ISBN: 978-4-909106025 C3051

GEOMATE Proceedings

20-22 November 2019

Hotel Continental
Fuchu Tokyo Japan

Edited by:
Zakaria Hossain
Shinya Inazumi
Jim Shiau

PROCEEDINGS OF THE NINTH INTERNATIONAL CONFERENCE – GEOMATE 2019
GEOTECHNIQUE, CONSTRUCTION MATERIALS AND ENVIRONMENT, TOKYO, JAPAN
20-22 NOVEMBER, 2019

Geotechnique, Construction Materials and Environment

Edited by

Prof. Zakaria Hossain
Department of Environmental Science and Technology
Graduate School of Bioresources
Mie University, Japan

Prof. Dr. Shinya Inazumi
Department of Civil Engineering
Shibaura Institute of Technology, Japan

Dr. Jim Shiau
School of Civil Engineering and Surveying
University of Southern Queensland, Australia

THE GEOMATE INTERNATIONAL SOCIETY

Published by:
The GEOMATE International Society
Tsu city, Mie, Japan
E-mail: society@geomate.org
http://www.geomate.org/

ISBN Number: 978-4-909106025 C3051

Table of Contents

Preface

Welcome to the GEOMATE 2019 - The Ninth International Conference on Geotechnique, Construction Materials and Environment, GEOMATE 2019, will be held in Hotel Continental Fuchu, Tokyo, Japan in conjunction with the Japan Association for Pulling-out Existing Piles, Mie University Research Center for Environmental Load Reduction, The GEOMATE International Society, The Society of Materials Science, Japan, The Useful Plant Spread Society, Japan, Glorious International, AOI Engineering, HOJUN, CosmoWinds and Beppu Construction, Japan.

On Friday 11 March 2011, at 14:46 Japan Standard Time, the northeast of Japan was struck and severely damaged by a series of powerful earthquakes which also caused a major tsunami. This conference was first dedicated to the tragic victims of the Tohoku-Kanto earthquake and tsunami disasters. The Geomate 2018 conference covers three major themes with 17 specific themes including:

- Advances in Composite Materials
- Computational Mechanics
- Foundation and Retaining Walls
- Slope Stability
- Soil Dynamics
- Soil-Structure Interaction
- Pavement Technology
- Tunnels and Anchors
- Site Investigation and Rehabilitation
- Ecology and Land Development
- Water Resources Planning
- Environmental Management
- Public Health and Rehabilitation
- Earthquake and Tsunami Issues
- Safety and Reliability
- Geo-Hazard Mitigation
- Case History and Practical Experience

Alike earlier conferences, this year we have received many paper submissions from different countries all over the world, including Australia, Bahrain, Bangladesh, Brazil, Canada, Colombia, Czech Republic, Egypt, France, India, Indonesia, Iran, Iraq, Israel, Japan, Kazakhstan, Lebanon, Malaysia, Nigeria, Pakistan, Philippines, Russia, Saudi Arabia, Singapore, South Korea, Taiwan, Thailand, Tunisia, Uganda, United Kingdom and Vietnam. The technical papers were selected from the vast number of contributions submitted after a review of the abstracts. The final papers in the proceedings have been peer reviewed rigorously and revised as necessary by the authors. It relies on the solid cooperation of numerous people to organize a conference of this size. Hence, we appreciate everyone who supports as well as participate in this joint conference.

Last but not least, we would like to express our gratitude to all the authors, session chairs, reviewers, participants, institutions and companies for their contribution to GEOMATE 2019. We hope you enjoy the conference and find this experience inspiring and helpful in your professional field. We look forward to seeing you at our upcoming conference next year.

Best regards,

Prof. Zakaria Hossain, Prof. Mie University, Japan

Prof. Dr. Shinya Inazumi, Shibaura Institute of Technology, Japan

Dr. Jim Shiau, University of Southern Queensland, Australia

Organization

Conference Honorary Chairmen:

Emeritus Professor Dr. Sohji Inoue, Mie University, Japan
Emeritus Professor Dr. Teruo Nakai, NIT, Japan
Emeritus Professor Dr. Fusao Oka, Kyoto University, Japan
Emeritus Professor Dr. Bujang B.K. Huat, UPM, Malaysia

Scientific Committees:

Conference Chairmen:

Prof. Dr. Shinya Inazumi, Shibaura Ins of Tech, Japan
Prof. Dr. Zakaria Hossain, Mie University, Japan

Conference Organizing Committee:

Prof. Dr. Shinya Inazumi, Shibaura Ins. of Tech., Japan (Chair)
Prof. Dr. Zakaria Hossain, Mie Univrsity, Japan (Chair)
Dr. Jim Shiau, USQ, Australia (Assiatant to General Chair)
Prof. Dr. M Ibn Ibrahimy, Prof., Int. Islamic Univ. (Co-Chair)
Prof. Dr. Toshinori Sakai, Mie University, Japan (Co-Chair)
Prof. Dr. Takamitsu Kajisa, Mie University, Japan (Co-Chair)
Dr. Vivi Anggraini, Lecturer, Monash Uni Malaysia (Co-Chair)
Dr. Masaaki Kondo, Mie University, Japan (Co-Chair)

National & International Advisory Committee:

Prof. Dr. Fumio Tatsuoka, Tokyo University of Science, Japan
Prof. Dr. Junichiro Takeuchi, Kyoto University, Japan
Prof. Dr. Kingshuk Roy, Nihon University, Japan
Prof. Dr. Sai Vanapalli, University of Ottawa, Canada
Prof. Dr. Musharraf Zaman, Univ. of Oklahama, USA
Prof. Dr. Rafiqul Tarefder, University of New Mexico, USA
Prof. Dr. M. Bouassida, National Sch. of Engg. of Tunis
Prof. Dr. L.R. Austriaco, Angles Univ. Found., Philippines
Prof. Dr. M. Ibn Ibrahimy, Int. Islamic Univ., Malaysia
Prof. Dr. Bujang B.K. Huat, Univ. Putra Malaysia
Prof. Dr. Nemy Banthia, Univ. of British Columbia, Canada
Prof. Dr. Ian Jefferson, Univ. of Birmingham, UK
Prof. Dr. John Bolander, Univ. of California, USA
Prof. Dr. Shamsul Chowdhury, Roosevelt Univ., USA
Prof. Dr. Isabel Pinto, University of Coimbra, Portugal
Prof. Dr. Mark Jaksa, University of Adelaide, Australia
Prof. Dr. Hj. Ramli Bin Hj. Nazir, UTM, Malaysia
Prof. Dr. M.S. Hossain, International Islamic Univ. Bangladesh
Prof. Dr. Suksun Horpibulsuk, Suranaree Uni of Tech, Thailand
Dr. Muzamir Hasan, Director, CERRM, Univ. Malaysia Pahang
Dr. Afshin Asadi, S/Lecturer, Int. College of Auckland, New Zealand

International Technical Program Committee:

Prof. Sai Vanapalli, University of Ottawa, Canada
Prof. Alaa Masoud, Tanta University, Egypt
Prof. Aly Ahmed, Beni-Suef University, Egypt
Prof. Aminaton Marto, Universiti Teknologi Malaysia, Malaysia
Prof. Bandari Shankar, Osmania University, India
Prof. Bashir Ahmed Mir, National Institute of Technology, India
Prof. Hamidi Abdul, Aziz, Universiti Sains Malaysia (USM), Malaysia
Prof. Hussein Elarabi, University of Khartoum, Sudan
Prof. M. Shohidullah Miah, International Univ. of Business Agriculture &Tech., Bangladesh
Prof. Michele, Casagrande, Pontifical University Catholic of Rio De Janeiro, Brazil
Prof. Radim Cajka, Technical University of Ostrava, Czech Republic
Prof. Rajaraman Jambunathan, AMET University, India
Prof. Reshma Chandran T., Global Institute of Architecture, India
Prof. Roslan Hashim, University of Malaya, Malaysia
Prof. Seyed Naser Moghaddas Tafreshi, K.N. Toosi University of Technology, Iran
Prof. Valeriy Perminov, Tomsk Polytechnic University, Russia
Prof. Quanmei Gong, Tongji University, China
A/ Prof. Abdoullah Namdar, Sichuan University, China
A/ Prof. Abdul Naser Abdul Ghani, Universiti Sains Malaysia, Malaysia
A/ Prof. Alaeddinne Eljamassi, Islamic University of Gaza, Palestine
A/ Prof. Alina Paranina, Herzen State Pedagogical University of Russia, Russia
A/ Prof. Ashraf Elmoustafa, Ain Shams Univeristy, Egypt
A/ Prof. Bindu C S, Cochin University of Science& Technology, India
A/ Prof. Chee-Ming Chan, Universiti Tun Hussein Onn Malaysia, Malaysia
A/ Prof. Chidanand Naik, Anjuman Instistute of Technology and Management, India
A/ Prof. Dahlia Hafez, Cairo University, Egypt
A/ Prof. Deepa G Nair, Isfahan University of Technology, India
A/ Prof. Dolrerdee Hormdee, Khon Kaen University, Thailand
A/ Prof. Farhad Behnamfar, Isfahan University of Technology, Iran
A/ Prof. Gabriela B. Cazacu, Geotech Dobrogea, Romania
A/ Prof. Hadi Khabbaz, University of Technology, Sydney (UTS), Australia
A/ Prof. Homayoon Ganji, Herat Univercity Badghis, Afghanistan
A/ Prof. Hudson Jackson, US Coast Guard Academy, United States
A/ Prof. Inazumi Shinya, National Institute of Technology, Akashi, Japan
A/ Prof. John Smith, RMIT University, Australia
A/ Prof. Kasinathan Muthukkumaran, National Institute of Technology, India
A/ Prof. Lindrianasari Lindrianasari, Universitas Lampung, Indonesia
A/ Prof. Mahdi Karkush, Baghdad University, Iraq
A/ Prof. Mohamed Redha Menani, Batna University, Algeria
A/ Prof. Navid Khayat, Ahvaz Branch, Islamic Azad University, Iran
A/ Prof. Salam, Bash AlMaliky, AlMustansiriya University, Iraq
A/ Prof. Shailesh Kumar Jha, Indian Institute of Technology, India
A/Prof. Teodor Lucian Grigorie, University of Craiova, Romania
A/Prof. Paresh Dalal, Shri Vitthalrao Shankarrao Naik Arts, Commerce and Science College, India
A/Prof. Muhammad Qasim, Abdul Wali Khan University Mardan, Pakistan
A/Prof. R. S. Ajin, GeoVin Solutions Pvt. Ltd., India
Dr. Abdul Karim M. Zein, University of Khartoum, Sudan
Dr. Abdull Halim Abdul, Universiti Teknologi MARA, Malaysia
Dr. Afshin Asadi, University Putra Malaysia, Malaysia
Dr. Ahmad Safuan A Rashid, Univeristi Teknologi Malaysia, Malaysia
Dr. Ahmad Safuan Bin A Rashid, Univeristi Teknologi Malaysia, Malaysia
Dr. Akindele Okewale, Federal University of Petroleum Resources, Nigeria
Dr. Akinola Johnson Olarewaju, Federal Polytechnic Ilaro, Nigeria
Dr. Ali Sobhanmanesh, Universiti Teknologi Malaysia (UTM), Malaysia
Dr. Alireza Bahiraie, Semnan University, Iran

Dr. Allan Manalo, Centre of Excellence in Engineered Fibre Composites, Australia
Dr. Aniza Ibrahim, National Defence University of Malaysia, Malaysia
Dr. Arif Ali Baig Moghal, King Saud University, Saudi Arabia
Dr. Aslan S. Hokmabadi, University of Technology, Sydney (UTS), Australia
Dr. Ather Ashraf, PUCIT, Old Campus Punjab University, Pakistan
Dr. Atsuko Sato, Cicil Engineering Research Institute for Cold Region, Japan
Dr. Ben-Hur Silva, Military Institute of Engineering, United States
Dr. Choy Soon Tan, Univeristi Teknologi Malaysia, Malaysia
Dr. David Thorpe, University of Southern Queensland, Australia
Dr. Delsye Ching Lee Teo, Universiti Malaysia Sarawak, Malaysia
Dr. Domenico Lombardi, University of Manchester, United Kingdom
Dr. Ehsan, Jorat Newcastle University, United Kingdom
Dr. Ganesh Kumar Shanmugam, National Institute of Ocean Technology, India
Dr. Helsin Wang, Institute of Bridge Engineering, Taiwan
Dr. Hossein Moayedi, Kermanshah University of Technology, Iran
Dr. Hossein MolaAbasi, Babol University of Technology, Iran
Dr. James Hambleton, University of Newcastle, Australia
Dr. James Hambleton, University of Newcastle, Australia
Dr. Janaka Kumara, Tokyo University of Science, Japan
Dr. Jirayut, Suebsuk Rajamangala University of Technology Isan, Thailand
Dr. Juhyung Lee, Korea Institute of Civil Engineering and Building Technology, South Korea
Dr. Jun Sugawara, Advision - WorleyParsons Group, Australia
Dr. Lamia Touiti Bouebdellah, Ecole Nationale d'Ingénieurs de Gabes, Tunisia
Dr. Luky Handoko, Universitas Atma Jaya Yogyakarta, Indonesia
Dr. M. Mohammad Ali, California Public Utilities Commission, United States
Dr. Marfiah Ab.Wahid, Universiti Technologi Mara, Malaysia
Dr. Maryam Naeimi, Semnan University, Iran
Dr. Mehdi Mokhberi, Islamic Azad University, Shiraz, Iran
Dr. Mohd Hairy Ibrahim, Sultan Idris Education University, Malaysia
Dr. Neelima Satyam, International Institute of Information Technology, India
Dr. Nor Zurairahetty Mohd Yunus, Univeristi Teknologi Malaysia, Malaysia
Dr. Siavash Zamiran, Southern Illinois University Carbondale, United States
Dr. Subha Vishnudas, Cochin University of Science and Technology, India
Dr. Sunggi Jin, SK E&C, South Korea
Dr. Sunil Pusadkar, Govt. College of Engineering, Amravati, India
Dr. Teresa Lopez-Lara, Universidad Autonoma De Queretaro, Mexico
Dr. Usama Juniansyah Fauzi, University of Tokyo, Japan
Dr. Yusep Muslih Purwana, Sebelas Maret University, Indonesia
Dr. Ana Almerich-Chulia, Universitat Politecnica de Valencia, Spain
Dr. Khor Shing Fhan, Universiti Malaysia Perlis, Malaysia
Dr. Afshin Asadi, International College of Auckland, New Zealand

Conference Correspondence:

Prof. Dr. Zakaria Hossain, Conference Chairman,
Dept. of Env. Sci. & Tech., Mie University, Japan,
E-mail: conference@geomate.org
Tel & Fax: +81-59-231-9578

Editorial Committee and Executive Committee:

Prof. Zakaria Hossain, Prof. Mie University, Japan
Prof. Sinya Inazumi, Shibaura Institute of Technology, Japan
Dr. Jim Shiau, University of Southern Queensland, Australia

Keynote Papers

9th Int. Conf. on Geotechnique, Construction Materials and Environment,
Tokyo, Japan, 20-22 November 2019, ISBN: 978-4-909106025 C3051

THE INFLUENCE OF TEMPERATURE AND MOISTURE ON THE BEHAVIOR OF FINE-GRAINED SOILS

Xingyi Wu[1], Junping Ren[1] and Sai K. Vanapalli[1]
Department of Civil Engineering, University of Ottawa, Ottawa, Ontario, Canada

ABSTRACT

The most widely used construction materials for various civil infrastructures is the naturally available, compacted and modified soils. Their behavior is influenced by environmental factors such as precipitation, evaporation and variations associated with the natural ground water table. The stability and deformation behavior are typically two key criteria that govern the design of these infrastructures. Soil is a complex material with different phases both in an unfrozen and frozen condition. The moisture content within the unfrozen and frozen soils is influenced by a wide range of negative and positive temperatures. The soil can be in a frozen or thawed, saturated or unsaturated condition or combinations of them due to the variations in temperature and moisture content. In other words, the hydro-mechanical behavior of soils is significantly influenced by freezing/thawing and wetting/drying processes. In this paper, the influence of variation of temperature and moisture content on the soil behavior is explained using the soil-water characteristic curve (SWCC) and soil-freezing characteristic curve (SFCC). The SWCC and SFCC are respectively used as tools in the prediction and interpretation of the behavior of unfrozen unsaturated soils and frozen soils. The focus of this paper is directed to understand the influence of wetting/drying, freezing, and freeze-thaw cycles on soil properties such as void ratio, hydraulic conductivity, shear strength, microstructure change and swelling behavior of expansive soils. Finally, the influence of temperature and moisture on the design of pile foundations in expansive soils is succinctly highlighted.

Keywords: Soil, Moisture, Temperature, Wetting-Drying, Freezing-Thawing

INTRODUCTION

The most widely used material in the construction of various engineered infrastructure is the soil, in its natural, compacted or modified form. For example, soils are compacted to form dams, canals, roads and railway subgrades, and waste containment structures such as soil covers and liners. The infrastructure constructed is typically in a state of the unsaturated condition during their service life. The variation of moisture content within the soil has a significant influence on the performance of these infrastructures.

The pore water in unfrozen unsaturated soils typically has a lower free energy in comparison to free water due to the interactions between soil particles, pore water and pore air. The soil-water characteristic curve (SWCC) defines the relationship between the free energy of pore water (or soil suction) and its amount in the unsaturated soil. The quantity of pore water can be represented by either gravimetric or volumetric water content or degree of saturation. The SWCC is a conceptual and interpretative tool for understanding the behavior of unsaturated soils [1]. For example, the SWCC has been used for predicting the hydraulic and mechanical properties of unsaturated soils, such as the hydraulic conductivity [2], shear strength [3], and modulus of elasticity [4].

The environmental impacts on soil behavior would be incomplete if only the influence of the variation of moisture content is considered. This is because phase changes of pore water (from liquid to solid or vice versa), which is the result of freezing and thawing of soils, has a significant impact on various soil properties are not considered. In the permafrost and seasonally frozen regions, frost penetration generally results in the freezing of the top layer of the soil which is close to natural ground level. For example, the frost penetration in northern Ontario, Canada can be deeper than 3 m; however, it is typically around 1 to 2 m in southern Ontario [5]. Similar or close to similar trends are observed in many other cold regions of the world.

The unfrozen water and pore ice typically coexist within a frozen soil. The relationship between unfrozen water content and the subzero temperature is defined as the soil-freezing characteristic curve (SFCC). Several researchers during the past five decades have investigated the similarity between SWCC and SFCC behavior [6], [7]. This background has provided a foundation for using SFCC as a tool for cold regions engineering applications by extending the mechanics of unsaturated soils, which will be highlighted and succinctly discussed in later sections of this paper.

There is an urgent need for both the researchers and engineers to better understand the influence of climate change and global warming effects on the engineering properties of unfrozen and frozen soils.

Lu et al. [8] estimated the possible variation of moisture contents within the soils of various regions of the world for the 21st century. Their study suggests significant widespread drying effects in most regions (e.g., Australia, America, Europe, and East Asia), while significant wetting is expected in some regions of East Africa, and central and south Asia. They also suggested that drying is related to precipitation reduction and temperature increase. In addition, soils in humid regions may undergo several wetting/drying (W-D) cycles due to high intensity rainfalls followed with periods of high temperature that contribute to significant evaporation. In addition, global warming effects are expected to contribute to widespread temperature variations in cold regions resulting in freeze-thaw (F-T) cycles. The focus of this paper is directed to understand the influence of freezing, F-T, and W-D cycles on soil properties which include void ratio, hydraulic conductivity, shear strength, microstructure change, and swelling behavior of expansive soils. Finally, the influence of variation of temperature and moisture content on the design of pile foundations in expansive soils is succinctly highlighted.

EFFECT OF FREEZING ON SOIL BEHAVIOR AND THE USE OF SFCC

Hydraulic Conductivity

The hydraulic conductivity of frozen soils near zero temperature is a key property required in water balance calculation in cold regions and is useful information in both engineering applications and agricultural management. It is also an important property in artificial ground freezing techniques. Ice crystals form in the pore spaces of the soil when it is subjected to freezing and block the pathways for water flow. As a result, the hydraulic conductivity of frozen soils is much lower in comparison to unfrozen soils. If the soil temperature falls further below subzero values, more ice will form in the soil pores. Due to this reason, the available unfrozen water films that facilitate free flow of water will substantially decrease. Therefore, hydraulic conductivity decreases further with a decrease in subzero temperature (or unfrozen water content). Fig. 1 summarizes the hydraulic conductivity behavior for various frozen soils.

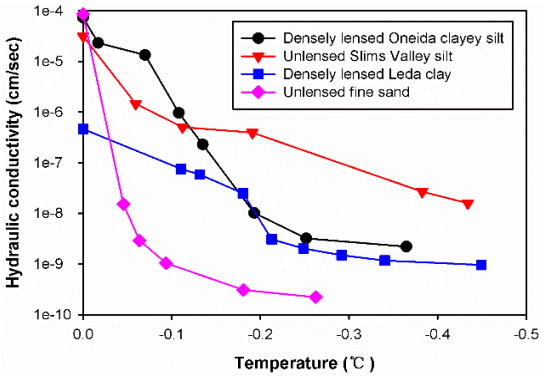

Fig. 1 Hydraulic conductivity of frozen soils [9].

The hydraulic conductivity of frozen soils is strongly dependent on the soil type. This is because the unfrozen water content, pore size distribution, void ratio, particle size, and surface area are dependent on the type of soil and influence the hydraulic conductivity. For example, most water available in sand freezes close to 0 °C. The amount of water in unfrozen sand below 0 °C is small; due to this reason the hydraulic conductivity of sand below 0 °C is low. On the other hand, an unfrozen clay has a low hydraulic conductivity. However, at temperatures below 0 °C, the hydraulic conductivity of clay is still relatively high in comparison to its unfrozen value since the clay contains unfrozen water and has continuous paths available for flow of water [9]. These observations can also be derived from the experimental results summarized in Fig. 1.

There are limited experimental studies in the literature that focus on the measurement of hydraulic conductivity of frozen soils. This may be attributed to difficulties associated with conducting and obtaining reliable experimental results. For this reason, hydraulic conductivity of frozen soils is estimated using relatively simple yet reliable models. The SFCC can be used as a tool for estimating the relationship between frozen hydraulic conductivity and subzero temperature. For example, Azmatch et al. [10] proposed a permeability function for partially frozen silt by using the saturated hydraulic conductivity and SFCC following two steps; which include; (i) the laboratory SFCC data points are fitted with the Fredlund and Xing [2] SWCC equation; and, (ii) the fitted curve is then used together with saturated hydraulic conductivity to estimate the hydraulic conductivity function for partially frozen silt by employing the Fredlund et al. [11] empirical equation.

Resilient Modulus

The resilient modulus (M_R) has been widely used as a key parameter for rational characterization of the resilient behavior of unbound base/subbase and subgrade soils subjected to traffic loading. These

unbound soils are porous media and contain a certain amount of water in their pore spaces. The phase change of pore water has a significant impact on the M_R of these soils. When pore water freezes, ice binds adjacent soil particles together, resulting in a dramatic increase in M_R. For example, Bigl and Berg [12] highlight the M_R of subbase and subgrade soils can increase approximately two orders of magnitude for frozen soils. Bosscher and Nelson [13] report a 20-fold increase in modulus for one type of frozen sand. Similar increases in moduli for frozen granular base soils were also observed by Cole et al. [14]. The pavement structure has relatively high stiffness and bearing capacity during the freezing process and at frozen state; due to this reason, overloading of the pavement structure is allowable in frozen soils without damages.

The SFCC has been used for estimating the M_R of frozen soils. Ren and Vanapalli [15] proposed a semi-empirical model for predicting $M_{R(\text{frozen})}$ for saturated soils. The model exploits the similarity between SWCC and SFCC, and uses cryogenic suction (ψ_{cryo}) and degree of unfrozen water saturation (S_u, which is the ratio of the volume of unfrozen water to the total water volume) for prediction. It is assumed that the rate at which ψ_{cryo} contributes towards frozen M_R can be related to S_u. The value of S_u varies from unity to a small value at large ψ_{cryo}. The semi-empirical model is expressed as:

$$M_{RSAT(\text{frozen})} = M_{RSAT(0℃)}(1+\chi\psi_{cryo}S_u^{\delta}) \quad (1)$$

where $M_{RSAT(0\ ^\circ C)}$ is the saturated M_R at 0 °C (MPa); χ and δ are fitting model parameters.

The above model works well for different types of saturated soils (e.g., see Fig. 2) and has a theoretical basis. However, the model is only applicable to saturated soils.

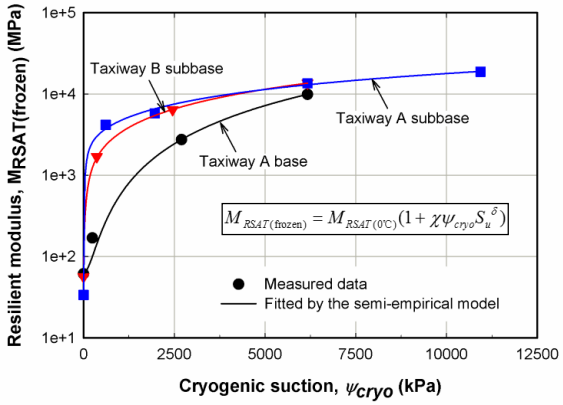

Fig. 2 Prediction of M_R of frozen saturated soils using the SFCC [15].

EFFECT OF F-T CYCLES ON SOIL BEHAVIOR

The effect of F-T cycles can be compared to the natural weathering process that has a significant influence on the behavior of various infrastructures that include the pavements, railroads, pipelines, and building constructions. The F-T cycles considerably change the soil physical property as their void ratio (density) and hydro-mechanical properties of soils; namely, hydraulic conductivity, shear strength, and stiffness.

Void Ratio (Density)

Previous studies show that F-T has a dual influence on soil density, i.e. loose soils tend to densify and dense soils become looser after F-T cycles [16]. Viklander [17] proposed a new term residual void ratio to explain this behavior associated with F-T cycles. The void ratios of different specimens show significant change after one F-T cycle; however, there is little or no change in void ratio for later F-T cycles. The initially loose soil experiences volume increase during freezing (due to ice-lensing) and decrease during thawing (due to the consolidation of soil matrix). Therefore, the density will increase and larger soil particles will come closer. On the other hand, the void ratio of an initially dense soil increases due to F-T, since particles of the soil cannot fall back to the same position after thawing, resulting in a net volume increase. Therefore, the soil structure is slightly looser in comparison to soil prior to soil freezing. The void ratios of the specimens reach a residual value after a certain number of F-T cycles, as shown in Fig. 3.

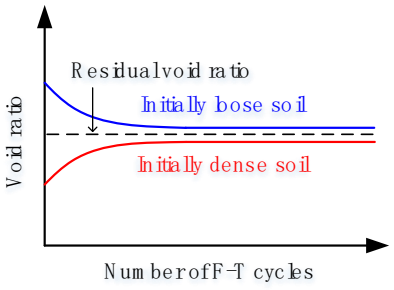

Fig. 3 Effect of F-T cycles on void ratio.

Hydraulic Conductivity

The F-T cycles typically weaken soil structure and contribute to more cracks and fissures. This leads to higher hydraulic conductivity after the soil is subjected to several F-T cycles. Fig. 4 highlights the effect of one- and three-dimensional F-T cycles on the hydraulic conductivity of three Wisconsin soils. The hydraulic conductivity test indicated that there was an

increase in vertical hydraulic conductivity of different types of fine-grained soils [18]. The increase in the hydraulic conductivity was attributed to the formation of polygonal shrinkage cracks and/or the reduction in the fine content in the pores of coarse fraction. The cracks and other structural changes can be observed using the scanning electron microscope (SEM). At low magnification, distinct cracks spaced at 0.5 mm were observed. However, at higher magnifications, voids of 0.005 mm were observed within the aggregates formed during the freezing process [19]. These results suggest F-T cycles can cause changes in both the macro- and micro-structure of fine-grained soils.

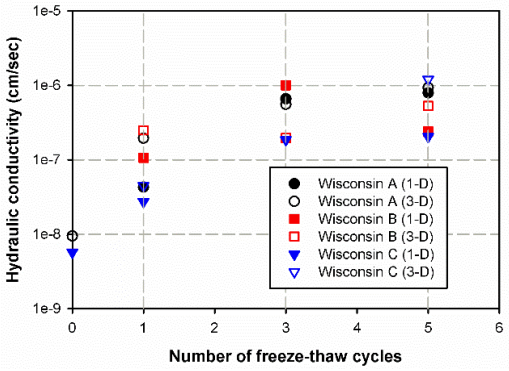

Fig. 4 Effect of F-T cycles on hydraulic conductivity [20].

Shear Strength

The soil particles are forced to separate from each other when water within the soil pore changes its phase to ice. This characteristic contributes to an increase in pore volume which results in swelling of frozen soils. The soil particles have a tendency to re-position to their original locations when the pore ice melts. However, this is not possible in dense soils. As a result, the original soil structure is typically weakened. In other words, the mechanical properties of soils are significantly influenced by F-T cycles.

From their studies, Formanek et al. [21] highlighted the loss of more than half of its original shear strength after the first F-T cycle for a silt loam. The second and third cycles contributed to a further loss, however, the lost of shear strength was not significant. Aoyama et al. [22] found the reduction in soil cohesion increased with a decrease in temperature, whereas little change was observed in friction angle after F-T cycles. Lerouil et al. [23] conducted shear strength tests on nine Champlain Sea clays after one F-T cycle. Results showed that freezing typically led to a drastic decrease in the undrained shear strength, and the frozen-thawed specimens presented a dilatant behavior similar to granular soils. Graham and Au [24] found that the F-T cycles produced increased compressibility and pore water pressure, and reduced strength at low stresses compared with the behavior of undisturbed Winnipeg clay. Kamei et al. [25] found that the unconfined compressive strength and durability decreased with an increase in the number of F-T cycles. The greatest reductions in both strength and durability were observed during the second F-T cycle; however, later F-T cycles only had a limited influence.

Wang et al. [26] investigated the mechanical properties of Qinghai-Tibet clay subjected to a maximum of 21 closed-system F-T cycles. The experimental results suggest a strong relationship between the failure shear strength and the number of F-T cycles. Figure 5 shows variations in cohesion and friction angle of the soil with respect to F-T cycles. These results suggest that the cohesion decreases dramatically with an increase in the number of F-T cycles, from 0.55 MPa to about 0.25 MPa after 15 cycles. On the other hand, the friction angle shows a dramatic increase. Similar trends of results were also reported by Ogata et al. [27].

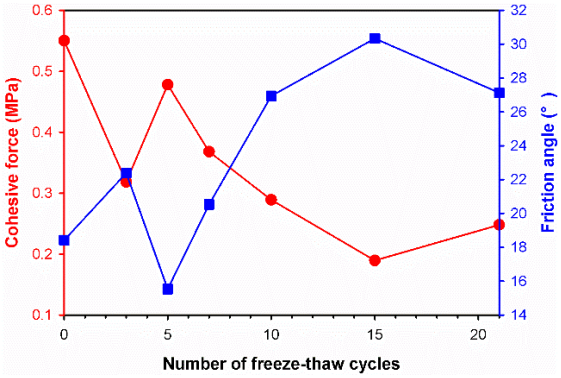

Fig. 5 Effect of F-T cycles on shear strength [27].

Resilient Modulus

The resilient response of compacted soils under cyclic loading is significantly influenced by soil structure. The M_R of soil typically decreases as F-T cycles weaken the soil structure. Culley [28] investigated the resilient strains and M_R of till specimens subjected to F-T cycles in a one-dimensional closed-system. The specimens were compacted to various densities and water contents. At water contents lower than the optimum water content, the decrease in M_R resulting from F-T cycles decreased as density increased. However, at water contents of optimum and higher, the detrimental F-T effect increased with an increase in the density. The water content at which the maximum F-T effect occurred increased as density increased, ranging from 1.5% less than optimum at 93% density to 1.5% greater than optimum at 100% density. These trends were also consistent for resilient strain.

Lee et al. [29] concluded from the M_R tests performed on five cohesive soils sampled from in-

service subgrades that the stress at 1% strain in the unconfined compression test ($S_{u1.0\%}$) was a good indicator of M_R, and proposed an empirical relationship between M_R and $S_{u1.0\%}$. The proposed relationship is applicable to both as-compacted and in-service subgrade soils. There was a negligible effect of F-T on M_R, when there was no ice lens formation, for soils having values of $S_{u1.0\%}$ less than approximately 55 kPa. The effect of F-T increased as the value of $S_{u1.0\%}$ increased. It was observed that a single cycle of F-T caused a 30% - 50% reduction in M_R. The M_R of various coarse- and fine-grained subgrade soils subjected to F-T cycles were presented by Simonsen et al. [30], the results indicated that all the soils exhibited a substantial reduction in M_R (approximately 20% - 60% depending on soil type) after F-T cycles.

Wang et al. [26] studies suggest decreases by 18%-27% for unfrozen soil M_R depending on confining pressure. The greatest changes in M_R in all the four soils studied with various confining pressures (i.e., 200, 400, 600, and 800 kPa) were obtained after the first F-T cycle (as shown in Fig. 6), suggesting significant disturbance during the first F-T cycle.

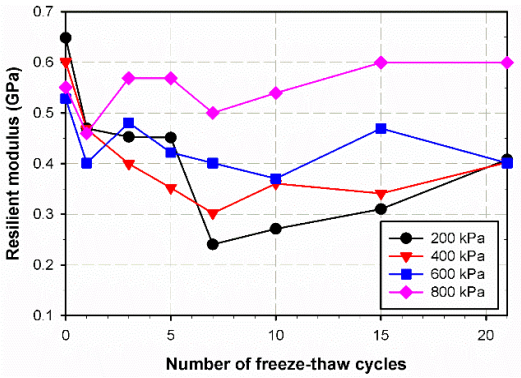

Fig. 6 Effect of F-T cycles on resilient modulus [26].

EFFECTS OF TEMPERATURE AND MOISTURE CHANGE ON THE BEHAVIOR OF EXPANSIVE SOILS

The Structure of Expansive Soil

The structure of expansive soil has a significant influence on its mechanical behavior. Tang et al. [31] studied pore size distribution (PSD) of an expansive soil by mercury intrusion porosimetry (MIP). The results of this study summarized in Fig. 7 shows two peaks suggesting it is bimodal in nature. The two peaks are around 30 μm and 7 nm, respectively. These two sizes of pores can be considered as macropores and micropores, respectively. Studies on different types of expansive soils showed similar results [32]–[34]. The soil structure with micro and macropores is typically referred to as the double structure in the literature.

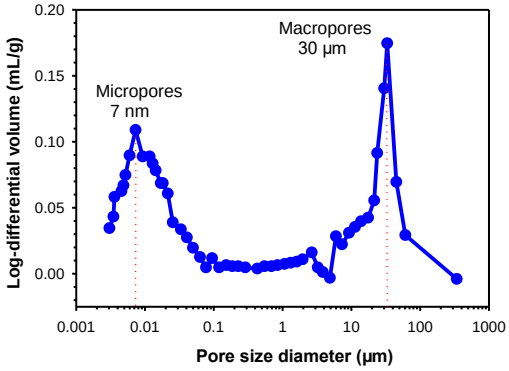

Fig. 7 Pore size distribution of an expansive soil [31].

The double structure can typically be attributed to the aggregation of elementary soil particles. For fine-grained soils, several factors including the water content and interparticle forces can facilitate particle aggregation. The soil particles get closer to each other during the drying stage due to an increase in suction associated with a decrease in water content. The positive ions of water (i.e., hydrogen ions) can be attracted to the negatively charged soil particle's edges when the distance between adjacent soil particles is smaller enough. In addition, the interparticle forces (e.g., van der Waals attraction and electrical double repulsion) contribute to the formation of aggregates. During the drying process, the water content decreases and the air content increases, resulting in an increase in the van der Waals attraction and drop of the electrical double repulsion. This results in the aggregation of clay particles [35]. On the contrary, during the wetting process, soil suction and van der Waals attraction between soil particles will decrease, and the electrical double layer repulsion will increase. In other words, the wetting process will destroy soil aggregates.

As shown in Fig. 8, the micropores are defined as pores in aggregates or intra-aggregates pores. The pores between aggregates (inter-aggregates) are the macropores. The double structure concept has been widely accepted to describe the behavior of expansive soils [36]–[38]. The micropores and macropores sizes are not unique values. Many factors including the soil type and the specimen preparation method may contribute to the different pore sizes.

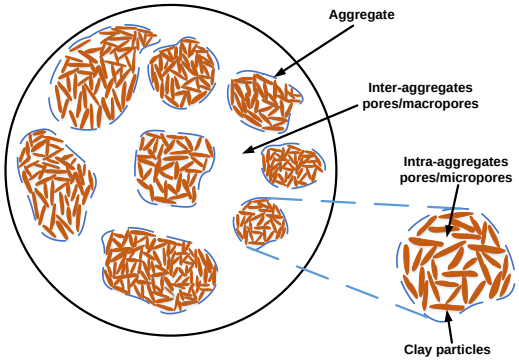

Fig. 8 The structure of aggregated soil [39].

The Volume Change Behavior of Expansive Soil

The effect of high temperature

The effects of high temperature (from 20 °C to several hundred degrees) on the deformation behavior of expansive soils have been studied by several researchers [40]–[42]. These studies suggest the influence of temperature on volume change behavior of expansive soils is affected by confining pressure and suction.

Romero et al. [40] used the Boom clay to study the volume change behavior by subjecting it to different stresses and temperature paths. The non-isotropic tests at constant suction and confining pressure were performed. The volume change of specimens under different thermal cycles is shown in Fig. 9. It can be seen that significant dilation occurs when temperature increases from 20 °C to 80 °C under both the values of suction investigated. However, when the temperature decreases from 80 °C to 20 °C, shrinkage was observed in the two specimens for both the suction values. It is of interest to note that the shrinkage is less in comparison to dilation.

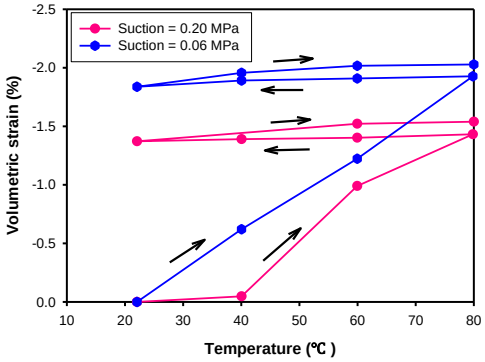

Fig. 9 Volumetric strain due to thermal cycling [40].

The temperature variation can contribute to significant changes in the soil structure. The clay minerals in the expansive soil typically expand and the adsorbed water could also enhance due to an increase in the temperature [43]. Romero attributed the irreversible strain to the possible rearrangements of particles at the macrostructural scale [40]. However, Tang et al. [42] found the effect of temperature depends on the stress state in the soil (e.g., confining stress and suction). The dilation phenomenon occurs under high suction and low confining pressure, and the volumetric strains are reversible. On the other hand, under low suction and high confining pressure condition, the test specimen contracts due to the influence of thermal cycles. The volumetric strain associated with this phenomenon is also irreversible.

Typically contraction is observed in a saturated soil with a low overconsolidation ratio when it is subjected to heating; however, the saturated soil with a high overconsolidation ratio will expand due to heating [43]. The effect is similar to that of the confining pressure on the unsaturated expansive soil. Tang et al. [42] suggested that soil aggregates weaken when soil is tested at low suction value; such a behavior may be attributed to an increase in water content.

An increase in temperature can result in expansion when the confining pressure is low and the suction is high. On the contrary, unsaturated expansive soil can be compressed under high confining pressure at low suction values.

The effect of wetting-drying (W-D) cycling

The volume change behavior of expansive soils resulting from W-D cycles is influenced by the number of W-D cycles, and W-D cycling pattern [44].

Tripathy and Subba Rao [44] conducted different swelling-shrinkage tests on a highly plastic expansive soil by controlling the height of samples. Samples were allowed to fully swell to the saturation and allowed to shrink to initial height or partially shrink to several predetermined heights that were larger than the initial heights of samples in each cycle. The height of samples after equilibrium condition was allowed to change from a smaller to a larger value (less shrinkage) or from a larger to a smaller value (greater shrinkage). From these studies, they found that if the greater shrinkage was applied to sample, a new swelling potential would establish, which means more swelling strains occurred along the first swelling path after the change. The swelling strains along the first swelling path were irreversible. The irreversible strains were reduced with an increase in the number of swell-shrink cycles. Only reversible strains occurred after five cycles. However, if the less shrinkage was applied to the samples, only reversible strain would immediately occur, without any irreversible strains.

The differences in the behavior of expansive soils can be attributed to changes in microstructure associated with the W-D cycles. Water was

progressively absorbed by the soil aggregates during the wetting process. The aggregates expanded due to an increase in water content, which closed the macropores. Therefore, during the wetting process, the volume of macropores decreased. The volume of micropores, however, did not change significantly. Therefore, during the hydration, the structure of the soil is going to be homogenous [32], [45].

The soil structure change that occurred due to hydration during W-D cycles may be considered as permanent. Therefore, the volumetric strain was reversible or elastic at each W-D cycles after equilibrium [46]. Seiphoori et al. [46] used MIP to test the microstructure of an expansive soil at several different stages of W-D cycles. The results summarized in Fig. 10 suggest that during wetting, the volume of the macropores decrease rapidly. However, the micropores were not affected by the hydration. The micropores in the soil were increased when it was close to the saturation condition. In the subsequent W-D cycles, three curves, C, D, and E were close to each other, which means the soil structure of the test specimen did not change significantly. In other words, the structure of the expansive soil was kept as homogenous during W-D cycles. Only reversible volumetric strain that occurred after W-D cycles can be attributed to the homogenous nature of the soil structure.

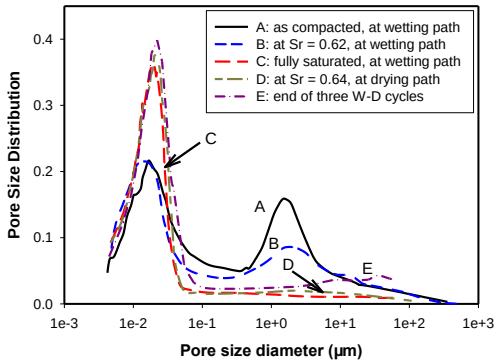

Fig. 10 Evolution of microstructure due to W-D cycles [46].

The Shear Strength of Expansive Soil

The effect of high temperature

The effect of high temperature on the shear strength of expansive soil is predominantly dependent on the degree of saturation and dry density [47], [48].

Wiebe et al. [48] conducted undrained triaxial shear tests on sand-bentonite mixtures with different degrees of saturation (i.e. 50%, 65%, 80%, and 98%) and under different temperatures (i.e. 26°C, 65°C, and 100°C). Fig. 11 summarizes these experimental results. The shear strength reduced with an increase in temperature when the soil was in a state of unsaturated condition. When the soil was nearly saturated, the effect of temperature on the strength can be considered negligible.

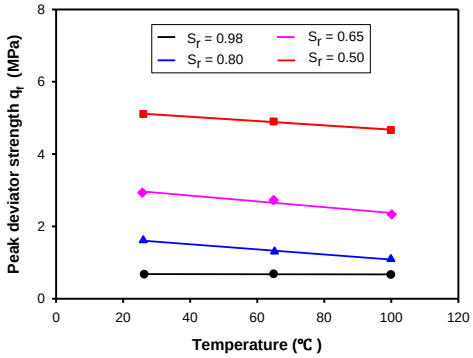

Fig. 11 Strength reduction due to temperature [48].

Gu et al. [47] used the micropenetrometer equipped with a series of penetration probes with different diameters ranging from 0.3mm to 1.0mm to test the resistance of a high liquid-limit clayey soil. The resistance can be used to indicate the structural strength of the soil. It is found that when the soil had high dry density, the resistance was reduced evidently with an increase in the temperature. For the soil at lower dry density, the resistance was only slightly influenced by temperature. Therefore, it can be concluded that the structural strength of dense soil decreases due to an increase in the temperature, while that of loose soil is not significantly influenced by temperature.

The soil strength originates from the strength of soil aggregates and forces between soil aggregates. Gu et al. [47] pointed out that soil aggregates will soften as a result of expansion and increase the intra-aggregate pore water pressure due to heating. This translates into a reduction in the soil strength. Another reason is that soil suction is reduced due to an increase in the temperature.

Wiebe et al. [48] suggest that soil pores and aggregates are small when the degree of saturation is relatively low; for this reason, suction in intra-aggregate pores will be high. The high suction is sensitive to the change of temperature, which contributes to a reduction in shear strength of the soil at low degrees of saturation.

For dense soils, the interparticle forces are significant due to the closer distance between soil particles. The effects of temperature on the interparticle forces will be more evident in dense soil in comparison to loose soil. Therefore, the shear strength of soil specimens at high dry density decreases significantly with an increase in temperature. However, the shear strength of specimens at low dry density is not significantly influenced by temperature [47].

The effect of W-D cycles

Yang et al. [49] found that the shear strength of expansive soils reduces due to the influence of W-D cycles. Zeng et al. [50] showed that soil cohesion decreases due to W-D, while the friction angle is relatively constant. They concluded that soil particles aggregate during the W-D cycles; due to this reason, the bonding between soil particles reduces and the shear strength decreases.

Goh et al. [51] measured the shear strength of sand-kaolinite mixtures at several different stages of W-D cycles. Some of the key results are summarized in Fig. 12. The peak soil strength after the first drying process is much higher in comparison to that after the first wetting. Although soil strength during the drying stage for the following subsequent cycles is higher than that during the wetting stage, the differences are not as significant as in the first cycle. The drying strengths of the second and third cycles are lower than that of the first cycle. On the other hand, the wetting strengths of the second and third cycles are higher than that of the first cycle. Tse and Ng [52] reported similar trends of results from their studies.

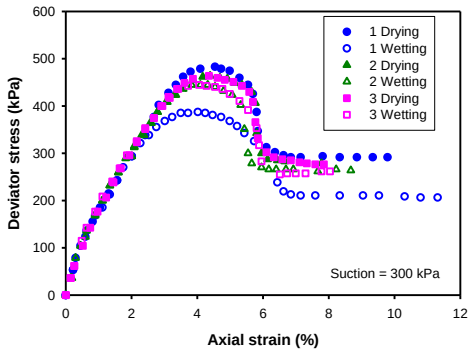

Fig. 12 Stress-strain relations during three W-D cycles [51].

Such a behavior may be attributed to the hysteretic characteristic of SWCC. The water content during the wetting stage is lower than that at the drying stage at the same suction. In other words, the area of water menisci that are in contact with soil particles or aggregates at the wetting stage is less than that at the drying stage. Therefore, the contribution of suction to soil strength during the wetting stage is lower in comparison to the drying path.

For obtaining SWCC, the boundary drying and wetting curves are obtained respectively by draining the initially saturated specimen to a totally dry condition and the initially dry specimen was wetted to saturation. The scanning curves were obtained from further drying or wetting cycles. The scanning curves are between the boundary drying and wetting curves. This means that at the same suction condition, soil water content on the scanning curves is higher and lower than that on the boundary wetting and drying curve, respectively [53]. The soil specimen followed the boundary curves under the first W-D cycle, while followed the scanning curves under the subsequent W-D cycles. As discussed earlier, more water menisci (or larger suction) contribute to an increase in soil strength. Therefore, soil strength during the subsequent W-D cycles was higher than that at the wetting path of the first cycle but lower than that at the drying path of the first cycle.

However, some other researchers suggest that soil strength increases with W-D cycles [54], [55]. Liu and Sun [55] studied the influence of W-D cycles on the loading and unloading behavior of a silty clay. It is found that the cyclic strength of the specimens subjected to W-D cycles is higher than that of the specimens at the initial state. Khoury and Miller [54] observed that the strength of the specimens that were subjected to W-D cycles is greater than that of specimens only subjected to drying at the same net normal stress and matric suction. Liu and Sun [55] suggested that the irreversible compaction due to W-D cycles increases as the interparticle forces contribute to higher shear strength. They also suggest that the strength may reduce due to an increase in water content; however, the influence of irreversible compaction outweighs effects of water content. Therefore, the shear strength was reinforced by W-D cycles.

In summary, there is no consensus about the influence of W-D cycles on the soil shear strength behavior. Further studies are necessary for a better understanding of the influence of W-D cycles on the microstructure and shear strength of expansive soils.

DESIGN OF PILE FOUNDATION IN EXPANSIVE SOILS CONSIDERING TEMPERATURE AND MOISTURE CHANGES

The energy piles are being used in some engineering practice applications; these piles use the thermal properties of the ground soils to exchange heat or cold energy between the ground soils and the superstructure. There is evidence from experimental studies that there will be thermal expansion or contraction of energy piles and surrounding soils due to the changes in temperature. This volume change can result in relative deformation along the soil-pile interface, which contributes to modifying the stress between piles and the surrounding soils. When soil expands due to an increase in temperature, positive friction typically occurs along the surface of the piles, resulting in the uplift of the pile foundations and damage the superstructure. These practical problems should be properly addressed when designing energy pile foundations [56].

Expansive soils expand with an increase in water content and contribute to an increase in the external lateral earth pressure, positive friction and pile uplift. Liu and Vanapalli [57], [58] proposed a simple constitutive framework for rational design piles in

expansive soils taking account of the variation of water content induced by infiltration. However, to date, the change in the behavior of soil and soil-pile interface due to W-D cycles has not been considered in the design of pile foundations in expansive soils extending unsaturated soil mechanics framework. The hysteresis of SWCC should also be considered to analyze the shear strength of soil and soil-pile interface. Although the hysteresis of SWCC has been considered in interpreting the strength of expansive soils [51], the strength of soil-pile interface considering different stages of SWCC has not been studied. Reliable behavior of pile foundations in expansive soils is possible by taking account of the influence of W-D history considering the hysteresis effects of SWCC.

SUMMARY

The soils and infrastructures are exposed to the influence of various environmental factors such as precipitation, evaporation, and temperature change. In other words, soils are likely to be subjected to freezing/thawing (F-T) and wetting/drying (W-D) cycles. It is anticipated that there will be frequent F-T and W-D cycles due to the anticipated climate change and global warming effects in the near future on our planet. In this paper, the influences of temperature and moisture variations on the soil behavior are succinctly reviewed. It is necessary to consider these influences for the rational design of infrastructures such as pile foundations. In addition, reliable constitutive models that take into account climate change and global warming effects should be proposed to facilitate reliable analysis of the behavior of soils and pile foundations.

The freezing process, W-D, and F-T cycles significantly influence the frozen and unfrozen soil properties. For example, frozen soils have low hydraulic conductivity, and high strength and stiffness, due to the formation of ice in soil pore spaces. The F-T cycles typically weaken soil structure and contribute to the formation of cracks and fissures within the soil mass. As a result, frozen-thawed soils typically have higher hydraulic conductivity and lower stiffness and bearing capacity. The temperature and W-D cycling have a significant influence on the behavior of expansive soils (e.g., swelling and shrinkage characteristics), and therefore on the design of pile foundations in expansive soils.

REFERENCES

[1] Vanapalli S.K., Fredlund D.G., and Pufahl D.E., The Influence of Soil Structure and Stress History on the Soil-Water Characteristics of a Compacted Till, Geotechnique, Vol. 49, Issue 2, 1999, pp. 143–159.

[2] Fredlund D.G., and Xing A., Equations for the Soil-Water Characteristic Curve, Can. Geotech. J., Vol. 31, Issue 4, 1994, pp. 521–532.

[3] Vanapalli S.K., Fredlund D.G., Pufahi D.E., and Clifton A.W., Model for the Prediction of Shear Strength with respect to Soil Suction, Can. Geotech. J., Vol. 33, Issue 3, 1996, pp. 379–392.

[4] Oh W.T., Vanapalli S.K., and Puppala A.J., Semi-empirical model for the Prediction of Modulus of Elasticity for Unsaturated Soils, Can. Geotech. J., Vol. 46, Issue 8, 2009, pp. 903–914.

[5] MTO (Ministry of Transportation of Ontario), Pavement Design and Rehabilitation Manual (Second Edition). Queen`s Printer for Ontario, Canada, 2013.

[6] Koopmans R.W.R. and Miller R.D., Soil Freezing and Soil Water Characteristic Curves 1, Soil Sci. Soc. Am. J., Vol. 30, Issue 6, 1966, p. 680-685.

[7] Ren J. and Vanapalli S.K., Comparison of Soil-Freezing and Soil-Water Characteristic Curves of Two Canadian Soils, Unpublished Work but Accepted, Vadose Zo. J., 2019.

[8] Lu J., Carbone G.J., and Grego J.M., Uncertainty and Hotspots in 21st Century Projections of Agricultural Drought from CMIP5 Models, Sci. Rep., Vol. 9, Issue 1, 2019, p. 4922.

[9] Burt T.P. and Williams P.J., Hydraulic Conductivity in Frozen Soils, Earth Surf. Process., Vol. 1, Issue 4, 1976, pp. 349–360.

[10] Azmatch T.F., Sego D.C., Arenson L.U., and Biggar K.W., Using Soil Freezing Characteristic Curve to Estimate the Hydraulic Conductivity Function of Partially Frozen Soils, Cold Reg. Sci. Technol., Vol. 83–84, 2012, pp. 103–109.

[11] Fredlund D.G., Xing A., and Huang S., Predicting the Permeability Function for Unsaturated Soils Using the Soil-Water Characteristic Curve, Can. Geotech. J., Vol. 31, Issue 4, 1994, pp. 533–546.

[12] Bigl S.R. and Berg R.L., Material Testing and Initial Pavement Design Modeling (No. CRREL-96-14), Cold Regions Research and Engineering Laboratory, Hanover, N.H, 1996.

[13] Bosscher P. and Nelson D., Resonant Column Testing of Frozen Ottawa Sand, Geotech. Test. J., Vol. 10, Issue 3, 1987, pp. 123–134.

[14] Cole D.M., Bentley D.L., Durell G.D., and Johnson T.C., Resilient Modulus of Freeze-Thaw Affected Granular Soils for Pavement Design and Evaluation. Part 3. Laboratory Tests on Soils from Albany County Airport (No. CRREL-87-2), Cold Regions Research and Engineering Laboratory, Hanover, N.H, 1987.

[15] Ren J. and Vanapalli S.K., Prediction of Resilient Modulus of Frozen Unbound Road Materials using Soil-Freezing Characteristic Curve, Can. Geotech. J., Vol. 55, Issue 8, 2018, pp. 1200–1207.

[16] Qi J., Ma W., and Song C., Influence of Freeze–Thaw on Engineering Properties of a Silty Soil, Cold Reg. Sci. Technol., Vol. 53, Issue 3, 2008, pp. 397–404.

[17] Viklander P., Permeability and Volume Changes in Till Due to Cyclic Freeze/Thaw, Can. Geotech. J., Vol. 35, Issue 3, 1998, pp. 471–477.

[18] Chamberlain E.J. and Gow A.J., Effect of Freezing and Thawing on the Permeability and Structure of Soils, Eng. Geol., Vol. 13, Issue 1–4, 1979, pp. 73–92.

[19] Othman M., Benson C., Chamberlain E., and Zimmie T., Laboratory Testing to Evaluate Changes in Hydraulic Conductivity of Compacted Clays Caused by Freeze-Thaw: State-of-the-Art, in Hydraulic Conductivity and Waste Contaminant Transport in Soil, ASTM International, 1994, pp. 227–254.

[20] Othman M.A., and Benson C.H., Effect of Freeze-Thaw on the Hydraulic Conductivity of Three Compacted Clays from Wisconsin, Transportation Research Board, Issue 1369, 1992, pp.118-125.

[21] Formanek G.E., McCool D.K., and Papendick R.I., Freeze-Thaw and Consolidation Effects on Strength of a

Wet Silt Loam, Trans. ASAE, Vol. 27, Issue 6, 1984, pp. 1749–1752.
[22] Aoyama K., Ogawa S., and Fukuda M., Temperature dependencies of mechanical properties of soils subjected to freezing and thawing, in Proc. 4th Int. Symposium on Ground Freezing, 1985, pp. 217–222.
[23] Leroueil S., Tardif J., Roy M., La Rochelle P., and Konrad J.M., Effects of Frost on The Mechanical Behaviour of Champlain Sea Clays, Can. Geotech. J., Vol. 28, Issue 5, 1991, pp. 690–697.
[24] Graham J. and Au V.C.S., Effects of Freeze-Thaw and Softening on A Natural Clay at Low Stresses, Can. Geotech. J., Vol. 22, Issue 1, 1985, pp. 69–78.
[25] Kamei T., Ahmed A., and Shibi T., Effect of Freeze–Thaw Cycles on Durability and Strength of very Soft Clay Soil Stabilised with Recycled Bassanite, Cold Reg. Sci. Technol., Vol. 82, 2012, pp. 124–129.
[26] Wang D.Y., Ma W., Niu Y.H., Chang X.X., and Wen Z., Effects of Cyclic Freezing and Thawing on Mechanical Properties of Qinghai–Tibet Clay, Cold Reg. Sci. Technol., Vol. 48, Issue 1, 2007, pp. 34–43.
[27] Ogata N., T. Kataoka, and A. Komiya, Effect of freezing-thawing on the mechanical properties of soil, in Proc. 4th Int. Symposium on Ground Freezing, 1985, pp. 201–207.
[28] Culley R.W., Effect of Freeze-Thaw Cycling on Stress-Strain Characteristics and Volume Change of a Till Subjected to Repetitive Loading, Can. Geotech. J., Vol. 8, Issue 3, 1971, pp. 359–371.
[29] Lee W., Bohra N.C., Altschaeffl A.G., and White T.D., Resilient Modulus of Cohesive Soils and the Effect of Freeze-Thaw, Can. Geotech. J., Vol. 32, Issue 4, 1995, pp. 559–568.
[30] Simonsen E., Janoo V.C., and U. Isacsson, Resilient Properties of Unbound Road Materials during Seasonal Frost Conditions, J. Cold Reg. Eng., Vol. 16, Issue 1, 2002, pp. 28–50.
[31] Tang L., Cong S., Ling X., Xing W., and Nie Z., A Unified Formulation of Stress-Strain Relations Considering Micro-Damage for Expansive Soils Exposed to Freeze-Thaw Cycles, Cold Reg. Sci. Technol., Vol. 153, 2018, pp. 164–171.
[32] Cui Y.J., Loiseau C., and Delage P., Microstructure changes of a confined swelling soil due to suction controlled hydration, in Proc 3rd Int Conf on Unsaturated Soils UNSAT. 2002., Vol. 2, 2002, pp. 593–598.
[33] Koliji A., Laloui L., Cusinier O., and Vulliet L., Suction Induced Effects on the Fabric of a Structured Soil, Transp. Porous Media, Vol. 64, Issue 2, 2006, pp. 261–278.
[34] Pedrotti M. and Tarantino A., A Conceptual Constitutive Model Unifying Slurried (Saturated), Compacted (Unsaturated) and Dry States, Geotechnique, Vol. 69, Issue 3, 2018, pp. 217–233.
[35] Ngoc T.P., Fatahi B., and Khabbaz H., Impacts of Drying-Wetting and Loading-Unloading Cycles on Small Strain Shear Modulus of Unsaturated Soils, Int. J. Geomech., Vol. 19, Issue 8, 2019, p. 04019090.
[36] Gens A. and Alonso E.E., A Framework for the Behaviour of Unsaturated Expansive Clays, Can. Geotech. J., Vol. 29, Issue 6, 1992, pp. 1013–1032.
[37] Langroudi A.A. and Yasrobi S.S., A Micro-Mechanical Approach to Swelling Behavior of Unsaturated Expansive Clays under Controlled Drainage Conditions, Appl. Clay Sci., Vol. 45, Issue 1–2, 2009, pp. 8–19.
[38] Ghiadistri G.M., Potts D.M., Zdravkovi L., and Tsiampousi A., A new double structure model for expansive clays, in Proc 7th Int Conf on Unsaturated Soils, 2018.
[39] Likos W.J. and Wayllace A., Porosity Evolution of Free and Confined Bentonites During Interlayer Hydration, Clays Clay Miner., Vol. 58, Issue 3, 2010, pp. 399–414.
[40] Romero E., Gens A., and Lloret A., Suction Effects on a Compacted Clay under Non-Isothermal Conditions, Geotechnique, Vol. 53, Issue 1, 2003, pp. 65–81.
[41] Villar M.V. and Lloret A., Influence of Temperature on the Hydro-Mechanical Behaviour of a Compacted Bentonite, Appl. Clay Sci., Vol. 26, Issue 1–4, 2004, pp. 337–350.
[42] Tang A.M., Cui Y.J., and Barnel N., Thermo-Mechanical Behaviour of a Compacted Swelling Clay, Geotechnique, Vol. 58, Issue 1, 2008, pp. 45–54.
[43] Baldi G., Hueckel T., and Pellegrini R., Thermal Volume Changes of the Mineral-Water System in Low-Porosity Clay Soils, Canada Geotech. J., Vol. 25, Issue 4, 1988, pp. 807–825.
[44] Tripathy S. and Subba Rao K.S., Cyclic Swell-Shrink Behaviour of a Compacted Expansive Soil, Geotech. Geol. Eng., Vol. 27, Issue 1, 2009, pp. 89–103.
[45] Wang Q., Cui Y.J., Tang A.M., Barnichon J.D., Saba S., and Ye W.M., Hydraulic Conductivity and Microstructure Changes of Compacted Bentonite/Sand Mixture During Hydration, Eng. Geol., Vol. 164, 2013, pp. 67–76.
[46] Seiphoori A., Ferrari A., and Laloui L., Water Retention Behaviour and Microstructural Evolution of MX-80 Bentonite During Wetting and Drying Cycles, Geotechnique, Vol. 64, Issue 9, 2014, pp. 721–734.
[47] Gu K., Tang C., Shi B., Hong J., and Jin F., A Study of the Effect of Temperature on the Structural Strength of a Clayey Soil Using a Micropenetrometer, Bull. Eng. Geol. Environ., Vol. 73, Issue 3, 2014, pp. 747–758.
[48] Wiebe B., Graham J., Tang G.X., and Dixon D., Influence of Pressure, Saturation, and Temperature on the Behaviour of Unsaturated Sand-Bentonite, Can. Geotech. J., Vol. 35, Issue 2, 1998, pp. 194–205.
[49] Yang H.P, Zhang R., and Zheng J.L, The Effect of Vertical Pressure on the Deformation and Strength of Expansive Soil During Cyclic Wetting and Drying, Chinese J. Geotech. Eng., Vol. 28, Issue 11, 2006, pp. 1936–1941. (in Chinese)
[50] Zeng Z.T., Lu H.B., and Zhao Y.L., Wetting-Drying Effect of Expansive Soils and its Influence on Slope Stability, Appl. Mech. Mater., Vol. 170–173, 2012, pp. 889–893.
[51] Goh S.G., Rahardjo H., and Leong E.C., Shear Strength of Unsaturated Soils under Multiple Drying-Wetting Cycles, J. Geotech. Geoenvironmental Eng., Vol. 140, Issue 2, 2014, p. 06013001.
[52] Tse E.Y.M. and Ng C.W.W., Effects of drying and wetting cycles on unsaturated shear strength, in Proc. 1st European conf. on unsaturated soils, 2008, pp. 481–486.
[53] Albers B., Main Drying and Wetting Curves of Soils: on Measurements, Prediction and Influence on Wave Propagation, Eng. Trans., Vol. 63, Issue 1, 2015, pp. 5–34.
[54] Khoury C.N. and Miller G.A., Influence of Hydraulic Hysteresis on the Mechanical Behavior of Unsaturated Soils and Interfaces, Geotech. Test. J., Vol. 35, Issue 1, 2011, pp. 135–149.
[55] Liu W.H. and Sun X.L., Comparison of Two Drying/Wetting Methods for Assessing the Influence of Drying/Wetting on the Mechanical Cyclic Behaviors of Soils, Iran. J. Sci. Technol. Trans. Civ. Eng., Vol. 41, Issue 3, 2017, pp. 297–303.
[56] McCartney J.S., Sánchez M., and Tomac I., Energy Geotechnics: Advances in Subsurface Energy Recovery, Storage, Exchange, and Waste Management, Comput. Geotech., Vol. 75, 2016, pp. 244–256.
[57] Liu Y. and Vanapalli S.K., Influence of Lateral Swelling Pressure on the Geotechnical Infrastructure in Expansive Soils, J. Geotech. Geoenvironmental Eng. ASCE, Vol. 143, Issue 6, 2017, p. 04017006.
[58] Liu Y. and Vanapalli S.K., Load Displacement Analysis of a Single Pile in an Unsaturated Expansive Soil, Comput. Geotech., Vol. 106, 2019, pp. 83–98.

9th Int. Conf. on Geotechnique, Construction Materials and Environment,
Tokyo, Japan, 20-22 November 2019, ISBN: 978-4-909106025 C3051

COMPRESSION BEHAVIOR OF ULTRA-SOFT SOIL WITH AND WITHOUT PREFABRICATED VERTICAL DRAIN

Suksun Horpibulsuk[1], Dong Huy Ngo[2], Apichat Suddeepong[3], Menglim Hoy[4], Artit Udomchai[5], Prajueb Doncommul[6], Runglawan Rachan[7] and Arul Arulrajah[8]
[1,2,4] School of Civil Engineering, Suranaree University of Technology, Thailand
[1,3,4,5] Center of Excellence in Innovation for Sustainable Infrastructure Development, Suranaree University of Technolgy, Thailand
[6] Mae Moh Mine Planning and Management Division, Electricity Generating Authority, Thailand
[7]Department of Civil Engineering, Mahanakorn Univ. of Technology, Thailand
[8] Department of Civil and Construction Engineering, Swinburne University of Technology, Australia

ABSTRACT

The compression behavior of ultra-soft soil with and without the prefabricated vertical drains (PVDs) at various water contents (w_i) was studied via a series of consolidation test and large-scale model tests. The compression curve of ultra-soft soil show an inverse S-Shaped due to the yield stress resisting deformation, which is similar to the pre-consolidation pressure for natural soil. Large settlements with the delay of excess pore pressures were observed, which is a distinct behavior of ultra-soft soil, especially at very high water content. The higher initial water content resulted in the longer delay of excess pore pressure dissipation. The ultra-soft soil was significantly improved by ground improvement with PVD, as evident by the significant reduction in w and increase in undrained shear strength (S_u). The S_u at various degree of consolidation could be approximated by the vertical effective stress (σ'_v) based on the SHANSEP and Asaoka's method. The outcome of this research will facilitate the geotechnical design of reclamation of ultra-soft dredged soil in Mae Moh mine and other similar soils.

Keywords: Ultra-soft soil; Large-scale model test; Prefabricated vertical drains; consolidation

INTRODUCTION

The Mae Moh mine is largest open-pit lignite mine in Southeast Asia, situated at Mae Moh district, Lampang province, Thailand. It is operated by the Electricity Generating Authority of Thailand (EGAT). Sump1 C1 is a low-lying area, located in the north of the Mae Moh mine with the total area of 80,000 m2. The soil erosion caused by the discharge of surface water along the mine slope were finally collected and formed up to approximately 38 m thickness of dredged soil deposits under water in sump 1 C1 for over decades.

According to the mine planning and development of EGAT, the mine will be excavated to a depth of approximately 500 m from original surface in the next 40 years. As a result, this mine will become the deepest open-pit lignite mine in the world. The excavated soil from mining activity will be transferred to dump in the Sump 1 C1. It will be subjected approximately 300 m of overburden material in the next 40 years. However, the dredged soil in the Sump 1 C1 is ultra-soft soil and possesses very low bearing capacity. Therefore, it is imperative to improve the existing ultra-soft dredged soil before commencing any construction activities in order to prevent any failure due to the mud flow.

Soil improvement techniques generally include soil replacement, preloading, stone column, and cement column, etc [1]-[4]. Among these methods, the preloading with prefabricated vertical drains (PVDs) is cost-effective and commonly used in land reclamation projects on ultra-soft soil deposits [5]-[8]. However, a few laboratory testing and field instrumentation have been conducted to study the performance of PVDs improved ultra-soft soil in dredged sump [2], [8]-[10]. The previous studies showed that the PVDs accelerate settlement, enhance shear strength, and reduce moisture content of the ultra-soft clay for a particular water content. However, the compression behavior of ultra-soft improved by PVDs at various initial water content have not been well examined.

In this study, the consolidation behavior of ultra-soft dredged soil with and without PVDs were studied. The distinct consolidation behavior especially excess pore pressure dissipation of ultra-soft clay was presented. The research outputs will facilitate geotechnical engineers to assess the compressibility of ultra-soft soil with and without PVDs, which can be applied to the ground improvement of ultra-soft soils in future dredging projects.

LABORATORY TEST

To study the consolidation behavior of the ultra-soft soil with and without PVDs, a series of consolidation test and large-scale model tests were conducted on the ultra-soft soil at various initial water contents.

Soil sample

The ultra-soft soil samples were obtained from a dredged pond - Sump 1 C1. The disturbed samples were collected from 1.5 m depth below the soil surface.

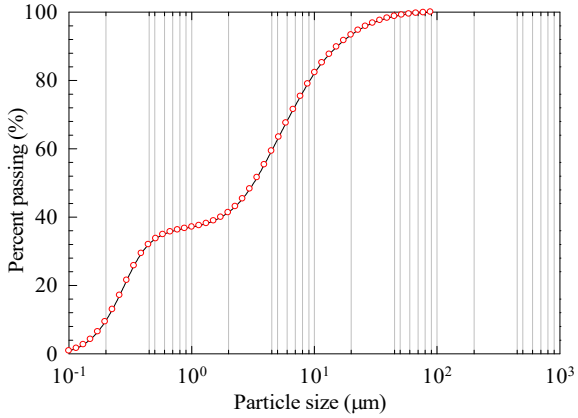

Fig. 1 Grain size distribution curve

The grain size distribution curve of the soil sample is shown in Fig. 1. The soil sample contained 41% clay and 58% silt with 1% sand. The liquid limit and the plastic limit were 57% and 26%, respectively. The specific gravity was 2.57. The natural water content was in the range of 114% - 170%. The in-situ strength was extremely low.

Consolidation test

The consolidation behavior of the sedimentation soil without PVDs were studied by conducting the Oedometer tests. Six samples were prepared by mixing the slurry thoroughly with a quantity of distilled water to reach the target initial water contents, which were 1.45, 1.79, 1.84, 1.97, 2.10, and 2.28 times the liquid limit. The remolded sample was then transferred into the consolidation ring. The consolidation sample was 105 mm in diameter and 20 mm in nominal height. After that the samples were then subjected to both low and high loads. A very low effective vertical stress of 0.5 kPa was first applied and gradually increased with following vertical stresses of 1 kPa, 1.5 kPa, 2.5 kPa, 3.5 kPa, 5.5 kPa, 7.5 kPa, 9.5 kPa, 12.5 kPa, 25 kPa, 50 kPa, 100 kPa, 200 kPa, 500kPa, 1000 kPa, 2000kPa, 4000 kPa. The duration of each loading step was fixed at 24 hours.

For each loading increment, the coefficient of permeability, k, was calculated by the following equation.

$$k = c_v \times m_v \times \gamma_w \quad (1)$$

where c_v is the coefficient of consolidation determined using the root time method proposed by Taylor (1942), m_v is the coefficient of volume change, and γ_w is the density of water.

Large – scale consolidation test

To investigate the compression behavior of ultra-soft soil improved by PVDs, the large-scale consolidation tests were conducted at the initial water contents of 120% and 180%.

The consolidation tank was made of stainless steel with an inside diameter of 495 mm and a height of 1200 mm, as shown in Fig. 2. During the test, the settlement was measured by two Linear Variable Displacement Transducers (LVDTs). Six saturated miniature pore pressure transducers (PPTs) were installed to measure excess pore water pressures at different positions. A total earth pressure cell was placed on the steel plate in order to control the pressure acting on the sample during the test. To reduce wall friction, the inner surface was smeared with lubricating oil beforehand.

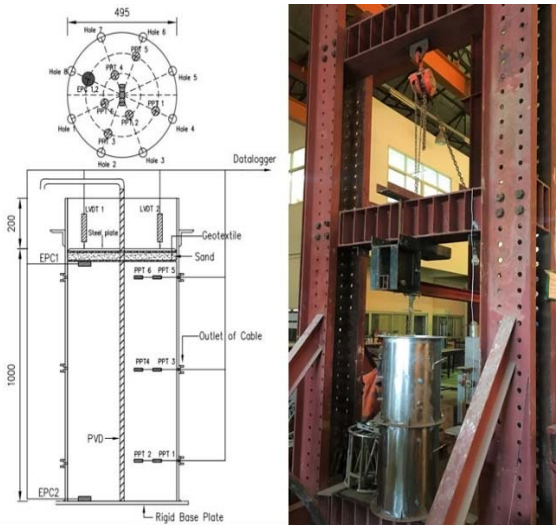

Fig. 2 Large scale of consolidation tank

For each test, the remolded sample was prepared by adding a sufficient amount of water to obtain the initial water content greater than its liquid limits and then thoroughly mixed by a mechanical mixer. The remolded soil was hence poured into the tank for about 1 month for sedimentation process. The final height of the soil in the consolidation tank was approximately 95 cm while the water contents of the soil in the 2 tested cases were respectively 120%, 180% after sedimentation time.

In this study, PVD Ali-drain type AD250 having 100 mm width and 5mm thickness was selected. After

the 1 month of sedimentation, a small aluminum mandrel with PVD inside was penetrated vertically into the ultra-soft soil. When the mandrel touched the bottom of the tank, it was slowly withdrawn from the soil. A 10 cm thick sand layer was then spread on the geotextile layer to prevent the soil squeeze out of the tank under the loading condition. A steel plate was placed on the top of soil to impose the same displacement.

After the assembling of the tank, three incremental vertical pressures (20 kPa, 40 kPa, and 80 kPa) were applied on the top of the soil layer. The step loading applied at the top of the soil is shown in Fig. 3. The large-scale consolidation test was allowed to drain only in one direction to the top surface. During the test, the settlement and the pore water pressure were automatically recorded in real-time with a data logger. The undrained shear strengths were measured after the end of consolidation at each loading step using a mini vane shear test apparatus.

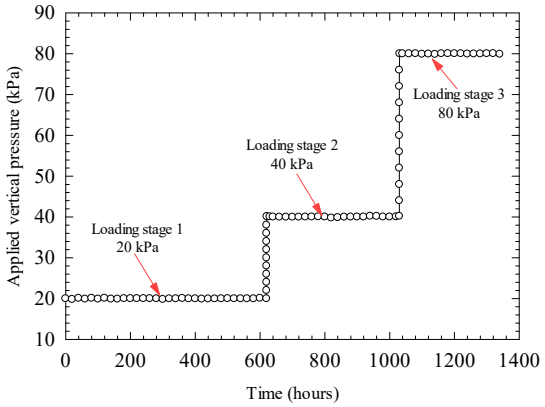

Fig. 3 Loading stages in 3 tested cases

RESULTS AND DISCUSSION

Consolidation test results

The consolidation curves in term of void ratio versus effective vertical stress in a semi-logarithmic (e vs log σ'_v) for six samples at different initial water contents are shown in Fig. 4. The consolidation behavior of the soil at various water content is an inverse S-shape, which is similar with Lianyungang, Baimahu clay and Kemen clay reported by [11]. The transitional stress separating small and large change in void ratio is defined as yield stress or suction pressure, which is similar to the pre-consolidation pressure for natural soil [11].

The relationship between the coefficient of permeability and void ratio of the ultra-soft soil at various water contents is shown in Fig. 5. The permeability significantly reduces with the reduction of void ratio. The non-linear relationship between e and log k for the Mae Moh soil samples can be represented by the following equation.

$$e = 141.84 \times k^{0.239} \quad (2)$$

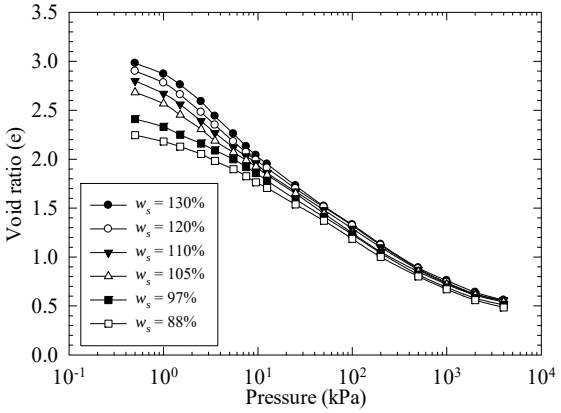

Fig. 4 Consolidation curve of sediment soil at different initial water contents

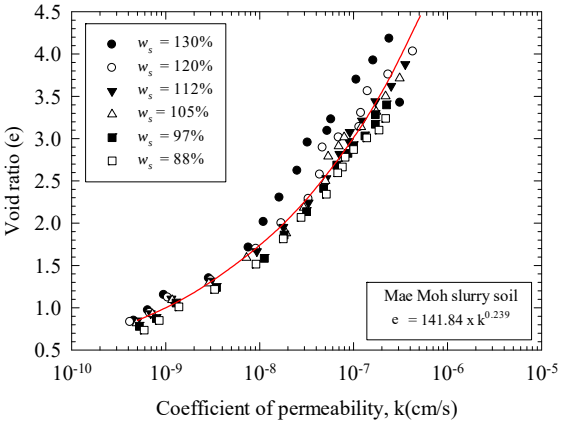

Fig. 5 e- log(k) relationship of sediment soil at different sedimentation water contents

Model test results

Settlement results

The relationship between the settlements versus time of two tested cases is shown in Fig. 6. The settlement occurred in the first loading stage (20 kPa) was much higher than the settlement induced in the second loading (40 kPa) and the last loading (80 kPa), respectively in both cases. The value of settlement reduced as the consolidation stress increased due to non-linear compression behavior of the ultra-soft soil [12]-[14].

The large settlements were observed in 2 cases, especially for case 2 with the initial water content of 180% that exhibited the highest value. The settlement of case 1 was in the order of 240 mm, which was about 27% of strain under the vertical consolidation stress of 80 kPa. The final settlement and the degree of consolidation of the soil at each stage of loading were predicted by using Asaoka's observational method [15], as presented in Fig. 7. The soil in case 1

achieved more than 90% the degree of consolidation in all stages of loading, which was about 90.65%, 94.33%, and 96.24% for consolidation stresses of 20 kPa, 40 kPa, and 80 kPa, respectively.

The measured settlements in case 2 were much higher than those in case 1, which was approximately 393.02 mm after 1362 hours of testing. A very large vertical strain of approximately 42% was developed at the end of consolidation test. Large settlements induced by PVDs in both cases proved the effectiveness of PVDs in improving the ultra-soft soil at different initial water contents. The degree of consolidation in case 2 in each loading stage was smaller than that in case 1. This indicates that the higher initial water content leads to the higher final settlement and the lower rate of consolidation settlement.

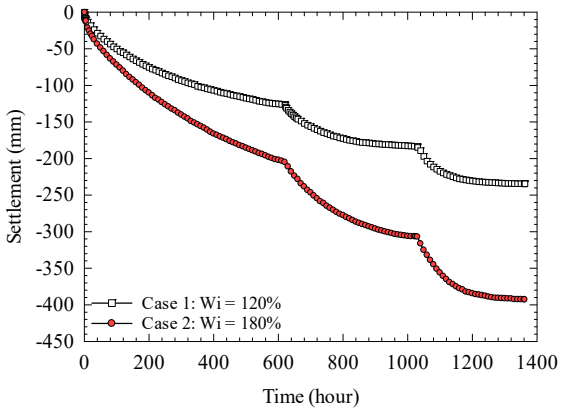

Fig. 6 Settlement versus with time curve measured from the model test of 2 cases under 3 loading stages.

Excess pore water pressure

The dissipation of excess pore water pressures from six transducers of case 1 and case 2 are shown in Figs. 8-9. In both cases, the initial excess pore water pressures (at time t = 0) measured from 6 PPTs were slightly lower than the total vertical stress. On the other hand, the excess pore water pressures recorded at the top (PPT 5, PPT 6) were different with those measured at the bottom of the tank (PPT 1, PPT 2), showing the different distribution of pressures on the soil along the depth possibly due to different drainage conditions.

It is of interest to note that only minimal pore pressure dissipation was recorded at six transducers in the early of loading stages, although the settlements took place during this time (Figs. 8-9). For instance, Fig. 6 shows that the settlement in case 2 after 50 hours was 53.61 mm, which was 30.89% of degree of consolidation, with the delay of excess pore water pressure during the first loading stage. The delayed time is defined as the transitional point from small change to large change in excess pore pressure. The delay of excess pore water pressures was also observed in the second and the last loading stage. It is noted that the delayed time tended to reduce with the increase of vertical consolidation pressure. The higher initial water content resulted in the longer delay of excess pore pressure dissipation. The delayed time observed in PWP 5 and PW6 of case 2 (Wi = 180%) was approximately 50 hours in the first loading, which was approximately 20 hours longer than that of case 1 (Wi = 120%). This delay in excess pore pressure dissipation with progressive settlement is the distinct behavior of ultra-soft clay which diverts from natural soft clay. This similar behavior was also noticed in the previous research reported by [6] , [8].

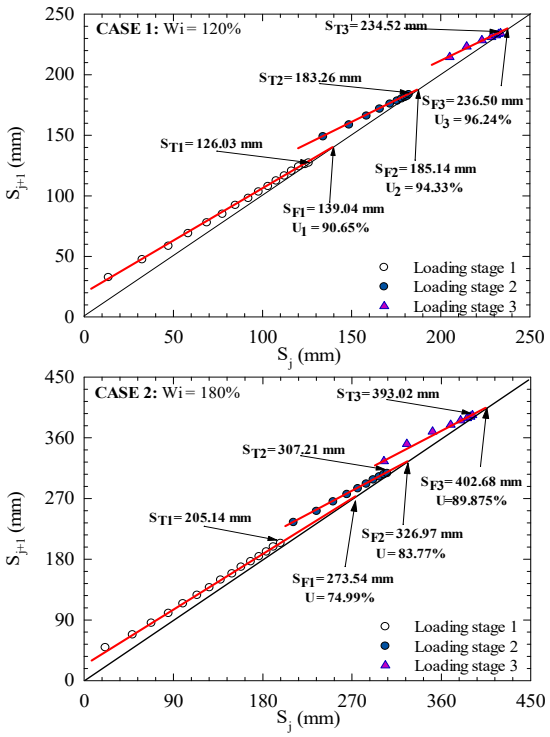

Fig. 7 The final settlement of each loading stage predicted by using Osaka's observation method

Beyond the delayed time, the pore water pressure reduced significantly (Figs. 8-9). At the same depth, the excess pore water pressures close to the PVD (PPT 2, PPT 4, and PPT 6) indicated a faster rate of dissipation than the others. Because the consolidation tank was tested under one-way drainage, the decrease of excess pore pressures observed from 2 PPTs at the bottom of tank (PPT 1 and PPT 2) were lower than those measured on the top of the tank.

Water content and undrained shear strength

The water contents of the ultra-soft soil in 2 cases were measured at various distances from the center of the vertical drains after the end of consolidation test at vertical stress of 80 kPa and compared with the initial water contents (w_i %), as shown in Fig. 10. A

significant reduction of the water content was noticed in both cases. The lowest water content was found near the PVDs, and the water content increased with the increasing radial distance from the PVD. For case 1 (w_i = 120%), the final water contents varied from 42.01% to 52.66%. It is noted that the reduction of water content in case 2 (w_i = 180%) was very large, which reduced by approximately 129% near the vertical drain.

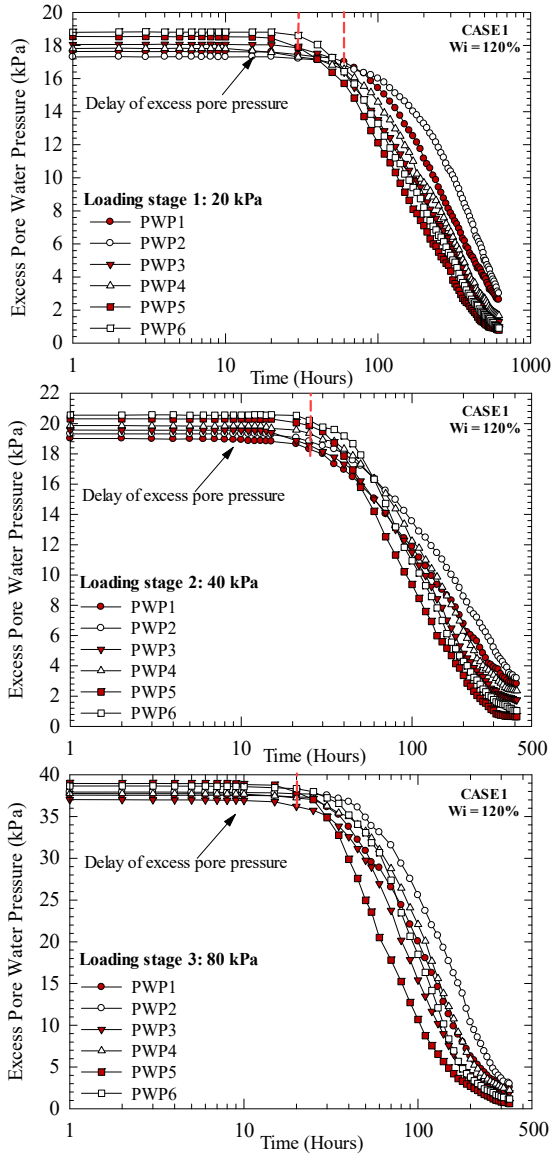

Fig. 8 Excess pore water pressure dissipation versus with time measured by pore pressure tranducer in case 1 (Wi = 120%)

The undrained shear strength (Su) of the soil in the middle of the soil layer in the tank was measured by using mini vane shear equipment. The higher water contents and lower initial undrained shear strengths were observed in case 2 when compared with the results in case 1. On the other hand, Fig. 10 shows that the undrained shear strength, S_u, versus the vertical effective stress, σ'_v. The vertical effective stress at the end of test of each vertical consolidation pressure was a product of the total vertical stress (σ_v) and the degree of consolidation (U) calculated using the Asaoka's observation method. It was evident that the undrained shear strengths is directly related to vertical effective stress ($\Delta\sigma'_v$). The Su versus σ'_v relationship was therefore developed based on the SHANSEP equation proposed by [16]:

$$\frac{S_u}{\sigma'_v} = 0.22 \quad (8)$$

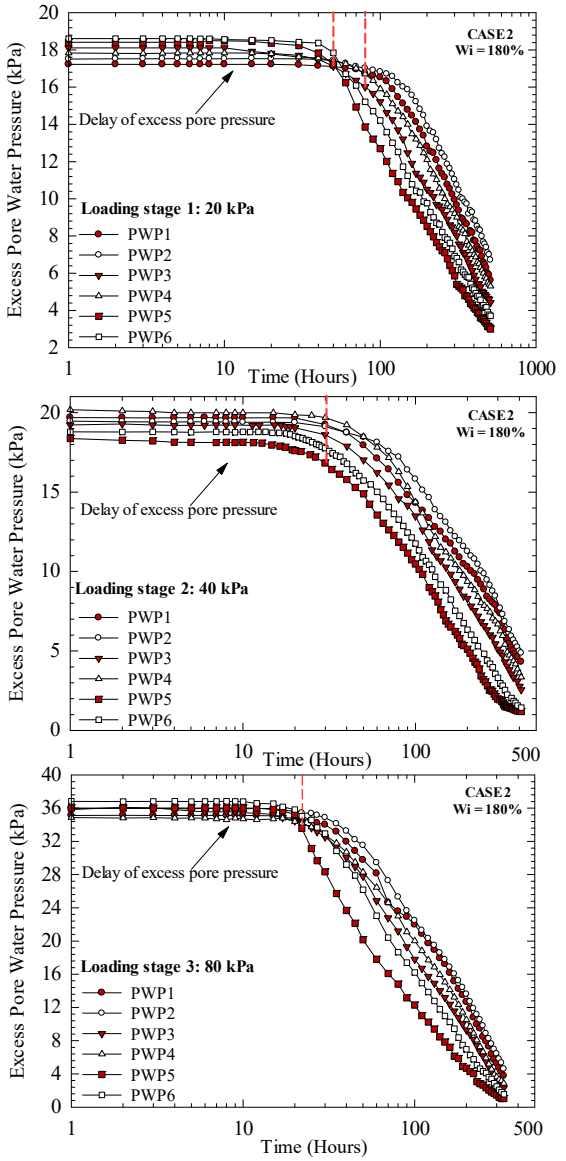

Fig. 9 Excess pore water pressure dissipation versus with time measured by pore pressure tranducer in case 2 (Wi = 180%)

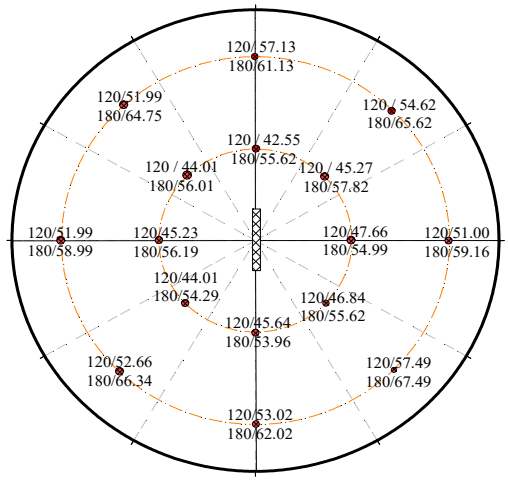

Fig. 10 Change of water content before and after consolidation time using PVDs in 3 cases

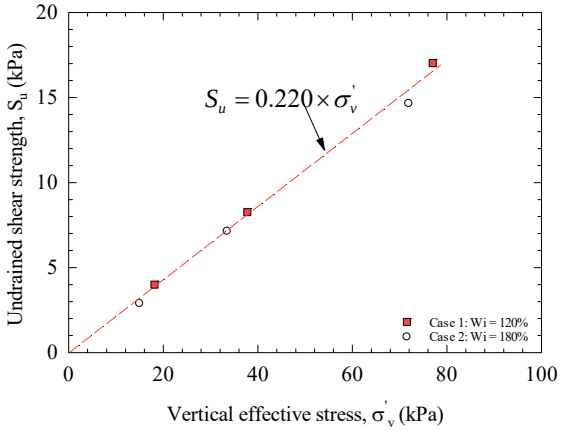

Fig. 11 Measured and predicted undrained shear strength in kPa during the consolidation process

CONCLUSION

This research studied the compression behavior of ultra-soft soil with and without using PVDs in Mae Moh mine, Thailand. The following conclusions can be drawn as follows:

- The consolidation curves of sedimentation soil without PVDs can be represented by the inverse S-shape from a very low (0.5 kPa) to very high vertical effective stresses.
- The large settlements for all cases were observed, especially for case 2 that exhibited the highest value after the consolidation stage of ultra-soft soil improved by PVDs. The test results indicated that the higher initial water content resulted in the higher settlement and the lower rate of consolidation settlement
- The distinct behavior of Mae Moh ultra-soft soil was the delay of excess pore water pressure at the initial stage of consolidation although the settlements had taken place. The higher initial water content resulted in the longer delay of excess pore pressure dissipation. Beyond the delayed time, the excess pore water pressures rapidly decreased with time.
- A significant reduction of water content and increase of undrained shear strength after testing highlighted the successful performance of PVDs on the improvement of the Mae Moh dredged soil. The equation for predicting undrained shear strengths at various vertical effective stress was developed based on SHANSEP's method.

REFERENCES

[1] Arulrajah, A., Nikraz, H., Bo, M., 2005. Finite element modelling of marine clay deformation under reclamation fills. Proceedings of the Institution of Civil Engineers-Ground Improvement, 9(3), 105-118.

[2] Choa, V., Bo, M., Chu, J., Soil improvement works for Changi East reclamation project. Proceedings of the Institution of Civil Engineers-Ground Improvement, 5(4), 2001, pp 141-153.

[3] Horpibulsuk, S., Phetchuay, C., Chinkulkijniwat, A., Cholaphatsorn, A., Strength development in silty clay stabilized with calcium carbide residue and fly ash. Soils and foundations, 53(4), 2013, pp 477-486

[4] Shen, S.L., Wang, Z.F., Horpibulsuk, S., Kim, Y.H. 2013. Jet grouting with a newly developed technology: the twin-jet method. Engineering Geology, 152(1), 2013, pp 87-95.

[5] Arulrajah, A., Nikraz, H., Bo, M., 2004. Factors affecting field instrumentation assessment of marine clay treated with prefabricated vertical drains. Geotextiles and Geomembranes. 22(5), 415-437.

[6] Bo, M., Choa, V., Wong, K., Reclamation and soil improvement on ultra-soft soil. Proceedings of the Institution of Civil Engineers-Ground Improvement, 9(1), 2005, pp 23-31

[7] Chen, J., Shen, S.L., Yin, Z.Y., Xu, Y.S., Horpibulsuk, S., Evaluation of effective depth of PVD improvement in soft clay deposit: a field case study. Marine Geo resources & Geotechnology, 34(5), 2016, pp 420-430.

[8] Chu, J., Bo, M., Choa, V., Improvement of ultra-soft soil using prefabricated vertical drains. Geotextiles and Geomembranes, 24(6), 2006, pp 339-348.

[9] Bo, M., Discharge capacity of prefabricated vertical drain and their field measurements. Geotextiles and Geomembranes, 2004.

[10] Chu, J., Bo, M., Choa, V., Practical considerations for using vertical drains in soil improvement projects. Geotextiles and Geomembranes, 22(1-2), 2004, pp 101-117.

[11] Hong, Z., Yin, J., Cui, Y.J., Compression

behavior of reconstituted soils at high initial water contents. Geotechnique, 60(9), 2010, pp 691-700.

[12] Fang, Z., Yin, J.H., Physical modelling of consolidation of Hong Kong marine clay with prefabricated vertical drains. Canadian Geotechnical Journal, 43(6), 2006, pp 638-652.

[13] Horpibulsuk, S., Liu, M. D., Zhuang, Z., Hong, Z.S., Complete compression curves of reconstituted clays. International Journal of Geomechanics, 16(6), 2016.

[14] Liu, M. D., Zhuang, Z., Horpibulsuk, S., Estimation of the compression behaviour of reconstituted clays. Engineering Geology, 167, 2013, pp 84-94

[15] Asaoka, A., 1978. Observational procedure of settlement prediction. Soils and foundations, 18(4), 87-101.

[16] Ladd, C. C., Foott, R., New design procedure for stability of soft clays. Journal of Geotechnical and Geoenvironmental Engineering, 1974, pp 100.

9th Int. Conf. on Geotechnique, Construction Materials and Environment, Tokyo, Japan, 20-22 November 2019, ISBN: 978-4-909106025 C3051

EVALUATION OF THE RELATIONSHIP BETWEEN THE DECREASE IN THE TENSILE LOAD OF GROUND ANCHORS AND GEOLOGICAL CONDITIONS

Mitsuru Yamazaki[1] and Toshinori Sakai[2]
[1] Central Nippon Highway Engineering Nagoya Company Limited, Japan;
[2] Graduate School of Bioresources, Mie University, Japan

ABSTRACT

Ground anchors (hereafter anchors) are structures used to stabilize landslides or cut slopes by transmitting a tensile load to the ground. The tensile load of an anchor is presumed to fall gradually as time passes and varies in the rate at which it declines. The decline of the tensile load of an anchor is expected to be caused by the relaxation of steel or the creep of the ground. This decrease is assumed to be large during the initial period within approximately 30 days after installation and is one index used to evaluate soundness at the maintenance stage. However, the degree to which the tensile load is impacted by specific geological conditions has not been clarified.

Thus, in this study, the relationship between the tensile load 30 days after installation, as obtained by measurements using load cells installed on the anchors, and the rock classification (representing the geological conditions) along the free length of the anchor was investigated. The results demonstrate that poorer geological conditions correspond to a greater decline in the tensile load of the anchor.

Keywords: Ground Anchor, Residual Tensile Load, Geological Condition, Rock Classification, Maintenance

INTRODUCTION

Since ground anchors (hereafter anchors) were first introduced in Japan in 1957, they have been frequently used in landslide and cut-slope stabilization countermeasures. An anchor is a structure consisting in part of a tension member installed in the ground such that one end is embedded in the ground whereas the other end is fixed at the ground surface. With the part between these ends free, the anchor adds a prestressing force (tensile load) to the tension members, stabilizing landslides or cut surfaces by sustaining the tensile load. Most of the anchor is located in the ground.

The tensile load of an anchor generally decreases gradually over time until it converges to a specified value under the action of the creep of the ground or the relaxation of the tension member after the introduction of an initial tensile load during anchoring, as shown in Figure 1 [1]. However, the tensile load of an anchor may not converge to a residual value if, immediately after the ground was excavated by cutting work, an unexpectedly large external force is produced by the geological conditions of the ground where the anchor was installed. Therefore, it is important to maintain anchors while appropriately monitoring their tensile loads.

Figure 2 shows the flow [2] of the tensile load management of anchors on expressways operated by the three Nippon Expressway Company Limited

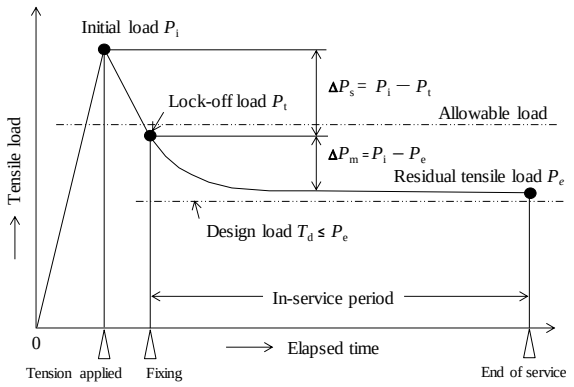

Fig.1 Tensile load acting on an anchor over time [1].

(NEXCO) companies. On such expressways, instruments used to measure the load (hereafter collectively referred to as the load cell) are installed at the construction stage on some of the anchors to monitor changes in the tensile load. At the service stage, measurement by the load cell is continued as required. After the load meters have ceased to function, lift-off tests are conducted as periodical detailed inspections to monitor the tensile load of the anchors (residual tensile load) and evaluate the soundness of the anchor [3].

Table 1 lists the standards [4] for the residual tensile load of an anchor and the corresponding

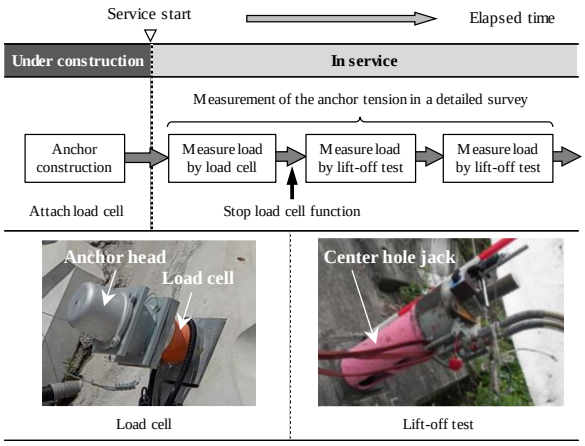

Fig.2 Management of anchor tension [2].

Table 1 Example of standards for the residual tensile load and soundness of an anchor [4]

Range of tensile load	Soundness	State	Example of action to be taken
	E^+	Risk of breakage	Emergency response
$0.9T_{ys}$	D^+	Possible dangerous state	Inplement a countermeasure
$1.1T_a$	C^+	Above allowable load	
T_a	B^+	–	Consider the need for measures by observation
T_d	A^+	Healthy	–
P_t	A^-	Healthy	–
$0.8P_t$	B^-	–	Consider the need for measures by observation
$0.5P_t$	C^-	Greatly reduced functionality	Inplement a countermeasure
$0.1P_t$	D^-	Nonfunctional	

T_{ys} : Yield point load, T_a : Allowable load, T_d : Design load, P_t : Fixed load

anchor soundness, which is generally used to evaluate the anchor function. Management of the residual tensile load of anchors is conducted by clarifying to what extent the tensile load has decreased from the lock-off load P_t when the anchor was constructed. This clarifies the characteristics of the relationship between the design load T_d, allowable load T_a, and yield point load T_{ys} and gives an indication of the appropriate treatment according to the situation. In addition to the measurement of the tensile load, a visual inspection for damage, such as the floating of anchor tops and the protrusion or sinking of tension members, is also conducted as part of anchor maintenance. However, the residual rate of the tensile load is only one index used to evaluate anchor function.

The geological conditions of the slope in which anchors are deployed vary according to the rock type (igneous, sedimentary, or metamorphic); the degree to which it is weathered; and the extent of the development of cracking, joints, and schistosity. Anchors are designed by performing boring surveys at multiple locations to geologically survey the ground where the anchors will be deployed, confirming the state of the geology, and assessing the depth of the slip plane that should be arrested. Moreover, the standards of the anchors and the number required are determined by considering the required arresting force calculated from the target safety factor. The geological conditions of the ground where the anchors are deployed presumably influences the tensile load of the anchors, both initially and in the long term. However, at this time, these factors are not considered during design and maintenance.

Takyu et al. [5] installed load cells on 57 of 1,130 anchors deployed as a large-scale landslide countermeasure and confirmed the tendency of the tensile load of the anchors to decline. They observed that 30 days after execution, the tensile load had decreased greatly at the end of the slope, where loose and weathered ground spread on the surface at the top of a slope that was cut to a shallow depth. The decrease in the tensile load was more than 10% of the lock-off load, and it was impacted by the geological conditions.

Yamazaki and Sakai [6] conducted a geological survey to study the relationship between the rock classification of the bedrock where anchors are installed and the initial decrease in the tensile load. They surveyed eight slopes without deformation for three types of rock: granite, sedimentary rock, and metamorphic rock. The results clearly showed that the reduction in the tensile load 30 days after installation increased as weathering advanced and cracking developed. In the sedimentary rock and metamorphic rock, which were remarkably brittle, the tensile load declined to between 80% and 85% of the lock-off load.

Fujiwara and Sakai [7] performed lift-off tests on all 18 anchors installed on a cut slope as part of an inspection of the tensile load on the anchors 10 years after their installation. The researchers obtained the residual rate of the tensile load, which fell from the center of the slope, where hard bedrock was distributed, toward the slope end, which was softened by the advance of weathering and the distribution of the surface soil. The average declines in the tensile loads in moderately weathered rock, severely weathered rock, and surface soil were 77%, 55%, and 50% respectively, demonstrating that the geological conditions at the installation site of the anchors impact the decline in the tensile load.

As demonstrated by these previous studies, the

tensile load of an anchor is thought to decline naturally under the impact of the geological conditions of the ground where they are installed, even in the absence of any unpredicted external force. However, although the residual rate of the tensile load of an anchor is one index used to evaluate its soundness, it is not clear to what extent the load declines under specific geological conditions. In this study, the relationship between the initial decline of the tensile load in the first 30 days after anchor installation and the geological condition was examined. This relationship was determined using the results of measurements by load cells installed on the anchors at the construction stage and the rock classification obtained by geological evaluation based on a boring survey and slope sketches.

STUDY METHOD

To correlate the decline in the anchor tensile load with the geological conditions, the rock classifications along the free length of the anchors on each of the slopes evaluated in this study were first determined. A detailed geological evaluation based on a boring survey was conducted on the cut slope and during the installation of the anchors. The evaluation of bedrock during a geological survey is typically accomplished using the rock classifications [8],[9] from Tanaka's extended method [10], and records of the evaluation of the borehole core and cut slope during excavation performed by such a method on each object slope were retained. A schematic of the rock classification [11] is shown in Table 2. This rock classification consists of a qualitative evaluation of three elements: the degree of weathering, the hardness of the rock masses, and the state of joints or cracked surfaces. These were compared with a variety of strength and physical constants.

The geological conditions of each slope were defined by broadly categorizing the rock as igneous, sedimentary, or metamorphic based on boring core data and cross sections used for the design and installation of the anchors performed at the construction and in-service stages and slope sketches drawn during excavation. The rock classifications, which were mainly bedrock, that were manifest on the anchor free lengths were divided into eight classes: C_H, C_H–C_M, C_M, C_M–C_L, C_L, C_L–D, D, and D (colluvium), including unconsolidated soil as colluvium.

To determine the tensile load of the anchors, measurement data from the load cells during the 30-day period after installation were used. These were evaluated using the residual rate $R_{pt} = P_e/P_t$ [%], where the residual tensile load P_e and the fixed anchor load P_t were obtained from these data.

Table 3 broadly classifies the slopes used to study the initial decline of the tensile load, the number of measurement data, and the geology. In this study, 30 slopes were examined using load cells installed in 170 locations. Stable slopes were studied where no deformation of the surface level or displacement was seen in dynamic observations. The anchors on each slope showed no damage or anomalies in their heads or pressure-bearing structures and no loss of function. The soundness of the anchors was evaluated based on their external appearance.

Table 2 Schematic of the rock classification [11]

Symbol	Pit wall, outcrop	Boring core	Herdness of rock fragments	Degree of weathering	State of cracked surface	Joint interval
D	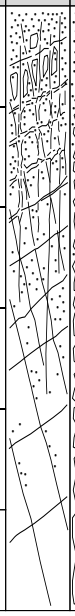		Can be crushed with fingers, easily broken	Soil, rock fragments in some places	Argillation, unclear crack	5 cm or less, crushed
C_L			Produces voiced sound with a hammer blow, collapses easily	Weathering until internal, argillation of rock-forming minerals	Argillation, clear crack	5–15 cm, many gravel and rock fragments
C_M			Voiced sound, fragile	Whole browning, noticeable alteration of rock-forming minerals	Many opening cracks, sandwich clay	5–30 cm, many rock fragments, short columnar joints
C_H			Slight metallic sound, unbreakable	Whole slight browning, slight alteration of rock-forming minerals	Contact to slight opening, sandwiched thin clay	15–30 cm, many short columnar joints
B			Metallic sound, unbreakable	Browing alog the crack, no alteration of minerals	Contact to slight opening, no clay	30–50 cm, many short columnar joints and poles
A			Metallic sound, unbreakable	Fresh, unweathered	Contact, no clay	50 cm or more, poles

Table 3 Geology of slopes and amount of data used to evaluate the decrease in the tensile load

Rock classification	Rock type	Geologic time	Number of slopes	Number of load cells
Igneous rock	Ryoke granite	Cretaceous	11	66
	Nohi rhyolite	Cretaceous	2	7
Sedimentary rock	Mino belt sandstone, shale	Jurassic	8	29
	Shimanto group snandstone, shale	Early Cretaceous to Paleogene	2	2
	Yasugawa group sandstone, shale	Jurassic	1	11
Metamorphic rock	Sanbagawa belt schist	Late Cretaceous to Paleogene	3	12
	Ryoke belt gneiss	Cretaceous	3	43
		Total	30	170

DECLINE IN THE TENSILE LOAD DURINGTHE 30-DAY PERIOD AFTER INSTALLATION

To assess the decline in the residual load of the anchors during the first 30 days after installation, the rock was classified as igneous, sedimentary, or metamorphic to discuss the relationship between the residual rate of the tensile load and the rock classification.

Igneous Rock

Figure 3 shows the residual rate R_{pt} [%] of the tensile load 30 days after anchor installation in igneous rock plotted against the rock classification. In cases where there were multiple measurements for a single slope, the plotted data point represents the average value of R_{pt}, and the range bars represent the maximum and minimum measured values. For cases with only one data point for a slope, the single measured R_{pt} is plotted individually. (The same applies below to Figs. 4 and 5.) Table 4 gives the R_{pt} values 30 days after installation and the rock classification of each slope.

In igneous rock in the C_H class, the average R_{pt} 30 days after installation was almost 100%, showing almost no decline in the tensile load. In the C_H–C_M and C_L–D classes, the decline was slightly larger than that for the C_H class; the average R_{pt} was between 96.2% and 99.1% and was consistently 95% or higher. In the case of the D class, the average R_{pt} value was between 92.0% and 97.8%, which was lower than that in bedrock. From C_L to D and D class, R_{pt} was scattered, and it took a minimum value of 85.4% in slope I-12.

Sedimentary Rock

Figure 4 shows the residual rate R_{pt} [%] of the tensile load 30 days after anchor installation in

Table 4 R_{pt} [%] 30 days after installation (igneous rock)

Slope No.	Design load T_d [kN]	Lock-off load P_t [kN]	Free length rock classification	Number of load cells	R_{pt} [%] after 30 days		
					MAX	AV	MIN
I-1	181.4	181.4	C_L-D	2	99.3	98.9	98.6
I-2	316.5	316.5	C_L	2	99.3	99.1	98.9
			C_L-D	3	98.2	96.9	94.8
I-3	850.0	850.0	C_H	3	98.4	97.7	96.9
			C_H-C_M	3	97.9	97.4	97.0
I-4	335.1	335.1	C_H	7	101.1	98.3	96.3
I-5	331.1	331.1	C_H	5	100.6	99.2	98.3
I-6	174.1	174.1	C_M	2	99.4	99.1	98.8
			C_H	3	99.4	99.0	98.4
I-7	190.0	190.0	C_H	5	102.9	100.6	98.4
I-8	650.1	650.1	C_M-C_L	5	96.9	96.2	94.8
I-9	514.8	514.8	D	5	96.1	95.3	94.2
I-10	766.8	766.8	D	17	97.2	95.9	94.1
I-11	408.1	426.0	C_M-C_L	4	100.9	97.8	93.9
I-12	367.8	367.8	D	3	97.9	92.0	85.4
I-13	374.4	374.4	D	4	98.2	97.8	97.4

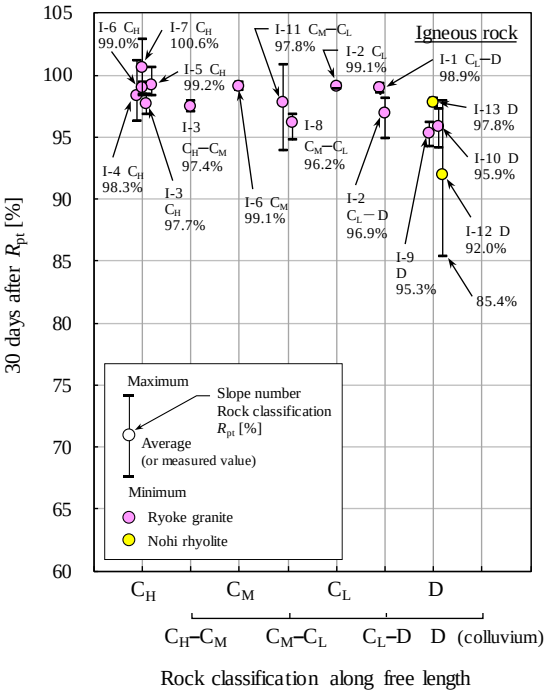

Fig.3 R_{pt} [%] 30 days after installation plotted against rock classification (igneous rock).

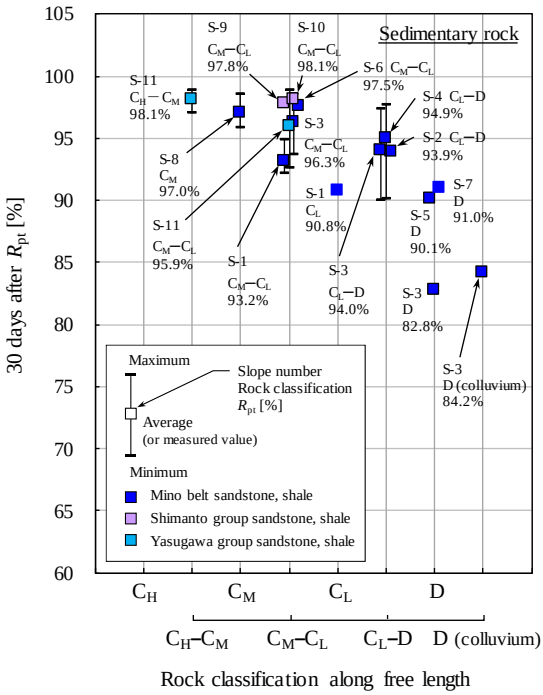

Fig.4 R_{pt} [%] 30 days after installation plotted against rock classification (sedimentary rock).

Table 5 R_{pt} [%] 30 days after installation (sedimentary rock)

Slope No.	Design load T_d [kN]	Lock-off load P_t [kN]	Free length rock classification	Number of load cells	R_{pt} [%] after 30 days		
					MAX	AV	MIN
S-1	341.9	341.9	C_L	1	–	90.8	–
	475.4	497.5	C_M-C_L	6	94.9	93.2	92.1
S-2	275.1	304.2	C_L-D	1	–	93.9	–
S-3	466.9	466.9	D	1	–	82.8	–
	880.6	880.6	C_M-C_L	3	98.5	96.3	93.7
	～	～	C_L-D	4	97.4	94.0	90.0
	440.0	440.0	D(colluvium)	1	–	84.2	–
S-4	804.1	804.1	C_L-D	6	97.7	94.9	90.1
S-5	639.9	639.9	D	1	–	90.1	–
S-6	362.5	347.1	C_M-C_L	1	–	97.5	–
S-7	159.2	152.2	D	1	–	91.0	–
S-8	329.3	319.2	C_M	3	98.6	97.0	95.8
S-9	528.9	527.3	C_M-C_L	1	–	97.8	–
S-10	617.1	615.2	C_M-C_L	1	–	98.1	–
S-11	724.0	744.5	C_M-C_L	5	98.9	95.9	92.6
	940.0	897.5	C_H-C_M	6	98.9	98.1	97.1

sedimentary rock plotted against the rock classification. Table 5 gives the value of R_{pt} 30 days after installation along with the corresponding rock classification for each slope.

The results indicate that in sedimentary rock from the C_H–C_M to D and D (colluvium) classes, as the geological conditions worsen, R_{pt} decreases more than in the corresponding case in igneous rock. For rock from slope S-11 from the C_H–C_M class, the average R_{pt} value after 30 days was high at 98.1%, and decreased in the sequence C_M, C_M–C_L, C_L, and C_L–D. On the three slopes with rock from the C_L–D class, the average R_{pt} value ranged from 93.9% to 94.9%, and even the minimum value remained at 90% or more. In the D and D (colluvium) classes, R_{pt} reached the lowest residual rate of between 84.1% and 91.0%, representing a large decline in the tensile load.

Metamorphic Rock

Figure 5 shows the residual rate R_{pt} [%] of the tensile load 30 days after anchor installation in metamorphic rock plotted against the rock classification. Table 6 gives the R_{pt} values 30 days after installation and the corresponding rock classification on each slope.

The results demonstrate that in metamorphic rock of rock classification from the C_H–C_M to D (colluvium) classes, R_{pt} was lower than that in igneous rock and sedimentary rock. In metamorphic rock from the C_H–C_M and C_M classes, the average R_{pt} value was high at 98.1% and 99.1%, but in the C_M–C_L class, it was slightly lower at 94.3% and 98.4%.

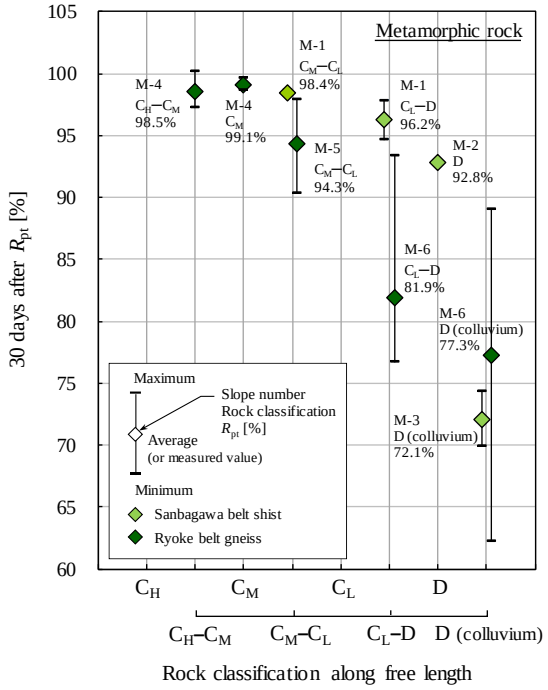

Fig.5 R_{pt} [%] 30 days after installation plotted against rock classification (metamorphic rock).

Table 6 R_{pt} [%] 30 days after installation (metamorphic rock)

Slope No.	Design load T_d [kN]	Lock-off load P_t [kN]	Free length rock classification	Number of load cells	R_{pt} [%] after 30 days		
					MAX	AV	MIN
M-1	639.7	447.8	C_L-D	6	97.8	96.2	94.6
			C_M-C_L	3	98.6	98.4	98.1
M-2	242.7	194.0	D	1	–	92.8	–
M-3	686.4	483.9	D (colluvium)	2	74.3	72.1	69.9
M-4	201.0	201.0	C_M	4	99.6	99.1	98.7
	136.0	136.0	C_H-C_M	5	100.2	98.5	97.3
M-5	872.8	920.4	C_M-C_L	24	97.9	94.3	90.3
M-6	795.4	830.1	C_L-D	6	93.4	81.9	76.7
			D (colluvium)	4	89.0	77.3	62.3

Then, for the C_L–D class, R_{pt} was less than 81.5%. For the D (colluvium) class, which represents colluvium along the free length of the anchor, R_{pt} was even smaller. The average R_{pt} values on slopes M-6 and M-3 were 77.3% and 72.1%, respectively, indicating a large decline in the tensile load.

SUMMARY

The tensile load of an anchor is impacted mainly by the slope on which the anchor is installed and the geological conditions of the slope. The decrease in the tensile load is related to the rock classification

along the free length, which was found to tend to increase with class in the order of C_H, C_M, C_L, and D.

In relatively good geological conditions (C_H, C_H–C_M, and C_M classes) in igneous, sedimentary, and metamorphic rock, R_{pt} 30 days after installation remained at 95% or higher. In particular, R_{pt} in granite of the C_H class was nearly 100%, and almost no decline in the tensile load occurred. In the C_M–C_L and C_L classes in every type of rock, R_{pt} values of less than 95% were observed. In sedimentary and metamorphic bedrock of the C_L–D and D classes that is weathered or cracked, the tensile load fell significantly. In sedimentary rock, anchors with R_{pt} of less than 85% appeared. In metamorphic bedrock of the C_L–D and D classes, the tensile load fell more than in igneous or sedimentary rock, and R_{pt} was lower than 80%. In metamorphic rock of the D (colluvium) class, where there is unconsolidated colluvium along the free length, the tensile load fell even more; R_{pt} 30 days after installation was lower than 80% on average, and anchors with the lowest observed R_{pt} value of less than 65% appeared.

It is thought that a factor represented by a variation in the decrease in the tensile load responded to geological conditions. Regarding the rock classification, three characteristics—the degree of weathering, the hardness of the rock mass, and the state of joints or cracks—were qualitatively evaluated; these characteristics are closely correlated with the decrease in the tensile load. To accurately estimate the decrease in the anchor tensile load, geological information must be incorporated into the model.

CLOSING REMARKS

To maintain anchors, it is necessary to evaluate not only their tensile load but also whether they function and the areal soundness of the entire slope. The results of this study demonstrate that the geological conditions (rock classification) impact the initial decline of the tensile load of an anchor. To maintain anchors, it is necessary to evaluate the decline of the tensile load shortly after installation as well as in the long term, 10, 20, and 30 years after installation. Clarifying the initial decline of the tensile load as performed in this study will permit the prediction of the long-term decline. In the future, methods of evaluating the relationship between the long-term decline in the tensile load and the geological conditions will be investigated, and the functionality of anchors after an extreme decline in the tensile load will be evaluated.

ACKNOWLEDGMENT

A part of work funded by JSPS under number of 19K04595. Thanks to the all research members of this project.

REFERENCES

[1] Japanese Geotechnical Society, Design and Construction Standards for Ground Anchor, The Commentary, 2012, pp.79-80.

[2] Fujiwara Y., Takemoto M., and Sakai T., A Study of Lift-off Test Method of Ground Anchors, Journal of Japan Society of Civil Engineers, Division C(Geotechnics), Vol.67, No.4, 2011, pp.558-568.

[3] Central Nippon Expressway Co., Ltd., Earthwork Construction Management Guidelines, 2017, pp.3-38 - 3-39.

[4] Public Works Research Institute, Japan Anchor Association, Maintenance Manual for Ground Anchor, 2008, pp.69-75.

[5] Takyu T., Shimoda K., Kawasaki H., and Tamura T., Change Over Time of Tension of Groud Anchors, The 65th Japan Society of Civil Engneers Annual Scientific Conference Abstract, 2010, pp.105-106.

[6] Yamazaki M., and Sakai T., Consideration about Initial Decrease of Tensile Load of Ground Anchor and Geological Condition, The 73th Japan Society of Civil Engneers Annual Scientific Conference Abstract, 2018, pp.855-856.

[7] Fjiwara Y., and Sakai T., A Maintenance of Ground Anchors Slope Based on Distribution Characteristics of The Residual Anchor Load, Journal of Japan Society of Civil Engineers, Division C(Geotschnics), Vol.74, No.3, 2012, pp.260-273.

[8] Japan Society of Engneering Geology, Rock Classification, Engineering Geology Special Issue, 1984, pp.103-118.

[9] Japan Construction Information Center Foundation(JACIC), Guidelines for Generating Boring Core Column Diagram, The Commentary, 1986, pp.17-20.

[10] Tanaka H., Primer of Geology for Civil Engineers, 1964, pp.25-49.

[11] Japan Society of Civil Engineers, Soft Rock Engineering -Fundamentals and Case Studies for Investigation, Design and Construction-, 1984, pp.1-6.

Technical Papers

Geotechnique

9th Int. Conf. on Geotechnique, Construction Materials and Environment,
Tokyo, Japan, 20-22 November 2019, ISBN: 978-4-909106025 C3051

EVALUATION OF AUXILIARY METHOD IN TUNNEL CONSTRUCTION ON MIXED FACE (SOIL-ROCK) CONDITION

Fahmi Aldiamar [1], Susy K. Ariestianty [2], Yusrizal [3] and Wida Nurfaida[4]
[1,2] Institute of Road Engineering (IRE), Ministry of Public Works and Public Housing (PUPR), Indonesia; [3,4] Directorate of General Highway (DGH), Ministry of Public Works and Public Housing (PUPR), Indonesia

ABSTRACT

Cisumdawu road tunnel is the first on going road tunnel built in Indonesia that located in Sumedang, West Java. The tunnel route lies in mixed soil-rock ground conditions that derived from young volcanic deposits of Tampomas Mountain. Based on the field investigation, tunnel area construction were passing through three soil types, i.e. firm to very firm silty clay (N-SPT values is 4-15), firm to very firm tuff-breccia (N-SPT value is 8-15), hard to very hard tuff-breccia (N-SPT values is 20-60). Boulder sizing from small size of 0.5m until 1.5m were found during excavation, while ground water level identified above the tunnel crown. Face stability and water inflow were main aspects to be considered and control during construction phase. Excavation method "three benches and seven steps" was selected and used in the construction of Cisumdawu road tunnel. Auxiliary methods of forepoling with a double layer scheme and GRF face-bolting as pre-support were applied to increase and maintain tunnel roof and face stability before excavation, while long drainage boring was conducted to lower ground water level and release pore water pressure acting to surrounding area of excavation. The deformation during excavation process was controlled and monitored by measuring the convergence that occur for each cycle and compare to the 3D numerical model using finite element method. The result indicate that the convergence was still under the limit criteria for deformation. The maximum value of convergence that has been measured is 3.3mm. This means that the excavation method and support system applied was sufficient.

Keywords: Tunnel, Mixed face, Auxiliary method, Forepoling

INTRODUCTION

Nowadays, the development of infrastructure for roads become one of the main focuses of Indonesian government policy, to support and improve the economy. In this development, the morphological and geological conditions often become the main issues that provoke challenges and constraint in road planning. Currently, tunnel construction began to be considered as an option and a part of road planning, especially in hilly or mountainous area. The application of tunnel construction is expected to provide a more convenient and safe route, as well as shorten the distance and travel time that will not affect and disrupt the condition of the surrounding environment.

Cisumdawu road tunnel becomes the first on going road tunnel that have been built in Indonesia as part of Cisumdawu toll road project (Section II of Tanjungsari - Sumedang) that will connect Cileunyi – Sumedang – Dawuan or connect Padaleunyi toll road with Palimanan-Kanci toll road. This tunnel project is located about 19 km from Cileunyi which is between Sta. 12+600 and Sta. 13+200, as shown in Fig. 1 The length of Cisumdawu road tunnel is about 472 m with diameter of 14 m, and height of 8.5 m and it is a twin tubes or double tubes tunnel that each tunnel consists of 2 lanes.

Fig. 1 Location of Cisumdawu road tunnel.

Geologically, route of Cisumdawu road tunnel lies on Undifferentiated Young Volcanic Product unit (Qyu) that consists of tuffaceous sand, lapilli, lava, agglomerate, as shown in Fig. 2 [1]. The volcanic material that forms the rock units surround Cisumdawu tunnel project is derived from Mt. Tampomas in the northeastern part. This unit forms a flat or low hill area covered by yellowish gray to reddish gray soil in the area between Bandung and Sumedang. Moreover, the older rock units that compose around the Cisumdawu tunnel, i.e.:

- Deep Sediment Deposit (Qol): well bedded tuffaceous clay, sandstones, conglomerate, and breccia. Dark clay contains plant remains and lignite.
- Undifferentiated Old Volcanic Product (Qvu): volcanic breccia, lahar, and lava repeteadly interlayered.
- Old Volcanic Products, Lava (Qvl): lava, showing columnar joints and sheeting. It is basaltic in composition and partly propylitized.
- Old Volcanic Products, Breccia (Qvb): volcanic breccia and lahar. The components consist of igneous rocks between andesite and basalt in composition.

Based on the regional geological map, there are several geologic structures that developed around the Cisumdawu road tunnel area and may affect the ground condition, such as a predicted fault lines directed north to south at west part and Lembang fault with direction of southwest to southeast that located about 3 km away. This tunnel will be construct at depth 14 m (the shallowest) and 52.8 m (deepest) from the ground surface, and the groundwater level will be above the tunnel.

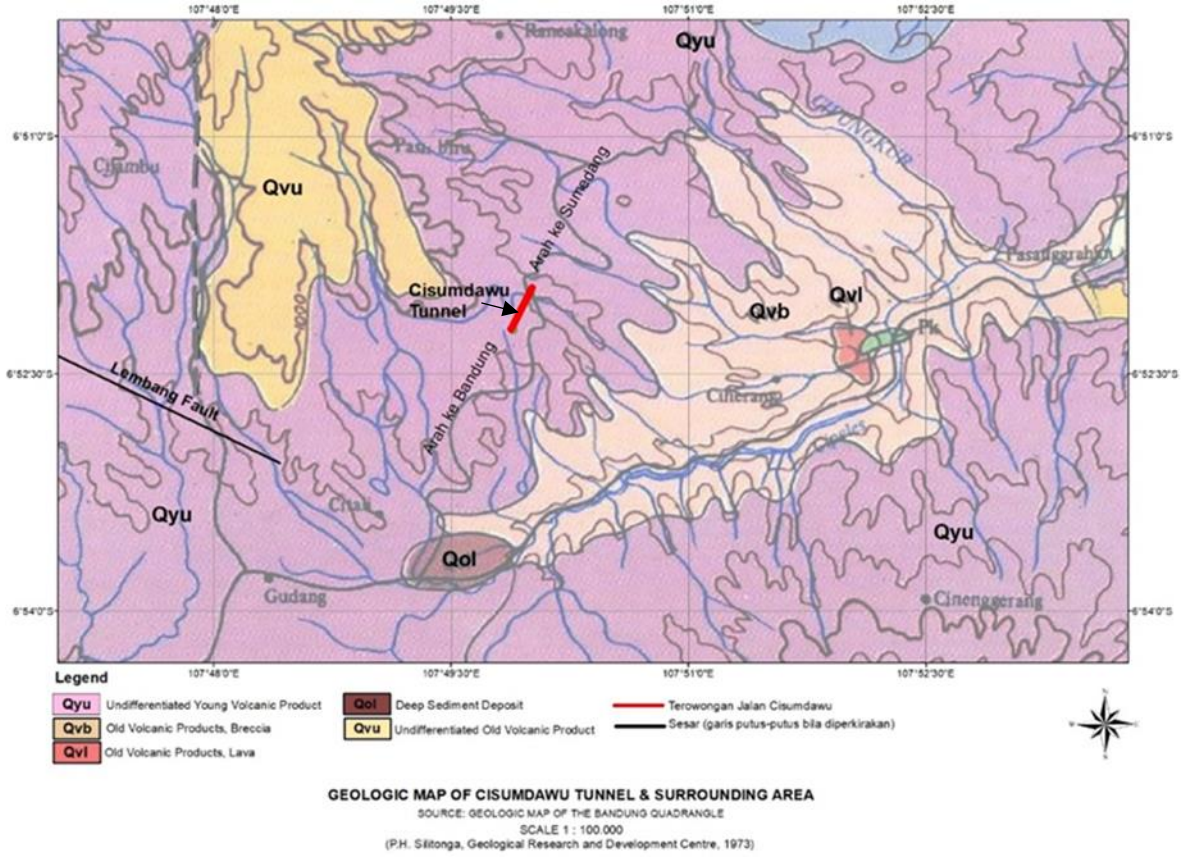

Fig. 2 Geological condition of Cisumdawu road tunnel.

Consequently, the tunnel route may traverse varying or mixed ground conditions. There are some issues that should be considered for tunneling in mixed ground condition, such as short stand up time of ground as well as ground water inflow that can reduce the strength and stability of ground. In order to overcome these problems, the application of an auxiliary method to improve the strength and stability of mixed face ground condition can be utilized. An auxiliary method is a secondary construction method adopted to ensure face stability and tunnel safety also to preserve the environment in cases where either conventional tunnel support or division of heading section do not provide effective solutions or disadvantageous [2]. At Cisumdawu road tunnel project, auxiliary method using fore-poling and face

bolt of GRF type as tunnel pre-support are applied. The excavation is carried out using 3 benches and 7 steps method that divided the tunnel face into 3 section/heading and then excavation is conducted with 7 stages sequentially [3].

To evaluate the performance and effectiveness of auxiliary method that applied in Cisumdawu road tunnel project, an empirical and numerical 3D analysis are carried out that will be discuss as follows.

METHODOLOGY

Field and Laboratory Data

Field investigations and laboratory testing have been carried out by the Cisumdawu Toll Road Project along the tunnel route area. Soil stratification can be identified based on soil consistency as the result of Standard Penetration Test (SPT) that is conducted in the drilling test according to [4] as shows in Table 1. Based on this correlation, the soil condition along Cisumdawu tunnel route was categorized as stiff to very hard soil that comprise of three soil layers (Fig. 3) as follow:

- First layer: soft to stiff clayey silt with N-SPT value between 4 – 15 and depth up to 22m from surface;
- Second layer: hard clayey silt with N-SPT value between 15 – 30 and depth of 5m – 28m beneath the first layer.
- Third layer: tuff with rock fragments sized from gravel to boulder with N-SPT value between 30 – 50 that underlying the second layer.

Table 1 Classification of fine-grained soils from N-SPT value [4]

Characteristics	Value of N-SPT	Category
Extrudes between fingers when squeezed	<2	Very soft
Remolded by light finger pressure	2 – 4	Soft
Remolded by strong finger pressure	4 - 8	Stiff
Indented by thumb	8 – 15	Very stiff
Indented by thumbnail	15 – 30	Hard
Difficult to indent by thumbnail	>30	Very hard

Soil consistency of Cisumdawu tunnel

Soil parameter used for numerical modelling are based on laboratory testing and also empirical correlation according to Standard Penetration Test (SPT) as seen in Table 2.

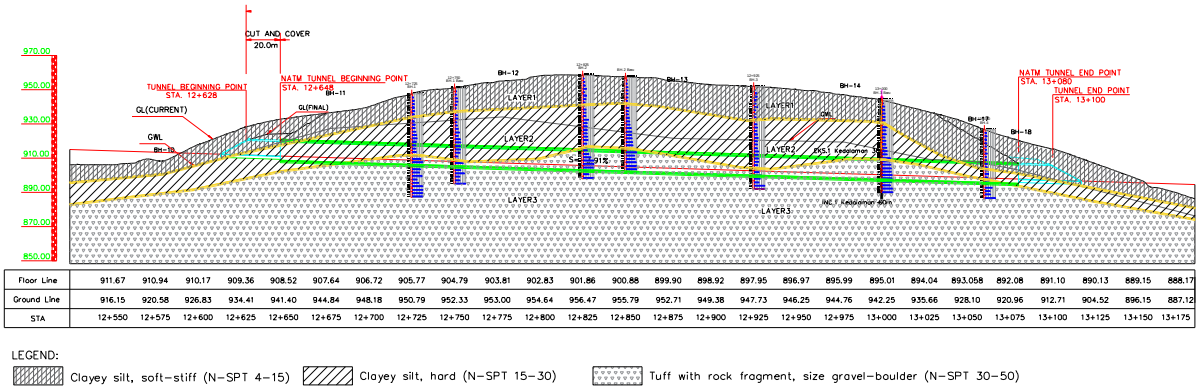

Fig. 3 Stratification of Cisumdawu tunnel route (longitudinal section).

Table 2 Soil parameter for numerical modelling using Mohr-Coulomb material model

Soil Description	N-SPT	γ (kN/m3)	c‘ (kPa)	ϕ’	E (kPa)	ν
Clayey silt, soft-stiff	4-15	16.7	40	26	15000	0.3
Clayey silt, hard	15-30	17	60	26	22000	0.3
Tuff with rock fragment, very hard	30-60	18	80	28	100000	0.3

In addition, the value of shear wave velocity of ground along Cisumdawu tunnel route was obtained from downhole seismic test. The test results show that shear wave velocity of the ground is range between 175m/sec–350m/sec and categorized by means medium soil class (SD) as shown in Table 3.

Table 3 Ground classification based on shear wave velocity [5].

Class	Average Shear Wave Velocity, (m/detik)	Average N-SPT Value	Average Undrained Shear Strength, S_u (kPa)
SA (Hard rocks)	> 1500	N/a	N/A
SB (Rocks)	750 - 1500	N/A	N/A
SC (Hard/very dense soils and soft rocks)	350 - 750	>50	≥100
SD (Medium soils)	175 - 350	15 - 50	50 - 100
SE (Soft soils)	< 175	<15	< 50
SF (Specific Soils)	Requires specific geotechnical / geophysical investigations		

Ground class of Cisumdawu tunnel

Ground Classification

Once the soil stratification of the tunnel route is identified, the next step is to determine the ground class, which in this study refer to [6]. The ground classification used in the technical guideline was adopted from the Japanese classification [2]. The primarily parameter used for determining the ground class were elastic wave velocity that obtained from seismic field test and the competence factor calculated from unconfined compressive strength divided by unit weight multiplied by the thickness of overburden (qu/(γ.H)). Elastic wave velocity of ground in Cisumdawu tunnel route was range between 1.9 km/sec to 2.5 km/sec (Fig. 4a) and the competence factor of 1. Therefore, the ground condition that traversed by Cisumdawu tunnel was considered to ground class of DII as shown in Fig. 4b.

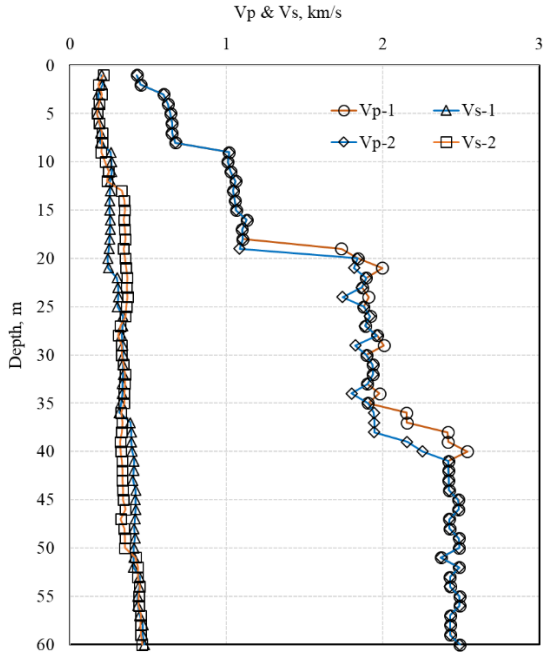

a. Seismic field test profile

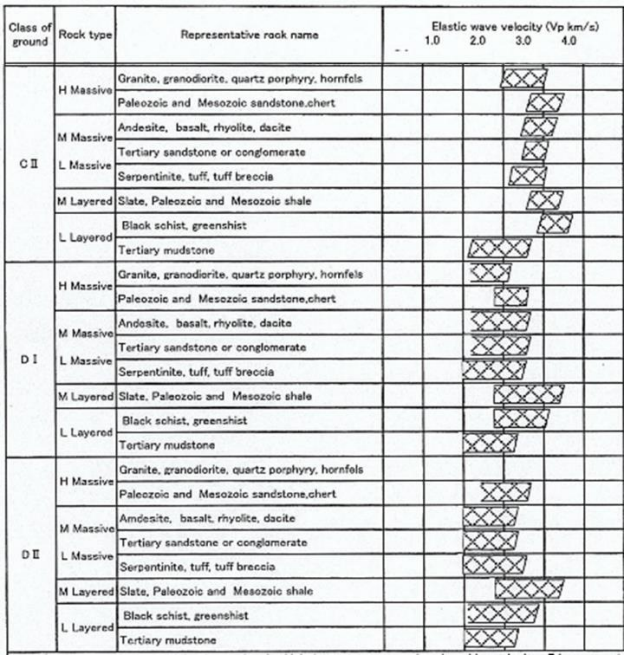

b. Ground classification (JSCE, 2007)

Fig. 4 Ground classification of Cisumdawu tunnel.

Excavation Method and Tunnel Support

Further, the excavation method of 3 bench and 7 steps was selected by contractor for constructing Cisumdawu tunnel and for more details it can be seen in Fig. 5. The tunnel face was divided into 3 bench and the excavation conducted on each bench gradually that is starting from the top roof. Besides of its ground condition, this excavation method was selected because it is expected may suitable either for good and bad geological conditions, proper for small as well as large tunnel section, also ensured a continuous and safe excavation works.

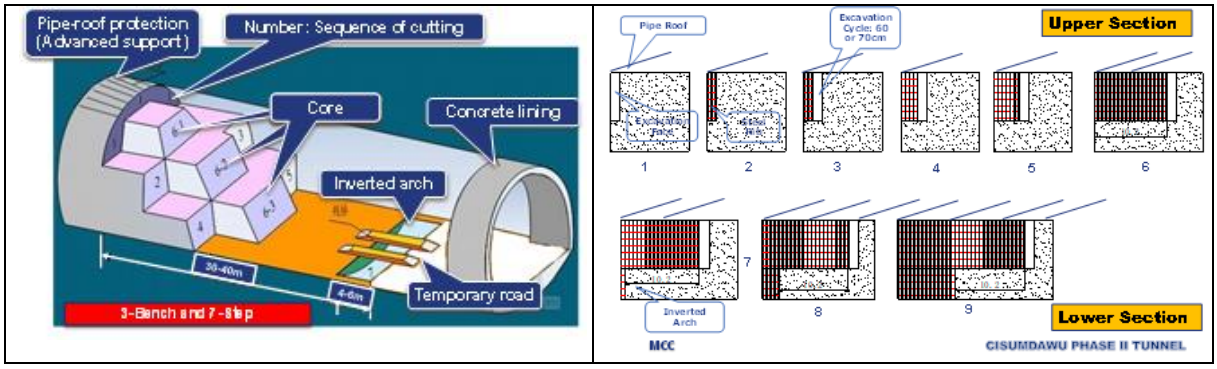

Fig. 5 Excavation stages of 3 bench 7 steps method of Cisumdawu tunnel project [3].

Typical tunnel support system that should be applied for ground class of DII were shotcrete, steel support and invert as shows in Table 4. In addition, auxiliary method was implemented to ensure tunnel face stability during tunnel excavation and the type of auxiliary method selected in Cisumdawu tunnel project were fore-poling, face bolt and drainage boring.

Fore-poling is installed before the excavation to increase the strength and stand-up time of the ground, and in addition face bolt of glass fiber reinforced plastic type was also applied. Drainage drilling or probe drilling was conducted in order to control ground water inflow i.e. 2 at each side of tunnel section and 1 at center of tunnel section. There were 3 type of fore-poling applied in this tunnel project that are varied according to the pipe diameter and its pattern shown in Table 5.

Table 4 Typical support pattern, lining and allowable deformation [2].

Class	Standard Round Length (m)	Rock Bolt			Area of Installation	Steel Support			Thickness of Shotcrete (cm)	Thickness of Lining		The Amount of Allowable Deformation (cm)
		Length (m)	Spacing Circum-ferential Direction (m)	Spacing Longitu-dinal Direction (m)		Top heading	Bench	Spacing (m)		Arch, Side Wall (cm)	Invert (cm)	
B	2.0	4.0	1.5	2.0	Top heading	-	-	-	10	40	-	0
C I	1.5	4.0	1.2	1.5	Top heading, bench	-	-	-	15	40	(45)	0
C II	1.2	4.0	1.2	1.2	Top heading, bench	H-150	-	1.2	15	40	(45)	0
D I	1.0	6.0	1.0	1.0	Top heading, bench	H-150	H-150	1.0	20	40	50	0
D II	1,0 or less	6	1.0	1,0 or less	Top heading, bench	H-200	H-200	1,0 or less	25	40	50	10

Cisumdawu tunnel

Table 5 Type of forepoling as auxiliary method applied for Cisumdawu tunnel project [3].

	Type 1	Type 2	Type 3
Schematic illustration	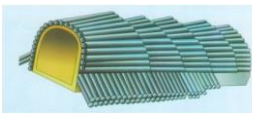	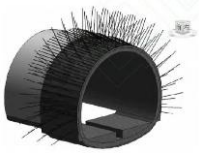	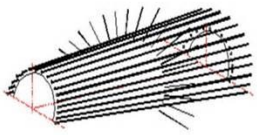
Pipe type	ϕ 114 mm, length 24m Placing in one row/single layer, angle 4°	ϕ 60.5 mm, length 5m Placing in two row/double layers, first layer at angle 30-40° with spacing of 50cm, second layer at angle 5-10° with spacing of 25cm	ϕ 114 + ϕ 60.5 mm, length 12m or 5m Placing in two row/double layers, first layer at angle 30-40° with spacing of 50cm, second layer at angle 5-10° with spacing of 25cm
Grouting direction	Longitudinal	Longitudinal + radial	Longitudinal + radial
Geological condition	Inlet & outlet portal	Sand layer, soft soil, boulder	Worst condition (muddy, weak)

DISCUSSION AND RESULT

To evaluate the appropriateness and performance of excavation method as well as tunnel support system that applied in Cisumdawu tunnel project, a numerical modelling was performed. The excavation method and tunnel support system that applied for constructing Cisumdawu tunnel have been described previously. The allowable deformation for ground class of DII with its typical tunnel support was stated of 10 cm empirically.

The geometry of numerical model for each layer and the tunnel support is shown in Fig. 6. The deformation occurs during the excavation proses is shown in Fig. 7. The excavation scheme is conducted by divided tunnel section into three bench with the core to maintain the tunnel face stability and the excavation performed according to time frame during construction as seen in Fig. 8.

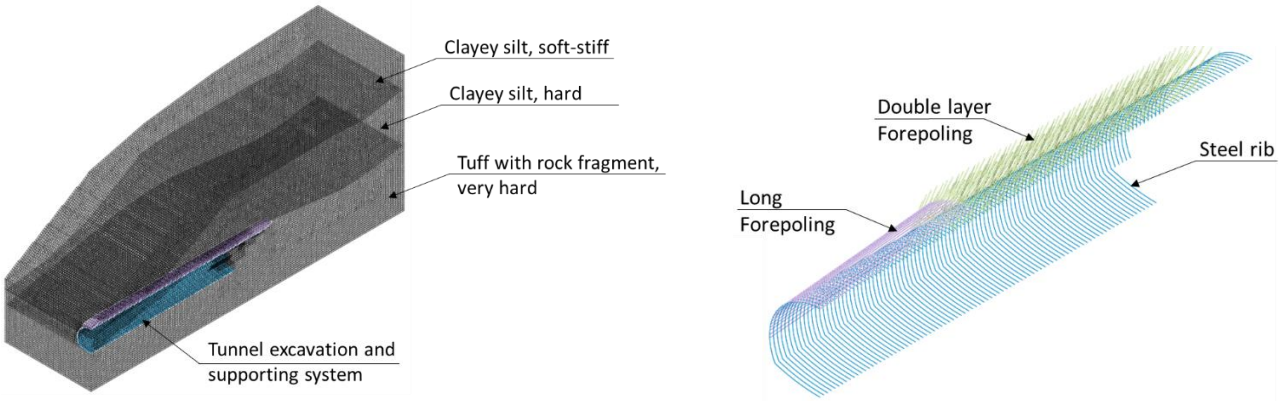

Fig. 6 Geometry of numerical model and tunnel support scheme of Cisumdawu tunnel.

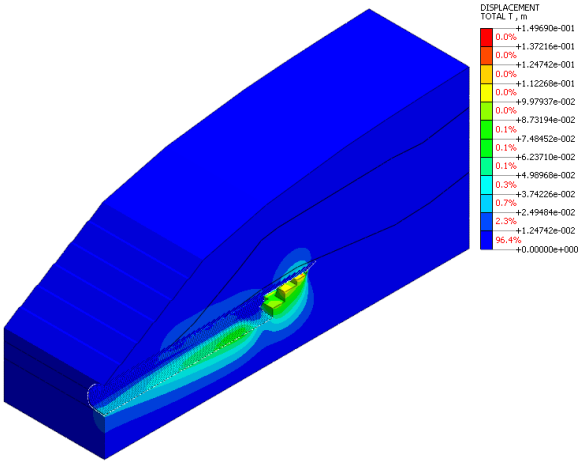

Fig. 7 Deformation caused by tunnel excavation process

In order to identify the appropriateness between the numerical model and the actual condition, the comparison of deformation scale is performed on the reference point of top of tunnel roof or crown as can be seen in Fig. 8. From the actual measurement, maximum value of roof displacement is 3.3 mm, while the deformation of numerical model slightly higher than the actual measurement as shown in Fig. 8. This result show that numerical modeling show a good correlation with actual vertical deformation.

Nevertheless, instrument for deformation measurement are placed after fore-poling, steel support and shotcrete applied for ground reinforcement. This is probably resulting to the small displacement during monitoring due to its elastic deformation and does not represent the actual deformation that occurs (accumulation of ground movement caused by excavation until reinforcement of steel support and shotcrete is installed).

The deformation result indicate that the convergence was still under the limit criteria for deformation which is less than 10 cm. The maximum value of vertical deformation that has been measured is very small. This means that the excavation method and support system applied was sufficient to keep the stability of the tunnel during construction.

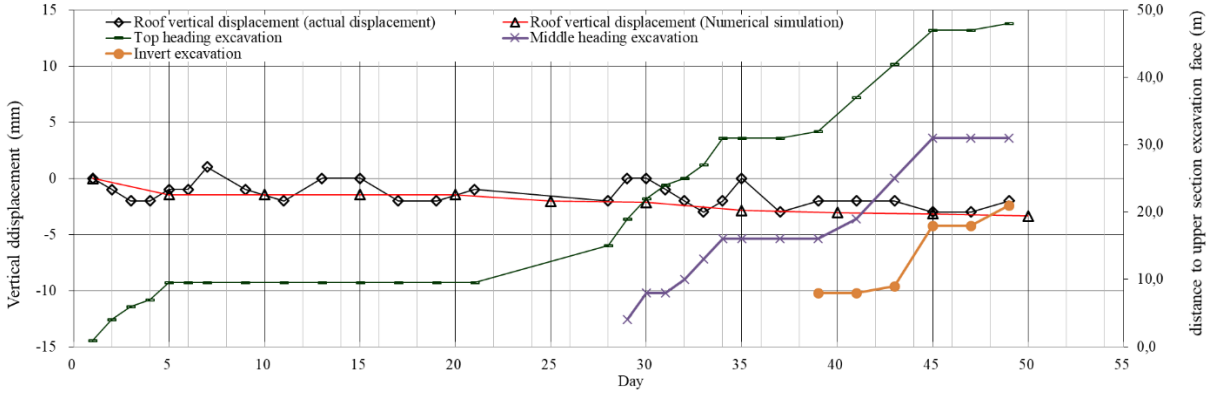

Fig. 8 Comparison of deformation on the tunnel crown.

CONCLUSIONS

The application of auxiliary methods to improve and ensure the stability of tunnel face using fore-poling, face bolt and drainage drilling prior to the excavation show effective performance. The overall evaluation against the performance of excavation methods and tunnel support system by numerical approaches using finite element method show a close result compare to the actual vertical deformation. It seems that Mohr Coloumb models could give a good result when soil parameters are conducted well and stage modelling is simulated according to actual phase of construction.

REFERENCES

[1] Silitonga, P.H. Geologic Map of the Bandung Quadrangle, Jawa. Bandung : Geological Research and Development Centre, 1973.

[2] Japan Society of CIvil Engineers. Standard Specifications for Tunneling-2006: Mountain Tunnels. Tokyo : JSCE, 2007.

[3] Metallurgical Corporation of China (MCC). Toll Road Development of Cileunyi-Sumedang-Dawuan Phase II Indonesia: Tunnel Construction Method Statement and Safety Report. Bandung : Sub Project Manager (PPK) of the Implementation of Cisumdawu Toll Road Project Phase II., 2016.

[4] National Standard Indonesia (SNI). Procedures for Recording and Approving the Results of Core Drilling, SNI 2436:2008.

[5] National Standard Indonesia (SNI). Procedures for Planning Earthquake Resistance for Structures of Buildings and Non-Buildings, SNI 1726:2012.

[6] Ministry of Public Works and Housing. Technical Guideline for Method Planning of Excavation and Tunnel Support System for Road Tunnel in Mixed Face Media. Jakarta : Ministry of Public Works and Housing, 2015.

9th Int. Conf. on Geotechnique, Construction Materials and Environment,
Tokyo, Japan, 20-22 November 2019, ISBN: 978-4-909106025 C3051

EVALUATION OF RELATIONSHIP BETWEEN DECREASE IN TENSILE LOAD OF GROUND ANCHORS AND THE GEOLOGICAL CONDITIONS

Mitsuru Yamazaki[1] and Toshinori Sakai[2]
[1] Central Nippon Highway Engineering Nagoya Company Limited, Japan;
[2] Graduate School of Bioresources, Mie University, Japan

ABSTRACT

Ground anchors (hereinafter anchors) are structures used to stabilize landslides or cut slopes by transmitting a tensile load to the ground. The tensile load of an anchor presumably falls gradually as time passes, and varies in the quantity at which it declines. The decline of the tensile load of an anchor is presumably caused by the relaxation of steel or creep of the ground. The decline of the tensile load of an anchor is assumed to be large at the initial period of about 30 days after execution, and is one index used to evaluate soundness at the maintenance stage. However, the degree to which the tensile load falls under specific geological conditions has not been clarified.

Thus, this paper studies the relationship of the tensile load during the 30 days period after execution as obtained by measurements using load cells installed on anchors with the rock classification (geological condition) on the anchor's free length. The results clarified the fact that the poorer the geological condition, the greater the decline of the tensile load of the anchor.

Keywords: Ground Anchor, Residual Tensile Load, Geological Condition, Rock Classification, Maintenance

INTRODUCTION

Since ground anchors (hereinafter anchors) were first introduced in Japan in 1957, they have been used many times in landslide and cut-slope stabilization countermeasure work. An anchor is a structure that fixes the ends of tension members in the ground while the other ends are fixed on the ground surface. With the part between these ends free, the anchor adds prestressing force (tension load) to the tension members to stabilize landslides or cut surfaces by sustaining their tensile loads. Most of each anchor is located in the ground.

The tensile load of an anchor generally falls gradually over time until it converges at a specified value under the action of the creep of the ground or the relaxation of tension members after it has been anchored introducting initial tension load as shown in Figure 1[1]. However, the tensile load of an anchor may not converge at a residual value under the action of an unexpectedly great external force as a result of the impact of the geology of the ground where the anchor was installed immediately after the ground was excavated by cutting work. Therefore, it is important to maintain an anchor while appropriately monitoring its tensile load.

Figure 2 shows the flow[2] of the tensile load management of anchors on expressways operated by the three Nippon Expressway Company Limited (NEXCO) companies. On expressways managed by NEXCO, instruments used to measure the load

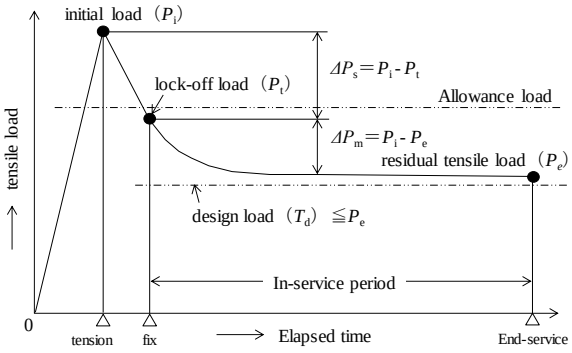

Fig.1 Change with time of tensile load acting on anchor[1].

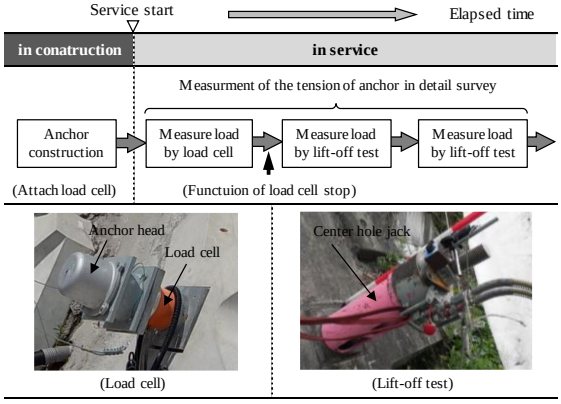

Fig.2 Management of anchor tention[2].

(hereinafter load cell) are installed at the construction stage on some of the anchors to monitor changes in the tensile load. At the service stage, measurement by the load cells is continued as required. After the functions of the load meters have been lost, lift-off tests are conducted as periodical detailed inspections to confirm the tensile load of the anchors (residual tensile load) in order to evaluate the soundness of the anchor functions [3]. Table 1 lists the standards[4] for the residual tensile load (tensile load) of anchors and anchor soundness that are generally used to evaluate anchor functioning. Management of the residual tensile load of anchors is conducted by evaluating the situation by clarifying to what extent the tensile load has declined from the lock-off load (Pt) when the anchor was constructed. This clarifies the characteristics of the relationship between the design load (Td), allowable load (Ta), and yield point load (Tys), and studies the treatment according to the situation. In addition to measuring the tensile load, anchor maintenance is conducted by visually inspecting for damage such as the floating of anchor tops and the protrusion or sinking of tension members. However, the residual rate of the tensile load is only one index used to evaluate anchor function.

Table 1 Standard of residual tensile load and soundness of anchor (example)[4]

Range of tensile load	Soundness	State	Example of deal
	E^+	There is a risk of break	Emergency response
0.9 Tys	D^+	There may be dangerous state	Inplement a countermeasure
1.1 Ta	C^+	It exceeds allowable load	
Ta	B^+	–	Consider the need for measures by observation
Td	A^+	Health	–
Pt	A^-	Health	–
0.8 Pt	B^-	–	Consider the need for measures by observation
0.5Pt	C^-	It has greatly reduced function	Inplement a countermeasure
0.1 Pt	D^-	Nonfunctional	

Tys:Yield Point load, Ta:Allowable load,
Td:Design load, Pt:Fixed load

On the other hand, the geological conditions of the slope where anchors are deployed vary according to whether the rock is igneous, sedimentary, or metamorphic, the degree to which it is weathered, and the extent of the development of cracking, joints, and schistosity. The anchors are designed by performing boring surveys at multiple locations as a geological survey of the ground where the anchors will be deployed, confirming the state of the geology, and assessing the depth of the slip plane that should be arrested. Moreover, the standards of and number of anchors are decided considering the required arresting force calculated by setting the target safety factor. The geological conditions of the ground where the anchors are deployed presumably influence the tension load of the anchors, both initially and in the long term. However, at this time, these factors are not considered during design and maintenance.

Takyu, Shimoda, Kawasaki, and Tamura[5] for installed load cells on 57 of 1,130 anchors executed as large-scale landslide countermeasure works, confirmed the tendency for the tensile load of anchors to decline. As a result, they pointed out that at 30 days after execution, the tensile load had fallen greatly at the end of the slope where loose ground and ground in a weathered state spread on the ground surface on top of a slope that was cut to a shallow depth. This quantity of decline was more than 10% of the lock-off load, and the decline of the tensile load was impacted by the geological conditions. Yamazaki and Sakai[6] conducted a geological survey to study the relationship of the rock classification of bedrock where anchors were installed with the quantity of initial decline of the tensile load on eight slopes without deformation for three types of rock: granite, sedimentary rock, and metamorphic rock. The results clearly showed that the quantity of decline of the tensile load at 30 days after execution increased as weathering advanced and cracking developed. In sedimentary rock and metamorphic rock, which were remarkably embrittled, the tensile load declined to between 85% and 80% of the lock-off load. Fujiwara and Sakai[7] performed lift-off tests of all anchors as part of an inspection of tensile load 10 years after execution on a cut slope where 18 anchors had been executed. The researchers obtained the residual rate of the tensile load, which fell from the center or the slope where hard bedrock was distributed toward the slope end, which was softened by the advance of weathering and the distribution of the surface soil. The average value of the decline in tensile load in moderately weathered rock, severely weathered rock, and surface soil was 77%, 55%, and 50% respectively, and it was pointed out that the geological conditions behind the anchors impacted the decline of the tensile load.

As this shows, the tensile load of anchors is thought to decline naturally under the impacts of the geological conditions of the ground where they are executed in the absence of any unpredicted external force. However, while the residual rate of the tensile load of an anchor is one index used to evaluate its soundness, it is not clear to what extent it declines

under specific geological conditions. This paper reports on a study of the relationship of the initial decline of the tensile load during 30 days after execution of the anchors with geological conditions. The study uses the results of measurements by load cells installed on the anchors at the construction stage and the rock classification obtained by the results of an evaluation of the geology based on a boring survey and slope sketches.

STUDY METHOD

To compare the decline of the anchor tensile load with geological conditions, first, rock classifications of the geology on the free length of the anchors on each of the slopes that were the object of the study were organized. A detailed geological survey based on the boring survey mentioned above was conductedon the cut slope and during the installation of the anchors. The evaluation of bedrock during a geological survey is typically accomplished using the rock classifications [8],[9] from Tanaka's extended method[10], and records of the evaluation of the borehole core and cut slope during excavation performed by such a method on each object slope were retained. The schematic rock classification[11] is shown in Table 2. This rock classification is a qualitative evaluation of three elements: degree of weathering, hardness of rock masses, and state of joints or cracked surface. These were compared with a variety of strength constants and physical constants.

Table 2 Schematic rock classification[11]

Symbol	Pit Wall, Outcrop	Bowring Core	Herdness of Rock Fragments	Degree of Weathering	State of Crack Surface	Joint Interval
D			crushed with fingers, easily broken	soil, rock fragments in some places	argillation, unclear crack	5 cm or less – crushed
C_L			voiced sound with a hammer blow, collapse easily	weathering until internal, argillation of rock-forming minerals	argillation, clear crack	5 to 15 cm, many gravel – rock fragments
C_M			voiced sound, fragile	whole browning, noticeable alteration of rock-forming minerals	many opening cracks, sandwich clay	5 to 30 cm, many rock fragments – short columner
C_H			slight metallic sound, unbreakable	whole slight browning, slight alteration of rock-forming minerals	contact – slight opening, sandwich thin clay	15 to 30 cm, many short columners
B			metallic sound, unbreakable	browing alog the crack, no alteration of minerals	contact – slight opening, no clay	30 to 50 cm, many short columners – pole
A			metallic sound, unbreakable	fresh, unweathered	contact, no clay	50 cm or over, pole

The geological conditions of each slope were defined by broadly categorizing the geology as igneous rock, sedimentary rock, or metamorphic rock using boring core data and cross sections used for the design and installation of the anchors performed at the construction stage and the in-service stage and slope sketches drawn during excavation. Then, the rock classifications that were mainly bedrock manifest on the anchor free lengths were divided into eight classes: C_H, C_H to C_M, C_M, C_M to C_L, C_L, C_L to D, D, and D(colluvium) including unconsolidated soil such as colluvium.

To determine the tensile load (residual tensile load) of the anchors, measurement data from load cells during the 30-day period after execution were used. These were compared with the parameter as the residual rate [Pe/Pt = Rpt (%)] of the tensile load (Pe) under the fixed anchor load (Pt) obtained from these data. As geological conditions, the rock classification of the bedrock distributed on the free length of the anchors classified into eight classes was used as the parameter.

Table 3 broadly classifies the slopes used to study the initial decline of the tensile load, the number of measurement data, and the geology. The study examined 30 slopes using load cells installed at 170 locations. Stable slopes were studied where no deformation of the surface level or displacement were seen in dynamic observations. The anchors on each slope had no damage or anomalies in their heads or pressure-bearing structures and no loss of function. The anchors were evaluated as sound based on their external appearance.

Table 3 Geology of slopes and number of deta used for consideration of decrease

Rock	Rock Type	Geologic Time	slope (number)	load cell (number)
Igneous rock	Ryoke granite	Cretaceous	11	66
	Nohi rhyolite	Cretaceous	2	7
Sedimentary rock	Mino belt sandstone, shale	Jurassic	8	29
	Shimanto group snandstone, shale	Early Cretaceous – Paleogene	2	2
	Yasugawa group sandstone, shale	Jurassic	1	11
Metamorphic rock	Sanbagawa belt schist	Late Cretaceous – Paleogene	3	12
	Ryoke belt gneiss	Cretaceous	3	43
		Total	30	170

DECLINE OF TENSILE LOAD DURING 30 DAYS PERIOD AFTER EXECUTION

Regarding the decline of the residual load of the anchors during the 30 days period after execution, the rock was classified as igneous rock, sedimentary rock, or metamorphic rock to discuss the relationship of the residual rate of the tensile load to the rock classifications.

Ignious Rock

Figure 3 shows the relationship of the residual rate [Rpt (%)] of the tensile load after 30 days in the igneous rock with the rock classification. Rpt in the rock classification of each slope was plotted by (in cases where there were multiple measurement data for one slope) using the average value in the center and the maximum and minimum values plotted above and below by bars linked by vertical lines. When there was only 1 datum, the Rpt of this measured value was plotted individually (the same applies below to the method of representing the relationship of Rpt to the rock classification). Table 4 shows the Rpt at 30 days after execution in the rock classification of each slope.

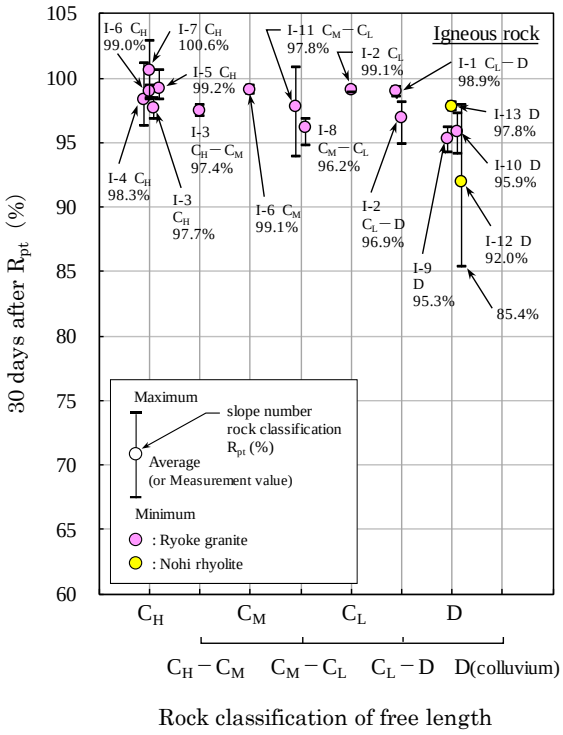

Fig.3 Relationship of R_{pt}(%) of after 30 days and rock classification (Igneous rock).

In the igneous rock, the average of Rpt at 30 days after execution in the C_H class showed almost no decline in the tensile load, and Rpt was almost 100%. In the range between C_H to C_M and C_L to D, the quantity of decline was slightly larger than for C_H, but the average Rpt was between 96.2% and 99.1% and remained at 95% or higher. In the case of rock classification D, the average Rpt was between 92.0% and 97.8%, which was lower than that in bedrock. From C_L to D with D class, Rpt was greatly scattered, and its minimum value was 85.4% in slope I-12.

Table 4 Rpt(%) at 30 days after consturuction (Igneous rock).

slope No.	Design Load Td (kN)	lock-off Load Pt (kN)	Free length Rock classification	load cell (number)	30 days after Rpt(%)		
					MAX	AV	MIN
I-1	181.4	181.4	C_L-D	2	99.3	98.9	98.6
I-2	316.5	316.5	C_L	2	99.3	99.1	98.9
			C_L-D	3	98.2	96.9	94.8
I-3	850.0	850.0	C_H	3	98.4	97.7	96.9
			C_H-C_M	3	97.9	97.4	97.0
I-4	335.1	335.1	C_H	7	101.1	98.3	96.3
I-5	331.1	331.1	C_H	5	100.6	99.2	98.3
I-6	174.1	174.1	C_M	2	99.4	99.1	98.8
			C_H	3	99.4	99.0	98.4
I-7	190.0	190.0	C_H	5	102.9	100.6	98.4
I-8	650.1	650.1	C_M-C_L	5	96.9	96.2	94.8
I-9	514.8	514.8	D	5	96.1	95.3	94.2
I-10	766.8	766.8	D	17	97.2	95.9	94.1
I-11	408.1	426.0	C_M-C_L	4	100.9	97.8	93.9
I-12	367.8	367.8	D	3	97.9	92.0	85.4
I-13	374.4	374.4	D	4	98.2	97.8	97.4

Sedimentary Rock

Figure 4 shows the relationship of the residual rate [Rpt (%)] of the tensile load after 30 days in sedimentary rock to the rock classification. Table 5 shows Rpt at 30 days after execution in the rock

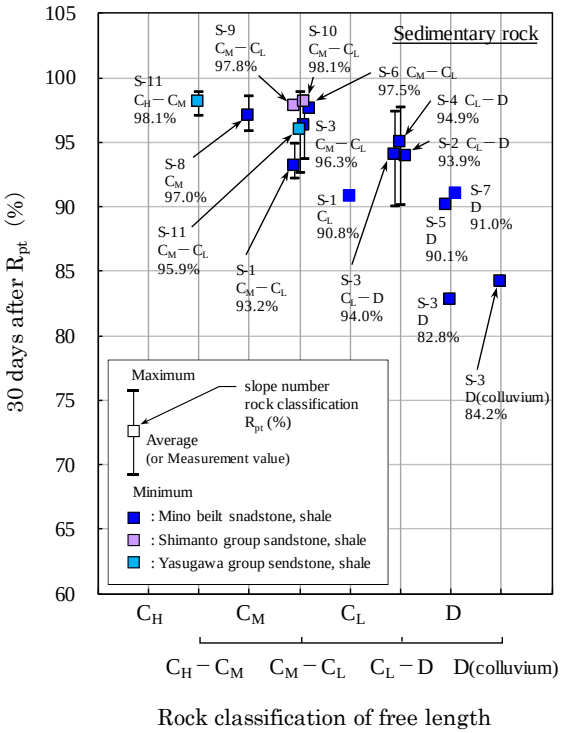

Fig. 4 Relationship of R_{pt}(%) of after 30 days and rock classification (Sedimentary rock).

classification on each slope.

This clearly shows that in sedimentary rock, from the C_H to D class (colluvium), as the geological conditions worsen, Rpt falls more than in igneous rock. On slope S-11 with rock class C_H to C_M, the average Rpt after 30 days was high at 98.1%, and fell in the sequence C_M, C_M to C_L, C_L, and C_L to D. On the three slopes with C_L to D class, the average of Rpt ranged from 93.9% to 94.9%, and even at the minimum value remained at 90% or higher. In D class and D (colluvium), Rpt had its lowest residual rate of between 84.1% and 91.0% (a significant decline in the tensile load).

Table 5 Rpt(%) at 30 days after consturuction (Sedimentary rock).

slope No.	Design Load Td (kN)	lock-off Load Pt (kN)	Free length Rock classification	Load cell (number)	30 days after Rpt(%)		
					MAX	AV	MIN
S-1	341.9	341.9	C_L	1	—	90.8	—
	475.4	497.5	$C_M - C_L$	6	94.9	93.2	92.1
S-2	275.1	304.2	$C_L - D$	1	—	93.9	—
S-3	466.9	466.9	D	1	—	82.8	—
	880.6	880.6	$C_M - C_L$	3	98.5	96.3	93.7
	～	～	$C_L - D$	4	97.4	94.0	90.0
	440.0	440.0	D(colluvium)	1	—	84.2	—
S-4	804.1	804.1	$C_L - D$	6	97.7	94.9	90.1
S-5	639.9	639.9	D	1	—	90.1	—
S-6	362.5	347.1	$C_M - C_L$	1	—	97.5	—
S-7	159.2	152.2	D	1	—	91.0	—
S-8	329.3	319.2	C_M	3	98.6	97.0	95.8
S-9	528.9	527.3	$C_M - C_L$	1	—	97.8	—
S-10	617.1	615.2	$C_M - C_L$	1	—	98.1	—
S-11	724.0	744.5	$C_M - C_L$	5	98.9	95.9	92.6
	940.0	897.5	$C_H - C_M$	6	98.9	98.1	97.1

Metermorphic Rock

Figure 5 shows the relationship of the residual rate [Rpt (%)] to the rock classification of the tensile load after 30 days in metamorphic rock. Table 6 shows Rpt at 30 days after execution in the rock classification on each slope.

This clearly shows that in metamorphic rock, from rock classification C_H to D (colluvium), Rpt declined in value from its level in igneous rock and sedimentary rock. In metamorphic rock, in the C_H to C_M and C_M classes, the average of Rpt was high at 98.1% and 99.1%; but in the C_M to C_L class, it began to fall slightly, to 94.3% and 98.4%. Then, from the C_L to D class, Rpt was clearly smaller than 81.5%. In D (colluvium), which is colluvium on the free length, Rpt was even smaller. The average of Rpt on slope M-6 was 77.3%, and the average of Rpt on slope M-3 was 72.1%. This indicates a large decline in the tensile load.

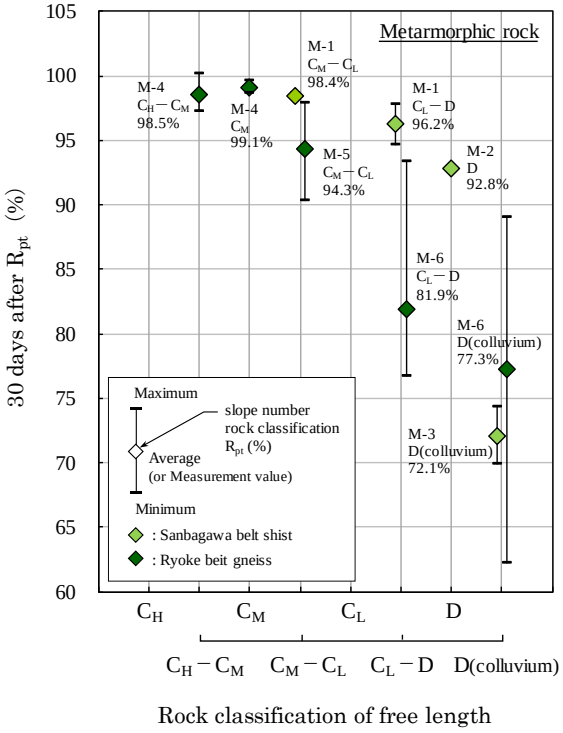

Fig. 5 Relationship of R_{pt}(%) of after 30 days and rock classification (Metamorphic rock).

Table 6 Rpt(%) at 30 days after consturuction (Metamorphic rock).

slope No.	Design Load Td (kN)	lock-off Load Pt (kN)	Free length Rock classification	load cell (number)	30 days after Rpt(%)		
					MAX	AV	MIN
M-1	639.7	447.8	$C_L - D$	6	97.8	96.2	94.6
			$C_M - C_L$	3	98.6	98.4	98.1
M-2	242.7	194.0	D	1	—	92.8	—
M-3	686.4	483.9	D(colluvium)	2	74.3	72.1	69.9
M-4	201.0	201.0	C_M	4	99.6	99.1	98.7
	136.0	136.0	$C_H - C_M$	5	100.2	98.5	97.3
M-5	872.8	920.4	$C_M - C_L$	24	97.9	94.3	90.3
M-6	795.4	830.1	$C_L - D$	6	93.4	81.9	76.7
			D(colluvium)	4	89.0	77.3	62.3

SUMMARY

The tensile load of anchors falls is impacted mainly by the slope on which the anchors are installed and the geological conditions of the slope. The quantity of decline in the tensile load is related to the rock classification at the free length, and this clearly tends to increase in the order of the C_H, C_M,

C_L, and D classes.

In relatively good geological conditions (C_H, C_H to C_M, and C_M classes) in igneous rock, sedimentary rock, and metamorphic rock, Rpt at 30 days after exection remained at 95% or higher. In particular, Rpt in granite of the C_H class was almost 100%, and almost no decline in the tensile load occurred. In the C_M to C_L and C_L classes in every geology, anchors with an Rpt lower than 95% began to appear. In bedrock of the C_L to D class and D class that is weathered or cracked, the tensile load fell significantly in sedimentary rock and metamorphic rock. In sedimentary rock, anchors with an Rpt lower than 85% appeared. In bedrock consisting of the C_L to D class and D class in metamorphic rock, the tensile load fell more than in igneous rock or sedimentary rock, and Rpt was lower than 80%. In the D (colluvium) class of metamorphic rock, where there is unconsolidated colluvium ground on the free length which was classified as D (colluvium) and the tensile load fell even more, Rpt at 30 days after execution was lower than 80% on average, and anchors with a lowest Rpt value of lower than 65% appeared.

It is thought that a factor represented by a variation in the quantity of decline of the tensile load according to geological conditions. As for the rock classification, three elements—degree of weathering, hardness of rock mass, and state of joints or cracks—are qualitatively evaluated, but they are closely correlated with the decline of the tensile load. In order to estimate the quantity of decline of the anchor tensile load, geological information is important.

CLOSING REMARKS

To maintain anchors, it is necessary to evaluate not only their tensile load but also whether they function and the areal soundness of the entire slope. This study showed that geological conditions (rock classification) impact the initial decline of the tensile load of anchors. To maintain the anchors, it is necessary to evaluate the long-term decline of the tensile load after execution and after 10 years, 20 years, and 30 years. Clarifying the initial decline of the tensile load as shown in this paper will permit the prediction of long-term decline. In the future, we wish to study methods of evaluating the relationship of the long-term decline of the tensile load with geological conditions, and the functions of anchors after an extreme decline in tensile loads.

REFERENCES

[1] Japanese Geotechnical Society, Design and Construction Standards for Ground Anchor, The Commentary, 2012, pp.79-80.

[2] Fujiwara Y., Takemoto M., and Sakai T., A Study of Lift-off Test Method of Ground Anchors, Journal of Japan Society of Civil Engineers, Division C(Geotecnics), Vol.67, No.4, 2011, pp.558-568.

[3] Central Nippon Expressway Co., Ltd., Earthwork Conatruction Management Guidelines, 2017, pp.3-38 - 3-39.

[4] Public Works Research Institute, Japan Anchor Association, Maintenance Manual for Ground Anchor, 2008, pp.69-75.

[5] Takyu T., Shimoda K., Kawasaki H., and Tamura T., Change Over Time of Tension of Groud Anchors, The 65th Japan Society of Civil Engneers Annual Scientific Conference Abstracs, 2010, pp.105-106.

[6] Yamazaki M., and Sakai T., Considertion about Initial Decrease of Tensile Load of Ground Anchor and Geological Condition, The 73th Japan Society of Civil Engneers Annual Scientific Conference Abstracs, 2018, pp.855-856.

[7] Fjiwara Y., and Sakai T., A Maintenance of Ground Anchors Slope Based on Distribution Characteristics of The Residual Anchor Load, Journal of Japan Society of Civil Engineers, Division C(Geotscnics), Vol.74, No.3, 2012, pp.260-273.

[8] Japan Society of Engneering Georogy, Rock Classification, Engineering Geology Spesial Issue, 1984, pp.103-118.

[9] Japan Construction Tnformation Center Foundation(JACIC), Guidelines for Generating Bowring Core Column Diagram, The Comentary, 1986, pp.17-20.

[10] Tanaka H., Primer of Geology for Civil Engineers, 1964, pp.25-49.

[11] Japan Society of Civil Engineers, Soft Rock Engineering -Foundamentals and Case Studies for Inventigation, Design and Construction-, 1984, pp.1-6.

9th Int. Conf. on Geotechnique, Construction Materials and Environment, Tokyo, Japan, 20-22 November 2019, ISBN: 978-4-909106025 C3051

A COMPARATIVE STUDY ON THE PERFORMANCE OF SOIL NAIL AND MICROPILE IN SOIL SLOPE STABILIZATION USING SPENCER'S METHOD

Lee Li Yong[1], Endene Emmanuel[2] and Vivi Anggraini[3]
[1,2,3] School of Engineering, Monash University, Malaysia

ABSTRACT

Reinforcing elements are introduced into steep and unstable slopes to create a stable and reinforced soil section that is able to resist soil mass movements. Soil nail is a commonly used reinforcing element in slope stabilisation owing to its efficiency and cost-effectiveness. Recently, micropile has emerged as an alternative slope reinforcing element to prevent slope failures. Previous studies have demonstrated the efficacy of each of the prementioned reinforcing element in various slope remedial works. However, limited studies can be traced in comparing their effectiveness in soil slope stabilization. Hence, this paper assessed and compared the performance of soil nail and micropile in soil slope stabilization using SLOPE/W software. A parametric study was performed to study the relationship between the geometric properties of the reinforcing elements such as the length, diameter, and inclination angle of the reinforcement bar with the slope Factor of Safety (FoS) based on Spencer's method. The results revealed that the reinforced slope FoS increases with increasing length and inclination angle of the reinforcement bar. However, the FoS was found to decrease as the reinforcement bar attained a certain optimum inclination angle. From the analysis, it is evident that micropile showed a better performance in soil slope stabilization compared to soil nail as micropile achieved a better FoS at a shorter length and smaller inclination angle.

Keywords: Soil slope stabilization; Soil nail; Micropile; Spencer's method; Limit equilibrium method; Slope stability analysis

INTRODUCTION

The rapid movement of earth materials down a natural or man-made slope under gravitational stresses is termed as slope failure or landslide. The influence of external stimuli such as earthquake, intense rainfall infiltration, fluctuation of groundwater level, soil erosion, disturbance due to construction activities, among others, can trigger the occurrence of slope failure [1]. In most tropical regions, rainfall-induced landslides commonly occur due to the infiltration of rainwater through the soil, hence the soil suction ability reduces, thus resulting in a decrease in the soil shear strength which eventually lead to slope failure [2]-[3]. The impact of slope failure is often detrimental as it leads to human casualties, severe destruction to existing building and infrastructures as well as disturbance to utilities and transportation networks [4]-[5].

Generally, reinforcing elements such as geosynthetics, soil anchors, soil nails, and micropiles are often introduced into unstable soil slopes to increase the soil shear strength and avoid further soil mass movements along definite rupture surface [6]. Soil nails have been widely employed in soil slope stabilization in comparison to other reinforcing elements owing to their low installation cost and ease of installation [7]-[8]. Likewise, during construction, it causes less environmental impact. Furthermore, the soil-nailed system provides early warning signs prior to failure due to its ductile failure mode [9]. Soil-nailed slope construction is commonly carried out by installing grouted steel bars into the existing slope to create a stable block of soil mass with improved shear strength [10]. The inclusion of steel bars also allows transfer of resisting tensile forces from the steel bar to the soil mass through the mobilization of friction along the nail-soil interface [11]. However, soil nails cannot be employed in a ground condition containing a significant quantity of rock or corestones as they cannot penetrate through such ground conditions [10]. Hence, reinforcing elements with similar properties and advantages to soil nails are extensively being sought. Micropiles serve as great alternative to soil nails as they can overcome the limitation of soil nails. They are capable of transferring the axial and lateral load to a more competent rock layer with side resistance developed along the micropile due to their construction technique [12]. Over recent years, numerous studies have been conducted to assess the efficacy of soil nails and micropiles in soil slope stabilization [7]-[8], [11], [13]-[18]. However, limited studies can be traced in comparing the performance of both reinforcing elements (soil nails and micropiles) in soil slope stabilization employing a limit equilibrium method.

Addressing the aforementioned research gap, this paper aimed at comparing the performance of two reinforcing elements (soil nail and micropile) in soil slope stabilization by employing a commercial SLOPE/W software package based on Spencer's method. The effects of geometric properties of the reinforcing elements such as length, diameter, and inclination angle of the reinforcement bar on the reinforced slope FoS were also explored to provide valuable insight on the relationship between the geometric effects of reinforcing elements and the reinforced slope FoS.

BACKGROUND OF SPENCER'S METHOD

The Spencer's method adopted in this analysis divides the assumed circular failure surface into few vertical slices and performs force equilibrium calculations on each slice. It then determines two safety factors with respect to moment, Fm and horizontal force equilibrium, Ff based on the ratio of interslice side shear to side normal forces. The relationship between the interslice side shear and side normal forces is represented in Eq.(1).

$$X = E\lambda f(x) \quad (1)$$

Where X is interslice side shear force, E is interslice side normal force, λ is the unknown constant to be determined and f(x) is a function.

The Spencer's method assumes a constant function f(x) and this implies that the interslice shear-normal ratio, λ is the same for all slices. Iterative procedures are performed and repeated subsequently until the two safety factors Fm and Ff converge at a constant λ.

METHODOLOGY

SLOPE/W version 2012 software package was employed to assess the safety factors of the natural and reinforced slopes using soil nails and micropiles by developing a 2D model. The geometry of the natural slope considered in the analysis is presented in Fig. 1. The height and width of the slope are 4m and 6m, respectively with an inclination angle of 33.69°. The soil parameters analysed in this study are typical residual soil properties which consist of a combination of silty sand and clayey sand present in natural soil slopes (refer to Table 1). The groundwater level was assumed to be 3m below the ground surface.

The slope stability analysis was conducted based on three stages. First, defining the basic components of the slope such as geometry, soil properties, pore water pressures, and imposed surcharge loading (refer to Fig. 1 and Table 1). This was followed by indicating the location and properties of the reinforcing elements. Three rows of soil nails were placed at a vertical spacing of 1.5m and horizontal spacing of 2m along the slope surface (refer to Fig. 2), while two battered micropiles were located at the middle of the slope with a horizontal spacing of 2m (refer to Fig. 3). The soil nail diameters used in the study were 20mm, 25mm, and 32mm, surrounded by 0.125m diameter of cement mortar. On the other hand, micropiles with diameters of 60.3mm, 73mm, and 88.9mm surrounded by 0.3m cement mortar were considered in the analyses. The analysis was then performed adopting Spencer's method. The geometric properties of the reinforcing elements such as the length and inclination angle varied in this study in order to assess their effects on the performance of reinforced slopes.

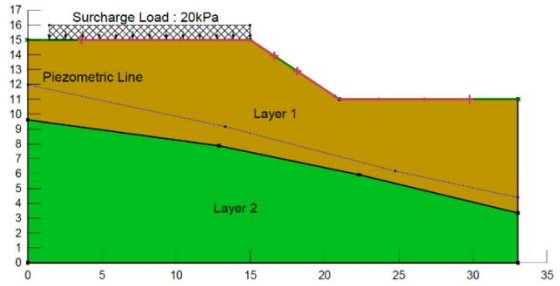

Fig.1 Geometry of natural slope.

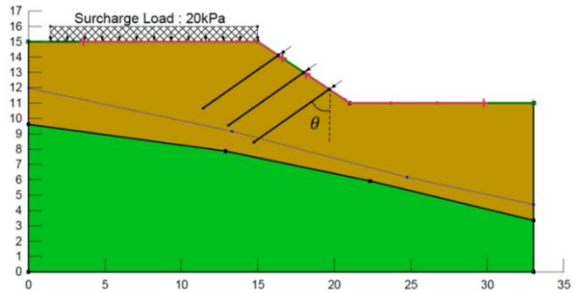

Fig.2 Slope reinforced with three rows of soil nails inclined at an angle θ to the vertical.

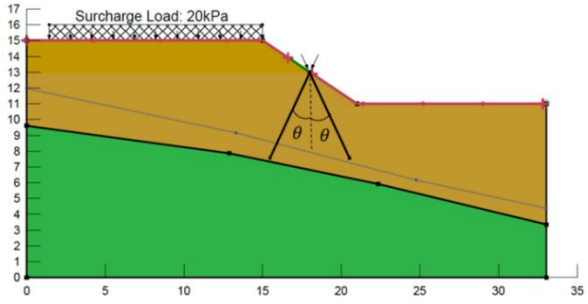

Fig.3 Slope reinforced with two micropiles battered at an angle θ to the vertical.

Table 1 Basic components of the slope.

	Parameter	Value	Unit
Slope geometry	Width ; Height	6 ; 4	m
	Width/height ratio	1.5	-
Layer 1	Material model	Mohr-Coulomb	-
	Unit weight	18	kN/m^3
	Cohesion	2	kPa
	Friction angle	20	°
Layer 2	Material model	Mohr-Coulomb	-
	Unit weight	19	kN/m^3
	Cohesion	5	kPa
	Friction angle	30	°
Imposed loading	Surcharge load	20	kPa

RESULTS AND DISCUSSIONS

Natural Slope

The FoS of the natural slope was found to be 0.846 from the analysis. This did not meet the FoS requirement for natural slope recommended by [19]-[20] of 1.3. Slope reinforcement measures should be applied to the natural slope to enhance its stability, and hence prevent future slope failure.

Soil-nailed Slope

Fig.4 a, b, and c depict the relationship between the FoS and soil nails inclination angle at 3m, 6m, and 9m length for reinforcement bar diameter of 20mm, 25mm, and 32mm, respectively. It can be observed that all three graphs portray a similar trend such that (i) the FoS increases and decreases after the soil nails attained an optimum inclination angle to the vertical and (ii) the FoS increases with increasing length of soil nails. The reinforced slope FoS is closely related to the mobilized tensile forces in individual soil nails. As the nail inclination angle increases, the tensile force of the individual soil nail increases until it reaches a maximum value and further decreases with increasing nail inclinations. These observations are consistent with the results reported by [21]-[22]. Also, the longer anchoring length of the soil nails embedded into a stronger soil strata layer and extended beyond the failure surface as compared to shorter soil nails contributes to a higher FoS. These results are in good agreement with the observations reported by [23]-[24]. However, the differences in the FoS for the three different reinforcement bar diameters (20mm, 25mm, and 32mm) at 3m, 6m, and 9m length appear to be insignificant. These results suggest that the soil nail reinforcement bar diameter does not show a pronounced effect on the reinforced slope FoS compared to its length.

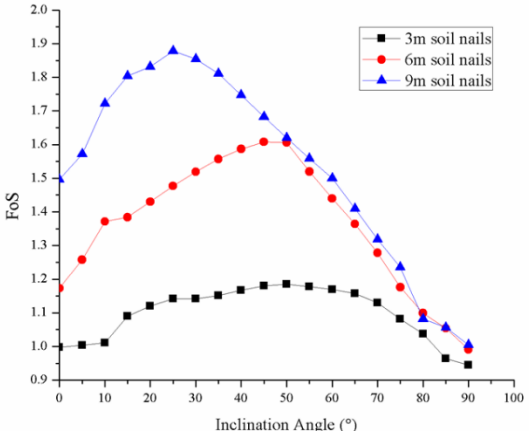

(a) Bar diameter 20mm.

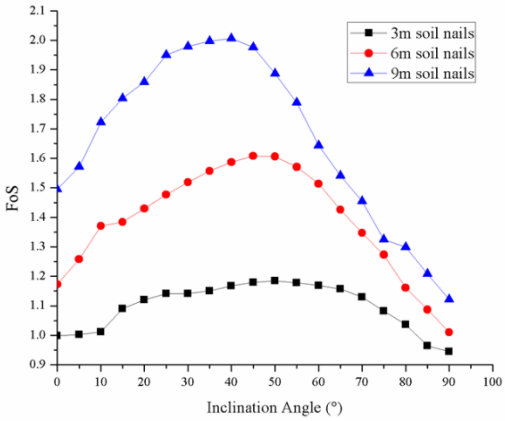

(b) Bar diameter 25mm.

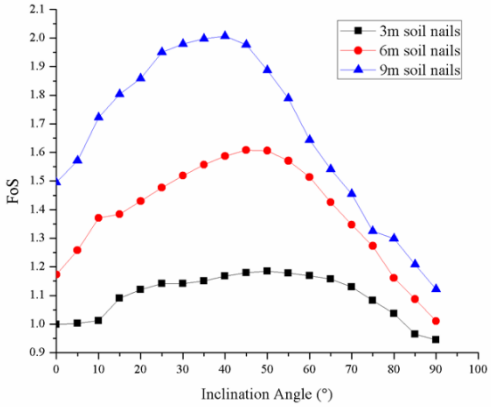

(c) Bar diameter 32mm.

Fig.4 FoS for soil-nailed slope with three different bar diameters at 3m, 6m and 9m length battered from 0 to 90° to the vertical.

Micropiled Slope

Fig.5 a, b, and c present the relationship between the FoS and micropiles inclination angle at 3m, 6m, and 9m length for reinforcement pipe outer diameter of 60.3mm, 73mm, and 88.9mm, respectively. All three graphs portray a similar trend such that (i) the inclination angle does not affect the FoS for slope reinforced with 3m micropiles (ii) the FoS for slope reinforced with 6m and 9m micropiles remains constant and decreases after attaining an optimum inclination angle and (iii) the FoS increases with increasing length of micropiles. The 3m micropiles with different reinforcement pipe diameter battered at varied inclination angle failed to extend beyond the circular failure surface, and this caused the FoS to remain as 1.267. Unlike soil nails, the shear forces developed along the micropiles also contributes to the FoS of reinforced slope. The mobilization of the two forces namely, shear and tensile forces along the micropiles increases and reduces after achieving an optimum inclination angle. As a result, the micropiles experienced reduced stiffness and consequently led to reduced slope stability [25]. Furthermore, the increment in FoS with increasing length of micropiles is probably due to (i) the longer embedment length of micropile into a more stable layer (layer 2) and (ii) the increased frictional resistance as a result of micropile-soil interactions. These observations are consistent with the results presented by [26]-[27]. Contrarily, the increasing reinforcement pipe diameter does not result in significant variations in the FoS, hence, the length of the micropile governs the reinforced slope FoS compared to the diameter of the reinforcement pipe.

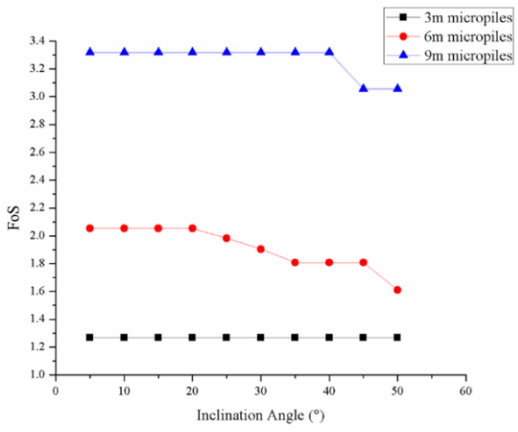

(a) Reinforcement pipe outer diameter 60.3mm.

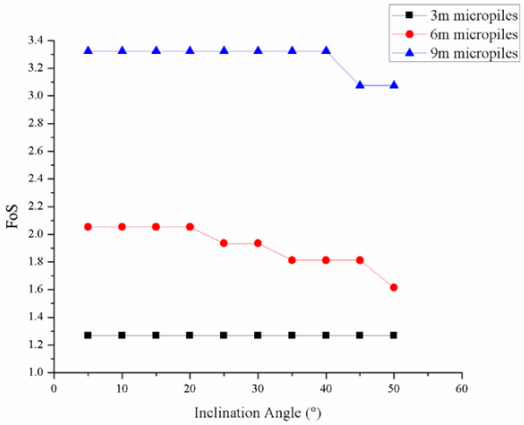

(b) Reinforcement pipe outer diameter 73mm.

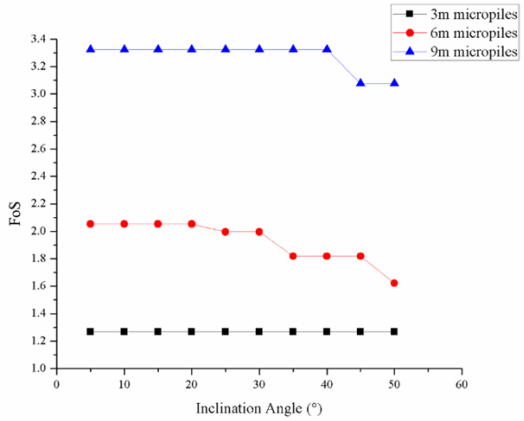

(c) Reinforcement pipe outer diameter 88.9mm.

Fig.5 FoS for micropiled slope with three different bar diameters at 3m, 6m and 9m length battered from 5 to 50° to the vertical.

Comparison between Soil-nailed Slope and Micropiled Slope

In general, micropiled slope achieved a higher FoS compared to soil-nailed slope and this is in line with the observations presented by [28]. The safety factors of micropiled slope satisfied the required reinforced slope FoS which is greater than 1.5 as specified by [19]-[20] at a shorter length (6m and 9m) and smaller optimum inclination angle (20° and 40°) relative to soil-nailed slope. This phenomenon can be attributed to the contribution of bigger grout diameter and reinforcement bar diameter of micropiles that resulted in the mobilization of higher shear and tensile capacity which can enhance the soil stability more effectively. Furthermore, the arrangement of micropiles with two legs affixed to a concrete cap beam at the ground surface (one leg sloping upward and the other leg sloping downwards) enable the micropiles to act in tension (upslope leg) and compression (downslope leg) at the same time [29].

This arrangement provides better resistance against the mobilizing forces developed along the potential failure surface. Moreover, the shear capacity of soil nails is normally ignored in the analysis as the contribution of shear capacity in improving the soil nail resistance is negligible [30]. This factor also constitutes one of the reasons for the lower safety factors of soil-nailed slope.

CONCLUSIONS

This study assessed the effectiveness of two reinforcing elements viz. soil nails and micropiles in soil slope stabilization by conducting slope stability analysis using SLOPE/W software package with reference to Spencer's method. The influence of the geometric properties of the reinforcing elements such as the length, diameter, and inclination angles on the reinforced slope FoS was evaluated accordingly. The following conclusions are established from the analysis:

1. Longer soil nails resulted in higher FoS due to their longer anchoring length that extends beyond the potential circular failure surface. The relationship between the FoS and soil nails inclination angle exhibited a negative parabolic curve such that the slope FoS increases and decreases after achieving an optimum inclination angle. This is attributed to the reduced mobilized tensile capacity of the soil nails. However, the diameter of the soil nails did not cause significant variation in the safety factors of the soil-nailed slope.
2. Micropiled slope showed a higher factor of safety with longer pile length as a result of increased frictional resistance developed along the longer micropiles and increased embedment length of micropiles into more stable soil strata. The 3m micropiles battered at different inclination angle failed to extend beyond the circular slip surface, and this caused the safety factors of the micropiled slope to remain constant at different inclination angles. Furthermore, the reduced mobilization of shearing and tensile forces along the micropiles after attaining an optimum inclination angle led to deterioration of the slope stability for slope reinforced with 6m and 9m micropiles. Similar to the soil-nailed slope, increasing reinforcement pipe diameter exhibited insignificant variations in the FoS of the reinforced slope.
3. Micropiles tend to have higher shear and tensile capacity relative to soil nails. This factor contributes to the higher safety factor of micropiled slope compared to the soil-nailed slope.

From the analysis, it can be concluded that micropiles showed a better performance in improving the stability of slope compared to soil nails.

ACKNOWLEDGMENTS

The authors express sincere thanks to the Abunde Sustainable Engineering Group for its valuable advice.

REFERENCES

[1] Zhou X. and Cheng H., Analysis of Stability of Three-dimensional Slopes using the Rigorous Limit Equilibrium Method. Engineering Geology, Vol. 160, 2013, pp. 21-33.
[2] Lee M.L., Gofar N. and Rahardjo H., A Simple Model for Preliminary Evaluation of Rainfall-induced Slope Instability. Engineering Geology, Vol. 108, 2009, pp. 272-285.
[3] Ali A., Huang J., Lyamin A., Sloan S., Griffiths D., Cassidy M. and Li J., Simplified Quantitative Risk Assessment of Rainfall-induced Landslides Modelled by Infinite Slopes. Engineering Geology, Vol. 179, 2014, pp. 102-116.
[4] Liu Y., Li H., Xiao K., Li J., Xia X. and Liu B., Seismic Stability Analysis of a Layered Rock Slope. Computers and Geotechnics, Vol. 55, 2014, pp. 474-481.
[5] Uhlemann S., Smith A., Chambers J., Dixon N., Dijkstra T., Haslam E., Meldrum P., Merritt A., Gunn D. and Mackay J., Assessment of Ground-based Monitoring Techniques Applied to Landslide Investigations. Geomorphology, Vol. 253, 2016, pp. 438-451.
[6] Bromhead E.N., Hosseyni S. and Torii N., Soil Slope Stabilization. In: Clague JJ, Stead D (eds) Landslides: Types, Mechanisms and Modeling, Cambridge University Press, 2012, pp. 252-260.
[7] Ghareh S., Parametric Assessment of Soil-nailing Retaining Structures in Cohesive and Cohesionless Soils. Measurement, Vol. 73, 2015, pp. 341-351.
[8] Zevgolis I. and Daffas Z., System Reliability Assessment of Soil Nail Walls. Computers and Geotechnics, Vol. 98, 2018, pp. 232-242.
[9] Sonjoy D. Soil nailing: An Innovative Ground Improvement Technology. Ground Improvement, 2014, pp. 152–158.
[10] Patel A., Geotechnical Investigations and Improvement of Ground Conditions. Woodhead Publishing, 2019, pp. 1-209.
[11] Wei W. and Cheng Y., Soil Nailed Slope by Strength Reduction and Limit Equilibrium Methods. Computers and Geotechnics, Vol. 37, Issue 5, 2010, pp. 602-618.
[12] Sun S.W., Zhu B.Z. and Wang J.C., Design

Method for Stabilization of Earth Slopes with Micropiles. Soils and Foundations, Vol.53, Issue 4, 2013, pp.487-497.

[13]Zhou Y., Cheuk C. and Tham L., Numerical Modelling of Soil Nails in Loose Fill Slope under Surcharge Loading. Computers and Geotechnics, Vol. 36, Issue 5, 2009, pp. 837-850.

[14]Kim Y., Lee S., Jeong S. and Kim J., The Effect of Pressure-grouted Soil Nails on the Stability of Weathered Soil Slopes. Computers and Geotechnics, Vol. 49, 2013, pp.253-263.

[15]Abdelaziz A., Hafez D. and Hussein A., The Effect of Pile Parameters on the Factor of Safety of Piled-slopes using 3D Numerical Analysis. HBRC Journal, Vol. 13, Issue 3, 2017, pp. 277-285.

[16]Deng D.P., Li L., Zhao L.H., Limit-Equilibrium Method for Reinforced Slope Stability and Optimum Design of Antislide Micropile Parameters. International Journal of Geomechanics, Vol. 17, Issue 2, 2017, pp. 1-10.

[17]Howe W.K., Micropiles for Slope Stabilization, in Proc. Biennial Geotechnical Seminar 2010, 2010, pp.78-90.

[18]Song Y., Hong W.P. and Woo K.S. Behavior and Analysis of Stabilizing Piles Installed in a Cut Slope during Heavy Rainfall. Engineering Geology, Vol. 129, 2012, pp. 56-67.

[19]JKR 21500-0011-10, Guidelines for Slope Design. Public Works Department Malaysia, 2010, pp.1-37.

[20] Geotechnical Engineering Office of Hong Kong, Geotechnical Manual for Slopes. The Government of the Hong Kong Special Administrative Region, 2011, pp.1-303.

[21]Rawat S. and Gupta A., Analysis of a Nailed Soil Slope using Limit Equilibrium and Finite Element Methods. International Journal of Geosynthetics and Ground Engineering, Vol. 2, Issue 34, 2016, pp.1-23.

[22]Alsubal S., Harahap I.S.H. and Babangida N.M., A Typical Design of Soil Nailing System for Stabilizing a Soil Slope : Case Study. Indian Journal of Science and Technology, Vol. 10, Issue 4, 2017, pp. 1-7.

[23]Zhang G., Cao J. and Wang L., Failure Behavior and Mechanism of Slopes Reinforced using Soil Nail Wall under Various Loading Conditions. Soils and Foundations Vol. 54, Issue 6, 2014, pp. 1175-1187.

[24]Tang O.L. and Jiang Q.M., Stability Analysis of Slope under Different Soil Nailing Parameters based on the Geostudio. International Journal of Geohazards and Environment, Vol. 1, Issue 2, 2015, pp.88-92.

[25]Sadek ., Shahrour I. and Mroueh H. (2006) Influence of Micropile Inclination on the Performance of a Micropile Network. Ground Improvement, Vol. 10, Issue 4, 2006, pp. 165-172.

[26]Yang S., Ren X. and Zhang J., Study on Embedded Length of Piles for Slope Reinforced with One Row of Piles. Journal of Rock Mechanics and Geotechnical Engineering, Vol. 3, Issue 2, 2011, pp. 167-178.

[27]Sun S.W., Wang W. and Zhao F., Three-dimensional Stability Analysis of a Homogeneous Slope reinforced with Micropiles. Mathematical Problems in Engineering, Vol. 2014, 2014, pp. 1-11.

[28]Matejcekova M., Study on the Effectiveness of Reinforcing Elements. Slovak Journal of Civil Engineering, 2007, pp. 13-19.

[29]Sabatini P.J., Tanyu B., Armour T., Groneck P. and Keeley J., Micropile Design and Construction. Report No. FHWA-NHI-05-039. National Highway Institute, Federal Highway Administration, 2005, pp.1-456.

[30]Liew S.S., Soil Nailing for Slope Strengthening, in Proc. Geotechnical Engineering 2005,2005, pp.1-9.

.

9th Int. Conf. on Geotechnique, Construction Materials and Environment, Tokyo, Japan, 20-22 November 2019, ISBN: 978-4-909106025 C3051

PORE-STRUCTURAL PARAMETERS OF VOLCANIC ASH SOIL: COMPARISON BETWEEN NON-DESTRUCTIVE AND INDIRECT METHOD

Arjun Baniya[1], Akihiro Matsuno[1] and Ken Kawamoto[1]
[1]Graduate School of Science and Engineering, Saitama University, Japan.

ABSTRACT

Mass transport within porous media is governed by their pore network, which is highly influenced by pore structure parameters such as pore size distribution, porosity, pore tortuosity and pore coordination number. Micro-focus X-ray computed tomography (MFXCT) has emerged as a powerful non-destructive tool for the direct visualization and better understand soil pore geometry. In this study, the soil-pore networks were visualized for volcanic ash soils from Nishi Tokyo, Japan. The study aimed to identify the pore structure parameters using a MFXCT system and compare the indirect pore parameters: equivalent pore diameter and tortuosity-connectivity parameter for gas flow. Both undisturbed and repacked samples were used for characterizing soil pore networking and structure. For repacked soil samples, particle size ($d \leq 2$mm) with field water content were used with different dry bulk densities by hand compaction. Soil samples were scanned by MFXCT system with various scanning resolutions and 3-dimensional models were reconstructed in the regions of interest (ROI). Soil pore-structural parameters effective pore radius, coordination number, and tortuosity were analyzed. Compare to the pore structure parameters of undisturbed samples the repacked samples showed less variation. The pore connectivity-tortuosity factors derived from MFXCT were well correlated with the indirect connectivity and tortuosities from measured soil gas diffusion. However, some variations in pore diameters were observed.

Keywords: Pore Structural Parameters, Microfocus X-ray Computed Tomography (MFXCT), Volcanic Ash soil, Gas Diffusion, Air Permeability

INTRODUCTION

Knowledge and understanding of gas transport processes in porous media are important for the environmental risk assessment and design of remediation methods at the contaminated sites. For examples, estimating emission of greenhouse gases from solid waste landfill site [1], [2], estimating contaminates at polluted sites and estimating aeration rates in agricultural soils [3]. Gas transport in soils occurs through the soil pore network, which is mainly controlled by soil pore structural parameters such as pore size distribution, pore tortuosity and pore coordination number. Nondestructive methods, such as an X-ray computed tomography (CT) has become a powerful technique to identify three-dimensional characterization of soil pore [4]–[6]. Till now, numerous studies have examined pore structural parameters based on the X-ray computed tomography (CT) about porosity [7], pore size distribution [8] and pore network tortuosity [9], [10]. However, there is limited number of studies on visualization and quantification of soil pore network and soil pore networks linked with the indirect pore parameters for gas flow based on measured gas diffusion coefficient and air permeability. [10] measured gas transport parameters (D_p and k_a) for Accusand (Unimin Corp., Ottawa, MN) and Granusil (Unmin Corp., Emmett, ID) and examined the correlations to pore structural parameters from X-ray CT analysis. They suggested that reasonably good agreement in tortuosity values obtained from CT analysis and from gas transport parameters. In this study, the soil-pore networks were visualized for volcanic ash soils using MFXCT system. The gas transport parameters of the soil samples (D_p and k_a) were measured in the laboratory. The objective of this study is to identify the pore structure parameters using a MFXCT system and compare with the indirect pore parameters such as equivalent pore diameter and tortuosity-connectivity parameter for gas flow. Accurate linking of pore structural parameters from MFXCT and gas transport parameters will allow easy and rapid quantification of important soil functional properties.

MATERIALS

For this study, a volcanic ash soil (Andsoils) collected from the grass-covered field at University of Tokyo agricultural site in Nishi-Tokyo, Japan was used. Both undisturbed and repacked soil sampled

Table 1. Basic physical and chemical properties of the soils (≤ 2mm fraction) used in this study.

Soil type	Particle size fraction %			ρ_s g cm^{-3}	ρ_d g cm^{-3}	Φ cm^3 cm^{-3}	ε_{FWC} cm^3 cm^{-3}	Soil condition
	Sand	Silt	Clay					
Volcanic ash soil (5 cm depth)	47	41	12	2.51	0.80	0.8	0.07	Undisturbed
					0.78	0.58	0.09	
					0.55	0.78	0.36	Repacked
					0.80	0.68	0.07	
Volcanic ash soil (50 cm depth)	49	40	11	2.73	0.49	0.82	0.21	Undisturbed
					0.49	0.82	0.21	
					0.49	0.82	0.21	Repacked
					0.55	0.80	0.11	

ρ_s : particle density, ρ_d : dry bulk density, Φ: total porosity, ε_{FWC} : air-filled porosity at field water content

Table 2. Scanning and analysis conditions for micro focus X-ray computed tomography.

Parameter	**Setting**			**Unit**
SR	12	30	50	µm/voxel
Average number for scanning		4		
View Number		3600		
FOV (X, Y)	12.0	31.0	50.8	mm
FOV (Z)	6.4	16.4	26.8	mm
Scaling Factor		150		
Image size of slice		1024×1024		voxels
Number of slices		540		
ROI		50×50×50		voxels
		100×100×100		
		200×200×200		
		300×300×300		

SR: scanning resolution, FOV: field of view, ROI: region of interest

from two depths: 5 cm and 50 cm depth below the surface were examined. The soils physical and chemical properties are shown in Table 1. Both undisturbed and repacked samples were used for characterizing soil pore networking. For repacked soil samples, particle size (d ≤ 2mm) with field water content (Samples below the 5 cm depth, w = 76 % and samples below the 50 cm depth w = 124 %) were prepared with various dry bulk densities (5 cm depth samples – 0.55 and 0.80 g cm^{-3} and 50 cm depth samples – 0.49 and 0.55 g cm^{-3}) by hand compaction. The samples were directly packed in an acrylic core of height 4.06 cm and diameter 5.61 cm. Undisturbed samples were used in the intact condition.

METHODOLOGY

Micro-focus X-ray CT Measurements and Analysis

Visualization of the soil pore structures was carried out using a microfocus X-ray CT (MFXCT) system (inspeXio SMX-90CT, Shimadzu Corp., Japan). At first, soil samples were scanned by MFXCT system with different scanning resolution 12, 30 and 50 µm/voxels. The scanned slices were reconstructed as a three-dimensional structure (Exfact VR 2.1, Nihon Visual Science, Inc., Japan) with different region of interest (50×50×50, 100×100×100, 200×200×200 and 300×300×300 voxels) and pore structural parameters such as pore radius, pore tortuosity and pore coordination number with a three-dimensional median axis (3DMA) method [6], [11] (EXFact analysis for porous

particles, Nihon Visual Science, Inc., Japan) were analyzed. The 3DMA package analyzes the CT data using the three steps: image segmentation, image skeletonization (construction of medial axis) and medial axis analysis. The details of the 3DMA package for X-ray CT analysis can be referred in earlier publications [6], [8]–[10]. For image segmentation, predetermined soil air-filled porosity at field water content was used to segment pore and grain spaces. The details of scanning and analysis conditions for the MFXCT system are summarized in Table 2.

Measurements of Gas Transport Parameters

After the MFXCT scanning, the tested same soil samples were reused to measure the gas transport parameters, such as the soil-gas diffusion coefficient, D_p (cm^2 s^{-1}) and air permeability, k_a (μm^2) at the constant room temperature of 20°C. The D_p was measured by using the diffusion chamber method [12]–[14]. Oxygen gas was used as a tracer gas and the change in the oxygen concentration was measured as a function of time in the diffusion chamber. In this study, the gas diffusion coefficient of oxygen in free air (D_0) at 20°C was taken as 0.20 cm^2 s^{-1} [12], [15] was used to calculate soil gas diffusivity. The k_a was measured by an air permeameter from the Darcy's equation [16] based on the pressure differences across the soil sample and viscosity of the air (1.86×10^{-5} Pa s).

The tortuosity-connectivity from gas transport was calculated by using previously developed simple power-law models [17] as equation (1) whereas equivalent pore diameters were predicted by using the relationship between diffusivity (D_p/D_o) and air permeability(k_a) [18] as equation (2) respectively.

$$X_G = log\left(\frac{D_p}{D_0}\right)/log\varepsilon \quad (1)$$

$$d_G = 2\sqrt{8k_a/(D_p/D_o)} \quad (2)$$

Where, X_G and d_G are the pore connectivity-tortuosity factor and equivalent pore diameter from gas flow.

RESULTS AND DISCUSSIONS

Figure 1 exemplifies the Multi-Planner Reconstruction (MPR), and binarized images at 5 cm depth of the undisturbed and repacked volcanic ash samples with different scanning resolution (SR). For each parameter, 3 ROIs were plotted and fitted under either normal or log normal scales. For each scanning conditions, the effective pore radius(r_{eff}) is fitted with log normal distribution curve whereas the pore coordination number and the pore tortuosity in z direction were fitted well by normal distribution curves.

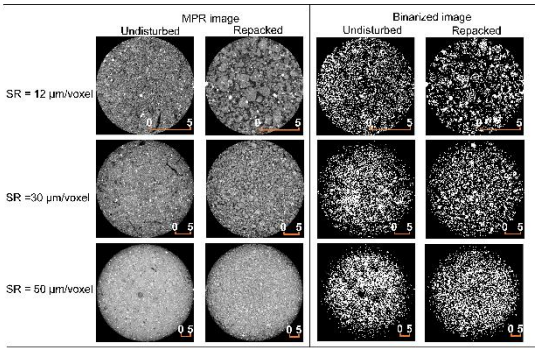

Figure 1. Multiplanar reconstruction image (MPR) and binarized images of undisturbed and repacked volcanic ash samples of dry bulk density 0.80 g cm^{-3}.

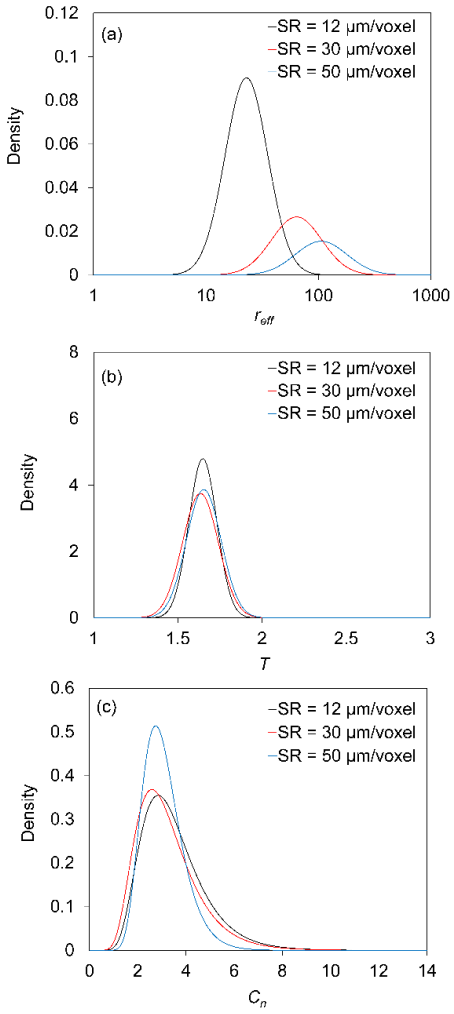

Figure 2. Distribution of pore structure parameters for undisturbed volcanic ash soils of dry bulk density 0.80 g cm^{-3} with different scanning resolution (SR). (a) effective pore radius (r_{eff}) (b) Pore Tortuosity(T) (c) Pore coordination number (C_n). (ROI = 200×200×200 voxels).

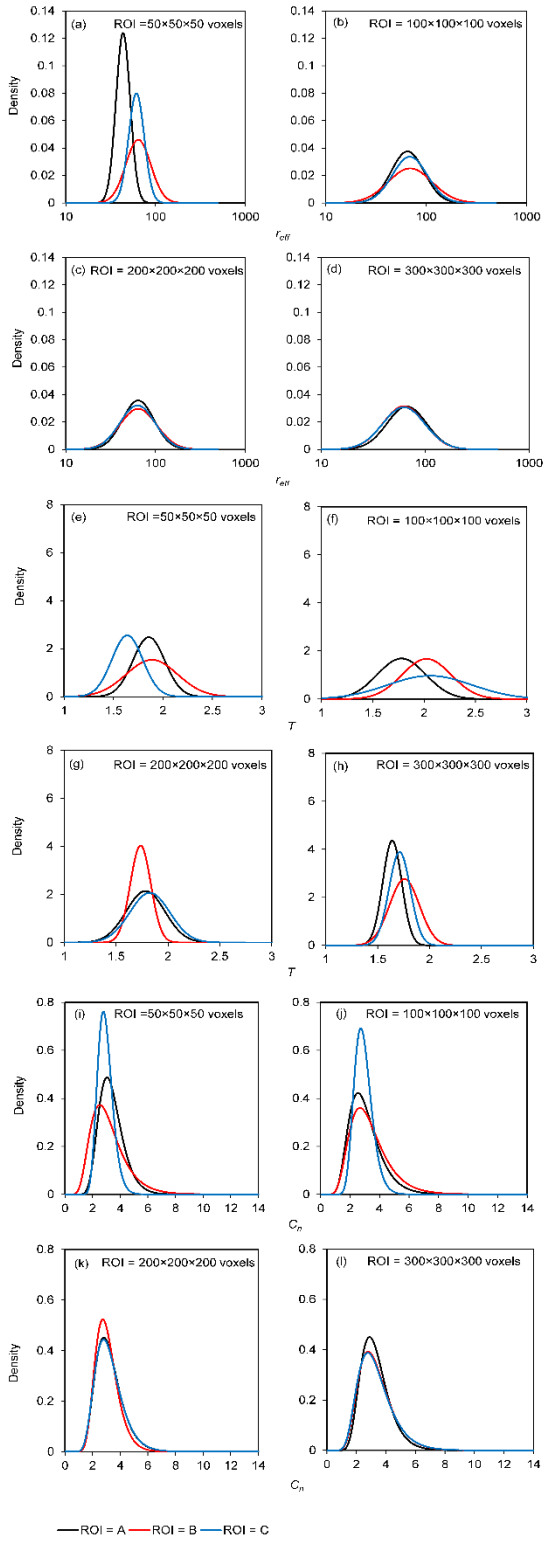

Figure 3. Distribution of pore structure parameters for undisturbed volcanic ash soils of dry bulk density 0.80 g/cm^3 with different region of interest (ROI) (SR 30 µm/voxel) : (a, e, i) ROI = 50×50×50voxels, (b, f, j) ROI = 100×100×100 voxels, (c, g, k) ROI = 200×200×200 voxels, and (d, h, l) ROI = 300×300×300 voxels and (a), (b), (c) and (d) are effective pore radius (r_{eff}), (e), (f), (g) and (h) are pore tortuosity(T), (i), (j), (k) and (l) are distribution of pore coordination number (C_n).

Typical examples of the effects of scanning resolution on the distribution of pore structure parameters are shown in Figure 2. The result shows that the effective pore radius (r_{eff}) is more depended on the SR in the MFXCT scanning compared to the pore tortuosity or the pore coordination number. This verified that lower SR size results in lowering the r_{eff}. All pore structure parameters for undisturbed and repacked samples varied depending on the ROI in the MFXCT scanning (Figure 3). However, such variations decreased with increasing ROI (typically, ROIs ≥ 100×100×100 voxels). For both undisturbed and repacked samples, ROI = 50×50×50 voxels showed high variation due to the limited number of pores in the analysis. The pore structure parameters are generally similar for ROI larger than 200×200×200 voxels. Sometimes, the larger voxels were not used in the analysis due to very large computational complexity for the pore structure analysis software used in the image analysis (EXFact analysis for porous particles, Nihon Visual Science, Inc., Japan). In this study scanning resolution 12 and 30 µm/voxel and ROI = 200 ×200×200 voxels were used for image analysis. Calculated mean (µ) and standard deviation (σ) values of pore structure parameters for undisturbed and repacked samples with different SR are summarized in Table 3. Compare to the undisturbed samples the repacked samples showed less variation of pore structure parameters. The pore tortuosity factors derived from MFXCT (T_{MFXCT}) were well correlated with the indirect connectivity tortuosities (X_G) from measured soil gas diffusion (Fig 4a and Fig 4b). The values that were not detected from the MFXCT analysis and that were not measurable because of low air permeability were not shown in Fig 4. [10] had also reported that reasonably good agreement between the pore characteristic parameter tortuosity determined from MFXCT analysis and from gas transport parameters. However, it was observed that there were some variations between effective pore diameters from MFXCT (d_{MFXCT}) and equivalent pore diameters for gas flow (d_G) estimated by gas transport parameters depending on scanning resolutions (ranging from 1:3 to 2:1 for SR =12µm/voxels and 1:1 to 5:1 for SR = 30µm/voxel) (Fig.4c and Fig. 4d). Similar findings were obtained in a previous study [19] for landfill cover soil (loam). This indicates that further improvements are needed to better correlate the pore diameter derived from MFXCT analysis with the equivalent pore diameter from gas flow measurements. Pores less than SR was not visualized due to limitations of MFXCT system.

Table 3. Mean values and standard deviations of undisturbed and repacked samples with different dry bulk density condition.

Sample	ρ_d gcm^{-3}	SR 12 µm/voxel						SR 30 µm/voxel					
		r_{eff}		T		C_n		r_{eff}		T		C_n	
		µ	σ	µ	σ	µ	σ	µ	σ	µ	σ	µ	σ
Undisturbed volcanic ash (5 cm depth)	0.80	30.5	14.1	1.54	0.05	3.49	1.33	95.0	52.2	1.58	0.06	3.07	0.85
	0.78	32.0	14.7	1.57	0.06	3.17	1.12	87.7	43.3	1.64	0.09	3.15	0.95
Repacked volcanic ash (5 cm depth)	0.55	32.2	15.3	1.69	0.09	3.07	0.89	121	61.4	1.58	0.06	3.29	1.07
	0.80	28.5	11.7	NP	NP	3.30	1.23	95.2	49.5	NP	NP	3.61	1.13
Undisturbed volcanic ash (50 cm depth)	0.49	32.9	15.8	1.77	0.20	3.16	0.95	106	59.2	1.76	0.15	3.22	0.91
	0.49	32.4	14.6	1.82	0.14	3.23	1.03	106	60.4	1.82	0.12	3.28	1.01
Repacked volcanic ash (50 cm depth)	0.49	32.3	15.7	1.86	0.17	3.20	1.01	105	56.0	1.87	0.17	3.25	1.04
	0.55	30.2	13.3	NP	NP	3.32	1.24	97.9	50.7	NP	NP	3.52	1.18

NP: calculation not possible from MFXCT, SR: scanning resolution, ρ_d: dry bulk density, r_{eff}: effective pore radius, *T: pore t*ortuosity, C_n: pore coordination number, µ: mean, σ: standard deviation

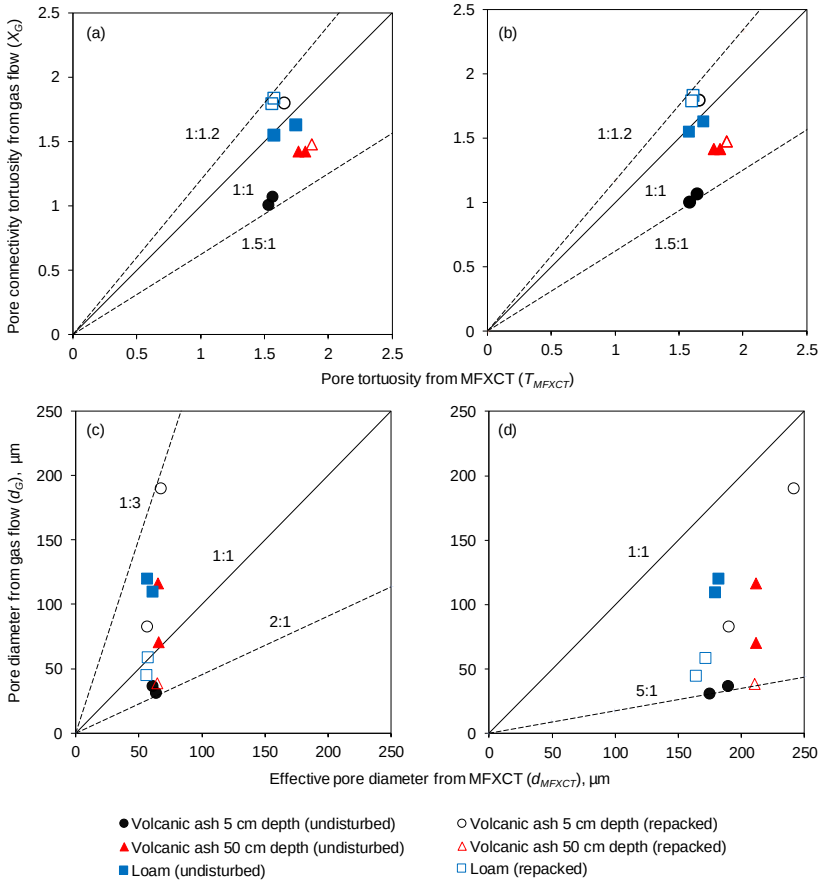

Figure 4. Comparison of pore connectivity tortuosity determined from MFXCT (X_{MFXCT}) and from gas transport parameters (X_G) (a) SR = 12 µm/voxel (b) SR = 30 µm/voxel. Comparison of pore diameter from MFXCT (d_{MFXCT}) and from gas transport parameters (d_G) (c) SR = 12 µm/voxel (d) SR = 30 µm/voxel. (Solid line represents 1:1 and dotted lines represents boundary lines)

CONCLUSIONS

By using microfocus X-ray CT system, soil pore networks of undisturbed and repacked volcanic ash soils with different scanning resolution (voxel) and different ROIs were visualized, and pore-structural parameters were analysed and these parameters were compared with the indirect pore structural parameters

obtained from gas flow methods. The major findings are:

(i) Effective pore radius (r_{eff}) is greatly affected by scanning resolution size compared to pore network tortuosity and coordination number. With the increasing analysis of volume (ROI), less variation of pore structure parameters was observed.

(ii) The pore tortuosity derived from MFXCT was well correlated with the indirect connectivity and tortuosities predicted by using soil gas diffusion. However, some variations in pore diameters were observed.

Measurement of pore network from MFXCT seems highly promising for further understanding of gas transport parameters.

ACKNOWLEDGMENTS

This study was partially supported by a JST-JICA Science and Technology Research Partnership for Sustainable Development (SATREPS) project and was made possible by the 'Providing New Insight into Interactions Between Soil Functions and Structure' (PROTINUS)-project in the framework of H2020

REFERENCES

[1] Kruse C. W., Moldrup P., and Iversen N., Modeling Diffusion and Reaction in Soils .2. Atmospheric Methane Diffusion and Consumption in a Forest Soil, Soil Science, Vol. 161, No. 6, 1996, pp. 355–365.

[2] Hamamoto S., Moldrup P., Kawamoto K., Wickramarachchi P. N., Nagamori M., and Komatsu T., Extreme Compaction Effects on Gas Transport Parameters and Estimated Climate Gas Exchange for a Landfill Final Cover Soil, Journal of Geotechnical and Geoenvironmental Engineering, Vol. 137, No. 7, 2011, pp. 653–662.

[3] Poulsen T. G., Blendstrup H., and Schjønning P., Air Permeability in Repacked Porous Media with Variable Structure-Forming Potential, Vadose Zone Journal, Vol. 7, No. 4, 2008, p. 1139.

[4] Otani J., Mukunoki T., and Obara Y., Application of X-Ray CT Method for Characterization of Failure in Soils., Soils and Foundations, Vol. 40, No. 2, 2000, pp. 111–118.

[5] Mees F., Swennen R., Geet M. Van, and Jacobs P., Applications of X-Ray Computed Tomography in the Geosciences, Geological Society, London, Special Publications, Vol. 215, No. 1, 2003, pp. 1–6.

[6] Hamamoto S., Moldrup P., Kawamoto K., Sakaki T., Nishimura T., and Komatsu T., Pore Network Structure Linked by X-Ray CT to Particle Characteristics and Transport Parameters, Soils & Foundations, Vol. 56, No. 4, 2016, pp. 676–690.

[7] Anderson S. H., Peyton R. L., and Gantzer C. J., Evaluation of Constructed and Natural Soil Macropores Using X-Ray Computed Tomography, Geoderma, Vol. 46, No. 1–3, 1990, pp. 13–29.

[8] Lindquist W. B., Venkatarangan A., Dunsmuir J., and Wong T., Pore and Throat Size Distributions Measured from Synchrotron X-Ray Tomographic Images of Fontainebleau Sandstones, Journal of Geophysical Research: Solid Earth, Vol. 105, No. B9, 2000, pp. 21509–21527.

[9] Lindquist W. B., Lee S.-M., Coker D. A., Jones K. W., and Spanne P., Medial Axis Analysis of Void Structure in Three-Dimensional Tomographic Images of Porous Media, Journal of Geophysical Research: Solid Earth, Vol. 101, No. B4, 1996, pp. 8297–8310.

[10] Naveed M. *et al.*, Correlating Gas Transport Parameters and X-Ray Computed Tomography Measurements in Porous Media, Soil Science, Vol. 178, No. 2, 2013, pp. 60–68.

[11] Lindquist W. B. and Venkatarangan A., Investigating 3D Geometry of Porous Media from High Resolution Images, Physics and Chemistry of the Earth, Part A: Solid Earth and Geodesy, Vol. 24, No. 7, 1999, pp. 593–599.

[12] Currie J. A., Gaseous Diffusion in Porous Media Part 1. - A Non-Steady State Method, British Journal of Applied Physics, Vol. 11, No. 8, 1960, pp. 314–317.

[13] Osozawa S., Measurement of Soil-Gas Diffusion Coefficient for Soil Diagnosis, SPCPG, Vol. 55, 1987, pp. 53–60.

[14] Rolston D. E. and Moldrup P., 4.3 Gas Diffusivity, Methods of Soil Analysis: Part 4 Physical Methods, Vol. methodsofs, 2002, pp. 1113--1139.

[15] Gliński J. and Stępniewski W., *Soil aeration and its role for plants*, 1985. CRC Press, Inc., 1985.

[16] Iverson B. V, Schjonning P., Poulsen T. G., and Moldrup P., In Situ, on-Site and Laboratory Measurements of Soil Air Permeability: Boundary Conditions and Measurement Scale, Soil Science, Vol. 166, No. 2, 2001, pp. 97–106.

[17] Buckingham E., Contributions to Our Knowledge of the Aeration of Soils, 1904. U.S. Dept. of Agriculture, Bureau of Soils, 1904.

[18] Millington R. J. and Quirk J. P., Formation Factor and Permeability Equations, Nature, Vol. 202, No. 4928, 1964, pp. 143–145.

[19] Baniya A., Matsuno A., and Kawamoto K., Characterization of Pore-Structure Parameters for Undisturbed and Repacked Soils at Filed Water Contents. Japan Geoscience Union Meeting, 2019.

9th Int. Conf. on Geotechnique, Construction Materials and Environment, Tokyo, Japan, 20-22 November 2019, ISBN: 978-4-909106025 C3051

PROPERTIES AND LIQUEFACTION RISK ON BULK CARGO CARRYING BUKIT GOH, KUANTAN BAUXITE; IN ACCORDANCE WITH IMSBC CODE

*Muzamir Hasan[1,2,3], Masitah Abdullah[2], Muhammad Fat-hi Al Juwaini Pahrol[1,2,3] and Masayuki Hyodo[4]

[1] Earth Resources & Sustainability Centre, University Malaysia Pahang, Malaysia
[2] Faculty of Civil Engineering & Earth Resources, University Malaysia Pahang, Malaysia
[3] Centre for Earth Resources Research & Management, University Malaysia Pahang, Malaysia
[4] Department of Civil and Environmental Engineering, Faculty of Engineering, Yamaguchi University, Japan

ABSTRACT

Bauxite is a raw material used in the production of alumina and, subsequently, aluminium. Like many metals, world demand for aluminium, and therefore bauxite, has grown substantially over the past 10 years in response to economic growth in emerging Asian economies. Bauxite is a relatively soft ore with a distinctive reddish brown colour. Bauxite ore from Malaysia exported to manufacturing country such as China to be processed into aluminium. Basic properties of bauxite are determined for exporting purpose in which several international specifications need to be followed while handling bauxite in order to ensure those raw materials are passing the standard to be imported. Laboratory test had been done to bauxite samples from Bukit Goh in Kuantan to determine its basic and morphological properties. It is found out that moisture content of raw Bukit Goh bauxite is higher compared to processed bauxite where it has the average of 24.33% over 7.16% only on the processed bauxite sample. For particle distribution, it shows that the processed bauxite has less fine particle compared to raw samples with the average of 16.60% compared to raw with 38.50%. Result from FESEM test proves that the lesser fine particle attached to the processed bauxite ore. Referring to the IMSBC Code, it can be stated that raw bauxite samples from Bukit Goh does not pass the standard. This is due to the presence of bulky fine particles which tend to absorb water more than granular particles that may lead to liquefaction to occur. Liquefaction during cargo transportation is high risk especially when there are strong current at the sea. In order to ensure the bauxite is passing the standard, beneficiation process must take place where it include washing, wet screening and mechanical or manual sorting.

Keywords: International Maritime Solid Bulk Cargoes (IMSBC) Code, Bauxite, Liquefaction

INTRODUCTION

Cargo liquefaction has been an arising issue since it is the major reason for numerous bulk carriers' capsizes. Many solutions have been adopted by researchers and seafarers to avoid these incidents which can be divided into experimental tests and numerical simulations [6] , [1]. The main cause of the problem is excess pore water pressure within the bulk cargo. The presence of unmanageable pore water pressure will weaken the microstructure of the soft soil particles, and it can make the unloading creep damage of soft soil extremely strong and even cause liquefaction [8]. The scenario is similar to liquefaction in solid bulk cargo. The ship's motion and the engine vibration during passage may cause particle rearrangement and compaction [3]. The gaps between the particles become smaller in the process, with the corresponding pore pressure progressively increasing [2]. As a result, the water holding ability of particles and the friction coefficient between cargoes decreases. In particular, the water in the interstellar spaces comes together to form a liquid layer that allows the cargo above to move relative to the cargo below – as if the two layers were part of a liquid and hence the term 'liquefaction'. Such a transition during ocean carriage can cause a sudden loss of stability of the carrying vessel. In the last ten years, more than ten ships capsized and sank due to a loss of hull stability attributed to the cargo liquefaction [4]. In addition, the problem of water pollution was widely reported by mainstream and social media. Bauxite is the major alumina (Al2O3) bearing ore used in the aluminum manufacturing industries. The bauxite containing less than 50% Al2O3 is called low-grade bauxite ore which is commonly used for the alumina-based abrasives and refractories productions. The alumina-silica and alumina-ferrite complexes are the foremost impurities present in the low-grade bauxite [9]. Aluminium is the most abundant metal in the crust of the earth and also can be recycled repeatedly while

maintaining its quality, so it is an environmentally friendly choice for many products. It does not rust, is not magnetic and it conducts both heat and electricity with ease. It is light and more easily shaped than many other metals while still staying remarkably strong [7]. Adaptable and practical, aluminium is often brought to our daily life through the process of aluminium extrusion. Besides smelter and manufacturing its own aluminium, Malaysia also exported the bauxite to China which is Malaysia's largest export destination. Due to strong demand from this country, Malaysia had to double and tripled the production of bauxite in order to meet the demand [10]. Thus, this study is carried out to determine does the bauxite production is achieved the IMSBC Standard or not for exporting where its basic properties; specific gravity, moisture content and particle size distribution is measured.

Percentage of moisture content of the sample does have a relationship with particle size distribution where the presence of fines particles will influence its water-holding properties [2]. Fine particles will increase total void ratio therefore increasing the capacity of the particles to store water. High moisture content as well as high value of specific gravity is not acceptable for solid bulk cargoes because it will be too risky to transport them.

OBJECTIVES OF THE STUDY

In general, this research aims to identify the geotechnical properties of raw and processed Kuantan bauxite by doing a laboratory test on Bukit Goh bauxite samples. In order to achieve the research aim, the following objectives had been established:

I. To determine basic properties of Bukit Goh, Kuantan bauxite
II. To determine morphological characteristics of Bukit Goh, Kuantan bauxite
III. To determine the suitability and quality of Bukit Goh, Kuantan bauxite according to IMSBC code.

SCOPE OF STUDY

The samples of bauxite ore were taken from Bukit Goh, Kuantan, Pahang which is located approximately 25km from Kuantan. A full laboratory scale test is carried out through this research in order to determine the correlation between the basic properties of Kuantan bauxite. The required testing are moisture content test, specific gravity test, sieve analysis test, field emission scanning electron microscope (FESEM) and x-ray fluorescence (XRF).

METHODOLOGY

In this study, to determine basic properties of bauxite sample, there are about five laboratory test and analysis done to 4 samples; 2 samples from Bukit Goh mine (M2L1 and M2L2) and 2 sample from stock pile (PTST1 and PTST2) to list out the required data. Sieving Analysis is done to determine particle size distribution of bauxite samples. Meanwhile, specific gravity of bauxite samples and moisture content determination is carried out to identify the specific gravity and moisture content present in the samples.

Meanwhile, for morphological study, samples is sent for FESEM test to have clear vision about the condition of bauxite particles under certain magnification while XRF test is conducted to identify the composition of elements and oxides of Bukit Goh bauxite

Table 1 Type of Test and Standard of Sample Tested

Soil Sample	Laboratory Tests	Standard
Bauxite (Bukit Goh)	Moisture Content Test	Geospec 3: Part 2; 5 Clause 3.2
	Specific Gravity Test	Geospec 3: Part 2; 7 Clause 3.4
	Particle Size Distribution	Geospec 3: Part 2; 8 Clause 3.5
	X-Ray Fluorescence (XRF)	QUANT-EXPRESS (Full Analysis) by XRF S8 Tiger
	Field Emission Scanning Electron Microscopic (FESEM)	By JSM 7800-F

RESULT AND DISCUSSIONS

Raw data of basic properties of the samples collected from laboratory test were analysed by referring to the formula and method stated in Geospec 3: Model Specification for Soil Testing. There are some standard and regulations that need to be follow by using IMSBC Code. Table 2 below shows the percentage of fine particles between raw and processed Bukit Goh Bauxite for four samples.

Table 2 Percentage of fine particles between raw and processed Bukit Goh Bauxite

Sample	Raw (%)	Processed (%)
M2L1	34	19
M2L2	40	24
PTST1	40	22
PTST2	40	18

Average fine particle	**38.50**	**16.60**

This test was conducted to evaluate the size characteristic of the Bukit Goh bauxite to determine whether it is safe to be exported undisturbed or otherwise. The deposits size that is permitted by IMSBC Code for fine particles content is between 10% to 30%. For bigger lumps; 2.5mm to 500mm, the suitable size for safe transportation is from between 70% to 90%

Referring to IMSBC Code, allowable size for cargo transportation is between 2.5 mm to 500 mm with total percentage of 70% to 90% lumps and only 10% to 30% powder. Based on the result analysis prove that the particle size distribution Bukit Goh bauxite's not in range the requirement size in IMSBC Code. The result proved that raw Bukit Goh bauxite's in average consist more than 30% fine particle and less than 70% coarse particle. Due to this situation, the moisture content of the raw bauxite will increase. Meanwhile, bauxite of the same sample that has been beneficiated has fine particle less than 30% which prove that beneficiation method can reduce the number of fine particles in bauxite.

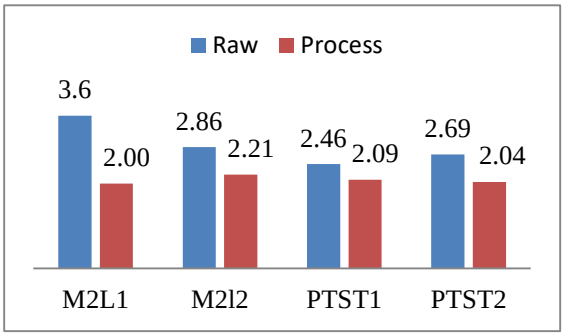

Figure 1 Tabulation of average specific gravity

The result from Small Pycnometer Test was collected and tabulated in Figure 1 for PTST1 and PTST2 are almost the same. Meanwhile, there is slightly difference in specific gravity for M2L1 and M2L2. The specific gravity of processed bauxite samples is slightly lower than the raw sample. Specific gravity for bauxite is between 2.0 – 3.0, thus the bauxite samples collected from Bukit Goh mine are still between the range of the study.

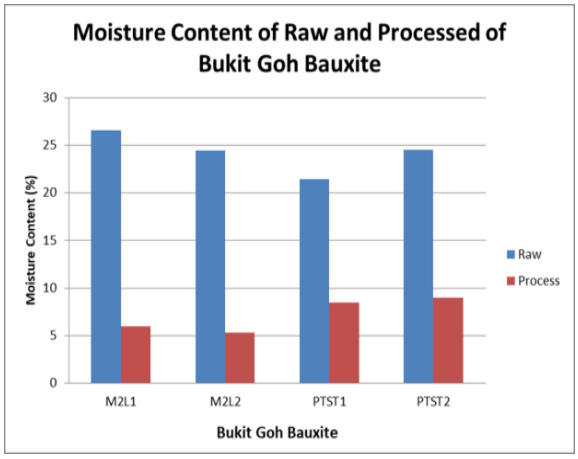

`Figure 2 Tabulation of average moisture content

From the comparison in the histogram in Figure 2, it shows that the moisture content of raw Bukit Goh bauxite is higher compared to processed bauxite where it has the average of 24.33% over 7.16% only on the processed bauxite sample. Due to higher moisture content, it clearly demonstrates that raw Bukit Goh bauxite have large amount of fine particle compared to coarse particle. Meanwhile, the moisture content for processed bauxite is within the allowable range in the IMSBC Code; 0%-10% which makes the bauxite safe to be exported [5].

Table 3 Raw and processed Bukit Goh Bauxite elements

Parameters	Unit	Raw	Processed
Iron (FE)	%	31.38	26.49
Aluminium (AL)	%	7.48	7.25
Titanium (Ti)	%	3.96	3.33
Silicon (Si)	%	0.50	0.44
Phosphorus (P)	%	0.40	0.41
Calcium (Ca)	%	0.09	0.11
Sulphur (S)	%	0.09	0.07
Chromium (Cr)	%	0.08	0.09
Manganese (Mn)	%	0.06	0.05
Zirconium (Zr)	%	0.05	0.05
Strontium (Sr)	%	0.02	0.02
Niobium (Nb)	%	0.02	0.02
Zinc (Zn)	%	0.01	0.02
Gallium (Ga)	ppm	69	79
Yttrium (Y)	ppm	35	48

Table 4 Raw and processed Bukit Goh Bauxite oxides

Parameters	Unit	Raw	Processed
Iron (III) Oxide	%	44.86	37.88
Aluminium Oxide	%	14.13	13.69
Titanium Dioxide	%	6.60	5.55
Silicon Dioxide	%	1.07	0.94
Phosphorus Pentoxide	%	0.91	0.93
Sulphur Trioxide	%	0.22	0.18
Calcium Oxide	%	0.13	0.15
Chromium (III) Oxide	%	0.12	0.13
Manganese Oxide	%	0.08	0.06
Zirconium Dioxide	%	0.07	0.06
Niobium Pentoxide	%	0.03	0.02
Strontium Oxide	%	0.02	0.02
Zinc Oxide	%	0.01	0.02

From Table 3, it shows that the quantity of Silicon (Si) is reduced from 0.50% to 0.44% and from Table 4, the amount of Silicon Dioxide (SiO2) or also known as silica is minimized from 1.07% to 0.94% after beneficiation process. Unfortunately, the value of aluminium element also decreases slightly from 7.48% to 7.25% although it has not much effects on the bauxite products. As mentioned before, the core target of washing bauxite is to decrease the amount of silica and improve the amount of aluminium. In addition, along with silica, the insoluble iron and titanium oxides in red mud will also be removed that will abolish lower grade fines and enhance the quality of bauxite

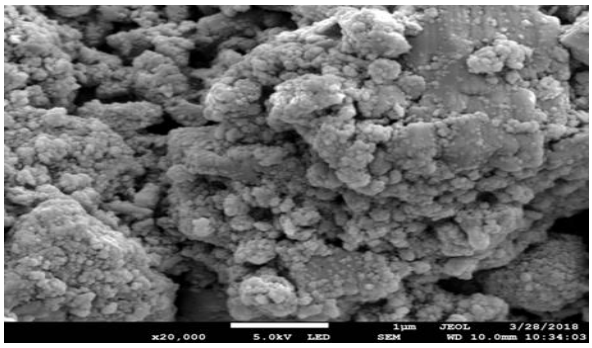

Figure 3 Raw Bauxite Morphology under 20000x magnification

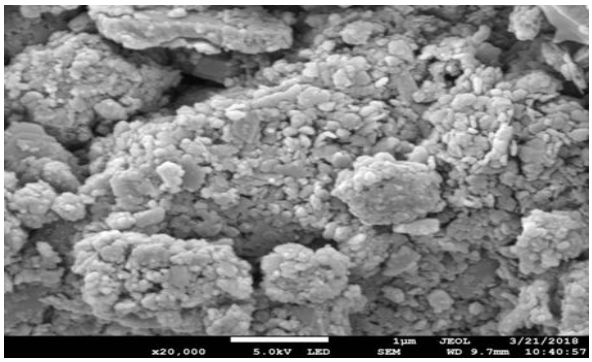

Figure 4 Process Bauxite Morphology under 20000x magnification

Clear image of particles started to be seen under 20000 x magnifications, fine particles attached to the bauxite sample are clearly can be seen for raw samples. This figure explained the main cause of high percentage of moisture content. Large amount of fine particles at the bauxite ore may result liquefaction to take place due to fine particles that have low anti-liquefaction characteristics compared with lump particles and granular particles. Clearly seen that the lesser fine particle attached to the processed bauxite ore. This proved the washing of bauxite can reduce the amount of fine particle in bauxite lump.

CONCLUSIONS

The potential liquefaction of bauxite cargoes has been the subject of a number industry bulletins in recent years. These concerns have been renewed following the recent sinking of the bulk carrier Bulk Jupiter reportedly carrying 46,400 MT of bauxite loaded at Kuantan in Malaysia [10]. Due to series of cargo liquefaction increased while shipping mineral ores, The Maritime Safety Committee of International Maritime Organization (IMO) has adopted the IMSBC Code to facilitate the safety of the cargo while transporting solid bulk. The main purpose of IMSBC Code is to provide a better guidance while handling solid bulk shipping in the cargo in terms of stowage and shipment. Thus, beneficiation process is a good method to reduce the fine particles in bauxite deposits that will minimize the dust pollution when transporting on land by lorries. This process also will decrease the water content of bauxite because there is a lesser fine particle content as well as improving the quality of bauxite that will be extracting into good quality aluminium. This study is focused on three basic properties which are particle size distribution, moisture content and specific gravity. Based on the results and discussion gained from the previous chapter, there are several conclusions that can be finalized as follow:

I. Results from the sieve analysis study concluded that the average fine particle sizes of raw bauxite are 38.50% which is higher than already processed bauxite sample with the average of 16.60%. Thus, by comparing to IMSBC Code, raw Bukit Goh bauxites are not fulfilling the maximum fine particle size passing of 30% requirement in the standard IMSBC Code and therefore it is not suitable to be exported.

II. From the outcome of beneficiation, the Bukit Goh bauxite has lower moisture content percentage with the value of 7.16% compared to raw bauxite with moisture content of 24.33% which exceed the 10% limitation. It is due to the lower content of fine particle in processed bauxite that absorbs less water.

III. The chemical properties of both raw and processed bauxite are tested by X-ray Fluorescence test. The Silicon (Si) element and

silicon dioxide that made up most of the fine particle in bauxite was reduced from 3.81% to 1.53% and 4.61% to 2.32% respectively.

IV. Study on morphological properties of Bukit Goh bauxite displays that the fine particles of raw bauxite is higher than the beneficiated bauxite. Clearly seen that the lesser fine particle attached to the processed bauxite ore resulting in lower absorption of moisture. All these basic properties are lead to lower risks of liquefaction to occur during bauxite cargoes transportation.

V. To be classified as Group C, the moisture content of bauxite must be within the 0% to 10%. For particle size, 70% to 90% for coarse lumps, varying between 2.5 mm and 500 mm and 10% to 30% for powder.

ACKNOWLEDGMENTS

The authors would like to acknowledge the Universiti Malaysia Pahang (UMP) and Japan International Cooperation Agency (JICA) for financing this research through the UMP Flagship Grant Scheme, Project Number RDU172205 and JICA International Grant, Project Number UIC181507, respectively. The cooperation given by all parties involved in this research is greatly acknowledged**.**

REFERENCES

[1] Bao, X., Zhiyang, J., Hongzhi, C., Xiangsheng, C., and Xiongyao, X. (2019). Soil Liquefaction Mitigation in Geotechnical Engineering: An Overview of Recently Developed Methods. Soil Dynamics and Earthquake Engineering 120: 273–91

[2] Buchanan, S.J., Kopittke, P.M, Menzies, N.W and So, H.B. 2010. Influence of texture in bauxite residues on void ratio, water holding characteristics and penetration resistence. Geoderma. (158): 421-426

[3] Daoud, S., Imen, S., Samir, E., and Mounir, B. (2018). Numerical Analysis of Cargo Liquefaction Mechanism under the Swell Motion. Marine Structures 57:52–71

[4] Hasan, M., Faez, A. A.,Moqsud, M. A., Tam, W. L. and Phang, B. Y (2017) Properties of Raw and Processed Bukit Goh Bauxite In Kuantan, Pahang In Accordance With IMSBC Code. In: Seventh International Conference on Geotechnique, Construction Materials and Environment, 21-24 November 2017, Mie, Japan. pp. 1-6

[5] IMO. 2011. International Maritime Solid Bulk Cargoes Code MSX. 393 (95)

[6] Ju, L., Dracos, V., Qing, W., Yongkui, W., and Yang, L. (2018). Numerical Investigation of Solid Bulk Cargo Liquefaction. Ocean Engineering 159:33–47

[7] Liu, Y., Ming, H. and Naidu, R. 2012. Surface electrochemical properties red mud (bauxite residue): Zeta potential. Journal of Colloid and Interface Science.394 (2013): 451-457

[8] Li, D., Farshad, A., Wei, H., Kejun, W., Xiaojia, D., Lin, L., and Haifei, J. (2019). Experiment Study of Lateral Unloading Stress Path and Excess Pore Water Pressure on Creep Behavior of Soft Soil. Advances in Civil Engineering 2019:1–9.

[9] Sukla, L. B., Pattanaik, A., and Pradhan, D. (2019) Advances in Beneficiation of Low-Grade Bauxite. In: Chesonis C. (eds) Light Metals 2019. The Minerals, Metals & Materials Series. Springer, Cham.

[10] The Bauxite Index. 2016. Bauxite mining. https://bauxiteindex.com/en/cbix/industry101/bauxite-101/bauxitemining#bauxite_101, (2016).

9th Int. Conf. on Geotechnique, Construction Materials and Environment, Tokyo, Japan, 20-22 November 2019, ISBN: 978-4-909106025 C3051

EFFECT OF CONSTRUCTION SEQUENCE ON THE PERFORMANCE OF GEOTEXTILE TUBES IN A CONTAINMENT BUND

J.W. Koh[1], K.E. Chua[2], H.M. Audrey Yim[3], S.H. Chew[4], and Z.X. Gng[5]
[1,3,4]Department of Civil and Environmental Engineering, National University of Singapore (NUS),
[2,5]Housing and Development Board (HDB), Singapore

ABSTRACT

Geotextile tubes (geotubes) filled with lightly cement-mixed soil (CMS) are used to construct a containment bund. The proposed containment bund was made of three layers of geotextile tubes, where each of the geotube was infilled to a height of 2m and stacked to form a 6m high containment bund in the shape of a triangular prism. Three geotubes were placed side by side to form the first layer of the containment bund. The shear strength development of the CMS of the first layer containment bund was evaluated using a modified mini Cone Penetration Test (CPT) after the infilling. The results suggested that the shear strength developed in the center geotube is generally lower than the edge geotubes. It was hypothesized that the edge geotubes, which were installed before the center geotube, hindered the dewatering action of the center geotube during its infilling process. Hence, a study on a scaled-down version of the three geotubes arrangement was conducted in the field with instrumentation. The hypothesis mentioned above was examined through the changes in volume and strain mobilised in the geotextile of geotube, the dewatering rate, and the shear strength development of the CMS, pore pressure and total pressure changes during infilling and dewatering phase of the geotubes. The study showed that the construction sequence of the geotubes indeed affects the shear strength development of the CMS.

Keywords: Geotextile tubes, Lightly cemented clay, Containment bund, Dewatering, Shear strength

INTRODUCTION

Sand is conventionally the preferred infill material of geotextile tubes (geotubes) to construct a stable containment bund. However, due to the shortage of sand in Singapore, lightly cement-mixed soil (CMS) is being studied as alternative infilling material for geotubes.

In one of Singapore's land reclamation projects, a containment bund was made up of three layers of geotubes, where each geotube was filled to a height of 2m and stacked to form a 6m high containment bund in the shape of a triangular prism as shown in Fig. 1. The first layer of the containment bund was made up of three geotubes placed side-by-side. After approximately three months since the infilling of the first layer of geotubes with CMS, the shear strength of the infill material was measured using a miniature Cone Penetration Test (CPT) equipment. It was found that the geotube in the center had a lower shear strength as compared to the edge geotubes. This was believed to be related to the construction sequence, where two edge geotubes were installed before the installation of the center geotube. A hypothesis was made that the installed edge geotubes somehow hindered the dewatering action of the center geotube during its infilling process.

In order to verify the proposed hypothesis, a field test with a scaled-down version of the three geotubes arrangement was conducted to simulate the actual large containment bund. These small geotubes were well-instrumented.

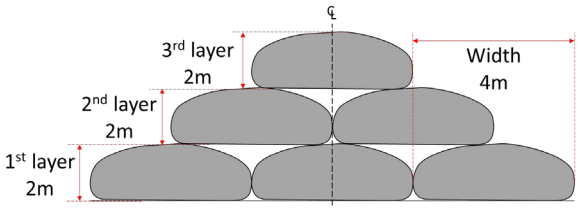

Fig 1 Cross section of geotubes containment bund (schematic).

MATERIALS

This section presents the materials used in this study. The properties of the geotextile, type of soil, cement, and monitoring instruments are elaborated.

Properties of Geotextile Materials

The scaled-down instrumented geotubes have a length of 2m and a circumference of 2.52m. The targeted height of the geotube was approximately 0.6m when fully filled. The geotube was made of Polypropylene (PP) woven geotextile, and the properties of the geotextile are tabulated in Table 1.

Table 1 Properties of geotextile material

Properties	Test Standard	Unit	Values
Tensile strength (MD/CD)	ISO 10319	kN/m	120/120
Elongation at break (MD/CD)	ISO 10319	%	20/15
Seam strength (CD)	ASTM D4884	kN/m	85
CBR puncture resistance	ISO 12236	kN	>14
Water permeability	ISO 11058	l/m^2/s	13
Pore size, O_{90}	ISO 12956	mm	<0.25

Properties of cement-mixed soil (CMS)

The Unified Classification of the soil used to produce the CMS infilling material is Sandy-Clayey SILT. The soil is then mixed with Ordinary Portland Cement (OPC). The cement content used was 7% to the dry unit weight of the soil. The bulk density of the CMS was determined to be 1.25 – 1.35 g/m^3.

Monitoring Instruments

The instrumentation plan for the geotextile tubes is shown in Fig. 2. All three geotubes were each instrumented with six strain gauges to capture the mobilized strains at the locations that were more prone to tearing.

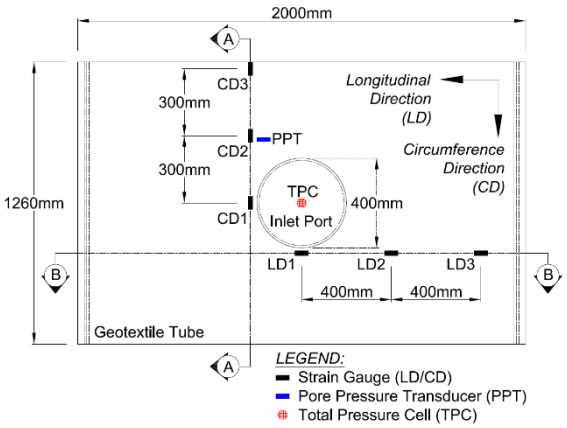

Fig. 2 Monitoring instruments layout on geotube when placed on flat (plan view).

Three strain gauges were attached in the circumferential direction (CD) and the other three were attached in the longitudinal direction (LD) as shown in Fig. 3. The strain gauges installation method proposed by Chew [1] was used in this study. Each geotubes was also fitted with one total pressure cell (TPC) and one pore pressure cell (PPT) near the bottom of inlet port to measure the variation of total pressure and pore water pressure with time, especially during the infilling process. A camera was used to capture the height change of the geotubes during the infilling and dewatering stages.

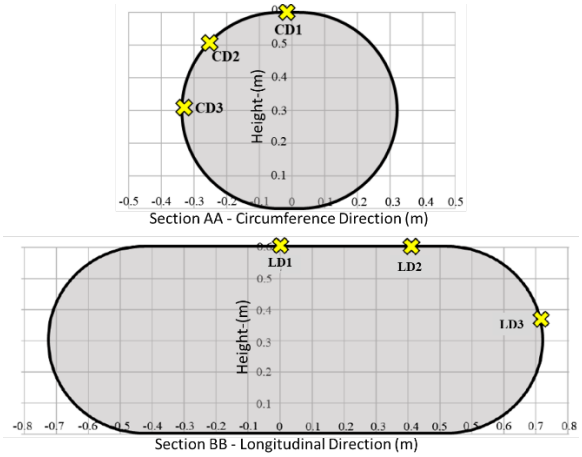

Fig 3 (Section AA & BB from Fig. 2) - Strain gauges location in CD & LD.

FIELD TEST SETUP & TEST PROCEDURE

The field test setup comprises of (a) a mixing pit with pump and pipeline, (b) the infilling and dewatering platform for the geotubes, and (c) a sump pit to collect the "dewatered" water from the geotubes. A layer of geomembrane was laid on the platform before the geotubes were laid on top of it. The geotubes were overlapped by up to 0.4m to simulate the actual construction conditions of the geotube containment bund. In addition, two levelling rods were positioned at both sides of the edge geotubes. The changes in height of the geotubes can then be analysed through the photos recorded by a camera positioned in front of the geotubes. Figure 4 shows the field setup mentioned above.

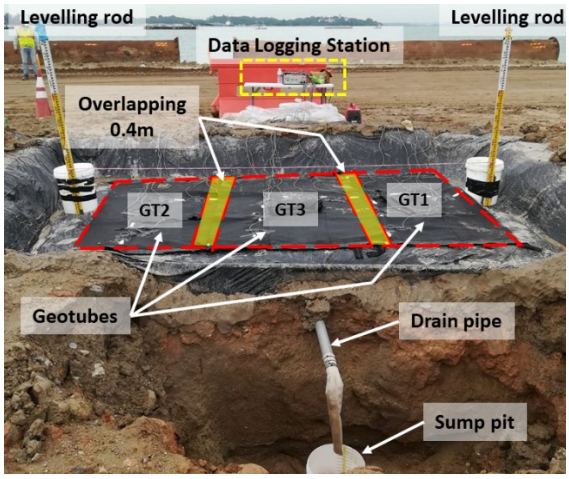

Fig. 4 Field Test Setup.

The field test began with the preparation of the CMS in the mixing pit. The infilling sequence followed with the first geotube on the right (GT1). After the GT1 had attained a height of 0.6m, the geotube on the left (GT2) was immediately infilled. Simultaneously, the water drained out from both of the geotubes during the dewatering process was collected in the sump pit. The volume of water collected was measured.

The infilling process of the center geotube (GT3) started after the dewatering process of the two edge geotubes (GT1 & GT2) ended. Similarly, the volume of water drained from the center geotube was measured. The entire infilling and dewatering process was recorded with a camera, which provides a record of the volume and height change of geotube with time. Fig. 5 illustrates the infilling sequence of geotubes.

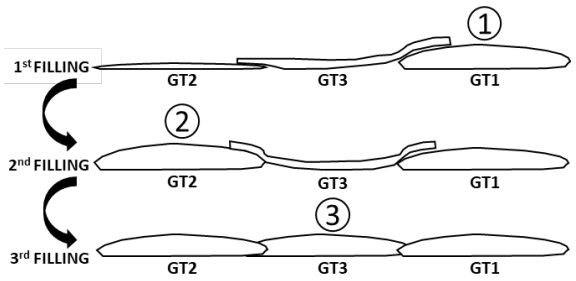

Fig. 5 Filling sequence (front view).

RESULTS & DISCUSSIONS

Changes in Shape, Height & Volume

Figure 6 shows the changes in height and shape of the geotubes with time. This enables the calculation of the change in volume of the geotubes with time by applying Eq. (1) proposed by Yee et al. [2]:

$$V_T = L_T {D_T}^2 \left[\left(\frac{h_T}{D_T}\right)^{0.815} - \left(\frac{h_T}{D_T}\right)^{8.6} \right] \quad (1)$$

where V_T is the volume of the geotube, L_T is the length of the geotube, h_T is the measured height of the geotube, and D_T is the theoretical diameter of the geotube. In this study, L_T = 2m and D_T = 0.802m.

The volume change of each geotube during the dewatering stage with infilling time is presented in Fig. 7. It illustrates that the results for GT1 and GT2 are consistent as they are identical in boundary condition at infilling and dewatering stages. It also clearly shows that the volume reduction of GT3 was much slower than that of GT1 and GT2. This suggests that the dewatering rate of the center geotube, GT3 was lower as compared to the edge geotubes. This suggestion can be further proved from the actual dewatering rate analysis of each geotube that will be presented in the next section.

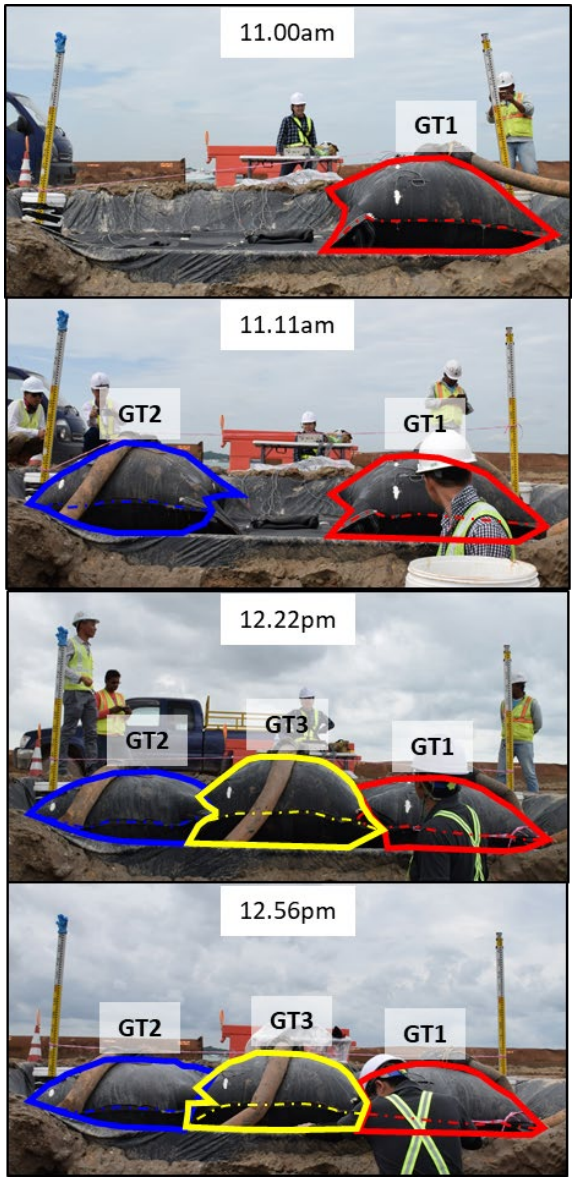

Fig. 6 Shape and height changes of geotubes.

Dewatering Rate

The dewatering rates of each geotube during the dewatering stage are plotted in Fig.8 using the recorded volume of effluent from the geotubes with time. For simplicity of calculation, the edge geotubes (GT1 and GT2) were assumed to have the same dewatering rate in this test. Hence, the volume of effluent collected from the edge geotubes (GT1 & GT2) was aggregated and the average volume was taken to compute the dewatering rate as they took place under the same period of time. From Fig. 8, the center geotube (GT3) showed a lower dewatering rate after 20 minutes as compared to that of the edge geotubes (GT1 & GT2). This matches the hypothesis in the earlier section and leads to the conclusion that the center geotube will be blocked or hindered by the edge geotubes, and thus the dewatering action will be

slowed down during the dewatering stage.

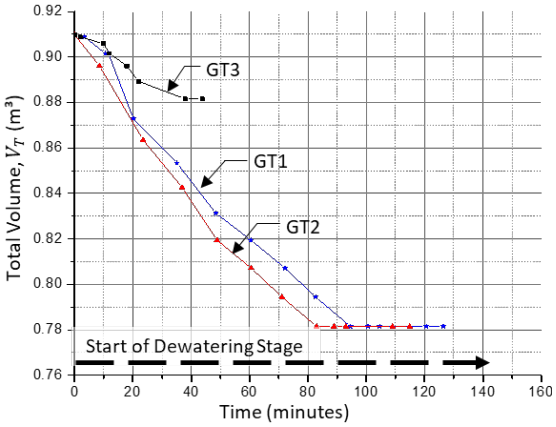

Fig. 7 Volume changes of geotubes over time of infilling.

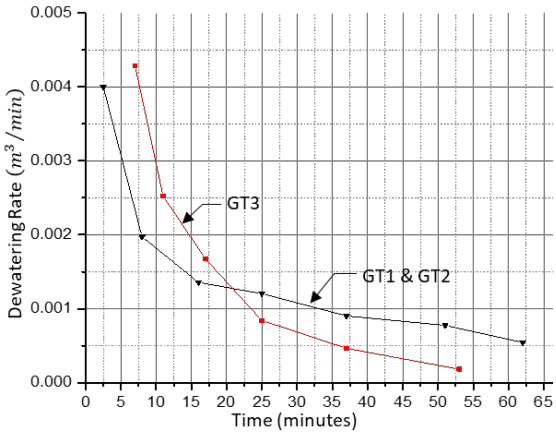

Fig. 8 Dewatering rate of geotubes.

Shear Strength Development

After infilling, the geotubes were left untouched for dewatering action and cementation reaction to take place. A modified mini Cone Penetration Test (CPT) was then conducted on the geotubes after 7 days and 28 days to ascertain the shear strength development of the infilled CMS. At 7 days, only one CPT testing point was conducted at each geotube, while two CPT testing points were conducted for each geotube at 28 days. Fig. 9(a) and Fig. 9(b) show the shear strength development of the CMS in the geotubes at 7 days and 28 days respectively.

The shear strength of the CMS at 7 days was in the range of 5kN/m^2 to 12kN/m^2 and increased to approximately 10kN/m^2 to 20kN/m^2 at 28 days. GT3 consistently had a lower shear strength at 7 days and 28 days than that of GT1 and GT2. This proves that the slow dewatering rate mentioned in the earlier section leads to a slightly lower shear strength development in GT3. It is also interesting to note that the shear strength at 7 days was uniformed with depth, while at 28 days, the CMS seemed to develop a higher shear strength with depth for all 3 geotubes.

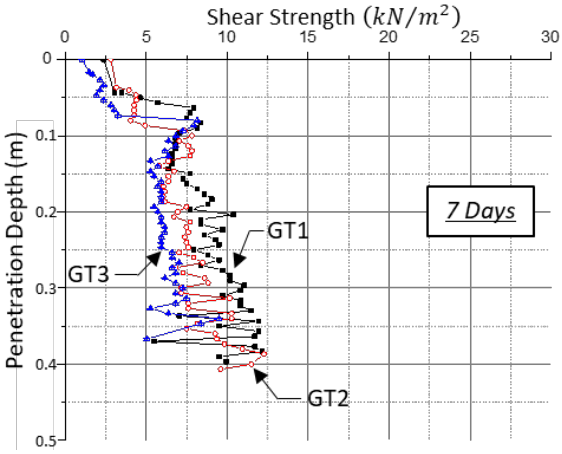

Fig. 9(a) Shear strength of infilling material at 7 days.

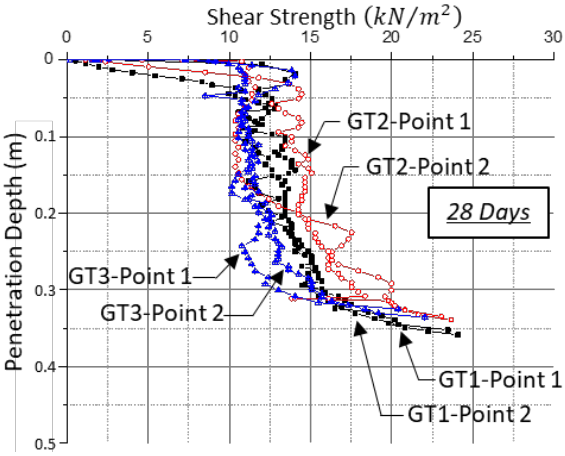

Fig. 9(b) Shear strength of infilling material at 28 days.

Mobilized Local Strain

The mobilized local strains in the circumferential and longitudinal direction on geotextile material of the geotubes are shown in Fig. 10(a) and Fig. 10(b) respectively. The strain data in both directions show that the highest local strain is generally generated at the moment when the maximum infilling height is attained. CD3-GT2 malfunctioned and thus has not been included in the analysis.

CD1-GT1 and LD3-GT1 registered the maximum local strain of 1.7% and 1.5% in circumferential and longitudinal direction respectively. This was because CD1-GT1 was attached nearest to the inlet port and LD3-GT1 was attached at the highest curvature point. Surprisingly, LD2-GT3 also registered the maximum local strain of 1.5% in the longitudinal direction. This could be due to the infilling sequence where the infilling of GT3 commenced immediately after GT1 and GT2 were fully filled. The edge geotubes would

have obstructed the expansion of GT3 in the circumferential direction leading to higher strain developed in the longitudinal direction for GT3 at that moment.

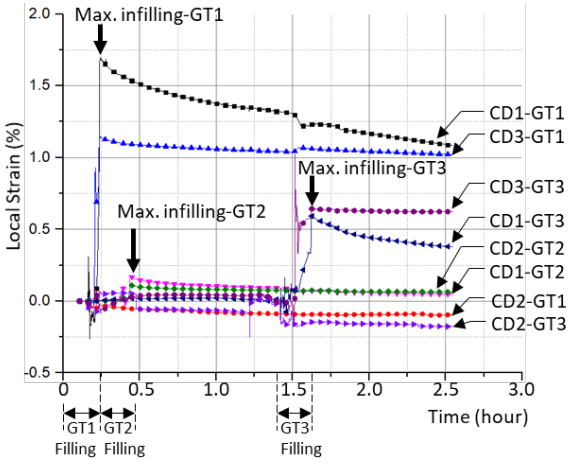

Fig. 10(a) Mobilized strain at CD on geotubes over time. (Refer to Fig. 3 for the location of the strain gauges)

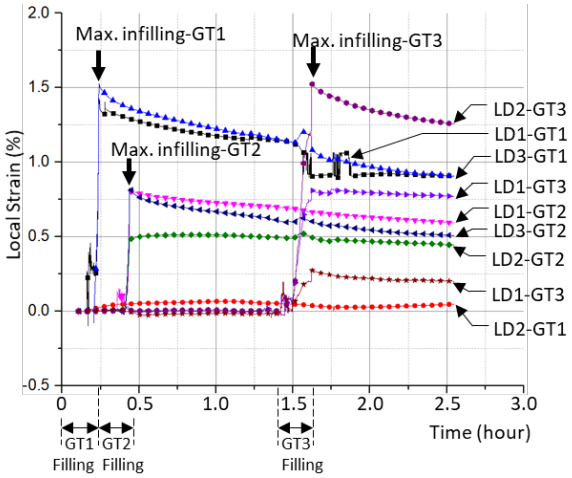

Fig. 10(b) Mobilized strain at LD on geotubes over time. (Refer to Fig. 3 for the location of the strain gauges)

Total Pressure & Pore Pressure

The total pressure in the geotubes during the test are shown in Fig. 11, with the times when the geotubes infilling took place indicated. It is shown that all geotubes registered the maximum total pressure at the end of infilling, and the total pressure subsequently gradually decreased with time.

The pore pressure measured within the geotubes with time is shown in Fig. 12. The maximum pore pressures of GT1 and GT2 were at the end of infilling when the geotubes were pumped to an approximate height of 0.6m. Subsequently, during the dewatering stage, the pore pressures decreased. However, the pore pressure in GT3 increases gradually with time even during the dewatering stage. This might due to a malfunction of the pore pressure transducer in the GT3.

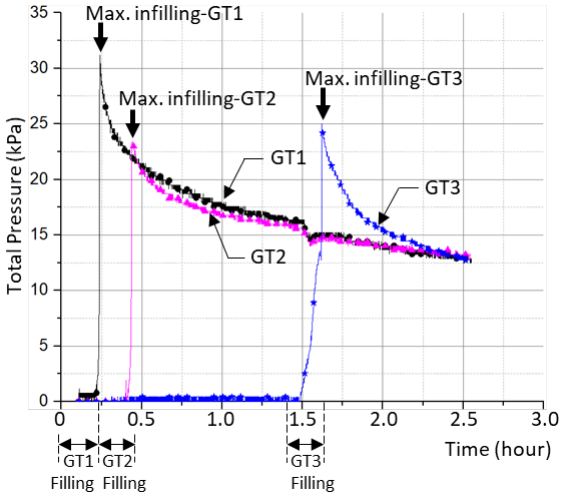

Fig. 11 Total pressure development of geotubes.

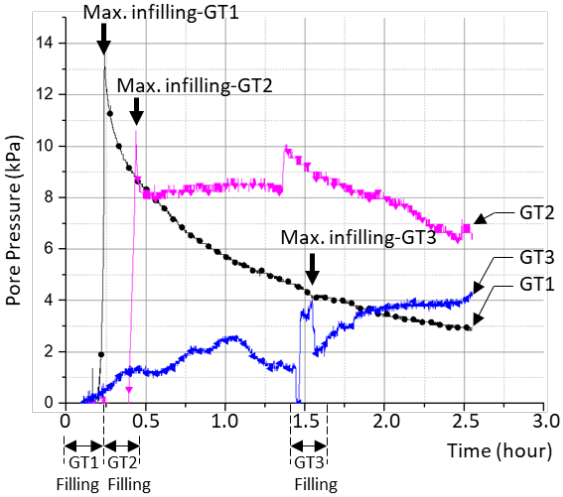

Fig. 12 Pore pressure development of geotubes.

CONCLUSION

A field test with scaled-down size geotubes filled with CMS material was conducted to model the effect of the construction sequence of the first layer of containment bund.

Three geotubes were modelled according to the actual construction sequence, where the two edge geotubes were installed first, followed by the center geotube. It was found that the volume reduction with time of the center geotube is generally slower than the edge geotubes. This is consistent with the observation that the dewatering rate of the center geotube is also the lower than the two edge geotubes.

The shear strength development of the CMS in the

geotubes further supports the finding above, where the center geotube had slightly lower shear strength amongst the three geotubes at 7 days and 28 days. It was also observed that the limited space for center geotube to expand sideways during the infilling stage caused the longitudinal direction of the center geotube to experience slightly higher strain as compared to that in the circumferential direction.

In conclusion, the construction sequence of the geotubes for the first layer in a containment bund would affect the behaviour of the geotubes, particularly the center geotube.

ACKNOWLEDGMENTS

The authors gratefully acknowledge the support of from Hyundai Engineering & Construction Co., Ltd. and Geoharbour Co., Ltd. for coordinating and carrying out the field tests reported in this study.

REFERENCES

[1] Chew, S.H., W.K. Wong, C.C. Ng, S.A. Tan, and G.P. Karunaratne., Strain Gauging Geotextiles Using External Gauge Attachment Method, ASTM Special Technical Publication 1379, 2000, pp. 97-112.

[2] Yee, T. W. & Lawson, C. R., Modelling the geotextile tube dewatering process, Geosynthetics International, 19, No. 5, 2012, pp. 339–353

9th Int. Conf. on Geotechnique, Construction Materials and Environment, Tokyo, Japan, 20-22 November 2019, ISBN: 978-4-909106025 C3051

STUDY ON THE PERFORMANCE OF SHALLOW SOIL MIXING WITH CEMENT

H.M. Audrey Yim[1], J.W. Koh[2], S.H. Chew[3], K.E. Chua[4], S.E. Danette Tan[5], and Y.S. Toh[6]
[1,2,3]Department of Civil and Environmental Engineering, National University of Singapore, Singapore;
[4,5,6] Housing and Development Board, Singapore

ABSTRACT

Shallow soil mixing (SSM) method with a low dosage of cement can be used to create a sufficiently strong platform for quick access onto grounds that have been recently reclaimed with soft clays. The effectiveness of the SSM method is dependent on the type, dosage and dosing method of cement, the mixing blade design, and the mixing sequence, etc. Hence, a laboratory-scale SSM apparatus was developed to simulate SSM in the field. The early strength development and uniformity of cement mixed soil (CMS) were evaluated by taking into consideration (a) Type of cement: CEM I vs CEM III/A, (b) Dosage of cement: 7% vs 3%, (c) Dosing method: 1-layer vs 2-layer mixing, and (d) Mixing blade design: without overlap between mixing blades vs overlapped mixing blades. Shear strength test results demonstrated that the shear strength development of CMS at an early stage is affected by the type, dosage, and dosing method of cement, while the uniformity of the CMS is affected by the dosage and dosing method of cement and the mixing blade design. From the laboratory test results, it is recommended that CEM III/A cement with 7% cement dosage, 2-layer of dosing method and overlapped mixing blades design parameters be used for SSM in the field to achieve high early strength gain and good uniformity cement soil mix.

Keywords: Shallow soil mixing, Early strength development, Uniformity

INTRODUCTION

In land reclamation, water bodies are usually reclaimed using fill materials such as sandy soils. However, due to the limited sources of sandy soil in Singapore, soft clays are used as the fill material instead. The major problem of using soft soils as the fill material is that it will undergo a substantial amount of settlement when loaded. Hence, ground improvement must be carried out to accelerate the consolidation and reduce post-construction settlement in the soft soil layer for the newly reclaimed land to gain enough strength for future use. However, to carry out ground improvement work on reclaimed land is also a great challenge as the ground improvement works also need a sufficiently strong working platform for machinery access.

One method of constructing the working platform for machinery access is to treat the top layer of the soft clay by mixing it with cement and creating a layer of cement-mixed soil (CMS). Some methods of introducing cement into the soft soils include Shallow Soil Mixing (SSM), jet grouting and Deep Cement Mixing (DCM). SSM and DCM both improve the geotechnical properties of soil by improving their undrained shear strength (Cu) and lowering compressibility [1]. SSM, however, is used to improve a large treatment area to a shallower depths (Fig. 1(a)), while DSM is used to treat soft soil to a greater depths with a smaller treatment area using column-by-column treatment arrangement. Fig. 1 illustrates this difference.

In the application that this study is concerned, since treatment to only the top shallow layer of soft soil is required, the use SSM to create a working platform for machinery access on ground recently reclaimed with soft soils will be discussed.

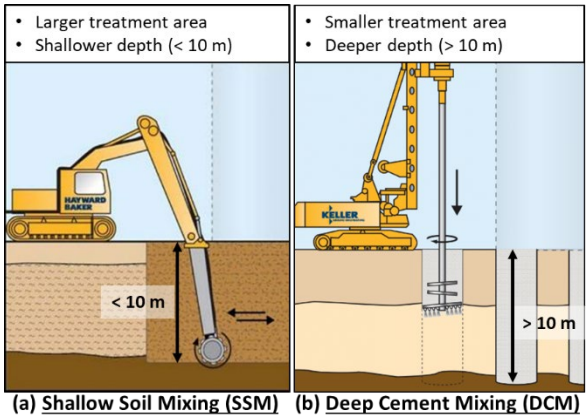

Fig. 1 Schematic illustration for Shallow Soil Mixing (SSM) and Deep Cement Mixing (DCM) [2].

Effectiveness of the SSM

Early strength of the CMS is very important for field implementation, as faster strength gained in the

CMS will allow early machinery access to the site. Existing literature reports that the parameters such as type of cement and dosage of cement affect the early strength development of CMS. Mixing uniformity is another key criteria for successful field implementation. A uniformed CMS will ensure uniformity in strength gained across the treatment area. The cement dosing method and mixing blade design are believed to be the parameters that will affect the uniformity of the CMS.

Hence, this study focuses on investigating the effect of the mentioned parameters on the early strength development and the uniformity of the CMS through a series of laboratory scale-SSM test.

Type of Cement

The two major standards used globally to categorise cement are (a) ASTM International standard, and (b) British Standard European Norm (BS EN). As early strength development is needed for the discussed application (which is the working platform at the shallow depth of soft soils), the type of cement mentioned in the two standards that are related to the early strength gain is as follows.

Referring to ASTM C150/150M, ASTM Type I cement is used for general purposes, while Type III is a rapid hardening cement with relatively high early strength gain. Fig. 2 shows the rate of strength development for various cement types according to ASTM, with higher the Tricalcium Silicate (C_3S) content in the cement composition providing higher early strength gain.

In the BS EN 197-1:2011, cement type is categorized based on the type of additional materials in the cement composition. The type of cement that provides high early strength gain is Portland cement (CEM I) and Silica fume cement (CEM II/A-D) as shown in Fig. 3. CEM I consists of 95-100% clinker, while CEM II/A-D consists of 90-94% of clinker and 6-10% of slica fume.

Blastfurnance cement (CEM III/A and CEM III/B) provides high long term strength development instead of high early strength gain. CEM III/A consists of 35-74% clinker and 36-65% granulated blastfurnance slag (GGBS), while CEM III/B consists of 20-34% of clinker and 66-80% of GGBS.

Cement Dosage

The effect of cement content on the unconfined compressive strength of Singapore Marine Clay is shown in Fig. 4. The strength of cement-treated clay increases with the amount of cement until a "saturated limit", beyond which there is no strength increment observed with additional cement [5]. For the current study, lightly cemented-clay with cement dosage ≤ 10% is adopted.

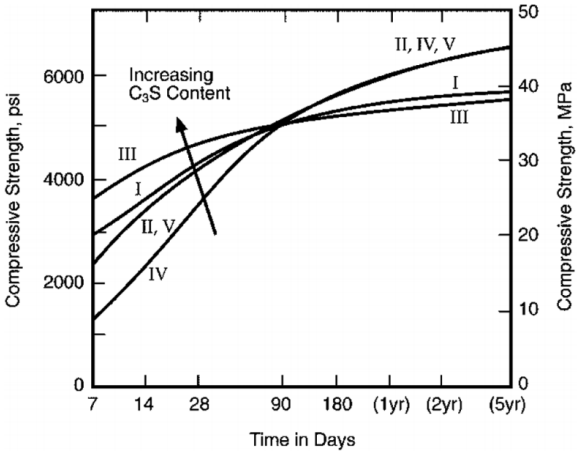

Fig. 2 Rates of strength development for concrete made with cement classified according to ASTM standard [3].

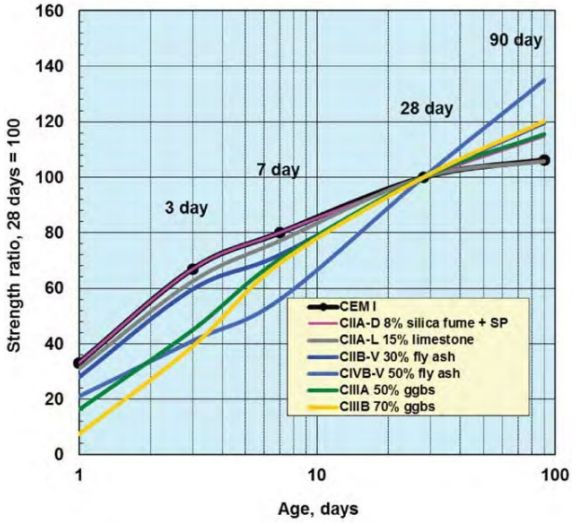

Fig. 3 Rates of strength development for concrete made with cement classified according to BS EN standard [4].

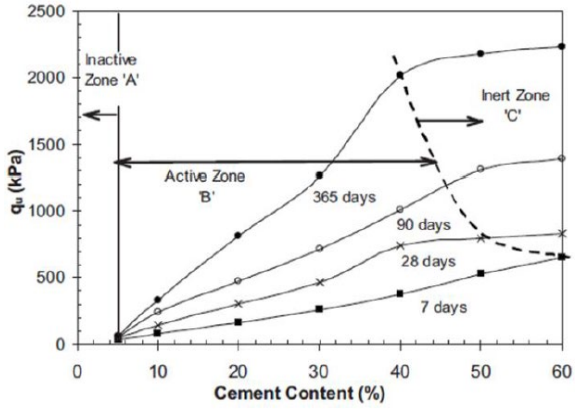

Fig. 4 The effect of cement content on the unconfined compressive strength of Singapore Marine Clay [5].

Cement Dosing Method

The effect of the number of cement layers placed in the soil specimen on the unconfined compressive strength of the CMS was earlier studied [6]. The study reported that the initial cement distribution is one of the dominant factors affecting the uniformity of the soil mix and demonstrated by the distribution of the strength of the CMS.

Mixing Blade Design

Several studies were carried out to investigate the operation techniques (e.g. mixing blade design) on the quality of the CMS [7]. Fig. 5 shows the influence of the number of mixer shafts on the strength of the CMS, where CMS improved by four mixer shafts show similar 7-day strength and higher 28-day strength compared to CMS improved by single mixer shaft.

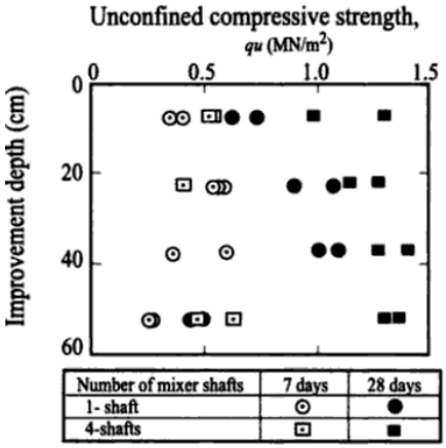

Fig. 5 Unconfined compressive strength achieved using a different number of mixer shafts [7].

MATERIALS & TEST SETUP

The materials and apparatus used in the laboratory-scale SSM test are elaborated in this section.

Properties of Soil

Kaolin Clay and Past Infilled Materials (PIM) were the two types of soils used in this study. PIM refers to excavated soils collected from construction activities that had been temporarily dumped into offshore containment sites and now dredged to be used as an alternative infill material for land reclamation.

The particle size distributions and the soil index properties of the soils used are shown in Fig. 6 and Table 1 respectively. It can be seen that while Kaolin clay is a uniform soil of silt-size, PIM is well-graded sandy-clayey silt.

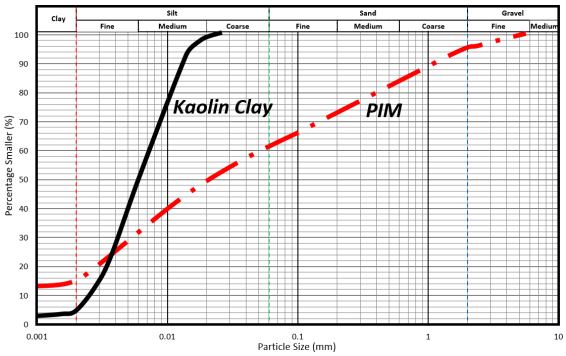

Fig. 6 Particle size distribution of Kaolin Clay and PIM.

Table 1 Soil index properties of Kaolin Clay and PIM

Properties	Kaolin Clay	PIM
Plastic Limit (PL)	40 %	28 %
Liquid Limit (LL)	80 %	67 %
Plasticity Index (PI)	40 %	39 %

Type of Cement

As Singapore adopts the BS EN standard, Cement CEM I and CEM III/A were used in this study. Although it was proven that the CEM I has a higher early strength gain, the use of CEM III/A is more environmentally friendly and cost-effective. There is approximately 11% reduction in the cost of concrete per 1 MPa of strength gained was documented when CEM III/A cement was used instead of CEM I cement [8].

Laboratory Scale SSM Apparatus

A laboratory-scale SSM apparatus was designed to model the SSM in a controlled environment. The SSM apparatus consists of two major components: (1) a 1200mm (length) x 400mm (width) x 400mm (height) rectangular soil container, and (2) motor-powered mixing blades as shown in Fig. 7. Three mixing blades were attached at equal spacing across the width (400mm) of the soil container, and each of the mixing blades had four cutting arms. Fig 8 illustrates two different lengths of the cutting arms (62mm and 75mm) attached on the mixing blades. It was postulated that a longer cutting arm could provide a better overlap between the blades and result in a more uniformed mix.

TEST PROCEDURE

Two dosing methods with slightly different test procedures were studied: 1-layer method and 2-layer method.

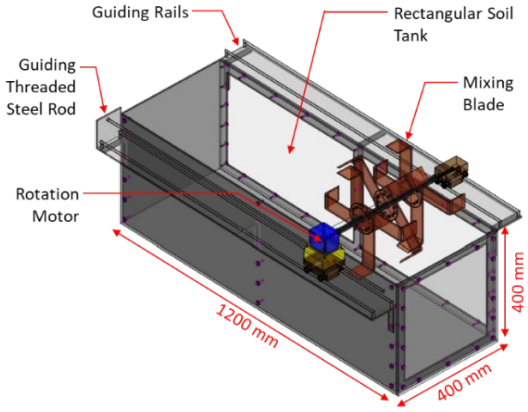

Fig. 7 Schematic diagram of the laboratory-scale SSM apparatus.

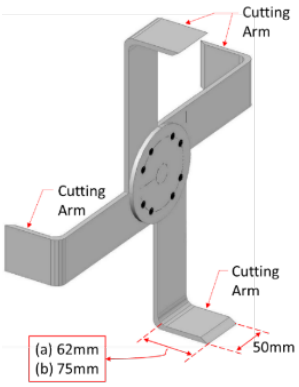

Fig. 8 Different lengths of cutting arm on a mixing blade.

1-layer Method

Soil was prepared to a water content of 1.2x its Liquid Limit (LL) and poured into the soil container. Cement slurry is then sprayed evenly onto the surface of the soil. The motor-powered mixing blades with the rotating cutting arms were subsequently activated to move back and forth the container 8 times.

2-layer Method

The effective treatment depth of 100mm in this study is to be divided into two layers. The first batch of the prepared soil (with a water content of 1.2x its LL) was poured into the soil container until the 50mm mark from the top of the container. The total amount of cement slurry was also divided into two equal portions, and the first portion of cement slurry was sprayed onto the first layer of soil surface.

Subsequently, the remaining batch of prepared soil was added to the top of the container. The second portion of cement slurry was then added onto the top surface of the soil. Finally, the motor-powered mixing blades were used to mix the soil uniformly, similar to the 1-layer method.

TEST PROGRAM

The first test series used Kaolin Clay (KC) with the 62mm cutting arms on the mixing blades. Effect of the dosing method of 1-layer vs 2-layers was studied in this phase. The second test series used PIM with the 75mm cutting arms on the mixing blades. In this phase, the effect of different dosing percentage was studied and evaluated. The parameters used in the first and second test series are listed in Table 2(a) and Table 2(b) respectively.

Table 2(a) First test series (Kaolin Clay and 62mm cutting arm).

Cement	Cement Dosage	Dosing Method	Test no.
CEM I	10%	1-layer	KC-1
		2-layer	KC-2
CEM III/A	10%	1-layer	KC-3

Table 2(b) Second test series (PIM and 75mm cutting arm).

Cement	Cement Dosage	Dosing Method	Test no.
CEM I	7%	1-layer	PIM-1
	3%	1-layer	PIM-2
CEM III/A	7 %	1-layer	PIM-3
	3%	1-layer	PIM-4

RESULTS AND DISCUSSIONS

The performance of the laboratory-scale SSM test is evaluated by the development of the undrained shear strength (Cu) of the CMS over time. Vane Shear Tests (VST) and miniature Cone Penetration Tests (CPT) were used to ascertaining the 3-day and 7-day Cu of the CMS at different locations in the soil container as shown in Fig. 9. The 28-day strength was not included as this study is concerned primarily with the early strength gain of CMS.

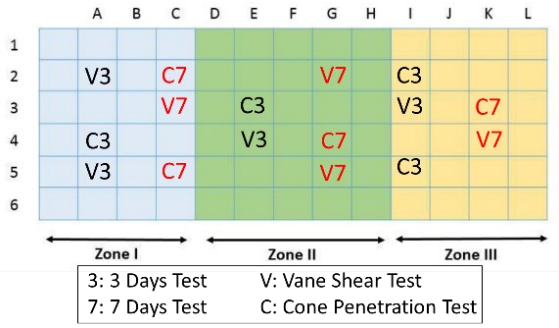

Fig. 9 Plan view for VST and CPT test points in soil container

The undrained shear strength (Cu) obtained for the Kaolin Clay CMS with depth at various locations for each test series are shown in Fig. 10(a) to Fig. 10(c).

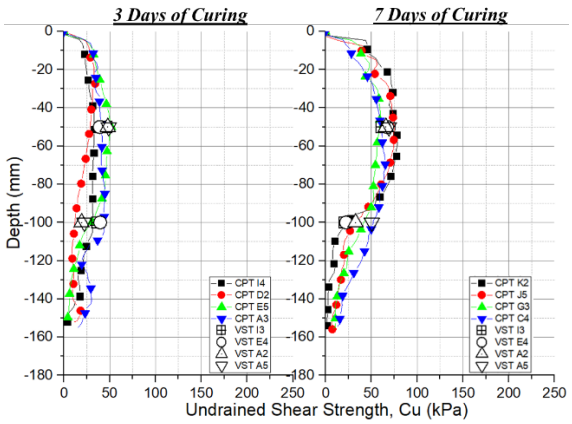

Fig. 10(a) Undrained shear strength, Cu, with depth of CMS for Test KC-1

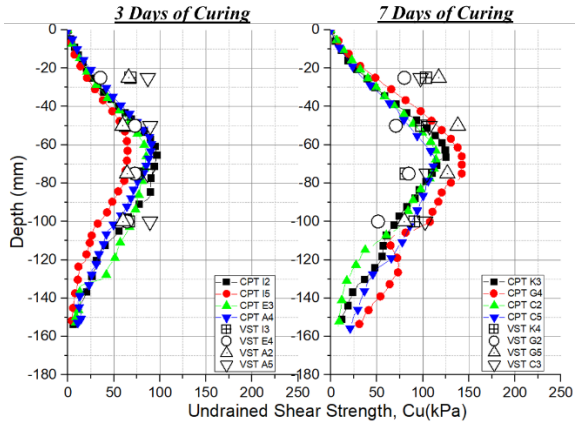

Fig. 10(b) Undrained shear strength, Cu, with depth of CMS for Test KC-2

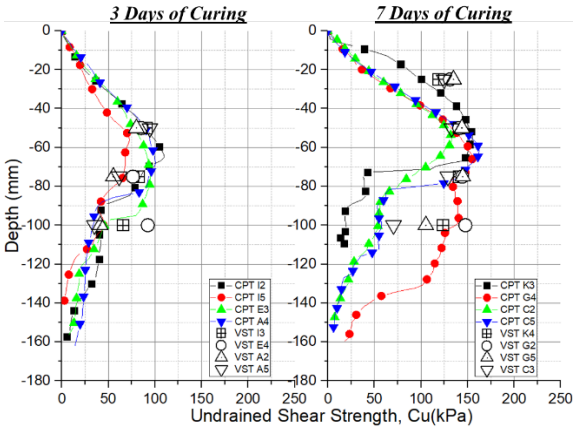

Fig. 10(c) Undrained shear strength, Cu, with depth of CMS for Test KC-3

The undrained shear strength (Cu) obtained for the PIM CMS with depth at various locations of each test series are shown in Fig. 11(a) to Fig. 11(d).

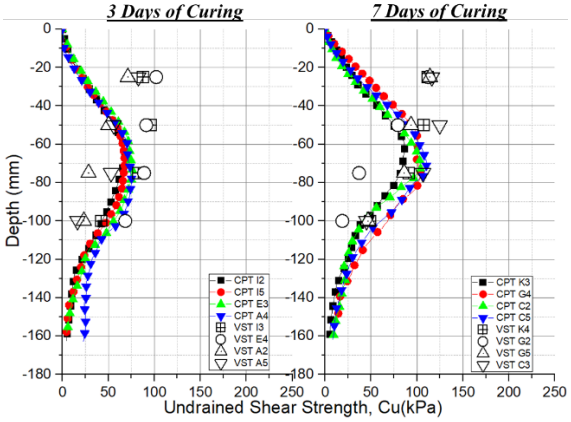

Fig. 11(a) Undrained shear strength, Cu, with depth of CMS for Test PIM-1

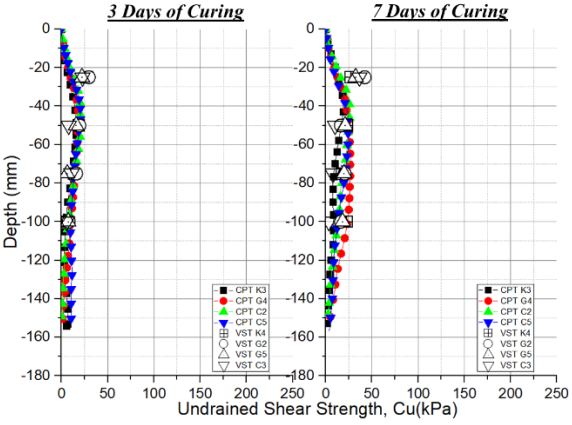

Fig. 11(b) Undrained shear strength, Cu, with depth of CMS for Test PIM-2

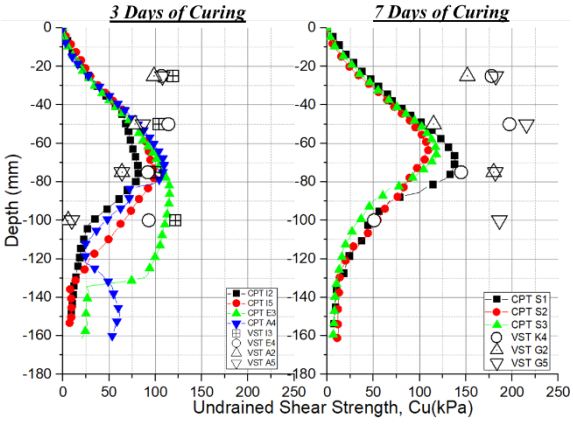

Fig. 11(c) Undrained shear strength, Cu, with depth of CMS for Test PIM-3

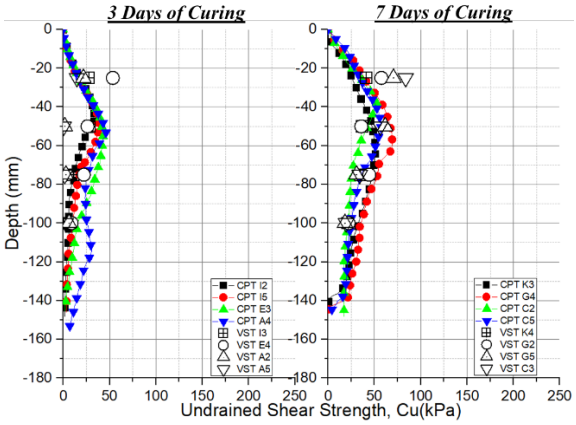

Fig. 11(d) Undrained shear strength, Cu, with depth of CMS for Test PIM-4

Effect of Cement Type

The effect of cement type on strength development can be observed by comparing the Cu distribution with depth in Test KC-1 and KC-3. In general, the 3-day Cu and 7-day Cu distributions of KC-3 are higher than in KC-1. Similar trends are observed in PIM-1 compared with PIM-3, and PIM-2 with PIM-4, where the Cu distribution of CMS with CEM III/A consistently have higher values compared to CEM I.

Effect of Cement Dosage

By comparing the Cu distributions with depth in PIM-1 with PIM-2, and the Cu distributions with depth in PIM-3 with PIM-4, it can be observed that using a higher dosage of cement gives a higher strength gain, which is expected.

Effect of Dosing Method

The results of higher Cu values observed in Test KC-2 as compared to KC-1 indicate that using the 2-layer dosing method provides more uniform strength gained in the CMS.

Effect of Mixing Blade Design

The first test series used 62mm cutting arms, while the second test series used 75mm cutting arms. Apart from differences in the cutting arms, a higher cement dosage was used in Test KC-1 than in PIM-1 is the cement dosage.

Although a higher cement dosage was used in KC-1, PIM-1 unexpectedly obtained higher Cu values at the corresponding location and time than that in KC-1. This proved that the increase in the uniformity of CMS is affected by the blade design such as the amount of overlap of the mixing blades.

CONCLUSION

A series of laboratory-scale SSM test was conducted successfully. In the study, CEM III/A cement shows more rapid strength development in the CMS as compared to CEM I cement, and that a higher cement dosage is an advantage for the development of strength gain. It was also concluded that the dosing method and mixing blade design are important in providing uniformed cement mixed soil. Therefore, for the cost-effectiveness of the SSM method to create a working platform at the top layer of soft soils, the cement dosing method and mixing blade design must be carefully planned as these two parameters impact the uniformity of CMS, which directly increase the overall strength gain across a large treatment area.

ACKNOWLEDGEMENTS

The authors gratefully acknowledge the efforts of Mr. Xu T.H. in completing this study.

REFERENCES

[1] Moseley M. P. and Kirsch K., Ground Improvements. Spon Press, Second Edition, 2004.
[2] Hayward Baker, 2012. Retrieved from Hayward Baker Keller Geotechnical Construction: http://www.haywardbaker.com/WhatWeDo/Techniques/GroundImprovement/WetSoilMixing/Imagery/2769.aspx.
[3] USBR, Concrete Manual, eighth edition, U.S. Bureau of Reclamation, Denver, CO, 1975, pp. 41-51.
[4] Clear C. A., Cementitious Materials and Early-Age Concrete Strength, Aggregates/Cementitious Materials, Concrete, June, 2012, pp. 21-22.
[5] Kamruzzaman A. H., Chew S. H. and Lee F. H., Structuration and Destructuration Behavior of Cement-Treated Singapore Marine Clay. Journal of Geotechnical and Geoenvironmental Engineering, Vol. 135, Issue 4, 2009, pp. 573-589.
[6] Chan C. M., Influence of Mix Uniformity on the Induced Solidification of Dredged Marine Clay. Environ Earth Sci, Vol. 71, 2014, pp. 1061-1071.
[7] Nishibayashi K., Matsuo T., Hosoya Y. and Kohinata T., Studies on Strength and Deformation Properties of Soils Stabilized with Cement, Obayashi Corporation Technical Research Report, No.30, 1985, pp. 123-127 (in Japanese).
[8] Kutlu O., Evaluation of the Technical and Economical Aspects of using type CEM III Cements in Concrete, Global Slag, 2008, Retrieved from: http://www.globalslag.com/magazine/articles/452-evaluation-of-the-technical-and-economical-aspects-of-using-type-cem-iii-cements-in-concrete

9th Int. Conf. on Geotechnique, Construction Materials and Environment, Tokyo, Japan, 20-22 November 2019, ISBN: 978-4-909106025 C3051

OPTIMISATION OF SENSOR LOCATIONS FOR RELIABLE AND ECONOMICAL EARLY WARNING OF RAINFALL-INDUCED LANDSLIDES

Abeykoon T[1], Gallage C[2] and Trofimovs J[3]
[1,2,3]Science and Engineering Faculty, Queensland University of Technology, Australia.

ABSTRACT

Rainfall-induced landslide monitoring and early warning is an effective technique for minimising potential landslide risks, especially in circumstances where structural countermeasures are not economically or technically feasible. In this regard, a number of methods have been developed to monitor susceptible slopes and warn against possible slope failures. The majority of real-time slope monitoring systems involve sensor networks that measure slope inclination/displacement, volumetric water content and rainfall, enabling the determination of pre-failure deformation. However, no systematic approach has been made to install such sensors in critical locations to enhance the cost-effectiveness of slope monitoring systems and the accuracy of landslide early warnings. This study has developed guidelines for a systematic approach for the determination of critical sensor installation points using RTK-GPS surface movement measurements, numerical transient seepage and slope stability analysis for the economic and technical optimisation of landslide monitoring and early warning systems.

Keywords: Rainfall-induced landslides, Landslide monitoring, Slope stability, Critical sensor locations

INTRODUCTION

Due to the adverse consequences, prevention and mitigation of rainfall-induced landslides are vital. Even though mechanical countermeasures such as retaining walls, soil hardening techniques and ground anchors are technically adaptable in rainfall-induced slope failure mitigation, practically such methods are commonly not feasible due to high costs, varying slope scales and potential risk factors in mechanical reinforcements. In these situations, continuous monitoring of slope behaviour provides an economical and slope-specific alternative for landslide risk mitigation [1]-[4].

In the context of landslide monitoring and early warning, the majority of early warning criteria are defined on time histories of rainfall intensities and real-time rainfall records (e.g.[5]). These rainfall based early warning techniques enable in advance detection of slope instabilities at a low cost and ease. However, such criteria are defined, assuming uniform rainfall conditions over the area of interest, which is usually in the range of several square kilometres [3]. Additionally, local topographical, geological and hydrological factors are not embedded in producing rainfall based landslide early warnings, which highly correlates with landslide initiation [6]. Therefore, the sole use of rainfall based early warning in evaluating slope instability risks in individual slopes becomes inadequate.

Furthermore, continuous monitoring of displacement or deformation provides a precursor to detect slope instabilities in advance via indices such as cumulative deformation and rate of slope deformation [3]. Hence, the reliability of landslide early warning systems can be improved by incorporating real-time deformation monitoring into the rainfall based landslide early warning systems. In that context, recent developments in multiple factors-based landslide early warning systems heightened the need for low cost, reliable and real-time sensor system.

In order to address the demand, a real-time slope monitoring system equipped with micro electro mechanical systems (MEMS) tilt sensors and volumetric water content (VWC) sensors was proposed by [2] to produce reliable early warnings for rainfall-induced landslides. MEMS technology enables the detection of rotation (or variation of tilt angle) in the unstable surface layers of slopes. Abeykoon [1], Uchimura [3], and Gallage [7] summarised case studies of tilt sensor monitoring systems and the variations of tilting rates during pre-failure and main failure stages, which facilitates the early warning of rain-induced slope failures.

However, in all aforementioned studies, sensors were randomly located, and no previous research to date has aimed to determine the optimum/critical sensor installation locations on the failing slopes. The scarcity of the fore-knowledge on the distinct sensor locations led to the installation of a large number of sensors, many of which were not effectively involved in producing early warnings (e.g. TS-4 and TS-5 sensor units were not detected any slope movement in the study conducted by [1]). Therefore, the optimum economic usage of the sensor system was not exploited.

The current study adopts a real-time monitoring system that consists of five MEMS tilt sensor units that are capable of transmitting real-time collected

data to an online web interface via a combination of wireless and mobile networks to investigate the critical locations of a slope to install sensor units. So that an efficient prediction of possible slope failures can be conducted reducing landslide risks. Further, by optimising the number of sensor units used in a given real-time slope monitoring system, the entire economic capability of the proposed tilt sensor system can be determined. Therefore this study provides novel insights into the low cost, reliable and real-time landslide monitoring and early warning systems.

STUDY AREA

The study area is located in Lake Baroon catchment, Maleny, Queensland, Australia (26.72 ^{0}S 152.87 ^{0}E). Mapleton - Maleny plateau, which has been documented as a highly susceptible area for rainfall-induced slope failures since the mid - 1950s. (e.g. [8]). Slope failures and mass movements of sediment into the waterways within the Lake Baroon catchment are recognised as a significant risk to water quality and the water storage capacity of Lake Baroon, which is used to supply water to South East Queensland. Approximately 170 mass movement landforms have been identified within the Lake Baroon catchment, and the study area is one such high-risk slope. This landslide site hosted a voluminous, single-failure rotational landslide in 2008 following heavy rainfall.

SOIL PROPERTIES

Index Properties

The soil extracted from the monitoring site was subjected to laboratory tests to determine the required soil properties for the numerical analysis. Table 1 summarises the results of the laboratory tests conducted to determine the index properties of the soil according to Australian standards.

Table 1 Soil index properties

Classification Test	Results
Grain size	% finer than 75 μm > 79%
Distribution	Clay % = 41.0 %
Atterburg Limits	LL = 67.2 %
	PI = 28.2 %
Linear Shrinkage	LS = 13.4 %

Strength Properties

Strength properties of the soil were determined by the direct shear test, in which all the samples were prepared to achieve a dry density of 1.25 g/cm^3 to replicate the in-situ dry density of the soil. Direct shear tests were conducted for four different water contents. Figure 1 shows the variation of apparent cohesion with gravimetric water content. However, the soil friction angle did not significantly vary with the gravimetric water content, which was determined as 15.9^0.

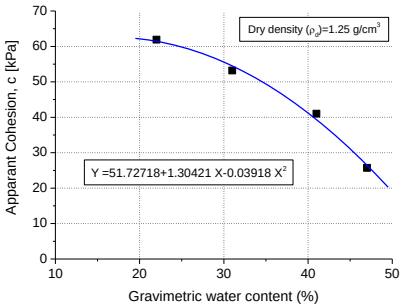

Fig. 1 The variation of apparent cohesion with gravimetric water content

Hydraulic Properties

A genetic-based neural network (GBNN) model was used for the determination of optimal weights of a neural network to predict the soil-water characteristic curve (SWCC) for this study. As defined by [9], five parameters; void ratio, initial water content, clay and silt fraction and the normalised logarithm of suction with respect to air pressure were used as the input neurons while the gravimetric water contents for input suction values are produced as the output neuron. Normalised input parameters were used for each arbitrary suction value. The input-hidden weight and the normalised input vectors were multiplied to obtain the input hidden neuron matrix, on which the sigmoidal activation function was applied to produce the output vector from hidden neurons. Then after the hidden output network weights were applied prior to de-normalising and descaling to obtain the final gravimetric water content. Figure 2 presents the F-X fit SWCC for the soil in the study area, derived from GBNN model [10].

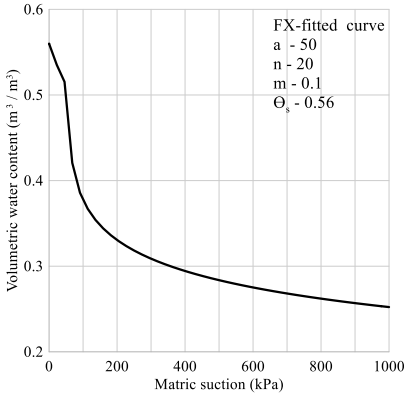

Fig. 2 Soil-water characteristic curve (SWCC) for the soil in the study area

Unsaturated coefficient of permeability function was defined using the SWCC predicted from GBNN model developed by [9] and the saturated permeability. The saturated permeability coefficient was chosen as 1 x 10^{-7} m/s.

METHODOLOGY

In order to determine the critical sensor installation locations for real-time monitoring of rainfall-induced slope failures, initially, the soil properties and sub-surface topography were determined by the laboratory experiments and ground penetrating radar (GPR) survey respectively. Moreover, to determine the predominant slope failure direction for 2-D stability analysis, previous slope failure occurrences along with the recorded RTK-GPS surface movement data were analysed. The obtained soil properties, topographical data were incorporated in the numerical model for stability analysis of 2-D cross-sections parallel to the predominant failure direction within the monitoring site.

Ground Subsurface Survey

A ground surface survey and a sub-surface GPR survey were performed to determine surface topography, and the depth of soil cover to bedrock on the site to evaluate the optimum positions for the monitoring stations using the numerical model. A base GPR transect was mapped downslope from the head of the main scarp to the toe of the site in an attempt to profile the sub-surface in the direction of the original mass movement. After characterising the soil profile by determining the interface between soil and underlying bedrock, four locations were selected to excavate pits for determining the composition of soil layers, soil layer thicknesses and verification of GPR survey results [1].

RTK-GPS Surface Movement and Elevation Monitoring

An array of surface survey points were installed, in order to monitor both horizontal and vertical ground displacement with millimetric accuracy. Less than 10 cm of downslope movement was recorded by individual points using the RTK-GPS system between installation survey points in April 2016 and October 2017. Figure 3 presents the cumulative movement data for these RTK-GPS surveys and summarises the total movement to October 2017. The data is presented as arrow vectors, which point in the direction of measured movement between the two surveys. The size of the arrow is scaled according to the amount of movement, with the larger yellow arrows indicating a larger amount of movement. For scale, the diameter of the orange dots represents a distance of 20 mm in the field, which is the conservative margin of error for measurements recorded by RTK-GPS equipment. Therefore, yellow vector arrows that fit within the 20 mm circle recorded movement within the error of the measuring technique, while arrows that extend outside the circle have recorded a significant movement which is outside the margins of measurement error. As depicted in Fig. 3, there were two main areas of movement during the RTK-GPS surface movement monitoring period.

Fig. 3 RTK-GPS movement map of the monitoring site highlighting the two circled areas with significant recorded movement

Previous Slope Failure Analysis

Several significant mass movements were recorded during the period following October 2017, including a rotational landslide (14th - 21st October 2017), a reactivation of rotational landslide (29th November - 1st December 2017), a debris flow and continued reactivation of landslide (16th February 2018), and a soil creep (9th - 16th March 2018) [1]. These slope instabilities highlighted that the steep upper slope is the most susceptible region for rainfall-induced slope failures. Also, inspections following the rotational landslide at the head scarp showed running and pooling water in the slide cracks. Hence, the sub-surface build-up of this groundwater during, and immediately following, heavy rain was identified as the trigger for landslides. During and immediately after the rainfall events, water infiltrates into the soil profile, largely through the macro-scale surface cracking, and concentrates above the bedrock and water saturated white clay horizon. Consequently, sliding is initiated at this sub-surface slide plane once the soil reaches its liquid limit (~60%) and surpasses the binding strength of the root system. Moreover, the inspection of the new landslide soil profile showed that the grass and tree roots were vertically oriented at the top of the soil profile. However, as tree roots approach the sub-surface slide plane, they were bent towards horizontal due to the shearing associated with the landslide movement. Therefore the observation indicates that the movement occurred at the base of the soil profile, which was acting as a fluid and rafting

slide blocks downslope, which also accounts for the back-rotated orientations of these blocks as soil blocks have come to rest.

The previous slope failure analysis, along with surface movement data, highlighted two areas with significant slope movement at the monitoring site, that includes steep upper slope (which had failed) and northern boundary of the monitoring site as shown in Fig 3. Therefore, a hypothesis was developed that sub-surface (ground) water flow drains from the steep upper slope to down towards the northeast of the monitoring site (Fig. 4A). This is contrary to the surface runoff which has formed a number of erosional gullies to either side of the largely displaced mid-slope that run toward the northeast and east (Fig. 4B).

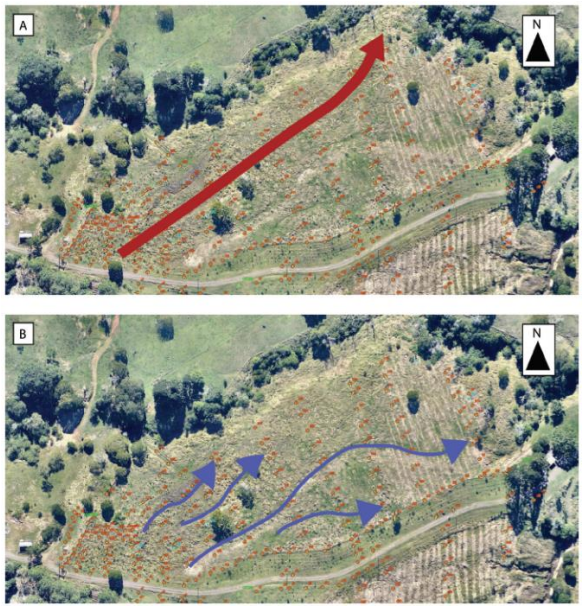

Fig. 4 (A) The hypothesised path of groundwater flow (B) Erosional gullies carved by surface runoff

Numerical Model

Transient seepage analysis and stability analysis were performed in order to determine critical locations of slope instability within the monitoring site. Transient seepage analysis was performed using Seep/W [11] allowing the analysis of wetting front movement and the excess pore-water pressure dissipation. The pore-water pressure profile computed for each time step from seepage analysis was then integrated into the stability analysis using Slope/W [12].

As depicted in Fig. 5, seven cross-sections parallel to predominant failure direction, which was determined through the hydrological (i.e. hypothesised groundwater flow and surface runoff) and previous slope failure analysis, were considered for the slope model. In the finite element modelling using Seep/W, each analysed cross-section consisted of approximately 1500 nodes and 1350 quadrilateral and triangular elements (Fig. 6). On the exposed slope surface, rainfall infiltration was simulated by applying water flux as a time-dependent function with the potential seepage face review. The sandstone bedrock located at approximately 4 m below the ground surface was assumed to be a low permeable layer, which was also justified by the presence of perched groundwater table during and immediately after the rainfall events. Saturated / Unsaturated material model was adopted for both the upper soil layer and the sandstone bedrock, using the hydraulic conductivity function and the water content function [11]. In defining the initial hydrological conditions, the groundwater table was assigned approximately 8 m below the ground surface. Since the initial groundwater table was located within the sandstone bedrock layer, perched groundwater table builds the pore-water pressure in the overlying soil layer in rainfall events, as observed in previous slope failures.

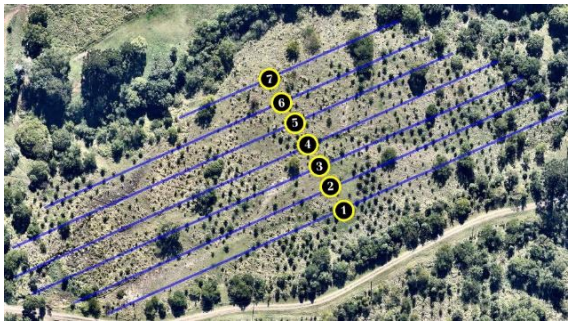

Fig. 5 Cross sections considered for the numerical analysis

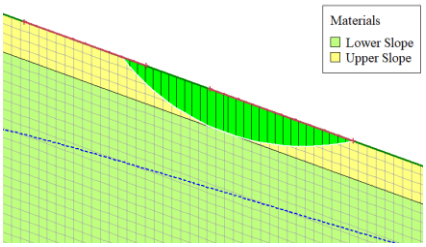

Fig. 6 Finite element mesh and the critical slip surface at the steep upper slope region in the cross section 4

The stability analysis was performed using the pore-water pressure profile developed by transient seepage analysis. Mohr-Coulomb material model was used by employing the laboratory determined shear strength parameters [12]. As shown in Fig. 6, in defining a slip surface for stability analysis, each cross section was analysed multiple times with different positioning of slip surfaces. The position of the critical slip surface with the lowest factor of safety was determined using the entry and exit slip surface condition, in which the entry and exit ranges of the

trial slip surface can be defined. The factor of safety (FS) values were determined using Morgenstern-Price's approach [12].

RESULTS

Validation of the Numerical Model

The developed numerical model was validated using the previous failure and the real-time monitoring data obtained from the real-time monitoring system installed in the study area. The real-time monitoring system is composed of five units of randomly positioned MEMS tilt sensors and VWC sensors, capable of continuously measuring the slope inclination and the soil VWC, respectively [1].

From the previous failure analysis, it was noted the majority of critical failure surfaces were laid within the upper clay layer, due to the low permeability of the sandstone bedrock or in other words shallow failures with a failure depth of 3 - 4 m were observed during the previous slope failures. Therefore, the failure depths, along with the locations of the previous slope failure, were accounted for validating the numerical model. Additionally, the VWC values at all the five sensor locations and the VWC values from the numerical model were compared to validate the developed numerical model. As shown in Fig. 7, the experimental VWC values at the TS-1 sensor location (at the steep upper slope) and simulated VWC values depicted a reasonable agreement, proving the accuracy of the numerical model.

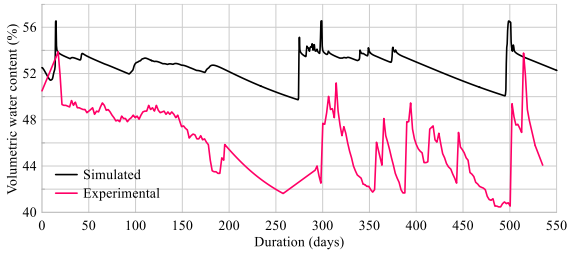

Fig. 7 Experimental and simulated volumetric water content values

Similarly, the VWC values obtained from the remaining sensor locations were also compared to validate the numerical model, which also showed an acceptable agreement. However, as depicted in Fig. 7, a slight lag on experimental VWC values were perceived due to the delay in response of the VWC sensor.

Determination of Critical Failure Locations

The FS value for various positions of entry and exit conditions for each cross section were obtained in order to analyse the critical locations of the study area. The FS variation produced from the numerical analysis showed significantly low values during the time periods with actual slope failures occurred, including October 2017, February 2018 and October 2018 failures, showing a reasonable agreement with the actual results. Figure 8 shows the variation of FS along with the rainfall (water flux) function applied to the exposed slope surface, for the steep upper slope region in the cross-section 4. Figure 9 presents the mean FS values for each location of the study area during the two-years. Therefore, as depicted in the previous failure analysis, the steep upper slope region in the study area has been determined as the most susceptible area for rainfall-induced slope failure.

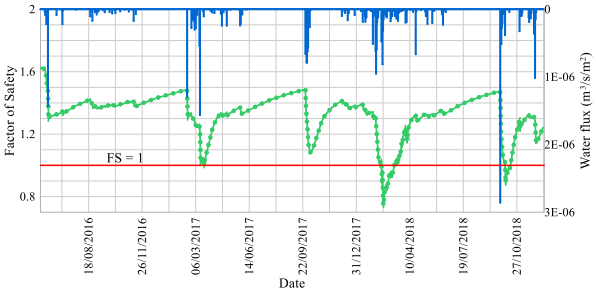

Fig. 8 FS and rainfall (water flux) variation in the steep upper slope section of cross-section 4

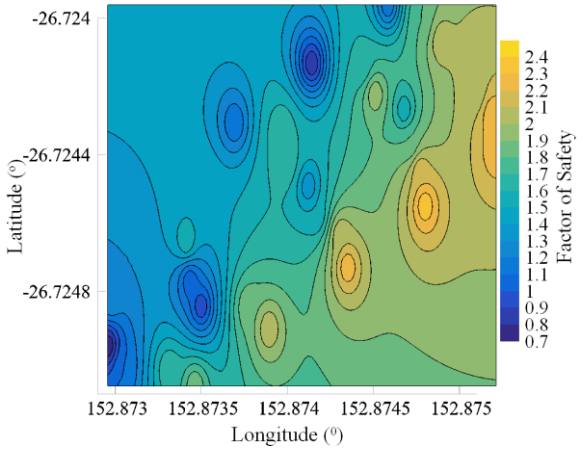

Fig. 9 Mean FS variation in the study area

Moreover, due to the low permeability of the underlying sandstone bedrock, a perched water table was exhibited within lower slope areas. As the rainfall infiltrates into the unsaturated soil zone, flow is moved down the slope creating a perched saturated zone. During the process, water flow moves either downwards into the adjacent unsaturated zone or exits from the exposed slope face, generating atypical pore water pressure conditions. Therefore, analysis of critical slip surfaces encountered intersection of phreatic water surface at multiple locations.

DISCUSSION

Strength and hydraulic properties of the soil become the fundamental requirements in numerical modelling a soil slope for stability. Even though the study adopted experimentally determined soil strength parameters, a GBNN based model was employed in evaluating VWC function, which provides an analytical alternative to obtain SWCC for soils.

Rainfall was applied as a water flux boundary condition to the numerical model in assessing slope stability under rainfall. However, the climatic and vegetation functions were not accounted for in the numerical analysis. Precipitation, air temperature, humidity, wind and solar radiation effects could be considered in developing a more accurate numerical model. Also, it should be noted that even though the study area was not densely vegetated, vegetation plays a vital role in slope stability under rainfall as the root system provides a reinforcement enhancing the slope stability. Therefore incorporating vegetation reinforcement into the numerical model may provide a more realistic evaluation of the critical failure locations.

CONCLUSIONS

The study developed a methodology to determine critical failure locations of a slope in advance so that the real-time slope monitoring instruments can be positioned at the critical locations, enhancing the cost-effectiveness of the monitoring system and reliability early warnings. In that regard, the study proposes a methodology with three steps that include the visual observation for the preliminary characterisation of the steeper regions of the slope, GPS surface movement monitoring to hypothesis the groundwater flow and predominant failure direction along with the susceptible moving areas within the slope and numerical analysis to confirm the critical failure locations. In the context of the current study, installation of sensor units in the regions with lower mean FS values will provide more cost-effective, economical, reliable and accurate landslide early warnings mitigating adverse impacts.

ACKNOWLEDGMENTS

The authors appreciate Seqwater, Australia, for its financial support for this study. Further, gratitude is extended to Mark Amos (Lake Baroon Catchment Care Group) for facilitating the installation of the monitoring system and providing site access at the convenience of QUT researchers. The management of Chuo Kaihatsu Corporation, Japan is greatly acknowledged for providing and installing the monitoring system for the in-kind research support to QUT. The first author acknowledges the scholarship for the doctoral degree received from QUT, Australia.

REFERENCES

[1] Abeykoon T., Gallage C., Dareeju B., and Trofimovs J., Real-time monitoring and wireless data transmission to predict rain-induced landslides in critical slopes. Australian Geomechanics Journal, Vol. 53 (3), 2018, pp. 61-76.

[2] Uchimura T., Towhata I., Anh T.T.L., Fukuda J., Bautista C.J.B., Wang L., and Seko I., Simple monitoring method for precaution of landslides watching tilting and water contents on slopes surface. Landslides, Vol. 7(3), 2010, pp. 351-357.

[3] Uchimura T., Towhata I., Wang L., Nishie S., Yamaguchi H., Seko I., and Qiao J., Precaution and early warning of surface failure of slopes using tilt sensors. Soils and Foundations, Vol. 55 (5), 2015, pp. 1086-1099.

[4] Gallage C., and Uchimura T., Investigation on parameters used in warning systems for rain-induced embankment instability, in Proc. the 63rd Canadian Geotechnical Conference (GEO2010), 2010, pp. 1025-103.

[5] Guzzetti F., Reichenbach P., Ardizzone F., Cardinali M., and Galli M., Estimating the quality of landslide susceptibility models. Geomorphology, Vol. 81, 2006, pp. 166-184.

[6] Chae B.G., and Kim, M.I., Suggestion of a method for landslide early warning using the change in the volumetric water content gradient due to rainfall infiltration. Environmental Earth Sciences, Vol. 66, 2012, pp. 1973-1986.

[7] Gallage C., Dareeju B., Trofimovs J., Wang L., and Uchimura T., Real-time monitoring and failure prediction of a slope due to rainfall - case study, in Proc. 9th International Conference on Sustainable Built Environment, 2018, pp.12-18.

[8] Ellison L. & Coaldrake J.E., Soil Mantle Movement in Relation to forest clearing in Southeastern Queensland. Ecology, Vol. 35, 1954, pp. 380-388.

[9] Johari A., Habibagahi G., and Ghahramani, A., Prediction of SWCC using artificial intelligent systems: A comparative study. Scientia Iranica, Vol. 18, 2011, pp. 1002-1008.

[10] Fredlund D.G., and Xing A., Equations for the soil-water characteristic curve. Canadian geotechnical journal, Vol. 31, 1994, pp. 521-532.

[11] GeoSlope International Ltd., Seep/W User's Guide for Finite Element Seepage Analysis. 2004.

[12] GeoSlope International Ltd., Slope/W User's Guide for Slope Stability Analysis. 2004.

9th Int. Conf. on Geotechnique, Construction Materials and Environment, Tokyo, Japan, 20-22 November 2019, ISBN: 978-4-909106025 C3051

EVALUATION OF DEBRIS FLOW CONTROL USING SABO FACILITIES BASED ON NUMERICA SIMULATIONS

Naomasa Honda[1]

[1] Faculty of Regional Environment Science, Tokyo University of Agriculture, Japan

ABSTRACT

The present paper describes predicting sediment runoff characteristics and evaluating debris flow control using such sabo facilities as check dams and channel works based on the numerical results of an actual mountain torrent and consider the changes of sediment transport modes. In Ohzedani River, which is a tributary of Sendai River in Tottori Prefecture in Japan, a very active sediment runoff was caused by the second Muroto typhoon in September 1961. A one-dimensional numerical simulation is conducted to investigate the variations of debris flow characteristics through a river reach with sabo facilities. The analytical results show that the debris flow discharge increased several orders of magnitude more than the water, and the sediment transport rate varies with river-bed slope and river width. A check dam is effectively reduced sediment transport when the initial river-bed slope of the deposition area at the dam's upstream was not steeper than the equilibrium slope of the debris flow. The flow path is fixed with channel works, which provide protection against debris flow flooding. The computational condition of the river-bed erosion depth greatly affected the numerical results.

Keywords: Sediment runoff characteristics, Debris flow control, Sabo facilities, Numerical simulation

INTRODUCTION

A large amount of sediment may be produced in areas where earth slides or hillside landslides might occur. Such sediment in steep area is supposed to be eroded and transported as debris flow during severe rains, and various disasters or geomorphic changes are caused by them. Sabo works such as hillside works, channel works and debris flow control dams have been constructed to defend against debris flow hazards.

Generally, sediment runoff modes depend upon such variables as topographical parameters, sediment characteristics, water supply, and so on. Debris flow is formed in the reach where unstable sediment exists and the river-bed slope is steeper than about 15 degrees [1], [2]. The sediment transport mode changes from a debris flow into general contact loads with decrease of river-bed slope [3]. A check dam impacts the sediment runoff, because the channel is wide and the river-bed slope is gentle upstream of the dam [4] [5].

In the present paper, the following problems are discussed: the characteristics of sediment runoff in an actual mountain torrent and such sabo facilities as check dams and channel works on the reductions of sediment runoff as well as on the prevention of debris flow hazards based on the changes of sediment transport modes.

This paper proposes a mathematical method that is composed of mass and momentum conservation equations for debris flow as well as erosion velocity formula on debris from river-beds and conduct a one-dimensional numerical simulation to investigate variations in the debris flow characteristics and the effects of debris flow control using sabo facilities. Such debris flow characteristics as flow depth, flow velocity, flow discharge, and sediment flux concentration can be predicted even if sabo facilities are constructed in a river reach.

This paper also discusses the effects of sabo facilities on sediment load and the mitigation of the hazards of potential debris flow.

METHOD AND PROCEDURE FOR STUDY

Governing Equations for Debris Flow

To analyze sediment transport in a river reach, one-dimensional equations for the flow of a sediment-water mixture developed by Egashira et al. is used [6]. The following are the mass conservation equations for the flow mixture and for sediment alone:

$$\frac{\partial h}{\partial t}+\frac{1}{B}\frac{\partial Bvh}{\partial x}=\frac{E}{c_*} \tag{1}$$

$$\frac{\partial \varepsilon ch}{\partial t}+\frac{1}{B}\frac{\partial \varepsilon cBvh}{\partial x}=E \tag{2}$$

where t is the time, x is the coordinate axis along the flow, h is the flow depth, B is the flow width, v is the flow velocity, E is the erosion velocity (its negative value designates the deposition), c is the sediment concentration by volume, ε is the correction factor

(Egashira et al. [7], $\varepsilon c = c_t$, c_t is the sediment flux concentration), and c_* is the sediment concentration of the river-bed layer. The following is the momentum conservation equation:

$$\frac{\partial v}{\partial t} + v\frac{\partial v}{\partial x} = g\sin\theta - \frac{1}{\rho_m h}\frac{\partial P}{\partial x} - \frac{vE}{c_* h} - \frac{\tau_b}{\rho_m h} \quad (3)$$

$$\rho_m = (\sigma - \rho)c + \rho \quad (4)$$

The second term on the right hand side of Eq. (3) is the pressure gradient and the third is the resistance due to the sediment erosion. g is the gravity acceleration, θ is the river-bed slope, P is the pressure, τ_b is the river-bed shear stress, ρ_m is the mass density of flow mixture defined in Eq. (4), σ is the mass density of gravel, and ρ is the mass density of water. The mass conservation equation of the river-bed sediment takes the following form:

$$\frac{\partial Z_b}{\partial t} = -\frac{E}{c_* \cos\theta} \quad (5)$$

$$\theta = \sin^{-1}\left(-\frac{\partial Z_b}{\partial x}\right) \quad (6)$$

where Z_b is the river-bed elevation, and θ is expressed by Eq. (6). As mentioned above, even though E and τ_b play an important role in the governing equations, no general formulas have been developed for them. The formulas for E [6] and τ_b [8] developed by Egashira et al., are used. Erosion velocity E is as follows:

$$\frac{E}{v} = c_* \tan(\theta - \theta_e) \quad (7)$$

$$\theta_e = \tan^{-1}\left\{\frac{(\sigma/\rho - 1)c}{(\sigma/\rho - 1)c + 1}\tan\phi_s\right\} \quad (8)$$

where θ_e is the equilibrium river-bed slope corresponding to the sediment concentration defined by Eq. (8), which was obtained by Takahashi's formula for the sediment concentration of debris flow [9], ϕ_s is the internal friction angle of the sediment. The following is river-bed shear stress τ_b:

$$\tau_b = \tau_y + \rho f v^2 \quad (9)$$

$$\tau_y = \left(\frac{c}{c_*}\right)^{1/5} \rho(\sigma/\rho - 1)cgh\cos\theta\tan\phi_s \quad (10)$$

$$f = \frac{25}{4}\left\{k_f\frac{(1-c)^{5/3}}{c^{2/3}} + k_g\frac{\sigma}{\rho}(1-e^2)c^{2/3}\right\}\left(\frac{h}{d}\right)^{-2} \quad (11)$$

In Eq. (9), τ_y is the yield stress caused by the particle to particle contacts defined in Eq. (10), and f is the friction factor defined as Eq.(11), where e is the restitution coefficient, d is the reference grain size, and k_f and k_g are coefficients: k_f=0.16, k_g =0.0828.

Outline of Ohzedani River Basin

Ohzedani River is one tributary of Sendai River in Tottori Prefecture in Japan that flows into the Japan Sea (Fig. 1). It has drainage of 3.2 km^2 and a river reach of 4.1 km. Its mean river-bed slope is 10.8 degrees, and its river-width changes irregularly (Figs. 2 and 3).

In this basin, the mountain slope is very steep, and weathering granites, which are susceptible to erosion, are widely distributed on the mountainside, and unstable sediment is liable to be produced in the drainage. Therefore, this torrent is designated as a river's stream that poses debris flow risks.

A very active sediment runoff was caused in September 1961 by the second Muroto typhoon in this basin. Debris flow arrived at the lowest stream reach near Kofune village (Fig. 1). However, the torrent didn't overflow its banks because a check dam and channel works, which were constructed at downstream

(a) Location of Tottri Prefecture in Japan

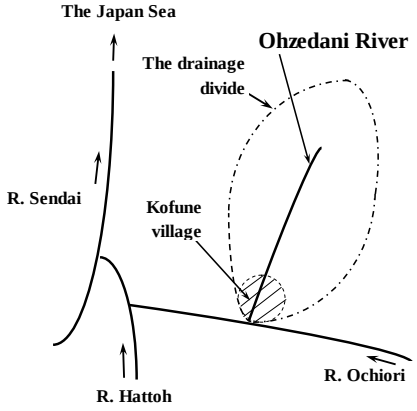

(b) Schematic diagram of Ohzedani River basin

Fig. 1 Lacation of Ohzedani River basin

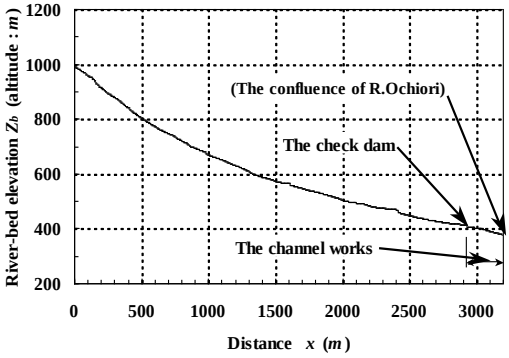

Fig. 2 Bed profile of Ohzedani River

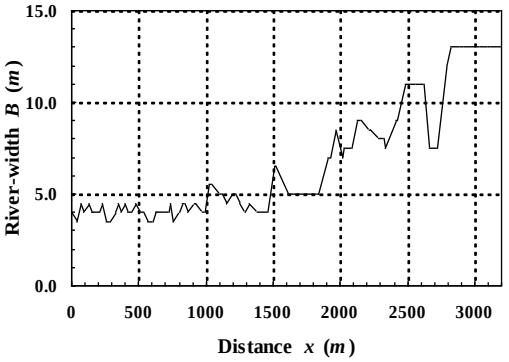

Fig. 3 Width of Ohzedani River

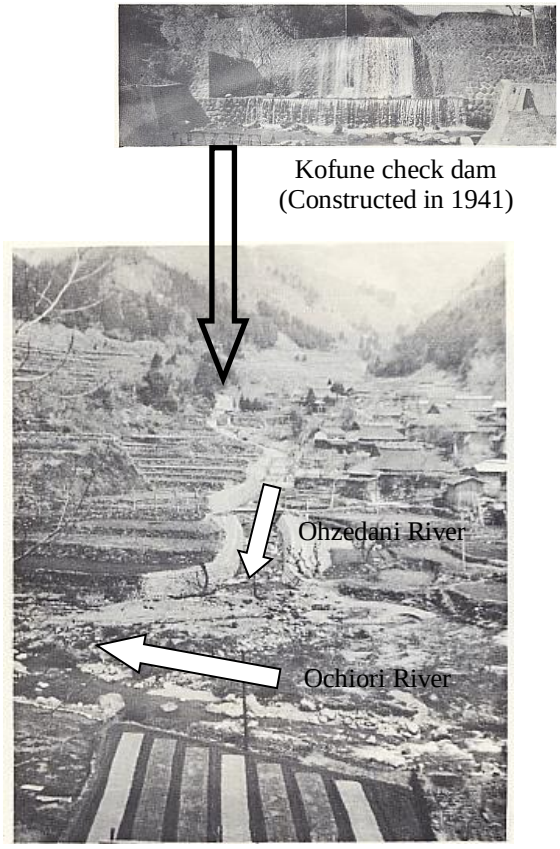

Photo 1 Sediment runoff from second Muroto typhoon in Ohzedani River

reach (Fig. 2), effectively reduced the sediment transport and controlled the debris flow (Photo 1).

Initial and Boundary Conditions of Computation

In this paper, 3,200 m long river reach that is 380 to 990 m above sea level from the point where the river-bed slope changes suddenly to the confluence of Ochiori River, is analyzed. The river-bed and river-width profiles are shown in Figs. 2 and 3.

In this reach, a check dam and channel works are located at the downstream reach (Fig. 2). The effective dam height of the sediment deposition was 5.5 m, and the width of the check storage was 53.0 m before September 1961. The channel works are 308 m long, 6.0 m wide, with a 3.0 m high embankment. In this study, the sediment transport for two cases were computed: 1) the existing stream conditions, and 2) under the investigation of the effect of sabo facilities on sediment transport by eliminating the check dam and the channel works.

There are no hillside landslide data at the upstream reach or river-bed erosion data throughout the reach. Therefore, this study has the following assumptions: the sediment is mainly supplied by the river-bed erosion in this calculation and estimate the critical erosion depth of the river-bed material based on numerical results.

There are no rainfall or runoff data at the reach's upstream end, too. Therefore, the upstream boundary inflow water discharge was estimated, based on the rainfall data of the drainage area. The maximum hourly precipitation was 58.0 mm in the September 1961 debris flow hazard. A rainfall intensity of this value is chosen, which yields 0.50m^3/sec at the reach's upstream end, using the rational formula with a drainage area of 0.05 km^2 and a runoff coefficient of 0.60. Such inflow water discharge is supplied constantly, and then sediment concentration, c_{in} is assumed to be 5 % by volume for convenience.

A finite difference method (the leap-frog scheme shown in Fig. 4) is used. The time and distance were discriminated as Δt= 0.025 seconds and Δx= 5.0 m. The following parameters are required for computation: σ= 2.70 g/cm^3, ρ= 1.17 g/cm^3 (the fine sand concentration into water is 10 % by volume), ϕ_s = 39.0 degrees, d= 5.0 cm and c_*= 0.50.

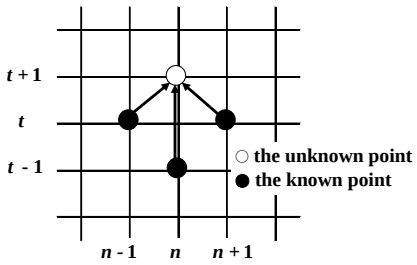

Fig.4 Schematic diagram of leap-frog scheme

RESULTS AND DISCUSSIONS

Existing Stream Conditions

Figure 5(a) shows the relationship between the critical erosion depth of the river-bed material and the flow depth in the channel works based on the numerical analyses with existing stream conditions. Figure 5(b) shows the relationship between the critical critical erosion depth and the total erosion.

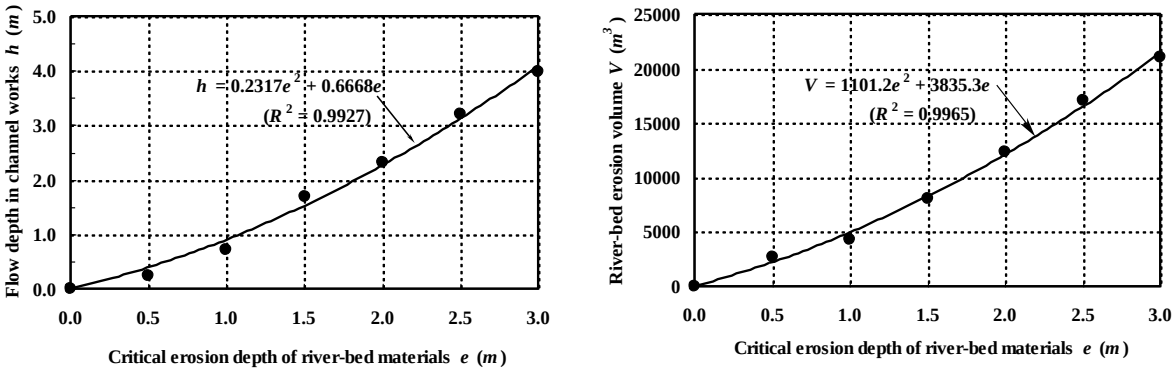

(a) Relationship between critical erosion depth of river-bed material and flow depth in channel works

(b) Relationship between critical erosion depth and total erosion volume

Fig. 5 Estimation of scale of debris flow at Ohzedani River

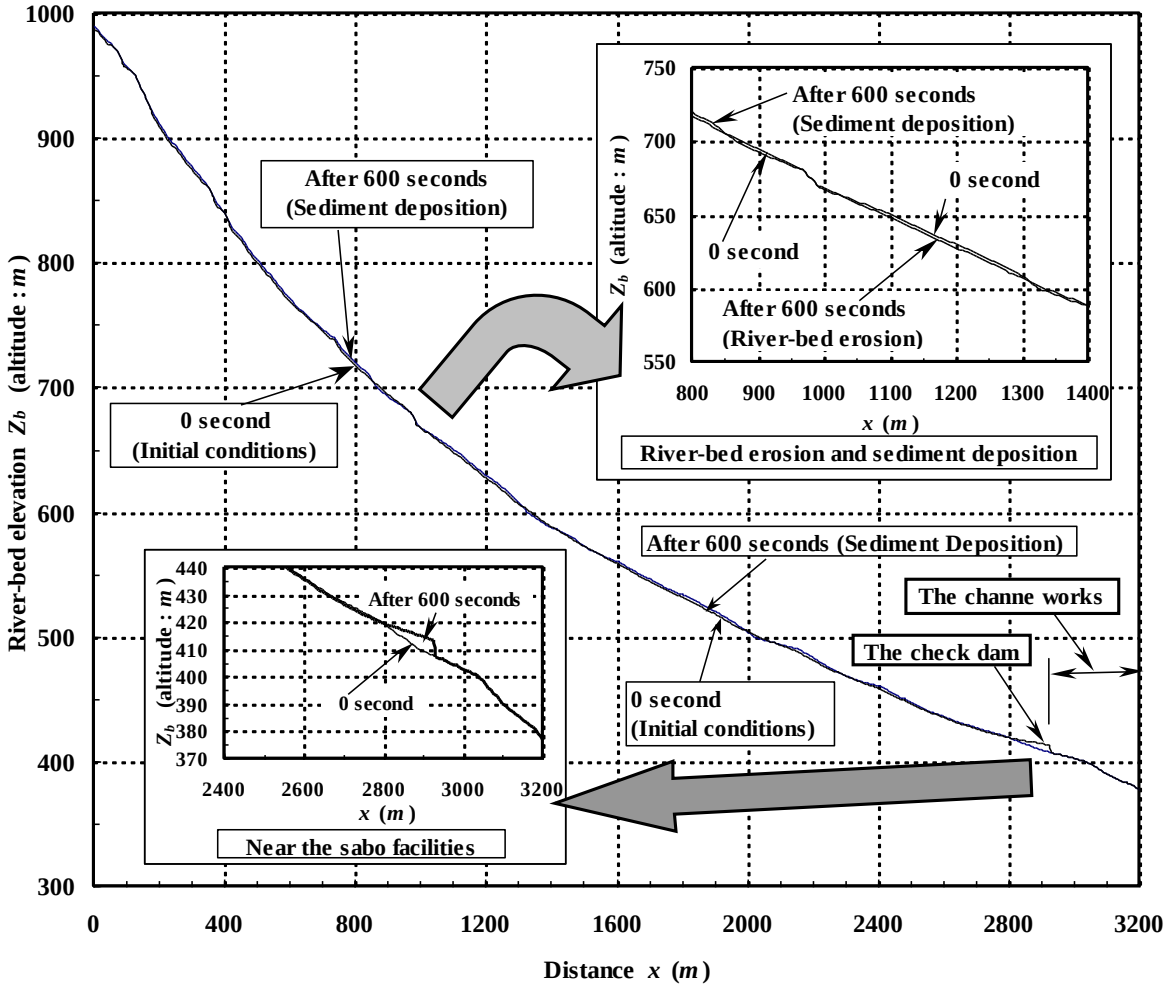

Fig. 6 Comparison of river-bed profiles between initial condition and calculation result after 600 seconds with water supply

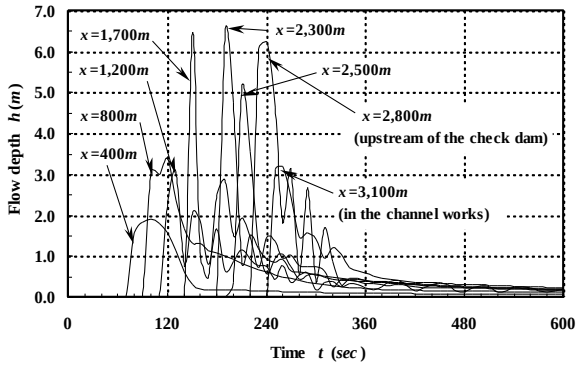

(a) Temporal changes of flow depth

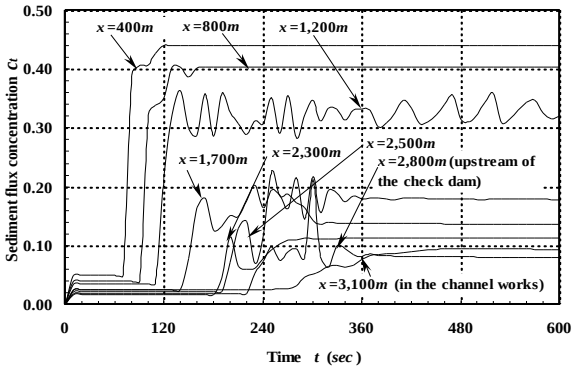

(b) Temporal changes of sediment flux concentration

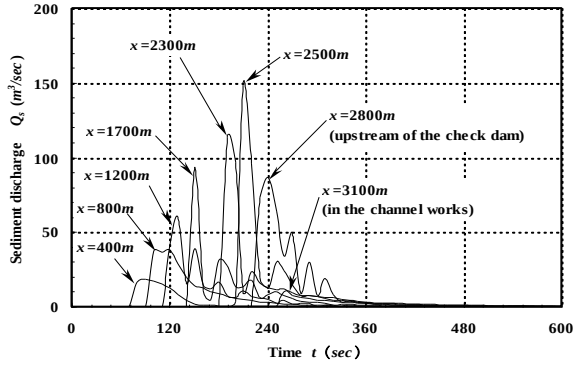

(c) Temporal changes of sediment discharge

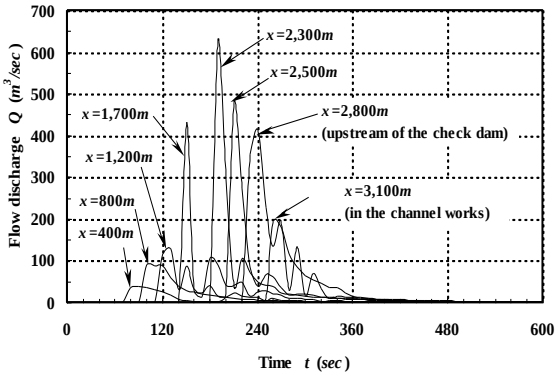

(d) Temporal changes of flow discharge

Fig.7 Temporal changes of debris flow characteristics rates: existing stream conditions

As shown in Fig. 5(a), when the critical erosion depth is shallower than about 2.5 m, the flow depth in the channel works is less than 3.0 m (it equals the embankment height of the channel works). Then the torrent doesn't overflow its banks.

As shown in Fig. 5(b), when the critical erosion depth is 2.5 m, the total erosion volume of the river-bed material is about 17,000 m^3. For the above reason, the scale of the debris flow at Ohzedani River is evaluated (the critical erosion depth and the total erosion volume of river-bed material).

Figure 6 compares the river-bed profiles between the initial condition and the calculation result after 600 seconds with a water supply when the river-bed's critical erosion depth was 2.5 m. Figures 7(a), (b) , (c), and (d) show the temporal changes of the flow depth, the sediment flux concentration, the sediment discharge, and the flow discharge of the sediment-water mixture at the cross-sections; x=400 m, x= 800 m, x=1,200 m, x=1,500 m, x=1,700 m, x=2,300 m, x= 2,500 m, x= 2,800 m (the upstream of the check dam) and x= 3,100 m (the downstream of the check dam and in the channel works).

The debris flow formed quickly after the water supply and the flow discharge increased several orders of magnitude more than the inflow water discharge (x= 400 m in Fig. 7(d)). The debris flow eroded the river-bed from the upstream end to the check dam's upstream (near x= 2,800 m) except the sediment deposition near x=800m (t= 600 seconds in Fig. 6) and the flow depth and discharge increased rapidly by entraining the river-bed material into the debris flow (x=1,700 m and x=2,300 m in Figs. 7(a), (c) and (d)). The sediment flux concentration at the upstream reach is very high, and the flow has debris flow characteristics in this region: x= 400 m, x= 800 m and x=1,200 m in Fig. 7(b)). But they decreased gradually in the midstream reach (x=1,700 m, x=2,300 m and x= 2,500 m in Fig. 7(b)), because the river-bed slope is milder, and the river-width is wider than the upstream reaches.

The debris flow front arrived up stream of the check dam after about 220 seconds with a water supply of x= 2,800 m (Fig. 7(a)), and the sediment began to be deposited on the check storage. The deposition height of the dam height was about 5.0 m,

and the sediment deposition volume on the check storage was about 4,700 m^3 after 600 seconds with a water supply of t= 600 seconds (Fig.6). The debris flow characteristics rate decreased sharply at the cross- section with the check dam due to the change of the transport mode from the debris flow into a conventional water flood with bed-load (x=3,100 m in Figs.7(a)～(d)). The total volume of the sediment-water mixture and the sediment alone, which arrived at the reach's downstream end after 600 seconds with the water supply, was about 10,000 m^3 and 950 m^3, respectively.

Evaluation of Debris Flow Control Using Sabo Facilities

The influence of sabo facilities on sediment transport can be investigated by evaluating the numerical results obtained by varying the initial conditions of the sabo facilities in the river reach. Figures 8(a), (b), (c), and (d) show the temporal changes of the rates of the debris flow characteristics at the cross-sections: x= 2,500 m, x= 2,800 m (upstream of the check dam), and x= 3,100 m (in the channel works) where the check dam and the channel works are eliminated. In these figures, broken lines illustrate the results by the existing stream conditions shown in Figs 7(a), (b), (c), and (d).

Based on these figures, if there is no sabo facility in the reach, the flow depth and flow discharge would amount to about 9.0 m and 360 m^3/sec at x= 3,100 m, respectively. In this calculation, a river-width of x=3,100 m was input as 6.0 m which is the same width of the channel works, and narrower than the local actual condition. Therefore, the torrent will actually overflow its banks near Kofune village. The channel works fix the flow path very well and provide much protection against debris flow flooding. The total volume of the sediment-water mixture and the sediment alone, which arrived at the reach's downstream end after 600 seconds with the water supply, was about 22,000 m^3 and 2,000 m^3, respectively. Therefore, sabo facilities satisfactorily reduced the sediment transport. Sediment deposition reduced the sediment transport, decreased the flow depth and flow discharge, and varies the sediment transport mode.

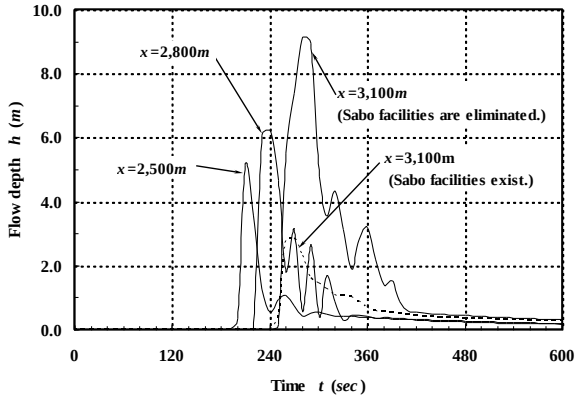

(a) Temporal changes of flow depth

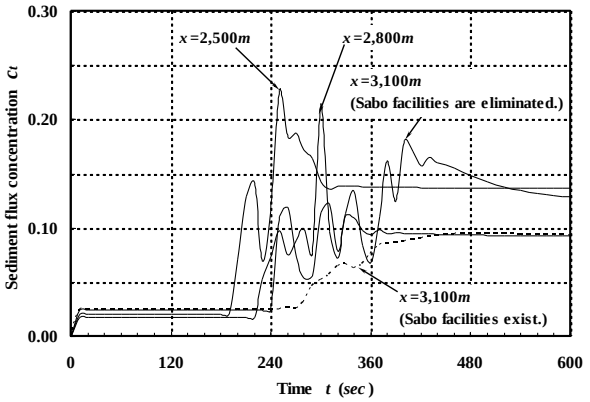

(b) Temporal changes of sediment flux concentration

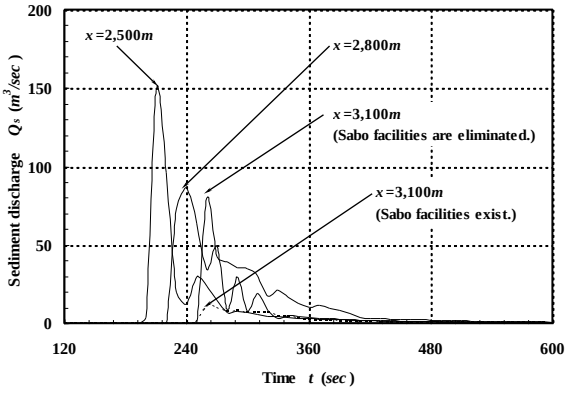

(c) Temporal changes of sediment discharge

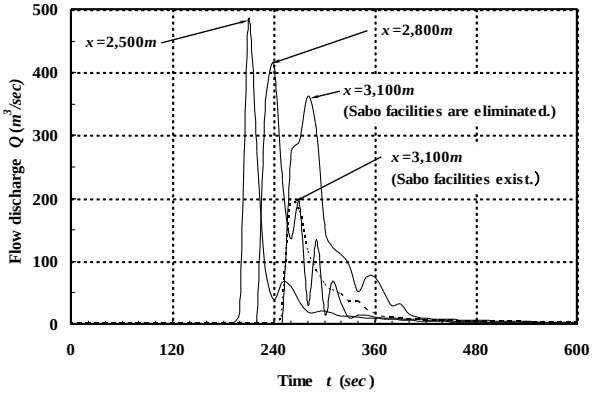

(d) Temporal changes of flow discharge

Fig. 8 Temporal changes of debris flow characteristics rates where sabo facilities are eliminated

CONCLUSIONS

In this paper, the characteristics of sediment runoff and the effects of debris flow control using sabo facilities were discussed, which was based on a numerical simulation and obtained the following interesting results.

1) The scale of debris flow at the Ohzedani River, which was evaluated to be the erosion volume of river-bed material, was about 17,000 m^3. The debris flow discharge increases by several orders of magnitude compared to water, and the sediment transport rate varies with river-bed slope and river width.

2) A check dam is quite effective to reduce sediment transport by depositing sediment on the check storage. The flow path is fixed very well with the channel works that provide much protection against debris flow flooding.

3) The proposed numerical method can reproduce actual sediment runoff processes in a mountain torrent where such sabo facilities as check dams or channel works are constructed. Predicting sediment runoff characteristics is useful and yields valuable results for the evaluation of debris flow control using sabo facilities. Such careful estimates are crucial because the erosion depth of river-beds affects these numerical results.

ACKNOWLEDGEMENTS

Part of the present study was supported by Strategic Research Project from Tokyo University of Agriculture.

REFERENCES

[1] Takahashi T., Study on the Deposition of Debris Flow (3) -Erosion of Debris Fan -. Annuals of Disaster Prevention Research Institute, Kyoto University, Vol. 25, Issue B-2, 1982, pp.327–348 (in Japanese with English abstract).

[2] Takahashi T. and Fu Kuang, Formation of Debris Flow on Varied Slope Bed. Annuals of Disaster Prevention Research Institute, Kyoto University, Vol. 29, Issue B-2, 1986, pp.343–359 (in Japanese with English abstract).

[3] Hashimoto H., Tsubaki T. and Hirano M., Sediment Gravity Flow on Relatively Gentle Slopes. Annual Journal of Hydraulic Engineering, Japan Society of Civil Engineering, Vol. 30, 1986, pp.235-240 (in Japanese with English abstract).

[4] Honda N. and Egashira S., Prediction of Debris Flow Characteristics in Mountain Torrents. The 1st International Conference on DFHM, American Society of Civil Engineering, 1997, pp. 707-716.

[5] Egashira S. and Honda N., Debris Flow Control with Sabo Dams. The 10th APD-IAHR Congress, Vol. 2, 1998, pp.180-187.

[6] Egashira S., Ashida K., Yajima H. and Takahama j., Constitutive Equations of Debris Flow. Annuals of Disaster Prevention Research Institute, Kyoto University, Vol. 32, Issue B-2, 1989, pp.487-501 (in Japanese with English abstract).

[7] Egashira S., Itoh T., Miyamato K. and Honda N., Importance of Correction Factor Associated with Sediment Concentration Profile in Debris Flow Simulation. 2th International Symposium on Flood Defence 2002, Vol.2, 2002, pp.1658-1666.

[8] Egashira, S., Miyamoto K. and Itoh T., Constitutive Equations of Debris Flow and Their Applicability. 1st International Conference on DFHM, American Society of Civil Engineering, 1997, pp. 340-349.

[9] Takahashi T., A Mechanism of Occurrence of Mud-Debris Flow and Their Characteristics in Motion. Annuals of Disaster Prevention Research Institute, Kyoto University, Vol. 20, Issue B-2, 1977, pp.405-435 (in Japanese with English abstract).

9th Int. Conf. on Geotechnique, Construction Materials and Environment, Tokyo, Japan, 20-22 November 2019, ISBN: 978-4-909106025 C3051

UNIT WEIGHT AND COMPRESSIVE STRENGTH OF SOFT BANGKOK CLAY STABILIZED WITH CALCIUM CARBIDE RESIDUE AND BOTTOM ASH

Teerat Tesanasin, Cherdsak Suksiripattanapong, Ratchanon Sakdinakorn, and Jaksada Thumrongvut
Faculty of Engineering and Architecture, Rajamangala University of Technology Isan, Thailand

ABSTRACT

Bottom ash (BA) and calcium carbide residue (CCR) are waste by-product form the Mae Moh power plant in Lamphang, and acetylene gas factory in Nakhon Pathom, respectively. This study investigated the possibility of using binder (B) which is a mixture of BA and CCR in order to improve the compressive strength of soft Bangkok clay. The variable used in this study is the SC: B ratios of 90:10, CCR : BA ratio of 70:30, 80:20, 90:10 and 100:0, water content of 1LL, 1.5LL and 2LL (LL is liquid limit of soft clay), and water to binder (W/B) ratio of 1. The 7-day total unit weight and 7-day unconfined compressive strength (UCS) of sample was evaluated. The test results show that the 7-day total unit weight of SC stabilized with CCR and BA samples increases slightly as the BA content increases for all water content because of lower specific gravity of BA. the compressive strength of soft Bangkok clay stabilized with calcium carbide residue and bottom ash tends to increase as the BA content increases because of the pozzolanic reaction resulting in the formation of calcium silicate hydrate (CSH).

Keywords: Soft Bangkok Clay, Calcium Carbide Residue, Bottom Ash, Compressive Strength

INTRODUCTION

The development of infrastructure (road, foundation, and bridges) on soft Bangkok clay has problems. This soil has high water content from 60-130 %, liquid limit is close to the water content which 70-120 % and plastic limit from 20-45 % [5] Ground improvement techniques have been employed to stabilize soft soil over the past three decades such as prefabricated vertical drain (PVD) [20], [6], grouting [21] and deep mixing (DM) [12]-[16]. The DM method has been used worldwide including Thailand, China, Sweden, Japan and Singapore. The cement column has previously been mixed with soft clay and cement. However, the use of conventional Portland cement will result in a large carbon footprint since the production of 1 ton of Portland cement releases about 1 ton of carbon dioxide [9].

Calcium Carbide Residue (CCR) an industrial waste generated from acetylene gas production, has a high calcium hydroxide [Ca(OH)2] content. CCR has been used as a binder to develop green stabilized pavement materials [7-11] and non-bearing masonry units [20]. Phetchuay et al. [21] and Arulrajah et al. [22] have recently used CCR for stabilization of natural soil and Construction and Demolition materials in pavement applications [23].

Bottom ash (BA) is a aluminosilicate-rich materials which is a by-product from electrical manufacturing factory, Mae Moh, Thailand. Chemical compositions of bottom ash is essentially the same as the fly ash which is the main aluminosilicate-rich material [30]. However, the compressive strength of BA was lower than that of fly ash because of larger particle size [31].

This study investigated the possibility of using binder (B) which is a mixture of BA and CCR in order to improve the compressive strength of soft Bangkok clay.The variable used in this study is soft clay:binder, CCR:BA ratio, water content, and water:binder ratio. The 7-day unconfined compressive strength (UCS) of sample was evaluated.

MATERIALS AND METHODS

Materials

Soft clay (SC)

Soft clay was collected at depth of 5-8 m from Khlong Toei, Bangkok, Thailand. Total unit weight (γ_t) = 15.97 kN/m^3, Specific gravity (Gs) = 2.68, Liquid limit (LL) = 63.93%, Plastic limit (PL) = 25.49% and Plasticity index (PI) = 38.44. Soft clay was classified as clay high plastic (CH) according to Unified Soil Classification System (USCS).

Bottom ash (BA)

Bottom ash (BA) is a by-product from electrical manufacturing factory Mae Moh, Lampang, Thailand. The chemical compositions of bottom ash are shown in Table 1. The sum of silica (SiO_2), alumina (Al_2O_3), and ferric oxide (Fe_2O_3) was 65.69% and Calcium

Oxide (CaO) was 21.76%. The BA can be classified as class C according to the standard ASTM C618 [1].

Calcium carbide residue (CCR)

CCR was collected from Sai 5 Gas Product Co., Ltd, Thailand. The CCR was oven-dried at 100 ºC for 24 h and was then passed through a No. 40 sieve (0.425 mm). The specific gravity is 2.32. The chemical composition of CCR is summarized in Table 1, indicating it has a very high CaO content of 75.96%.

Table 1 Chemical composition of BA and CCR

Chemical composition (%)	BA	CCR
SiO_2	36.33	9.81
Al_2O_3	13.71	4.64
Fe_2O_3	15.65	2.03
CaO	21.76	75.96
SO_3	10.15	2.58
K_2O	1.5	N.D.
TiO_2	0.54	1.86
LOI	N.D.	3.12

Mixing proportions

The soft clay was prepared at water content of 1LL, 1.5LL and 2LL (LL is the liquid limit). The SC:binder (CCR and BA) was fixed at 90:10. The water:binder ratio was 1. The CCR:BA ratios were 100:0, 90:10, 80:20, and 70:30 by total weight. Firstly, the CCR, BA, and water were mixed for 2 minutes and then these mixture was added into the SC and mixed for about 3 minutes. Next the homogeneous sample was moved into a cylinder diameter of 36 mm and height 72 mm and cured at room temperature for 24 hours. After that the sample was removed from mold and then wrapped with plastic and store in room temperature. Compressive strength of soft Bangkok clay stabilized with calcium carbide residue and bottom ash at curing 7 day was evaluated by unconfined compressive strength (UCS) according to ASTM D2166 [3]

RESULTS AND DISCUSSION

Total Unit Weight of Soft Bangkok Clay Stabilized with Calcium Carbide Residue and Bottom Ash

Figure 1 shows 7-day total unit weight of SC stabilized with CCR and BA at different LL. The 7-day total unit weight of SC stabilized with CCR and BA samples increases slightly as the BA content increases for all water content because of lower specific gravity of BA. For example, The 7-day total unit weight of SC stabilized with CCR and BA samples at LL=1 was 16.05, 16.43, 16.52 and 16.81 kN/m^3 for BA content of 0, 10, 20 and 30%, respectively. The water content has an effect on the 7-day total unit weight of SC stabilized with CCR and BA samples. The 7-day total unit weight of SC stabilized with CCR and BA samples reduces as water content increases due to high porosity from water.

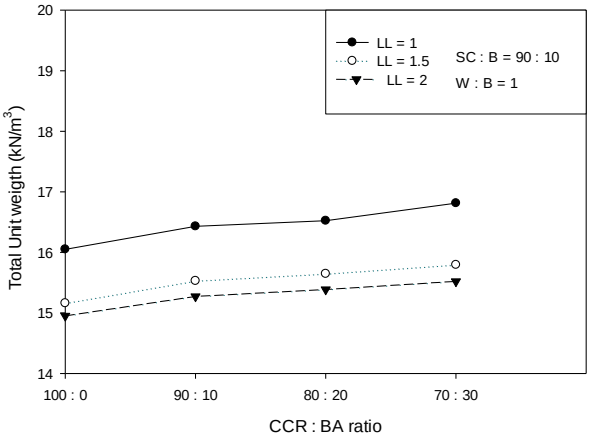

Fig. 1 7-day total unit weight of SC stabilized with CCR and BA at different LL

Compressive Strength of Soft Bangkok Clay Stabilized with Calcium Carbide Residue and Bottom Ash

Figure 2 shows 7-day compressive strength of SC stabilized with CCR and BA at different LL. It was found that the 7-day compressive strength of SC stabilized with CCR and BA increases as BA content increases. This is because Ca (OH_2) from CCR can react with Si and Al form BA, resulting in the formation of calcium silicate hydrate (CSH). The 7-day compressive strength of SC stabilized with CCR and BA decreases as water content increases. For example, The 7-day compressive strength of SC stabilized with CCR and BA samples at CCR:BA of 70:30 was 177.16, 42.97 and 34.76 kN/m^2 for water content of 1LL, 1.5LL and 2.0LL, respectively. The maximum 7-day compressive strength of SC stabilized with CCR and BA samples was found at CCR:BA of 70:30 and water content of 1LL which offers maximum 7-day compressive strength of 177.16 kPa. Table 2 illustrated standard deviation (SD) of SC stabilized with CCR and BA at different LL. The SD of SC stabilized with CCR and BA

ranged from 0.3 to 8 kPa. This low SD values confirmed variation of results.

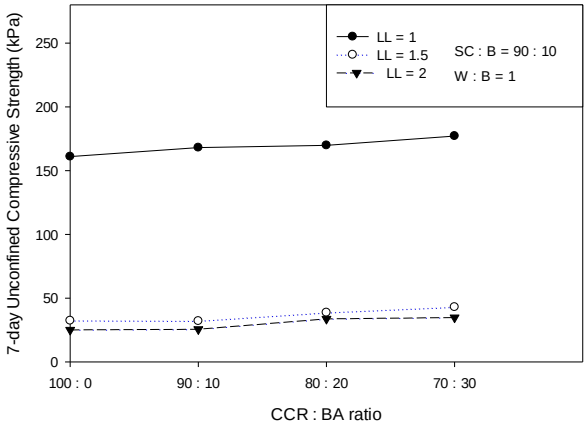

Fig. 2 7-day compressive strength of SC stabilized with CCR and BA at different LL

Table 2 Standard deviation of SC stabilized with CCR and BA at different LL

ITEM		CCR : BA			
		100:0	90:10	80:20	70:30
1LL	Sample 1	156	175	171	169
	Sample 2	161	164	167	177
	Sample 3	166	166	169	185
	mean	161	168	169	177
	SD	5	6	2	8
1.5LL	Sample 1	32.4	32	37.7	43.3
	Sample 2	32.4	31	42.3	45.5
	Sample 3	31.9	33.6	36	39.4
	mean	32.2	32.2	38.7	42.7
	SD	0.3	1.3	3.3	3.1
2LL	Sample 1	26.2	30.3	34.6	35
	Sample 2	27.4	21.9	34.8	33
	Sample 3	22.1	24.9	30.2	34.8
	mean	25.2	25.7	33.2	34.3
	SD	2.7	4.3	2.6	1.1

CONCLUSIONS

The paper investigated the possibility of using a binder material which is a mixture of Bottom Ash (BA) and Calcium Carbide Residue (CCR). The experiments were conducted only for one Soft Clay to Binder ratio, SC:B ratio of 09:10 at various CCR to BA ratios, CCR:BA of 70:30, 80:20, 90:10 and 100:0 at water content of 1LL, 1.5LL and 2LL (LL is liquid limit of soft clay), and water to binder (W/B) ratio of 1. The outcome of the research indicate that the total unit weight of SC stabilized with the binder increases slightly with increasing the water content, the compressive strength increases with increasing the BA content.

ACKNOWLEDGMENTS

This work was financially supported by the Thailand Research Fund under the Research and Researcher for Industry (RRi) program Grant No. RTA MSD61I0083. The authors acknowledge the financial support from the Rajamangala University of Technology Isan.

REFERENCES

[1] American Society for Testing and Materials (2015). ASTM C618. Standard specification for coal fly ash and raw or calcined natural pozzolan for use in concrete. ASTM International.

[2] American Society for Testing and Materials (2015). ASTM D388. Standard classification of coals by rank. ASTM International.

[3] American Society for Testing and Materials (2000). ASTM D2166. Standard Test Method for Unconfined Compressive Strength of Cohesive Soil. ASTM International.

[4] American Society for Testing and Materials (2011). ASTM D2487. Standard practice for classification of soils for engineering purposes (unified soil classification system). ASTM International.

[5] Bergado, D, T., Ruenkrairergsa, T., Taesiri, Y., Balasubramaniam, A, S. (1999). Deep soil mixing used to reduce embankment settlement. Ground Improvement (1999) 3, pp. 145-162

[6] Chen, J., Shen, S-L., Yin, Z-Y., Ye-Shuang Xu, Y-S., Horpibulsuk, S., 2016. Evaluation of effective depth of PVD improvement in soft clay deposit: a field case study. Marine Georesources and Geotechnology. 34(5), 532-541.

[7] Chindaprasirt, P. Jaturapitakkul, C., Chalee, W., Rattanasak, U., 2009. Comparative study on the characteristics of fly ash and bottom ash geopolymers. Waste Management, 29(2), 539-543.

[8] Chindaprasirt, P.C., T. Hatanaka, S. Cao, T. 2011. High-Strength Geopolymer Using Fine High-Calcium Fly Ash. Journal of Materials in Civil Engineering, 23(3), 264-270.

[9] Cong, M., Longzhu, C., Bing, C. (2014). Analysis of strength development in soft clay stabilized with cement-based stabilizer. Construction and Building Materials, pp. 354-362.

[10] Davidovits J. (1999) Chemistry of geopolymer systems, terminology, Geopolyme 1999.

[11] Horpibulsuk, S., Miura, N., Nagaraj, T.S., 2003. Assessment of strength development in cement-admixed highwater content clays with Abrams' law as a basis. Geotechnique, 53 (4), 439–444.

[12] Horpibulsuk, S., Miura, N., Koga, H., Nagaraj, T.S., 2004. Analysis of strength development in

deep mixing – a field study. Ground Improv. 8 (2), 59–68.
[13] Horpibulsuk, S., Rachan, R., Raksachon, Y., 2009. Role of fly ash on strength and microstructure development in blended cement stabilized silty clay. Soils Found. 49 (1), 85–98.
[14] Horpibulsuk, S., Rachan, R., Suddeepong, A., 2011a. Assessment of strength development in blended cement admixed Bangkok clay. Constr. Build. Mater. 25 (4), 1521–1531.
[15] Horpibulsuk, S., Rachan, R., Suddeepong, A., Chinkulkijniwat, A., 2011b. Strength development in cement admixed Bangkok clay: laboratory and field investigations. Soils Found. 51 (2), 239–251.
[16] Jamsawang, P., Poorahong, H., Yoobanpot, N., Songpiriyakij, S., Jongpradist, P. (2017). Improvement of soft clay with cement and bagasse ash waste. Construction and Building Materials 154 (2017), pp. 61-71
[17] Phetchuay, C., Horpibulsuk, S., Arulrajah, A., Suksiripattanapong, C., Udomchai, A. (2016). Strength development in soft marine clay stabilized by fly ash and calcium carbide residue based geopolymer. Applied Clay Science, pp. 134-142
[18] Porbaha, A., Shima, M., Miura, H. and Ishikura, K. (1999). Dry jet mixing method for liquefaction remediation. Dry Mix Methods for Deep Soil Stabilization, 27-32.
[19] Wu, H-N., Shen, S-L., Ma, L., Yin, Z-Y., Horpibulsuk, S., 2015. Evaluation of the strength increase of marine clay under staged embankment loading: a case study. Marine Georesources and Geotechnology. 33(6), 532-541.
[20] Shen, S.L., Wang, Z.F., Horpibulsuk, S., Kim, Y.H., 2013a. Jet grouting with a newly developed technology: the twin-jet method. Eng. Geol. 152 (1), 87–95.
[21] Kampala A, Horpibulsuk S. Engineering properties of calcium carbide residue stabilized silty clay. Journal of Materials in Civil Engineering, ASCE 2013:25(5);632-644.
[22] Kampala A, Horpibulsuk S, Chinkulkijniwat A, Shen SL. Engineering properties of recycled calcium carbide residue stabilized clay as fill and pavement materials. Constr Build Mater 2013;46:203–10.
[23] Kampala A, Horpibulsuk S, Prongmanee N, Chinkulkijniwat A. Influence of wet-dry cycles on compressive strength of calcium carbide residue-fly ash stabilized clay. Journal of Materials in Civil Engineering, ASCE 2014;24(1):633-643.
[24] Horpibulsuk S, Phetchuay C, Chinkulkijniwat A. Soil stabilization by calcium carbide residue and fly ash. Journal of Materials in Civil Engineering, ASCE 2012;24(2):184-193.
[25] Horpibulsuk S, Phetchuay C, Chinkulkijniwat C. Soil stabilization by calcium carbide residue. J Mater Civ Eng 2012;24(2):184–93.
[26] Horpibulsuk, S., Munsrakest, V., Udomchai, A, Chinkulkijniwat, A. and Arulrajah, A. (2014), "Strength of sustainable non-bearing masonry unit manufacturing from calcium carbide residue and fly ash", Construction and Building Materials, Vol.71, pp.210-215
[27] Phetchuay, C., Horpibulsuk, S., Suksiripattanpong, C., Chinkulkijniwat, A., Arulrajah, A. and Disfani, M.M. (2014). Calcium carbide residue: Alkaline activator for clay-fly ash geopolymer. Construction and Building Materials, 69:285-294.
[28] Arulrajah A, Mohammadinia A, Phummiphan I, Horpibulsuk S, Samingthong W. Stabilization of recycled demolition aggregates by geopolymers comprising calcium carbide, fly ash and slag precursors. Construction and Building Materials (Tentatively accepted for publication); 2016.
[29] Du, Y-J, Jiang, N-J. Liu, S-Y, Horpibulsuk, S. and Arulrajah, A. (2016) "Field evaluation of soft highway subgrade soil stabilized with calcium carbide residue", Soils and Foundations (accepted 18 December 2015; in press).
[30] Boonserm K, Sata V, Pimraksa K and Chindaprasirt P, 2012, Improved geopolymerization of bottom ash by incorporating fly ash and using waste gypsum as additive. Cement and Concrete Composites, 34(7): 819-824.
[31] Chindaprasirt, P., Jaturapitakkul, C., Chalee, W. and Rattanasak, U. (2009). Comparative study on the characteristics of fly ash and bottom ash geopolymers. Waste Management, vol.29 (2), pp. 539-543.

9th Int. Conf. on Geotechnique, Construction Materials and Environment, Tokyo, Japan, 20-22 November 2019, ISBN: 978-4-909106025 C3051

EXPERIMENTAL STUDY ON BEHAVIOUR OF VERTICALLY LOADED PILED RAFTS RESTING ON SATURATED CLAYEY GROUND

Lua Hoang[1, 2] and Tatsunori Matsumoto[1]
[1]Faculty of Geosciences and Civil Engineering, Kanazawa University, Japan; [2]Thuyloi University, Vietnam

ABSTRACT

When designing piled raft foundation (PR) on clayey ground, it is necessary to understand time-dependent behaviour of the foundation because stresses and strains in clayey ground will change for a long time after the construction, due to consolidation processes. This paper, therefore, aims to investigate long-term behaviour of PRs through small-scale physical modelling. In the experiments, the model ground was prepared by consolidating a slurry mixture of Kasaoka clay and silica sand. The model foundations consisted of a square raft having a width of 125 mm and 4 or 9 piles having a length of 150 mm. For the loading test of PR, vertical load was increased by multiple steps and each load step was maintained to observe the long-term behaviour. The experimental results show that, the piles effectively suppress the settlement of the foundation for relatively smaller loads. In primary consolidation stage, the pile resistance increases while the raft resistance decreases with elapsed time. This is caused by the dissipation of pore water pressure and the corresponding increase of effective stresses of soils below the raft base. In secondary consolidation stage, the resistances of both the raft and piles are stable while creep settlement continues. In general, the PR with 9 piles reduces settlement significantly, compared to the 4-pile PR.

Keywords: Piled raft, Clayey ground, Experiment, Consolidation, Pore water pressure

INTRODUCTION

In recent years, there has been an increasing need to construct heavy structures, especially in urban areas. To support these structures, piled raft (PR) is a favourable foundation type because of its cost effectiveness and safety, as both raft and piles share the load together.

Behaviours of PRs in clay have been investigated in many researches. In most of these researches, numerical methods were used to solve the behaviour. Physical modelling of PRs in clay subjected to vertical loads were carried out in a few researches ([1], [2] and [4]). These experiments aimed to investigate immediate behaviour of PRs until the end of construction, disregarding long-term behaviour after full construction load was achieved. However, if a PR is located on saturated clayey ground, the foundation will continue to settle for a very long time after the construction, due to primary consolidation process and creep behaviour of the ground.

Hence, one of the main purposes of this research is to study time-dependent behaviour of piled raft foundations in saturated clay through small-scale physical modelling. In this paper, focuses are placed on the settlement of foundation, and on the change of load sharing by the raft and piles with time due to primary and secondary consolidation processes. Two PRs with different numbers of piles were carried out to investigate effect of pile number on long-time load distribution and settlement of PRs.

EXPERIMENT DESCRIPTION

Model Ground

Preparation of the model grounds

Clay ground was prepared in a cylindrical chamber of height 420 mm and diameter 420 mm. The soil used for the model ground was a mixture of Kasaoka clay powder and silica sand #6.

The model ground was prepared as follows: Firstly, Silica sand #3 was poured into the chamber, and compacted in saturated condition until it reached a high relative density, D_r, of 81% and a thickness of 50 mm for a bottom drainage layer. This drainage layer was considered as a stiff layer. Secondly, in a rectangular basin, Kasaoka clay powder and Silica sand #6 were mixed at a dry mass ratio of 1:1 (K50S50). Water was then added to the mixed soil to have a soil slurry with a water content of 1.3 times the liquid limit, *LL*. This soil slurry was poured into the chamber to have an initial thickness of 370 mm. The soil then left to consolidate under its self-weight for two days. After that, a surface layer of silica sand #6 of thickness 10 mm was placed on the clay to provide the top drainage layer, and a rigid circular loading plate was placed on the top. Next, vertical load on the loading plate was increased to consolidate the soil one-dimensionally in several steps, up to a vertical stress of 100 kPa. Each load step was maintained until degree of consolidation reached 90% following the

one-dimensional consolidation theory of Terzaghi. The final load step was kept for an additional week to have higher degrees of consolidation. Finally, the consolidation pressure was removed and the ground was allowed for swelling process in 10 days.

Soil property investigation

T-bar tests, cone penetration tests (CPTs) and unconfined compression tests (UCTs) were carried out immediately after completion of the load test of each model foundation. In each model ground, two T-bar tests (T1 and T2) were conducted at the locations far from the load test area in order to estimate undrained shear strength of the original model ground without effect of loading test of PR. Three T-bar tests (T3, T4 and T5) were carried out at the locations beneath the raft base (loading area) in order to obtain effect of the load test of PR on the ground strength. Three CPTs were also conducted in one experiment. Figure 1(a) shows the locations of the T-bar tests and the CPTs in the two experiments. Undrained shear strength, c_u, was deduced from the average stress acting on T-bar cylinder, $q_{u\ T\text{-}bar}$, or from the cone tip resistance, $q_{u\ cone\ tip}$, using empirical equations [3] indicated in Fig. 1(b).

As for UCTs, soil specimens were sampled from different depths of each model. Locations of the specimens were also selected at, near and far from the loading area (Fig. 1(a)). c_u was estimated from unconfined compression strength, q_u, as $c_u = q_u/2$.

Figure 1(b) shows the distributions of c_u of the model grounds with depth obtained from the three different methods. The c_u varied with depth, and similar results were obtained for both the model grounds. c_u of the original model ground could be expressed approximately by the following equation:

$$c_u\ (\text{kPa}) = 9\ (\text{kPa}) + z\ (\text{mm}) \times 0.04\ (\text{kPa/mm}) \qquad (1)$$

To obtain other properties of the model grounds, laboratory soil tests such as oedometer, Atterberg limits, density and water content tests were conducted, and the results are summarised in Table 1.

Table 1 Properties of the model ground soil

Parameter	Notation and unit	Value
Density of soil particle	ρ_s (Mg/m^3)	2.653
Saturated density	ρ_{sat} (Mg /m^3)	1.98
Liquid limit	LL (%)	33.9
Plastic limit	PL (%)	13.6
Compression index	C_c	0.291
Swelling index	C_s	0.055
Water content*	w (%)	26.2
Void ratio*	e	0.7

* after consolidating with vertical pressure of 100 kPa

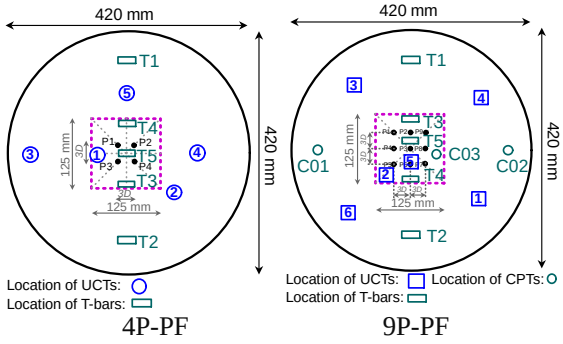

(a) Location of T-bar tests, CPTs and UCTs

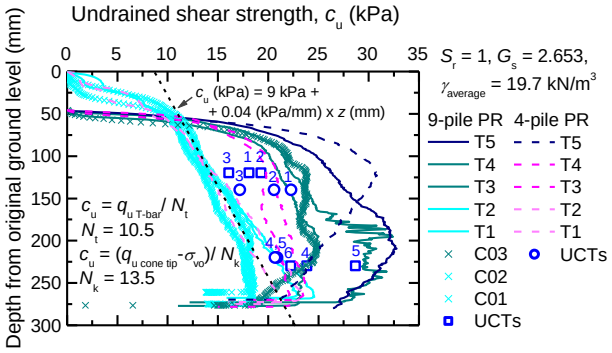

(b) Variation of undrained shear strength with depth

Fig. 1 Distribution of c_u with depth.

Model Foundations

Model piles used in this study were ABS (Acrylonitrile Butadience Stayrene) solid bars (Fig. 2(a)) having a diameter D of 10 mm and a length L of 150 mm. Young's modulus E_p and Poisson's ratio ν of the model piles are 2920 N/mm^2 and 0.406, respectively. In order to measure axial forces along each pile, strain gauges (SGs) were attached on the pile shaft at 4 different levels as shown in Fig. 2(a). Model raft was a square aluminium plate with a thickness of 12 mm and a width of 125 mm (Fig. 2(b)). The raft could be regarded as rigid.

In the experiments, the foundation models included unpiled raft (UR), single pile (SP), 4-pile pile foundation (4P-PF) and 9-pile pile foundation (9P-PF).

Figure 2(c) and (d) show the dimensions of the pile foundation models. Both the pile foundations (PFs) had the same centre-to-centre pile spacing, s of 3D.

Test Procedure

Figure 3 shows the set-up of an experiment. The loading system in the experiment included an air cylinder to apply constant vertical load, a load cell to measure the applied load and 4 dial gauges to measure settlements of the foundation. One pore water pressure transducer and one earth pressure cell were installed at the centre locations of the raft base.

Prior to the load test of PFs, vertical static load tests on single pile and unpiled raft in undrained

condition were carried out to obtain bearing capacity of each element and to determine the magnitude of the vertical load to be applied on the piled rafts.

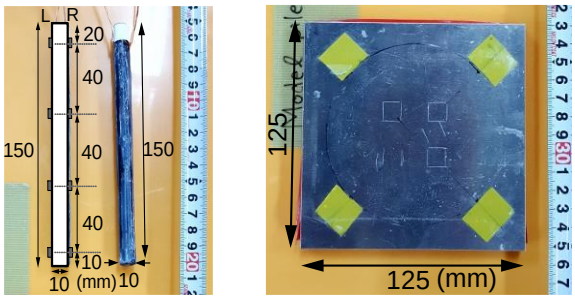

(a) Model piles and locations of SGs (b) Model raft

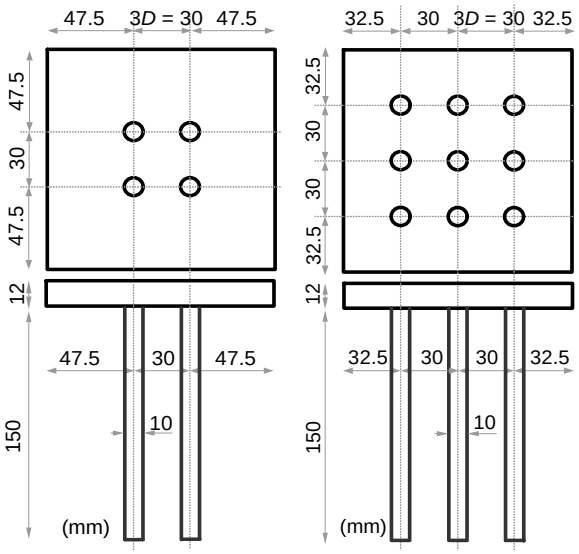

(c) 4P-PF (d) 9P-PF

Fig. 2 Model piles, raft and pile foundations.

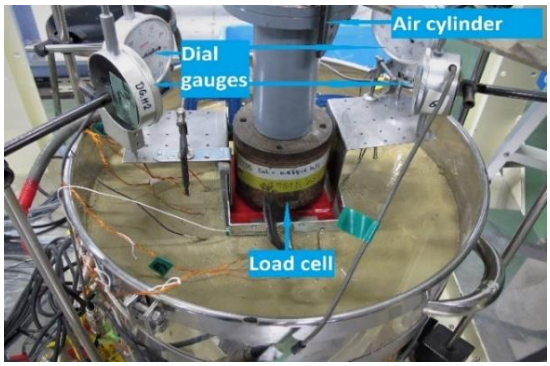

Fig. 3 The set-up of an experiment.

As for the load tests of the pile foundations, the piles were firstly jacked into the ground one by one with a centre-to-centre pile spacing, *s*, equal to 3*D*. Thereafter the raft was placed on the pile heads with a gap of around 5 mm from the raft base to the ground surface, and vertical static loading of the pile group (PG) was conducted in a displacement-controlled manner. The PG changed to piled raft (PR) after the raft base touched the ground surface. In the piled raft condition, vertical load was increased by 4 steps on 4P-PR and 5 steps on 9P-PR in a load-controlled manner. Each load step was maintained for a reasonable time to obtain the long-term behaviour of the foundation.

EXPERIMENTAL RESULTS

Bearing Capacity of Single Pile and Unpiled Raft

Figure 4 shows the results of vertical load tests of the single pile (SP) and the unpiled raft (UR). The bearing capacity of UR and SP were about 2100 N and 100 N, respectively. The sum of bearing capacity of UR and 4 times of a SP or 9 times of a SP was 2500 N or 3000 N, respectively. Based on these results, the load steps applied on the 4P-PR were determined to be 750 N, 1250 N, 2000 N and 2500 N respectively, corresponding to 30% (Factor of safety F_S = 3.3), 50% (F_S = 2), 80% (F_S = 1.25) and 100% (F_S = 1.0) of the predicted total bearing capacity. For 9P-PR, the same 4 load steps were applied in order to compare with 4P-PR. One more final load step, P = 3000 N, corresponding to 100% of the predicted capacity of 9P-PR was additionally applied.

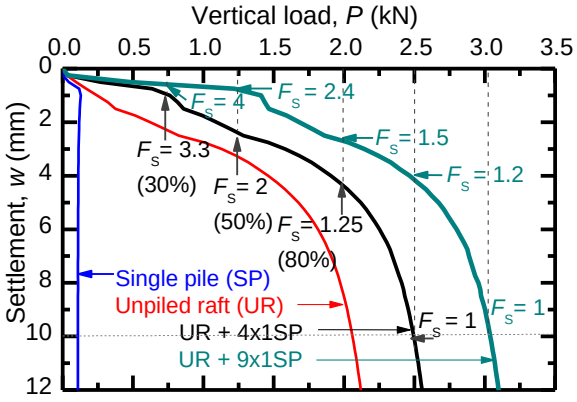

Fig. 4 Load settlement relations of SP and UR.

Settlement and Pile Respond in PR Condition

Immediate behaviour - the time of increasing load

Figure 5(a) shows the relationship between the applied load, *P*, and the settlement, *w*, of the 4P-PR. Figures 5(b), 5(c) and 5(d) are zoom-ins of the periods of increasing load of the first 3 steps of the 4P-PR. Figure 6(a) shows the change of excess pore water pressure (PWP) and settlement with whole experimental duration of the 4P-PR. Figures 6(b), 6(c) and 6(d) are zoom-ins of the periods of increasing applied load of the first 3 steps. Figures 7 and 8 are the corresponding results of the 9P-PR.

It is noticed that the authors do not zoom-in the remained load steps due to the space limitation.

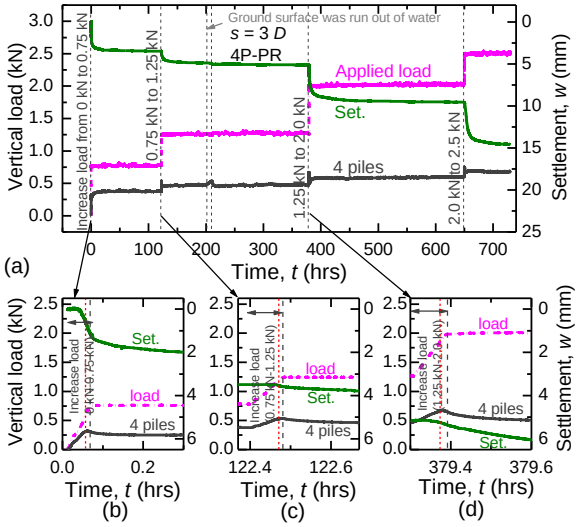

Fig. 5 Changes with time of load and settlement of 4P-PR: (a) full-time of loading test; (b), (c) and (d) zoom-in the duration of increasing the applied load.

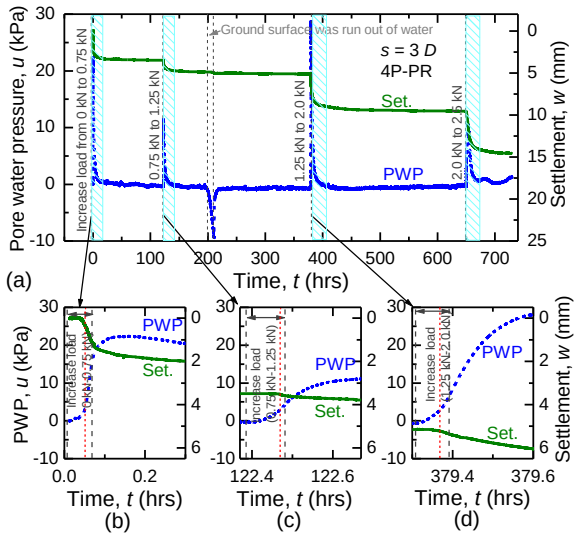

Fig. 6 Changes with time of PWP and settlement of 4P-PR: (a) full-time of loading test; (b), (c) and (d) zoom-in the duration of increasing the applied load.

Let us focus first on the results of the 4P-PF. It should be noted that the bearing capacity of a single pile was around 100 N. The applied load, P = 750 N, in the 1st loading step was less than 9 times of the bearing capacity of a SP, and almost a double of 4 times of the bearing capacity of a SP.

Figure 5(b) shows that, at early stages of increasing load, the increase of the settlement was minor. The reason for this phenomenon is that, when the initial small loads were applied, the resistance of piles increased rapidly to support the load, and the increase of pile resistance was almost equal to the increase of the applied load.

Hence, the piles effectively suppressed the settlement of the foundation in this stage. The foundation then started settling under undrained condition while the pile resistance increased to a peak in this loading stage. After the pile resistance reached the peak, the settlement of the foundation continued rapidly, and pile resistances reduced. The raft load is obtained as the difference of the applied load and the pile resistance.

Let us look at Fig. 6(b). It is clearly seen that PWP started increasing when the undrained settlement started, and PWP increased sharply after the pile resistance reached the peak. The measured results also indicated that when the PWP reached the peak, the pile resistance decreased to a lowest value in this loading stage. Similar trends were measured for the other loading stages (Figs. 5(c), (d) and Figs. 6(c), (d)).

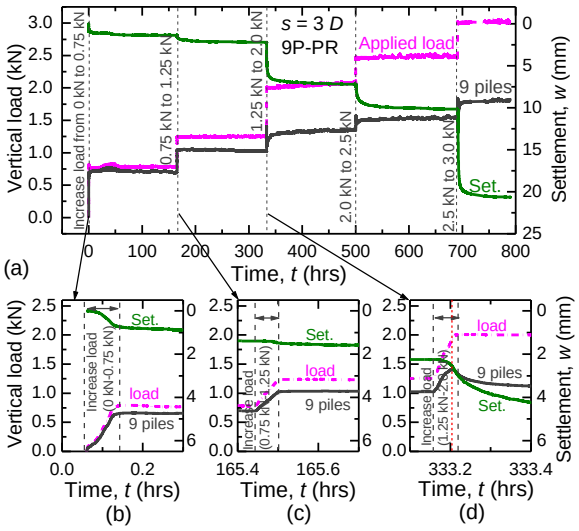

Fig. 7 Changes with time of load and settlement of 9P-PR: (a) full-time of loading test; (b), (c) and (d) zoom-in the duration of increasing the applied load.

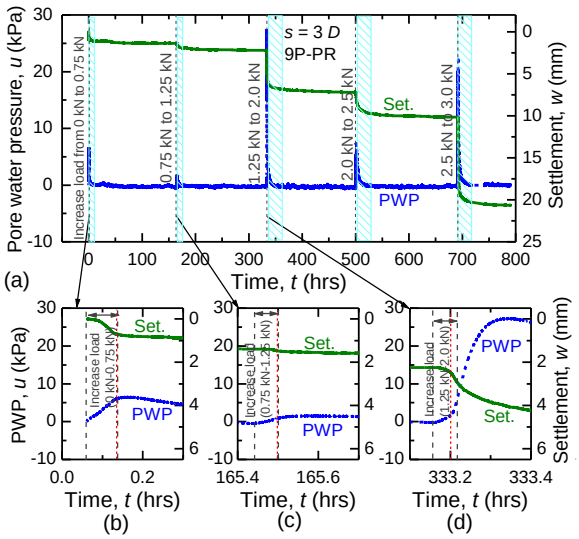

Fig. 8 Changes with time of PWP and settlement of 9P-PR: (a) full-time of loading test; (b), (c) and (d) zoom-in the duration of increasing the applied load.

Let us turn to the results of 9P-PR. Comparing the results of 9P-PR with the results of 4P-PR, in the 1st (Fig. 7(b)) and 2nd (Fig. 7(c)) loading steps, the settlements of 9P-PR were much smaller (about a half of 4P-PR) and the reduction of pile resistance after reaching the peak did not occur. Figures 8(b) and 8(c) also indicate that the increments of PWPs beneath the raft base of 9P-PR were quite small in these stages. The reason for the differences is that the 9P-PR had larger number of piles, therefore the applied loads were mainly carried by the piles in these loading stages.

In the 3rd, 4th and 5th load steps where P was sufficiently large compared with the bearing capacity of 9 times of a SP, the results of the 9P-PR clearly have similar trends to the results of 4P-PR.

It is interesting to notice that in both the foundations, the peak pile resistances increased with increasing the applied loads. For example, the peak pile resistances, in the four load steps of P = 0.75, 1.25, 2.0 and 2.5 kN, were 0.32, 0.53, 0.68 and 0.75 kN for 4P-PF, and 0.66, 1.02, 1.42 and 1.57 kN for 9P-PF, respectively. For 9P-PR, when the applied load increased to 3 kN, the resistance of the 9 piles reached a peak of 1.85 kN which was a double of the resistance of 9 single piles. The increase of the pile resistances with increasing the applied loads is caused by increase of effective stresses in the ground, which will be explained in the next section.

Long-term behaviour - primary consolidation stage

The PWP dissipated after increasing the applied load and returned to the steady state. These time durations could be regarded as primary consolidation stages (highlighted areas on Figs. 6(a) and 8(a)). It is seen from these figures that the settlement rates in the primary consolidation stages were proportional to the dissipation rates of the PWP, and considerable parts of settlements occurred in these stages.

The changes of load sharing with time of 4P-PR and 9P-PR are shown in Fig. 9(a) and Fig. 10(a), respectively. Fig. 9(b) is a zoom-in of the first load step, and Figs. 10(b) and 10(c) are zoom-ins of the first and the third load steps, respectively. Figs. 9(b), 10(b) and 10(c) clearly show that, during the primary consolidation stages, the load supported by the raft decreased while the load supported by the piles increased with the elapsed time. The magnitude of the increment of pile resistance during the primary consolidation stage was roughly proportional to the increment of PWP during the load increasing stages. Hence, this phenomenon is caused by the consolidation process of the ground. The dissipation of the PWP causes the corresponding increase of the effective stress in the ground, resulting in the increase of pile resistances. Similar trends were measured in the other load steps.

Let us look back at Fig. 1(b), in which c_u of the model grounds with and without effect of the loading tests of PRs were presented.

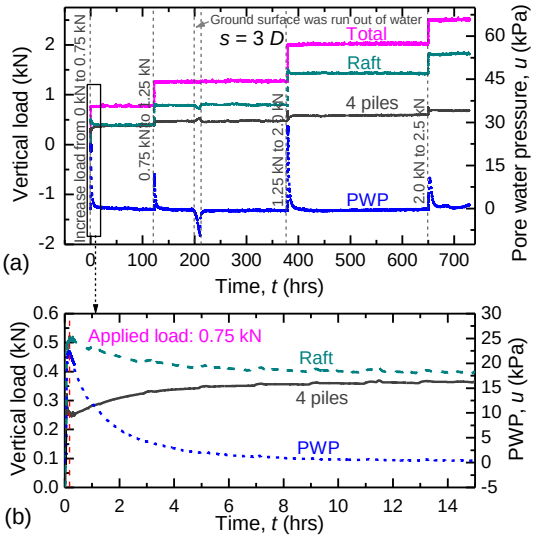

Fig. 9 Load transfer with time of 4P-PR: (a) full-time; (b) zoom-in of the first loading step.

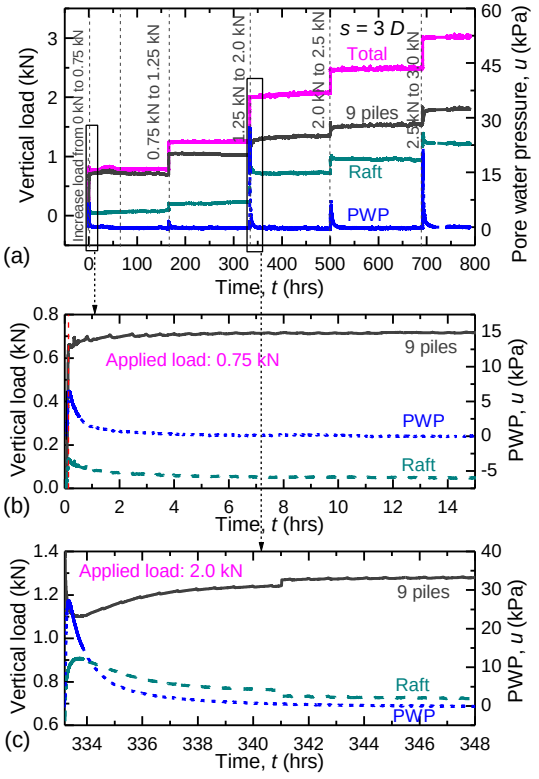

Fig. 10 Load transfer with time of 9P-PR: (a) full-time; (b) and (c) zoom-ins of the first and third loading steps, respectively.

It is clearly seen from the figure that, after the load test of PRs, within a depth of 190 mm from the raft base (≃ 1.5 times of the raft width), c_u was higher at the raft edge areas (T3, T4 and C03) and was highest at the centre area of the raft base (T5), in comparison with the original state (T1 and T2, C01 and C02). Furthermore, c_u beneath the centre of the raft base was much greater than c_u of the original ground within a

depth of 75 mm for the 4P-PR, and of 150 mm for the 9P-PR. For deeper depths, the difference of c_u between the loading area and the original area became smaller with increasing depth. The results indicate that the area affected by loading of 9P-PR was deeper than that of 4P-PR. The results of UCTs also presented similar trends. Therefore, it is clear that the consolidation process increased the ground strength and stiffness.

Long-term behaviour - secondary consolidation stage

After the primary consolidation stages, the foundation continued to settle due to the creep phenomenon of the ground. This phenomenon was seen clearly from Fig. 6(a) for 4P-PR and Fig. 8(a) for 9P-PR. Here let us define the creep settlement index, C_{cs}, as follows where B is the raft width:

$$C_{cs} = \mathrm{d}(w/B)/\mathrm{d}(\log t) \quad (2)$$

In 4P-PR, C_{cs} for the 4 load steps of P = 0.75, 1.25, 2.0 and 2.5 kN were 0.00057, 0.0014, 0.0017 and 0.0165, respectively. The corresponding values for 9P-PR were 0.0005, 0.0021, 0.0118 and 0.0083. For the applied load of 3.0 kN, C_{cs} of 9P-PR was 0.0162. Basically, C_{cs} became larger as larger load was applied.

Load Distribution in Piled Raft Foundations

Figure 11 shows the proportions of loads shared by the raft and the piles with elapsed time in cases of (a) 4P-PR and (b) 9P-PR. Please notice again that the raft resistance includes the uplift force due to PWP.

In both the foundations, the proportion of the load supported by the raft decreased in the primary consolidation stages meanwhile the opposite trend was seen in the proportion of the load carried by the piles. This is due to the dissipation of the PWP at the raft base as described in the previous section. In the all secondary consolidation stages of 4P-PR, the proportions of loads shared by the raft and the piles were stable with time, although the creep settlement of the foundation continued. For the secondary consolidation stages of 9P-PR, the proportion of the load supported by the raft increased slightly in the 1st and 2nd loading stages, in which the applied load was mainly carried by the piles. In the 3rd, 4th and final load steps, the trend of load sharing of 9P-PR became similar to the trend of 4P-PR.

In general, the proportion of the load supported by the raft increased with increasing the applied load, and the raft supported considerable parts of the applied load at relative larger loads.

It is interesting that, at the final stages, the measured results show that, the average load supported by each pile in both the PRs (175N for 4P-PR and 195N for 9P-PR) are much higher than the bearing capacity of a single pile (100N).

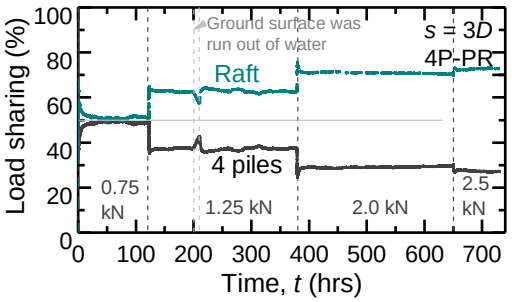

(a) 4P-PR

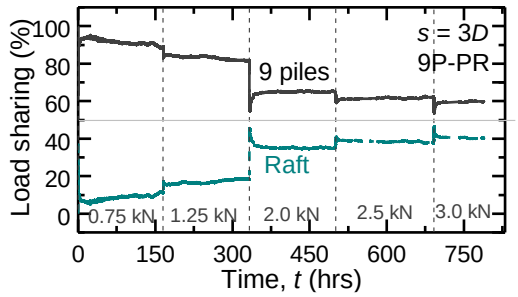

(b) 9P-PR

Fig. 11 Load sharing ratio with time in the PRs.

CONCLUDING REMARKS

In this paper, long-term behaviours of PR models in a saturated clay was investigated through a small-scale physical modelling.

Main findings from this study are as follows:

(1) Piles effectively suppressed the settlement of the foundation for relatively smaller loads.
(2) Stresses from the raft base cause consolidation of the ground. Consequently, the effective stresses in the ground increase, resulting in the increase of the pile resistance.
(3) After the primary consolidation stages, the creep settlement continued, the loads supported by both the raft and the piles were stable.
(4) The proportion of the load supported by the raft increased with increasing the total applied load.

REFERENCES

[1] Cooke R.W., Piled Raft Foundations on Stiff Clays - A Contribution to Design Philosophy. Geotechnique, Vol.36, Issue 2, 1986, pp.169-203.
[2] Horikoshi K. and Randolph M.F., Centrifuge Modelling of Piled Raft Foundations on Clay. Geotechnique, Vol.46, Issue 4, 1996, pp.741-752.
[3] Low H.E., Lunne T., Andersen K.H., Sjursen M.A., Li X. and Randolph, M.F., Estimation of Intact and Remoulded Undrained Shear Strengths from Penetration Tests in Soft Clays. Geotechnique, Vol.60, Issue 11, 2010, pp.843-859.
[4] Rodriguez E., Cunha R.P. and Caicedo B., Conference proceedings, in Proc. 9th Int. Conf. on Physical Modelling in Geotechnics, Vol.2, Issue 21, 2018, pp.1407-1412.

9th Int. Conf. on Geotechnique, Construction Materials and Environment, Tokyo, Japan, 20-22 November 2019, ISBN: 978-4-909106025 C3051

COMPRESSIVE STRENGTH OF LATERITIC SOIL IMPROVED WITH BAGASSE ASH AND CALCIUM CARBIDE RESIDUE

Nuttapol Triamcherdtiwong, Cherdsak Suksiripattanapong, Jaksada Thumrongvut and Piyathida Yoosuk
Faculty of Engineering and Architecture, Rajamangala University of Technology Isan, Thailand

ABSTRACT

This research aims to study compressive strength of lateritic soil improved with bagasse ash and calcium carbide residue as a non-bearing interlocking blocks. Binder (B) is the mixture of bagasse ash (BA) and calcium carbide residue (CCR). The Bagasse ash is a waste from sugar industry in Nakhon Ratchasima province. The calcium carbide residue is a by-product from the acetylene gas factory in Nakhon Pathom province. This research studied the influence of laterite soil to binder ratios of 90/10, 80/20, 70/30 and 60/40, the CCR:BA ratios of 100/0, 90/10, 80/20 and 70/30 and curing time of 7 days. The compacted sample was 50 mm in diameter and 100 mm in height under modified Proctor energy. The unconfined compressive strength of laterite soil mixed with bagasse ash and calcium carbide residue increased with increasing in curing time. This research enables bagasse ash and calcium carbide residue as a construction material, which reduces the use of cement.

Keywords: Compressive Strength, Bagasse Ash, Calcium Carbide Residue, Interlocking Block

INTRODUCTION

Interlocking blocks are one of the most popular construction materials. In general, the interlocking block production process uses soil, cement and water. The mixture is extruded with a compression machine. [1]. However, the cement production process requires a large energy. (Burning raw materials at a temperature of around 1450 ºC). This process will result in a large carbon footprint since the production of 1 ton of Portland cement releases about 1 ton of carbon dioxide [2].

Calcium carbide Residue (CCR) is a by-product of the production of acetylene gas used in cutting, welding metal and other industries. For the production of acetylene gas in Thailand, it produces CCR about 21,500 tons per year and is constantly increasing and increasing each year [3]. CCR has been used as a binder to develop green stabilized pavement materials [4-8] and non-bearing masonry units [9]. Phetchuay et al. [10] and Arulrajah et al. [11] have recently used CCR for stabilization of natural soil and Construction and Demolition materials in pavement applications [12].

Bagasse ash (BA) is a waste from the burning of sugarcane for electricity. BA is left from the production process in order to produce approximately 424,700 tons of electricity per year [13]. Particles of bagasse ash are large and high porosity. Bagasse ash has main aluminosilicate-rich material which can be classified as Class N pozzolanic materials according to ASTM C 618.

The objective of this research is to study the possibility of using industrial wastes, CCR and BA, to be used as cementing materials. This research studied the influence of laterite soil to binder ratios of 90/10, 80/20, 70/30 and 60/40, the CCR:BA ratios of 100/0, 90/10, 80/20 and 70/30 and curing time of 7 days. The compacted sample was 50 mm in diameter and 100 mm in height under modified Proctor energy. This research enables bagasse ash and calcium carbide residue as a construction material, which reduces the use of cement.

MATERIALS AND METHODS OF TESTING

Materials

Lateritic soil (LS) was obtained from Sikhio District, Nakhon Ratchasima. The specific gravity of LS is 2.72. the liquid limit and the plastic limit of LS are 32 and 21, respectively. This soil can be classified as clayey sand (SC) according to the Unified Soil Classification System (USCS).

Calcium carbide Residue (CCR) was collected from Sai 5 Gas Product Co., Ltd, Thailand. The CCR was oven-dried at 100 ºC for 24 h and was then passed through a No. 40 sieve (0.425 mm). The specific gravity is 2.24. The chemical composition of CCR is summarized in Table 1, indicating it has a very high CaO content of 75.96%.

Bagasse ash (BA) is a waste from the burning of sugarcane for electricity, the Khonburi sugar factory. The chemical composition of bagasse ash was shown in Table 1. It can be seen that the BA has SiO_2 of 70.91 and Al_2O_3 of 4.28, respectively. BA can classified as type N according to ASTM C 618.

Table 1 Chemical composition of CCR and BA

Chemical composition (%)	CCR	BA
SiO_2	9.81	70.91
Al_2O_3	4.64	4.28
Fe_2O_3	2.03	6.61
CaO	75.96	8.91
SO_3	2.58	0.56
K_2O	N.D.	3.48
TiO_2	1.86	N.D.
LOI	3.12	3.28

Sample preparation

The LS mixed CCR and BA sample is a mixture of LS, CCR, BA, and water. Binder (B) is a mixture of CCR and BA. The LS/B ratios were varied at 90/10, 80/20, 70/30 and 60/40. The CCR:BA ratios were 100/0, 90/10, 80/20 and 70/30. Modified Proctor compaction effort in accordance with ASTM D1557-12 was used to compact the LS mixed CCR and BA sample. Next the LS mixed CCR and BA sample was prepared by static compression with a 50 mm in diameter and a 100 mm in height using a cylindrical split mold. Then, the specimens were wrapped in clear vinyl to prevent moisture loss throughout curing. These specimens were subjected to 7-day unconfined compressive strength (7-day UCS) tests with reference to ASTM D2166 at water content of 0.8OWC, OWC and 1.2OWC (OWC=optimum water content).

TEST RESULT

Compaction of Lateritic soil with calcium carbide residue and bagasse ash

Fig. 1 shows the relationship between dry unit weight and water content of LS mixed with CCR and BA at the LS/B ratios of 90/10, 80/20, 70/30 and 60/40 and the CCR/BA ratios of 100/0, 90/10, 80/20 and 70/30. The test results show that the maximum dry unit weight of the LS mixed with CCR and BA sample was 18.03 kN/m^3 at LS/B ratio of 90/10 and CCR/BA ratio of 80/20. This is because LS has a higher specific gravity than CCR and BA. The minimum dry unit weight of the LS mixed with CCR and BA sample was 13.83 kN/m^3 at LS/B ratio of 60:40 and CCR/BA ratio of 70/30.

–

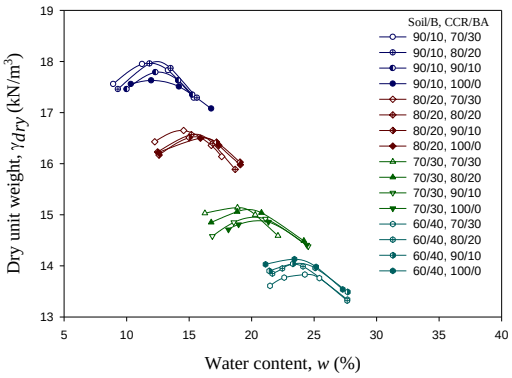

Fig. 1 The relationship dry unit weight and water content of LS mixed with CCR and BA at different LS/B ratios of and the CCR/BA ratios

Compressive strength of lateritic soil mixed with calcium carbide residue and bagasse ash

Fig. 2-5 show the compressive strength of LS mixed with CCR and BA at the LS/B ratios of 90/10, 80/20, 70/30 and 60/40 and the CCR/BA ratios of 100/0, 90/10, 80/20 and 70/30 and water content of 0.8OWC, OWC and 1.2OWC. The test results showed that the compressive strength of LS mixed with CCR and BA at 0.8OWC and 1.2OWC was less than that of LS mixed with CCR and BA at OWC (about 30%). For all LS/B ratios and CCR/BA ratios, the highest 7-day compressive strength of LS mixed with CCR and BA sample was found at LS/B ratio of 90/10, CCR/BA ratio of 70/30 and water content of OWC which offered maximum 7-day UCS of 2.56 MPa.

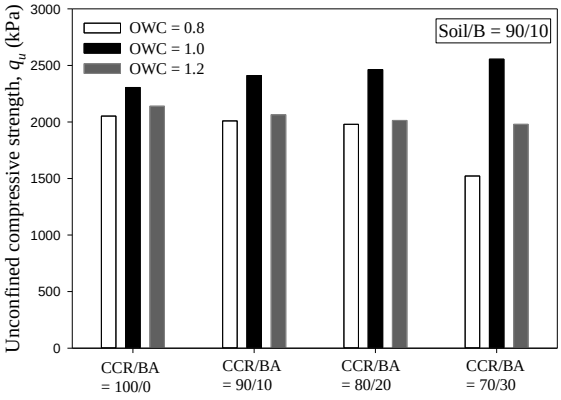

Fig. 2 Compressive strength of lateritic soil mixed with calcium carbide residue and bagasse ash at the Soil/B ratio of 90/10.

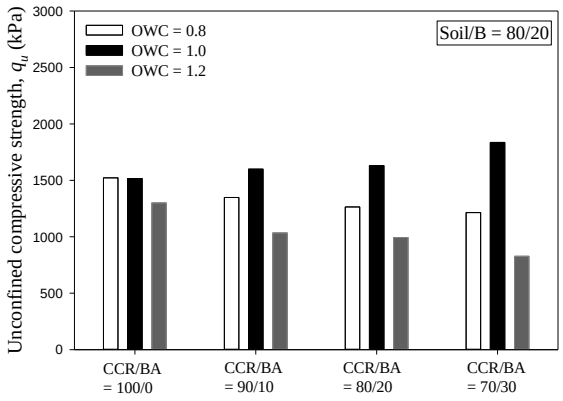

Fig. 3 Compressive strength of lateritic soil mixed with calcium carbide residue and bagasse ash at the Soil/B ratio of 80/20.

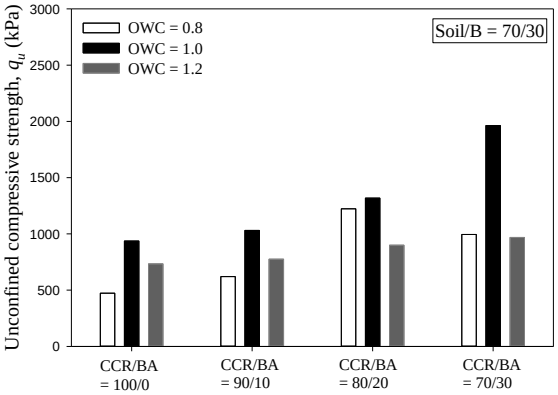

Fig. 4 Compressive strength of lateritic soil mixed with calcium carbide residue and bagasse ash at the Soil/B ratio of 70/30.

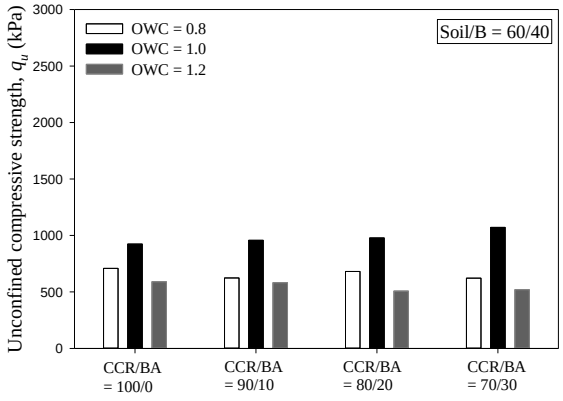

Fig. 5 Compressive strength of lateritic soil mixed with calcium carbide residue and bagasse ash at the Soil/B ratio of 60/40.

CONCLUSIONS

This research evaluated the 7-day compressive strength of lateritic soil mixed with calcium carbide residue and bagasse ash for construction materials. The results of the study can be summarized as follows.

1. The maximum dry unit weight of the LS mixed with CCR and BA sample was 18.03 kN/m^3 at LS/B ratio of 90/10 and CCR/BA ratio of 80/20. This is because LS has a higher specific gravity than CCR and BA.
2. The compressive strength of LS mixed with CCR and BA at 0.8OWC and 1.2OWC was less than that of LS mixed with CCR and BA at OWC (about 30%).
3. The highest 7-day compressive strength of LS mixed with CCR and BA sample was found at LS/B ratio of 90/10, CCR/BA ratio of 70/30 and water content of OWC which offered maximum 7-day UCS of 2.56 MPa and met the TIS 58-2533 standard [11], which specified the compressive strength of more than 2.5 MPa (about 2.4%).

ACKNOWLEDGMENTS

This research has been supported by the Research and Industrial Research Development Project (WPO), the Office of Research Fund (TRF) and would like to thank Rajamangala University of Technology Isan Nakhon Ratchasima for its research tools.

REFERENCES

[1] Suksun H., Varagorn M., Artit U., Avirut C., Arul A. (2014)., “Strength of sustainable non-bearing masonry units manufactured from calcium carbide residue and fly ash”. Construction and Building Materials, 71, pp.210–215.

[2] Sumi S. and Priscila N.M. B. (2018)., “Chemical stabilization of rammed earth using calcium carbide residue and fly ash”. Construction and Building Materials, 169, pp.364–371.

[3] Horpibulsuk S., Munsrakest V., Udomchai A., Chinkulkijniwat A. and Arulrajah A. (2014)., “Strength of sustainable non-bearing masonry units manufactured from calcium carbide residue and fly ash”. Construction and Building Materials, 71, pp.210-215.

[4] Kampala A, Horpibulsuk S. Engineering properties of calcium carbide residue stabilized silty clay. Journal of Materials in Civil Engineering, ASCE 2013:25(5);632-644.

[5] Kampala A, Horpibulsuk S, Chinkulkijniwat A, Shen SL. Engineering properties of recycled calcium carbide residue stabilized clay as fill and pavement materials. Constr Build Mater 2013;46:203–10.

[6] Kampala A, Horpibulsuk S, Prongmanee N, Chinkulkijniwat A. Influence of wet-dry cycles on compressive strength of calcium carbide residue-fly ash stabilized clay. Journal of Materials in Civil Engineering, ASCE 2014;24(1):633-643.

[7] Horpibulsuk S, Phetchuay C, Chinkulkijniwat A. Soil stabilization by calcium carbide residue and fly ash. Journal of Materials in Civil Engineering, ASCE 2012;24(2):184-193.

[8] Horpibulsuk S, Phetchuay C, Chinkulkijniwat C. Soil stabilization by calcium carbide residue. J Mater Civ Eng 2012;24(2):184–93.

[9] Horpibulsuk, S., Munsrakest, V., Udomchai, A, Chinkulkijniwat, A. and Arulrajah, A. (2014), "Strength of sustainable non-bearing masonry unit manufacturing from calcium carbide residue and fly ash", Construction and Building Materials, Vol.71, pp.210-215

[10] Phetchuay, C., Horpibulsuk, S., Suksiripattanpong, C., Chinkulkijniwat, A., Arulrajah, A. and Disfani, M.M. (2014). Calcium carbide residue: Alkaline activator for clay-fly ash geopolymer. Construction and Building Materials, 69:285-294.

[11] Arulrajah A, Mohammadinia A, Phummiphan I, Horpibulsuk S, Samingthong W. Stabilization of recycled demolition aggregates by geopolymers comprising calcium carbide, fly ash and slag precursors. Construction and Building Materials (Tentatively accepted for publication); 2016.

[12] Du, Y-J, Jiang, N-J. Liu, S-Y, Horpibulsuk, S. and Arulrajah, A. (2016) "Field evaluation of soft highway subgrade soil stabilized with calcium carbide residue", Soils and Foundations (accepted 18 December 2015; in press).

[13] Chaiyanunt R., Pongsiri T., Weerachart T., and Chai J. (2013)., "Use of calcium carbide residue and bagasse ash mixtures as a new cementitious material in concrete". Materials and Design, 46, pp.106–111.

[14] Thai Industrial Satandard. 2553. Standard for Hollow Non-Load-Bearing Concrete Masonry Unit (TIS. 58-25533).

9th Int. Conf. on Geotechnique, Construction Materials and Environment, Tokyo, Japan, 20-22 November 2019, ISBN: 978-4-909106025 C3051

EVALUATION OF NUMERICAL APPROACH IN SLOPE STABILITY ANALYSIS CONSIDERING LARGE DEFORMATION OF GEO-MATERIALS

Nafisa Tabassum[1], Md. Aftabur Rahman[2], Mohammed Russedul Islam[3]

[1]Graduate Student (M.Sc Engg. Candidate), Chittagong University of Engineering & Technology, Chattogram-4349, Bangladesh, Email: nafisa_t@cuet.ac.bd
[2]Faculty, Department of Civil Engineering, Chittagong University of Engineering & Technology, Chattogram-4349, Bangladesh, Email: maftabur@cuet.ac.bd
[3]Faculty, Department of Civil Engineering, Military Institute of Science & Technology, Mirpur Cantonment, Dhaka-1216, Bangladesh, Email: ce_russel@yahoo.com

ABSTRACT

Geo-hazards associated with slope failure so far considered to be one of the most devastating natural disasters, responsible for damage to infrastructures and people are buried alive under scratched mass. The extent of slope failure not only limited to the small distance from the source but also extend to several kilometers in the extreme scenario. Rapid urbanization in recent years also increases the fatality and destruction. Numerous researches have been conducted to get the insight of slope failures for rational mitigation of associated hazards. Among several analysis approaches, numerical simulations of the scaled model is a robust way to describe the slope failures realistically. However, large deformation in such geo-disaster problem restricts the use of the traditional grid-based method. Considering the constraints of the mesh-based method, the particle-based method gets the attraction in slope failure analysis owing to its inherent features of capturing large deformation. Smoothed Particle Hydrodynamics (SPH), which was originally developed for astrophysical problems is nowadays used extensively in geo-disaster analysis from small scale model analysis to simulate real disasters. This paper presents a brief review of different numerical modeling in SPH environment for analyzing slope failure, their applications & limitations. The development, validation, application & advantages of SPH method, its numerical errors & treatment procedures, soil constitutive model are also discussed. Findings from various research articles regarding dry & saturated soil, rainfall, earthquake influence on soil mass are also summarized here which supports the SPH method as an appropriate numerical method for analyzing slope instability problem.

Keywords: Slope-stability, Large deformation, Mesh-free method, Smoothed Particle Hydrodynamics, Scaled model

INTRODUCTION

Slope failure associated disasters are considered to be one of the most fatal natural disasters, responsible for the loss of life and property. To be specific, mountainous areas are most vulnerable to this kind of disaster. Among many causes, torrential rainfall and extreme natural hazards like earthquake, volcanic eruptions, and tornados are the prime factors to trigger the failure of slopes. Landslide and debris flows are also the results of slope failures. Extensive research works have been conducted to understand the insight of failures for rational mitigation of such hazards.

Experimental investigation is the traditional way and numerous works have been conducted in the last decade to find the clue behind the slope failure. However, the lack of facilities for large scale experimental investigation is the main drawback of such research methodology and in many cases, difficult to capture the real scenario [1]. Concurrently, development of technological setups, numerical simulations and validation with analytical models have recently become an attractive concern and proven to be useful for most of the analysis of real slope failures and also used to grasp the insight mechanics of slope failures. Application of similarity law also justify the numerical modeling of real instances.

Traditional grid-based numerical tools, especially the Finite Element Method (FEM) is the mostly used numerical framework in geotechnical engineering. The discretization of the entire model into finite elements and simple framework for numerical integration makes it a robust numerical system. However, the distortion of finite elements under large deformation is a serious problem for the convergence of solutions, and to the extreme cases, blow up of the entire system can occur. The large deformation in slope failures, therefore, faces numerical instability by FEM simulation and therefore, an alternative approach is necessary. Pointing this technical difficulties and development of modern computational tools attract the use of mesh-less

numerical methods for large deformation analysis. To date, a number of mesh-less methods have been developed keeping facility to handle large deformation of materials. Hence, the application of particle methods in slope stability analysis is becoming a promising tool in geotechnical engineering. Some notable particle methods are Discrete Element Model (DEM), Discontinuous Deformation Analysis (DDA), Material Point Method (MPM), Smoothed Particle Hydrodynamics (SPH). Among the particle-based methods, SPH is a newly developed numerical framework and extensively used in large deformation analysis. The adaptive and true particle nature with no connectivity between particles make it a robust tool for simulation of large deformation problems. Several frameworks for slope stability analysis with wide variety of material modeling soil water coupling, and continuous development of more sophisticated simulation justify the suitability of SPH in slope stability analysis. Considering the above, a compilation of different aspects of SPH simulation to analyze slope failure is necessary. Therefore, this research paper aims to bring the to-date SPH slope stability simulations in one platform so that further improvement of SPH can be done and also supports this as a prospective tool for future research works. The findings and critical thinking of major approaches are discussed in the subsequent writings.

BACKGROUND OF SPH

SPH was first developed to analyze the astrophysical cases [2], [3] and later extended to the diverse field of engineering, especially free surface simulations [4], [5], viscous analysis [6], [7], heat transfer problems [8] etc. Subsequently, this numerical tool has been applied in the field of geotechnical engineering, more especially, large deformation analysis of geomaterials [9]-[27]. The fundamentals of SPH is written in the following section.

FUNDAMENTALS OF SPH

In the SPH method, the entire computational domain is the summation of discrete points, generally called particles. These particles possess certain volume and mass of the material, having physical properties such as velocity, acceleration, density, stress, etc. The field variables $f(x)$ at any point x of the problem domain are computed by using an interpolation method over its neighboring particles belonging to its influence domain. The basic formulation of SPH is given in the following equation:

$$\boldsymbol{f(x)} = \int_{\Omega} \boldsymbol{f(x')\, W(x - x', h)\, dx'} \tag{1}$$

where, h = smoothing length, W = smoothing or kernel function, x = position vector of particles.

The continuous integral representation shown in Eq. (1) can be further approximated by taking summation over the neighboring particles in the support domain as follows:

$$\boldsymbol{f(x)} = \sum_{j=1}^{N} \frac{\boldsymbol{m_j}}{\boldsymbol{\rho_j}} \boldsymbol{f(x_j)} \mathbf{W}(\boldsymbol{x - x_j, h}) \tag{2}$$

where, $\boldsymbol{j = 1, 2, \ldots, N}$ indicates neighboring particles of the particle at $\boldsymbol{x}$ within the support domain, $\boldsymbol{x}$ = concerning particle, $\boldsymbol{x_j}$ = neighboring particle, $\boldsymbol{m_j}$ = mass of the particle and $\boldsymbol{\rho_j}$ = density of the particle $\boldsymbol{j}$.

The smoothing function $\boldsymbol{W}$ must satisfy unity condition, delta function and compact support condition:

$$\int_{\Omega} \boldsymbol{W(x - x', h)\, dx' = 1} \tag{3}$$

$$\lim_{\boldsymbol{h \to 0}} \boldsymbol{W(x - x', h) = \delta(x - x')} \tag{4}$$

$$\boldsymbol{W(x - x', h) = 0} \text{ when } \boldsymbol{|x - x'| > kh} \tag{5}$$

where, $\boldsymbol{k}$ = constant, $\boldsymbol{kh}$ specifies the non-zero or effective length of the kernel function at point $\boldsymbol{x}$. Interaction between SPH particles takes place when they belong to each other's influence domain. Larger smoothing length generates smoother behavior than smaller smoothing length.

Different types of smoothing kernels are available for implementation into SPH code. These are: Bell-shaped function [2], Gaussian Kernel [3], Cubic Spline function and Super-Gaussian Kernel [28], Quadratic function [29] etc. Cubic spline function, proposed by Monaghan and Lattanzio [28] is the most widely used owing to its convergence nature and the first derivatives of the kernel is also stable and do not cause any unphysical response.

The SPH formulation of the Navier-Stokes equation is written in the following equation:

$$\frac{\boldsymbol{D\rho_i}}{\boldsymbol{Dt}} = \sum_{j=1}^{N} \boldsymbol{m_j}\, (\boldsymbol{v_i^{\alpha} - v_j^{\alpha}}) \frac{\boldsymbol{\partial W_{ij}}}{\boldsymbol{\partial x_i^{\alpha}}} \tag{6}$$

$$\frac{\boldsymbol{Dv_i^{\alpha}}}{\boldsymbol{Dt}} = \sum_{j=1}^{N} \boldsymbol{m_j} \left(\frac{\boldsymbol{\sigma_i^{\alpha\beta}}}{\boldsymbol{\rho_i^2}} + \frac{\boldsymbol{\sigma_j^{\alpha\beta}}}{\boldsymbol{\rho_j^2}} + \boldsymbol{C_{ij}^{\alpha\beta}} \right) \frac{\boldsymbol{\partial W_{ij}}}{\boldsymbol{\partial x_i^{\beta}}} + \boldsymbol{g_i^{\alpha}} \tag{7}$$

Where, σ = total stress tensor, g = acceleration due to gravity, $C_{ij}^{\alpha\beta}$ = stabilization term which is used for removing the tensile instability and stress fluctuation. The expression of total stress tensor can be adopted from an appropriate constitutive model applicable in the SPH framework.

Finally, the governing and constitutive equations are integrated to update the particle positions and their properties. Among several time integration approaches, Leapfrog algorithm is the most efficient one. In this method, the field variables, which include density (ρ), velocity (v), position (x) and stress tensor ($\sigma^{\alpha\beta}$) of a particle are updated by half a time step as follows:

$$\boldsymbol{\rho}_{n+\frac{1}{2}} = \boldsymbol{\rho}_{n-\frac{1}{2}} + \Delta \boldsymbol{t} \left(\frac{\boldsymbol{D\rho}}{\boldsymbol{Dt}}\right)_{\boldsymbol{n}} \quad (8)$$

$$\boldsymbol{v}_{n+\frac{1}{2}} = \boldsymbol{v}_{n-\frac{1}{2}} + \Delta \boldsymbol{t} \left(\frac{\boldsymbol{Dv}}{\boldsymbol{Dt}}\right)_{\boldsymbol{n}} \quad (9)$$

$$\boldsymbol{x}_{n+1} = \boldsymbol{x}_{n} + \Delta \boldsymbol{t} \boldsymbol{v}_{n+\frac{1}{2}} \quad (10)$$

$$\boldsymbol{\sigma}^{\alpha\beta}_{n+\frac{1}{2}} = \boldsymbol{\sigma}^{\alpha\beta}_{n-\frac{1}{2}} + \Delta \boldsymbol{t} \left(\frac{\boldsymbol{D\sigma}^{\alpha\beta}}{\boldsymbol{Dt}}\right)_{\boldsymbol{n}} \quad (11)$$

where, Δt= time step, n defines the present time t, $(n+1)$ defines the onward time $(t+\Delta t)$.

SPH IN LARGE DEFORMATION ANALYSIS

Modeling Dry Granular Flow

A breakthrough in the application of SPH in large deformation geotechnical problem was first developed by Bui, Fukagawa, Sako and Ohno [10] though some works on dealing solid elements were available before this works. Both the cohesionless and cohesive soils were taken into consideration with appropriate constitutive laws. An elasto-plastic Drucker Prager model was chosen to define soil particles and both the non-associated and associated plastic flow rules were implemented in the SPH framework and justified with several applications. The failure of the soil column owing to the instantaneous breakdown of the assembly were simulated and insight of different material types and analysis criteria were evaluated. No significant distortion was found between the experimental and numerical simulation of granular materials; however, instability of simulation was seriously seen for cohesive soils. Therefore, a rational technique was developed to generate additional artificial stress so that clumping and instability of the assembly can be avoided. The results after the treatment were found compatible with experimental results. The works are notable as the detailed discussion of different types of soils and different schemes for keeping numerical stability has been developed and a well-documented reference for the further research works. However, the entire simulation considers dry soil properties and in-situ scenario of saturated soil model is not explicitly discussed. Following the primary development of Bui, Chen and Qiu [13] developed an SPH model in three dimensions to examine the flow of granular materials. The collapse of a 3D soil block was simulated and flow pattern was validated with the conventional flow trace. Besides, granular column collapse of different aspect ratios was simulated and an attempt was made to develop a correlation between aspect ratio and final run-out. Aspect ratio of initial soil mass play an important role in landslide and debris flow dynamics and therefore, the findings on relation between aspect ratio and final run-out length is a notable contribution in large deformation geotechnical simulation. The impact of smoothing length on the outcomes was also critically discussed.

The development of slope stability analysis by SPH has been greatly accelerated with the development of 3D slope simulation of different types of geomaterials [14]. Two 3D slope cases with different geometric configurations are conducted to analyse the final profile, slip surface and distance of soil mass and compared with the 2D cases. Moreover, three slope shapes (concave, common and convex) are taken into consideration. The plastic area of the convex slope is much thicker than the concave one whereas the common slope plastic area takes position between concave and convex. For concave and common slopes, the translational distance of slope toe and the settlement distance of slope top are smaller than the 2D case. An opposite phenomenon is observed for convex slope. The 3D case is found to be more evident for both concave and convex sub-bases. The slip surface of the convex sub-base looks alike down-beating wing with a symmetrical shape whereas it is like a rising wing for concave sub-base. Side slope of concave sub-base and top corner of convex sub-base are subjected to instability and deformation. However, the corner toe of both sub-bases is found safe. This development is worthy to analyse the real landslide and debris flows. However, the effect of constitutive laws and soil-water coupling is not considered in the current paper, which is the major constraints of the practical application of the developed procedure.

Modeling Saturated Soils

However, modelling of slopes considering only dry flow is not realistic all the time. Generally, slope failures are greatly linked with pore water occupied in the void space of soils. Therefore, pore water contribution is a prime requirement for modelling real slope. In the case of slope stability analysis, the Factor of Safety (FoS) of the slope is necessary. Considering this real case, a methodology was developed to simulate slopes with different configurations and FoS was estimated [15]. The unique contribution is that the effective stress concept is applied in the SPH formulation for more realistic modeling. A pore water pressure equation is developed and incorporated in the SPH framework. The simulated FoS was found compatible with the available analytical models for both dry and saturated soils. Not only the

homogenous soils but also the slope with non-homogenous soils were simulated and the entire failure process was captured, which is the main findings of the developed procedure. SPH simulation shows a clear failure surface in the form of a thin layer of plastic strain localization which agrees well with the Bishop's modified method's critical slip surface. Conversely, a little greater slip circle and thicker shear band layer were observed in FEM. FEM simulation was ceased at a definite displacement of soil, while the entire flow process was simulated by the developed model.

Following this work, an improved version of SPH incorporating hydrostatic pore water pressure was developed to simulate an embankment having two sloping sides with a high groundwater table [12]. An investigation was carried out to check the influence of dilatancy angle on the collapse mechanism of the slope. Then, a comparison was made between slip surface outcomes and traditional LEM results (Bishop's modified method). For high dilatancy soils, the new SPH method satisfies somewhat more or less the same slip surface as created by LEM, but for low dilatancy soil, it underestimates the failure zone. It is found that with an increase of dilatancy angle, failure zone and slip surface contracted, and total displacement of the slope increased. The improved model can be applied in general for large deformation as well as post failure simulation and slope stability is considered to be an ideal case to implement the developed idea.

Coupled Analysis

In the earlier works of Bui, Sako and Fukagawa [16], they consider soil and water element separately and the soil-water interaction is given by seepage force following Darcy's law. Erosion of soils owing to the water flow is simulated and a representative solution was found.

Zhang and Maeda [17], [18] conducted a two-phase and three-phase SPH simulation to find out the influence of heavy rainfall on the behaviour and collapse mechanism of slope and levee. The maximum of volume water content was found smaller for drained condition than undrained condition, indicating that undrained condition act as a factor for slope instability. To verify the model test, a simulation process was done in two parts: with and without considering air effect. For the case of no air effect, higher intensity takes less time for saturation than lower intensity which satisfies the model test. Erosion takes place easily on the surface of the slope as the saturation zone starts from the slope model surface. Again, maximum shear strain is found to occur around the center face of the slope. Slip surface is formed for high-intensity rainfall rather than low intensity. Swelling of soil due to pore water pressure is severe for the undrained condition than drainer condition. While considering air effect in simulation, it takes a longer time for saturation than before as air particles slow down the infiltrating process in the soil mass. Again, the concentration of the air bubble is found higher near the slope surface and it rises with time.

Li, Huang, Maeda, Zhang and Saito [19] conducted a two-phase-coupled SPH simulation by using Zhang and Ikariya's proposed constitutive model [20]. Simulation of a dike failure due to water level-up is conducted to evaluate the seepage operation, maximum shear strain distribution, pore water pressure and slip surface. Influence of rainfall intensity using this model is then compared to the model test for 120 min. Soil particle exhibits a very small pressure around the surface, leading to liquefaction. For small intensity (30 and 60 mm/h), dry soil mass is found inside the slope, but soil mass gets nearly fully saturated for high intensity (90 and 120 mm/h). Finally, the proposed model is applied to analyse the failure mechanism of dike due to rainfall with low and high intensities. Simulated infiltrated area and surface infiltration match the model test. The rainfall produces an unsymmetrical shear strain to the symmetric dike. With an increase in rainfall intensity, shear strain enhances. Between the two shear strains, one is developed on the dike surface due to suction reduction. Another one is occurred inside the dike because of seepage force. In the infiltration process, the surface is prone to fail if a shear strain is developed on the surface.

Grabe and Stefanova [21] extended the SPH method to perform a coupled analysis of saturated soils considering deformable soils. An erosional dam break test simulation was performed and a comparison was made with the experimental results of Fraccarollo, Capart and Young [22], [23]. It is observed that sand particles are subjected to sudden hydraulic impact just after the moment of removing a retaining wall, causing the sand particles to get displaced and liquified. The displacement is severe at the dam breakfront. The hydraulic jump and velocity distributions are found consistent with the experimental outcomes.

Earthquake-Induced Slope Failures

A shaking table test was chosen for comparison and verification of the SPH model [24] . The SPH simulation generates horizontal and vertical displacements, velocities, at three defined points like the shaking table test. The displacement, as well as velocity values from the physical test correlate well with numerical results.

Bui, Fukagawa, Sako and Okamura [25] proposed an advanced SPH method in conjunction to conduct the progressive failure of a slope subjected to seismic loading. Laboratory experiments were also conducted for verification of numerical performance. In the experiment, the slope model experiences horizontal seismic shaking by a vibration generation machine. In

simulation, this seismic condition is created by applying seismic acceleration directly to the horizontal of each SPH particle as the external load, rather than shaking. SPH can predict the final slope configuration fairly well with the experimental test. Slope failure in the experiment produced four sliding surface and rotational blocks whereas SPH simulation resulted in one sliding surface and rotational block. Again, the failure surface of the last failure mode of the experiment is found to be a straight line, while the failure surface is almost circular in case of simulation. From the horizontal and vertical displacements of the sliding mass at the center of the slope, it is seen that the experimental results underestimated the simulation performance. Furthermore, the slope failure in the experiment started at about 1s later than that in simulation. Ono [26] conducted a simulation using a Corrective SPH (CSPH) method to investigate the large and discontinuous failure of slope initiated by an earthquake. The vertical stress distribution for three different types of particle spacing (0.5 m, 1.0 m and 2.0 m) is obtained properly. Failure lines emerged at the same place whereas the width of the slip line and displacement of sliding soil mass are different for all cases. The larger the particle spacing, the greater the kernel smoothing length. Larger particle spacing reduces the spatial resolution of the SPH simulation.

CONSTITUTIVE MODELS

In any numerical approach, the most difficult part is to characterize its materials. Even in SPH analysis, a proper constitutive relation is necessary to solve the momentum equation. Mixture of wide range particles, varity of packing's, geological formation, weathering etc. are the main factors which makes soil as most complicated one to model in any numerical scheme. Besides, its behavior under different loading conditions and presence of water in pore space are responsible for complicated behavior of soils. Therefore, actual modeling of soil is practically impossible. Keeping this critical point, researcher developed some simplified model to account for soil particles. A very simple way to consider soils as purely elastic solid models. Based on the experimental results, it is more rational to consider an elastic perfectly plastic model for geomaterials. From this perspective, elasto-plastic Drucker Prager model is one of the widely used rheological models that used in many SPH simulations. The traditional Mohr-Coulomb failure law is also used for some soil modeling. However, the concept of finite strain sometimes restrains the use of those elastic and/or elasto-plastic models. Likewise, real slope failures are mostly saturated flows and contain many other substances with the soil. Defining those complicated scenarios can be done by considering viscous flow model. For rapid flow model, either Newtonian or Dilatant Fluid model is proven to be an effective option. In addition, Bingham model or Hershel-Bulkey model are also used in SPH simulations. Recently, some other models like viscoplastic model, Hyperbolic model, mixture model have gained attraction and implemented in SPH code.

Application of SPH In Real Simulation

Dai, Wang, Huang, Song and Iio [27] conducted a three-dimensional SPH simulation to investigate the post-failure features of two typical landslides in Kyushu Region, Japan induced by the Kumamoto earthquake in 2016. For landslide near the Aso Bridge, the simulated run-out distance (364.5 m) agrees fairly well with the field data (395 m). Again, for landslide in the northeast of the Aso Volcanological Laboratory of Kyoto University, the run-out distance from simulation (70.3 m) was found in good agreement with the surveyed field data (65 m).

Huang, Zhang, Dai and Xu [11] conducted a physical model test along with a soil–water-coupled numerical simulation to analyse flow processes in liquefied soils. Displacements and velocity data matched well for both cases. Finally, a practical example of liquefaction occurred in northern Sweden causing an embankment failure was taken for simulating the actual flow caused by liquefaction. Proposed SPH method closely agrees with the actual field flow mode and distance triggered by liquefaction.

CONCLUSIONS

The success of the SPH method in diversified fields has been witnessed by the world yet many challenges are remaining. This paper summarizes the SPH method for slope stability analysis and it's so-far development and applications in short. Some remarkable works related to the slope failure simulations were discussed critically. However, the scope of this paper limits the detailed discussion of SPH.

REFERENCES

[1] Rahman M. A. and Konagai K., Substantiation of debris flow velocity from super-elevation: a numerical approach, Landslides, Vol. 14, No. 2, 2017, pp. 633–647.
[2] Lucy L. B., A numerical approach to the testing of the fission hypothesis, Astron. J., Vol. 82, No. 12, 1977, pp. 1013–1024.
[3] Gingold R. A. and Monaghan J. J., Smoothed particle hydrodynamics: theory and application to non-spherical stars, Mon. Not. R. Astron. Soc., Vol. 181, 1977, pp. 375–389.
[4] Monaghan J. J., Simulating Free Surface Flow With SPH, J. Comput. Phys., Vol. 110, No. 2, 1994, pp. 399–406.
[5] Monaghan J. J. and Kocharyan A., SPH

simulation of multi-phase flow, Comput. Phys. Commun., Vol. 87, No. 1–2, 1995, pp. 225–235.
[6] Takeda H., Miyama S. M. and Sekiya M., Numerical Simulation of Viscous Flow by Smoothed Particle Hydrodynamics, Prog. Theor. Phys., Vol. 92, No. 5, 1994, pp. 939–960.
[7] Morris J. P., Fox P. J. and Zhu Y., Modeling Low Reynolds Number Incompressible Flows Using SPH, J. Comput. Phys., Vol. 136, No. 1, 1997, pp. 214–226.
[8] Cleary P. W. and Monaghan J. J., Conduction Modelling Using Smoothed Particle Hydrodynamics, J. Comput. Phys., Vol. 148, No. 1, 1999, pp. 227–264.
[9] Liu G. R. and Liu M. B., Smoothed Particle Hydrodynamics: A Meshfree Particle Method, World Sci. , Singapore, 2003, pp. 1-449.
[10] Bui H. H., Fukagawa R. Sako K. and Ohno S., Lagrangian meshfree particles method (SPH) for large deformation and failure flows of geomaterial using elastic-plastic soil constitutive model, Int. J. Numer. Anal. Methods Geomech., Vol. 32, No. 12, 2008, pp. 1537–1570.
[11] Huang Y., Zhang W., Dai Z. and Xu Q., Numerical simulation of flow processes in liquefied soils using a soil-water-coupled smoothed particle hydrodynamics method, Nat. Hazards, Vol. 69, No. 1, 2013, pp. 809–827.
[12] Bui H. H. and Fukagawa R., An Improved SPH method for saturated soils and its application to investigate the mechanisms of embankment failure: Case of hydrostatic pore-water pressure, Int. J. Numer. Anal. Methods Geomech., Vol. 37, No. 1, 2011, pp. 31–50.
[13] Chen W. and Qiu T., Numerical Simulations for Large Deformation of Granular Materials Using Smoothed Particle Hydrodynamics Method, Int. J. Geomech., Vol. 12, No. 2, 2011, pp. 127–135.
[14] An Y., Wu Q., Shi C., and Liu Q., Three-dimensional smoothed -particle hydrodynamics simulation of deformation characteristics in slope failure, Géotechnique, Vol. 66, No. 8, 2016, pp. 670–680.
[15] Bui H. H., Fukagawa R., Sako K. and Wells J. C., Slope stability analysis and discontinuous slope failure simulation by elasto-plastic smoothed particle hydrodynamics (SPH), Géotechnique, Vol. 61, No. 7, 2011, pp. 565–574.
[16] Bui H. H. Sako K. and Fukagawa R., Numerical simulation of soil-water interaction using smoothed particle hydrodynamics (SPH) method, J. Terramechanics, Vol. 44, No. 5, 2007, pp. 339–346.
[17] Zhang W. and Maeda K., SPH simulations for slope and levee failure under heavy rainfall considering the effect of air phase, Computer Methods and Recent Advances in Geomechanics, 2014, pp. 1465–1470.
[18] Zhang W. J. and Maeda K., The Model Test and SPH Simulations for Slope and Levee Failure under Heavy Rainfall Considering the Coupling of Soil, Water and Air, Soil Behavior and Geomechanics, 2014, pp. 538–547.
[19] Li Z., Huang Y., Maeda K., Zhang W. and Saito H., Numerical analysis on seepage failures of dike due to water level-up and rainfall using a water–soil-coupled smoothed particle hydrodynamics model, Acta Geotech., Vol. 11, No. 6, 2016, pp. 1401–1418.
[20] Zhang F. and Ikariya T., A New Model for Unsaturated Soil Using Skeleton Stress and Degree of Saturation As State Variables, Soils Found., Vol. 51, No. 1, 2011, pp. 67–81.
[21] Grabe J. and Stefanova B., Numerical modeling of saturated soils based on smoothed particle hydrodynamics (SPH): Part 2: Coupled analysis, Geotechnik, Vol. 38, No. 3, 2015, pp. 218–229.
[22] Capart H. and Young D. L., Formation of a jump by the dam-break wave over a granular bed, J. Fluid Mech., Vol. 372, 1998, pp. 165–187.
[23] Fraccarollo L. and Capart H., Riemann wave description of erosional dam-break flows, J. Fluid Mech., Vol. 461, 2002, pp. 183–228.
[24] Hamada M., Sato H. and Kawakami T., A consideration of the mechanism for liquefaction-related large ground displacement, Proceedings of the 5th US Japan Workshop on Earthquake Resistant Design of Lifeline Facilities and Countermeasures for Soil Liquefaction, Salt Lake City, USA, 1994, pp. 217–232.
[25] Bui H. H., Fukagawa R., Sako K. and Okamura Y., Earthquake Induced Slope Failure Simulation by SPH, Fifth Int. Conf. Recent Adv. Geotech. Earthq. Eng. Soil Dyn., 2010.
[26] Ono Y., SPH Simulation of Earthquake-induced Slope Failure, 15th World Conf. Earthq. Eng., 2012.
[27] Dai Z., Wang F., Huang Y., Song K. and Iio A, SPH-based numerical modeling for the post-failure behavior of the landslides triggered by the 2016 Kumamoto earthquake, Geoenvironmental Disasters, Vol. 3, No. 1, 2016.
[28] Monaghan J. J. and Lattanzio J. C., A refined particle method for astrophysical problems, Astron. Astrophys., Vol. 149, No. 1, 1985, pp. 135–143.
[29] Johnson G. R. and Beissel S. R., Normalized Smoothing Functions for SPH Impact Computations," Int. J. Numer. Methods Eng., Vol. 39, No. 16, 1996, pp. 2725–2741.

9th Int. Conf. on Geotechnique, Construction Materials and Environment, Tokyo, Japan, 20-22 November 2019, ISBN: 978-4-909106025 C3051

A GEOSTATISTICAL APPROACH TO DEVELOP THE SOIL ZONATION MAP: AN APPLICATION FOR CHATTOGRAM CITY

Nafisa Tabassum[1], Md. Aftabur Rahman[2], Md. Nasir Uddin[3], Probal Singha[3]
[1]Graduate Student (M.Sc Engg. Candidate), Chittagong University of Engineering & Technology, Chattogram-4349, Bangladesh, Email: nafisa_t@cuet.ac.bd
[2]Faculty, Department of Civil Engineering, Chittagong University of Engineering & Technology, Chattogram-4349, Bangladesh, Email: maftabur@cuet.ac.bd
[3]Former Undergraduate Student, Department of Civil Engineering, Chittagong University of Engineering & Technology, Chattogram-4349, Bangladesh

ABSTRACT

The rapid urbanization and industrial evolution of the developing cities is commonly seen all over the world. This development results construction of new infrastructures and industries are always in a hurry to build structures at the earliest time. However, lack of proper geotechnical data makes it always cumbersome to get the idea of the sub-surface condition which is a prime importance for the construction of new structures. Considering the current burning scenario, this research work aims to develop a comprehensive procedure for the preparation of soil zonation map by using geostatistical tools. Therefore, the spatial distribution of geotechnical sub soil characterization of chattogram city which is 2nd largest and the major port city of Bangladesh located between 22.13º and 22.28ºN latitude and between 91.45º and 91.54ºE longitude with 168.1 square kilometer divided into 41 wards are presented and soil zonation map at depth 3m to 9m is developed using spatial analyst tools with corresponding SPT -N values. The prepared zonation map is afterward validated with the second data set to implicitly justify the suitability of the proposed approach. Based on the comparison between the predicted and real values, the proposed method provides a better agreement and can be a plausible option for the development of soil zonation map.

Keywords: SPT, soil zonation map, Chattogram, IDW, geostatistical analysis

INTRODUCTION

Before the construction of any structure, the soil condition of the proposed area must be known. Actual geotechnical data, which is an important parameter to develop any kind of civil engineering construction is not only easily available but also expensive due to costly boring technique. Sub-surface investigation, which is to date the sophisticated exploration system, consists of determining the profile of the natural soil deposits at the site, and determining properties of the soils by laboratory analysis [1] . A soil profile and soil zonation maps can be a useful means to understanding and evaluating the suitability and sustainability of the proposed structure because it provides information about soil suitability, soil behaviour for current and future use, basis for monitoring and formulating land use strategies. The soil profile modelling is a useful option to mitigate geotechnical hazards. Having a proper soil profile of a certain location, the geological condition of that location can be known. However, for getting preliminary idea of a proposed site, it is not economical to conduct geotechnical investigation all the time. Rather, an alternative approach needs to be developed to qualitatively justify the geotechnical condition of sub-surface [2]. Experimental and numerical simulation is not justified here to get such rational information's. Besides, statistical formulation based on random data sets can be a good option to prepare spatial distribution of any quantity [3]. For soil profile, SPT, N is a critical parameter and implicitly used to determine the necessary parameters for determination of bearing capacity of soils. Therefore, feeling the necessity of the current situation, an attempt is made to prepare spatial distribution of soil profile by using SPT, N values. Afterward, the prepared map is validated with the field data set. The subsequent sections describe the detailed procedure of the developed methodology.

BACKGROUND AND STUDY AREA

Chattogram, the second largest city and the major commercial hub of a geographically important country named Bangladesh. The Government of Bangladesh is going ahead taking many development projects and some mega projects such as Elevated Express Road, Outer Ring Road, Expansion of Port, and Deep Seaport in Sonadia Island, Chattogram -

Cox's Bazar Railway etc.. Moreover, the city is growing day by day. Based on these developments and extension of the city, a number of infrastructure, buildings and associated structure will be required in coming days. All these leads to our comment that Chattogram is destined to grow and became more populous in the coming days. These will create demand for more housing and utility of infrastructure. To fulfil these needs an important task is geological and geotechnical investigation. Therefore, GIS based SPT-N zonation maps can be useful tools in the subsurface exploration system.

The geographical location of Chattogram Metropolitan Area (CMA) is between 22.13º and 22.28ºN latitude and between 91.45º and 91.54ºE longitude. It has an area about 168.1 square kilometers and divided into 41 wards. The city is located on the bank of Karnaphuli River. The Bay of Bengal is on western side and hilly terrain on the north side adds to its beauty. Much of Chattogram Division is located within the ecological Indo-Burma zone on the boundary of the India plate and Burma Plate. The current population of the city is 8.6 million as per census 2017. The natural harbor of Chattogram has been a gateway to the historic region of Bengal for centuries. It is a prominent trading center and the oldest living city of Bangladesh. In the current research, about 450 soil investigation reports, related to the already constructed/proposed buildings and other engineering structures, were used as the sources from which the geotechnical properties of the soil, for the region of study area (CMA) were extracted. The location of the study area is shown in the Fig.1.

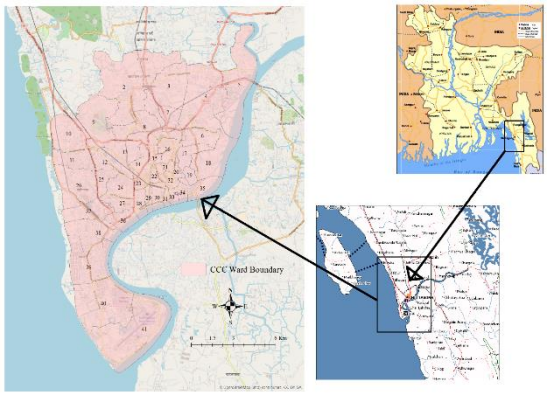

Fig. 1 Study Area.

METHODOLOGY

The data extraction process used in the current study involved in two approaches. The first approach was achieved using the arduous manual extraction of the data from the soil reports available in many different forms and locations. Afterward, statistical model was developed to prepare the spatial distribution of the selected locations.

Several types of interpolation techniques exist for geo-statistical and spatial analysis. Inverse Distance Weighting (IDW) is a interpolation technique, which was used to characterized the Standard Penetration Test SPT-N value to produce the soil zonation maps .The Spatial Analyst Inverse Distance Weighting(IDW) technique was deemed the most suitable method to represent the SPT-N value data in the study area. The mandatory fields in the process include the input point features, the z value (SPT-N) and the output raster name. Therefore, the IDW interpolation method was used to spatially analyze the produced SPT-N value zonation maps. It determines the cell values by using a linear-weighted combination of set of sampled points. The IDW method is a deterministic interpolation technique which creates maps or interpolated surface, based on mathematical formulas and measured points. The interpolation, in turns, predicted the values of the cells at the specific locations that lacked sampled points and also predict unknown attributes at particular location. The main aim of this process was to provide new geotechnical properties in locations where there were no geotechnical data existed.

The GIS methodology, using ArcMap 10.5 formed the second complementary part of the main methodology. This technique can produce zonation maps which can categories the properties of soil in the study area. Standard Penetration Test SPT-N values were used as the key data for the production of the GIS-based soil zonation maps. This procedure enables the interpolation (generation) of the new SPT-N values in the areas that lacked sampled SPT-N data. Such Interpolation is important in any attempt to solve problems or, at a very least reducing the escalating of for soil investigation.

To prepare such soil profile map, a total of 450 sub-soil reports were collected and N values were updated with locations. For current research, the soil profiles at 3m, 6m, and 9m were chosen and N values at those depths were separated and synchronized in GIS environment. Later, IDW technique was employed to prepare spatial distribution of the quantity over the CMA. The location of the collected sampling points are shown in Fig.2.

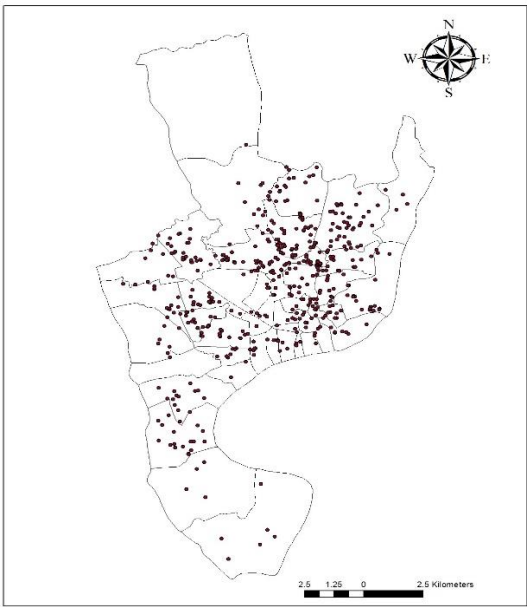

Fig. 2 Distribution of borehole over the city.

RESULTS AND DISCUSSIONS

SPT, N values were represented on the Geographic Information System (GIS) and IDW analysis was conducted to develop the GIS based soil zonation maps. This zonation maps characterized the soil of the CMA area using the interpolation techniques in the spatial analyst in GIS. GIS based SPT-N values zonation maps were obtained for three different depths are 3m, 6m, and 9m.

Zonation map at different depths

Fig 3 depicts Zonation map at 3m depth from existing ground surface. The maximum area covered pink color for which the dominant SPT-N value range is 4 – 10. This range of SPT-N represent very loose to loose type soil and very soft to stiff type soil. The minimum area covered green color for which the SPT-N range is 30 -50 .This range of SPT-N represent dense type soil. The maximum area of Ward No 2,5,10,21,26,30,33,38,39,40 fall in the range of SPT-N ,4 – 10 . This map suggest that at shallow depth the soil are very loose and soft types.

In Fig.4, it is represented the soil zonation map at 6m depth from existing ground surface. The maximum area covered pink and also yellow color. The SPT-N range for pink color 4- 10 for which the soil is very loose to loose, very soft to stiff type soil. Maximum area of ward No 10, 35, 36, 37, 38, 39, 40, 41 fall in this range. The area covered yellow color also remarkable for which the SPT-N range is 10-30, 10 to 30 SPT-N range indicates medium dense, very stiff type soil. This map suggest that from the low N value in the shallow depths towards higher value of N in the deeper depth. The soil is transition from loose to medium dense, soft to stiff type soil.

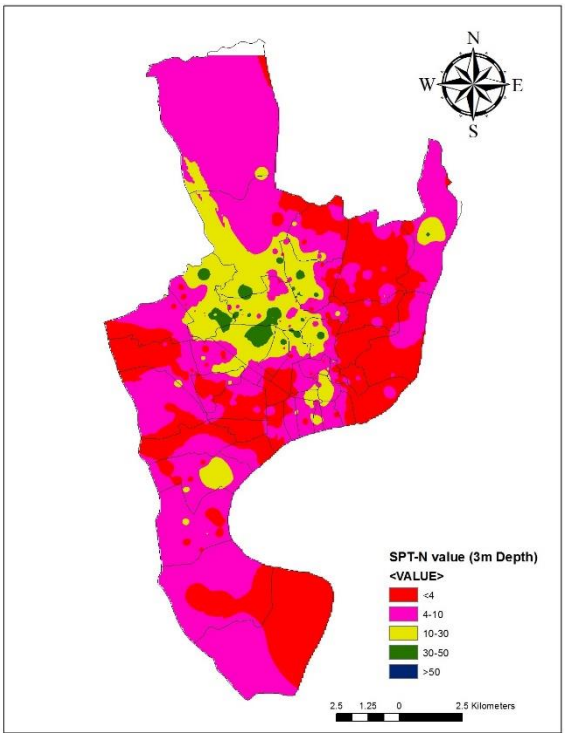

Fig. 3 Soil zonation at 3m depth.

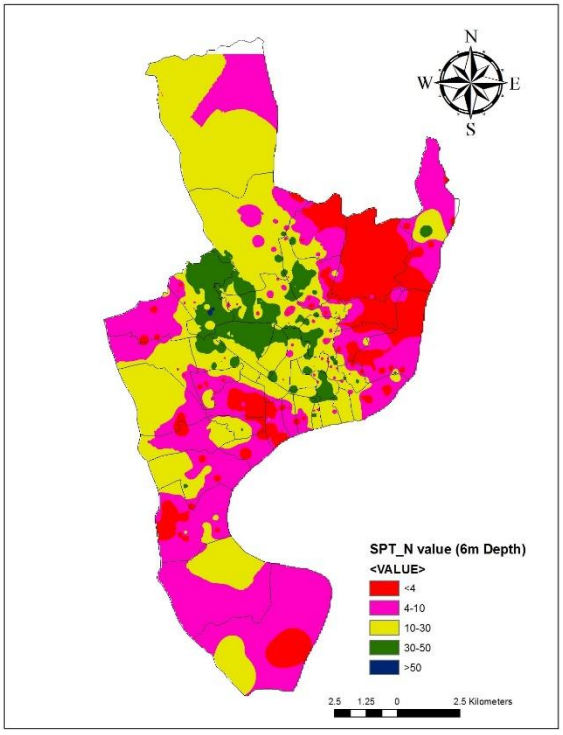

Fig. 4 Soil zonation at 6m depth.

In Fig.5, it is represented the soil zonation map at 9m depth from existing ground surface. The maximum area covered by yellow color. The SPT-N range for yellow color is 10 – 30 for which the soil is medium dense, very stiff type soil. Maximum area of ward No 1,2,26,27,28,29,30,36,38,40 fall in this

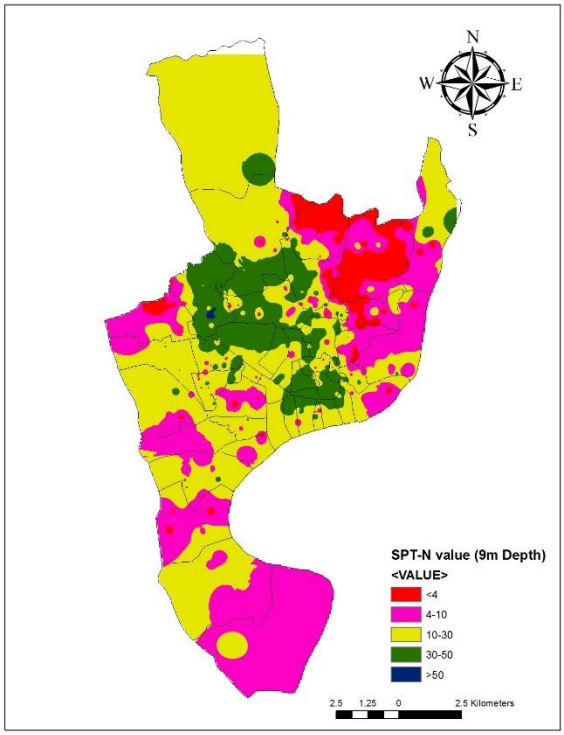

Fig. 5 Soil zonation at 9m depth.

range. The area covered by green for which SPT-N range 30 -50 large then above shallower depth. This map suggest that from the low N value in the shallow depths towards higher value of N in the deeper depth. The soil is transition from loose to dense, soft to very stiff type soil.

Cross-validation Validation curve for zonation map of 3m depth is plotted in Fig.6 between predicted N value and actual N value. The R-squared value of best fit line is 0.827 and considered to be satisfactory for such highly non-linear datasets.

The validation curves for 6m and 9m depths were also plotted in Fig. 7 and Fig.8 , respectively. In all cases, the R-squared value was found nearly 0.8, which portrays quite good match between actual and predicted values.

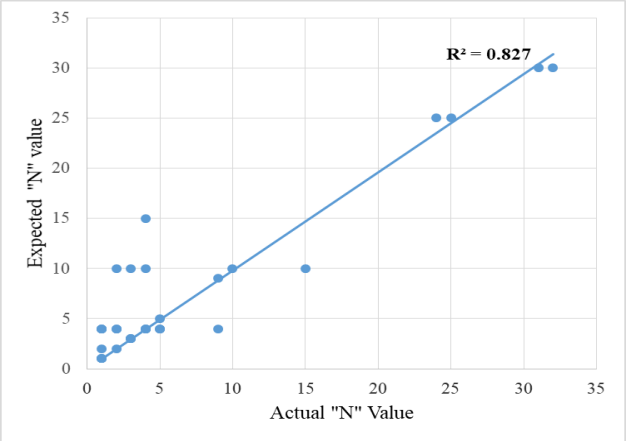

Fig. 6 Validation curve for zonation map at 3m.

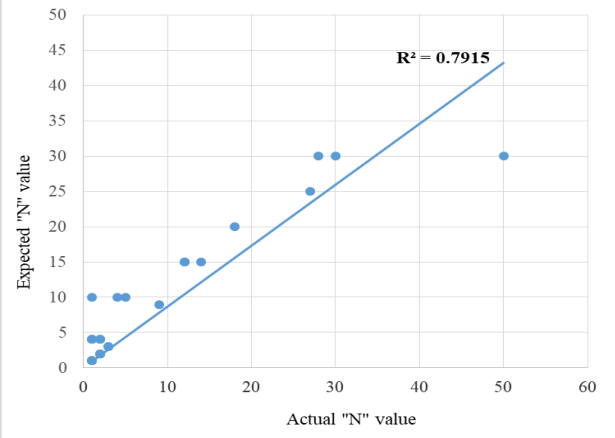

Fig. 7 Validation curve for zonation map at 6m.

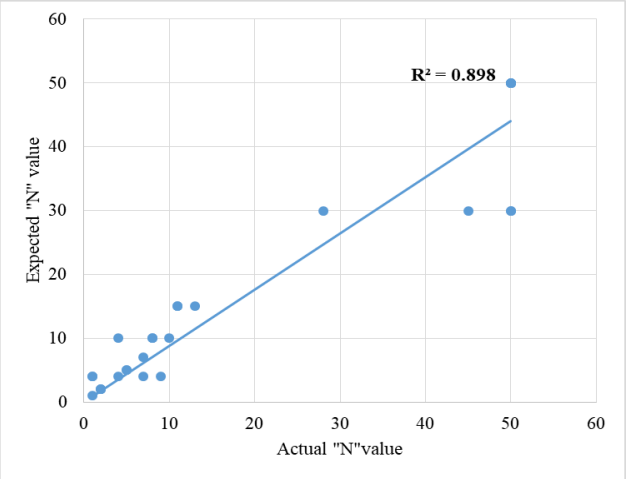

Fig. 8 Validation curve for zonation map at 9m.

CONCLUSIONS

Due to scarcity of sufficient borehole location and lack of additional information and also soil variation from place to place, it is difficult to analyze soil profile of Chattogram City Corporation area of 41 wards. The data for the current study were collected from reliable sources related to the already erected building and others engineering structure. The study has two scope, first scope represented soil type, properties of soil, depth and the second scope represented Geographic Information System (GIS), which was conducted to develop GIS-based SPT-N value soil zonation maps. These zonation maps characterized the soil in Chattogram City using the interpolation techniques in the Spatial Analyst in GIS. The soil profile of Chattogram City consists of very loose to loose type soil at shallow depth with lower SPT-N value. A layer of medium dense type soil occurs beneath the loose layer with a higher SPT-N value. Very dense type soil is located underneath this layer with SPT-N value 50 or greater than 50.

The overall result of the study will help in future expansion and development process, construction of infrastructure,general planning, sustainable land use and management. The analyze of the soil beside Karnaphuli river which is the most important river of the city and Bay of Bengal would be helpful for the construction of hydraulic structure or other structure and further development of river and sea shore. The identified hotspot location will help to future development of any civil engineering structure on specified location.

REFERENCES

[1] Miller BA, Schaetzl RJ , The historical role of base maps in soil geography. Geoderma ,2014, 230–231:329–339.

[2] Al-Ani H, Oh E, Chai G GIS-based examination of peats and soils in Surfers Paradise, Australia. Soil Sci Annu, 2014, 65:29–38

[3] Abdel Rahman MAE, Tahoun S GIS model-builder based on comprehensive geostatistical approach to assess soil quality. Remote Sens Appl Soc Environ, 2018.

9th Int. Conf. on Geotechnique, Construction Materials and Environment,
Tokyo, Japan, 20-22 November 2019, ISBN: 978-4-909106025 C3051

DYNAMIC INTERACTION BETWEEN STEEL CASING AND EXISTING PILE WHEN PULLING-OUT EXISTING PILES

Shuichi Kuwahara [1], Shin-ichi Hamaguchi [1], Yoshikazu Shimada [1],
Ken-ichi Shishido [1] and Shinya Inazumi [2]
[1] Japan Association for Pulling-out Existing Piles, Japan
[2] Shibaura Institute of Technology, Japan

ABSTRACT

Many urban areas in Japan are located on soft ground and there are many buildings with pile foundations. Therefore, when dismantling a building, it is necessary to remove the pile (existing pile) designated as industrial waste remaining in the ground. There is a method of crushing and removing the pile as a method of removing the existing pile, but there is a problem of vibration and noise. Therefore, in many existing pile drawing methods, the outer circumference of the pile is drilled by the steel casing, and the existing pile is pulled out by cutting the boundary between the pile and the surrounding ground. Among them, when pulling out the existing pile that exists diagonally due to the pressure in the soil or the construction failure, it is confirmed that the steel casing follows the sloped pile when inserted into the ground. However, the dynamic mechanism of this phenomenon is unknown because the situation in the ground cannot be observed visually. Therefore, in this study, we will use MPS-CAE simulation to clarify visually and quantitatively the dynamic mechanism along the existing pile in which the steel casing is inclined when inserted into the ground, which occurs in the realization site.

Keywords: Insolubilization treatment, Insolubilization mechanism, Metal-insolubilizing material, Leaching test, Contaminated soil

INTRODUCTION

In Japan, with the rapid economic growth, demand for offices and commercial facilities increased rapidly, and construction of high-rise buildings that could effectively utilize narrow land proceeded. However, it is thought that the aging of those structures built in the same period will be concentrated, and that rebuilding demand will increase. In addition, the disaster prevention awareness of the people has been raised by the topic of the Tohoku region Pacific offshore earthquake that occurred on March 11, 2011, and by the Tokyo metropolitan area earthquake, the Tokai earthquake, the Tonankai earthquake, and the Nankai earthquake that are said to have a high probability of occurrence. It is thought that it is increasing the demand for rebuilding of aging structures. Furthermore, it is thought that not only because of deterioration but also because facilities are being reduced due to obsolescence and population decline are factors that accelerate the increase in demand for rebuilding structures.

Many urban areas in Japan are located on soft ground and there are many structures using pile foundations. Therefore, it is necessary to remove not only the existing structure but also the existing piles supporting the structure, in order to newly utilize the land where the existing structure exists. In addition, because existing piles are treated as industrial wastes that are generated as a result of business activities and defined by the Waste Disposal Act, it is a problem to leave them in the ground [1]-[3]. Furthermore, in the land sale transaction and so on, a problem has actually occurred as a “hidden trap”. Therefore, it can be said that removal of existing piles is essential [1]-[3].

As methods of removing the existing pile, there are the method of crushing and removing the pile with a rock auger and the method of cutting out the friction between the pile and surrounding ground by a cylindrical steel casing [1]-[3]. However, in these methods, vibration and noise generated during construction works often become a big problem. Furthermore, in these methods, there are cases where the pencil part and flange at the tip of the pile cannot be removed, which means that industrial waste is left in the ground, so it can be said that these methods also have problems with the environment.

Therefore, pulling out of piles is now being adopted at many sites. At the beginning of the work for pulling out the pile, the outer periphery of the pile is drilled with the steel casing, but at this time the situation in the ground cannot be visually checked, so various examinations have to be carried out to check the inside situation. However, because many on-site surveys cannot be performed in terms of time and money, computer-based simulations can provide a visual and efficient evaluation.

In this study, the authors will clarify the mechanism of the behavior that occurs in the

realization site that the steel casing follows the existing pile when the steel casing is inserted into the ground by verifying the behavior of the ground and the pressure distribution using MPS-CAE [4]-[5].

ANALYSIS CONDITIONS IN MPS-CAE

Outline of MPS-CAE of steel casing drilling

In the case of removing an existing pile work, the inside of the steel casing and its surroundings are filled with muddy water because the water is discharged from the lower part of the steel casing while penetrating the steel casing (see Fig. 1).

In this analysis, the authors set the state that the existing pile area up to the depth of 15,000 mm was filled with muddy water particles, and carried out the analysis to make rotational penetration of the steel casing to the depth of 10,000 mm. In addition, the existing pile in this analysis has a foot protection part at the depth of 16,100 mm or deeper, and the steel casing is not penetrated to the foot protection part at the lower end of the existing pile. The authors will analyze two patterns in which the inclination angle of the existing pile is inclined 0° and 2° from the vertical direction.

Parameter setting for muddy water particles

Table 1 shows the material parameters for the mud water in MPS-CAE. The parameter setting was performed with the mud water to be analyzed as the Bingham fluid. Regarding the density and plastic viscosity, the authors measured the density of the mud collected from the hole of the existing pile at the site of the removing work of the existing pile, and set the plastic viscosity by measurement using a Brookfield's B-type viscometer. In addition, the yield value gives the measurement result 10 Pa of the yield value of drilling mud obtained by measurement with a double cylinder type rotational viscometer from previous researches [1]-[3].

Modeling method of existing pile and steel casing

The existing piles and steel casings were created according to the actual dimensions using 3D-CAD based on the shape of the steel casing used at a certain field site and the removed existing piles. From Figs. 2 and 3, the existing piles in this analysis are existing piles with a foot protection part, and the steel casing is cylindrical. In addition, the steel casing was set as the wall boundary, and the characteristics were determined not by the material parameters but by the contact angle between the liquid and the wall boundary. According to previous researches, the contact angle between water and stainless steel is 45° to 58°, and the analysis results when the contact angle is set to 45° and 58° did not show a large difference.

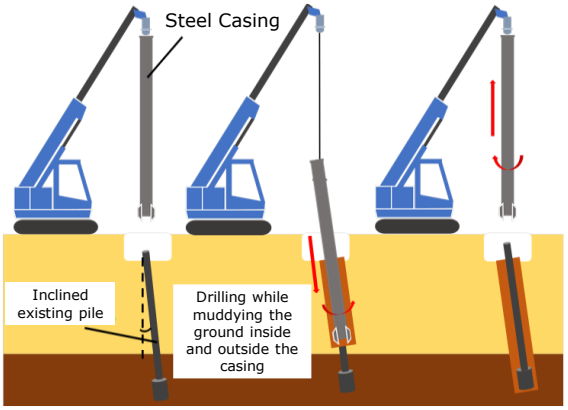

Fig. 1 State of muddy water on the ground

Table 1 Material parameters of muddy water particles

	Density (kg/m³)	Plastic viscosity (Pa·s)	Yield value (Pa)
Muddy water	1200	6.92	10

The authors reproduced steel casing as 50° [6]-[7]. Table 2 shows the penetration speed and rotational speed of the steel casing.

MPS-CAE SIMULATION FOR STEEL CASING DRILLING

Velocity of muddy water particles according to drilling depth

The cross section color-coded by the vertical velocity at the depth of 5 and 8 m is shown in Fig. 4. Particles close to red have velocity components in the vertical upward direction, and particles close to blue have velocity components in the vertical downward direction. From Fig. 4 (a) and (c), in the case of an inclination angle of 0°, particles with similar velocity components are evenly distributed, but from Fig. 4 (b) and (d), in the case of an inclination angle of 2°, the distribution of velocity of muddy water in the vertical direction was confirmed on both sides of the existing pile.

Pressure gradient acting between muddy water particles according to drilling depth

The cross section color-coded by the pressure acting at the depth of 5 and 8 m is shown in Fig. 5. From Fig. 5 (a) and (c), when the inclination angle is 0°, almost the same pressure is received as a whole, and no pressure gradient is generated. However, according to Fig. 5 (b) and (d), when the steel casing is inserted into the existing sloped pile, the pressure increases in the process of narrowing the gap between

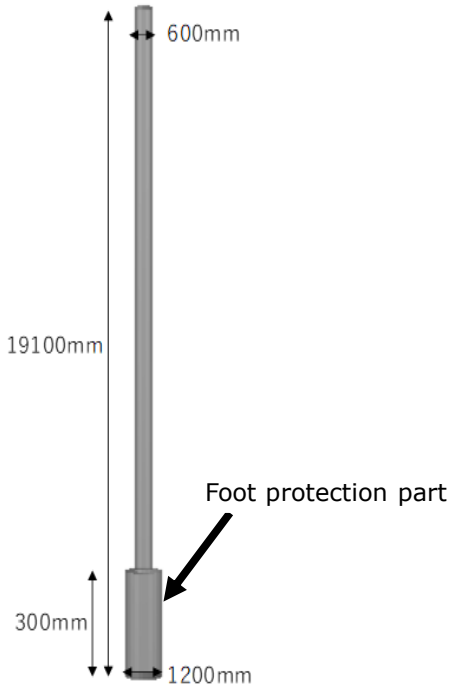

Figure 2 Existing pile

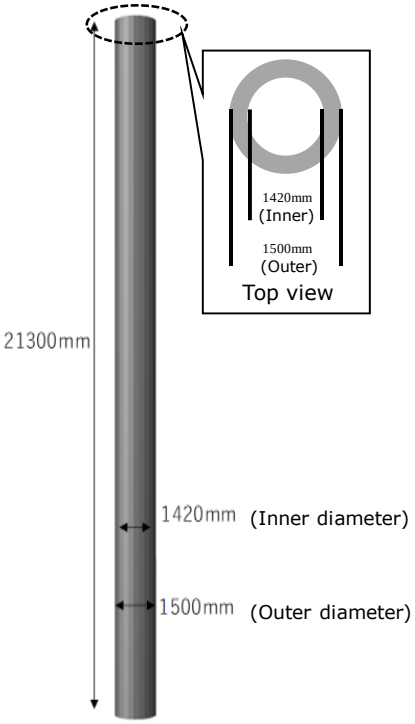

Fig.3 Steel casing

Table 2-Parameters of MPS-CAE steel casing

	Rotational speed (rpm)	Penetration speed (m/min)
Steel casing	15	0.5

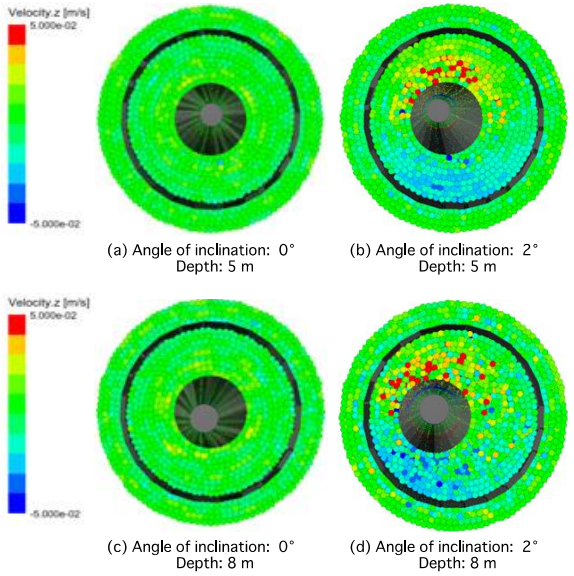

Fig. 4 Velocity of muddy water particles (vertical direction)

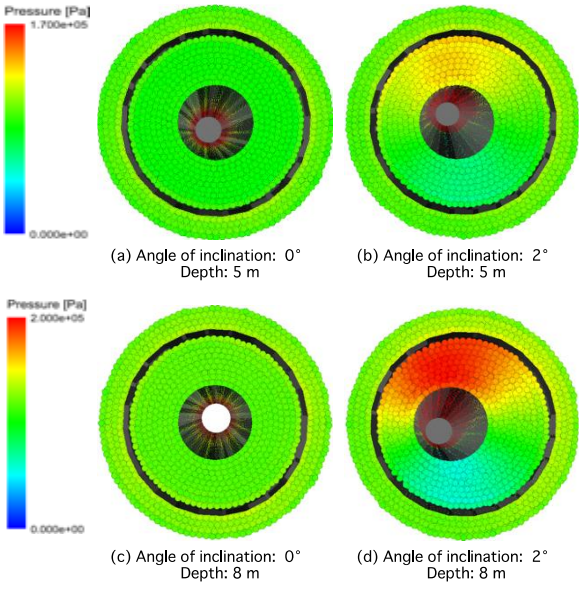

Fig. 5 Pressure gradient of muddy water particles

the pile and the steel casing, and the pressure decreases in the process of widening the gap There is a pressure gradient. It is considered that this is caused by the mud water rotating together under the influence of the rotation of the steel casing.

A co-rotation is a phenomenon in which they (this case is both steel casing and muddy water) move together due to the frictional force generated between the steel casing and the muddy water. From Figs. 4 and 5, when the existing pile is inclined, muddy water particles inside the steel casing show different behavior compared to the case of 0°. It has been

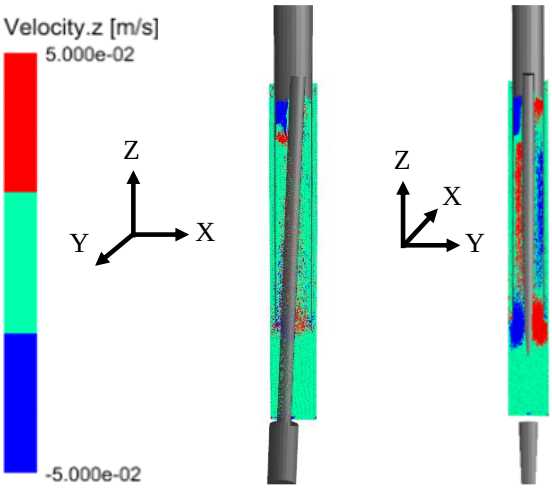

Fig. 6 Vertical velocity of muddy water particles (vertical cross section)

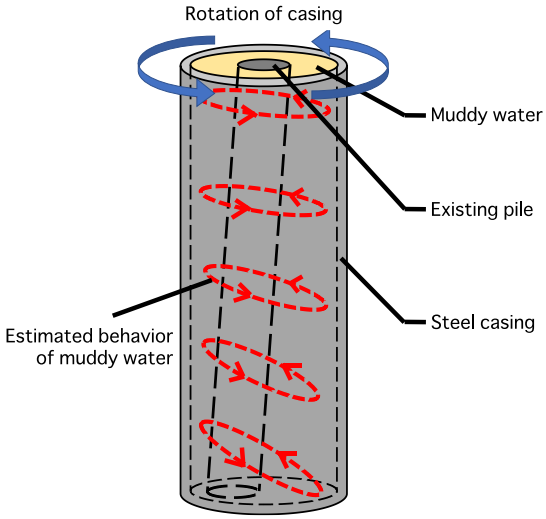

Fig. 7 Estimated behavior of muddy water particles

confirmed that the muddy water particles have a vertical upward velocity at high pressure and a vertically downward velocity at low pressure, in addition to co-rotation by the rotational force of the steel casing. This is due to the fact that the muddy water particles subjected to high pressure try to move in a spiral trajectory toward the released ground surface (upward direction) so that the pressure gradient disappears.

MECHANISM OF STEEL CASING FOLLOWING INCLINED EXISTING PILE

The vertical cross section obtained by cutting the analysis target in the X-Z plane is shown in Fig. 6 (a), and the vertical cross section obtained by cutting in the YZ plane is shown in Fig. 6 (b). Red particles have vertically upward velocity components, and blue particles have vertically downward velocity components. From Fig. 6 (b), it can be understood that the vertical velocity of the muddy water is different on both sides of the existing pile. First, due to the rotation of the steel casing, the muddy water inside rotates together. When the existing pile is inclined, the gap between the steel casing and the pile becomes different as the penetration depth of the steel casing gets deeper, and a pressure gradient as shown in Fig. 5 (b) and (d) occurs. That is, in addition to the rotational speed of the steel casing due to the co-rotation of the steel casing, it has a vertically upward velocity at high pressure and a vertically downward velocity at low pressure, resulting in the pressure gradient of the mud in the steel casing as shown in the figure. As shown in Fig. 7, spiral co-rotation occurs. In addition, the steel casing is considered to be along an inclined pile so that the pressure gradient produced is eliminated.

CONCLUSIONS

In this study, the authors aimed to clarify the mechanism of the behavior of a steel casing along the existing inclined pile confirmed in the field by performing the MPS-CAE analysis. An MPS-CAE analysis was performed by inserting a steel casing into the ground to an inclined existing pile, and the behavior and pressure gradient of muddy water mainly in the casing were visually represented. It was possible to deduce the mechanism of behavior of the casing along the sloped existing pile, which has not been elucidated yet by separating and examining the behavior of the mud particles and the pressure gradient for each depth.

Until now, the co-rotation phenomenon of muddy water has not been captured in a positive image. There are many cases where the existing piles remain in the unhealthy condition as shown in Figure 2.1. If cracks and joints are not properly joined, penetration may occur while rotating the casing, which may further damage the pile. That is, at the time of casing penetration, the lower part of the existing pile is not yet cut off and fixed to the surrounding ground, but the upper part is forced by the rotation of the casing due to the co-rotation of muddy water, resulting in the existing pile Is considered to be in a twisted condition and to be broken. However, in this research, it is concluded that the phenomenon that the casing follows the sloped existing pile cannot occur because the pressure gradient does not occur if the muddy water does not rotate together and the muddy water does not move vertically due to it.

(1) By using MPS-CAE to visually represent the behavior and pressure gradient of muddy water particles in the steel casing, it is possible to simulate steel casing drilling in existing pile drawing-out work.

(2) The phenomenon along the existing pile in which the steel casing is inclined causes spiral co-rotation due to the influence of the pressure gradient of the muddy water in the steel casing, and the steel casing is gradually inclined along the pile in which the pressure gradient disappears.

REFERENCES

[1] Kuwahara, S. and Inazumi, S.: Settlement of surrounding grounds due to existence of pile pulling-out holes, International Journal of GEOMATE: Geotechnique, Construction Materials and Environment, Vol.16, Issue 54, pp.81-85, 2019.

[2] Kuwahara, S., Hamaguchi, S., Shimada, Y. and Inazumi, S.: Construction theories and examples for method of powerfully chucking the tip of existing pile at removal of existing piles, Japanese Geotechnical Journal, Vol.14, No.1, pp.69-76, 2019.

[3] Inazumi, S., Namikawa, T., Kuwahara, S. and Hamaguchi, S.: Influence of pulling out existing piles on the surrounding ground, International Journal of GEOMATE: Geotechnique, Construction Materials and Environment, Vol.13, Issue 35, pp.16-21, 2017.

[4] Darko, V., Vedran B. and Boris, S.: Analytical modelling in low-frequency electromagnetic measurements of steel casing properties, NDT & E International, Vol.40, Issue 2, pp.103-111, 2007.

[5] Kim, S.J., Kim, S.G., Oh, K.S. and Lee, S.K.: Excitation force analysis of a powertrain based on CAE technology, International Journal of Automotive Technology, Vol.9, Issue 6, pp.703-711, 2008.

[6] Sulskya, D., ChenbH, Z. and Schreyerc, H.L.: A particle method for history-dependent materials, Computer Methods in Applied Mechanics and Engineering, Vol.118, Issues 1–2, pp.179-196, 1994.

[7] Tanaka, M. and Masunaga, T.: Stabilization and smoothing of pressure in MPS method by Quasi-Compressibility, Journal of Computational Physics, Vol.229, Issue 11, pp.4279-4290, 2010.

9th Int. Conf. on Geotechnique, Construction Materials and Environment, Tokyo, Japan, 20-22 November 2019, ISBN: 978-4-909106025 C3051

A STUDY OF THE COMPACTED KHON KAEN LOESS PARAMETER FOR THE DESIGN OF GRAVITY WALL

W. Phimonnok[1], R. Nuntasarn[2] and S. Tirapat[3]
[1,2,3] Faculty of Civil Engineer, Khon Kaen University, Thailand

ABSTRACT

This paper presents the testing of retaining walls on the compacted Khon Kaen Loess by using the physical models. The specification of this research is to compact Khon Kaen Loess in the box size 100x100x100 cm to achieve the dry density of 1.91 t/cu.m, which is the 90% of the maximum dry density by the modified method. Moreover, the moisture content of this compacted Khon Kaen loess was 11.85%. The effective friction angle (ϕ′) and effective cohesion (c′) of this compacted Khon Kaen loess at saturated condition was 29 degree and 12 kPa, respectively. The soil sample was compacted in five layers in the box, and the thickness of each layer was 45 cm. The dry density of each layer was examined by the sand cone method. The retaining the wall, a gravity wall, wherein the size of the 15x30x50 cm, was installed in the box to determine the stability of the retaining wall. The horizontal force was applied by using the pneumatic jack. The weight plate was applied to the top of the retaining wall as a vertical force. The horizontal and vertical movement was measured by using LDVT. The soil- concrete interaction was determined from the relationship between the horizontal pressure and the vertical pressure.

Keywords: Retaining Walls, Compacted Khon Kaen Loess, Physical Models, Soil- Concrete interaction

INTRODUCTION

The structure of Khon Kaen Loess is loose like a honeycomb as classified as silty sand (SM) or clayey sand (SC). The sand grains may be bonded by clay silt or iron oxide (Fe2O3). As a moisture content increases, the bonding between sand grain was destroyed, which causes to loss of the shear strength and collapses suddenly.

Barden et al. [1] studied loess structure by collecting soil samples from around the world. The predominant of loess is sand, whereas clay particles or silt particles or chemical cementing agents like calcium carbonate or iron oxide is the bonding. The cause of collapsing loess can be classified as 3 characteristics.

1. The structure is unsaturated and unstable. Easily to destroyed.
2. Excessive applied stresses destroy the soil structure, which causing subsidence.
3. The increasing of moisture content dissolves the bonding and making void ratio decrease. As a consequence of compact soil.

Collapsible soil always found in arid areas and semi-arid areas. The soil in this climate is mostly unsaturated by deep groundwater level. The moisture content of the soil in the summer season is about 3-5% and in the rainy season is about 10-12%.

Udomchoke [2] found that Khon Kaen loess is collapsible soil with a very severe degree of collapse. Moreover, the shear strength parameters of Khon Kaen loess are decreased when the moisture content is increased.

Gasaluck [3] found that loess is cover in many areas of northeastern Thailand. This loess has a relatively high permeability, which soil moisture content is easily increasing.

Muktabhant [4] present that the color of the soil in Khon Kaen province, especially in Khon Kaen University, is red. With a mixture of fine sandy loam, silt and clay are the caused of windblown as known as loess. The thickness of the soil layer is about 4 - 8 meters. According to USCS, Khon Kaen loess was classified as SM, SC or SM-SC with 13 - 19% of LL, 11 - 14% of PL, 0 - 5% of PI and specific of gravity between 2.60-2.72.

The purpose of retaining wall construction is to prevent lateral movement of soil. Application of retaining walls is in engineering works, such as embankment, excavation work, bridges, and waterproof structures. Das [5] suggested the smallest dimension of the retaining wall as shown in Fig.1.

The failure mode of a retaining wall can be classified into 4 categories, which is overturning, sliding, bearing capacity failure, and deep-seated shear failure, as shown in Figure 2. As the acting force on the retaining wall as shown in Fig. 3, safety factor against overturning about the toe, sliding and the bearing capacity as present in equation (1), (2) and (3), respectively. The minimum factor of safety against overturning, sliding and the bearing capacity is 2, 1.5 and 3, respectively

$$FS_{(overtruning)} = \frac{\sum M_R}{\sum M_O} \quad (1)$$

Where;

$\sum M_R$ = sum of the moments resist overturn about point C

$\sum M_O$ = sum of the moments overturn about point C

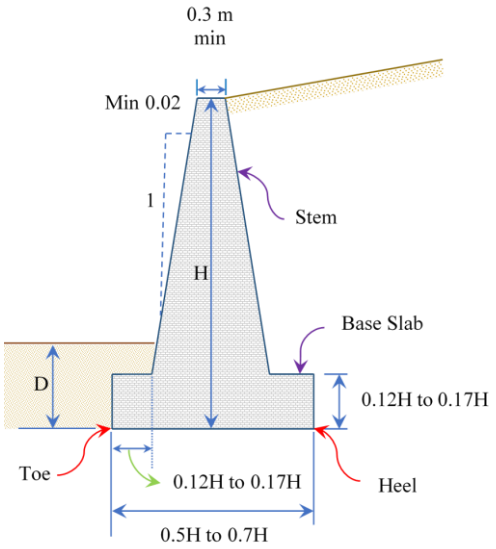

Fig. 1 Smallest dimensions of gravity retaining wall.

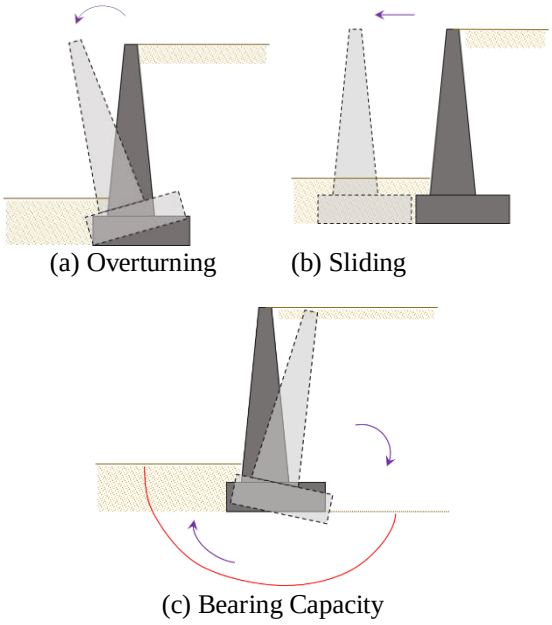

Fig. 2 Failure ode of retaining wall.

$$FS_{(sliding)} = \frac{\sum F_{R'}}{\sum F_d} \quad (2)$$

Where;

$\sum F_{R'}$ = sum of the horizontal resisting forces.

$\sum F_d$ = sum of the horizontal driving forces.

$$FS_{(\text{bearing capacity})} = \frac{q_u}{q_{\max}} \quad (3)$$

Where;

q_u = ultimate bearing capacity

q_{max} = maximum pressures

At present, many projects are using Khon Kaen loess as backfill. Therefore, this study investigates the physical modeling of retaining wall on compacted Khon Kaen loess. The Khon Kaen loess was compacted to 90% of the maximum dry density by the modified method on the wet side. Moreover, the gravity retaining wall is precast concrete.

APPARATUS

Modeling gravity retaining wall was 0.15 m wide, 0.50 m long and 0.30 m high as illustrated in Fig.4. The tank size is 1.0x1.0x1.0 m in width, length, and depth, respectively.

Fig. 4 Model gravity retaining wall.

The loading equipment as shown in Fig. 5 consists of

(1) A pneumatic system controls the horizontal load by using speed as 1 mm/min.

(2) A proving ring was used to measure the horizontal load.

(3) The 4 LDVTs were used to determine the vertical and horizontal displacement

(4) Weight plates were used as vertical loading.

(5) Two soil pressure transducers were used to measure the passive pressure

METHODOLOGY

Khon Kaen loess was determined the basic properties to classify according to [6]. Moreover, the soil-water characteristic curve (SWCC) was examined from the pressure plate. The soil structure and chemical

analysis were determined from scanning electron microscope (SEM) and EDX, respectively. Besides the undrained shear strength of compacted soil was investigated from the direct shear test. The samples to do SEM, EDX, direct shear test and modeling were prepared to compaction 90% wet side of maximum dry density by modified compaction.

(a) soil pressure transducers (b) LVDT

(c) Weight plates

Fig. 5 Apparatus

.

Three vertical loaded were examined to physical retaining wall modeling, which is 100, 200, and 400 kg.

Step I: Khon Kaen loess was compacted 90% of maximum dry density at the wet side in the tank. A soil sample was compacted in 5 layers 9 cm thickness for each layer. Then the dry density was checked by the sand cone method.

Fig. 6 This is preparation of Soil sample

Step II The speed of pneumatic was adjusted to be 1 mm./min.

Step III Two earth pressure cells, the modeling gravity retaining wall, four LDVTs were installed in the tank. The vertical loads applied at the top of the modeling. Then the test was started immediately.

Fig. 7 The Adjustment of Pneumatic.

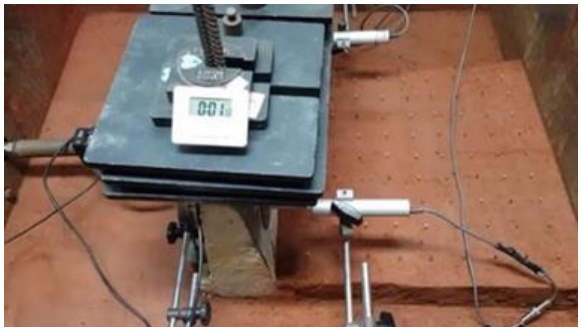

Fig. 8 Test running

RESULTS AND DISCUSSION

The sieve analysis and hydrometer analysis present that the predominant of Khon Kaen loess is sand, whereas silt and clay are the binders, as shown in Table 1. Moreover, the EDX's result, as present in Table 2 showed the high percentage of iron. Therefore, the iron oxide is also the binder. Khon Kaen loess was classified as silty sand (SM) according to [6]. The comparison between disturbed and undisturbed Khon Kan loess was shown in Fig. 9. There are various sizes of the void in both samples. But there is numerous void in an undisturbed sample rather than a disturbed sample. Besides, the structure of the undisturbed sample is flocculated, while the structure of the disturbed sample is dispersed. The test result of the soil water characteristic curve (SWCC) was shown in Fig. 10. there are two air-entry values and two residual points. The first and second air-entry values are 3 and 450 kPa, respectively. Moreover, the first and second residual degrees of saturation are 42% and 16%, respectively.

Table 1 Basic properties of Khon Kean Loess.

Properties	
Liquid limit (LL), %	16.5
Plastic limit (PL), %	NP
Plasticity index (PI), %	-
Specific gravity	2.65
Optimum moisture content (OMC), %	7.22
Maximum dry density (γ_d), t/m^3	2.12
Sand (%)	55
Silt (%)	30
Clay (%)	15
USCS classification	SM

Table 2 EDX's Result

Element	Weight%	Atomic%	
O K	60.16	59.37	SiO_2
Na K	0.10	0.10	Albite
Mg K	0.06	0.06	MgO
Al K	8.74	8.62	Al_2O_3
Si K	25.93	25.59	SiO_2
K K	0.09	0.09	MAD-10 Feldspar
Ca K	0.09	0.09	Wollastonite
Ti K	0.69	0.69	Ti
Fe K	4.15	4.09	Fe
Totals	100.00		

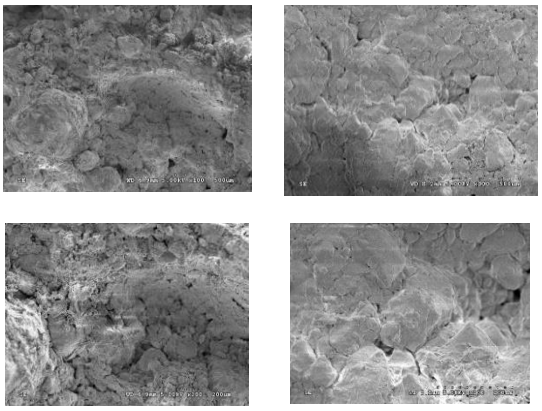

(a) Undisturbed Sample (b) Disturbed Sample

Fig. 9 Soil Structure

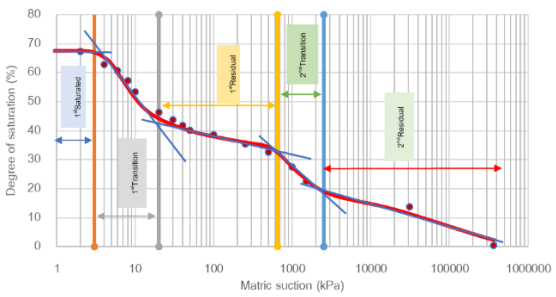

Fig. 10 The soil-water characteristic curve (SWCC)

Direct Shear Test (UU test)

According to the direct shear test as shown in Fig. 11. The total cohesion and the total friction value is 27 deg and 12 kPa, respectively.

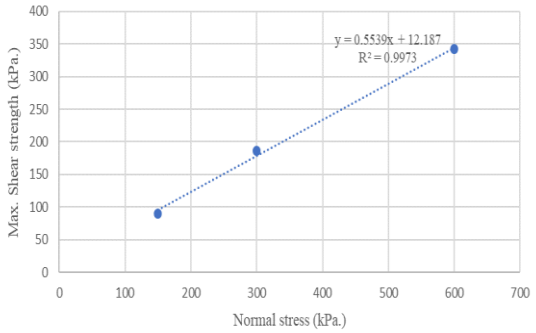

Fig. 11 This is result of direct shear.

Physical Model Test

The relationship between the different active and passive pressure (P_a-P_p) and the vertical displacement, as shown in Fig.12 showed that the retaining wall was uplift and going to overturning. The data of pressure of uplifting were provided in Table3. The retaining wall was going to overturning due to the soil in front of retaining wall cannot be moved anymore. Because of the soil reached passive pressure (the failure). The passive pressure at the uplift point, which read out from earth cell pressure, was quite constant at 2.6 kPa, as shown in Table 3. Therefore, the Rankine passive earth pressure coefficient, K_p, equal to 3.5888. Due to the soil thickness in front of the retaining wall was 7 cm, and the total density was 2.11 t/m^2. Due to the effective vertical stress was 0.72 kPa. The retaining wall was sliding due to the driving pressure (P_d) equal to the active pressure (P_a) minus passive pressure (P_p) and kinetic friction between the base of retaining wall and soil (F_k) as shown in equation (4).

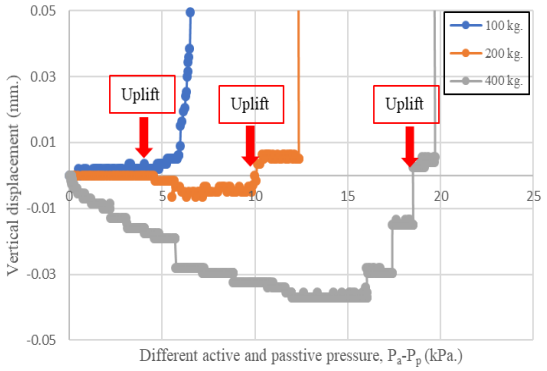

Fig. 12 The relationship between the different active and passive pressure (P_a-P_p) and the vertical displacement.

Table 3 Lateral pressure on the retaining wall at uplift point

σ_v		P_a	P_p	T	FS
kg.	kPa.	kPa.	kPa.	kPa.	
100	13.08	7.92	2.72	5.20	1.26
200	26.16	13.16	2.54	10.63	1.93
400	52.32	18.53	2.53	16.00	2.12

$$P_d = P_a - P_p - F_k \quad (4)$$

Where
P_d = the driving pressure
P_a = the acting pressure
P_p = the passing pressure
F_k = the kinetic friction between the base of retaining wall and soil

Given
T = different pressure between active and passive pressure

Therefore

$$P_d = T - F_k \quad (5)$$

$$T = P_d + F_k \quad (6)$$

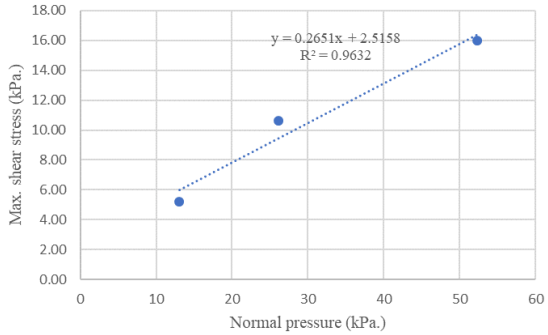

Fig. 13 The relationship between normal pressure (N) and T

The plot between the normal pressure (N) and T as shown in Fig. 13 give a good linear relationship as present in equation (7).

$$T = 2.5158 + 0.2651N \quad (7)$$

Where
N = the normal pressure

Equation (6) equal to (7) therefore

P_d = 2.5158 kPa

And
F_k = 0.2651N kPa
Where $F_k = \mu_k.N$
Hence $\mu_k = \tan(\delta'_k) = 0.2651$
Sine δ'_k = 14.85 deg.

According to the direct shear result, the friction angle (ϕ) equal to 29 deg. Therefore, the ratio between δ_k:ϕ of compacted Khon Kaen loess equal to 0.5.

The passive failure plane, as shown in Fig. 14, presents the failure angle (θ) equal to 31 deg. According to [7], the passive failure planes is (45-ϕ/2). Therefore, the friction angle (ϕ), which was back-calculate from the passive failure plane, is similar to the result of the direct shear test. Moreover, the maximum horizontal movement was 0.07 m or 15.9%strain at failure, as shown in Fig. 15.

All test series was terminated because of overturning. The lateral pressure at the failure shown in Table 4. The maximum factor safety against the overturning was 1.65. According to Table 3, the maximum factor safety against overturning at the uplift point was 2.12, which is over the specification.

Fig. 14 Passive plan failure

Fig. 15 Horizontal movement

Table 4 This is Lateral pressure on the retaining wall at failure.

	σ_v	P_a	P_p	FS
kg.	kPa.	kPa.	kPa.	
100	13.08	12.13	2.72	0.81
200	26.16	15.03	2.90	1.30
400	52.32	23.75	3.26	1.65

CONCLUSIONS

The predominant of Khon Kaen loess is sand, whereas silt, clay, and iron oxide are the binders. The structure of the undisturbed sample is flocculated, while the structure of the disturbed sample is dispersed. The total cohesion and the total friction value is 27 deg and 12 kPa, respectively. According to the physical modeling found that the ratio between δ angle and ϕ angle equal to 0.5.

ACKNOWLEDGMENTS

Acknowledgment is given to the SIRDC - Sustainable Infrastructure Research and Development Center, Khon Kaen University, for the support of this research.

REFERENCES

[1] Barden, L., McGown, A., and Collins, K. The collapse mechanism in partly saturated soil. Engineer Geology 1973 February. pp 305-317

[2] Udomchoke, V. 1991, Origin and Engineering Characteristics of the Problem Soil a in the Khorat Basin, Northeastern Thailand, Ph.D. dissertation, Asian Institute of Technology, Bangkok, Thailand.

[3] Gasaluck W., 1999., Influence of moisture content on bearing capacity of Khon Kaen loess. The 5th national convention on civil engineering, Pataya,Thailand.

[4] Muktabhant Ch., 2009., Soil Mechanics., Khon Kaen University -1st edition, Khon Kaen, Thailand.

[5] Das, B.M., 2011., Principles of Foundation Engineering – 7th editions.

[6] American Society for Testing and Materials. (D2487-98). Standard practice for classification of soils for engineering purposes (Unified Soil Classification System).

9th Int. Conf. on Geotechnique, Construction Materials and Environment, Tokyo, Japan, 20-22 November 2019, ISBN: 978-4-909106025 C3051

A STUDY OF THE TENSILE STRENGTH OF VEINS AND ITS INFLUENCE ON ROCK MASS STRENGTH

Nikhil Tukaram Urmale and John Victor Smith
School of Engineering, RMIT University, Australia

ABSTRACT

Rock mass strength models include open discontinuities but typically do not include discontinuities that have been sealed by precipitation of minerals. These veins can represent significant weaknesses in a rock mass yet are not accounted for in most rock mass models. The Warramboo magnetite deposit in South Australia is hosted by a strong gneiss rock mass with a low level of open joints. Veins are relatively abundant throughout the rock mass. The distribution of veins has been analysed from the database of core drilled at the project site. Samples of veins of various mineral types have been collected and tested for tensile strength. Sample strength was measured by direct tension in a Shimadzu 50 kN loading machine. Initial results indicate that the veins do not contribute a significant weakening effect to the rock mass. The test result showed that the veins have a significant tensile strength which varies between 3 MPa to 9 MPa. But the majority of the samples failed in rock rather than on the vein itself. The observed tensile strength values for the veins are not significantly less than the tensile strength of the host rock gneiss.

Keywords: Tensile strength, Vein, Rock mass, Gneiss

INTRODUCTION

Deformation of rock commonly creates fractures. The aperture of the fracture can be closed by the precipitation of minerals to form a vein [1]. The influence of open fractures, known as discontinuities, on rock mass strength is well known [1]. Some of the open discontinuities may actually be veins which have become open due to the weakness of the mineral fillings. However, the impact of sealed discontinuities, such as veins, on the strength of a rock mass is usually neglected.

An investigation into the significance of veins and vein-parallel open discontinuities is needed to improve methods of rock-mass strength determination. Veins are common in mineralized systems and have the portiential to create weakness in the rock mass that could affect the stability of excavated slopes and affect the selection of blasting methods. Various studies have been done on the characteristics of vein systems but their effect on the strength of rock masses has not generally been considered. This study will investigate the topic using an extensive drill hole database from the feasibility studies of a major proposed mine in South Australia.

A previous study by one of the authors investigated the role of foliation in the gneiss in forming discontinuities in the rock mass of this deposit [2]. The purpose of the present study is to investigate the potential for veins in the rock mass to represent a weakness that could affect stability of the large slopes of the proposed mine open pits (Fig. 1). For this research, rock core samples were collected from the proposed Warramboo magnetite iron ore mine on the Eyre Peninsula of South Australia. Samples containing sealed veins were tested in the RMIT University laboratory to determine the tensile strength of rock samples with an intact vein. This was done by performing a direct tensile test on all the samples by keeping the orientation of the vein at 90° following methods developed in previous studies [3].

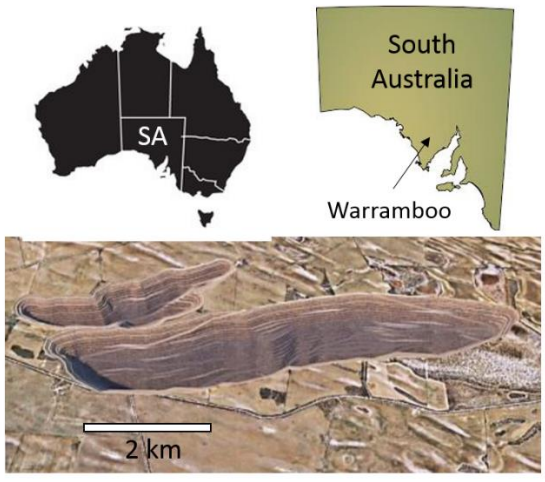

Fig. 1 Location of the Warramboo Iron Project and proposed final pits (Iron Road Limited).

VEINS IN ROCK MASS

The influence of veins and vein-parallel open discontinuities on rock mass strength has been

generally overlooked while significance is predominantly given to open discontinuities such as joints and faults [4]. Most well-known rock mass classification schemes do not recognize veins and vein-parallel open discontinuities as important characteristics influencing the mechanical behavior of a rock mass. The Rock Mass Rating (RMR) system only briefly considers the surface coating of open discontinuities that may be related to the mineralogy of the veins [5]. Similarly, in the GSI and Q rock mass classification systems, only minor attention is given to the texture of vein infilling material and surface characteristics of the discontinuity [6,7]. Although these rock mass classification schemes do consider some aspects of veins in the form of the surface characteristics of open discontinuities, the tensile strength of the mineral infilling in sealed veins is not considered.

VEINS

Veins have been studied in detail for their geological origins and implications for fluid flow through fractured rock. For example, synkinematic quartz veins formed from dissolved minerals transported to growth sites in fractures by the transient pathway created by intragranular, trans-granular and intergranular dilation [8]. Many different vein mineralogies occur and each vein system differs in its formation and therefore each vein may have different mechanical behaviour.

Many experiments have been carried out on veins using techniques such as X-ray diffraction to identify vein minerals and investigate the mechanical behaviour of veins [9]. In another study, triaxial compression stress result showed that an intact veined rock sample behaved differently from the intact rock without veins [4]. It was also observed that the infilling material may have intermediate or even high tensile strength, sometimes higher than the parent rock [10]. If the strength of infilling material is greater than parent rock, then it does not pose a great threat to the stability but when the infill is weaker then it has potential to be a weakness in the rock structure.

Studies have been carried out to find out the relationship between the rock strength anisotropy and vein emplacement. The results showed that the rock mass has greater rock strength in the direction perpendicular to weaknesses such as foliation than parallel to it [11]. The most important study done very recently about veins and vein-parallel open discontinuities significance in the rock mass stability [12]. That study investigated vein characteristics, discrete vein networks, vein thickness, orientation, and mineralogy prior to the triaxial compression testing. It was observed that the vein orientation with respect to the direction of loading was the most important factor for a vein to take part in the fracturing of the rock specimen [12] That study did not explain the characteristics of different vein types and was unable to demonstrate the relation between vein mineralogy, vein thickness, and strength of rock specimens.

Numerous studies have been done to determine the significance of joints and other open discontinuities for rock mass strength but very less research is done to determine the role of veins and vein-parallel open discontinuities in rock mass strength. The role played by veins and vein-parallel open discontinuities in slope stability and underground excavation require further investigation. For this, the tensile strength of veins may play an important role in the strength of the rock mass and, if the tensile strength of the veins is low, may downgrade the overall strength of the rock mass.

VEINS IN THE WARRAMBOO DEPOSIT

In the preliminary stage of this research, an extensive drill hole database from the feasibility studies of a major proposed iron ore mine in South Australia was analyzed. In total, a database of 63 drill holes was studied. Each drill hole ranged from 180m to 700m in length. A detailed study of the core log record database was made. All the discontinuities were recorded alongside comparing them with the photographs of all the core boxes.

Also, a detailed study was done on veins, considering its mineral classification, thickness, and their characteristics whether they are open or sealed. It was observed that there are 21379 discontinuities present in the complete database of which 4307 are veins, which comprises of more than 20% of all the discontinuities observed (Fig. 2).

Chlorite, carbonate, sericite, and quartz were the major infill minerals observed in the veins at 43%, 30%, 12%, and 5%, respectively. Epidote, gypsum, pyrite, hematite, clay, feldspar and limonite were the other minerals observed.

Carbonate and chlorite are most abundant veins and more than 80% of these veins were recorded as open, whereas quartz infill had less than 17% open (Table 1). The open conditions of the rock mass at vein may act as an indicator of strength for the rock mass. So, from the data, it was observed that veins

may represent additional weakness to rock structure stability and need to be considered while determining the stability of rock structure.

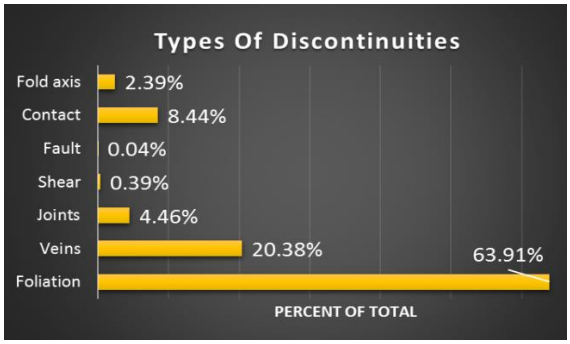

Fig. 2 Relative proportions of discontinuity types in the rock mass at Warramboo Iron Project.

Table 1 Vein mineralogy types and proportions.

Minerals	Total mineral veins	Mineral veins (%)	Open veins (%)	Sealed veins (%)
carbonate	1310	30.4%	81.4%	18.6%
chlorite	1851	43.0%	88.9%	11.1%
sericite	504	11.7%	82.1%	17.9%
quartz	195	4.5%	16.9%	83.1%
clay	148	3.4%	98.0%	2.0%
epidote	98	2.3%	30.6%	69.4%
gypsum	117	2.7%	76.9%	23.1%
pyrite	53	1.2%	56.6%	43.4%
hematite	22	0.51%	77.3%	22.7%
feldspar	3	0.07%	0.0%	100.0%
limonite	6	0.14%	83.3%	16.7%

METHODOLOGY

Sample Selection

The specimens for the research were collected from the drill core repository of the Warramboo iron ore project on Eyre Peninsula South Australia. The deposit is hosted by high-grade metamorphic rock, mainly gneiss [2]. Gneiss is a coarse-grained rock comprising mainly quartz and feldspar and generally of high strength.

The selection of the specimens was done from the extensive drill hole collection from the feasibility study of the proposed mine. The total length of core studied for the research is approximately equal to 25.6 km. The specimens with intact veins were selected after comparing the database and the photographs of the core boxes.

Sample Preparation

Specimens for the tensile test were prepared from the 60mm diameter original core specimens in the following steps:

Drilling

30mm diameter pedestal-mounted diamond drill was used to drill the specimen from the main sample in such a way that the vein plane is perpendicular to the direction of the drilling (Fig. 3A). The tensile strength of a discontinuity tends to decrease with the increase in the relative orientation of the discontinuity relative to the direction of the load applied [3].

Cutting

The cylindrical specimens were made flat at each end using a rock cutting diamond blade saw. The specimens were then kept in the oven for 24 hours at 100°C to dry.

Sandblasting

The end caps were prepared from 4 cm wide T-Bar. The long bar was cut at the 4 cm interval and then the cementing surface was sandblasted to remove any oil or grease present on the surface. This process is important for the strong adhesion of the specimen with the end caps.

Cementing

The specimens were cemented to the end caps using the Araldite 420 adhesive. The specimens were clamped on both the ends and kept for curing for 1 week after the application of the adhesive.

Although samples of a range of sizes were produced, a previous study of direct tensile testing methods found that there was no significant difference in the tensile strength of samples with different sizes [13].

Test Method

To gain a deeper insight into the vein strength and its influence on the overall rock strength, it was important to know the strength and behavior of the

vein in tension. In order to find the tensile strength of veins the direct tensile strength testing method was selected as it has the ability to provide the most valid results [14].

In direct tensile testing, the failure occurs in tension at the weakest link of the rock sample and is not affected by any other factors if the test is done properly. Whereas, for indirect tensile tests such as the Brazilian test, the compression force must overcome the frictional forces at grain boundaries in order to initiate tensile force. Due to this reason, the Brazilian test tends to yield higher strength values than the direct tensile strength [15].

Specimens were prepared from 60mm diameter core specimen, so the new specimen size is smaller than the original specimen, which makes it difficult to perform Brazilian or the point load test on the specimen.

Laboratory investigation of rock sample containing intact veins has been carried out using SHIMADZU universal testing equipment, which has the maximum capacity of 50 kN and was used for the tensile testing of 9 specimens.

Some specimens were loaded at the rate of 1 mm/min and others were loaded at 0.05mm/min rate. The specimens were tested with different arrangements at various stages of the research. Following are the ways in which specimens were tested:

Direct clamping

Only one sample was tested in this arrangement (Fig. 3B). The specimen was not perfect cylinder, the ends of the sample were not parallel because of which there was stress concentration at the edges of the specimen and the sample failed at one of the edges. So, in order to solve the issue of stress concentration a small chain system was used.

Small chain assembly

Small chain arrangement used 2 D-shackles on both the ends of the sample caps which were clamped to the testing machine (Fig. 3C). With this arrangement, two samples failed on the vein but the other six samples failed in rock, which may have been partly due to stress concentrations [16].

Long chain assembly

In order to stress alignment, samples which had failed in rock were re-glued and again tested with long chain arrangement (Fig. 3D). This arrangement is intended to ensure the center of mass of the specimen is in line with the tension of the testing machine.

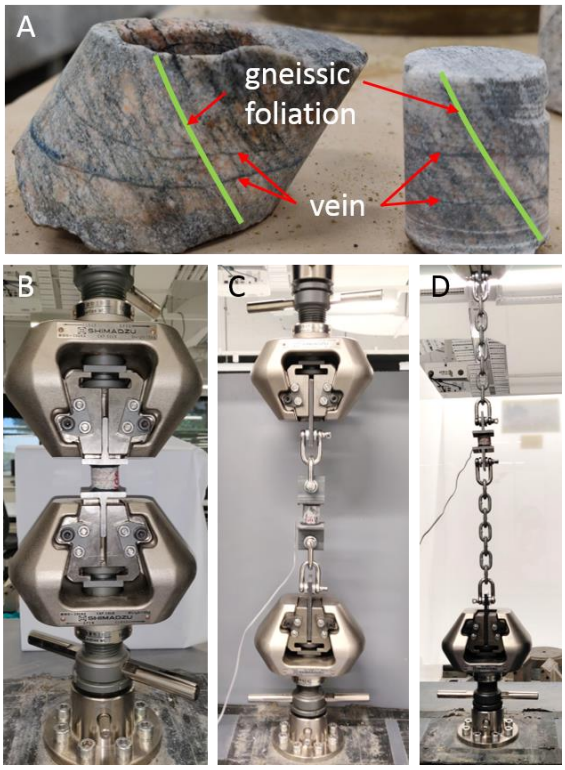

Fig. 3 A) Core sample of foliated gneiss which has been re-cored perpendicular to veins. Method of direct tensile strength experiment (Shimadzu 50 kN). B) Direct clamping, C) short chain assembly and D) long chain assembly.

Trimming of samples in dog bone shape

The cylindrical specimen can fail near the ends due to stress concentration. Fairhurst [17] observed that the stress concentration can be reduced if the end caps have sample dimensions that of the specimen. But due to the very small size of the present samples with a radius of around 25mm, it was very difficult to prepare a cap of at a smaller dimension

It was observed that the dog bone shape of sample reduces the stress concentration at the edges so three samples were trimmed around the vein to form a dog bone shape and tested with the previous long chain arrangement.

RESULTS

Most samples failed in rock at the end of the sample rather than in the vein (Fig. 4). These failures were observed to have relatively high tensile strength value. The highest tensile strength was observed was 14.25 MPa. Other samples failed between 3 MPa to 10 MPa range. Considering the magnitude of force at which the samples failed, the veins are inferred to have significant strength.

Even in the four samples which failed on the vein, the failure was observed at reasonably high tensile stress. These veins have significant tensile strength ranging from 3 to 9 MPa. They are not very weak and have considerable strength in tension.

Table 2 Direct tensile test results.

Sample ID	Vein Mineral	Test Number	Set-up*	Tensile strength (MPa)	R/V *
4	Sericite	1	S	7.07	R
		2	L	6.22	R
19B	Carbonate	1	S	14.25	R
		2	L	8.96	V
92	Carbonate	1	S	9.03	R
		2	L	3.45	R
106A	Epidote	1	S	9.62	R
106B-I	Chlorite	1	D	7.69	R
		2	L	9.00	R
106B-II	Chlorite	1	S	7.12	R
		2	L	7.29	R
107	Chlorite	1	S	3.12	V
110-I	Chlorite	1	S	4.52	V
110-II	Hematite	1	S	7.66	R
		2	L	5.04	V

* D=direct clamping, S=short chain assembly, L=long chain assembly. R=failure in rock, V= failure on vein.

DISCUSSION

Typically, the tensile strength of rock mass can be estimated as about 1/10th it's UCS value [18]. The Warramboo gneisses have been reported to have UCS strength ranging from 56 to 187 MPa [2]. This would correspond approximately to a range of 6 to 19 MPa of tensile strength. This is similar to the range of tensile strength for gneiss given in reference sources as 5 to 20 MPa [19]. The tensile strength for all the specimens tested falls close to this range.

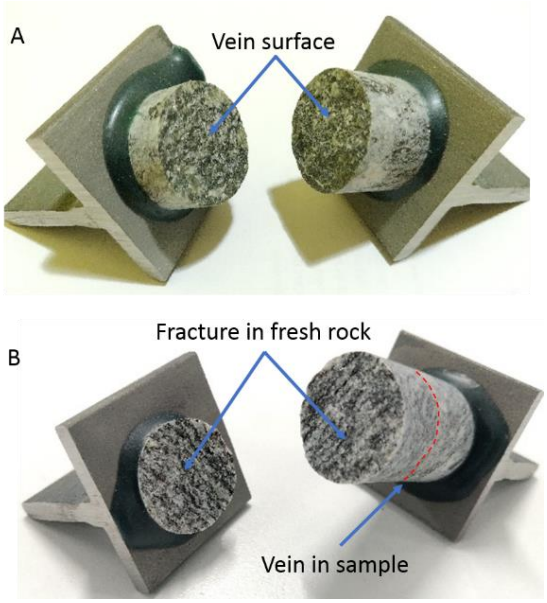

Fig. 4 Completed direct tensile tests. A) Failure on the vein. B) Failure in the rock.

In cases where the specimen failed in rock rather than on the vein the specimens were re-tested with a long chain assembly. In two cases this led to specimen failure on the vein which is attributed to the benefit of improved force alignment in the long chain assembly.

The eleven samples that failed in rock rather than on the vein had an average tensile strength of 8 MPa. This value is at the low end of the expected range of tensile strength of gneiss. The four samples that failed on the vein had an average tensile strength of 5 MPa. This value is at the low end of the range of tensile strength expected for gneiss. So, the vein samples behaved similarly to the parent rock in tension.

CONCLUSIONS

In this research, a study of core samples obtained from a proposed iron ore mine in Eyre Peninsula South Australia was conducted. For this research, all the samples tested for tensile strength have been gneisses with a range of vein mineral fillings.

From the laboratory testing, it was observed that the veins have shown significant tensile strength. The tensile strength of veins observed from the tests is generally comparable to the typical tensile strength of a gneiss. Also, the samples which failed in rock rather than on the veins imply that the veins were not excessively weak in those cases. Failure of the

specimens in rock at the ends of the samples may be due to stress concentrations which will be investigated in future work. The vein tensile strength measurements and the tendency of some samples to fail on rock rather than on the vein indicates that the veins are not highly significant weaknesses in the rock.

ACKNOWLEDGMENTS

The assistance of Mr. Larry Ingle, General Manager of the Iron Road Limited is appreciated for data access, site visit support and access to samples.

REFERENCES

[1] Priest, S. D., Fluid flow in discontinuities, Discontinuity Analysis for Rock Engineering, Dordrecht, Springer Netherlands, 1993, pp. 340-381.

[2] Smith, J. V., Rock structure characterization of a magnetite gneiss with foliation-parallel discontinuities for footwall slope design, International Journal of Rock Mechanics and Mining Sciences, Vol. 108, 2018, pp.105-117.

[3] Dan, D. Q., Konietzky, H. and Herbst, M., Brazilian tensile strength tests on some anisotropic rocks, International Journal of Rock Mechanics and Mining Sciences, Vol. 58, 2013, pp. 1-7.

[4] Turichshev A. and Hadjigeorgiou J., Quantifying the effects of vein mineralogy, thickness, and orientation on the strength of intact veined rock, Engineering Geology, Vol. 226, 2017, pp. 199-207.

[5] Bieniawski Z. T., Rock mass classification in rock engineering applications, Procedings of the Symposium on Exploration for Rock Engineering. Balkema, 1976, pp. 97-106.

[6] Barton N., Lien R. and Lunde J., Engineering classification of rock masses for the design of tunnel support. Journal of the International Society of Rock Mechanics / Felsmechanik / Mécanique des roches Vol. 6, Issue 4, 1976, pp. 189-236.

[7] Hoek E. and Brown E.T., Practical estimates of rock mass strength, International Journal of Rock Mechanics and Mining Sciences, Vol. 34, Issue 8, 1997, pp. 1165-1186.

[8] Smith J. V., Textures recording transient porosity in synkinematic quartz veins, South Coast, New South Wales, Australia. Journal of Structural Geology, Vol. 27, Issue 2, 2005, pp. 357-370.

[9] Sekine K. and Hayashi K., Residual stress measurements on a quartz vein: A constraint on paleostress magnitude, Journal of Geophysical Research, Solid Earth (B1), 2009, pp. 114.

[10] Shang J., Hencher S.R. and West L.J., Tensile strength of geological discontinuities including incipient bedding, rock joints and mineral veins. Rock Mechanics and Rock Engineering, Vol. 49, Issue 11, 2016, pp.4213-4225.

[11] Vishnu C.S., Lahiri S. and Mamtani M.A., The relationship between magnetic anisotropy, rock-strength anisotropy and vein emplacement in gold-bearing metabasalts of Gadag (South India). Tectonophysics, Vol. 722, 2017, pp. 286-298.

[12] Turichshev, A. and Hadjigeorgiou J., Triaxial compression experiments on intact veined andesite, International Journal of Rock Mechanics and Mining Sciences, Vol. 86, 2016, pp. 179-193.

[13] Rund M., Procházka R., Konopík P., Džugan J. and Folgar H., Investigation of Sample-size Influence on Tensile Test Results at Different Strain Rates, Procedia Engineering, Vol. 114(C), 2015, pp. 410-415.

[14] Hoek E., Fracture of anisotropic rock, Journal of the South African Institute of Mining and Metallurgy, Vol. 64, Issue 10, 1964, pp. 501–518.

[15] Gorski B., Conlon B. and Ljunggren B., Determination of the direct and indirect tensile strength on cores from borehole KFM01D. Svensk Kärnbränsle-hantering AB Report, 2007.

[16] Feng, X.-T., Rock Mechanics and Engineering Volume 2: Laboratory and Field Testing, CRC Press. 2017.

[17] Fairhurst C., Laboratory measurement of some physical properties of rock. The 4th US symposium on rock mechanics (USRMS), American Rock Mechanics Association. 1961.

[18] Perras M. and M. Diederichs M., A Review of the Tensile Strength of Rock: Concepts and Testing." An International Journal, Vol. 32, Issue 2, 2014, pp. 525-546.

[19] MatWeb Mechanical characteristics of Gneiss. from http://www.matweb.com/search/data-sheet.aspx?MatGUID=e936e661999e4f11a3ffab78355dec78. Accessed 10 June 2019.

9th Int. Conf. on Geotechnique, Construction Materials and Environment, Tokyo, Japan, 20-22 November 2019, ISBN: 978-4-909106025 C3051

BEARING CAPACITY ANALYSIS OF EMBEDDED SPREAD FOUNDATION USING RIGID PLASTIC FINITE ELEMENT ANALYSIS WITH NONLINEAR CONSTITUTIVE EQUATION

Kazuhiro KANEDA[1], Masamichi AOKI[1]
[1]Reseacher, Takenaka Corporation, Japan

ABSTRACT

The Architectural Institute of Japan's guidelines for building foundation design provide a formula for calculating the ultimate vertical bearing capacity. With a wider footing, the ultimate bearing capacity becomes smaller than that obtained using Terzaghi's formula for sandy grounds owing to the decrease in the inertial friction angle or progressive failure. Furthermore, the ultimate bearing capacity of embedded and inclined loads have not been clarified. In this study, the rigid plastic finite element method is used to calculate the ultimate bearing capacity of a large foundation against inclined and embedded loads.

Keywords: Embedded spread foundation, Ultimate bearing capacity, Rigid plastic finite element method, Inclined load

INTRODUCTION

The calculation of the ultimate bearing capacity of soil is important when designing a building [1]. The formula for calculating the ultimate bearing capacity of building foundations is specified in the guideline published by the Architectural Institute of Japan (AIJ) [2]. These formulae are based on both experimental and theoretical considerations of risk avoidance. Researchers have applied the rigid plastic finite element method (RPFEM) to this problem. For example, the bearing capacity under squeeze breakdown of clayey soils was last discussed at Geomate2017 [3]. Further, the bearing capacity of footing in a two-layered clayey soil system was discussed at Geomate2018 [4]. The inclined bearing capacity was also investigated in some specific cases.

The calculation for the bearing capacity of a spread foundation uses the coefficients of bearing capacity N_c, N_γ, and N_q. In equation (1), which is proposed by the AIJ, the size effect is considered using the parameter η that reflects the effect of the constraint stress of the inertial friction angle for only N_γ and not for N_c and N_q.

$$q_u = i_c \alpha c N_c + i_\gamma \beta \gamma_1 B \eta N_\gamma + i_q \gamma_2 D_f N_q \quad (1)$$

where q_u (kN/m^2) is the beating capacity; $\eta = (B/B_0)^{-1/3}$, where B is the foundation width and B_0 = 1 m; $i_c = i_q = (1\text{-}\theta/90)^2$; $i_\gamma = (1\text{-}\theta/\varphi)^2$; θ = tan(H/V) is the inclined angle (°), where H and V are respectively the horizontal and vertical load; D_f (m) is the embedded height; and γ_1 and γ_2 (kN/m^3) are unit weights.

Furthermore complicated loads that could occur during an earthquake (e.g., vertical or horizontal moment and eccentric load) should be considered when calculating the bearing capacity. In the present study, RPFEM is used to calculate the ultimate bearing capacity of a large foundation against embedded and inclined loads using a high-order function.

ANALYSIS CONDITIONS

In this study, the effect of an embedded load is assumed for the overload of surrounding soils. Figure 1 shows the analysis mesh for B = 1 m. The mesh size is changed according to the foundation width. For the plane strain condition, a rigid footing is modeled. A increasing vertical load was applied to the footing to calculate a ultimate vertical bearing capacity. The soil strength is φ = 30° and 40°, soil density is γ = 18 kN/m^3, footing strength is c = 100 MPa, and embedded height is D_f = 1–5 m. Table 1 lists the analysis conditions. A high-order function is used in the soil constitutive model [5] to evaluate φ reduction under high constraint stress as follows.

$$f(\boldsymbol{\sigma}) = aI_1 + (J_2)^n - b = 0 \quad (2)$$

where I_1 and I_2 are stress invariants and a and n are material parameters.

In a previous study, the material parameters for φ = 30° and 40° were respectively a = 0.175, b = 1.5, and n = 0.52 and a = 0.237, b = 1.5, and n = 0.52 [6]. These values are determined to fit the bearing capacity of various foundation widths calculated using the AIJ's formula. The bearing capacity of an inclined load (θ = tan^{-1}(H/V), where H and V are respectively the horizontal and vertical load) was also simulated.

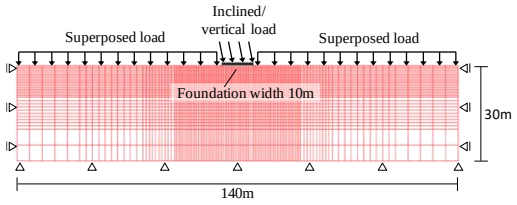

Fig. 1 Analysis model (B = 10 m).

Table 1 Analysis conditions

Foundation width (m)	1, 3, 10, 30
Embedded length (m)	0, 1, 2, 5
Inclined load (°)	0, 10, 20

ANALYSIS RESULTS

Figure 2 shows the relationship between the bearing capacity value and the foundation width for θ = 0. The figure indicates that equation (1) can be well reproduced by RPFEM using a higher-order function between 1 and 30 m for the foundation width. Figure 3 shows the shear strain contours at failure for B = 10 m, D_f = (a) 0 m and (b) 5 m. When the surcharge load on the top of the soil surrounding the footing was applied as the embedded load, the shear strain at the footing edge at failure with the embedded load is smaller than that in the case without an embedded load and the distribution area of slip failure tends to become slightly larger. The effect of N_q was discussed using q_uD_f (results with embedded load) - q_{u0} (results for D_f = 0). Figure 4 shows the relationship between q_uD_f - q_{u0} and embedded length for both φ = 30° and 40° using the AIJ's and the Japan Road Association's guidelines [7]. The effect of increased bearing capacity of D_f is smaller than that in the case of the AIJ's guideline. However, the effect of increased bearing capacity of D_f is almost the same in the case of the Japan Road Association's guideline for both φ = 30° and 40°. The modification coefficient S_q = $(q/q_0)^{-1/3}$ = $(\gamma D_f/10)^{-1/3}$ for N_q was adopted in the Japan Road Association's guideline. Figure 4 shows the relationship between H/V_m and V/V_m (where V_m is the ultimate vertical bearing capacity for H = M = 0) for both φ = 30° and 40° for the AIJ's guideline and Nova's equation with M = 0, μ = 0.5, and β = 1.0 (3) [8].

$$\left(\frac{H}{\mu Vm}\right)^2+\left(\frac{M/B}{\phi Vm}\right)^2=\left(\frac{V}{Vm}\right)^2\left(1-\frac{V}{Vm}\right)^{2\beta} \quad (3)$$

$$\left(\frac{H}{0.5Vm}\right)=\left(\frac{V}{Vm}\right)\left(1-\frac{V}{Vm}\right) \quad (4)$$

i_q obtained using the AIJ's guideline (black line) is much larger than that obtained in the RPFEM results. When the foundation width B is small and D_f is large, the results approached those obtained using Nova's equation.

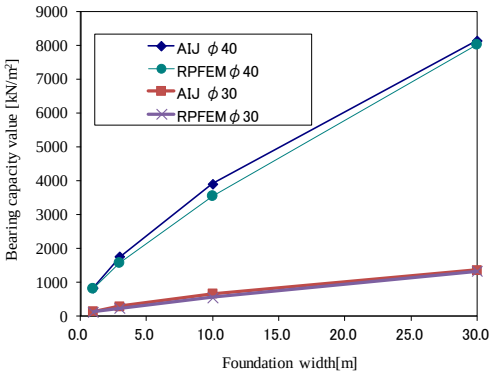

Fig. 2 Relationship between bearing capacity value and foundation width.

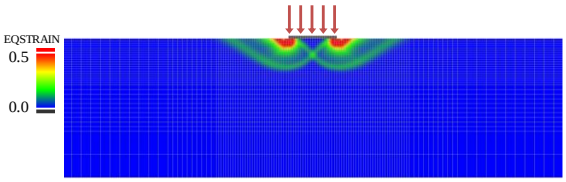

(a) φ = 30°, B = 10 m, and D_f = 0 m

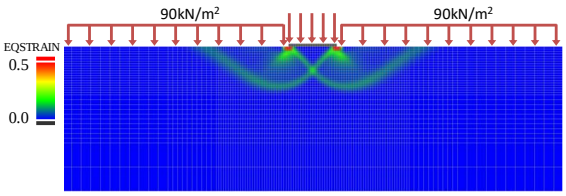

(b) φ = 30°, B = 10 m, and D_f = 5 m

Fig. 3 Shear strain contours at failure.

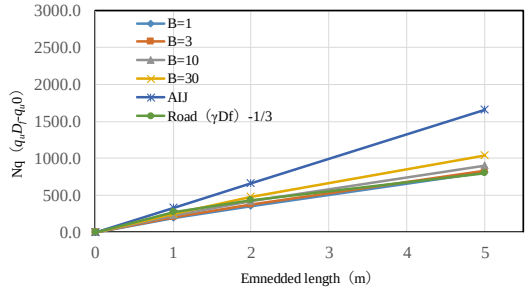

(a) φ = 30°

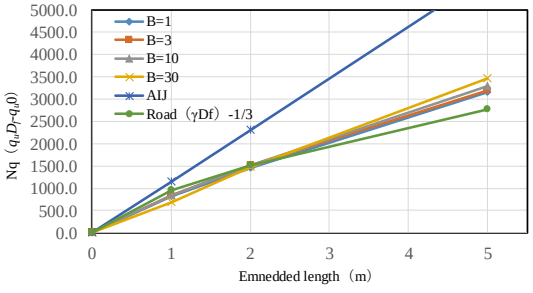

(b) φ = 40°

Fig. 4 Relationship between N_q and embedded length.

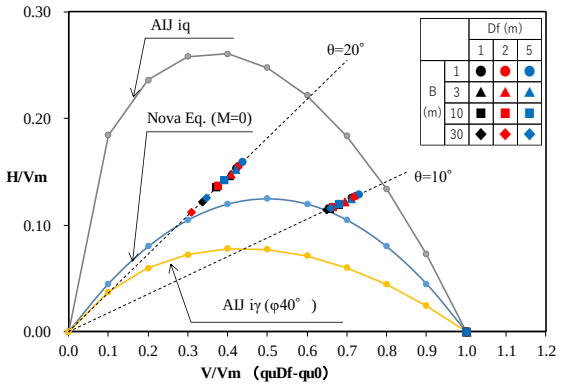

(a) φ = 30°

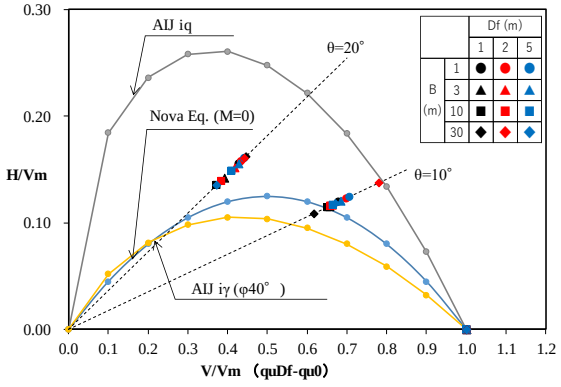

(b) φ = 40°

Fig. 5 Relationship between H/V_m and V/V_m.

REMARKS

Numerical simulations of the vertical and inclined bearing capacity of an embedded footing were conducted using RPFEM considering the size effect. When using a high-order function for the size effect, the obtained vertical bearing capacity is smaller than that obtained using the Drucker Prager model with increasing foundation width. Although the size effect for an embedded foundation is not considered in the current AIJ guideline, the results obtained in this study clearly indicate that the size effect should be considered.

REFERENCES

[1] Terzaghi, K. and Peck, R.B.: Soil Mechanics in Engineering Practice, John Wiley & Sons, pp. 472-569, 1967.

[2] Architectural Institute of Japan, AIJ (1988, 20011), Recommendations for design of building foundation, pp. 105-111, 2001. (in Japanese)

[3] Kaneda, K., Aoki, M., Tanikawa, T. and Ohtsuka, S.: Ultimate vertical bearing capacity of clayey footing under squeeze breakdown using rigid-plastic finite element method, 7th International Conference on Geotechnique, Construction Materials and Environment, Mie, Japan, Nov. 21-24, 2017, ISBN: 978-4-9905958-8-3 C3051.

[4] Kaneda, K., Aoki, M. and Ohtsuka, S.: Ultimate bearing capacity of footing of two layered clayey soil system by rigid-plastic finite element method, 8th International Conference on Geotechnique, Construction Materials and Environment, Kuala Lumpur, Malaysia, Nov. 20-22, 2018, ISBN: 978-4-909106001 C3051.

[5] Hoshina, T., Ohtsuka, S. and Isobe, K., Ultimate bearing capacity of ground by rigid plastic finite element method taking account of stress dependent non-linear strength property, Journal of Applied Mechanics, Vol. 6, pp. 191-200, 2011.

[6] Kaneda, K. and Aoki, M.: Study of vertical bearing capacity of spread foundation using rigid plastic FEM (part 1 and 2), Summaries of technical papers of annual meeting in Architectural Institute of Japan, pp. 601-604, 2016. (in Japanese)

[7] Japan Road Association: Specifications for highway bridged (Part IV Substructures), pp. 204-207, 2017.

[8] Nova, R. and Montrasio, L.: Settlement of shallow foundations on sand, Geotechnique, Vol. 41, No. 2, pp. 243-256, 1991.

9thInt. Conf. onGeotechnique, Construction Materials andEnvironment,
Tokyo, Japan,20-22 November 2019, ISBN: 978-4-909106025C3051

THE EFFECT OF UPWARD FLOW OF WATER TO TILT AND SETTLEMENT OF SHALLOW FOUNDATION

Rina Yuliet[1], Fauzan[2*], Abdul Hakam[3] and Mas Mera[4]
[1]Doctoral Program, Department of Civil Engineering, Engineering Faculty, Andalas University, Indonesia;
[1,2,3,4]Departmen of Civil Engineering, Engineering Faculty, Andalas University, Indonesia

ABSTRACT

Large soil deformation can occurs allowing the structure to settle and tilt when the soil supporting a building or other structures liquefies and loses strength. The presence of excess pore water pressure below ground surface indicates that upward flow is taking place and liquefaction occurs. Dissipation of excess pore water pressure will be accompanied by densification of the soil and settlement of the surface. Liquefaction first developed in a sand layer several meters below ground and then propagated upward flow water through overlaying sand layer. In this paper, the effect of upward flow of water will be discussed based on laboratory experiment results. The soil samples used are varies from coarse sands, medium sands and fine sands according to United Soil Classification System. The results of study show that the size of sand particles greatly affects the stability of the foundation due to upwards flow of water. The shallow foundations on fine sand are more susceptible to settlement and tilt compared to foundations on coarse sand at the same seepage velocity.

Keywords: Upward flow, Tilt, Settlement, Shallow foundation

INTRODUCTION

Upward flow of water is formed when excess pore water pressure develops at some depth. If the upward gradient is large enough, flowing water will lift up soil particles, with homogeneous soil. This can produce extensive quicksand conditions. However, it is likely that the flow will break through to the surface in places where the top layer is very thin or where there are cracks or other weaknesses in superficial soil. Soil particles are brought up with water in these locations and will be left on the surface when the sand boils. Sand boils indicates that liquefaction has occurred.

The liquefaction in Padang city due to the last 7.6 SR earthquakes of 30 September 2009 was identified by numerous sand boils [1] and [2]. Based on field observations and laboratory testing conducted on soil samples in Padang city is found that the fine sand grains of the sites are more than 65%, where this types of soils susceptible to liquefaction criteria [3]. One of the studies conducted to evaluate the potential of liquefaction in Padang city was carried out at the Nurul Haq Shelter. Based on N-SPT data, the soil condition at the Nurul Haq Shelter between the depths of 11.55 m and 29.55 m has a high potential of liquefaction [4].

When soil that supports buildings or other structures liquefies and loses strength, large soil deformations can occur, allowing the structure to settle and tilt (Fig. 1).

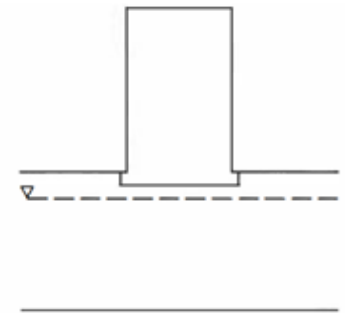

a. Without upward flow of water

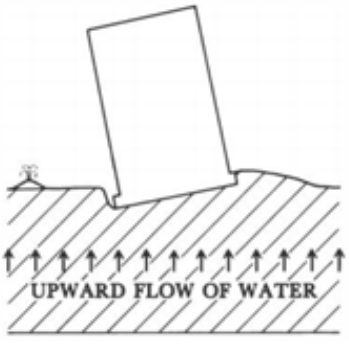

b. Upward flow of water

Fig. 1 Tilt of building with shallow foundation (Youd, 1984b in [7])

Based on the available geotechnical data and information from the site observations following the 2009 Padang earthquake, the ground settlement and sand boiling generally occurred in the populated areas up to 5 km from coastal line, with a significant damage to the city infrastructures. Many buildings, located near the river front experienced foundation movement due to ground settlement [3]. For this reasons of sand soil near the beach and on the riverbank of the Padang city area need to be examined from the effect of upward flow.

The objective of this investigation is to study the effect of the particle size distribution and dry density on the critical hydraulic gradient due to upward flow are then explained the effect on tilting and settlement of shallow foundation. It is known that have different sizes, and these characteristics also have a significant effect on its engineering behavior.

LITERATURE REVIEW

The key parameters affecting liquefaction induced settlement and tilting of shallow foundation, namely (a) increase contact pressure, decreasing ground water table depth and thickness of the non liquefied; (b) increase eccentric mass and distance ratio due to the tilt angel of the building; and (c) the safety factors against vertical load and dynamic overturning moment [6].

According to previous studies, there are three variables that cause strength reduction of Non Cohesive soil, namely the fine content, relative density of the soil and hydraulic gradient on the soil sample. Soil with a fine fraction and coarse fraction are vulnerable to increase in hydraulic conductivity that resulting decrease in the soil strength from its initial value [5]. Non Cohesive soil and relatively permeable soil overlaying the liquefied material causes a general settlement of the ground, with uniformity of the settlement depending on the degree of homogeneity of the material [7].

If water is seeping, the effective stress at any point in a soil mass will differ from that in static case. The effective stress will decrease due to upward flow of water. The effective stress at a point located at a depth z measured from the surface of a soil layer is reduced by an amount $iz\gamma_w$ because of upward flow of water. If the rate of seepage and thereby the hydraulic gradient gradually are increase, a limiting condition will be reached, at the point the effective stress will be zero. Where critical hydraulic gradient for zero effective stress. Under such situation, soil stability is lost. This situation is referred to as boiling or a quick condition.

RESEARCH MEHODOLOGY

The research was carried out with a series of simple model test at the Soil Mechanics Laboratory, Department of Civil Engineering Andalas University of Padang. Soil used for the test was collected in Muaro Baru area is located close to the coastline of Padang city (Fig. 2), and in riverbank area of Gurun Laweh Naggalo with a distance of ± 5 km towards the coastline of Padang city (Fig. 3). Soil sample used in this investigation is a disturbed sample, taken at a depth 30 cm from soil surface in Muaro Baru area and on the riverbank of the Gurun Laweh Nanggalo area.

The sieve analysis test was carried out in both locations of soil sampling. In this study a Unified Soil Classification System (USCS) used are to determine group symbol and group name. The sample of sand soil used was soil fraction or component for sand according Table 1. The dry unit weights test of granular soil also carried out for each soil fraction according Unified Soil Classification System (USCS).

Fig. 2 Location of soil sampling in the Muaro Baru area of Padang city

Fig. 3 Location of soil sampling in the Gurun Laweh Naggalo area of Padang city

Table 1 Soil fraction according Unified Soil Classification System (USCS)

Soil Fraction	Size range
Coarse Sand (CS)	No. 4 (4.75 mm) to No. 10 (2 mm)
Medium Sand (MS)	No. 10 (2 mm) to No. 40 (0.425 mm)
Fine Sand (FS)	No. 40 (0.425 mm) to No. 200 (0.075 mm)

Schematic diagram of experiment system can be seen in Fig 4. The experiment do not attempt to simulate an earthquake but to examine the effect of upward flow to settlement. All dimensions in millimeters and small prototypes.

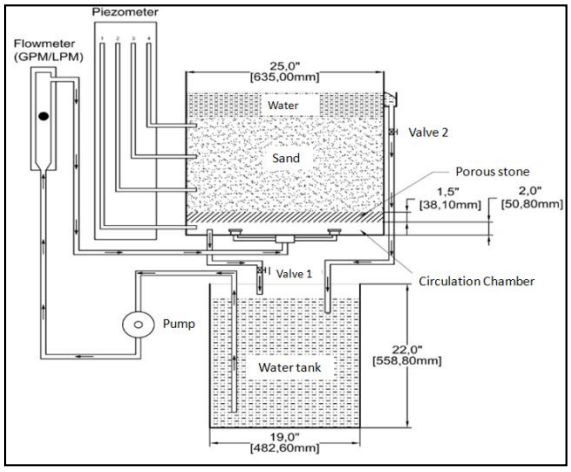

Fig. 4 Schematic diagram of experiment system

RESULT AND DISCUSSION

The grain size characteristics of a soil are given on the Table 2 and the grain-size distribution curve is show in Fig. 5.

Table 2 Sieve analysis

Sieve size	Sieve opening	% Finer			
		Original sand MB	Oroginal sand GLN	FS-MB	FS-GLN
	10	100	100	100	100
4	4.75	100	100	100	100
10	2	100	80.5	100	100
20	0.841	99	46.3	95.9	43.1
40	0.42	95.8	28.4	0	0
100	0.149	5.1	4	0	0
200	0.075	1.4	2.9	0	0

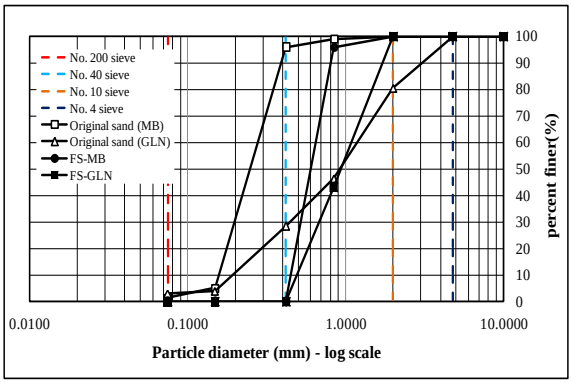

Fig. 5 Grain size distribution of sands in Muaro Baru beach and sands in riverbank area of the Gurun Laweh Naggalo.

A particle-size distribution curve can be used to determine the parameters following.

The coefficient of uniformity (C_u) is

$$C_u = \frac{D_{60}}{D_{10}} \quad (1)$$

The coefficient of gradation (C_c) is

$$C_c = \frac{D_{30}^2}{D_{60} \times D_{10}} \quad (2)$$

Where

D_{10} = Grain diameter (in mm) corresponding to 10% passing
D_{60} = Grain diameter (in mm) corresponding to 60% passing.
D_{30} = Grain diameter (in mm) corresponding to 30% passing.

Based on results of the particle-size analysis then the soil in Muaro Baru and Gurun Laweh Naggalo can be classified as on the Table 3 below :

Table 3 Classify the soil by USCS

Parameters	Muaro Baru (MB)	Gurun Laweh Naggalo (GLN)
% passing No. 200 sieve	1.4	2.9
% retained on No. 4 sieve	0	0
D_{10} (mm)	0.16	0.18
D_{30} (mm)	0.19	0.44
D_{60} (mm)	0.27	1.3
C_u	1.7	7.2
C_c	0.84	0.82
Group symbol	SP (Poorly Graded Sand), C_u<6 and/or 1 > C_c > 3	SP (Poorly Graded Sand), C_u<6 and/or 1 > C_c > 3

The classification results according to USCS show that the sand in the Muaro Baru area and Gurun Laweh Naggalo are both Poorly Graded sand (SP). Fig. 6 and Fig. 7 show photograps of sand soil fraction samples

(a) (b)

Fig. 6 Sand particle in Muaro Baru area (a) Medium Sands (b) Fine Sand

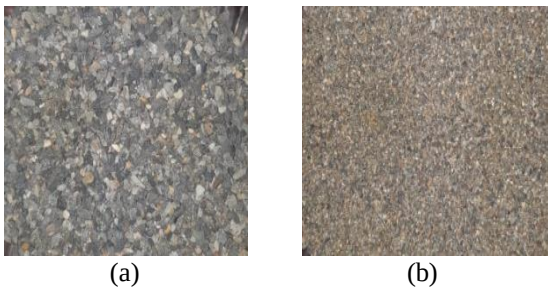

(a) (b)

(c)

Fig. 7 Sand particle in Gurun Laweh Nanggalo area (a) Coarse Sand (b) Medium Sand (c) Fine Sand

The dry unit weight (γ_{dry}) and saturated unit weight (γ_{sat}) of sand fraction in the Muaro Baru and Gurun Laweh Naggalo area shown in Table 4 below.

Table 4 Dry unit weight and saturated unit weight in Muaro Baru and Gurun Laweh Area.

Area	Sand fraction	Dry unit weight, γ_{dry} (gr/cm^3)	Saturated Unit Weight, γ_{sat} (gr/cm^3)
Muaro baru (MB)	Medium Sand	1.13	-
	Fine Sand	1.15	1.76
Gurun Laweh Naggalo (GLN)	Coarse Sand	1.36	1.41
	Medium Sand	1.35	1.60
	Fine Sand	1.32	-

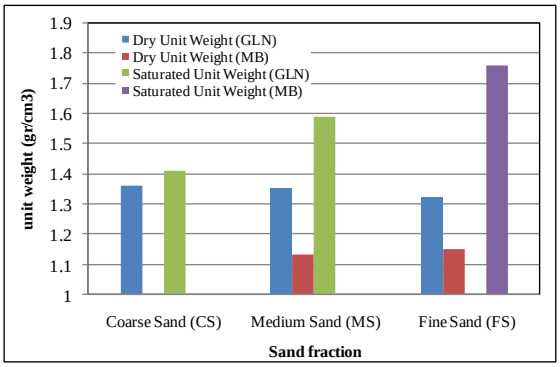

Fig. 8 The unit weight versus sand fraction

From Figure 8 it can be concluded that the size of the sand fraction does not affect the value of dry unit weight and value of the dry unit weight of river sand greater than the dry unit weight of the beach sand. The saturated unit weight value of fine sand is greater than medium sand and coarse sand.

For the model test, the first condition of the material used is fine sand from the Muaro Baru area (Fig. 9 and Fig. 10), while for the second condition the material used was a combination of medium sand with coarse sand from the Gurun Laweh Nanggalo (Fig 11 and Fig. 12). A square foundation measuring 15 cm x 15 cm with a weight of 3080 kg located at ground level. The following are pictures that show the initial conditions and the final conditions of the test.

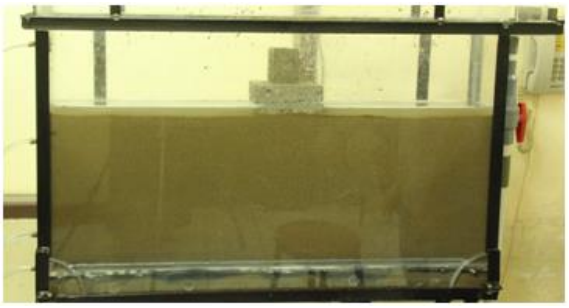

Fig. 9 Initial condition model test for fine sand

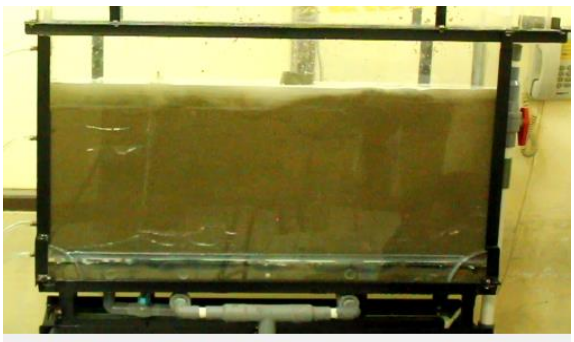

Fig. 10 Final condition model test for fine sand

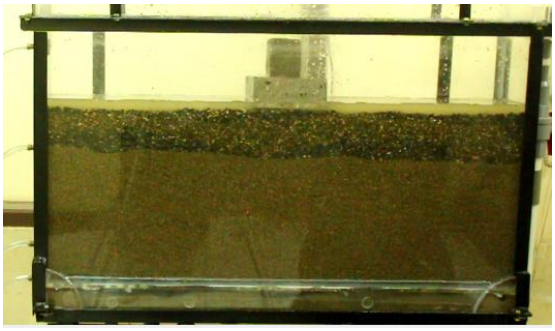

Fig. 11 Initial condition model test for combination of the coarse sand with medium sand

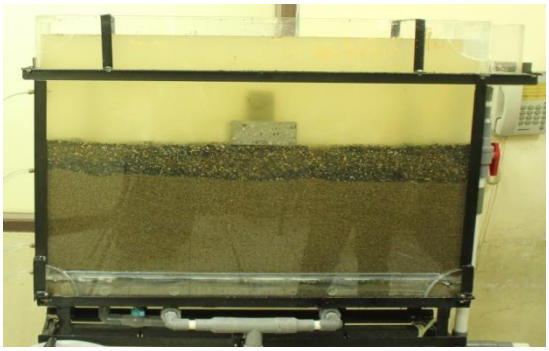

Fig. 12 Final condition model test for combination of the coarse sand with medium sand

In Figure 9, the initial water level is at elevation 38.8 cm (Fig 13a), the ground level is at an elevation of 36.8 cm and the thickness of the soil is 33.8 cm. In the Figure 11, the initial water level is at elevation 41 cm (Fig 13b), the ground level is at an elevation of 39 cm and the total thickness of the soil is 36 cm where the thickness of coarse sand and medium sand respectively 8 cm and 28 cm.

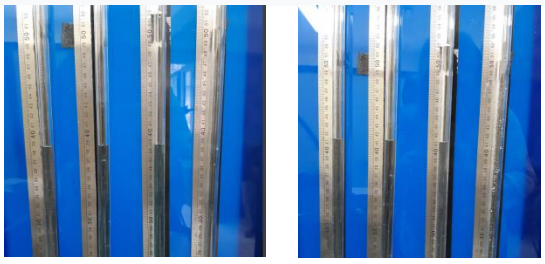

a b

Fig. 13 Initial condition water level

From the results of observations of the two conditions there is a significant difference between in the final condition in Figure 10 and final condition in the Figure 12. In the first conditions where the material is fine sand there is a settlement and tilt on the foundation. whereas in the second condition where the material is coarse sand and sand, there is no settlement and tilt at all.

CONCLUSIONS

From the results of the study it can be concluded that :

- The sand fraction in the coastal area is dominated by fine sand and medium sand while in the river area the sand fraction is dominated by medium sand and coarse sand while fine sand is less.
- The dry unit weight of the sand in the coastal area is smaller than the dry unit weight of sand in the river bank.
- The size of sand particles greatly affects the stability of the foundation due to upwards flow of water, where the foundation which is on fine sand is more susceptible to settlement and tilt.

ACKNOWLEDGMENTS

The authors would like to acknowledge the funding support provided by Andalas University, Padang, Indonesia.

REFERENCES

[1] Tohari, A., K. Sugianti and E. Soebowo, Liquefaction Potential at Padang City : A Comparison of Predicted and Observed Liquefactions During The 2009 Padang Earthquake. Riset Geologi dan Pertambangan Vol. 21 No. 1 (2011), 7 - 8.

[2] Hakam, A., Soil Liquefaction in Padang due to Padang Earthquake 30 September 2009. Civil Engineering Dimension, Vol. 14 No. 2, September 2012, 64-68, ISSN 1410-9530 print/ISN 1975-570X online.

[3] Hakam, A., and E. Suhelmidawati. Liquefaction Due to September 30th 2009 Earthquake in Padang. Procedia Engineering 54, pp.140 – 146.

[4] Yuliet, R., Fauzan, A. Hakam and H. Riani, Structural Evaluation Of Nurul Haq Shelter Building Constructed On Liquefaction Prone Area In Padang City – Indonesia. International Journal Of Geomate, July 2019, Vol.17, Issue 59, Pp.106-114

[5] Ke, L. and Takashi, A., Strength reduction of cohesionless soil due to internal erosion induced by one-dimensional upward seepage flow. Soil and Foundation 2912:52(4):698-711.

[6] Tokimatsu, K., K. Hino, H. Suzuki, K. Ohno, S. Tamura and Y. Suzuki. (n.d)., Liquefaction-induced settlement and tilting of buildings with shallow foundations based on field and laboratory observation. Soils and Foundations 2015;55(6):1501–1511.

[7] National Academies Press, Liquefaction of Soil During Earthquakes, 1985, http://nap.edu/19275

9th Int. Conf. on Geotechnique, Construction Materials and Environment,
Tokyo, Japan, 20-22 November 2019, ISBN: 978-4-909106025 C3051

STABILIZATION OF RIMBO PANJANG PEAT SOIL USING LIGHTWEIGHT MATERIALS MIXED WITH CEMENT AS SUBGRADE FOR ROAD PAVEMENT

*Elsa Eka Putri[1], Rina Yuliet[2], Lusia Elfina Harris[3] and Jodin Makinda[4]

[1,2]Faculty of Engineering, University of Andalas, Indonesia; [3]Public Works Agency and Spatial Planning, Riau, Indonesia; [3]Faculty of Engineering, Universiti Malaysia Sabah, Malaysia

ABSTRACT

Most of the road constructions in Riau Province are built on problematic and poor peat soil. This is one of the reasons why roads in this province do not last long according to their design. The aim of this research is to improve the engineering properties of the peat soil obtained from Rimbo Panjang, by using lightweight materials such as Bagasse and Sawdust Ash mixed with Portland Cement so that they meet the conditions stipulated as subgrade for road pavement layer. The tests conducted include determination of the physical properties of the peat soil such as Water Content, Organic Content, Ash Content, Unit Weight, Specific Gravity, Atterberg Limit and Dry Density, and engineering properties such as CBR and Unconfined Compressive Strength. A total of 18 CBR and 24 Unconfined Compressive Strength samples were prepared and tested. Results obtained showed the increases the Dry Density, CBR value and Unconfined Compressive Strength. The highest increment is observed on peat soils that mixed with 15% Cement with Unconfined Compressive Strength of 92 kN/m^2, Dry Density of 0.53 gr/cm^3 and CBR value of 4.67 %. It is followed by peat soils that mixed with 15% Cement and 20% Bagasse Ash with Unconfined Compressive Strength of 82 kN/m^2, Dry Density of 0.5 gr/cm^3 and CBR value of 4.56%. By comparison, Bagasse Ash shows a better result than Sawdust Ash in stabilizing Rimbo Panjang peat soils.

Keywords: Stabilization, Bagasse Ash, Sawdust Ash, Cement, CBR, Unconfined Compressive Strength

INTRODUCTION

Peat soil is soft soil with an organic content of >75% (Department of Settlement and Regional Infrastructure, 2004). Peat soil has low bearing capacity, high compressibility and low shear strength [1].

Most of the road constructions in the Riau Province area are built on peat soil. This is one of the reasons why roads in the Riau Province do not last long according to their design. During rainy season, peat soil will be saturated with water, while in the dry season, peat soil will compress due to the loss of water from the pores. This causes damage to the road construction due to the expansion and shrinkage of the soil surface. Typical illustration of peat soil can be seen in fig. 1 below.

Fig.1 Peat Soil at Rimbo Panjang, Riau Province

For this reason, peat soils found in the Riau Province, especially in the Rimbo Panjang area need to be stabilized and improved so that they are in accordance with the conditions stipulated as subgrade for pavement layers. One of the stabilizing methods is by using lightweight materials. Bagasse ash and sawdust ash as lightweight materials mixed with Portland cement were chosen to be investigated in this research. Mixing the peat soil with lightweight materials were not expected to add the weight of the peat soil itself. Moreover, the purpose of adding cement to the mixes is to increase the binder properties of the peat soil mixtures.

The objective of this investigation is to study the properties of stabilizing peat soils with lightweight materials namely bagasse ash (BA) and sawdust ash (SA) mixed with Portland cement (PC). In addition, the study aims to determine to what extent can these new mixtures improve the engineering properties, i.e. California Bearing Ratio (CBR) and unconfined compressive strength (UCS), as subgrade for pavement layers.

LITERATURE REVIEW

Department of Settlement and Regional Infrastructure defines peat as a part of soft soil consisting of inorganic clay and organic clay [2], forms mainly of plant debris in various levels of decomposition [3], and has a density ranges from 1.4 to 1.5 [2]. Peat also has a dark brown to black colour, distinctively scented with decaying plants, hollow consistency without showing obvious plasticity and fibrous to the amorphous texture [3].

Weathering of organic materials is the main process that forms this soil [4]. Due to this, the content of organic matter in peat soil is higher than 75%, consisting of fibrous material produced by the accumulation of half decaying plant debris in an environment with low oxygen level [1]. This type of soil has a field CBR value of less than 2% [5].

Higher groundwater level resulting in higher water content of the peat soil. It can be visualized, identified and observed by their dark brown colour [6].

Sawdust used in this research was obtained from a factory that manufactures frames, doors and windows. Sawdust ash is a lightweight material thus it is expected not to overburden the load on peat soil. A study by Munthe (2012) found that the use of sawdust ash increases the value of the UCS and cohesion of clay soil, moreover, the addition of 12% SA reduces the permeability and the plasticity index and increases the shear strength and the maximum dry density [7]. SA used in this study can be seen in Figure 2.

Fig. 2 Sawdust Ash (SA)

Bagasse ash (BA) used in this research was obtained from sugar cane drinks seller at a local market. The use of BA produced from the remnants of sugar cane helps in reducing the environmental impact caused by garbage dumping on the street and open areas. Similar to SA, BA is also a lightweight material that might not increase the load on peat soil.

A previous study by Yuliet et al. (2006) on the use of BA and cement as stabilization material for clay soils proven to reduce soil expansion and increase the CBR value [9]. Whereas Rezki and Roesyanto (2014) concluded that a mixture of BA and cement increases the compressive strength and maximum dry weight of clay soil. BA used in this study can be seen in Figure 3 [10].

Fig. 3 Bagasse Ash

Soil which in its original state is poor can be changed through compaction, adding aggregates or other materials so that it can be used as subgrade for pavement. Soil stabilization is one of the common methods used to improve the properties of existing soil to meet the technical demands [11]. According to the Department of Settlements and Regional Infrastructure (2002d), there are five methods to improve the subgrade properties that have been accepted and applied in Indonesia. Such as a material replacement, counter berms, surcharging, for stage construction and the use of lightweight material [12].

RESEARCH METHODOLOGY

The research was carried out at the Material Testing Technical Implementation Unit of the Public Works and Spatial Planning of Riau Province. BA, SA and Cement are varied to be mixed with peat soil in order to achieve higher CBR value and unconfined compressive strength (q_u) values for pavement subgrade.

Peat soil was collected from Km. 18. Pekanbaru-Bangkinang road, Riau Province which is ± 100 m from the main road. Peat soil used in this investigation is in a disturbed condition, taken at a depth of 40 cm to 60 cm. Peat soil is dried for four weeks, the roots are removed then filtered with sieve no. 4.

Bagasse ash used in this investigation was derived from the surrounding waste. Bagasse ash was air dried then burnt in the drum. The ash derived is then ground with 12 kg grinder for 10 minutes. The use of bagasse ash as additional material to stabilize the peat soil was then implemented according to the Guidelines issued by the Department of Settlements and Regional Infrastructure No: Pt T-10-2002-B regarding Geotechnical Guidelines 4 Road Construction Design and Construction in Soft Soil [2].

The sawdust powder was derived from the wood cutting process from the sawmilling process. The use of sawdust ash to stabilize the peat soils

was implemented according to the Guidelines issued by the Department of Settlements and Regional Infrastructure using the same aforementioned guideline. As with bagasse ash, sawdust ash was also through the process of burning and grinding.

Cement used in this investigation was Type 1 Portland Cement from Padang Cement Factory based on the Procedure of Land Stabilization with Portland Cement for Roads and Base Coarse Manual, Road Book no. 6 Department of Public Works Directorate General of Highways No: 002-06/BM/2006.

Peat soil was mixed with various materials such as bagasse ash, sawdust ash and cement in different percentage variations as seen in Table 1.

Table 1: Variation of materials studied

SAMPLES	Portland Cement (PC) in Peat	Baggage Ash (BA) in Peat	Sawdust Ash (SA) in Peat
P	-	-	-
P15BA	-	15%	
P15PC	15%	-	
P15PC10BA	15%	10%	
P15PC20BA	15%	20%	
P15PC30BA	15%	30%	
P15SA	-	-	15%
P15PC10SA	15%		10%

RESULTS AND DISCUSSION

The physical and mechanical properties of the peat can be seen in Table 2.

Table 2. Properties of Rimbo Panjang Peat Soil

Parameter	**Value**
CBR Lab, (%)	4.50
UCS, q_u (kN/m^2)	52
Undrained Shear Strength, S_u (kN/m^2)	26
Maximum Dry Density, ρ_d (gr/cm^3)	0.48
Optimum Water Content, w (%)	106.50
Liquid Limit	131.10
Plastic Limit	101.24
Plasticity Index	29.86
Natural Water Content (%)	324.66
Dry Air Water Content (%)	21.50
Ash Content (%)	66.34
Organic Content (%)	33.66
Specific Gravity	1.5
Weight/Volume (gr/cm^3)	0.4

Based on the results, Rimbo Panjang peat soils can be categorized as 'high ash' due to the ash content of >15%. Moreover, from the previous report by the Department of Settlements and Regional Infrastructure (2004) [5], it classifies the Rimbo Panjang peat soil as organic clay because of the organic content was in the range of 25% -75%.

Dry Density vs. Moisture Content

Figure 4 shows the relationship between the moisture content against the dry density for various variations of peat soils stabilized with bagasse ash and Portland cement.

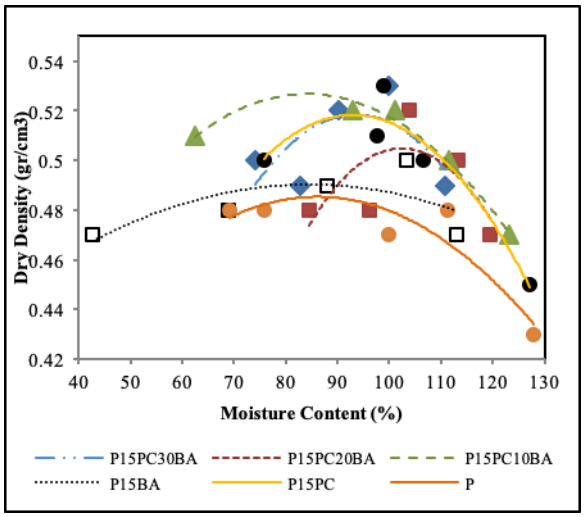

Fig. 4 Dry Density vs. Moisture Content of Peat Stabilized with BA and PC

It can be seen from Figure 4 that the maximum dry density increases in all mixes compared to the control sample. The highest increment is observed in peat soil + 15% PC + 10% BA, where the value increases from 0.480 gr/ cm^3 to 0.528 gr /cm^3, obtained at optimum water content (w) of 84%.

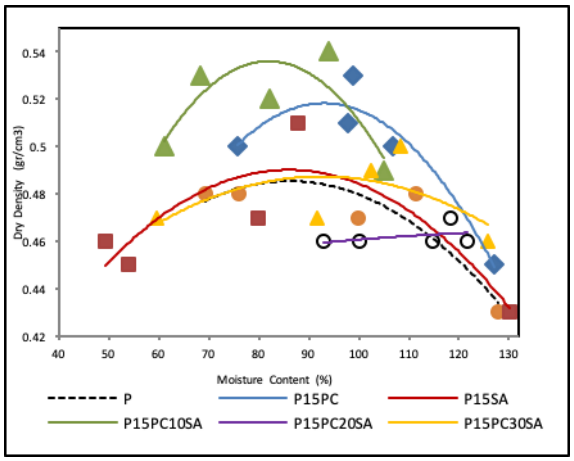

Fig. 5. Dry Density vs. Moisture Content of Peat Soil Stabilized with SA and PC

Figure 5 shows the relationship between the moisture content against the dry density for

various variations of peat soils stabilized with SA and PC from the compaction test.

It can be seen that the maximum dry density increases in all mixes. The highest increment is observed in peat soil + 15% PC + 10% SA, where the value increases from 0.480 gr/ cm^3 to 11.67 gr /cm^3, obtained at optimum water content (w) of 81%.

Relationship Between CBR Value (%) and Dry Density (gr/cm^3)

Figure 6 shows the relationship between CBR value and dry density. It can be observed that the CBR value and dry density increase in all mixes. The highest increment is observed in peat soil + 15% BA (P15BA), where the CBR value rises by 1.49% from 4.50% to 5.99% and the maximum dry density increases by 4.17 % from 0.48 gr/cm^3 to 0.50 gr/cm^3.

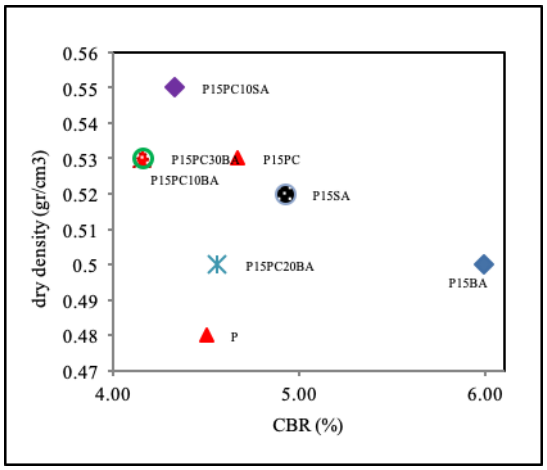

Figure 6. Relationship Between CBR Value and Dry Density of Peat Soil Stabilized with BA and PC

Meanwhile, Peat soil stabilizes with 15%PC and 10%SA achieved the highest density at 4.3%CBR value which is above the minimum value of CBR subgrade i.e 3%.

Relationship between UCS, q (kN/m^2) value and Dry Density (gr/cm^3)

Figure 7 shows the relationship between dry density and UCS. It can be seen that the UCS and the dry density increases in all mixes. The highest value of the UCS is 92 kN /m^2 observed in a mixture of peat soil + 15% PC. This a 76% increment compared to the UCS of Peat soil at 52 kN/m^2. Moreover, the highest value of the maximum dry density is 0.55gr/cm^3 occurs in a mixture of peat soil + 15% PC + 10% SA, increasing by 15 gr/cm^3.

Thus, it can be concluded that the variation with the highest dry density and UCS achieved at Peat soil stabilize with 15%PC+10%SA.

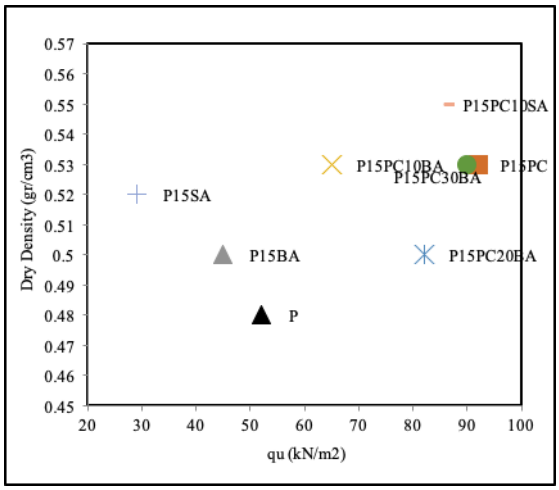

Fig. 7 Relationship Between UCS and Dry Density of Peat Soil Stabilized With BA, SA and PC

Relationship Between CBR Value (%) and UCS, q_u (kN/m^2)

Figure 8 shows the relationship between CBR and UCS.

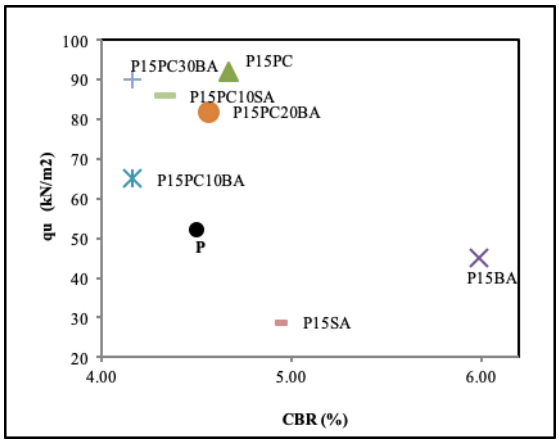

Fig. 8 Relationship Between CBR Value and UCS for Peat Soil Stabilized With BA, SA and PC

It can be seen from Fig.8 that the UCS and the CBR value increase in all stabilize variation mixes. The highest value of UCS observed is 92 kN/m^2 occurs in a mixture of peat+15%PC, which is increased by 40 kN/m^2. Meanwhile, the highest increase in CBR value occurred in a mixture of peat soil + 15%BA where the CBR value increased by 1.49% from 4.50% to 5.99%.

Referring to Fig. 7, peat soil stabilizes with 15%PC+10SA (P15PC10SA) achieved the highest dry density and as shown in Fig.8, the same sample achieved CBR value of 4.33%, which is above the minimum value of CBR design for pavement thickness.

Stress and Strain RELATIONSHIP

The relationships between stress and strain for various variations of the mixture of peat and cement were presented in Figure 9 where the increase in UCS is observed in all mixtures. The highest increment is observed on peat soil+15% PC at 96 kN/m^2, an increase of 125% compared to the lowest strength of Peat soil itself with a value of 48 kN /m^2.

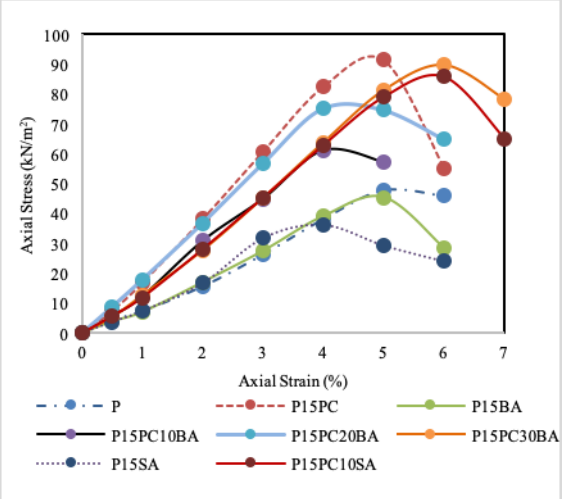

Figure 9. Stress and Strain Relationship for Peat Soils Stabilized with PC, BA and SA.

The highest increment is observed on peat soil+15% PC+ 10% SA at 96 kN/m^2, an increase of 147% compared to the an increase of 121% compared to the peat soil without stabilized materials. Then it was followed by peat soil + 15% PC + 30% BA at 94 kN/m^2, an increase of 121% compared to the peat soil without stabilized materials.

Cross-Examination of the Values of UCS, Dry Density and CBR.

In this study, a cross-examination was carried out to determine which of the mix variations could be implemented in the field as summarized in Table 4. For comparison purpose, the control sample is also included.

It can be observed that the optimum mixture is peat soil + 15% PC with unconfined compressive strength of 92 kN/m^2, dry density of 0.53 gr /cm^3 and CBR value of 4.67 %, followed by the peat soil + 15% PC + 20% BA with unconfined compressive strength of 82 kN/m^2, dry density of 0.5 gr /cm^3 and CBR value of 4.56 %.

Table 4. Cross-examination of the Values of UCS (q_u), Dry Density and CBR

No	Mix Variation	q_u (kN/m^2)	C_u	Dry Density (gr/cm^3)	CBR (%)
1	Peat Soil	52	26	0.48	4.50
2	Peat Soil + 15%PC	92	46	0.53	4.67
3	Peat Soil + 15% BA	45	22.5	0.5	5.99
4	Peat Soil + 15%PC+10% BA	65	32.5	0.53	4.16
5	Peat Soil + 15%PC+20% BA	82	41	0.5	4.56
6	Peat Soil + 15%PC+30% BA	90	45	0.53	4.16
7	Peat Soil + 15% SA	28	14	0.52	4.92
8	Peat Soil + 15%PC+10% SA	86	43	0.55	4.33

From the mixed variations, the selection of which mix should be implemented in the field should be based on; i) CBR value; higher CBR value of the subgrade is considered better and more economical because of its larger bearing capacity thus reduces the need of thicker pavement layer above it. Of the two mixed variations, the highest CBR value was a mixture of peat soil + 15% PC with a CBR value of 4.67%., ii) Ease in workmanship ; as it determines the success of a job in the field as the suitable mix could avoid constant technical and non-technical disruption to the construction works and iii) Human Resources or skilled workers whom are capable to carry out the job in the field.

CONCLUSIONS

From the results of research and discussion, some conclusions can be drawn;

- An increase in observed in the value of dry density, CBR value and unconfined compressive strength of the peat soil for all mixes.
- The most optimum mixture is peat soil + 15% PC with unconfined compressive strength of 92 kN/m^2, dry density of 0.53 gr /cm^3 and CBR value of 4.67 %, followed by peat soil + 15% PC + 20% BA with unconfined compressive strength of 82 kN/m^2, dry

density of 0.5 gr /cm^3 and CBR value of 4.56 %.

- Addition of bagasse ash gives better results than sawdust ash in stabilizing peat soil.
- Because bagasse ash used was not filtered with a 200 sieve, they lack the binding capacity, thus they only function as filler.

ACKNOWLEDGMENTS

The author would like to acknowledge the Program Bantuan Seminar Luar Negeri, Faculty of Engineering, Andalas University, Padang, West Sumatera, Indonesia for funding of this research.

REFERENCES

[1] Vishwanath, G., Pramod, K.R., Ramesh, Dr.V. (2014). Peat Soil Stabilization with Rice Husk Ash and Lime Powder. International Journal of Innovation and Scientific Research. ISSN 2351-8014.9(2):225-227,2014.

[2] Department of Settlement and Regional Infrastructure (2002c). Pt M-01-2002-B Geotechnical Guide 3 Soft Soil Investigation Laboratory Testing.

[3] Department of Settlement and Regional Infrastructure (2004). Pd T-06-2004-B Planning Road Construction on Peat with Pre-loading Method.

[4] Rakhman, Yunan A. (2002). Stabilisasi Tanah Gambut Rawa Pening Dengan Semen Dan Gypsum Sintetis ($CaSO4.2H_2O$). Tesis. Universitas Diponegoro, Semarang

[5] Ministry of Public Works Directorate General of Highways (2010). Technical Specifications 2010 (Revision 3). Jakarta.

[6] Kolay, P.K., Sii, H.Y. and Taib, S.N.L. (2011). Tropical Peat Soil Stabilization using Class F Pond Ash from Coal-Fired Power Plant. International Journal of Civil and Environmental Engineering 3:2 2011.

[7] Munthe, MTN. (2012). Perbaikan Tanah Lempung Menggunakan Abu serbuk kayu. Tugas Akhir. Universitas Atmajaya, Yogyakarta

[8] Wong, L.S., Roslan, H. and Faisal, H.A. (2008). Behaviour of Stabilized Peat Soil in Unconfined Compression Test. American J. of Engineering and Applied Sciences. 1(4):274-279,2008.

[9] Yuliet, R., Andriani., Karisfa, Dona H. (2006). Stabilisasi Tanah Dengan Menggunakan Semen Dan Abu Abu Ampas Tebu Sebagai Subgrade Jalan. Jurnal Rekayasa Sipil. Vol. 2. No. 2. Oktober 2006.

[10] Rezki, A. (2014). Kajian Kuat Tekan Bebas pada Tanah Lempung yang Distabilisasi dengan Abu Ampas Tebu dan Semen. Tugas Akhir. Universitas Sumatera Utara, Medan.

[11] Department of Public Works (2006a). 002-01 / BM / 2006. Manual of Subbase Work (Book 1) General

[12] Departemen Permukiman dan Prasarana Wilayah (2002d). Pt T-10-2002-B Panduan Geoteknik 4 Desain dan Konstruksi.

Table 3; Stress-Strain Value

Strain (%)	Stress (kN/m2)							
	P	P15PC	P15BA	P15PC10BA	P15PC20BA	P15PC30BA	P15SA	P15PC10SA
0	0.000	0.000	0.000	0.000	0.000	0.000	0.000	0.000
0.5	4.230	7.393	3.877	5.633	8.803	5.283	3.700	5.637
1	7.360	16.827	7.010	12.270	17.877	12.713	7.360	11.913
2	15.610	38.167	16.997	30.877	36.777	27.757	16.655	28.103
3	26.300	60.787	27.477	44.987	56.663	45.320	31.790	45.330
4	38.240	82.590	39.087	61.180	75.113	63.897	36.200	62.913
5	47.925	91.483	45.407	57.177	74.663	81.390	29.265	79.040
6	45.925	55.247	28.287		64.895	89.860	23.960	85.863

9th Int. Conf. on Geotechnique, Construction Materials and Environment, Tokyo, Japan, 20-22 November 2019, ISBN: 978-4-909106025 C3051

ALGORITHMS DEVELOPED FOR TWO PROTOTYPES OF AIRBORNE VISION-BASED CONTROL OF GROUND ROBOTS

Ilan Ehrenfeld[1], Oleg Kupervasser[1,2], Hennadii Kutomanov[1], Vitalii Sarychev[2], and Roman Yavich[1]
[1] Department of Mathematics, Ariel University, Israel; [2] TRANSIST VIDEO LLC, Skolkovo, Russia

Abstract

Unmanned autonomous robots will be widely used very soon for land use, treatment, and monitoring. Our and the other groups already described technologies, that can be used for such robots (Kupervasser et al., International Journal of GEOMATE, May, 2018 Vol.14, Issue 45, pp.10-16; Djaja et al., International Journal of GEOMATE, Aug, 2017, Vol.13, Issue 36, pp.31-34). We continue developing these technologies and present here new patented technology of airborne vision-based control of ground robots. The main idea is that robot's "eyes" is not located on robot, but are independent autonomous system. As a result, the "eyes" can go up and observe the robot from above. We present in this paper algorithms used for two real physical prototypes of a such system.

Keywords—visual navigation; ground robots; tethered platform; airborne control; prototype; vision-based navigation

INTRODUCTION

Unmanned autonomous robots will be widely used very soon for land use, treatment, and monitoring. Our and the other groups already described technologies, that can be used for such robots [1,2].

The most popular outdoor robots are currently robot-lawnmowers. Current robot-lawnmowers need for staked border wires. They have random navigation methodologies. They are inconvenient, static, expensive technology.

You can see the following citation from "THE ROBOT REPORT: TRACKING THE BUSINESS OF ROBOTICS" [3]:

"... Too expensive for most home use, not professional enough for industrial use, robotic lawnmowers have yet to become as commonplace as Roombas, But a new crop of consumer manufacturers is quietly making inroads by providing more bang for the buck."

".., Friendly Robotics and their line of Robomowers, $2,000, and Husqvarna and their Automower line, $2,200, have been around for a few years but never hit consumer traction outside of Europe (Husqvarna has sold over 100,000 of their Automowers), partly because of their high price, mulching clumps, inability to handle high grass, need for staked border wires, and their random navigation methodologies."

The solution of the problem is vision-based navigation [4-6]. Vision-based navigation of robots is similar to human navigation by the help of eyes vision. However, we do not eyes on the robot. We put eyes on a top and from the top robot can see itself and its motion. We use airborne terrestrial robots control (Figure 1).

We continue developing these technologies and present here new patented technology of airborne vision-based control of ground robots [7-10]. It is planned to develop a software package including approaches for comprehensive video navigation solution of ground robot from top position (tethered drone, balloon, tower, antenna on the ground robot) and a physical prototype (camera on the top position, ground robot, ground station with computer) controlled by this software.

The system relates to the control systems of automated devices and may be used for the coordination of the ground movable automated devices (automated transport, automated agricultural machines, municipal and aerodrome vehicles, garden lawnmowers and so on), hereinafter referred to as the robots.

The invention essence is the system of navigation [1-10] and intercoordination of one or more roots located on the controlled area including one or more robot tracing devices on the suspended platforms, natural or artificial markings, central module for robot coordination and orientation detection to which the information is transferred from all the tracing devices, charger and the system is equipped with the central calculation module located on the suspended platform, on the ground, on the charger or on the robot designed with the possibility to detect the coordinates, to orient the system and to form the control commands based on the information received from all the above described devices.

The technical result is the development of the robot efficient coordination using the devices located on the towers or the aerial apparatuses tracing the robots on the controlled area and supervising their environment including natural and artificial markings. One of the developments is to take into account delays in the control system. The technical result coincides with the engineering challenge.

This visual system can also be used for preventing collision of ground robot with children or animals. Also we can use this visual system for security purposes.

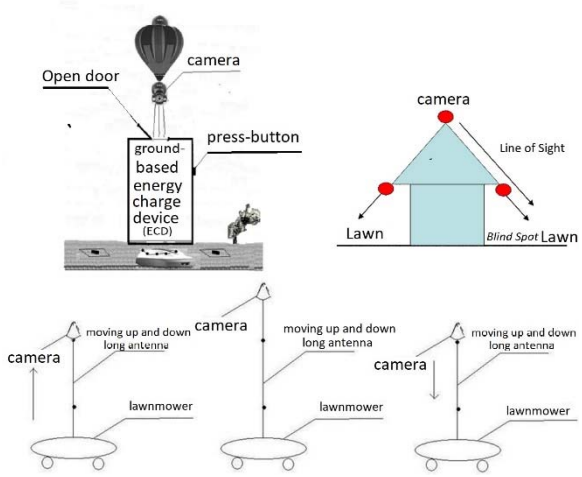

Fig. 1. Airborne terrestrial robots control, some possible camera dispositions

The system (the proof of concept) was defined to work as follow:

1. A toy car will simulate the lawnmower.
2. The car will be controlled by a software that will connect to a webcam that watch all the area.
3. There will be two options to drive the car:
    a. A random movement
    b. A user predefined route
4. For random route, the user will define on the live video:
    a. The edges of the area (practically close to the edge of the frame).
    b. Using lines and squares, areas in the frame that the car can't go to.
5. For predefine route, the user will define on the live video:
    a. Continues and close route that is starting at the location of the car and end about the same location.
    b. The user will use lines to draw the route.
6. The software will receive the life video from the webcam
7. The software will analyze the location and orientation of the car.
8. The software will instruct the car what to do next according to its analyzing and the user definition.

The paper is constructed as following:

Section 1 is the introduction and includes a description of the system.

Section 2 provides a system overview.

Section 3 describe the software.

Section 4 describes the algorithms in use.

SYSTEM OVERVIEW

System Components

The following figure describe the system components (Figure 2):

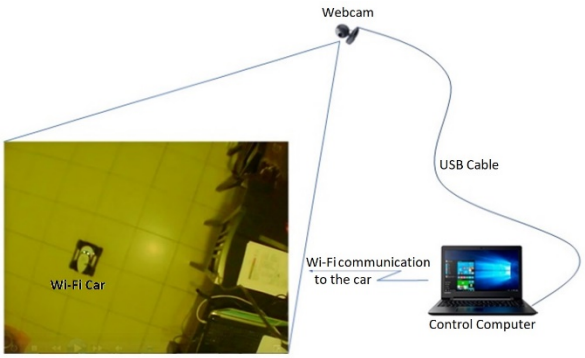

Fig. 2. The system components

SOFTWARE DESCRIPTION

Software General Description

Following is a list of the components in the system:

- Car – A game car of type iSpy. This car has Wi-Fi communication and an API to be controlled from a computer.
- Webcam – connected to the computer by USB cable.
- Control Computer – A computer running the software we developed. This computer connected to the webcam to get a live video of the area and give instructions to the car using Wi-Fi communication.

The software (Figure 3) is written in Python. Is build out of two files:

- ColorTrack.py – main file. This file contains all the flow control, logics, computer vision and the UI
- carControl.py – This file is where the communication with the car is done.

The following paragraph describe shortly the carControl.py structure. All the rest of the description in this document exist in ColorTrack.py file.

The carControl build as a class with regular __init__ function, where all the initializations for this class happened.

There is the "run" function. This is the thread control function. This function run in endless loop and wait for a command. A command received in the self.move variable. When this variable set to something that is different from "no" (no command), it will run a function according to the command:

- moveForCalib – This function use for calibration of a strait move.
- turnForCalib – This function use for calibration of a turn.
- goForward – Move forward function. It receives, as input, the distance to move in pixels and calculate the time to move and send by Wi-Fi the right command to the car.
- goBackword – Move backward function. It receives, as input, the distance to move in pixels and calculate the time to move and send by Wi-Fi the right command to the car.
- goLeft – Turn left function. It receives, as input, the angle, in degrees, for turn and calculate the time to move and send by Wi-Fi the right command to the car.
- goRight – Turn right function. It receives, as input, the angle, in degrees, for turn and calculate the time to move and send by Wi-Fi the right command to the car.

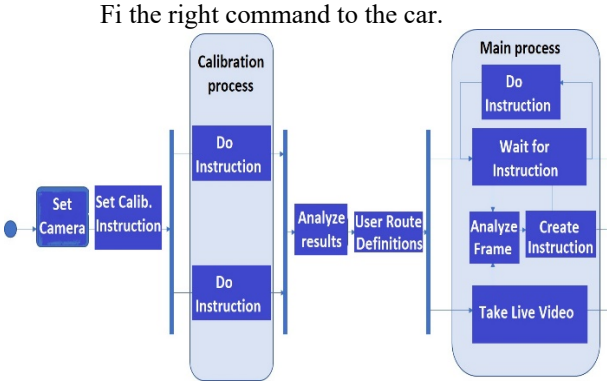

Fig. 3. State Diagram

Software Flowchart

In this paragraph we show the flowcharts of the software (Figures 4-6). It starts with the start flowchart and then show separately the flow for route mode driving and for random mode driving.

In the flowcharts, a rectangle that represent a function in the software, the function name is written in red and in parenthesis in the rectangle.

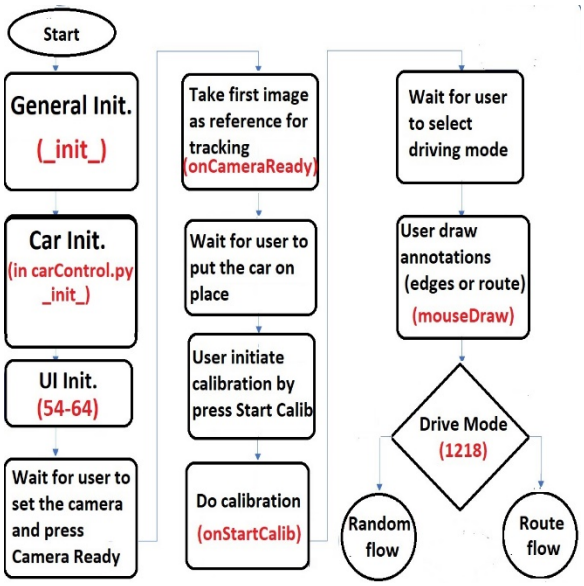

Fig. 4. Start Flowchart

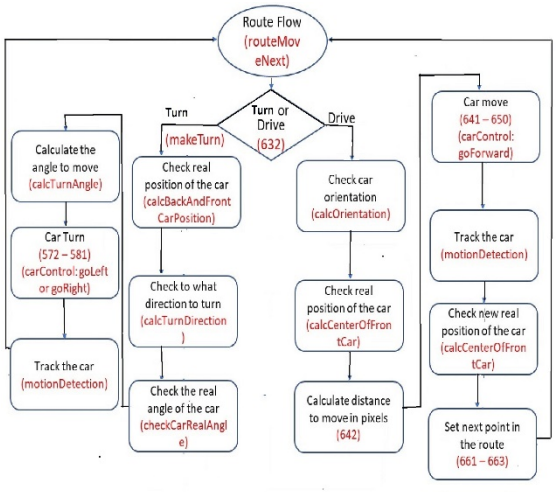

Fig. 5. Route Mode Drive Flowchart

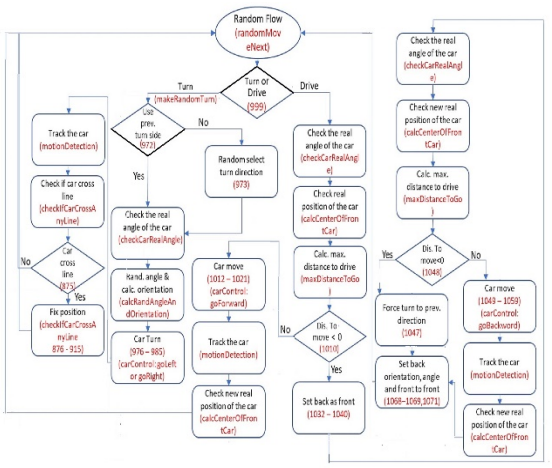

Fig. 6. Random Mode Drive

ALGORITHMS AND CALCULATIONS DESCRIPTION

Tracking Algorithm

The tracking algorithm is based on Motion Detection. It is based on OpenCV and example from OpenCV.org for implementation of motion detection.

Following is description of the algorithm:

1. Save an image of the area with no moving object in it – this image will be the reference image.
   a. In our case that's done when the user is press <Camera Ready> in function "onCameraReady"
2. The rest of the algorithm is implemented in the function "motionDetection". For each image the algorithm does:
   a. Change the image to gray level image
   b. Apply a Gaussian Blur on the gray level image
   c. Calculate absolute differentiation from the reference image
   d. Apply binary threshold for the result (will get black and white image where the different between the images is greater than threshold)
   e. Apply filter to reduce noises (dilate filter function from OpenCV) – the result is kept in image called "mask" (the masked image)
   f. The rest of the steps in this algorithm are implemented in function "showTrackingResults"
      i. Using OpenCV function "findContours" we find the contours of all the objects in the mask image
      ii. Using OpenCV function "max" we select the biggest object in the image
      iii. Using OpenCV function "minAreaRect" we define and save the enclosing rectangle of the car

Movement Calculations

General

All movement logics are based on the orientation of the car relatively to the images axes. We use in the software two parameters to describe the orientation:

1. carOrientation: this is the general direction of the car. The orientation names are:
   a. NW – north west
   b. NE – north east
   c. SE – south east
   d. SW – south west
2. carAngle: this is the exact angle of the car. We calculate it relatively to its general direction in the image. In other words, the angle of the car will always be in the range of 0-90 degrees.

The axes, the general directions and their names and the angle location for each direction is shown in figure 7.

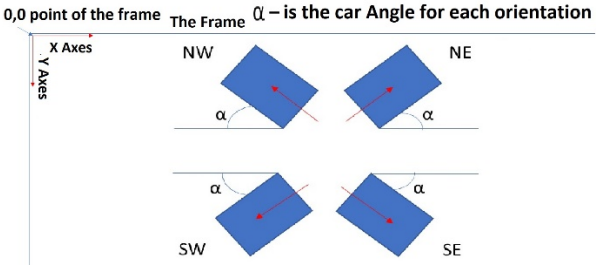

Fig. 7. The axes, the general directions and their names and the angle location for each direction

The frame of the car, which hold in array variable carBox in the software, is defined by 4 points. The first point (located in place 0 in the carBox array) will always be at the lowest point. From there the other points are kept clockwise as shown in figure 8.

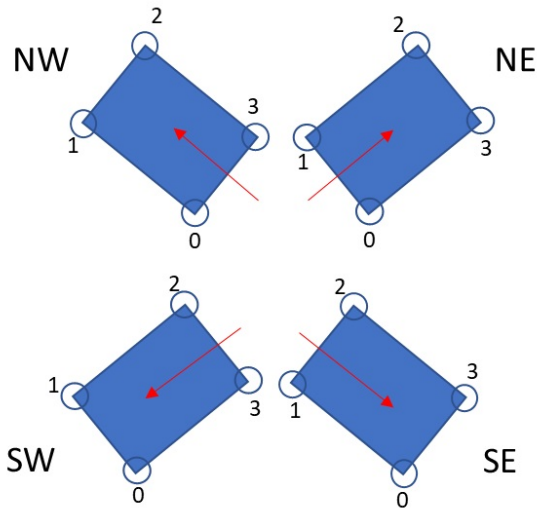

Fig. 8. The frame of the car is defined by 4 points

General Help Calculations

Based on the above explanation here are explanations on some help calculations done during the the flow of the software:

1) CALCULATING THE POSITION OF THE CAR

The position of the car is defined as the center of the front line of the car:

1. According to the orientation of the car (NW, NE, SE or SW) select the two points represent the front of the car:
   a. NW – points 1 and 2
   b. NE – points 2 and 3
   c. SE – points 3 and 0
   d. SW – points 0 and 1
2. Calculate the middle of this segment

2) CALCULATE THE REAL ANGLE OF THE CAR

1. According to the orientation of the car choose the two points along the car
2. Calculate the line angle = atan(dy/dx)

3) INTERSECTION BETWEEN TWO SEGMENTS

This calculation is implemented in function "find_intersection". It is based on an algorithm in Andre LeMothe's. The implementation was taken from [11].

There, you can also find a detailed explanation of the algorithm.

Route Mode Help Calculations

Now as we have the above help calculations and according to the above explanation on the orientations calculations such as: what side to turn, what is the angle of the turn are become straightforward.

To calculate the distance to drive to the next point is the Euclidean distance between the current location point to the destination location point.

Random Mode Help Calculations

1) TO CHECK IF THE CAR IS ON ONE OF THE LINES

1. Go over all the lines the user created on the video
2. For each line:
   a. Each two adjacent points, of the car, determined as a segment
   b. For each segment check intersection with the line

2) CALCULATE THE MAXIMUM DISTANCE THE CAR CAN MOVE

This calculation is implemented in function "maxDistanceToGo".

1. Check the shortest distance to the edge of the frame
2. Keep this distance in minDis variable
3. Go over all the lines the user created on the video
4. For each line:
   a. Create a vector for each side of the car:
      i. Example of a side: if the car orientation is NW one side will be points 2 and 3 and the other side will be 1 and 0
      ii. The vector goes from the back of the car to the front and on until the edge of the frame. For NW orientation, for example, the vector direction will be from point 3 to point 2 and the other vector will be from point 0 to point 1.
   b. For each segment check intersection with the line
   c. If there is intersection, calculate the distance to the line
   d. If the distance is smaller than minDis, keep this distance as the new minDis.

FUTURE PLANS AND CONCLUSION

We plan to create much more complicated prototype using Kamin grant (Israel).
The plane consists of the next stages:

1. Creating programs of video-navigation for airborne control from towers of ground robots on flat ground surface
2. Design and integration of robotic system: observation towers, controlling center, and ground robots
3. Testing robotic system and computer program, errors correction of robotic system and computer program
4. Rewriting programs for video-navigation than airborne control is made from tethered platform (drone or balloon) and ground robots on not-flat surface
5. Modernization of robotic system: creation of observation tethered platform (drone or balloon) and modernization of ground robots for not-flat surface
6. Testing robotic system and computer program, errors correction of robotic system and computer program

This system may be used for a wide class of robots: automated lawnmowers, robots for cleaning the rooms, tractors, snow-removal, garbage disposal and flushing vehicles, vehicles for people and goods transportation, agricultural and municipal vehicles, transport and so on. This system may be used for extra-terrestrial robots on other planets, for instance, for Mars rovers.

The system easily stays within the frames of the "smart home" or even "smart city" enabling to coordinate simultaneously a lot of actions, robots and other control objects and to solve many tasks - for instance, not only navigation but detection.

References

1. Oleg Kupervasser, Vitalii Sarychev, Alexander Rubinstein and Roman Yavich, ROBUST POSITIONING OF DRONES FOR LAND USE MONITORING IN STRONG TERRAIN RELIEF USING VISION-BASED NAVIGATION, International Journal of GEOMATE, May, 2018 Vol.14, Issue 45, pp.10-15:
2. Djaja et al., International Journal of GEOMATE, Aug, 2017, Vol.13, Issue 36, pp.31-34
3. "THE ROBOT REPORT" TRACKING THE BUSINESS OF ROBOTICS, 2012 http://www.therobotreport.com/news/robot-lawnmowers-still-a-work-in-progress
4. Oleg Kupervasser, Ronen Lerner, Ehud Rivlin and Hector Rotstein Error Analysis for a Navigation Algorithm based on Optical-Flow and a Digital Terrain Map In the Proceedings of the 2008 IEEE/ION Position, Location and Navigation Symposium, P.1203-1212
5. Kupervasser O. Yu., Rubinshtein A.A., Correction of Inertial Navigation System's Errors by the Help of Video-Based Navigator Based on Digital Terrarium Map "Positioning" Vol.4 No.1, February 2013
6. Kupervasser O.Yu. Computer programs "Video-navigation of UAV over relief" Part 1, Part 2 The certificates on the state registration of the computer programs № 2016613306, 2016613305 It is registered in the register of the computer programs of Federal service on intellectual property, patents and trade marks, Russia, on March, 24, 2016 http://www1.fips.ru/Archive/EVM/2016/2016.04.20/DOC/RUNW/000/002/016/613/305/document.pdf http://www1.fips.ru/Archive/EVM/2016/2016.04.20/DOC/RUNW/000/002/016/613/306/document.pdf
7. Ilan Ehrenfeld, Max Kogan, Oleg Kupervasser, Vitalii Sarychev, Irina Volinsky, Roman Yavich, Bar Zangbi, "Visual navigation for airborne control of ground robots from tethered platform: creation of the first prototype", Proceeding of the IEEE International Conference on New Trends in Engineering and Technology, September 2018, GRTIET, Tirupathi, Chennai, Tamil Nadu, India, http://grt.edu.in/news/international-conference-on-new-trends-in-engineering-and-technology-icntet-2018/
8. Kupervasser O.Yu., Kupervasser Yu.I., Rubinstein A.A., Russian Utility model: Apparatus for Coordinating Automated Devices, Patent № 131276, Russia, on Nov, 12th, 2012
9. Kupervasser O.Yu., Kupervasser Yu.I., Rubinstein A.A., German Utility model: Vorrichtng fur Koordinierung automatisierter Vorrichtungen. Patent Nr. 21 2013 000 225. It is registered in Germany Jul, 10, 2015
10. Kupervasser O.Yu., Franch Utility model application: Coordination System for Ground Movable Automated Devices. Utility model, publication number 3037157, Jun, 04, 2016, http://bases-brevets.inpi.fr/en/document-en/FR3037157.html?s=1482862654519&p=5&cHash=1f6f99c78cfb2124b5accb92be338388
11. "How do you detect where two line segments intersect?",https://stackoverflow.com/questions/563198/whats-the-most-efficent-way-to-calculate-where-two-line-segments-intersect

9th Int. Conf. on Geotechnique, Construction Materials and Environment, Tokyo, Japan, 20-22 November 2019, ISBN: 978-4-909106025 C3051

INFLUENCE OF THE FOUNDATION SIZE ON COLLAPSIBLE KHON KAEN LOESS

R. Thongpong[1] and R. Nuntasarn[2]
[1,2] Faculty of Civil Engineer, Khon Kaen University, Thailand

ABSTRACT

This paper presents the behavior of shallow foundation had a maximum load at 20 T/m^2,cast-in-situ sample for simulate old buildings at Khon Kaen University. Due to Khon Kaen loess in dry conditions have a high load capacity. However, these buildings are suffered when the soil under a shallow foundation is soaked. The volume of soil is significantly reduced, or soil is a collapse. Since the structure of this soil is a honeycomb structure, which is unstable. The size of a shallow foundation in Khon Kaen University has a variety of sizes depending on the service load. Almost the size foundation was designed by using soil parameters at the dry condition rather than a wet state. Therefore this research investigates the influence of the foundation size for bearing capacity on Khon Kaen loess in dry and wet conditions. The foundation sizes in this research are 1x1 meter and 1.2x1.2 meter, which is seated at a depth of 1.00 meters from the ground surface. Moreover, the site of testing is at Khon Kaen University. The study also considers the settlement of foundations — sudden subsidence from wet soil conditions and shear failure mode of soil. The Results on the experiment is the size of the foundation has an effect of subsidence. Larger more settlement at equal pressure and mode of shear failure is a local failure from both foundations. Suggest to prove in this study will be tested in dry condition.

Keywords: Shallow foundation, Khon Kaen Loess, Settlement, Soil parameters, Shear failure mode of soil

INTRODUCTION

The most buildings in Khon Kaen University have been built for a long time. The foundation of these old building was shallow with various sizes and depths. Due to the dry condition, the Khon Kaen loess has high strength. The foundation is the part of the structure used to support the entire building and transfer the load to the soil. Therefore engineering should be considered the engineering properties of the Khon Kaen loess to design the size of the foundation. Therefore this study investigates the effect of the foundation size on the bearing capacity at the same depth. Two sizes of the shallow foundation were 1x1 m, and 1.2x1.2 m at 1.00 m depth were studied. The result can be used in the design and actual operation, including repair and improve the strength of buildings. Moreover, this result can be worth the investment.

The objective of this paper is:

1. To study the behavior of the foundation size affecting the load capacity from the actual size foundation test
2. To study and compare the relationship between load-bearing capacity and settlement of foundations
3. To study the surface pattern caused by the mode of shear failures of soil

Udomchoke (1991) [1] explained about soil more very severe. Which can be considered that the wind-blow soil such as Khon Kaen loess have a sudden collapse. (Collapse Soil) In this type of soil is found in the arid area to the semi-arid area. Soils in this climate are mostly unsaturated. Because the underground water level is quite deep. In addition, the moisture content of the soil in the field of summer is about 3-5%. And in the rainy season is about 10-12%.

Ahmad et al. (2009) [2] presents an estimate of soil load capacity. From tests in the field and from the laboratory. To compare tests for determining the load carrying capacity of soil in the field and in the laboratory tests. The test in field is tested in 3 different areas. Depth are 2.5 meters and a circular steel sheet with an area of 1000 square centimeters. The unconfined compression test determined the shear strength of the soil sample. The results from field tests and laboratory tests, as shown in Table 1.

Table 1 Result from filed and laboratory test

Result	BH		
	1	2	3
Field Test Ks (kPa/m)	145283	152323	163443
Field Test q_{all} (kPa)	302.6	317.3	340.5
Laboratory Test (kPa)	276	320	401

The values obtained in the laboratory can confirm the determination of the load capacity from field tests, which can predict the load capacity in foundations which avoids surveying the entire area and saves both cost and time.

Briaud and Gibbens (1999) [3] used five concrete

footings sized 1x1, 1.5x1.5, 2.5x2.5, 3x3(South), and 3x3(North) m, all thick 1.5 m., and embedded 0.75 m in silty sand with a relatively constant profile of SPT blow count equal to 20 bpf. The water table deeps 4.9 m. The pressure versus settlement curves obtained from the load tests is shown in Fig. 1 the pressure under the footing was normalized by the average limit pressure of pre-boring pressure-meter tests performed within the depth of influence of the footing next to the footing. The settlement was normalized by the footing width. Fig. 2 shows that the normalization brings the five normalized curves into a narrow band. Therefore, in this case, the normalized curves are independent of footing width and can be represented by a unique curve.

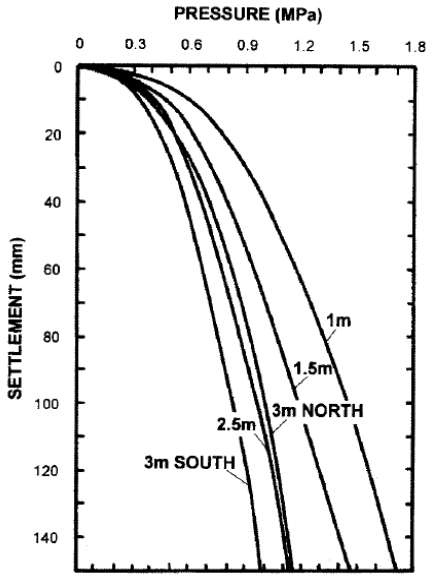

Fig. 1 The pressure versus settlement curves

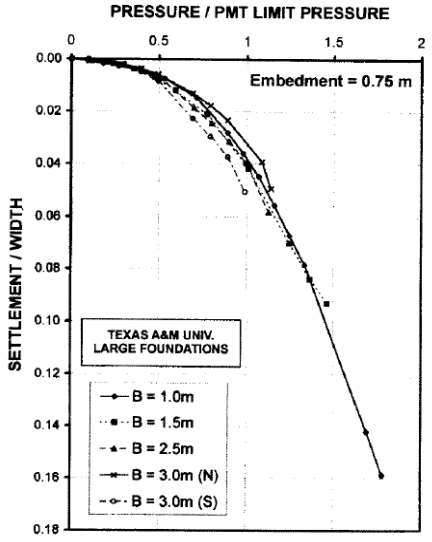

Fig. 2 The pressure/PMT versus settlement/width curves

Sanjeev et al. (2013) [4] made to study the bearing capacity and settlement characteristics of footings for develop an equation for predicting ultimate bearing capacity of two layered soils based on the test data. The footings subjected to central vertical load and resting on layered soil with the help of model tests, because in case of layer soil plate load test, the layer thickness is 2B or more, the effect of both layer will not be effected, However in case of actual large size footing the effect of lower layer will exist, Hence safe bearing capacity change. The tank size was 2000mm x 2000mm x1500mm (Length x Width x Depth). The depth below the base of the footing up to which the gravel is used is called as top layer thickness, and it thickness was varied as, 0.5B, 1.0B, 1.5B, and 2.0B, where B is the width of the plate. A total of 18 tests were conducted. For each test, load versus settlement curves were plotted and with the help of load-settlement curves, the ultimate bearing capacity of soil is determined. And the results of the tests on the field obtained

1) Same depth of sand, gravel layer. The load-bearing capacity will increase when the size of the plate load test increase, and the settlement decrease when increasing the size of the plate load test.

2) The gravel layer has a layer of sandy soil supported below. The load-bearing capacity increase when the gravel layer thickness is an increased in the test too. Moreover, the settlement is reduced.

3) The load-bearing capacity of the soil layer when L = 2B has a slightly different value from the other thickness on the gravel layer and the load-bearing capacity is constant.

Kim et al. (2017) [5] present that shallow foundations are usually located in the unsaturated area with high groundwater levels. This study investigated the influence of rainwater infiltration on subsidence behavior of shallow foundations by using numerical analysis to compare the numerical solution with experimental data from the field load test. The relative importance of density, rainwater falling in the area, and groundwater levels affecting the settlement of shallow foundations. Different groundwater levels that facilitate the absorption of rainfall, which requires numerical methods to calculate. General soil properties of the soil that are mostly residential in Korea is classified as the same type for use in numerical analysis. The study has a particular interest in the process of analyzing the flow of rain in the soil and soil deformation. The relationship between the load capacity and the subsidence obtained from that numerical method is currently consistent with field testing. The results of the parameterized study showed that the density of rainfall an important in the subsidence behavior of shallow foundations. In unsaturated soil with water changes in subsidence values during the rain have also been effective. The high groundwater levels show the affecting the change of gravity between soil grains (matric suction). Besides, it was found that the load capacity of the soil was high. Will have less permeability in the amount

of rainfall compared to the permeability of large amounts of rainfall the bearing capacity of the soil will be less. As shown in Figure 3 and 4 graph shows the relationship between settlement and stress occurring under a rainfall of two type soil conditions.

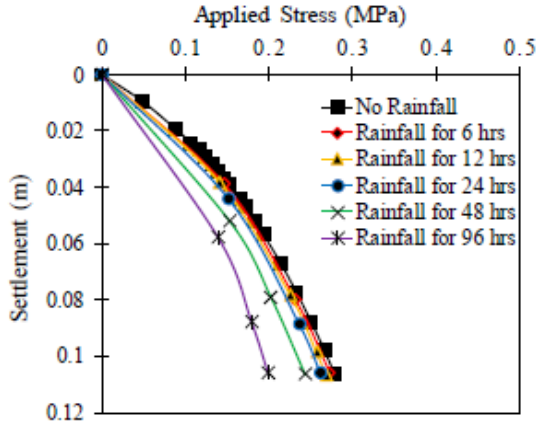

Fig. 3 Footing 5x5 m. Settlement and stress occurring under rainfall of soil type A.

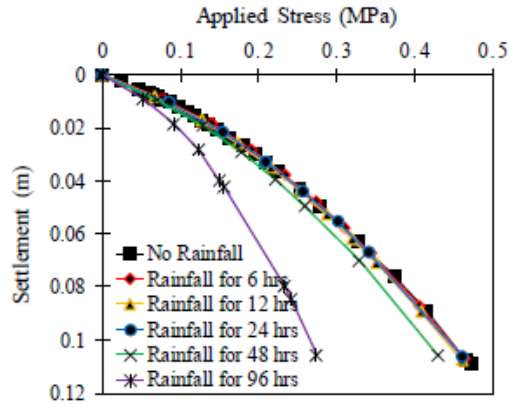

Fig. 4 Footing 5x5 m. Settlement and stress occurring under rainfall of soil type B.

METHODOLOGY

Isolated spreading footing -When the structure had a separate pillar that is reasonably separated. Where the load that is taken into the column was not very high and the soil layer is strong. Therefore, the area for weight loss does not require much space. The design is single footing for each column loading, which is economical and easy to constructed. In practice, these foundations are usually designed when the load-bearing area is not more than 10 square meters or the base area. Total not exceeding 50 percent of the building area. The characteristics of a single footing are shown in Fig. 5

Field test - The shallow foundation size of 1.0 x 1.0 m, and 1.2 x 1.2 m was installed at a depth of 1.00 m from the ground surface. Due to the limitation of the dead load, which is a pile, the maximum pressure was 20 ton per square meter. 50-ton hydraulic jack capacity was used to take pressure at 20 T/m^2 to the foundation size by size. Twenty piles were used as a dead load for 1.0 x 1.0 m, and Twenty nine piles were used as a dead load for 1.2 x 1.2 m. The equipment for settlement measurement was four LVDT attached to the reference beam at the corner of the foundation. Moreover, modes of shear failure surface measurement by elevation changing before and after taking a load to the foundation. It used ten footplates left and right of foundation long 3 times of wide foundation. The installation of the apparatus is detailed in Fig. 6, and Fig. 7.

Fig. 5 The single footing.

Fig. 6 LVDT Installation.

This study investigated the behavior of the foundation in a wet condition. The load increment in this study was 2 T/m2, and the load was maintained for 60 min. The maximum applied load was 20 T/m^2. After loading, the settlement was recorded at 1, 2, 4, 8, 15, 30, and 60 min each cycle of the load. The failure was defined as a total settlement of 25 mm. In addition, recommendations of European Committee for Standardization on Differential Settlement Parameters. [6] However, although the foundation reached the failure, the pressure was still applied to achieve 20 T/m^2.

In this study, the mode of shear failure was

studied by record the elevation of the ground surface as shown in Fig.8

Fig. 7 Footplate Installation.

After loading of to 20 T/m2, the foundation was prepared to soak condition — Embankment small dirt around the foundation for pit water. As shown on Fig. 9

In time soak condition maintain load 20 T/m2 all the time. Record settlement 30, 60, 90, 120, 150, 180 min that end of the circle for test 1.0x1.0 m, and 1.2x1.2 m to analyze behavior. Note 1x1 m. not soak condition.

Fig. 8 Recording ground surface settlement.

EXPERIMENT RESULTS

Basic Properties of Khon Kaen loess shown in Table 1. According to the hydrometer and sieve analysis found that Khon Kaen loess was classify as SM

Table 1 Basic Properties of Khon Kaen loess

Properties	
Liquid limit (LL), %	16
Plastic limit (PL), %	13.4
Plasticity index (PI), %	2.6
Specific gravitat	2.66
e	0.8
Dry density (γ_d), kPa	15.65
Sand (%)	60
Silt (%)	20
Clay (%)	20
USCS classification	SM

Moisture content at field test foundation shown in Table 2. The initial degree of saturated of both test was 32%, approximately

Table 2 Moisture content at field

Foundation (m^2)	%m Initial	%m Soak	Sr% Initial	Sr% Soak
1.0 x1.0	10	-	33.25	-
1.2x1.2	9.45	20.92	31.42	69.54

Fig. 9 Soak condition

The results of foundation size 1x1 m and 1.2x1.2 m are shown in Fig. 10 and Fig. 11, respectively. The failure load of foundation size 1x1 m and 1.2x1.2 m was 8 and 10 ton/m2, respectively. Moreover, the settlement at the pressure of 20 ton/m^2 of foundation size 1x1 m, and 1.2x1.2 m was 55 and 60 mm, respectively. According to the result, there is no significant value load failure and settlement at a load of 20 ton/m^2 for both sizes of the foundation.

Moreover, the relationship between pressure and settlement for both sizes of foundation prior soaked show the local shear failure. After soaked, the foundation was settlement about one time in three hours, as shown in Fig. 11.

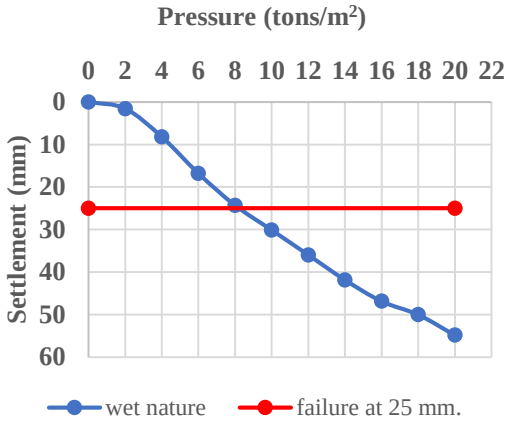

Fig. 10 Foundation 1x1 m.

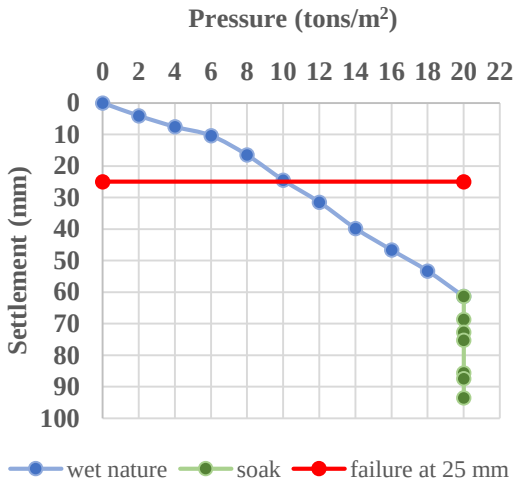

Fig. 11 Foundation 1.2x1.2 m.

The elevation of the surface shown in Fig.12 and Fig. 13 respective from 1x1 m and 1.2x1.2 m foundation. The surface movement also showed the local shear failure, which was agreed with the relationship between pressure and settlement

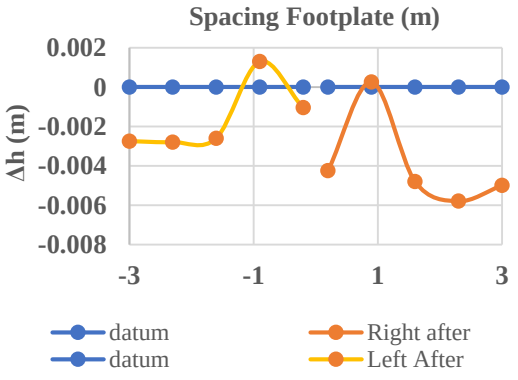

Fig. 12 Surface changing from foundation 1x1 m.

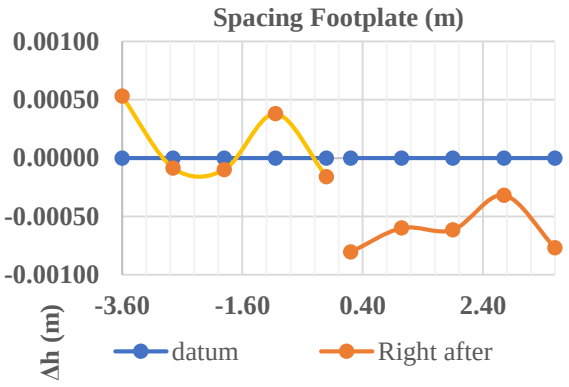

Fig. 13 Surface changing from foundation 1.2x1.2 m

DISCUSSION

The comparison of experimental results between two sizes of the foundation was present in Fig. 14. The graph shows no significant difference result between the two sizes of the foundation. The initial degree of saturation was slightly different.
Both of failure mode was a local shear failure, which is consistent with the surface displacement. Moreover, after soaking 3 hours the settlement was gained approximately 1 time. The rate of settlement was 0.05 mm per second.

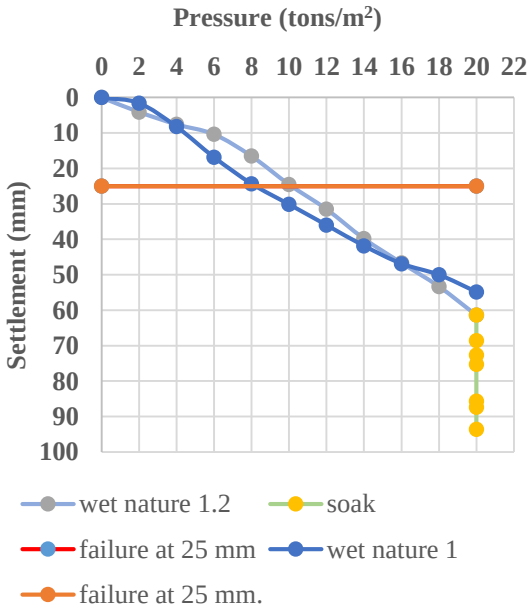

Fig. 14 Compare curve between 1.2x1.2 and 1x1 m.

CONCLUSIONS

The test result present that the size of the foundation does not affect the bearing capacity in the wet condition of Khon Kaen loess in this research. It may be the size of the foundation in this study is slightly different. Moreover, this study found that the failure mode of the foundation is local shear. Further

work, this study will investigate the shear strength parameter of Khon Kaen loess under saturated and unsaturated condition. Then the prediction bearing capacity from [7] and [8] will be compared with the field result. Meanwhile, the standard penetration test will also perform.

ACKNOWLEDGMENTS

Acknowledgment is given to the SIRDC - Sustainable Infrastructure Research and Development Center, Khon Kaen University, for the support of this research.

REFERENCES

[1] Udomchoke, V. 1991, Origin and Engineering Characteristics of the Problem Soil a in the Khorat Basin, Northeastern Thailand, Ph.D. dissertation, Asian Institute of Technology, Bangkok, Thailand.

[2] Ahmad, A.A., Qasim, A.J., and Ali, A.J., 2009. "Evaluation of Bearing Capacity from Field and Laboratory Tests", Eng. &Tech. Journal, Vol.27, No.3, 2009.

[3] Briaud, J.-L., and Gibbens, R. M. (1999). "Behavior of five large spread footings in sand." J. Geotech. Geoenviron. Eng., 125(9), 787–796.

[4] Sanjeev, K.V., Pradeep, K.J., and Rakesh, K., 2013. "Prediction of bearing capacity of granular layered soil by plate load test", International Journal of Advanced Engineering Research and Studies E-ISSN2249–8974.

[5] Kim, Y.; Park, H.; Jeong, S. Settlement Behavior of Shallow Foundations in Unsaturated Soils under Rainfall. Sustainability 2017, 9, 1417

[6] Das, B.M., 2012., Principles of Foundation Engineering – 8th editions

[7] TERZAGHI, K. (1943). Theoretical Soil Mechanics, Wiley, New York.

[8] MEYERHOF, G. G. (1963). "Some Recent Research on the Bearing Capacity of Foundations," Canadian Geotechnical Journal, Vol. 1, No. 1, pp. 16–26.

9th Int. Conf. on Geotechnique, Construction Materials and Environment, Tokyo, Japan, 20-22 November 2019, ISBN: 978-4-909106025 C3051

INFLUENCE OF A SHALLOW FOUNDATION DEPTH ON THE COLLAPSIBLE KHONKAEN LOESS

K. Piyasawat and R. Nuntasarn
Department of Civil Engineering, Faculty of Engineering, Khon Kaen University, Thailand

ABSTRACT

This research studied the bearing capacity and settlement of a shallow foundation on Khon Kaen loess. The bearing capacity and settlement of a shallow foundation was tested in the field by a static load test, at various depths for both natural and wet conditions. The foundation,1.0 x 1.0 m, seated at a depth of 1.0 meters and 1.5 meters. The foundation at a depth of 1.0 m was investigated only the wet condition but the foundations at a depth of 1.5 m were investigated in wet and dry condition. Four dial gauges were installed at the four corners of the foundation to measure the settlement due to the loading. The settlement of a 20 ton/m^2 load was observed in this study. The test result showed that the settlements of foundation at 1.5 m depth were 9 and 73 mm for dry and wet conditions, respectively and the settlement in a wet condition of foundation at 1.0 m depth was 55 mm. According to the theory, the deeper foundation has less settlement. Therefore the saturation degree was considered. The saturation degree of soil under foundation depth of 1.0 and 1.5 m was 30 and 33%, respectively. Hence it can be concluded that the degree of saturation of Khon Kaen loess is more effect to the bearing capacity rather than the depth of foundation.

Keywords: Shallow foundation, Bearing capacity, Collapsible soil, Khon Kaen loess, Static load test

INTRODUCTION

Loess is fine-grain soil which occurs extensively on Northeast Thailand. Loess has high bearing capacity when it is in a dry condition, but it has low bearing capacity when it is in a wet condition. That causes trouble in construction working.

Foundation is one of the most important structure because the vertical load of the building was transferred to the foundation. Therefore, the bearing capacity has to carry the apply load from the building.

In the past, the foundation of the building in Khon Kaen University usually used a shallow foundation because the strength of the soil is very high in the dry season. Without the consideration of the parameters in wet condition, therefore many buildings in Khon Kaen was damage due to the leaking water.

Hence, this study investigated the bearing capacity and settlement of shallow foundation on Khon Kaen loess at various depth for both natural and wet condition.

LITERATURE REVIEW

Udomchoke [1] present that the shear strength parameters of Khon Kaen loess are decreased when the moisture content is increased. Moreover, it also found that Khon Kaen loess is collapsible soil.

W.Gasaluck and R.Nuntasarn [2] present that Khon Kaen loess has a moderate degree of collapse. However, the collapse index of Khon Kaen loess is decreased by compaction at 95% by modified method. The strength of Khon Kaen loess is very high when the moisture content is low. Nevertheless, when the moisture content increases, the cohesion and friction angle are decrease and also damage to the building.

Hu Zhang et al. [3] study soil deflection in permafrost area with plate load test. Use the triangle plate and analyze by Burgers Viscoelasticity Model. This study also found that the frost heave effect on the rate of settlement. The rate of settlement increase with the ground surface temperature increase.

Bowles [4] The elastic settlement of a shallow foundation can be estimated by using the theory of elasticity (Se). The differential of the depth that the foundation seat effect on the settlement. The same type of soil will give the same modulus of elasticity and Poisson' s ratio. The net applied pressure on the foundation and depth factor are decrease when the depth of the soil increases. According to the theory, the deeper foundation has a less elastic settlement.

APPARATUS

In this study, the precast concrete size 1.0x1.0x 0.25 m was used as isolate shallow foundation, as shown in Fig 1. The counterweight was a group of pile size 0.35x0.35x5.0 m, as shown in Fig 2. Moreover, the load column, the capacity of 500 kN,

was used to measure the applied load. The settlement of the foundation was examined by using 4 Kyowa LVDTs. All electronic devices were connected to UCAM data logger, as shown in Fig 3, to record all data.

The ground surface settlement was also observed by used Leica sprinter digital levels, as shown in Fig. 4.

Fig. 1 Shallow foundation size 1 m x 1 m

Fig. 2 Electronic devices

METHODOLOGY

Khon Kaen loess was excavated at a depth of 1.0 and 1.5 m with a width of 1.4 m. Then the precast concrete as isolated spread footing was installed in the pitch. Four LVDTs were installed at the four corners of the foundation to measure the settlement due to loading. Hydraulic jack was installed at the center of the foundation for increase pressure during testing. The incremental loading was 2 ton/m^2. Reading out data from data logger at 0, 1, 2, 4, 8, 15, 30, and 60 minutes and repeat every tested pressure. In addition, footplates were installed at the side of the shallow foundation to measure ground surface displacement by Leica sprinter digital levels. The ground surface settlement was determined every loading. The foundation was soaked 3 hours, as shown in Fig.5 after pressure reach 20 tons/m^2. The pressure at soaked condition was maintained at 20 tons/m^2; meanwhile, the settlement of foundation was also measured every 30 mins.

Fig. 3 Counterweight

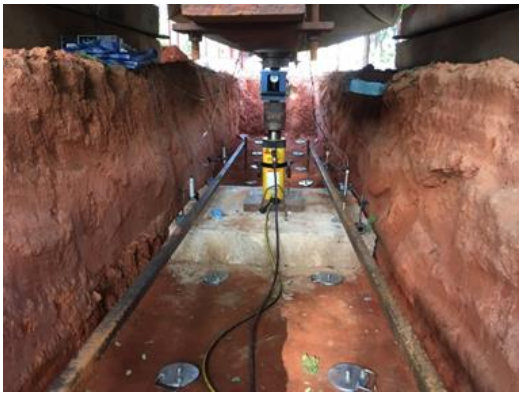

Fig. 4 The installation of the devices

Fig. 5 Soaked

LABORATORY RESULTS

The basic properties of Khon Kaen loess were present in Table 1. Khon Kaen loess was classified as

silty sand (SM) according to [4]. The majority of Khon Kaen loess is sand. The grain size distribution curve, as shown in Fig 6, was determined from sieve analysis and hydrometer analysis. The Atterberg limit, which is a liquid limit and plastic limit, showed a plasticity index of 2.6%. The specific gravity of 2.66.

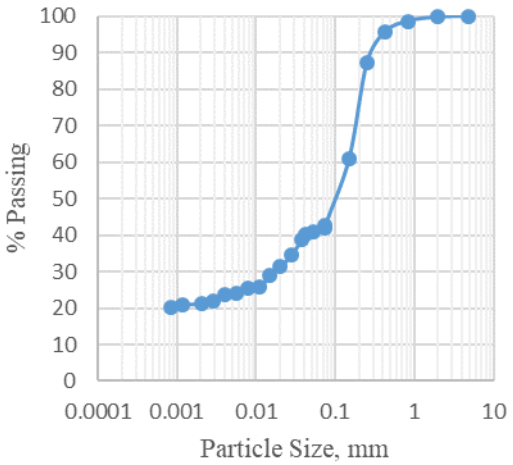

Fig. 6 Grain size distribution curve

Table 1 Basic property of Khon Kaen loess

Property	
USCS	SM
Specific gravity, G_s	2.66
Liquid limit, LL (%)	16
Plastic limit, PL (%)	13.4
Plasticity index, PI	2.6
% Passing #4	100
% Passing #200	42.74
% Silt	21.75
% Clay	20.99

FIELD TEST RESULT

There were three foundations at the same size as 1.0x1.0x0.25 m. The first foundation was studied at a depth of 1.0 m in the wet condition. The initial degree of saturation was 30%. The relationship between settlement and pressure was illustrated in Fig. 7. As the definition of the foundation failure at 25 mm settlement, the failure load was 8 t/m^2. Moreover, the graph presents the bearing capacity failure mode as a local shear failure, which agreed with the ground surface displacement, as shown in Fig. 8.

The second foundation was studied at a depth of 1.5 m in the dry condition. The initial degree of saturation was 16%. The load and settlement curve, as illustrated in Fig. 9, was not present the failure load. Since the maximum applied load in this study was 20 ton/m^2. However, the failure occurs after soaking for approximately 1 hour. The settlement rate of the foundation after soaking was 17.64 mm/hr. Moreover, the graph presents the bearing capacity failure mode as a local shear failure, which agreed with the ground surface displacement, as shown in Fig. 10.

The third foundation was studied at a depth of 1.5 m in the wet condition. The initial degree of saturation was 33%. As the definition of the foundation failure at 25 mm settlement, the failure load was 5 t/m^2. The settlement rate of the foundation after soaking was 9.71 mm/hr. Moreover, the graph also presents the bearing capacity failure mode as a local shear failure, which agreed with the ground surface displacement, as shown in Fig. 12.

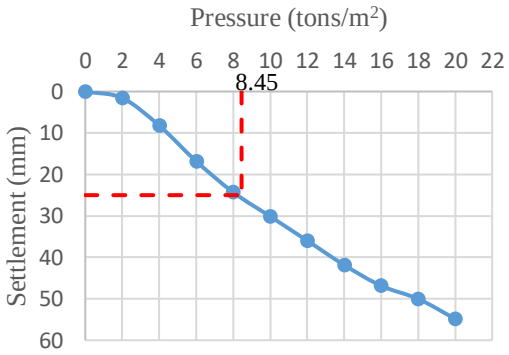

Fig. 7 Load - settlement curve of the first foundation

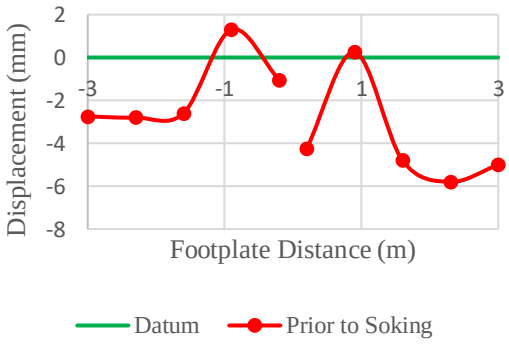

Fig. 8 Ground surface displacement of the first foundation

DISCUSSION

The comparison results between the first and the third foundation, which had the similar degree of saturation (approximately 32%) but different of the seating depth (Df), as shown in Fig. 13 found that

- The first and third foundation settlement at a pressure of 20 tons/m^2 before soak is 54.8 and 73.31 mm, respectively.

- The failure load at 25 mm settlement of the first and third foundation was 8 and 4.79 ton/m^2, respectively.

According to the theory, the foundation that seat on the deeper had a high bearing capacity and small settlement. However, the test shows otherwise. It might be the initial degree of saturation of the third foundation was higher than the first. Therefore, it can be concluded that the depth of the foundation was not entirely affected on the bearing capacity of Khon Kaen loess. However, the primary effect on the bearing capacity of Khon Kaen loess is the degree of saturation or moisture content of the soil.

The comparison results between the second and the third foundation, which had the same depth but different degree of saturation, as shown in Fig. 13 found that

- The saturation degree of the second and the third foundation was 16 and 33%, respectively.
- The second and the third foundation settlement at a pressure of 20 tons/m^2 before soaking was 9.06 and 73.31 mm, respectively.
- After soaking for 3 hours, the second and the third foundation settlement increased to be 61.97 and 102.43 mm, respectively.
- The incremental settlement of the second and the third foundation was 709.52 and 33.78%, respectively.
- The settlement rate of the second and the third foundation was 17.64 and 9.71%, respectively.
- The final moisture content of the second and the third foundation was 27.3 and 22.5%, respectively.

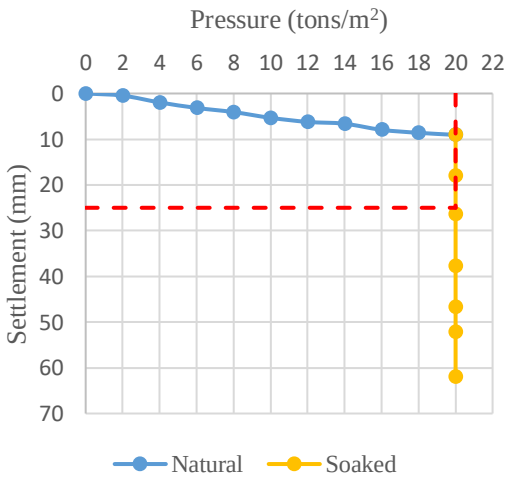

Fig. 9 Load settlement curve of the second foundation

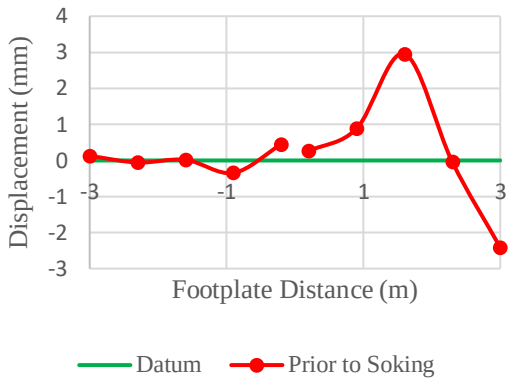

Fig. 10 Ground surface displacement of the second foundation

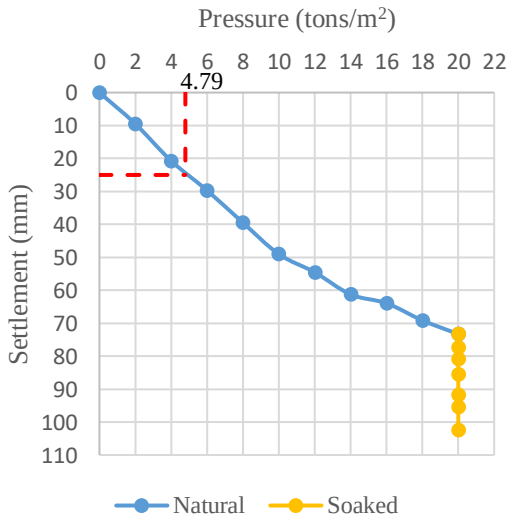

Fig. 11 Load settlement curve of the third foundation

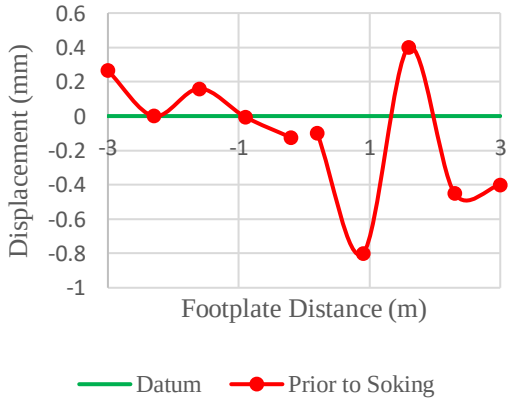

Fig. 12 Ground surface displacement of the third foundation

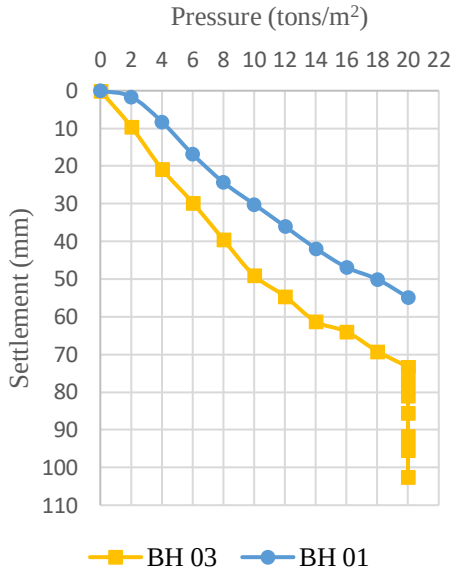

Fig. 13 Compare load settlement curve BH 01 and BH 03

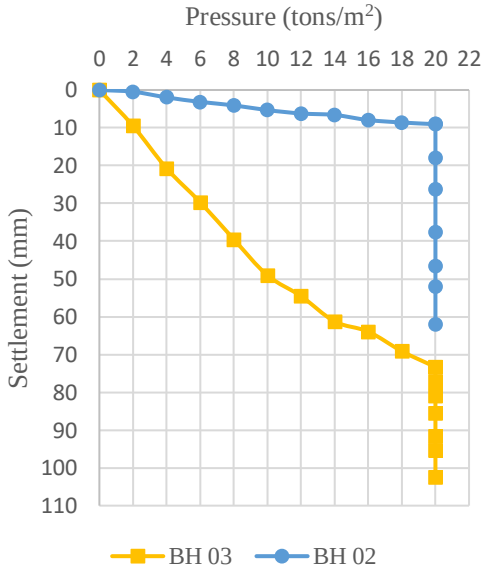

Fig. 14 Compare load settlement curve BH 02 and BH 03

CONCLUSIONS

The test results showed that the mode of failure was local shear failure. Moreover, the depth of the foundation was not entirely affected on the bearing capacity of Khon Kaen loess. However, the primary effect on the bearing capacity of Khon Kaen loess is the degree of saturation or moisture content of the soil.

ACKNOWLEDGMENTS

Acknowledgment is given to the SIRDC - Sustainable Infrastructure Research and Development Center, Khon Kaen University, for the support of this research.

REFERENCES

[1] Udomchoke V., Origin and Engineering Characteristics of the Problem Soil a in the Khorat Basin, Northeastern Thailand, Ph.D. dissertation, Asian Institute of Technology, Bangkok, Thailand, 1991.

[2] H. Zhang, J. Zhanga, K. Zhangb, B. Zhengc, Long-term plate load tests in permafrost region on the Qinghai-Tibetan
Plateau, Cold Regions Science and Technology 143, 2017, 105–111.

[3] Gasaluck W., Nuntasarn R., Behavior of Khon Kaen Loess due to High Moisture Content, Proceeding of the Eighth National Convention on Civil Engineering, The Engineering Institute of Thailand under H.M. The King's Patronage and Department of Civil Engineering, Khon Kaen University, Khon Kaen, 2002, pp. GTE 458-463

[4] American Society for Testing and Materials. (D2487-98). Standard practice for classification of soils for engineering purposes (Unified Soil Classification System).

[5] BOWLES, J. E. (1987). "Elastic Foundation Settlement on Sand Deposits," Journal of Geotechnical Engineering, ASCE, Vol. 113, No. 8, pp. 846–860

9th Int. Conf. on Geotechnique, Construction Materials and Environment, Tokyo, Japan, 20-22 November 2019, ISBN: 978-4-909106025 C3051

PRELIMINARY EXAMINATION ON IN-SITU MEASUREMENT OF NEEDLE PENETRATION RESISTANCE

Makiko Kobayashi[1], Hiroyasu Ishii[1], Tadafumi Fujiwara[1], Tomoyuki Aoki[1] and Kiyonobu Kasama[2]
[1]Technology Center, Taisei Corporation, Japan
[2]Department of Civil and Environmental Engineering, Tokyo Institute of Technology, Japan

ABSTRACT

Taking specimens from bored sample and conducting unconfined compression strength (USC) tests are common practice for strength estimation of cement improved soils. According to a Japanese practical guideline, 27 strengths in every 500 cement improved soil columns are recommended as a frequency of quality check for in-situ soil mixing method. On the other hand, the authors recognize that this frequency is the minimum level to estimate cement improvement works; it is clear that conducting more testing is ideal for further estimation to enhance work efficiency and to review design criteria. With these backgrounds, the authors are focusing on in-situ measurement of needle penetration resistance, i.e. a possible index to represent unconfined compressive strength, because it may realize multi point measurements without stepwise labors such as obtaining bored cores at site, bringing them to laboratory and shaping them to form UCS specimen. This paper deals with a fundamental study on in-situ measurement of needle penetration resistance on borehole walls prepared in cement improved layers. Using the prototype tool we have carried out the needle penetration tests in a model ground to obtain 100 trial measurements. In the same time, 2 cylindrical samples of the same model ground were prepared to measure each 25 needle penetration resistances on its surface by a conventional penetration system. Through the examination, we have found that both the measurements were consistent with each other. The results also revealed that required time for one measurement was just 72 seconds that may be effective for multi measurements at sites investigation.

Keywords: Improved soil, Penetration test, Unconfined compression strength, Quality management

INTRODUCTION

Taking specimens from bored sample and conducting unconfined compression strength (UCS) tests are most widely used for strength estimation of cement improved soils. For example, according to a quality management standard of deep mixing methods in Japan, 27 strengths in every 500 cement improved soil columns, adding 9 in another 250 columns, are recommended as a frequency of quality check in practice. While the standard is often referred to in practical works, the authors recognize that more testing is ideal for further estimation to enhance work efficiency and to review design criteria. On this occasion, just increasing the number of UCS test may be the simplest and easiest approach; it should be noted that several work steps, as described in the followings, are required before getting one UCS test result.

1) obtaining bored samples after solidification of cement improved soils
2) bringing them to laboratory
3) shaping them to form UCS test specimen
4) setting them on a test apparatus and conducting UCS test

Since these would make UCS unsuitable for multi-point investigation, we have been studying extensive application of a needle penetration resistance which can get a possible index to represent UCS. As an alternative method of strength estimation of cement improved soils, we have proposed an in-situ measurement tool which measures needle penetration resistance efficiently on borehole walls prepared in cement improved layers.

In this paper, we firstly explain conventional needle penetration tests and introduce a prototype tool which measures needle penetration resistance on borehole walls. Then we secondarily implement it to trial measurements in a model ground and estimate the results to evaluate efficiency and accuracy of the new method.

PROPOSAL OF NEW NEEDLE PENETRAION TEST

Conventional needle penetration tests

The needle penetration test, specified in Japanese Geotechnical Society Standard (JGS 3431-2012) [1], is a non-destructive test that has been designed to provide quick strength estimation for soft rocks and cement improved soils. In this test, the needle penetration resistance (N_p) is obtained as a penetration load divided by a penetration length. 10 mm penetration is normally employed as a standard length. The test method was originally established in

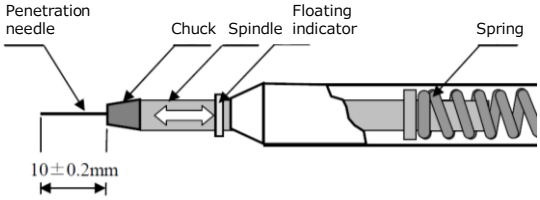

a) Portable type

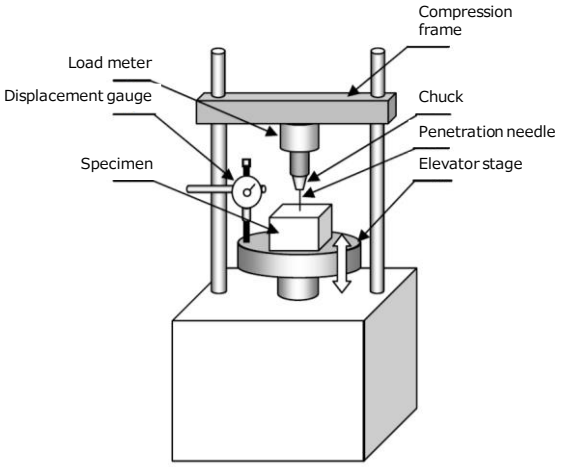

b) Desktop type

Fig. 1 Needle penetration test apparatus

Japan, and now used practically and academically in other countries. Recently a study by Ulusay et al. (2012) developed a more generalized empirical relationship for indirect estimation of the UCS from N_p based on a total of 725 UCS-N_p data pairs obtained from soft rocks to very weak rocks [2]. Kahraman et al. (2017) investigated the predictability of coal strength based on N_p and a conversion factor, 0.35, for UCS- N_p linear ration was proposed for coal samples [3].

Two types of test apparatus are currently available as shown in Fig. 1, respectively.

A portable needle penetration test apparatus (Fig. 1a, hereinafter referred to portable type) is housed in a light weight casing and composed of the spring which is contracted in proportion to the penetration load during manual operation. The needle can be pushed into in-situ ground or bored samples in core containers by hand. When the needle penetration length reaches 10mm, or the penetration load reaches the maximum value, N_p can be quickly specified by reading the penetration length and load. While a typical merit of a portable type is easiness of handling and operation, accuracy of measurement is less because rate and angle of penetration is not strictly controlled.

A desktop needle penetration test apparatus (Fig. 1b, hereinafter referred to desktop type) controls the needle penetration rate at 20±5 mm/min and measures needle penetration load by an electronic cell in laboratory. In contrast to a portable type, it is possible

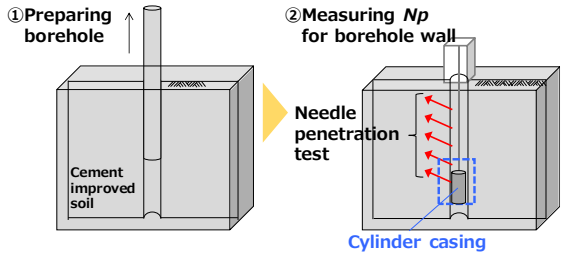

Fig. 2 Process of measuring N_p by borehole type

Fig. 3 Prototype tool

to record penetration load-length curves and obtain more reliable N_p. On the other hand, several work steps are required before conducting loading tests such as bringing sample to laboratory, shaping them to form specimen and setting them on a test apparatus, resulting in less easiness of handling and operation.

Proposal of borehole type

Considering the present two types of penetration test apparatus, we have studied concept of another method and pictured a new procedure as shown in Fig. 2. It is reasonable to be described as “a borehole type”, for which we can expect easiness of operation as well as accuracy of measurement. With further studies in detail parts, we have manufactured a prototype tool as depicted in Fig. 3. The main cylindrical casing of the tool has a diameter of 108 mm and a length of 443 mm, in which the following functions are built along with a needle penetration device:

- CCD camera (see Fig. 3A) which monitors needle penetration progress,
- reaction force device (see Fig. 3B) which pushes

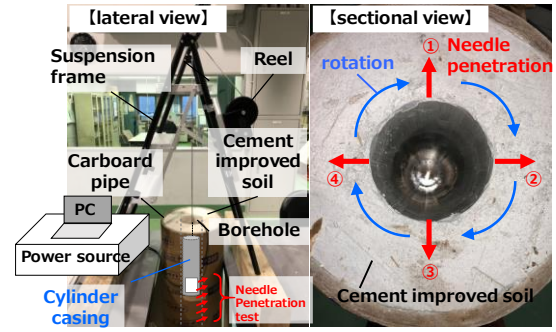

a) Borehole type

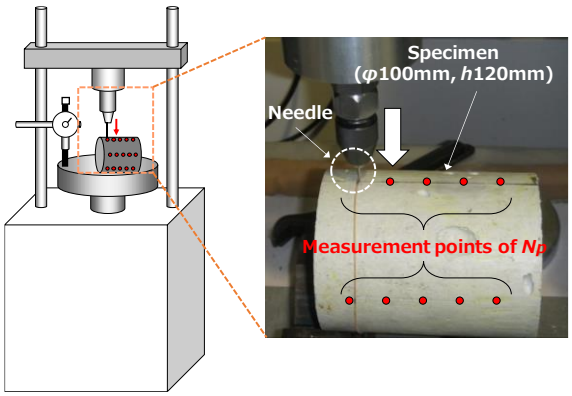

b) Desktop type

Fig. 4 Outline of laboratory tests

Table 1 Mix proportions

1. Clay slurry			
Kaolin powder (kg/m^3)	Silica sand (kg/m^3)	Water content (%)	Water (kg/m^3)
13.0	5.6	70	13.0
2. Cement slurry			
Water cement ratio (%)	Cement (kg/m^3)	Water (kg/m^3)	
60	3.2	1.9	

the main casing onto a borehole wall to fix its position

- and rotation wheels (see Fig. 3C) which adjust directions of penetration.

LABORATORY TESTS

Experimental outline

In order to evaluate efficiency and accuracy of the borehole type, we have planned the needle penetration tests as the followings:

a) Cement improved soil (a diameter of 300 mm and a length 1000 mm) keeping a borehole (a diameter of 114 mm) are prepared in a cardboard

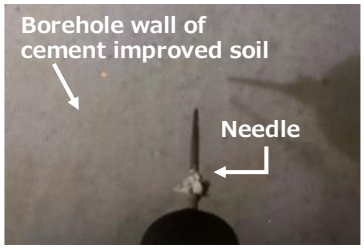

a) Before penetrating

b) Penetrating in progress

Photo 1 Images of needle penetration

to take 100 measurements of N_p by the borehole type (see Fig. 4a)).

b) Two cylindrical specimens (each diameter of 100 mm and length 120 mm) of the same model ground are prepared to conduct each 25 measurements of N_p on its surface by the desktop type (see Fig. 4b)).

Model ground preparation

Table 1 shows mix proportions with which the model ground and two cylindrical specimens were prepared. The followings are the preparation procedure:

1) Kaolin powder and silica sand were mixed with water to produce clay slurry for 5 minutes.
2) Cement was mixed with water to produce cement slurry for 1 minute.
3) The cement slurry was poured into the clay slurry, and then they were mixed to produce cement improved soil for 1 minute.
4) The cement improved soil was poured into the clearance between the cardboard pipe and the polyvinyl chloride pipe which was inserted to create a borehole.
5) The polyvinyl chloride pipe was pulled out to produce borehole walls at the material age of one day.
6) In addition, the improved soil was poured into cylindrical molds to create specimens used for desktop type measurement.

Test results

Photo 1 shows examples of images during needle penetrating which are captured by CCD camera. These images indicate that the needle penetration of

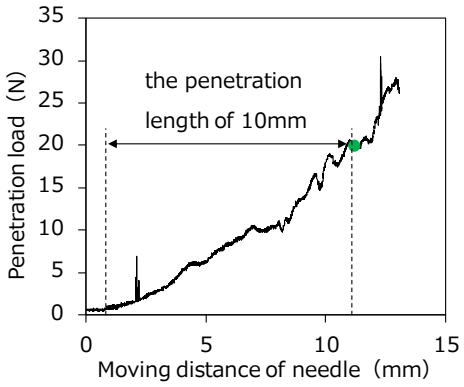

a) Borehole type

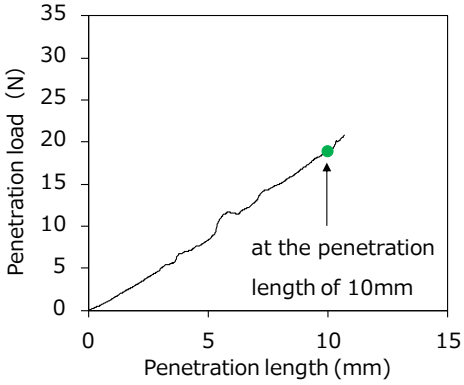

b) Desktop type

Fig. 5 The relationship between the penetration length and the penetration load

the borehole type was successfully controlled in a borehole.

Fig. 5 shows examples of the penetration load which are measured by using a) the borehole type and b) the desktop type, respectively. In case of the borehole type, the penetration load is referred to "moving distance of the needle" because the needle started to move forward from a setback position in the cylindrical casing. Accordingly, as indicated in the Fig. 5(a) the penetration length was defined in the range where a certain level of load was detected. In case of desktop type, the tip of needle was firstly set on the surface of specimen and the needle penetration was started. Therefore, the penetration load is referred to "penetration length" as shown in Fig. 5 (b). It seems that the borehole type may still have rooms to be mechanically improved because i) there are remarkable variances in some length-load curves and ii) non-liner relationships of length-load curves are observed which are not consistent with results by the desktop type. On the other hand, the trial measurements revealed that required time for one measurement was just 72 seconds; this allows us to consider that such an efficient operation using the borehole type would contribute for challenge of multi measurements in ground improvement practice.

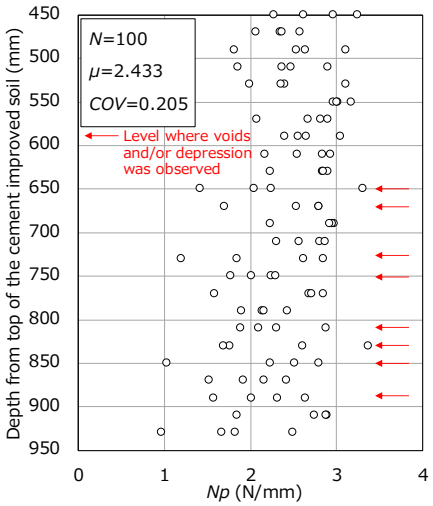

a) Borehole type

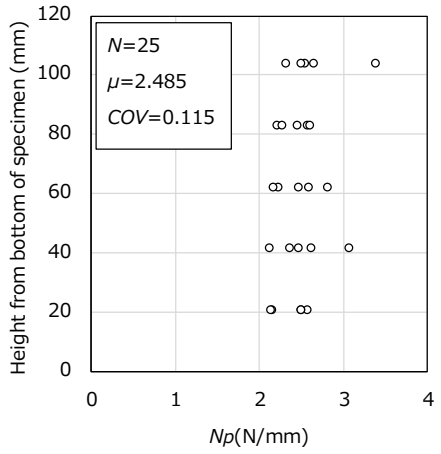

b) Desktop type (No.1 specimen)

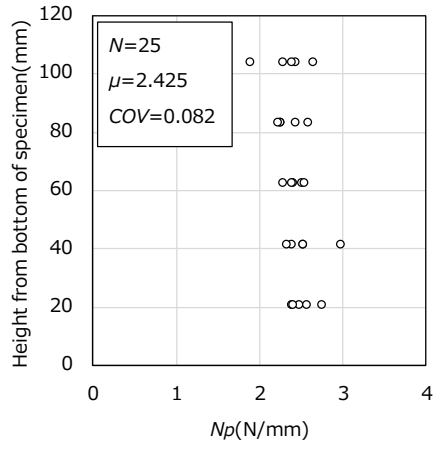

c) Desktop type (No.2 specimen)

Fig. 6 Results of N_p

Fig. 6 shows the distributions of N_p obtained from a) the borehole type, b) the desktop type (No.1 specimen) and c) the desktop type (No.2 specimen), respectively. It is clear the distribution of N_p by the

a) Depth of 670mm

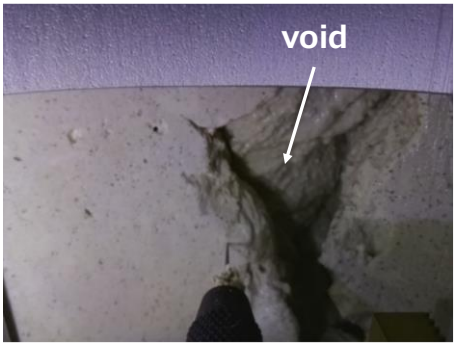

b) Depth of 890mm

Photo 2 Images monitored by camera

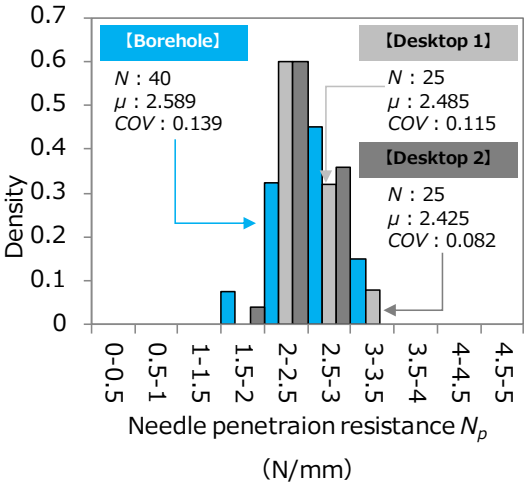

Fig. 7 Density distribution of each N_p

borehole type is more significant than ones by the desktop type. Furthermore, it may be said that the main distribution range of N_p by the borehole type is 2 to 3 N/mm having the additional distribution in the smaller range from 1 to 2 N/mm. Consequently, the coefficient variation of N_p by the borehole type is approximately twice as much as those measured by the desktop type.

In order to investigate the cause of the wider distributions of N_p, we have reviewed images captured by CCD camera during the penetration test. Photo 2 shows example images at a) depth of 670mm and b) depth of 890mm, respectively. Many voids and depressions were observed on the borehole walls which might have been created during the model ground preparation. This indicates that the cement mixed soil in these areas might be less compacted which may result in less strength. These kinds of the image were confirmed at many levels in the cement improved soil as indicated by the arrows in Fig. 6a. This leads us to consider the cement improved soil below 650mm may have been prepared improperly due to work difficulties affected by the deeper part of the carbonate pipe.

Finally, we reconfirmed the N_p by removing data below the 650 mm and the density distribution, defined as the frequency divided by its total number of data, was obtained as shown in Fig. 7. The remaining 40 measurements of N_p gives us the coefficient of variation of 0.139. It results that a frequency distribution of N_p by the borehole type is almost equivalent to one by the desktop type; the borehole type may be able to measure N_p of the model ground without a substantial difference from the desktop type.

CONCLUSIONS

In this study, we conducted needle penetration tests to evaluate efficiency and accuracy of the borehole type which was newly proposed as a device suitable for multi-point measurements. The following conclusions were obtained:

- The needle penetration of the borehole type was successfully controlled in a borehole, even though it has rooms to be mechanically improved.
- A frequency distribution of N_p can be obtained by the borehole type which is almost equivalent to one by the desktop type.
- Required time for one measurement of N_p was just 72 seconds by the borehole type, suggesting that it may be effective for multi measurements in fields.

In addition to the present work, we are focusing on upgrade of estimation formula of UCS based on N_p [4] and expecting better accuracy of UCS estimation. We wish these studies would be the first step of the development of a new system which can contribute to detailed analysis of ground improvement practice.

ACKNOWLEDGMENTS

This work was supported by grants from Japan Institute of Country-ology and Engineering.

REFERENCES

[1] The Japanese Geotechnical Society, Japanese

Geotechnical Society Standard -Geotechnical and Geoenvironmental Investigation Methods-, Vol. 3, 2018.

[2] Ulusay, R. and Erguler, Z.A., Needle penetration test: Evaluation of its performance and possible uses in predicting strength of weak and soft rocks, Engineering Geology, Vol. 149-150, 2012, pp. 47-56.

[3] Kahraman, S., Aloglu, A.S., Aydin, B. and Saygin, E., The needle penetration test for predicting coal strength, the Journal of the Southern African Institute of Mining and Metallurgy, Vol. 117, 2017, pp. 587-591.

[4] Kobayashi, M., Ishii, H. and Fujiwara, T., Fundamental study on strength evaluation of cement treated sand using needle penetration test, Proceedings of the 13th National Symposium on Ground Improvement, 2018, pp. 169–172. (in Japanese)

9th Int. Conf. on Geotechnique, Construction Materials and Environment, Tokyo, Japan, 20-22 November 2019, ISBN: 978-4-909106025 C3051

COMPARISON OF MACROPORE STRUCTURE AND NETWORK OF AUTOCLAVED AERATED CONCRETE (AAC) BLOCKS USING MICRO-FOCUS X-RAY CT

Akihiro MATSUNO[1], Shin ISHIZUKA[1], Trong Lam NGUYEN[2], Van Tuan NGUYEN[2], Hoang Giang NGUYEN[2], and Ken KAWAMOTO[1,2]

[1]Graduate School of Science and Engineering, Saitama University, Japan

[2]National University of Civil Engineering, Vietnam

ABSTRACT

Autoclaved Aerated Concrete (AAC) is a lightweight cementitious material and has a unique structure characterized by a solid skeleton and pores (porous media). Currently, AAC is widely used in many building applications all over the world due to its advantages such as low density and thermal conductivity, high heat resistance, and so on. However, the quality of AAC including internal pore structure and network is highly dependent on materials and manufacturing process. In this study, using two different AAC block samples manufactured in Japan and Vietnam (JP-AAC and VN-AAC, respectively), 3-dimensional macropore structure and network (typical in > 30 μm diameters) were visualized and analyzed using a microfocus X-ray CT (MFXCT). The final goal of study is to characterize structure and network of macropores in AAC and to correlate the macropore characteristics to mass transport processes in AAC. First, the tested samples (~ 5 cm dimension cube) were scanned with different scanning resolution (SR) with 12, 30 and 50 μm /voxel and region of interest (ROI) with 300 voxels. Then, the pore structural parameters such as effective pore radius (r_{eff}), coordination number (N), and tortuosity in z direction (T_{zz}) were analyzed. The results show the difference in SR greatly affected the Mean value of r_{eff} for both JP-AAC and VN-AAC. A relatively difference can be observed in the Mean value and Standard Deviation (SD) of T_{zz}. For JP-AAC, the T_{zz} showed a SD ranging from 0.33 to 0.54. On the other hand, the measured T_{zz} for VN-AAC showed a SD ranging from 0.35 to 0.49.

Keywords: Autoclaved Aerated Concrete (AAC), Macropore structure, Macropore network, Micro-focus X-ray CT system (MFXCT),

INTRODUCTION

Autoclaved Aerated Concrete (AAC) is a lightweight cementitious material and has a unique structure characterized by a solid skeleton and pores (porous media). Currently, AAC is widely used in many building applications all over the world due to its advantages such as low density and thermal conductivity, high heat resistance, and so on [1].

A typical process for the production of AAC includes hydrothermal treatment of a mixture of quartz sand, lime, cement, gypsum and other additives at high temperature (typically, 180–200°C) under saturated steam pressure, which results in the formation of crystalline calcium silicate hydrates, namely, tobermorite ($Ca_5Si_6(O,OH,F)_{18}5H_2O$) [2]. Therefore, due to the influence of the manufacturing process, multiple pores are generated.

The diameter (d) of the pores is classified into Micropores of d <10 μm and Macropores of d≥10 μm. Micropores are mainly composed of Tobermorite. SEM images show the layered structure of Tobermorite [3]. Trong [4] shows the distributions of Pore size and pore volume of Japanese-made AAC (JP) and Vietnamese-made AAC (VN1 and VN2) measured by Mercury Intrusion Porosity (MIP). The pore size distribution of JP and VN1 are bimodal, whereas the curves of VN2 are almost single peak. However, the volume of fine pores with the pore radius of around 10 nm, is much higher in JP (about 0.594 ml/g) than that in VN1 (about 0.372 ml/g). That is the reason why, a clear difference was seen at d <10 μm in JP, VN1 and VN2, but no significant difference was seen at d≥10 μm of the MIP measurement.

However, although AAC possesses a clear difference in Micropore, up to now, only a few studies have shown differences due to differences in the manufacturing process at the macropore level.

Therefore, the purpose of this research is to visualize and analyze the structure of macropore level with Micro-Focus X-ray CT (MFXCT). That is visualization and analysis of structures of macropores using a MFXCT system and particle/pore network analysis software. On the other hand, the structure and network of pore of AAC control physical properties such as surface area, water retention, thermal conductivity, and gas diffusion. Therefore, macropores analysis results can be used to model

mass transfer coefficients (including water retention capacity) that control physical properties, and for quality control.

METHODS

First, the target materials are AAC from Japan (manufactured by Asahi Kasei Corporation): JP-AAC and AAC from Vietnam: VN-AAC1. The macropores of these two samples did not differ much with the naked eye.

These air-dried materials were cut on a rectangular solid so that the volume could be seen. The weight of the air-dried condition was then measured. The samples were then saturated to fill all the pores with water. From this saturated condition, water was removed by suction pressure method (pressure chamber method). The suction pressure is based on the relationship (1) of the pore diameter and the matrix potential by capillary action,

$$H = \frac{0.3}{d} \qquad (1)$$

where H is the matrix potential and d is the pore size. From this, the matrix potential H=-300 cm H_2O (ε_{300}) corresponding to the macropores (d> 10 μm or r> 5 μm) was calculated.

Scanning conditions for MFXCT system (inspeXio SMX-90CT, Shimadzu Co Ltd. Japan) include Energy level is 90 kV, 110 μA, View number is 1800, Average number is 4, Scan number is 1, Image size is 1024x1024 pixels, Scaling factor is 150, Scanning Resolution (SR) is 12, 30, 50 μm / voxel, FOV (XY) is 12.3, 30.7, 51.2 mm and FOV (Z) is 6.5 in Field of view (FOV), 16.2, 27.0 mm, and the number of slices is 541.

The CT image data of the sample scanned by MFXCT system was reconstructed and then analyzed by ExFact VR 2.1 (Nihon Visual Science Inc., Japan). Region of interest (ROI) is 300 voxels. The CT image data in this range was imaged into 8 bits and then binarized. The threshold value of luminance as a reference of the binarization is a value at ε_{300}, which is set to each of JP-AAC and VN-AAC1 samples. The threshold value as a reference of the binarization is a value at ε_{300}, which is set to each of JP-AAC and VN-AAC1 samples. From the above, the locations of macropores and solid and micropores of 8-bit CT image data could be seperated.

Next, the effective pore radius (r_{eff}) of Macropores is shown using ExFact VR 2.1.r_{eff} is the pore radius calculated by assuming each pore as a sphere. At the same time, Numbers of pores connected to a pore, the Coordination number (N), and Tortuosity (T_{zz}), which characterizes the tortuous path of pore, are shown.

T_{zz} is defined in (2).

$$T_{ZZ} = \frac{L}{L_s} \qquad (2)$$

where L is the actual path, and L_s is the shortest path.

RESULTS AND DISCUSSION

Table 1 shows the results of the porosity (φ) according to the dry density ρ_d (g/cm^3) and mineral density ρ_s (g/cm^3) of JP-AAC and VN-AAC1 samples and each condition.

Table 1 Comparison of density and porosity between JP-AAC and VNAAC1 samples

Items	ρ_d (g/cm^3)	ρ_s (g/cm^3)	φ (Total)	φ (ε_{300})
JP-AAC	0.50	2.15	0.77	0.34
VN-AAC1	0.53	2.71	0.80	0.46

According to Table 1, ρ_d is almost the same between JP-AAC and VN-AAC1 samples, in which ρ_s is larger in VN-AAC1 sample. It is found that Total φ is almost the same, and φ at ε_{300} is larger in VN-AAC1 sample.

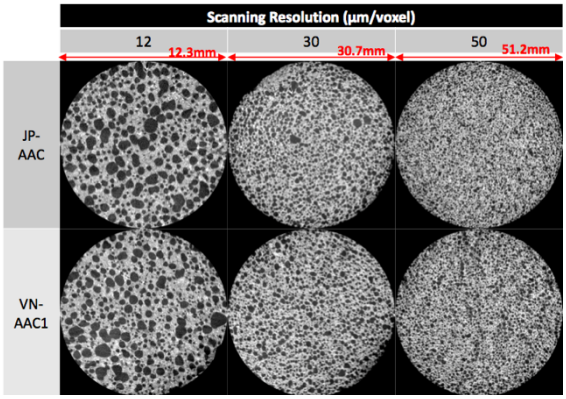

Fig. 1 MPR image (Brightness Level, Range: Auto).

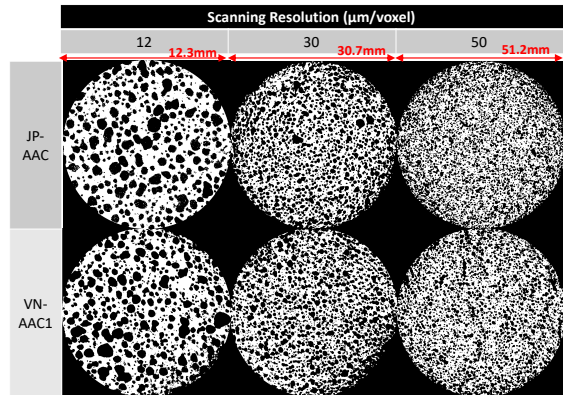

Fig. 2 MPR image (binarized with ε_{300}).

Fig. 1 shows a comparison of MPR images of (Brightness Level, Range: Auto) between JP-AAC and VN-AAC1 samples. With observed by the naked eye, no big difference can be seen in each SR. However, Fig. 2 shows a comparison of binarized MPR images with ε_{300}. The black zone shows macropores, and The white zone shows solids and micropores. Also, no big difference is seen in each SR.

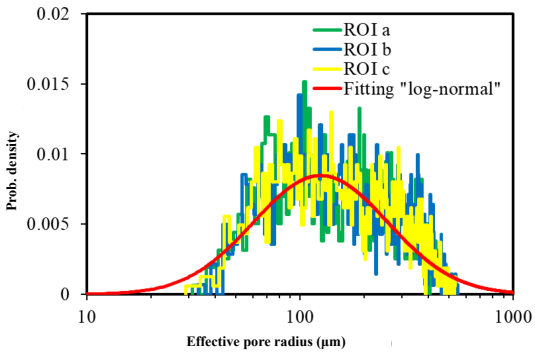

Fig. 3 Distribution of Effective pore radius (r_{eff}).

Fig. 3 shows an example of JP-AAC's Prob. Density and r_{eff}. From this, from the method of [5], three normal distribution curves were fit with ROI = 300 voxels. This result is given in Fig.4. Similarly, Fig.5 and Fig.6 show N and T_{zz} (All paths) are shown, respectively, where 3 normal distribution curves of the same posision of ROI = 300 voxels are fit. These fitting are based on the Shapiro-Wilk test, ANOVA test, and Kruskal-Wallis test ([6, 7]). Table 2 and Table 3 show the mean value (Mean) and standard deviation (SD) of r_{eff}. Similarly, Table 4 and Table 5 show the mean value (Mean) and standard deviation (SD) of T_{zz}.

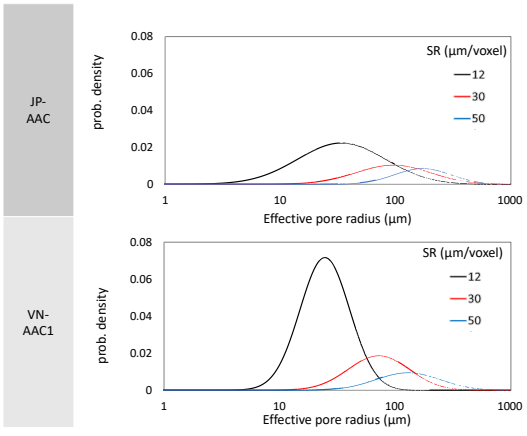

Fig. 4 Normal distribution of Effective pore radius (r_{eff}).

Table 2 Comparison of Mean value of r_{eff}

SR μm	12 Mean	30 Mean	50 Mean
JP-AAC	186.1	301.0	412.5
VN-AAC1	149.2	358.9	562.5

Table 3 Comparison of Standard Deviation (SD) of r_{eff}

SR μ m	12 SD	30 SD	50 SD
JP-AAC	115.9	164.6	228.1
VN-AAC1	107.9	221.3	347.4

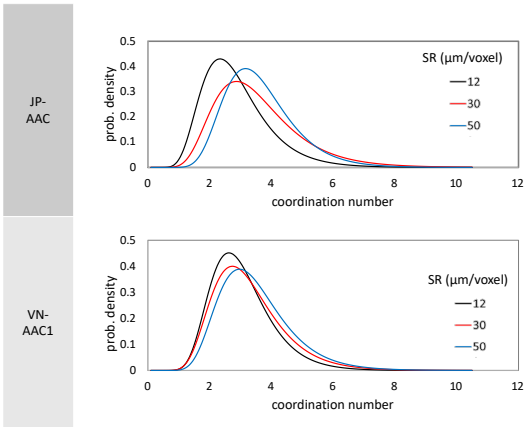

Fig. 5 Normal distribution of coordination number (N).

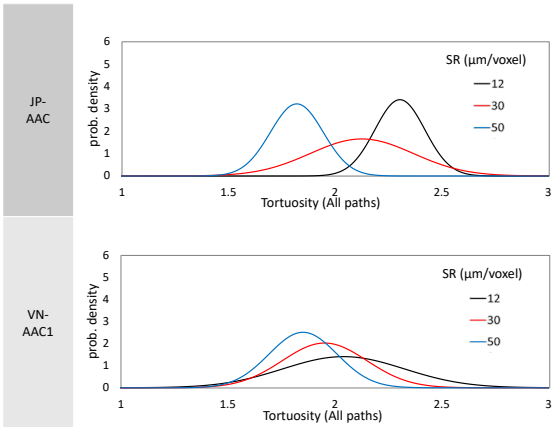

Fig. 6 Normal distribution of T_{zz} (All paths).

Table 4 Comparison of Mean value of T_{zz} (All paths)

SR	12	30	50
	Mean	Mean	Mean
JP-AAC	3.04	2.33	2.05
VN-AAC1	2.33	2.24	2.08

Table 5 Comparison of Standard Deviation (SD) of T_{zz} (All paths)

SR	12	30	50
	SD	SD	SD
JP-AAC	0.54	0.46	0.33
VN-AAC1	0.49	0.43	0.35

These data show no significant difference of N between JP-AAC and VN-AAC1 samples. Besides, in SR = 30, 50 of r_{eff}, the JP-AAC sample has a larger variation than the VN-AAC1 sample, and Mean is also larger in the VN-AAC1 sample. The difference in SR limits the minimum resolution, which may result in this, but the VN-AAC1 sample is larger. According to [5], there is a positive correlation between the r_{eff} and the air permiability, so it is considered that the VN-AAC1 sample is a material that is easier to ventilate.

Moreover, T_{zz} is larger in the JP-AAC sample at SR = 12, 30 and almost the same in SR = 50. However, T_{zz} of the JP-AAC sample is higher than that of the VN-AAC1 sample. According to [8], it is shown that T_{zz}, when converted, is close to the measured value of the gas diffusion coefficient. Moreover, since this T_{zz} is higher in the JP-AAC sample than in the VN-AAC1 sample, low air permeability is expected, and the heat insulation is considered to be higher than in the VN-AAC1 sample. In addition, the VN-AAC1 sample is expected to have low thermal insulation in comparison, and it can be said that it is a material suited to the conditions of high temperature and humidity in Vietnam, compared to the JP-AAC sample.

CONCLUSIONS

Focusing on the same macropores of JP-AAC and VN-AAC1 in appearance, to scan and visualize these by MFXCT system, then to use software and analyze the particle / pore network. The result is that r_{eff} is about 50-57 μm larger for VN-AAC1 sample and N is almost the same, and that T_{zz} is 0.03-0.05 for JP-AAC sample. From this, it is considered that a clear difference between JP-AAC and VN-AAC1 samples of the pore network of macropore.

Acknowledgments

This research was supported by JST-JICA Science and Technology Research Partnership for Sustainable Development (SATREPS) project (No. JPMJSA1701).

This Research grant is the Research Management Bureau, Saitama University (FY2018-FY2019)

REFERENCES

[1] van Boggelen, W., and van Boggelen, J. Sustainable building solutions with new generation autoclaved aerated concrete panel applications. ce/papers, Vol. 2, Issue 4, 2018, pp.513-525.

[2] Matsui, K., Kikuma, J., Tsunashima, M., Ishikawa, T., Matsuno, S.-y., Ogawa, A., and Sato, M. In situ time-resolved X-ray diffraction of tobermorite formation in autoclaved aerated concrete: Influence of silica source reactivity and Al addition. Cement and Concrete Research,Vol. 41, Issue 5, 2011, pp.510-519.

[3] Liu, Y., Leong, B. S., Hu, Z.-T., and Yang, E.-H. Autoclaved aerated concrete incorporating waste aluminum dust as foaming agent. Construction and Building Materials,Vol. 148, 2017, pp.140-147.

[4] Nguyen T. L., Asamoto, S., and Matsui, K. Sorption isotherm and length change behavior of autoclaved aerated concrete. Cement and Concrete Composites,Vol. 94, 2018, pp.136-144.

[5] Hamamoto, S., Moldrup, P., Kawamoto, K., Sakaki, T., Nishimura, T., and Komatsu, T. Pore network structure linked by X-ray CT to particle characteristics and transport parameters. Soils and Foundations,Vol. 56, Issue 4, 2016, pp.676-690.

[6] Luo, L., Lin, H., and Li, S. Quantification of 3-D soil macropore networks in different soil types and land uses using computed tomography. Journal of Hydrology,Vol. 393, Issue 1-2, 2010, pp.53-64.

[7] Paradelo, M., Katuwal, S., Moldrup, P., Norgaard, T., Herath, L., and de Jonge, L. W. X-ray CT-Derived Soil Characteristics Explain Varying Air, Water, and Solute Transport Properties across a Loamy Field. Vadose Zone Journal,Vol. 15, Issue 4, 2016.

[8] Arjun Baniya, K. K., Shoichiro Hamamoto, Toshihiro Sakaki, Takeshi Saito, Karin Müller, Per Moldrup, and Toshiko Komatsu. Linking Pore Network Structure Derived by Micro-focus X-ray CT to Mass Transport Parameters in Differently Compacted Loamy Soils. Soil research, 2019, accepted.

9th Int. Conf. on Geotechnique, Construction Materials and Environment, Tokyo, Japan, 20-22 November 2019, ISBN: 978-4-909106025 C3051

RECYCLED GYPSUM AND RICE HUSK ASH AS ADDITIVES IN THE STABILIZATION OF EXPANSIVE SOIL

Jomari F. Tan[1], Mary Ann Q. Adajar[1]
[1]Department of Civil Engineering, College of Engineering, De La Salle University, Philippines

ABSTRACT

Expansive soils pose great risk to the structural integrity of many overlying structures. Given the impracticality of mechanical means of ground improvement in smaller projects, chemical stabilization is preferred. An economic and sustainable way of improving weak soils can be achieved with waste utilization of discarded materials as enhancing additives. Clay loam from Kauswagan, Lanao del Norte were treated with varied proportions of recycled gypsum and rice husk ash. Evaluation of the effectiveness of the admixtures were done based from criteria and laboratory tests listed by NSCP 2010 Section 303.5 and ASTM D4609. Addition of gypsum as lone additive increases plasticity, while further addition of RHA finally diminishes plasticity. Compaction characteristics at 15% gypsum + 10% RHA had maximum dry density increased by 1.918 kN/m^3 and optimum water content decreased by 26%. While overall decrease in swelling was observed, only specimens with 15% gypsum + 10% RHA were considered non-expansive (EI < 20) by NSCP 2010. Mean compressive strengths of specimen were enhanced with a peak value of 1.128 MPa at 15% gypsum. Considering criteria from ASTM D4609 and NSCP Section 303.5, an admixture combination of gypsum and RHA can be considered effective in improving expansive soils.

Keywords: Expansive soils, Recycled gypsum, Rice husk ash, Soil stability, Expansion index

INTRODUCTION

Expansive soils are a type of soil which exhibit significant changes in volume. Comprised primarily from volcanic material, its composition enables this change as manifested through a cyclic shrink-swell behavior. Climatic conditions influence the soil condition due to its dependence on moisture [1]. Torrid weather facilitates shrinking in soil, while heavy rainfall triggers consequent ground swelling. This soil characteristic is primarily determined by certain clayey minerals such as kaolinite and montmorillonite, components which allow greater water absorption [2]. Repeated shrink-swell cycles eventually result to differential ground movement, causing varying degrees of damage to overlying structures. Conventional solutions to poor soil conditions often implement soil replacement with better quality fill or compaction using heavy equipment. Despite their effectiveness, these practices raise concerns on their environmental footprint and economic viability. A more practical solution can be found through chemical soil stabilization. In this method, an additive is applied to the soil to improve engineering properties. Based from the National Structural Code of the Philippines, improvement by chemical means is recommended when designing foundations [3] to prevent potential damages to houses and buildings. Additives in soil stabilization often contain cementitious or pozzolanic properties which are known catalysts in improving soil conditions. While materials such as lime and cement are established additives already, these promote excessive carbon dioxide emissions during production, leaving a great environmental impact in the process. Waste and other discarded materials can be considered cheaper and more sustainable options.

Gypsum is chemically known as calcium sulfate. As an industrial material, gypsum is commonly used in cement and drywall production. Discarded forms of gypsum can be sourced from waste plasterboards and manufacturing rejects. Originating in Japan, the practice of recycling gypsum was done in response to the growth of their construction industry beginning in 1970 [4]. It has been used in ground improvement for road embankments and highways. Its cementitious properties were found to induce strength development in past studies [5],[6].

Challenges may be encountered with gypsum as a lone stabilizer in wet environments. Previous studies raised the necessity for a solidification agent to improve its performance as a stabilizer [5]. A second additive should be paired with recycled gypsum to achieve better soil conditions.

Rice husk is the most abundant agricultural waste in the Philippines. While its original form provides little to no beneficial or nutritional use, its incinerated form exhibits good characteristics. Rice husk ash contains rich amounts of silica and aluminum which exhibit pozzolanic properties that can facilitate strength development [7]. Moreover, RHA costs less and is produced in greater quantities compared to other chemical additives. Commonly, RHA is being used as fertilizer, fuel, or partial cement replacement.

The main objective of this study is to examine the effectiveness of a recycled gypsum-RHA mix in mitigating volume change and improving strength of expansive soils. Evaluation of results shall be measured using engineering properties such as Atterberg Limits, Maximum Dry Density (MDD), Optimum Moisture Content (OMC), Expansion Index (EI) and Unconfined Compression Strength (UCS). The study also determines the physical and chemical composition of the tested expansive soil and each additive. Finally, the study aims to find the best gypsum-RHA mix proportion that yields the most desirable result in reducing swelling and enhancing compressive strength.

Repurposing waste gypsum for soil stabilization is necessary given that its disposal poses harmful impacts to the environment. Organic materials may react with sulfates in discarded gypsum to form hydrogen sulfide gas. Hence, recycling gypsum reduces its environmental impact. Moreover, the use of RHA is highly encouraged, given that the Philippine rice production marks at 2 million tons annually [8]. The measure presented by this study leans towards low-cost sustainable approaches to improve weak expansive soils and to provide alternate disposal options for discarded materials.

MATERIAL AND METHODS

Source of Expansive Soil

The soil to be investigated in this experiment was gathered from Kauswagan, a coastal municipality located in the province of Lanao del Norte in the Philippines. The specimen belongs under the Adtuyon soil series which was initially identified in barangay Adtuyon in the municipality of Pangantucan in Bukidnon. This soil series is characterized to have been developed from volcanic deposits which consist of basalt and andesite boulders. surface soils were observed to be brown, friable, and granular like clay. Meanwhile, the subsoil is generally darker in color with hints of reddish tint in some cases. Possessing clayey properties, the subsoil is plastic in the presence of moisture, but hard and brittle in dry conditions [9]. Moist soil samples changed the color into a darkened pale brown mixture (Fig 1a). A sticky and viscous texture was also observed among all test specimens. This was indicative of the cohesive trait found in all clayey and expansive soils. Dry samples exhibit significant cracking and reduction in volume, indicating its shrink-swell tendencies (Fig 1b).

Source of Recycled Gypsum

Recycled gypsum was sourced from a small wet market stall which sells the powder as plaster for nearby construction projects. Recycled gypsum is typically prepared from three different sources. Waste are obtained from excess and rejected plasterboard from manufacturing, new construction, and demolition. Contaminants from nails, screws, paint, wall coverings etc. are removed prior to recycling process. The collected waste gypsum is pulverized into powder form and is typically heated at 130℃ to 160℃ depending on the preference of the recycling company.

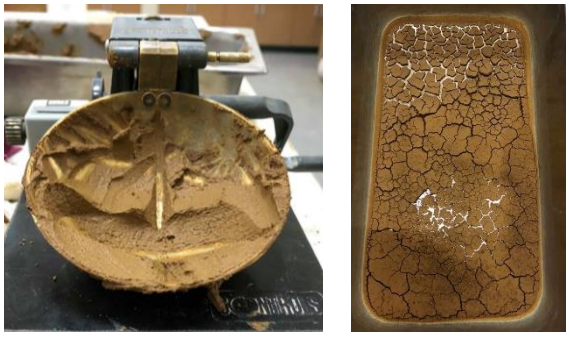

a) moist soil b) dry soil

Fig. 1 Moist and dry soil samples from the study

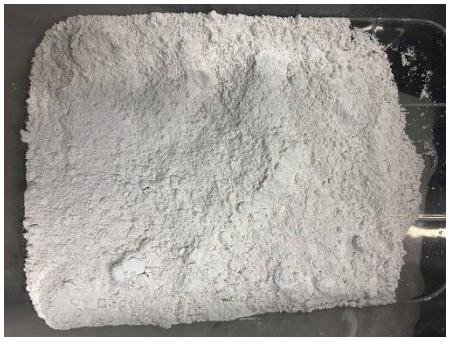

Fig. 2 Recycled gypsum samples used in the study

Source of Rice Husk Ash

Rice husk ash was obtained from Restored Energy Biomass Power Plant in Muntinlupa City, Metro Manila. The rice husk sourced from the plains of Nueva Ecija were incinerated by the said company at a fixed high temperature to create power using biomass energy [10]. The byproduct of this process yields roughly textured ash. The material was sourced from a lone power plant to preserve the consistency of its properties. Moreover, the ash samples were stored away from environments which may compromise its quality.

Experimental Procedure

Before proceeding with the primary laboratory tests required to determine additive effectiveness, test soil samples were subjected for verification on its expansivity in accordance with standards set by Section 303.5 of the NSCP 2010 [3].

Fig. 3 Rice husk ash samples used in the study

Parameters given by the NSCP criteria were obtained using ASTM laboratory tests. Section 303.5 indicates that expansive soils can identified through its plasticity and particle size characteristics. Table 1 enumerates the required values that would classify a test soil sample as expansive.

Table 1 NSCP Criteria to Identify Expansive Soils

Parameter	Criteria
Liquid Limit, LL (%)	Greater than 50
Plasticity Index, PI (%)	Greater than 15
Percentage of soil particles passing the #200 sieve (%)	More than 10% of the particles pass the #200 sieve
Percentage of soil particles less than 5μm in size (%)	More than 10% of the particles are less than 5μm in size
Expansion Index, EI	Greater than 20

The laboratory tests performed on untreated and treated samples are enumerated in Table 2. These procedures were based from ASTM standards to establish a reference in evaluating the index properties and potential for shrink-swell behavior of tested samples.

Table 2 Laboratory procedures based from ASTM standards to determine index properties and potential for shrink-swell behavior

Laboratory Test	ASTM Standard
Specific Gravity Test	ASTM D854
Grain Size Analysis (Mechanical and Hydrometer Method)	ASTM D422
Liquid Limit Test	ASTM D4318
Plastic Limit Test	ASTM D4318
Expansion Index Test	ASTM D4829

The effectiveness of recycled gypsum and RHA as additives were tested as per provisions indicated by ASTM D4609. The criteria for assessing the test samples is summarized in Table 3.

Table 3 Laboratory procedures based from ASTM standards to evaluate the effectiveness of recycled gypsum and RHA as admixtures.

Parameter	Criteria
Liquid Limit, LL (%)	Significant reduction
Plasticity Index, PI (%)	Significant reduction
Maximum Dry Density, MDD (kN/m^3)	Increase by 80kg/m^3 (0.785 kN/m^3)
Optimum Moisture Content, OMC (%)	Decrease by 15%
Unconfined Compressive Strength, q_u (kPa)	Increase by 345 kPa

Five experimental trials were performed for each soil-additive mixture. The test results from ASTM D4609 and ASTM D4829 were the basis for assessment on the effectiveness of the additives. The admixture is only considered effective when the sample meets the required value for expansion index and unconfined compressive strength.

Mixture Preparation

The tests were divided into two sets: gypsum-only and gypsum-RHA mixtures. Both mixture sets were made by replacing varying percentages of the soil volume with the admixture. Calculations were based from the index properties of the soil and the additives. Both sets were mixed with gypsum at percentages of 5%, 10% and 15%. For the gypsum-RHA set, the rice husk ash was mixed at a constant percentage of 10%. Mixtures were cured for minimum period of 16 hours prior to performing laboratory tests.

TEST RESULTS

Soil Classification

Table 4 displays the resulting index properties of the test soil sample required for classifying the soil.

Table 4 Summary of Soil Classification

Parameter	Criteria	Result	Remarks
Liquid Limit, LL (%)	> 50	64.78	Pass
Plasticity Index, PI (%)	> 15	18.64	Pass
Percentage passing #200 sieve (%)	> 10%	59.14	Pass
Percentage less than 5μm (%)	> 10%	0.00	Fail
Expansion Index, EI	> 20	98	Pass
USCS Classification	MH (high plasticity silt)		

The results indicated that the soil sample did not meet the criterion on particle size. However, the rest of the index properties classified the test soil as expansive as the value of the expansion index governs. The EI value of the test soil was found at 98. Based from the USCS Classification, Kauswagan soil is classified as MH (high plasticity silt).

Evaluation of Additives as Stabilizing Agents

Atterberg Limits

Atterberg limits are threshold markers which indicate the moisture content values which represent the transition of soil from one consistency to another. Table 5 provides the average values for the each Atterberg limit tested for the soil-additive mixtures. ASTM D4609 states that a soil additive is deemed effective when significant reduction in liquid limit and plasticity index.

Table 5 Atterberg Limits of Soil-Additive Mixtures

Mixture	Liquid Limit (%)	Plastic Limit (%)	Plasticity Index (%)
Kauswagan Soil	64.776	46.847	17.929
5% Gypsum	79.060	42.937	36.122
10% Gypsum	75.326	39.851	35.747
15% Gypsum	71.815	37.486	34.329
5% Gypsum + 10% RHA	59.372	36.237	23.135
10% Gypsum + 10% RHA	56.184	36.828	19.356
15% Gypsum + 10% RHA	53.270	36.887	16.383

Test results show the trend in liquid limit values in the two set of additive proportions follow distinct behaviors. The inclusion of gypsum in the plain soil increased the liquid limit of the soil, yet a gradual increase in gypsum resulted into incremental decrease in liquid limit. A decrease is usually expected when introducing stabilizer agents, but several studies have reported the reverse occurrence [11],[12]. Gypsum used in construction manifests its ability to improve strength at high moisture content since its composition allows higher water absorption capacity. The eventual decrease in liquid limit with increase in gypsum was due to reduction of clay particles.

On the other hand, samples with a constant 10% RHA content saw a general decrease in liquid limit with the increase in gypsum content. RHA does not exhibit plasticity when exposed to moisture. Further soil particle replacement with the addition of non-plastic ash was a cause of the eventual decrease in plasticity.

Compaction Characteristics

Soil compaction demonstrates the relationship between densifying effect of repeated mechanical effort and the amount of moisture present in soils. Compaction parameters – maximum dry density and optimum moisture content – indicate the condition required to reach the most compact state of soil. Table 6 presents the values of these compaction parameters obtained using the proctor method.

Table 6 Compaction Values of Soil-Additive Mixes

Mixture	Maximum Dry Density (kN/m^3)	Optimum Moisture Content
Kauswagan Soil	11.916	42.415%
5% Gypsum	12.185	41.184%
10% Gypsum	12.405	39.940%
15% Gypsum	12.627	37.168%
5% Gypsum + 10% RHA	13.384	34.279%
10% Gypsum + 10% RHA	13.729	32.626%
15% Gypsum + 10% RHA	13.835	31.395%

ASTM 4609 requires a decrease of 15% for optimum moisture content and increase in $80kg/m^3$ for maximum dry density. When converted into kN/m^3, the required increase in density is 0.785 kN/m^3. A maximum decrease of 12.37% in moisture content for gypsum-only specimen and 25.98% for gypsum-RHA specimen was observed. Moreover, increases of 0.711 kN/m^3 and 1.918 kN/m^3 were obtained for gypsum only and gypsum + 10% RHA samples respectively. The resulting values suggest that 15% gypsum was nearly statistically effective in stabilizing the tested soil, but a minimum content of 5% gypsum + 10% RHA was adequate to be considered effective. However, it should be noted that the conditions from ASTM D4609 were suggested values to ensure experimental error did not affect results. Individual trial results were found to be consistent in values, which allows the additives to be considered effective.

Unconfined Compressive Strength

The unconfined compression strength of a given soil specimen is the peak axial stress resisted by an unconfined cylindrical soil specimen. The absence of confining pressure in the specimen eases the determination of the undrained shear strength. Figure 4 displays the trend between the strength of each soil-additive mixture and the curing period. The weekly values indicate that longer curing improves strength.

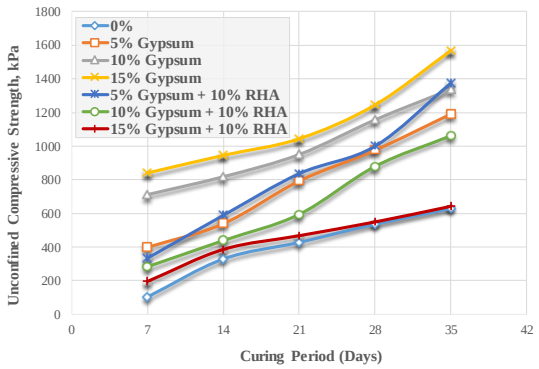

Fig. 4 Unconfined compressive strength of soil-additive mixtures vs. curing period

Reconstituted laboratory samples cannot recreate strength at in-situ conditions. However, particle rearrangement occurs when the remolded specimens were kept undisturbed during curing period. Constant moisture and composition when curing allows partial strength gains [13].

ASTM D4609 considers an additive effective when UCS increases by at least 345 kPa (50psi). The results shown by Figure 5 show that UCS of gypsum-only increase significantly with addition of gypsum for all curing period. Meanwhile, Figure 6 indicates that adding gypsum-RHA mix initially increases strength before decreasing eventually.

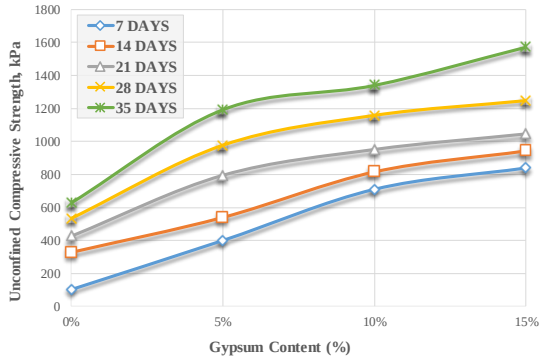

Fig. 5 UCS values of gypsum-only soil specimen vs. gypsum content

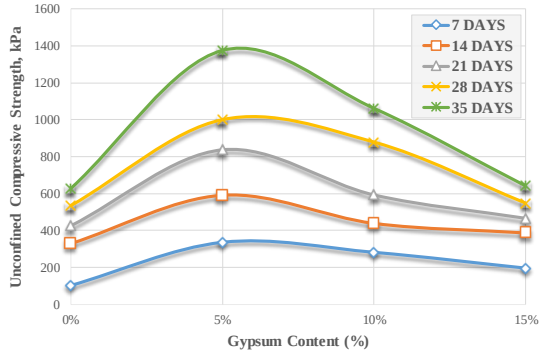

Fig. 6 UCS values of gypsum-only soil specimen vs. gypsum content

Gypsum has cementitious characteristics which enabled samples to gain strength over time. However, RHA is a non-cohesive material which deterred the strength development of the soil over time, resulting to the decrease for gypsum-RHA specimen.

Expansion Index

Expansion index measures the swelling potential of a given specimen. NSCP 2010 Section 303.5 defines EI as the determinant of the expansiveness of a given soil. The section states that a value exceeding 20 is considered expansive. Identifying the degree of expansiveness of a soil type is an important task in geotechnical engineering, considering the risks posed by weak soils to overlying structures. This parameter influences design considerations in foundations. Table 6 provides the mean expansion indices of each mixture.

Table 6 Expansion Index of Soil-Additive Mixtures

Mixture	Expansion Index	Potential Expansion
Kauswagan Soil	98	High
5% Gypsum	72	Medium
10% Gypsum	54	Medium
15% Gypsum	33	Low
5% Gypsum + 10% RHA	52	Medium
10% Gypsum + 10% RHA	28	Low
15% Gypsum + 10% RHA	11	Very Low

The EI of the soil saw a diminishing trend with each addition of gypsum and rice husk ash into the specimen. Introducing 15% gypsum reduced EI from 98 to 33, while adding 10% RHA decreased EI further to 11. An expansion index of 11 is considered non-expansive by NSCP 2010. The significant dip in expansiveness of the specimen was a consequence of clay particles replaced by material with either cementitious or non-plastic properties. The soil contains large portions of clay particles which can be linked to its high plasticity and expansion index. The calcium content of gypsum promoted particle hardening which limited the soil swelling. Moreover, RHA possessed good adsorption capacity which limited the attraction of water with clay particles when the specimen was fully inundated, eventually reducing EI into 11.

CONCLUSION

The summation of findings from the conducted study which introduced recycled gypsum and rice husk ash into expansive soil conclude the following:

Initial addition of gypsum increased liquid limit by 22%. However, a mixture of 15% gypsum and rice husk ash decreased liquid limit by 11.5%. This behavior cannot confirm the effectivity of the admixtures in diminishing plasticity of soil. Favorable results were found with compaction characteristics, with gypsum providing an increase in dry unit weight by 0.71 kN/m^3 and a decrease in OMC by 12.37%. Gypsum + RHA was more effective with improvements of 1.918 kN/m^3 and 26% respectively. Gypsum also greatly enhanced strength of 35-day samples with 15% gypsum providing 945 kPa mean increase compared to untreated samples. Slight increases in strength were observed with gypsum-RHA treated specimen, but improvement lessens with added gypsum content. Highest reduction in expansion index was achieved with 15% gypsum + RHA from 98 to 11. This is considered non-expansive based from NSCP Section 303.5.

Future work on this research are encouraged to focus on shear strength of soil based on short-term and long-term loading scenarios. Other agricultural wastes may also be considered as complementary to recycled gypsum.

REFERENCES

[1] Shi, B., Chen, S., Han, H., & Zheng, C. (2014). Expansive Soil Crack Depth under Cumulative Damage. *The Scientific World Journal*.

[2] Cokca, E. (2001). Use of Class C Fly Ashes for the Stabilization of an Expansive Soil. *Journal of Geotechnical and GeoenvironmentalEngineering*.

[3] ASEP. (2010). National Structural Code of the Philippines 2010, Chapter 3: Earthworks and Foundations.

[4] Ahmed, A. & Issa, U. (2014). Stability of soft clay soil stabilised with recycled gypsum in a wet environment. *Soils and Foundations*, *54*(3), 405-416.http://dx.doi.org/10.1016/j.sandf.2014.04.09

[5] Ahmed, A., Ugai, K., & Kamei, T. (2011). Investigation of recycled gypsum in conjunction with waste plastic trays for ground improvement. *Construction and Building Materials*, *25*(1), 208-217. http://dx.doi.org/10.1016/j.conbuild mat.2010.06.036

[6] Sivapullaiah, P. & Jha, A. (2014). Gypsum Induced Strength Behaviour of Fly Ash-Lime Stabilized Expansive Soil. *Geotechnical and Geological Engineering*, *32*(5), 1261-1273. http://dx.doi.org/10.1007/s10706-014-9799-7.

[7] Della, V., Kuhn, I., & Hotza, D. (2002). Rice husk ash as an alternate source for active silica production. *Materials Letters*, 818-821.

[8] Belonio, A. (2014). *Utilization of Rice Husks in the Production of Renewable Energy.* PHIL SCAT.

[9] Carating, R., Galanta, R., & Bacatio, C. (2014). *The Soils of the Philippines.* Quezon City: Springer.

[10] Marsh, D. (2008). WRAP: Comprehensive life-cycle analysis of plasterboard. *Global Gypsum Magazine*, 24-26. Retrieved from https://www.ct.gov/deep/lib/deep/waste_management_and_disposal/solid_waste_management_plan/gypsumwallboard/jan2010/wrap_-_comprehensive_life-cycle_analysis_of_plasterboard_may_2008. pdf

[11] Degirmenci, N. (2008). The using of waste phosphogypsum and natural gypsum in adobe stabilization. *Construction and Building Materials*, *22*(6), 1220-1224. http://dx.doi.org/10.1016/j.conbuildmat.2007.01.027

[12] Kumar, S., Dutta, R., & Mohanty, B. (2014). Engineering Properties of Bentonite Stabilized with Lime and Phosphogypsum. *Slovak Journal of Civil Engineering*, 35-44.

[13] Das, B. (2010). *Principles of Geotechnical Engineering.* Stamford, CT: Cengage Learning.

9th Int. Conf. on Geotechnique, Construction Materials and Environment, Tokyo, Japan, 20-22 November 2019, ISBN: 978-4-909106025 C3051

ALLOWABLE SOIL BEARING CAPACITY REFERENCE FOR QUEZON CITY, PHILIPPINES

Jonathan R. Dungca[1]
[1]Faculty, De La Salle University, Philippines

ABSTRACT

Quezon City is the largest city in the National Capital Region of the Philippines. This city has several other cities and provinces that bound it. North Caloocan and the province of Bulacan bound the northern portions of the city. The eastern side of the city is bounded by Marikina city, the city of Manila and the province of Rizal. Mandaluyong, Pasig and San Juan bound the southern portions of the city. And finally, the western portions of the city are bounded by the cities of Valenzuela and South Caloocan. This paper provides the estimated allowable soil bearing capacity at different locations within the city. The allowable soil bearing capacity is being used by structural engineers when determining the required sizes of the shallow foundation for the structures that they are going to build. Several borehole data were collected to estimate the geotechnical parameters. The geotechnical parameters such as the angle of internal friction, cohesion, and unit weight were estimated using the SPT values derived from the collected borehole data. These geotechnical parameters were then used to estimate the allowable soil bearing capacity using Terzaghi equation for bearing capacity. The final output is a map of the city showing the contours of different colors which correspond to the different values of the allowable soil bearing capacities. Due to the presence of Guadalupe tuff formation at shallow depths, the estimated allowable soil bearing capacity ranges from a low od 100 kPa near the ground surface to as high as 1000kPa at a depth of five meters.

Keywords: Soil Bearing Capacity, Foundation Design, Standard Penetration Test, Geotechnical Properties

INTRODUCTION

Quezon City is located near the center of Metro Manila, towards the northeastern portion of the metropolis. It is bordered by Manila City in the southwest, Caloocan City and Valenzuela city in the west and northwest, San Juan City and Mandaluyong City in the south, while Pasig City and Marikina City in the southeast. It has a total land area of 161.126 km^2, which is one-fourth the area of the National Capital Region of the Philippines.

Quezon city is underlain by a thick sequence of predominantly water laid tuff and tuffaceous clastics collectively known as the Guadalupe Tuff Formation. The formation consists of lithified volcanic ash, lapili and crystal sands. Beds rich in sand and not directly derived from volcanic activity are common, especially in the upper section. They are generally compacted and slightly lithified or cemented by precipitated silica and/or clay. The underlying Tuff bedrock is generally well consolidated and cemented, however, varying degrees of chemical decomposition and disintegration are indicated at different intervals in the section with beds alternating with hard and unaltered layers [1].

There are 130 borehole locations that were used in this study. Borehole data from standard penetration tests (SPT) were collected within the city. The distribution of these data points is shown in Figure 1.

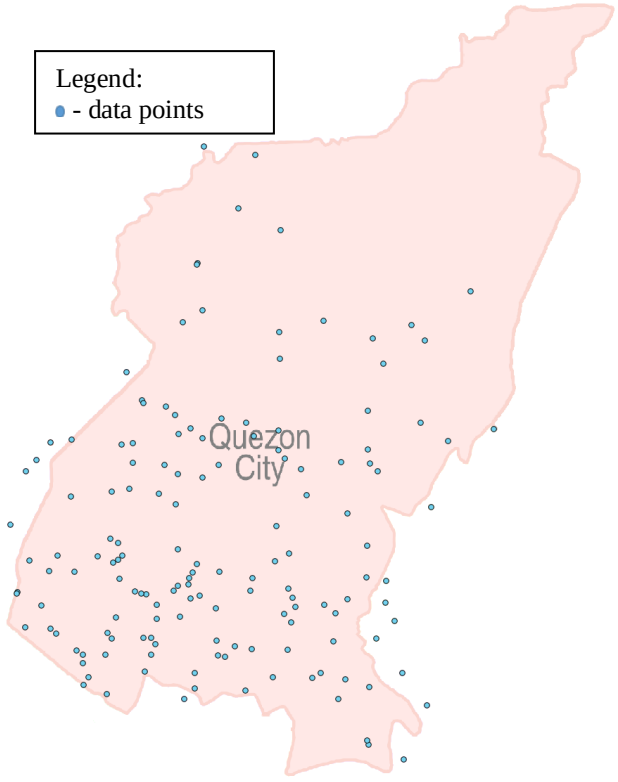

Fig. 1 Distribution of soil data in Quezon City

GEOTECHNICAL CHARACTERISTICS

The northern section of Quezon City is predominantly composed of silty sand, and high plasticity silts and clay up to the second meter; well-graded sand, low plasticity silts, and high plasticity silts and clays are the dominant soil type in the succeeding depths. Minor presences of poorly-graded sand and clayey sand are also observed. The central section is predominantly underlain by well-graded sand, silty sand, and high plasticity silts and clay with minor presences of clayey sand and low plasticity silt. Traces of well-graded gravel and poorly-graded sand are also observed. The southwestern section is predominantly underlain by silty sand, high plasticity silts and clays for depths reaching two meters; well-graded sand, low plasticity silts and high plasticity clays dominate the succeeding depths. Minor presence of clayey sand is observed as well as traces of poorly-graded sand and organic materials. The southeastern section is predominantly underlain by silty sand, high plasticity silts and clays up to a depth of two meters; well-graded sand, low plasticity silts and high plasticity clays dominate the lower depths. Minor presence of clayey sand is observed as well as traces of poorly-graded sand [2]. Table 1 further shows the distribution of the different soil types of both sections in varying depths up to a depth of five (5) meters. Table 2 shows the relevant design parameters that can be used for the designs of foundation in this area.

In soil sampling procedure, all sections are generally done by SPT up to the 2nd meter with mixed preference of SPT and RQD in the 3rd meter, and then the use of RQD in the succeeding depths.

Table 1 Soil type distribution for the (a) northern, (b) central, (c) southwestern and (d) southeastern sections of Quezon City

(a)

SYMBOL	DEPTH				
	1m	2m	3m	4m	5m
GP	0.00	0.00	0.00	0.00	0.00
GW	0.00	0.00	0.00	0.00	0.00
GM	0.00	0.00	0.00	0.00	0.00
GC	0.00	0.00	0.00	0.00	0.00
SP	5.88	5.88	0.00	0.00	0.00
SW	0.00	5.88	17.65	23.53	17.65
SM	35.29	17.65	0.00	0.00	0.00
SC	5.88	11.76	0.00	0.00	0.00
ML	5.88	5.88	5.88	17.65	23.53
MH	29.41	23.53	29.41	11.76	11.76
CL	0.00	0.00	0.00	0.00	0.00
CH	17.65	29.41	47.06	47.06	47.06
OR	0.00	0.00	0.00	0.00	0.00

(b)

SYMBOL	DEPTH				
	1m	2m	3m	4m	5m
GP	0.00	0.00	0.00	0.00	0.00
GW	0.00	0.00	0.00	0.00	2.94
GM	0.00	0.00	0.00	0.00	0.00
GC	0.00	0.00	0.00	0.00	0.00
SP	2.94	0.00	0.00	0.00	0.00
SW	2.94	14.71	14.71	35.29	35.29
SM	29.41	23.53	29.41	11.76	11.76
SC	5.88	2.94	2.94	2.94	0.00
ML	0.00	11.76	11.76	14.71	8.82
MH	20.59	17.65	11.76	8.82	2.94
CL	0.00	0.00	0.00	0.00	0.00
CH	38.24	29.41	29.41	26.47	38.24
OR	0.00	0.00	0.00	0.00	0.00

(c)

SYMBOL	DEPTH				
	1m	2m	3m	4m	5m
GP	0.00	0.00	0.00	0.00	0.00
GW	0.00	0.00	0.00	0.00	0.00
GM	0.00	0.00	0.00	0.00	0.00
GC	0.00	0.00	0.00	0.00	0.00
SP	2.50	0.00	0.00	0.00	0.00
SW	2.50	12.50	17.50	30.00	35.00
SM	32.50	32.50	27.50	7.50	7.50
SC	5.00	10.00	5.00	0.00	0.00
ML	0.00	10.00	17.50	20.00	22.50
MH	30.00	12.50	7.50	10.00	7.50
CL	0.00	0.00	0.00	0.00	0.00
CH	25.00	22.50	25.00	32.50	27.50
OR	2.50	0.00	0.00	0.00	0.00

(d)

SYMBOL	DEPTH				
	1m	2m	3m	4m	5m
GP	0.00	0.00	0.00	0.00	0.00
GW	0.00	0.00	0.00	0.00	0.00
GM	0.00	0.00	0.00	0.00	0.00
GC	0.00	0.00	0.00	0.00	0.00
SP	2.70	0.00	0.00	0.00	0.00
SW	8.11	16.22	24.32	29.73	29.73
SM	18.92	24.32	10.81	8.11	10.81
SC	2.70	2.70	2.70	5.41	2.70
ML	16.22	10.81	16.22	13.51	16.22
MH	32.43	24.32	10.81	2.70	0.00
CL	0.00	0.00	0.00	0.00	0.00
CH	18.92	21.62	35.14	40.54	40.54
OR	0.00	0.00	0.00	0.00	0.00

Table 2 Design parameters for foundation design

SYMBOL	DESCRIPTION	TYP. UNIT WEIGHTS										
		Abv. GWT (kN/m^3)			Blw. GWT (kN/m^3)			emax			emin		
GP	Poorly Graded Gravel	17.5	-	20.5	19.5	-	22.0	0.48	-	0.48	0.18	-	0.18
GW	Well-Graded gravel	17.5	-	22.0	19.5	-	23.5	0.52	-	0.85	0.32	-	0.54
GM	Silty Gravel	16.0	-	20.5	19.5	-	22.0	0.60	-	0.64	0.25	-	0.33
GC	Clayey Gravel	16.0	-	20.5	19.5	-	22.0	0.60	-	0.72	0.33	-	0.34
SP	Poorly-Graded Sand	15.0	-	19.5	19.0	-	21.0	0.34	-	0.85	0.13	-	0.54
SW	Well-Graded Sand	15.0	-	21.0	19.0	-	23.0	0.52	-	0.90	0.32	-	0.48
SM	Silty Sand	12.5	-	21.0	17.5	-	22.0	0.60	-	0.90	0.33	-	0.48
SC	Clayey Sand	13.5	-	20.5	17.5	-	21.0	0.60	-	0.80	0.33	-	0.48
ML	Low Plasticity Silt	11.5	-	17.5	12.5	-	20.5	0.60	-	1.36	0.33	-	0.83
MH	High Plasticity Silt	11.5	-	17.5	11.5	-	20.5	0.60	-	1.10	0.33	-	0.60
CL	Low Plasticity Clay	12.5	-	17.5	11.5	-	20.5	0.69	-	1.10	0.34	-	0.60
CH	High Plasticity Clay	12.5	-	17.5	11.0	-	19.5	1.02	-	1.36	0.54	-	0.83
OR	Organic Materials	11.5	-	12.5	11.5	-	16.5	0.60	-	0.92	0.33	-	0.54

METHODOLOGY

Quezon City has an approximate land surface area of 160 square kilometers. a density of 0.80 borehole locations per square kilometer was used to describe the geotechnical characteristics and possible foundation design parameters of the said area. Borehole logs were collected for a total of 130 locations all over Quezon City.

The amount of borehole logs alone is not the only criterion in gathering data for the study. It is just as important as, that the locations of the borehole logs be properly distributed. To check their distribution, each of the locations of the borehole logs was plotted in a map of Quezon City. After this, the distribution was visually inspected and the areas that needed more data were determined. Aside from these, borehole logs that seemed erroneous were removed and disregarded.

In properly designing shallow foundations, the geotechnical characteristics and allowable bearing capacity of the soil must be known. This is because the design would largely depend on the strength and the behavior of the soil. The bearing capacities are computed using the SPT-N values found in the borehole logs which were corrected using the procedures discussed in [1], [3]-[5], also shown in Equation 1.

$$N_{60} = \frac{E_m C_B C_S C_R C_N N}{0.6} \qquad \text{(Eq. 1)}$$

Where: N_{60} is the corrected SPT-N value (blows/ft), E_m is the hammer efficiency, C_B is the borehole diameter correction, C_S is the sampler correction, C_R is the rod length correction, C_N is the overburden pressure correction and N is the SPT-N recorded in the field.

The corrected SPT, N_{60}, values were then used to compute for various geotechnical parameters such as relative density, undrained shear strength and angle of internal friction using different correlation factors [6]-[10]. As such, the group computed the ultimate bearing capacity. The Terzaghi's and Vesic's bearing capacity formulas, shown on Equations 2 and 3 respectively, were used to achieve this [11]- [13].

$$q_{ult} = 1.2cN_c + \gamma D_f N_q + 0.4\gamma B N_\gamma \qquad \text{(Eq. 2)}$$

where: q_{ult} is the ultimate bearing capacity, γ is the effective unit weight, B is the width of foundation, D_f is the depth of foundation below ground surface, N_c, N_γ and N_q are the Terzaghi's factors.

$$q_{ult} = c' N_c s_c d_c i_c b_c g_c + \sigma'_{zD} N_q s_q d_q i_q b_q g_q + 0.5\gamma' N_\gamma s_\gamma d_\gamma i_\gamma b_\gamma g_\gamma \qquad \text{(Eq. 3)}$$

Where: s_c, s_q, s_γ are shape factors; d_c, d_q, d_γ are depth factors; i_c, i_q, i_γ are load inclination factors; b_c, b_q, b_γ are base inclination factors; and g_c, g_q, g_γ are ground inclination factors.

A factor of safety of 3.0 was divided to ultimate bearing capacity to determine the allowable soil bearing capacity of the soil. The allowable soil bearing capacities at different locations were then plotted on to the maps at 1-meter, 2-meters, 3-meters , 4-meters and 5-meter depths. Contour maps were created to visually classify and analyze the allowable bearing capacities at different locations in Metro Manila.

BEARING CAPACITY ESTIMATES

The allowable soil bearing capacity of Quezon City at one-meter depth from the ground surface is in the range of 200 to 300 kPa, as represented by the color red in Figure 2. The north, southwest, and some scattered portion of the center part of the city has bearing capacity values of 100 to 200kPa. Compared to other cities in Metro Manila, this is quite high for the first meter depth.

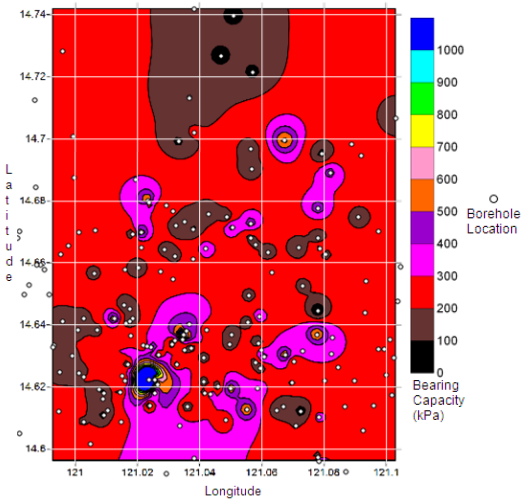

Fig. 2 Soil bearing capacity at 1-meter depth

At a depth of two meters from the ground surface, as shown in Figure 3, a significant increase in allowable soil bearing capacity is observed. The allowable soil bearing capacity is in the range of 400 kPa to 500 kPa. This is dominant on the central to the eastern side of the city. The northern and some parts of the south-eastern part of the city have a bearing capacity of 300 kPa. The north- western part of the city has reached 600 kPa. It is also seen that there are certain portions that already reached more than 1000 kPa, specifically the south-western part of the city. Those with high bearing capacities are those in the higher elevation areas.

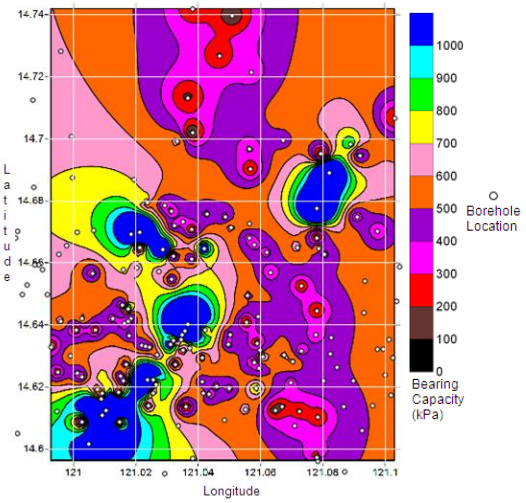

Fig. 3 Soil bearing capacity at 2-meter depth

At three-meter depth, there is a further increase in the allowable soil bearing capacity, as shown in Figure 4. Majority of the bearing capacity that was computed is now split into three ranges: 700 to 800 kPa, 800 to 900 kPa, and more than 1000 kPa. The north and southeast part of the city has the least bearing capacity of around 600 kPa, while the central, southwest, and east part of the city now has the strongest, with more than1000 kPa. One can observe that it still follows the trend that as the elevation increases, the bearing capacity also increases.

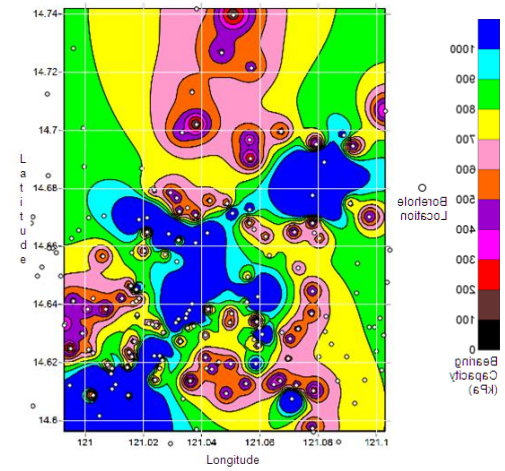

Fig. 4 Soil bearing capacity at 3-meter depth

An even larger increase in the allowable soil bearing capacity in the whole vicinity of Quezon City is seen at four-meter depth from the ground surface, as shown in Figure 5. Take note of the south portion though, as the bearing capacity decreased from 1000 kPa to an average value of 500 to 600 kPa. Since the rock formation at this area has lower RQD index as seen from the borehole logs, the equivalent bearing capacity is much smaller compared to the layer above it.

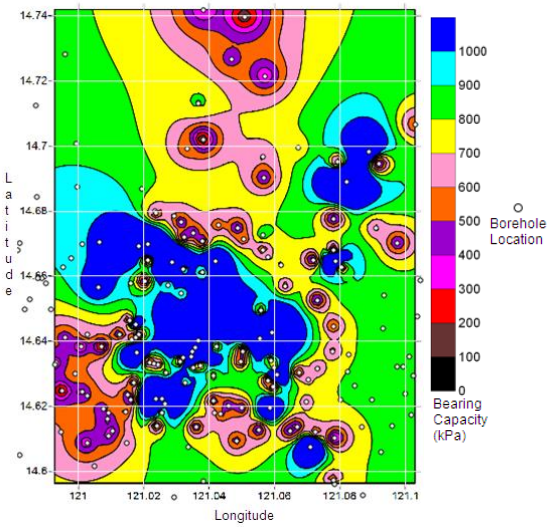

Fig. 5 Soil bearing capacity at 4-meter depth

At 5 meters depth from the ground surface, as shown in Figure 6, there is a further increase in the allowable soil bearing capacity, wherein the 800 kPa to over 1000 kPa range is the dominant allowable soil bearing capacity. The lowest capacity easily seen here is the 400 kPa (violet) in the southwest and south parts of the city, while the highest still remains at those positions that are high in elevation, which are in the central and western parts of the city.

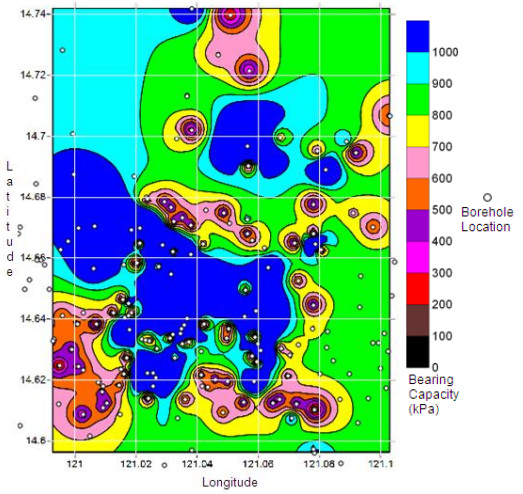

Fig. 6 Soil bearing capacity at five-meter

Figure 7 shows the geological map of Metro Manila [14]. Quezon City is in the central part of Metro Manila. Quezon City has a different surface geology compared to its neighboring cities. Tuff was primarily observed in this area, and rock formations are common below the surface. SPT blows depend on the amount of deposits that are present and increase as the soil goes deeper. SPT refusal was achieved at shallow depths of 2 to 3 meters in the outer regions and as shallow as the ground surface in the inner regions.

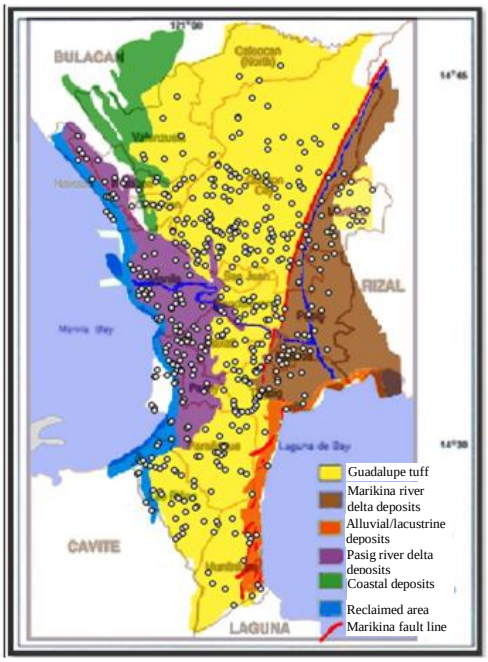

Fig. 7 Geologic Map of Metro Manila [13]

Since the surface geology of this area is reported as tuff, it can be generalized that the city is mostly made up of rocks. In accordance to this, the allowable soil bearing capacities of the rocks should have high values compared to soils and it is in this premise that the estimated soil bearing capacities in the different areas in Quezon city are relative high.

CONCLUSIONS

Borehole logs were collected for a total of 130 locations all over Quezon City, Philippines. Maps were also created in order to show the locations of the collected boreholes throughout the city.

Using a spreadsheets, different geotechnical properties of the collected boreholes were computed. Some examples of this are the unit weight and the angle of internal friction. Also using the same spreadsheet, the allowable soil bearing capacity of the entire Quezon City was estimated and evaluated per meter depth until a depth of 5 meters. Contour maps of the allowable bearing capacities at each of the depths were also made and analyzed.

Because of the shallow rock formations beneath the surface of the city, high allowable soil bearing capacities were observed at shallow depths. It is recommended to place the foundations on these refusal levels since it is more than capable of carrying loads that are suited for shallow foundations. Nevertheless, caution must be taken when placing structures in these areas, as the Valley Fault System is nearby, making the area prone to earthquakes.

The soil in the Quezon City area shows an increasing trend in the bearing capacity at every meter deeper. High-rise building can be easily built in the area without many struggles in the foundation design. Because of this, settlement in the said area can be considered minimal, thus, structures can be built confidently to resist such phenomena. This reference can be used by structural engineers and city engineers in properly designing the foundation of structures and can also be used for disaster mitigating activities of the city.

REFERENCES

[1] Dungca J. R., Concepcion I., Limyuen M. C. M., See T. O., and Vicencio M. R., Soil Bearing Capacity Reference for Metro Manila Reference. International Journal of GEOMATE, Vol. 12, Issue 32, 2017, pp.5-11.

[2] Dungca J. R., and Galupino J. G., Quezon City Soil Profile Reference. International Journal of GEOMATE, Vol. 16, Issue 58, 2019, pp.48-54.

[3] Clayton CRI " SPT Energy Transmission:Theory, Measurement, and Significance", Ground Engineering, Vol. 23, No. 10, 1990, pp 35-43.

[4] Skempton AW " Standard penetration Test Procedures and the Effects in Sands of Overburden Pressure, Relative Density, Particile Size, Aging and Over Consolidation" Geotechnique, Vol 36, No. 3 1986, pp. 425-447.

[5] Tokimatsu k and Seed HB "Simplified Procedures for the Evaluation of the Settlements in Clean Sand. Report No. UCB/EERC-84/16. University of California , Berkely, CA, 1984.

[6] Das B. "Fundamentals of Geotechnical Engineering, 3rd Ed., Toronto, Canada, Thomson Learning, 2008

[7] Coduto DP " Foundation Design Principles and Practices, 2nd Ed., New Jersey, USA, Rentice Hall, 2001.

[8] Sowers G. and Sowers G. "Introductory soil Mechanics and Foundation, New York, USA Macmillan, 1961.

[9] Gibbs HJ and Holtz WG "Research on Determining the Density of Sands by Spoon Penetration Testing, In the Proceedings of the 4th

International Conference on Soil Mechanics, Vol. 1, London, 1957, pp. 35-39.
[10] Kulhawy FH and Mayne PW "Manual on Estimating Soil Parameters for Foundation Design. Report No. EL-6800, Electric Power Research Institute, Palo, Alto, CA, 1990.
[11] Terzaghi K, "Theoretical Soil Mechanics", John Wiley, 1943. Terzaghi K, "Theoretical Soil Mechanics", John Wiley, 1943.
[12] Vesic' AS "Analysis of Ultimate Loads of Shallow Foundations," ASCE Journal of the Soil Mechanics and Foundation Division, 1973, Vol. 99, No. SM1, pp. 45-73.
[13] Vesic' AS "Bearing Capacity of Shallow Foundations," Foundation Engineering Handbook. 1st ed., p 121-147, Winterkorn, Hans F. and Fang, Hsai-Yang, eds., Van Nostrand Reinhold, New York., 1975.
[14] Oca G. "The Geology of Greater Manila and Its Bearing to the Catasthropic Earthquake of August 2, 1968" the Philippine Geologist, Vol 22 No. 4, pp. 171-192.

9th Int. Conf. on Geotechnique, Construction Materials and Environment,
Tokyo, Japan, 20-22 November 2019, ISBN: 978-4-909106025 C3051

FIELD OBSERVATIONS OF STEEL STRIP REINFORCED SOIL WALLS CONSTRUCTED USING DIFFERENT EMBANKMENT MATERIALS

Akinobu OGASAWARA[1], Yusuke GOTO[1], Shunzo KAWAJIRI[2], Hijiri HASHIMOTO[3],
Takayuki KAWAGUCHI[2], Dai NAKAMURA[2] and Satoshi YAMASHITA[2]
[1]Graduate School of Engineering, Kitami Institute of Technology, Japan;
[2]Faculty of Engineering, Kitami Institute of Technology, Japan;
[3]Civil Engineering Research Institute for Cold Region, Japan

ABSTRACT

Currently, the reinforced earth construction method using the steel strip reinforcement, which is the most frequently used in Japan, has been carried out in many snow-covered cold districts such as Hokkaido, but there have been reported some cases of deformation attributable to the freezing of back fill materials. However, the detailed mechanism of the deformation in the steel strip reinforced soil wall is still unclear.

In this study, we constructed a steel strip reinforced soil wall of full scale size by using a good-quality back fill material and a back fill having freezing property, intentionally deformed the reinforced soil wall using a freezing back fill by infiltration of cold air during winter, and examined the effect of tension acting on the reinforcement material at that time on the deformation of the reinforced soil wall. As a result, it was confirmed that a large tensile force acts on the reinforcing material laid in the embankment having a high freezing property when the soil behind the wall panel freezes up under the condition that a certain degree of overloading pressure acts on the reinforcing material.

Keywords: Reinforced Soil Walls, Snowy Cold Areas, Deformation Behavior, Freezing and Thawing

INTRODUCTION

The reinforced soil wall method using the steel strip reinforcement was developed in France in 1963, and it is the reinforced soil wall method which is adopted most frequently in Japan at present. A number of construction projects have been carried out in snow-covered cold areas in Japan, but there have been reports of changes caused by the freezing of embankment materials [1]. Photo 1 shows two cases which are considered to have been deformed by freezing. However, it can be confirmed that the wall panel was broken at the connection between the wall panel and the reinforcing material, and the wall panel was dropped off. In the steel strip reinforced earth wall construction method, even when the deformation occurs by the external force such as earthquake or record rainfall, it is an extremely rare phenomenon that the wall panel falls out as shown in Photo 1. In addition, the fall of wall panels like Photo 1 is a problem comparable to earthquakes and recorded rainfall in snow-covered cold districts because it is difficult to grasp signs at present and occurs during the snow melting season. When a freezing force acts on a wall panel in severe winter, a relatively large force is expected to act on the reinforcing material. However, there are many questions about the detailed mechanism of the change, such as at what timing the freezing force acts and whether the reinforcing material will not be pulled out before breaking.

In this study, the full-scale size steel strip reinforced soil wall was constructed by using good quality back fill material and back fill material with freezing property. The full-scale reinforced soil wall was constructed in Kitami-city, Hokkaido (E143˚53’44.9’’ N43˚48’14.4’’). The tensile force

Photo 1 Deformation case of reinforced soil walls

acting on the reinforcing material and the deformation mode of the reinforcing soil wall were measured when the embankment of the actual large-scale steel reinforcing soil wall frozen up. This paper reports the measurement results from November 2017 to May 2019.

OUTLINE OF REINFORCED SOIL WALLS

Photo 2 shows the construction process of the constructed full-scale steel reinforced soil wall. Fig. 1 is a schematic diagram summarizing the dimensions of the reinforced soil wall and the installation location of the measuring instrument in the A-A cross-section of Photo 2d). Fig. 2 and Fig. 3 compare the particle size distributions and compaction curves of the two types of embankment materials used, respectively. Case A is a soil with a high freezing property classified as fine-grained gravel sand as a filling material. Case B is a soil with low freezing property classified as gravel sand.

The wall panel of the steel strip reinforced soil wall uses 1.5×1.5×0.14 m concrete skin, and the reinforcement uses 0.06×4.5 to 5.5×0.004 m steel strip (Photo 2b). Six reinforcements are attached to the uppermost wall panel and four reinforcements are attached to the other wall panels. In each case, after arranging the panels in one row, the reinforcement was placed by rolling to a height at which the reinforcement was laid to a finished thickness of 0.25 m (Photo 2c). This operation was repeated to construct a reinforced soil wall having a height of 6 m and an extension of about 34 m. In addition, each case is partitioned by providing a buffer area with a width of about 1 m (Photo 2d)).

As shown in Fig. 1, in addition to a thermocouple

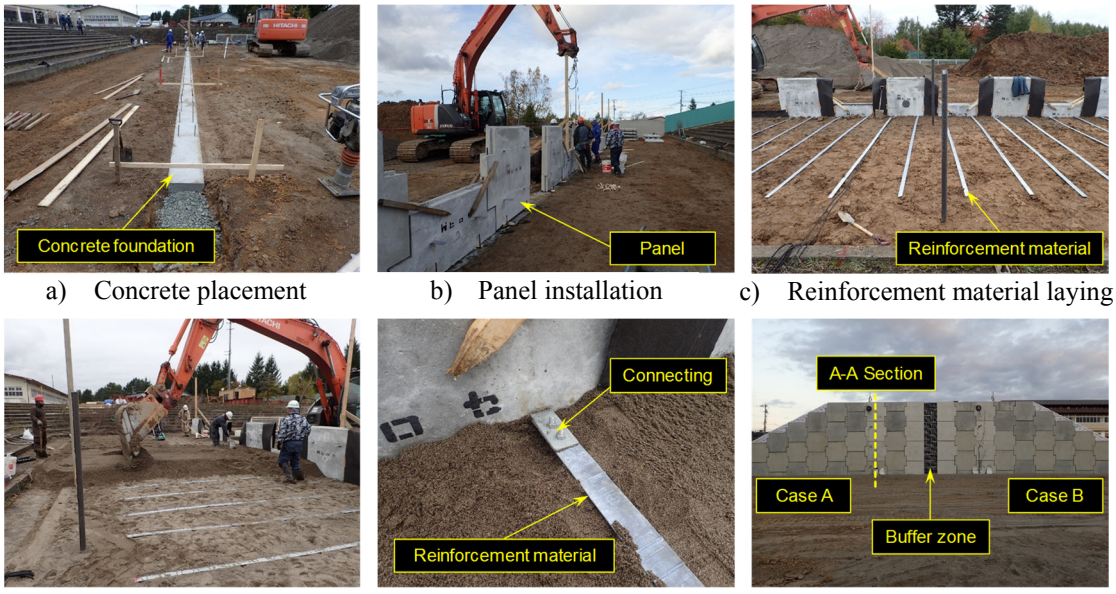

a) Concrete placement b) Panel installation c) Reinforcement material laying

d) embankment material spreading e) Connection of panel and reinforcement material f) Situation after completion

Photo 2 Construction situation of full-scale steel strip reinforced soil walls

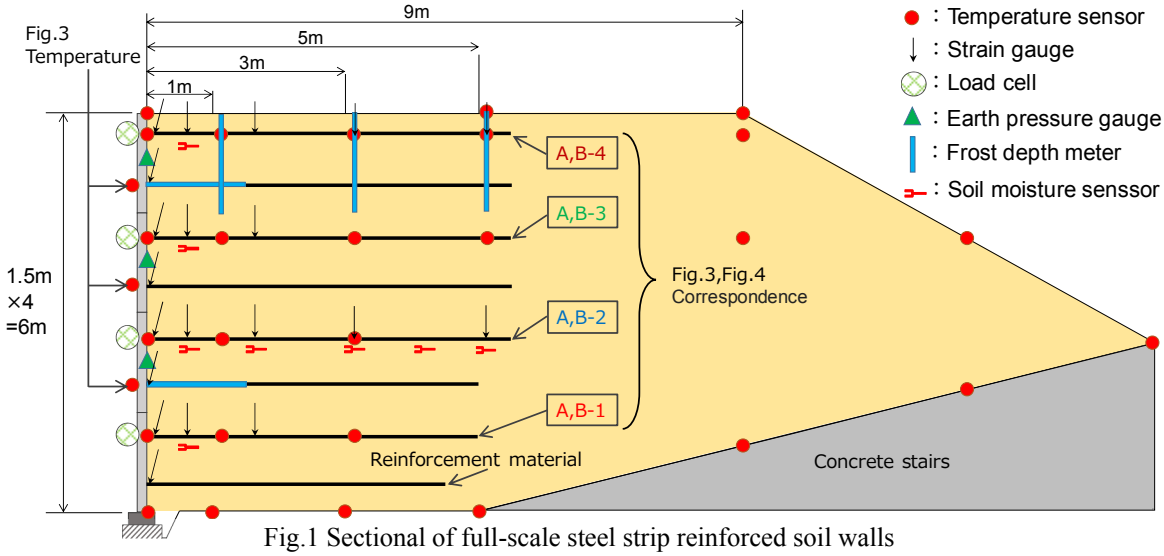

Fig.1 Sectional of full-scale steel strip reinforced soil walls

for temperature measurement, a methylene blue freezing depth meter is installed in the reinforced soil wall to grasp the shape of the freezing line. In each case, a reinforcement material to which a strain gauge is attached is connected to the upper part of the wall panels 1 to 4, a soil moisture sensor is arranged in the periphery of the reinforcement material, and an earth pressure gauge is arranged in the wall panels 2 to 4.

Fig. 4a) and b) show the distribution of dry density, ρ_d and water content, w in the reinforced region obtained from RI measurement [2], respectively. RI measurement was carried out at 9 points in the transverse direction at a wall height of 1 m at the time of construction of the reinforced soil wall. Case A, which is composed of an embankment material having a high freezing property, has a larger variation of ρ_d than that of case B, and it is possible to confirm a lowered region of ρ_d on the back surface of the wall panel having $Y = 2$ to 4 m. On the other hand, in the case B, although the value of ρ_d is large at the center of the reinforcement region, the extreme lowering region of ρ_d cannot be confirmed at the rear surface of the wall panel, and in case A, w is slightly low at the lower portion of the reinforcement region.

In case A, the average value of the number of 54 points was ρ_d=1.43g/cm^3, w=23.1%, and D_c=83.1%. Note that, D_c (%) is ρ_d /ρ_{dmax} *100. In case B, ρ_d=1.47 g/cm^3, w=5.5%, D_c =85.0%. In both cases, D_c is lower than the standard value (D_c > 95.0%) in current

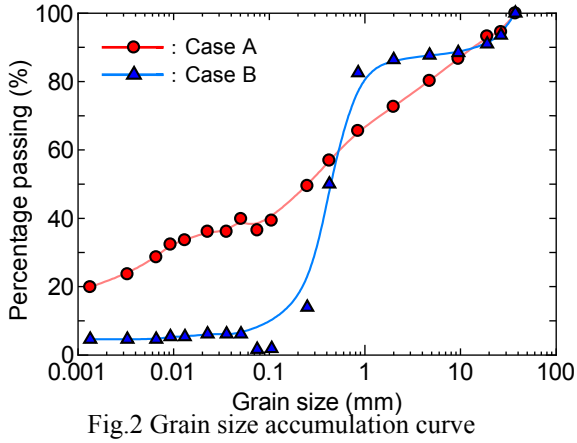

Fig.2 Grain size accumulation curve

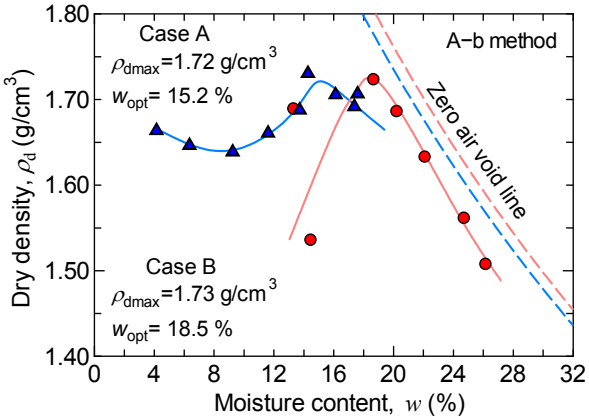

Fig.3 Compaction curve

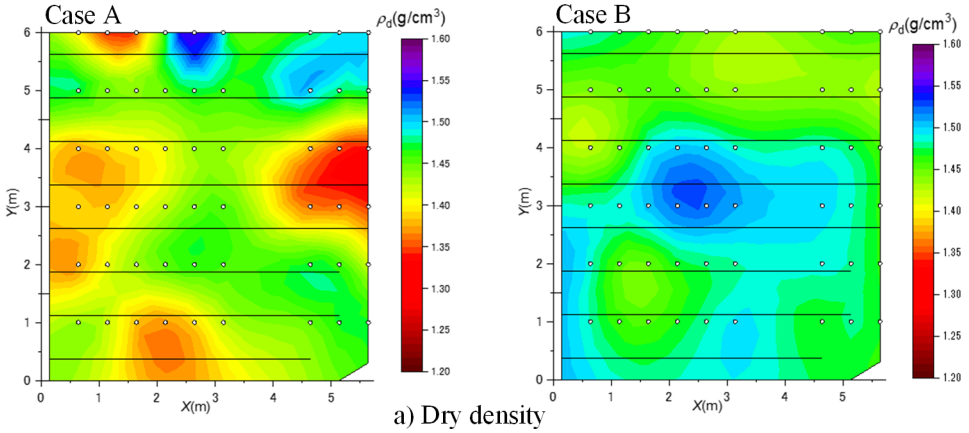

a) Dry density

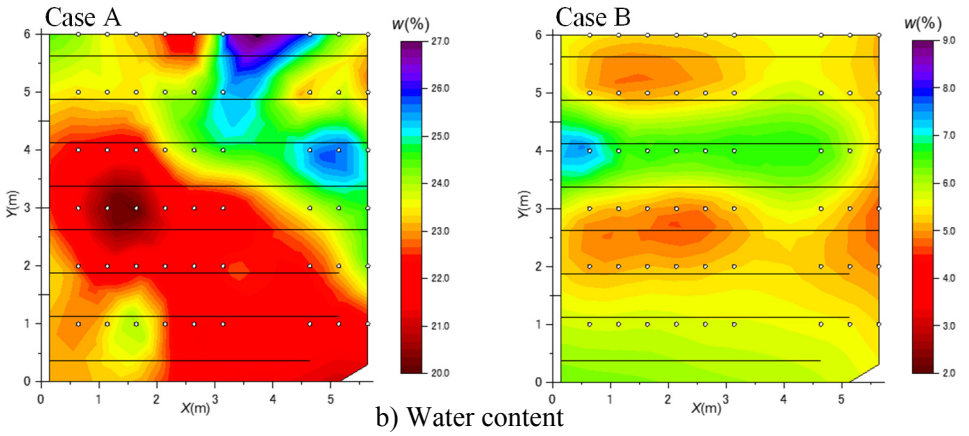

b) Water content

Fig.4 Distribution of dry density and water content

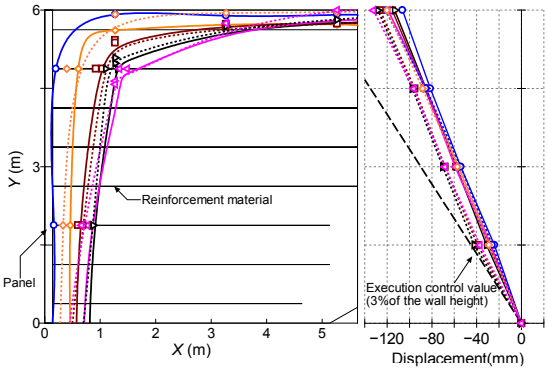

Fig.5 Change of freezing front and panel displacement in Case A

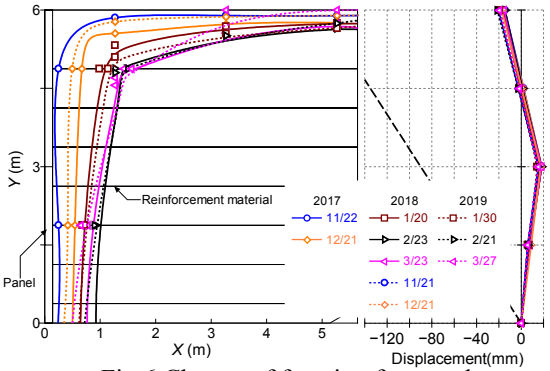

Fig.6 Change of freezing front and panel displacement in Case B

Design Manual [3].

FIELED OBSERVATION REAULTS IN THE FREEZING PERIOD

(1) Freezing condition of backfill, panel displacement

Figs. 5 and 6 show the frozen line and the change of the wall surface displacement in the reinforced soil wall cross sections of Case A and Case B, respectively. Wall displacement was measured periodically at a total station. The frozen line represents the 0° C. line estimated by the freeze depth meter. Looking at changes in the frozen line, in both case A (Fig. 5) and B (Fig. 6), the frozen line has a shape parallel to the crown and the wall surface because cold air enters the wall surface and the crown of the backfill. In addition, in the shoulder portion of the reinforced soil wall, cold air enters from both directions of the crown and the wall surface. Therefore, the freezing lines are not parallel [4][5], and the freezing depth reaches about 1.5 m at the maximum from the wall surface. In both 2018 and 2019, the depth of freezing was almost the same.

As for the change of the horizontal displacement of the wall panel, in case A (Fig. 5), all the wall panels are displaced forward at the stage of 2017/11/22. However, it does not reach 3% of the wall height, which is the construction management value. As shown in Fig. 4, it is expected that the reason for this is that there was a locally lowered portion of ρ_d in the backfill soil near the wall surface. Thereafter, it can be seen that in case A, as the frozen line progresses to the backfill soil, the level of the wall panel in the forward direction increases. In addition, the displacement is larger in 2019 than in 2018.

Next, in case of B, although the freezing line is located at the same position as in case A, the horizontal displacement of the wall panel in the forward direction (Fig. 6) is not measured.

(2) Force acting on the reinforcement material

Fig. 7 compares the measured values of Case A as typical data of the outside air temperature by thermocouples installed on wall panels, and the measured values of load meters connected to reinforcements installed on each stage of wall panels. The initial value of the load cell is acquired during construction. In Case A, the tensile force was applied to the reinforcement material in accordance with the decrease of outside air temperature in both 2017-2018 and 2018-2019. This is because the inside of the reinforced soil wall freezes due to a decrease in the outside air temperature, and the soil freezes up to generate the soil pressure. A large tensile force is applied to the reinforcing members (A-1, A-2) of panel 1 and the second stage in which the upper loading pressure is large. The direction of action of the freezing pressure generated in association with the freezing is perpendicular to the freezing line. Therefore, it is considered that the tensile force increased in the wall panel under the reinforced soil wall in which the frozen line shown in Figs. 5 and 6 were relatively parallel to the wall panel.

In 2018-2019, a tensile force of about 44 kN at the maximum was exerted on the first stage A-1, which had a large overload pressure, and the tensile force increased to a value close to 44.4 kN when the allowable stress level of the reinforcement used in this study was converted into a load. This is probably due to the large wall surface displacements associated with freezing in 2018-2019.

It is expected that the restraint pressure acting on the reinforcement material is small in the panels 3 and 4 (A-3 and A-4) having a small tensile force due to a small overburden pressure, thereby reducing the pulling resistance of the reinforcement material, and excessive tensile force is not generated because the reinforcement material is pulled out.

Next, in case B, since the filling material having a low freezing property is used, the volume changes of the backfilling soil due to freezing is extremely small. From this, it is considered that the generation amount of the upward freezing pressure for pulling out the reinforcing material is small, and the tensile force does not act on the reinforcing material.

From the above results, in order to estimate the

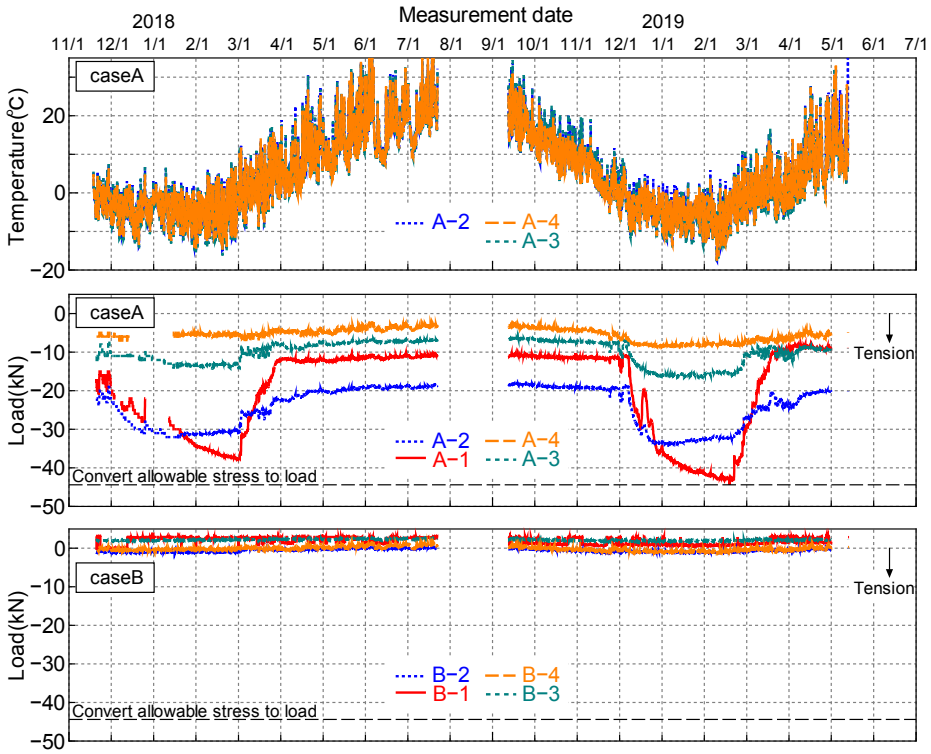

Fig.7 Seasonal change of outside temperature and load of reinforcement material

magnitude of the tensile force acting on the reinforcing material, it is important to estimate the frozen region inside the reinforcing soil wall. Therefore, in this study, the reproducibility of the frozen wire estimation using the commercially available two-dimensional heat conduction analysis software was examined.

(3) Freezing condition of backfill soil by two-dimensional thermal conductivity analysis

For the analysis carried out in this study, commercially available two-dimensional thermal conductivity analysis software TEMP /W [6][7] were used. The analytical model reproduced the reinforced soil wall. Table 1 summarizes the thermos-physical properties of the materials used in the analysis. Thermo-physical property values of ground materials were estimated from the calculation formulas shown by Kersten Equation [8] (thermal conductivity) and Ifuku be [9] (volume heat capacity), which can be calculated using only dry densities and water content ratios as parameters. In this study, the average values of the dry density and the water content ratio shown in Fig. 4 were used as parameters. Fig. 7 shows the temperature distribution on the day (February 21, 2019) when the maximum freezing depth parallel to the wall panel was recorded in Case A in 2019, out of the results of analyzing the temperature change in the reinforced soil wall using the measured wall surface and top edge as external force conditions. The results confirm that the temperature sensor in the reinforced soil wall is generally consistent.

From the results of this analysis, it was found that the frozen lines were present in parallel in the wall panels of the first and second steps, as shown in the transition of the frozen lines estimated in Fig. 5. That is, when the outside air temperature can be correctly set in addition to the dry density and the water content ratio of the reinforced soil wall to be targeted, it can be said that the frozen region of the reinforced soil wall can be estimated with a certain degree of accuracy by using commercially analysis software.

Figure 8 shows the results of an analysis of the external temperature of 1976-1977, which was the lowest temperature in the history of observation in Hokkaido City, on the wall panel. Figure 7 shows the results of the analysis on the same day (February 21, 1997). The frozen line parallel to the wall panel travels into the approximately 40 cm reinforced soil wall. In the future, the estimation of the progress process of the freezing line in the reinforced soil wall in which the wall surface panel dropped out is tried by giving the outside air temperature in the region in which the disaster case actually occurred.

CONCLUSIONS

(1) The deformation of the wall surface during the winter period in which the cold air infiltrates, when the embankment material having a high freezing property is used, becomes larger in the forward direction compared to the case of the embankment material having a low freezing property.

(2) It was found that the soil behind the wall panel

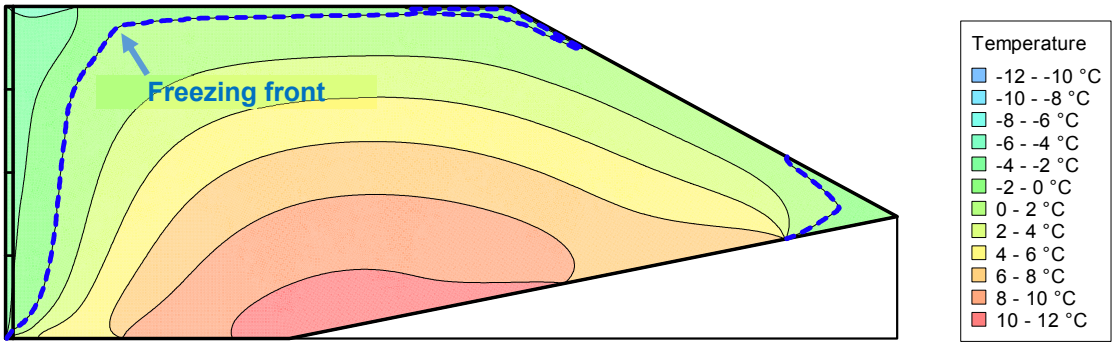

Fig.8 Temperature distribution in 2019 by two-dimensional thermal conductivity analysis

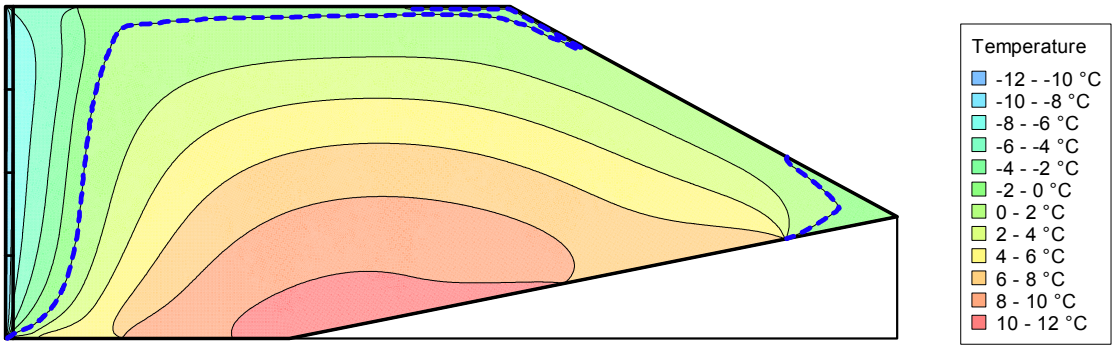

Fig.9 Temperature distribution in 1977 by two-dimensional thermal conductivity analysis

freezes up, especially under the condition that a certain restraining force is applied, and a large tensile force acts on the reinforcing material laid in the embankment material having a high freezing property at the position where the frozen wire enters in parallel with the wall panel.

ACKNOWLEDGMENTS

Mr. Naoki Shimura and other members of HIROSE REINFORCED SOIL corporation gave great cooperation on the construction of reinforced soil walls. Furthermore, with regard to the construction of reinforced soil walls, we obtained the cooperation of Mr. Uno and other BIHORO CARGO CAR corporation member. We express my deep appreciation.

REFERENCES

[1] Hashimoto, H., Kawajiri, S., Kawaguchi, T., Hayashi, T., Hayashi, H., Damage to the Terre-Arrme reinforced soil wall due to frost heaving, Japan Society of Civil Engineers Proceedings, Vol.73. 2017.

[2] Japanese Geotechnical Society, Test method for soil density using nuclear gauge, JGS1614-2012. 2013.

[3] Reinforced soil wall (Terre Armee) design・execution manual, Public Works Research Center, pp. 116-117, pp. 250-251.

[4] Suzuki, T., Uno, H., Sawada, S., Adachi, K., Freezing Front and Frost Heaving Pressure in Multi Anchored Retaining Wall, Japan Society of Civil Engineers Proceedings, No.645/III-5, pp. 281-290, 2000.

[5] Kawaguchi, T., Nakamura, D., Kawajiri, Shunzo., Yamashita, S., Kobayashi, S., Sasaki, T., Hayashi, T., Adachi, K., Amamiya, S., Harada, M., Freezing and Thawing Behavior of Reinforced Soil Walls Built in a Cold Region, Geosynthetics Engineering Journal, Vol.29, pp. 147-154, 2014.

[6] Thermal Modeling with TEMP/W., GEO-SLOPE International Ltd, 2007.

[7] Hayashi, K., Suzuki, T., Toyota, K., Study on the Shape of Freezing Front and Frost Heave Damage of Box-culvert Structure - Inspection by 2-dimensional FEM Heat Conduction Analysis -, Japan Geotechnical Journal, Vol. 4, No. 2, pp. 147-156, 2009.

[8] M. S. Kersten., Thermal properties of Soils, University of Minnesota, Institute of Technology, Engineering Experiment Station, Bulletin No28, 1949.

[9] Ifukube, M. Studies on Frost Heave, Frost Penetration and Ratio of Replacement to Prevent Frost Damage of Roads in Hokkaido. Public Works Research Institute, Vol.26,1962.

9th Int. Conf. on Geotechnique, Construction Materials and Environment, Tokyo, Japan, 20-22 November 2019, ISBN: 978-4-909106025 C3051

UNIAXIAL COMPRESSION TEST WITH VARYING SILICA SAND CONTENT, PARTICLE SIZE AND TEMPERATURE

Shin-ichi Kanazawa[1], Masaki Yanai[1], Nozomi Ichikawa[1], Naoki Muto[1],

Senri Kobayashi[1] and Koji Ishiyama[2]

ABSTRACT

At present, underground geological disposal at depths greater than 300 m is considered a viable disposal option for high-level radioactive waste generated from the reprocessing of spent fuel used in nuclear power plants. In geological disposal, bentonite is employed as the primary component of buffer material filling gaps between waste and geologic rock. Bentonite has remarkable water absorption swelling and low permeability characteristics. Bentonite buffers are generally mixed with silica sand to improve workability and economy. However, specification details have yet to be completely determined. It is anticipated that the buffer material will be exposed to high temperature due to the heat generated by the vitrified solid. This study aims to understand the mechanical properties of bentonite buffer material by employing uniaxial compression tests after applying temperatures between 30 ℃ to 90℃ to bentonite specimens with different silica sand contents and particle sizes. Results of the experiment confirmed that uniaxial compressive strength tends to decrease with higher blending ratios of silica sand greater particle sizes and temperatures.

Keywords: Bentonite, Geological disposal , temperature, Uniaxial compression test

1. INTRODUCTION

At present, the use of bentonite as a buffer material for geological disposal is being examined. Bentonite fills gaps due to its water intake swelling properties and low permeability, thus preventing the leakage of groundwater contaminated with high levels of radiation. In Japan, various tests, such as swelling pressure tests and uniaxial compression tests, have helped to characterize swelling performance and mechanical properties of bentonite [1]. In addition, workers have examined the method for mixing silica sand with bentonite from the viewpoint of workability and economic efficiency. However, complete specifications for this method have yet to be determined. In this study, to understand the mechanical properties of bentonite buffer material, uniaxial compression tests were conducted by applying temperatures in the range of 30℃ to 90℃ to bentonite specimens with different silica sand contents and particle sizes.

2. TEST METHOD

The initial conditions were set at a dry density of 1.6 Mg/m^3 and a saturation of 30%. Temperatures of 30 ℃, 50 ℃, 70 ℃ and 90 ℃ were applied to bentonite (Kunigel V1) with No. 3, 5 and 8 silica sand ratios of 20%, 30% and 40%. Table 1 summarizes the physical and chemical properties of Kunigel V1 and silica sand.

Table 1 Physical and chemical properties of Kunigel V1 and silica sand

soil particle density(Mg/m^3)	2.61
Montmorillonite content(%)	51
Silica sand No. 3 particle density(Mg/m^3)	2.691
Silica sand No. 5 particle density(Mg/m^3)	2.62
Silica sand No. 8 particle density(Mg/m^3)	2.701
Silica sand No. 3 particle size(mm)	1.2~2.4
Silica sand No. 5 particle size(mm)	0.3~0.8
Silica sand No. 8 particle size(mm)	0.08~0.2

2.1 Sample preparation method

A mixed sample of bentonite and silica sand was prepared at ratios of 6:4, 7:3, and 8:2 for Kunigel V1 and silica sand particle sizes, nos. 3, 5, and 8. The montmorillonite content of bentonite in Table 1 was measured with reference to the Methylene Blue adsorption measurement method [3] of AIST. The properties of each sample are

shown in Tables 2, 3, and 4.Equation (1) was used for the effective clay density[4] of JAEA.

$$\rho_e = \frac{\rho_d(100 - R_s)}{(100 - \frac{\rho_d R_s}{\rho_s})} \quad (1)$$

(1) where, ρ_e : effective clay density , ρ_d :dry density, ρ_s : soil particle density of silica sand, R_s : silica sand mixing ratio

Table 2 Properties of each sample at the 6:4 mixing ratio

silica sand No.	No.3	No.5	No.8
Mixed soil particle density(Mg/m^3)	2.64	2.612	2.644
Void ratio	0.650	0.632	0.653
Effective clay density(Mg/m^3)	1.260	1.270	1.258

Table 3 Properties of each sample at the 7:3 mixing ratio

silica sand No.	No.3	No.5	No.8
Mixed soil particle density(Mg/m^3)	2.632	2.610	2.635
Void ratio	0.645	0.631	0.647
Effective clay density(Mg/m^3)	1.363	1.371	1.362

Table4 Properties of each sample at the 8:2 mixing ratio

silica sand No.	No.3	No.5	No.8
Mixed soil particle density(Mg/m^3)	2.623	2.609	2.625
Void ratio	0.639	0.631	0.641
Effective clay density(Mg/m^3)	1.453	1.458	1.452

2.2 Water content adjustment

The water content of the mixed samples was adjusted to a saturation of 30%. The water content was measured using a microwave oven (500 W, 15 min) to shorten the time.

2.3 Specimen molding

The sample was divided into five layers, placed in the mold, and compacted. Afterwards, static compaction (40 MPa, 10 min) was applied with a hydraulic jack to produce the test specimen.
Equations (2) and (3) were used for the mass of the specimen, assuming that the volume of the specimen was constant.

$$e = \frac{\rho_s}{\rho_d} - 1 \quad (2)$$

$$S_r = \frac{w\rho_s}{e\rho_w} \quad (3)$$

(2) where, e:void ratio, ρ_s:soil particle density, ρ_d: dry density ; (3)and where, Sr : degree of saturation, w:water content , ρ_s : soil particle density e: void ratio, ρ_w : water density (1.00Mg/m^3).

2.4 Temperature change

Specimen temperature was achieved by curing the sample for 1 day in a constant-temperature water tank. A water interception sheet prevented the specimen from touching the water.

2.4 Uniaxial compression test

The compression test was carried out at a fixed loading speed of 0.4 (mm/min). An electric screw jack system of 10 kN capacity was employed as a testing machine. A schematic diagram of the tester is shown in Fig. 1.

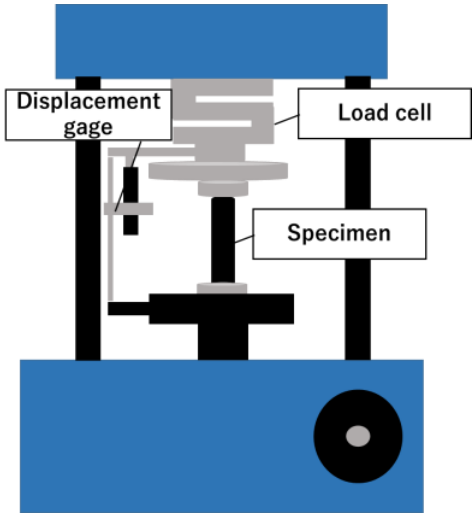

Fig.1 Schematic diagram of the test machine

3. TEST RESULTS AND DISCUSSION

Fig. 2, Fig. 3, and Fig. 4 show the results of the uniaxial compression tests in which the temperature and silica sand content were varied according to silica sand particle size. Fig. 5, Fig. 6, and Fig. 7 show the results of the uniaxial compression test in which the temperature and the type of silica sand particles were varied for each silica sand content.

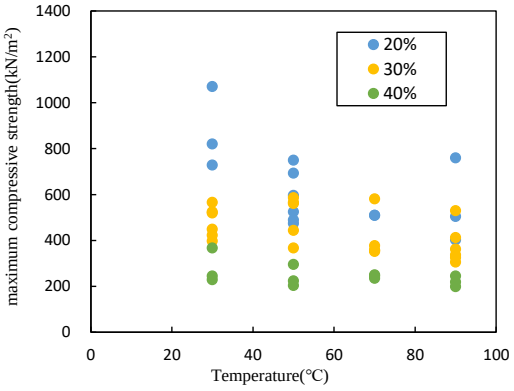

Fig.2 Relationship between temperature and maximum compressive strength (Silica sand No.3)

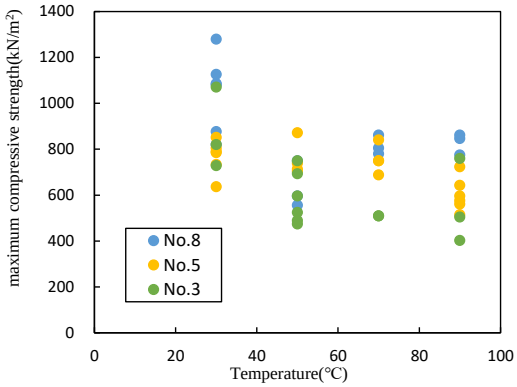

Fig.5 Relationship between temperature and maximum compressive strength (6:4)

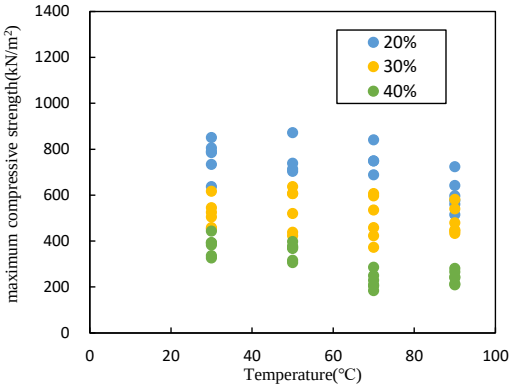

Fig.3 Relationship between temperature and maximum compressive strength (Silica sand No.5)

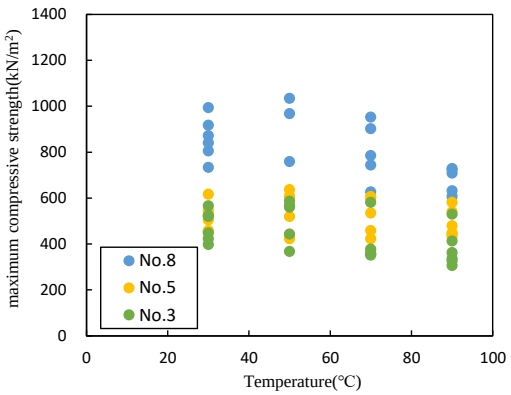

Fig.6 Relationship between temperature and maximum compressive strength (7:3)

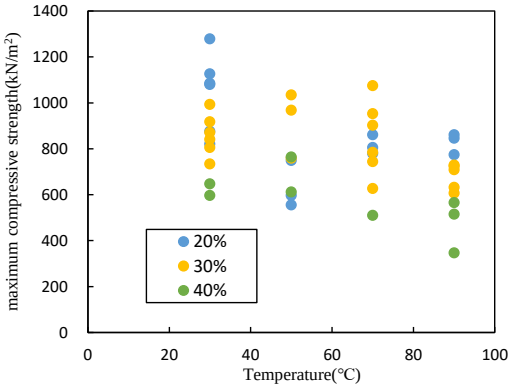

Fig.4 Relationship between temperature and maximum compressive strength (Silica sand No.8)

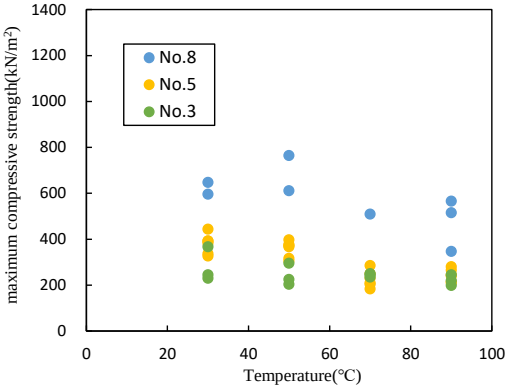

Fig.7 Relationship between temperature and maximum compressive strength (8:2)

3.1 Results of tests varying silica sand content, silica sand particle size, and temperature

Figs. 2 to 7 illustrate that maximum

compressive strength decreases linearly with increasing temperature under all conditions. Fig. 9 shows the changes in the modulus of elasticity for silica sand No. 3 at different compositions, and Fig. 11 shows the changes in the elastic modulus of silica sand for a silica sand composition of 40% with varying silica sand particle size (Nos. 3, 5, or 8). The elastic modulus demonstrated the same tendency as compressive strength with increasing temperature. The same tendency was also observed under other conditions. There are several possible reasons why the maximum compressive strength and elastic modulus decrease. The first is the expansion of the specimen volume. Fig. 8 shows the rate of volume change of silica sand No.3 at different temperatures and silica sand contents. Fig. 10 shows the volume change rate with temperature for a silica sand content of 40% and different silica sand particle sizes (Nos. 3, 5, or 8). Figs. 8 and 10 confirm that the rate of volume change tends to increase with rising temperature during curing. Therefore, it is possible that at higher temperatures, with a lower dry density and smaller cracks, strength characteristics were lower. Expansion of the specimen may be caused by the difficulty in discharging the pore water and air expanded by heat due to bentonite's low water and air permeability. The effects of cracks caused by drying shrinkage of the specimen surface could also be a factor. As temperature increased during curing, the amount of evaporation from the surface of the specimen increased, and the number of cracks due to drying shrinkage also increased, which may have decreased material strength. For this test, specific cracks inside of the specimen were not confirmed. However, that interior cracks were generated was confirmed due to the remarkable shrinkage after curing, especially on the specimen surface. Since this effect increases with temperature, compressive strength is also considered to decrease as the temperature increases.

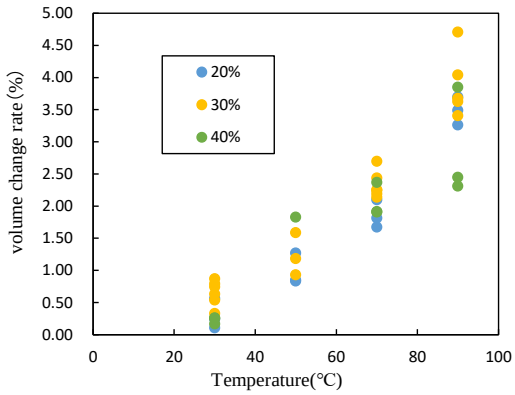

Fig.8 Relationship between temperature and volume change rate (Silica sand No.3)

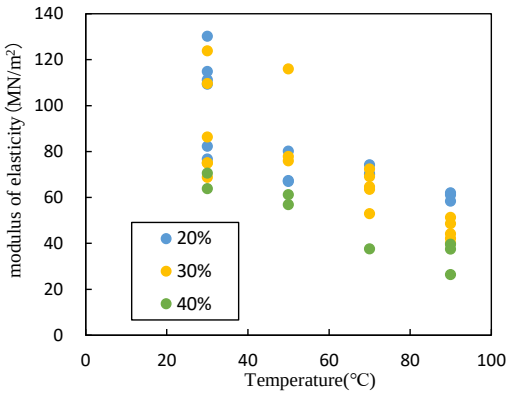

Fig.9 Relationship between temperature and the modulus of elasticity (Silica sand No.3)

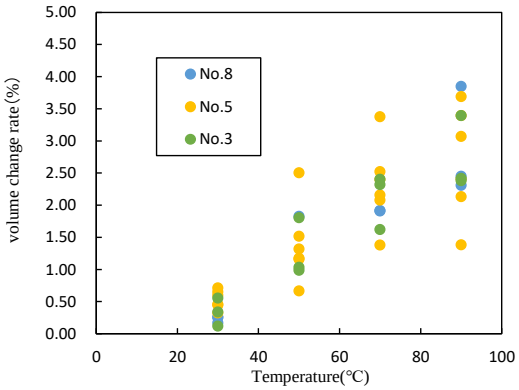

Fig.10 Relationship between temperature and volume change rate (6:4)

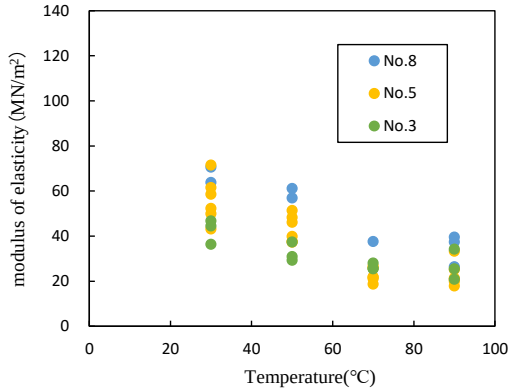

Fig.11 Relationship between temperature and the modulus of elasticity (6:4)

3.2 Results of tests in which the silica sand content and silica sand particle size (Nos. 3, 5, or 8) at each temperature were varied

Figs. 12 and 13 show the relationship between silica sand particle size (Nos. 3, 5, or 8) and

maximum compressive strength at temperatures of 30 ° C, 90 ° C and silica sand contents of 20%, 30% and 40%. Both figures confirm that maximum compressive strength increased as the particle size of silica sand decreased. The increase of maximum compressive strength with the decrease of silica sand particle size may result from a smaller particle size The increase of the maximum compressive strength with the decrease of the silica sand particle size considered to be the increase of the forming pressure by the decrease of the silica sand particle size. These results also confirmed that the smaller the silica sand particle size, the higher the strength, under constant silica sand content. This is due to suction. Suction is the attractive force of pore water to soil particles in dry unsaturated soil and is calculated as the difference between pore air and water pressures. Generally, the greater the suction, the more the apparent adhesive force, and the better the strength and deformation characteristics. In other words, the smaller the particle size of silica sand, the larger the area of contact between silica sand and water. Therefore, it is considered that the smaller the particle size of silica sand, the greater the strength. Figs. 14 and 15 show the relationship between silica sand content and maximum compressive strength at temperatures of 30 ° C and 90 ° C and silica sand numbers of 3, 5 and 8. In both figures, the maximum compressive strength decreases with increasing silica sand content. With this result, compaction is considered the cause. According to Masuda et al[4], at higher montmorillonite contents, the compaction property worsens, and the molding pressure can be reduced by increasing the silica sand mixing ratio. In this case, montmorillonite content decreases with increasing silica sand content, and the strength is considered to decrease because the energy of compaction is reduced.

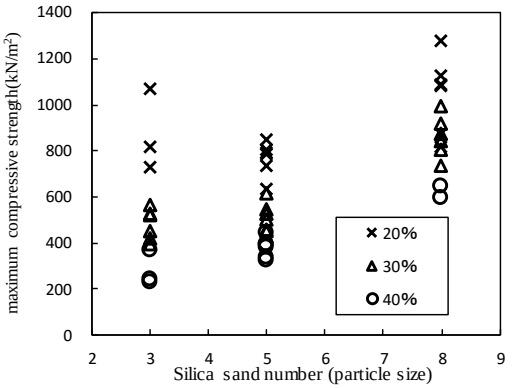

Fig.12 Relationship between silica sand number and maximum compressive strength (30℃)

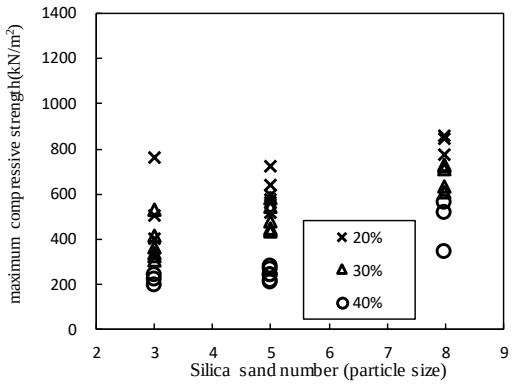

Fig.13 Relationship between silica sand number and maximum compressive strength (90℃)

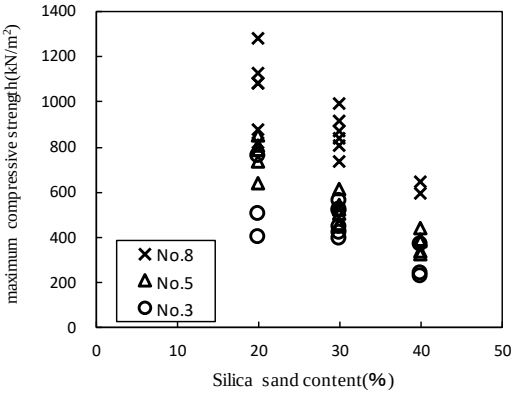

Fig.14 Relationship between silica sand content and maximum compressive strength (30℃)

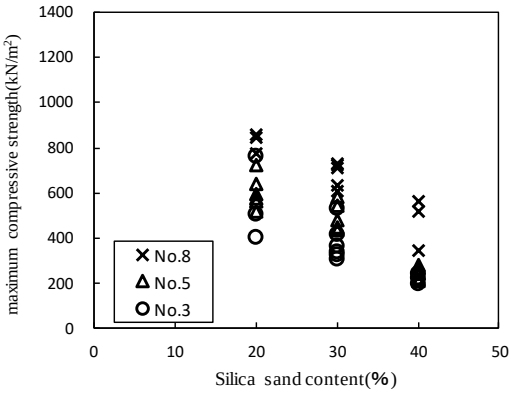

Fig.15 Relationship between silica sand content and maximum compressive strength (90℃)

4. CONCLUSION

In this study, uniaxial compression tests investigated the mechanical properties of bentonite mixed with silica sand, considering the effects of

temperature. The findings obtained in this study are as follows.

(1) As temperature rises, the dry density of the bentonite mixed with silica sand decreases due to volume expansion caused by expanded pore water and air exiting the specimen. In addition, cracks occur on the surface and inside of the specimen due to drying shrinkage. Based on the above, maximum compressive strength is also considered to decrease.

(2) As the silica sand number increases, suction between silica sand particles increases. Maximum compressive strength is considered to further increase with this increase.

(3) Montmorillonite content decreases with increasing silica sand content. It is conceivable that the compressive strength of the specimen is decreased by reducing the energy used on the compression molding for higher sand specimens, compared to when the sand ratio is low.

The above results experimentally demonstrate the temperature dependence of bentonite mixed with silica sand and that suction and montmorillonite content affect strength characteristics. In future work, it is desirable to improve the accuracy of the data by continuously carrying out tests. Furthermore, when considering re-submergence of a geological disposal facility after construction, it is likely that not only the mixing ratio of silica sand and silica sand particle size, but also change in the degree of saturation affect the strength characteristics. Therefore, change in the degree of saturation of bentonite specimens with different silica sand contents and particle sizes should be tested. In addition, by considering the effect of heat generated from high-level radioactive waste, we hope that the uniaxial compression test with temperature change applied to the silica-sand mixed bentonite specimen will contribute to the performance design of bentonite buffer material from the viewpoints of workability, economy, and thermal conductivity.

5. REFERENCES

[1] Japan Nuclear Cycle Development Institute (1999): Technical confidence on the disposal facilities for high level radioactive wastes 2nd Report.

[2] Horiuchi Y., Takagi T., Method of the methylelene blue adsorption test for bentonite at AIST., Research Materials of the Geological Survey of Japan., No.555(2012).

[3] Japan Nuclear Cycle Development Institute (1999): Engineering technology for geological disposal

[4] JIS A 1216:2009, Method for uniaxial compression test**.**

[5] Masuda R., Amemiya K., Chijimatsu M., Adachi K., Komine H., Study on the influence of a specification of buffer material on the compaction characteristics., Journal of JSCE., No.772/III-68, pp.157-171, 2004

9th Int. Conf. on Geotechnique, Construction Materials and Environment, Tokyo, Japan, 20-22 November 2019, ISBN: 978-4-909106025 C3051

THE SWELLING BEHAVIOUR OF BENTONITE BUFFER MATERIAL CONSIDERING THE EFFECT OF TEMPERATURE

Shin-ichi Kanazawa[1], Senri Kobayashi[1], Nozomi Ichikawa[1], Naoki Muto[1], Manaki Yanai[1] and Koji Ishiyama[2]
[1]National Institute of Technology, Fukushima College, Japan; [2]Nishimatsu Construction CO.,LTD

ABSTRACT

In the nuclear fuel cycle of nuclear power generation, reprocessing generates high-level radioactive waste. Geological disposal is a widely accepted disposal method for high-level radioactive waste. This method can isolate waste from the human environment for a very long time. Geological disposal utilizes bentonite as a buffer material in order to suppress the transfer of radioactive materials to groundwater. In practice, waste may be exposed to a high-temperature environment due to decay heat or geothermal heat, or heated groundwater may permeate the water. Nonetheless, few studies consider the effect of heat on bentonite, and it is difficult to understand the long-term swelling performance of bentonite material under these conditions. Therefore, it is necessary to investigate the effect of temperature on bentonite. In this study, swelling properties of bentonite were investigated by performing a swelling pressure test considering temperature history and temperature change. Results demonstrated that swelling pressure tended to increase with increasing temperature. Furthermore, a threshold value for the equilibrium swelling pressure may exist.

Keywords: bentonite, swelling pressure, temperature, geological disposal, High-level radioactive waste

INTRODUCTION

In the nuclear fuel cycle, which reuses nuclear fuel, radioactive effluent is generated when uranium and plutonium are extracted. The mixture of radioactive effluent and glass into canister is called high-level radioactive waste. In Japan, geological disposal is employed for the safe disposal of high-level radioactive waste. It is believed that this method can safely dispose of high-level radioactive waste via the multiple barrier system, which combines an engineered barrier system and a natural barrier system. In Japan, Bentonite is used as a buffer material. Since bentonite has swelling properties, low permeability, and cation exchange properties, it is expected to fill gaps, control transfer of radioactive material, and control groundwater invasion. In the actual disposal environment, the buffer material is exposed to high temperatures. Because of this, it is necessary to examine the effects high temperature on the buffer. High temperature environments arise from the decay heat of the vitrified body, the geothermal energy of the rock mass, permeation of heated groundwater. However, there are few studies considering the effect of heat on bentonite, which poses a problem or understanding the material swelling performance of the long-term. In this study, the swelling characteristics of bentonite were investigated using a swelling pressure test and considering the temperature history of the buffer material exposed to high temperatures and the infiltration of heated groundwater.

MATERIALS AND METHODS

Materials

In this study, a 70% bentonite and 30% silica sand mixture was used, because of its excellent workability and economy. The mixture comprised Kunigel V1 for bentonite and sillica sand particle size diameter of 212 μm or less. Table 1 shows the physical properties of Kunigel V1. The samples were placed in stainless steel vats and heated in a drying oven at 30 ° C, 60 ° C and 100 ° C for 14 or 90 days, respectively, to obtain the temperature history. Since the water content of the sample after drying was as low as 1 ~ 2%, and the preparation of the sample was difficult, the water content of the sample was adjusted using ion exchange water. The sample was then placed in a desiccator until the reaching nearly uniform water content. The temperature history and test conditions for each heating period are summarized in Tables 2, 3 and 4. The montmorillonite content shown in Tables 2, 3 and 4 is the value of a mixed sample of bentonite and silica sand. The montmorillonite content was determined by the boiling method of methylene blue adsorption determination in [3].

Table 1 The physical properties of Kunigel V1

Properties	Kunigel V1
soil particle density (Mg/m^3)	2.61
montmorillonite content(%)	51.0

Table 2 Test conditions (No history)

Properties	No history
water content (%)	6.95~9.20
void ratio	0.647
degree of saturation (%)	28.3~37.5
montmorillonite content(%)	35.7

Table 3 Test conditions (Heating period of 14 days)

Properties	30℃	60℃	100℃
water content (%)	3.00	1.72~4.00	1.62~6.95
void ratio	0.647	0.647	0.647
degree of saturation (%)	12.2	13.2~16.3	16.7~28.3
montmorillonite content(%)	35.7	34.3	34.3

Table 4 Test conditions (Heating period of 90 days)

Properties	30℃	60℃	100℃
water content (%)	4.00	2.54	4.40
void ratio	0.647	0.647	0.647
degree of saturation (%)	16.4	10.5	18.2
montmorillonite content(%)	32.1	32.9	32.1

Method for Producing Test Material

Specimens with a dry density of 1.6 Mg/m3, a diameter of 28 mm, and a height of 10 mm were prepared by static consolidation using the mixtures prepared by the above method. Each specimen was treated with a given temperature history described above. The mass assigned to the specimen was calculated for each test condition such that the dry density was 1.6 Mg/m3 when compacted to the target specimen height. Test equipment consisted of a hydraulic jack, a reaction frame, and a piston, which can load a maximum pressure of 100 MPa. First, the sample was put into a metal mold with an inner diameter of 28 mm. A compaction rod was put into the mold. Then, the piston was lowered to the upper part of the compaction rod. The specimen was then compressed and molded using a hydraulic jack so that the sample height was 10 mm. The compaction pressure was about 8MPa, and the pressure retention time was 10 minutes. After unloading, the compaction rod was removed, and testing was performed with the specimen in the mold.

Test Method

The main components of the swelling pressure testing equipment are a reaction frame, load cell, compressor, air cylinder, displacement gauge, water tank, temperature control tool, and thermocouple, as shown in the schematic diagram, Fig. 1. The piston of the testing machine can load at maximum of 1 tf using compressed air. The load cell is connected to a data logger and a PC, and data can be collected every second. The specimen was moved to the pedestal of the tester for each mold, and the upper and lower pedestals were fixed with screws. A membrane filter and a porous metal were inserted as filter materials between the specimen and the pedestal. The piston was lowered to the top plate of the testing machine, and the vertical displacement was fixed by a clamp knob. The initial vertical pressure was defined as the vertical pressure at this time. The initial vertical pressure was about 50 N. After this, ion exchange water warmed to the target test temperature was supplied to a water tank, and the specimen wetted to start the swelling pressure measurement. The water supply was applied only from the underside of the specimen, as ground water only permeate from one side of the buffer material in the actual disposal environment. The test water temperature was controlled by a hot water circulator (or a heater and a thermocouple) so that the water temperature was ± 3 °

C of the target temperature. Temperature was measured by the thermocouple. The reason why the temperature control was carried out by either a hot water circulation equipment or a heater and a thermocouple is that, when the temperature of the test water was high, it dropped to less than -3 ° C of the target temperature during its transfer through a hose. Therefore, hot water circulation equipment was only used for tests using 30 ° C water. At 60 ° C and 100 ° C, a heater and thermocouple was used. To suppress evaporation from the water surface during testing, an evaporation inhibitor (pp sphere) was set up, and ion exchange water, heated to a target temperature, was injected as needed so that the water level could be maintained at about 50 mm from the upper part of the specimen. In addition, to confirm that the specimen position was maintained during the test, a displacement meter was installed on the upper part of the specimen, and the displacement amount during the test was measured. A displacement gauge capable of measuring up to a minimum of 0.001 mm was used. The test period was about 1 to 2 weeks, during which time the swelling pressure of bentonite was considered to reach equilibrium. After the completion of the test, each specimen was immediately sliced into 2 mm sections, and the water content distribution at each height was measured. The test results showed that the maximum swelling pressure and the equilibrium swelling pressure correlated with temperature.

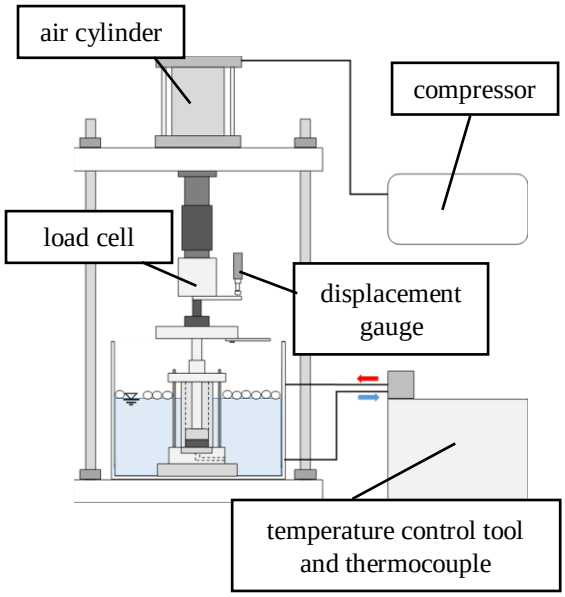

Fig. 1 Swelling pressure tester

RESULTS AND DISCUSSION

Changes in Swelling Pressure with Time

Figures 2 to 8 shows changes in swelling pressure over time.

In all test results, the swelling pressure rapidly increased after receiving water, decreased after reaching the peak swelling pressure, and then increased again to reach the equilibrium state. Under some test conditions, the swelling pressure at equilibrium was larger than at the initial peak. Pressure peaked about 7 hours after the start of the test at 30 ° C and about 0.3 hours after the start of the tests at 60 ° C and 90 ° C. The slope of the initial swelling pressure graph, which increase with increases temperature, indicates that with higher temperature, the time until the swelling pressure reaches the equilibrium state decreases. In addition, for tests at 90 ° C, the swelling pressure after the peak repeatedly increased and decreased by about 100kPa.

That the time until the swelling pressure reaches the equilibrium state becomes shorter as the temperature rises is thought to be facilitated by a faster hydration reaction with rising temperature. Bentonite swells when water molecules enter between the layers of montmorillonite crystals due to the hydration reaction between interlayer cations and solution water. In addition, the hydration reaction is accelerated at higher temperatures. Therefore, the hydration reaction likely advanced more rapidly as the temperature rose. The reaction ended when the hydration number reached the upper limit, and the swelling pressure reached equilibrium state.

The reason that the swelling pressure after the peak repeatedly increased and decreased by about 100kPa at the test temperature of 90 ° C is likely caused by the use of a heater and a thermocouple for temperature control of the test water. The heater cools after reaching the target temperature, and when the temperature decreases by about 3 ° C from the target temperature, the heater repeatedly activates to control the temperature. Since the time course of the swelling pressure after the peak agrees with the heating and cooling cycles of the heater, swelling pressure likely changes due to the change in the temperature.

Maximum Swelling Pressure

Maximum swelling pressure increased with increasing temperature under all test conditions. In addition, maximum swelling pressure of samples with temperature history decreased slightly at a test temperature of 30 ° C, and increased by about 100 ~ 200kPa at test temperatures of 90 ° C and 60 ° C. This suggests that the higher the test temperature, the greater the effect on the maximum swelling pressure of samples with temperature history, regardless of the

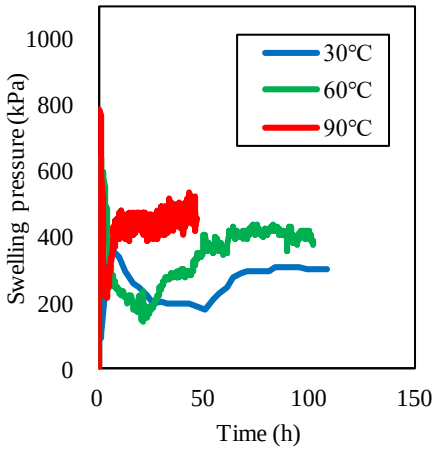

Fig. 2 Samples with no history

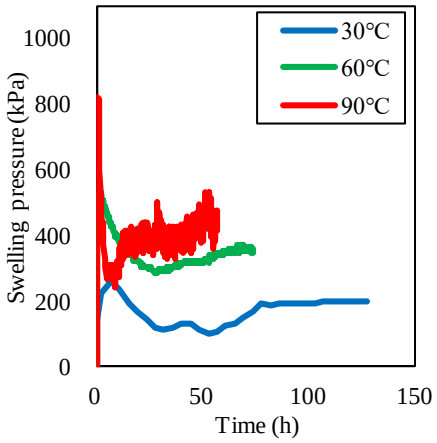

Fig. 3 Heating period of 14 days and temperature history of 30 ° C

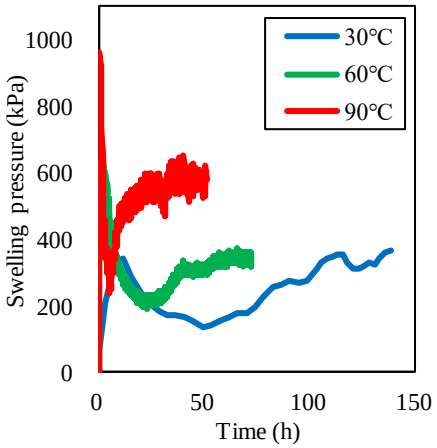

Fig. 4 Heating period of 14 days and temperature history of 60 ° C

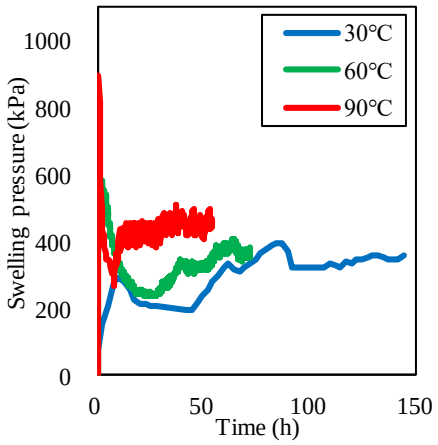

Fig. 5 Heating period of 14 days and temperature history of 100 ° C

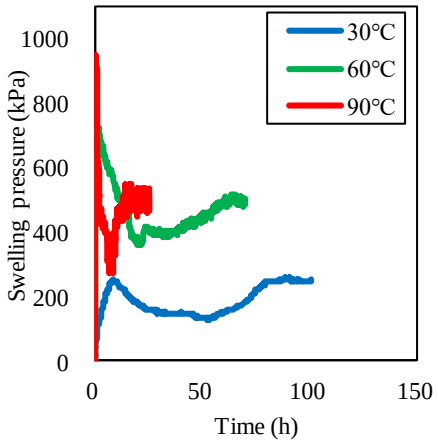

Fig. 6 Heating period of 90 days and temperature history of 30 ° C

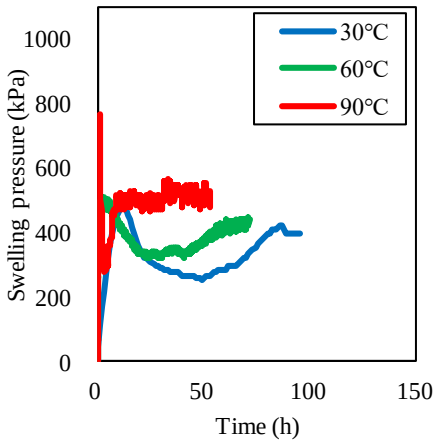

Fig. 7 Heating period of 90 days and temperature history of 60 ° C

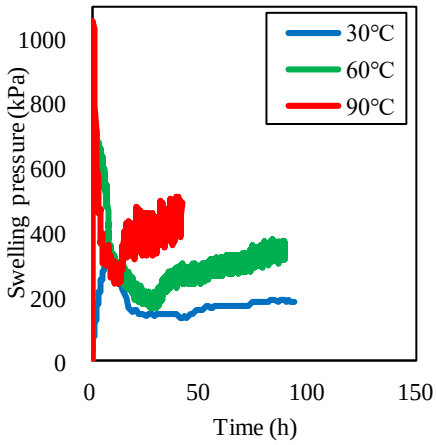

Fig. 8 Heating period of 14 days and temperature history of 100 ° C

heating period or specific temperature history.

The increase in maximum swelling pressure is caused by the expansion of the diffusion electric double layer and the increase in osmotic pressure. First, we will discuss the expansion of the diffusive electric double layer. Since the surface of clay minerals is charged, an electric double layer is formed. Debye distance (1/κ) is defined as a parameter representing the thickness of the electric double layer. Equation (1) is Debye distance magnitude.

$$\frac{1}{\kappa} = \sqrt{\frac{\varepsilon_r \varepsilon_0 kT}{2e^2 n_0 z^2}} \quad (1)$$

where e:elementary charge, n0: ion molar concentration, z: valence of ion, εr: dielectric constant, ε0: dielectric constant of vacuum, k: Boltzmann constant, and T: absolute temperature. Debye distance increases with increasing absolute temperature. Overlapping electric double layers generate repulsive forces, and as the Debye distance increases, the area where the electric double layers overlap grows larger. Therefore, it is thought that the repulsive force and the swelling pressure both increased.

Secondly, we consider osmotic pressure. Bentonite swells by the hydration reaction of water molecules with interlayer cations. Large osmotic pressure is considered to be generated by the ion concentration difference between the ion exchange water and montmorillonite layers. Since the osmotic pressure increases with increasing temperature, it is likely that the swelling pressure increases because water molecules entry between the layers becomes easier.

The decrease in the maximum swelling pressure of the sample with a temperature history of 30 ° C is thought to be due to the decrease in the montmorillonite content of the sample with increasing temperature history. As the montmorillonite content decreased by about 3% in the 14- day history period and by about 2% in the 90- day history period, the maximum swelling pressure of the sample during the 90- day history period is thought to be lower than that of the sample without a temperature history. However, clay minerals may be altered by drying if the water content falls below 7%. Since the water content of the sample taken out of the drying furnace after the temperature history was as low as 1 ~ 2%, the decrease of montmorillonite content is considered to be due to the alteration of bentonite by drying. Necessary future analysis should include examination of temperature history application to prevent sample drying and clarify the causal of montmorillonite content reduction. Since the maximum swelling pressure increases at the test temperatures of 60 ° C and 90 ° C, further collection of data is necessary.

Equilibrium Swelling Pressure

The equilibrium swelling pressure increased with increasing temperature, and the swelling pressure tended to increase more slowly than the maximum swelling pressure under all test conditions. A sample with a history temperature of 60 ° C shows a larger equilibrium swelling pressure than a sample without a temperature history. In addition, it was confirmed that the equilibrium swelling pressure of the sample with a temperature history decreased by about 100kPa at the test temperature of 30 ° C.

First, the expansion of the diffusion electric double layer is considered to cause an increase in the equilibrium swelling pressure with the rise in temperature. The previous section explained that the diffusion electric double layer expands with rising temperature, a trend observed even to equilibrium swelling pressure. The repulsive forces are considered to increases due to the expansion of the electric double layer and the equilibrium swelling pressure increases due to the repulsive force of the particles.

The gradual increase in swelling pressure compared with the increase in maximum swelling pressure is thought to be due to the decrease in osmotic pressure and dehydration of interlayer water. Although the osmotic pressure increased with increasing temperature, the osmotic pressure likely decreased because water entered the interlayer and the ion concentration difference between the peripheral solution and the interlayer decreased. As for the dehydration of the interlayer water, the increase in the swelling pressure likely slowed, due to the separation of the interlayer cations and hydrated water molecules with increasing temperature. A TG (thermogravimetric decrease) index exists, which illustrates the relation between temperature and mass. In this, TG is defined as a method to measure the mass of the sample as a function of temperature, while the

temperature of the sample is changed according to a fixed program. By this method, weight reduction was confirmed even at temperatures below 100 ° C. in [5]. The higher the test temperature, the more the water molecules in the montmorillonite layers become dehydrated, because higher temperatures enhance dehydration. Therefore, the tendency of the equilibrium swelling pressure to increase became less pronounced the distance between layers decreased. However, since the rate of the hydration reaction and the time until specimen saturated are unknown, it is necessary to estimate from the water content distribution of the specimen in the initial stage of swelling by changing the duration of the swelling pressure test.

The decrease in equilibrium swelling pressure at a test temperature of 30 ° C for samples with a temperature history (regardless of the specific temperature history or heating period) is likely caused by the decrease in montmorillonite content due to the temperature history. However, since the swelling pressure increased at a test temperature of 90 ° C and a hysteresis temperature of 60 ° C, it is necessary to continue testing and data collection.

CONCLUSIONS

In this study, the swelling pressure test was used to understand the swelling characteristics of bentonite buffer material, considering temperature history and temperature change.

First, it was confirmed that the swelling pressure rapidly increased at the start of water supply, decreased after reaching the peak swelling pressure, and then increased again to reach the equilibrium state. This tendency was confirmed in all test conditions. It was also confirmed that the slope of the graph in the initial stage of swelling increased and that the time to reach the equilibrium state was shorter with increasing test temperature.

Second, the maximum swelling pressure tended to increase as the temperature of the test water increased. Expansion of the diffusion electric double layer and an increase in the osmotic pressure are considered as important factors for this.

Thirdly, the equilibrium swelling pressure tended to increase with increasing temperature of the test water. This is likely due to the expansion of the diffusion electric double layer.

Finally, various condition tests will be conducted in the future to understand the swelling characteristics of bentonite.

REFERENCES

[1] H12 report Project Overview Report, Japan Nuclear Cycle Development Institute, pp.IV22-IV32, 2000.4

[2] Nozomi Ichikawa, Shin-ichi Kanazawa, Hisashi Hayashi, Koji Ishiyama and Atsushi Iizuka, Swelling characteristics of bentonite due to difference in water quality, Environmental Ground Engineering Symposium 12th, pp.557-560,2017.9

[3] Yu Horiuchi and Tetsuichi Takagi, Method of the methylene blue adsorption test for bentonite at AIST, Journal of Geological Survey of Japan, no.555, 2012

[4] Masanobu Onikata, Characteristics and Application of Bentonite, Journal of the Clay Science Society of Japan Volume 46 Issue 2, pp.131-138, 2007.8

[5] Ritsuro Miyawaki, Takashi Sano, Fumihiko Ohashi, Masaya Suzuki, Toshihiro Kogure, Taiga Okumura, Jun Kameda, Takuya Umezome, Tsutomu Sato, Daisuke Chino, Kaori Hiroyama, Hirohisa Yamada, Kenji Tamura, Kazuya Morimoto, Seiichiro Uehara and Tamao Hatta, Some Reference Data for the JCSS Clay Specimens, Journal of the Clay Science Society of Japan Volume 48 Issue 4, pp.158-198, 2010

[6] Nozomi Ichikawa, Shin-ichi Kanazawa, Hisashi Hayashi, Naoki Muto and Koji Ishiyama, Swelling pressure Characteristic of bentonite buffer considering temperature change, Journal of Japan Society of Civil Engineers, pp.33-34, 2018.8

[7] Hideo Komine, Ryoya Ohashi, Kazuya Yasuhara and Satoshi Murakami, Theamal influencea on swelling-pressure and swelling-deformation of bentonites and its factors, Journal of JSCE of Japan Vol.63 No.3, pp.731-741, 2007.8

[8] Jun Kodama, Kakuichiro Adachi, Ryo Tanabe, Eriko Suzuki and Shigehiro Yamamoto, Swelling characteristics of bentonite-silica mixture under high temperature, Journal of JSCE of Japan No.764, pp.319-328, 2004.6

[9] Yukihisa Tanaka and Kunihiko Nakamura, Effect of seawater and high-temperature history on swelling characteristics of bentonite, Journal of JSCE of Japan No.806, pp.93-111, 2005.12

9th Int. Conf. on Geotechnique, Construction Materials and Environment, Tokyo, Japan, 20-22 November 2019, ISBN: 978-4-909106025 C3051

DETECTION OF CONCEALED ACTIVE FAULTS BY MICROTREMOR AT RIVER WATER DISAPPEAR SECTION

Minoru Yamanaka[1], Shuichi Hasegawa[1] and Shuichi Miyaji[2]
[1]Kagawa University, Japan; [2]Chiken Inc. Ltd., Japan

ABSTRACT

Big earthquake caused by unknown active fault occurs frequently in recent years in Japan. A surface earthquake fault which develops in an alluvial fan above the earthquake source fault becomes indefinitely by erosion and accumulation during repeated floods. An existence of the concealed active fault is very difficult to distinct by topography investigation in the alluvial fan. On the other hands, a river water disappears into underground during a dry season. This phenomenon is considered as a change of depth of permeable layer at a concealed active fault crosses. Therefore it is necessary to survey the suddenly change of the layer in order to detect the distribution of concealed active fault along the river at the alluvial fan.

In this study, the microtremor measurement as new geophysical exploration technique in order to detect the concealed active fault were carried out at 2 river sites where the distribution of two active faults is revealed yet. As a result of this study, the principal peak frequency changes largely at the river water disappear section, and it can be clear that there is meaningful difference in the depth of basement rock at the location of the estimated fault.

Keywords: Physical exploration, Active faults, Microtremor, Vibration analysis, River

INTRODUCTION

Big earthquakes caused by an active fault such as the 2016 Kumamoto Earthquake or the 2018 Hokkaido Eastern Iburi Earthquake occurred frequency in Japan. Many active faults are distributed over about 2000 points over Japan. A trace of active fault is not clear on an alluvial fan or an alluvial low plain, then it is difficult to detect the active fault in the topography [1].

A mysteries phenomenon that a river water disappears continuously from a riverbed at a certain section occurs frequency in a small river during dry season. The authors consider that this phenomenon which river water disappears into underground happens by difference of depth of permeable layer at a concealed active fault crosses [2], [3].

The boring exploration and the reflective exploration method, etc. are used as a conventional active fault detection method [4], but these methods are needed many days and expensive cost, and more these methods cannot carried out easily for detection of an active fault. Therefore development of new detection method of active fault is expected.

The purpose of this study is to estimate on application of microtremor measurement as the new geophysical exploration method to detect a concealed active fault at river water disappear section. It can be considered that it's possible to detect the sudden depth change of stratum from the difference in the vibration characteristics gained by setting some microtremors along the traverse line which crossed an active fault.

In this study, the microtremor measurements was carried out at 2 river sites where the distribution of the active fault is revealed yet and is not yet. And change of the principal peak frequency and difference in the depth of the basement rock at the location of active fault were discussed.

DETECTION METHODS OF ACTIVE FAULT BY GEOPHYSICAL EXPLORATION

So many researches on survey method of an active fault distribution were carried out until now [5], [6]. Geophysical exploration is used widely as a method to grasp a location or an extension of active fault and to clear a property of active fault under an alluvial plains covered by thick accumulated layer in particular [7]-[9]. But a trench and boring survey within shallow layer as a survey method of active fault is not enough because a fault displacement is very small or almost zero at ground surface in an alluvial plain.

Generally, seismic reflection survey, acoustic survey, electric survey, electromagnetic survey, gravity survey and radio-metric survey etc. can be listed as geophysical exploring methods for active fault investigation. But these methods can't carried out easily because of its necessary days and much expense. The authors proposed the microtremor as a survey method to detect an active fault more easily and conveniently [10]. The microtremor has utilized widely on in the field of the geophysical exploration [11], but it seems that the application study of microtremor to detect a concealed active fault under alluvial plain is very few [12].

DISAPPEAR OF RIVER STREAM AT CONCEALED ACTIVE FAULTS

River water disappears frequency into underground during a dry season at a small river which flows on an alluvial fan, and this phenomenon is called as "*Segire*" in Japanese [13]. The authors supposed that *Segire* is related closely to a change in the stratum structure. It is considered that *Segire* occurs because of sudden change of the depth or thickness of stream strata at the cross part of concealed active fault.

ACTIVE FAULT AND SEGIRE IN KAGAWA PREFECTURE

Takamatsu Plain

Outline of geology

Takamatsu plain is formed at the alluvial fan by Koto river mainly, and the flood plain by Kasuga river and Shin river is distributed at the east area. Headwaters of Koto river is located at Sanuki mountains in toward to south of the plain. The gravel composed of Izumi layer group is accumulated mainly in the riverbed.

The geological feature is divided roughly into the alluvium layer, Mitoyo layer group and basement rock (granite) from the ground surface. The low permeability layer with much fine soil particles is distributed in the boundary of the alluvium layer and Mitoyo layer group. The thickness of aquifer in the upper part is about 20 m of depth.

Nagao fault

Nagao fault is located in the south in Takamatsu plain. This fault is distributed over eastern and western direction, and is about 20 km of length. Nagao fault inclines toward the south side, and is reverse fault which rises to south side. The unit length of displacement is estimated to be 0.5-2.0m with the right-lateral strike-slip component [14], [15].

Segire of Koto river

Segire phenomenon occurs sometimes at the middle reaches area along Koto river in Takamatsu plains. A section of *Segire* of Koto river is about 2 km in length. The low fault scarp and flexure by the active fault isn't confirmed along the *Segire* section.

Marugame Plain

Outline of geology

Doki river which flows from Sanuki mountains forms Marugame plain. The geological feature of Marugame plain consists of the alluvial fan with gravel mainly, Mitoyo layer group which is alternation of gravel, sand and cohesive soil strata, and granite as a basement rock.

Okada fault and Kami-hogunji fault

Okada and Kami-hogunji faults are distributed in the south-eastern area in Marugame plain. The length is short, and is spread in NW-SE direction. For Kami-hogunji fault, the length on ground surface is about 5 km, the ground level rises at north side, and the inclination of fault plane is unclear.

Segire of Doki river

Segire occurs at 2.8 km in length along middle reaches of Doki river during a dry season. The low fault scarp and flexure is not confirmed along the *Segire* section. The depth of granite (basement rock) is more than 50 m at the downstream side of *Segire* point in Doki river according to the past boring data.

Furthermore the sudden change of depth of the engineering base surface is estimated around this *Segire* according to the microtremor carried out in Marugame plane [16]. The distribution of concealed active fault at near of *Segire* is suggested.

MICROTREMORE INVESTIGATION

Investigation Site

Koto river

Segire points where river water disappears at Koto river was investigated 3 times from June, 2012 to January, 2013. These *Segire* points were divided into 2 section with the stable section where *Segire* occurs continuously and the unstable section intermittently during this investigation period.

Doki river

According to reports on occurrence of *Segire* by Ministry of land, infrastructure, transport and tourism Shikoku regional development bureau from 2004 to 2017, it was revealed that there are an unstable section and a stable section of *Segire* at the middle reaches in Doki river.

Method of Microtremor

Microtremors measurement was used McSEIS-MT NEO (OYO Corp.) which is possible to measure an acceleration of three direction (2 horizontal and 1 vertical). The main axis of the measurement correspond to the north, and it was set levelly in a flat surface on the ground. Measurement time is about 40 minutes for 1 point. A spectrum analyzed a measured data was performed a smoothing process by Pazen window of band width 0.3 Hz.

RESULTS OF MICROTREMOR

Site at Koto River

Fig.1 shows the measuring points of microtremor investigation at Koto river. Total of 11 points of K1-

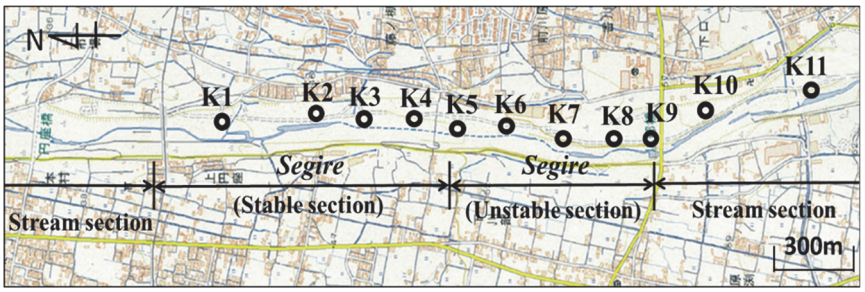

Fig.1 *Segire* section and microtremor measurement points at Koto river

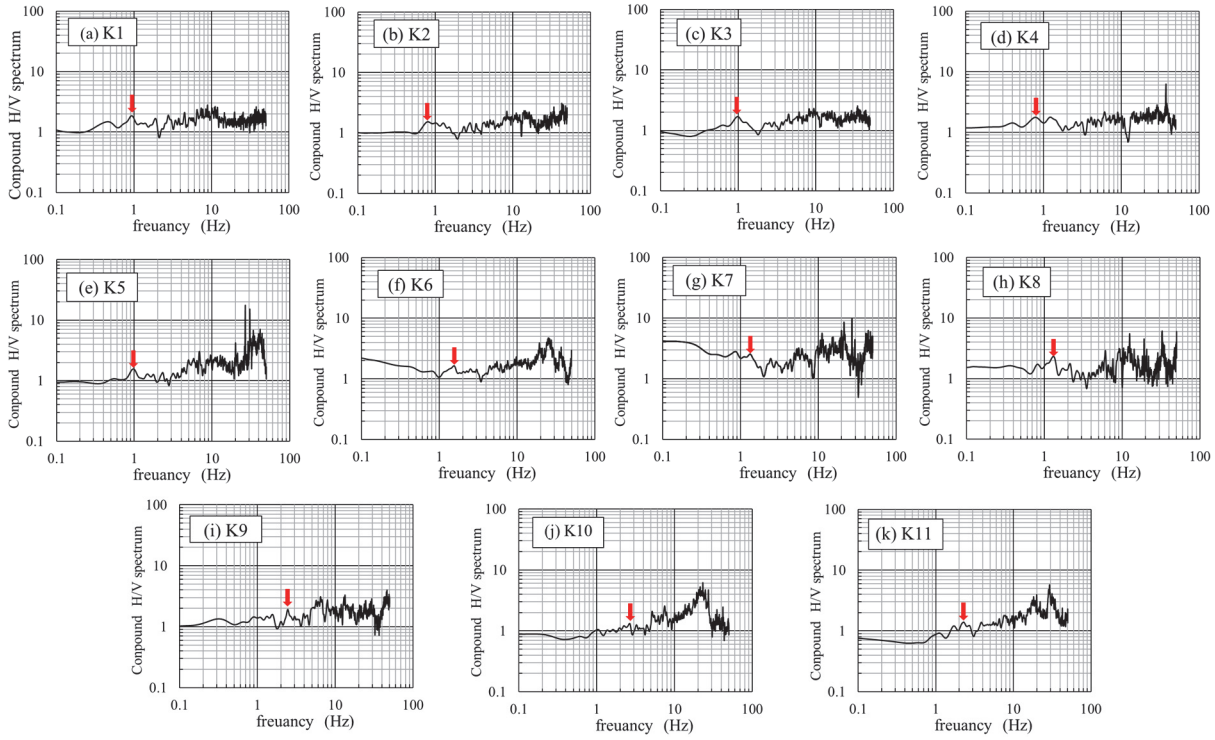

Fig. 2 Compound H/V spectrum obtained by microtremor investigation in Koto river

K11 were set on the flood plain along these two sections and at its upstream side.

Fig.2 (a)-(k) show the compound H/V spectrum obtained by microtremor investigation in Koto river. The composed H/V spectrum is obtained that the square root of summation of square of EW and NE directional (horizontal) spectrum is divided by UD directional (vertical) spectrum. The frequency in the first peak from low frequency side which reflects the depth of granite (basement rock) is indicated by the red arrow. The value of composed H/V spectrum is relatively small, but it is revealed that the first peak indicates around the frequency 1-3Hz at each spot.

Fig.3 shows change the first peak frequency at Koto river. This is about 1 Hz at K1 to K5 point where ranges in the stable section of *Segire*, is about 1.5 Hz at K6 to K8 where ranges in the unstable section of *Segire*, and is over 2 Hz at K9 to K11 where streams river water. It can be say the first peak frequency decreases meaningfully at *Segire* section.

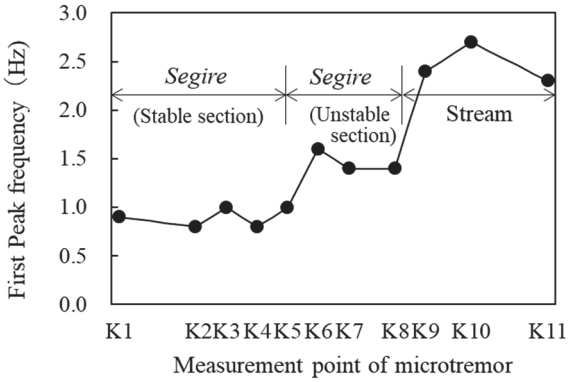

Fig. 3 Change of first peak frequency at Koto river

Site at Doki River

Fig.4 shows the measuring points of microtremor investigation at Doki river. Total of 11 points of D1-D11 on the flood plain along these two sections.

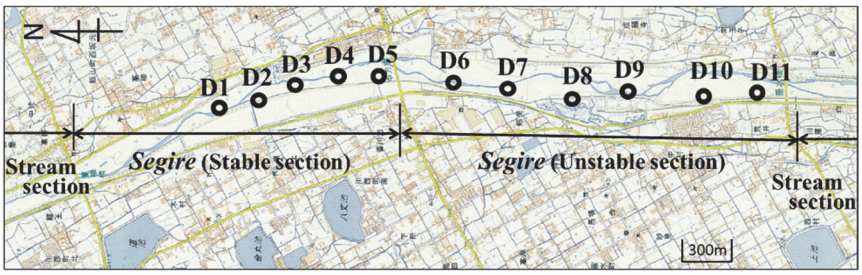

Fig.4 *Segire* section and microtremor measurement points at Doki river

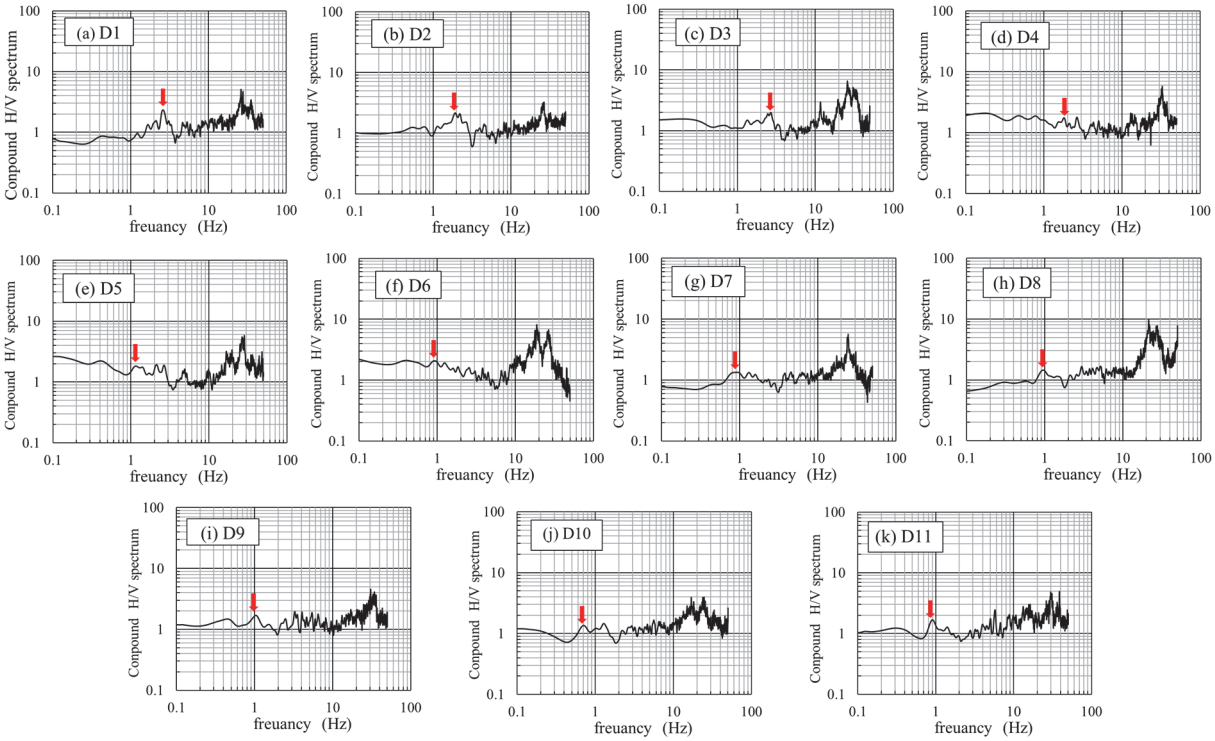

Fig. 5 Compound H/V spectrum obtained by microtremor investigation in Doki river

Fig.5 (a)-(k) show the compound H/V spectrum obtained by microtremor at D1 to D11 points in Doki river. The first peak frequency indicates by the red arrow, the red arrow indicates from about 1 to 3.

Fig.6 shows change the first peak frequency at Doki river. The peak frequency is about 2.7 Hz at D1 to 1.3 Hz at D4 where ranges in the stable section of *Segire*, and is about 0.9 to 0.7 at D6 to D11 where ranges in the unstable section of *Segire*.

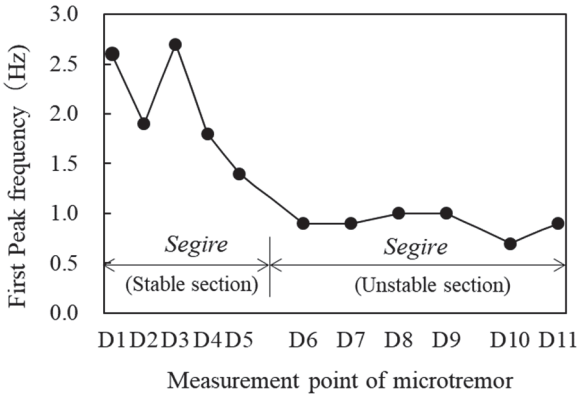

Fig. 6 Change of first peak frequency at Doki river

Estimation of Depth of Concealed Active Fault

If the equation $H=V_s/4f$ defined as 1/4 wavelength law which calculates a thickness of surface layer of ground composed with 2 layers is used, the thickness H becomes so large when a peak frequency f changes so small. Because *Segire* stable section could assume that the depth of basement rock which is the concealed active fault is relatively deep, it means that distribution of concealed active fault is harmonized with the estimated result.

CONCLUSIONS

Microtremors measurement was carried out at the river water disappeared section "*Segire"* in Koto river and Doki river in Kagawa Pref., Japan where can expect crossing of unknown concealed active fault.

As a result of this study, the followings could be obtained;

1) The first peak frequency is about 1 Hz in the stable section of *Segire*, is about 1.5 Hz in the unstable section of *Segire*, and is over 2 Hz at streaming water in Koto river.
2) The peak frequency is about 2.7 Hz at the stable section of *Segire*, and is about 0.9 to 0.7 in the unstable section of *Segire* in Doki river.
3) The first peak frequency decreases meaningfully at *Segire* section at both rivers.
4) The stable section of *Segire* could assume that the depth of basement rock which is the concealed active fault is relatively deep, it means that distribution of concealed active fault is harmonized with the estimated result by 1/4 wavelength law.

ACKNOWLEDGMENTS

The authors would like to appreciate Mrs. Ting Wang of former master course student, and Mr. Ryo Hayashibara and Mr. Shinkichi Natsumeda of former bachelor course student of Kagawa University for their support of microtremor survey in this study.

REFERENCES

[1] Takahashi T., Mimoto K. and Hayakawa T., Present State of Applications of Geophysical Methods to Characterization of Active Faults, Journal of Japan Society of Engineering Geology, Vol.38, N.3, 1997, pp.118-129 (in Japanese)

[2] Hasegawa S., Yabuguchi M., Nonomura A. and Yamanaka M., Research on active faults in Takamatsu and Marugame Plains, Proc. of Annual Conference of Shikoku Branch of Japanese Geotechnical Society, 2013, pp.73-74 (in Japanese).

[3] Wang T., Hasegawa S., Nonomura A., Yamanaka M. and Miyaji S., Preliminary Report on New Active Faults in Takamatsu and Marugame Plains, Kagawa Prefecture, Proc. of Annual Conference of Japan Society of Engineering Geology, 2017, pp.265-266 (in Japanese).

[4] Takahashi T., Nozaki K., Shima H., Yamane M. and Igarashi T., Field Experiments of Various Geophysical Methods at the Nojima Fault, Butsuri-Tansa, Vol.49, No.6, 1996, pp.498-510 (in Japanese with English abstract)

[5] Ishiyama T. and Sato H., Active faults explored by Shallow Seismic Reflection Surveys: A decade perspective and future research directions, Butsuri-Tansa Vol.59, No.6, 2006, pp.515-524 (in Japanese with English abstract)

[6] Ito T., Sato H. and Ikawa T., New Scope for the Study of Structural Geology added by the Seismic Reflection Method, The memoirs of the Geological Society of Japan, No.50, 1998, pp.177-192 (in Japanese with English abstract).

[7] Putra R.R., Kiyono J., Yoshimoto Y., Ono Y. and Syahril, Determined Soil Characteristic of Palu in Indonesia by using Microtremor Observation, Int. Jour. of GEOMATE, Vol.10, No.2, 2016, pp.1737-1742.

[8] Arai H. and Tokimatsu K., S-Wave Velocity Profiling by Inversion of Microtremor H/V Spectrum, Bulletin of the Seismological Society of America, Vol.94, No.1, 2004, pp.53-63.

[9] Putra R.R., Estimation of Vs_{30} Based on Soil Investigation by using Microtremor Observation in Pading, Indonesia, Int. Jour. of GEOMATE, Vol.13, Issue 38, 2017, pp.135-140.

[10] Hasegawa S., Yamanaka M., Hayashibara R. and Wang T., Microtremor Measurement along River with Disappeared Water Zone to Detect Covered Active Fault, Proc. of Annual Conference of Shikoku Branch of Japanese Geotechnical Society, 2017, pp.79-80 (in Japanese).

[11] Kojima K. and Yamanaka H., Estimation of Quaternary Structure of Fukui Plain based on Microtremor Observation, Journal of Japan Society of Civil Engineers, No.752/I-66, 2004, pp.217-225 (in Japanese with English abstract).

[12] Iwatate T., Ooka A. and Enomoto T., Characteristics in Ashiya-Nishinomiya Area, Comprehensive urban studies, No.61, 1996, pp.5-23(in Japanese with English abstract).

[13] Moriwaki R., Kamei Y. and Fujimori Y., Influence of Surface Water on Heat Environment around Rivers, Journal of Japan Society of Civil Engineers, Vol.68, No.4, 2012, pp.I_1747-I_1752, (in Japanese with English abstract).

[14] Sangawa A., Fault Topography of the Northern Foot of the Asan Mountains, Journal of Tohoku Geography, Vol.25, No.3, 1972, pp.157-164 (in Japanese with English abstract).

[15] Sugiyama T., Sangawa A., Tamura E., Tsuyuguchi K., Fujikawa S., Hasegawa S., Ito T. and Okitsu M., Recent rupture history of the Nagao Fault in Kagawa Prefecture, Annual Report on Active Fault and Paleoearthquake Researches, No.1, 2001, pp.175-198 (in Japanese with English abstract).

[16] Hasegawa S., Saito A., Yamanaka M. and Hayashi K., Application of Surface Wave Surveying to Active Faults Research, Proc. of the 12th Japan Earthquake Engineering Symposium, Paper No.66, 2005, pp.370-373 (in Japanese with English abstract).

9th Int. Conf. on Geotechnique, Construction Materials and Environment, Tokyo, Japan, 20-22 November 2019, ISBN: 978-4-909106025 C3051

PERFORMANCE EVALUATION OF PEAT WITH LOCAL SPECIAL CEMENTS, *GGBFS*, AND SUPERPLASTICIZER

Ahmad Numan[1], Fahmi Aldiamar[1] and Hirochika Hayashi[2]
[1]Institute of Road Engineering (IRE), Bandung, Indonesia; [2] Civil Engineering Research Institute for Cold Region (CERI), Sapporo, Japan

ABSTRACT

Road construction over peat is a big challenge in Indonesia because it still requires the right technology to be applied. One of the options for bearing capacity improvement for peat is through deep cement stabilization in the form of columns that requires extensive research. A laboratory study of unconfined compressive strength (*UCS*) of cemented peat is fundamental to formulate a suitable and economical mix design of stabilized peat columns. The use of Ground Granulated Blast Furnace Slag (*GGBFS*) reduces the consumption of cement so that efficiency is expected in the construction. This paper aims to evaluate the increase of *UCS* between original peat from Ambarawa, Indonesia and peat stabilized with several special cements produced in Indonesia, Ordinary Portland Cement (*OPC*), mixture of *OPC* with *GGBFS*, and including superplasticizer (*SPC*) as additives. To characterize the strength behavior of cemented peat, 28 different mix designs of the cemented peat were prepared and tested in unconfined compression tests. The results revealed that specimen with a mix design of 50% binder dosage (25% *OPC* and 25% *GGBFS*) by mass of wet peat and 2.5% superplasticizer by mass of binder gave the highest unconfined compressive strength of 416.1 kPa after 7 air-curing days and 1034.6 kPa after 28 air-curing days which show the effectiveness of strength incremental for bearing capacity improvement.

Keywords: Cement stablilization, Ground granulated blast furnace slag, Superplasticizer, Peat, Unconfined compressive strength.

INTRODUCTION

Indonesia cover more than 18 million hectares of peat making it the third largest country in the world in terms of peat deposit [1]. Peat originates from plant and denotes the various stages in the humification process where the plant structure can be discerned [2]. Some key problems related to peat are low shear strength, low bearing capacity and high compressibility leading to excessive settlements [3]. It is a growing challenge in Indonesia as a developing country to construct a road over peat which has very soft consistency hence low bearing capacity also large and differential deformation were incurred as a result. Many options available to overcome those concerns, one of them is through deep cement stabilization in the form of columns which requires extensive research in particular for low bearing capacity problems. Foundations constructed using deep cement stabilization techniques have been applied to support structures, embankments and excavations in countries like Japan, Scandinavia, the United States, and central Europe [4]. The properties of the improved soil column may reflect the characteristics of the native soil, mixing method, and the binder characteristics [5].

Hence a laboratory study of *UCS* of cemented peat is fundamental to formulate a suitable and economical mix design of stabilized peat columns.

Table 1 Soil consistency from unconfined compressive strength value, q_u [6]

Consistency	q_u (kPa)
Very Soft	< 24
Soft	24 - < 48
Medium	48 - < 96
Stiff	96 - < 192
Very Stiff	192 - < 383
Firm	> 383

The aim of this paper is to evaluate the increase of *UCS* between original peat with a number of ordinary and special cements produced in Indonesia, slag, and including additives.

METHODOLOGY

A laboratory mixing test was performed on Indonesian peat with several special cements produced in Indonesia, *OPC*, mixture of *OPC* with *GGBFS*, and included superplasticizer as additive which all specimens were tested for unconfined compression tests.

Peat properties

Peat samples for the laboratory test was collected from Ambarawa, Central of Java, Indonesia. Table 2 shows engineering soil properties of the peat sample which resulted in a high water content of over 200%, ignition loss of over 90% and low pH value of 1.6.

In this study, the content of addition cement ratio, defined in Eq. (1), were 10%, 15%, 20%, 25%, 30%, 40% and 50%. Where, WC is the dry weight of the cement and WP is the wet weight of peat.

$$\text{Addition Cement Ratio (\%)} = (W_C / W_P) \times 100 \qquad (1)$$

Table 2 Engineering properties of peat sample

Specific gravity, Gs	1.81
Water Content, Wn (%)	218.6
Ignition loss L_i (%)	92.9
PH	1.6
Degree of decomposition (Von Post)	H7 - H10
Unconfined Compression Strength *UCS*, q_u (kPa)	4 - 6

Characteristic of Cements and Slag

Three types of special cements, *OPC*, and *GGBFS* were used as the binder. Table 3 shows chemical composition of these cements and slag.

Table 3 Chemical composition of used cements and G*GBFS*

Type of Cement	Specific surface area (cm2/g)	Chemical Composition (%)					
		SiO_2	Al_2O_3	CaO	SO_3	Fe_2O_3	MgO
OPC	3970	19.7	5.5	64.2	2.0	3.4	1.7
Special Cement A	3610	19.2	4.9	64.4	2.1	3.3	1.5
Special Cement B	3700	n/a	n/a	n/a	1.70	n/a	n/a
Special Cement C	3770	27.0	9.4	54.6	1.2	2.4	1.9
GGBFS	3880	34.8	14.8	45.2	1.7	1.3	1.0

Test Procedure

To characterize the strength behavior of cemented peat, 28 different mix designs of the cemented peat were prepared and tested for unconfined compression tests. Three cylindrical specimens (triplo) were made for each mix design, as a measure to minimize errors.

Since there have not been any standard method in Indonesia to test cemented peat specimens for each mix design, the tests were conducted according to [7] a standard defined by the Japanese Geotechnical Society. Specimens 5.2 cm in diameter and 10.4 cm in height were made as follows. First, peat and cement slurry with W/C (W: weight of water, C: dry weight of cement) of 0.60 for each addition cement ratio were poured into an electric mixer and mixed well for 10 minutes. Next, the mixture was put in a mold in three layers, without compaction. Then, the specimens were tamped to avoid voids.

The method for unconfined compression test refers to [8] and the test was conducted after 3, 7, 14 and 28 air-curing days.

RESULTS AND DISCUSSION

Strength of *OPC* and special cement-treated peat

Figure 2 shows the relationship between the addition of cement ratio and the *UCS* value of stabilized peat using *OPC*, special cement A, special cement B, and special cement C after 3, 7, 14, and 28 days curing respectively. The *UCS* value of stabilized peat increased roughly with the increase of the addition cement ratio. It can be seen that the *UCS* value of stabilized peat varied depending on the type of cement. 50% addition cement ratio gave the best result of *UCS* value. In cases which *OPC* was used, the maximum *UCS* value was 268 kPa. Special cement A performed better than *OPC* with 371 kPa of maximum *UCS* value but Special cement C gave best performance with 428 kPa of *UCS* value. Special cement B had the lowest value of maximum *UCS* with 205 kPa.

Fig. 1 Unconfined compression tests were conducted for each specimen.

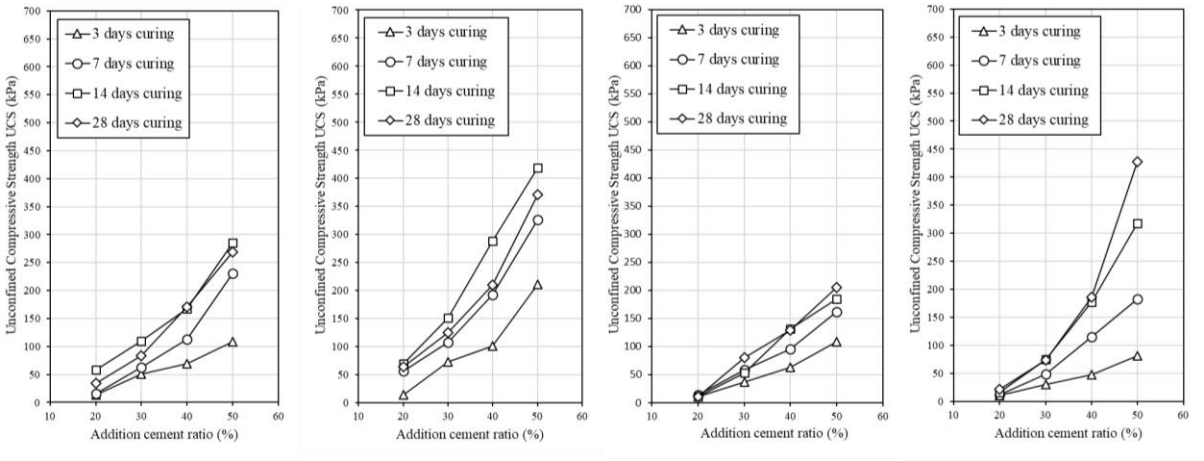

(a) *OPC* (b) Special cements A (c) Special cements B (d) Special cements C

Fig. 2 Relationship between Cement Ratio and *UCS* of stabilized peat.

Strength of *OPC* with *GGBFS*-treated peat

Granulated Blast Furnace Slag (*GBFS*) sometimes simply referred to as slag, is a glassy granular material formed when molten blast-furnace was rapidly chilled, as by immersion in water. It is the residue of combustion in the furnace of steel refining process or by-products of the steel plant. The mineralogical composition and reactivity of the slag vary depending on the rate of cooling after leaving the blast furnace (1500 °C). Slow cooling results in a crystalline, quite unreactive slag, while rapid cooling produces an amorphous, glassy, latent reactive slag. Granulated blast furnace slag is a product of fast cooling and is thus a latent reactive slag [9]. *GBFS* forming elements are lime, silica and alumina has a chemical composition that does not differ from natural mineral compunds found in *OPC*.

GGBFS is a *GBFS* which has been finely grounded. It has cementitious properties like cement and can serves as an adhesive aggregate. On a certain finer condition of *GGBFS* after being grounded, it can be a substitute for *OPC* in a wide range of equal mass replacement ratios. The use of *GGBFS* reduces the consumption of cement hence construction is expected to be more efficient, which is the aim of the second series trial.

The ratio of the cementitious binder was maintained at a ratio of 50% to the wet weight of peat (since 50% addition cement ratio gave the best result of *UCS* value in previous trial). The binding material consisting *OPC* cement and *GGBFS* was then varied according to the composition shown in Fig. 3.

The test results of compressive strength using a combination of variations in the composition of *OPC* and *GGBFS* showed that variations in the ratio of addition cement in a mixture of binding materials did not have a significant effect as seen on Fig. 4. The maximum *UCS* value was 330 kPa at 25% addition cement ratio (in this case is *OPC*) at 28 days curing time. The performance is quite satisfying since the cases in which *OPC* was used, the maximum *UCS* value was 268 kPa with a 50% addition cement ratio. With less cement ratio (25% from wet weight of peat) combined with *GGBFS*, the *UCS* value is bigger.

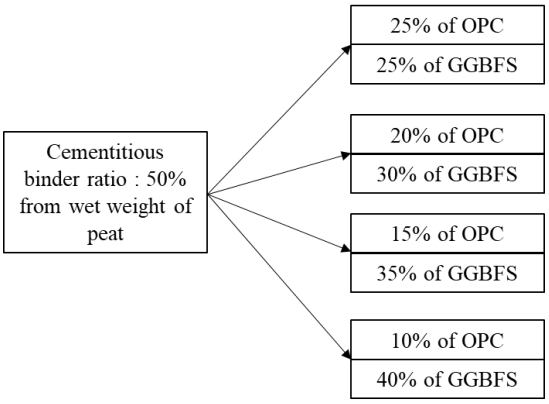

Fig. 3 Variations of cementitious binder ratio

Strength of *OPC* with *GGBFS* and superplasticizer-treated peat

The last trial aimed to have higher *UCS* value with less amount of cement addition ratio. The basic method to increase the strength of concrete is using less W/C. In this case, to have higher mechanical strength of cement-treated peat, the same method was used. The problem which appeared was the lower workability caused by clogging in Deep Concrete Mixing (*DCM*) machine pipe. To extend workability retention, acrylic polymer-based superplasticizer as a chemical admixture was used in this trial.

1% and 2.5% dosage of superplasticizer from the total weight of cementitious binders were used in this

trial. For a 1% dosage superplasticizer, the W/C was lower down to 0.37 and for 2.5% dosage plasticizer, W/C was lower down to 0.30.

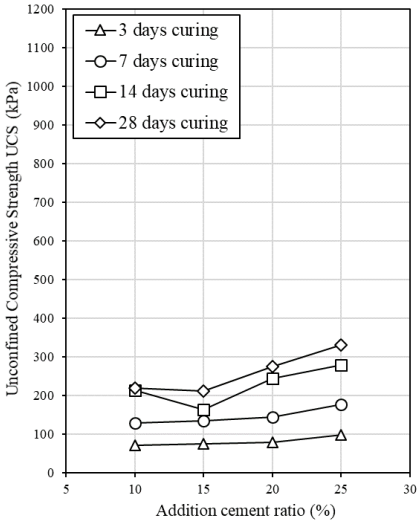

Fig. 4 Relationship between Cement Ratio and *UCS* of stabilized peat using *OPC* with *GGBFS*.

The compressive strength significantly increased along with the amount of addition ratio of superplasticizer as seen in Fig. 5 and Fig. 6 although variations of addition cement ratio in a mixture of binding materials did not contribute significant effect for the addition of 1% superplasticizer.

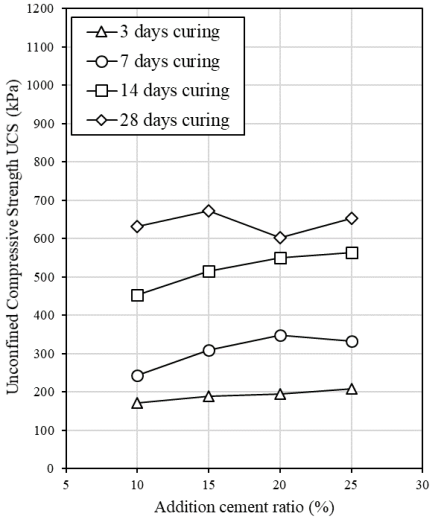

Fig. 5 Relationship between addition cement ratio and *UCS* of stabilized peat using *OPC* with *GGBFS* and 1% superplasticizer.

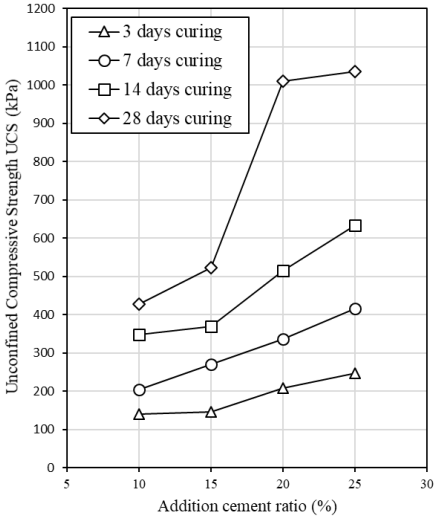

Fig. 6 Relationship between addition cement ratio and *UCS* of stabilized peat using *OPC* with *GGBFS* and 2.5% superplasticizer.

Gain strength of stabilized peat

In the case of all specimens, the *UCS* after 28 days curing increased from 3 days curing as shown in Fig. 2, Fig. 4, Fig. 5 and Fig 6. To clarify this trend, the relationship between the *UCS* after 3 days and 28 days is shown in Fig. 7. The *UCS* after 28 days curing ranged from 1.6 to 4 times the *UCS* after 3 days curing.

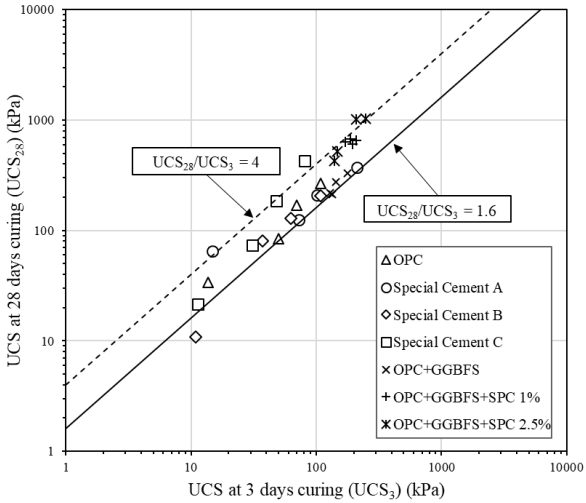

Fig. 7 Relationship between *UCS* of stabilized peat after 3 days and after 28 days curing.

The general in-situ *UCS* ranges from 200 to 500 kPa which is commonly used in Japan [10]. In Scandinavia countries, the general value is from 100 to 200 kPa. The difference in the strength naturally causes differences in the relative stiffness of stabilized and unstabilized soils, which strongly influences the overall behavior of the improved

ground as a system [4]. In-situ *UCS* is generally between 1/2 and 1/5 (ave. is 1/3) of laboratory *UCS* due to mixing accuracy of in-situ mixing is lower than laboratory mixing [9]. Hence, the laboratory *UCS* value was expected to be around 300 ～ 1500 kPa when the target of improvement is to prevent lateral slip flow or the site condition consists of peat and soft clay.

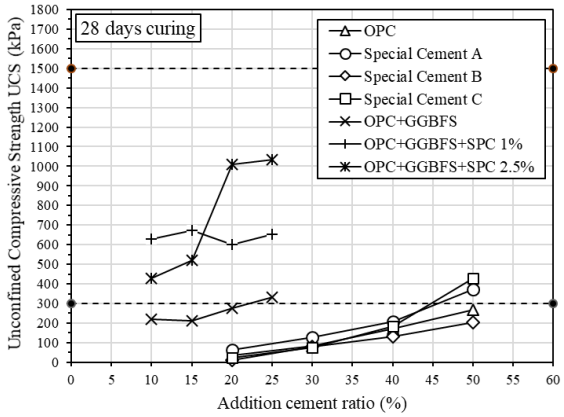

Fig. 8 Relationship between cement ratio and lab. *UCS* of stabilized peat.

The results revealed that specimen with a mix design of 50% binder dosage (25% *OPC* and 25% *GBFS*) by mass of wet peat and 2.5% superplasticizer by mass of binder gave the highest unconfined compressive strength of 1034.6 kPa after 28 air-curing days which shown the effectiveness of strength incremental for bearing capacity improvement as seen in Fig. 8.

CONCLUSIONS

In this study, peat from Ambarawa, Indonesia was stabilized with different amount of binder, primarily consisting of several special cements produced in Indonesia, Ordinary Portland Cement (*OPC*), and mixture of *OPC* with Ground Granulated Blast Furnace Slag (*GGBFS*). Ground Granulated Blast Furnace Slag (*GGBFS*), an industrial waste was found to be suitable for use in stabilizing peat through a number of experiments. The use of *GGBFS* reduces the consumption of cement so that efficiency is expected in the construction.

The design compressive strength will vary based on the purpose and target strength of soil improvement. Hence, if all test results were formulated at 28 days curing time as shown in Fig. 8, a cement ratio above 50% was needed for Special Cement A and Special Cement C to meet the requirement of laboratory compressive strength design range **(**300 ～ 1500 kPa). Whereas, if a mixture of ***OPC*** with ***GGBFS*** were used then the use of a 25% cement ratio can fulfill the common value of laboratory compressive strength design range. Then, the use of superplasticizer additives can be used if a high compressive strength value above 400 kPa is needed.

Because the experiment is limited for laboratory conditions, the result needs to be confirmed for actual field conditions in future work.

REFERENCES

[1] Institute of Road Engineering (IRE), GeoGuide 1, Occurrence & General Nature of Soft Soils. Indonesian Geoguides, Road embankments on Soft Soils, 2001, pp. 41.

[2] Hartlen, J. and W. Wolski, Embankments on Organic Soils. 1st Edn. Elsevier Science B.V., Amsterdam, Holland. ISBN: 0-444-88273-1, 1996, pp. 6.

[3] Huat, B. B. K., Afshin Asadi, & Sina Kazemian, Experimental Investigation on Geomechanical Properties of Tropical Organic Soils and Peat, American Journal of Engineering and Applied Sciences, 2(1), 2009, pp. 184-188.

[4] Kitazume, M., and Terashi, M., The Deep Mixing Method, 2013, pp. 12, 143.

[5] Bruce, D., An introduction to the deep mixing methods as used in geotechnical applications. Volume III. The verification and properties of treated ground. Report No. FHWA-RD-99-167, US Department of Transportation, Federal Highway Administration, 2001.

[6] Terzaghi. K., and R.B. Peck, Soil Mechanics in engineering practice, New York: Wiley, 1967.

[7] Japanese Geotechnical Society (JGS), Practice for Making and Curing Stabilized Soil Specimens without Compaction (JGS 0821-2009), 2016.

[8] Badan Standar Nasional (BSN), Metode Uji Kuat Tekan Bebas Tanah Kohesif (SNI 3638:2012), 2012.

[9] Axelsson A., Johansson S., and Anderson R., Stabilization of Organic Soils by Cement and Puzzolanic Reactions, Feasibility Study, Report 3, Swedish Deep Stabilization Research Centre, 2002, pp. 19.

[10] Civil Engineering Research Institute for Cold Region (CERI), Manual for Countermeasure for Peat Soft Ground, 2017.

9th Int. Conf. on Geotechnique, Construction Materials and Environment, Tokyo, Japan, 20-22 November 2019, ISBN: 978-4-909106025 C3051

EFFECTS OF THE MEDIAN TECTONIC LINE ON SHIKOKU EXPRESSWAYS

Hironobu Ito[1], Shuichi Hasegawa[2], Junji Uchida[1]
[1] West Nippon Expressway Engineering Shikoku Co. Ltd, Japan; [2] kagawa University, Japan

ABSTRACT

In the Shikoku region, the Median Tectonic Line, which is a large-scale tectonic line, extends in the east-west direction. Shikoku region are built close to the Median Tectonic Line. This causes various problems from the construction stage to the maintenance stage on the expressway. Soil structures such as cuttings and tunnels in fragile fractured zones affected by the Median Tectonic Line collapsed or deformed at the construction stage. In addition, clay minerals such as Smectite and Illite produced by hydrothermal alteration form slip clay of landslide because shear strength decreases. Also, they exhibit swelling properties. It causes the roadbed in the tunnel to ridge. Besides these effects, hydrothermal alteration produces pyrite in the soil. When pyrite comes in contact with air and groundwater, sulfuric acid is generated to form acidic soil. On cut slopes where acid soils are distributed, poor vegetation will cause slope failure during rainfall. In this paper, we report several cases in which those Median Tectonic Line affected the expressways in Shikoku region.

Keywords: Median Tectonic Line, Cut slope, Landslide, Hydrothermal alteration

1. Introduction

The Median Tectonic Line is a large fault that divides southwest Japan into the Ryoke zone on the north side and the Sanbagawa body on the south side, and in the Shikoku region, it was an active fault that has active right lateral faulting in the Quaternary.

Yadabe et al. (2000)[1] suggest that the heterogeneity of the deep underground may suggest the influence of past large-scale landslides, fault movements and hydrothermal alteration.

In Hasegawa (2002)[2], there is a high possibility that the granite body is hidden Shikoku Southwest Japan Outer Zone. These igneous activities may provide a site of slope change (geographical predisposition) by constructing a prototype of the Shikoku mountain range by uplift, and also a geological predisposition by bedrock degradation accompanied by hydrothermal alteration Point out to offer.

Tamura et al. (2007)[3] What is the mineral composition of the landslide clay of the cut slope along the Median Tectonic Line and the clays around it Similar to the mineral composition of the hydrothermal alteration fault fracture zone, there are many alteration zones and clay veins on the slope of the cut surface, and the hydrothermal alteration also extends to the landslide point. From these facts, on the expressway constructed near the Shikoku Median Tectonic Line, uneven rock mass was distributed deep in the underground area under the influence of hydrothermal alteration, and many problems of hydrothermal alteration clay and fracture zone occurred.

2. Cut slopes affected by fault fracture zone

The case of Tokushima Expressway Hanazono district is introduced as an example affected by the fault fracture zone by the Median Tectonic Line.

The Tokushima Expressway Hanazono district is a district where several occurrences of deformation occurred and measures were taken each time.

Since the cut slope is planned on the Median Tectonic Line, fault fracture zone clay is excavated. Therefore, this change has been going on for a long time.

Fig.1 Location map of the Hanazono area

There is a steel tower at the top of the cut slope. In addition, there was no time for construction. For this reason, the earth removal method was not adopted. Therefore, measures are taken such as ground anchors and catchment wells.

Pic.1 Full view at Hanazono area

2.1 Hanazono district topography, geology summary

The topology of the Hanazono area of almost parallel to the Yoshinogawa River along the southern rim of the Sanuki Mountain Range, and the slope of the cutting is on the Mino fault, one of the active faults in Median Tectonic Line, as shown in Fig.1.

The Mino fault is located on the northern bank of the Yoshinogawa River, and it consists of the following four formations: 1) Izumi Group at the Cretaceous, late Mesozoic as a basement rock, 2) Dotyu Formation, at Pliocene to Middle Pleistocene, 3) the middle or lower terraced sediments at late Pleistocene, and 4) the Alluvial Formation at Holocene, as shown in Fig.2,3.

The geology consists of the fan-shaped gravel formation at the Cenozoic Quaternary and the mudstone formation of the Izumi Group at Cretaceous, Mesozoic as shown in Fig. 1, and there is a fault crush zone of partly degraded mudstone between them, as shown in Fig.4.

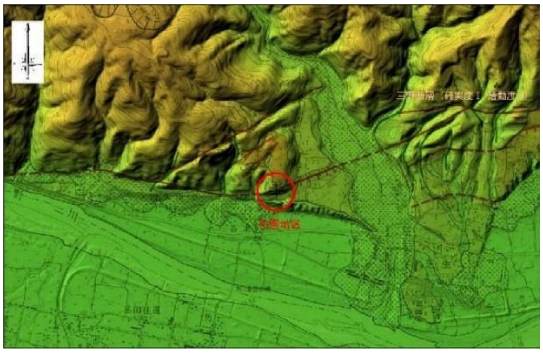

Fig.2 Around the topographic map

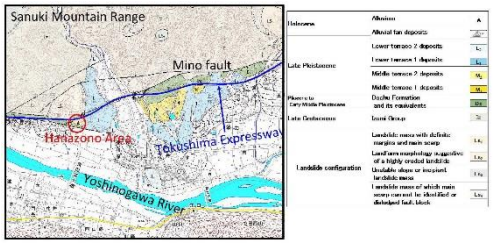

Fig.3 Surrounding geological map

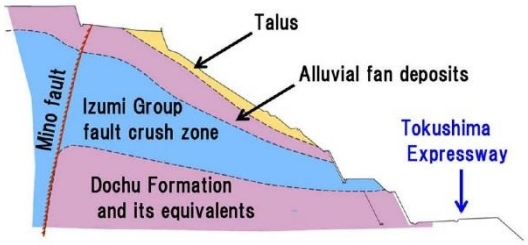

Fig.4 Geologic cross section

2.3 Deformations during construction

In Hanazono area, we began cutting works from July 1997, but when the cumulative rainfall reached 190 mm because of the rainy season in July 1997, a deformation occurred at STA 339 where the town road crossed. So a small-scale ground anchor work was done as a measure countermeasures. In September 1998, the cumulative rainfall reached 557 mm due to a typhoon attack,5 Moreover, landslide cracks were observed at around the tower of mobile phone and cracks at the structures such as retaining walls. The landslide scale by this deformation was a medium-sized landslide block, as shown in Fig4. As a temporary countermeasure against this landslide deformation. As a permanent countermeasure ground anchors were installed through the reverse winding construction method, and two collection wells were also installed (total 34m long). The expressway opened to traffic in March 2000.

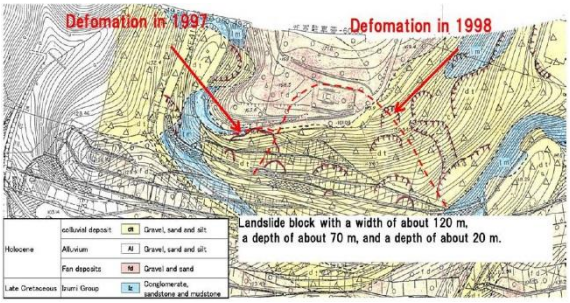

Fig.5 Landslide area map

2.4 Predisposition and attraction of collapse in Hanazono district

The following events were considered as landslide factors. The predisposing factor is the distribution of fragile fractured zones of the Mino fault and the mudstone of the Izumi group The main fault fracture zone clay and the stratum composed of fan beds and diluvial beds are distributed, and it can be mentioned that the shear strength constant was originally low.

3. The effect of clay minerals on tunnel construction

Matonoo tunnel (extension: 213.5 m) is located in Nakanoshou-cho, Shikoku Chuo, Ehime Prefecture

as shown in Fig.5, within the Shredding zone of the Median Tectonic Line (outbound lane 222 m) and in the Fault fracture zone (inbound lane 205 m) It is a tunnel built on.

At the top of the mountain, there is a transmission tower, and at the top of the tunnel is Route 319, and at the bottom of the west slope is Mishima Nishi Junior High School.

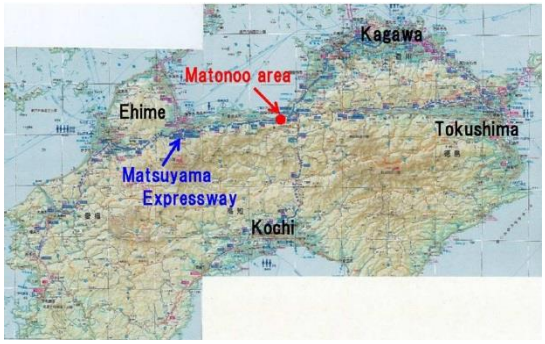

Fig.6 Location map of the Hanazono area

The construction of the relevant tunnel was started in January 1980 as Shikoku's first expressway construction, but landslide fluctuation became apparent along with the tunnel construction, and it took about 40 months to construct the landslide countermeasure construction tunnel. Was completed.

Guide drilling was started in April 1980, but it was difficult to drill at the point where it was more than 20 meters long and drilling was discontinued. After that, I adopted the concept of NATM and changed it to construction with shotcrete. After completion of the outbound lane mountain tunnel, landslides were activated by inbound lane tunnel excavation, and it was estimated that the tunneling and landslide behavior were linked, so the excavation was temporarily suspended, and landslide countermeasure work was carried out. In order to prevent landslides, we have put in place prevention pile and we used a combination of earth filling and drainage boring. As a result of the countermeasure construction, the inbound lane was completed in December 1982. Landslide movement has become apparent again from the time the drilling passes near the summit, but by extending the tunnel at the west wellhead by 10 m and adding a fill-up work and drainage bore, July 1983 outbound lane was also completed. The Matonoo Tunnel was completed in February 1984, but ongoing inspections and dynamic observation in the tunnel are still being conducted.

3.1 Geomorphology and geology of Matonoo area

Matonoo area is located at the end of the ridge between the Otani River, which flows steeply from the Pope Mountains, which is a branch of the Ishizuchi Mountains, and the Ishibe River. The boundary between mountains and plains that are clearly divided by the Ishizuchi fault, as shown in Fig.7,8.

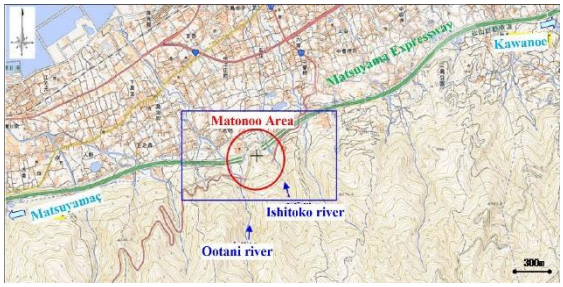

Fig.7 Topographical map around Matonoo area

Fig.8 Topographical map around Matonoo area

The Ikeda fault also runs parallel to the east-west direction to the north of the Ishizuchi fault. Along these faults, plateau-like separation hills remain at the foot of the mountain and fault ridges are partially formed near the boundaries. The separation hills in the Motonoo area are sedimentary deposits of old cliffs and extend northward in a peninsular manner.

On the other hand, in the valleys found on both sides of the hill, the fan-shaped ground of the new-age fan deposits spreads to the north and leads to the alluvial plain. The geology of the area is based on crystalline schists in the Sanbagawa belt originating from pre-lived sediments and sandstone and mudstone in the Upper Cretaceous Izumi Group, and these are Quaternary ancient cliff cones above them It is a geology covered by sediments and fan deposits.

Fig.9 Surrounding geological map

The geology of the area is based on crystalline schists in the Sanbagawa belt originating from pre-lived sediments and sandstone and mudstone in the Upper Cretaceous Izumi Group, and these are

Quaternary ancient cliff cones above them It is a geology covered by sediments and fan deposits.

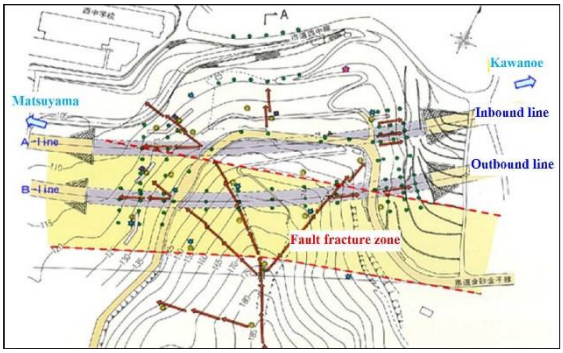

Fig.10 Map plan matonoo area

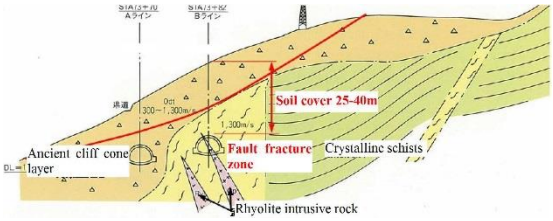

Fig.11 Geologic cross section matonoo area

Bedrocks are divided by a narrowly defined central tectonic line extending diagonally below the route.

Bordering it, the north side is sandstone and mudstone of Izumi Group, and the south side is pelitic crystal schist of Sanbagawa belt. These basement rocks are widely fractured by faulting. In addition, a rhyolitic dike assumed to have been intruded in the Neogene along the fracture zone was recognized, and the horned to sediment-like formation was remarkable, and in part the clayification generated by hydrothermal alteration progressed doing, as shown in Pic 2.

Pic. 2 Penetrating into the shatter zone Rhyolite dike

Since the loose paleo cliff sediment layer of the intervening and relative density of the above fault fracture zone is present thickness 20m ~ 30m, these geological conditions are predisposed to landslide occurrence.

3.2 Predisposition and attraction of collapse in Matonoo district

The predisposition of landslides includes the formation of an old cliff cone layer with the intervention of the low engineering strength including clay minerals affected by hydrothermal alteration and the origin of these geology.

In addition, the low terrain conditions of the side friction of the ridge are considered to be one of the predispositions. As a landslide inducement, since the tunnel excavation and landslide variant from the variable background is closely related, the loosening of the ground due to the thin tunnel excavation becomes an incentive, a plurality of landslides in the vicinity of the stratum boundary is considered to have occurred.

4. Distribution of acidic soils by the influence of hydrothermal alteration

The acidic soil, the soil in which the pH is low, refers to the soil pH of the soil suspension is 7.0 or less.

Acidic soil, vegetation failure in greening the surface, elution of acidic water, causing problems such as plate blister and concrete deterioration of the foundation ground.

The mechanism by which the acidic soil is generated is that the pyrite-containing soil is oxidized to form sulfuric acid, and pyrite (sulfide ore) retains the crystal structure at the time of formation in the deep underground, but the atmosphere (It is generally known that in the weathered layer near the surface, which is easily accessible to oxygen) and surface water, it is converted to chemically stable sulfur that is compatible with this environment.

Pyrite, a source of acid soil, is strongly influenced by marine sedimentary rocks and sediments, and also by volcanic activity, and Quaternary volcanic geology that had large scale volcanism with caldera formation It has been confirmed in the hydrothermal alteration zone.

There are few cases where acid soil is a problem in Shikoku so far, because it is characterized by the geology where the acid soil has been reported so far and there is hardly any geology corresponding to that feature in Shikoku.

Acidic soil is considered to be characterized by the geologic age that occurs, and is often sedimentary rock of marine origin, and its geologic age has been geological since the Tertiary. However, strata and rocks distributed in Shikoku are strata groups mainly composed of Mesozoic and Paleozoic that are distributed in a zonal belt structure. In addition, hydrothermal alteration is considered to be influenced by the Quaternary volcanic origin geology, etc. where large-scale volcanism with caldera formation was strongly influenced by volcanic activity. It is pointed out that the geology affected by the hydrothermal alteration is overlooked because the Quaternary volcanoes are not distributed in Shikoku and the distribution of the

Neogene igneous rocks is also small. Because of that, until now, the fault of acid soil in Shikoku has not received much attention.

However, on the large-scale cut slopes associated with the construction of the Shikoku Expressway, obstacles in the acid soil have become apparent, and in November 2006 the Takamatsu Expressway Naruto to Itano Vegetation failure is said to have spread as much as about 33,000 m2, and poor reforestation such as poor growth of vegetation and discoloration and deterioration of concrete have been confirmed.

Pic. 3 Poor vegetation due to acidity

Pic. 4 Concrete deterioration by acid soil

Pic. 5 Discoloration of concrete by acid soil

4.1 Distribution of acid soil in Shikoku

The distribution of acid soils of 3.9 or less, which is a very strong acid soil in Shikoku, is shown in Fig.1. According to the results, acid soil is concentrated along the Median Tectonic Line, and it occurs along the geological boundary at other points. Focusing on the geology zone, it has been confirmed that the rock types do not depend on granite, conglomerate, sandstone, shale and rock types, including the Izumi Group, the Sanbagawa Belt and the Shimanto Belt.

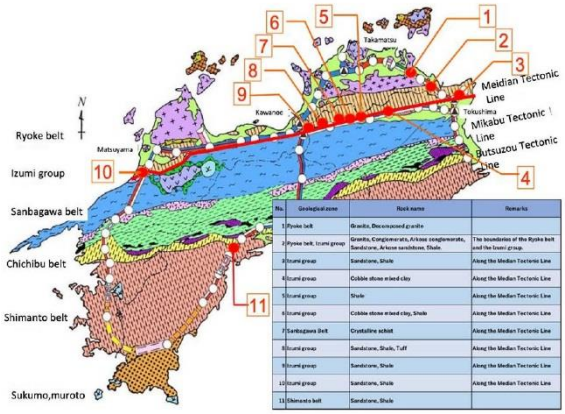

Fig.12 Distribution of acid soil in Shikoku

The distribution of acid soil in Shikoku is also confirmed in areas where geology other than marine clay is distributed. Sandstone of the Izumi group is distributed on the slope No.2 in Fig.11 in areas showing strong acidity, pyrite is identified along with illite and quartz of clay minerals. In addition, in many slopes where geology other than marine clay origin is distributed among other slopes, it is confirmed along the stratum boundary. It can be said that this is likely that the hot water that has flowed into the fault fracture zone deep in the fault contributes to the formation of pyrite. Therefore, it can be said that pyrite is generated near the Median Tectonic Line of Shikoku and other tectonic lines, etc., and acidic soil is likely to be distributed on cut slopes where large-scale excavation has been conducted.

5. Conclusion

In this paper, we report various problems caused by the influence of the Median Tectonic Line in Shikoku. Those problems were constructed in the era when the various effects of the Chuo Tectonic Line were not recognized. At present, there are many findings obtained by constructing expressways in Shikoku, but even at this stage, the detailed mechanism of landslides, especially the origin of deep slip surfaces that form large-scale landslides, has not been fully elucidated. is there. It is important

to solve these problems, and it is important to apply them to construction and maintenance based on the knowledge obtained so far.

REFERENCES

[1] R.Yatabe, K.Yokota, T.Ishii, T.Yuube, General characteristics of landslides in Shikoku region, Journal of the Landslide Society, vol.37.No.3, 2000, pp.50-56.

[2] S.Hasegawa, Middle Miocene Hydrothermal alteration as a predisposing factor of landslides in Shikoku,Japanese Geotechnical society Sikoku branch Geotecnical disaster problem papers, vol.1, pp47-54.

[3] E.Tmaura, S.Hasegawa, H.Watanabe, K.Miyata, R.Yatabe, J.uchida, Effect of Hydrothermal Alteration on landslide along the Median Tectonic Line, **J**ournal of the Landslide Society, vol.44.No.4, 2007, pp.18-32.

9th Int. Conf. on Geotechnique, Construction Materials and Environment, Tokyo, Japan, 20-22 November 2019, ISBN: 978-4-909106025 C3051

INVESTIGATION OF PHYSICAL MODEL ON SOFT SOIL REINFORCED BY RIGID INCLUSIONS UNDER CYCLIC LOADING

Nipun Insog[1], Suriyavut Praai[2], Chaisit Pengjan[3], Chaiwat Saengsrichan[4] and Orianne Jenck[5]
[1, 3, 4]School of Engineering, University of Phayao, Thailand;
[2]GWR Research Unit, School of Engineering, University of Phayao, Thailand;
[2, 5]3SR Laboratory, UMR 5521 CNRS, Grenoble-Alpes University, Grenoble cedex 9, France

ABSTRACT

Soft soil reinforced by rigid inclusion is one of the methods to homogenize and reduce the settlements of earth structures. Various cases of structures under cyclic loading are commonly encountered in the practice, which requires the understanding of this technique under cyclic and/or dynamic loading. This paper is aimed to present a series of experimental studies performed at 1g laboratory scale to simulate soft soil reinforced by rigid inclusions subjected to cyclic loading. Tests were performed with two kinds of embankment or load transfer platform (LTP), i.e., sand and gravel. The parametric study performed with this physical model allowed us to study the influence of the sequence of cyclic loading at the surface of the load transfer platform. The experimental results highlighted the efficiency of load transfer and the accumulation of the settlements during the cyclic loading.

Keywords: Rigid inclusions, soft soil reinforcement, efficiency, cyclic loading

INTRODUCTION

Constructions of roads, railways and other engineering structures in areas, where loose or soft cohesive deposits are found, usually involve with problems such as excessive settlements, deformations and stability problems. These problems have been one of the major challenge for infrastructure planning and implementation.

An interesting– alternative construction technique on soft soil reinforced by rigid inclusions involving granular platforms is widely implemented across the world due to rapid construction, low cost and small total/differential settlements ([1], [8]-[10], [12]-[14]). This technique consists in driving a rigid pile network through the soft soil layer, in order to transmit the loads towards a more competent stratum (in general, the substratum is situated at a depth of a few meters up to 15-20m). The rigid piles can also have pile caps or enlarged heads, in order to increase the surface covered by the piles. This technique is different from those of classical deep foundations, because the piles are not directly connected to the superstructure: a load transfer platform (LTP) or an embankment is built over the improved soil layer, where shearing mechanisms termed as “arching effects” take place. This arching effect partially transmits the load from the surface to the piles, thus permitting to reduce and homogenize the surface settlements. An additional geosynthetic layer can also be placed at the platform base. This layer takes part to the load transfer due to the membrane effect.

The French project ASIRI (Amélioration des Sols par Inclusions Rigides) has brought responses concerning the behaviour of pile improved geotechnical structures and recommendations for the design and installation were published ([7]). However, these studies were only focused on the case of monotonic loading. In case of cyclic loading, a principal citation work in laboratory scale, carried out by Heitz et al. [4], is relevant to the case of dynamic cyclic loading with high frequencies (1-5 Hz). Special investigations have also been performed to described the cyclic mechanism of a granular earth-platform with rigid pile reinforcement by centrifuge modeling ([1], [12]), but only few number of cycles have been prescribed. Houda et al. [5]-[6] also investigated the physical evidence of the effect of vertical cyclic loading (N<50) on soil improvement by rigid piles with a small-scale laboratory experiment. Many such mechanisms, i.e., the use of granular layer, geosynthetic reinforcement, are sophisticated and their description by means of analytical design scheme remains problematic.

This paper describes some of experimental results carried out from a series of experimental observations on soft soil reinforcement by rigid inclusions subjected to cyclic loading using a 3D small-scale physical model. The effects of two kinds of embankment over the soft soil, preloading and boundary conditions are described.

PHYSICAL MODELLING

Test set-up

In order to study the behavior of soft soil reinforcement by rigid inclusions, a 3D laboratory

physical model has been developed (Fig. 1), according to [2], [5]-[6]. This model is under normal gravity at 1/10th scale on the lengths. The device consists of a rigid steel tank of 1x1 m^2. It contains 16 steel pipes with a diameter of 40 mm and a height of 600 mm. In this approach, the modeled inclusions have to be sufficiently rigid and experienced insignificant deformation. Then, the steel pipes were filled with a concrete mix at compressive strength of 23.5 MPa (cube at 28 day). The inclusions were spaced in a square mesh of 200 mm, center to center. In plane surface covered by the inclusions (or pile caps), a recovery ratio (α) can be expressed as;

$$\alpha = \frac{A_p}{A} \quad (1)$$

where A_p is the inclusion section and A is the unit cell surface. Therefore, this spacing provides a recovery ratio equal to 3.14 %. In addition 4 half-inclusions were arranged along an edge of the work, behind a window made of acrylic which allows the observation of deformation. A major disadvantage of this 1-g model is that a small scale model may not entirely respect the prototype due to the scaling law. However, this model can provide a first step for a qualitative analysis of the mechanical behavior of soft soil reinforcement by rigid inclusions. In addition, the parametric experimental studies obtained from this model can be used as a database to calibrate and verify the numerical models ([5], [6]).

The device is instrumented with force sensors at the top of the inclusions and settlement sensors at the base of the granular platform. The load transfer platform (LTP) has a thickness of 300 mm in this part of the study. The loading (monotone or cyclic) was applied to the surface via a cushion under air pressure (P_m), allowing the application of a uniform vertical load over the entire section of the device.

The complex analysis of soil-structure interactions that develop in this model requires appropriate instrumentation. For this study, the following parameters were measured in the central zone, far from the boundaries:

- Forces transmitted to the top of the four central incluaions are measured by 5 kN force sensors; F1, F2, F3 and F4
- Settlement of soft soil was measured at two points (D1 and D2) by 50 mm – displacement transducers.

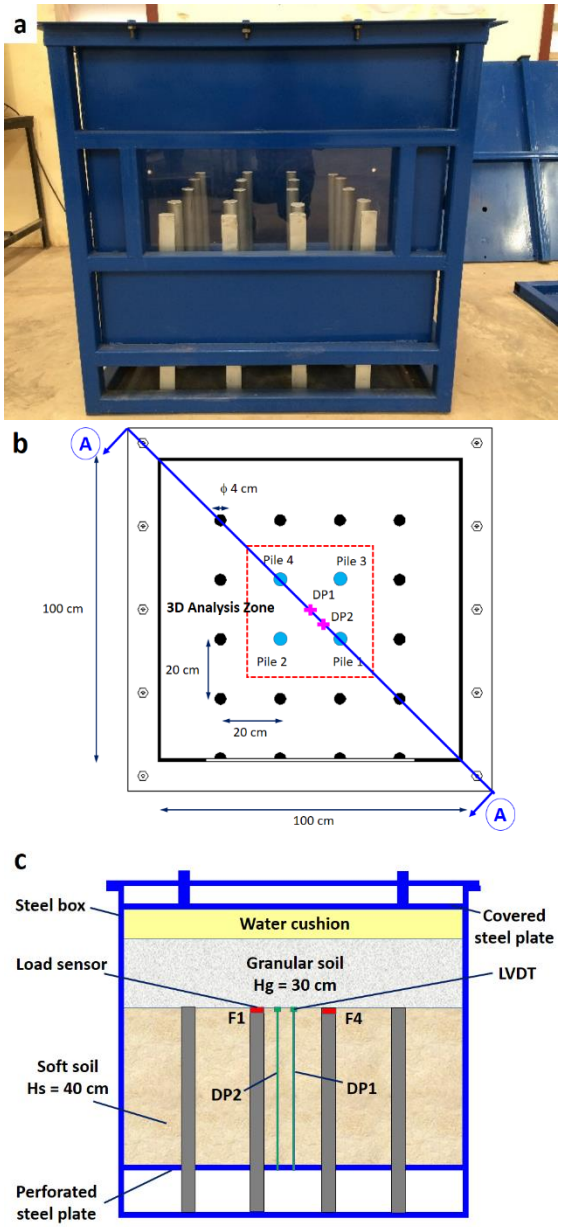

Fig. 1 (a) Photograph of the model; (b) schematic plane view of test set-up; (c) cross section of test set-up with instrumentation

Materials

The soft soil used in this study was simulated by a mixture of expanded polystyrene balls, sand and water (Fig. 2a). Fig. 2b shows the grain size of the soft soil (a mixture of polystyrene balls and sand) in this study. This mixture can represent the compressibility characteristics similar to the real soft soil. This analogue soil also provides an advantage of being easy to set-up and of having a homogeneous density. In addition, a satisfying repeatability from one experiment to another can be achieved.

Soft soil was prepared with the ratio of sand:

water: polystyrene balls at 40: 4: 1 by weight. The presence of the water contributed to the homogenization of the sand with polystyrene. The average density of the mixture in this study was 5.8 kN/m^3.

An embankment of 0.3 m height as a LTP was constructed over the soft soil layer reinforced by the inclusions. Two kinds of embankment or load transfer platform, i.e., sand and gravel, with grain size D_{50} of 1.2 mm and 3.4 mm, respectively, were used. The sand was prepared by the pluviation and tamping methods providing the average unit weight of 16.67 kN/m^3. The friction angle of 45° was examined from triaxial test. While gravel was prepared by tamping method which gave the average unit weight of 15.4 kN/m^3. With this unit weight, the friction angle of 35° could be achieved.

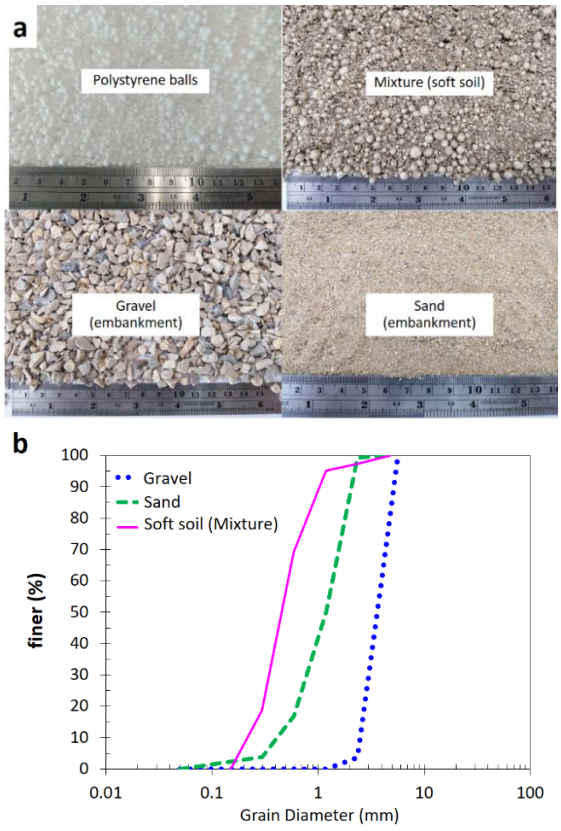

Fig. 2 Materials and Grain size distribution of materials used in this study.

Test program

Table 1 summarizes the preliminary test campaign with different loading conditions in this study. The test set-up was first performed by:

- Filling the model with soft soil
- Construction of the embankment layer
- Placing the air cushion on the top of the embankment
- Closing the tank with the covered steel plate
- Consolidation as a result of the weight of embankment for 12 hours.
- Application of loading, P_m.

Three levels of loading P_m = 5, 15 and 25 kPa, for 3 hours each, followed by an unloading to P_m = 0 kPa for monotonic test series were performed. In case of cyclic loading, two patterns (P_m between 2-15 and 15-25 kPa) with the period of 8 min were applied.

Table 1 Program of experimental tests

Test	Type of embankment	P_m (kPa)	Number of cycles
M_s	Sand	5-15-25	-
M_g	Gravel	5-15-25	-
Cy_s1	Sand	5-15	500
Cy_s2	Sand	15-25	500
Cy_g1	Gravel	5-15	500
Cy_g2	Gravel	15-25	500

TEST RESULTS

Fig. 3 shows typical results under monotonic loading of the test M_S. After a consolidation period of 12 hours, the step of loading (5, 15 and 25 kPa) was applied. The forces on the four central inclusions and the displacements were measured. The values of F_i (in this study, i from 1 – 4, Fig. 3b) were not different and indicated that the distribution of the load in the system was homogeneous. The settlements measured beneath the embankment showed a prominent value at mid-span (DP1, Fig. 3c). A small increase in settlements was observed when P_m was kept constant for 3 hours.

Fig. 3d shows the average efficiency of the four central inclusions as a function of time. The efficiency of the system (E) can be defined as the ratio of the load acting on the inclusion (F) to the total load applied on a unit cell (weight of embankment (W) and surface pressure, P_m):

$$E = \frac{F}{W + P_m} \quad (2)$$

In this study, after finishing the construction of embankment, the consolidation period of 12 hours was performed. At this stage an inclusion only supported the weight of embankment for a unit cell of A = 0.04 m^2). Then, the application of surface pressure, P_m was performed. It can be seen that at the beginning of applying the surface pressure, P_m = 5 kPa, while the surface pressure was applied, the force on the inclusion did not increased coincidently. The

increase rate of force on the inclusion was slower than that of the surface pressure. After that the mobilization of the force took place.

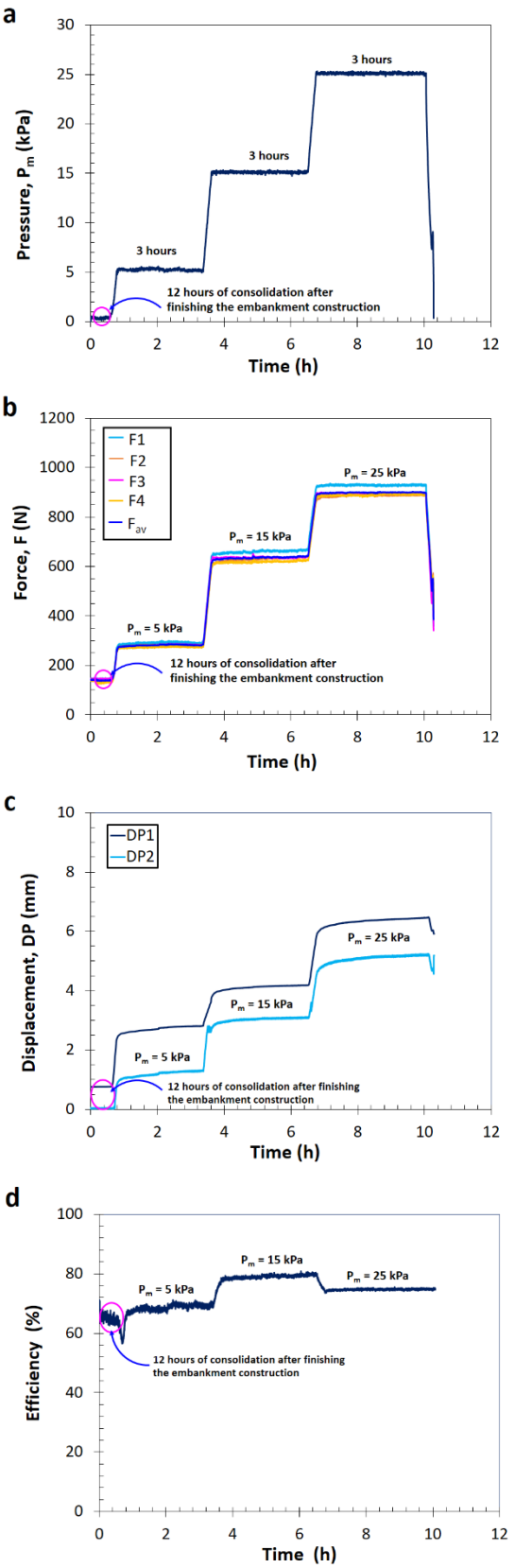

Fig. 3 Monotonic test, M_s, on sand embankment.

The increase in surface pressure at P_m = 5 kPa provided an increase in the average efficiency of 68%. When P_m = 15 kPa was applied, the average efficiency could reach 80%. However, the average efficiency decreased to 75% when applying P_m = 25 kPa.

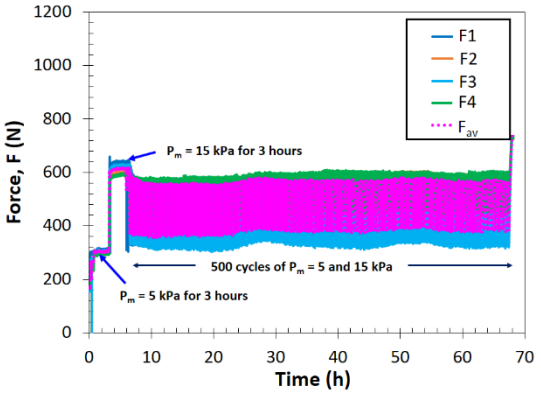

Fig. 4 Evolution of force on the head of four central inclusion with sand embankment (test Cy_s1)

The cyclic tests of two kinds of embankment were performed with the same geometrical configuration. Two patterns of load sequence (monotonic and cyclic) were performed. The effect of stress level, at which the cyclic loadings of 500 cycles were performed, was highlighted. Before applying the cyclic loading, each test experienced the static loading for three hours. Fig. 4 shows the forces on the inclusions of the test Cy_s1 consisting of applying two stages of static loading P_m = 5 kPa and then P_m = 15 kPa followed by an application of cyclic loading by means of ΔP_m = 10 kPa (P_m = 5 and 15 kPa). During cyclic loading, the variation of the forces measured on each inclusion could be found. However, the force repartition on the four inclusions could be satisfactory. The maximum difference of 12 % between the average value (F_{av}) and the value of F_i on each inclusion was found (the maximum difference of 10% was reported by [5], [6]).

Fig. 5 shows the evolution of average efficiency of four central inclusions as a function of number of cycles for two kinds of embankment. These average values were computed by taking into account the center of cycle. It can be seen that the initial values of efficiency of gravel embankment were lower than those of sand embankment due to the friction angel. Starting with the low level of cyclic loading (P_m = 5 and 15 kPa), the efficiency of 79% and 70% could respectively be found for sand (Cy_s1) and gravel (Cy_g1) embankments. During cyclic loading, there was no significant variation in efficiency for both

kinds of embankment. Okkay et al., [11] performed a centrifuge model and reported that the loading-unloading cycles did not influence the behavior of pile group on soft soil. Their results also showed the similar efficiency values for monotonic and cyclic loading tests.

When starting with the higher level of cyclic loading (P_m = 15 and 25 kPa), the average efficiency decreased slightly as a function of number of cycles. In comparison between two embankments, a higher reduction rate in efficiency was observed on gravel embankment (Fig. 5b). The efficiency started at 64 % after the consolidation period of 12 hours and then decreased until reaching 58 %.

When considering the settlement of the system, Fig. 6 shows the satisfactory repeatability of the monotonic loadings before applying the cyclic loadings. The application of cyclic loading induced an accumulation of settlement. The accumulation settlement due to cyclic loading on gravel embankment (Fig. 6b) was found to be greater than that on sand embankment as a result of low efficiency.

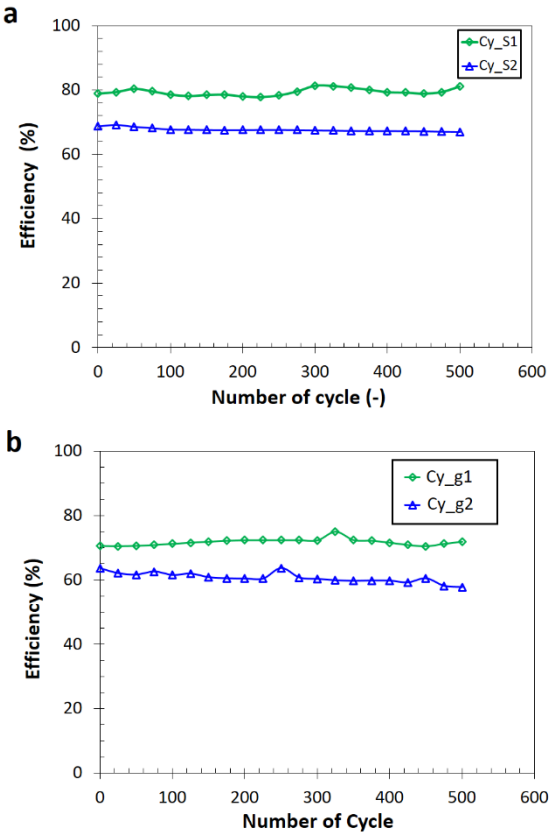

Fig. 5 evolution of the average efficiency at the head of four central inclusions as a function of number of cycles: (a) sand embankment; (b) gravel embankment.

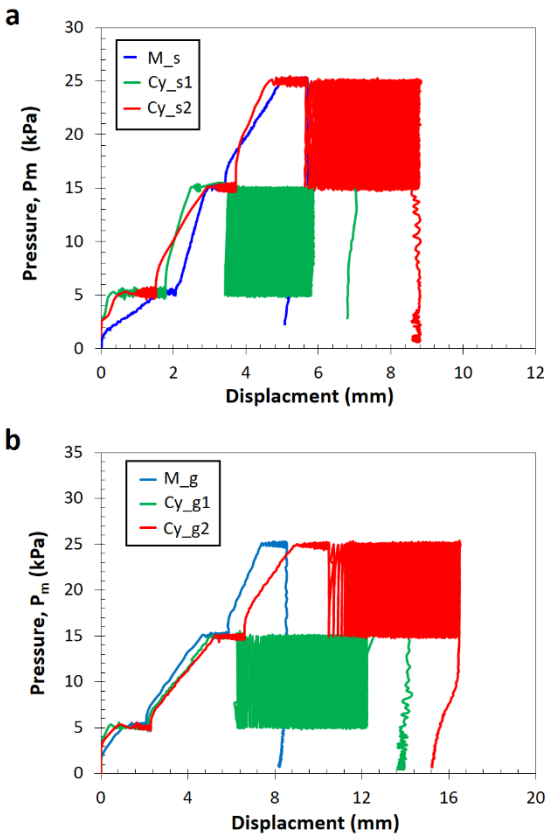

Fig. 6 Settlement evolution with the applied surface pressure: (a) sand embankment; (b) gravel embankment.

CONCLUSIONS

Based on experimental investigation on soft soil reinforced by rigid inclusions in laboratory scale, the preliminary results for two kinds of embankment were presented and analyzed. With 1-g scale model, a drawback still exists because of the scaling law. However, a parametric study obtained from this model allows access to a better understanding of the mechanical behavior of soft soil reinforced by rigid inclusions. This includes the constitution of a large experimental studies to develop and validate numerical approaches.

Monotonic test results serving as the reference tests consisted of applying three levels of surface pressure (5, 15 and 25 kPa) and each loading level was kept constant for 3 hours. On both kinds of embankment, the efficiency increased as a function of applied surface pressure for a certain values. When P_m = 25 kPa was applied, a reduction in efficiency could be observed. The average efficiency of gravel embankment was less than that of sand embankment as a result of unit weight and friction angle.

Under cyclic loading, at low level of surface pressure (5 and 15 kPa) the evolution of average efficiency as a function of number of cycles had no significant variation on both embankments. This is in accordance with the results carried out by centrifuge tests [11]. Comparing the basal settlement between two kinds of embankment, low density and low friction angle could induce more settlement accumulation.

ACKNOWLEDGMENTS

Financial support from University of Phayao under the contract No. RD61091 and Junior Fellowship Program 2019 by Campus France Thailand is gratefully acknowledge. The authors are also grateful to 3SR Laboratory, Grenoble for the technical support.

REFERENCES

[1] Blanc M., Rault G., Thorel L., and Almeida M., Centrifuge investigation of load transfer mechanisms in a granular mattress above a rigid inclusions network. Geotext and Geomembrane, Vol 36, 2013, pp. 92–105.

[2] Da Silva Pinto C., Almeida M., Almeida M.C.F., Jenck O., Briancon M., Houda M. and Emeriault F., Physical model studies on piled embankments with and without geosynthetics, Conference proceedings, in Proc. 10th Int. Conf. on Geosynthetics, 2014, pp. 1-8.

[3] Dinh A.Q., Etude sur modèle physique des mécanismes de transfert de charge dans les sols renforcés par inclusions rigides. Application au dimensionnement. PhD thesis, Ecole des Ponts, Paris, France (in French), 2009.

[4] Heitz C., Luking J. and Kempfert H.G., Geosynthetic reinforced and pile supported embankments under static and cyclic Loading. Proceedings of the 4th European Geosynthetics Conference Euro-Geo4, Edinburgh, UK. UK Chapter of the International Geosynthetic Society, Blackburn, UK, paper number 215.

[5] Houda M., Jenck O. and Emeriault F., Physical evidence of the effect of vertical cyclic loading on soil improvement by rigid piles: a small-scale laboratory experiment using digital image correlation. Acta Geotechnica, Vol. 11, Issue 2, 2016, pp. 325–356.

[6] Houda M., Jenck O. and Emeriault F. Rigid pile improvement under vertical cyclic loading: 1g laboratory small-scale modelling. Int. J. of Physical Modelling in Geotechnics, 19(2), 2019, pp. 89-103.

[7] IREX, Recommendations for the Design, Construction and Control of Rigid Inclusion Ground Improvements: ASIRI National Project. Presses des Ponts, Paris, France, 2012.

[8] Jenck O., Dias D. and Kastner R., Two-dimensional physical and numerical modeling of a pile-supported earth platform over soft soil. J. of Geotechnical and Geoenvironmental Engineering, Vol. 133, Issue 3, 2007, pp. 295–305.

[9] Jenck O., Dias D. and Kastner R., Three dimensional numerical modelling of a piled embankment. International Journal of Geomechanics, Vol. 9, Issue 3, 2009, pp. 102-112.

[10] Kongkitkul W., Chaiyaporn U., Youwai S. and Jongpradist P., Role of geogrids in load transfer of pile-supported embankments. Ground Improvement, Vol. 165, Issue G14, 2012, pp. 239-248.

[11] Okyay U.S., Dias D., Thorel L. and Rault G., Centrifuge modeling of a pile-supported granular earth-platform. J. of Geotechnical and Geoenvironmental Engineering, Vol. 140, Issue (2), 2014.

[12] Nunez M., Dias D., Kastner R., Poilpre C., Soft ground improved by rigid vertical piles. Experimental and numerical study of two real cases in France. Proc. of the 6th Int. Conf. on Case Histories in Geotechnical Engineering. Arlington VA. 2008. p.1-10

[13] Van Eekelen S.J.M., Bezuijen A., and Van Tol A.F., Model experiments on piled embankments. Part I. Geotextiles and Geomembranes, Vol. 32, 2012, pp. 69–81.

[14] Van Eekelen S.J.M., Bezuijen A. and Van Tol A.F., Model experiments on piled embankments. Part II. Geotextiles and Geomembranes, Vol. 32, pp. 82–94.

9th Int. Conf. on Geotechnique, Construction Materials and Environment, Tokyo, Japan, 20-22 November 2019, ISBN: 978-4-909106025 C3051

A NON-DESTRUCTIVE METHOD FOR INVESTIGATING SOIL LAYERS OF AN INDIVIDUAL VULNERABLE SLOPE

Eko Andi Suryo[1], Yulvi Zaika[1], Chaminda Galage[2] and Bambang Trigunarsyah[3]
[1]Faculty of Engineering, Brawijaya University, Indonesia; [2,]Science and Engineering Faculty, QUT, Australia; [3]Construction and Project Management, RMIT, Australia.

ABSTRACT

Soil stability analysis becomes main concern in the preliminary design of new construction project. In a critical soil slope, the stability can be affected by the additional load and water infiltration significantly. This is due to additional overturning moment and decreasing of shear strength of the slope material. In such scenario, the non-destructive soil investigation method is needed to analyze the stability. This paper examines the use of Electrical Resistivity Tomography (ERT) to investigate soil layers in a critical slope and to measure parameters of soil shear strength indirectly. Two ERT methods used in this research were dipole-dipole array and square array resistivity (SAR). The results of ERT were verified using geotechnical testing (Bore-hole and Standard Penetration Test) results by investigating the presence of high porosity and water content with soil resistivity. The results of Dipole-dipole array and SAR at selected locations are consistent and suggest a possible crack at the location was reflected by the low soil resistivity value. Furthermore, the results of the SAR confirmed the existence of the deep crack as a continuance of visible cracks on the surface. The results of ERT can be used to detect deep cracks in the subsoil if ERT is conducted in the wet seasons, due to the existence of infiltrated rainwater. Due to the limitations of this technique, the ERT result should be interpreted cautiously. The study demonstrated the benefits of the use of electrical resistivity for the detection of soil layers in residual soil slope.

Keywords: Soil layers detection, Electrical resistivity tomography, Geotechnical investigation, Soil crack

INTRODUCTION

Analyses in stability of slope can be well undertaken by knowing the soil layers underground. Including cracks in soil slopes that has a significant effect on rain-induced slope instability. The stability of slopes associated with surface cracks and rain-water infiltration, has been widely investigated [1], [2], [3], [4], [5]. Surface cracks in soils can be easily seen. In contrast, it is difficult to detect deep cracks unless special equipment for subsoil investigations, such as geophysical tools, is used. The application of geophysical methods may be useful for subsoil investigations, especially at the reconnaissance stage. Based on different physical principles, there are three techniques that can be used to identify soil cracks are based on seismic refraction, electromagnetic wave refraction, and electrical resistivity.

Ground investigations using Electrical Resistivity Tomography (ERT), have been used by [6], [7], [8], [9], [10], [11]. The electrical resistivity method determines the soil type by using electrical resistances differences in different soil types. The flow of an electrical current can move through a soil due to electrolytic action. Water content and the concentration of salts will then measure the resistivity of soil. For example, a saturated soil with a high void ratio would be detected as having low resistivity, due to the significant quantity of pore water and free ions in the water.

Samouëlian et al. [6] have reviewed the application of ERT for characterization of soils, including the early detection of soil layers. Colangelo et al. [12] have used ERT to obtain information on the deep characteristics of landslide bodies, such as sliding surface location and thickness of the slide materials, by comparing information with previous geological maps. Some researchers have attempted to verify the results of geophysical application by using in-situ geotechnical tests such as Standard Penetration Test (SPT) and Dynamic Cone Penetrometers test (DCPT) by [11], [13], [14].

Although attempts at soil characterization have been made, to integrate the results of geophysical application testing and geotechnical data, there is still a lack of investigations of soil slopes associated with deep cracks using ERT, field and laboratory geotechnical testing. This paper discusses the results of soil investigations to detect soil layers with deep cracks on unsaturated residual soil slopes using an electrical resistivity tomography (ERT). The results then being verified using data from field and laboratory geotechnical testing.

SITE CHARACTERISTICS

A residual soil slope in the hilly terrain of East Java Province in Indonesia was selected for this study as shown in Fig. 1. This slope is located at a high seismically active zone [15] and experience a high

average annual rainfall of about 2,700 mm [16]. Figure 2 shows the distribution of slope angle in the study area. The result of a land survey conducted on the slope was used to generate the geometry of slope along AA' with the average slope angle being measured at 20^0.

There is evidence of past rainfall-induced residual soil slope failures in the study area. Local authorities had reported that areas downstream of the targeted slope had experienced a sliding one year before this research was conducted by [17]. Some surface cracks subsequently emerged on the upper side of the soil slope.

There were three profile lines (see Fig. 1), each 150 m long and separated by a distance of 5 m (from A to A'), with one profile line (line 4) of 100 m crossing the other profile lines (from C to C'). To obtain a sub-soil resistivity profile for the slope, an ERT survey using the Dipole-Dipole array method was conducted along profile lines 1, 2, 3, and 4 with 15 electrode points at a spacing of 10 m. The total length of each profile line, from A to A', was 150 m.

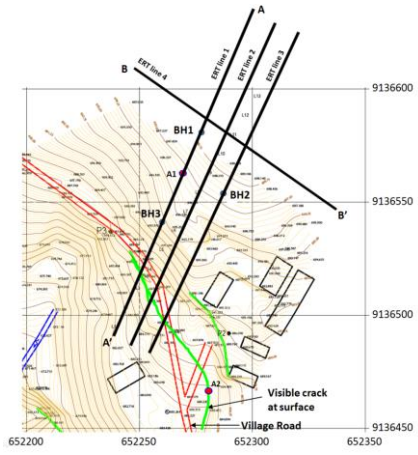

Fig. 1 Map of the study area showing ERT and borehole locations (BH)

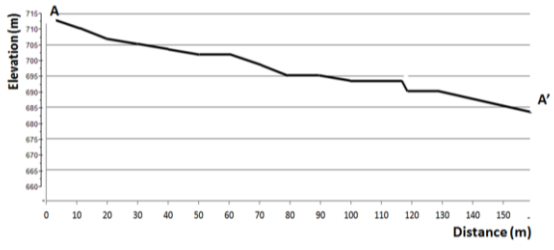

Fig. 2 Cross section long A-A' of the selected slope

METHODOLOGY

To provide electrical resistivity and soil parameters, two soil investigation methods were used in the study: field and laboratory geotechnical testing; and Electrical Resistivity Tomography (ERT).

From the field and laboratory geotechnical testing, selected relevant soil parameters were measured such as water content, porosity and clay content. The electrical resistivity of the subsoil identified the location and provided geometrical information relating to subsoil cracks [6], [7], [8], [9, [10], [11]. Soil resistivity can be affected by soil water content, porosity, and clay content. Sub-surface cracks or deep cracks can be associated with high porosity and high water content in wet seasons, providing low resistivity. The location of deep cracks was confirmed when a low resistivity value was found in the subsoil, in association with high porosity, high water content, and low clay content. The results of SPT test and other laboratory tests conducted on soil samples obtained from the bore-holes were used to verify the location of the deep cracks detected by ERT.

Geotechnical Test Method

In this study, geotechnical investigations carried out in the selected slope in order to characterize the sub-surface soils. Three borehole tests were conducted at BH1, BH2 and BH3, as shown at Fig. 1. At every 2 m depth interval in each borehole, an SPT test was performed following the procedure of the American Society for Testing and Material (ASTM) Standard. Soil samples collected at every 1 m depth in each borehole were used to determine water content, specific gravity, Atterberg limits, dry unit weight, grain size distribution, and shear strength using direct shear test in the laboratory following ASTM testing procedures.

Geophysical Application Method

ERT was used for subsurface exploration along four profile lines at observed slope locations, as illustrated in Fig 1. The objective of the ERT was to detect deep cracks in the upper side of the soil slope. Two ERT methods used in this research were Dipole-dipole array and Square array.

Dipole-dipole array provides the highest resolution, when compared with other arrays such as Wenner arrays and Schlumberger arrays, most sensitive to vertical resistivity boundaries as is needed for deep-crack detection [18], [19], [20], more efficient for delineating the direction of faults [20], suitable for vertical structures, vertical discontinuities, and cavities [21], produced a better lateral extension of the subsurface features [22]. Therefore, in this research, the ERT survey was carried out using the Dipole-dipole array method along the profile lines (shown in Fig. 1) at an acceptable inter electrode spacing of 10 m, as applied by [12]. To gain comprehensive results, there were three profile lines, each 150 m long, with a 5 m spacing.

An ERT survey using the Dipole-Dipole array can be conducted on the profile lines on the slope. A

direct current (D.C.) is driven into the ground through particular electrode position as shown in Fig. 3 to initiate electrical responses (labelled C1, C2, P1 and P2) are put in place. The 45-degree angle is used to plot the pseudo section data point. The electrical current is activated to measure soil resistivity which is recorded using the resistivity meter device.

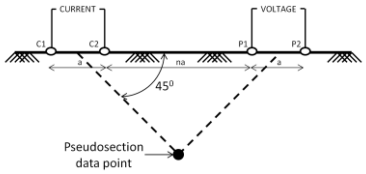

Fig. 3 Basic Dipole-dipole array method configuration

The next step requires that the electrodes are moved across the surface, following marked locations to measure all subsurface data points. For example, Fig. 4 illustrates the 3rd step of taking measurements to get data at selected locations; whereas C1 and C2 are inserted in the same poles, the P1 and P2 electrodes are moved to pole numbers 5 and 6.

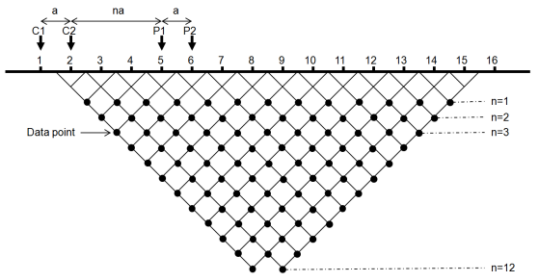

Fig. 4 Third measurement step using the Dipole-Dipole array method

Possible location of deep crack can be interpreted from the ERT result by detecting the zone with lower resistivities. The low resistivity value can be an indication of increased water content due to higher porosity in that zone. However, clay content of the soil matrix also affects soil resistivity. A mobile cloud of additional ions can be formed around each clay particle by the ion exchange properties of clay. As these ions will facilitate easy flow of electrical current, the electrical resistivity in fine-grained soils, such as clay, is always lower than expected [23]. Therefore, the results from ERT need to be verified using a geotechnical test, to ensure that the deep crack has shown a low resistivity value due to high porosity.

To obtain detailed identification of deep cracks in subsoils, ERT application using Square array Resistivity (SAR) technique was used in the potential soil cracks zone detected from Dipole-Dipole array method. Basically, the principle of SAR is similar to Dipole-Dipole array, but in SAR the configuration is modified into a square and rotated measurement [24]. As shown in Fig. 1, there were two locations for the SAR: at the middle of Profile Line 1 (location A1) and on the nearby visible surface crack (location A2).

In general, the nature of anisotropy can be interpreted as cracks in a soil layer. SAR techniques can be used to determine the direction of vertical cracks in the soil [24], [25], [26]. The SAR technique was selected for use in this study to support the result of Dipole-dipole array method by indicates the existence of anisotropy in the soil with low resistivity value.

The SAR technique characterizes the soil crack by using minor resistivity, which indicates the angle direction of the soil crack and the influential depth of the crack zones. The measurement is obtained by inserting four electrodes into the ground following the square array illustrated in Fig. 5. In this square array, the measurement point is located at the centre of the square. The azhimuth of the measurement is represented by the line connecting the current electrodes (A and B).

An incremental array size (a) from 2 m to 12 m was used. The plot of pseudosection data points is located at a 45-degree angle from the horizontal line between the electrode pole and the centre. Therefore, the depth of the measured data point (D) will be determined by:

$$D = \frac{1}{2}a\sqrt{2} \quad (1)$$

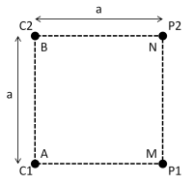

Fig. 5 Azimuthal square array configuration

In accordance with the electrode configuration of the square array as shown in Fig. 5, the value of apparent resistivity ρa is calculated as:

$$\rho_a = \frac{K\,\Delta V}{I} \quad (2)$$

Where:

ρ_a = resistivity (Ω m)
K = geometric factor
ΔV = potential difference between P1 and P2 (volts)
I = electric current (amps)

Furthermore, the geometric factor, K, can be substituted with the side length of square (a):

$$K = \frac{2\pi a}{2-\sqrt{2}} \quad (3)$$

Changes in the rotation angle (azimuth) can be made in 15º increments to 360º, in accordance with the rules of the British National Grid (BNG). Therefore, 24 parts with different resistivity values can be obtained at every depth.

This SAR method will produce decreasing resistivity values if there is a crack inside the

subsurface layer. Such a medium is called anisotropic and will produce an ellipse resistivity value plotted in polar coordinates, as shown in Fig. 6a. If the observed ground has an isotropy medium, the relationship will be seen as rounder as illustrated in Fig. 6b. The direction of the observed crack can be determined by viewing the results of a polar graph at each point of measurement, with the direction of the crack coinciding with the minor axis. If the polar graph is an ellipse-shape, then a crack can be found.

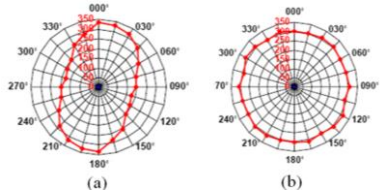

Fig. 6 Polar graphics of azimuthal square array

However, Busby and Jackson [25] have stated that to be assumed as anisotropy, an ellipse polar graph has to have a coefficient of anisotropy of more than 1.16, based on the ratio of minor and major axis:

$$\lambda = \sqrt{\frac{p_l}{p_t}} \quad (4)$$

RESULTS AND DISCUSSION

Detection of Possible Crack Location based on Soil Resistivity

Figure 7 presents the ERT Dipole-dipole array results, showing the soil resistivity distribution of the subsurface soil in the study area. A significant variation in soil resistivity at different depths along the profile lines can be observed. The soil resistivity in the area ranges from 1 to 2000 Ωm, indicating a wide variation in soil type, clay content, porosity, and water content. In general, low soil resistivity was measured for the surface soil layers (5 – 10 m depth). This would be due to high water content in the surface soil, as this test was conducted in the rainy season.

Local zones with very low resistivity (3 – 30 Ωm) could be potential locations for cracks. Soil crack zones have very high porosity and high water content in the rainy season, as rain water can easily seep into the cracks. This hypothesis was justified in profile line 1 (Fig. 7.a), as the visible surface crack coincided with the very low resistivity zone in the subsoil. However, it was not possible to perform a resistivity test in the vicinity of the surface crack in profile line 2 (Fig. 7.b) and profile line 3 (Fig. 7.c), due to the accessibility issues in the area.

The low resistivity zones at the horizontal distance (from A) between 60 m to 130 m and at depth 2 to 12 m, were consistent in all profiles. This suggests possible transverse cracks in this area, as shown in profile line 4 (Fig. 7.d) that crosses over the three other profile lines. This possible transverse crack can also be observed in Fig. 7.d, whereas a local zone with very low soil resistivity was found at the horizontal distance (from B) between 35 m to 55 m and at depth 2 to 12 m.

Possible cracks could be investigated by using the results of SAR technique in the selected locations, as shown in Fig. 8. It was found that: at location A1, cracks in the soil were detected in a direction of 135° from the north, 0 to 5.65 m deep; at location A2, a non linear crack direction was found. From the surface to a depth of 1.41 m, the crack began at an angle of 165˚ from the north (N 165 E). From the depth of 1.41 m to 4.24 m, the direction of the crack changed to an angle of 180˚ from the north (N 180 E). Then from a depth of 4.24 m to 5.65 m, the crack direction was found to lie between an angle of 180˚-195˚ from the north (N 180-195 E).

The results of Dipole-dipole array and SAR at A1 are consistent and suggest a possible crack at this location was reflected by the low soil resistivity value. The results of the SAR conducted at A2 confirmed the existence of the deep crack as a continuance of visible cracks on the surface (see Fig. 1).

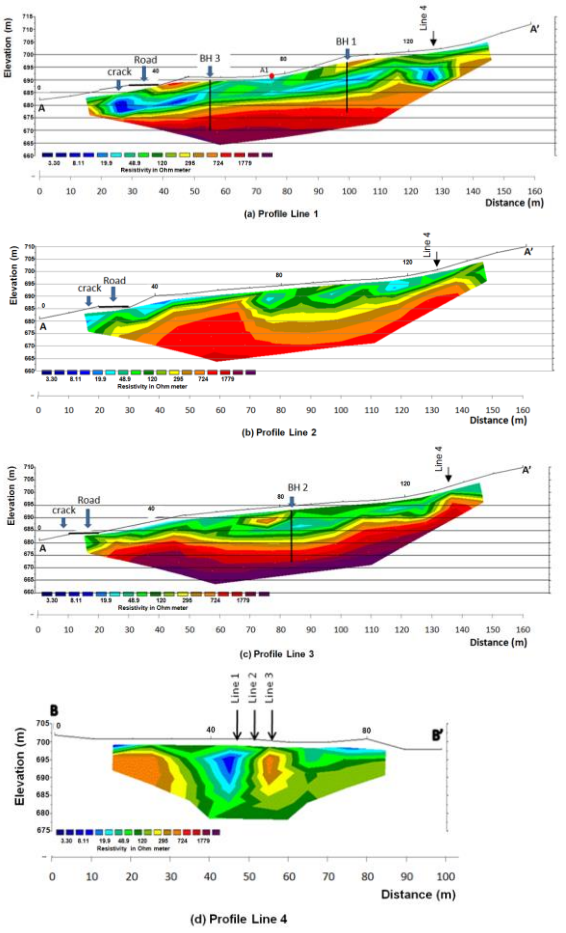

Fig. 7 The visual results of ERT of four profile lines

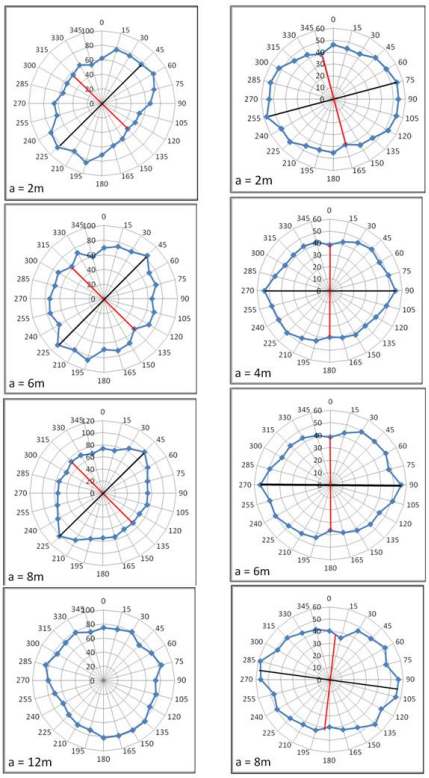

(a) A1 location results (b) A2 location results

Fig. 8 Results of SAR Technique

Verification of possible crack location using geotechnical data

Since soil resistivity is affected by clay content and soil density, in addition to soil water content, it is important to use the measured soil parameters such as density, grain-size distribution and water content of the soil in the site, to verify the size and location of the cracks detected by ERT. The existence of cracks can be determined by the presence of high porosity and water content in the wet season. Verification was undertaken to all Bore Hole (BH-1, BH-2 and BH-3).

At bore hole location 1 (BH-1), it can be seen that a low soil resistivity zone was found at a depth of 6 m to 10 m (less than 50 Ωm), as illustrated in Fig. 9. At this depth, there was an average volumetric water content of 65%, and an average clay content of 20%. Therefore, the low resistivity at the depth 6 m to 10 m could have been mainly due to the high-water content, rather than an effect of the clay content. Based on the above information, it might be concluded that a deep crack could be located at the depth of 6 m to 10 m. It was further confirmed that the soil at 6 m to 10 m depth has a high porosity and low unit weight of around 68% and 14 kN/m3, respectively. Similar analyses were undertaken for BH-2 and BH-3 whereas possible crack location at a depth of 7 m to 9 m in BH-2 and at 2 m to 5 m depth in BH-3.

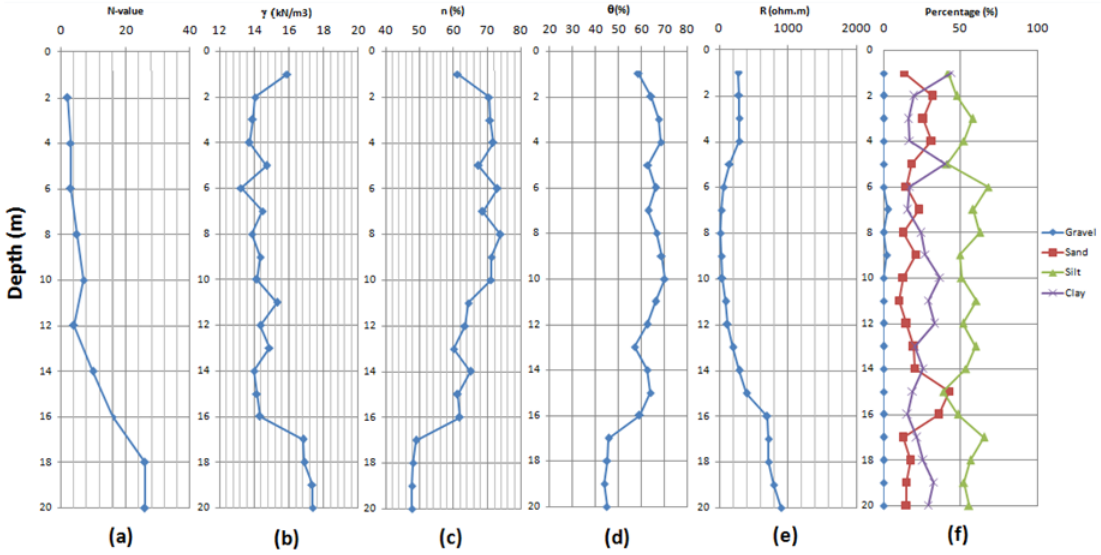

Fig. 9 Soil parameters at BH-1: (a) N-value, (b) Unit weight, (c) Porosity, (d) Volumetric water content, (e) Resistivity, (f) Grain-size distribution

CONCLUSIONS

The following conclusions can be drawn from this study that the results of ERT can be used to detect deep cracks in the subsoil if ERT is conducted in the wet seasons, due to the existence of infiltrated rainwater. However, the ERT result should be interpreted cautiously due to its limitations.

ACKNOWLEDGEMENTS

The authors are grateful to Trihanyndio Rendy Satrya, Munthoha, Dwadesa Wanana and Umar Cs. from ITS Surabaya, for their assistances in geotechnical interpretations; Dr. Arief Rachmansyah and Fajar Rakhmanto from Brawijaya University their assistances in the geophysical application.

REFERENCES

[1] Baker, R., 1981. Tensile Strength, Tension Cracks, and Stability of Slopes. Japanese Society of Soil Mechanics and Foundation Engineering. 21(2), 17.

[2] Lee, F.H., Lo, K.W., Lee, S.L., 1988. Tension Crack Development in Soils. Journal of Geotechnical Enineering. 114(8), pp. 915-929.

[3] Chowdhury, R.N., Zhang, S., 1991. Tension Cracks and Slope Failure. Slope Stability Engineering, Proc. International Conference, pp. 27-32.

[4] Yao, H.L., Zheng, S.H., Chen, S.Y., 2001. Analysis of the slope stability of expansive soil considering cracks and infiltration of rainwater. Chinese Journal of Geotechnical Engineering. 23(5), pp. 606-609.

[5] Li, J., 2009. Field experimental study and numerical simulation of seepage in saturated/unsaturated cracked soil. The Hong Kong University of Science and Technology. Hong Kong. PhD Thesis.

[6] Samouelian, A., Cousin, I., Richard, G., Tabbagh, A., Bruand, A., 2003. Electrical resistivity imaging for detecting soil cracking at the centimetric scale. Soil Science Society of America Journal. 67(5).

[7] Friedel, S., Thielen, A., Springman, S.M., 2006. Investigation of a slope endangered by rainfall-induced landslides using 3D resistivity tomography and geotechnical testing. Journal of Applied Geophysics. 60, pp. 100 – 114.

[8] Tabbagh, J., Samouelian, A., Tabbagh, A., Cousin, I., 2007. Numerical modelling of direct current electrical resistivity for the characterisation of cracks in soils. Journal of Applied Geophysics. 62, pp. 313 – 323.

[9] Oh, A., Sun, C., 2008. Combined analysis of electrical resistivity and geotechnical SPT blow counts for the safety assessment of fill dam. Environmental Geology

[10] Zhu, T., Feng, R., Hao, J., Zhou, J., Wang, H., Wang, S., 2009. The Application of electrical resistivity tomography to detect a Buried Fault: A case study. JEEG.14(3), pp. 145 – 151.

[11] Sudha, K., Israil, M., Mittal, S., Rai, J., 2009. Soil characterization using electrical resistivity tomography and geotechnical investigations. Journal of Applied Geophysics. 67, pp. 74 – 79.

[12] Colangelo, G., Lapenna, V., Loperte, A., Perrone, A., Telesca, L., 2008. 2D Electrical resistivity tomographies for investigating recent activation landslides in Basilicata region (southern Italy). Annals of Geophysics. 51, 275-285.

[13] Braga, A., Malagutti, W., Dourado, J., Chang, H., 1999. Correlation of electrical resistivity and induced polarization data with geotechnical survey standard penetration test measurements. Journal of Environmental and Engineering Geophysics. 4, pp. 123–130.

[14] Giao, P.H., Chung, S.G., Kim, D.Y., Tanaka, H., 2003. Electrical imaging and laboratory resistivity testing for geotechnical investigation of Pusan clay deposits. Journal of Applied Geophysics. 52, pp. 157–175.

[15] USGS, n.d. Seismotectonics of the Indonesian Region. Retrieved August 11th, 2010, from http://earthquake.usgs.gov/earthquakes/world/indonesia/seismotectonics.php

[16] Lavigne, F., Suwa, H., 2004. Contrasts between debris flows, hyperconcentrated flows and stream flows at a channel of Mount Semeru, East Java, Indonesia. Geomorphology. 61, pp. 41-58

[17] Rahmansyah, A., 2010. Laporan Kemajuan Hibah Kompetitif Penelitian Strategis Nasional Batch-1 (Suryo, E.A., trans.). FTUB.

[18] Griffiths, D.H., Barker, R.D., 1993.Two-dimensional resistivity imaging and modelling in areas of complex geology. Journal of Applied Geophysics. 29, pp. 211–226.

[19] Zhou, W., Beck, B.F., Stephenson, J.B., 1999. Reliability of Dipole-Dipole electrical resistivity tomography for defining depth to bedrock in covered karst terranes. Environmental Geology. 39 (7), pp. 760-766.

[20] Santos, F.A.M., Perea, H., Massoud, U., Plancha, J.P., Marques, J., Cabral, J., 2009. Journal of Geophysics and Engineering. 6, pp. 390-400.

[21] Hack, R., 2000. Geophysics for slope stability. Surveys in Geophysics. 21, pp. 423-448.

[22] Neyamadpour, A., Wan Abdullah, W.A.T, Taib, S., Neyamadpour, B., 2010. Comparison of Wenner and Dipole-Dipole arrays in the study of an underground three-dimensional cavity. Journal of Geophysics and Engineering. 7, pp. 30-40.

[23] Zhdanov, M.S., Keller, G.V., 1994. The Geoelectrical methods in geophysical exploration. Elsevier, Amsterdam

[24] Senos Matias, M.J., 2002. Square array anisotropy measurement and resistivity sounding interpretation. Journal of Applied Geophysics. 49, pp. 185 – 194.

[25] Busby, J., Jackson, P., 2006. The Application of time-lapse azimuthal apparent aesistivity measurement for the prediction of coastal cliff failure. Journal of Applied Geophysics. 59, pp. 261 – 272.

[26] Schmutz, M., Andrieux, P., Bobachev, A., Montoroi, J.P., Nasri, S., 2006. Azimuthal resistivity sounding over a steeply dipping anisotropic formation: A case history in Central Tunisia. Journal of Applied Geophysics. 60, pp. 213 – 224.

9th Int. Conf. on Geotechnique, Construction Materials and Environment, Tokyo, Japan, 20-22 November 2019, ISBN: 978-4-909106025 C3051

ESTIMATION OF THE INSTABILITY OF SLOPE SURFACE LAYER BY ELASTIC WAVE ATTENUATION CHANGING WITH SOIL MOISTURE AND DEFORMATION

Shangning Tao[1], Taro Uchimura[2], Makoto Fukuhara[1] and Junfeng Tang[1]

[1]Graduate School of Science and Engineering, Saitama University, Japan
[2] Faculty of Engineering, Saitama University, Japan

ABSTRACT

This paper proposes a method to estimate the instability of the slope surface layer by elastic wave attenuation which changes with soil moisture and deformation. The objective of this study is to investigate the effect of soil moisture and deformation on wave attenuation of soil. Two experiments were conducted, the first one was a laboratory experiment using a multi-layer shear model, and the second one was an on-site monitoring wave attenuation with soil moisture. In laboratory experiments, wave attenuation at various soil moisture and deformation were measured. The relationships between wave attenuation and soil moisture were found to have hysteresis, that is, difference paths were observed in rain and drain process. The attenuation of wave energy increased about 20%~40% when the VWC grew up near saturation. With increasing the displacement, the wave attenuation also increased, and the wave energy ratio dropped by 40% during a 3 mm of displacement. The results of on-site monitoring showed that wave attenuation decreased with the increasing soil moisture in the rain events and increased during the drain stages. Since most of the rain-induced landslides start failure in nearly saturated conditions, and the elastic wave attenuation in soil can indicate the status of saturation, monitoring elastic wave in the surface layer of slope can detect its instabilities.

Keywords: Landslide, Early warning, Wave propagation, Attenuation

INTRODUCTION

Rainfall-induced landslide occurred commonly in mountainous areas and caused severe human and infrastructure damages[1],[2],[3],[4]. Most of the Rainfall-induced landslide occur at shallow depths, generally less than 3 m[5][6]. In Japan the average depth is 1.2m, 90% is under 2.5m, 500,000 potentially dangerous slopes exist[7][8].

Early warning system can help people safely escape from the dangerous area. It is an economic and effective method to prevent and mitigate rainfall-induced landslide. Rainfall threshold has been used to predict the slope failure[9][10]. The current early warning systems are mainly focused on monitoring the slope's movements by MEMS (Micro Electro Mechanical Systems) tilt sensors or inclinometers and soil moisture by volumetric water content sensors[11],[12]. To cover a wide area of potential danger slope, a large number of tilt sensors would be required[13]. An alternative method to predict slope failure method applied elastic wave propagation in soil has been proposed, which can detect the soil moisture and deformation of a wide area slope. Irfan and Uchimura found that the velocities of both of shear wave(S-wave) and compression wave(P-wave) velocities decreased with increasing degree of saturation by laboratory triaxial tests[14],[15],[16]. In a series model tests, elastic wave velocity has been observed that it responded sensitively to soil moisture content and deformation [17],[18],[19]. Thus, many studies were conducted focusing on the velocities of elastic wave, however, precise measurement of travel time is needed to measure the wave velocities.

In this paper, a method using wave attenuation is presented to monitor slope deformations and soil moisture variations. It is an application of geometric spreading, which is as the wave moves away from the source, the area that the wave energy covers becomes larger and thus wave intensity decreases, and wave energy loss due to inelastic material behavior or internal friction during wave propagation [20]. Laboratory experiments using Multi-layer shear model were conducted, wave attenuation affected by shear forces and corresponding with deformations on every layer, and the soil moistures in wet and dry processes have been investigated. To investigate the behavior of elastic wave propagation in slope surface layer, an elastic wave monitoring system including one exciter and several revivers have been developed and installed in a nature unstable slope. Wave attenuation and soil moisture were analyzed.

METHODOLOGY OF MODEL TEST

The material used in this study is comprised of Silica sand No4, No5, No7 and No8 mixed with ratio of 1:1:3:1 to be near the particle size distribution of soils of the typical natural slopes. It had a dry density around 1.481 g/cm^3. It's minimum and maximum dry density were found out to be 1.308 g/cm^3 and 1.707 g/cm^3 (Figure 1). The relative density was 50% and Volume Water Content was 7.4% at the initial state.

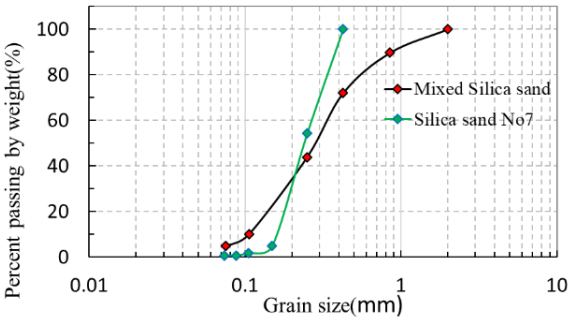

Fig. 1 Grain size accumulation curve

The Multi-layer shear model is shown in Figure 4. It is a model including 20 layers with a total height of 1m to simulate a part of slope surface layer. Every layer has a height of 0.05m, length of 0.6m and width of 0.54m. Shear force is applied on every interface between the layers by air cylinders to simulate the shear force corresponding to the slope angle. Displacement meters are also set at every layer. Rainfall intensity of 60mm/h is given with a nozzle controlled by constant water pressure. Rainwater infiltrates into the top layer of model and drains out from the bottom. Elastic wave is generated by exciter (Figure 2) and detected by receivers (Figure 3). Exciters, receivers and soil moisture sensors are set in the model.

The elastic wave attenuation is defined by the wave energy ratio, calculated by

$$\text{Energy ratio} = E_n/E_0 (\text{n=1,2, 3…}) \quad (1)$$

where E_0 is energy of the receiver near the exciter (r0 in figure 4), E_n is others receiver' energy which far away from exciter(r1~r8). Energy is defined as

$$E = \sum_{f=1}^{f=3000} \left(\frac{1}{2}\right) * 4\pi^2 \rho (f * A_f)^2 \quad (2)$$

where ρ is the density of material, f is frequency, A_f is the amplitude of wave. Frequency is resolved from 1~3000Hz by FFT (Fast Fourier Transformation).

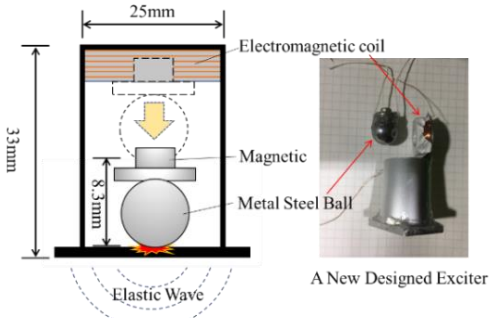

Fig. 2 Exciter used to generate pulse elastic wave. The mass of metal steel boll is 16.95g, the free drop height is 8.3mm.

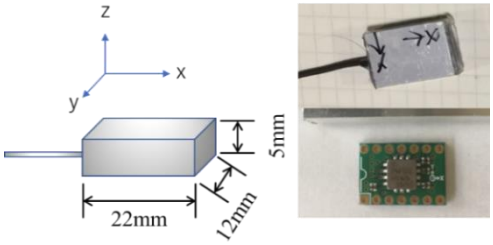

Fig. 3 Receiver is 3- axis MEMS accelerometers (ADXL354), used to detect elastic wave.

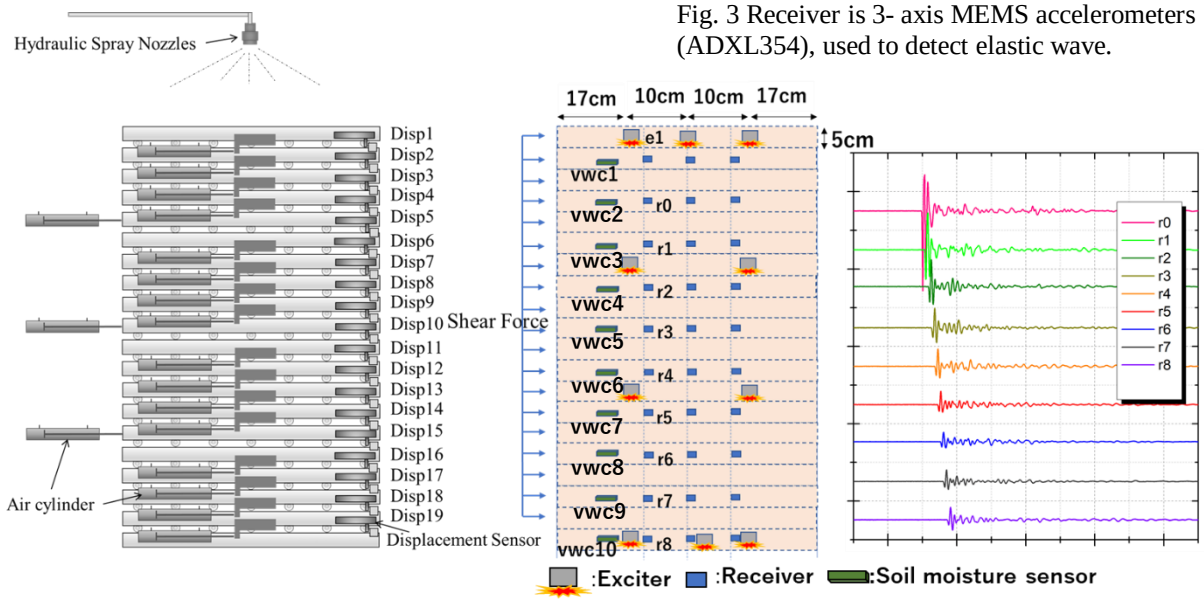

Fig. 4 Multi-layer shear model (left); Sensors layout in soil(middle); Waveform of One pulse wave which generated by exciter e1 and detected by receivers r0~r8(right).

TEST CONDITIONS

Table 1 Test conditions

Test Case	Moisture Control	Slope Angle	Shear Displacement
1	Rain/Drain	0	0
2-1	Rain/Drain	27	0
2-2	Rain/Drain	29	0
2-3	Rain/Drain	31	0
3	Constant	33	5cm

Three test cases were conducted with the conditions in Table 1. In Test Case 1, slope angle was zero, it means no shear force put on any layer of the model. Rainfall was applied for 4 hours until VWC (Volume Water Content) became stable, then rainfall was stopped, and water was drained out by gravity about 20hours (Figure 5a). In Test Case 2, the slope angle was set to be 27, 29, and 31-degree. Displacement was not found changing during the artificial rainfall(24hours) and drain(24hours) events. In Test Case 3, the slope angle was set to 33-degree (Figure 7). No rain was applied but the displacement continuously increased until failure.

RESULTS

Figure 5a shows the changes of wave energy ratio with VWC during the rainfall and drain event in the time series observed in Test Case1. It took 4 hours rainfall to make the VWC be stable, and more than 20 hours to drain the water out. The deeper from the surface, the higher moisture was observed. Figure 5b shows energy ratio changes in the time series. With soil moisture increased in the rainfall event, the energy ratio decreased. During the drain stage, energy ratio increased. Figure 5c and 5d show the energy ratio at every receiver against the VWC averaged between the nearer and farther receivers. The energy ratio reduced 20%~50% when the VWC grew up from 0.1 to 0.25 m^3/m^3.

Effects of soil moisture on the wave energy ratio could be explained by matric suction. When the soil moisture becomes higher, the matric suction decreases, and the weaker of force between soil partials results in lower of wave energy propagation. There is hysteresis in the path of energy ratio and VWC between rainfall and drain event. This may be related to the hysteresis observed in the relationship between soil moisture and matric suction.

The response of energy ratio at different shear force corresponding to slope angle during rainfall and drain event is shown in Figure 6, which is the results of the Test Case 2. The stronger shear force applied, the lower energy ratio is observed. Wave energy ratio reduced 20%~40% when shear force increases from 27 to 31degrees. For example, in Figure 6a, at the 0.1 m^3/m^3 of VWC, when shear force was set to 27-degrees, 29-degrees and 31-degrees, the energy ratio decreased from 0.18, 0.14, and 0.11, wave energy ratio reduced from 22% to 38%.

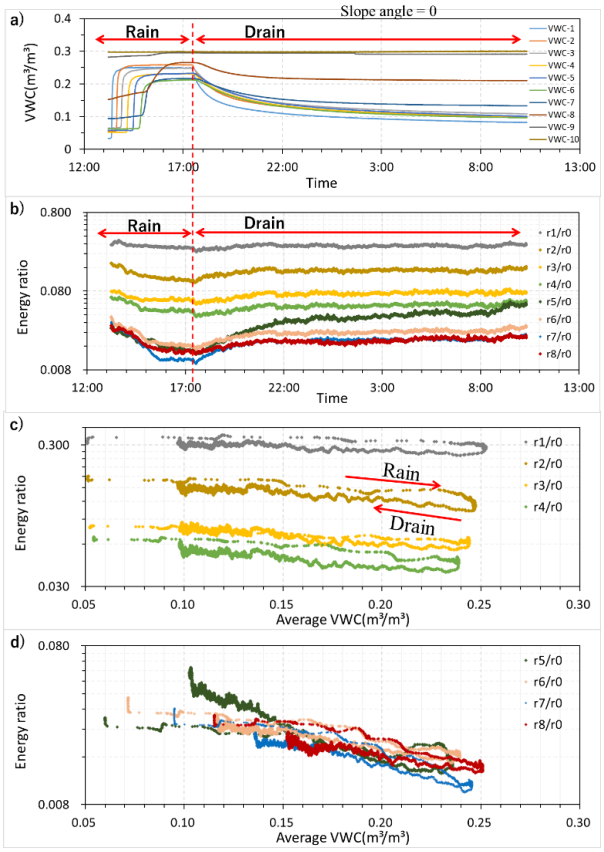

Fig. 5 Energy ratio changes with VWC (slope angle = 0)

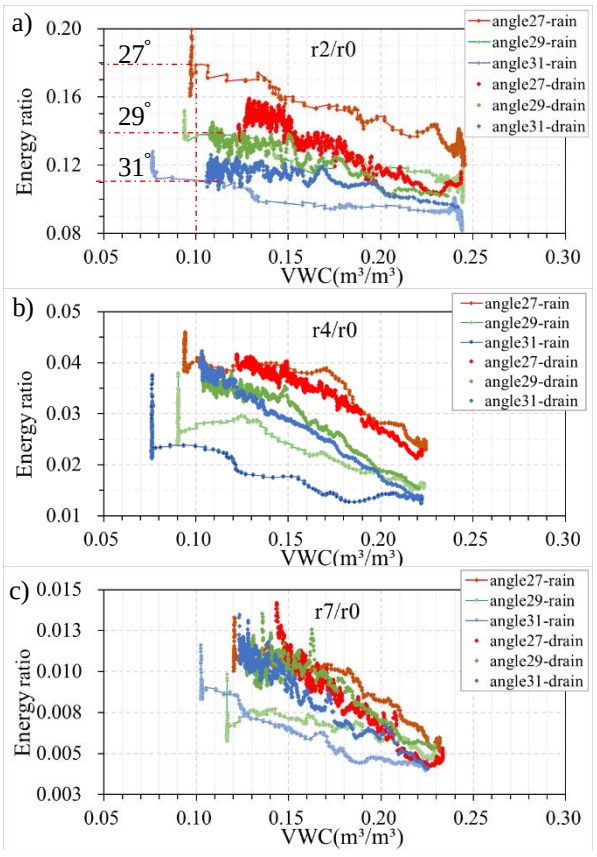

Fig.6 Energy ratio changes with VWC (slope angle = 27, 29,31)

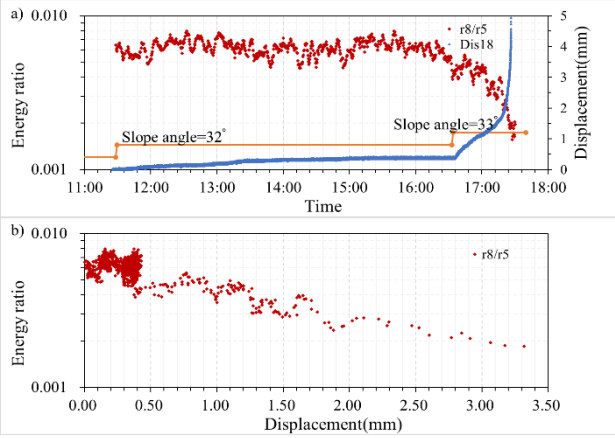

Fig.7 Elastic wave energy ratio changes with displacement

Figure 7a shows the response of wave energy ratio and displacement during shearing in the Test Case 3. VWC did not change in this test. After the shear force was set corresponding to the slope angle of 33-degree, the displacement started with an average 0.3cm/h of moving speed, then accelerated and finally failed, which observed at the displacement sensor No18, so energy ratio of r8/r5 was analyzed. With the increasing displacement, the wave energy ratio also decreased rapidly. Figure 7b shows the wave attenuation against the displacement. Wave energy ratio dropped by 50% during a 3 mm of displacement.

ELASTIC WAVE MONITORING ON-SITE

To investigate the behavior of elastic wave propagation in natural slope surface layer, elastic wave monitoring has been conducted at a slope located at Aso-shi, Kumamoto, Japan. This slope was suffered from the 2016 Kumamoto Earthquakes and some big cracks appeared on the slope surface. It is a typically unstable slope.

Figure 8 shows elastic wave monitoring devices. It has a fully automatic to generate elastic wave by exciter, measure the wave signal by receivers. It includes a controller and data collection device, an exciter, 4 receivers, and a VWC sensor. Exciter is made with a Solenoid Electromagnet, which is controlled by the controller, it can generate pulse elastic wave per 10 minutes. Receivers are 3- axis MEMS accelerometers, ADXL354, a production of Analog Devices. The controller and data collection device control the timing of exciter, handle the wave data received by the receiver with a 7kHz of sampling rate, and store wave data into SD card. The VWC sensor is a soil moisture sensor EC-5 to measure the volume water content in the soil. The power is supplied by the arrangement of lead-acid battery, which is charged by a solar panel (Figure 9), to be continually running for a long term.

Figure 9 shows the elastic wave monitoring system installed on an unstable slope. Dotted line in the photo shows the survey line of elastic wave. Sensors and exciter were set in the underground. The exciter and VWC sensor were installed at a depth of 0.2 m. The receiver (CH1) was set at a horizontal distance of 0.01 m and a depth of 0.1 m from the exciter. Receiver (CH3) has a horizontal distance of 0.2 m from the exciter and a depth of 0.1 m; receiver (CH5) has a horizontal distance of 0.2 m from the exciter, a depth of 0.4 m; receiver (CH6) was installed at a depth of 0.1 m at a horizontal distance of 1.5 m from the exciter.

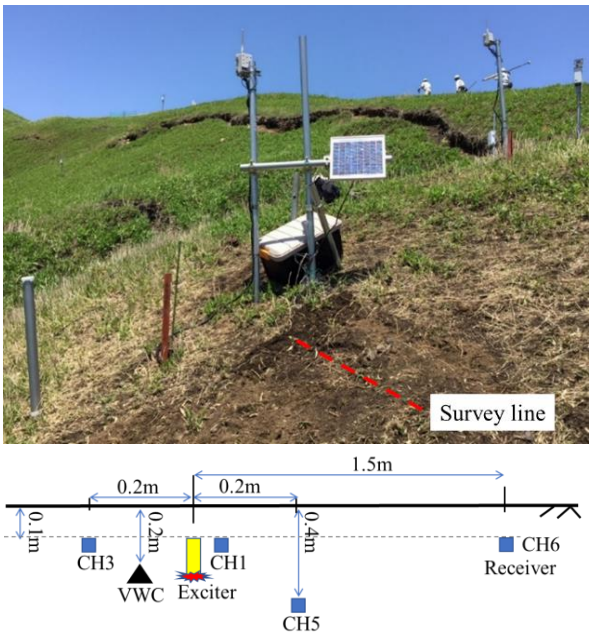

Fig. 9 Elastic wave monitoring system installed on an unstable natural slope. Dotted line shows the survey line of elastic wave. The layout of sensors and exciter underground.

Fig.8 Elastic wave monitoring devices. It can automatically generate elastic wave and measure wave signal.

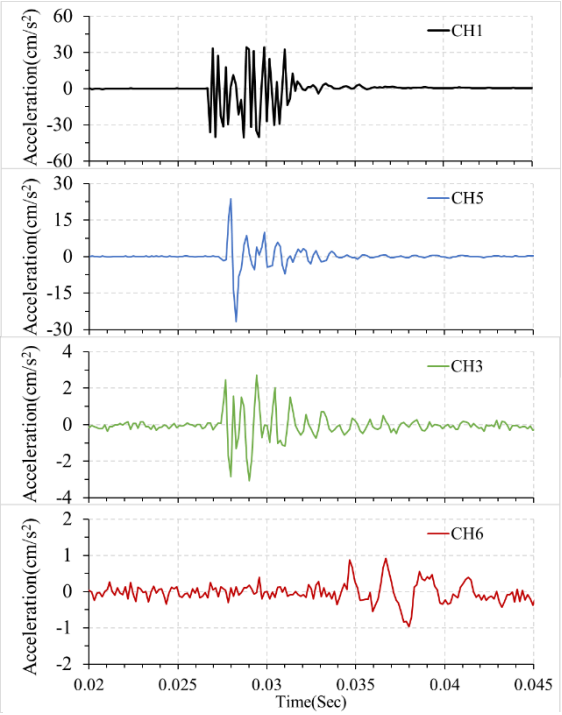

Fig.10 Examples of waveforms of a pulse elastic wave observed by receivers.

Figure10 shows the examples of waveforms of a pulse elastic wave observed by received by each acceleration sensor. CH1, the nearest with exciter, could detect the strongest signal around 30 cm/s^2, whereas CH6, the farthest from the exciter, detected the weakest signal around 1 cm/s^2. It indicates that wave amplitudes reduced quickly with distance.

Figure 11 shows VWC and energy ratio plot in time series from 2018/9/24 to 2018/12/20. In the dry process, the energy ratio of the elastic wave tends to increase with the decrease of VWC. On the contrary, in the wet process (rainfall events), the energy ratio of the elastic wave tends to decrease with the increase of VWC.

Figure 12 shows energy ratio response with VWC. Wet process is the cases of rain event, the dry process is a drain event. In CH5/CH1, wave energy ratio dropped down 60% when VWC increased from 0.39 to 0.41 m^3/m^3. In CH3/CH1, wave energy ratio dropped down 70% when VWC increased from 0.39 to 0.44 m^3/m^3. Whereas CH6, the farthest from the exciter, not clear changes trend. Hysteresis had been observed in CH3/CH1, that is similar to the results in laboratory experiments.

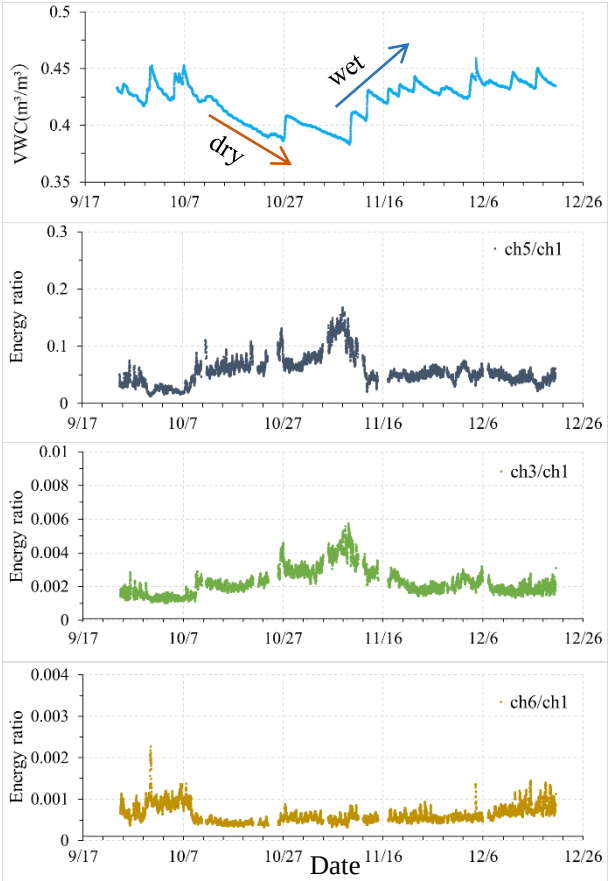

Fig.11 VWC and energy ratio plot in time series. Elastic wave data was collected from 2018/9/24 to 2018/12/20 on-site.

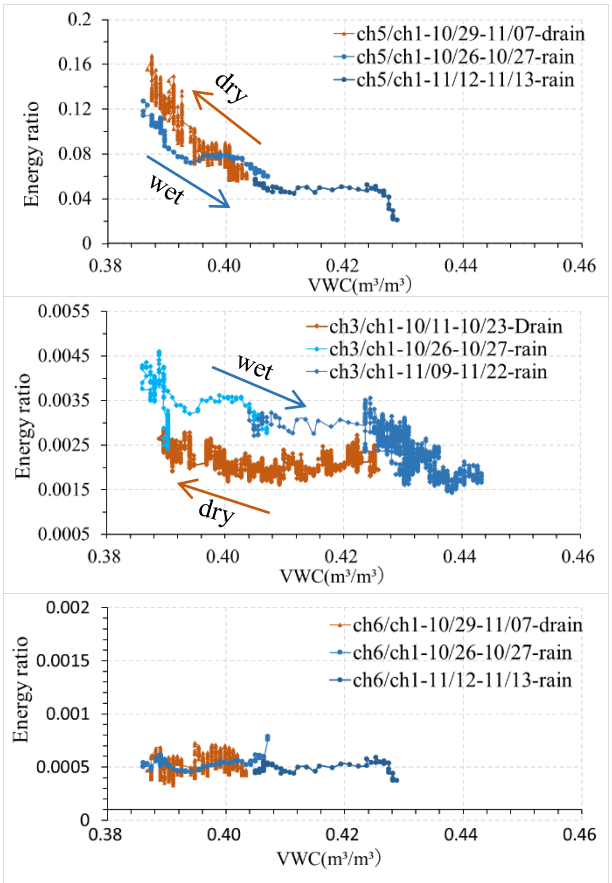

Fig.12 Energy ratio responses with VWC. Wet and dry process are the cases of rain event and drain event.

CONCLUSION

In this research, a method using elastic wave attenuation to predicts slope failure is presented. Laboratory experiment using multi-layer shear model was conducted to observe the changes of elastic wave propagation in slope surface layer. The results show that the wave attenuation increased with the increasing soil moisture, the wave energy reduced by 20%~50% when the VWC grew up from 0.1 to 0.25 m^3/m^3. The stronger shear force applied, the lower energy ratio observed. With increasing the displacement, the wave attenuation also increased.

An elastic wave monitoring system including one exciter and several revivers have been developed and installed in a nature unstable slope. The results show that wave attenuation behaviors with soil moisture on-site is similar to laboratory experiments.

Monitoring wave attenuation in slope surface layer can indicate the status of saturation state and shear deformation. Slope instabilities may be predicted based on its historical record.

ACKNOWLEDGMENT

The research is supported by Grants-in-Aid for Scientific Research of Japan Society for the Promotion of Science (JSPS), Research Fellowships of Japan Society for the Promotion of Science for Young Scientists (DC2), and River and Sabo Technology Open Research and Development System of the Ministry of Land, Infrastructure Transport and Tourism.

REFERENCE

[1] D. J. Varnes, “Landslide Types and Processes,” *Highw. Res. Board Spec. Rep.*, no. July, pp. 1–4, 1978.

[2] P. Lumb, “Slope failures in Hong Kong,” *Q. J. Eng. Geol. Hydrogeol.*, vol. 8, no. 1, pp. 31 LP – 65, Feb. 1975.

[3] H. Rahardjo, X. W. Li, D. G. Toll, and E. C. Leong, “The effect of antecedent rainfall on slope stability,” *Geotech. Geol. Eng.*, vol. 19, no. 3–4, pp. 371–399, 2001.

[4] E. W. Brand, J. Premchitt, and H. B. Phillipson, “Relationship between rainfall and landslides in Hong Kong,” *Proc. 4th Int. Symp. Landslides, Toronto, 1984*, no. January 1984, pp. 276–284, 1984.

[5] B. S. A. Anderson and N. Sitar, “Analysis of rainfall-induced debris flows,” *Int. J. Rock Mech. Min. Sci. Geomech. Abstr.*, vol. 33, no. 3, p. A106, 1996.

[6] C. W. W. NG and Y. W. PANG, “Influence of Stress State on Soil-Water Characteristics and Slope Stability,” *J. Geotech. Geoenvironmental Eng.*, vol. 126, no. February, pp. 157–166, 2000.

[7] T. ONODERA, R. YOSHINAKA, and H. KAZAMA, “SLOPE FAILURES CAUSED BY HEAVY RAINFALL IN JAPAN,” *J. Japan Soc. Eng. Geol.*, vol. 15, no. 4, pp. 191–200, 1974.

[8] T. Uchimura *et al.*, “Precaution and early warning of surface failure of slopes using tilt sensors,” *Soils Found.*, vol. 55, no. 5, pp. 1086–1099, 2015.

[9] G. Iiritano, P. Versace, and B. Sirangelo, “Real-time estimation of hazard for landslides triggered by rainfall,” *Environ. Geol.*, vol. 35, no. 2–3, pp. 175–183, 1998.

[10] P. Aleotti, “A warning system for rainfall-induced shallow failures,” *Eng. Geol.*, vol. 73, no. 3–4, pp. 247–265, 2004.

[11] T. Uchimura *et al.*, “Simple monitoring method for precaution of landslides watching tilting and water contents on slopes surface,” *Landslides*, vol. 7, no. 3, pp. 351–357, 2010.

[12] T. Uchimura, L. Wang, J. P. Qiao, and I. Towhata, “Miniature ground inclinometer for slope monitoring,” *Proc. 14th Asian Reg. Conf. Soil Mech. Geotech. Eng.*, 2011.

[13] L. Wang *et al.*, “An early warning monitoring of Earthquake-induced slope failures by monitoring inclination changes in multi-point tilt sensors,” vol. 19, no. September, pp. 251–256, 2018.

[14] M. Irfan and T. Uchimura, “Modified triaxial apparatus for determination of elastic wave velocities during infiltration tests on unsaturated soils,” *KSCE J. Civ. Eng.*, vol. 20, no. 1, pp. 197–207, 2016.

[15] M. Irfan, T. Uchimura, and Y. Chen, “Effects of soil deformation and saturation on elastic wave velocities in relation to prediction of rain-induced landslides,” *Eng. Geol.*, vol. 230, no. July, pp. 84–94, 2017.

[16] M. Irfan and T. Uchimura, “Helical filter paper technique for uniform distribution of injected moisture in unsaturated triaxial specimens,” *Soils Found.*, vol. 55, no. 4, pp. 749–760, 2015.

[17] Y. Chen, T. Uchimura, M. Irfan, D. Huang, and J. Xie, “Detection of water infiltration and deformation of unsaturated soils by elastic wave velocity,” *Landslides*, vol. 14, no. 5, pp. 1715–1730, 2017.

[18] Y. Chen, M. Irfan, T. Uchimura, G. Cheng, and W. Nie, “Elastic wave velocity monitoring as an emerging technique for rainfall-induced landslide prediction,” *Landslides*, vol. 15, no. 6, pp. 1155–1172, 2018.

[19] Y. Chen, M. Irfan, T. Uchimura, Y. Wu, and F. Yu, “Development of elastic wave velocity threshold for rainfall-induced landslide prediction and early warning,” *Landslides*, vol. 16, no. 5, pp. 955–968, 2019.

[20] P. Bormann, E. Engdahl, and R. Kind, “Seismic Wave Propagation and Earth models,” 2012, p. p36.

9th Int. Conf. on Geotechnique, Construction Materials and Environment, Tokyo, Japan, 20-22 November 2019, ISBN: 978-4-909106025 C3051

THREE-DIMENSIONAL ANALYSES OF EXISTING TUNNEL RESPONSES DUE TO ADJACENT LOADED PILES ROW

N. Heama[1], P. Luepersert[1], S. Suwansawatt[1]
[1]Faculty of Engineering, King Mongkut's Institute of Technology Ladkrabang, Bangkok, Thailand

ABSTRACT

In urban area, Tunnel Boring Machine shield (TBMs) is recommended to construct a tunnel to solve the traffic congestion problems. Although the tunnel is generally aligned under the major road to avoid the building, a new adjacent infrastructure such as flyovers, elevated trains, crossing bridge and tall building are continually construction as the same time. In the soft ground condition as Bangkok, Thailand, the pile foundations as pile foundations are used to support the new infrastructures. Then, the existing tunnel is inevitably affected by the adjacent piles row under loading. Many researches use the three-dimension finite element method (3D FEM) to investigate the effect of loaded pile row on existing tunnel. However, a few researches study the influence of number of piles in term of fully effect on existing tunnel. Thus, this study focused on the effect of the various pile row conditions, the number and spacing of 1 m loaded bore pile (D_P) in single row are varied, on existing tunnel by PLAXIS 3D Version 2018. The cases study was divided into pile length of 17.35 m (short pile row case) and 57 m (long pile row case). The properties of Bangkok sub soil and data of MRTA Blue line project were used in this study. The results obtained from 3D models were shown in terms the maximum of tunnel deformations (ΔC and ΔE) and additional structure forces in tunnel lining (ΔN and ΔM). The number and spacing of pile in row for modeling in which the tunnel response become constant are 11, 7, 5 and 5 piles with $3D_P$, $4D_P$, $5D_P$ and $6D_P$, respectively. The pile row lengths considered from monitoring plane (L/2) at which the maximum changes in tunnel diameter become constant are 15 m with respect to the number and spacing of pile in row.

Keywords: 3D FEM, Adjacent Piles row, Existing tunnel, Embedded pile

INTRODUCTION

The tunnel construction with Tunnel Boring Machine shield (TBMs) play an important role to solve the traffic congestion problems in the urban development. Generally, the tunnel is aligned under the major roads to avoid their effect on adjacent structures. Simultaneously, a new adjacent infrastructure such as flyovers, elevated trains, crossing bridge and tall building are also constructed to be the urbanization. In the soft ground condition as Bangkok, Thailand, the pile foundations are required to support the infrastructures. Then, the adjacent piles under loading is inevitably affected on the existing tunnel. Thus, an evaluation of the effect of loaded pile on the stability and integrity of tunnel is essential.

The many researches use a three-dimension finite element (3D FE) method to investigate the influence of this problems [1]-[5]. In the Bangkok, Thailand, the effect of adjacent single pile under loading on existing tunnel in Bangkok soft clay was studied [6], [7]. However, the effect of single loaded pile on existing tunnel is hardly ever met in engineering practice. With characteristic of tunnel structure (a longer underpass containing a road), the pile row condition with various numbers of piles in single row is often affected on the existing tunnel. Only a few researches studied the impact on the existing tunnel due to loaded pile row. In previous research, the two-dimension finite element (2D FE) under plane strain condition was considered to analyze the pile row and existing tunnel problem. The pile row in 2D FE under plane strain condition must be used the transformation technique to convert the properties or sizes of pile row [8], [9]. Besides, the interaction between soil and pile in the 2D plane strain analysis cannot evaluate [10]. Therefore, the 3D FE method is needed to analyze the effect of piles on existing tunnel. Heama [11] studies the number of loaded piles in row is great enough to evaluate the fully effect on existing tunnel in cases studies with Bangkok clay parameters by 3D FEM. In this analysis, the pile spacing was kept witch $3D_P$, and the analysis results were presented in terms of only the fully maximum tunnel deformations.

This research has a goal of understanding the influence of number and spacing of adjacent piles in row on the tunnel response**.** Various number and spacing of piles in single row are considered by using the 3D FE method. The Bangkok subsoil obtained the data from the Mass Rapid Transit Authority (MRTA) projects were considered in this study. The results are presented in terms of tunnel deformation and additional forces in tunnel lining.

CHARACTERISTICS OF THE CASE STUDIES

The data of the MRTA blue line project was chosen to be the case study in this analysis. The modeling of the tunnel lining was simulated into the continuous lining. The outer diameter of tunnel, D_T, of 6.3 m, lining thicknesses, T, of 0.3 m, and the tunnel depth (from ground surface to the center of the tunnel), Z_T, of 20.5 m are fixed throughout this study. The distance between edge of tunnel and edge of pile, C, are fixed at 0.5 m. The bored pile dimeter, D_P, of 1.0 m and the pile lengths of 17.35 m and 57 m are defined. The pile spacing, S, are varied witch $3D_P$, $4D_P$, $5D_P$ and $6D_P$ as shown in Fig 1.

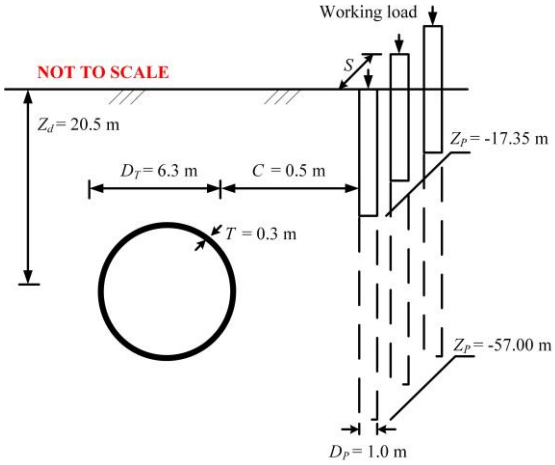

Fig. 1 Geometrical parameters

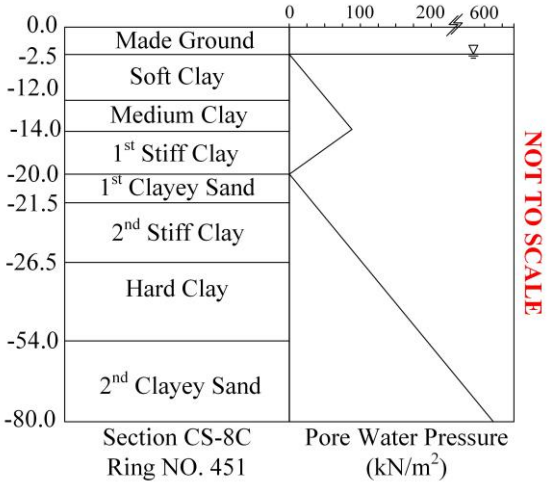

Fig. 2 Bangkok subsoil and pore water pressure profiles

The soil profile at Sukhumvit Station obtained forms a part of the Mass Rapid Transit Authority (MRTA) Blue Line Project was considered. Geological conditions can be divided into (1) Made Ground or fill material at 0–2.5 m, (2) Soft Clays at 2.5–12 m, (3) Medium Clays at12–14 m, (4) First Stiff Clays at 14–20 m, (5) A thin seam of First Clayey Sand is found at 20-21.5 m, (6) Second Stiff Clays at 21.5-26.5 m, (7) Hard Clays at 26.5-54 m and then (8) Dense Sand at 54–80 m. A typical pore water pressure profile in Bangkok is a piezometric drawdown, as shown in the Fig. 2.

FINITE ELEMENT METHOD

Constitutive model and material properties

The finite element (FE) method based on software PLAXIS 3D is used for investigating the impact of adjacent row pile under loading on existing tunnel. The made ground layer was assumed by hardening soil model (HS). The hardening soil with small strain stiffness (HSS) was assumed to simulate as all layers below the made ground layer. The tunnel geometry is comprised the grouting and lining layers, the details will be described in section numerical procedure. The soil and grouting layers were simulated by the solid elements or the 10-node tetrahedral elements. the tunnel lining and EPB were considered into the 6-node triangular plate elements. In this study, the bore piles were modeled by the embedded pile (*EP*) as the function in PLAXIS 3D. The *EP* is attractive method to reduce the complexity of the solid pile models [13]. An *EP* were modeled by the beam elements or 3-node line element. The soil properties were obtained from the MRTA projects and laboratory testing data [14], [15]. The tunnel lining, tail void grouting layer and bored pile are assumed to be linear elastic. The material parameters of FE analysis are summarized in Table 1, Table 2 and Table 3. The interface friction value (R_{inter}) between surrounding soil and the structural elements (EPB, tunnel lining or bored piles) was chosen to be 0.9 [16].

Finite element mesh

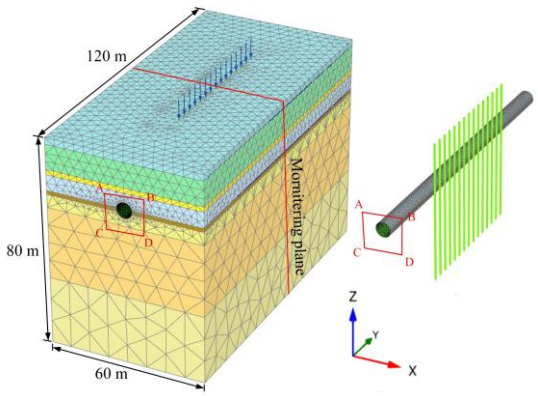

Fig. 3 models and meshes

The dimension of FE mesh in the transverse direction of 60 m (≈$9.5D_T$), the longitudinal direction of 120 m (≈$19D_T$) and vertical direction of 80 m

(≈12.5D_T) were shown in Fig. 3. The boundary size of FE meshes are lager to avoid the boundary effect [17]. The FE models were meshed with the 420,000 elements and 550,000 nodes were approximately. For boundary conditions, the lateral movement was fixed in x and y directions while vertical displacement in z-direction was allowed. The bottom of the models was restrained against displacements in all directions.

Table 1 Parameter for Hardening Soil Model (HSM)

Layer	Soil type	γ_b (kN/m³)	c' (kPa)	$\emptyset'$ (°)	Ψ' (°)	E_{50}^{ref} (MPa)	E_{oed}^{ref} (MPa)	E_{ur}^{ref} (MPa)	v_{ur}	m	K_0^{nc}	R_f	Analysis type
1	Made Ground	18	1	25	0	45.6	45.6	136.8	0.2	1	0.58	0.9	Drained
2	Soft Clay	16.5	5	27	0	5	5	15	0.2	1	0.6	0.9	Undrained
3	Medium Clay	17.5	15	27	0	20	20	100	0.2	1	0.6	0.9	Undrained
4	1st Stiff Clay	19.5	25	28	0	60	60	180	0.2	1	0.5	0.9	Undrained
5	1st Dens Sand	19	0	33	5	80	80	240	0.2	0.5	0.55	0.9	Drained
6	2nd Stiff Clay	20	30	28	0	60	60	180	0.2	1	0.5	0.9	Undrained
7	Hard Clay	20	40	28	0	60	60	180	0.2	1	0.5	0.9	Undrained
8	2nd Dens Sand	20	0	36	5	80	80	240	0.2	0.5	0.5	0.9	Drained

Table 2 Parameter for Small Strain Stiffness (SS)

Layer	Soil type	G_{max} (MPa)	$\gamma_{0.7}$ (%)
1	Made Ground	Hardening Soil Model (HSM)	
2	Soft Clay	15	0.08
3	Medium Clay	45	0.11
4	1st Stiff Clay	80	0.12
5	1st Dens Sand	200	0.014
6	2nd Stiff Clay	80	0.12
7	Hard Clay	130	0.15
8	2nd Dens Sand	240	0.02

Table 3 Material properties

	Young modulus [E] (kN/m³)	Poisson's ratio [ν]	Unit weight [γ] (kN/m³)
Tunnel lining	31 x 10^6	0.20	24
Bore pile	31 x 10^6	0.20	24
EPB shield	210 x 10^6	0.28	78
Grouting layer	1 x 10^6	0.30	21

Numerical procedure

The simulation process was divided into two stages. The tunneling process with EPB shield proposed by the study of Lueprasert [18] was simulated in the first stages. The measured data of MRTA project were investigated by [19]. At the considered section of MRTA project (CS-8C), face pressure of 150 - 200 kPa are applied on the face of shield (applied pressure of 150 kPa at the crown and linearly increased to 200 kPa at the invert of tunnel). The grouting pressure of 200 kPa was applied on the perimeter of the excavation zone with uniformly distributed pressure. The measured data of MRTA project was considered and compared with the tunneling results. In the second stage, the pile row located on the one side of existing tunnel was modeled. The applied working loads on pile were calculated based on the alpha method with safety factor of 2.5 [20]. The working load of 1,406 kN and 4,905 kN applied on pile length of 17.35 m and 57 m, respectively. The wished-in-place pile row is considered in this study. The FE models were calibrated by comparison between the numerical results and in-situ measurements of surface settlement and static pile load test at the section CS-8C and Sukhumvit Soi 23, respectively [21].

ANALYSIS RESULTS

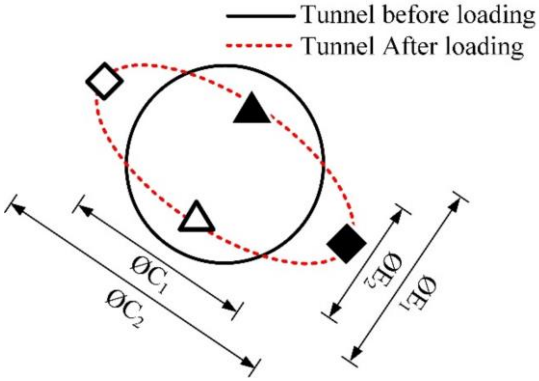

Fig. 4 Positions to observe the structural forces in tunnel lining and tunnel deformations

In this section, the results were discussed in terms of the maximum tunnel deformations and additional forces in tunnel lining. The maximum changes of tunnel diameter were calculated in terms of both the maximum contraction change (ΔC) and the maximum extension change (ΔE) inferred from assessment of the unsymmetrical distortion of shell structure shapes or the out-of-roundness [22]. The ΔC and ΔE represent the largest shortening and extending of the tunnel diameter due to loaded pile row. The calculation of the ΔC and ΔE were shown in Eq. (1) and (2). When $\emptyset_1$ and $\emptyset_2$ are tunnel diameters before and after the effect of pile rows under loading, respectively.

ΔE = maximum extension changes of tunnel dimeter

$$\Delta E = \emptyset E_2 - \emptyset E_1 \quad (1)$$

ΔC = maximum extension changes of tunnel dimeter

$$\Delta C = \emptyset C_2 - \emptyset C_1 \quad (2)$$

For changes in lining forces, axial force and bending moment were obtained at the same position of the maximum changes of tunnel diameter as shown in Fig. 4.

Models calibrations

The model parameters and numerical procedure were calibrated by the comparison between the computed results from FE analysis and in-situ measurements data. Figure 5a shows the measured of ground surface settlements at the section CS-8C and numerical results in tunneling stage. The contraction ratio of 0.4% and volumetric strain of 5.5% applied in grouting layer are used to model in tunneling process. The results of pile under loading simulation is illustrated in Fig. 5b. The result of FE analysis and the pile head settlement from the static pile loaded test is satisfaction. Note that the results were obtained from only single pile under loading simulation without tunneling**.**

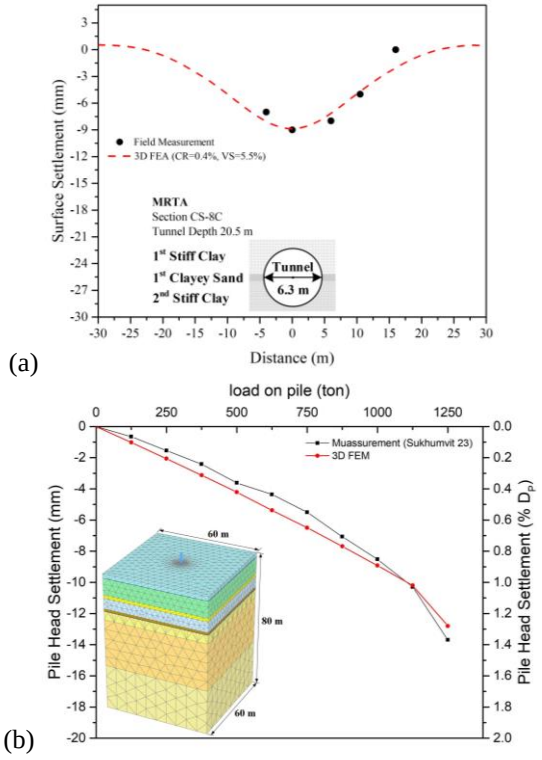

Fig. 5 The model parameters and numerical procedure (a) calibration of tunneling process (b) calibration of pile simulation

Tunnel deformations

Figure 6 depicts the maximum tunnel deformations due to nearby pile row under loading for various number of piles in row and pile spacing. The negative sign is the maximum contraction change (ΔC) and positive sign is the maximum extension change (ΔE) in y-axis. The distribution patterns of analysis results are similar in both of effect of short pile row (CASE 1) and long pile row (CASE 2). The magnitudes of ΔC and ΔE gradually increase with increasing pile number and decrease with increasing pile spacing and the effect of long pile row is larger than short pile row. In CASE 1 and CASE 2, the impact of adjacent loaded pile with various numbers and spacings of piles on ΔC and ΔE becomes constant when the number of piles is more than 11, 7, and 5 piles in row for pile spacing of $3D_P$, $4D_P$ and both of $5D_P$ and $6D_P$, respectively. In consideration of length of pile spacing (L), the pile row lengths considered from monitoring plane (L/2) at which the maximum changes in tunnel diameter become constant are 15 m, 12 m, 10 m, 12 m in case of $3D_P$, $4D_P$, $5D_P$ and $6D_P$, with 11, 7, 5 and 5 piles, respectively.

It is postulated that the pile row lengths considered from monitoring plane (L/2) at which the maximum changes in tunnel diameter become constant are 15 m with respect to the number and spacing of pile in row.

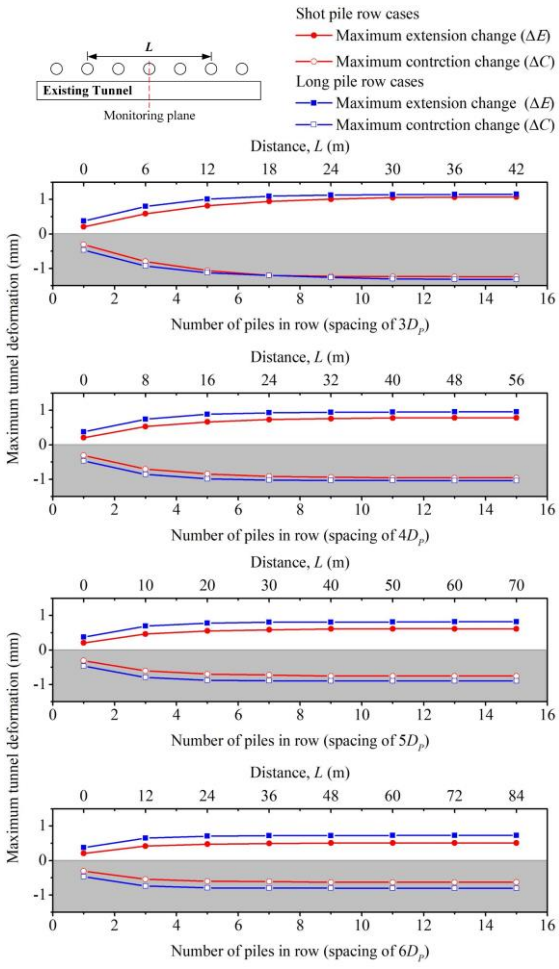

Fig. 6 Maximum tunnel deformations

The value of distortion degrees of maximum contraction change (β) is range of 40^0-45^0 and 30^0-35^0 for the distortion degrees of maximum extension change (α) as shown in Fig. 7.

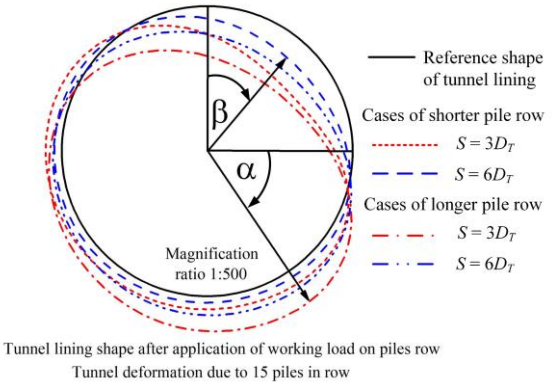

Fig. 7 Change of lining tunnel diameters distortion

Change of lining forces

The additional lining forces due to the effect of number of piles in row and pile spacing were investigated at the same position of maximum tunnel deformations. Figure 8 and 9 show the changes of axial forces and bending moment (the negative and positive signs referred the increasing of compression and tensile bending moment, respectively). The case of adjacent loaded pile spacing of $3D_P$ and $6D_P$ are only presented in this study. In short pile row case (CASE 1), change of axial forces (ΔN) and the change of bending moment (ΔM) decrease with increasing pile spacing. CASE 1, the increasing axial forces at the ΔC axis and the ΔE axis increase 5 to 90 and 10 to 200 kN, respectively. While the additional bending moment decrease -2 to -18 at the ΔC axis and increase 1 to 20 at the ΔE axis. With increasing 3 and 5 piles in row, the ΔN and ΔM dramatically increases. The maximum values of ΔN and ΔM become constant or remains unchanged with the 11 and 5 piles for pile spacing of $3D_P$ and $6D_P$, respectively. The results in this section again confirm that the pile row lengths considered from monitoring plane (L/2) at which the maximum changes in lining become constant are 15 m and 12 m in case of $3D_P$ and $6D_P$, with 11 and 5 piles as same as the results in terms of tunnel deformation. For long pile row (CASE 2), a similar tendency to can be observed.

It again confirms that the pile row lengths considered from monitoring plane (L/2) of 15 m with respect to the number and spacing of pile in row should be modeled to obtain the constant or fully effect on tunnel response due to adjacent loaded pile row.

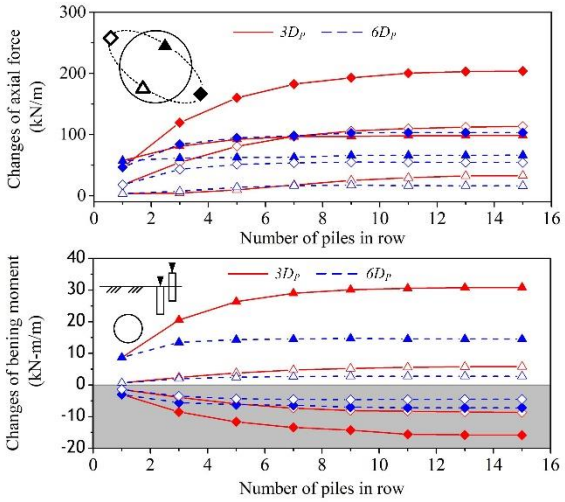

Fig. 8 Change of lining forces in cases of short pile row

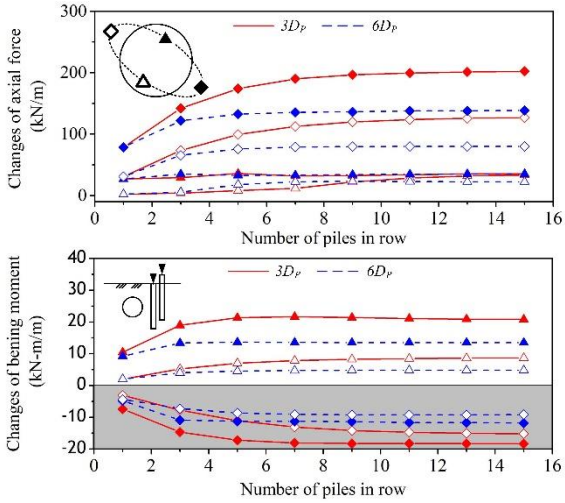

Fig. 9 Change of lining forces in case of long pile row

CONCLUSIONS

This paper studies the effect on existing tunnel due to adjacent loaded pile row in terms of short and long pile row by 3D finite element method. The tunnel deformations and changes of lining forces are observed. The main results of the analysis are as follows:

1. It is postulated that the pile row lengths considered from monitoring plane (L/2) at which the maximum changes in tunnel diameter become constant are 15 m with respect to the number and spacing of pile in row. The number and spacing of pile in row for modeling in which the tunnel response become constant are 11, 7, 5 and 5 piles with $3D_P$, $4D_P$, $5D_P$ and $6D_P$, respectively

2. The increasing of structural forces in the tunnel lining due to adjacent pile row under loaded should be paid attention. In tunnel lining design, the designer should be considered the possible increasing structural forces in the future construction. Otherwise, the lining must be checked if it can resist the additional forces and tunnel deformation in terms of serviceability and safety.

ACKNOWLEDGMENTS

The authors fund by Faculty of Engineering, King Mongkut's Institute of Technology Ladkrabang, Ladkrabang Underground and Tunneling Innovation Center (LUTIC) and 1D2 Group Co. Ltd. under Grant KREF035001.

REFERENCES

[1] Schroeder F. C., Potts D. M., and addenbrooke T. I., The influence of pile group loading on existing tunnels, Geotechnique, Vol. 54, Issue 6**,** 2004, pp. 351-362.

[2] Abdel-Meguid M., Rowe R. K., and Lo K. Y., 3D effects of surface construction over existing subway tunnels, Geomechanics, Vol.2, 2002, pp. 447-469.

[3] Yao J., Taylor R. N., McNamara A. M., The effects of loaded bored piles on existing tunnels, in: Geotech. Asp. Undergr. Constr. Soft Gr. – 6th Int. Symp., 2008, pp. 735–741.

[4] Arunkumar S., and Ayothiraman R., Effect of vertically loaded pile on existing urban tunnel in clay, in: Proc. of Indian Geotechnical, Mumbai, India, 2010, pp.751-754.

[5] Lueprasert P., Jongpradist P., Charoenpak K., Chaipanna P., and Suwansawat S., Three-dimensional finite element analysis for preliminary establishment of tunnel influence zone subject to pile loading, Maejo Int. J. Sci. Technol., Vol 9, 2015, pp. 209–223.

[6] Lueprasert P., Jongpradist P., Jongpradist P., and Suwansawat S., Numerical investigation of tunnel deformation due to adjacent loaded pile and pile-soil-tunnel interaction, Tunn. Undergr. Space Technol., Vol 70, 2017, pp. 96–109.

[7] Heama N., Jongpradist P., Lueprasert P., and Suwansawat S., Investigation on tunnel responses due to adjacent loaded pile by 3D finite element analysis, International Journal of GEOMATE, Vol.12, Issue 31, 2017, pp. 83–90.

[8] Potts,D. M., and Zdravkovic´ L., Finite element analysis in geotechnical engineering: Theory, London: Thomas Telford, 1999.

[9] Potts D. M., and Zdravkovic´ L., Finite element analysis in geotechnical engineering: Application. London: Thomas Telford, 2001.

[10] Chai J. C., Shrestha S., Hino T., Ding W. Q., Kamo Y., and Carter J., 2D and 3D analyses of an embankment on clay improved by soil–cement columns, Comput. Geotech., Vol 68, 2015, pp. 28-37.

[11] Heama N., Jongpradist P., Lueprasert P., and Suwansawat S., Investigation on pile-soil-tunnel interaction due to adjacent loaded pile row by 3D FEM, in Proc. 4th Int. Conf. on engineering, Applied Sciences and Technology, 2018, pp. 792-795.

[12] Mass Rapid Transit Authority of Thailand, Restrictive Guideline for Protection Zone in Blue Line Project, Engineering Specifications for MRT Tunnels, Bangkok, Thailand, 2009.

[13] Tschuchnigg F., and Schweiger H. F., The embedded pile concept – Verification of an efficient tool for modelling complex deep foundations, Comput. Geotech., Vol 63, 2015, pp. 244–254.

[14] Rukdeechuai T., Jongpradist P., Wonglert A.. and Kaewsri T., Influence of soil models on numerical simulation of geotechnical works in Bangkok subsoil, EIT Research and Development J., 2009, Vol 20, Issue 3, pp. 17-28.

[15] Likitlersuanga S., Teachavorasinskuna S., Surarakb S., Ohc E., and Balasubramaniamc A., Small strain stiffness and stiffness degradation curve of Bangkok Clays, Soils and Foundations, Vol 53, Issue 4, pp. 498-509.

[16] Brinkgreve R., Engin E., and Swolfs W., PLAXIS 3D Version 2013 manual, 2013.

[17] Mroueh H., and Shahrour I., A simplified 3D model for tunnel construction using tunnel boring machines, Tunn. Undergr. Space Technol., Vol 23, 2008, pp. 38–45.

[18] Lueprasert P., Jongpradist P., and Suwansawat S., Tunneling simulation in soft ground using shell elements and grouting layer, International Journal of GEOMATE, Vol.12, Issue 31, 2017, pp. 51–57.

[19] Suwansawat S., Earth Pressure Balance (EPB) Shield Tunneling in Bangkok: Ground Response and Prediction of Surface Settlements Using Artificial Neural Networks, Ph.D. Thesis, Massachusetts Institute of Technology, USA, 2002.

[20] Skempton A. W. Cast in-situ bored piles in London Clay, Géotechnique, Vol 9, 1959, pp. 153–173.

[21] Supawo S., Project Report: Settlement Prediction of Large-Diameter Bored Pile in Bangkok Soils, Thesis, Khon Kaen University, Thailand, 2015.

[22] European Committee for Standardization (CEN), Design of steel structures, Part 1–6 general rules: Supplementary rules for shell structures, Eurocode 3, Brussels, Belgium, 1999.

9th Int. Conf. on Geotechnique, Construction Materials and Environment, Tokyo, Japan, 20-22 November 2019, ISBN: 978-4-909106025 C3051

ASSESSMENT OF LANDSLIDE SUSCEPTIBILITY: A CASE STUDY OF CARABAO MOUNTAIN IN BAGUIO CITY

Miller DL. Cutora[1], Mary Ann Q. Adajar[2], Maria Cecilia R. Paringit[3], and Eleazar H. Santiago[4]
[1,2,3,4]Civil Engineering Department, De La Salle University, Manila, Philippines

ABSTRACT

Baguio City is one of the most visited places in the Philippines especially during summer season. Due to its topography, soil characteristics, land use classification, and exposure to different calamities immense rainfall, Baguio City is prone to landslide. Lack of information and warning system regarding rainfall puts a challenge to decrease casualties and losses. The study evaluated in this study is a portion of the Carabao Mountain located in Baguio City. The degree of saturation of the soil and the imposed loading due to land use are considered as the main external factors for assessing the stability of earth slopes. Mohr-Coulomb failure criteria parameters are used in the determination of initial factor of safety. Using different scenarios, a general factor of safety is obtained and then use to develop a landslide susceptibility map. The loading imposed by land use developments such as settlement and road networks induce a great impact on the weight carried by the underlying soil which results to a greater decrease of factor of safety. The impact of the saturation as an added weight to the soil is lower as compared to the loading of structures. The general factor of safety indicates that as the degree of saturation of soil increases, the moderate susceptible area increases, and some are close to high susceptible degree with factor of safety close to a value of 1, which is located at residential zone. Possible addition of loading may decrease further the factor of safety which will cause landslide.

Keywords: Degree of saturation, Factor of safety, Land use, Landslide, Slope stability

INTRODUCTION

The City of Baguio is popularly known as the Summer Capital of the Philippines and as the City of Pines. It is a highly urbanized city in the Northern part of Luzon in the Philippines. Baguio City has a flying distance of 206 km and about a driving distance of 250 km from Manila City, the Capital City of the Philippines. Baguio City is nestled on Cordillera Mountain Range with elevation ranging from 900 to 1,600 m above sea level. Due to its geographical location in a very high plateau, Baguio is commonly exposed to storms and heavy rainfalls. With such, landslide is very prevalent in the City. Shown in Table 1 is the lists of reported landslide incidents during typhoons according to City Disaster Risk Reduction and Management Council (CDRRMC) of the City of Baguio.

Landslide is a hazard that causes properties to a massive damage, and sometimes the cause of life loss. Landslides may be induced or triggered by other natural activities such as immense rain or earthquake. During storms or heavy rainfalls as well as during earthquake, landslides are prevalent to the City of Baguio, which causes some of the thoroughfare to stop their operations as well as cause damage to different properties. The closure of road arteries put a challenge in the supply of food and other commodities of the city which causes establishments to close.

Table 1 Landslide statistics during typhoons in Baguio City [CDRRMC Baguio]

Typhoon (Local)	Date	Landslide
Florida	July 11 – 14, 2006	53
Emong	May 13, 2009	1
Kiko	August 10, 20019	2
Pepeng	October 02 – 04, 2009	97
Juan	October 15 – 21, 2010	2
Mina	August 26 – September 02, 2011	16
Pedring	September 26 – 28, 2011	3
Gener	July 28 – August 03, 2012	10
Labuyo	August 09 – 13, 2013	5
Luis	September 15, 2014	1
Mario	September 18 – 22, 2014	26
Ineng	August 20 – 24, 2015	5
Lando	October 14 – 23, 2015	80

Landslides cause damage to buildings, infrastructure, agricultural land and crops. Landslides and slope stability are two important issues to consider in planning cities located in mountainous regions. Rainfall-induced landslide hazard has been growing all over the world, due to the fast population increase, often accompanied by uncontrolled urban

sprawl [1]. In regions where urban residential areas coincide with mountainous terrains, the risk is higher for people and the economic costs include relocating communities, repairing physical structures, and restoring water quality in streams and rivers [2].

Landslide is one of the causes of deaths in the city during calamities. The susceptibility to landslide of areas is high due to the formation of the terrain, type of soil, as well as changes in land use. Lack of information and warning system regarding rainfall puts a challenge to the fight to decrease casualties. Susceptibility maps that may be used as tools for predicting movement of soil for warning system implementation will be needed.

Baguio City is prone to landslide due to its topography, soil characteristics, land use, as well as natural factor such as rainfall. The Mines & Geosciences Bureau of Cordillera Administrative Region (MGB-CAR) of the Department of the Environmental and Natural Resources (DENR) GeoHazard Map that will present the susceptible areas to landslide with consideration of assessment parameters. The assessment was done with the geologists' perception with the defined tools. Upon the evaluation of the existing parameters, the assessment tools lack technical aspect, specifically the inclusion of soil strength parameters, and some relevant triggering mechanisms such as the land use of the area, and the development of the saturation of soil due to the immense rainfall.

With these considerations, this study investigates if a slope is susceptible to failure using soil parameters related to slope stability and will incorporate the additional assessment tools, which will improve the existing susceptibility map. In addition, the landslide susceptibility levels and the areas that are of high susceptibility levels during massive rainfall is identified.

This study is geared to create assessment tool for rainfall-induced landslide and identify the landslide susceptible areas at Baguio City for planning and preparedness. To attain this goal, the stability of the identified sloping areas was assessed and evaluated considering the geotechnical characteristics of the ground and incorporating other triggering factors like saturation of the soil due to rainfall, presence of vegetation, and land use-imposed loading. Using a Quantum Geographic Information System (QGIS), a free and open-source GIS program, a landslide susceptibility map is developed for rapid assessment.

RAINFALL INDUCED LANDSLIDES

Slope failures occur frequently during or following period of heavy rainfall [3]. The infiltration of rainwater causes a reduction in this negative pore water pressure and an increase in the soil unit weight (due to an increased saturation [4]), both of which have a destabilizing influence. Rainfall-initiated landslides continue to inflict damages and and take the lives of people at any places throughout the world. According to [5], rainfall-initiated landslides involve highly dynamic hydrologic, earth surface, and ecological processes that persist over a range of spatial and temporal scales; however, guidance for overcoming these challenges has been elusive. Based on the study of [6], the process for quantitative risk assessment are seepage analysis, slope stability assessment, and risk assessment. The triggering mechanisms for a rainfall induced landslide have also been highlighted by the pore water pressure distributions at failure [6]. When the pore water pressure reaches a critical state, the effective shear strength of the soil diminished, inducing the landslide's formation [7].

LANDSLIDE SUSCEPTIBILITY ASSESSMENT

Numerous methods and practices such as frequency ratio, logistic regression, spatial regression, geographically weighted regression, and analytical hierarchy process, ordered weighted averaging, fuzzy logic and artificial neural networks [8] are used as landslide assessment tools.

The stability index is defined as the probability that a location is stable assuming uniform distributions of parameters over the uncertainty ranges. It does not predict that shallow translational slope movements will occur, but it forecasts that if they do, where they are more likely to initiate given the assumptions and input parameters used in the analysis [3].

According to the study of [9], an approach for establishment of an analytical risk assessment model to evaluate the risk index for soil erosion by water is proposed, in which the remote sensing, GIS, the analytical hierarchy process (AHP), and modeling techniques are integrated through investigation of soil erosion by water. The risk assessment model constructed through this approach in this study can be consistently used for understanding of the risk or potential of soil erosion by water, under either current site conditions or assumed certain changes of pertinent dominating factors, in a large area of interest.

The study of [10] aimed to develop a landslide model by using GIS and remote sensing techniques for landslide susceptibility mapping. The study employs several parameters with weights which are assigned according to the potential cause of landslide.

The studies investigated and analyzed the selected areas with different methodologies in generating the tools in identifying the state of a slope. This considers assessment scores to generate the stability score of the areas investigated. These studies served as a guide in generation and improvement of the slope stability assessment tools and scores in this study, which will be used together with slope stability analysis.

GEOHAZARD ASSESSMENT OF BAGUIO CITY

With the expertise and perception of the trained Geohazard Assessment Team of MGB-CAR, it was limited to the barangays and other areas of recent typhoon and dependent on the eighty-three observation stations in landslide-prone areas. This assessment is the basis for the formulation of the existing geohazard (landslide) map of the City of Baguio as shown in Fig. 1.

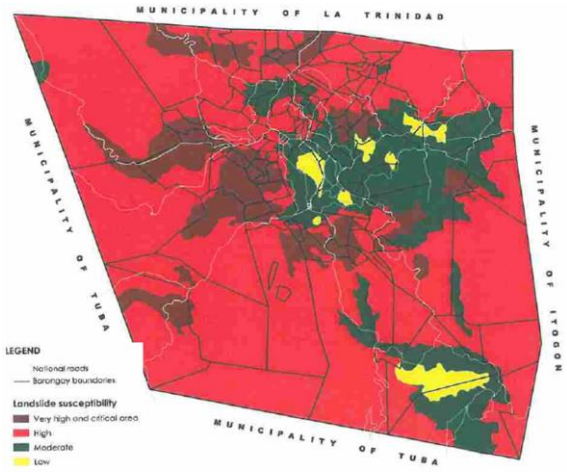

Fig. 1 GeoHazard map of Baguio City [11].

RAINFALL WARNING SYSTEM

A warning system was established by the Philippine Atmospheric, Geophysical, and Astronomical Service Administration (PAG-ASA) for monitoring, alert and evacuation purposes. This system is presented in three different colors which is presented in Table 3. These new color-coded advisories aimed to help the communities and concerned government agencies prepare for floods, landslides and dam spills.

Table 3 PAG-ASA Warning system.

Color Code	Rainfall Intensity, mm/hr	Rainfall Type	Remarks
Yellow	7.5 to 15.0	Heavy	Monitor
Orange	15.0 to 30.0	Intense	Alert
Red	more than 30.0	Torrential	Evacuation

METHODOLOGY

The study employed descriptive and analytical research. Descriptive research was used to describe, classify, measure and compare the present state of the area for the identification of scores for the different assessment tools. Analytical research was used to analyze the current situation of the area and make critical evaluation as to the susceptibility of the area to landslide based on the assessment tools.

Population and Locale of the Study

Baguio City occupies about 57 square kilometers of hilly land in the southwestern portion of the Cordillera Central mountain range in northern Luzon in the Philippines. It is completely surrounded by the province of Benguet, bordered by the municipality of Tuba to the south and west, by Itogon to the east and to the north by Benguet's capital, La Trinidad. The weather follows the typical Philippines' seasons: Dry Season from October to May and Wet Season from June to September.

As of 2015 census as per Philippine Statistics Authority - Cordillera, Baguio has a population of 345,000 which is about 20 percent of the region's population. The population density during that time is about 6,005 persons per square kilometer. The average annual population growth rate is 2.36 [13].

The research covered the north - left portion of the Central Business District of the City of Baguio, since these areas are of high density, and prone to landslide as per CDRRMC of Baguio City as shown in Fig. 2. This area is popular by its name as the Carabao Mountain which was intended to be the pastureland of the Camdas Clan. The portions of the Carabao Mountain considered are Quirino Hill and Pinget area which is limited by the yellow boundaries.

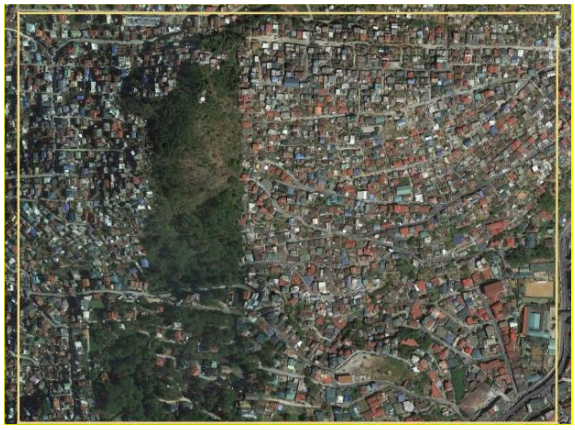

Fig. 2 Carabao Mountain, Baguio City

Research Design

The study evaluated the state of the slope with the aid of computer program and incorporating the effects of triggering factors. Figure 3 summarizes the research design of the study.

The geotechnical data was requested from BIP Steadfast Grounds Inc. The soil data available are the

Standard Penetration Number (SPT) and unit weight. The topographic map was issued City Planning and Development Office. The data acquired was aided with site inspection and inputs from MGB.

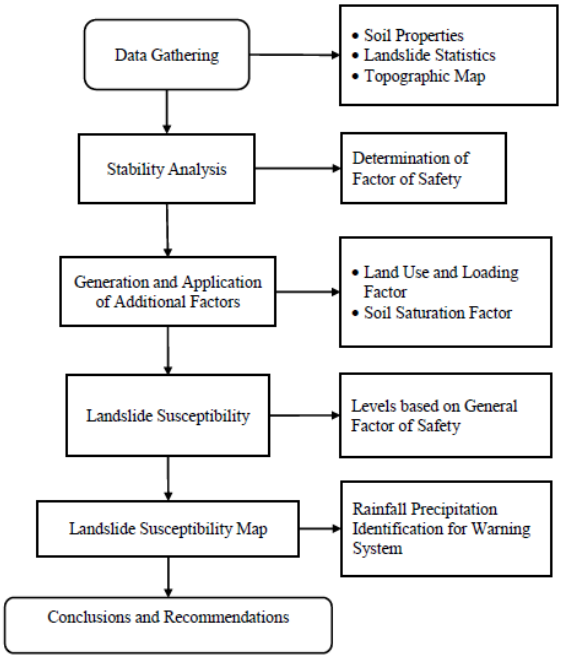

Fig. 3 Research design

Slope Stability Analysis

The area considered is about 1000m × 760m. The area was divided into 10m × 10m grids, while sections for slope stability analysis are of 20m intervals and using the topographic map as elevation guide. The factor of safety for the two columns of grids considered 1 section for analysis. The division was based on sections with slopes.

The SPT was used in predicting the value of soil shear strength parameters namely, cohesion and angle of internal friction, which are the parameters of Mohr-Columb Failure Criteria.

The data was processed and analyzed using the GEO-SLOPE: SLOPE/W software. The slope was analyzed whether it is safe or susceptible to landslide. The input parameters are the cohesion, angle of internal friction, and unit weight of soil, as well as the topography of the slope. The stable slopes were further processed by considering other triggering factors in the form of landslide assessment additive factors.

Landslide Assessment Tools

The addition of loading will decrease the strength of soil, therefore the value of the factor of safety will decline. These additional factors are the land use change in form of vegetation, settlement and roads, and rainfall which will increase the unit weight of soil due to the saturation.

There are several methods available to weight the evaluation criteria including direct ranking, swing weights ranking, rating, pairwise comparison, trade off analysis, and qualitative translation. This study employed the use of additional rating method.

The values of the additional factors were generated based on the difference of factor of safety of the initial state of the slope and the slope affected by the triggering factors. These values underwent regression process to identify possible relationship with the parameters. The regression model defines the formula which determined the values of the additional factors for the tools which was used for the assessment.

General Factor of Safety, FS_G

The General Factor of Safety was obtained from the sum of the initial factor of safety from slope stability analysis and external factors as presented in Eq. (1). This was derived by the methodology employed by [10] which is the summation of impact of every factor.

$$\boldsymbol{FS_G = FS + L_i + S_i} \quad (1)$$

Where:

$\boldsymbol{FS_G}$ = General Factor of Safety
$\boldsymbol{L_i}$ = Land Use and Loading Tool
$\boldsymbol{S_i}$ = Saturation of Soil due to Rainfall Tool

The values were then evaluated to generalize the susceptibility levels of the area and compare it to Table 4.

Table 4 Susceptibility Levels

Factor of Safety	Color Coding	Susceptibility Level	Remarks
1.5 ≤ FS	Yellow	Low Susceptible	Safe (as suggested by design criteria)
1.0 ≤ FS ≤ 1.5	Orange	Moderate Susceptible	Relatively Safe
FS < 1.0	Red	High Susceptible	Under State of Failure

Landslide Susceptibility Map

The evaluated scores and identified hazard prone areas at different group of rainfall intensities criteria were digitized using QGIS for easier view and appreciation. The scale of the map was based on the proximity of the span of the test evaluation. Evacuation site was recommended from the analysis of the proposed area. An evacuation site is sitting at the safe or almost flat zone that is free from landslide and accessible to different utilities and needs.

Rainfall Intensity and Warning System

The slopes ponding time and infiltration capability was determined based on the criteria of Green and Ampt parameters for the subsurface soil with soil type that is ML or Silty Loam. The parameters were used to generate different values of ponding time and the saturation depth of the soil as the time of constant rainfall increases. The values were examined and compared with PAGASA rainfall warning system for developing the warning systems which will be used for landslide susceptibility maps during rainfall, as well as the response guidelines by the CDRRMC.

RESULTS AND DISCUSSIONS

Soil Data

The data obtained from BIP Steadfast Ground Inc. includes standard penetration test (SPT) number, *N*, unit weight of the soil, γ, specific gravity, G_S, compression index, C_C, liquid limit, *LL*, plasticity index, *PI*, and moisture content, *w*, and percent finer than the No. 200 sieve. The data which were used for the study are the unit weight, and Standard Penetration Test (SPT) number which was used for calculating the cohesion and angle of internal friction. The type of soil in the area is ML which is classified as Silty Loam. The SPT data considered is about 1.5 m (5 feet) below the ground surface. Inverse-distance weighing interpolation method [14] is used to assume the soil data which represents the soil properties that are along the critical slope.

Land Use Assessment Additive Factor, L_i

The three different land use factors that are considered are vegetation (open space and with trees), road network, and settlement (buildings). For the generation of the factor, it will consider a 10 m tributary width for load distribution.

Table 5 Distributive Load for Land Use Impact and Land Use Tool (L_i)

Details	Distributive Load	L_i
Vegetation		
Open Space/grassland	0.0 kN/m	0.000
Pine Trees	141.9 kN/m	-0.081
Road Network		
Reinforced Concrete Pavement	67.2 kN/m	
Converted Truck Load	130.0 kN/m	
Total	197.2 kN/m	-0.136
Factored Residential Load (3 storeys)		
Dead Load	360.0 kN/m	
Live Load	91.2 kN/m	
Total	451.2 kN/m	-0.390

Saturation od Soil Assessment Additive Factor, S_i

The saturation of soil additive was based on the degree of saturation of the soil. With the preliminary values of soil parameters and computing the values of void ratio (e) and degree of saturation (S), the value of soil unit weight with different saturation was calculated which must be higher than the saturation level of the soils being considered that is about 70%.

Table 6 Saturation of Soil Tool (S_i)

Degree of Saturation	S_i
70%	0.000
80%	-0.018
90%	-0.036
100%	-0.054

General Factor of Safety

Using Eq (1), the general value of the factor of safety combined with the external factors were identified. The addition of the land use additive was added first. By using the available satellite imagery by google earth, the portions of the different land use were established. This data was added to the initial factor of safety and to the different saturation levels of the soil.

The color coding established in Table 4 was used for easier construction of maps as presented in Figure 5.5. Majority of the area are safe, but as the saturation increases some are already exposed to danger since the value of the lowest factor of safety for saturation values of 70%, 80%, 90%, and 100%, are 1.061, 1.043, 1.025, and 1.007, respectively. The critical area or the area with lowest factor of safety was highlighted in Fig. 4 is at Barangay Pinget, Baguio City. Portions that are close to a value equal to 1 are already at the verge of failure, necessary precautions and engineering interventions must be accounted.

Susceptibility Maps of the Area

The map was created using Quantum Geographic Information System (QGIS). Color coding specified in Table 4 was used to identify the level of susceptibility of respective area.

Figure 4 is layered with the actual satellite map, presents the level of susceptibility of the area to landslide due to varying saturation of the soil. The areas that are still in yellow code are still safe. Some areas are near the critical value which is 1 presented in orange color, therefore needs caution when massive rainfall occurs. Based map developed, the critical portion is residential area which is located at Barangay Pinget, Baguio City. If the area exceeds the assumed loadings, there will be a decrease in the factor of safety which will now result to soil slip failure, mass movement or landslide.

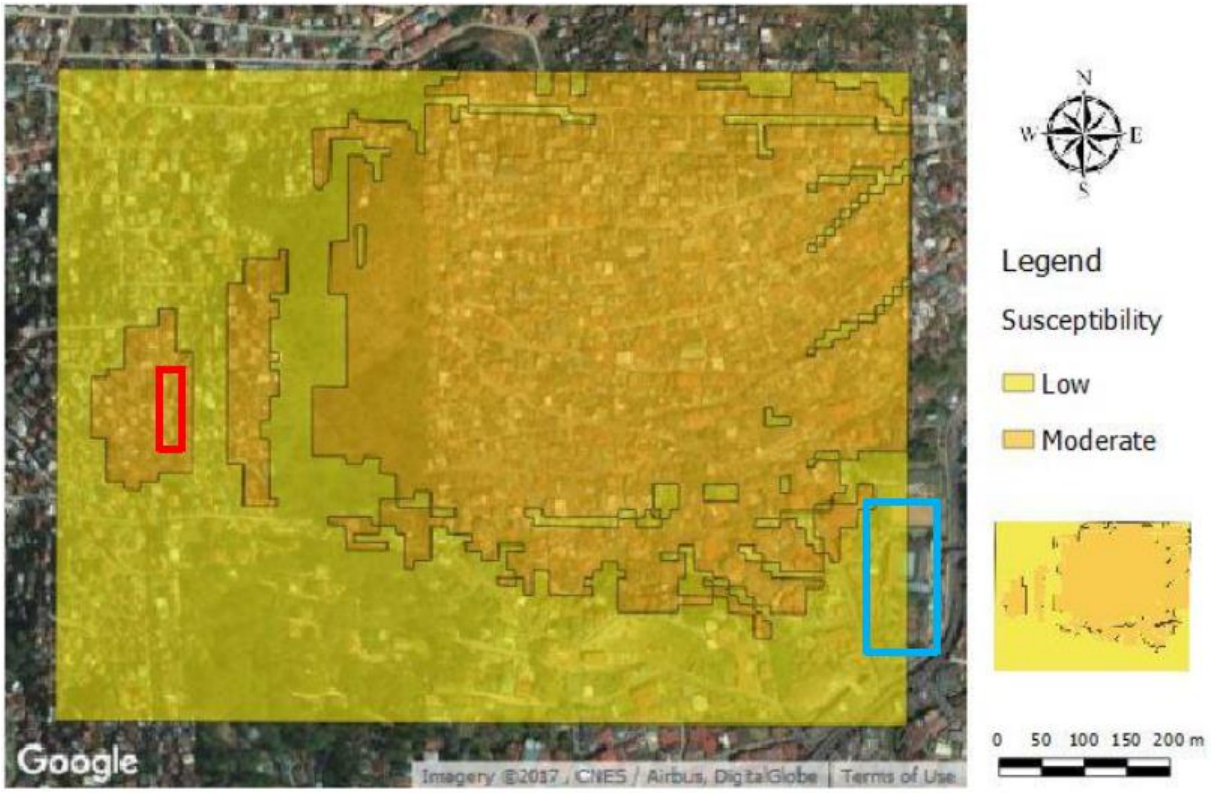

Fig. 4 Landslide Susceptibility Map

The area which is under moderate susceptibility is increasing as the value of saturation increases. The areas that are now susceptible to landslide are portions of Barangay Pinget and Barangay Quirino Hill in Baguio City.

Time of Ponding for Different Rainfall Intensities

Based on the values of ponding time, the values for rainfall intensity which is 20 and 30 are 56.26 and 21.55 mins, respectively. It can be noticed that the time for the surface to be saturated is quite long before infiltration occurs. Comparing to the warning system of PAGASA, 15 to 30 mm/hr precipitation is under the orange rainfall advisory. On the other hand, the rainfall intensity which is 40 and above has a shorter period of time of ponding, thus, infiltration is accelerated. According to [14], a continuous rainfall of 40 mm or over will cause slope failures. Comparing to the warning system of PAGASA, greater than 30 mm/hr precipitation is under red rainfall advisory. At this level of precipitation, the depth of soil under saturation state escalate as time increases, thus the early warning system of PAGASA might be adopted for landslide warning system.

At 40 mm/hr or more rainfall, the soil will begin to saturate, therefore, the factor of safety of the soil will be the general factor of safety that considers saturated soil additive, which is presented as the saturated soil susceptibility map. At this rainfall precipitation, evacuation at the susceptible areas such as Barangay Quirino Hill and Portions of Barangay Pinget must be raised for safety of the residences.

CONCLUSIONS

This study was intended to predict the possible role of external factors such as land use and saturation of soil due to rainfall on the factor of safety of slopes which is the deterministic factor of stability of earth slopes. Based on the results, land use loading and saturation of soil reduce the shear strength of the soil thus reducing the factor of safety of the soil.

For rapid assessment, the study considered land use tool and saturation of soil tool. As factors to slope stability, these tools are additives to the initial factor of safety. The values of additives are 0, -0.081, -0.136, and -0.390 for open space/grassland, vegetation (trees), road network and residential structures, respectively for land use tool. While 0, -0.018, -0.036, and -0.054 for initial, 0.8, 0.9, and 1.0 degree of saturation, respectively for saturation of soil tool.

The loading imposed by land use developments such as settlement and road networks induce great impact on the weight carried by the underlying soil which results to a greater decrease of factor of safety that is about 0.39. The impact of the saturation as an

added weight to the soil is lower as compared to the loading of structures since it only decreases the factor of safety to about 0.054.

The area that is close to the critical factor of safety which is 1 is a residential area located at Barangay Pinget, Baguio City as presented in Figure 4 which is highlighted in red box, thus addition of loading on that area would be risky. The residential areas at Barangay Quirino Hill, Baguio City, highlighted in blue box, are already below the ideal factor of safety which is 1.5. This implies the possibility of landslide in the area, especially if the load in the area is higher than the assumed values. The map generated can used as a guide in identifying the areas that are susceptible to landslide.

This landslide susceptibility map shall be used together with warning system for necessary actions during immense rainfall.

The warning system of PAGASA which is Red Warning will be adopted for precipitation which is 40 mm/hr and above. At this level, upon the release of thePAGASA warning, the preemptive action will be an immediate evacuation rendered by the concerned government bodies such as CDRRMC.

REFERENCES

[1] Greco, R., Giorgio, M., Capparelli, G., and Versace, P., Early warning of rainfall-induced landslides based on empirical mobility function predictor, Engineering Geology, Volume 153, 2013, pp. 68-79.

[2] Dragicevic, S., Lai, T., and Balram, S., GIS-based multicriteria evaluation with multiscale analysis to characterize urban landslide susceptibility in data-scarce environments, Habitat International, Volume 45, Part 2, 2015, pp. 114-125.

[3] Rabonza, M.L. (2014). Shallow landslide susceptibility mapping for selected areas in the Philippines severely affected by super typhoon Haiyan.

[4] Adajar, M.A.Q. and Cutora, M.D.L., The Effect of Void Ratio, Moisture Content, and Vertical Pressure on the Hydrocompression Settlement of Copper Mine Tailing, International Journal of GEOMATE, Volume 14, 2018, pp. 82-89

[5] Sidle, R.C. and Bogaard, T.A., Dynamic earth system and ecological controls of rainfall-initiated landslides, Earth-Science Reviews, Volume 159, 2016, pp. 275-291.

[6] Ali, A., Huang, J., Lyamin, A.V., Sloan, S.W., Griffiths, D.V., Cassidy, M.J., and Li, J.H., Simplified quantitative risk assessment of rainfall-induced landslides modelled by infinite slopes, Engineering Geology, Volume 179, 2014, pp. 102-116.

[7] Fang, H., Cui, P., Pei, L.Z., and Zhou,X.J., Model testing on rainfall-induced landslide of loose soil in Wenchuan earthquake region, Natural Hazards and Earth System Sciences, Volume 12, 2012, pp. 527-533.

[8] Akinci, H., Dogan, S., Kilicoglu, C., and Temiz, M., Production of landslide susceptibility map of Samsun (Turkey) City Center by using frequency ratio method, International Journal of the Physical Sciences, Volume 6(5), 2011, pp. 1015-1025.

[9] Wu, Q. and Wang, M., A framework for risk assessment on soil erosion by water using an integrated and systematic approach, Journal of Hydrology, Volume 337, 2007, pp. 11-21.

[10] Pareta, K. and Pareta, U., Landslide modeling and susceptibility mapping of Giri River Watershed, Himachal Pradesh (India), International Journal of Science and Technology, Volume 1, No. 2, 2012, pp. 91-104.

[11] The City Government of Baguio. Baguio City Ecological Profile, 2017.

[12] Mines and Geosciences Bureau – Cordillera Administrative Region, Department of Environment and Natural Resources, MGB-CAR, DENR (2015). Results of the Mines and Geosciences Bureau's Updating of 1:10,000 Scale Detailed Landslides and Flood Hazard map of Baguio City, Benguet Province

[13] Philippine Statistics Authority (2016). Population of the Cordillera Administrative Region (based on the 2015 census of population)

[14] Lu, G.Y. and Wong, D.W, An adaptive inverse-distance weighting spatial interpolation technique, Computers & Geosciences, Volume 34, 2008, pp. 1044-1055.

[15] Ministry of Land, Infrastructure and Transport Infrastructure Development Institute – Japan (2004, March). Development of warning and evacuation system against sediment disasters in developing countries.

9th Int. Conf. on Geotechnique, Construction Materials and Environment, Tokyo, Japan, 20-22 November 2019, ISBN: 978-4-909106025 C3051

EFFECT OF THE INDUCED ANISOTROPY ON THE STIFFNESS OF FLY-ASH TREATED SOILS

Valentina Guerrero[1], Jhon Roldán[1] and Javier Camacho-Tauta[1]
[1]Faculty of Engineering, Universidad Militar Nueva Granada, Colombia

ABSTRACT

Granular materials conforming geotechnical structures use to be subjected to typically anisotropic loading conditions. For this reason, it is reasonable to consider the influence of a variety of stress combinations on the elastic parameters effectively used in design of these types of structures. Elastic parameters in soils can be evaluated in laboratory by imposing different stress conditions while strains in two directions are carefully measured. In this work, it was evaluated the effect of the stress-induced anisotropy on the vertical stiffness of a granular material treated with fly ash. On this purpose, a Bishop & Wesley triaxial cell was used to apply different stress conditions on soil specimens while deformations were measured by local sensors in order to obtain the small-strain moduli under unloading and reloading compression. Results exhibit the relationship between the induced stress anisotropy and soil stiffness for different fly-ash contents of the specimens. Finally, the results were compared against a model that allows taking into account the stress anisotropy on the stiffness.

Keywords: Anisotropy, Shear modulus, Small-strain, Stiffness

INTRODUCTION

The stiffness of soils is a function of different characteristics that depend of density, particle shape, grain-size distribution, accommodation structure of particles, among others [1], [2]. Inherent anisotropy is a result of the formation process of the soil deposit, mainly due to particles shape and their orientation. The soil is subjected to horizontal and vertical stresses of different magnitude along its history. Such stresses generate stress-induced anisotropy. The degree of anisotropy is affected by the stress path imposed to the soil mass [3]–[5].

In laboratory, stress-induced anisotropy in soils can be evaluated by tests procedures in which different combination of stresses are applied while small strains are measured carefully by local sensors [6]. Strains can be categorized as small when they are lower than 10^{-3}% [7].

There are different consitutive models to evaluate the effect of the stress-induced anisotropy on the soil stiffness [8]–[11]. Li and Zeng [12] state that the construction of earth structures induce anisotropic conditions on soils. For this reason, some authors have studied the influence of the stress anisotropy on the shear modulus [3], [13]. It is well recognized that the maximum shear modulus (G_{max}) mainly depends on the void ratio (e) and the mean effective stress (p') [14]–[16]. A model able to include the effect of the particle shape, grain-size distribution and the stress anisotropy could be useful to this more general condition [13].

This work deals with the evaluation of the effect of the stress-induced anisotropy on the stiffness of a sand treated with fly ash. The methodology includes physical characterization of mixtures with different percentages of fly ash and compaction of soil specimens. These specimens were tested in a Bishop & Wesley triaxial cell equipped with local sensors. Soil stiffness was measured under different compression effective stress conditions. Results were compared against a model that includes the anisotropic effect of stresses [13]. It was found the relationship between the degree of anisotropy and the shear modulus for the different soil mixtures.

MATERIALS, EQUIPMENT AND METHODS

This section describes the materials used in the experimental work and the methods to obtain the soil properties. The materials used are sand and fly-ash. The description of equipment and methods is focused on the characterization of the shear modulus. Also, the model used for analysis is described in this section.

Materials

It was used a colluvial granular material coming from sandstone rocks [17]. The grain-size distribution (Fig. 1) was measured using the ASTM D422 standard method [18]. Specific gravity of solids (G_s) and plasticity limits (LL and PL) were obtained by the standard methods ASTM D854 [19] and ASTM D4315 [20], respectively. In addition, the modified compaction test ASTM D698 [21] was used to obtain the maximum dry unit weight (γ_{dmax}) and the optimum water content (ω_{opt}). Table 1 presents the results of the physical characterization of the soil.

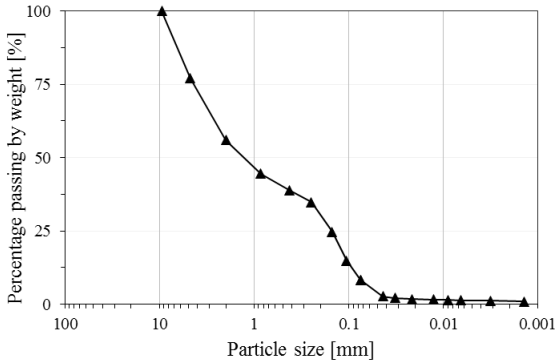

Fig. 1 Grain-size distribution of the soil.

Table 1 Physical properties of the soil.

Parameter	Unit	Value
G_s	-	2.52
C_u	-	31.3
C_c	-	0.20
d_{50}	*mm*	1.25
ω_{opt}	*%*	11.8
γ_{dmax}	kN/m^3	19.5
LL	*%*	*NP*
PL	*%*	*NP*

The fly-ash comes from a local thermoelectric plant (Termopaipa). This fly-ash classifies as a F-type ash. The main components are SiO_2 and Al_2O_3. Also, the components include quartz, mullite, hematite and a low percentage of CaO_2 [22].

Equipment

The Bishop & Wesley triaxial cell is a triaxial apparatus capable of imposing independent control of vertical and radial stresses on a cylindrical soil specimen. The device comprises three automatic pressure-volume controllers (cell pressure, back pressure and vertical pressure) with 0.1 kPa and 1 mm^3 accuracy. The set of sensors is composed by a submersible load cell (8kN capacity), a radial and two axials local LVDT sensors (0.1 µm accuracy) and a pore pressure sensor (0.1 kPa accuracy). Figure 2 shows the local sensors installed in a soil specimen before closing the triaxial cell.

Experimental method

Five specimens of 70mm in diameter and 140 mm in height were prepared by compaction. Specimens were compacted with optimum water content using an energy amount equivalent to the modified Proctor test ASTM D698 [21]. Each specimen was compacted with different fly-ash content (0%, 4%, 8%, 12% and 16%). Figure 3 shows two examples of the specimens prepared.

Fig. 2 Local sensors installed on the soil specimen.

a) b)

Fig. 3 Specimens: a) 0% fly-ash; b) 16% fly-ash.

Once the specimen was prepared and installed in the triaxial cell, the saturation process was applied until obtaining a B-Skempton parameter above 0.98. At this point, the specimen was consolidated under isotropic conditions of 50 kPa. Then, cycles of loading and unloading with different deviatoric levels (q) under constant radial cell pressure were applied to the specimen. Given the low amount of strain imposed on the specimen, a new confining pressure of 100 kPa was applied for consolidation and a loading-unloading cycle was applied. The procedure was repeated for 200 kPa confining pressure. For each cycle the deviatoric stress was increased by 50 kPa being the maximum deviatoric stress depending on the confining pressure.

Anisotropic model for soil stiffness

The model used to evaluate the effect of anisotropy is presented in Eq. (1) [13].

$$G_{\max} = A \cdot f(e) \cdot \left(\frac{p'}{Pa} \right)^{n} \cdot (\eta'+1)^{\alpha_1 \cdot \alpha_2} \quad (1)$$

Where A and n are model parameters obtained by experimental correlation, $f(e)$ is an empiric function of void ratio, p' is the effective mean stress, Pa is the atmospheric pressure equivalent to 100 kPa, $\eta'=q/p'$ is the anisotropy ratio, α_1 and α_2 are parameters depending of the coefficient of uniformity (C_u), the mean grain size (d_{50}) and the particle shape. The following empiric void ratio function was used in this paper [23]:

$$f(e) = e^{-1,29} \quad (2)$$

The model estates different values for α_1 and α_2 when different grain distributions and particle shapes are involved. However, in this case it is used a single value of the exponent α given the insignificant variation in the grain characteristics of the soil mixtures studied.

RESULTS AND DISCUSSION

By direct measurement of vertical and radial strains with local sensors during the unloading-reloading cycles, it was possible to compute the small-strain shear moduli for each radial confinement and anisotropy ratio. Figure 4 shows the stress-strain curves for each specimen and radial confinement. As can be seen, deviatoric stress is increased by 100 kPa intervals and then unloaded 50 kPa. The procedure is repeated different times depending on the confining pressure but ensuring positive deviatoric stress.

The response of the soil is the axial strain, given the test is stress controlled. Also, the pore pressure exhibits a variation because the tests were done under undrained conditions. The added fly-ash produced a stiffening of the soil depending on its percentage and hence the soil without treatment showed greater axial strains. The specimen with 16% added fly-ash presented lower strain levels, which means a stiffer material.

Figure 5 shows the stress paths in the p' - q plane. Despite the cyclic nature of the deviatoric stress, the path did not presented accumulation of pore pressure per cycle, which is an evidence of the small-strain regime. Figure 5a) shows the stress path for the untreated material and Fig. 5b) shows the stress path for the soil with 4% added fly-ash.

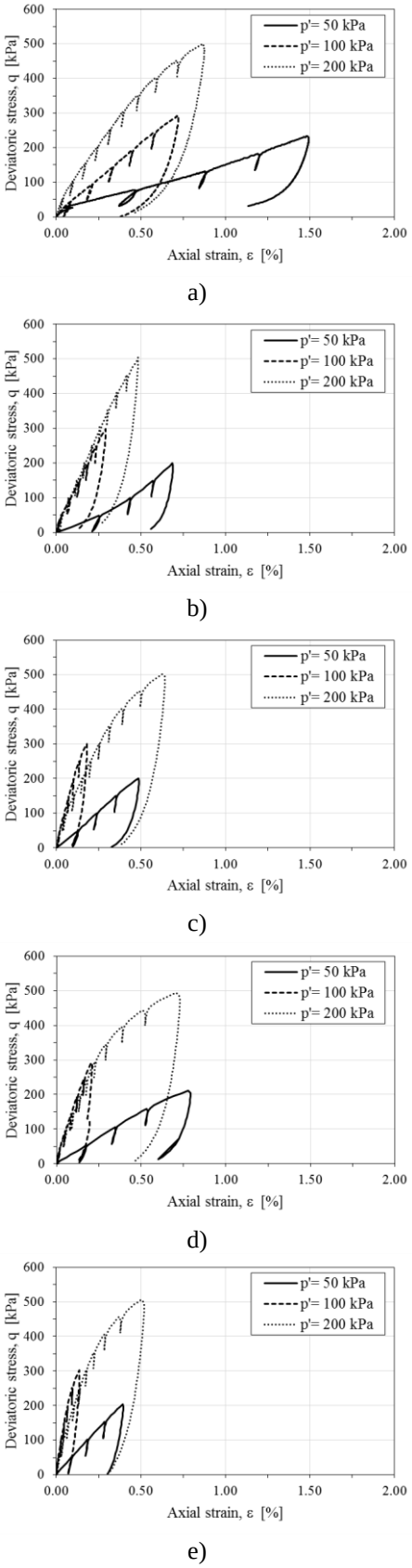

Fig. 4 Loading-unloading cycles for different fly-ash content: a) 0%, b) 4%, c) 8%, d) 12%, e) 16%.

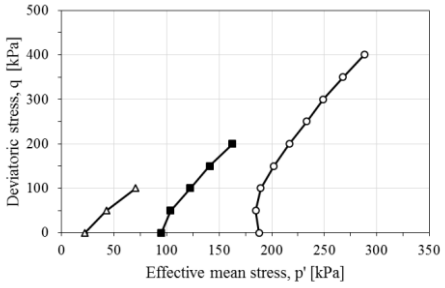

a)

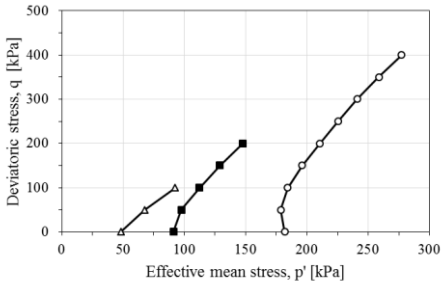

b)

Fig. 5 Effective stress-paths: a) 0% fly-ash content; b) 4% fly-ash content.

Computed shear moduli for the different specimens are plotted as a function of the anisotropy ratio in Fig. 6. In all the cases, the shear modulus is higher as the anisotropy ratio increases. The effect of the fly-ash is notorious when compared with the untreated specimen (Fig. 6a). However, this positive effect does not increase for higher fly-ash contents. It suggests that the optimum fly-ash content (from the point of view of stiffness) is around 4%. The fly-ash used has low content of CaO_2 and therefore its pozzolanic effect is limited. Additional fly-ash does not increase the cementation of the soil, but the resulting higher fine content transforms the soil into a more compressible material. In addition, high contents of fly-ash do not increase the stiffness at high confinement at the same rate as for los and medium confinement.

Figure 7 presents the same data but organized by confinement. This arrangement shows that high fly-ash content (16%) increases the shear modulus in specimens at low confinement level (Fig. 7a) and at medium confinement level (Fig. 7b) but for 200 kPa, 8% is the optimum fly-ash content (Fig. 7c). The gradual positive effect of the added fly-ash is clear in Fig 7a, but as the confinement level increases the influence of higher amount of fly-ash is less clear.

Experimental data was used to obtain by curve fitting the parameters of the model in Eq. 1. Table 2 shows the parameters for the five mixtures and their respective correlation coefficient (r^2). The best adjustment was for the soil with no fly-ash addition. In general, the correlation coefficient goes down as the addition of fly-ash increases

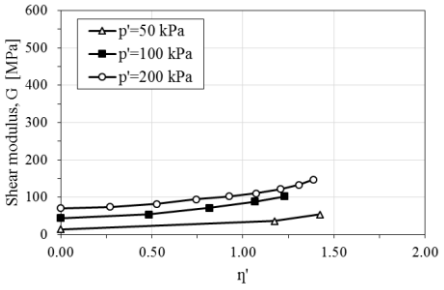

a)

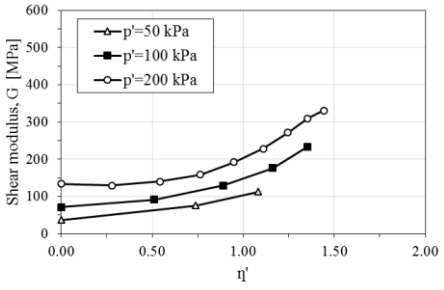

b)

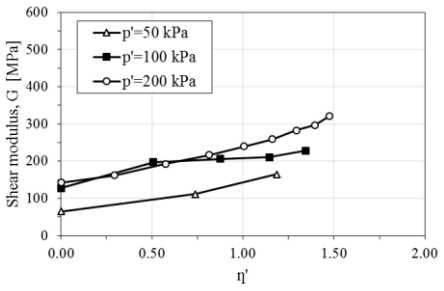

c)

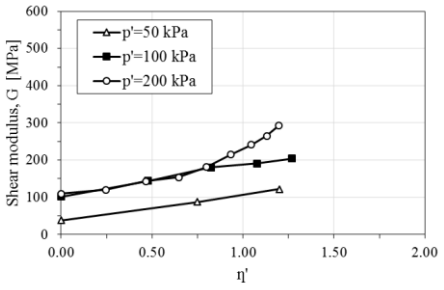

d)

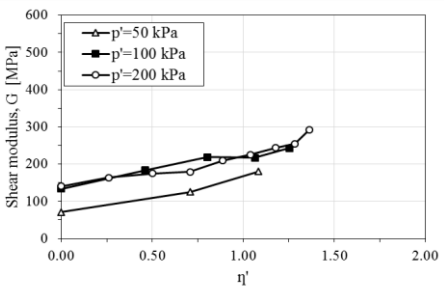

e)

Fig. 6 Shear modulus as a function of anisotropy ratio and confinement stress for different fly-ash content: a) 0%, b) 4%, c) 8%, d) 12%, e) 16%.

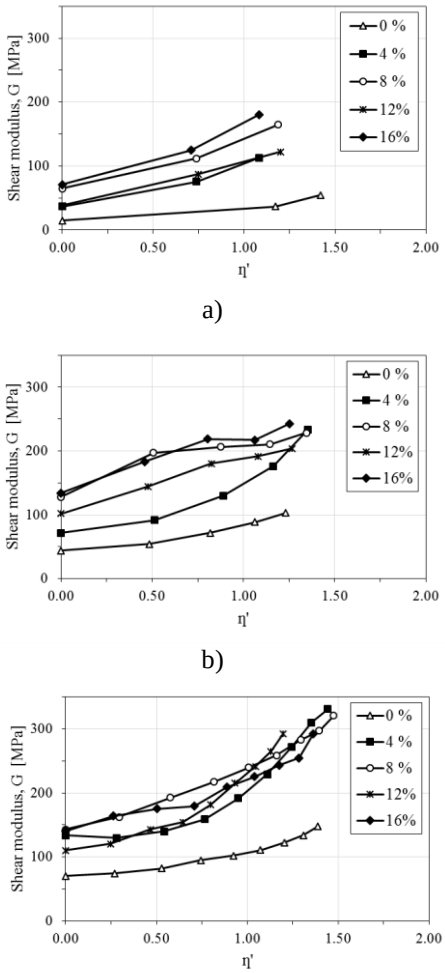

Fig. 7 Shear modulus as a function of the anisotropy ratio and fly-ash content for different confinement stresses: a) 50kPa. b) 100kPa. c) 200 kPa.

Table 2 Parameters of the anisotropic model.

Fly-ash content (%)	A (MPa)	n	α	r^2
0	5.49	0.70	0.55	0.93
4	20.93	0.96	0.67	0.76
8	46.00	0.62	0.54	0.63
12	*26.35*	*0.76*	0.69	0.55
16	*37.62*	*0.48*	*0.56*	*0.61*

Well correlation coefficient could be due to a better application of this model for sands. The parameter α did not showed a trend but oscillated in a narrow range, which is caused by the no variation of the shape and gradation of the sand. The significant difference in the A value is a result of the stiffening caused by the addition of fly-ash. The parameter n does not show a trend but most of the values differ from the usual exponent, which is near 0.5.

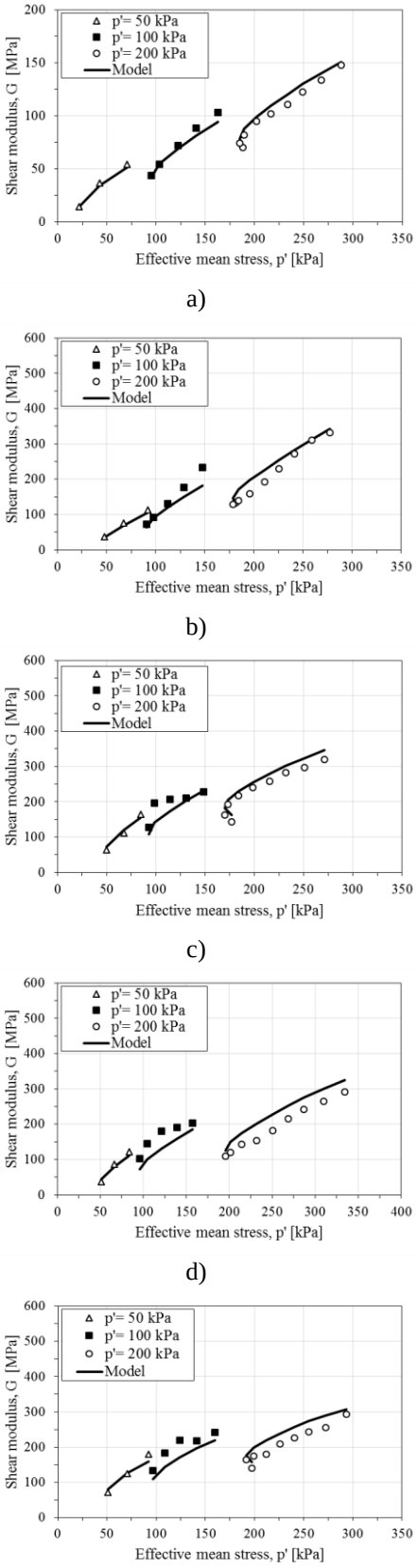

Fig. 8 Experimental shear modulus and comparison against anisotropic model for fly-ash content: a) 0%, b) 4%, c) 8%, d) 12%, e) 16%.

CONCLUSIONS

An experimental campaign to study the improvement of a sand by adding fly-ash was carried out and results were presented in this paper. The use of an instrumented stress-path triaxial cell let to measure the evolution of the shear modulus respect to different fly-ash contents, anisotropic conditions and confinement levels.

The type of fly-ash used in this work contains a low pozzolanic effect and therefore the optimum amount of addition is not high. More fly-ash than the necessary could produce a contrary effect.

A shear modulus model considering the effect of stress-induced anisotropy was used satisfactorily. The parameters found for the different soil mixtures contributed to reveal the effect to the fly-ash and the degree of stress anisotropy on the soil stiffness.

ACKNOWLEDGMENTS

This paper is a result of the research project IMP-ING-2932 funded by the Research Vice-presidency of the Universidad Militar Nueva Granada.

REFERENCES

[1] H. C. Chang, "Physical and Mathematical Modeling of Coarse-Grained Soils," University of Washington, 2004.

[2] S. Chummuneerat and P. Jitsangiam, "Permanent Deformation Behavior of a Cement-Modified Base Course Material," *Procedia Eng.*, vol. 143, pp. 42–50, 2016.

[3] M. Hu, C. O'Sullivan, R. Jardine, and M. Jiang, "Stress-induced anisotropy in sand under cyclic loading," *Granul. Matter*, vol. 12, no. 5, pp. 469–476, Oct. 2010.

[4] B. Schädlich and H. F. Schweiger, "Influence of Anisotropic Small Strain Stiffness on the Deformation Behavior of Geotechnical Structures," *Int. J. Geomech.*, vol. 13, no. 6, pp. 861–868, Dec. 2013.

[5] Y. H. Wang and C. M. Mok, "Mechanisms of Small-Strain Shear-Modulus Anisotropy in Soils," *J. Geotech. Geoenvironmental Eng.*, vol. 134, no. 10, pp. 1516–1530, Oct. 2008.

[6] X. Zeng and B. Ni, "Stress-Induced Anisotropic Gmax of Sands and Its Measurement," *J. Geotech. Geoenvironmental Eng.*, vol. 125, no. 9, pp. 741–749, Sep. 1999.

[7] M. Vucetic and R. Dobry, "Effect of Soil Plasticity on Cyclic Response," *J. Geotech. Eng.*, vol. 117, no. 1, pp. 89–107, Jan. 1991.

[8] F. Emeriault and C. S. Chang, "Anisotropic Elastic Moduli of Granular Assemblies from Micromechanical Approach," *J. Eng. Mech.*, vol. 123, no. 12, pp. 1289–1293, Dec. 1997.

[9] P.-Y. Hicher and C. S. Chang, "Anisotropic Nonlinear Elastic Model for Particulate Materials," *J. Geotech. Geoenvironmental Eng.*, vol. 132, no. 8, pp. 1052–1061, Aug. 2006.

[10] E. Tutumluer and U. Seyhan, "Characterization of Cross-Anisotropic Aggregate Base Behavior From Stress Path Tests," *Recent Adv. Mater. Charact. Model. Pavement Syst.*, pp. 18–34, Dec. 2003.

[11] J. Young-Hoon, L. Jae-Hoon, and C. Choong-Ki, "Evolution of Fabric Anisotropy in Granular Soils under Triaxial Loadings," *GeoCongress*, pp. 1–4, 2006.

[12] B. Li and X. Zeng, "Effects of fabric anisotropy on elastic shear modulus of granular soils," *Earthq. Eng. Eng. Vib.*, vol. 13, no. 2, pp. 269–278, Jun. 2014.

[13] M. Payan, A. Khoshghalb, K. Senetakis, and N. Khalili, "Small-strain stiffness of sand subjected to stress anisotropy," *Soil Dyn. Earthq. Eng.*, vol. 88, pp. 143–151, Sep. 2016.

[14] R. Chaney, K. Demars, V. Jovičić, and M. Coop, "The Measurement of Stiffness Anisotropy in Clays with Bender Element Tests in the Triaxial Apparatus," *Geotech. Test. J.*, vol. 21, no. 1, p. 3, Mar. 1998.

[15] T. B. Edil and G.-F. Luh, "Dynamic Modulus and Damping Relationships for Sands," *Dyn Earthq Eng*, pp. 394–409, Jun. 1978.

[16] B. O. Hardin and F. E. Richart, "Elastic Wave Velocities in Granular Soils," *J. Soil Mech. Found. Div.*, vol. 89, no. 1, pp. 33–66, 1963.

[17] O. Coronado, B. Caicedo, S. Taibi, A. G. Correia, and J.-M. Fleureau, "A macro geomechanical approach to rank non-standard unbound granular materials for pavements," *Eng. Geol.*, vol. 119, no. 1–2, pp. 64–73, Apr. 2011.

[18] ASTM international, *D422 - Standard Test Method for Particle-Size Analysis of Soils*. 2007.

[19] ASTM international, *D854 - Standard Test Methods for Specific Gravity of Soil Solids by Water Pycnometer 1*. 2014.

[20] ASTM international, *D4315 - Standard Test Methods for Liquid Limit, Plastic Limit, and Plasticity Index of Soils*. 2010.

[21] ASTM international, *D698 - Standard Test Methods for Laboratory Compaction Characteristics of Soil Using Standard Effort (12 400 ft-lbf/ft3 (600 kN-m /m3))*. 2014.

[22] J. Camacho-Tauta, O. Reyes-Ortiz, A. Viana Da Fonseca, S. Rios, N. Cruz, and C. Rodrigues, "Full-scale Evaluation in a Fatigue Track of a Base Course Treated with Geopolymers," *Procedia Eng.*, vol. 143, pp. 18–25, 2016.

[23] D. C. F. Lo Presti, M. Jamiolkowski, O. Pallara, A. Cavallaro, and S. Pedroni, "Shear modulus and damping of soils," *Géotechnique*, vol. 47, no. 3, pp. 603–617, Jun. 1997.

9th Int. Conf. on Geotechnique, Construction Materials and Environment, Tokyo, Japan, 20-22 November 2019, ISBN: 978-4-909106025 C3051

FOUNDATION DESIGN AND SLOPE FAILURE PROTECTION FOR A LARGE COMMUNITY BUILDING IN KHANOM, NAKHON SI THAMMARAT

Chollada Kanjanakul[1]
[1]Department of Civil Engineering, College of Industrial Technology and Management, Rajamangala University of technology Srivijaya Country, Thailand

ABSTRACT

In geotechnical engineering, the bearing capacity of soil to support the building loads applied to the ground and slope failure behaviour analysis have significance for design protection in important buildings (e.g., roads, dams, soil embankment), and land filling procedure before construction in Thailand. Frequent landslides and mistake on foundation design occur in khanom, causing property damage and loss of human life. This paper aimed to analyze ultimate bearing capacity of soil and study the influence of unsaturated slope stability on a hill range in one particular southern part of Thailand (Khanom district in Nakhon Si Thammarat province). A GIS survey, the area's geology, geotechnical laboratory results and rainfall intensity were carried out and analyzed in order to verify the use of factor of safety for an early warning indicator. Moreover, the research focuses on designing foundation and calculation ultimate bearing capacity of soil that necessary for a site engineer at large communication building in khanom, Nakhon si thammarat. In the analysis result, suitable shallow foundation is 0.7 x0.7 m^2 of square footing put on lower soil (SM) 70 cm with the ultimate bearing capacity 82.54 t/m^2.

Keywords: Factor of Safety, Bearing Capacity, Foundation Design, Slope Failure Protection, Finite Element Method

INTRODUCTION

Foundation design process is the most significant part of any structure because foundation gets the load of the total building [1]. The main objective of foundations is to structurally support the building by transferring the loads of the building through the surrounding soil. There are difficult to determine the exact ultimate bearing capacity of shallow foundation, because of variability parameters in unsaturated soil slope such as permeability behaviour (e.g., rainfall characteristics, the amount of water in the soil and suction drawn on a curve called Soil Water Characteristic Curve (SWCC), k-function), soil properties (e.g., unit weight, angle of friction, cohesion of soil), hydrogeology (e.g., hydraulic conductivity, moisture content, groundwater table), and others such as vegetation cover. Overall, rainwater infiltration is among the most significant triggering factors [2].

The mistake on foundation design lead to loss of properties and human life. The two standard to be satisfied in the analysis and design of a shallow foundation in Khanom slope are A mechanical behaviour based on the basic physical properties (grainsize distribution, sieve analysis, atterberg's limits) and permeability behaviour in slope stability analysis landslide triggering by rain infiltration.

Unstandard laboratory testing that determines soil properties and wrong procedure from the laboratory testing that determines the type of soil lead to mistake in soil data base and waste the time to design construction for building.A bearing capacity analysis for a shallow foundation has been necessitated by the result of soil laboratory at khanom site.

Determining permeability function at a site can be measured directly through various in-situ and laboratory tests [3]. Chollada K., Tanan C., and Panupong T. [4] used the temporal pore water pressure distributions derived from the seepage analysis. Slope stability analysis with regard to the outcome of Factor of safety (F.S.) was produced for case study area. These result indicated that unsaturated slope at case study area in Southern part of Thailand will collaps at 50 hours with the average factor of safety (F.S.) = 0.940.

In this research, the permeability function from soil laboratory were used as input parameters to estimate surface infiltration rates for slope stability analysis. SEEP/W was employed to model fluctuations in pore-water pressure during a rainfall, using the computed water infiltration rates as surface boundary conditions. SLOPE/W was then carried out to compute their factors of safety. Slope at the site became unstable (F.S. less than 1) at 80 hours.

This research focuses on determining the ultimate bearing capacity of shallow foundation on soil structure and factor of safety on slope stability analysis at Khanom in the Nakhon-Si-Thammarat province of Thailand for the construction of 45 large community houses and early warning of landslides.

DESCRIPTION OF THE STUDY AREA

This paper aimed to study and analyze the influence of unsaturated-soil slope stability on a khanom hill range in one particular southern part of Thailand. A GIS survey, the area's geology geotechnical laboratory results and rainfall intensity data with regard to the outcome of calculated F.S. were carried out and analyzed in order to verify the use of FS_{cr} for an early warning indicator. the slope geometry in this study were based on typical residual soils in the tropical region and the works by Chollada K. [5]. Two types of soil samples were collected: Lower layer samples, to evaluate physical and basic engineering properties such as sieve analysis (D_{10},D_{30},D_{60}), grain size distribution (Cu,Cc), and atterberg's limits (LL,PL,PI) ; and Upper layer samples, to evaluate the effective soil cohesion, soil unit weight and undrained shear strength of soil for estimating dimension for foundation design.

Plate. 1 Study site at Nakhon Si Thammarat.

Parameters affecting shallow foundation design and landslide occurrences, such as slope geometry, related geotechnical and laboratory data, and rainfall intensity are usually needed in analytical processes that will describe in methodology (Fig 1).

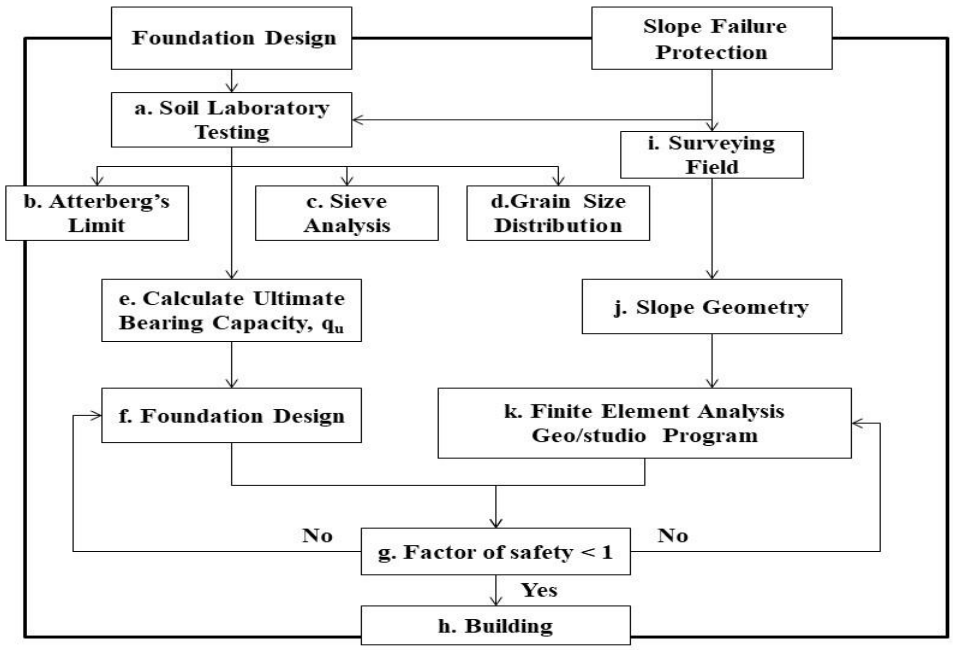

Fig. 1 Methodology.

Bearing Capacity

The ultimate bearing capacity aims at determining the load that the soil under the foundation can handle before shear failure [1]. Some studies on stability of foundations have been reported by [6]-[8]. This paper attempts to report on analysis of shallow foundations on soil slope in Nakhon Si Thammarat. The subject shows that the majority of the bearing capacity theories involve heterogeneous soils under the foundations. Soil properties were used for the bearing capacity analysis, and therefore analytical solutions, like Terzaghi's bearing capacity theory, matched with the experimental results. [9] Developed the bearing capacity expression for footing design as follow:

$$q_{ult} = c\,N_c + q\,N_q + 0.5\,\gamma\,B\,N_\gamma \quad (1)$$

Where

q_{ult} is the ultimate bearing capacity
c is cohesion of soil, γ is soil unit weight of soil
B is width of footing

N_C, N_q, Nγ is Terzaghi's bearing capacity factors depend on soil friction angle (ϕ)

[10] recommends that for the computation of ultimate bearing capacity of a shallow foundation in general shear failure, following Equation may be used:

$$q_{ult} = S_C W_C c N_c + S_q W_q q N_q + S_\gamma W_\gamma 0.5 \gamma B N_\gamma \quad (2)$$

Where

q_{ult} is the ultimate bearing capacity
c is cohesion of soil, γ is unit weight of soil
B is width of footing

N_C, N_q, Nγ is Terzaghi's bearing capacity factors depend on soil friction angle (ϕ)

S_C, S_q, Sγ is shape correction factors where

$$S_C = 1 - \frac{B}{L}\left(\frac{N_q}{N_C}\right) \text{ for rectangle shape} \quad (3)$$

$$S_C = 1 - \left(\frac{N_q}{N_C}\right) \text{ for circular shape} \quad (4)$$

$$S_q = 1 + \frac{B}{L}(\tan\varphi) \text{ for rectangle shape} \quad (5)$$

$$S_q = 1 + \tan\varphi \text{ for circular shape} \quad (6)$$

$$S_\gamma = 1 - 0.4\frac{B}{L} \text{ for rectangle shape} \quad (7)$$

$$S_\gamma = 0.6 \text{ for circular shape} \quad (8)$$

W_C, W_q, Wγ is water correction factors where

$$W_C = 1.0 \quad (9)$$

for water table below and upper foundation

$$W_q = 1.0 \quad (10)$$

for water table below foundation

$$W_q = 1.0 - (0.5)\left(\frac{a}{D_f}\right) \quad (11)$$

for water table upper foundation

$$W\gamma = 0.5 \quad (12)$$

for water table upper foundation

$$W\gamma = 0.5\left(1 + \frac{d}{B}\right) \quad (13)$$

for water table lower foundation

Unified Soil Classification System (USCS)

The Unified Soil Classification System is a soil classification system used in geotechnical engineering to explain the type and grain size of a soil. In USCS system, the basic physical parameters that can be used to identify soil characteristics and behaviour are D_{10}, D_{30}, and D_{60} (Sieve analysis laboratory), Cu and Cu (Grainsize distribution laboratory) and LL, PL and PI (Atterberg limits laboratory). The details are described below.

Sieve Analysis

Sieve Analysis is a procedure for determining the particle size distribution of a granular material to pass through a series of sieves of progressively smaller mesh size and weighing the amount of material that is stopped by each sieve as a fraction of the whole mass. The results of a sieve analysis are plotted as a grain size distribution curve and analyzed to determine the soil gradation of the particular soil [11]. A particle-size distribution curve can be used to determine the following parameters for a given soil:

A. Effective size (D_{10} , D_{30} , and D_{60}): This parameter is the diameter in the particle-size distribution curve corresponding to 10%, 30% and 60% finer. The effective size of a granular soil is a good measure to estimate the hydraulic conductivity and drainage through soil.

B. The uniformity coefficient, C_u is a crude shape parameter and is defined as

$$C_u = \frac{D_{60}}{D_{10}} \quad (14)$$

where D_{60} is the grain diameter at 60% passing, and D_{10} is the grain diameter at 10% passing.

C. The coefficient of gradation, C_c is a shape parameter and is calculated using the following equation:

$$C_C = \frac{(D_{30})^2}{D_{10}D_{60}} \quad (15)$$

Where D_{60} is the grain diameter at 60% passing, D_{30} is the grain diameter at 30% passing, and D_{10} is the grain diameter at 10% passing.

Atterberg's limits

Aterberg limits method is a standard measure of the water content of fine-grained soils. Atterberg defined the boundaries of four states (solid, semi-solid, plastic and liquid) in terms of limits as follows:

- *Liquid Limit (LL),* determines the water content at which the behavior of a clayey soil changes from plastic to liquid. Liquid Limit can be determined using the Casagrande cup method when the soil specimen is just fluid enough for a groove to close when jarred in a specified manner.

- *Plastic Limit (Pl)* is defined as the moisture content where the thread breaks apart at a diameter of 3.2 mm (about 1/8 inch). A soil is considered non-plastic if a thread cannot be rolled out down to 3.2 mm at any moisture possible.

- *Plasticity Index (PI)* is calculated as the Plastic Limit subtracted from the Liquid Limit and is an important value when classifying soil types.

METHODOLOGY

Fig. 1: Three stages were conducted in this research: (i) Determining soil laboratory testing; (ii) Slope stability analysis from SEEP/W and SLOPE/W; (iii) Calculated ultimate bearing capacity and foundation design**.** These are described in more details in next section, thus:

Determining Physical Parameters Result from In-Situ Soil Sampling Laboratory on Study Area

In this topic, result from soil sampling are significant on the stability of foundation design

- Result from soil sampling laboratory

From laboratory result, SM Soil properties (Lower layer) Liquid Limit (LL) obtained from Atterberg limits laboratory testing (ASTM D 4318-04) are: 36.7 , Plastic limit (PL); 26.37, and 10.33, Plastic Index (PI).

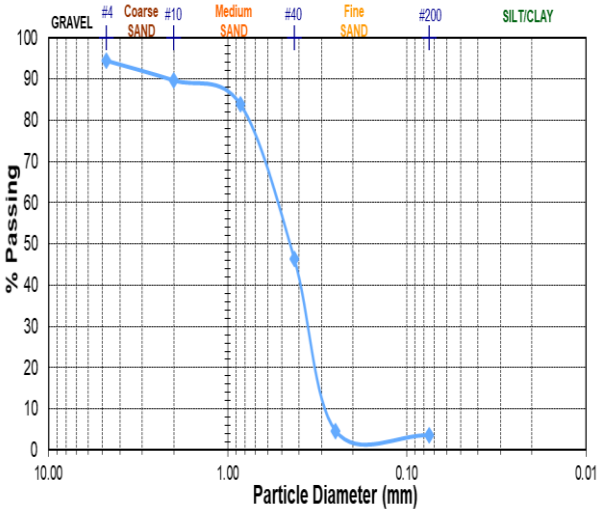

Fig. 2 Grain size distribution for lower layer

As shown in Fig. 2**,** Soil properties size fom lower layer in mm such that 10%, 30% and 60% of particles are finer than this size ($D_{10,}$ D_{30} and D_{60}) from Sieve Analysis laboratory testing are: 2.00, 0.08 and 0.3. The coefficient of uniformity (C_U) are 0.15 and 1.01, the coefficient of curvature (C_C). From upper layer laboratory test, SP Soil properties (Upper layer) Liquid Limit (LL) obtained from Atterberg limits laboratory testing (ASTM D 4318-04) are: 35.5 , Plastic limit (PL); 30.14, and 5.36, Plastic Index (PI).

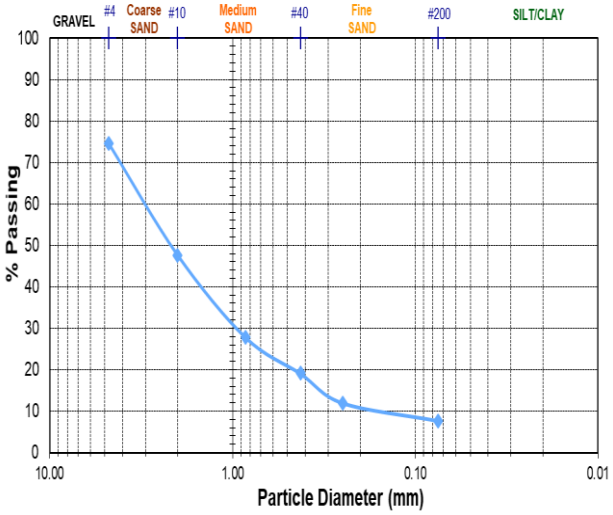

Fig. 3 Grain size distribution for upper layer

As shown in Fig. 3**,** Soil properties size from upper layer in mm such that 10%, 30% and 60% of particles are finer than this size ($D_{10,}$ D_{30} and D_{60}) from Sieve Analysis laboratory testing are: 2.00, 0.80 and 0.25. The coefficient of uniformity (C_U) are 0.125 and 1.28, the coefficient of curvature (C_C).

Estimation Water Volume Change Characteristics of Soil from Seep/w Results and Calculation Factor of safety (F.S.) from SLOPE/W Results

the slope geometry in this study were based on typical residual soils in the tropical region and the works by [4]. the study slope to be used in the mathematical models. There is a 80 m thick silty sand (SM) soil layer. The slope height is 80 m and the slope degree 27°. In the finite element analysis, the slope profile was divided into meshes of equal quadrilateral elements with a total number of more than 1,000 elements. The rainfall intensities 6-36 mm/hr used in the sensitivity analysis were adopted from the intensity-duration-frequency (IDF) curve for the southern part of Thailand. Boundary conditions utilized for the transient seepage analysis are: Zero flux for the lower horizontal and the left vertical bed boundaries (there is no seepage through the base of the soil slope) and a rainfall intensity Ir for the upper horizontal boundary.

Calculated Ultimate Bearing Capacity and Foundation Design

Fig. 4 idealizes the foundation to be used in the mathematical models. There is a 70 cm thick graded sand (SP) of upper soil layer with the soil unit weight 2.6 t/m^3 , cohesion of soil 0 and soil friction angle 25° In lower layer of soil, there is silty sand (SM) soil with the soil unit weight 2.68 t/m^3 , cohesion of soil 10.5 and soil friction angle 14°

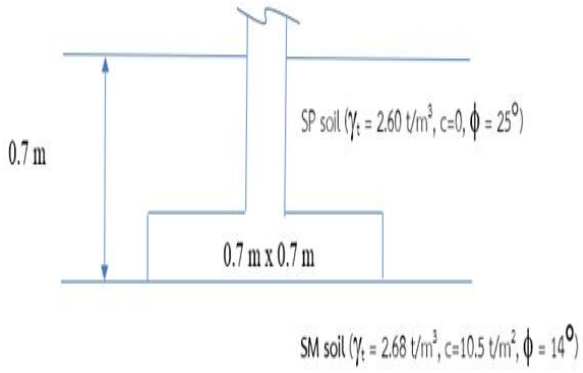

Fig. 4 Foundation and soil property of the site.

- Step by step bearing capacity problem solver

Step1 Find N_c, N_q, N_γ (In silty sand soil: ϕ=14°) N_c=11, N_q=4, N_γ=1.2

Step2 Find S_c, S_q, S_γ (Shape correction) When BxL = 0.7x0.7 m^2

$S_c = 1-\frac{B}{L}(\frac{N_q}{N_c})=0.63$

$S_q = 1+\frac{B}{L}\tan\phi = 1.25$

$S_\gamma = 1-0.4\frac{B}{L} = 0.60$

Step3 Find q_{ult}

$q_{ult} = S_C\, cN_c + S_q\, qN_q + S_\gamma \frac{1}{2}\gamma BN_\gamma$

$q_{ult} = 82.54$ t/m^2

soil laboratory parameters and Terzaghi's bearing capacity theory was adopted to calculate the ultimate bearing capacity for foundation design. The results were showing the ultimate bearing capacity 82.54 t/m^2

RESULT AND DISCUSSION

Two stages were conducted in this topic: (i) Results from slope stability analysis; (ii) Results from the soil sampling laboratory for foundation design. These are described in more details in the next paragraph:

Results for The Khanom Case Study

A GIS survey, the area's geology, geotechnical laboratory results and rainfall intensity were carried out and analyzed in order to verify the use of factor of safety for an early warning indicator. Program SEEP/W was used to model fluctuations in pore-water pressure with rainfall intensities from the Thailand's intensity-duration-frequency curve, using the computed water inltration rates as surface boundary conditions. The program SLOPE/W were calculate factors of safety and time when slope become unstable. Results for the Khanom case study show that slope at the site became unstable at 80 hours with the factor of safety (F.S.) = 0.960.

Results from The Soil Sampling Laboratory for Foundation Design.

The basic properties results from the soil sampling laboratory (Sieve Analysis, Grain Size Distribution, Liquid Limit, Plastic Limit, Shrikage Limit) for upper and lower soil layer were compared were shown in Table.2 for estimating dimension for foundation design that necessary for an engineer at Khanom site.

Table 2 The Soil Sampling Laboratory for Foundation Design.

Sample	Case Study	Case Study
Soil Properties	Position	Position
	Khanom (Lower layer)	Khanom (Upper layer)
Liquid Limit (LL %)	36.7	35.51
Plastic Limit (PL %)	26.37	30.15
Plastic Index (PI %)	10.33	5.36
Soil Classification	Silty-Sand (SM)	Graded-Sand (SP)
The coefficient of uniformity, Cu	0.15	0.125
The coefficient of curvature, Cc	0.01	1.28
D10	2.00	2.00
D30	0.08	0.80
D60	0.3	0.25

CONCLUSIONS

This paper focuses on determining factor of safety on slope stability analysis and the ultimate bearing capacity of shallow foundation on soil structure at Khanom in the Nakhon-Si-Thammarat province of Thailand for the construction of 45 large community houses and early warning of landslides. SEEP/W was employed to model fluctuations in pore-water pressure during a rainfall, using the computed water infiltration rates as surface boundary conditions. SLOPE/W was then carried out to compute their factors of safety. Increasing rainfall intensity induces increased matric suction and decreased shear strength in soil mass. Increasing amount of moisture from the rainfall leads to reduced slope stability. The F.S. is an inverse relationship with rainfall precipitation, moisture content and coefficient of permeability changes. Slope at the site became unstable at 80 hours with the factor of safety (F.S.) = 0.960. It can be used as an early warning indicator for landslide. For suitable shallow foundation in this case study, The results were showing 0.7 x 0.7 m^2 of square footing put on lower soil (SM) 70 cm the ultimate bearing capacity 82.54 t/m^2.

ACKNOWLEDGMENTS

I am very grateful to the Thailand Royal Irrigation Department is kindly acknowledged for providing the30-year monthly rainfall data in its vicinity. Thanks are due to a former RMUTSV Trang lecturer,

Mr.Daniel Edward Guiney, in rendering helpful reviews and in polishing up somewhat the English of the paper.

REFERENCES

[1] Abhishek Arya. and Ameta N.K., Bearing capacity of foundation review paper. American journal of engineering research (AJER), Vol. 6, Issue 7, 2017, pp.42-45.

[2] Tung Y.K. and Chan G. C. C., Stochastic analysis of slope stability considering uncertainty of soil-water retention characteristics, Proceeding of The International Conference on Applications of Statistics and Probability in Civil Engineering, Vol.1and 2, 2003, pp.1409–1414

[3] Lu N. and Likos W.J., Unsaturated Soil Mechanics. John Wiley & Sons, Inc., Hoboken, New Jersey. 2004.

[4] Chollada K., The comparison between soil sampling and unsaturated soil hydraulic database (UNSODA), Proceeding of The Eight International Conference-Geomate, Geotechniue, Construction materials and Environment, November 20-22, Kuala lumpur, Malaysia, pp.23-29. 2018.

[5] Chollada K., Quantifying uncertainty of natural slope stability analysis for landslide warning system. Ph.D. Thesis. Prince of Songkla University, Songkla, pp.1-60. 2016.

[6] Terzaghi, K., Theoretical Soil Mechanics, John Wiley and Sons Inc. New York. 1943.

[7] Vesic, A. S., Analysis of Ultimate Loads of Shallow Foundations. Journal of the Soil Mechanics and Foundation Engineering Division, ASCE, Vol.99, 1973, No. SM1, Proc. Paper 9480, pp 45-73.

[8] Akpila, S.B., ThankGod, O., and Igwe, A., Bearing Capacity and Settlement Analysis of a Shallow Foundation on Reclaimed Sand Overlying Soft Clay, Journal of Scientific and Industrial Studies, Vol.6, 2008, No.9, pp 84-89.

[9] Terzaghi, K., Die Berechung der Durchlaessigkeitsziffer des Toneseaus dem Varlauf der hydrodynamischen spannugser schinungeen. Sitzungsberichte de Akadennie der wissehsahaften Abt., II a, Vol. 132,1943, Vienna.

[10] IS :6403-1981. Code of practice for determination of bearing capacity of shallow foundations

[11] Holtz, R. and Kovacs, W., An Introduction to Geotechnical Engineering, Prentice-Hall, Inc. ISBN 0-13-484394-0, 1981

9th Int. Conf. on Geotechnique, Construction Materials and Environment, Tokyo, Japan, 20-22 November 2019, ISBN: 978-4-909106025 C3051

EFFECT OF CHLORIDE AND SULPHATE ON COMPRESSIVE STRENGTH OF BANGKOK CLAY ADMIXED CEMENT

Worawit Phojan[1], Haruetai Maskong[2] and Anuchat Leeanansaksiri[3]
[1,3]Department of Civil Engineering, Faculty of Engineering, North Eastern University, Thailand;
[2]Center for Water Engineering and Infrastructures Research (CWEIR), King Mongkut's University of Technology North Bangkok, Thailand

ABSTRACT

The paper presents the results of an experimental investigation on the influence of salt content on the unconfined compressive strength of Bangkok clay admixed with cement. The soil sample was added with sodium chloride (NaCl) and sodium sulphate ($NaSO_4$) at varying salt content of 3%, 5%, 10% and 15% by weight of soil. Based on the results of the study, it was found out that as the salinity increases, the diffusion double layer decreases. Hence, resulting to a decrease on the liquid limit (LL), plastic limit (PL), and plasticity index (PI). Moreover, at a certain moisture content, cement content, and curing time, the unconfined compressive strength of saline (sodium chloride and sodium sulphate) Bangkok clay admixed cement decreases with the increase of salt content. It was observed that the compressive strength of Bangkok clay admixed cement mixed with sodium sulphate ($NaSO_4$) exhibited higher compressive strength than the one mixed with sodium chloride (NaCl) for all curing times and mixing ratios. Moreover, it was noted that it has compressive strength than the natural clay admixed with cement.

Keywords: Sodium chloride, Sodium sulphate, Bangkok clay, Diffusion double layer

INTRODUCTION

Bangkok and its metropolitan areas are well known as soft clay. Bangkok clay occurred from the accumulation of subsoil layer by layer at the points of low lands or estuary caused by water flow. It is found that Bangkok and its metropolitan consist of soft clay with high moisture content and large settlement. This soft clay becomes harder in accordance with the depth consisted of sand and gravel layers alternatively deep into the ground until the rock layer. Bangkok clay is classified as non- to low swelling [1] as per free swelling test [2].

Nowadays, before the construction of buildings, roads, or embankments in the area of soft clay, chemical soil improvement is the popular solution to be used. This method uses soft clay mix with cement to improve the engineering properties of soil admixed cement. However, in the nature, there always be many kinds of mixed substances embedded in the soil which provide some effects to the engineering properties of the soil such as chemical substances, organics, salts (sulphate and chloride), acidity, basicity, etc. These chemical substances help enhance the properties of soft clay.

The effect caused by chloride and sulphate are one of the factors that causes some problems in soil admixed cement improvement such as reduction in soil bearing capacity and compressive strength. Hence, the investigation or prevention from the damages which could happen from sulphate and chloride are very important factors and should not be missed in the improvement of soil admixed cement properties. Davidson [3] reported that the chemical composition of soils causes soil particle to have reactions with cement in different forms subjected to anion (negative ion) in the soil particles, especially for organic soils, the reaction will be changed such as slow stabilization. Whereas, the soil consisted of sulphate will be swelled causing its compressive strength to be reduced. Sherwood [4] studied about the influence of organic matters by finding the relationship between the compressive strength and the pH value of soil admixed cement obtained by the combination of soil and cement in the ratio of 1:10.. The results showed that if pH is less than 12.1, it means that the soil consists of organic substances consequently slow down the solidification of soil admixed cement and significantly reduce the compressive strength even if the same cement content is maintained.

This paper aims to study about the influences of salts (chloride and sulphate) on unconfined compressive strength of soft clay admixed cement considering the cement ratio, type of salt, and curing time.

MATERIAL AND METHODOLOGY

Soil Samples Preparation

The unconfined compressive strength of saline soft clay is discussed (chloride and sulphate). The

soil samples used in this study were collected from Soi Sukhumvit 103, Bang Na District, Bangkok, Thailand at 3-5 meters depth. Soil samples were brought and placed under the sun until it become dry. A rubber hammer was used to break the soil samples into pieces and sift through the sieve No.20 to remove the shells, roots, and other waste materials in the soil samples. Subsequently, the soil samples were mixed with water until its liquidity index is equal to 1.5 times the moisture content. Then, the sample is mixed with Portland cement type I subject to some variables (cement content, chloride and sulphate content, and curing time). Salt components consisted of sodium chloride and sodium sulphate.

Table 1: Test and soil samples used in the test

Soil cement sample		
Variable	No.	Note
Soil sample	1	Clayey soil at Soi Sukhumvit 103, Bang Na District, Bangkok, Thailand
Chloride and sulphate	2	Sodium chloride and sodium sulphate
Moisture content	1	Moisture content with the Liquidity Index = 1.5%
Cement content	3	10%, 20%, and 30% by weight of soil
Chloride and sulphate content	5	0%, 3%, 5%, 10%, and 15% by weight of soil
Curing time	4	7, 14, 28, and 60 days
Number of sample	3	Three samples per test

Soil admixed cement, chloride, and sulphate sample preparations

Table 1 shows the detail of the soil sample used in this test. The soil sample passed through the sieve No.20 in order to adjust the level of water content until its liquidity index (LI) equals to 1.5%. Then the cement content was varied at 10%, 20%, and 30% by weight of soil. The chloride and sulphate content were also varied from 0%, 3%, 5%, 10%, and 15% by weight of soil. Altogether, mix the component samples for about 10 minutes until it becomes homogenous. Subsequently, put the soil sample in a cylinder with a 45 mm diameter and 90 mm height. Then the sample in 3 layers, and one layer needs to be compacted for 30 time to remove air from the soil. Prepare at least 3 soil samples for each test. Remove the cylinders after 24 hours and then the samples were wrapped using a food preservation film. Then cure the sample in the water for about 7, 14, 28, and 60 days. After curing, take the soil samples to the laboratory and test its unconfined compressive strength.

Unconfined compressive strength

Prior to the compressive strength test, the diameter, height, and weight of the samples were recorded. The measurement should be detailed until 0.1 mm by using a Vernier Caliper. The pressing speed of the unconfined compression testing machine was set at 1.4 (please indicate the unit). During the test, record the new height of the sample in order to determine the maximum value of unconfined compressive strength. Then the average of the test results obtained in the 3 samples with the same curing time were determined.

RESULTS AND DISCUSSION

Fundamental properties of soil

The soil sample used in this study has liquid limit and plastic limit of 64.5% and 30%, respectively. Its specific gravity is 2.68, and is classified as clay high plasticity (CH). Based on the Unified Soil Classification System (USCS), this type of soil has electrical conductivity (EC) of 1.8 dS/m, and according to the US Soil Salinity Laboratory Staff 1954, it can be counted as a saline soil [5].

Table 2: Salinity of soil and its influence on plants [5]

EC (dS/m)	Salt content (%)	Salinity	Influence on plants
<2	< 0.1	Not salty	No influence on plants
2–4	0.1– 0.2	Slightly salty	Grow slowly
4–8	0.2– 0.4	Moderate salty	Limit the growth of many kinds of plants
8–16	0.4– 0.8	Very salty Absolutely salty	Only salt-tolerant plants can grow
>16	>0.8	Very salty Absolutely salty	Only some salt-resistant plants cannot grow

Influence of salt content to physical properties of soil

Figure 1 shows that as the salt content increases, the liquid limit (LL) and plastic limit (PL) decreases, and the resulting plasticity index (PI) also decreases since the liquid limit (LL) of soil is occupied by shearing resistance and diffuse double layer

thickness [6]. The salinity components mixed in the sample consisted of cation (positive ion) in the form of sodium (Na+).

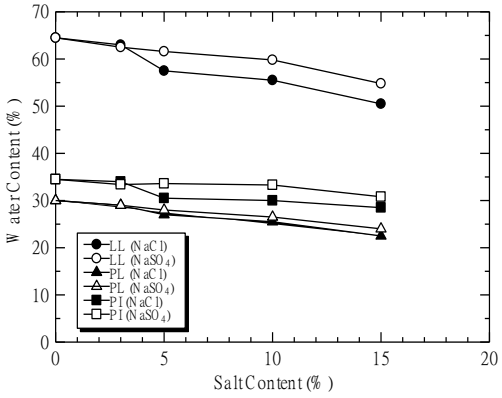

Fig. 1 Influence of salt content on Atterberg's limit.

When the cation gets melt in the water, it goes and sticks into the space between soil particles so that the soil particles moved closely to each other; and the diffuse double layer thickness decreases, resulting to a decreases in the liquid limit (LL).

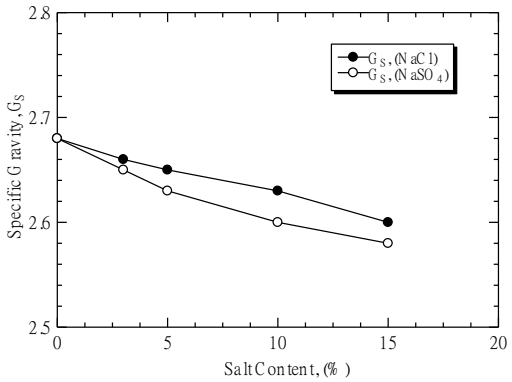

Fig. 2 Influence of salinity on specific gravity

Figure 2 shows about the influence of salinity on specific gravity. When salt content increases, it causes the specific gravity to decreases since salts (sodium chloride and sodium sulphate) are chemical substances consisted of specific gravity less than soil. The addition of salts into the soil causes organic substances to occur, hence, causes a decrease specific gravity.

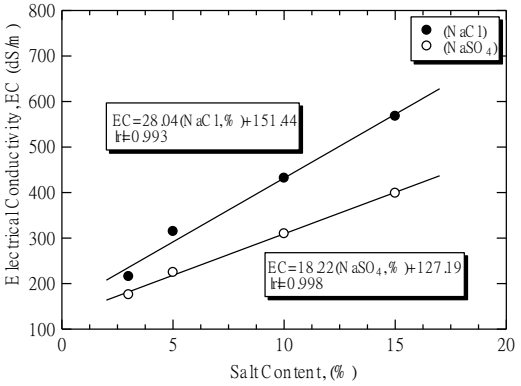

Fig.3 Relationship between salt content and electrical conductivity

Figure 3 illustrates the relationship between electrical conductivity (EC) and salt content added into the soil sample. The results show that when NaCl in added, the electrical conductivity is higher than adding $NaSO_4$ since $NaSO_4$ causes the soil to become more acidity than NaCl. Moreover, NaCl is the salt which can melt easily in water, resulting to a higher electrical conductivity in the soil than using $NaSO_4$.

Influence of salt content to the unconfined compressive strength of soil cement

Figure 4 proves about the test results when using 10%, 20%, and 30% of cement content and 81.75% of moisture content (LI=1.5) at various curing times. It shows that when mixing soil admixed cement with NaCl more than 3% by weight of soil, its unconfined compressive strength is lower than the unconfined compressive strength of the natural soil admixed cement at all curing times since the positive ion (cation) in NaCl causes soil particles get swelled. At the same moisture content and curing time of soil mixed with NaCl, its unconfined compressive strength decreases in accordance with the increase of salt content because at the same moisture content the low salinity soil will provide low value of e/e_L (matric suction). The bonding strength between soil particles happened from the hydration reaction, are similar to each other since the hydration reaction varies as a function of moisture content.[7]

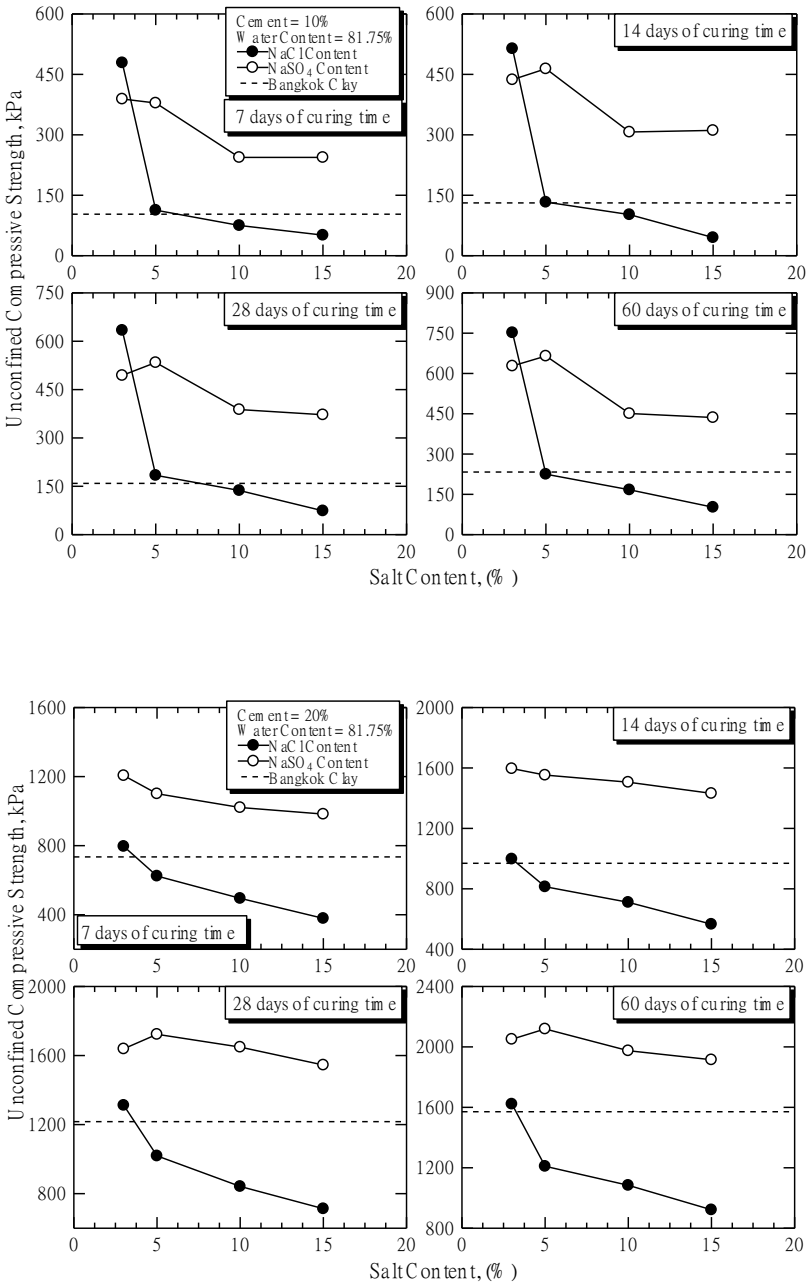

Fig.4 Influence of salt content on compressive strength of Bangkok clay

In the soil sample contained $NaSO_4$, its unconfined compressive strength decreases as the amount of salt content increases. All mixing ratios have unconfined compressive strength higher than the natural clayey soil admixed cement at all curing periods. When using 10% of cement content, soil admixed cement mixed with $NaSO_4$ exhibited higher unconfined compressive strength than natural soil at all curing periods and the differentiation of unconfined compressive strength decreases in accordance with the increase of 20% and 30% of cement content. The increase of $NaSO_4$ content causes the unconfined compressive strength to decreased because sulphate reacts with calcium hydroxide ($Ca(OH)_2$ and the calcium aluminate hydrate which occurred from the reaction between water and cement (hydration reaction) causes the strength of cement to decreases and the compressive strength of soil admixed cement also decreases.

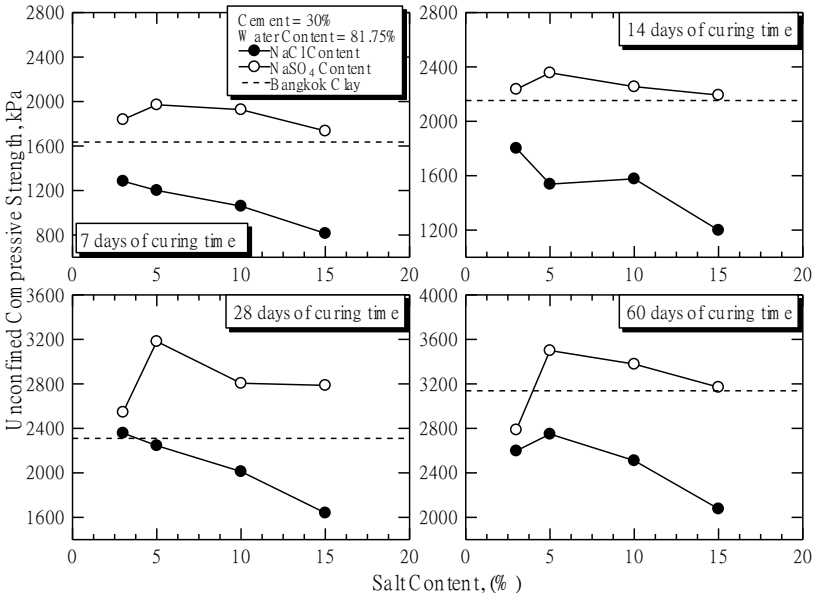

Fig.4 Influence of salt content on compressive strength of Bangkok clay (Cont.)

Compressive strength development on soft clay admixed cement

Figure 5 shows the types of salt influence on unconfined compressive strength of soft clay admixed cement at varying salt contents and varying curing times using cement content at 10%, 20%, and 30% by weight of soil. From the test results, it was found that the unconfined compressive strength increases accordingly with the increase of curing time for all mixing ratios; however, the compressive strength of soil cement mixed $NaSO_4$ resulted to a higher compressive strength than mixing with NaCl at all curing times and varying salt contents.

CONCLUSION

The increase of salinity in soil sample causes diffusion double layer to decrease leading the liquid limit (LL), plastic limit (PL), and plasticity index (PI) decrease**.** At a particular moisture content, cement content, and curing time, the unconfined compressive strength of saline (sodium chloride and sodium sulphate) soft clay admixed cement decreases in accordance with the increase of salt content because sodium chloride (NaCl) influences the soil particles disperse (specific surface becomes larger), whereas sodium sulphate ($NaSO_4$) causes to have a kind of crystal called Ettringite**.** This kind of crystal causes soil to disperse larger when hydration reaction happens**.** However, at the same level of salinity, the soil admixed cement mixed with sodium sulphate ($NaSO_4$) provides the unconfined compressive strength higher than soil admixed cement mixed with sodium chloride (NaCl) for all mixing ratios and curing times, and also higher than the unconfined compressive strength of natural clay admixed cement**.**

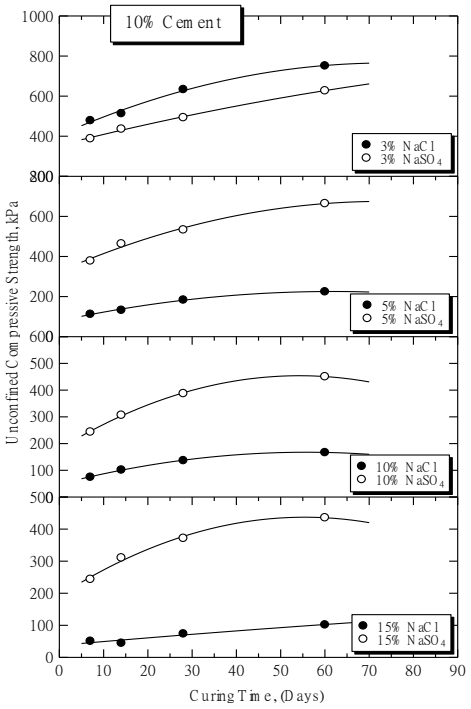

Fig. 5 Compressive strength development on Bangkok clay admixed cement at various curing time

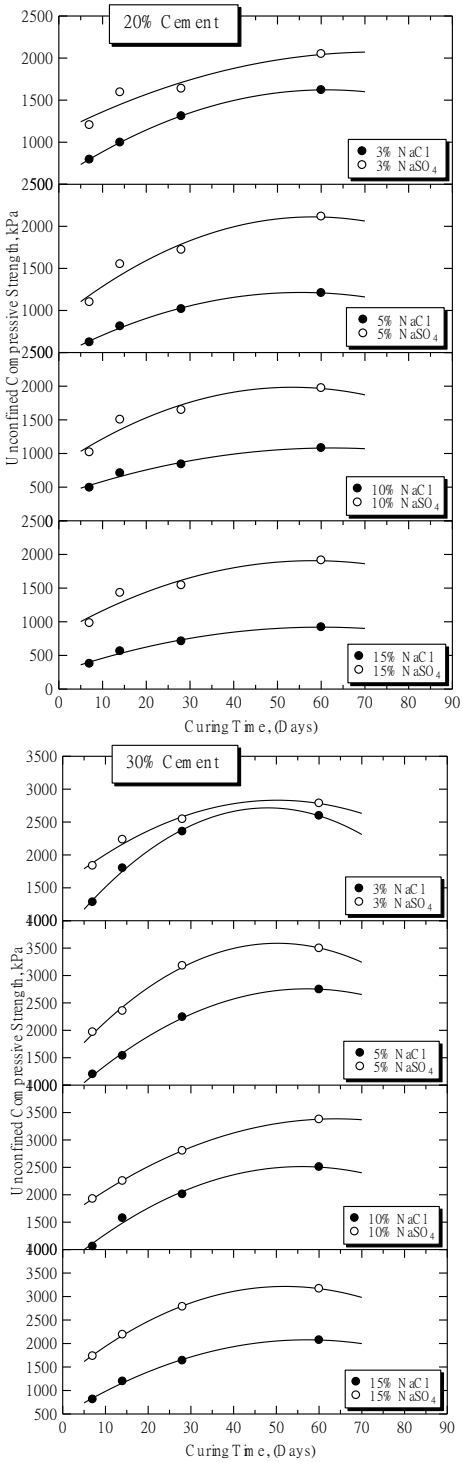

Fig.5 Compressive strength development on Bangkok clay admixed cement at various curing time (Cont.)

ACKNOWLEDGMENTS

The Authors would like to express their sincere thanks and gratitude to the Department of civil engineering, Faculty of engineering, North Eastern University, Khonkaen, Thailand.

REFERENCES

[1] Horpibulsuk, S., Rachan, R., and Suddeepong, A. (2011). "Assessment of strength development in blended cement admixed Bangkok clay", Construction and Building Materials, 25(4): 1521-1531

[2] Prakan, K. and Sridharan, A. (2004). Free swell ration and clay mineralogy of fine-grained soils, Geotechnical Testing Journal, ASTM, 27(2), 220-225.

[3] Davidson, D.T. (1961). Soil stabilization with Portland cement. Highway Research Board: 200 p.

[4] Sherwood, P.T. (1958). The effect of Sulphates on Cement Stabilization Clay. Highway Research Board, Bulletin. 198 : 45 – 54.

[5] United States Salinity Laboratory Staff.1954. Diagnosis and improvement of saline and alkali soils. US Department of Agriculture, Agricultural Handbook No. 60. Washington: US Government Printer.

[6] Sridharan, A. and Rao, G. (1975). Mechanisms controlling the liquid limit of clay. Proc. Conf. an Soil Mechanics and Foundation Engineering, Istanbul, Vol.1,pp.65-75.

[7] Horpibusuk, S., Phojan, W., Suddeepong, A., Chinkulkijniwat, A., and M.D. Liu. "Strength development in blended cament admixed saline clay". Applied Clay Science. 55, 2012, pp. 44-52.

9th Int. Conf. on Geotechnique, Construction Materials and Environment, Tokyo, Japan, 20-22 November 2019, ISBN: 978-4-909106025 C3051

THE INFLUENCE OF ROCK SLOPE SCALES ON THE STABILITY AND FAILURE MECHANISMS

Maged Al Mandalawi[1], Mohannad Sabry[2], Manar Sabry[3] and Mays Sabry[4]
1) Faculty of Science and Technology, Federation University, Australia, 2)School of Civil Engineering, Western Sydney University, Australia3) Pavement Management Service, Sydney and 4)Faculty of Engineering and Information Technology, The University of Technology, Australia

ABSTRACT

This paper demonstrates the influence of slope geometry and scale of the joint networks on the stability and the failure mechanisms in discontinues rock masses. These analyses based on finite element method (FEM) to calculate the factor of safety (FOS) and to simulate the explicit discontinuities deformations for different scales of rock masses. The study was carried out through examples of regular jointed models having different slope heights and an irregular jointed slope. The result shows that the slope stability decreases with increased scale and that the irregular columnar joints are more unfavorable to the slope stability than the regular ones. Furthermore, the failure mechanism appears shifting from structurally controlled for the 50m slope towards a step-like failure path for the 100m and 200m slopes.

Keywords: Rock slopes Stability, Failure mechanisms, Finite Element Method, Shear strength reduction factor

INTRODUCTION

In rock mechanics of both natural and engineering slopes, many studies have provided the influence of geological structures on slope stability. These discontinuities respond significantly to any change of stresses and loadings applied to rock masses (Brady and Brown, 2004; Bandis et al., 1983). This response changes the distribution of stresses to extend further to the next areas of the rock masses and other discrete pre-existing structures. These residual stresses could allow shear/tensile through intact rock and shear along discontinuities to create new fractures or initiate failures.

In geotechnical investigations of rock failures, many mechanisms primarily depend on the geometry of geological structure and change in slope scale. It has also been long observed from slope and other failures that the influence of discontinuities is not the same at different scales of excavations (Hamma et al., 2009). With increased slope angle or depth, comes an increased risk of slope failure (Sjoberg, 1999). Usually, at smaller slope scales, discontinuities may exert greater influence on behavior than rock properties. In small slopes, failure mechanisms such as planar wedges, which are controlled by joints, are common. In large scale slopes the pre-existing structures and the new fractures created by redistribution of stresses in slope surface probably congregate to develop a circular failure, combined failure or unidentified failure mechanisms.

Many failures of rock slopes appear to occur by sliding along major individual discontinuities such as fault planes and bedding planes, or along combinations of these planes (Stacy, 2006). As the scale increases, more complex mechanisms such as step-path failures and rotational shear failure, which combine failure along discontinuities with shearing through intact rock bridges, begin to occur (Eberhardt et al., 2004). These complex mechanisms can follow overall curved paths that can be similar to those encountered in soils. Toppling and columnar flexural bending or buckling are other failure mechanisms that can occur with increasing slope scale.

Rock discontinuities include joints, bedding planes, dykes, fractures, faults, shear zones, cleavages, foliations, stratums contacts and other geological structures, whose strength is lower than the intact rock. Most discontinuities increase the permeability of rocks, resulting in even lower strength. Thus, rock discontinuities are typically governing the overall behaviour of the rock masses (Zhao, 2004). Sjoberg (1996) indicated that pre-existing fractures in the rock mass and their characteristics were the most important factors contributing to potential slope failures, along with the hydrologic conditions at the mine. A recent study with more details (Xu et al. 2013) emphasised that the failure of rock slope depended on the size of discontinuities, and showed that both tensile and shear damages at the weakest element were the trigger for the failure surface initiation in the rock slope.

This paper inspects the effect of the geometry of slope on its stability. In open cut mine, the geometry of slope could be defined by height, width, bench face, interramp and slope angles. The rock masses of slope include the geological structure and intact rock. The geological structure in rock masses may vary in different scales, ranging from micro cracks having length of a few millimeters to many kilometers, such as the Paroo fault which strikes in south George Fisher and south-west of Handlebar Hill open cut mines at Mt. Isa (Long, 2010). From the study, it is found that the geometry of slope controls the behaviour of rock slope at different scales associated with the critical mechanism of rock failure. Paper size is 210mm×297mm of A4 paper. Please save to MS Word templates directory. Use 10 point Times New Roman font throughout the paper including text inside figures and tables. Single line spacing is mandatory. Try to avoid Underline or Bold within texts.

The top margin is 30mm while the left, right, and bottom margins are 25 mm. Headings should be left justified and without number. Leave one line between headings and the first paragraph and no space before succeeding paragraphs. Indent the first line of the paragraph by 5mm. All text should be left and right justified. Footnotes and underlines are not allowed.

THE SLOPE STABILITY ANALYSIS METHOD IMPLEMENTED IN THIS STUDY

The numerical models in this investigation are two dimensional finite element stress analysis using Rocscience/Phase2 program. Application of the finite element method (FEM) to problems of blocky rock masses as explicit modelling of the behaviour of individual joints can be used for practical engineering in blocky rock masses (Hamma et al., 2009). Geotechnical engineers have used different failure criteria for rock slopes. One of the techniques is the shear strength reduction (SSR) approach. SSR is simple in concept, which systematically reduces the shear strength envelope of material by a factor of safety, until deformations are unacceptably large or solutions do not converge (Hamma et al., 2005).

The SSR technique for slope stability analysis can be used to verify the stress reduction factor (SRF). The critical SRF is the one that brings the slope to failure, namely the factor of safety. The shear strength parameters of all slope materials will be reduced until the critical SRF is found. Use at most three levels of headings that correspond to chapters, sections and subsections. The first level headings for chapter titles should be in 10pt, bold, justified, and upper case font. Leave one blank line before and after the first level headings, respectively.

Finite Element Analyses for Models at Different Scales

The effect of slope scale on its stability was numerically experimented through five models. The change in safety factor and the failure mode of rock masses were verified in these samples when slope dimension increased. The strength parameters required to define the material properties dialog for discontinuities and intact rock are explained in Table 1. Shear strength reduction factor (SRF) was established within a tolerance of 0.001 for initial estimate of SRF =1 when setting the shear reduction dialog of the project.

The rock mass is assumed to be homogenous and rock slopes are dry. For all five models, the same discrete joint sets networks are used as shown in Table 1. One joint set dips at an angle of 36o (clockwise from the horizontal axis), while the other dips at 80o. The spacing of each joint set was assumed to follow a normal distribution with a mean of 4m and standard deviation of 1.0m. Both joint sets having infinite lengths that can form discrete elements through the rock block. The slope angle is 76o and the heights are 10m, 20m, 50m, 100m and 200m, respectively, for the five models. The FEM meshes for the five slopes are shown in Fig. 1.

The factor of safety was calculated during the numerical simulation and the failure mechanism was analysed for each of the models. Table 2 is the factors of safety obtained for each slope with the same infinite two joint sets and rock mass parameters.

Failure Mechanisms of Slopes with Regular Joints

Phase2 program was run to predict the behaviour of intact rock and fracture developments in these models. Figs. 2a to 2e are the modelling results of FEM-SSR.

The distributions of shear strains obtained from the numerical simulations are shown in Figs. 2a through 2e. Contours of shear strains in discontinuous rock mass in Fig. 2a indicate a highest shear strain zone above the toe at the intersection of the two joint sets, namely largest shear deformation in this zone for the 10m slope. Fig. 2b reveals the high shear strain zone at the toe controlled by two parallel 36o joints near the toe and an 80 o joint at the toe. At Fig. 2c for the 50m slope, the contours indicate large blocks shearing extending up through the intact rock and controlled by the joints. While in Figs. 2d and 2e, there are indications of more shearing through intact rocks and a step-wise shear strain contour at the bottom of the high strain band that is parallel to the 36° joints and the steps are

parallel to the 80o joints, suggesting a step failure coupled with intact rock shearing. The band in Fig. 2d expands much larger than in Fig. 2e.

It was found that the shear strain level formed above the toe is much higher, suggesting higher shear stress levels in those locations. Thus, unstable zones would be progressively initiated there. At lower slope heights, the slopes are stable (Figs. 2a and 2b), refer to Table 2.

When the slope is higher, the deformation expands till exceeding the limit, or slope failure as in the case of Fig. 2c. It may be concluded that the slope scale and joint sets control the development of unstable rock zone. While the high shear strain contours in Figs. 2d and 2e are in more structural rock masses (joint sets) and the dislocations have acquired approximate step path of failure

Table. 1 Mechanical properties of intact rock and joints used in Phase2 models

Material	Properties	Comments
Spears Siltstone	**Unit weight = 0.0272 MN/m^3** **Young's Modulus = 22 MPa** **Poisson's ratio = 0.2** **Tensile strength residual = 0.1 MPa** **Dilation angle = 2^o** **Internal friction angle = 33^o** **Cohesive force = 0.1 MPa**	**Based on Mohr-Coulomb criterion.**
Joint set 1	**Dip angle = 36^o** **Spacing = 4m (mean)** **Normal stiffness = 100 MPa/m** **Shear stiffness = 10 MPa/m** **Tensile strength = 0 MPa** **Cohesive force= 0.1 MPa** **Internal friction angle = 18^o** **Joint end condition = All closed**	**Parallel statistical joint model.**
Joint set 2	**Dip angle = 80^o** **Spacing = 4m (mean)** **Normal stiffness = 100 MPa/m** **Shear stiffness = 10 MPa/m** **Tensile strength = 0 MPa** **Cohesive force= 0.1 MPa** **Internal friction angle = 18^o** **Joint end condition = All closed**	**Parallel deterministic joint model.**

Table. 2 Factor of safety of the homogeneous cross-jointed slopes

Slope height (m)	Factor of safety
10	**2.46**
20	**1.34**
50	**0.81**
100	**0.54**
200	**0.32**

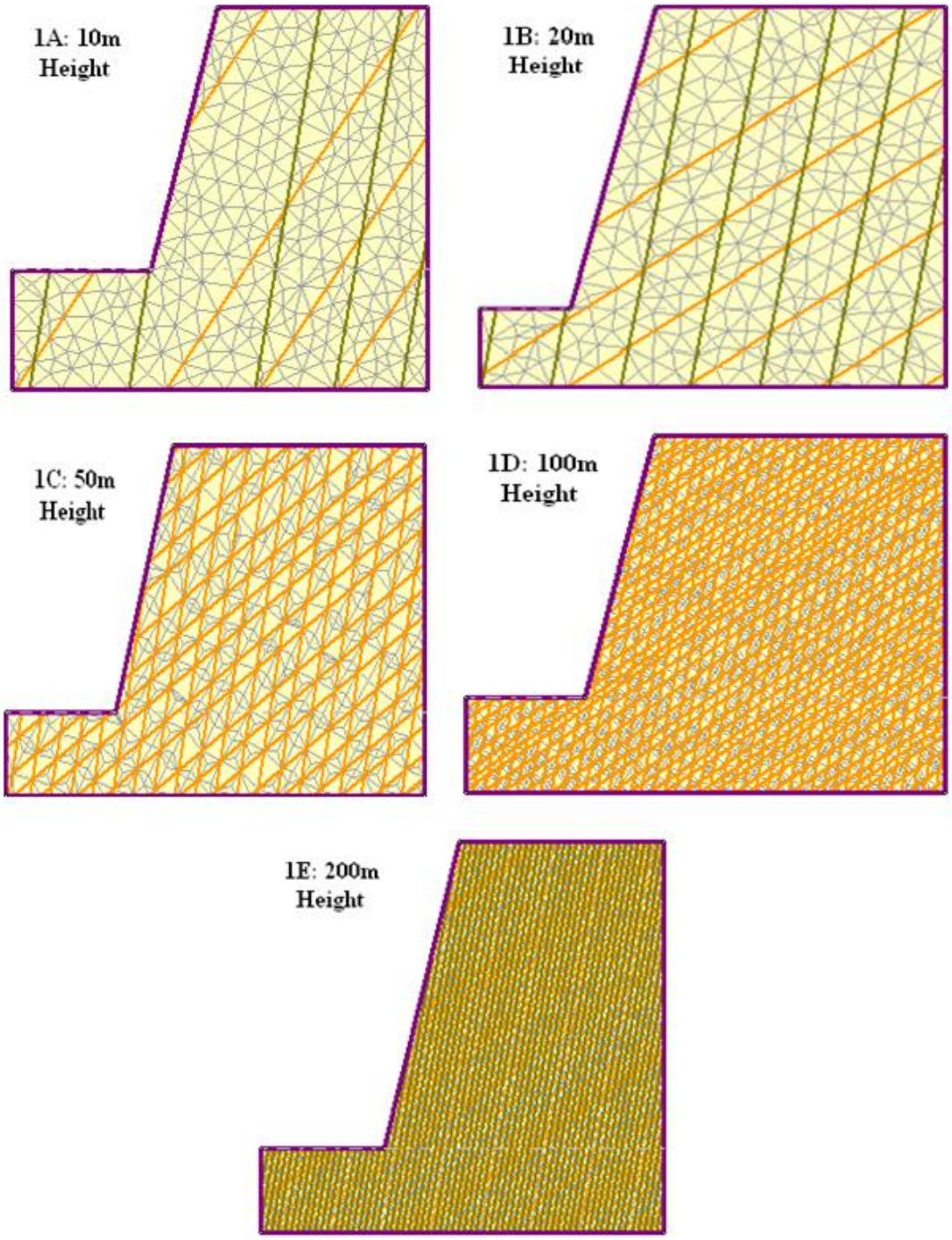

Fig. 1 Models of different scales used in this study

When the slope is higher, the deformation expands till exceeding the limit, or slope failure as in the case of Fig. 2c. It may be concluded that the slope scale and joint sets control the development of unstable rock zone. While the high shear strain contours in Figs. 2d and 2e are in more structural rock masses (joint sets) and the dislocations have acquired approximate step path of failure.

The mechanical properties of the rock mass is obviously influenced by the presence of joint sets and, more joint sets provide more possibilities of potential slide planes for rock blocks to slide and fall (Zhao, 2004). Initiations and progression of shear strain along joints were followed by block movements and the involvements of further development of more shearing through intact rock.

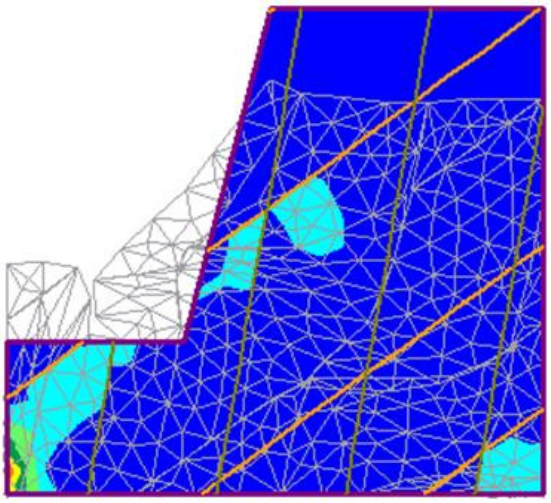

Fig. 2a Shear strain development of 10m height slope

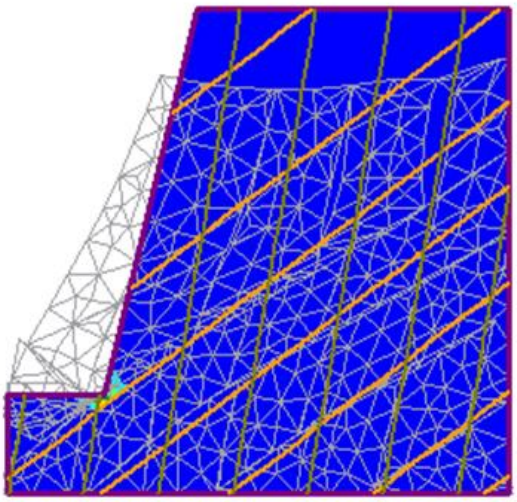

Fig. 2b Shear strain development s of 20m height slope

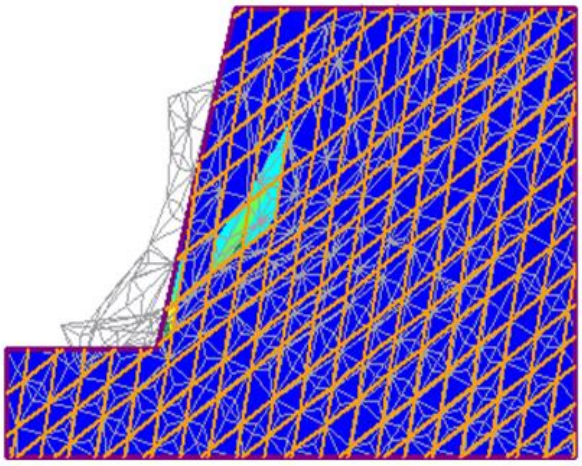

Fig. 2c Shear strain development of 50m height slope

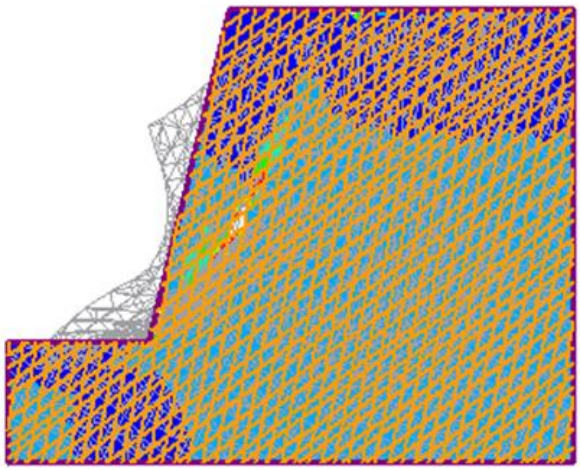

Fig. 2d Shear strain development of 100m height slope

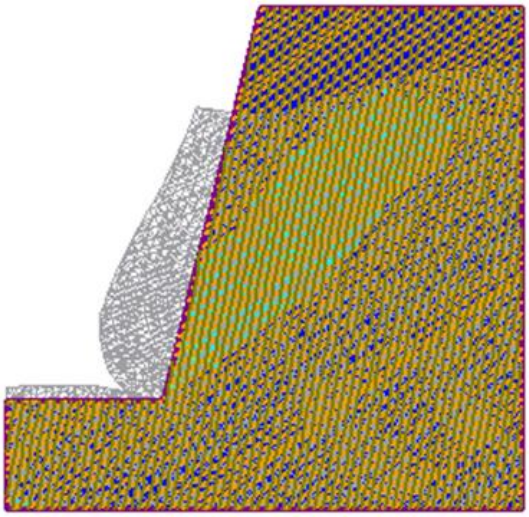

Fig. 2e Shear strain development of 200m height slope

The patterns of the deformation vectors for rock masses in term of the total displacements and joints slip directions are demonstrated in Figs. 3a to 3e.

Figs. 3a to 3e clearly show the displacement vectors and the directions of block sliding. The slip of the rock mass during SSR method application was deliberate as red arrows.

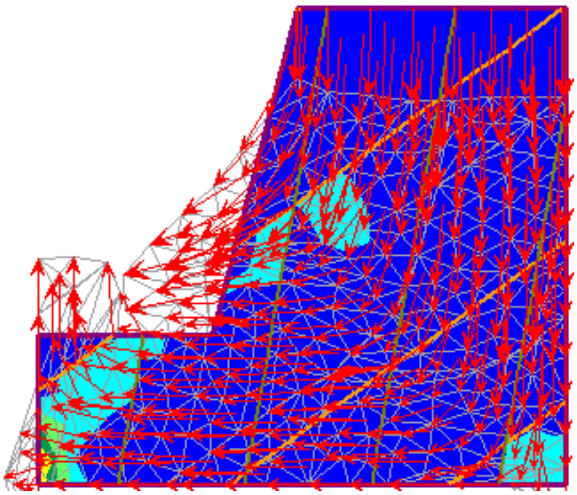

Fig. (3a) Displacement vectors and slip directions of joints of 10m slope

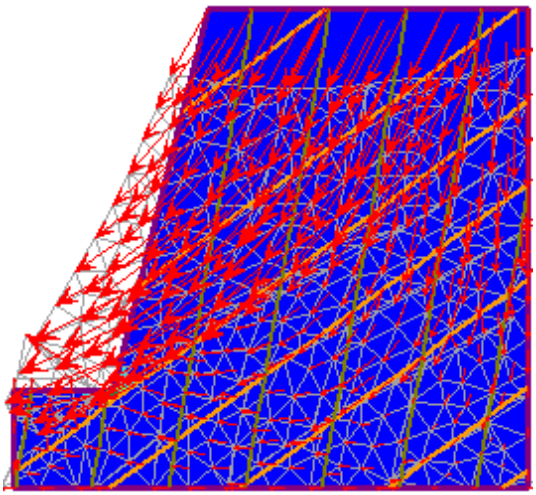

Fig. (3b) Displacement vectors and slip directions of joints of 20m slope

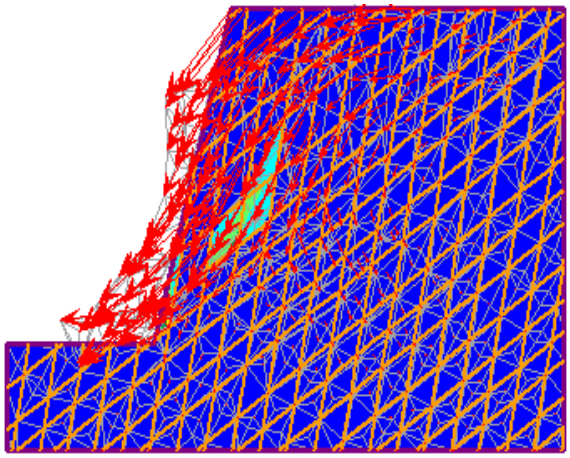

Fig. 3c Displacement vectors directions joints of 50m slope

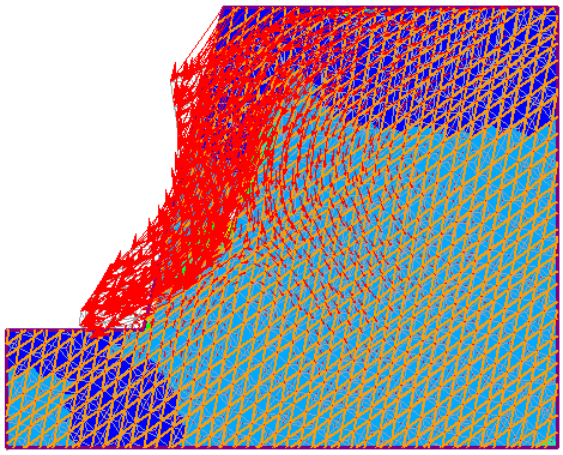

Fig. 3d Displacement vectors directions and slip of and slip of joints of 100m slope

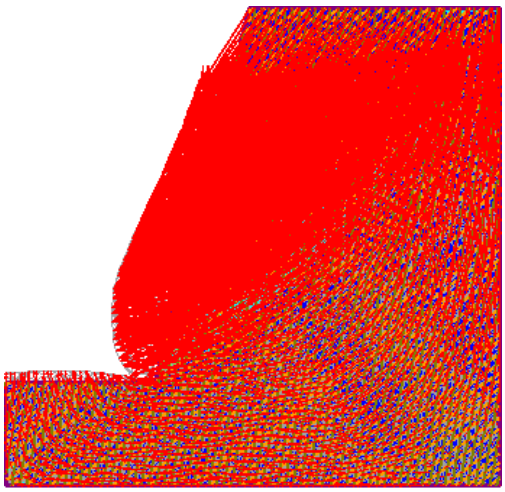

Fig. 3e Displacement and joints slip direction of 200m slope

Failure Mechanisms of Slopes with Irregular Joints

In this section, an irregular columnar joints voronoi network is introduced to obtain the influence of irregular joint patterns on slope stability. The same material properties composed the slope of 200m height and 76o slope angle (Case E in Fig. 1), is adapted to analyse the behaviour of irregular discontinuity. The numerical analysis result shows a FOS of 0.36 for the irregularly jointed slope. Fig. 4 (a) is the shear strain where the green legend represents largest shear strain and (b) is the total displacements.

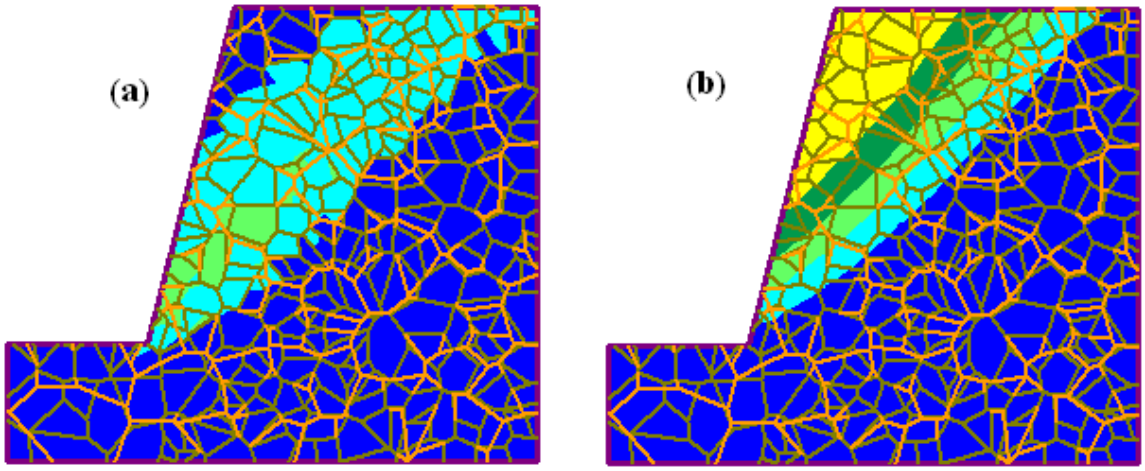

Fig. 4 Visualised slope with irregular voronoi- joints, slope angle 76o, slope height 200m and FOS is 0.36 (a) maximum shear strain, (b) total displacement.

DISCUSSION AND CONCLUSION

The factor of safety values in Table 2 clarify that when slope height increases, factor of safety reduces, and the mechanisms of failures (Cases C to E, refer to Figs. 2c-2d and Figs. 3c-3d.) have been varied with the slope scales. The finite element analysis using SSR method has demonstrated the influence of slope scales and joint patterns on the slope stability.

For the examples used in this study, the slope of 10 m height, the simulated results indicates that the area above the toe has the highest shear strain along a joint. Consequently, this area of the 10m slope is most critical. For the 20 m height slope in Fig. 2b, the simulation reveals a high shear strain zone controlled by joints near the toe. More recently, Xu et al., (2013), however, suggested that shear stress level and normal stress level might have significant effect on the long term behavior of rock mass with discontinuities of low strength.

As the height increases in Fig. 2c, further blocks are involved in the sliding and the critical failure surface developed from the initial local shear failure along the joint and near the toe. The contours of maximum shear strain indicate a rock failure mechanism involving structural movements and failure through intact rock. With further increasing the slope height, a composite failure surfaces become visible through the toe as illustrated in Fig. 2d. Fig. 2e shows maximum strain contours for the slope of 200 m height, suggesting a step failure coupled with intact rock shearing.

In the process of rock slope investigation for failure modes, it can be shown that these mechanisms depend on change in the scale of slope and geological structure. The stability of the minor slopes is controlled by small-medium geological structures, for example, joints control the slope failure mechanisms in wedge and planner slips along the intersection line of two structural features. In large scale slopes, failure occurs may involve in two or more interacted failure modes, such as step failure coupled with the intact rock shearing founded in this model study. Previously, Sjoberg (1996) stated that rotational shear failure in large scale slope, would probably primarily involve failure along pre-existing discontinuities with perhaps some portion of the failure surface going through intact rock. Recently, Ma et al., (2013) simulated numerical models for the progressive failure of rock slopes involving a complex non-linear evolution from initiation, through propagation to crack.

This study indicates that the scale of the slope remarkably influences the factor of safety, the higher the slope is, the less stable it becomes as shown in

Fig. 5. Moreover, the existence of the regular joint sets in the rock mass can significantly affect the mechanical behavior of rock slope and degrade the factor of safety (FOS). While the irregular joints further increase the slope instability and reduce the factor of safety (FOS) as shown in Fig. 6.

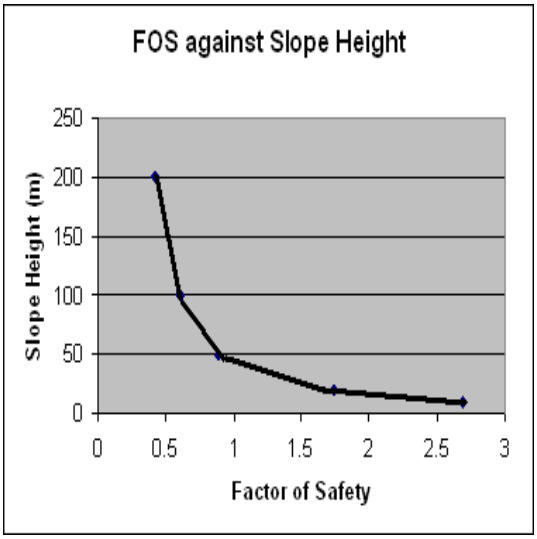

Fig. 5 Shows factor of safety against slope heights.

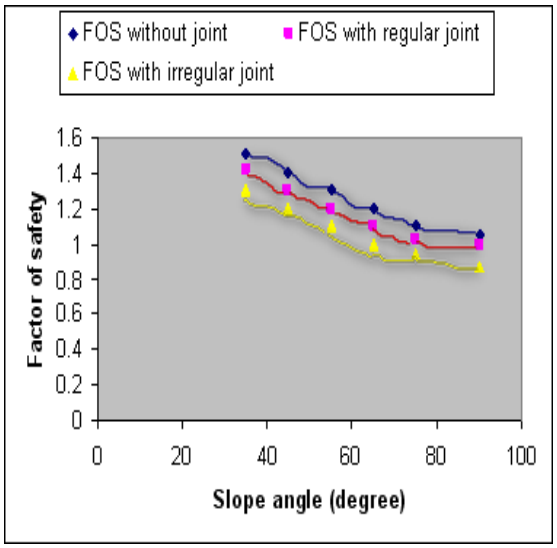

Fig. 6 Shows factor of safety of intact, regular and irregular jointed slopes.

REFERENCES

[1] Brady, B.H. and Brown, E.T, Rock mechanics: for underground mining. Springer Science & Business Media, 2013.

[2] Bandis, S.C. Lumsden, A.C. and Barton, N. R, Fundamentals of rock joint deformation. In International Journal of Rock Mechanics and Mining Sciences & Geomechanics Abstracts (Vol. 20, No. 6, 1983, pp. 249-268).

[3] Hammah, R.E., Yacoub, T. and Curran, J.H, Variation of failure mechanisms of slopes in jointed rock masses with changing scale. In Third Canada-US rock mechanics symposium, Toronto, Canada, Paper (Vol. 3956), 2009.

[4] Sjöberg, J. Analysis of large scale rock slopes. Doctoral dissertation, Luleå tekniska universitet, 1999.

[5] Stacey, T.R, Considerations of failure mechanisms associated with rock slope instability and consequences for stability analysis. Journal of the Southern African Institute of Mining and Metallurgy, 106(7), 2006, pp.485-493.

[6] Eberhardt, E., Stead, D., Karami, A. and Coggan, J, Numerical analysis of brittle fracture propagation and step-path failure in massive rock slopes. In Proceedings of the 57th Canadian Geotechnical Conference, Québec City, Que, 2004, pp. 24-27.

[7] Zhao, J. Rock Mechanics for Civil Engineers. Rock Mechanics, chapter 5 Introduction, lecture note in Rock Mechanics and Tunneling, School of Architecture, Civil and Environmental Engineering, Lausanne Federal Institute of Lausanne, 2004.

[8] Sjöberg, J. Large scale slope stability in open pit mining: a review. Luleå tekniska universitet, 1996.

[9] Xu, T., Xu, Q., Tang, C. A. and Ranjith, P.G, The evolution of rock failure with discontinuities due to shear creep. Acta Geotechnica, 8(6), 2013, pp.567-581.

[10] Long, R.D, The Paroo Fault and the Mount Isa copper orebodies; a revised structural and evolutionary model, Mt Isa. Queensland, Australia, Doctoral dissertation, James Cook University, 2010.

[11] Hammah, R.E., Yacoub, T.E., Corkum, B.C. and Curran, J.H, The shear strength reductionmethod for the generalized Hoek-Brown criterion. In Alaska Rocks 2005, The 40th US Symposium on Rock Mechanics (USRMS). American Rock Mechanics Association, 2005.

[12] Zhao, J. Rock Mechanics for Civil Engineers. Rock Mechanics, chapter 5 Introduction, lecture note in Rock Mechanics and Tunneling, School of Architecture, Civil and Environmental Engineering, Lausanne Federal Institute of Lausanne, 2004.

[13] Ma, K., Tang, C.A., Li, L.C., Ranjith, P.G., Cai, M. and Xu, N.W. 3D modeling of stratified and irregularly jointed rock slope and its progressive failure. Arabian Journal of Geosciences, 6(6), 2013, pp. 2147-2163.

9th Int. Conf. on Geotechnique, Construction Materials and Environment, Tokyo, Japan, 20-22 November 2019, ISBN: 978-4-909106025 C3051

PIV ANALYSIS OF THE SANDY SOIL TRANSPORTATION INDUCED OCEAN WAVE ON WAVE FLUME EXPERIMENT

Tatsuya Matsuda[1], Kinya Miura[1], Keita Anai[1] and Rintaro Takayanagi[1]
[1]Department of Architecture and Civil Engineering, Toyohashi University of Technology, Japan

ABSTRACT

Sandy soil transportation in seabed induced ocean wave is caused by complex interactions between shear stress and effective stress change due to seepage force. This study investigated the soil movement phenomena under various soil density condition that focused on the influence of the Shields number and the excess pore water pressure ratio using the wave flume experiment device. Particle Image Velocimetry (PIV) analysis was also done to quantitatively evaluate soil movement. In the case of the loose density of soil, liquefaction occurred with the phase difference of the pore water pressure fluctuation and the accumulation by residual pore water pressure. The soil particles showed the elliptical movement similar to water particles. On the other hand, in the case of medium-dense soil, the soil was moved to the offshore direction due to flow velocity in the ground surface when the effective stress decreased near the surface layer due to the phase difference of the pore water pressure fluctuation. Especially, the ground surface layer was moved in a body. As PIV analysis result, the upward velocity of soil particles is suggested as near as its a seepage flow velocity of the geomaterial.

Keywords: Wave flume experiment, Sedimental transportation, Shear stress, excess pore water pressure, PIV

INTRODUCTION

The Sediment transportation induced by ocean wave is an important problem for disaster prevention and the environment in the coastal area. In past studies on the scour and erosion, many researchers thought the application of a tractive force about the prediction of topographical changes due to water flow [1]. The geotechnical researchers have focused on the stress change in seabed induced by wave [2]–[5]. However, Flow movement of soil, sediment induced by sea wave is caused by a complex interaction between traction force and seepage force.

The authors have conducted a series of wave flume experiment with movable bed focusing on the influence of the traction and seepage forces for soil movement phenomena [6]. The experimental results for stress change induced by wave were validated with the exact solution which was derived by means of u-p formulation of the seabed as a two-phase material consisting of solid and fluid.

This study has investigated the soil movement phenomena under various soil density condition that focused on the influence of the Shields parameter and the excess pore water pressure ratio. Particle Image Velocimetry (PIV) analysis was also done to quantitatively evaluate soil movement.

OUTLINE OF EXPERIMENT

Experimental device and Measurement tools

Figure 1 shows the schematic diagram of wave flume channel. This channel has 25 m length, 0.6 m width and 1.0 m height. The movable bed area was installed in the channel. The length is 2.5 m and the depth is 0.2 m. The Hydraulic condition was taken into consideration Froude's similarity law. Similarity rate was set $\lambda_L = 1/25$.

During the experiment, the wave propagation was measured above the sediment area by using a capacity type wave gauge and an electromagnetic velocity meter. The pore water pressure in the ground was also measured using pore water pressure sensors. The measurement point of pore water pressure was shown by points in Figure 1. The experiments were recorded using a high-speed camera and a video camera to observe sediment transportation.

Selection of seabed material

It has a limit to applying the geometry scale of the geomaterial according to the Froude's similarity law: For example, geomaterial in model sediment is classified as silt ($D_{50}|m$ = 0.008 mm) when the prototype is fine sand ($D_{50}|p$ = 0.2 mm). Therefore, this study used Dean Number to select of the geomaterial [7]. Dean Number is a dimensionless fall speed parameter, given as the follows Eq. (1);

$$\left\{w/(H/T)\right\}_p = \left\{w/(H/T)\right\}_m \quad (1)$$

where, w, H, and T are vertical fall speed of soil

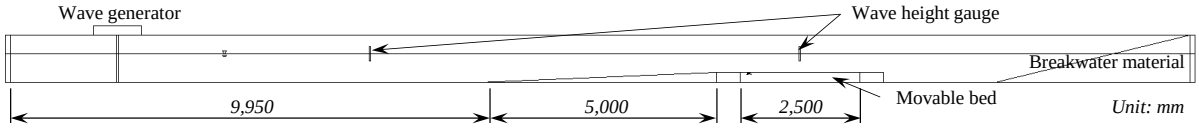

Fig. 1 Schematic diagram of the wave flume device.

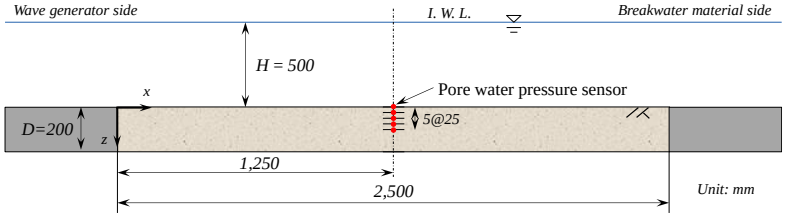

Fig. 2 Schematic diagram of movable bed.

particle in the fluid, wave height and wave period, respectively. The subscript of *p* and *m* means prototype and model. The vertical fall speed of sediment can be calculated using Hallermeier's Relationship as follows Eq. (2);

$$w = \frac{\left[\left(\rho_s - \rho_w\right)\cdot g\right]^{\frac{7}{10}}\left(D_{50}\right)^{\frac{11}{10}}}{6\left(\nu\right)^{\frac{2}{5}}} \quad (2)$$

there, ρ_s, ρ_w, ν and g are soil particle density, water density, the coefficient of kinematic viscosity (= 1.0×10^{-6} m^2/s) and gravitational acceleration, respectively. The geomaterial in the model which is applied to the Dean Number is classified as fine sand ($D_{50}|m$ = 0.075 mm) when the prototype is fine sand ($D_{50}|p$ = 0.2 mm). The characteristic of geomaterial is same between prototype and model.

Experimental condition

Table 1 shows the physical parameters of the geomaterial of sediment. In this experiment, the silica sand No.8 which is applied to Dean Number used. The movable bed was constructed to control the relative density D_r about 55%: Case1 and 67 %: Case2 with a saturated condition.

Table 2 shows the wave conditions. The wave condition is referenced by the book that was discussed liquefaction in seabed induced by the ocean wave, which is published from JSCE [8]. The regular wave was generated for 20 minutes and its acting the movable bed.

Data arrangement with the wave phase angle

Fourier transform was used in the frequency analysis of the time history data obtained from the

Table 1 Physical parameter of silica sand No.8

	Silica sand No.8
Mean diameter, D_{50} (mm)	0.090
Maximum void ratio, e_{max}	1.353
Minimum void ratio, e_{min}	0.706
Coefficient of permeability, k (m/s)	2.00×10^{-5}

Table 2 Wave condition

	Prototype (model)
Wave period, T (s)	8.0 (1.6)
Wave height, H (m)	3.5 (0.14)
Wave length, L (m)	70.0 (2.8)
Water density, ρ_w (kg/m^3)	1,000

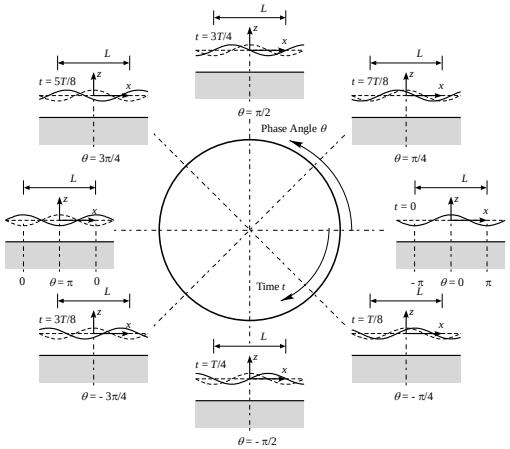

Fig. 3 Definitions of the water level using the phase angle.

experimental results and the data were arranged using a wave phase angle based on the wave duration. These procedures enabled the generalization of the results. Phase angle was defined on the basis of water level, which was

defined. Fig. 3 presents a conceptual diagram of the water level. Experimental data that from 60 to 120 s from the start of the experiment was used because the data became stable.

EXPERIMENTAL DATA ANALYSIS

Calculation of excess pore water pressure ratio

The excess pore water pressure ratio was calculated as follows a formula:

$$\Delta u_e / \sigma_0' = \left(p_n - p_{surface} \right) / \sigma_0' \quad (3)$$

where Δu is an excess pore water pressure and σ_0' is initial effective stress.

The excess pore water pressure ratio is showing the change in the effective stress state of the ground. The excess pore water pressure ratio equal to 1.0 mean that the sediment becomes liquefaction state. The excess pore water pressure was calculated as the pore water pressure at each point on the ground: p_n minus pore water pressure in the ground surface: $p_{surface}$.

Calculation of bed shear stress

The waves interact with the seabed sediment mainly through the bed shear stress. The bed shear stress was suggested by Jonsson [9] as follows Eq. (4);

$$\tau = \frac{1}{2} \rho_w f_w u_b^{\ 2} \quad (4)$$

where f_w is a wave friction factor and u_b is an amplitude of near-bed wave-orbital velocity.

A different measure of the balance between driving and stabilizing forces on sand grains at the bed was suggested by Madsen and Grant [10] as follows Eq. (5);

$$\psi = \frac{\tau}{\left(\rho_s / \rho_w - 1 \right) gd} \quad (5)$$

where, ψ is known the Sields parameter.

Eq. (4) and q. (5) give Eq. (6);

$$\psi = \frac{1}{2} \frac{f_w u_b^{\ 2}}{\left(\rho_s - 1 \right) gd} \times Sign\left(u_b \right) \quad (6)$$

EXPERIMENTAL RESULT AND DISCUSSION

Excess pore water pressure ratio change

Fig. 4 shows the change in the excess pore water pressure ratio. In the Case1, liquefaction has occurred at t = 49 s with the phase difference of the pore water pressure fluctuation and the accumulation by residual pore water pressure. On the other hands in Case2, Accumulation of residual excess pore pressure was observed before t = 30 s. After then, the stabilized amplitude of excess pore water pressure was observed. Hereafter, this paper shows the analyzed result in detail of Case2.

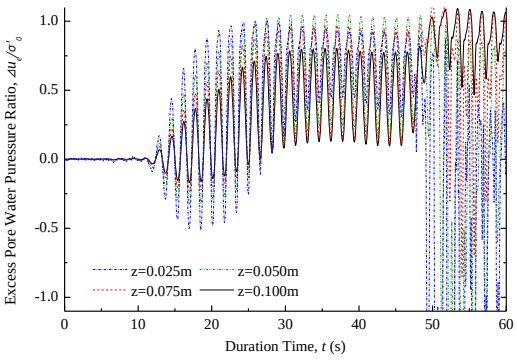

(a) Case1, D_r = 55 %

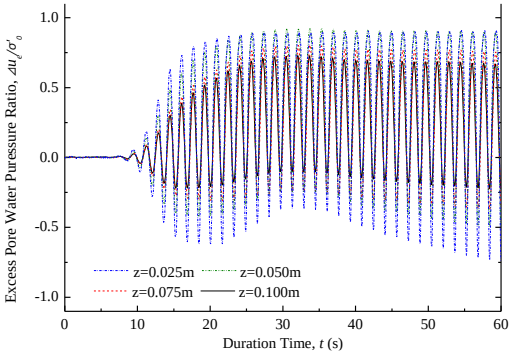

(b) Case2, D_r = 67 %

Fig. 4 The change in the excess pore water pressure ratio from 0 to 60 s.

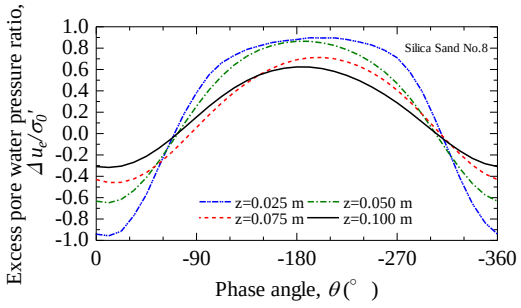

Fig. 5 The change in the excess pore water pressure ratio that is analyzed from one minute after 60 to 120 s.

Fig. 5 shows the change in the excess pore water pressure ratio that is analyzed of data that during one minute after 60 to 120 s from the start of the experiment. The excess pore water pressure ratio became maximum when the wave level became minimum at the phase angle θ = -180 degree. The reason for generating the excess pore water pressure that a difference of the phase angle of water pressure propagation was generated between the surface and the internal of the seabed. The effective stress was decreasing induced by wave action. The maximum excess pore water pressure ratio generated about 0.896 at z = 0.025 m.

Shields parameter and Excess pore water pressure ratio

Fig. 6 shows the relationship between the Shields parameter and excess pore water pressure ratio in Case2. The critical Shields parameter of fine sand is ± 0.05. The positive value is showing the wave flow in an inshore direction.

The excess pore water pressure ratio rising, and the near-seabed flow velocity is generated in the offshore direction opposite to the traveling direction of the wave at the timing of temporary instability in the ground surface.

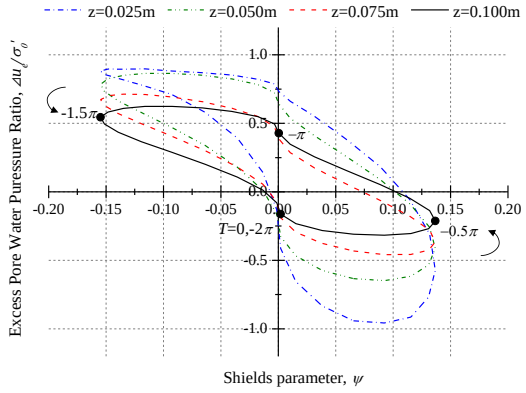

Fig. 6 The relationship between the Shields parameter and the excess pore water pressure ratio in Case2.

Observed sediment movement by PIV analysis

For the observation of sediment motion, PIV analysis was done. PIV analysis is an image analyzed method based on inferring in what direction and in what amount a part of an image has moved between two successive instants. The sediment transportation was recorded by a high-speed camera load a telephoto lens. The analysis was performed with soil particles as the target.

Fig. 7 shows the motion velocity vector of sediment that is calculated by PIV analysis. Color contour shows the velocity value; Maximum velocity as 0.3 m/s (red color), Minimum velocity as 0.0 m/s (blue color).

As a result of PIV analysis, the sediment surface was moved uniformly due to wave motion. The velocity vector is upward at the phase angle where the excess pore water pressure ratio increases. On the other hand, when the excess pore water pressure decreases, the velocity vector turns downward.

The movement velocity of the sediment is evaluated quantitatively. Fig. 8 shows the data extraction area. The velocity data were averaged in 1 mm steps from the ground surface, with the range of the center of the photograph, which is less affected by lens distortion.

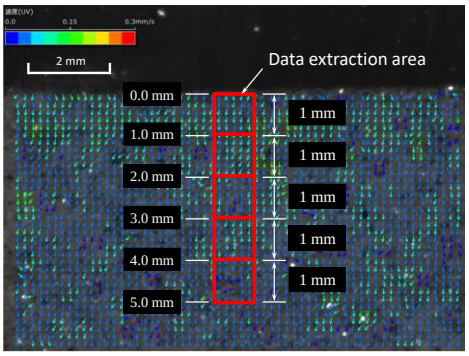

Fig. 8 PIV analysis result; The upper right figure shows a zoomed view of the dotted line position in the center of the whole.

Fig. 9 shows the movement velocity of the sediment in the horizontal direction, and Fig. 10 shows the movement velocity of the sediment in the vertical direction. Fig. 11 shows the relationship between the movement velocity of the sediment in the horizontal and in the vertical direction.

The maximum upward velocity became about 0.06 m/s when θ = -135 degree. Then, the horizontal velocity in the offshore direction was generating about 0.02 m/s. On the other hands, the downward velocity in a vertical direction was generated when the excess pore water pressure ratio decreases. The maximum downward velocity became about -0.12 m/s when θ = -315 degree. Then, the horizontal velocity in the inshore direction was generating about 0.04 m/s.

The surface-bed was transporting with influences of the bed shear stress, and seepage force with the excess pore water pressure change. The upward velocity of soil particles is suggested as near as its a seepage flow velocity of the geomaterial.

CONCLUSIONS

Sandy soil transportation in seabed induced ocean wave is caused by complex interactions between shear stress and effective stress change due to seepage force.

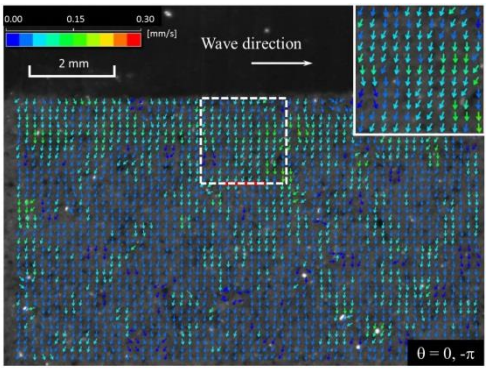

(a) θ = 0 deg.

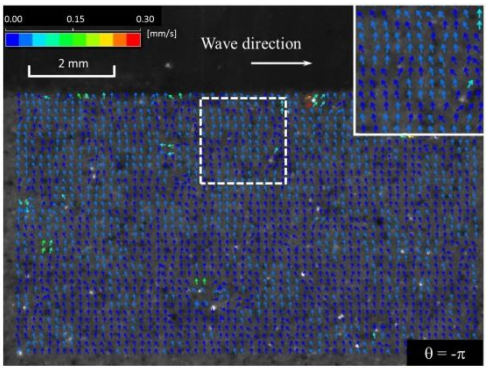

(e) θ = -180 deg.

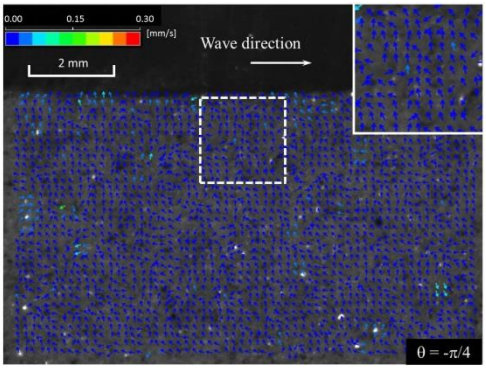

(b) θ = -45 deg.

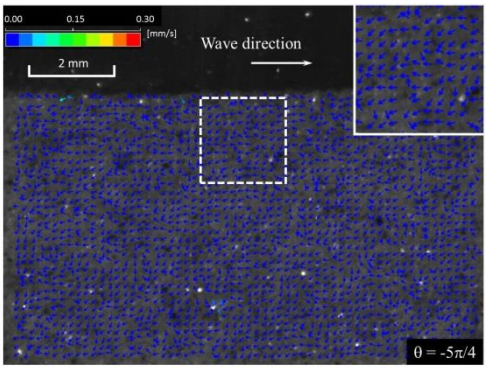

(f) θ = -225 deg.

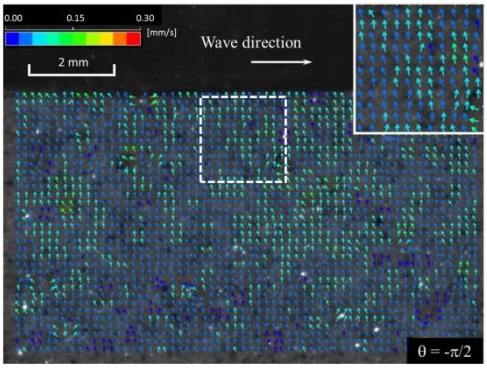

(c) θ = -90 deg.

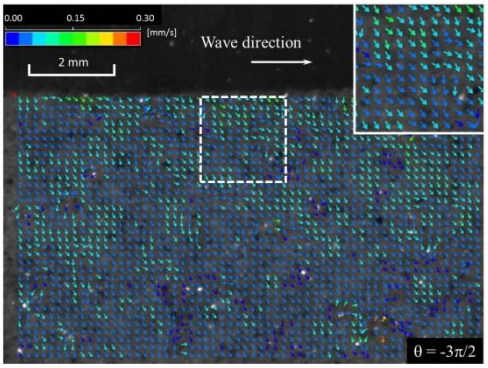

(g) θ = -270 deg.

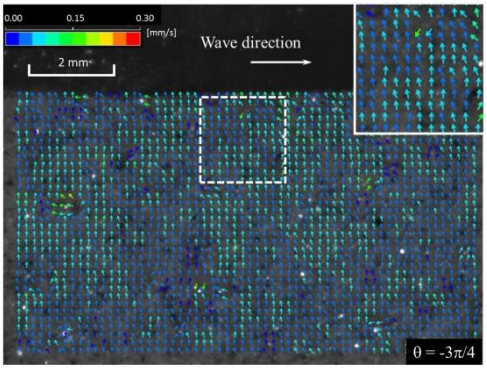

(d) θ = -135 deg.

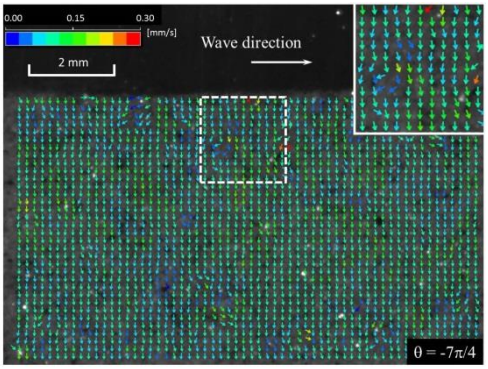

(h) θ = -315 deg.

Fig. 7 PIV analysis result in Case2; The upper right figure shows a zoomed view of the dotted line position in the center of the whole.

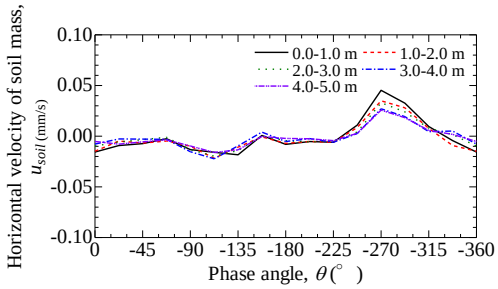

Fig. 9 The movement velocity of the sediment in the horizontal direction in Case2.

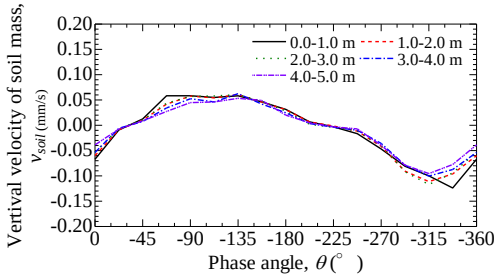

Fig. 10 The movement velocity of the sediment in the vertical direction in Case2.

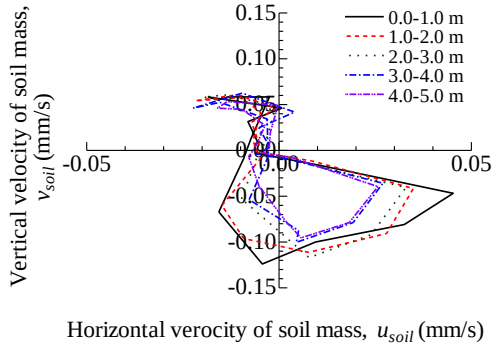

Fig. 11 Relationship between the movement velocity of the sediment in the horizontal and in the vertical direction in Case2.

This study investigated the soil movement phenomena under various soil density condition that focused on the influence of the Shields number and the excess pore water pressure ratio using the wave flume experiment device. PIV analysis was also done to quantitatively evaluate soil movement. The results obtained indicate as follows;

- In the case of medium-dense soil, the bed shear stress on the ground was acting in an offshore direction when the effective stress decreased with excess pore water pressure increase near the surface layer due to the phase difference of the pore water pressure fluctuation.
- As PIV analysis results, the surface-bed was transporting with influences of the bed shear stress, and seepage force with the excess pore water pressure change. The upward velocity of soil particles is suggested as near as its a seepage flow velocity of the geomaterial.

ACKNOWLEDGMENTS

The authors are grateful to the Japan Society for the Promotion of Science for its financial support with Grant-in-Aid for Research Activity Start-up 26889035 and Grants-in-Aid for Scientific Research (C)17K06553.

REFERENCES

[1] Nielsen, P, Robert, S., Moeller-Christiansen, B, Oliva, P., Infiltration effects on sediment mobility under waves. Coastal Eng., Vol. 42, 2001, pp. 105-114.

[2] Madsen, O. S., Wave Induced Pore pressures and Effective Stresses in a Porous Bed, Geotechnique, Vol.28, No.4, 1978, pp. 377-393.

[3] Yamamoto, T., Sea Bed Instability from Waves, Proceedings, 10th Annual Offshore Technology Conference, Paper No.3262, Vol.1, 1978, pp.1819-1824.

[4] Zen, K. and Yamazaki, H., Mechanism of wave-induced liquefaction and densification in seabed, Soils and Foundations, Vol.30, No.4, 1990, pp. 90-104.

[5] Miura, K., Asahara, S., Otsuka, N. and Ueno, K., Formulation of ground for coupled analysis of seabed response to wave loading, Proceedings of Geotechnical Engineering symposium, Vol.49, 2004, pp. 233-240 (in Japanese).

[6] Matsuda, T., Miura, K., Sato, J., Isayama, K. and Sawada, Y., ater pressure change in movable bed regarding similarity law for geamaterial by Dean Number on wave flume experiment, Journal of Japan Society of Civil Engineers, Ser. B2 (Coastal Engineering), Vol. 73, Issue 2, 2017, pp. I_1117-1122.

[7] Dean, R. G., Heuristic models of sand transport in the serf zone, Proc. Conf. Eng. Dyn. in Surf zone, 1973, pp. 208-214.

[8] JSCE, Coastal Wave - Analytical methods for the interaction among waves, structures and seabed -, 1994, pp.781-783 (in Japanese).

[9] Jonsson, I. G., Wave boundary layers and friction factors, Proc. 10th Coastal Eng. Conf., ASCE, 1966, pp. 127-148.

[10] Madsen, O. S. and W. D. Grant, Quantitative description of sediment transport, Proc. 15th Coastal Eng. Conf., ASCE, 1976, pp. 1093-1112

9th Int. Conf. on Geotechnique, Construction Materials and Environment, Tokyo, Japan, 20-22 November 2019, ISBN: 978-4-909106025 C3051

EFFECTS OF VOID UNDER THE SLAB OF THE NAILED-SLAB PAVEMENT SYSTEM DUE TO THE SOIL STRESS

Anas Puri[1*], Muhammad Toyeb[2]
[1]Associate Professor Department the of Civil Engineering Universitas Islam Riau, Pekanbaru, Indonesia
[2]Research Assistant Department of Civil Engineering, Universitas Islam Riau, Indonesia

*Corresponding Author Email: anaspuri@eng.uir.ac.id

ABSTRACT

Nailed-slab System is not a soil improvement method, but rather as an alternative method to improve the performance of rigid pavement on soft soils. The end of the slab of this system is the critical structural element. The void under the end of slab is to be potential to develop because of vehicle wheel paths. If the void is developed under the end of slab, the performance of Nailed-slab Pavement System may be decreased. This research is aimed to learn the effects of the void under the end of the slab due to the soil stress. The numerical analysis will be conducted to investigate the performance of the system. The soil and structural properties of Nailed-slab is based on the previous research on the soft clay. The dimension of the void will be varied in the direction of wide and depth of the void. A standard wheel load 40 kN is set on the end of the slab as a distributed load in 30 cm diameter. Soil stress will be investigated and discussed. Results show that significant effects occur in the soil stress due to the increase of void dimension. Void causes tension stress in the soil. Hence, the void under the slab affects the distributed load stresses to be dominantly resisted by the slab.

Keywords: *rigid pavement, void under slab, soil stress*

INTRODUCTION

The soil under the pavement slab is an important thing in bearing the stress due to traffic loads. Compacted soil tends to transfer the stress relatively uniform in the soil. Voids could occur under the pavement slab of the Nailed-slab System. In case there is a void under the slab, the stress will distribute in non-uniformly in the soil. Concentrated stress will cause maximum stress in the soil. Otherwise, the void can cause decreasing contact area between slab and soils. Hence, the soil bearing will decrease and the slab deflection will increase.

Previous researchers concerned only in normal soil condition under the pavement slab with no voids ([1] - [10]). Soil stress under the Nailed-slab System can be done by a finite element method ([10], [11], [12]).

The critical structural element of the Nailed-slab System is the end of the slab [3]. The void under the end of the slab tends to be more potential developed rather than in the other area. It is important to know what the effects of the void under the slab due to the soil. This research is aimed to investigate the effects of the void under the pavement slab of the Nailed-slab System due to the soil stress. The considered load will be a compression load on the edge of the slab.

METHODOLOGY

This research used soil and a one pile row Nailed-slab structural data from Puri [10]. There was the dense sand layer below the soft clay. The considered load 40 kN was an edge load on the pavement slab. The boundary condition of the soil is shown in Figure 1.

The dimension of Nailed-slab model is 6.0 m x 1.2 m and 0.15 m slab thickness. The slab is supported by 5 piles in a row. Pile diameter was 0.20 m. Pile spacing was 1.20 m. The pile-slab connections were monolithically. The pile length was 1.50 m. The models were analyzed by 2D finite element method. In 2D FEM plain strain analysis, the soft clay was modeled by Mohr-Coulomb in un-drained condition. All structural elements were modeled by plate element in linear-elastic behavior. Lean concrete was modeled by soil with the linear-elastic non-porous material. Soil parameters and idealization of structural elements are presented in Table 1 and 2 respectively.

The void was set under the end of edge slab (actually under the lean concrete). The dimension of voids were varied in 4 variations by depth, h vs. width, w (5 cm x 10 cm; 10 cm x 15 cm; 25 cm x 30 cm; 50 cm x 55 cm). Figure 2 shows the types of void shape and dimension.

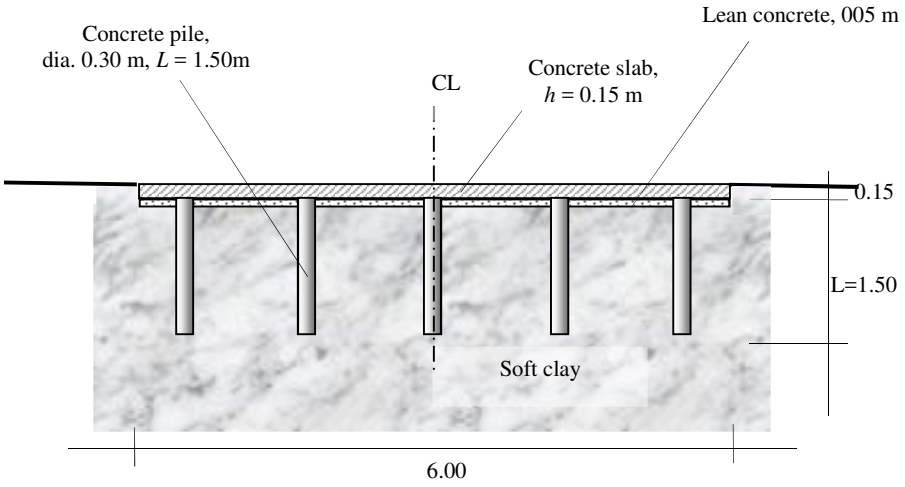

Unit in m. unscale

Fig. 1 Schematic model of Nailed-slab without a void.

Table 1 Model and parameters of soil [10]

Parameters	Name/ Notation	Soft clay	Unit
Material model	Model	Mohr-Coulomb	-
Material behavior	Type	*Un-drained*	-
Saturated density	γ_{sat}	16.30	kN/m^3
Dry density	γ_d	10.90	kN/m^3
Young's Modulus	E	1,790.00	kPa
Poisson's ratio	v	0.45	-
Un-drained cohesion	c_u	20.00	kPa
Internal friction angle	ϕ	1.00	^{o}
Dilatancy angle	ψ	0.00	^{o}
Initial void ratio	e_0	1.19	-
Interface strength ratio	R	0.80	

Table 2 Model and parameters of structural elements in FEM 2D plain strain [10]

Parameters	Name/ Notation	Lean concrete	Structural elements		Unit
			Slab	Pile	
Material model	Model	Volume element	*Plate*	*Plate*	-
Material behavior	Type	Elastic	Elastic	Elastic	-
Normal stiffness	EA	-	4,554,000	738,528	kN/m
Flexural rigidity	EI	-	8,539	5,649.74	kNm^2/m
Equivalent thickness	D	-	0.15	0.3	m
Weight	W	-	3.60	0.9	kNm/m
Poisson's ratio	v	0.2	0.15	0.20	-
Unit weight	γ	22	24	24	kN/m^3
Young's Modulus	E	17,900	25,300	19,600	MN/m^2
Interface strength ratio	R	0.80	0.80	0.80	-

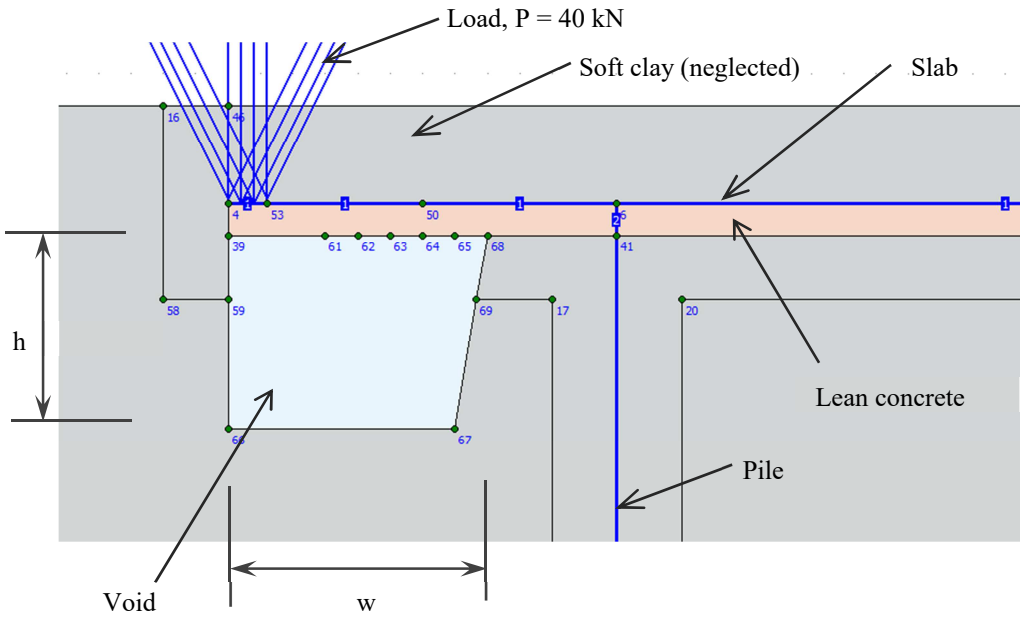

Fig. 2 Typical model of void shape and dimension under the end of edge slab.

RESULTS AND DISCUSSIONS

Figure 3 shows the effective stress of soil in the base of the void. In the normal condition (0 x 0 void), there was the effective stress in compression condition. Otherwise, in case there was a void under the slab, the effective stresses were changed to be in tension condition. This is not beneficial for the soil because soil cannot bear the tension stress. It is evident that the void causes negative effects the soil stress. Soil can easily fail in tension stress condition. Effective stress of soils tends to be relatively constant by increasing the void dimension. Hence, the distributed load stresses to be dominantly resisted by the slab.

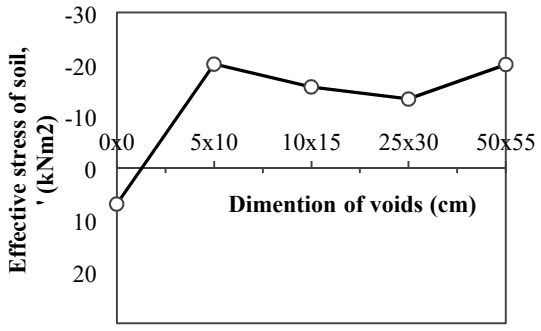

Fig. 3 Effective stress of soil vs. dimension of the void.

Figure 4 shows the effective stress distribution of soil around the void 10 cm x 15 cm. Tension stress condition occurred around the end of the slab and in the right base of the void. The other void dimensions had similar behavior.

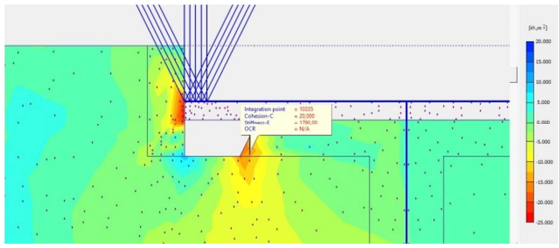

Fig. 4 Effective stress distribution of soil around the void 10 cm x 15 cm.

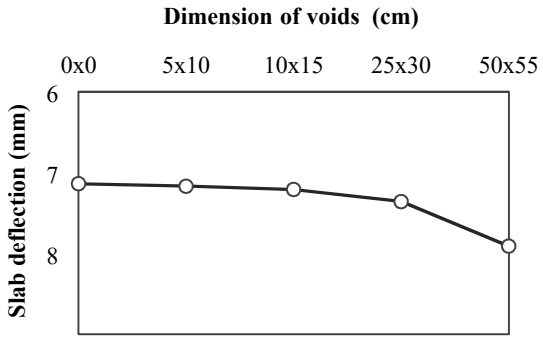

Figure 5. The relation between slab deflection and voids dimensions.

Figure 5 shows the relation between slab deflection and voids dimensions. Because of the distributed load stresses was dominantly resisted by the slab, the slab deflection tends to increase the void dimension. Changing the effective stress of soil around the void affects the increasing slab deflection insignificantly. Loading stresses were distributed dominantly in the slab through bending moments. Hence, the slab dominates to resist this bending moment by its resistance moment. Since the bigger void dimension under the slab, the distributed stress load was dominantly bear by the slab.

CONCLUSIONS

The void under the slab can change the effective stresses of soil in compression to be in tension condition. It is not beneficial for the soil because soil cannot bear the tension stress. It is evident that the void causes negative effects on soil stress. Effective stress of soils tends to be relatively constant by increasing the void dimension. Hence, the void under the slab affects the distributed load stresses to be dominantly resisted by the slab. Further research should be done to investigate the inner forces of structural elements.

ACKNOWLEDGMENTS

Authors to thanks for supporting by Research Institutes and Community Service (LPPM) and the Laboratory of Civil Engineering Computational of Universitas Islam Riau.

REFERENCES

[1] Hardiyatmo, H.C., Method to Analyze the Deflection of the Nailed Slab System, IJCEE-IJENS, Vol 11. No. 4, 2011, pp. 22-28. http://ijens.org/IJCEE%20Vol%2011%20Issue%2004.html.

[2] Puri, A., Hardiyatmo, C. H., Suhendro, B., Rifa'i, A., Experimental Study on Deflection of Slab which Reinforced by Short Friction Piles in Soft Clay. In Proc. of 14th Annual Scientific Meeting (PIT) HATTI, 2011, Yogyakarta, 10-11 February, pp. 317-321 (in Indonesian).

[3] Puri, A., Hardiyatmo, H.C., Suhendro, B., Rifa'i, A., Contribution of Wall Barrier to Reduce the Deflection of Nailed-Slab System in Soft Clay. In Proc. of 9th Indonesian Geotech. Conf. and 15th Annual Scientific Meeting (KOGEI IX & PIT XV) HATTI, Jakarta, 7-8 December 2011, pp. 299-306 (in Indonesian).

[4] Puri, A., Hardiyatmo, H. C., Suhendro, B., & Rifa'i, A., Determining Additional Modulus of Subgrade Reaction Based on Tolerable Settlement for the Nailed-slab System Resting on Soft Clay. International Journal of Civil and Environmental Engineering IJCEE-IJENS, 12 (03), 2012, pp. 32-40. http://ijens.org/IJCEE%20Vol%2012%20Issue%2003.html.

[5] Puri, A., Hardiyatmo, H. C., Suhendro, B., & Rifa'i, A., Application of The Additional Modulus of Subgrade Reaction to Predict The Deflection of Nailed-slab System Resting on Soft Clay Due to Repetitive Loadings. In Proc. of 16th Annual Scientific Meeting (PIT) HATTI, 2012, pp. 217-222.

[6] Puri, A., Hardiyatmo, H. C., Suhendro, B., & Rifa'i, A., Application of Method of Nailed-slab Deflection Analysis on Full Scale Model and Comparison to Loading Test. In Proc. the 7th National Conference of Civil Engineering (KoNTekS7), Surakarta, October 2013, pp. G201-G211.

[7] Puri, A., Hardiyatmo, H.C., Suhendro, B., Rifa'i, A., The Behavior of Nailed-slab System on Soft Clay Due to Repetitive Loadings by Conducting a Full-Scale Test. IJCEE-IJENS, Vol. 14 No. 06, 2014, pp. 24-30. http://ijens.org/IJCEE%20Vol%2014%20Issue%2006.html.

[8] Puri, A., Hardiyatmo, H.C., Suhendro, B., Rifa'i, A., Pull out Test of Single Pile Row Nailed-slab System on Soft Clay, Proc. The 14th International Conference on Quality in Research (QiR), Universitas Indonesia, Lombok, 10-13 August 2015, pp. 63-68.

[9] Puri, A., Hardiyatmo, H.C., Suhendro, B., Rifa'i, A., Validating The Curve Of Displacement Factor Due To Full Scale Of One Pile Row Nailed-Slab Pavement System. International Journal of GEOMATE, Vol.17, Issue 59, 2019, pp.181-188. DOI: https://doi.org/10.21660/2019.59.65815

[10] Puri, A., Behavior of Pavement of Nailed-slab System on Soft Clay, *Dissertation*, Doctoral Program of Civil Engineering, Universitas Gadjah Mada, 2015, Yogyakarta.

[11] Puri, A., Suhendro, B., & Rifa'i, A., Effects Of Vertical Wall Barrier On The Rigid Pavement Deflection Of Full-Scale 1-Pile Row Nailed-Slab System On Soft Sub Grade. International Journal of GEOMATE, Vol. 12 Issue 32, 2012, pp. 25-29. DOI: http://dx.doi.org/10.21660/2017.32.6577

[12] Puri, A., and Mildawati, R., Investigasi Numerik Perkerasan Jalan Sistem Pelat Terpaku terhadap Variasi Dimensi Struktur. BENTANG Jurnal Teoritis dan Terapan Bidang Rekayasa Sipil, 7 (01), 2019, pp. 1-7. (in Indonesian). http://jurnal.unismabekasi.ac.id/index.php/bentang/article/view/1594

9th Int. Conf. on Geotechnique, Construction Materials and Environment, Tokyo, Japan, 20-22 November 2019, ISBN: 978-4-909106025 C3051

A DETERMINISTIC APPROACH OF GENERATING EARTHQUAKE LIQUEFACTION SEVERITY MAP OF MINDORO, PHILIPPINES

John Guinto[1], Mariz Espinoza[1], Joey Grimaldo[1], Daniel Juan[1], Michael Mapacpac[1], and Nolan Concha[1]
[1]FEU-Institute of Technology, Philippines

ABSTRACT

An essential component in decision making for site planners is the availability of risk maps to various geological hazards. Liquefaction in particular can be devastating and impose disastrous damage to existing structures built in earthquake prone areas like the province of Mindoro. Through the aid of in situ data, a simplified method of evaluating earthquake induced liquefaction potential was carried out in this study. This is to address the difficulty and high cost necessary to carry out the development of a liquefaction risk map. Borehole data were collected from different locations in Mindoro and the earthquake liquefaction severity index in each location were calculated using deterministic approach. Results showed that different levels of liquefaction severity were obtained in various areas of Mindoro. There were locations exhibiting manifestations of surface liquefaction due to 7.1 Mw earthquake with a peak ground acceleration of 0.4g. The generated liquefaction severity maps can be utilized as baseline information in selecting appropriate geotechnical intervention for soil improvement and stabilization. Further, the indices can be used as additional dimension of evaluating the holistic reliability of existing engineering structures.

Keywords: Borehole, Liquefaction, Liquefaction Severity Index, Risk Map

INTRODUCTION

The Philippine Archipelago is located within the Pacific Ring of Fire. For this reason, the country is vulnerable to two natural hazards characteristic of this region that are significant to this study – earthquakes and soil liquefaction. Earthquakes, which is the shaking of the earth's surface due to the sudden release of energy in the lithosphere, often causes soil liquefaction. Soil liquefaction takes place when ground movements or earthquakes cause an increase in water pressure that turns the solid ground into a liquid-like state. The shaking of the ground disrupts the soil by increasing the spaces between grains, which in turn lessens soil cohesion, making the soil lose its bearing capacity or strength [1]. These disturbances in the ground lead to a significant problem for areas at risk for soil liquefaction - multi-story buildings and other infrastructures experience the sudden loss of support of the soil underneath it that may cause buildings to collapse. Owing to the Philippines' location in the Pacific Ring of Fire, a record number of earthquakes occurs almost every day in parts of the Philippines, but most are imperceptible tremors that people are entirely unaware of. Because of this, the impact and risks brought upon by soil liquefaction often have devastating results due to people being unaware that they are in risk zones.

There are a number of measures that can be done to lessen the impact and risk that this hazard can incur to a community. This phenomenon can be mitigated, through soil stabilization and a number of ground improvement techniques. Such as accelerating the dissipation of pore water pressure by inducing radial drainage through sand or stone columns, inducing cohesion into the soils or jet-grouting which also increases the density and strength, injection of chemical additives, and liquefaction mapping through hazard indexing. There are several approaches on how to develop liquefaction map by means of: First, Probability of Liquefaction by Chen and Juang [2], Iwasaki et-al. Liquefaction Potential Index [3], Liquefaction severity index by Sonmez and Gokceoglu [4]. In this study, the approach of liquefaction severity index proposed by Sonmez and Gokceoglu [4] will be used for probability and severity mapping. This introduces the probability of liquefaction equation based on the factor of safety to the liquefaction potential index concept. Rearranging the classification of liquefaction severity was done by considering Chen and Juang's probability of liquefaction classes based on P_L values. For this research, the Mindoro province were evaluated for generation of the liquefaction severity map by considering earthquake scenario of Mw=7.1 based from the destructive 1994 Mindoro earthquake.

Mindoro in particular is the seventh largest island in the Philippines by land area with a total of 10,571 square kilometers and is prone to Earthquakes [5]. However, no disaster mitigating methods due to earthquake liquefaction was carried out in the province. The absence of a liquefaction map might

impose devastating impact on built environment resulting to damage to structures and intangible losses.

To address this, this study aims to develop earthquake liquefaction severity map to identify liquefaction prone areas and measure the severity of liquefaction when an earthquake of various magnitudes occurs in the province. The generated map can be utilized as baseline information to develop appropriate mitigation techniques to lessen the risk of earthquake liquefaction. A rapid and inexpensive assessment of the degree of liquefaction can be carried out in a timely and convenient approach with the aid of the generated maps.

EXPERIMENTAL PROGRAM

This presents the procedures that the researchers have undergone to achieve the objectives of this study. The data gathered from the geotechnical reports were used for the calculation of the factor of safety against liquefaction (F_L) to the calculation of the probability of liquefaction (P_L) and the liquefaction severity index (LSI) as shown in Fig. 1. These will be used to determine if the soil in the Province of Occidental Mindoro is liquefiable or not liquefiable using earthquake magnitude 7.1 and to determine the severity of liquefaction in each location.

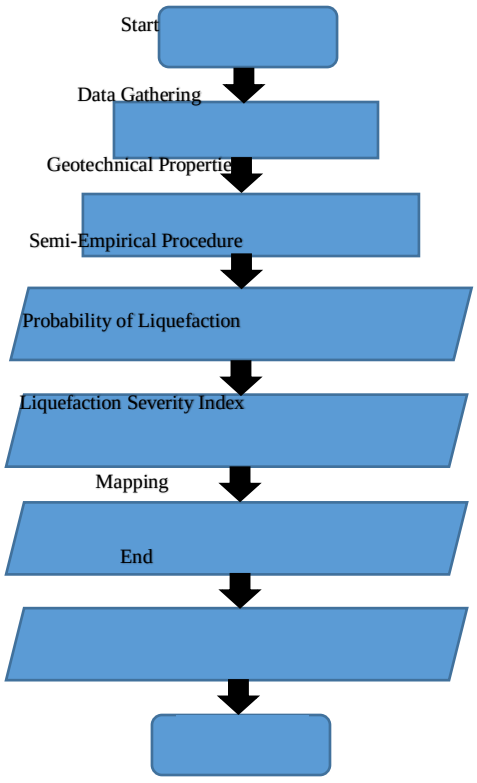

Fig. 1 Liquefaction Mapping Generation

A quantitative research that focused on computational techniques for the investigation with regards to liquefaction is used in this study. The geotechnical properties gathered from geotechnical reports was tabulated in Microsoft Excel to obtain the vertical pressure, pore water pressure, effective pressure, and the factor of safety against liquefaction at every 1.5 m layer. The susceptibility of liquefaction was based on the factor of safety against liquefaction by Idriss and Boulanger [6]. The Probability of Liquefaction (P_L) and the Severity of Liquefaction at each location was based on the Liquefaction Severity Index by Sonmez and Gokceoglu [4] which uses P_L values by Chen and Juang.

The Probability of Liquefaction by Chen and Juang based on $\mathbf{P_L}$ values were considered in rearranging the classification of liquefaction severity. An equation proposed by Juang et al. [2] was introduced by Sonmez and Gokceoglu to overcome the use of linear relation for impact of the factor of safety on liquefaction potential [4]. Table 1 shows the classification of the severity index.

Table 1 Classification of Liquefaction Severity Index

Liquefaction Severity Index	Classification
$L_s = 0$	Non-Liquefiable
$0 < L_s < 15$	Very Low Liquefaction Severity
$15 < L_s < 35$	Low Liquefaction Severity
$35 < L_s < 65$	Medium Liquefaction Severity
$65 < L_s < 85$	High Liquefaction Severity
$85 < L_s < 100$	Very High Liquefaction Severity

$$\mathbf{FS} = \frac{\mathbf{CRR_m}}{\mathbf{CSR}} \quad (1)$$

$$\mathbf{L_S} = \int_0^{20} \mathbf{P_L(z)W(z)dz} \quad (2)$$

$$\mathbf{P_L(z)} = \frac{1}{1+\left(\frac{F_L}{0.96}\right)^{4.5}} \text{ for } \mathbf{F_L \leq 1.411} \quad (3)$$

$$\mathbf{P_L(z) = 0} \text{ for } \mathbf{F_L > 1.411} \quad (4)$$

$$\mathbf{W(z) = 10 - 0.5z} \text{ for } \mathbf{z < 20m} \quad (5)$$

$$\mathbf{W(z) = 0} \text{ for } \mathbf{z > 20m} \quad (6)$$

RESULTS AND DISCUSSION

Geotechnical Assessment

Considering the geotechnical properties of Occidental, Mindoro, this study analyzes the factors of safety against liquefaction (F_L), the probability of liquefaction (P_L) and corresponding liquefaction severity indices for an earthquake having magnitude 7.1. The number of borehole logs on each municipalities of Occidental Mindoro are shown in Fig. 2.

Fig. 2 Map of Occidental Mindoro.

The data gathered from the Province of Occidental Mindoro was evaluated based from the water content, number of blows, N-values, and the depth of soil. The number of blows is the most dominant geotechnical characteristic because it affects the whole computation for Cyclic Resistance Ratio (CRR). The water content, specific gravity of soil and the depth of soil is important for computing the Vertical Pressure, Pore Water Pressure, and Effective Pressure which will contribute to the computation of the Cyclic Shear Ratio (CSR). The CSR and CRR values will help us obtain the factor of safety for each 1.5 m layer. Considering different factors needed in this study, a total of 73 boreholes were used as shown in Table 2.

Table 2 Borehole Distribution in Occidental, Mindoro

List of Municipalities	No. of Boreholes
Abra de Ilog	11
Calintaan	4
Magsaysay	9
Mamburao	12
Paluan	9
Rizal	1
Sablayan	13
San Jose	8
Sta. Cruz	6
Total No. of Boreholes	73

Based from the geotechnical report, the water content and n-values were used to solve the vertical pressure, pore water pressure, and effective pressure as shown in Table 3.

Table 3 Geotechnical Properties

DEPTH	WATER CONTENT	N-VALUE	VERTICAL PRESSURE	PORE WATER PRESSURE	EFFECTIVE PRESSURE
1.5	100	22	14.07	4.41	9.65
3	100	18	35.54	19.13	16.41
4.5	98	28	57.12	33.84	23.27
6	100	11	78.59	48.56	30.03
7.5	100	11	100.07	63.27	36.79
9	100	7	121.55	77.99	43.56
10.5	100	6	143.02	92.70	50.32

Semi-Empirical Procedure

A Semi-Empirical Procedure based on Idriss and Boulanger was used in this study to calculate the safety factor against liquefaction refer to Eq. (1). In determining the Factor of Safety, the values of the reduction factor (r_d), Magnitude Scaling Factor (MSF), equivalent clean sand standard penetration resistance value ($N_{1(60)CS}$), cyclic shear stress ratio (CSR), and cyclic resistance ratio (CRR) will be obtained as shown in Table 4. The soil is susceptible to liquefaction if $FS \leq 1$ or otherwise, it is not susceptible to liquefaction if $FS > 1$.

Table 4 Result of Factor of Safety at Magnitude 7.1

DEPTH	CSR	CRRm	FS
1.5	2.51	1.41	0.56
3	3.73	0.27	0.07
4.5	4.23	0.49	0.12
6	4.51	0.13	0.03
7.5	4.68	0.12	0.03
9	4.80	0.10	0.02
10.5	4.89	0.09	0.02

The table above shows the result of the factor of safety at magnitude 7.1. This table shows that with an increasing depth the reduction factor decreases and as CSR is greater than that of CRRm, the value of the factor of safety against liquefaction is less than 1 and is identified as a liquefiable layer, or otherwise, a non-liquefiable layer.

Liquefaction Severity Index

The factor of safety against liquefaction can be used to calculate the probability of liquefaction and the liquefaction severity index refer to Eq. (2), (3), (4), (5), (6) and as shown in Table 6.

Table 6 Computation of LSI for GPA 0.4g corresponding to Mw=7.1

DEPTH	Z	H	w(z)	$P_L(z)$	LSI
1.5	0.75	1.50	9.63	0.13	1.81
3	2.25	1.50	8.88	0.73	9.65
4.5	3.75	1.50	8.13	0.60	7.31
6	5.25	1.50	7.38	0.87	9.66
7.5	6.75	1.50	6.63	0.88	8.79
9	8.25	1.50	5.88	0.91	8.02
10.5	9.75	1.50	5.13	0.92	7.05
				∑LSI =	52.29

Level of Liquefaction Severity: MODERATE

Mapping

The probability of the soil to liquefy and the severity of liquefaction for each location was obtained in terms of LSI values of 9 municipalities having 73 boreholes around Occidental Mindoro. The maps of LSI values were generated for the province to show the distribution of the probability and severity of liquefaction as shown in Fig. 3 and Fig. 4. The probability map and the severity map will help identify liquefaction prone areas and measure the severity of liquefaction when an earthquake of various magnitudes occurs in the province.

The maps of LSI generated for the Province of Occidental Mindoro representing the probability of liquefaction and the levels of severity of liquefaction for an earthquake magnitude of Mw=7.1. The levels of severity as shown in Table 1. Abra De Ilog has 70-78% probability of liquefaction though the severity level varies from low to medium, Calintaan has 0-2.575% probability of liquefaction and the severity level varies from very low to low, Magsaysay has 0-66.15% probability of liquefaction and the severity level varies from very low to medium, Mamburao has 0-85.75% probability of liquefaction and the severity level varies from low to medium, Paluan has 0-41% probability of liquefaction and the severity level varies from very low to medium, Rizal has 11.25% probability of liquefaction and the severity level is low, Sablayan has 0-91.71% probability of liquefaction and the severity level varies from very low, low, and medium, Sta. Cruz has 0-83.20% probability of liquefaction and the severity level varies from low to medium, San Jose has 0-73.59% probability of liquefaction and the severity level varies from very low, low, and medium. Based on the analysis, Abra De Ilog, Magsaysay, Mamburao, Sablayan, Sta. Cruz, and San Jose has high probability of liquefaction while Calintaan, Paluan, and Rizal has low probability of liquefaction. Sablayan has the highest probability of liquefaction due to a smallest value of FS and as observed from the data, the least number of blows results to a smaller value of FS. Also, the effective pressure and depth of the soil affects the probability of liquefaction. The deeper the depth, the larger the pressure and at the same time has the least number of blows results to a higher probability of liquefaction as observed in the data. The factors that contributed to the level of liquefaction severity is the LSI value at every 1.5 m layer. The summation of all LSI values at each location results to the level of liquefaction severity.

As a result, the category of high to very high liquefaction severity were not observed for the earthquake scenario Mw=7.1. The factors that affects the severity of liquefaction are the depth of the midpoint of the soil layers, the thickness of the soil layer, and the probability of liquefaction. The higher the probability of liquefaction at a certain layer and the nearer it is to the ground results to a higher chance of having larger LSI values. Majority of the studied areas in the province are in moderate liquefaction severity as described by the LSI values. Furthermore, the severity of liquefaction in Occidental Mindoro ranges from very low to medium liquefaction severity although it is susceptible to liquefaction. Municipalities with low chance of liquefaction is because of the not existing ground water table at a depth of 10.5 m which means a dry soil in that certain depth and a shallow ground water table has very high chance to liquefy. It can be

observed in the probability map that a high chance of liquefaction would likely to occur in some of the areas in Occidental Mindoro while it can be observed in the severity map that most of the areas is not that severe when liquefaction would occur during seismic events.

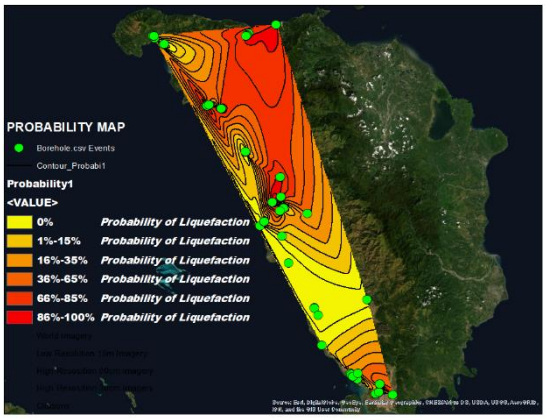

Fig. 3 Liquefaction Probability Map of Occidental Mindoro at EQ Magnitude 7.1

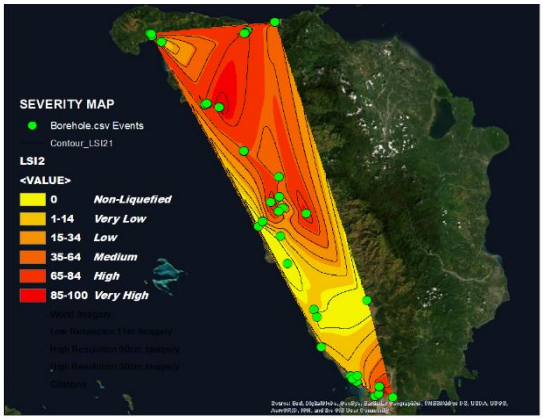

Fig. 4 Liquefaction Severity Map of Occidental Mindoro at EQ Magnitude 7.1

CONCLUSION

The soil properties were investigated in the Province of Occidental Mindoro to show manifestation of soil liquefaction during seismic events. It was observed that majority of the municipalities have high degree to liquefaction as described by P_L values, and the severity of liquefaction is not that severe in a 7.1 earthquake magnitude as described by LSI values. The Probability and Severity Map were able to provide a rapid and inexpensive assessment of the degree of liquefaction in a timely and convenient approach, which are essential to structural engineers in improving the safety matters of any structures to be built and developed in the Province of Occidental Mindoro.

ACKNOWLEDGMENTS

Special thanks to DPWH Occidental Mindoro who provided necessary geotechnical data needed in order to support our study.

REFERENCES

[1] Rahman, Md Zillur, Sumi Siddiqua, and ASM Maksud Kamal. "Liquefaction hazard mapping by liquefaction potential index for Dhaka City, Bangladesh." *Engineering geology* 188 (2015): 137-147.

[2] Juang, C. Hsein, Tao Jiang, and Ronald D. Andrus. "Assessing probability-based methods for liquefaction potential evaluation." *Journal of Geotechnical and Geoenvironmental Engineering* 128, no. 7 (2002): 580-589.

[3] Iwasaki, Toshio, Tadashi Arakawa, and Ken-Ichi Tokida. "Simplified procedures for assessing soil liquefaction during earthquakes." *International Journal of Soil Dynamics and Earthquake Engineering* 3, no. 1 (1984): 49-58.

[4] Sonmez, H., and C. Gokceoglu. "A liquefaction severity index suggested for engineering practice." *Environmental Geology*48, no. 1 (2005): 81-91.

[5] Garcia, Ian Frederic P., Jesse Thaddeus M. Go, Rio Jasmin D. Go, Paoala Beatrize B. Suspine, and Nolan C. Concha. "Earthquake liquefaction susceptibility mapping of Pasig City." In 2017IEEE 9th International Conference on Humanoid, Nanotechnology, Information Technology, Communication and Control, Environment and Management (HNICEM), pp. 1-5. IEEE, 2017.

[6] Idriss, I. M., and R. W. Boulanger. "Semi-empirical procedures for evaluating liquefaction potential during earthquakes." *Soil dynamics and earthquake engineering* 26, no. 2-4 (2006): 115-130.

9th Int. Conf. on Geotechnique, Construction Materials and Environment,
Tokyo, Japan, 20-22 November 2019, ISBN: 978-4-909106025 C3051

THE INCREASING OF UNDRAINED SHEAR STRENGTH AND SHEAR MODULUS OF SOFT BANGKOK CLAY BY SILICA POWDER USING UNCONFINED COMPRESSION TEST WITH BENDER ELEMENT

Pithan Pairojn[1]
[1] Faculty of Science, Chandrakasem Rajabhat University, Thailand

ABSTRACT

The present study aims to increase the undrained shear strength and shear modulus of soft Bangkok Clay soil by silica powder when they were subject to unconfined compression test with the bender element. The shear wave velocity was measured using a pair of bender elements installed at the top cap and pedestal of the unconfined cell. The undrained shear strength was conducted step by step so that the variation of shear modulus could be determined. The undrained shear strength was carried out at the strain rate of 1% per minute during which the shear modulus was continuously recorded. The result found that when the soil was mixed with silica powder an increased rate, the undrained shear strength and shear modulus were increased but the strain was decreased. Therefore, the improvement of soil quality using silica powder can be increased the efficiency of the construction such as embankment and road construction.

Keywords: Undrained shear strength, Shear modulus, Bangkok Clay, Silica powder, Bender element

INTRODUCTION

At present, the construction in the central region of Thailand, such as road construction, slope construction, etc., has been damaged due to soil foundations that are soft clay (Bangkok soil), especially roads along the canal (Fig. 1). Therefore, requires the design and construction of roads to be appropriate according to the engineering principles which cause the collapse of roads along the irrigation canal caused by

1. Infrastructure construction and buildings in soft clay areas where soft clay layers are characterized by varying depth.
2. The rapid drop of water level in the irrigation canal (Sudden drawdown) from normal use with water supplying into the canal or during the extreme drought that farmers will accelerate pumping water into the garden or farmland area (Fig. 2) or in the late rainy season, early in the winter, the water in the canal will be drained faster, which will give the opportunity to the collapse of the riverbank slope in this regard. The behavior of river bank collapse due to the rapid decrease of water level, especially the clay bank soil slopes so that water and pressure caused water to flow out. If the water pressure is high enough, it will cause the river bank slopes and roads along the canal to collapse.
3. Longer summer months as a result of global climate change directly affect the collapse of river bank slopes and roads along the irrigated canal due to lack of water in the canal that will help push or support the bank slopes to stabilize.

This research focuses on improving soft soils by using additional mixtures, which the researcher uses silica powder because it is cheap, easily available, can fill the gap between soil mass and can increase the undrained shear strength and shear modulus of soft soil. The silica powder is not very expensive compared to other additive mixtures. Therefore, the construction of roads or roads along the canal can use clay mixed with silica powder for the efficiency, the investment value and the reduction of soil collapse [1]-[4].

Fig. 1 Damage of roads along the canal.

Fig. 2 Rapid drop of water level in the irrigation canal.

METHODOLOGY

Use at most three levels of headings that correspond to chapters, sections and subsections. The first level headings for chapter titles should be in 10pt, bold, justified, and upper case font. Leave one blank line before and after the first level headings, respectively.

Unconfined Compression Test with Bender Element

The researcher developed the unconfined compression test with bender element (UCTwBE) by using the unconfined compression test of ELE International to install the axial force transducer and axial displacement transducer of Kyowa (Fig. 3).

Fig. 3 Unconfined compression test with bender element.

Bender Element

Install the bender element to measure small strain modulus. The Bender element converts the Eletro-mechanical system by converting mechanical energy (Vibration) into electrical energy. On the other hand, it converts electrical energy into mechanical energy. The bender element is characterized by two piezo ceramic plates attached together, can be both a transmitter and receiver (Fig. 4). Since the bender element is a material that resists electricity, therefore, the use must be careful about short-circuiting, the need to have electrical insulation because of moisture by using epoxy coating around the bender element (Fig. 5).

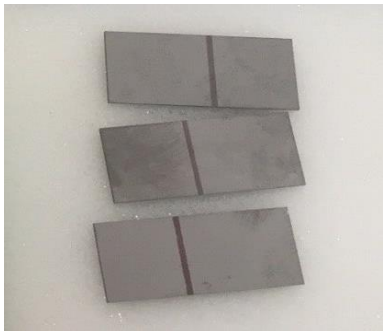

Fig. 4 Sample of bender element T226.

Fig. 5 Connecting the power cable to the bender element.

Signaling and Recording Equipment

Install the equipment for wave signal transmission using NI CompactDAQ Set (Fig. 6), which is installed with NI9237, NI9215, NI9263, NI9915, Function generator, Amplified voltage and DC supply 24V 5A for control and recording with CRU-Bender Recorder from LabView program (Fig. 7).

Fig. 6 NI CompactDAQ Set.

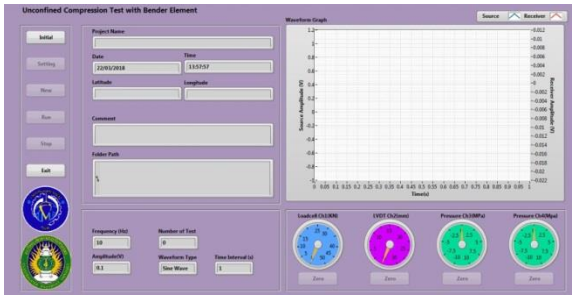

Fig. 7 CRU-Bender Recorder program.

Soil Properties Testing

Collect soil samples for testing as clay at Bang Khen in Bangkok, Thailand at a depth of 0-5 meters (13° 53’ 03" N, 100° 36’ 19" E) with engineering Properties as shown in Table 1.

Table 1 Engineering properties of clay samples

Property	Standard	Value
Water content, W_c (%)	ASTM D4959-00	20-21
Total unit weight, γ_t (t/m^3)	ASTM D4253-00	1.95
Liquid limit, LL (%)	ASTM D4318	53
Plastic limit, PL (%)	ASTM D4318	28
Plasticity index, PI (%)	ASTM D4318	25
Specific gravity, G_s	ASTM D854-00	2.56

Mixing Clay with Silica Powder

Compaction of clay as standard ASTM D698-12e2 standard test methods for soil using standard effort [5] by mixing normal water and mixing silica powder by 5% to 50% of water weight, respectively. Silica powder in Thailand is easy to find because Thailand has a lot of paddy so it can be synthesized into silica powder. Mix together (Figs. 8 and 9) and cut samples according to ASTM D2166-00 standard test method for unconfined compressive strength of cohesive soil [7] as shown in Fig. 10, installed with the UCTwBE to find undrained shear strength and shear modulus values.

Fig. 8 Mixing silica powder.

Fig. 9 Standard compaction test.

Fig. 10 Soil sample cutting.

Determination of Undrained Shear Strength

When cutting samples obtained from soil compaction tests Installed with the unconfined compression test with bender element (Fig. 11). The undrained shear strength can be obtained from Eq. (1) according to the standard ASTM D2166-00 Standard Test Method for Unconfined Compressive Strength of Cohesive Soil [6].

$$S_u = q_u / 2 \quad (1)$$

Where S_u = Undrained shear strength (kPa), q_u = Unconfined compressive strength (kPa).

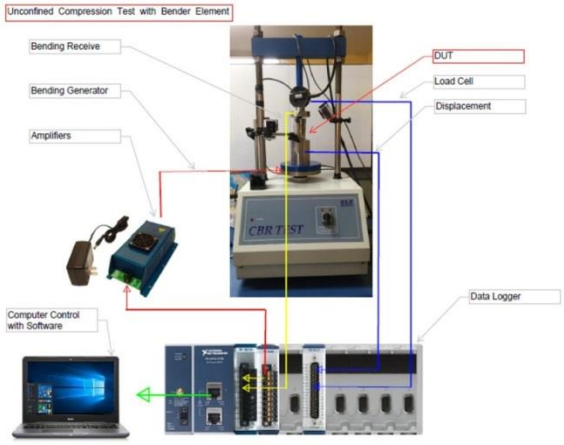

Fig. 11 The system of unconfined compression test with bender element.

Determination of Shear Wave Velocity and Shear Modulus

Shear Wave Velocity

During the testing of soil compression (Fig. 12), the sine waveform is generated and transmitted by a 20V pp 1 kHz frequency signal from the function generator and sent via the transmitter at the base through the soil sample to the receiver at the top cap when the shear wave travels through the soil sample. The shear wave velocity can calculate as Eq. (2) [7]-[8].

$$V_s = L / t \quad (2)$$

Where V_s = Shear wave velocity (m/s), L = Distance between transmitter and receiver (m), t = The travels time of wave between transmitter and receiver peak-peak (s).

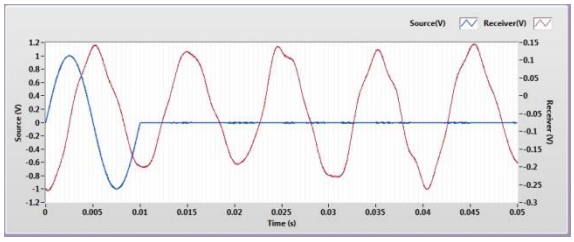

Fig. 12 Shear wave from the test of mixing silica powder by 30%.

Shear Modulus

When the shear wave velocity is obtained, then the small-strain shear modulus can be obtained from Eq. (3).

$$G_{max} = \rho V_s^2 \quad (3)$$

Where G_{max} = Shear modulus (MPa), ρ = Soil density (kN/m^3), V_s = Shear wave velocity (m/s).

RESULTS AND DISCUSSION

Result of Undrained Shear Strength

Figure 13 showed that the undrained shear strength of the soil mixed with silica 50% of water weight was the highest about 69.25 kPa. Which is greater than the soil mixed with water about 30.34 kPa, which is about 2 times at optimum moisture content (OMC).

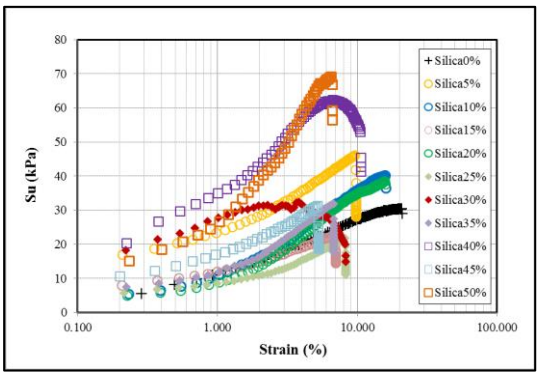

Fig. 13 Undrained shear strength of soil.

Figure 14 showed that the shear wave velocity of the soil mixed with silica 5% of water weight was the highest about 436.58 m/s. Which is greater than the soil mixed with water about 211.39 m/s, which is about 2 times at optimum moisture content (OMC).

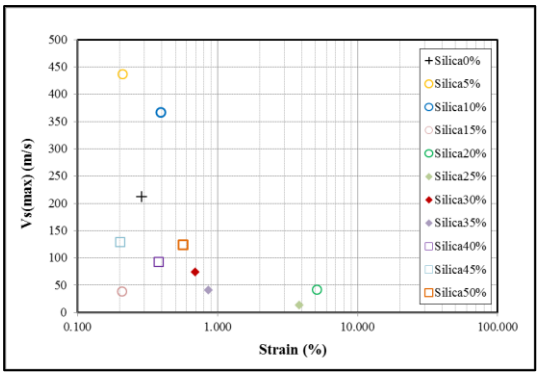

Fig. 14 Shear wave velocity of soil.

Figure 15 showed that the shear modulus of the soil mixed with silica 5% of water weight was the highest about 4,117.09 MPa. Which is greater than the soil mixed with water about 933.91 MPa, which is about 4 times at optimum moisture content (OMC).

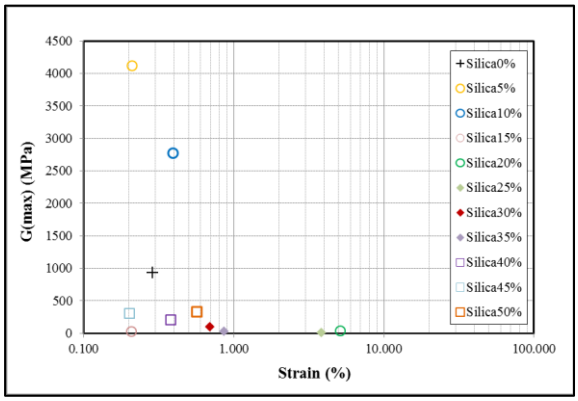

Fig. 15 Shear modulus of soil.

CONCLUSION

The results of the research concluded that improvement of soil quality by using silica powder approximately 5-10% of water weight as an additive during soil compaction in construction can increase the efficiency of the pavement to have undrained shear strength and shear modulus rather than soil mixed with water. Therefore, silica powder can be used to improve soil quality by mixing it as an additive during soil compaction. The unconfined compression test with bender element developed by the researcher can be used to determine the undrained shear strength and shear modulus. Thus, reducing time and cost savings in soil testing. It can be used to solve problems during construction, so it is an innovation that is suitable for engineers, designers, field engineers and supervisors. In future research, the researcher will conduct on the modification of soil chemical structure by mixing silica powder.

ACKNOWLEDGMENTS

The author would like to acknowledge the Chandrakasem Rajabhat University Research Grant, which collectively funded this project.

REFERENCES

[1] Barnes G., Workability of Clay Mixtures. Applied Clay Science, Vol. 153, 2018, pp. 107-112.

[2] Goodarzia A., Akbari H.R., and Salimi M., Enhanced Stabilization of Highly Expansive Clays by Mixing Cement and Silica Fume. Applied Clay Science, Vol. 132, Issue 133, 2016, pp. 678-684.

[3] Istratea O., and Chen B., Structure and Properties of Clay/Recycled Plastic Composites. Applied Clay Science, Vol. 156, 2018, pp. 144-151

[4] Mousavi S.E., and Karamvand A., Assessment of Strength Development in Stabilized Soil with CBR Plus and Silica Sand. Journal of Traffic and Transportation Engineering, Vol. 4, Issue 4, 2017, pp. 412-421.

[5] ASTM International, ASTM D 698-12e2 Standard Test Methods for Laboratory Compaction Characteristics of Soil Using Standard Effort, 2019, pp. 1-13.

[6] ASTM International, ASTM D 2166-00 Standard Test Method for Unconfined Compressive Strength of Cohesive Soil, 2000, pp. 1-6.

[7] Pairojn P., The Simple Method of Shear Wave Velocity Profile from Explosion Source in Surin, Thailand. International Journal of GEOMATE, Vol. 16, Issue 58, 2019, pp.184-189.

[8] Pairojn P., and Pedrung S., An identification of shear wave velocity of soft bangkok clay using unconfined compression test with bender element, in Proc. 23rd National Conf. on Civil Engineering, 2018, pp. 1-10.

9th Int. Conf. on Geotechnique, Construction Materials and Environment, Tokyo, Japan, 20-22 November 2019, ISBN: 978-4-909106025 C3051

EVALUATION OF GROUNDWATER FLOW CHARACTERISTICS BY VOLTAGE DIFFERENCE METHOD ELECTRICAL PROSPECTING

Shuichi MIYAJI[1], Hisayuki NAKANE[1], Itsuo KAWASAKI[2], Yoshihiro NAGANO[2], Shuichi HASEGAWA[3] and Minoru YAMANAKA[3]
[1] Chiken Inc. Ltd., Japan; [2] Japan Crust Research co., ltd, Japan; [3] Faculty of Eng., Kagawa University, Japan

ABSTRACT

Evaluation of groundwater flow channel is very important for utilization and conservation of groundwater resources, safety and economical construction work, and protection of soil and groundwater against pollution. Although electric prospecting has long been used to evaluate the groundwater flow path, its interpretation is comparatively hard, because resistivity depends on groundwater as well as soils and bedrock.

The voltage difference method is an electrical prospecting method that obtains the resistivity change rate in addition to the normal resistivity, and by promoting forced polarization, it is possible to improve the estimation accuracy of the distribution and properties of the groundwater flow path. In this study, the relationship between resistivity change rate and groundwater flow and the relationship between the groundwater yield by observation holes was verified at the site where the groundwater survey such as electrical prospecting, boring survey and pumping test was conducted. As a result, the following was found. (1) The estimation interpretation of groundwater flow area is improved by resistivity change rate rather than resistivity. (2) The resistivity change rate and the yield may have a positive correlation.

This paper reports the effectiveness of the voltage difference method confirmed from the verification results of the research.

Keywords: groundwater flow, voltage difference method, electrical prospecting, resistivity, resistivity change rate

INTRODUCTION

No clear definition is given for the groundwater flow layer, so-called "water path", but it is qualitatively considered as "a place where groundwater is concentrated and flowing in the aquifer" [1]. Groundwater is divided into soil water that exists in the interstices of soil particles and fissure water that exists in the fissures of bedrock. When the fissure is large and continuity is good, it forms “water flow” [2].

Excessive groundwater use and inadequate construction work in the aquifer will cause various groundwater troubles such as depletion of groundwater resources, land subsidence, and diffusion of soil and groundwater contamination. Therefore, proper evaluation of the groundwater flow layer is very important for the appropriate development, utilization and maintenance of groundwater resources, safe and economical construction work, and environmental protection.

Electrical prospecting is used as a method to spatially understand the distribution and properties of the groundwater flow layer. Electrical prospecting is a physical exploration that applies a direct current to the ground and analyzes the resistivity characteristic of the ground from the potential formed. The ground has different resistivity depending on the types of minerals that make up sediments and rocks, and the ion concentration and amount of water that fills the pores between mineral particles, and the underground structure can be approximately estimated from the resistivity distribution [3]. Electrical exploration was introduced to Japan in the 1920s and used for groundwater surveys. Later, with the advancement of computer technology and simulation technology in the 1970's, complex underground structure analysis has become possible [4].

The normal electrical prospecting evaluates that the low resistivity zone is groundwater area. However, in general, the cohesive soil layer also has a low resistivity zone, and it is difficult to estimate the location and range of the groundwater flow layer from the resistivity distribution. The voltage difference method is a method to emphasize the forced polarization phenomenon, and in addition to the resistivity, the rate of resistivity change can also be obtained. As a result, it is possible to improve the estimation accuracy of the distribution and properties of the groundwater flow layer.

This paper indicate that the voltage difference method is effective for the appropriate evaluation of the groundwater flow layer from the case study.

VOLTAGE DIFFERENCE METHOD

Voltage difference method electrical prospecting is one of the forced polarization methods (IP method:

Induced Polarization Method) of electrical prospecting. This method can promote the forced polarization phenomenon by the same survey line and make the groundwater flow range clearer.

Principle

Induced polarization phenomenon

When an electric current is applied to rocks and ores, the electrical phenomenon observed as lagging response potential is called forced polarization. When groundwater flows in the fissures in rocks and pores in sediments below the ground, electrical interaction occurs at the boundary between minerals and groundwater. Normal water is electrically neutral, but when anions are left on the mineral surface, the water flow carries many cations, causing a bias in the distribution of cations and anions in the pore water (Fig.1) [5].

Voltage difference method

The voltage difference method carries out exploration twice on the same survey line and promotes forced polarization of the groundwater flow layer. The apparent resistivity value (ρ_a) of the ground by the electrical survey is not limited to the electrode arrangement, but as shown in the Eq. (1), linear relationship is established between the load current (I) and the measured potential (V) ($V_1 / I_1 = V_2 / I_2$).

$$\rho_a = \alpha \frac{V}{I} = \alpha k \qquad (1)$$

Here, ρ_a : apparent resistivity, V : measured potential, I : load current, α : proportional constant, k : constant

Since the ground acts as a dielectric, it is also known that a forced polarization phenomenon occurs due to the load current (I) ($V_1 / I_1 > V_2 / I_2$) [6]. If there is a groundwater flow layer, the potential of Eq. (2) is generated around "Groundwater flow", and the measurement V decreases due to this effect.

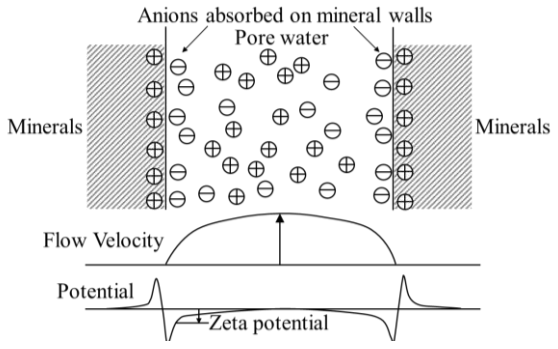

Fig. 1 Model for adsorption of ions in water to mineral surfaces

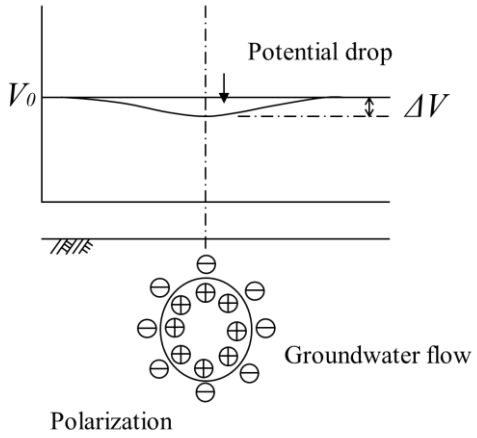

Fig. 2 Potential drop model in groundwater flow

$$E(\Delta V) = \frac{\Delta P \cdot D \cdot \zeta \cdot \rho_w}{4\pi \cdot \eta} \alpha \Delta P \qquad (2)$$

Here, E : flow potential, ΔP : water pressure, D : dielectric constant of the fluid, ζ : zeta potential, ρ_w : specific resistivity of groundwater, η : viscosity coefficient of groundwater

If laminar flow exists in the ground, it is considered that the generated polarization is released with the water flow, then a new charge starts, and the amount of current is absorbed continuously (Fig.2). On the other hand, if there is no water flow even in saturated ground, the polarization is put in a steady state is kept, and no voltage drop occurs. Therefore, the more pronounced the groundwater flow, the more the forced polarization phenomenon is emphasized, and the estimation accuracy of the water movement range in the ground improves.

Difference between conventional IP method and the voltage difference method

In the conventional IP measurement, the load voltage is returned to 0 after boosting to point A (V_1). At this time, if there is a dielectric (groundwater fluidized bed) on the ground, a dielectric potential is generated as a result, current I_0 (point C) at load voltage V = 0 is measured, and corresponding V_0 (measured voltage) is measured. The result is $\rho_a = \alpha (V_0 / I_0)$ (Fig.3).

The voltage difference method measures the measured current (I_2) by reducing the pressure to point B (V_2) immediately after point A (V_1) of the conventional IP method measurement. At this time, the pressure reduction path AB in the presence of the dielectric follows a path different from the pressure rising path OA, and it is considered that the following $\Delta\rho_a$ occurs (Eq. (3) (4)).

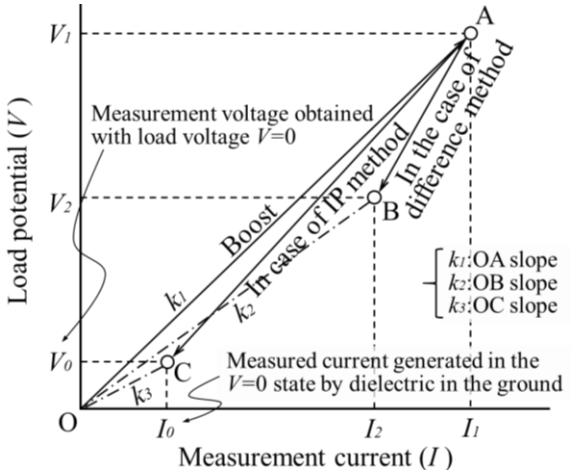

Fig. 3 Measurement principle of the voltage difference method

$$\left(k_1 = \frac{V_1}{I_1}\right) \neq \left(k_2 = \frac{V_2}{I_2}\right) \quad (3)$$

$$\Delta\rho_a = \rho_2 - \rho_1 = \alpha(k_2 - k_1) < 0 \quad (4)$$

In the case of voltage drop due to groundwater flow, even if the measurement is $V_1 = V_2$. It is assumed that $I_1 < I_2$ ($V_1 / I_1 > V_2 / I_2$), and the resistivity change rate can be taken out. Therefore, reducing the pressure from V_1 to V_2 has the effect of amplifying the specific resistance difference value.

Exploration method

The exploration is performed according to the following procedure, and the exploration are performed twice on the same survey line. The electrode arrangement in measurement uses Wenner method, which has high horizontal sensitivity, and Ertran method which has high vertical sensitivity. In addition, electrode spacing and survey line length should be set with a margin for accurate analysis of exploration depth and exploration target range. The exploration cross section image and the survey instrument are shown below (Fig. 4, Table 1).

1) Set a survey line to a predetermined route
2) Electrode placement
3) Cable attachment and wiring, and grounding resistance check
4) Initial measurement
5) Difference measurement (The search condition is the same as 4))
6) After data check, equipment removal

Analytical method

The normal resistivity cross section is analyzed from the initial measurement, and the resistivity change rate cross section is analyzed from the initial measurement and the differential measurement.

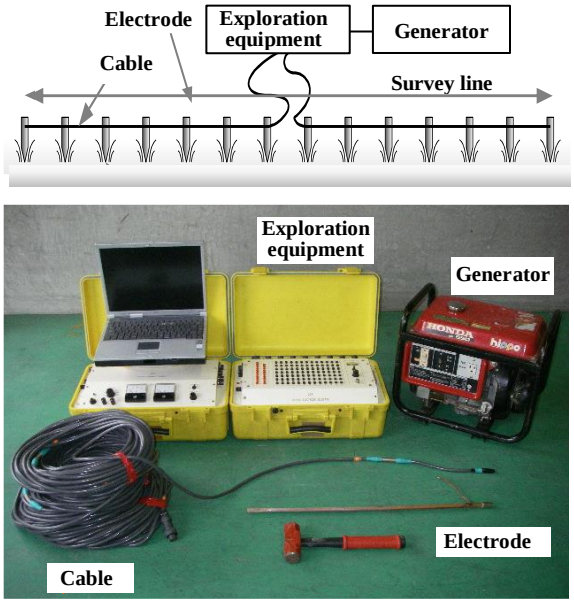

Fig. 4 Exploration image and measuring equipment

Table. 1 Measurement equipment specifications

Exploration equipment	
Name	JCR CH-97T・C CURRENT SOURCE
Manufacturing	Japan Crust Research co., ltd.
Max output	600V (1.25A)
Control	Automatic control by PC
Power supply (Generator)	
Name	HONDA EG-550
Manufacturing	Honda Motor Co., Ltd.
Rated output	Single-phase 100V 550VA (60Hz)
Exploration cable	
Name	Exploration cable with electrode
Manufacturing	Japan Crust Research co., ltd.
Size	ϕ 10mm
Exploration electrode	
Name	S-shaped ground rod (SF-600 Made of copper)
Manufacturing	NICHIDO DENKO Co., Ltd.
Size	ϕ 10mm, L=600mm

Resistivity cross section

In the analysis, apparent resistivity values are calculated from measured values of Wenner and Ertran method, and then apparent resistivity cross sections of both arrays are analyzed. Cross-sectional

analysis is performed from the apparent resistivity values of both arrays. For cross-sectional analysis, two-dimensional inverse analysis consisting of finite element method and nonlinear least squares method is conducted [7] [8].

Resistivity change rate cross section

The resistivity change rate ($\Delta\Omega$) is taken from the difference ($\Delta\rho$) of the resistivity values obtained by difference measurement (Eq. (5) (6)). If rate of change would become higher, the possibility of pressurization in the groundwater would be higher as a result it is judged that there is a confined groundwater or groundwater flow layer.

$$\Delta\rho = \rho_1 - \rho_0 \quad (5)$$

$$\Delta\Omega = -(\Delta\rho / \rho_0) \times 100 \quad (6)$$

Here, ρ_0 : resistivity at initial measurement, ρ_1 : resistivity at difference measurement, $\Delta\rho$: resistivity difference, $\Delta\Omega$: resistivity change rate (%)

CASE STUDY

The voltage difference electrical prospecting was applied to shallow terraces of surface rock, and the relationship between the survey results and groundwater flow characteristics was verified.

Geological setting

The site is located on a river terrace about 230 m above sea level. Bedrocks are interjected sandstone and mudstone and are covered by terrace soil layers of cohesive soil to gravel with a thickness of about 3-5m (Fig.5).

The mainly groundwater consists of free groundwater distributed around GL-3 to 5m. From the drilling conditions, the aquifer is presumed to be a gravel layer at the base of the terrace sediments or in fissures in weathered bedrocks (Fig.6).

Survey methods

Electrical prospecting overview

The exploration method was as described above. The survey lines were arranged in two lines so that they almost coincide with the previous boring points (Table.2, Fig.5).

Boring survey

All-core boring of φ 66 mm was conducted at two locations where groundwater flow can be expected in the electrical prospecting (Table. 3, Fig. 5). After the investigation, the hole was expanded to φ 116 mm and used as a test hole for the pumping test described later.

Pumping test

Pumping tests were conducted in accordance with JGS 1315-2012, and pumping and water level observation were conducted with a single hole. In the test, a 100 mm diameter perforated pipe with an aperture rate of 10% was inserted to carry out stepwise pumping up to the estimated critical pumping capacity. The critical pumping capacity was estimated from the relationship between stable water level and pumping capacity.

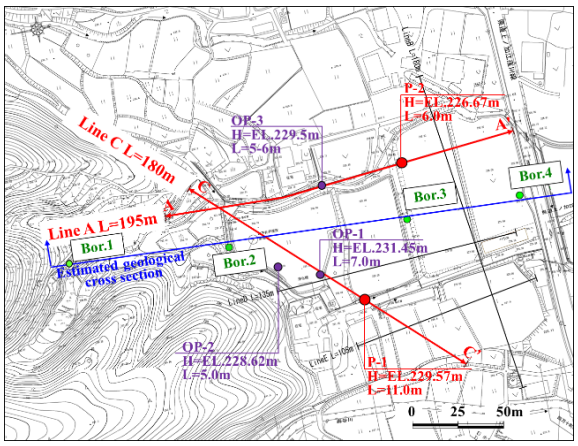

Fig. 5 Survey line and boring survey position

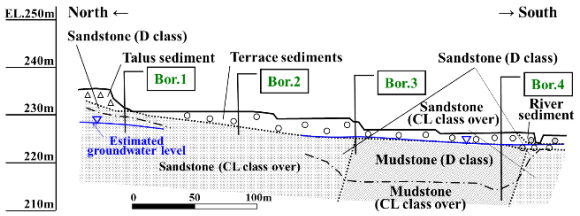

Fig. 6 Estimated geological section (NS direction)

Table. 2 Exploration specifications

Line name	Line length	Electrode spacing	Number of electrodes
A	195 m	3 m	66 points
C	180 m	3 m	61 points

Table. 3 Boring survey specifications

Point name	Hole height (EL.m)	Depth (m)	Hole diameter (mm)
P-1	229.57	11.00	66
P-2	226.67	6.00	66

Result

Exploration result and interpretation section

The exploration result was colored the resistivity distribution by the initial measurement and was overlaid to the resistivity change rate of 10% or more with a contour, and the geologic interpretation was added to it. In both the A and C survey lines, the surface layer of 3 to 4 m has a resistivity of 50 to 700 Ωm, and the depth of more than 4 m has a resistivity of 50 to 2000 Ωm (Fig. 7). The bedrock shallower than GL-10-15m has a low resistivity band with a resistivity of 50-200 Ωm. The resistivity change rate is distributed in the relatively high range of about 10 to 20% on the electrode No. 10 to 45 of Line A and No. 0 to 10, 30 to 40 of line C. Geological interpretation was comprehensively judged based on existing geological data.

Electrical prospecting result of the boring point

In addition to the boring points of P-1 and P-2 investigated this time, data of three boring surveys of OP-1 to 3 exist near the survey line in the survey site. The resistivity change rate is the same at 50 to 300 Ωm at all points, but the resistivity change rate is as high as 10-20% at P-1 and about 10% of P-2, others less than 10% (Table. 4).

Table. 4 Exploration result of survey hole point

Point name	Hole height (EL.m)	Depth (m)	Resistivity (Ωm)	Resistivity change rate (%)
P-1	229.57	11.00	100-300	10-20
P-2	226.67	6.00	25-300	10
OP-1	231.45	7.00	100-200	10<
OP-2	228.62	5.00	100-200	10<
OP-3	229.5	5-6	50-150	10<

Note: The depth of OP-3 is estimated by listening.

P-1 and P-2 were the only points where groundwater could be pumped at the survey point. In addition, as a standard which can carry out a pumping test, it was set as the state where the stable groundwater level was maintained by the yield of several L / min.

Relationship between core properties and yield and resistivity change rate

P-1 is a softly gravel mixed silt with a low water content throughout the 5.0 m of the surface layer. It is a weathered mudstone in the form of rock fragments and angular gravel between 5.0 and 10.0 m in depth and becomes weakly weathered rock from 10.0 m or less in depth (Fig. 8). The surface 1.5 m of P-2 is a silty sand between. Between the depth 1.5 to 6.0 m is a weathered sandstone and a weathering mudstone

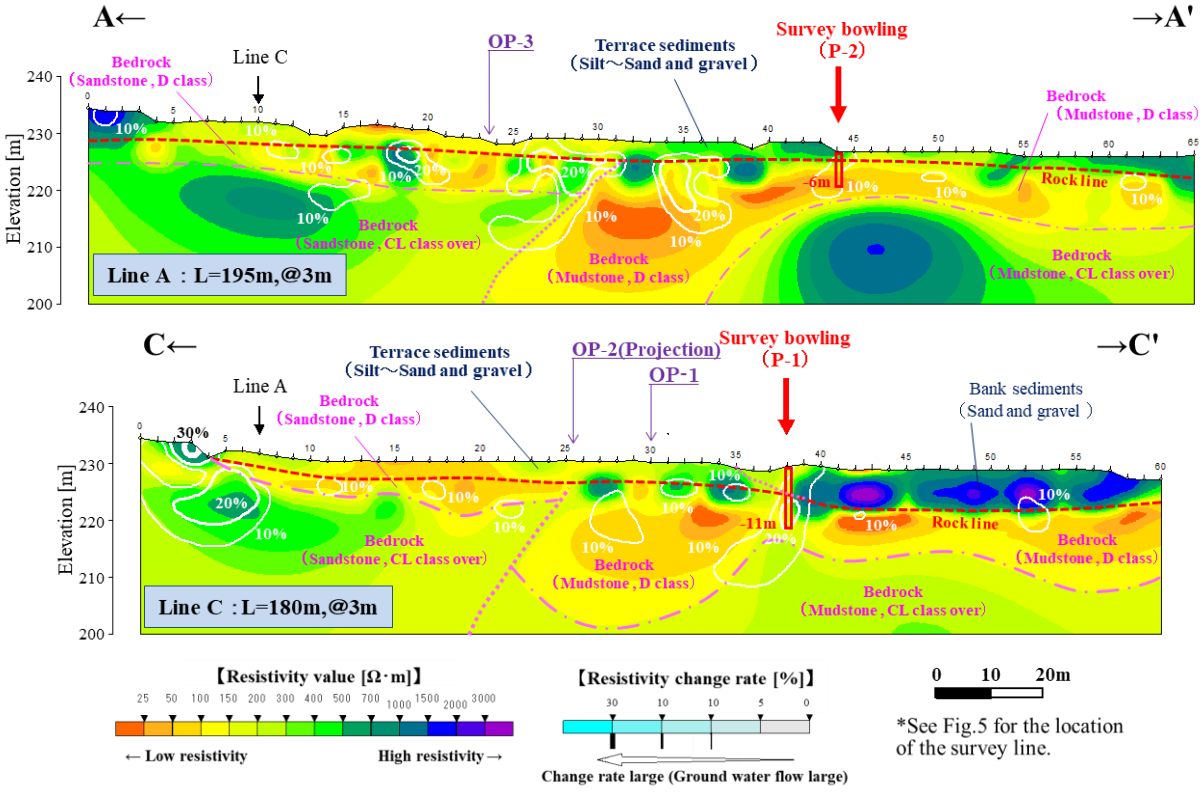

Fig. 7 Resistivity and resistivity change rate distribution and interpretation

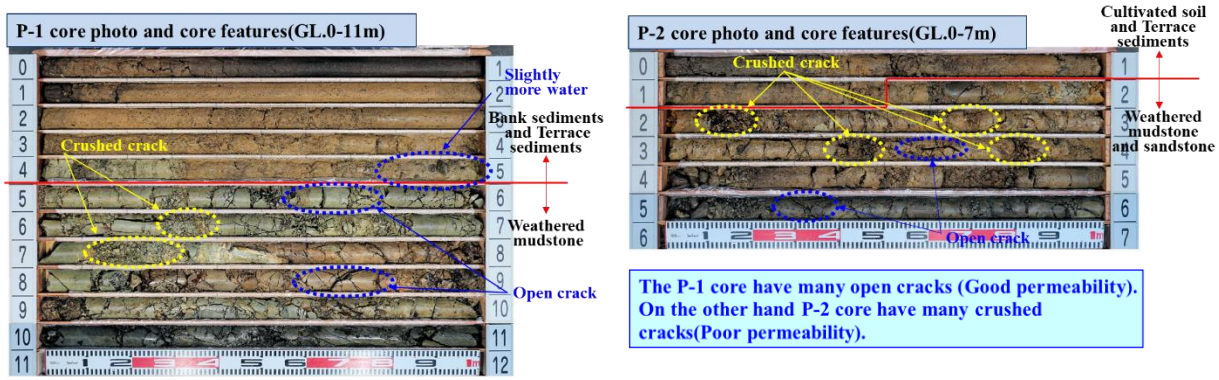

Fig. 8 Core properties of P-1 and P-2

from a rock fragment to angular gravel. As for rock fractures, P-1 tends to have many open cracks and P-2 tends to have few open cracks. At the time of the survey, the water level in the borehole was located near GL-5m for P-1 and 1.5m for P-2 and both were in the bedrock.

The critical yield of P-1 was as high as 8.35 L/min, and P-2 was as small as 3.05 L / min. The resistivity change rate of P-1 is mostly 20% or more in the bedrock, but P-2 is only 10%.

CONSIDERATION

The resistivity change rate distribution can be roughly compared with the groundwater flow range, and it is inferred that there is correlation between the magnitude of the change rate and the yield.

1) P-1 and P-2 had a resistivity change rate in the range of 10 to 20%, therefore it is a high possibility that the groundwater flow layer exists. While OP-1, OP-2 and OP-3 do not show clear change in resistivity change rate, and it is assumed that groundwater flowability is low.
2) The resistivity change rate may be positively correlated with the magnitude of the yield under almost the same weather conditions. Therefore, it is considered possible to estimate the permeability of the ground and the amount of yield water by the resistivity change rate at the point.

SUMMARY

The comparison with other groundwater survey indicates that the voltage difference method electrical prospecting is effective as an evaluation tool of groundwater flow characteristics.

1) The ordinary electrical prospecting is a limit to estimating the groundwater flow range and flow path, but it is considered that the estimation accuracy is improved by analyzing the resistivity change rate of the voltage difference method.
2) The resistivity change rate of the voltage difference method may be correlated with the yield. Therefore, it may be a quantitative evaluation index of groundwater fluidity.

ACKNOWLEDGMENTS

The authors are very grateful to the local people and related party for supporting the present work.

REFERENCES

[1] Isamu Kayane., Groundwater and topography science Introduction to hydrology, Kodansha Academic Paperback, 2158, 2013, pp.43-45.
[2] Makoto Nishigaki supervised Symbiotic-type groundwater technology utilization study meeting., Basic concept of groundwater use in cities, 2007, pp.9-10.
[3] The Society of Exploration Geophysicists of Japan., Graphic physics exploration, 1989, pp.53-54.
[4] Hiromasa Shima., Kazuhiko Kajima., Hideki Kamiya., New Electrical Exploration Method for Construction, Disaster Prevention and Environment Resistivity Image Profiling, Kokon Shoin Co., Ltd., 1995, pp.5-8.
[5] Tadashi Nishitani., Tomoki Tsutsui., Shinya Sakanaka., You are also a try Physics exploration, GIHODO SHUPPAN Co., Ltd., 2007, pp.91.
[6] Wait J.R., A theoretical study of induced electrical polarization, Geophysics23, (1), 1958, pp.144-153
[7] Yutaka Sasaki., Automatic Interpretation of Resistivity Sounding Data over Two dimensional Structures (1), Butsuri-Tanko; Geophysical Exploration, Vol. 34, No. 5, 1981, pp.341-350.
[8] Yutaka Sasaki., Automatic Interpretation of Resistivity Sounding Data over Two dimensional Structures (2), Butsuri-Tanko; Geophysical Exploration, Vol. 34, No. 6, 1981, pp.422-434.

9th Int. Conf. on Geotechnique, Construction Materials and Environment, Tokyo, Japan, 20-22 November 2019, ISBN: 978-4-909106025 C3051

EFFECTS OF PULVERIZED MUSSEL SHELL ON THE PROPERTIES OF EXPANSIVE SOIL

Dianne Angela V. Montefrio [1*], *Ralph Joseph P. Santos* [1*], *Gene Harvey J. Solis* [1*], *John Michael P. Zacarias* [1*]

Dr. Maria Cecilia Marcos[2] ,[1]Department of Civil Engineering, College of Engineering, Adamson University, Ermita, Manila, Philippines, 1000

ABSTRACT

This study determined the effects of pulverized mussel shell on the properties of expansive soil. The expansive soil was collected from the vicinity of Taytay, Rizal. The mussel shell pulverized into different stages and passed the #200 sieve were used in the experimentation. The index properties and physical properties of the soil, determined as Plastic Limit, Liquid Limit, Plasticity Index, Shrinkage limit, Specific Gravity and Shear Strength, classified the soil to be SC Soil and were obtained in accordance with American Standard for Testing and Materials (ASTM). The Expansive soil was mixed with the pulverized mussel shell at different percentages (3%, 6% and 9%) by weight of the expansive soil. Index Properties test were conducted on the expansive soil alone, and with pulverized mussel shell to determine the changes to be dealt with the index properties of soil. Unconsolidated Undrained Triaxial Test was conducted on the expansive soil alone and with pulverized mussel shell to determine its shear strength. The test results of the study showed that with increasing amount of pulverized mussel shell, the expansive soil's moisture content decreased, specific gravity of expansive soil increased, Liquid Limit decreased, Plastic Limit increased, Plasticity Index decreased, Shrinkage Limit increased and the shear strength of the soil increased.

Keywords: Mussel, Triaxial, Expansive Soil, Shear Strength

INTRODUCTION

Several problems are encountered during the early stages of Construction whether it is vertical or horizontal. A major dilemma revolves about the type of soil present on the site. Structures built on soils that possess weak engineering properties are generally prone to foundation problems, for instance, the clayey soil which is not a good scenario in any construction works. Structure built under this condition experiences failure in the foundation due to low bearing capacity and shear strength. [1-3]

Clay mineral such as Smectite which is composed of Montmorillonite and Bentonite, makes the soil shrink or swell making it an expansive soil. When this type of soil is subjected to an increase in moisture content, swells, and shrinks when water escaped from it. [3-4] This soil is considered problematic because it tends to lose its strength when there is a significant change in its moisture content. When such soil expand, cracks on structures such as building foundations, roadways, and bridges that was built on it may occur, as well as pipes buried within it may be misaligned, causing leaks and adverse effect to series of pipe systems. [5]

In order to improve the properties of expansive soil, stabilizing the soil is necessary; this can be done through Chemical Stabilization. The most common Chemical Stabilizer is lime. Application of this material to expansive soil is proven to reduce the swelling and shrinkage capacity of soil, thus improving the properties of the soil. Commercially available lime is mostly made up of Calcium Carbonate and as the world continues to seek for a more economical soil stabilizer, Mussel Shell, which is composed of 95-99% Calcium Carbonate, arises as a possible soil stabilizer. [6].

METHODOLOGY

Researh Design

This study takes on the experimental method in determining the effects of pulverized mussel shell in the properties of expansive soil. The foresighted method according to key is suitable in a research study that intends to maintain control over all factors that may affect the result of an experiment. By adapting this method, the researchers determined what factors are to be controlled and what are to be manipulated in this study and attempt to determine what may occur. The problems in this research study were answered by depending largely on the collection of data from the series of laboratory test through which were measures of the effects of pulverized mussel shell in the properties of expansive soil.

Materials

Mussel Shell

The Mussel Shells were collected from a mussel shell product supplier from Bacoor, Cavite and were pulverized to obtain a particle size of not greater than the no. 200 sieve (0.075-mm opening).

Expansive Soil

The expansive soil was mapped out through the aid of soil map and soil survey from the Bureau of Soil and the soil was collected from Taytay, Rizal. A depth of 0.5 meter from the natural grade line was excavated before gathering the soil sample.

Preparation of Raw Materials

The Mussel Shell was collected from mussel shell product supplier from Bacoor, Cavite. It was cleaned to remove any organic matter from the shell. It was also washed with water and detergent to remove any unpleasant smell from the mussel flesh. The mussel shell was then air-dried and prepared for crushing. Safety equipment was used by the researchers such as safety goggles, mask, gloves, etc. in crushing the mussel shell.

The obtained pulverized mussel shell undergoes 2 stages of crushing. On the first stage, the shell was crushed by the use of roller compactor in order to obtain small particles sizes. The gathered crushed particles proceeded to the second stage of crushing with the use of willey-mill to produce a smaller particle sizes that passed through the #200 sieve. Shells that passed through sieve no. 200 (0.075-mm opening) were used in the study. After pulverizing the mussel shell, it was then incorporated to the soil, 0%, 3%, 6%, and 9% by weight and laboratory tests were performed.

Laboratory Tests

Physical Properties

To determine the physical properties of the soil samples laboratory tests for Moisture Content; ASTM D2216 – 10 Standard Test Method for Laboratory Determination of Water (Moisture) Content of Soil and Rock by Mass, Particle Size; ASTM D422 – 63 (Reapproved 2007) Standard Test Method for Particle-Size Analysis of Soils and Specific Gravity; ASTM D854-10 Standard Test Methods for Specific Gravity of Soil Solids by Water and Soil Classification; ASTM D2487 Practice for Classification of Soils for Engineering Purposes (Unified Soil Classification System) were conducted.

Index Properties

To determine the index properties of the soil samples laboratory tests for Plastic and Liquid Limit; ASTM D4318 – 00 Standard Test Method for Liquid Limit, Plastic Limit and Plasticity Index of Soils and Shrinkage Limit; ASTM D4943-02- Standard Test Method for Shrinkage Factors of Soils by the Wax Method were conducted.

Mechanical Properties

To determine the mechanical property of the soil samples laboratory tests for Shear Strength; ASTM D2850 – 03a Standard Test Method for Unconsolidated – Undrained Triaxial Compression Test on Cohesive Soil was conducted.

DATA AND RESULTS

Physical Properties

Soil Classification

In the Classification of Soils, the values of $D_{60,}$ $D_{30,}$ $D_{10,}$ Cu and Cc were computed. The values of liquid limit, plastic limit and plasticity index of the control soil are used to classify the soil. The coarse fraction is 78.158% which is greater than 50 % which means the soil is coarse grained. The gravel fraction is 1.354% which is lesser than 50 % which means the soil is sand. The A line is computed to be 40.384 so the plasticity index plots above the A line. Based from the Unified Soil Classification System, the soil sample is classified with a group name of Clayey Sand with a group symbol of SC. With the value of plasticity index and percent finer of 0.02 mm, the clay activity which was computed to be 6.025 this falls under the smectite category. The clay minerals composed in the soil is mostly smectite which is either montmorillonite or bentonite which are expansive clay minerals.

Particle Size Distribution

Table 1 presents the result of the particle size distribution for coarse grain soils. A total of 798.59 g of soil was tested. The sieve numbers used were 4, 10, 40 and 200 with sieve openings of 4.75 mm, 2.00 mm, 0.425 mm, and 0.075 mm respectively. The percent passing in #4 sieve is 98.646 %, 83.429 % in #10 sieve, 47.457% in #40 sieve and 15.078% in #200 sieve. The highest amount of soil was retained in sieve #40. From this test, the soil is mainly sand.

Table 1. Results of Mechanical Sieve Analysis

Sieve number	Mass of soil (g)	Cumulative mass of soil passing (g)	Cumulative mass of soil retained (g)	Percent passing (%)
4	10.81	787.78	10.81	98.646
10	118.33	669.45	129.14	83.829
40	296.77	372.68	425.91	46.667
200	198.25	174.43	624.16	21.842
PAN	174.43	0	798.59	0
Total	798.59			

Table 2 shows the result of hydrometer analysis for the clay particles contained in the expansive soil. A total of 50 g of soil that passed #200 sieve was tested. The hydrometer is read at 2 minutes, 5 minutes, 15 minutes, 30 minutes, 60 minutes, 250 minutes and 1440 minutes. The hydrometer readings are 355, 33, 31, 29, 27, 24 and 22 respectively.

Table 2. Results of Hydrometer Analysis

Time (min)	R	L (cm)	D (m)	P (%)	P' (%)
2	35	10.595	0.03116	13.741	62.912
5	33	10.921	0.02001	12.852	58.840
15	31	11.247	0.01172	11.962	54.768
30	29	11.573	0.00841	11.073	50.696
60	27	11.899	0.00603	10.184	46.624
250	24	12.388	0.00301	8.863	40.576
1440	22	12.714	0.00127	7.96	36.444

From table 2, The diameter of soil particles at every time are computed and they are 0.03116 mm, 0.02001 mm, 0.01172 mm, 0.00841 mm, 0.00603 mm, 0.00301 mm and 0.00127 mm respectively. The percent passing with respect to every diameter is 62.912 %, 58.840%, 54.768%, 50.696%, 46.624%, 40.576% and 36.444%. The percent passing with respect to the percent of #200 sieve are 13.741%, 12.852%, 11.962%, 11.073%, 10.184%, 8.863% and 7.96% respectively. By interpolation, the percent finer than 0.002 mm is 8.338%.

Moisture Content

The control specimen obtained the highest moisture content of 53.438% while the soil with 9% pulverized mussel shell has the lowest moisture content of 50.049%. With these, the moisture content of the soil decreases as the amount of pulverized mussel shell increases. When a stabilizer is added, flocculation-agglomeration causes the clay particles to clump together to form large particles resulting to decrease in the surface area which leads to the decrease in the moisture content.

Specific Gravity

In Figure 1 the results showed that the soil alone (control sample – serves as a basis for comparison) gained lower specific gravity than of those with pulverized mussel shell. The control sample has 2.56 specific gravity while the specific gravity of soil solids with 3%, 6%, and 9% ranges from 2.6 to 2.67. Both values of Control and Variable samples fall under the category of clay soils. The increase in specific gravity upon the addition of pulverized mussel shell means a decrease in organic content. According to (Huang,P., et.al), soils with high organic content have a specific gravity ranging from 1.0 to 2.0, and soils with high mineral content have a specific gravity of greater than 2.0. From the results obtained, both Control and Variable Soils have specific gravity of greater than 2.0, which means they have high mineral content.

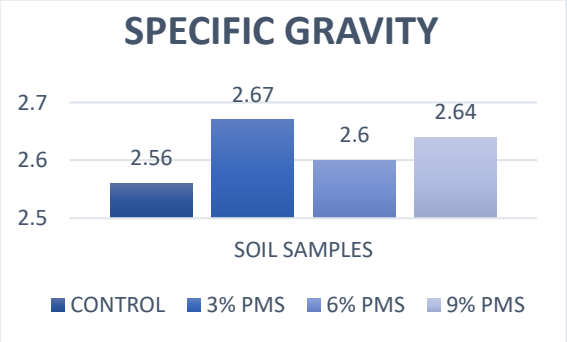

Figure 1. Specific Gravities of Soil Samples

Index Properties

Table 3 presents the summary of results for the Liquid Limit, Plastic Limit, Plasticity Index and Shrinkage Limit for the control sample, the 3%, 6% and 9% pulverized mussel shell

Table 3. Summary of Results of Liquid Limit, Plastic Limit, Plasticity Index, Shrinkage Limit

Index Property	Control Soil	3%	6%	9%
Liquid Limit (%)	75.32	64.17	59.29	53.31
Plastic Limit (%)	25.08	36.97	37.52	38.77
Plasticity Index (%)	50.24	27.2	21.77	14.54
Shrinkage Limit (%)	11.4	15.08	22.45	24
Plasticity	Very High	High	High	Medium

Based on Table 3, the results showed that the control soil has a higher value of liquid limit than those of soil with additional mussel shell and further addition of mussel shell results to a decrease in the value of the liquid limit. The highest liquid limit value was obtained from the control soil and the lowest liquid limit value was obtained from the soil with 9%

pulverized mussel shell. Soils with liquid limit higher than 50 usually have higher inherent swelling capacity and all soil samples fall under this condition.

Addition of mussel shell on the soil gave a higher value of plastic limit than of the control. As the pulverized mussel shell increase, the obtained value of plastic limit increased as well. The highest plastic limit was obtained upon the addition of 9% pulverized mussel shell to the soil with 38.77% plastic limit and the lowest value was obtained on the control soil with 25.08% plastic limit. The plastic limit of soil with 3%, 6%, and 9% have almost the same values as of each other.

The plasticity index of the soil alone has the highest value of plasticity index among the soil with pulverized mussel shell. The plasticity index decreased as the pulverized mussel shell was increased. The value of control soil with 50.24% plasticity index falls under soil with very high plasticity, and upon the addition of 3% and 6% pulverized mussel shell, the soil falls under the category of high plasticity. The addition of 9% pulverized mussel shell made the soil to fall under the category of medium plasticity.

The control soil has the lowest shrinkage limit while the soil with 9% pulverized mussel shell has the highest shrinkage limit. Based from the results, the shrinkage limit of the soil increases when the amount of the pulverized mussel shell increases. Flocculation-agglomeration produces a change in texture of clay soils. The clay particles tend to clump together to form a larger particles, thereby decreasing in liquid limit, increasing the plastic limit, decreasing the plasticity index and increasing the shrinkage limit of soils.

Mechanical Property

Figure 2 presents the undrained shear strength of the soil with 3%, 6%, and 9% pulverized mussel.

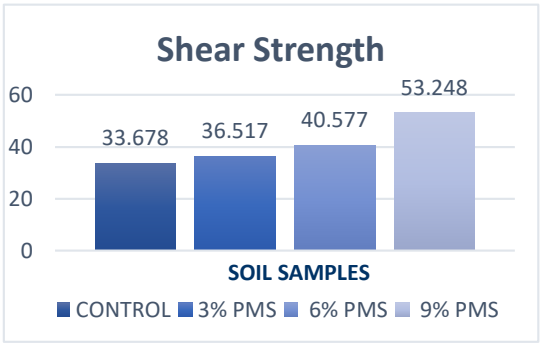

Figure 2. Undrained Shear Strength of Soil

The undrained shear strengths of the soil samples were computed to be 33.678 kpa, 36.517 kpa, 40.577 kpa and 53.248 kpa respectively. The results showed that addition of Pulverized mussel shell to the expansive soil increased its shear strength.

Resulting Undrained shear strength can be used used to calculate the unconfined compression strength which is used to classify the consistency of the soil. Table 4 shows the equivalent values of Unconfined Compression Strength of the obtained Unconsolidated Undrained Strength. Based from table 4, the expansive soil alone with 67.356 Kpa has a consistency of medium. Addition of 3% and 6% of pulverized mussel shell, with corresponding values of 73.034 Kpa and 81.154 Kpa, produced a consistency same as the expansive soil alone which is medium. On the other hand, addition of 9% pulverized mussel shell to the expansive soil improved its consistency from medium to stiff, with a value of 106.496 Kpa.

Table 4. Unconfined Compression Strength Value of Soil

Sample	c_u (KN/m^2)	q_u (KN/m^2)	Consistency
Control	33.678	67.356	Medium
3% PMS	36.517	73.034	Medium
6% PMS	40.577	81.154	Medium
9% PMS	53.248	106.496	Stiff

CONCLUSIONS

The study found out the effects of pulverized mussel shell on the properties of expansive soil. Based on the findings, it can be concluded that the moisture content of the soil decreased as the amount of pulverized mussel shell increased. It can be deduced that the specific gravity of expansive soil increased upon the addition of pulverized mussel shell. After the addition of pulverized mussel shell, the soil's specific gravity still falls under the average range of values of specific gravities for soils.

When pulverized mussel shell is mixed with the expansive soil, the liquid limit decreases while the plastic limit increases which results to the decrease in plasticity index. The plasticity index of expansive soil alone is classified to be very high plasticity and the addition of 9% pulverized mussel shell improved its plasticity index to medium plasticity.

It can be concluded that the shrinkage limit of the expansive soil increased upon the addition of pulverized mussel shell therefore, decreasing the shrink swell capacity of the expansive soil.

The addition of pulverized mussel shell improved the shear strength of the soil and the addition of 9% pulverized mussel shell yielded the most significant change. By the addition of 9% pulverized mussel shell, the shear strength of the expansive soil increased by 58.109%. The expansive soil's consistency improved from medium to stiff with the addition of 9% pulverized mussel shell.

RECOMMENDATIONS

From the results and experiences gained in this study, the following recommendations are drawn:

1. Unconsolidated Undrained Test is the only test that is used. It is recommended to conduct another test like unconfined compression test for further details of the strength capability of pulverized mussel shell as an additive for soil stabilization.

2. The percentages by weight of pulverized mussel shell used were 3%, 6% and 9%. The shear strength's trend up to 9% is still increasing. It is recommended to test another samples with pulverized mussel shell greater than 9% to determine whether the 9% addition is the percentage of pulverized mussel shell that yields the optimum increase in shear strength of the expansive soil.

ACKNOWLEDGMENTS

The researchers would like to acknowledge the support of the people who made this research possible.

They would like to express their deepest gratitude to their academic advisers, Engr. Crispin S. Lictaoa, and Dr. Ma. Cecilia M. Marcos, for their patience, vast knowledge, and commitment in helping them throughout the course of the research study.

They would also like to express their sincere gratitude to Mr. Mar Mercado for his time, patience, guidance and dedication in helping the researchers in their series of tests

Above all, they would like to express their sincerest gratitude to God, the Father, who provided the things and people that they were thankful for. For with Him, all things are possible.

REFERENCES

[1] Gungat, L., Putri, E. E., and Makinda, J.,Effects of oil palm shell and curing time to the load-bearing capacity of clay subgrade. Precedia Engineering, 54, 2013, pp.690-697.

[2] Jones, L. D., and Jefferson, I..,Expansive soils, ICE Publishing, 2012, pp 413-441.

[3] Ramesh, P., Rao, A. N., and Murthy, N. K., Efficacy of Sodium Carbonate and Calcium Carbonate in Stabilizing a Black Cotton Soil, 2012.

[4] Petry, T. M., and Armstrong, J. C.,Stabilization of expansive clay soils. Transportation Research Record, 1219, 1989.

[5] Roohbakhshan, A., and Kalantari, B.,Effect of lime and waste stone powder variation on the pH values, moisture content and dry density of clayey soil., International Journal of Advances in Applied Sciences, 3(1), 2014, pp. 41–46.

[6] Kocaman, S., Ahmetli, G., Cerit, A., Yucel, A., and Gozukucuk, M., Characterization of Biocomposites Based on Mussel Shell Wastes., World Academy of Science, Engineering and Technology, International Journal of Chemical, Molecular, Nuclear, Materials and Metallurgical Engineering, 10(4), 2016, pp 438-444.

[7] Das, B. M., and Sobhan, K., Principles of Geotechnical Engineering., Cengage Learning., 2013, pp. 266-285.

[8] Rogers, J. D., Olshansky, R., and Rogers, R. B., Damage to foundations from expansive soils. Claims People, 3(4), 1993, pp 1-4.

9th Int. Conf. on Geotechnique, Construction Materials and Environment, Tokyo, Japan, 20-22 November 2019, ISBN: 978-4-909106025 C3051

VISUALIZATION OF CEMENT DEEP MIXING CONSTRUCTION PROCESS BY INCORPORATING INFORMATION AND COMMUNICATION TECHNOLOGY (ICT)

Hong-Son Nguyen[1], Yuji Adachi [1], Takuma Kizuki[1], Hiroyuki Maeba[1], Shinya Inazumi[2]
[1]Hazama Ando Corp., Japan; [2] Shibaura Institute of Technology, Japan

ABSTRACT

In the deep mixing improvement method, soil-cement columns are installed in to an invisible ground, therefore it is impossible to visually confirm the circumstance of the constructions process. As the results, the inadequacy of construction data management and quality control of the constructed soil-cement columns may happen following re-construction of the columns, and structures failures/damages in some cases. By incorporating the information and communication technology (ICT), authors have invented and developed a system to visualize the construction process of the deep mixing work in real-time, namely "3D Pile Viewer". This system consists of two functions that are the positioning guidance and the visualization of the construction information. The former has been developed by using the combination of the global navigation satellite system (GNSS) or the total station (TS), and the tilt sensor. The latter is to create three-dimensional model of all information during construction such as depth, electrical current value, amount of slurry, rotation speeds, etc., then sharing via internet. By introducing the newly developed system to various actual construction sites Japan and oversea, the practical performance of the system and its advantages have been confirmed.

Keywords: Deep mixing method, Soil-cement column, Information communication technology, Construction information modelling, 3D Pile Viewer.

INTRODUCTION

Developing new infrastructure on a soft ground often faces many difficulties. To ensure the stability of the structure, reduce the large settlement, and mitigate liquefaction, the soft ground is normally required to strengthen. Among numerous soft ground improvement methods have been developed and applied worldwide, the cement deep mixing method that is a deep in-situ soil stabilization technique using cement as a binder is one of the most effective method. This method was mainly developed and practiced in Japan and Nordic countries until the end of the 1980s, but became very popular over the world recently [1].

Generally, the method consists of a deep mixing machine and a binder plant. The deep mixing machine is composed of one or several mixing shafts with a motor and gear box are installed at the top, and a set of mixing blades are mounted at the bottom. As for supplying cement slurry, a swivel joint is installed at the top of the shaft(s) for slurry supply and set of outlets is made at the bottom for binder injection. A mixing execution procedure ordinarily includes penetration of the mixing blades into the ground while rotating the mixing shaft(s) until designated depth, and then withdrawal of the mixing blades to the ground surface, the slurry could be injected to the ground during the penetration stage or withdrawal stage, or both. After one execution, a column shaped of treated soil-cement is constructed in the invisible ground. When implementing the construction work, the stabilized soil-cement columns must be installed to satisfy both geometric plan including location, depth, verticality, and the quality specified in the design. In order to ensure that operational parameters such as penetration and withdrawal speeds, rotational speed, amount of slurry and current value must be monitored and displayed continuously in control room and cabinet of machine during soil-cement installation [1]. However, those quality control parameters could be evaluated only after finishing working day and limited inside the construction area. If the construction parameters are properly recognized, displayed, shared, and evaluated in real time among related parties, then get the feedback immediately, the failure of column installation could be early fixed and prevented from repetition. Furthermore, a great amount of labor is required to collect the necessary information from a huge amount of numerical data to properly evaluate the construction process and then make the daily report.

On the other hand, the application of information and communication technology (ICT) become very popular recently in the construction industry. There are techniques to input the design data into the construction machines, then using these data for guidance or controlling the machines have been developed and applied in the practices [2], [3]. Additionally, the Japanese Ministry of Land, Infrastructure, Transportation and Tourism (MLIT)

has been positioned "1st for the productivity revolution" from 2016 onward, and has begun efforts to promote "i-Construction" to improve the productivity by incorporating ICT into all processes of construction including investigation, survey, design, construction, inspection, maintenance and so on [4]. In which, the ground improvement work by the deep mixing method is not out of the scope.

Based on the above-mentioned background, we have invented and developed a system called "3D Pile Viewer" [5] that is able to visualize all operational control parameters in three dimensions and shares real-time information among related parties even during the execution. This paper will introduce this system and its practical application on construction sites.

CONSTRUCTION INFORMATION VISUALIZATION SYSTEM (3D PILE VIEWER)

As shown in figure 1, the system has two main functions that are (1) positioning guidance function and the (2) data visualization function.

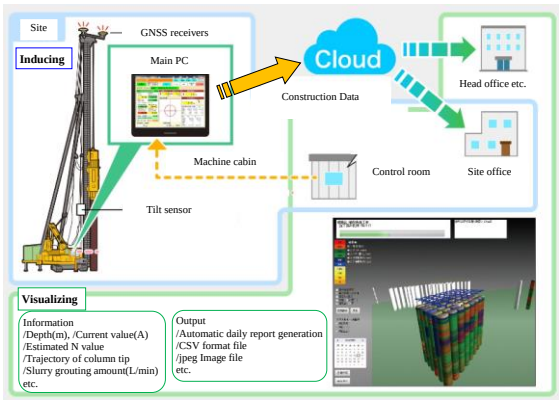

Fig. 1 Configuration of the system

Positioning guidance function

The function is configured by using global navigation satellite system (GNSS) or total station (TS), and tilt sensor measurement data to ensure the soil-cement columns are installed correctly as per the geometric plan as in the design. At first, three-dimensional designed data of the columns are registered into the system, then positioning work of every column is guided by GNSS or TS, and its verticality is controlled by tilt sensor during the construction process. Fig.2 shows the deep mixing machine attached with the instruments, two GNSS receivers are installed at the top and one tilt sensor (2 axes) is set at the bottom of the leader, and one computer and data communication antenna are mounted in cabin. In the computer monitor, the current position of casing rod(s) or mixing shaft(s) is displayed in comparison with the pre-registered designated position, and the other operational parameters are also presented (Fig. 3). The positioning guidance function allows to avoid geometric miss-installation of the treated soil-cement columns often caused by human errors. Moreover, the verticality of the column also is monitored instantaneously by obtaining measure data of the tilt sensor.

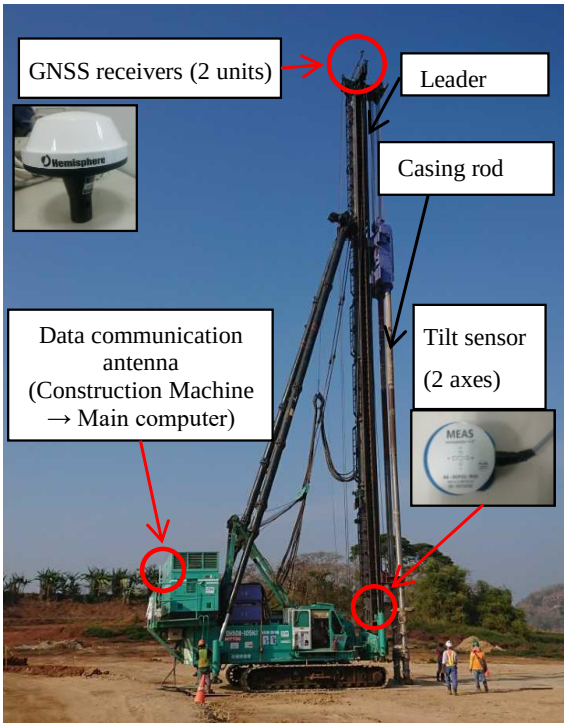

Fig. 2 Construction machine with attached instruments

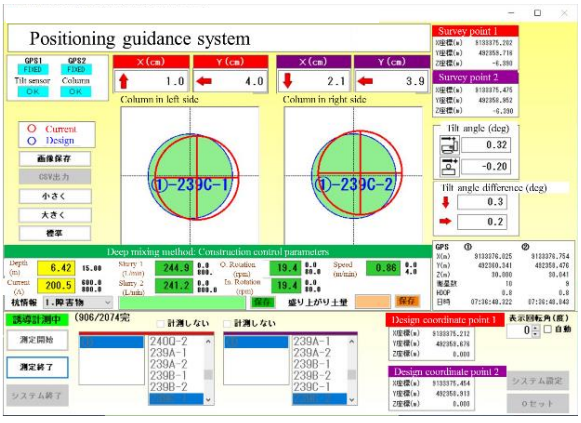

Fig. 3 Monitor screen in the machine cabin

Information visualization function

The second function of the system allows three-dimensional visualization and immediately evaluation by seeing the kinetic measurement

construction management data such as penetration/withdrawal depth, velocity, discharge amount of slurry, rotation speed of mixing blades, current value generating in the motor, ground properties, etc. In the meantime, the information is uploaded in to a Cloud from the main computer set up in the control room via internet. Consequently, all the construction measuring information are shared in real time among the parties related to the project. An example of the visualization screen is shown in figure 4, in which, the soil-cement columns are displayed in three-dimension on the left side. All the columns have been geometrically arranged conforming to the designed layout, the measured information of the columns have been constructed and the done part of the ongoing column are categorized and represented in a range of color. The columns and a part of column that are in white color have not been constructed. On the right side, all the distribution with depth of the recorded data of any target column are plotted in corresponding graph. By incorporating the ICT such as the Cloud and internet services, the construction situation and the changing of the ground properties are clearly visualized and evaluated in real-time; therefore, it is able to provide instruction then obtain feedback instantly during the construction process.

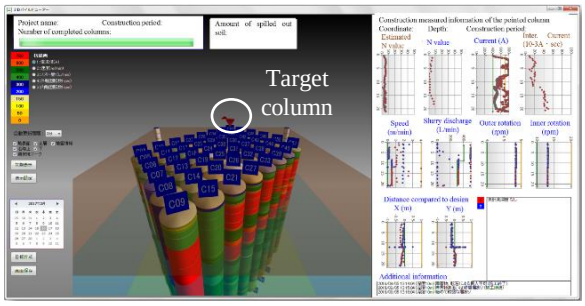

Fig. 4 The screen representing the visualization function of the system

APPLICATION AT THE CONSTRUCTION SITES

The above construction information visualization system has been introduced in several real construction projects in Japan, and oversea. The practical performance of the system is discussed here.

Katagishi high coastal embankment

As a restoration work after the Great East Japan Earthquake and Tsunami in 2011, an embankment of 800m long and 14.5m high (figure 5) is being built in Katagishi coastal zone in Iwate prefecture to prevent from the similar level of tsunami in the future [6]. A soft ground consisting of lose sand, and soft to medium silty clay is existing underneath the embankment.

Fig. 5 Location of the embankment

In figure 6, a complex ground improvement work including sand drain method and cement deep mixing method have been illustrated. The sand drain used at the center part to accelerate the consolidation settlement. The cement deep mixing method is performed at the embankment edges to increase stability, against liquefaction and to reduce settlement amount. In the design, the soil-cement columns with diameter of 2.0m are installed until maximum of 33.6m below the ground surface. The designed strength of the treatment soil-cement columns is different between sea side and land side. Moreover, the soil-cement columns were divided in to three patterns, the 1st pattern is a wall block type of soil column arrangement with 20cm overlapping up to the end of the upper lose sand layer as for liquefaction countermeasure, the 2nd pattern containing the columns are installed until the end of the upper silty clay layer against instability, and the tip of columns belonging to the 3rd pattern is set to reach the bearing layer to reduce settlement. Fig. 7 illustrates the geometric arrangement of soil-cement columns.

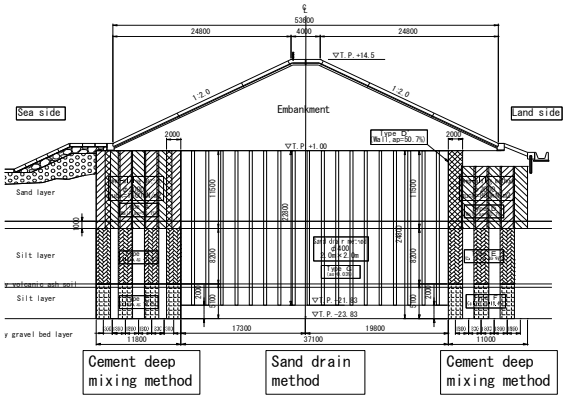

Fig. 6 Typical cross-section of embankment

To conform to the above-mentioned design specification, Deep Cement Stabilization method (DCS) has been selected. The DCS method has advantages in construction of large diameter and

extreme depth, as well as suitable for the ground containing sand and gravel layers [6].

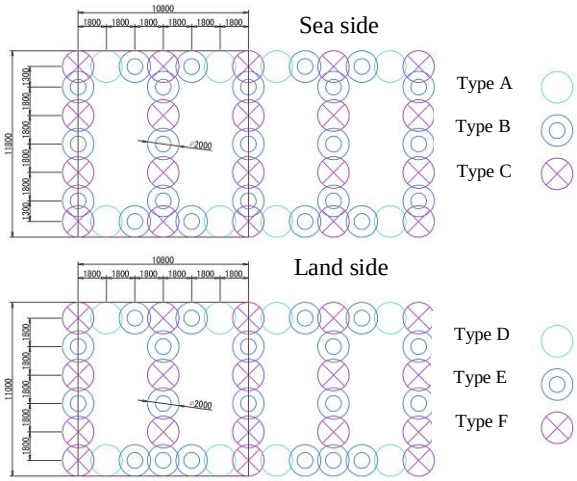

Fig. 7 Layout of soil-cement columns

As previously mentioned, the deep mixing work is quite complicated in this project. It is a challenge for controlling the quality during construction, therefore, the newly developed construction information visualization system has been introduced. Fig. 8 shows the captured screen of the system presenting the construction information of deep mixing work in this project. Since the designed layout and depth of all soil-columns were registered into the system in advance, so it is easy to guide the soil-cement columns to install correctly, and to be ensure overlapping between the columns have been made. Besides that, the soil-cement columns have been constructed in high quality without any mistake relating to the designed strength because all construction parameters are monitored in real-time allowing the engineers to control, evaluate, and give further instruction instantly during construction stage.

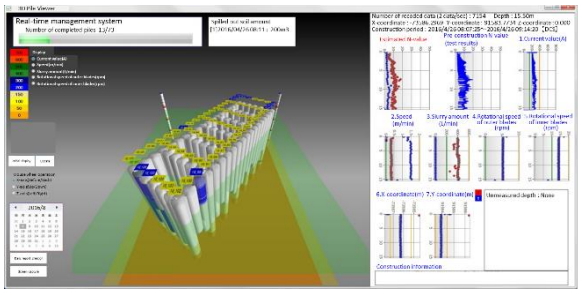

Fig. 8 The screen of visualization system applied in the Katagishi embankment.

Yokokan Minani-Sakae Interchange and Junction

This is a construction project of substructures of Yokokan Minani-Sakae Interchange (IC) and Junction (JCT) on the National Route No. 468 (figure 9). As showing in figure 10, the structure foundation is placed on a very soft ground containing a high-water content peaty soil with N-value of 0 from the ground surface to 7.0m depth, under that layer is the soft silt layer up to 18.0m depth with N-value range from 0 to 2, and below that is mudstone with N-value lager than 50 considering as the bearing stratum.

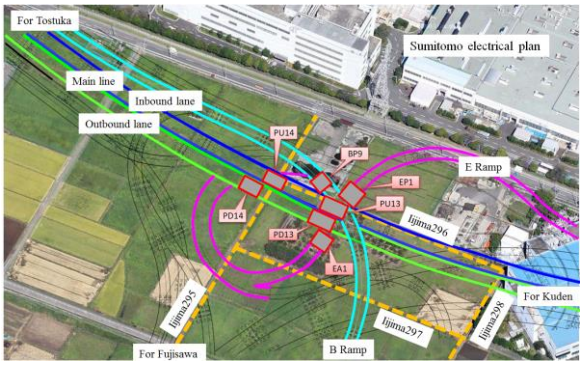

Fig. 9 Plan view of the project.

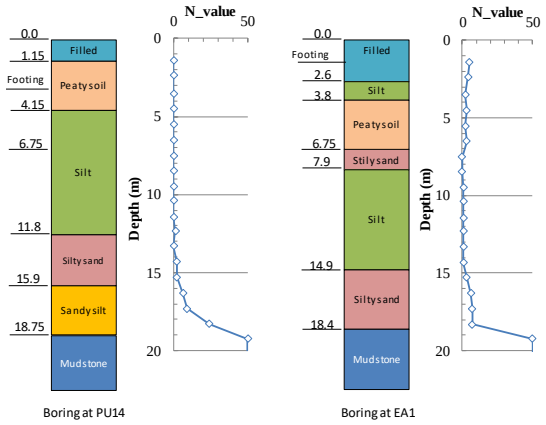

Fig. 10 Boring investigation results

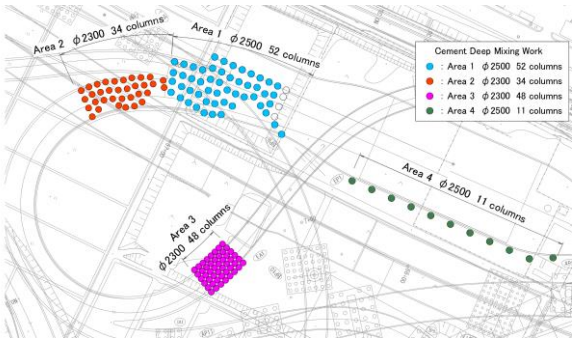

Fig. 11 The ground improvement plan

In order to increase the stability and reduce the consolidation settlement of the ground under the embankment of the IC and ramp sections, the ground

improvement by cement deep mixing (DCS method) was adopted. As showing in figure 11 and table 1, the cement deep mixing work was designed to perform in four areas with different geometric arrangement, diameter, design strength, length, and number of soil-cement columns. And the overlap among the columns was particularly designed in the area 3. In the design, the soil-columns are required to install to the designate depth or approach the Mudstone stratum. The penetration depth where the current value of motor is over 700A, or speed of the penetration is 10cm/minute is judged as the bearing stratum.

Table 1 Quantity and specification of soil-columns

Location	Diameter (mm)	Design strength (kN/m^2)	Length (m)	No. of columns
Area 1	2500	600	18.5	52
Area 2	2300	600	17.7	34
Area 3	2300	1000	18.7	48
Area 4	2500	600	19.5	11
Total				145

To comply with the design and the judgment specification, it would be not easy and takes time and effort to manage quality during construction process when applying the conventional construction management method, because the construction process is required to control uninterruptedly with high accuracy. For this reason, the new development construction information visualization system was introduced to overcome the difficulty as well as enhance the construction control more reliably and efficiently. The application of the system, for instance, is presented in figure 12. It is clearly seen that the deep mixing work had finished in the area 3, is ongoing in the area 4, and have not started in the area 2 and 1 yet. In addition, when the measurement current value data is chosen to illustrate in the three-dimensional screen, the parts having current value larger than 700A occur not only at the bottom but also in the upper parts of many columns. According to the specification, the construction of those columns might be ended shallowly. However, when that abnormal high current value was shown in the construction information visualization system the previous soil investigation data and others related information are checked immediately. After that, the inhomogeneous ground strata were confirmed, then resulted in continuation of the improvement works in those columns until the designed depth.

In conjunction with visualization of the construction information, a formula converts current value measured during construction to the N-value was included in the system to instantaneously estimate the N-value of the ground at the point where the soil-cement column installation was implemented. The conversion formula is established by doing statistical analysis on the soil investigation boring data and the construction information of the test column near the boring location. The conversion formula has been validated for the ground consisting of peaty, clayey, and silty soil [5], [7].

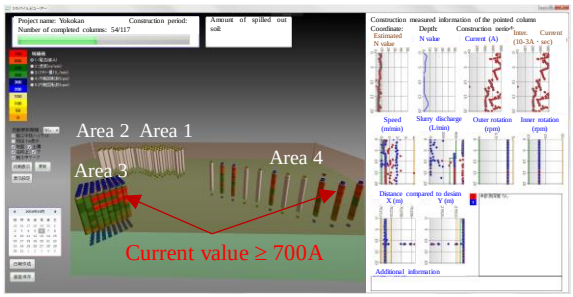

Fig. 12 The application of the visualization system in Yokokan Minani-Sakae.

Through this project, the accuracy of the system was confirmed by comparison with the conventional management method, the geometrical installation deviation due to human error could be prevented, and the construction process could be smoothly carried out providing that all the quality control information is visible in real-time. On the other hand, for the 1st time it came into notice that the data communication did not operate normally due to orientation of the construction machine and the antenna. The shortcoming was addressed properly confirming the alignment in the setting manual.

Wonogiri Multi-Purpose Dam

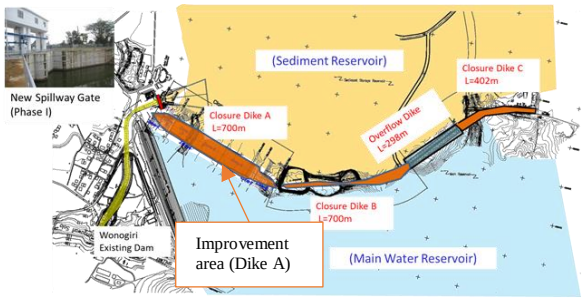

Fig. 13 Outline of closure dikes in Wonogiri dam.

Recently, the construction of closure dikes is being implemented in Wonogiri multi-purpose dam in Center Java, Indonesia with the aim of reducing sedimentation that are dramatically increasing every year and might cause serious effects on the intake. The outline of the project is presented in figure 13, the closure dikes are constructed to prevent sediments inflow from the Kudwan River into the Wonogiri dam reservoir and to discharge the sediment to the downstream side via the new flushing spillway. The top elevation and the height of closure dikes are

EL+140.0m and approximately 7.0m, respectively. Since the foundation of the closure dike A mainly consists of very soft to soft clay, silty clay sediment deposited in the dam reservoir, the ground improvement by the cement deep mixing method (CDM) is applied to secure stability against sliding and consolidation settlement. The cement deep mixing machine for on-land works having two mixing shafts is adopted in this project.

The layout of the soil-cement columns and longitudinal profile of closure dike A are shown in figure 14. The improvement ratio of 32.0% was required resulting in more than 5000 soil-cement columns are necessary to be installed. Because the depth of soft clay layer varies from 0.0 m to 24.0m in longitudinal section, the largest depth of soft clay layer is at the center of the closure dike A, and it reduces toward both left and right sides. Therefore, the improvement depth was designed from 6.0m to 24.0m corresponding to the changing of the soil profile. The typical cross-section of the deep mixing soil improvement is shown in figure 15.

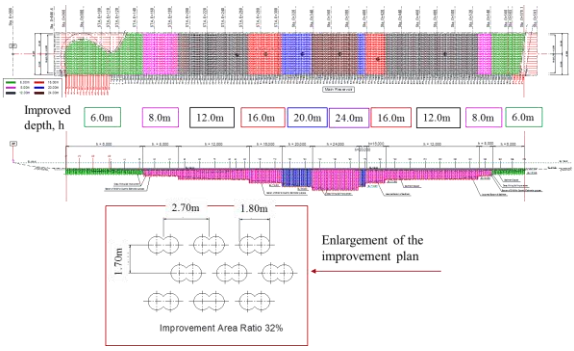

Fig. 14 Plan view and longitudinal profile of the soil improvement work in closure dike A.

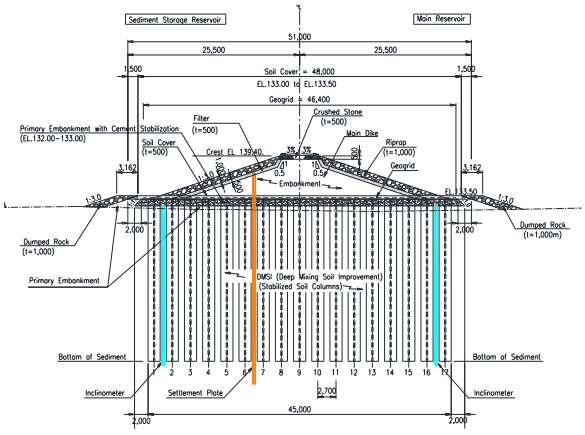

Fig. 15 Typical cross-section of closure dike A

In addition to the ordinary operational parameters, the soil-cement column finished depth that is embedded 0.5m into the bearing layer must be strictly controlled in the construction. Generally, the bearing layer is specified when the current value is larger than 300A continuously for at least one minute. To deal with that high criterion, the newly developed three-dimensional construction information visualization system is introduced. Fig. 16 is an example of the capture screen of the system applied in the project, in which, only the soil-cement columns belonging to the section 267 are chosen to display on the screen. Although all the columns in the section were designed to stop at the same depth, the different finished depth of each column was constructed actually in reality is clearly recorded and presented. Moreover, abnormal increasing of electrical current value at middle of 10 columns in the right side was recognized while it did not occur in the left. If the construction visualization system had not been adopted, those columns in the right would have been judged to end at the middle. However, similar to the Yokokan Minami-Sakae IC and JTC, the inhomogeneous geological condition was evaluated immediately, and then the construction process continued until reaching the real bearing stratum. The additional two borings positioned in each side were carried out instantly to clarify the abnormality. The boring data as illustrated in figure 17 indicates that there is a thin layer of dense silty sand to gravely sand with N-value of 30 exists at 5.0 to 7.0m deep.

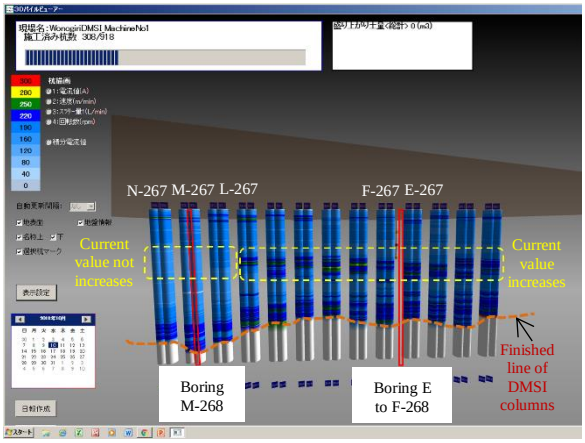

Fig. 16 The screen capture of the visualization system

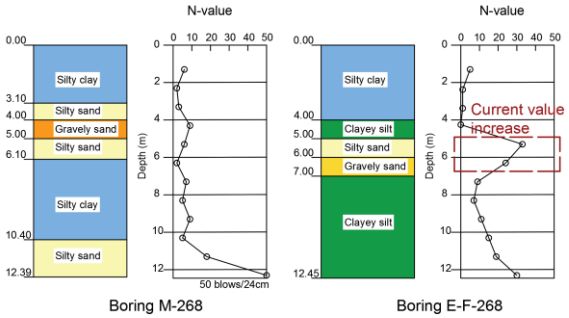

Fig. 17 Boring data at the section 267~268

The advantage of the construction information visualization system incorporating ICT could be confirmed successfully through this project. The construction progress and change in bearing layer depth were easy visualized and shared among the involved parties in real-time via internet and Cloud service. On the contrary, the issue in the operation of the system and downloading data due to huge number of soil-cement columns and the internet environment is not fast enough as in Japan was understood. Additionally, it is barrier to local staffs operating the system because only Japanese language is available at the current state.

CONCLUSIONS

By actively introducing ICT to develope the three dimensional visualization system for the deep mixing method, then applying in the real construction sites, the following advantages can be acquired.

1. The quality magament parameters/information obtaining during the construction process is visually displayed in three dimension and sharing in real time making it more easy to understand the construction situation and the alteration of the original ground condition to compare with conventional magament method.

2. It is expected that accurancy and efficiency of the construction management will improve. The human errors can be minimized and amount of labor for making daily report has been reduced drastically.

3. It raises the awareness of the contractor regarding the quality control and management, results in providing highly reliable products.

However, some shortcomings still remains in the application at the actual construction sites. For example, the system needs to improve to operate smoothly when large amount of treated columns are registered, and operating in the weak internet enviroment. Futhermore, the location of the tip of the column is calculated using measurment data of the tilt sensors attaching on the leader with the assumption that the leader and the mixing shaft(s) are integrated based on the position leader on the ground surface. In reality, there is a certain play between the two, and as the depth increases, there is a possibility that the deviation from the measured value increases.

REFERENCES

[1] Kitazume M., Terashi M., The Deep Mixing Method, CRC Press, 2017, pp.1-26.
[2] Bjork BC., Information Technology in Construction: Domain Definition and Research Issues, International Journal of Computer Integrated Design and Construction, SETO, London, Vol. 1, Issue.1, 1999, p.1-16
[3] Peansupap V., Walker DHT, Information Communication Technology (ICT) Implementation constraints: A Construction Industry Perspective, Engineering Construction & Architectural Management, Vol.13, Issue 4, 2006, p.364-379
[4] Japanese Ministry of Land, Infrastructure, Transportation, and Tourism i-Construction Committee, i-Construction: Construction Site Productivity Revolution, 2016 (in Japanese)
[5] Inazumi S., Adachi Y., Kizuki T., Tsuchiya T., Funahashi M., Development of Construction Information System and Estimation of N Value by Current Value Measurement on Ground-Improvement Work, Construction Robotics, 2019, p.1-14.
[6] Kizuki T., Sawaguchi H., Imai T., Takaue T., Tsuchiya J., Inazumi S., An Introduction of Real-Time Management System for Applying Deep-Mixing Method with Large Diameter and Improvement Depth (DCS method), Journal of the Japanese Society of Material Science, Vol. 67, No.1, 2018, p.93-98 (in Japanese)
[7] Funahashi, M., Inazumi, S., Kizuki, T., Adachi, Y., Tsuchiya, J. and Ishimaru, K., Development of Real-time Visualization Technology for Ground Improvement Works by Measuring Kinetics of the Ground, Geo-Environmental Engineering 2017, Proceedings of the 16th Global Joint Seminar on Geo-Environmental Engineering, pp.67-72, 2017.

9th Int. Conf. on Geotechnique, Construction Materials and Environment, Tokyo, Japan, 20-22 November 2019, ISBN: 978-4-909106025 C3051

AN EXPERIMENTAL STUDY ON THE REDUCTION EFFECT OF SETTLEMENT WITH STIFFNESS OF THE SOIL FLOW PROTECTOR

Jae-won Yoo[1], Su-won Son[2], Min-su Seo[3] and Hwa-ni Jo[4]
[1,3]Research Institute of Industrial Technology, Pusan National University, South Korea;
[2,4] Department of Civil Engineering, Pusan National University, South Korea

ABSTRACT

The embankment is settled by different reasons. But the settlement hardly occurs in structures supported by pile foundation such as an abutment, culvert. Such a settlement difference causes a cavity in the lower part of the bottom of the structure. In order to prevent problems caused by cavity under the structure supported by pile foundation, soil flow protector (briefly called 'FLP'), which can be easily installed on the side of a structure, was developed. In this study, a laboratory model tests were carried out to analyze the reduction effect of settlement with stiffness of the FLP. As a results of the behavior in the ground showed that the installation of the FLP reduced the settlement of the lateral ground and prevented the leakage of lateral ground soil into the cavity. The results of the laboratory model test showed that the settlement depending on the stiffness of the FLP was reduced by average 28.4 % in flexible and average 50.0 % in stiffness compared with non-reinforcement, indicating that the higher the stiffness of FLP, the more effective for settlement reduction. And the results of the photo-analysis of deformation due to stiffness showed that if the stiffness of the FLP is high enough, the passive earth pressure area is generated in the upper part, which will be advantageous for the stability.

Keywords: Cavity, Settlement, Soil flow protector, Stiffness, Laboratory model test

INTRODUCTION

The embankment is settled by a consolidated settlement over time, drying shrinkage due to soil drying, poor compaction during construction, soil compression due to overburden load. But the settlement hardly occurs in structures supported by pile foundation such as an abutment, culvert. Such a settlement difference causes a cavity in the lower part of the bottom of the structure. As a result, groundwater and soil are inflowed by the cavity generated in the lower part of the structure. And soil discharged from the lateral ground to the cavity accelerates the settlement of the lateral ground of the structure, resulting in a larger settlement.

For these problems, [1] confirmed that cavity occurred under the bottom of the structure due to poor compaction of the backfill material and also settlement of ground caused by compression, corrosion of the head of the pile foundation. They also indicated that the penetrated groundwater into the cavity is the reason of erosion of the ground. Furthermore, [2], [3] summarized the main causes and ranking of the each step. They mentioned that cavity is occurred due to the compressive embankment, short connection slab, defective backfill material. Additionally, it has been reported that the lateral expansion due to horizontal earth pressure [4], cavities created at the bottom of connecting slabs [5], and soil erosion incurred by water infiltration may lead to further issues.

In addition, [6] and [7] pointed to the consolidated settlement of the ground as a major cause of the differential movement of the bridge connection. And [8] observed the tendency of road surface settlement after opening the highway and analyzed that the small settlement difference in the connection section of the structure also causes inconvenience to the driving of the driver.

Until now, however, there are no measures to prevent problems caused by cavities in the lower part of the structure when designing and constructing at home and abroad. Therefore, after the occurrence of the problem, there is no clear solution except for temporary measures such as filling (grouting) or continuous paving overlay.

Therefore, in order to prevent problems caused by a cavity under the structure supported by the pile foundation, FLP, which can be easily installed on the side of a structure, was developed. The FLP is designed to produce similar downward movement as the settlement of the ground. Therefore, the stability against the lateral earth pressure is maintained even after the cavity occurred.

In this study, the laboratory model test was carried out to compare and analyze the settlement behavior according to FLP thickness, installation length. And analysis of the results showed that the reduction effect of the settlement was affected by the change of the stiffness of the FLP.

COUNTERMEASURES METHOD WITH CAVITY GENERATION

Case of cavity and differential movement

As shown in Fig. 1, groundwater is gathered and the head of the pile is damaged by the cavity in the lower part of the box structure. In addition, settlement of the lateral side of the structure and the difference in settlement of the connecting part pavement cause the differential movement. Such differential movement causes settlement and cracking of the pavement.

(a) Cavity generation

(b) Failure with cavity generation

(c) Differential movement

Fig.1 Cavity generation and problems

Features of FLP

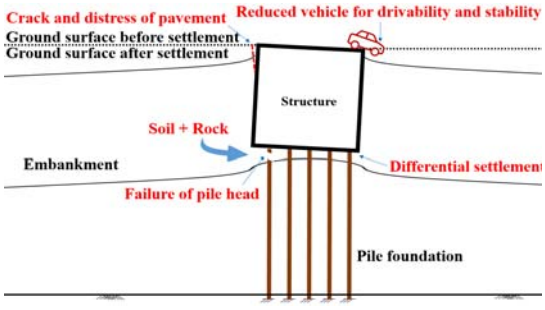

(a) Problems with cavity generation

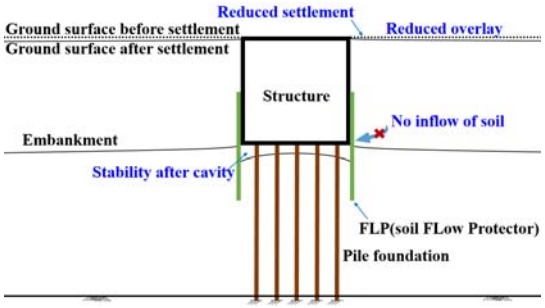

(b) Countermeasures for cavity generation

Fig.2 A schematic diagram of problems and countermeasures method with cavity generation [9]

As shown in Fig. 2 (a), the problems caused by the cavity in the lower part of the structure include reduced vehicle drivability and stability due to cracks and damage of the pavement, damage of the pile head due to the inflow of soil into the lateral ground, and the differential settlement of the structure. As shown in Fig. 2 (b), the countermeasure against this is to reduce the settlement of the lateral ground even after the cavity occurs by installing FLP on the side of the structure and to secure the stability by preventing damage of the pile head caused by the soil introduced into the cavity.

LABORATORY INDOOR MODEL TEST

Equipment of tests

Plane strain model soil-tank

The plane strain soil box applied in this study is shown in Fig. 3. In order to satisfy the plane strain condition, a wall of the plane strain model soil-tank was formed with transparent acrylic with a thickness of 30 mm, and the device was constructed to prevent deformation by further reinforcing 280 mm x 380 mm spacing in width and height, respectively. A vibration motor capable of generating vibrations was installed in the lower part of the plane strain model soil-tank, and spring was installed to facilitate transmission of the generated vibration.

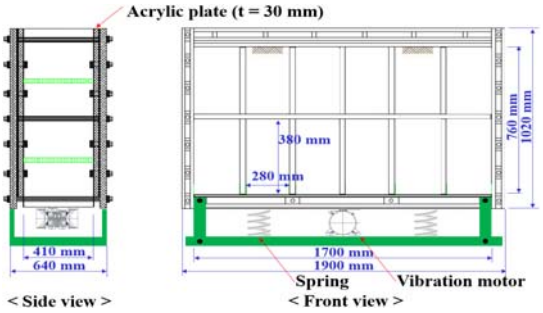

Fig.3 Side view and front view of plain strain soil tank

Dimension of model

As shown in Fig. 4, the dimensions of the box structure model are made of transparent acrylic with a thickness of 20 mm and its width x length x height are 408 mm x 350 mm x 340 mm, respectively. The actual structure is supported on a solid ground by pile foundation. In this study, however, it is fixed to the upper frame of the soil box to prevent settlement of the box structure by vibration. As shown in Fig. 5, an acrylic plate with a thickness of 3 mm (flexible) and 10 mm (stiff) were used for the FLP model and the horizontal length is 408 mm, 1 mm shorter on both sides to avoid friction with the width of the soil box (410 mm).

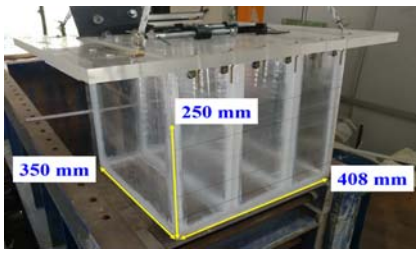

Fig.4 Test model of box structure

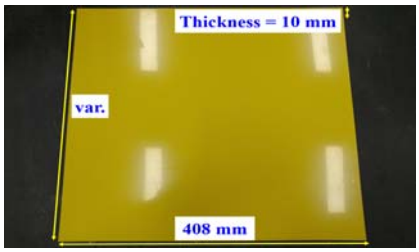

(a) Flexible

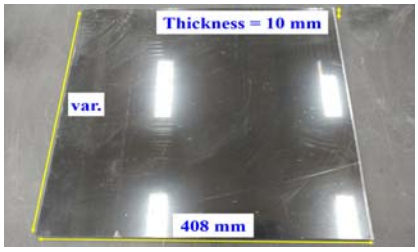

(b) Stiff

Fig.5 Test model of flexible and stiff FLP

Ground material

The ground material used when creating the ground is Jumun-jin standard sand and physical properties are shown in Table 1. Sandy soil such as Jumun-jin standard sand varies in density depending on the height of falling (Fig. 6(a)), and the mechanical properties also vary as the density changes (Fig. 6(b)), so the ground should be formed by keeping the density constant during the test. In this study, we used a sanding device to create with the ground with constant density with river sand method [10], [11], [12] at the falling height of 0.1 m, and the dry density at this time is 1.487 g / cm^3 on average.

Table 1 Physical characteristics of Jumun-jin standard sand

Description	Index	Property
Specific gravity	G_s	2.65
Water content	w_n (%)	0.9
Average particle size	D_{50}	0.580
Effective particle size	D_{10}	0.448
Uniformity coefficient	C_u	1.370
Coefficient of curvature	C_g	0.960

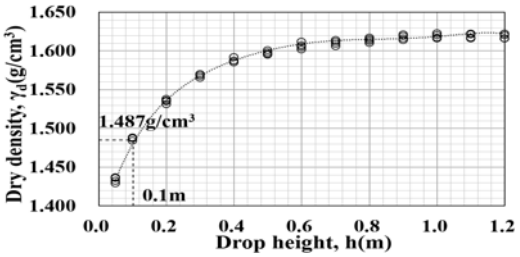

(a) Dry density relative to drop height

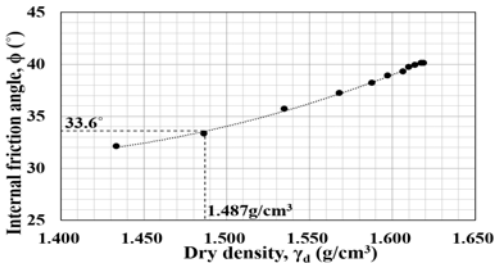

(b) Internal friction angle relative to dry density

Fig.6 Mechanical properties of Jumun-jin standard sand relative to drop height

Method of model tests

Considering the location where the box structure is installed, sand was installed up to the height where the bottom of the FLP was installed, then the FLP was installed and grease was applied between the wall of the soil box wall and the FLP. After that, sand was installed up to the height of the bottom of the box structure so that there is no difference in the earth pressure between the back surface and the front surface of the FLP, and then grease was applied in advance to the contact surface of the box structure and the soil inflow cut off, and a box structure was installed in order to prevent the penetration of sand and minimize friction.

In order to analyze the behavior of FLP due to the

settlement of the ground, the settlement was generated by force using a vibration motor. After the vibration occurred at each time, the settlement at regular intervals from the box structure was measured and averaged at the front, back and middle of the wall of the soil box. The experiment was terminated based on when the settlement due to vibration was almost converged. And Fig. 7 shows the installation of the box structure and FLP and the completion of ground creation.

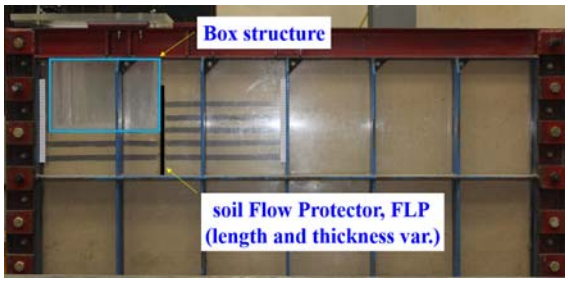

Fig.7 Front view of box structure and FLP after ground construction

Types of test

The tests were conducted under different installation conditions in order to check the effect of the FLP. The thickness of the FLP was divided into 3 mm, 10 mm and the installation length of the FLP was divided into 100 mm, 300 mm and 500 mm in order to analyze the behavior of the ground depending on the stiffness. Table 2 shows the types of model tests.

Table 2 Types of model test

Contents	Stiffness of FLP	Thickness of FLP (mm)	Length of FLP (mm)
Non	Non-reinforcement	-	-
S_100	Stiff	10	100
S_300			300
S_500			500
F_100	Flexible	3	100
F_300			300
F_500			500

Results of test

Fig. 8 shows the settlement of the lateral ground depending on 60 s, 120 s, 180 s, 360 s, 720 s and 1440 s, vibration time for each types of model test. The results show that the settlement tends to converge after 1440 s of vibration time, and the ground behavior was compared and analyzed based on the vibration time of 1440 s.

The settlement results for each types of model test are shown in Fig. 9.

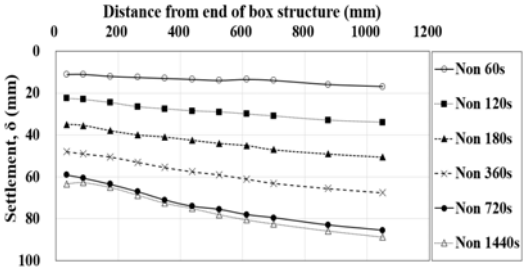

Fig.8 Settlement by vibration times

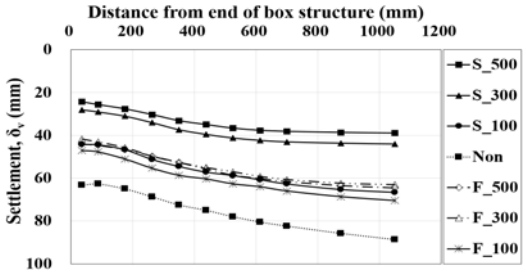

Fig.9 Settlement by types of model test (after 1440 s of vibration time)

ANALYSIS OF RESULTS

Ground behavior with installation

Table 3 Settlement with installation of FLP

Distance from end of box structure (mm)	Settlement		Ratio of Settlement S_300 / Non
	Non	S_300	
35.0	63.3	28.0	0.442
87.5	62.7	29.0	0.463
175.0	65.0	31.0	0.477
262.5	68.7	34.0	0.495
350.0	72.5	37.3	0.515
437.5	75.0	39.5	0.527
525.0	78.0	41.2	0.528
612.5	80.5	42.3	0.525
700.0	82.4	43.0	0.522
875.0	85.8	43.6	0.508
1050.0	88.7	44.0	0.496

In order to analyze the behavior of the ground according to the FLP installation, the settlement when the FLP is not installed (Non) and the FLP length is 300 mm (S_300) was shown in Table 3. The results show that, when the FLP is installed, the settlement was analyzed to be reduced by 44.2 ~ 52.8 % (50.0 % on average). As shown in Fig. 10(a), in the case of non-reinforcement, the inflow of soil into the cavity occurs as the ground sinks. Therefore, the installation of the FLP reduces the settlement of the lateral ground and prevents the leakage of lateral ground soil into the cavity.

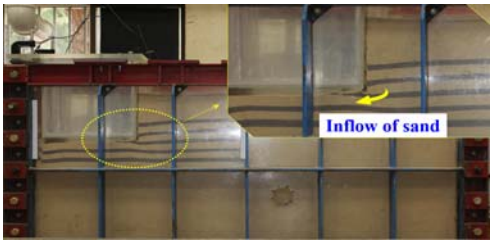

(a) Non

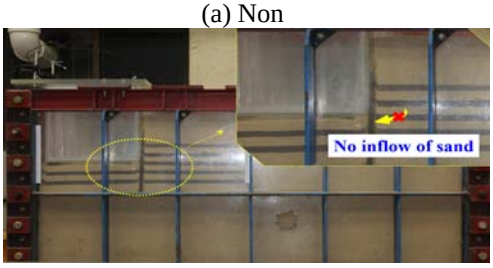

(b) S_300

Fig.10 Soil behavior in the cavity with installation of the FLP

Ground behavior with stiffness

Table 4 Settlement with stiffness of FLP

Distance from end of box structure (mm)	Settlement			Ratio of Settlement	
	Non	F_300	S_300	F_300 / Non	S_300 / Non
35.0	63.3	41.7	28.0	0.659	0.442
87.5	62.7	43.1	29.0	0.687	0.463
175.0	65.0	45.7	31.0	0.704	0.477
262.5	68.7	49.7	34.0	0.724	0.495
350.0	72.5	52.7	37.3	0.727	0.515
437.5	75.0	55.1	39.5	0.734	0.527
525.0	78.0	57.1	41.2	0.732	0.528
612.5	80.5	59.2	42.3	0.735	0.525
700.0	82.4	60.7	43.0	0.737	0.522
875.0	85.8	62.4	43.6	0.727	0.508
1050.0	88.7	63.1	44.0	0.711	0.496

In order to analyze the ground behavior according to the stiffness of the FLP, the thickness of the FLP was divided into 3 mm (F_300) and 10 mm (S_300) as shown in Table 4. As a result, the settlement was reduced by average 28.4 % in flexible and average 50.0 % in stiffness compared with non-reinforcement, indicating that the higher the stiffness of FLP, the more effective for settlement reduction. Fig. 11 shows the deformation after final settlement according to the stiffness of the FLP. It was found that the FLP displacement in a flexible case did not occur in the upper part, and displacement of about 20.0 mm occurred in the lower part. In the case of stiff, however, a displacement of about 4.0 mm occurred towards the back and the structure at the same time in the upper part and lower part of the FLP, respectively. Therefore, if the stiffness of the FLP is high enough, the passive earth pressure area is generated in the upper part, which is considered to be advantageous for the stability.

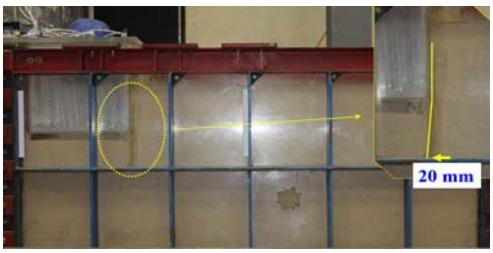

(a) F_300 (flexible)

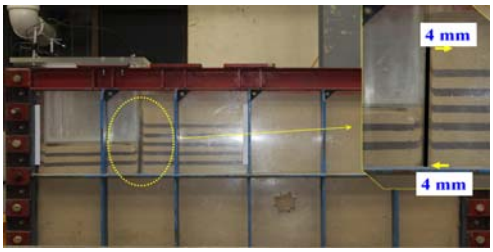

(b) S_300 (stiff)

Fig.11 Deformation shape with stiffness of the FLP

Ground behavior with stiffness change by length

In order to analyze the ground behavior according to the difference of stiffness with the change of length of the FLP, the length of the FLP was divided into 100 mm, 300 mm and 500 mm with the stiffness, the results are shown in Table 5. In this case, if the length is changed, the flexural rigidity also changes. As a result, the settlement is decreased by average 25.7 %, average 50.0 % and average 55.6 % in the stiffness as the length is increased, and it is effective to decrease the settlement as the length increases. However, in ductility, average 20.9 %, average 28.4 % and average 27.0 % decrease in length is not effective in decreasing the settlement because the stiffness decreases with increasing length. Therefore, in order to reduce the settlement effectively, it is necessary to sufficiently secure the flexural rigidity according to the length.

CONCLUSION

In this study, a laboratory model tests were carried out to analyze the reduction effect of the settlement with the stiffness of the FLP. The results are as follow:

The results of the laboratory model test showed that the installation of the FLP reduced the settlement by 50.0 %. The results of the photo analysis of the behavior in the ground showed that the installation of

Table 5 Ratio of settlement with stiffness change by length

Distance from end of box structure (mm)	Ratio of Settlement					
	F_100 / Non	F_300 / Non	F_500 / Non	S_100 / Non	S_300 / Non	S_500 / Non
35.0	0.742	0.659	0.695	0.700	0.442	0.384
87.5	0.760	0.687	0.712	0.709	0.463	0.409
175.0	0.785	0.704	0.718	0.719	0.477	0.426
262.5	0.806	0.724	0.723	0.746	0.495	0.442
350.0	0.809	0.727	0.726	0.753	0.515	0.458
437.5	0.804	0.734	0.742	0.762	0.527	0.467
525.0	0.803	0.732	0.752	0.753	0.528	0.471
612.5	0.795	0.735	0.748	0.754	0.525	0.468
700.0	0.801	0.737	0.748	0.761	0.522	0.464
875.0	0.800	0.727	0.740	0.761	0.508	0.451
1050.0	0.795	0.711	0.728	0.751	0.496	0.440

the FLP reduced the settlement of the lateral ground and prevented the leakage of lateral ground soil into the cavity.

The results of the laboratory model test showed that the settlement depending on the stiffness of the FLP was reduced by average 28.4 % in flexible and average 50.0 % in stiffness compared with non-reinforcement, indicating that the higher the stiffness of FLP, the more effective for settlement reduction. And the results of the photo-analysis of deformation due to stiffness showed that if the stiffness of the FLP is high enough, the passive earth pressure area is generated in the upper part, which will be advantageous for the stability.

ACKNOWLEDGMENTS

This research was supported by Basic Science Research Program through the National Research Foundation of Korea (NRF) funded by the Ministry of Education (No. 2018R1D1A1B07048553 and (No. 2019R1I1A1A01060584).

REFERENCES

[1] White, D.J., Mekkawy, M.M., Sritharan, S., and Suleiman, M.T. (2007), ""Underlying" Causes for Settlement of Bridge Approach Pavement Systems", Journal of performance of constructed facilities, ASCE, Vol.21, No.4, pp.273-282.

[2] Briaud, J., James, R.W., and Hoffman, S.B. (1997a), NCHRP Synthesis of Highway Practice 234: Settlement of Bridge Approaches (The Bump at the End of the Bridge), Transportation Research Board, National Reseach Council, Washington, D.C., pp.75.

[3] Briaud, J., Maher, S.F., and James, R.W. (1997b). "Bump at the End of the Bridge", Feature article, Civil Engineering, ASCE, Vol.67, No.5, pp.68-69.

[4] James, R.W., Zhang, H., and Zollinger, D.G. (1991). Observations of severe abutment backwall damage, Transportation Research Record 1319, Transportation Research Board, pp.55-61.

[5] Schaefer, V.R. and Koch, J.C. (1992). Void Development Under Bridge Approaches, Report No. SD90-03, South Dakota Department of Transportation, Pierre, pp.147.

[6] Im, Y. J., Choi, Y. C. and Lee, H. S.(2009), "Occurrence of steps in roads and countermeasures", Journal of the Korean Society of Road Engineers, Vol.11, No.3, pp.5-12. (in Korean)

[7] Kim, N. Y., Jeong, J. H., Nam, M. S. and Kim, H. J.(2012), "Analysis of the cause of settlement in the backfill part of bridge connection part", Journal of the Korean Geotechnical Society, Vol.28, No.4 pp.22-24. (in Korean)

[8] Jeong, J. H., Jo, S. M., Kim, H. J., Jeong, G. J., Park, J. G. and Kim, D. S.(2005), The Evaluations and Managements of Long-Term Settlement for the Highway on the Soft Grounds, Road Traffic GE-05-11, Korea Highway Corporation Road Traffic Institute. (in Korean)

[9] Yoo, J. W., Im, J. C., Choi, M. B. and Park, D. H.(2018), A Numerical Study on the Settlement Behavior of Soft Ground by Installation of Soil Flow Proctor, KSCE 2018 Convention, Vol.2018, No.10. pp.632-633. (in Korean)

[10] Ko, H. S., Im, J. C., Park, L. K. and Oh, M. L. (1996), "Model Tests on the Behaviour of Sandy Ground during Tunneling", Journal of the Korean Society of Civil Engineers, Vol.1996, No.2, pp.371-374. (in Korean)

[11] Son, J. H., Im, J. C., Park, L. K. and Lee, T. H.(2003) " A Study on the Group Effect of Micropiles installed beneath Shallow Foundations", Journal of the Korean Society of Civil Engineers, Vol.2003, No.10, pp.3354-3357. (in Korean)

[12] Bautista, F. E., Park, L. K., Im, J. C. and Lee, Y. N.(2006), "Variation of Earth Pressure Acting on Cut-and-Cover Tunnel Lining with Settlement of Backfill", Journal of the Korean Geotechnical Society, Vol.22, No.6, pp.27-40. (in Korean)

9th Int. Conf. on Geotechnique, Construction Materials and Environment, Tokyo, Japan, 20-22 November 2019, ISBN: 978-4-909106025 C3051

IDENTIFICATION OF MASS MOVEMENT (LIQUEFACTION) HAZARD IN SIBALAYA CENTRAL SULAWESI INDONESIA

Ihwan fauzi[1], Rudy Febrijanto [2], Cahya Ahmad Gumilar[3] and Tiya Rosdianti Utari[4]

[1,2,3,4] Institute of Road Engineering, Agency for Research and Development, Public Work Minister, Indonesia

ABSTRACT

The Palu earthquake magnitude 7.4 on the 28th September 2018 has impacted a liquefaction process in several areas in Central Sulawesi. One of the areas affected by the disaster was Sibalaya, Sigi District. Liquefaction phenomena as an earthquake-induced effect in loose saturated soils is considered very dangerous for structures founded over such materials. The common practice for liquefaction potential assessment recommends geological survey and field testing such as more cost-effective method is the use of geophysical methods which are not destructive and faster. Regional geological mapping was carried out with a direct survey of the Sibalaya area affected by liquefaction. One of the geophysical methods that can find out the subsurface profile is resistivity method. This study aims to describe the soil resistivity in the Sibalaya area. The resistivity method used is 1D as many as 4 points in the direction of the direction of land shift. Mapping on the surface using UAV photogrammetry to determine the distance of shifting of the land. The resistivity method results found that the dominant lithology was sand with gravel and grit to a depth of 30 meters with average resistivity values ranging from 1.38 Ωm-6246 Ωm. Where the resistivity value of 1.38 Ωm-11.5 Ωm is categorized as silty clay layer and 11.5 Ωm-6246 Ωm is a layer of sand with a mixture of various materials such as gravel or silt. The difference in the initial ground level with the land that has collapsed ranges from 10 m with the results of the situation mapping.

Keywords: Liquefaction, Lithology, Resistivity, UAV photogrametry

INTRODUCTION

The earthquake that shocked Palu and Donggala which occurred on September 28, 2018 with an epicenter location 26 km north of Donggala, Central Sulawesi, magnitude 7.4 with OT 17:02:45 WIB which occurred at a depth of 11 km was a shallow earthquake due to the Palu Koro fault activity. The active fault of Palu-Koro extends with the north-east direction splitting the area of Palu City [1]. This fault is inside one system with North Sulawesi subduction lanes in part north and Matano fault in the south .

The earthquake has caused infrastructure damage in the form of buildings, roads, river and bridges that are quite severe and triggered a collapse / landslide slope , and resulted in a tsunami in the coastal area of the Palu bay [2] and resulted in liquefaction in the Petobo, Balaroa, Jono Oge and Sibalaya areas [3].

Liquefaction phenomena as an earthquake-induced effect in loose saturated soils is considered very dangerous for structures founded over such materials. Liquefaction occurs when the soil's shear strength plummets due to an increase in pore water pressure induced by dynamic loading . This event is problematic in geotechnics since it can cause failure in structures founded on liquefiable soils. One of the affected areas of liquefaction which will be discussed in this paper is the Sibalaya area, located in Sigi Regency, within ± 30 km south of Palu City.

Electrical resistivity tests are being used for geophysical characterization but the electrical properties of soils can also describe the subsurface lithology of each layer of soil. Soil physical properties relevant for studying electrical resistivity may be controlled by the compaction process because soil structure [4]. Geophysical method is field testing which more cost-effective, not destructive and faster. The use of this technique for *in situ* prospection allows characterizing wide open areas and large depths. Measurements were made namely 1D (dimension) electrical resistivity using 4 iron electrodes to induce electricity flow to the subsurface. Configuration measurements made are wenner with the characteristic distance of each electrode that is plugged in the same length

LOCAL GEOLOGY OF SIBALAYA

Investigation of local geology in the affected areas of Sibalaya liquefaction is carried out by conducting a visual investigation of the type of soil or rocks scattered in that location, by determining the direction and position of rock layers and also identifying the geological structure occurring in the investigation area, especially after the earthquake in the area. Donggala. Fig 1 is a result of gological investigation in affected area of Sibalaya

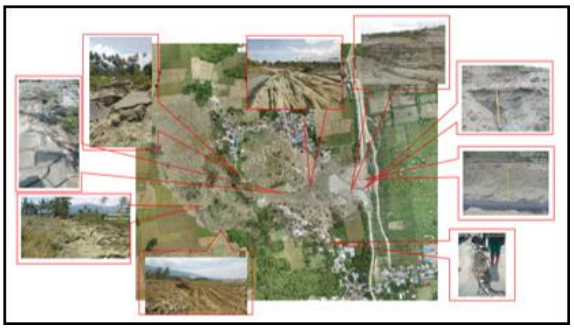

Fig 1. Results of local geological investigations in the Sibalaya area

Based on morphology, the location of Sibalaya is located in a depressed area and forms a pattern of trellis river flow, where there is only one main river (Palu river) with the presence of small rivers whose flow leads to the Palu river. The pattern of trellis river flow generally occurs in areas that have complex geological structure processes.

The main geological structure formed in the Sibalaya area is the presence of horizontal drift faults located on the right and left side of the Palu river, so that the Sibalaya area is located in the area of decline or the Depression which is increasingly narrowing towards the south. The fault was characterized by the presence of triangular facet which is a macro characteristic of Fault in the western part of Sibalaya, and mountains with steep slopes formed in the eastern part of the Sibalaya location that shows ini Fig 2.

Fig. 2 The existence of a triangular facet

Based on the results of the local geological investigation of the Sibalaya area it was found that the Sibalaya location was dominated by sand material with the presence of mixed deposited conglomerates and in some locations this conglomerate was deposited relatively at the bottom of the sand, with sand thickness varying between 1.8 - 2.4 m. The sand material is very loose / decomposed so that it makes the material vulnerable to the liquefaction process.

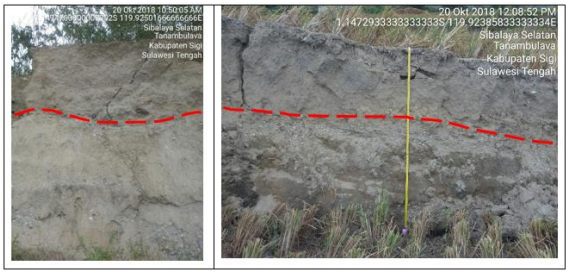

Fig. 3 The existence of sand and conglomerates

At the location of the investigation it was also found the emergence of mud material consisting of clay and silt that appeared around the cracks with the condition of the mud being wet due to the presence of water. The thickness of the mud that appears varies between 20 cm - 100 cm. The mud was identified in the upstream part of the Sibalaya liqueurfaction site on slope outcrops that experienced landslides, while in the lower reaches of Sibalaya it was found on the surface of lowland and in natural watersheds.

In making a local geological map a topographic map or detailed contour map with a scale ranging from 1: 1000-1: 2000 is needed. The contour map of the Sibalaya area is obtained based on the results of measurements using UAV planes with a map of the following:

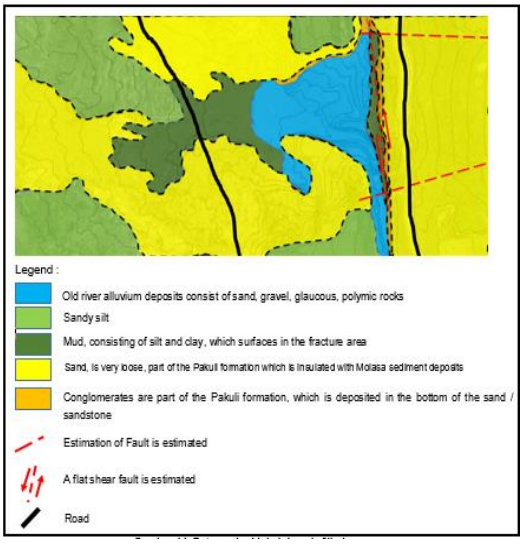

Fig. 4 Local geological map of the Sibalaya area

THEORETICAL FRAMEWORK

Liquefaction Potential Assessment

Liquefable soils according to [5] The first step in engineering assessment of the potential for "triggering" or initiation of soil liquefaction is the determination of whether or not soils of "potentially liquefiable nature" are present at a site. This, in turn,

raises the important question regarding which types of soils are potentially vulnerable to soil liquefaction.

It has long been recognized that relatively "clean" sandy soils, with few fines, are potentially vulnerable to seismically induced liquefaction. There has, however, been significant controversy and confusion regarding the liquefaction potential of silty soils (and silty/clayey soils), and also of coarser, gravelly soils and rockfills.

Coarser, gravelly soils are the easier of the two to discuss, so we will begin there. The cyclic behavior of coarse, gravelly soils differs little from that of "sandy" soils, as Nature has little or no respect for the arbitrary criteria established by the standard #4 sieve. Coarse, gravelly soils are potentially vulnerable to cyclic pore pressure generation and liquefaction. There are now a number of well-documented field cases of liquefaction of coarse, gravelly soils. These soils do, however, often differ in behavior from their finer, sandy brethren in two ways: (1) they can be much more pervious, and so can often rapidly dissipate cyclically generated pore pressures, and (2) due to the mass of their larger particles, the coarse gravelly soils are seldom deposited gently and so do not often occur in the very loose states more often encountered with finer sandy soils. Sandy soils can be very loose to very dense, while the very loose state is uncommon in gravelly deposits and coarser soils

Mass Movement

Mass movement eventually caused by a highly erosive precipitation as a climate variable to determine its type and magnitude [6]. But some mass movement likes liquefaction may occur during Earthquake [7], slope failure as a mass movement could be initiate by a trigger mechanism which is a discrete, identifiable event or influence its mass movement. A very effective trigger mechanism are tropical cyclones and earthquakes [8].

Sibalaya mass movement where its topography such as along ridges amplified ground acceleration of earthquake-triggered landslides, different with a landslides rainfall-triggered which occur lower on slopes, depends on groundwater discharge area [9]. Geotechnical investigations conducted to the landslide revealed that large volumes of highly sensitive clays (quick clays) known molase, were mobilized in the later stages of the landslide as mass movement [10]. Boreholes and static cone penetration tests conducted to assess the liquefaction susceptibility during earthquakes [11].

Photogrametry UAV

Unmanned Aerial Vehicles (UAVs) are increasingly used for surveying in widespread and operational for several applications [12], [13] rapidly across many civil application domains including real-time monitoring, providing wireless coverage, remote sensing, search and rescue, delivery of goods, security and surveillance, precision agriculture, civil infrastructure inspection [14], land rights[15] and hazard as well . it is very efficiency and flexibility for observing geological processes and acquiring data from different attached instruments, allowing especially wide application in the field of photogrammetry and remote sensing. Close range aerial photogrammetry, processed by modern computer vision approaches, allows the derivation of a digital elevation model at very high resolution [10].

Aerial photo survey activities are carried out to create topographic maps and situations from the results of the latest aerial photography by using a Unmanned Aerial Vehicle. The mapping location is in Sibalaya Village, Tanambulaya District, Sigi Regency, Central Sulawesi. The area to be surveyed is ± 580 Ha. The survey location is an area of settlements and rice fields. The aircraft used was Dadali X8 with a fixed wing/delta wing type autopilot control system.

The technical specifications of this work are as follows:

1) Fixed Wing Drone equipment with an autopilot and remote control navigation system,
2) Camera device, has a 20 MPixel sensor
3) The value of GSD (Ground sampling Distance) <10 cm / pixel
4) 70-80% Overlap and 50-60% Sidelap

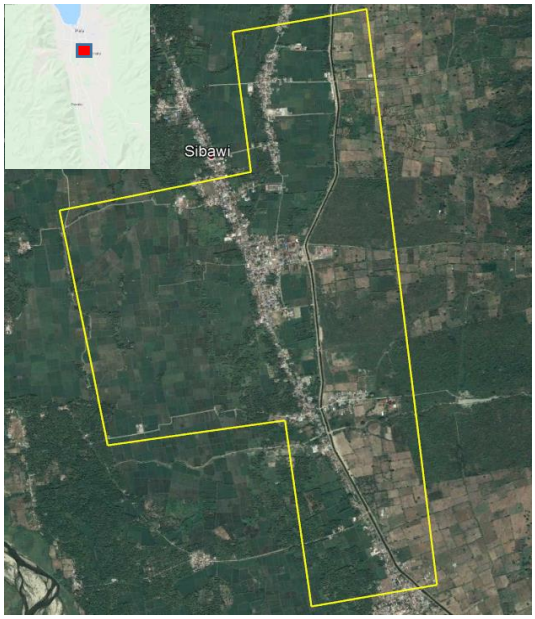

Fig. 5 Location of aerial photo surveys in Sibalaya.

GCP (Ground Control Point) are used to geo-referencing [16]. A pre-mark is installed as a GCP which becomes a reference / position controller in the Air Triangulation process. Ground control measurement using Geodetic GPS. Data acquisition

using Drones is carried out after all pre-marks are installed. Fig. 6 shows distribution of premark.

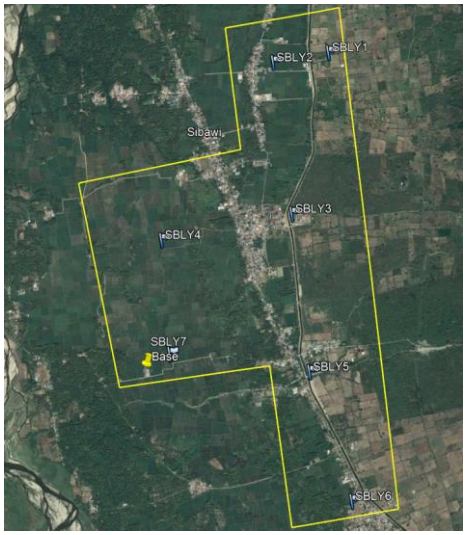

Fig. 6 The location of the pre-mark point in the Sibalaya.

Air triangulation, aerial photography is possible to calculate 3-dimensional coordinates for elements of each object. In the process several points are needed with known positions that appear on some photos. These points are the control points that are an important part of the air triangulation process. The process of implementing air triangulation is carried out automatically through the application program with the following stages and illustrations:

- Automatic identification of tie point points and ground control points based on image matching
- Perform a bundle leveling count that is equipped with a self-calibration count to obtain the optimal camera calibration value
- Look at the RMS value that shows the precision of the count and cannot be more than 3 x GSD

Digital Terrain Model (DTM) is 3-dimensional data that represents the surface state of the object covered. DTM is raster data with cell size of 1 mm on a map scale, which is obtained automatically with stereo matching techniques and continued with semi-automatic data editing.

Fig. 7 Plan for UAV flyways.

Fig. 7 is track as a plan for UAV flyways to make sure image can be captured follows the technical specification.

Electrical Resisitivity Method

Geophysical methods can provide information on subsurface conditions through measurements on the surface, including resistivity, electromagnetic induction, ground-penetrating radar, magnetometry, self-potential, seismic, gravity, radioactivity, nuclear magnetic resonance, induced polarization, etc [17].

Geological subsurface mapping is done by the type of resistivity method [18], measurements are made by energizing electric current (I = Ampere) to the earth and observing the potential difference (V = Volt), obtained by the value of rock resistance (Ohm) from equation :

$$V = I. R \quad (1)$$

Information:
V: measured potential difference (volts)
I : the amount of current sent (Amper)
R : rock resistance (Ohm)

The type of resistance value ($\boldsymbol{\rho}$a) is influenced by the relationship between the magnitude of the value of rock resistance (R) and the measured depth (a) and geometric. Material type resistance is defined as:

$$\boldsymbol{\rho} = R. A / L \quad (2)$$

Where:
$\boldsymbol{\rho}$: material type resistance (Ohm-m)
R: measured electrical resistance (Ohm)
L: length (m)
A: cross-sectional area (m^2)

The Wenner electrode arrangement, the geometric correction factor is 2 $\boldsymbol{\pi}$ a and the resistivity value of the type is obtained from the formula:

$$\boldsymbol{\rho} a = 2. \boldsymbol{\pi} a. R \quad (3)$$

Where:
$\boldsymbol{\rho}$a : pseudo-type resistance value (Ohm-m)
2 $\boldsymbol{\pi}$ a : geometric correction factor (m)
a :the electrode spacing (m)
R :rock resistance (Ohm)

This resistivity method uses a Wenner configuration. The Wenner four-pin method is the most commonly used technique for soil resistivity measurements [19]. The distance between electrodes, which is considered recommendable for various depth. The distance of each electrode in the Wenner configuration is always the same for each displacement. The farther the distance between the electrodes the deeper the depth will be. The

illustration of the Wenner configuration is shown in Figure 8

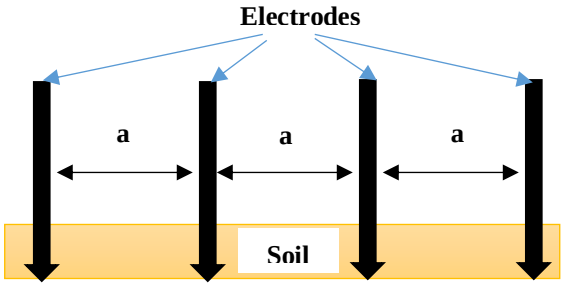

Fig 8. Ilustration of Wenner configuration

Concept of measuring the geoelectric resistance type (resistivity) [20], among others:

1) Resistance-mapping
   a. Measurements to obtain information about variations in lateral resistivity.
   b. Measurement at several points with fixed electrode spacing
   c. The electrode spacing is changed to obtain lateral variations at different depths

2) Resistivity-sounding or VES (Vertical Electrical Sounding) estimation
   a. Measurements to obtain information about resistivity variations vertically
   b. Measurement at one fixed point (sounding point) with varying electrode spacing
   c. Pseudo-type resistance data as an electrode space function
   d. VES data plots a pseudo-type resistance log (a) with a log spacing the current electrode (a)
   e. VES curve describes type resistance as a function of depth at the point of measurement (sounding)
   f. Modeling 1 D

Based on the value of the type of resistance carried out subsurface geological interpretation to be able to estimate the thickness, type of rock and its spread. The type of resistivity values measured on the tool, mapped and depicted two-dimensional resistivity contours (2 D) with the direction of the horizontal axis X and Z depth using IP2WIN software for VES measurements. In this paper rockworks version 15 software is used to better describe the subsurface section with an interpolation system for each resistivity value at the subsurface.

RESEARCH METHODOLOGY

The measurement location is shown in Figure 9, where resistivity testing is carried out in 4 points. The reason is done in that place because it can still be reached, it is considered safe if measurements are taken and it is considered sufficient to determine the objectives to be obtained. The length of the stretch reaches 150 meters to find up to 50 meters below the surface, so a wide and straight surface is needed.

Fig. 9 Location of acquisition resistivity method

RESULT AND DISCUSSION

Photogrametry UAV

GCP coordinates are determined from the processing of GPS observation data with BM Reference 'Base' points located in the location of Sibalaya Village. Result of GCP measurement can be found at table 1. This result is used for georeferencing

Table 1 GCP coordinates GPS observations

Name	N(m)	E(m)	h(m)
base	9872285	824306.5	126.758
sbl1	9874762	825563.1	145.3254
sbl2	9874720	825382.1	137.2652
sbl3	9873450	825462	150.2309
sbl4	9873279	824750.5	130.3463
sbl5	9872222	825569.6	150.3849
sbl6	9871118	826121.1	150.0124
sbl7	9872301	824547.1	127.0146

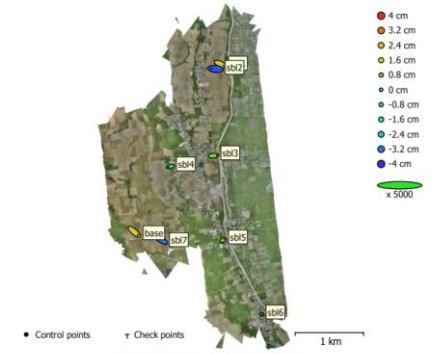

Fig. 4. GCP locations and error estimates.
Z error is represented by ellipse color. X,Y errors are represented by ellipse shape.
Estimated GCP locations are marked with a dot or crossing.

Count	X error (cm)	Y error (cm)	Z error (cm)	XY error (cm)	Total (cm)
8	1.89491	1.10807	2.11531	2.19511	3.04845

Table 4. Control points RMSE.
X - Easting, Y - Northing, Z - Altitude.

Fig. 10 Georeferencing accuracy with GCP point

Fig. 10 shows spread of premark and result of triangulation. RMSE for total accuracy is 3.0485 cm means that UAV survey could be use for precise scale map (1:1000). Fig. 11 shows imagery and contour map from UAV fotogrametric survey. Digital Elevation Model (DEM) of liquefaction in Sibalaya showed at Fig. 12.

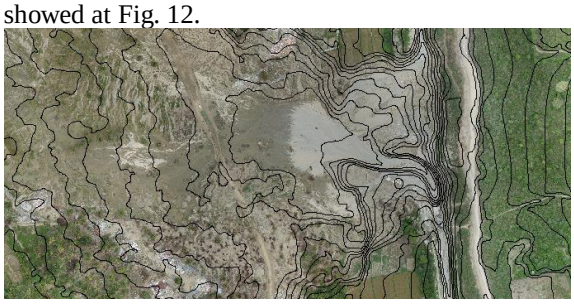

Fig. 11 Georeferencing accuracy with GCP point

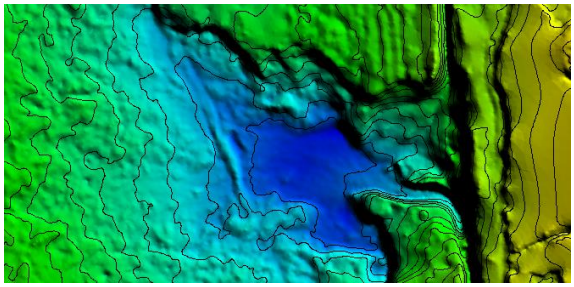

Fig.12 DEM of soil surface as a result of classification

Electrical Resistivity Method

The results of the geological mapping in which the majority of lithology that forms the Sibalaya area is sand with several other forming lithologies found in the area such as conglomerates, gravels, and other molasses sediments found in the Pakuli formation. So that the resulting resistivity value will be of great value because the main lithology of the location is sand. The results of processing using IPI2WIN are in table 1 where there is a column of depth and resistivity, while the lithology column is the result of interpretation.

Where the resistivity value of 1.38 Ωm-11.5 Ωm is categorized as silty clay layer and 11.5 Ωm-6246 Ωm is a layer of sand with a mixture of various materials such as gravel or silt. At GL-0 point the interpretation results are in table 2 with the largest resistivity value of 3718 Ωm which is included in mixed sand lithology and the resistivity value of 1.38 Ωm is interpreted as silty clay lithology

Table 2 The results of the interpretation at GL-0

Hole	Depth (m)	Rho (Ohm.m)	Lithology	Description
GL-0	0	293	Mixed Sand	Sand with a mixture of various materials such as gravel or silt
GL-0	0.224	183		
GL-0	0.668	3718		
GL-0	1.73	196	Silty Clay	Silty Clay
GL-0	50	1.38		

The depth of 0.224 -0.668 meters still considered one layer with a resistivity value of 293 29m and 183 Ωm which is thought to be soil and gravel in the area. After that at a depth of 0.668 meters up to 1.73 meters filled with a layer of molasses consisting of a mixture of sand lithology and conglomerates with poor gradations so that the value of the resistivity is 3718 Ωm. The next layer with a resistivity value of 193 µm at a depth of 1.73 meters - 33.9 meters is thought to be the lithology of a sandy silt where the resistivity value is not too large as sand and too small like silt. The sand contained in this layer can be caused by the layer above it in the form of a layer of molasses which is deposited on the lithology. Furthermore, with a resistivity value of 1.39 Ωm at a depth of 33.9 - 50 meters, it is assumed that the layer contains a lot of water content because the resistivity value is small compared to the others. The lithology that can be estimated for this layer is silt with a lot of water content which can also be called a aquifer zone.

In GL-1 the results of the interpretation are in table 3. The largest resistivity value of 5879 Ωm is interpreted as gravel found in the dominating sand layer, then the smallest resistivity value is 2.99 Ωm which is interpreted as a more conductive silty clay lithology. Fig. 13 Show the stratigraphic section of electrical resistivity from measurement.

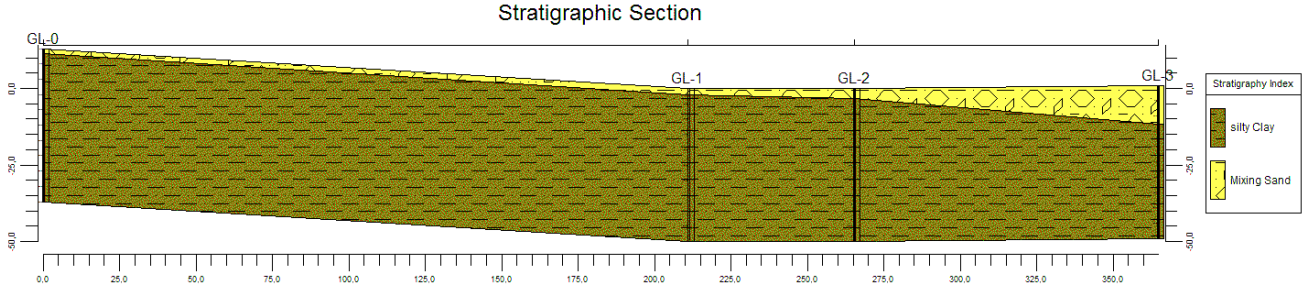

Fig.13 Stratigraphic section of electrical resistivity

Table 3 The results of the interpretation at GL-1

Hole	Depth (m)	Rho (Ohm.m)	Lithology	Description
GL-1	0	76.2	Mixed Sand	Sand with a mixture of various materials such as gravel or silt
GL-1	0.228	1936		
GL-1	0.554	46.7		
GL-1	2.21	5879		
GL-1	50	2.99	Silty Clay	Silty Clay

Resistivity values at depths of 0 - 0.554 meters are 76.2 Ωm and 1936 Ωm which is assumed that this layer is a pile of land which is buried beneath. Depth of 0.554 - 2.21 meters has a resistivity value of 46.7 Ωm which is assumed that in this layer there is silt with a little sand inside. The next layer with a resistivity value of 5879 Ωm at a depth of 2.21 - 5.82 meters is thought to be a layer of molasses with sand lithology with a conglomerate mixture so that the resistivity value is high. The depth of 5.82 - 50 meters with a resistivity value of 2.99 µm is thought to be a wet silt layer and contains a lot of water in it so that the resistivity value is small.

Table 4 The results of the interpretation at GL-2

Hole	Depth (m)	Rho (Ohm.m)	Lithology	Description
GL-2	0	335	Mixed Sand	Sand with a mixture of various materials such as gravel or silt
GL-2	0.24	5825		
GL-2	0.656	88.4		
GL-2	3.35	6246		
GL-2	50	11.5	Silty Clay	Silt Clay

Interpretation of results at the point of GL-2 contained in Table 4 with a resistivity value worth 6246 Ωm largest and the smallest is worth 11.5 Ωm. Resistivity values of 335 Ωm - 5825 Ωm are considered in one layer, namely the uppermost layer consisting of sand, gravel, and also conglomerate debris that can be seen from the surface and located at a depth of 0 - 0.656 meters. This measurement area is a landslide area so that a lot of material is carried from above to the middle area (GL-2). The value of resistivity 88.4 Ωm at a depth of 0.656 - 3.35 meters is thought to be a sand silt layer considering that from the GL-1 point there are also layers with almost the same resistivity value range. The next layer with a resistivity value of 6246 Ωm at a depth of 3.35 - 9.57 meters is thought to be a mixture of sand molasses and conglomerates with poor gradations so that the resistivity value is large. The last layer with a resistivity value of 11.5 Ωm from a depth of 9.57 - 50 meters is thought to be a silt layer.

Table 5 The results of the interpretation at GL-3

Hole	Depth (m)	Rho (Ohm.m)	Litologi	Deskripsi
GL-3	0	117	Mixed Sand	Sand with a mixture of various materials such as gravel or silt
GL-3	3.55	22.4		
GL-3	5.5	98.1		
GL-3	12.6	35.2		
GL-3	50	2.81	Silty Clay	Silt Clay

Table 5 describes the results of the GL-3 point interpretation. The resistivity value of GL-3 tends to be smaller than the previous geoelectric measurement because a day before the measurement takes place rain with high rainfall so that it can increase the amount of water below the surface which is more conductive. Depth 0 - 12.6 meters is considered to be the same layer with a resistivity value of 22.4 Ωm - 117 Ωm. The depth of 12.6 - 50 meters is considered to be the same layer only different from the water content contained in it where a small resistivity value has more water content than the others. The alleged lithology in this layer is silty clay or mud. Fig. 13 shows result of geotechnical borehole.

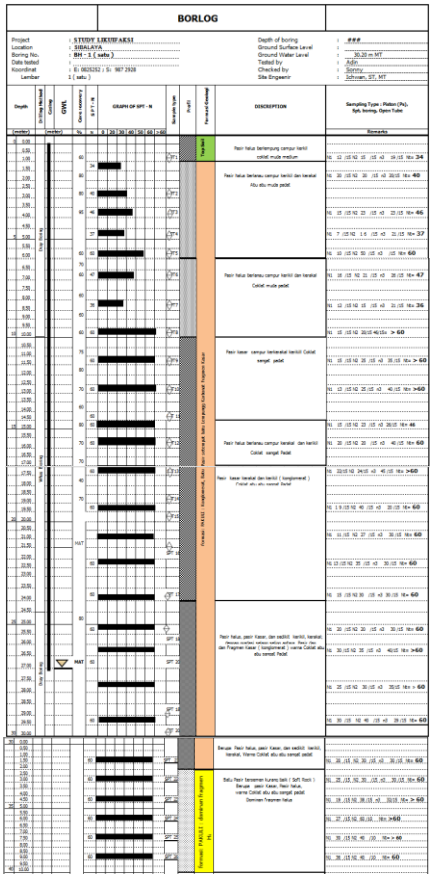

Fig. 13 Bore log Sibalaya Liquefaction

CONCLUSIONS

The dominant Sibalaya location is sand material that is loose/decomposed. There is a minor geological structure proven by the presence of line scratches and building shifts due to the presence of horizontal faults. There is a change in topography in the location area with a 10 meter decrease from the initial condition before the disaster occurs.

There are 3 main layers that make up the surface of the Sibalaya area. Aquifer zone (saturated layer of water) in the upper Sibalaya area (GL-1) at ± 30 meters depth while in the lower Sibalaya area (GL-4) around ± 6 meters. In general, the soil layer around the Sibalaya liquefaction zone consists of fine-grained to coarse material with loose properties (N-SPT 7-10), from rather dense to solid (N-SPT 16-47) and very dense (N-SPT> 50).

ACKNOWLEDGMENTS

The researcher would like to express his deep gratitude towards the Institute of Road Engineering, Agency for Research and Development, Public Work Minister, Indonesia for funding and supporting the research.

REFERENCES

[1] S. Pakpahan *et al.*, "Analisis Kegempaan di Zona Sesar Palu Koro, Sulawesi Tengah," *J. Lingkung. dan Bencana Geol.*, vol. 6, no. 3, pp. 253–264, 2015.

[2] D. G. Lintern, D. C. Mosher, and M. Scherwath, "SC," *Geol. Soc. London, Spec. Publ.*, 2019.

[3] B. Tandigala, "Dampak Bencana Gempa Bumi , Likuifaksi , Tsunami Sulawesi Tengah," Palu, 2019.

[4] V. Gingine, A. S. Dias, and R. Cardoso, "Compaction Control of Clayey Soils Using Electrical Resistivity Charts," *Procedia Eng.*, vol. 143, no. Ictg, pp. 803–810, 2016.

[5] K. O. Cetin, A. Kammerer, A. K. Consulting, J. M. Pestana, and M. F. Riemer, "Recent Advances in Soil Liquefaction Engineering and Seismic Site Response Evaluation," no. January 2014, 2001.

[6] D. M. Johnston, *Expansive Soils and Clays*, no. January 2013. 2014.

[7] T. R. Walter, J. Salzer, N. Varley, C. Navarro, R. Arámbula-mendoza, and D. Vargas-bracamontes, "Geomorphology Localized and distributed erosion triggered by the 2015 Hurricane Patricia investigated by repeated drone surveys and time lapse cameras at Volcán de Colima , Mexico," *Geomorphology*, vol. 319, pp. 186–198, 2018.

[8] J. P. Terry, "Tropical cyclones: Climatology and impacts in the South Pacific," *Trop. Cyclones Climatol. Impacts South Pacific*, no. January 2007, pp. 1–210, 2007.

[9] M. A. Brideau and N. J. Roberts, *Mass Movement in Bedrock*, no. October 2017. 2014.

[10] Y. Yamada *et al.*, "Submarine mass movements and their consequences," *Submar. Mass Movements Their Consequences - 5th Int. Symp.*, no. May 2014, pp. 1–12, 2012.

[11] S. Gupta, R. Sundaram, and S. Gupta, "Liquefaction Susceptibility Study At Commonwealth Games Village , Delhi," vol. 201309, pp. 4–7, 1986.

[12] R. El Meouche, I. Hijazi, P. A. Poncet, M. Abunemeh, and M. Rezoug, "UAV photogrammetry implementation to enhance land surveying, comparisons and possibilities," *Int. Arch. Photogramm. Remote Sens. Spat. Inf. Sci. - ISPRS Arch.*, vol. 42, no. 2W2, pp. 107–114, 2016.

[13] A. Gruen *et al.*, "Joint Processing of Uav Imagery and Terrestrial Mobile Mapping System Data for Very High Resolution City Modeling," *ISPRS - Int. Arch. Photogramm. Remote Sens. Spat. Inf. Sci.*, vol. XL-1/W2, no. September, pp. 175–182, 2013.

[14] H. Shakhatreh *et al.*, "Unmanned Aerial Vehicles (UAVs): A Survey on Civil Applications and Key Research Challenges," *IEEE Access*, vol. 7, pp. 48572–48634, 2019.

[15] P. Odwe, A. Mwasumbi, and R. Wayumba, "Application of Unmanned Aerial Vehicles in Strengthening Land Rights for the Youths in Kenya," *Strengthenning L. Gov. Africa*, 2017.

[16] V. Peterman and M. Mesarič, "Land Survey From Unmaned Aerial Veichle," *ISPRS - Int. Arch. Photogramm. Remote Sens. Spat. Inf. Sci.*, vol. XXXIX-B1, no. September, pp. 447–451, 2012.

[17] B. Allred *et al.*, "Agricultural Geophysics," pp. 1–4, 2016.

[18] H. S. Mesbah, E. A. Morsy, M. M. Soliman, and K. Kabeel, "Joint application of Geoelectrical Resistivity and Ground Penetrating Radar techniques for the study of hyper-saturated zones. Case study in Egypt," *NRIAG J. Astron. Geophys.*, vol. 6, no. 1, pp. 256–266, 2017.

[19] A. S. Soewaeli, "Menentukan Kedalaman Air Tanah Dengan Pengukuran Geolistrik Di Daerah Tonga , Padang Lawas , Sumut Geoelectrical Measurement on Determine Groundwater Depth in Tonga Area , Padang Lawas , North Sumatera," *J. Sumber Daya Air*, vol. 10, no. 1, pp. 57–70, 2014.

[20] H. Grandis, *Pengantar Pemodelan Inversi Geofisika*, no. 80. 2009.

9th Int. Conf. on Geotechnique, Construction Materials and Environment,
Tokyo, Japan, 20-22 November 2019, ISBN: 978-4-909106025 C3051

EFFECT OF CEMENT SOIL STABILIZATION ON THE PREVENTION OF SOIL OUTFLOW FROM BACK OF THE BRIDGE ABUTMENT

Yuko Ishida[1], Shoki Takayama[2], Kazuyuki Izuno[3], Yoshifumi Satofuka[4],
Taizo Kobayashi[5] and Ryoichi Fukagawa[6]
[1]kinugasa Research Organization, Ritsumeikan University, JAPAN;
[2-6] Fuculty of Science and Engineering, Ritsumeikan University, JAPAN

ABSTRACT

In recent years, heavy rains have frequently occurred in Japan, and a large amount of soil, rocks, and trees that were dislodged by landslides have flowed into rivers, causing damage to bridges. When a bridge is blocked by driftwood and boulders, the river water overflows onto and around the bridge abutment and the back face banking of the abutment is eroded, rendering the bridge impassable. We propose cement soil stabilization as a countermeasure to the erosion for the back of abutments. In this study, channel experiments on a 1:15 scale into the effect of cement soil stabilization were carried out. It was observed that erosion started from the downstream corner of the abutment when the overflow water returned to the river at the downstream point. In addition, when the back face banking of the abutment was strengthened with the minimum addition amount of concrete (set as 50 kg/m3) and cured for approximately two days, erosion was inhibited in both the reinforced back face banking and the unimproved levee.

Keywords: Overflow water, Erosion, Back of the abutment, Cement soil stabilization,

INTRODUCTION

In recent years, large-scale rainfall has increased in Japan due to the effects of climate change. It has been reported that trees and rocks have flowed into rivers from collapsed slopes due to heavy rainfall, causing damage to bridges. Driftwood and boulders accumulate between the bridge piers, that block the flow of the river and wash out the bridge or erode a levee and a back face banking of the bridge abutment. Bridges are vital parts of roads and railways; when they are damaged, traffic obstacles occur, which significantly affects evacuation, isolates villages, and hinders post-disaster recovery. As an example, the Yuyabashi Bridge over the Ohmata River in Kumano City, Mie Prefecture, was damaged by Typhoon Talas in 2011. Drifts were deposited on the bridge, and water overflowing from the upstream embankment eroded the ground. On the back face banking of the abutment, the ground was eroded by up to approximately 5.0 m, making the bridge impassable (Fig. 1).

In this study, we focus on the erosion of the back face banking of the abutment by overflow water. Abutments are generally constructed by excavating a space enclosed by inserted steel sheet piles, and space is then backfilled with on-site soil (Fig. 2). Because the enclosed working space is narrow and the abutment is a hindrance, backfill soil is difficult to compact and tends to be a weak spot. Therefore, we propose the use of cement soil stabilization for the shallow ground to improve the ground strength of the back face banking of the abutment, thereby preventing erosion. In this paper, we clarify the erosion process due to overflow water by a basic water channel model experiment, and also examine the erosion prevention effect of the ground improvement.

Fig. 1 Erosion at the left bank of the Yuya bridge (provided by Dr. Kenji Okajima Mie Univ.)

Fig. 2 Construction space by excluding water using steel sheet pile

PREVIOUS STUDY

Various damage has occurred at the back face of abutments. Such as subsidence of embankment at the boundary between the different material characteristics of the structure (abutment) and the ground (back face banking of the abutment) caused by an earthquake, or the erosion of the embankment caused by tsunami or flood.

Ikemoto et al. devised a method of creating a column-like reinforced body using cement-based material as a measure to prevent the settling of the rear surface of the abutment during earthquakes and verified the effect by shaking table tests [1]. Their studies have been put to practical use in JR East as a method for preventing subsidence back face banking of abutments on railroad bridges, and show the effectiveness of ground improvement using cement-based materials. However, the effects of erosion are not discussed in their study. It is therefore necessary to separately consider the effectiveness of the ground surface erosion prevention which this study targets, the construction range of the improvement body, and the construction method.

There are few research cases on erosion and runoff of back face banking of the abutment and concrete measures. The development of effective measures with excellent workability and economy should be promoted. There are approximately 700,000 road bridges over two meters in length, and approximately 160,000 road bridges over 15 meters in length; half of them will have existed for 50 years or more by the mid-2020s [2]. Considering that there is a large number and age range of existing bridges, it is desirable to upgrade to a structure that is resistant to disasters as efficiently as possible while maintaining and managing them. In this study, when considering countermeasure works, we placed emphasis on three points: (1) low material cost; (2) low construction cost; and (3) the possibility of implementation at the same time as routine maintenance. The surface of the abutment approach section is often asphalt-paved, and the pavement is subjected to repair work such as replacement over a fixed period as it deteriorates. Therefore, the above three points may be satisfied by constructing the shallow ground in the lower part of the road body at the same time as the renovation of the pavement.

EXPERIMENTAL OUTLINE

Experiment model

The experiment simulated the upper part of the embankment in the cross-section of the river in order to investigate the influence of a rising water level and overflow on the erosion of the embankment, especially around the abutment. The open channel used for the experiment has a length of 13,000 mm, a width of 500 mm, a height of 350 mm, and a slope of 5°. Among them, a 1333 mm section (model scale: 1:15, actual scale: 20.0 m) was closed to simulate a bridge with a width of 333 mm (actual scale: 5.0 m) and the upper part of the left bank levee. The bridge model made combined the following four parts (Fig. 3): the wall of the inverted T-abutment modeled in a simple box shape; the bridge girder; the panel simulating a blockage between the bridge pier and abutment; and the floor board of the width of the channel. The bridge model was placed at the center of the experimental section in the extension direction and fixed to the bottom of the water channel. The part of the free board of the levee (the revetment top end to the levee top end) and the surface of the embankment was assumed to be bare ground, and the embankment surface was assumed to be horizontal. The image of the experimental model on the actual embankment is shown in Fig. 4, and the experimental model is shown in Fig. 5. Silica sand No. 7 was used as the embankment material, and it was designed so that the optimum water content ratio w = 10% and the compaction degree Dc = 85%. The thickness of one layer was 50 mm and layers were compacted to a predetermined volume.

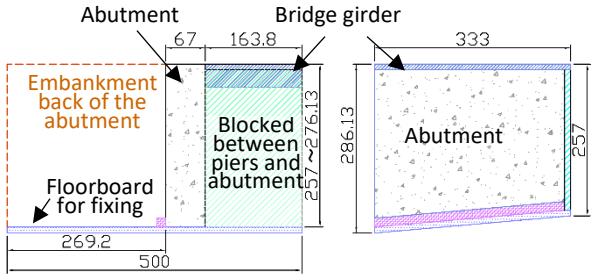

Fig. 3 Bridge model

Fig. 4 Revetment and Free board of a levee

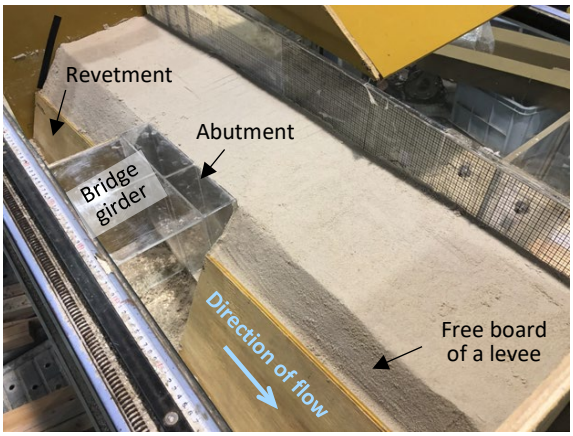

Fig.5 Experimental model （Case 1）

Experiment case

In this paper, we report four cases of experiments. The differences in the experimental conditions are shown in Table 1. In the experiments of Case-1 and Case-2, the effect of the countermeasure is considered from the difference of the erosion process depending on with or without the countermeasure with a similar flow rate. Additionally, in the experiments of Case-2, Case-3, and Case-4, the influence of the flow rate is considered from the difference of the erosion process of the same condition ground improvement part when the flow rate is different.

Table 1 The main difference between the four cases

	Soil stabilization	Curing period （ days）	Flow rate （ m^3/s）
CASE-1	Without	—	2.00×10^{-2}
CASE-2	With	2	1.77×10^{-2}
CASE-3	With	3	2.34×10^{-3}
CASE-4	With	3	2.18×10^{-4}

Blast furnace cement type B was used as the stabilizer for ground improvement, and the amount to be added was set to 50.0 kg/m3, which was considered the minimum additional amount necessary to be sure of an accurate mix of stabilizer and untreated soil [3]. The improvement range was the entire back face banking of the abutment, and the improvement depth was 80 mm (actual scale: 1.2 m). The usual method of mixing requires stabilizer to be spread onto the target ground and mixed with the ground material using a shovel-loader. However, in this experiment, the soil of the ground improvement target area was put into a bucket and mixed thoroughly with the stabilizer. Subsequently, the prescribed amount of improved soil was returned to the target area and compacted. If the cement setting time (approximately 2 hours) is exceeded, the cement stabilized soil loses its strength significantly. It is therefore desirable that the time from mixing to compression be within approximately one hour. Consequently, the ground improvement was carried out in a timely manner. Generally, it takes seven days for the strength development of the stabilizer to become stable; however, we set the curing time to between two and three days to impose a more severe condition in these experiments.

The flow velocity was targeted at approximately 3.0 m/s based on the references [4]. Based on equation (1), the flow amount was adjusted so that the overflow water depth around the bridge center was approximately 60 mm, and the design standard flow amount simulating a flood was 2.00 × 10-2 m3/s. In Case 3 and Case 4, the flow rate is changed. The pump used in these experiments caused an error in the flow setting depending on the water supply condition, so the flow rate during the experiment was measured every time.

$$v = \sqrt{gh} \tag{1}$$

$$\frac{h_m}{h_p} = L_r \tag{2}$$

in which v is the average flow velocity (m/s) , g is gravitational acceleration (m/s^2), and h is water depth (m), h_m is the water depth of the model (m), h_p is the water depth of the prototype (m), L_r is the model scale .

Measuring equipment

In order to quantitatively evaluate the amount of displacement of the embankment, inclinometers (PMP-S5HT) were installed at symmetrical positions on the upstream and the downstream sides, centering on the center of the abutment. The two-dimensional (2-D) diagram of the inclinometer installation position is shown in Fig. 6. These inclinometers detect inclination in one direction by the leaf spring pendulum method, to an effective inclination angle

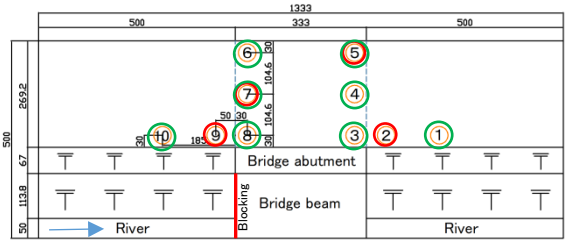

Fig. 6 Tilt sensor arrangement plan
（Case-1: ①②③④⑤⑥⑦⑧⑨⑩
Case-2 : ①②③④⑦⑧⑨⑩
Case-3 : ①②③⑤⑥⑧⑨⑩）

of ± 5°. They were installed with the condition that when they incline toward the downstream side, the output change is positive; their bases were embedded to a depth of 100 mm. The external dimensions [5] and the interpretation of the direction of inclination are shown in Fig. 7.

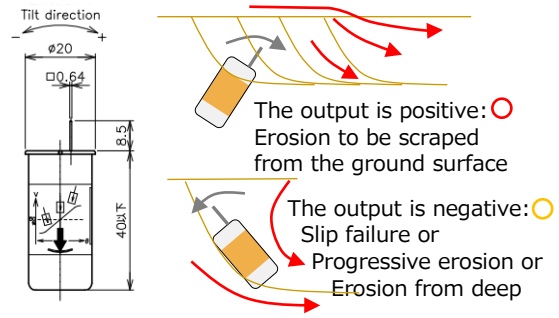

Fig. 7 Tilt direction and interpretation of results

RESULTS AND DISCUSSION

The results of Case-1

The state after the water flow is shown in Fig. 8, and the tilt fluctuation around each measurement point is shown in Fig. 9. The overflow water reached the end of the downstream embankment adjacent to the abutment 6 s after the onset of the overflow, and the erosion started approximately 1 s later (Fig. 8). The erosion area expanded from that position and the embankment at the installation position of the downstream inclinometer (2, 3, 4, 5) flowed out 17 s after the start of the overflow. Subsequently, the eroded area expanded downstream and upstream.

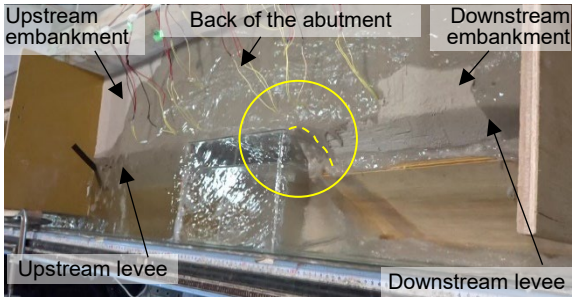

Fig. 8 Start of erosion (After overflow 6 s)

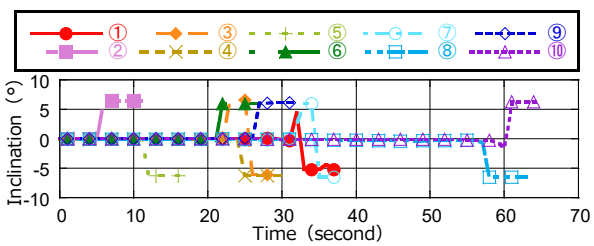

Fig. 9 Tilt fluctuation (Case 1)

The red circle in Fig. 7 shows that the upper part of the inclinometer fell towards the downstream side. The inclination direction of the inclinometer at each point was uneven, and the characteristic tendency was not found in the erosion direction.

The results of Case-2

The state after the water flow is shown in Figs. 10 and 11, and the tilt fluctuation around each measurement point is shown in Fig. 12. The erosion of the embankment started after The overflow water reached the end of the downstream embankment adjacent to the abutment as with Case 1. However, the subsequent erosion process was different from Case 1, and the erosion near the back face of the abutment did not progress rapidly.

The downstream levee was notably eroded by the surface flow, and the erosion progressed slowly at the boundary between the ground improvement part adjoining the abutment and the downstream embankment (Fig. 10). Furthermore, the erosion of the upstream embankment progressed (yellow in Fig. 11) and the embankment just under the improved part was washed away. However, the unified improved part showed resistance to erosion and remained in its former position by the frictional resistance of the abutment and the water channel wall. Inclinometers 3, 4, 5, and 6 (red in Fig. 11) of the improved part started to gradually incline at approximately 2 min and 40 s from the start of overflowing, and they greatly inclined downstream all at once after 3 min and 27 s. Because the four inclinometers showed the same behavior at the same time, it is clear that the ground improvement part became integrated (Fig. 12). Inclinometer 8 (blue in Fig. 11) in the upstream embankment part continues to incline gently from approximately 2 minutes and 27 s to the end of the experiment. Comparing with Case 1, in which the same position embankment was washed away 60 s after the start of overflow, this result shows the unimproved embankment on the upstream side increased its resistance for erosion.

The direction of inclination of the inclinometers is analyzed in order to consider the state of erosion. The green circle in Fig. 7 shows that the upper part of the inclinometer fell towards the downstream side when the inclinometer started to move. With only inclinometers 2 and 7, close to the improved part, did the lower part of the inclinometer fall towards the downstream side. It is inferred that it moved along with the sliding soil due to the strong flow from upstream to downstream. With the other inclinometers, their upper parts fell towards the downstream side. It is inferred that deep progressive

erosion was suppressed and the influence of erosion from the ground surface was larger.

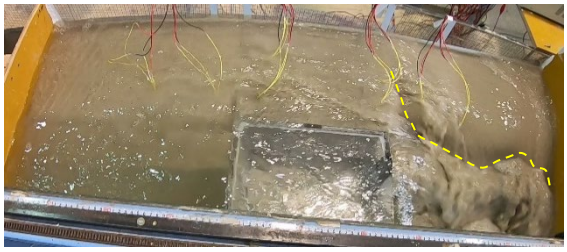

Fig. 10 Erosion at the boundary of the downstream

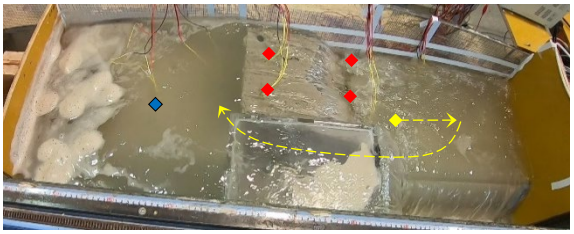

Fig. 11 Broken ground improvement part and process of displacement (After overflow 3 min 40 s)

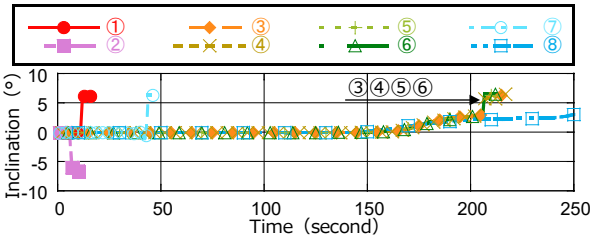

Fig. 12 Tilt fluctuation (Case 2)

Effectiveness of ground improvement

Case 2 was carried out with the conditions of the minimum amount of cement addition and two days of curing. From the results of Case 2, it was confirmed that the ground improvement was integrated, and the erosion was suppressed more than in Case 1, which was without improvement. Although the improved part settled and inclined because the foundation ground supporting the improved ground had been lost, if the foundation ground remained, there is a fair possibility that it would maintain its function as a road on the embankment adjoining the abutment. There is room for consideration of the improvement ground range, such as the downstream embankment adjacent to the abutment, because erosion proceeds from weak areas such as the boundary between the abutment and the embankment, or the boundary between the improved part and the unimproved embankment.

In addition, the result from improving the ground of the embankment adjoining the abutment, the unimproved embankment became more resistant to erosion. It was considered that the cause of this phenomenon was affected by the following: the resistance to erosion of the improved part increased compared to the case without improvement; and the penetration of the improved part was suppressed. Moreover, because the improved part was not eroded, the flow of the overflow water and the progress of erosion became reduced compared with the unimproved case.

The results of Case-3 and Case-4

In both Case 3 and Case 4, significant time passed before the water level rose and overflow occurred because of the low rate of flow, with the result that penetration and erosion of the upstream levee preceded other areas of erosion (Fig. 13). It is thought that the erosion was accelerated because the formwork moved by compaction energy at the time of formation of the levee and the ground adjoining the revetment loosened. After the erosion area approached the bottom of the upstream levee, the unimproved ground immediately below the improved ground adjoining the abutment was eroded in the downstream direction, and a water flow analogous to a tunnel penetrated underneath the improved part (Fig. 14). The erosion gradually progressed at the boundary between the improved part and the levee on the downstream side until approximately 1 min and 20 s (in Case 3), and 2 min and 30 s (in Case 4), after the start of overflow. Subsequently, the erosion area did not expand because the water flowed through the tunnel in Case 3, and the downstream embankment was completely washed away by the water flow in Case 4, so the experiment was ended.

Fig. 13 Scour-like erosion and flow at the upstream side (Case 3)

Fig. 14 Improved soil after the experiment (Case 4)

In both cases, inclinometers 3, 4, and 5 in the improved part were not displaced (Figs. 15-16). The cause of displacement of inclinometer 6 in the improved part close to the upstream revetment in Case 3 is that the base of the improved part was slightly eroded by the water flow.

The results show when the flow volume is low (the flow velocity is low), the embankment erosion by the penetration on the upstream side is notable, and the erosion progresses in the riverbed direction. In addition, because the amount of overflow water is small, the amount of erosion at the downstream embankment is small. Erosion was observed at the boundary with the improved part and the unimproved embankment, however, the improved part adjoining the abutment almost became integrated with the structure and remained consolidated.

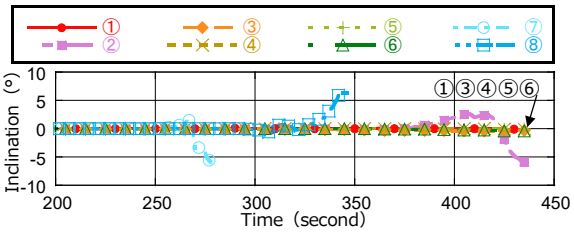

Fig. 15 Tilt fluctuation (Case 3)

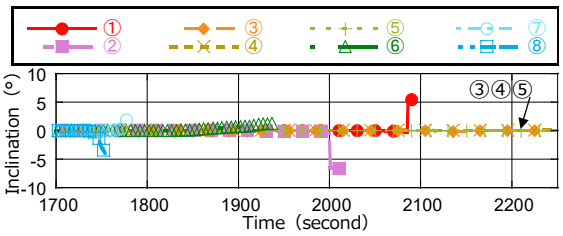

Fig. 16 Tilt fluctuation (Case 4)

CONCLUSIONS

In this study, four experiments were conducted to examine the resistance to erosion of soil stabilized by a cement-based solidifying material. Under the conditions of this experiment, it was found that to carry out ground improvement of the embankment adjoining the abutment, erosion can be suppressed, the ability to maintain function as a road is improved, and the suppression effect can be expected also against the erosion of the surroundings of the abutment.

Progression of erosion at the boundary between the ground improvement section and the embankment was confirmed. The overflow water from the river embankment due to the blockage of the bridge significantly eroded the downstream embankment, especially near the abutment. If the flow rate is small, the risk of seepage failure on the levee increases on the upstream side. Therefore, countermeasures for the upstream and downstream levee near the abutment are also desirable.

In the future, under the condition that the foundation ground does not run off, it is necessary to consider the amount of cement to be added, curing conditions, and ground improvement range, to resist against larger flow rates and longer overflow times.

ACKNOWLEDGMENTS

This work was partially supported by JSPS KAKENHI Grant Number 17H03299. We would like to thank Mr. Noriaki Nakanishi of Fukken Co., Ltd. for much advice on the countermeasure method and the experimental plan. We are also grateful to Keiji Asada the Engineering Center of Ritsumeikan University for the experimental bridge model building. We wish to thank Atsuyuki Shimizu who is a graduate, Yuuki Tasaki and Toshiya Nakauchi who are the undergraduate students of Science and Engineering of Ritsumeikan University cooperating in the water channel experiments.

REFERENCES

[1] Hirofumi Ikemoto, Hideaki Takahashi, Experimental study on method for controlling settlement of backfill of abutment, JR EAST Technical Review, No.52, 2015, pp.41-46.

[2] Subcommittee on bridge management system Committee of Structural Engineering Japan Society of Civil Engineers, The bridge management system –Practice and Methodology-, Structural Engineering Series 25, 2016, p.1.

[3] The Kino river basin committee on Ministry of Land, Inflastructure, Transport and Tourism Kinki Regional Development Breau, The conference document 4 for the Sixth the Kino river basin committee " The flow velocity at the time of flooding in the Kino River, 2001, p.5. https://www.kkr.mlit.go.jp/wakayama/ryuiki_iinkai/ryuiki/comm06/pdf/data4/data4.pdf （2018.5.24access）.

[4] The soil stabilization technology curation exploratory committee on Earthwork laboratory of Road Research Department of Nippon Expressway Research Institute Company Limited, Soil stabilization processing technology for road construction, Nippon Expressway Research Institute Company Limited, 2017, pp.49,90,121.

[5] Midori Precisions Co., Ltd., Contactless (Hall IC) Inclinometer Sensor"PMP-SxxHT Series, n.d., pp.1-2.

9th Int. Conf. on Geotechnique, Construction Materials and Environment,
Tokyo, Japan, 20-22 November 2019, ISBN: 978-4-909106025 C3051

A STUDY ON THE EFFECT OF FLOODING DEPTHS AND DURATION ON SOIL SUBGRADE PERFORMANCE AND STABILITY

Muhd Shahril Nizam Ismail[1], *Abdul Naser Abdul Ghani[2] Zuhayr Md Ghazaly[3], Muawia Dafalla[4]

[1,2]School of Housing, Building and Planning, Universiti Sains Malaysia, Malaysia; [3]School of Environmental Engineering, Universiti Malaysia Perlis, Malaysia; [4]Bugshan Research Chair in Expansive Soils, King Saud University, Saudi Arabia.

ABSTRACT

In the event of flooding, the road infrastructure especially the subgrade will be affected in terms of its capacity to support the pavement. It is well known that subgrade deterioration will eventually cause pavement failure. However, little is known on how the subgrade reacts to different flooding conditions especially in terms of the depth and duration of the floods. The aims of this study are to evaluate the moisture content variation and strength of the subgrade using the flood simulation model. The pavement loading characteristics are referred to the Manual on Flexible Pavement Design published by the Malaysian Public Works Department (ATJ 5/85 Rev. 2013). The flood parameters used for this experimental model are based on actual data of flooding events from 1991 to 2014. It includes the parameters of flood water level, flood duration and repeated flooding. The samples were exposed to flooding for a duration of 3, 24 and 48 hours for unrepeated flooding and 2, 5, and 24 hours for repeated flooding. Flood water levels were set to 0.3 m, 0.6 m and 1 m. This study shows that there is a strong relationship between moisture content and subgrade strength. The increase in the duration of the flooding affected the performance of the subgrade due to the increasing moisture content. The study also revealed that the rate of deterioration in subgrade strength for second flooding events is 30% less than for first flooding events. The result of this experiment will be used to develop the basis for including flooding characteristics in the modified California Bearing Ratio test for soils in flood prone areas.

Keywords: Moisture content, Flooding, road subgrade, California Bearing Ratio

1. INTRODUCTION

The economic development of a country can be assessed by the connectivity of its different regions by means of roads and railways. Thus, the construction of road infrastructure is one of the important civil engineering works undertaken for interconnecting the different places in a country [1]. For a developing country like Malaysia damage to road infrastructure due to natural disasters such as flooding commonly result in a huge expenditure for rehabilitation and road works [2]. The foundation soil supporting the pavement is called the subgrade. In the design of flexible pavements, the CBR test is the most widely performed method to estimate the strength values of the road subgrade and sub-base. These CBR values enable the design of a suitable thickness for the base and pavement layers. As the performance of a constructed road essentially depends on the various parameters e.g. subgrade material, materials used in different layers of the pavement and the traffic loading, the selection of appropriate subgrade materials with better quality is very important for getting a superior performance [3]. The destructive effect of moisture on pavement performance is an important consideration especially as the monsoon season is an annual occurrence. Furthermore, it affects the long-term performance of granular or stabilized base and sub-base, and of the sub-grade [4]. When the road is inundated for an extended time, the materials in each layer of the pavement become saturated, and then as the floodwaters drain, the subgrade soils begin to shrink and subside. [2]. A study by Ismail et al. [5] on flood depths and duration found that the average flash flood occurs in less than 6 hours in most locations in Malaysia, but flash floods duration may exceed 6 hours with the flood water level above 1.0 m due to heavy rain and high tidal level. In contrast, the average monsoon flood duration is two days with an average flood water level of 1.0 m, depending on rainfall conditions. In addition, repeat flooding frequently happens within a month of the first flooding event. There are several studies by previous researchers on the effect to the soil subgrade due to the duration and flooding depth. According to Alam and Zakaria [6], the period of inundation by floodwater affects the strength of pavement layers significantly and in the case of surface layers the strength also reduces substantially. Other researchers like Fairweather and Yeaman [7] concluded that the effect of flood on the road pavement structure

deterioration shows a good relationship between strain and moisture in the subgrade layer and poor relationship between surface layer strain and moisture. This manuscript presents a general overview on the following issues regarding road infrastructure especially how the subgrade will be affected in terms of its capacity to support the pavement. It is well known that subgrade deterioration will eventually cause pavement failure. However, little is known about how the subgrade reacts to the different flooding conditions, especially the depth and duration of the floods. The focus is determine the moisture content and strength of the subgrade from actual flood events using a flood simulation model. At the end, this experiment will be used to develop the basis for including flooding characteristics in the modified California Bearing Ratio Figure 1 is a typical road inundation during a monsoon flood.

Fig. 1: Typical road inundation during monsoon flood. (Source: Department of Irrigation and Drainage Malaysia)

2. EXPERIMENTAL SET UP

An experimental program was planned to study the effect of flood events on subgrade soil performance on a reduced scale in the laboratory. The first phase was specimen and test preparations and the second phase was the preparation of an experimental model section. The proposed test is called a Flood Simulation Model (FSM). The samples of sub-grade soil were taken from quarries that supply soil which is usually used as the embankment soil in road works. The soil samples were approved according to the Standard Specification for Road Works - Section 2: Earthworks by the Public Work Department (PWD), Malaysia. The properties of the soil samples are shown in Table 1 and the physical and mechanical properties of the soil samples were determined according to the Unified Soil Classification System (ASTM D2487). The tested soils were found and can be classified in the group of "Well-graded sand''.

Table 1: Basic Properties of soil Sample

Soil properties	Value
Specific Gravity	2.65
Moisture content	12%
Adjustment moisture content	14.5 %
Maximum dry density	1.92
Ph value	5.04
Organic Content	1.69%
Liquid limit	45%
Plastic limit	Non-Plastic
Plasticity index	Non-Plastic
Grading	SW

2.1 Specimen and Test Preparation

Initially, experiments such as the Atterberg limit, sieve analysis and index properties were conducted to determine the properties of the soil. Soil with a total mass of 4956g with an optimum moisture content at 12% was compressed in the mould using Static Compression with Tamping [8] for unflooded and unrepeated flood sample. For repeated flood events a soil sample with total mass of 5067 g with adjustment optimum moisture content at 14.5% was used. 80 specimens were prepared in total, and the specimens were intended for control, unrepeated flood and repeated flood.

2.2 Flood Simulation Model (FSM)

The flood parameters used in this experimental model were based on actual data of flooding events from 1991 to 2014. The data on flood statistics were obtained from an annual flood report issued by for the Department of Irrigation and Drainage Malaysia. Only complete information was considered in the study. It includes the parameters of flood water level; flood duration and repeated flooding were identified based on the high frequency of flood cases. The samples were exposed to flooding for a duration of 3, 24 and 48 hours for unrepeated flooding and 2, 5, and 24 hours for repeated flooding. Table 2 which shows the flooding characteristics of the flood simulation model. The percentages of adjustment moisture content were determine based on the duration estimated within a day-10 using an outdoor moisture content test (refer Figure 6). The purpose of the outdoor moisture content test is to determine the reduction of moisture content after the soil sample was submerged. In this test, the soil sample is submerged for 24 hours and then placed in an outdoor area for an estimated reduction of the moisture content in one month (refer to Figure 2).

Table 2: Flooding characteristics of FSM

Types of flooding	Duration flooding (Hours)	Water level (Meter)	Duration repeated flooding (Days)
Unrepeated flooding	3,24 and 48	0.3,0.6, and 1.0	_
First repeated flooding	2,5 and 24	0.3,0.6, and 1.0	2 days
Second repeated flooding	2,5 and 24	0.3,0.6, and 1.0	2 days

(a) (b)

Fig 2: (a) Specimen under water to simulate flood and (b) placed in outdoor area

To clarify the methodology of the research, this study focuses only on one type of conventional flexible pavement: granular base. Table 3 shows the loading characteristics of the flood simulation model for the purpose of calculating the loading characteristics to simulate the load of the pavement structure on the subgrade layer to represent the actual flooding event. These calculations have been designed based on typical conditions for roads and highways in Malaysia as referred to the Manual for Flexible Pavement Design published by the Malaysian Public Works Department. Pavement structure has slightly different characteristics due to unknown variables and several factors such as environmental and weather conditions. The design of actual pavement structures depends on the types of local material and the design approval from local authorities.[9]. Figure 3 shows the layout of the apparatus for FSM. All specimens will be tested referring to a modified soaking procedure from Malaysian Standard MS 1056: 2005 (Confirmed:2013), Soils for Civil Engineering purposes, Part 4. After that, the California Bearing Ratio (CBR) test was carried out to determine the strength of the subgrade soil [8].

Table 3: Loading characteristics of FSM

Level	Pavement structure (kg)	Flood water level (kg)	Total weight (kg)
0.3 m	17.6 kg	5.4 kg	23 kg
0.6 m	17.6 kg	10.8 kg	28.4 kg
1m	17.6 kg	18 kg	35.6 kg

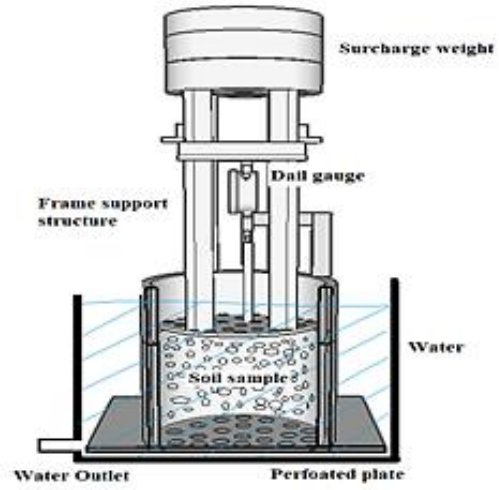

(a)

(b)

Fig. 3. Set up of the flood simulation model configuration: (a) diagram model (b) photograph

In this study, regression models were established to show the relationship between dependent variables and independent variables. Correlation equations are developed by performing single linear and multi linear regression analysis using Microsoft Excel tool pack analysis. Firstly, simple linear regression analysis (SLRA) was carried out by considering the moisture content as the independent variable (IV) and CBR values as dependent variables (DV). Secondly, a multiple linear regression analysis (MLRA), was determined by considering first and second repeated events as independent variables (IV) and CBR values as dependent variables (DV). The scatter diagrams are presented in Figures 5 and 9.

3. RESULT AND DISCUSSION

3.1 Unrepeated Flood

The results of CBR strength and moisture content values presented in Figure 4 illustrate the comparison between unflooded and flooded conditions. The soil samples were flooded for 3, 24 and 48 hours for unrepeated floods. From the combo chart, the vertical left and right axes represent the CBR value and moisture content (MC). It shows the CBR value for unflooded condition is relatively higher than the CBR value for flooded condition due to the saturated duration for flooded soil. Obviously, the presence of water when the soil was flooded for 3, 24 and 48 hours contributes to the decreasing of soil strength and performance. The soil had been losing strength starting in the 2-hour flood when it is compared to the unflooded condition. In addition, in the 48 hours of flooded condition at flood level 1.0 m, the value of CBR was reduced from 20% to 18%.

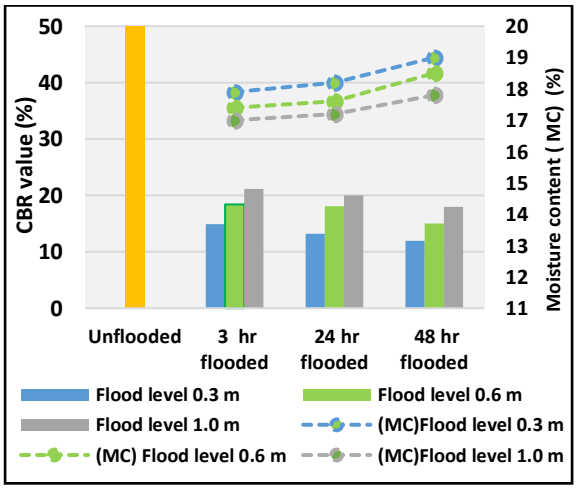

Fig. 4: Comparison of CBR value and water content of unrepeated flood samples.

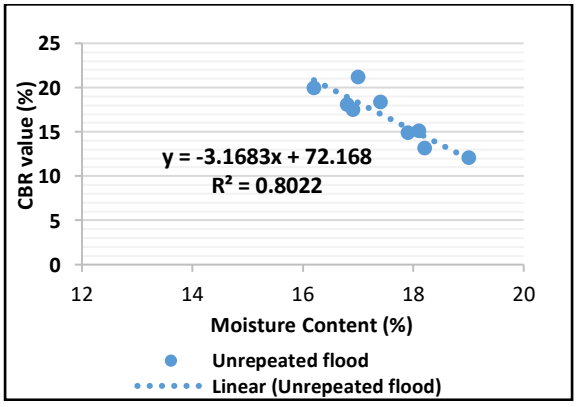

Fig 5: Relation between moisture with CBR value of unrepeated flood

Figure 5 presents the model developed for CBR values where the coefficient of correlation R^2 was found to be 0.82. Thus, moisture content has a high influence on the CBR value and the linear regression equation for unrepeated flood is CBR value (inundation) = -3.1683(MC) + 72.168

3.2 Repeated Flood

The outdoor moisture content test is a process by which soils decrease the moisture content in the specified volume. In this test, the focus is on observing the reduced effect water content from the outdoor condition for the soil sample. Figure 6 shows the result of the outdoor moisture content test for one month and the figures are given as percentages of the moisture content. It can be seen that the percentage of moisture content slightly increased to 20.2 % after a 24 hour soaking. Otherwise, there was a minimal decrease in the percentage of moisture content in the day-1 to day-30 tested samples and the average percentage reduction in water content is 0.4 % per day. However, this is dependent on the weather factor and the outdoor environment. The typical weather condition in Malaysia is uniform temperature and high humidity which is the one major factor contributing to the fluctuation in the rate of the soil moisture content. In a general overview, it shows that the moisture content will return to its original rate of 12% on day-16. Therefore, it can be concluded that the repeated flood after day-16 can be categorised as unrepeated flood. The moisture in the soil will return to its original value.

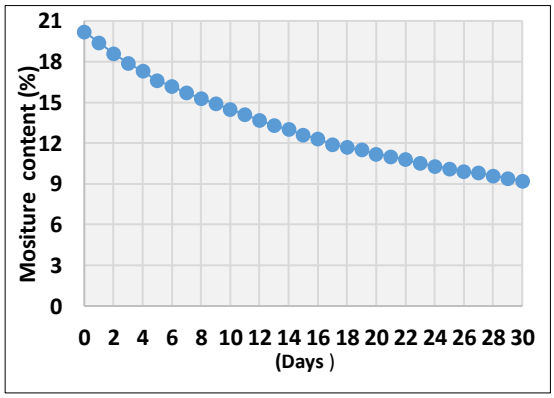

Fig. 6: Percentages moisture content of outdoor test

The result of CBR strength and moisture content presented in Figure 7 illustrates the comparison between unflooded and flooded condition. From the combo chart, the vertical left and right axes represent the CBR value and moisture content (MC). The soil samples were flooded for 2, 5 and 24 hours for the first repeated flooding condition. It shows that the CBR value for unflooded condition was 41% and in the first repeated flood for 2 hours at

flood water levels 0.3 m, 0.6 m and 1.0 m, the CBR values were 15.4%, 17% and 18% respectively. In addition, at 5 hours on flood water levels 0.3 m, 0.6 m and 1.0 m, the CBR values were 16%, 17% and 19% respectively. The unflooded samples mostly showed better performance in their strength and the CBR strength probably can be increased with suitable compaction of the soil tested. However, for 24 hours flooding at flood levels 0.3 m, 0.6 m and 1.0 m the CBR values were 17.9%, 16.5% and 22% respectively. The average CBR strength was reduced in 2 hours flooding to 24% and subsequently the CBR value also reduced in the 5 to 24-hour floods compared to the unflooded sample. The CBR strength increased by 2.9% after flooding for 2 hours at flood level 1.0 m. The moisture content values in the combo chart show the fluctuation pattern of the result.

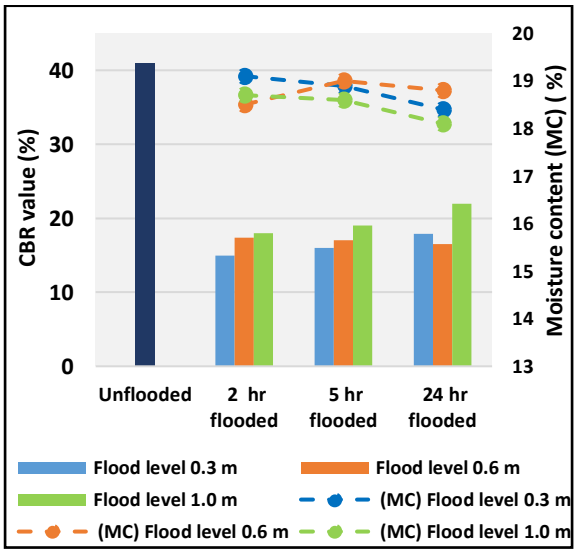

Fig 7: Comparison of CBR value and water content of first repeated flood samples.

In contrast, the combo chart in Figure 8 shows the second repeated flood condition is seen differently compared to the unflooded and flooded conditions. From the combo chart, the vertical left and right axes represent the CBR value and moisture content (MC). The soil samples were similar with the first repeated flood in which the soil samples were flooded for 2, 5 and 24 hours. It shows that the CBR value for unflooded condition was 41% and in the first repeated flood for 2 hours at flood water levels of 0.3 m, 0.6 m and 1.0 m, the CBR values were 11.9%, 12.6% and 14% respectively. It follows that, for 5 hours at flood water levels of 0.3 m, 0.6 m and 1.0 m the CBR values were 12.3%, 13% and 14.3% respectively. However, for 24 hours at flood levels 0.3 m, 0.6 m and 1.0 m the CBR values were 14.3%, 15.4% and 17% respectively. In the second repeated flood case, the moisture content increased in the 5 hour flood at flood levels 0.3 m and 0.6 m, to 20.7% and 20% respectively. This condition may be due to the subgrade of the soil becoming saturated because of the number of floods and the loads used during the FSM in the soil sample affecting the absorption of moisture content.

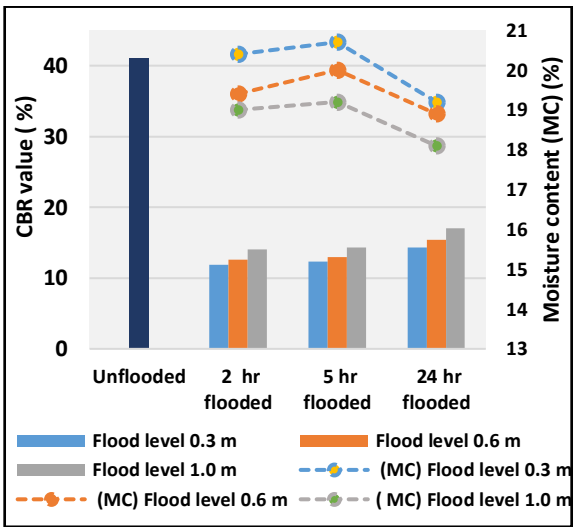

Fig 8: Comparison of CBR value and water content of second repeated flood samples.

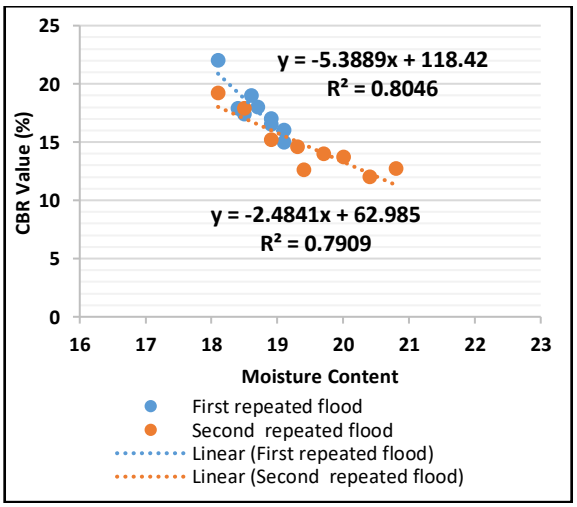

Fig 9: Relation of CBR value and water content of repeated flood.

From Figure 9 it is observed that there is a multi linear relationship between the moisture content and CBR value in repeated flood events. In general, as moisture content increases the subgrade strength decreases, indicating a linear relationship exists between these two parameters. From linear regression the coefficient of correlation R^2 for these two parameters in first and second repeated floods were found to be 0.80 and 0.79 respectively.

5. CONCLUSION

This study was carried out to evaluate the moisture content variation and strength of the subgrade using the FSM. It can be concluded that:

i) Based on experimental results and linear regression this study shows that there is a good relationship between moisture content and subgrade strength. A linear relationship exists between moisture content and subgrade strength with a coefficient of correlation on unrepeated flood, first and second flood events, R^2 = 0.80, 0.80 and 0.79 respectively. It illustrates that the increase in the duration of the flooding affects the performance of the subgrade due to the increasing moisture content.

ii) The study also revealed that the rate of deterioration in subgrade strength for the second flood is 30% less than for the first repeated flood.

As described, the selection of the type of soil in this study is relevant as the impacts of flood depths or water flow under hydraulic gradient is significant. Furthermore, clayey soils of low hydraulic conductivity will require extended time for soil moisture content to change. The decease of CBR value and shear strength does not happen immediately. It's due to shear force generated by the friction and adhesion between particles of soil. In addition, pore water pressure dissipation is also corresponded to time factor.

For future works, this study will continue to investigate the effect of the period for inundated roads and recurring inundation and how these could affect the whole road structural systems in different localities and sub-grade properties.

6. ACKNOWLEDGEMENTS

This study is supported by the Universiti Sains Malaysia and FRGS grant no: 1 /2017-203/PPBGN/6711611.

7. REFERENCES

[1] Lakshmi S. M.,Subramanian S., Lalithambikhai M.,Vela A. M. , and Ashni M., "Evaluation of Soaked and Unsoaked Cbr Values of Soil Based on the Compaction Characteristics,"*Malaysian Journal of Civil Engineering*, vol. 28, no. 2, 2016.

[2] Ghani A.N.A.,Roslan N.I., and Hamid A. H. A., "Road Submergence During Flooding and Its Effect on Subgrade Strength," *Int. J. of GEOMATE*, vol. 10, no. 21, pp. 1848-1853, 2016.

[3] Roy T. K. , "Influence of sand on strength characteristics of cohesive soil for using as subgrade of road," *Procedia-Social and Behavioral Sciences*, vol. 104, pp. 218-224, 2013.

[4] *Manual For The Structural Design Of Flexible Pavement*, 2013.

[5] Ismail M. S. N., Ghani A. N. A, and Ghazaly Z. M., "The Characteristics of Road Inundation During Flooding Events In Peninsular Malaysia," *International Journal*, vol. 16, no. 54, pp. 129-133, 2019.

[6] Alam M. and Zakaria M., "Design and construction of roads in flood affected areas," *Engineering Concerns of Flood*, pp. 91-99, 2002.

[7] Fairweather H. and Yeaman J., "A study of the parameters affecting the performance of roads under an extreme rainfall event," *Int. J. of GEOMATE*, vol. 7, no. 1, pp. 955-960, 2014.

[8] *Soils for Civil Engineering Purposes -Test method - Part 4: Compaction-related tests* 2013.

[9] Atkins H. N., *Highway materials, soils, and concretes*, 4th edition ed. Prentice Hall, 2003.

9th Int. Conf. on Geotechnique, Construction Materials and Environment,
Tokyo, Japan, 20-22 November 2019, ISBN: 978-4-909106025 C3051

GIS FOR COASTAL HAZARD ANALYSIS

A. B. Sambah[12*], F. Miura[3], D. O. Sutjipto[1], T. D. Lelono[1]
[1]Faculty of Fisheries and Marine Science, University of Brawijaya, Indonesia
[2]Marine Resources Exploration and Management Research Group, University of Brawijaya
[3]Faculty of Engineering, Yamaguchi University, Japan

ABSTRACT

Coastal areas have been used as a settling ground for human population as they provided abundant fisheries and marine resources and possibilities for business sectors. Coastal hazards cause loss of life and the degradation of coastal environment. It defined as physical phenomena that expose a coastal area to risk of property damage. Coastal areas are frequently changing, in which natural hazards such as tsunamis is one of the sources. The management of coastal hazard currently has become an important aspect for coastal planning in order to improve the resilience of society to coastal hazards. Coastal disaster management can be done based on the risk analysis using several vulnerability and risk parameters. The current research tried to analyze the potential risk area due to tsunami hazard using the parameter of vulnerability in the coastal area of East Java Indonesia. Risk map produced from the geospatial database analysis in the concept of the geographical information system (GIS). Risk assessment combines the outputs of vulnerability assessments and the hazard, in which the topography elevation, type of building, land cover, coastal vegetation density, and the type of coastline build the vulnerability map. Historical data of some tsunami events indicates that some of the damage caused by the coastal elevation as one of the physical parameters of tsunami vulnerability, as well as social parameters. The study describes an important result related to multi-criteria processing in predicting the tsunami risk area. GIS plays as important approaches in combining the geospatial database of each parameter and displays it in geographical perspective.

Keywords: Geographical information system, hazard, tsunami, risk, vulnerability

INTRODUCTION

The development of coastal areas today is more focused on the consideration of environmental degradation. Various kinds of hazard threats to the coastal environment, such as natural disasters and other natural phenomena, are also considered in the management of coastal areas. Coastal areas are one of the areas that are susceptible to environmental damage, both caused by the pressure of human activities and the consequences of natural disasters.

Coastal hazards can be defined as physical phenomenon that exposes a coastal area to risk of property damage, loss of life and environmental degradation. In the term of coastal zone management, coastal hazard management has become an increasingly important aspect. This is important to improve the resilience of society to coastal hazards. Possible management options include the design of coastal structures, application of natural coastal green for coastal protection, various accommodation approaches as well as a managed infrastructure in the area close to the coastline. For overcoming coastal hazards, it is also important to have early warning systems and emergency management plans in order to be able to address sudden and potential disastrous hazards i.e. major flooding events, tsunami, or hurricane. Events as the 2004 Indian Ocean earthquake and tsunami, the Hurricane Katrina affecting the southern USA in 2005, the cyclone Nargis affecting Myanmar in 2008, the 2011 Tohoku, Japan earthquake and tsunami, and also the 2018 Sulawesi, Indonesia earthquake and tsunami provides clear examples of the importance of timely coastal hazard management.

The purpose of mitigation is not only to minimize the loss of property damage but also minimize the damages of environmental due to development. Disaster mitigation program also important approaches in order to avoid impacts by not taking actions, to reduce impacts by rehabilitation the affected environments or constructing long-term maintenance operations, and compensating for impacts by providing substitute environments for resources.

Through human history, developing technology has increased the range of adaptation options in the face of coastal hazards, and there has been a move from retreat and accommodation to hard protection and active seaward advance via land claim as exemplified by the Netherlands [1].

in general coastal hazards can be grouped into five main impacts, usually with several contributing

processes causing cumulative harm; (1) coastal erosion and coastline stability (including the area of river mouths, tidal inlets and cliffs) from waves, storm tide, changes in sediment budgets, river floods, coastal structures, storm water, and sea-level rise; (2) coastal flooding cause from storm tide, river floods, tsunami, and sea-level rise; (3) the level of groundwater in the coastal area due to storm tide, intense rainfall, sea-level rise, and salinization; (4) recreational activities together with hazards arising from surf zone conditions (e.g. rips, wave conditions, long-wave surges); (5) oceanic activities together with marine navigation hazards arising from wave conditions, storm tide, strong winds, long-wave surges and also tsunami.[2].

The application of Geographical Information System (GIS) for disaster research provides an important integrated contribution in order to assess the risk of the coastal area due to the natural disaster [3]. The development of satellite remote sensing technology and its applications enable the use of satellite imagery for mapping the distribution of an area damaged by a disaster. Satellite images have the advantage of being able to deliver simultaneous images of wide areas [4]-[5]-[6]. In addition, with the aid of the GIS, spatial multi criteria analysis helps prioritize the decision-making process using spatial database. Spatial multi criteria analysis is vastly different from conventional Multi Criteria Decision Making (MCDM) techniques, due to the inclusion of an explicit geographic element.

GIS mapping of tsunami vulnerability has also applied using the Shuttle Radar Topography Mission (SRTM) to obtain the topographic data of the study area [7]-[8]. Another geospatial analysis approach has applied soil type, urban form and social type system for the potential natural hazard mapping [9] and has assessed the tsunami vulnerable area by comparing building damage map with the physical topography data includes elevation, land use, and the distance from the coast [10]. Mapping of the 2011 Tohoku earthquake tsunami inundation and run-up by in-situ survey also has been published in order to develop create appropriate disaster mitigation concepts [11].

This study tried to apply several physical topography data for analyzing coastal hazard and its affected areas, especially caused by the tsunami disaster using GIS approach.

METHOD

Study Area

The analysis was applied in three different case study areas around the coastal area of Indonesia in order to know the different result of applying physical topographic dataset. The area includes the coastal area of Java Island and divided into the western part of Java which is represented by Banten Regency areas, the eastern part of Java Island which represent by Banyuwangi Regency, and also Malang regency area which represents the area that directly faces to the Indian Ocean. The study area as describe on Fig. 1.

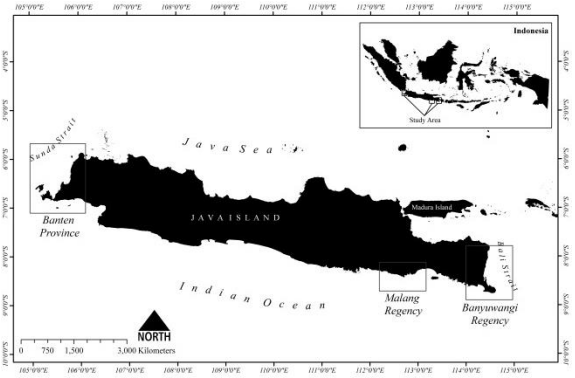

Fig. 1 Study area

Dataset

Physical data set for assessing the affected area of tsunami disaster in all coastal areas of case study was collected. This dataset includes topography elevation, slope, building area, coastal proximity and coastal type, and also population density as well. For providing the physical topographic parameters, the dataset of The ASTER Global Digital Elevation Model (ASTER GDEM) version 2 was collected from *https://gdex.cr.usgs.gov/gdex/*. This data are available from the Land Processes Distributed Active Archive Center (LP DAAC). Moreover, The NASA Shuttle Radar Topographic Mission (SRTM) also collected for preparing topographic elevation dataset. SRTM has provided digital elevation data (DEMs) for over 80% of the globe and distributed by USGS and is available for download from the National Map Seamless Data Distribution System, or the USGS ftp site. The SRTM data is available as 3 arc second and downloaded from *http://srtm.csi.cgiar.org/srtmdata/*.

In addition to provide land use map that describe also the building areas, Sentinel 2 satellite image was applied. Sentinel-2 is a European wide-swath, high-resolution, and multi-spectral imaging mission. The full mission specification of the twin satellites flying in the same orbit but phased at 180°, is designed to give a high revisit frequency of 5 days at the Equator. Sentinel-2 carries an optical instrument payload that samples 13 spectral bands: four bands at 10 m, six bands at 20 m and three bands at 60 m spatial resolution. The orbital swath width is 290 km [12]. This data was collected from *https://scihub.copernicus.eu/dhus/#/home.*

The type of coastal, distance from coastline to hinterland (coastal proximity), and other land use

feature were created from vector data of base map. This data was collected from Indonesia Geospatial Information Agency. Dataset that used in the analysis as described in Table 1, Table 2, and Table 3.

Table 1 Specification of DEM data

	Aster GDEM	SRTM
Data source	ASTER	Space shuttle radar
Generation and distribution	METI/NASA	NASA/USGS
Release year	2009 ~	2003 ~
Data acquisition period	2000~ongoing	11 days (in 2000)
Posting interval	30m	90m
DEM accuracy (stdev)	7-14m	10m
DEM coverage	83°N~83°S	60°N~60°S

Table 2 Specification of satellite image data

Satellite specification			
Data source	The Copernicus Sentinel-2 mission		
swath width	290 km		
revisit time	10 days at the equator with one satellite, and 5 days with 2 satellites under cloud-free conditions which results in 2-3 days at mid-latitudes		
coverage limits	56°S~84°N		
Sensor specification			
No	Band	Wave length (µm)	Spatial resolution
1	Band 2 – Blue	0.490	10m
2	Band 3 – Green	0.560	10m
3	Band 4 – Red	0.665	10m
4	Band 5 – Vegetation Red Edge	0.704	20m
5	Band 6 – Vegetation Red Edge	0.740	20m
6	Band 8 – NIR	0.835	10m
7	Band 8a – Vegetation Red Edge	0.865	20m

Table 3 Specification of vector base map data

Location	Type	Scale	Coordinate system
Banten, Malang, and Banyuwangi, Indonesia	**Point type:** boundaries of administrative areas, road edge, elevation, buildings **Line type:** Shoreline, water, road edge, boundaries of administrative areas **Polygon type;** Boundary of the district	1:25000	UTM WGS 88, Zona 48 S

Data Analysis

As one of the potential natural disasters that affect to the dynamic of coastal area, the affected area due to tsunami could be assess through the analysis of risk and vulnerability. In order to analyse this assessment, all parameters will be analyzed using GIS. GIS helps in the integration of all dataset geographically.

DEM dataset collected will be calculated for producing topographic elevation data and slope. This elevation and slope data will then be analyzed spatially based on the risk standard and vulnerability of these two parameters to produce a map of coastal area vulnerability to tsunami hazards. DEM data will be visualized using surface analysis in GIS as well as the slope was created from the DEM data. DEM data will be visualized using surface analysis in GIS as well as the slope was created from this DEM data.

The distance from coastline to the hinterland (coastal proximity) and the radius zone from river was calculated and created using vector base map of the study area and analyzed through multi-ring buffer of proximity analysis in GIS. In order to set the radius number of coastal proximity for assessing the risk area due to tsunami, Eq. (1) was applied.

$$log X_{max} = log 1400 + {}^{4}/_{3}\, log\left({}^{Y_0}/_{10}\right) \quad (1)$$

In which, X_{max} is represent the maximum reach of the tsunami over land, and Y_0 is the height of the tsunami at the coast. For applying this algorithm, a set of tsunami historical data which describe the information of maximum run-up in the area of study was collected. The class number of this coastal proximity was different for three research areas. Type of coastline was created also using vector base map of the study area by digitizing polyline data of the coastline and categorized it based on the coastal morphology type.

For preparing the land use data and build area of the study area, Sentinel-2 satellite image was analyzed using image classification process. The satellite image processing starts with the computation of TOA (Top of Atmosphere) Reflectance. The numeric digital counts (CN) of each pixel image (*i*,*j*) and each spectral band (*k*) are converted in TOA reflectance (ρ). This conversion takes into account the equivalent extra-terrestrial solar spectrum (*Es*), the incoming solar direction defined by its zenith angle (θs) for each pixel of the image and the absolute calibration (*Ak*) of the

Multispectral Instrument (MSI). As explained in Sentinel-2 technical guides [13], The TOA conversion equation as described in Eq. (2).

$$\boldsymbol{\rho_k(i,j)} = \frac{\boldsymbol{\pi \times CN_{k.NTDI}(i,j)}}{\boldsymbol{A_{k.NTDI} \times E_S \times d(t) \times \cos(\theta_s(i,j))}} \qquad (2)$$

where:
$CN_{k.NTDI}$ is the equalized numeric digital count of the pixel (*i,j*) with NTDI, the number of Sentinel-2 TDI lines. E_s is the equivalent extra-terrestrial solar spectrum and depends on the spectral response of the Sentinel-2 bands. The component *d(t)* is the correction for the sun-Earth distance variation (as described in Eq. (3)). It utilises the inverse square law of irradiance, under which, the intensity (or irradiance) of light radiating from a point source is inversely proportional to the square of the distance from the source [13].

$$\boldsymbol{d(t)} = \frac{\boldsymbol{1}}{\boldsymbol{(1-0.01673 \times \cos(0.0172 \times (t-2)))^2}} \qquad (3)$$

Where :
t is the Julian Day corresponding to the acquisition date. 0.01673 is the Earth orbit eccentricity. 0.0172 is the Earth angular velocity (radians/day). The parameters *Ak* and *Es* are provided by the GIPP and are also included in the ancillary data of the Level-1 products. The sun zenith angles are determined at this level too. A sun angle grid is computed by regularly down-sampling the target geometry (Level-1C tile). The cosine of the zenith angle *θs* is defined at each point of the grid using the ground coordinates and the datation of the corresponding pixel acquisition.

Reflectance value, often between 0 and 1, is converted into integer values, in order to preserve the dynamic range of the data by applying a fixed coefficient (1000 by default). This reflectance value was used as standard value in image classification process in which the supervised classification method was applied using several training area.

All geospatial databases will be analyzed through a spatial overlay process, where all parameters were in the form of a raster data base and processed based on the standard value of each parameter, as illustrated in Table 4 and Table 5. Analysis carried out through GIS with a pixel-based weighted overlay process. The weights of the parameter were constructing using pair-wise comparison matrix of Analytical Hierarchy Process (AHP) method.

Table 1 The physical vulnerability value range for elevation, slope, and landuse

Vulnerability class	Elevation (m)[1]	Slope (%)[2]	Landuse[3]
High	<5	0-2	Urban
Slightly high	5-10	2-6	Agriculture
Moderate	10-15	6-13	Bare soil
Slightly low	15-20	13-20	Water
Low	>20	>20	Forest

[1][4]
[2][5]
[3][6]

Table 2 The physical vulnerability value range for coastline distance, river distance, and coastal type

Vulnerability class	Coastline distance (m)[4]	River distance (m)[5]	Coastal type[5]
High	<293	0-100	V bay
Slightly high	293-514	100-200	U bay
Moderate	514-762	200-300	Cape
Slightly low	762-1032	300-500	Straight
Low	>1032	>500	Neutral

[4] Based on Eq. 1 calculations and it will be different result for different study area
[5] [7]

RESULT AND DISCUSSION

This study was one of the approaches in the integrated coastal hazard assessment, in which the analysis for describing the affected area caused by tsunami wave was studied. Analysis of all disaster risk parameters in this study obtained thematic maps of each parameter. This map illustrates the potential areas affected by the tsunami disaster. To get a conclusion of the risk area based on a combination of all parameters, a spatial overlay process for all parameters was carried out, with the multiplication concept of each pixel of parameter with its weight. The weight of each parameter was obtained from expert judgment and calculated based on the AHP approach. The conclusion of this calculation is the form of pair-wise comparison matrix with the required consistency ratio of less than 10% (2.9%), as explained in Fig. 2. The result of AHP calculation through pair-wise comparison matrix described that the elevation was parameters with the highest weight that affect the creating of risk maps. In contrast, the parameter of river distance was the lowest. In the future analysis, the different type of landcover would be important to be separated. The area with a high density of vegetation would be included in the low class of tsunami risk compare with the bare land.

In the application of parameter's weight for creating risk area map, a research on tsunami vulnerability in Alexandria was applied all parameter in equal weight due to the limitation of knowledge regarding to the study area [14]. The use of pair-wise comparison matrix in weight calculation also applied in the tsunami vulnerability mapping along coastal area of Miyagi Prefecture, Japan and. illustrated a similar pattern of tsunami vulnerability

area to the real tsunami inundation area during the 2011 Tōhoku's tsunami [15].

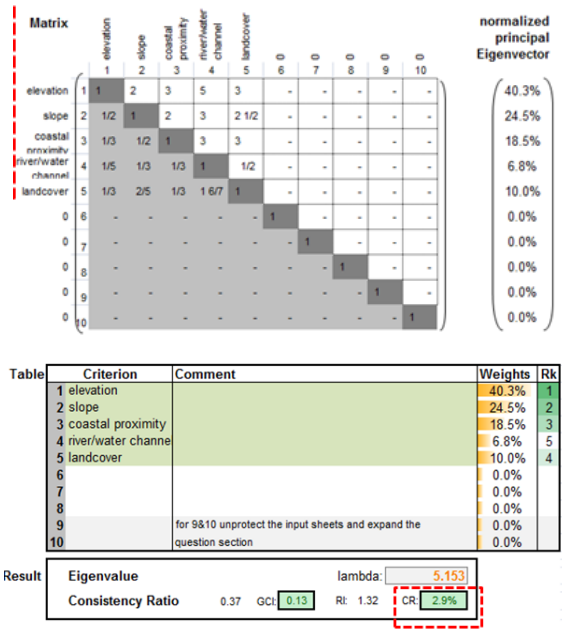

Fig. 2 Pair-wise comparison matrix and normalized principal eigenvector

The result of the analysis as describe on Fig. 3, Fig. 4, and Fig. 5. The map shows that in general the high risk areas were mostly found in the coastal area with the sloping coast type. Elevation and slope play an important role in determining the stability of the terrain in the coastal [16]. The research of tsunami vulnerability along coastal area of Bali, Indonesia described that the distribution of vulnerability is not uniform and physically it is highly influenced by the distance from coastline to the hinterland, topography elevation, and also slope [17]. The most risk area due to tsunami disaster in depends on the direction of tsunami source or the epicentre of the earthquake.

The results of this study illustrate that areas with low vegetation density, high distribution of build area, flat areas, and areas close to large rivers will have greater disaster risk. The existence of rivers in the coastal area will enable it to act as the successor to the tsunami wave that comes and takes it far towards the land until it reaches a certain elevation.

The outputs of the tsunami hazard analysis are very much dependent on data availability and the application of methods. The approaches range from simple empirical methods to sophisticated numerical simulations. Empirical methods use simplified formulas to derive tsunami hazard maps. In general, information on the elevation and the distances from coastline are applied in combination with empirical formulas to estimate the inundated areas on coastal areas [18].

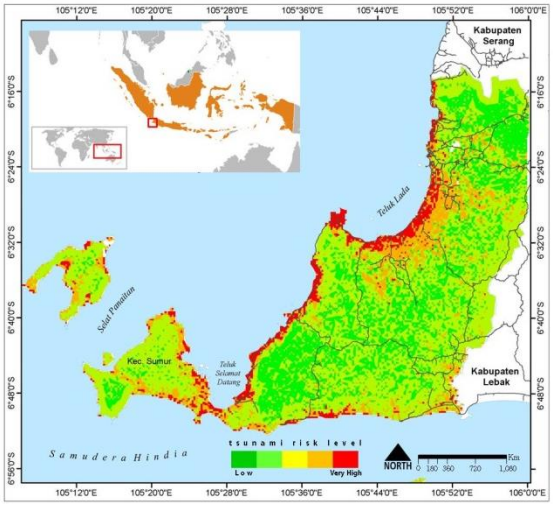

Fig. 3 Tsunami risk area in the coastal area of Banten, Indonesia

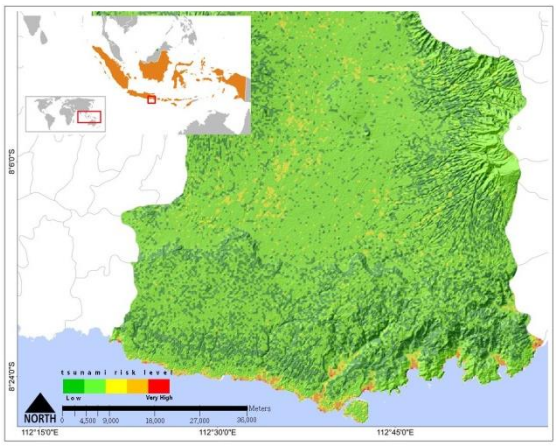

Fig. 4 Tsunami risk area in the coastal area of Malang, Indonesia

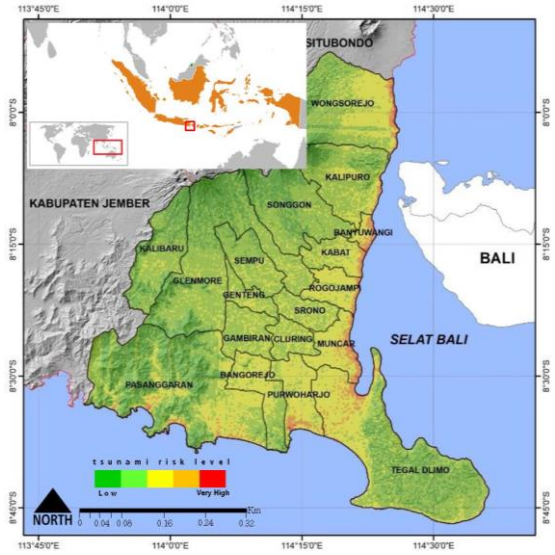

Fig. 5 Tsunami risk area in the coastal area of Banyuwangi, Indonesia

CONCLUSIONS

Risk and vulnerability assessment is one of the important steps in contributing the information regarding to the coastal hazard analysis. The concept and methods have been applied to compare the importance of using risk parameters by testing them in three different coastal regions. From the analyses key parameters are derived and integrated for assessing the risk and vulnerability map. The result will be act an important role for effective early warning system. In the future work, the social and ecological parameter will be an important parameter for analysis.

ACKNOWLEDGMENTS

Authors are thankful to Laboratory of Marine Resources Exploration, University of Brawijaya Indonesia and Laboratory of Disaster Prevention System, Yamaguchi University, Japan. We also thank to Indonesia Geospatial Information Agency for providing the basic map of the study area, METI/NASA for Aster GDEM data, NASA/USGS for SRTM data, and ESA for Sentine-2 data.

REFERENCES

[1] Van Koningsveld, M.; Mulder, J.P.M.; Stive, M.J.F.; van der Valk, L., and van der Weck, A.W., Living with sea-level rise and climate change: a case study of the Netherlands. Journal of Coastal Research, Vol. 24, 2008, pp. 367–379.

[2] https://www.niwa.co.nz/natural-hazards/hazards/coastal-hazards

[3] Sambah A.B., Miura F., Guntur, and Fuad., Integrated Satellite Remote Sensing And Geospatial Analysis For Tsunami Risk Assessment, International Journal of GEOMATE, Vol.14, Issue 44, 2018, pp.96-101.

[4] Karen, E., Joyce K. C., Wright S., Samsonov V., and Ambrosia V. G., Remote Sensing and the Disaster Management Cycle, In Advances in Geoscience and Remote Sensing, edited by G. Jedlovec. Croatia: InTech, 2009.

[5] Yamazaki, F., Kouchi K., and Matsuoka M., Tsunami Damage Detection Using Moderate-Resolution Satellite Imagery, Proceeding of the 8th U.S. National Conference on Earthquake Engineering, San Francisco, CA, April 18–22, 2006.

[6] Yamazaki, F., and Matsuoka, M., Remote sensing technology in post-disaster damage assessment, Journal of Earthquakes and Tsunamis, World Scientific Publishing Company, vol. 1, no. 3, 2007, pp. 193-210.

[7] Sinaga, T.P., Adhi, N., Yang-Won, L. and Yongcheol, S., GIS Mapping of Tsunami Vulnerability: Case Study of the Jembrana Regency in Bali, Indonesia, KSCE Journal of Civil Engineering, Vol. 15, No. 3, 2011, pp. 537-543.

[8] Abu Bakar Sambah Fusanori Miura, Remote Sensing and Spatial Multi-Criteria Analysis for Tsunami Vulnerability Assessment, Disaster Prevention and Management, Vol. 23 Issue 3, 2014, pp. 271 – 295.

[9] Hsien, L.C. and Sheng, C.H., The Use of Spatial Analysis Techniques In Mapping Potential Natural Hazard Areas: A Case Study of Taiwan", Procedia Environmental Sciences, Vol. 10, No. Part B, 2011, pp. 1092-1097.

[10] Gokon, H. and Koshimura, S., Mapping of Building Damage of The 2011 Tohoku Earthquake Tsunami in Miyagi Prefecture, Coastal Engineering Journal, Vol. 54, No. 1, 2012, pp. 126-138.

[11] Mori, N., Takahashi, T., Yasuda, T. and Yanagisawa, H., Survey of 2011 Tohoku earthquake tsunami inundation and run-up, Geophys. Res. Lett, Vol. 38, 2011, L00G14.

[12] Sentinel-2 User Handbook. Issue 1 Rev 2. ESA Standart Document. European Space Agency, 2015.

[13] https://sentinel.esa.int/web/sentinel/technical-guides/sentinel-2-msi/level-1c/algorithm

[14] Eckert, S., Jelinek, R., Zeug, G. and Krausmann, E., Remote sensing-based assessment of tsunami vulnerability and risk in Alexandria, Egypt", Applied Geography, Vol. 32 No. 2, 2012, pp. 714-723

[15] Sambah A.B. and Miura F., "Remote Sensing and Spatial Multi-Criteria Analysis for Tsunami Vulnerability Assessment", Disaster Prevention and Management, Vol. 23 (3), 2014, pp. 271–295.

[16] Yashon O. Ouma, and Tateishi R., Urban Flood Vulnerability and Risk Mapping Using Integrated Multi-Parametric AHP and GIS: Methodological Overview and Case Study Assessment, Water, Vol. 6, 2014, pp. 1515-1545.

[17] Eddy, GIS in Disaster Management: a Case Study of Tsunami Risk Mapping in Bali, Indonesia, Masters (Research) Thesis, 2006, Jamas Cook University, Australia.

[18] Strunz, G., Post, J., Zosseder, K., Wegscheider, S., Muck, M., Riedlinger, T., Mehl, H., Dech, S., Birkmann, J., Gebert, N., Harjono, H., Anwar, H. Z., Sumaryono, Khomarudin, R. M. and Muhari, A., Tsunami risk assessment in Indonesia, Natural Hazards and Earth System Science, Vol. 11, 2011, pp. 67-82.

9th Int. Conf. on Geotechnique, Construction Materials and Environment, Tokyo, Japan, 20-22 November 2019, ISBN: 978-4-909106025 C3051

DIAPHRAGM WALL DISPLACEMENT WITH UPLIFT CONSIDERATION FOR VERY DEEP BASEMENT EXCAVATION IN SOFT BANGKOK CLAY

Wanchai Teparaksa[1], Jirat Teparaksa[2] and Mike Sinkinson[3]
[1]Faculty of Engineering, Chulalongkorn University, Thailand; [2] Strategia Engineering Consultant Co., Ltd., Thailand; [3]Thai Bauer Co., Ltd., Thailand

ABSTRACT

High-rise condominium is being constructed in Bangkok city center, Thailand. It consists of six underground basement floors (B1-B6) planned to be underground automated car park as this system provides much more parking spaces than the conventional which requires many ramps to access to basement floors. To provide space for automatic car park system, basement floors number B2, B3 and B5 were taken out of the design leaving only B1 (-3.20 m), B4 (-10.85 m) and B6 (-16.50 m). The maximum depth of excavation is -21.00 m which is desired for lift pit while the normal depth of excavation is -19.50 m. Diaphragm wall of 0.80 m and 1.20 thick were used as a soil retaining structure with five layers of temporary bracing strut. At the center strip of the basement floors in the longitudinal side, it is a void space throughout six basement slab causing weaker system of diaphragm wall. Therefore, the thickness of diaphragm wall was revised to be 1.20 m with band beams as a strengthener to resist the lateral earth pressure. Since the depth of excavation was deep, the effect of uplift pressure was also considered. The Finite Element Method (FEM) was conducted to predict the behavior and displacement of the diaphragm wall with the Mohr-Coulomb soil modeling as a failure criteria. During the construction, the displacement of the diaphragm wall was recorded and was compared with the FEM result. The predicted value by FEM agreed well with the field performance.

Keywords: Diaphragm wall, basement construction, finite element method, wall displacement, deep excavation

INTRODUCTION

High-rise residential building with six floors of substructure is being constructed in Bangkok city center. Basement floor of this building is desired to be an underground automatic carpark. This system maximize parking space by eliminating driving path and ramps. In order to provide space for automated car park system, basement floor number B2, B3 and B5 were taken out of the design leaving only B1 (-3.20 m), B4 (-10.85 m) and B6 (-16.50 m). General depth of excavation is -19.50 m while the maximum depth of excavation is -21.00 m in lift pit area. Diaphragm wall (D-Wall) of 0.80 m and 1.20 m thick were employed as a soil retaining structure. The former was intended for the general excavation area while the latter was designed for lift pit area due to higher induced bending moment. The tip of D-Wall is penetrated in the hard clay layer at -35.00 m. There were five temporary bracing strut layers at – 2.00, -5.50, -9.00, -12.50 and -15.80 m.

Typical sections of bracing system and basement structure are presented in Fig 1 and Fig 2. In this project, car lift was located closed to diaphargm wall leaving the opening (6.40 x 7.60 m) at every basement floor as can be seen in Fig 2. Special band beam was designed to transferr axial force from the retaining structure to the basement slab.

The research work for study the behavior and performance of diaphragm wall for basement construction in Bangkok subsoil with various conditions was presented by Teparaksa[1],[2],[3].

This paper presents the performance and behavior of the diaphragm wall. The lateral displacement of diaphragm wall is predicted by FEM analysis by simulating the construction sequence in the analysis. The lateral wall displacement was monitored during excavation and casting the basement floor. The FEM prediction was compared and discussed with the field performance.

SOIL AND GROUND WATER CONDITIONS

Two boredholes of 70 m deep were carried out to investigate soil condition for underground structural design. It consists of a 11.5 m thick very soft Bangkok clay layer followed by soft clay layer to -15.0 m deep. The medium stiff clay and very stiff clay are encountered from -14.0 to -17.0 and -17.0 to -20.5 m, respectively. From -20.5 m to -24.0, a 3.5-m-thick very stiff clay layer was found. The first dense sand layer was at -24.0 to -28.0 m while the second sand layer was at -30.0 to -34.0. After the second dense sand layer, it was a hard clay layer where the tip of diaphragm wall is penetrated into. Fig 3 shows illustration of soil profile and engineering properties.

Groundwater condition of Bangkok soft clay is hydrostatic strating from -1.0 m. The deep well pumping in the past had promoted under drainage of the soft and the first stiff clay. The piezometric level of Bangkok aquifer was reduced and was constant at -23.0 m [1] causing advantages to geotechincal engineers such as higher effective stress and dry condition during underground construction. However, 20 years ago, Thailand's government prohibited deep well pumping to solve the problem of land subsidence promoting an increase in piezometric level up to -13.0 m as presented in Fig 4 [4].

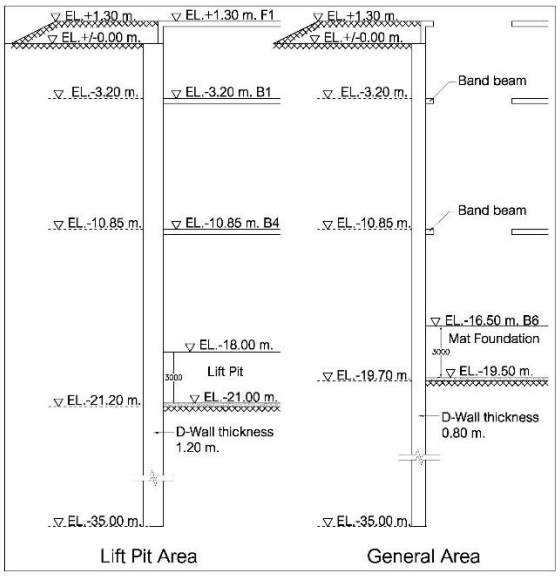

Fig. 1 Typical section of bracing system

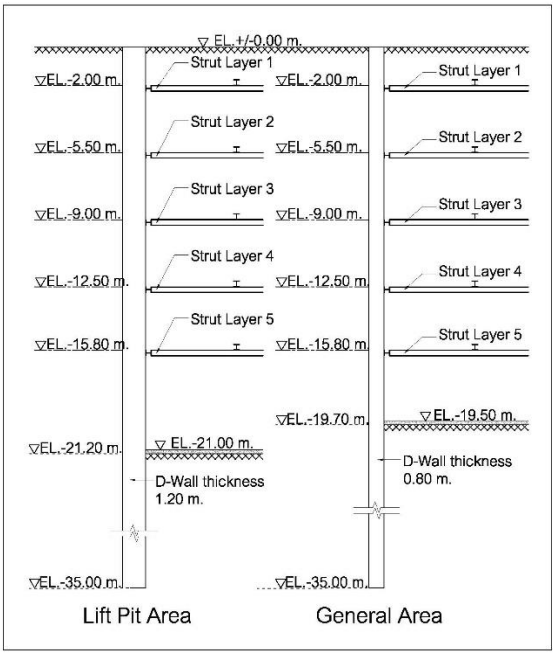

Fig. 2 Typical section of basement

Fig. 3 Soil Profile

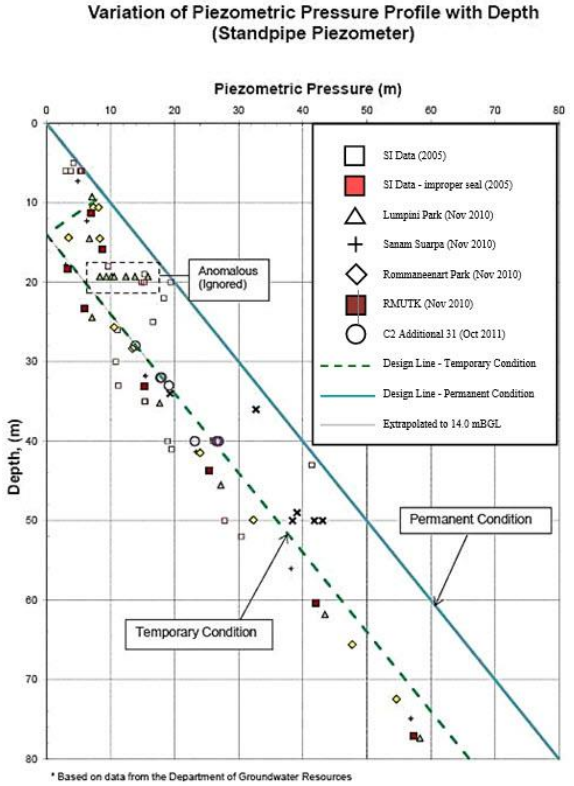

Fig. 10 Recent Bangkok groundwater conditions data [2]

ANALYSIS OF DIAPHRAGM WALL BEHAVIOR BY FINITE ELEMENT METHOD

Design Criteria of Diaphragm Wall

The behavior of diaphragm wall can be predicted by numerical analysis by means of Finite Element Method (FEM). The result of FEM analysis of diaphragm wall behavior is presented in term of bending moment and shear force induced in the diaphragm wall as well as lateral displacement. The soil modeling is one of the main parameters for FEM analysis. The step of soil excavation, bracing installation, as well as preloading in the strut system are simulated in the FEM analysis. The casting of base slab, basement floor and the step of removal of strut system are also have to be designed and combined in the FEM analysis of diaphragm wall. In this project, the PLAXIS 2D [5] program wa used as the FEM program analysis to predict the diaphragm wall behavior. In this regards, the bending moment, shear force and lateral displacement can be determined at all construction steps.

The Mohr-Coulomb soil modeling was emloyed. The Undrained Young's modulus (Eu) of each clay layer was correlated with undrained shear strength (Su) while in the sand layer, the drained modulus (E') was correlated with the Standard Penetration Test (SPT) N-value.

The correlation of Eu and Su as well as E' and N-value can be conducted as follows.

- For soft to medium clay layer, Undrained Young's modulus
  (EU) = 500 – 700 Su (Undrained Shear Strength)
- Stiff to very stiff silty clay layer
  Eu = 1000 Su
- Sand layer
  E' = 2000(N) SPT-N-Value (kN/m^2)

The above correlations between Eu-Su, and E'-N(value) are based on the back analysis from various basement excavation projects by means of FEM analysis compared with field measurement proposed by Teparaksa [6].

Surcharge on the diaphragm wall

The ground surface surcharge behind the diaphragm wall during construction was assumed at 10 kN/m^2 to simulate possible loads such as truck traffic and loading of materials. However, the surcharge value affects the diaphragm wall behavior in inducced bending moment, shear force and lateral displacement. The appropriate value have to be selected. In authors experience, 10 kN/m^2 is closed to real situation. This ground surface was applied during excavation, basement casting and completion of the basement work.

Groundwater table

The ground water in Bangkok subsoil condition is in the draw down condition due to deep well pumping. Recently, as the deep well pumping is not allow, the recent ground water table was at -13 m. below ground surface. The original design of D-Wall length was only 25 m deep. However, according to uplift calculation, the safety factor against uplift was too low. Therefore, length of D-Wall was lengthened to be penetrated in the hard clay layer at -35 m just before the construction of D-Wall.

FEM ANALYSIS RESULTS

All the construction sequences were taken into the account in FEM analysis using Mohr-Coulomb as a failure criteria. The first stage was first excavation just little below the first temporary bracing strut. The second was the first strut layer installation and excavation to litle below the second strut layer. The process continued until reaching the final depth. The deformed mesh at this stage is shown in Fig. 5. At final depth, the mat footing was casted followed by removal oftemporary bracing strut layer 5 and 4. respectively. The bracing layer 3 can be removed after casting of basement slab B4. The process continued until the ground floor slab was casted as shown in Fig. 6.

In FEM, all the basement floors were modelled. This was intended to determine the axial forces in basement for band beam design. The design and construction of band beam was complicated. Stirrup of band beam was casted with the D-wall during D-Wall construction and was then pulled out during basement construction to combine with the transverse reinforcement which would act against horizontal force. The band beam was 3 m high. Fig 7 and 8 show the photos of band beam construction. This project was one of the very first projects in Thailand with band beams as a force transfer structrure.

Fig 9 presents the envelop of bending moment diagram induced in the diaphragm wall with all excavation steps including soil excavation and bracing installation until casting the foundation. The upward construction including casting base slab, removing of bracing as well as basement casting are also included in the envelope.

Diaphargm wall reinforcement was designed based on this bending moment envelop. It can be seen that the capacity of reinforcement covers all the construction sequences.

DIAPHRAGM WALL DISPLACEMENT AND TRIGGER LEVEL AND SAFETY CONTROL

Inclinometers were installed in the diaphragm wall to monitor wall deflection. The safety control and monitoring criteria were proposed in terms of trigger level as shown in Table 1. During construction inclinomter data was recorded and compared with the analysis as shown in Fig 10. It can be observed that the performance of diaphargm wall agreed well with the FEM analysis. It should be noted that the latest reading was during the third bracing strut removal. The basement construction is not yet finished.

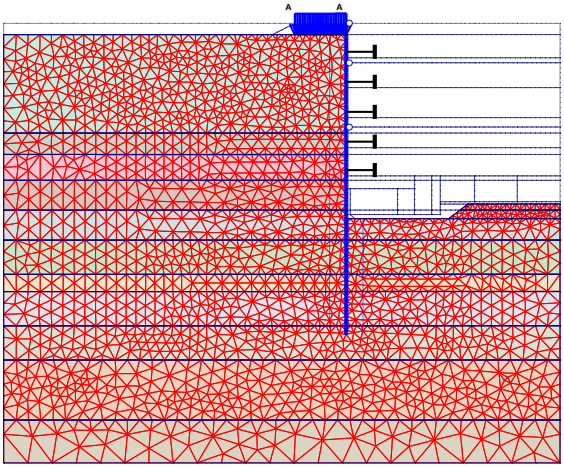

Fig. 10 Deformed mesh at the final depth of excavation in lift pit area.

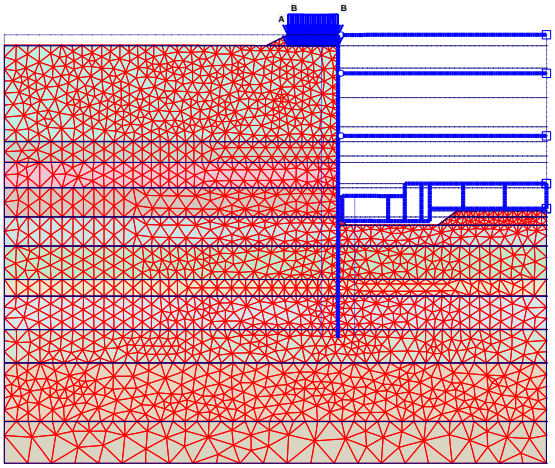

Fig. 6 Deformed mesh at final step

Fig. 7 Band beam during construction

Fig. 8 Band beam during construction

Table 1 Trigger level and safety control

Trigger Level	Inclinometer Movement (mm)		Safety Crteria
	General Area	Lift Pit Area	
Alarm Level (70 % of DV)	37.65	31.39	Inform designer to review CS
Alert Level (80 % of DV)	43.02	35.87	Inform all parties to review CS
Action Level (90 % of DV)	48.40	40.36	Stop construction and revise the CS
Maximum	53.78	44.84	

Note: DV = Design Value, CS = construction sequence.

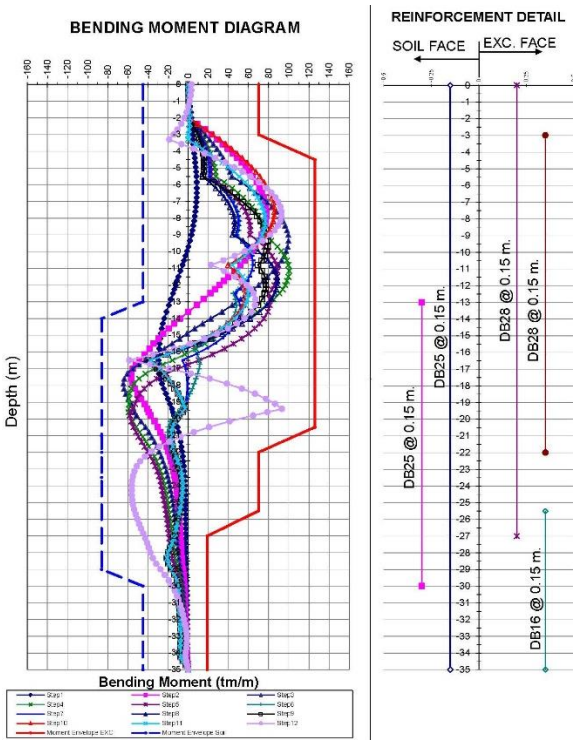

Fig. 9 Bending moment induced in diaphragm wall and reinforment

SAFETY AGAINST UPLIFT PRESSURE

The maximum depth of excavation of this project was -21 m. The illustration of sand layer where uplift pressure occurs is shown in Fig 11. The pressure occurs in sand layer at EL.-45.0 to EL.-47.0 m. Uplift pressure based on D-Wall tip of -35 m was estimated to be 320 kN/m^3 while the overburden stress of soil is 501.3 kN/m^3 and 473.2 kN/m^3 at general area and lift pit area, respectively. Thus, the safety factor against uplift is 1.57 and 1.47 which is higher than the required minimum value, 1.30.

The original design of D-Wall was only 25.0 m in length. The safety factor against uplift was too low. Thus, the d-wall tip was lengthened to -35.0 m to be penetrated in the hard clay layer. In addition, the groundwater of Bangkok keeps raising due to prohibition of deep well pumping. It is important to consider uplift issue for deep excavation in the future.

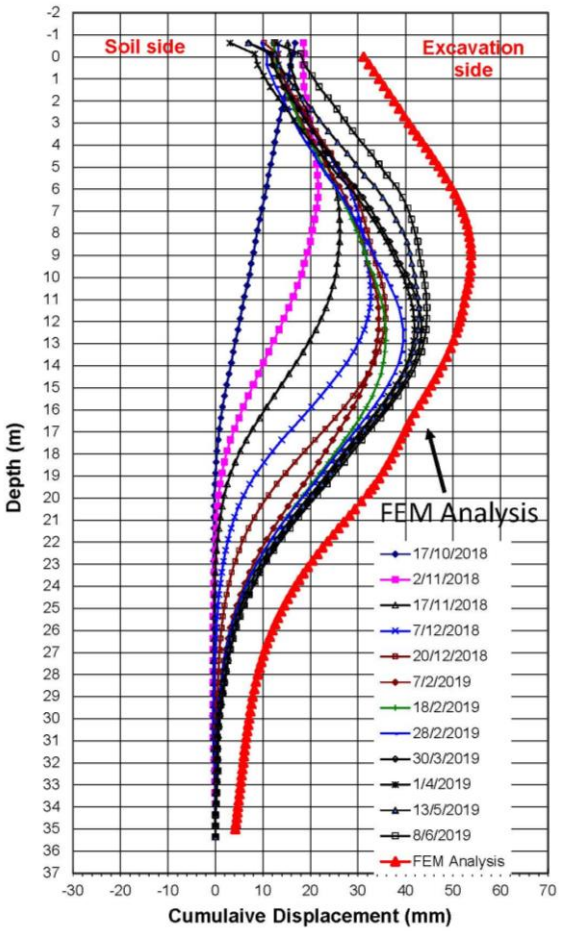

Fig. 10 Diaphragm wall displacement monitoring data and FEM analysis

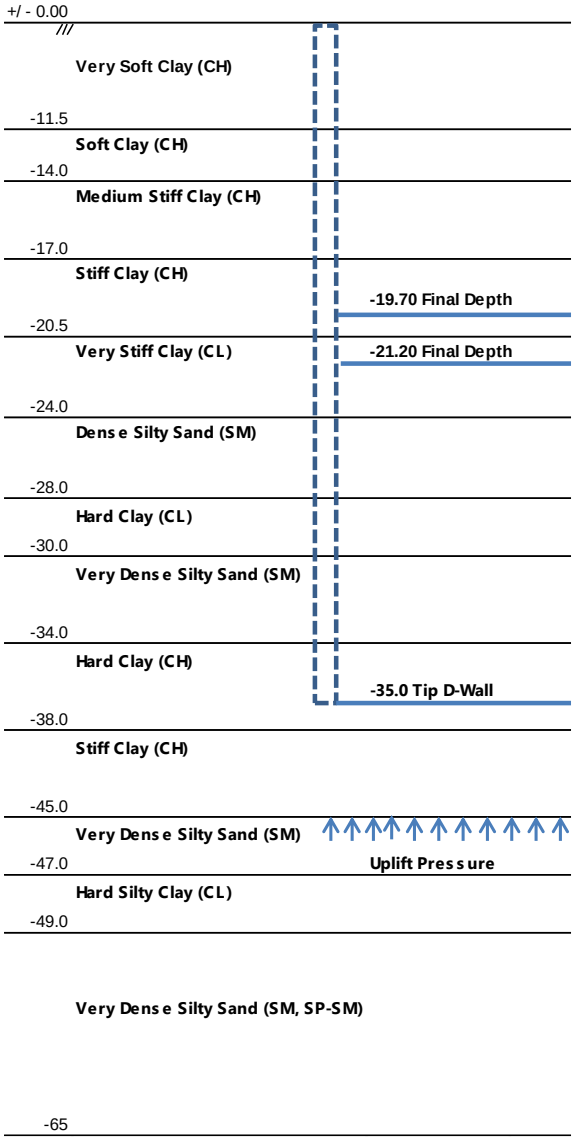

Fig. 11 Illustration of uplift pressure in sand layer

CONCLUSIONS

The underground basement construction was designed to be underground automatic carpark of the high-rise residential building. It consisted of six baseement floors using diaphragm wall as a soil retaining structure. However, to minimize space for automatic system, floor B2, B3 and B5 was cleared leaving only B1, B4 and B6. In addition, the car lift was located closed to the diaphargm wall promoting opening throught out the underground basement from B6 to ground floor. Band beam was designed to resist and transfer force to the basement slab. Safety against uplift was checked.

The behavior of diaphargm wall was predicted by means of FEM analysis with Mohr-Couloub failure criteria. All the construction sequences were simulated in the FEM. The diaphargm wall behavior and displacement were predicted and compared with the field monitoring data from inclinometer installed in the diaphragm wall. The FEM result agreed well with the field performance.

REFERENCES

[1] Teparaksa W., Principal and application of instrumentation for the first MRTA subway project in Bangkok, 5th International Symposium on Field Measurement in Geomechanics, Singapore, 1999.

[2] Teparaksa W, “Deep Basement Construction of Bank of Thailand Along Chao Phraya River closed to Tewavej Palace and Bangkhunphrom Palace”, Proc. of the 18th International Conferences on Soil Mechanics and Geotechnical Engineering, Paris, 2013.

[3] Teparaksa W, P. Sontiprasart, N. Prachayaset and S. Keawsawasvong. “Impact Assessments of the Deep Basement Construction in the MRT Protection Zone”, The 28th KKHTCNN Symposium. Civil Engineering, Bangkok, Thailand, 2015.

[4] Teparaksa W., and Teparaksa J., Comparison of Diaphragm Wall Movement Prediction and Field Performance for Different Construction Techniques. Underground Space, 2019.

[5] Brinkgreve, R.B.J., PLAXIS 2D Version 8 Manual, A.A. Balkema Publishers, 2002.

[6] Teparaksa W, Displacement analysis of diaphragm wall for subway construction, The 7 th National convention in the Civil Engineering Bangkok,2001

9th Int. Conf. on Geotechnique, Construction Materials and Environment, Tokyo, Japan, 20-22 November 2019, ISBN: 978-4-909106025 C3051

USE OF FLY ASH BASED GEOPOLYMER FOR STABILIZATION OF EXPANSIVE SOIL

Opu Chandra Debanath[1], Md. Aftabur Rahman[2] and Sultan Mohammad Farooq[2]
[1]Graduate Student, Department of Civil Engineering, Chittagong University of Engineering & Technology, Bangladesh
[2]Faculty, Department of Civil Engineering, Chittagong University of Engineering & Technology, Bangladesh

ABSTRACT

Expansive soil is considered as one of the most problematic soil in geotechnical engineering arena due to its swell-shrinkage behavior. In developing countries like Bangladesh, coal-based power plant is increasing day by day which leads to generate large amount of fly ash. Geopolymer stabilization is a suitable way to improve the properties of such soil which utilize the Fly Ash (FA) as a binder with some chemical additives. This research represents the laboratory investigation on expansive soil stabilized with fly ash based geopolymer. In this Consequence, synthesized expansive soils has been treated with FA treated geopolymer at different mix ratios and engineering properties of such treated soils are examined through laboratory investigation. Besides, swelling index, which is one of the major indicator for differentiating expansive soils are also experimentally determined. The significant increase of unconfined compressive strength and reduction of Modified free swell index is observed on geopolymer treated expansive soil compared to its original condition. To be specific, an optimum amount of 20% stabilizing agent is found to improve the swelling behavior of expansive soils.

Keywords: Fly ash, Expansive soil, Geopolymer Stabilization, Modified free swell index

INTRODUCTION

Foundations on problematic soils is always a concern in geotechnical engineering. Among several problematic soils, expansive soils is one of the most unreliable soils for safe foundation design due to its swell-shrink behavior. The Na^+ based clay minerals which expand in the presence of water exhibits huge swelling pressure. This swelling pressure is responsible for damage of foundations, roads, embankments etc. Considering the risk of failure of structures on expansive soils, researchers have been trying to found some efficient and economical remedial measures. To date, several approaches were developed and suitability of those methods have been validated by experimental and in-situ applications. Partial replacement of expansive soils with non-expansive soil is one way to stabilize the problematic soils. Concomitantly, treatment of expansive soils with stabilizing agent(s) is a clever approach in rational mitigation of the associated problem. Some common stabilizing agents are Ordinary Portland Cement (OPC), lime, Ground Granulated Blust Furnace Slag (GGBFS), Fly Ash (FA) etc. All the same, the stabilizing agent itself is not capable of improving the properties of soils owing to the lack of binding agent. With the current scenario, adding some additives with the stabilizing agent accelerate binding nature and expedite strength gain in many instances. OPC is so far the mostly available and viable stabilizing agent used to improve the soils. However, Use of OPC associated with some environmental issues, like the cement production discharge CO_2 around 5% of total CO_2 released into air [1]. Keeping the current scenario in mind, an alternative approach of using environmental friendly agent is suitable over the conventional approach. FA, which is the industrial by-product can be a good option considering no threat for environment and safe disposal. Chemical additives i.e. geopolymer based treatment is necessary to be added to the FA to make it active in the bonding. The chemical reactions of Geopolymerization process is entirely different from conventional Portland cement/lime type admixtures. Polymerization process includes a very first chemical reaction of Si-Al minerals in presence of alkali activators (Sodium/potassium hydroxide and sodium silicate), which results a 3D polymer ring and chain type structure having Si-O-Al-O bonds [2].

Expansive soil treatment by 9% of GGBFS and cement by-passes dust mix was found to reduce swelling index and pressure [3]. Cokca, Yazici & Ozaydin [4] found that 15% of Granulated blast furnace slag-cement (GBFSC) admixture is optimum for lowering swelling percentage up to 10 times of untreated expansive soil having high swelling potential. Yadu & Tripathi [5] used GGBFS to stabilize expansive soil and found 9% admixture as optimum which increase the UCS around 28% of untreated soil. the presence of

expansive clays are generally found in steppe climate zone where the precipitation is much less compared to evapotranspiration [6]. In Bangladesh presence of expansive soil was found in several locations named as Joydevpur, Savar, Lalmai Hills of Cumilla and some part of Rajshahi and Tangile [7].

Summarizing the above discussions, an attempt was made to check the effectiveness of fly ash based geopolymer for stabilizing a laboratory synthesized expansive soil. The performance of geopolymer binder was evaluated based on its improvement of strength and swelling properties. The subsequent sections describe in detail the outcomes of the current study.

MATERIALS

Expansive Soil

The expansive soil used for this study was synthesized artificially in laboratory. Firstly, a suitable clayey soil was collected near the coastline of Bangladesh and 5% of commercial grade Bentonite was blended with pulverized clay soil to generate expansive behavior. The nature of expansive soil was medium expansive as per IS: 1498-1970 [8]. The geotechnical properties of medium expansive soil are listed in table 1 and the particle size distribution is shown in Fig. 1.

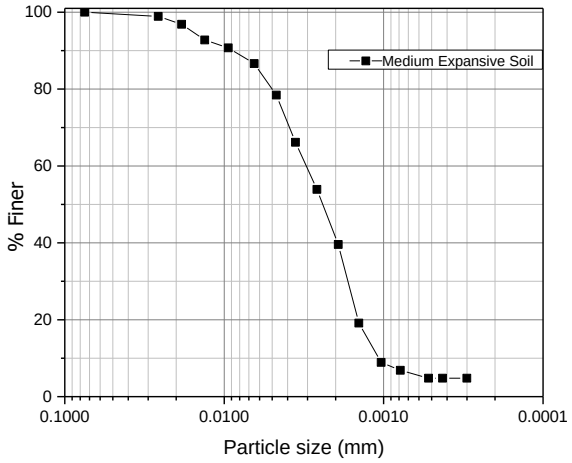

Fig. 1 particle size distribution of used soil.

Geopolymer

The main constituents of geopolymer used for soil stabilization is alkali activators and binder materials. The function of alkali activators is to stimulate the reaction of polymerization process. In present study, sodium silicate (Na_2SiO_3) solution and sodium hydroxide (NaOH) pallets were collected from local supplier to prepare alkali activator of geopolymer. Equal proportion of Sodium hydroxide and sodium silicate was mixed to prepare alkali activator solution prior to use and 10% of this solution was used in geopolymer. Class F fly ash was used as binder. Table 2 represents the properties of fly ash. A total of five mix ratios from 10% to 30% by weight of fly ash was replaced with natural soils, while the amount of alkali activator was kept fixed for all cases.

Table 2 Properties of Fly ash

Specific Gravity	Fineness (cm^2/g)	SiO_2 (%)	Fe_2O_3 (%)	Al_2O_3 (%)
2.22	2325	62.1	6.6	22.4

TEST PROGRAM

Series of experimental program was run on geopolymer treated and untreated synthesized expansive soil. In this study, dosage of geopolymer indicates the amount of fly ash present in geopolymer such as 10% geopolymer treated soil means the mixture have 10% fly ash, 10% alkali solution and 80% dry soil. where the 0% geopolymer denoted as the untreated soil.

firstly, required amount of fly ash and soil was mixed in dry condition through a mixture machine. Alkali activator solution was gradually applied thereafter and mixed until a homogeneous mixture is obtained.

Compaction test was performed maintaining standard effort (600 kN-m/m3) for each mix combination to find the optimum moisture content and maximum dry density. Figure 2 represents the compaction curve of different soil-geopolymer mix.

The samples for unconfined compressive strength (UCS) test were prepared in laboratory according to the standard procedure of ASTM D 1632 [9] maintaining the optimum moisture content and maximum dry density obtained from compaction curve. Three identical samples were tested under compression loading for each case and the average value was taken. The UCS test was performed on both untreated and treated soil samples immediately after preparation which is reported as 0 days strength.

In addition, the strength development with the time was also checked. For this, UCS samples were warped with thin cling film and preserved in desiccator to check the strength after 7days and 28 days.

Table 1 Geotechnical properties of used soil

Liquid Limit (%)	Plastic Limit (%)	Plasticity Index (%)	Swelling Pressure (kPa)	Specific Gravity	Clay (%)	Silt (%)	Sand (%)	USCS Classification
42	19	23	81	2.56	9.0	91	--	ML

The swelling parameter of expansive soil was determined in terms of modified free swell index (MFSI). To observe the effect of geopolymer stabilization, modified free swell index test was performed after 28 days curing age. The soils were oven dried, pulverized to pass through 425-micron sieve and 10 grams of soil was dispersed in distilled water and placed on a 100 ml graduated cylindrical jar. The MFSI is calculated as the ratio of equilibrium sediment volume (V_d) of dispersed soil to its dry weight [10].

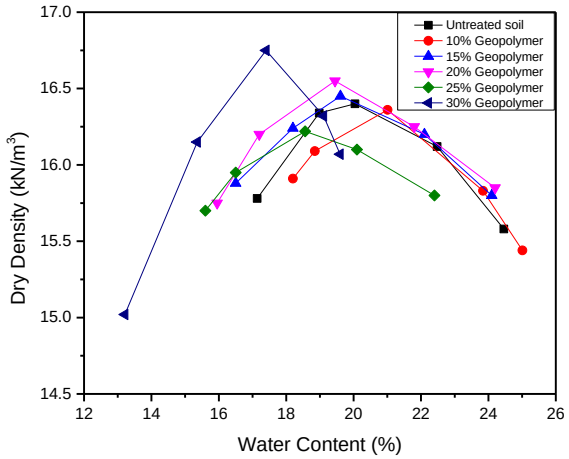

Fig. 2 Compaction curve of different soil-geopolymer mix.

RESULTS AND DISCUSSION

The influence of various geopolymer dosage on artificial expansive soil was evaluated in terms of UCS and MFSI. The general trend of compaction test is not clear, though increased dry density was seen with the increment of geopolymar content. Concurrently, moisture content shows slight decreasing trend with the variation of geopolymer content. The variation of strength and swelling behavior of geopolymer stabilized expansive soil are explained separately as following:

Effect of Stabilization on Unconfined Compressive Strength

The UCS of untreated expansive soil was found 88 kPa and remain constant with curing time. The effect of geopolymar was compared by normalizing its strength with the untreated soils. Figure 3 represents the variation of normalized compressive strength of geopolymer treated soil at different curing age.

The strength gaining rate of geopolymer treated expansive soil is observed to very low at 0 days curing. At any particular geopolymer dosage UCS increase continuously with curing age which indicates that, the curing time have significant effect on strength development. For 20% geopolymer stabilized soil UCS is only found 1.7 which increased up to 2.8 and 4.2 times after 7 and 28 days, respectively. The maximum normalized UCS was found as 4.2 at 28 days for 20% geopolymer content

The experimental results also show the decrement of normalized UCS after 20% of geopolymer content. Similar trend of unconfined compressive strength development was also reported for fly ash - lime treated expansive soil [11]. Cementation of soil particles happens in treated soil matrix due to stabilization with chemical additives up to a certain percentage of admixture.

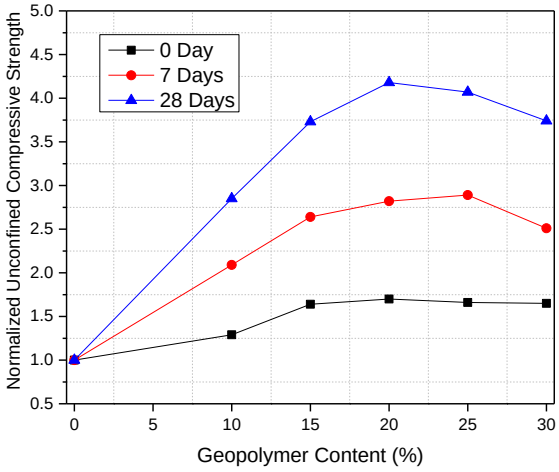

Fig. 3 Effect of Geopolymer content on Normalized UCS of expansive soil.

It was observed that during stabilization of expansive soil with increasing percentage of admixture, the soil particles become more granular in shape [12]. However, for higher percentage the above-mentioned process reach saturation level and excess additive remains unbonded that reduce overall strength level of soil [13].

Effect of Stabilization on Modified Free Swell Index

Figure 4 represents the variation of modified free

swell index with the variation of geopolymer content. The figure indicates that as the percentage of geopolymer increases the modified free swell index of soil decreases.

The MFSI of untreated expansive soil is found 1.75 and that of treated soil is observed to vary from 1.55 to 1.2 due to variation of geopolymer content from 10 to 30%. However, A steep reduction of modified free swell index has been noticed for geopolymer content up to 15% and the reduction rate becomes slower thereafter.

The fly ash provides multivalent cation to soil which results flocculation and reduce water affinity of expansive soil. When such non expansive admixture is added to soil, the swelling behavior of expansive soil decreases to some extent [11].

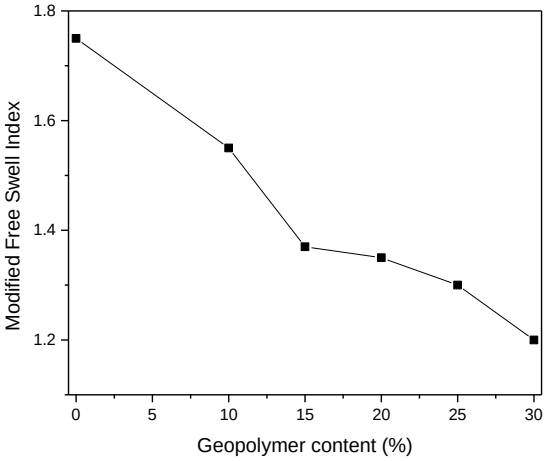

Fig. 4 Variation of modified free swell index with geopolymer content.

CONCLUSIONS

The Effect of various percentage of geopolymer on strength and swelling properties of expansive soil was investigated experimentally. The major conclusions are listed below:

1. Addition of geopolymer dosage increase the dry density of treated soil while the optimum moisture content decreases.
2. The swelling behavior of geopolymer treated soil reduced substantially with the increment of fly ash content in geopolymer.
3. Strength gaining of geopolymer treated expansive soil is time dependent. After 28 days curing the unconfined compressive strength is almost 4.2 times of instant strength.
4. The maximum unconfined compressive strength of treated expansive soil is found for observed for geopolymer having 20% fly ash content and 10% alkali activator solution.
5. Based on experimental study 20% geopolymer dosage can be taken as optimum dosage for stabilization of expansive soil.

REFERENCES

[1] Worrell E., Price L., Martin N., Hendriks C., and Leticia O.M., Carbon Dioxide Emission from the Global Cement Industry. Annual Review of Energy and The Environment, Vol. 26, Issue 1, 2001, pp. 303-329.

[2] Davidovits J (1999) Chemistry of Geopolymeric Systems, Terminology. Proceedings of Geopolymer, Vol. 99, Issue 292, 1999, pp. 9-39.

[3] Al-Rawas A. A., Microfabric and Mineralogical Studies on the Stabilization of an Expansive Soil Using Cement By-pass Dust and Some Types of Slags. Canadian Geotechnical Journal, vol. 39, Issue 5, 2002, pp. 1150–1167.

[4] Cokca E., Yazici V., & Ozaydin, V.,Stabilization of Expansive Clays Using Granulated Blast Furnace Slag (GBFS) and GBFS-Cement. Geotechnical and Geological Engineering, vol. 27, Issue 4, 2009, pp. 489–499.

[5] Yadu L., & Tripathi R. K., Effects of Granulated Blast Furnace Slag in the Engineering Behaviour of Stabilized Soft Soil," Procedia Engineering, vol. 51, 2013, pp. 125–131.

[6] Neeraja D., & Narsimha A. R., Use of Certain Admixtures in the Construction of Pavement on Expansive Clayey Subgrades. International Journal of Engineering Science and Technology, vol. 2, Issue 11, 2010, pp. 6108–6114.

[7] Khan A. J., Ameen S. F., and Abedin M. Z., Effects of Sand Layer on Swelling of Underlying Expansive Soil. Fifteenth International Conference on Soil Mechanics and Geotechnical Engineering, 2001, pp. 1767-1770.

[8] IS: 1498-1970, Classification and Identification of Soils for General Engineering Purposes. Bureau of Indian Standards, New Delhi, 2000, pp. 1-24.

[9] ASTM D1632-17, Standard Practice for Making and Curing Soil-Cement Compression and Flexure Test Specimens in the Laboratory. ASTM International, West Conshohocken, PA, 2017.

[10] Sivapullaiah P., Sitharam T., & Subba Rao K., Modified Free Swell Index for Clays. Geotechnical Testing Journal, Vol. 10, Issue 2, 1987, pp. 80-85.

[11] F. Zha, S. Liu, Y. Du, and K. Cui, Behavior of Expansive Soils Stabilized with Fly Ash. Natural Hazards, vol. 47, no. 3, 2008, pp. 509–523.

[12] Basma A. A., & Tuncer E. R., Effect of Lime on Volume Change and Compressibility of Expansive Clays. Transportation and research record, vol. C, Issue 1295, 1991, pp. 52–61.

[13] Bell F. G., Lime Stabilization of Clay Minerals and Soils. Engineering Geology, Vol. 42, Issue 4, 1996, pp. 223-237.

9th Int. Conf. on Geotechnique, Construction Materials and Environment, Tokyo, Japan, 20-22 November 2019, ISBN: 978-4-909106025 C3051

RELATIONSHIP BETWEEN DRAINAGE DENSITY AND DEGREE OF DISSECTION OF LARGE-SCALE LANDSLIDES IN SHIKOKU, JAPAN

*Daisuke KANBARA[1], Shuichi HASEGAWA[2], Atsuko NONOMURA[2], Makoto YANAGIDA[3] and Matsuri KIMURA[1]
[1]Yonden Consultants Co., Inc, Japan, [2]Kagawa University, Japan; [3]Hanshin Consultants Co., Ltd, Japan

ABSTRACT

A geomorphic approach is essential for landslide investigation because it represents different topographies from the surrounding slopes. Yanagida and Hasegawa first proposed a relational expression between the formation age of landslides and the degree of dissection by using carbon-14 dating and volcanic ash to compare the age of formation. As a result, it became possible to estimate landslide age even for landslides whose formation age is unknown.

In this study, the relationship between the degree of dissection and drainage density, which are both indicators of landslide topography, by using digital elevation model (DEM) data. We determined the relationship between drainage density and degree of dissection for 17 landslides in Shikoku in Southwest Japan, where the degree of dissection was already known from previous studies. An approximate relationship between the drainage density (V_1, km^{-1}) and the degree of dissection (D, %) of landslide bodies can be expressed as $D = e^{0.72V_1}$.

Keywords: Landslide, DEM, Drainage density, Degree of dissection, Relative drainage density

INTRODUCTION

Landslide is defined as "A general term covering a wide variety of mass-movement landforms and processes involving the downslope transport, under gravitational influence, of soil and rock material en masse" [1], and landslides play a significant role in terrain formation in mountainous areas [2]. Most landslide topographies are inferred to have been formed by strong triggers. If a landslide has stabilized, dissection of the surface landslide topography and the landslide mass will begin [3]. The topographic development of a landslide is therefore important information when evaluating the stability of the landslide [4, 5].

In recent years, research on landslide analysis using digital elevation model (DEM) data acquired by aviation laser surveying has been ongoing [6]. The use of this type of data enables researchers to conduct topographic analyses over wide areas much faster than could be done manually. It has also become possible to extract drainage and inclination information with good reproducibility. Research and development has been generally been conducted to extract high risk area from surrounding slopes by using multiple parameters, including landslide micro topography. For example, the Slope Stability Evaluation (SSE) model using satellite data and geographical information has been developed [7].

The formative age of landslides is estimated by ^{14}C dating of wood fossils in landslide deposits and identification of volcanic ash that covers or is part of the landslide deposits [8, 9]. Yanagida and Hasegawa [10] focused on the erosion of the topography of a landslide similar to the terrace analyzed by Suzuki [11] and Ota and Ikura [12], and they estimated the correlation between the formation age of the landslide and the degree of dissection. In addition, Kanbara et al. [13] identified landslide ages by using volcanic ash and improved the accuracy of the relationship between topographical analysis and landslide age. Inagaki et al. [14] have reported that landslide topographies with older formative ages are more stable.

On the other hand, Tsukamoto et al. [15] and Tsukamoto and Noguchi [16] regard the collapse of mountains as valley development. I In other words, the development of valleys can be regarded as a slope dissection process. Landslides have been regarded as a rejuvenation of river systems in mountains [17], and landslide topographies have been considered as slopes with drainage density smaller than that of the surrounding area [18]. Hasegawa et al. [19] and Kinoshita et al. [20] developed a method for evaluating slope failure using drainage density and reported that the larger the drainage density, the larger the collapse density.

In this study, we focused on valley development (drainage density) and examined the relationship between the dissection rate of landslide topography and drainage density. The examinations were conducted by using a DEM in conjunction with available data to make determining the relationship between the degree of dissection and drainage density

as simple and easy as possible.

STUDY AREA

We have collected information on 17 landslides whose formative ages were inferred by using ^{14}C dating and volcanic ash in Shikoku, southwest Japan (Fig. 1).

On the 17 sites, landslides 1 to 13 were reported by Yanagida and Hasegawa [10], and 14 to 17 were reported by Kanbara et al. [13].

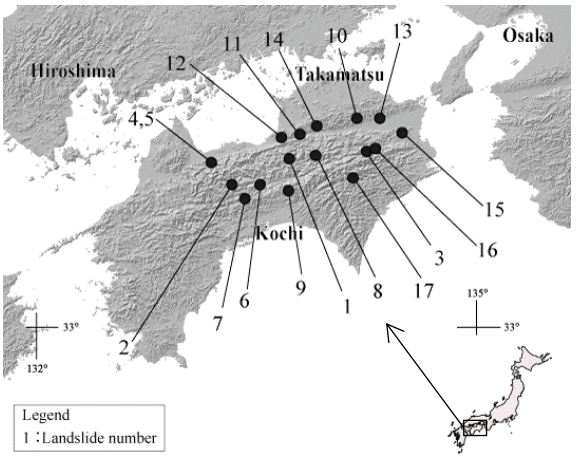

Fig. 1 Study area

METHODS

DEM Data and Analysis Software

The 10-m resolution DEM data used for topographical analysis were acquired from the Geospatial Information Authority of Japan (https://fgd.gsi.go.jp/download/menu.php). ILWIS 3.3 Academic, a published source code, was used for the analysis of drainage density.

Degree of Dissection of Landslide

We have used the method described by Yanagida and Hasegawa [10]. The degree of dissection (D, %) as the ratio of the dissection surface area (S_1, km^2) to the landslide mass surface area (S_2, km^2) are defined as follows.

Degree of dissection*(D)* = Area of dissection *(S_1)* / Area of landslide topography *(S_2)* (1)

Figure 2 shows an example of the measurement method. First, we transcribed the landslide mass onto 25,000:1 topographical maps and obtained the surface area of landslide unit 1 (S_2=0.71km^2) using the Auto Cad LT (Auto Desk) surface area calculation function. Next, we have conducted photographic interpretations of dissections using 10,000:1 scale aerial photographs, transferred them to 25,000:1 topographic maps, and thereby obtained the dissection surface area of landslide unit 1 (S_1=0.04 km^2) with the Auto Cad LT (Auto Desk) surface area calculation function. The degree of dissection was then calculated as $D=S_1/S_2$=0.04/0.71 or about 6%.

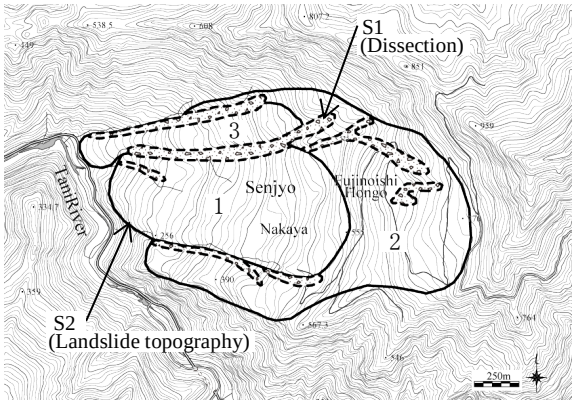

Unit 1, D = 6%; unit 2, D = 12%; unit 3, D = 26%.
S_1, Area of dissection (km^2);
S_2, Area of landslide topography (km^2); and
D, Degree of dissection of the landslide topography (%) ($D = S_1 / S_2$).

Fig. 2 Method for evaluating the degree of dissection of a landslide

Drainage Density

Mean curvature

Mean curvature defined as the average of the maximum and minimum values of the curvature of all measurement lines passing through a point on a curved surface, is used as an indicator of topographic unevenness. We have extracted the valleys, which determined the mean curvature (H), by using the equation (2) [21].

$$H=\frac{h_{xx}\left(1+h_y^2\right)+h_{yy}\left(1+h_x^2\right)-2h_xh_yh_{xy}}{2\left(1+h_x^2+h_y^2\right)^{3/2}}, \quad (2)$$

where h is elevation and

$$h_x=\frac{\partial h}{\partial x},\ h_y=\frac{\partial h}{\partial y},\ h_{xx}=\frac{\partial^2 h}{\partial x^2},\ h_{yy}=\frac{\partial^2 h}{\partial y^2},\ \text{and}\ h_{xy}=\frac{\partial^2 h}{\partial x\partial y}.$$

We set the mean curvature at H>0.10 following Nonomura et al. [22]. We optimized the line width to one pixel following Kinoshita et al. [20] (Fig. 3).

Calculation of drainage density

Drainage density represents the degree of development of the river drainage in an area, and

erosion becomes stronger as drainage density increases [23]. The valleys were evaluated by counting the number of pixels contained in the extracted valleys. Following equation (3) was used to determine of drainage density.

$$\text{Drainage density } (V_1)\ (\text{km}^{-1}) = \frac{\text{Total extension of the extracted valley(km)}}{\text{Basin area}\left(\text{km}^2\right)} = 100 \times \frac{\text{Total number of valley pixels contained in the extracted valleys}}{\text{Total number of basin area pixels}} \quad (3)$$

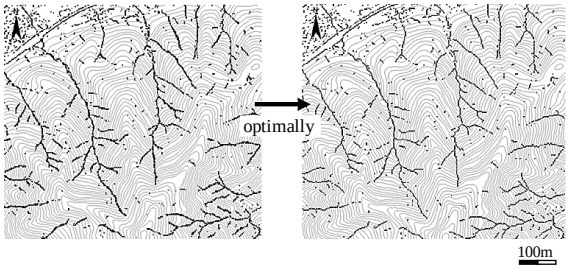

Before optimization After optimization

Fig. 3 Optimization of a valley

Degree of relative drainage density

The physical properties of the bedrock strongly influence the topography [24], and they are considered to control the development of the valley surface [25]. Therefore, in 17 landslides evaluated in this study, we decides to the relative drainage density with the surrounding slope (E) in order to reduce the influence of differences in bedrock (equation (4)).

Relative drainage density *(E)*
= drainage density of landslide bodies (V_1)
/ drainage density of surrounding slope (V_2) (4)

RESULTS

The surrounding slopes were chosen to examine the relative drainage densities of selected landslides (Fig. 4).

The drainage density and the degree of dissection of selected landslide topographies of the 17 landslides are shown in Table 1. The drainage networks determined by using the DEM were in agreement with the degree of dissection determined by using the aerial photographs. Scattered valleys were identified as undissected slopes in aerial photo interpretation.

DISCUSSION

Relationship between Drainage Density and Degree of Dissection

The relationship between drainage density and degree of dissection was examined for 17 landslides at some places in Shikoku, Southwest Japan. Figure 5 shows that the drainage densities increased according to the degree of dissection in landslides 1 to 17. In other words, after landslide formation, the drainage density is reset to almost zero.

Table 1 Measurement results of the degree of dissection (*D*), drainage density (V_1), and relative drainage density (*E*).

No.	Landslide	Age (year) [10],[13]	Degree of dissection (*D*)(%) [10],[13]	Drainage density (V_1)(km^{-1})	Relative drainage density (*E*)
1	Taira	$200\sim300\times10^3$	33.0	3.5	0.7
2	Kuromaru	9,340 ± 170	8.5	5.6	1.1
3	Morito	15,400 ± 400	16.0	2.8	0.9
4	Shimotsuike	2×10^3	1.0	2.8	0.6
5	Yoshii	1,970 ± 130	1.0	0.7	0.1
6	Shimojizoji	$100\sim200\times10^3$	17.0	3.1	0.9
7	Amou	350±80	1.0	2.2	0.3
8	Kuki	$2\sim5\times10^3$	2.2	1.6	0.2
9	Higashiterauchi	$30\sim150\times10^3$	9.0	2.2	0.8
10	Nagamine	1×10^6	100	6.3	1.5
11	Inokubo	30×10^3	10.0	3.3	1.0
12	Sanokamiura	5×10^3	1.0	0.1	0.3
13	Kirihata	1×10^6	100	6.1	1.1
14	Ikeda-shinyama	500×10^3	96.0	6.1	1.6
15	HigashiOkubo	$7\sim29\times10^3$	10.6	2.3	0.5
16	Koune	$7\sim16\times10^3$	9.3	2.4	0.6
17	Nakauchi	$7\sim29\times10^3$	10.3	3.0	0.9

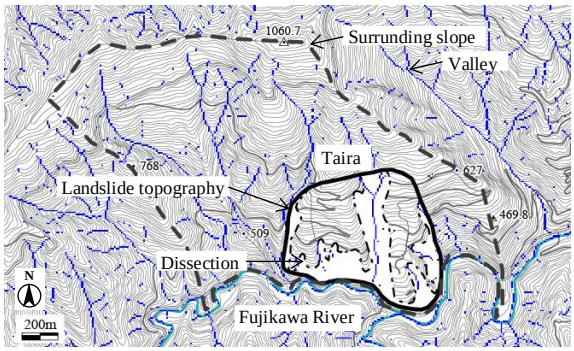

No. 1 Taira
Degree of dissection=33.0%,
Drainage density=3.5%,
Relative drainage density=0.7

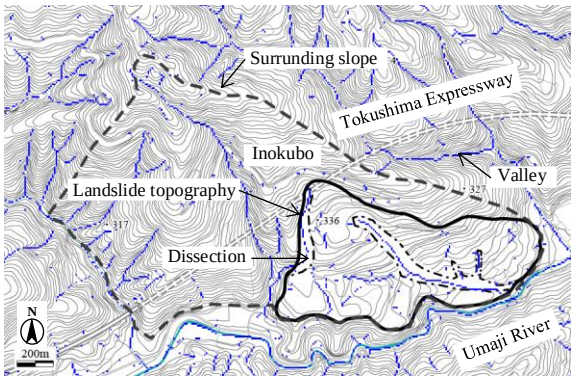

No. 11 Inokubo
Degree of dissection = 10.0%,
Drainage density = 3.3%,
Relative drainage density = 1.1

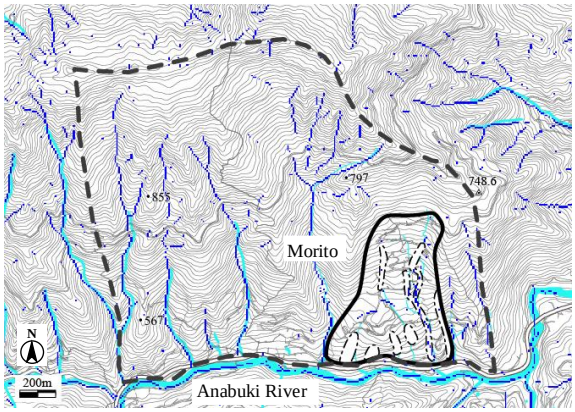

No. 3 Morito
Degree of dissection = 16.0%,
Drainage density = 2.8%,
Relative drainage density = 1.0

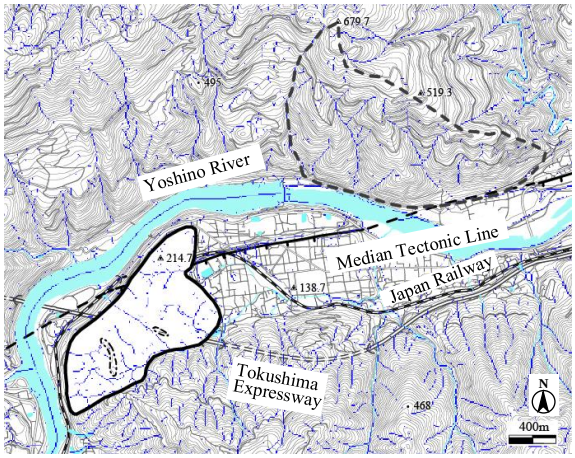

No. 14 Ikeda-shinyama
Degree of dissection = 96.0%,
Drainage density = 6.1%,
Relative drainage density = 1.6

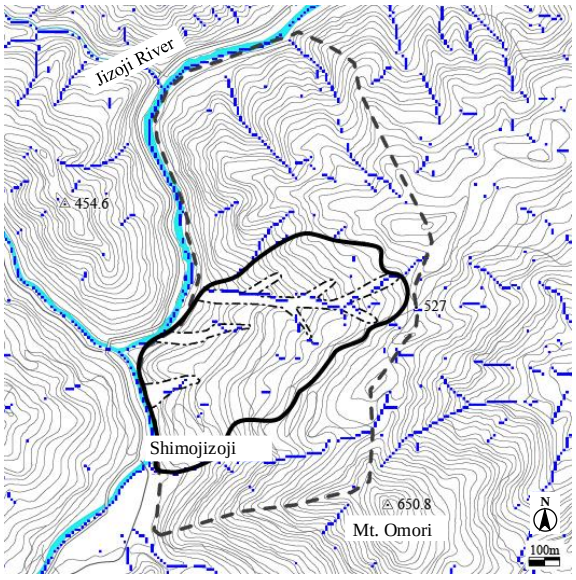

No. 8 Shimojizoji
Degree of dissection = 17.0%,
Drainage density = 3.1%,
Relative drainage density = 1.0

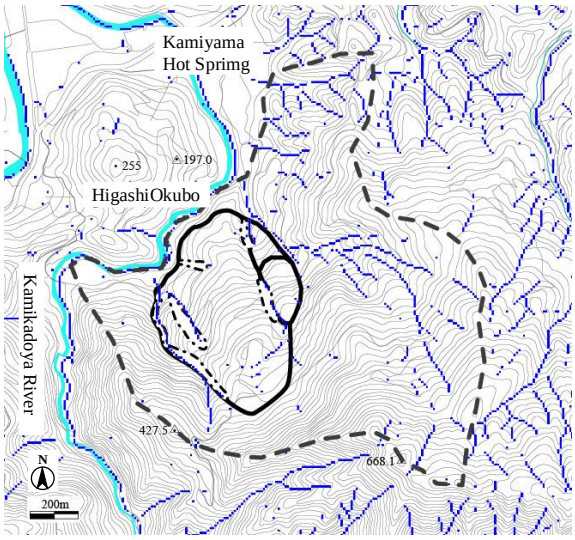

No. 15 HigashiOkubo
Degree of dissection = 10.6%,
Drainage density = 2.3%,
Relative drainage density = 0.6

Fig. 4 Analysis results examples

It shows that the dissected valleys in landslide bodies then start to develop, and as a result, drainage density starts to increases. The exponential relationship shown in Figure 5 can be expressed as $D = e^{0.72V_1}$ and can be used to evaluate dissected landslides.

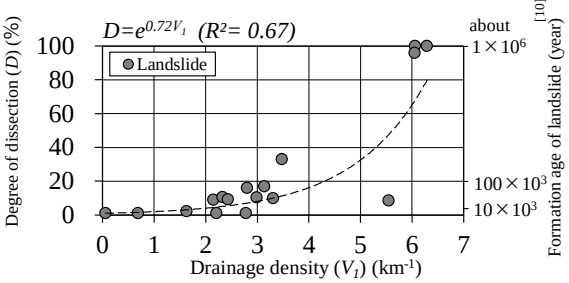

Fig. 5 Relationship between drainage density and degree of dissection (landslides 1-17)

Relationship between Relative drainage density and Degree of dissection

The relationship between relative drainage density and degree of dissection is shown in Figure 6. The degree of dissection increases as the relative drainage density increases, and the exponential relationship can be expressed as $D = e^{2.9E}$. The drainage density of most landslides selected in this study was less than 1. The relative drainage density of completely eroded landslides tended to be greater than 1, which was larger than the drainage density of the surrounding slopes.

We originally thought the drainage density and the relative drainage density would be different because the bedrocks in these landslides are different, but the graphs show a similar relationship (Figs. 5, 6). All the bedrock of the selected landslides are composed of Mesozoic and Paleogene hard bedrock.

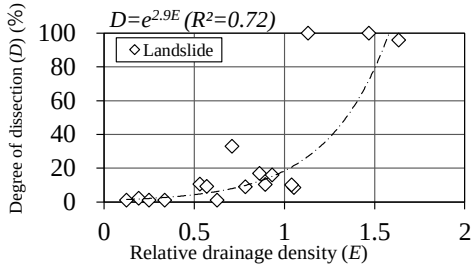

Fig. 6 Relationship between relative drainage density and degree of dissection (landslides 1-17)

CONCLUSION

We have examined the relationship between the degree of dissection and drainage density by using 10-m DEM data. The results are as follows:

1) The drainage density of landslide bodies gradually increased after the formation of landslide topographies. The older the landslide, the higher the drainage density.
2) The degree of dissection increased as the relative drainage density increased. The relative drainage density of completely eroded landslides tended to be greater than the drainage density of the surrounding slopes.
3) With this method, the relationship between drainage density and degree of dissection can be used as a guideline for landslide development in Shikoku, southwest Japan. Applicability of the method to other places is a research subject in the future.

REFERENCES

[1] Jackson J.A., Glossary of Geology, Fourth Edition, American Geological Institute, 1997, 769p.
[2] Machida D., Large-scale rockslides, avalanches and related phenomena, Japan geomorphological union, Vol.5-3, 1984, pp155-178.
[3] Ueno S., Influence of geological factors on configuration and scale of landslide, Journal of the Japan Landslide Society, Vol.38 No.2, 2001, pp.105-114.
[4] Terado T. and Katto J., The "Ancient Landslides" and their Backgrounds in the Central Area of Shikoku Mountains, Japan - A Case Study of the Drainage Basin of Nakatsu River, Kochi Prefecture -, Selected Papers in Honor of Prof. Jiro Katto, Geology and Paleontology of the Shimanto Belt, 1980, pp.17-26.
[5] Higaki D., Slope evolution processes of the Choja landslide, Southwest Japan, Journal of Japan landslide society, Vol.29-2, 1992, pp.12-19.
[6] Kasai M., Ikeda M., Fujisawa K., Matsuda M. and Suzuki Y., Observation of the landslide development process by analysis of LiDAR-derived DEMs, Journal of Japan landslide society, vol.45, No.2, 2008, pp.118-124.
[7] Obayashi S., Kojima H., and Fujii K., improvement of the accuracy for extracting areas in danger of the landslide using satellite multispectral data, Proceedings of the Japan Society of Civil Engineers, No. 534, VI-30, 1996, pp.173-184.
[8] Abe S., Moriya H. and Moriai T., A Geological Factor in the Large-Scale Rock-Slides in the Ou Mountains –In the Westernmost Part of the Ou Mountains in Akita Prefecture-, Journal of the Japan Society of Engineering Geology, 35-5, 1994, pp.15-26.
[9] Yagi H., Soda T., Inokuchi T., Haraguchi T. and Ban M., Catastrophic Collapse of Mt. Zao and Mt. Shirataka and Their Chronologic Timing, The Quaternary Research, 44(4), 2005, pp.263-272.

[10] Yanagida M. and Hasegawa S., Morphological dating and dissection process of landslide. Poc.7th International Conference & Field Workshop on Landslides, S.Novosad & P.Wager (ed.), Balkema, 1993, pp.117-122.
[11] Suzuki T., Rate of erosion in strato-volcanoes in Japan, Volcanol Social Japan Second Ser. Vol.14, 1969, pp133-147.
[12] Ota Y. and Ikura K., Dissection of Pleistocene Marine Terraces by Paleolandslides on the Nishi-tsugaru Coast, Northern Japan, Geographical review of Japan, 72A-12, 1999, pp.829-848.
[13] Kanbara D., Onishi K., Nishizaka N., Yanagida M. and Hasegawa S., Relations of the age of landslide generation and the topographic dissection, abstracts of the 55th annual meeting of the Japan Landslide Society, 2016, pp.136-137.
[14] Inagaki S., Okubo T., Hasegawa S. and Yatabe R., Stability of old landslide, The Japan geotechnical society, Soil mechanics and foundation engineering, No.53-7, 2005, pp.17-19.
[15] Tsukamoto Y., Hiramatsu S. and Shinohara S., Study on the growth of stream channel (III)-Relationship between 0 (zero) order channels and landslides, Journal of the Japan Society of Erosion Control Engineering, 89, 1973, pp.11-20.
[16] Tsukamoto Y. and Noguchi H., Study on the Growth of Stream Channel (VIII) Characteristics of basin morphology in equilibrium stage, Journal of the Japan Society of Erosion Control Engineering, 113, 1979, pp.6-9.
[17] Nakamura S., Landslide, Iwanami, 254p.
[18] Japan Society of Engineering Geology, Slope Geology Reserch Trends Future Prospects, 2000, 294p.
[19] Hasegawa S., Mimura A., Ranjan K., Yamanaka M. and Nonomura A., Relation between Drainage Density and Volume of Rainfall Triggered Landslides, the Japanese Geotechnical Society - Proceedings of the symposium on slope failure mechanism and stability assessment for rainfall and earthquakes-, 2009, pp.301-306.
[20] Kinoshita H., Hasegawa S., Nonomura A. and Yanamaka M., Drainage Density as Slope Failure Susceptibility Index in Small Catchment Are, Journal of the Japan Society of Engineering Geology, 59-6, 2019, pp.472-484.
[21] Nishida K., Kobashi S. and Mizuyama T., DTM-based Topographical Analysis of Landslides Caused by an Earthquake, Japan Society of Erosion Control Engineering, Vol.49, No.6, 1997, pp.9-16.
[22] Nonomura A., Hasegawa S., Matsumoto H., Takahashi M., Masumoto M. and Fujisawa K., Curvature derived from LiDAR digital elevation models as simple indicators of debris-flow susceptibility , journal of mountain science 16(1), 2019, pp.95-107.
[23] Suzuki T., Introduction to Map Reading for Civil Engineers Vol.3, 2000, 942p.
[24] Yanagida M., Fujiwara O., Goto N. and Sasaki T., A New Definition of Hills in terms of Relative Relief and Drainage Density, Journal of Geography, 113(6), 2004, pp.835-847.
[25] Suzuki, T., Tokunaga, E., Noda H. and Arakawa H., Effects of rock strength and permeability on hill morphology Trans. Japan Geomorph.Union, 6, 1985, pp.101-130.

9th Int. Conf. on Geotechnique, Construction Materials and Environment, Tokyo, Japan, 20-22 November 2019, ISBN: 978-4-909106025 C3051

EVALUATING HYDRAULIC AND MECHANICAL PROPERTIES OF NATURAL PREFABRICATED VERTICAL DRAIN (PVD) ON A LABORATORY SCALE

Dea Pertiwi[1] and Maulana Iqbal[1]
[1]Institute of Road Engineering (IRE), Bandung, Indonesia

ABSTRACT

Rapid development in urban areas requires reliable technology but still puts forward the environment issues. Synthetic Prefabricated Vertical Drain (PVD) commonly used in accelerating settlement over soft soils tend to not easily decomposed in soil after the service period has been exceeded, thus storing plastic waste under the ground. Local materials such as coconut fibers and jute woven fibers that can be cultivated in Indonesia are promising option because of its easily biodegradable characteristic. To check their performances, series of laboratory test of hydraulic and mechanical properties using geosynthetic testing apparatus were conducted. The test revealed that natural PVD tested with geosynthetic testing apparatus gives high tensile strength and permittivity. However, its laboratory discharge capacity is ten times lower than synthetic PVD if tested in horizontal condition using water flow (in-plane) capacity apparatus (EN ISO 12958). Considering the good performance of natural PVD in field in accelerating embankment settlement over soft soils especially due to its nature capillarity characteristic, specific laboratory test standards for natural PVD are needed, and the range of test results must be distinguished from synthetic PVD.

Keywords: PVD, Natural fibers, Hydraulic properties, Soft soils, Laboratory test

INTRODUCTION

Synthetic Prefabricated Vertical Drain (PVD) technology made from polymer has been widely recognized as one of soil improvement technologies with the main function of dealing with the problem of settlement over soft soil by accelerating the consolidation process. The demand for the use of PVD technology in Indonesia is very large because soft land areas in Indonesia estimated to cover some 20 million hectares or around 10% of Indonesia's land area [9]. Preloading with PVD is one of the technologies used, in addition to the use of other soil improvement technologies.

In addition to synthetic drains, natural-based drains often used outside Indonesia i.e. Japan, Korea, Bangladesh, India mainly due to consideration of environmental preservation. The advantages of drains made from natural materials are non-toxic, recyclable, high absorbency, the disintegration time in the soil is relatively fast due to biodegradable properties. Thus, in less than 1 year the drain material will be decayed in the soil. This advantage is very suitable for dense urban areas because the location of the former drain installation can be used for other underground constructions.

However, their application is still very limited because they are usually composed of individual fibers with large openings which allows fine soils trapped while discharging pore pressure, so that they are reducing the hydraulic conductivity of the drain [11].

Jute drains was first developed in 1994 and named Fiberdrain [2]. They were used in seaward runway construction in Singapore. Later, jute drains also developed in India and named PJVD or Prefabricated vertical Jute Drains and modified into braided sheath (filter) named as Brecodrain [3] which prioritizes the efficient manufacturing stage and withstand buckling very well [4], [7]. In Srilanka jute PVD named as VFD or Vertical Fiber Drain [8]. In Indonesia the development of jute drains began in 1990s and applied in reclamation, road and highway project.

Studies related to natural fibers was conducted on a laboratory scale to find the most suitable material for PVD by varying materials, geometry and configuration to obtain model with best technical performance.

METHODOLOGY

In this study, the parameters that determine the specifications of the natural drains are described. If referring to [5], then all tests refer to EN ISO standard of testing, although some of samples are also tested using ASTM standard. Fifteen drain models were evaluated using the variations shown in Table 1. The materials used are coconut fiber for core and jute sheath for filter, webbing density 5,6 and 7,8 weft thread per inch, number of filter layers are 1 and 3, numbers of coir rope are 3 and 6.

Drain width are 6 cm, 9 cm, 9,5 cm and 10 cm. Four last model variation (Model 6) were made from coconut coir core and recycled synthetic fibers to compare their performance.

Table 1. Drain models and testing standard

Property	Model name	Testing Standard
Drain composite		
Width	Model 1	EN ISO 9863-1
Thickness	Model 1-a	EN ISO 9863-1
Tensile strength in longitudinal direction	Model 1-b Model 1-c	EN ISO 10319
Elongation at maximum tensile force	Model 1-d Model 1-e Model 1-f	EN ISO 10319
Discharge capacity, straight	Model 1-g Model 1-h Model 3 Model 6	EN ISO 12958
Drain filter	Model 6a Model 6b	
Width	Model 6c	EN ISO 9863-1
Mass per unit area	Model 6d	EN ISO 9864
Pore size, O_{90}		EN ISO 12956
Velocity index (vh_{50})		EN ISO 11058
Tensile strength in longitudinal direction		EN ISO 10319
Tensile strength in cross direction		EN ISO 10319

Natural Drain Characteristic

At the beginning, materials tested for drain filter were woven jute fiber and woven hemp fiber, whilst material for drain core are coconut fiber and non woven jute. Visually, hemp fiber is finer and has higher density than jute. Hemp has pore opening size of ± 0.1 mm (Fig. 1b), while jute has larger pore opening size of ± 0.5 mm as presented in Figure 1c.

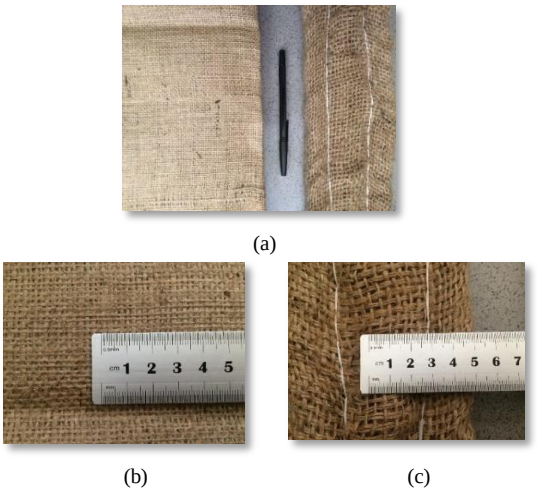

(a) (b) (c)

Fig. 1 Visualization of studied PVD: (a) comparisan between hemp (left) and jute (right) weaving; (b) density of hemp fiber ±0,1 mm; (c) density of jute fiber ±0,5 mm.

The opening size of hemp is more uniform than jute. Nevertheless, jute fibers are rougher, thicker and have higher tensile strength. Furthermore, only jute fibers were studied. Because coconut fiber raw material is easy to obtain while non-woven jute is not, then only coconut fiber is studied as PVD core material.

Drain Properties

Required testing parameters for synthetic PVD refers to European standards [5] are only tensile strength, seam strength, in-plane water flow capacity in straight and buckled conditions, opening size and elongation. Testing of tensile strength, grab strength, puncture strength and tear strength of drain filter are not required because they are not determinant of performance.

For natural PVD, as reviewed by [3] in [6] and by [10], the determinant parameters of performance are thickness at confining pressure of 20 kPa, mass per unit area, tensile strength and elongation, opening size, permeability, and drainage capacity. If referring to the EN ISO standard, testing the strength of the PVD filter (pull, grab, puncture, tear) are not required.

Study by [2] examined the components that need to be considered in testing natural drains, i.e. thickness, compressibity, tensile strength and durability. The measurement of thickness of coconut coir and jute filter revealed that thickness did not change after being tested for 30 seconds. Meanwhile, the thickness of non-woven coconut fiber and hemp filter showed no change after 60 seconds. By following ASTM D 5199-01 (2006) and/ or EN ISO 9863-1990, it is recommended to measure the thickness drains at the end of 60 seconds, after giving a normal load of 2 kPa.

Compressiblity

The results of the study from [2] shows that non-woven coconut coir has maximum compressibility, while woven coconut coirs have lower compressibility. The woven jute or hemp are more compressible than the woven coconut coir . However, it should be noticed that when testing woven fibers, compressibility can drop drastically to below 6 kPa.

Tensile Strength

From several related studies of tensile strength, it was summarized that for geotextiles made from woven natural fibers, width-length ratio of specimen does not affect the tensile strength. If the width is left constant and the length is changed, then strain will experience a linear variation.

The test speed between 2 mm/minute to 300 mm/minute does not have a significant effect on the strength and strain of natural fibers. While the test

speed below 2 mm/minute results decreasing in strength and strain. On the contrary at test speed above 300 mm/minute increases slightly. This makes the natural fibers different from synthetic.

For soaked test specimens, strength will decreases and strain increases.

Durability

Research by [1] on the durability of coconut coir and jute forms was carried out at controlled temperatures and humidity. The effects of variations in pH values, salt water, wet-dry processes, soil types (sand and clay), organic content in the soil, and installation in different climatic conditions were examined. The results revealed that design life of coconut coir is more than a year, while jute had two or three years. Durability test can be carried out by grab test, immersion in acid solution (pH = 3), alkaline solution (pH = 12) or kept in clay soil in a separate containers. Core and filter are tested separately.

RESULTS AND DISCUSSION

Development of Specification of Natural PVD

Studies are made for 15 natural PVD models with variation and testing standard explained in Table 1. As a comparison, the test results of more than 20 specimens of synthetic PVD were also evaluated. Synthetic PVDs are made of polypropylene material, polypropylene-polyethylene, polyolefin and high-density polyethylene (HDPE). Figure 2 and Figure 3 compares the characteristics of natural PVD with synthetic PVD when testing discharge capacity refers to EN ISO 12958 (Geotextiles and geotextile-related products - Determination of water flow capacity in their plane) measured at 20 kPa, 100 kPa, 250 kPa and 350 kPa confining pressure and hydraulic gradients of 0,1 and 1,0.

From the relationship between dicharge capacity and confining pressure during the test, it was known that discharge capacity of both type decreased as pressure increasing. Discharge capacity of synthetic PVD is 10 times greater than natural PVD. PVD with non woven jute core (Model 3) has the largest value because the core has greater capillary than coconut fiber.

Discharge capacity of natural PVD tested in i = 1,0 and 20 kPa (low confining pressure) ranged between 0,0568 to 0,3040 litre/m.sec, in 350 kPa confining pressure ranged between 0,0027 to 0,0242 litre/m.sec. Synthetic PVD tested in i = 1,0 and 350 kPa confining pressure ranged between 0,050 to 0,240 litre/m.sec.

As reviewed by [11] the difference between discharge capacity from different studies are understandable because of the varying drain models and testing apparatuses. However, in all case, discharge capacity tend to reduces significanly as the confining pressure increases.

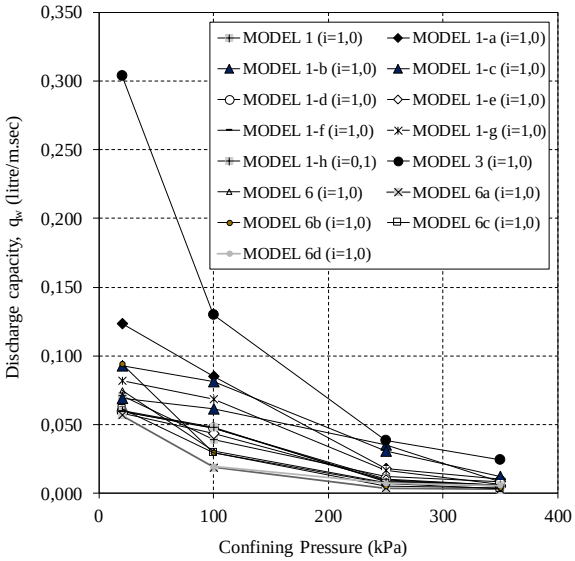

Fig. 2 Relationship between confining pressure and discharge capacity of natural PVD models tested in hydraulic gradients 1,0.

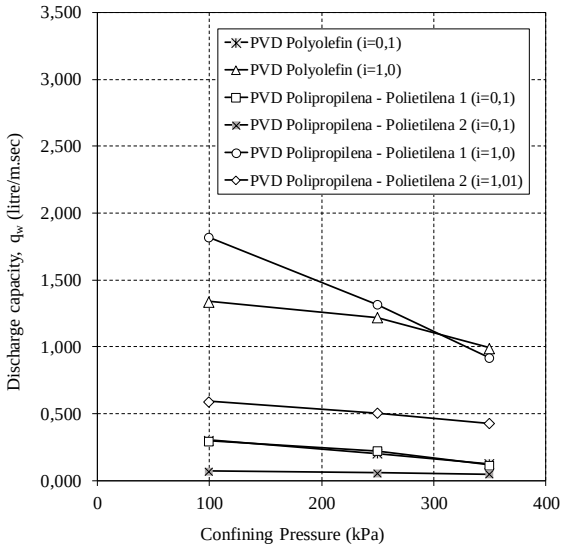

Fig. 3 Relationship between confining pressure and discharge capacity of synthetics PVD models tested in hydraulic gradients 1,0.

The low value of discharge capacity of natural drains analyzed due to sample placed horizontally, not vertically while tested which is against the ability of natural drain capillary forces. Natural fiber relies to its capillary, so testing a sample in a vertical position and confined with soil is recommended.

Tensile strength of PVD in machine direction and tensile strength of PVD filter in machine and cross-machine direction are three requirements for testing

synthetic PVD in the laboratory referring to EN ISO 10319. Figure 4 and Figure 5 shows relationship between discharge capacity and tensile strength of natural PVD and synthetic PVD.

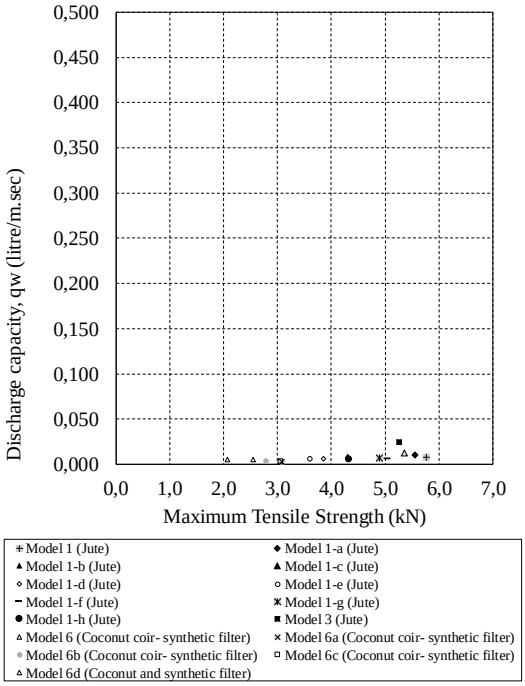

Fig. 4 Relationship between maximum tensile strength and discharge capacity of natural PVD models.

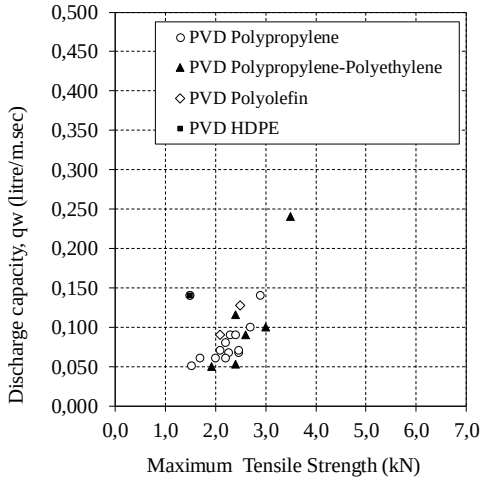

Fig. 5 Relationship between maximum tensile strength and discharge capacity of synthetic PVD models.

Required strength of synthetic PVD filters ≥ 3 kN/m, while for PVD installation depth > 25 m and in soft soils, required cross-machine direction strength is ≥ 6 kN / m [5]. Tensile strength of natural PVD ranged between 3,5 to 6,0 kN/m and the combination with synthetic filter ranged between 2,0 to 5,8 kN/m (requirements ≥ 1,5 kN/m), whilst synthetic PVD ranged between 1,5 to 3,5 kN/m. If correlated with field construction, jute PVD will have sufficient tensile strength to prevent the materials from damage during installation and during their design life.

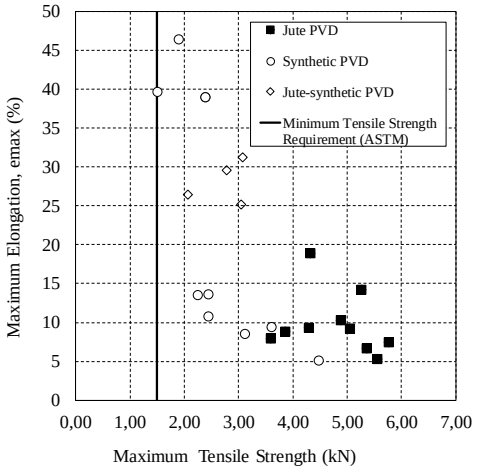

Fig. 6 Relationship between maximum tensile strength and maximum elongation of PVD.

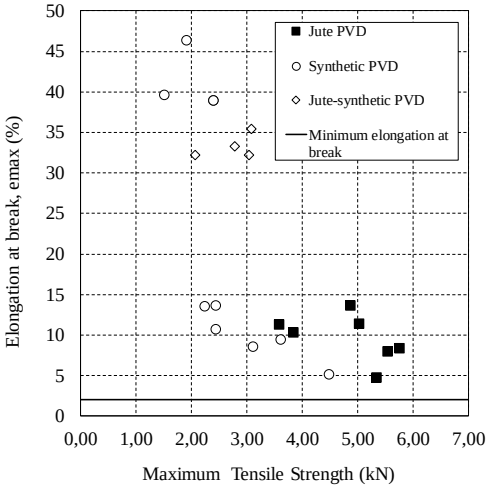

Fig. 7 Relationship between maximum tensile strength and elongation at break of PVD.

Maximum elongation and elongation at-break refers to EN ISO 10319 are presented in Figure 6 and Figure 7. Elongation at-break requirement for synthetic PVD is ≥ 2% on the weakest element and ≤ 10% in testing pressure of 0,5 kN. Minimum tensile strength required is > 1,5 kN on the weakest element and PVD structures are not allowed to break (BS EN 15237-2007).

From Figure 5, it was found that maximum elongation of natural PVD ranged between 3,5 to 5,5%, whilst natural PVD combined with synthetic filter ranged between 2,0 – 3,2%. Maximum elongation of synthetic PVD ranged between 1,5 to 4,5%, lower that natural PVD.

It can be concluded that in terms of mechanical

and hydraulic properties, natural PVD (jute PVD) has good tensile strength and elongation performace despite its lower disharge capacity value when tested with geosynthetics testing apparatus in the laboratory.

Thickness and mass per unit area refers to EN ISO 9863-1. The thicker and heavier filter material, the higher cost of preparing raw material. Figure 8 presents relationship between PVD thickness and amout of discharge capacity. To increase efficiency, it is recommended to use models that have moderate discharge capacity but less thick. the thickness ranged between 5 to 10 mm. Mass per unit area ranged between 150 to 350 gram/m'. Figure 9 presents the results.

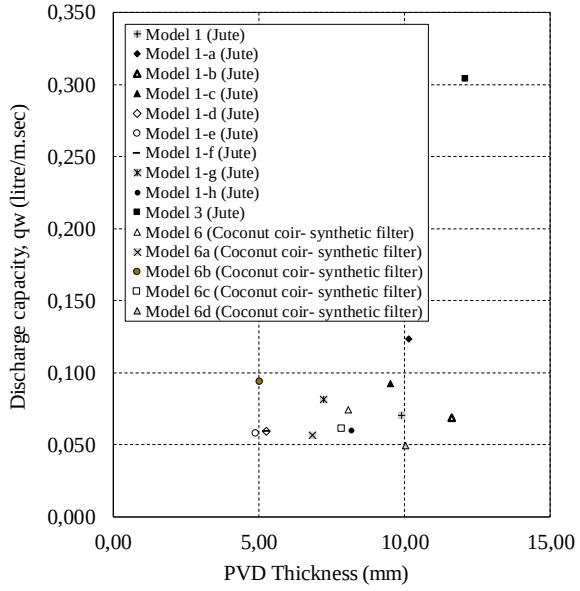

Fig. 8 Relationship between PVD thickness and discharge capacity.

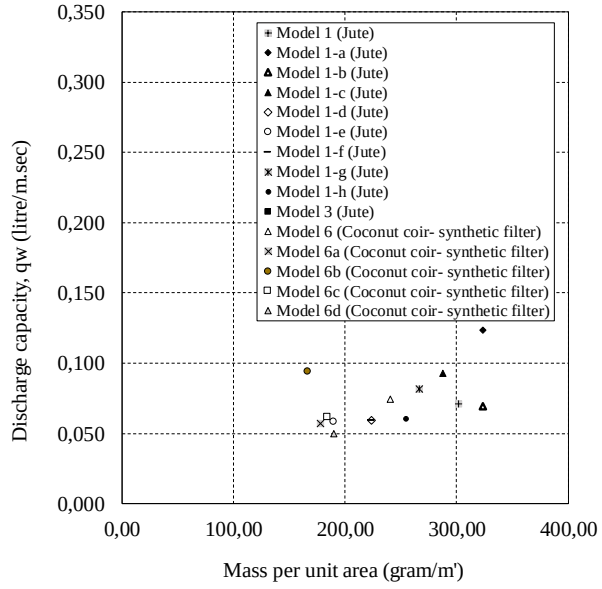

Fig. 9 Relationship between mass per unit area of PVD and discharge capacity.

Last parameter observed is velocity index, refers to EN ISO 11058 (Fig. 10). It was found that vh50 of natural PVD and PVD with recycled synthetic filter are ≥ 1 mm/sec. Value of vh50 ranged between 27 to 120 mm/sec. The greater filter pore size, the higher vh50. Table 2 summarized the overall results of the tested natural PVD compared with synthetic PVD specifications

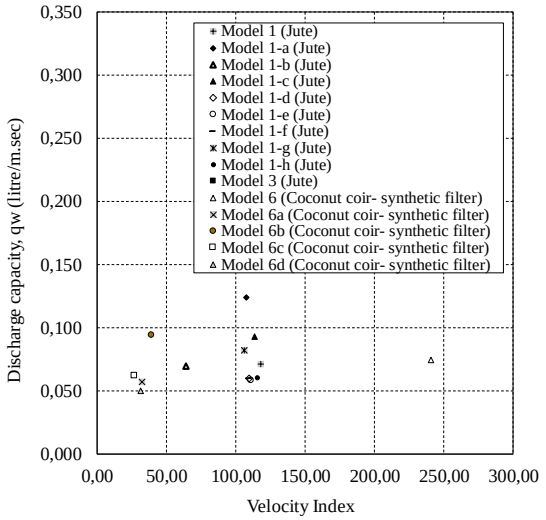

Fig. 10 Relationship between velocity index and discharge capacity.

CONCLUSION

Laboratory test results summarized that PVD model with the best performance is Model 1h with 1 layer of jute, 6 ropes of coconut fiber and filter webbing density of 5,6 feed / inch). The model gives high tensile strength and velocity index but lower mass per unit area an thickness so that it is still efficient. However discharge capacity of natural PVD is relatively lower than synthetic PVD, possibly due to placement of sample in testing apparatus is against capillarity force of natural fibers.

Testing of natural PVD needs to be accompanied by special procedures for sample preparation and initial conditioning (soaking the sample) before tested. If natural PVD is retested, the result will not similar with previous test because natural fibers are inhomogeneous.

Compared with specification for synthetic PVD, some values meet specifications, but some are differ from synthetic PVD, therefore the testing standard and minimum value of natural PVD should be made separately.

Testing in a large-scale radial consolidation apparatus in the laboratory which confined with soils, is highly recommended rather than tested in-plane water flow capacity apparatus.

Table 2. PVD Specifications

Testing properties	Specification of Synthetics PVD (ASTM)		Specification of Synthetics PVD (BS EN 15237, 2007)		Proposed specification (obtained from this study	
	Value	Test method	Value	Test method	Value	Test method
Composite						
Tensile strength	≥ 1500 N (≥ 1,5 ken)	ASTM D 4595	> 1,5 kN, longitudinal direction	EN ISO 10319	> 2,0 kN	EN ISO 10319
Tensile strength at elongation ≤10%	≥ 1300 N (≥ 1,3 kN)	ASTM D 4595	Not required	-	Not required	
Seam strength		-	≥ 1 kN/m	EN ISO 10321	Not required	
Type of polymer	PP / PET	-			Jute, Coconut Coir	
Width	100 ± 5 mm	ASTM D 3774	-	EN ISO 9863-1	60 – 100 mm	EN ISO 9863-1
Thickness	2,5 - 5,0 mm	ASTM D 5199	-	EN ISO 9863-1	7,0 – 17 mm	EN ISO 9863-1
In-plane water flow capacity, *straight*	≥ 1 x 10^{-6}	ASTM D 4716	As designed	EN ISO 12958	As designed	EN ISO 12958
In-plane water flow capacity in 200 kPa, *buckled*	-	-	As designed	EN ISO 12958	As designed	N/A
In-plane water flow capacity in100 kPa, *buckled*	-	-	-	-	As designed	N/A
Elongation at maximum tensile force (at-break)	-	-	≥ 2%	EN ISO 10319	≥ 3,5%	EN ISO 10319
Elongation at 0,5 kN	-	-	≤ 10 %	EN ISO 10319	≤ 10 %	EN ISO 10319
Filter						
Tensile strength	≥ 4 N	ASTM D4595			≥ 4 N	EN ISO 10319
Grab strength	≥ 330 N	ASTM D 4632	-	-		
Puncture strength	≥ 100 N	ASTM D 4833	-	-		
Tear strength	≥ 100 N	ASTM D 4533				
Opening size, O_{90}	-	-	80 μm	EN ISO 12956	> 300 μm	EN ISO 12956
Opening size, O_{95}	50 – 90 μm	ASTM D 4751	-	-		
Permeability	≥ 1 x 10^{-4} m/sec	ASTM D4491	-	-		
Tensile strength	-	-	3 kN/m*	EN ISO 10319	≥ 3 kN/m	EN ISO 10319
Velocity index (vh_{50})	-	-	1 mm/sec	EN ISO 11058	26,8 – 117,75 mm/sec	EN ISO 11058

For further development, the influence of soil clogging on the discharge capacity of natural PVD should be examined, due to jute filter opening size could not prevent soil penetrating into internal part of PVD at larger load increments.

REFERENCES

[1] Balan, K. Venkatappa, R.G., Durability of Jute Fabric. Proc. Int. Seminar and Technomeet on Environmental Geotechnology with Geosynthetics (Eds). ASCE/CBIP, New Delhi,1996, pp348-357.

[2] Balan, K., Natural Fibres in Geotechnical Engineering, Journal of Research Innovations in Engineering and Technology Issues 2 Volume 2, ISSN 2321- 6603, July – Desember 2015.

[3] Banerjee, P.K., Characteristics of the Brecodrain for Soft Soil Consolidation, Proc. Geosyn. Asia'97, Bangalore, 1: VI. 3–24.1997.

[4] Banerjee, P.K., Kumar, J.P.S., Production Method and Characteristics of Braided PVD, Indian Journal of Fibre and Textile Research Vol. 25, September 2000, pp. 182 – 194.

[5] BSI, Execution of Special Geotechnical Works – Vertical Drainage, BS EN 15237:2007, British Standard, United Kingdom, 2007.

[6] Ghosh, M., Choudhury, P.K., Suitability of Natural Fibres In Geotextile Applications. IGC 2009, Guntur, India. 2009.

[7] IJIRA. Project Completion Report. Manufacture of Jute Braided Cloth by Appropriate Design Incorporation in Braiding Machines. Jute Technology Mission (Mini-mission IV, DDS 7.1), Project No. 4. Indian Jute Industries Research Association, 2008.

[8] Intercoirlanka. Vertical Fiber Drains (VFD's). http://www.intercoirlanka.com/geo-textiles/2016/9/2/vertical-fiber-drains. 2017.

[9] IRE, Geoguide 1 Occurrence and General Nature of Soft Soils, Road Embankment on Soft Soils, Institute of Road Engineering. November 2001.

[10] Khan, A.J., Performance of A Prefabricated Vertical Jute Drain In A Remolded Soft Soil, Proc. of Bangladesh Geotechnical Conference. 2009.

[11] Nguyen, T.T., Indraratna B., Carter, J.P., Influence of Soil Clogging on the Performance of Jute Fibre Drains in Ballina Clay, 13th ANZ Geomechanics, Australia New Zealand Conference on Geomechanics, Perth, 1-3 April 2019.

9th Int. Conf. on Geotechnique, Construction Materials and Environment, Tokyo, Japan, 20-22 November 2019, ISBN: 978-4-909106025 C3051

EVALUATION OF ELASTIC AXIAL STIFFNESS REFERS TO TENSILE STRENGTH TESTING OF GEOGRIDS AND NON-WOVEN GEOTEXTILES

Dea Pertiwi[1] and Fahmi Aldiamar[1]
[1]Institute of Road Engineering (IRE), Bandung, Indonesia

ABSTRACT

Over the last several years geosynthetics are widely used for soil reinforcement in many cases of embankment over soft soil material or steep slope construction. Mechanisms of reinforcement that expected are lateral resistance through friction between geotextile and soil/aggregate and reducing the potential bearing surface failure plane to develop higher surface shear strength. In design phase, reinforced slopes are currently analyzed using modified limit equilibrium slope stability methods, while for complex cases numerical model is commonly used for determining required tensile strength within factor of safety assigned in the design requirements. In most cases, elastic axial stiffness (E.A.) as input parameter in finite element method is determined from typical strain distribution of geogrids or non-woven geotextiles in soil foundations, with the value less than 2%, which are provided by manufacturers and assumed to be linear elastic. To confirm those assumptions, several tensile strength test of geogrids and non-woven geotextiles are conducted according to ASTM D4595-17 procedures. Proposed elastic axial stiffness and typical strain distribution for numerical model described in this paper to guide the designer for selecting proper input design parameter.

Keywords: Non-woven geotextiles, Geogrids, Soil reinforcement, Elastic axial stiffness, Strain distribution

INTRODUCTION

Geosynthetics have been utilized in most of soil improvement techniques as a soil reinforcing systems to escalate the bearing capacity of the soil and reduce settlement. Geosynthetics are also commonly used as separator, filtration, drainage, erosion control and even shore protection. For separator purposes, requires high tensile strength geosynthetics whilst for erosion control requires high permeablity geosynthetics. Many types of geosynthetics are available in the engineering process (geogrid, geotextile, geocell, geomembrane, etc.).

Required tensile strength within factor of safety assigned in the design requirements are often analyzed using numerical models to simplify the complexity of calculations. Elastic axial stiffness (E.A.) as input parameter in finite element method is assumed from typical strain distribution of geogrids or non-woven geotextiles with the value less than 2% which are provided by manufacturers and assumed to be linear elastic [2]. For non-woven fabrics. However, generalization or assumption should not made for determining E.A. due to different properties of geosynthetics used in the design.

METHODOLOGY

Several studies showed that geosynthetics were applicable as reinforcement, particularly in embankment over soft soil. Most of them designed with numerical model using finite element method due to calculation complexity. However parameter that often used is ultimate tensile strength, whilst strain or elongation parameters rarely considered in the design or decided based on asumption, as mentioned in [1], [2], [4] and [10]. In Plaxis reference manual geotextile is introduced as a tensile element i.e. E.A [5]. To avoid using assumptions in determining the value of E.A a number of tensile strength data from laboratory Wide-Width Tensile Test (ASTM D 4595/ISO 10319) results of geosynthetic non woven and geogrid were collected and studied. By using a correlation between maximum tensile strength and elongation at break in machine (MD) and cross-machine direction (CMD), axial stiffness or E.A. can be calculated using Eq. (1) [5].

$$EA = \frac{F}{\Delta l / l} \qquad (1)$$

The axial stifness is the ratio of the axial force (F) per unit width and the axial strain ($\Delta l/l$). l is grip to grip separation at the start position of testing. Δl is the elongation, derived from the difference between length of sample after being pulled and l.

Then using a simple embankment model, finite element modeling was carried out with varied E.A. and tensile strength parameters of geogrid and non-woven geotextiles in order to provide guidance for designer to select proper input of E.A. parameter particularly in numerical analysis.

Geosynthetics Properties

Geogrids and non-woven geotextiles are flexible elements with a normal stiffness and no bending stiffness [5]. Maximum tensile strength (F_{max}) parameters from Wide-Width Tensile Test were used to calculate E.A. use Eq. (1). Geogrids are open grid-like materials of integrally connected polymers and are stronger than most geotextiles. Compared to geotextiles, geogrids have low strain. However, it can withstand heavy tension loads without much deformation [7]. Geogrids evaluated in this study were uniaxial and biaxial as shown in Fig. 1c.

Geotextiles are defined as permeable textile used with foundation soil, rock, earth, and any other. There are two types of geotextiles, i.e. woven and non woven geotextiles.Woven geotextiles are cloth-like fabrics, and tend to have high tensile strength but relatively low strain compared to non-woven geotextiles [6]. Non-woven geotextiles studied in this paper were PP (Polypropylene) as shown in Fig.1a and PET (Polyethylene) as shown in Fig. 1b that assemblied by mechanically-bonded, needle-punched or thermal-bonded methods.

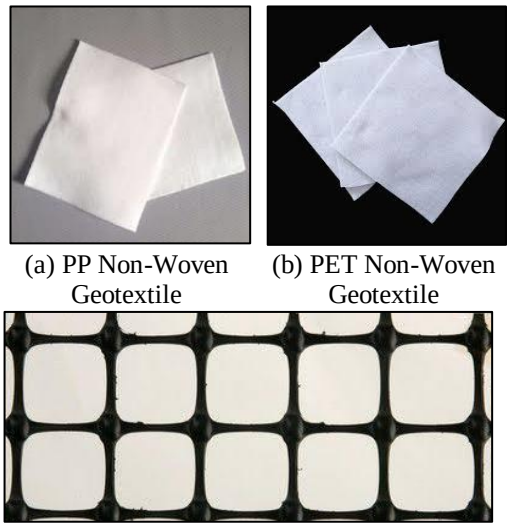

(a) PP Non-Woven Geotextile (b) PET Non-Woven Geotextile

(c) Geogrid

Fig. 1 Types of geosynthetics used in study.

Figure 2 and Fig. 3 each shows the relationship between normal force and strain from a number of geogrids and non-woven geotextiles data from laboratory test results of Wide-Width Tensile Strength referring to [3] and [9]. The graphs informed that different types of geotextiles and geogrids yields different strain pattern and have different maximum strain. Therefore tensile strength for design should not obtained at ultimate (T_{max}) and at 2% strain as stated in [1], but also at maximum strain (ε_{max}). Although for non-woven geotextiles the axial stiffness is usually not considered since these elements typically served at separating layers [8], in this study, the parameters were evaluated and compared with geogrids.

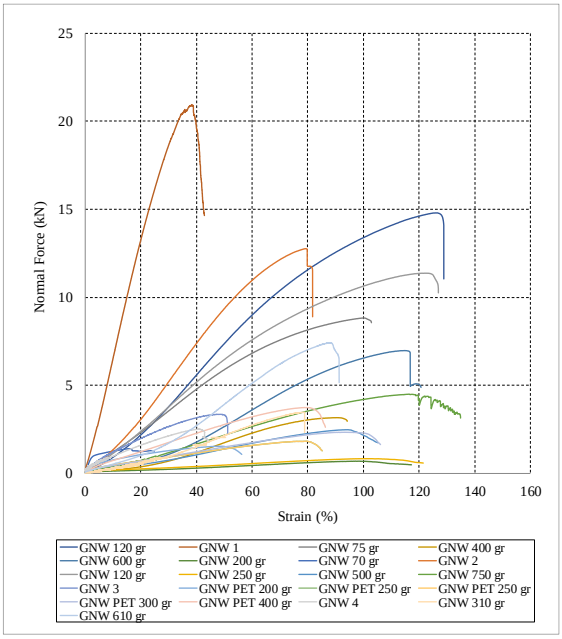

Fig. 2 Strain and force relationship of non-woven geosynthetics.

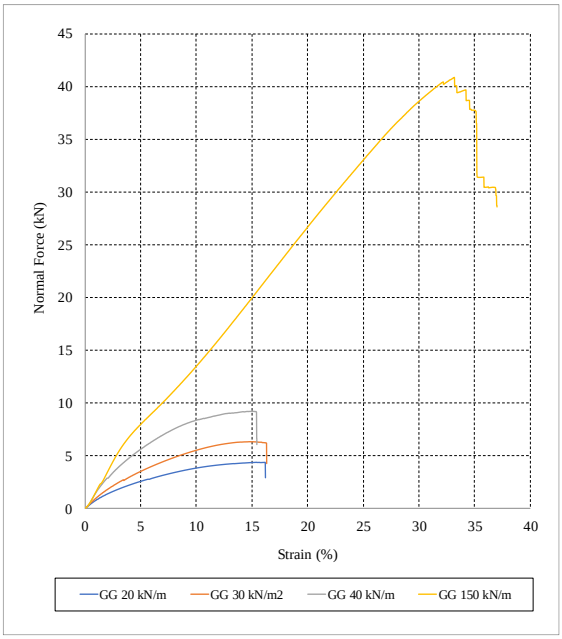

Fig. 3 Strain and force relationship of geogrids.

Finite Element Modelling

Geosynthetics modelling

Geogrids are used to model soil reinforcements, whilst non-woven geotextiles are used to model soil

separator or filtration. Both was modeled using elastoplastic constitutive model with the parameters elastic axial stiffness, E.A. and maximum axial force, N_p entered in units of force per unit width. N_p also is ultimate tensile strength of the geosynthetics.

Embankment modelling

The 2 m embankments with 1,5H : 1V slopes as presented in Fig. 4 was evaluated in this study. The water level was at 0,00 level (critical condition). A surcharge of 12 kN/m^2 has been used for modelling the traffic load. As the model is symmetric with respect to center line, half of the embankment is modeled in analysis. The numerical modeling using commercial Finite Element Method (FEM) package (PLAXIS version 9) is employed for performing the analyses.

In the first model safety factor of road embankment without geosynthetic placed between the base of embankment and overlaying clay layer evaluated. After that, placement of PP Non Woven Geotextile, PET Non Woven Geotextile and Geogrid at base of embankment (Fig. 4) conducted to evaluate increase of safety factor and also displacement on each of geosynthetic in horizontal and vertical direction.

The material properties used for the model are presented in the Table 1. Model material used is Mohr-Coloumb, since it has been considered as a first order approximation of real soil behavior and main focus of research are stability of embankment.

Table 1 Soil parameters of underlaying layer and embankment

Soil parameters	Underlaying layer	Embankment
γ dry (kN/m^3)	14	18
γ wet (kN/m^3)	16	20
Young's modulus, E_{ref} (kN/m^2)	2.000	10.000
Poisson's ratio, ν	0,3	0,3
Cohesion, c_{ref} (kN/m^2)	5	10
Friction angle, ϕ (°)	20	30
Dilatancy angle, Ψ (°)	0,0	0,0

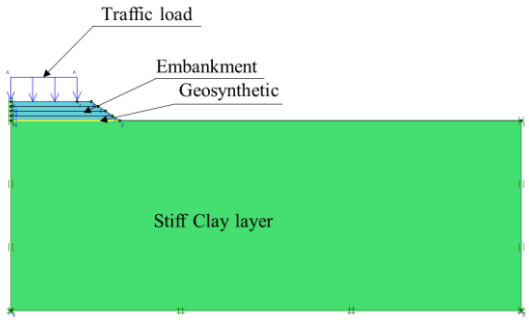

Fig. 4 Geometry model for evaluating effect of geotextiles and geogrid

RESULTS AND DISCUSSION

Figure 5a shows the relationship between E.A., calculated using Eq.(1) and maximum tensile strength of PP non woven geotextiles tested in Machine Direction (MD). The graph showed that EA and maximum tensile strength are linearly distributed. For tensile strength 0-10 kN, E.A. ranges from 50 - 400 while for > 10 kN E.A. ranges from 400 - 800. So when designing geotextiles as separators, E.A. entered as input parameters should be less than 800.

Figure 5b shows the relationship between E.A., calculated using Eq.(1) and maximum tensile strength of PP non woven geotextiles tested in Cross-Machine Direction (CMD).

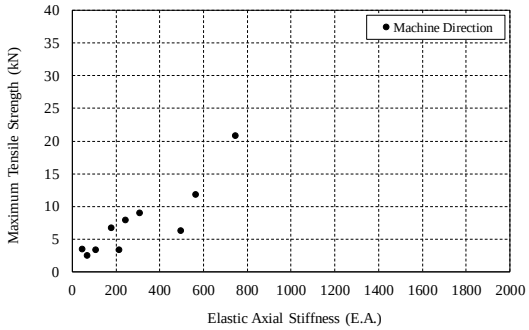

(a) Tested in Machine Direction

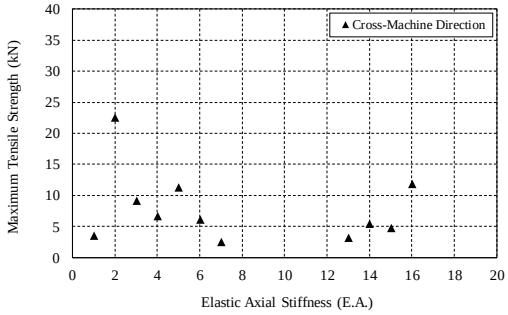

(b) Tested in Cross-Machine Direction

Fig. 5 Elastic axial stiffness (E.A.) and maximum tensile strength of PP non-woven geotextiles.

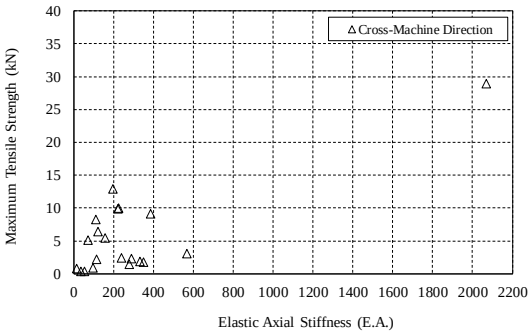

(a) Tested in Machine Direction

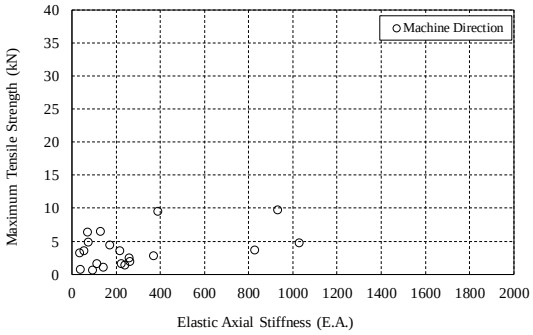

(b) Tested in Cross-Machine Direction

Fig. 6 Elastic axial stiffness (E.A.) and maximum tensile strength of PET non-woven geotextiles.

In contrast to the results of MD test, E.A. tend to have lower ranges i.e. 1 - 12 and uneven data distribution. Therefore it is recommended to use the results of the MD test for design, and because the installation of geotextiles in the field is at longitudinal direction.

The relationship between E.A and the maximum tensile strength for PET non-woven geotextiles shown in Fig. 6 explains that E.A. in MD test is twice higher than in CMD (transverse direction) However, there is a maximum tensile strength of non woven geotextiles which has a greater tensile strength when tested in MD. Compared with PP geotextile, PET geotextile has higher E.A. up to 1000 for maximum tensile strength up to10 kN.

Although geogrid data are less than non-woven geotextile data, Fig. 7 summarized that the distribution of E.A. to the maximum tensile strength of the geogrid is also linearly distributed. Geogrids tested in MD (Fig. 7a) tend to give the same tensile strength and E.A. distribution with those tested in the CMD (Fig. 7b), except for some types of geogrids that have higher tensile characteristics than the general type of biaxial geogrid.

From the data studied here, it can be concluded that for maximum or ultimate tensile strength up to 10 kN, E.A. ranged from 600 – 1600 and for ultimate tensile strength 15 – 35 kN, E.A could reached until 13000.

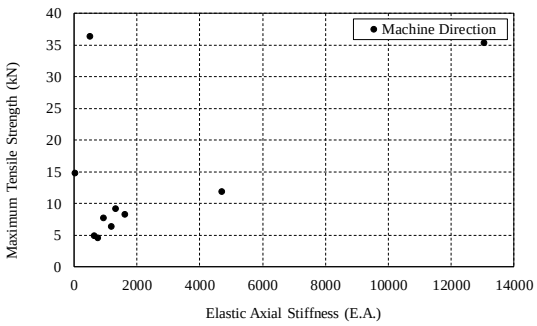

(a) Tested in Machine Direction

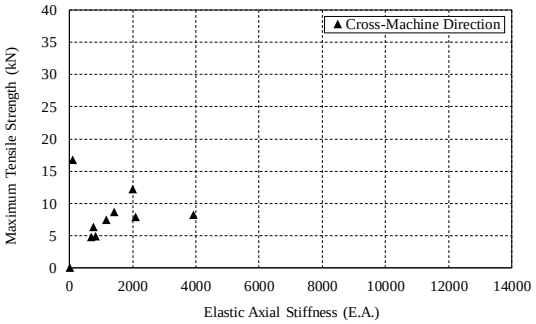

(b) Tested in Cross-Machine Direction

Fig. 7 Elastic axial stiffness and maximum tensile strength of geogrid.

Figure 8 showed that the design with geogrid should enter the input value of E.A. which is quite high. Since the laboratory result for geogrids with high tensile strength (tensile strength > 20kN) are limited, E.A. value resulting a lower result than equation approach. This may lead to unrealistically E.A. value that could lead error result when using geogrid elastoplastic model.

Assesment the effect of geosynthetics layers

To assess the effect of geosynthetics layer on road embankment, 4 type of FEM condition namely road embankment without geosynthetic, using PP and PET non woven geotextile and also geogrids conducted using different elastic axial and ultimate tensile strength parameter as seen in Table 2. Each of FEM model resulting on increase of safety factor in accordance to increase of tensile strength used (Fig. 9). Increase of tensile strength also effectively reduce horizontal displacement acting on geosynthetics (Fig. 10).

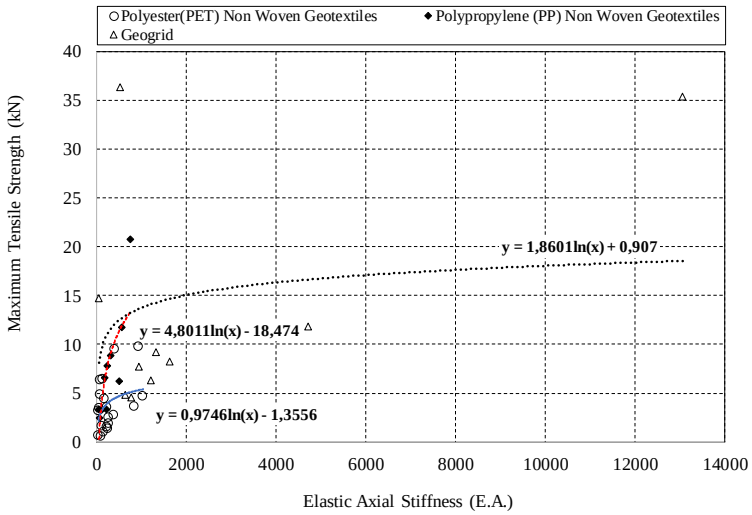

Figure 8. Equation approach for determining E.A. from laboratory tensile strength test of non-woven geotextiles and geogrids

PP and PET non woven geotextile for separator purpose had relatively small tensile strength (less than 20 kN) which resulting in small increase of safety factor and relatively large horizontal displacement, while geogrids using 25 kN and 35 kN resulting higher safety factor and smaller horizontal displacement (Table 2). Vertical displacement for each model resulting a similar result which mean that for this case, increase of tensile strength did not influence the vertical displacement of geosynthetics.

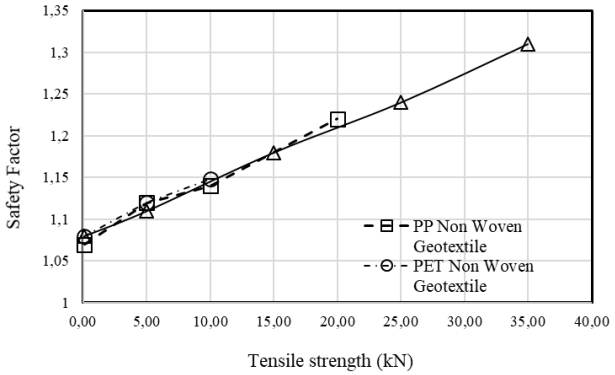

Fig. 9 Result of safety factor and increase of tensile strength

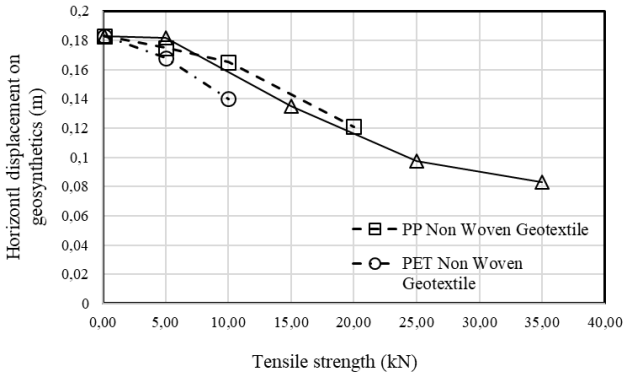

Fig. 10 Result of horizontal displacement on geosythetics and increase of tensile strength

Result of stability analysis (Fig. 11) showed a circular failure deformation mechanism and position of geosynthetic that placed between embankment and original ground are cut off the circular failure plane. Position of geosyntetic for embankment reinforcement is critical to be observe due to the misplaced of it could resulting in ineffective use of soil reinforcement.

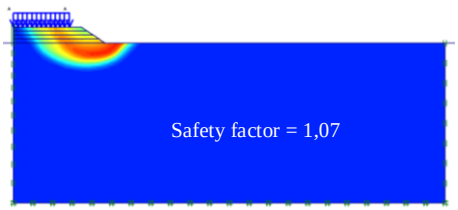

(a) FEM model without geosynthetic

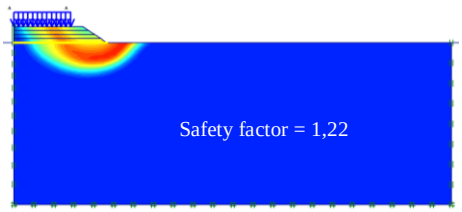

(b) FEM model using PP Non Woven Geotextile 20 KN/m

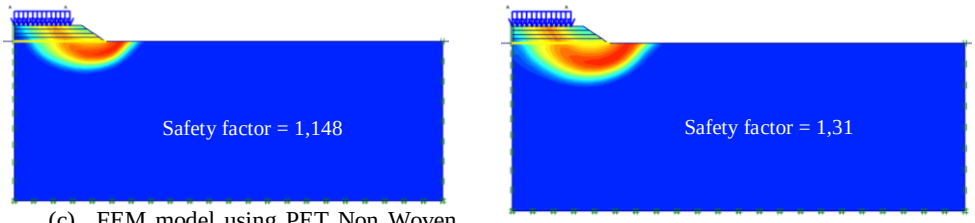

(c) FEM model using PET Non Woven Geotextile 10 kN/m

(d) FEM model using Geogrids 35 KN/m

Figure 11. Stability analysis using FEM according to each model variation

Table 2 Results of simulation and proposed E.A for design

Condition	Ultimate tensile strength (kN)	Elastic Axial (E.A.) Stiffness modeled Refers to Eq. 1	Height of embankment (m)	Traffic load (kPa)	Safety Factor	Horizontal displacement of geosynthetic (m)	Vertical displacement of geosynthetic (m)
Without Geosynthetic	-	-	2	12	1,07	-	-
PP Non Woven Geotextile	0,10	47,879	2	12	1,07	0,183	0,435
	5,00	132,860	2	12	1,12	0,175	0,437
	10,00	376,427	2	12	1,14	0,165	0,438
	20,00	3.021,716	2	12	1,22	0,121	0,425
PET Non Woven Geotextile	0,10	4,453	2	12	1,08	0,183	0,435
	5,00	679,419	2	12	1,12	0,168	0,433
	10,00	114.869,198	2	12	1,148	0,14	0,424
Geogrids	0,10	0,648	2	12	1,08	0,183	0,435
	5,00	9,029	2	12	1,11	0,182	0,435
	15,00	1.951,736	2	12	1,18	0,135	0,428
	25,00	421.902,462	2	12	1,24	0,0976	0,416
	35,00	91.201.735,520	2	12	1,31	0,0828	0,418

CONCLUSIONS

Numerical model using FEM for several model of geosynthetic use for road embankment show a good result and increase of ultimate tensile strengh resulting increase of safety factor and also reduce horizontal displacement.

Proposed elastic axial stiffness and typical strain distribution for numerical model described in this paper are expected to guide the designer for selecting proper input design parameter. Hence, result gained from this research are basically customized for specific type of geogrid. Evaluation for non woven or geogrid material with different characteristics should be conducted to evaluate their behaviour.

REFERENCES

[1] Abu-Farsakh, M., Coronel J, Tao M., Effect of Soil Moisture Content and Dry Density on Cohesive Soil–Geosynthetic Interactions Using Large Direct Shear Tests. Journal of Materials in Civil Engineering ASCE, July 2007, pp 540 – 549.

[2] Abu-Farsakh, M., Chen, Q., Sharma, R., and Zhang, X., Large-Scale Model Footing Tests on Geogrid Reinforced Foundation and Marginal Embankment Soil, Geotechnical Testing Journal, Vol. 31, No. 5, 2008, pp. 413-423.

[3] ASTM D 4595, Standard Test Method for Tensile Properties of Geotextiles by the Wide-Width Strip Method, American Society for Testing and Materials, 2017.

[4] Bergado D.T., Teerawattanasuk C, 2D and 3D Numerical Simulations of Reinforced Embankments on Soft Ground, Geotextiles and Geomembranes 26, 2008, pp. 39-55.

[5] Brinkgreve R.B.J, Broere W., Plaxis 2D – Version 9.0 Part 2 Reference Manual, ISBN-13:978-90-76016-06-1, 2008, pp. 3.56.

[6] Brown, L., Geosynthetics Materials: What Are They? How Are They Used?, Abbotsford, British Columbia, Ministry of Agriculture and Lands. 2006.

[7] FHWA, Geosynthetics Reinforced Steep Slopes, FHWA/TX-14/0-6792-1, Federal Highway Administration, March 2016, pp 43.

[8] Fine Software, Axial Stiffness of Geosynthetics, https://www.finesoftware.eu/help/geo5/en/axial-stiffness-of-geosynthetics-01/.

[9] ISO 10319:2015, Geosynthetics - Wide-Width Tensile Test, International Organization for Standardization, 2015.

[10] Siavoshnia M., Kalantari F., Shakiba A., Assesment of Geotextile Reinforced Embankment on Soft Clay Soil, The 1st International Applied Geological Congress, Department of Geology Islamic Azad University – Mashad Branch, Iran, 26-28 April 2010

9th Int. Conf. on Geotechnique, Construction Materials and Environment, Tokyo, Japan, 20-22 November 2019, ISBN: 978-4-909106025 C3051

NUMERICAL AND ANALYTICAL STUDY OF STABILITY OF AN EXISTING MULTI-LAYERED ROADSIDE SLOPE WITH THE VALIDATION BY A PHYSICAL MODEL

Nishat Nawal[1], Monjurul Mozid[2], Md. Ibrahim Khalil Porag[3], S.K. Tamheedul Islam[4] and Hossain Md Shahin[6]

[1,2,3,4]Graduated student, Department of Civil Engineering, MIST, Mirpur Cantonment, Dhaka-1216, Bangladesh.
[6] Professor, Department of Civil Engineering, IUT, Board Bazar, Gazipur, Bangladesh.

ABSTRACT

This study focuses on the stability analysis of an existing roadside slope near Mirpur Cantonment area, Dhaka. Both numerical and analytical approach was adopted to examine the roadside slope against failure. For numerical analysis, Plaxis 2D was used [1][2]. Mohr-Coulomb failure criteria was adopted as the material model for various layers of the slope. Analytical studies were conducted following the limit equilibrium method [3] as stated by Bishop [4], Fellenius [5] and Janbu [6] using the GEO 5. To obtain the parameters undisturbed samples were collected with boring and triaxial drain tests, consolidation tests and other laboratory tests were conducted. To visualize the failure pattern and validate the numerical model and analytical study, a physical model test was carried out. The two layered physical model was constructed with a slope angle similar to the existing roadside slope using same soil of the site. It was observed from the numerical simulation and analytical analysis that slope starts to fail at an angle of 45^0. This phenomenon is also validated by the observation from mobilized section of the slope in the physical model in saturated condition.

Keywords: Slope stability, Mohr-Coulomb Failure criteria, Limit equilibrium analysis, Plaxis 2D, GEO 5, Physical model.

INTRODUCTION

From geological and geographical point of view, Bangladesh is intensely vulnerable for slope failure for many reasons. In present time, the country is facing problems regarding slope failure which has become a common phenomenon. This project work was based on the stability analysis of a connecting road which is vulnerable due to heavy vehicle movement and also for the landslide because the road is surrounded by a lake in both sides. So, this road is prone to failure because of the buoyancy effect due to the pore water pressure generated at the slope.

METHODOLOGY

Digital survey was carried out at the first stage to determine the existing soil profile. Soil samples were collected from selected road side slope area. A borehole was set at a depth of 48 feet and six samples were collected from the borehole at an interval of 8 feet. Various laboratory tests were conducted by the procedures specified in ASTM standard, such as Grain size analysis (ASTM D422-63), Atterberg limit (ASTM D 4318-00), specific gravity test by water pycnometer (ASTM D 854-02), Hydrometer analysis, triaxial test, consolidation test, direct shear. Sub-soil characteristics of the slope were determined based on these test results.

To observe the failure pattern and comparison between analytical and numerical analysis and also for evaluating the stability of the slope in terms of factor of safety, a small-scale physical model was constructed in two layers, the same as in existing slope in the site. It consists of silty sand layer at bottom and clayey silt layer at top. Tests were carried out with two slope angles of 30^0 and 45^0.

Figure1: Small scale physical model for 30° slope

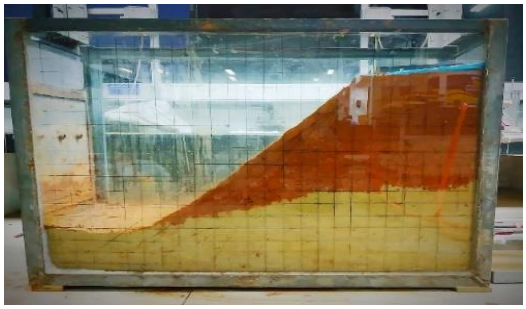

Figure 2: Small scale physical model for 45° slope

Experimental Procedures

Seepage water pressure

Two buckets were installed at a height of 2 m. The water flowed through the pipes into the soil at a low velocity, which were controlled by the valves. The water entered in the soil by seepage, and pore water pressure was created.

Figure 3: Set up for applying seepage water

Change in water level

Water level was changed at an interval of 30 minutes from bottom to mid height of the slope. this process was done to observe the watering and dewatering effects on the slope.

Figure 4: Initial height of water. Water was kept in this level in the first stage.

Figure 5: Dewatering process. Height of the water level was changed through this process.

Surcharge load

Surcharge loading was installed on the slope to observe the effect. Total loading of 120 kg was applied on the slope gradually. The loads were placed on a wooden plank to distribute the load uniformly over the slope.

Figure 6: Applied 120 kg surcharge load. The loads were balanced by placing them on wooden pieces, to keep them steadier.

Artificial rainfall

Artificial rainfall was introduced to the face of the slope to observe the impact of the rainfall. The grated bucket or sprinkler was used for application of rain fall. For 30-degree slope, 13.5 mm/min and for 45-degree slope, 11.11 mm/min water was applied at an interval of 1 hour for 5 times.

Figure 7: Application of artificial rainfall.

Limit equilibrium method

To model in GEO5, there are some components need to be considered. Initially the problem definition of geometry of the slope was inputted. As the soil layer was taken as multi material layer, the soil type was classified and their property was defined in the particular region in the model. Computing the load as worst condition surcharge load was applied on the upper portion of the slope which was indicated as stress applied on the road. As in the selected site, there

was a lake just beside the slope, water level is defined keeping a variation for observing the fluctuation of FOS in different condition.

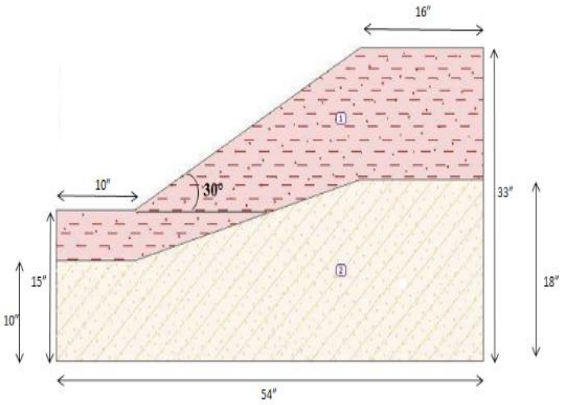

Figure 8: Geometry of the slope for 30^0 angles

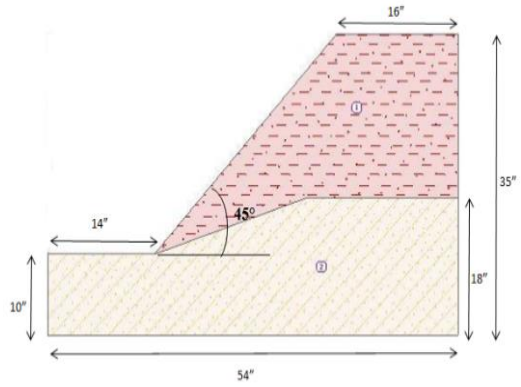

Figure 9: Geometry of the slope for 45^0 angles

Surcharge load

To keep similarity of stress with the selected site in the model 6 KPa is applied to consider it as a surcharge pressure and to compare the factor of safety at different water level for the same surcharge pressure. The value of surcharge pressure is taken as the worst condition.

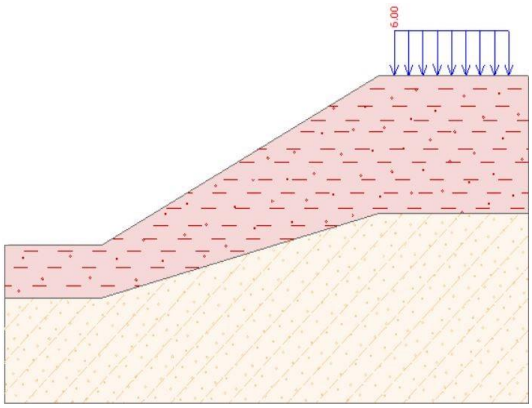

Figure10: Geometry of the slope (30°) with surcharge pressure

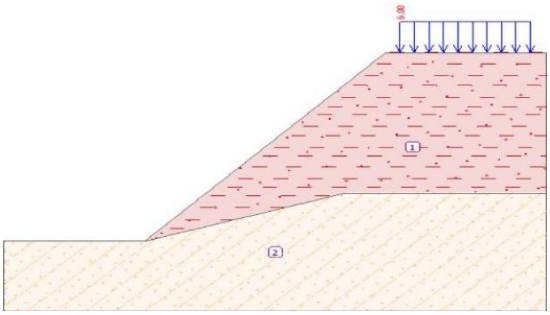

Figure11: Geometry of the slope (45°) with surcharge pressure

Water level variation

In this case water level variation was kept considering two seasonal occurrences. In dry season water level decreases with time and in rainy season water level increases. In this model three different condition is considered keeping the water level at bottom, mid top and top of the slope. Top of the slope is applied for the worst condition in rainy season. If flood occurs, comparing the fluctuation of factor of safety in the slope is the purpose of keeping water level at the top of the slope. The level of water in 30° & 45° slope is represented in table 1

Table1: Water level variation in $30^0$and 45^0 slopes

Water Level	30° slope	45° slope
Bottom	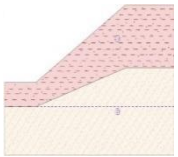	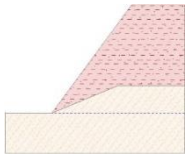
Mid Top	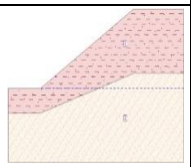	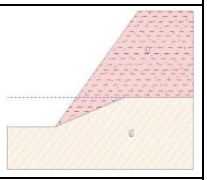
Top	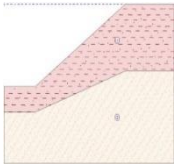	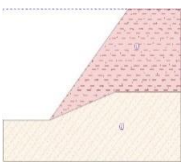

Finite Element Method

In this study, for determining the stability of the slope by numerical analysis method, PLAXIS 2D was used. PLAXIS version 8.2 has been used for numerical modeling. There are 2 different model for 30 degree and 45 degree. Height, distance, slope angle is same

as defined in GEO 5 and model type is Plain strain and 15 nodal. Since the study slope was not axisymmetric, plain strain type model was selected from the dropdown. Dimensions were in meters giving the real geometry of the considered in two different sections.

Material properties

To determine the failure criteria of the road side slope, the properties of the soil was determined by the lab tests**.**

Table 2: Parameters acquired from lab test for clayey silt

Parameters	Value
Unsaturated Unit weight (kN/m^3)	16
Saturated Unit weight (kN/m^3)	17.5
Cohesion, C (kPa)	1.1
Friction angle, ϕ (Degree)	28
Poisson's Ratio, v_u	0.35
Elastic Modulus, E_u (kPa)	12000

Table 3: Parameters acquired from lab test for silty sand

Parameters	Value
Unsaturated Unit weight (kN/m^3)	17
Unit weight (kN/m^3)	18.5
Cohesion, C (kPa)	0.88
Friction angle, ϕ (Degree)	33
Poisson's Ratio, v_u	0.35
Elastic Modulus, E_u (KPa)	20000

Conditions in PLAXIS 2d

Table 4: Applied conditions for the calculations

Material type condition	Undrained
Soil model type	Mohr Coulomb elasto-plastic constitutive soil model
Boundary condition	Fixed at the bottom of the FE model
Restrains	Standard fixities
Applied external load	5 Kpa (calculated from surcharge load obtained from the axle load)
Meshing size	Very fine mesh
Level of ground water taken in to consideration	Three different level was considered. First one was at mid height of the slope, second one was at the toe of the slope (dry season) and third one was at the top of the slope (rainy season)
Calculation type chosen for phase-1	Consolidation; time:30 days for clayey silt layer.
Calculation type chosen for phase-2	Consolidation; time: 2 days for clay layer.
Calculation type chosen for phase-3	Plastic; load: -5kpa

RESULTS

Observations from small scale physical model

For30^0 slope

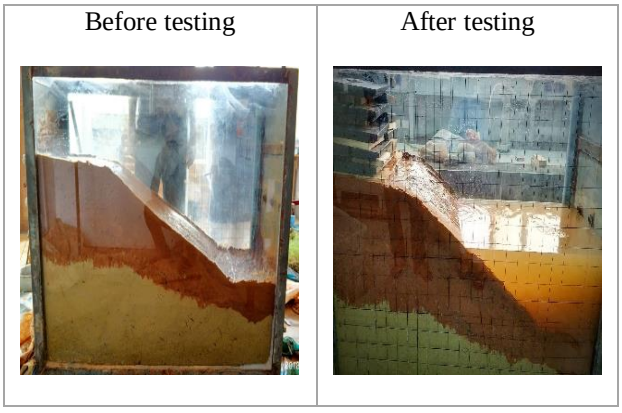

Figure12: Conditions of the 30^0 slope, before and after the testing. There were no changes after testing in the slope except for the surface erosion created by the artificial rainfall.

For 45^0 slope

All the test procedures were applied on the 45^0slope and after 48 hours, it was observed that, sand boiling was occurring at the downslope surface. the sand boiling leads to cracks on the lower soil surface of the slope. piping occurred inside the silty sand, which was observed. sand particles started entering into the clayey silt layer, and cracks were widening by time.

Figure13: Sand boiling at the lower soil surface.

Figure14: Piping action in the silty sand layer.

Figure15: Generation of cracks at the toe of the slope.

It was observed that the cracks lead to the top of the slope. The upper soil layer settled down at a visible rate, and the surcharge loads leaned towards the slope. Within 3 minutes, the top of the slope failed drastically, although the surcharge loads bumped on the slope and slightly restrained a chunk of clayey silt layer from failing. So, it can be said that, for slope angle of 45-degree failure occurs vulnerably.

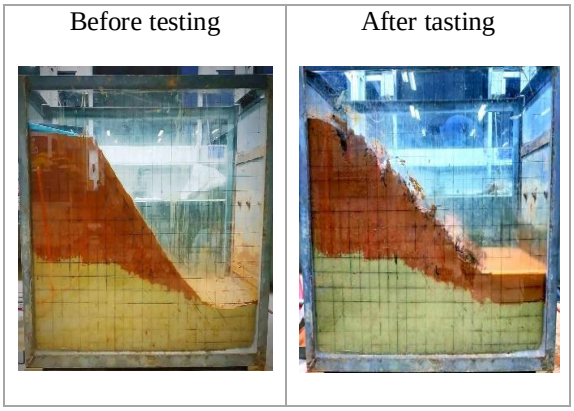

Figure16: Conditions of the 45^0 slope, before and after the testing.

Results from Limit Equilibrium Method

Table 5: factor of Safety was found for 30^0 slope

Methods	FOS	
	Bottom	Mid Top
Bishop	0.97	0.89
Janbu	0.97	0.88
Spencer	0.96	0.88
Morgenstern Price	0.97	0.88

Table 6: factor of Safety was found for 45^0 slope

Methods	FOS	
	Bottom	Mid Top
Bishop	2.00	1.76
Janbu	2.00	1.76
Spencer	1.99	1.75
Morgenstern Price	2.00	1.76

Results from Finite Element Method

Total displacements could be observed for water level at mid height and water level at lower height in both 30^0 and 45^0 slopes.

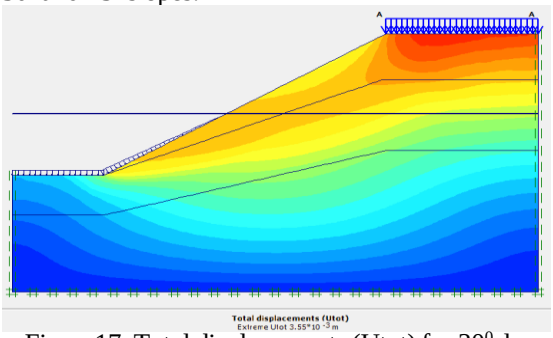

Figure17: Total displacements (Utot) for 30^0slope was found $3.55*10^{-3}$m for water level at mid height.

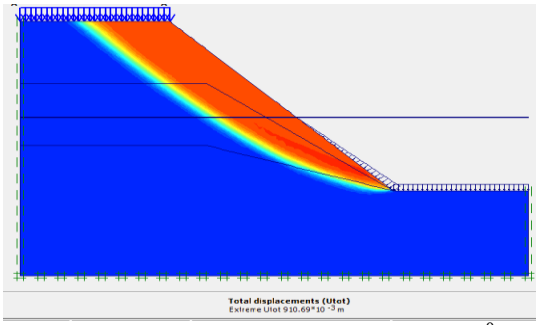

Figure18: Total displacements (Utot) for 45^0slope was found $910.69*10^{-3}$m for water level at mid height.

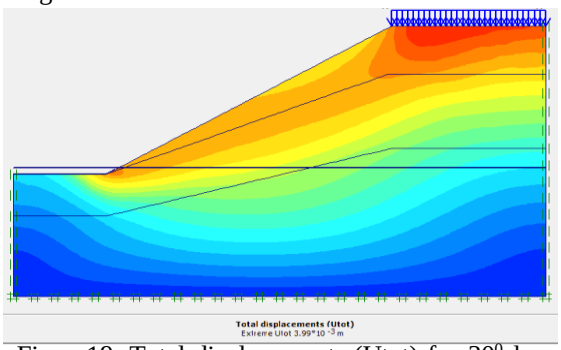

Figure19: Total displacements (Utot) for 30^0slope was found $3.99*10^{-3}$m for water level at lower height.

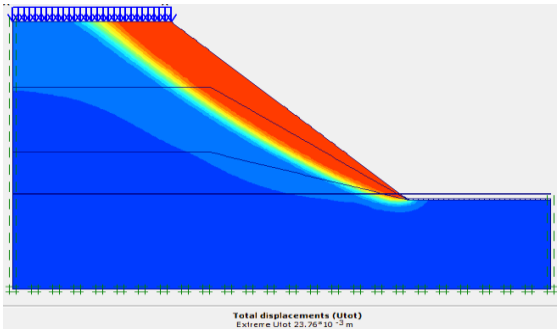

Figure20: Total displacements (Utot) for 45^0slope was found $23.76*10^{-3}$m for water level at lower height.

CONCLUSION

From the physical model, it was observed that when slope angle was 30º, settlement occurred in the ground, however, no visible failure pattern was observed. On the other hand, for the slope angle of 45º, a slope failure is seen and the pattern of slope was rotational non-circular failure. Depending on the slope angle, the deformation of the ground varied. Moreover, surface cracks, boiling of sand and formation of sinkholes behind the edge of the slope were also observed in the physical model tests.

The failure pattern and failure slope angle from physical model coincides with the analytical and numerical analysis. In the numerical analyses the failure pattern was also rotational non-circular when slope angle was 45º, but a negligible amount of settlement occurred when slope angle was 30ºthe same as the physical model tests.

In analytical analyses with different water levels, the factor of safety varied from 1.75 to 2.10, when slope angle was 30º. In contrast, for different water levels, the factor of safety varied from 0.88 to 1.05 when slope angle was 45º, which indicated the failure of the slope which coincides the results of the physical model tests.

REFERENCES

[1] F. Ali & Farah, Elias & H. Fadi. 2014; Slope Stability Analysis Using Numerical Modelling. *American Journal of Civil Engineering*. 2. 60-67.

[2] Plaxis bv., 2012b, PLAXIS 2D 2012 - Reference Manual, The Netherlands.

[3] Duncan J.M; State of the art: Limit equilibrium and finite element analysis of slopes.;*Journal of Geotech Engineering., Vol. 122 (7), 1996, 577-596*

[4] Bishop, A.W. (1955) The Use of Slip Circles in the Stability Analysis of Earth Slopes. Geotechnique, 5, 7-17.

[5] Fellenius, W. (1927) Erdstatische Berechnungen mit Reibung und Kohasion (Adhasion) und unter Annahmekreiszylindrischer Gleitflachen. Ernst & Sohn, Berlin.

[6] Janbu, N. 1954. Stability analysis of slopes with dimensionless parameters. Harvard Soil Mechanics Series,46, 811.

9th Int. Conf. on Geotechnique, Construction Materials and Environment, Tokyo, Japan, 20-22 November 2019, ISBN: 978-4-909106025 C3051

DEFORMATION ON EMBANKMENTS DUE TO SLAKING PHENOMENON AND ITS COUNTERMEASURE

Andius Dasa Putra[1] and Mamoru Kikumoto[2]
[1]Department of Civil Engineering, Faculty of Engineering, University of Lampung, Indonesia
[2] Institute of Urban Innovation, Yokohama National University, Japan

ABSTRACT

Geotechnical issues have increased in the last two decades since sedimentary rocks material such as mudstone or shale has been widely used as embankment material. They, however, tend to be weathered once they are immersed in the water. This phenomenon is a kind of weathering processes known as slaking and may cause a reduction of stiffness and peak strength. This paper, in order to evaluate the slaking induced deformation, a number of one-dimensional compression slaking tests and scanning electron microscopy (SEM) tests to observe the physical morphology of mudstone were performed. These data confirm that slaking in crushed mudstone is accompanied by a variation in the particle size distribution during wetting and drying cycles, and a variation in grading results in an irreversible change in mechanical characteristics, such as the reference packing density. Since the particle size distribution was transformed under confined stress constant occurs without a change in the maximum particle size, it can be described by existing indexes of grading such as breakage parameter *Br*. Furthermore, to eliminate the deformation behavior of sedimentary rocks, changing the particle size distribution in the beginning by applying loading/unloading history before slaking cycle has exhibited the significant result. The compressibility during wetting and drying cycle decreases to 50% of conventional compression by applying this countermeasure method. In earth construction works, the process of roller compaction is necessary in order to encourage the particle crushing. Proper compaction can control the occurrence of slaking under wetting and drying cycle so that volumetric compression does not occur easily.

Keywords: mudstone, slaking, particle size distribution, one-dimensional compression, deformation

INTRODUCTION

Soft sedimentary soft rock such as mudstone or shale are highly susceptible to weathering. They have a tendency to slake and soften when immersed into the water and as a result their strength diminishes gradually with time. Due to this natural behavior, mudstone material has been mostly disposed as waste material. However, while dealing with economic considerations and environmental concerns, several earth constructions projects propose to utilize the crushed mudstones or shales as embankment materials. Since large embankment made of these materials was considered, long term stability problem may possibly occur to slaking [1] - [3]. One of these embankments located on the Tomei expressway in Makinohara district in Japan failed during the earthquake in 2009, with subsequent field investigation and analysis identifying the primary cause to be slaking of the mudstone [4]. The cross section of Tomei expressway after and before collapse is shown in Fig. 1. The slaking behavior of mudstone has been studied experimentally [5] - [7] through slake-durability tests and other similar tests, in which a number of wetting and drying cycles are applied to evaluate the weathering resistance of weak rocks such as shales, mudstones and siltstones. This has demonstrated that slaking cycles significantly affect the degradation process and evolution of particle size distribution in such rocks [8] – [10]. Particle size distribution characteristics such as the gradation of weak rock tend to transform in response to slaking induced by wetting and drying, and this will ultimately affect the mechanical behavior as the material after slaking is quite different from the original material [11], [12]. Weak rocks may lose their strength or stiffness through slaking, as this usually results in a gradation with small particle sizes.

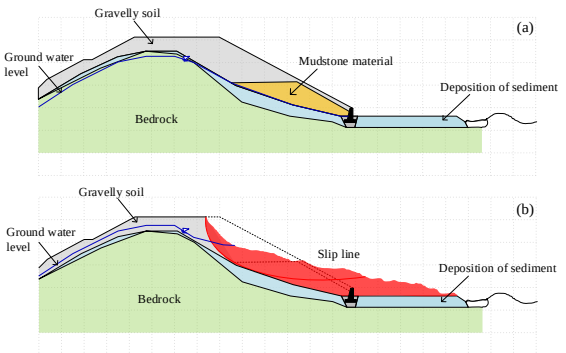

Fig. 1 Cross section of Tomei expressway fault after and before the earthquake in 2009

Such variation in mechanical characteristics during slaking can directly affect the deformation and failure behavior of the ground, but so far, most studies have only looked at the role of slaking in the evolution of the particle size distribution or the change in behavior of weak rocks. As there has been little discussion of the deformation behavior that is directly induced by slaking, this paper attempts to address the slaking-induced deformation based on the one-dimensional compression slaking tests and to propose a rational way to eliminate the issues of the granulated weak rocks in earth construction projects.

MATERIALS AND METHODS

Weak rock materials

The tested materials presented in this paper has originated from several embankments which caused deformation issues due to slaking phenomena. Kakegawa mudstone was derived from the embankment on Tomei expressway in Japan. Hattian Bala mudstone was obtained from a natural dam which was generated by Kashmir earthquake 2005 that locates at 3.5 km of Karli River in Pakistan. In addition, to investigate the rational countermeasures to the issues related with the weak rocks in embankments, loading histories (loading/unloading) were applied before the wetting and drying cycles. The test was carried out on Nou mudstone since the deformation issues in the field has occurred due to slaking. The particle size distribution of mudstone specimens at the initial state of the one-dimensional compression slaking test was a unit grading having a diameter of 0.85-2.00 mm (passed by sieve no. 10 and restrained by sieve no. 20 ASTM [14]). The physical surface morphology and general properties of the material are summarized in Fig. 2 and Table 1.

Several mechanisms of the slaking of weak rocks were attributed to the compression of air entrapped in the intra-granular pores of the particles [5]. Moreover, the size and the roughness of the pore boundaries have dominant effects on the resistance of particles against slaking. Therefore, it is necessary to explore the surface characteristics of the granulated weak rocks through SEM (Scanning Electron Microscopy) analysis using the same particle size distribution for one-dimensional compression slaking test.

Table 1 General properties of weak rocks materials

Properties	Kakegawa	Hattian Bala	Nou
Particle density (gr/cm^3)	2.65	2.75	2.69
Max. Void ratio (e_{max})	1.83	1.09	1.97
Min. Void ratio (e_{min})	1.29	0.79	1.40

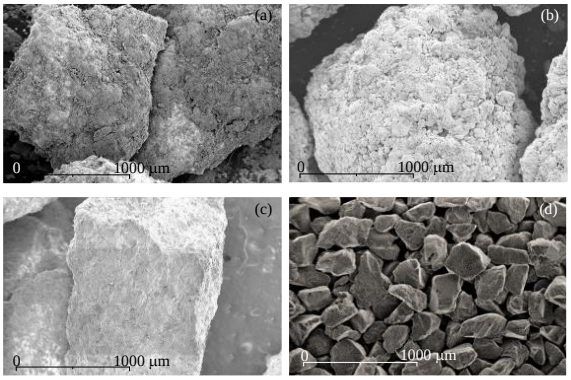

Fig. 2 Physical surface appearance of granulated mudstone magnified to 50 x: (a) Kakegawa; (b) Nou; (c) Hattian Bala and (d) Toyoura sand

Slaking under Confined Condition: One-Dimensional Compression Slaking Tests

In order to evaluate the slaking induced deformation on mudstone, a one-dimensional compression test that incorporates wetting and drying cycles [11] was modified. The schematic setup of testing apparatus is shown in Fig. 3, and consisted of: a measuring system (left), loading system (centre), and wetting and drying paths (right). The specimen container was a rigid steel cylinder with dimension of 60 mm in diameter and 40 mm high, with porous stones installed on the top and bottom loading plates, respectively. For testing, dried specimens were first installed in the steel cylinder, after which the load cell and contact-type displacement gauge were installed and initialized. The initial height of the specimen was measured to determine the initial void ratio, and then a vertical stress was applied in stages (9.8, 19.6, 39.2, 78.5, 157, 314, 628, 1256 kPa) by a pneumatic cylinder by way of a loading rod. The time for each loading was set to 30 min, as compression of the specimen immediately occurred and the volumetric behavior did not appear time dependent during the compression stage. After reaching a prescribed vertical stress, a wetting and drying cycle was carried out while keeping the vertical stress constant.

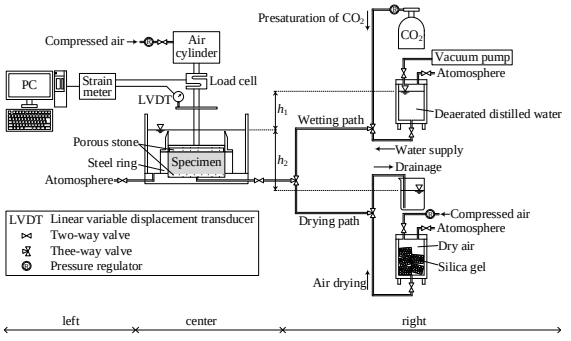

Fig. 3 The schematic of one dimensional compression slaking test

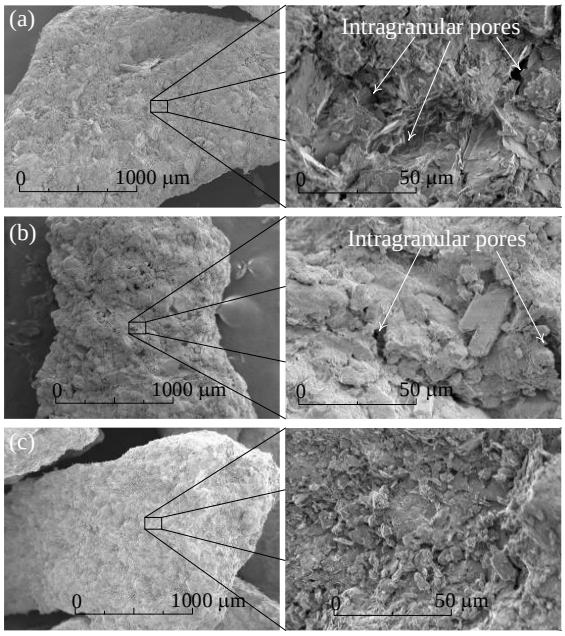

Fig. 4 SEM images of the weak rocks: (a) Kakegawa mudstone; (b) Nou mudstone and (c) Hattian Bala mudstone.

The wetting process started by permeating carbon dioxide slowly through the specimen without changing the void pressure for 30 min to remove any air, after which distilled water was permeated through the specimen by a slight difference in water level between the water tank and specimen container (h1) until the specimen was fully submerged. After leaving the specimen submerged for 6 h, the drying process was commenced by draining the void water from the specimen for 30 min through light difference (h2) in water level. Silica gel packs were then set around the steel cylinder of the specimen container, and dried air was slowly permeated through the specimen for 48 h to ensure it was completely dry. This cycle of wetting and drying was repeated three times, during which time the volumetric behavior was observed. Following the final drying process, the specimen was oven-dried and then sieved using only horizontal circular movements without any tapping impulse being added.

RESULTS AND DISCUSSIONS

Intra-granular pores

Several different mechanisms of the slaking of weak rocks have been pointed out in past studies. One of the slaking mechanisms is attributed to the compression of air entrapped in the intra-granular pores of the particles. The effect of the geometry of the intra-granular pores and revealed that the size of the pores and the roughness of the pore boundaries have dominant effects on the resistance of particles against slaking [5], [13]. The surface characteristics of the granulated mudstones were explored through SEM. The low-magnification images of each specimen on the left side in Fig. 4 clearly expose that clay-sized particles that produce a rough surface texture. It is note that the particles of the Kakegawa and Nou mudstone there is a particularly pronounced accumulation of tiny particles, with apparent intra-granular pores appearing to form within each bulk particle (the right side in Fig. 4.). In comparison, the surface texture of the Hattian Bala mudstone looks relatively smoother, but is still rougher than that of the Toyoura sand presented in Fig. 2.

Deformation on Weak rocks due to Slaking

The test result of one dimensional compression slaking for the crushed Kakegawa and Nou mudstones under a vertical effective stress σ_v' of 314 and 1256 kPa are shown in Figs. 9 and 10, respectively, whereas the results for the crushed Hattian Bala mudstone under a vertical effective stress σ_v' of 314 kPa are provided in Fig. 11. It is evident from this that the particle size distributions of the crushed Kakegawa was transformed after compression, and that mudstone types experience particle breakage during one-dimensional compression. It is also clear that there is a slightly greater change in particle size distribution at 1256 kPa, and so the evolution of grading due to particle breakage is related to an increase in the stress level. The effect that changes in grading due to slaking have on the mechanical characteristics were investigated by monitoring the maximum and minimum void ratios of the Kakegawa mudstones, Nou mudstone and Hattian Bala mudstone after each cycle of wetting and drying. As seen in Fig. 5 to Fig. 7, the maximum and minimum void ratios decrease by almost the same amount until the third cycle. For the Hattian bala mudstone, these ratios remain almost constant, while in the Kakegawa and Nou mudstone they slightly decrease. The crushed Hattian Bala mudstone, however, retains its original void ratios, and does not seem to exhibit any particle breakage under a stress of less than 314 kPa (Fig. 7).

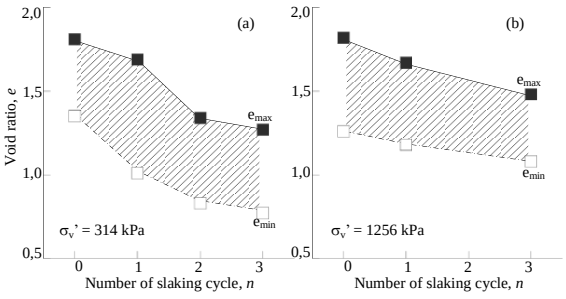

Fig. 5 Changes in void ratio (e) during slaking cycles (n) of Kakegawa mudstone

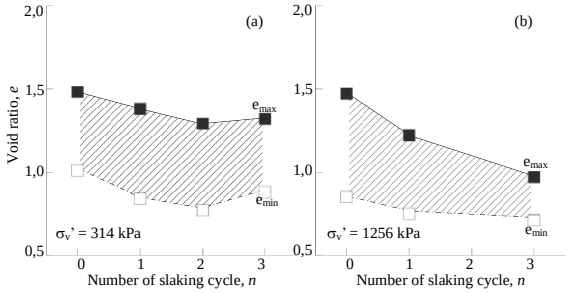

Fig. 6 Changes in void ratio (*e*) during slaking cycles (*n*) of Nou mudstone

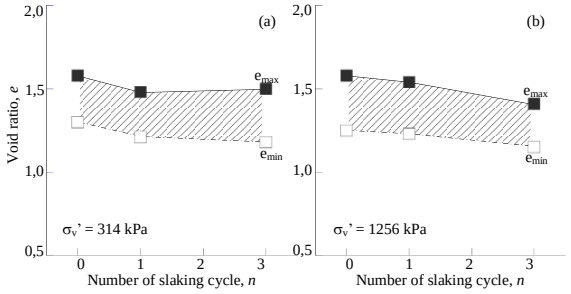

Fig. 7 Changes in void ratio (*e*) during slaking cycles (*n*) of Hattian Bala mudstone

Furthermore, the Hattian Bala mudstone particles did not contain any intra-granular pores (Fig. 4(c)), which would explain why there is so little change in particle size distribution during wetting and drying cycles shown by the breakage parameter (B_r) value. Figures 9, 10 and 11 exhibit the relationships between the vertical effective stress σ_v', number of wetting and drying cycles *n*, void ratio *e* and breakage parameter B_r for the all crushed mudstone, respectively. The upper figures ((a) and (b)) illustrate the behavior in compression, whereas the lower figures ((c) and (d)) show the variation in grading based on the B_r value. From the behavior of the Kakegawa mudstone shown in Fig. 9, it is clear that the value of B_r (Fig. 9(c)) increases to 0.12 at 314 kPa and to 0.19 at 1256 kPa, which is consistent with particle crushing theory. The compression line in the semi-logarithmic plot of *e* and log σ_v' also becomes steeper, which further confirms that particle crushing occurred [8]. After wetting and drying, the B_r value increased to 0.44 (Fig. 9(d)) and the specimen experienced significant compression, to the extent that the decrease in void ratio was greater than 0.6. For the crushed Nou mudstone, the results for which is summarized in Fig. 10, the B_r value increases from 0.21 to 0.25 at 314 kPa but decreases from 0.35 to 0.29 at 1256 kPa during wetting and drying. It was confirmed that particle breakage increases the proportion of fine particles to fill the void space between larger particles without considerably changing the maximum particle size.

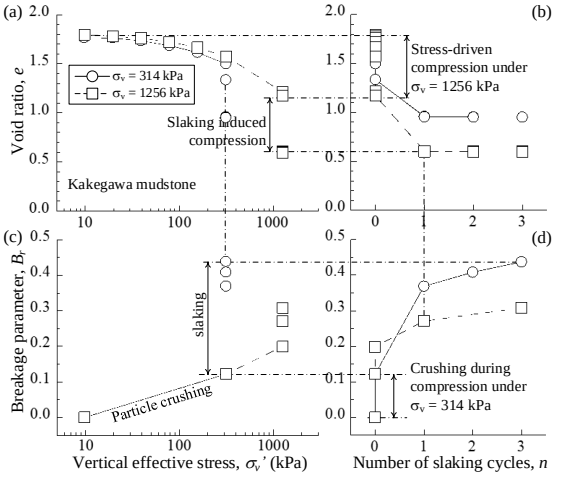

Fig. 8 Changes in the compressive properties and particle size of the Kakegawa mudstone

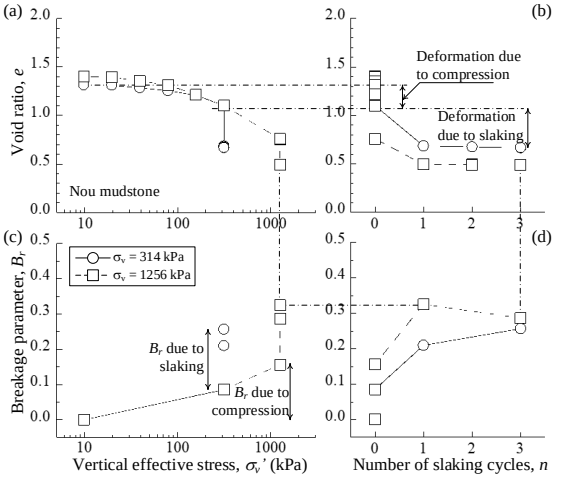

Fig. 9 Changes in the compressive properties and particle size of the Nou mudstone

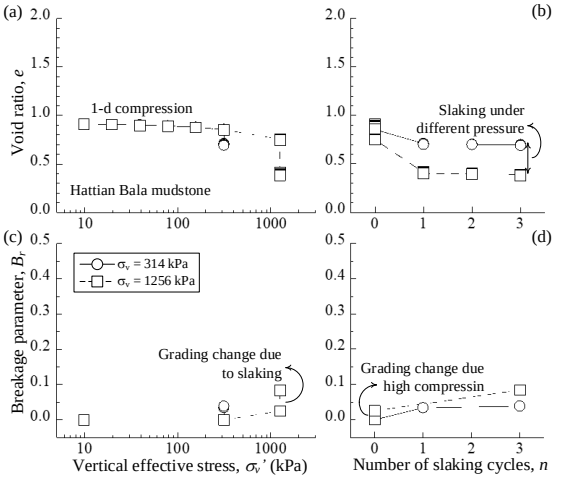

Fig. 10 Changes in the compressive properties and particle size of the Hattian Bala mudstone

The decrease in void ratio e (volumetric compression) were not significant, comparing to the Kakegawa mudstone. In contrast, the increase in Br of the crushed Hattian Bala mudstone (Fig.11) was almost zero during the compression stage at 314 kPa and slightly increase due to high compression at 1256 kPa. The compression line in the e-ln σ_v' plane was comparatively flat. This indicates that the variation in Br during wetting and drying is small. It can be inferred that slaking induced by wetting and drying cycle under a constant vertical effective stress causes substantial compression of geo-materials derived from mudstone.

An Effort to Eliminate the Deformation on Weak Rocks

A rational countermeasure technique is needed for reducing the deformation due to slaking on the earth construction project. A number of one-dimensional compression slaking test has been performed on Nou mudstone to get a better understanding related to these circumstances. The effect of loading/unloading compression history before wetting and drying cycle applied is one technique to consider. The procedure for the loading stage was similar with the previous one-dimensional compression slaking test already explained. Except for the effect of loading/unloading, after the high compression of 1256 kPa is applied for 30 min, then followed with the unloading process to 314 kPa for 30 min. Further, the wetting and drying cycles were applied as one cycle. The combination loading patterns in this section are summarized in Table 2. The particle size distribution (PSDs) changes of each case patterns of the test are shown in Fig. 12. It is significant that the PSD curve after loading history (case 7 and case 8) almost similar, despite the initial void ratios are different. It is inferred that the void ratio did not significantly affect to the grading changes. In spite of the high compression applied on the specimen, the final grading change (case 7 and case 8) almost similar with the test result of one-dimensional compression slaking under constant vertical effective stress at 314 kPa (case 3).

The total volume compression between case 3 and case 7 (Fig. 13(a)) also exhibit similar behavior, even though in case 7 the high compression stress has been applied in the beginning. It is pointed out that during the earth construction utilizing the geomaterial which has slaking properties, paying attention to roller compaction throughout the embanking work enhances the crushing of particles, controlling the occurrence of slaking under cyclic wetting and drying so that volumetric compression does not occur easily.

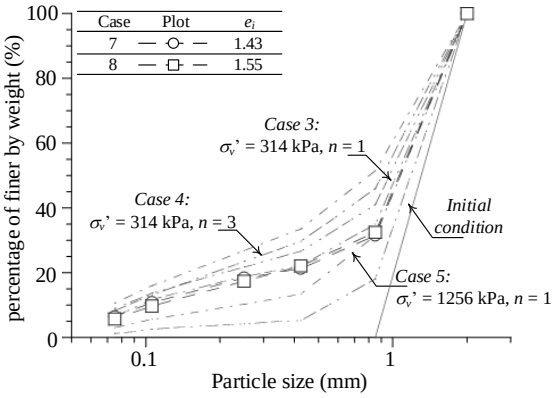

Fig. 11 The particle size distribution changes during stress history applied

Table 2 The one dimensional compression slaking testing series of Nou mudstone

case	1	2	3	4	5	6	7	8
e_i	1.3	1.5	1.3	1.3	1.4	1.4	1.4	1.6
σ_v'	314				1256		1256 - 314	
n	0	1	1	3	1	3	1	1

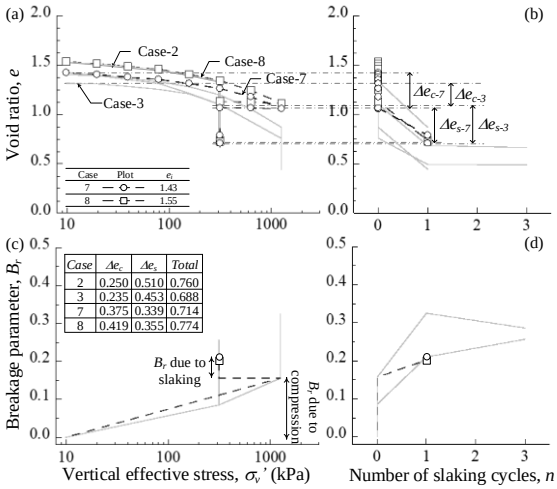

Fig. 12 Change in compressive properties during the stress history (loading/unloading) of Nou mudstone

CONCLUSIONS

In order to investigate the deformation due to slaking behavior, a number of one-dimensional compression slaking tests has performed in this paper. The surface morphology of mudstone based on SEM result indicated the different slaking and deformation behavior caused by the intra-granular pores within particle. The transformation of particle size distribution due to slaking is influenced by the existences of intra-granular pores. As a result, it causes an irreversible change in the mechanical properties of weak rocks attributable to variation in

the density compaction. Moreover, the changes in particle size distribution as an evolution grading during compression can increase the compressibility of weak rocks, with wetting and drying cycles causing significant compression even if the effective stress remains constant. Since the evolution of particle size distribution under confined stress constant occurs without a change in the maximum particle size, it can be described by existing indexes of grading such as breakage parameter B_r. A countermeasures technique of the deformation behavior of weak rocks was performed in this study. Changing the particle size distribution in the beginning by applying loading/unloading history before wetting and drying cycle has exhibited the significant result. The compressibility during wetting and drying cycle decreases to 50% of conventional compression by applying this countermeasure method. In earth construction works, the process of roller compaction is necessary in order to encourage the crushing of particle. A proper compaction can control the occurrence of slaking under wetting and drying cycle so that volumetric compression does not occur easily.

ACKNOWLEDGMENTS

Finally, authors would like to extend their appreciation and thanks to the earthworks research section of the NEXCO Research Institute for providing mudstones specimens. The first author is grateful to the University of Lampung and Yokohama national University for supporting and research collaboration. This research is financially supported by JSPS KAKENHI Grant Numbers 24360192, 16H06099 provided to the second author.

REFERENCES

[1] Walkinshaw, J. L. and Santi, P. M., Shales and other degradable materials, Landslides: Investigation and Mitigation, Special Report 247, Transport Research Board, National Research Council, National Academy Press, 1996, pp. 555-576.

[2] Yoshida, N., Enami, K. and Hosokawa, K., A staged compression-immersion direct shear test on compacted crushed mudstone, Journal of Testing and Evaluation, Vol 30 No. 3, 2002, pp. 239 – 244.

[3] Santi, P. M., Field methods for characterizing weak rock for engineering, Environmental & Engineering Geoscience, Vol. 12 No. 1, 2006, pp. 1–11.

[4] Yasuda, S., S. Yokota, H. Nakamura, and K. Inou., Reduction of static and dynamic shear strength due to the weathering of mudstones, Proceedings of the 15th World Conference on Earthquake Engineering, Lisboa, 2012, pp. 4-11

[5] Vallejo, L. E., Welsh, R. A. Jr., Lovell, C. W. and Robinson, M. K., The Influence of Fabric and Composition on the Durability of Applachian Shales, Rock for Erosion Control. ASTM STP 1177, Charles H. McElroy and David A. Lienhart, Eds., American Society for Testing and Materials, Philadelphia, 1993, pp. 15-28

[6] Santi, P. M., Improving the jar slake, slake index and slake durability tests for shales, Environmental and Engineering Geoscience. Vol. IV. No. 3, 1998, pp. 385-396

[7] Yoshida, N. and Hosokawa, K., Compression and shear behavior of mudstone aggregates, Journal of Geotechnical and Geoenvironmental Engineering, ASCE, Vol. 130, No. 5, 2004, pp. 519-525

[8] Kikumoto, M., Putra, A. D., Fukuda, T, Slaking and deformation behavior, Géotechnique, Vol. 66, No. 9, 2016, pp. 771-785

[9] Sadisun, I. A., Shimada, H., Ichinose, M. and Matsui, K., Study on the physical disintegration characteristics of Subang claystone subjected to a modified slaking index test, Geotechnical and Geological Engineering, Vol. 23, No. 3, 2005, pp. 199-218

[10] Gautam, T and Shakoor, A., Slaking behavior of clay-bearing rocks during a one-year exposure to natural climatic conditions, Engineering Geology, Vol. 166: 2013, pp. 7-25

[11] Putra, A. D and Kikumoto, M., Weathering-induced deformation of geomaterials derived from weak rocks, ARPN Journal of Engineering and Applied Sciences, Vol. 12 No. 12, 2017, pp.3858-3868

[12] Pappas, D. M. and Vallejo, L. E., The settlement and degradation on nondurable shales associated with coal mine waste embankments, International Journal Rock Mechanics and Mineral Sciences, Vol. 34, No. 3-4, 1997, pp. 241.e1-241.e13

[13] Vallejo, L.E. and Murphy, A. S., Fractal Pores and the Degradation of Shales, Fractals; Theory and Application in Engineering. M. Deking et.al. (eds), 1999, pp. 229-243.

[14] ASTM D6913-04, Annual Book of ASTM Standards, ASTM Int., 2004

9th Int. Conf. on Geotechnique, Construction Materials and Environment, Tokyo, Japan, 20-22 November 2019, ISBN: 978-4-909106025 C3051

SEDIMENT FLOW CHARACTERISTICS AROUND CYLINDRICAL STRUCTURE REGARDING SEABED EFFECTIVE STRESS RESPONSE

Anh Quang TRAN[1], Kinya MIURA[2], Tatsuya MATSUDA[2] and Taiki MURAKAMI[1]
[1]Graduate School of Architecture and Civil Engineering, Toyohashi University of Technology, Japan
[2]Department of Architecture and Civil Engineering, Toyohashi University of Technology, Japan

ABSTRACT

Stability of onshore and offshore structures subjected to stormy ocean waves is influenced by the soundness of seabed foundation ground, as well as the intensity of wave pressure acting directly on the structures. The seabed soundness would be affected by the change of the seabed surface elevation caused by erosion and/or deposition of sediment. The fluctuating effective stress in the seabed ground, which is induced by sea wave loading, would cause the reduction in seabed stiffness, and then the sediment flow and related scouring of seabed must be also affected by the effective stress fluctuation. In the present study we propose a calculation method for sediment traction flow on seabed around cylindrical structures. The calculation method that we used comprises with linear wave theory, pore-linear-elasticity theory for seabed medium, and empirical sediment traction flow model regarding seawater flow velocity. Although the intensity of sediment traction flow is mainly a function of seawater flow velocity, the sediment traction flow must be also influenced by the soundness of seabed ground. In the present study we calculated sediment flow and associated erosion-deposition around upright cylindrical structures of several types. The characteristic behavior of sediment flow was clarified.

Keywords: Sediment flow, Erosion-deposition, Cylindrical structure, Reflected-diffracted wave, Effective stress

INTRODUCTION

When seabed surface is subjected to water pressure change induced by sea wave loading, the fluctuation of pore water pressure and related effective stress are propagated along depth through seabed ground, where the seabed behaves as multi-phase porous continuum. The fluctuation of effective stress causes the reduction of the seabed stiffness, and then liquefaction or fluidization of seabed material may occur under stormy wave conditions. Some damaged structures which were affected by the destabilization of seabed ground have been reported [1]. On the other hand the destabilization of seabed ground would have effects on the sediment flow, and related scouring.

We focus on the sediment flow that is mobilized by traction force from seawater flow; suspended sediment and sheet flow are out of scope of the present study. Although the sediment traction flow is mainly a function of seawater flow velocity, the sediment traction flow would be also influenced by the soundness of seabed ground even under the same seawater velocity on seabed; the sediment flow in a particular direction would be enhanced by the reduction of effective stress near surface. Miura, Morimasa, Otsuka, Yamazaki and Konami [2] explained the combined effect of seawater velocity and effective stress induced by variation of water pressure on sediment flow, and qualitatively examined the direction of sediment flow average per cycle. Tran, Miura, Matsuda and Yoshino [3] proposed an analytical method regarding the effective stress response of seabed for sediment traction flow, and the method was applied to the seabed subjected to travelling wave and stationary wave near line structures. They clarified the characteristics of erosion-deposition behavior of sediment flow quantitatively; the sediment was deposited near nodes, on the other hand seabed was eroded near loops near line structures. In the present study we modify the analytical method and apply it to the sediment traction flow behavior around cylindrical structures.

ANALYSIS METHOD

The analysis method used consists of three processes: a sea wave analysis, a response analysis of seabed ground to sea wave loading, and an evaluation of sediment flow on seabed.

Sea Wave Analysis

The behavior of sea wave was analyzed in the framework of linear theory for small amplitude waves.

Incident plane wave

The incident wave travelling along x-axis is expressed by seawater surface elevation η_i and

velocity potential ϕ_i; flow velocity vector v_i and water pressure p can be calculated as the derivatives of velocity potential ϕ_i;

$$\eta_i(x,y,t) = \frac{H}{2} e^{i(\lambda x - \omega t)} \quad \because \lambda = \frac{2\pi}{L}, \quad \omega = \frac{2\pi}{T} \tag{1a}$$

$$\phi_i(x,y,z,t) = i\frac{gH}{2\omega}\frac{\cosh\lambda(h+z)}{\cosh\lambda h} e^{i(\lambda x - \omega t)} \tag{1b}$$

$$v_i = -\phi_{i,i}, \quad p = \rho_w\left(\dot{\phi}_i - gz\right) \tag{2}$$

where H, λ, and ω are wave height, wave number, and angular frequency, respectively. And ρ_w is density of seawater, and g is gravity acceleration.

Travelling and stationary waves

The geometry of upright cylindrical structures is presented in Fig. 1 with an incident plane wave. Two extreme cases were considered for comparison. One is zero-radius (no-structure) case in Fig. 2(b): travelling wave simply appears without reflection or diffraction. The other is infinite radius (line structure) case in Fig. 2(c), where stationary wave appears without diffraction. The travelling wave is expressed by Eq. (1b), and the stationary wave is expressed by the following Eq. (3).

$$\begin{aligned}\phi &= \phi_i + \phi_s \\ &= i\frac{gH}{2\omega}\frac{\cosh\lambda(h+z)}{\cosh\lambda h}\left\{e^{i[\lambda(x-R_o)-\omega t]} + e^{i[\lambda(-x+R_o)-\omega t]}\right\} \\ &= i\frac{gH}{2\omega}\frac{\cosh\lambda(h+z)}{\cosh\lambda h}\cos\lambda(x-R_o)\cdot e^{-i\omega t}\end{aligned} \tag{3}$$

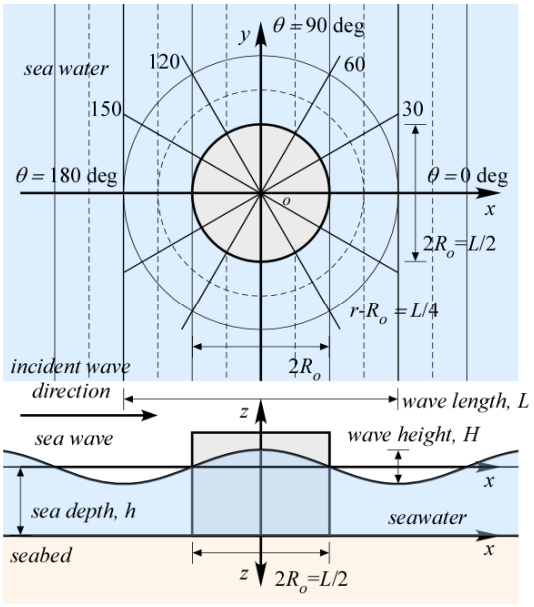

Fig. 1 Upright cylindrical structure

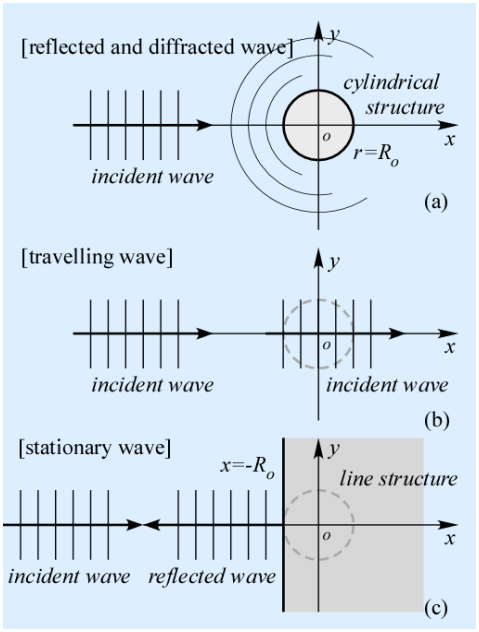

Fig. 2 (a) Reflected-diffracted waves for cylindrical structure, (b) Travelling, (c) Stationary wave for line structure

Reflected-diffracted wave for circular cylinder

For the cylindrical structure, the reflected-diffracted wave was generated as a response to the incident plane wave as shown in Fig. 2(a). For the upright cylinder of R_o in radius, MacCamy and Fuchs [4] succeeded in deriving velocity potential according to no-flow condition in radial direction on the side surface as follows

$$v_r = -\partial(\phi_i + \phi_{rdc})/\partial r = 0; \quad (r = R_o) \tag{4}$$

$$\begin{aligned}\phi_{rdc} = &-i\frac{gH}{2\omega}\frac{\cosh\lambda(h+z)}{\cosh\lambda h} \\ &\times\left[\sum_{k=-\infty}^{\infty}\frac{J_k'(\lambda R_0)}{H_k^{(1)\prime}(\lambda R_0)}H_k^{(1)}(\lambda r)\left(ie^{i\theta}\right)^k\right]e^{-i\omega t}\end{aligned} \tag{5}$$

where J_k is Bessel function of first order, and $H_k^{(1)}$ is Hankel function of first order.

In the present study, an ocean wave field with uniform depth of 20m was assumed, and an incident plane wave of wave height H of 10m, period T of 13m, and wave length L of 167.5m, was employed, regarding the sea wave condition set up for cooperative study by JSCE Committee [5].

Seabed Response Analysis

The effective stress response of seabed ground to sea wave loading on surface is analyzed with poroelastic continuum model within the framework of linear elastic theory [6]. In the model, seabed material is modeled as a binary phase material

consisting with solid phase and fluid phase (mixture of pore water and pore air), and the interaction between the two phases is combined as permeability. Miura, Asahara, Otsuka and Ueno [7] examined the applicability of the poroelastic continuum model and associated formulations under extensive conditions, according to that we employed the u-p formulation under quasi-dynamic, one-dimensional condition in the present study. For a uniform seabed layer with infinite thickness, the fluctuating pore water pressure Δp and associated vertical effective stress $\Delta\sigma_v$ can be calculated as follows.

$$\Delta p(z,t) = \Delta p_o \frac{1}{B_f + E_u}\left(B_f + E_u e^{-\zeta z}\right)e^{-i\omega t}$$
$$\sigma_v(z,t) = \Delta p_o \frac{E_u}{B_f + E_u}\left(1 - e^{-\zeta z}\right)e^{-i\omega t} + (\rho_t - \rho_f)z \qquad (6)$$
$$\because\ \Delta p_o e^{-i\omega t} = \rho_w \dot{\phi};\ z = -h \ \text{(on seabed surface)}$$
$$\zeta = \sqrt{i\omega h_v}$$

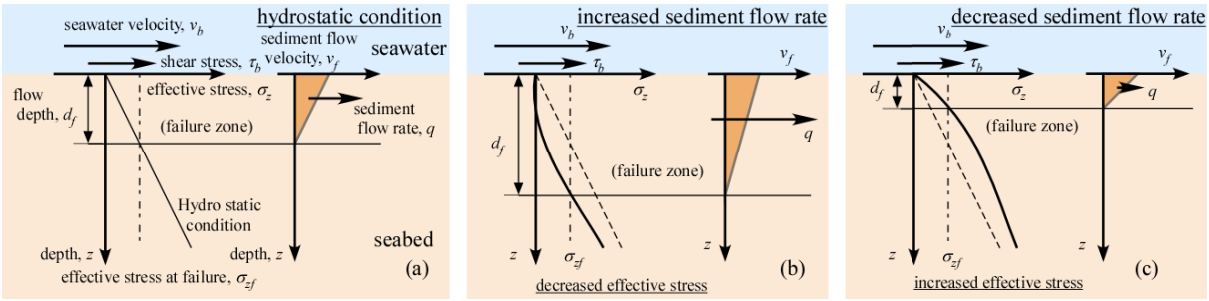

Fig. 3 Sediment flow intensity: (a) hydrostatic pressure condition, (b) decreased effective stress condition, (c) increased effective stress condition

Amount of sediment flow

The surface shear stress τ_b, that is traction force per specific seabed surface area, was assumed to be proportional to the seawater velocity v_b squared as expressed in Eq. (7), where dimensionless coefficient C_b of 1/40 was introduced.

$$\tau_b = C_b \rho_w v_b^{\,2} \qquad (7)$$

The sediment would be fluidized within the layer of d_f in thickness, where shear stress τ_b exceeds shear resistance τ_f which is calculated as a function of effective stress σ_z and internal friction angle ϕ_e as shown in Eq. (8). Finally the fluidization depth d_f can be determined.

$$\tau_f = \sigma_z(z,t)\cdot\tan\phi_e,\quad \tau_b = \tau_f$$
$$\therefore\ \sigma_z(d_f,t) = \tau_f / \tan\phi_e \qquad (8)$$

Then we assumed that the distribution of sediment flow velocity v_f within the fluidization layer was triangular along depth as shown in Fig. 3. Thus the amount of sediment flow vector per unit width q (m^2/s) can be calculated with Eq. (9), where the dimensionless coefficient C_q was introduced for the difference between seawater velocity v_b and sediment flow velocity v_f. The value of C_q was assumed to be 1/2.5.

$$q = \frac{1}{2} d_f v_f = \frac{1}{2} d_f C_q v_b \qquad (9)$$

As explained schematically in Fig. 3, the amount of sediment flow vector q would be rather dependent on effective stress distribution. Figure 3(a) shows the case of hydrostatic effective stress. If the effective stress decreases, the fluidized shear zone becomes thicker and thus q becomes larger as in Fig. 3(b). On the other hand, if the effective stress increases, the fluidized shear zone becomes thinner and thus q becomes smaller as in Fig. 3(c). It should be noted that even under the same seawater velocity

In the present study, it was assumed that for typical uniform loose sand, uniaxial stiffness of solid phase E_u is $1.40\text{x}10^5$kN/m^2, average stiffness of fluid phase B_f is $0.933\text{x}10^5$kN/m^2, and hydraulic consolidation coefficient H_v is $1.75\text{x}10^{-3}$ s/m^2 (see [5,7] for detailed explanation).

Evaluation of Sediment Flow on Seabed

The sediment flow and related variation of seabed surface elevation, that is erosion and/or deposition, was calculated in an empirical manner based on the concept of Shields Number, regarding the effective stress response in seabed ground (see Fig. 3).

v_b, sediment flow is dependent on effective stress.

Sediment storage rate: erosion-deposition

As shown in Fig. 4, the rate of sediment storage designated as Q (m/s) can be calculated from the total balance of inflow and outflow in both x- and y-directions to/from an infinitesimal rectangular area.

$$Q = -\frac{q_{x(x+\Delta x/2,y)} - q_{x(x-\Delta x/2,y)}}{\Delta x} - \frac{q_{y(x,y+\Delta y/2)} - q_{y(x,y-\Delta y/2)}}{\Delta y} \rightarrow -\left(\frac{\partial q_x}{\partial x} + \frac{\partial q_y}{\partial y}\right) \quad (\Delta x \rightarrow 0, \Delta y \rightarrow 0) \tag{10}$$

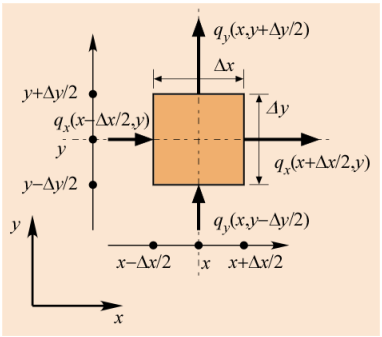

Fig. 4 Calculation of sediment storage from the balance of inflow and outflow to/from infinitesimal rectangular area

The positive and negative values of sediment storage rate Q correspond to deposition and erosion, respectively. The sediment flow velocity vector q and storage rate Q both can be integrated during a sea wave period T for evaluating the accumulated sediment flow behavior; the accumulated integrated values were designated as q_T (m^2) and Q_T (m), respectively.

EXAMINATION OF CALCULATED BEHAVIOR AND DISCUSSION

Sea Wave Behavior around Cylindrical Structure

Figure 5 shows sea wave behaviors along radial directions both in front and back of the cylindrical structure of R_o/L=1/4; the variation of seawater surface elevation along radial direction are drawn in 8 sections of wave period T. For comparative examinations, the travelling wave and the stationary wave are shown in front of the structure (Fig. 5(a): θ =180deg), and the travelling wave is shown in back of the structure (Fig. 5(b): θ =0deg). In the front of cylindrical structure, loop appears on the structure side surface, and node and loop are repeated along

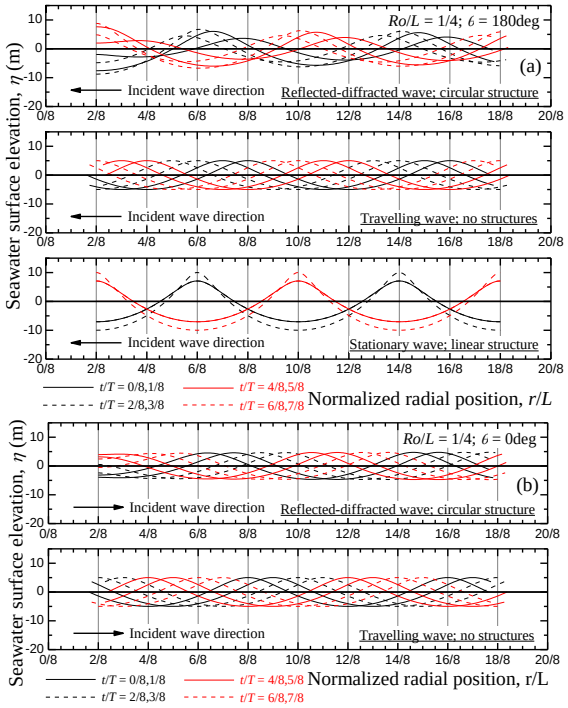

Fig. 5 Behavior of sea surface along radial direction: (a) front of structure, θ =180deg, (b) back of structure, θ =0deg

the radial direction. Though the loop and node are not clear compared with the stationary wave near line structure, characteristic behavior of stationary wave can be recognized in Fig. 5(a). In back of the structure, sea wave behavior is similar to that of travelling wave with somewhat smaller wave height and a phase lag of about T/4 compared with the travelling wave in Fig. 5(b).

Sediment Flow and Storage: Erosion and Deposition around Cylindrical Structure

Behavior in radial direction

Figure 6 shows sediment flow behaviors along radial direction both in front and back of a cylindrical structure of R_o/L=1/4; the variations of accumulated sediment flow vector q_T and sediment storage Q_T are shown in 8 sections of wave period T. For comparative examinations travelling wave and stationary wave are also shown in the figure. In structure front (θ=180deg) radial component of sediment flow vector q_{Tr} is fluctuating but consistently positive. This feature means that the sediment flows away from the structure, and the flow direction is in the opposite of the incident wave travelling direction. The behavior of sediment storage Q_T shows that the seabed is eroded on the side surface, and however, the sediment deposits around the node apart from the structure surface by L/4. The erosion and deposition are seen clearly in

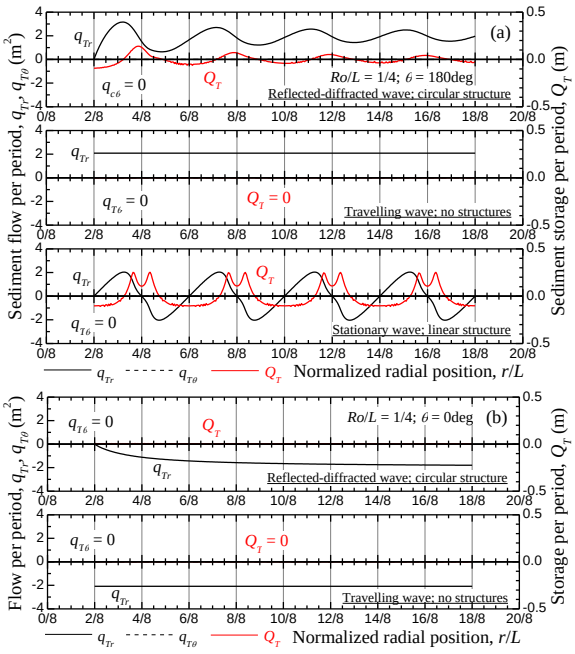

Fig. 6 Behavior of sediment flow on seabed along radial direction: (a) front of structure, θ=180deg, (b) back of structure, θ=0deg

the case of stationary wave, and the erosion and deposition are repeated along the radial line in front of the structure.

On the other hand, in back of cylindrical structure (θ=180deg), q_T is not fluctuating and consistently negative. This means that the sediment flows toward the structure in the opposite of the incident wave travelling direction. As Q_T is negligibly small, the erosion or deposition wouldn't occur in structure back.

Behavior in circumferential direction

Figure 7(a) shows the behavior of sediment flow and associated storage of sediment on the side wall of the cylindrical structures with different diameters. On the side wall (r=R_o) sediment flows only in circumferential direction. Although the sediment flow is somewhat influenced by the structure size, $q_{T\theta}$ is anti-symmetry and positive on the right hand side but negative on the left hand side in the top of Fig. 7(a). It is suggested that the sediment flows accumulatively for back to front on the structure side surface. The behavior of Q_T tells that notable erosion (Q_T<0) occurs near structure front (θ=180deg), its intensity is equivalent to that in the case of stationary wave.

Figure 7(b) shows the sediment flow behavior on the concentric circle apart from the structure side surface by a quarter of wavelength (r=R_o+L/4). The behavior of $q_{T\theta}$ shows the circumferential flow from structure back to front as similar to the case of on the side surface (r=R_o). The radial flow of sediment q_{Tr} is positive near structure front but negative near the perpendicular directions (θ=+90 or –90deg). On the concentric circle (r=R_o+L/4), notable deposition of sediment (Q_T>0) is recognized around structure front (θ=180deg).

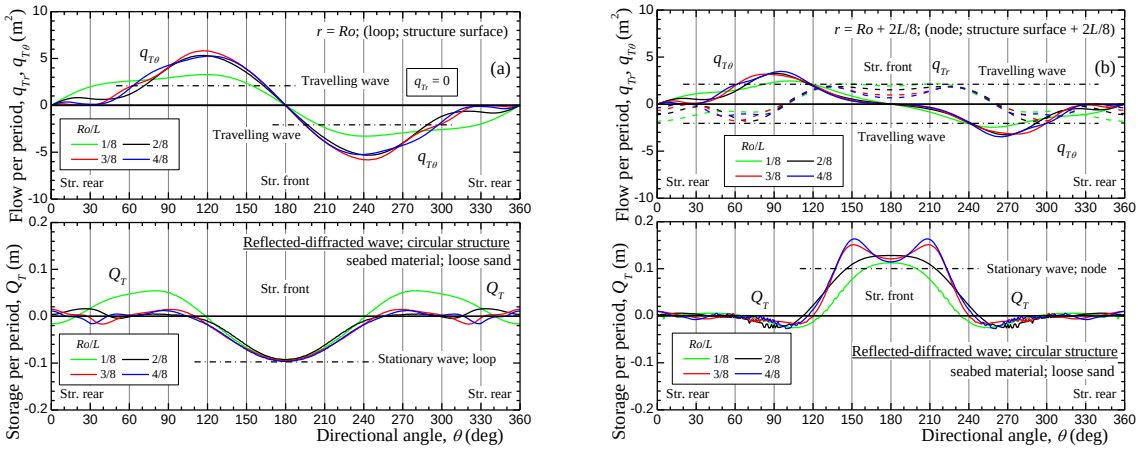

Fig. 7 Behavior of sediment flow along circumferential direction:
(a) (on structure side surface: loop) r=R_o, (b) (on concentric circle: node) r=R_o+2L/8

Plane view of the sediment flow

Figure 8 shows the plane view of sediment flow and associated storage of sediment near the cylindrical structure of R_o = L/4. The red vector indicates the direction and intensity of accumulated sediment flow q_T, and color gradation and contour lines indicate the intensity of sediment storage Q_T. Without structures, the incident wave and travelling wave generate uniform sediment flow with no-storage, in the opposite direction to the incident wave as shown in Figs. 7(a, b) (see [3]). As a result

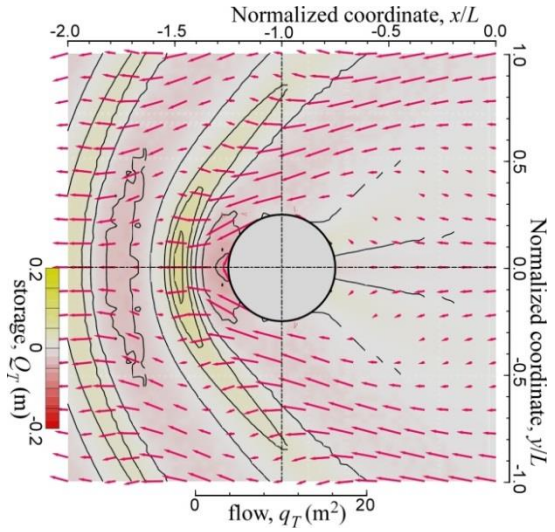

Fig. 8 Plane view of sediment flow and its storage around cylindrical structure: $R_o/L=L/4$

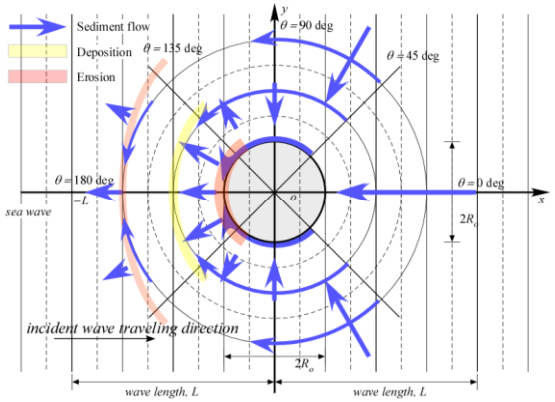

Fig. 9 Schematic explanation of sediment flow behavior around cylindrical structure: $R_o/L=L/4$

of the disturbances by the cylindrical structure, sediment storage occurs, and erosion and/or deposition are caused.

Figure 9 explains the sediment flow behavior schematically, where arrows are for accumulated sediment flow vector q_T; the thickness of the arrows roughly corresponds to the intensity of q_T. The curved lines indicate the storage of sediment Q_T; the thickness of the lines corresponds to the intensity of Q_T; and light red and light yellow are for erosion (Q_T<0) and deposition (Q_T>0), respectively. Overall behavior of the sediment flow can be explained as follows. Sediment flows toward the structure in the wide range including structure back (−90deg <θ <+90deg). The sediment flows from back to front along structure side surface: the flow is followed by the radial, flows away from the structure in the range including the structure front (120deg<θ<240deg). It should be noted that the erosion and deposition on the parabolic lines are repeated in the wide range of the structure front, which occurs under the influence of sea wave behavior similar to stationary wave with loops and nodes (see Figs. 5, 6). It would be important that the notable erosion on the structure front side surface possibly destabilizes the structure.

CONCLUSIONS

We explained the analysis method comprised with "the linear wave theory analysis", "effective stress analysis by poroelastic model" and "empirical evaluation method for traction sediment flow", and the sediment flow characteristics when the plane wave meets upright cylindrical structure was examined.

ACKNOWLEDGMENTS

The authors are grateful to the Japan Society for the Promotion of Science for its financial support with Grant-in-Aid for Research Activity Start-up 26889035 and Grants-in-Aid for Scientific Research (C)17K06553.

REFERENCES

[1] Oka F., Yashima A., Miura K., Ohmaki S. and Kamata A., Settlement of Breakwater on Submarine Soil Due to Wave-induced Liquefaction, 5th ISOPE, Vol.2, 1995, pp.237-242.

[2] Miura K., Morimasa S., Otsuka N., Yamazaki H. and Konami T., Combined Effect of Flow Velocity and Water Change on Wave-induced Seabed Destabilization, J. of Japan Society of Civil Engineers, Ser. B2 (Coastal Engineering), Vol.66, Issue 1, 2010, pp.851-855 (in Japanese).

[3] Tran, A., Q., Miura, K., Matsuda, T., and Yoshino, T., Sediment Flow Characteristics on Seabed Subjected to Stationary Waves with Diagonal Incident Wave Loading Near Line Structures, Proc 8th Int Conf on Geotechnique, Construction Materials and Environment, Kuala Lumpur, Malaysia, 2018, pp.379-384.

[4] MacCamy, R. C. and Fuchs, R. A., Wave forces on piles; a diffraction theory, Tech Memo, No.69, Beach Erosion Board, 1973, pp.1-17.

[5] Coastal Engineering Committee, Coastal Wave, Japan Society of Civil Engineers, 1994, pp.430-503 (in Japanese).

[6] Yamamoto T., H. S. L. Koning and E. Van Hijum, On the Response of a Pore-elastic Bed to Water Waves, J. of Fluid Mechanics, Vol. 87, Part 1, 1978, pp.193-206.

[7] Miura K., Asahara S., Otsuka N. and Ueno K., Formulation of Ground for Coupled Analysis of Seabed Response to Wave Loading, Proceedings of Symposium on Geotechnical Engineering, Vol. 49, 2004, pp.233-240 (in Japanese).

9th Int. Conf. on Geotechnique, Construction Materials and Environment, Tokyo, Japan, 20-22 November 2019, ISBN: 978-4-909106025 C3051

CARACTERIZATION OF CEMENTITIOUS BACKFILL WITH HIGH SULPHUR CONTENT

Daniela Ionescu[1], Joe Petrolito[2] and David Morton[3]
[1]School of Mathematical Sciences and Engineering, [2]School of Leadership, [3]School of Molecular Sciences, La Trobe University, Australia

ABSTRACT

The extraction and use of mineral resources are critical to modern societies. New technologies and practices have ensured the development of the mining industry. Currently, the industry is striving to become more efficient and more environmentally-friendly. This paper reports on the effect of chemical and mineralogical changes (weathering due to sulphate attack) with time on the mechanical properties of backfills. Fines, sulphide-rich gold tailings from the local Fosterville Mine, were mixed with varied cementing binders for the purpose of this study. Sulphate resistant binders (fly ash, ground granulated blast-furnace slag, silica fumes) were used in addition to general purpose cement to identify the effects of the binder and the age of the hardened cemented paste on the mechanical properties, as well as the effect of sulphate attack on these properties. The findings to date show that there is potential to replace current backfill materials with cemented paste backfill to increase mine productivity and ore profitability.

Keywords: Binder type, Cemented paste backfills, Mining stopes, Sulphite Resistant Binders, Sulphide tailings

INTRODUCTION

Mining gold is a multi-billion dollar activity in many countries around the world. In Australia, gold extraction has a long history in Bendigo and its surroundings. In this area, the rich gold-bearing quartz reefs are hosted by tightly forded Ordovician (480 Mya) marine sediments [1]. Recent drilling and bulk sampling by Kirkland Lake Gold Ltd at their operation at Fosterville Gold Mine (FGM) have shown that the gold resources exceed 1.03 million ounces in this region, and more than half of the estimated gold reserve has an average grade of 58.8g/t [2]. Furthermore, high-grade gold resources at relatively shallow depths were also reported [2].

FGM is located about 155 km north of Melbourne, in Central Victoria. It uses open stoping mining with delayed backfill in its operation as shown in Fig. 1. This method employs blasting to create a void called a stope. The ore from the stope is removed using drilling and blasting, then is transported to the extraction plant to separate the gold. Subsequently, the created void is backfilled with waste rock (rockfill, RF) and cemented rockfill (CRF), which is left to cure. The CRF backfill is used to increase the recovery of ore by minimising the requirement of leaving ore pillars, and provides ground support for the mine structures and a safe working environment. In addition, the CFR backfill minimises the risk of surface subsidence due to underground stopes, provides a disposal site for the waste rocks, and controls ore dilution from hanging wall and footwall. This extraction technique is considered one of the

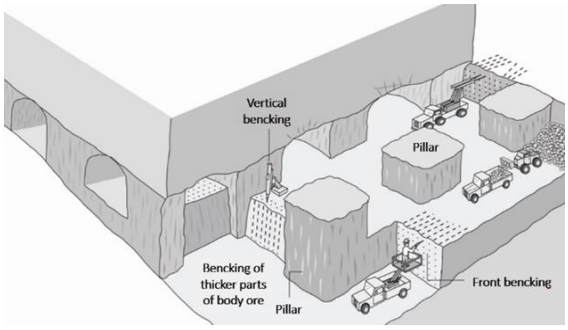

Fig. 1 Diagram of open stoping mining method.

better choices for mining steeply dipping tabular ore bodies [3]-[5], as is the case at FGM, and it also provides a good production and ore recovery rate. Annually, around 80,000 m^3 of voids are backfilled using a proportion of 75% CRF and 25% RF.

Whilst the current CRF backfilling method is considered to be working effectively, the operators at FGM have observed that when a new stope is created by blasting, hardened fill material from the adjacent stope can collapse [5]-[8]. This results in dilution of the ore, decreasing the productivity of the mine operation and increases the cost of ore processing. Furthermore, the ore extraction adjacent to newly CFR stopes is delayed by about a month, due to curing time required by the cemented rock fills to achieve the needed strength.

Farsangi [5], Belem and Benzaazoua [6], Kockler [7], Emad *et al.* [8], [9], Yumlu[10], and Miller *et al.* [11] have reported that vibrations from blasting are the main cause of collapse for CRF stopes.

However, the strength of cemented rockfill stope is affected by the type of binder, mix proportions, and the gradation and maximum particle size of the waste rock [12], [13]. In addition, factors such as cohesion and stiffness, and the size of the backfilled stope affect the strength of CRF [3], [6, [8].

More than three decades ago, new backfilling methods were introduced in underground open stoping mining with delayed backfill operations. One of these methods uses cemented paste backfill, which has gained worldwide acceptance in recent years as an integral part of underground mining processes. Cemented paste backfill (CPB) is a heterogeneous material made of tailing having about 70 % - 80 % solid content, water and a hydraulic binder [14]. This developing technology has both economic and environmental benefits [15]. Hence, FGM operators have commissioned this study to identify if cemented paste backfill provides higher strength for the exposed stopes, a faster curing time to enable a reduction in gold extractions costs and an increase in the operation productivity when compared with the current CRF backfill system.

This paper discusses the results of a continuing study at La Trobe University into the use of fine tailings supplied from FGM for cemented paste backfill. FGM has an annual production of about 606300 tones per year, which is expected to increase in the near future. The gold processing plant grinds the ore so about 80% of its mass is smaller than 75 μm. Flotation is then used to extract the gold locked within the pyrite/arsenopyrite minerals. The stream of tailings resulting from the gold production consists of 30% solids, and it is discarded in the tailings storage facility to desiccate. A significant volume of tailing results from the gold production, and hence FGM operators are interested in finding environmentally-friendly ways to use this waste material, while increasing their productivity and minimizing production costs.

MATERIAL REQUIREMENTS

Cemented paste backfill takes the form of a non-Newtonian fluid consisting of the full mine tailings that is mixed with a binding agent and water, and it has the consistency of a fine slurry [14], [15]. The pumping of the CPB is done over relatively long distances through the mine and then into the open stope [14]. Therefore, the mix should have a slump value of around 200 mm [16]. Typically, CPB contains about 75-85% by weight tailings, around 3-6% by weight cement and water to form the dense, pumpable mix [17], [18]. To increase the pumpability of the mix, researchers have suggested that tailings should have a minimum of 15% of the solid particles finer that 20μm, as this allows the surface tension of the water to form a lubricating film on the paste grains [18], [19].

In terms of the compressive strength of CPB, the water to cement ratio influences the unconfined compressive strength (UCS), as is the case for concrete. A higher ratio lowers the strength, due to the increase in porosity that typically is around 30% [17]. Furthermore, sulphate or sulphide minerals present in gold mine tailings reduce the strength of CPB and increase setting time of the mix [20].

EXPERIMENTAL PROGRAM

The physical characteristics of the materials used in the study were determined in accordance with relevant Australian Standards [21]. The governing factors were the compliance with current specifications and the feasibility of obtaining an acceptable and economic material.

Tailings

Considering the economic aspects, the supplied tailings used in this study were 'moist' tailings that were reclaimed from one of the two TSF currently used at FMG. The chemical composition of the tailings used in this study is presented in Table 1. Tailings were sampled from both the entrance and exit to/from the ponding area of Hunt's TSF to provide a better picture on the gradation of the supplied tailings. Figure 2 shows that the particle size distribution of the tailings fit between close boundaries. The coarser tailings were sampled from the entrance into the sedimentation pond and the finer tailings were collected from the exit. The content finer than 20 μm was about 35% - 41%. Hence, these tailings are ideal for the production of CPB. The moisture content of the desiccated tailings varied from 22.6% for the coarser tailings to 31.3 % for the finer tailings, while the specific gravity of the tailings varied from 1.39 to 1.46 for the finer and coarser tailings, respectively.

Table 1 Main chemical properties of the tailings supplied from Fosterville Gold Mine

Chemical component/compound	Content (wt.%)
$(K)(Al)xSiO_2$	35-45
$CaSO_4.2H_2O$	30
$FeOOH.0.4H_2O$	~1-5
FeS	0.5-1
$Fe(AsO_4).2H_2O$	0.1-0.5
H_2SO_4	0.5
As^{5-}	0.2-0.3
Fe^{3+}	0.1-0.2
FeAsS	0.1-0.2
Sb_2O_3	0.1-0.2

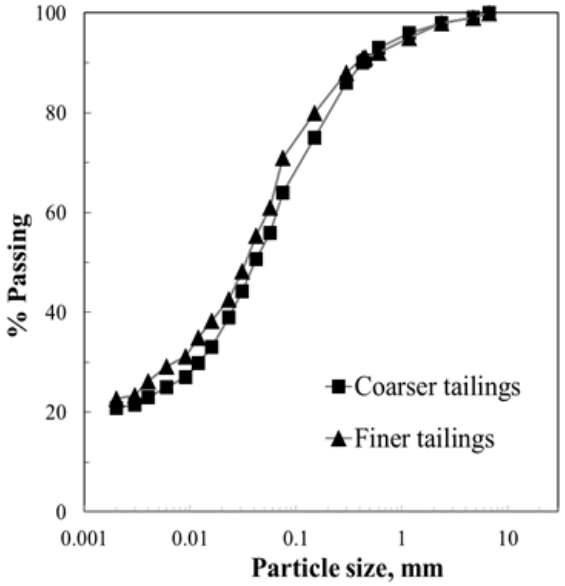

Fig. 2 Particle size distribution of tailings supplied from Hunt's tailing storage facility at FGM.

Binder

General-purpose Portland cement (type GP) was used for the control mix. To check the effect of binder type on the mechanical properties of CPB, three supplementary cementitious materials were also used in various proportions. These cementitious materials were class F fly ash (FA), ground granulated blast-furnace slag (GGBS) and silica fumes (SF). Past research [13], [22], [23] showed that CPB achieved acceptable strength even when the binder proportion was as low as 3% - 7% by weight. Hence, the binder content was limited to 5% in this study, and the following blends of cementitious materials were used:

- 5% General purpose Portland cement (5GP, the control mix)
- 3% Fly Ash + 2% GP Portland cement blend (3FA-2GP)
- 1% Silica Fume + 4% GP Portland cement blend (1SF-4GP)
- 4% Ground Granulated Blast-furnace Slag + 1% GP Portland cement blend (4GGBS-1GP).

Mix proportioning and specimen preparation

The required quantities of tailings, binder and water that were used for each batch type are summarized in Table 2. The moisture content of the supplied tailings was taken into account to achieve the required workability for a 200 mm slump [16]. The four batches were mixed in a flat pan mixer following the standard procedure for concrete preparation in the laboratory [24]. Compressive and indirect tensile strength specimens were prepared using the standard concrete molds corresponding to each test. Molds were removed after 24 hours, and specimens were placed in plastic containers and closed tightly. The specimens were dry-cured at room temperature until the test time (i.e., 7, 14 and 28 days), to simulate the underground environment where CPB would be placed. After the required curing times, the CPB specimens were subjected to various tests.

Table 2 Proportions of materials for the proposed mixes

Material	Mix type			
	5GP	3FA-2GP	1SF-4GP	4GGBS-1GP
Tailings (kg)	93.5	93.5	93.5	93.5
GP (kg)	10.8	4.1	8.0	2.2
FA (kg)	-	6.5	-	-
SF (kg)	-	-	2.2	-
GGBS (kg)	-	-	-	8.0
Water (L)	14	14	14	14

STRENGTH OF CEMENTED PASTE BACKFILL

One of the functions of CPB is to provide ground support to create a safe working environment, as well as to minimise surface subsidence. Hence, it is expected that the CPB would have reasonable strength for both short-term operations and the long-term management of backfilled stopes. The strength tests were performed following the standard procedure for laboratory measurement of concrete strength [25], [26].

Compressive strength of CPB

The variation of the compressive strength with the curing time is presented in Fig. 3. It should be observed that the partial replacement of general purpose cement with fly ash and silica fume caused a reduction in the compressive strength of about 36% - 45% and 12% - 35%, respectively when compared with the control batch prepared with GP cement. This reduction was independent of the age of the CPB. This shows that the hydration of the binder containing fly ash and silica fume was adversely affected by the sulphate content present in the supplied tailings. In contrast, partial replacement of GP cement with blast-furnace slag resulted a strength that is 2 to 3 times higher than the strength of the control batch (5GP). Typically, GGBS is used as a partial replacement for GP to produce sulphate-resistant concrete, and hence the test results were expected. It is interesting to note that the 4GGBS-1GP batch displayed a 16%

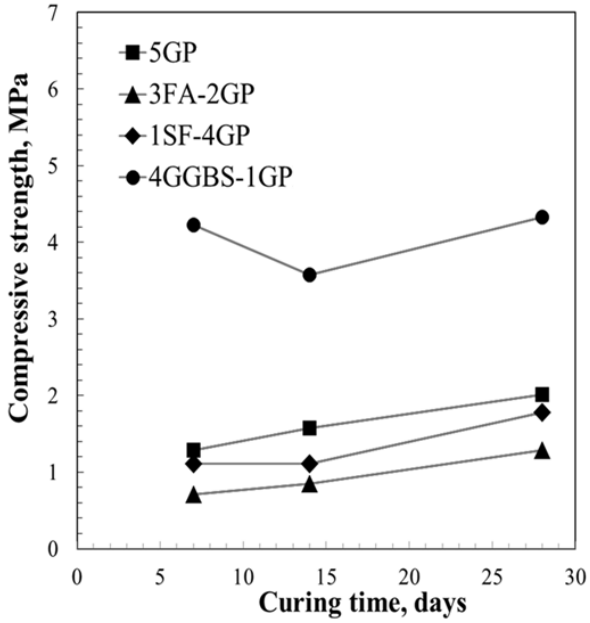

Fig. 3 Effect of binder type and proportion on the compressive strength of the proposed cemented paste backfills.

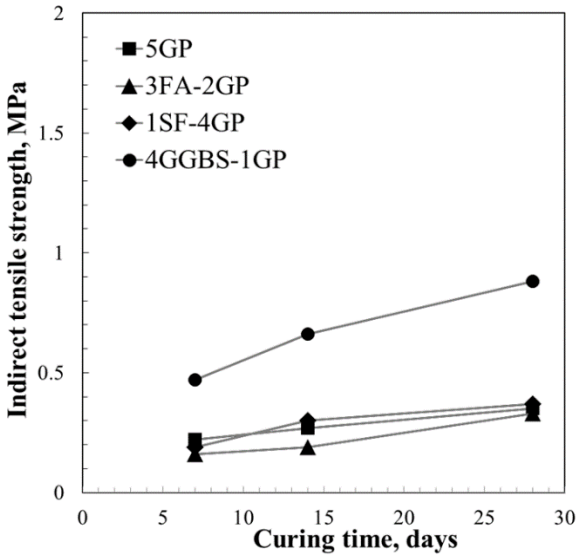

Fig. 4 Effect of binder type and proportion on the indirect tensile strength of the proposed cemented paste backfills.

reduction in compressive strength at 14 days. However, the loss in strength is recovered after longer curing times.

Indirect tensile strength of CPB

Another function of CPB is to provide stability for the freshly exposed stope during blasting processes, thereby avoiding dilution of the gold ore. Thus, it is expected that the CPB would have reasonable tensile strength, especially for short-term operations, to resist vibrations from blasting processes. The variation of indirect tensile strength with curing time is presented in Fig. 4. Similar trends were observed as for compressive strength, and the trends were independent of the age of the CPB. The partial replacement of general purpose cement with fly ash caused a strength reduction of about 15% - 28%. Interestingly, the effect of partial replacement of the general-purpose cement with silica fume caused an insignificant change in the strength when compared with the control batch (5GP). As expected, the highest indirect tensile strength was displayed by the batch containing GGSB, which had a strength of 2 to 2.5 times higher than the control batch (5GP). Furthermore, the rate of strength increase was highest for the 4GGBS-1GP batch.

CONCLUSIONS AND RECOMMENDATIONS

The effects of various binders on the strength of cemented paste backfill produced with tailings from a gold processing plant were discussed in this paper, and the following conclusions can be drawn.

Partial replacement of GP cement with FA resulted in lower compressive and indirect tensile strengths when compared with the CPB produced only with GP cement, and this result was independent of the curing time of the mix. Similar outcomes were obtained when GP cement was partially replaced with SF, although the change in the indirect tensile strength was minimal.

As expected, partial replacement of GP cement with GGBS resulted in a CPB with significantly higher compressive and indirect tensile strengths. In addition, the rate of increase of the indirect tensile strength was highest for this batch (4GGBS-1GP). Hence, the use of the GGBS binder as a partial replacement for GP cement proved to be the optimal cemented material for production of CPB using sulphide-rich gold tailings from FGM.

However, further research is needed on the elastic properties of the proposed mixes to enable numerical modelling of the performance of CPB in a practical mine to be undertaken. Furthermore, as the effect of sulphide has a detrimental long-term effect on the strength of CPB, this aspect needs to be further investigated.

ACKNOWLEDGMENTS

The authors gratefully acknowledge the help provided by Fosterville Gold Mine with the supply of materials. The assistance with preparation and testing provided by Mr Adam Dare, Mr David Osborne, Mr Zac Pentreath and Ms Laura Sonnberger is also acknowledged.

REFERENCES

[1] Ionescu, D., Evans, T. and Kilpatrick, A., Engineering applications of a mining by-product, in Proc. of the Int. Civ. Engg. Conf. on Sust. Dev. in the 21st Cent., 2003, pp. 437-442.

[2] Kirkland Lake Gold, News release, TSX:KL, 8 Aug. 2017, Toronto, Ontario

[3] Yu, T.R., Some factors relating to the stability of consolidated rockfill at Kidd Creek, in Proc. of the 4th Int. Symp. on Min. with Bckfl., 1989, pp. 279-286.

[4] Annor, A.B., A study of the characteristics and behaviour of composite backfill material, Ph.D. thesis, McGill University, Montreal Canada, 1999.

[5] Farsangi, P.N., Improving cemented rockfill design in open stoping, Ph.D. thesis, McGill University, Montreal, Canada, 1996.

[6] Belem, T. and Benzaazoua, M., An overview on the use of paste backfill technology as a ground support method in cut-and-fill mines, in Proc. of the 5th Int. Symp. on Grd. Sup. in Min. and Undgrd. Constr., 2004, pp. 637-650.

[7] Kockler, M., Design of cemented rockfill spans for longhole stoping at the Rain Mine, Carlin, Nevada, Ph.D. thesis, University of Idaho, 2007.

[8] Emad, M.Z., Mitri, H.S. and Henning, J.G., Some factors affecting cemented rockfill failure in longhole mining, in Proc. of the 20th Int. Symp. on Mine Plang. and Equip. Select., 2011, pp. 163-174.

[9] Emad, M.Z., Mitri, H.S. and Henning, J.G., Effect of blast vibrations on the stability of cemented rockfill, Int. J. Ming., Reclam. and Env., Vol.26, Issue 3, 2012, pp. 233-243.

[10] Yumlu, M., Backfill practices at Çayeli Mine, in: 17th Int. Ming. Congr. and Exhib. of Turkey, 2001, pp. 333-340.

[11] Miller, F., Potvin, Y. and Jacob, D., Laser measurement for open stope dilution, CIM Bull. Vol.85, Issue 962, 1992, 96-102.

[12] Mitchell, R.J., Olsen, R.S. and Smith, J.D., Model studies on cemented tailings used in mine backfill, Can. Geotech. J., Vol.19, Issue 1, 1982, 14-28.

[13] Fall, M., Benzaazoua, M. and Saa, E.G., Mix proportioning of underground cemented tailings backfill. Tunlg. and Undgrd. Spc. Techn., Vol.23. 2008, 80-90.

[14] Brackebusch, F., Basics of paste backfill systems, in Proc. of the Int. J. of Rock Mech. and Ming. Sci. and Geomech. Abstr., No.3, 1995, 122A.

[15] Sivakugan, N., Veenstra, R. and Naguleswaran, N., Underground mine backfilling in Australia using paste fills and hydraulic fills, Int. J. of Geosynt. and Grnd. Engg., Vol.1, Issue 2, 2015, 1-7.

[16] Canadian Standards Association, Methods of test and standard practices for concrete-Slump test, CSA A23.2-5C 2009, Cement Association of Canada, Mississauga, 2009

[17] Amaratunga, L. and Yaschyshyn, D., Development of a high modulus paste fill using fine gold mill tailings, Geotech. and Geol. Engg., Vol.15, Issue 3, 1997, 205-219.

[18] Sivakugan, N., Rankine, R.M., Rankine, K.J. and Rankine, K.S., Geotechnical considerations in mine backfilling in Australia, J. of Clean. Prod., Vol.14, Issues 12–13, 2006, 1168-1175.

[19] Kesimal, A., Yilmaz, E., Ercikdi, B., Alp, I. and Deveci, H., Effect of properties of tailings and binder on the short-and long-term strength and stability of cemented paste backfill, Mat. Letr., Vol.59, Issue 28, 2005, 3703-3709.

[20] Li, W. and Fall, M., Sulphate effect on the early age strength and self-desiccation of cemented paste backfill, Constr. and Build. Mat., Vol.10, No.6, 2016, 296-304.

[21] Standards Australia, AS1289 Methods of Testing Soils for Engineering Purposes, Standards Australia, Sydney.

[22] Fall, M., Benzaazoua, M. and Ouellet, S., Experimental characterization of the influence of tailings fineness and density on the quality of cemented paste backfill, Minrl. Engg, No.18, 2005, 41-44.

[23] Benzaazoua, M., Belem, T. and Bussière, B., Chemical factors that influence the performance of mine sulphidic paste backfill, Cem. and Concr. Resch., No. 32, 2002, 1133-1144.

[24] Standards Australia, Methods of testing concrete - Preparation of concrete mixes in the laboratory, AS 1012.2, Standards Australia, Sydney, 2014.

[25] Standards Australia, Methods of testing concrete Compressive strength tests - Concrete, mortar and grout specimens, AS 1012.9, Standards Australia, Sydney, 2014.

[26] Standards Australia, Methods of testing concrete - Determination of indirect tensile strength of concrete cylinders (Brasil or splitting test), AS 1012.10, Standards Australia, Sydney, 2000 (R2014).

9th Int. Conf. on Geotechnique, Construction Materials and Environment, Tokyo, Japan, 20-22 November 2019, ISBN: 978-4-909106025 C3051

INFLUENCE OF CHEMICAL PROPERTIES AND MINERAL CONTENTS ON SANDSTONE STRENGTH

Haryati Awang[1], Nor Hayati A Hamid[2] and M Idris Ali[1], Noram I Ramli[1], Ramadhansyah PJ[1]
[1]Faculty of Civil Engineering & Earth Resources, Universiti Malaysia Pahang, Malaysia; [2]Institute for Infrastructure Engineering & Sustainable Management, Universiti Teknologi MARA, Shah Alam, Malaysia

ABSTRACT

Malaysia is a country which experiencing wet tropical weathering. Rock material in this country is affected by weathering action as they exposed to the weathering process throughout the year. In verifying the material properties of rock, laboratory tests are needed to ensure a safe design of structures and foundations.This paper presents the results of laboratory investigation of chemical properties, mineralogical content and mechanical properties of the rocks and the influence of the chemical and mineral contents to the rock strength. This experimental works is about to investigate the significant of chemical content to the rock strength particularly in sedimentary rock of sandstone type. For this purpose, Alkali Silica Reactivity (ASR), Petrographic Image Analysis, Unconfined Compression Strength (UCS), Shear strength and Tensile strength tests were carried out. The correlations between the chemical properties, petrographic characteristics (minerals) and engineering properties of sixteen sandstones samples by simple regression analysis and bar chart were presented. Abundance of quartz mineral, carbonate minerals and cement in the sandstone increase the rock strength, and reduction of easily dissolve mineral like carbonate minerals, reduced the strength of the rocks. This study also suggested that the ASR has less significant to the Shear strength and uniaxial compression strength as the quantity of these deleterious minerals such as opal, chalcedony, volcanic glass, cristobalite, tridymite and cryptocrystalline quartz are very low compared to main minerals.

Keywords: Mineral content; Strength properties; Weathering; Chemical properties; Sandstone

INTRODUCTION

In tropical country like Malaysia, weathering plays important role in determining the strength of rock. However, rock strength is also influenced by the rock type either it is in the group of igneous, sedimentary or metamorphic. Among these rocks, sedimentary rock with its physical characteristics of bedding, lamination and clastic grains provide an easy way that prone to weathering, thus weaken the rock mass and material. According to [1], [2] properties such as porosity, density, chemical content, mineralogy and degree of cementation are related to the rock strength. These rocks with their own chemical properties and mineral content could influence the rock strength as rock is composed of minerals. Mineral bond in rocks is known as cementation. Strength of rock increase proportionally with the degree of cementation [3], the minerals bond in rocks. According to [4], chemical composition of rocks influences its surface energy and its chemical reactivity. The chemical functionalities in rocks play a predominant role in rock strength. Aggregates containing certain constituents can react with alkali hydroxides in concrete [5]. The reactivity is potentially harmful only when it produces significant expansion. Alkali silica reaction (ASR) is chemical reactions which occur between certain reactive minerals in some aggregates and alkali in the pore solution of concrete. According to [6] the ASR results from the reaction of disordered forms of silica minerals in aggregates and the hydroxyl ions (OH–) in the pore fluid of concrete.

Even though many researches have been done to relate mineral contents and the mechanical properties of rocks [6],[7],[8], the relationship between the chemical properties and sedimentary rock strength is still not well identified. Most of the researches explained no conclusive finding on rock strength for the three types of rocks; igneous, sediment and metamorphic rock based on chemical and mineral contents of rocks. This paper is presented to identify the relationships between the chemical properties and mineral contents on the strength of weathered sandstone that widely distributed in tropical country like Malaysia. The results of this study could be used to estimate the strength of sandstone for future development in weathered environment like Malaysia

.

MATERIAL AND METHODS

A number of sixteen (16) sandstone rock cores were collected from the area of Jerantut in the state

of Pahang, Malaysia for this study. The strength tests that were carried out are uniaxial compressive strength, Triaxial Shear test, Direct Shear tests and indirect tensile strength (Brazilian) tests. The test for uniaxial compression strength was according to the ASTM D7012 specification. This test method covers the determination of the strength of intact rock core specimens in uniaxial compression load. Triaxial shear tests have been used to gain an understanding of rock behaviour under a three-dimensional state of stress and to verify, and even validate, mathematical expressions that have been derived to represent rock behaviour in analytical and numerical models. It is through the results of triaxial tests that yield strength criteria have been developed and material specific strength characteristics are determined. The parameters obtain from this test are the friction angle and cohesion in relation to the following equation:

$$\tau = \sigma \tan\theta + c \qquad (1)$$

where; τ is shear strength; σ is shear stress; ɵ is friction angle and *c*, is cohesion of rock material.

Direct shear strength test of rock core is purposely to establish the shear strength properties of discontinuities in rock. These core samples were to be tested for their shear strength along selected fracture plane (existing natural joint) and under a specified normal stress. Throughout the shearing process, the normal stress was maintained at constant level and as such this test is also termed as *single-stage direct shear* test in accordance to ASTM D5607-08. Data obtained from the test were shear behaviour (shear stress vs. shear displacement), peak shear strength, and the corresponding horizontal displacement where the peak strength occurs.

The tensile test method is also referred as Brazilian test where cylindrical intact rock specimens are loaded at diametrically –opposed surfaces by a uniformly distributed, radial stress (ASTM D3967-08). It is an indirect measurement of tensile strength of rocks by applying compressive on the rock samples. The parameters obtain from this test are the relation between splitting tensile and load applied, diameter and length of sample as following:

$$\sigma = \frac{2P}{\pi DL} \qquad (2)$$

where; σ is splitting tensile strength; *P* is maximum load; *H* is height and *D* is diameter of rock material. For chemical contents and mineralogical analysis, Alkali Silica Reactivity (ASR) test was measured the result of reaction of an aggregate with alkali where the procedure is recognized by as ASTM-C289-07. The potentially alkali reactive rocks are not used for the production of aggregates because deleterious aggregates will affect the soundness of concrete structures and adversely impact the construction industry. The objective of this test is to assess the potential alkali-aggregate reactivity of sandstone samples. Another test is petrographic analysis recognised by ASTM- C295-08 for mineral composition identification in sandstone.

RESULT AND DISCUSSIONS

Strength properties

Results from the laboratory experiments for strength properties are given in Table 1. The values in the tables shows the UCS was collected from uniaxial compressive strength test while the triaxial test provide parameters for cohesion (c) and friction angle (θ^o). The parameter collected from the direct shear test for discontinuities or joint on the rock core is named as friction angle at joint (θ^o).

Table 1 Results of strength properties for sandstone

Sample	σ_{UCS}, (MPa)	c, (MPa)	θ (°)	Θ at joint (°)	$\sigma_{tensile}$, (MPa)
1	22.0	5	47	35.87	7.62
2	23.0	7	28	42.16	16.46
3	40.0	-	-	39.50	25.56
4	20.0	5	47	42.16	6.66
6	33.7	-	-	37.85	2.81
7	107.1	-	-	36.12	6.24
8	16.3	8	0	28.01	14.52
9	81.6	-	-	35.36	13.42
10	202.0	-	-	36.62	9.36
11	98.0	-	-	41.15	23.37
12	63.8	-	-	26.57	7.90
13	17.0	3	62	26.57	6.43
14	4.3	1.5	22	30.16	12.38
15	193.0	15	68	39.50	3.02
16	167.0	28	52	38.80	14.42

Chemical properties and mineral content

Results for mineral contents were collected from petrographic analysis and alkali silica reactivity tests were tabulated as in Table 2. Distribution of minerals in sandstone that composes of quartz, carbonate matrix, calcite, rock fragments and accessory minerals is presented in Fig.1. Among these minerals quartz shows the highest content in sandstone with range from 18.5% to 92.4%, followed by carbonate matrix, 2.1% to 86.4% and rock fragments, 1% to 80.9%. Calcite and

accessories minerals presents lowest in sandstone ranges from 2% to 16% and 0.5% to 1.1% respectively. The mineral distribution of sandstone is similar as discussed in petrographic [4], confirmed that the samples are sandstone. In some cases, like in sample 1 to sample 6 the calcite mineral is absent. The high content of quartz in sandstone is due to the nature of sedimentation of weathered parent rock such as granite with high contain of quartz that broken to small particle called as sand. This quartz grains were transported by the weathering agent like water, glacier or wind to be deposited and cemented as sandstone.

Correlation between mineralogy and strength properties

Relationships between the percentages of the main minerals and uniaxial compressive strength (UCS)
The relation between the percentages of the main minerals and uniaxial compressive strength (UCS) is given in Fig. 2. As can be seen in this figure, quartz (Q) have a very important role in strength increment in Sandstone. In contrast the carbonate mineral (CM) have a very important role in strength reuction. The reason on why mineral can easily

Table 2 Results of mineral content and chemical properties of sandstone

Sample	Weathering Grade	Petrographic Analysis				Alkali Silica Reactivity	
		Mineral Composition (%)				Average concentration of dissolved silica in NaOH (%)	Potential Reactivity specification
		Q	CM	C	R		
1	II	53.9	41.7	-	3.5	0.9	0.042
2	1	66.4	25.9	-	6.9	0.8	0.051
3	1	-	86.4	-	13.6	-	0.219
4	1	65.9	27.1	-	6.5	0.5	0.043
6	1	-	18.5	-	80.9	0.6	0.014
7	1	-	56.2	-	43.3	0.5	0.039
8	1	92.4	1.6	3.9	1.5	0.6	0.121
9	1	54.2	43.0	-	4.0	0.5	0.136
10	1	18.5	79.1	-	1.5	0.6	0.251
11	1	81.9	10.8	5.9	1.0	0.4	0.204
12	II	70.9	19.4	-	9.3	1.2	0.292
13	1	82.0	2.1	12.4	2.4	1.1	0.006
14	1	84.0	2.3	11.0	2.2	0.5	0.177
15	1	76.3	4.1	16.2	2.75	0.65	0.150
16	1	42.2	52.1	2.0	3.2	0.5	0.065

Note: Q=quartz; CM=Carbonate matrix and cement; C= Calcite; R= Rock fragments; A= Accessory minerals

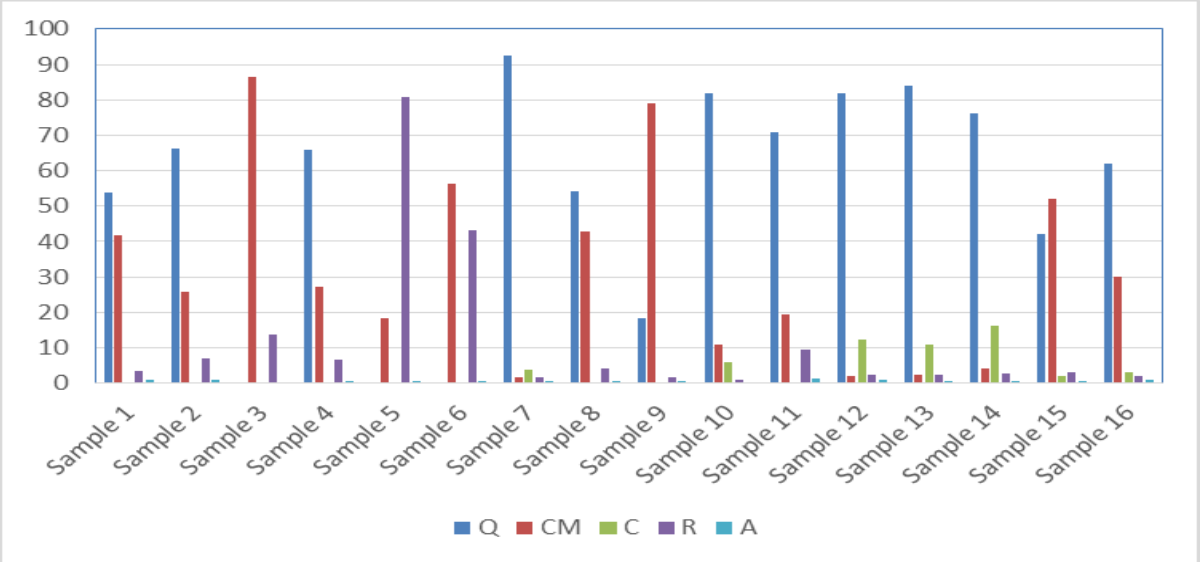

Figure 1: Distribution of minerals in the sandstone rock material

react with and wash away thus weakened the material. The strong correlation between quartz content the increasing of quartz increased the strength and increasing of carbonate mineral decreased the strength of sandstone is that quartz is a high resistance mineral to weathering agent. Meanwhile, carbonate dissolve in water. So that quartz will stay longer in the rock as part of mineral composition and strengthen the rock material while carbonate will and compressive strength is validated by many researchers [10,11].

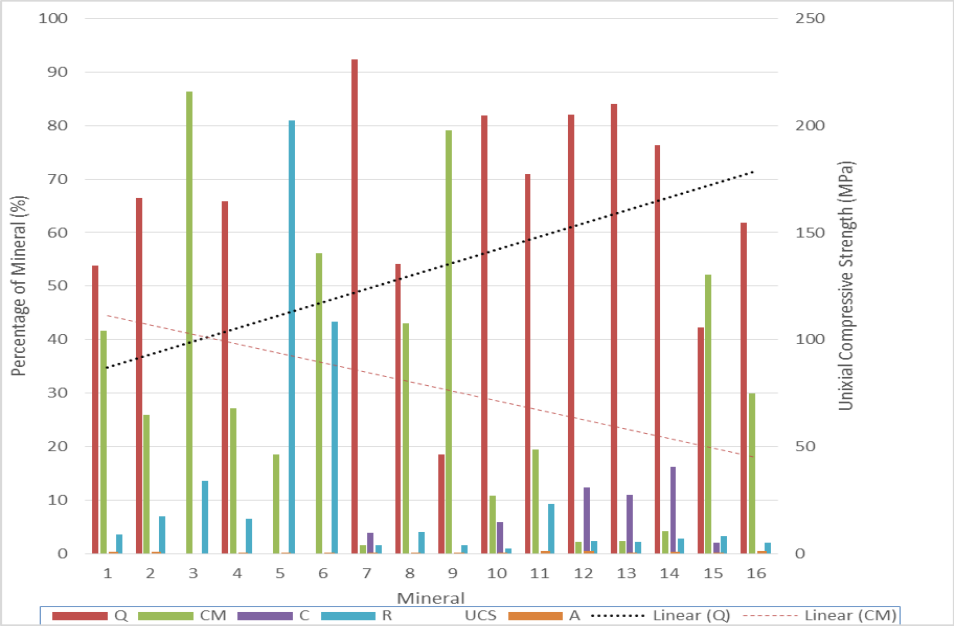

Figure 2: Relationship between the percentage of minerals and the uniaxial compressive strength

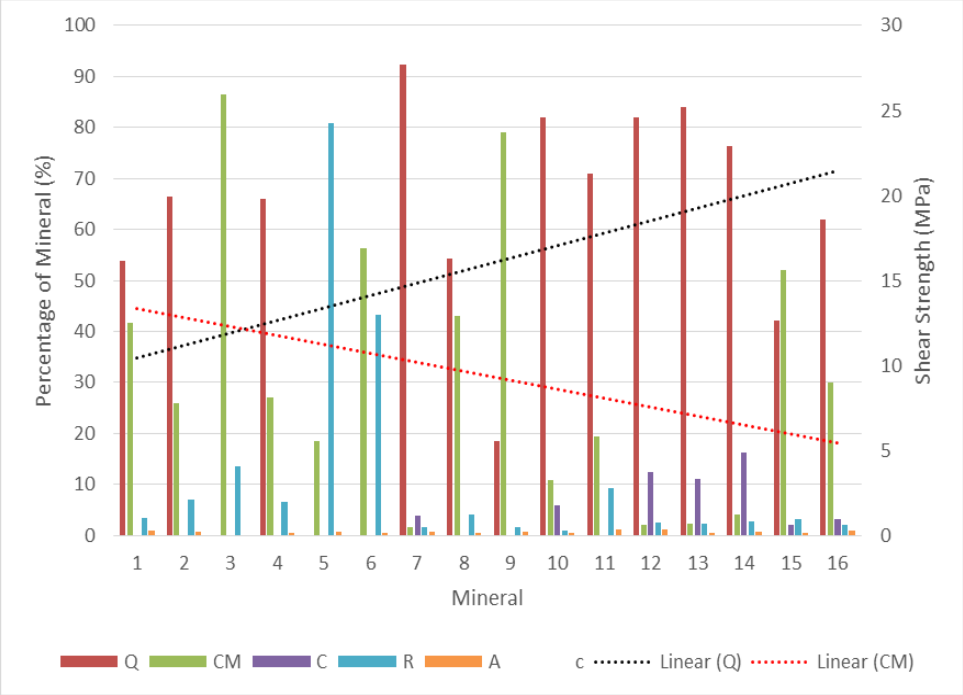

Figure 3: Relationship between the percentage of minerals and the shear strength

Relationships between the percentages of the main minerals and shear strength

The relation between the percentages of the main minerals and shear strength is given in Fig. 3. Similar to UCS quartz also have a very important role in shear strength increment in Sandstone. The carbonate mineral (CM) have a very important role in strength reduction. The reason on why the

increasing of quartz increased the strength and increasing of carbonate mineral decreased the strength of sandstone is that quartz is a high resistance mineral to weathering agent such as water, wind or heat. Meanwhile, carbonate mineral will wash away thus weakened the material. can easily react with and dissolve in water. So that quartz will stay longer in the rock as part of mineral composition and strengthen the rock material while carbonate will wash away thus weakened the material.

strength of rock material due to that the The hydroxyl ions usually originate from the sodium and potassium alkalis in the Portland cement during hydration. The reaction produces a gel-like material that can be expansive when exposed to water. Reactive silica materials that can cause deleterious expansion listed in decreasing order are: opal, chalcedony, volcanic glass, cristobalite, tridymite and cryptocrystalline quartz [7] These ASR minerals are not abundance in the sandstone and thus, will not influence the strength of the rock.

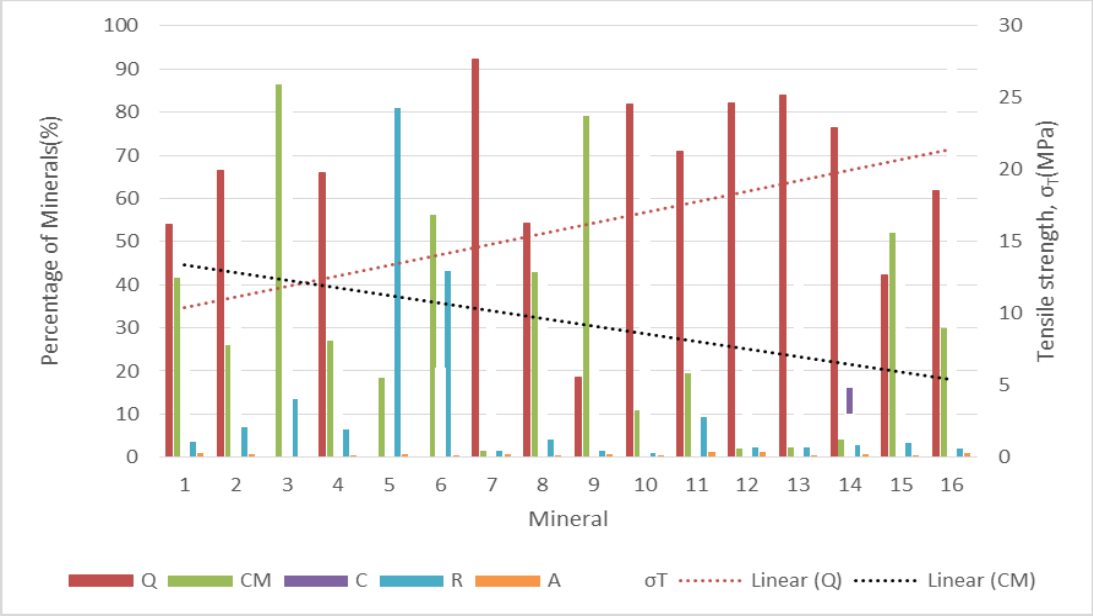

Relationships between the percentages of the main minerals and tensile strength

In the case of indirect tensile strength, the relationship follows the same trend, where the tensile strength increase with the increment of percentage of quartz mineral and the tensile strength reduce with the reduction of the percentage of carbonate mineral in the sandstone as shown in Fig.4. The composition of quartz mineral in sandstone strengthen the rock as quartz is a strong mineral with hardness of 7 however samples with low percentage of carbonate mineral weakened the sandstone with the same reason that the carbonate mineral can easily dissolve in water when react with water. Furthermore, the hardness of the carbonate mineral is less than 3.

Correlation between Alkali Silica Reactivity (ASR) and Strength Parameters

The relationships between ASR and UCS; ASR and shear strength; and ASR and tensile strength showed poor correlations as the R^2 is 0.13, 0.034 and 0.063 respectively as shown in Fig 5. This indicates that the ASR is less significant to the

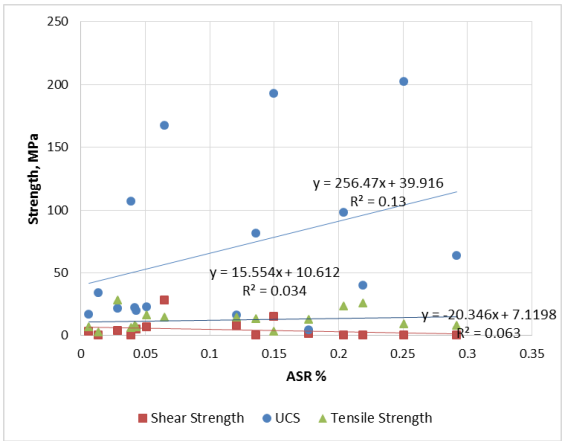

Figure 5: Relationships between the ASR and strengths of sandstone**.**

CONCLUSIONS

The correlations between the minerals and the strengths of sandstone rock samples were determined by simple regression analysis and bar charts. The first conclusion of the study is, quartz (Q) have a very important role in uniaxial

compressive strength increment in sandstone meanwhile the carbonate mineral (CM) have a very important role in strength reduction. The same trend also followed by the correlation with shear strength and tensile strength. Secondly, the percentage of strong minerals (i.e. quartz and cement) and weak minerals (i.e. carbonate minerals) can have opposite effects on the strength parameters of the rocks. The strength increases as the quartz and cement content increases. Thirdly, the relationships between ASR and UCS; ASR and shear strength; and ASR and tensile strength showed poor correlations between them as the ASR minerals is not abundance in sandstone and presents in very small amount .

ACKNOWLEDGMENTS

Please make sure you register before the registration deadline for your papers to be included in the proceedings and to be evaluated for conference awards. This is strictly necessary for logistics and smooth operation of the conference. Those who register and make payment after the registration deadline will not be guaranteed that their papers are included in the proceedings. Try to follow the reference style below.

REFERENCES

[1] Franklin, J. Suggested methods for determining water content, porosity, density, absorption and related properties and swelling and slake-durability index properties. Int. J. Rock Mech. Min. Sci. and Geomech. , 16, 1979, pp. 141-156

[2] Mc Neilly, M..F.. Ground support design and analysis: Exchange place station improvements. Proceedings of the North American Tunneling Conference 2004, 17-22 April 2004, Atlanta, Georgia, USA

[3] Pettijohn, F.J., Potter, P.E., Siever, R. Sands and Sandstones, Springer Science & Business Media, 6 Dec 2012 - Science - 631 pages

[4] Kosmatka, S.H. Diagnosis and control of alkali-aggregate reactions in concrete: Portland Cement Association. 1997. Pp. 1-23.

[5] Yusof, N. and Zabidi, H. Correlation of mineralogical and textural characteristics with engineering properties of granitic rock from Hulu Langat, Selangor. Procedia Chemistry, 19, 2016. pp. 975-980.

[6] Hobbs, D.W. (1990). Alkali-silica reactions. In Standards for Aggregates, ICE Publishing. 1988. pp. 1-192.

[7] Ng Tham Fatt, John K. Raj & Azman A. Ghani. Potential Alkali-Reactivity of Granite Aggregates in the Bukit Lagong Area, Selangor, Peninsular Malaysia. Sains Malaysiana 42(6)(2013). pp. 773–781

[8] Tayebeh Keikha, Hamed A. Keykha. Correlation between Mineralogical Characteristics and Engineering Properties of Granitic Rocks. Electronic Journal of Geotechnical Engineering · January 2013, Vol. 18 [2013], Bund. S, pp 4055-4065

[9] Wenjuan Sun, Linbing Wang, Yaqiong Wang. Mechanical properties of rock materials with related to mineralogical characteristics and grain size through experimental investigation: a comprehensive review. Frontiers of Structural and Civil Engineering, September 2017, Volume 11, Issue 3,, pp 322–328.

[10] Gunsallus K L, Kulhawy F H. A comparative evaluation of rock strength measurements. International Journal of Rock Mechanics and Mining Sciences & Geomechanics Abstracts, 1984, 21(5): 233– 248 20.

[11]Tuğrul A, Zarif I H. Correlation of mineralogical and textural characteristics with engineering properties of selected granitic rocks from Turkey. Engineering Geology, 1999, 51(4): 303–317

9th Int. Conf. on Geotechnique, Construction Materials and Environment, Tokyo, Japan, 20-22 November 2019, ISBN: 978-4-909106025 C3051

NUMERICAL ANALYSIS ON MECHANISM OF DEWATERING AS A MITIGATION METHOD AGAINST LIQUEFACTION IN SOFT GROUND

Yukihiro Morikawa[1], Ho Cho[2]
[1,2] Department of Civil Engineering, Nagoya Institute of Technology, Japan

ABSTRACT

In recent years, liquefaction due to major earthquake caused serious damages to many infrastructures and houses around the world. In order to protect people's daily life and infrastructure from the disaster, development of effective and economical countermeasure against liquefaction that can be applied to existing houses is becoming increasingly important. Although many liquefaction countermeasures have been developed by many researchers, most of them require large construction machines and are costly, which limits their application to existing structures. For this reason, a liquefaction countermeasure, called as groundwater-level decreasing method, has been proposed in Japan. This method has already been put into practice and the construction of the countermeasure has finished several years ago. The purpose of this method is to change a liquefied layer to a non-liquefied layer by lowering the groundwater level. Yet the performance of this method has not been fully evaluated quantitatively. Therefore, in this paper, numerical analysis using FEM method was carried out to evaluate the liquefaction damage before and after the lowering of groundwater level. The calculation is conducted with 2D soil-water coupling finite element-finite difference (FE-FD) analysis based on a rotating-hardening elastoplastic constitutive model. From the analyses, it is found that the effective stress of the ground below under-groundwater level increases significantly because of the lowering of groundwater-level, resulting in an increase in resistance to liquefaction and mitigating the settlement damage of liquefiable ground.

Keywords: Liquefaction, FEM, Countermeasure, groundwater-level decreasing method

1. INTRODUCTION

In recent years, the liquefaction occurred seriously in the world, e.g., 1995 Southern Hyogo Prefecture Earthquake, 2004 Mid Niigata Prefecture Earthquake, 2011 off the Pacific coast of Tohoku Earthquake, 2011 Canterbury earthquake, 2016 Kumamoto Earthquake, and 2018 Hokkaido Eastern Iburi Earthquake. In particular, the liquefaction damages in Tohoku Earthquake (2011) [1]-[2] were the heaviest recoded ever in Japan history. As shown in Fig. 1, one of the damage site, the liquefaction area covered 600 km along the Northeast coast of Japan and about 27,000 houses experienced severe damaged.

Therefore, development of effective and economical countermeasure against liquefaction for existing houses is very important and urgently needed. In this study, particular attention is paid to the performance of the groundwater-level decreasing method that has been already put into practical use as a countermeasure against liquefaction with numerical tests. In this method, continue drainage of groundwater is necessary so that the effective stress of ground can be increased and the excess pore water pressure can be dissipated quickly in a wide area with relative low cost. It is thought that these effects are effective not only for the large main shock, but also for multiple aftershocks in a short period of time.

The purpose of the research is to evaluate quantitatively the performance of the method that is still not enough at current stage. In this study, numerical analysis is conducted on the liquefaction damages of the ground in Ibaraki prefecture, Japan, dynamic FEM method considering the main shock and aftershocks in a unified way. The earthquake waves in the calculation were recorded in the Tohoku Earthquake (2011). In the analysis, a series of repeated dynamic-static analyses, considering not only the earthquake loading but also the static consolidation after each earthquake shock, are conducted in a sequential way just the same as the scenario happened in the Earthquake.

Fig. 1 Liquefaction damage in the 2011 off the Pacific coast of Tohoku Earthquake

2. ANALYSIS METHOD

The numerical analyses to evaluate the effect of a liquefaction countermeasure were conducted by a 2D/3D soil-water coupled finite element method program named as DBLEAVES [3] using based on the Cyclic Mobility model [4]. The applicability and the accuracy of the DBLEAVES has been firmly verified by shaking table tests for piles [5]-[8] and various liquefaction case histories [9]-[11].

Cyclic Mobility model is a kind of rotating-hardening elastoplastic model based on Cam-clay model [12]. It can consider properly the effects of stress-induced anisotropy, density and structure of soils in a unified way by introducing concept of subloading yield surface [13] and superloading yield surface [14], as shown in Fig. 2.

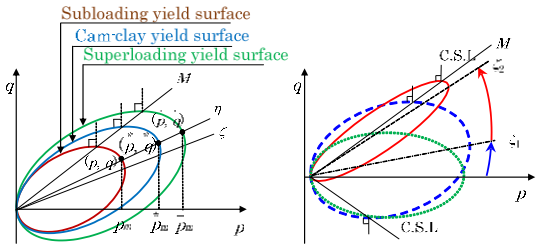

Fig. 2 Concept of Cyclic Mobility model [11]

The DBLEAVES can reproduce or predict accurately the overall mechanical behavior during and after the earthquakes, including the liquefaction and consolidation in repeated earthquake vibrations by describing properly the mechanical behaviors of soil subjected to monotonic/cyclic loading under drained/undrained conditions. In particular, the study of re-liquefaction using DAVLEAVES taking into account aftershocks [11], it was possible to reproduce the same phenomena as the observed phenomena, especially, a liquefaction happened easily by a small aftershock when the ground was not recovered from the damage by main shock and the range of liquefaction is expanded by aftershocks. For more detailed information about DBLEAVES and Cyclic Mobility model can be referred to references [3]-[4].

3. NUMERICAL ANALYSIS CONDITION

3.1 Investigated Site and Analyses Mesh for FEM

The investigated site, located at Ibaraki prefecture, experienced serious liquefaction damage during the 2011 off the Pacific coast of Tohoku Earthquake. Figure 3 shows the FEM mesh used in the calculation based on boring survey. The model ground consists of filling soil (Fs: 3.5 m), loose sand (As: 5.5 m) and dense sand (Ds: 11.0 m), and there is an embankment with a height of 1.0 m and a width of 60 m on the ground.

The ground area considered in the FEM analysis is 120 m in width and 20 m in depth, each mesh has width of 0.50 m and depth of 0.50 m. Here, the ground water level is set at -1.0 m of the ground level. In the case of dynamic analyses, an equal displacement boundary is adopted at side boundaries (x direction) to deal with the energy dissipation problem caused by artificial boundaries used in FEM. The bottom is assumed to be fixed in all directions.

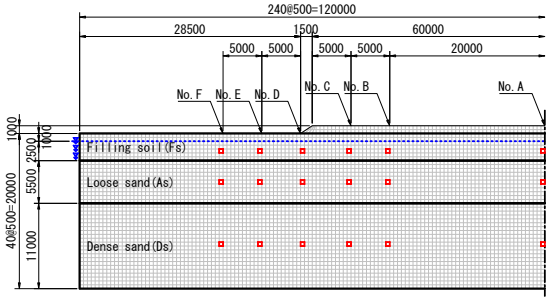

Fig. 3 FEM mesh for calculation

3.2 Earthquake Waves

The earthquake motion in N-S direction recorded at Hasaki-2 923m below the ground surface at Ibaraki Prefecture in the 2011 off the Pacific coast of Tohoku Earthquake (Tohoku wave) is selected to be the input earthquake motion in analyses, as shown in Fig. 4. A maximum acceleration of the main shock was 0.62 m/s^2 and that of aftershock was 0.94 m/s^2. The interval between the main shock and aftershock was approximate 24 minutes.

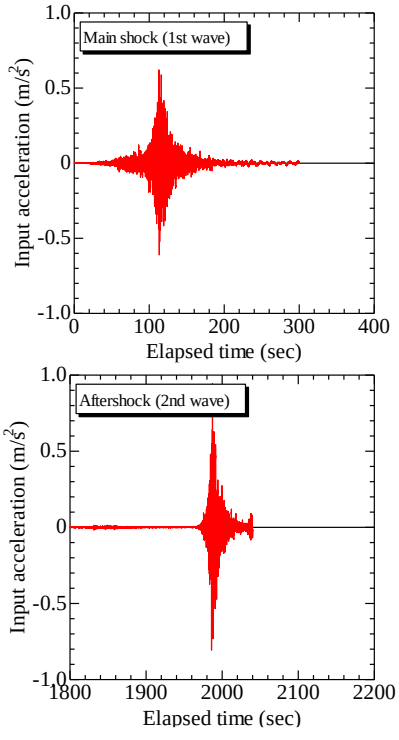

Fig. 4 Earthquake waves for calculation

3.3 Simulation Scenario

By lowering the groundwater level, it is expected that the effective stress of the ground can be increased in addition to the excess pore water pressure (EPWP) being dissipated quickly. Therefore the following four cases were carried out to evaluate the liquefaction damage before and after lowering the groundwater level:

Case A (Water Level: G. L. -1.0m): This is a basic case for unimproved ground.

Case B (Water Level: G. L. -2.0m): In this case, the groundwater level is lowered by 1.0m but initial effective stress is kept the same.

Case C1 (Water Level: G. L. -3.0m): In this case, the groundwater level is lowered by 2.0m but initial effective stress is kept the same.

Case C2 (Water Level: G. L. -3.0m): In this case, the groundwater level is lowered by 2.0m while the initial effective stress is increased accordingly.

In all cases, the calculation is conducted using the same Tohoku wave: (1) main shock, (2) 1440 seconds consolidation, (3) aftershock, (4) consolidation until the settlement of the ground ceased completely (50 years later).

3.4 Material Parameters

The material parameters used in calculation are shown in Table 1. The parameters of the embankment on the ground are the same values as the filling soil. Here, the initial effective stress in each ground is given as the vertical stress in the central part of each ground with the coefficient of earth pressure at rest K0 of 0.5. Near the investigated site, standard penetration test was conducted, and it was possible to obtain a columnar section, N value and unit weight. However, data other than N value and unit weight (such as result of tri-axial test with undrain cyclic loading of soils and permeability test) were not available, some of these parameters were determined with reference to the standard penetration tests and those of Toyoura sand. Therefore, studies in this paper is a numerical experiment on a virtual ground rather than a simulation for liquefaction damage that actually occurred in the 2011 off the Pacific coast of Tohoku Earthquake .

Figure 5-1 to 5-3 shows the simulation results of the element behavior in undrained cyclic loading test when the cyclic stress ratio is set to 0.10. From the results, it is known that the strain accumulates as the number of cyclic loading increases, and liquefaction accompanied by cyclic mobility occur in the filling soil and loose sand. However, liquefaction will not occur easily in the dense sand.

Table 1 Material parameters

	Filling soil	Loose Sand	Dense sand
Compression index λ	0.026	0.022	0.017
Swelling index κ	0.005	0.004	0.003
Stress ratio at critical state R_f	3.000	3.840	4.600
Void ratio e_0 (p'=98kPa on N.C.L)	0.550	0.550	0.470
Passion's ratio ν	0.300	0.300	0.300
Degradation parameter of over-consolidation m	0.100	0.100	0.100
Degradation parameter of structure a	2.200	2.200	2.200
Evolution parameter of anisotropy b_r	1.500	1.500	1.500
Unit weight γ (kN/m^3)	18.62	19.31	17.84
Permeability k (m/sec)	5.0E-5	5.0E-5	5.0E-5
Initial structure R^*_0	0.800	0.800	0.800
Initial degree of over-consolidation $1/R_0$	6.000	8.000	10.000
Initial anisotropy ζ_0	0.000	0.000	0.000

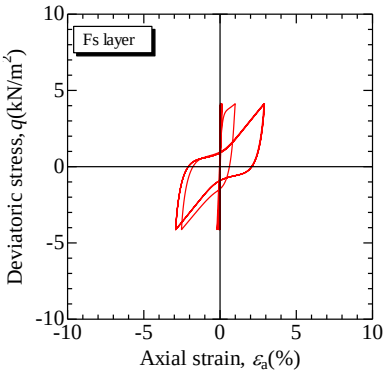

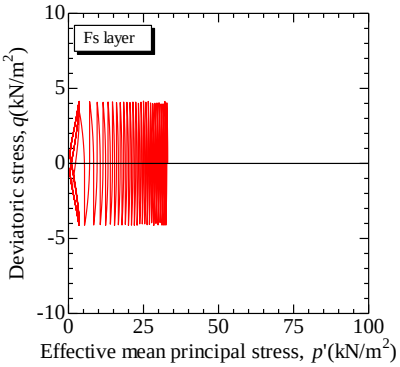

(a) Filling soil: Fs

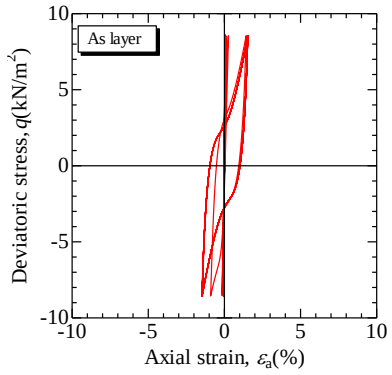

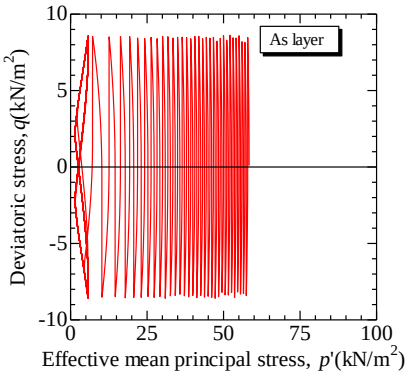

(b) Loose sand: As

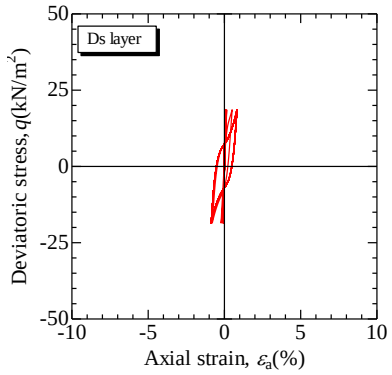

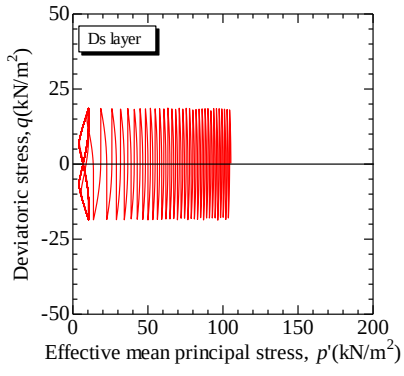

(c) Dense sand: Ds

Fig. 5 Simulated element behavior of soils

4. RESULT AND DISCUSSIONS

Figure 6 and 7 shows the calculated excess pore water pressure ratio (EPWPR) at the center of embankment (Point A) and the distribution of EPWPR in Case A. Here, Case A is the basic case, and the measurement points (Point A to F) are shown in Fig.3. EPWPR is defined as the ratio of excess pore water pressure to the initial vertical effective stress. Therefore, EPWPR reaching 1.0 means that the soil is liquefied completely.

From the results, it is known that the liquefaction damage in non-embankment area is greater than that in embankment area. This is the effect of the initial effective stress due to embankment loading. In addition, it is also known that the liquefaction damage is expanding due to the aftershock. This result is clear seen in Fig. 7, that is, EPWPR increased greatly due to the aftershock.

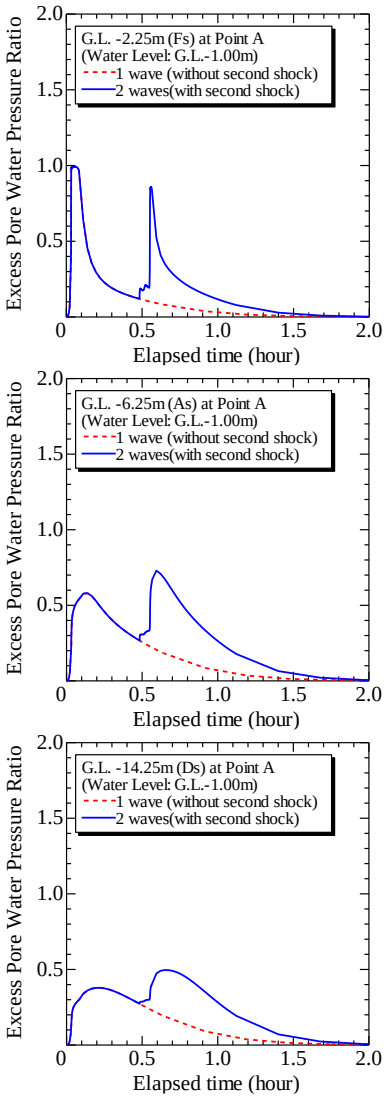

Fig. 6 Time history of EPWPR at Point A (center of embankment) in Case A

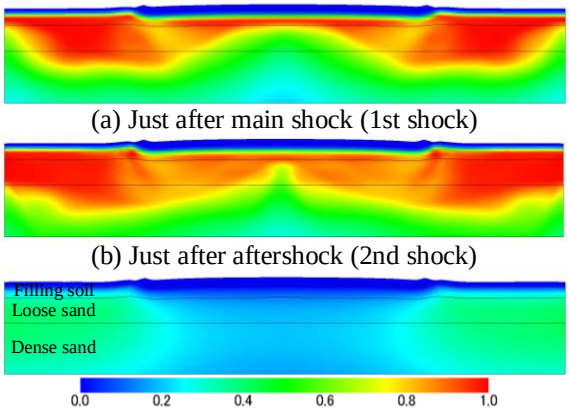

(a) Just after main shock (1st shock)

(b) Just after aftershock (2nd shock)

(c) 33 minutes after aftershock

Fig. 7 Distribution of EPWPR in Case A

Figure 8 shows EPWPR of loose sand at Point F (10 m from the toe of slope), where the liquefaction damage is large. As mentioned above, these cases have different groundwater depths, but have the same initial effective stress. From the results, it is known that EPWPR deceased due to the lowering of groundwater level, and that EPWP dissipated much faster.

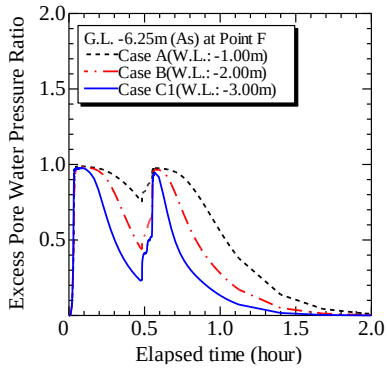

Fig. 8 Effect of groundwater level on EPWPR (Point F: 10 m from toe of the slope)

Figure 9 shows the comparison of EPWPR at Point F in Case C1 and C2. These cases have same groundwater depth in each case, but have the different initial effective stress. From the results, it is known that the countermeasure effect, such as suppression of excessive pore water pressure and early dissipation, is further enhanced by the increase of the initial effective stress compared to the case where only the groundwater level is lowered.

Figure 10 shows distributions of displacement vector in Case C1 and C2. In Case A, it is known that the outer side of the embankment is greatly uplifted right after liquefaction, and then settlement due to consolidation with dissipation of EPWP.

Therefore, it is clear that the ground deformation due to liquefaction is largely suppressed by the decrease of the groundwater level and the increase of the initial effective stress.

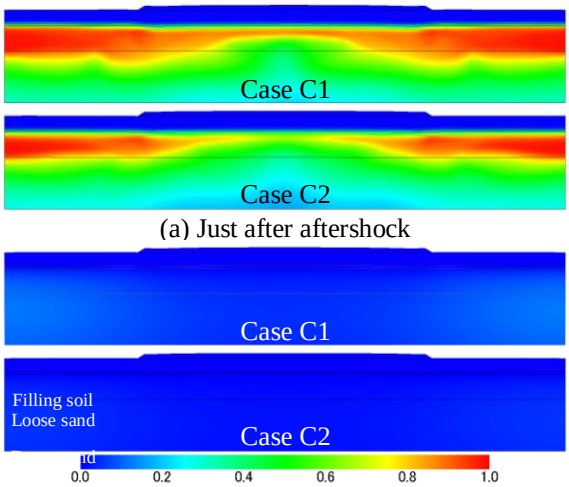

(a) Just after aftershock

(b) 33minutes after aftershock

Fig. 9 Distribution of EPWPR in Case C1 and C2

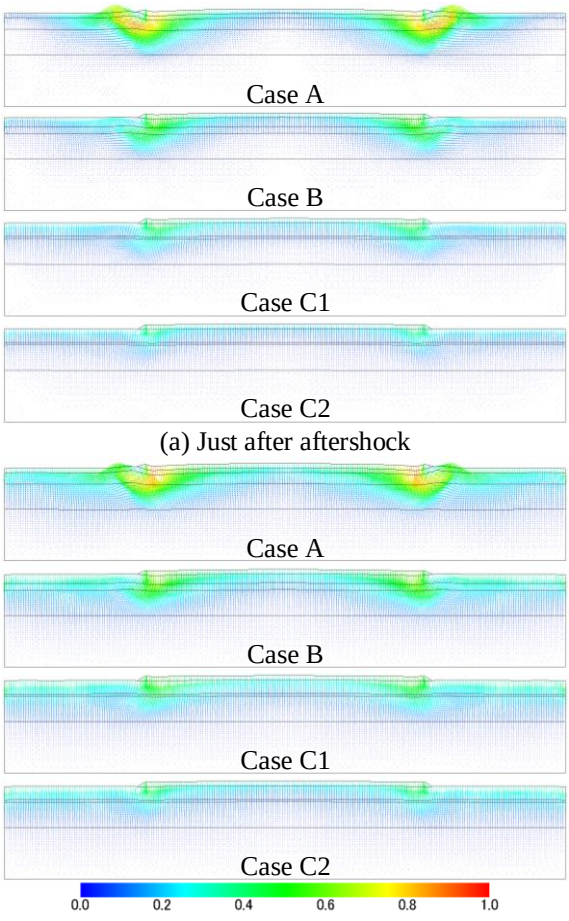

(a) Just after aftershock

(b) 50years after aftershock

Fig. 10 Distributions of displacement vector

5. CONCLUSIONS

In this study, 2D soil-water coupled finite element-finite difference analyses based on Ciclic Mobility model were conducted to evaluate the liquefaction damage before and after lowering the groundwater level. The following conclusions can be obtained:

1. According to the calculated results, even if the initial effective stress does not increase, liquefaction damage can be greatly reduced only by lowering the groundwater level with 1 to 2 m.

2. If the effective stress of the ground also increases in addition to the lowering of groundwater level, the effect of the coutermeasure against liquefaction will be further enhanced.

ACKNOWLEDGMENTS

We would like to give thanks to Mr. S. Maemoto and Nakanihon Engineering Consultants Co., Ltd for providing the necessary data used in this research.

REFERENCES

[1] M. Kazama: Overview of the damages of The 2011 Off the Pacific Coast of Tohoku Earthquake and its geotechnical problems, Japanese Geotechnical Journal, Vol. 7, No. 1, pp. 1-11, 2012.

[2] F. Oka, N. Yoshida, S. Kai, T. Tobita, Y. Higo, N. Torii, S. Kagamihara, N. Nakanishi, S. Kimoto, Y. Yamakawa, Y. Touse, R. Uzuoka and T. Kyoya: Reconnaissance Report of Geotechnical Damage due to the 2011 off the Pacific coast of Tohoku Earthquake - Northern Area of Miyagi Prefecture -, Japanese Geotechnical Journal, Vol. 7, No. 1, pp. 37-55, 2012.

[3] Y. Bin: Experiment and Numerical Simulation of Repeated Liquefaction -Consolidation of Sand, Doctoral Dissertation, Gifu University, 2007.

[4] F. Zhang, B. Ye, T. Noda, M. Nakano and K. Nakai: Explanation of Cyclic Mobility of Soils: Approach by Stress-Induced Anisotropy, Soils and Foundations, Vol.47, No. 4, pp.635-648, 2007.

[5] X. Bao, Y. Morikawa, Y. Kondo, K. Nakamura and F. Zhang: Shaking table test on reinforcement effect of partial ground improvement for group-pile foundation and its numerical simulation, Soils and Foundations, Vol. 52, No. 6, pp. 1043-1061, 2012.

[6] F. Zhang, R. Oka, Y. Morikawa, Y. Mitsui, T. Osada, M. Kato and Y. Wabiko: Shaking Table Test on Superstructure-foundation-Ground System in Liquefiable Soil and Its Numerical Verification, Geotechnical Engineering Journal of the SEAGS & AGSSEA, Vol. 45, No. 2, pp. 1-6, 2014.

[7] K. Hamayoon, Y. Morikawa, R. Oka, F. Zhang: 3D dynamic finite element analyses and 1 g shaking table tests on seismic performance of existing group-pile foundation in partially improved grounds under dry condition, Soil Dynamics and Earthquake Engineering, Vol. 90, pp. 196-210, 2016.

[8] K. Hamayoon, Y. Morikawa, Guanlin Ye and Feng Zhang: Liquefaction-Induced Buckling Failure of Group-Pile Foundation and Countermeasure by Partial Ground Improvement, International Journal of Geomechanics (ASCE), 19(5): 04019020, pp. 1-16, 2019.

[9] Y. Morikawa, X. Bao, K. Maeda, T. Imase and F. Zhang: Importance of liquefaction analysis considering re-liquefaction due to aftershock of earthquake, Japanese Geotechnical Journal, Vol. 7, No. 2, pp. 389-397, 2012.

[10] Y. Morikawa, Y. Tanaka, K. Maeda and H. Cho: Countermeasure against liquefaction using drainage diaphragm wall focused on the effect of dissipation of water pressure, Journal of JSCE, Ser. A2, Vol. 71, No. 2, pp. I_437-I_448, 2015.

[11] Y. Morikawa, H. Sakaguchi, A. Taira and H. Cho: NUMERICAL ANALYSIS ON MECHANISM OF LIQUEFACTION NOT ONLY IN MAIN EARTHQUAKE BUT ALSO IN AFTER SHOCK, International Journal of GEOMATE, Vol.14, Issue 45, pp. 58-65, 2018.

[12] Roscoe K. H., Schofield A. N. and Thurairajah A.: Yielding of clays in states wetter than critical, Geotechnique 13 (3), pp.211-240, 1963

[13] K. Hashiguchi and M. Ueno: Elastoplastic constitutive laws of granular material, Constitutive Equations of Soils, Pro. 9th Int. Conf. Soil Mech. Found. Engrg., Spec. Ses. 9, Murayama, S. and Schofield, A. N. (eds.), Tokyo, JSSMFE: pp. 73-82, 1977.

[14] A. Asaoka, M. Nakano, T. Noda: Superloading yield surface concept for the saturated structured soils, Proc. of the Fourth European Conference on Numerical Methods in Geotechnical Engineering-NUMGE98, pp. 232-242, 1998.

9thInt. Conf. on Geotechnique, Construction Materials and Environment, Tokyo, Japan, 20-22 November 2019, ISBN: 978-4-909106025C3051

NUMERICAL SIMULATION OF THE SETTLEMENT BEHAVIOUR OF PLANAR AND 3D GEOGRID REINFORCED SAND BED

Femy M.Makkar[1], Sreya M.V.[2], Chandrakaran S.[3]and Sankar N.[4]
[1]Assistant Professor, Amaljyothi College of Engineering, Kanjirappally, Kerala, India
[2] Research Scholar, National Institute of Technology Karnataka, Surathkal, India
[3,4] Professors, National Institute of Technology Calicut, Kerala, India

ABSTRACT

Geosynthetics have been proved as a bona fide engineering material and a good alternative to the conventional design techniques in the field of geotechnical engineering. They are widely used for the construction of retaining walls, pavements, embankments and shallow foundations etc. The performance of geosynthetic reinforced soil structure greatly depends on the form (such as discrete, planar, vertical, cellular, 3D etc.) in which it is used. In this paper, the settlement behaviour of a model footing resting on sand bed reinforced with planar geogrid and three dimensional geogrid are numerically simulated using Plaxis 3D software. The behaviour of sand bed was modelled by Mohr Coulomb model. The planar geogrid and 3D geogrid were modelled in Auto CAD 3D and imported into Plaxis 3D and assigned the properties of geogrid structural element available in Plaxis. A uniformly distributed pressure was applied on the top of a plate element to simulate the load on model footing. The numerical analysis showed that the presence of geosynthetic reinforcement in sand bed improved the bearing capacity and reduced the settlement of model footing. However, geogrid in three dimensional form gave better results compared to planar geogrid. A single layer of 3D geogrid provided at an optimum embedment depth improved the load carrying capacity of soil by 66% and the settlement of footing was reduced by 30% compared to single layer planar geogrid reinforced sand bed.

Keywords: 3D geogrid, Load carrying capacity, Numerical modelling, Plaxis 3D, Settlement

INTRODUCTION

Reinforced soil foundation has been widely used in various geotechnical engineering applications, since it is a cost effective solution to increase the bearing capacity and reduce the settlement of shallow foundations. The concept was first demonstrated by Vidal [19] by incorporating galvanized steel strips in cohesionless soil to improve its mechanical properties. Later, the development of geosynthetics from strong and durable polymers changed the trend to planar geotextiles and geogrids. The performance of geosynthetic reinforced soil foundation has been investigated by several researchers [1], [3], [5] - [6], [11], [17] - [18], [20]. Several numerical studies are also performed by researchers to investigate the behaviour of reinforced soil foundation with planar geotextile or geogrid as reinforcement [3] – [4], [9] – [10], [15], [20].

Reinforcements in three dimensional forms are the recent trend in the construction of reinforced soil system. A few studies on the behaviour of soil reinforced with 3D inclusions are reported by [2], [12], [14], [21] – [22]. These reinforcements give the advantages of conventional planar reinforcements along with the passive resistance offered by the additional third dimension. The behaviour of three dimensional geocell reinforced soil has been numerically studied by [7] – [8], [16]. In the present investigation, the load-settlement behaviour of shallow footing resting on planar geogrid reinforced soil and 3D geogrid reinfored soil are numerically simulated and compared using plaxis 3D software.

NUMERICAL MODELLING

The laboratory plate load test conducted by Makkar et al., [13] in a steel tank of 750 mm x 750 mm x 750 mm was simulated in the numerical modelling. The model footing used was 150 mm square in size and 25 mm thick. To simplify the computational effort, only one quarter portion of the test model was modelled using Plaxis 3D software due to symmetry. In order to simulate the behaviour of soil, a suitable material model and appropriate material parameters has to be assigned to the geometry. The Mohr Coulomb model was used to simulate the behaviour of infill soil. The linear elastic- perfectly plastic Mohr Coulomb model requires a total of five parameters, namely, Young's modulus, E (kN/m^2); poisson's ratio, ν; cohesion, C (kN/m^2); friction angle. Φ (◦); and dilatancy angle, ψ(◦). The shear strength properties of the sand were determined from direct shear tests. The Young's modulus of sand bed modelled is directly taken from the pressure- settlement curve of plate

load test on unreinforced sand bed. The footing was modelled as a plate element. The behaviour of plate element is defined by the parameters Young's modulus and Poisson's ratio. The planar geogrid and 3D geogrid were used as the reinforcing material, and they are modelled in Auto CAD 3D and imported in to Plaxis 3D. Later, it was defined as the geogrid structural element by assigning the value of axial stiffness (EA).

After assigning the appropriate material properties for soil and structural elements, finite element meshes were generated. In the present study relatively coarser mesh was chosen for the analysis. In order to simulate the load on the model footing, a uniformly distributed pressure was applied on the top of the plate element and the corresponding settlements were found out. The displacement along bottom boundary was restrained both in horizontal as well as vertical direction. The displacement along side boundaries were restrained only in the horizontal direction, such that displacements were allowed to occur in vertical direction. Fig. 1 shows the plaxis 3D models of planar geogrid reinforced soil and 3D geogrid reinforced soil. The material properties assigned for the soil and structural elements are given in Table.1.

(a)

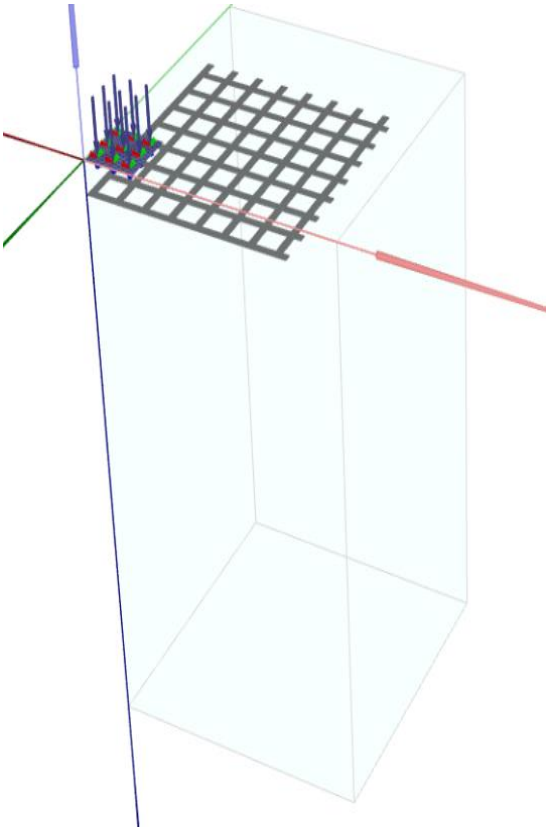

(b)

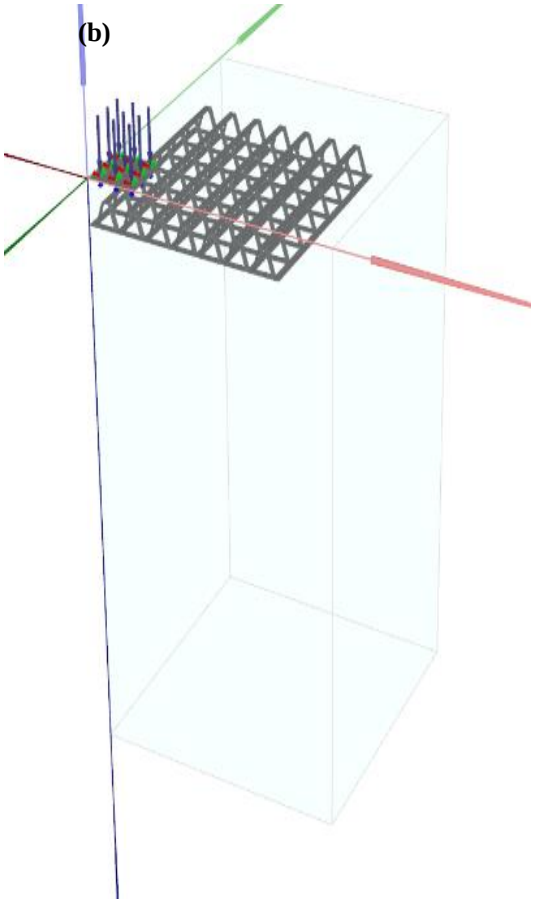

Fig.1 plaxis 3D models of (a) Planar geogrid reinforced soil; (b) 3D geogrid reinforced soil

Table 1 Material properties

Parameters	Value
Sand	
Young's modulus, E	3600 kPa
Poisson's ratio, υ	0.3
Cohesion, C	1 kPa
Angle of internal friction, ϕ	40.4◦
Dialatancy angle,ψ	0◦
Model footing	
Young's modulus, E	2 x 10^6 kPa
Poisson's ratio, υ	0.3
Geogrid	
Axial stiffness, EA	250kN/m

RESULTS AND DISCUSSIONS

The numerical models developed in the present investigation were validated with the experimental results reported by Makkar et al. [13]. Fig.2. shows the pressure-settlement curve for planar geogrid reinforced soil and 3D geogrid reinforced soil obtained from numerical study and reported by Makkar et al. [13]. From the graph, it is clear that the

(b)

results are in close agreement with each other. Table.2 gives the bearing capacity obtained from the numerical analysis and from the literature. Fig.3 shows the displacement contour for planar geogrid reinforced soil and 3D geogrid reinforced soil at an embedment depth of 0.25B.

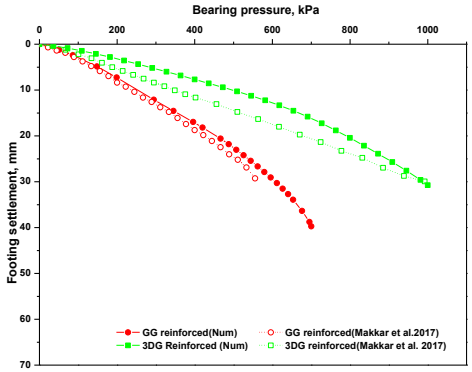

Fig.2 Pressure-settlement curve for planar geogrid and 3D geogrid reinforced soil

Table 2 Bearing capacity obtained for planar geogrid and 3D geogrid reinforced soil

Type	Makkar at al. 2017	Numerical	% error
Geogrid reinforced	510	540	5.9
3DG reinforced	840	900	7.1

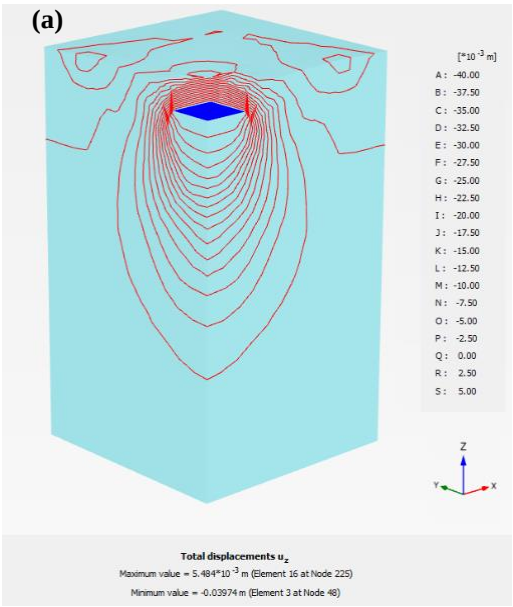

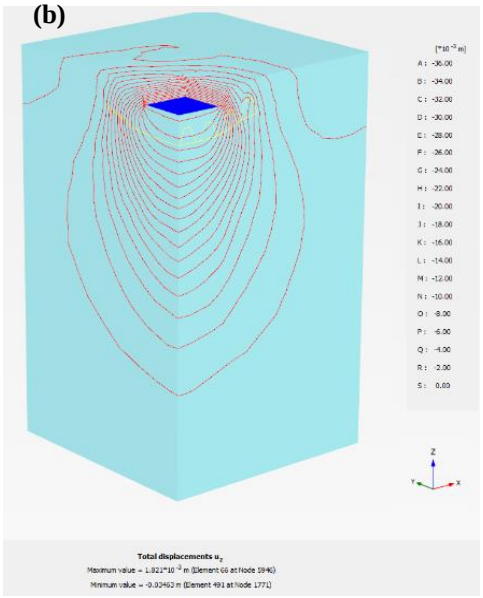

Fig.3 Displacement contour for (a) Planar geogrid reinforced soil; (b) 3D geogrid reinforced soil

The bearing capacity of reinforced soil has been taken as the bearing pressure corresponding to 25 mm footing settlement. To get the maximum benefit, the reinforcement should be placed at an optimum depth from the base of the footing. The effect of embedment depth of reinforcement on the bearing capacity and settlement was studied by placing the reinforcements at depths of 0.1B, 0.25B, 0.5B, and 0.75B, where, B is the width of model footing. Fig.4. shows the variation of Bearing capacity ratio (BCR) with reinforcement embedment depth (u/B). BCR is defined as the ratio of bearing capacity of reinforced sand bed at a given settlement to the bearing capacity of unreinforced sand bed at the same settlement. From Fig.3, it can be seen that the BCR is increased up to an embedment depth of 0.25B and thereafter, it decreases for both type of reinforcement. The reason is that, in order to develop the maximum interfacial frictional resistance, sufficient overburden pressure is required above the reinforcement which is attained at an embedment depth of 0.25B. Further increase in the depth of reinforcement reduces the bearing capacity improvement due the excessive settlement of thicker layer of soil above the reinforcement. It can also see that the bearing capacity improvement is higher for 3D geogrid reinforced soil compared to planar geogrid reinforced soil bed for all embedment depth. The beneficial advantage of conventional planar reinforcement along with the confinement effect of soil with in the cells of 3D geogrid imparts higher bearing capacity to the 3D geogrid reinforced soil. The bearing capacity improvement by 3D geogrid reinforced soil was 66% more than planar geogrid

reinforced soil, when both of them are placed at the optimum embedment depth of 0.25B.

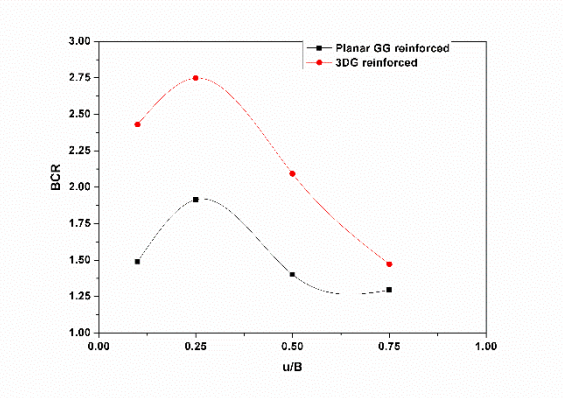

Fig.4 Variation of BCR with embedment depth

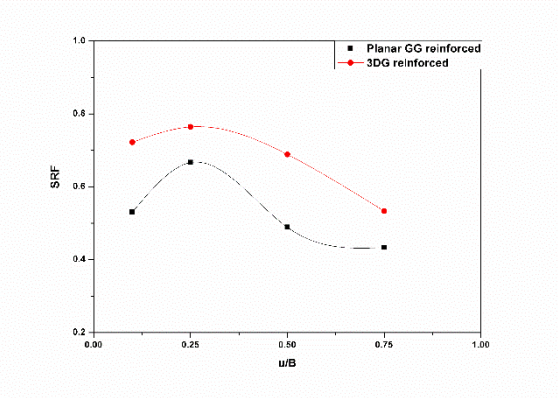

Fig.5 Variation of SRF with embedment depth

Considerable amount of reduction in the settlement of footing was observed with the provision of reinforcement. However, the footing resting on 3D geogrid reinforced soil shows more reduction in the settlement compared to planar geogrid. To quantify the reduction in settlement, a non dimensional parameter Settlement Reduction Factor (SRF) was introduced. SRF is defined as follows:

$$SRF = {(Su - Sr)}/{Su} \qquad (1)$$

Where, Su- settlement of unreinforced soil at a given pressure

Sr –Settlement of reinforced soil at the same pressure

The SRF was calculated for a normalized settlement of 30% of unreinforced sand bed. Fig.5 shows the variation of settlement reduction factor with embedment depth of reinforcement. The maximum reduction in the settlement was observed at an embedment depth of 0.25 times the width of footing for both type of reinforcement. At the optimum embedment depth, a single layer of planar geogrid reinforcement reduced the settlement of footing by 66%, while single 3D geogrid layer reduced the settlement by 77% compared to unreinforced soil. The model footing resting on 3D geogrid reinforced soil shows 30% more reduction in the settlement of footing compared to planar geogrid reinforced soil.

CONCLUSIONS

- 3D geogrid reinforced soil shows better performance compared to planar geogrid reinforced soil in improving the bearing capacity and settlement characteristics of model square footing.
- 66% improvement in bearing capacity was observed with single layer 3D geogrid reinforced soil compared to planar geogrid reinforced soil.
- The settlement of the model footing resting on 3D geogrid reinforced soil bed was reduced by 30% compared to planar geogrid reinforced soil.
- The optimum depth of embedment of single layer of reinforcement was obtained as 0.25 times the width of footing, in terms of bearing capacity and settlement improvement.

REFERENCES

[1] Abu-farsakh M.,Chen Q., Sharma R., An Experimental Evaluation of the Behavior of Footings on Geosynthetic Reinforced Sand. Soils and Foundations, Vol. 53, Issue 2, 2013, pp.335–348.

[2] Alamshahi S., Hataf N., Bearing Capacity of Strip Footings on Sand Slopes Reinforced with Geogrid and Grid-Anchor. Geotextiles and Geomembranes, Vol. 27, Issue 3, 2009, pp.217–226.

[3] Boushehrian J. H., Hataf N., Experimental and Numerical Investigation of the Bearing Capacity of Model Circular and Ring Footings on Reinforced Sand. Geotextiles and Geomembranes, Vol. 21, 2003, pp. 241–256.

[4] Chung W., Cascante G., Experimental and Numerical Study of Soil-Reinforcement Effects on the Low-Strain Stiffness and Bearing Capacity of Shallow Foundations. Geotechnical and Geological Engineering, Vol. 25, 2007, pp. 265–281.

[5] El Sawwaf M., Nazir, Behavior of Eccentrically Loaded Small-Scale Ring Footings Resting on Reinforced Layered Soil. Journal of Geotechnical and Geoenvironmental Engineering, Vol. 138, 2012, pp. 376–384.

[6] Guido V. A., Chang D. K., Sweeney A. Comparison of Geogrid and Geotextile Reinforced Slabs. Canadian Geotechnical Journal, Vol . 23, 1986, pp. 435-440.

[7] Hegde A., Sitharam T. G., Experimental and Numerical Studies on Footings Supported on Geocell Reinforced Sand and Clay Beds. International Journal of Geotechnical Engineering, Vol. 7, Issue 4, 2013, pp. 346-354.

[8] Hegde A., Sitharam T. G., 3-Dimensional Numerical Modelling of Geocell Reinforced Sand Beds. Geotextiles and Geomembranes, Vol. 43, 2015, pp. 171–181.

[9] Kurian N. P., Beena K. S., Kumar R. K., Settlement of Reinforced Sand in Foundations. Journal of Geotechnical and Geological Engineering , Vol. 123, Issue 9, 1997, pp. 818–827.

[10] Laman M., Yildiz A., Numerical Studies of Ring Foundations on Geogrid- Reinforced Sand. Geosynthetics International , Vol. 14, Issue 2, 2007, pp. 52–64

[11] Latha G. M., Somwanshi A., Effect of Reinforcement Form on the Bearing Capacity of Square Footings on Sand. Geotextiles and Geomembranes, Vol. 27, Issue 6, 2009, pp. 409–422

[12] Lawton E., Li C., Merry S. M., Performance of Spread Footings on Subgrades. Proceedings of the Symposium on Engineering Geology and Geotechnical Engineering, Vol. 34, 1999, pp. 245–256.

[13] Makkar F. M., Chandrakaran S., Sankar N., Behaviour of Model Square Footing Resting on Sand Reinforced with Three-Dimensional Geogrid. International Journal of Geosynthetics and Ground Engineering, Vol. 3, Issue 3, 2017, DOI 10.1007/s40891-016-0083-1.

[14] Mosallanezhad M., Hataf N., Ghahramani A., Three Dimensional Bearing Capacity Analysis of Granular Soils Reinforced with Innovative Grid-Anchor System. Iranian Journal of Science & Technology, Transaction B: Engineering, Vol. 34, 2010, pp. 419-431

[15] Raghavendra H. B., Effect of Properties and Length of Reinforcement on Load-Carrying Capacity of Reinforced Soil Beds. Ground Improvement, Vol. 9, Issue 3, 2004, pp. 121–126.

[16] Saride S., Gowrishetti S., Sitharam T. G., Puppala A. J., Numerical Simulation of Geocell-Reinforced Sand and Clay. Ground Improvement, Vol. 162 , Issue G14, 2009, pp. 185–198.

[17] Tavanagar Y., Shooshpasha I., Experimental and Numerical Study of Bearing Capacity and Effect of Specimen Size on Uniform Sand with Medium Density Reinforced with Nonwoven Geotextile. Arabian Journal of Science and Engineering, Vol. 41, Issue 10, 2016, pp. 4127–4137.

[18] Vinod P., Bhaskar A. B., Sreehari S., Behaviour of a Square Model Footing on Loose sand Reinforced with Braided Coir Rope. Geotextiles and Geomembranes, Vol. 27, Issue 6, 2009, pp. .464–474.

[19] Vidal H., The Principle of Reinforced Earth. Highway Research Record, Vol. 282, 1969, pp. 1–16.

[20] Yetimoglu T., Wu J. T. H., Saglamer A., Bearing Capacity of Rectangular Footings on Geogrid-Reinforced Sand. Journal of Geotechnical Engineering, Vol. 120, Issue 12, 1994, pp. 2083–2099.

[21] Zhang M. X., Zhou H., Javadi A. A., Wang Z. W. Experimental and Theoretical Investigation of Strength of Soil Reinforced with Multi-Layer Horizontal – Vertical Orthogonal Elements. Geotextiles and Geomembranes, Vol. 26, 2008, pp. 1–13.

[22] Zhang M. X., Qiu C. C., Javadi A. A., Zhang S. L., Model Tests on Reinforced Sloped Embankment with Denti-Strip Inclusions under Monotonic Loading. KSCE Journal of Civil Engineering, Vol. 18, Issue 5, 2014, pp. 1342–1350.

9th Int. Conf. on Geotechnique, Construction Materials and Environment, Tokyo, Japan, 20-22 November 2019, ISBN: 978-4-909106025 C3051

PARTICULATE MECHANICS PARAMETERS FOR GEOTECHNICAL AND AGRICULTURAL ENGINEERING APPLICATIONS

Joash Bryan Adajar[1], Irene Olivia Ubay[2], Zhiwei Zeng[2], Marolo Alfaro[2], and Ying Chen[2]
[1,2]Department of Civil Engineering, Faculty of Engineering, University of Manitoba, Manitoba, Canada

ABSTRACT

Discrete Element Method (DEM) is a numerical technique that uses particulate mechanics in simulating the discontinuous behavior of granular materials. DEM presents the advantage of modelling granular materials in a particulate level allowing specification of particle geometry including how their contacts interact. However, identifying microparameters to accurately simulate the behavior of particulate materials is challenging. This paper presents the determination of material microparameters for geotechnical and agricultural engineering applications using various calibration methodologies and laboratory tests. Sensitivity analyses were performed to develop a systematic calibration approach. For agricultural engineering application, crop residue microparameters that can be used for tillage simulations are identified. Linear contact model was used to describe the behavior of crop residue particles. Particle stiffness and friction were determined by simulating ring and direct shear tests. Tillage simulations can provide information on the dynamics of soil-tool-residue interactions. For geotechnical engineering application, microparameters of the constituents of a particular earth fill dam, such as rockfill and clay soil, were identified. Linear-based contact models such as rolling resistance and parallel-bond models were explored. Direct shear and triaxial tests were simulated to determine the microparameters of rockfill (particle stiffness, friction, and rolling resistance coefficient) and clay (particle stiffness, friction, bond strength, and bond stiffness). Microparameters were used to model the observed slope movements (landslide) of the earth fill dam. The model provided information on the velocity and runout distance of the landslide which are important for risk assessment. Calibration methodologies performed were successful in identifying appropriate microparameters which can be used to improve the reliability of large-scale models.

Keywords: Particulate, DEM, Landslide, Tillage, Calibration

INTRODUCTION

The discrete element method (DEM) is a numerical process that uses particulate mechanics to model the discontinuous response and behavior of granular materials when subjected to various conditions. It simulates the mechanical behavior of a particulate system by using a collection of distinct particles that interacts with each other [1]. DEM is a useful tool for simulating physical processes that involves separation of material constituent particles [2]. It has been used effectively in various fields like construction and building materials, agriculture, geotechnical, mining, mechanical, and industrial engineering.

The accuracy of DEM simulations are dependent on the input parameters. A challenge that researchers confront in using DEM is the identification of microparameters that define the behavior of particle interactions. There are not a lot of laboratory tests that can quantify material microparameters. These microparameters should also be able to compensate for the simplifications that were made on the particle geometry used in the model. Common approach to characterize material microparameters is through a back-calculation or calibration process wherein results of actual and simulated laboratory tests are matched. This paper focused on the identification of microparameters of materials necessary for a particular agricultural and geotechnical engineering application. For agricultural application, micro-parameters of crop residue and its interface with soil were identified. These microparameters are necessary to accurately simulate the tillage process and observe soil-toil-residue interactions. For geotechnical application, microparameters of the two components of a particular earth fill dam, clay and rockfill, were determined. Clay and rockfill microparameters were used in making a model that can simulate the observed excessive movement (landslide) of the dam slope. The model helped in understanding better the dynamics of the soil flow.

AGRICULTURAL APPLICATION

Tillage simulations are performed in order to observe and understand soil-tool-residue interactions during the tilling process. Comprehensive knowledge on soil-tool-residue interactions during tillage is significant in the design and optimization of high-efficiency soil-engaging tools [3]. For the development of an accurate DEM soil-tool-residue model, microparameters of agricultural soil, crop residue, and their interface are necessary. This paper only focused on the calibration of microparameters of crop residue and its interface with soil.

Ring Shear Test (RST)

Ring shear test was physically conducted and simulated with DEM to identify crop residue macro and microparameters. Measured shear strength macroparameter was the internal friction angle of the crop residues. Crop residues tested were canola, corn, flax, oats, and wheat.

For the RST model, the ring shear device was modelled using four walls having similar dimensions as the actual device. A total of 9,680 spheres of uniform particle size of 2 mm diameter was used to represent the crop residue. Figure 1 shows the DEM model of the RST. Same testing parameters as the actual test was assigned in the model to simulate the shearing process

Linear contact model was assigned to describe crop residue particle behavior. Microparameters calibrated for the linear contact model were particle stiffness (k) and friction coefficient (μ). Sensitivity analyses were performed to identify the influence of those parameters on the simulated material shear strength. Figure 2 displays the results of the sensitivity analyses and it shows that μ was a more influential microparameter. μ was chosen for calibration in order to match the actual and simulated RST results. The value of k for the crop residues is 7.5e3 N/m. Governing μ for flax and wheat are 0.425 and 0.025, respectively. For canola, corn, and oats, μ was 0.05. As an example, comparison of measured and simulated failure envelopes for flax are shown in Fig. 3. Similar behaviors having good agreements have been observed on the other crop residues. Computed values of the measured and simulated internal friction angles are listed in Table 1.

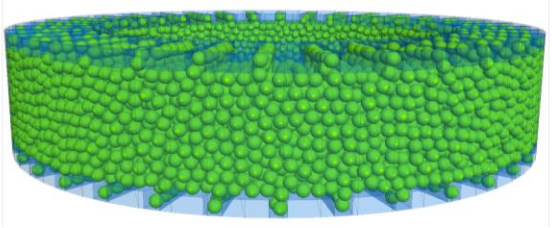

Fig. 1 Ring shear test DEM model.

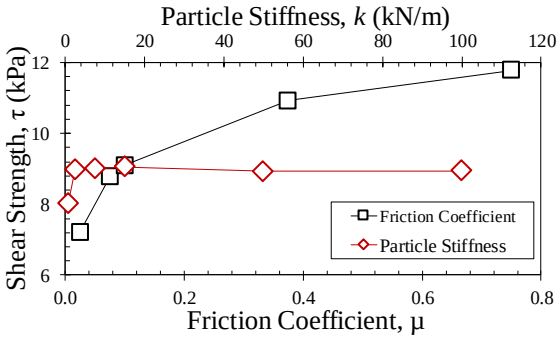

Fig. 2 Influence of μ and k on RST model results.

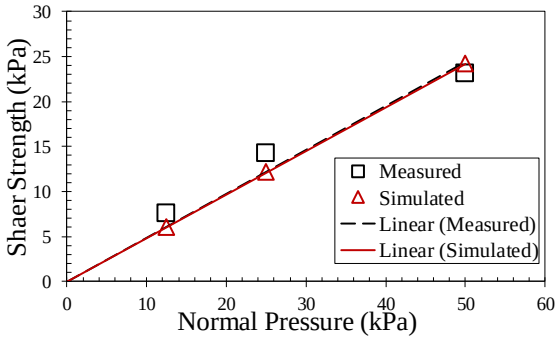

Fig. 3 Derived failure envelopes for RST of flax.

Table 1 Calculated internal friction angles.

Residue	Internal Friction Angle	
	Measured	Simulated
Flax	26°	25.8°
Canola	18.9°	19°
Corn	18.8°	19°
Oats	18.9°	19°
Wheat	16.4°	16.7°

Direct Shear Test (DST)

Direct shear test was carried out to characterize the shear strength macroparameter, interface friction angle, between the crop residues and agricultural soil. It was then simulated to back-calculate soil-residue interface microparameters. Agricultural soil used was classified as sandy loam having a composition of 70% sand, 14% clay, and 16% silt [4]. Crop residues tested were also canola, corn, flax, oats, and wheat. For the physical direct shear test, soil and crop residues were placed at the bottom and upper shear box, respectively. This was done to ensure that the shear plane will develop at the interface of the two materials.

To simulate DST, four walls were used to model the shear box. Two cylindrical walls of the same diameter and height to the actual equipment were generated to serve as horizontal enclosures. Two disks were generated to represent the top and bottom covers. Spherical balls having a uniform diameter of 2 mm were used to represent both the soil and crop residue particles. The compression and shearing of materials were simulated using the same testing parameters as the actual experiment. Figure 4 shows the sheared condition of the DST model.

Linear contact model was once again designated on the crop residue particles. Initial microparameter values set were the same values identified from the RST model. For the soil particles, linear parallel-bond model (LPBM) was assigned. Microparameter values used for the soil particles are listed in Table 2. Nandanwar et al. [4] calibrated the microparameters of the same soil used in this research with triaxial test simulations.

Sensitivity analyses on the direct shear test model were performed. It was observed that both μ and k was influential for DST simulations (Fig. 5). Calibration approach considered was to maintain the μ obtained from RST and perform bulk of the adjustments on k. This yielded results that are still valid for the RST model since it was only dependent on μ. Interface microparameters between crop residues and soil particles were computed with the surface inheritance approach defined in the DEM software used. In this approach, k of the two different particles are expected to behave in series while the smaller value between the μ governs upon contact.

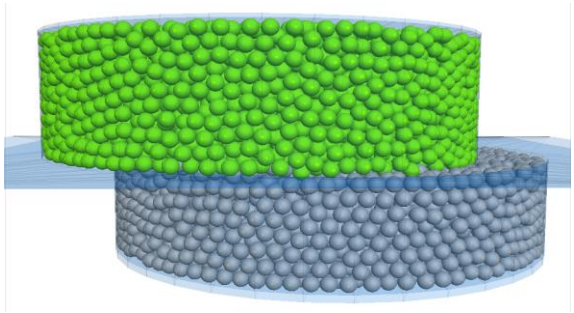

Fig. 4 Direct shear test DEM model.

Table 2 Soil microparameters [4].

Parameters	Units	Value
Particle Normal Stiffness (k_n)	N/m	5.4e3
Particle Shear Stiffness (k_s)	N/m	2.57e3
Friction (μ)	-	0.7
Bond Normal Stiffness ($\bar{k}_n$)	Pa/m	1.25e10
Bond Shear Stiffness ($\bar{k}_s$)	Pa/m	5.95e9
Bond Normal Strength ($\bar{\sigma}_c$)	Pa	2e4
Bond Shear Strength ($\bar{c}$)	Pa	2e4
Bond Radius Ratio	-	0.5

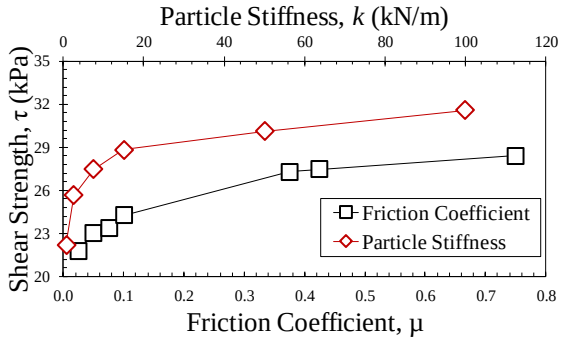

Fig. 5 Influence of μ and k on DST results.

The final microparameters of crop residue and its interface with soil are listed in Tables 3 and 4. An example comparison of the derived failure envelope for both the simulated and measured DST is shown in Fig. 6. Good agreement can be observed on the computed interface friction angles (Table 5).

Table 3 Crop residue microparameters.

Crop residue	$k_n = k_s$ (N/m)	μ
Flax	1e4	0.425
Corn	5e4	0.05
Canola	5e4	0.05
Oats	5e3	0.05
Wheat	2.125e4	0.025

Table 4 Soil-residue interface microparameters.

Material		k_n	k_s	μ
Crop	Soil	(N/m)	(N/m)	
Flax	Sandy Loam	7e3	4.1e3	0.425
Corn		9.7e3	4.9e3	0.05
Canola		9.7e3	4.9e3	0.05
Oats		5.2e3	3.4e3	0.05
Wheat		8.6e3	4.6e3	0.025

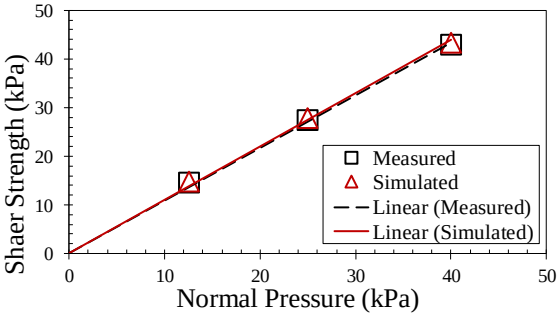

Fig. 6 Derived failure envelopes for DST of flax.

Table 5 Calculated interface friction angles.

Material		Interface Friction Angle	
Crop	Soil	Measured	Simulated
Flax	Sandy Loam	47.4°	47.7°
Canola		43.6°	43.9°
Corn		44.4°	43.9°
Oats		41.3°	41.5°
Wheat		41.6°	41.5°

Tillage Simulation

The microparameters identified in the previous section can be used to help improve the accuracy of soil-tool-residue interactions in simulations of tillage in agricultural fields (Fig. 7). One example of a soil-tool-residue model was the straw-sweep-soil model developed by Zeng et al. [3] (Fig. 8). The dynamics of soil and oats straw can be studied and predicted as it gets ploughed by a sweeping tool with the help of the model. It was able to quantify and observe information like residue cover, kinetic energy, and soil/straw moving area, velocity, acceleration, displacement, and movement trajectory. The model developed can also be used for other tilling equipment and can help in improving their design and performance when it comes to straw management.

Fig. 7 Tillage in agricultural fields [5].

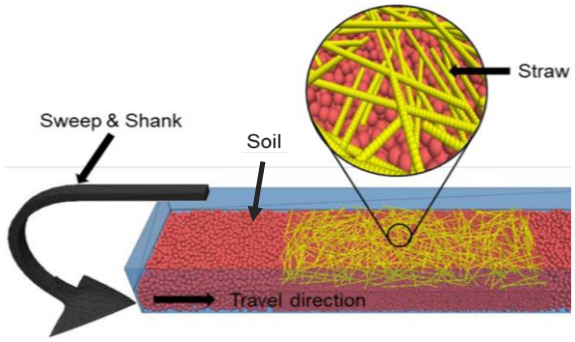

Fig. 8 Straw-sweep-soil DEM model [3].

GEOTECHNICAL APPLICATION

Excessive soil movements were observed in a particular earth fill dam in Canada. Developing a landslide DEM model is beneficial in order to observe the dynamics of the soil flow and predict the possible behavior of a future landslide. Information that can be derived from landslide models can be used for risk assessment and planning of mitigation measures. Major constituents of the earth fill dam were compacted clay, as its core, and rockfill, as its protective layer. Microparameters of these two materials were identified to aid in the development of a landslide model. Calibration methodology carried out in determining the microparameters are discussed in the succeeding sections.

Large-scale Direct Shear Test (LDST)

Alfaro et al. [6] carried out experimental testing using a large-scale direct shear box to measure the shear mobilization of rockfill materials. The shear box has a diameter of 600 mm. LDST results presented in the research were used as the basis for the calibration of rockfill microparameters.

Similar process as the DST model discussed previously was followed in creating the shear box. However, cylindrical walls having larger diameters and heights were generated for the LDST model. Spherical particles having 25 mm diameters were used to represent rockfill particles. Figure 9 shows the LDST DEM model developed. Similar testing parameters as the actual experiment were considered for the simulation of the shearing process.

Rolling resistance linear contact model was assigned for the rockfill particles. A rolling resistance coefficient (μ_r) was introduced to represent the angular nature of rockfill particles. μ_r is significant in modelling materials of high shearing resistance due to particle shape angularity.

Similar to the observed influence of k and μ from the previous DST model, both parameters are also influential on the simulation results of LDST. μ_r and μ were adjusted to match the shear strength at the end of the test, while calibration of k focused on matching the rate of increase or development of shear strength as the material was being sheared. After calibration, good correlation can be observed on the measured and simulated stress-strain relationships (Fig. 10). Characterized rockfill microparameters are listed in Table 6.

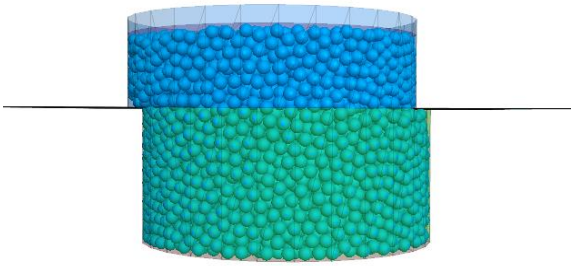

Fig. 9 Large-scale direct shear test DEM model.

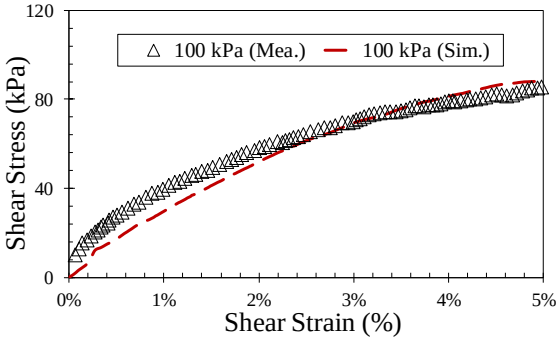

Fig. 10 Rockfill stress-strain relationship.

Table 6 Rockfill microparameters.

Parameters	Value	Units
Particle Stiffness (k)	3e5	N/m
Friction (μ)	1	—
Rolling Resistance (μ_r)	0.2	—

Triaxial Test (TT)

The clay material used for dam construction was classified as lacustrine clays of high plasticity [7]. Clay stress-strain behavior and shear strength macroparameters were obtained by carrying out undrained consolidated triaxial test. For the TT model, three walls were generated; one cylindrical wall to radially confine the material, and two disks to confine and strain the material vertically. 5,155 spherical particles having 5 mm diameters were generated to represent clay. Figure 11 shows the developed TT DEM model. For simplification and to mimic the zero volumetric strain throughout the shearing process, a strain-controlled boundary condition was assigned on the three walls [8].

Linear parallel-bond was the chosen contact model for the particles. Upon the execution of preliminary simulations, it was observed that parallel-bond microparameters ($\bar{k}$ and $\bar{c}$) dictate the peak shear strength. On the other hand, linear contact microparameters (k and μ) control the critical-state shear strength. With the said findings, calibration methodology considered was to match the measured peak shear strength by adjusting $\bar{k}$ and $\bar{c}$, while the measured critical-state shear strength was matched by adjusting k and μ. The model was able to match the identified peak and critical-state points in the deviator stress (q) vs mean effective stress (p') graph (Fig. 12). Good agreement can be observed on the comparison of the measured and simulated stress-strain relationships (Fig. 13). Identified clay microparameters are listed in Table 7.

Fig. 11 Triaxial test DEM model.

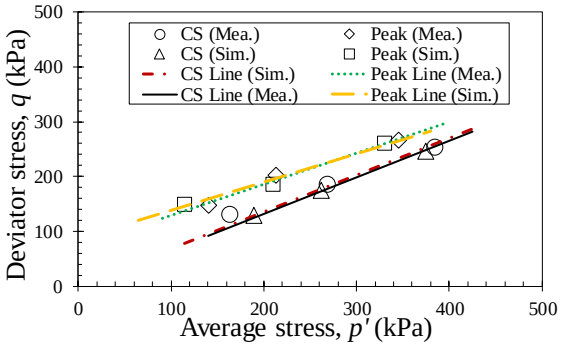

Fig. 12 Critical-state and peak stress points.

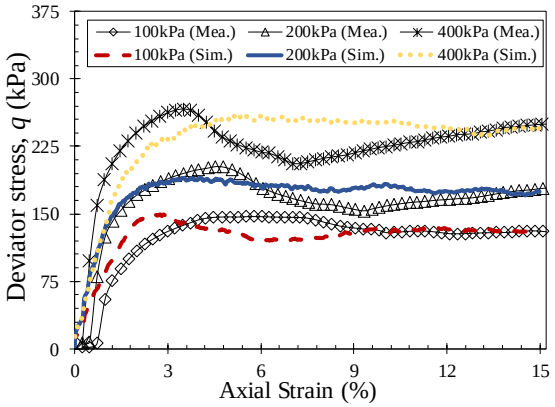

Fig. 13 Clay stress-strain relationships.

Table 7 Clay microparameters.

Parameters	Value	Units
Particle Stiffness (k, $k_n = k_s$)	3.5e4	N/m
Friction (μ)	0.15	—
Radius Multiplier	1	—
Bond Stiffness ($\bar{k}, \bar{k}_n = \bar{k}_s$)	1e9	Pa/m
Bond Strength ($\bar{c}$)	1.1e5	Pa

Landslide Simulations

The 3D digital terrain model that shows the landslide that occurred in the dam slope can be viewed in Fig. 14, wherein the observed dam crest depression is encircled.

Fig. 14 Dam post-landslide digital terrain model.

The clay and rockfill microparameters can be used to aid in the development of the landslide DEM model. The landslide model was able to recreate the post-failure soil flow of the earth fill dam slope. Figure 15 shows the model condition after the landslide runout or when soil flow movement has stopped. It displays the z-displacement (m) contour where depression and bulging on the dam crest and toe, respectively, can be observed. Simulated movement or changes in the model topography have good agreement on the post-landslide topography observed from the 3D digital terrain model. This validates the improved reliability of a landslide DEM

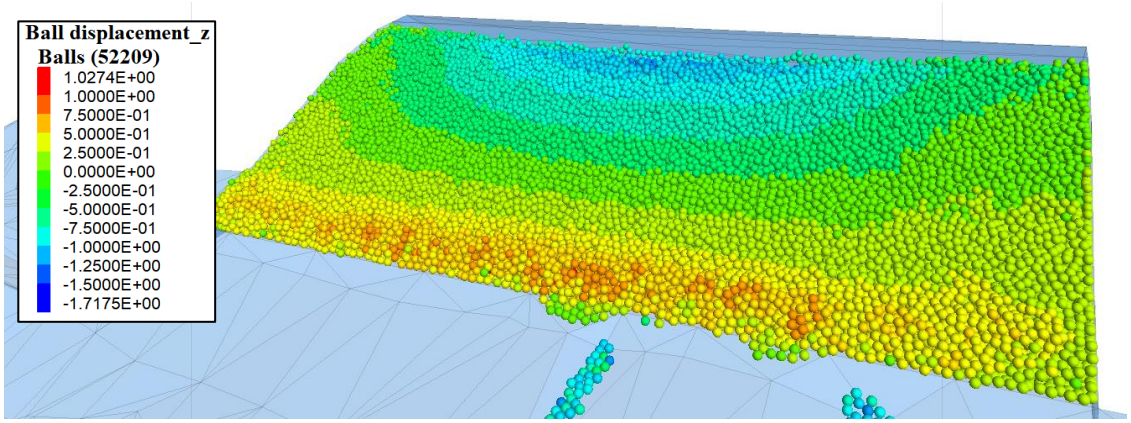

Fig. 15 Landslide DEM model.

model with input microparameters calibrated from the laboratory tests considered in this paper. The model can be used to simulate potential future landslides at the vicinity, which can give researchers insights on the behavior of the soil flow. Information on the velocity of different portions and overall kinetic energy of the moving soil mass can also be extracted from the model. These information are helpful in the design of possible mitigation structures or in identifying the extent of the area that can possibly be affected.

CONCLUSIONS

There are different methods that can be explored to calibrate and back-calculate material microparameters. The use of direct shear, ring shear, and triaxial test for microparameter calibration purposes has been found to be effective in this research. The laboratory test DEM models were able to simulate the macroscopic behavior of the materials which were obtained from carrying out actual laboratory tests. From the different calibration methodologies performed, it can be concluded that the sensitivity and behavior of microparameters are complicated making it impossible to define a robust or general approach for the calibration and identification of its values. The influence of the contact model microparameters varies for different laboratory test simulated. It is recommended to perform sensitivity analysis and design an effective calibration approach based from the results.

Presented tillage and landslide simulations highlighted the applicability of identified microparameters on a broader research that involves large-scale physical processes. Results of the landslide simulation reaffirmed that the calibration approach followed in this research can successfully characterize microparameters which can improve the reliability of the model.

Identified microparameters in this research should be used with caution. It is important to take note that characterized microparameters are considered as apparent microparameters that are only applicable for material models having identical cases and conditions as what is presented in this research. Differences in model behavior may be observed upon the use of different particle geometry and distributions.

REFERENCES

[1] Cundall P. A. and Strack O. D. L., A Discrete Numerical Model for Granular Assemblies, Geotechnique, Vol. 29, No. 1, 1979, pp. 47–65.

[2] Mei C. J., Determination of Microparameters for Discrete Element Modelling of Granular Materials with Varying Particle Size Using One-Dimensional Compression Testing, Masters Thesis, University of British Columbia, 2017.

[3] Zeng Z. and Chen Y., Simulation of Straw Movement by Discrete Element Modelling of Straw - Sweep - Soil Interaction, Biosystems Engineering, Vol. 180, 2019, pp. 25-35.

[4] Nandanwar M. and Chen Y., Modeling and Measurements of Triaxial Tests for a Sandy Loam Soil, Canadian Biosystems Engineering, Vol. 59, No. 1, 2017, pp. 2.1-2.8.

[5] Verner A., Vertical Tillage not just for Row Crops, Hay & Forage Grower, Issue 2017, pp. 35.

[6] Alfaro M. C., Blatz J. A., Abdulrazaq W. F. and Kim C. S., Evaluating Shear Mobilization in Rockfill Columns used for Riverbank Stabilization, Canadian Geotechnical Journal, Vol. 46, No. 8, 2009, pp. 976–986.

[7] Alfaro III M., Blatz J., Alfaro M. and Ubay I. O., Stability Assessment of Aging Earth Fill Dam, Conference Proceedings, In Canadian Geotechnical Conference (GeoOttawa), 2017.

[8] Yang G., Yu T. and Liu H., Numerical Simulation of Undrained Triaxial Test Using 3D Discrete Element Modeling, Conference Proceedings, In GeoHunan Internation Conference (ASCE), 2011, No. 222, pp. 99–106.

9th Int. Conf. on Geotechnique, Construction Materials and Environment, Tokyo, Japan, 20-22 November 2019, ISBN: 978-4-909106025 C3051

STABILIZATION OF MARGINAL CRUSHED ROCK USING CEMENT AND FLY ASH AS A GREEN BASE COURSE MATERIAL

Mathagul Metham[1] Wutthiwat Mangkornngam[2] Akepong Sedthamanop[1] and Cherdsak Suksiripattanapong[2*]

[1] Bureau of Road Construction 2, Department of Highways, Thailand
[2] Department of Civil Engineering, Faculty of Engineering and Architecture, Rajamangala University of Technology Isan, Thailand, corresponding author: cherdsak_2526@hotmail.com, cherdsak.su@rmuti.ac.th

ABSTRACT

The use of marginal materials stabilized by cement for base course applications has grown rapidly. Marginal materials consist of marginal crushed rock (MCR), marginal lateritic soil (MLS), and reclaimed asphalt pavement (RAP). However, the use of cement will release high CO_2 causing greenhouse effect. This research investigates stabilization of marginal crushed rock using cement (C) and fly ash (FA) as a green base course material. FA used as pozzolanic binders was obtained from Mae Moh power plant in Thailand. The physical and engineering properties of MCR stabilized by OPC-FA were evaluated according to the specification of Department of Highways in Thailand. The influencing factors studied included binder content of 1%, 3% and 5% by weight of the crushed rock material, C/FA ratios of 100/0, 90/10, 80/20, 70/30, 60/40, and 50/50, and curing time of 7. The optimum ingredient of MCR stabilized by B was found at binder content of 3%, and C/FA ratios of 70/30. This research enables FA, which is a residue material, to be used as a green base course material.

Keywords: marginal crushed rock, binder, cement, fly ash

INTRODUCTION

Transportation is significant for development of country. Roadways and Highways are one major mode of transportation. According to the Ministry of Transportation (2013), it was found that total of roads in Thailand were 115,707 km, divided into Department of Highways, 68,253 km and 47,454 km of the Department of Rural Roads. Figure 1 shows characteristic of road structure. Generally, roadways are constructed in four layers which composed of subgrade, subbase, base and surface layer. An available material at the road construction site is used for road construction. However, some of available material does not typically meet the standard requirement as base materials. Marginal available materials can be effectively improved by chemical stabilizing agents with an additive, such as Portland Cement (PC) [1-4], lime and bitumen. However, the production of 1 ton of OPC releases about 1 ton of carbon dioxide, resulting in a significant amount of greenhouse gas into the atmosphere [5-15].

Fly ash (FA) is a aluminosilicate-rich materials which is a by-product from electrical manufacturing factory, Mae Moh, Thailand. The objective of this research is to investigate the possibility of using fly ash (FA) to improve compressive strength of marginal crushed rock (MCR) as a green pavement materials. The influential factors studied include MCR:binder ratios and cement:FA ratio. Unconfined compressive strength (UCS) of MCR mixed with cement and fly ash was investigated and compared the results with the standard of the Department of Highways, Thailand. The microstructural analyses of BA geopolymer stabilized MLS via scanning electron microscopy (SEM) were carried out to enlighten the role of influence factors. This research enables FA, which is a residue material, to be used as a green base course material.

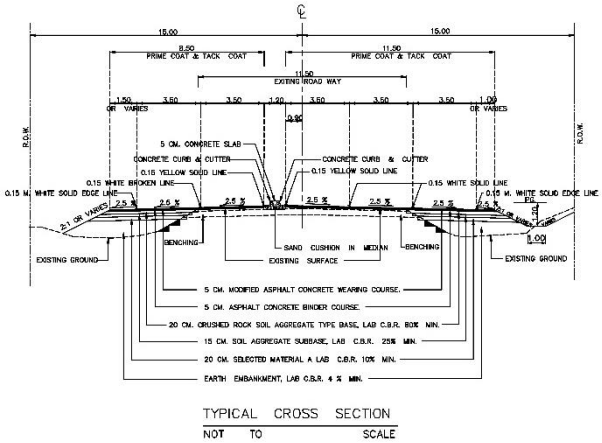

Figure 1 Characteristic of road structure

MATERIALS AND METHODS OF TESTING

Material

The marginal crushed rock (MCR) was collected from Nakhon Ratchasima province, Thailand. Figure 2 shows the grain size distribution of the MCR. The MCR is classified as GC in accordance with the Unified Soil Classification System. The maximum dry unit weight and optimum water content under modified Proctor energies of MCR were 2.308 gm/m^3 and 5.2%, respectively (Figure 3).

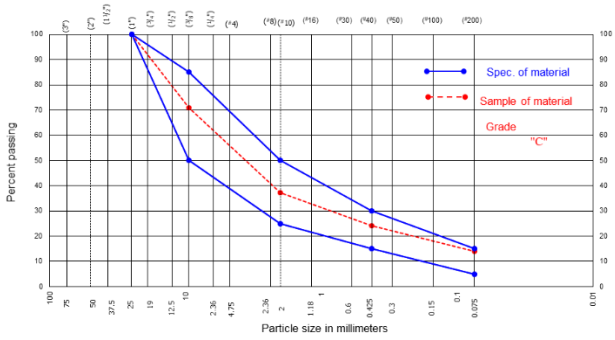

Figure 2 grain size distribution of the MCR

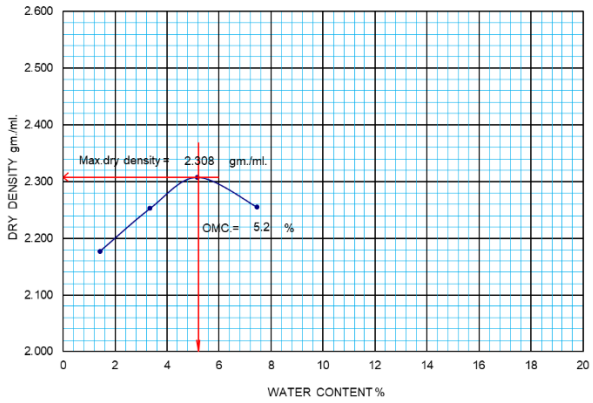

Figure 3 Compaction curves of MCR

Portland Cement Type 1 (OPC) has a specific gravity (Gs) = 3.10. The chemical composition of OPC are shown in Table 1. It is found that the main chemical composition of OPC was calcium oxide (CaO) content which was 75.96%

Fly ash (FA) was culledted from Mae Moh Power Plant, Lampang, Thailand. It is found that FA has brown color FA has a specific gravity (Gs) = 2.31. The chemical composition of FA by using X-Ray Fluorescence Spectrometer (XRF) technique. According to ASTM C618 is shown in Table 1. It can be soon that the amount of SiO_2 + Al_2O_3 + Fe_2O_3 is 67.31% by weight. The calcium oxide (CaO) content was 30.24% and Loss of Ignition (LOI) was 0.42 by weight. This fly ash is classified as a Class C fly ash.

Table 1 Chemical Properties of OPC and FA

Chemical composition	OPC (%)	FA (%)
SiO_2	9.81	47.51
Al_2O_3	4.64	13.14
Fe_2O_3	2.03	6.66
CaO	75.96	30.24
SO_3	2.58	ND
K_2O	1.62	1.63
NO_2	0.24	0.40
LOI	3.12	0.42

Sample preparation

The composition of marginal crushed rock (MCR) stabilized with cement (C) and fly ash (FA) sample was MCR, C, FA and water. Binder (B) is a mix of C and FA. The B content was added by 0, 1, 3, and 5% by weight of MCR. The C/FA ratios were 100/0, 90/10, 70/30, 60/40, and 50/50. Mixing ratio used in the study are shown in Table 2. The MCR and B were mixed until an observable consistency was observed for 2 minutes. The optimum water content was added and 5 minutes mixed. Under modified Proctor energies in preventing liquid evaporation, compaction was continued immediately thereafter. The mixture was then compacted in a standard mould of 101.6 mm in diameter and 116.4 mm in height. The Unconfined Compressive strength (UCS) specimens were wrapped in clear vinyl, after that cured at room temperature for 7 days.

Table 2 Mixing ratio used in the study

Mixed proportion	OPC (%)	FA (%)
M1	100	0
M2	90	10
M3	80	20
M4	70	30
M5	60	40
M6	50	50

TEST RESULT

Compaction of MCR mixed with C and FA

Fig. 4 shows the compaction results of MCR mixed with C and FA at the B content of 1%, 3%, and 5% and C/FA ratios of 100/0, 90/10, 70/30, 60/40, and 50/50. It can be seen that the maximum dry unit weight of MCR mixed with C and FA increases as B content increases because of the higher specific gravity of C. The optimum water content of MCR

mixed with C and FA was about 4.1-4.85%. The maximum dry unit weight of MCR mixed with C and FA was 2.288 gm/m^3.

Table 3 The compaction results of MCR with C and FA

	MDD (gm/m^3)			Optimum water content (%)		
	1 (%)	3 (%)	5 (%)	1 (%)	3 (%)	5 (%)
M1	2.236	2.261	2.257	4.85	4.40	4.33
M2	2.245	2.260	2.288	4.80	4.30	4.29
M3	2.28	2.254	2.268	4.60	4.28	4.20
M4	2.268	2.255	2.260	4.55	4.20	4.20
M5	2.273	2.263	2.257	4.50	4.15	4.18
M6	2.259	2.246	2.256	4.40	4.10	4.10

Compressive strength of MCR mixed with C and FA

Figures 4 indicate the 7-day Compressive strength of MCR mixed with C samples at various at the B content of 1%, 3%, and 5% and C/FA ratios of 100/0, 90/10, 70/30, 60/40, and 50/50. The 7-day compressive strength of MCR mixed with C and FA increases with the increase in binder (C and FA). The 7-day UCS of MCR mixed with C and FA samples at B content of 5% and C/FA ratios of 100/0 give the highest UCS values, Which is about 40 ksc. The 7-day UCS values of MCR mixed with C and FA at B content greater than 3% are also met the minimum strength requirement for UCS of 17 ksc specified by the Department of Highways, Thailand. The optimum ingredient of MCR stabilized by B was found at binder content of 3%, and C/FA ratios of 70/30.

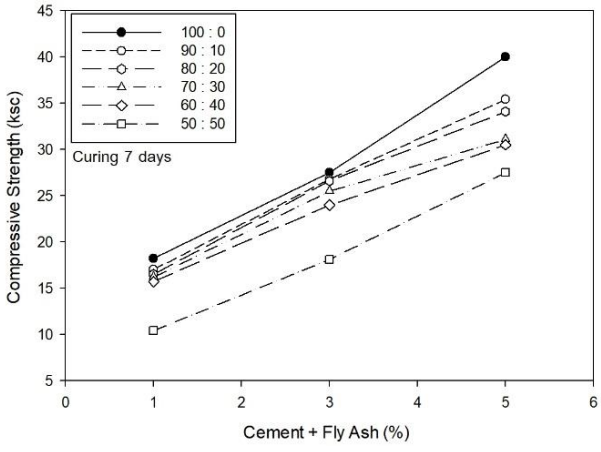

Figure 4 Compressive strength of MCR mixed with C and FA

CONCLUSIONS

The marginal crushed rock mixed with cement (OPC) and fly ash (FA) as a green base course material is presented in this study.

1. The maximum dry unit weight of MCR mixed with C and FA increases as B content increases because of the higher specific gravity of C.

2. The optimum water content of MCR mixed with C and FA was about 4.1-4.85%. The maximum dry unit weight of MCR mixed with C and FA was 2.288 gm/m^3.

3. The 7-day UCS of MCR mixed with C and FA samples at B content of 5% and C/FA ratios of 100/0 give the highest UCS values, Which is about 40 ksc.

ACKNOWLEDGMENTS

This research has been financial supported by Department of Highways, Thailand and authors would like to acknowledge Rajamangala University of Technology Isan, Nakhon Ratchasima for the facilities support

REFERENCES

[1] Chinkulkijniwat, A., and Horpibulsuk, S. (2012). Field strength development of repaired pavement using the recycling technique. Quarterly Journal of Engineering Geology and Hydrogeology, 45(2), 221–229.

[2] Baghini, M.S., Ismail, A., Naseralavi, S.S. and Firoozi, A.A. (2016). Performance evaluation of road base stabilized with styrene–butadiene copolymer latex and Portland cement. International Journal of Pavement Research and Technology, 9 (2016), pp. 321–336.

[3] Jitsangiam, P. and Nikraz, H. (2013). Coarse bauxite residue for roadway construction materials. International Journal of Pavement Engineering, 14(3), pp. 265–273.

[4] Saghafi, B., Al Nageim, H. and Atherton, W. (2013). Mechanical Behavior of a New Base Material Containing High Volumes of Limestone Waste Dust, PFA, and APC Residues. Journal of Materials in Civil Engineering, 25(4), pp. 450-461.

[5] Phummiphan, I., Horpibulsuk, S., Phoo-ngernkham, T., Arulrajah, A., and Shen, S.-L. (2017). Marginal Lateritic Soil Stabilized with Calcium Carbide Residue and Fly Ash Geopolymers as a Sustainable Pavement Base Material. Journal of Materials in Civil Engineering, 29(2)

[6] Phummiphan, I., Horpibulsuk, S., Rachan, R., Arulrajah, A., Shen, S.-L., and Chindaprasirt, P. (2018). High calcium fly ash geopolymer stabilized lateritic soil and granulated blast

furnace slag blends as a pavement base material. Journal of Hazardous Materials, 341, 257-267.

[7] Suksiripattanapong, C. Horpibulsuk, S. Chanprasert, P. Sukmak, P. Arulrajah, A. Compressive strength development in fly ash geopolymer masonry units manufactured from water treatment sludge, Construction and Building Materials. 82 (2015) 20–30.

[8] Suksiripattanapong, C. Horpibulsuk, S. Boongrasan, S. Udomchai, A. Chinkulkijniwat, A., and Arulrajah, A. Unit weight, strength and microstructure of a water treatment sludge–fly ash lightweight cellular geopolymer. Construction and Building Materials, 94, (2015) 807–816.

[9] Phetchuay, C., Horpibulsuk, S., Arulrajah, A., Suksiripattanapong, C., Udomchai, A. (2016). Strength development in soft marine clay stabilized by fly ash and calcium carbide residue based geopolymer. Applied Clay Science, pp. 134-142

[10] Kampala A, Horpibulsuk S. Engineering properties of calcium carbide residue stabilized silty clay. Journal of Materials in Civil Engineering, ASCE 2013:25(5);632-644.

[11] Kampala A, Horpibulsuk S, Chinkulkijniwat A, Shen SL. Engineering properties of recycled calcium carbide residue stabilized clay as fill and pavement materials. Constr Build Mater 2013;46:203–10.

[12] Kampala A, Horpibulsuk S, Prongmanee N, Chinkulkijniwat A. Influence of wet-dry cycles on compressive strength of calcium carbide residue-fly ash stabilized clay. Journal of Materials in Civil Engineering, ASCE 2014;24(1):633-643.

[13] Horpibulsuk S, Phetchuay C, Chinkulkijniwat A. Soil stabilization by calcium carbide residue and fly ash. Journal of Materials in Civil Engineering, ASCE 2012;24(2):184-193.

[14] Horpibulsuk S, Phetchuay C, Chinkulkijniwat C. Soil stabilization by calcium carbide residue. J Mater Civ Eng 2012;24(2):184–93.

[15] Horpibulsuk, S., Munsrakest, V., Udomchai, A, Chinkulkijniwat, A. and Arulrajah, A. (2014), "Strength of sustainable non-bearing masonry unit manufacturing from calcium carbide residue and fly ash", Construction and Building Materials, Vol.71, pp.210-215

9th Int. Conf. on Geotechnique, Construction Materials and Environment, Tokyo, Japan, 20-22 November 2019, ISBN: 978-4-909106025 C3051

STATIC PILE LOAD TEST: INTERNATIONAL PRACTICE REVIEW AND DISCUSSION ABOUT THE EUROPEAN AND JAPANESE STANDARDS

Fabien Szymkiewicz [1], Taisuke Sanagawa[2] and Hidetoshi Nishioka[3]
[1]IFSTTAR, Université Paris-Est, France; [2]Railway Technical Research Institute, Japan, [3]Chuo University, Japan

ABSTRACT

This publication aims to describe the European and Japanese standards in order to discuss about the ongoing project of revision of the Japanese standard for static pile load tests, keeping in mind that the future version of this standard will have to take into accounts Japanese past experience, as well as the future needs to adapt to overseas practices, if necessary, for economical purposes. To do so, the different derived parameters that can be obtained by carrying out a static pile load test on a vertically loaded pile (instrumented or not) are described. Then, the current practice for static pile load tests in Japan is described, and the main current overseas practices (with an extra focus on the European practices) are inventoried, and their differences (if any) with the Japanese practice are highlighted. Finally, these differences are discussed, and their importance assessed for a possible integration in the future Japanese standard, that could this way be seen for an oversea point of view as viable and legitimate alternative to the other and until now more common practices.
Keywords: Piles, Load Test, State of the Art, Standardisation

INTRODUCTION

Static pile load tests are usually time consuming, difficult, and expensive. It necessitates thorough soil investigations and detailed planning, as well as involving skilled and dedicated staff.

However, such tests are the most reliable way to assess correctly the ultimate bearing capacity of piles and their behavior. Depending on the level of monitoring put into action, shaft resistance and base resistance can be differentiated, and even unit shaft friction can be measured. Also, depending on the testing protocol chosen, different behaviors can be studied in detail, such as creep, cyclic behavior, or tensile strength.

Moreover, while these kinds of tests are often performed to verify a design hypothesis for a particular project, they can and should always be used to create and continuously improve databases used to build the design rules for deep foundations, increasing the accumulated experience and hence the robustness and reliability of these design rules. This should in time translate into improved design standards, saving natural resources, and making the solutions proposed overseas more attractive and competitive.

Therefore, having a complete and well detailed test standard that is thoroughly linked to the design standard is a necessity.

This publication aims to first inventory the current practices for static pile load tests in Japan as well as overseas (mainly in the USA and in Europe), then to describe the ongoing project of revision of the Japanese standard for static pile load tests, keeping in mind that the future version of this standard will have to take into accounts Japanese past experience, as well as the future needs to adapt to overseas practices, if necessary, for economical purposes.

In this paper, only the compression load test is described with a focus mainly centered on:
(1) The distance between test pile and reaction piles,
(2) Loading protocols
(3) Failure criteria of pile loading tests.

MAIN MEASURED AND DERIVED PARAMETERS

Two main categories of tests can be carried out: non instrumented or instrumented tests. The purposes of these two kinds of tests are different, with the instrumented test evidently giving more information on the behavior of the pile.

Non Instrumented Test

This is the simplest test carried out on piles, giving also least information on the behavior the pile.

The first information available when performing a static load test is the load-displacement curve. This curve gives rough information about the behavior of the pile.

However, as this curve depend on the nature and state of the soil, as well as on the piling method and the pile geometry (Fig. 1), and furthermore on the loading procedure, its use is clearly limited to the determination of the bearing capacity or the validation of the design behavior of the pile for

control tests.

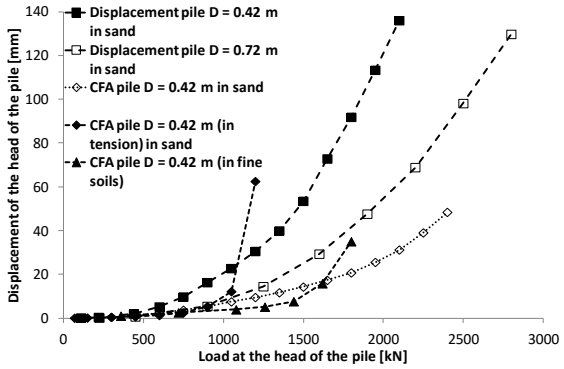

Fig. 1 Examples of load-displacement curve for different piles and sites.

The only other information given by a non instrumented test is the time-displacement curve and the load-creep rate curve, which can be used to determine the creep load of the pile (Fig. 2).

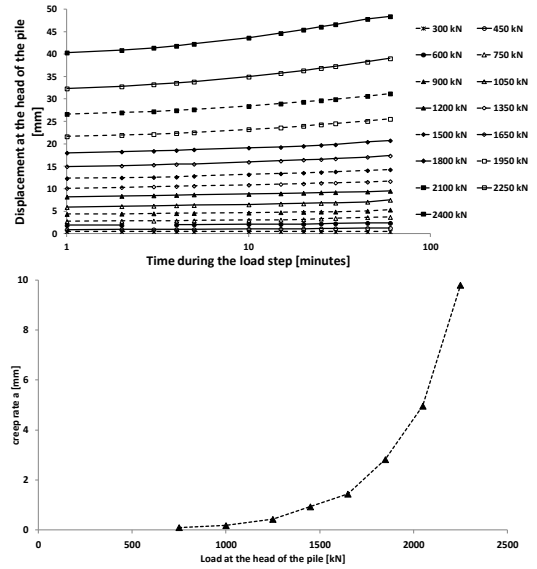

Fig. 2 Evolution of the displacement rate and creep rate during a load test.

Instrumented Test

Instrumented tests give away much more detailed information on the behavior of the pile.

Piles can be instrumented with strain gauges, vibrating wires or any other mean of achieving strain measurements, and also with embedded load cells (these are however much rarer).

Embedded load cells, when used, are often placed at the base of the pile, to measure directly the effort at this level, and therefore to distinguish the base resistance of the pile from its shaft resistance. However, this is relatively costly, and the quality of the concrete around this cell is often not as good as expected due to the presence of the cell, and therefore giving lower than expected results.

The distribution of the shaft resistance as well as the base resistance can also be determined by measurement of the strain at different depths. By knowing the strains at different depths, one can evaluate distribution of the efforts along the pile (Fig. 3), and from there determine the t-z curves (Fig. 4).

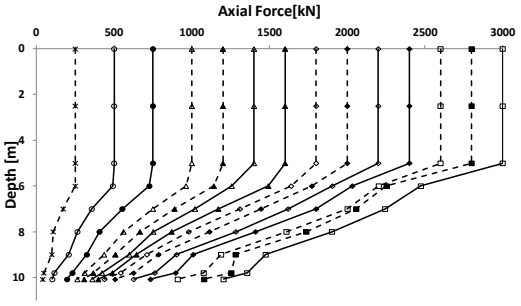

Fig. 3 Evolution of the distribution of the efforts along the shaft during a load test.

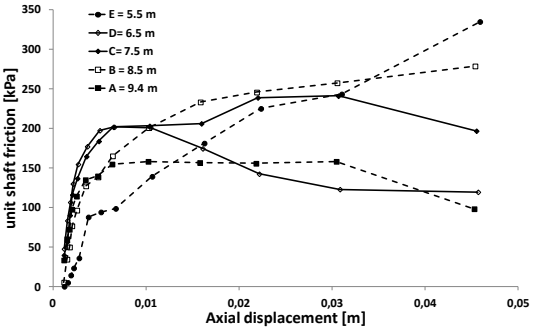

Fig. 4 *t-z* curves achieved from an instrumented load test.

To determine load from strain, the cross section and the pile material modulus of elasticity have to be assessed and all the materials present in the pile shall be considered. Strain sensors close to the pile head can be used to do this, if the geometry of the cross section and its composition is constant along the depth. Compression test on cored samples can also be considered. It is important to keep in mind that the type of strain sensor used has an impact on the modulus to take into account.

TESTING PROCEDURES OF JAPANESE STANDARD

History of Standard Revision

In Japan, the first standard "Method for Static Axial Compressive Load Test of Single Piles" was published in 1972 by the Japanese Geological Society (JGS). This standard has been revised twice in 1993 and 2002. And the third revision committee was established in 2018, and the discussion is still continuing now. In this chapter, the testing

procedures of the current standard revised in 2002 is mainly mentioned.

Distance Between Test Pile and Reaction Piles

Usually, the reaction device can be tension piles or anchors. In the JGS standard (2002), the following rules are defined as such: "As a general rule, the distances between the centers of the test pile and the tension piles (or anchors) shall be more than 3 times the maximum diameter of the test pile, and also more than 2.5 meters." (Fig. 5).

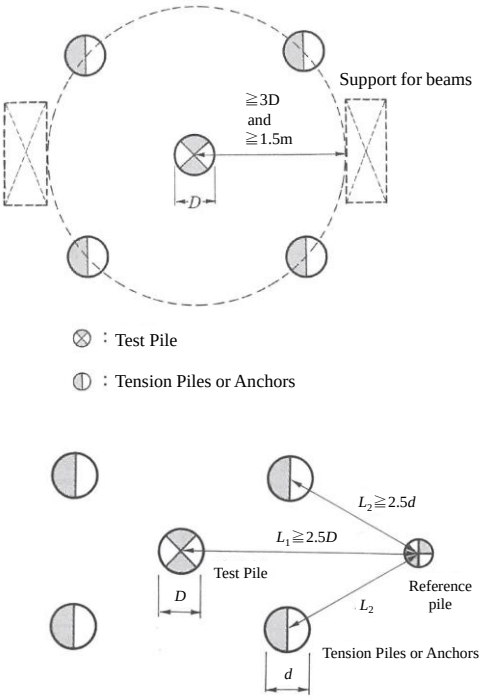

Fig. 5. Distance between the support point or tension piles (or anchors) and the test pile.

The rule of "more than 3 times the maximum diameter of the test pile" has been traditionally used since the first edition of the standard in 1972. In the revision of 2002, the experiment using model piles and the re-analysis of the data of the bi-directional load tests using the actual piles were conducted. As a result, it became clear that when this rule was satisfied, it did not have a big influence on the value of the second limiting resistance force which will be described later, and therefore this rule was judged to be appropriate for the purpose of assessing the resistance of the pile.

Time of testing

It seems reasonable to think that a waiting period of more than 5 days for the piles in sandy soil is needed, and a period of more than 14 days is necessary for the piles in cohesive soil.

Loading method

In the JGS standard, four loading methods are defined as shown in Fig. 6. These are classified into "step loading method" in which load holding is performed step by step and "continuous loading method" without load holding. In addition, two methods of "single cycle" and "multi cycle (not less than 4 cycles)" are defined respectively. The continuous loading method is a new loading method added as a revision in 2002 seen as a method suitable for reproducing the load condition acting in the short term such as seismic action.

Also, if the step loading method is applied, the load holding time for new loading steps is defined as "a constant period not less than 30 minutes". Regarding the validity of this load holding time, it was carefully examined at the time of revision in 1993. Thirty-four test cases with a load holding time of 120 minutes were collected and "the limit-resistance" and "the second-limit-resistance", which will be described below, were calculated. Then, when the load holding time is virtually shortened, it is calculated how much these errors occur. The result shows that the error is large when the load holding time is about 10 minutes, but the error has converged to several percent in about 30 minutes. As a result, it was judged that a rule of "not less than 30 minutes" is enough for the duration of a load step for engineering applications.

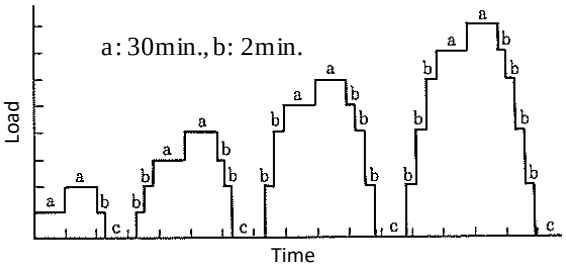

Fig. 6. Procedure of multi cycles loading method.

Failure Criteria of Pile Loading Tests

In JGS standard, two failure criteria are defined, and called "the first-limit-resistance" and "the second-limit-resistance", which is defined by the 1993 revision.

"The first-limit-resistance shall be defined as the load at the point of maximum curvature which appears clearly in the log *t* - log *z* curve.

"The second-limit-resistance shall be defined as the largest load measured within the displacement of the pile toe less than 10 % of the pile toe diameter." In the design standards for each field (railway, road, port etc.), the second-limit-resistance is considered

as the bearing capacity, and used for deriving the estimation formula of bearing capacity from the database of the loading tests.

Table 1 Distance between the test pile and the reaction device

Reaction device	NFP 94-150-1 [2]	NF EN 61773 [6]	ICE Specifications [5]	SIA 267/1 [4]	EA Piling [3]	GCP-18 [9]	ASTM D1143_07 [8]	NF EN ISO 22477-1 [7]
Dead load	N/A	N/A	At least 1.3 m	2.5 m or 2.5 time D *	2.5 m or 2.5 time D *^	3 m or 5 time D *^	1.5 m	2.5 m or 2.5 time D *^
Vertical tension piles (shorter than the test pile) or Vertical tension piles (longer)	2 m or 1.5 e *+	2 m or 1.5 e *+	2 m or 3 time D_{max} *+	N/A	2.5 m or 2.5 time D *^	3 m or 5 time e *^	2.5 m or 5 time D_{max} *^	2.5 m or 2.5 time D *^
			At least 5 time D_{max} *+		2.5 m or 2.5 time D *^			4 m or 5 time D *^
Raking piles	N/A	N/A	N/A		N/A	N/A	N/A	N/A
Vertical anchors	N/A	N/A	N/A	N/A	3 m under the base and 3 m or 3 D from the shaft *	N/A	N/A	N/A
Raking anchors	3 m both ways	N/A	N/A	N/A		N/A	N/A	3 m both ways

* whichever is the greatest
\+ from center to center
^ from edge to edge
e is the sum of the diameters of the test pile and the reaction pile
D is the diameter of the test pile

OVERSEA LOADING PROCEDURES AND REACTION DEVICES SETUPS

In this section, the main differences between several loading procedures are presented, mainly from Europe (French standard NF P 94-150-1 [2], German recommendations on piling [3], Swiss standard SIA 267/1 [4], ICE Specifications for piling and embedded retaining walls [5], European standard on Overhead lines – testing of foundations for structures [6], the European standard (also ISO) on static compression load testing NF EN ISO 22477-1 [7]) and USA (the Standard Test Methods for Deep Foundations Under Static Axial Compressive Load D 1143-07 [8] and the Geotechnical Control Procedure GCP-18 [9]) as well as the expected impact on the result.

Reaction Devices

Usually, the reaction device can be dead load or tension piles or anchors. Alternatively, in some cases, an existing structure situated over the test pile can be used. Moreover, for piles with a very high loading capacity, embedded jacks can be used.

When using dead load, tension piles or anchors, special attention should be paid to the distance between the test pile and the reaction piles (or anchors), so as to minimize the influence of the reaction system on the test pile, during the setup and the loading sequences.

Table 1 summarizes some of the practices in Western countries.

It can be seen that there are some notable differences between the different procedures, especially when a dead load is used. However, for more common reaction devices using vertical tension piles, characteristic values tend to stand out

Table 2 Recommended waiting time between the realization of the pile and the load test

Type of piles	NFP 94-150-1 [2]	NF EN 61773 [6]	ICE Specifications [5]	SIA 267/1 [4]	EA Piling [3]	GC P-18 [9]	ASTM D1143_07 [8]	NF EN ISO 22477-1 [7]
Displacement piles	7 to 28 days without any other precisions	7 (non cohesive soils) to 21 (cohesive soils) days	12 hours	At least 10 days in saturated clayey soils	3 (non cohesive soils) to 21 (cohesive soils) days	7 days	3 to 30 days without any other precisions	7 (sandy soils) to 28 (cohesive) days
Cast in place piles (bored)		14 days	4 days		N/A			7 (sandy soils) to 21 (cohesive) days

Time of Testing

The period of time between the day of the completion of installation of the test pile and testing is an important factor, for two reasons:

(1) In the case of displacement piles, this period allows for the dissipation of any excess pore pressures due to the installation of the pile;

(2) In the case of a cast in place pile, this period allows for the strength of concrete to build up so as to ensure that the pile shall not be damaged during the test.

No clear pattern can be extracted from the analysis of the different standards and recommendations: nevertheless, it seems reasonable to think that a waiting period of 14 days for bored piles is enough to reach a sufficient concrete strength, and a period of 21 days is sufficient for displacement piles. Table 2 summarizes the recommended intervals in Western countries.

Size of Pile Related to Piles Project

This question is of great importance, when the objective of the test is to verify a design hypothesis: indeed, the ratio diameter to length has a direct impact on the performance of the pile, as the rigidity of the pile change with it. Moreover, quality of concreting at the base can also be impacted by the diameter: for some execution methods, base resistances for large diameter are smaller than for smaller diameter.

Therefore, it seems logical to keep the test piles founded at the same level and in the same soils as the project piles, with a diameter as close as possible to the diameter of the project piles.

Loading Sequence and Load Steps Durations

The international (meaning not Japanese) standards and recommendations cited in this paper offer two different approaches for performing a maintained load compression test: with or without cycles.

Some standards are offering the possibility to perform a one cycle procedure, whereas the others offer a multi-cyclic procedure only, or both. Most of the procedures use the displacement rate as a criterion to increase the duration of the load step, so as not to allow a change of load step without stabilization of the pile. The magnitude of the load steps is mostly adjustable.

It is important to note that these differences in the procedures may be explained by the necessity to adapt to the local design method, as well as to the purpose of the test. When a sudden increase appears in the duration of a load steps, it is usually because the pile has to be tested at the working load. Then the magnitude and duration of the steps vary again to assess the overall bearing capacity. However, these changes in the loading pattern are detrimental to other aspects, like the determination of the critical load, which can be used in some countries for serviceability limit state. This is the case in France, for example, where the national standard reflects this particular need, by fixing the length and duration of all the load steps.

Moreover, some standards allows, like the Japanese one, the possibility to carry out test at a constant rate of penetration. However, it is very uncommon and will not be described here.

Failure Criterion

The most widely accepted failure criterion is the load at 10 % displacement of the diameter. However, some other standards recommend a higher displacement (to 15 %) or a combination of the

displacement rate and a percentage of the diameter in terms of displacement.

Table 3 Key points of the loading procedures

	NFP 94-150-1 [2]	NF EN 61773 [6]	ICE Specifications [5]	SIA 267/1 [4]	EA Piling [3]	GCP-18 [9]	ASTM D1143_07 [8]	NF EN ISO 22477-1 [7]
Cycles (number)	Multi-cyclic (2)	1 or more	1 or more	Multi-cyclic (3)	Multi-cyclic (2)	Multi-cyclic (3)	1 or more	1 or 2
Typical length of a load step	60 min	3 to 10 min	10 to 360 min	90 min	N/A	30 min	20 to 60 min	60
Shortening of a load step	no							Yes
Criterion for the shortening	/							Disp. rate
Prolonging a load step	no			Yes				
Criterion for lengthening	/		Overall head displacement	D, load applied			Overall duration	
				+ displacement rate				
step of equal magnitude	yes	no	no	no	no	no	no	not if multi-cyclic

CONCLUSION

In this paper, we described the Japanese standard (JGS standard) of the compression pile loading test, and compared with international standards.

The revision work of JGS standards is currently ongoing, and harmonizing with overseas standards, including ISO, is one of the important viewpoints, for economical reasons for instance. In addition, it is necessary to consider the situations unique to Japan. One is the very large earthquake action in the Japanese standards for seismic design, and the other is the interaction between the installed pile and the neighboring structures in very narrow places such as renewal projects.

Comparisons of the different procedure tend to show clear similarities between the different practices, from which we can conclude that the Japanese method and its interpretation of the results is already transposable overseas.

It is still expected that this paper will be useful for the revision of the JGS standards and further improvement of pile foundation design standards.

ACKNOWLEDGEMENTS

The authors would like to acknowledge the work of the members of the JGS Pile Loading Standards Revision Committee and especially its Chairman, Professor Kikuchi.

REFERENCES

[1] Japanese Geotechnical Society, Method for Static Axial Compressive Load Test of Single Piles, 2002.

[2] AFNOR, Essai statique de pieu isolé sous compression axiale. French Standard NF P 94-150-1, 1999.

[3] DGGT, Recommandations on Piling (EA Pfähle), 496 pages, 2013.

[4] SIA, Geotechnical Design – Supplementary Specifications, Swiss Standard, SIA 267/1, 2003.

[5] ICE, Specifications for piling and embedded retaining walls, second editions, 2009.

[6] AFNOR, Overhead lines: Testing of foundations for structures, European standard, 1997.

[7] AFNOR, Geotechnical investigation and testing -- Testing of geotechnical structures -- Part 1: Testing of piles: static compression load testing, European Standard, NF EN ISO 22477-1.

[8] ASTM, Standard Test Methods for Deep Foundations Under Static Axial Compressive Load, American Standard, 2007.

[9] State of New-York, Geotechnical Control Procedure 18 (GCP-18), 2015.

9th Int. Conf. on Geotechnique, Construction Materials and Environment, Tokyo, Japan, 20-22 November 2019, ISBN: 978-4-909106025 C3051

COMPARISON OF DIFFERENT METHODS FOR ANALYSIS OF COMBINED PILED RAFT FOUNDATION

Irfan Jamil[1], Irshad Ahmad[2], Muhammad Shoaib Khan[3]
[1,2]Department of Civil Engineering, UET Peshawar, Pakistan;

ABSTRACT

In a combined piled raft foundation (CPRF) both raft and piles take their share of total load applied. However, in practice, the contribution of raft in taking load is usually ignored and the load is assumed to be totally supported on piles. This way of CPRF becomes excessively conservative and uneconomical. To economize the design, relative load sharing of raft and piles in CPRF has to be found. In this connection, different simplified methods have been developed- each one with some limitations. In this study, three simplified methods have been applied to two cases of pile raft system. These methods are Randolph, Poulos-Davis-Randolph and Modified Poulos-Davis-Randolph. The first case is a hypothetical case consisting of a 12 m. x 12 m. raft supported on a square group of nine piles. The second case study is an actual eight story building to be constructed in Peshawar, Pakistan. The building is supported on pile raft system, with raft resting on very soft clay underlain by dense sand. The two case studies are also modelled in finite element program PLAXIS-3D. The results of all the simplified methods are comparable with PLAXIS-3D. However, results of the Randolph method are much close to PLAXIS-3D for the two cases studied. Furthermore, it is also shown that piles in a piled raft system can be used as a "stress reducers" as well as a "settlement reducers".

Keywords: Analytical methods, Raft, PLAXIS-3D, Stress reducers, Settlement reducers.

INTRODUCTION

CPRF system consists of three foundation bearing elements Piles, Raft and Supporting Soil. The thickness of Raft, Length and dimension of Pile, location of Piles in Raft, the soil Properties and Stiffness of pile and raft play a crucial role in the analysis and design of CPRF foundation [11]. Applied load from the superstructure are transferred to soil through these foundations bearing elements Raft and Pile by taking into account interaction between these foundations bearing elements. There are mainly two types of interaction which are Pile-to-Pile interaction and Pile-to-Raft Interaction. These interaction factors are highly dependent upon elastic modulus of soil, S/d ratio of piles and length of piles. Ignoring these interactions will lead to unsafe design and will underestimate settlement and bending moments in raft [1].

Every element in a piled raft system have their advantages. Raft can contribute in taking some percentage of load and can reduce substantially differential settlement depending upon raft thickness. Piles can be used as a "stress reducers" as well as a "settlement reducers" [5], [2] in addition to increase in bearing capacity of soil. Taking into account these contribution of both elements, piled raft foundation can be made very economical in terms of no of piles, length of piles and reinforcement in raft.

Researchers have put their efforts to solve problem of load sharing and analysis of CPRF like (Poulos and Davis, 1980 [3]; Randolph, 1994 [4] and Burland, 1995 [5]) have proposed some simplified methods involving a number of simplifications. Other approximate methods like "strip on springs" proposed by Poulos [6] in which raft is represented by Strip and Piles as Springs and "plate on springs" method proposed by Clancy and Randolph [7] in which raft is represented by Plate and Piles as Springs. Finite Elements software's like SAP2000 (Method proposed by Nguyen) [8], and PLAXIS-3D foundation (Brinkgreve and Broere, 2004) [9] can provide a good option for numerical analysis.

For structure design of raft in a piled raft system, there are several simplified approaches, which includes Burland [5] method and Winkler model for piled raft foundation system (WMPR) method [12]. These methods can provide reasonable results for preliminary analysis of raft in a piled raft system.

Randolph Method (1994)

In this method response of equivalent raft with single pile is used to predict response of whole CPRF system. Using stiffness of raft in isolation and pile group stiffness, combined piled raft stiffness can be calculated. Using this method, we can estimate percentage load taken by piles and raft and average settlement of whole CPRF system. To incorporate variation of stiffness along depth of soil, Randolph include stiffness of soil along the pile shaft, at pile head and pile tip. Randolph do not consider flexibility of raft and strength properties of soil (Cohesion, friction angle).

Poulos-Davis-Randolph Method (2001)

Tri-linear settlement curve is used to establish this method. Using this method, we can find a point (load "P1") at which pile capacity is fully mobilized and ultimate capacity "Pu" of CPRF. Using stiffness of Pile group "K_p" and stiffness of raft "K_r" combined piled raft stiffness can be calculated "K_{pr}". Using this method, load sharing percent between piles and raft can be estimated. Pile raft interaction factor and stiffness of raft can be calculated from Randolph method and elastic theory respectively (Mayne and Poulos, 1999) [12]. The Combined piled raft stiffness can be calculated as follow:

$$K_{pr}=\frac{(K_p+K_r(1-2\alpha_{rp}))}{(1-\alpha_{rp}^2*\frac{K_r}{K_p})} \quad (1)$$

In this equation, Kp is the pile group stiffness, kr is only raft stiffness and αrp is pile-raft interaction factor.

Modified Poulos-Davis-Randolph Method

For this method, a hyperbolic settlement curve for piled raft system is used instead of tri-linear settlement curve. Also, in this method, Stiffness of raft and piles will change according to the applied load. Using this method, we can find allowable settlement for CPRF and load level at which piled raft system gets non-linear and subsequently non-linear behavior of piled raft system can be capture. In order to avoid plastic behavior of CPRF system, it is focused not to exceed the non-linear load level.

Burland Method

One of the simplified approach for geotechnical and structure design of piled raft system. This approach is applicable only, when piles are developing their full geotechnical capacity. In this method, load is calculated corresponding to allowable settlement of raft out of total load. The remaining excess load is assumed to be carried by piles. Bending moments in raft of piled raft system can be calculated using a reduced column load "Qr" which is given by equation. 2.

$$Qr=Q-0.9Psu$$

where "Q" is total column load and "Psu" is the pile geotechnical capacity without factor of safety.

Winkler Model For Piled Raft System (WMPR)

WMPR method is based on Randolph method. Adjusted Stiffness's for piles and raft can be calculated based on settlement results of Randolph method and assign as Winkler Springs in any FEM software. Pile-pile and pile-raft interaction factors were incorporated while finding these stiffness's. Bending moments in raft of a piled raft system can be calculated using this simplified approach.

METHODOLOGY

For this research, the above-mentioned methods were applied on two case studies. The first case study is a typical piled raft of 12mx12m supported on a square group of nine piles while second case study is an actual piled raft of eight story building to be constructed in Peshawar, Pakistan. Both case studies were also analyzed using FEM software PLAXIS-3D. In second case study analysis of unpiled raft were also performed to show usage of piles as a "Stress Reducers" and "Settlement Reducers".

Case Study (1)

First case study consists of 12mx12m raft with nine piles as shown in Figure 1 and 2.

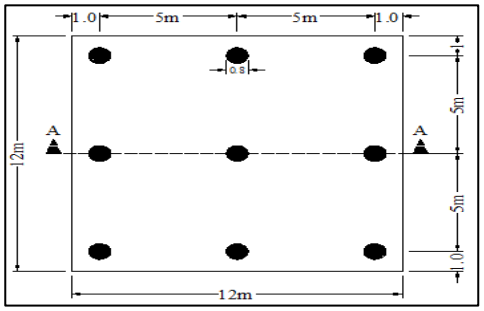

Fig. 1 Piled raft Layout

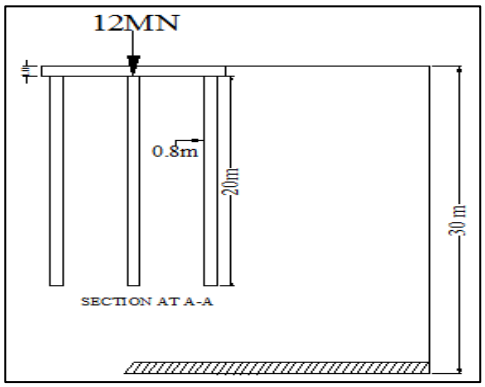

Fig. 2 Piled raft Layout cross-section

The Soil, pile and raft properties selected are shown in Table 1, 2 and 3 respectively. Similarly, PLAXIS 3D meshed and general model is shown in Figure 3 and 4.

Table 1 Soil Properties

Properties	Value
Soil modulus, E_s	50 [MPa]
Cohesion of soil, c_u	50 [KPa]
Poison's ratio of soil, υ_s	0.45
Angle of internal friction, ϕ	0 [degrees]
Unit weight	γ_{sat} = 20 [KN/m^3] γ_{unsat}=19 [KN/m^3]
FE model	Elasto-plastic [Mohr-coulomb]

Table 2 Pile Properties

Properties	Valve
Modulus of elasticity, Ep	30 x 10^7 [KN/m^2]
Diameter of pile, d_p	0.8 [m]
Length of pile, L	20 [m]
Unit weight, γ	25 [KN/m^3]
Poison's ratio of pile, υ_s	0.3
FE model	Linear isotropic

Table 3 Raft Properties

Properties	Valve
Modulus of elasticity, Er	3 x 10^7 [KN/m^2]
Thickness, d	1 [m]
Unit weight, γ	25 [KN/m^3]
Poison's ratio of raft, υ_r	0.3
Length and breadth of raft, Lr and Br	12 x 12 [m]
FE model	Linear isotropic

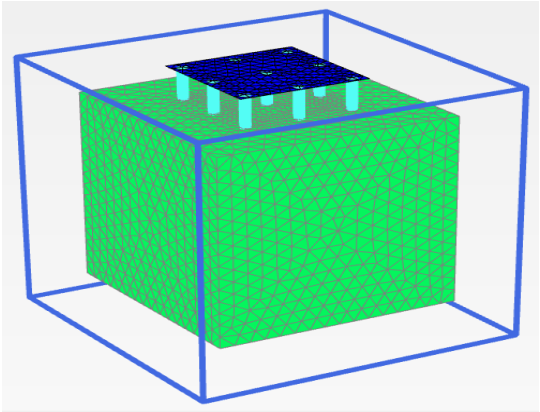

Fig. 3 PLAXIS 3D Meshed model (top soil is hidden for clarification)

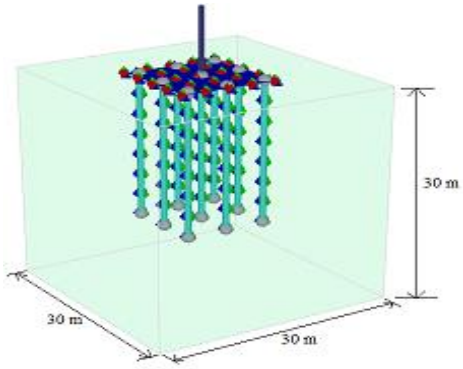

Fig. 4 PLAXIS 3D Piled raft model

Analysis Results of Case Study 1

Result of performed analysis are shown in Table 4. All methods show that more than 20 percent load is taken by raft supported on soil. In all methods, PLAXIS 3D is the most accurate approach for finding settlement and load taking percentages.

Table 4 Analysis result of Case Study (1)

Method	Percentage load taken by piles (%)	Settlement (mm)
Randolph Method	**78**	**7.22**
Poulos-Davis-Randolph Method	**61**	**5**
Modified Poulos-Davis-Randolph Method	**75**	**8.6**
PLAXIS-3D Approach	**76**	**8.7**

Case Study (2)

For second case study, piled raft of eight story building which was to be constructed in Peshawar is selected. Raft dimension was 32mx83m with 132 piles underneath. Diameter of piles is 0.6 m with embedded length is 25 m. Architectural 3D view of the proposed constructed building is shown in Figure 5. Raft layout and position of piles are shown in Figure 6. Geotechnical Profile of the proposed site is also shown in figure.7. A 15m soft clayey soil layer is present at the top, which makes the foundation design challenging. PLAXIS 3D models are shown in Figure 8 and 9.

Fig. 5 Architectural 3D view of eight story building

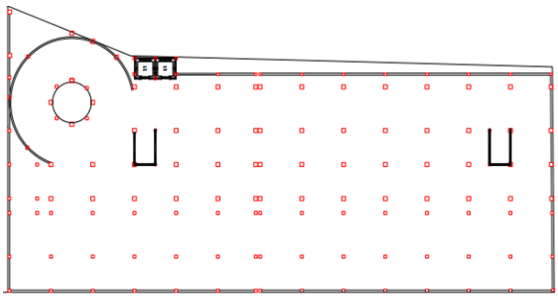

Fig. 6 Case 2 Piled raft Layout

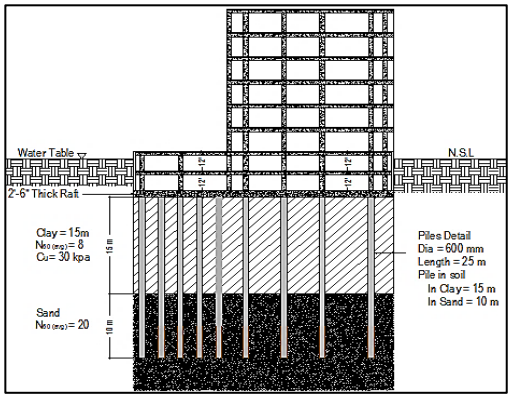

Fig. 7 Cross-section of case study 2 Piled raft

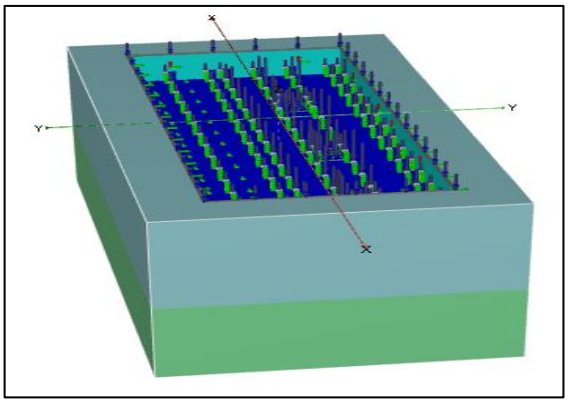

Fig. 8 PLAXIS 3D case study 2 model

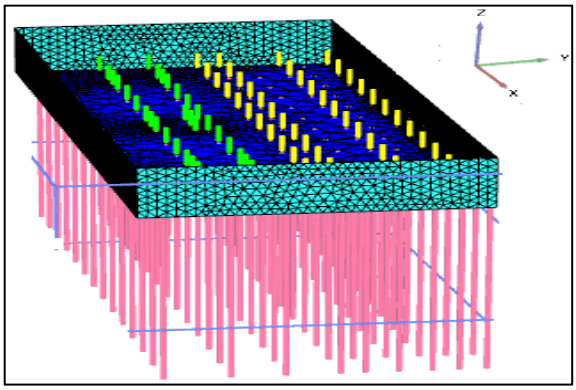

Fig. 9 PLAXIS 3D meshed model case study 2

Analysis Results of Case Study 2

By analyzing the piled raft using different methods along with PLAXIS-3D, analysis result are tabulated in Table 4.

Table 5 Analysis result for case study 2

Method	Percentage load taken by piles (%)	Settlement (mm)
Randolph Method	**80**	**61.5**
Poulos-Davis-Randolph Method	**64**	**45.45**
Modified Poulos-Davis-Randolph Method	**60**	**91**
PLAXIS-3D Approach	**76**	**67.5**

Piles as a "Stress and settlement reducers"

Analysis were performed for raft an isolation to show piles as "settlement reducers" and "stress reducers". Settlement of piled raft with piles and without piles are shown in Table 5. Usage of piles as a "Stress reducers" was shown by taking two cross-section of bending moment from PLAXIS-3D analysis, one on two story side while other on eight story side as shown in Figure 7 and 8, respectively.

Table 6 Piles as a "Settlement reducers"

Model	Settlement [mm]	Differential settlement [mm]
With piles	**67.5**	**81**
Without piles	**127.4**	**131**

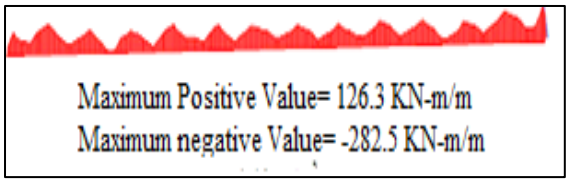

(a) With Piles

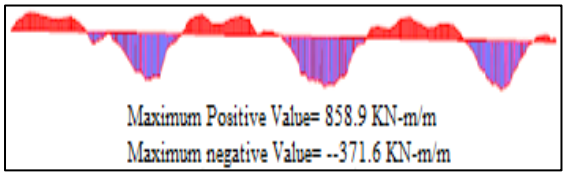

(b) Without Piles

Fig. 10 Cross-section for M11 moment on two story Side

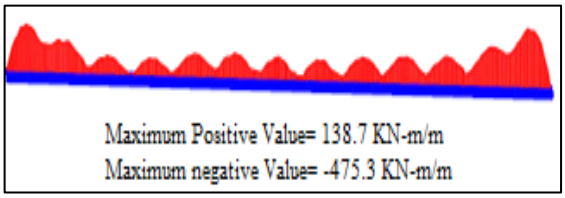

(a) With Piles

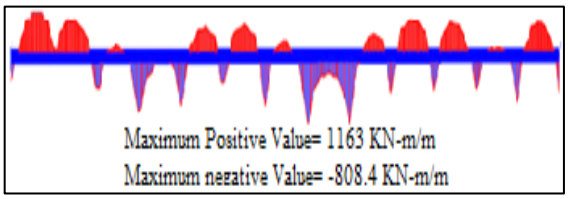

(b) Without Piles

Fig. 11 Cross-section for M11 moment on eight story Side

CONCLUSIONS

The analysis conducted shows Randolph method gives results which are much closed to numerical model result as compared to other methods. For preliminary analysis of piled raft design, Randolph method is recommended. Piles in addition to geotechnical advantage, can also be used to reduce state of stress in raft and settlement of piled raft foundation. Piled raft foundation can be make very economical by incorporating these aspects in piled raft design.

REFERENCES

[1] Poulos, H. G. "Methods of analysis of piled raft foundations." A Report Prepared on Behalf of Technical Committee TC18 of Piled Foundations (2001).

[2] Mandolini, A., Di Laora, R. and Mascarucci, Y., 2013. Rational design of piled raft. Procedia Engineering, 57, pp.45-52.

[3] Poulos, Harry George, and Edward Hughesdon Davis. Pile foundation analysis and design. No. Monograph. 1980.

[4] Randolph, M.F., 1994. Design methods for pile group and piled rafts. In Proc. 13th Int. Conf. on SMFE (Vol. 5, pp. 61-82).

[5] Burland, J. B. "Piles as settlement reducers." In The 8th Italian Conference on Soil Mechanics. 1995.

[6] Poulos, H.G., 1991. Analysis of piled strip foundations. Comp. Methods and Advances in Geomechs, 1, pp.183-191.

[7] Clancy, P. and Randolph, M.F., 1993. An approximate analysis procedure for piled raft foundations. International Journal for Numerical and Analytical Methods in Geomechanics, 17(12), pp.849-869.

[8] Nguyen, D.D.C., Jo, S.B. and Kim, D.S., 2013. Design method of piled-raft foundations under vertical load considering interaction effects. Computers and Geotechnics, 47, pp.16-27.

[9] Brinkgreve, R.B.J. and Broere, W. eds., 2004. Plaxis: 3D Foundation-Version 1. AA Balkema.

[10] Poulos, H.G., 2001. Piled raft foundations: design and applications. Geotechnique, 51(2), pp.95-114.

[11] Mayne, P.W. and Poulos, H.G., 1999. Approximate displacement influence factors for elastic shallow foundations. Journal of Geotechnical and Geoenvironmental Engineering, 125(6), pp.453-460.

[12] Jamil, Irfan., and Ahmad, Irshad., 2019. Bending moments in raft of a piled raft system using Winkler analysis. *Geomechanics and Engineering*, *18*(1), pp.41-4

9th Int. Conf. on Geotechnique, Construction Materials and Environment,
Tokyo, Japan, 20-22 November 2019, ISBN: 978-4-909106025 C3051

STUDY ON THE CHANGE OF SOFT SOIL SHEAR STRENGTH AND STIFFNESS IN HO CHI MINH CITY UNDER THE EXTENSION STRESS PATHS FOR DEEP EXCAVATIONS CALCULATION

Trung Ngo Duc[1], Phan Vo[2] and Thanh Tran Thi[3]
[1] Civil Engineering Department, Van Hien University, Ho Chi Minh City, Vietnam,
[2] Ho Chi Minh City University of Technology, Vietnam,
[3] The Industrial University of Ho Chi Minh City, Vietnam

ABSTRACT

In urban areas, underground space is growing up and deep excavations are often used to solve this problem. In Ho Chi Minh City, deep excavation is often constructed in areas close to existing buildings, infrastructure or public services, so limiting the displacement of the retaining wall and surface subsidence is very important to ensure that the surrounding works are not affected or affected by the level of permission. In order to analyze the displacement and deformation of the excavation pit, it is necessary to determine the soil characteristics of the excavation pit foundation for inclusion in the soil models. However, the construction design of the project is mainly taken from normal geological experiments, yet it does not describe the behavior of the surrounding soil. Therefore, the problem is to use an experimental model with a reasonable stress path to determine input parameters that are appropriate to the behavior of the ground around the pit, expressed by the change the stiffness of the soil during the excavation work, which the current experimental process is considered unchanged. This paper uses triaxial tests to evaluate the shear strength behavior of soft soil in Ho Chi Minh City with stress paths for calculation deep excavations. The experiments were carried out on an undraining fixture scheme of 50, 100, 200kPa pressure ratings to determine the shear strength and deformation modulus parameters of the E_{50} during the unloading process.

Keywords: strain, stress paths, nonlinearity, deep excavation, soil model, unloading

INTRODUCTION

In recent years, the demand for underground space has been increasing in urban areas. Deep excavations are often used to solve this problem. In Ho Chi Minh City, deep excavations have usually constructed in areas close to existing buildings, infrastructure or public services, so it is important to limit the displacement of retaining walls and surface settlement. to ensure the surrounding buildings are not affected or affected by the permitted level.

Due to the lack of laboratory data in the room, engineers often use conventional geological test data or correlate design parameters from available parameters and are often limited to simple model land in design of deep excavations. In fact, the construction of excavation can be considered a loading and unloading problem for the ground, this unloading changes the deformation stress state in the ground. If the correlation is irrelevant or determine parameters from test with improper stress paths, the engineer often faces the problem of deformation the actual deep excavations will be different from the predicted value.

Deep excavations is influenced by geotechnical conditions, the most important calculation is the control of horizontal displacement of the retaining wall at the lowest level, so it is necessary to determine the actual stress state of the soil around the deep excavations.

Many studies [11] have divided the area affected by the excavation process into four parts, as shown in Figure 1.

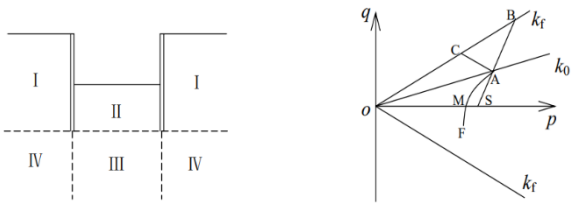

Fig. 1 Area of influence of deep excavation and stress paths

Zone I: when removing soil out of the excavation, horizontal displacement of the retaining wall will occur and horizontal stress decreases while vertical stress remains unchanged. Stress paths as the AC segment in Figure 1.

Zone II: during excavation, vertical stress decreases and lateral stress increases due to wall displacement, reduced soil strength, and ductile region may appear at the bottom of the pit. The stress path for this region is represented by the AMF segment in Figure 1.

Zone III: During the excavation process, vertical stress decreases continuously; horizontal stress

changes a little; and stress path is shown in the AS segment in Figure 1.

Region IV: Vertical stress is basically constant; there is a slight change in horizontal stress; the main shaft of the stress is deflected by shear; and the stress path is still near the AC segment in Figure 1.

The most significant effect on the deformation of the deep excavation is Zone I and Zone II, in which Zone I is the main factor causing horizontal displacement and Zone II causing bottom heave, which has important effects on deformation of deep excavation. Zone I and Zone II correspond to stress paths AC and AMF. In the AMF, the AM part is the unloading part and the MF part is loaded, which can be analyzed by a general geotechnical model. The AC line is the horizontal unloading stress line. Unlike AB stress lines in conventional experiments, there are different behaviors and stress paths.

In practice, the soil productivity change is very complicated. It can be seen that in order to analyze the behavior of Zone I (behind the retaining wall) and Zone II (at the bottom of the excavation pit), the analysis of soil strength and stiffness parameters of these two areas is a major issue focus on solving.

In order to have accurate data on the deformation of the excavation, it is necessary to have the soil characteristics of the area around the excavation to provide input data to be included in the calculation models. However, the current design of construction activities is mainly taken from normal geological tests, not describing the behavior of the land around the excavation pit. Therefore, the question is to use an experimental model with a reasonable stress path to determine the input parameters in accordance with the behavior of the ground around the excavation, expressed through change soil stiffness during excavation, which the current experimental procedure is considered to be constant.

In this study, the author performed a series of three undrained triaxial tests (CU) on 27 soft soil samples with a depth of 4 to 24m with load levels of 50, 100, 200 kPa, respectively, with the stress paths. Different stresses for evaluating shear and stiffness behavior of soft soil in Ho Chi Minh City.

APPARATUS

The test was carried out with the load frame system of Humboldt (USA) according to ASTM D4767. This system includes pressure, deformation, pressure and volume sensors connected to ADAM View 32-channel datalogger system. Advantech Adam view software allows collecting data from sensors over time. The system is connected to the computer via a network card to allow chamber pressure control and testing to be performed automatically from the beginning to the end.

Fig. 2 Humboldt tri-axial equipment system

Principles for design of the compression cell of the experiment with loading models based on Bishop and Wesleys's hydraulics (1975) [7] to control the different stresses during the unloading experiment.

Testing samples and testing parameters according to different stress paths shows in Table 2. A total of 27 soft soil samples were tested, of which 18 samples of very soft clays and 9 samples of soft clays, experimented according to the stress paths. The stress program is as follows:

- Conventional triaxial compression model (CTC - increase σ_1 and fixed σ_3): Saturated soil samples are isotropic consolidation and undrained samples according to the usual compression schedule: 9 samples;
- Triaxial drag model (RTE - reduced σ_1 and fixed σ_3): Saturated soil samples are isotropic consolidation and non-draining samples according to vertical stress reduction schedule: 9 samples;
- Model of cell pressure reduction (RTC - reduction σ_3 and fixed σ_1): Saturated soil samples are isotropic consolidation and non-draining samples according to horizontal stress reduction schedule: 9 samples;

Table 1 Soil parameters for soft soil in HCMC. Ho Chi Minh City and the stress paths in the tri-axial test

Depth [m]	Stress paths	Test No.	W_n [%]	γ_n [kN/m^3]	σ_c [kPa]
Very soft clays					
4÷6	CTC	1	88.55	15.7	50
		2	88.38	16.0	100
		3	81.47	15.9	200
	RTE	4	88.55	15.7	50
		5	88.38	16.0	100
		6	81.47	15.9	200
	RTC	7	88.55	15.7	50
		8	88.38	16.0	100
		9	81.47	15.9	200
12÷14	CTC	10	78.87	15.6	50
		11	78.70	15.4	100
		12	75.80	15.9	200
	RTE	13	78.87	15.6	50

		14	78.70	15.4	100
		15	75.80	15.9	200
	RTC	16	78.87	15.6	50
		17	78.70	15.4	100
		18	75.80	15.9	200
Soft clays					
18÷20	CTC	19	71.83	15.6	50
		20	62.86	15.7	100
		21	65.89	15.6	200
	RTE	22	71.83	15.6	50
		23	62.86	15.7	100
		24	65.89	15.6	200
	RTC	25	68.45	15.8	50
		26	65.76	15.7	100
		27	65.76	15.9	200
24÷26	CTC	28	50.14	16.4	50
		29	66.27	16.6	100
		30	54.21	16.7	200
	RTE	31	50.14	16.4	50
		32	66.27	16.6	100
		33	54.21	16.7	200
	RTC	34	50.14	16.4	50
		35	66.27	16.6	100
		36	54.21	16.7	200

ANALYSIS AND EVALUATION OF TESTING RESULTS

Stress and strain relationship (q-ε_1)

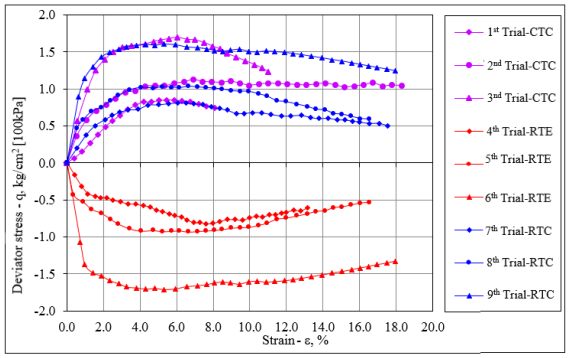

Fig. 3 Relationship (q - ε) of stress paths at depths 4-6m

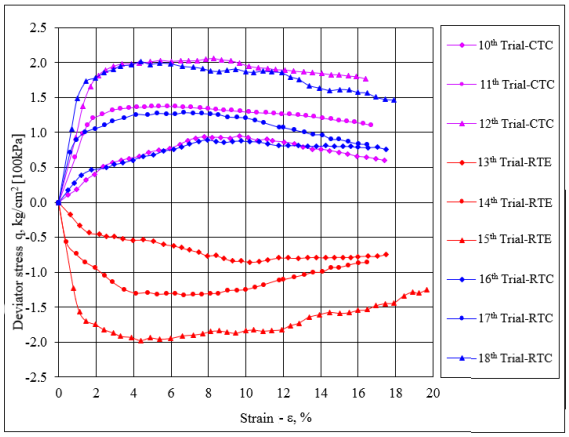

Fig. 4 Relationship (q - ε) of stress paths at depths 12-14m

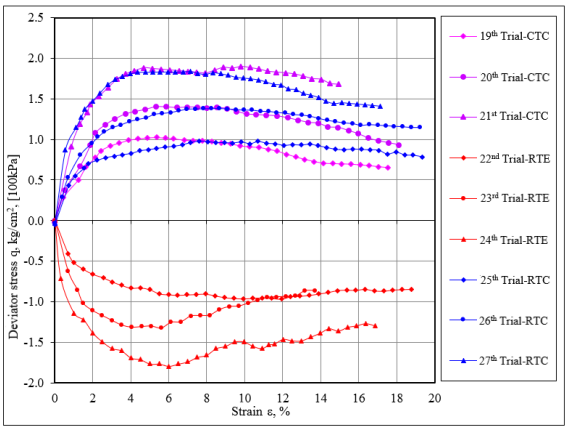

Fig. 5 Relationship (q - ε) of stress paths at depths 18-20m

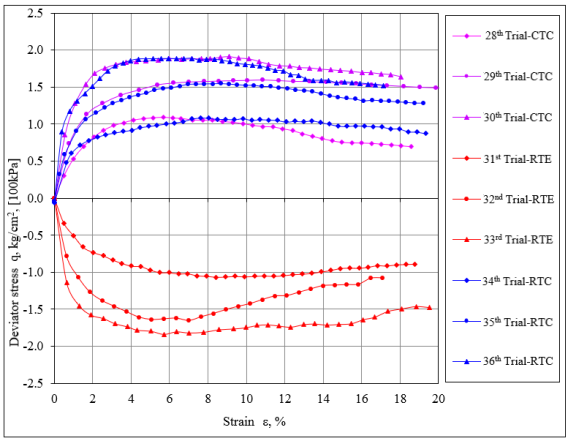

Fig. 6 Relationship (q - ε) of stress paths at depths 24-26m

In the above section, the triaxial test according to the three stresses CTC, RTE and RTC is performed with the CU diagram. The relationship of stress - deformation and change of pore water pressure with deformation with the above 3 stress paths at the cell pressure levels (σ_3) are respectively 50kPa, 100kPa and 200kPa are shown from Figure 3 to Figure 6.

In conventional triaxial compression test with CTC stress curve, stress relationship - deformation is progressively nonlinear and deformed with increasing deviation stress until the sample is destroyed, value maximum deviation stress increases with cell pressure level. The pore water pressure is always positive and also increases immediately along with the deformation in the axial stress increase process.

In contrast, for the RTE stress paths in a triaxial tensile test, the pore water pressure decreases at low stress levels and gradually increases at higher stress levels. The initial pressure of the pore water is negative and the positive sign is changed according to the increase of the deviation stress due to the reduction of σ_1. Therefore, the destructive stress and the change of pore water pressure for triaxial tensile tests also depend on the stress paths. Experimental results with RTE stress paths show that axial strain corresponding to maximum stress increases with cell

pressure and pore water pressure represents elasticity, which corresponds to the corresponding. The expansion of volume of ground soil outside reality when unloading during construction of excavation pits. This expansion behavior may be partly explained by the change in the pore water pressure of the soil sample at the end of the saturation and consolidation period during shear stress. In most cases, these soil samples were damaged by declining deformation. The destruction of the sample is seen in the middle of the sample like the bottleneck shape as shown in Fig. 7. It can be seen that, during the increase in stress, the pore water pressure also increases similarly corresponding to each stress paths. The destructive pattern when deforming is about 6 ÷ 8%.

Testing results show that in the axial stress strain RTE paths, it increases more slowly than CTC stress paths, especially shown at the maximum cell pressure level, which means that the initial tangent modulus is higher in the RTE stress paths and has a lower value for the CTC stress paths. From this, it can be concluded that the elastic parameters depend on the initial stress and strain modulus paths in the process of unloading.

Fig. 7 Sample destruction by RTE (left picture) and RTC stress path (right picture)

With the triaxial compression stress paths reducing horizontal stress RTC, when the horizontal stress is reduced during the sample cutting process, the deformation also increases but is slower than the deformation compared to CTC stress paths, so the strain deformation modulus The intention to calculate deep excavation by HS model has much greater results than CTC stress paths due to the curvature of stress strain relationship with greater slope. The pore water pressure in the RTC route is opposite to the CTC stress path but has a significantly smaller magnitude and has a different nonlinearity, this pressure gradually increases to the destructive threshold of the sample and decreases when the sample starts destructive. Testing results indicate that the parameter values determined from the strain stress relationship of the ground soil depend on the stress path of the triaxial test. Different stress paths will give different shear strength values and the deformation characteristics of soil samples will change as cell pressure increases. The initial deformation module E_i in experiments with unloading path is also of different value than when determining from the usual tri-axial compressive stress paths. Therefore, with the problem of designing deep excavations, the determination of input parameters with appropriate stress paths will give economical and safety results.

Analysis of deformation modules of stress paths

The relation (q, ε_1) Figure 3 to Figure 6 calculate the deformation module E_{50} of soft clays samples at different depths and different cell pressures as determined stiffness parameters of HS model. The results are shown in Table 2.

The magnitude of the E_{50} strain module increases gradually with depth. At the same depth, the distortion module will also have a greater value if tested with a larger cell pressure level.

Testing results show that the stiffness of soil depends on the stress paths. With HDS, the selection of stiffness parameters in the displacement calculation should be taken from the test with the unloading stress paths.

Table 2 E_{50} deformation modules from CTC, RTE and RTC stress paths

		RTE	RTC	CTC		
Depth [m]	σ_c [kPa]	E_{50} [kPa]	E_{50} [kPa]	E_{50} [kPa]	$\frac{E_{50,RTE}}{E_{50,CTC}}$	$\frac{E_{50,RTC}}{E_{50,CTC}}$
Very soft clays						
4÷6	50	3611	3494	2085	1.73	1.68
	100	8202	7495	4774	1.72	1.57
	200	14528	13997	8553	1.70	1.64
12÷14	50	2750	2968	1853	1.48	1.60
	100	11575	9427	5981	1.94	1.58
	200	15194	17774	9389	1.62	1.89
Soft clays						
18÷20	50	5811	5391	3673	1.58	1.47
	100	8640	6442	4510	1.95	1.48
	200	14652	14121	9273	1.58	1.52
24÷26	50	4579	4201	2861	1.60	1.47
	100	7765	7026	4922	1.58	1.43
	200	16688	15107	9161	1.82	1.65

The difference in the value of the elastic modulus according to the stress paths can be explained by the dependence of the elastic modulus according to each stress paths on the plastic strain level. The magnitude of plastic deformation depends on the flexible potential function and flexible flow function. Thus, the elastic modulus of the ground at some point has only one value in the state without deformation. When the ground is deformed, the value of the elastic modulus decreases with a degree of dependence on the stress path. The value of the elastic modulus of the

ground soil is determined by the initial slope of the strain-strain relationship curve in such a conventional tri-axial compression test that results in a large error in the calculation. Therefore, it is recommended to use the value of the elastic module from the unloading tri-axis compression test.

With triaxial test according to RTE and RTC stresses, the results of the deformation modulus are much larger than those calculated from the test results according to the normal tri-axial compressive stress path:

$$\frac{E_{50,RTE}}{E_{50,CTC}} \approx \frac{E_{50,RTC}}{E_{50,\mathrm{RTC}}} = [1.48 \div 1.57] \quad (1)$$

Shear strength of soil with different stress paths

From the above diagrams of stress-strain relationship (Figure 3 to Figure 6), destructive contour lines can be drawn to determine the effective shear resistance parameters for soil layers as follows:

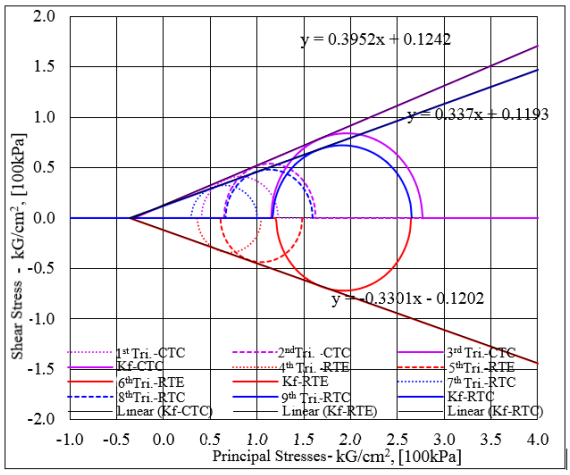

Fig. 8 Mohr circle according to stress paths at depth of 4-6m

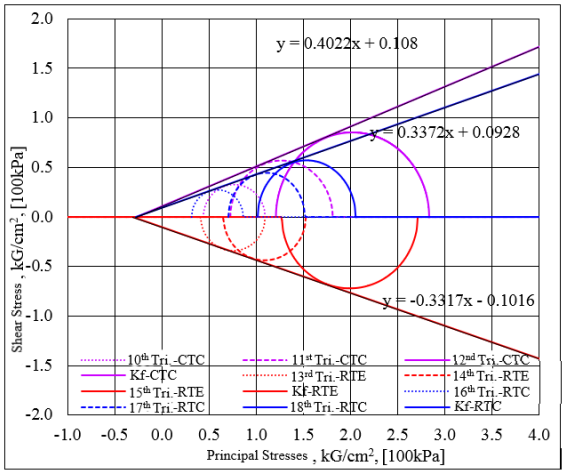

Fig. 9 Mohr circle according to stress paths at depth of 12-14m

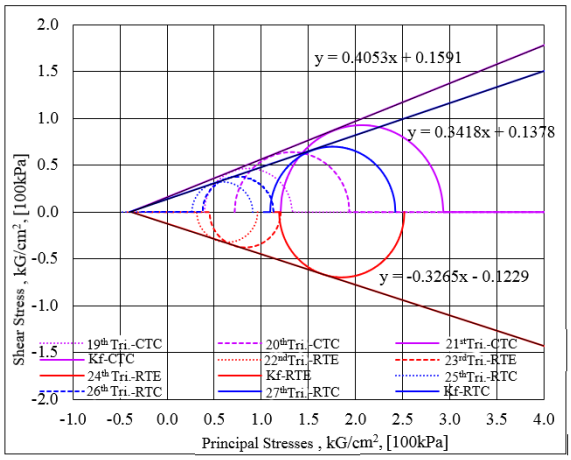

Fig. 10 Mohr circle according to stress paths at depth of 18-20m

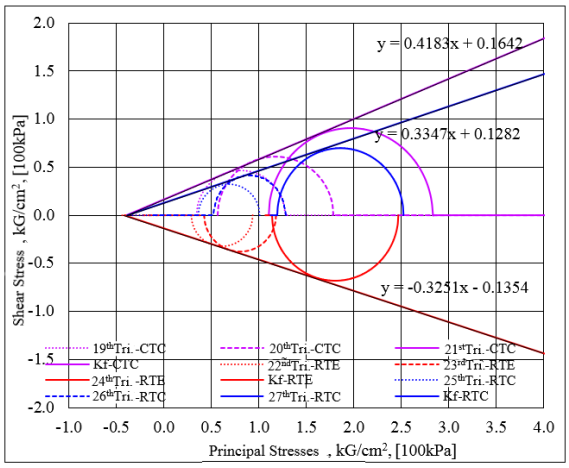

Fig. 11 Mohr circle according to stress paths at depth of 24-26m

The slope of the K_f destructive lines according to the stress paths is clearly different.

The effective friction angle of the RTE and RTC unloading route is similar and smaller than the CTC schedule. For each load level, the stress circle of RTE and RTC routes is back to the origin of the coordinates compared to the normal tri-axial compression stress paths CTC.

From the diagrams of Figure 8 to Figure 11, determine the effective shear strength parameters of the soil as shown in Table 3.

Table 3 Value of c' and φ' of soft soil in HCMC. according to stress paths

Depth [m]	Stress paths	*c'* [kPa]	*Δc'* [%]	*φ'* [^{0}]	*Δφ'* [%]
Very soft clays					
4÷6	CTC	13.58		21.56	
	RTC	11.21	0.83	18.62	0.86
	RTE	11.17	0.82	18.26	0.85
12÷14	CTC	13.87		21.90	
	RTC	11.12	0.80	18.63	0.85

	RTE	11.39	0.82	18.35	0.84
Soft clays					
18÷20	CTC	15.32		22.00	
	RTC	12.45	0.81	18.87	0.86
	RTE	12.17	0.79	18.08	0.82
24÷26	CTC	14.94		22.70	
	RTC	11.72	0.78	18.51	0.82
	RTE	11.64	0.78	18.01	0.79

From the results of the analysis, it can be seen that the effective friction angle of the ground (φ') in the three-axis test calculated by RTE and RTC is similar and smaller than that determined by the usual triaxial compression stress paths (CTC), this value is about 15% to 23% smaller:

$$\frac{\varphi'_{RTE}}{\varphi'_{CTC}} \approx \frac{\varphi'_{RTC}}{\varphi'_{CTC}} = 0.77 \div 0.85 \quad (2)$$

Experimental results show that the effective shear strength (φ') of soft soil in HCMC declined from 15% to 23% under the unloading stress schedule in case of deep excavations.

CONCLUSIONS

- Behavior of soil depends greatly on stress paths. Determining the shear strength parameters as well as the stiffness parameters for the deep excavation problem should be determined from the tri-axial experiment with the unloading stress paths because these experiments describe the actual working state of the ground during the construction process
- The results show that experiments with different stress paths will give different shear resistance values and strain characteristics will change with cell pressures. In the experiment with the unloading schedule, the shear resistance of the soil is significantly reduced compared to the conventional tri-axial compression test, because the excavation process is the process of unloading so the horizontal displacement of the soil will cause the soil to deteriorate (soft soil when digging).
- The effective friction angle of the ground (φ') in the tri-axial test calculated by RTE and RTC is similar and smaller, determined by the usual tri-axial compression stress path (CTC), which is smaller between 15% and 23%:

$$\frac{\varphi'_{RTE}}{\varphi'_{CTC}} \approx \frac{\varphi'_{RTC}}{\varphi'_{CTC}} = 0.77 \div 0.85$$

- Deformation modulus of soil also depends on stress paths. The linear sand deformation module of the triaxial test reduces the stress greater than the conventional triaxial test. Triaxial test according to RTE and RTC stresses results in equivalent modulus of modulus but larger than conventional tri-axial CTC stress path. With soft soil, scale ranges from [1.48 ÷ 1.57] times:

$$\frac{E_{50,RTE}}{E_{50,CTC}} \approx \frac{E_{50,RTC}}{E_{50,CTC}} = 1.48 \div 1.57$$

REFERENCES

[1] ASTM D 4186 – 89 (Reapproved 1998), *Standard Test Method for One-Dimensional Consolidation Properties of Soils Using Controlled-Strain Loading;*

[2] BS 1377:2016, Methods of test for soils for civil engineering purposes;

[3] Balasubramaniam, A. S.; Waheed-Uddin, Deformation characteristics of weathered Bangkok Clay in triaxial extension, Géotechnique Volume 27 issue 1, 1977, pp. 288-234;

[4] Becker P. (2008), Time and stress path dependent performance of excavations in soft soils, 19th European Young Geotechnical Engineers' Conference 3-6 September 2008, Gyor, Hungary;

[5] Bishop, A. W. and Garga, V. K., Drained Tension Tests on London Clay, Géotechnique Volume 19 issue 2, June 1969, pp. 309-313;

[6] Bishop, A.W. and Henkel, D.J., The measurement of soil properties in the triaxial test, London : E. Arnold, 1962, ©1957.

[7] Bishop, A.W. and Wesley, L.D. (1975), A Hydraulic Triaxial Apparatus for Controlled Stress Path Testing, Geotechnique, vol. 25(4), pp. 657–670;

[8] Duncan, J.M. and Chang, C.Y. (1970). Non-linear analysis of stress and strain in soils, Journal of Geotechnical Engineering, ASCE, vol. 96(5), pp. 1629–1653**.**

[9] Parry, R.H.G. and Nadarajah, V. (1974). Anisotropy in a natural soft clayey silt, Engineering Geology, vol. 8, pp. 287–309.

[10] Taha, M.R., Mofiz, S.A., Hossain, M.K. and Asmirza, M.S. (1999). Model simulation of residual soil in triaxial extension tests. Proc. of the Fifth Geotechnical Eng. Conference, Geotropika-99, pp. 105–114.

[11] Wong, K. S. (2009), A Short Course on Deep excavations, New Zealand;

9th Int. Conf. on Geotechnique, Construction Materials and Environment, Tokyo, Japan, 20-22 November 2019, ISBN: 978-4-909106025 C3051

QA/QC PLAN AND EVALUATION OF CHARACTERISTIC VALUE FOR DEEP CEMENT MIXING

S.H. Chew[1], H.M. Audrey Yim[1], J.W. Koh[1], K.E. Chua[2] and Z.X. Gng[2]
[1]Faculty of Engineering, National University of Singapore, Singapore; [2]Housing and Development Board, Singapore

ABSTRACT

Deep cement mixing (DCM) is widely used to improve the strength and stiffness of soil by mixing it with cement. When DCM is used as a low permeability barrier for water cut off, permeability must be tested in addition to the usual strength values. One concern in DCM construction is the quality assurance and quality control (QA/QC) of this technique to ensure uniformity along the DCM column. It is even more crucial when low permeability is required for the DCM column to be used as a seepage cutoff in an earth bund, in addition to its strength requirement. In this application, the DCM columns require low permeability and adequate strength. In this paper, two QA/QC aspects will be evaluated: the operational control and the evaluation of the treated DCM column. The operational control in terms of mixing time, cement content, rotation speed and mixing energy will be studied to gain understanding on how strength and permeability changes with the variability of the soil with depth. A rational QA/QC plan will be briefly proposed to ensure a consistent and rational method is developed for the evaluation of the strength and permeability variation of the treated soils over the area and over the depth. These will help in the development of acceptable characteristic value for the geotechnical parameters of soils treated with DCM (in line with Eurocode 7).

Keywords: Deep Cement Mixing, Soil Improvement, Permeability, Quality, Eurocode 7

INTRODUCTION

Deep cement mixing (DCM) is widely used to improve the strength and stiffness of soil by mixing it with cement and its application has gained popularity over the years in Singapore [1]. When installed in an earth bund, the DCM not only improves the stability of the slope but also act as a low permeability barrier for water cutoff if the earth bund is used to retain water, for example in a reservoir. When DCM is used as a low permeability barrier for water cut off, permeability must be tested in addition to the usual strength values.

When used to increase stability, there is usually no limit in strength requirements for the DCM column. However, a higher strength implies a more brittle behavior and the likelihood of crack formation when the DCM column is subjected to higher loads. This is not acceptable if the DCM columns are used as a seepage cutoff. Hence, the strength of the DCM columns needs to be capped.

One concern in DCM construction is the quality assurance and quality control (QA/QC) of this technique to ensure uniformity along the DCM column. It is even more crucial when low permeability is required for the DCM column to be used as a seepage cutoff in an earth bund, in addition to its strength requirement. In this application, the DCM columns require low permeability and adequate strength.

In this paper, two QA/QC aspects will be evaluated: the operational control and the evaluation of the treated DCM column. The operational control in terms of mixing time, cement content, rotation speed and mixing energy will be studied to gain understanding on how strength and permeability changes with the variability of the soil with depth. A rational QA/QC plan will be briefly proposed to ensure a consistent and rational method is developed for the evaluation of the strength and permeability variation of the treated soils over the area and over the depth. These will help in the development of acceptable characteristic value for the geotechnical parameters of soils treated with DCM (in line with Eurocode 7).

The results, values, and parameters presented and suggested in this paper are only indicative and are intended to illustrate principles. They do not refer to any specific project and should not be used contractually.

PROPOSED QA/QC CONTROL FOR ACTUAL WORKS

Two QA/QC aspects will be evaluated: the operational control and the evaluation of the treated DCM column strength and permeability.

(a) Operational QA/QC Control

The operational control in terms of mixing time, cement content, rotation speed and mixing energy are to be studied to gain understanding on how strength and permeability changes with the variability of the soil with depth.

To ensure the installation of good quality DCM columns, stringent operational controls are to be set up. For every column installation, a digitized record of the mixing efficiency, in terms of mixing time, cement content and mixing energy, etc. are to be recorded. Contractors will be required to submit records of the DCM column installation and compare that with the designed operation curves. These operation curves must be established with a site trial. An example of a design operation curve is shown in Fig. 1(a), (b) and (c). The values in this figure are only indicative.

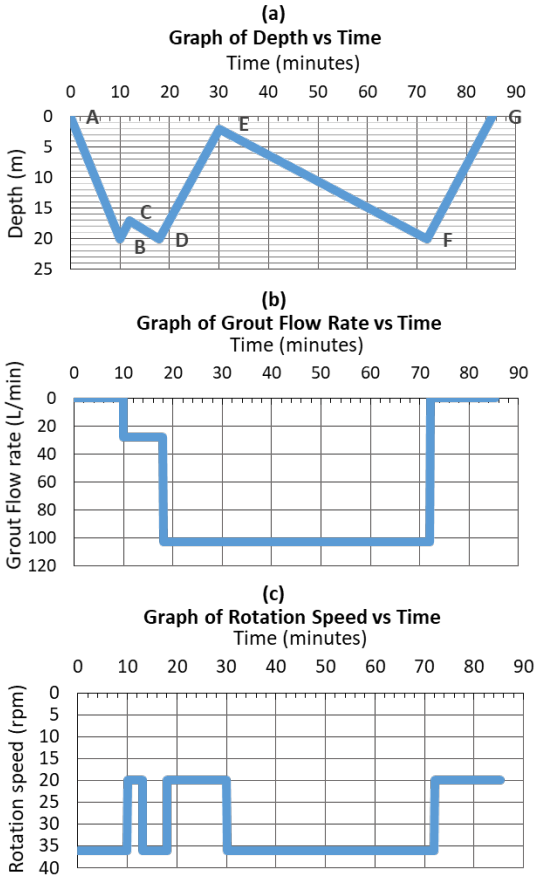

Fig. 1 Example of a design operation curve.

In Fig. 1(a), the vertical axis is the depth of penetration, while the horizontal axis is the time. Fig. 1(b) and (c) are the grout flow rate with time and the mixing blade rotation speed with time respectively.

Based on this information, the amount of cement mixed with the soil at a depth of interest can be evaluated based on the grout flow rate at that depth. The calculated rate of mixing and cement used must be consistent with the design value. Any variation will suggest that the column was not properly installed, and remedial action could be necessary.

(b) End Result Evaluation

The properties of Singapore Marine Clay treated with cement mixing has been well studied [2], [3]. However, due to the changes in soil profile with depth in the ground and differences in operation parameters, the quality, and properties of the DCM columns can vary greatly from laboratory studies.

To understand the long-term characteristics of the DCM columns, the qualities of the DCM columns were inspected by coring the completed columns after 91 days. The conventional method of using only absolute average strength values often indicate highly varied and inconsistent results and will result in difficulty to access the overall performance of the DSM columns. In addition, permeability is usually not tested or specified. Hence, an improvement to the QA/QC criteria is needed.

To provide consistent and representative quality sampling, the DCM treated area will be divided into sections of 100m along the cutoff wall.

Coring tests

The quality of DCM columns is to be inspected by coring the completed columns throughout the depth. The coring shall consist of at least two cored locations per section of 100m along the cutoff wall.

Representative zones along DCM columns

Sampling at 1.5m intervals will be conducted along each cored location of the selected DCM column. Unconfined compressive strength tests will then be carried out for all cored samples, while permeability tests will be carried out on five selected samples per cored location.

Acceptance criteria for DCM column

The acceptance criteria for the cored sampled obtained from the selected DCM column are as follows:

(1) The minimum unconfined compressive strength (UCS) for all the samples must be greater than 200 kPa, while the maximum UCS for all the samples must be less than 450 kPa;
(2) At least 70% of the total number of cored samples have to attain a UCS between 250 kPa and 350 kPa;
(3) Lower bound limit: not more than 15% of the total number of cored samples are to attain a UCS between 200 kPa and 250 kPa;
(4) Upper bound limit: not more than 15% of the total number of cored samples are to attain a UCS between 350 and 450 kPa;
(5) For the five samples per cored location tested for

permeability, the average permeability for all five samples must be less than 10^{-9} m/s. No single permeability value should be more than 10^{-7} m/s.

PRELIMINARY DCM SITE TRIAL DESIGN

Before implementation of the actual works, a site trial was conducted to determine the optimal cement dosage and operation parameters in order to achieve the stringent strength and permeability requirements. Too high a cement dosage will likely lead to a higher strength but more brittle behavior of the DCM; which is not acceptable in this case. The site trial, as compared to laboratory tests mix results, is also more representative of the actual DCM construction as it considers variability in the actual DCM behavior due to installation methods.

The DCM columns for the site trial were installed beneath the site's existing seabed, with the top level of the columns at -7.5 mCD and the toe level at -23.5 mCD, resulting in a design column length of 16m. The ground consists soft marine CLAY (M) overlaying fluvial CLAY/SILT (F2) and fluvial SAND (F1) and underlined by the original formation of sandy SILT residual soils (RS). Figure 2 shows two reference borelogs with respect to the DCM columns installed in the site trial.

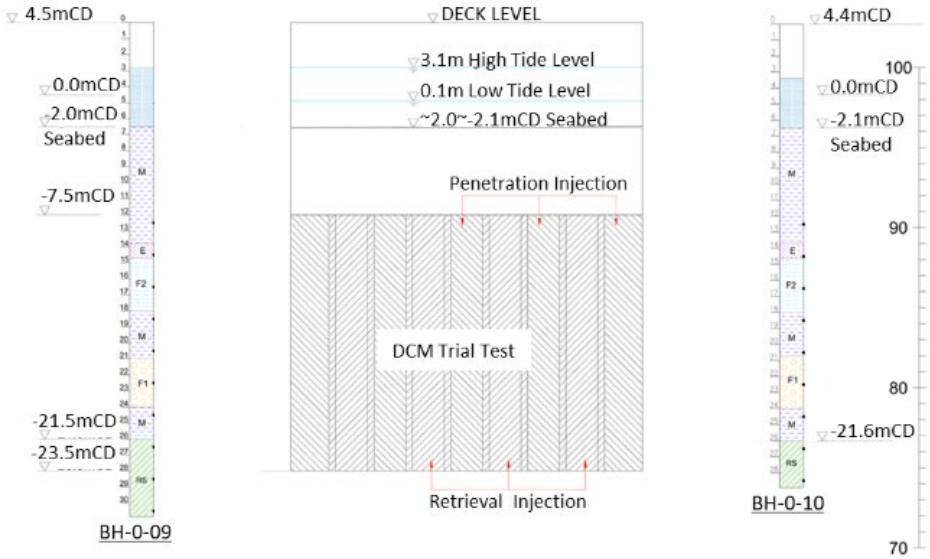

Fig. 2 Reference borelogs for site trial.

The DCM columns were constructed using four mixing blades, resulting in four overlapping columns that form a 2.8m by 2.8m block. A total of 18 DCM blocks with varying cement dosage and installation method (penetration/retrieval injection of cement) were installed for the site trial as shown in Fig. 3. All blocks were installed within a week. As shown in Fig. 3, the DCM blocks labelled with circles represent the DCM columns constructed with a cement dosage of 120 kg/m^3 of treated soil volume. Similarly, the DCM blocks labelled with stars and triangles represent cement dosages of 140 kg/m^3 and 160 kg/m^3 respectively. All mentioned above are for the retrieval injection installation method. The other DCM blocks that were not labelled were constructed using the penetration injection method, and will not be discussed in this paper.

The operational QA/QC control will be closely monitored during the construction of these blocks, and the cored samples obtained from the completed DCM columns after 28 and 91 days will be tested for strength and permeability.

SITE TRIAL RESULTS

Two QA/QC aspects will be evaluated: the operational and end result. However, this paper will only summarize the 28 and 91-day results.

(a) Operational QA/QC Control

The operation parameters of every DCM block constructed were recorded and monitored. One of the actual operational curves is shown in Fig. 4.

For the site trial, the preliminary set of key operational parameters adopted were as follows:

(1) The maximum main penetration and withdrawal rate should not be more than 0.5 m/min.

(2) The grout flow rate should not be less than 100 *l*/min for the main penetration and withdrawal steps.

(3) The blade rotation speed should not be faster than 40 rpm for the penetration step and 30 rpm for the withdrawal step.

(4) The current supplied to the four blades must be more than 300A and less than 1200A for all effective penetration and withdrawal steps.

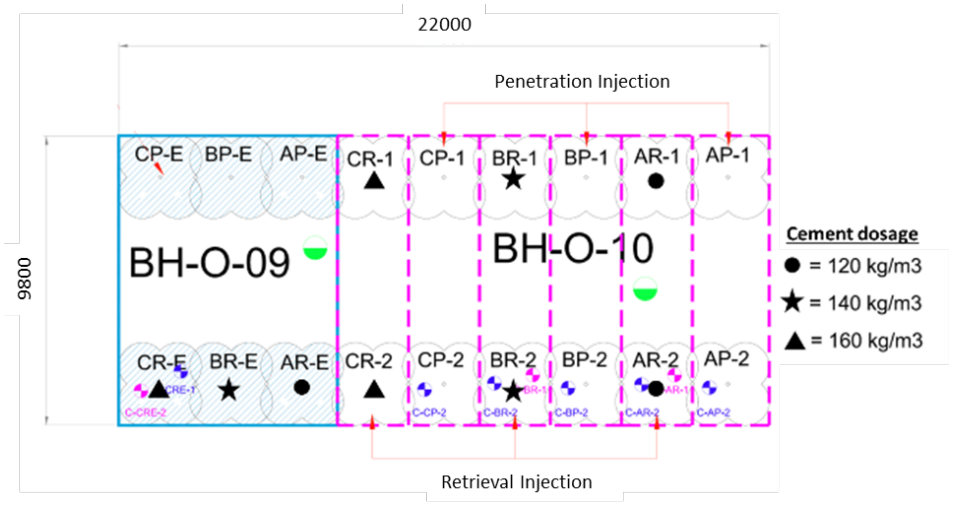

Fig. 3 DCM site trial plan

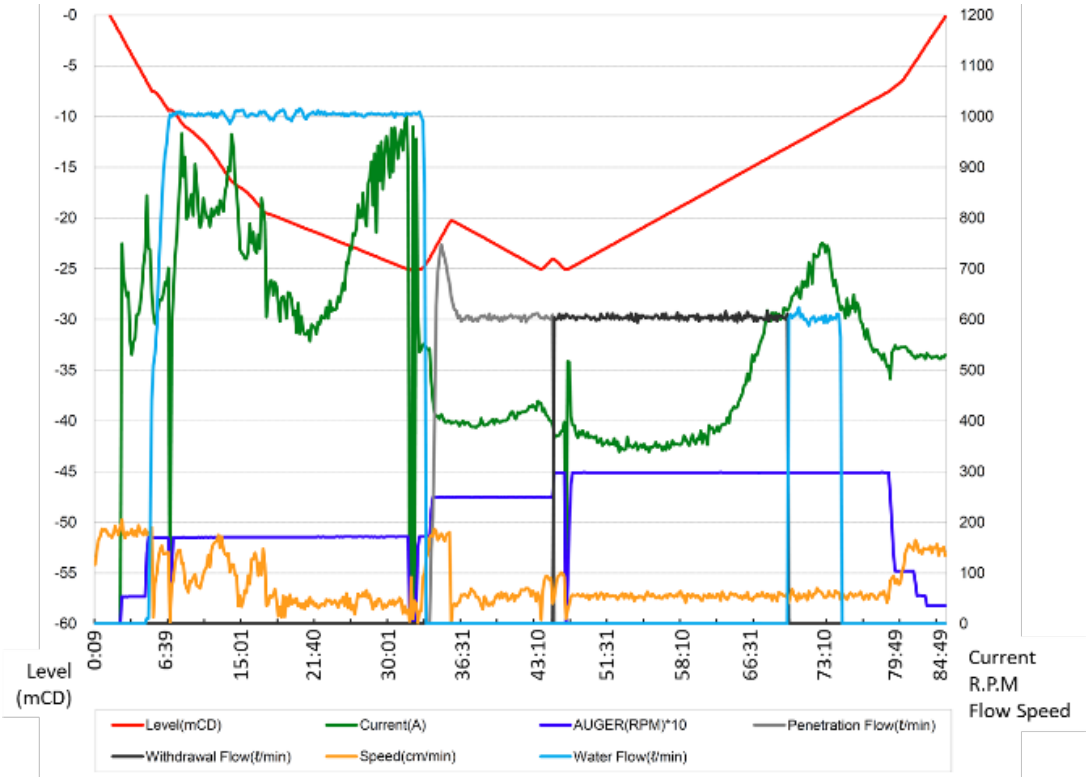

Fig. 4 Actual DCM site trial operation curve.

Every DCM block was found to satisfy and/or are close to the limiting operational parameter values stated above. Hence, if the core strength and permeability results satisfy the minimal specification requirement, the above operational parameter values will indicate the minimum requirement needed to achieve a good quality DCM block. Otherwise, if the core strength and permeability results do not satisfy the requirements, the above operational parameters have to be adjusted accordingly.

(b) End Result Evaluation

The recovered cored samples comprised of cement mixed with the different types of in-situ soils occurred through the depth of the DCM columns. This ranged from M (clay) to F1 (sand) and RS (residual soils). Different strengths and permeability values were obtained for the different soil mixes even when the cement dosage is kept constant throughout the depth.

Unconfined Compressive Strength (UCS)

For ease of comparison, the 28 day and 91 day UCS results have been plotted with depth for the cement dosages of 120, 140 and 160 kg/m^3 and are shown in Fig. 5, 6 and 7 respectively. In general, the 91-day results show an increase in UCS as compared to the 28-day result. However, the increase in strength resulted in a more brittle behavior in DCM column as observed from the increase in stiffness and reduction in elastic strain limit and failure strain. In addition, all the samples had exhibited a UCS higher than the allowable maximum limit of 450 kPa. This implies that cracks may develop in the DCM columns due to shrinkage. This could affect the overall permeability of the DCM columns, leading to its inability to function as a seepage cutoff wall.

By comparing the UCS result with depth for a constant cement dosage, it can be observed that the UCS varies greatly in the different soil types, and the DCM column does not have a uniform strength throughout its depth. In addition, for the same soil type treated with a constant cement dosage, the UCS results obtained also varied greatly as shown in the clay (M) layers treated with a cement dosage of 140 kg/m^3 shown in Fig. 6. This indicates that the operational QA/QC control is not adequate and further refinement is necessary.

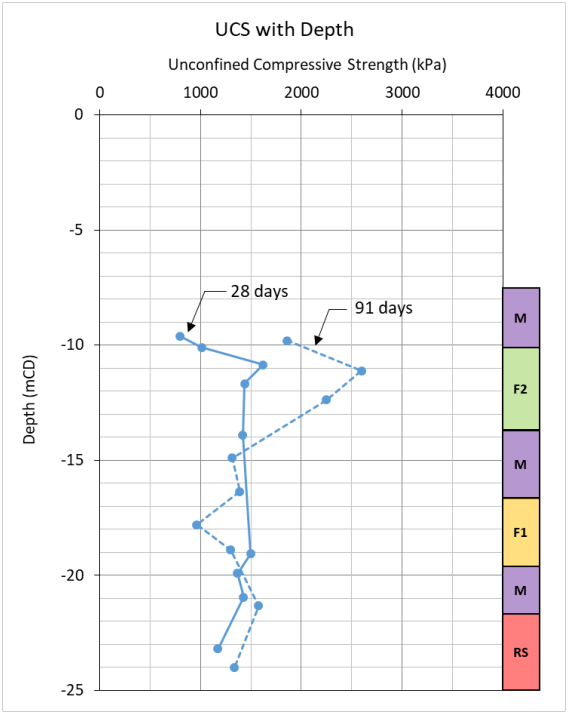

Fig. 5 UCS with depth for the cement dosage of 120 kg/m^3 of treated soil.

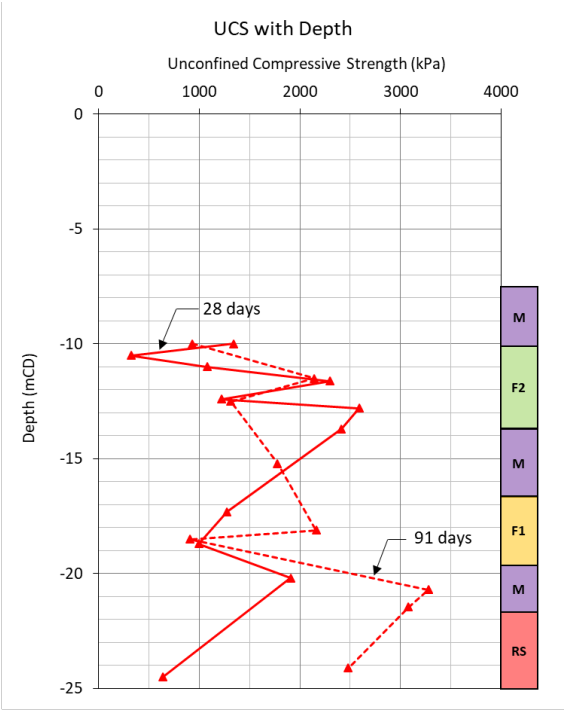

Fig. 6 UCS with depth for the cement dosage of 140 kg/m^3 of treated soil.

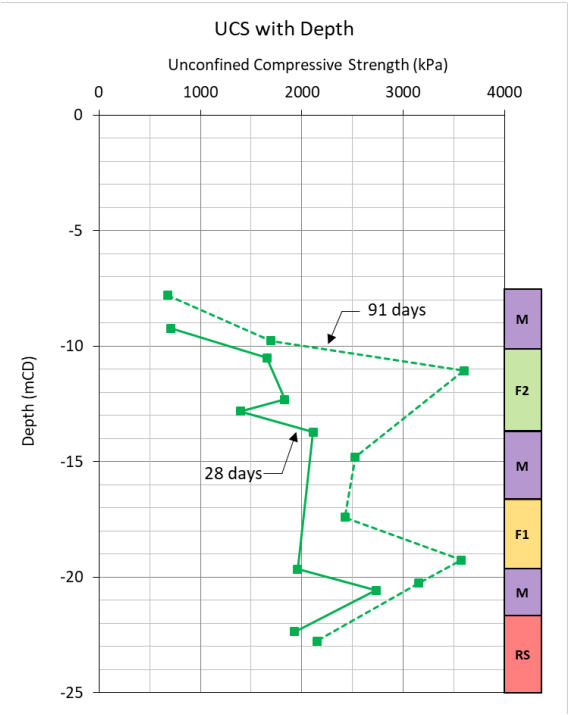

Fig. 7 UCS with depth for the cement dosage of 160 kg/m^3 of treated soil.

Permeability

Triaxial permeability tests were carried out for some of the cored samples. The permeability results at the various depths of the DCM columns have been plotted in Fig. 8.

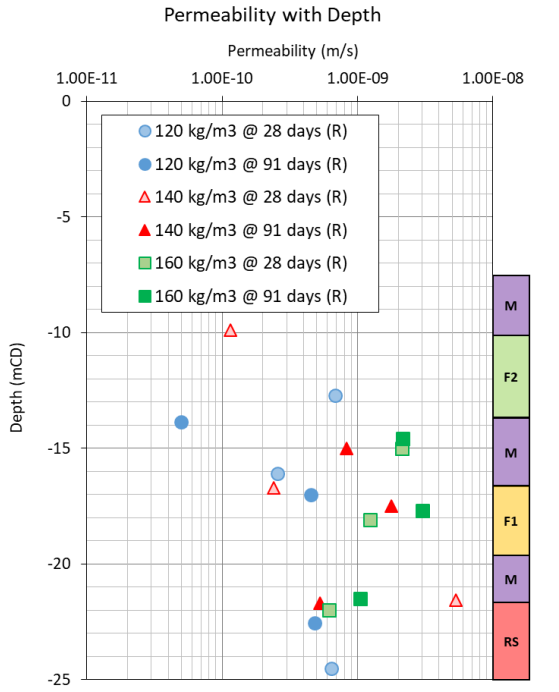

Fig. 8 Triaxial permeability tests result for some of the cored samples.

The permeability test results show that the core samples obtained from the DCM columns constructed with a cement dosage of 120 kg/m^3 were able to meet the permeability requirements of less than 10^{-9} m/s after 28 days and 91 days of curing. The permeability test results obtained from the DCM columns constructed with a cement dosage of 160 kg/m^3 was not satisfactory as it had obtained higher permeability values than the required. In addition, it was also observed that the sand (F1) layer tended to have higher permeability results. This is due to a lot more granular particles present in this layer.

A summary table of the UCS and permeability tests result obtained from the three different cement dosage of DCM core samples is shown in Table 1.

CONCLUSION

A quality assurance and quality control (QA/QC) plan for the construction of a DCM cutoff wall was proposed and consisted of two components: the operational mixing control the end result check.

To ensure the adequacy of the QA/QC plan, a site trial was conducted before the actual site works. Another objective of the site trial is to determine the optimal cement dosage and operation parameters in order to achieve the stringent strength and permeability requirements.

It was found that the DCM design implemented for the site trial did not fulfilled the DCM strength and permeability requirements. As observed from the non-uniform UCS results obtained through the DCM depth, different cement dosage may be required for the different soil types.

As such, the proposed QA/QC plan is not suitable. Additional site trials should be carried out to further refine the operation process such that good quality DCM columns with adequate strengths and low permeabilities can be constructed. This will enable the satisfactory performance of the DCM columns to improve slope stability and function as a seepage cutoff wall.

Table 1 Summary of UCS and permeability tests result.

Cement Dosage	Remarks	
	Unconfined Compressive Strength	Permeability
120 kg/m³	Almost all samples obtained higher than the upper limit of 450 kPa	All samples lower than $10\times^{-9}$ m/s
140 kg/m³		Average at 2.5×10^{-9}
160 kg/m³		Average at 1.7×10^{-9}

REFERENCES

[1] Tan T.S., Goh, T.L., and Yong, K.Y., "Properties of Singapore Marine Clays Improved by Cement Mixing", ASTM Geotechnical Testing Journal, Vol. 25 Issue 4, 2002.

[2] Kamruzzaman, A.H.M., Chew, S.H., and Lee, F.H., "Structuration & Destructuration Behavior of Cement-Treated Singapore Marine Clay", ASCE Journal of Geotechnical and Geoenvironmental Engineering, Vol. 135 no. 4, 2009.

[3] Chew, S.H., Kamruzzaman, A.H.M., and Lee, F.H., "Physiochemical and Engineering Behaviour of Cement-Treated Clay", ASCE Journal of Geotechnical and Geoenvironmental Engineering, Vol. 130 no.7, 2004.

9th Int. Conf. on Geotechnique, Construction Materials and Environment, Tokyo, Japan, 20-22 November 2019, ISBN: 978-4-909106025 C3051

GEOTHERMAL ENERGY PILE-SOIL INTERACTION UNDER MECHANICAL LOADING AND THERMAL CYCLES

Alitking Anongphouth[1], Pooneh Maghoul[2] and Marolo Alfaro[3]
[1,2,3]Faculty of Engineering, University of Manitoba, Canada

ABSTRACT

Harvesting shallow geothermal energy for heating and cooling building spaces in winter and summer is considered environmentally friendly and renewable. Recently, geothermal energy piles have been used as heat exchanger elements in ground source heat pump systems to exchange heat with the ground underneath buildings for heating and cooling purposes. However, imposing thermal cycles on such piles may result in possible adverse effects on their structural and geotechnical performance. Comprehensive understanding of the behavior of these geothermal energy piles; therefore, is vital for their successful applications. This paper aims to investigate the geothermal energy pile-soil interaction subjected to a combination of mechanical loading and thermal cycles. Coupled thermo-hydro-mechanical (THM) finite element analyses were carried out on a generic geothermal energy pile using local climatic and geological conditions in Winnipeg. Numerical results are presented in this paper in terms of pile head displacements, strains, and stresses developed in the pile, as well as shaft friction and effective radial stresses along the pile-soil interface. The effects of heating and cooling on the ultimate geotechnical pile capacity are also presented. Based on the numerical results, it was found that the thermo-mechanical loads have considerable effects on the geothermal energy pile responses.

Keywords: Geothermal energy pile, Pile-soil interaction, Thermal cycles, Coupled THM modeling

INTRODUCTION

In recent years, geothermal energy piles or simply energy piles have been increasingly used as ground heat exchangers in ground source heat pump (GHSP) systems to harness shallow geothermal energy for building heating and cooling purposes. The systems are considered renewable and environmentally friendly. The energy piles are structural piles with heat exchange pipes (loops) attached inside the rebar cages before casting concrete. They serve as structural elements to support the buildings and also as ground heat exchangers to exchange heat between the buildings and the underlying ground. Using working structural piles as ground heat exchangers; however, has raised concerns about possible adverse effects of thermal loads on the structural and geotechnical performance of the piles. This means that thermally loading the piles may lead to over-stressing, loss of load-carrying capacities of the piles, and excessive settlements. Energy piles were first used in the construction industry in Austria more than three decades ago [1]. Their use then has spread throughout Europe and to North America in recent years. Nonetheless, there is still limited understanding of their behavior under the combined effects of thermal and mechanical loads. This paper aims to numerically investigate the behavior of the energy pile subjected to thermo-mechanical loads and under local climatic and geological conditions in Winnipeg, Manitoba, Canada.

NUMERICAL MODEL DESCRIPTION

Axisymmetric thermo-hydro-mechanical (THM) finite element analyses using PLAXIS 2D-2018 were carried out. Note that in this paper the negative sign (-) is used for compression and positive sign (+) is used for tension. A generic energy pile was hypothesized based on local ground conditions and pile foundation engineering practice in Winnipeg. The pile was assumed to have a diameter of 0.8 m and a length of 20 m. It was installed through Winnipeg lacustrine clay with a pile toe embedded 5 m into very dense silt till.

Material Characteristics

For numerical modeling, the soil profile was simplified based on [2] and consists of three main layers. The first layer is Winnipeg lacustrine clay, from 0 to 15 m below ground level (bgl). This layer is underlain by silt till, from 15 to 21 m bgl. Below this silt till is dolomitic limestone bedrock, extending to a great depth. The groundwater table is at 3 m bgl. For constitutive material models, the concrete energy pile was modeled as non-porous (solid) elastic material using the linear elastic model (LEM). Hardening soil with small strain stiffness model (HSSM) was used for the clay and till. The LEM was also used for the dolomitic limestone. Table 1 gives a summary of some material parameters used for numerical modeling.

Table 1 Some material parameters used for numerical modeling of the Winnipeg energy pile

Parameter	Winnipeg clay	Silt tilt	Dolomitic limestone	Concrete pile
Hydraulic conductivity, k_x, k_y (m/day)	$6.70x10^{-5}$	0.028	8.64	-
Specific heat capacity, c_s (kJ/t/°C)	830	720	1300	800
Thermal conductivity, λ_s (kW/m/°C)	$1.2x10^{-3}$	$1.5x10^{-3}$	$2.3x10^{-3}$	$1.8x10^{-3}$
Soil density, ρ_s (t/m^3)	1.83	2.34	2.45	2.55
Linear thermal expansion coefficient, α_{sL} (1/°C)	$5x10^{-6}$	$5x10^{-6}$	$5x10^{-6}$	$10x10^{-6}$

Model Setup and Boundary Conditions

The pile was assumed to be located right underneath the center of the building with a width of 30 m and without any basements. With these assumptions, the axisymmetric finite element model was used. The model domain was set at a distance of 50 m (> 2L) and 75 m (> 3L) for the side and bottom boundaries; respectively, as illustrated in Fig. 1. These distances were considered to minimize the potential effects of the assumed boundary conditions. The model domain was divided into zones for discretization in which very fine mesh sizes were used for the pile body, along the pile-soil interface, and around the pile toe in order to ensure that there were enough elements to capture the correct pile behavior. Coarser mesh sizes were used for the zones further away from the pile.

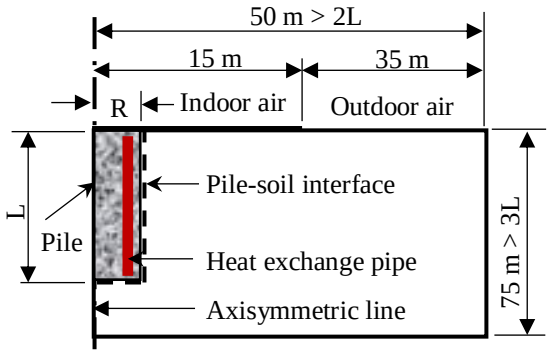

Fig. 1 Axisymmetric geometry setup (not to scale).

Free displacements were allowed at the top boundary. Both vertical and horizontal displacements were restrained at the bottom. Only vertical displacements were allowed at the left- and right-hand side boundaries. Drainage was allowed at the top and right-hand side boundaries. A closed flow boundary was assigned along the axisymmetric line and the bottom boundary. The heat flow was closed at the left- and right-hand sides. At the top boundary, the indoor air temperature was used as a boundary condition inside the building with a constant temperature of 20°C. The outdoor air temperature corresponding to climate variation was used as a boundary outside the building. A constant ground temperature of 7°C was assigned at the bottom boundary. The initial ground temperature for the entire model domain was also set at 7°C which was approximately the undisturbed average ground temperature in the Winnipeg area [3], [4].

A mechanical load of -1300 kN (compression), corresponding to the stress on the pile head of -2586 kPa, was applied in a drained manner and maintained on the pile head. In addition to this mechanical load, the energy pile was also subjected to thermal cycles due to heating and cooling by the circulating heat-carrying fluid in the heat exchange pipe installed inside the pile. In this study, a change of temperature of the fluid in the pipe inside the pile as a function of time from 0 to 40°C was used, as shown in Fig. 2. The convective boundary condition (line-based internal thermal boundary which implies a circular shell in the axisymmetric models) at 70 mm from the pile shaft was used to represent the heat exchange pipe. It was assumed that the changing pattern of the temperature in the pile with time followed the rising and falling pattern of the seasonal air temperature. The assumption was made based on the field observation by [1] on the operational energy geostructures. In the simulations, the energy pile was subjected to six heating-cooling cycles, corresponding to six years of heating and cooling of the building. Here, the term at the end of heating (EOH) means the pile was heated to the maximum temperature (the peak). Likewise, the term at the end of cooling (EOC) means the pile was cooled to the minimum temperature (the trough) in the particular year.

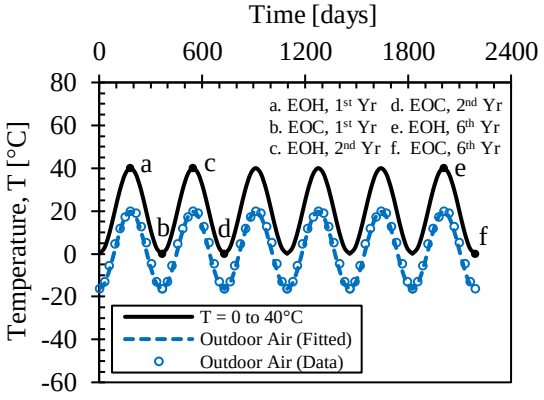

Fig. 2 Outdoor air temperature variation and thermal cycles applied to the pile starting from the first of January.

NUMERICAL RESULTS AND DISCUSSIONS

Temperature Distributions

Temperature profiles along the pile-soil interface were relatively constant, except reductions or roll-offs near the pile ends due to mechanisms of heat transfer at these locations. There were little changes (increased from 38.5 to 38.7ºC and from 7.9 to 8.9ºC) in the maximum temperature values at the EOH and EOC from the first to sixth year, respectively. Nonetheless, the ground temperatures seemed to increase marginally with time (overall ground warming over time). This was due to the influence of heat loss through the ground floor slab that accumulated in the ground underneath the building with time and also due to the imbalance in thermal loads during heating and cooling periods in relation to the initial ground temperature. Fig. 3 shows the horizontal temperature profiles at the mid-depth of the pile from the pile center to 15 m away at the EOH and EOC. As seen in the figure, large changes in the ground temperatures only occurred within a distance of about 2 m (≈ 2.5D) from the pile center.

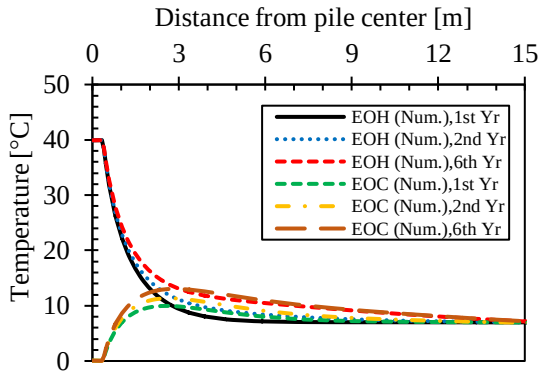

Fig. 3 Temperature profiles at the mid-depth of the pile from the pile center to 15 m away at the EOH and EOC in the 1st, 2nd, and 6th year.

Excess Porewater Distributions

Thermally induced excess porewater pressures (EPWPs) were induced in the clay layer with low permeability. There were no EPWPs induced in the till layer located below -15 m because of its high hydraulic conductivity. Heating induced negative EPWPs and cooling produced positive EPWPs. As shown in Fig. 4, the maximum negative values of EPWPs at the EOH were -9.1, -8.8, and -7.5 kPa in the first, second, and sixth year, accordingly. The reduction in EPWPs may be partially due to the consolidation. Another reason may result from the lesser temperature difference between the pile and surrounding ground at the EOH due to overall ground warming. The opposite occurred during cooling in which the negative EPWPs were generated with the maximum values of 5.2, 5.7, and 6.6 kPa at the EOC in the first, second, and sixth year, respectively. The negative EPWPs somewhat increased with time from the first to the sixth year, resulting from the larger temperature difference between the pile and surrounding ground at the EOC due to overall ground warming.

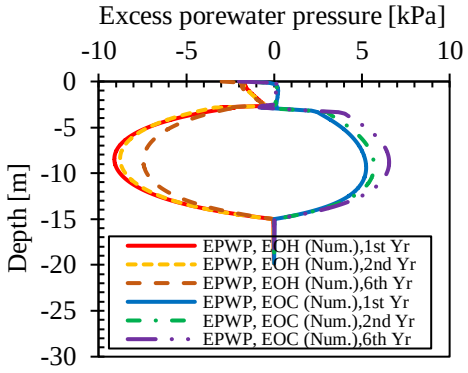

Fig. 4 Thermally induced excess porewater pressures (EPWPs) along the pile-soil interface at the EOH and EOC in the 1st, 2nd, and 6th year.

Pile Head Vertical Displacements

Figure 5 shows the simulated vertical pile head displacements (settlements and uplifts) for six-year heating and cooling cycles. The mechanical load (M) caused a pile head settlement of -1.89 mm (-0.24% D). The thermal cycles caused to pile head displacements to move downwards gradually (a phenomenon of ratcheting settlements). This was because of the cyclic accumulated plastic strains in the surrounding soils. The dissipations of excess porewater pressures in the clay may also contribute to the continuing settlements. At the EOH in the first to sixth year, the uplifts of the pile head of 2.78 mm and 0.52 mm were obtained, a drop of 81.3%. On the other hand, the settlements at the EOC in the first to the sixth year were -4.18 mm and -5.91 mm (-0.74% D), increasing by 41.4%.

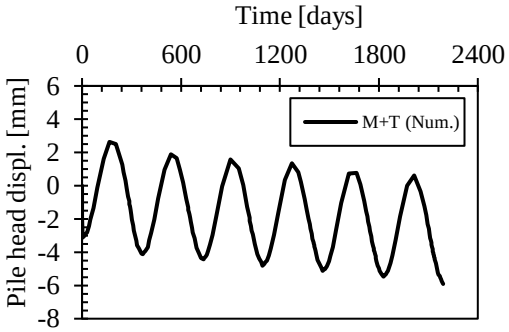

Fig. 5 Pile head vertical displacements (uplifts and settlements) during six thermal cycles.

Pile Axial Strains

The mechanical load (M) produced contractive strains (negative) in the entire pile as shown in Fig. 6. In contrast, heating induced expansive strains (positive) in the pile as shown in Fig. 7(a). The strains at the EOH in the sixth year were generally higher than in the 1st year. Similar to the M load, cooling induced contractive strains in the pile as shown in Fig. 7(b). As seen in the graph, lower contractive strains were observed at the EOC for the higher simulated times.

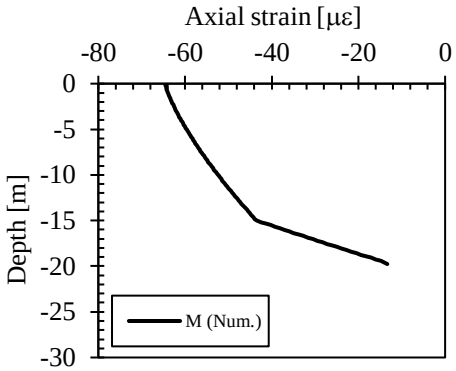

Fig. 6 Axial strain profiles due to the mechanical load (M) only.

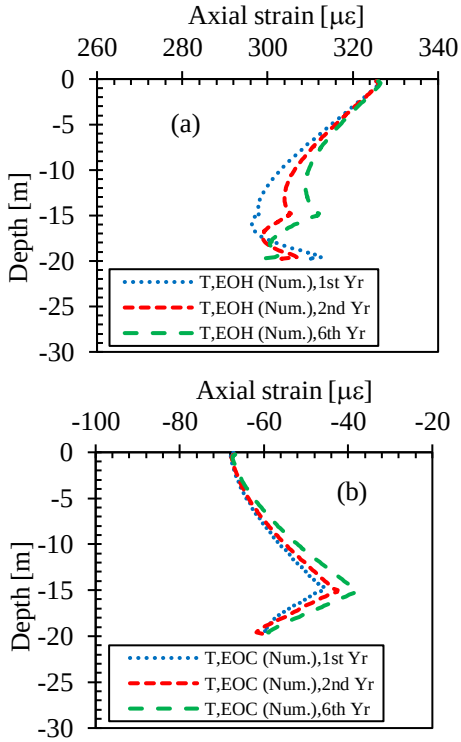

Fig. 7 Axial strain profiles (a) thermal load (T) at the EOH and (b) at the EOC in the 1st, 2nd, and 6th year.

Pile Axial Stresses

The M load of -1300 kN on the pile head induced compressive stresses in the pile, which were plotted in all figures for reference as shown in Fig. 8 and Fig. 9. In these figures, the mechanically induced stresses transferred mostly into the till layer, located below -15 m, beneath the Winnipeg lacustrine clay. Heating induced axial compressive stresses in the pile, which is similar to the effect of the mechanical load. The maximum thermally induced compressive stresses, as shown in Fig. 8(a), were -1391 kPa at the EOH in the first year. This value reduced to -1302 kPa in the sixth year. As shown in Fig. 8(b), at the EOH, the axial compressive stresses increased in the pile as a result of thermo-mechanical loads. This was because heating induced additional compressive stresses in the pile.

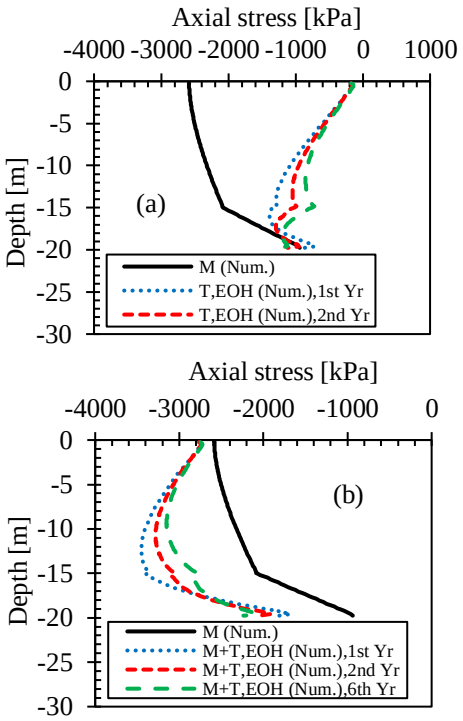

Fig. 8 Axial stress profiles (a) thermal (T) and (b) thermo-mechanical (M+T) at the EOH in the 1st, 2nd, and 6th year.

On the other hand, cooling generated axial tensile stresses in the pile in contradiction to the effect of the mechanical load as shown in Fig. 9(a). The maximum thermally induced tensile stresses located at about -15 m were 982 kPa and 1290 kPa at the EOC in the first and sixth year, accordingly. This shows an increase in the maximum thermally induced tensile stress of 31.4% from the first to sixth year. As shown in Fig. 9(b), there were large reductions of the axial compressive stresses in the pile for the combined effects of mechanical load and thermal cooling.

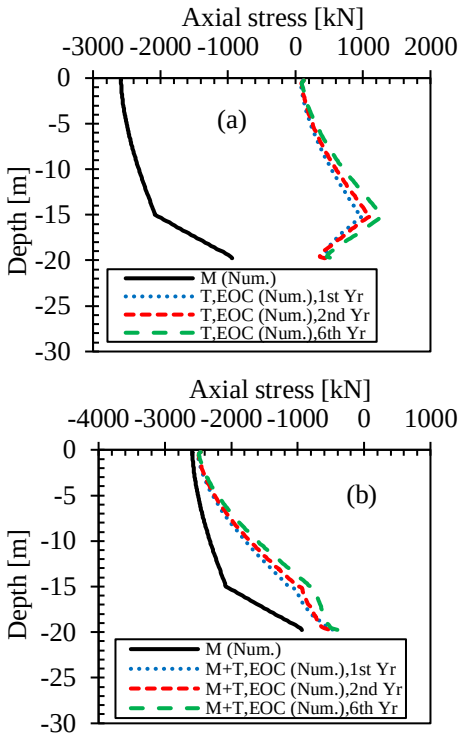

Fig. 9 Axial stress profiles (a) thermal (T) and (b) thermo-mechanical (M+T) at the EOC in the 1st, 2nd, and 6th year.

Mobilized Shaft Friction

Figure 10 shows the mobilized shaft friction along the pile-soil interface at the EOH and EOC in the first, second, and sixth year. It was observed that the M load induced positive skin friction along the whole pile length. Larger values were mobilized in the till layer below -15 m depth than in the overlying clay layer. This is because the till has much higher stiffness and strength. At the EOH, as shown in Fig. 10(a), the shaft friction in the upper two-thirds of the pile reduced and resulted in small negative values. In the lower one-third; the shaft friction increased considerably. Conversely, at the EOC, the shaft friction increased in the upper two-thirds portion, but it reduced in the lower one-third part where the pile was installed through the till layer as shown in Fig. 10(b). Some irregularities in shaft friction in the till were observed as shown in the graphs. This may be due to a sudden change in the soil stiffness from a very low value in the clay to a very high value in the till and also high permeability of the till which somehow caused oscillations in the THM computations.

Mobilized Effective Radial Stresses

Mobilized effective radial stress profiles along the pile-soil interface at the EOH and EOC are shown in Fig. 11. In Fig. 11(a), heating generally caused the effective radial stresses to increase along the entire pile length. There were marked rises in the till layer, and again, some irregularities in the radial stresses were noticed which may be due the same reasons explained earlier in the mobilized shaft friction section. Cooling did the opposite to the heating in which the radial effective stresses reduced in the lower two-thirds of the pile in the till layer but slightly increased in the upper two-thirds as shown in Fig. 11(b). This later stress increase was due to the stress redistributions to somewhat compensate the reduction in stresses at the lower part of the pile and at the pile toe at the EOC. The change in effective radial stresses could be caused by a change in a lateral soil pressure coefficient (K) due to relative thermal expansions or contractions of the pile and the surrounding soils.

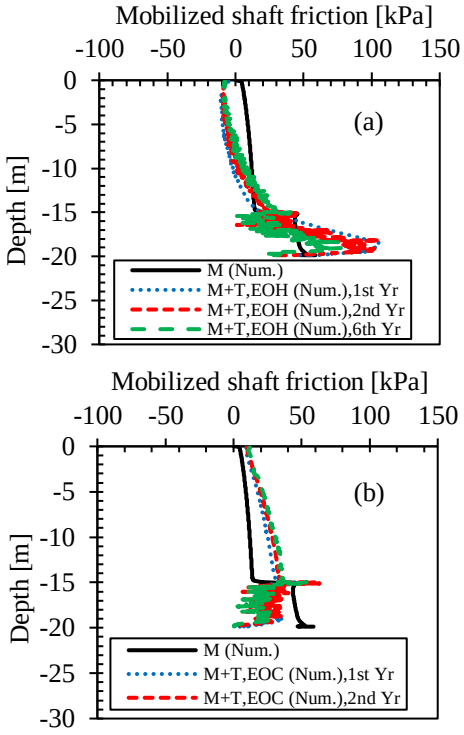

Fig. 10 Mobilized shaft friction profiles along the pile-soil interface (a) at the EOH and (b) at the EOC in the 1st, 2nd, and 6th year.

Thermal Effects on Geotechnical Pile Capacities

As shown in Fig. 12, a geotechnical pile capacity was generally increased upon heating. At the EOH, the ultimate pile capacity, determined using the 10% D failure criterion [5], increased by 12%. On the other hand, cooling caused the ultimate pile capacity to reduce. The reduction of 9% was observed at the EOC. The reason for the increase in ultimate geotechnical capacities of the piles during heating was mainly due to the increase in effective radial stresses along the pile. When the pile was heated, it would try to expand

vertically and radially. The radial expansion, in this case, could not fully mobilize because of the restriction of the surrounding soils. Consequently, higher radial stresses were developed along the pile-soil interface, leading to an increase of the ultimate geotechnical capacity of the pile. The opposite reason seemed to be valid when the pile was cooled. In addition, because of the contraction (moving upwards) of the pile toe during cooling, there was a reduction of the end-bearing stress which could also contribute to the decrease in the ultimate geotechnical capacity of the pile at the end of cooling.

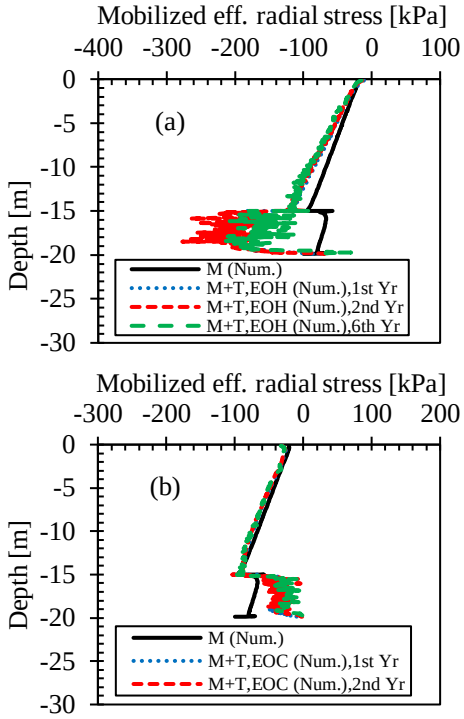

Fig. 11 Mobilized effective radial stress profiles along the pile-soil interface (a) at the EOH and (b) at the EOC in the 1st, 2nd, and 6th year.

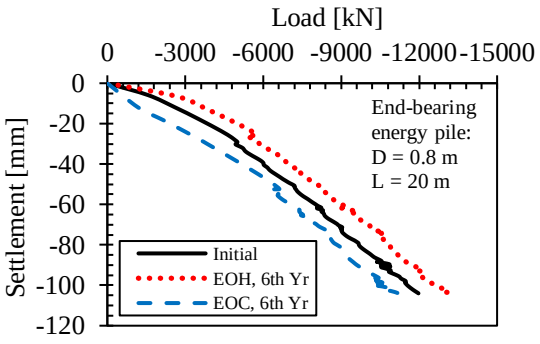

Fig. 12 Load-settlement curves simulated at the initial stage, at the EOH and EOC in the 6th year.

CONCLUSIONS

Temperature changes in the pile had significant effects on its displacements, strains, and stresses. In general, heating caused the pile to expand. These expansions resulted in expansive strains in the pile. If the pile cannot expand freely due to the shaft friction and end restraints, thermal compressive stresses would be generated in addition to the mechanically induced stresses. Therefore, for the thermal and mechanical combined effects, the compressive loads in the pile would be higher during heating. Cooling caused reverse effects in which the pile contracted. In consequence, compressive strains were generated and led to the tensile stresses build up in the pile. Therefore, the compressive stresses in the pile were less for the combined thermo-mechanical effects. In terms of pile head displacements, heating produced uplifts of the pile head while cooling caused settlements. The settlements kept on increasing with increasing thermal cycles (ratcheting settlements).

The heating-cooling cycles of the pile also affected the surrounding ground temperatures to some distances which were dependent on the simulation times. Excess porewater pressures were generated in the clay with low hydraulic conductivity. The mobilized shaft friction and the effective radial stresses along the pile-soil interface were also affected by the temperature changes to some extent.

Geotechnical pile capacities generally increased during heating but reduced during cooing. For the Winnipeg energy pile, the ultimate pile capacity increased at the end of the heating by about 12% but decreased at the end of cooling by about 9%.

REFERENCES

[1] Brandl H., Energy Foundations and Other Thermo-Active Ground Structures, Géotechnique, vol. 56, no. 2, 2006, pp. 81–122.

[2] Baracos A., Shields D. H., and Kjartanson B., Geological Engineering Report for Urban Development of Winnipeg, Department of Geological Engineering, University of Manitoba, 1983.

[3] Ferguson G., and Woodbury A. D., Subsurface Heat Flow in an Urban Environment, J. Geophys. Res. Solid Earth, vol. 109, no. B2, 2004, pp. 1–9.

[4] Mitalas G. P., Calculation of Below-Grade Residential Heat Loss - Low-Rise Residential Building, ASHRAE Trans., vol. 93, 1987, pp. 743–783.

[5] EN 1997-1, Eurocode 7 Geotechnical Design, Part 1_General Rules. European Committee for Standardization, 2004.

9th Int. Conf. on Geotechnique, Construction Materials and Environment,
Tokyo, Japan, 20-22 November 2019, ISBN: 978-4-909106025 C3051

TESTS OF FIBER REINFORCED CONCRETE COMPOSITE SLABS ON THE SUBSOIL

Radim Cajka[1], Petr Mynarcik[1], Zdenka Neuwirthova[1], Zuzana Marcalikova[1] and Michal Kropacek[1]
[1] Faculty of Civil Engineering, VSB - Technical University of Ostrava, Czech Republic

ABSTRACT

Interaction between the soil and the structure is complex problematic. For the better understanding of the behaviour of the flat concrete slab in contact with the subsoil series of tests were performed in the Faculty of Civil Engineering in Ostrava in the Czech Republic. This article focuses on the fibre reinforced concrete flat slab with dimensions 2000 x 2000 x 150 mm loaded by vertical and horizontal force. This loading is typical for building in undermined areas. The article describes the course, results and the evaluation of the experimental test, which was performed on special test equipment Stand over a four day period. Slab was exposed to constant load of 100 kN in vertical direction and about 50 kN in horizontal direction. The deformations of the top surface of the slab were monitored by many sensors in both directions. Concrete deformation and cracks was also observed during the experiment. Deformation curves in the selected cross-section of the slab were evaluated from the measured data. Together with experiment the laboratory tests were performed from the same dough of concrete like the slab itself. The laboratory results are also present. The slab is compared to the vertically loaded slab with same characteristics.

Keywords: Fibre-reinforced concrete composite, soil-structure interaction, vertical and horizontal loading, sliding joint, punching

INTRODUCTION

This article deals with slab-soil [1-3] using fiber reinforcement concrete (FRC) [4-7]. A specific research task is focusing to horizontal loading with sliding joint [8]. This problematic is typical for undermined areas and mining activities, which affect the landscape on the surface [9]. As a result of deep mining, terrain deformations gradually occur on the surface. Terrain deformation can be described by the following parameters: slope, curvature, displacement, and horizontal displacement. This is mainly the region Ostrava-Karviná region in the Czech Republic. Friction and significant normal forces occur between the foundation structure and the subsoil as a result of deep mining and the terrain deformations.

Possible solutions to this problem include a sliding joint design - sliding joints from an asphalt belt [8], which was used in the present experimental program. The idea of using an asphalt belt as a sliding joint comes from the 70's of the 20th century. The first experiments have already been implemented by Balcarek and Bradac [8]. However, the number of experiments and horizontal / vertical load configurations was limited. With regard to the development of materials engineering and properties of asphalt belt, the performed experiments give insufficient results for further research.

The selected board composite is FRC. FRC has improved mechanical properties compared to plain concrete. FRC belongs to the group of fiber concrete. The fiber concrete group is divided according to the material used, the shape and length of the wire in the concrete mixture [11-13]. An important factor is the dosage amount of wires in the concrete mixture. The FRC has typically a better tensile strength and toughness. The actual determination of the responsibility and mechanical testing of FRC are dedicated experts in researches and recommendations [14-17]. In particular, there are a number of approaches that differ in the test configuration to determine the tensile strength. The scope of the tests and the description of the mechanical properties are also influenced by the used design procedure. Research in the field of concrete structures and punching of concrete slabs are also related [18-24].

Fig. 1 Special testing device Stand.

FRC typical applications include the construction of industrial floors and foundations. This also falls within the research area. The slab-subsoil interaction needs to be taken into account while designing industrial floors [25-26]. Analytical and numerical methods are used to solve this problem [27-29]. Numerical methods based mainly on finite element method (FEM) finds wider application with the development of computer technologies. It is important to use a suitable interaction system between the upper structure, foundation and subsoil in the computational model of construction when solving a task. Interaction occurs in the interconnection system, where physical, geometric and design nonlinearities are also included in the calculation.

EXPERIMENTAL PROGRAM

The experimental program involves testing two fiber-concrete slabs interacting with the subsoil. The tests variants of the experiments differ in the load character. The experimental tests are performed on a specialized test facility, the so-called Stand [30] shown in Fig. 1.

The plate tests are also supplemented by laboratory testing to determine mechanical properties. Special testing equipment Stand allows to test the interaction of concrete slab with subsoil. The test device can develop a vertical load up to 1000 kN using a hydraulic press [30]. The device was specially modified by adding horizontal hydraulic cylinders to develop a horizontal loading in addition to vertical loading. Improved device can develop a horizontal load up to 295 kN. The test equipment includes a data logger for evaluating deformations using up to 24 track sensors. Tested slab has dimensions 2000 x 2000 mm with height 150 mm. Used concrete mixture is described in Tab. 1.

Table 1 Material composition of concrete.

Description	Type/Amount
Consistency	S3
Maximum grain	CEM I 42.5
Minimal cement content	300 kg
Water Factor: *v / c*	0,6
Aggregates 0/4	870 kg
Aggregates 4/8	150
Aggregates 8/16	820 kg
Water	189 l
Plasticizer	2.9 l

The Dramix® 3D 65/60 BG fiber type was used in dosage 25 kg/m^3. The basic material characteristics of the wires are given in Tab. 2. These wires ends with double bending, their shape is shown in Fig. 2.

The first experiment was focused on tracking the vertical deformation of the plate using the deformation sensors and the load capacity of the plate. The loading of the FRC was in steps of 75 kN / 30 min to its maximum bearing capacity. The second part of the experiment attempted to approximate the conditions corresponding to the undermined area. Sliding joint was created between the FRC slab and subsoil using asphalt strips and underlay concrete width 50 mm. A horizontal load was caused by a gradual increase of horizontal load of about 50 kN with two hydraulic cylinders from one side of the plate. One hydraulic cylinder exerted a load of about 25 kN. This load was kept constant throughout the experiment. Uniform transmission of this load was ensured by a specially designed construction created for this type of experiment. Construction consists of mounting frame, hydraulic cylinder brackets and support frame.

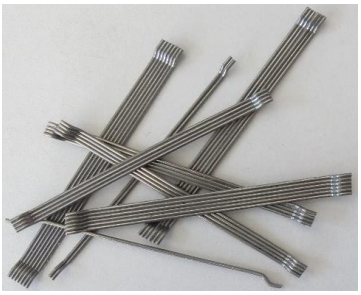

Fig. 2 Shape of fibers Dramix® 3D 65/60 BG.

Table 2 Fiber properties Dramix® 3D 65/60 BG.

Description	
Length [mm]	60
Diameter [mm]	0.9
Aspect Ratio	67
Tensile strength [N/mm^2]	1160
Effect on consistency [s]	8
Impact on concrete strength [kg/m^3]	15
Modulus of elasticity [GPa]	200

LABORATORY TEST OF FRC

The experimental tests of the plates are supplemented by laboratory tests. Samples for laboratory tests were performed at the same time as casting slabs from the same batch of mixture. The following characteristics were tested in laboratory: compressive strength on cube ($f_{c,cube}$), compressive

strength on cylinder ($f_{c,cyl}$), Modulus of elasticity ($E_{c,cyl}$), transverse tensile strength perpendicular to filling direction ($f_{ct,split,A}$), transverse tensile strength parallel ($f_{ct,plit,B}$), three point bend test with no cut for a span 500 mm ($f_{c,fl,3B600BZ}$) and four point bend test for span 500 mm ($f_{c,fl,3B600BZ}$).

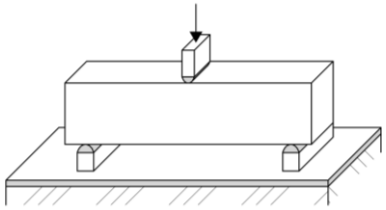

Fig. 3 Three-point test scheme.

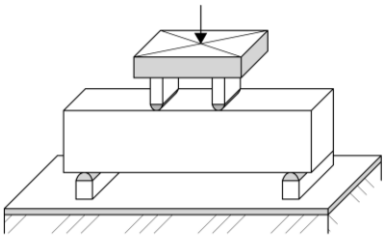

Fig. 4 Four-point test scheme.

The test scheme is shown on Fig. 3 and Fig. 4. Laboratory test results are given in Table 3 in summary.

Table 3 Laboratory test results.

Notation.	Number samples	Min. value	Max. value	Medium value
$f_{c,cube}$	12	24.5	37.4	30.4
$f_{c,cyl}$	12	20.3	27.9	23.5
$f_{ct,split,A}$	12	2.1	3.2	2.6
$f_{ct,split,B}$	12	1.4	3.3	2.1
$E_{c,cyl}$	6	15.6	24.5	19.3
$f_{c,fl,3B600BZ}$	5	4.0	4.4	4.2
$f_{c,fl,4B600BZ}$	4	2.6	4.0	3.6

The influence of wire orientation results has showed during the testing. The tensile strength perpendicular to the filling direction was bigger than in parallel direction. The modulus of elasticity is only 19.3 GPa. With comparison of bending tests, it is seen that the strength of the four-stroke test is smaller. Typical course of load-displacement diagrams from performed bending tests is on Fig. 5.

FRC SLAB OF EXPERIMENTS

The first performed experiment is a variant with a vertical load. Vertical deformation was observed during the experimental testing using 24 tensometers (Fig. 6). The vertical loading was performed in steps 75 kN / 30 min until the maximum bearing capacity reached. The loading process is in Fig. 7.

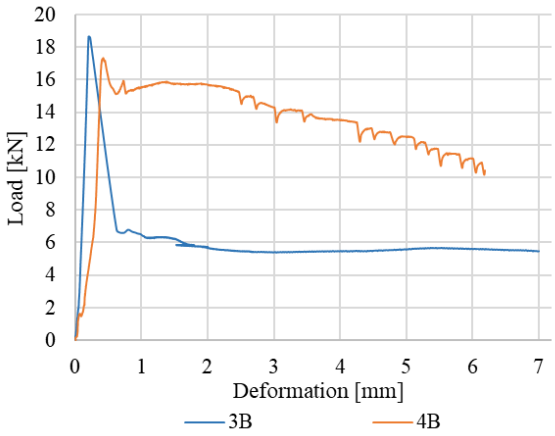

Fig. 5 Typical load-displacement diagram for three and fourth-point bending test.

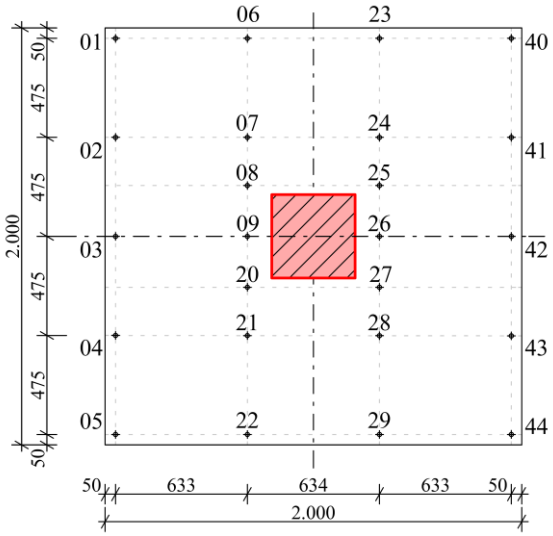

Fig. 6 Placement of vertical deformation sensors for vertical loading.

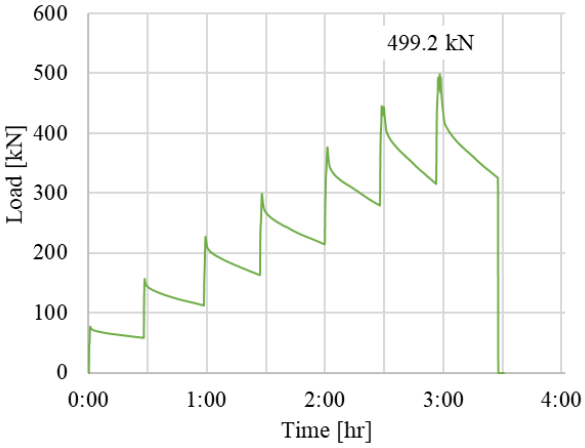

Fig. 7 Loading process.

The vertical deformation in cross-sections and maximum bearing capacity were evaluated based on

measured data. The deformation of vertical sensors for selected cross-section are displayed at Fig. 8. Maximal measured vertical deformation was 26.72 mm in sensor 09. The lifting of edges occurs at higher load intensities. Maximum lifting was observed in sensor 42 at amount of 13.06 mm. Maximum bearing capacity of the slab was reached in 7th loading step under load of 499.2 kN.

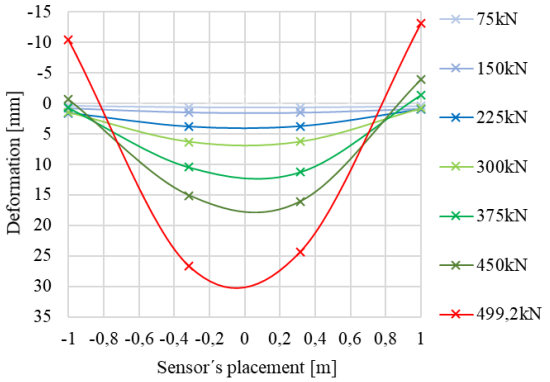

Fig. 8 Deformation in cross-section for potentiometers 03-42.

Gradual decrease in bending stiffness is well visible from Fig. 8. The decrease was caused due to the gradual development of cracks in concrete. The cracks in concrete can be seen in Fig. 9.

Fig. 9 Deformation of the slab for constant increase of vertical force.

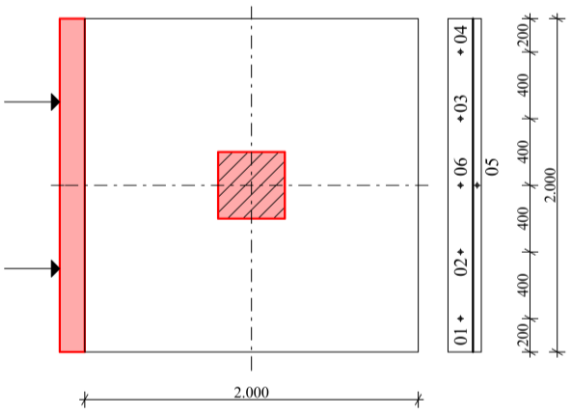

Fig. 10 Location of horizontal measuring potentiometers for horizontal loading experiment.

The second experiment contained the combination of the vertical and horizontal loading. The experiment also included the sliding joint created by the asphalt belt and the concrete bed width 50 mm. The experimental testing scheme is in Fig. 10.

Constant load of size 100 kN was maintained in vertical direction using hydraulic piston. This force represents the load from the upper structure. Furthermore, a horizontal load of about 50 kN was applied from one side of the plate using two hydraulic cylinders. The horizontal load represents the effects caused by undermining. This load was kept constant throughout the experiment. Uniform transmission of this load was ensured by a specially designed construction created for this type of experiment. The horizontal displacement between the concrete bed layer and the FRC was monitored from the other side of the board. The vertical and horizontal deformation was recorded by data logger every 5 minutes. The experiment scheme is drawn in Fig. 11. The ambient temperature, temperature in the middle of slab and temperature at the edge of the slab to verify slab temperature stability were measured every 15 minutes. The ambient temperature was reaching 5-22°C during experiment. The temperature in the middle of slab was around 10°C and the temperature at the edge of the slab was slightly higher about 13°C. The experiment took 4 days.

Fig. 11 Positioning of the sensores for experment with horizontal load.

The final horizontal displacements are at Fig. 12. Course of the ambient temperature and the temperature in the middle of slab are at Fig. 13.

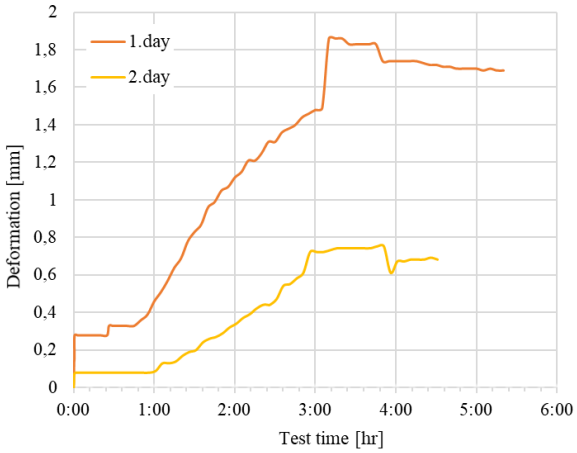

Fig. 12 Horizontal deformation corresponding to 06 sensor.

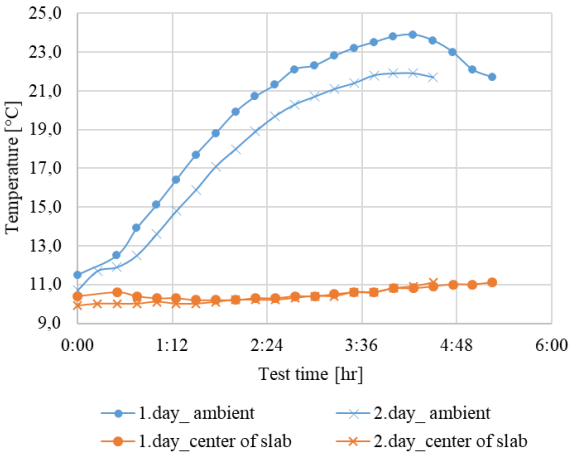

Fig. 13 Temperatures course.

CONCLUSIONS

The article is focused on interaction of slab and subsoil. The performed experiment focused on application of FRC for horizontal loading. Experiment was performed on slab with dimension 2000 x 2000 mm and height 150 mm. The special testing equipment Stand was used for testing. The sliding joints was used among the specifics of the experiment. Experimental testing proved increase of total bearing capacity and ductility of tested slabs already at dosage of 25 kg/m^3 fibres in previously tested slab [10]. The cracking and destruction of FRC occurred gradually. The use of sliding joint was confirmed in case of horizontal loading. The laboratory program can be also described as very usefull since it allows to describe in detail the mechanical properties of FRC, which are necessary for follow-up tasks for research like numerical modeling of the task which will be performed in the future by the authors of article.

ACKNOWLEDGMENTS

This outcome has been achieved with the financial support of MEYS by the project of "The conceptual research and development 2019" in the Faculty of Civil Engineering, VŠB TU – Ostrava.

REFERENCES

[1] Hegger J., Ricker M., Ulke B. and Ziegler M., Investigations on the punching behaviour of reinforced concrete footings, Engineering Structures, Vol. 29, Issue 9, 2007, pp. 2233-2241, DOI: 10.1016/j.engstruct.2006.11.012.

[2] Hegger J., Sherif A. G. and Ricker M., Experimental investigations on punching behaviour of reinforced concrete footings, ACI Structural Journal, Vol. 103, Issue 4, 2006, pp. 604-613.

[3] Cajka R., Labudkova J. and Mynarcik P., Numerical solution of soil - foundation interaction and comparison of results with experimental measurements, International Journal of GEOMATE, Vol. 11, Issue 1, 2016, pp. 2116-2122, DOI: 10.21660/2016.23.1208.

[4] Katzer J., and Domski J., Quality and mechanical properties of engineered steel fibres used as reinforcement for concrete, Construction and Building Materials, Vol. 34, 2012, pp. 243-248.

[5] Holschemacher K., Mueller T. and Ribakov Y., Effect of steel fibres on mechanical properties of high-strength concrete, Materials & Design, Vol. 31, Issue 5, 2010, pp. 2604-2615.

[6] Sucharda O., Pajak M., Ponikiewski T. and Konecny P., Identification of mechanical and fracture properties of self-compacting concrete beams with different types of steel fibres using inverse analysis, Construction and Building Materials, Vol. 138, 2017, pp. 263-275, DOI: 10.1016/j.conbuildmat.2017.01.077.

[7] Zaborski A., Constitutive model for restricted compression of fiber concrete, Cement, Wapno, Beton, Vol. 2016, Issue 1, 2016, pp. 46-52.

[8] Balcarek V. and Bradac J., Utilization of bitumen insulating stripes as sliding joints for buildings on undermined area, Journal Civil Engineering, Vol. 2, 1982 (In Czech).

[9] Mateckova P. et al, Design of foundations with sliding joint at areas affected with underground mining, IOP Conf. Ser.: Earth Environ. Sci, Vol. 143, Issue 1, 2018, DOI: 10.1088/1755-1315/143/1/012006.

[10] Sucharda O., Bilek V., Smirakova M., Kubosek J. and Cajka R., Comparative evaluation of mechanical properties of fibre-reinforced concrete and approach to modelling of bearing capacity ground slab, Periodica Polytechnica

Civil Engineering, Vol. 61, Issue 4, 2017 pp. 972-986, DOI:10.3311/PPci.10688.

[11] Koniki S. and Ravi P. D., A study on mechanical properties and stress-strain response of high strength concrete reinforced with polypropylene–polyester hybrid fibres, Cement, Wapno, Beton, Vol. 2018, Issue 1, 2017, pp. 67-77.

[12] Kasagani H. and Rao C. B. K., The influence of hybrid glass fibres addition on stress – Strain behaviour of concrete, Cement, Wapno, Beton Vol. 2016, Issue 5, 2016, pp. 361-372.

[13] Sucharda O., Lehner P., Konecny P. and Ponikiewski T., Investigation of Fracture Properties by Inverse Analysis on Selected SCC Concrete Beams with Different Amount of Fibres, Procedia Structural Integrity, Vol. 13, 2018, pp. 1533-1538, DOI: 10.1016/j.prostr.2018.12.313.

[14] Sucharda O. and Bilek V., Aspects of Testing and Material Properties of Fiber Concrete, 25th Concrete Days 2018, Solid State Phenomena, Vol. 292, pp. 9-14 DOI:10.4028/www.scientific.net/SSP.292.9.

[15] Kormanikova E. and Kotrasova K., Elastic mechanical properties of fiber reinforced composite materials, Chemicke Listy, Vol. 105, Issue 17, 2011.

[16] Dramix® steel fiber concrete reinforcement - Bekaert.com, https://www.bekaert.com.

[17] Pazdera L., Cajka R., Topolar L., Mateckova P., Bilek V. and Sucharda O., Measurement and Utilization of Acoustic Emission for the Analysis and Monitoring of Concrete Slabs on the Subsoil, Periodica Polytechnica Civil Engineering, Vol. 63, Issue 2, 2019, pp. 608-620, DOI: 10.3311/PPci.12695.

[18] Aboutalebi M., Alani A. M., Rizzuto J. and Beckett D., Structural behaviour and deformation patterns in loaded plain concrete ground-supported slabs, Structural Concrete, Vol. 15, Issue 1, 2014 pp. 81-93, DOI:10.1002/suco.201300043.

[19] Halvonik R. and Fillo J., The Maximum Punching Shear Resistance of Flat Slabs, Procedia Engineering, Vol. 65, 2013, pp. 376-381, ISSN 1877 – 7058.

[20] Halvonik J., Hanzel J. and Majtanova L., Punching Resistance of Column Basis, Advances and Trends in Engineering Sciences and Technologies II, 2017, pp. 93-98, 2nd International Conference on Engineering Sciences and Technologies (ESaT), Slovakia 2016.

[21] Halvonik J. and Majtanova L., Experimental Investigation of the Maximum Punching Resistance of Slab-Column Connections, Slovak Journal of Civil Engineering, Vol. 26, Issue 3, 2018, pp. 22-28, DOI: 10.2478/sjce-2018-0017.

[22] Sucharda O., Smirakova M., Vaskova J., Mateckova P., Kubosek J. and Cajka R., Punching Shear Failure of Concrete Ground Supported Slab, International Journal of Concrete Structures and Materials, Vol. 12, Issue 1, 2018, DOI:10.1186/s40069-018-0263-6.

[23] Ricker M. and Siburg C., Punching shear strength of flat slabs – critical review of Eurocode 2 and fib Model Code 2010 design provisions, Structural Concrete, Vol. 17, Issue 3, 2016, pp. 457-468.

[24] Siburg C. and Hegger J., Experimental investigations on the punching behaviour of reinforced concrete footings with structural dimensions, Structural Concrete, Vol. 15, Issue 3, 2014, pp. 331-339, DOI: 10.1002/suco.201300083.

[25] Cajka R. and Labudkova J., Dependence of deformation of a plate on the subsoil in relation to the parameters of the 3D model, International Journal of Mechanic, Vol. 8, Issue 1, 2014, pp. 208-215, ISSN: 19984448.

[26] Hrubesova E., Lahuta H., Duris L. and Jaafar M., Mathematical modeling of foundation-subsoil interaction, International Multidisciplinary Scientific GeoConference Surveying Geology and Mining Ecology Management, SGEM, Vol. 2, Issue 1, 2015, pp. 437-444.

[27] Hrubesova E., Mohyla M., Lahuta H., Bui T.Q. and Nguyen P. D., Experimental analysis of stresses in subsoil below a rectangular fiber concrete slab, Sustainability (Switzerland), Vol. 10, Issue 7, 2018, DOI: 10.3390/su10072216.

[28] Ibrahim M. Metwally, Three-dimensional finite element analysis of reinforced concrete slabs strengthened with epoxy-bonded steel plates, Advances in Concrete Construction, Vol. 2, Issue 2, 2014 pp. 91-108, DOI:10.12989/acc.2014.2.2.091.

[29] Cajka R., Comparison of the calculated and experimentally measured values of settlement and stress state of concrete slab on subsoil, Applied Mechanics and Materials, Vol. 501-504, 2014, pp. 867-876, DOI: 10.4028/www.scientific.net/AMM.501-504.867.

[30] Cajka R., Krivy V. and Sekanina D., Design and Development of a Testing Device for Experimental Measurements of Foundation Slabs on the Subsoil, Transactions of the VSB - Technical University of Ostrava, Civil Engineering Series, Vol. 11, Issue 1, 2011, pp. 1-5, DOI: 10.2478/v10160-011-0002-2.

9th Int. Conf. on Geotechnique, Construction Materials and Environment, Tokyo, Japan, 20-22 November 2019, ISBN: 978-4-909106025 C3051

STABILITY ASSESSMENT OF AN AGING EARTH FILL DAM CONSIDERING ANISOTROPIC BEHAVIOUR OF CLAY

Irene Olivia Ubay[1], Moises Alfaro III[2], Marolo Alfaro[3] and James Blatz[4]
[134]Faculty of Engineering, University of Manitoba, Canada; [2]KGS Group, Canada

ABSTRACT

Anisotropic behaviour of the clay core, blanket, and foundation of an aging water retaining earth fill dam may be a result of environmental loading. The repeated wetting-drying and freezing-thawing cycles produce fissures that can cause degradation of strength with time. The compaction of clay core and clay blanket during the construction of the dam may also play a significant role in its anisotropic behaviour. Undisturbed clay samples taken from field investigations of an existing aging water retaining earth fill dam were tested in the laboratory to obtain the parameters used in the numerical modeling. A testing program was implemented in order to determine the soil classification along with mineralogy, strength, and deformation characteristics of the collected clay samples. Laboratory tests include index property tests, Scanning Electron Microscopy (SEM) tests, X-Ray Diffraction (XRD) tests, one-dimensional consolidation oedometer tests, consolidated drained direct shear tests, and isotropically consolidated undrained triaxial compression tests. Results from slope stability analyses to assess the aging earth dam, using parameters from laboratory investigation results, are presented in this paper.

Keywords: Anisotropy, Earth fill dam, Stability, Clay core, Clay blanket

INTRODUCTION

Anisotropic soils have directionally dependent properties. Anisotropy is sometimes referred to as the difference of a physical soil property along different directions. Most natural clay has a particle arrangement or fabric that is initially anisotropic due to its platy particle shape and deposition process. Repeated expansion and contraction of clays due to wetting-drying and freezing-thawing can also cause fissures leading to mechanical anisotropy. Fissures tend to create planes of weaker strength and higher permeability in clays [1]. Anisotropy in structural composition, mechanical behavior, and shear strength of Lake Agassiz clays had been studied extensively by different researchers and was thought to influence embankment performance [2]–[6].

Despite the increasing awareness of anisotropy in geotechnical engineering, most geotechnical design approach would typically describe soil as isotropic due to convenience or lack of information. Research is currently ongoing to evaluate the stability of earth dams in hydroelectric generating stations considering anisotropic behaviour as part of its periodic dam safety review. It will also aid in evaluating long-term performance of earth dams and in carrying out proactive rehabilitation, if the performance does not meet current dam safety standards. This paper presents the stability assessment of an aging earth dam considering clay anisotropic behaviour using parameters determined from laboratory test results performed on undisturbed samples taken from field investigations.

SITE INVESTIGATION AND SOIL SAMPLING

An aging water-retaining earth fill dam that was constructed in the 1950s with an upstream inclined clay core. The local clay material used in the construction of the dam was classified as high plasticity lacustrine clay, often described as highly fissured in nature with nuggetty or crumbly appearance.

Undisturbed soil sampling of the clay core and foundation were completed during the fall season when the ground was still unfrozen. Continuous soil sampling by means of a Hollow Stem Auger (HSA) using Shelby tubes with a diameter of 102 mm (4 in) was used to collect samples from predetermined borehole locations.

Shelby tube samples of the clay foundation were obtained from test pits. These samples have two orientations: vertical and inclined. Vertical Shelby tube samples were simply pushed perpendicular into the test pit floor. Inclined Shelby tube samples were pushed into the wall of a test pit with an angle of inclination of 53° from the horizontal, as shown in Fig. 1.

Soil sampling of the clay blanket was done during the winter season as the frozen reservoir allowed the drilling equipment to be appropriately positioned over borehole locations. Typical 76 mm (3 in) diameter Shelby tubes on a track-mounted piston sampler was used to collect clay blanket samples. Multi-directional sampling of the clay core and blanket were not performed to reduce further disturbance in these locations.

Fig.1 Shelby tube clay foundation sample with inclined orientation

EXPERIMENTAL INVESTIGATION

Several laboratory tests were conducted to determine the index properties, deformation characteristics, mineralogy, and strength characteristics of the collected clay core, blanket, and foundation samples. Tests were in accordance with ASTM standards.

Index Properties and Deformation Characteristics

The index properties of the tested samples are shown in Table 1. Extruded clay core samples were a mottled mix of brown and grey with random silt lenses and silt pockets. It had a matted texture with medium to stiff consistency. Clay blanket samples were brown in color, with soft to medium consistency in the upper layer; and mottled mix of brown and grey with stiff to very stiff consistency from 0.6 m and below. The clay foundation samples were mottled mix of brown and grey in color with random silt pockets and was intensely fissured. All tested samples were classified as "fat clay" of high plasticity (CH) according to the Unified Soil Classification System (USCS). Deformation characteristics were based on one-dimensional consolidation (oedometer) test results.

Particle Orientation and Mineralogy

Scanning Electron Microscope (SEM) with back-scattered electron and Energy Dispersive X-ray (EDX) system was used to examine the particle orientation of the prepared carbon coated specimens. SEM images of the clay core (Fig. 2) displayed an edge-to-edge contact and slight particle orientation whereas clay blanket samples (Fig. 3) showed that most particles formed broad overlapping sheets. Images of clay foundation samples (Fig. 4) show predominantly edge-to-edge contacts with random non-clay particles without a preferred alignment or orientation.

X-ray diffraction (XRD) testing was performed to determine the mineralogical composition of the clay and non-clay constituents of the samples. Figure 5 shows XRD results from clay core, foundation, and blanket. All samples show the same mineralogical composition. Clay minerals present are mostly interlayered smectite and illite, with some kaolinite, mica and traces of attapulgite. Non-clay minerals are composed of quartz, feldspar, and dolomite. The clay was thought to be an expansive type as the dominant clay mineral was smectite. Observed non-clay minerals such as quartz and feldspar are typical composition of silt, consistent with the observed of silt pockets. Similar findings were also reported by Baracos [2] found in his study on Lake Agassiz clay and by Loh and Holt [6].

Table 1 Soil properties of tested samples

Properties	Clay Core	Clay Blanket	Clay Foundation
Moisture content (%)	39	41	38
Liquid limit (%)	85	82	89
Plasticity index (%)	60	57	61
Specific gravity	2.72	2.68	2.70
Minus #200, <0.075mm (%)	100	100	100
Clay fraction, <0.002mm (%)	74	71	75
Activity	0.81	0.80	0.81
Apparent preconsolidation pressure (kPa)	150	170	200
Slope of NCL, λ	0.125	0.145	0.124
Slope of NCL, κ	0.024	0.042	0.028

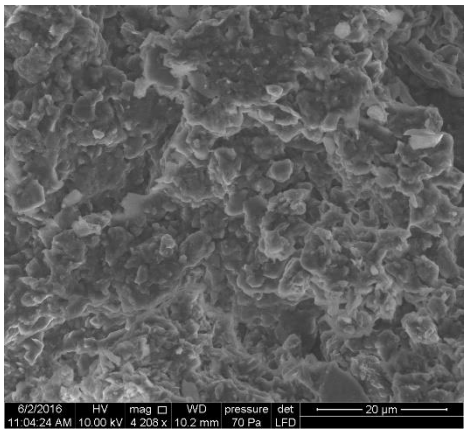

Fig.2 SEM image of clay core.

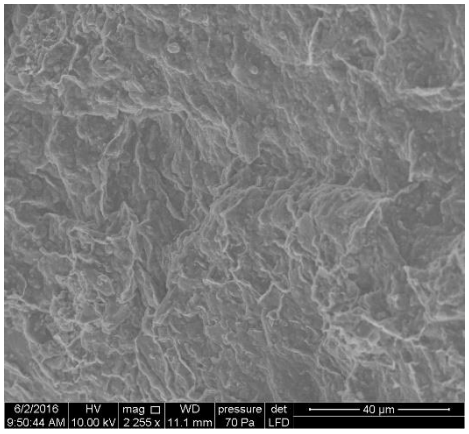

Fig.3 SEM image of clay blanket.

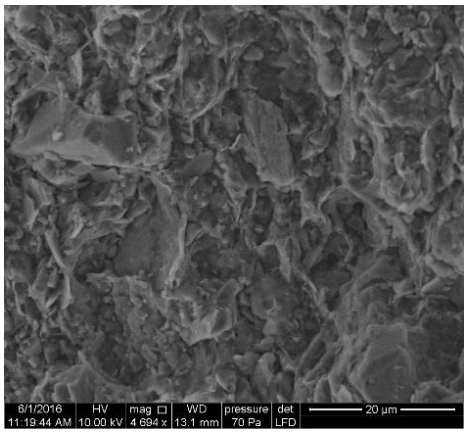

Fig.4 SEM image of clay foundation.

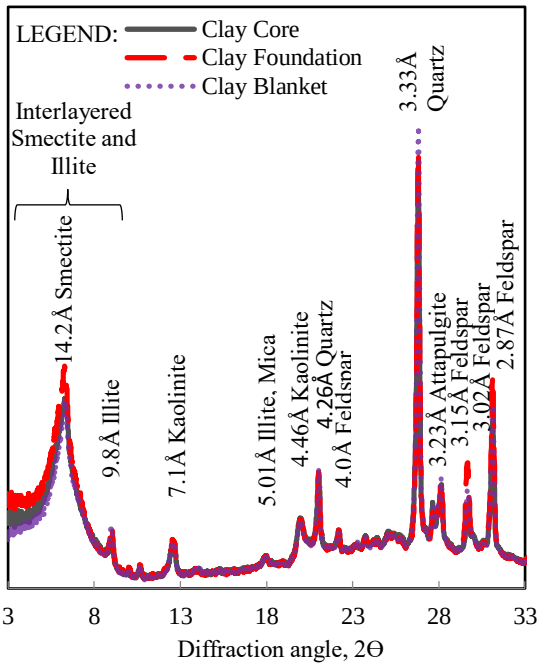

Fig.5 XRD results from clay core, blanket, and foundation.

SHEAR STRENGTH PARAMETERS

Multi-directional shearing tests were conducted to determine strength anisotropy. Vertical clay foundation Shelby tube samples determined cross shear strengths from isotropically consolidated undrained triaxial compression (CIU) tests. Inclined Shelby tube samples of clay foundation that underwent CIU testing provided horizontal shear strength values. For clay core and clay blanket test specimens, cross-shear strengths were determined from CIU tests. As it was not possible to obtain inclined samples from the clay core and blanket, horizontal shear strengths were determined by means of consolidated drained (CD) direct shear testing from vertical Shelby tube samples. Residual strengths were determined from direct shear tests. Multiple reversal method was used wherein clay samples were repeatedly sheared until 100 % strain was reached, which corresponded to about 63 mm of displacement.

Undrained shear testing results are shown in Fig. 6, Fig. 7, and Fig. 8 for clay core, blanket, and foundation samples, respectively. Figure 6 shows that clay core samples sheared at a mean effective stress between 100 kPa to 300 kPa exhibit an isotropic elastic behaviour ($m\Delta p \approx \Delta u$), with a slight anisotropy observed when the clay core was sheared under a lower confining stress less than 100 kPa. This could be due to the tendency of fissured materials to dilate. Clay blanket samples also show slight elastic anisotropy as seen in Fig. 7. Both vertical and inclined clay foundation samples show elastic anisotropy as shown in Fig. 8. Inclination of stress paths to the left ($m>1$) indicated that the sample had higher horizontal stiffness than its vertical counterpart [4]. Specimens sheared higher than 300 kPa behaved typically for a normally consolidated specimen.

The clay core and blanket CIU results exhibited a more uniform failure envelope compared to the clay foundation, which exhibited a bilinear failure envelope. Higher frictional resistance was observed for confining stresses less than 100kPa, and decreased as the confining stress increased. The bilinear failure envelope was thought to be attributed to the intense fissuring of the clay foundation leading to an increase in dilatancy under lower stress levels [7]

The stress-strain behavior from drained shear strength test results conducted on all samples is seen in Fig.9. The foundation clay and clay blanket behaved similarly as both underwent strain softening as compared to the clay core. This behaviour could be attributed to the fissured nature of the clay blanket and foundation.

Cross-shear and horizontal shear strength parameters were interpreted using Critical State Soil Mechanics (CSSM) approach and summarized in Table 2. Strength anisotropy is evident having cross shear strength values different that horizontal shear strength in all tested clays. Clay core and blanket

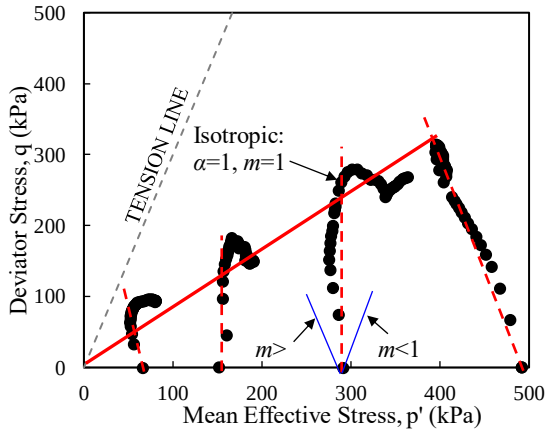

Fig.6 Clay core CIU triaxial test results.

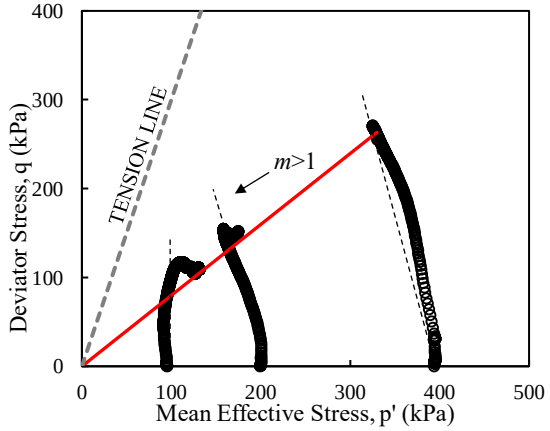

Fig.7 Clay blanket CIU triaxial test results.

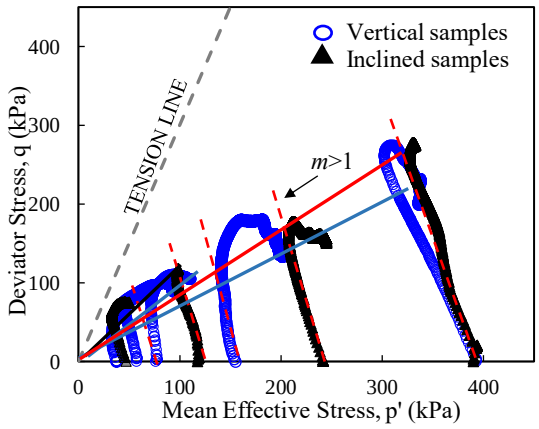

Fig.8 Clay foundation CIU triaxial test results.

samples have higher cross shear strength than that along the horizontal shear plane and the values are independent of the stress range. Clay foundation results show that in addition to anisotropic strength, shear strength values were dependent on the stress range, which indicated a bilinear failure envelope. For both cross shear and horizontal shear, the strengths were higher at a lower confining stress and decreased as the confining stress was increased. Strength anisotropy seem to decrease as the confining stress increased as expressed in the decreased difference in shear strength values. The bilinear failure envelope could be once again due to the dilatancy behaviour of the intensely fissured clay foundation.

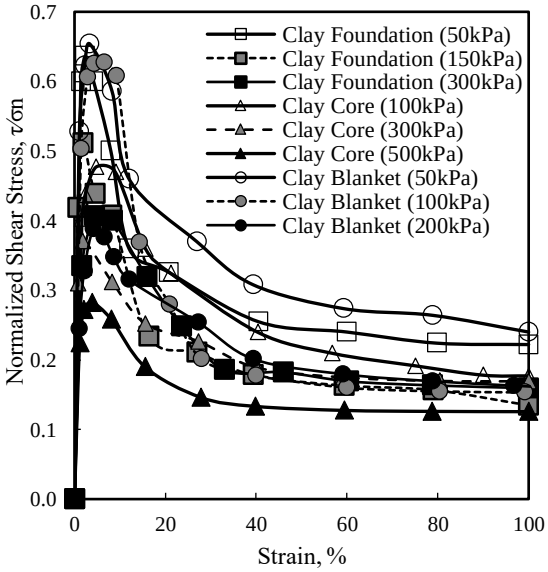

Fig.9 Stress-strain behavior from CD direct shear tests.

Table 2 Summary of estimated effective shear strength parameters

Stress Range (kPa)	Clay Core		Clay Blanket		Clay Foundation	
	CS	HS	CS	HS	CS	HS
<100	19	13	21	17	24	29
>100	19	13	21	17	18	16
Residual		8		9		7

Note: CS = cross shear, φ' (deg), HS = horizontal shear, φ' (deg)

NUMERICAL MODELING

Numerical modeling was implemented using the GeoSlope 2018 program suite in order to evaluate the stability of the earth fill dam using a 2-dimensional plane strain model. The location of the phreatic surface was determined using the steady-state seepage analysis in SEEP/W and was confirmed by readings from vibrating wire piezometers installed on site. Finite element method (FEM) of stress distribution method was performed using SIGMA/W to establish in-situ stresses conditions. Results from the stress distribution and seepage analysis were imported in the SLOPE/W slope stability analysis.

The dam of interest has two sections, depending on the foundation conditions. Section A has a clay

foundation that stretches from the upstream to the downstream side of the dam, overlying dense silty sand. Section B has an absence of an impermeable natural clay layer with only a layer of dense silty sand and gravely sand underneath the dam. In order to control seepage in this section, a compacted clay blanket was placed in the upstream side and was tied into the inclined clay core. Irregular movement was observed in the upstream section of Section B despite its good performance for over fifty years.

Post peak or critical state shear strength parameters were used in the numerical modeling as the clay materials in the dam were thought to have reached its fully-softened condition over the years. Cohesion was assumed to be zero for fully softened shear strengths of fissured clays [8]. Two cases of slope stability analyses were conducted. Case 1 considered the anisotropic strength model for clay materials to simulate the difference in strength along the cross-shear and horizontal direction. Case 2 used Mohr-Coulomb strength model with parameters based on the shape of the postulated slip surface. Cross-shear strength was assigned for the clay core whereas the clay blanket used horizontal shear strength values. Clay foundation horizontal shear strengths were inputted using a bilinear soil model for Case 2. Input parameters used in the numerical modeling can be seen in Table 3.

Table 3 Input parameters for numerical modeling

Parameters	Clay Core	Clay Blanket	Clay Foundation
γ (kN/m^3)	17	17	17
υ	0.35	0.45	0.35
λ	0.125	0.145	0.124
κ	0.024	0.042	0.028
c' (kPa)	0	0	0
$\Phi'_{cross\text{-}shear}$ (°)	19	21	18
$\Phi'_{horizontal}$ (°)	13	17	16
$\Phi'_{bilinear}$ (°)	n/a	n/a	29,16

The results of the SLOPE/W slope stability analyses are presented in Table 4. The calculated factors of safety (FS) indicate that the use of anisotropic soil analysis (Case 1) tend to generate lower values for both dam sections compared to Case 2. Results also show that the upstream slope was more critical than the downstream side for both sections of the dam using either Case 1 or 2, primarily due to the geometry of the inclined core. Moreover, the upstream side of Section B had a factor of safety value less than unity (FS = 0.99) when anisotropy was considered. This corresponds to the observed irregular movement in this section, which could be a precursor to instability. The results were compared to the following safety criteria: a factor of safety of 1.5 against normal water level load cases, and a value of 1.0 considering normal water levels and seismic loading. It is evident that the upstream slope does not pass the safety criteria, with Section B as the most critical. Proactive rehabilitation measures in this dam is on-going in order to address this. The results of the analyses performed also indicated that considering anisotropic behaviour in clay was a better representation of the dam as the numerical model was able to capture the observed behaviour on site. The critical slope stability results for both Sections A and B can be seen in Fig. 9 and Fig. 10, respectively.

Table 4 Factor of safety values from slope stability analyses

	Section A		Section B	
Case	U/S	D/S	U/S	D/S
Case 1	1.31	2.37	0.99	2.88
Case 2	1.48	2.37	1.15	2.88

Note: U/S = upstream, D/S = downstream

CONCLUSION

Observations from site investigation and soil sampling indicated that the clay core, blanket and foundation of an aging water-retaining dam had fissured structures. The clay foundation fissuring was more intense than the clay in other locations and had more silt pockets. Despite the difference in the degree of fissuring, all tested samples were similar in terms of structural and mineralogical composition. The micro fabric of the clay was considered anisotropic from interlayered smectite and illite. The presence of silt could also influence the anisotropic behaviour of the clay foundation in general such as in terms of strength and permeability.

Experimental investigation indicated that other than anisotropy in its mineralogical composition, the undrained and drained strength of the materials used in construction of old earth fill dams were anisotropic. Strength anisotropy was evident in all tested clay as samples had different cross shear and horizontal shear strength values. Clay core and clay blanket samples have higher cross shear strength than that along the horizontal shear plane. Intense fissuring of the clay foundation resulted to a bilinear failure envelope, while the clay core and clay blanket had a more uniform failure envelope.

The slope stability analysis considering strength anisotropy was a better representation of what was observed on site concerning the aging earth dam in this study. Based on site exploration, laboratory investigation, and numerical modeling analysis, the dam operator and owner have carrying out proactive measures in order to meet current dam safety standards.

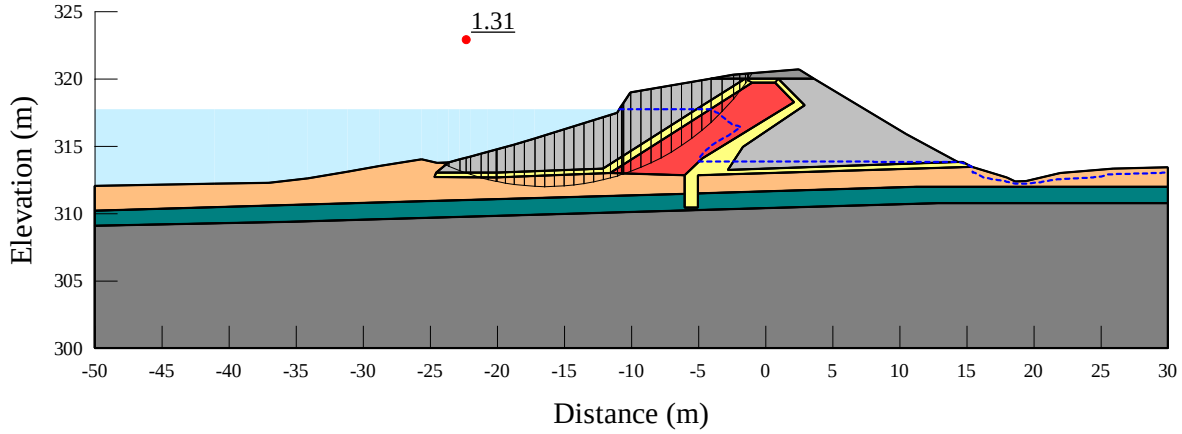

Fig.9 Slope stability analysis for Section A using Case 1.

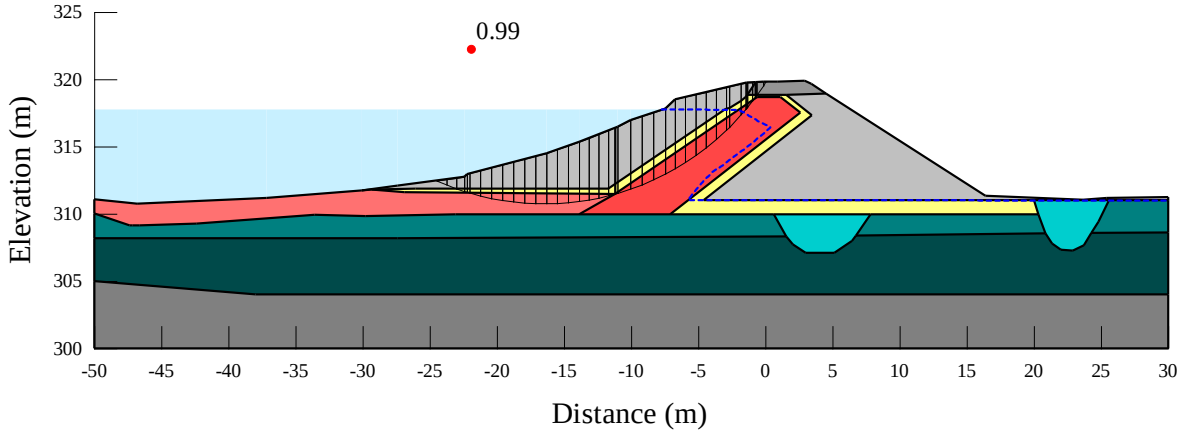

Fig.10 Slope stability analysis for Section B using Case 1.

REFERENCES

[1] McGown A. and Radwan A. M., The Presence and Influence of Fissures in the Boulder Clays of West Central Scotland, Canadian Geotechnical Journal, vol. 12, 1975, pp. 84–97.

[2] Baracos A., Compositional and structural anisotropy of Winnipeg soils - a study based on scanning electron microscopy and X-ray diffraction analyses, Canadian Geotechnical. Journal, vol. 14, 1977, pp. 125-137.

[3] Freeman W. S. and Sutherland H. B., Slope Stability Analysis in Anisotropic Winnipeg Clays, Canadian Geotechnical Journal, vol. 11, 1974, pp. 59–71.

[4] Graham J. and Houlsby G. T., Anisotrophic elasticity of a natural clay, Geotechnique, vol. 33, 1983, pp. 165–180.

[5] Graham J., Embankment stability on anisotropic soft clays, Canadian Geotechnical. Journal, vol. 16, 1979, pp. 295–308.

[6] Loh A. K.and Holt R. T., Directional Variation in Undrained Shear Strength and Fabric of Winnipeg Upper Brown Clay, Canadian Geotechnical. Journal, vol. 11, 2011, pp. 430–437.

[7]Yoshida N., Morgenstern R., and Chan D. H., Finite-element analysis of softening effects in fissured, overconsolidated clays and mudstones, Canadian Geotechnical Journal, vol. 28, 1991, pp. 51–61.

[8] Rivard P. J.and Lu Y., Shear strength of soft fissured clays, Canadian Geotechnical Journal, vol. 15, 1978, pp. 382–390.

9th Int. Conf. on Geotechnique, Construction Materials and Environment, Tokyo, Japan, 20-22 November 2019, ISBN: 978-4-909106025 C3051

RAINFALL-INDUCED DEFORMATION BEHAVIOR OF CRACKS ON BROWN COAL OPEN PIT BATTER IN AUSTRALIA

Lei Zhao [1], Greg You [1]
[1] School of Science, Engineering and Information Technology, Federation University Australia, Australia;

ABSTRACT

After a 26mm rainfall in 24 hours, noticeable ground movements were observed on the north batter at Maddingley Brown Coal Open Pit Mine, Victoria, Australia in February 2014. The batter is brown coal sandwiched by confining beds. Cracks manifested on the north batter months before the rainfall event, and then an emergency buttress was immediately constructed to maintain the batter stability. A three-dimensional geologic model is developed to study the rainfall-induced ground movement in this paper. The finite element program encoded in Plaxis 3D is employed to conduct the complex two-phase (fluid-solid) coupled numerical simulation. It is found that the simulated deformation is well agreed with the observed data from field survey markers. There are ground movements along the length of cracks on both sides with larger movement towards the pit bottom. These movements are the results of the combined reactions of surface run-off and sudden increased underground water level. The 26mm rainfall event did not cause instability of the batter.

Keywords: Crack, Rainfall, Deformation, Brown Coal, Open-Pit Mining

INTRODUCTION

Brown coal is won by open pit mining in Victoria, Australia, benefiting from its shallow depth and thick seam. A number of open pit walls and permanent batters have been formed due to the open pit mining activity lasting for a century in this area. Depth and size of mining excavations are still increasing, it was reported [1] that Loy Yang Brown Coal Open Cut in Latrobe Valley, Victoria, had reached a depth of 200 meters. As a result, the slope instability has become a major risk of geo-hazard in Victoria Brown Coal Open Pits. Although, different from the hazards kinds [2] caused by underground coal mining, the batter instability issues of open pits often result in serious casualties, property loss, and environmental damage [3]-[4]. Also, coal batter failures have been reported from time to time in Victoria brown coal open pits. A block failure occurred in the northeast batter at the Yallourn East Field Mine on 14th November 2007 as shown in Fig.1. It was a very large failure, approximately 80m high and 500m long, and about six million cubic meters of materials were encompassed [6]. This failure caused Yallourn river diverted into the mine site that resulted in over $200 million costs to the mine and an immediate loss of one-fifth of Victorian power generation capacity [7]. A clear understanding of coal batter failure mechanism is crucial in slope instability control and prediction. Though groundwater pressure, coal joints, the shear strength of batter composition, batter slope and height are generally known as the factors involved in the batter instability problem, it is a challenge to adequately interpret batter failures due to the complex interaction of those factors. Owing to the quick-growth computer technique, numerical simulation has become a promising way to solve such kind of problem. The numerical simulation method can analyze batter stability under the conditions as close to reality as possible by employing full-scale three-dimensional model and high-performance computers. Over past years, number of scholars [8]-[12] studied slope instability using numerical simulation method, and the outcomes were positive. The numerical simulation method has become a reliable way to solve the complicated geotechnical problems.

Fig. 1 Yallourn batter sliding on 14th November 2017 [5]

In Victorian brown coal mines, batter movements and failures observed are roughly attributed to circular type sliding of overburden faces and block type sliding of brown coal faces [13]-[14]. Brown coal batter with overburden tends to lead a circular

sliding while the coal batter after overburden removal has a blocking slide trend at Maddingley brown coal mine [15]. Brown coal block sliding is a unique and common failure type in this region after overburden removal. Block failure occurred not long after cracks (opened joints) emerging on coal batter surface or heavy rainfall event in Victorian brown coal open pits, as reported in Yallourn mine in 1950 [14] and 2007 [6].

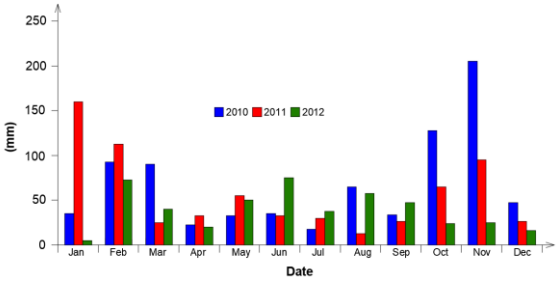

Fig. 2 Monthly rainfall values (mm) for 2010, 2011 and 2012- Bacchus Marsh, Victoria

In Maddingley brown coal (MBC) mine, where this study is based on, a block failure occurred in the southern wall of the open pit in October 1994 which caused a water leakage along cracks from the adjacent Parwan Creek; cracks were observed in the northern batter in November 2013, and then an emergency buttress was immediately constructed to maintain batter stability. The further development of the cracks had been well controlled in the northern batter with the buttress, but horizontal movements along cracks were monitored immediately after a 26mm rainfall in February 2014. In previous studies, high tensile strain behind the batter and high shear strain underneath the coal seam could be developed after the overburden is stripped in the north batter, and cracking propagation was a result of stress relief due to the overburden removal [15]; rainfall event can accelerate the cracking propagation process [16]. The observed cracks on north batter of MBC did not penetrate the coal batter as high tensile strains are generally developed at the surface of the coal seam due to its low-modulus, ductile nature [6]. On the other hand, the high tensile strain could lead to the open of pre-existing joints in the coal seam. It is also interesting to note that batter failures are prone to occur in summer or close to summertime in Victoria. There is high precipitation in summer in Victoria, Australia. Figure 2 shows the distribution of precipitation in Bacchus Marsh from 2010 to 2012, where MBC mine site is located. This study interprets how opened cracks deform under a 26mm rainfall condition by developing and simulating a three-dimensional geologic model of the north batter of Maddingley brown coal mine. The batter is sandwiched by confining beds, and there are opened joints in the coal seam.

MADDINGLEY BROWN COAL OPEN PIT OVERVIEW

Geology and Hydrogeology of MBC Mine Site

MBC is a typical Victorian Brown Coal Open Pit, located on the southern outskirts of the township of Bacchus Marsh, Victoria, Australia. Open pit mining was commenced in the 1940s, and simultaneous coal excavation (on the north batter) and waste landfill operation (in the south of pit bottom) are in progress in MBC at present. Three main formations (Fig.3) constitute the typical sandwiched MBC brown coal batter. The top formation consisting of sands, silts and clays is Fyansford Formation (overburden), with a thickness of 5m to 20m; the middle Maddingley Brown Coal Seam Formation consists predominantly of brown coal, which is in a thickness of between 35m and 60m; underlying coal seam is Werribee Formation consists predominantly of silty clays and silty sands, fine to medium grained sands and minor sandy gravels. Description of the main hydro-stratigraphic units underlying the site is summarized in Table 1.

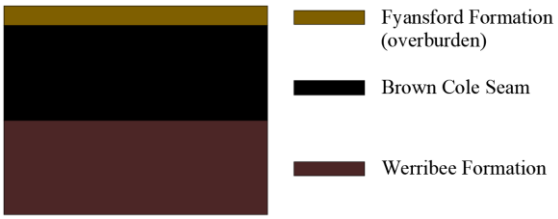

Fig. 3 Geologic formations of MBC

Table 1 Main Hydro-stratigraphic Units in MBC

Hydro-stratigraphic Unit	Function Within the Regional Groundwater System
Fyansford Formation;	Unconfined Aquifer
Brwon Coal Seam;	Aquitard and confining Aquifer
Werribee Formation.	Confined Aquifer

MBC Brown Coal Characterizations

Victorian brown coal is a material with high organic content and low permeability [17]-[18], whose strength is between normal engineering soil and rock, and its stiffness is similar to very stiff clay. It is also a highly deformable and low-density material. The unit weight of saturated MBC brown coal is about 11.5kN/m^3 while the dry unit weight is about 5kN/m^3. The low density means the batter

stability is very susceptible to the water pressure from groundwater or rainfall runoff, and the deformable character tends to cause the formation of cracks and open of existing joints in Victorian brown coal [6].

Fig. 4 Major cracks on North Batter in November 2013

Northern Batter of MBC

Stripping and mining operations were commenced on the north batter in MBC in early 2013, and before that the north batter was stable for many decades. It was a single bench, about 25m high and extended over approximately 150m in length orientated from west to east, at a slope angle >80 degree. Cracks (Fig. 4) were observed on the surface of north batter in November 2013, which was located about 20m from the batter crest, when there was a large scale of overburden stripping commenced in early 2013 and minimal mining of coal. The length of these cracks was almost throughout the overall length of the batter, and the width was from a trace to approximately 150mm. The cracks opened wider in the east than in the west as there was an old 5m high buttress left at the toe of the western end of the batter. An emergency buttress was constructed immediately after the observation of these cracks. From the monitored data, movements were well controlled benefitting from the construction of the emergency buttress, except some new minor cracks appeared in the south of the cracks (Fig. 5).

Ground Deformation Monitoring System

Eight survey markers were installed along the major cracks in November 2013 to monitor the ground movement. The locations of these survey markers (from Marker 1 to Marker 8) were demonstrated in Fig.6.

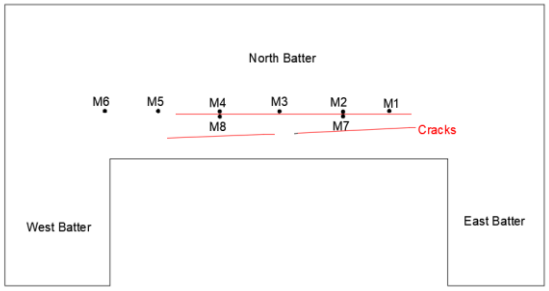

Fig. 5 Survey markers (M1 – M8) on MBC north batter

Monitored Ground Movement Induced by Rainfall Event

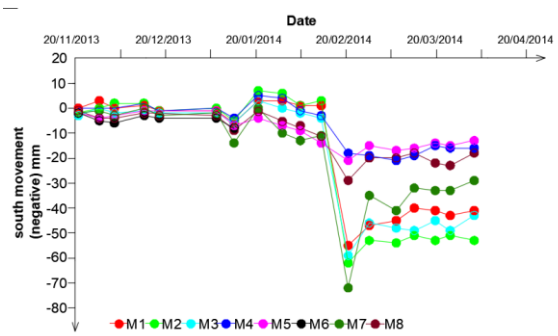

Fig.6 Monitored ground deformation on North Batter (no data for M6)

From the monitored data (Fig.6), the ground deformation on the north batter was well controlled within 10mm in both north and south directions in the following three months after the installation of survey markers. However, a 26mm rainfall occurred on 14 February 2014 (one day after the buttress was fully completed), and noticeable movements (Fig.6, south movement is negative and north positive) were observed. The movements were 56mm, 65mm, 55mm, 15mm, 7mm, 61mm and 18mm towards pit bottom (south), seen from survey marker 1 to 8 respectively (survey marker 6 was destroyed prior to the rainfall event due to mining).

NUMERICAL SIMULATIONS

In this paper, a three-dimensional geological model of MBC north batter with cracks was developed to study the ground movement under

rainfall event. This model was developed based on the MBC north batter on 13 February 2014 at that moment the emergency buttress was in position. One day later, a 26mm rainfall event occurred. Figure 7 shows the geometry of the model that is 400m in length from west to east and 250m in width from north to south. The model covers the north batter, east batter and west batter of MBC open pit.

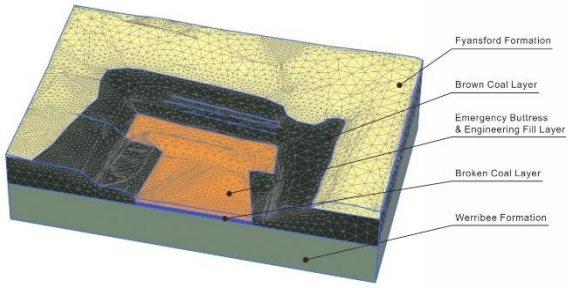

Fig.7 Three-dimensional model of north batter (meshed)

The model consists of 5 layers, which are, from top to bottom, Fyansford Formation (overburden, RL 87m to RL 100m), brown coal layer (RL 50m to RL 87m), emergency buttress (RL 60m to RL 72m) and engineering fill layer (RL 55m to RL 60m), broken brown coal layer (RL 50m to RL 55m), and Werribee Formation (RL 0m to RL 50m). Groundwater flows towards pit bottom. Based on the measured borehole logs in the field, the top groundwater level is set at RL 92m in the Fyansford Formation at the initial state, which flows down to the pit bottom (RL 60m). The cracks constructed in the model include the major crack and the subsequent minor cracks, which are shown in Fig.8. The major crack is approximately 20m back from the coal face, and the two minor cracks are located on the south of the major one. The cross-section view of cracks is shown in Fig.9.

Fig.8 Aerial view of cracks on the north batter surface

The numerical simulation is a two-phase procedure. The first phase is defined as initial gravity calculation phase which simulates the initial state of the model; the second phase is a fully coupled flow-deformation calculation phase that is to simulate the deformation of the model under the defined condition of a 26mm rainfall evenly distributed in 24 hours. The mechanics of soils and brown coals adopted in this numerical simulation are listed in Table 2.

Table 2 Mechanical prosperities adopted in the three-dimensional simulation

Parameters	Unit	Fyansford Formation	Brown Coal	Buttress and Fill	Broken Brown Coal	Werribee Formation
Drainage Type	-	Drained	Undrained A	Drained	Drained	Drained
Saturated unit weight	kN/m^3	19	11.5	18	11.5	20
Unsaturated unit weight	kN/m^3	16	5	15	5	17
Young's modulus	MPa	130	37	15	37	95
Poisson's ratio	-	0.3	0.27	0.3	0.27	0.3
cohesion	kPa	9	174	5	20	5
Friction angle	degree	27	33	30	33	30
Horizontal permeability k_x	m/d	0.0086	0.0086	0.1	0.1	0.00086
Horizontal permeability k_y	m/d	0.0086	0.0086	0.1	0.1	0.00086
Vertical permeability k_z	m/d	0.00086	0.00086	0.1	0.1	0.00086

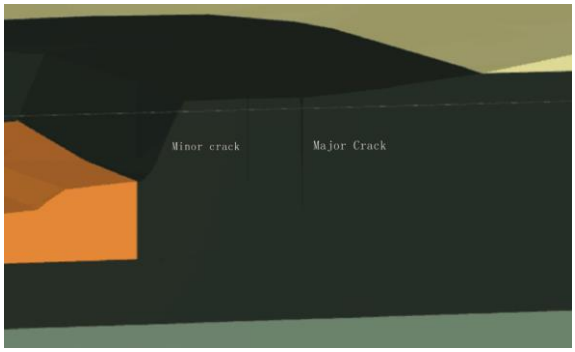

Fig.9 Cross-section view of cracks

RESULTS AND DISCUSSION

From the results of simulation, noticeable movements are generated along the length of both sides of cracks in the direction perpendicular to the cracks after the 26mm rainfall event, while no apparent lateral movements in the direction parallel to the cracks (Fig.10). The monitored data of deformation after the rainfall event was recorded by survey markers installed along the major crack (four on north side, two on south, two on lateral). The magnitude of monitored deformations are 56mm, 65mm, 55mm, 15mm, 7mm, 61mm and 18mm from marker 1 to 8, respectively, excluding Marker 6 that was damaged and no data available. The simulated movements of the seven markers are 48mm, 52mm, 44mm, 32mm, 4mm, 28mm, and 8mm correspondingly, which are shown in Fig.11. The simulated result is in good agreement with the monitored, with comparatively less southern movements than the observed data except for Marker 4.

The largest movement towards open pit (south) appears close to the north of the major crack, reaching up to 52mm. Deformations around 28mm towards open pit are seen in the north of the two minor cracks, whereas in the opposite side (south) of the minor cracks, smaller movements of less than 8mm towards north are simulated. These movements between the

major and minor cracks are the overlapping effects of both south and north movements resulted from the major and minor cracks after rainfall. There is up to 24mm positive (towards north) movement in the central south of the major crack, where exists a gap between the two minor cracks. Thus, there is less effect from the minor cracks.

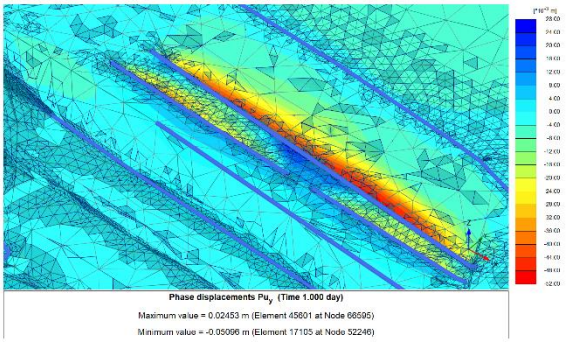

Fig.10 Movement of cracks after a 26mm rainfall in 24hours

The ground appears to move towards the centerline of the crack and the deformation in the north of crack is larger than that in the south. The ground movements mainly concentrate in the vicinity of cracks, and there is no noticeable movement in other parts of the batter. It is inferred that the surface run-off entering cracks exerts a hydrodynamic force on the initially unsaturated surface brown coal that could be pushed move along the direction of rainfall run-off; as a result, the deformation tends to move towards the centerline of the crack. The overall water flow is towards pit bottom (or towards south); thus the suddenly increased groundwater level in the cracks and brown coal increase the south-direction hydrodynamic force and horizontal hydrostatic water pressure to the brown coal, which could result in that the south-direction movement is larger than north-direction. From the simulated results, the groundwater level increased in the coal layer north of the minor cracks, but not of the south part. Therefore, the movements in the north of the minor cracks are larger than that of the south. The deformation generated around the major crack is larger than the deformation around the minor cracks. It is inferred that the deformation could be larger with the increase of the crack's depth. In summary, the movements are the results of the combined reactions of surface run-off and suddenly increased groundwater level. Although noticeable deformation is generated after the rainfall, the batter is still in a safe state after the rainfall event. It would benefit from the support of the emergency buttress, the moderate rainfall intensity and the short duration of the rainfall.

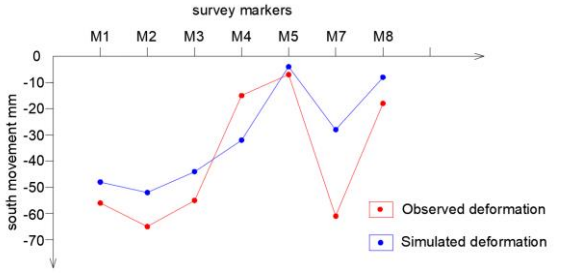

Fig.11 Comparison of observed and simulated movements along the crack

CONCLUSIONS

A three- dimensional model was developed using Plaxis 3D to study the effects of rainfall on batter movement in a Victorian brown coal open pit. The following conclusions can be made.

1. The simulated deformation is well agreed with the observed data from the seven field survey markers, which in turn verifies the three-dimensional numerical model developed.

2. From the simulation, the 26mm precipitation in 24hours results in noticeable movements on both sides along the cracks, while no apparent movements are seen in either lateral side of cracks or other parts in the batter. The overall movement is towards the pit bottom. The ground tends to move towards the centerline of the crack, and the deformation is larger in the north of the crack than in the south. The deformation generated around the major crack is larger than the deformation around the minor cracks.

3.These movements are the results of the combined reactions of surface run-off and suddenly increased groundwater level. This 26mm rainfall event did not cause the batter instable. A further study is to address what is the relationship between rainfall and potential block failure of brown coal batter.

ACKNOWLEDGMENTS

The authors sincerely express their appreciation to the support of this research project from Maddingley Brown Coal Pty Ltd., in particular, to Mr. Tim Tillig, the Environmental, Quality & Safety Officer.

This study is supported by the Australian Research Training Program (RTP) Scholarship and Federation University Australia George Collins Memorial Scholarship.

REFERENCES

[1] Langmore D., Latrobe Valley Open Cuts: Wastelands or treasured assets? [online], Planning News, Vol. 42, Issue 11, 2016, retrieved from: https://search.informit.com.au/documentSummary;dn=509945601620014;res=IELENG

[2] Zhang J.J., Xu K.L., You G., Wang, B.B., and

Zhao L., Causation Analysis of Risk Coupling of Gas Explosion Accident in Chinese Underground Coal Mines, Risk Anslysis, Vol. 39, Issue 7, 2019, pp. 1634-1646.

[3] Ayalew L., The effect of seasonal rainfall on landslides in the highlands of Ethiopia, Bulletin of Engineering Geology and the Environment, Vol. 58, Issue 1, 1999, pp.9-19.

[4] Chae B.G., Park H.J., Catani F., Simoni A., and Berti M., Landslide prediction, monitoring and early warning: aconcise review of state-of-the-art, Geosciences Journal, Vol. 21, Issue 6, 2017, pp.1033-1070.

[5] Petley D., Landslides that make you gasp part 1: Yallourn. Blogsphere, 2017, retrieved from: https://blogs.agu.org/landslideblog/2017/05/18/yallourn/

[6] Mining Warden, Yallourn Mine Batter Failure Inquiry, 2008, retrieved from: https://www.parliament.vic.gov.au/papers/govpub/VPARL2006-10No156.pdf

[7] Sullivan T., Lessons from the Yallourn Batter Failure Inquiry. Australian Geomechanics Society 2011, retrieved from: https://australiangeomechanics.org/meetings/lessons-from-the-yallourn-batter-failure-inquiry/

[8] Chang K.T. and Huang H.C., Three-dimensional analysis of a deep-seated landslide in central Taiwan, Environmental Earth Sciences, Vol. 74, Issue 2, 2015, pp.1379-1390.

[9] Ozbay A., and Cabalar A.F., FEM and LEM stability analyses of the fatal landslides At Çöllolar open-cast lignite mine in Elbistan, Turkey, Landslides, Vol. 12, Issue 1, 2015, pp.155-163.

[10] Jamsawang P., Boathong P., Mairaing W., and Jongpradist P., Undrained creep failure of a drainage canal slope stabilized with deep cement mixing columns, Landslides, Vol. 13, Issue 5, 2016, pp.939-955.

[11] Usluogullari O.F., Temugan A., and Duman E.S., Comparison of slope stabilization methods by three-dimensional finite element analysis, Natural Hazards, Vol. 81, Issue 2, 2016, pp.1027-1050.

[12] Göktepe F. and Keskin I., A Comparison Study between Traditional and Finite Element Methods for Slope Stability Evaluations, Journal of the Geological Society of India, Vol. 91, Issue 3, 2018, pp.373-379.

[13] Washusen J.A., and Fraser C.J., Stability control and monitoring in deep Latrobe Valley Open Cuts, The Aus.I.M.M Conference, Melbourne, Vic, 1982, pp 87-95.

[14] Learmonth A.P., Geomechanics Working in the Power Industry, The National Engineering Conference, Melbourne, 1985, pp 10-18.

[15] Zhao L., and You G., Cracking Mechanism Along the North Batter of Maddingley Brown Coal Open Pit Mine, Victoria, Australia, In: Wasowski J., Giordan D., Lollino P. (eds) Engineering Geology and Geological Engineering for Sustainable Use of the Earth's Resources, Urbanization and Infrastructure Protection from Geohazards. GeoMEast 2017. Sustainable Civil Infrastructures, 2018, pp. 115-129.

[16] Zhao L., and You G., Stability study on the northern batter of MBC Open Pit using Plaxis 3D, Arabian Journal of Geoscience, Vol. 11, Issue 6, 2018.

[17] Xue J., and Tolooiyan A., Reliability analysis of block sliding in large brown coal open cuts, ACEM' 12 The 2012 World Congress on Advances in Civil, Environmental, and Materials Research. Korea:Techno-Press, 2012, pp.1578-1587.

[18] Liu K., Mackay R., Xue J., and Tolooiyan A., Experimental study of brown coal hydraulic behavior at low confining stress, Unsaturated soils: research and applications- proceedings of the 16th International Conference on Unsaturated Soils, Sydney, 2014, pp 1125-1130.

9th Int. Conf. on Geotechnique, Construction Materials and Environment, Tokyo, Japan, 20-22 November 2019, ISBN: 978-4-909106025 C3051

STABILIZATION OF CLAYEY SOILS USING POWDERED MARINE SHELLS

Giancarlo P. Ventura[1], Ma. Michaela B. Biscocho[1] and Jose Maria Ferdinand V. Calaunan[1]
[1]Institute of Civil Engineering, University of the Philippines Diliman, Philippines

ABSTRACT

The Philippines, as an archipelago, is surrounded by different bodies of water. Along with these are the abundant marine resources the country has such as mussels, oysters, and scallops. These marine organisms are widely used especially in the food industry. Upon consumption, the shells of these species are being put into waste, which in turn, causes issues regarding disposal of these organic wastes. With this, the study aims to analyze the effectiveness of powdered marine shells as soil stabilizers by identifying the changes in the unconfined compressive strength, plasticity index, and activity number, brought about by increasing marine shell concentration specifically 0%, 4%, 6%, and 8%. Application of increasing shell concentration yielded the following effects: increasing trend of unconfined compressive strength, decreasing values of plasticity index, and lower activity number. The significant increase in unconfined compressive strength of the soil changes the stiffness of the soil from a medium state to a very stiff state. The reduction of plasticity index changes the soil property from very high plasticity to high plasticity. Consequently, the decreasing activity number alters the soil from normal to inactive, lowering the swelling potential of the soil. Both stabilized and unstabilized soil samples underwent scanning electron microscopy (SEM) analysis to see the effect of the marine shells on the soil particle structure. The application of calcined marine shells and consequent increase in shell concentration lead to the clustering of the soil particles with the aid of connectors, reducing the intergranular voids, and further strengthening the soil.

Keywords: Marine shell, Stabilization, Compressive strength, Plasticity index, Activity number

INTRODUCTION

The history of aquaculture is known to be very rich in the Asia and the Pacific with Southeast Asia producing 10.2% of this resource (Silpachai, 2001). The Philippines is the largest contributor in Southeast Asia with 33.6% in production (Silpachai, 2001). In the 1930s, the production of these resources was originally confined in the Manila Bay area but with the help of technological advancements, oyster and mussel farming eventually became widespread in the country. At present, the Philippines specializes in the production of oysters and green mussels, producing approximately 12,000 MT in 1987 (Aypa, 1990) and still growing rapidly until today with farms ranging from 300 to 1,000 m^2 (Yap, 1999).

Along with the flourishing economy of oyster and mussel farming comes the issue of the disposal of these organic wastes. After these have been consumed, shells go straight to landfills and cause problems with increased microbiological activity, the introduction of diseases and parasites and the production of anoxia in the sediments and bottom water in turn leading to the production of toxic substances such as hydrogen sulfide (OSPAR, 1998). Because of these, the marine shell waste's potential for use must be explored, specifically to clayey soils [5].

Shells have been used as heterogeneous catalysts for biodiesel production [2], an alternative liming material for increasing crop productivity [4], and substitute aggregates in mortar (Yoon, et al., 2004). These studies have shown that the main material in shells that increases its potential for use is calcium carbonate ($CaCO_3$), a material also found in lime which is commonly used in soil stabilization. Lime is one of the most commonly used soil stabilizers [1]. However, its helpfulness in the engineering industry causes environmental problems such as the demolition of natural ecosystem and the consumption of huge amounts of energy (Lee, et al., 2008). This serves as another motivation for researchers to explore the use of marine shells as soil stabilizer so as to limit the use of lime in the field.

The researchers aim to analyze the effectiveness of powdered marine shells as soil stabilizer. This is done by identifying the changes in unconfined compressive strength, plasticity index, and activity number of the soil when stabilized with marine shells. This objective is achieved by varying the amount of concentration of powdered marine shells, and analyzing their effects on the clayey soil. The effect of powdered marine shells to soil particle structure shall also be taken into consideration. All of the experiments will be done to both stabilized

and unstabilized soils for comparison to validate the study's effectiveness.

METHODOLOGY

Sample Acquisition

Clayey soil sample was provided by Geotechnics Philippines, Inc. from an area in Sikatuna Village, Quezon City, Philippines. The marine shells were obtained from Dampa sa Libis Restaurant in Libis, Quezon City, Philippines. A mixture of oyster, mussel, and scallop shells weighing 5.5 kg were acquired.

Soil Sample Preparation

The soil sample was cleaned by removing plastic, glass, and other materials that mixed up with the soil. The sample was then passed through Sieve No. ⅜ and oven-dried for 24 hours to remove excess moisture and to declump the particles for sieving. A mortar and pestle was then used to declump the soil further in preparation for preliminary soil investigation.

Preliminary Soil Investigation

The grain size analysis involves the use of a set of sieves to separate soil particles into different size ranges. The mass of particles in each range was then determined using a mass balance. The experiment was done as guided by ASTM D6913-04.

The Atterberg Limits such as liquid limit and plastic limit were obtained, following the standard method indicated in ASTM D4318-10. Consequently, the plasticity index and activity number were calculated to correlate these with different engineering behaviors.

Two classification systems were used to classify the soil. These are the USCS and AASHTO Soil Classification System. Both systems are used to classify mineral and organo-mineral soils for engineering purposes based on laboratory determination of particle-size characteristics, liquid limit, and plasticity index.

The laboratory test for the generation of compaction curve is based from the Standard Test Methods for Laboratory Compaction Characteristics of Soil using Standard Effort provided in ASTM D698-07. This test method covers laboratory compaction methods used to determine the relationship between molding water content and dry unit weight of soils compacted in a 4-in. (101.6-mm) diameter mold with a 5.50-lbf (24.5-N) rammer dropped from a height of 12.0 in. (305 mm) producing a compactive effort of 12,400 ft-lbf/ft^3 (600 kN-m/m^3).

Shell Cleaning

The shells were washed using water and brushes to free the shells from dirt and dust. The clean shells were sun-dried for 2 days then oven-dried at 110^{0}C for 2 hours [6]. This method for cleaning was taken from a study by Rashidi, et al. (2011).

Fig. 1 Marine shell samples after oven-drying

Shell Crushing

The shells were then crushed and grounded using a ball mill located in the Pilot Plant of the UP Department of Mining, Metallurgical, and Materials Engineering. It was crushed in the ball mill in two batches, revolving for 30 minutes per batch. The product of this process is the shell in powder-like form.

Calcination

After the powdered shells have been obtained, they were placed in the furnace at UP Department of Mining, Metallurgical, and Materials Engineering and in the Environmental Engineering Laboratory for calcination. To avoid contamination, the shells were placed in 30 milliliter porcelain crucibles. The furnace was set at 850^{0}C for 4 hours, as done in the study by Buasri, et al. (2013). The shells were passed through Sieve No. 100 for particle size uniformity. The shells were then stored in airtight plastic bags to prevent carbonation.

X-ray Fluorescence

X-ray Fluorescence (XRF) analysis is an analytical technique used to determine the chemical composition of the shells. This process was done to verify the presence of CaO after calcination. The XRF analysis was done in the National Institute of Geological Sciences in UP Diliman.

Soil Stabilization

The weight of the oven-dried soil and powdered shells was predetermined depending on the required concentration needed in the mixture. The mixture was then dry-mixed for 1 minute using the mortar mixer. The mortar mixer used is located in the Construction Laboratory in UP Institute of Civil Engineering. The obtained optimum moisture content by weight of the mixture was added to the soil in a thin stream and mixed for 5 minutes. The mixture was then transferred to a bowl and immediately covered with a plastic bag to prevent the loss of moisture and carbonation.

Unconfined Compression Test

The unconfined compression test is used to determine the stress-strain behavior of a given sample. ASTM D2166 and D5102-09 are used for cohesive soils and soil-lime mixtures respectively. Samples were compressed using an Instron 3366 UTM located in the Construction Laboratory in UP Institute of Civil Engineering, at a rate of 2% per min. The compression stops at an axial strain of 15% and 5% for unstabilized and stabilized soil respectively, or until the load values decrease, whichever happens first. The cylindrical mold used had a diameter of 2 inches and a height of 4 inches. An improvised rammer was also made using a PVC pipe and a tamping rod. To be able to maintain a standard effort of 12,400 ft-lbf/ft^3 given the dimensions of the instruments, the number of blows is recomputed, resulting to 12 blows per layer for 3 layers. After extrusion of the soil specimens from the mold, they were immediately stored in airtight plastic bags to prevent the loss of moisture and carbonation. The plastic bags were then stored in an airtight, and moisture-proof container at room temperature for a curing period of 7 days.

Atterberg Limits

With the addition of calcined marine shells to the clayey soils, stabilization at 4%, 6%, and 8% shell concentrations produce different effects on the soil. These alterations on the properties per concentration are expressed in terms of the changes in their respective liquid limits, plastic limits, plasticity indices, and activity numbers.

Scanning Electron Microscopy

The Scanning Electron Microscopy (SEM) was used to obtain the micrographs of both stabilized and unstabilized soil samples. These were determined to compare the differences on the textural characteristics and the particle structure of the soil specimens. The magnification used for all samples are 2000x and 5000x. This laboratory test is done at the Department of Chemical Engineering in UP Diliman using Hitachi S-3400N.

RESULTS AND DISCUSSION

Preliminary Investigation

Sieve analysis determines the particle-size distribution for coarse-grained particles of the soil. The results of the sieve analysis of unstabilized soil are noted to have a 53.68% finer than Sieve No. 200. The coefficient of uniformity (Cu) is 8.732 while the coefficient of curvature (Cc) is 1.031. Since the uniformity coefficient of the unstabilized soil is greater than 6 and the coefficient of gradation is within the range of 1 to 3, the soil is well graded. The liquid limit test is done and using the multipoint method. With the equation of the best-fit line from the liquid limit graph, the water content corresponding to 25 blows is considered to be the liquid limit of the unstabilized soil, obtaining a value of 81. The plastic limit is considered to be the average of the two values, 33.33 and 34.88, which is 34. The plasticity index is 47, considering it with a very high plasticity. The activity number is calculated to be 0.8756 and is known to be a normal clay soil with minerals of illite in it. Given these values, the classification of the soil is CH or High-Plasticity Clay according to USCS, and A-7-5 consisting of clayey soils according to AASHTO Soil Classification System. The standard proctor test was performed to obtain the optimum moisture content of the unstabilized soil, which is 32%.

X-ray Fluorescence

Table 1 shows the results of the X-ray Fluorescence as performed in the National Institute of Geological Sciences. It was verified that the $CaCO_3$ in the shell was transformed to CaO by the calcination process. The calcined shells contain 95.22% CaO.

Table 1 X-ray Fluoresence Results

Component	T1 (%)	T2 (%)	T3 (%)	Ave
CaO	93.25	98.06	94.33	95.22
MgO	5.02	0.00	3.91	2.98
SiO_2	0.67	0.81	0.86	0.78
Sr	0.23	0.25	0.25	0.24
Fe_2O_3	0.49	0.43	0.36	0.43
S	0.16	0.19	0.13	0.16
P	0.09	0.12	0.04	0.08
Ti	0.08	0.11	0.10	0.10
Mn	0.01	0.02	0.02	0.02

Unconfined Compression Test

The unconfined compression test was done using 2-inch molds and the improvised rammer. Table 2 shows the summary of the maximum compressive stress reached by the soil specimens and their corresponding consistencies.

Table 2 Summary of Compressive Strength

% Shell	Compressive Strength (MPa)			
	T1	T2	T3	Ave.
0%	0.095	0.096	0.079	0.090
4%	0.132	0.135	0.158	0.142
6%	0.189	0.143	0.158	0.163
8%	0.203	0.208	0.224	0.212

As seen in Table 2, the relationship of the compressive stress and the concentration has an increasing trend and to be able to identify if the increase in compressive strength is statistically significant, the data is analyzed using one-way analysis of variance (ANOVA) using Minitab 18.

The Tukey Pairwise post hoc test will be done to analyze where the differences occur in the data. Running one-way ANOVA, results show that there is a significant difference in the values as shown in Figure 2.

One-way ANOVA: 0%, 4%, 6%, 8%

Method

Null hypothesis	All means are equal
Alternative hypothesis	Not all means are equal
Significance level	α = 0.05

Equal variances were assumed for the analysis.

Factor Information

Factor	Levels	Values
Factor	4	0%, 4%, 6%, 8%

Analysis of Variance

Source	DF	Adj SS	Adj MS	F-Value	P-Value
Factor	3	0.022979	0.007660	31.91	0.000
Error	8	0.001920	0.000240		
Total	11	0.024899			

Fig. 2 One-way ANOVA results

The one-way ANOVA results show that the P-value is less than 0.05 therefore rejecting the null hypothesis that all means are equal. The Tukey post hoc test then determines where the differences occur. The results are shown in Figure 3.

Tukey Pairwise Comparisons

Grouping Information Using the Tukey Method and 95% Confidence

Factor	N	Mean	Grouping
8%	3	0.21191	A
6%	3	0.1632	B
4%	3	0.14186	B
0%	3	0.09001	C

Means that do not share a letter are significantly different.

Fig. 3 Results of Tukey Post Hoc Test

Minitab groups the data in letters to show whether or not the means are significantly different. Comparing the data relative to the unstabilized soil represented by 0%, all 3 concentrations have a significant difference with 0%.

Figures 4, 5, 6, and 7 show the stress-strain curves of the soil specimens. All of the stress-strain curves exhibit strain softening with the sudden decrease in compressive stress with increase in compressive strain after reaching a peak in stress. Strain softening often occurs for specimens that do not fail homogeneously. This is the case for all soil specimens since all failed due to a barreling failure.

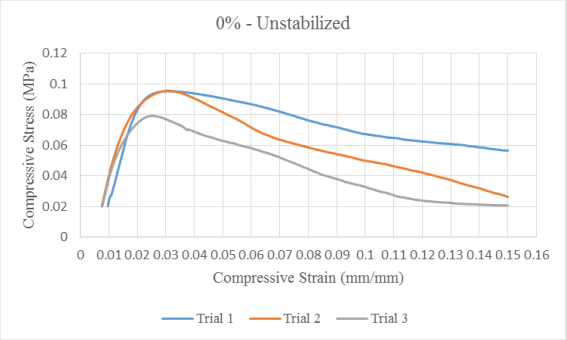

Fig. 4 Stress-Strain curve of unstabilized soil

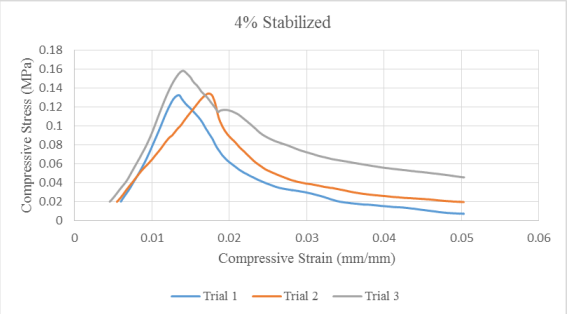

Fig. 5 Stress-Strain curve of 4% stabilized soil

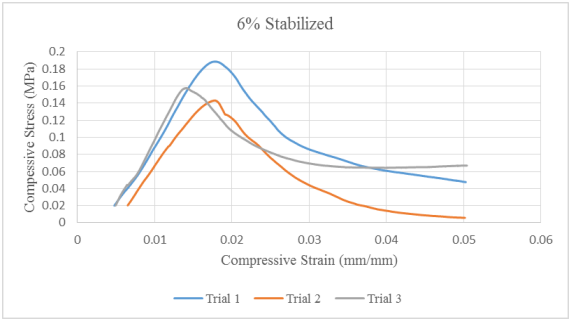

Fig. 6 Stress-Strain curve of 6% stabilized soil

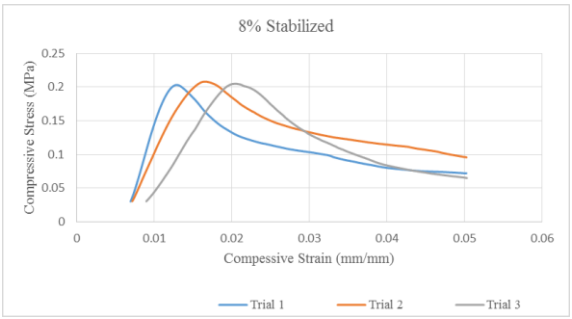

Fig. 7 Stress-Strain curve of 8% stabilized soil

The elastic moduli of the stress strain curves were computed to further verify the increase in stiffness of the soil sample with the addition of marine shells. For all points in all the stress-strain curves, the elastic modulus was approximated by solving for the ratio of the stress and strain. Table 3 contains the summary of elastic moduli values.

Table 3 Summary of Young's moduli

%	Young's Modulus (MPa)			
Shell	T1	T2	T3	Ave.
0%	2.669	3.425	3.329	3.141
4%	4.397	4.601	5.355	4.784
6%	5.372	4.123	5.532	5.009
8%	5.915	5.723	4.406	5.348

An increasing trend in Young's modulus values can be observed based from the average of the moduli of the three trials. The more closely packed the soil particles are, the higher the value of the modulus of elasticity, therefore the increase in soil stiffness is verified.

Atterberg Limits

As expected from previously discussed references, there was a decrease in the plasticity index of the soil, implying the reduction of the soil's expansivity. Table 4 shows the summary of results for Atterberg limits.

Table 4 Results of Atterberg Limits

%	Atterberg Limit			
Shell	LL	PL	PI	A
0%	81	34	47	0.8756
4%	75	36	39	0.7266
6%	72	35	37	0.6893
8%	74	38	36	0.6707

The plasticity index of unstabilized soil fell under clays of very high plasticity. The stabilized soils were classified under soils of high plasticity with their plasticity indices falling in the range of 20 to 40. The reduction of plasticity index also decreases the activity number of composite materials. The activity number indicates the swelling potential of the soil. As the marine shell concentration increases, the activity number decreases. From an activity number of 0.8756, the unstabilized soil is a normal type of soil in terms of its activity. However, the rest of the concentrations for the stabilized soils yield activity numbers less than 0.75. Because of this, the soils have turned to inactive clayey soils, and therefore lowering its swelling potential. The application of marine shells as soil stabilizer causes this alteration and gives us an idea of how susceptible to swelling the soil is.

Scanning Electron Microscopy

The unstabilized and stabilized soils were subjected to the scanning electron microscope to clearly visualize the microstructures, its arrangement and assemblage. These micrographs were generated with both magnifications of 2000x and 5000x. Figure 8 shows the micrographs for 5000x.

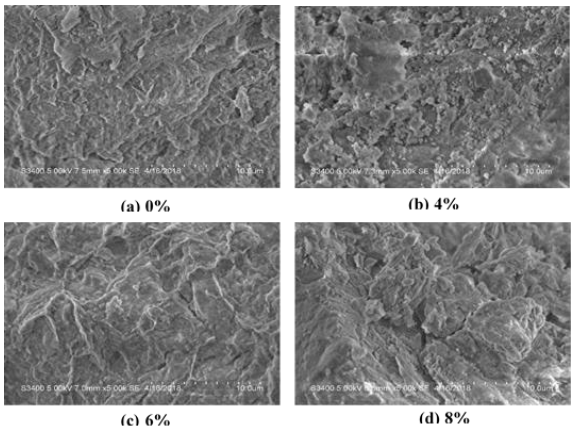

Fig. 8 Scanning Electron Micrographs: 5000x

For the unstabilized soil, sharp edges are seen, as well as crystal-like structures, indicating its initial arrangement as clayey soil. The 4% stabilized soil showed the dispersal of rounded and subangular

particles, reduced the presence of sharp-edged particles but exposes the intergranular voids. The rounded particles were combined with the irregularly-shaped particles, forming various lines and making the 6% stabilized soil more homogeneous. Clustering of these molecules into bigger particles evidently showed the clumping and binding of particles in 8% stabilized soil. For the overall arrangement, the application of marine shells and consequent increase in shell concentration to the soil exhibited the binding of the soil particles with the aid of connectors, reducing the intergranular voids, and therefore strengthening the soil.

Soil Application Assessment

For subbase and base materials, the National Lime Association recommends unconfined compressive stress values ranging from 0.345 MPa to 0.9 MPa, for soil-lime mixtures cured for 8 days. Based from the unconfined compressive strengths obtained from curing the samples for 7 days, the requirements were not met. With this, it is recommended to have longer curing periods for soil-shell mixtures since this may be a factor in the increase of strength.

The Department of Public Works and Highways Blue Book also set the requirements for suitable embankment materials. The soil used for homogenous embankment must not have more than 15% of its mass passing Sieve No. 200. Also, the material should have a plasticity index and liquid limit not more than 6 and 30, respectively. Using obtained data, it was found that the soil was not a suitable material for homogenous embankment.

Finally, using requirements for zoned embankments as specified in the Earthworks Materials Specification of the Australian Rail Track Corporation, it was found that only part of the requirements for zone D were met by the values obtained in the study.

CONCLUSIONS

The potential for the use of marine shell is explored as it is made up of a useful product, specifically the calcium carbonate ($CaCO_3$), a chemical compound also found in lime. This study was conducted to identify the changes in some mechanical properties of clayey soils upon stabilization with various shell concentrations.

With the aid of X-ray fluorescence, it was verified that the calcined marine shells from a mixture of waste mussels, oysters, and scallops are composed of 95.22% CaO by weight.

The unconfined compressive strength of the unstabilized soil significantly increased with that of all the stabilized soils. From the medium consistency given by the unstabilized soil, the soil improved to a very stiff consistency due to 8% marine shell concentration. In addition to that, the plasticity index decreases as the marine shell content increases, changing the soil from a classification of very high plasticity to high plasticity. Consequently, the reduction of plasticity index also decreases the activity number of the soil. The unstabilized soil is a normal type of soil, in terms of its activity. All stabilized soils yielded activity numbers less than 0.75, reclassifying the soils to an inactive type, and therefore lowering its swelling potential.

The stress-strain curves displayed a strain softening behavior due to the barreling failure of the soil specimens. The elastic moduli of the soils were also obtained and it was found that there was an increase in its value, supporting the unconfined compressive strength results showing the increase in stiffness of the clay.

The application of calcined marine shells leads to the clustering of the soil particles with the aid of connectors, reducing the intergranular voids, and further strengthening the soil.

REFERENCES

[1] Bell, F.g. “Lime Stabilization of Clay Minerals and Soils.” Engineering Geology, vol. 42, no. 4, 1996, pp. 223–237.

[2] Buasri, Achanai, et al. “Calcium Oxide Derived from Waste Shells of Mussel, Cockle, and Scallop as the Heterogeneous Catalyst for Biodiesel Production.” The Scientific World Journal, vol. 2013, 2013, pp. 1–7.

[3] Habiba Afrin. (2017). A Review on Different Types Soil Stabilization Techniques. International Journal of Transportation Engineering and Technology. Vol. 3, No. 2, 2017, pp. 19-24

[4] Lee, Chang Hoon, et al. “Effects of Oyster Shell on Soil Chemical and Biological Properties and Cabbage Productivity as a Liming Materials.” Waste Management, vol. 28, no. 12, 2008, pp. 2702–2708.

[5] Mokhtar, Madiha, et al. “An Experimental Study on Dust Shell as an Admixture in Soft Soil Stabilization.” ARPN Journal of Engineering and Applied Sciences, vol. 11, no. 11, ser. 2016, June 2016. 2016.

[6] Rashidi, N. A., et al. “A Study of Calcination and Carbonation of Cockle Shell.” International Journal of Chemical, Molecular, Nuclear, Materials and Metallurgical Engineering, vol. 5, no. 12, ser. 2011, 2011.

9th Int. Conf. on Geotechnique, Construction Materials and Environment, Tokyo, Japan, 20-22 November 2019, ISBN: 978-4-909106025 C3051

UNDRAINED TRIAXIAL COMPRESSION BEHAVIOR OF CARBON-DIOXIDE-HYDRATE-BEARING SAND AND ITS CONSTITUTIVE MODELING

Hiromasa Iwai[1] and Takaya Kawasaki[2]
[1] Nagoya Institute of Technology, Japan; [2] Nagoya Railway Company, Japan

ABSTRACT

Recently, carbon-dioxide-hydrate (CDH) has attracted attention from the viewpoint of the energy and environmental related issues in geotechnical engineering, since a larger amount of CO_2 gas can be captured in form of the CDH and it can be stored beneath submarine sediments. In order to achieve the reduction of the CO_2 gas emission, it is important to understand the mechanical response of CDH-bearing soils such as stress-strain relations and deformation behavior. Further, a constitutive model for CDH-bearing soils will be also required for numerical simulations to evaluate the safety and the geotechnical risk of CDH-bearing sediments. In the present study, we have proposed a new constitutive equation considering the hydrate morphology, and then the proposed model is applied to the past experimental results of CDH-bearing sand specimens; a series of undrained triaxial compression tests were conducted by the author myself. The result shows that the proposed constitutive equation well fit both the stress-strain curves and the effective stress path of CDH-bearing specimens.

Keywords: Carbon dioxide hydrate, Triaxial compression test, Elasto-plastic constitutive model, CCS

INTRODUCTION

Gas hydrates (GHs) are compounds which the cage-like structure of water molecules traps guest gas molecules inside and solidifies under low temperature and high-pressure conditions. In the past decades, the mechanical properties of soil materials containing GHs have been investigated by many researchers. Methane hydrates(MHs)-bearing marine sediments, for example, have been recognized as an important geomaterial in terms of energy geotechnics, since a large amount of methane gas is trapped inside MHs. Recently, not only MHs but also carbon dioxide hydrates (CDHs) have attracted attention from the viewpoint of carbon dioxide (CO_2) gas emission, because the CDHs can store an enormous volume of CO_2 gas inside its cage-like solid structure. In addition, the formation of CDHs in marine sediments can also be used as one of the methods for enhanced MHs recovery. At present, the method considered to be the mainstream of MHs production is "depressurization method" in which the pore pressure of MH reservoir is reduced to a pressure where MHs cannot exist as a solid phase; MHs dissociates into water and methane gas. In this depressurization method, however, the recovery rate of the MHs may decrease due to the endothermic reaction of MH dissociation. Fig. 1 shows a schematic drawing of MHs production with simultaneous formation of CDHs in marine sediments. The simultaneous formation of CDHs with MHs dissociation will prevent temperature decrease and it will lead to continuous methane gas production.

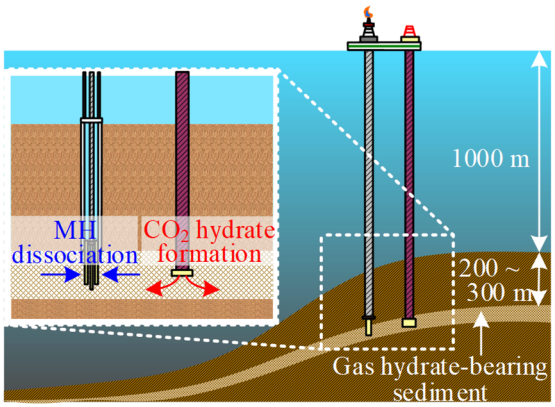

Fig. 1 Schematic drawing of MHs production and simultaneous formation of CDHs in marine sediments

This method not only contributes to the enhanced recovery of MHs, but also it is expected as one of the technologies for carbon capture and storage (CCS). For example, Inui and Satoh (2006)[1], Inui (2011)[2] and Nakashima et al. (2013)[3] focus on sequestering CO_2 in form of CDH state beneath the seafloor. In this method, CO_2 is injected into the unconsolidated sand layer under low temperature and high-pressure conditions where the CDH can be generated, and it reacts with pore water in the sediment. The CDH storage is expected to be able to stably store a large amount of CO_2 gas in a long period with a smaller volume. It is, therefore, important for MHs production and carbon dioxide storage to clarify the fundamental mechanical characteristics of the submarine sediments containing CDHs.

In the present study, undrained triaxial compression behavior of CDH-bearing sand are investigated by means of a comparative study of the experimental results and the results of the constitutive model. For the experimental results, the result presented by Iwai et al. (2018)[4] is referred; they carried out a series of undrained triaxial compression tests on the CDH-bearing sand specimens. As for the constitutive modeling, we propose an elasto-plastic constitutive equation for GH-bearing sediments considering the different type of morphology of GHs, and the proposed model is then applied to the experimental results of Iwai et al. (2018)[4].

SUMMARY OF THE UNDRAINED TRIAXIAL COMPRESSION TESTS ON CDH-BEARING SAND

In order to have further knowledge of CDH-bearing sediments, Iwai et al. (2018)[4] carried out a series of undrained triaxial compression tests on synthetic CDH-bearing sand specimens. They used a high-pressure and low-temperature triaxial testing apparatus which can reproduce an environment where GHs can exist stably [5]. Fig. 2 shows the view of the experimental apparatus. The details of the equipment can be found in the paper by Iwai et al. (2016)[5] or Iwai et al. (2018)[4].

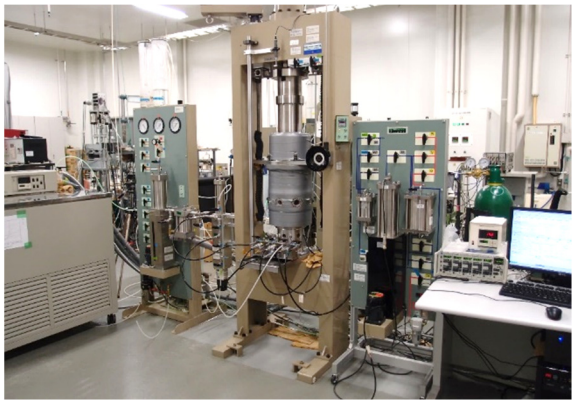

Fig. 2 View of the experimental apparatus

They conducted the tests for a total of six cases with different hydrate saturations; one of these cases is the sample without CDHs, that is, just water-saturated sand. The initial mean effective stress is 2.0MPa and the back pressure is set to be 10MPa in all the cases. The strain rate is constant at 0.1%/min. From the undrained compression test, it is found that both stiffness and strength increase with an increase in total hydrate saturation. The stress ratio at the critical state becomes M=1.20 in all cases and it seems to be independent on the hydrate saturation when it is less than about 50%; when the hydrate saturation is larger than about 50%, on the other hand, the critical stress ratio becomes larger than that of the host geomaterial. As to the dilatancy behavior, the positive excess pore water pressure was observed at the early stage of the shearing. The maximum value of the excess pore water pressure seems not depending on the hydrate saturation, while the negative value of the excess pore water pressure at the end of the shearing clearly depends on the hydrate saturation.

CONSTITUTIVE MODELING CONSIDERING GAS HYDRATE MORPHOLOGY

In general, the mechanical behavior of GH-containing soil changes depending on the content of GH in pore spaces; the strength and the stiffness increase with the increase in hydrate content. On the other hand, the past researches have also found that there are obvious differences in the peak strength, the stiffness and the dilatancy behavior among GH-bearing samples even though they have the same degree of hydrate saturation (e.g., Hyodo et al., 2014[6]; Miyazaki et al., 2016[7]). Some researchers have pointed that those differences may come from the difference in hydrate morphology, that is, pore-filling (PF) type, load-bearing (LB) type, and cementing (CM) type as shown in Fig. 3 (i.e., Waite et al., 2009[8]). Various constitutive equations have been proposed by many researchers (e.g., Kimoto et al., 2007[9]; Klar et al., 2010[10]), however, nothing considers differences of the hydrate morphology into the constitutive model. In order to make the constitutive model which can express the stress-strain relations and deformation behavior of GH-bearing sediments more precisely, we propose the new model for GH-bearing sediments considering the variation of the hydrate morphology.

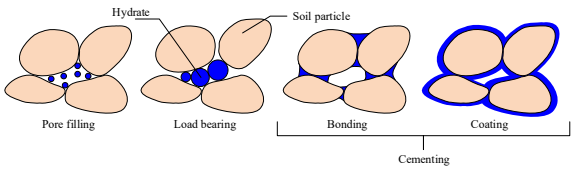

Fig. 3 Three types of GHs morphology

Basic settings of each GHs morphology

At first, the total hydrate saturation is defined as follows:

$$S_r^H = V^H / V^v \tag{1}$$

in which V^H is the volume of the hydrate phase in the pore space and V^v is the volume of the void,

respectively. In the present study, we newly propose the hydrate saturation for each hydrate morphology assuming that there three different types of the hydrate morphology. The total hydrate saturation S_r^H is divided into three parts, that is, CM-type, LB-type, and PF-type.

$$S_r^H = S_{CM}^H + S_{LB}^H + S_{PF}^H \tag{2}$$

$$S_{CM}^H = \alpha S_r^H, \quad S_{LB}^H = \beta S_r^H, \quad S_{PF}^H = \gamma S_r^H \tag{3}$$

$$0 < \alpha, \beta, \gamma < 1, \quad \alpha + \beta + \gamma = 1 \tag{4}$$

in which α, β, γ are the ratio of each hydrate morphology with respect to the total hydrate saturation, and the total should be equal to 1.

Yield function and plastic potential function

Uchida et al. (2012)[11] have developed the methane hydrate critical state (MHCS) model based on the concept of the critical state of soil mechanics. In a similar manner to Uchida et al. (2012)[11], the following yield function is used in the present study.

$$f = g = q^2 + M^2 p' \left[p' - R\left(p_c' + p_{CM}' + p_{LB}' \right) \right] \tag{5}$$

where q is the deviator stress, M is the stress ratio at the critical state of the host material, p' is the mean effective stress, p_c', p_{CM}', and p_{LB}' are the hardening parameters that expand the original yield function: modified Cam-clay model. In the present study, the associated flow rule is adopted to evaluate the plastic strain vector. The plastic potential function g, therefore, is the same function as the yield function f. The parameter R is the sub-loading surface ratio proposed by Hashiguchi (1989)[12] and its evolution law is given by:

$$dR = -m_R \left[\left(p_c' + p_{CM}' + p_{LB}' \right) / p_c' \right] \ln R \left| d\boldsymbol{\varepsilon}^p \right| \tag{6}$$

where m_R is a fitting parameter and $d\boldsymbol{\varepsilon}^p$ is the increment of the plastic strain vector. The schematic drawing of the yield surface is shown in Fig. 44.

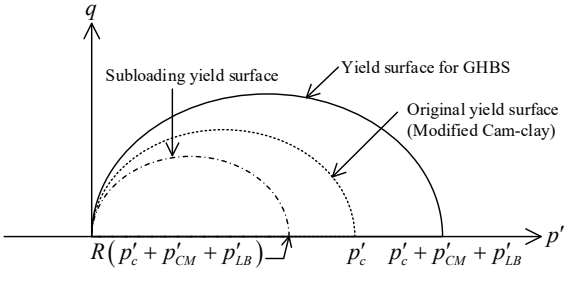

Fig. 4 Yield function [11]

By using the associated flow rule in the presenting model, the plastic strain increment vector can be expressed as follows.

$$\left\{ d\varepsilon_v^p \;\; d\varepsilon_v^p \right\}^T = \left\{ \partial f / \partial p' \;\; \partial f / \partial q \right\}^T \tag{7}$$

Hardening parameters

Consolidation yield stress

The hardening parameter p_c' is the effective consolidation yielding stress which represents an isotropic strain hardening behavior of the soil. As for the hardening rule, the conventional relationship between the p_c' and the plastic volumetric strain is adopted as follows:

$$dp_c' / p_c' = (1+e) d\varepsilon_v^p / (\lambda - \kappa) \tag{8}$$

where e is the void ratio, λ is the compression index, κ is the swelling index, and $d\varepsilon_v^p$ is the increment of the plastic volumetric strain.

Hardening parameters of gas hydrates

In order to express the greater strength and the dilatancy of GH-bearing sediments comparing with that of sand without hydrates, the additional hardening parameters p_{CM}' and p_{LB}' are newly introduced to the yield function, which expands the original yield function to the right-hand side. The p_{CM}' and p_{LB}' are the function of each of the hydrate morphology; the different type of morphology will involve the different hardening behavior.

$$p_{CM}' = a_{CM} \left(S_{CM}^H \right)^{b_{CM}} \tag{9}$$

$$p_{LB}' = a_{LB} \left(S_{LB}^H \right)^{b_{LB}} \tag{10}$$

In which a_{CM}, b_{CM}, a_{LB}, and b_{LB} are the fitting parameters controlling the expansion of the yield function. These parameters are determined so that the degree of material hardening becomes much larger in the CM-type than that in the LB-type.

Hydrate morphology transition by shearing

The hardening parameters p_{CM}' and p_{LB}' increase or decrease with the changes in the total hydrate saturation and the hydrate morphology ratio. Each hydrate morphology ratio will vary due to shearing and deformation of void spaces even if the total hydrate saturation is constant. The following assumptions in regard to the morphology transition are adopted.

- First, the CM-type changes into the LB-type due to crush and breakage of the hydrates bonding with soils particles as shown in Fig. 5. Thus, the increment of the CM-type ratio α is given by the following equation as depending on the shear strain.

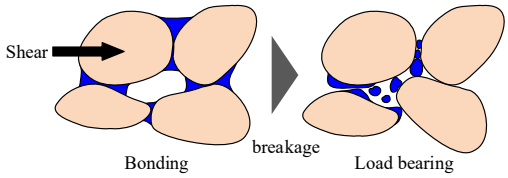

Fig. 5 Morphology transition from CM-type to LB-type

$$d\alpha = -m_\alpha \alpha \left| d\varepsilon_d^p \right| \tag{11}$$

where m_α is a material parameter which determines the transition rate from the CM-type to the LB-type.

- The second assumption is that the LB-type and the PF-type of the hydrate morphology mutually changes with increase and decrease in the volume of void. The LB-type changes into the PF-type in the case of the volume expansion: positive dilatancy. In contrast, the PF-type changes into the LB-type when it is compression: negative dilatancy. This transition between the LB-type and the PF-type is schematically illustrated in Fig. 6.

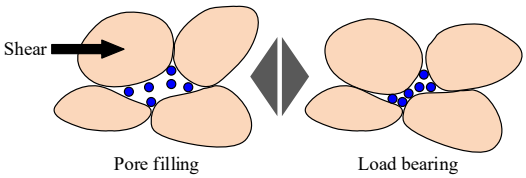

Fig. 6 Morphology transition between LB-type and PF-type

As shown in Fig. 6, the ratio of the PF-type γ depends on the volume of the pore space, and the increment of the ratio $d\gamma$ is defined as the function of the plastic volumetric strain increment (positive in compression)

$$d\gamma = -m_\gamma \gamma d\varepsilon_v^p \tag{12}$$

in which m_γ is a material parameter which determines the transition rate between the LB-type and the PF-type of the morphology.

Since the summation of the morphology ratio is equal to one as shown in Eq. (1), the increment of the morphology ratio of the LB-type $d\beta$ is expressed by the following equation.

$$d\beta = -d\alpha - d\gamma \tag{13}$$

Considering Eq. (8)~Eq. (12) gives the evolution laws for the hardening parameters p'_{CM} and p'_{LB} as

$$dp'_{CM} = a_{CM} b_{CM} \left(\alpha S_r^H\right)^{b_{CM}-1} \left(\alpha dS_r^H - m_\alpha \alpha \left| d\varepsilon_d^p \right| S_r^H\right) \tag{14}$$

$$dp'_{LB} = a_{LB} b_{LB} \left(\beta S_r^H\right)^{b_{LB}-1} \left\{\beta dS_r^H - \left(d\alpha + d\gamma\right) S_r^H\right\} \tag{15}$$

MODEL APPLICATION

In this chapter, the performance of the proposed model evaluated by comparing with the past experimental data by Iwai et al. (2018)[4]. The model is applied to the results of undrained triaxial compression tests for CDH-bearing sand samples, and mechanical behavior such as the undrained shear strength and the effective stress path is investigated.

Material parameters

The material parameters for the constitutive model are listed in Table 1. The parameters from the initial mean effective stress p'_0 to the initial void ratio e_0 are determined based on the experimental results; the initial void ratio varies depending on the experiment condition. The parameters for the hardening rules are determined so that the model results fit that of the experiment.

Table 1 Material parameters

Parameters		value
Initial mean effective stress [MPa]	p'_0	2.0
Poisson's ratio	ν	0.2
Stress ratio at the critical state	M	1.20
Compression index	λ	0.16
Swelling index	κ	0.004
Initial void ratio	e_0	variable
Initial yield stress	p'_{c0}	11.0
Material constant for sub-loading surface	m_R	15.0
Transition parameter (CM → LB)	m_α	1.0
Transition parameter (PF ↔ LB)	m_γ	7.0
Hardening parameter for p'_{CM}	a_{CM}	21.0
Hardening parameter for p'_{CM}	b_{CM}	1.0
Hardening parameter for p'_{LB}	a_{LB}	6.0
Hardening parameter for p'_{LB}	b_{LB}	1.0

Initial hydrate morphology ratio

In addition to the material parameters, the initial ratio of each hydrate morphology α_0, β_0, and γ_0 should be determined. It is preferable that the initial morphology ratio is directly determined by visualizing the microscopic structure of soil particles and hydrates. In the present study, however, the initial ratio is treated as the fitting parameter and it is

determined so that the results by the constitutive model fits the experimental data because of the lack of research data on the microstructure of the hydrate morphology. Table 2 shows the initial void ratio of each case, the total hydrate saturation, and the initial morphology ratio. In determining the initial ratio, we use the following findings obtained from the past researches.

[1] All the type of the hydrate morphology, that is, the CM-type, the LB-type and the PF-type, exist at the initial state.

[2] The increase in the strength and the positive dilatancy becomes greater in the order of CM > LB > PF-type of the hydrate morphology.

[3] The proportion of the LB-type and the CM-type increases as the total hydrate saturation increases. Furthermore, the CM-type becomes dominant when the total hydrate saturation increases much more.

Table 2 Total hydrate saturation and the initital morphology ratio

e_0	p'_0 [MPa]	S^H_r [-]	α_0	β_0	γ_0
0.74	2.0	0.0	-	-	-
0.74	2.0	25.8	0.1	0.3	0.6
0.73	2.0	27.8	0.1	0.3	0.6
0.74	2.0	36.3	0.1	0.4	0.5
0.74	2.0	42.2	0.1	0.4	0.5
0.74	2.0	56.9	0.1	0.4	0.5

RESULT AND DISCUSSION

The comparison result of the stress-strain relation and the effective stress path between the experiment and the constitutive equation is shown in Fig. 7~Fig. 9. As mentioned in the previous section, the undrained shear characteristics of the CDH-bearing specimens are that the maximum deviator stress increase with an increase in the total hydrate saturation. From the effective stress path, it can also be found that the increase in the mean effective stress after reaching the point of the phase change becomes larger with the increase in the total hydrate saturation; the degree of the positive dilatancy depends on the total hydrate saturation. It should be noted that the negative dilatancy in the early stage of the shearing is almost the same regardless of the hydrate saturation.

First, the stress-strain curves of the proposed model fit the shape of the experimental curves very well. The maximum deviator stress, that is, the undrained shear strength obtained from the constitutive model increases with the increase in the total hydrate saturation. For the case where the hydrate saturation is 56.9%, the maximum deviator stress at closely matches the experimental and analytical results, but the initial stiffness is greater in the model than that of the experiment. Secondly, in the stress path, it is found that the mean effective stress initially because of the negative dilatancy and the minimum value of the mean effective stress is almost the same in each case. The model result supports the fact that the degree of the negative dilatancy at the early stage of the shearing independent on the hydrate saturation. In contrast to that, the positive dilatancy increases after the phase change in all cases, and the increase to reach the critical state is also well consistent with the behavior of the experiment. The reason for this is that the PF-type is the predominant morphology at the initial stage and the plastic strain is easy to progress because of the less bonding effect of hydrates. The PF-type morphology gradually shifts to the LB-type as the increase in the plastic volumetric strain by the shearing, and it comes to exhibit the positive dilatancy more clearly.

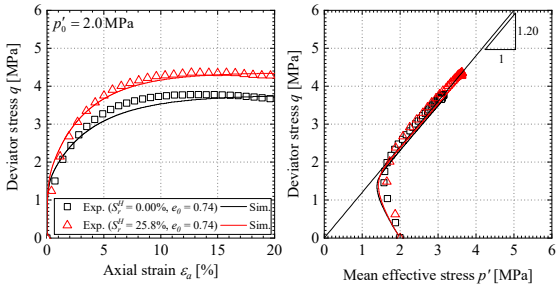

Fig. 7 Comparison of the constitutive model with undrained triaxial compression test (1)

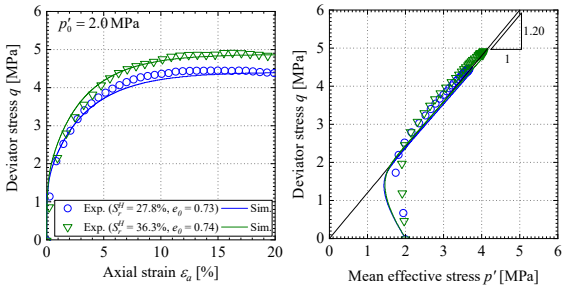

Fig. 8 Comparison of the constitutive model with undrained triaxial compression test (2)

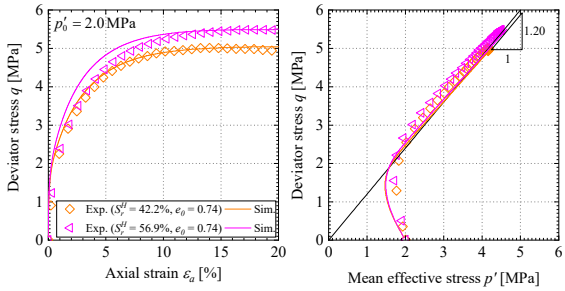

Fig. 9 Comparison of the constitutive model with undrained triaxial compression test (3)

CONCLUSIONS

In order to clarify the mechanical behavior of synthetic CDH-bearing sand under undrained conditions, we performed a comparative study of the experimental result and the element simulation by the proposed constitutive model. As for the constitutive model, the difference of the hydrate morphology was taken into account for the hardening parameters. The main findings of this study are summarized below:

- The maximum shear strength increases with the increase in the total hydrate saturation. The result is the same as the past experiment results of methane hydrate-bearing specimens.
- The positive excess pore water pressure, that is, the negative dilatancy, can be found in the early stage of the loading, and the maximum value of the pore water pressure seems to be independent on the total hydrate saturation. It implies that the PF-type, which has little hardening effect on the CDH-bearing sand, is the dominant hydrate morphology at the beginning of the shearing.
- The positive dilatancy, on the other hand, clearly depends on the total hydrate saturation. The hydrate morphology of the PF-type changed into the LB-type as the increase in the plastic volumetric strain by the shearing.
- The proposed constitutive model well fits both the stress-strain relation and the effective stress path by considering the difference of the initial hydrate morphology and its transition.

REFERENCES

[1] Inui M. and Sato T., Economical feasibility study on CO_2 sequestration in the form of gas hydrate under the seafloor, Journal of the Japan Society of Naval Architects and Ocean Engineers, Vol.3, 2006, pp.35-46.

[2] Inui M., Sato T., Komai T., and Kagemoto H., Experiments and Numerical Simulations of Hydrate Formation in Sand Sediment Simulating Sub-Seabed CO_2 Storage in the form of Gas Hydrate., Journal of MMIJ 2011;127:194–201. doi:10.2473/journalofmmij.127.194.

[3] Nakashima T, Sato T, Inui M. Numerical Modeling of Hydrate Formation in Sand Sediment Simulating Sub-Seabed CO_2 Storage in the form of Gas Hydrate. Energy Procedia 2013;37:5986–93.

[4] Iwai H., Konishi Y., Saimyou K., Kimoto S., and Oka F., Rate effect on the stress-strain relations of synthetic carbon dioxide hydrate-bearing sand and dissociation tests by thermal stimulation, Soils and Foundations, Vol 2018;58:1113–32.

[5] Iwai H, Saimyou K, Kimoto S, Oka F. Development of a temperature and pressure controlled triaxial apparatus and dissociation tests of carbon dioxide hydrate containing soils. Japanese Geotechnical Society Special Publication 2016;2:518–21.

[6] Hyodo M, Li Y, Yoneda J, Nakata Y, Yoshimoto N, Kajiyama S, et al. A comparative analysis of the mechanical behavior of carbon dioxide and methane hydrate-bearing sediments. American Mineralogist 2014;99:178–183.

[7] Miyazaki K, Oikawa Y, Haneda H, Yamaguchi T. Triaxial Compressive Property of Artificial CO_2-Hydrate Sand. International Journal of Offshore and Polar Engineering 2016;26:315–20.

[8] Waite WF, Santamarina JC, Cortes DD, Dugan B, Espinoza DN, Germaine J, et al. Physical properties of hydrate-bearing sediments. Reviews of Geophysics 2009;47.

[9] Kimoto S, Oka F, Fushita T, Fujiwaki M. A chemo-thermo-mechanically coupled numerical simulation of the subsurface ground deformations due to methane hydrate dissociation. Computers and Geotechnics 2007;34:216–228.

[10] Klar A, Soga K, Ng MYA. Coupled deformation–flow analysis for methane hydrate extraction. Géotechnique 2010;60:765–76.

[11] Uchida S, Soga K, Yamamoto K. Critical state soil constitutive model for methane hydrate soil. Journal of Geophysical Research: Solid Earth 2012;117.

[12] Hashiguchi K. Subloading surface model in unconventional plasticity. International Journal of Solids and Structures 1989;25:917–945.

9th Int. Conf. on Geotechnique, Construction Materials and Environment, Tokyo, Japan, 20-22 November 2019, ISBN: 978-4-909106025 C3051

EXAMINATION OF CALCITE PRECIPITATION USING PLANT-DERIVED UREASE ENZYME FOR SOIL IMPROVEMENT

Heny Sulistiawati Baiq[1,2], Hideaki Yasuhara[1], Naoki Kinoshita[1], Heriansyah Putra[3], and Erni Johan[4]
[1]Department of Civil and Environmental Engineering, Ehime University, Japan
[2]Faculty of Civil Engineering, State Polytechnic of Semarang, Indonesia
[3]Department Civil and Environmental Engineering, IPB University, Indonesia
[4]Agriculture Faculty, Ehime University, Japan

ABSTRACT

Enzyme-mediated calcite precipitation (EMCP) method has been established for soil improvement technique. This study discussed the possibility of plant-derived urease enzyme as bio-catalyst. The urease enzyme was utilized for hydrolysis of urea, which causes the supply of calcium ions to precipitate calcium carbonate. Extract of cabbage and soy pulp without purification were utilized as a substitute for commercial urease enzyme product. The solution was composed of 15 g/L crude extract, 1 mol/L urea, and calcium chloride. Test tube experiment and mineralogy analysis of precipitated materials were conducted. The mineralogy and morphology of precipitated calcite were confirmed by using X-Ray Diffraction (XRD) and Scanning Electromagnetic (SEM) tests. The precipitation ratio of crude extract as the replacement of the urease enzyme was more than 60% of the maximum theoretical mass. The calcite mineral was formed as the precipitated materials revealed from the mineralogical and morphological analyses, which concludes that crude extract from cabbage and soy pulp should be a potential material for sources of urease enzyme.

Keywords: Plant-derived urease, Crude extract, Calcite precipitation, Soil improvement

1. INTRODUCTION

Calcite precipitation method was establish for improving the mechanical properties of soil [1, 2, 3], for reducing the permeability of porous materials [4-8] for increasing shear strength and stiffness of soil [1-8], for decreasing the swelling potential of clay soil, and for mitigating the liquefaction potential [2, 3]. Specifically, microbial-induced carbonate precipitation (MICP) may be used to improve the engineering properties of soil, such as shear strength, stiffness, and permeability of the soil [4, 10]. In this method, bacterial cells, e.g., Sporosarcina pasteurii, has been utilized to hydrolyze urea into ammonium and carbonate ions [7,10,11]. The produced carbonate ions may be precipitated as calcite crystal in the existence of calcium ion. However, the complexity of mechanical and hydraulic properties of soil may not be easy to control because it may be impossible to constrain the extinction and/or the generation of living bacteria in natural environments [8]. Examination of other alternative methodology for calcite precipitation technique is necessary.

Recently, enzyme-mediated calcite precipitation (EMCP) technique have been investigated [3, 8, 9, 12] to enhance the mechanical properties of soil. Urease enzyme from jack beans may be used to dissociate urea into ammonium and carbonate ions instead of bacteria. Using enzyme may be more straightforward than using bacterial because the biological treatment does not need to be considered [13]. The calcite precipitation should occur after the chemical reaction between the powdered urease enzyme mixed with urea and calcium chloride. The method using urease enzyme with purification is expensive when purchased from a commercial supplier. However, the utilization of the enzyme is very effective for laboratory-scale models [13]. The reaction of calcite formation are shown in the following equations:

$$CO(NH_2)_2 + 2H_2O \xrightarrow{\text{Urease}} 2NH_4^+ + CO_3^{2-} \quad (1)$$

$$CaCl_2 \longrightarrow Ca_2^+ + 2Cl^- \quad (2)$$

$$Ca_2^+ + CO_3^{2-} \longrightarrow CaCO_3 \text{ (precipitated)} \quad (3)$$

Urease enzyme has been found in various bacteria, fungi, and higher plants. Some of the studies have used plant-derived urease enzyme to increase the shear strength of the soil. Watermelon seed crude extract and urea may be effective to induce the precipitation of calcium phosphate compound. The maximum UCS using the method is 125.6 kPa after 28 days of curing [16]. Meanwhile, plant-derived urease enzyme has a limited lifespan; its activity, and function decrease with time. This limited lifespan is beneficial in soil improvement as the enzyme can naturally degrade and eliminate the long-term effect on the environment [14, 15].

The current study aims to obtain new sources of urease enzyme as a replacement of the purified

enzyme. The crude extract of cabbage and soy pulp, which are both waste materials, was selected in this work and was examined to produce calcite precipitation. Test-tube experiments were performed to determine the effect of the crude extract and to evaluate the material precipitation. The XRD and SEM tests were conducted to observe the effects of crude extract on the mineralogy and morphology of the precipitated materials. This study mainly focuses on replacing commercial urease enzyme with crude extract of cabbage. The use of waste materials may result in lowering the cost and the negative impacts on environments. The current method may be used to increase the soil strength as soil improvement. The schematic of soil improvement with plant-derived urease is shown in Fig. 1.

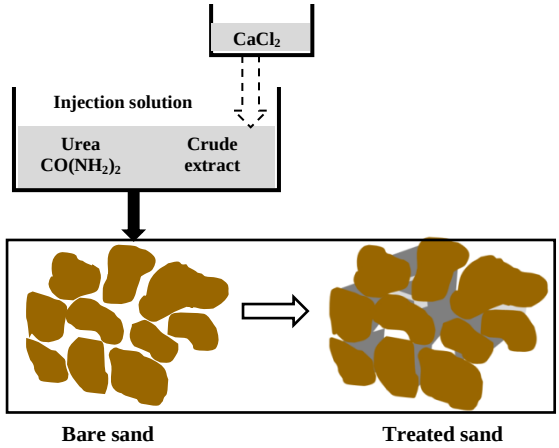

Fig. 1 Schematic of soil improvement using calcite precipitation with plant-derived urease enzyme

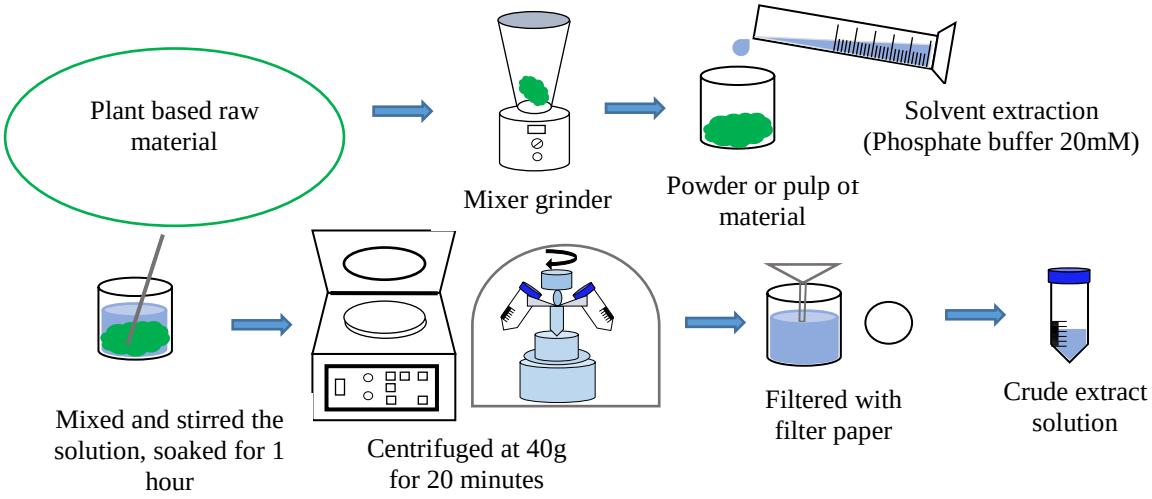

Fig. 2 Procedures of the make the crude extract

2. METHODOLOGY

2.1 Extraction of Urease Enzyme

The crude extract from plant-derived urease was performed as follows: the plant-based raw material was finely ground using a mixer grinder, and 1.5 g of the pulp or powder was soaked in 0,1L of solution with 20mM buffer phosphate as a solvent extraction for 1 hour with occasional agitation. The suspension was then centrifuged, stirred at 40 g for 20 minutes and the clear or slightly turbid solution without dregs was produced, and then filtered using filter paper (pore size 11μm) to remove the undissolved particles of crude extract. The procedures to make a crude extract from the plant-based raw material are illustrated in Fig. 2.

2.2 Test-Tube Experiment

In this experiment, the precipitation of calcium carbonate was evaluated directly in transparent test tubes. The solution consisted of 15 g/L of crude extract and 1mol/L urea and calcium chloride. Urea-$CaCl_2$ was mixed with distilled water. The combination of Urea-$CaCl_2$ and the crude extract source of urease solution were mixed thoroughly to make a total solution volume of 30 mL and allowed to react until the system reached the steady state. During the entire curing time, the test tubes were kept in a box without shaking, and the samples were always cured at a room temperature of 20°C. The precipitation of $CaCO_3$ was produced after curing time (2 weeks), and the solution was filtered with filter paper. The procedures of a test-tube experiment with crude extract are illustrated in Fig. 3. The particles deposited on the filter paper and the particles remained in the tubes were dried at 60°C

for 24 hours. The precipitation ratio, which is the ratio of actual mass of the precipitated materials to the theoretical mass of the maximum precipitation of calcium carbonate, is determined as the equation below:

$$\textbf{precipitation ratio}\ (\%) = \frac{\textbf{actual mass}\ (a_m)}{\textbf{theoretical mass of}\ CaCO_3 (t_m)} \quad (4)$$

$$t_m = C \times V \times M \quad (5)$$

Where a_m is mass of the precipitated materials obtained from the test (g); t_m theoretical mass of $CaCO_3$ (g); C is concentration of the solution (mol/L); V is the volume of the solution (L); and M is molar mass of $CaCO_3$ (100.087 g/mol).

The comparison of the precipitation ratio between commercial urease enzyme and plant-derived urease enzyme was conducted to determine the effect of the crude extract used in this work.

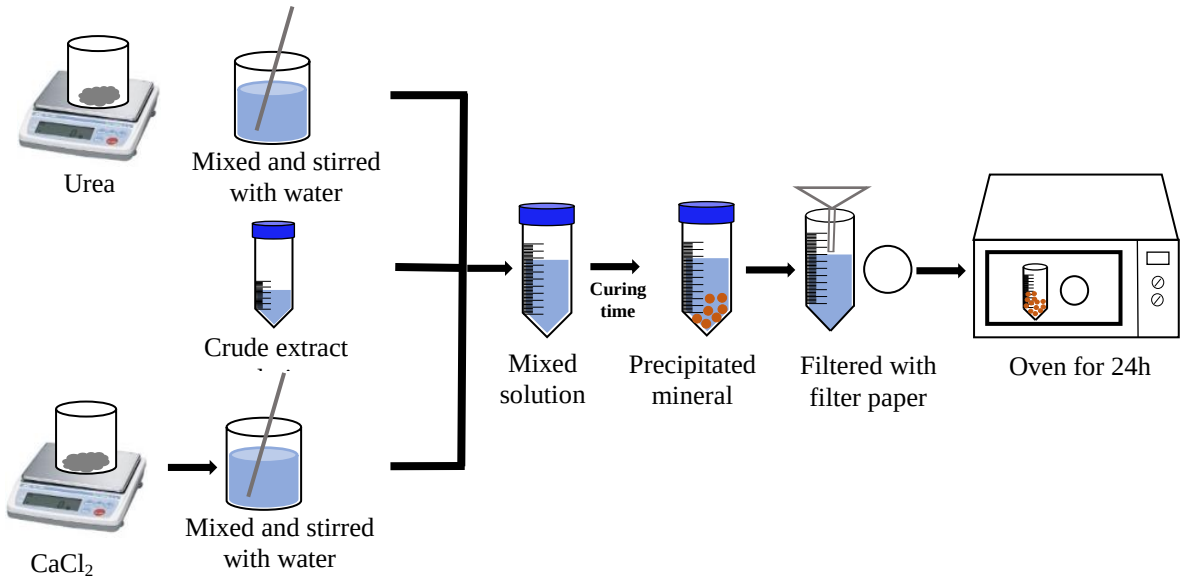

Fig. 3 Procedures of test tube experiments

3. RESULTS AND DISCUSSION

The addition of the crude extract of cabbage and soy pulp as a replacement of urease enzyme for the test-tube experiment may be effective to produce precipitation. The precipitation ratios of various sources of urease enzyme with concentration 1 mol/L of urea-$CaCl_2$ and 15 g/L of urease for several curing time were evaluated. A summary of the precipitation ratio obtained from the experiments are shown in Fig. 4.

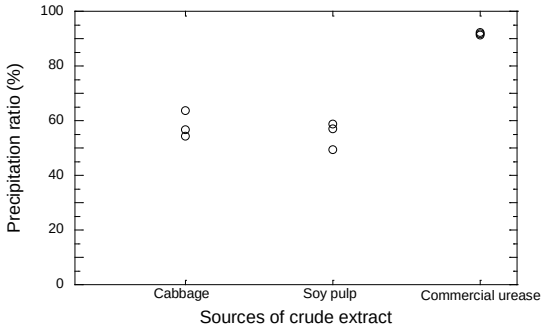

Fig. 4 The comparison test-tube experiment result between plant-derived urease and commercially of urease enzyme.

According to Fig. 4, the average of the precipitation ratio from the crude extract of cabbage and soy pulp is more than half of the precipitation ratio of the purified commercial product.

The addition of crude extract from cabbage and soy pulp should be effective to produce mineral precipitation.

The precipitation was assessed by X-Ray Diffraction (XRD) to confirm the occurrence of mineral. The obtained results are shown in Figure 5. The x-axis of XRD graph analysis indicates the 2θ of minerals while the y-axis represents the intensity. The main peak intensity of the materials was plotted on the curve and was compared with the intensity of the main peak of calcium carbonate. The growth of the crystal phase was observed by SEM, which is shown in Fig. 6. In Fig. 6(a), the crystal structure image of the precipitated materials obtained using the crude extract of cabbage is obvious, and in Fig. 6(b) rhombohedral precipitation is obtained when using the crude extract of soy pulp. The rhombohedral shape of precipitated material was also apparent when the extract of cabbage without purification is used to replace the commercial urease enzyme. Furthermore, the agglomeration form is also promoted in addition to rhombohedral shape. The using of extract soy pulp without purification

also has the significant effect on the precipitated material. The polymorph and agglomeration carbonate precipitated are obtained. The different shape of precipitated material resulting from the use of cabbage and soy pulp may be affected by the urease activity in the cabbage higher than soy pulp. Hence, the crystallization process on the soy pulp hasn't completed yet in the curing time of 2 weeks. The previous research reported that the delaying of precipitated process may promote the agglomeration form in the precipitated material [20].

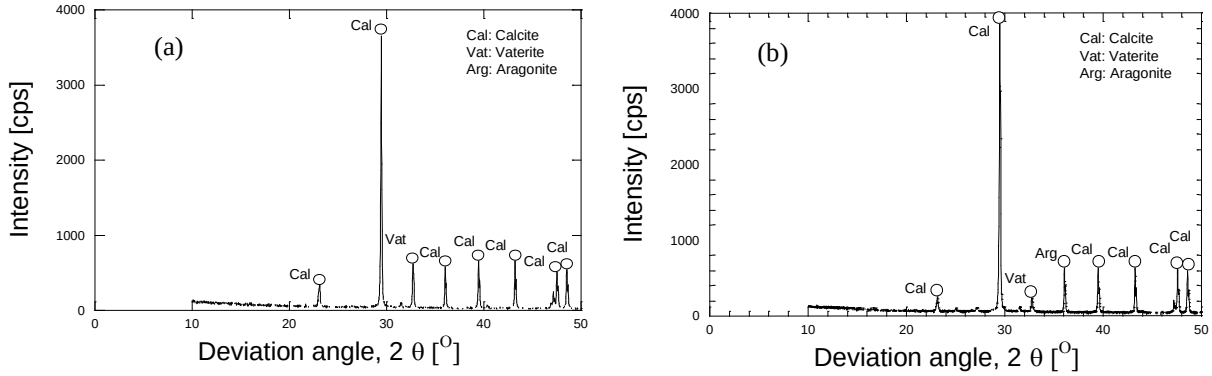

Fig. 5 X-Ray Diffraction (XRD) spectra confirming the polymorph of crystals: (a) cabbage (b) soy pulp

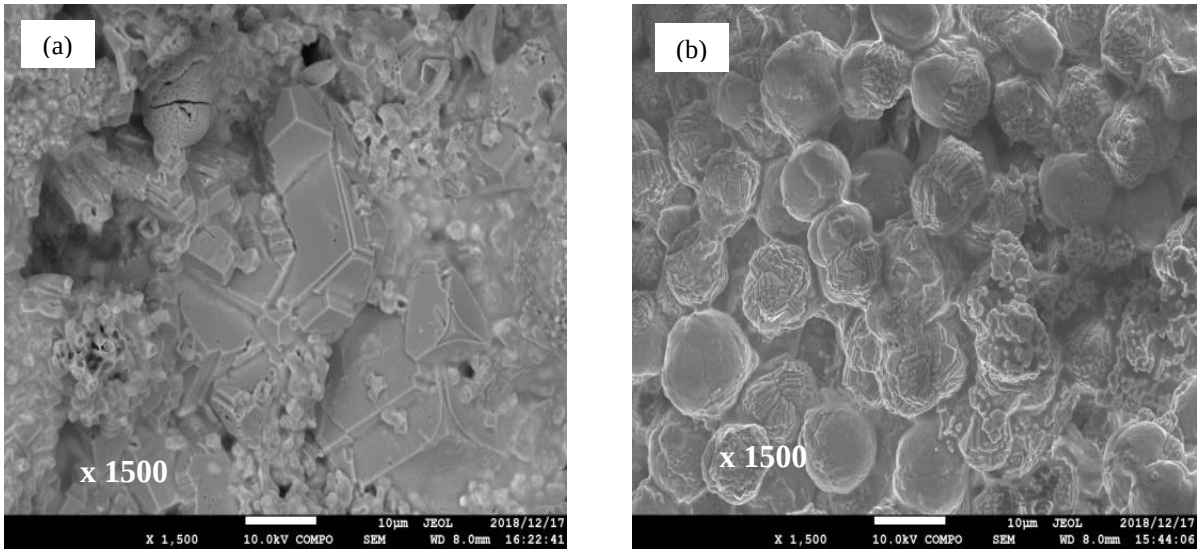

Figure 6. SEM images of calcium carbonate precipitated: (a) crude extract of cabbage (b) the crude extract of soy pulp

4. CONCLUSIONS

The possibility of plant-derived urease enzyme as bio-catalyst in enzyme-mediated calcite precipitation (EMCP) method has been evaluated. Development of alternative sources for urease enzyme, which are cost-effectiveness and easy to be controled in the natural environment, is the crucial issue in the sustainability of calcite precipitation technique. In this study, the applicability of extract of cabbage and soy pulp as the bio-catalyst instead of the commercial urease enzyme was examined. The results of the test-tube experiment show that the precipitated materials of 40-60% are achieved using the cabbage and soy pulp without purification as the bio-catalyst. The mineralogical analysis of precipitated material using XRD confirms that the polymorph of calcite, aragonite, and vaterite are promoted. The SEM analysis has shown that the utilization of cabbage and soy pulp results in the different shape of precipitated material. The cabbage promotes the rhombohedral crystal, and the polymorph precipitated material is promoted by the utilization of soy pulp. The results of this study indicate that the plant-derived urease enzyme using the crude extract of cabbage and soy pulp is the potential source for urease enzyme in the EMCP method.

5. ACKNOWLEDGMENTS

This work has been partly supported by a research grant from the Penta-Ocean Construction Co. Ltd. Their support is gratefully acknowledged.

6. REFERENCES

[1] Akiyama, M. and Kawasaki, S. (2012), "Microbially mediated sand solidification using calcium phosphate compounds," Engineering Geology, 137, 29-39.

[2] Ivanov, V. and Chu, J. (2008), "Applications of microorganisms to geotechnical engineering for bioclogging and biocementation of soil in situ," Reviews in Environmental Science and Biotechnology, 7(2), 139-153.

[3] Putra, H., Yasuhara, H., and Kinoshita, N. (2017). "Optimum condition for the application of enzyme-mediated calcite precipitation technique as soil improvement method," in Advanced Science Engineering Information Technology. Vol. 7, No. 6.

[4] Harkes, M.P., van Paassen, L.a., Booster, J.L., Whiffin, V.S., and van Loosdrecht, M.C.M. (2010), "Fixation and distribution of bacterial activity in sand to induce carbonate precipitation for ground reinforcement," Ecol. Eng., 36(2), 112-117.

[5] Van Paassen, L.a., Harkes, M.P., Van Zwieten, G.a., Van Der Zon, W.H., Van Der Star, W.R.L. and Van Loosdrecht, M.C.M. (2009), "Scale up of BioGrout: A biological ground reinforcement method", Proceedings of the 17th International Conference on Soil Mechanics and Geotechnical Engineering: The Academia and Practice of Geotechnical Engineering, Alexandria, Egypt, October, pp. 2328-2333.

[6] Sidik, W.S., Canakci, H., Kilic, I.H. and Celik, F. (2014), "Applicability of biocementation for organic soil and its effect on permeability." Geomech. Eng., Int. J., 7(6), 649-663.

[7] Whiffin, V.S., van Paassen, L.a. and Harkes, M.P. (2007), "Microbial carbonate precipitation as a soil improvement technique," Geomicrobiol. J., 24(5), 417-423.

[8] Yasuhara, H., Hayashi, K., and Okamura, M. (2011). Evolution in mechanical and hydraulic properties of calcite-cemented sand mediated by biocatalyst. Geo-Front. 2011, 3984–3992.

[9] Yasuhara, H., Neupane, D., Hayashi, K. and Okamura, M. (2012), "Experiments and predictions of physical properties of sand cemented by enzymatically-induced carbonate precipitation," Soil Found., 52(3), 539-549.

[10] DeJong, J. T., Mortensen, B. M., Martinez, B. C., and Nelson, D. C. (2010). Bio-mediated soil improvement. Ecol. Eng. 36, 197–210.

[11] Martinez, B. C., DeJong, J. T., Ginn, T. R., Montoya, B. M., Barkouki, T. H., Hunt, C., et al. (2013). Experimental optimization of microbial-induced carbonate precipitation for soil improvement. J. Geotech. Geoenviron. Eng. 139, 587–598.

[12] Neupane, D., Yasuhara, H., Kinoshita, N., and Unno, T. (2013). Applicability of enzymatic calcium carbonate precipitation as a soil-strengthening technique.

[13] Knorr, B., 2014. Enzyme-induced carbonate precipitation for the mitigation of fugitive dust. A thesis for the degree Master of Science. Arizona State University.

[14] Marzadori, C., Miletti, S., Gessa, C., Ciurli, S., 1998. Immobilization of jack bean urease on hydroxyapatite: urease immobilization in alkaline soils. Soil Biol. Biochem. 30, 1485–1490.

[15] Pettit, N.M., Smith, A.R.J., Freedman, R.B., Burns, R.G., 1976. Soil urease: activity, stability, and kinetic properties. Soil Biol. Biochem. 8, 479–484

[16] Dilrukshi, R.A.N., Watanabe, J., Kawasaki, S. (2015), Sand cementation test using plant-derived urease and calcium phosphate compound. Mater. Trans. 56 (9), 1565–1572.

[17] Chung, F.H. Quantitative interpretation of X-ray diffraction patterns of mixtures. III. Simultaneous determination of a set of reference intensities. J. Appl. Crystallogr. 1975, 8, 17–19.

[18] Chipera, S.J., Bish, D.L. Fitting full x-ray diffraction patterns for quantitative analysis: a method for readily quantifying crystalline and disordered phases. Adv. Mater. Phys. Chem. 2013, 3, 47–53.

[19] Connolly, J.R. Introduction quantitative x-ray diffraction methods. fundamentals of x-ray powder diffraction; Nuevo Mexico University: Albuquerque, NM, USA, 2012.

[20] Putra, H., Yasuhara, H., and Kinoshita, N., Neupane, D., Lu, C.W., (2017). "Effect of magnesium as substitute material in enzyme-mediated calcite precipitation for soil-improvement technique," in Bioengineering and Biotechnology. Vol. 4.

9th Int. Conf. on Geotechnique, Construction Materials and Environment, Tokyo, Japan, 20-22 November 2019, ISBN: 978-4-909106025 C3051

AN EXPERIMENTAL STUDY ON THE EVOLUTION OF UNSATURATED SOIL PARAMETERS DUE TO VARIOUS DEGREE OF SATURATION

Galih Bhekti Sula Pratama[1], Roh Santoso Budi Waspodo[1], and Heriansyah Putra[1]
[1]Department of Civil and Environmental Engineering, Faculty of Agricultural Technology and Engineering, IPB University (Bogor Agricultural University), Bogor, Indonesia

ABSTRACT

Landslide is a natural disaster that often occurs in Indonesia, which is associated with the rainy season. Infiltration of water from rainfall increases the degree of saturation; thus, the reducing of the shear strength parameters of soil and promote the imbalanced of the slope. Understanding of slope failure of the mechanism is the main challenge in the slope stability analysis due to rainfall. The evolution of the engineering properties of soil as the effect of water infiltration during the rainfall should be fixed. Undisturbed samples of well-graded silty sand (SW-SM) and silty sand (SM) from the site are used as the soil sample in this study. In this study, the experimental works are conducted to evaluate the evolution of unsaturated soil parameters, i.e., suction, cohesion, and internal friction angle in various degree of saturation. The filter paper tests are conducted to evaluate the matric suction of soil and develop the soil water characteristic curve (SWCC). Shear strength parameters of soil sample are examined using direct shear test method with the normal stress of 0.5, 1.0, 1.5 kgf. The results of this study show that the correlation of various degree of saturation and evolution of matric suction and shear strength parameters. The increase in the degree of saturation brings about the reduction in suction and shear strength parameters.

Keywords: Unsaturated soil, Shear strength, Suction, Slope stability

INTRODUCTION

Landslide is a geological phenomenon and one of the most scattered disasters on various surfaces of the earth. This phenomenon is indicated by the presence of large-scale soil movements, both in the form of rock falls, slope failures or shallow discharge flows, which can occur inland, coast and sea environments [1]. Landslide is a natural disaster that often occurs in Indonesia, which is associated with the rainy season [2]. Infiltration of water from rainfall increases the weight and degree of saturation of the soil [3], [4]. This condition is corresponding to reduce the suction of the soil . Decreasing suction of the soil, can make the normal stress of the soil decrease and result in the decrease of soil shear strength. Finally, it will promote the imbalanced of the slope [5]

Research about the landslide induced by rainfall has been studied extensively [2]-[17]. Understanding of slope failure mechanism is the main challenge in the slope stability analysis due to rainfall. The evolution of the engineering properties of soil as the effect of water infiltration during the rainfall should be fixed. In this study, Undisturbed samples such as well-graded silty sand (SW-SM) and silty sand (SM) from the site are used as the soil sample. The experimental works are conducted to evaluate the evolution of unsaturated soil parameters, i.e., suction, cohesion, and internal friction angle in various degree of saturation. The filter paper tests are conducted to evaluate the matric suction of soil and develop the soil water characteristic curve (SWCC). Shear strength parameters of soil sample are examined using direct shear test method with the normal stress of 0.5, 1.0, 1.5 kgf. Finally, all data were analyzed, and the mechanism of slope failure has known. Hence, the slope failure can be predicted, and the effect of the landslide can be minimized.

METHODOLOGY

Material

Undisturbed samples from Raya Puncak street were collected in March 2019 as the specimen of this experimental work. The undisturbed samples are well-graded silty clay (SW-SM) and silty clay (SM) that classified by USCS method.

Soil Water Characteristic Curve (SWCC)

The soil-water characteristic curve (SWCC) expresses the relationship between matric suction and gravimetric water content, volumetric water content or saturation [18]. The SWCC is a fundamental soil characteristic, which is necessary to determine parameters of many processes in the soil such as infiltration, drainage, solute movement, and water

availability for plants. It is also an essential tool in the study of the strength and deformation of unsaturated soil [19], [20].

In this study, Whatman 42 filter paper based on ASTM D5298-2003 was used to measure the evolution of the matric suction in various degree of saturation of the soil. The scheme of the filter paper method is depicted in Figure 1. Two blocks of the soil samples were prepared inside the core cutter cylinder as the container. Three layers of filter paper were put between the soil samples. The sample was kept in the vacuum condition for 7 days to approach the equilibrium condition. The initial and final mass of the soil samples and filter paper were measured to know the water content of each case and develop the degree of saturation.

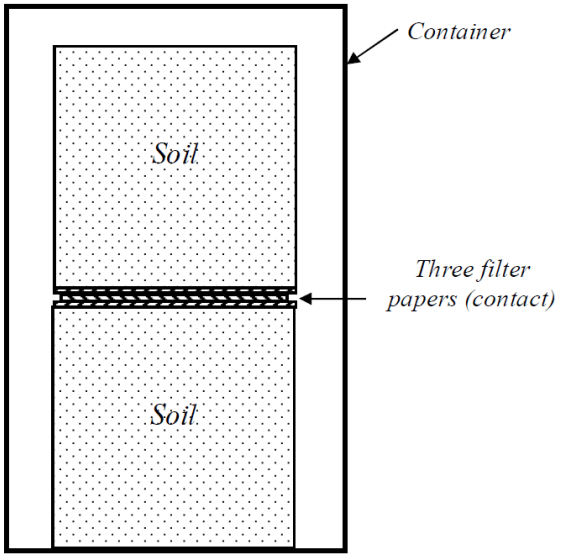

Fig. 1 Scheme of the filter paper method [21]

A calibration curve based on ASTM D5298-03 in Figure 2 is used to obtain the matric suction from the water content of the filter paper.

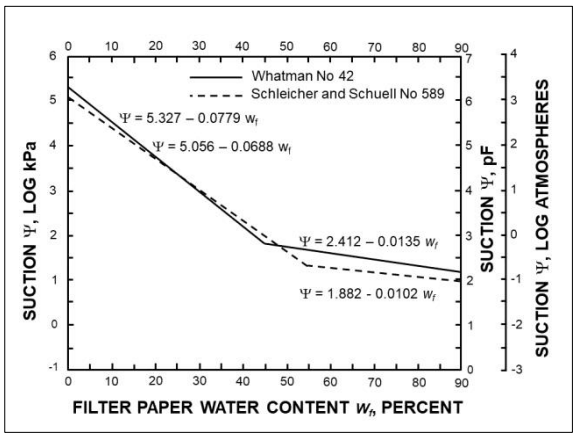

Fig. 2 Calibration curve for the matric suction [21]

Direct Shear Test

The direct shear test is a laboratory test that used to measure the shear strength parameters of soil such as cohesion and internal friction angle [22]. In this study, the direct shear test was performed on silty sands in several degrees of saturation condition. It conducted according to the ASTM standard for the direct shear test (ASTM D3080-11).

The test is performed on three specimens for each sand from a remolded soil sample. The specimen is placed in a shear box which has two stacked rings to hold the sample. The contact between the two rings is at approximately the mid-height of the sample. The normal stress of 0.5, 1.0, 1.5 kgf is applied vertically to the specimen, and the upper ring is pulled laterally until the sample fails, or through a specified strain.

The load applied and the strain induced is recorded at frequent intervals to determine a stress-strain curve for each confining stress. Several specimens are tested at varying confining stresses to determine the shear strength parameters, the soil cohesion (c) and the angle of internal friction, commonly known as friction angle (ϕ). The results of the tests on each specimen are plotted on a graph with the peak (or residual) stress on the y-axis and the confining stress on the x-axis. The y-intercept of the curve which fits the test results is the cohesion, and the slope of the line or curve is the friction angle.

Fig. 3 Direct shear test tool

Experimental Condition

Experimental conditions for matric suction test and shear strength test experiments to evaluate the effect of degree of saturation on soil parameters changes are beginning from wet condition to dry condition (drying process) — each experiment conducted in five various degrees of saturation. Undistributed samples are used for matric suction test, and remolded samples are used for the shear strength test. Each soil samples are modified on wetting weight using oven to obtained various condition. The degree of saturation can be measured by knowing the specific gravity and initial condition

of the soil. A formula to measure the degree of saturation refers to Eq. (1).

$$Sr = \left(\frac{Wb - Ww}{V - \left(\frac{Wd}{Gs}\right)}\right) \quad (1)$$

where ;
Sr : the degree of saturation
Ww : wet weight
Wd : dry weight
Gs : specific gravity
V : volume of specimen

RESULT AND DISCUSSION

Laboratory Test

The laboratory test results for physic and mechanical properties of soil are present in Table 1. Two types of soil were examined in this work. The saturation condition was obtained in the initial state.

Table 1 Physic and mechanical properties of two type soil samples

Parameters	SW-SM	SM
Spesific gravity, Gs [-]	2,593	2,508
Initial water content, *w* [%]	62,5	52
Initial saturation, Sr [%]	86,2	92,7
Porosity, n [-]	0,70	0,63
Dry density, γ_d [g/cm^3]	0,83	1,02
Permeability, k [cm/s]	0,35	0,0036
Liquid limit, LL [%]	56,7	66,6
Plastic limit, PL [%]	32,3	34,2
Plasticity index, PI [%]	24,4	32,4

Two types of soil were classified based on the USCS (United States Classification Soil) method by using grain size distribution data and atteberg limit test data. Soil 1 was classified as well-graded silty sand with SW-SM symbols. Soil 2 was classified as silty sand with SM symbol. Grain size distribution curve for soil 1 and soil 2 are depicted in Fig. 4 and Fig. 5. All of the curves was fitted with the unimodal method by using Soil Vision program. Vision for two types of soil are depicted in Fig. 6

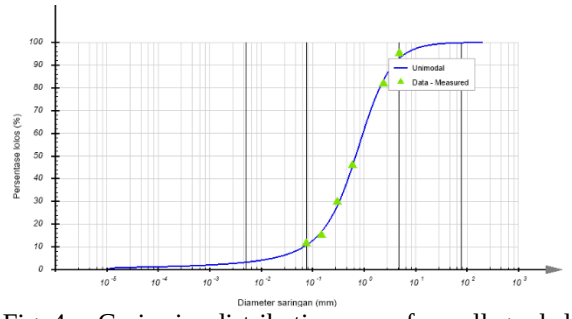

Fig. 4 Grain size distribution curve for well-graded silty sand (SW-SM)

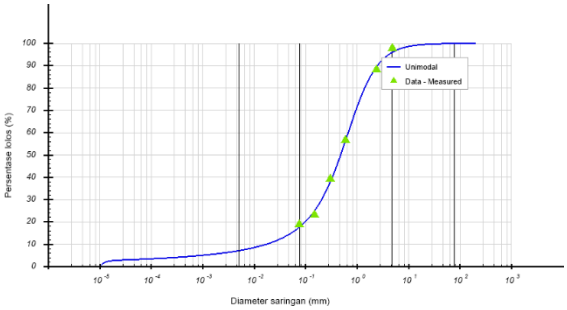

Fig. 5 Grain size distribution curve for silty sand (SM)

(a) (b)

Fig. 6 (a) Well-graded silty sand, (b) Silty sand

Evolution of Matric Suction

Filter paper method was conducted in various degree of saturation. Five conditions were obtained in this test for each type of soil. The drying method was used to reduce the water content for each condition. Each condition after drying was used in the filter paper test. Table 2 presents the matric suction for each type of soil sample in several conditions of the degree of saturation. Calibration curve in Figure 2 is used to obtain the matric suction.

Table 2 Summary result for matric suction test of two type of soil

Cases	Well-graded silty sand		Silty Sand	
	Sr [%]	Matric Suction [kPa]	Sr [%]	Matric Suction [kPa]
1	75,2	4,8	86,1	17,3
2	62,8	14,1	66,2	796,4
3	51,0	1786,8	59,2	2814,6
4	38,7	5181,4	26,3	96764,5
5	25,0	38297,5	24,7	106361,6

Soil Vision program was performed to fit the soil-water characteristic curve (SWCC) from the matric suction experimental data. The fitting curves are depicted in Fig. 7 for well-graded silty sand (SW-SM) and Fig. 8 for silty sand (SM). In these cases, 3 formulas are used to fit the SWCC curve. They are Freedlund and Xing,Van Genucthen, Brooks and Corey. The highest coefficient of the determinant (R^2) for each equation is picked for the fitting of SWCC. The highest R^2 for each SWCC curves is Freedlund and Xing formulas. The value is 0,9032 for well-

graded silty sand and 0,9708 for silty sand.

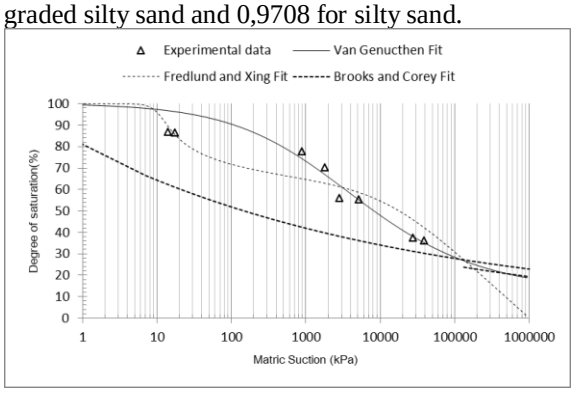

Fig. 7 SWCC for well-graded silty sand (SW-SM)

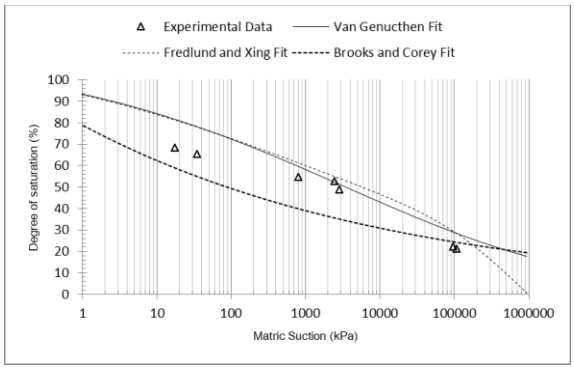

Fig. 8 SWCC for silty sand (SM)

Evolution of Shear Strength Parameters

The direct shear test was conducted in various degree of saturation. Five conditions of the degree of saturation were obtained in this test for each type of soil. Three remolded samples for each condition are used as a specimen of the test. The dry density of initial condition for each soil type is used as a control when the samples are remolded. Table 3 and 4 present the result of shear strength test for well-graded silty sand (SW-SM) and silty sand (SM). There is a change of soil shear strength parameter for each condition of the degree of saturation. The value of cohesion achieved in less than 1 kN/m^2 for each soil. This result confirmed that soil with sand type has a little cohesion value . It can be caused by the surface roughness of the soil [23].

Table 3 Summary result for the shear strength test of well-graded silty sand (SW-SM)

Cases	Dry density (γ_d) [gr/cm^3]	Saturation (Sr) [%]	Cohesion (c) [kN/m^2]	Internal friction angle (φ) [°]
1	0,83	9,4	0,29	11,3
2	0,83	32,7	0,26	9,7
3	0,83	45,9	0,24	10,2
4	0,82	88,8	0,19	10,2
5	0,81	90,2	0,09	6,3

Table 3 Summary result for the shear strength test of silty sand (SM)

Cases	Dry density (γ_d) [gr/cm^3]	Saturation (Sr) [%]	Cohesion (c) [kN/m^2]	Internal friction angle (φ) [°]
1	1,05	22,7	0,71	11,3
2	1,09	49,3	0,58	16,7
3	1,07	58,2	0,53	16,5
4	1,06	71,9	0,46	12,1
5	1,00	92,7	0,42	9,94

Both table 2 and 3 show that the internal friction angle has constant values, relatively.Value of internal friction angle for well-graded silty sand is about 6,7˚ until 11.3˚, and internal friction angle for silty sand is about 9.94˚ until 16.7˚. The change of internal friction angle value caused by dissimilarity of dry density of the soil.

Fig. 9 presents the evolution of cohesion for each soil type in various degree of saturation. Saturation of the soil effect on the change of cohesion. The increasing degree of saturation of the soil corresponding to reducing the value of cohesion. Well-graded silty sand has a value of cohesion lower than silty sand. It caused by the grain size of the soil. Silty sand has more fine materials than well-graded silty sand so it will affect the cohesion of the soil. It appropriate for the research conducted by Nugroho 2011. If a soil has more fine materials, it will increase the cohesion of the soil [24]

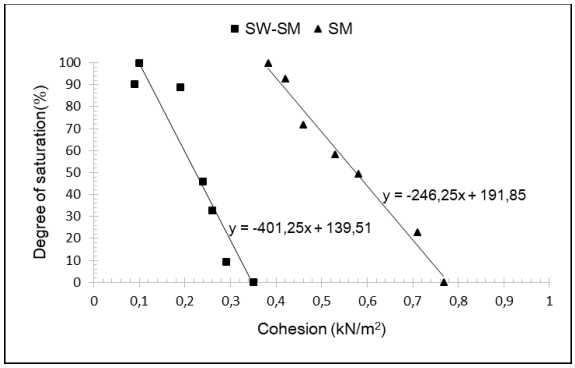

Fig. 9 Evolution of cohesion for each soil type

Correlation of Saturation, Matric Suction, and Cohesion

Shear stress is essential parameter in geotechnical engineering. SWCC that expresses the relationship between matric suction and gravimetric water content, volumetric water content or saturation is the primary tool to predict shear strength parameter in

unsaturated soil. Beside cohesion and internal friction angle, the value of matric suction also affects on shear stress of unsaturated soil.

Fig. 10, and Fig. 11 present the change of cohesion and matric suction effected by soil saturation changes. Fig. 10 curves for well-graded silty sand and Fig. 11 curves for silty sand. There is a correlation between the various degree of saturation and the evolution of matric suction and shear strength parameters. The increase in the degree of saturation brings the reduction in suction and shear strength parameters. The shear strength of the soil increases as matric suction increases. It has similarity with research conducted on sandy clay soil [24]

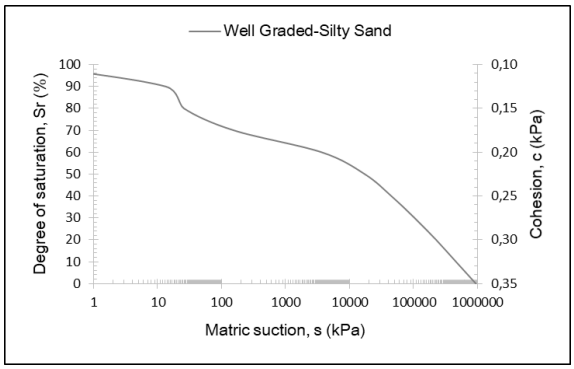

Fig. 10 Correlation between saturation, matric suction and cohesion on well-graded silty sand (SW-SM)

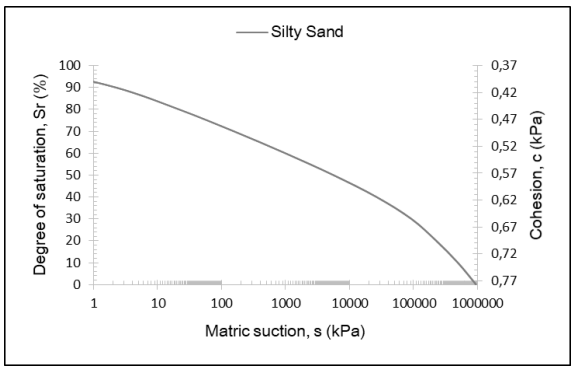

Fig. 10 Correlation between saturation, matric suction and cohesion on silty sand (SM)

CONCLUSIONS

The effect of infiltration induced by rainfall on the unsaturated soil parameters was evaluated. Laboratory experiments are conducted to obtain the significant effect of soil parameters changes influenced by soil saturation. Soil Vision knowledge-based system was used to give an approximation of the entire soil water characteristic curve (SWCC) using a proper curve fitting equation which represents measurable data points. In this study, Freedlund and Xing equation was utilized. Based on the results of fitting of SWCC, the value of correlation coefficient (R^2) is 0,9032 for well-graded silty sand and 0,9708 for silty sand.

The results of this study show that there is a correlation between the various degree of saturation and evolution of matric suction and shear strength parameters. The increase in the degree of saturation brings about the reduction in suction and shear strength parameters.

REFERENCES

[1] Cruden D M, A Simple Definition of A Landslide, Bulletin International Association for Engineering Geology, Vol 43, 1991, pp. 22-29

[2] Pramusandi S, Rifa'i A, Suryolelono K B, Determination of Unsaturated Soil Properties and Slope Deformation Analysis due to the Effect of Varies Rainfall, Poli Teknologi, Vol 10, Issue 1, 2011, pp. 9-21

[3] Pierson T C, Piezometric Response to Ainstorms in Forested Hillslope Drainage Depressions, Journal of Hydrology. Vol 19, 1980, pp. 1–10.

[4] Huang L J, Lin X S, Study on Landslide Related to Rainfall. Journal of Xiangtan Normal University (in Chinese, Natural Science Edition), Vol 24, Issue 4, 2002, pp. 55- 62.

[5] Hardiyatmo H C, Tanah Longsor Dan Erosi, Kejadian dan Penanganan., 2006, Gadjah Mada University Press.

[6] Lim T T, Rahardjo H, Chang M F, Fredlund D G, Effect of Rainfall on Matric Suction in a Residual Soil Slope. Canadian Geotechnical Journal. Vol. 33, Issue 4, 1996, pp. 618-628

[7] Muntohar A S, Liao H J, Rainfall Infiltration: Infinite Slope Model for Landslides Triggering by Rainstorm, Natural Hazards, Vol 54, Issue 3, 2010, pp. 967-984.

[8] Muntohar A S, Ikhsan J, Liao J H, Influence of Rainfall Patterns on the Instability of Slopes, Civil Engineering Dimension, Vol 15, Issue 2, 2013, pp. 120-28.

[9] Muntohar A S, Ikhsan J, Soebowo E, Mechanism of Rainfall Triggering Landslides in Kulonprogo Indonesia. Geo-Congress 2013 © ASCE 2013, 2013, pp. 452-461.

[10] Muntohar A S, Muhammad Uradi, Fourie A, Development A Boundary of Rainfall-Induces the Stability of A Residuals Soils Slope in Northern Territory Australia, Seminar Nasional Geoteknik 2014 Yogyakarta, 2014, pp. 133-137.

[11] Karnawati D, Pengaruh Kondisi Vegetasi Dan Geologi Terhadap Gerakan Tanah Dengan Pemicu Hujan. Media Teknik, Vol 3, 2006, pp. 12-22.

[12] Mustafa M R, Isa M H, Rezaur R B, Rahardjo H, Data-Driven Modelling for Pore Water Pressure Variation Responses to Rainfall.

Sustainable Development, Vol 1, 2015, pp. 447-55.

[13] Rahardjo H, Leong E C, Rezaur R B, Studies of Rainfall-induced Slope Failures, Proceedings of the national seminar, Slope, 2002, pp. 15-29.

[14] Wang, Gonhui, Suemine A, Furuya G, Kaibori, M, Sassa K, Rainstorm-Induced Landslides at Kisawa Village Tokushima Prefecture, Japan, August 2004, Landslides, Vol 2, Issue 3, 2005, pp. 235-242.

[15] Haryanti, Sri, Suryolelono K B, Jayadi R, Analisis Pengaruh Karakteristik Hujan Terhadap Gerakan Lereng, Jurnal Ilmiah Semesta Teknika, Vol 13, Issue 2, 2010, pp. 105-15.

[16] Rifa'i A, Effect of Matric Suction Changes on Unsaturated Soil Parameter Slope Stability Analiysis due to Rainfall, Seminar Nasional-1-BMTTSSI-Konteks, Sumatera Utara, 2011, G15-G23.

[17] Suradi M, A. Fourie C, Beckett, Buzzi. O, Rainfall-Induced Landslides: Development of a Simple Screening Tool Based on Rainfall Data and Unsaturated Soil Mechanics Principles, Unsaturated Soils: Research & Applications. (April 2016), 2014, pp. 1459-1465.

[18] Xiaoli F., Shao M, Lu D, Wang H, Soil Water Characteristic Curve Measurement Without Bulk Density Changes and Its Applications in The Estimation of Soil Hydraulic Properties. Geoderma. Vol 176, Issue 178, 2011, pp. 1-8.

[19] Vanapalli S K, Fredlund D G, Putahi D E, Clifton A, The Model for Matric Prediction of Shear Strength with Respect to Soil Suction, Canadian Geotechnical Journal, Vol 33, 1996, pp. 329-392.

[20] Gerard A, Miller, Khoury Charbel N, Muraleetharan Kanthasamy K, Chunyang L, and Kibbey Tohren C G, Effect of Soil Skeleton Deformation on Hysteretic Soil Water Characteristic Curve : Experiments and Simulations, Water Resources Research, Vol 44, 2008, pp. 1-10.

[21] Putra H, Rifa'i A, Sujono J, Silarukmi, A, Analysis of Unsaturated Soil Parameters as Slope Stability Mitigation, Jurnal Teknologi, Vol 79, Isuue 7-2, 2017, pp. 21-27

[22] Price D G, De Freitas M H, Engineering Geology : Principles and Practice, 2009, Springer, pp. 450.

[23] Braja D M, Advanced Soil Mechanics. 2008, Taylor Francis

[24] Nugroho S A, Putra A I, Ermina R, Korelasi parameter kuat geser tanah hasil pengujian triaksial dan unconfined compression strength (UCS), Jurnal Sains dan Teknologi. Vol 11, Issue 1, 2012, pp. 1-10

[25] Pujiastuti H, Rifa'i A, Adi A D, Farhani T F, The Effect Of Matric Suction On The Shear Strength Of Unsaturated Sandy Clay, International Journal of GEOMATE, Vol 14 , Issue 42, 2018, pp. 112-119.

9th Int. Conf. on Geotechnique, Construction Materials and Environment, Tokyo, Japan, 20-22 November 2019, ISBN: 978-4-909106025 C3051

EFFECT OF CROSS-SECTIONAL SHAPE ON PILLAR STRENGTH

Greg You[1], Dake Zhao[1], Shuo Liu[1] and Zhou Gao[1]
[1]Federation University Australia, Ballarat, Victoria, Australia

ABSTRACT

Pillars of different cross-sectional shapes are widely used in civil and mining engineering. Are different shapes affecting the strength of pillars? Three cross-sectional shapes were designed in this study, which are circular, rectangular and square, and of the same height (150 mm) and the same cross-section area (1963.5mm^2). They were mortar pillars. The diameter of circular specimens is 50 mm, the width and depth of rectangular specimens are 62.67 mm×31.33 mm and the widths of square specimens are 44.31 mm. Uniaxial compressive strength (UCS) and point load strength tests were conducted for 36 specimens to comparatively analyse the effect of different shapes. From this study, it is found that the rectangular pillar has the highest average strength in both UCS and point load strength, while the square pillar has the lowest in both. Both the UCS and point load strength increase with the increase of density of pillars for the three shapes.

Key words: Cross-sectional shape, Pillar strength, Uniaxial compressive strength, Point load strength index

INTRODUCTION

Pillar is a common load-bearing structure in civil and mining engineering. Pillar can be made of steel, masonry, concrete and reinforced concrete in civil engineering, but rock pillars are universally used in underground mines to take the advantage of the self-supporting capacity of rock. Pillars can have different cross-sectional shapes, including circular, square and rectangular. Strength of pillar is an important parameter in pillar design and its application. Does different cross-sectional shape affect the strength of pillar?

Shape effect, which is referred to the pillar width (w) to height (h) ratio, is reported in literature [1]. The strength of pillar (s_p) in coal and hard rock can be calculated using empirical formulas. Coal pillar strength is related to the compressive strength (σ_c) of coal and the shape (w/h) of pillar as shown in Eq. (1) [2].

$$s_p/\sigma_c = 0.778 + 0.222w/h \quad (1)$$

Esterhuizen, Dolinar and Ellenberger [3] reported that pillar strength is influenced by its volume and its shape. The shape effect on the stability of hard rock pillar can be empirically assessed using the ratio of width to height (w/h). When the $w/h > 2$, the likelihood of pillar failure is seldom [4]. Hence, pillar strength, s_p, can be calculated using Eq. (2).

$$s_p = k\, w^{\alpha}/h^{\beta} \quad (2)$$

Where k is a parameter related to the strength of rock, α and β are parameters related to the geomechanical conditions of rock mass [3].

Shown in Table 1 are the average, minimum and maximum w, h and w/h of 91 pillar layouts in 34 mines in the USA [3]. All of the pillar layouts are successful in providing global stability by supporting overburden load up to the ground surface. Pillar failure will occur when a pillar has reached its peak load bearing capacity. As indicated by Eq. (1)-(2), a declining w/h may cause the strength of pillar to rapidly decrease and the potential of pillar failure to increase.

Table 1 Width to height ratio of stone pillar [3]

Dimension	Average	Minimum	Maximum
Pillar width (ft)	43.0	15.0	70.5
Pillar height (ft)	36.5	15.8	124.6
w/h ratio	1.41	0.29	3.52

Del Viso, Carmona and Ruiz [5] studied cube and cylinder specimens, and found that (1) the compressive strength of cubes is higher than that of cylinders, (2) there are different crack patterns between the cubes and cylinders, and (3) the micro cracking is denser in the cubes than in the cylinders specimen. The diameter and height of cylinders were 75mm×150mm and 100mm×200mm, and the dimension of cubes were 33mm×33mm, 50mm×50mm, 67mm×67mm and 100mm×100mm, where the cross-sectional area (CSA) of each specimen is different.

While the shape effect of pillars has attracted many studies, they appear mainly focusing on the w/h ratio. In addition, the w/h ratio of rock pillars ranges from 0.29 to 3.52 with an average of 1.41 in 34 underground mine applications [3]. Its inverse (e.g. h/w) is required greater 2.0 by test standards governing uniaxial compressive strength test [6]. To

better understand the shape effect, this study aims to investigate the effect of different cross-sectional shapes on the strength of pillars of the same height and the same CSA.

RESEARCH METHODOLOGY

Laboratory experiments employed in this study are uniaxial compressive strength (UCS) tests [7] and point load strength index tests [8] according to Australian Standards (AS) [6], [9], [10].

Experimental design

Design of pillar shapes

To investigate the effect of shapes on pillar strength, three different cross-sectional shapes, namely circular, rectangular and square, are selected. All specimens have the same length of 150 mm and the same cross-sectional area of 1963.5 mm^2. The diameter of the circular cross-section is 50 mm, the width of the square one is 44.31mm, and the rectangular cross-section is designed at a width/depth ratio of 2:1, or 62.67mm×31.33mm (Fig. 1).

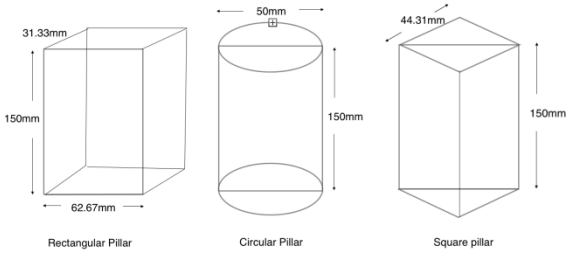

Fig. 1 Shapes and dimensions of the test specimens designed for the study.

Design of the mortar formula

Cement, fine sand and coarse sand are employed to mix the mortar specimens. Water to cement ratio commonly ranges from 0.4 to 0.7 to mix mortar. A water to cement ratio of 0.6 is used for this study. In accordance with mortar mix proportions guidance, cement to sand ratio is 1 cement: 3 sand (60% fine sand and 40% coarse sand) [11]. Thus, the mortar mix formulation is defined as 0.6 water: 1.0 cement: 1.8 fine sand: 1.2 coarse sand. Shown in Fig. 2 are the 18 mixed specimens prepared for the UCS tests. The mixed specimens were cured for 28 days in a curing tank at constant temperature of 21.5℃. The same procedure was followed for the specimens used in the point load strength index tests.

Fig. 2 Model mortar pillars prepared for the UCS tests.

Laboratory test

The procedures of sample preparation and UCS test of specimens were conducted in compliance with the Method 9: Compressive strength tests-Concrete, mortar and grout specimens [9]. In the meantime, the specimens also meet the dimensional requirements specified in the Methods of testing rocks for engineering purposes (Method 4.2: Determination of uniaxial compressive strength) [6]. Liu [7] conducted the UCS tests in this study.

Gao [8] conducted the point load strength tests in this study according to the Methods of testing rocks for engineering purposes (Method 4.1: Determination of point load strength index) [10]. The diametric test method is used as the length to diameter ratio of the circular specimens is three.

TEST RESULTS

Uniaxial compressive strength (UCS) test

18 specimens were tested for UCS, which are six each for square, rectangular, and circular cross-sectional pillars. The test results are tabulated in Tables 2-4, respectively.

Table 2 UCS experimental results of square cross-sectional pillars

No.	Weight, g	Density, kg/m^3	Maximum load, kN	UCS, MPa
1	640	2097.97	44.1	21.70
2	640	2085.17	47.5	23.26
3	636	2089.85	46.1	22.84
4	631	2051.08	42.9	20.97
5	639	2090.83	48.5	23.84
6	618	2003.53	NA	NA

Table 3 UCS experimental results of rectangular cross-sectional pillars

No.	Weight, g	Density, kg/m^3	Maximum load, kN	UCS, MPa
1	633	2099.28	39.4	19.67
2	637	2071.52	49.9	24.37

3	633	2092.86	42.5	21.11
4	637	2094.88	50.6	25.15
5	646	2132.25	55.1	27.34
6	626	2073.40	36.9	18.35

Table 4 UCS experimental results of circular cross-sectional pillars.

No.	Weight, g	Density, kg/m^3	Maximum load, kN	UCS, MPa
1	610	2147.28	38.7	20.37
2	603	2098.99	39.7	20.86
3	610	2106.39	50.9	26.46
4	600	2093.56	NA	NA
5	603	2092.76	NA	NA
6	603	2081.37	NA	NA

Point load strength test

18 specimens were conducted using the diametric point load tests. The point load test results are recorded in Tables 5-7 for square, rectangular, and circular cross-sectional pillars, respectively. The point load strength index was calculated as follows [10]. Firstly, the uncorrected point load strength (I_s, MPa) is calculated by Eq. (3).

$$I_s = \frac{P \times 1000}{D_e^2} \quad (3)$$

Where, P is the load at failure, kN; D_e is the "equivalent core diameter" derived from the Eq. (4), mm.

$$D_e{}^2 = \frac{4 \times A}{\pi} \quad (4)$$

Where, A = CRA, mm^2.

Secondly, the point load strength index, $I_{s(50)}$, is calculated by Eq. (5).

$$I_{s(50)} = I_s \times \left(\frac{D_e}{50}\right)^{0.45} \quad (5)$$

Table 5 Point load test results of square cross-sectional pillars.

No.	Load, kN	D_e, mm	Weight, g	Density, kg/m^3	I_s	$I_{s(50)}$
1	5.5	50.93	650	2162.18	2.12	2.14
2	5.5	50.81	644	2142.56	2.13	2.15
3	4.4	50.84	639	2113.59	1.70	1.72
4	5.0	50.85	649	2146.19	1.94	1.95
5	4.6	50.71	641	2131.55	1.79	1.80
6	5.0	50.64	645	2150.59	1.95	1.96

Table 6 Point load test results of rectangular cross-sectional pillars.

No.	Load, kN	D_e, mm	Weight, g	Density, kg/m^3	I_s	$I_{s(50)}$
1	4.5	50.55	644	2154.24	1.74	1.75
2	5.8	50.84	655	2171.52	2.25	2.26
3	5.3	50.59	651	2184.29	2.07	2.08
4	4.5	50.44	634	2139.91	1.77	1.77
5	5.7	50.71	645	2163.42	2.22	2.23
6	5.3	50.53	643	2157.81	2.08	2.09

Table 7 Point load test results of circular cross-sectional pillars.

No.	Load, kN	D, mm	Weight, g	Density, kg/m^3	I_s
1	4.3	49.40	605	2158.26	1.76
2	5.0	49.57	613	2172.11	2.04
3	5.0	49.38	615	2170.98	2.05
4	5.5	49.49	613	2173.60	2.25
5	5.0	49.46	623	2182.28	2.05
6	4.0	49.37	608	2151.70	1.64

ANALYSIS

The average UCS and the average point load strength index, $I_{s(50)}$, are tabulated in Table 6 for the square, rectangular and circular pillars, respectively. It is interesting to know that the rectangular pillar has the highest strength in both the UCS and point load strength index, while the square pillar has the lowest. However, the difference is not big: the average UCS of rectangular pillars is 0.63% higher than the UCS of square pillars, and the $I_{s(50)}$ is 4.05% higher.

Table 8 Average UCS and $I_{s(50)}$ of square, rectangular and circular pillars

Shape	UCS, MPa	$I_{s(50)}$	Remark
Square	22.52	1.952	Lowest in average UCS and $I_{s(50)}$
Rectangular	22.67	2.031	Highest in average UCS and $I_{s(50)}$
Circular	22.56	1.964	

Shown in Figs. 2-3 are the UCS-density and $I_{s(50)}$-density curve, respectively. The data appear scattered in a narrow band and trend linearly,

indicating that both UCS and $I_{s(50)}$ increase with the increase of density.

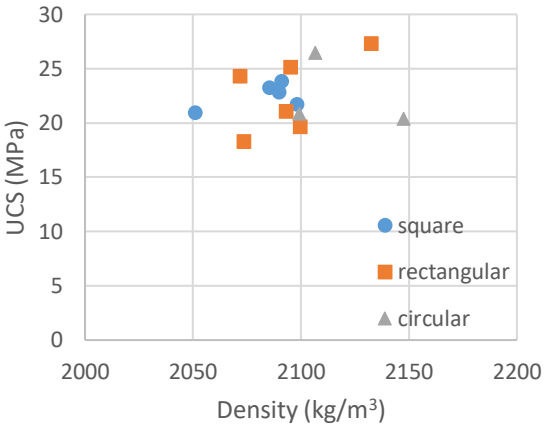

Fig. 3 UCS – density curve of square, rectangular and circular pillars.

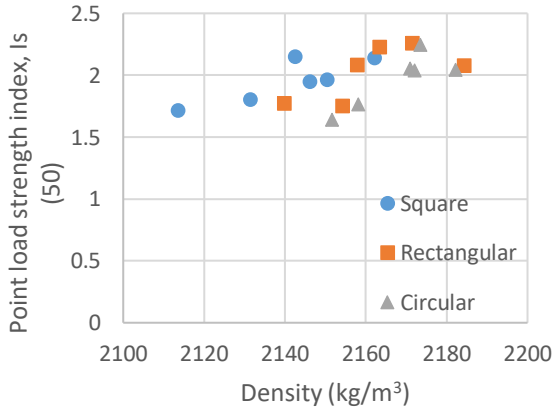

Fig. 4 Point load strength index – density curve of square, rectangular and circular pillars.

CONCLUSION

36 laboratory tests have been conducted to investigate the effect of cross-sectional shapes on the UCS and point load test strength of pillars. The model pillars were made of mortar and the three different cross-sectional shapes are square, rectangular and circular. From the study, it might be concluded that the cross-sectional shapes have some effect on the strength of mortar pillars.

Through the comparative analyses of the average uniaxial compressive strength and point load strength of the three different shapes of pillars, the rectangular specimens have both the highest uniaxial compressive strength and the highest point load strength. On the other hand, the square specimens have the lowest in both strength. However, the difference may not be significant in the uniaxial compressive strength.

Both the uniaxial compressive strength and the point load strength increase with the increase of the density of pillar for all the three different cross sectional shapes.

REFERENCES

[1] Qasim, O., 2018, A Review Paper on Specimens Size and Shape Effects on the Concrete Properties, International Journal of Recent Advances in Science and Technology, 5(3): 13 – 25.Awal A.S.M.A, Hosseini H. and Hossain M.Z., Strength, Modulus of Elasticity and Shrinkage Behaviour of Concrete Containing Waste Carpet Fiber, International Journal of GEOMATE, Vol. 9, Issue 17, 2015, pp. 1441-1446.

[2] Hustrulid, W., 1976, A review of coal pillar strength formulas. Rock Mechanics and Rock Engineering, pp. pages 115-145.Author H., A Book New York Publisher, Year, pp.1-200.

[3] Esterhuizen, G., Dolinar, D., & Ellenberger, J., 2008, Pillar Strength and Design Methodology for Stone Mines. Proceedings of the 27th International Conference on Ground Control in Mining, July 29 - July 31, 2008, Morgantown, West Virginia. Peng SS, Mark C, Finfinger GL, Tadolini SC, Khair AW, Heasley KA, Luo-Y, eds., Morgantown, WV: West Virginia University, 2008; :241-253Kimura S., Journal Paper Title, J. of Computer Science, Vol. 1, Issue 2, 1987, pp. 23-49.

[4] Martin, C., & Maybee, W. (2000). The strength of hard-rock pillars. Rock Mechanics and Mining Sciences, 37 (2000), pp 1239-1246. Hossain M.Z. and Awal A.S.M.A., Experimental Validation of a Theoretical Model for Flexural Modulus of Elasticity of Thin Cement Composite, Const. Build. Mat., Vol.25, No.3, 2011, pp.1460-1465.

[5] del Viso, J., Carmona, J., & Ruiz, G., 2008, Size and Shape Effects on the Compressive Strength of High Strength Concrete, Cement and Concrete Research, 38(3), pp386-395.

[6] AS4133.4.2 -1993, 1993, Methods of testing rocks for engineering purposes, Method 4.2: Determination of uniaxial compressive strength, Australian Standard.

[7] Liu, S., 2017, Effect of Pillar Shape on the Uniaxial Compressive Strength, Honours thesis, Federation University Australia, Victoria, Australia, June 2017.

[8] Gao, Z., 2017, Effect of pillar shapes on the Point load strength, Masters thesis, Federation University Australia, Victoria, Australia, November 2017.

[9] AS1012.9 – 2014, 2014, Method of testing concrete, Method 9: Compressive strength tests-Concrete, mortar and grout specimens, Australian Standard.

[10] AS4133.4.1 -1993, 1993, Methods of testing rocks for engineering purposes, Method 4.1: Determination of point load strength index, Australian Standard.

[11] Cement Australia Pty Limited, 2011, General purpose cement, page 4.

9th Int. Conf. on Geotechnique, Construction Materials and Environment, Tokyo, Japan, 20-22 November 2019, ISBN: 978-4-909106025 C3051

EVALUATING MSE WALL DEFORMATION USING TERRESTRIAL LASER SCANNING AND FINITE ELEMENT MODELLING

Devon Adamson[1], Marolo Alfaro[1], James Blatz[1], and Kent Bannister[2]
[1]Civil Engineering Department, University of Manitoba, Canada; [2]TREK Geotechnical Inc., Canada

ABSTRACT

Mechanically Stabilized Earth (MSE) walls are now commonly used as retaining structures in bridge-approached embankments. They have an ability to accommodate more deformations without structural distress and are cost-effective compared to conventional concrete gravity retaining structures. Engineers prefer to monitor the deformations of the wall during and after construction to verify their design. Instrumentation and/or surveying techniques are commonly used to monitor deformations of structures. Current measuring methods are in discrete locations of the walls and do not provide movement profile of the entire wall. In this study, Terrestrial Laser Scanning (TLS) technique was used to monitor the deformations of newly-constructed MSE walls. TLS uses lasers to create a 3D point cloud in a 360° range of its surroundings with their relative X,Y,Z coordinates. Post-processing of the data in its subsequent computer software register all scans of the wall and develop them into a larger project point cloud. The point clouds are used to determine the deformations from periodic scans. The use of Finite Element Modelling (FEM) will be develop and calibrate the measured deformations into a model of the site. Once calibrated, the numerical model will be used to investigate important factors affecting the performance of the MSE walls. The vertical settlements observed from the TLS compared to the modelling analysis were in agreement with the behavior as well as the magnitudes, 50mm and 106mm in centre and critical sections for TLS and 57mm and 111mm for the modelling respectively.

Keywords: Terrestrial Laser Scanning, Finite Element Modelling, MSE Walls, Deformation

INTRODUCTION

A bridge interchange project began construction in April 2018 to extend across an existing high-speed roadway. The interchange was first proposed as commuter traffic in the area has increased to a point where safety and environmental concerns required action. The bridge interchange has 2 lanes of traffic for the 80km/h speed limit roadway travelling East-West and 2 lanes for the neighbourhood street Northbound and one lane for Southbound at 60km/h. The new bridge has three lanes over the existing roadway. The bridge structure is supported by a total of 21 Cast-In-Place (CIP) belled piles. Approach fills for the bridge are approximately 8 to 9 m high and have an MSE wall face running parallel to the high-speed roadway.

The approach fills are supported by a total of 240 vibration-compacted stone columns (120 each at the North and South Abutments). A study has been undertaken to determine if Terrestrial Laser Scanning (TLS) can provide a reliable and applicable surveying technique to measure movements in the MSE wall and whether Finite Element Modelling (FEM) can predict the actual movements of the wall during and after construction.

Soil stratigraphy observed at site from previous test holes found silty clay overlying clay till. The properties of the silty clay is generally highly plastic and stiff, with a soft transition layer above the till. The clay till is silty with trace to some sand and gravel, has low plasticity, and ranges from firm to very stiff depending on depth **[1]**.

Fig. 1 South Abutment MSE Wall

TLS DETAILS

TLS is a surveying tool that with lasers can measure coordinates of its surroundings in a 3D space by shooting out a web or mesh of data points. The collection of these data points is called a “point cloud” and with the addition of pictures taken by the scanner, objects and surfaces in the point cloud are colourized, replicating the site conditions. Scanning larger objects and areas is done by performing multiple scans along the desired object/surface (in this case it is the MSE wall of a bridge interchange) and then register each scan together using identical targets in each point cloud. These targets can either be cooperative targets like spheres and placards, or

identifiable targets like edges and planes on the bridge structure **[2]**. Registering together the multiple scans create a "project point cloud" which can be used for design, such as settlements and displacements, preliminary site conditions, and inspections for structure integrity **[3]**

The scanner used for the project is the *FARO Focus X330* and uses the software *FARO Scene* for processing the data. The specifications of the scanner includes a ranging error of 0.3mm at 10m with 90%, and a max scan distance of 330m. FARO Scene allows the user to combine scans into the project point cloud by using Target and Cloud-to-Cloud registration. Target registration best fits the scan clouds together using the identical targets for alignment in an X,Y,Z coordinate space. Cloud-to-Cloud registration is a finer registering tool that using the computer software's algorithm, will input parameters such as number of iterations, search distance between data points, and subsampling distance to align point clouds together based on the criteria. After registration is completed, a registration report is produced to show the mean point error, maximum point error, and minimum overlap percentage of data points. This report will allow the user to determine if the registration satisfies the error tolerance required for the application. If the error is out of tolerance, re-registering different targets than aligned previously or using a different registration tool will be required. If the amount of error is accepted, measurements are reported with the registration errors to detail the accuracy of the results. An example of a finished project point cloud is provided in Fig. 2.

Fig. 2 Project Point Cloud of MSE Wall

FINITE ELEMENT MODELLING

FEM is implemented into preliminary design work for its capabilities to simulate foundation soil behavior. FEM is a great tool when there is sufficient testing for soil properties and site conditions are well known. The model will only produce results based on the user parameters. Therefore, the parameters should be carefully selected to best represent site conditions and should not use conservative values without justification as model results will lose validity.

A numerical model was developed using the computer software program Geostudio 2019. The model was built using Geostudio's SIGMA/W model component, running different analysis types to determine the short-term and long-term deformation behaviour of the walls. By using this software, a limitation on the deformation analysis is that Geostudio does not have 3D capabilities and therefore, conversion into 2D parameters is required. Stone columns in the foundation design are spaced in triangular and rectangular grids, expressed in axisymmetric parameters. Using the equivalent area method, the columns are treated as a solid wall with plane strain conditions. This conversion equation is designated as Eq. (1) **[4]**

$$\mathbf{D'} = \frac{\pi \mathbf{D^2}}{4d} \quad (1)$$

Where D = diameter of column, d = spacing of columns, and D' = equivalent diameter of column

Since the orientation of the wall is planar and surcharge loading from the backfill is applied normal to the wall, the assumption for foundation design characteristics to be represented in plane strain may be acceptable.

METHODOLOGY

The laser scanning occurs during construction and post-construction of the wall to determine the displacements of the wall as backfill material is built up in lifts for each row of wall panels is placed (clay material for the embankment and granular material for behind the wall). The scanning schedule began while the first row of panels was erected to establish a baseline for following scans. During construction, it is recommended to scan each row of panels being placed with monthly scans after it has been completed **[5]**. With that in mind, scanning was performed for the completion of the first row, last row, and one intermediate row (May 9, May 25, and June 2, 2018). Post construction was limited to two scans in the summer (July 05 and August 28) with two more scheduled in the summer of 2019 (May 07 and August 06) following the spring thaw to observe and longer term settlement.

The scans were registered using multiple spheres and placards set up around the wall. The wall required multiple scans to gather data points for each panel surface. To reduce bounce back error, each successive scan shall maintain an incident angle of 45° between one another; therefore more scans were required in the range from 4-6. For the scanner to orient itself with the other scans, each scan will need to reference at least 3 targets for X,Y,Z coordinate alignment **[6]**. However, aligning targets in a single line should be avoided as there will be more uncertainty in the control target locations.

FEM of analysis begins with an in-situ phase, establishing initial stress conditions and Pore-Water Pressure (PWP) conditions of the site. This dictates the rate and volume of consolidation the foundation material encounters during construction. Initial stress conditions were formulated from the soil layers, material properties and initial PWP conditions were from an assumed initial phreatic surface. This was set at 505.4m, taken from previous water elevations observed in borehole logs. Following the in-situ phase, subsequent analyses model the effects of the reinforced backfill material during erection of the MSE wall and the clay fill used for the approach embankment; analyses classified in 4 stages: Lift 1, Lift 2, Lift 3, and Lift 4. The analysis type for the staged backfill loading is Load/Deformation as the scope of this paper is to determine the magnitudes of vertical movement and compare how accurate the model is to the TLS results. Boundary conditions include Fixed X/Y movement along the bottom of the clay till and a Fixed X movement along the sides of the model layers. The model boundaries were stretched out far enough that they had no effect on the settlement foundation due to the backfill layers.

The output reports from the model include settlement along the MSE wall plane and cross-sections at the centre of the wall and at the edge of the wall slope section. The particular sloped section is where stormwater and sewer pipes run underneath the stone columns, preventing the columns from reaching till, resulting in the critical section of the wall. Models for each analysis are provided in Fig. 3, 4, and 5.

The model was analyzed using effective-drained conditions with the parameters outlined in Table 1. The parameters were determined reviewing previously completed soils lab testing and recommended modelling values, made available by the foundation design report **[1]**. Effective-drained conditions were considered since preliminary design modelling is used to predict the magnitude of settlement the structure will encounter during its service life. The use of stone columns in the design also act as vertical drains, allowing the PWP to dissipate quickly for immediate consolidation. The subsoil and backfill material were modelled with Linear-Elastic criteria as the stress conditions the materials are loaded with are estimated to be below the yield strength of the soil. Modified Cam Clay (MCC) parameters were used for the soft silty clay layer as MCC can better predict soil behaviour for slightly over-consolidated clay than the linear-elastic model.

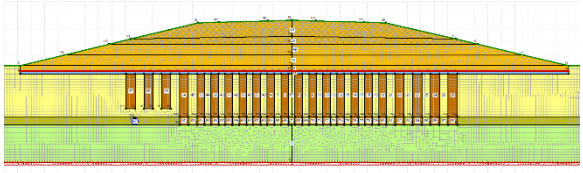

Fig. 3 Model of MSE Wall Cross-Section

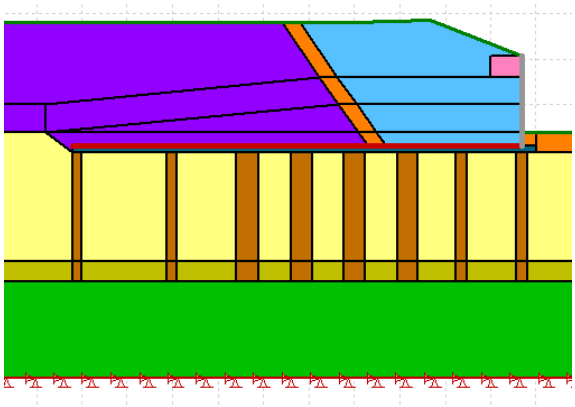

Fig. 4 Model Profile at the Centre of the MSE Wall

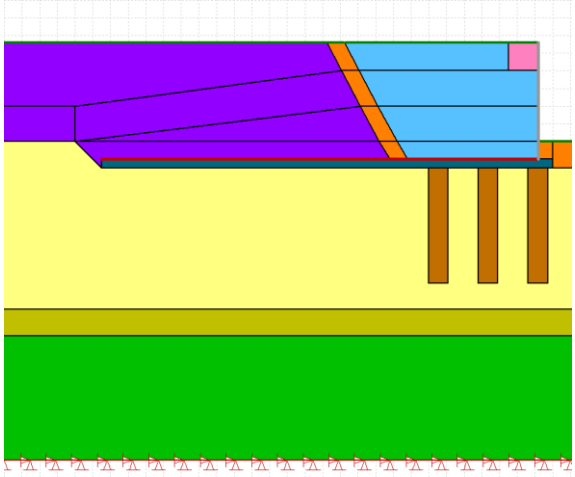

Fig. 5 Model Profile at the Critical Section of the MSE Wall

The south abutment has a larger embankment, allowing it to be more susceptible to settlement, resulting in a more critical case than the north abutment. Therefore, modelling was focused on just the south abutment.

Table 1 Model Parameters for Subsoil and Backfill Material

Material	Model	E'(kPa)	Φ(°)	γ(kN/m^3)	ν	λ	κ	e	OCR
Clay Fill	Linear-Elastic	20,000		18	0.334				
Granular Fill	Linear-Elastic	60,000		21	0.334				
Reinforced Granular Fill	Linear-Elastic	60,000		21	0.334				
Stone Columns	Linear-Elastic	60,000		21	0.334				
Silty Clay	Linear-Elastic	15,000		18	0.334				
Soft Silty Clay	Modified Cam Clay		20	18	0.334	0.17	0.036	1	1.2
Clay Till	Linear-Elastic	60,000		21	0.334				

Table 2 Model Parameters for Structural Beams

Material	E' (MPa)	Cross-Sectional Area (m^2)	Moment of Inertia (m^4)
MSE Wall Panel (concrete)	23,478	0.45	0.0035
Geosynthetic (Tensar BX1500)	492	0.004	0

DEFORMATION ANALYSIS RESULTS

TLS Results

The settlement analysis from TLS in this paper will include the three construction scans and the two post-construction scans from the summer of 2018. The parameters for each of the scans was set to a resolution of 44MPts and a quality of 4x to minimize noise and error for each scan **[7]**. Since the bridge deck is expected to exhibit minimal movements and it has been constructed prior to wall erection, it was used as a reference target for deformation analysis. The bridge deck is expected to have a final settlement magnitude of 20mm **[1]**. Control targets were surveyed using Real-Time Kinematics (RTK) which causes the satellites to communicate to the rover station, providing the UTM coordinates of its position. Communication error between the satellites and rover and duration of the rover stationed over a reference location, 2D errors can range from 3-10mm, 1D errors range from 6-14mm, and 3D errors range from 9-20mm. Therefore, the movement from the bridge deck is within the error tolerance of the RTK measurement and is accepted for reference.

The results generated from the TLS will be represented in seven different locations: three spaced out between the bridge deck and wall descent on the East and West side (total of six) and one in the centre of the wall, as shown in Fig. 6.

1D Settlement Analysis

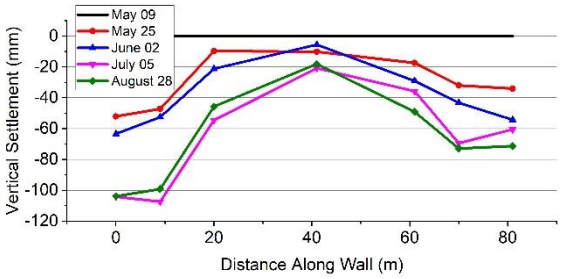

Fig. 6 Terrestrial Laser Scanning Results for Settlement along Wall

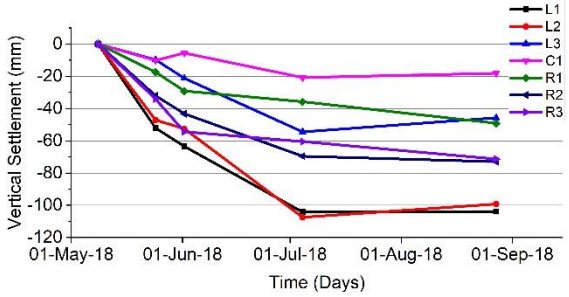

Fig. 7 Terrestrial Laser Scanning Results for Rate of Settlement Plot

The settlement profile of the south abutment resembles a 'W' pattern, greater magnitudes of settlement outside of the bridge deck section, and lower amounts of settlement in the centre of the wall. Stone columns were placed primarily in the area where higher embankments were planned (near the centre of the wall) with embankment height reducing near the edges. The 'W' pattern observed indicates the influence of the stone columns in the centre of the embankment.

As shown in the settlement profile, the largest movement exhibited by the wall was 107mm on July

5th, 2018 between the slope of the wall and the bridge deck. August 28 at the same location was measured at 99mm of settlement, causing some concern over the amount of error induced in the measurements. Since both measurements are within 10mm to each other, it is reasonable to assume settlements are low in that area and are largely complete. Measurement error is also evident in other locations that appear to have upheave between successive scan dates which would also be assumed to have minimal movement between measurements. This is consistent with design estimates relative to the MSE wall settlement (settlement was projected to be completed shortly after wall construction due to the PWP dissipation effects of the stone columns).

Finite Element Modelling Results

Settlement results were measured underneath the load transfer pad (granular base on top of the stone columns) and are presented below

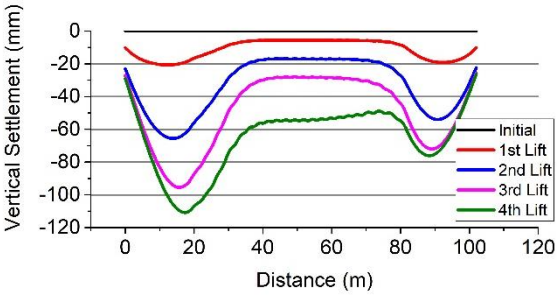

Fig. 8 Finite Element Results for Settlement Cross-Section along Length of Wall

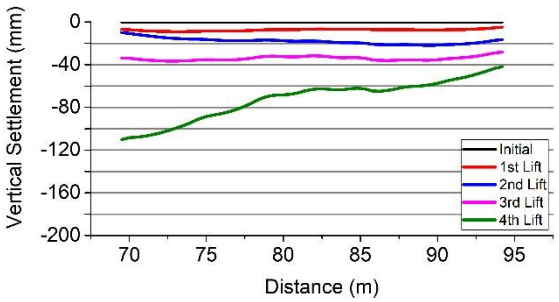

Fig. 9 Finite Element Modelling Results for Settlement Profile along Centre of Wall

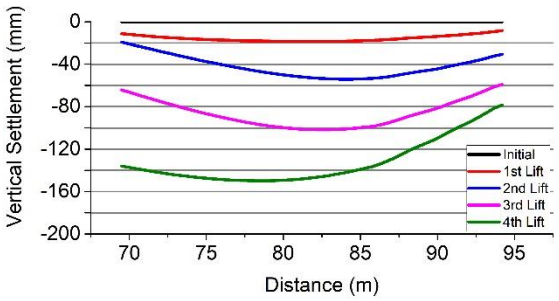

Fig. 10 Finite Element Modelling Results for Settlement Profile Overlying Pipe Section

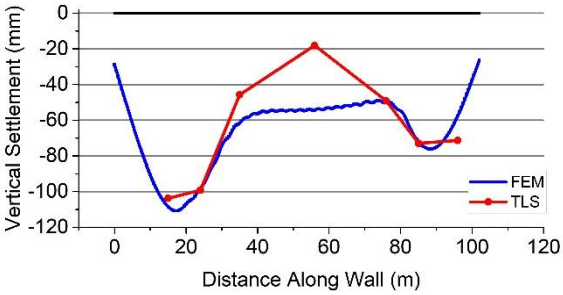

Fig. 11 Vertical Settlement Cross-Section August 28 Scan (TLS) vs 4th Lift (FEM)

From the cross-sectional settlement figure, the behaviour or trend of the wall is very similar to the TLS as it settles in a 'W' shape with most of the settlement occurring just outside of the stone columns. As well, the most settlement occurs on the left side of the wall, located above the pipes. The short columns not drilled to till are the big influence for the additional 30mm of settlement of difference between the two sides. Additionally, the amount of settlement in the centre of the wall slopes down towards the left side because of less reinforcement in the subsoil. Fortunately, it is a small difference of 10mm over 40m of wall so the implications of differential settlement underneath the bridge deck will be negligible (consistent with design intent).

When comparing the magnitudes of settlement to the TLS results, the prediction from the model is within a reasonable estimate of what was observed. The May 25 scan in Fig. 8 is taken when the second lift was installed, June 2 when the third lift was installed, and July 5 and August 28 for the final lift. The model estimates a larger amount of settlement than the TLS for the first three lifts being erected which should be expected as the model is assuming completely drained conditions for soil consolidation. When comparing the final lift with the TLS as seen in Fig. 11, the model settlements are more comparable to the observed survey measurements on the extents of the wall, however the centre of the wall is predicted to settle another 30mm. This is interesting as the stone columns underneath the wall in that section will allow for immediate settlement. The soil settling more than double what it has already moved is unreasonable and therefore, error in the measurements, the presence of the belled piles behind the wall, and/or the transformation from 3D to 2D conditions has influenced the results of the settlement behaviour.

Figures 9 and 10 represent the settlement underneath the approach embankment settlement with the last point on the right of the graph is the wall settlement. First looking at movement underneath the centre of the wall, the settlement is consistent

throughout the length of the granular pad up until the final lift is installed. The most settlement occurs where it is reinforced with two spaced out columns where it reaches a maximum of 126mm. For the critical section, ground settled in a more 'U' shape, with the most settlement occurring past the columns in the centre of the pad with 160mm. The reduced number of columns greatly impacts the amount of settlement occurring as the entire section settles at least 10cm, compared to the centre of the wall where approximately 80% of the soil underneath the granular pad won't settle more than 10cm.

For confirmation of representing the wall settlements in a cross-section and profile, comparing the last point in the profile graphs with settlement at the same location on the cross-section plot will be observed. The profile models calculated wall settlements to be 50mm and 106mm for sections at the centre and critical sections of the wall respectively. Comparing that to the cross-section model, values of 57mm and 111mm are within 7mm of each other which is very reasonable to assume that the plane strain transformations into each 2D model was consistent with depicting the site conditions.

RECOMMENDATIONS

From comparing the observed TLS results with the calculated FEM results, the behaviour and magnitude of the settlements were similar as both methods displayed a 'W' pattern of movement. The maximum settlements in both TLS and FEM were 103mm and 111mm, respectively. There was great disparity between the results for the centre of the wall with results of 21mm and 57mm for TLS and FEM, respectively. More information on the collection of measurements should be examined. With the limitations of FEM and the errors incurred by the TLS, the results both methods produced are satisfactory for evaluating the performance of bridge interchange projects.

The use of plane strain parameters for 2D modelling seems reasonable in predicting the settlement behaviour of the wall but for research interests, a 3D model would be interesting to observe the movement without assuming plane strain conditions. Another interest would be how the PWP would affect the rate of settlement during construction. The stone columns accelerates the dissipation of PWP but the soil around the short columns would not drain out as quickly and therefore may not reach the settlements as depicted by effective drained conditions.

REFERENCES

[1] TREK Geotechnical Inc., "Saskatoon Interchanges Project Geotechnical Design Report for McOrmond Interchange - REVISION 4," Winnipeg, 2017.

[2] T. Knaak, "Structural Wall Monitoring (#1017) rev: C," Certainty 3D, Orlando, 2017.

[3] L. Truong-Hong and D. Laefer, "Application of Terrestrial Laser Scanner in Bridge Inspection: Review and an Opportunity," in *37th IABSE Symposium on Engineering for Progress, Nature and People*, Madrid, 2014.

[4] N. N. S. Yapage, D. S. Liyanapathirana, R. B. Kelly, H. G. Poulos and C. J. Leo, "Numerical Modeling of an Embankment over Soft Ground Improved with Deep Cement Mixed Columns: Case History," *Journal of Geotechnical and Geoenvironmental Engineering*, vol. 140, no. 11, pp. 1-10, 2014.

[5] I. Scotland, N. Dixon, M. Frost, R. Wackrow, G. Fowmes and G. Horgan, "Measuring Deformation Performance of Geogrid Reinforced Structures using a Terrestrial Laser Scanner," in *10th International Conference of Geosynthetics*, Berlin, 2014.

[6] D. F. Laefer and D. Lennon, "Viability Assessment of Terrestrial LiDAR for Retaining Wall Monitoring," in *GeoCongress 2008 : Geosustainability and Geohazard Mitigation*, New Orleans, 2008.

[7] FARO, "Laser Scanner Best Practices," 10 January 2019. [Online]. Available: https://knowledge.faro.com/Hardware/3D_Scanners/Focus/Laser_Scanner_Best_Practices. [Accessed 02 May 2019].

9th Int. Conf. on Geotechnique, Construction Materials and Environment,
Tokyo, Japan, 20-22 November 2019, ISBN: 978-4-909106025 C3051

MODELLING OF GRANULAR PILE COLLAPSE BY USING MATERIAL POINT METHOD AND DISCRETE ELEMENT METHOD

Yi Yang[1]

[1]Department of Civil Engineering, Chu Hai College of Higher Education, Hong Kong, China

ABSTRACT

Granular debris flows can be observed in many regions of the world. The process is accompanied with large deformation and phase transitions from solid to fluid states. In this paper, material point method (MPM) and discrete element method(DEM) are used to identify the flow mechanism and energy dissipation from continuum to discrete perspectives. These two methods are also compared from many aspects. In addition, this study will be helpful for the future combined MPM and DEM study.

Keywords: material point method; discrete element method; granular pile collapse

1. INTRODUCTION:

Granular materials are important constituents in many fields. Understanding the evolution of internal structures of granular flows will certainly help the description and prediction of nature geophysical hazards in mountainous areas. Although extensive researches have been carried out worldwide to study different aspects of granular-type debris flows, the fundamental initiation and propagation mechanisms are not yet fully understood. Existing theoretical models and numerical approaches are not captured all the key features of debris flows, especially for the large deformation and phase transition analysis [1]. In current paper, we focus on the numerical part to describe and predict the flow mechanism and patterns.

Numerical models have been adopted and developed to fully describe the mechanism of debris flows over decades [2-11]. Due to the inherent multiscale feature of debris flows, these numerical methods can be mainly divided as continuum, discontinuum and multiscale methods [11].

Continuum approaches are only used when the scale separation between grain-scale and macro-scale is very large [8]. The most commonly adopted continuum methods for simulating debris flows include the finite element method (FEM) [3], smooth particle hydrodynamics (SPH) [2,12], material point method (MPM) [8,9,13] , etc. Soga and his colleagues (2015) have reviewed the numerical techniques for modeling large deformation landslide problems and summarized their advantages and limitations. The MPM is a particle-based method that represents the material as a collection of material points, and Newton's laws of motion determine their deformations. It combines the advantages of Eulerian and Lagrangian approaches to elimate the mesh distortion. Meanwhile, the application of boundary conditions is more straightforward than SPH method. During the last decade, MPM has been applied to solve large deformation geotechnical problems, which include granular flows, retaining walls, slopes, anchors and others [8,14,15]. Most of previous publications consider the soil as a single-phase material.

The discrete element method (DEM) proposed by Cundall and Strack [16] are capable of simulating the granular material as a discontinuous system. DEM is a robust research tool to explore the behavior of dry granular materials at the grain scale. Within the last two decades, DEM has been used to study the fundamental mechanisms of landslides from 2D to 3D [17-19]. The modeling of granular flow using DEM is a possible way to study the complicated behavior of landslides. Its drawback is that it is difficult to consider the presence of water in granular flows, which cannot explain the high mobility of debris flows [20].

In the current paper, we study the pile collapse problems by using MPM and DEM respectively to capture the similarities and differences. We compare in detail the evolution of the profile of the granular pile to observe the energy dissipation and other physical indexes for different approaches.

2. NUMERICAL SET UP:

Initially, a granular packing with 5200 particles is randomly generated by YADE with a mean particle radius 2.2275×10^{-3}m. Then, all particles will be allowed to fall by gravity force to generate a mimicking sample with the dimensions 0.2×0.4m. The density and friction coefficient are 2600 kg/m^3 and 0.4 respectively. Additionally, a MPM packing with the same geometry is set up. The initial numerical sample for DEM and MPM can be seen in Fig. 1.

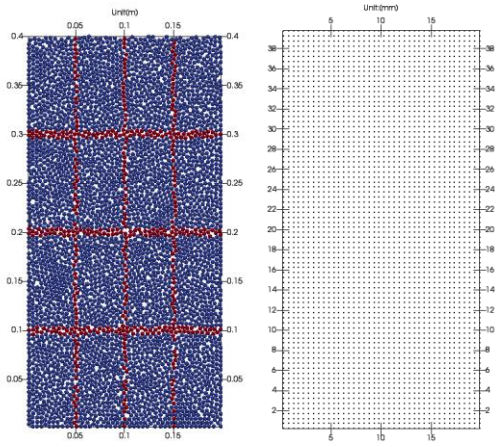

Fig. 1: Initial geometry and dimensions of the granular pile collapse

It can be found that the difference between the DEM and MPM is clear at the initial collapse part in Fig. 2. DEM will show a much more reliable simulation where the particles will abruptly flow down. In MPM all the simulations show a continuous feature.

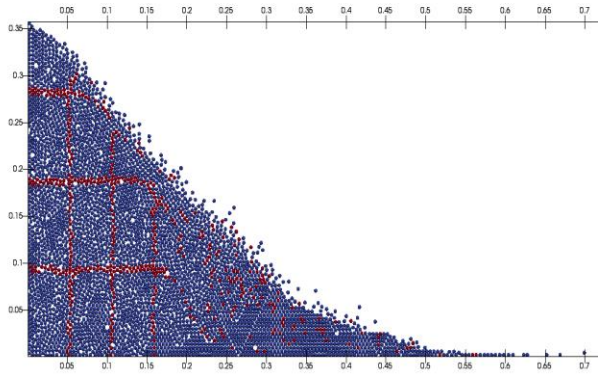

(a) DEM

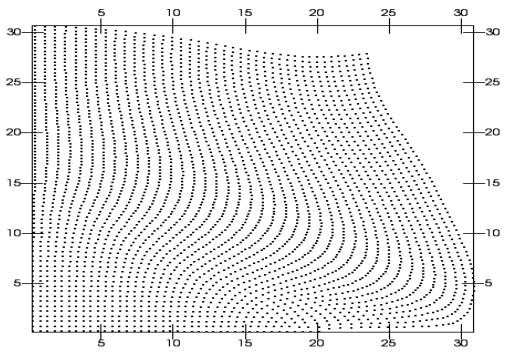

(b) MPM

Fig.2: Initial collapse between DEM and MPM

In Fig.3, it can be found that the final deposition of both numerical approaches is similar. This part proves MPM is useful for simulating large deformation problems in geotechnical engineering. And the computing efficiency of MPM is better than DEM. By using DEM, we can obtain a lot of physical quantities at a mesoscale. For example, in Fig. 4 it can be easily predict the displacement vectors by DEM.

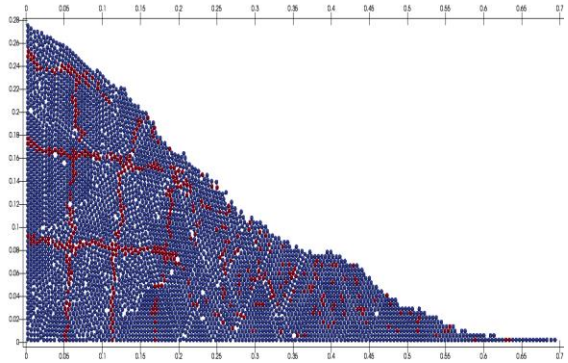

(a) DEM

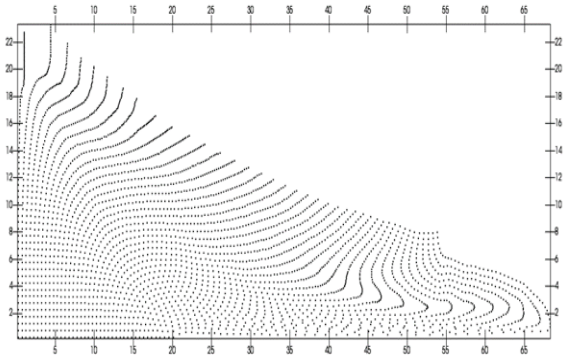

(b) MPM

Fig. 3: Final Profile of the granular collapse.

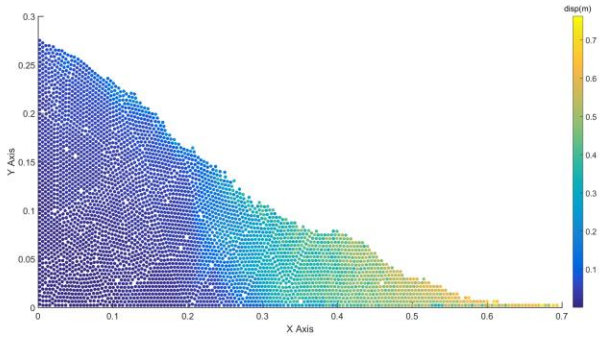

Fig. 4: Evolution of displacement by DEM

3. CONCLUSIONS:

This work shows a comparison study between MPM and DEM. DEM is better for simulating the granular pile collapse problems at the initial stage. Moreover, DEM can also provide a lot mesoscale information. A similar result at the final stage can be found by MPM and DEM. The efficiency of MPM is better than DEM. Additionally, this study will be benefited for the later couple approach between MPM and DEM.

4. ACKNOWLEDGEMENT:

The work described in this paper was financially supported by the Research Grant Council of the Hong Kong SAR Government through the project UGC/FDS13/E06/18.

5. REFERENCES:

[1] Iverson, R. M. (1997). "The physics of debris flows." Reviews of Geophysics, 35(3), 245-296.

[2] Bui, H. H., Fukagawa, R., Sako, K., and Ohno, S. (2008). "Lagrangian meshfree particles method (SPH) for large deformation and failure flows of geomaterial using elastic–plastic soil constitutive model." International Journal for Numerical and Analytical Methods in Geomechanics, 32(12), 1537-1570.

[3] Chen, H., Crosta, G., and Lee, C. (2006). "Erosional effects on runout of fast landslides, debris flows and avalanches: a numerical investigation." Géotechnique, 56(5), 305-322.

[4] Denlinger, R. P., and Iverson, R. M. (2001). "Flow of variably fluidized granular masses across three-dimensional terrain: 2. Numerical predictions and experimental tests." Journal of Geophysical Research: Solid Earth, 106(B1), 553-566.

[5] Hungr, O. (2008). "Simplified models of spreading flow of dry granular material." Canadian Geotechnical Journal, 45(8), 1156-1168.

[6] Hutter, K., Wang, Y., and Pudasaini, S. P. (2005). "The Savage–Hutter avalanche model: how far can it be pushed?" Philosophical Transactions of the Royal Society of London A: Mathematical, Physical and Engineering Sciences, 363(1832), 1507-1528.

[7] Leonardi, A., Wittel, F. K., Mendoza, M., Vetter, R., and Herrmann, H. J. (2016). "Particle–Fluid–Structure Interaction for Debris Flow Impact on Flexible Barriers." Computer-Aided Civil and Infrastructure Engineering, 31(5), 323-333.

[8] Soga, K., Alonso, E., Yerro, A., Kumar, K., and Bandara, S. (2015). "Trends in large-deformation analysis of landslide mass movements with particular emphasis on the material point method." Géotechnique, 66(3), 248-273.

[9] Yerro, A., Alonso, E., and Pinyol, N. (2016). "Run-out of landslides in brittle soils." Computers and Geotechnics, 80, 427-439.

[10] Zhao, J., and Shan, T. (2013). "Coupled CFD–DEM simulation of fluid–particle interaction in geomechanics." Powder Technology, 239, 248-258.

[11] Liu, C., Sun, Q., & Yang, Y. (2017). Multi-scale modelling of granular pile collapse by using material point method and discrete element method. Procedia Engineering, 175, 29-35.

[12] Bonet, J., and Kulasegaram, S. (2000). "Correction and stabilization of smooth particle hydrodynamics methods with applications in metal forming simulations." International Journal for Numerical Methods in Engineering, 47(6), 1189-1214.

[13] Sulsky, D., Chen, Z., and Schreyer, H. L. (1994). "A particle method for history-dependent materials." Computer methods in applied mechanics and engineering, 118(1-2), 179-196.

[14] Coetzee, C., Vermeer, P., and Basson, A. (2005). "The modelling of anchors using the material point method." International Journal for Numerical and Analytical Methods in Geomechanics, 29(9), 879-895.

[15] Więckowski, Z., Youn, S. K., and Yeon, J. H. (1999). "A particle-in-cell solution to the silo discharging problem." International Journal for Numerical Methods in Engineering, 45(9), 1203-1225.

[16] Cundall, P. A., and Strack, O. D. (1979). "A discrete numerical model for granular assemblies." Géotechnique, 29(1), 47-65.

[17] Liu, Z., and Koyi, H. A. (2013). "The impact of a weak horizon on kinematics and internal deformation of a failure mass using discrete element method." Tectonophysics, 586, 95-111.

[18] Liu, Z., and Koyi, H. A. (2013). "Kinematics and internal deformation of granular slopes: insights from discrete element modeling." Landslides, 10(2), 139-160.

[19] Utili, S., Zhao, T., and Houlsby, G. (2015). "3D DEM investigation of granular column collapse: evaluation of debris motion and its destructive power." Engineering Geology, 186, 3-16.

[20] Legros, F. (2002). "The mobility of long-runout landslides." Engineering Geology, 63(3), 301-331.

9th Int. Conf. on Geotechnique, Construction Materials and Environment, Tokyo, Japan, 20-22 November 2019, ISBN: 978-4-909106025 C3051

THREE-DIMENSIONAL STABILITY OF CIRCULAR OPENING

Ji-Sung Lee[1], Mohammad Hassan[1] and Jim Shiau[1]
[1]School of Civil Engineering, University of Southern Queensland, Australia

ABSTRACT

The stability of a circular opening trapdoor in undrained cohesive soils was numerically investigated. Three-dimensional (3D) numerical simulations were performed to analyze the stability of a circular trapdoor with a series of opening diameter-to-depth ratios and soil properties. The shear strength reduction method (*SSRM*) built in finite difference method (*FDM*) is employed to determine the *FoS* solutions, which are functions of the depth ratio and stability number. The results are compared to numerical solutions from previous related studies and other published literatures. The numerical results were presented in the form of factor of safety that is a function of the depth ratio and the shear strength ratio. Practical examples were used to demonstrate how to use the design charts and equations in practice. The investigation of *FoS* suggested that the 3D circular opening results are almost twice larger than those in 2D plain strain. The strong arching effects has been noted for deeper cases, and the corresponding failure mechanism has not been observed.

Keywords: Sinkhole, Circular opening, FLAC 3D, Finite Difference Method, Surface failure extent

INTRODUCTION

The stability of the trapdoor was initiated by Terzaghi [1], which experimentally investigated the effect of the distributed stress in sand and defined the active and passive trapdoor failure. He described the active mode as surcharge or overburden pressure, and passive mode as an uplifting force, such as an anchor. In principle, there are two key elements that stimulate an underground cavity's failure, one being the overburden pressure (γH) and the other the surcharge load (σ_s). It is not unusual in geotechnical engineering analysis and design, to consider a greenfield condition (σ_s=0), with some examples being in Taylor's original slope stability charts [2]. Without considering weathering effects, a failure may occur due to overburden pressure (γH) above a cavity in the ground, which is a typical condition in the analysis of natural sinkholes and longwall mining.

Taylor's stability charts are one of the principal tools used in analysing slope stability problems, and they are still popular with engineers in the field. Using the limit equilibrium method, the stability of slopes is a function of the slope height (H), slope angle (β), and soil properties, such as the unit weight (γ) and undrained soil shear strength (S_u) [3], [4]. The undrained stability number introduced by Taylor is presented in Eq. (1), which can be used to investigate the stability of soil overlying a cavity.

$$N_s = \frac{S_u}{\gamma H \times FoS} \tag{1}$$

Craig [5] employed a large centrifuge model to investigate the critical stability of a circular cavity. In this investigation, Craig [5] used the lower and upper bond technique to estimate the stability of a shallow trapdoor (between 0.5-1.5) and concluded that, for a depth ratio greater than 1, the theoretical results are not valid. This approach to the problem has been continued and expanded in the finite element limit analysis (*FELA*) research by Yang et al. [6], Auguard et al. [7], Drumm et al. [8], Martin [9] and most recently by Keawsawvong et al. [10].

Recent studies have been conducted using a shear strength reduction method by Shiau et al. [11], to investigate tunnel heading stability in homogeneous cohesive soil. What was notable about this study is that the strength ratio defined following Taylor's [1] stability approach, was where the factor of safety became the function of the depth ratio (H/W) and the soil strength ratio ($S_u/\gamma W$).

This paper investigates the study of cavity's stability underlying homogeneous clay in an unsupported greenfield condition in a realistic three-dimensional circular opening condition. In this paper, shear strength reduction techniques are used to study the three-dimensional failure mechanisms of a circular trapdoor by using *FLAC*, a finite difference program. The stability results are presented in the form of a factor of safety and a failure extent ratio for various dimensionless ratios and verified by using the finite element limit analysis technique with upper and lower bound theorems.

The numerical results of three-dimensional circular trapdoor are compared with 3D square and rectangular results and 2D results which were obtained earlier in other available solutions. In addition, the practical examples are provided to illustrate the use of the charts and tables.

PROBLEM DEFINITION

The sinkhole propagation process is a complex for estimating by the numerical analysis. It is impossible to predict the actual propagation of the sinkhole occurrence. Hence, this study assumes an idealised three-dimensional horizontal trapdoor and that the propagation process is at the last stage where the cavity is big enough to cause a collapse failure.

Figure 1 presents a conceptual horizontal trapdoor problem underlying undrained homogeneous clay layer with constant unit weight (γ) and shear strength (S_u).

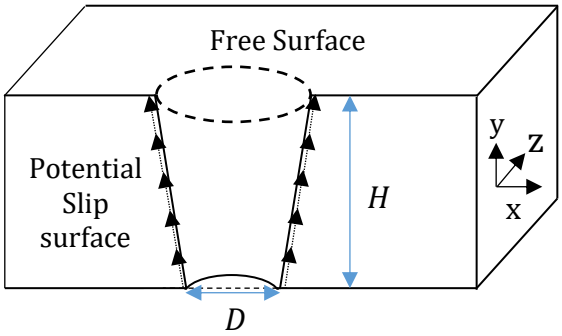

Fig. 1 An idealized sinkhole problem

The three-dimensional soil body is modelled as uniform Tresca material, which is the same as Mohr-Coulomb material when the soil friction angle (ϕ) is zero. The opening of the cavity is assumed to be horizontal, with the radius represented by (D) in the x direction and the height represented by (H) in the z direction.

An extensive range of depth ratios (H/D= 1 to 6) and shear strength ratios ($S_u/\gamma D$= 0.2 to 2) were selected for covering the wide range of parametric studies. Note that the shear strength ratio is defined following Taylor's method and the *FoS* can be defined as a function of the shear strength ratio ($S_u/\gamma D$) and the depth ratio (H/D). This relationship is shown in Eq. (2).

$$FoS = f\left(\frac{S_u}{\gamma D}, \frac{H}{D}\right) \quad (2)$$

MEDLLING TECHNIQUE

The trapdoor stability in undrained cohesive soil were examined using shear strength reduction method (*SSRM*) and 2D and 3D finite difference software. Built-in *FISH* scripts were also developed for the problem to facilitate the auto mesh generation, and hence allow parametric studies to be conducted efficiently. Internal verification and model validation of the solution revealed that results from full, half or quarter meshes were almost identical. This has greatly improved the level of confidence in the current 3D development.

Figure 2 shows the typical quarter mesh of circular trapdoor problem. Although the mesh shows perfect square cubes, *FLAC 3D* uses a mixed discretisation technique of various element shapes such as wedges, pyramids, bricks and tetrahedrons to form and solve the problem [12].

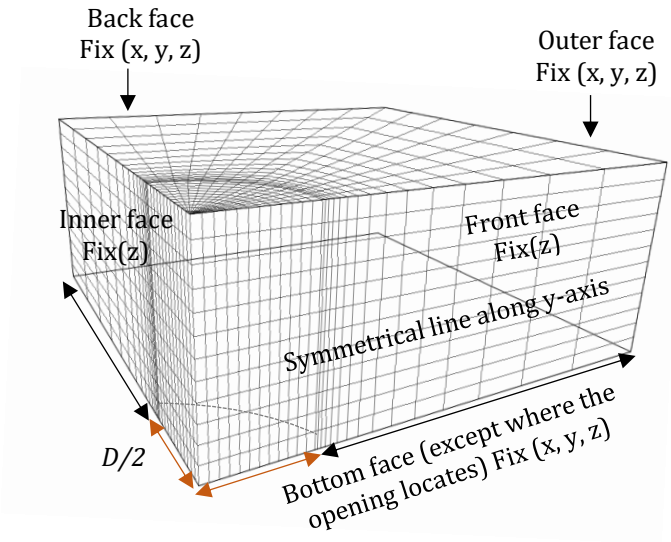

Fig. 2 Typical quarter mesh and boundary condition

This study conducted the stability analysis of three-dimensional circular trapdoor in undrained homogeneous layer of clay using the shear strength reduction method (*SSRM*). The velocity and displacement plots of the finite difference method represented to determine the surface subsidence due to collapse of the sinkhole. The results of the study are compared with other existing studies.

RESULTS AND DISCUSSION

A combination of wide range of depth ratio (H/D= 1-6) and strength ratio ($S_u/\gamma D$) utilizes to investigate all possible situations associated with the trapdoor stability. The factor of safety (*FoS*) results obtained by utilizing the shear strength reduction method in 3D finite difference method software which discussed previously. The factor of safety results of this investigation are presents in tables 1.

Figure 3 shows the comparison of the effect of shear strength rate ($S_u/\gamma D$) on factor of safety (*FoS*) with circular opening and various opening ratios (L/W) which were obtained from Shiau et al. [13]. The various range of the L/W ratio represent the square opening and the rectangular opening. The length (L) indicates the horizontal length of the cavity, the width (W) indicates the vertical length of the cavity.

Table 1 *FoS* results for *H/D*=1-6 and $S_u/\gamma D$=0.2-2.

H/D	FoS					
	SR =0.2	SR =0.6	SR =0.73	SR =1.0	SR =1.5	SR =2.0
1	0.84	2.51	3.06	4.19	6.28	8.38
1.5	0.81	2.43	2.96	4.06	6.08	8.12
2	0.75	2.26	2.75	3.77	5.64	7.53
2.5	0.69	2.09	2.52	3.47	5.12	6.94
3	0.64	1.92	2.33	3.20	4.72	6.43
3.5	0.59	1.75	2.15	2.97	4.38	5.94
4	0.55	1.66	2.02	2.77	4.16	5.53
4.5	0.52	1.53	1.89	2.59	3.89	5.19
5	0.49	1.47	1.79	2.45	3.66	4.89
5.5	0.46	1.39	1.69	2.32	3.48	4.64
6	0.44	1.32	1.61	2.20	3.30	4.41

*SR= $S_u/\gamma D$.

Figure 3 shows a linear correlation between *FoS* and shear strength ratio ($S_u/\gamma D$) for all values of square and rectangular opening (*L/W)* and circular opening. As expected, *FoS* increases as the shear strength of the soils $S_u/\gamma D$ increases.

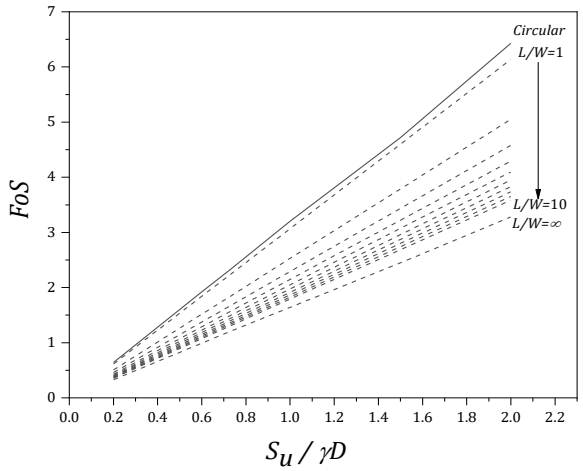

Fig. 3 Effect of $S_u/\gamma D$ (*H/D*=3)

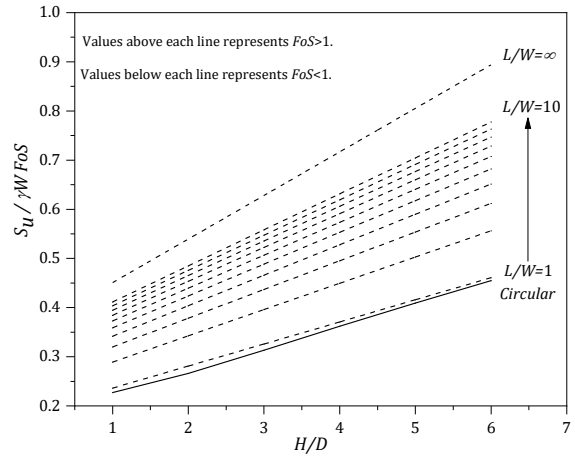

Fig. 4 Failure envelope (*L/W*=1 to *L/W*= ∞ and circular opening trapdoor)

Given the linear relationship in Fig. 3, a failure envelope or critical strength ratio ($S_u/\gamma DFoS$) is presented in Fig. 4. The shear strength ratio is normalised with respect to *FoS*, and therefore represents a critical condition where the *FoS* =1. Fig. 4 is particularly important for designers because it represents the critical value of each parameter. The values above each line indicate a safe working zone (*FoS* >1), while the values below indicate an unsafe zone (*FoS* <1). Closer inspection of the figure reveals that the value of ($S_u/\gamma DFoS$) increases as the depth ratio (*H/D*) increase. The line of the circular opening problem is below the all of the square trapdoor problems from Shiau et al. [13] study. It shows the similar trends as the square opening trapdoor problem as shown in Fig. 4.

A linear regression analysis was employed to develop a practical design equation covering geometrical parameter *H/D*. The linear function was used to yield an accurate curve-fitting of original *FoS* solutions with r^2 = 0.996. This is shown in Eq. (3).

$$\frac{S_u}{\gamma D \times FoS} = \left(\frac{0.0453H}{D} + 0.1812 \right) \quad (3)$$

Equation 3 can be used to obtain critical parameters such as undrained shear strength (S_u), depth (*H*) and opening radius (*D*).

Table 2 shows the used data for plotting circular trapdoor in Fig 4.

Table 2 Data used for Fig. 4 (Circular opening).

H/D	$S_u/(\gamma D\ FoS)$
1	0.239
1.5	0.247
2	0.266
2.5	0.289
3	0.313
3.5	0.340
4	0.362
4.5	0.387
5	0.409
5.5	0.432
6	0.455

ARCHING MECHANISM

The arching effect is a phenomenon of redistribution of the stresses from yielding soil particles into non-yielded adjacent soil body. In general, the arching support can develop due to material property, geometrical shape or combination of both. In Mohr-Coulomb failure criterion, the shear stress (τ) is a function of normal stress (σ), the internal frictional angle (ϕ) and soil cohesion (c). Thus, the shear strength is represented by the following Eq. (4):

$$\tau = c + \sigma \tan \phi \quad (4)$$

For cohesive soils such as undrained clay where the friction angle (ϕ) is zero, the shear strength of the soil will be determined by soil cohesion (c) value. A better understanding of the arching support can be explained by studying the soil's failure mechanism. Fig. 5 presents vertical velocity contours for a shallow (H/D =4) and deep case (H/D =4.5).

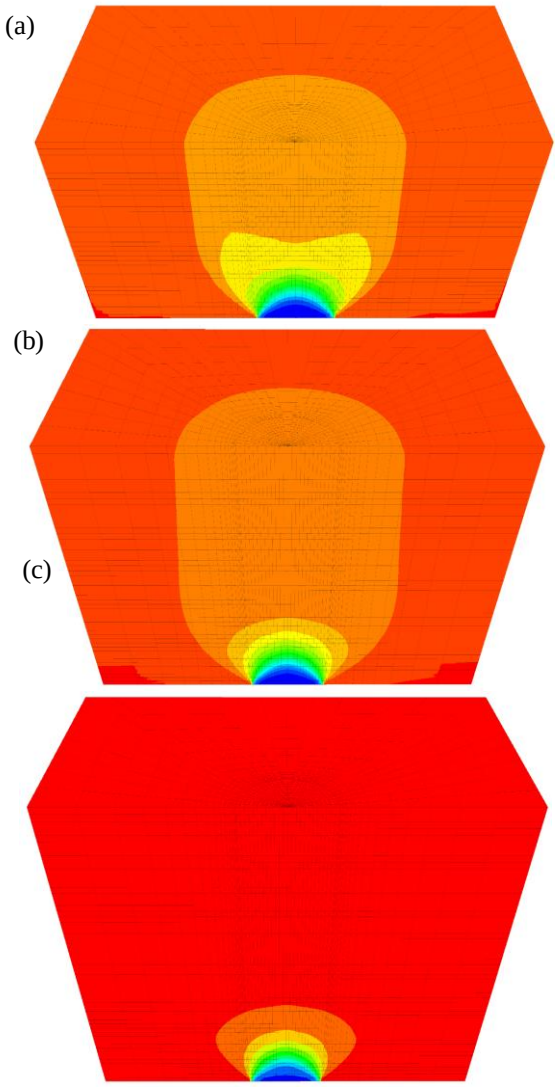

Fig. 5 Contour plots of the vertical velocity of *(a)* H/D=3, *(b)* H/D=4 and *(c)* H/D=5

As shown in Fig. 5, for deeper case (H/D=5), the failure does not extend to the ground surface. It implicates that the strong arching support is developed near the cavity in the deeper cases, resulting in a local failure.

The arching development also can be seen from the *FoS* results presented in Tables 1. It is noted that the rate of change of *FoS* starts to decrease for deeper cases. In addition, the stress distribution plot shown in Fig. 6, suggest that there is a change in vertical stress across the soil heights above the cavity.

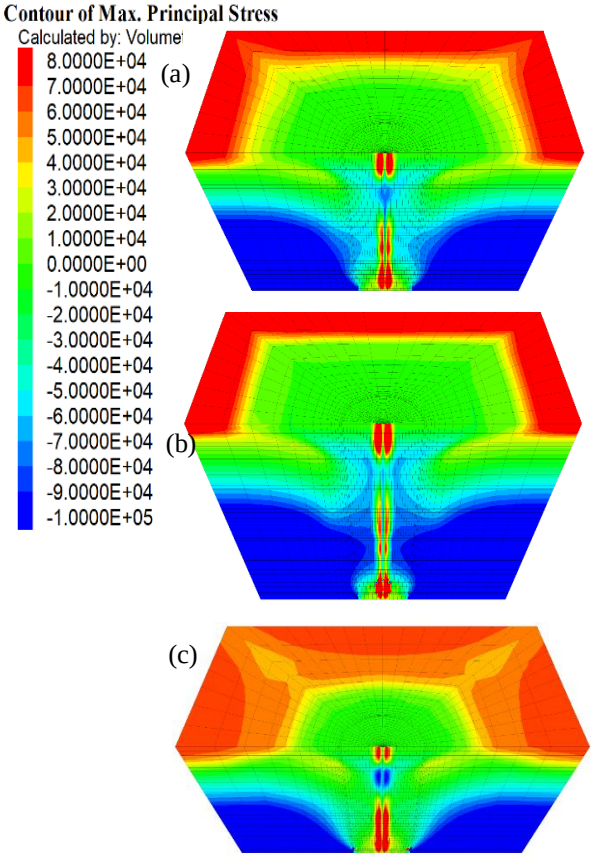

Fig. 6 Contour plots of principal stress of *(a)* H/D=3, *(b)* H/D=4 and *(c)* H/D=5

The transformation of compressive stress to tensile stress suggests that the vertical stress (σ_v) above the trapdoor is less than the total overburden pressure (γH) due to the load being redistributed in deeper case. This finding agrees with the observations in real engineering cases which assumes that the deeper tunnels are safer.

RESULT VERIFICATION

The use of *SSRM* and *FoS* is prevalent in slope stability analyses, however, this process is uncommon when it comes to estimating the stability of underground cavities. Owing to the lack of published literature for comparison, it was decided that the current 3D results obtained are to be compared with 2D and 3D *FDM* as well as 2D upper bound and lower bound solutions using the finite element limit analysis by Shiau et al. [13]. Fig. 7 shows such a comparison.

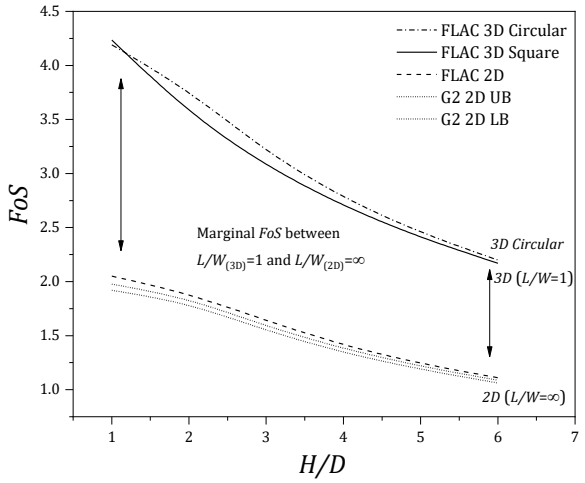

Fig. 7 Comparison of *FoS* results from 2D and 3D analyses (for $S_u/\gamma D$=1)

Fig. 7 shows that the results of 3D circular opening are similar to the 3D rectangular which has a significant variance between 3D and 2D. Table 3 shows the values used to plot Fig. 7.

Table 3 *FoS* results of *FLAC* 3D circular and rectangular, *FLAC* 2D and *FELA UB* and *LB* for $S_u/\gamma W$=1 [13]

H/W	FDM_{3D} Circular	FDM_{3D} Rectancular	FDM_{2D}	$FELA_{2D}$ LB [13]	$FELA_{2D}$ UB [13]
1	4.19	4.23	2.05	1.92	1.98
2	3.77	3.56	1.89	1.80	1.85
3	3.20	3.07	1.64	1.55	1.59
4	2.77	2.70	1.41	1.34	1.38
5	2.45	2.41	1.24	1.19	1.21
6	2.20	2.17	1.11	1.06	1.09

The results presented in table 3 shows that the *FoS* of 3D circular opening analyse is approximately two times higher than those 2D solutions. This is not particularly surprising, as a two-dimensional analysis will always yield conservative results when compared to a three-dimensional analysis. This finding can significantly reduce the estimation cost for practical purposes

DESIGN CHARTS AND EQUATION

The design charts and equations has been presented as a result of the factor of safety. A huge range of design charts for *H/D* = 1 to 6 are shown in Fig. 8.

The design chart is represented by the general equation to cover all possible depth ratios. Equation 3 which introduced earlier can be further transformed into Eq. (5) to determine *FoS* for known design parameters such as *H/D* and $S_u/\gamma D$.

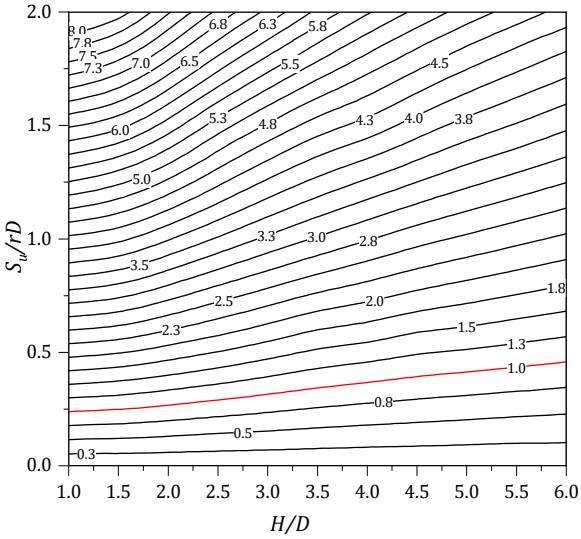

Fig. 8 Design chart for trapdoor stability.

$$FoS = \frac{S_u/\gamma W}{\left[\frac{0.0453H}{D} + 0.1812\right]} \quad (5)$$

Eq. (5) can be very useful in the early design stage for engineers because it allows them to determine the *FoS* when other parameters are available.

RPACTICAL EXAMPLES

Workability of the stability design charts and equations can best demonstrate through a number of examples, as follows.

Example 1 – determine the factor of safety (FoS)

Assume the sinkhole which has no internal pressure and no surcharge pressure, determine the factor of safety for the cavity. The following information is provided:

H=16m, *D*=4m, γ= 18 kN/m3 and S_u=72 kPa.

1. Given, *H/D*=4 and $S_u/\gamma D$=1, Eq. (3) returns a FoS approximately 2.76.

2. Using Fig. 8, a value of *FoS*=2.81.

3. An actual *FoS* value from the *FLAC* analysis is 2.77.

The results obtained from Eq. (5) and the Fig. 8 shows highly agreement with the actual analysis results.

Example 2 – determine the critical depth ratio (H/D)

In the case of the deep sinkhole, what would be the critical depth (H) required to maintain FoS of 1 with the following given parameters:

S_u= 162 kPa, D=30 m, γ= 18 kN/m3.

1. Given the parameter, $S_u/\gamma DFoS$ =0.3.

2. Using Eq. (3), the depth (H) is calculated to be 78.68m. Converting the result in terms of a depth ratio, H/D=2.62.

3. Using Fig. 4, H/D is estimated as a 2.8.

CONCLUSION

A series of 3D circular opening numerical models were investigated to analyse the stability of the trapdoors with various depth ratios in undrained cohesive soil. Numerical results were obtained by utilising the shear strength reduction method in the finite difference method software *FLAC* 3D. In order to efficiently perform parametric analyses, a *FISH* script was developed to enable auto mesh generation and solver. The following conclusions can be drawn based on this study:

- The *FoS* study showed that the 3D circular opening results were close to the 3D square opening (L/W=1).

- Strong soil arching was observed for deep trapdoors (H/D > 4.5) in the 3D circular trapdoor study, resulting in local failure mechanisms.

Although the study has investigated the stability in form factor of safety and the surface failure extent of sinkhole, there is certain limitation which is not considering the surcharge. Despite of the limitation, this study contributes to the understanding of the failure mechanism and arching effects in 3D circular opening problem. Further research is required to investigate the impact of surcharge load (σ_s) and support load (σ_t) for the development of sinkhole in undrained clay.

REFERENCES

[1] Terzaghi, K., Stress distribution in dry and saturated sand above a yielding trap-door, in Proceedings of The International Conference of Soil Mechanic, Harvard university Press, Cambridge, vol. 1, no. 4, 1936, pp. 307-311.

[2] Taylor, D. W., 'Stability of earth slopes', Journal of Boston Society Civil Engineers, vol. 24, no. 3, 1937, pp. 197-247.

[3] McCarthy, D. F., 'Essentials of soil mechanics and foundations', Sixth edition, Prentice Hall, New Jersey, USA, 2002.

[4] Baker, R., A second look at

[5] Taylor's stability chart, Journal of Geotechnical and Geoenvironmental Engineering, vol. 129, no. 12, 2003, pp. 1102-8.

[6] Craig, W., Collapse of cohesive overburden following removal of support, Canadian Geotechnical Journal, vol. 27, no. 3, 1990, pp. 355-64.

[7] Yang, M. Z. and Drumm, E. C., Stability evaluation for the siting of municipal landfills in karst, Engineering Geology, vol. 65, no. 2-3, 2002, pp. 185-95.

[8] Augarde, C. E., Lyamin, A. V. and Sloan, S. W., Prediction of undrained sinkhole collapse, Journal of Geotechnical and Geoenvironmental Engineering, vol. 129, no. 3, 2003, pp. 197-205.

[9] Drumm, E. C., Aktürk, Ö, Akgün, H and Tutluoğlu, L., Stability charts for the collapse of residual soil in karst, Journal of Geotechnical and Geoenvironmental Engineering, vol. 135, no. 7, 2009, pp. 925-31.

[10] Martin, C, Undrained collapse of a shallow plane-strain trapdoor, Geotechnique, vol. 59, no. 10, 2009, pp. 855-63.

[11] Keawsawasvong, S and Ukritchon, B., Undrained stability of an active planar trapdoor in non-homogeneous clays with a linear increase of strength with depth, Computers and Geotechnics, vol. 81, 2017, pp. 284-93.

[12] Shiau, J, Hassan, M. M. and Hossein, Z., Stability charts for unsupported square tunnels in homogeneous undrained clay, International Journal of Geomate, vol. 15, no. 48, 2018, pp. 195-201.

[13] Abbasi, B, Russell, D and Taghavi, R., FLAC 3D mesh and zone quality'. Proceedings of the 3rd International FLAC/DEM Symposium, China, 2013. http://www.itasca.com.au/proceedings-of-the-3rd-international-flacdem-symposium%E2%80%8F

[14] Shiau, J, Asadi, F and Hassan, M. M., Finite element limit analysis of undrained trapdoor stability, International Journal of Geomechanics (to submit), 2019.

9th Int. Conf. on Geotechnique, Construction Materials and Environment, Tokyo, Japan, 20-22 November 2019, ISBN: 978-4-909106025 C3051

DETERMINATION OF CRITICAL TUNNEL HEADING PRESSURE

Fadhil Al-asadi[1] and Jim Shiau[1]
[1]School of Civil Engineering and Surveying, University of Southern Queensland, Australia

ABSTRACT

One of the main problems when constructing a tunnel is to ensure the stability of the tunnel heading. Many researchers have attempted to develop and elaborate the methods for tunnel stability calculation. In a similar form to traditional bearing capacity calculations, tunnel heading pressures can be analysed using the minimum supporting pressure σ_t, Such an equation is of the form: $\sigma_t = -cF_C + \sigma_s F_s + \gamma D F_\gamma$, where c and γ are the effective cohesion and the soil unit weight respectively, σ_s is the possible surcharge loading on the ground surface, D is the height of the tunnel and F_c, F_s and F_γ are the stability factors which are functions of soil frictional angle and tunnel depth ratio. For a series of tunnel diameter-to-depth ratios and material properties, this paper analyses the tunnel stability factors for the determination of tunnel supporting pressures σ_t. Both rigorous lower and upper bound solutions of stability factors are obtained by using novel finite element limit analysis techniques. For practical use, tunnel stability factors are presented in the form of figures and equations.

Keywords: Tunnel Heading, Upper Bound, Lower Bound, Finite Element Limit Analysis, Tunnel Stability Factors.

INTRODUCTION

Excavations for tunnel construction and underground mining in soft ground inevitably induces ground movement and may affect the existing underground infrastructure and surface structures. Ensuring tunnel face stability is directly related to the safety of the adjacent buildings and successful construction of a tunnel or mine.

Experimental tests and analytical approaches such as limit equilibrium methods and limit analysis methods are widely used in the analyses of tunnel face stability in cohesive-frictional soils. [1] was one of the first to propose a model for assessing the stability under drained conditions. He considered the limit equilibrium of a sliding wedge at the tunnel face. [2] proposed a 2D logarithmic spiral model. [3] derived the limit support pressure for tunnel face failure by assuming that the failure zone was a half sphere, a half circle, or a quarter circle. [4] applied the wedge model to calculate the limit support pressure in the homogeneous stratum. [5] extended the wedge model to a layered stratum. The other theoretical methods are the limit analysis methods

(Based on the upper and lower bound theorems of plasticity). [6] derived the limit support pressure for an unlined cavity in a dry cohesionless material. [7] derived upper bound solutions for the limit support pressure from assuming three failure mechanisms based on the movement of rigid blocks with conical shapes in frictional material. [8] investigated the stability of a plane strain circular tunnel in cohesive-frictional soils using finite element limit analysis methods.

The most recent publications are based on this new approach, and further developments have been produced on the stability of circular and square tunnels in cohesive-frictional soil subjected to surcharge loading [9-10].

The idea of considering drained stability based on a single equation was first suggested by [11] they proposed a formula for shield tunnels in dry sand as; $\sigma_t = \sigma_s F_s + \gamma D F_\gamma$.This formula was extended by [4] to cover cohesive-frictional soils by proposing an equation of the form: $\sigma_t = -cF_C + \sigma_s F_s + \gamma D F_\gamma$. However, the results produced were limited and were not ready for practical application. It is therefore the aim of this study to focus on finding the rigorous *UB* and *LB* values of the stability factors (F_c, F_s and F_γ) so that accurate minimum supporting pressure required to maintain the stability of the tunnel face in cohesive-frictional soils can be determined using a wide range of design charts and tables

PROBLEM DEFINITION AND METHODOLOGY

The layout of a plane strain heading stability problem is shown in Figure 1. The problem is similar to a long wall mining or any flat wall in an underground excavation. The heading has a height D and a cover C. The ground around the excavation is modelled as a uniform Mohr-Coulomb material with a cohesion c, friction angle ϕ, and unit weight γ.

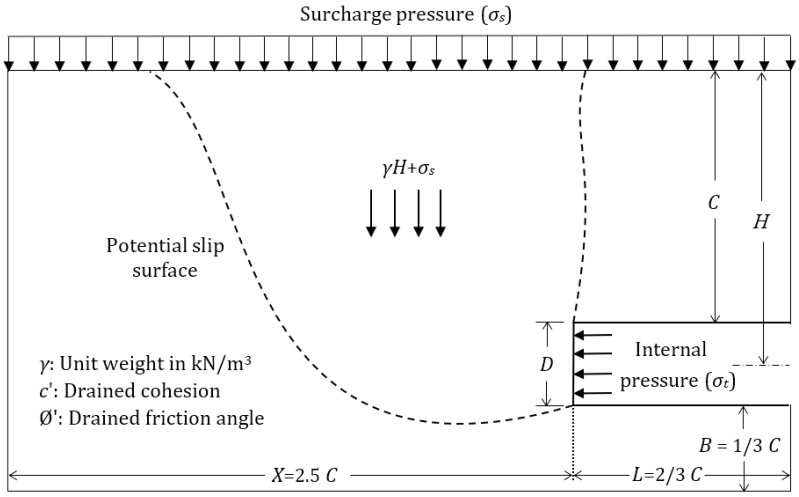

Figure 1. Problem definition

The face of the heading is free to move and is subject to normal stress representing an internal pressure σ_t. The ground surface is horizontal and subject to a vertical surcharge σ_s. The boundary condition of the problem was defined such that the bottom boundary of the model was fixed in both vertical and horizontal directions, while the left and the right boundary of the problem was allowed to move only in the vertical direction. Also, the rigid, smooth tunnel lining is achieved by constraining the movement in the vertical direction.

Figure 2 shows an example of the plane strain condition in *FELA* [12]. The soil mass was discretized as triangular elements. Three iterations of adaptive meshing with the number of elements increasing from 2000 to 5000 were used to obtain the solution. The size of the problem domains was chosen to be large enough that the plastic yielding zone was contained within the domain and did not intersect the boundaries. This would ensure that no influence of the domain size on the computed solutions.

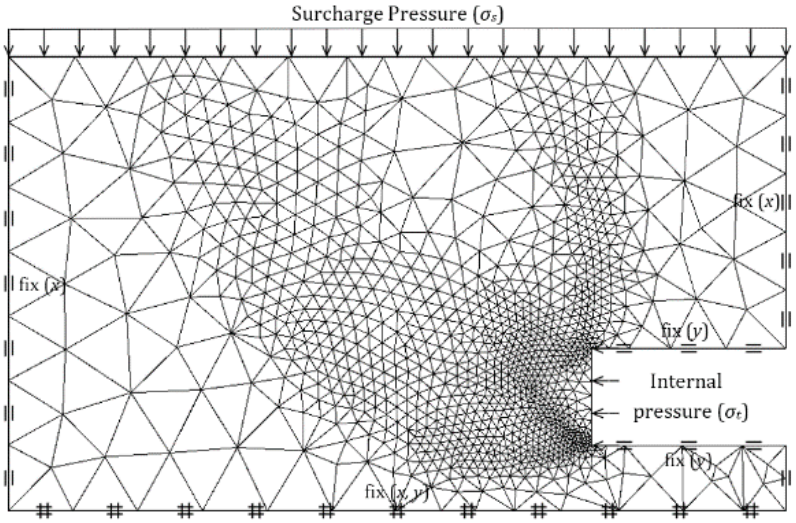

Figure 2. Adaptive mesh used for the problem

In *FELA* modelling, the solution is obtained by applying the load multiplier method, where a unit load is applied and amplified until a state of failure is induced. The internal pressure σ_t is optimised using both upper and lower bound simulations. To compute the bound solution of the stability factors (F_c, F_s and F_γ), zero value of the unit weight γ, the surcharge σ_s and the cohesion c are imposed respectively in the program runs. Similar to Terzaghi's bearing capacity equations, the three factors are functions of the depth ratio *C/D* and the soil friction angle ϕ. With the three factors, critical support pressures can be calculated by the method of superposition. The obtained results (F_c, F_s and F_γ) are compared and validated by using the existing published solution.

DISCUSSING THE TUNNEL STABILITY FACTORS (F_γ, F_s and F_c)

Numerical analyses were performed to calculate the upper bound (*UB*) and the lower bound (*LB*) limits of the stability factors (F_c, F_s, and F_γ) for various depth ratios *C/D* and angles of internal friction ϕ. Since the lower bound theorem offers a safe assessment of the limit pressure for a stability problem, the computed lower bound results of the stability factors were chosen in all equations and design charts. They can be used to assist designers and practising engineers in the evaluation of tunnel heading stability.

The stability factors for cohesion (F_c)

The *FELA* method used in this study produces different curves of F_c for different depth ratios *C/D*. In figure 3, F_c decreases as ϕ increases for all values of *C/D*. This indicates that the effect of soil cohesion diminishes as the soil friction angle increases. It is interesting to see that all curves merge into a single line at approximately ϕ = 30 degree. A double logarithmic regression analysis was employed to develop equation 1. The correlation coefficient r^2 = 0.996.

$$F_c = [-0.24 \times \ln(C/D) + 1.11] + [(-0.49 \times \ln(C/D) + 1.18) \times \ln(tan\emptyset)] \quad (1)$$

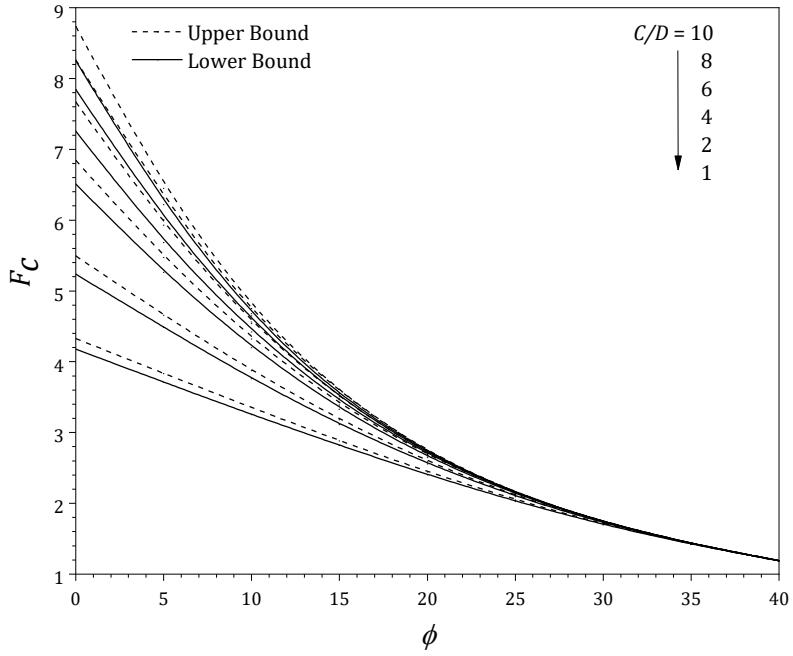

Figure 3. F_c vs ϕ for various depth ratios (*C/D* = 1-10).

The stability factors for surcharge (F_s)

Figure 4 shows that, for any given depth ratio, the maximum value of the surcharge stability factor (F_s) is one. When the internal friction angle (ϕ) of the soil is equal to zero, i.e. undrained condition, the value of F_s is equal to one. This indicates that, for the undrained condition without volume loss during shearing, the stability results is independent of the loading direction. With increasing angle of internal friction ϕ, the value of F_s decreases and merges into one line at ϕ = 35 degree. It is interesting to see that F_s approaches to zero for large values of ϕ, which indicates that surcharge loading σ_s has little contribution to the support pressure when the value of ϕ is large.

A double regression analysis (exponential and logarithmic) was employed to develop equation 2. The correlation coefficient r^2 = 0.991.

$$F_s = [0.056 \times (C/D) + 1.16] \times e^{[(-3.33 \times \ln(C/D) - 5.97) \times tan\emptyset]} \quad (2)$$

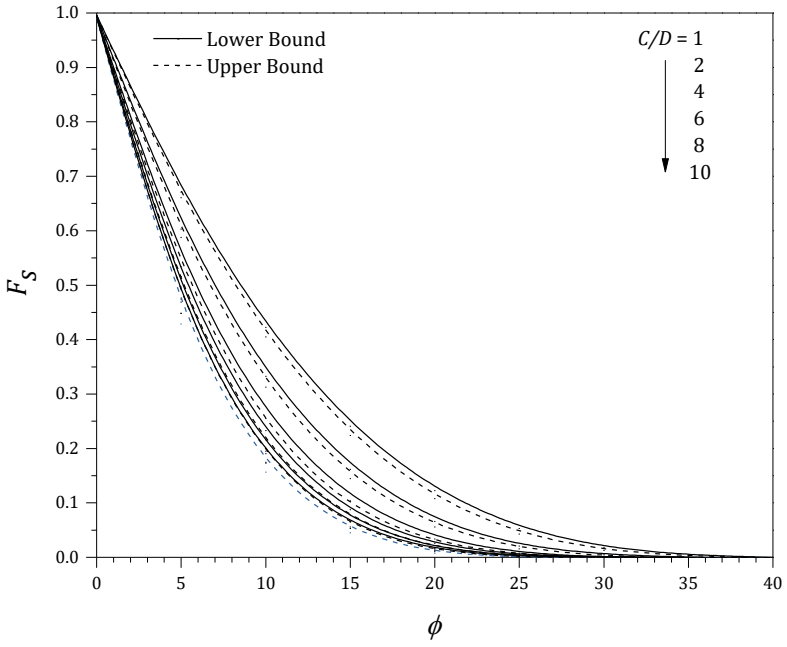

Figure 4. F_s vs ϕ for various depth ratios (C/D = 1-10).

The stability factors for unit weight (F_γ)

Tunnel stability factors based on theoretical analyses and numerical models results were discussed by Atkinson and Potts (1977), Atkinson and Mair (1981), Vermeer et al. (2002) and others. It was concluded that the values of F_γ depend only on the angle of internal friction (ϕ) and are independent of the depth of the tunnel. However, the present study produces different curves of F_γ for different depth ratios when the friction angle of the soil equal or less than 25˚. This is a significant finding for the current study based on the novel *FELA* approach.

In general, F_γ decreases as ϕ increases. A double regression analysis (Exponential and Logarithmic) was employed to develop equation 3. The correlation coefficient $r^2 = 0.983$.

$$F_\gamma = [-0.016 \times \ln(C/D) + 0.143] \times tan\emptyset^{[-0.347 \times \ln(C/D) + 0.994]} \quad (3)$$

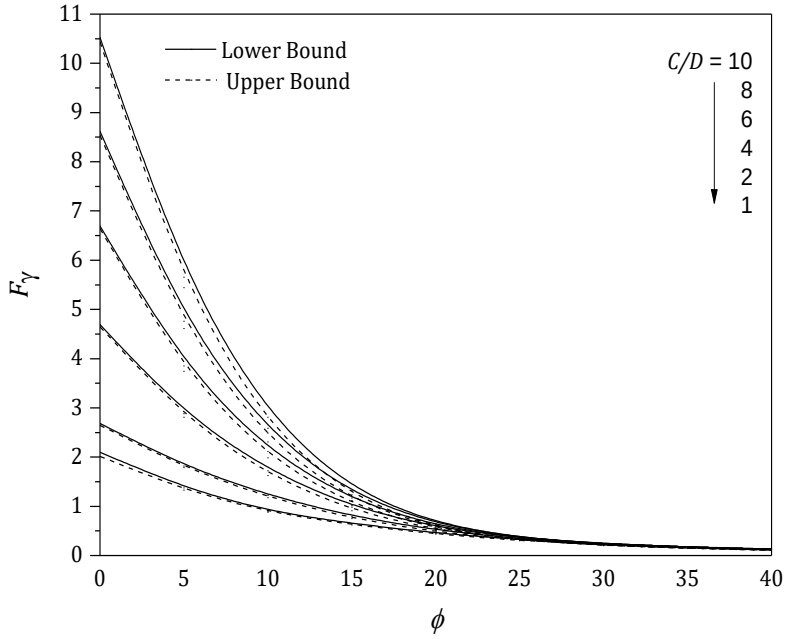

Figure 5. F_γ vs ϕ for various depth ratios (C/D = 1-10).

PRACTICAL USES AND EXAMPLES

The usefulness of the tunnel stability factors is best demonstrated through some examples. Since the lower bound theorem offers a safe assessment of the limit pressure for a stability problem, all stability factors and equations have been derived by double regression analysis based on *LB* results. The following examples demonstrated using *LB* results.

Example 1

Given soil cohesion (c) = 45 kPa, friction Angle (ϕ) = 0°, unit weight of soil (γ) = 18 kN/m^3, surcharge surface load (σ_s) = 40 kPa. The tunnel height (D) = 6m and the depth of the soil above the tunnel (C) =18m. It is required to determine the minimum support pressure at collapse.

Solution:

1. Using equations (1, 2 and 3) with C/D = 3 and ϕ = 0, F_c = 6.0, F_s = 1 and F_γ = 3.6.
2. $\sigma_t = -cF_c + \sigma_s F_s + \gamma D F_\gamma = -(45 \times 6.0) + (40 \times 1.0) + (18 \times 6 \times 3.6) = 158.8$ kPa
3. An actual *LB* analysis of this case gives a σ_t of 153.50 kPa.

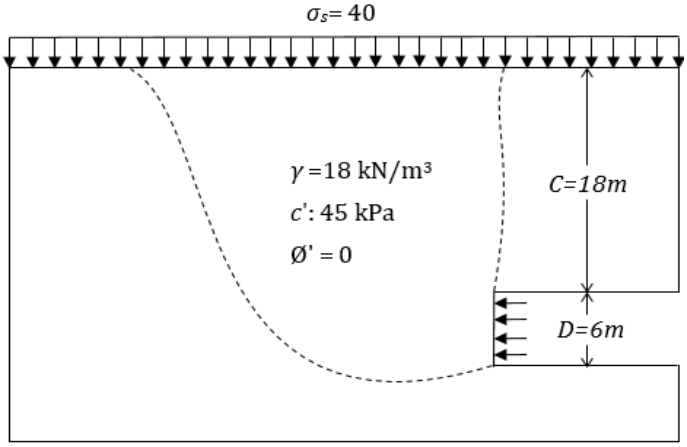

Figure 6. Statement of the problem for Example 1

Example 2

Given soil cohesion (c) = 0 kPa, friction Angle (ϕ) = 35°, unit weight of soil (γ) = 18 kN/m^3, surcharge surface load (σ_s) = 0 kPa. The tunnel height (D) = 6m and the depth of the soil above the tunnel (C) = 36m. It is required to determine the minimum support pressure at collapse.

Solution:

1. Using equations (1, 2 and 3) with C/D = 6 and ϕ = 35°, F_c = 1.43, F_s = 0 and F_γ = 0.171.
2. $\sigma_t = -cF_c + \sigma_s F_s + \gamma D F_\gamma = (0 \times 1.43) + (0 \times 0) + (18 \times 6 \times 0.171) = 18.47$ kPa
3. An actual *LB* analysis of this case gives a σ_t of 18.50 kPa.

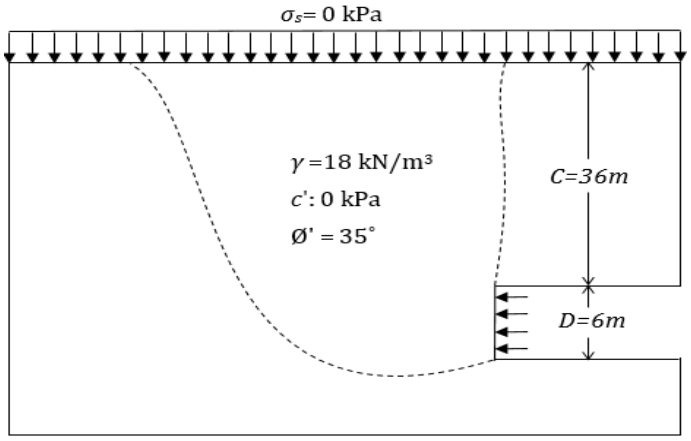

Figure 7. Statement of the problem for Example 2

CONCLUSION

In order to study the face stability of tunnel heading in cohesive-frictional soils, numerical simulations through finite element limit analyses were performed. The limit support pressure of the tunnel face for the limit conditions are of the main concerns. A series of numerical simulations in different soils (ϕ = 0 - 40) for various depth ratios (*C/D*) were performed to calculate tunnel stability factors (F_c, F_s, and F_γ). With the three factors, the minimum support pressures can be calculated using the principle of superposition ~ a similar approach to Terzaghi's bearing capacity equations. The current approach is convenient for practical engineers as it is user friendly in estimating the support pressure. Some future work may include the preparation of a comprehensive of design tables.

REFERENCES

[1] Horn, N 1961, 'Horizontal earth pressure on the vertical surfaces of the tunnel tubes', in *Proceedings of the National Conference of the Hungarian Civil Engineering Industry*, Budapest, pp. 7–16 (in German).

[2] Murayama, S, Endo, M, Hashiba, T, Yamamoto, K & Sasaki, H 1966, 'Geotechnical aspects for the excavating performance of the shield machines', in *The 21st annual lecture in meeting of Japan Society of Civil Engineers*, p. 265

[3] Krause, T 1987, 'Schildvortrieb mit flüssigkeits- und erdgestützter Ortsbrust', *Mitteilungen des Instituts für Grundbau und Bodenmechanik der Technischen Universität Braunschweig*, no. 24.

[4] Anagnostou, G & Kovári, K 1996, 'Face stability conditions with earth-pressure-balanced shields', *Tunnelling and Underground Space Technology*, vol. 11, no. 2, pp. 165-73.

[5] Broere, W 2001, 'Tunnel face stability & new CPT applications', PhD thesis, Delft University of Technology.

[6] Atkinson, JH & Potts, DM 1977, 'Stability of a shallow circular tunnel in cohesionless soil', *Geotechnique*, vol. 27, no. 2, pp. 203-15.

[7] Leca, E & Dormieux, L 1990, 'Upper and lower bound solutions for the face stability of shallow circular tunnels in frictional material', *Geotechnique*, vol. 40, no. 4, pp. 581-606.

[8] Lyamin, AV & Sloan, SW 2000, 'Stability of a plane strain circular tunnel in a cohesive-frictional soil', in *Developments in theoretical geomechanics : proceedings of the Booker Memorial Symposium*, Sydney, N.S.W., Australia, pp. 139-54.

[9] Yamamoto, K, Lyamin, AV, Wilson, DW, Sloan, SW & Abbo, AJ 2011a, 'Stability of a circular tunnel in cohesive-frictional soil subjected to surcharge loading', *Computers and Geotechnics*, vol. 38, no. 4, pp. 504-14.

[10] Yamamoto, K, Lyamin, AV, Wilson, DW, Sloan, SW & Abbo, AJ 2011b, 'Stability of a single tunnel in cohesive–frictional soil subjected to surcharge loading', *Canadian Geotechnical Journal*, vol. 48, no. 12, pp. 1841-54

[11] Atkinson, JH & Mair, RJ 1981, 'Soil mechanics aspects of soft ground tunnelling', *Ground Engineering*, vol. 14, no. 5.

[12] OptumG2 2014, Optum Computational Engineering, Version 1.2014.10.1, Newcastle, Australia.

Construction Materials

9th Int. Conf. on Geotechnique, Construction Materials and Environment,
Tokyo, Japan, 20-22 November 2019, ISBN: 978-4-909106025 C3051

ADHESIVE STRENGTH OF INJECTABLE INORGANIC ANCHOR MATERIAL IN CONCRETE

Hidenori Tanaka[1], Hayata Yanagihara[2] and Nobuyuki Sasaki[3]
[1]National Institute of Technology, Gunma College, Japan; [2,3] Former students, Japan

ABSTRACT

We have used some organic materials to connect between steel anchors and concrete structures. They are very useful to repair the cracks in concrete and to glue the steel or another organic materials to concrete structures. But, we don't apply them in water or upward injection. Especially, we couldn't fill them sufficiently in case of the upward injection. Some crucial incidents are reported because of non-filling area in hole which have to be filled with anchor materials. And then, new inorganic anchor material has been developed as applications for construction under sea water level or upward injection. However, the adhesive strength of it to concrete or steel anchor hasn't been cleared sufficiently. We carried out the adhesive strength tests (punching out shearing) between steel anchor including anchor material and concrete by using amsler testing machine. The experimental factors are diameter of injection hole, injection length, type of steel anchor, axial eccentricity of steel anchor, treatment of side surface in hole. According to the results, we found that there were some fracture modes due to some experimental factors. In cases of short injection length and round steel anchor, Adhesive interfacial fracture between steel and anchor material or between anchor material and concrete tended to be occurred. Bond-splitting fracture including cone shape fracture was shown in treatment of side surface in hole.

Keywords: Adhesive strength, Inorganic material, Fracture modes, Numerical analysis, Damage Mechanics

INTRODUCTION

We have used organic material like epoxy and urethane resin to glue steel or plastic to concrete structures. Especially, epoxy resin is useful for cracking repair or injectable material. But, these materials have some flaws for example, deterioration by UV light, nonconformity under water construction, non-filling in case of the upward injection in hole.

We have tried to adopt the inorganic material which could make up for defects as the injectable anchor material to connect to a steel anchor and concrete structures in case of the thin thick structures.

Generally speaking, Adhesive strength has been easily defined by interfacial area of two materials or hypothesis of shear or diagonal fracture (45 degree). But, we have to consider fracture modes that defined Interfacial of material, shear fracture of injectable material and bond-splitting fracture of concrete [1].

In this study, we conducted some experiments to clear the adhesive strength between steel anchor and injectable material, or injectable material and concrete block considering fracture modes by punching out shearing test. Here, the experimental factors are diameter of injection hole, injection length, type of steel anchor, axial eccentricity of steel anchor, treatment of side surface in hole.

We also showed the results of basic numerical analysis about fracture by axisymmetric problem.

ADHESIVE STRENGTH TEST

In this research, we used cylindrical concrete specimen (outer diameter = 150 mm). And, the compressive strength is 50 (N/mm^2) of concrete and 55 (N/mm^2) of injectable material.

The specimen was shown in Figure 1. And, we adopted the displacement control method by amsler. The velocity was 2.0 (mm/min). The concept of loading (punching out) was shown in Figure 2.

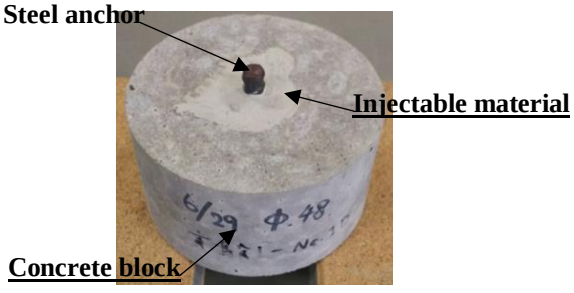

Fig.1 Specimen

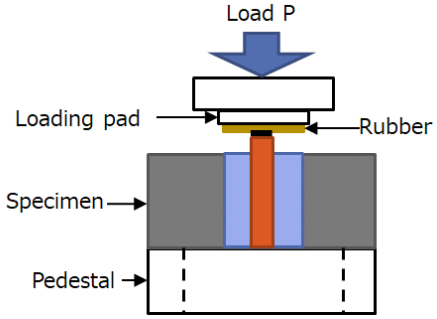

Fig.2 Loading method

Previous researches were carried out by the pulling off test which needed the special steel jigs and tools [1]-[3].Generally, The mechanism of adhesive was defined by shear behavior within a material or interfacial border between two materials. In case of isotropic material, we could apply punching out test to this research from point of theoretical and economical view. We found out that there were same fracture modes in pulling off or punching out. And, we targeted the concrete structure under 100 (mm) thickness. These were main difference between previous researches and ours.

Experimental factors

We focused on four experimental factors in this study. First, we used round and deformed bar as a steel anchor. Second, we changed the diameter and the length of injectable anchor material [2],[3]. Third, the eccentricity of steel anchor form center of hole which is equal to the center of injectable material. And fourth, we checked the influence to adhesive strength with or without side surface treatment of injectable material in hole.

The third and fourth factors also were difference between previous documents [2],[3].

Results of experiment

Influence of steel anchor

The load and displacement relation was shown in Figure.3. The maximun load of deformed bar was eleven times bigger than that of round bar. The interfacial fracture mode was occurred between round bar and injectable material (refer to Figure 4) .

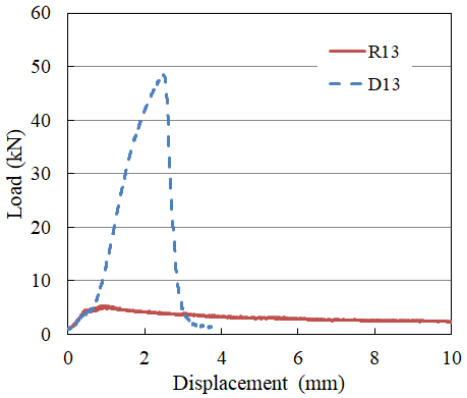

Fig.3 Load and displacement

On the other hand, The bond-splitting fracture mode was shown between deformed bar and injectable material including concrete block (refer to Figure 5). We used a deformed bar succeeding experimental cases as the steel anchor.

Fig.4 Bottom surface of specimen (R-bar)

Fig.5 Bottom surface of specimen (D-bar)

Influence of injectable diameter and length

We showed the influence of injectable diameter and length on the maximum load (refer to Figure 6).

We found out two main fracture modes whether the injectable length was less than 55 (mm) or not. It was bond-splitting fracture under 55 (mm) length. And then, In case of more than 65 (mm) length, it was founnd not only the bond-splitting but also the cone shape fracture. The cone shape fracture mode was shown in Figure 8 and 9.

The influence of injectable diameter on the maximum load has not been cleared. However, the maximum load in case of 60 (mm) diameter was the smallest, because the curve was bifurcated two peaks under 55 (mm) length (refer to Figure 7) .

The maximum load trended to be in inverse proportion to the injectable dimameter in cases of more than 65 (mm) length.

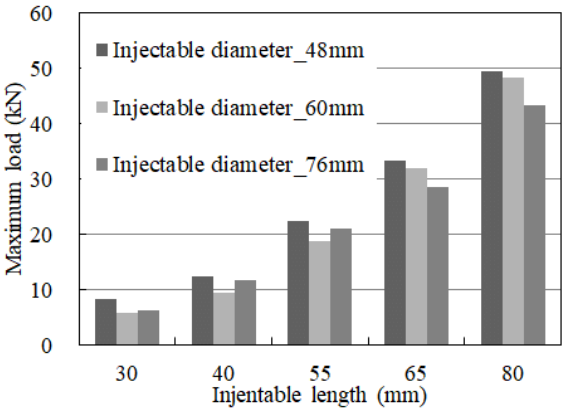

Fig.6 Maximum load and injectable length, diameter

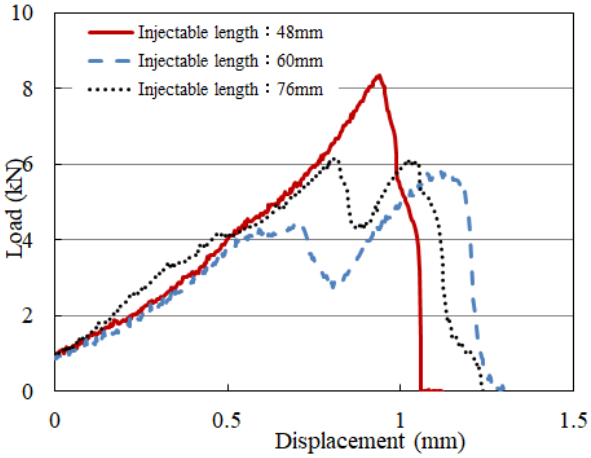

Fig.7 Load and displacement (length=30 (mm))

Becase the height of cone shape became lower in inverse proportion to the injectable diameter, the total area against the load got smaller (refer to Figure 8 and 9) . We thought that was main reason.

Fig.8 Cone shape fracture (ℓ=65 (mm),d=60 (mm))

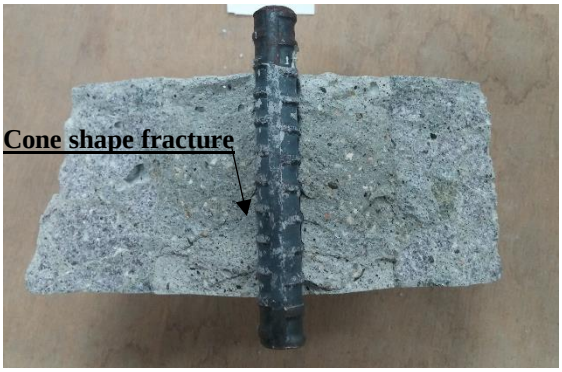

Fig.9 Cone shape fracture (ℓ=65 (mm),d=80 (mm))

Influence of the eccentricity of steel anchor in hole

We had to check the influence of the eccentricity of steel anchor on adhesive strength in order to avoid the inconsistency of steel anchor position in hole.

The e of legend in Figure 10 notes that the eccentricity value from center of hole.If there were 8 (mm) eccentricity from center, The maximum load was about 30 percent smaller than that of center and the bifurcation was occurred in the curve (refer to Figure 10).

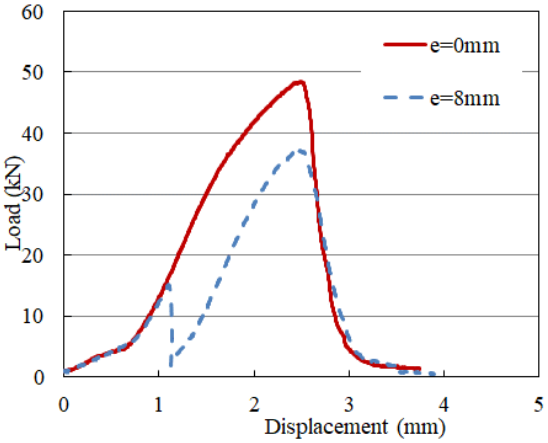

Fig.10 Load-displacement curve (eccentricity of bar)

I thought that it was caused by the shift from bond-splitting to cone shape fracture. At first, the bond-splitting was occurred and next, the mechanism of fracture was shifted to the cone shape mode (refer to Figure 11). The standard case was bond-splitting mode in Figure 12.

Fig.11 Bottom surface of specimen (e=8 mm)

Fig.12 Bottom surface of specimen (e=0 mm)

Influence of treatment of side surface of hole

Most of the time, The suface treatment in hole

was carried out by brush to improve the adhesive strength between injectable material and concrete [4]. In this research, we did the surface treatment by brush and checked the influence of that. There were about 17 percent difference with or without treatment on maximum load in Figure 13.

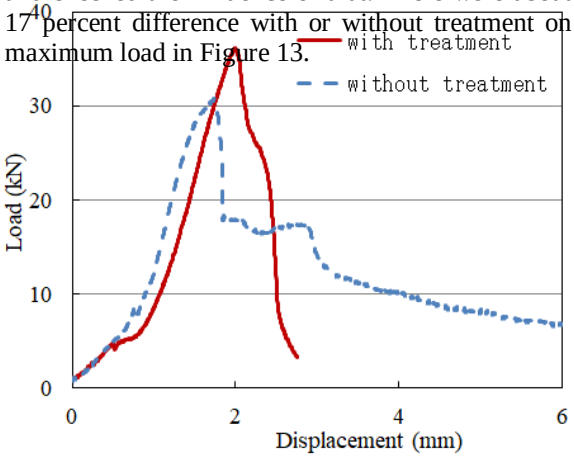

Fig.13 load and displacement (treatment)

Fig.14 Without treatment

Fig.15 With treatment

The fracture modes were shown in Figure 14 and Figure 15 respectively. The interfacial fracture was occurred between injectable material and concrete without treatment. On the other, the bond-splitting fracture was occurred with treatment. It was found that the fracture mode was shifted with or without treatment of surface in hole.

NUMERICAL ANALYSIS (FIRST VERSION)

In this section, we showed the results of numerical analysis that was applied to damage mechnics [5]. And, we conducted numerical analysis by finite element method considering axisymmetric problem to evaluate the basic fracture mode which was so called the interfacial border fracture.

Constitutive equation

It was important to evaluate the equivalent stress and strain of material in numerical analysis. The constitutive equation was defined as followed [6].

$$F = F_p(\bar{\sigma},\gamma,D) + F_D(Y;p,D) = \bar{\sigma}_{eq} - \gamma - \sigma_y + \frac{S_1}{(S_2+1)(1-D)}\left(\frac{Y}{S_1}\right)^{S_2+1} \quad (1)$$

Where, F_p is the potential for the growth of plastic strains, which is a function of the effective stress $\bar{\sigma}$, the plastic hardening parameter γ and the scalar damage variable D.

F_D is the potential for the evolution of damage which is a function of the strain energy release rate Y, the equivalent plastic strain and the damage variable p.

In the formulation of the constitutive equation, the yield function is assumed as follows:

$$f = F_p = \bar{\sigma}_{eq} - \gamma - \sigma_y = 0 \quad (2)$$

$$\bar{\sigma}_{eq} = \sigma_{eq}/(1-D) \quad (3)$$

$$\sigma_{eq} = \alpha I_1 + \left(J_2^{'}\right)^{1/2} \quad (4)$$

Where the following notations are used. $\bar{\sigma}_{eq}$;effective Drucker-Prager's equivalent stress, σ_y ;the yield stress, ; α material parameter, I_1 ;the first invariant of stress and $J_2^{'}$;the second invariant of deviatoric stresses.

$$dD = \left(\frac{Y}{S_1}\right)^{S_2} dp \qquad Y = \frac{\sigma_{eq}^{\ 2}}{2E(1-D)^2} \quad (6)$$

$$d\sigma = (1-D)d\bar{\sigma} - \bar{\sigma}dD = D_{epd}d\varepsilon$$

$$\mathbf{D}_{epd} = \left[(1-D)\mathbf{C} - \left\{(1-D)\mathbf{C}\frac{\partial F_p}{\partial \bar{\boldsymbol{\sigma}}} + \bar{\boldsymbol{\sigma}}\frac{\partial F_D}{\partial Y}\right\}\frac{\left(\frac{\partial F_p}{\partial \bar{\boldsymbol{\sigma}}}\right)^T\mathbf{C}}{H + \left(\frac{\partial F_p}{\partial \bar{\boldsymbol{\sigma}}}\right)^T\mathbf{C}\frac{\partial F_p}{\partial \bar{\boldsymbol{\sigma}}} - \frac{\bar{\sigma}_{eq}}{1-D}\frac{\partial F_D}{\partial Y}}\right] \quad (7)$$

D_{epd} meant elasto-plastic and damageable stiffness tensor, C is general elastic tensor.

We used the same relationship between equivalent stress and strain both injectable material and concrete. Because the compressive strength and these mechanical properties were almost same value. The basic prameters were shown in Table 1.

Figure 16 showed the compressive stress test of concrete specimen comparing with the numerical constitutive equation (MODEL in Fig.16).

Table 1 Material parameters

Parameter	Value
E (Young Modulus)	30.0 (kN/mm^2)
ν (Poisson's ratio)	0.17
α (equivalent stress)	0.72
σ_y (yield stess)	0.75 (N/mm^2)
K (plastic hardening)	40.0 (N/mm^2)
n (plastic hardening)	0.215
S_1 (damage paremeter)	0.000215 (N/mm^2)
S_2 (damage parameter)	1.55

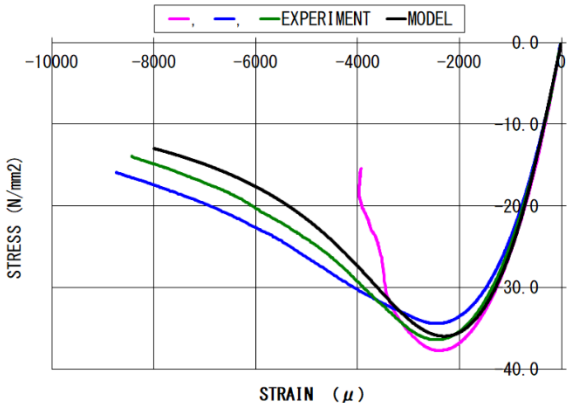

Fig.16 stress-strain cure (concrete)

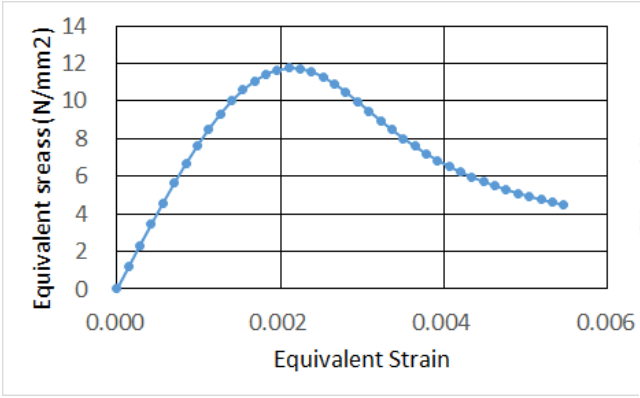

Fig.17 Equivalent stress-strain curve

Examle of analysis

We took the specimen without steel bar as the example of analysis. Because it was needed to confirm the basic fracture mode between injectable material and concrete. The final state was shown in Figure 18.The analysis model was half considering axisymmetric (refer to Figure19) .

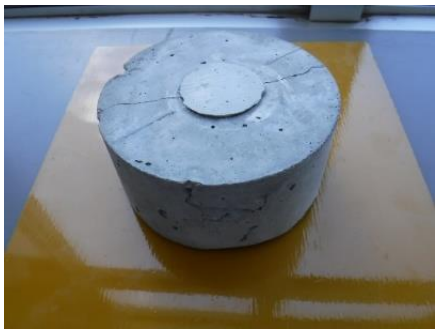

Fig.18 Bottom of specimen (example)

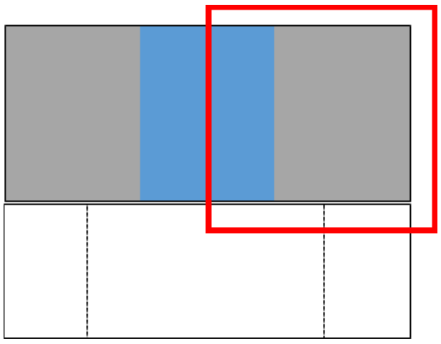

Fig.19 Analysis area (1/2model)

The analysis was based on elasto-plastic problem [7]. We used Von Mises type as the yield function.

Result of analysis

The distribution of equivalent stresses were shown in Figure 20. The analysis was carried out to controll the displacement at the top of injectable material. We showed each distribution of stresses from the top to the bottom in proportion to controlled displacement (refer to Figure 20,Numit:(N/mm^2)).

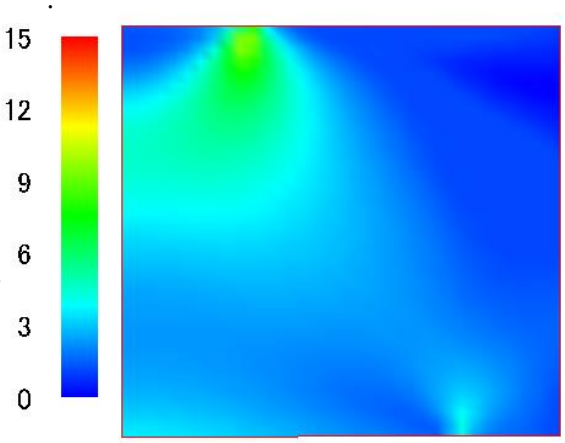

Fig.20 Distribution of equivalent stress No.1

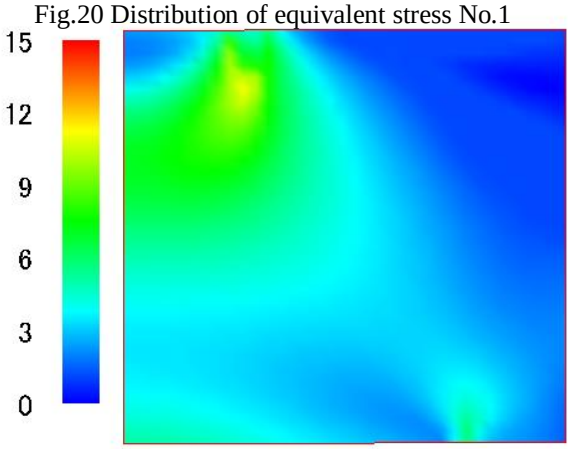

Fig.20 Distribution of equivalent stress No.2

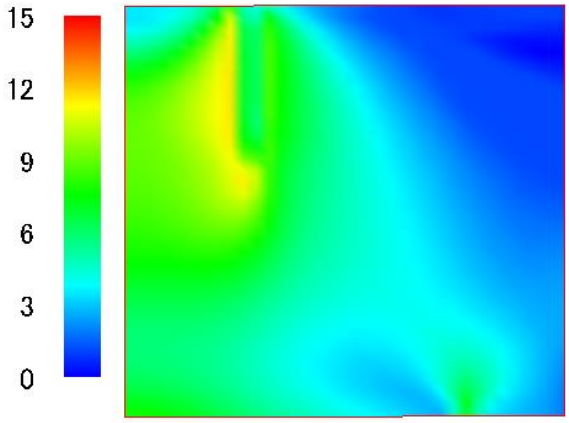

Fig.20 Distribution of equivalent stress No.3

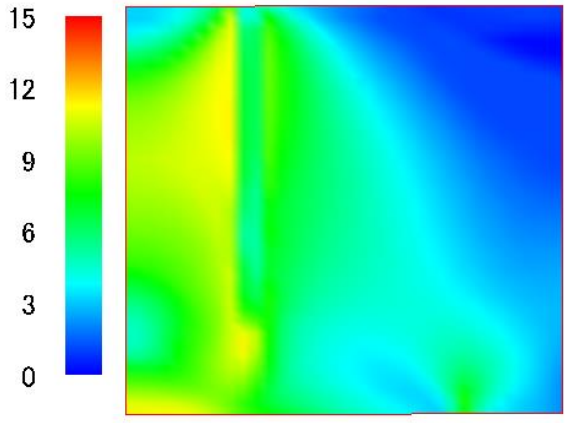

Fig.20 Distribution of equivalent stress No.4

CONCLUSIONS

The knowledge found in this research were as below.

(1) The mixed fracture modes of bond-splitting and cone shape were found over 65 (mm) length of injectable material.

(2) The maximum load was decreased about 30 percent because of the eccentricity of steel anchor.

(3) The fracture mode was shifted from the interfacial to the bond-splitting with or without the treatment of surface in hole. And, the maximum load of with the treatment was 17 percent bigger than that of without.

(4) The crack was occurred along the border of injectable material and It had good response to the experimental result.

(5) We have the plan to change the strength of concrete and the shape of side surface in hole.

(6) It needs to improve the relationship between equivalent stress and strain about concrete and injectable material.

(7) We will try to carry out the analysis including steel anchor and various strength of concrete.

ACKNOWLEDGMENTS

Authors appreciate Sumitomo Osaka Cement Co.,Ltd. for providing the injectable inorganic anchor material so called “Ceme-force Anchor “.

REFERENCES

[1] Shigehiro Ando, Katsuhiko Nakano, et al, Relationship between crack width of concrete an retention ratio of ultimate load for cast-in-place anchor and inorganic post-installed anchor, Architecture of Technology and design, Vol.25,Issue 59,2019,pp51-54.

[2] Akihiro Kawakami, Kazuhiro Watanabe, et al, Characteristics of post-installed rapid hardening cement bonded anchor Part3, Summaries of technical papers of annual meeting Architectural Institute of Japan, 2013, pp79-80.

[3] Shigehiro Ando, Katsuhiko Nakano,et al, Influence of environment and construction condition on the adhesive strength of post – installed rapid hardening cement bonded anchor, Proceedings of the Japan Concrete Institute,Vol.35, No.2, 2013,pp.535-540

[4] Design and construction guideline of post-installed anchor and continuous fiber reinforcement, Ministry of Land, Infrastructure, Transport and Tourism, July, 2006

[5] J.Lemaitre, A course on Damage Mechanics, Springer, August, 1990

[6] Hidenori Tanaka, Yutaka Toi, Adhesive Failure Analysis of Structural Elements Reinforced with Carbon Fiber Sheet, Transaction of the Japan Society of Mechanical Engineers, Series A, Vol.72, No.724,2006,pp.198-204

[7] EA de Souza Neto, D Peric, DRJ Owen, Non-linear finite element method, June,2012

9th Int. Conf. on Geotechnique, Construction Materials and Environment, Tokyo, Japan, 20-22 November 2019, ISBN: 978-4-909106025 C3051

EFFECT OF CURING PERIOD ON THE PROPERTIES OF CONCRETE

M. A. Rahman [1], M. A Rasid [2], Rita Khatun[3] & Sabuj Chakma[4]

[1] WRP, Institute of Water Modelling (IWM, Dhaka, Dhaka,
[2] Civil Engineering, DUET Gazipur,Gazipur,
[3] Engineering, MECTECH Corporation Ltd, Dhaka,Dhaka,
[4] RHD, Roads & Highway Department, Khagrachhari,

ABSTRACT

Concrete's strength is derived by the hydration of cement particles which requires sufficient moisture. Curing can be considered as a way of moisturizing the concrete for the hydration process. The principal objective of this study is to find the effect of curing period on the properties of concrete. The curing period of concrete has been kept variable through this study. The properties of materials are determined according to ASTM specification and only one mix proportion is used. In this study, a series of concrete cylinders have been cast and cured for 0, 3, 7, 14, 21 and 28 days. Each specimen has been tested after 28-days and basic properties of concrete such as compressive strength, tensile strength and modulus of elasticity have been determined. Mix proportion of concrete has been considered as 1:2:4 by volume and ratio of water cement has been used 0.5 by weight. Specimens have been immersed in fresh water for curing process. It has been observed from the study that the compressive and tensile strength both increases linearly and gradually with the increase of curing periods respectively. Also increasing rate of tensile strength is slower for short period rather than long period.

Keywords: Curing; Concrete strength; Hydration; Compressive and Tensile strength.

INTRODUCTION

Concrete is a mixture of cement, water and aggregate which produces firm and hard mass making it durable. The quality and durability of concrete depend both on the quality and properties of ingredients and method of preparation, placing, curing and environmental conditions to which it is exposed over its service life.

In the practical, higher water-cement ratio is used where the concrete remains open to atmosphere. The water used in the concrete evaporates and quick surface drying of concrete results extraction of moisture from the concrete mix. Remaining water in the concrete is not sufficient for effective hydration. Extra water must be added for the proper hydration during a specified period to replenish the loss of water by absorption and evaporation. (Shetty, 2005)

The strength of concrete starts developing immediately after settling is completed which continues for an indefinite period at a rate gradually diminishing with time. 80-85% of the strength is attained within first 28 days and hence this strength is considered to be the design criterion. Submerged method is the most effective method of curing during laboratory tests.

Objectives

- Study the effect of curing period on the compressive strength of concrete.
- Find the effect of curing period on the modulus of elasticity of concrete.

MATERIALS AND METHODOLOGY

The Second Level Headings

The strength of concrete is greatly influenced by the properties of ingredients in the concrete mix. Cement, Fine Aggregate, Coarse Aggregate and Water are generally used in concrete:

Cement

Holcim is one of the world's leading cement, for this study Holcim ordinary Portland cement has been used. Its specific gravity ranges from 3.12 to 3.16 and weight 1208 kg/m3 (94lb/ft3). The specific gravity of cement used in this study is 3.15.

Fine Aggregate

Fine aggregate passes through a 4.75 mm IS sieve and contains material permitted by the specifications. The fine aggregate that has been used in this study was mix of 50% Sylhet sand and 50% local sand. The value of F.M of combined fine aggregate is 2.59 where the F.M of fine sand is 1.86 and coarse sand is 3.32

Coarse Aggregate

Most of the coarse aggregate are retained on the 4.75mm IS sieve and contain material permitted by specifications. Generally, brick chips are used as coarse aggregate. Brick chips are prepared by crushing

first class bricks and 3/4" down grade chips are selected for this study.

Table 1: Properties of brick

Compressive strength	35.1 (MPa)
Absorption capacity	8.45% (by weight)

Properties of Coarse Aggregate
The test method for sieve analysis of coarse aggregate conforms to the ASTM standard requirements of specification C136. Maximum size of coarse aggregate was 3/4".

Table 2: Properties of coarse aggregate

Common properties	Brick aggregate
Dry unit weight	18.62
Absorption capacity (%)	12.47
Bulk specific gravity (S.S.D)	1.92
F.M	6.54

Water

Water is essential for concrete to initialize chemical reaction with cement, to wet the aggregate, and to lubricate the mixture for workability. Since the quality of water effects the strength it is necessary to ensure fresh water. Normally, drinking water is used for mixing. Water having harmful ingredients such as contamination, salt, oil, sugar or chemical is deleterious to the setting properties of cement. It can damage the affinity between the aggregate and cement paste also adversely affect the workability of mixture.

PREPARATION OF TEST SPECIMENS

Quality of concrete requires careful care exercised at every stage of concrete manufacturing. The various stages of casting test specimens are batching, mixing, placing and compacting, and curing.

Batching

The correct method of measuring the materials is weigh batching. For important concrete, invariably, weigh batching system is should be adopted. In this study weigh batching has been used for measuring water cement ratio and volume batching is used for measuring the materials.

Mixing

Tilting type mixer machine has been used for the study to mix up the concrete. After loading the mixer machine, the mixing process should be continued till a thoroughly and properly mixed concrete is obtained. Speed of this mixer machine was about 15-20 rpm. Mixing time was 5-6 minutes.

Placing and Compacting

After mixing the concrete is placed in a cylindrical mold in three layers. Each layers compacted by a 25mm bar with rounded end. Compaction is accomplished by doing external work on the concrete. In this study compaction was done by manually. In the process of placing and mixing, air might have been trapped in the concrete. If the air is not removed entirely, the strength of concrete will decrease significantly.

Curing of Concrete

During the first few days and weeks, fresh concrete gains strength rapidly. Structural design is usually based on the 28-days strength, about 70 percent of which is reached at the end of first week after casting. The final concrete strength depends largely on the conditions of moisture and temperature during this initial period.
In this study water curing method was used for curing of concrete. Test specimens have been immersed in curing tank for 3-days, 7-days, 14-days, 21-days, 28-days. Some specimens have been immersed for 25-days which have not been immersed in water for first 3-days after casting. Some specimens have been immersed for 21-days which have not been immersed in water for first 7-days after casting. Some specimens have allowed for no curing totally.

TESTING OF CONCRETE SPECIMENS

Testing of harden concrete plays an important role in controlling and confirming the quality of cement concrete work. Following tests have been commonly used to determine the properties of hardened concrete.

Test for Compressive Strength

Compression test is the most common test on hardened concrete. In this study cylindrical specimens have been used. The size of the cylinder specimens is 6 in. dia. and 12 in. height. Universal testing machine has been used for loading which is illustrated in Fig 1. Capacity of the testing machine 1000 KN and rate of loading is 250 KN/minute. The test method conforms to the ASTM standard requirements specification C39 for cylinder. The compressive strength of test specimens of concrete has been determined at 28-days but different curing periods have been used for different specimen.

Fig 1: Photo view of set up of compressive strength

Test for Modulus of Elasticity

The modulus of elasticity is determined by subjecting a cylinder specimen to uniaxial compressing and measuring the deformation by means of dial gauges fixed between certain gauge lengths showing in Fig 2. Dial gauge reading divided by gauge length will give the strain and loads are divided by area of cross section will give the stress. A series of reading is taken and stress-strain relationship is established. Thus, the modulus of elasticity Ec (N/mm2), that is, the slope of the initial straight portion of the stress-strain curve, is seen to increase as the strength of concrete increases. The modulus of elasticity values obtained will usually be less than moduli derived under rapid load application (dynamic or seismic rate, for example) under slow load application (extended load duration) provided another test condition have been kept the same.

Fig 2: Photo view of set up for modulus of elasticity test

RESULTS AND DISCUSSIONS

Compressive Strength of Concrete

The compressive strength of concrete varies with the change of curing period. In this study it has been obtained that the variation is linear (**Error! Reference source not found.**). The result of compressive strength of concrete are summarized in **Error! Reference source not found.**.

Table 3: Test result of compressive strength

Curing Period (day)	Compressive Strength (MPa)
No curing at all	15.67
3	17.68
7	17.25
14	20.08
21	22.46
28	24.31

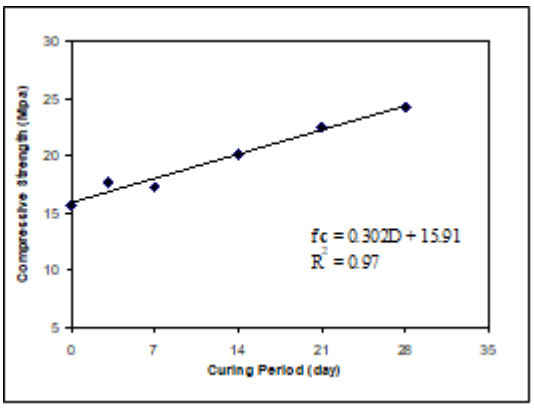

Fig 3: Relation between the compressive strength and curing period.

The following equation is suggested to express the relationship

$$f_c^{'} = 0.302D + 15.91 \quad (1)$$

Where, f_c'= Compressive strength of concrete in Mpa, D= Curing period in day.

From the test results we obtain that the specimen which were cured for 0, 3, 7, 14, 21 days attained 65%, 69%, 74%, 82%, 91% strength as compared to the strength of 28 days cured specimen. The strength of concrete increases almost linearly with the curing period, so from the experimental data it can be say that proper curing up to a specified period is must be required for attaining the desired strength of concrete.

Modulus of Elasticity of Concrete

The modulus of elasticity is determined by the formula, $f_c^{'} = \frac{2P}{\pi LD}$ (Hossain. N, Concrete structure)

The modulus of elasticity is affected by curing period but no relationship can be defined with such limited number of experimental data. The variation of modulus of elasticity is shown in

The result of modulus of elasticity is summarized in **Error! Reference source not found.**.

Table 4: Test result of modulus of elasticity

Curing Period (day)	Modulus of elasticity (Mpa)
No curing at all	45,880
3	42,700
7	44,350
14	42,610
21	45,630
28	44,400

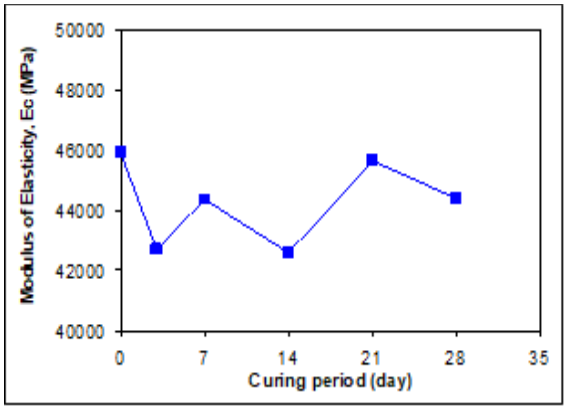

Fig 4: Variation of modulus of elasticity with curing period.

RELATION BETWEEN COMPRESSIVE STRENGTH AND TENSILE STRENGTH

Depending on the curing variation the relation between compressive strength and the tensile strength is established. The relation is shown Fig 2

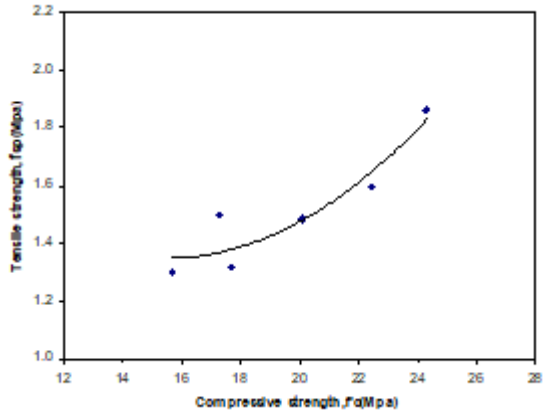

Fig 2: Relation between Compressive strength and Tensile strength in different curing period

Result show that the tensile strength is increasing with the increasing of compressive strength. This rate of increasing is lower than the increasing rate of compressive strength. The curve shows that the rate of increasing of tensile strength is lower in less compressive strength and higher in larger compressive strength.

$$f_{sp} = 0.0061f_c'^2 - 0.188f_c' + 2.8 \quad (2)$$

Where,
f_{sp}= Tensile strength of concrete (MPa)
f_c'= Compressive strength (MPa)

CONCLUSIONS

Concrete is the most widely used construction materials. When other factors remain same the quality control is the main factor to get good concrete. Curing of concrete is crucial to attain the desired strength of concrete. Concrete hardens and gains strength as it hydrates. The hydration process continues over a long period of time. It happens rapidly at first stage and slows downward trend as time increases. However, hydration occurs only if water is available and if the concrete temperature remains within an appropriate range. During the curing period initially, concrete surface needs to be kept moist to permit the hydration process. So, it is clear that for attaining desired strength, the concrete must be cured sufficiently up to a specified time period.

The main objective of this project work is establishing a relationship among curing period and different properties of concrete. Analysing the result, it has been figured out that

(i) Compressive strength increases linearly up to 28 days with the increasing in curing periods and compressive strength can be determined by using the equation

$$f_c^{'} = 0.302D + 15.91$$

(ii) Tensile strength increases gradually with the increasing in curing periods, the increasing rate is lower in short curing period becomes higher in longer period and the tensile strength can be determined by using a two-degree equation

$$f_{sp} = 0.0061f_c'^2 - 0.188f_c' + 2.8$$

ACKNOWLEDGMENTS

At first authors are grateful to almighty Allah for giving the strength and courage that we have completed the study successfully. The completion of this study involves contribution and assistances from many individuals. First of all, we would like to express our invaluable profound gratitude to our supervisor Dr. M.A. Rashid, Professor, Department of Civil Engineering, Dhaka University of Engineering and Technology (DUET) for his valuable continuous guidance, helpful suggestion and constant encouragement throughout the thesis. His generous suggestions and directions during this period have led to the completion of this thesis. We are also grateful to him for acquainting us with the world of advanced technology.

Finally, the authors would like to convey their thanks to the Department of civil Engineering. They also express their sincere gratitude to Dhaka University

of Engineering and Technology (DUET), Gazipur, for providing the necessary fund to fulfil the entire project.

Table 5: Table of the test results

Curing period (day)	Compressive Strength, f_c' (MPa)	Tensile strength, f_{sp} (MPa)	Modulus of elasticity, E_c (MPa)	Unit Weight Kn/m^3	Water absorption (By weight)	Ratio $f_{sp}/\sqrt{f_c'}$	Ratio $E_c/\sqrt{f_c'}$
No curing at all	15.67	1.30	45880	19.80	12.56%	0.083	11590
3	17.68	1.32	42700	20.20	13.78%	0.074	10155
7	17.25	1.50	44350	20.21	13.85%	0.087	10680
14	20.09	1.48	42613	21.42	12.75%	0.074	9508
21	22.46	1.60	45633	20.30	13.15%	0.071	9628
28	24.31	1.86	44400	20.73	13.13%	0.076	9005
Curing period: 4th to 28th days	20.77	1.42	49120	21.10	13.78%	0.068	10778
Curing period: 8th to 28th days	21.72	1.40	45237	20.95	12.89%	0.064	9707

REFERENCES

[1] Aziz, M.A (1973) "Engineering Materials" 1st Edition.

[2] Carino,N.J and Meeks,K.W (2000) "Curing of High Performance Concrete for

[3] Hossain, N.M "Structural Concrete"1st edition.

[4] Hilsdorf and Burieke, (1992), "Influence of Initial Curing on Concrete

[5] Nevil, A.M "Properties of Concrete" Third edition, London, Pitman Publishing Limited (119-339)

[6] Nilson, H.A and Darwin.D. (1997), "Design of concrete structures"12th edition, Printed in Singapore.

[7] Shetty M.S. "Concrete technology" second edition published by S.Chand & Company Ltd India.

[8] Uddin, S and Amin, A.F.M S, (1998) "Effect of Curing Period on the Compressive Strength of Concrete"

9th Int. Conf. on Geotechnique, Construction Materials and Environment, Tokyo, Japan, 20-22 November 2019, ISBN: 978-4-909106025 C3051

COMPRESSIVE STRENGTH OF CONCRETE WITH SEAWATER AND POWDERED EGGSHELLS AS PARTIAL REPLACEMENT FOR CEMENT

Bernardo A. Lejano[1], Rev Jacob D. Barron[2], Philip Daniel T. Saludo[2], Jericho Mari C. Tugade[2], and Ken L. Yokohama[2]
[1]Faculty, Gokongwei College of Engineering, De La Salle University, Philippines;
[2]Student, Gokongwei College of Engineering, De La Salle University, Philippines

ABSTRACT

In efforts to generate sustainable concrete, alternative mixing constituents are used. In this study, the use of powdered eggshells as partial cement replacement and seawater as freshwater replacement were explored. The experiment consisted of two phases. First phase was the investigation of 50-mm mortar cube specimens to determine the effect on the compressive strength of mortars with 5% cement replacement with powdered eggshells that were heated at varying temperatures and duration. In the preparation of powdered eggshells, the heating duration was varied at 3, 6, and 12 hours while the temperature was varied at 100^{O}C and 200^{O}C. Base on the compressive strength test results, it was determined that heating of powdered eggshells at 100^{O}C for 12 hours achieved the highest compressive strength. Results of Scanning Electronic Microscope (SEM) showed that there was formation of fiber-like structures for mixes with powdered eggshell. This is believed to be the cause of increase in strength. For the second phase, the better heating method of powdered eggshells that was determined from the first phase was adopted and was used as mixing guide for the cylindrical concrete specimens. The three water-cement ratios used in making the concrete cylinders were 0.4, 0.5 and 0.6. All water-cement ratios of concrete cylinders cured for 28 days exhibited increased compressive strength as powdered eggshells were added as partial cement replacement. It was also determined that the compressive strength further increased when both seawater and powdered eggshells were utilized in concrete. An increase up to 36.4% was observed.

Keywords: Cement Replacement, Compressive Strength, Concrete, Eggshells, Seawater

INTRODUCTION

The versatility of eggs as food and other usage resulted to large volume of production which in turn produces a lot of eggshell waste. In poultry hatchery plants alone, huge volume of eggshells is produced. Currently the most viable disposal is throwing them into landfill sites. Eggshells are composed of 97% calcium carbonate [1], one of the main components of cement. Hence, several researches have been conducted regarding the utilization of powdered egg shells as a partial replacement for cement in concrete. These eggshells were either, air-dried, sun-dried or oven-dried before being grounded into powder. Although there are contradicting reports, results of some researchers [2]-[4] have shown that concrete with powdered eggshells have produced higher compressive strength than conventional concrete.

Another aspect of this research is the water used in concrete. Currently, the use of seawater in concrete is not allowed as stipulated in most building codes worldwide. However, shortage of freshwater is already experienced in certain areas even though they are close to the seashore. In addition, the increasing demand for water and the rising global temperatures also increase the cases of freshwater shortage. Thus the use of seawater in concrete production is worthy to investigate. Concrete with seawater as ingredient may be possible to use in structural application [5].

With the foregoing statements, this study is conducted to determine whether the utilization of eggshells and seawater are suitable alternative materials in the production of concrete; powdered eggshells as partial replacement for cement and seawater as a substitute for freshwater. The specific objectives are the following: (a) To determine the temperature and duration of heating of powdered eggshells that will produce mortar with the highest compressive strength; (b) To determine the effects of powdered eggshells and seawater on the compressive strength of concrete; and (c) To determine whether the concrete with powdered eggshells and seawater will be cost efficient.

The possible use of eggshells and seawater would be beneficial in protecting the environment. Partially replacing cement with powdered eggshells will not only address eggshell waste disposal but also reduce cement consumption. Cement production is one of the largest sources of carbon dioxide emissions, thus reduction of cement consumption will result to reduction of carbon

dioxide emissions. Ultimately, the use of eggshells and seawater would also address the sustainability of environmental resources. This is also in line with other researches utilizing other waste materials like fly ash, powdered mussel shells, and others as possible partial cement replacement [6].

METHODOLOGY

The experimental program was divided into two phases. The first phase is the test of mortar specimens while the second phase is the test of concrete specimens.

The production of mortars had different duration and temperature of heating of powdered eggshells. The duration and temperature of heating that yielded the highest compressive strength of mortar was used in the mix design of concrete.

Preparation of Eggshells

The chicken eggshells that were used were obtained from an egg hatchery plant. The hatchery plant produced eggs from a specific type of chicken called Gallus Domesticus or also known as Broiler chickens. The eggshells were subjected to initial disinfection process. This process involved cleaning with water until unnecessary substances are removed, especially the soft membranes. The eggshells were air dried for 24 hours. Then they were crushed, grinded, heated and sieved through a 100 μm sieve, similar to previous research in preparing powdered mussel shells [6]. The crushed eggshells were then placed inside the oven having two different heating temperatures, 100°C and 200°C, and three different duration of heating, particularly 3, 6, and 12 hours. Heating the crushed eggshells was done to determine the optimum duration and temperature to enhance the strength of the mortar specimens.

First Phase: Test of Mortar Specimens

The mortar samples used for compressive test were 50 mm cube specimens. The mortar cubes had a sand to cement ratio of 2.75 to be mixed at a water-cement ratio (W/C) of 0.5. All proportions are by weight. Furthermore, a 5% constant partial replacement of the total weight of cement with powdered eggshell was adopted based on the findings of previous researches [2], [3].

Thirty two (32) cases of mortar cubes were prepared to evaluate effects of the four parameters considered. For each case, 5 specimens were tested, for a total of 160 specimens. Shown in Table 1 are the codes used for naming the different cases of mortar specimens. The name of the specimens was based on the parameters in the following order: heating temperature of eggshells, type of water, curing age, and duration of heating of eggshells.

Table 1 Codes for naming the mortar specimens

Temperature (^{o}C)	Water Type	Curing (days)	Duration (Hours)
100	F=freshwater	7	III=3
200	S-seawater	28	VI=6
			XII=12

The code names were based on the four parameters. For example, the mortar specimens with code name 100F7-III is identified as follows: the first code "100" refer to 100^{O}C heating temperature, the second code "F" means that freshwater was used, the third code "7" refers to specimens cured for 7 days, and the last code "III" means the heating durations was 3 hours. There were also specimens without cement replacement. The codes used for these specimens were only the water type and curing age, that is, F7, F28, S7, and S28. For the specimens with powdered eggshells that were not heated, "0" was added for the heating duration, that is, F7-0, F28-0, S7-0, and S28-0. It should be noted that specimens F7 and F28 served as the control specimens for 7-day and 28-day curing, respectively.

Scanning Electron Microscope (SEM) analysis was done to the mortar specimens to determine the microscopic structural changes that occurred due to the presence of powdered eggshells and seawater.

Second Phase: Test of Concrete Specimens

Concrete cylindrical specimens measuring 100 mm in diameter by 200 mm in height were prepared with the following parameters considered: water-cement ratio, W/C (0.4, 0.5 and 0.6); type of water (freshwater or seawater), and with or without cement replacement. Table 2 shows the codes used in naming the specimens. For example, a specimen named 0.4FX refers to concrete specimen with W/C=0.4, "F" for freshwater, and "X" for no partial replacement of cement.

Table 2 Codes for naming the concrete specimens

W/C	Water	Cement Replacement
0.4	F=freshwater	X=None
0.5	S=Seawater	E=With
0.6		

The adopted percentage of partial cement replacement with powdered eggshells was also 5%. The preparation of powdered eggshells used in this phase was one that produced the highest compressive strength in the mortar test in phase 1. For the parameters considered, 12 cases of concrete mixes were prepared. Five concrete cylinders had to be made for the compression strength test, for a total

of 60 concrete cylindrical specimens.

After mixing the concrete, fresh concrete properties (slump, wet density and air content of the concrete) were evaluated. Curing of concrete was done for 28 days. Freshwater was used in curing concrete. After curing the specimens were subjected to compressive strength test.

RESULTS AND DISCUSSION

The main output of this research is the evaluation of the effects of powdered eggshells and seawater on the strength of mortar and concrete. In addition, other data and experiment results will be presented in this section.

Properties of Materials Used

Table 3 shows the properties that were obtained from the raw materials used in this research. The raw materials are Portland cement, fine aggregates (sand), coarse aggregates (gravel), and water. These properties were needed in designing the mix proportion of mortar and concrete.

Table 3 Properties of materials used

Material Properties	Values
Specific gravity of Cement	3.16
Specific gravity of CA	2.804
Specific gravity of FA	2.353
Absorption of CA (%)	1.18
Absorption of FA (%)	3.80
Dry-rodded density of CA (kg/m^3)	1813
Fineness modulus of FA	2.76
Density of seawater (kg/m^3)	1025.8
Salinity of Seawater (%)	3.7

Note: FA=fine aggregates, CA=coarse aggregates

Table 4 Properties of powdered eggshells

Classification of Powdered Eggshells	SG
Air-dried eggshells for 24 hours	2.466
Heated at 100^{o}C for 3 hours	2.393
Heated at 100^{o}C for 6 hours	2.466
Heated at 100^{o}C for 12 hours	2.505
Heated at 200^{o}C for 3 hours	2.495
Heated at 200^{o}C for 6 hours	2.486
Heated at 200^{o}C for 12 hours	2.534

Note: SG=specific gravity

The material property of eggshell was measured in terms of the specific gravity. Shown in Table 4 are the values of the specific gravity of powdered eggshells as affected by heating temperature and duration. It may be noticed that the specific gravity increased as the heating temperature and duration were increased.

Results of Tests of Mortar Specimens

The variation of temperature and duration of heating of the powdered eggshells for the mortar cubes affected their compressive strength. The compressive strength data were statistically analyzed using the software ANOVA in order to determine whether the differences within the each case are significant or not. The result of the analysis says that the strengths of the specimens in each case (5 specimens per case) are statistically similar. Furthermore, the average strength per case is statistically different from the other cases. This statistically verifies that the addition of powdered eggshells and use of seawater have an effect on the strength of mortar specimens.

Compressive strength of mortar specimen at 7 days

Shown in Table 5 is the summary of the average compressive strengths of the mortar cubes and their corresponding percentage difference with respect to the control specimens (F7).

Table 5 Compressive strength of mortar at 7 days

Specimen Case	Compressive Strength (MPa)	Percentage Increase
F7 (control)	12.42	0.0%
F7-0	15.33	23.4%
100F7-III	13.38	7.7%
100F7-VI	16.43	32.3%
100F7-XII	15.73	26.7%
200F7-III	13.62	9.7%
200F7-VI	13.88	11.8%
200F7-XII	13.35	7.5%
S7	11.08	-10.8%
S7-0	15.83	27.5%
100S7-III	9.86	-20.6%
100S7-VI	15.37	23.8%
100S7-XII	12.32	-0.8%
200S7-III	9.86	-20.6%
200S7-VI	11.77	-5.2%
200S7-XII	16.49	32.7%

The partial replacement of air-dried powdered eggshells (F7-0) resulted to a stronger mortar cubes by 23.4% compared to the control specimen at 7 days. It was also noticed that the strength decreased by 10.8% when seawater was added by comparing F7 and S7. Among the mortars mixed with freshwater, the highest increase was for 100F7-VI,

which was 32.3% greater than the control mortar (F7). As for the mortars mixed with seawater, the highest increase was for 200S7-XII, which was 32.7% greater than the control mortar (F7).

Although, the strength of mortar cubes has increased in the freshwater group, there was a decrease in strength in some mortar cubes in the seawater group. This may mean that the certain combinations of seawater and powdered eggshell tend to decrease the strength development at 7 days.

Compressive strength of mortar specimen at 28 days

Shown in Table 6 is the summary of the compressive strength of 28-day mortar specimens.

Table 6 Compressive strength of mortar at 28 days

Specimen Case	Compressive Strength (MPa)	Percentage Increase
F28 (control)	18.09	0.0%
F28-0	20.24	11.9%
100F28-III	18.92	4.6%
100F28-VI	19.53	8.0%
100F28-XII	23.86	31.9%
200F28-III	20.60	13.9%
200F28-VI	21.22	17.3%
200F28-XII	24.64	36.2%
S28	20.26	12.0%
S28-0	19.58	8.2%
100S28-III	23.87	32.0%
100S28-VI	26.46	46.3%
100S28-XII	26.90	48.7%
200S28-III	21.77	20.3%
200S28-VI	23.17	28.1%
200S28-XII	16.76	-7.4%

The compressive strength gathered from the 28-day mortar cubes had generally exhibited increase in strength compared to the 7-day age mortar cubes. In contrast to the 7-day mortar cubes, the use of seawater increased the strength by 8.2% by comparing F28 and S28. Powdered eggshells exposed to longer duration of heating resulted to higher strength, except for the seawater group with the powdered eggshells exposed to 200^{O}C. This may indicate that overheating the powdered eggshells results to quality degradation. This is further manifested in 200S28-XII, which resulted to strength lower than the control specimen.

For better visualization of the trend of the 28-day compressive strength as affected by powdered eggshell and seawater, the data in Table 6 are plotted in Figure 1 as bar graph.

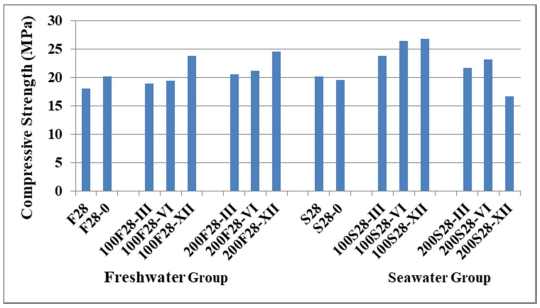

Fig. 1 Plot of 28-day compressive strength of mortar specimens

A trend of increasing strength can be seen in the Fig.1. The freshwater and seawater groups, show in increasing strength with the increase in heating duration for those exposed to 100^{O}C. Also, using seawater as substitute to freshwater further increased the strength of the mortar cubes. Furthermore, 100S28-XII produced the highest strength, an increase of 48.7%. Based on the test results, the most promising preparation of powdered eggshells is by heating at 100^{O}C for 12 hours.

Results of Tests of Concrete Specimens

Mix designs based on 0.4, 0.5 and 0.6 water-cement ratio were made for the experimental program. The designed mix proportions are shown in Table 7. The powdered eggshells that were used were heated at 100^{O}C for 12 hours.

Table 7 Mix proportion per cubic meter of concrete

W/C	Water (kg)	Cement (kg)	Gravel (kg)	Sand (kg)
0.4	221	553	1126	451
0.5	218	432	1090	471
0.6	205	342	1131	620

The resulting fresh concrete properties of the different mixes were almost the same. The average values obtained were as follows: slump=74mm, air content=2.4%, and wet density=2363kg/m^3. It appears that the powdered eggshells and seawater have little effect on the properties of fresh concrete.

Shown in Table 7 is the summary of the average compressive strength of concrete specimens as affected by seawater and powdered eggshells. Also indicated in the Table 7 are the percentage increases with respect to the control specimens (0.4FX, 0.5FX, and 0.6FX). Statistical analysis was also done similarly to what was done in the mortar. The results also validated the similarity of results of strength test per case, and the significant different

between cases. To have a good visualization of the results, a graphical representation of Table 8 is presented in Figure 2.

Table 8 Compressive strength of concrete

Specimen Case	Compressive Strength (MPa)	Percentage Increase
0.4FX	30.38	0.0%
0.4FE	34.96	15.1%
0.4SX	37.51	23.5%
0.4SE	38.42	26.5%
0.5FX	27.28	0.0%
0.5FE	29.31	7.4%
0.5SX	34.00	24.6%
0.5SE	37.21	36.4%
0.6FX	24.73	0.0%
0.6FE	25.07	1.4%
0.6SX	25.28	2.2%
0.6SE	28.53	15.4%

Note: F=freshwater, S=seawater, X=no replacement, E=cement replacement with powdered eggshells

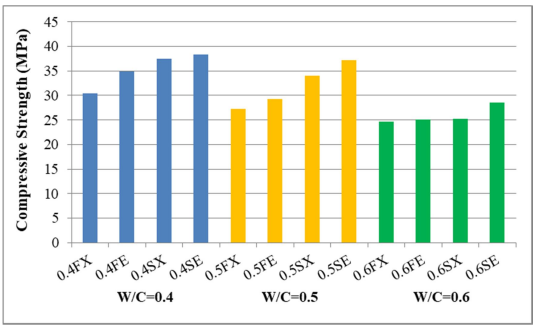

Fig. 2 Plot of 28-day compressive strength of concrete specimens

The results validated the known concept that as the W/C decreases, the strength of concrete increases. In general, the use of powdered eggshell increased the concrete strength. It seems that it is more effective at lower W/C (0.4 and 0.5). Furthermore, the use of seawater in mixing of concrete resulted to a higher strength. Among the concrete specimens, the highest increase was for 0.5SE at 36.4%. For concrete mixed with freshwater, the highest increase was for 0.4FE at 15.1%.

Results of SEM Analysis

Mortar samples were subjected to the scanning electron microscope (SEM) analysis. Typical results are presented in Fig.3. The picture at the top in the Fig.3 is a 3500 magnification of the mortar without eggshells, mixed with freshwater, and cured for 28 days. The picture at the bottom of Fig.3 is a 3500 magnification of the mortar with powdered eggshells, mixed with seawater, and cured for 28 days. Comparison of the two pictures showed fiber-like microscopic structures that were found only on specimens containing powdered eggshells. These fiber-like structures were formed on grain surfaces like needles with sharp ends and were seen gathering in void spaces. It is believed that the increase in strength is caused by these fibers. More of these fibers were observed to be present when seawater was used.

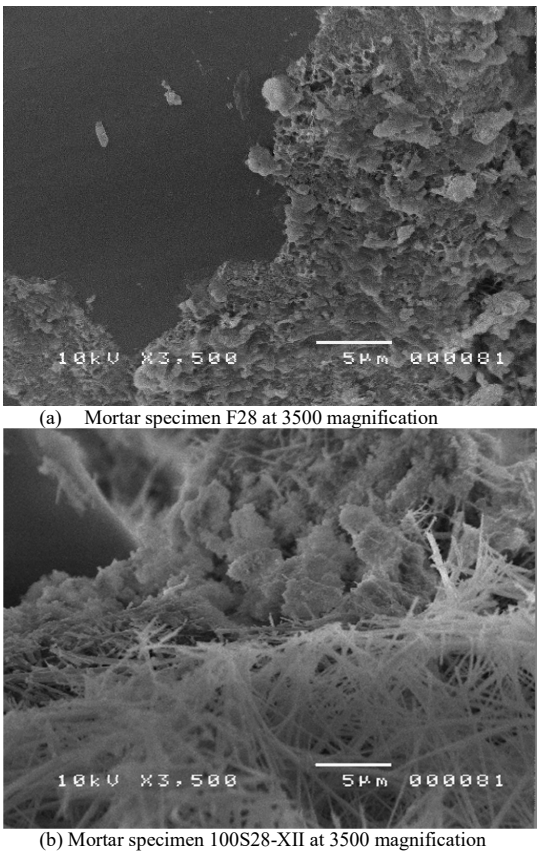

(a) Mortar specimen F28 at 3500 magnification

(b) Mortar specimen 100S28-XII at 3500 magnification

Fig. 3 SEM comparison of mortars without and with powdered eggshells

Cost Analysis Results

Determining the effect of seawater and powdered eggshells on the cost of concrete is necessary for commercial and economical applications. The unit cost of each material used is tabulated in Table 9. Since seawater can be freely obtained from the seaside, the assumed cost was zero. Powdered eggshells can be assumed to cost zero but since it involved the process of cleaning, crushing, grinding and heating, it was estimated to cost 4.30 Php/kg.

Table 9 Unit cost of materials used

Material	Cost per Kilogram
Portland Cement	5.250 Php/kg
Sand	0.530 Php/kg
Gravel	0.661 Php/kg
Freshwater	0.035 Php/kg
Seawater	0.000 Php/kg
Eggshell Powder	4.300 Php/kg

Table 10 Cost analysis of concrete

Specimen Case	Cost /Volume (Php/m^3)	Cost Efficiency (Php/MPa)
0.4FX	3885	128
0.4FE	3859	110
0.4SX	3893	104
0.4SE	3867	101
0.5FX	3236	119
0.5FE	3212	110
0.5SX	3244	95
0.5SE	3220	87
0.6FX	2870	116
0.6FE	2854	114
0.6SX	2878	114
0.6SE	2861	100

With the unit cost of the materials known, the cost of concrete per cubic meter can be easily calculated. Table 10 shows these values for the different specimen case. Lower W/C resulted to more expensive concrete. However, the addition of powdered eggshells and seawater lowered the cost of concrete. Enumerated also is the cost-efficiency which can be calculated by simply dividing the cost with the measured strength of the specimen. The lowest value is the most cost- efficient. Among the specimen considered, the specimen with W/C=0.5, using seawater, and with powdered eggshells (0.5SE) is the most cost efficient.

CONCLUSIONS

The use of powdered eggshells as partial replacement for cement and seawater as a substitute for freshwater were found to be suitable alternatives for conventional concrete materials. However, certain combination of powdered eggshells and seawater tends to delay the strength development as manifested in the results of strength test of 7-day mortar specimens. On the other hand, the 28-day mortar specimens generally resulted enhanced strength due to the addition of both powdered eggshells and seawater. It was also observed that the powdered eggshell produced the highest mortar strength (among those tested) when heated at 100^{O}C for 12 hours.

The strength of concrete increased when powdered eggshell were used, especially when W/C is low. The strength further increased when using both seawater and powdered eggshells. Among those tested, the highest obtained is for concrete with W/C=0.5, using seawater, and with powdered eggshells. The increase was 36.4%.

Utilizing seawater and powdered eggshells in concrete was determined to be cost-efficient, and most cost-efficent at W/C=0.5.

ACKNOWLEDGMENTS

The authors express their gratitude to the faculty and staff of the Civil Engineering Department of De La Salle University (DLSU) for all their help and support. The authors also acknowledge the support of the other DLSU offices. Special appreciation is also due to the parents of the students who participated in this research.

REFERENCES

[1] Hunton P., Research on Eggshell Structure and Quality: A Historical Overview. Brazilian Journal of Poultry Science, Vol.7, No.2, 2005, pp. 67-71.

[2] Yerramala A. Properties of Concrete with Eggshell Powder as Cement Replacement. The Indian Concrete Journal, Vol. 88, No.10, 2014, pp. 94-102.

[3] Dhanalakshmi M., Sowmya N.J., and Chandrashekar A., A Comparative Study on Egg Shell Concrete with Partial Replacement of Cement by Fly Ash. International Journal for Research in Applied Science & Engineering Technology. Vol. 3, No. 11, 2015, pp. 12-20.

[4] Asman, N.S.A., Dullah, S., Ayog J., Amaludin, A., Amaludin, H., Han, L.C., and Baharum, A., Mechanical Properties of Concrete using Eggshell Ash and Rice Husk Ash as Partial Replacement of Cement. MATEC Web of Conferences, 103, 01002. 2017.

[5] Lejano B. and Roxas C.L., Influence of Seawater on the Strength of RC Beams and Corrosion Behavior of Steel", International Journal of GEOMATE, Vol. 14, Issue 42, 2018, pp. 58-64.

[6] Gagan J. and Lejano B., Optimization of Compressive Strength of Concrete with Pig-Hair Fibers as Fiber Reinforcement and Green Mussel Shells as Partial Cement Substitute, International Journal of GEOMATE, Vol. 12, Issue 31, 2017, pp. 37-44.

9th Int. Conf. on Geotechnique, Construction Materials and Environment, Tokyo, Japan, 20-22 November 2019, ISBN: 978-4-909106025 C3051

AN INVESTIGATION ON THE PRODUCTION OF STABILIZED CLAY BRICKS (UNFIRED BRICKS) WITH MIOCENE CLAY AND WASTE MATERIALS

Rashed, M. [1]; Sadiek, K.N.[1]; Kandeel, A.M.[2]; El Mahllawy, M.S.[2], and Mohsen, S. A[1].
[1]Alexandria University, Faculty of Science, Geology Department, Egypt; [2] Housing and Building National Research Institute, Cairo, Egypt

ABSTRACT

In Egypt, conventional clay bricks produced from clay with a high firing temperature is a common construction materials. The clay bricks industry consumes a significant amount of energy and releases a large quantity of gases to the atmosphere leading to environmental and economic problems. The stabilized clay bricks are an unfired clay bricks produced from mixture of clay, stabilizing materials and wastes. The current study evaluates the feasibility of using waste materials such as electric arc furnace slag (EAF slag) and calcrete dust (CD) with Miocene clay deposits for production of stabilized clay bricks. The use of waste materials can achieve economic benefits (reduction in raw material and energy required) and environmental benefits.

Experimental investigations were carried out to explore the effect of wastes addition in different clay-based mixes at different ratios. Ordinary Portland Cement (OPC), gypseous hydrated lime (GHL) and sands were added in the studied formulations. The ingredients of each mix were molded in a cylindrical metal mold under compression of 100kg/cm^2 then cured in a plastic container for 14, 28, and 60 days. As the curing days increase, the gypsum transformed into ettringite and the calcium-silicate-hydrate (C-S-H) phase well-formed as shown from the X-ray diffraction (XRD) analysis and Scanning Electron Microscopy (SEM). That can be visualized also on the enhancement of the physico-mechanical properties. The results show that the pozzolanic reaction and cation exchange played an important role in particles agglomeration and stabilization. Also, the addition of EAF slag as an additive material enhances the durability of stabilized clay specimens more than the addition of calcrete dust.

Keywords: Miocene clays**,** Unfired bricks, EAF slag**,** Pozzolanic reaction

INTRODUCTION

In Egypt, clay deposits are widely distributed. One of these deposits is the Miocene clay which is widely exposed especially at the east of Western Desert. The traditional application of clays is many, but one of the most is clay bricks making. The increasing consumption of suitable clay deposits may lead to the decrease in their resources. Therefore, the improvement of some useless clays should be target. This may be carried out through some additives and /or treatments. The common and most of building bricks in the world are conventional fired bricks which produced when clay particles bond to one another at high temperatures, forming a glassy material, which, upon cooling, displays high strength and durability properties. High temperatures required to melt SiO_2 which mean high energy cost associated with brick production. In addition to cost, challenges facing the modern brick industry include shortages of raw material and environmental impacts of production due to the generation of a significant amount of carbon dioxide (CO_2) to the environment, which accounted for around 5% of global man-made CO_2 emissions [1]. The catastrophic consequences of the greenhouse gas emission from the traditional brick industry have considerably contaminated the surroundings with smog, fog, acid rains, global warming and climate change. These dangerous impacts of the bricks manufacture have been encouraged to find new building technologies which have a low environmental impact. The use of stabilized unfired clay bricks for masonry construction may solve these problems [2]. Due to problems with shrinkage and swelling of clays and changes in material properties, it is tried to stabilize the mixtures realized with clay using cement, lime and sand as binder, and also the addition of some industrial waste materials.

Stabilization which characterized by pozzolanic properties can bind soil particles together as the pozzolanic reaction is the reactions between lime, water, soil silica and alumina that form various cementing-type materials such as calcium-silicate-hydrates (C-S-H) and calcium-aluminate-hydrates (C-A-H) which can bind soil particles together and at the same time reduce water absorption by clay particles [3]. The clay minerals and amorphous materials are the only important sources of calcium-silicate-hydrates (C-S-H) and calcium-aluminate-

hydrates (C-A-H) in most soils. The same hydrates are formed during the hydration of Portland cement.

Now in the worldwide, there is a sizeable body of research completed on the possibility of utilizing unfired clay bricks for masonry building wall construction. These researches concern with the use of some secondary materials and wastes types (environmental approach) as partial substitutes for primary clay (economical approach) and stabilizing agents for the manufacture of unfired clay bricks. Yin sung, [4] produced bricks from reservoir harbor sediment mixed with fly ash. Oti [2] produced unfired clay brick by recycling a Ground Granulated Blast Furnace Slag (GGBS) activated with an alkaline lime and Portland cement combined with clay soil. Vinai [5] studied the production of bricks using coal combustion residues together with cement, lateritic clayey soil and sand. Smeu [6] tried to stabilize the mixtures made from clay by using cement, lime and sands as a binder, and also added sawdust in each batch made. El- Mahllawy [7] studied the activation of granulated blast-furnace slag on the properties of unfired eco-friendly clay brick. It is observed from his study that the addition of quick lime and cement kiln dust (CKD) to the granulated blast-furnace slag improved the investigated engineering properties of the unfired stabilized specimens due to the pozzolanic reaction. Tao [8] studied the possibility of using sandy soil as the main raw material in making unfired bricks. The results show that unfired brick specimens with the addition of Ground Granulated Blast Furnace Slag (GGBS) tend to achieve better mechanical properties when compared with the specimens that added cement alone. El-Mahllawy [9] evaluated the feasibility of stabilizing clay bricks with application added cement alone. marble cutting waste (MCW). The results demonstrate that the utilization of MCW incorporating up to 15% hydrated lime for the stabilized clay brick production is feasible.

So, this work aims to investigate the using feasibility and characteristics of selected Egyptian industrial and quarry waste in clay-based mixes for producing eco-friendly clay brick. This is to provide technical solution that will enable the brick industry to develop commercially and using wastes in a useful application.

MATERIALS AND METHODS

Materials

The materials used for the current research consisted of clay and sand, from wadi El Natrun area (wadi El-Farigh depression). The wadi el Natrun area is covered by Miocene sediments (Moghra formation, Raml member). Facies of Raml member are represented by, ferruginous quartz arenite, calcareous subarkosic arenite and shales. Loose sands dominate the examined sequence and commonly pale yellow and frequently stained by iron oxides. They are fine to coarse grained, moderately well sorted and vary from subrounded to subangular.

Clay of Raml member are grey, greyish to light green and moderately hard occasionally contain streaks and spots of gypsum. The clay minerals of the clay include montmorillonite, illite and kaolinite in a decreasing order of abundance [10].

Also, Ordinary Portland cement (OPC), gypseous hydrated lime (GHL), electric arc furnace slag (EAF slag) and calcrete dust (CD).

Methods of Investigation

Laboratory methods

The physical properties of clay samples (Water content, Grain size analysis Atterberg Limit, Unit weight and Specific gravity) are determined according to ASTM. Also, Unit weight and Grain size analysis of the sand samples were determined.
Ordinary Portland cement (OPC), gypseous hydrated lime (GHL), calcrete dust (CD), and electric arc furnace slag (EAF slag) were crushed and ground, if necessary, then passed through 0.5 mm sieve diameter.

The prepared specimens were tested for water absorption, bulk density and compressive strength at the end of curing periods (14, 28 and 60 days) according to ASTM standards and evaluated in accordance with The Egyptian Code for the Building by the stabilized and compressed earth soil [11].

The used material and the made unfired clay specimens were analyzed by powder X-ray diffraction (XRD) for mineralogical characterization. The chemical composition (major oxides) of the starting materials was determined by X-ray fluorescence (XRF). Scanning electron microscope (SEM) technique was used to investigate micro structure and morphological feature of the tested samples.

Mix compositions and specimen preparation

In order to investigate the effect of the used stabilizers on the properties of the unfired stabilized clay specimens, three system were studied: reference sample, calcrete dust system and steel slag system. Seven suggested mixtures from the three systems were studied namely C (Control mix), L1, L2, L3 (Calcrete system) and S1, S2, S3 (Slag system) as shown in Table 1.

The prepared mixtures were homogenized for 5 min, and then mixed with a suitable amount of water about (15%) to reach a wetting mixture. The water/solid ratio was adjusted to achieve ease molding as to match processing technology for the

clay brick manufacturing in Egypt. Immediately after mixing, the materials were compressed into steel mold cylinders by using a hydraulic compaction machine under pressure of 100kg/cm^2.The compacted cylinder was left in the mold under pressure for about 5 second in order to allow for dissipation of pore pressure, thus enabling test specimen stability and/or relaxation. The specimens were then extruded using a steel plunger. Thereafter, the demolded prepared specimens were labelled and placed in sealed plastic box. The specimens were moist (cured) for 14, 28 and 60 days in a plastic box at temperature of about 35^{o}C ± 2 and humidity about 83% ± 2. This was done to avoid sample carbonation that is common with most stabilized soil-based systems, where lime reacts with carbon dioxide to form calcium carbonate instead of forming cementitious reaction products (C-A-H, C-A-S-H, C-S-H among other complex compounds).

Table 1 Composition, proportion (wt.%) and pH of the studied mixes

Mix code	Clay(C)%	Sand (S)%	GHL%	OPC%	CD%	EAF slag%	pH
C	50	25	15	10	----	-----	13.0
L1	50	20	15	10	5	-----	13.4
L2	50	15	15	10	10	-----	13.3
L3	50	20	15	5	5	-----	13.1
S1	50	20	15	10	----	5	13.3
S2	50	15	15	10	----	10	13.4
S3	50	20	15	5	----	5	13.2

RESULTS AND DISCUSSION

Characteristics of the used materials.

The results of grain size analysis indicated that the percentage of clay particle size is approximately 47 % in the clay sample used in this work. This percentage met the required guideline for the minimum clay contents required for the production of red clay bricks [12]. Moisture content ranges between 7.76 and 9.7%. Specific gravity ranges between 2.76 and 2.91. The unit weight of the clayey soil ranges between 1.60 and 1.72 gm/cm^3. Depending on the obtained data of moisture content, unit weight, and specific gravity, the void ratio of the clay samples ranges between 0.82 and 0.93. The porosity (η) ranges between 45 and 48%. Sand samples are classified according to the Unified Soil Classification into poorly graded sand (SP).

XRD analysis show the predominance of montmorillonite over the other clay minerals. On other hand, the kaolinite and illite minerals, as well as the non-clay minerals such as quartz and hematite, were present as trace amounts. Also, The XRD pattern shows that the gypseous hydrated lime composes of gypsum, anhydrite and portlandite [Ca $(OH)_2$], while EAF slag compose mainly of calcium iron oxide, wustite (FeO), and calcium silicate ($CaO.SiO_2$). The XRD pattern of (CD) shows that it is composed of calcite and dolomite and a minor amount of quartz. The chemical composition and loss on ignition (LOI) of the used materials are depicted in Table 2.

Table 2 Chemical composition in terms of oxide content, loss on ignition (wt.%).

Oxide %	GHL	OPC	EAF Slag	CD
SiO_2	4.06	20.59	16.00	18.90
Al_2O_3	1.01	4.02	4.85	2.06
Fe_2O_3	0.13	3.31	34.80	1.28
CaO	41.50	62.71	34.90	42.80
MgO	0.81	1.95	4.39	2.55
Na_2O	0.29	0.47	Nil	0.39
K_2O	0.21	0.18	0.09	0.35
P_2O_5	0.03	Nil	0.38	0.07
TiO_2	Nil	Nil	0.92	0.31
MnO	Nil	Nil	1.49	Nil
SO_3	24.70	2.95	0.38	0.47
Cr_2O_3	Nil	Nil	0.64	Nil
Cl^-	Nil	Nil	Nil	0.10
L.O.I	27.10	3.81	0.25	30.50

Characteristics of the Cured Specimens

i) Control system (C): It is observed from the XRD pattern as shown in figure 1,2, that the examined specimens of mix C for 14 day have illite, gypsum, quartz, calcite and calcium silicate hydrate (C-S-H) phase. Also, with increasing the curing days from 28 up to 60 days, gypsum ($CaSO_4.2H_2O$) begins to decrease due its consuming in the formation of ettringite ($3CaO.Al_2O_3.3CaSO_4.32H_2O$) until it is completely disappeared at 60 curing days. Furthermore, the quartz peak intensity decreased with increasing curing day, which may be due to its sharing in (C-S-H) formation or agglomeration of particles in the mix.

ii) EAF Slag system (S1, S2 and S3): It is observed that ettringite phase is formed earlier in mix S2 as compared to the other mixes (S1 and S3) at 14 curing days. C-S-H is detected at 14 and 28 curing day at (10% OPC) while it is not detected at 60 curing day at (5% OPC). The appearance of kaolinite mineral in mix S3 means that it does not share with any cementitious phase formation. It is expected that mix S2 will show superior physico-mechanical properties as well as the all mixes in slag system.

iii) Calcrete dust system (L1, L2 and L3): It is observed that ettringite phase is not detected at 14 day but with progressing curing days, gypsum consumed to form ettringite. Also, C-S-H phase is not formed in mix L3 (5% OPC) this may be due to the shortage of OPC content and related hydration phase $Ca(OH)_2$ while it detected at 14 and 28 curing days at (10% OPC). It is observed that with increasing calcrete dust, C-S-H decrease. This is may be due to that Ca^{+2} found in $CaCO_3$ is not easy to be solubilized in the media so the calcrete dust acts as a filler rather than a pozzolanic material.

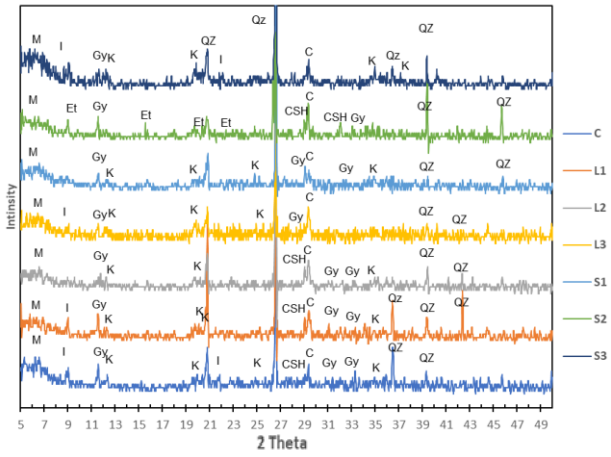

(Et: Ettringite, M: Montmorillonite, Qz: Quartz, Gy: Gypsum, I: Illite, C: Calcite and CSH: Calcium silicate hydrate).

Fig. 1 XRD patterns of the 14 days cured specimens of different mixes.

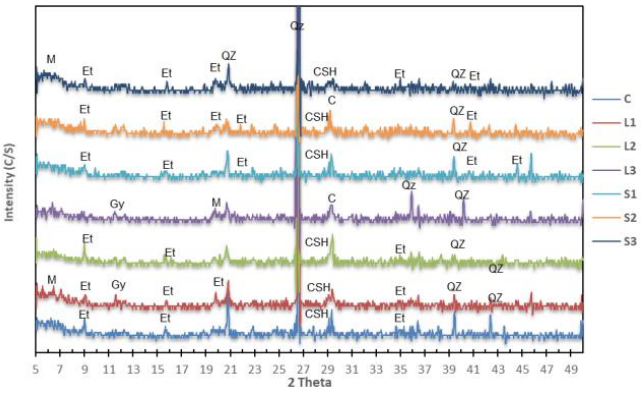

(Et: Ettringite, M: Montmorillonite, Qz: Quartz, Gy: Gypsum, I: Illite, C: Calcite and CSH: Calcium silicate hydrate).

Fig. 2 XRD patterns of the 60 days cured specimens of different mixes.

The results of SEM technique of the lab specimens (C, L1, L2, S1, S2 and S3), cured for 60 days which are more representative for the formation of cementitious material and ettringite phase show, a well cemented structure and the quartz grain is surrounded by a matrix composed of a mix of clay particles and the formed phases (ettringite and C-S-H) as shown in figure 3. On the other hand, pozzolanic reaction will promote a more compacted microstructure with less pores, and fractures, resulting from the stronger bonds formed during the hydration process and the possibility of additional pozzolanic C–S–H, and therefore deliver better mechanical and physical properties and durability to the bricks. While mix L3 cured for 60 days shows a poorly-cemented structure and a number of unfilled pores as shown in figure 4. The gypsum is appeared as radiated needles on the surface and around the clay particle (matrix).

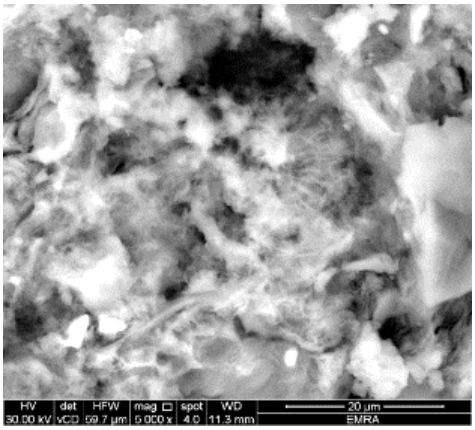

Fig. 3 SEM images of mix S2, show C-S-H gel and ettringite (needle -like structure) phase at high magnification.

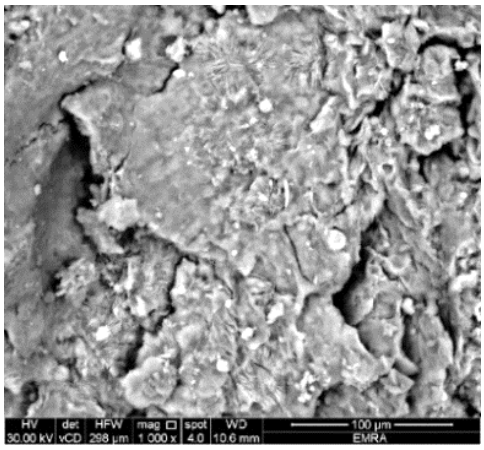

Fig. 4 SEM images of mix L3 shows a poorly cemented structure and gypsum (radiated needle -like structure).

Physico-mechanical properties of the lab specimens

Compressive strength

It is observed generally that compressive strength increases significantly with prolongation of curing days. Figure 5 show that highest compressive strength is gained by the (C, L1, L2, S1 and S2) cured specimens due to the addition of cement (10%) that has a positive effect on the strength. This is attributed to the continuous hydration forming more C-S-H as binding agent. Also, the results explained that the loss of strength in mix L3 and S3 is due to the low content of OPC. It is noticed that the strength of mix S2 has the highest compressive strength which attributed to pozzolanic activity of slag. Furthermore, cation exchange between the soil and the steel slag was identified as the major factor that influenced the modification of the engineering properties of the clayey soil by the addition of steel slag [13]. Also, the progressive increase in the compressive strength can be explained by the formation of ettringite on the expense of gypsum content. It is observed that when industrial waste gypsum is combined with Portland cement to solidify soil, the strength of the solidified soil will be much higher than that when Portland cement is used only, because of the effect of ettringite on filling pores.Indeed, the increase in compressive strength values is particularly important when the amount of $CaSO_4.2H_2O$ increases to an extinct limit [14]. Based on the test results, all stabilized specimens cured for 14, 28 and 60 days achieved the ECBS requirements.

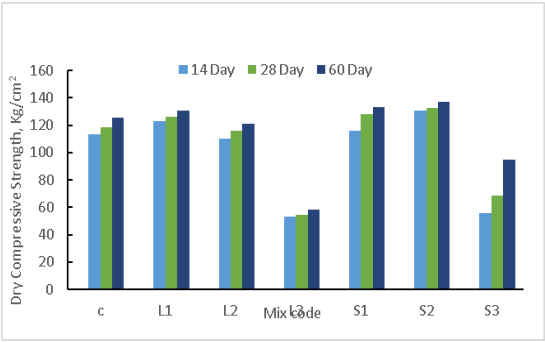

Fig. 5 Dry compressive strength of specimens at various curing days.

Water absorption

In all case, water absorption decreases with increasing in curing days of the cured specimens as shown in figure 6. The results show that amount of the absorbed water decreased as the cement (OPC) content increased (10%) giving evidence that the cement (OPC) plays a significant role in the impermeability of the tested specimens. The best value was found in the S2 specimens (10% EAF slag) cured for the 60 days. This is probably due to the pozzolanic reaction development as detected previously in the XRD patterns which leads to the formation and accumulation of cement phases that close some of the open pores then decreases their affinity to absorb water and also may be due to the formation of ettringite which fill pores.

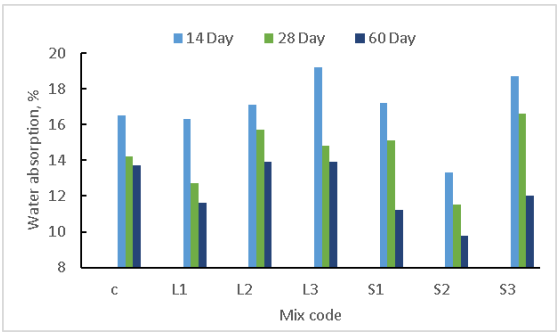

Fig. 6 Water Absorption of specimens at various curing days.

Bulk density

In terms of bulk density of the unfired stabilized clay specimens, it is increased with curing days as shown in figure 7. The highest value was achieved by specimens of the mixture S2 at the end of 60 curing days. The specimens of the mix L3 show the lowest density rather than the other mixes. The bulk density increases are indicative for the pozzolanic reaction progressing and phases formation. In other words, as the Portland cement content increases, the bulk density increases giving evidence for densification.

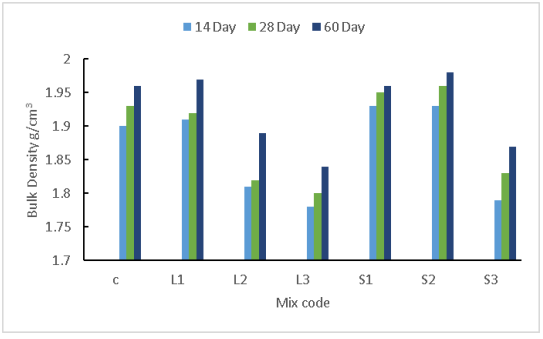

Fig. 7 Bulk density of specimens at various curing days.

CONCLUSIONS

The current study evaluates the feasibility of using waste materials (electric arc furnace slag EAF slag), calcrete dust CD) for production of stabilized clay bricks. From the present work, it can be concluded that:

1- With increasing curing days, the calcium silicate hydrate phase well-formed and increased, gypsum transformed into ettringite and the peak intensities of quartz and kaolinite decrease due to its contribution towards the formation of C-S-H phase as well as quartz particles agglomeration which reflected on the physico-mechanical properties that enhanced with increasing the curing days which attributed to the formation of calcium silicate hydrate (C-S-H) gel which act as a binding material and also due to the formation of ettringite which fill the open pores .

2- The decreasing in OPC affected negatively on the significant properties of the unfired stabilized montmorillonite clay specimens.

4- Calcrete dust has no pozzolanic activity and it act primary as a filler in the mix. Increasing the addition of CD on the expense of sand at mix L2 has a negative effect on specimen properties, while slag has more pozzolanic activity rather than calcrete dust and reference mix. This is reflected on the mechanical properties of S specimens especially S2 (10% EAF slag)

REFERENCE LIST

[1] Federico, L. M., Chidiac, S. E., and Drysdale, R. G. The use of waste material in the manufacturing of clay brick" 10th Canadian Masonry Symposium, Banff, Albert, (2005).

[2] Oti, J. E., Kinuthia, J. M., and Bai, J. Unfired clay bricks: From laboratory to industrial production. Proceedings of the Institute of Civil Engineers: Engineering Sustainability, vol. 162, No.4, 2009, pp. 229-237.

[3] Oti, J. E., The development of unfired clay building materials for sustainable building construction. Ph.D thesis. Welsh Assembly Government (WAG), Department for Environment, Sustainability and Housing. Collaborative Industrial Research Project (CIRP), 2010.

[4] Yin-Sung, H., Bing-Jean, L., and Henry, L., Mixing reservoir sediment with fly ash to make bricks and other products. International Ash utilization symposium, Center of applied Energy, University of Kentucky, 2003, 89p.

[5] Vinai, R., Lawane, A., Minane, JR., and Amadou, A., Coal combustion residues valorisation: research and development on compressed brick production. Constr Build Mater, Vol. 40, 2013, 1088–96.

[6] Smeu, S., Gal, A., and Badea, C., Environmental_friendly_buidling_materials. Journal of Environment, Vol.3, No.3, 2014, pp.47-50.

[7] El-Mahllawy, M. S., Kandeel, A. M., Engineering and mineralogical characteristics of stabilized unfired montmorillonitic clay bricks." HBRC JOURNAL Vol.10, No.1, 2014, pp. 82-91.

[8] Tao, G., Pan, Y., Qiao, Z., and Jiang, C., Utilization of sandy soil as the primary raw material in production of unfired bricks. Advances in Materials Science and Engineering ,2018,1-11.

[9] El-Mahllawy, M. S., Kandeel, A. M., Abdel Latif, M.L., and El Nagar A. M., The Feasibility of Using Marble Cutting Waste in a Sustainable Building Clay Industry. Recycling, Vol.3., No.3, 2018, 13p.

[10] El-Sherbini, M. E., Stratigraphic analysis of the Neogene succession at Wadi El-Farigh, west Nile Delta, Egypt. M.Sc. Thesis, Fac. Sci. Mansoura Iniv.,1988, 187P.

[11] Egyptian Code for the Building by the Soil (ECBS). The building by the stabilized and compressed earth blocks 2016, 1, 1-144.

[12] Oladeji, O. S., and Akinrinde, A. F., Performance Characteristics of stabilized clay bricks using additives, Int. Journal of Engrg Research and Applications, Vol.3, 2013, pp. 806-810.

[13] Akinwumi, I., Soil Modification by the Application of Steel Slag. Rperiodica polytechnica, 2014, pp. 371-377.

[14] Huan, X. (2000). Available from: https://www. Research gate. net/ publication / Strength enhancement effect of ettringite in soil stabilization.

9th Int. Conf. on Geotechnique, Construction Materials and Environment, Tokyo, Japan, 20-22 November 2019, ISBN: 978-4-909106025 C3051

THE COMPRESSIVE STRENGTH AND DURABILITY OF CONCRETE WITH COCONUT SHELL ASH AS CEMENT REPLACEMENT

Mary Ann Adajar [1], Joenel Galupino[1], Jilliane Faye Aguilon[2], Cielo Frianeza[2], Jan Brayden Sy[2], and Paul Adrian Tan[2]
[1]Faculty, De La Salle University, Manila, Philippines
[2]Undergraduate student, De La Salle University, Manila, Philippines

ABSTRACT

The durability of concrete is the ability to withstand induced damages over a long period of time. It can be measured by sorptivity, or rate of water absorption, and resistance to sulfate attack (RSA). Concrete with larger voids is more susceptible to deterioration through absorption of chemicals, such as sulfate found in soil and seawater, which forms gypsum and ettringite. Gypsum and ettringite cause reduction of strength, cracking, and expansion of concrete. To improve the durability of concrete exposed to sulfate, the National Structural Code of the Philippines (NSCP) suggests increasing the strength of concrete to 31 MPa, which would require more cement; thus, increasing the cost of concrete. This study aims to investigate the effects of partially replacing cement with coconut shell ash (CSA) in terms of its compressive strength, sorptivity, and RSA. CSA in this study was classified as a Class N pozzolan, a cementitious material that will make a cheaper substitute for ordinary Portland cement (OPC). Results showed that the sorptivity of all concrete with CSA is within the acceptable limit. Based on the relationship of compressive strength with the CSA content, the optimum percentage replacement of OPC with CSA is 10%. From statistical analysis, it was determined that there is no significant difference in the compressive strength and expansion of concrete between the conventional and 10% CSA concrete. The strength of 10% CSA concrete is 92.10% of the strength of conventional concrete. The study reveals that CSA at 10% cement replacement is an effective pozzolan, which neither compromises the compressive strength and RSA of concrete.

Keywords: Coconut Shell Ash, Compressive Strength, Sorptivity, Resistance to Sulfate Attack

INTRODUCTION

The durability of concrete is the ability to withstand induced damages over a long period of time. There are multiple parameters in which the durability of concrete can be measured, two of which are sorptivity and resistance to sulfate attack (RSA). Sorptivity, or rate of water absorption, is when water undergoes capillary suction within the pore spaces of concrete. Durability is highly dependent on the capacity of concrete microstructure to absorb water [1]. This implies that concrete with greater voids between particles is highly susceptible to chemicals, such as sulfate ions. Sulfate ions that penetrate the concrete and incorporated with free lime and alumina would yield gypsum and ettringite, which causes expansion and deterioration of concrete. Most soils in the ground contain the element sulfate in different forms [2]. Since most of the concrete structures, like foundations, are exposed to the soil in its entire lifespan, protection against sulfate attack is important to ensure that reduction of strength, cracking, and expansion of the concrete does not occur especially on concrete exposed to soil with high salinity level. To improve the durability of concrete exposed to sulfate, the National Structural Code of the Philippines (NSCP) suggests increasing the strength of concrete to 31 MPa, which would require a smaller water-cement ratio. Hence, more ordinary Portland cement (OPC) is required, increasing the cost of concrete. A lower water-cement ratio leads to a decrease in total porosity and pore median of concrete [3]. Thus, decreasing water-cement ratio decreases voids and increases strength and durability due to less water penetration but increases also the cost of concrete. One way to lessen the cost of concrete without sacrificing the strength or durability is to partially replace OPC with a cheaper cementitious substitute. Several studies make use of waste materials that contain pozzolanic property as a substitute for cement in concrete. Fly ash [4], rice husk ash [5], palm oil fuel ash [6], and coconut shell ash [7] are some examples of viable substitute for cement.

The partial replacement of OPC with coconut shell ash (CSA) in concrete was found to be effective in reducing the cost of concrete and environmental pollution due to the accumulation of agricultural wastes as it incorporates recycling of wastes [8]. This study aims to investigate if the effects of substituting OPC with CSA will produce acceptable results in terms of concrete compressive strength, sorptivity, and resistance to sulfate attack.

COCONUT SHELL ASH

The Philippines is one of the major suppliers of coconut in the world, producing more than 15 million tons of coconut annually or 26.4% of coconuts worldwide [9]. There are currently 500 million coconut trees in the Philippines that contribute to 10.4 million tons of biomass annually [10]. An estimated area of 178,180 hectares is allocated for approximately 23,329,000 coconut trees in Quezon province. The coconut shells used for the study were collected from a local farm in this province. The shells underwent calcination to produce CSA in uncontrolled combustion which lasted for 4 hours. The calcined coconut shells were then crushed and ground to produce CSA. To control the effect of fineness on the performance of CSA, only samples that passed through the No. 200 sieve was used for experimentation. The material was oven-dried for 24 hours prior to experimentation to maintain moisture content less than 3% as required by ASTM C618.

EXPERIMENTAL PROGRAM

Mixing and Curing of Concrete Test Specimens

In this study, CSA was used as partial replacement of cement in the concrete mix. The CSA content used for experimentation were 10%, 20%, 30% and 40% of cement by weight. The concrete material will be termed as the CSA concrete. Specimens without CSA were also prepared which serves as the control specimen and represents the conventional concrete. Concrete materials were proportioned in accordance with ACI 211.1. The water-cement ratio of 0.6 was maintained in all concrete mixes. Table 1 shows the concrete batch mix proportion for cylindrical specimens while Table 2 shows the mortar batch mix proportion for mortar prisms. The mixing, curing, and molding of the concrete specimens was in accordance with ASTM C192.

Table 1 Concrete mix proportion

CSA content	Water (kg)	Cement (kg)	CSA (kg)	Gravel (kg)	Sand (kg)
0%	3.76	6.67	0.00	19.45	14.61
10%	3.76	6.37	0.30	19.45	14.61
20%	3.76	6.03	0.64	19.45	14.61
30%	3.76	5.64	1.02	19.45	14.61
40%	3.76	5.20	1.47	19.45	14.61

Table 2 Mortar mix proportion

CSA content	Sand (g)	Cement (g)	Water (g)	CSA (g)
0%	3850.0	1400.0	952.0	0.0
10%	3850.0	1337.1	952.0	62.9
20%	3850.0	1265.9	952.0	134.1
30%	3850.0	1184.9	952.0	215.1
40%	3850.0	1091.7	952.0	308.3

Compressive Strength Test

To determine the compressive strength of CSA concrete, a total of 150 cylindrical specimens with dimensions of 100 mm diameter and height of 200 mm were prepared and subjected to a uniaxial compression test in accordance with ASTM C39. The uniaxial compression test was conducted after the 7th, 14th, 21st, 28th, 50th, and 90th curing age. The 50^{th} and 90^{th} curing periods were conducted to determine the long-term compressive strength of CSA concrete.

Sorptivity

Sorptivity of CSA concrete was determined using cylindrical concrete specimens with a diameter of 100 mm and a height of 50 mm in accordance with ASTM C1585. The sorptivity test was done after the 28^{th}-day curing period. This was done by submerging 1mm to 3mm of the samples in water and computing the absorption using the mass difference at different intervals until 9 days. Linear regression analysis was applied to experimental results to measure the initial (1st day of testing) and secondary sorptivity (2nd to 9th day of testing) of the specimens.

Resistance to Sulfate Attack

Resistance to sulfate attack (RSA) was done by measuring the length change of mortar prisms with dimensions of 25 mm by 25 mm x 275mm in accordance with ASTM C1012. RSA was also measured through a mass change of cube specimens with a side dimension of 100mm following the procedure described in the study of Wang, Zhou, Meng, and Chen (2017) [11]. The specimens were submerged in a sulfate solution after the 28^{th}-day curing period. The sulfate solution has a 5% concentration where 50g of anhydrous sodium sulfate was diluted for every 950g of water. Hence, the exposure class, based on the concentration of the sodium sulfate, is classified as S3 [14]. The measurement of expansion through length and mass were conducted once a week until 9 weeks.

TEST RESULTS

Pozzolan Classification

To determine the pozzolan classification of CSA, the chemical composition, obtained using Energy Dispersive X-Ray Analysis (EDX), was compared with the chemical requirements for calcined natural pozzolan in accordance with ASTM C618. The oxides formed in calcinating the raw materials of OPC such as calcium oxide, silicon oxide, aluminum trioxide, and iron oxide, are also found in CSA. As shown in Table 3, CSA contains 80.02% of a combined chemical compound of SiO_2, Al_2O_3, and Fe_2O_3. Hence, it signifies that the pozzolanic activity is greater. Silicon dioxide in OPC, commonly known as silica, is the main component that is responsible for the strength of concrete and mortar at an early age; thus, the abundance of silica in CSA denotes that it is a cementitious material and it can be used as a substitute of OPC. Based on chemical properties requirements as stated in ASTM C618, CSA can be classified as Class N pozzolan. The loss on ignition is below the 10% criteria for Class N pozzolan. This denotes that the amount of unburnt carbon in CSA is very minimal. This is a desirable property of Class N pozzolan because if the percentage of loss on ignition is greater than 10%, it indicates that the pozzolan has an abundance of unburnt carbon that could decrease the pozzolanic activity [7]. A decrease in pozzolanic activity can lead to a decrease in the strength of the concrete. On the other hand, the moisture content of CSA is greater than the minimum requirement for Class N pozzolan; thus, oven drying before use of CSA is recommended.

Table 3 Chemical properties of CSA

Chemical Compound	CSA %	Class N Pozzolan* %
Silicon dioxide (SiO_2)	60.91	
Aluminum trioxide (Al_2O_3)	17.38	
Iron Oxide (Fe_2O_3)	1.72	
SiO_2 *plus* Al_2O_3 *plus* Fe_2O_3	80.02	70 min.
Sulfur trioxide (SO_3)	0.5	4 max.
Calcium oxide (CaO)	0.84	
Moisture Content	4.58	3 max.
Loss on Ignition	5.54	10 max.

*Standard requirements as per ASTM C618

Compressive Strength of CSA Concrete

The CSA concrete samples were subjected to a uniaxial compressive test to obtain their corresponding strengths on the 7th day until the 90th day of curing. This test was done before conducting sorptivity and RSA tests to verify whether the CSA concrete samples passed the required compressive strength. Figure 1 shows the collective compressive strength results from the 7th to 90th-day curing period. It can be observed that the compressive strength of the samples increases with the curing time. However, as the CSA content increases in the concrete, the compressive strength tends to decrease.

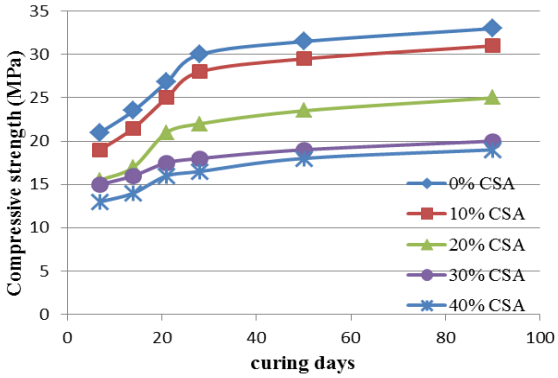

Fig. 1 Compressive strength of CSA concrete

Statistical Analysis of Compressive Strength

The Two-Tailed T-test is applied to the compressive strength test results of the concrete cylinders. Comparing the compressive strength of CSA concrete specimens with that of the control specimens, the computed T-critical value is 1.8331; while the *p*-value is below 0.5, which implies that the probability of the observed results due simply to chance is very low. The T-values of specimens with 10% CSA from 7 to 90 days curing period is less than the T-critical; hence, the compressive strength of concrete with 0% CSA and 10% CSA concrete is statistically the same and the replacement of OPC with 10% CSA did not affect the compressive strength. Thus, increasing the CSA content until 10% would significantly decrease the cost of concrete while retaining the identical strength performance it has to the conventional concrete.

Response surface methodology (RSM) was used to determine the optimum CSA replacement based on the compressive strength obtained at all curing days. The statistical method revealed that 10% CSA generated the highest compressive strength among all the other concrete design mixtures while the 40% CSA mix obtained the lowest compressive strength. It can be inferred that the optimal CSA content based on compressive strength is 10%. Empirical model as shown in Eq. (1) was derived from RSM in order to predict the compressive strength of concrete with CSA at any curing period. Using the formulated model, the compressive

strength of 10% CSA concrete is 92.10% of the strength of the conventional concrete at 28th-day curing period.

$$fc = 15.81 - 0.111(x) + 0.70(t) - 7.020\times10^{-3}(x)(t) - 0.022(x^2) - 9.758\times10^{-3}(t^2) - 2.173\times10^{-5}(x^2)(t) + 5.956\times10^{-5}(x)(t^2) + 4.096\times10^{-4}(x^3) + 4.45\times10^{-5}(t^3) \quad (1)$$

where:
fc = compressive strength of concrete at x% CSA, in MPa
x = CSA replacement in decimal (i.e. 10% is 0.1)
t = curing days of concrete, in days

Sorptivity of CSA Concrete

The slope of the linear trendline of the initial and secondary absorption versus the square root of time is the sorptivity of the specimen. A typical test result is shown in Fig. 2. In all test trials, the initial rate of water absorption, which was taken on the 1st day of experimentation, is greater than the secondary sorptivity, which was taken at the 2nd to 9th day of experimentation, because the empty pores of the sample are being filled with water more rapidly. However, at the stage of the secondary sorptivity, the pores are already filled with water which causes the sample to have a lower sorptivity as time progresses. Figure 3 shows the collective sorptivity results for all CSA concrete samples. It can be observed from the graph that the sorptivity increases as the amount of CSA in concrete increases at the stage of initial sorptivity. This implies that conventional concrete absorbs less water for a certain duration that it is exposed to water. The sorptivity for all samples is acceptable since all concrete specimens passed the acceptable limit which is 6 mm/hr$^{1/2}$ [12].

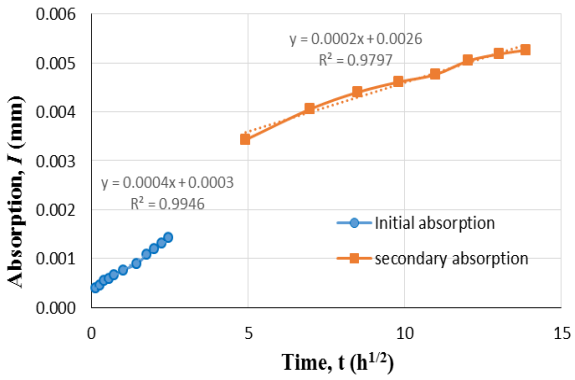

Fig. 2 Typical absorption result of CSA concrete

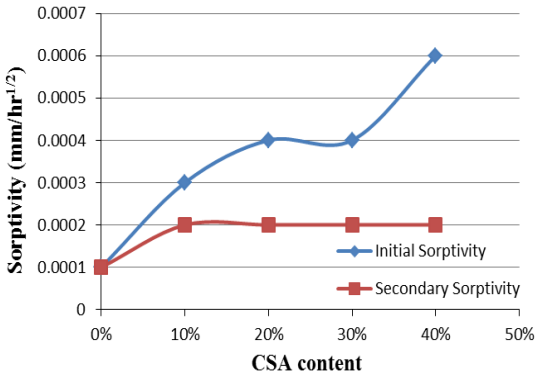

Fig. 3 Sorptivity of CSA concrete

Resistance to Sulfate Attack of CSA Concrete

Gypsum, a form of sulfate, is usually added to the production of cement to prevent the flash setting and improve the performance of concrete; furthermore, it is composed of hydrated calcium and sulfate. On the other hand, sulfate combined with alumina and calcium produces ettringite, which is normally present in concrete at early ages of the concrete [13]. However, an excessive amount of ettringite on the void spaces of the concrete cause deterioration, in the form of expansion, in concrete and mortar.

The length change or expansion of CSA mortar prisms was obtained to determine if the samples would not go over the NSCP limit for concrete susceptible to sulfate attack. Since the solution wherein samples were submerged contains 5% sodium sulfate (exposure class S3), the limit is 0.1% in 18 months [14]. Figure 4 shows the relationship of the length change of CSA mortar prisms with the time when it is immersed in a sodium sulfate solution. It can be observed that as the time of immersion increases, the expansion increases as well. Moreover, the expansion of mortar also increases as the CSA content increases. It can be observed that at the 9th week, the mortar with 0% and 10% CSA surpassed the acceptable limit while the expansion of other CSA content exceeded the limit at the 7th and 8th week. Previous research showed that it took 49 days for the conventional concrete mortar to reach 0.1% expansion when submerged in a 5% sodium sulfate solution [15]. In this study, the limit of 0.1% expansion is attained sooner than 18 months even for mortar without CSA.

The expansion of CSA concrete cubes in terms of mass change was obtained to determine the effect of sulfate attack on the exposure of concrete to saline soil and groundwater or saltwater containing sodium sulfate in its aqueous state. The test results are presented in Fig. 5. It can be observed that the

mass change is directly proportional to its time of exposure. As the CSA content increases, the expansion in terms of mass change also increases as time progresses.

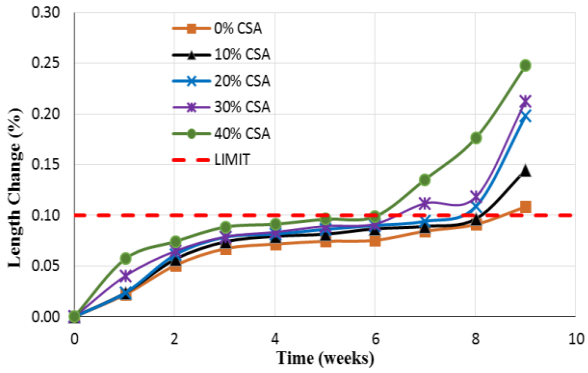

Fig. 4 Length change of CSA mortar prism

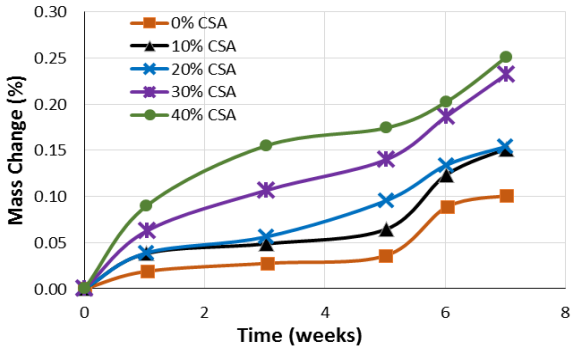

Fig. 5 Mass change of CSA concrete

The microstructure of CSA concrete after exposure to sulfate solution

The microstructure of CSA concrete after exposure to sulfate solution is shown in Fig. 6. Since sulfate can only be detrimental to concrete in its aqueous form, sulfate will only cause deterioration if it seeps through the void spaces and bond with the excess calcium oxide, also known as lime, and alumina in the concrete. It can be observed that there is needle-like particles, ettringite, between the void spaces of CSA concrete. Ettringite is a compound composed of calcium, sulfate, and aluminate. The sulfate interacted with the free lime and alumina in the concrete, from the OPC and CSA, which resulted in ettringite that was displaced into the intergranular and trans-granular voids and caused expansion of the concrete. This expansion in the concrete can be detrimental and cause spalling, onion peeling, or scaling. Furthermore, ettringite is expansive; hence, if it expands, it can lead to the cracking of the concrete, which ultimately decreases its strength [16].

Gypsum is also present in the concrete together with ettringite in between the voids, which was produced when the free calcium ions in the concrete mix reacted with the sulfate ions. Gypsum is expansive and has a softening effect that can cause strength loss [16]. However, the cause of the expansion of the concrete immersed in the sulfate solution is not exclusive to the expansive property of gypsum and ettringite. The tensile stresses that may have accumulated in the concrete could have also caused the expansion. The cracking of concrete could lead to bigger void space wherein the sulfate could penetrate the concrete and cause more expansion due to ettringite and gypsum.

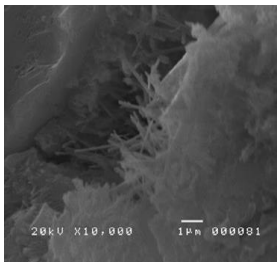

a.) conventional concrete (0% CSA)

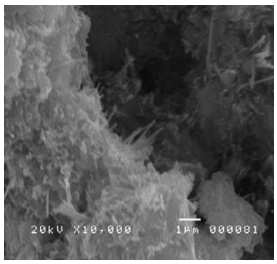

b.) 10% CSA

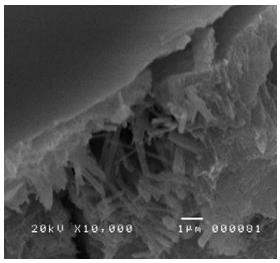

c.) 20% CSA

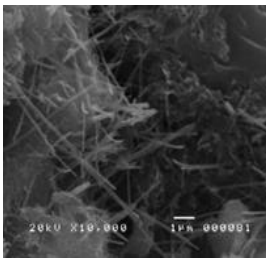

d.) 30% CSA

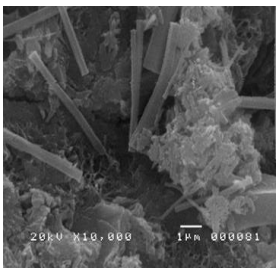

e.) 40% CSA

Fig. 6 Microstructure of CSA concrete after exposure to sulfate solution.

CONCLUSIONS

Based on the experimental results, the following conclusions can be drawn:

Coconut shell ash (CSA) contains 80.02% of the combined silicon dioxide, aluminum trioxide, and iron oxide classifying it as Class N pozzolan. The high pozzolanic activity makes it suitable to be used

as a replacement for ordinary Portland cement (OPC).

Increasing CSA content increases sorptivity and makes it more susceptible to sulfate attack. The sorptivity of the conventional concrete and all CSA concrete mixture up to 40% CSA is deemed to be acceptable and is less than the limit which is $6mm/hr^{1/2}$.

There is no significant difference between the conventional and 10% CSA concrete in terms of compressive strength at all curing ages. The compressive strength of concrete with 10% CSA is 92.10% of the compressive strength of the conventional concrete.

The microstructure of the CSA concrete after immersion in the sulfate solution shows the presence of ettringite and gypsum, which causes softening and expansion effect in the concrete. The limit of 0.1% expansion was attained sooner than 18 months even for mortar without CSA.

The results obtained proved that CSA is suitable to replace OPC because it passed the criteria to classify it as a cementitious material, however, the optimal percentage of replacement of OPC that will not affect the durability and strength of concrete should be observed. The optimum level of CSA content as replacement of OPC is 10% wherein the durability and strength are acceptable. CSA concrete can be used as an economical approach in having an acceptable level of durability of concrete structures without increasing the cement usage in any construction project; however, it is recommended that further study on the long term behavior of hardened concrete, specifically on its resistance to sulfate attack, be conducted.

REFERENCES

[1] Zhang Z.P. and Zong L., Evaluation of Relationship Between Water Absorption and Durability of Concrete Materials. Advances in Material Science and Engineering, Vol. 2014, Article ID 650373, 2014, pp. 1-8.

[2] Prasad J., Jain D.K., and Ahuja A.K., Factors Influencing the Sulfate Resistance of Cement Concrete and Mortar. Building and Housing, 7, 2006, pp. 259-268.

[3] Zivica V., Effects of the Very Low Water/Cement Ratio, Construction and Building Materials, Vol. 23, 2009, pp. 3579-3582.

[4] Thomas M., Optimizing the Use of Fly Ash in Concrete, Portland Cement Association, Publication IS 548, 2007, pp. 1-24.

[5] Zaree S.A., Ameri F., Dorostkar F., and Mojtaba, A., Rice Husk Ash as Partial Replacement of Cement in High Strength Concrete Containing Micro Silica: Evaluating Durability and Mechanical Properties, Elsevier, Case Studies in Construction Materials 7, 2017, pp. 73 – 81.

[6] Awal A.S.M., Ibrahim M.H.W., Ali A.Z.M.A., and Hossain, M.Z., Mechanical Properties and Thermal Properties of Two-Stage Concrete Containing Palm Oil Fuel Ash, Int. Journal of GEOMATE, April 2017, Vol. 12, Issue 32, pp. 166-175.

[7] Nagarajan V.K., Devi S.A., Manohari S.P., Santha M.M., Experimental Study on Partial Replacement of Cement with Coconut Shell Ash in Concrete. Int. Journal of Science and Research, 3(3), 2014, pp. 651-661.

[8] Desai B.M., Umravia N., and Gujarat K.B., Experimental Study on Concrete by Partial Replacement of Cement with Coconut Shell Ash Incorporating Steel Fibres: A review. Int. Journal for Research in Applied Science & Engineering Technology, 5(3), 2017, pp. 161-164.

[9] World Atlas, The World Leaders in Coconut Production. Retrieved date: June 10, 2017, from http://www.worldatlas.com/articles/the-world-leaders-incoconut-production.html.

[10] Zafar S., Agricultural Wastes in the Philippines, 2015. Retrieved June 10, 2017, from http://www.bioenergyconsult.com/agricultural-resources-in-philippines/

[11] Wang D., Zhou X., Meng Y., and Chen Z. Durability of Concrete Containing Fly Ash and Silica Fume against Combined Freezing, Thawing and Sulfate Attack. Construction and Building Materials, 2017, pp. 398-406.

[12] Alexander M., Durability indexes and their use in concrete engineering. 2004, Retrieved June 5, 2017, from http://demo.webdefy.com/rilem-new/wpcontent/uploads/2016/10/pro036-02.pdf

[13] Portland Cement Association, Ettringite Formation and the Performance of Concrete, Concrete Information, 2001.

[14] Association of Structural Engineers of the Philippines, National Structural Code of the Philippines, 2015: Building, Towers, and other Vertical Structures, 7th ed., Vol 1, 2015.

[15] Ferraris C., Stutzman P., Peltz M., and Winpigler J., Developing a More Rapid Test to Assess Sulfate Resistance of Hydraulic Cements. Journal of Research of the National Institute of Standards and Technology, 110(5), 2005, pp. 529-540.

[16] Tian B., and Cohen M., Does Gypsum Formation during Sulfate Attack on Concrete Lead to Expansion? Cement and Concrete Research, 30, 1999, pp. 117-123.

9th Int. Conf. on Geotechnique, Construction Materials and Environment, Tokyo, Japan, 20-22 November 2019, ISBN: 978-4-909106025 C3051

EFFECTS OF MINERAL AND CHEMICAL ADMIXTURES ON THE RHEOLOGICAL PROPERTIES OF SELF COMPACTING CONCRETE

Nolan C. Concha[1] and Melito A. Baccay[2]
[1]Faculty, FEU-Institute of Technology, Philippines
[2]Faculty, Technological University of the Philippines, Philippines

ABSTRACT

One of the most significant innovations on the workability of concrete that was achieved in recent years is self-compacting concrete (SCC). This desirable performance can be attained through the addition of admixtures to enhance its properties. In this study, superplasticizers were blended with fly ash and air entraining admixtures and were tested for Slump Flow, V-Funnel, L-Box, U-Box, and Screen Stability tests based on the European Federation of National Associations Representing for Concrete (EFNARC) specifications and guidelines for SSC. Based on the results of the study, Fly ash with spherical smooth texture enhances the lubrication between the concrete particles while the air-entrainer provides microscopic bubbles acting as ball bearings between aggregates. The best result was obtained in the specimens containing 5.0% superplasticizers due to its dispersibility effect and reduced flow resistance. In general, the air entraining agent blended with 3.7% superplasticizer exhibited the best performance in all workability test conducted.

Keywords: Viscosity; Yield stress; Self-compacting concrete; Rheology; dispersibility

INTRODUCTION

The introduction of chemical and mineral admixtures in the fundamental components of self-compacting concrete (SCC) has been used to enhance further the desirable properties of the freshly mixed concrete. SCC is a special concrete mixture exhibiting superior material homogeneity and workability requiring less to no form of external compaction [1]. Even without the aid of a compactor, a concrete is able to pass through corners of forms through its own mass. Such condition is essential in developing designs of SCC mixture. However, there is a limited number of study as to this area of concrete technology and thus require further research to completely describe the behaviour of SCC [2]. In the preparation of SCC, the material proportions of the mix are an essential component [3-6]. The compactness of concrete attributed by well distributed aggregates imparts strength to the concrete. The efficiency of the concrete in flowability is affected much by tuning the coarse aggregates spacing that depends on sizes and volume of cement in the mixture.

The rheological performance of SCC is much affected by the proportioning of the material components in the preparation of the mixture [7]. All normal concrete fine aggregates including crushed or rounded either siliceous or calcareous fine aggregates can be used in SCC. In order to develop a self compacting concrete of desirable quality, the moisture content of sand must be carefully checked and must be regarded into account. The volume of sand less than 0.125 mm must be taken as powder and is essential for the consistency of SCC. The small quantity of accumulated powders, resulting from the binders and the used of fine aggregates, must be achieved to avoid segregation with a recommended value of 500-600 kg/m3 [8]. Almost every type of coarse aggregates is appropriate for the production SCC, where the angular coarse aggregates develop the mechanical interlocking performance of the particles resulting to better strength, whilst rounded aggregates enhanced the flowability attributed by the lesser build-up of frictional stresses. The average largest aggregate size is normally 16-20 mm but particle sizes of 40 mm and up have been utilized in SCC. Well-graded aggregates are of vital importance in the production of SCC, while gap graded aggregates may exhibit more internal resistance and provide flow reduction. The volume content of the coarse aggregates usually varies between 50 to 60% of the total volume of solids in concrete [9]. When the amount of coarse aggregates in concrete go beyond the recommended limit (50-60%), the chance between aggregate particle contact or collision develop quickly and may result in higher susceptibility to blockage when the concrete move through gaps between rebars [10]. Mineral admixtures were incorporated as well in the SCC mix to further enhance the desirable properties of concrete. Rice husk ash can improve the resistance to

segregation and plastic viscosity of the mixture [11]. The concrete also exhibited chloride ion resistance and drying shrinkage with the addition of ground granulated furnace slag in the design mix [12]. The use of waste marble powder of up to 0.60 in ratio with cement produced better workability and compressive strength in the development of eco-efficient SCC [13].

To investigate the effects of blending admixtures on the rheology of self-compacting concrete, various concrete mixtures with different dosages of admixtures was prepared. The results can be used as baseline information for the identification of the most appropriate proportion for self-compacting concrete, decrease the duration of construction, and minimizes the use of external vibrators.

EXPERIMENTAL PROGRAM

Materials and Specimens

The primary objective of this research is to measure the rheological properties of self-consolidating concrete using the EFNARC criteria and examine the influence of added admixture in the concrete mix. All locally available concrete materials were tested to meet the structural standards established by the American Society for Testing and Materials (ASTM). In order to meet the requirements for SCC, superplasticizer was added to the concrete mix in gradual amounts. Adjustments as recommended by the EFNARC trouble shooting guide was carried out correspondingly to develop the desired SCC mix. The workability performance of the freshly mixed concrete having 3.7 % and 5.0% superplasticizers blended binary with Fly ash, Retarding, and Air-entraining admixtures were tested for V-Funnel, Slump Flow, L-Box, U-Box, and Screen Stability tests. Two SCC proportions with different amounts of superplasticizers was derived using the recommended material design proportions provided by the American Concrete Institute (ACI). These design mixes were used as benchmark proportions to investigate the influence of various admixtures when blended with superplasticizers. Using the general criteria for Self-Compacting Concrete, test specimen with varied admixture dosage was designed and tested in three trials for viscosity and flowability performance. Linear regression analysis was implemented to develop various linear models describing the correlation of the variation of mineral and chemical admixtures on the workability of concrete.

EXPERIMENTAL RESULTS

Rheological Tests of Blended Superplasticizer and Fly Ash

Typical quantity of fly ash ranging from 15-25% was used to partially replace the cement in the concrete mixture. This amount is found to be sufficient without providing undesirable effects in the mechanical properties of hardened concrete. Various experimental tests were carried out to evaluate the performance of the samples in passing, filling, and resistance to segregation abilities with the results reflected in Table 1. The design proportions in the table contains an increasing volume of fly ash and it is apparent from the measured values that the greater the quantity of this additive in the design proportion, the better will be the filling ability of the resulting SCC mix. Fig. 1 shows a direct correlation between fly ash volume and the flow spread of freshly mixed concrete. The addition of fly ash in the mixed resulted to better flowability performance of SCC.

Table 1 Test Results of SCC with Blended Fly Ash

Fly Ash (kg/m^3)	FILLING ABILITY				PASSING ABILITY				SEGREGATION RESISTANCE	
	Slump Flow (550-850 mm)		V-Funnel (0-8 sec)		L-Box (0.8-1.0)		U-Box (0-30mm)		Screen Stability (0-15%)	
	SCC1	SCC2	SCC1	SCC2	SCC1	SCC2	SCC1	SCC2	SCC1	SCC2
20.20	561	591	6.25	6.08	0.81	0.90	27.0	21.5	12.11	13.47
24.24	577	608	6.15	6.01	0.81	0.91	27.0	19.5	12.65	13.11
28.28	569	615	6.15	6.05	0.83	0.94	27.5	19.0	12.33	14.00
32.32	583	611	5.92	5.54	0.84	0.91	27.0	21.0	12.73	13.94
36.36	579	619	5.83	5.21	0.85	0.93	26.0	20.0	13.00	14.02
40.40	589	622	5.58	4.89	0.83	0.93	26.0	20.0	12.95	15.31
44.44	596	629	5.41	5.13	0.85	0.92	26.0	20.5	13.44	14.88
48.48	600	623	5.38	4.56	0.88	0.93	25.5	19.0	13.63	15.22
52.52	598	638	5.44	4.78	0.89	0.93	25.0	19.5	13.94	16.35
56.56	612	631	5.39	4.45	0.89	0.95	23.5	18.5	13.79	15.93
60.60	620	645	5.33	4.33	0.91	0.94	22.5	18.0	13.86	16.12

Legend: ■ - Passed ■ - Failed

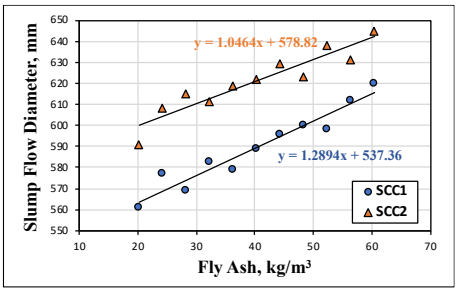

Fig. 1 Fly Ash vs Slump Flow

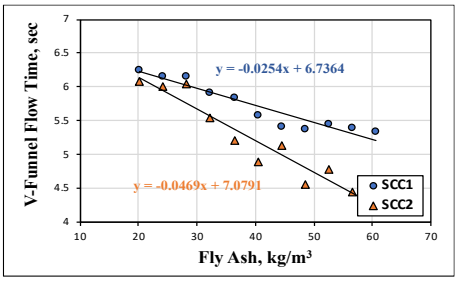

Fig. 2 Fly Ash vs V-Funnel

All samples satisfactorily met the minimum standard flow of 550 mm with SCC2 having the highest amount of fly ash registered the highest flow diameter. This observation is being justified by the time-based parameter considering a decrease in time of the concrete to move in the V-Funnel test. It is also evident and important to note that under the V-Funnel test, each SCC proportion consistently provides a declining flow time values having a strong correlation coefficient as shown in fig. 2. The dominating rounded structure of the particles of fly ash associated with mainly glassy texture and composition of its surface as shown in fig. 3 has significantly affected the flow time values of the concrete containing fly ash. Fly ash in rounded and particulate geometry can enhance flowability by its ball bearing effect between aggregate particles [14]. The increased ball bearing effect of the particle imparts better lubrication and reduces the cohesion between particles allowing it to flow freely and provides lesser recorded time.

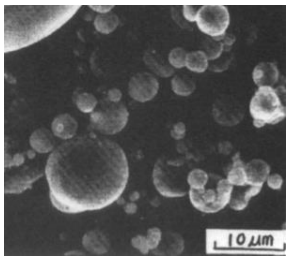

Fig. 3 Fly Ash under Scanning Electron Micrograph [14]

Ouchi et al. [15] had established the correlation between the flowing ability of fresh concrete and the amount of superplasticizer. It has been reported that the ratio of flow diameter and V-Funnel flow time could be an index of dispersibility of the concrete components. The dispersibility values of the samples tested increases with the amount of fly ash introduced in the mix with a remarkable correlation coefficient. The particulate form of the fly ash has glassy texture and are charged negatively. With this, it has lesser capacity in absorption relative to the particles of Portland cement. The quantity of adsorbed superplasticizer in the cement mixed with fly ash varies largely on the substituted fraction of the Portland cement with fly ash [16]. Superplasticizers tend to increase the dispersing effect between solid particles and since fly ash is weak to adsorb it, the adsorption effect has been given to the cement particles allowing a higher dispersibility. Fly ash can also reduce the water requirement of the mortar mixtures since porous particles can be attributed to the absorption of water. This property has a substantial effect on the behavior of the fresh concrete.

The coarse aggregates sizes were limited to a maximum of 20 mm in diameter to improve the passing ability of the mixture. Each passing ability test showed impressive results indicating a well-achieved self-compacting concrete proportion. Fig. 4 shows the behavior of the design mixes in relation with L-box and U-box tests and both regression lines demonstrate a consistent concrete behaviour in the two sample groups. As the distance between the particles decreases, the potential for blocking increases due to the particle collisions and internal stresses. The presence of excess water developed in the mixture due to the amount of fly ash and the considerable powder content maintained sufficient gap between aggregates thereby reducing interparticle interaction and build up. The aggregates in the samples having the least amount of fly ash developed a less spaced particles that is highly susceptible to collision, thus obtaining the most undesirable values.

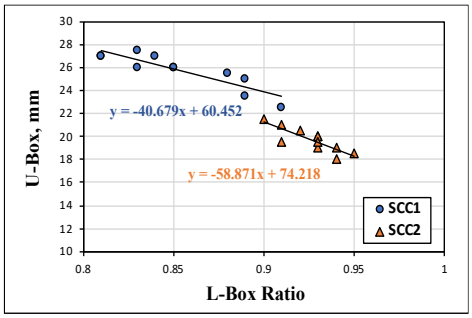

Fig. 4 L-Box vs U-Box

The viscosity of concrete dictates its segregation resistance and the more viscous the resulting mixture, the lesser will be the likelihood of its components to segregate. Fig. 5 provides a picture of the behavior of the mixture when tested using the screen stability. The given data established evident correlation between the values obtained and the quantity of fly ash blended in the concrete. Most of the calculated percentages in the mixtures indicates a susceptible chance to material segregation. Consistency is essentially related on the thickness and cohesiveness of the mixture of concrete. These properties can be enhanced by lessening the excess amount water and increasing the volume of cement. The SCC samples having the greatest amount of fly ash excessively increased the free water content and reduced cohesiveness of the mixture.

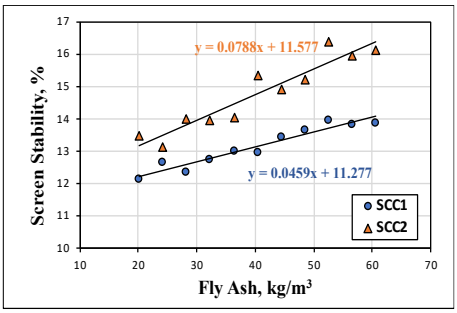

Fig. 5 Fly Ash vs Screen Stability

Rheological Tests of Blended Superplasticizer and Air Entraining Admixtures

This section discusses the final set of SCC designed samples with the addition of varying amounts of air entraining admixtures. Similar proportions of concrete components and superplasticizer were prepared and tested for filling ability, passing ability, and segregation resistance requirements as shown in table 2. The mixture in each SCC design contains an increasing amount of air entraining admixture. In the slump flow test, the spread of the concrete in each sample satisfactorily met the acceptance criteria and this shows that the blending promotes better and smooth horizontal free flow of the mixture. As observed in the table, the increasing amount of air entrainer corresponds to a better slump flow result and is consistently exhibited in the two SSC design groups as shown in fig. 6. Stabilizing the air void system in the fresh concrete would permit relatively free motion of fresh concrete in shear. The drastic change in the air bubbles as contributed by the increase in the air-entraining dosage resulted to desirable effect on the flow efficiency of SCC. The entrained air also increases the paste volume and tends to increase the distances between solid particles. This in turn reduced the interparticle friction and interaction allowing the fresh concrete to flow easily in the slump flow test.

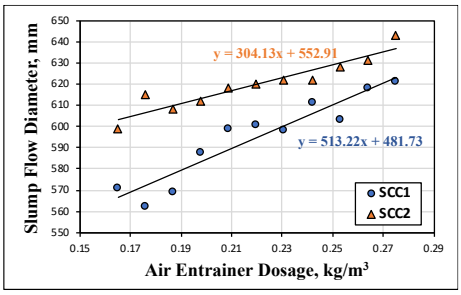

Fig. 6 Air Entrainer vs. Slump Flow

With the low results in the recorded data of the time-based V-Funnel test, the samples displayed better fluidity and efficient flow ability. Fig. 7 shows the declining flow time with the increasing dosage of air entrainer. This implies that the fresh concrete was able to flow easily due to low flow resistance and minimal frictional stresses developed between concrete particles.

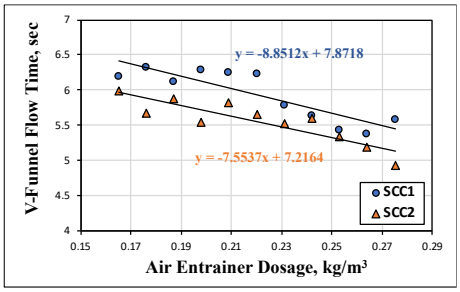

Fig. 7 Air Entrainer vs V-Funnel

The entrained bubbles in the mixture considerably modified the flow characteristics of the mixture yielding a well-performed SCC. It can be seen in fig. 8 the relationship between the increased dosage of the admixture and the dispersibility of the mixture. The addition of superplasticizers in the mixture as well imparts dispersion effect in the particles creating a significant dispersibility results. The entrained bubbles allowed deformation under compression and slippages of neighboring particles offering smooth translation of the concrete particles.

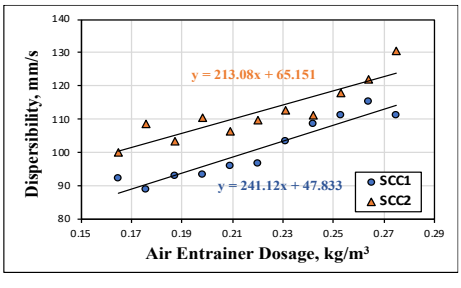

Fig. 8 Air Entrainer vs. Dispersibility

Table 2 Test Results of SCC with Blended Fly Ash

Air Entrainer (kg/m^3)	FILLING ABILITY				PASSING ABILITY				SEGREGATION RESISTANCE	
	Slump Flow (550-850 mm)		V-Funnel (0-8 sec)		L-Box (0.8-1.0)		U-Box (0-30mm)		Screen Stability (0-15%)	
	SCC1	SCC2	SCC1	SCC2	SCC1	SCC2	SCC1	SCC2	SCC1	SCC2
0.165	571	599	6.19	5.99	0.71	0.78	28.50	24.50	10.56	13.32
0.176	562	615	6.33	5.67	0.74	0.84	27.00	22.50	11.88	13.56
0.187	569	608	6.11	5.88	0.80	0.71	23.00	27.50	11.72	13.12
0.198	588	612	6.29	5.54	0.79	0.87	24.00	22.50	12.12	14.00
0.209	599	618	6.24	5.81	0.83	0.90	22.44	20.00	12.45	14.19
0.220	601	620	6.22	5.66	0.83	0.90	21.50	21.50	12.47	14.33
0.231	598	622	5.78	5.53	0.85	0.89	22.50	22.00	12.63	14.55
0.242	611	622	5.63	5.59	0.83	0.93	21.00	18.50	13.33	14.22
0.253	603	628	5.43	5.33	0.87	0.88	22.50	20.50	13.71	14.67
0.264	618	631	5.37	5.18	0.87	0.92	19.00	19.50	13.12	14.51
0.275	621	643	5.58	4.92	0.89	0.94	20.50	20.00	13.75	14.73

Legend: ■ - Passed ■ - Failed

When the entrained air content is increased, the effect of further increased in the electrostatic attraction between the cement and other small particles was counteracted by greater reduction in the mechanical interlocking due to the lubricating effect of the bubbles. The group of samples was also tested for passing ability requirements. According to Chia [1] entrained air bubbles were able to perform effectively as deformable and elastic ball bearings, reducing internal friction in the fresh concrete. It can be seen that the samples having the highest amount of air entrainer registered the best results among the samples. The augmented ball bearing behavior of the bubbles imparts better lubrication and reduces the friction between particles allowing it to flow freely and pass over the apparatus. The impressive ability of the concrete to flow over complex forms is described by the results in the L-box and U-box tests depicted in fig. 9. Again, the lubrication and minimal development of friction due to the ball bearing behaviour of the entrained bubbles enable the freshly mixed concrete to flow and pass successfully over the L-Box and U-Box apparatus.

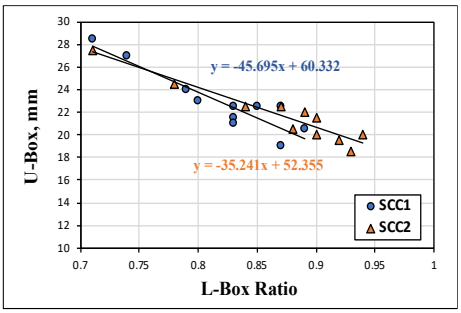

Fig. 9 L-Box vs. U-Box

Fig. 10 presents the increasing values in the screen stability test with the amount of air entrainers mixed in the concrete. This has been regularly observed in each SCC design groups. It can be seen that a less stable distribution in the composition of concrete was provided by the corresponding increase in the dosage of the admixture. Among the design proportions prepared, SCC2 having the most amount of air entrainer exhibits a possible chance to segregation.

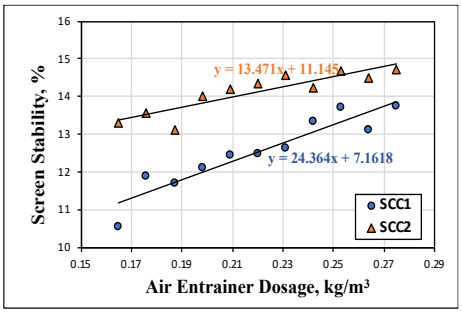

Fig. 10 Air Entrainer vs Screen Stability

CONCLUSIONS

The blending of fly ash and superplasticizer demonstrates a remarkable performance in the filling ability and passing ability of the self-compacting concrete. This is due to the roller bearing effect of the smooth spherical surface of the fly ash. Most of the tests conducted for these workability parameters were fulfilled establishing a concrete with high flowability. Consequently, the blending significantly reduced the viscosity of the mixture producing a concrete susceptible to segregation. It is advisable to blend these two admixtures in their minimum recommended amounts to maintain the overall workability performance of SCC.

To produce SCC having a uniform material distribution, one of the two admixtures is sufficient for the purpose. With the increasing amount of air entrainer in the production of self-compacting concrete, the design mixes performed efficiently in

the three workability parameters. The blending of air entraining admixture and superplasticizer significantly enhanced the ability of the concrete in passing, filling and resistance to segregation. The blending should be done such that the proportions of each admixture fall within the middle range of the recommended dosage.

REFERENCES

[1] Seng CK. Workability and stability of lightweight aggregate concrete from rheology perspective (Doctoral dissertation).

[2] Ozawa K. Evaluation of self-compactability of fresh concrete using the funnel test. InProceedings of Japan society of Civil Engineers 1995 (Vol. 25, pp. 59-75).

[3] Shi C, Wu Z, Lv K, Wu L. A review on mixture design methods for self-compacting concrete. Construction and Building Materials. 2015 Jun 1;84:387-98.

[4] Concha N, Oreta AW. A model for time-to-cracking of concrete due to chloride induced corrosion using artificial neural network. InIOP Conference Series: Materials Science and Engineering 2018 Oct (Vol. 431, No. 7, p. 072009). IOP Publishing.

[5] Concha NC, Oreta AW. Bond Strength Prediction Model of Corroded Reinforcement in Concrete Using Neural Network. International Journal Of Geomate. 2019 Feb 1;16(54):55-61.

[6] Concha N, Oreta AW. A model for time-to-cracking of concrete due to chloride induced corrosion using artificial neural network. InIOP Conference Series: Materials Science and Engineering 2018 Oct (Vol. 431, No. 7, p. 072009). IOP Publishing.

[7] Le HT, Müller M, Siewert K, Ludwig HM. The mix design for self-compacting high performance concrete containing various mineral admixtures. Materials & Design. 2015 May 5;72:51-62.

[8] Poppe AM, De Schutter G. Influence of the Nature and the Grading Curve of the Powder on the Rheology of Self-Compacting Concrete. Special Publication. 2001 Jun 1;200:399-414.

[9] Santamaría A, Orbe A, Losañez MM, Skaf M, Ortega-Lopez V, González JJ. Self-compacting concrete incorporating electric arc-furnace steelmaking slag as aggregate. Materials & Design. 2017 Feb 5;115:179-93.

[10] Saak AW, Jennings HM, Shah SP. New methodology for designing self-compacting concrete. Materials Journal. 2001 Nov 1;98(6):429-39.

[11] Le HT, Ludwig HM. Effect of rice husk ash and other mineral admixtures on properties of self-compacting high performance concrete. Materials & Design. 2016 Jan 5;89:156-66.

[12] Zhao H, Sun W, Wu X, Gao B. The properties of the self-compacting concrete with fly ash and ground granulated blast furnace slag mineral admixtures. Journal of Cleaner Production. 2015 May 15;95:66-74.

[13] Alyamac KE, Ghafari E, Ince R. Development of eco-efficient self-compacting concrete with waste marble powder using the response surface method. Journal of cleaner production. 2017 Feb 15;144:192-202.

[14] Nawa T. State-of-the-art report on materials and design of self-compacting concrete. InProc. of the International Workshop on Self-Compacting Concrete 1999 (pp. 160-190).

[15] Ouchi CW. Flowability of fresh mortar in self-compacting concrete using fly ash. InPRO 42: 1st International RILEM Symposium on Design, Performance and Use of Self-Consolidating Concrete-SCC'2005, China 2005 (Vol. 42, p. 261). RILEM Publications.

[16] Kong D, Du X, Wei S, Zhang H, Yang Y, Shah SP. Influence of nano-silica agglomeration on microstructure and properties of the hardened cement-based materials. Construction and Building Materials. 2012 Dec 1;37:707-15.

9th Int. Conf. on Geotechnique, Construction Materials and Environment, Tokyo, Japan, 20-22 November 2019, ISBN: 978-4-909106025 C3051

AN IMPROVED PREDICTION MODEL FOR BOND STRENGTH OF DEFORMED BARS IN RC USING UPV TEST AND ARTIFICIAL NEURAL NETWORK

Nolan C. Concha[1] and Andres Winston C. Oreta[2]
[1]Faculty, FEU-Institute of Tech., Philippines
[2]Faculty, De La Salle University, Philippines

ABSTRACT

The composite action of reinforcement in the surrounding concrete involves a complex and non-linear mechanism. Inadequate understanding of the underlying interactions may lead to designs with insufficient amount of bond resistance of reinforcing bars in concrete structures. To investigate the effects of various parameters on the bond strength of steel bars in concrete, 54 cube samples with varying embedded reinforcements and strengths were prepared. The samples were cured for 28 days and tested using ultrasonic pulse velocity (UPV) test for sample homogeneity and single pull out test for bond strength. Data gathered in the experiment were used in the development of bond strength model as a function of compressive strength, concrete cover to rebar diameter ratio, embedment length, and UPV using artificial neural network (ANN). Of all the bond strength models considered from various literatures, the neural network model provided the most satisfactory prediction results in good agreement with the bond strength values obtained from the experiment. The UPV parameter was found to be one of the most significant predictors in the neural network model having a relative importance of 20.57%. This suggest that the robust prediction performance of the bond model was attributed to this essential component of the model. The proposed model of this study can be used as baseline information and rapid non-destructive assessment for zone wise strengthening in reinforced concrete.

Keywords: Bond strength; Artificial neural network; Ultrasonic pulse velocity; Parametric analysis

INTRODUCTION

One of the essential components that must be achieved for structural design is the bond strength of the steel reinforcement to the enveloping concrete. The resistance of the rebar against slipping from embedment due to pulling force is defined as bond strength. The composite action between steel and the enveloping concrete may be may be destroyed by the inadequate bond resistance and may result to concrete brittle failure [1]. The bond does not only ensure the composite action but also controls structural behavior of the reinforced concrete. There are numerous number of researches embarking on bond behavior of steel bars in concrete are available in the literature. Results recorded from experiments of these studies were used to develop analytical and empirical models. Due to the complex non-linear relationships that exist in the rebar and concrete, several ideal assumptions were adopted to simplify the systems involved in the development of the models. These estimates however insufficiently represent the existing underlying mechanism of bond strength in reinforced concrete. As a result, the derived bond equations provided estimates that are in good agreement only within the framework of their study. It is therefore indispensable to consider other modelling techniques that are powerful enough to generally adopt with the complex behavior of bond strength in reinforced concrete.

A convenient and precise way to model the complex interactions in such intricate systems is by means of artificial neural network [2-6]. There is no need to consider ideal assumptions to simplify the modelling approach as the neural network process raw data from actual experiments. Through the aid of a set of input-output data, a system of interconnected neurons can be developed that is capable of predicting variables from a certain set of inputs. In this work, novel prediction model of bond resistance of reinforcing rebars in reinforced concrete using neural network will be developed. A greater number of variables will be considered in the modeling including concrete compressive strength, tensile capacity of concrete, homogeneity of concrete using ultrasonic pulse velocity, rebar diameter, embedment length and concrete cover. The performance of the model will be compared to other available bond strength models in the literature. Multiple regression model will also be derived for comparison.

BOND STRENGTH MODELS

The bond strength of reinforced concrete members depends on many different variables such as compressive strength, rebar size, length of embedment, type of loading (dynamic or static), development length, and bar spacing. The use of pull out test played a vital role in the development of bond strength model. In the study of Hadi [7], 14 simple pull out tests were performed in measuring the bond strength of 500 MPa grade steel embedded in a 70 MPa concrete compressive strength. Different bar diameters from 12 mm to 36 mm were used having concrete cover of 120 mm and 150 mm. The derived model using regression analysis is given in eqn 2. The equation is dependent on the compressive strength of concrete (f'c), concrete cover (c), diameter of the rebar (d_b), and the length of embedment (L_d). The bond strength equation was compared with other established models and comparison showed that among the models considered, the proposed model provided the best prediction values in agreement with the experimental results.

$$u = 0.08305\sqrt{f'c}\left(22.8 - 0.208\frac{c}{d_b} - 38.212\frac{d_b}{L_d}\right) \quad (1)$$

Unlike any other studies that focus on bond strength, the study of Yalciner et al [8] made use of multiple linear regression in order to model an equation for the ultimate bond strength(τ_{bu}) that is dependent to compressive strength (f'c) of concrete and the cover (c) to bar diameter (D) ratio. An increase in concrete compressive strength and concrete cover would also result to an increase in bond strength. Moreover, it was found out that an increase in the compressive strength with constant concrete protective cover resulted to higher bond strength than a constant compressive strength with increasing the concrete protective cover. Using multiple linear regression, the following equations with high correlation coefficient values were established:

$$\tau_{bu} = -2.7143 + 0.3621 f'c + 2.3296\left(c/D\right)\left(R^2 = 0.96\right) \quad (2)$$

A larger number of variables were considered in the study of Diab et al [9] on bond performance and ultimate design of bond stress of normal and high strength concrete. Samples having different compressive strength (f_{cu}), concrete cover (c), size of the bar (d_b), length of embedment (L_d), rib height (h_r), and rib spacing (s_r) were tested using single and double pull out tests. The bond stress equation of samples having compressive strength of 80 MPa was developed using multiple regression as shown in eqn 3. The reliability of this equation was validated using values recorded from experiments and compared with forecasted values provided by other available models. There is a satisfactory agreement of the proposed equation as described by the average value of actual to predicted bond strength ratio of 0.89.

$$\tau_{pr} = \sqrt{f_{cu}}\left[0.08262 + 0.09234\left(c/d_b\right) + 1.6038\left(d_b/L_d\right) + 0.6318\left(h_r/s_r\right)\right] \quad (3)$$

In most of the studies enumerated for bond strength models, other equally important factors were not considered such as tensile strength and homogeneity of concrete. Thus, the results of the studies do not provide a substantial and complete discussion of the composite action between steel and concrete. Further, the derived models can only be applied to specific cases of bond strength to which the models were calibrated. In most of the studies involving non-linear relationships of multiple variables like bond stress, several ideal assumptions were usually adopted to reduce the complexity of the system in the modeling process. In order to avoid these simplifications that may reduce the reliability of results, a more powerful modelling approach such as artificial neural network must be used.

EXPERIMENTAL PROGRAM

Materials and Specimens

In designing the correct proportion of concrete, raw materials need to exhibit desirable properties to ensure beneficial effect to the design mixture. With the advent of available standard testing procedures and duly accepted gaging criteria, this study was able to measure the physical properties of the materials used and found to be in good conditions for the production of concrete. Water used in the mix was in good quality and free from contaminants. The density and water absorption of the coarse aggregates used were 1572.028 kg/m^3 and 0.402% respectively. These values were measured in accordance with ASTM C127-04. Using ASTM C127-04a and ASTM C136, the density, water absorption, and fineness of fine aggregates were respectively measured to be 1533.801 kg/m3, 3.2 %, and 2.673. Three distinct designs of concrete mixtures were prepared based on target compressive strengths of 21 MPa, 28 MPa, and 35 MPa. Using a slump interval between 25mm and 100mm, 2% entrapped air, and estimated water cement ratios of 0.68, 0.57, and 0.47, three design mixes shown in table 1 were obtained. A total of 54 cube samples having side length of 200 mm with embedded reinforcement were prepared for the conduct of pull out test. Variation in rebar diameter (16mm, 20mm, and 25mm), concrete cover (60mm, 70mm, and 80mm), and embedment length (50mm, 75mm, and 100mm) were used in this study.

Table 1 Concrete design proportions and strengths

Design Mix	W kg/m^3	C kg/m^3	CA kg/m^3	FA kg/m^3	f'c (MPa)	ft (MPa)
1	189	301	1018	866	22	2.08
2	189	359	1018	806	29	2.61
3	190	436	1018	726	36	3.14

Testing of Specimens

Immediately after molding and finishing, cube and cylindrical specimens were cured by immersing the samples in water for 28 days (ASTM C31). The dimensions of the cylindrical samples were 6 inches in diameter and 12 inches in height. After the specified age of curing period have been reached, the cylindrical samples were tested in three trials for compressive strength (ASTM C39) and tensile strength (ASTM C496) of concrete using the universal testing machine. To assess the quality of concrete, ultrasonic pulse velocity test was carried out to all the cube samples (ASTM C597). All lateral faces of the specimen were applied with liquid coupling material for better contact between the coupler and surface of the sample. The transducer and receiver of the UPV apparatus was placed in direct set up. Lastly, standard single pull out test (ASTM C234-91A) was conducted in all the concrete cube samples to measure the maximum force necessary to pull the rebar from the concrete as shown in fig.1. Bond strength between the rebar and enveloping concrete was obtained by taking the ratio of the stress load and the surface area of steel bar which is in contact with the concrete.

Fig. 1 Concrete cube sample under pull out test

EXPERIMENTAL RESULTS

Experimental Data Statistics

The statistics of 54 samples tested for ultrasonic pulse velocity and pull out tests were determined. The statistical description includes the mean, standard deviation, sample variance, maximum value, and minimum value of the geometric attributes and measured strengths of the samples. The maximum pulse velocity was 4537 km/s while the minimum velocity was 4009 km/s. These values were measured from samples having 36 MPa and 22 MPa compressive strengths respectively. The observed values were reasonable since higher compressive strengths imply more solid or compact internal structure of the sample. The signal generated by the UPV apparatus travels faster in solid medium thus providing larger values of pulse velocity. The UPV standard deviation of 128.56 km/sec suggests that the measured UPV values of the samples were roughly close to the average UPV value of 4355 km/sec. Less variability in the measured values were also observed as describe by a relatively small COV of only 3%. In the bond strength however, a larger dispersion in the measured values were observed as indicated by large SD of 6.376 MPa and COV of 46.7%.

NEURAL NETWORK MODELLING

Framework of the Neural Network Model

The bond strength model was a function of 6 independent variables namely compressive strength (f'c), tensile strength (ft), embedment length (ld), rebar diameter (ϕ), concrete cover (cc), and ultrasonic pulse velocity (UPV). These variables were individually represented by 6 distinct nodes in the input layer of the neural network. To develop a simple ANN model, only one hidden layer was used with varying number of hidden nodes between 3 to 6. A single node in the output layer represents the bond stress in the model. Neural network architecture having 6 input nodes, 2 hidden layer neurons, and 1 output node was represented as N 6-2-1. Four ANN structures were developed having different number of nodes in the intermediate layer. The variation in the nodes was carried out to explore a better neural network topology. Feedforward backpropagation algorithm was used as the learning algorithm in the derivation of the models with hyperbolic tangent sigmoid function $f(n)=2/(1+e-2n)^{-1}$ as the neural activation function. This transfer function calculates a layer output that returns value between -1 to 1. Threshold criteria of 100000 cycles or an error tolerance value of 0.001 were used to terminate the simulation process. A few number of nodes in the hidden layer was considered to avoid overfitting in the development of the model. Early stopping in the testing phase was also carried out to further improve the generalization of the model.

ANN Model Experimental Data and Simulations

The least number of training data pairs that will provide unique approximation must not be less than the number of weights and biases associated with the neural network model [10]. Carpenter and Hoffman [11] further suggest that 20-50% overdetermined

ANN model tends to provide satisfactory prediction performance. The bond strength model in this study involved six predictors, one hidden layer, and one output node. This neural network structure (N 6-5-1) with five nodes in the hidden layer and using 20% overdetermined network required a minimum number of input-output data pairs between 42 to 50 [12].

The correlation coefficient (R) and the mean squared error (MSE) were used as performance metrics in selecting the best bond strength model. The best neural network structure among the variations considered will have the least MSE and the closest R value to 1.0. As shown in table 2 were the results of MSE and R of the four distinct ANN model architectures having different number of nodes in the hidden layer. It is evident that N 6-6-1 model provided the best performance among all the models considered in the simulation. After all the data in the output layer were transformed in their corresponding physical attributes, the errors can be calculated by subtracting the experimental values from the estimated values provided by each model. The measured errors in the predicted values of N 6-6-1 model were the least errors relative to the other neural network architectures inasmuch as the model obtained the least MSE of 1.491. Further, a better agreement between the experimental and predicted values of N 6-6-1 model was expected owing to its high Pearson correlation coefficient R equal to 0.981. Having these desirable results, the developed model successfully learned from the simulation given a limited number of experimental data.

Table 2 Variation of ANN models

Model	Number of hidden nodes	Performance criteria	
		MSE	R
N 6-3-1	3	5.247	0.938
N 6-4-1	4	3.413	0.957
N 6-5-1	5	2.287	0.972
N 6-6-1	6	1.491	0.981

Connection Weights and Biases of N 6-6-1 Model

After a series of simulations of different ANN architectures, the N 6-6-1 model emerged as the best performing architecture. The model has six normalized nodes in the input layer representing compressive strength of concrete (f'c), tensile strength of concrete (ft), embedment length (Ld), rebar diameter (ϕ), concrete cover (cc), and ultrasonic pulse velocity (UPV). The weights and biases of this network model upon simulation were shown in table 3. Using the causal inference procedure developed by Garson [13], the relative importance of each parameter was also reflected in the table. Apparently, the rebar diameter was the most significant predictor in the model having a relative importance of 29.29% followed by compressive strength (16.78%), and concrete cover (16.63%). This was reasonable since the bond strength in reinforced concrete is largely influenced by the change of these three parameters. The least significant predictor on the other hand was the UPV having a relative importance of only 8.32%.

Table 3 Connection weights and biases of N 6-6-1 model

Hidden Nodes	**Input Layer**						**Output Layer**
	f'c	**ft**	**L_d**	**ϕ**	**cc**	**UPV**	
1	1.2359	0.97265	-3.488	-0.7465	0.8836	0.7632	0.8562
2	-1.5151	-1.3295	-2.7982	0.01032	-0.69229	0.10122	-0.2242
3	0.25005	-0.3640	3.1946	2.3349	-0.99424	0.28041	-0.3132
4	-3.1719	-1.4096	1.0701	-2.4758	0.62345	-4.111	-0.6295
5	-1.8764	-1.253	0.74373	-2.1176	-0.6216	-0.6828	0.7191
6	-0.0100	-0.8921	-0.3019	-0.3384	-0.9233	0.5979	-0.3561
Biases	-5.4397	2.5168	-1.1038	-3.5886	-1.9855	-1.7898	0.12035
Rel. Impt.	16.78	13.43	15.15	29.29	16.63	8.32	

Prediction Performance of N 6-6-1 Model

Fig. 2 shows the comparison of the N 6-6-1 model predictions to the experimental values for both training and test data. The results obtained in both data sets were significantly correlated as described by their respective Pearson's correlation coefficients of 0.99 and 0.90. A vast majority of the plotted points was very close to the measured bond strength. Based almost lied on the perfect line with an average prediction error of 6.86%. Roughly 90% of the predicted values of the model lied within the 10% error. Maximum and minimum errors of 64% and 0.01% respectively were observed in the estimated values. An average ratio between the experimental and predicted values of 0.998 was further obtained. This result suggests that the estimated bond strength on these desirable results, the derived ANN model

exhibited a robust prediction performance

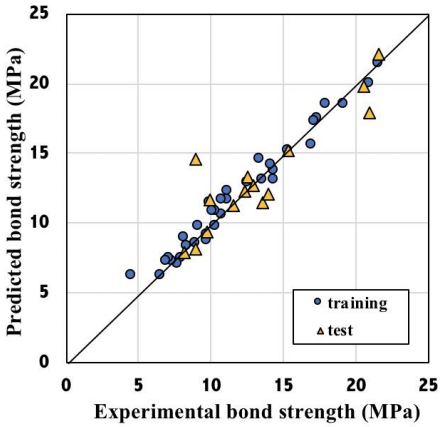

Fig. 2 ANN model predictions of bond strength

Comparison Between N 6-6-1 Model and Other Bond Strength Models

The performance of N 6-6-1 model was compared with other existing models developed by Hadi [7], Yalciner et al [8], Diab et al [9], and the developed model using multiple linear regression. Data sets in each study were consolidated and used to test the prediction performance of each bond strength model. Fig. 3 shows the plotted points of the experimental data against predicted values provided by the aforementioned models. A 45° line, also called the perfect line, was drawn in the figure to clearly observe the fitness of the models in estimating the bond strength of a given set of input parameters. The better the prediction, the closer will be the point to the perfect line. The scatter plot diagram displayed large dispersion of collected data sets from different studies. The figure suggests that, in general, the models performed satisfactory only within the set of data in which the models were respectively calibrated. Most of the models provided significant deviations from the perfect line for values beyond the framework of their study. These undesirable attributes showed poor generalization of the models considered. It may be because of the ideal assumptions made in the modelling process that may not be the actual underlying behavior of the interactions involved in the system. The model developed by Yalciner [8] exhibited the largest recorded average error of 75%. While the model developed by Diab [9] included the largest number of parameters, the average prediction error was 49%. In fact, Hadi's [7] model involving four independent variables offered better approximations providing a mean error of only 48% in the predictions. This observation implies that the superiority of the model does not rely on the number of variables involved in the modelling process but by how significant is the contribution of each variable in the model. Looking closely on the plots of the proposed N 6-6-1 model, majority of the points showed relatively small deviations from the perfect line and obtained a correlation coefficient of 0.855. Among all the models considered in this study, the proposed ANN model gave the least average prediction error of only 29%. The maximum and minimum correlation coefficients were 0.855 and 0.062 respectively. About 72% of the consolidated data sets from various studies considered were captured by the ANN model with an error within ±20%.

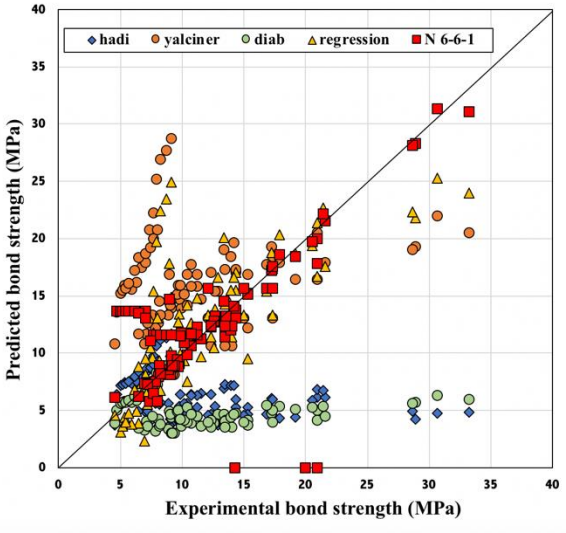

Fig. 3. Bond predictions using different models

CONCLUSIONS

Upon training various neural network architectures, N 6-6-1 model was found to be the best performing architecture having six input nodes, one hidden layer with five nodes, and one output node. The model was able to provide satisfactory prediction results capturing 72% of the data from experiments conducted and from various literatures with an error of at most 20%. Model comparison further showed that the proposed N 6-6-1 model provided the best prediction performance against other existing models considered in this study. The superiority was achieved since no simplified ideal assumptions were considered and only experimental results were used in the simulation process. This shows the power of artificial neural network in modelling highly complicated interactions using a limited source of experimental data.

The compressive and tensile strengths of concrete, concrete protective cover, and ultrasonic pulse velocity offered direct correlation with the bond strength behavior of reinforced concrete. The bond stress however decreases as the rebar diameter and embedment length of reinforcement increases. This observation was attributed by the lateral contraction of the rebar due to Poisson's ratio. The derived model

can be considered as rapid and convenient approach to estimate the bond strength of concrete. The results of the model can be used as baseline information in the design of reinforced concrete structures and other engineering applications involving bond strength.

REFERENCES

[1] Rao GA, Pandurangan K, Sultana F, Eligehausen R. Studies on the pull-out strength of ribbed bars in high-strength concrete. InProc. of FraMCoS-6 2007 (pp. 295-301).

[2] Concha NC. Rheological Optimization of Self Compacting Concrete with Sodium Lignosulfate Based Accelerant Using Hybrid Neural Network-Genetic Algorithm. In Materials Science Forum 2016 (Vol. 866, pp. 9-13). Trans Tech Publications.

[3] Concha NC, Oreta AW. Bond Strength Prediction Model of Corroded Reinforcement in Concrete Using Neural Network. International Journal Of Geomate. 2019 Feb 1;16(54):55-61.

[4] Concha N, Oreta AW. A model for time-to-cracking of concrete due to chloride induced corrosion using artificial neural network. InIOP Conference Series: Materials Science and Engineering 2018 Oct (Vol. 431, No. 7, p. 072009). IOP Publishing.

[5] Rinchon JP, Concha NC, Calilung MG. Reinforced concrete ultimate bond strength model using hybrid neural network-genetic algorithm. In2017IEEE 9th International Conference on Humanoid, Nanotechnology, Information Technology, Communication and Control, Environment and Management (HNICEM) 2017 Dec 1 (pp. 1-6). IEEE.

[6] Concha NC, Dadios EP. Optimization of the rheological properties of self-compacting concrete using neural network and genetic algorithm. In 2015 International Conference on Humanoid, Nanotechnology, Information Technology, Communication and Control, Environment and Management (HNICEM) 2015 Dec 9 (pp. 1-6). IEEE.

[7] Hadi MN. Bond of high strength concrete with high strength reinforcing steel.2008. vol. 2, pp. 143-147

[8] Yalciner H, Eren O, Sensoy S. An experimental study on the bond strength between reinforcement bars and concrete as a function of concrete cover, strength and corrosion level. Cement and Concrete Research. 2012 May 1;42(5):643-55.

[9] Diab AM, Elyamany HE, Hussein MA, Al Ashy HM. Bond behavior and assessment of design ultimate bond stress of normal and high strength concrete. Alexandria Engineering Journal. 2014 Jun 1;53(2):355-71.

[10] Carpenter, W. C., and Barthelemy, J., Common misconceptions about neural networks as approximators, J. Comput. Civ. Eng., 1994, 83 , 345 – 358.

[11] Carpenter, W. C., and Hoffman, M. E., Training backprop neural networks, AI Expert, March 1995, 30–33.

[12] Oreta AW, Kawashima K. Neural network modeling of confined compressive strength and strain of circular concrete columns. Journal of Structural Engineering. 2003 Apr;129(4):554-61.

[13] Garson, G. D., Interpreting neural-network connection weights, AI expert, 1991,6(4), 46-51.

9th Int. Conf. on Geotechnique, Construction Materials and Environment, Tokyo, Japan, 20-22 November 2019, ISBN: 978-4-909106025 C3051

APPLICATION OF TAILINGS AS THE SUBSTITUTION MATERIAL OF FINE AGGREGATE IN THE HOT ROLLED SAND SHEET

Yogi Priyo Pradana [1*], *Heriansyah Putra[1*], Tri Sudibyo[1], Devyan Meisnnehr[1], Kamal Hassan Iskandar[1]
[1]Department of Civil and Environmental Engineering, Faculty of Agricultural Engineering and Technology, IPB University, Indonesia 16680

ABSTRACT

In numerous mining process, tailing continue to be produced in large quantities and stored in massive ponds while posing environmental hazards. This paper presented the utilization of tailing as the substitution material of fine aggregate in the sand sheet of road construction. Several amounts of tailing are substituted to modify the gradation of the fine aggregate. The gradation analyses are conducted to evaluate the effect of the substitution of tailing on the gradation distribution of the mixed material. The Marshall tests are also conducted to asses the impact of tailing substitution on the strength of the hot rolled sand sheet. The gradation analysis shows that the substitution of 50% tailing has a significant effect on the distribution of mixed materials. The coefficient of uniformity, Cu, and coefficient of the curve, Cc of 4.82 and 1.72 are obtained, respectively. The mechanical test results using the Marshall test shows that the substitution of 50% tailing brings about a significant improvement in the strength of the hot rolled sand sheet. The strength of hot rolled sand sheet increase 100% or 2-fold higher compared than those without the tailing is obtained. The results of this study have indicated that the gold mining waste of tailing may be viable as the substitution material for road construction.

Keywords: Tailing, gradation analyses,marshall test, strength

INTRODUCTION

The development of infrastructure, especially road infrastructure in Indonesia in recent years, has increased. Since 2014, the Ministry of PUPR through the Directorate General of Highways has successfully completed the construction of 3432 km of national roads including roads on the borders of Papua, Kalimantan, and NTT. In addition, 941 km of new toll roads have been built with the final target of 2019 reaching 1,852 km [1]. In 2016, the total length of national roads that have been built was 47,017.28 km [2]. Hence, the material needs, especially asphalt constituents materials such as sand and gravel, also increase.

Until now, many the innovation of materials for roads, especially roads made from asphalt such as the use of resin as a substitute for conventional asphalt has been found by researchers [2]. Reclaimed asphalt (utilization of stripping and asphalt reprocessing materials) [7], utilization of used tire waste on asphalt [4], foam asphalt in road construction, and other innovative materials [6]. There are two conditions that must be considered in innovating road construction materials are the level of material effectiveness and sustainability. One alternative material that meets both of these criteria is tailings.

Tailings have the potential as an alternative material in construction materials such as mixtures of concrete and asphalt. Tailings, as a mixture of construction materials, has a good impact on the environment because tailings are waste from the rest of metal mining and minerals [5]. Aschuri and Yamin [1] show that the tailings on the base material and sub-base material gave an excellent effect on CBR values along with increasing use of 45% tailings. Whereas 5% by weight of cement replaced by tailings on mortar making will increase mortar compressive strength by 108.45% compared to more than compressive strength without tailings [5].

This paper aims to explain the ability of tailings as fine aggregate substitution and determine the optimum percentage of tailings in hot mix asphalt.

METHODOLOGY

Gradation Analysis

The strength and elegance of a pavement construction are very dependent on the aggregate quality, carrying capacity of the soil and the type of asphalt used as the primary material to bind the materials needed to obtain a hardened, durable, strong and rough hardening. The two types of pavement commonly used are flexible pavements that use asphalt as a binder and rigid pavements that use cement as an aggregate binder. With aggregate as the main component of the highway, pavement consists of coarse aggregates and fine aggregates that have each according to the specifications used the test is carried out by aggregate gradation test using fine and coarse aggregates using a shaker. The basic references used in this test are AASHTO T-27-74, and ASTM C-126-46. HRSS (Hot Rolled Sheet

Sheet). Requirements for gradation of the HRSS class with a filter size of 0.075 mm are 4-14% passed. Requirements for class HRRS B with a filter size of 0.075 mm are 8-18% escaped. The percentage of tailings used is 0%, 25%, 50%, and 75%. Experiments from this HRSS can require angularity to provide a mixture that is stronger and more resistant to deformation. While HRSS can be made with or not approved coarse aggregate, depending on the gradation of sand available.

Trial Mix

This examination is intended to determine the resilience (stability) of the plastic melt (flow) of the asphalt mixture, while the purpose of this test is to obtain an asphalt mixture that meets the requirements set out in the planning criteria. The procedure carried out in this experiment included: test specimen preparation, mixture preparation, and mixed preparation. In compaction procedures, the type of impact used is collision for light traffic.

Marshall Test

The Marshall test aims to determine the characteristics of a flexible tapper. The Marshall method consists of Marshall tests and Marshall parameters, which are explained as follows:

a.Marshall Test

Mixed design based on the Marshall method invented by Bruce Marshall. The Marshall test aims to measure the durability (stability) of an aggregate and asphalt mixture against the flow (plastic). Flow is defined as a change in deformation or strain of a mixture from no load, to maximum load. Marshall equipment is a press equipped with a Proving ring with a capacity of 22.2 KN (5000 lbs.) and flow meter. Proving ring is used to measure the value of stability, and a flow meter to measure plastic melt or flow. Standard cylindrical standard Marshall specimens with a diameter of 4 inches (10.16 cm) and a height of 2.5 inches (6.35 cm).

b. Marshall Test Parameters

The properties of paved mixtures, can be seen from the Marshall test parameters, including:

1. Marshall stability

According to The Asphalt Institute, Mudianto (2004), stability is the ability of asphalt mixture to withstand deformation due to load which works without permanent deformation like waves, groove or bleeding which is expressed in units of kg or lb. Value stability is obtained from the results of direct reading on the Marshall tool Test when doing Marshall testing.

Stability value too high will result in the pavement that is too stiff, so the durability is reduced.

2. Melt (Flow)

Like the way to obtain stability values, the flow value is the value of each indicated by the dial needle (inside mm) when doing Marshall testing. A mixture of those who have low melting will be more rigid and tend to experience early cracking at the age of service, while value high melting indicates the mixture is plastic.

3.Marshall quotient

Marshall Quotient is the result of a comparison between stability with the flow. The higher the MQ, the more it will be high stiffness of a mixture and the more vulnerable the mixture is against cracks. Here is the equation for the MQ value:

$$MQ = \frac{S}{F}$$

MQ : Marshall Quotient (kg/mm)
S : Corrected stability value (kg)
F : flow value (mm)

4. Asphalt / Void Filled with Asphalt (VFA)

Filled cavity Void Filled with Asphalt (VFA) is percent the cavity between the aggregate particles (VMA) filled by asphalt, not including asphalt absorbed by the aggregate.

5. Void in Mineral Aggregate (VMA)

Intergroup cavity (VMA) is the cavity space between particles aggregate on the pavement, including air cavities and asphalt volumes effective (excluding aggregate absorbed asphalt volume).

6. Air cavity in mix / Voids in Mix (VIM)

The air cavity in the mixture (VA) or VIM in the paved pavement mixture consists of air space between the asphalt-coated aggregate particles.

RESULTS AND DISCUSSION

Manufacture of Hot Rolled Sand Sheet asphalt, starting with the determination of tailings content, namely 0%, 25%, 50%, 75%. The level indication is viewed from the increasing value of Cu (Coefficient Uniformity) and Cc (Coefficient Curve). Coefficient Uniformity, namely sand gradation coefficient, and Coefficient Curve, namely curvature cohesion on the graph obtained. At 0% tailing content Cu value of 1.32 and Cc is 0.96. At 25% tailings content Cu value of 2.65 and Cc is 1.74. The 50% tailings content of Cu is 4.83 and Cc is 1.72. At tailings content 75% Cu value is 4.19 and Cc is 1.60. This increase affects the size of the cavity in the mixture and determines the workability (ease of work) and the stability of the mixture. The following graph increases the graph of each level

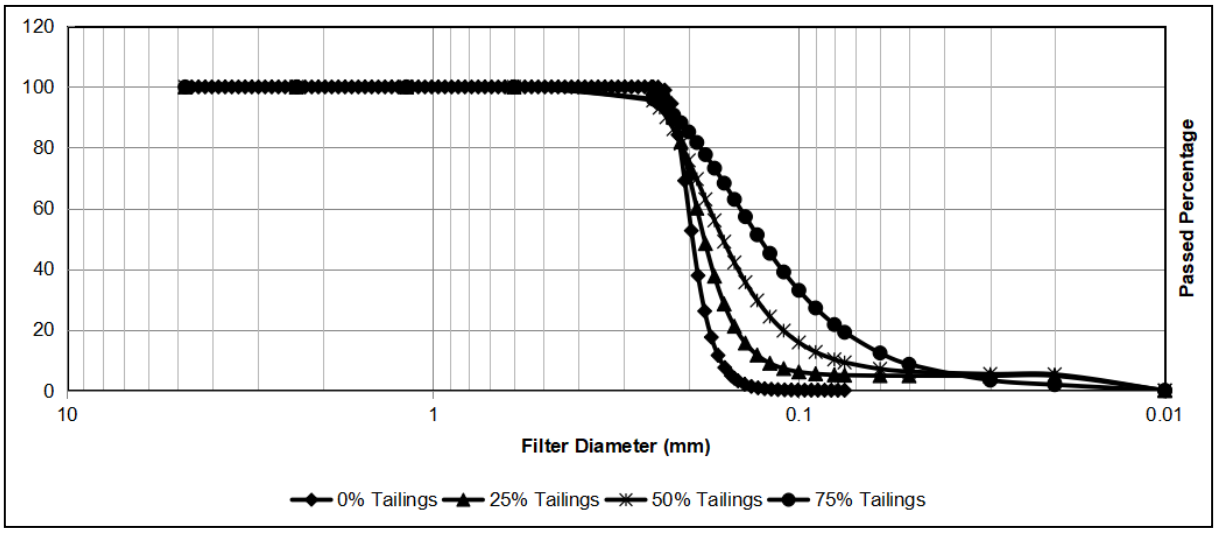

After that, the test was carried out with an aggregate gradation test which used fine and coarse aggregates using a shaker. The basic reference used in this test is PB-0201-76, AASHTO T-27-74, ASTM C-126-46. HRSS (Hot Rolled Sand Sheet). At 0% percent tailing content escapes 0.075 mm diameter by 0.11% and does not meet the requirements as HRSS. In the tailings content, 25% escaped the 0.075 mm diameter by 9.97% and fulfilled the requirements as HRSS. The 50% tailings content escapes 0.075 mm diameter by 15.69% and meets the requirements as HRSS. At tailings levels of 75% escaped 0.075 mm diameter by 21.31% and did not meet the requirements as HRSS. Requirements for class HRSS A with a filter size of 0.075 mm are 4-14% passed. Requirements for class B, HRRS B, with a filter size of 0.075 mm are 8-18% escaped. The aggregate grading test results are presented in the following table 1:

The results of testing the asphalt with the trial mix method for pavement obtained the optimum level of 50% tailings with a doubling or 100% increase in strength with 0% tailings content as a control. The increase was marked by the marshal quotient value, at 0% tailing levels only reaching a value of 65.118 kg / mm. Whereas the 50% tailings content reached 136.7 kg / mm. The value of other test results also increases, such as the stability and flow that originally only reached 459.598 kg and 7mm, increasing to 872.69 kg, 6.5mm. According to SNI 03-6749-2008, the results have requirements as HRSS (Hot Rolled Sand Sheet) with a minimum value of marshal quotient and stability of 80 kg / mm and 200 kg.

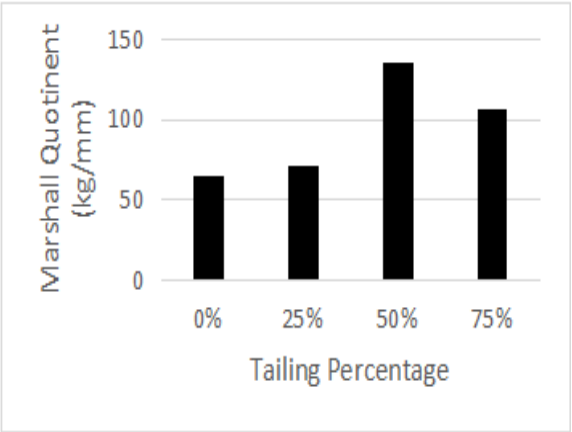

Figure 2 Marshall Test Results

The results of the study indicate that there is an effect of the coefficient of fine aggregate uniformity value (Cu) on road stability. The aggregate mixture with 50% tailings content has the highest stability value with the highest Cu value. This can occur because the value of Cu illustrates the distribution of the size of the grain in the aggregate. The higher the value of Cu, the higher the distribution of the size of the aggregate granules, the higher the aggregate density. In addition, after testing Marshall each level and tested for hardness. The optimum level of the tailing's mixture can be seen with the strong mixture sample holding the Marshall pavement test. The strongest level and the least damage compared to the other levels is 50% tailing substitution. The following samples are tested for each level of tailings.

HRSS is generally used for road planning with traffic that is not too high (≤ 500,000 SST), but can also be used for temporary maintenance or repair work in higher traffic.

Figure 3 Sample Condition after Marshall Test is Conducted, (a) Sample with 0% tailings (b) Sample with 25% tailings (c) Sample with 50% tailings (d) Sample with 75% tailings

CONCLUSION

The conclusions that can be taken in this study are:

1.The greater the value of Cu, the greater the size of the aggregate grain so that the aggregate density gets higher.

2.The value of Cu, Cc, stability, the highest quotient marshal and qualify as meeting the requirements as Hot Rolled Sand Sheet (HRSS) is a mixture of 50% tailings.

3.The optimum content of the tailing's mixture as 50% fine aggregate substitution with a 2-fold increase or a 100% increase

REFERENCES

[1] Aschuri I,, Yamin A., The Waste of Materials on Road Pavement Construction in Indonesia.

[6] at the National Institute of Technology Malang, 2016

[7] Widayanti A., Soemitro RAA., Ekaputri JJ., Suprayitno H., Characteristics of materials for the formation of reclaimed aspalt from national roads Proceedings of the Eastern Asia Society for Transportation Studies, Eastern Asia Society for Transportation Studies,2011, Vol. 8, Pp. 283

[2] Baihaqi A, Setyawan A, Djumari. Analysis of workability index on asphalt (asphalt resin) as an asphalt substitute binder. Civil Engineering Matrix Journal, 2015, Vol 3, Issue 4, Pp 1083-1089.

[3] Indrayati EW., Susanto HA., Study of rheumatic properties of asphalt with the addition of used tire waste. Journal of Engineering Dynamics,2015, Vol 11, Issue 1, Pp 24-28.

[4] Pandeleke RE., Assessment of the benefits of tailings for construction building materials, TEKNO Journal, 2010, Vol 7, Issue 52, Pp 75-80.

[5] Purwanto D., Sudhana P., Use of Foamed Bitumen for Road Construction. Paper. In: National Seminar on Innovation and Technology Applications in Industries

in the eastern Java province, Infrastructure & Facility Asset Management Journal, 2017, Vol 1, Issue 1, Pp 11-22.

9th Int. Conf. on Geotechnique, Construction Materials and Environment,
Tokyo, Japan, 20-22 November 2019, ISBN: 978-4-909106025 C3051

MICROMECHANICAL MODELING OF TENSILE STRENGTH OF SHORT RANDOM CARBON FIBER REINFORCED CONCRETE

Gilford B. Estores[1] and Bernardo A. Lejano[2]

[1]Faculty, Mapua University, Philippines; [2]Faculty, De La Salle University, Philippines

ABSTRACT

The accurate prediction on the response of the composite material is difficult to achieve due to the complexity of its mechanical properties. However, such complexity can be understood well using the micromechanical analysis. One of the most important goals of micromechanical analysis is to predict the failure and strength of the composite material on the basis of the geometries and properties of the matrix and the fibers. This study aims to develop a simplified micromechanical model that predicts the direct tensile strength of a randomly oriented short Carbon Fiber Reinforced Concrete (CFRC) using the modified rule of mixtures based on the assumptions that CFRC will fail by fiber failure mode and with the perfect interfacial bond between the matrix and the fibers. PAN-based High Tensile short carbon fibers distributed randomly in 3D with low fiber volume fractions (V_f) of 0.10%, 0.15%, 0.20%, 0.25% and 0.30% were used in this study. Fiber lengths (L_f) of sizes 19mm, 30mm, and 38mm were used. The designed compressive strength considered for each fiber volume fraction and fiber length was 21MPa, 28MPa, and 35MPa. There were three samples of specimens considered for each case. Each case was tested for cylindrical compressive strength and direct tensile test. Test results showed that the tensile strength of CFRC was optimum at V_f = 0.10% and L_f = 38mm. Finally, good agreement has been observed between the experimental tensile strength and predicted tensile strength using the micromechanical model.

Keywords: Micromechanical Analysis, Tensile Strength, Short Randomly Oriented Composites, Carbon Fiber Reinforced Concrete

INTRODUCTION

The micromechanical analysis is developed to understand well the complex mechanical properties of the combined materials known as a composite material. Within the composite material, it deals more on the stress and strain transfer within the fibers and the matrix. The inputs in the micromechanical analysis of composites are the fiber properties, matrix properties, a geometric configuration that would result in the uniaxial strengths and fracture toughness of the composite material. However, it is believed that the central parameter in micromechanical modeling is the fiber content and the matrix [1].

The fiber's length inclusion in composite material may be classified as continuous or short. Fiber is considered short if its length is less than its critical length. For increased fiber length, the strain difference tends to become smaller until equal strain can be attained between the fibers and the matrix. At this point of equality in failure strain, the fiber length is called the critical fiber length.

Unlike the continuous fiber composites, the mechanical properties of the short-fiber composites are very different due to their fiber's orientation. The orientation of short fibers may be aligned discontinuous, off-axis aligned discontinuous, and randomly oriented discontinuous. If the fiber's orientation in a composite is random, there are two considerations that must take into account. If the fiber length is less than the thickness of the part, the fibers are randomly oriented in 3D, but if the fiber length is greater than the thickness of the part, the fibers are randomly oriented in 2D. A random discontinuous fiber composite is indeed different from those of unidirectional continuous fiber-reinforced concrete. The tensile strength of the random discontinuous fiber is at its optimum as the content of the fiber increases and then tends to decrease [2].

According to Fu and Lauke [3], the modified rule of mixtures is usually used to estimate the direct tensile strength of short-fiber composites by presuming a perfect interfacial bond among the matrix and the fibers. The modified rule of mixture is actually the extension of the simple rule of mixture in which modification focuses on factors such as fiber length and fiber orientation.

It is believed that the accurate prediction of the failure and strength of composite materials is difficult to achieve. Thus, it is necessary that the failure mechanisms both on the fiber and matrix level should be understood. Fracture of the composite happens when either the fiber or the matrix fails. There are two possible failures for typical composites as shown in Fig. 1.

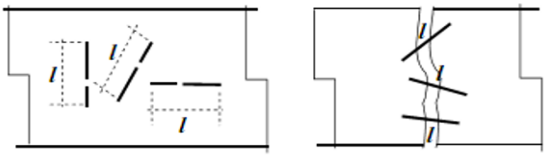

(a) (b)

Fig. 1 Typical failures for typical composite: (a) Fiber failure mode (b) Matrix failure mode

The first type is the fiber failure mode, where the failure strain of the matrix is larger than the failure strain of the fiber. This implies that the stress in the fiber portion at fracture must be larger than the stress in the matrix portion of the composite volume after the fracturing of all fibers so that the fibers will actually be reinforcing. On the other hand, the second type is the matrix failure mode, where the failure strain of the fiber is larger than that of the matrix. This assumes that the fiber has to carry the whole load when the matrix fails.

Some theories for unidirectional fiber-reinforced composites were derived from micromechanics simple rule of mixtures. However, the simple rule of mixtures does not apply for short randomly oriented fiber composites because it does not consider the fiber-matrix interaction effects and the fiber orientation at a given dimension (2D or 3D). From these considerations, a researcher like Curtis et al. modified the rule of mixtures by introducing factors such as fiber length efficiency factor and fiber orientation factor. The ultimate tensile strength of a short discontinuous and random composite can be calculated using the modified rule of mixtures developed by Curtis et al. [4].

METHODOLOGY

Materials

The composite material used in this study is Carbon Fiber Reinforced Concrete (CFRC). The carbon fiber type used was 0.111mm thick chopped PAN-based high tensile (HT) strength. The fiber lengths used in this study were 19mm, 30mm, and 38mm. The tensile strength (F_t), modulus of elasticity (E), specific gravity (SG) and other properties of the PAN-based HT carbon fibers considered are shown in Table 1.

Table 1 Properties of PAN-based HT carbon fibers

L_f (mm)	F_t (MPa)	E (MPa)	SG	Width (mm)
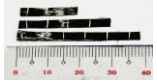	4510	231000	1.8	3.0

The concrete matrix is consists of cement, fine aggregates, coarse aggregates, superplasticizer, and water. A Portland cement that meets ASTM standard specification C595 [5] was used. Crushed coarse aggregates with a maximum size of 19mm having an absorption of 1.01% and a mass density of 1592 kg/m^3 were used. Fine aggregates with a mass density of 1551 kg/m^3, and having a 3.01% water absorption and fineness modulus of 2.40 were used. A superplasticizer was added to ensure the workability of fresh CFRC mix. The water used was of good quality.

Specimens and Testing

The different cases of fiber volume fractions (V_f) and fiber lengths (L_f) combination used in this study are presented in Table 2. Three specimens were prepared for each case of CFRC composites both in compression and tension. All these CFRC specimens were tested and compared to the plain concrete specimen.

Table 2 Cases of the CFRC specimens

Case No.	L_f, mm	V_f, %	Case No.	L_f, mm	V_f, %
1	19	0.10	24	38	0.20
2	30	0.10	25	19	0.25
3	38	0.10	26	30	0.25
4	19	0.15	27	38	0.25
5	30	0.15	28	19	0.30
6	38	0.15	29	30	0.30
7	19	0.20	30	38	0.30
8	30	0.20	31	19	0.10
9	38	0.20	32	30	0.10
10	19	0.25	33	38	0.10
11	30	0.25	34	19	0.15
12	38	0.25	35	30	0.15
13	19	0.30	36	38	0.15
14	30	0.30	37	19	0.20
15	38	0.30	38	30	0.20
16	19	0.10	39	38	0.20
17	30	0.10	40	19	0.25
18	38	0.10	41	30	0.25
19	19	0.15	42	38	0.25
20	30	0.15	43	19	0.30
21	38	0.15	44	30	0.30
22	19	0.20	45	38	0.30
23	30	0.20			

The design mix of the CFRC composite was based on the compressive strengths 21MPa (Cases 1-15), 28MPa (Cases 16-30), and 35MPa (Cases 31-45) with a water-cement ratio of 0.68, 0.57 and 0.48,

respectively considering the slump requirement that ranges from 25mm to 100mm, and 2% entrapped air. Moreover, partial replacements of the sand by the carbon fibers are made in the design mix. Then the workability of each mix was checked using the slump test in accordance with ASTM C143 [6].

The compressive strength specimens were tested using 100mm x 200mm cylinders in accordance with ASTM C39-05 [7] after 28 days of curing period. Likewise, the tensile strength specimens employing a dumbbell form with a critical section of 75mm x 50mm, and a gauge length of 300mm were also tested on the same curing period. The set-up for the tensile strength test and its corresponding failure mode at the critical section are shown in Fig. 1.

Fig. 1 Tensile strength test set up and failure mode

Micromechanical Analysis

Since the composite material involved in this study is CFRC, its ultimate tensile stress is best determined by micromechanics equation. In this study, the fiber failure mode is considered because short carbon fibers were used for CFRC. Short fibers favor a fiber failure where the matrix failure strain is assumed to be greater than the failure strain of the fiber. On the practical point of view, fiber failure means composite failure. Such fiber failure mode is based primarily on the assumption that since PAN-based carbon fibers filament has a very small diameter despite their very high tensile strength, they tend to break first before the concrete matrix does upon the pull-out test.

The modified rule of mixtures by Curtis et al. is generally expressed as,

$$\sigma_{ult} = \chi_1 \chi_2 V_f \sigma_{fu} + \sigma_{mu} V_m \quad (1)$$

where χ_1 denotes the effect of fiber's orientation, χ_2 denotes the effect of fiber's length. V_f is the volume of fraction percentage of fiber's inclusion, V_m is the volume of fraction percentage of the matrix, σ_{fu} is the fiber's ultimate tensile stress, and σ_{mu} is the matrix ultimate tensile stress. For three-dimensional (3D) random fiber orientation, the value of χ_1 is 0.20 [8]. While χ_2 is computed as,

$$\chi_2 = 1 - \frac{s_c}{2s} \quad \text{when } s > s_c \quad (2)$$

$$\chi_2 = \frac{s}{2s_c} \quad \text{when } s < s_c \quad (3)$$

where s denotes the fiber aspect ratio and s_c denotes the critical aspect ratio. The critical aspect ratio is the ratio between the critical fiber length l_c and the fiber diameter d. The critical fiber length can be computed as,

$$l_c = \frac{\sigma_{fu} d}{2\tau_y} \quad (4)$$

where σ_{fu} is the fiber's tensile stress and τ_y denotes the interfacial shear stress. The diameter, d of the chopped PAN-based carbon fiber in tow is computed using the equivalent diameter equation [9] given by,

$$D_e = \sqrt{\frac{4m_f}{\pi l \rho_f}} \quad (5)$$

where m_f = mass of the chopped carbon fibers, ρ_f = mass density of chopped carbon fiber, l = total length of the sample carbon fiber used.

RESULTS AND DISCUSSIONS

Influence of Fiber Volume Fraction and Fiber Length to Tensile Strength of CFRC Composite

Generally, the fiber volume fraction strongly affects the tensile strength of the CFRC. Most of the cases of V_f and L_f mix have satisfied and significantly increased the tensile strength of CFRC in relation to their control specimens. The effect of fiber volume fraction to the tensile strength of CFRC at cases L_f = 19mm, L_f = 30mm, and L_f = 38mm are shown in Fig. 3(a), Fig. 3(b), and Fig. 3(c), respectively.

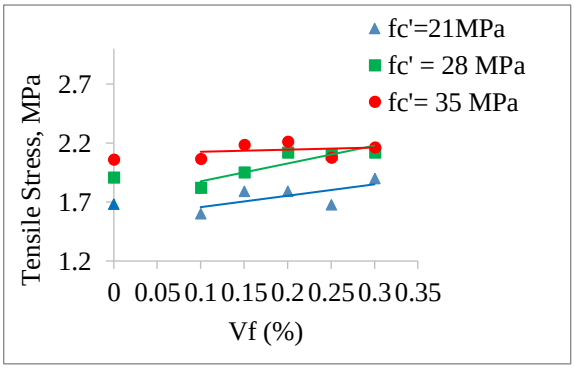

(a)

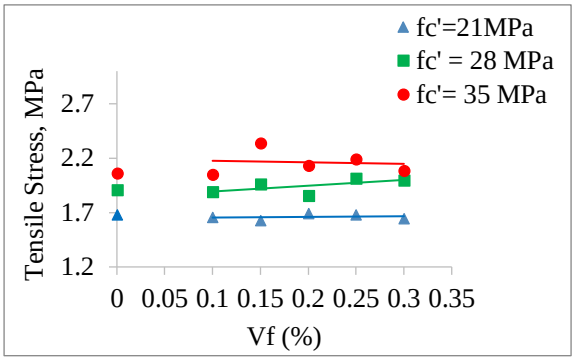

(b)

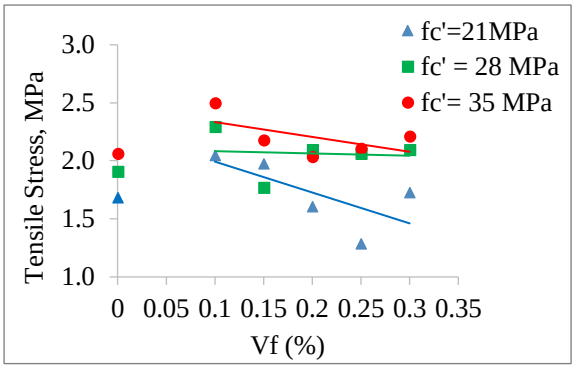

(c)

Fig. 3 Influence of fiber volume content to tensile stress of CFRC at (a) L_f =19mm (b) L_f = 30mm (c) L_f = 38mm

The addition of 19mm fiber length in concrete as shown in Fig. 3(a), the tensile strength tends to increase with increased fiber volume fraction particularly at f_c'=21MPa and at f_c'=28MPa.

With the addition of L_f =38mm as shown in Fig. 3(c), the tensile stress tends to decrease at increased fiber volume fraction in all cases of designed compressive strengths, while no trend was observed in the 30mm fiber length as shown in Fig. 3(b). However, 38mm fiber length at 0.10% fiber volume fraction has its tensile strength increased significantly to 2.047 MPa, 2.293 MPa, and 2.498 MPa by 21.63%, 19.99%, and 21.14% respectively as compared to their corresponding control specimens.

It is also noticeable from the findings that only the addition of L_f = 19mm at V_f = 0.30% and the addition of L_f = 38mm at V_f = 0.10% satisfy the compressive strength of CFRC, while most of the V_f cases for L_f = 19mm and V_f cases for L_f =38mm satisfy and significantly increased the tensile strength of CFRC. This indicates that the compressive strength of CFRC is relatively less affected by the addition of fibers as compared to the tensile strength of CFRC. This finding agrees to the report of ACI 544 [10] where the recommended fiber length of carbon fiber may vary from 5mm to 50mm, but preferably on 19mm or 38mm. In addition, Tezuka et al. [11] claimed that to achieve high strength in CFRC, use a chopped strand of carbon fibers with an average length based on the maximum aggregate size to be used as a minimum, but, more preferably not less than twice the maximum aggregate size. This refers to the fiber lengths 19mm and 38mm since the maximum aggregate size used in this study was 19mm.

Micromechanical Modeling

Assumptions

The micromechanics modeling of the ultimate tensile strength of the CFRC composites is based on the assumptions that the CFRC base material will fail by fiber failure mode during the tensile test and is linearly elastic until failure. It is also assumed that the fibers' strength is uniform, and the fibers and matrix are perfectly bonded at their interface. The errors are assumed to distribute normally with zero mean and variance.

In this study, the ultimate tensile strength of the CFRC composites was calculated by micromechanics analysis using the modified rule of mixtures. Although the ultimate tensile strength of a composite is difficult to achieve accurately, the modified rule of mixture is selected because it is the most appropriate for composite material at fiber failure mode. Figure 4 shows the fiber failure mode of different tensile strength specimens used in this study. It can be seen that most of the chopped carbon fiber breaks when the ultimate tensile strength of the CFRC specimens is reached.

Fig. 4 Fiber failure mode of tensile strength specimens

Modified rule of mixtures

The observed tensile strength was plotted against the cases of the specimens and compared with the modified rule of mixtures equation by Curtis et al. as shown in Fig. 5. The ultimate tensile stress of the CFRC composites using this model was computed by Eq. (1). Varying parameters are χ_2 and s. χ_2 is computed using Eq. (3), and s is the ratio of L_f and d. While L_f, V_f, V_m, and σ_{mu} are the experimental data. Constant parameters such as χ_1 = 0.20, τ_y = 2.3 MPa, σ_{fu} = 4510MPa, l_{fc} = 755.52mm, d = 0.771mm were also used as part of the micromechanics modeling.

The value of χ_1 is based on 3D random fiber orientation, τ_y = 2.3MPa and σ_{fu}= 4510MPa are the carbon fiber properties found in Table 1, and the l_c and d values are computed using Eq. (4) and Eq. (5), respectively.

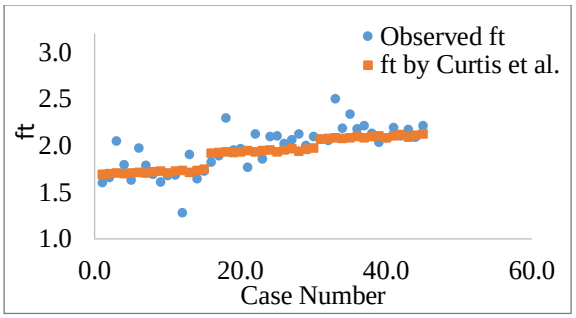

Fig. 5 Scatter plot of ultimate tensile stress for the observed and modified rule of mixtures model against cases of specimen

The Curtis et al. model was compared to the observed tensile stress as presented in the scatter plot above. Although there are cases where the tensile stress is extreme, its scatter is acceptable at the coefficient of variance (CV) of 12.23% which is less than the required maximum CV = 15%. Generally, the model appeared to have a good agreement. This only implies that the modified rule of mixture by Curtis et al. appeared to be an appropriate model for predicting the tensile strength of CFRC base material.

Modified Curtis et al. model

Despite good agreement observed from the plot as shown in Fig. 5, there are still some observed values that deviate largely from the modified rule of mixtures. However, most of these values increased significantly the tensile strength of CFRC. To address this increased effect, a tensile modification factor (k_m) that relates the observed and predicted values for tensile strength of CFRC was determined by

$$k_m = ft / \sigma_{ult} \tag{6}$$

In this study, the computed tensile strength of CFRC composite is denoted by f_{tc} and is expressed as

$$f_{tc} = k_m \sigma_{ult} \tag{7}$$

Equation 7 is considered in this study as the Modified Curtis et al. model, where k_m is the modification factor for tensile strength computed by Eq. (6) and σ_{ult} is the tensile strength derived from the modified rule of mixtures by Curtis et al. However, due to the difficulty in testing the direct tensile strength of the concrete matrix σ_{mu}, it is best expressed as a function of its compressive strength. The relation of the direct tensile strength to the compressive strength of the control specimens (f_{cm}) was denoted by k_t and expressed as

$$k_t = \sigma_{mu} / \sqrt{f_c} \tag{8}$$

The observed (σ_{mu}) values of the direct tensile strength were utilized to calculate the numerical value of k_t as shown in Table 3.

Table 3 Results of the estimated coefficient for direct tensile strength in plain concrete

Control Case	σ_{mu}	f_{cm}	k_t
0-21	1.6833	20.17	0.375
0-28	1.9111	27.82	0.363
0-35	2.0622	35.78	0.345
		mean	0.361

Consequently, the direct tensile strength of the concrete matrix is then expressed as

$$\sigma_{mu} = 0.361\sqrt{f_{cm}} \tag{9}$$

This estimated coefficient of compressive strength to determine the direct tensile strength of normal plain concrete is within the range cited in ACI Code 318-89 [12], where the coefficient of $\sqrt{f_c}$ ranges 0.247 to 0.412 for f_c in MPa.

With the inclusion of Eq. (9) to the Eq. (1), it becomes

$$\sigma_{ult} = \left[\chi_1 \left(\frac{L_f}{d} \right) \tau_y V_f + 0.361\sqrt{f_{cm}} V_m \right] \tag{10}$$

Substituting Eq. (10) to Eq. (7), the Curtis et al. model is modified to

$$f_{tc} = k_m \left[\chi_1 \left(\frac{L_f}{d} \right) \tau_y V_f + 0.361\sqrt{f_{cm}} V_m \right] \tag{11}$$

where k_m = 1.0245 computed by Eq. (6) using the data from Fig. 5, χ_1= 0.20 for 3D fiber orientation, τ_y = 2.3 MPa for UT70-20 PAN-based carbon fibers, and d = 0.771 mm computed from Eq. (5), and V_m = 1-V_f.

Residual Analysis

The residual output of tensile strength using the Modified Curtis et al. model is presented in Fig. 6. It is shown here the error between the observed tensile

strength and predicted tensile strength computed from the Modified Curtis et al. model given by Eq. (11). Using this modified model the CV was reduced from 12.23% to 8.24%. This means that the scatter for tensile strength using the modified Curtis et al. model is acceptable.

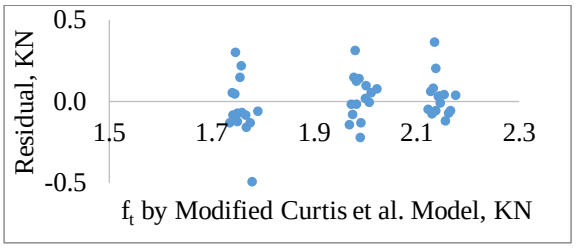

Fig. 6 Residual plot of tensile strength using a modified Curtis et al. model

The residual plot for predicted tensile strength of CFRC composites shown in Fig. 6 are clustered into three groups based on the three designed compressive strengths (21, 28, 35MPa) considered in this study, but the pattern appears to be fairly random. This means that in general, the errors are approximately normally distributed with constant variance. This implies that the modified Curtis et al. model use to predict the tensile strength of the CFRC composite follows a normal distribution and fits the observed data satisfactorily. It is noticeable that the residuals are ranging only from -0.495 to 0.364. This range of error is obviously small. This indicates that the tensile strength of CFRC composites can be predicted satisfactorily under given limitations of the Modified Curtis et al. model.

CONCLUSIONS

Test results show that the compressive strength of CFRC in each case of designed compressive strength are consistently satisfied with the addition of L_f = 38mm at V_f = 0.10%. Test results also show that the tensile strength of CFRC is optimum at V_f = 0.10% and L_f = 38mm.

A Modified Curtis et al. model to predict the tensile strength of CFRC composite is developed based on the micromechanics equation of Modified Rule of Mixtures by Curtis et al. model. This model is significantly acceptable and can be used to predict the tensile strength of the CFRC composites, but it is applicable only for UT70-20 PAN-based chopped carbon fibers distributed randomly in 3D with low fiber volume content ranging from 0.10 % to 0.30 %. This model also applies to CFRC composites with normal compressive strength. The fiber length in CFRC composite must be limited to 19mm, 30mm, and 38mm.

ACKNOWLEDGMENTS

The carbon fiber employed in this study was UT70-20 TORAYCA. The authors would like to thank Mapua University, DOST-ERDT, and Alphatec Chemical Corp. for their great support in this study.

REFERENCES

[1] Nilsson, T., Micromechanical Modelling of Natural Fibers for Composite Materials, Department of Construction Sciences Structural Mechanics, Lund, Sweden, 2006, pp. 37-57.

[2] Lu, Y., Mechanical Properties of Random Discontinuous Fiber Composites Manufactured from Wetlay Process, MS Thesis, Virginia Polytechnic Institute and State University, Blacksburg, Virginia, 2002.

[3] Fu, S.Y. and Lauke B., Effects of Fiber Length and Fiber Orientation Distributions on the Tensile Strength of Short-fiber-reinforced Polymers. Composites Science and Technology, Vol. 56, 1996, pp. 1179-1190.

[4] Curtis, P.T., Bader, M.G. and Bailey, J.E., The Stiffness and Strength of a Polyamide Thermoplastic Reinforced with Glass and Carbon Fibers. Journal of Material Science, Vol. 13, 1978, pp. 377-390.

[5] ASTM C 595, Standard Specification for Blended Hydraulic Cement, ASTM Standards in Building Codes, Vol. 1 (43), 2006

[6] ASTM C 143, Standard Test Method for Slump of Hydraulic Cement Concrete, ASTM Standards in Building Codes, Vol. 1 (43), 2006.

[7] ASTM C 39-05, Standard Test Method for Compressive Strength of Cylindrical Concrete Specimens, ASTM Standards in Building Codes, Vol. 1 (43), 2006.

[8] Thomason J. L. and Vlug, M.A., Influence of Fiber Length and Concentration on the Properties of Glass Fibre-reinforced Polypropylene: Part 1. Tensile and Flexural Modulus, Composites Part A, Vol.27A, 1996, pp. 477-484.

[9] Sommerville, P., Understanding Fiber Diameter Measurement, Fundamental Principles of Fibre Fineness Measurement, Part 2. AWTA Ltd., 2002, pp. 1-5.

[10] ACI Committee 544, "State-of-the-art Report on Fiber Reinforced Concrete", 2000, ch. 4.

[11] Tezuka M, Awata M and Shiraki A, Carbon Fiber-Reinforced Concrete and Method for Preparing the Same, United States Patent, Patent Number 5685902, 1997.

[12]ACI committee 318, Building Code Requirements for Reinforced Concrete (ACI 318-89) and Commentary (ACI 318R-89), ACI, Detroit, Michigan, revised 1992.

9th Int. Conf. on Geotechnique, Construction Materials and Environment, Tokyo, Japan, 20-22 November 2019, ISBN: 978-4-909106025 C3051

PREPARATION OF GEOPOLYMER CEMENT FROM SIMULATED LUNAR ROCK SAND USING ALKALI FUSION

Kazuki Sakamoto[1], Takaaki Wajima[1]
[1]Graduate School of Science and Engineering, Chiba University, Japan

ABSTRACT

In this study, we tried to convert simulated lunar rock sand into geopolymer cement by alkali fusion with sodium hydroxide. Space development is currently being conducted in various countries. For construction on the moon, it is difficult to bring all the construction materials from the earth, and development of construction materials made from lunar resources is required. The authors have succeeded in making geopolymer cement from crushed stone dust using alkali fusion. Therefore, there is a possibility that geopolymer cement used for construction material can be made from lunar rock sand, abundantly present on the lunar surface, using the same method.

In this experiment, simulated lunar rock sand was fused with NaOH by changing the mixing ratio of the sand and sodium hydroxide, heating temperature, heating time in vacuum or air atmosphere, and the reaction in vacuum and air was compared and examined. As a result, it was found that the elution contents of Si and Al in the fused sand into acid solution increased with increasing the temperature, NaOH addition and heating time of alkali fusion, and the fused reaction in vacuum atmosphere is different from that in air atmosphere.

Keywords: Lunar Rock Sand, Alkali Fusion, Geopolymer Cement, Vacuum Atmosphere

INTRODUCTION

Space exploration with unmanned spacecraft for space development is currently active in various countries. The moon is satellite of the planet earth, the nearest astronomical object, and development as a base for space development is planned. In the development plan, when a large-scale base is built on the moon, it is difficult to transport all building materials from the earth. Therefore, the development of building materials made from lunar resources is required.

In this study, we focused on lunar rock sand (Regolith) which is abundant on the lunar surface. Regolith is the sand that covers the surface of the moon with a thickness of several meters and is mainly composed of SiO_2 and Al_2O_3 in the form of alumino-silicate minerals, such as anorthite and augite. In our previous studies, the authors have succeeded in making geopolymer cements from rock dust, discharged from a quarry, using alkali fusion [1, 2]. Although ordinary Portland cement is mainly solidified by the formation of needle-like calcium silicate hydrate (C-S-H), geopolymer cement is mainly solidified by the polymerization of silicate ions bridged by metal ions, such as Al^{3+}, Fe^{3+} and so on, which is similar to the reaction of zeolite synthesis [3, 4]. It would be possible to make geopolymer cement which can be used as a building material by using the same method for lunar rock sand abundantly present on the moon.

Therefore, in this study, we tried to make geopolymer cement by reacting simulated lunar rock sand with sodium hydroxide in air and vacuum. We prepared the precursor of geopolymer fused by changing the mixing ratio of sodium hydroxide, heating time and temperature in air and vacuum, and compare the reaction to make geopolymer cement.

EXPERIMENT

Sample

Simulated lunar rock sand (FJS-1, CSP Japan, Inc.) was used in this study. The chemical composition is mainly composed of 42% of SiO_2, 13% of Al_2O_3, 12% of CaO, 15% of FeO and 8% of MgO.

Preparation of fused dust

The sand and sodium hydroxide powder are mixed in a weight ratio of 1: 0.25 to 1: 2, put in a platinum crucible, and heated up to setting temperature (300 to 500 °C) in 10 min in air and vacuum atmosphere. After heating for 0 to 120 min, it cooled naturally at room temperature, recovered fused dust as a powder, and the mineral phase was identified by a powder X-ray diffractometer (MiniFlex 600, Rigaku).

In order to confirm the possibility of making geopolymer cement, the soluble elements, Si, Al, Fe, Mg and Ca, in the sample were examined. 0.1 g of the fused dust prepared under each condition is added into 20 mL of 1 M HCl solution, shaken at room temperature for 6 h, centrifuged, and the contents of Si, Al, Fe, Mg and Ca in the supernatant were measured by an atomic absorption spectrophotometer (Perkin Elmer, AAnalyst 200) to calculate the solubility (*S*) using the following equation;

$$S = C \times V/w \quad (1)$$

where C is the concentration of each element in the supernatant (mg/L), V is the volume of HCl solution, and w is the weight of the fused sand.

Preparation of geopolymer cement

Preparation of geopolymer cement was performed using the fused sand. The raw sand, water and the fused sand were mixed to prepare the mixtures of 5 g weight, and the mixing ratios used in this study are 1:1:2, 1:1:3 and 2:1:2. The mixture was formed into a mold (ϕ 25 mm $\times$5 mm) and allowed to stand at 80 ℃ in air atmosphere and cure for 1 or 7 days at 80 ºC.

Strength test

The obtained geopolymer cement were subjected to strength tests using a strength tester (ZT series ZTA-500N, IMADA). The sharp point attachment was inserted into the sample at a speed of 30 mm/min to measure the strength when the sample broke. Strength tests for the Portland cement were carried out to compare strength. Portland cement was prepared at water-cement ratio (W/C) = 40 %, formed in a mold and was cured at room temperature for 7 days.

RESULTS AND DISCUSSION

Mixing Ratio

The XRD patterns of the fused sands prepared by changing the mixing ratio in (a) air and (b) vacuum are shown in Fig. 1. The experimental conditions are a heating temperature of 500 ° C and a heating time of 60 minutes. In simulated lunar rock sand, the peaks of anorthite and augite were confirmed. In the sands after alkali fusion, the peaks of anorthite and augite in the sand disappeared and the peaks of sodium silicate were confirmed in both air and vacuum.

The solubility of each element dissolved from the fused sand prepared by changing the mixing ratio in (a) air and (b) vacuum are shown in Fig. 2. In both air and vacuum, as the amount of sodium hydroxide was increased, the solubilities of all elements increased and became almost constant above a mixing ratio of 1: 1. It is considered that almost all elements in the sand was converted into soluble phases by alkali fusion in air and vacuum.

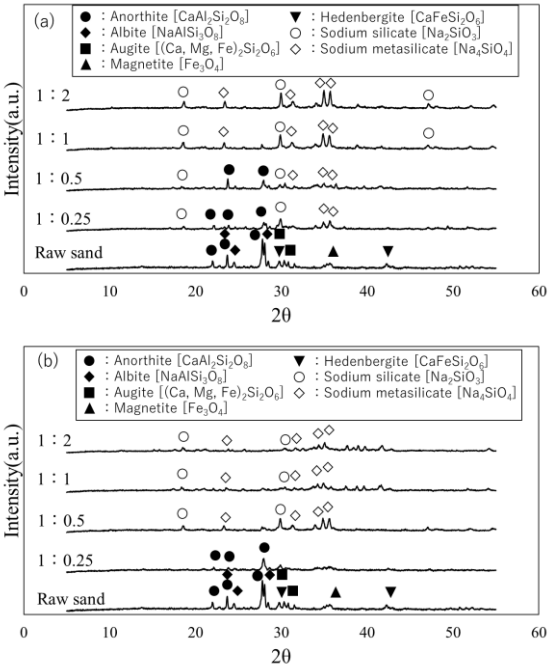

Fig. 1 The XRD patterns of the fused sand prepared by changing the mixing ratio in (a) air and (b) vacuum

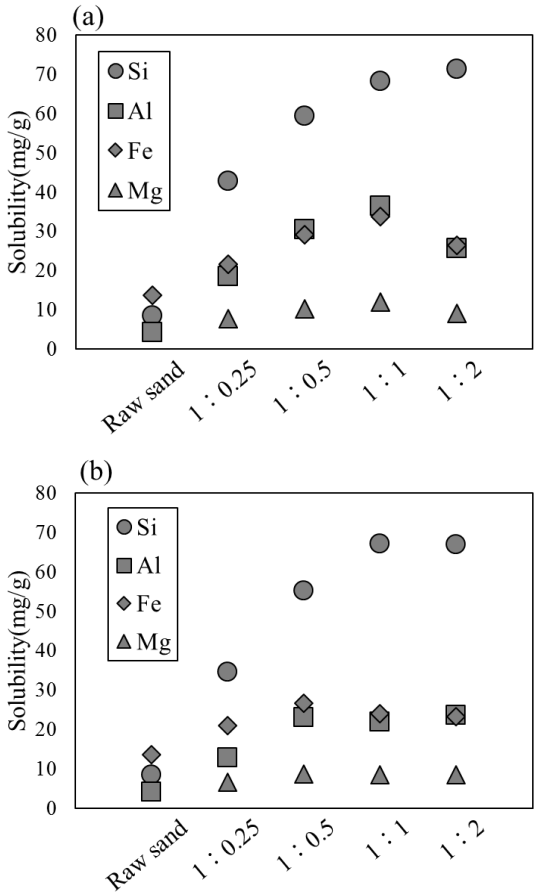

Fig. 2 The solubility of each element dissolved from the fused sand prepared by changing the mixing ratio in (a) air and (b) vacuum

Heating Time

The XRD patterns of the fused sand prepared by changing the heating time in (a) air and (b) vacuum are shown in Fig. 3. The fused sand was prepared at the ratio of raw sand: sodium hydroxide = 1: 0.5 at 500 ° C. In the air, as the heating time increased, the peaks of minerals observed in the sand disappeared, and the peak of sodium silicate was confirmed. In the vacuum, as the heating time became longer, the mineral peak observed in the sand disappeared except anorthite, the peaks of anorthite gradually decrease, and the sodium silicate peak was confirmed at more than 5 min.

The solubilities of each element dissolved from the fused sand prepared by changing the heating time in (a) air and (b) vacuum are shown in Fig.4. The solubilities of Si and Al rose and became constant in 10 min, in both air and vacuum. The soluble amounts of Si and Al from the fused sand in air are higher than those in vacuum, which would be caused by remaining anorthite. There was no change in the dissolved amount for Fe, Mg and Ca of all samples.

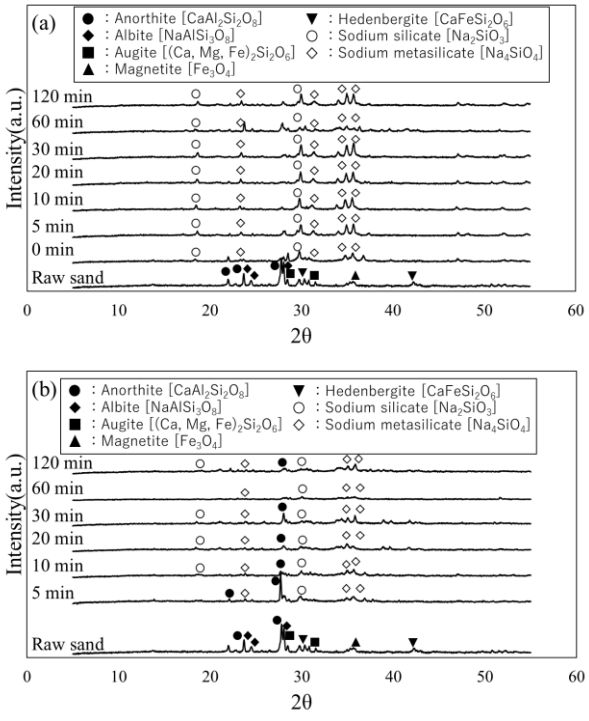

Fig. 3 The XRD patterns of the fused sand prepared by changing the heat time in (a) air and (b) vacuum

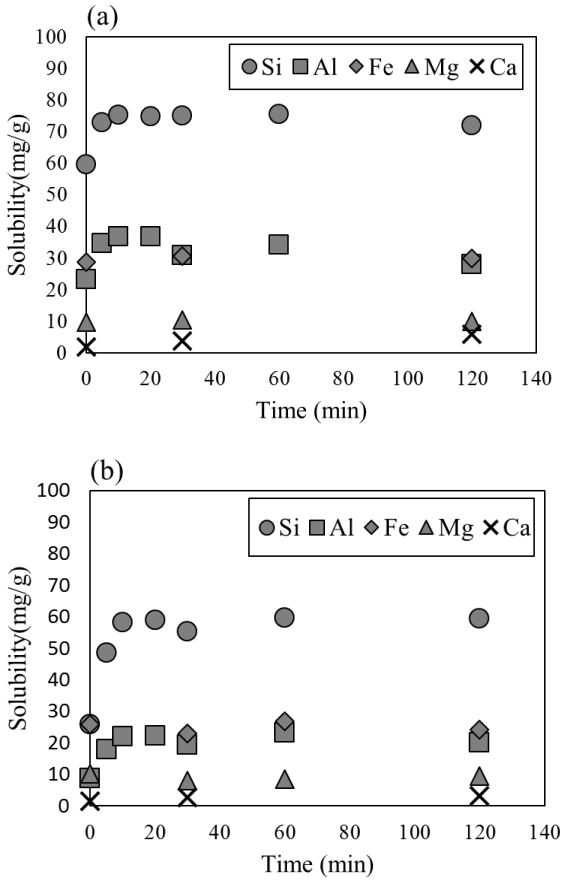

Fig. 4 The solubilities of each element dissolved from the fused sand prepared by changing the heating time in (a) air and (b) vacuum

Heating temperature

The XRD patterns of the fused sand prepared by changing the heating temperature in (a) air and (b) vacuum are shown in Fig. 5. The fused sand was prepared at the ratio of raw sand: sodium hydroxide = 1: 0.5 for 60 minutes. In both air and vacuum, the mineral peaks in the sand disappeared as the heating temperature was raised, and the peaks of sodium silicate were confirmed.

The solubilities of each element dissolved from the fused sand prepared by changing the heating temperature in (a) air and (b) vacuum are shown in Fig. 6. The solubilities of each element increased with increasing the heating temperature in both air and vacuum. At 300 °C, in the air, the fused sands have quadruple higher solubility than that of the raw sand, while in the vacuum, the fused sands have about double higher solubilities than that of the raw sand.

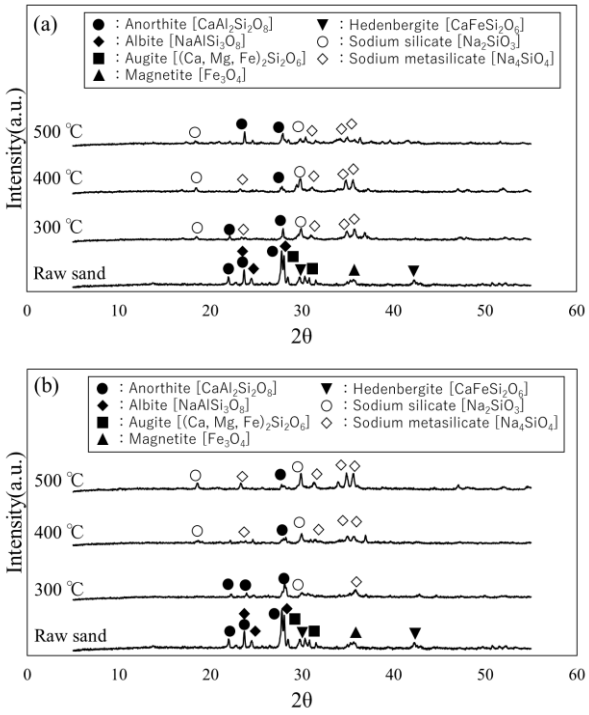

Fig. 5 The XRD patterns of the fused sand prepared by changing the heating temperature in (a) air and (b) vacuum

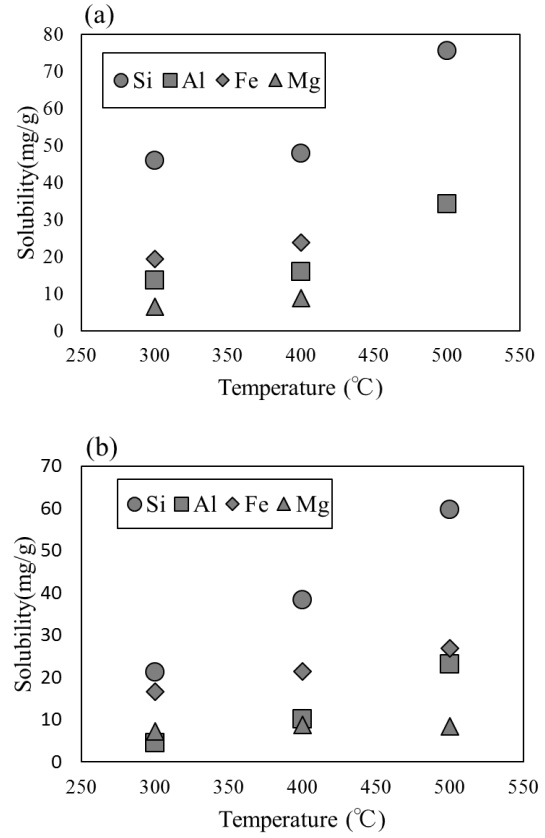

Fig. 6 The solubilities of each element dissolved from the fused sand prepared by changing the heating temperature in (a) air and (b) vacuum

From these results, it is possible to convert the sand into a soluble material including sodium silicate using alkali fusion in vacuum atmosphere, and a high soluble material can be prepared when the mixing ratio is 1:1, heating time is 10 min, and heating temperature is 500 ºC.

Preparation of geopolymer cement

The photograph of the product after 1 and 7 days from (a) fused sand in air and (b) fused sand in vacuum is shown in Fig. 7. After 1 day, hardened product was confirmed using the fused sand in the air, while the products from the fused sand in vacuum are slightly soft. After 7 days, all the products were hardened.

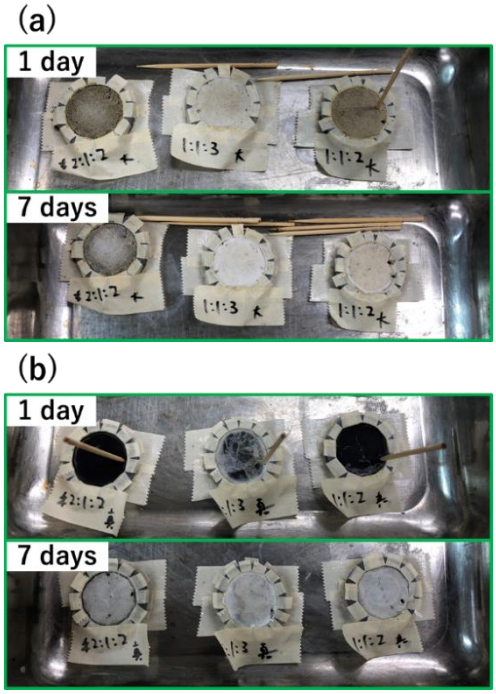

Fig.7 The photograph of the product after 1 and 7 days from (a) fused sand in air and (b) fused sand in vacuum

Strength test

The result of the strength test for the product prepared from (a) fused sand in air and (b) fused sand in vacuum is shown in Fig. 8. It was confirmed that the strength increased as the curing time was prolonged in all the products. The product with the highest strength was obtained using the fused sand prepared in the air atmosphere at the mixing ratio of 2: 1: 2.

The product using the fused sand prepared in a vacuum atmosphere at a mixing ratio of 2: 1: 2 had the highest strength (120 N) among the product from fused sand in vacuum.

Portland cement indicate higher strength (500 N) than the obtained products. The highest strength of the obtained product is 200 N, which is less than half as strong as the Portland cement.

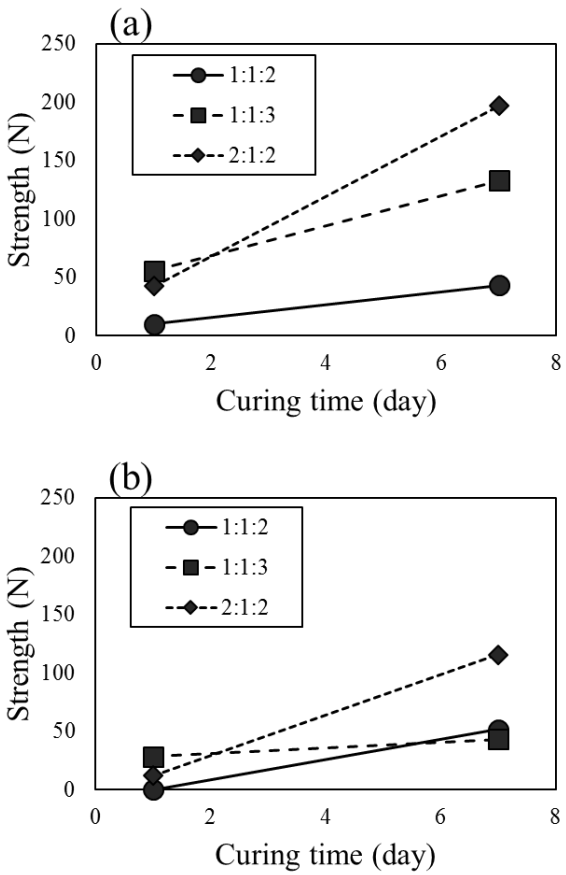

Fig. 8 The result of the strength test for the product from (a) fused sand in air and (b) fused sand in vacuum

CONCLUSIONS

An attempt was made to prepare geopolymer cement by alkali fusion of simulated lunar rock sand with sodium hydroxide. Alkali fusion with sodium hydroxide allows conversion to a highly soluble fused sand even under vacuum. It was found that a high soluble fused sand can be produced with a mixing ratio of 1: 1, a heating temperature of 500 ° C, and a heating time of 10 min.

We succeeded in making a hardened geopolymer cement by mixing the raw sand, water and fused sand. The strength of 200 N was confirmed with the geopolymer cement prepared at a mixing ratio of 2:1:2, using the fused sand prepared in the air atmosphere. Since this strength of the obtained product is about half the strength of the Portland cement, it is necessary to improve the strength.

REFERENCES

[1] K. Sakamot and T. Wajima, Preparation of Geopolymer Cement from Crushed Stone By-Product Using Alkali Fusion, International Journal of GEOMATE, Vol.17, Issue 63, 2019, pp.17-22.

[2] G. Davis, C. Montes and S. Eklund, Preparation of lunar regolith based geopolymer cement under heat and vacuum, Advances in Space Research, 59, 2017, pp. 1872 – 1885.

[3] Melkon T., Gunther M. and Stefan K. H., Relation of water adsorption capacities of zeolites with their structural properties, Microporous and Mesoporous Materials 264, 2018, pp. 70–75.

[4] G. Habbib, S. Oliver, M. Yvan and K. Philippe, The Reconstruction of Natural Zeolites, Kluwer Academic Publishers, Dordrecht, pp. 1-20.

9th Int. Conf. on Geotechnique, Construction Materials and Environment, Tokyo, Japan, 20-22 November 2019, ISBN: 978-4-909106025 C3051

FIELD PULL-OUT EXPERIMENTS OF FLIP-TYPE GROUND ANCHORS INSTALLED IN DRY SAND GROUND

Shota Yoshida[1], Tatsunori Matsumoto[2], Kazuki Komura[3] and Takayoshi Yoshida[4]
[1,2]Graduate School of Science and Technology, Kanazawa University, Japan; [3]Obayashi Corp., Japan; [4]Daisho Co., Ltd., Japan

ABSTRACT

The fundamental mechanisms of the pull-out resistance behaviour of flip-type anchors have not been fully understood enough to apply them on sites. In this research, pull-out experiments of 5 types of actual flip-type anchors were conducted in a field. Model ground was prepared in a test pit of 4 m in length, 4 m in width and 2.5 m in height. Sand was put into the test pit by layers of 0.25 m. Each soil layer was tamped to have a relative density of 80%. Flip-type anchors were embedded at different depths during the preparation of the ground. Anchor heads were set as "opened" or "closed". After the completion of the ground, flip-type anchors were also driven into the ground at different depths. The anchors were pull-out by means of a jack with measurement of pull-out displacement. As for the anchors buried with "opened" head condition, the maximum pull-out force, F_{max}, got larger as the embedment depth got deeper or as the anchor size got bigger. In contrast, the maximum pressure, p_{max} (F_{max}/project area of anchor), got larger as the anchor size becomes smaller. F_{max} of "closed" or "driven" anchors were about 80% of F_{max} of the corresponding "opened" anchor. The experimental results are presented in detail and discussed in the paper.

Keywords: Ground anchor, Field experiment, Pull-out experiment, Sand ground.

INTRODUCTION

Recently, easier and faster countermeasures for slope failures related to heavy rains are required.

Flip-type ground anchor (flip anchor, hereafter) is one type of end-anchors that are often used for reinforcing or stabilising slopes. As shown in Fig. 1, the flip anchor is driven directly into the ground with a driving rod to a designated depth. Then the anchor is pulled with a jack using a pulling rod connected to the flip anchor head. Hence, the flip anchor is an easy and fast solution for countermeasures of slope failures.

The biggest difference between soil nailing and the flip anchor is that there is no need to fill borehole with grout in case of the flip anchor, because pull-out force of the flip anchor does not depend on the friction resistance of the anchor rod, but on the pull-out bearing force acting on the anchor head from the ground above the anchor head.

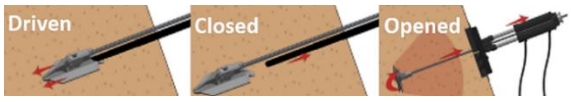

Fig. 1 Procedure of installing a flip-type anchor [1].

Although there are some previous laboratory experiments using model ground and model anchors as in [2]-[4], design guidelines of flip anchors have not been fully established in Japan due to a lack of experimental data and records. Therefore, pull-out experiments on various flip anchors with different installation methods and anchor head conditions were carried out in sand ground in a field, to provide performances of the flip anchors.

OUTLINE OF THE FIELD EXPERIMENT

Model Ground

Model sand ground was prepared in a test pit of 4 m in length, 4 m in width and 2.5 m in height in a field (Fig. 2).

Fig. 2 Test pit for model ground in field.

Table 1 shows the physical properties of river sand used for the model ground. The model ground consisted of 10 layers of 0.25 m thick. Each sand layer was compacted using a vibration tamper to have a relative density, D_r, of around 80% and a dry density, p_d, of around 1.745 t/m^3.

Two series of experiments were carried out in the model grounds named "Ground 1" and "Ground 2".

Table 1 Physical properties of sand used for the model ground

Density of soil particles, ρ_s (t/m^3)	2.688
Max. dry density, ρ_{dmax} (t/m^3)	1.833
Min. dry density, ρ_{dmin} (t/m^3)	1.463
Max. void ratio, e_{max}	0.837
Min. void ratio, e_{min}	0.466

Figure 3 shows the distribution with depth of the water content, w, of each ground. The water contents of the ground 1 and the ground 2 were similar having w around 5.5%.

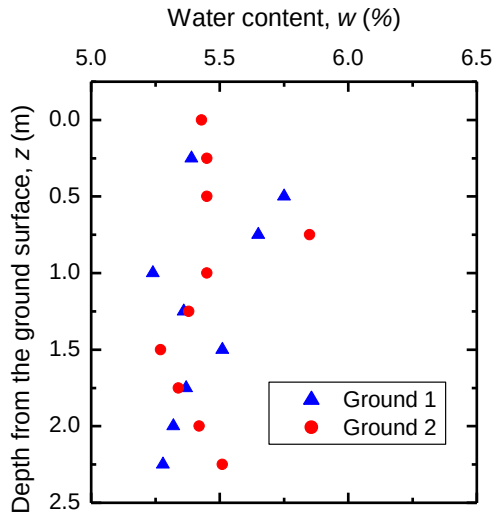

Fig. 3 Water contents of model grounds.

Figures 4 and 5 are distributions of total density, ρ_t, and dry density, ρ_d, of each ground. There is not a clear difference of the ground conditions between the ground 1 and the ground 2.

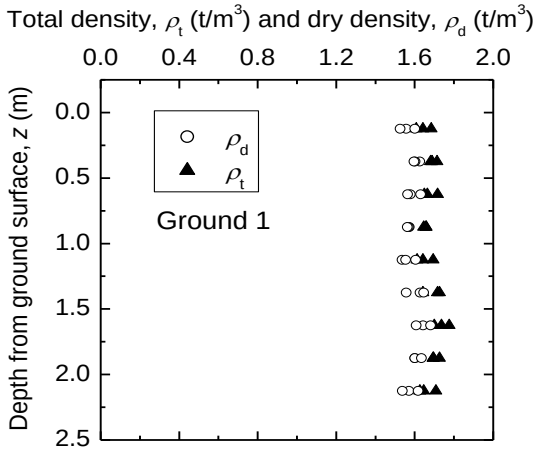

Fig. 4 Distributions of soil densities in the ground 1.

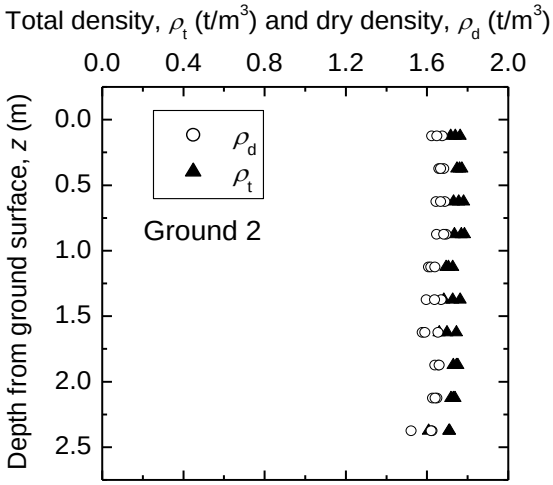

Fig. 5 Distributions of soil densities in the ground 2.

Portable dynamic cone penetration tests (DCPs) were also conducted in the model ground 1. In the DCPT, a cone having a diameter of 25 mm was driven with a hammer having a mass of 5 kg and a free-falling height of 500 mm.

Figure 6 is N_d-values of the ground 1. Here, N_d is the blow count required for the penetration of 100 mm of the cone.

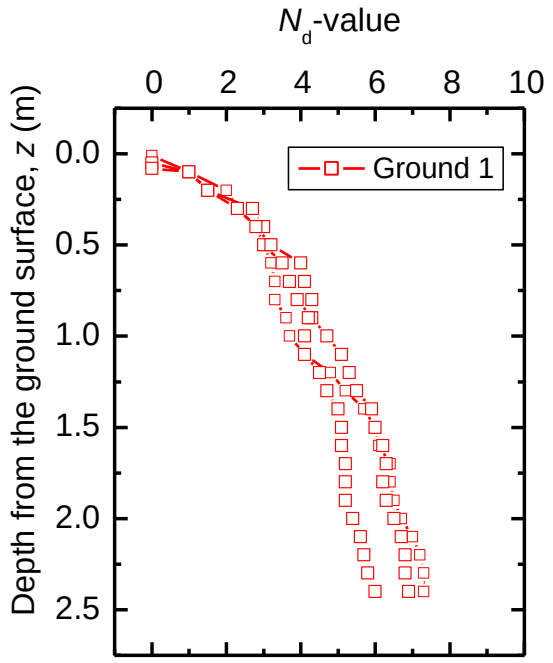

Fig. 6 N_d-values in the ground 1.

Although DCPT was not conducted in the ground 2, it could be judged that the conditions of the ground 2 are almost equal the conditions of the ground 1, based on the results of Figs. 3, 4 and 5.

Used Anchors

Figure 7 shows five flip anchors used for the experiments. They have different sizes and different projection areas, *A*.

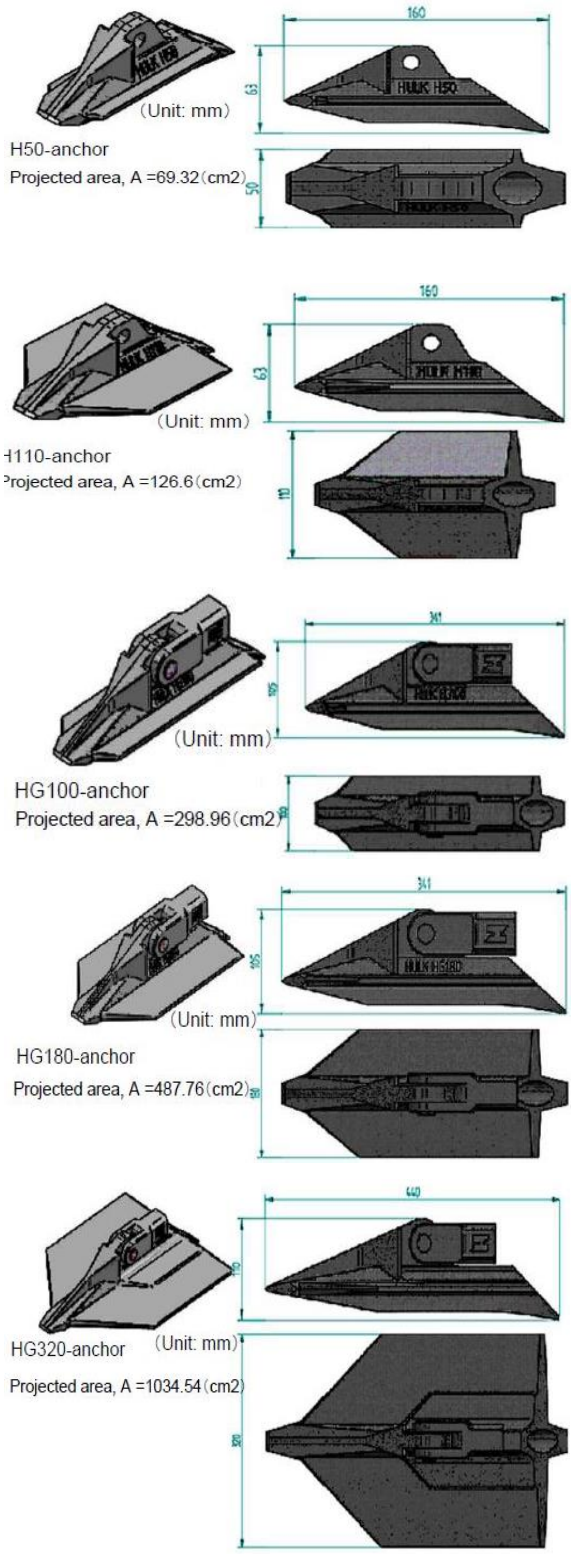

Fig. 7 Flip-anchors used in experiments [1].

Cases of Experiments

Table 2 and Table 3 list experimental cases in the ground 1 and the ground 2, respectively.

Table 2 Experimental cases in the ground 1

Case	Anchor type	Depth, z (m)	State	Max. force F_{max} (kN)
G1_C01	HG100	1.5	OP	30.63
G1_C02	H50	2.0	OP	12.28
G1_C03	H110	2.0	OP	20.06
G1_C04	H110	1.5	OP	14.28
G1_C05	H50	1.5	OP	10.31
G1_C06	HG100	2.0	OP	42.88
G1_C07	HG100	2.0	OP	42.88
G1_C08	HG180	2.0	OP	67.39
G1_C09	HG180	1.5	OP	42.88
G1_C10	HG320	1.01	D	18.38
G1_C11	HG180	1.34	D	42.88
G1_C12	HG100	1.33	D	21.44
G1_C13	H110	1.41	D	11.86
G1_C14	H50	1.41	D	9.66

NB OP: Opened CL: Closed D: Driven

Table 3 Experimental cases in the ground 2

Case	Anchor type	Depth, z (m)	State	Max. force, F_{max} (kN)
G2_C01	H110	1.5	CL	16.34
G2_C02	H110	1.0	OP	8.58
G2_C03	H50	1.0	OP	5.20
G2_C04	H50	1.5	CL	10.86
G2_C05	HG180	2.25	CL	50.20
G2_C06	HG320	2.25	CL	90.30
G2_C07	HG100	2.25	OP	50.20
G2_C08	HG180	2.25	OP	70.10
G2_C09	HG100	2.25	CL	45.00
G2_C10	HG320	2.25	OP	106.50

Experimental Procedure

First, anchors were set in the ground at designated depths with opened (OP) or closed (CL) anchor head condition while soil layers were being made (Figs. 8 and 9).

Each anchor was pulled out with a hydraulic jack, and the pull-out force, *F*, and the upward displacement, *w*, were measured with a load cell and an encoder (Fig. 10).

In case of the ground 1, five flip anchors were driven into the ground (G1_C10 to C14) after the completion of the pull-out experiments of G1_C01 to C09, and the pull-out experiments the driven anchors were carried out similarly.

In case of the ground 2, pull-out experiments of the buried anchors (G2_C01 to C10) were carried out .

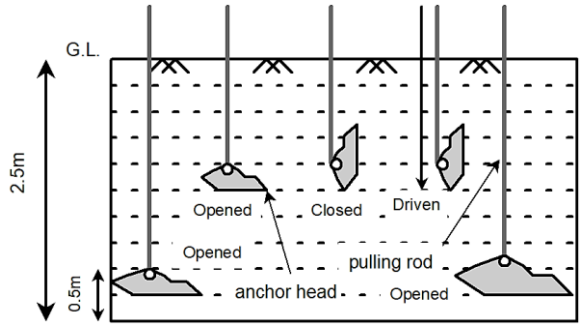

Fig. 8 Installed anchors in the ground.

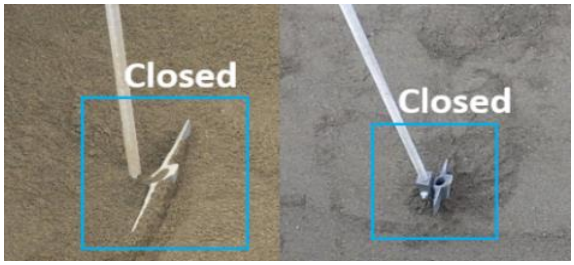

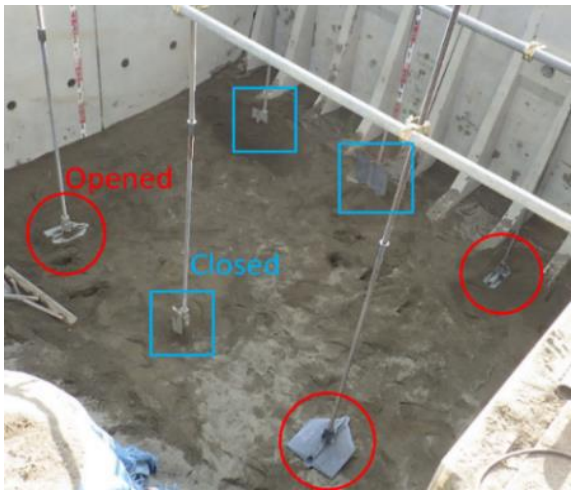

Fig. 9 Anchors set in the ground with opened or closed conditions.

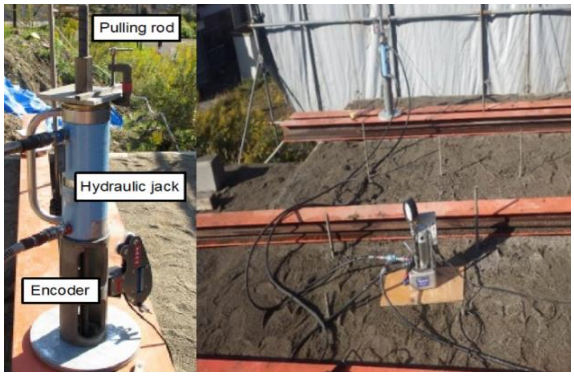

Fig. 10 Equipment for pull-out experiment.

EXPERIMENTAL RESULTS

Figures 11 and 12 show comparisons of relationships between the pull-out force, *F*, and the upward displacement, *w*, of each opened anchor. The pull-out force got larger as the size of anchors (projection area) got bigger. Similar tendency was observed for the closed anchors, as shown in Fig. 13.

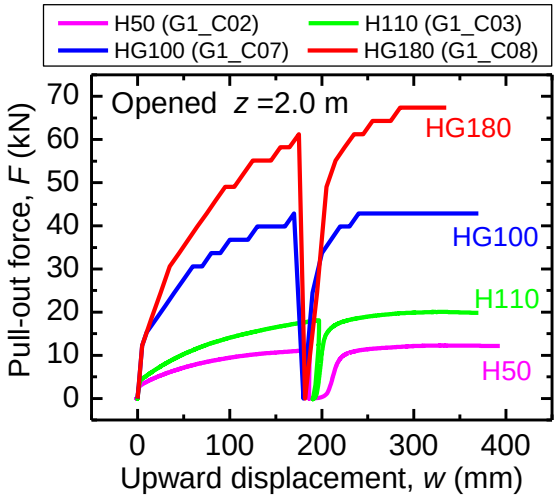

Fig. 11 Pull-out force versus displacement of each opened anchor buried at *z* = 2.0 m.

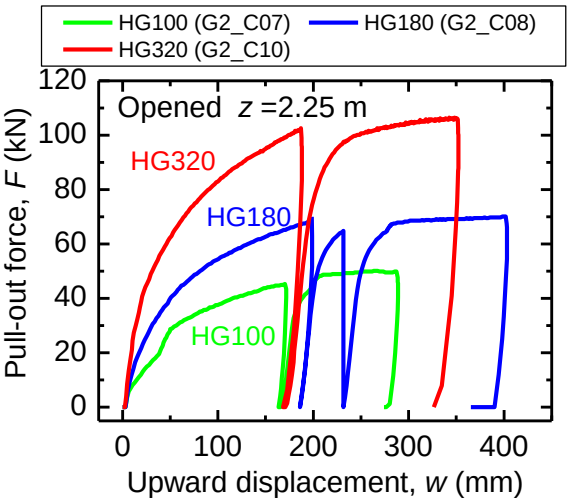

Fig. 12 Pull-out force versus displacement of each opened anchor buried at *z* = 2.25 m.

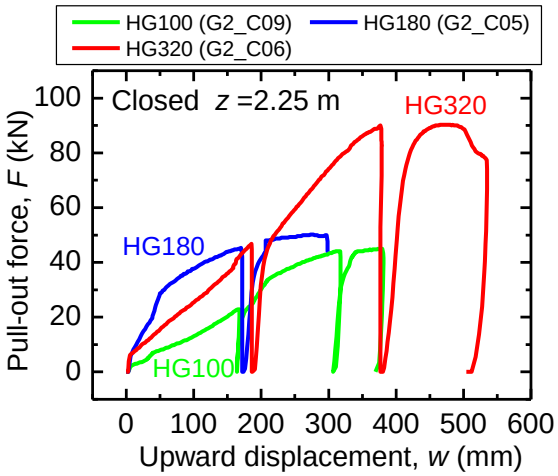

Fig. 13 Pull-out force versus displacement of each closed anchor buried at z = 2.25 m.

Figure 14 shows comparison of F versus w of opened HG100 anchor buried at different depths. As expected, the anchors got larger pull-out force when they were installed deeper in the ground.

Figure 15 is the relationship of maximum pull-out force, F_{max}, and embedment depth, z. F_{max} gets larger as the anchor size becomes larger at any depth.

Figure 16 shows the maximum pull-out stress, $p_{max} = F_{max}/A$, acting on each size of anchor at each depth. Contrary to the tendency of the maximum pull-out force, p_{max} becomes smaller as the anchor size becomes larger.

Figures 17 and 18 compare F versus w of flip anchors with opened and closed head conditions. It can be seen that although the stiffness ($\Delta F/\Delta w$) of the closed anchors are smaller than those of the opened anchors, the maximum pull-out forces of the closed anchors attain to about 80% of those of the opened anchors in both cases.

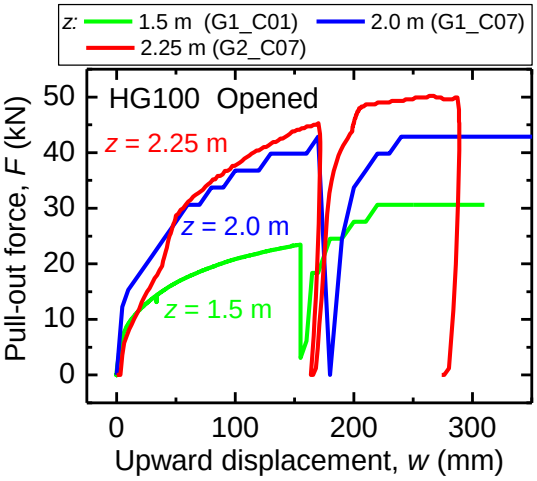

Fig. 14 Pull-out force versus displacement of opened HG100 anchor buried at different depths.

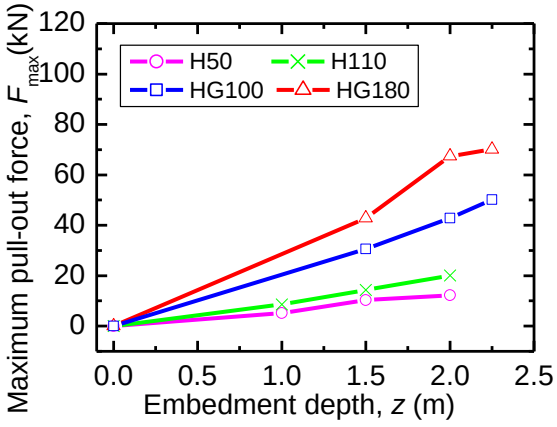

Fig. 15 Maximum pull-out force versus embedment depth of each anchor.

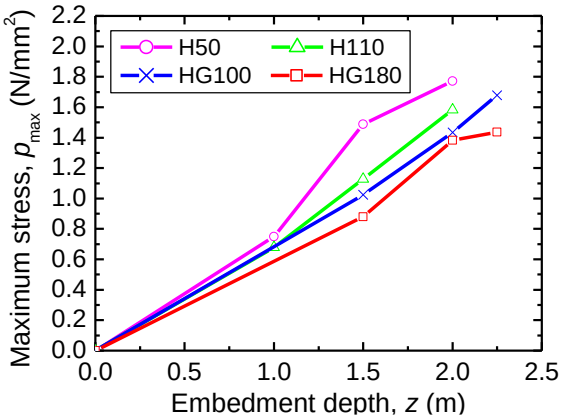

Fig. 16 Maximum pull-out stress of each anchor.

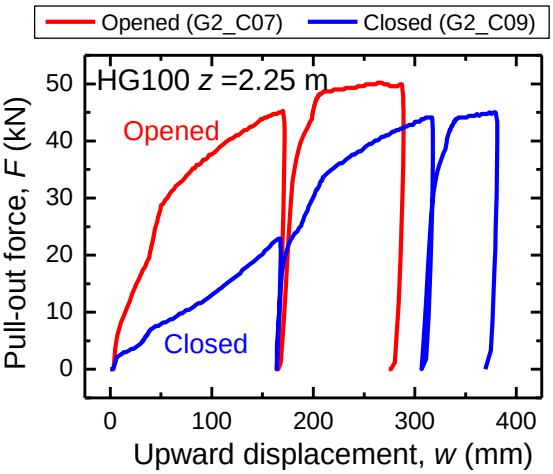

Fig. 17 Pull-out force versus displacement of opened and closed HG100 anchors buried at z = 2.25 m.

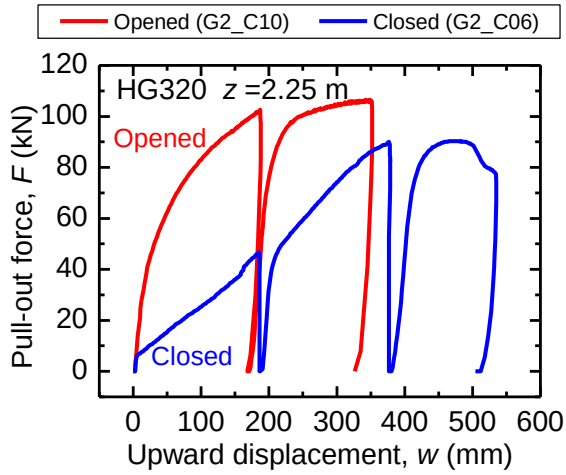

Fig. 18 Pull-out force versus displacement of opened and closed HG320 anchors buried at z = 2.25 m.

Figures 19 compares F versus w of opened and driven H50 anchors. Figure 20 is similar comparison for H110 anchor. Except for the early stage of loading, the stiffness of the driven anchors are comparable to that of the opened anchors, and the maximum pull-out force of the driven anchors attains to about 80% of that of the opened anchors.

In practical installation process, anchors are normally driven into the ground, not buried in advance. Therefore, how close the F_{max} of driven anchors approaches to the F_{max} of opened anchors, which is regarded as ideal values, is the most important concern in design of the flip anchors.

From these results, design values for F_{max} of the driven flip anchors could be around 80% of the ideal F_{max} of the corresponding opened anchors.

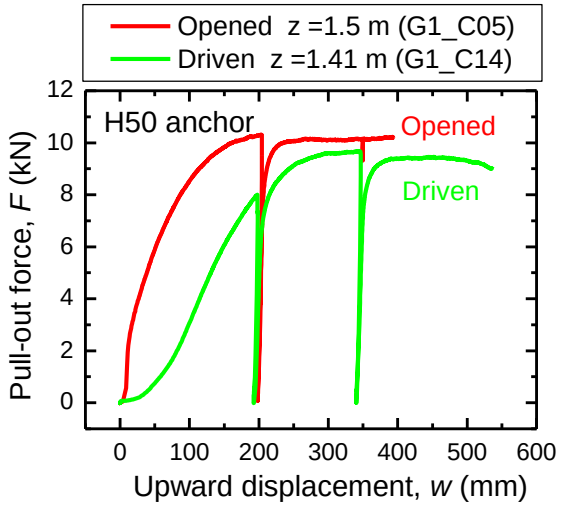

Fig. 19 Pull-out force versus displacement of opened and driven H50 anchors (z = 1.5 m and 1.41 m).

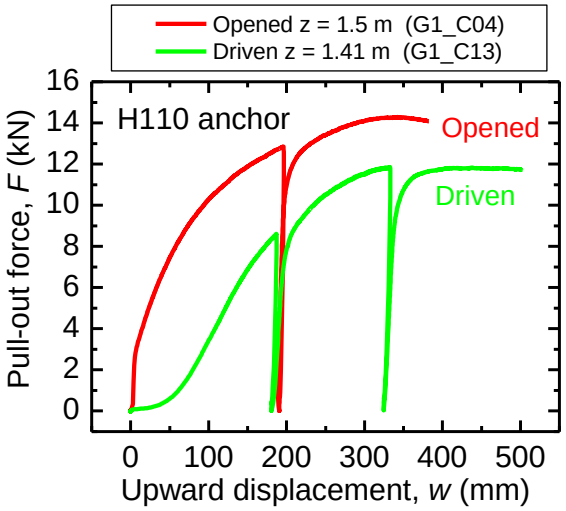

Fig. 20 Pull-out force versus displacement of opened and driven H110 anchors (z = 1.5 m and 1.41 m).

CONCLUSIONS

Pull-out experiments of flip-type anchors in sand ground in a field were carried out in this study. Main experimental parameters were embedment depth, anchor size, anchor head condition (opened or closed), installation method (buried or driven).

The maximum pull-out force, F_{max}, of buried opened anchor increases as the anchor size increases. Contrary to the tendency of F_{max}, the pressure, p_{max} (= F_{max}/A), becomes smaller as the anchor size becomes larger. So installing multiple smaller anchors is more effective than installing one big anchor.

Interestingly, stiffness ($\Delta F/\Delta w$) of buried closed anchors and driven anchors is smaller than that of buried opened anchors, but F_{max} of buried closed anchors and driven anchors attains to about 80% of F_{max} of buried opened anchors.

REFERENCES

[1] Anchoring Rope and Rigging Pty Ltd, 2019. Hulk Earth Anchors, http://www.hulkearthanchors.com

[2] Tanaka, T. & Sakai, T. (1987). A trap-door problem in granular materials: Model test and FEA, Irrigation Engineering and Rural Planning, No. 11, pp 8-23.

[3] Tanaka, T. & Sakai, T. (1987). A trap-door problem in granular materials: Model test and FEA, Irrigation Engineering and Rural Planning, No. 11, pp 8-23.

[4] Shota Y., Kazuki K., Tatsunori M. and Takayoshi Y (2019). Pull-out experiment of two-dimensional model flip-type ground anchors installed in dry sand ground. GEOTEC HANOI 2019.

9th Int. Conf. on Geotechnique, Construction Materials and Environment, Tokyo, Japan, 20-22 November 2019, ISBN: 978-4-909106025 C3051

FINITE DIFFERENCE APPROXIMATION FOR SOLVING TRANSIENT HEAT CONDUCTION EQUATION OF THE BRICK

Dalal Adnan Maturi [1]

[1]Departement of Mathematics, Faculty of Science, King Abdulaziz University, P.O.Box 42664,Jeddah 21551, Saudi Arabia

ABSTRACT

In this paper, we studied the numerical approximation of transient heat conduction equation of the brick .Brick is a natural building material used in construction, usually shaped in parallel, made of clay, sand and water, with a small amount of hay (crushed and soft straw) added to the clay block before cutting bricks to dry it under the sun. The bricks are strongly resistant and are not easily affected by weather. We applied the Finite differences method to the thermal conductivity equation for bricks. The technique is described and illustrated with a numerical example. The obtained solutions are compared with the available exact solutions and the solutions obtained by Finite difference method Results showed that Finite difference method is a very promising method for obtaining approximate solutions to transient heat conduction equation of the brick. As evidenced by numerical results obtained from brick in resistance to external factors such as rain, air, sounds and others.

Keywords: Finite Difference Method,Transient Heat Conduction Equation, Brick, Matlab.

INTRODUCTION

Finite difference method is one of several techniques for obtaining numerical solution of partial differential equation. Finite difference method describe functions as discrete values across a grid and approximate their derivatives as differences between points on the grid. Knowing a little about how difference methods are formulated and in what regimes they are stable can help save a lot of time, both in the design of finite differencing algorithms, and in the time that they take to run, the finite difference approximations for derivatives are one of the simplest and of the oldest methods to solve differential equations.

We need a fast, realistic and reliable method to solve the heat conduction equation of the Brick.

Advantages of using clay brick:

• very lite:

Its weights are 40-55% less than other building materials, which reduces loads on concrete foundations for construction.

• Heatproof:

It consists of thermal insulating materials more than any other materials, which saves 40% of the electrical energy.

• High pressure:

It has a high pressure equivalent to three times the other building materials. It is used to build the bearing walls without columns.

• Fire resistance:

It is incinerated in ovens with a temperature of more than 1000 ° C, which gives immunity against fire and reduce its spread in buildings and facilities.

Resists moisture leakage:

It has a low water absorption rate of not more than 12% which prevents moisture leakage.

• Soundproof:

Features a high rate of sound absorption.

• Ease of work:

Helps in the ease of construction and electrical wiring and plumbing for light weight and the presence of spaces.

• Low maintenance costs:

Free of salt, which increases its age, prevents corrosion and maintains its color and shape and does not require maintenance.

FINITE DIFFRENCE METHOD FOR HEAT CONDUCTION EQUATION

The linear second order partial differential equation

$$Au_{xx} + 2Bu_{xy} + Cu_{yy} + Du_x + Eu_y + Fu + G = 0$$

as a parabolic equation if $B^2 - AC = 0$. A parabolic equation holds in an open domain or in a semi-open domain.

The partial differential equation governing the flow of heat in the rod is given by the

parabolic equation

$$\boldsymbol{u_t = c^2 u_{xx},\ \ 0 \le x \le l,\qquad t > 0.}$$

Where $\boldsymbol{c^2}$ is a constant and depends on the material properties of the rod.

The heat conduction equation of the Brick

$$\boldsymbol{u_t = (0.0038)u_{xx}}$$
$$\boldsymbol{u(0,t) = u(1,t) = 0, \forall t \in (0, t_F)}$$
$$\boldsymbol{u(x,0) = u_0(x),\quad \forall x \in [0,1],}$$

Where t_F Denotes the terminal time for the model. Here without loss of generality, we assume that the spatial domain is $[0, 1]$.
At first divide the physical domain $(0, t_F) \times (0, 1)$ by $N \times J$ uniform grid points

$$t_n = n\Delta t, \Delta t = \frac{t_F}{N}, n = 0, 1, \cdots, N,$$
$$x_j = j\Delta x, \Delta x = \frac{1}{J}, j = 0, 1, \cdots, J.$$

Then, we denote the approximate solution $u_j^n \approx u(x_j, t_n)$ .At an arbitrary point (x_j, t_n) . To obtain afinite difference scheme, we need to approximate the derivatives in (1) by some finite differences. (Explicit scheme)
Substituting

$$u_t(x_j, t_n) \approx (u_j^n - u_j^{n-1})/\Delta t,$$
$$u_{xx}(x_j, t_n) \approx (u_{j+1}^n - 2u_j^n + u_{j-1}^n)/(\Delta x)^2,$$

Into (1), another difference scheme for (1) can be constructed as:

$$\frac{u_j^n - u_j^{n-1}}{\Delta t} = \frac{u_{j+1}^n - 2u_j^n + u_{j-1}^n}{(\Delta x)^2}, \quad 1 \le j \le J-1, 1 \le n \le N.$$

SEVERALS EXAMPLES

(i) Example1. Find the solution of the heat conduction equation of the Brick

$$u_t = (0.0038)u_{xx} \quad 0 < x < 1, \quad t > 0;$$
$$u(0, t) = u(1, t) = 0, \quad t > 0;$$
$$u(x, 0) = 2\sin(\pi x/2) - \sin \pi x + 4 \sin 2\pi x, \quad 0 \le x \le 1.$$

Applying the finite difference method using Matlab, then the result show as follows.

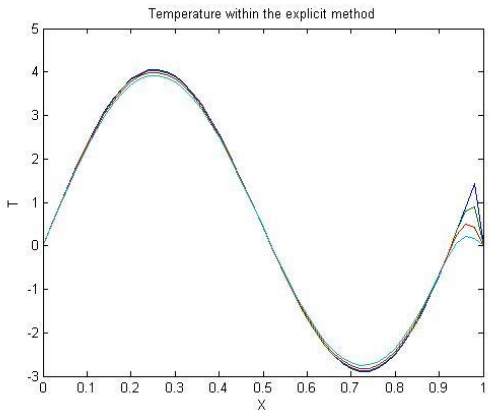

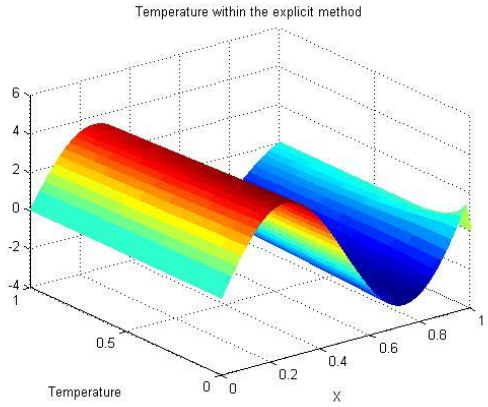

Fig.1 Temperature distributions at several times for the heat conduction of the Brick for example 1.

(ii) Example2. Find the solution of the heat conduction equation of the Brick

$$u_t = (0.011)u_{xx} \quad 0 < x < 1, \quad t > 0;$$
$$u(0, t) = u(1, t) = 0, \quad t > 0;$$
$$u(x, 0) = \sin \pi x, \quad 0 \le x \le 1.$$

Applying the finite difference method using Matlab, then the result show as follows.

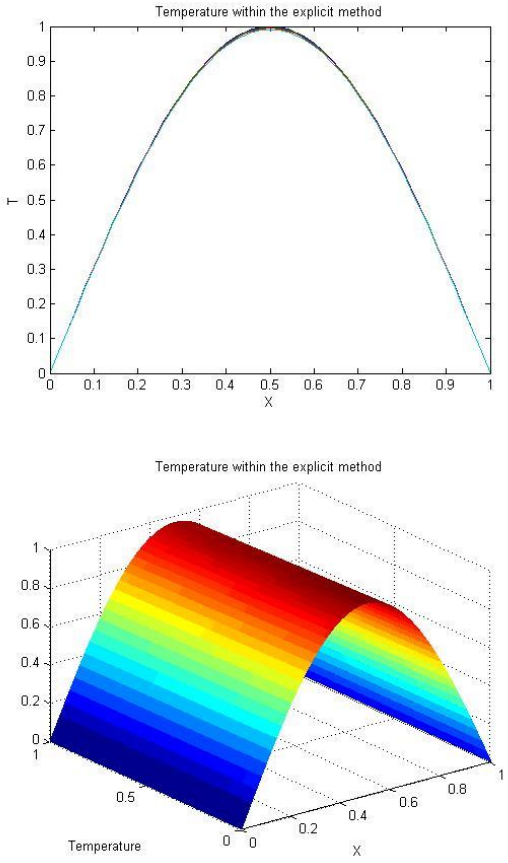

Fig.2 Temperature distributions at several times for the heat conduction of the Brick for

example 2.

(iii) Example3. Find the solution of the heat conduction equation of the Brick

$$u_t = (0.0038)u_{xx} \quad 0 < x < 1, \quad t > 0;$$
$$u(0,t) = u(1,t) = 0, \quad t > 0;$$
$$u(x,0) = \sin 2\pi x - \sin 5\pi x, \quad 0 \le x \le 1.$$

Applying the finite difference method using Matlab, then the result show as follows.

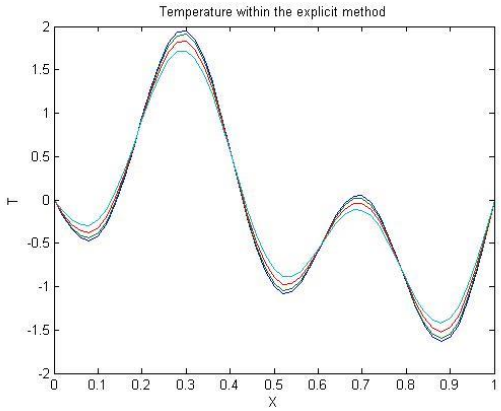

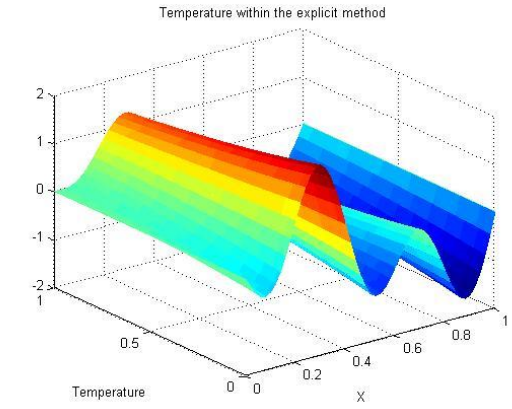

Fig.3 Temperature distributions at several times for the heat conduction of the Brick for example 3.

(iv) Example4. Find the solution of the heat conduction equation of the Brick

$$u_t = (0.0038)u_{xx} \quad 0 < x < 1, \quad t > 0;$$
$$u(0,t) = u(1,t) = 0, \quad t > 0;$$
$$u(x,0) = \sin(x) - 3\cos 4x, \quad 0 \le x \le 1.$$

Applying the finite difference method using Matlab, then the result show as follows.

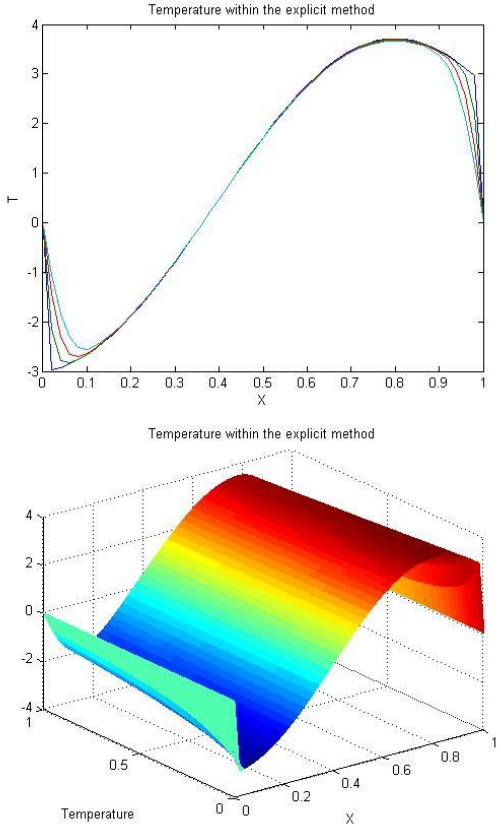

Fig.4 Temperature distributions at several times for the heat conduction of the Brick for example 4.

(v) Example5. Find the solution of the heat conduction equation of the Brick

$$u_t = (0.0038)u_{xx} \quad 0 < x < 1, \quad t > 0;$$
$$u(0,t) = u(1,t) = 0, \quad t > 0;$$
$$u(x,0) = x(1-x), \quad 0 \le x \le 1.$$

Applying the finite difference method using Matlab, then the result show as follows.

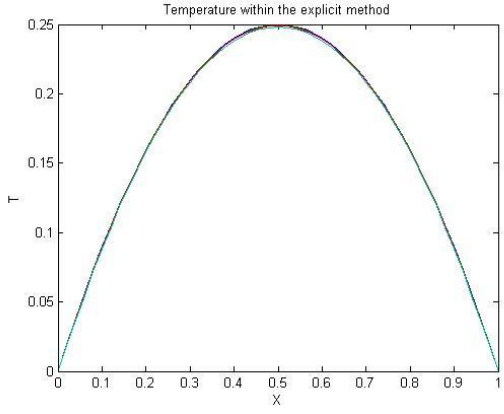

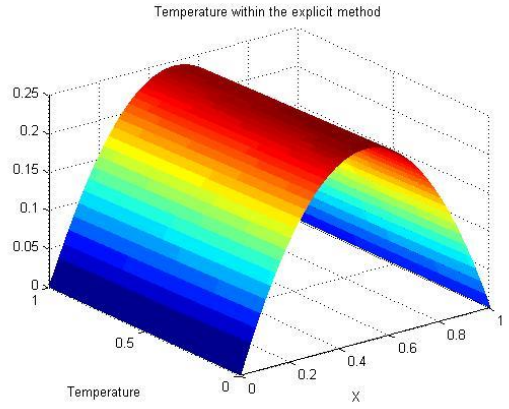

Fig.5 Temperature distributions at several times for the heat conduction of the Brick for example5.

CONCLUSION

In this paper, the calculations were performed by the MATLAB program for the programming and the corresponding evolutionary laws on the basis of the one-dimensional mathematical model of one-dimensional thermal conductivity using the Finite differences method of solving the heat-conduction equation for the bricks. All the examples show that the finite difference method is a powerful mathematical tool to solve the heat conduction equation for bricks. The graphic shapes we have provided to determine the higher resolution and simplicity of the proposed method. In addition, it should be noted that the method described can be easily circulated to build more heat for different materials. This work focuses on bricks because it is resistant to high temperatures, friction and various chemical effects. It is used in the construction of heaters and lining furnaces used in the iron and steel industry in the iron and steel industry and the non-ferrous industries such as copper, zinc and lead in the manufacture of cement, lime and glass.

ACKNOWLEDGEMENTS

This paper was supported by the Deanship of Scientific Research (DSR), King Abdulaziz University, Jeddah.

REFERENCES

[1] William. F. A., Numerical Methods for Partial Differential Equations. Academic Press, New York, NY, 3rd edition, 1992.

[2] Jim. D., and H.H. R., On the numerical solution of heat conduction problems in two and three space variables. Trans. Amer. Math.Soc., 82:421–439, 1956.

[3] A.R. Mitchell and D.F. Griffiths. The Finite Difference Method in Partial Differential Equations. John Wiley & Sons, Chichester, 1980.

[4] A.R. Mitchell and D.F. Griffiths. The Finite Difference Method in Partial Differential Equations. John Wiley & Sons, Chichester, 1980.

[5] Dalal A.M, Amani.Z.B., Badreeh.M. G., Numerical Solution of Volterra Integral Equation of Second Kind Using Implicit Trapezoidal, Journal of Advances In Mathematics, Vol8,No.2,pp.1540-1553,2014.

[6] Dalal .A. M., Adomian Decomposition Method of Fredholm Integral Equation of the Second Kind Using Maple, Journal of Advances In Mathematics, Vol9, No.1, pp.1868-1875,2014.

[7] Dalal. A.M., Application of Adomian Decomposition Method for Solving of Fredholm Integral Equation of the Second Kind, European Journal of Science and Engineering, Vol9, No.2, pp.1-9,2014.

[8] Dalal.A.M., Adomian Decomposition Method for Solving of Fredholm Integral Equation of the Second Kind Using Matlab, International Journal of GEOMATE, Dec. 2016, Vol. 11, Issue 28, pp.2830-2833.Special Issue on Science, Engineering and Environment, ISSN: 2186-2990, Japan.

[9] Dalal A.M. and Honida M.M., Numerical Solution of System of Three Nonlinear Volterra Integral Equation Using Implicit Trapezoidal, Journal of Mathematics Research, Vol.10, No. 1, February 2018, ISSN 1916-9795 E-ISSN 1916-9809.

[10] Dalal.A.M., Finite Difference Method for Solving Heat Conduction Equation of The Granite, International Journal of GEOMATE, Sept. 2019, Vol. 17, Issue 61, pp.135-140.Special Issue on Science, Engineering and Environment, ISSN: 2186-2982(P),2186-2990(O), Japan.

9th Int. Conf. on Geotechnique, Construction Materials and Environment,
Tokyo, Japan, 20-22 November 2019, ISBN: 978-4-909106025 C3051

POST-FIRE BEHAVIOUR OF CONCRETE-FILLED STEEL CIRCULAR TUBE COLUMNS UNDER AXIAL COMPRESSION

Kamonwan Prathumwong[1], Jaksada Thumrongvut[2*] and Cherdsak Suksiripattanapong[3]
[1,2,3] Department of Civil Engineering, Faculty of Engineering and Architecture,
Rajamangala University of Technology Isan, Nakhon Ratchasima, 30000, Thailand

ABSTRACT

This paper presents experimental studies on the post-fire behavior of concrete-filled steel tube (CSFT) columns under axial compression. The structural responses and axial load capacity of CSFT columns after exposure to elevated temperatures are investigated and discussed. All of the specimens are 750 mm in height, the nominal diameter of the circular columns is 150 mm, and have compressive strength of 18 MPa. The primary test parameters are wall thicknesses of the circular tubular (3.0 mm, 4.5 mm and 6.0 mm) and three different exposure to elevated temperatures (400°C, 600°C and 800°C). The results of these tests showed that the load-axial shortening relationship of the CSFT columns have a linear elastic response up to 80-90% of axial load capacity. After the axial load capacity is reached, the load-axial shortening curves are rarely becoming a nonlinear manner. The failure mechanism of CSFT columns is local buckling of the steel tubular walls and compressive crushing of the concrete core. It is also shown that the axial load capacity and ductility of the post-fire test columns are decreased significantly compared to the columns at ambient temperature, depending mainly on the elevated temperature and wall thickness of steel tubular. In addition, by comparing the axial load capacity of the experimental results with those obtained from the ACI design equation, the comparison results indicate that calculation formula in ACI code unconservative predicts the axial load capacity of the CSFT columns after exposure to elevated temperatures. Finally, the residual strength ratios are modified to both strength of concrete and steel tube under ambient temperature, and analyzed to evaluate the effect of post-fire behavior on the axial capacity of CFST columns.

Keywords: Concrete-filled tube columns, Circular tube, Axial compression, Post-fire behavior, Elevated temperature

1. INTRODUCTION

Concrete-filled steel tube (CFST) column is a type of composite columns in which the combined action of concrete and cold-formed steel circular and rectangular tubes leads to an exceptional structural behavior [1]. The axial load capacity of the CFST column increases due to the passive confinement that the steel tube generates on the concrete core [2]. Meanwhile, the local buckling failure of the steel tube is restrained by the concrete core which prevents it from suffering this phenomenon inwards. This fact reveals that the concrete retards the wall buckling and temperature rise of steel tube, and considerably enhances seismic resistance and inelastic deformation capacity in compression and combined loads [3]. Also, CFST members have many advantageous features at ambient temperature for structural applications, such as high stiffness and ductility, large energy absorption for earthquake-resistant properties, excellent fire resistance behavior without external prevention, the axial capacity of the CFST column is more than that achieved by reinforced (RC) columns with similar cross-section size, and reduced cost and time management in construction because formworks are not necessary for the construction process [4-11].

Over the last 20 years, the research and development on the mechanical behavior of CFST columns have advanced considerably in several countries [12]. Many research investigations have been conducted to study the structural response of CFST structural members under axial compression and flexure at the ambient temperature [13-20]. However, some attention has been reported on the fire behavior and performance of CFST columns or their residual properties after exposure to elevated temperatures [21-22]. Ordinarily, a deterioration in the properties of CFST columns occurs when it exposed to fire. In addition, the CFST members are loss in strength and ductility of the steel tube, reduction of compressive strength and modulus of the concrete core [23]. At elevated temperatures in case of fire, the assessment of CFST columns is much more complicated comparing to ambient temperature. Also, in order to create further confidence in the CFST columns after exposure to high temperatures, it is necessary to enhance knowledge of structural responses, particularly the post-fire behavior of CSFT columns subjected to axial compression. Consequently, this research aims to present the experimental results on post-fire behavior of CSFT columns, and to evaluate the axial load capacity of

test members after exposure to elevated temperatures. Eventually, comparisons with the prediction of axial load capacity by using ACI code provisions with consideration effect of residual strength of materials are also performed.

2. EXPERIMENTAL PROGRAM

2.1 Specimen Configuration

A total of 24 columns were prepared in the Department of Civil Engineering at Rajamangala University of Technology Isan. All circular columns had a height of 750 mm, the nominal diameter of the circular columns was 150 mm. The average 28-day compressive strength of concrete was 18 MPa. The main parameters were the wall thicknesses of the circular tube (3.0 mm, 4.5 mm and 6.0 mm) and three different temperatures. The maximum temperatures were 25°C, 400°C, 600°C and 800°C, respectively. The temperature of 25°C denoted the ambient temperature. Two specimens of each set were tested to determine the average axial load capacity. A summary of the nominal dimensions of CFST columns under different temperatures is presented in Table 1. The CFST columns were classified into 3 groups with thicknesses of steel tubular.

Table 1 Summary of test information

Specimen	t (mm)	D (mm)	L (mm)	T (°C)	D/t	Concrete		Steel Tube	
						A_c (mm^2)	f_c' (MPa)	A_{st} (mm^2)	f_y (MPa)
C18-3.0-025	3.0	150	750	25	50.0	19,607	18.2	1,529	370.2
C18-3.0-400	3.0	150	750	400	50.0	19,607	18.2	1,529	370.2
C18-3.0-600	3.0	150	750	600	50.0	19,607	18.2	1,529	370.2
C18-3.0-800	3.0	150	750	800	50.0	19,607	18.2	1,529	370.2
C18-4.5-025	4.5	150	750	25	33.3	19,483	18.2	2,272	347.5
C18-4.5-400	4.5	150	750	400	33.3	19,483	18.2	2,272	347.5
C18-4.5-600	4.5	150	750	600	33.3	19,483	18.2	2,272	347.5
C18-4.5-800	4.5	150	750	800	33.3	19,483	18.2	2,272	347.5
C18-6.0-025	6.0	150	750	25	25.0	18,942	18.2	3,001	366.7
C18-6.0-400	6.0	150	750	400	25.0	18,942	18.2	3,001	366.7
C18-6.0-600	6.0	150	750	600	25.0	18,942	18.2	3,001	366.7
C18-6.0-800	6.0	150	750	800	25.0	18,942	18.2	3,001	366.7

Each CSFT column is labeled according to its 28-days compressive strength of cylinder concrete, thickness of the steel tube and maximum heating temperature, respectively. For example, consider column C18-3.0-600; C represents the circular CSFT column, 18 is the compressive strength in MPa, 3.0 is the thickness of the steel tube in millimeter and 600 is the maximum heating temperature in Celsius. Also, the average mechanical properties of the compressive strength concrete at the age of 28 days and steel tube were performed according to ASTM procedures, and given in Table 1.

2.2 Fire Exposure and Test Setup

In the fire exposure process, heat treatment of CSFT columns was performed using the gas furnace at the Department of Ceramic Design in Rajamangala University of Technology Isan. The specimens were moved into position inside the furnace, as presented in Figure 1. Eight gas burners were set up in the furnace chamber and it can be adjusted individually to generate a uniform temperature. Dual thermocouples were fixed to the lower and upper inner furnace and were used to observe the furnace temperature. A heating rate was set at 10°C/min [24]. The furnace temperature was uniform increased to a target temperature (400°C, 600°C and 800°C). After the furnace temperature reached the target temperature, the furnace was maintained at a constant temperature phase for 3 hours to ensure that the CFST columns were heated equally and obtain a stable residual strength [25]. Then, the furnace was turned off and natural air cooling was used to cool down until ambient temperature.

Fig. 1 Exposure to elevated temperatures of column

The CFST columns were tested under an axial compression load. A 2,000 kN capacity Universal Testing Machine (UTM) with displacement control was used to apply the compressive load monotonically until failure. The load arrangement and test setup can be seen in Figure 2. The column was set up in a vertical position and the steel bearing plates were placed between the column and the top and bottom crosshead of the UTM. Two linear variable differential transducers (LVDT) were used to monitor overall axial shortening. Before the beginning of each test, a preload of approximately 20% of the predicted axial load capacity of the columns was applied in order to reduce the friction between the steel bearing plates and the columns, and to balance the uneven top and bottom surfaces. The specimens were loaded at a very slow rate, was increased at a constant rate up to axial load capacity, such that the axial load, the axial shortening of the columns were automatically recorded by a KYOWA EDX-10 Series data acquisition unit. Additionally, the local tube wall buckling and the axial load capacity were carefully observed.

Fig. 2 Post-fire test of CFST member

3. TEST RESULTS AND DISCUSSIONS

3.1 Behavior Curves and Failure Mode

The term “short column” refers to a compression member which can attain its axial load capacity, known as the squash loads (P_{Test}), without buckling of the columns. The typical structural behavior of the tested CFST column at ambient temperature and after different elevated temperatures are obtained in Figure 3 by relations between the axial load and axial shortening. It can be seen that the CFST column at ambient temperature and after exposure to elevated temperatures showed a linear elastic behavior up to 80-90% of their axial load capacity. After that, as the load continued to increase and reached the ultimate load, the curves are gradually becoming nonlinear due to the start of the cracking of the concrete underneath the applied load and the local yielding of the steel tube [12].

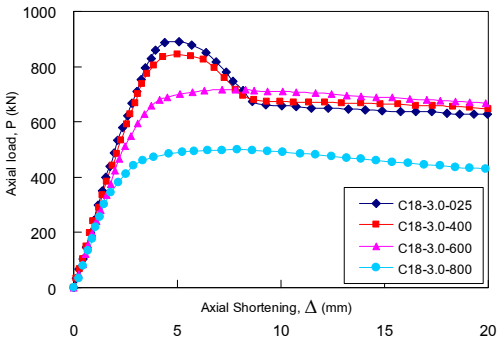

(a) t = 3.0 mm

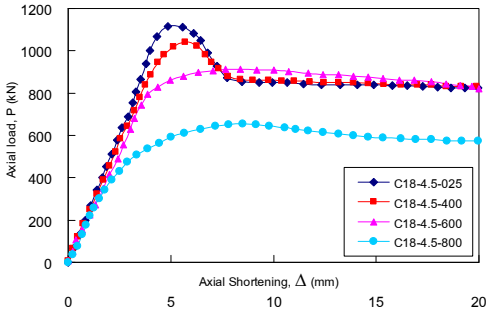

(b) t = 4.5 mm

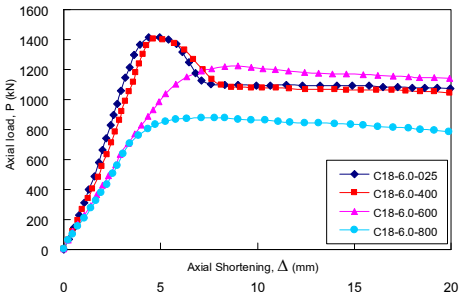

(c) t = 6.0 mm

Fig. 3 Axial load-axial shortening curves of columns after exposure to elevated temperatures

According to the test results, the axial load-axial shortening curves of the CFST columns heated to 400°C are similar to the those CFST columns at ambient temperature (25°C). Thus, it is evident that there is no obvious deterioration of the mechanical properties of CFST columns at 400°C. In contrast, when the temperature increased to 600°C and 800°C, the ascending and descending line stages of the axial load-axial shortening curves became much less distinct, and the axial load capacity also decreased. This result is similar to that reported in previous research on the strength development of recycled

aggregate CFST stub columns [24]. Figure 4 shows a typical failure mode of the HSCFT column. The failure mechanism of the columns was identified as the crushing of concrete core and the yielding of steel tube. This indicates that the concrete core in these locations was contained by the steel tube, in turn providing large axial deformability to the columns [2].

Fig. 4 Failure modes of CFST columns after different elevated temperatures

3.2 Residual axial load capacity and comparison ACI

3.2.1 Residual strength of concrete

When concrete is exposed to an extreme heat sources, the physical and chemical responses occur at elevated temperatures, for instance, dehydration of cement paste, loss of moisture [26]. Figure 5 represents the residual strength ratio of normal strength concrete (ϕ_c) as a function of the elevated temperatures [27].

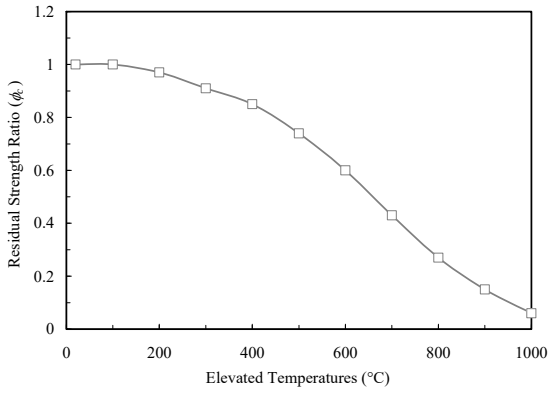

Fig. 5 Residual strength ratio versus elevated temperatures curve of concrete [27]

3.2.2 Residual strength of steel

In general, the residual strength ratio of steel after elevated temperatures can be estimated. The steel recovers most of its strength and stiffness natural air cooling [28]. Nevertheless, the higher elevated temperatures achieved in steel, the residual strength of steel is reduced, especially when the elevated temperatures in steel exceeds 500°C [29]. In this study, the residual strength ratio of steel is assumed to follow the test data reported by Neves *et al*. [28]. Figure 6 shows a residual strength ratio versus elevated temperatures curve of steel.

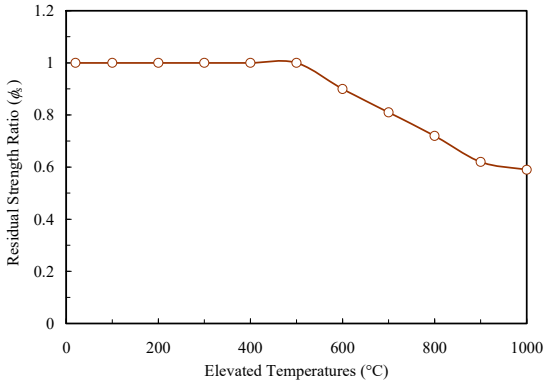

Fig. 6 Residual strength ratio versus elevated temperatures curve of steel [28]

3.2.3 Residual axial load capacity of CFST column

In the proposed approach, a simplified equation to assess the residual axial load capacity of post-fire CFST column is presented. The residual axial load capacity of CFST columns after exposure to elevated temperatures could be evaluated by using the composite design equation under ambient conditions, as recommended in the ACI code [30]. The residual strength ratio of concrete and steel will be multiplied by the strength of concrete and steel under ambient temperature, respectively. Consequently, the residual axial load capacity of CFST columns after exposure to elevated temperatures is given by:

$$P_u = \phi_c 0.85 f_c' A_c + \phi_s f_y A_s \quad (1)$$

where P_u is defined as the residual axial load capacity of CFST columns after exposure to elevated temperatures, ϕ_c is the residual strength ratio of concrete and ϕ_s is the residual strength ratio of steel tube.

From the analytical results, the comparison of residual axial load capacity of CFST columns between the test values and the modified the ACI design equation are presented in Table 2. The

comparison of results shows that modified ACI design equation closely predicts with a difference of 2-5%. This indicates that the modified ACI design equation with residual strength ratio can adequately predict the axial load capacity of the CFST columns after exposure to elevated temperatures.

Table 2 Comparison of the residual load capacity obtained from test and modified ACI Eq.

Specimen	P_{Test}	P_u	P_{Test} / P_u
C18-3.0-025	888.7	886.0	1.03
C18-3.0-400	849.9	821.0	1.04
C18-3.0-600	716.5	689.4	1.04
C18-3.0-800	500.0	477.2	1.05
C18-4.5-025	1,114.1	1,087.6	1.02
C18-4.5-400	1,079.4	1,042.9	1.04
C18-4.5-600	913.6	889.4	1.03
C18-4.5-800	657.0	633.1	1.04
C18-6.0-025	1,415.1	1,390.3	1.02
C18-6.0-400	1,403.0	1,346.8	1.04
C18-6.0-600	1,225.2	1,164.3	1.05
C18-6.0-800	885.7	848.6	1.04

CONCLUSIONS

The conclusions from the experimental studies are summarized as follows.

1) The structural performance of CFST columns after exposure to elevated temperatures have a linear elastic behavior up to 80-90% of their axial load capacity. Then, the behavior of the columns is gradually becoming nonlinear with the strain-softening type. Failure mechanism of the CFST columns are identified as the crushing of concrete core and the localized buckling of steel tube.

2) There is no obvious deterioration of the mechanical properties of CFST columns at 400°C. In contrast, when the temperature increased to 600°C and 800°C, the ascending and descending line stages of the axial load-axial shortening curves became much less distinct, and the axial load capacity also decreased.

3) Good agreement is evaluated between the predicted residual load capacity using the modified ACI design equation and the experimental results.

ACKNOWLEDGMENTS

The authors would like to acknowledge the financial support provided by the Thailand Research Fund (TRF): Research and Researchers for Industries (RRI). The authors are grateful to Faculty of Engineering and Architecture, Rajamangala University of Technology Isan for facilities and equipment provided.

REFERENCES

[1] Han, L.H., Li, W. and Bjorhovde, R., Developments and advanced applications of concrete-filled steel tubular (CFST) structures: Members. Journal of Constructional Steel Research, Vol. 100, 2014, pp. 211-228.

[2] Thumrongvut, J. and Tiwjantuk, P., Strength and axial behavior of cellular lightweight concrete-filled steel rectangular tube columns under axial compression. Materials Science Forum, Vol. 941, 2018, pp. 2417-2422.

[3] Thumrongvut, J. and Seangatith, S., Axial load capacity of cellular lightweight concrete-filled steel square tube columns. Central Europe towards Sustainable Building (CESB 2016): Innovations for Sustainable Future, Czech Republic, 22-24 June 2016, pp. 1312-1319.

[4] Elremaily, A. and Azizinamini, A., Behavior and strength of circular concrete-filled tube columns. Journal of Constructional Steel Research, Vol. 58, Issue 12, 2002, pp. 1567-1591.

[5] Liu, D., Gho, W.M. and Yuan, J., Ultimate capacity of high-strength rectangular concrete-filled steel hollow section stub columns. Journal of Constructional Steel Research, Vol. 59, Issue 12, 2003, pp. 1499-1515.

[6] Giakoumelis, G. and Lam, D., Axial capacity of circular concrete-filled tube columns. Journal of Constructional Steel Research, Vol. 60, Issue 7, 2004, pp. 1049-1068.

[7] Xiao, Y., He, W. and Choi, K., Confined concrete filled tubular columns. Journal of Structural Engineering, Vol. 131, Issue 3, 2005, pp. 488-497.

[8] Seangatith, S. and Thumrongvut, J., Behaviors of square thin-walled steel tubed RC columns under direct axial compression on RC core. Procedia Engineering, Vol. 14, 2011, pp. 513-520.

[9] Chen, B., Liu, X. and Li, S.J., Performance investigation of square concrete-filled steel tube columns. Journal of Wuhan University of Technology-Mater. Sci. Ed., Vol. 26, Issue 4, 2011, pp. 730-736.

[10] Ding, F., Liu, J., Liu, X., Yu, Z. and Li, D., Mechanical behavior of circular and square concrete filled steel tube stub columns under local compression. Thin-Walled Structures, Vol. 94, 2015, pp. 155-166.

[11] Buachart, C., Hansapinyo, C. and Ueatrongchit, N., Analysis of square concrete-filled cold-formed steel tubular columns under axial cyclic loading. International Journal of GEOMATE, Vol. 15, Issue 47, 2018, 74-80.

[12] Thumrongvut, J., Seangatith, S., Siriparinyanan, T. and Wangrakklang, S., An experimental behaviour of cellular lightweight concrete-filled steel square tube columns under axial compression. Materials Science Forum, Vol. 860, 2016, pp. 121-124.

[13] Uy, B., Strength of short concrete filled high strength steel box columns. Journal of Constructional Steel Research, Vol. 57, Issue 2, 2001, pp. 113-134.

[14] Han, L.H., Yang, Y.F. and Tao, Z., Concrete-filled thin walled steel RHS beam-columns subjected to cyclic loading. Thin-walled Structures, Vol. 41, Issue 9, 2003, pp. 801-833.

[15] Lue, D.M., Liu, J.L. and Yen, T., Experimental study on rectangular CFT columns with high-strength concrete. Journal of Constructional Steel Research, Vol. 63, Issue 1, 2007, pp. 37-44.

[16] Zhang, S. and Liu, J., Seismic behavior and strength of square tube confined reinforced-concrete (STRC) columns. Journal of Constructional Steel Research, Vol. 63, Issue 9, 2007, pp. 1194-1207.

[17] Chang, X., Ru, Z.L., Zhou, W. and Zhang, Y.B., Study on concrete-filled stainless steel-carbon steel tubular (CFSCT) stub columns under compression. Thin-Walled Structures, Vol. 63, 2013, pp. 125-133.

[18] Ananthi, B.G. and Knight, S., Experimental and theoretical study on cold-formed steel box stub columns under uniaxial compression. Arabian Journal for Science and Engineering, Vol. 39, Issue 10, 2014, pp. 6983-6993.

[19] Wang, W.H., Han, L.H., Li, W. and Jia, T.H., Behavior of concrete-filled steel tubular stub columns and beams using dune sand as part of fine aggregate. Construction and Building Materials, Vol. 51, 2014, pp. 352-363.

[20] Lu, Y., Li, N., Li, S. and Liang, H., Behavior of steel fiber reinforced concrete-filled steel tube columns under axial compression. Construction and Building Materials, Vol. 95, 2015, pp. 74-85.

[21] Han, L.H. and Huo, J.S., Concrete-filled hollow structural steel columns after exposure to ISO-834 fire standard. Journal of Structural Engineering, Vol. 129, Issue 1, 2003, pp. 68-78.

[22] Liu, F., Gardner, L. and Yang, H., Post-fire behaviour of reinforced concrete stub columns confined by circular steel tubes. Journal of Constructional Steel Research, Vol. 102, 2014, pp. 82-103.

[23] Short, N., Purkiss, J. and Guise, S., Assessment of fire damaged concrete using colour image analysis. Construction and Building Materials, Vol. 15, 2001, pp. 9-15.

[24] Li, W., Luo, Z., Tao, Z., Duan, W.H. and Shah, S.P. Mechanical behavior of recycled aggregate concrete-filled steel tube stub columns after exposure to elevated temperatures. Construction and Building Materials, Vol. 146, 2017, pp. 571-581.

[25] Mohamedbhai, G.G. Effect of exposure time and rates of heating and cooling on residual strength of heated concrete. Magazine of Concrete Research, Vol. 38, Issue 136, 1986, pp. 151-158.

[26] Xiaoyong, L. and Fanjie, B. Residual Strength for Concrete after Exposure to High Temperatures. Innovative Computing and Information (ICCIC 2011). Communications in Computer and Information Science, Vol. 232, 2011, Springer, Berlin, Heidelberg.

[27] EN 1992-1-2, Eurocode 2. Design of Concrete Structures Part 1-2: General Rules - Structural Fire Design, European Committee for Standardization, Brussels, 2004.

[28] Neves, I.C., Rodrigues, J.C. and Loureiro, A.P. Mechanical properties of reinforcing and prestressing steels after heating. Journal of Materials in Civil Engineering, Vol. 8, Issue 4, 1996, pp. 189-194.

[29] Yao, Y and Hu, X.X. Cooling behavior and residual strength of post-fire concrete filled steel tubular columns. Journal of Constructional Steel Research, Vol. 112, 2015, pp. 282-292.

[30] ACI Committee 318, Building Code Requirement for Structural Concrete and Commentary. Farmington Hills: ACI Committee 318-11, 2011.

9th Int. Conf. on Geotechnique, Construction Materials and Environment, Tokyo, Japan, 20-22 November 2019, ISBN: 978-4-909106025 C3051

EXPERIMENTAL STUDY ON INFILLING BEHAVIOR OF PLASTOC GROUT IN VOIDS WITH CHANGING HEIGHT

Hiroyasu Ishii[1]
[1]Technology Center, Taisei Corporation, Japan

ABSTRACT

The most effective measure to deal with underground voids is infilling with an engineering material; fluidized cement mixtures have been widely used due to easiness of placing, i.e. just pumping out to allow gravitational flow in voids. However, the mixtures spread mainly downwards in voids; they may spread to unintentional directions or spill out to adjoining land before infilling up in target areas. Then another engineering material, plastic grout, may contribute to improve work efficiency and infilling quality. Due to its characteristics in fresh state, plastic grout spread in voids under infilling pressure, and stay in place when infilling is stopped. In this paper, the author raises an attention to actual infilling behavior of plastic grout affected by change of void heights and shows simplified infilling tests with four model voids having 7.8 m in length, 0.3 m in width and 0.25 to 0.15 m in height. Each infilling was conducted from center of the model and allowed to spread in two directions along the length. It was experimentally demonstrated that; i) grout spreads uniformly in two directions when void height is uniform, ii) grout spreads more in direction with larger heights of voids. Also, the author proposed a simple estimation method to predict the infilling volume in each direction, and the validity of the method was confirmed by comparing with the testing results.

Keywords: Ground improvement, Cement grout, Model tests, Void filling

INTRODUCTION

Underground voids, created by human activity or natural phenomena, may cause land cave-ins or collapses at surrounding surface that may result in hampering construction activities or damage nearby structures. Underlying voids are also created beneath structures intentionally in some construction works as a part of efficient work processes.

In both the above cases, the most effective and popular measure to deal with voids is infilling with an engineering material; fluidized cement mixtures have been widely used due to easiness of placing; we may just pump it out to allow gravitational flow in voids [1], [2], [3]. However, the mixtures spread mainly downwards in voids; they may spread to unintentional directions or spill out to adjoining before infilling up in target areas.

Then another engineering material, plastic grout, may contribute to improve work efficiency and infilling quality in place of fluidized cement mixtures. Due to its characteristics in fresh state, plastic grout spreads in voids with infilling pressure, and stay in place when infilling is stopped even though gravitational force may work. Taking advantage of these characteristics, plastic grout have been already applied to some practices [4], [5], [6].

In case of practical application of plastic grout for void filling, execution details such as positioning of supply pipes, volumes from each supply pipe, order of infilling etc. have to be planned to complete the work effectively and efficiently. It is important that plastic grout behavior during infilling process should be well estimated in advance and reflected to the execution plans. For this purpose, numerical simulation based on fluid mechanics may be one of effective tools for this purpose and the author already conducted some applicability studies by dealing experimental results as verification data [7]. In mean time, it is clear that simple methods to estimate reaches of plastic grout under certain conditions can also be helpful for parametrical studies in practice.

The present study aims to clarify engineering properties of plastic grout and to contribute to better achievement for infilling works. In this paper, a focus is put to basic infilling behavior of plastic grout in a simplified model considering changes of void heights. Firstly, two engineering materials, namely fluidized cement mixture and plastic grout, are reviewed. Secondly, four infilling model tests using plastic grout are explained. Finally, the tests results are shown and discussed to propose a simple estimation method to predict reaches of the plastic grout observed in the simplified model tests.

EINGINEERING MATERIALS FOR VOILDS FILLING

Fluidized cement mixture

A fluidized soil-cement mixture normally consists of surplus soils, water and cement with which mix

(a) Spread in table flow test (*C.F.* = 200 mm)

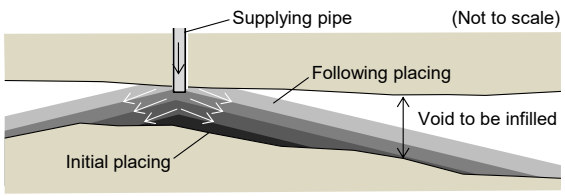

(b) Schematic behavior in sectional view

Fig. 1 Characteristics of fluidized cement mixture.

(a) Spread in table flow test (*C.F.* = 120 mm)

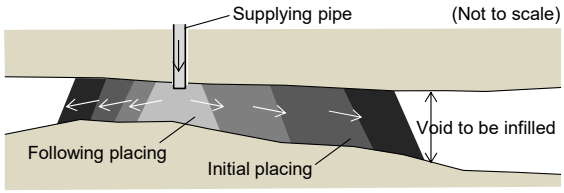

(b) Schematic behavior in sectional view

Fig. 2 Characteristics of plastic grout.

proportion is designed to secure fluidity as well as to prevent material segregation (see Fig.1(a)).

Fluidity is normally confirmed by cylinder flow tests in which i) sample is prepared in casing with the diameter and the height of 80 mm set on a flat plate, ii) then the casing is vertically lifted up to allow sample to spread in circle on the plate, iii) diameters of sample are measured in two directions and iv) a cylinder flow index (*C.F.*) is identified by averaging. Typical range of *C.F.* for fluidized soil cement mixtures are 180~300 mm to secure good flowability.

When it is utilized for void filling, fluidized cement mixture is normally dumped in place, or supplied through supplying pipes. Then, it gravitationally flows to cover wider area of subjected voids as depicted in Fig 1(b). While this contributes better work efficiency, there are some demerits of fluidized cement mixtures under certain construction conditions, as described in the followings:

- Due to gravitational flow, fluidized cement mix flows downwards; it may spread to unintentional directions or spill out to adjoining land before infilling up in target areas.
- After placing, fluidized cement mix gets solidified in conical shape with flow angle. It is usually 3~10%, which creates unfilled space immediately below void ceiling.

Plastic grout

A typical plastic grout consists of cement, water and plastic agents, such as a sodium silicate or clay minerals. Such grouts have recently been used in construction works as an effective method for infilling in place of fluidized cement mixtures. As shown in Fig. 2(a), typical *C.F.* of plastic grout is 80–120 mm in contrast with 180 mm or more for conventional flowable mixtures. As illustrated in Fig. 2(b), the plastic grout is pushed forward by the following mass when injected into voids, which is different from flow behaviors seen with conventional gravitational placement. As a result, the voids can be filled to full height with a lower probability of leaving major voids.

Plastic grout is first prepared in separate solutions, namely cement solution and plastic solution. These are pumped separately from batching plant to infilling work places, then mixed together in line type mixers immediately before infilling. This procedure enables delivery of the solutions by pipes over a long-distance and suggests us a major advantage in comparison with fluidized cement mixtures.

During maturing period after infilling, plastic grout hardens with the help of cement hydration to reach an unconfined compressive strength of approximately 1 MN/m^2 or more according to mix design.

Void filling behavior of plastic grout

While the above merit of plastic grout during infilling work, the author points out a particular infilling behavior to which a certain attention needs to be paid during practical application. As depicted in Fig.2 (b), plastic grout tends to extent infilling areas where void height is relatively large. This highlights

an importance of proper execution plans for infilling works which requires a number of supply pipes to cover infilling areas. It is inferred that improper plane arrangement of supply pipes and wrong order of placing work may leave some areas not to be infilled. This leads us to recognize importance of knowledge about actual behavior of plastic grout subjected to infilling works.

METHODOLOGY OF INFILLING TEST

Outline

The aim of the present model testing is to clarify basic behaviors of plastic grout when implemented for simplified model voids with changing height. The results are also referred to for verification of a simple calculation method to predict the reaches of plastic grout in the simplified model voids.

Considering simplicity of testing conditions and easiness of preparation, model voids were prepared in commercially available U shape drain concreates as shown in Fig.3 and 4. 13 drain concretes were connected in line to create a space with 7,800 mm in length, 300 mm in width and 300 mm in height. Infilling was conducted from center of the model, and allowed plastic grout to spread in both right and left side along the length.

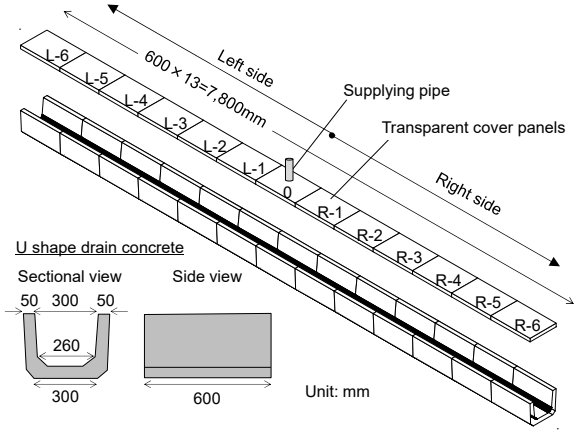

Fig. 3 Model void fabricated using 13 U shape drain concretes.

Fig. 4 Model void preparation

Testing conditions and procedure

Four model voids, as illustrated in Fig. 5, were prepared. Case 1 has a uniform height, Case 2 and 4 have shrinking heights and Case 3 has an enlarging height, respectively. By laying the 10~25 mm size gravel on the bottom of U shape drain concretes, the heights of the void were changed from 150 to 250 mm. While the first case was to observe balanced reaches in both the sides, the other cases let grout reaches more in the right or left side. Accordingly, the positions of the infilling pipe was set on the center

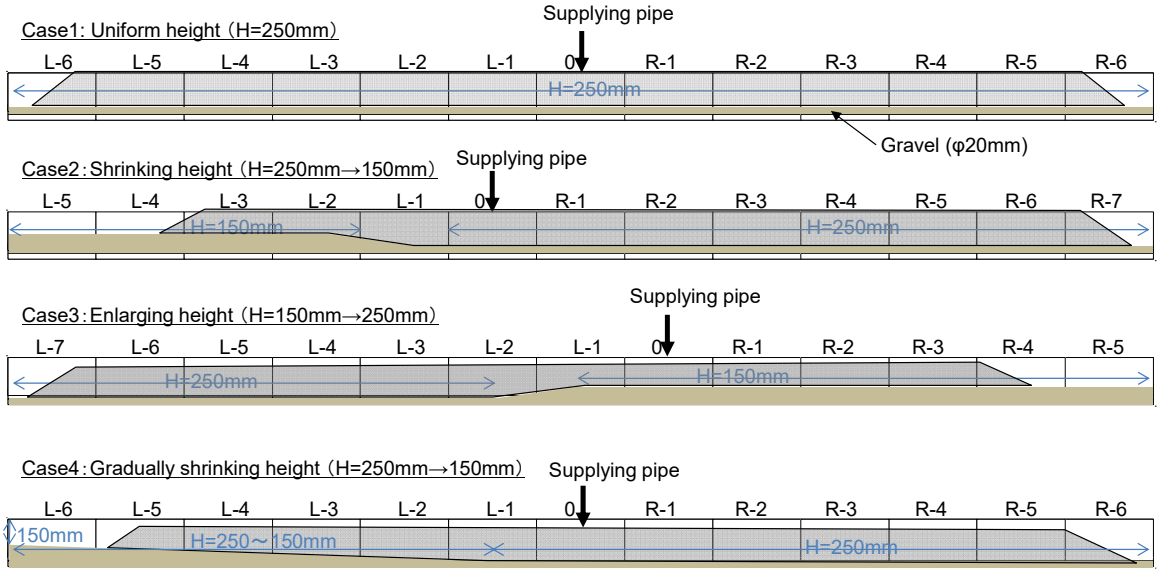

Fig. 5 Sectional view of model voids.

Table 1 Mix proportion of plastic grout used for filling tests (per 1,000L)

Solutions	Materials	Mix description	
A	Cement	320kg	390L
	Solution B	60L	
	Retarder	2L	
	Water	226L	
B	Bentonite	47kg	590L
	Water	571kg	
C	Sodium silicate	20L	

Measured properties:
C.F. = 130-145mm
Vane shear resistance = approximately 200N/m^2
(measured by miniature vane shear apparatus)

unit or neighboring ones according to each condition.

Table 1 shows the mix proportion of plastic grout used for the tests. Among various mix proportions proposed by researchers and practitioners, the mix proportion in Table 1 has been proposed by the author in which two plastic agents, namely clay and chemical type, are utilized. The author recognizes that the simultaneous use of the plastic agents helps plastic properties in fresh state kept longer, contributing better applicability for large scale infilling works in which significant amount of plastic grout needs to be supplied from one infilling pipe.

While plastic grout is often used for infilling in submerged condition, the present tests were conducted without water to allow us to observe the behavior of plastic grout very clearly and easily. During the infilling with the rate of 120 L/min, the grout reaches were recorded by the following methods.

i) The area where the plastic grout reached were confirmed through the transparent cover panels and were marked directly with 2 minutes interval.
ii) Thermocouples placed on the bottom gravel monitored changes of temperature to confirm the arrival of grout by sensing sudden change of temperature.

Finally in each case, infilling was terminated when the plastic grout reached one end wall.

RESULTS AND DISCUSSION

Test results

Fig. 6 shows the plastic grout observed through the transparent cover panels. The area where the plastic grout closely contacted the transparent cover panels was easily identified and horizontal moves of the area were successfully recorded.

Fig. 7 shows the temperature changes recorded during Case 1. In this case, the atmospheric temperature, approximately 23 degrees Celsius, suddenly decreased to below 20 degrees Celsius which allow us to confirm arrival of plastic grout. Comparing the left and right-side results, the times of temperature change are almost simultaneous at the record points with same distance from the infilling

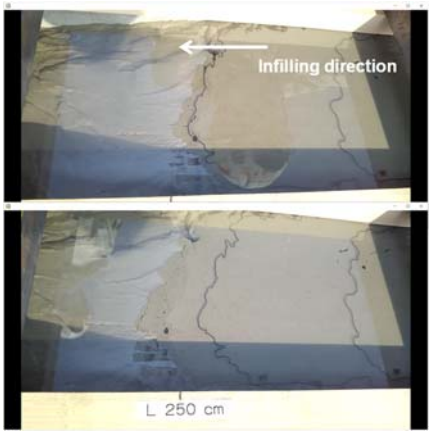

Fig. 6 Observation of grout spread through transparent cover panel (30 seconds gap between the top and bottom photos).

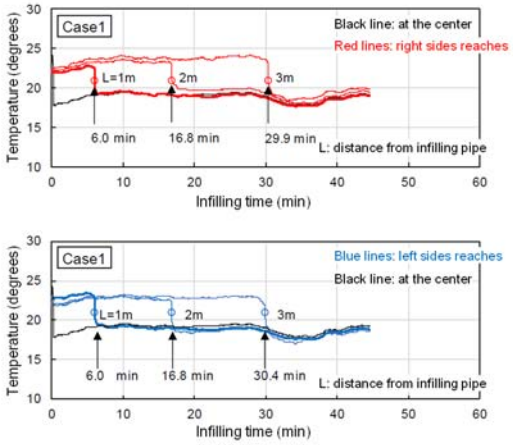

Fig. 7 Temperature changes recorded with thermocouples in Case 1.

Fig. 8 Plastic grout after test (left side of Case 1).

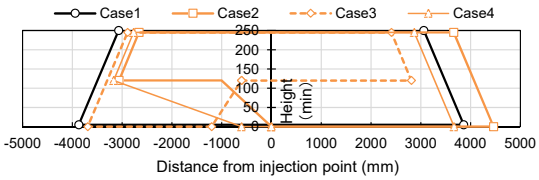

Fig. 9 Shapes of supplied plastic grout after tests.

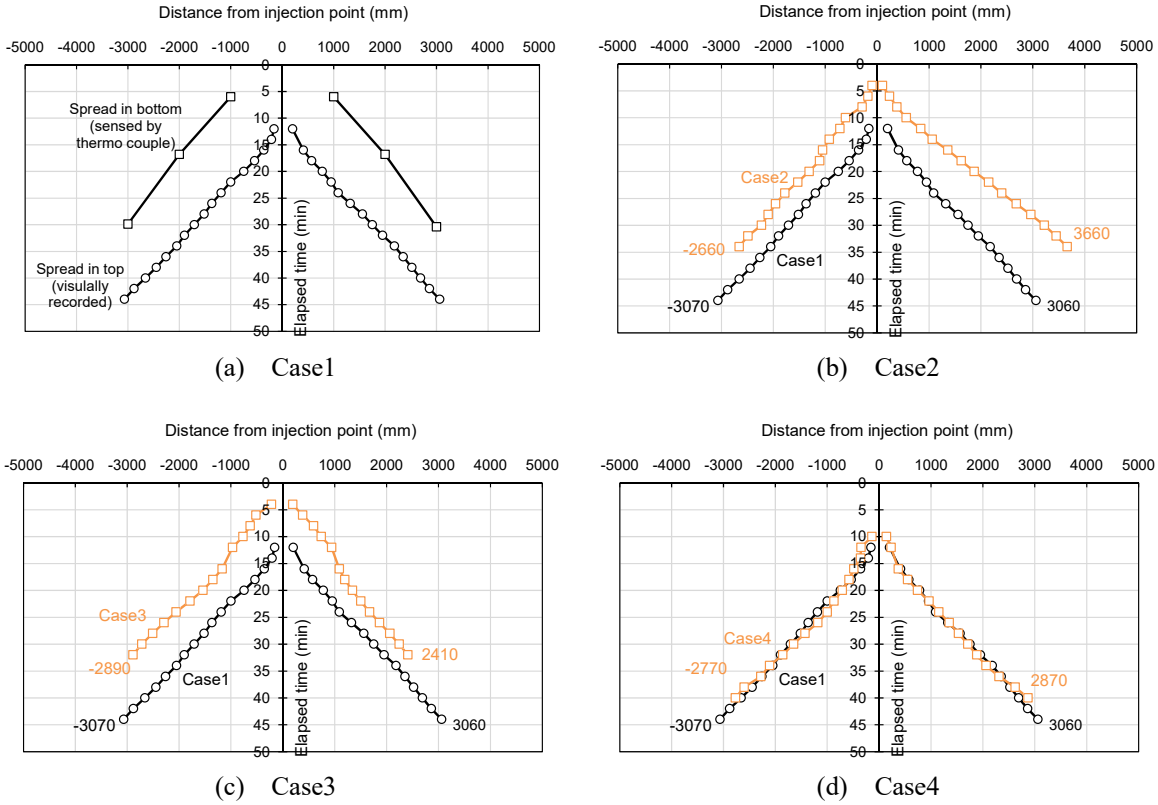

Fig. 10 Observed right/left side spread of plastic grout.

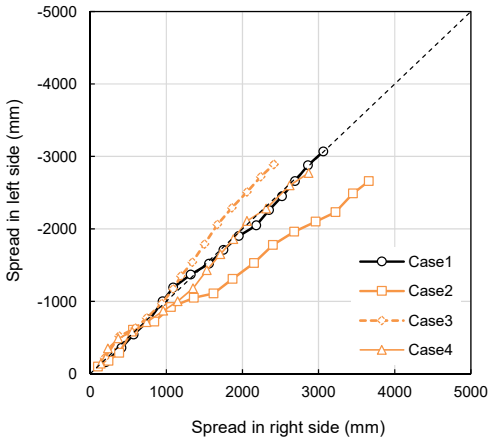

Fig. 11 Relationships between reaches in right and left side obtained from infilling tests.

pipe. This demonstrates that the plastic grout was equally spread in left/right side.

After each test, the transparent cover panels were removed to observe the reaches of the plastic grout as shown in Fig.8, and the observational results were summarized in Fig. 9. While left/right reaches in Case 1 are equal in length from the infilling pipe, the right side reaches in Case 2 ~ 4 are larger or smaller than the left ones.

To examine the filling process in more detail, the elapsed changes of reach which the plastic grout achieved are depicted in Fig. 10. Here, the result from Case 1 were compared in Fig. 10(a) with the estimation based on the temperature change sensed by thermocouples and other results of Cases 2~4 were compared in Fig.10(b)~(d) with those of Case 1. Consequently, relationships between reaches in left and right side were compared in Fig. 11. From these results, it is confirmed that:

- From the comparison between results of Case 1, it is confirmed that the gap of reaches in bottom and top tends to decrease. This infers that tip gradient of the plastic grout got steeper as the infilling proceeds.
- In Case 2 and 3, the infilling of plastic grout proceeded equally in left/right side till 10 minutes in Fig.10 (till approximately 800 mm reach in Fig. 11) and unequally afterwards. This demonstrates that changes of void height clearly affected the advance rate of the plastic grout reaches.
- In Case 4 where the void height gradually changes, the deference between left/right side reaches were not significant.

Simple estimation

Fig. 12 shows a schematic view of the simple calculation model to predict plastic grout reaches in left and right side. The basic principle is to identify the reaches so that each reach generates an equivalent pressure at the infilling pipe. Here, pressure distributions are calculated based on the following

assumption:

a) When a mass of plastic grout advances in void, shear resistance reacts on a surrounding area touching with void surface.
b) The magnitude of shear resistance is identified by shear resistance measured by miniature vane shear apparatus.
c) The amount of pressure generated in a calculation element (*dP*), is calculated as the shear resistance divided by the sectional area of the element.
d) A pressure distribution is calculated by integrating *dP* among the reach of plastic grout.

To estimate the present 4 cases, the differences of void height were referred to in calculations and relationships between left and right reaches were summarized in Fig.13. It is notified that the simple calculation reasonably represents the unbalanced reaches observed in the tests. Even though influence of gravity force should be considered especially in the cases when void foundation is inclined, the present simple model is expected to be utilized in practical works.

CONCLUDING REMARKS

Through the present test results and discussion, the following conclusions are obtained.

- By conducting a series of simplified infilling tests using U shape drains, the influence of changing heights of void on plastic grout reaches was successfully demonstrated.
- The proposed simple calculation model is effective to predict reaches of plastic grout observed in the tests.

The author recognizes that that the present study of the simple calculation is just the first step based on two directional advances of plastic grout. The extension of the model to multi-dimensional behavior is the next step of the research aiming at developing a tool for infilling works in practice.

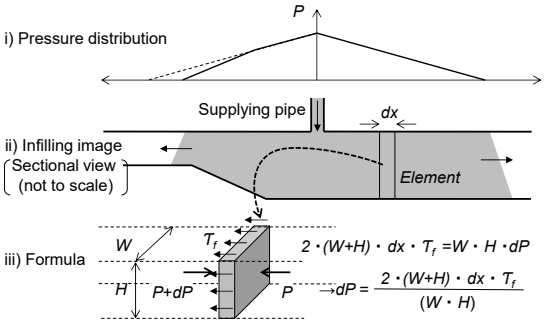

P: pressure
τ_f: friction between grout layer and U shape channel for which vane shear resistance of plastic grout, see Table 1, substituted in this study.

Fig. 12 Schematic model of simple calculation for left/right side reaches.

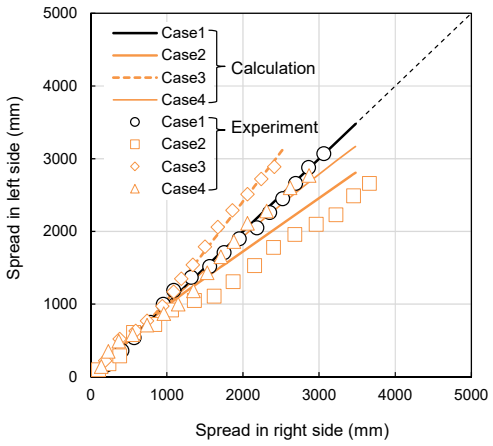

Fig. 13 Relationships between reaches in right and left side obtained from infilling tests and simple estimation.

REFERENCES

[1] Miki, H., Iwabuchi and J., Chida, S., New soil treatment methods in Japan, The 2nd International Symposium Treatment and Recycling of Materials for Transport Infrastructure, C189, 2005,
[2] Carsana M. and Bertolini L., Fluidized soil-cement mixes for backfilling of flooded cavities, Materials and Structures, Volume 45, Issue 1-2, pp.53-65, 2012.
[3] Matsui H., Ishii H., Furukawazono K. and S. Onitsuka, Backfilling of intake and discharge structures using fluidized soil-cement mixture with air foam and fly ash. Geotechnics for Sustainable Infrastructure Development - Geotec Hanoi, pp.759-764, 2016.
[4] Sakamoto A, Yamada N, Sugiura K and Hamada M, An integrated cavity filling technique for abandoned underground room and pillar lignite mines and underground quarries, Post-Mining, pp.16-17, 2005.
[5] Ishii, H., Kimura, M. and Koyama, F., Construction of immersed tunnel foundation using plastic grout, Proceedings of 15th Asian Regional Conference on Soil Mechanics and Foundation Engineering, 2011.
[6] Ishii H., Hanyuu T. and Kitazume M., Execution and applicability study of boulder mound improvement by injecting plastic grout, Japanese Geotechnical Journal, Vol.11, No.4, pp.327-339, 2016 (in Japanese).
[7] Ishii H., Kitazume,M., Full-scale modeling tests and numerical simulation of infilling behavior of plastic grout, Japanese Geotechnical Society Special Publication, Volume 2, Issue 63, pp.2133-2137, 2016.

9th Int. Conf. on Geotechnique, Construction Materials and Environment, Tokyo, Japan, 20-22 November 2019, ISBN: 978-4-909106025 C3051

PERFORMANCE OF CONCRETE MIXED WITH FLY ASH AND PLASTIC WHEN EXPOSED TO FIRE

Joenel Galupino[1], Mary Ann Adajar[1], Erica Elice Uy[1], Nicole Clarice Koa[1], Angel Lisette Lao[1], Rachelle Nicole Lao[1], and Jiro Charles Mikail Tan[1]
[1]Civil Engineering Department, De La Salle University, Manila, Philippines

ABSTRACT

Due to the negative environmental impacts of concrete production, several studies have explored other concrete materials, specifically plastic aggregates and fly ash. However, previous studies have focused on evaluating the alternative concrete for its strength properties and none for its performance during extreme events, such as a fire. Thus, this study sought to further validate the feasibility of alternative concrete by investigating its strength properties in conjunction with its post-fire performance. The concrete specimens were made by replacing sand with HDPE pellets by volume of fine aggregates, and cement with class F fly ash by weight of the binder. The parameters investigated were compressive strength (fc'), post-fire relative residual strength (RRS) and fire resistance rating (FRR). The compressive strength tests were done on cylindrical specimens at varying curing periods (7, 14, 28, and 120 days), while fire performance tests were done on specimens cured for 28 days. The specimens were fired on one surface in a small-scale furnace. The fired cubes were then tested for compressive strength to obtain the RRS. The results show that to have comparable or increased strength than conventional concrete. Using the optimization model, response surface method, the optimum mix was garnered. This study is a stepping stone towards acceptance of the alternative concrete in the Philippines.

Keywords: Plastic, Fly Ash, Fire, Post-Fire Performance, Philippines

INTRODUCTION

The Philippines is considered one of the developing countries and, currently, one of its priorities is to develop its infrastructure, thus, it is noticeable that more projects are being constructed. More construction project entails more concrete is being used. Concrete is among the widely used structural materials due to its versatile properties, however, it has a negative environmental impact due to the production of some of its components, such as cement. Cement production is energy-intensive and emission-intensive because of the amount of heat needed during manufacturing. Moreover, the production of a ton of cement requires 4.7 million BTU of energy or 400 pounds of coal, which has an effect on the environment [1].

Many studies have been conducted locally in the use of waste materials as a substitute for some of the construction materials [2-8], such as fly ash. An option towards more sustainable concrete production is replacing energy-intensive cement with supplementary cementitious materials (SCM) that are industrial by-products. Apart from economic and environmental benefits, SCMs enhance the strength and durability of concrete [9-11]. Being comprised of cement and aggregate, both of which containing inert materials, concrete is virtually non-combustible [12]. However, despite such attributes, concrete exposed to elevated temperatures still undergoes significant changes in its mechanical properties. Also, the inclusion of fly ash in the concrete mix can improve the performance of concrete at elevated temperatures or its fire performance [13].

Aside from fly ash, another way to make concrete more sustainable is by substituting natural aggregates with less energy-intensive and sustainable materials, such as plastic. Currently, a growing number of researches have examined the feasibility of using waste plastic in concrete. Different plastic types have been investigated for their feasibility as aggregate, fibre, or filler for concrete, including polyethylene terephthalate (PET), polyvinyl chloride (PVC), high density polyethylene (HDPE), low density polyethylene (LDPE), expanded polystyrene (EPS), glass-reinforced plastic (GRP), polycarbonate (PC), and polypropylene (PP) [14]. In this study, the focus is on using HDPE as fine aggregates. This is due to the limited number of studies on that type as compared to PET and EPS, as well as the vast usage of HDPE in the Philippines.

In light of these two approaches towards sustainable concrete material, the researchers recognized that there is a gap in the current studies. Most published literature on the use of HDPE as fine aggregates has dealt with testing the mechanical properties only. Little has been done to assess other properties.

Based on the 2015 Annual Accomplishment Report of the Bureau of Fire Protection, fire incidents

in the country increased from 15,879 to 17,138, where 8,501 were related to structural fires. Estimated property damage of 3.62 billion was reported in the same year. Additionally, in 2012, the annual worldwide economic and human costs of fire-related casualties were estimated to amount to billions of dollars due to damaged property. Though no recent fire has been classified as a disaster, fire makes structures dangerous to public welfare due to hazards posed by structural failure, which is caused by the weakening of its materials. This has led to numerous efforts such as emergency responses and disaster risk reduction, but these may still not be enough to reduce the unpredictable effects of fire. As such, the disastrous impact of fire on livelihood and properties poses the need to investigate the fire resistance of concrete as the structural material.

As one of the primary objectives, the study evaluated the fire-resistance rating of alternative concrete. With the intended use as non-load bearing exterior walls, the specimens were not loaded during fire testing and only one face was exposed to fire. To save on material while still enabling comparison with the standards, the fire-resistance rating was determined for an effective wall thickness of 50 mm only, which has a standard fire rating of 30 minutes [15].

The researchers sought to integrate the growing body of knowledge from the two approaches in promoting concrete's sustainability, with the ultimate goal of producing a structural material that maximizes the use of waste materials without compromising its fire resistivity and strength. Since the addition of fly ash has been proven to enhance the fire performance of conventional concrete, it was anticipated that it would improve the fire resistance of the alternative concrete, thus permitting a higher plastic percentage replacement while still having an acceptable fire resistance and strength.

By determining the fire-resistance rating and post-fire residual strength of the concrete, the researchers were able to assess the fire performance of the alternative concrete as compared to conventional concrete. This provided information on the effects of fire on the structural integrity of this alternative material. Since the risk of fire is inevitable in any structure, studying the fire performance of building materials is relevant in the present and the future. The investigation of these properties is valuable in ensuring the safety of occupants in concrete structures and progressing towards sustainable concrete production.

The results lay the groundwork for future studies that aim to improve the performance of the alternative material. These add to existing literature that investigated the feasibility of concrete with HDPE aggregates, and of using fly ash to improve fire performance. It served as a stepping stone towards accepting HDPE concrete as a building material, particularly in the Philippines where fire incidence is high. The goal of reducing plastic waste and the negative impacts of fire on structures was also fulfilled.

METHODOLOGY

The study dealt with the investigation of the strength performance of concrete with fly ash and recycled HDPE plastic aggregates through an experimental method of research. This was done by assessing the effect of varying amounts of substitution of fly ash and HDPE on the compressive strength of the concrete and fire performance.

There were 2 independent variables: the percentage of HDPE substitution and the percentage of fly ash substitution. The percentage of HDPE substitution were 0%, 5%, 10% and 15% by volume of fine aggregates. The level of substitution cannot be increased further due to the adverse effect of HDPE on the compressive strength of concrete.

Second, the percentage of fly ash substitution were 0%, 30%, and 60% by weight of the total binder. From past studies on concrete, fly ash was found to increase the residual strength of concrete at high levels of substitution – ranging from 20% to 60% by weight of the binder.

The main parameters that were investigated in this study were the compressive strength (fc'), post-fire relative residual strength (RRS), and the fire-resistance rating (FRR). Cylindrical specimen with 100 x 200-mm dimension were tested for compressive strength after curing for 7, 14, 21, 28, and 120 days. For the fire performance, 50-mm cube specimens that were cured for 28 days were tested for compressive strength, while a corresponding mix subjected to fire exposure was used to determine RRS and FRR. The results with and without fire exposure were compared to evaluate the relative strength loss. The specifications of the materials used are shown in Table 1.

With 2 independent mix design variables, fly ash and HDPE percent substitution, at 3 and 4 levels, respectively, giving a total of 12 types of mixes.

The preparation of the samples was divided into 3 batches based on the amount of fly ash substitution (0%, 30%, 60%). The concrete specimens were mixed and cast in accordance with ASTM C192 and ASTM C39 in the form of 100 x 200-mm cylindrical specimens and 50-mm cube specimens. After 24 hours of being cast, the specimens were removed from the molds and placed in a water bath at room temperature.

Compressive Strength

The cylindrical specimens were used to assess the compressive strength of the alternative concrete. Before placing in the cylindrical molds, the freshly mixed concrete was tested for the slump in

accordance with ASTM C143 and adjustments were made to achieve a workable concrete mix. The hardened concrete was tested for their compressive strength in accordance with ASTM C39, at different curing days, namely, 7, 14, 21, 28 and 120 days. The 28th-day strength was the basis for assessing the effect of the substitutions on the compressive strength of concrete.

Table 1. Specifications of Materials Used

Gravel	Gravel from Montalban, PH with max. size of 19 mm.
Sand	Natural sand from Pampanga, PH.
HDPE Plastic Pellets	Pellets approx. 3 mm in length and diameter, recycled from various HDPE products like post-consumer plastic.
Cement	Cement Type 1P Portland Cement
Fly Ash	Class F Fly Ash. As per ASTM C618, Class F has pozzolanic properties, less than 5% of CaO and more than 50% of SiO2+Al203+Fe2O3.
Water	Clean tap water.

Fire Resistance Rating

For the standard fire tests, the 50-mm cubes were used. After curing for 28 days, the cube specimens underwent fire testing in a small-scale test furnace, as shown in Fig. 1. The specimens were placed in the furnace starting from ambient temperature and heated through the ASTM E119 time-temperature curve. With a thermocouple attached to the unexposed surface of the specimen, the temperature of the specimen was monitored until the temperature was 139°C greater than the initial temperature, signifying the end of the test. This time in minutes was taken as the fire-resistance rating (FRR) of the specimen. Afterward, the specimen was taken out from the furnace to cool for 24 hours at room temperature before undergoing compression testing.

During the fire resistance test, physical observations were noted during and after the test. This includes hearing any explosive spalling of the samples during the test and investigating the physical appearance of the fired samples, such as the occurrence of cracks and shrinkage.

Optimization

Further analysis was made through the graphs of the strength development, fire-resistance rating, and the individual effect of each substitution on the response variables. With the objective of finding the optimum amount of percent substitutions, the response surface method (RSM) analysis was carried out. A response surface model equation was developed for each response variable.

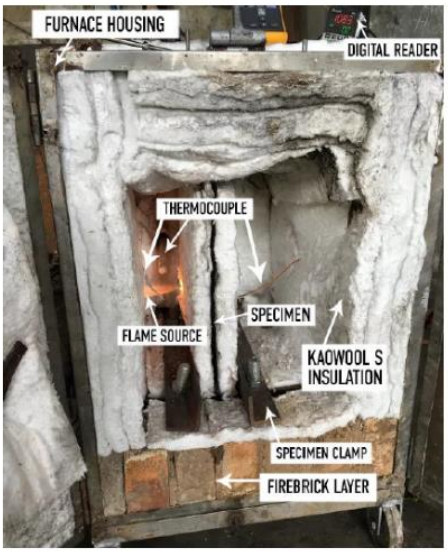

Figure 1. Small-scale furnace for fire testing [16]

RESULTS AND DISCUSSIONS

Compressive Strength Tests

A large portion of the concrete strength developed in the first 14 days of curing, ranging from 12.95% to 54.65% increase from 7th-day strength, the data is shown in Table 2. It was observed that the concrete with higher fly ash content had a higher percentage increase in the strength after 28 days. The addition of fly ash improved long-term strength. The rate of strength increase of Portland cement concrete slows down, the opposite happens to fly ash concrete due to the continued pozzolanic reaction with water in the later ages.

Table 2. Compressive strength of the specimen

MIX	Compressive Strength, MPa				
	7	14	21	28	120
0F-0H	29.65	33.49	34.02	34.20	34.38
0F-5H	15.69	18.41	20.91	28.57	28.63
0F-10H	23.69	34.87	38.52	38.60	38.89
0F-15H	23.76	27.48	31.14	30.89	31.32
30F-0H	20.42	27.91	31.76	33.73	34.34
30F-5H	15.76	21.43	26.79	27.09	28.19
30F-10H	13.54	19.16	21.00	24.92	26.47
30F-15H	14.41	20.68	22.29	22.91	25.40
60F-0H	8.22	12.71	17.17	17.39	19.94
60F-5H	10.48	14.75	17.82	20.50	22.45
60F-10H	8.06	11.77	16.03	17.54	19.79
60F-15H	9.40	14.08	16.96	20.47	21.95

It is possible that the strength of the 30F and 60F samples may still increase significantly beyond 120 days.

Concrete cylinder samples with 60% fly ash show failure in columnar vertical cracking from top to bottom of the concrete, the crack started from the top

cap down to the bottom cap without forming well-defined cones on either end. With concrete samples that fail due to shearing means that the concrete is likely to have a high sand content.

0F, 30F-0H and 30F-5H samples characterized as a failure with side fractures are visible at the top. This failure pattern occurs commonly in samples subjected to compression tests with unbonded caps, which is the case for this study.

It can be observed that as the percentage of fly ash substitution increases, the failure pattern is more severe. For samples with no fly ash substitution, the failure is only caused by the unbonded caps used in the compression test. Hence, there is a strong bond between the aggregates. For samples with 60% fly ash substitution, the failure pattern illustrates a columnar failure, similar to a system of continuous parallel cracks in the direction of compression.

It is clear that replacing cement with fly ash had an adverse effect on the 28th day compressive strength, regardless of the HDPE content. Since the graph displays the 28th-day compressive strength which is considered early strength, this trend is consistent with the study conducted by Johari et. al (2011), where fly ash was found to reduce the early strength of concrete but improves the long term strength.

Relative Residual Strength (RRS) and Fire Resistance Rating (FRR)

The relative residual strength (RRS) represents the remaining strength after fire exposure, relative to equivalent unfired samples. The fire-resistance rating is the time before failure as defined in ASTM E119. It represents how fast the heat can conduct through the concrete. The results are shown in Table 3.

Table 3. Relative residual strength (RRS) and Fire resistance rating (FRR) Results

Mix ID	RRS, %	FRR, min.
0F-0H	77.07	15.75
0F-5H	81.88	6.28
0F-10H	66.12	8.66
0F-15H	86.2	9.49
30F-0H	52.36	12.16
30F-5H	70.83	10.64
30F-10H	82.74	8.38
30F-15H	64.77	10.68
60F-0H	47.22	9.28
60F-5H	70.23	15.06
60F-10H	62.96	15.28
60F-15H	53.59	9.05
Minimum	47.22	6.28
Maximum	86.2	15.75

According to the International Building Code (2012), the standard fire-resistance rating for 50-mm thick concrete specimens is 30 minutes. The FRR that was attained in the test was only half of this value (15.753 minutes). A possible reason for this low value is due to the smaller scale testing equipment that was used. Since the test furnace has already been used several times since its fabrication, the quality of the results could not have been as accurate as its initial testing.

For concrete with 0% HDPE, only charring occurred and surface spalling was negligible.

However, for concrete with 5% and 10% HDPE, there was a small part that melted away. For concrete with 15% HDPE, there was a significant reduction in the size of the concrete and a large part of the cube was burnt.

It can be inferred that the surface spalling of concrete depends on the amount of HDPE. The higher the HDPE content, the more concrete was melted or stripped off. This was probably due to the melting of the plastic pellets that comprise the concrete matrix. Since the furnace temperature was observed to reach 400-600°C at failure, this was sufficient to melt the HDPE

The effect of fly ash on the RRS was quite similar to the effect on fc'. All mixes except for the 10H samples decreased in RRS when fly ash replacement was increased from 0% to 30%. By contrast, the 10H mix had a peak RRS at 30%. Notably, all combinations decreased in RRS at 60% fly ash substitution. Overall, the fly ash negatively affected the concrete except for 10H samples which benefited from 30% fly ash substitution.

For the 0H samples, increased fly ash substitution resulted in a decrease in FRR. It was at its highest when no fly ash was present in the mix. It was the opposite for the 5H and 10H samples, where increased fly ash resulted in a higher fire-resistance rating.

Although the 5H samples attained a greater FRR at 30F, both 5H and 10H samples obtained similar FRR at 60F. For the 15H samples, however, the fly ash content did not significantly affect the FRR.

Overall, the control concrete attained the highest FRR and adding fly ash to the 0H concrete adversely affected the FRR. However, when the concrete was mixed with HDPE at 5% and 10%, the fly ash improved the FRR of the alternative concrete.

In light of both the RRS and FRR, it appears that the 30F-5H and 60F- 5H samples were the best performing alternative mixes in terms of fire performance.

Response Surface Methodology

One of the main objectives of this study was to build a model that would be useful in predicting the compressive strength, given the mix proportion of HDPE and fly ash as well as finding the optimum mix proportions for a given response criterion. Shown in Figure 2-4 are the 3D-surface plots generated for the

compressive strength (fc'), post-fire residual strength (RRS), and fire resistance rating (FRR), as a function of the percent substitution of FA and HDPE.

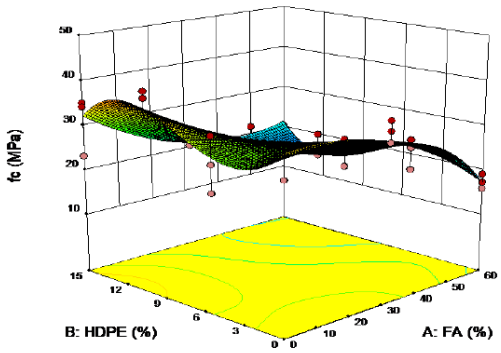

Figure 2. 3D surface plot showing the 28th-day compressive strength as a function of fly ash and HDPE percent substitution

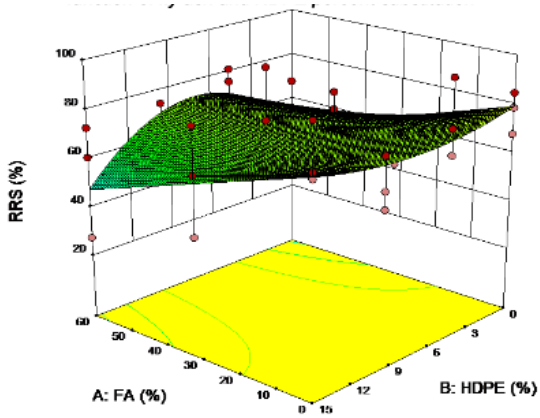

Figure 3. 3D surface plot showing the relative residual strength as a function of fly ash and HDPE percent substitution

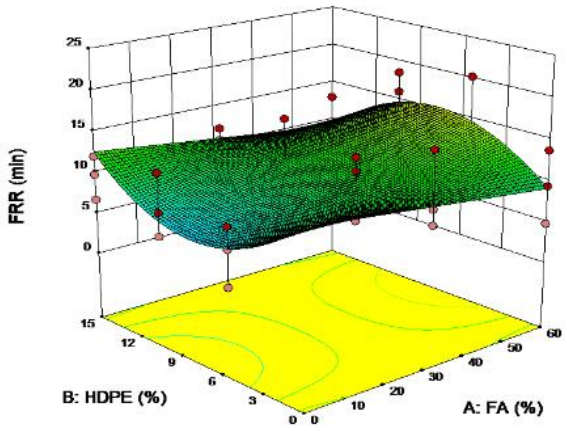

Figure 4. 3D surface plot showing the fire-resistance rating as a function of fly ash and HDPE percent substitution

Different models were investigated, but based on the adjusted r-squared, the quadratic model was found to be the most suitable. The backward elimination analysis was used to increase the precision of the model.

Before proceeding to optimization, the fitted models were examined to ensure that they give sufficient approximation of the results obtained in the experimental conditions.

The fitted models were examined to ensure that they give sufficient approximation of the results obtained in the experimental conditions.

Validation

The actual and predicted values of the responses obtained using the three model equations are graphically presented in Figures 5a-5c, where the predicted values were plotted against the actual values later and a 45-degree line was used as a reference of equality between the two values.

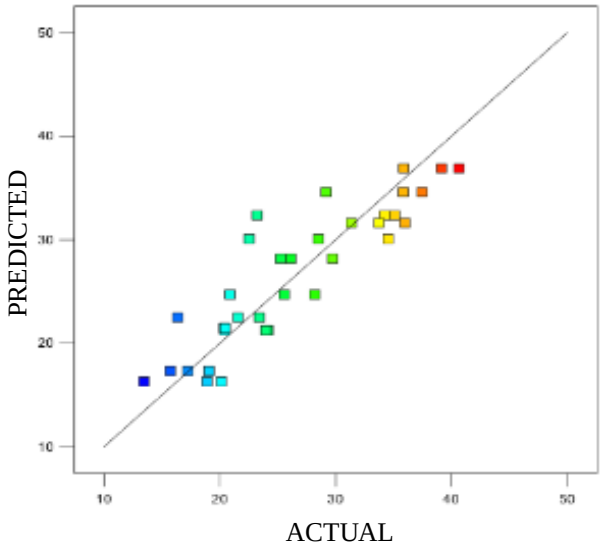

Figure 5a. Predicted vs. actual plots of compressive strength

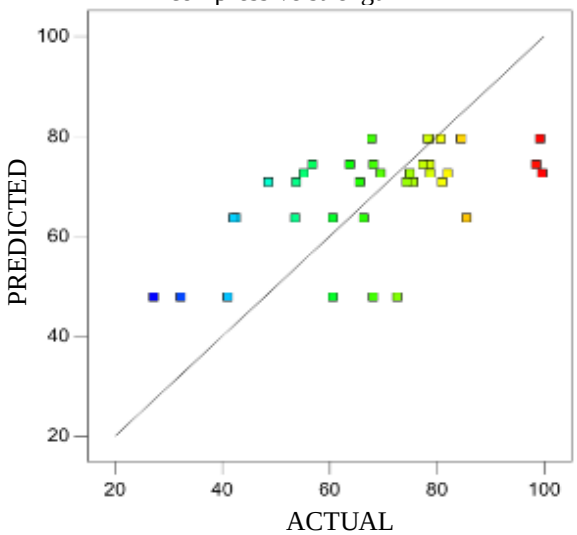

Figure 5b. Predicted vs. actual plots of relative residual strength

It could be noted that due to the large variation in the responses for the RRS and FRR, the predicted values may be far off some of the actual values, which explains the low adjusted R-squared values. In Fig. 5a-5c, this was illustrated by the scattered behavior of the values around the equality line. For the fc', the points lied close to the equality line, which means the model has high accuracy in predicting the fc'.

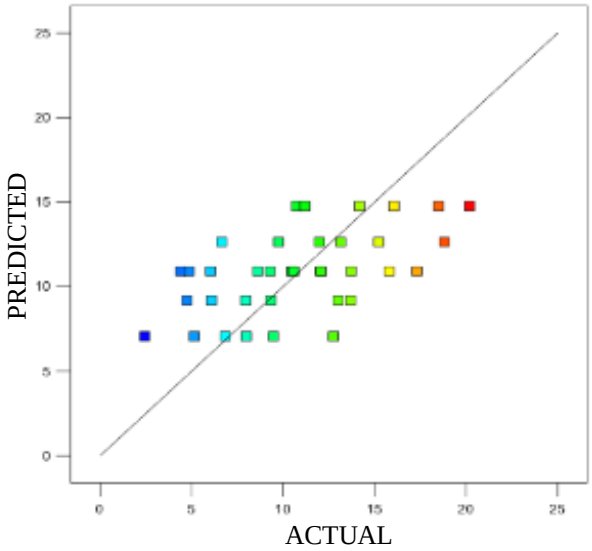

Figure 5c. Predicted vs. actual plots of fire-resistance rating

CONCLUSIONS

The majority of the concrete strength development occurred in the first 14 days of curing, with percentage increases relative to 7 days ranging from 12.95% to 54.65%. After 28 days, concrete with higher fly ash content showed a higher rate of increase due to delayed pozzolanic reaction of fly ash with water. The control concrete exceeded the target compressive strength of 25 MPa with an average strength of 34.20

MPa. Among the alternative concrete mixes, 0F-10H attained the highest strength with 38.60 MPa while 60F-0H attained the lowest strength with 17.39 MPa. HDPE as fine aggregate replacement slightly increased or did not have a significant effect on the strength. This may be attributed to the size of the HDPE pellets which were larger than sand - thus leading to a strength increase in spite of their lower density. By contrast, fly ash as cement replacement decreases the strength, which was consistent with previous studies that observed Class F fly ash to be detrimental to the 28th-day compressive strength.

Cubes with 60% fly ash substitution were observed to be vulnerable to explosive spalling, whereas cubes with higher HDPE content were more vulnerable to surface spalling, as exhibited by a large reduction in size after fire exposure. Replacement of up to 5% HDPE increased the RRS. By contrast, fly ash generally decreased the RRS except for 10H samples which increased at 30% fly ash. At HDPE levels of 5%, 10%, 15%, the peak RRS was at fly ash levels of 60%, 30%, and 0%, respectively. It was surmised that at higher HDPE content, lower fly ash content was more favorable for the RRS. The control concrete attained the highest FRR with 15.75 minutes. Among the alternative concrete mixes, the 60F-5H and 60F-10H performed best with 15.06 minutes and 15.28 minutes, respectively. Similar to the RRS, the effect of fly ash on the FRR varied according to the HDPE content. Generally, the fly ash improved the FRR of 5H and 10H samples, while decreased those of 0H samples and did not affect those of 15H samples.

Using the response surface method, model equations were developed for use in predicting the compressive strength, relative residual strength, and fire resistance rating of concrete at different levels of HDPE and fly ash percent substitution. A quartic model was formed for fc' while cubic models were formed for the RRS and FRR. All models were validated for the assumptions of response surface methodology.

REFERENCES

[1] Rubenstein, M. (2012). Emissions from the Cement Industry. Retrieved June 14, 2017, from Columbia University.

[2] Dungca, J.R., Galupino, J.G. (2016). Modeling of permeability characteristics of the soil-fly ash-bentonite cut-off wall using response surface method. International Journal of GEOMATE, 10 (4), pp. 2018-2024.

[3] Dungca, J.R., Galupino, J.G. (2017). Artificial neural network permeability modeling of soil blended with fly ash. International Journal of GEOMATE, 12 (31), pp. 76-83.

[4] Dungca, J., Galupino, J., Sy, C., Chiu, A.S.F. (2018). Linear optimization of soil mixes in the design of vertical cut-off walls. International Journal of GEOMATE, 14 (44), pp. 159-165.

[5] Dungca, J.R., Galupino, J.G., Alday, J.C., Barretto, M.A.F., Bauzon, M.K.G., Tolentino, A.N. (2018). Hydraulic conductivity characteristics of road base materials blended with fly ash and bottom ash. International Journal of GEOMATE, 14 (44), pp. 121-127.

[6] Elevado, K., Galupino, J., & Gallardo, R. (2018). Compressive Strength Modelling of Concrete Mixed with Fly Ash and Waste Ceramics using K-Nearest Neighbor Algorithm. International Journal of Geomate, 15(48), 169-174.

[7] Elevado, K., Galupino, J., & Gallardo, R. (2018). Artificial neural network (ANN) modelling of concrete mixed with waste ceramic tiles and fly ash. International Journal of GEOMATE, 15(51), 154-159.

[8] Galupino, J.G., Dungca, J.R. (2015). Permeability characteristics of soil-fly ash mix. ARPN Journal of Engineering and Applied Sciences, 10 (15), pp. 6440-6447.

[9] Sumer, M. (2012). Compressive strength and sulfate resistance properties of concretes containing Class F and Class C fly ashes. Construction and Building Materials, 531-536.http://blogs.ei.columbia.edu/2012/05/09/emissions-from-the- cementindustry/

[10] Johari, M. M., Brooks, J., Kabir, S., & Rivard, P. (2011). Influence of supplementary cementitious materials on engineering properties of high strength concrete. Construction and Building Materials, 25, 2639-2648. doi: 10.1016/j.conbuildmat.2010.12.013

[11] Gonen, T., & Yazicioglu, S. (2006). The influence of mineral admixtures on the short and long-term performance of concrete. Building and Environment, 42(8), 3080-3085. doi: 10.1016/j.buildenv.2006.10.019

[12] Khoury, G. A. (2000). Effect of fire on concrete and concrete structures. Progress in Structural Engineering and Materials, 2, 429-447.

[13] Nadeem, A., Memon, S., & Lo, T. (2014). The performance of Fly ash and Metakaolin concrete at elevated temperatures. Construction And Building Materials, 62, 67-76. doi: 10.1016/j.conbuildmat.2014.02.073

[14] Saikia, N., & de Brito, J. (2012). Use of plastic waste as aggregate in cement mortar and concrete preparation: A review. Construction and Building Materials, 385-401.

[15] International Code Council. (2012). International Building Code. Retrieved July 24, 2017, from International Code Council: https://ia800807.us.archive.org/19/items/gov.law.icc.ibc.2012/icc.ibc.2012.pdf

[16] Relucio Jr., A., Lim, M. J., Palaypayon, P. A., Ngo, T. C., & Kalaw, E. E. (2016, August). Design and Fabrication of a Test Set-up for the Fire Testing of Structural Materials. Manila, Philippines.

9th Int. Conf. on Geotechnique, Construction Materials and Environment, Tokyo, Japan, 20-22 November 2019, ISBN: 978-4-909106025 C3051

EFFECTS OF ANTI-CRACKING AGENT TO ASPHALT COMPOSITE USING CONTINUOUS CONSTRUCTION METHOD

Aisha Marie Castillo[1], Joshua Mendoza[1], Franchette Coleen Presto[1], John Paul Villa[1] and Albert Griño Jr[2]
[1]Graduate Student, Adamson University, Philippines; [2]Faculty, Adamson University, Philippines

ABSTRACT

Reflective cracks is one of the most common types of distress failure in the cement treated base(CTB) in pavement. These cracks can be seen as a reflection from the base to the surface layer which can affect the performance and durability of hot-mix asphalt pavement. The base layer can be treated with lime, however, this process is not effective to eliminate the reflective cracks. This paper presents the effects of gypsum, potassium sulfate and silicate mineral powder as anti-cracking agent in asphalt composite used in continuous construction method. The anti-cracking agent was composed of 65% silicate mineral powder, 20% gypsum, and 15% potassium sulfate. The cement mixture was mixed with varying weight fractions (0%, 3%, 6%, 9%) of the anti-cracking agent. The initial, final setting time and compressive strength of the asphalt composite with anti-cracking agent (0%, 3%, 6%, 9%) were determined in accordance to American Standard for Testing and Materials (ASTM). The Vicat needle test result showed that the anti-cracking agent increased the final setting time up to 29.17% when the weight fraction of the anti-cracking agent was 3%. On the other hand, the compressive strength test showed increase in the strength by 21.27% for the 6% mixture in comparison to that of the control. The optimum percentage of anti-cracking agent is 6% since it gained the maximum compressive strength which implied a higher quality of cement treated base.

Keywords: Anti-Cracking, Asphalt Pavement, Gypsum, Continuous Construction Method, Silicate Mineral Powder

INTRODUCTION

Asphalt concrete pavements are not simply a thin covering of asphalt concrete over soil— they are engineered structures composed of several different layers. Because asphalt concrete is much more flexible than Portland cement concrete, asphalt concrete pavements are sometimes called flexible pavements [1]. Reflective cracking of asphalt concrete (AC) overlays is one of the most extensive pavement distress and damage mechanisms in composite pavement structures [2].

Reflective cracking is one of the most common failure modes of roads and is mainly caused by traffic loading and thermal variations [3]. Reflective cracks allow water to penetrate the surface and migrate into the aggregate base and subgrade, weakening those layers. Reflective cracks are more than an aesthetic concern; they eventually weaken the overall pavement structure and reduce ride quality [4]. These kinds of cracks are difficult to prevent, thick overlays or reconstruction is the usual solution.

Several approaches have been made to properly address the problem of reflective cracks in pavement with cement-treated base. One of these is by using or adding an anti-cracking agent. This study used gypsum, potassium sulfate and silicate mineral powder as an anti-cracking agent in asphalt mixture.

Another approach used in this study was the implementation of new construction method, Continuous Construction Method (CCM). This new method differs from the traditional construction method mainly in the construction process. Traditionally, the Cement Treated Base (CTB) need to be cured for 3 to 7 days after paving to secure strength, this procedure was canceled in CCM and the asphalt mixture was paved immediately after the construction of CTB. This study is significant to the construction industry since the addition of anti-cracking agent can be used to improve the quality of the pavement and to increase the structural capacity of the road.

BACKGROUND OF THE STUDY

Last 2009, an anti-split agent for materials such as lime and coal ash was invented by Kaiyan Tan, Junqi Chen, Zhiyuan Chen, Yongjun Song, Runxi Cheng and Wei Zeng [5]. This agent mainly comprises of silicate mineral powder, gypsum or chemical engineering waste residue phosphogypsum and an alkali metal substance containing SO_3, wherein the tri-calcium silicate content of the silicate mineral

powder is more than 55%. Usually, these limes and coal ash materials' early strength are significantly low making the anti-cracking performance of the material poorer. However, after mixing the said anti-split agent, the researchers have come up with positive results that improved the anti-crack performance of the material and thereby lowering the construction cost and obtaining good economic benefits.

Five years later, Jia Li, Jianmin Zi, Lei Mao and Tao Hu developed a low-cost anti-cracking agent by using the chemical waste phosphogypsum. According to their research, the principle is to stimulate pozzolanic reaction to occur between the phosphorus gypsum (calcium sulfate dihydrate) and lime by using alkaline binder lime. Shrinkage caused by the temperature and humidity change reduced significantly because of the certain amount of expansion and densification generated by the substances in the pozzolanic reaction, Aft ($3CaO•Al_2O_3•3CaSO_4•32H_2O$) and AFm ($3CaO•Al_2O_3•CaSO_4•32H_2O$). Having said that, the researchers achieved the purpose of reducing road base cracking, therefore, prolonging roadway service life.

The aforementioned studies were the basis in reinventing an anti-cracking agent, which comprises of 65% silicate mineral powder, 20% gypsum and 15% potassium sulfate.

METHODOLOGY

Research Design

This experimental study tackled the effects of using anti-cracking agent and continuous construction method in asphalt composite with cement-treated base to minimize reflective cracks.

The experimental factor in this study was the anti-cracking agent, comprised of 65% silicate mineral powder or talc powder, 20% gypsum and 15% potassium sulfate. The criterion for the effectiveness of anti-cracking agent and continuous construction method in asphalt composite with cement-treated base are as follows: setting time test and compressive strength test.

The researchers produced four batches each for setting time test and compressive strength test. Batch 1-4 contained 0%, 3%, 6% and 9% respectively. Each batch for setting time test and compressive strength test comprised of three trials per anti-cracking addition. The asphalt composites were tested on the 7th, 14th and 28th day after the construction.

Research Procedure

Preparation of anti-cracking agent

The anti-cracking agent used in this study was composed of 65% silicate mineral powder or talc powder, 20% gypsum and 15% potassium sulfate. The locally available form of gypsum was Plaster of Paris which had 75% of its water evaporated. Thus, gypsum was reproduced by adding 75% of water in Plaster of Paris. The chemicals were mixed evenly in a container using a stirring rod.

Preparation of cement-treated base

The mix proportion used for mechanical property Test was 4 parts Type 1 Portland cement, 16 parts Class F fly ash and 80 parts gravel. Batch formulation for 12 trials were composed of 4 kg of cement, 6 kg of fly ash and 91 kg of gravel. The gradations of gravel used were G1, ¾ and ¼ with a proportion of 30:25:45.

Preparation of CCM Constructed Asphalt Composite

Hot-mix asphalt mixture comprised of 79% sand, 19% 3⁄8 gravel, 2% hydrated lime and 5.7% asphalt cement with a compressive strength of 200 psi. The asphalt composite was consisted of hot-mix asphalt mixture, tack coat and cement-treated base. The following series of steps were used for CCM constructed asphalt composite: (1) A 20 cm cement-treated base was placed in a cylindrical mold, (2)The layer was consolidated by rodding 25 times around the layer, (3) The sides of the mold were tapped 10-15 times with the mallet after each layer in order to close any insertion holes formed by the rod, (4) The tack coat was then applied after compaction, and (5) Before the initial setting time of the base, the 6.5cm hot mix-asphalt mixture was paved and compacted immediately. Compaction for asphalt concrete was also 25 blows using hammer.

Setting time test

The setting time test was conducted in accordance with the ASTM C191-08 "Standard Test Methods for Time of Setting of Hydraulic Cement by Vicat Needle" [6]. A vicat apparatus was used to test the setting time of the samples with varying amount of anti-cracking agent. The role in set-retarding and water-reducing of the anti-cracking agent in cement are tested by following these procedures: (1) 300g of cement was mixed with 30% of water and varying amount of anti-cracking agent, (2) The mold was filled with cement paste. The top of the specimen if necessary was smoothed with one or two light touches of the pointed end of the trowel. The specimen remained in the conical mold supported by

the glass plate throughout the test period, (3) The specimen was set in the moist cabinet for 30 minutes after molding without being disturbed (4) The penetration of the 1mm needle at this time and every 15 minutes thereafter was determined until a penetration of 25mm or less was obtained (5) The needle of the rod was lowered until it rest on the surface of the cement paste for the penetration test. The setscrew was tightened and the initial reading was obtained (6) The rod was released quickly by loosening the setscrew and allowed the needle to settle for 30 seconds. No penetration test shall be made closer than 6.4mm form any previous penetration and no penetration test shall be made closer than 9.5mm from the inside of the mold.

Compressive strength test

It was performed on the 7th, 14th and 28th day after construction of asphalt composite. The following series of steps were used for compressive test: (1) The hot-mix asphalt was separated from the cement treated base by means of cutting (2) Cement treated base was weighed and measured before it was then placed on the Universal Testing Machine (3) The load was applied until the specimen fails, and recorded the maximum load carried out by the specimen during the test. The compressive strength can be calculated using Eq.1.

$$\sigma = \frac{P}{A} \quad (1)$$

where:
σ = compressive strength, psi (kPa)
F = maximum load carried by the batch, lbf (kN)
A = cross-sectional area of the batch, in^2 (m^2)

RESULTS AND DISCUSSION

Setting Time Test Results

Table 1 Setting Time Results

Anticracking Content(%)	Initial Setting Time(mins)	Final Setting Time(mins)
0	165	240
3	241	310
6	180	265
9	177	255

As seen in Table 1 the result of setting time test obtained for all of the samples with varying amount of anticracking agent. Relative to the control, all of the samples were higher for both initial and final setting time. This only indicates that the anticracking agent can extend the setting time of the cement in the concrete mix. The highest initial and final setting time were obtained at 3% with a value of 241 minutes and 310 minutes, respectively. At 3% in comparison to the control there is a substantial increase of 46.06% for the initial and 29.17% for the final setting time.

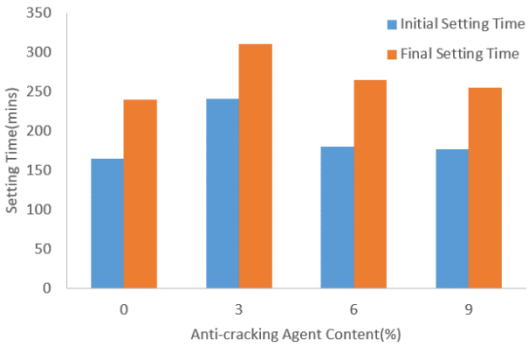

Fig. 1 Setting Time Test Results

The delay in setting time of these batches as seen in Figure 1 was caused by the reaction formed between the anti-cracking agent particularly gypsum and tricalcium aluminate that is already present in cement. Suryakanta [7] affirms this study in which gypsum reacts with tricalcium aluminate quickly to generate calcium sulfoaluminate hydrate which deposits and forms a protection film on the cement particles to hinder the hydration of tricalcium aluminate and delay the setting time of cement. Prolonged setting time of cement implies that the longer it is for the cement to set, the longer the time for the continuous construction to be executed.

Although, the results showed inconsistent increment as the anti-cracking mixture addition increases. From zero to three percent, the initial and final setting time increased but partially decreased from three to nine percent. This, on the other hand, was particularly caused by the potassium sulfate and talc powder in the anti-cracking agent. Hewlett [8] proved this result in his study that determined the effect of potassium sulfate in the setting time of cement paste. The results in his study showed that adding 0.88% of potassium sulfate would give 66.67% and 32.56 % decrease in the initial and final setting time respectively while adding 1.48% potassium sulfate would lead to 91.67% and 90.70% decrease in the initial and final setting time respectively.

Moreover, Woo and Ryu [9] examined the potential use of talc as a substitute for cement and found out that the setting time for all the specimens were shortened compared to the one without talc powder. This implies that talc and potassium sulfate

could increase the setting time of cement thereby making it difficult for the continuous construction method to be performed.

The batch that showed the most significant result based from the setting time test was the cement with 3% anti-cracking agent addition. Among all the batches with agent addition, this batch gained the highest increase in setting time compared to the control that has 0% addition.

Compressive Strength Test Results

Table 2 Compressive Strength Test Results

AC Content (%)	Compressive Strength (MPa)		
	7th day	14th day	28th day
0	4.594	5.025	7.084
3	4.722	5.188	8.357
6	4.875	5.277	8.591
9	4.707	5.217	8.334

As seen in Table 2 the result of the compressive strength test obtained for all of the samples with varying amount of anticracking agent. It was found out that all the batches with varying amount of anti-cracking agent implied a significant increment relative to the control batch. Higher strength results implied higher quality of cement treated base.

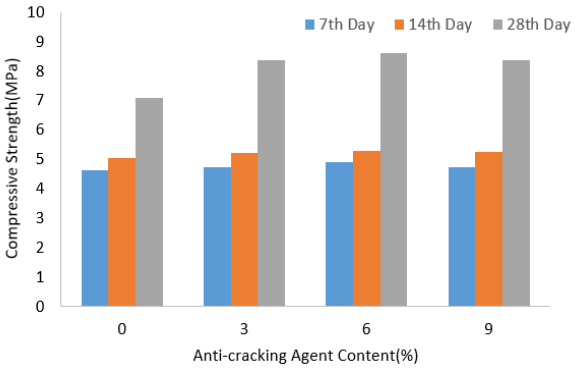

Fig. 2 Compressive Strength Test Results

Also, the test results have shown that an increase in compressive strength by 21.27% for the 6% mixture relative to the control as shown in Figure 2. It can be noted that 6% anticracking addition gained obtained the highest increment with 4.875 MPa, 5.277 MPa and 8.591 MPa on its 7th, 14th and 28th day.

According to Lim and Zollinger [10], most specifications require the minimum design strength of CTB in the range of 350 to 500 psi (2.4 to 3.4 MPa). On the other hand, Portland Cement Association [11] stated that typical cement contents that range from 3 to 10 percent will have a resulting 7-day compressive strength of 300 to 800 psi. But, since the researchers adopted the design mix used in the study of Li, Zi, Mao and Hu [12], the resulting compressive strength of their control was set as the standard which is 650 psi (4.48 MPa) on the 7th day.

A study was conducted by Halaweh [13] on the effect of potassium sulfate in the compressive strength of different cements and concluded that specimen with 5% potassium has a slightly higher strength compared to the control from 0-60 days. But beyond 60 days, it appeared that the sulfate content of 3.6% generated the highest strength.

Meanwhile, Sabouang, Mbey, Liboum, Thomas and Njopwouo [14] made a study about the effect of talc powder as a potential raw material for the formulation of cementitious materials in the year 2014. The compressive strength test results of their study varied from 3.35 MPa (cement with 0% added talc) to 4.50 MPa (cement with 20% added talc). According to them, the addition of talc powder in cement causes more cement phase formation and thereby leading to strength increment.

In line with this, Woo and Ryu [9] also proved the significant strength improvement of concrete by replacing plain mix with fine grains of talc at the rate of 10%, 20% and 30%.

The implementation of continuous construction method to the batches with anti-cracking agent addition also greatly contributed to its strength increment. Li [12] added phosphogypsum as anti-cracking agent and obtained 0.89% and 5.30% increase on the 7th and 28th day of the CCM constructed pavement respectively. Meanwhile on our results, the maximum increase we have attained are 6.12% on the 7th day, 5.01% increase on the 14th day and 21.27% increase on the 28th day.

However, strength of the mixture gradually decreased from six to nine percent. This was caused by excessive amounts of gypsum and potassium sulfate in the mixture. Studies conducted by Halaweh [13] and Sabouang [14], mentioned above had already clarified certain limitations in the dosages of the chemicals used. In addition to that, Suryakanta [7] also mentioned that if the content of gypsum exceeds the limit of 3-5% of the cement's mass, it would certainly lower the strength of cement and lead to poor dimensional stability.

CONCLUSION

Several approaches has been made to effectively eliminate the cracks in asphalt pavement with cement-treated base, one of these is by adding lime in the base. In line with this, the production of gypsum,

silicate mineral powder and potassium sulfate as an anti-cracking agent in asphalt mixture using continuous construction method has shown great potential in eliminating or minimizing cracks significantly because of the certain properties that these chemicals have. The Vicat needle test result showed that the anti-cracking agent increased the final setting time up to 29.17% when the weight fraction of the anti-cracking agent was 3%. On the other hand, the compressive strength test showed increase in the strength by 21.27% for the 6% mixture in comparison to that of the control. The optimum percentage of anti-cracking agent is 6% since it gained the maximum compressive strength which implied a higher quality of cement treated base. For further studies, the researchers recommend to perform bonding property test between the asphalt mixture and cement treated base in order to further determine the effectiveness of continuous construction method.

ACKNOWLEDGMENTS

The authors would like to acknowledge the financial support given by the Center for Research and Development (CRD) of Adamson University. Also, we would like to recognize the help of Ms. Malou S. Guelos of Socor Construction Corporation for giving us the asphalt supply, and ARDI Development and Construction, Inc. for giving us the access to their site and some of their construction materials.

REFERENCES

[1] NCHRP 9-33. A manual for design of hot mix asphalt with commentary, Report 673, Transportation Research Board, National Research Council, Washington, DC, 2011.

[2] Dave E. V. and Buttlar, W. G., Thermal reflective cracking of asphalt concrete overlays, International Journal of Pavement Engineering, Vol. 11, Issue 6, 2010, pp.477-488.

[3] Gonzalez-Torre, I., Calzada-Perez, M. A., Vega-Zamanillo, A., Castro-Fresno, D., Evaluation of reflective cracking in pavements using a new procedure that combine loads with different frequencies, Construction and Building Materials, Vol. 75, 2015, pp.368-374.

[4] Blackenship, Phil., Reflective Cracking Relief Interlayer for Composite Pavements, Asphalt: Magazine of Asphalt Institute: 17-20. 2007.

[5] Tan, Kaiyan et al. Reinforced anti-split agent for materials such as lime and coal ash. CN101402515 (A), Hubei Gezhouba Testing Co Ltd, 20 July 2011. Google Patents, https://patents.google.com/patent/CN101402515A/en.

[6] ASTM C191-08, Standard Test Methods for Time of Setting of Hydraulic Cement by Vicat Needle, ASTM International, West Conshohocken, PA, 2018.

[7] Suryakanta, 8 Factors Affecting Setting and Hardening of Cement, CivilBlog.Org. N.p., 22 Sept. 2016. 27 Feb. 2017.

[8] Hewlett, P., Lea's chemistry of cement and concrete", Butterworth-Heinemann, 2003.

[9] Woo, J. K. and Ryu, H. G., A Study on Using Possibility of Talc Powder as Concrete Admixture, Journal of the Korea Institute of Building Construction, Vol. 6, Issue 4, 2006, pp. 93-98.

[10] Lim, S., and Zollinger, D. G., Estimation of the Compressive Strength and Modulus of Elasticity of Cement-Treated Aggregate Base Materials, Transportation Research Record, Volume 1837, Issue 1, 2003, pp. 30-38.

[11] Portland Cement Association, Soil-Cement technology for Pavements: Different Products for Different Applications." Retrieved from: http://pca-se.org/wp-content/uploads/2015/06/IS327.pdf, 2005.

[12] Li, J., Yong, Z., Lei, M., Jianmin., Z., Tao, Hu, Laboratory Research on the Application of Phosphogypsum as an Anti-Cracking Agent in a Cement-Treated Base, CICTP 2014.

[13] Halaweh, M., Effect of alkalis and sulfates on Portland cement systems, 2006.

[14] Ngally Sabouang, C. J., Mbey, J. A. Liboum, Thomas, F., Njopwouo, D., Talc as raw material for cementitious products formulation, Journal of Asian Ceramic Societies, Volume 2, Issue 3, 2014, pp 263-267.

9th Int. Conf. on Geotechnique, Construction Materials and Environment, Tokyo, Japan, 20-22 November 2019, ISBN: 978-4-909106025 C3051

RESISTIVITY AGAINST SULFATE ATTACK OF CONCRETE WITH HDPE AS PARTIAL SUBSTITUTE FOR FINE AGGREGATES

Richard De Jesus[1], Grant Yves M. V. Borbon[2], Kenrick F. Go[2], and Rockwell M. G. Jardiniano[2]
[1]Faculty, De La Salle University, Philippines; [2] De La Salle University, Philippines

ABSTRACT

High-Density Polyethylene (HDPE) when used as partial substitute of fine aggregates in concrete is investigated to determine if it addresses sulfate attack in concrete. Since HDPE is known to be resistant against chemical compounds including sodium sulfate, it is hypothesized in this study that sulfate attack problems in concrete will be lessened by incorporating HDPE in concrete mix. Mechanical properties of concrete were determined to ensure that HDPE is limited to an amount where there will be no serious compromise to strength, hence, compressive, and split tensile test are included in the study. To determine the influence of HDPE in addressing sulfate attacks, length change of mortar specimen is investigated using ASTM C1012 (length change of mortar exposed to sulfate solution). Scanning Electron Microscopy (SEM) is also employed to qualitatively assess the microstructure of concrete with HDPE exposed to sulfate attacks. Mechanical test results showed that increasing HDPE did not adversely affect the compressive strength. However, there was a decrease observed in tensile strength. To achieve balance between mechanical properties, HDPE replacement of fine aggregates was set at 10% by weight of fine aggregates. The mortar bar test demonstrated that increasing HDPE resulted to an increased resistivity against sulfate attacks. SEM have also shown reduction in voids and ettringite with increasing HDPE content.

Keywords: HDPE in concrete, Sulfate attack, Mortar bar test, Ettringite, Alternative concrete

INTRODUCTION

Among the causes of deterioration in concrete is sulfate attack [1]. In coastal regions, sulfates from groundwater seeps through the pores in concrete and reacts with cement mix. These sulfate ions react with aluminates in concrete which forms gypsum and ettringite that causes concrete expansion [2]. Concrete exposed to environment with high sulfate compounds are vulnerable to sulfate attacks and so are concrete in contact with soil abundant with sulfate contents. Aggregates may also contain sulfuric compounds that may initiate sulfate attacks if such aggregates are used in the production of concrete. Sulfate attacks is a potential problem in concrete hence, it must be addressed.

Sulfate attack may be caused externally, when sulfate-containing water seeps through concrete, or internally, when sulfate-rich aggregates are used. When sulfate ions react with aluminates in concrete, ettringite and gypsum are formed. These two cause a reaction that involves cracking, expansion, loss of bond between cement paste and aggregates, and/or alteration of paste composition. When cement paste is altered, monosulfate is converted into ettringite then into gypsum [3]. This takes up calcium from CaOH and CSH hence affecting the mechanical properties of concrete [4] & [5]. Consequently, the formation of ettringite causes expansion and cracking in concrete [4].

Other than contributing to helping save the environment by utilizing waste materials such as HDPE, high density polyethylene (HDPE) has been shown to have combative properties against sulfate attacks. ISO 10358 [6] stated that HDPE possesses higher chemical resistance compared to other polymers, particularly against sulfuric acid. Polymer impregnation was also shown to enhance the chemical resistance of concrete [7]. HDPE are plastics made up of polymer molecules linked together. Hence, when used in concrete as partial substitute for aggregates, HDPE can aid in lessening the deterioration brought about by sulfate attacks.

Study of [8] used PET bottles as component of concrete and had shown that the reduction brought by sulfuric acid to crushing load, and weight loss was lessened. Moreover, [9] showed that the use of PET as aggregates in concrete improved acid resistance of concrete. And [10] employed HDPE as coarse aggregates replacement in concrete and showed that with 10% and 20% replacement, compressive strength is comparable to that of normal concrete. Thisstudy investigated the impact of using HDPE in concrete to combat the effects of sulfate attacks in concrete using mortar-bar test (ASTM C1012) reinforced by spectron electron microscopy (SEM). Additionally, it will seek to establish the desirable amount of HDPE as partial replacement of fine aggregates in concrete without compromising the mechanical properties.

MATERIALS AND METHODS

The HDPE used in this study was in pelletized form bought commercially. It was checked with sieve No. 4 to determine its' suitability as a fine aggregate material. It has a specific gravity of 0.80, as provided by the supplier. Coarse and fine aggregates were sourced from a local hardware store. Upon checking experimentally, the specific gravities of fine aggregates and coarse aggregates are 2.34, and 2.81 respectively. Type I Portland cement was utilized in the preparation and making of concrete in this research. Utilization of HDPE as fine aggregates substitute were done in 5% to 20% by weight at 5% interval. For each strength test, three (3) specimens were prepared. Cylinders of size 100mm x 200mm was used for both compression and split tension test. Two sets of strength tests were conducted – the first set involves strength tests for concrete specimens cured in water while the second set involves the same strength tests but for concrete specimens submerged to sulfate solution. The duration of curing in water and in sulfate solution is 28 days.

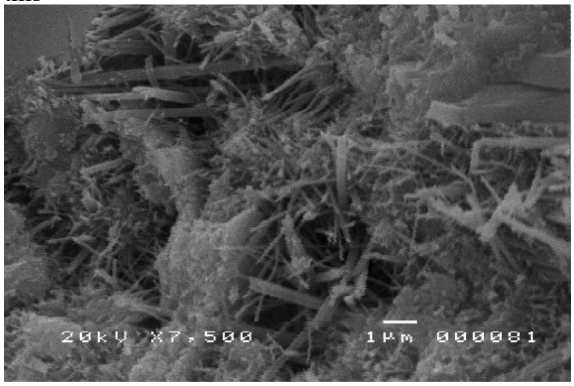

Figure 1. SEM of mortar with 0%HDPE (00HDPE)

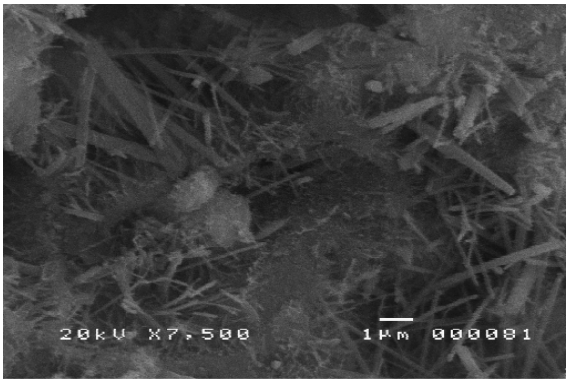

Figure 2. SEM of mortar with 5%HDPE (05HDPE)

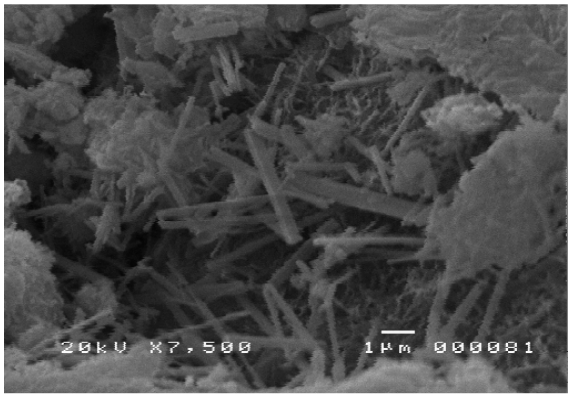

Figure 3. SEM of mortar with 10% HDPE (10HDPE)

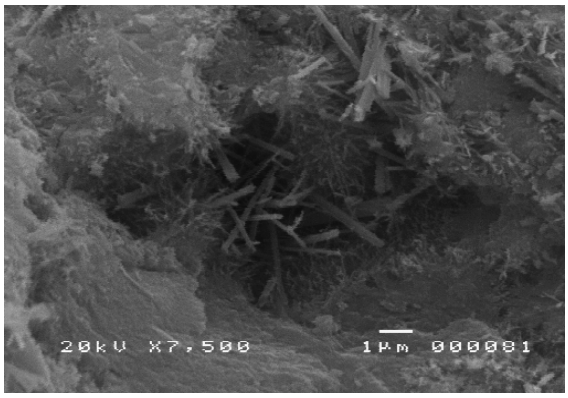

Figure 4. SEM of mortar with 15% HDPE (15HDPE)

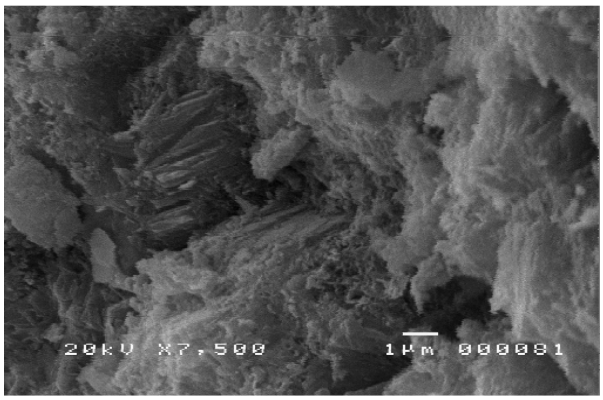

Figure 5. SEM of mortar with 20% HDPE (20HDPE)

Table 1. Concrete design mix (as per ACI 211.1)

Component (kg)	00HDPE	05HDPE	10HDPE	15HDPE	20HDPE
Water	205.00	205.00	205.00	205.00	205.00
Cement	379.63	379.63	379.63	379.63	379.63
Coarse Aggregates	1009.20	1009.20	1009.20	1009.20	1009.20
Fine Aggregates	691.30	656.73	622.17	587.60	553.04
HDPE	0.00	11.80	23.60	35.30	47.20

Table 2. Average compression and split tension strength (in MPa) of samples exposed to sulfate solution

% HDPE	Compression (MPa)		% reduction (pre to post-sulfate)	Tension (MPa)		% reduction (pre to post-sulfate)
	Pre-Sulfate	Post-Sulfate		Pre-Sulfate	Post-Sulfate	
00HDPE	36.43	32.45	11.0%	2.37	2.05	13.5%
05HDPE	39.15	37.80	3.4%	2.31	2.16	6.5%
10HDPE	35.53	34.66	2.4%	2.27	2.21	2.7%
15HDPE	44.48	40.11	9.8%	2.21	2.18	1.3%
20HDPE	42.36	41.07	3.0%	2.17	2.14	1.3%

The mortar bar test involves measurement of length change of mortar specimens in accordance with ASTM C1012 [11]. Three mortar specimens, in rectangular prism of size 25mm x 25mm x 285mm, were prepared in varying HDPE content, from 0% to 20% at 5% interval. One set of all mortar samples were prepared with 3 specimens per mix. Initial length reading was done before curing the specimen to sodium sulfate solution. Measurement of final length change was conducted after 28 days of curing. Concrete mix design was made in accordance with ACI 211.1 and the design mix is shown in Table 1. Mortar mix was designed in accordance with ASTM C305 [12].

DATA AND ANALYSIS

Strength Test Results

The result of strength tests for compression and tension is shown in Table 2. Reduction in strength is observed for concrete exposed to sulfate solution (post-sulfate samples) compared to unexposed ones (pre-sulfate samples). As mentioned earlier, the formation of gypsum during sulfate attacks takes up calcium from CaOH and CSH in hydrated cement paste hence, affecting the strength of concrete. It can be observed from test results that for both compression and tension tests, these drops in strength caused by exposure to sulfate solution decreases as HDPE increases. Post-sulfate samples have demonstrated an increase in strength properties, both in compression and tension, with increasing HDPE.

Length Change Of Mortar Bars

After immersing mortar bars to sulfate solution for 28 days, the final length is measured using a length comparator. The table below shows the average length change per mix. Mortar mix includes a control sample (i.e. 00HDPE) and samples with varying HDPE (from 5 to 20%).

Table 3. Length change of mortar bars

% HDPE	Average length change
00HDPE	0.0209
05HDPE	0.0213
10HDPE	0.0144
15HDPE	0.0103
20HDPE	0.0063

It is apparent from this test that HDPE influenced the resistance of mortar bar specimens against length expansion attributed to sulfate attack. This result supported the hypothesis of the study that HDPE, when mixed into concrete, will provide resistance against sulfate attacks.

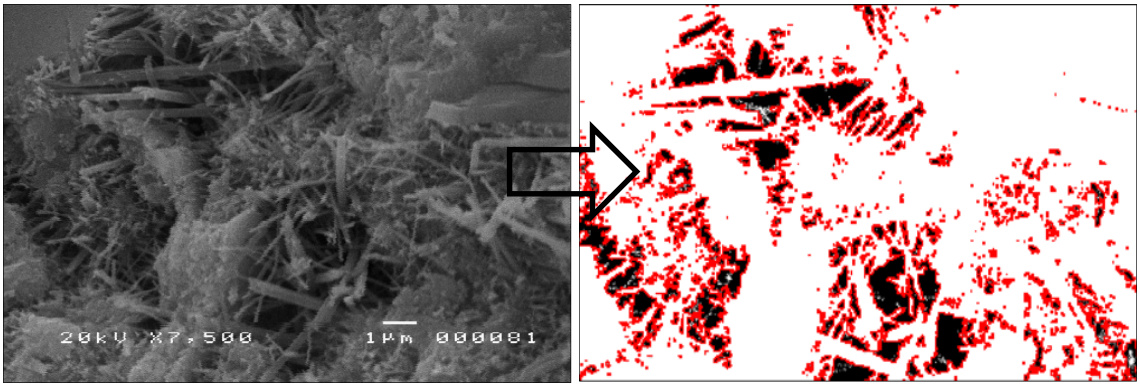

Figure 6. Conversion of SEM micrographs into 'imageJ' image to calculate area of voids (00HDPE)

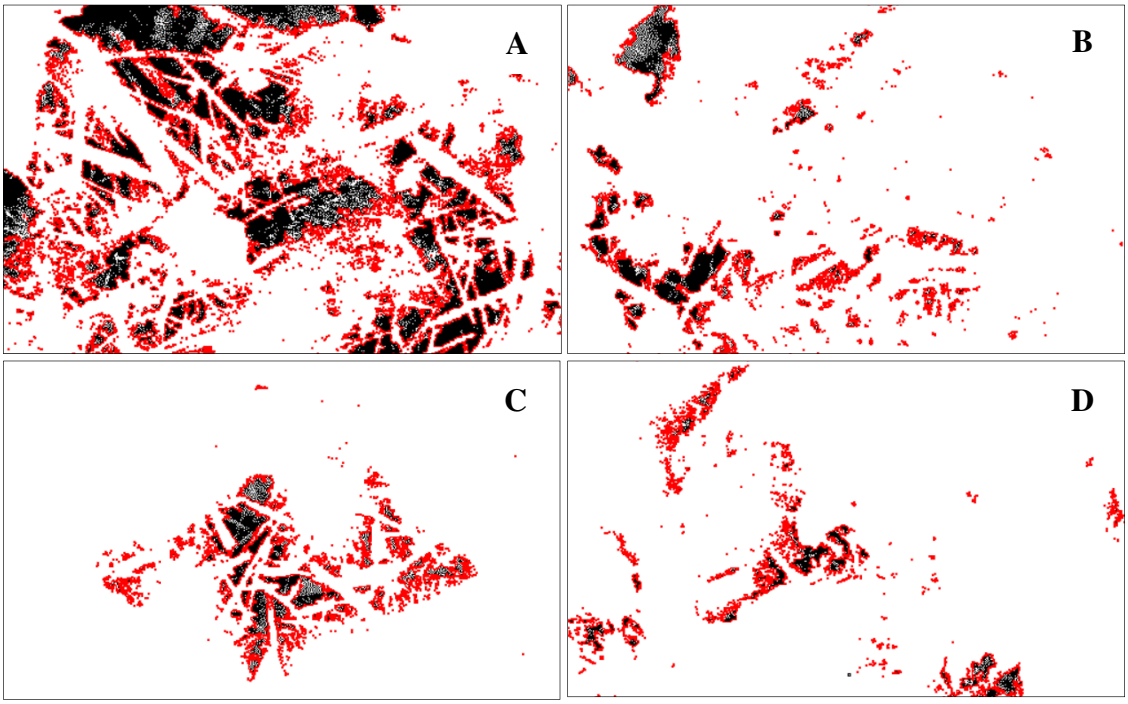

Figure 7. 'ImageJ' image for (a) 05HDPE, (b) 10HDPE, (c) 15HDPE, and (d) 20HDPE

Spectron Electron Microscopy

As earlier mentioned, sulfate attacks in concrete happens when sulfate ions react with aluminates to form ettringite and gypsum which are responsible for concrete expansion leading to cracking. This study attempted to look for the formation of ettringite after exposing concrete specimens to sulfate solution for 28 days. Formation of ettringites are expected to be more common on areas with wide spaces, like cracks and voids, as the formation of ettringite crystals require space. Figures 1 to 5 show ettringite formation (needle-like crystals in the micrographs) typically along the void regions. These micrographs also exhibited lessening amount of ettringite formation with increasing HDPE amount. It can also be noticed that voids were reduced with increasing HDPE.

These micrographs support the results of length expansion by mortar bar test which implies that increasing HDPE contributes to the reduction of ettringite and correspondingly, reduction in voids and size resulting to reduced length expansion as shown by mortar bar tests. Using ImageJ, a platform for processing scientific images, quantification of area of ettringite and voids from SEM images were computed and shown in Table 4. This table provides number to support the study claim that SEM results showed reduction in the amount of ettringite and voids as a consequence of increasing HDPE in concrete. Figures 6 and 7 were the result of ImageJ reduction of SEM images into calculable areas for voids. Images in black are the voids while red spots mark the boundaries. Similar procedure was done to calculate the ettringite areas. Ettringite and voids calculation show that with increasing HDPE, both areas of ettringite and voids decreases.

Table 4. Computation of ettringite and void area using ImageJ

% HDPE	Ettringite Area (μm^2)	Void area (μm^2)
00HDPE	91.962	23.689
05HDPE	113.345	37.646
10HDPE	74.306	8.883
15HDPE	37.731	6.668
20HDPE	10.184	4.680

CONCLUSIONS

In order to address the potential deterioration that can be brought about by sulfate attacks in concrete, the use of HDPE in concrete was explored. This study investigated the mechanical properties of concrete with varying HDPE used as partial substitute for fine aggregates. Concrete mix with 5% to 20% HDPE at 5% interval were assessed. HDPE significantly reduces the tensile strength of concrete but in compression, no impact was observed for the compressive strength property. Exposure to sulfate solution, to simulate sulfate attacks, revealed that both compressive and tensile strength properties decreased but HDPE in increasing amounts, have shown to have the potential to arrest the impact of sulfate attacks.

Length change of mortar bars exposed to sulfate solution were also evaluated. The change in length decreases as the amount of HDPE increases. To explain this further, SEM images of concrete samples with varying HDPE were taken. From SEM micrographs, the formation of ettringite and development of voids (or cracks) in concrete have decreased with increasing HDPE. These are significant demonstration of HDPE providing resistance against sulfate attacks.

REFERENCES

[1] Attiogbe, E. K. and Rizkalla, S. H., Response of Concrete to Sulfuric Acid Attack, ACI Materials Journal, 1988, pp. 481-488.

[2] Allen, T., Concrete in coastal structures, London, England, Thomas Telford Ltd, 1998.

[3] Collepardi, M., A state-of-the-art review on delayed ettringite attack on concrete, Cement and Concrete Composites, Vol. 25, Issues 4-5, 2003, pp. 401-407.

[4] Bai, J., Durability of sustainable concrete materials, Sustainability of Construction Materials, 2009, pp. 239–253.

[5] Chen, J.K., Qian, C., and Song, H., A new chemo-mechanical model of damage in concrete under sulfate attack, Construction and Building Materials, 115, 2016, pp. 536-543.

[6] ISO 10358, Plastic pipes and fittings – Combined chemical resistance classification table, Geneva, Switzerland: ISO/IEC, 1993.

[7] Pacheco-Torgal, F., and Jalali, S., Sulphuric acid resistance of plain, polymer modified, and fly ash cement concretes, Construction and Building Materials, 23(12), 2009, pp. 3485-3491.

[8] Araghi, H., Nikbin, I., Reskati, S., Rahmani, E., and Allahyari, H., An experimental investigation on the erosion resistance of concrete containing various PET particles percentages against sulfuric acid attack, Construction and Building Materials, Vol. 77, 2015, pp. 461-471.

[9] Nikbin, I., Rahimi, S., Allahyari, H., and Fallah, F., Feasibility study of waste Poly Ethylene Terephthalate (PET) particles as aggregate replacement for acid erosion of sustainable structural normal and lightweight concrete, Journal of Cleaner Production, Vol. 126, 2016, pp. 108-117.

[10] Rahim, N. L., Salehuddin, S., Ibrahim, N. M., Amat, R. C. and Jalil, M. F. A., Use of plastic waste (High Density Polyethylene) in concrete mixture as aggregate replacement, Advanced Materials Research, Vol. 701, 2013, pp. 265-269.

[11] ASTM C1012, Standard Test Method for Length Change of Hydraulic-Cement Mortars Exposed to a Sulfate Solution, ASTM International, PA, USA, 2014.

[12] ASTM C305, Practice for Mechanical Mixing of Hydraulic Cement Pastes and Mortars of Plastic Consistency, ASTM International, PA, USA, 2014.

9th Int. Conf. on Geotechnique, Construction Materials and Environment,
Tokyo, Japan, 20-22 November 2019, ISBN: 978-4-909106025 C3051

ASSESSMENT OF TESTING PROTOCOLS FOR BAMBOO FOR TENSION PARALLEL TO FIBER

Martin A. De La Cruz[1], Luis F. Lopez[2], Richard M. De Jesus[3], and Lessandro E. O. Garciano[3]
[1, 3]De La Salle University (Manila), Philippines; [2] Base Bahay Inc., Philippines

ABSTRACT

To determine tension parallel to fiber properties of Bamboo, one can employ ISO 22157. However, several studies highlighted some challenges in using the method such as premature failure of testing due to force at clamping and slipping failure at the grips. Hence, this study aims to look for a solution to address these challenges. This study investigated, both qualitatively and quantitatively, three testing protocols in determining bamboo's tensile strength parallel to fiber – (1) ISO 22157, (2) a modification of ASTM D143, and (3) Pittsburgh Method. The success rate, test duration, load rate and transmission, specimen preparation, equipment fabrication, and execution of the three protocols were compared. The physical properties of bamboos, such as moisture content, density, and shrinkage, were also measured in the study. The results of the study showed that the modified ASTM D143 test is the most viable method to use in testing the tensile strength parallel to fiber of bamboos. Modified ASTM D143 produced the highest tensile strength with value equal to 100.36 MPa, compared to specimen tested under ISO 22157 with tensile strength only reaching 94.11 MPa, while Pittsburgh Test produced the lowest tensile strength of 76.78 MPa. Modified ASTM D143 also yielded the lowest confidence interval which implied good consistency. Modified ASTM D143 is the recommended test protocol based on the results of this study as it gained the highest success rate during testing, lowest testing duration and the easiest to execute.

Keywords: Bamboo, Tensile strength parallel to fiber, ISO 22157, ASTM D143, Pittsburgh method

INTRODUCTION

Bamboo is used as an alternative to wood and it has been considered as "poor man's timber" [1]. Its reputation changed in recent times with the technological developments and researches [2] and [3] which led to different uses of bamboo such as ceilings, floorings, cabinetry, furniture, and even, a base of a bicycle ([4]-[8]). Bamboo is a renewable material, being one of the fastest growing plants in the world. It can be harvested at an age as early as 3 years compared to timber which takes about 25 years to mature and be harvested [9]. Since bamboo is technically a grass, thus it regenerates faster. In 2004, ISO published ISO 22157-1 (Bamboo - Determination of physical and mechanical properties) with 2 parts: Requirements, and (2) Laboratory Manual. Also, it has published ISO 22156 Bamboo - Structural Design. One of the properties that [10] determines is the tension parallel to the fiber. However, this test method exhibited some notable shortcomings: specimen clamped at the grips failed due to the force of gripping, and slipping at the grips [1] & [11].

Study of [12] also observed similar issues and additionally noticed that it also has problems with specimen orientation noting that reduction should be made in the tangential direction of the specimen so as not to remove the extreme inner and outer culm wall fibers from the test coupon.

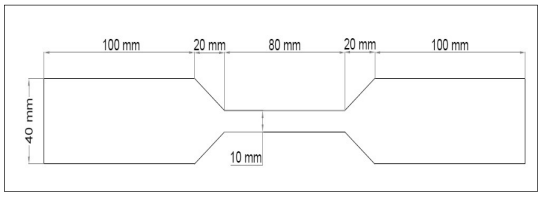

Figure 1. ISO 22157 (TP1) specimen

According to [13], adjustments should be made to ISO 22157 in determining properties of bamboo to make sure that the cause of failure is tension and not failure due to compression because of the grip issues. Study of [14] recommended the adaptation of [15] ASTM D143 for tension parallel to fibers test.

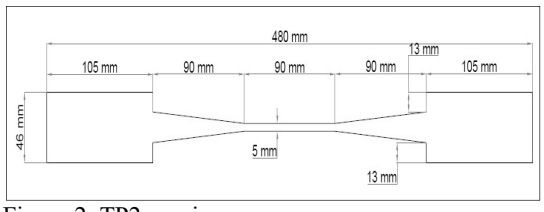

Figure 2. TP2 specimen

It is evident that there is a need for modifications in ISO 22157 to address concerns about testing of tension parallel to fiber. Since before making any recommendation to ISO 22157, verification of a new test protocol is needed, it is the aim of this study to

Table 1 Tensile strength (parallel to fiber) summary of test results

Test Protocol	Average Tensile Strength, MPa	R_k, MPa	Moisture Content, %	Density ρ (kg/m^3)	Shrinkage, %
TP1	94.11	44.86	10.95	682.48	1.40
TP2	100.36	62.67	10.95	682.48	1.40
TP3	76.78	43.45	10.95	682.48	1.40

assess three testing protocols: (1) ISO 22157 itself, (2) a modification of ASTM D143, and (3) Pittsburgh Method - a test adopted from [1]; in determining bamboo's tensile strength parallel to fiber.

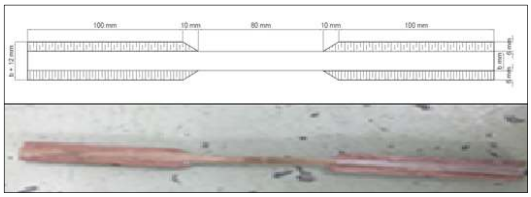

Figure 3. TP3 specimen

MATERIALS AND METHODS

Materials and Equipment

The material used in the study is a homegrown bamboo known as "kawayang tinik" (*Bambusa blumeana)* which was sourced from Tarlac, Philippines. The specimen came from several culms of the said specie. Testing was done using a Shimadzu UH-1000kNI universal testing machine equipped with finely-tuned control loading rate settings and is available locally. The number of specimens tested for each protocol is 25.

Testing Protocols (TP)

TP1: ISO 22157

For this protocol, the specimen used has a measure of the gauge area of 10 mm in width, and a length of 80mm (Fig. 1). The ends of the test specimen were shaped to ensure failure at the gauge portion. The node of the bamboo is taken to be exactly at the middle of the gauge length. Notably, the whole specimen is slightly curved. The specimen was cut using a handsaw. In this test, the load was applied constantly at a constant rate of 2.0 mm/min.

TP2: Modified ASTM D143

The second testing protocol is a modification of ASTM D143 which, without modification, is specifically for test of tension parallel to grain for small clear specimens of timber. The modification comes in the form of special grips which is attached to the testing machine to lessen failures. The specimen was cut using a table saw because the specimen profile requires high precision (Fig. 2). Load rate of 1 mm/min is applied for this test.

TP3: Pittsburgh Method

Pittsburgh method is a test protocol adopted from [1]. The specimen (Fig. 3) of the method have a rectangular cross section dimension with breadth equal to the culm wall thickness (t), and width (b) equal to one-half the culm wall thickness or less. The specimen width did not exceed 20 mm and included one node in the gauge section. The gauge length was set at 80 mm. The gripped ends of radially oriented test pieces have softwood tabs laminated to the breadth dimension using a coconut lumber with a thickness 6mm. The load rate of the test was set at 5mm/min.

RESULTS AND DISCUSSION

Table 1 shows the tensile strength of each protocol and the average value of moisture content, density, and shrinkage of all specimen. Pittsburgh Method has the least tensile strength average while the modified ASTM produced the highest tensile

strength. Table 2 summarizes all tensile strength test results, characteristic value, allowable stress and confidence interval.

Modes of Failure

TP1: ISO 22157

For the ISO test, there were five mode of failures observed during testing: bearing, shear, premature cracking or cracking in grips, tension (parallel to fiber) failure on node or brittle tension, and splintering tension (parallel to fiber) failure. Out of 25 specimens, 17 (68%) failed in tension (parallel to fiber) while 8 (32%) failed in non-tension mode.

TP2: Modified ASTM D143

There were three mode of failures observed in the test: tension brittle, splintering tension parallel, and

Table 2 Tensile strength (parallel to fiber) values for three (3) testing protocols

Test Protocol	Range (MPa)	Average (MPa)	Rk (MPa)	Allowable Stress (MPa)	Confidence Interval (MPa)	Confidence Interval Range@ 95% confidence level, MPa
TP1	51.72-145.18	94.11	44.86	9.97	12.89	81.22-106.99
TP2	49.65-131.84	100.36	62.67	13.93	10.09	90.27-110.45
TP3	42.71-102.36	76.78	43.45	9.66	13.59	66.22-93.40

Table 3 Qualitative comparison of three (3) testing protocols

Testing Protocol	Success Rate	Test duration < 5 min?	Specimen Preparation Difficulty	Needs accessory?	Test Difficulty
TP1	68%	Yes	Mid	No	Mid
TP2	76%	No	High	Yes	Easy
TP3	48%	Yes	Mid to High	No	Mid

shear failure. Out of 25 specimens, a total of 19 (76%), failed in tension (parallel to fiber), 6 specimens (24%) failed in shear.

TP3: Pittsburgh Method

There were two failures observed in the test: tension (parallel to fiber) failure on node, and bearing failure. Out of 25 specimens, 12 (48%) failed in tension parallel, 13 specimens (52%) did not fail in tension (parallel to the fiber) but instead, failed in bearing failure mode.

Qualitative Analysis

Table 3 shows the success rate of the testing protocols. The most successful testing method is TP2 with 76% (19/25). The least successful method is TP3 with 48% (12/25).

It is observed that TP2 has the fastest average testing time with 258 seconds. TP1 and TP3 take 534 and 682 seconds, respectively, to complete the test. This is attributed to the difference in load rates between test protocols. Additionally, for TP1 and TP3, it was observed that the load-displayed values were fluctuating and is attributed to the clamping at the grips. During test, the grips compressed the specimens and when the specimen gets thin as a result of compression, slipping at the grips happen, thus, the fluctuation of values. At the beginning of the tests for TP1 and TP3, it took time for the load to increase as the clamps need to grip the specimen firmly. Qualitative observations for all test protocols were summarized in Table 3.

The preparation of specimen is very important to obtain the expected failure. For TP1, the preparation of the specimen is the easiest since its specimen's width is larger compared to the other TPs. The specimens for TP2 were the most difficult to prepare since it needs precise and careful preparations as it demands that the part where the gadget and the specimen comes into contact must be parallel to make sure the load distribution is equal. For TP3, preparation was rated between medium and high. It is easier than TP2 test since it is much easier to cut but tedious due to the addition of tabs.

TP1 and TP3 did not require additional grips as the testing machine's grip is sufficient to conduct the tests. For TP2, however, extra grips were fabricated for better clamping. TP2 is the easiest test to execute as the additional grips made the setup for clamping easy. TP1 and TP3 made the setup for clamping extra difficult as the testing machine's grip requires manual adjustment for the specimen to be perfectly aligned with the load direction.

CONCLUSIONS

Among three testing protocols investigated, modified ASTM D143 Test (TP2) produced the highest tensile stress reading at 100.36 MPa compared to ISO 22157 (TP1) with 94.11 MPa, and Pittsburgh Method (TP3) with 76.78 MPa. TP2 also produced the most consistent results with the lowest confidence interval.

From the results summarized above, it is concluded that the Modified ASTM D143 test (TP2) is the most recommended method to use. It has the highest success rate, lowest test duration, and the easiest to execute. The only downside is the demand for careful attention during the preparation of the specimen. The second recommended protocol is the ISO 22157 (TP1) based on its success rate, test duration, and specimen preparation. The least recommended method is the Pittsburgh method (TP3) because of the lowest success rate, long test duration, and tedious specimen preparation.

REFERENCES

[1] Mitch, D., Splitting capacity characterization of bamboo culms, Master's thesis, University of Pittsburgh Honors College, Pennsylvania, USA, 2009.

[2] Janssen, J, Bamboo in building structures. Doctorate thesis, Eindhoven University of Technology, Netherlands, 1981. Retrieved March 3, 2017, from http://alexandria.tue.nl/extra3/proefschrift/PRF3B/8104676.pdf.

[3] Atanda, J., Environmental Impacts of bamboo as substitute construction material in Nigeria. Case Studies in Construction Materials 3, 2015, pp. 33-39.

[4] Alipon, M., Bauza, E., and Sapin, G., Development of Floor Tiles from Philippine Bamboos. Philippine Journal of Science Vol. 140, Issue 1, 2011, pp. 33-39.

[5] Marquez, C., Improving and maintaining productivity of Bambusa blumeana for quality shoots and timber in Iloilo and Capiz, the Philippines, Australian Centre for International Agricultural Research, 2006.

[6] Razal, R., Bantayan, R., Delgado, T., and Elec, J., Bamboo Poles for Engineered-Bamboo Products Through Improved Clump Management and Harvesting: Lessons for the Philippines, Ecosystems & Development Journal, Vol. 4, Issue 1, 2013, pp. 39-49.

[7] Schau, E., Chang, Y., Scheumann, R., and Finkbeiner, M., Manufactured products - how can their life cycle sustainability be measured? A case study of bamboo bicycle, Conference proceedings, in 10th Global Conference on Sustainable Manufacturing, 2012.

[8] Malab, S., and Zafaralla, J., Engineered kawayan technology promotion and investment options for commercialization, Monograph, Mariano Marcos State University, 2006, 11p.

[9] Gutu, T., A Study on the Mechanical Strength Properties of Bamboo to Enhance Its Diversification on Its Utilization, International Journal of Innovative Technology and Exploring Engineering Vol. 2, Issue 5, 2013, pp. 314-319.

[10] ISO 22157, Bamboo – Determination of physical and mechanical properties, Geneva, Switzerland: ISO/IEC, 2004.

[11] Bartoli, G., ISO Standards of Bamboo, Paper presented at Performance of Joints in Bamboo Structures Conference, Italy, 2005.

[12] Richard, M., and Harries, K., On inherent bending in tension tests of bamboo, Wood Science and Technology, Vol. 49, 2015, pp. 99–119.

[13] Valdes, D., and Zapata, D., Test procedures for determining the physical and mechanical properties of bamboo, National University of Colombia, Bogota, 2004.

[14] Trujillo, D. and Lopez, L., Bamboo material characterization, Nonconventional & Vernacular Construction Materials Vol. 1, 2016, pp. 365-392.

[15] ASTM D143, Standard Test Methods for Small Clear Specimens of Timber. ASTM International, West Conshohocken, PA, 2007.

9th Int. Conf. on Geotechnique, Construction Materials and Environment, Tokyo, Japan, 20-22 November 2019, ISBN: 978-4-909106025 C3051

UTILIZATION OF PHILIPPINE GOLD MINE TAILINGS AS A MATERIAL FOR GEOPOLYMERIZATION

Erica Elice S. Uy[1], Mary Ann Q. Adajar[1], Hannah Eunice V. Beltran[1], Camille Allysa L. Calicdan[1], Tony Rose E. Duran[1] and Caryl David G. Ramos[1]
[1]Department of Civil Engineering, Philippines

ABSTRACT

Mining minerals results to a waste material called mine tailings. In the Philippines, these waste materials are considered as valueless and are just stored at tailing dams. The increasing demand of gold minerals in the country can cause an increase in production of these waste materials. This can lead to a shortage in storage facilities. With this, this study used Philippine gold mine tailings as a material for geopolymerization. The process of geopolymerization produces a cementitious material with properties substantially comparable to those of a conventional cement. It occurs after an aluminosilicate material reacts with an alkali hydroxide or silicate solution. In this study, gold mine tailings was mixed with the alkaline solution, or the combination of the 10-molar sodium hydroxide solution (10M NaOH) and the water glass solution (WGS), to produce the geopolymer. A total of four-mix proportion of WGS-to-10M NaOH and alkaline solution-to-mine tailings (AS-to-MT) was tested in this study. The compressive strength of each mix proportion were compared. Based on the results, highest compressive strength has a mix proportion of AS-to-MT ratio of 0.35 and the WGS-to-10M NaOH solution ratio of 2.5. X-Ray Diffraction was also performed to determine the chemical compound present in the gold mine tailings used. The results show that aluminum and silicon compounds are present in the material, hence, making the gold mine tailings viable for geopolymerization.

Keywords: Gold Mine Tailings, Geopolymerization,Geopolymer Binder, Waste Material

INTRODUCTION

The increase in mining of minerals such as gold and copper resulted to the growth of waste materials such as mine tailings. These materials are considered as valueless and are always stored in tailing dams. Shortage in storage facility can be a problem due to the increase in mine tailings. As a result, several studies proposed the application of mine tailings for embankment material [1]-[3]. Another promising application is by utilizing mine tailings as a material for geopolymerization which can result to a geopolymer binder. Geopolymerization is a process that produces a cementitious material with properties substantially comparable to those of conventional cement. In a study done by Hardjito, Wallah, Sumajouw, and Rangan (2004), they used geopolymer paste instead of cement paste, but applied the usual methods of creating concrete in manufacturing a type of geopolymer concrete [4]. Based in their results, the geopolymer paste works similarly to a normal cement paste as it binds all the other ingredients together, such as the coarse and fine aggregates, to form the geopolymer concrete. There are several researches that already claimed that mine tailings can be used as a material geopolymerization. Rösner (1999) investigated the geotechnical, mineralogical, and geochemical parameters of gold mine tailings found in South Africa was investigated in the research [5]. A semi-quantitative X-Ray Diffraction (XRD) method was performed. This method is a common technique which identifies the phase and structural characteristics of crystalline solids [6]. Based on the result of the analyses of Rösner, gold mine tailings have high quartz content with an average of 78%. After thorough investigations, it was also revealed that the major chemical element of gold mine tailings found in the East Rand area was silica or SiO_2, with an average of 81.6%. Ahmari, J. Zhang, and L. Zhang (2011) also investigated the feasibility of fly ash modified mine tailings-based geopolymer concrete as an alternative construction material [7]. They discovered that mine tailings have significantly high silicon to aluminum ratio (Si-to-Al) and can be adjusted by using fly ash (ASTM Class F). In the study, the chemical composition of mine tailings and fly ash was compared. It was observed that mine tailings have more SiO_2 content and have less Al_2O_3 content than fly ash, thus, resulting to a greater Si-to-Al ratio. More of their test results revealed that the properties of the mine tailings-based geopolymers were intensively affected by the Si-to-Al ratio and alkalinity of the material, as well as its curing time, especially during the first week. Nevertheless, Ahmari et al. (2011) came to the conclusion that mine tailings may be used as the base material in creating a geopolymer concrete [7].

Moreover, Ahmari and Zhang (2012) tested the feasibility of environment-friendly bricks made through the geopolymerization of copper mine tailings [8]. Unlike the conventional method of brick production, but similar to the production of geopolymer concrete, these environment-friendly bricks were produced by combining the tailings sample with an alkali solution. These bricks were tested under water absorption and unconfined compression tests. The results showed that the use of copper mine tailings in the production of environment-friendly bricks using geopolymerization technology met the ASTM requirements. It is therefore the objective of this study to investigate the potential of the gold mine tailings form the Philippines as a material for geopolymer. Specifically, establish the most appropriate ratio of the alkaline reagent and gold mine tailings to be able to create a geopolymer binder.

GEOPOLYMERIZATION

Geopolymerization occurs after an aluminosilicate material reacts with an alkali hydroxide or silicate solution [9]-[10]. Aluminosilicate materials are minerals composed of compounds with aluminum and silicon; examples of this type of materials include fly ash and mine tailings [11]. Likewise, examples of an alkali hydroxide or silicate solution would be sodium hydroxide (NaOH), and sodium silicate (Na_2SiO_3) solutions, respectively. The mixture of the alkali hydroxide and silicate solutions is collectively known as the alkaline solution or alkaline reagent. The chemical reaction between the wet (alkaline solution) and dry (aluminosilicate material) constituents causes an amorphous gel to harden and condense into a geopolymer binder.

GOLD MINE TAILINGS

The gold mine tailings sample was from a mining site at the Northern Province of Luzon, Philippines. The index properties of the sample were first established based in ASTM standards. The results are tabulated in Table 1. X-Ray Diffraction (XRD) analysis was performed in order to identify the presence of crystalline compounds in the mine tailings sample. The result is shown in Fig. 1. The peaks on the XRD graph suggest that the material is crystalline, while if the lines are somehow flat, the material is amorphous. Based on Fig. 1, the gold mine tailings contain crystalline compounds. Additionally, illite, kaolinite, montmorillonite, and quartz were present in the mine tailings sample. Quartz has a chemical composition of SiO_2 which shows the presence of silicon compounds in the sample. However, no aluminum compound of Al_2O_3 was identified; thus, the aluminum may be amorphous which is desirable for geopolymerization. The XRD results of the mine tailings used in this study shows that aluminum and silicon compounds are present in the material, hence, making the gold mine tailings viable for geopolymerization. To further investigate if the material is amorphous X-Ray Fluorescence (XRF) was also performed. It is a non-destructive procedure that performs the quantitative analysis of elemental composition in which the amount of aluminum (Al) and silicon (Si) present in the mine tailings sample can be found [12]. This was done by displacing the electrons from their atomic positions through a discharge of energy from the apparatus. This energy is identified by the detector to categorize the material by element [13]. The XRF analysis identified the major elemental components of the mine tailings. The top two major elemental components found in the mine tailings sample are silicon (Si) with 61.848% and aluminum (Al) with 12.867%. Since the XRF shows the presence of aluminum, it confirms with the XRD result that this aluminum oxide is amorphous.

Table 1. Index Properties of Gold Mine Tailings

Material	Properties	Values
Gold Mine Tailings	Specific Gravity	2.63
	Liquid Limit	27
	Plastic Limit	22
	Plasticity Index	3
	Linear Shrinkage	3
	Uniformity Coefficient	2.47
	Coefficient of Curvature	1.93
	Soil Classification	Uniformly graded ML

GEOPOLYMERIZATION OF GOLD MINE TAILINGS

The gold mine tailings was first stored in dry condition before the preliminary experiments and the production of the geopolymer binder. The sample was dried in an oven for 24 hours then placed in a plastic container to prevent the absorption of moisture in the atmosphere. Compacted lumps of mine tailings that resulted after the oven-drying were crushed using the mechanical crusher to ensure uniformity of the particle sizes. The texture of the sample after crushing was soft and fine, with physical properties similar to that of cement powder.

Gold Mine Tailings and Alkaline Reagent

An alkali solution was needed to initiate the geopolymerization process of gold mine tailings. A combination of the water glass solution (WGS) and the 10M NaOH was established as the alkaline reagent to create a geopolymer. For the geopolymerization of the gold mine tailings, an alkaline solution-to-mine tailings (AS-to-MT) ratio is also needed to ensure that the geopolymer can develop a capacity to hold compressive stress. The WGS used in this study was composed of 14.65% of Na_2O, 34.13% of SiO_2 and 51.22% of water. The 10M NaOH solution was made from 97%-98% pure sodium hydroxide pellets that were dissolved in distilled water. The ratio of the alkaline solution-to-aluminosilicate material affects the strength of the geopolymer. As the ratio increases, the strength also increases [15]. Based on previous researches, in order to form a geopolymer the WGS-to-10M NaOH ratio can be 1.0 or 2.5 [14]-[15]. Hence, the WGS-to-10M NaOH ratios that were used in this study were 1.00 and 2.50 to ensure that geopolymerization can occur. The alkaline reagent produced by combining the 10M NaOH and WGS is recommended to be prepared at least 24 hours before use [16]-[18]. For the alkaline solution-to-mine tailings (AS-to-MT) ratio, a value of 0.35 and 0.45 was implemented. These ratios were based on previous researches from Aleem and Arumairaj (2012), Patankar, Ghugal, and Jamkar (2014a) and Patankar, Ghugal, and Jamkar (2014b) where they used 0.35 as the AS-to-MT ratio; while Patankar, Ghugal, and Jamkar (2014b) used 0.35, 0.40 and 0.45 as their AS-to-MT ratio, and the results of their study showed that the ratio 0.45 resulted to the samples with the greatest compressive strengths [14], [15], [19].

Preliminary Experiment

A preliminary procedure was made to determine whether the gold mine tailings would react with the alkaline reagent to form a geopolymer and hence, if it would harden, Fig. 2. This is due to the fact that, although some studies have shown to use copper mine tailings to successfully produce geopolymer bricks, it cannot be guaranteed that the same reaction would happen to the gold mine tailings used in this study considering it was obtained from a different source and could possibly be of a different composition, especially the level of aluminum and silica content, both of which are vital to the geopolymerization of the material [8].

Five 50x50mm cubes of geopolymer binders were produced as seen in Fig. 2. The geopolymer binder was produced through the combination of the aluminosilicate material and the alkaline solution. This is analogous to cement paste or the product of the combination of water and cement powder. The geopolymer binder specimens were hand mixed to ensure a uniform consistency of the mixture, since the use of mechanical mixer did not effectively mix the ingredients well. The addition of water was limited to observe medium workability. As a result, four trial mixtures were successfully produced from the combination of the WGS-to-10M NaOH and AS/MT ratios. A minimum of ten 50-mm mortar cubes for each trial mix were made; therefore, an estimated total volume of $1.25x10^{-3}$ m^3 of geopolymer binder per trial was produced. The summary of the materials needed is tabulated in Table 2.

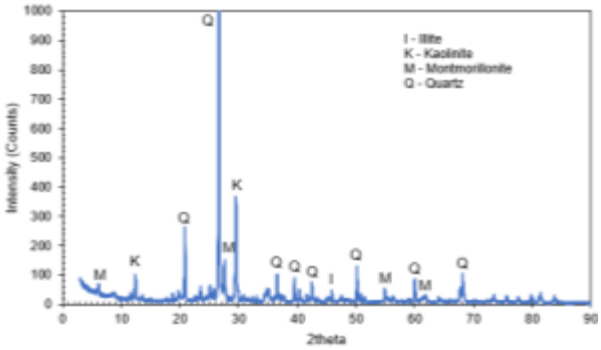

Fig. 1 XRD Results of Mine Tailings.

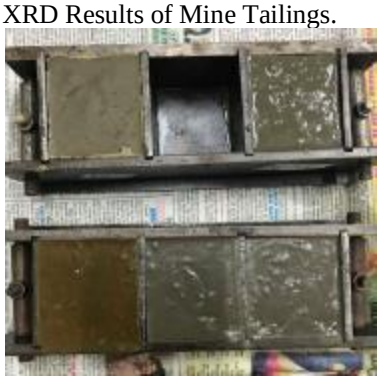

Fig. 2 Preliminary of Geopolymer Binder Samples

Table 2. Mix Proportions of Geopolymer Binder

Materials	Weight Proportions (kg)			
Trial	1a	1b	2a	2b
WGS-to-10M NaOH	1.00		2.50	
AS / MT	0.35	0.45	0.35	0.45

These specimens were heat cured for a temperature of 60ºC for 24 hours after casting in cube molds for at least 5 days, since the specimens were still moist after few days of production. The total number of created specimens for geopolymer binders was 42, wherein at least 10 cube samples were made for each ratio (Fig. 3). The cubes were tested in an unconfined compression test to determine the compressive strength of the geopolymer binder. Five samples for each ratio were first tested on the 7th day, while the remaining

samples were tested on the 28th day.

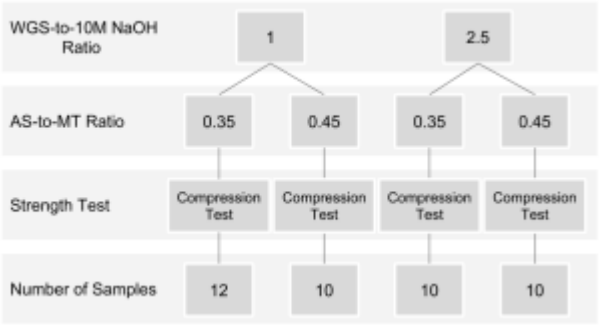

Fig. 3 Actual Number of Samples

Fig. 4 Testing of Geopolymer Binder

RESULTS AND DISCUSSION

The WGS-to-10M NaOH ratios used in this study were 1.00 and 2.50. The WGS, also known as sodium silicate solution, used in this study was composed of 14.65% of Na_2O, 34.13% of SiO_2 and 51.22% of water. Meanwhile, the 10-molar concentration of the NaOH was produced by mixing 400 grams of NaOH micropearls per 1L of the solution. Furthermore, the AS-to-MT ratios used were 0.35 and 0.45. The alkaline solution was mixed a day prior to the mixture of the wet and dry ingredients [17]. Consequently, four trial mixtures were produced based on the combination of the given ratios. Ten 50-mm mortar cubes of each trial were produced whose mix proportions may be found in Table 3. The specimens were heat cured at a temperature of 60ºC for about 24 hours after casting and setting in the cube molds for 5 days. Based on the results of the unconfined compression test, Binder 2a possessed the highest unconfined compression strength both on the 7th and 28th days, with a value of 1.541 MPa, and 1.636 MPa, respectively. These results may be seen in Table 4 and Fig. 4. Binder 2a has an AS-to-MT ratio of 0.35, and WGS-to-10M NaOH ratio of 2.5. Comparing the two ratios for AS-to-MT of 0.35 and 0.45, it shows that the amount of alkaline solution, that is 35% of the amount of mine tailings, is enough to produce a binder. However, increasing the amount of solution to 45% decreases the strength of the binder. WGS, which is used as a binder or adhesive, is required to have a greater amount than the 10M NaOH. This is to ensure the adhesivity of the binder and its ability to set.

Table 3. Mine Tailings-Based Geopolymer Binder Mix

Sample ID	MT (g)	AS (g)	H_2O (g)	AS-to-MT	WGS-to-10M NaOH
Binder 1a	2834	992.5	114.8	0.35	1
Binder 1b	2224	1000	96.6	0.45	1
Binder 2a	2224	778.2	90	0.35	2.5
Binder 2b	2444	1100	106.3	0.45	2.5

On the other hand, 10M NaOH is also used to increase the strength of the binder, but excessive 10M NaOH may result to the occurrence of efflorescence as observed in the preliminary investigation for the production of geopolymer binder (Fig. 5).

Fig. 5 Occurrence of Efflorescence

Table 4. Summary of Compression Test Results

Sample ID	Unconfined Compression Strength, MPa			
	Day 7	Std. Dev.	Day 28	Std. Dev.
Binder 1a	1.225	0.291	1.626	0.380
Binder 1b	0.831	0.413	1.362	0.137
Binder 2a	1.541	0.207	1.636	0.304
Binder 2b	1.155	0.478	1.237	0.201

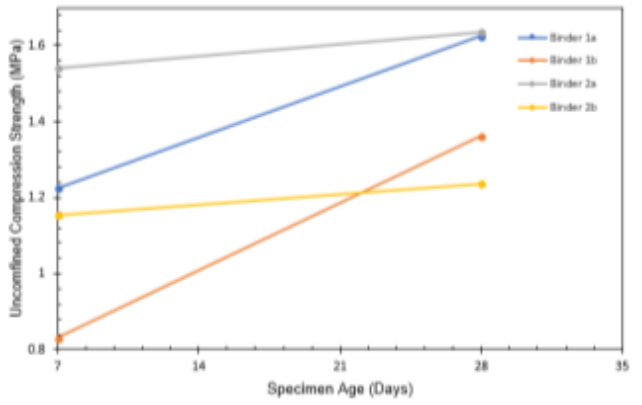

Fig. 6 Relationship between Unconfined Compression Strength and Specimen Age

This is the result of some of the sodium hydroxide solution not reacting completely with the mine tailings. A study by Zhang et al. (2014) suggests that the presence of efflorescence in geopolymers could pose negative effects to its compressive strength development especially when exposed to humid environments [20]. The test results of their study show that the geopolymer binder samples subjected to the occurrence of efflorescence have lower strength values compared to the samples without efflorescence products. Moreover, Zhang et al. (2014) explained that the specimens produced with a higher amount of additional water might have a higher porosity which may lead to the formation of higher efflorescence products within the pores, which then translates to a higher inner stress [20]. They proposed that this eventuality could account for the low strength of the geopolymers with efflorescence. The load-deformation curve of the mine tailings-based geopolymer binder may be seen in Fig. 6.

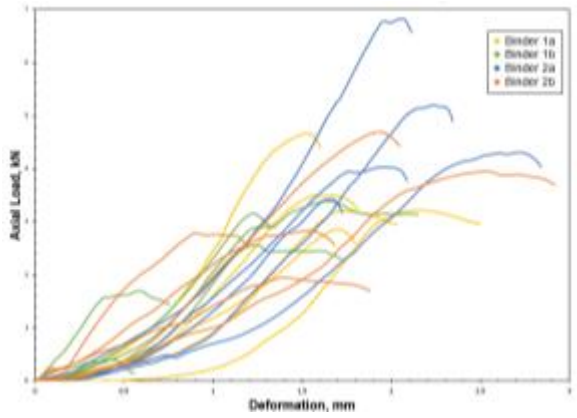

Fig. 7 7th Day Compressive Test

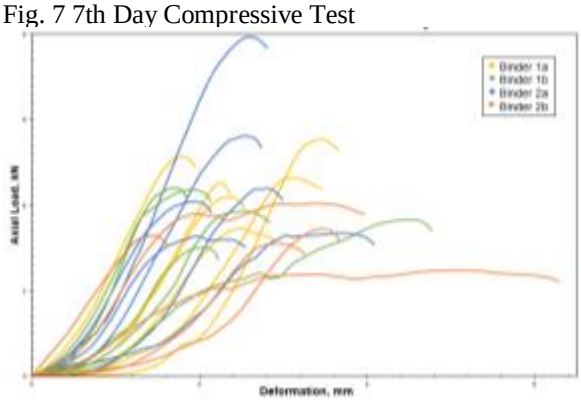

Fig. 8 28th Day Compressive Test

This shows the relationship between the applied axial load and the corresponding deformation at the 7th day of binders 1a, 1b, 2a, and 2b. Binders 1a, 1b, and 2b show steeper slopes than binder 2a. This means that there is gradual deformation as the axial load is applied. However, binder 2a is more flexible in handling the axial load and can still resist greater magnitudes. Binder 2a also produced the greatest unconfined compressive strength at the age of 7 days as seen in Fig. 7. For the 28th day unconfined compression test found in Fig. 8, the load-deformation curve has steeper slope than that of the 7th day. Binders 1b and 2b show a lesser value of maximum applied axial load thus lesser unconfined compressive strengths. These two mixes, binders 1b and 2b, with the AS-to-MT ratio of 0.45 showed that too much alkaline solution may result to a more workable mixture, but binder specimens with lesser compressive strength. The amount of alkaline solution must be adequate to produce the geopolymerization. Binders 1a and 2a presented lesser steep graphs, but, binder 2a resisted a greater load. Thus, the ratio combination that will be used for the mine tailings-based geopolymer concrete is binder 2a, which consists of 0.35 as AS-to-MT ratio and 2.5 as WGS-to-10M NaOH. The summary of these compression strengths is found in Table 4 with its corresponding standard deviation.

CONCLUSIONS

Gold mine tailings were used to produce a geopolymer. Preliminary investigations on the mine tailings sample revealed that the gold mine tailings obtained was a fine-grained, poorly-graded soil having particles with roughly the same sizes or shapes, and may then be considered as uniformly graded inorganic silt with low plasticity (ML) with a specific gravity of 2.63. The average liquid limit of the gold mine tailings was found to be 27, while the average plasticity index was 3; on another hand, the plastic limit and linear shrinkage were found to be 22 and 3, respectively. Furthermore, the XRD analysis showed that the gold mine tailings sample is viable aluminosilicate material for geopolymerization since it has aluminum and silicon compounds in their crystalline forms. This was further verified when the XRF analysis was conducted. This also revealed that the two major elements present in the mine tailings specimen are silicon (Si) with a percentage quantity of 61.85%, and aluminum (Al) with 12.87%. The results show that aluminum and silicon compounds are present in the material, hence, making the gold mine tailings viable for geopolymerization. For the production of the geopolymer binder, four proportion combinations of WGS-to-10M NaOH and AS-to-MT ratio were used to create ten 50mm x 50mm cubes for each ratio combination. After 5 days of setting in the molds, the cubes underwent heat curing for 24 hours using an oven temperature of 60^{o}C. An unconfined compression test was conducted to determine the compressive strength of the geopolymer cubes. The highest compressive strength obtained among the tested binders had a WGS-to-10M NaOH ratio of 2.5 and a AS/MT ratio of 0.35, with a value of 1.541 MPa on the 7th day, and 1.636 MPa on the 28th day. Based on the

results, gold mine tailings has a potential to be used as a material for geopolymerization which can result to a geopolymer binder. For further studies, the binder can be mixed with concrete. The mixture is limited to non-load bearing structures based on its compressive strength.

ACKNOWLEDGMENTS

The authors would also like to thank the Civil Engineering Department of De La Salle University for their support in the research.

REFERENCES

[1] Adajar, M. A. Q. and Zarco, M. A. H. (2016). Predicting the Stress-Strain Behavior of Mine Tailings using Modified Hyperbolic Model. International Journal of GEOMATE, 10(21), 1834-1841.

[2] Adajar, M. A. Q. and Zarco, M. A. H. (2014). An Empirical Model for Predicting Hydraulic Conductivity of Mine Tailings. International Journal of GEOMATE, 7(2), 1054-1061.

[3] Uy, E. E. S. and Adajar, M. A. Q. (2017). Assessment of Critical-State Shear Strength Properties of Copper Tailings. International Journal of GEOMATE, 12(32), 12-18.

[4] Hardjito, D., Wallah, S. E., Sumajouw, D. M., & Rangan, B. (2004). On the Development of Fly Ash-Based Geopolymer Concrete. ACI Materials Journal, 101(6), 467-472.

[5] Rösner, T. (1999). The environmental impact of seepage from gold mine tailings dams near Johannesburg, South Africa (Unpublished master's thesis). University of Pretoria.

[6] Dutrow, B., & Clark, C. (2017, September 28). X-ray Powder Diffraction (XRD). Retrieved October 06, 2017, from https://serc.carleton.edu/research_education/geochemsheets/tech niques/XRD.html

[7] Ahmari, S., Zhang J., & Zhang L. (2011). Synthesis and characterization of fly ash modified mine tailings-based geopolymers. Construction and Building Materials. 25(9). 3773-3781.

[8] Ahmari, S., & Zhang, L. (2012). Production of eco-friendly bricks from copper mine tailings through geopolymerization. Construction and Building Materials, 29, 323-331.

[9] Ren, X., Zhang, L., Ramey, D., Waterman, B., & Ormsby, S. (2014). Utilization of aluminum sludge (AS) to enhance mine tailings-based geopolymer. Journal of Materials Science, 50(3), 1370-1381.

[10] Provis, J. L., & Deventer, J. S. (2009). Geopolymers: structures, processing, properties and industrial applications. Oxford: Woodhead.

[11] Dungca, J. R. and Codilla II, E. E. T. (2018). Fly-Ash-Based Geopolymer as Stabilizer for Silty Sand Embankment Materials. International Journal of GEOMATE, 14(46), 143-149.

[12] Wirth & Barth, 2018 Wirth, K., & Barth, A. (2018, June 20). X-Ray Fluorescence (XRF). Retrieved June 29, 2018, from https://serc.carleton.edu/research_education/geochemsheets/techniques/XRF.html

[13] Guthrie & Ferguson, 2017 Guthrie, J. M., & Ferguson, J. R. (2017, June 2). Overview of XRF. Retrieved June 29, 2018, from http://archaeometry.missouri.edu/xrf_overview.html

[14] M. I., & Arumairaj, P. D. (2012). Optimum mix for the geopolymer concrete. Indian Journal of Science and Technology, 5(3), 2299-2301.

[15] Patankar, S. V., Ghugal, Y. M., & Jamkar, S. S. (2014a). Mix Design of Fly Ash Based Geopolymer Concrete. In ResearchGate. Retrieved October 8, 2017, from https://www.researchgate.net/publication/275340304_Mix_Design_of_Fly_Ash_Based_Geopolymer_Concrete

[16] Rangan, B. V. (2008). Low-Calcium, Fly-Ash-Based Geopolymer Concrete. Concrete Construction Engineering Handbook.

[17] Rangan, B. V. (2009). Engineering properties of geopolymer concrete. Geopolymers, 211-226.

[18] Hardjito, D., & Rangan, B. (2005). Development And Properties Of Low-Calcium Fly Ash-Based Geopolymer Concrete (Master's thesis, Curtin University of Technology). Perth, Australia. Retrieved from https://espace.curtin.edu.au/bitstream/handle/20.500.11937/5594/19327_downloaded_stream_419.pdf?sequence=2&isAllowed=y

[19] Patankar, S. V., Ghugal, Y. M., & Jamkar, S. S. (2014b). Effect of Concentration of Sodium Hydroxide and Degree of Heat Curing on Fly Ash-Based Geopolymer Mortar. Indian Journal of Materials Science, 2014, 1-6.

[20] Zhang, Z. H., Yang, T. & Wang, H. (2014), 'The effect of efflorescence on the mechanical properties of fly ash-based geopolymer binders', in ST Smith (ed.), 23rd Australasian Conference on the Mechanics of Structures and Materials (ACMSM23), vol. I, Byron Bay, NSW, 9-12 December, Southern Cross University, Lismore, NSW, pp. 107-112.

9th Int. Conf. on Geotechnique, Construction Materials and Environment, Tokyo, Japan, 20-22 November 2019, ISBN: 978-4-909106025 C3051

THE INFLUENCE OF UTILIZATION OF FLY ASH AND RECYCLED COARSE AGGREGATE TO THE STRENGTH OF PERVIOUS CONCRETE

Eva Arifi[1], Evi Nur Cahya[2]
[1]Civil Engineering Department, Brawijaya University, Indonesia;
[2] Water Resources Engineering Department, Brawijaya University, Indonesia

ABSTRACT

This paper investigates the strength performance of pervious concrete which utilizes recycled coarse aggregate and fly ash to promote sustainable pavement construction. Recycled coarse aggregate was obtained from parent concrete with around 225 kg/cm2 of compressive strength. Fly ash was used as supplementary material for cement, while to evaluate the strength of pervious concrete using recycled coarse aggregate, 0%, 50%, and 100% of recycled aggregate was prepared to replace natural coarse aggregate. Result shows that fly ash improves compressive strength and tensile strength of pervious concrete for natural coarse aggregate. Moreover, it also shows that utilization of recycled aggregate indicates significant influence to replace specific natural coarse aggregate to the strength of pervious concrete.

Keywords: Pervious concrete, fly ash, recycled coarse aggregate, compressive strength, splitting tensile strength

INTRODUCTION

Pervious pavement is made so that water can flow through the pavement structure as it has more pores than normal concrete [1]. As the development of urban areas has significantly increased and caused change of land use, resulted increasing surface runoff. As a green alternative to conventional pavements with high void content, pervious concrete allows water to infiltrate through the pavement thus reducing the runoff [2]. The void content of pervious concrete closely relates to the strength of concrete [3]. The advantages of pervious concrete using as road pavement are lower density, lower cost due to lower cement content, lower thermal conductivity, relatively low drying shrinkage, no segregation and capillary movement of water. It also has better insulating characteristics than conventional concrete because of the presence of large voids [4].

As natural aggregate continue to deplete in the recent years, while demolition of old building also increases, the utilization of recycled aggregate offers sustainable construction. Many research have been recorded that recycled aggregate have lower quality than natural aggregate. Recycled aggregates are more porous due to containing mortar from their parent concrete compare to natural aggregate. McGovern [5] has been reported that recycled aggregate has a water absorption rate of between 5-6%, whereas recycled fine aggregate has a water absorption rate of 9-10%, while natural aggregates has a water absorption rate of about 1-2%, therefore the application of recycled aggregate are commonly for low quality concrete [6].

In the other hand, with the increased amount of fly ash generated each year as an environmental pollutant, the utilization of fly ash has drawn researchers interests. In fact, it is proved the most effective of utilization fly ash is in concrete and cement [7], [8]. It is well documented that fly ash as cement replacement improves durability and workability of concrete [9]-[12]. Furthermore, in recycled aggregate concrete, the utilization of fly ash reduces drying shrinkage of concrete [13]. Thereby, the experiment on the influence of utilization of fly ash and recycled coarse aggregate on the strength of pervious concrete is conducted.

EXEPERIMENTAL METHOD

Material Used

To investigate the strength of pervious concrete, recycled coarse aggregate were reclaimed from crushed concrete with 225 kg/cm2 as parent concrete average compression strength. The natural coarse aggregate and recycled coarse aggregate are presented in Fig. 1 dan Fig. 2, respectively. Table 1 showed the physical properties of natural coarse aggregate and recycled coarse aggregate used in the experiment. It is clear that natural coarse aggregate used in the experiment has higher oven-dry density compared to recycled coarse aggregate. However, the water absorption indicated that natural coarse aggregate more porous compared to recycled coarse aggregate. Portland pozzolan cement was used in the experiment with water-to-cement ratio was set to 0.3.

Fly ash Type C also used in the experiment as partial replacement of portland pozzolan cement.

Fig 1. Natural coarse aggregate used in the experiment

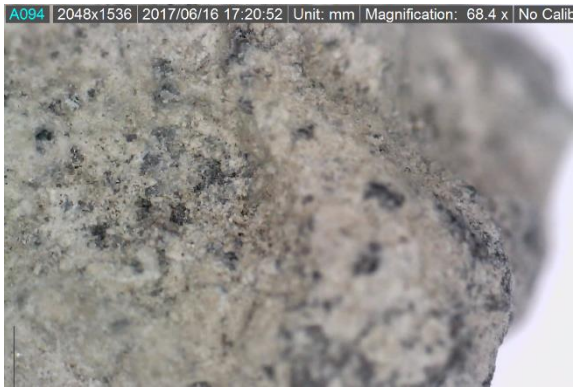

Fig 2. Recycled coarse aggregate used in the experiment

Table 1 Properties of natural and recycled coarse aggregate used in the experiment

Properties	Oven-dry density (g/cm^3)	Water absorption (%)
NCA	1.51	15.023
RCA	1.46	5.18

NCA : Natural Coarse Aggregate
RCA : Recycled Coarse Aggregate

Mix Proportion

The mix proportions of pervious concrete in this study are described in Table 2. The cement-to-aggregate ratio of pervious concrete was set to 1:4 with 0% of fine aggregate used in the experiment. The recycled coarse aggregate replaced 0 %, 50% and 100% of natural aggregate while 0%, 15% and 25% of fly ash were used to replaced Portland pozzolan cement by weight.

Table 2 Mix proportion of pervious concrete

Mix No	NCA/RCA (%)	Cement (%)	Fly Ash (%)
R0F0	100/0	100	0
R0F15	100/0	85	15
R0F25	100/0	75	25
R50F0	50/50	100	0
R50F15	50/50	85	15
R50F25	50/50	75	25
R100F0	0/100	100	0
R100F15	0/100	85	15
R100F25	0/100	75	25

Compressive and Splitting Tensile Strength Test

Compressive strength test and splitting tensile strength were conducted at age 28day to evaluate the performance of hardened pervious concrete using cylinder specimens with diameter of 15 cm and 30 cm height according to ASTM C39 and ASTM C496 standards for cylindrical concrete specimens.

RESULTS AND DISCUSSION

Compressive Strength

The effect fly ash as partial replacement of cement on compressive strength of pervious concrete using recycled aggregate was illustrated in Fig. 3. It indicated that the utilization of fly ash in pervious concrete using natural coarse aggregate significantly improved the compressive strength. 15 % of fly ash increased compressive strength of pervious concrete using natural aggregate up to 83.65%, while 25% of fly ash increased 149.49% of compressive strength compared to natural aggregate pervious concrete with 0% of fly ash.

Figure 3 also illustrated the effect of utilization of recycled coarse aggregate to replace specific natural coarse aggregate. It shown that 50% and 100% recycled coarse aggregate to replace specific natural aggregate with 0% of fly ash indicated to improve compressive strength up to 76.18% and 71.88%, respectively. However, in 15% of fly ash to replace cement, 50% of recycled coarse aggregate to replace specific natural coarse aggregate the compressive strength increased 16.62% the compressive strength of pervious concrete, while 100% recycled coarse aggregate lower the compressive strength of pervious concrete instead. In contrary with the 0% of fly ash that recycled coarse aggregate to replace specific natural coarse aggregate tends to improve its

compressive strength, 25% of fly ash significantly decreased pervious concrete compressive strength when percentage of recycled coarse aggregate was increased.

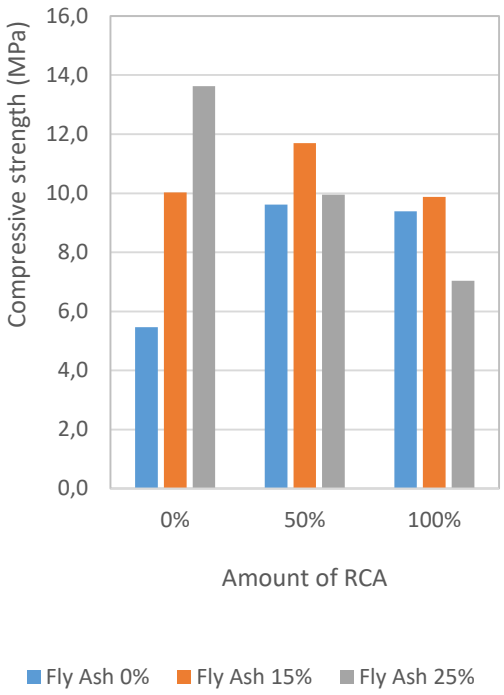

Fig 3. Compressive strength of pervious concrete

Splitting Tensile Strength

The result of splitting tensile strength test of pervious concrete with the effect of utilization of fly ash and recycled coarse aggregate to the strength of previous concrete are presented in Fig. 4. It indicated that the utilization of fly ash in pervious concrete using natural coarse aggregate significantly improved the splitting tensile strength. 15 % of fly ash increased splitting tensile strength of pervious concrete using natural aggregate up to 57.035%, while 25% of fly ash increased 94.93% of splitting tensile strength compared to natural aggregate pervious concrete with 0% of fly ash.

Figure 4 also illustrated the effect of utilization of recycled coarse aggregate to replace specific natural coarse aggregate to its splitting tensile strength. It shown that 50% and 100% recycled coarse aggregate to replace specific natural aggregate with 0% of fly ash indicated to improve splitting tensile strength up to 101.21% and 61.78%, respectively. However, in 15% of fly ash to replace cement, 50% of recycled coarse aggregate to replace specific natural coarse aggregate the splitting tensile strength increased 32.7% the splitting tensile strength of pervious concrete, while 100% recycled coarse aggregate increased the splitting tensile strength of pervious concrete 13.01%. Instead, 25% of fly ash significantly decreased pervious concrete splitting tensile strength when percentage of recycled coarse aggregate was increased compared to 0% of fly ash.

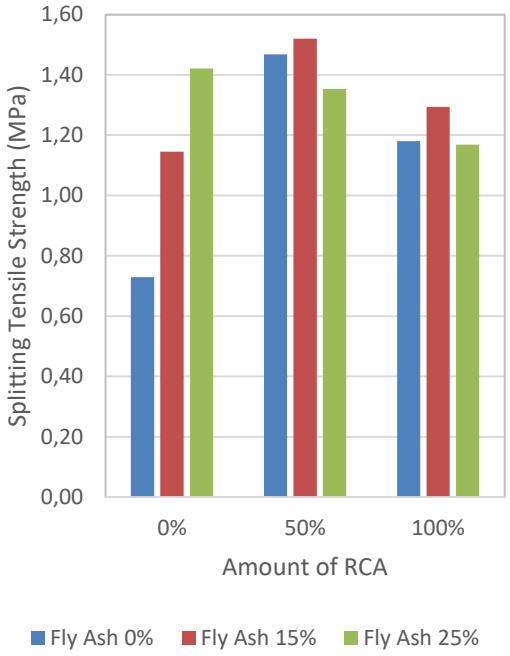

Fig 4. Splitting tensile strength of pervious concrete

CONCLUSION

Compressive strength test and splitting tensile strength test of pervious concrete were examined to investigate the utilization of fly ash and recycled coarse aggregate. The following conclusions are drawn from the test result :

1. The utilization of recycled coarse aggregate to replace selected natural coarse aggregate increases compressive strength and splitting tensile strength of pervious concrete
2. Utilization of fly ash up to 25 % to replace cement improves compressive strength, splitting tensile strengh and flexural strength of pervious concrete using natural coarse aggregate. However, replacing natural coarse aggregate with recycled coarse aggregate up to 50% improves the strength of pervious concrete, particularly in 15% of fly ash to replace cement.

REFERENCES

[1] Agar-Ozbek Ayda S. , Weerheijm J., Schlangen E., Klaas van Breugel, Investigation of Porous Concrete with Improved Strength: Testing at

Different Scales, Const. Build. Mat., Vol 41, 2013, pp. 480-490.
[2] Rizvi R., Tighe S.L., Norris J., Henderson V., Incorporating Recycled Concrete Aggregate in Pervious Concrete Pavements, Pavement Evaluation, Performance and Management Session of the Annual Conference of The Transportation Association of Canada
[3] Lian C., Zhuge Y., Beecham S., Constr. Build. Mat., Vol. 25, 2011, pp. 4294-4298.
[4] Praveenkumar P., Santosh, M.M.,Study on The Properties of Pervious Concret, International Journal of Engineering Research & Technology, 2014.
[5] McGovern M., Recycled Aggregate for reinforced concrete, in *Concrete Technology Today*, Vol. 23, No. 2, Portland Cement Association, Illinois, 2002, pp. 5-6
[6] Tam WYV, Tam CM, Wang Y., Constr. Build. Mat., Vol. 21, 2007, pp. 1928-1939.
[7] Ahmaruzzaman M., Prog. Energy Combust. Sci., Vol. 36 No. 3, 2010, pp. 327-363.
[8] Cao. D., Selic E., Herbell JD., J. Zhejiang Univ. Sci. A., 9(5), 2008, 681-687.
[9] Nath P., Sarker P., Procedia Eng., Vol 14, 2010, pp. 1149-1156.
[10] Nath P., Sarker P., KSCE J Civ. Eng., Vol 17 No. 6, 2013, pp. 1437-1445.
[11] Naik TR., Sivasundaram V., Singh SS., Use of high-volume class F fly ash for structural grade concrete, Transportation Record No. 1301, TRB, National Research Council, Washington, D.C., 1991, pp. 40-47.
[12] Mokarem DW., Development of concrete shrinkage performance specifications, Dissertation, Faculty of the Virginia Polytechnic Institute and State University, 2002.
[13] Arifi E., Zacoeb A., Shigeishi M., International Journal of GEOMATE, Vol. 7 No. 1, 2014, pp. 1009-1016).

9thInt. Conf. onGeotechnique, Construction Materials andEnvironment,
Tokyo, Japan,20-22 November 2019, ISBN: 978-4-909106025C3051

CONCRETE MIXTURE WITH COCONUT FIBER AND BENTONITE TO REDUCE THE VALUE OF GROUNDING RESISTANCE: VALUE CREATION OF COCONUT FIBER WASTE IN TROPICAL COUNTRIES

Yul Martin[1], Diah Permata[2], Alimuddin[3], Mustofa[4], Lindrianasari[5]
[1,2,3]Faculty of Engineering University of Lampung, Indonesia,
[4]Faculty of Mathematics University of Lampung, Indonesia,
[5]Faculty of Economics and Business, University of Lampung, Indonesia

ABSTRACT

The purpose of this study is to create added value in coconut fiber waste that is commonly found in tropical countries, especially in Indonesia. This study analyzes the change in foundation resistance value by using concrete mixed with bentonite and coconut fiber and finding out the best mixture to reduce the earth resistance value. The highest percentage change in resistance value is 72% with an average resistance value of 45,896 Ω that is using concrete mixed with bentonite 30% from the amount of cement and coconut fiber 1.5% from the concrete volume which is 25 x 25 x 30 cm. The use of coconut fibers is very effective as one of the additives mixed into concrete as a grounding uffer grounding system. Aside from being effective, the use of coconut fiber is also economical because of its high availability at low prices. This study contributes to the use of coconut fiber to reduce the value of grounding resistance. This study also shows that the value of grounding resistance is influenced by the amount of resistance of soil types that can be reduced by adding bentonite. There are 4 variations of concrete used, namely concrete mixed with 30% bentonite, concrete mixed with 30% bentonite and coconut fiber 300 gr, concrete mixed with 30% bentonite and coconut fiber 150 gr, and concrete mixed with coconut fiber 300 gr. The best concrete variation to reduce the value of grounding resistance is 30% bentonite mixture and 300 gr coconut fiber. This research has succeeded in finding that coconut fiber waste can provide more benefits in the form of a decrease in soil resistance to ensure the safety of the electrical system.

Keywords: Grounding resistance, Concrete, Bentonite, Coconut fiber

INTRODUCTION

A good and effective grounding system has a role in security and protection in electric power systems, especially when there are land-related disturbances so that losses can be reduced and even avoided. When there is a disruption in the electric power system, with the grounding system, the disturbance currents that arise can be quickly flowed into the ground and spread in all directions [1].

The grounding system serves as a safeguard against devices that use electricity as a source of energy. Several factors can influence the value of grounding resistance including soil type, soil salinity, soil temperature, soil moisture and chemical content in the soil. The existence of several of these factors causes the value of grounding resistance not in accordance with existing standards. In areas that have high soil type resistance, it is often difficult to achieve small earth resistance values according to the standard [2].

There are several ways to condition the soil so that the location of the electrodes that will be planted has low and standard soil type resistance, one of which is the addition of additives to the soil. These additives can be in the form of gypsum, salt, zeolite, charcoal powder, and bentonite. Addition of bentonite additives and coconut fiber waste into the concrete to influence the increase in water absorption in the concrete so that the value of the resulting earth resistance will be more stable. From the results of this research, it is expected that the bentonite and coconut fibers mixed into the concrete can improve the value of ground resistance and later can be used as a reference in planning or installing ground systems [3].

BASIC THEORY

Grounding system is one of the factors that has an important role in efforts to protect the electric power system when there is interference caused by excess current and voltage. When there is interference with the electrical equipment, the grounding system will flow the fault current quickly to the ground and spread in all directions. In other words, the grounding system will provide the equipment to be protected from the negative impact of excess voltage.

Concrete

Concrete is a homogeneous mixture between

cement, water and aggregate. The characteristics of concrete are high crushed stress and low tensile stress. Concrete is a function of its constituent material consisting of hydraulic cement (Portland cement), coarse aggregate, fine aggregate, water, and added material (admixture or additive) [5]. The advantage of using concrete is that it has a wider surface so that it can absorb more water and be able to keep soil moisture longer.

Bentonite

Bentonite is a type of clay which mostly contains more than 85% montmorillonite with minerals such as quartz, calcite, dolomite, feldspars, and other minerals [see 6]. Based on the type, bentonite is divided into two, namely Na-Bentonite and Ca Bentonite. Comparison between Na + cations and Ca + cations contained therein is quite high, and the colloidal suspension has a pH of 8.5 to 9.8. Fig 1 shows the bentonite powder and Figure 2 shows the chemical structure of the bentonite powder

Fig.1 Bentonite

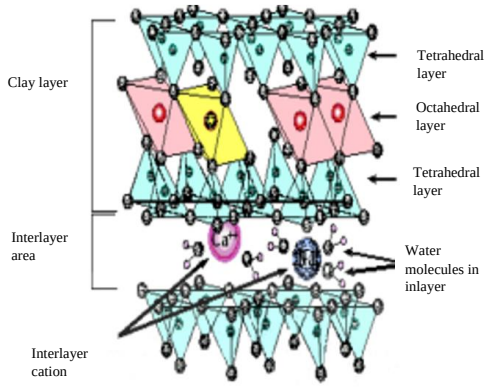

Fig.2 Structure of Bentonite

Coconut fibers

Coconut fiber is one of the bio-mass that is easily obtained and utilized because it can withstand the water content and chemical elements of fertilizers and can neutralize the acidity of the soil. Coconut fibers consist of fiber (fiber) and cork (pitch) which connects one fiber to another fiber. Coconut fibers consist of 75% fiber and 25% cork. Nutrient content that is owned by coconut fibers either macro or micro turns out to be needed by plants.

Macro and micro nutrients contained in coconut fiber include (K) Potassium, (P) Phosphorus, (Ca) Calcium, (Mg) Magnesium, (Na) Sodium and several other minerals. But of the many nutrients that cocopeat has, it turns out that the most abundant amount is the element K (potassium). Fig. 3 shows the coconut powder used for mixing bentonite.

Coconut fiber is very preferred as an absorber because it contains cellullose which in its molecular structure contains carboxyl groups and leginins containing phenoelat acids which take part in metal binding. Cellullose and liginin are biopollymers associated with heavy metal processes

Fig.3 Coconut fiber

Uffer grounding system

Uffer grounding is an electrode wrapped in concrete like a building foundation that is in direct contact with the earth to be used as grounding. This concept is based on concrete conductivity and its large surface area so that it can handle very high current loads [7][8]. Fig.4 Shows grounding system using the uffer grounding method

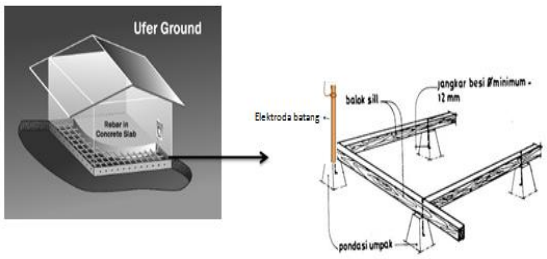

Fig.4 Uffer grounding[8]

EXPERIMENT

Based on literature study research, this research design uses concrete that is volume (25 x 25 x 30) cm and planted at a depth of 50 cm and uses copper-coated electrodes that are 16 mm in diameter and 50 cm in length. Before the research design used

additives added to the grounding system using the grounding fermentation system, the preliminary data was collected using pure concrete without additives. Measuring the value of grounding resistance using pure concrete was carried out five months before measuring the value of grounding resistance using concrete mixed with bentonite additives and coconut fiber waste so that the value of pure concrete resistance with the value of concrete resistance mixed with the additives could not be compared because the treatment between the two was different.

Comparison of material for pure concrete is (cement: sand: gravel = 1: 2: 4) the measurement of the value of grounding resistance in this study is using the three points method [9][10]. Fig.5 shows how earth measurements use the 5 points method

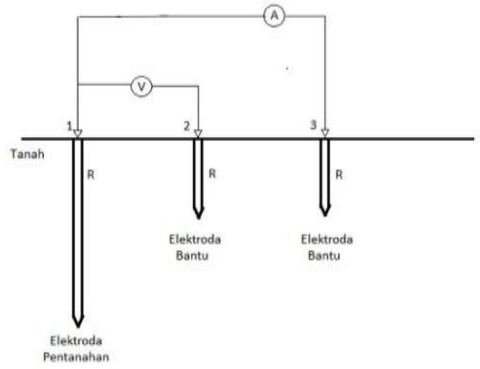

Fig.5 Three points measurement method

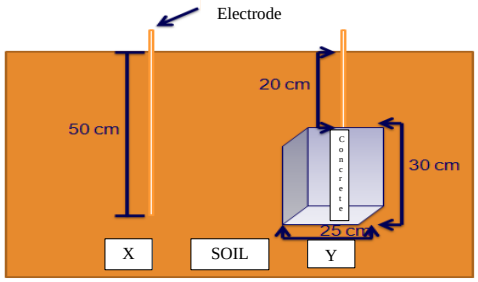

Fig.6 Visualization of testing grounding holes with pure concrete

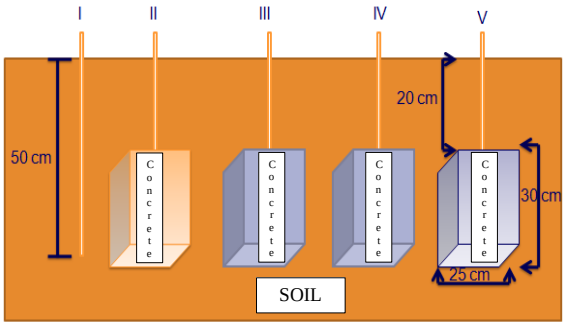

Fig. 7 Visualization of testing of grounding holes with concrete mixed with additives

There are 4 types of concrete mixed with bentonite additives which will be used. First, with the composition of the concrete mixture is mixing bentonite 30% from the amount of cement. Both donit and coconut fiber waste with the composition of the concrete mixture is mixing bentonite 30% of the amount of cement and adding coconut fiber waste 1.5% which is 300 gr.

The third with the composition of the concrete mixture is mixing 30% bentonite from the amount of cement and the addition of coconut fiber waste 0.75% (ie 150 gr). The fourth with the composition of the concrete mixture is the addition of 1.5% coconut fiber waste, namely 300 gr. The following is the research design of the grounding system using concrete mixed with bentonite and coconut fiber [11]

Note:
I= Grounding hole without concrete or without substance additives.
II= Grounding hole using concrete (bentonite: cement: sand: gravel = 0.3: 0.7: 2: 4) and the addition of coconut fiber waste 1.5%, 300 gr.
III= Grounding hole using concrete (bentonite: cement: sand: gravel = 0.3: 0.7: 2: 4) and the addition of coconut fiber waste 0.75% which is 150 gr.
IV= Grounding hole using concrete (cement: sand: gravel = 1: 2: 4) and the addition of coconut fiber waste 1.5% which is 300 gr.

RESULT AND DISCUSSION

The value of grounding resistance in accordance with the PUIL standard, namely ≤ 5Ω is used as a security system for devices with a power source for interference caused by short circuit or lightning. To reduce the value of grounding resistance by several methods, one of them is by adding additives to ground earthing.

Testing of Ground Resistance

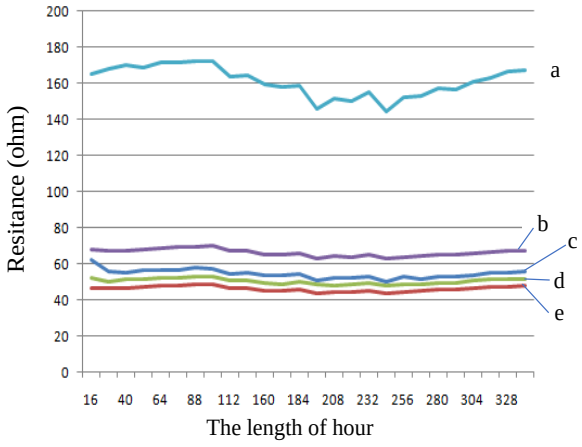

Note:
a = 30% bentonite composition
b = concrete composed of 30% bentonite and 300gr fibers
c = bentonite 30% concrete composition and 150gr fibers
d = 300gr concrete fiber composition
e = Soil

Fig. 8 Graph comparison of measurement results of grounding resistance by composition of bentonite and coconut fiber waste

Figure 8 shows a graph of the comparison of the results of measuring the value of earth resistance from concrete variations which are composed of bentonite and coconut fiber waste. From the figure, it can be seen that the value of the resistance on the ground looks fluctuating, while the variation of the concrete mixture of bentonite and coconut fiber waste looks more stable.

The average value of grounding resistance from the composition of concrete that is composed produces different grounding resistances, namely 54.546 Ω for bentonite composition 30%, 45.889 Ω for bentonite compositions 30% and coconut fibers 300 gr, 50.192 Ω for bentonite compositions 30% and 150 gr of coconut fiber, 66,157 Ω for coconut fiber compositions 300 gr, and 162,2 Ω for grounding prisoners.

Results of Percentage Changes in Land Detention Value

Calculation of the percentage change in value of grounding resistance to obtain how much the change in the percentage value of grounding prisoners between land using bentonite and coconut fiber waste which is composed of concrete with the value of grounding resistance without using concrete or additives is as follows:

$$\% \text{ Change } R = (R\_X - R\_Y) / R\_X \times 100\%$$

Note:
Rx = value of grounding resistance without additives
Ry = value of grounding resistance with additives

Table 1 Percentage change in value of grounding resistance

Item	R (Ω)	Change R (%)
I	54,546	66%
II	45,896	72%
III	50,192	69%
IV	66,158	59%
V	161,2	-

Note:
I = Grounding of concrete is composed of 30% bentonite mixture.

II = Grounding of concrete is composed of 30% bentonite mixture and addition of coconut fiber waste 300 gr.

III = Grounding hole of concrete composed of 30% bentonite mixture and addition of coconut fiber waste 150 gr.

IV = Grounding of a mixture of compressed concrete added coconut fiber waste 300 gr.

V = Grounding hole without concrete or without additives.

Table 1 show the percentage change in the value of the largest grounding resistance, namely with concrete which is composed of 30% bentonite and the addition of coconut fiber waste 300 gr is 72%. The difference in the percentage change value of grounding resistance from concrete which is composed of 30% bentonite from the addition of coconut fiber waste 150 gr and 300 gr is not too significant, namely with each change in the percentage value of 69% and 72%.

Comparison of the percentage change in the value of grounding resistance between concrete which is composed of 30% bentonite and concrete that is composed of coconut fiber waste 300 gr is the value of each change in percentage of 66% and 59%. From these data it can be concluded that using concrete that is composed of bentonite and coconut fiber waste is better with the percentage change in the value of grounding resistance higher than that of only bentonite and coconut fiber waste. To be clearer in comparing the percentage change in value of grounding resistance can be seen in the Fig 9.

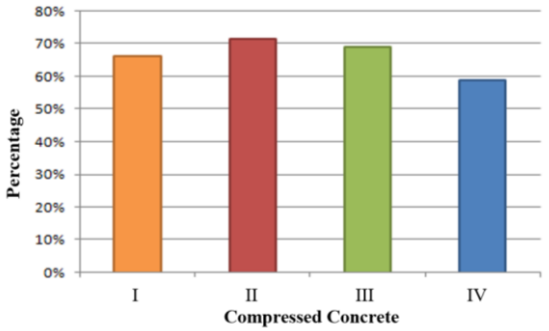

Fig.9 Percentage change in value of grounding resistance

Pure Concrete Test Results

Fig.10 Graph of the measurement results of grounding pure concrete resistance

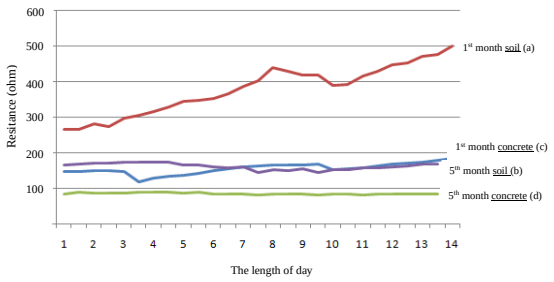

Pure concrete testing is the preliminary data from this study which has been carried out for five months from October 2017 to March 2018 and is measured 14 days in the first month and the fifth month in the morning and evening. This pure concrete testing is

planted at the same depth of 50 cm and the same volume of concrete is 25 x 25 x 30 (cm). This is to find out the testing of grounding prisoners using concrete for a longer period of time.

Figure 10 shows the results of pure electrode testing in the first 14 days. In the figure there is a decrease in the value of soil resistance in the first month (a) where on the first day measured 266 and on the 14th day measured by 499 Ω on the first month, and decreased resistance on the fifth month (b) on the first day measured by 165 and on the 14th day measured by 167. These results indicate that even in wet environmental conditions in tropical countries (such as in Indonesia) the resistance of pure concrete has decreased. Condition (a) and (b) occurs when the electrodes are directly implanted into the ground without concrete (see picture 6 [X]).

Meanwhile, electrodes implanted into concrete showed lower resistance, i.e. in the first month (c) the measured value on the first day was 147 Ω to the 14th day measured at 185 Ω. Testing the value of pure earth ground resistance in the fifth month (d) looks more stable than the first month which is around the earth resistance value of ± 85 Ω. These conditions (c) and (d) occur when electrodes are implanted into pure concrete before they are implanted into the ground (see figure 6 [Y]).

Discussion of Uffer Grounding

Uffer grounding is an electrode wrapped in concrete like a building foundation that is in direct contact with the earth to be used as a grounding resistance system. Concrete is composed of materials in the form of cement, sand, and gravel with a ratio of 1: 2: 4. Where cement itself is composed of several ingredients, namely as showes at table 4

Table 2 Chemical composition of Portland cement

Oksida	Persen (%)
Kapur (CaO)	60 – 65
Silica (SiO_2)	17 – 25
Alumunia (Al_2O_3)	3 – 8
Besi (Fe_2O_3)	0,5 – 6
Magnesia (MgO)	0,5 – 4
Sulfur (SO_3)	1 – 2
($Na_2O + K_2O$)	0,5 – 1

Source: Tjokrodimuljo, 1996 [12].

Table 2 the main ingredients of cement are lime and silica (clay). Limestone is the main source of compounds of calcium carbonate (CaCO3). Therefore, when cement is made as one of the concrete forming materials it will increase Ca + 2 levels while CO3-2 and if it reacts with H2O to H2CO3, it can eventually break down into CO2 and water vapor [13] [14].

CaCO3 + 2H + Ca + 2 + CO2 + H2O

The concrete structure that contains cement, creates concrete pore spaces, especially water binding pores which can reduce resistance through the role of water as an electrolyte. Whereas clay is the main source of silica compounds. Silica compounds have the ability to absorb large amounts of water because they have a large surface and large pore volume. In addition, when concrete becomes a solid object it will have absorption characteristics that can absorb water for a long time and maintain substances around it so that it can retain moisture in the soil [5].

This research uses 50 cm long and 16 mm diameter rod electrodes which are bound to an iron frame 8 mm in diameter and then wrapped with concrete mixed with bentonite and coconut fiber waste. The electrodes were planted at a depth of 50 cm and the volume of concrete was 25 x 25 x 30 cm with four different methods of mixing additives namely concrete plus bentonite 30% from the amount of cement, concrete plus bentonite 30% from the amount of cement and adding coconut fiber waste 1.5 % is 300 gr, concrete plus bentonite 30% of the amount and the addition of coconut fiber waste is 0.75% which is 150 gr, and concrete plus coconut fiber 1.5% is 300 gr. From the variations in the addition of zat additives so that the best final results are known.

The use of coconut fiber waste is used to increase water absorption and compressive strength of the concrete so that the value of grounding resistance will be better than without the addition of coconut fibers. Addition of coconut fiber waste must be limited because it will affect the compressive strength of the concrete itself. The best addition of coconut fiber waste is 0% - 3% of the concrete volume. In this study with the volume of concrete 25 x 25 x 30 cm, the amount of addition of coconut fiber waste which must be limited to 1.5% is ± 316 gr.

The addition of coconut fiber waste was varied to 0.75% and 1.5% in mixing electrodes with bentonite 30% of the amount of cement. From the addition of the two variations of coconut fiber addition, we should know the best mixture of coconut fiber waste. From the results of measurements obtained by the addition of 30% bentonite from the amount of cement and coconut fiber waste of 1.5%, 300 gr mixed into the concrete has the best value of detention, namely the value of the average resistance 45,896 Ω.

CONCLUSION

The purpose of this study is to create added value in coconut fiber waste that is commonly found in tropical countries, especially in Indonesia. This study analyzes the change in foundation resistance value by using concrete mixed with bentonite and coconut fiber and finding out the best mixture to reduce the soil resistance value. The best concrete variation to reduce the value of grounding resistance is 30%

bentonite mixture and 300 gr coconut fiber. This research has succeeded in finding that coconut fiber waste can provide more benefits in the form of a decrease in soil resistance to ensure the safety of the electrical system. In other words, this grounding system can secure electrical equipment.

Based on the some conclusions are obtained as follows:

(1) Concrete has the ability to maintain the water content in it and is able to maintain the surrounding soil moisture and the effect of adding bentonite and coconut fibers to the concrete can increase water absorption in concrete resulting in better grounding resistance than without addition of bentonite or coconut fibers only.
(2) In this study, the best composition of the mixture was 30% mixed bentonite concrete from the amount of cement and the addition of 1.5% coconut fiber at a volume of 25 x 25 x 30 cm which had a better average value of grounding resistance, 45,896 Ω.
(3) Concrete which is composed of bentonite and coconut fiber waste has a lower grounding resistance value of 45,896 Ω compared to concrete which is only bentonite composition which is 54,546 Ω or coconut fiber waste is 66,158 Ω.

ACKNOWLEDGMENTS

We are appreciate of the support provided for this work by faculty of engineering, university of lampung. This work was also partially supported by Environment science of the post doctoral.

REFERENCES

[1] Hutauruk, T.S. Neutral Strengthening of Power Systems and Equipment Strengthening. Erlangga. 1991
[2] National Standardization Agency. General Requirements for Electrical Installation. Jakarta. 2000.
[3] Martin, Yul. Improved Grounding Prisoners Using Activated Bentonites. Electrician, Journal of Electrical Engineering and Technology. 2016.
[4] Carrijo, O.A., Liz, R.S., Makishima, N. Fiber of Green Coconut Shell as Agriculture substratum, Brazilian Horticulture, 20, 533-535. 2002.
[5] SNI 7604: 2014. Portland Composite Cement. National Standardization Agency. 2014.
[6] Kusrini, Neneng. Utilization of Bentonite, Limestone and Building Debris to Increase Tropical Soil Capacity in Reducing Grounding Resistance. (Thesis). University of Lampung. 2018.
[7] Department of Public Works. General Road and Bridge Specifications, PU Research and Development Agency, General Department, Jakarta. 2010.
[8] Juarez, Gil. Grounding systems. Sections 24, Standard Handbook for Electrical Engineers. 2006.
[9] National Standardization Agency. Procedures for Mixing Lightweight Concrete with Light Aggregates. SNI 03-3449-2002. Jakarta: Department of Public Works. 2002.
[10] National Standardization Agency. How to Test Specific Gravity and Absorption of Fine Aggregate Water. SNI 1970: 2008. Jakarta: Department of Public Works. 2008.
[11] Effendi, H. Review of Water Quality for Management of Aquatic Resources and Environment. Fifth print. Yogyakarta: Kanisius. 2003.
[12] Tjokrodimulyo, Kardiyono. Concrete Technology. Publisher Bureau of Civil Engineering Department, UGM Faculty of Engineering, Sleman, Special Region of Yogyakarta. 2007.
[13] Junardana, IGN. Differences in Salt Addition with Addition of Bentonite to Groundwater Resistant Value in Grounding Systems. Volume 4, No.1. 2005.
[14] IEEE Std 142TM-2007. IEEE Recommended Practice for Grounding of Industrial and Commercial Power Systems. Institute of Electrical and Electronics Engineers, New York, USA. 2007.

9th Int. Conf. on Geotechnique, Construction Materials and Environment, Tokyo, Japan, 20-22 November 2019, ISBN: 978-4-909106025 C3051

EXPERIMENTAL STUDY OF CORNER BEAM-COLUMN JOINT WITH FUSE-BAR DESIGNED EC8 UNDER CYCLIC LOADING

N.H. Hamid[1], N.F. Hadi[2], H. Awang[3] and N. Ibrahim[1]
[1]Institute For Infrastructures Engineering, Sustainable and Management (IIESM), Universiti Teknologi Mara, 40450 Shah Alam, Selangor, Malaysia
[2]Faculty of Civil Engineering, Universiti Teknologi MARA, 40450 Shah Alam, Selangor, Malaysia.
[3]Faculty of Civil Engineering and Earth Resources, Universiti Malaysia Pahang, 26600 Pekan, Pahang, Malaysia

ABSTRACT

A superassembalage of corner beam-column joint specimen equipped with fuse-bars were designed, constructed, tested, analyzed, modelled using Ruaumoko 2D program and validated is presented. The full-scale of corner beam-column joint was designed using Eurocode 8 (seismic code of practice) under Ductility Class Medium (DCM). Experimental results such as hysteresis loops, stiffness, ductility and equivalent viscous damping have higher values than the corner beam-column joint which designed using BS8110 (non-seismic code of practice). The ductility with 2.69 was achieved at 2.5% drift (lateral displacement) when applied in-plane lateral load to the specimen. The fuse-bars were placed inside the corner beam-column joint acted as energy dissipator which can reduce the structural damages and at the same time to increase the rigidity and stiffness of structures by producing bigger hysteresis loops. This loops can contribute to higher value of equivalent viscous damping of the structures. Subsequently, the experimental hysteresis loops was modelled using HYSTERES program in Ruaumoko folders and validated with experimental hysteresis loops. There is good correlation and agreement between them. Therefore, this hysteresis loops can be used to model the real RC frame and tested under different level of earthquake excitation.

Keywords: corner beam-column joint, fuse-bars, Ductility Class Medium, ductility, stiffness

INTRODUCTION

Currently, there are a lot of research which had been conducted on super-assemblage and sub-assemblage of beam-column joint under in-plane lateral cyclic loading using different seismic code of practices and philosophies. There are three types of beam-column joints mainly corner, exterior and interior joints [1]. Initially, the beam-column joints were designed using non-seismic code of practice subjected to gravity loads only and tested under reversible vertical cyclic loading [2,3]. Later on, more experimental studies were conducted to investigate the exterior non-seismic precast RC beam-column joint and corner beam-column joints with floor slabs [4,5,6]. In seismic design, ductility is the main parameter to determine the survivality of the structures under earthquake attack. In order to obtain higher ductility, rectangular spiral transverse reinforcements and FRP bars were used [7,8], mechanical anchorage [9], different arrangement of detailing [10] and fuse-bars [11]. The validation between experimental results and modeling results of seismic behavior of beam-column joints need to be carried out [12,13,14].

Following the past earthquake events, there were a lot of structural damages especially at beam-column joints. Several methods had been used to repair and retrofit the beam-column joints such as ferrocement layers [15], CFRP composite [16,17], combination of GFRP sheets and steel cage [18], prestressed steel angles [19] and CFRP and steel plate [20]. However, it is important to design the RC beam-column joint using current seismic code of practice such as Eurocode 8, NZ3101, UBC 2004, FEMA 276 and others international seismic code of practice. Previous had been conducted on RC interior beam-column joint with fuse-bars designed using Eurocode 8 [11] and this paper will present the seismic behavior of RC corner beam-column joint with fuse-bars. The detail designed of beam-column joints, construction of specimen, experimental set-up and analysis of results in terms of hysteresis loops, lateral strength capacity, stiffness, ductility and equivalent viscous damping will be presented in the following section.

DESIGN BEAM-COLUMN JOINT USING EC8

Figure 1 shows the plan view of the two-storey school building with the locations of exterior, interior and corner beam-column joints. The exterior beam-column joint connected with two parallel beams and one column, meanwhile the interior joint has one perpendicular beam, two parallel beams and one column. The corner beam-column joints has two beams with perpendicular with each other and one

column. The RC corner beam-column joint is equipped with fuse-bars and designed using EC8. Figure 2 shows the 3D corner beam-column joint seats on the foundation beam which bolted to the strong floor. Figure 3 shows the 25mm diameter of fuse-bars with reduce section of 20mm at the middle. This fuse-bar is acting as passive energy dissipater where during earthquake it will behave in elastic behavior and yielded the earliest as compared to other reinforcement bars.

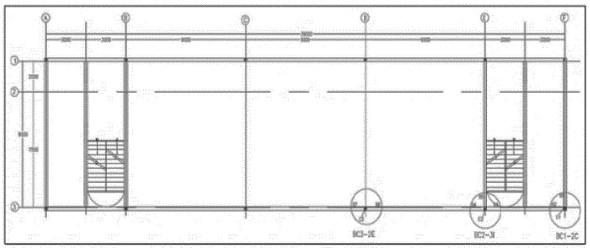

Fig. 1: Plan view of two-storey school building

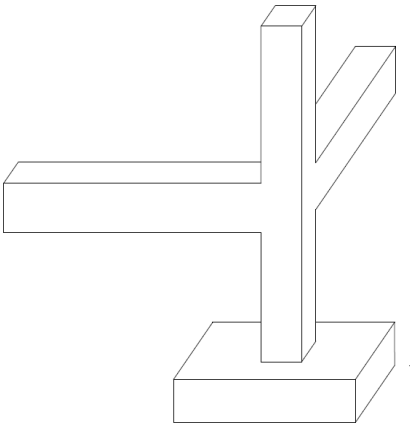

Fig. 2: 3D corner beam-column joint

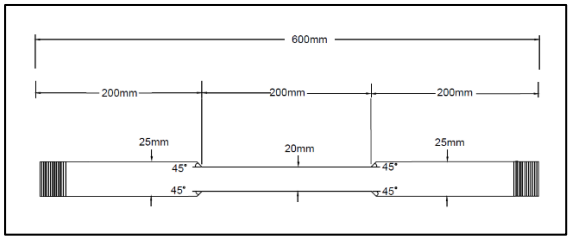

Fig. 3: Fuse-bars inserts inside corner joint.

CONSTRUCTION OF SPECIMEN

Figure 4 shows the construction of RC corner beam-column joint which seated on the foundation beam. Foundation beam was constructed before preparing the reinforcement bars cages for the column. After that formwork was prepared and nailed to the reinforcement cages prior to pouring the wet concrete into the column. Then, let the wet concrete curing for 3 days before dismantle the formwork and the hardened concrete achieved 40% of its compressive strength.

Fig. 4: Pouring of wet concrete into formwork on corner beam-column joints at construction site.

Figure 5 shows the installation of fuse-bars inside the RC corner beam-column joints before pouring the wet concrete into two perpendicular beams. Figure 6 shows column with foundation was lifted to the strong floor before construction of RC corner beam-column joint. After the installation of fuse-bars, formworks were built along the two beams and columns. Subsequently, wet concrete was poured into the formwork and dismantle formwork after its achieved 40% compressive strength. The specimen was ready for experimental set-up and calibration.

Fig. 5: Installation of fuse-bars at corner joint

Fig. 6: Construction of corner beam-column joints inside the Heavy Structural Laboratory.

EXPERIMENTAL SET-UP AND PROCEDURE

Figure 7 shows the RC corner beam-column joint specimen is ready for instrumentation, calibration and testing. Figure 8 shows the systematic arrangement of linear potentiometers which labelled LVDTs to measure the vertical deformation on the column and lateral displacement on two beams. Double load actuator was applied at top of the column using displacement control method. Data logger was used to record the displacement, load and strain in the reinforcement bars. This specimen will be tested under quasi-static in-plane lateral cyclic loading using the loading regime as shown in Figure 9.

Fig. 7: Specimen is ready for testing.

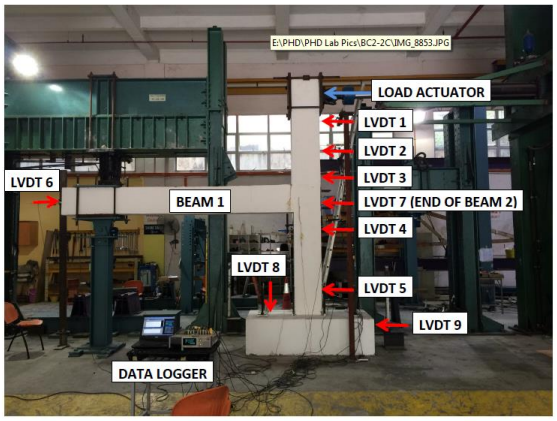

Fig. 8: Systematic arrangement of LVDTS along the column and beams.

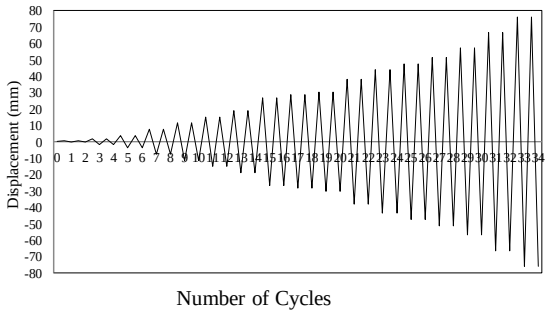

Fig. 9: Loading regime for testing the specimen

EXPERIMENTAL RESULT AND ANALYSIS

The experimental work was conducted in the Heavy Structural Laboratory, Faculty of Civil Engineering, Universiti Teknologi MARA, Malaysia. The specimen was applied quasi-static in-plane lateral cyclic loading using double actuator under displacement control. The lateral displacement is converted into drift by dividing the displacement with effective height of the actuator from strong floor and multiplying by one hundred percent. The specimen was tested from ±0.01% drift until ±2% drift using the loading regime as shown in Figure 9. The RC corner beam-column was failed at 2% drift and lost its lateral strength The photo graphic visual observation of damages was taken, the seismic parameter such as hysteresis loops were recorded, lateral strength capacity, stiffness, ductility and equivalent viscous damping were calculated and analyzed.

Hysteresis loops

Hysteresis loops is one of the important graph that measured and recorded using experimental work. The graph load versus displacement was plotted during testing starting from ±0.01%, ±0.05, ±0.10%, ±0.20%, ±0.50%, ±0.75%, ±1.00%, ±1.15%, ±1.25%, ±1.35%, ±1.50%, ±1.75% and ±2.00% drift. Two cycles of loading and unloading were imposed for each drift. Figure 10 shows the shape of the hysteresis loops where it started with linear behavior, non-linear and experienced the strength degradation starting from ±1.50% until ±2.00% drift.

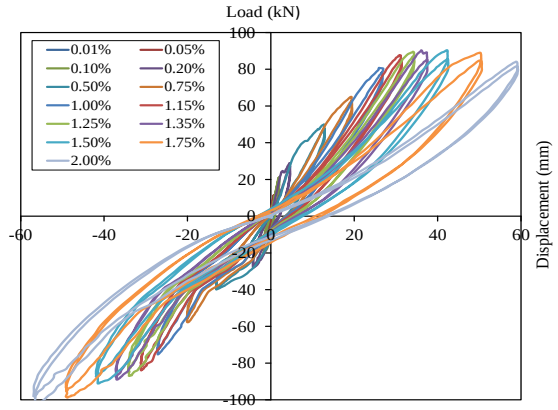

Fig. 10: Hysteresis loops under cyclic loading

Visual Observation of Damages

Figure 11 shows the overall cracks at beam-column joint interfaces starting from -0.2% drift until -1.5% drift. Vertical cracks were observed at beam-column interfaces and horizontal cracks were occurred at column. The measured cracks width were 12mm and the joint started to loss its lateral strength. Figure 12 exhibits the vertical and horizontal cracks were occurred on the vertical and horizontal surfaces

of the beam starting from -0.2% until +1.0% drift. It was also observed that the cracks were around the horizontal beam. Figure 13 displays the spalling of concrete underneath the beam-column joint at +1.75% drift. The opening and closing the gaps of the cracks made the concrete cover spalling and felt down to the strong floor.

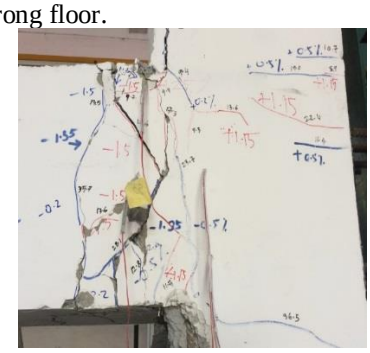

Fig.11: Vertical cracks on the beam-column interfaces at -1.5% drift

Fig. 12: Vertical and horizontal cracks were occurred on the beam starting from+0.5% drift

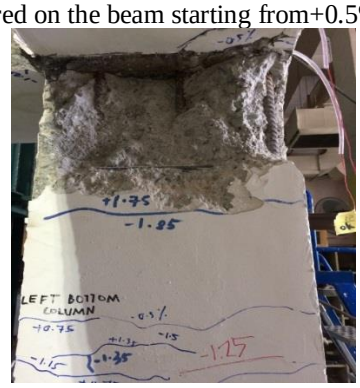

Fig. 13: Spalling of concrete occurred at +1.75%

Lateral Strength Capacity

Figure14 shows the "backbone curve" or graph of load vs displacement for 1st cycle. Based on the graph, the H_u and Δ_u were estimated at 90.79kN and 42.22mm, respectively. Therefore, the value of Hy, taken as 75% of Hu is 67.79kN with the projection of displacement being 27mm making it the yield displacement (Δ_y). Meanwhile, in the pulling direction, Hu and Δu is about -102.66kN and -56.37mm, respectively. The H_y was estimated at -76.7kN while Δ_y at -38mm. Figure 15 shows the lateral strength capacity for second cycle. In pushing direction, H_u was estimated as 87.20kN and Δ_u at 34.26mm. Therefore, Δy was estimated at 27mm. In the pulling direction, Δy was estimated at -36.50 mm. This was taken based on the value for Hu at -98.08kN and Δ_u at -56.95mm.

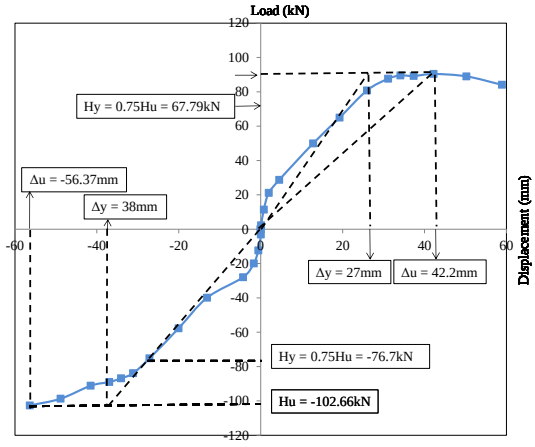

Fig. 14: Lateral strength capacity for the first cycle

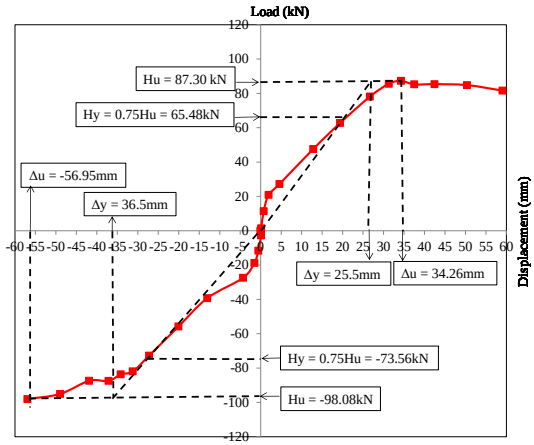

Fig 15: Lateral strength capacity for second cycle.

Stiffness

Stiffness of the structures can be classified into elastic stiffness (K_e), secant stiffness (K_{sec}) and effective stiffness (K_{eff}). Figure 16 shows the equation of stiffness using lateral strength capacity of RC corner beam-column joint. The elastic stiffness has the highest value, followed by effective stiffness and secant stiffness has the lowest value. Figure 17 shows the values of these stiffness versus drift starting from 0.01% drift until 2.0% drift for first and second cycle. The highest value of stiffness occurred in first cycle in pushing direction.

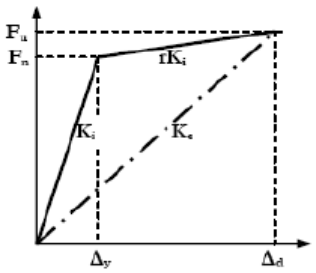

Fig 16: Definition of stiffness

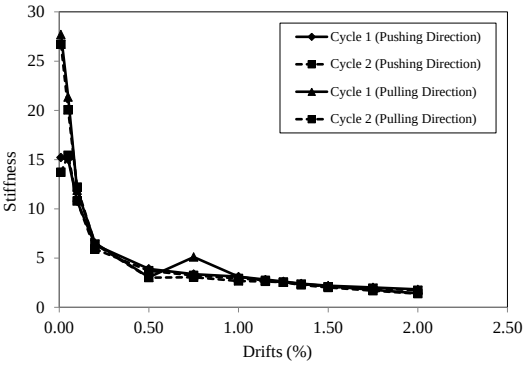

Fig. 17: Stiffness of corner beam-column joint for the 1st and 2nd cycle of each drift.

Ductility

Ductility can be defined as the capacity of a structure or its members to undergo large inelastic deformations beyond the initial yield deformation without losing much of its load carrying capacity or without rupture before failure [21]. Table 1 tabulates the values of ductility for the first and second cycles in pushing and pulling directions. The highest value of ductility for corner joint is 2.69 at 2.00% drift for the 1st cycle in pushing direction. It means that when ductility higher than 2, the building will be able to withstand moderate or severe earthquake excitations.

Table 1: Ductility for the First and Second Cycles in Pushing and Pulling Directions

Target Drift (%)	Pushing Direction		Pulling Direction	
	Cycle 1	Cycle 2	Cycle 1	Cycle 2
0.01	0.00	0.01	0.00	0.00
0.05	0.03	0.04	0.02	0.02
0.10	0.09	0.09	0.06	0.06
0.20	0.21	0.22	0.15	0.15
0.50	0.58	0.61	0.47	0.47
0.75	0.88	0.92	0.72	0.72
1.00	1.18	1.00	0.98	0.97
1.15	1.42	1.27	1.12	1.12
1.25	1.56	1.49	1.23	1.22
1.35	1.71	1.63	1.33	1.33
1.50	1.93	1.79	1.50	1.50
1.75	2.29	2.02	1.76	1.75
2.00	2.69	2.40	2.04	2.03

Equivalent Viscous Damping

The equivalent viscous damping corresponding to the hysteretic response, the concept of dissipated and stored energy has been used [22]. Equivalent viscous damping ratio can be calculated by dividing the total area under hysteresis loops with strain energy under triangle area and multiplying by 100. The fatter the hysteresis loops, more work done by the structures before it started to collapse. The best shape of the hysteresis loops is the flag shape which contribute from post-tensioned tendons. Table 2 shows the values of equivalent viscous damping for the 1st and 2nd cycle starting from 0.01% drift until 2.00% drift. The highest value of the equivalent viscous damping is 2.05% which occurred at 2.00% drift under the 1st cycle.

Table 2 Equivalent viscous damping corner joint

Drift (%)	Cycle 1	Cycle 2
	ζeq	
0.01	0.06	0.11
0.05	0.10	0.15
0.10	0.15	0.20
0.20	0.25	0.30
0.50	0.55	0.60
0.75	0.80	0.85
1.00	1.05	1.10
1.15	1.20	1.25
1.25	1.30	1.35
1.35	1.40	1.45
1.50	1.55	1.60
1.75	1.80	1.85
2.00	2.05	2.10

CONCLUSIONS

Based on the visual observation of damages, experimental data and analysis of result, the following conclusions can be drawn;

1) The corner beam-column with fuse-bars can shift the diagonal cracks from the intersection beam-column joint to the interface and spalling of concrete at the bottom beam.
2) The maximum lateral strength capacity of the joint is 102.66 kN in pulling direction for the first cycle at 2.00% drift.
3) The stiffness of the corner beam-column joint become the highest at elastic region before 0.20% drift and reduce starting from 0.50% until 2.00% drift.
4) The highest value of ductility for corner joint is 2.69 at 2.00% drift for the 1st cycle in pushing direction which meaning to say that the structures survive under moderate and strong earthquake excitation.
5) The highest values of equivalent viscous damping is 2.05% at 2.00% drift.

ACKNOWLEDGMENTS

Special thanks go to the Ministry of Higher Education (MoHE) under Fundamental Research Grant Science

(FRGS) and RMC (Research Management Center), Universiti Teknologi MARA for funding this research work. Gratitude and appreciation go to the laboratory staff for their invaluable assistance during the course of this experimental research work.

REFERENCES

[1] Uma S.R., Sudhir D.R., and Jain K. Seismic Behaviour of Beam-Column Joints in Reinforced Concrete Moment Resisting Frames, Document No: IITK-GSDMA-EQ32, Vol 1.0, Final Report :A-Earthquake Codes, 2004.

[2] Pampanin S., Calvi G.M. and Moratti M., Seismic Behaviour of RC Beam-column Joints Designed For Gravity Loads, 12th European Conference on Earthquake Engineering, 2002, Paper Reference 726.

[3] Hamid N.H. Seismic Performance of Beam-column Joints in Reinforced Concrete Buildings Subjected to Reversible Vertical Cyclic Loading, Malaysian Journal of Civil Engineering, Vol. 22, Issue 2, 2010, pp 264-290.

[4] Ghani K.D. and Hamid N.H. Experimental Investigation on A Non-seismic Precast RC Beam-column Exterior Joint Under Quasi-static Lateral Cyclic Loading, Safety and Security Engineering, WIT Transactions on the Built Environment, Vo. 134, 2013, pp 827-837.

[5] Sangjoon P and Khalid M.M., Experimental Investigation for Non-ductile RC Corner Beam-column Joints wit floor slabs, Journal of Structural Engineering, American Society of Civil Engineering (ASCE), 2013, Vol.13, Issue. 9 pp1-14.

[6] Wang H., Marino E.M., Pan P., Liu H and Nie X., Experimental Study of A Novel Precast Prestressed Reinforced Concrete Beam-to-column Joint, Engineering Structures, Vol. 156, 2018, pp 68-81.

[7] Azimi M.A., Adnan A., Tahir M.M., Sam A.R., Razak S.M., Seismic Performance of Ductility Classes Medium RC Beam-column Connections with Continuous Rectangular Spiral Transverse Reinforcement, Latin American Journal of Solids and Structures, ISSN 1679-7817, Vol. 12, No. 4, 2015, pp787-807.

[8] Athira P. and Remya R., Behaviour of Corner Beam-column Joint with Rectangular Spiral Reinforcement and Longitudinal FRP bars, International Research Journal of Advanced Engineering and Science, ISSN No: 2455-9024, Vol. 2, Issue 2, 2017, pp 160-165.

[9] Rajagopal S. and Prabavathy S., Seismic Behaviour of Exterior Beam-column Joints Using Mechanical Anchorage Under Reversal Loading: An Experimental Study, IJST, Transactions of Civil Engineering, Vol. 38, No. 2, 2014, pp 345-358.

[10] Kalaivani M., Ramesh S. and Angu Senthil K., Performance Evaluation of Corner RC Beam-Column Joints with Different Reinforcement Detailing Subjected to Cyclic Loading, International Journal for Research in Applied Sciences and Engineering Technology, ISSN No: 2321-9653, Vol. 6, Issue No. 10, 2018, pp129-133.

[11] Yahya S.M., Hamid N.H. and Hadi N.F., Seismic Performance of Interior Beam-column Joint With Fuse-Bar Designed Using EC8 Under In-plane Lateral Cyclic Loading, ISBN No. 978-93-84422-57-8, Proceedings of 2015 International Conference on Disaster Management in Civil Engineering, Phuket, Thailand, 2015, pp1-7.

[12] Basha A.M. and Fayed S., Behaviour of RC Eccentric Corner Beam-Column Joint Under Cyclic Loading: An Experimental Work, Civil Engineering Journal, Vol.5, No. 2, 2019, pp295-308.

[13] Metelli G., Messali F., Beschi C and Riva P., A model for Beam-column Joints of Existing RC Frame Subjected to Cyclic Loading, Engineering Structures, Elsevier, Vol. 89, 2015, pp79-92.

[14] Gregoria M.K., Demitrios M.C. and Nikos D.L., Assessment of RC Exterior Beam-column Joints Based on Artificial Neural Networks and other methods, Engineering Structures, Vol. 144, 2017, pp 1-18.

[15] Ibrahim G.S. and Osman A.S., Experimental Behaviour of Full-scale Exterior Beam-column Space Joints Retrofitted by Ferrocement Layers Under Cyclic Loading, Case Studies in Construction Materials Journal, Elsevier, Vo. 8, 2018, pp 61-78.

[16] Saleh H.A., Tarek H.A., Youset A.A. and Nadeem A.S., Seismic Rehabilitation of Corner RC Beam-column Joints Using CFRP Composites, Journal of Composition for Construction, ASCE, Vol. 14, No. 6, 2010, pp681-692.

[17] Murat F., Lawrence F.K. and Abdul Hamid Z., Pre 1970s RC Corner Beam-column Slabs Joints: Seismic Adequacy and Upgradability with CFRP Composites, The 14th World Conference on Earthquake Engineering, October 2008, Beijing China.

[18] Esmaeel E., Kong F.T., Fakhruddin D. and Sassan E., A combination of GFRP Sheets and Steel Cage For Seismic Strengthening of Shear-Deficient Corner RC Beam-column Joints, Composite Structures, Vol. 159, 2017, pp206-219.

[19] Jalil S., Abdollah H., and Mohammad S.M., Seismic Retrofit of External RC Beam-column Joints Enlargement Using Prestressed Steel Angles, Engineering Structures, Vol. 81, 2014, pp265-288.

[20] Hamid N.H., Hadi N.D., and Ghani K.D., Retrofitting of Beam-column Joint Using CFRP and Steel Plate, International Science Index, Vol. 84, 2013, 783-788.

[21] Ninad P.P., Rajguru R.S. and Mehetre, Ductility Requirements of Earthquake Resistant Reinforced Concrete Buildings, International Journal of Innovation in Engineering Sciences and technology, Civil, Vol.1, Issue No.1, 2015, pp1-5.

[22] Jacobsen L.S., Steady Forced Vibrations as Influenced by Damping, ASME Transaction 1930, 52(1): 169-181.

9th Int. Conf. on Geotechnique, Construction Materials and Environment, Tokyo, Japan, 20-22 November 2019, ISBN: 978-4-909106025 C3051

COMPRESSIVE STRENGTH AND WORKABILITY OF CEMENT MORTAR CONTAINING RECYCLED ASPHALT PAVEMENT

Jirayut Suebsuk[1] and Panupong Panpipat[2]
[1,2]Department of Civil Engineering, Faculty of Engineering and Architecture,
Rajamangala University of Technology Isan, Thailand

ABSTRACT

This article presents the compressive strength and workability of cement mortar (CM) containing recycled asphalt pavement (RAP) as fine aggregate replacement. The effect of RAP replacement, water to cement ratio, curing time, and aggregate water absorption on compressive strength and flow workability are reported. The results showed that the mixing water and mixing time play a significant role in the compressive strength and unit weight of CM containing RAP. The RAP has higher the water absorption and slower rate of water absorption than those of sand. The flow workability of CM increases with RAP replacement due to the unabsorbed water at the initial mixing stage. The main negative factors affected the compressive strength of CM containing RAP as a fine aggregate replacement was revealed. The unabsorbed water at the initial state of mixing before hardening causes increased flow workability and decreased compressive strength. The modified water to cement ratio was recommended for the mix design of CM containing RAP. The findings from this research will promote the mix design approach of CM containing RAP as a fine aggregate replacement for moving toward increased applications of recycled materials in a sustainable manner in civil engineering construction.

Keywords: Compressive strength, Flow workability, Cement mortar, Recycled asphalt pavement

INTRODUCTION

The recycled or reclaimed asphalt pavement (RAP) is pavement materials containing asphalt binder and selected aggregate. The RAP is from constructions and rehabilitation of damaged asphalt pavement road. The recycled asphalt pavement mixture and in-situ pavement recycling base course are increasingly used during recent years [1-3]. It is due to the substantial saving in cost and conservation of natural aggregate source. The RAP has been successfully repurposed in the mix asphalt for new paving applications [1, 4]. Although RAP can be used to replace virgin aggregates for new hot mix asphalt concrete with high percentage replacement [1, 5-6], the remaining RAP poses an environmental problem in many developing and developed countries including Thailand. The good use of RAP in civil engineering application is to reuse it in the concrete pavement for disposing the excess RAP. The RAP can improve the performance and cost effectiveness of the new concrete pavement.

The properties of RAP depend on the source of aggregates used in asphalt pavement mixtures. In Thailand, three main types of aggregates are used for preparing the asphalt concrete by Department of Highway and Department of Rural Roads; those are limestone, granite, and basalt. Moreover, the variation in characteristics of RAP is due to the type of mix, asphalt mix consistency, bitumen content, and milling procedure. Typical size of RAP produced from cold milling process is between 0.1-25 mm in size [7-9].

Previous research studied the engineering properties and feasibility of using RAP as fine and coarse aggregates replacement in the concrete application, including concrete slab for pavement [9]. Huang et al. [7] presented the schematic behavior of concrete containing RAP that the asphalt forms a thin film at the interface of cement binder and aggregate. The asphalt interface is useful in resisting the crack propagation through the aggregate. The crack development occurs along with the asphalt film, which more energy dissipation is higher than those of normal concrete. The reduction in compressive strength and increase in toughness have been observed for the laboratory test on concrete containing RAP. Generally, strength and stiffness of concrete depend on the asphalt binder in RAP [10-14]. The performance of concrete containing RAP can be improved with the use of fly ash as indicated by the measurements of porosity and permeability. Concrete containing RAP enhances the ductility and strain capacity of concrete. This improvement in property can be useful for application such as rigid pavement, road, or railway base [15-16].

The present study aimed to investigate the strength formation mechanisms of CM containing RAP under various RAP replacements, water to cement ratio, curing time. The flow workability and compressive strength were carried out for fresh and harden mortar, respectively. The different water

absorption between natural sand and RAP, which is a key point of workability of CM containing RAP has been studied and discussed. The mixing and effective waters have been defined separately. The strength-effective water to cement ratio law of CM containing RAP is satisfied with the traditional Abrams' law. This study has significant impacts on vibrating support applications (such as concrete pavement, road or railway base) by using CM containing RAP as fine aggregate replacement.

MATERIALS AND METHODS

Materials

The Portland cement type I used in this study is, according to ASTM C150/C150M. The clean sand and the RAP were collected from a stockpile of the Department of Highway (DOH), Thailand. The RAP consisted of crushed Basalt rock, which is a very common dark-colored volcanic rock composed of calcic plagioclase, clinopyroxene and iron ore, with asphalt binder. Only 45% of raw RAP from stockpile passes through 4.75 mm sieve. This portion is defined as a fine RAP. The particle size distribution curves of sand and fine RAP are shown in Fig. 1. The particle size of fine RAP is larger than that of the ASTM C33 upper bound, while the particle size of natural sand is on the lower bound of ASTM C33. However, the RAP passed 4.75 mm-sieve was used to replace the natural sand as fine aggregate in this study. The fine RAP, composed of approximately 4.8% bitumen content, was determined by the extraction method recommended by McDaniel and Anderson [17]. The physical properties of the aggregate are listed in Table 1.

Methods of study

The CM samples were prepared using natural sand and fine RAP as aggregate. Twenty-five mix proportions were used in this study, as shown in Table 2. The CM with the percentage of RAP is denoted by M†R**, which † is water to cement ratio and ** is the percentage of RAP replacement. The cement paste is prepared at any water to cement ratio (*w/C*) as reference.

The natural sand and RAP were prepared and mixed at dry state in practice. The mixing water (w_{mix}) included the water counting for reacting with the cement (w) and compensated water for aggregate as SSD state (w_{SSD}). The water absorption (A) from Table 1, according to ASTM C128 was used to determine the compensated water for mix design. The flow test of fresh mortar was investigated according to ASTM C109. Moreover, the flow loss test with time was performed on fresh mortar to investigate the setting time and variation of workability with elapsed time.

Table 1 Properties of aggregates

Properties	Sand	RAP	RAP*
Fineness modulus	2.38	3.91	3.80
Specific gravity (G_s)	2.62	2.66	2.82
Unit weight (kg/m^3)	1,647	1,442	1,632
Water absorption (%)	1.15	2.56	2.31

* RAP without Asphalt determine by the extraction method recommended by McDaniel and Anderson [29]

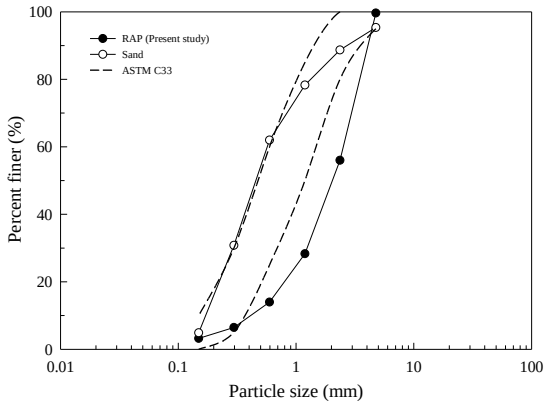

Fig. 1 Particle size distribution curves of aggregate

The mortar samples of 15x15x15 mm were demolded after 24 hours and immediately wrapped with the vinyl sheet then cured under room temperature. The unit weight of harden mortar was measured before the compression test. The compressive strength was measured at a specific curing time using the 600 kN universal testing machine (UTM) according to ASTM C109. The strength was the average value of five samples.

RESULTS AND DISCUSSION

Flow workability of fresh mortar

The twenty-five test results of flow of mortar are represented in Fig. 2. The water in mix proportions with *w/C* between 0.40 and 0.50 is inadequate for workability. The zero percentage of flow was observed for *w/C* of 0.40. The appropriate *w/C* is between 0.50 and 0.70. The percentage of the flow of mortar with 25% to 100% RAP replacement passes the requirements by ASTM C109.

The flow of mortar for all aggregate types depends on the *w/C* [18]. The higher the *w/C*, the higher the mortar flow. Quiroga [19] found that the concrete mixtures optimized for maximum packing density produced poor workability and high susceptibility to segregation, which was possibly due to the reduced spacing and increased friction between aggregates. For the same reason, the increase in the volume fraction of aggregate in mortar generally results in a reduced flow. Hu and Wang [20] presented in the same way that the flow workability depends mainly on the fineness modulus (FM) which was possibly

Table 3 Mix proportions

Sample ID	Absolute amount (g)				*w/C*
	C	*S*	*RAP*	w_{mix}	
M0.40R0*	100	275.00	-	43.14	0.40
M0.40R25	100	206.25	68.75	44.18	0.40
M0.40R50	100	137.50	137.50	45.21	0.40
M0.40R75	100	68.75	206.25	46.24	0.40
M0.40R100	100	-	275.00	47.27	0.40
M0.45R0*	100	275.00	-	48.14	0.45
M0.45R25	100	206.25	68.75	49.18	0.45
M0.45R50	100	137.50	137.50	50.21	0.45
M0.45R75	100	68.75	206.25	51.24	0.45
M0.45R100	100	-	275.00	52.27	0.45
M0.50R0*	100	275.00	-	53.14	0.50
M0.50R25	100	206.25	68.75	54.18	0.50
M0.50R50	100	137.50	137.50	55.21	0.50
M0.50R75	100	68.75	206.25	56.24	0.50
M0.50R100	100	-	275.00	57.27	0.50
M0.60R0*	100	275.00	-	63.14	0.60
M0.60R25	100	206.25	68.75	64.18	0.60
M0.60R50	100	137.50	137.50	65.21	0.60
M0.60R75	100	68.75	206.25	66.24	0.60
M0.60R100	100	-	275.00	67.27	0.60
M0.70R0*	100	275.00	-	73.14	0.70
M0.70R25	100	206.25	68.75	74.18	0.70
M0.70R50	100	137.50	137.50	75.21	0.70
M0.70R75	100	68.75	206.25	76.24	0.70
M0.70R100	100	-	275.00	77.27	0.70

* is control sample

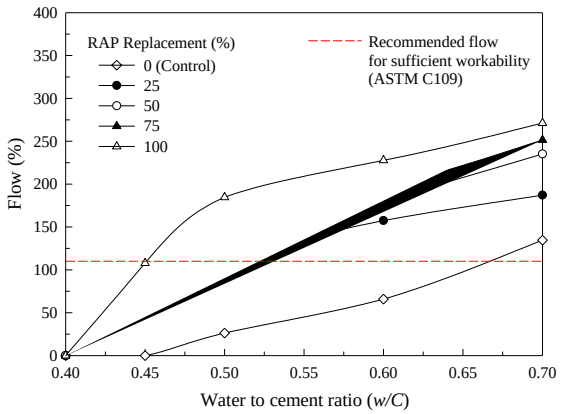

Fig. 2 Flow workability of CM containing RAP

due to the size of the aggregate. Although the RAP is rougher than that of sand and the RAP replacement tends to induce the increased volume fraction of aggregate due to the lower unit weight of RAP when compared with that of sand, the percentage of mortar flow increases directly with RAP replacement due to the effect of aggregate type. This unique behavior is different from past work by Hu and Wang [20]. RAP replacement affects the increasing flow of fresh mortars. At a particular mixture, RAP in the proportion increases both friction and the average size of aggregate which are represented by the higher FM when compared with sand but flow workability increases with the RAP replacement. This unique behavior can be revealed by the effect of water absorption, which is presented in the next section.

Compressive strength

The compressive strengths of CM at 7, 28, and 60 days of curing are presented in Fig. 3. For inadequate zone (*w/C* = 0.4 – 0.5), the compressive strength increased with 25% of RAP replacement then the strength dropped with the increase in RAP replacement. This pattern was observed for all the curing ages. The compressive strength development with curing time was observed for both RAP replacement and control samples.

The water to cement ratio of 0.45, which is an optimum point provided the maximum compressive strength for CM containing RAP. While the optimum point of control CM was observed at *w/C* of 0.5, these investigated results are in line with other past research [21-22]. The 7 and 28 days compressive strength of M†R25 and M†R50 passed the minimum requirement of Portland CM specified for high-speed railway application [22] for *w/C* of 0.40, 0.45, 0.50 and 0.60. The compressive strength varied according to the flow workability. However, the compressive strength of mortar decreased slightly, related to the RAP replacement.

The results of the unit weight of harden mortar are shown in Fig. 4. The unit weight decreased with increasing RAP replacement compared with those of M†R0 series (control mortar). It was due to the bulk unit weight of fine RAP lower than that of sand (*vide* Table 1). The maximum unit weight for RAP replacement was observed for the sample with *w/C* of 0.45. The bulk unit weight of mortar decreased with increasing w/C due to the pores of cement paste [23]. The mixing water in Table 2 includes the water reacted with cement and water that fills the pore of sand and RAP for SSD state. The experiment result conforms with the flow workability. However, the mixing water and mixing time played a significant role in the compressive strength and unit weight. The modified water absorption test was performed under various soaking time at 3, 6, 12, and 24 hours to investigate the variation of workability with mixing time.

Although the SSD-water absorption of RAP was higher than that of sand (*vide* Table 1), the percentage of flow increased with increase in the amount of RAP in mix proportion for *w/C* of 0.45 to 0.70. The rate of water absorption with the time of sand and RAP were different. The water absorption of sand and RAP under various elapsed times is shown in Fig. 5. The initial rate of water absorption of RAP for 1.5 hours (90 minutes) to 12 hours was slower than that of sand but gradually increased for 12 to 24 h. The compensated water, which was not fully absorbed at the initial mixing stage, is defined as free water. The additional percentage of flow composes of the percentage of flow due to reacted water and free

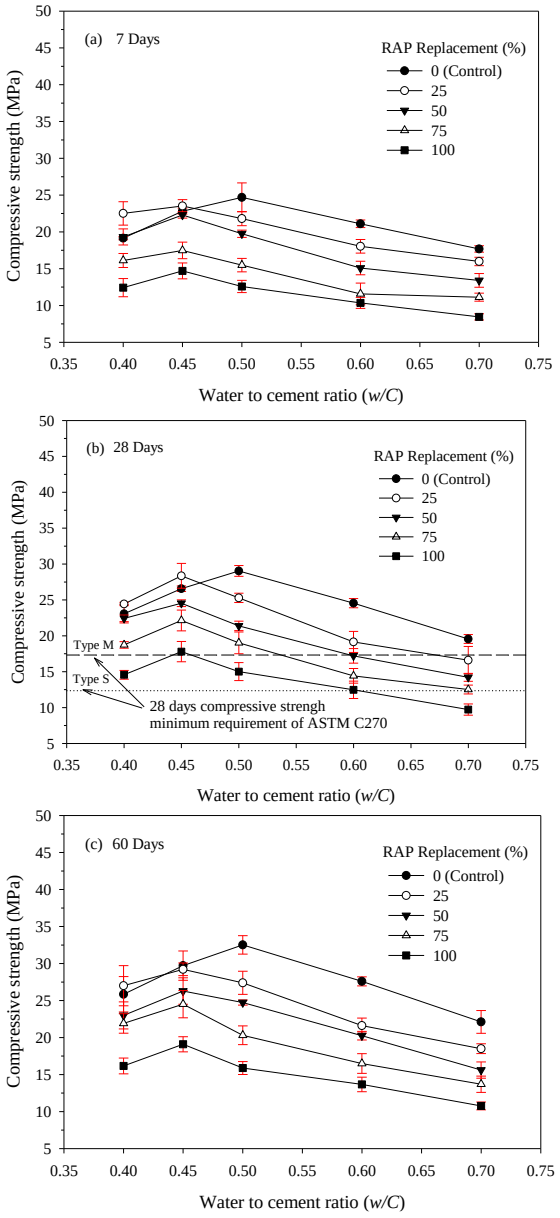

Fig. 3 Compressive strength of mortar for w/C of 0.40-0.70 at various RAP replacements and curing time

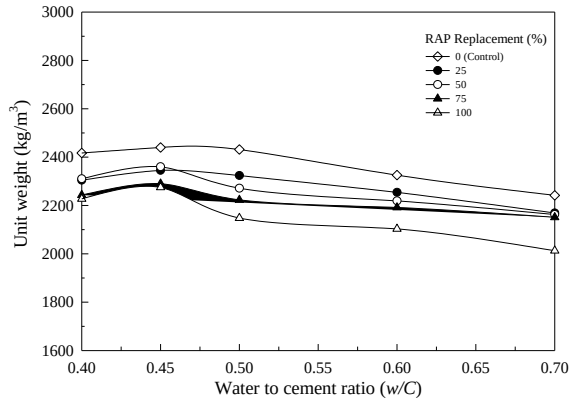

Fig. 4 Unit weight of harden CM containing RAP

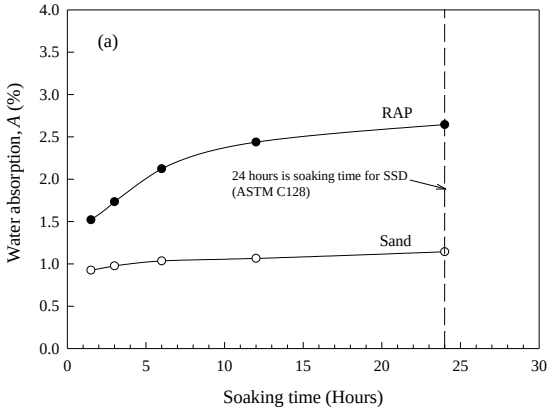

Fig. 5 Water absorption characteristic of sand and RAP

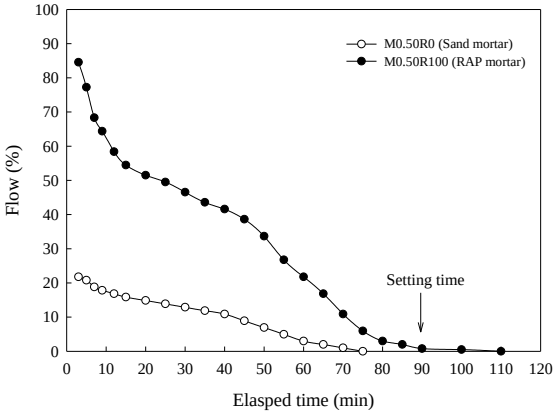

Fig. 6 Flow workability of mortar loss with elapsed time

water. The flow workability of mortar loss proved this assumption with elapsed time, as shown in Fig. 6 for sand and RAP mortars. The setting time of sand and RAP mortar were observed for 90 minutes of elapsed time. While the flow workability of RAP mortar was higher than that of sand mortar, it decreased rapidly with elapsed time. This result revealed that the increasing flow workability of mortar with RAP replacement was mainly affected by the free water at mixing time. The growing free water induces the decreasing compressive strength due to the increasing *w/C*. The effective water (*w**), which is a summation of reacted water and free water at 90 minutes of mixing time, is recommended for the analysis of strength development in CM contacting RAP.

Strength development with curing time

The compressive strengths increased with curing time for all of the RAP replacements. Fig. 7 presents the strength development of mortars in terms of curing time. The curves of strength development with curing time were the same for all mixtures. The compressive strength from the hydration reaction of cement increased up to the 28 days of curing; then the strength development curves went flat. At the early

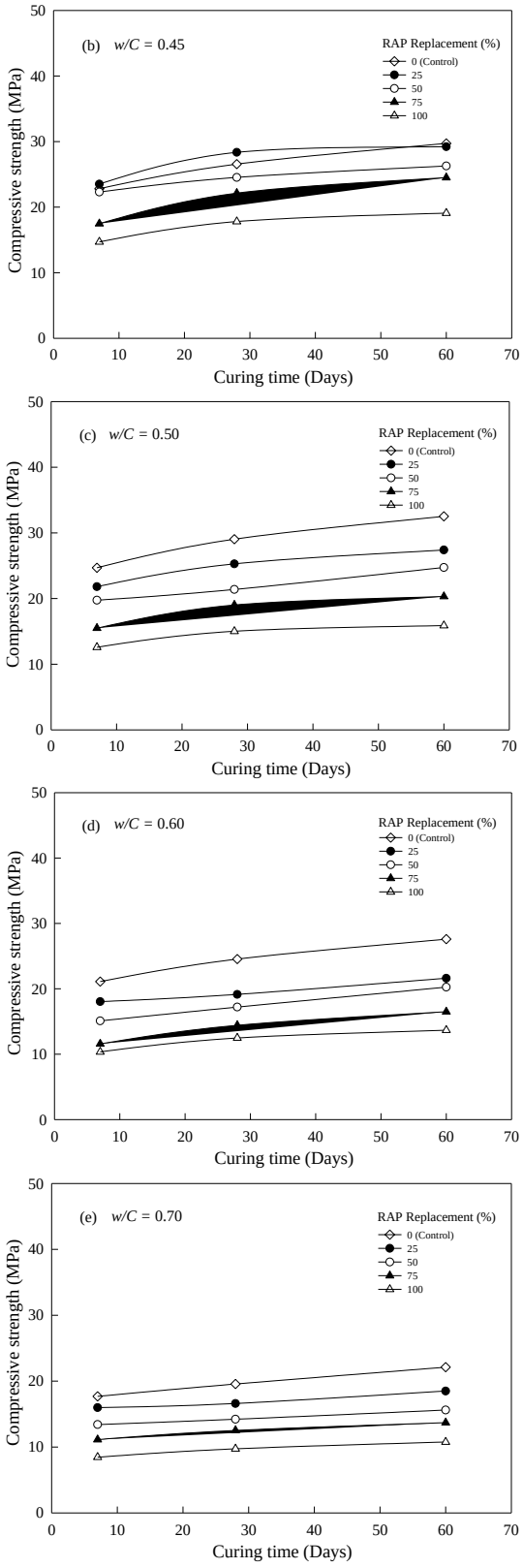

Fig. 7 Strength developments with curing time of sand and RAP mortar

ages of curing (7 days), the compressive strength of M†R25 and M†R50 were higher than those of control mortar (M†R0) for *w/C* of 0.40 and 0.45 while the compressive strength of other series was lower than the control mortar. At the long terms strength (60 days), the strength was mainly dependent on the RAP replacement as fine aggregate. The higher RAP lowered the strength.

CONCLUSIONS

A series of laboratory test was conducted to assess the strength mechanism of concrete mortar containing RAP instead of natural sand. The influence factors studied were mix proportions (RAP replacement, water to cement ratio), and curing time. The flow workability of CM increases with RAP replacement due to the free water, which is the compensated water, not fully absorbed at the initial mixing stage. The effective water to cement ratio (*w*/C*) is recommended for strength analysis. The compressive strength varies according to the flow workability. The compressive strength of mortar decreases slightly, related to the RAP replacement. However, the 7 and 28 days compressive strength of M†R25 and M†R50 passed the minimum requirement of Portland CM specified for railway application [22] for *w/C* of 0.40, 0.45, 0.50 and 0.60.

ACKNOWLEDGMENTS

This research is supported by Rajamangala University of Technology Isan Contact No. NKR2561REV030.

REFERENCES

[1] Zaumanis, M., and Mallick, R.B., Review of very high-content reclaimed asphalt use in plant-produced pavements: state of the art, International Journal of Pavement Engineering, Vol.16, No.1, 2015, pp.39–55.

[2] Suebsuk, J., Suksan, A., and Horpibulsuk, S., Strength assessment of cement treated soil/reclaimed asphalt pavement (RAP) mixture, International Journal of GEOMATE, Vol.6, No.2, 2014, pp.878-884.

[3] Suebsuk, J., Horpibulsuk, S., Suksan, A., Suksiripattanapong, C., Phoo-ngernkham, T., and Arulrajah, A., Strength prediction of cement-stabilised reclaimed asphalt pavement and lateritic soil blends, International Journal of Pavement Engineering, Vol.20, No.3, 2019, pp.332–338.

[4] Mangiafico, S., Benedetto, H.D., Sauzéat, C., Olard, F., Pouget, S., Dupriet, S., Planque, L., and Van Rooijen, R., Statistical analysis of the influence of RAP and mix composition on

viscoelastic and fatigue properties of asphalt mixes, Materials and Structures, Vol.48, 2015, pp.1187-1205.

[5] Visintine, B., Khosla, N. P., and Tayebali, A., Effects of higher percentage of recycled asphalt pavement on pavement performance, Road Materials and Pavement Design, Vol.14, 2013, pp.432-437.

[6] Yu, B. G., X, Wu, M & Ni, F., Application of a high percentage of reclaimed asphalt pavement in an asphalt mixture: blending process and performance investigation, Road Materials and Pavement Design, Vol.18, No.3, 2017, pp. 753-765.

[7] Huang, B., Shu, X., and Burdette, E.G., Mechanical properties of concrete containing recycled asphalt pavements, Magazine of Concrete Research, Vol.58, No.5, 2006, pp. 313-320.

[8] Al-Oraimi, S., Hossam, F., and Hago, H.A., Recycling of reclaimed asphalt pavement in Portland cement concrete, Journal of Engineering Research, Vol.6, No.1, 2009, pp. 37–45.

[9] Hossiney, N., Tia, M., and Bergin, M.J., Concrete containing RAP for use in concrete pavement, International Journal of Pavement Research and Technology, Vol.3, No.5, 2010, pp. 251-258.

[10] Mathias, V., Sedran, T., and Larrard, F., Recycling reclaimed asphalt pavement in concrete roads, Proc., International RILEM Conference on the Use of Recycled Materials in Buildings and Structures, pp.66-75.

[11] Huang, B., Shu, X., and Li, G., Laboratory investigation of Portland cement concrete containing recycled asphalt pavements, Cement and Concrete Research, Vol.35, No.10, 2005, pp. 2008-2013.

[12] Huang, B., Shu, X., and Burdette, E.G., Mechanical properties of concrete containing recycled asphalt pavements, Magazine of Concrete Research, Vol.58, No.5, 2006, pp.313-320.

[13] Katsakou, M., and Kolias, S., Mechanical properties of cement-bound recycled pavements, ACI Materials Journal, Vol.160, No.4, 2007, pp. 171-179.

[14] Topcu, I., and Isikdag, B., Effects of crushed RAP on free and restrained shrinkage of mortars International Journal of Concrete Structures and Materials, Vol.3, No.2, 2009, pp.91-95.

[15] Li, G., Zhao, Y., Pang, S. S., and Huang, W., Experimental study of cement-asphalt emulsion composite, Cement and Concrete Research, Vol.28, No.5, 1998, pp.635-641.

[16] Tompkins, D., Khazanovich, L., Darter, M. I., and Walter, F., Design and construction of sustainable pavement, Transportation Research Board, Record No.2098, 2009, pp.75-85.

[17] McDaniel, R.S., and Anderson, R.M., Recommended use of reclaimed asphalt pavement in the superpave mix design method: technician's manual, West Lafayette, IN: North Central Superpave Center, 2011.

[18] Haach, V. G., Vasconcelos, G., and Lourenço, P. B., Influence of aggregates grading and water/cement ratio in workability and hardened properties of mortars." Construction and Building Materials, Vol.25, 2011, pp.2980–2987.

[19] Quiroga, P.N., The effect of aggregate characteristics on the performance of Portland cement concrete, PhD Dissertation, The University of Texas at Austin, Austin, TX., 2003.

[20] Hu, J., and Wang, K., Effects of aggregate on flow properties of mortar, Proc., the 2005 Mid-Continent Transportation Research Symposium, Iowa State University, pp.1-8.

[21] Rao, G.A., Generalization of Abrams' law for cement mortars, Cement and Concrete Research, Vol.31, No.3, 2001, pp.495–502.

[22] Qiang, W., Peiyu, Y., Ruhan, A., Jinbo., Y., and Xiangming, K., Strength mechanism of cement-asphalt mortar, Journal of Materials in Civil Engineering, Vol.23, No.9, 2011, pp.1353-1359.

[23] Espino, E.I., An investigation into the relation between the strength and density of normal concrete." Master Thesis, University of Illinois, Urbana, Illinois, 1966.

9th Int. Conf. on Geotechnique, Construction Materials and Environment, Tokyo, Japan, 20-22 November 2019, ISBN: 978-4-909106025 C3051

EFFECT OF ASSOCIATED CATIONS ON CHLORIDE PENETRATION INTO CONCRETE

Nattapong Damrongwiriyanupap[1], Worajak Janwaen[1], Suchart Limkatanyu[2] and Yunping Xi[3]
[1]School of Engineering, University of Phayao, Thailand; [2]Faculty of Engineering, Prince of Songkla University, Thailand; [3]College of Engineering and Applied Science, University of Colorado, Boulder, USA

ABSTRACT

This study aims to investigate the effect of cations associated in three different chloride solutions, NaCl, CaCl2, and MgCl2, on the rate of chloride penetration into concrete. Chloride ponding test was conducted at 15 and 30 days of exposure. The concentration profiles of various ions were undertaken including Cl-, Na+, K+, Mg2+ and the effect of different cations on the diffusion rate of chloride ion into concrete was systematically studied. The test results showed that cations in different chloride solutions have strong influence on the diffusion rate of chloride ions. The rate of chloride penetration in order of fastest to slowest was CaCl2, NaCl, and MgCl2, respectively. The experimental data were compared to numerical results obtained from a numerical model developed based on the Nernst-Planck equation which took into account the ionic coupling effects among ions in chloride solutions and ions in concrete pore solution, Na+, K+, and OH-, and a satisfactory agreement was observed.

Keywords: Chloride, Concrete, Deicing salts, Associated cations.

INTRODUCTION

It has been established for several years in the research studies that chloride is one of the most significant causes of corrosion of steel in reinforced concrete structures. This deleterious effect can reduce the load-bearing capacity, service life, and aesthetics of structures subjected to chloride environments such as bridge decks, parking garages, and marine/offshore structures. Also, the degradation due to corrosion is one of the long-term durability problems for reinforced concrete structures. This study focuses on penetration of deicing salts which are considered as one of the chloride sources. Chloride based deicers are widely used for ice and snow control on roads and bridges in snow-belt regions. In some areas, one mile of four-lane roadways requires the application of more than 100 metric tons of deicing salts each year. About 15.4 million tons of road salts used annually in the U.S. for deicing of highways and roadways [1]. In general, different deicers are frequently used on the same areas for ice and snow control, for example, magnesium chloride solution is used before a snow storm for ice control, and calcium chloride solid salt is used during the snow storm for snow control. As a result, multiple species of deicing salts coexist on the surface and penetrate into concrete simultaneously. The studies of the effect of deicing salts and chloride solutions on concrete have been done by some researchers. Al-Hussaini et al. [2] conducted the experimental study on the effect of free chloride ion source mixed in cement mortar. Two different types of chlorides, NaCl and $CaCl_2$, were selected in the study. They found that NaCl presented more free chloride ion than $CaCl_2$ at all concentration, from 0.5% to 2% by mass of cement, and pH of cement mortars were lower in the case of NaCl. As a result, cement mortars mixed with NaCl can accelerate the corrosion mechanism when compared with $CaCl_2$. In contrast to Arya et al. [3] study, $CaCl_2$ had greater effect than NaCl in terms of producing more free and bound chloride ions when mixed and immersed in specimens. Also, they found from the thin cement pate specimens immersed in 20 g/l of different types of chloride solutions that associated cation in solutions was one of the most important factors affecting on chloride binding capacity. The highest free chloride content was found from the specimens immersed in $MgCl_2$ solution and it decreased in the order of $MgCl_2$ > NaCl > Sea-water > $CaCl_2$. Similar to bound chloride content, $MgCl_2$ had the highest binding capacity and it ranked as $MgCl_2$ > $CaCl_2$ > NaCl > Sea-water. In terms of total chloride content, it can be ordered as $MgCl_2$ > $CaCl_2$ > NaCl > Sea-water.

In this study, three different types of deicers with different associated cations were selected to investigate how these ions affect the chloride ingress rate in concrete. The laboratory tests were conducted to evaluate the penetration of three types of chloride-based deicers, i.e. 3% NaCl, 3% $CaCl_2$, and 3% $MgCl_2$. The study was performed in terms of ponding test. This method was chosen because, in reality, deicing salts are applied on the top surface of concrete structures and then ingress into the bottom where reinforcing steels were located.

EXPERIMENTAL PROCEDURE

The mix proportions with two different water-cement ratios, 0.55 and 0.65, used in this study. After 28 days of curing time, all specimens were immersed in water for 30 days to achieve saturation. The chloride ponding test in this study was conducted in saturated condition so that the effect of moisture was not considered. In order to perform chloride ponding test, the ponding reservoirs were designed by using 5" tall plastic sleeves cut from PVC concrete cylinder molds with 4" diameter. Then, PVC sleeves were put on the top of concrete specimens for 2" in depth so that this created the 3" reservoir. Steel band clamps were used to tighten the PVC sleeves and concrete specimens in order to prevent leakage. A bead of silicone was added around the interface between sleeve and specimen to further prevent water leakage and create watertight compartment for chloride solution at the top of specimen as seen in Fig. 1.

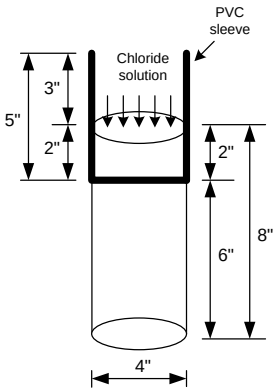

Fig. 1 A concrete sample prepared for the chloride ponding test.

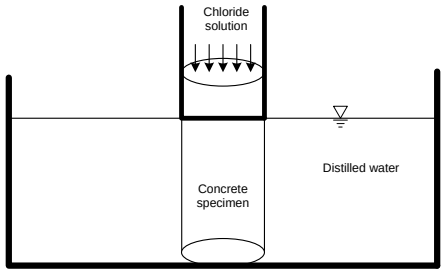

Fig. 2 Chloride ponding test set up.

Once the silicone had dried, all specimens were exposed to chloride solutions. The three different types of chloride solutions, as mentioned above, were ponded on top of samples. The bottom face of specimen was exposed to distilled water so that there would be no moisture effect due to moisture gradient as shown in Fig. 2. The samples were removed from the solutions after 15 and 30 days. The chloride concentration was measured by samples of concrete powder collected at various depth from the surface exposed to chloride solutions. The total chloride contents were obtained from concrete powder samples by using the rapid chloride test instrument.

RESULTS AND DISCUSSION

As mentioned previously, total chloride concentration is analyzed by using the Rapid Chloride Test Water-soluble (RCTW) method [4]. The results of this electrochemical analysis were represented in mille Volt (mV) which is responded to chloride concentration at each depth of concrete specimen. Total chloride profiles are illustrated in Figs. 3 through 6. Figs. 3 and 4 are plotted for specimens with 0.55 w/c exposed to chloride solutions, and Figs. 5 and 6 are represented for samples with 0.65 w/c.

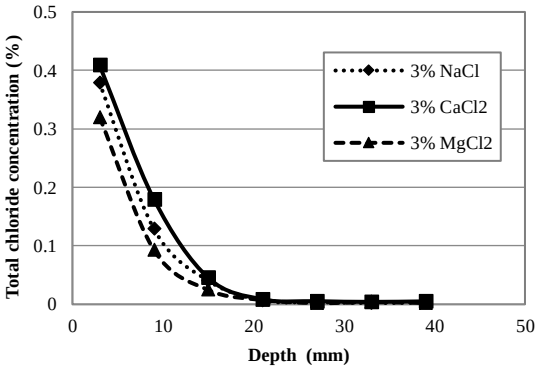

Fig. 3 Chloride profiles of concrete specimen at 15 days of exposure with 0.55 water-cement ratio.

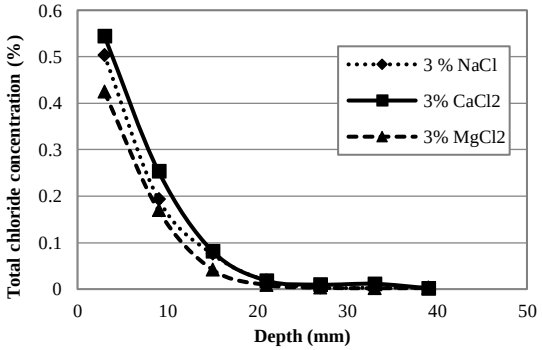

Fig. 4 Chloride profiles of concrete specimen at 30 days of exposure with 0.55 water-cement ratio.

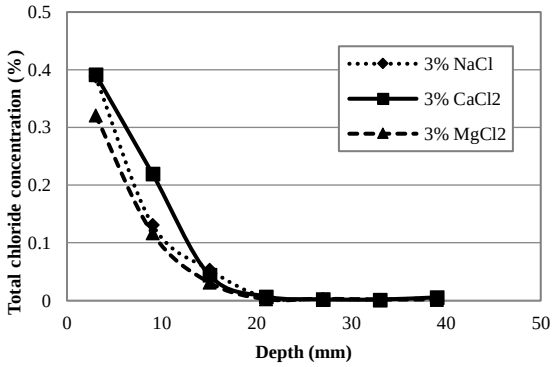

Fig. 5 Chloride profiles of concrete specimen at 15 days of exposure with 0.65 water-cement ratio.

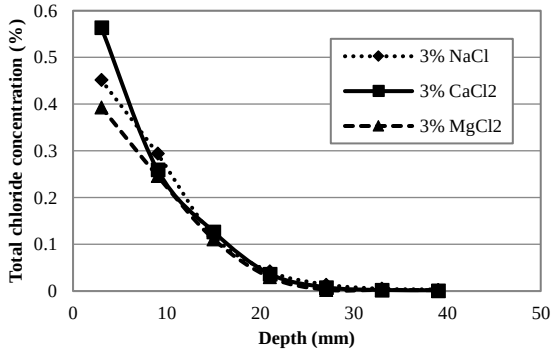

Fig. 6 Chloride profiles of concrete specimen at 30 days of exposure with 0.65 water-cement ratio.

It can be observed from the profiles in Figs. 3, 4, 5, and 6 that the chloride concentrations contribute from 3% $CaCl_2$ solution tend to be the highest when compared with 3% NaCl and 3% $MgCl_2$, at the same depth. This is because 3% solid $CaCl_2$ salt diluted in water produces higher chloride ions than 3% NaCl and 3% $MgCl_2$. The extraction of these three chloride-based salts in solution can be described as Eqs. (1), (2), and (3). In order to compare the test results with numerical results, 3% NaCl, 3% $CaCl_2$, and 3% $MgCl_2$ by weight diluted in 1 liter of distilled water can be converted into mol/l as 0.513, 0.270, and 0.148, respectively. One can see from the Eqs. (1), (2), and (3) that 3% $CaCl_2$ can extract chloride ions higher than 3% NaCl and 3% $MgCl_2$ and 3% $MgCl_2$ produces the smallest amount of chloride ions in solution. This means, at the fixed depth, the highest total chloride concentration is found in the case of 3% $CaCl_2$ and the lowest one occurs in the case of $MgCl_2$.

$$\underset{(0.513\ mol/l)}{3\%\,NaCl} \rightarrow \underset{(0.513\ mol/l)}{Na^+} + \underset{(0.513\ mol/l)}{Cl^-} \quad (1)$$

$$\underset{(0.270\ mol/l)}{3\%\,CaCl_2} \rightarrow \underset{(0.270\ mol/l)}{Ca^{2+}} + \underset{2(0.270\ mol/l)}{2Cl^-} \quad (2)$$

$$\underset{(0.148\ mol/l)}{3\%\,MgCl_2} \rightarrow \underset{(0.148\ mol/l)}{Mg^{2+}} + \underset{2(0.148\ mol/l)}{2Cl^-} \quad (3)$$

To compare experimental data with numerical results, chloride diffusion in concrete is simulated using the Nernst-Planck equation which is dependent on diffusion mechanism due to concentration gradient and migration due to ionic interaction. The flux equation of each ionic species is expressed as,

$$J_i = -D_i\left(\frac{\partial C_i}{\partial x} + \frac{z_i F}{RT}\frac{\partial \phi}{\partial x}C_i\right) \quad (4)$$

where C_i is the concentration, D_i is the diffusion coefficient, z_i is the charge number, F is the Faraday's constant, R is the gas constant, T is the temperature, Φ is the electrostatic potential, and index i represents for the *i-th* species. Theoretically, the Nernst-Planck equation can be used to explain the penetration of multi-types of chloride solutions into concrete. This is because each type of salt has different associated cations that affect in the second term, migration process, of the Nernst-Planck equation. In order to verify the experiments, the test results of concrete specimens exposed to chloride solutions with 0.55 water-cement ratio at 15 and 30 days of exposure are plotted compares with the numerical results obtained by the Nernst-Planck equation. Figs. 7 and 8 show the total chloride profiles obtained from the experiment compared with the numerical results. It is noticed from these figures that the total chloride concentrations obtained from the experiment agree very well with numerical results. The present model can be used to simulate not only chloride diffusion but also other chemical species. Due to test data available for cation species, Na+ and K+, the concentration profiles of sodium and potassium predicted by this present model are compared with the test data obtained from concrete specimens with 0.55 water-cement ratio exposed to three different chloride solutions at 15 days of exposure as illustrated in Figs 9 through 11. As seen, the trends of sodium and potassium profiles resulting from ponding test match the prediction model. However, the concentration values of these ions deviate from the model in cases of specimens exposed to 3% $CaCl_2$ and 3% $MgCl_2$. A good agreement can be observed in case of concrete sample exposed to 3% NaCl. From the comparison point of view, it can be concluded that the cations associated in chloride solution have influence on the penetration of chloride ions into concrete structures.

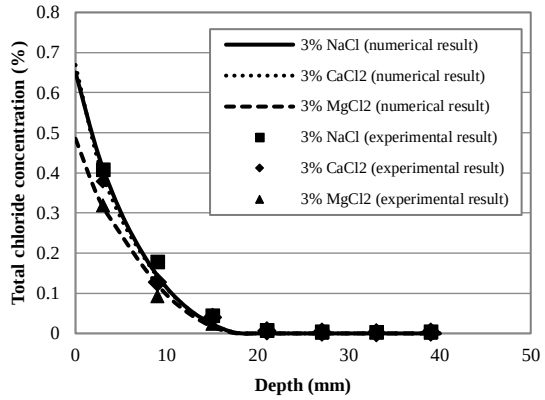

Fig. 7 A comparison between numerical and experimental result of specimens at 15 days of exposure.

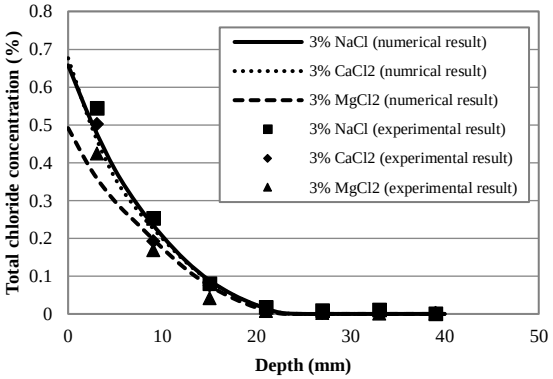

Fig. 8 A comparison between numerical and experimental result of specimens at 30 days of exposure.

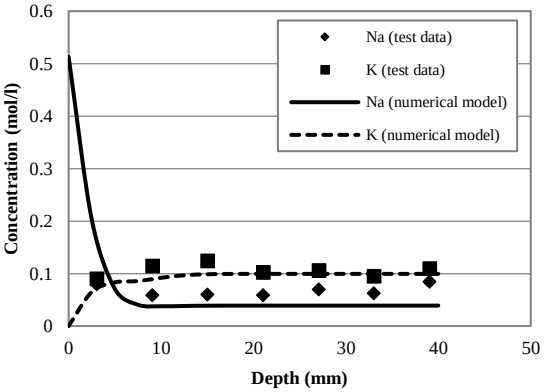

Fig. 9 A comparison between numerical and experimental result of specimens exposed to 3% NaCl at 15 days of exposure.

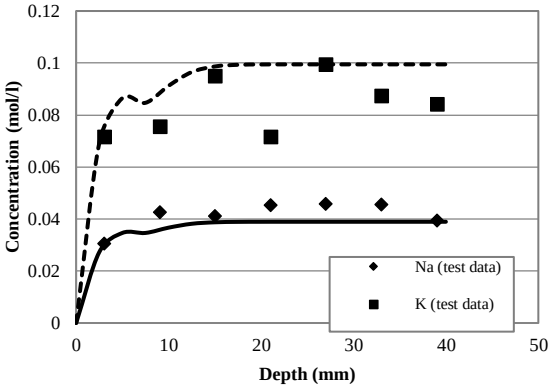

Fig. 10 A comparison between numerical and experimental result of specimens exposed to 3% $CaCl_2$ at 15 days of exposure.

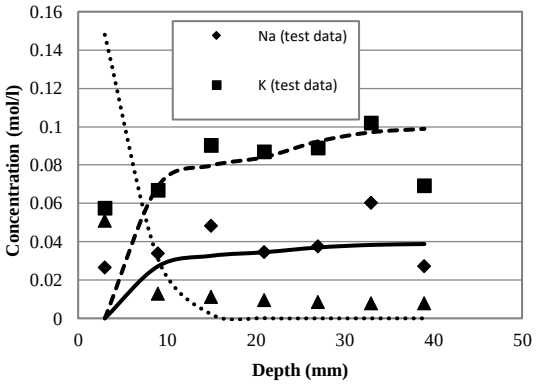

Fig. 11 A comparison between numerical and experimental result of specimens exposed to 3% $MgCl_2$ at 15 days of exposure.

CONCLUSIONS

1. An experimental study was conducted on the penetration of various types of deicing salts into concrete. Three different types of deicers, chloride-based salts, were selected to investigate the influence of associated cations on diffusion rate of chloride solutions.

2. Concrete specimens were divided into three groups exposed to six different chloride solutions that is 3% NaCl, 3% $CaCl_2$, and 3% $MgCl_2$.

3. In order to investigate only the diffusion mechanism of the effect of cations associated in chloride solutions, the moisture effect is neglected so that the experiment was performed in saturated condition.

4. The experimental results show that cations associated in chloride solutions have significant effect on the penetration rate of chloride ions. This can be summarized in the order of $CaCl_2$ > NaCl > $MgCl_2$ from the fastest to slowest chloride penetration.

5. The experimental results are compared to the numerical results obtained from the Nernst-Planck model which accounts for the interaction between

ions and a good match is obtained in a case of total chloride concentration. The good trends of sodium and potassium profiles obtained from the experiment can be observed when compared to the mathematical model.

ACKNOWLEDGMENTS

This work was financially supported by the TRF New Research Scholar Grant no. MRG6180056. The part of the present work was also supported by the European Commission Research Executive Agency via the Marie Skłodowska-Curie Research and Innovation Staff Exchange Project (689857-PRIGeoC-RISE-2015) and the Industry Academia Partnership Programme-2 (IAPP1617\16) "Development of Sustainable Geopolymer Concrete." The authors also would like to acknowledge the support of the Department of Civil Engineering, School of Engineering, University of Phayao, Thailand.

REFERENCES

[1] Basu R., Breshears J.S., and Clausen E.C., Calcium Magnesium Acetate at Lower Production Cost: Production of CMA Deicer from Biomass, Federal Highway Administration, Virginia Report No. FHWA-RD-98-055, 1999.

[2] Al-Hussaini, M.J., Sangha, C.M., Plunkett, B.A., and Walden, P.J., The effect of chloride ion source on the free chloride ion percentages in OPC mortars, Cement Concrete Res., 20(5), 1990, 739-745.

[3] Arya, C., Buenfeld, N.R., and Newman, J.B., Factors Influencing Chloride-Binding in Concrete, Cement Concrete Res., 20, 1990, 291-300.

[4] Damrongwiriyanupap, N., Modeling the Penetration of Multi-Species Aggressive Chemicals into Concrete Structures, Ph.D. Dissertation, University of Colorado, Boulder, Colorado, USA, 2010.

9th Int. Conf. on Geotechnique, Construction Materials and Environment, Tokyo, Japan, 20-22 November 2019, ISBN: 978-4-909106025 C3051

UNCONFINED COMPRESSIVE STRENGTH OF CLAY REINFORCED WITH KEROSENE-TREATED COIR FIBER

Lestelle Torio-Kaimo[1], Annamarie M. San Diego[1], Matthew Travis Alcantara[1]
[1]Geotechnical Engineering Group, Institute of Civil Engineering, University of the Philippines Diliman, Quezon City 1101

ABSTRACT

The need for ground modification is more prevalent as the availability of good site conditions decrease. Among the available methods of ground modification, soil reinforcement is emerging as a promising alternative. Fiber reinforcement involves mixing fibers with soil to improve its strength characteristics. Natural fibers have the following advantages over synthetic: affordability, bulk availability, and eco-friendliness. Coir fiber has the greatest tensile strength and slowest rate of biodegradation among natural fibers. This study presents the effect of kerosene-coated coir on strength and stress-strain response of a cohesive soil. Preliminary soil tests were performed and the soil was classified as CH or high-plasticity clay. Water absorption capacity tests revealed that kerosene reduces moisture intake of coir by up to 170%. Reconstituted samples, with fiber concentrations ranging from 0% to 2% by dry weight of soil, were tested for unconfined compressive strength in optimum moisture and dry states. Results showed that incorporation of coir improved the strength and stress-strain response of high-plasticity clay by as much as 52% compared to unreinforced samples. Aside from increasing peak strength, addition of coir also improved the post-peak behavior of the samples. Results show improved ductility in the coir-reinforced samples tested at optimum moisture condition. An increase in the elastic modulus, by as much as 78%, was also observed. These improved performance was exhibited at 1.5% fiber content. Dry samples tested show that addition of coir caused a 43% strength gain. However, dry samples exhibited brittle failure and minimal post-peak shear resistance, regardless of fiber content

Keywords: Soil reinforcement, Coir fiber, Clay reinforcement, Ground modification

INTRODUCTION

Ground modification refers to a variety of techniques used to improve the engineering characteristics of the ground. It can be used in various soil conditions such as collapsible soils, expansive soils, soft soils, or soils with inadequate mechanical properties. One method of modifying the ground is the use of reinforcing elements in the form of strips, bars, sheets, membranes, and fibers.

Fiber reinforcement involves mixing natural or synthetic fibers with soil, where the fibers act as tensile resisting elements that improve soil strength. The primary advantages of natural fibers are that they are cheap, abundantly available, and biodegradable. In the Philippines, the locally available natural fibers include abaca, coir, banana, pineapple, and bamboo. Among these natural fibers, coir has the greatest tensile strength and has the slowest rate of biodegradation [1]. Coir is useful in practical applications as a geotextile material. The fibers are twined and woven into "coco nets" which are primarily used for erosion control. Other coir products include coir mattresses, coir tufted mats, coir ropes, and coir logs.

The Philippines, being a tropical country, is abundant in coconut trees. In 2015, the Philippine Coconut Authority reported a total of 3.517 million hectares planted with coconuts in the country. This area is also 26% of the country's total agricultural land. The average nut production is 14.902 billion nuts/year.

In the context of sustainable development, coir fiber is a promising soil reinforcement material because it is indigenous, abundantly available, cheap, and environment-friendly. It can be a cost-effective alternative to commercially available additives such as cement and lime. Coir fiber reinforcement can be used in cases where mixing with fibers can be done onsite, such as in pavement subgrade, small embankments, and engineered fill.

Processing of coir contributes to rural employment and income generation. Large-scale utilization of coir can expand the market for the country's coir industry.

Lastly, there is a need to find a suitable treatment method that will increase the life span of coir fibers. To serve its intended purpose as soil reinforcement for a longer duration, a protective coating may be required.

Coir, just like any natural fiber, gradually loses strength over time. Depending on the duration of use,

it may require a physical coating to protect it from moisture-induced degradation. In this context, this paper presents the results of an experimental investigation on the effect of coated coir fiber reinforcement on the strength and stress-strain response of local clayey soil.

The primary objective of the research is to study the effect of kerosene-coated coir fiber reinforcement on the strength of clayey soil. To attain this, it is necessary to investigate effect of kerosene coating on water absorption capacity of coir, examine effect of coir on the unconfined compressive strength of soil and the soil stress-strain response, and, evaluate effect of coir on soil samples tested at optimum moisture content and dry state.

FIBER REINFORCEMENT IN SOIL

Hausmann [2] classified ground modification techniques into four: mechanical modification, hydraulic modification, physical and chemical modification, and modification by inclusions and confinement.

Mechanical modification involves increasing the density of soil by compaction, which requires mechanical energy. This is achieved through plate vibrators, impact rollers, and special techniques like vibro-flotation and blasting. Hydraulic modification involves removal of pore water from the ground using vertical drains or wells. Physical and chemical modification is the use of additives mixed or blended with soil. Natural soils, cement, fly-ash, and limestone are some examples of soil additives. Modification by inclusions and confinement is the use of strips, meshes, bars, fabrics, and fibers to reinforce the soil.

Soil reinforcement by inclusions has the ability to improve strength and stability, reduce settlements, improve bearing capacity, and reduce lateral deformation [3]. One method of reinforcing soil is with the use of fibers. Nature provides an example of this in the roots of trees stabilizing near-surface soil with low shear strength. The roots are distributed randomly within the soil mass and act as tension members to improve the strength characteristics of the soil [4].

The stabilizing effects of plant roots may be replicated artificially with the use of natural or synthetic fibers. Randomly distributed fibers (RDFs) are mixed with soil in the same manner as an additive. Unlike traditional geosynthetics, they are not oriented in a specific direction. The main advantages of RDFs are the relative isotropy of the soil mass and the absence of predefined planes of weakness [5].

Fiber

Shukla [4] defines fiber as a unit of matter characterized by fineness, flexibility, and high ratio of length to diameter. Fibers fall under two categories: synthetic and natural. Examples of synthetic fibers are glass fibers, polypropylene (PP) fibers, polyester (PET) fibers, polyethylene (PE) fibers, metal fibers, carbon fibers [4]. Natural fibers include coir, jute, palm fibers, sisal fibers, bamboo fibers, banana fibers, manila fibers, and cotton fibers.

The advantages of natural fibers are strength, bulk availability, affordable cost, and environmental-friendly characteristics. Unlike synthetic fibers, natural fibers do not contribute to greenhouse gas emissions in construction.

Some practical disadvantages of natural fibers are variability of the fiber geometry and biodegradability. Most natural fibers except coir are not durable in alkaline environments. Natural fibers exhibit gradual loss of strength over time, with rate of strength loss varying across fiber types [4].

Fiber Treatment

The issue of biodegradability can be overcome by suitable fiber treatment methods. These modification techniques can make natural fibers on par with or even superior to synthetic fibers. Unnikrishnan [6] provides some possible treatment methods for natural fibers. These are alkali treatment, enzyme treatment, UV grafting with monomers, treatment using chemicals, natural anti-microbial finishing, vegetable oils, and physical coatings.

Physical coatings modify the surface of fibers using synthetic polymers or resins. By physically preventing the entry of moisture into the fiber, this technique improves the durability of natural fibers [6].

A study by T. Sanyal and K. Chakraborty [7] found that bitumen coating applied on jute geotextiles could defer degradation by 3 to 4 years. However, bitumen affects the flexibility and drapability of the geotextile. H.N. Ramesh and K.V. Manoj Krishna [1] conducted water absorption studies on coir coated with kerosene, bitumen, and varnish. After 365 days of submergence, kerosene and bitumen coated coir fibers showed decreased water absorption, with kerosene providing the highest reduction in moisture intake compared to uncoated coir. Varnish, on the other hand, did not exhibit significant difference.

Coconut Coir as Soil Reinforcement

Coir is a fiber extracted from the outer husk of coconuts. There are two types of coir: brown fibers

from mature coconuts and white fibers from young coconuts. Brown fibers are thick and have strong resistance to abrasion. White fibers have a smooth and fine surface, but are also weaker than brown fibers [8].

Coir has the greatest tensile strength of most natural fibers [4]. It contains 40% lignin and 54% cellulose [9]. Its high amount of lignin, a complex hydrocarbon polymer, is what makes coir degrade slower than other natural fibers. Lignin makes the stem rigid and protects the fiber against biological attack [6]. Coir fibers may be used in engineering applications for a period of 1 to 2 years [4].

Several researches have investigated coir as randomly distributed fiber on different types of soil. Laboratory tests including triaxial tests, unconfined compression tests, and California bearing ratio tests showed significant results on the effect of coir inclusion.

Sujatha et al. [10] studied the influence of randomly distributed coir fiber on the compaction characteristics, stress-strain behavior, and unconfined compressive strength of highly compressible clay. The soil sample has a liquid limit of 53 and plasticity index of 38. Compaction tests were performed to determine the optimum moisture content (OMC) and maximum dry density (MDD) of unreinforced and reinforced samples. Study showed that OMC increased and MDD decreased with the inclusion of coir. The increase in OMC was attributed to the tendency of coir fibers to absorb moisture. Replacement of fibers in the soil matrix caused a decrease in mass occupied in the standard volume, explaining the decrease in MDD.

Unconfined compression tests were carried out to determine the effect of coir fiber on stress- strain behavior and unconfined compressive strength of the soil sample. Four fiber concentrations were studied: 0%, 0.25%, 0.5%, 0.75%, and 1%. Addition of coir fiber resulted to an increase in unconfined compressive strength, with the optimum fiber content being 0.75%. Beyond 0.75%, clumping of fibers was observed and resulted to a decrease in strength. Figure 1 shows that stress-strain of soil shifted to a more plastic behavior.

Devdatt et al. [11] made an experimental study on expansive soil mixed with varying concentrations of coir (0% to 1%). Results of compaction tests revealed a decreasing trend in OMC and increasing trend in MDD with addition of coir. Soaked and unsoaked California bearing ratio (CBR) tests were also conducted. Results exhibited a linearly increasing trend in both soaked and unsoaked CBR value. A similar study by Peter et al. [12] investigated the behavior of soft soil stabilized with varying concentrations of coir pith (0% to 3%) and coir fiber (0% to 1%) by conducting California bearing ratio (CBR) tests and static triaxial tests. The optimum stabilization scheme found in the study was 2% coir pith and 6% short coir fiber, which exhibited the greatest improvements in CBR value. Stress-strain curves from triaxial testing revealed a more ductile behavior in the coir-stabilized sample. The combined treatment of coir pith and fiber also increased the elastic modulus by 1.74 MPa.

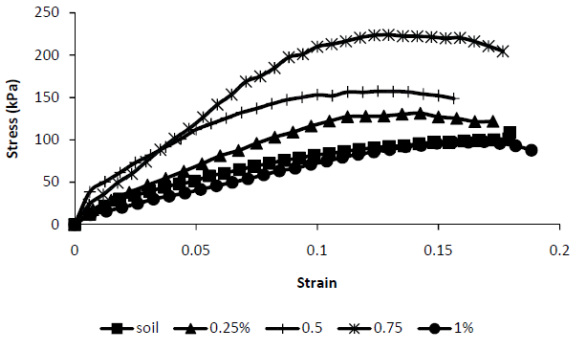

Fig.1 Stress-strain Plots of Unreinforced and Coir-Reinforced Samples [11]

In a study by Sivakumar Babu, et.al. [13], the effect of coir fiber parameters on strength and stiffness of sandy soil was studied. Triaxial tests were performed for varying confining pressures, fiber lengths, fiber contents, and fiber diameters. Fiber contents varied from 0% to 2.5% by weight of soil. Test results showed that deviator stress at failure increased as the fiber content increased. This was observed in all variations of confining pressures. The optimum coir content corresponding to the maximum strength improvement was at 2% to 2.5%. The researchers also noted that preparing specimens beyond 2.5% fiber content was quite difficult. Coir fibers grouped according to diameter (0.15, 0.25, and 0.35 mm) were also tested to observe the effect of fiber diameter on strength of soil. For both confining pressures of 50 and 100 kPa, the deviator stress at failure increased with increasing fiber diameter. This was attributed by the researchers to the increase in pullout resistance for fibers with larger diameter.

Fiber diameter and content was also kept constant while lengths were varied (10, 15, 25, and 30 mm). The maximum strength improvement was exhibited by samples with 15 mm fibers. Short fibers (10 mm) have less area in contact with soil, resulting to less pullout resistance and less strength gain. Preparing samples with longer (30 mm) fibers was reported to be difficult, making them ineffective as reinforcements.

Sivakumar Babu, et.al, [14] conducted an experimental investigation on the use of coir for

improving expansive black cotton soil. The degree of improvement in strength, shrinkage, swelling, and compressibility due to addition of fibers was measured. Length of coir fibers were kept at 15 mm, since this was the optimum length found in Sivakumar Babu and Vaseduvan's related study on coir-fiber reinforced sand.

Test results revealed the following: (1) deviator stress at failure increased with increasing fiber content; (2) deviator stress increased with increasing fiber diameter; (3) cohesion and friction angle increased as fiber content increased; (4) coir fibers reduced soil swell potential and compression index. The study concluded that coir as randomly distributed fiber contributes significant improvement in expansive black cotton soils.

Another study by Dasaka and Sumesh [15] evaluated the effect of coir on the stress-strain response of a reconstituted fine-grained soil. Unconfined compression tests and unconsolidated-undrained (UU) triaxial tests were performed using fiber contents in the range of 0% to 2% by dry weight of soil. Results of the study show that unconfined compressive strength (UCS) increased with increase in fiber dosage. At 1.5% fiber content (optimum), the UCS of reinforced soil is more than twice that of unreinforced soil. However, the study also found that UCS of soil reinforced with 30-mm length fibers is less than that of unreinforced soil. The researchers recommend using 15 mm fiber lengths when forming 38 mm-diameter soil specimens.

From triaxial test results, it was found that peak deviator stress and major principal stress at failure increased with increase in fiber dosage for all confining pressures. Cohesion and friction angle both increased significantly. Cohesion achieves maximum value at 1.5% fiber content. Friction angle, on the other hand, steadily increased with increase in fiber content. Researchers also noted an overall shift to ductile behavior in the stress-strain response of coir-reinforced samples.

In both UCT and UU triaxial tests, addition of coir fiber in the range of 1.5% to 2% was reported to produce significant improvement in the soil. Fiber dosages less than 1.5% exhibit minimal strength improvement. For dosages greater than 2%, specimen preparation becomes too difficult because of fiber agglomeration.

Ramasubbarao [16] investigated the effect of kerosene-coated randomly distributed coir fibers on highly compressible clay. Using fiber length of 5 mm and varied fiber contents (0.5%, 1%, and 1.5%), the optimum coir content was found to be 1% based on peak compressive strength. Stress-strain response shifted from brittle to a more ductile one with addition of coir. The researcher also performed water absorption capacity tests on uncoated and coated fibers, where it was found that kerosene coating significantly reduced the moisture absorption of coir.

METHODOLOGY

The research focused on soil improvement with respect to unconfined compressive strength. Initial steps were acquisition and preparation of the soil samples, kerosene, and coir. Local clayey soil used in the study was obtained from Sikatuna Village, Quezon City. Coir fibers were obtained from a small-scale farm in Dolores, Quezon. Preliminary soil tests were conducted on oven-dried soil for classification purposes. All tests are performed according to ASTM standards. Coir fibers were cut to a fixed length and coated with kerosene. Coated and uncoated fibers were subjected to water absorption capacity tests. Standard proctor test provided the maximum dry density and optimum water content of the soil sample. Coated fibers were added to soil in varying concentrations. Reconstituted samples were prepared using the soil-fiber mixes. The orientation of the fibers due to the soil mixing process cannot be controlled.

Unconfined compression tests were conducted on soil samples at optimum moisture condition. Stress-strain plots were generated and compressive stresses at maximum load were obtained. Statistical analysis was performed on the data to determine the optimum fiber concentration. The long-term performance of coir fibers as reinforcement was not investigated.

RESULTS AND DISCUSSION

Soil Analysis

Laboratory tests were performed for characterization of the soil sample. The tests include sieve analysis, Atterberg limits tests and standard proctor test. Results of the said tests were used to classify the soil sample according to the Unified Soil Classification System. Table 1 shows the results of the tests performed.

Fiber Testing

Water absorption capacity tests were carried out to determine if a physical coating can help defer the degradation of coir by reducing moisture intake. Figure 2 illustrates the effect of kerosene coating on the water absorption behavior of coir. It is evident that kerosene-coated fibers have significantly lower water absorption level than uncoated fibers. There is also a steep increase in water absorption at the beginning of the test. As immersion time increased, water

absorption capacities leveled off, approaching equilibrium.

Table 1 Index properties of soil sample used

Soil Property	Soil Sample
Passing #4 sieve	99.97%
Passing #10 sieve	94.45%
Passing #20 sieve	85.23%
Passing #200 sieve	53.68%
Liquid Limit	80
Plastic Limit	35
Plasticity Index	45
USCS	CH
Max. Dry Unit Weight	12.05 kN/m^3
Optimum Moisture Content	31.15%

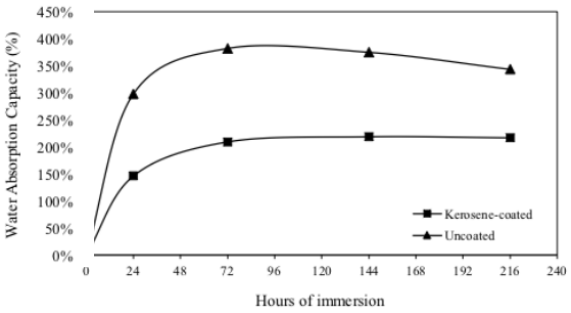

Fig.2 Effect of Kerosene Coating on Water Absorption Capacity of Coir

Unconfined Compression Strength

A total of 25 reconstituted samples of unreinforced and reinforced clay were tested for unconfined compressive strength immediately after preparation. The samples after failure were oven-dried to determine water content. Table 2 presents the average values of maximum load and its corresponding compressive strength at maximum load and water content for each fiber concentration.

Table 2 Mean values of maximum load for each fiber concentration

Fiber Concentration (%)	Average Max Load (N)	Stress at Max Load (MPa)	Water Content (%)
0	264.65	0.132	34.50
0.5	303.75	0.150	33.08
1.0	371.74	0.183	34.09
1.5	406.06	0.200	32.98
2.0	320.69	0.158	33.75

From figure 3, it can be observed that strength of reinforced samples has significant difference from that of unreinforced samples. This can be said for all fiber concentrations. Furthermore, the maximum strength improvement was seen in the 1.5% coir-reinforced group. It also shows that compressive strength values increased as fiber content increased. At the optimum fiber content of 1.5%, average unconfined compressive strength was increased by 52% compared to plain samples. The strength increase can be attributed to the pull-out resistance of the coir fibers during compression.

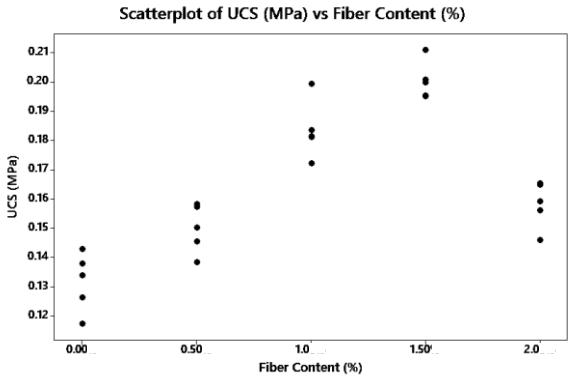

Fig.3 Plot of the compressive strength obtained for each samples

Sample preparation at 2% fiber content was made difficult by the clumping of coir fibers. Failure mostly occurred in the weak regions of the samples where fiber agglomeration was observed. This explains the decrease in strength from 1.5% to 2% fiber concentration. Still, samples with 2% coir exhibited higher compressive strength than unreinforced samples.

Typical results of the stress versus strain response for various fiber concentrations are presented in figure 4. Resulting stress-strain curves for the 25 samples are shown in figure 5.

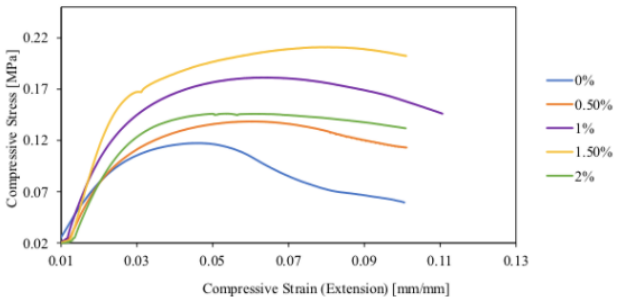

Fig.4 Typical Stress-strain Curve of Soil for Different Fiber Concentrations

Peak strengths for all the samples occurred at about 4% to 7% strain. Aside from increasing peak strength, coir fiber reinforcement was also found to improve the post-peak behavior of the soil. Compared to plain samples, coir-reinforced samples exhibited less reductions in strength after peak. Soil with coir

behaved more like a ductile material.

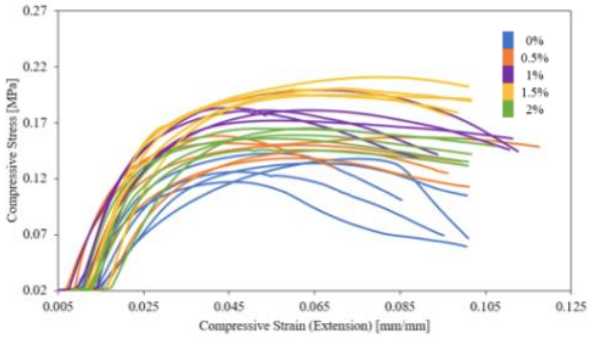

Fig.5 Stress-strain Curves of Soil for Different Fiber Concentrations

The elastic modulus of all the samples were obtained by from the stress-strain curves. The mean values are presented in Table 3.

Table 3 Mean elastic moduli for different fiber concentrations

Fiber Concentration (%)	Elastic Modulus (MPa)
0	5.73
0.5	8.34
1	9.94
1.5	10.21
2	8.09

The same trend in the case of peak compressive strength was observed in the elastic modulus of the groups. Values steadily increased from 0% to 1.5%, where the maximum improvement was observed. Addition of 1.5% coir resulted to a 78% increase in elastic modulus compared to plain soil. At 2% coir, there was also a decrease from the maximum value seen at 1.5% coir.

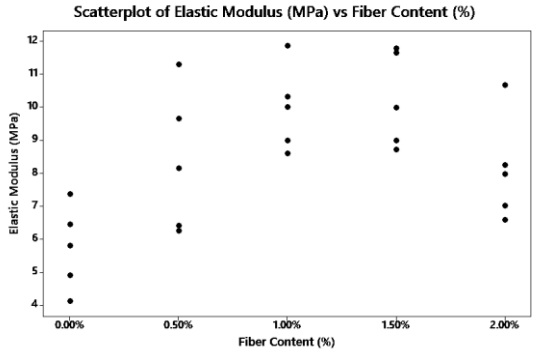

Fig.6 Elastic modulus of samples with different fiber content

Failure Patterns

Figure 7 presents the failure patterns of samples under unconfined compression test. A well- defined shear plane was observed in the 0% and 0.5% reinforced samples. In contrast, samples with 1% and 1.5% coir exhibited bulging failure and formation of small cracks. The samples at the optimum fiber content showed minimal signs of failure compared to plain samples. As the fiber content increases, failure would happen slowly and the sample behaves like a ductile material. The increased ductility due to fiber reinforcement allows the samples to bear stress even after peak. At 2% fiber content, it was observed that failure mostly occurs in the regions where fiber has agglomerated, contributing to the lower compressive strength.

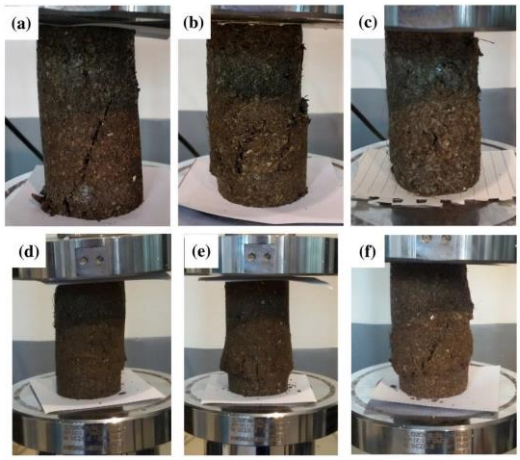

Fig.7 Typical Failure Patterns: (a) 0%, (b) 0.5%, (c) 1%, (d) 1.5%, (e) 1.5%, (f) 2%.

CONCLUSION

The present study investigated the effect of kerosene-coated coir fiber on strength and stress-strain characteristics of a reconstituted cohesive soil sample. The soil sample was classified as high-plasticity clay and found to have a maximum dry density of 12.05 kN/m^3 and optimum moisture content of 31.15%.

The use of kerosene as protective coating significantly lowers the water absorption capacity of coir by up to 170%. It was proven to be an effective protective coating to reduce moisture-induced coir degradation.

Coir fiber reinforcement was found to be beneficial to clayey soil. The maximum strength improvement was at 1.5% fiber content, with a 52% increase in strength compared to unreinforced soil. However, fibers tend to clump together at fiber concentration of 2%, resulting to a decrease in strength from the average strength at 1.5%. Still, 2% reinforced samples have higher compressive strengths than samples with 0% coir. Addition of coir fiber limited post-peak strength reduction in the soil.

From the stress- strain graphs, it was observed that samples with coir exhibited improved ductility. A 78% increase in soil elastic modulus was also observed at the optimum fiber content. Well-defined shear failure planes were seen in the 0% and 0.5% samples. At higher fiber concentrations, failure occurs slowly and minimal signs of failure were observed.

RECOMMENDATIONS

The researcher recommends that experiments can be conducted to determine the effectiveness of kerosene coating on preserving coir fibers under buried conditions over a long period of time. Furthermore, tensile strength tests can be performed to determine if kerosene has any effect on coir tensile strength. It is also suggested to know the applicability of coir on other soil types such as silts and sands may also be studied. For a more in-depth experimental study, shear strength tests such as triaxial compression tests and direct shear tests may be used to evaluate coir as soil reinforcement. California bearing ratio tests may be used to determine the effect of coir on weak subgrade. Swell index tests may also be done for expansive soils mixed with coir. The effect of varying coir fiber parameters (e.g. length, diameter) on the strength improvement may also be further studied. Additionally, regression models may be proposed to quantify the effect of fiber parameters on the shear strength of soil.

REFERENCES

[1] Ramesh, H. N. and Manoj Krishna, K.V. (2011) Performance of coated coir fibers on the compressive strength behavior of reinforced soil, International Journal of Earth Sciences and Engineering, Vol. 4, No. 6, 26-29.

[2] Hausmann, M. (1990) Engineering Principles of Ground Modification, McGraw-Hill, Inc., Singapore, 4-7.

[3] Singh, A., Ali Jawaid, S.M. and Chaurasia Shree Ram. (2016) Techniques to improve the strength of ground, International Journal for Research in Applied Science & Engineering Technology (IJRASET), Vol. 4, No. 4, 754-760.

[4] Shukla, S.K. (2017) Fundamentals of Fibre-Reinforced Soil Engineering, Springer Nature Singapore Pte Ltd., 23-44.

[5] Sadek, S., Najjar, S. and Freiha, F. (2010) Shear strength of fiber-reinforced sands, Journal of Geotechnical and Geoenvironmental Engineering, Vol. 136, No. 3, 490- 499.

[6] Unnikrishnan, S. (2014) Natural fibres in engineering applications: an overview, International Journal of Scientific & Engineering Research, Vol. 5, No. 7, 260-265.

[7] Sanyal, T. and Chakraborty, K. (1994) Application of bitumen - coated jute geotextile in bank-protection works in Hoogly estuary, Geotextiles and Geomembranes, Vol. 13, 127-132.

[8] Ali, M. (2010) Coconut fibre - a versatile material and its applications in engineering, Proceedings Second International Conference on Sustainable Materials and Technologies, Universita Politecnica delle Marche, Ancona, Italy, June 2010.

[9] Rao, G.V. and Balan, K. (2000) Coir Geotextiles - Emerging Trends. The Kerala State Coir Corporation Limited, Alappuzha, Kerala, India.

[10] Sujatha, E., Saisree, S., Prabalini, C. and Aysha Rasana, Z. (2017) Influence of random inclusion of coconut fibres on the short-term strength of highly compressible clay, IOP Conference Series: Earth and Environmental Scienc.

[11] Devdatt, S., Shikha, R., Saxena, A.K. and Jha, A.K. (2015) Soil stabilization using coconut coir fibre, International Journal for Research in Applied Science & Engineering Technology (IJRASET), Vol. 3, No. 9, 305-309.

[12] Peter, L., Jayasree, P., Balan, K. and Alaka Raj, S. (2014) Laboratory investigation in the improvement of subgrade characteristics of expansive soil stabilised with coir waste, Transportation Research Procedia 17, 558-566.

[13] Sivakumar Babu, G.L. and Vasudevan, A.K. (2008) Strength and stiffness response of coir fiber-reinforced tropical soil, Journal of Materials in Civil Engineering, Vol. 20, No. 9, 571-577.

[14] Sivakumar Babu, G.L., Vasudevan, A.K. and Sayida, M.K. (2008) Use of coir fibers for improving the engineering properties of expansive soils, Journal of Natural Fibers, Vol. 5, No. 1, 61-75.

[15] Dasaka, S.M. and Sumesh, K.S. (2011) Effect of coir fiber on the stress-strain behavior of a reconstituted fine-grained soil, Journal of Natural Fibers, Vol. 8, No. 3, 189-204.

[16] Ramasubbarao, G. (2014) Strength behaviour of kerosene coated coir fiber-reinforced expansive soil, Facta Universitatis Series: Architecture and Civil Engineering, Vol. 12, No. 2, 113-120.

[17] Budhu, M. (2011) Soil Mechanics and Foundations, John Wiley & Sons, Inc., USA.

[18] Craig, R.F. (2004) Craig's Soil Mechanics, Spon Press, New York.

[19] Das, B. (2014) Principles of Geotechnical Engineering, 7th Edition, Cengage Learning, USA.

[20] Ramasubbarao, G. (2014) Strength behaviour of kerosene coated coir fiber-reinforced expansive soil, Facta Universitatis Series: Architecture and Civil Engineering, Vol. 12, No. 2, 113-120.

9th Int. Conf. on Geotechnique, Construction Materials and Environment,
Tokyo, Japan, 20-22 November 2019, ISBN: 978-4-909106025 C3051

STUDY ON ENGINEERING APPLICATION OF CRUSHED SHELL PARTICLES FOR THE CONSTRUCTION MATERIALS

Ryota Morizaki[1], Kaoru Kobayashi[2], Kenjiro Honda[3] and Wataru Miyazaki[4]
[1,2]Ibaraki University, Japan; [3,4] A×C corp., Japan

ABSTRACT

Scallop shells are by-products of fishery and are stock piled around the fishing ports such as Hokkaido. Effective method(s) of their disposal and utilization have not been established as yet. These pileups cause a disagreeable odor and destruction of landscapes. There have been few attempts to effectively use scallop shells as a construction material. Crushed scallop shell particles (hereinafter referred to as crushed shell particles) in actual construction have only been effectively used as a mixture material in caisson fillings, and quay-wall back fillings in fishing ports. It is necessary to utilize a significant amount of scallop shells for construction, because problems that arise due to the pileup of scallop shells has not been solved yet. This study confirmed the specific characteristics of the crushed shell particles considering particle size via laboratory experiments, and analytically evaluated the applicability of crushed shell particles as an improvement material considering shear strength and permeability for soft ground, based on their circular slip calculation and one-dimensional effective stress analysis. This study elucidated the potential of the crushed shell particles as highly effective construction material. The utilization of crushed shell particles may significantly contribute to the promotion of a recycling society promotion.

Keywords: Crushed shell particles, Construction materials, Particle size, Shear strength, Permeability

INTRODUCTION

In recent years, research on effectively utilizing waste resources [1] is being increasingly carried out in the field of civil engineering for constructing a recycling society [2]. Scallop shells are the by-products of the fishery industry, and one such utilizable waste resource. Shells account for a large percentage of landing. Fig. 1 shows year-wise landing amount of scallops in Japan [3]. Landing amount of scallops in 2014 was 560,000. Because scallop shells account for approximately half of mass of scallops [4], their shells amounted to 280,000 in number. A large amount of these scallop shells is piled up (Fig. 2) [5] in the open areas surrounding the fishing ports, because disposal method for scallop shells have not been established yet. These pileups cause a disagreeable odor and destruction of landscapes. The use of scallop shells which pile up around fishing ports effectively use considered environment has been required to convert into a recycling society in Japan by using as construction materials.

Attempts have been made to effectively use scallop shells because their primary chemical component is calcium carbonate [6] providing them strength. Crushed scallop shells particles (hereinafter referred to as crushed shell particles) can be effectively used in mixtures for caisson fillings [7] and quay wall back fillings in the fishing ports [8]. However, till date, the effective use of scallop shells is restricted as a mixing material with sand and concrete aggregates. A larger number of effective utilization methods is required to solve the problem.

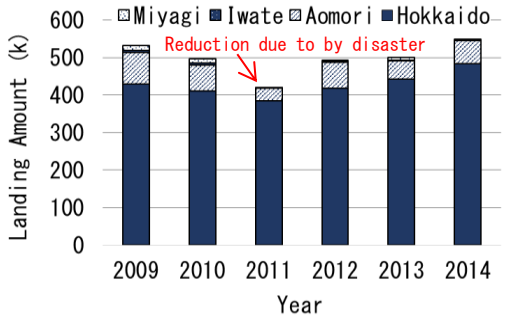

Fig. 1 Landing amount of scallops in Japan [3].

Fig. 2 Pileup of scallop shells [5].

Therefore, the purpose of this study is to effectively utilize scallop shells for construction materials. This study confirmed the specific shear strength characteristics of the crushed shell particles considering particle size on triaxial compression.

Circular slip calculation and one-dimension effective stress analysis in this study analytically evaluated the countermeasure effect considering shear strength and permeability for soft ground countermeasure. This study elucidated that the crushed shell particles have high potential for use as effective construction materials. The utilization of crushed shell particles is expected to contribute greatly to the promotion of recycling society.

BASIC CHARACTERISTICS OF CRUSHED SHELL PARTICLES

The proposed methods of crushing the scallop shells in construction include the use of heavy machinery such as bulldozers and crushing stone factories [9]. In recent years, adjustable rotary crushers are used for the purpose that aid in monitoring the particle size of crushed material [10], [11]. Rotary crusher is an on-board type equipment (it can be easily moved on a truck and belt conveyor) and can be effectively used on-site. Its use also makes it possible to reduce the cost of transporting a large amount of piled shells to the crushing plant.

Fig. 3 shows particle size accumulation curve. The scallop shells from the Aomori prefecture were used in this study. The shells were washed with water to remove impurities such as salt, and then dried in a drying oven at 80°*C* for 24 *h*. They were cooled to approximate room temperature, and crushed using a small crusher. Particle size analysis [12] was conducted to understand particle size character of crushed shell particles. Crushed shell particles sieved, and divided into three categories based on the particle size: less than 2 mm, less than 4.75 mm, and less than 9.5 mm to understand particle size characteristics. In addition, the same tests were carried out using silica sand No. 6 to compare the strength characteristics of crushed shell particles with general sandy soil. 50% particles size (D_{50}) of less than 2 mm, less than 4.75 mm, and less than 9.5mm are 0.8 mm, 1.6 mm and 2.0 mm, respectively. D_{50} of crushed shell particles are larger than silica sand No.6.

Table.1 shows the soil test results of the samples. Crushed shell particles have many voids when they are crushed, because the void ratio e and saturation permeability k_s (only less than 9.5 mm) of crushed shell particles having a flat shape are larger than that of sand. The particle density ρ_s is also found to be about the same as or slightly larger than that of sand.

SPECIFICITY CHARACTERISTICS OF CRUSHED SHELL PARTICLES IN TRIAXIAL COMPRESSION TEST

Materials

Fig. 4 shows three types of crushed shell particles in triaxial compression test [12]. The materials used

Table 1 The soil test results of sample

Sample	Crushed shell particles			Silica sand No. 6
	Less than 2 mm	Less than 4.75 mm	Less than 9.5 mm	
Particle density ρ_s (g/cm^3)	2.698	2.718	2.739	2.689
Water content ratio W_n (%)	0.2	0.2	0.2	0.5
Maximum void ratio e_{dmax} (–)	1.671	1.381	1.218	1.050
Minimum void ratio e_{dmin} (–)	1.227	0.788	0.705	0.629
Dry density ρ_{d60} (g/cm^3)	1.198	1.342	1.433	1.868
Permeability K_s (m/s)	–	–	3.34×10^{-1}	1.62×10^{-4}

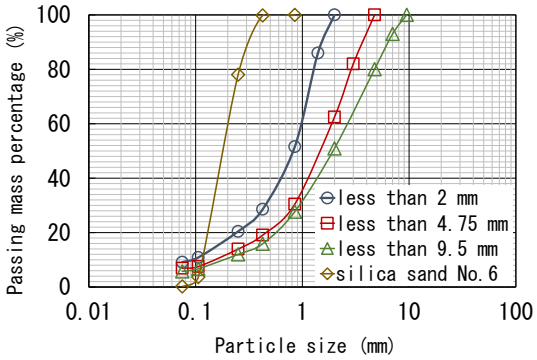

Fig. 3 Particle size accumulation curve.

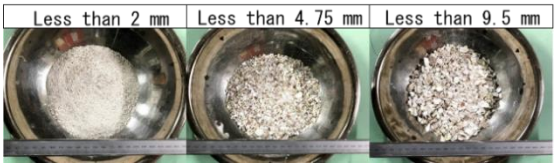

Fig. 4 Three types of crushed shell particles in triaxial compression test.

had three types of crushed shells with different particle sizes as compared to silica sand No. 6. The particle sizes of crushed shell particles are less 2 mm, less 4.75 mm, and less 9.5 mm in the sample (diameter 5 cm, height 10 cm) used in the triaxial compression test. Fig. 3 and Table 1 show Particle size accumulation curve and physical properties obtained by particle size analysis of the crushed shells and silica sand No. 6. The maximum and minimum void ratio materials were calculated from the maximum and minimum density tests of sand respectively [12].

Method

Table 2 shows the soil test results of the sample. To prepare the specimens, a rubber sleeve of thickness 0.3 mm was placed in two molds of diameters 50 and height 100 mm, and negative pressure was applied. Samples in the dry condition were filled and compacted in five layers using the air drop method to obtain a relative density of D_r = 60 %. Then, the saturation of the specimens was attempted using the CO_2 method (back pressure of 100 kPa, pore pressure coefficient of $B \geqq 0.95$). Then, isotropic

consolidation was performed at effective confining pressures of σ_c' = 50, 100, and 200 kPa. Axial compression was performed at an axial strain of ε_a = 15 % under undrained conditions while measuring the pore water pressure u with the shaft strain rate set to 0.1 %/mm.

Result

The specificity characteristics of the crushed shell particles were grasped for each shell particle size in this test. Fig. 5 shows the relationship between the deviator stress q vs axial strain ε_a. Fig. 6 shows the relationship between the excess pore pressure Δu vs axial strain ε_a. The deviator stress q at the axial strain ε_a = 15 % is followed by Case G, Case D, Case A, and Case J in a descending order, based on the effective confining pressure σ_c' = 50 kPa. All crushed shell particles had a larger deviator stress q than silica sand No. 6. The larger the size of crushed shell particles, the more remarkable the difference is. This behavior of the deviator stress q showed the same tendency at effective confining pressures σ_c' = 100 kPa and 200 kPa. The influence of the particle size on the excess pore water pressure Δu was basically not observed. The excess pore water pressure Δu depends on the effective confining pressure σ_c'.

Fig. 7 shows the strength parameters total stress and effective stress. Crushed shell particles have both internal frictional angle φ' and soil cohesion c'. It means crushed shell particles have different strength characteristics in contrast to a sand material with only internal friction angle φ'. Compared with the strength parameters (c', φ') of silica sand No. 6, the crushed shell particles show large values. This tendency is more remarkable with an increasing particle size.

Discussion

The specificity characteristic of crushed shell particles may affect the behavior and strength parameters in the triaxial test. The maximum and minimum density tests of sand suggested a dry density ρ_{d60} of the crushed shell particles. The samples with a relative density D_r = 60 % as a standard were prepared in a mold of 5 cm diameter and 10 cm height. Dry densities ρ_{d60} of less than 2 mm, less than 4.75 mm, less than 9.5 mm, and silica sand No. 6 were 1.227 g/cm^3, 1.342 g/cm^3, 1.433 g/cm^3, and 1.868 g/cm^3, respectively. The larger the dry density ρ_{d60}, larger is the particle size. Therefore, it is considered that the deviator stress q becomes larger at the same relative density. In addition, the crushed shell particles have both internal frictional angle φ' and soil cohesion c' owing to the surface roughness and cementation due to calcium carbonate of main component. The component of soil cohesion c' exerts resistance in the shallow layer slip. The component of internal frictional angle φ' in the deep layer slip.

Table 2 The soil test results of sample

Case	A	B	C	D	E	F	G	H	I	J	K	L
Sample	Less than 2 mm			Less than 4.75 mm			Less than 9.5 mm			Sillica sand No.6		
Effective confining pressures σ_c'(kPa)	50	100	200	50	100	200	50	100	200	50	100	200

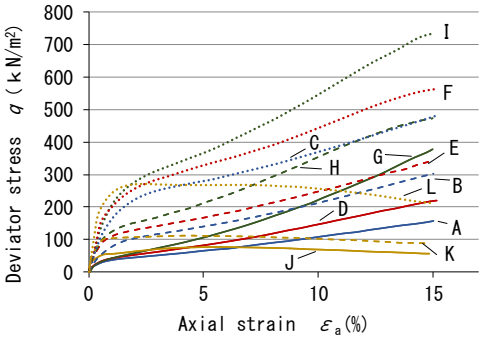

Fig. 5 Deviator stress q vs. axial strain ε_a.

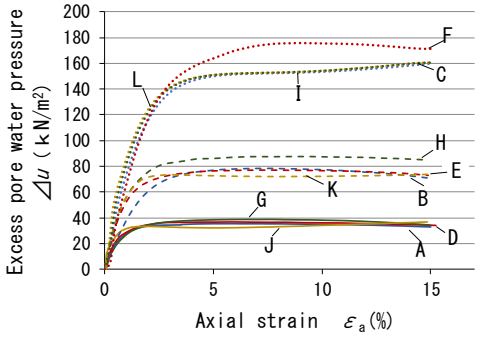

Fig. 6 Excess pore pressure Δu vs. axial strain ε_a.

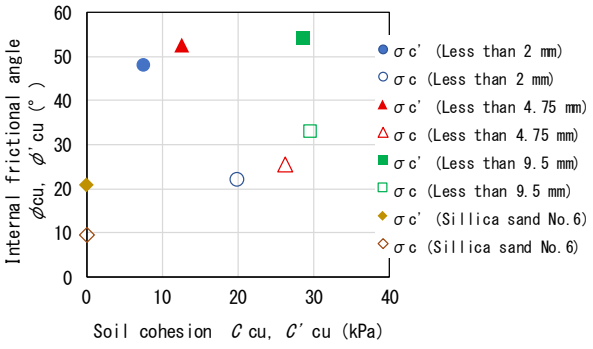

Fig. 7 Strength parameters total stress σ_c and effective stress σ_c'.

POTENTIAL INVESTIGATION OF CRUSHED SHELL PARTICLES AS CONSTRUCTION MATERIALS

Estimation of Circular Slip

Analysis conditions

Fig. 8 shows the embankment model; the ground configuration used in the trial is where the embankment is built on soft ground with a supporting ground. This analysis assumed that ground improvement construction on the sea was performed using the soft ground improvement method and the sand compaction pile (SCP) method because the crushed shell particles can effectively exert strength and permeability as a pile in case they have a flat shape. As the triaxial test results, the soft ground between the crushed shell pile or sand pile was considered as composite ground considering the obtained strength parameters. The improvement rate for a satisfying safety factor $F_s \geqq 1.2$ was calculated using the modified Fellenius method [13].

$$F_s = \frac{\text{Resistance force}}{\text{Sliding force}} = \frac{\sum\{cl + (W\cos\alpha - ul)\tan\varphi\}}{\sum W\sin\alpha} \quad (1)$$

where u is the average pore water pressure of the split plane, l is slip surface length of the split plane, W is the soil unit weight of the split plane, and α is the slip surface inclination angle of the split plane. The required shear strength τ [14] of the composite ground considering the improvement rate to show the resistance value was calculated by

$$\tau = (1 - a_s)\left(c_0 + kz + \frac{\mu_c \Delta\sigma_z \Delta c}{\Delta p} U\right) + \left(\gamma_s z + \mu_s \Delta\sigma_z\right) a_s \tan\varphi_s \cos^2\theta \quad (2)$$

where τ is the average shear strength on the slip surface, a_s is the improvement rate, c_0 is the undrained shear strength of the soft ground at $z = 0$, k is the strength increase rate in the depth direction, and z is the vertical coordinate; μ_c is the stress concentration factor for the soft ground part, $\Delta\sigma_z$ is the vertical stress increment caused by the external force on the slip surface, $\Delta c/\Delta p$ is the strength increase rate of the soft ground, and U is the average compressive density; and γ_s is the unit weight of the sand pile, μ_s is the sand stress reduction coefficient for the pile, φ'_s is the internal friction angle of sand pile, and θ is the angle of the sliding surface with the horizontal plane.

There is no strength increase at the time of embankment loading because the average compaction density $U = 0$. The stress sharing ratio n was calculated as $n = 3$ using the calculation formula [15] provided in the SCP method. The internal friction angle $\varphi'_s = 30°$ of sand piles was selected from the previous construction cases [14]. The internal friction angle φ'_s of sand piles was set to a low value considering construction uncertainty. The resistance and sliding forces of the slip surface were obtained from the same arc center and arc radius for easy comparison. Based on the above conditions, circular slip estimation was performed to identify the resistance force provided by the crushed shell pile in comparison to that provided by the sand pile (SCP).

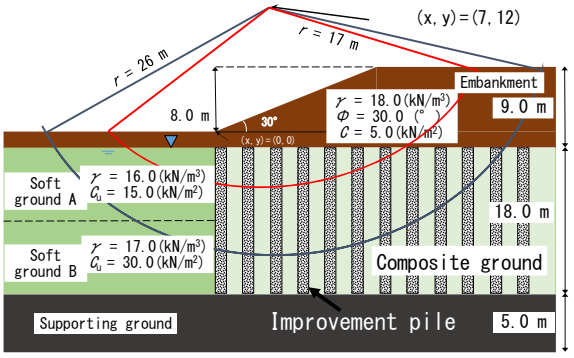

Fig. 8 Embankment model.

Table 3 Results of circular slip analysis

Resistance force (kN/m) / Sliding force (kN/m)	Shallow circle radius	Deep circle radius
No improvement	956 / 1884	1129 / 1962
Sand pile a_s = 30 %	1528 / 1884	2596 / 1962
Sand pile a_s = 90 %	2291 / 1884	3526 / 1962
Less than 2 mm Shell pile a_s = 30 %	2376 / 1884	4014 / 1962
Less than 4.75 mm Shell pile a_s = 30 %	2437 / 1884	4086 / 1962
Less than 9.5 mm Shell pile a_s = 30 %	2630 / 1884	4458 / 1962

Analysis result

Table 3 summarizes the results of the circular slip estimation. The resistance force showed a tendency of increasing in both the shallow and deep layers for the same improvement rate a_s when the crushed shell particles were used for the composite ground as the pile. In particular, the larger the particle sizes of crushed shell particles, the higher was the resistance force. Further, the resistance force of the crushed shell particles had a larger value than the resistance of sand, which implies the strength parameters (c', φ') obtained from the triaxial compression test is effective as a soft ground improvement method because strength parameters (c', φ') considered in equation (1) increases the resistance force by adding to the shear strength τ of the composite ground calculated from equation (2). For comparison of the improvement rate a_s, it was necessary to use the crushed shell particle piles for both shallow and deep arcs with an improvement rate a_s = 30 % to satisfy the safety factor F_s = 1.2.

On the other hand, sand piles were necessary for a deep arc with an improvement rate a_s = 30 % and with a shallow arc with an improvement rate a_s = 90 % (construction with improvement rate a_s = 90% is impossible). The improvement rate a_s is decreased to ensure that the resistance force of crushed shell piles is large enough to secure the crushed shell

particles with an internal friction angle φ' and soil cohesion c' according to the triaxial compression test. The internal friction angle φ' works more effectively on soft ground and gets deeper due to the relationship with the effective confining pressure σ_c'. The soil cohesion c' works effectively on the soft ground in the shallow layer.

From the above, it is possible to use crushed shell particles as effective construction materials as a countermeasure for soft ground because the crushed shell particles showed exert both depth and shallow of the layer slip by resistance having strength parameters (c', φ').

One-Dimensional Effective Stress Analysis

Analysis condition

Table 4 summarizes the parameters for effective stress analysis. One-dimensional effective stress analysis was performed using analysis code LIQCA2D16 [16]. An effective stress analysis confirms whether crushed shell particles considering high permeability and strength parameters (c', φ') larger than sand have the effect as SCP for liquefaction; it was assumed that the soft ground was totally replaced with crushed shell particles (less than 9.5 mm). The liquefaction layer was the cyclic elastic-plastic constitutive model modeled 24 m and the non-liquefaction layer was an elastic model modeled in 5 m. The analysis parameters are taken from Oka et al.'s study [17]. The saturated permeability coefficient k_s and the fracture stress ratio M_f changed, as shown in Table 5, because the various dynamic tests for grasping the dynamic strength and deformation characteristics were not conducted. The saturated permeability coefficient k_s was determined by the soil permeability test; the fracture stress ratio M_f was calculated from the internal friction angle φ' obtained by the triaxial compression test using

$$M_f = \frac{2\sqrt{6}\sin\varphi'}{3 - \sin\varphi'} \quad (3)$$

The input seismic wave was a Level 2 earthquake movement inland type 1 of the concrete standard specification [18]. The effective stress reduction ratio effective stress decreasing ratio (ESDR) is calculated using equation (4) to judge the liquefaction suppression effect of crushed shell particles.

$$ESDR = 1 - \frac{\sigma_m'}{\sigma_{m0}'} \quad (4)$$

where σ_{m0}' is the initial average effective stress and σ_m' is the average effective stress at a certain time. Complete liquefaction shows $ESDR$ = 1.0.

From the above condition, effectiveness as a countermeasure for the liquefaction of crushed shells particles as construction materials for liquefaction were examined from *ESDR* by comparing it with no improvement measures.

Table 4 Parameter for effective stress analysis

	No improvement	Crushed shell particles (less than 9.5 mm)
Compression index λ (–)	0.025	
Swelling coefficent κ (–)	0.0025	
Normalized initial shear modulus G_0/σ'_{m0} (–)	563.3	
Saturated permeabillty coefficent k (m/s)	1.00×10^{-5}	3.34×10^{-1}
Initial void ratio e_0 (–)	0.8	
Failure stress ratio M_f (–)	1.158	1.813
Phase transformation stress ratio M_m (–)	0.909	
Material parameter B_0^* (–)	1800	
Initial value of B_0^* B_1^* (–)	50	
Material parameter providing the rate of disapperace of anisotropy C_d (–)	2000	
Cofficient of dilatancy D_0^* (–)	1	
Cofficient of dilatancy n (–)	2.2	
Quasi-overconsolidation ratio OCR (–)	1	
Plastic shear strain γ_r^p (–)	0.005	
Elastic shear strain γ_r^E (–)	0.1	

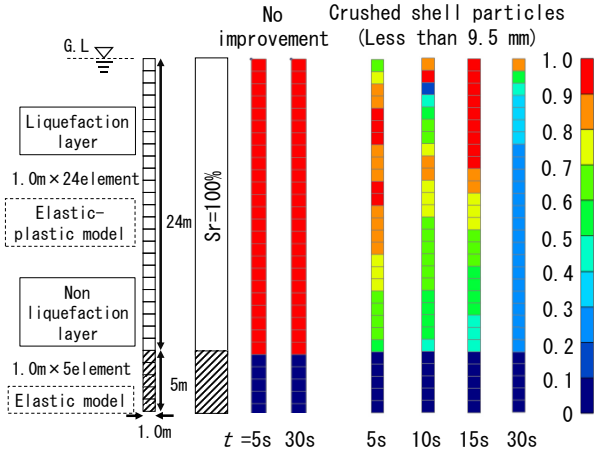

Fig. 9 Analysis result of *ESDR*.

Analysis result

Fig. 9 shows the analysis result of *ESDR*. The *ESDR* with no improvement showed a high value for the shallow and deep elements at any times from the occurrence of the earthquake, which implies sand liquefaction occurred in this analysis. On the other hands, the *ESDR* of crushed shell particles (less than 9.5mm) showed a low value under the same conditions; this means crushed shell particles suppressed liquefaction. In detail, the *ESDR* of the crushed shell particles increased in the shallow element at t = 5 s , 10 s, and 15 s before the earthquake happens, and it finally decreased both the shallow and deep elements at t = 30 s. The reason why crushed shell particles can have suppression for liquefaction more than no improvement is that crushed shell particles are related to the particle size, surface roughness and cementation due to calcium carbonate of main component. The saturated permeability

coefficient k_s of the crushed shell particles was obtained from the soil permeability test is larger than no improvement because larger particle size makes permeability larger. The fracture stress ratio M_f of the crushed shell particles was obtained from triaxial compression test showed large internal friction angle. The influence of the two factors on the crushed shell particles helped suppress liquefaction. Therefore, crushed shell particles can be employed as a construction material because they showed a liquefaction suppression effect to make the *ESDR* value of no improvement ground low.

The results of the one-dimensional effective stress analysis indicate that crushed shell particles can be possibly employed as construction materials owing to its liquefaction suppression effect.

CONCLUSIONS

This study obtained the following results to validate the use of crushed shell particles as construction materials.

(1) Crushed shell particles can have a large value of deviator stress q and strength parameters (c', φ') because of the surface roughness and cementation due to calcium carbonate of main component.

(2) Crushed shell particles can exert a resistance force effectively at depth and shallow layer due to strength parameters (c', φ') in the improvement pile in estimate of the circular slip.

(3) Crushed shell particles can exert the liquefaction suppression effect due to the saturated permeability coefficient k_s and fracture stress ratio M_f in a one-dimensional effective stress analysis.

For wider implementation, the influence of the chemical component in the crushed shell particles—made of calcium carbonate owing to its strength—and the detailed strength characteristics of the crushed shells particles need to be obtained via investigation and examination at the particle level.

REFERENCES

[1] Ministry of the Environment: About the Treatment of Fishery Waste http://www.env.go.jp/hourei/11/000083.html (accessed on April 4, 2019).

[2] Ministry of the Environment: A New Challenge to Recycling Society (accessed on April 4, 2019).

[3] Aomori Scallop Distribution Promotion Association: Scallop Production Volume Attachment Table by Year, http://www.aomori-hotate.com/ (accessed on April 4, 2019).

[4] Agency Fishing Port and Fisheries Division of the Japanese Institute of Fisheries Infrastructure and Communities: Guidelines for Fishery Construction Using Hokkaido Scallop Shells, 2007, pp.2-5.

[5] Investigation for Utilization as Asphalt Pavement Aggregate Scallop Shell Powder: Masaaki Tsuji, Tomohiko Katou, Sinya Ono 2010.

[6] Basic Characteristics of FRP with Scallop Shells as the Filler: Takashi Hirose, Masanori Kushibiki, Hiromi Tushima and Katuji Shibata,Japan Society of Material Cycles and Waste Management, Vol.22, No.2, 2011, pp.87-92.

[7] Ohno Gen: Effective Utilization of Scallop Seashells as a Caisson Intermediate Material, Journal of the Japan Society of Civil Engineers, Vol. 95, No 9, 2010, p27.

[8] Yukio Tsubota, Saeki Kimiyasu: Inclusion of Aquatic by- Fundamental Study on Effective Utilization to Sand (Part 2) - Internal Friction Angle of Sand Mixed with Scallop Shell -, Annual Journal of Civil Engineering in the Ocean, 2005, pp. 862-866.

[9] Tsubasa Koguchi: Promotion of Recycling of Fishery Byproducts ~A Caisson Filling Material for Scallop Shells ~, Construction Recycle, Vol.33, 2005, pp.10-13.

[10] Toshimitu Ohnishi, Shigeyuki Yokota, Tadashi Yamauchi and Hiroshi Kawakami: Efforts to Recycle Concrete Waste, Japan Society of Civil Engineers 60th Annual Scientific Lecture, 2005, pp. 889-890.

[11] Yamauchi Tadashi, Kiyomiya Osamu, Hisao Takahashi and Akira Yoshikazu:Study about the Application of the Concrete that Uses Scallop Shell as Fine Aggregate to Port Structures, Concrete Journal, Vol.47, No.3, 2009,pp. 24-31.

[12] The Japanese Geotechnical Society: Method and Explanation of Foundation Material Test, 2009, pp. 151, 575–582.

[13] Kakuichirou Adachi: Text Series Civil Engineering11 Geotechnical Mechanics, Kyoritsu Publication, 2002, pp.89-107.

[14] The Ports and Harbours Association of Japan, Technical Standards and Commentaries for Port and Harbour Facilities in Japan (Frist Volume), 1994, pp.459-461.

[15] Tsunehiro Sakaiya, Mitsuru Takahashi, Tsutomu Sakakibara and Takatoshi Noguchi: Improvement Effect Evaluation of Low-Replacement-Ratio SCP Method with RI-CPT, Journal of the Society of Materials Science, Japan, Vol.61, No.1, 2012, pp.68-73.

[16] LIQCA Liquefaction Geo Research Institute, LIQCA2D16・LIQCA3D2016(2016 Published Version) , 2016.

[17] Fusao Oka, Sayuri Kimoto: Study on Liquefaction Suppressed Effect by Unsaturation of the Ground, Association for Disaster Prevention Research, Vol.36, 2013, pp.11-12.

[18] Japan Society of Civil Engineers: Concrete Standard Specifications, 2002, pp.7-9.

9th Int. Conf. on Geotechnique, Construction Materials and Environment, Tokyo, Japan, 20-22 November 2019, ISBN: 978-4-909106025 C3051

ULTRASONIC PROTECTIVE IMPREGNATION OF POROUS CONSTRUCTIONS AND NATURAL MATERIALS

Valery Tsaplev[1], Sergey Konovalov[1], Roman Konovalov[1,2] and Sergey Nikolaev[2]
[1]Electroacoustics and Ultrasonic Engineering, Saint Petersburg Electrotechnical University "LETI", Russia;
[2]Devices and Methods of NDT, Emperor Alexander I St. Petersburg State Transport University, Russia

ABSTRACT

The results of the experimental and theoretical studies of the acoustical flows in the porous or microcrumbling building and natural materials are presented. Building constructions, walls or foundations of concrete, brick or natural facing stone material being porous media absorb water due to the natural capillary effect. This happens mostly in countries with humid climates and if the faces of building structures are not protected by a waterproof layer. The damp penetrates into the foundation if the waterproofing layer between the foundation and the wall is damaged, the damp comes up the wall due to the natural capillary effect. Just the same, if the protective covering of the concrete or brick wall is damaged, they begin to absorb the damp from the air, growing damp by and by and worsening their protective properties. There exist different ways to restore damaged waterproofing layers. One possible way is to impregnate walls or/and foundations by some special hydrophobic liquid using the ultrasound. Being then dried out, the elements of constructions become water-repellent, do not absorb damp more and remain dry. The usage of the ultrasound makes the impregnation much more effective and fast, being at the same time the nondestructive method. The speed of the penetration depends on the porosity or microcrack or porosity factor. The paper presents the results of the study of the dependence of the velocity of the hydrophobic liquid movement from the average diameter of the capillaries and from the acoustical intensity.

Keywords: Ultrasonic impregnation, Porosity, Building materials, Capillary effect, Nondestructive protection

INTRODUCTION

It is possible to accelerate the impregnation and to increase its efficiency using ultrasound. The effect of saturation of porous media by the liquid in the ultrasonic field is based on the fact, That the acoustic pressure causes acoustic flow in the liquid. That is why the ultrasonic oscillations essentially help the liquid to move into the pores or capillaries of the material. The effect is strong within the wide range of frequencies and intensities of sound. The effect is well known. It is so called "ultrasonic capillary effect". This effect was first opened in the USSR, described by Konovalov and Germanovitch [1] and was also studied by Prokhorenko and Dezhkunov [2,3], ets.

The effect essentially increases after the arrival of cavitation. The essence of this effect is that the depth and the velocity of movement of the liquid into the capillaries increase significantly under the influence of cavitation in comparison with the influence of the acoustic radiation field.

FLOWS IN WALLS AND BRICS

The impregnation in the presence of ultrasonic oscillations is widely used in electronic and chemical-engineering industry. As a rule, it is used in plants, where it is possible to submerge the detail fully into the impregnating bath filled with the liquid and having the high power ultrasonic transducer inside the bath.

The main goal of our investigation was to study the process of liquid penetration in real, not in laboratory conditions. It is quite clear, that the concrete foundation or the brick wall cannot be submerged into the bath. Obviously, we had to look for some other engineering solution.

The main goal of our investigation was to study the process of liquid penetration in real, not in laboratory conditions. It is quite clear, that the concrete foundation or the brick wall cannot be submerged into the bath. Obviously, we had to look for some other engineering solution.

Figure 1 shows our design [4]. The ultrasonic vibrator 1 is mounted upright near the wall 2, subject to impregnation. The liquid 3 (special silicone hydrophobic liquid) forms an intermediate layer between the emitting surface of the vibrator and the wall. A special elastic rubber U-tank 4 prevents liquid leakage from the layer. This U-tank forms a kind of a small caisson. The tank is feeded by the liquid from a special feeding service tank (not shown in the figure). The vibrator is firmly attached to the wall (the attaching construction is not shown in the figure), but it is necessary to control the layer thickness. This thickness must be quite definite – it is very important. The

vibrator is excited by means of the power ultrasonic generator 5, that has the self-tuning circuit. The depth *L* of liquid penetration into the porous material (brick) was measured by pulse ultrasonic method.

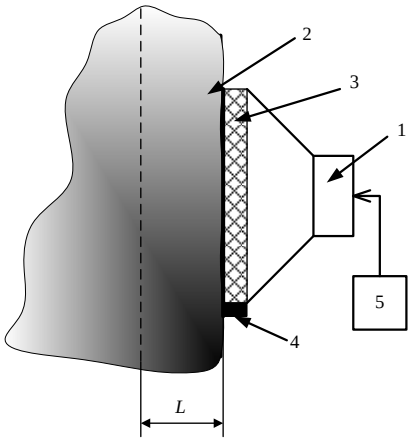

Fig. 1. Experimental setup

The main goal of this work is to compare this depth of the liquid penetration into different types of bricks under the influence of ultrasound of different power and different frequency.

EXPERIMENTAL RESULTS

Three types of porous material were used for the experiment. These were bricks, and their properties one can see in the following table.

Table 1 Specimen properties

№	Density ($\times 10^3$ kg/м^3)	Aver. grain diam. (мм)	Mean capillary diameter (mm)	Density (%)
1	3.4	0.35	0.02	8
2	2.9	0.5	0.05	17
3	1.8	1.0	0.17	38

The filling liquid was a special organic-silicon hydrophobic solution "Gifob" (density $\rho=1.07\cdot10^3$ kg/m^3, viscosity $\eta=0.19\cdot10^{-3}$ Ps), the temperature t=+20±2 C°).

First it was necessary to compare the theoretical velocity of ultrasound in the porous partially filled material with experimental. Different authors proposed various theoretical models for the velocity of elastic wave. The best approaches were obtained by Sato [5] and Gilberstein [6].

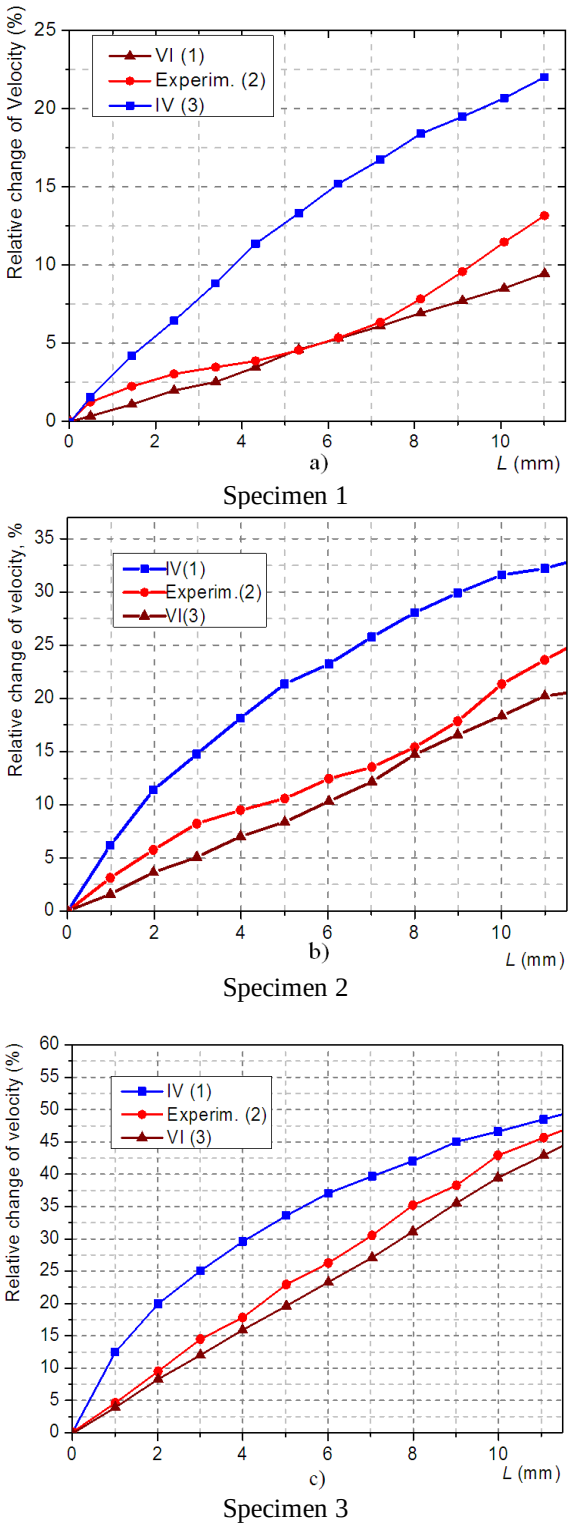

Fig. 2. Calculated and experimental changes of ultrasound velocity from the depth of filling (L). IV and VI correspond to [5] and [6] respectively

Approximation by Sato [5] is the following:

$$C_x = C_0\{1 - z\cdot\frac{\varphi}{2}[\frac{(1-k)(1+\sigma_1)}{2(1-2\sigma_1)+k(1+\sigma_1)} + \quad (1)$$

$$+10\frac{1-2\sigma_1}{7-5\sigma_1} - (1-D)]\}$$

where: $k = \frac{\rho_2 C_{2l}^2}{\rho_1 C_0^2}$;

C_0 – longitudinal velocity of elastic wave in porous media;

σ_1 – Poisson's ratio for 3*D* infinity media;

φ – porosity;

k – bulk elastic modulus of the liquid, filling capillaries, to that of continuous media;

D – density of the liquid to that of continuous media ratio;

z - depth of penetration factor.

Gilberstein [6] proposed the following approximation:

$$C_x = \frac{C_0}{\sqrt{\frac{1-zQ}{1-1{,}08zQ}(1+1{,}08zQS)}}, \quad (2)$$

$$S = \frac{1+2\sigma_1(1-\sigma_1)}{1-\sigma_1},$$

where C_0 – longitudinal velocity of elastic wave in porous media;

σ_1 – Poisson's ratio for 3*D* infinity media;

Q – total volumes of holes to that of material;

z – depth of penetration factor.

One can see from figure 2, that the model, proposed by Gilberstein fits very good with experiment.

The experiment showed, that the intensity of filling the specimen by liquid increases with increasing of the ultrasonic field power. This effect can be seen from figures 3, 4 and 5. Figure 3 shows the dependences of time of filling from the depth of penetration for different frequencies – 20 kHz, 60 kHz and 100 kHz and different values of power for the specimen № 1. Different values of electric amplitude on transducer – 100 V, 370 V and 780 V correspond to different values of sound-energy-flux density. These values are $2\cdot10^4$ Wt/m^2, $4\cdot10^4$ Wt/m^2 and $8\cdot10^4$ Wt/m^2, correspondingly. All The measurements were carried out below the threshold of cavitation. This level for this type of the hydrophobic liquid was about $8.4\cdot10^4$ Wt/m^2. The increase of the sound intensity causes the increase of the impregnation velocity, but it is quite necessary to avoid cavitation, because cavitation demolishes the water-repellent properties of liquid.

The increase of the impregnation time is caused by the growth of the ultrasound frequency, which leads to the wave decrement. This causes the reduction of the ultrasonic power as the depth of filling increases. As a result, the time of impregnation increases.

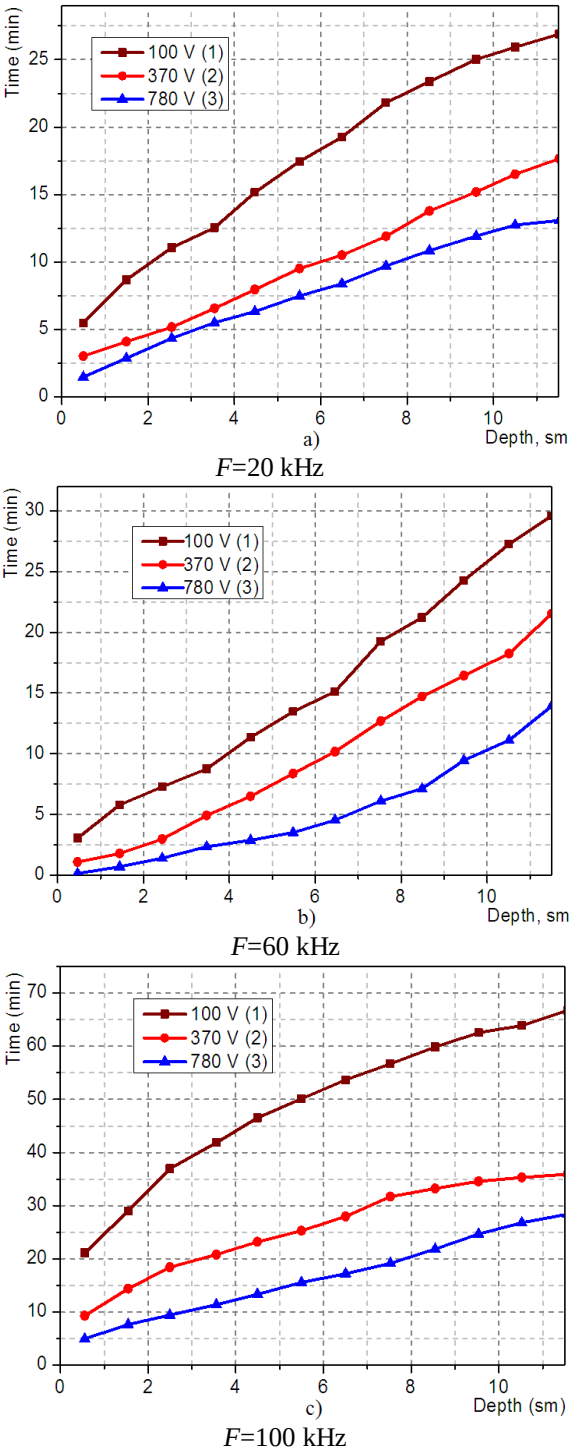

Fig. 3. Times (*t*) of filling specimen № 1, *L*=12 sm

The interpretation of the fill-up time of the porous material from the frequency shows, that the time grows as the frequency increases. That is illustrated by figures 5,6 and 7. At the beginning of the process the velocity of flow is proportional to the ultrasonic

frequency, but then the time of filling up slows down due to reduction of power.

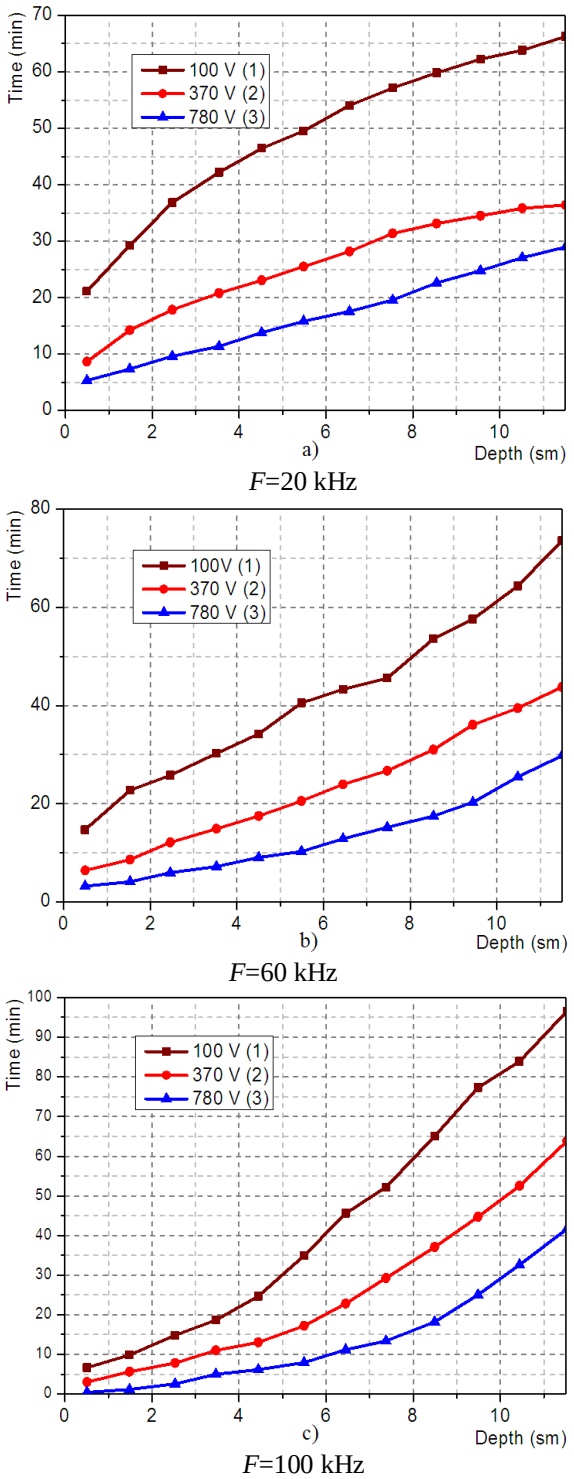

Fig. 4. Mean times (*t*) of filling specimen № 3, *L*=12 sm for different frequencies and different signal amplitudes

Figure 5 shows the dependence of the average filling-up time from the depth of penetration at different frequencies (20 kHz, 60 kHz and 100 kHz) and different signal amplitudes (100 V, 370 V and 780 V, that correspond to values of sound-energy-flux density of $2 \cdot 10^4$ Wt/m^2, $4 \cdot 10^4$ Wt/m^2 and $8 \cdot 10^4$ Wt/m^2.

Figure 5 is for specimen №1, *L*=12 sm, figure 6 is for specimen №2, *L*=12 sm and figure 7 shows these dependences obtained for specimen №3, also for *L*=12 sm.

All dependences are in good accordance with those of figures 2, 3 and 4.

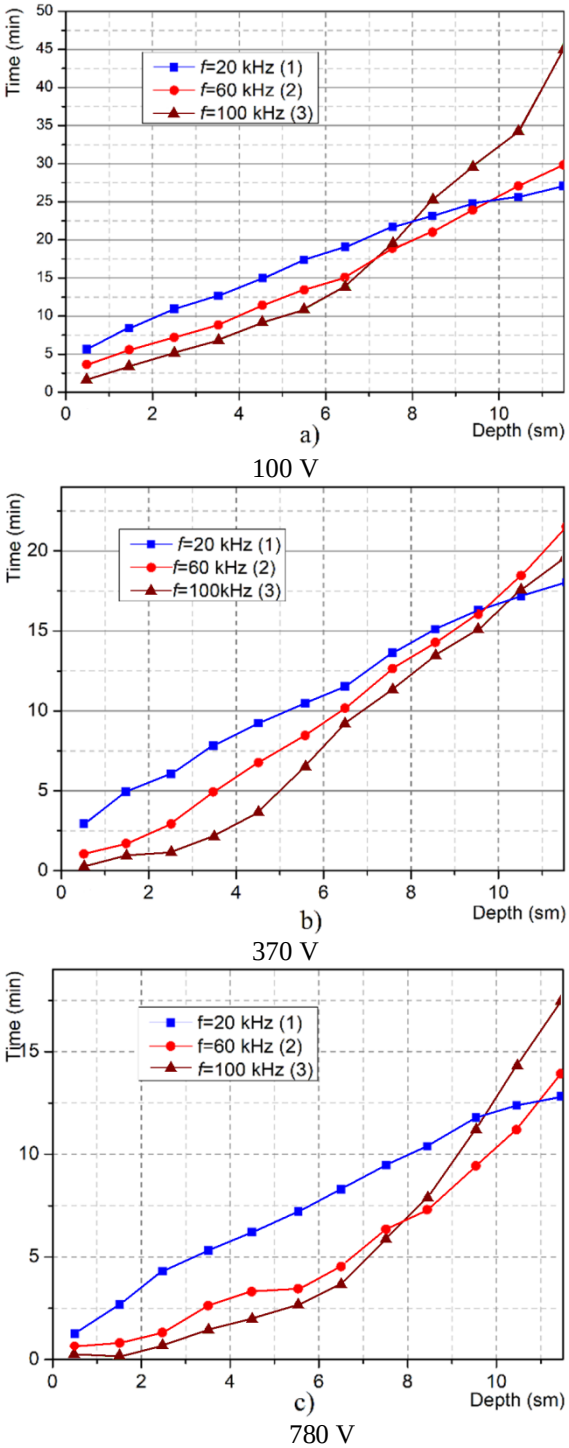

Fig. 5.Times (t) of filling specimen №2, *L*=12 sm for different frequencies and different signal amplitudes

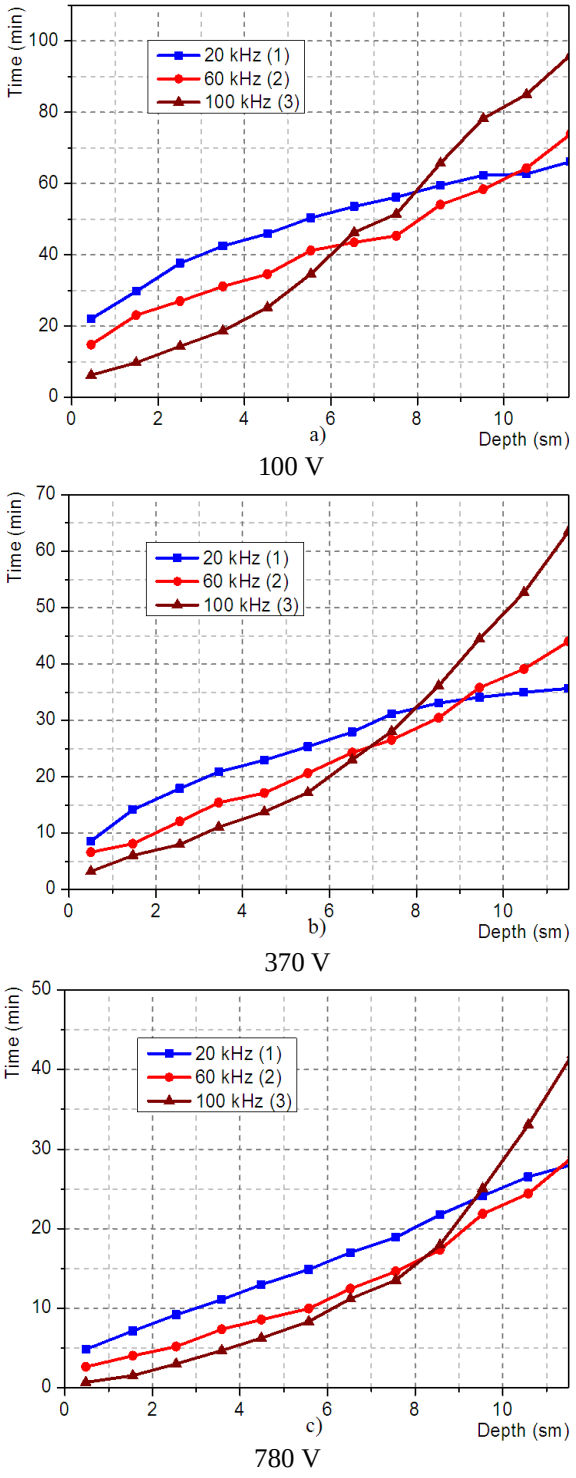

Figure 6. Mean times (t) of filling specimen № 3, L=12 sm for different frequencies and different signal amplitudes

DISCUSSION OF RESULTS

Our theoretical and experimental studies have found that in most solution-saturated samples the velocity of elastic longitudinal waves is higher than in dry ones. The total increase of the sound velocity in filled bricks reaches 13-50%. relatively dry bricks, depending on the brand of material.

From the theoretical and experimental results obtained, one can see that the best match of the measured values of the longitudinal wave velocities with the theoretical ones for various brick samples is obtained by the Hilberstein formula.

In bricks there is usually a more or less natural increase in speed with saturation.

One can also notice that with a small filling of capillaries (up to 10-20 mm), the change in speed is more abrupt than with further saturation.

With an average pore filling (up to 30-70 mm), the velocity usually increases smoothly, but when saturation reaches the values over 80 mm, the sound velocity increases sharply. It should be noted that in samples with higher porosity the velocity changes more smoothly, while in samples with lower porosity more sharp and significant changes are observed.

With the gradual saturation of the bricks with liquid, an uneven increase of the velocity is usually observed. At the stage of ultimate saturation, associated with a sharp transition of the system to a new physical state, usually there comes an abrupt change in speed.

In General, the nature of the change in the saturation velocity can be explained from the point of view of the contact model, i.e. is associated with a change in the contact area.

However, a significant role is also played by the nature of the links, their rigidity, so the reasons for the change in speed are often more complex than in the simplified model.

The velocities of longitudinal elastic waves in water-saturated materials are determined by the following:

a) the elasticity of the skeleton and fluid, as well as porosity;

b) lithological features of rocks affecting the state of elastic bonds (mainly composition and type of cement).

While the first factor is quantifiable, the second is much more difficult to account for. Note that in natural conditions the velocity of longitudinal elastic waves is affected by a number of other factors (pressure, temperature, etc.).

Measurements of the velocity of ultrasonic oscillations in various depths of fill brick mortar showed the impermanence of the velocity of propagation of the oscillations. This is due to the heterogeneity of the brick material.

The statistical analysis of the results showed that the confidence interval of the measured values varies depending on the frequency of ultrasonic vibrations. As the frequency increases, the confidence interval of the measured velocity values decreases.

For combining on the same physical principle of impregnating the material hydrophobic solution and simultaneously to control the depth of penetration of

this impregnation was carried out by additional experimental research of ultrasonic impregnation of porous material by hydrophobic solution. During the experiments it was found that the filling of the brick increases with increasing power of the ultrasonic field. However, the increase in power at certain values can cause cavitation of the hydrophobic solution.

The obtained results show that the time of filling the brick increases with increasing frequency: the increase in impregnation time is associated with an increase in the frequency of the acoustic signal, which leads to weakening of the signal. This in turn leads to decrease of the acoustic power along with increase in the depth of the brick filling respectively, a decrease in the rate of impregnation.

The time of filling the porous material is also related to the adsorption forces in the capillaries of the brick. This is due to the change in the capillary volume, which affects the mechanism of rigid friction of the wall surface. When the diameter of the capillary decreases, the number of rubbing areas of the surface of the capillaries increases, which leads to an increase in the slowing down of the velocity of the liquid along the capillary of the porous material.

CONCLUSION

In conclusion we can say, that the results of this investigation provide new possibilities to water-repellent treatment of brick walls and concrete foundations. The time of hydrophobic liquid fill-up under the influence of ultrasound is about 8-10 times less than without the ultrasound, in the course of natural capillary seepage. Generally speaking, the ultrasonic effect on the fluid flow is complex. The acceleration of the rate of the impregnation can be explained by different effects. Among these effects the most important ones seem to be the capillary wall vibrations, the influence of ultrasound on the meniscus in the capillary channel, changes in physic-chemical properties of the fluid, acoustical pressure and cavitation.

Similar results were obtained for different other porous materials, including concrete, ceramics, and some natural porous materials, such as marble and polycrystalline rocks, some natural facing materials.

It should be noted that the majority of theoretical works in both seismic and acoustic literature are devoted to the study of the propagation velocities of longitudinal and only in some cases transverse waves, and usually idealized media were considered.

Therefore, it became necessary to analyze the basic theoretical expressions derived for different types of aggregates, in terms of their applicability to the characteristics of porous materials, and to find out to what extent the available theoretical provisions are linked to the experimental data.

Our future work deals only with studies related to the study of elastic properties of porous media containing different types of hydrophobic liquids.

The use of ultrasonic technologies is not limited to hydrophobic water-repellent impregnation of building structures. For the operation of stationary mining, fixed with concrete, it is often necessary forced repair of concrete support, caused by the destruction of its individual sections. That is why it seems possible to prevent impregnation of the concrete lining workings by hydrophobic liquid using the ultrasonic technologies. High efficiency and manufacturability, small consumption, low cost and environmental solutions and liquids allow us to hope for their use in the extraction of minerals both open and underground methods [7]. Solutions of the corresponding consistencies and liquids in combination with acoustic technologies can be used for fixing the walls of mine workings, and also for strengthening of the massif of rocks, including water-saturated (siltstone, mudstone, sand and others).

ACKNOWLEDGMENTS

The authors would like to thank the members of the Department of Electroacoustics and Ultrasonic Engineering of the Saint Petersburg Electrotechnical University “LETI” for useful discussions.

REFERENCES

[1] E.G. Konovalov, I.N. Germanovitch, “Ultrasonic capillary effect”, *Docl. Ac. Sci. BSSR* 8, v.6, 492-496 (1962) (Rus)

[2] P.P. Prokhorenko, N.V. Dezhkunov, *Ultrasonic capillary effect and its application to non-destructive testing*, v.3, Moscow (1982)

[3] N.V. Dezhkunov, “Cavitation mechanism of ultrasonic influence on rising of liquid in capillary”,in *Some problems of heat- and mass exchange*, p. 178-181, Minsk (1978)

[4] V. Tsaplev, A. Sarvin and S. Nickolaev, “Using of ultrasound for water-repellency treatment of concrete walls and foundations”, *20th Cement and Concrete Science Conference*, p. 156-159, Sheffild University, UK, (11-12 September 2000)

[5] I. Sato, “Velocity of elastic waves propagates in media with small holes”, *Bull.Tokyo Univ. Earthquake Res. Inst*., 30 (3) (1952)

[6] P.G. Gilberstein, I.I. Gurvitch, “Velocities of elastic waves in perforated materials for seismic simulation”, *Izvestia of Institutions of Higher Education, ser. Geol. and Exploration*, 5 (1962) (Rus)

[7] V. Tsaplev, V. Zverevich, G. Zhukov, “Use of acoustic technologies for antiseptic and waterproofing treatment of mine openings and building structures”, *Mine surveying and subsurface use*, 2 (76) (2015), p. 20-24, http: //www.geomar.ru (Rus)

9th Int. Conf. on Geotechnique, Construction Materials and Environment, Tokyo, Japan, 20-22 November 2019, ISBN: 978-4-909106025 C3051

SUSTAINABLE UTILIZATION OF INDUSTRIAL BY-PRODUCTS FOR STABILIZATION OF RECYCLED CONSTRUCTION AND DEMOLITION AGGREGATES

Alireza Mohammadinia[1], Arul Arulrajah[2], Suksun Horpibulsuk[3] and Melvyn Leong[4]
[1,2]Faculty of Science, Engineering and Technology, Swinburne University of Technology, Australia;
[3]School of Civil Engineering, Suranaree University of Technology, Thailand; [4]Geofrontiers Group Pty Ltd., Australia

ABSTRACT

Conventionally, high-quality quarry materials are used in pavements and railway substructure. Traditional building materials is becoming scarce in some regions. Moreover, rate of consumption of high strength aggregates is increasing rapidly in different industries. The use of traditional quarry materials at current rate of consumption is unsustainable from both environmental and cost perspective. Chemical stabilization has been extensively applied for improving the mechanical properties of the recycled construction and demolition (C&D) aggregates. However, the high carbon footprint burden imposed by use of conventional binders for stabilization increases the overall cost and decreases the sustainability of the construction activities. Alternatively, industrial by-products which are rich in alumina, silica and calcium are a strong potential replacement for Portland cement and lime stabilization with no carbon footprints. In addition, the stiffness of the mixtures can be optimized to increase the serviceability of the stabilized materials under repeated loadings.

Keywords: recycled waste materials, alkali activation, stabilization, resilient modulus

INTRODUCTION

It has been well established that light stabilization of construction and demolition (C&D) aggregates can potentially be utilized as a low-carbon alternative to quarry aggregate materials [1, 2]. However, the stabilized layer are often show low tolerance of flexibility and can cause progressive failure after crack propagation in the stabilized layer [3]. Unbound granular mixtures have the potential to absorb minor differential displacement by rearrangement in the soil matrix known as "self-healing" capability [4]. However, the developed crack in stabilized material can cause progressive settlement leading to failure.

The stabilization is often targets to increase the modulus of a structural layer in order to reduce the overall thickness and consequently the cost of construction [5]. However, brittle failure of heavily stabilized layers have limited their use in design procedures of road authority design approaches [6]. Hence, a definition for lightly stabilized layer (i.e. modified layer) have been recommended to reduce the binder content to moderate the impact of the local failures in the structural layer that will lead to excessive settlement [6].

Reducing the cement percentage results in reduction in number and area of contact points throughout the stabilized soil matrix and consequently increases the localized pressure which in turn accelerate the local failure in the soil structure. It is noteworthy that general Portland cement is often used in these studies for creating the stabilized layer [6-8]. Considering higher aggregate crushing value of C&D aggregates, researchers have attempted to reduce the amount and stiffness of binders to moderate the homogeneity of the stabilized C&D materials [9, 10].

The size variation of solid binder gels in low-calcium and high calcium systems and stiffness variation of these bounds can significantly impact the load-bearing and deterioration of the stabilized layer under repeated loadings [3]. The impact of binder chemistry on flexural compressional behavior of lightly stabilized C&D aggregates have been studied in this research.

MATERIALS AND METHODS

Despite the increase in the rate of recycling solid waste, the C&D waste production stream has also increased leaving the rate of disposal to landfills unchanged [11]. Approximately, 50% of the C&D waste generation is disposed to landfills in Australia [12]. Crushed brick (CB) and Recycled Concrete Aggregate (RCA) comprise the majority of the C&D waste stream and was used for this research.

Industrial by-products was used for stabilization of the recycled aggregates as low-cost and sustainable alternative to general Portland cement. Fly ash (FA) is a rich source of Alumina for producing aluminosilicate gel in a low calcium system [13]. However, the combination of high calcium precursors such as ground granulated slag (S) can be beneficial to implement the stable C-S-H gel as well as

aluminium-substituted C-A-S-H gels [14].

Recycled materials

Granular aggregates

Crushed brick (CB) and Recycled Concrete Aggregate (RCA) have been collected from a recycling facility in Melbourne, Australia. The aggregates have a nominal size of 20 mm with less than 5% of fine content (Fig.1). The materials are classified as well-graded gravel and fit within the envelope suggested by local road authority [15]. Both CB and RCA have acceptable durability with a Los Angeles abrasion value of 35 and 31 respectively.

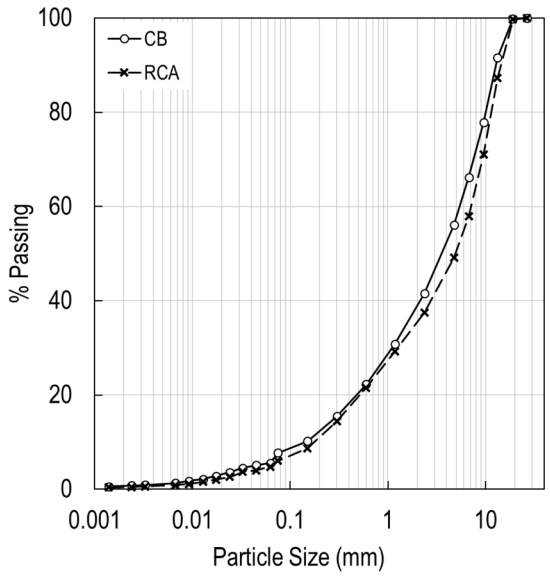

Fig. 1 Particle size distribution of C&D aggregates

Industrial by-products

Low calcium class F FA with mean diameter of 36 µm and slag with mean diameter of 20 µm was procured locally as low carbon alternatives for Portland cement. The chemical composition and physical properties of FA and S are presented in Table 1 and Table 2 respectively.

Table 1 Chemical composition of FA and S

Chemical	FA (wt.%)	Slag (wt.%)
AL_2O_3	25.56	13.8
SiO_2	51.11	34.2
CaO	4.3	43.1
Fe_2O_3	12.48	0.4
K_2O	0.7	0.4
MgO	1.45	5.4
Na_2O	0.77	0.1
SO_3	0.24	0.8
LOI[a]	0.57	1.8

Table 2 Physical specification of FA and S

Specification	FA	Slag
Diameter at 10% - D_{10} (µm)	7.2	6.4
Diameter at 50% - D_{50} (µm)	35.8	20.5
Diameter at 90% - D_{90} (µm)	69.1	54.6
Mean Diameter (µm)	35.0	20.7
Specific Gravity, G_s	2.3	3.15
Bulk density (Mg/m^3)	0.90	0.88
Solubility in water (g/L)	< 10	< 1
pH (25°C)	10	12

The scanning electron microscope (SEM) image of the precursors are presented in Fig.2. The FA particles are spherical and need a high pH to dissolve and start the activation. Aluminosilicate gels are often spiky and create a bridge between the particles while the calcium silicate hydrate (C-S-H) gel are bulky. Combination of the two gels are often create a dense and well-connected matrix.

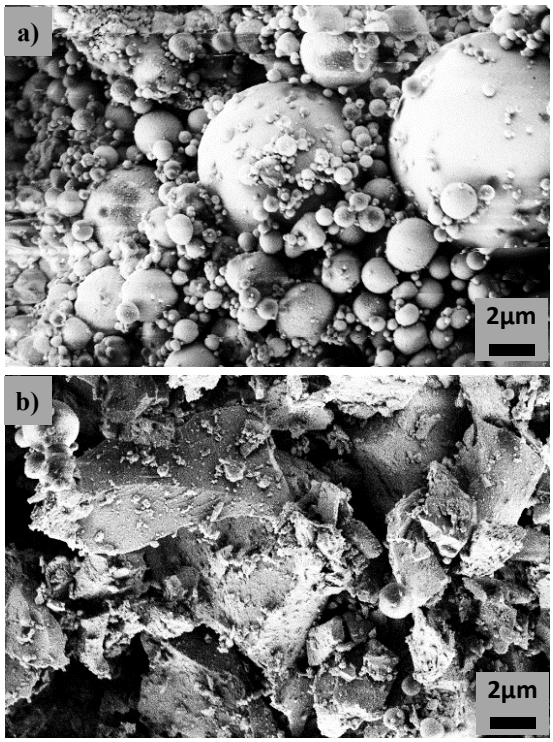

Fig. 2 SEM image of the precursors a) FA and b) S

Alkaline activators

To activate the precursors in room temperature, a 8 molar solution sodium hydroxide (NaOH) in combination with grade D solution of sodium silicate (Na_2SiO_3) was used. The ratio of silicate to hydroxide solution was kept under 2.5 : 1.0 as a result of study performed by Mohammadinia, et al. [3].

Experimental program

Advanced geotechnical tests

The basic characteristics of the C&D aggregates have been detailed in the research performed by the authors [3]. Complementary advanced testing such as repeated load triaxial (RLT) test have been performed to evaluate the compressional resilient modulus of the stabilized materials under repeated loading according to AASHTO T 307 [16]. In addition, four-point beam testing was performed on the stabilized materials to compare the static flexural strength (Modulus of rupture) as well as flexural resilient modulus.

The repeated loading nature in the moving load in transportation geotechnics comprise a complex combination of shear and moment and the impact of these loadings can have different impact on the stabilized layer [17]. Hence, the four-point beam was designed (Fig.3) to create a zone of pure moment where the specimen experience pure moment under repeated loads [18]. The modulus of rupture is determined under monotonic loading [19]:

$$f_{cf} = \frac{PL\,(100)}{BD^2} \quad (1)$$

Where f_{cf} is modulus of rupture (MPa), P is maximum applied load (kN) and *L, B and D* are average span length, width and height of the beam in mm. The resilient modulus will then be performed at a fraction of maximum load (70% of peak load in this case) to evaluate the deterioration of modulus over time. Once the beam reaches half of the initial modulus, the beam is considered to reach end of its serviceability. However, a brittle failure is often observed close to the halfway point of initial resilient in the beam [18].

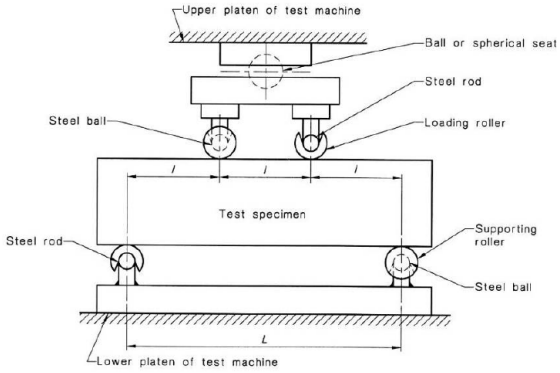

Fig. 3 Schematic of four-point beam test setup [19]

Preparation of specimens

In this research, 10% additive precursor based on dry mass of CB and RCA was mixed with blend for consistency among the blends. The dry precursors have been mixed thoroughly and was mixed with the diluted activator in a mixer to create a lean mortar. The remaining water content was mixed with the aggregates and cured for 3-4 hours to allow for aggregates water absorption before mixing. The mortal and wet aggregates have been mixed thoroughly and was placed in layers into the moulds.

The triaxial specimens with a diameter of 100±0.5mm were compacted in 8 layers of 25 mm (specimen height = 200±1mm) in a split mould at modified energy of compaction and optimum moisture content. The moisture content was limited to the value obtained from the compaction curves in order to demould the sample instantly after compaction. The samples were wrapped in plastic sealing and were cured in a moisture chamber for 7 days before testing. The height of each sample was monitored for swelling which was limited to 0.2 to 0.6 mm (less than 0.3% strain).

Two beam samples were compacted in a rectangular prism mould (400±1mm × 100±0.5mm × 100±0.5mm) in three layers using under compaction technic suggested by Vallejo [20]. A haversine dynamic load with a frequency of 2 Hz including a 250 ms worth of loading and 250 ms of rest at a minimum sitting pressure (Fig.4).

The recoverable mid-span deformation of the beam is used to calculate the resilient modulus under repeated loading. Hence, a small sitting area for the tip of LVDT should be prepared to avoid unnecessary drop in resilient modulus. The average modulus calculated at first 50 cycles are determined as the initial modulus of the beam and will be used to determine the fatigue life of the specimen.

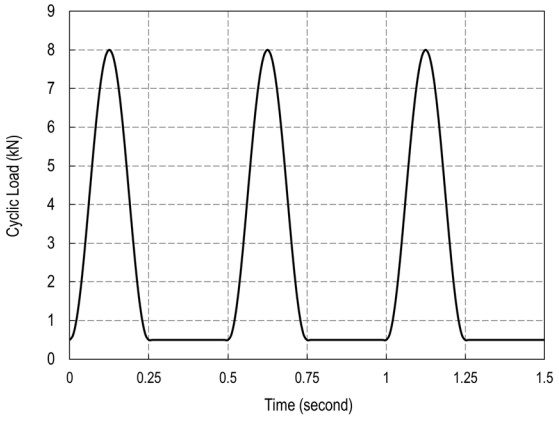

Fig. 4 Typical haversine loading of Fatigue beam test

RESULTS AD DISCUSSIONS

Repeated load triaxial test

The compressional average resilient modulus (R_m) of stabilized CB and RCA over 65 stress combination have been reported in Fig.5. The addition of FA showed negative impact on the compressional

resilient modulus. Addition of 10% FA had limited impact on uniaxial strength improvement as well as resilient modulus of the C&D aggregates as discussed by Mohammadinia, et al. [3]. The beam samples prepared with this blend have failed prior to loading due to low shear strength.

The low strength development at low-calcium systems that rely on alominosilicate gel activation have been reported previously [21]. On the other hand, using a high calcium-based precursors like slag have resulted in rapid strength and stiffness gain. It worth noting that at 10% of stabilization, the compressional resilient modulus between CB and RCA are very close which suggest it is mainly controlled by binder rather than the aggregates in the blend.

Considering the high stiffness of these blends and relatively low-stress level of the RLT testing regime, it is evident that the samples have remained in the elastic zone and the bound between the aggregates have not been broken. On the other hand, the mixed system of FA and S mixtures show similar resilient modulus levels and also lower stiffness compared to that of the higher calcium systems.

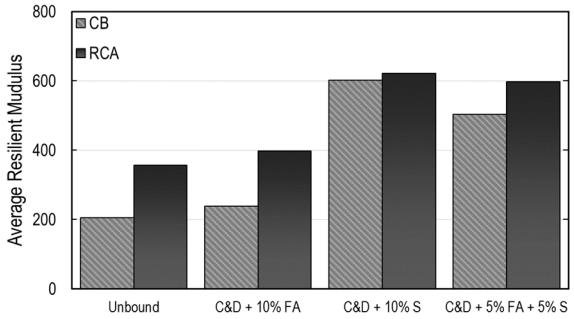

Fig. 5 *Rm* of 7-day cured stabilized C&D aggregates

Four-point beam test

The modulus of rupture of the stabilized samples have been reported in Table 3. The Monotonic loading of the first of two beams reveals the peak load that the beam can carry before failure under pure moment. The relation between compressive strength and modulus of rupture of the stabilized materials is depicted in Fig.6. The samples show a similar behavior at failure under uniaxial compressive strength and flexural peak load. However, the stress levels as high as the peak load is hardly reached in railway and road layers. Yeo [18] suggest a reduced fraction of peak load to be utilized to assess the behavior of the stabilized layer. This fraction should be selected to push the stabilized materials out of the elastic zone and still low enough to avoid premature failures in the stabilized layer. For this research, 70% of the peak load have been used to evaluate the fatigue behavior of the stabilized materials.

Table 3 Four-point beam test results

Sample Designation	Modulus of rupture (MPa)	Flexural Modulus‡ (MPa)
CB + 10% S	1.68	11,113
CB + 5% FA + 5% S	1.90	8,784
RCA + 10% S	1.90	14,274
RCA + 5% FA + 5% S	2.10	12,088

‡ The initial flexural modulus was calculated as the average of second 50 cycles performed at 70% of peak load from rupture test.

On top of quick setting time of specimens stabilized with S, Fig 6 shows that although the rapid strength gain and stiffness improvement in high calcium system stabilized aggregates is desirable, these blends are susceptible to brittle failure under flexural loadings. Although the peak of compressive strength for both C&D aggregates stabilized with S is higher compared to the respective blends stabilized with combination of FA and S, the modulus of rupture at the peak of flexural strength for specimens stabilized with S are lower.

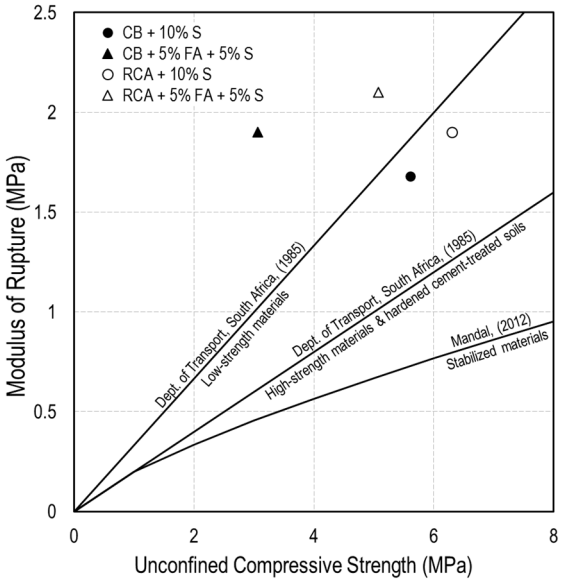

Fig. 6 comparison between modulus of rupture and uniaxial strength of stabilized C&D aggregates

This theory is confirmed by the deterioration rate observed in the four-point beam flexural fatigue test (Fig.7). The higher initial resilient modulus (Table 2) is mainly due to higher stiffness and higher Young modulus of the high-calcium systems. However, the brittle behavior of these samples results in quick deterioration of the gel which in turn amplify the reduction in resilient modulus which resulted in failure of CB + 10%S and RCA + 10%S at cycle number 253 and 403, respectively.

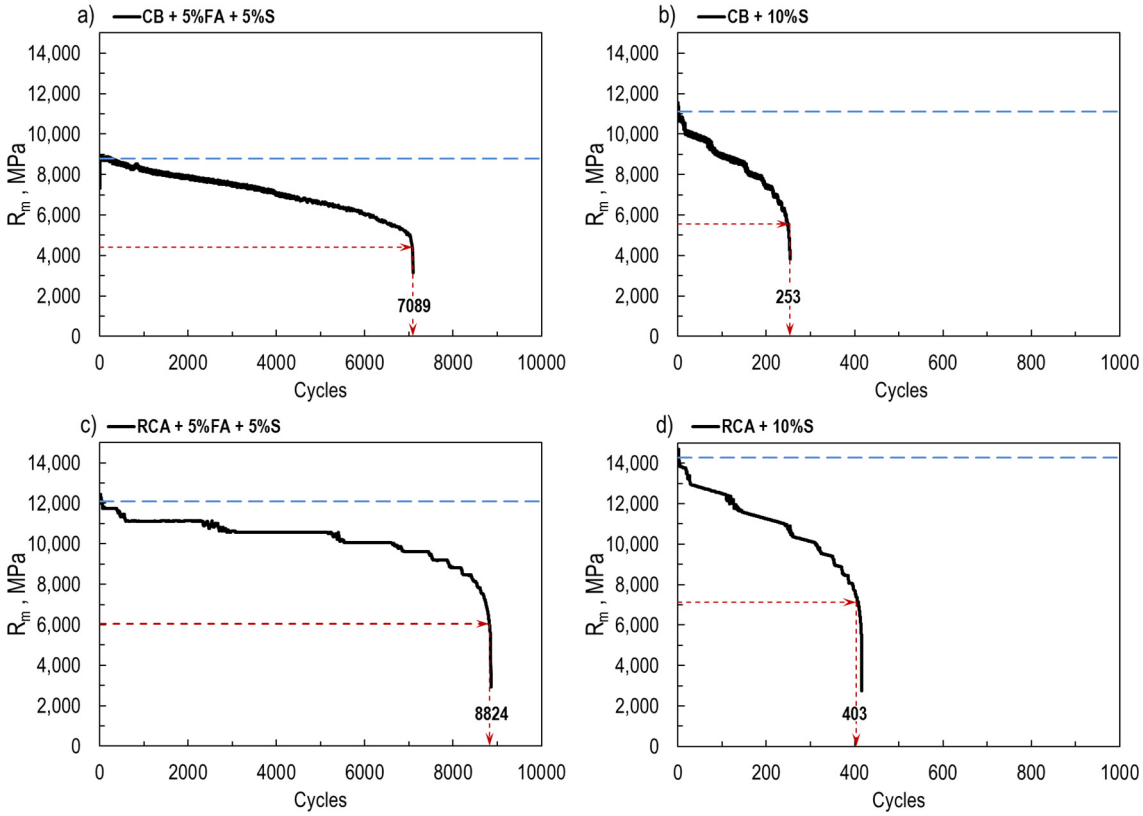

Fig. 7 Four-point beam flexural fatigue test on lightly stabilized C&D materials

In contrast, samples stabilized with FA and S with lower initial stiffness and lower resilient modulus can sustain longer at elastoplastic repeated loading region with minimum deterioration. CB + 5%FA + 5%S and RCA + 5%FA + 5%S have persisted under the repeated loading up to cycles 7089 and 8824 respectively.

It should be noted that at 10% additive content, the stabilized materials behavior, particularly in flexural loading, is governed by the binder behavior. This is particularly important to note that despite the lower compressive strength of stabilized CB blends compared to that of RCA, lower durability of the CB aggregates is less significant under flexural loading conditions.

CONCLUSIONS

The sustainable use of C&D aggregates have often limited to low bearing capacity layers in railways and pavement construction. Utilization of industrial by-products have been researched as an environmental friendly approach for stabilizing solid waste aggregates. Understanding the stiffness and resilient modulus of the binders as well as the geo-materials generated for construction of stabilized layers can potentially promote utilization of C&D aggregates in railway capping layer and pavement construction activities.

Furthermore, the loading condition and the stress levels induced to the intended stabilized layer can significantly affect the behavior of the materials. Resilient modulus of the stabilized layers in pavement and railway structures is not only relying on the stiffness of the geo-materials but also relies on the thickness of the layer.

Additionally, the lack of flexibility in the stabilized layer can lead to progressive and potentially sudden failure of the layer while gradual deterioration can often be rectified. In this research, the fatigue life behavior of the two stabilizing precursors were compared to demonstrate the advantages and disadvantages of the stabilization process.

ACKNOWLEDGMENTS

This research was conducted by the Australian Research Council Industrial Transformation Training Centre for Advanced Technologies in Rail Track Infrastructure (IC170100006) and funded by the Australian Government. The authors would like to thank Alex Fraser Group for providing the demolition aggregates used in this research.

REFERENCES

[1] A. Lopez-Uceda, F. Agrela, M. Cabrera, J. Ayuso, M. López, Mechanical performance of roller compacted concrete with recycled concrete aggregates, Road Materials and Pavement Design 19(1) (2018) 36-55.

[2] A. Arulrajah, M.M. Disfani, H. Haghighi, A. Mohammadinia, S.J.C. Horpibulsuk, B. Materials, Modulus of rupture evaluation of cement stabilized recycled glass/recycled concrete aggregate blends, 84 (2015) 146-155.
[3] A. Mohammadinia, A. Arulrajah, I. Phummiphan, S. Horpibulsuk, M. Mirzababaei, Flexural fatigue strength of demolition aggregates stabilized with alkali-activated calcium carbide residue, Construction and Building Materials 199 (2019) 115-123.
[4] S. Kakuturu, L.N. Reddi, Evaluation of the parameters influencing self-healing in earth dams, Journal of geotechnical and geoenvironmental engineering 132(7) (2006) 879-889.
[5] Y.H. Huang, Pavement analysis and design, 1993.
[6] B. Vuong, R. Brimble, Austroads repeated load triaxial test method: Determination of permanent deformation and resilient modulus characteristics of unbound granular materials under drained conditions, (2000).
[7] S. Chakrabarti, J. Kodikara, Basaltic crushed rock stabilized with cementitious additives: compressive strength and stiffness, drying shrinkage, and capillary flow characteristics, Transportation research record 1819(1) (2003) 18-26.
[8] A. Litwinowicz, A. Brandon, Dynamic flexure testing for prediction of cement-treated pavement life, 17TH ARRB CONFERENCE, GOLD COAST, QUEENSLAND, 15-19 AUGUST 1994; PROCEEDINGS; VOLUME 17, PART 2, 1994.
[9] J.H. Beeghly, Recent experiences with lime-fly ash stabilization of pavement subgrade soils, base and recycled asphalt, Proceedings of the International Ash Utilization Symposium, University of Kentucky, Lexingston, USA, Oct, 2003, pp. 20-22.
[10] D. Xuan, L. Houben, A. Molenaar, Z. Shui, Cement treated recycled demolition waste as a road base material, Journal of Wuhan University of Technology-Mater. Sci. Ed. 25(4) (2010) 696-699.
[11] J. Pickin, P. Randell, J. Trinh, B. Grant, Australian National Waste Report 2018, Department of the Environment and Energy; Blue Environment Pty Ltd, 2018, pp. 1-126.
[12] J. Pickin, P. Randell, J. Trinh, B. Grant, National Waste Report 2018, Department of the Environment and Energy, 2018.
[13] R.J. Myers, S.A. Bernal, R. San Nicolas, J.L. Provis, Generalized structural description of calcium–sodium aluminosilicate hydrate gels: the cross-linked substituted tobermorite model, Langmuir 29(17) (2013) 5294-5306.
[14] A. Fernández‐Jiménez, F. Puertas, I. Sobrados, J. Sanz, Structure of calcium silicate hydrates formed in alkaline‐activated slag: influence of the type of alkaline activator, Journal of the American Ceramic Society 86(8) (2003) 1389-1394.
[15] VicRoads, Section 812 : Crushed Rock for Pavement Base and Subbase, in: Victoria (Ed.) 2011.
[16] AASHTO T 307, Standard method of test for determining the resilient modulus of soils and aggregate materials, AASHTO T 307-99,, AASHTO, American Association of State and Highway Transportation Officials, 2007.
[17] Y. Momoya, E. Sekine, F. Tatsuoka, Deformation characteristics of railway roadbed and subgrade under moving-wheel load, Soils and Foundations 45(4) (2005) 99-118.
[18] R. Yeo, The Development and Evaluation of Protocols for the Laboratory Characterisation of Cemented Materials, Austroads, 2008, p. 89.
[19] Standards Australia, Methods of testing concrete, Method 11: Determination of the modulus of rupture, Standards Australia, 2000.
[20] L.E. Vallejo, Interpretation of the limits in shear strength in binary granular mixtures, Canadian Geotechnical Journal 38(5) (2001) 1097-1104.
[21] H. Xu, J. Van Deventer, The geopolymerisation of alumino-silicate minerals, International journal of mineral processing 59(3) (2000) 247-266.

9th Int. Conf. on Geotechnique, Construction Materials and Environment, Tokyo, Japan, 20-22 November 2019, ISBN: 978-4-909106025 C3051

HIGH CALCIUM FLY ASH GEOPOLYMER CONTAINING NATURAL RUBBER LATEX AS ADDITIVE

Prinya Chindaprasirt[1] and Charoenchai Ridtirud[2*]
[1]Khon Kaen University, Faculty of Engineering, Department of Civil Engineering, Sustainable Infrastructure Research and Development Center, Khon Kaen, Thailand; [2] Rajamangala University of Technology Isaan, Faculty of Engineering, Department of Civil Engineering, Thailand
*Corresponding author, Email: Charoenchai.ri@rmuti.ac.th

ABSTRACT

This research studied the use of natural rubber latex as an additive in high calcium fly ash geopolymer. The high calcium fly ash geopolymer with natural rubber latex (medium ammonia concentrated latex type) content of 0, 1, 2, 3, 5 and 10 % by weight of fly ash was incorporated in the mixtures. Setting time, workability, absorption, apparent porosity, compressive strength, flexural strength, and surface abrasion resistance were tested. The test resulted shows that the optimum latex content was 1.0 % of fly ash to obtain mortar with improved mechanical properties and a slight reduction in workability, and an increase in setting time.

Keywords: Geopolymer, Fly ash, Rubber, Setting time, Medium ammonia concentrated latex

INTRODUCTION

Geopolymer is an aluminosilicate material consisting of a structure of amorphous and semi-crystalline phases. The substrate used in geopolymer production can be liberated from the particle surface with the use of base solution at both room temperature and moderate temperatures of 40-80 °C. Consequently, the geopolymerization leads to the reaction, which forms aluminosilicate chain. The material sets and endures compressive strength well [1].

The high calcium fly ash consists of a high CaO content and is categorized as type C fly ash. The high CaO content gives a higher self-cementitious property for high calcium fly ash. [2]. The high calcium content also leads to the shortening of the setting time[3] and comparable strength development to the class F fly ash. The main advantages of using high calcium fly ash are increase in the degree of hydration at the early age and the hardening and gain in strength at ambient curing temperature without the use temperature heat curing [4, 5].

The mechanical property of geopolymer mortar and concrete is similar to the mechanical property of those from Ordinary Portland cement [6]. One of the outstanding properties of geopolymer is the high strength gain in a short period when the heat is used to accelerate the reaction [7, 8]. This is suitable for precast concrete, which is in high demand in the market. The fly ash geopolymer can resist acidic and alkaline environments better than Portland cement products because it has a strong structure of aluminosilicate [9, 10] with excellent fire resistance [7, 11]. However, there are reports that geopolymer concrete exhibits higher brittleness than OPC concrete [12, 13] and to improve brittleness, elastomeric latexes can be applied to the geopolymer system [14]

Elastomeric latex is a natural or synthetic polymer having elastic properties. The use of elastomeric latex improves the durability in concrete [15, 16], and increases the flexural strength [17]. It also decreases absorption, improves workability, resists chemical aggressions, and reduces brittleness [14]. In general, there are two basic elastomers for cement mixes viz.., natural rubber latex (NRL) and synthetic rubber latexes (SRL). These elastomers affected the property of concrete in a similar way. The advantage of NRL is that it is readily usable and consumes less processing and energy in the production than that of synthetic rubber latex.

Moreover, the synthetic rubber latex cost is high as it required additional processing and other natural resources[18]. Very few researchers have studied the use of NRL with geopolymer. Lee (2016) used Styrene-butadiene with geopolymer [19] and found that it significantly increased the flexural strength in the order of 50%.

Generally, the use of NRL with OPC needs to be mixed with non-ionic surfactant to avoid agglutination when it is mixed with water and cement [20, 21]. However, geopolymer has high alkalinity, and the anion is similar to that of NRL. Therefore, it should distribute itself well in the geopolymer system. The basically sound properties of geopolymer could thus be improved with the incorporation of rubber latex. This research is thus aimed to study the properties of geopolymer mortar incorporating NRL.

The setting time, water absorption, abrasion resistance, compressive strength, direct tensile strength and bending strength were tested.

EXPERIMENTAL DETAILS

Materials

The high calcium fly ash was from Mae Moh power station in the north of Thailand. The oxide composition of fly ash is summarized in Table 1 and its X-ray diffraction (XRD) is shown in Fig.1. Scanning Electron Microscopy (SEM) results as shown in Fig. 2 showed that the fly ash particles were spherical. The fly ash was relatively fine with 24% retained on sieve No. 325 (45 µm), the median particle size of 15.6 µm, and a specific gravity of 2.64. The particle size distribution also revealed that 76% of fly ash particles were smaller than 50 µm as shown in Fig. 3.

The NRL (medium ammonia concentrated latex type) was used as an additive to improve the properties of geopolymer mortar. The properties of concentrated latex are presented in Table 2. Sodium silicate solution (Na_2SiO_3) and sodium hydroxide solution (NaOH) with Na_2SiO_3 to NaOH ratio of 0.33 were used as alkali activators. The low Na_2SiO_3 to NaOH ratio was selected for reason of environmental concern. Sodium hydroxide solutions with 6, 8, 10, and 12 molars (M) concentrations were prepared using sodium hydroxide flakes of 97% purity and distilled water. Sodium silicate with 15.32% Na2O, 32.87% SiO_2 and 51.80% H_2O by weight was used. The fine aggregate was local river sand in saturated surface dry condition with a specific gravity of 2.62 and a finesse modulus of 2.95.

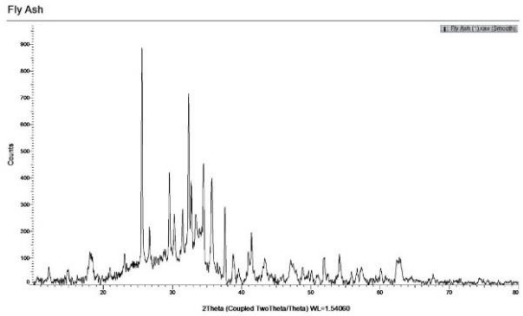

Fig. 1 X-ray diffraction of Fly ash.

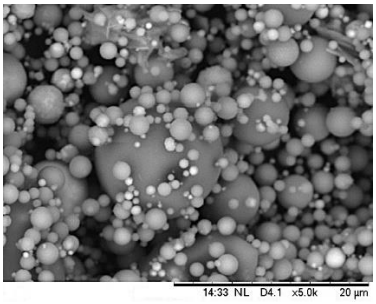

Fig. 2 Scanning Electron Microscopy of Fly ash.

Table 1 Chemical composition and properties of Fly ash

Chemical composition)wt(%	Fly ash
SiO_2	35.86
CaO	23.31
Al_2O_3	16.27
Fe_2O_3	14.06
SO_3	8.00
K_2O	1.62
TiO_2	0.44
MnO_2	0.16
SrO	0.14
As_2O_5	0.05
Rb_2O	0.02
ZrO_2	0.03
Cr_2O_3	0.02
LOI[a]	0.50

[a]Loss on ignition

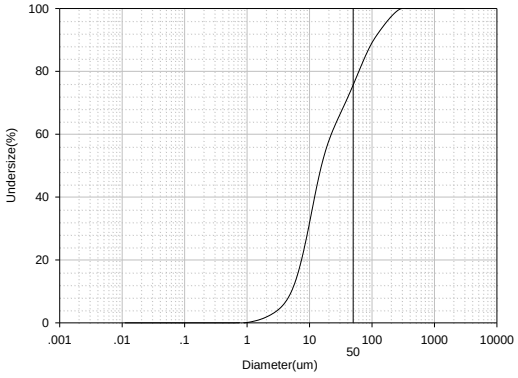

Fig. 3 Particle size distribution of Fly ash.

Table 2 Properties of natural rubber latex

Property	Value
Total solid content	62.05
Dry rubber content	60.35
Non-rubber content	1.70
pH	10.10
Volatile fatty acid number)VFA(	0.041
Mechanical stability time)sec(	685
Ammonia content)NH_3(%	0.50
Color	Milky white

Mix proportion and specimen preparation

In this study, geopolymer mortars were prepared. The ratios of sand to fly ash of 2.75, liquid to fly ash ratio of 0.6 and Na_2SiO_3 to NaOH ratio of 0.33 were used for all mixtures with the NRL addition of 0, 1, 2, 3, 5 and 10 % by weight of fly ash.

For mixing, fly ash and sodium hydroxide were mixed for 5 minutes. Sand was added at this stage and the mixing was done for another 2 minutes. The premixed rubber latex and sodium silicate were then added, and the mixing was continued for three more minutes. For mortar, the fresh geopolymer mortar was tested for flow in accordance with ASTM C1437-15 (2015) and setting time in accordance with ASTM C807-13 (2013). The fresh mortar was then cast in 50x50x50 mm cubic moulds as described in ASTM C109/C109M-16a (2016). The mortar was also cast in 100x100x100 mm cube mold for abrasion test and 40x40x160 mm prism for the flexural strength test. All specimens were covered with plastic sheets and left in a controlled 25 °C and 50 % R.H. room for 24 hours. They were then demolded and wrapped with plastic sheets to prevent moisture loss and stored in a 25 °C and 50 % R.H controlled room until the testing age.

Testing procedure

The workability of the mortar mix was tested using the flow of mortar following the ASTM C109 / C109M - 16a (2016) The setting time of the mortar was tested in accordance with the ASTM C807-99 (1999) The compressive strength and tensile strength of mortar were tested at the ages of 7 and 28 days in accordance with ASTM C109 / C109M - 16a (2016) and ASTM C307 – 03 (2012). The reported strengths were the average of three tests.

The abrasion resistance of mortars was determined according to ASTM C944 / C944M – 12 (2012) with a normal load on the specimen surface of 98 N for 2 minutes. The absorption of mortar was also tested using 50 mm cube specimen oven dried at 85 °C for 24 hours with immersion time of 48 hours. The reason for applying 85 °C was to avoid the effect of high temperature on geopolymer structure [19].

RESULT AND DISCUSSION

Setting time and flow

The results of setting time and flow of mortar are shown in Table 3. The increase in NRL content resulted in longer initial and final setting times due primarily to the reduced increased water content of system as rubber latex contained some water. Without rubber latex additive, the initial and final setting times of geopolymer mortar were 60 and 105 mins and conformed with the previously reported results [22]. The addition of 10% rubber latex slightly increased these values to 87 and 135 mins.

With regards to the flow of mortar, the increase in the rubber latex content decreased the flow of fresh mortar. The flow of mortar without rubber latex additive was 20.6 cm and reduced to 11.4 cm with 10% NRL. The NRL was a high viscosity liquid, and thus its presence reduced the workability of mixture.

Table 3 Setting time and flow of geopolymer mortars

Rubber Latex (%)	Setting time (min)		Flow (cm)
	Initial	Final	
0	60	105	20.6
1	62	120	18.1
2	65	122	17.2
3	67	125	17.0
5	80	130	14.5
10	87	135	11.4

Absorption and apparent porosity

The results of absorption and apparent porosity of mortar are shown in Fig. 4. The incorporation of 1.0 % rubber latex resulted in the reduced apparent porosity and absorption of mortar. The reduced porosity indicated the filling of pore with rubber latex. As the particles of rubber latex were between 50-100 nanometers. The cavity of paste is slightly larger at between 100 picometers to several hundred nanometers [23].

However, when the rubber latex additive was increased, the absorption and apparent porosity of mortar started to decrease. The optimum amount of rubber latex was 1.0% and the increase in the additive beyond this level resulted in the surplus rubber latex in the matrix. The increased latex particles resulted in the increases in non-homogeneity, interface, and the gap between rubber latex and paste as shown in Fig. 5 The reduced absorption was one of the important factors that improved chemical absorption resistance ability of specimen[24]. The addition of 1% rubber latex decreased the absorption and porosity of specimen at the age of 28 days by 0.7% and 3%, respectively. The geopolymer mortar containing appropriate amount of rubber latex could enhance the absorption characteristics of mortar. In addition, the experiment also showed that the absorption improved with age due to the continued reaction of geopolymer and the forming of additional calcium silicate hydrate (C-S-H) and calcium aluminosilicate hydrate (C-A-S-H) and sodium aluminosilicate hydrate (N-A-S-H) in the geopolymer matrix [25]. When the age of specimen increased, the matrix of the sample became denser and the apparent porosity decreased by 9-16

%.

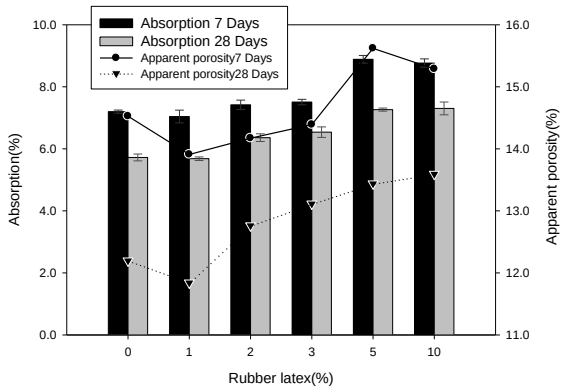

Fig. 4 Absorption and apparent porosity of geopolymer mortar at 7 and 28 days

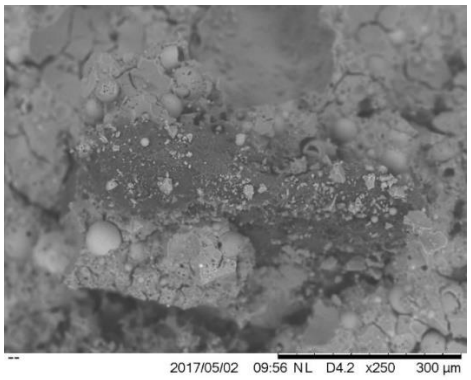

Fig. 5 SEM of rubber latex particle and geopolymer matrix

Compressive strength

The results of the compressive strength of geopolymer mortars are shown in Fig. 6. The optimum amount of latex was 1% and this produced mortar with increased compressive strength. The addition of latex beyond this level resulted in a decrease in compressive strength. A small amount of latex could fill the pore of matrix and make the mortar denser. The filling of pore at this level reduced the void in the matrix and slightly increased the compressive strength. The addition of more latex started to reduce the compressive strength due to increases in rubber particle, interface, and gap between rubber particle and paste. The compressive strength results agreed with the porosity which showed that the lowest porosity (optimum) was with the incorporation of 1% NRL. The reduction in the mechanical properties with increased NRL content complies with other reported results on the use of elastomer[16, 19] .Under the compression loading, the additional rubber latex and interface resulted in additional internal tensile strain resulting in a decrease in the compressive strength of mortar. The 7-day compressive strength of 1% latex sample was optimum at 30.0 MPa and this reduced to 7.0 MPa with the incorporation of 10 % latex.

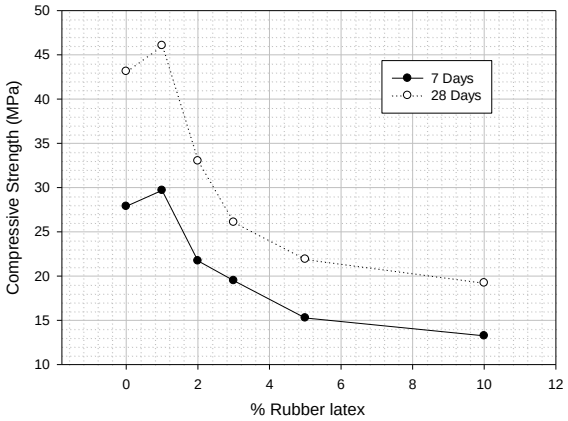

Fig. 6 Compressive strength of NRL modified geopolymer mortar at 7 and 28 days

Flexural Strength

The results of flexural strength of geopolymer mortars are shown in Fig. 7. At the age of 7 days, the flexural strengths of specimens containing 1-3 % NRL were approximately the same with that without NRL. The good performance of samples with a small amount of NRL followed similar trend to that of the compressive strength. However, at the age of 28 days, the increase in the amount of NRL reduced the flexural strength of sample. The incorporation of rubber latex seemed to have an adverse effect on the flexural strength of the mortar particularly for the samples with high strength normally obtained with advanced age. In this test, there is an indication here that the benefit of incorporation of a small amount of NRL on the flexural strength was more pronounce at the low strength level, i.e. at the early age of sample of 7 days.

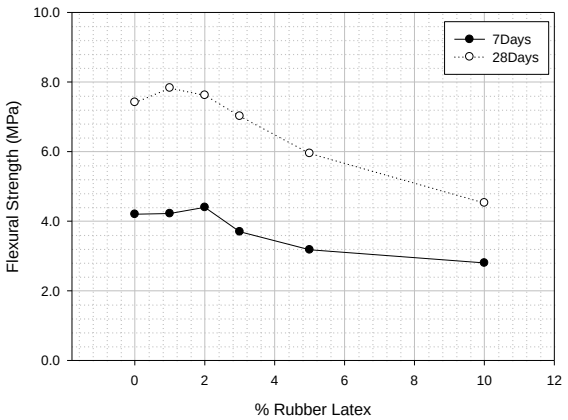

Fig. 7 Flexural strength of NRL modified geopolymer mortar at 7 and 28 days

Surface abrasion resistance

The result of abrasion resistance as shown in Fig. 8 follows the same trend as that of compressive strength. The surface abrasion resistance has been shown to relate to the compressive strength of samples [26]. In this research, the optimum NRL content of 1 % resulted in the lowest surface abrasion weight loss which corresponded to the highest compressive strength. The optimum amount of NRL addition resulted in the filling of pore of geopolymer paste and thus enhanced the properties of the mixture. The presence of NRL has also been shown to increase the absorption of impact and the impact resistance of samples [27]. The better characteristics of absorbing energy rendered the sample with increased resistance to the abrasion action of the rotation and impact of rotating cutters and decreased the surface abrasion weight loss as shown in Fig.8. As already pointed out that the increase in the NRL resulted in the non-homogeneity, interface, and gap between rubber latex and paste. In addition, the incorporation of more than 1 % NRL resulted in surplus NRL and reduced amount of paste for the basic strength unit as it reduced the amount of fly ash in the system. In some cases, the surplus NRL was prone to adhere to each other and this larger particle caused the weakness in the matrix. The results thus confirm that resistance to the surface abrasion is related to the strength of materials as indicated by the direct relation to the compressive and tensile strength of the samples.

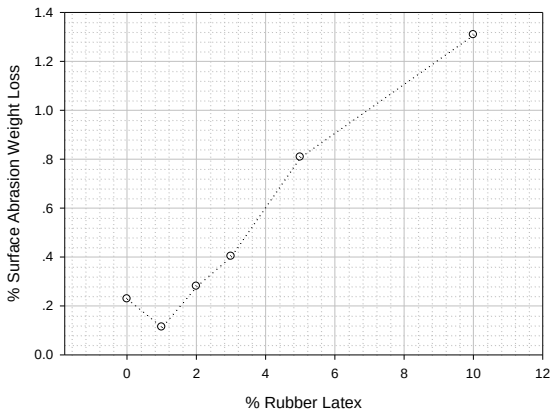

Fig. 8 Surface abrasion weight loss of rubber modified geopolymer mortar at 28days

CONCLUSIONS

Based on experiment result, the following conclusion can be made:

(1) The incorporation of natural rubber latex (NRL) increased the setting time of geopolymer mortar due to the increase in the water content of the system. The flow of mortar decreased with increasing NRL content as the NRL was a high viscosity fluid and thus increased the viscosity of system.

(2) The incorporation of 1% of NRL was optimum for the geopolymer mortar system to obtained reductions in apparent porosity and absorption of specimens. This would have a positive effect on the durability of the samples as the decreased apparent porosity and low absorption would lower the chemical absorption of sample.

(3) The compressive, and flexural strength tests confirmed that the optimum amount of NRL addition was 1%. This produced mortar with increased strengths due to the filling of pore and associated improved mechanical properties. The incorporation of NRL beyond this level resulted in the surplus NRL and reduction the strengths of mortar was observed. The surplus NRL resulted in increases in non-homogeneity, interface, and gap between rubber latex and paste. In addition, the amount of geopolymer gel was also reduced as the amount of rubber was increased.

(4) The results also confirmed that the resistance to surface abrasion was highest with the incorporation of optimum amount of NRL of 1%, which resulted in the lowest surface abrasion loss.

Overall, the results showed that NRL could be used as additive in the high-calcium geopolymer with optimum content of 1% by weight of fly ash. The geopolymer mortar with 1%NRL showed improved properties with increased in strengths (compressive, and flexural strengths), increased resistance to surface abrasion, and reduced porosity and absorption.

ACKNOWLEDGMENTS

This research was supported by Faculty of Engineering, Rajamangala University of Technology Isan. We thank our colleagues from Sustainable Infrastructure Research and Development Center SIRDC, Khon Kaen, Thailand. who provided insight and expertise that greatly assisted the research.

REFERENCES

[1] Davidovits, J., et al., '99 Geopolymer International Conference Proceedings1999: Cordi-Géopolymère SARL.

[2] R.C.Joshi and R.P.Lohtia, Fly ash in concrete prodution, properties and uses. Advances in concrete technology. Vol. 2. 1997, 1079 LH Amsterdam The Netherlands: Gordon and breach science publishers.

[3] Wongkvanklom, A., et al., Setting time, compressive strength and sulfuric acid resistance of a high calcium fly ash geopolymer containing borax. Engineering and Applied Science Research, 2017. 45(2): p. 6.

[4] Chindaprasirt, P., T. Chareerat, and V. Sirivivatnanon, Workability and strength of

coarse high calcium fly ash geopolymer. Cement and Concrete Composites, 2007. 29(3): p. 224-229.
[5] Chindaprasirt, P. and U. Rattanasak, Improvement of durability of cement pipe with high calcium fly ash geopolymer covering. Construction and Building Materials, 2016. 112(Supplement C): p. 956-961.
[6] Wongpa, J., et al., Compressive strength, modulus of elasticity, and water permeability of inorganic polymer concrete. Materials & Design, 2010. 31(10): p. 4748-4754.
[7] Cheng, T.W. and J.P. Chiu, Fire-resistant geopolymer produced by granulated blast furnace slag. Minerals Engineering, 2003. 16(3): p. 205-210.
[8] Songpiriyakij, S., et al., Compressive strength and degree of reaction of biomass- and fly ash-based geopolymer. Construction and Building Materials, 2010. 24(3): p. 236-240.
[9] Bakharev, T., Resistance of geopolymer materials to acid attack. Cement and Concrete Research, 2005. 35(4): p. 658-670.
[10] Bakharev, T., Durability of geopolymer materials in sodium and magnesium sulfate solutions. Cement and Concrete Research, 2005. 35(6): p. 1233-1246.
[11] Kong, D.L.Y., J.G. Sanjayan, and K. Sagoe-Crentsil, Factors affecting the performance of metakaolin geopolymers exposed to elevated temperatures. Journal of Materials Science, 2008. 43(3): p. 824-831.
[12] Noushini, A., et al., Compressive stress-strain model for low-calcium fly ash-based geopolymer and heat-cured Portland cement concrete. Cement and Concrete Composites, 2016. 73: p. 136-146.
[13] Pan, Z., J.G. Sanjayan, and B.V. Rangan, Fracture properties of geopolymer paste and concrete. Magazine of Concrete Research, 2011. 63(10): p. 763-771.
[14] Muhammad, B., Technology, Properties and Application of NRL Elastomers. Advanced Elastomers - Technology, Properties and Applications2012.
[15] Abdullah, S., Characteristics and performance of concrete modified with prepackaged polymer-modified mortar, 2008, Ph. D. thesis, Universiti Teknologi Malaysia, Skudai, Malaysia.
[16] Ismail, M., B. Muhammad, and N.A. Mohamad, Durability Performance of Natural Rubber Latex Modified Concrete. Malaysian Journal of Civil Engineering, 2009. 21(2): p. 195-203.
[17] Ramakrishnan, V., et al., Latex-modified Concretes and Mortars1992: Transportation Research Board, National Research Council.
[18] Thomas, S., et al., Natural Rubber Materials : Volume 1: Blends and IPNs2013: Cambridge : Royal Society of Chemistry.
[19] Lee, N.K., E.M. Kim, and H.K. Lee, Mechanical properties and setting characteristics of geopolymer mortar using styrene-butadiene (SB) latex. Construction and Building Materials, 2016. 113: p. 264-272.
[20] Khamput, P. and K. Suweero, Properties of Mortar Mixing with Medium Ammonia Concentrated Latex. Energy Procedia, 2011. 9: p. 559-567.
[21] Nadarajah, M. and U.G. Fernando, Development of natural rubber latex Portland cement mixes for engineering applications. Journal of the Rubber Research Institute of Sri Lanka, 1978. 55: p. 5-12.
[22] Al-Majidi, M.H., et al., Development of geopolymer mortar under ambient temperature for in situ applications. Construction and Building Materials, 2016. 120: p. 198-211.
[23] Riley, V.R. and I. Razl, Polymer additives for cement composites: a review. composites, 1974. 5(1): p. 27-33.
[24] Thokchom, S., P. Ghosh, and S. Ghosh, EFFECT OF WATER ABSORPTION, POROSITY AND SORPTIVITY ON DURABILITY OF GEOPOLYMER MORTARS. ARPN Journal of Engineering and Applied Sciences, 2009. 4(7): p. 5.
[25] Phoo-ngernkham, T., et al., The effect of adding nano-SiO2 and nano-Al2O3 on properties of high calcium fly ash geopolymer cured at ambient temperature. Materials & Design, 2014. 55: p. 58-65.
[26] Yan, B., P. Duan, and D. Ren, Mechanical strength, surface abrasion resistance and microstructure of fly ash-metakaolin-sepiolite geopolymer composites. Ceramics International, 2017. 43(1, Part B): p. 1052-1060.
[27] Ohama, Y., Handbook of polymer-modified concrete and mortars properties and process technology1995, Park Ridge, New Jersey, U.S.A.: Noyes Publications. 245.

9th Int. Conf. on Geotechnique, Construction Materials and Environment, Tokyo, Japan, 20-22 November 2019, ISBN: 978-4-909106025 C3051

MOISTURE SUSCEPTIBILITY OF SUPERPAVE ASPHALT MIXTURE WITH RUBBER POLYMER MODIFIED ASPHALT BINDER

Ekarizan Shaffie[1], Ahmad Kamil Arshad[1], Juraidah ahmad[2] Anizahyati Alisibramulisi[1] and Ramadhansyah Putra Jaya[3]

[1] Institute for Infrastructure Engineering and Sustainable Management (IIESM), UiTM, 40450, Selangor, Malaysia

[2] Faculty of Civil Engineering, Universiti Teknologi MARA (UiTM), 40450, Selangor, Malaysia

[3] Faculty of Civil Engineering & Earth Resources, Universiti Malaysia Pahang, 26300 Gambang, Pahang, Malaysia

ABSTRACT

Moisture susceptibility or known as stripping are very common road distress in tropical country and it is a safety treat to road users. Polymer modified asphalt binder has been conducted previously to find an alternative material in pavement construction that can be used as new improvement for asphalt mix design. This research was carried out to determine the potential benefits of rubber polymer as modifier to enhance the properties and strength of the bituminous road. In this study, three different types of dense graded Superpave HMA mix were developed consists of unmodified asphalt binder (Control) mix, Rubber Polymer Modified Asphalt binder (RMB) mix and Rubber Polymer Modified Asphalt binder with Hydrated Lime (RMBL) mix. This research evaluates the physical properties and moisture susceptibility performance of dense graded Superpave-designed HMA mix. Laboratory tests, i.e. aggregate testing and Superpave volumetric properties were performed to evaluate the physical properties of these mixtures. The Moisture Susceptibility Test (AASHTO T283) was used to characterize stripping performance of dense graded Superpave HMA mixes. The addition of 4 percent 40-mesh tyre crumbs by weight of asphalt binder into asphalt binder were used to prepare rubber polymer modified asphalt binder. 1 percent Hydrated lime by total weight of aggregate was added into the aggregate to improve the bond between aggregate particles and, thereby mitigating moisture damage. Results from the study revealed that, all the mixes passed the Superpave volumetric properties criteria which indicate that these mixtures were good with respect to durability and flexibility. The addition of rubber polymer significantly enhances the properties of asphalt mixtures. The moisture susceptibility result showed that RMB mix demonstrates better resistance to stripping than those prepared using Control mix. While the addition of hydrated lime as antistripping additive with rubber polymer into bituminous asphalt binder would improve the stripping performance of HMA mixes which indicated that RMBL has the most potential to improve stripping resistance eventually increasing the life span of the pavement and reduce premature pavement failure. Therefore, rubber polymer has high potential recycling market value which can be used as additive to, reduce temperature susceptibility, improve adhesion and cohesion properties and further enhance performance of Superpave designed pavement in tropical climate.

Keywords: Moisture susceptibility, Superpave, Volumetric Properties, Stripping, Consensus Properties

INTRODUCTION

Malaysia being in tropical climate receives a significant amount of rainfall throughout the year. Climatic factor such as temperature and moisture and high traffic impact stress have profound effect on the durability of hot mix asphalt (HMA) pavements against pavement failures. The selection of poor-quality material may also affect the overall performance of the pavement including stiffness, stability, durability, workability, fatigue resistance, frictional resistance and resistance to stripping [1,2]. Stripping happens when water infiltrates between an asphalt film and the aggregate surface, and replaces the asphalt aggregate's coating. This situation causes a loss of bond between the aggregate and the asphalt cement [3,4]. The most serious consequence of stripping is the loss of strength and integrity of the pavement. Stripping failures within the asphalt pavement structure can translate into various types of pavement failure such as fatigue cracking, rutting, raveling and potholes. This condition makes the driving comfort and safety of the drivers in dangerous. The damage of asphalt pavements due to moisture also can significantly increase the maintenance costs of a pavement and ultimately, reduce the life of the pavement. Due to these problems, it has been seen increased interest to improve HMA mixture properties for better performance and safe riding comfort.

Currently, there are a number of additives that are available that can be added to the Hot Mix Asphalt (HMA) mixture as a solution to the stripping problem and hence, create a high performance pavements characteristics. For many years' polymers are used as additives to modify asphalt cement to increase the high temperature stiffness of the HMA mixture which can reduce the probability of pavement failures. Many studies explored the effects of polymer/additives on the properties of conventional. Results showed that the incorporation of polymers to also has beneficial effects

on asphalt binders on road pavement. It would decrease the thermal susceptibility and permanent deformation under load (rutting) and increased the resistance to low-temperature cracking. It also brings greater adhesion to aggregate [5,6]. Hydrated lime and Portland cement are the most effective antistripping fillers. It can considerably improve the stripping resistance characteristics of asphalt mixtures [7]. Study conducted by Huang (2010) studied the moisture susceptibility of hot-mix asphalt (HMA) containing hydrated lime [8]. They concluded that the strong interaction between hydrated lime and can improve the bond between aggregate particles and, thereby mitigating moisture damage. Researchers found that the mixes containing hydrated lime and liquid anti-stripping agent are stiffer, less susceptible to rutting, moisture damage and cracking. Studies have shown that lime reduces the potential for moisture to disrupt the adhesive bond that exist between the and aggregate [9]. In this study, the usability of rubber polymer in asphalt mixture and the effectiveness of hydrated lime additives on the HMA mixes was also investigated in term of moisture susceptibility or stripping performance. Finally, this research will investigate and show that the use of hydrated lime as antistripping additives and the modification of the asphalt binder by using rubber polymer will reduce the stripping problem.

METHODOLOGY

Materials

Granite aggregate and two types of asphalt binder; unmodified asphalt binder of penetration grade 80/100 and rubber polymer modified were used in this study. The aggregates were obtained from Hanson Quarry, Semenyih. The aggregate undergone and satisfy the Jabatan Kerja Raya (JKR) material specification test and also Superpave recommended evaluation tests. Consensus aggregate test; Flat and Elongated Particles (ASTM D4791), Fine Aggregate Angularity (AASHTO TP33), Clay Content (ASTM D2419) are performed to assure that the selected aggregate is acceptable for the mix design. Source properties tests; Toughness (ASTM C131), Soundness (ASTM C88), Deleterious Material (ASTM C142) are used to qualify local source of aggregate.

Rubber Polymer Modified binder used in this study was produced by modifying of PEN 80/100 with 4 percent 40-mesh tyre crumbs by weight of asphalt binder. A high shear mixer was used for blending tyre crumb particles into the asphalt binder. An acceptable tyre crumb particle dispersion was achieved by operating the high shear mixer at 175 ºC and 1500-2000 rpm.

Hydrated lime was used as an antistripping additive. In this study, 1 percent Hydrated lime by total weight of aggregate was added in a 1.5 percent water by total weight of aggregate. Dry hydrated lime was initially added to the dry aggregate. Water was then added then thoroughly mixed to provide a good coating of lime on the aggregate surface. The aggregate was then placed in the oven for drying and heating purposes.

Mix design

The Superpave mix design procedure[10] was used to determine the aggregate gradation and optimum asphalt binder content. The major steps involved in volumetric testing and analysis process are (i) selection of materials; (ii) selection of aggregate gradation; (iii) selection of optimum asphalt binder content; and (iv) evaluation of moisture susceptibility of the design mixture. Three different mix were developed in this study; unmodified asphalt binder (control) mix, rubber polymer modified asphalt binder (RMB) mix and rubber polymer modified asphalt binder with hydrated lime (RMBL) mix.

To select the aggregate gradation, three trial blends were established mathematically by combining the gradations of individual stockpiles into a single blend. This step consists of blending available aggregate stockpiles at different percentages to arrive at aggregate gradations that meet Superpave requirements for each blend. The initial trial content for the three blends was estimated to 4.5%. Two samples from each trial blends were compacted using Superpave Gyratory Compactor (SGC). The SGC compact the samples at an angle of 1.25 gyration, pressure of 600 kPa and a speed of 30 rpm. In this study, the number of gyrations for initial compaction, design compaction, and maximum compaction were N_{ini} = 8 gyrations, N_{des} = 100 gyrations and N_{max} = 160 gyrations were used. Each sample was compacted to the design number of gyrations, with sample height data collected during the compaction process. Superpave gyratory compaction data was analyzed by computing the estimated bulk specific gravity, corrected bulk specific gravity, and corrected percentage of maximum theoretical specific gravity for each desired level of gyration. Superpave mix design volumetric properties criteria such as voids in mineral aggregates (VMA), voids filled with asphalt (VFA), and dust proportion (DP) were established on a four percent (4%) air void content at N_{des} by using the N_{ini} and N_{des} gyration levels previously determined from the design traffic level. The corrected volumetric parameters were compared to the Superpave specification requirements. The design aggregate gradation that "best" meets the criteria was selected for determining the optimum asphalt binder content.

Once the design aggregate gradation was selected from the trial blends, samples were compacted at varying asphalt binders content. The mixture properties were then evaluated to determine optimum asphalt binder content. A minimum of two samples were compacted at the trial blend's estimated asphalt content, at ± 0.5% of the estimated asphalt content, and at +1.0% of the estimated asphalt content. Samples were prepared and tested in the same manner as the samples in the "Selection of design Aggregate Structure" section. The volumetric properties were

calculated at N_{des} for each asphalt binder content. All other mixture properties (%VMA, %VFA, $\%G_{mm}$ at N_{ini}, $\%G_{mm}$ at N_{max} and dust proportion) were checked at the design asphalt binder content to verify that they meet the established criteria. After the trial blend and design asphalt binder content were selected, two additional samples were compacted to N_{max} (160 gyrations) and then compared to Superpave criteria. Superpave specifies a maximum density of 98% at N_{max}. Specifying a maximum density at N_{max} prevents design of a mixture that will compact excessively under traffic become plastic and produces permanent deformation. Since N_{max} represents a compactive effort that would be equivalent to traffic much greater than the design traffic, thus excessive compaction will not occur.

Moisture Susceptibility test

Modified Lottman Test (AASHTO T283) was used to evaluate moisture induced damage of compacted samples. For the compacted samples testing method requires six samples of 150 mm diameter and 95mm height for each mixture which were randomly assigned to two groups of three numbers. One group as control sample (dry conditioning) and kept at room temperature, while the other (second group) was treated through wet conditioning. During conditioning, samples were subjected to 10-26 inHg pressure for 5 to 10 minutes under vacuum saturation. Strength for both Modified Lottman Test was obtained by determined the ratio of mean strength of conditioned samples to the mean strength of dry samples to measure moisture susceptibility of the mixes. The Tensile Strength ratio (TSR) values in the test are an indication of the potential for moisture damage. Higher TSR value indicates greater resistance of the mix to moisture damage. Tensile strength ratio (TSR) was used with 80% as the boundary between mixtures resistant and sensitive to moisture [11].

RESULTS AND DISCUSSION

Aggregate Testing

In Superpave mix, the aggregate was tested in term of consensus and source aggregate properties testing in order to achieve high performance of HMA. The results of the consensus and source aggregate properties testing are summarized in Table 1. Based on the obtained results, the value for both consensus and source properties are acceptable and fulfilled the Superpave mix design criteria. Thus, the sample from HQP Semenyih can be used in Superpave mix design and also suitable for used in the road work.

Table 1: Aggregate Specification Test Results

Reference		Test Method	Results	Criteria
Consensus Properties	ASTM D 4791	Flat or Elongated Particles in Coarse Aggregate	Flakiness Index: 7.71% Elongation Index: 9.16%	< 20%
	AASTHO TP 33	Fine Aggregate Angularity	49.18%	>45%
	ASTM D 2419	Sand Equivalent Test	46.23%	> 45%
Source Properties	AASTHO T 96	Toughness	23.30%	< 45%
	ASTM C88	Soundness Test	Fine aggregate: 4.82% Coarse aggregate: 3.25%	>10% to 20%
	ASTM C142	Deleterious Materials	Clay lumps for each aggregate size: 1.18 mm: 0.4% 4.75 to 9.5 mm: 0.2% 9.5 to 19 mm: 0.2%	>0.2% to 10%

Superpave Mixture Design

This study uses a grading NMAS 19mm and calculations were made based on the average between the upper limit and lower limit of the grading. Three trial blends were evaluated mathematically combining the gradations of individual stockpiles into a single blend gradation to determine the best aggregate structure. The Superpave combined gradation for each blend is shown in Table 2 and the gradation chart for the all blends was plotted and is shown in Figure 1.

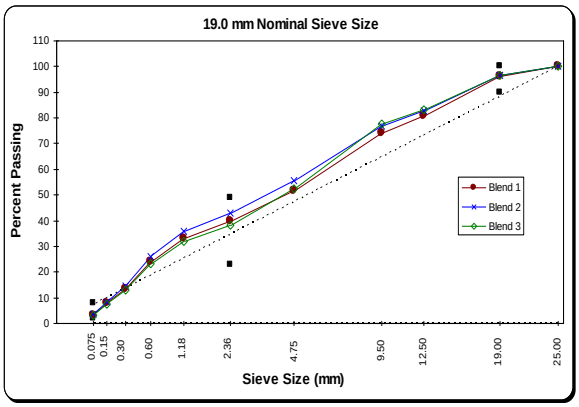

Fig. 1: Aggregate Structure Gradation

Table2: Aggregate Gradation

Sieve size	Individual gradation			Combined gradation			
	#3/4 (a)	#3/8 (b)	Dust (c)	**Blend 1** 39%(a)+ 17%(b)+ 44%(c)	**Blend 2** 35%(a)+ 17%(b)+ 48%(c)	**Blend 3** 34%(a)+ 24%(b)+ 42%(c)	Superpave control points
25.0mm	100.0	100.0	100.0	**100.0**	**100.0**	**100.0**	**100**
19.0mm	89.9	100.0	100.0	**96.1**	**96.5**	**96.6**	**90-100**
12.5mm	50.4	100.0	100.0	80.7	82.6	83.1	-
9.5mm	34.0	100.0	100.0	74.3	76.9	77.6	-
4.75mm	3.8	38.3	99.6	51.8	55.6	52.3	-
2.36mm	2.0	2.7	87.4	**39.7**	**43.1**	**38.0**	**23-49**
1.18 mm	1.8	2.0	73.0	33.2	36.0	31.8	-
600	1.7	1.9	52.4	25.0	27.1	23.9	-
300	1.6	1.6	28.7	13.5	14.6	13.0	-
150	1.6	1.5	15.6	7.7	8.3	7.5	-
75	0.9	1.2	6.2	**3.3**	**3.5**	**3.2**	**2 - 8**

Traffic level was selected based on common traffic level operating on most Malaysia highways. In this study, the traffic will be limited to medium to high roadway application. The initial trial content for the three blends was estimated to 4.5%. Each samples were compacted to N_{design} gyrations and the volumetric properties : Voids in Mineral Aggregate (VMA), Voids

Filled with Aggregate (VFA), air voids (AV) and dust proportion (DP) of the mixtures were determined. Table 3 shows the estimated blend properties. Results indicate that All mix gradations mixtures met the Superpave volumetric requirements and were qualified to become the design aggregate gradation.

Table 3: Summary of Estimated Blend Properties

Superpave mix design properties	Control	RMB	RMBL	Criterion
%Trial asphalt content	4.5	4.5	4.5	-
% Est. asphalt content	5.1	4.9	4.5	4.0%
%VMA	15.05	14.69	15.40	min 13
%VFA	73.4	72.4	74.0	65-76
Dust Proportion	0.8	0.8	0.9	0.6-1.2
%Gmm@Nini	88.4	88.9	88.7	≤89

Determination of optimum asphalt binder content

Further evaluation of this data is to determine the optimum asphalt binder content of the mixtures to achieve 4% air voids (96% G_{mm}) at N_{design}. Selection of the optimum asphalt binder content consists of varying the amount of in the design aggregate gradation to obtain acceptable volumetric properties when compared to the established mixture criteria based on the SGC samples with 4% air voids. The volumetric properties evaluation is one of the major components in determining stability and durability of asphaltic mixtures. The volumetric properties of all mixtures are presented in Table 4 and it can be concluded that all the mixture properties meet the Superpave Criteria. The optimum asphalt binder content of 5.3 %, 5.2% and 4.5% were the values that corresponds to 4.0% air voids at N_{des}=100 gyrations for unmodified asphalt binder (Control), rubber polymer modified asphalt binder (RMB) and rubber polymer modified asphalt binder with hydrated lime (RMBL) respectively. Results revealed that the RMBL mix use less binder compared to Control and RMB. However, all the Superpave volumetric mix design properties for each mixture were found very close to the target value, which implied that the design mixture was good with respect to durability and flexibility.

Table 4: Summary of Volumetric Properties of Superpave Mixtures

Mix design properties	Control	RMB	RMBL	Criterion
% AC	5.3	5.2	4.5	-
%VMA	15.7	15.5	15.5	min 13
%VFA	74.6	72.0	74.4	65-76
%DP	0.7	0.7	0.7	0.6-1.2
$\%G_{mm}@N_{ini}$	88.6	88.8	88.9	≤89
$\%G_{mm}@N_{max}$	96.9	96.5	96.8	≤98

Moisture susceptibility

The last step in the Superpave mix design system is the evaluation of moisture susceptibility of the design mixture. This step is accomplished by performing Modified Lottman test (AASHTO T283) in order to determine the effect of rubber polymer modifier on moisture susceptibility of asphalt mixtures and to determine the effect of hydrated lime as antistripping additive on moisture susceptibility of asphalt mixtures modified with rubber polymer.

Indirect Tensile Strength (IDT)

Table 5 and Figure 2 shows summary of the indirect tensile strength (IDT) results of dry conditioned and wet conditioned sample for subsets with and without antistripping additives. For the dry conditioned samples, rubber polymer modified asphalt binder with lime (RMBL) mix has the highest IDT of 1.416 MPa, followed by rubber polymer (RMB) mix 1.204 MPa, unmodified asphalt binder (Control) mix 1.124 MPa. All the values are reasonable when compared to the result reported by Epps et al., [12] which indicates that dry conditioned tensile strength ranges from 0.54 MPa to 1.88MPa. While, the IDT of the wet conditioned samples ranged from 0.958 MPa to 1.341MPa. The results of IDT of wet conditioned samples showed a similar trend with the dry conditioned samples which showed the RMBL has the highest IDT.

Table 5: Summary of the indirect tensile strength (IDT) results

Mix Design	Unconditioned			Conditioned			TSR (%)
	Air Voids (%)	ITS (Mpa)	ITS_{Ave} (Mpa)	Air Voids (%)	ITS (Mpa)	ITS_{Ave} (Mpa)	
Control	7.4	1.262	1.124	7.5	1.012	0.958	85.3
	6.8	0.972		7.1	0.964		
	7.3	1.137		6.5	0.899		
RMB	6.7	1.112	1.208	6.9	0.977	1.059	87.6
	7.5	1.240		6.7	1.138		
	6.7	1.273		7.2	1.061		
RMBL	7.4	1.537	1.416	6.9	1.224	1.341	94.7
	7.0	1.412		7.4	1.549		
	6.9	1.299		6.9	1.249		

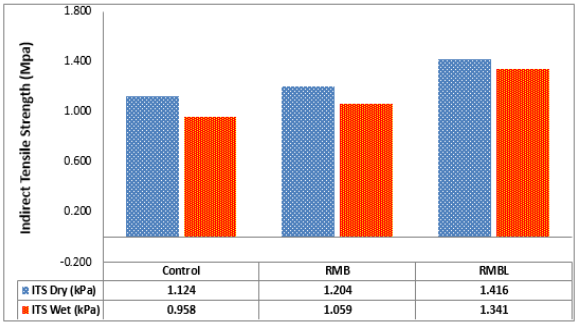

Fig. 2: Indirect Tensile Strength of Dry conditioned and Wet Conditioned samples

Tensile Strength Ratio (TSR)

The Tensile Strength Ratio (TSR) value in the modified Lottman test is an indication of the potential for moisture damage. Higher TSR value indicates greater resistance of the mix to moisture damage. A minimum TSR criterion of 80 percent was adopted for Superpave mix design AASHTO T283. Figure 3 shows the TSR for subsets with and without antistripping additive. The TSR value shows that there is no damage caused by moisture induced for all mixes since TSR

values significantly higher than 80%. The test results show that mixes of RMBL has the highest value of 94.7%, followed by RMB 87.6%, and Control 85.3%.

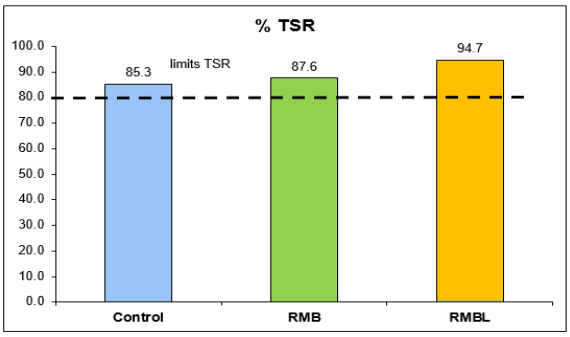

Fig. 3: The Results of Modified Lottman Test (TSR value)

Effect of moisture conditioning on moisture susceptibility of asphalt mixtures

Moisture conditioning has a significant effect on the stripping potential. This was true by the laboratory test results obtained from Modified Lottman test which indicated that the indirect tensile strength (IDT) of the wet conditioned samples was lower than dry conditioned samples. The statistical test analysis was undertaken to look at the effects of wet conditioned strength versus dry conditioned strength for each mixture. A paired sample t-test was done to compare the mean dry conditioned to the mean wet conditioned. The null hypothesis for this analysis was that the mean difference in the mean strength for both dry conditioned and wet conditioned data was equal (H_o: Dry conditioned strength = Wet cconditioned strength). The results of these analyses show the p-values of 0.00 was less than $\alpha = 0.05$, indicate that the null hypothesis was rejected. In other words, the hypothesis that the mean difference between dry conditioned and wet conditioned samples is significant. This analysis indicates that moisture conditioning has a significant effect on the stripping potential of the mixes. This means the environmental conditioning procedures in AASHTO T283 reduced the tensile strength of the mixtures.

Effect of rubber polymer modifier on moisture susceptibility of asphalt mixtures

It could be seen that rubber polymer (RMB) mixes gave better performance compared to unmodified (Control) mixes. It is because the addition of rubber polymer into asphalt binder also enhances the indirect tensile strength towards the moisture susceptibility. The enhancement of the performance to resist the tensile stress is because of rubber polymer reinforcement. The statistical test analysis was carried out to look at the effects of rubber polymer modified asphalt binder (RMB) mix versus unmodified asphalt binder (Control) mix. A paired sample t-test was used to compare the mean RMB mix to the mean Control mix. The results show the p-values of 0.05 was less than the $\alpha = 0.05$. The differences in TSR values of samples made with an unmodified asphalt binder (Control) and rubber polymer modified asphalt binder (RMB) were found to be statistically significant. Therefore, incorporation of rubber polymer as a modifier will improve the strength. This was true because rubber polymer absorbs the asphalt binder that needed to coat the aggregate thus improving the stripping resistance. In general, it can be concluded that mixes prepared using rubber polymer modified asphalt binder showed an improvement in performance and showed better resistance to stripping than mixes prepared using unmodified asphalt binder.

Effect of hydrated lime as antistripping additive on moisture susceptibility of asphalt mixtures modified with rubber polymer

The purpose of adding hydrated lime as antistripping additives was to improve bonding between asphalt binder and aggregate. It could be seen that the rubber polymer asphalt with hydrated lime mixes give better performance compared to the mixes having unmodified asphalt binder. The addition of hydrated lime as an antistripping additive has significantly improved the TSR and the stripping resistance. The enhancement of the performance to resist the tensile strength towards the moisture induced damage might be explained by the fact that hydrated lime contains calcium which increases interaction between aggregate surface and asphalt binder, so it improves the bond between and aggregate. Some States reported that modifications made to hot mix asphalt with hydrated lime will add years to its life [13]. These modifications can reduce stripping, rutting, cracking, and aging. Hydrated lime substantially improves and also works much better in conjunction with polymer additives, helping to create pavement systems that will perform to the highest expectations for many years[14]. The statistical test analysis was undertaken to look at the effects of hydrated lime as antistripping additive on unmodified asphalt binder mix and rubber polymer modified asphalt binder mix. A paired sample t-test was also used to compare the mean unmodified asphalt binder (Control) mix with the mean rubber-polymer modified asphalt binder with hydrated lime (RMBL) mix. The p-values of 0.003 for RPMBL were less than the $\alpha = 0.05$. These results indicate that the null hypothesis was rejected. Rejection H_o indicated that the mean difference between mixes of UMB with RMBL is significant. Therefore, incorporation of hydrated lime in to rubber polymer mix as an additive will enhances the indirect tensile strength towards the moisture susceptibility. It can be concluded that mixes prepared using rubber polymer modified asphalt binder with hydrated lime showed an improvement in performance and showed better resistance to stripping than mixes prepared without hydrated lime.

CONCLUSION

The research had conducted a comprehensive laboratory experimental tests to determine and evaluate the suitability of Superpave system using

local aggregates, to evaluate the stripping performance of rubber polymer modified asphalt mixes and also to evaluate the effectiveness of antistripping additive on the HMA mixes. Superpave consensus and source aggregate properties results showed that local aggregates meet both aggregate properties requirement which indicated that Hanson quarry, Semenyih has a good quality aggregate. Thus, the aggregate and locally aggregate gradations are acceptable and suitable for used in road works. Whereas, for the performance results, the incorporation of rubber polymer modified asphalt binder to bituminous mixes increases the strength. This shows that, incorporation of rubber polymer does improve the stripping resistance. It is also evident from the results, that the introduction of hydrated lime has significantly improved the TSR values of the mixes and reduces the moisture susceptibility of the HMA mixture. In term of knowledge contribution, this study contributes and proof the suitability of the new Superpave system can give better performance especially in reducing pavement failures. The used of hydrated lime and rubber polymer as additives can improved the pavement performance through their ability to improve the properties of the and resulting asphalt concrete mix that is moisture insusceptible.

ACKNOWLEDGMENT

Special thanks to the financial support for this work from Universiti Teknologi MARA (UiTM). The provided experimental facilities and assistance during the work progress were gratefully appreciated.

REFERENCES

[1] M. R. Kakar, M. O. Hamzah, and J. Valentin, "A review on moisture damages of hot and warm mix asphalt and related investigations," *J. Clean. Prod.*, vol. 99, pp. 39–58, 2015.

[2] C. Gorkem and B. Sengoz, "Predicting stripping and moisture induced damage of asphalt concrete prepared with polymer modified bitumen and hydrated lime," *Constr. Build. Mater.*, vol. 23, no. 6, pp. 2227–2236, Jun. 2009.

[3] S. Amelian, M. Manian, S. M. Abtahi, and A. Goli, "Moisture sensitivity and mechanical performance assessment of warm mix asphalt containing by-product steel slag," *J. Clean. Prod.*, vol. 176, pp. 329–337, 2018.

[4] P. Mirzababaei, "Effect of zycotherm on moisture susceptibility of Warm Mix Asphalt mixtures prepared with different aggregate types and gradations," *Constr. Build. Mater.*, vol. 116, pp. 403–412, 2016.

[5] M. Singh and P. Kumar, "Laboratory Study on Bitumen Modification for Improved Physical , Rheological Properties and the Effect of Short Term Ageing," *25th ARRB Conf.*, pp. 1–13, 2012.

[6] E. Shaffie, J. Ahmad, A. K. Arshad, D. Kamarun, and H. Awang, "Investigation on rutting performance of nanopolyacrylate and natural rubber latex polymer modified asphalt binder mixes," *J. Teknol.*, vol. 78, no. 7–3, pp. 11–15, 2016.

[7] E. Shaffie, A. K. Arshad, J. Ahmad, and W. Hashim, "Evaluation of moisture-induced damage of dense graded and gap graded asphalt mixture with nanopolymer modified binder," *IOP Conf. Ser. Earth Environ. Sci.*, vol. 140, no. 1, 2018.

[8] B. Huang, X. Shu, Q. Dong, and J. Shen, "Laboratory Evaluation of Moisture Susceptibility of Hot-Mix Asphalt Containing Cementitious Fillers," *J. Mater. Civ. Eng.*, vol. 22, no. 7, pp. 667–673, 2010.

[9] H. Özen, "Rutting evaluation of hydrated lime and SBS modified asphalt mixtures for laboratory and field compacted samples," *Constr. Build. Mater.*, vol. 25, no. 2, pp. 756–765, Feb. 2011.

[10] AASHTO, *Standard Specification for Transportation Materials and Methods of Sampling and Testing, Part 2A, 24th Edition. Washington, D.C.* 2004.

[11] AASHTO, *Resistance of compacted Hot Mix Asphalt (HMA) to Mixture-Induced Damage. AASHTO T283-07.* 2008.

[12] J. Epps, A.John, Sebaly, E.Peter, Penaranda, "Compatibility of a Test for Moisture – Induced Damage with Superpave Volumertic Mix Design," 2000.

[13] D. Lesueur, J. Petit, and H.-J. Ritter, "The mechanisms of hydrated lime modification of asphalt mixtures: a state-of-the-art review," *Road Mater. Pavement Des.*, vol. 14, no. 1, pp. 1–16, 2013.

[14] G. Kollaros, E. Kalaitzaki, and A. Athanasopoulou, "Using Hydrated Lime in Hot Mix Asphalt Mixtures in Road Construction American Journal of Engineering Research (AJER) Open Access Using Hydrated Lime in Hot Mix Asphalt Mixtures in Road Construction," no. July, 2017.

9th Int. Conf. on Geotechnique, Construction Materials and Environment, Tokyo, Japan, 20-22 November 2019, ISBN: 978-4-909106025 C3051

IMAGE ANALYSIS FOR QUANTIFICATION OF LOCAL SCALING ON CONCRETE SURFACE

Liangjun Hu[1], Isamu Yoshitake[2] and Tomoyuki Maeda[3]
[1, 2] Graduate School of Sciences and Technology for Innovation, Yamaguchi University, Japan;
[3] Institute of Technology, Penta-Ocean Construction, Japan

ABSTRACT

Surface deteriorations such as scaling on concrete happen due to environmental factors such as frost damage and chemical corrosion. Such surface deteriorations in the freeze-thaw test are generally quantified by weight loss and/or decrease of dynamic modulus of elasticity. However, it is difficult to examine these properties of huge concrete blocks such as tunnel lining sidewall. It is hard to quantify local scaling accurately because the current visual inspection methods are based on the slight loss of concrete surface subjected to the scaling. An image analysis has been developed to assess the deterioration of concrete surfaces accurately and efficiently. This image analysis is applicable for quantitative evaluation of the surface quality, including local scaling and surface holes. This study conducted a freeze-thaw test on mortar specimens with artificial surface holes. The paper presents the influence of surface holes on local scaling, which was quantified by the image analysis based on RGB values in the colored photograph. The results indicate that the image analysis is valid to detect and quantify the area of scaling, including invisible micro-scaling. It was concluded that surface holes negatively affect the scaling of concrete. A degradation grade scale based on the area-ratio, including surface holes, is proposed for evaluating local scaling appropriately.

Keywords: Image Analysis; Local Scaling; Bugholes; Freeze-Thaw Cycles

INTRODUCTION

Freeze-thaw (F-T) damage of concrete generally happens by surface scaling and internal damage [1, 2]. Concrete scaling, progressive removal of small flakes or chips of binder [3], is caused by frost damage, chemical sulfate attack, physical salt attack, and pumping effect [4–7].

Conventional evaluation methods for the F-T damage include weight loss and/or decrease of dynamic modulus of elasticity. However, it is difficult to examine these properties of huge concrete blocks such as tunnel lining.

Grading method based on a visual inspection is occasionally used to assess surface quality of concrete. ACI Committee 116 report (ACI 116R) [8] describes concrete scaling as local flaking or peeling away of the near-surface portion of hardened concrete or mortar. According to the report, “light”, “medium”, “severe” and “very severe” are defined by the loss of surface mortar down to depths of less than 5 mm, 5-10 mm, 5-10 mm to 10-20 mm around aggregates, and greater than 20 mm, respectively. ASTM C 672/C 672M [9] gives the visual rating-scale of surface scaling, as shown in Table 1. This grading method provides a quick and convenient way to evaluate surface scaling. However, these visual grading methods may be varied by inspectors, and it may cause subjective and inaccurate evaluation. Both the ACI 116R and ASTM 672/C 672M assess surface scaling based on depth. Most local scaling on concrete surface is caused from the loss of light depth. It may be hard to quantitatively evaluate such local scaling in the general way. Hence, a quantitative evaluation method for local scaling is necessary to assess the deterioration of concrete appropriately.

IMAGE ANALYSIS

Image analysis methods are developed initially to detect deteriorations such as the bugholes. Detailed surveying is a conventional and reliable way to detect bugholes. However, it requires much human resource and takes a long inspection time. Image analyses based on thresholding are generally used to detect and evaluate the surface bugholes, but the detection accuracy of the thresholding method is not always adequate since the stains on concrete. A simple detection method having sufficient accuracy is preferable for the actual application.

The colored image analysis Concrete Vision Evaluation (CVE) developed by our lab is based on red/green/blue (RGB) value of color photographs taken by a commercial digital still camera. Each pixel in a color image consisted of the red (R), green (G) and blue (B) color. Therefore, each pixel has a specific RGB value.

The image analysis to detect and evaluate bugholes is described as follows [10]:

1. Select a typical bughole in evaluated photographic image, and the RGB values of the pixels are determined as reference numbers of red/green/blue.
2. The RGB values of each pixel in the photographic image are compared with the reference number of RGB.
3. When all RGB values of a pixel is low than the reference criteria, the pixel is estimated as an element of the photographic image of the bugholes.
4. When multiple pixels showing a bughole are adjacent to each other, they are combined and estimated as a larger photographic image of the bughole.
5. The dimensions and X-Y coordinates of estimated bugholes are automatically calculated by counting pixels. The reference length is determined by recalculating the pixels of photographic image of a steel ruler in evaluated photographic image.

A comparative test conducted by Yoshitake *et al*. [10] shows that even invisible bugholes (diameter < 1 mm) can be detected in the developed system, whereas such bugholes are hardly detected in detailed visual survey. Further information on image analysis CVE can be found in the previous papers [10, 11].

With the benefits of high accuracy and efficiency, therefore, the image analysis is applicable to detect local scaling deteriorations. This study employs the image analysis to quantify the scaling area-ratio to evaluate the local scaling on concrete/mortar surface.

Table 1 Visual rating scale of ASTM C 672/C 672M

Rating	Condition of surface
0	no scaling
1	very slight scaling (3 mm [1/8 in.] depth, max, no coarse aggregate visible)
2	slight to moderate scaling
3	moderate scaling
4	moderate to severe scaling
5	severe scaling (coarse aggregate visible over entire surface)

RESEARCH SIGNIFICANCE

Bughole often appears on concrete surface. It is considered as an aesthetic problem rather than a durability problem. However, Saorin *et al*. [12] mentioned that the surface finishing of a concrete element might relate to the external and internal porosities with the mechanical and durability properties. Maeda *et al*. [13] addressed that the bugholes reduces the thickness of the concrete cover and probably causes an increase of permeability, which may accelerate the process of deterioration. Hence, it is necessary to investigate the effect of surface bugholes on durability.

A F-T test on concrete blocks (30 cm × 30 cm × 75 cm) was conducted to examine the local scaling of bugholes. In the 300 F-T cycles, concrete specimens were stored in a cooling chamber, and saltwater were sprayed on vertical surface of the specimens. The image analysis was performed to detect the surface deteriorations during the F-T test.

Surface scaling is observed as local flaking of the near-surface portion of mortar. The image analysis emphasizes on the image color of concrete surface and the scaling. This study conducted a F-T test on mortar specimens having artificial holes to confirm the actual application of the color image analysis method for quantitative evaluation of surface deterioration. This paper discusses the influence of surface holes due to the local scaling.

TEST PROGRAM

Mortar Specimens

Mortar materials used in this study were sea sand (density 2.58 g/cm^3) and ordinary Portland cement (density 3.16 g/cm^3) defined in the Japan Industrial Standard (JIS R 5210). Water-cementitious material ratio and cement/sand mass ratio of mortar were 0.45, 1:2, respectively. The mortar had a compressive strength of 45 MPa at the age of 28 days.

To make surface holes, the mortar was cast in a steel mold (150 mm × 150 mm × 60 mm) with wood plates at the bottom having various sizes of round screws, as shown in Fig. 1. Every three of specimens with the same hole size, including hole diameter of 2 mm, 4.5 mm, 6.9 mm, 9.4 mm, 14 mm, and no holes, as given in Table 2. Figure 2 shows the specimens demolded at the age of 1 day. After that, the perimeter of testing surface was covered with an aluminum tape as a dike shown in Fig. 3. In addition, an adhesive was employed to bond aluminum tape to the surface.

Freeze-Thaw Test

All specimens were subjected to 100 F-T cycles. In the F-T test, mortar specimens retained 4 % calcium chloride water of 6 mm depth and were placed in a cooling chamber. The freezing temperature was -15 ^{o}C for 16 hours, while thawing was performed in a natural ventilation condition for 8 hours. A digital camera recorded the surface

Fig. 1 Steel mold with wood plates having various sizes of round screws

Table 2 Hole size of specimens

Specimen	Hole size (mm)	
	Diameter	Depth
1 2 3	-	-
4 5 6	2	0.5
7 8 9	4.5	1.2
10 11 12	6.9	1.9
13 14 15	9.4	2.5
16 17 18	14	3.7

conditions with a shooting distance of 400 mm, as shown in Fig. 4.

RESULTS AND DISCUSSIONS

After the F-T test, surface scaling was evaluated by both visual inspection methods and the image analysis method.

Evaluation by Visual Inspection

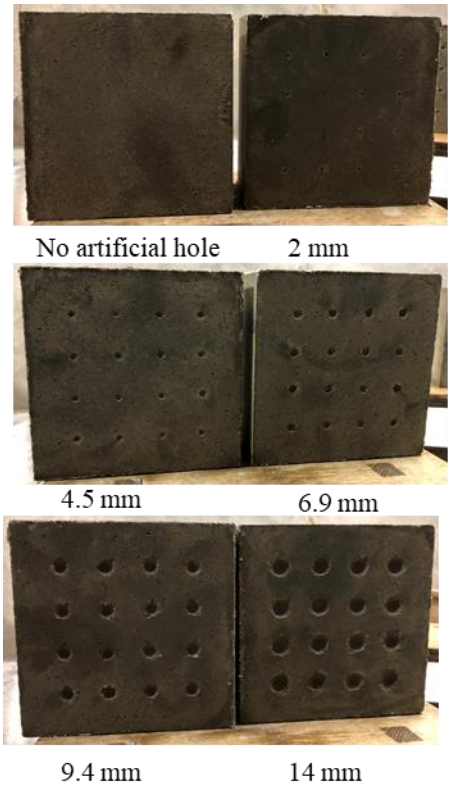

Fig. 2 Surfaces of mortar specimens with holes in various diameters

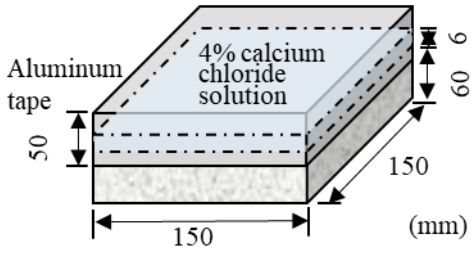

Fig. 3 Mortar specimen in the F-T test

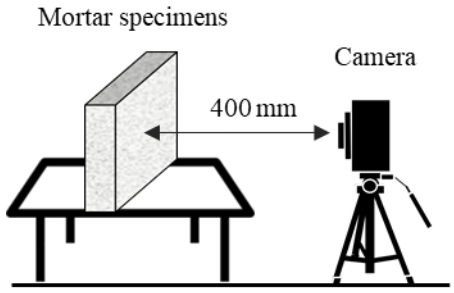

Fig. 4 Photographic test condition

Table 3 gives the rating grade by the visual inspections. Based on the ACI criterion, all mortar specimens indicated “light scaling” since the loss of

Table 3 Visual evaluation by ACI 116R and ASTM C 672/C 672M

Specimen	ACI 116R	ASTM C 672/C 672M
1	light	1
2	light	1
3	light	1
4	light	1
5	light	1
6	light	1
7	light	1
8	light	1
9	light	1
10	light	1
11	light	1
12	light	1
13	light	1
14	light	1
15	light	1
16	light	1
17	light	1
18	light	1

surface mortar down to depths is less than 5 mm. Moreover, based on the visual rating scale of ASTM C 672/C 672M, all mortar specimens were rated as level 1 because scaling depths were lower than 3 mm. These visual evaluation methods evaluate the local scaling in a general way and ignore the deterioration area.

Evaluation by Image Analysis

Deterioration area-ratio

The deterioration area-ratio r_d is defined as

$$r_d = \frac{S_d}{S}, \quad (1)$$

where S_d is the total area of pixels estimated as holes and scaling, and S is the evaluation area of a graphical image used in the image analysis.

The deterioration area-ratios of test surfaces before and after 100 F-T cycles (r_{d0} and r_{d100}) were performed by the image analysis, and their relationship is shown in Fig. 5. Specimen 1-2, 4-6, 7-9, and 10-11, having the same size of surface holes, respectively, showed less deterioration during the F-T cycles. The observation implies that the degradation of the surface with small holes can be negligible.

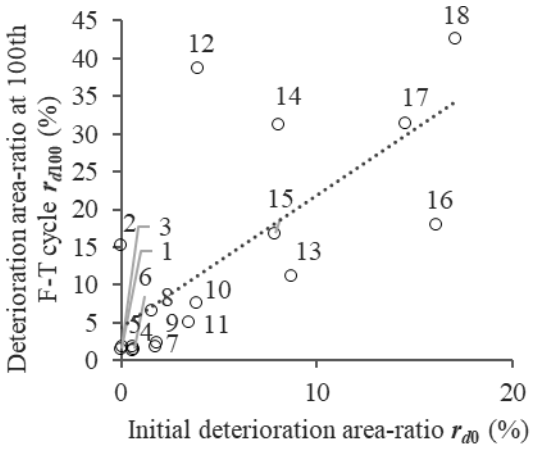

Fig. 5 Relation of deterioration area-ratio before and after 100 F-T cycles

Scaling area-ratio

Scaling area-ratio r_s occurring in the 100 F-T cycles is calculated as follows:

$$r_s = r_{d100} - r_{d0} \quad (2)$$

Figure 6 shows the relation of initial deterioration area-ratio r_{d0} and scaling area-ratio r_s. Specimen 1 and 3-11 indicated slight scaling. On the other hand, Specimen 14-15 and 17-18 had severe scaling around their larger surface-holes. The observations confirm the former F-T test result of concrete. That is, the local scaling may occur at the edge of bugholes subjected to multi-directional frost damages while the surface having fewer bugholes shows hardly local-scaling. Therefore, it can be concluded that the local

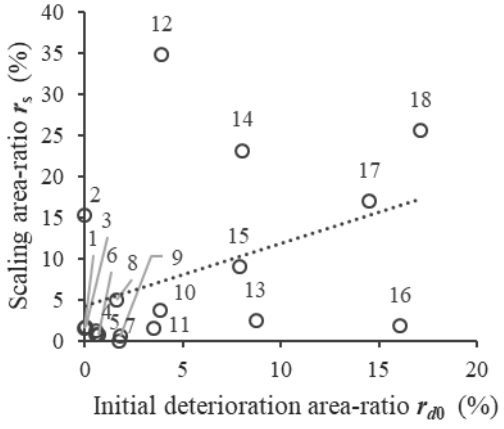

Fig. 6 Relation of initial deterioration area-ratio r_{d0} and scaling area-ratio r_s in 100 F-T cycles

scaling is affected by surface bugholes. The initial surface quality problems such as surface bugholes and spalling, has possible to increase the permeability of concrete and to accelerate the penetration of chloride ion.

Degradation grade scale based on the area-ratio

To evaluate surface deterioration precisely, the present study proposes a grading scale based on the area-ratio given in Table 4.

Table 4 Degradation grade scale based on deterioration area-ratio r_d

Grade	r_d	Surface condition
0	≤ 0.01%	no deterioration
1	≤ 1%	very slight deterioration
2	≤ 5%	slight to moderate deterioration
3	≤ 10%	moderate
4	≤ 20%	moderate to severe deterioration
5	>20%	severe deterioration

For grade 0, deterioration area-ratio under 0.01% is acceptable while the image analysis can detect invisible bugholes and holes caused by the scaling (< 1 mm). The degradation is not so important for the evaluation of the surface quality. The grade 1-4 refer to the hole area-ratio of Specimen 4-6, 7-12, 13-15, 16-18, respectively. For severe deterioration grade 5, scaling area-ratio is over than 20%.

According to the degradation grade scale, the tested mortar specimens were rated in Table 5. It assesses the degradation of specimens concisely and precisely based on the area-ratio. This grading scale is a complement with visual inspection methods by scaling depth though further investigation is needed to validate the application of the proposed deterioration grade scale.

Figure 7 shows the processed image of Specimen 18 before and after the F-T test. The scaling, occurring around holes in a slight depth, was detected by the image analysis. It is confirmed that the image analysis is applicable to quantify surface deteriorations.

CONCLUSIONS

Table 5 Deterioration grade of mortar specimens

Specimen	Before F-T test		100th F-T cycle	
	r_{d0}	Grade	r_{d100}	Grade
1	0	0	1.6	2
2	0	0	15.3	4
3	0	0	1.8	2
4	0.6	1	1.3	2
5	0.6	1	1.8	2
6	0.7	1	1.5	2
7	1.7	2	1.8	2
8	1.6	2	6.6	3
9	1.8	2	2.4	2
10	3.9	2	7.6	3
11	3.5	2	5	2
12	3.9	2	38.6	5
13	8.7	3	11.2	4
14	8.1	3	31.2	5
15	7.9	3	16.8	4
16	16.1	4	18	4
17	14.5	4	31.5	5
18	17.1	4	42.6	5

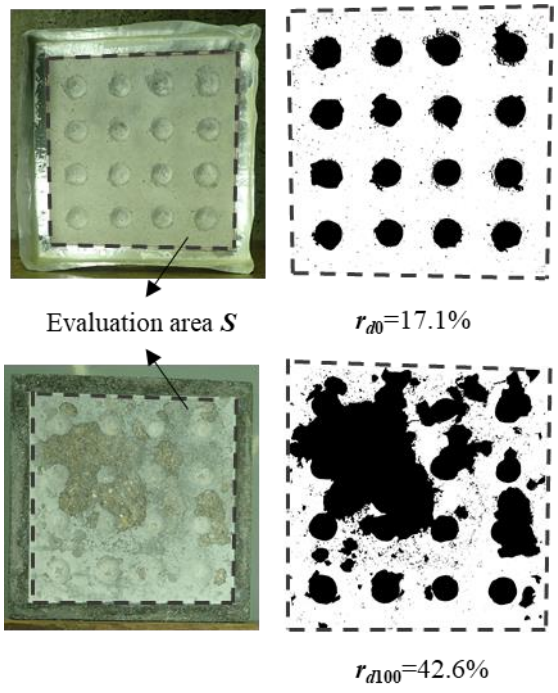

Fig. 7 Processed images of Specimen 18 by image analysis before and after 100 F-T cycles

The conclusions of this study are summarized as follows.

(1) The image analysis provides a quantitative evaluation method for local scaling of concrete surface. It is applicable for detection of the deteriorations including invisible surface scaling under the F-T cycles.

(2) The local scaling is affected by initial surface holes or bugholes before F-T test.

(3) The proposed grading-scale based on the area-ratio is useful for evaluation of surface deterioration.

The image analysis in this study can quantify surface deterioration by using two-dimensional area. It may be a complement for the conventional visual inspection methods by scaling depth. To validate the proposed scale, further research and practical application study are needed.

ACKNOWLEDGMENTS

The authors gratefully acknowledge Gifu Kogyo and APTECH for technical support. We also thank to Mr. M. Fujiwara, Mr. S. Ono (Penta-Ocean Construction), Mr. M. Hieda and Mr. H. Huang (Yamaguchi University) for their continuous support.

REFERENCES

[1] Setzer M.J., Basis of testing the freeze-thaw resistance: surface and internal deterioration, Frost Resistance of Concrete, Vol. 34, 1997, pp.157‑173.

[2] Pigeon M., Marchand J., Pleau R., Frost resistant concrete, Construction and Building Materials, Vol. 10, Issue 5, 1996, pp.339–348.

[3] Valenza J.J., Scherer G.W., Mechanism for salt scaling, Journal of the American Ceramic Society, Vol. 89, Issue 4, 2006, pp.1161–1179.

[4] Valenza J.J., Scherer G.W., Mechanism for salt scaling of a cementitious surface, Materials and Structures, Vol. 40, Issue 3, 2007, pp.259–268.

[5] Çopuroğlu O., Schlangen E., Modeling of frost salt scaling. Cement and Concrete Research, Vol. 38, Issue 1, 2008, pp.27–39.

[6] Bassuoni M.T., Rahman M.M., Response of concrete to accelerated physical salt attack exposure, Cement and Concrete Research, Vol. 79, 2016, pp.395–408.

[7] Liu Z., Hansen W., Wang F., Pumping effect to accelerate liquid uptake in concrete and its implications on salt frost durability, Construction and Building Materials, Vol. 158, 2018, pp.181–188.

[8] ACI Committee 116, American Concrete Institute 2000, Cement and concrete terminology, American Concrete Institute, Farmington Hills, Mich, 2000.

[9] ASTM C672 / C672M-12, Standard Test Method for Scaling Resistance of Concrete Surfaces Exposed to Deicing Chemicals, ASTM International, West Conshohocken, PA, 2012.

[10] Yoshitake I., Maeda T., Hieda M., Image analysis for the detection and quantification of concrete bugholes in a tunnel lining, Case Studies in Construction Materials, Vol. 8, 2018, pp.116–130.

[11] Maeda T., Harada S., Moriuchi M., Digital image analysis of concrete bugholes under vibrating consolidation, Journal of the Society of Materials Science, Japan, Vol. 66, Issue 3, 2017, pp.205–210. (In Japanese)

[12] Benito Saorin F., Miñano Belmonte I., Parra Costa C., QSI methods for determining the quality of the surface finish of concrete, Sustainability, Vol. 10, Issue 4, 2018, pp.931.

[13] Maeda T., Honma H., Hirano M., Yoshitake I., Permeability of tunnel lining with air/water bubbles on concrete surface, in Proc. ASEA-SEC-2, 2014, pp.321–326.

9th Int. Conf. on Geotechnique, Construction Materials and Environment, Tokyo, Japan, 20-22 November 2019, ISBN: 978-4-909106025 C3051

EXPERIMENTAL STUDIES OF HYDROGEOCHEMICAL INTERACTIONS OF SEAWATER AND CEMENT CONCRETES: IMPACTS ON STRENGTHS AND DURABILITY

Moshood N. TIJANI, Adedayo A. ADESIYAN, John H. ARUWA and Nnamdi OBINI
Faculty of Science, University of Ibadan, Ibadan – Nigeria

ABSTRACT

This study examines the hydrogeochemical processes associated with cement concrete–seawater interactions vis-à-vis strengths and durability of the cement concretes. A total number of 46 samples each of moulded concrete cubes (100mm x 100mm x 100mm) and cylinders (200mm x 100mm) using freshwater with mix ratio of cement, sand and gravel at 1:1:2 were cured in seawater while 32 control samples of both cubes and cylinders were cured in freshwater. Crushing and strength tests were undertaken while hydrochemical analyses of major cations and anions in the curing fresh and seawater were undertaken at the end of the prescribed curing duration of 15, 30, 60, 75, 90, 120, 135, 150 and 180 days. The crushing strength tests revealed a higher compressive strength of 18.6 – 56.9 N/mm^2 and tensile strength 1.4 – 3.2 N/mm^2 for specimens cured in freshwater compared to the samples cured in seawater with compressive strength of 16.3 – 41.8 N/mm^2 and tensile strength of 1.4 – 3.01N/mm^2. The decrease in strengths for seawater cred samples, correspond to decreases in Na^+ from 12,475mg/l to 7,250.4mg/l and decrease in Cl^- from 26,000mg/l to 17,160.2mg/l and at the same time with increase in Ca^{2+} from 382mg/l to 695.4 mg/l and increase in CO_3^{2-} from 122mg/l to 788.1 mg/l; indicative of ion exchange processes. The overall evaluation revealed that ion exchange processes, formation of crystallized chloride salts through ingress of chloride ions into concrete pore system and the formation of gypsum salts through sulphate attack are responsible for the observed strength weakening of concretes.

Keywords: Hydrogeochemical interactions, Seawater, Concretes, Strengths.

INTRODUCTION

Worldwide, the vast majority of infrastructural development has found concrete useful as an important building component. However, concrete are a composite construction material composed of cement and other cementing materials [1]. Generally, the strength of concrete structures (compressive and tensile strengths) depends mainly on the proportion of its ingredient particles i.e. cement, sand, coarse aggregates etc and it is affected by the nature of the mix, water-cement ratio, method of curing, physical properties of coarse and fine aggregates and cement types [2].

Most large cities of the world are situated within coastal settings with massive infrastructural development due to high economic potentials vis-à-vis international trades. However, the durability of concrete structures, i.e. the ability to resist the effects and influences of the environment while performing the desired functions are found to be greatly compromised under such coastal marine environment. This is largely due to the fact that the coastal and offshore concrete structures are exposed to the combined effects of a number of physical and chemical deterioration processes notably: chemical action of seawater constituents on cement hydration products, alkali-aggregate expansion, corrosion of embedded steel in reinforced or pre-stressed members, and physical erosion due to wave action and floating objects [2].

Generally, no matter its composition, water plays a big role in concrete production especially during curing since good curing practice enhances the strength and durability of concrete structures. However, there is a great variability in the concentrations of chemical elements in fresh and sea water, as seawater contains high percentage of chloride, sodium, magnesium, calcium and potassium with total salinity of about 3-5%.

A number of studies had revealed long-term negative impacts of seawater on the strengths and durability of concrete structures in coastal environments [3]–[4]. However, the chemical nature of concrete deterioration is often unappreciated [5] due to lack of detail understanding of chemical interactions between the components of the cement concretes and mixing or curing fluids.

Nonetheless, the combined damaging effects of the chemical action of seawater in form of sulphate attack through crystallization and chloride attack on the steel reinforcement are said to be the major problems associated with concrete structures either built in seawater or cast or cured with seawater [6].

Thus, this paper experimentally, studied the effects of seawater chemistry on the strengths (compressive and tensile) and durability of concretes. This by extension assesses the variations in concrete strengths with recourse to the chemistry of the curing fluids and durations / age to understand some of the controlling hydrogeochemical processes responsible for the strengths deterioration.

EXPERIMENTAL SET-UP

The experimental set-up of this study involved casting of concrete cubes and cylinders using a mix ratio of ordinary Portland cement, sand and gravel at 1:1:2 and cured in seawater and control freshwater in order to assess the possible impacts on compressive strength (Fc) and splitting tensile strength (Ft).

Concrete Mix Design and Strength Tests

A total of seventy-eight (78) concrete moulds` consisting of 46 samples each of moulded concrete cubes (100mm x 100mm x 100mm) and cylinders (200mm x 100mm) at mix ratio 1:1:2 using freshwater were employed in this study. Thirty-two (32) control samples (16 cubes and 16 cylinders) mixed with freshwater and cured in freshwater were also employed (Fig. 1).

Crushing and strength tests, using ELE - Testing Machine (Model ADR-2000), were undertaken at the end of the prescribed curing duration of 15, 30, 60, 75, 90, 120, 135, 150 and 180 days. The fresh water used for mixing and curing the concrete samples was devoid of impurities making them fit for drinking according to ASTM C190, and the seawater containing about 21,000 mg/l of dissolved salts with a pH value of about 8.0 was used.

Fig 1 Moulded cubes and cylinder concrete specimens

All the required materials for preparing concretes were weighed as regards the required proportions while the samples were removed after 24h of casting into the curing liquid until the prescribed testing durations of 15, 30, 60, 75, 90, 120, 135, 150 and 180 days. At the end of the prescribed curing duration, compressive and splitting tensile strength tests were conducted on the cubes and cylinders in accordance with BS 1881 part 116 and 117 (1983) using ELE International-Testing Machine (Model ADR-2000) (Fig. 2).

Fig 2 Loaded concrete cube specimen for Compressive strength test

The respective compressive and splitting tensile strengths in N/mm^2 for the test specimens were calculated using Eq. 1 and 2:

$$\boldsymbol{F_c = P/10} \quad (1)$$

$$\boldsymbol{F_t = 2P/\pi LD} \quad (2)$$

where; F_c = Compressive strength, F_t = Splitting tensile strength, P = Applied load / crushing load, L = length of the sample (mm), D = cross sectional dimensions or diameter (mm).

Hydrochemical Analyses of Curing Fluids

About 600 litres of seawater collected from Aivorji Beach, Badagry, Lagos and freshwater from a borehole at the Department of Civil Engineering, University of Ibadan were tested for their in-situ and laboratory physico-chemical parameters (pH, EC, TDS and major cations and anions prior to concrete moulding and curing.

Furthermore, at the end of each of the prescribed curing durations samples of the curing fluids were collected and tested for physico-chemical parameters and laboratory analyses of major cations and anions. Inductively, couple plasma atomic absorption spectrometry (ICP-AES was used for Ca^{2+}, Mg^{2+} and flame photometer for Na^+ and K^+. Also Cl^-, HCO_3^-, and CO_3^- were determined by titration while colorimeter method was employed for SO_4^{2-} and PO_2^{3-}.

The hydrochemical data alongside the strength test data were subsequently subjected to statistical evaluation, presentations using bivariate plots and interpretations in order to draw reliable deductions/ inferences.

RESULTS AND DISCUSSION

Generally, it was observed that concrete cubes (CU_{SW}) and cylinder (CY_{SW}) samples cured in seawater had darker surfaces compared to CU_{FW} and CY_{FW} (cube and cylinder cured in control fresh

water). Also, crystallized salts deposits were noticed on the surfaces of CU_{SW} and CY_{SW} samples.

Compressive Strength, Fc and Splitting Tensile Strength, Ft of the Concrete Moulds

Table 1 presents the results of the compressive strength (Fc) tests for CU_{SW} and CU_{FW} and that of the splitting tensile strength (Ft) tests for CY_{SW} and CY_{FW} at the end of the different curing durations. The results of the crushing strength tests revealed a higher Fc of 18.6 – 56.9 N/mm^2 and Ft of 1.4 – 3.2 N/mm^2 for CU_{FW} and CY_{FW} specimens cured in freshwater when compared to the CU_{SW} and CY_{SW} samples cured in seawater with Fc of 16.3 – 41.8 N/mm^2 and Ft of 1.4 – 3.01N/mm^2. This is a clear indication of the negative impact of seawater on strengths of the cement concretes. For the Fc, CU_{SW} initially gained strength and reaches a peak value of 32.9 N/mm^2 at 90 days which can be attributed to progressive hydration during setting and curing with resultant improved strength development. However, a decrease in Fc by 120 days (21.7N/mm^2) and 135 days (15.9 N/mm^2) can be associated with interaction of the seawater with the hydrated components of the concrete with resultant disintegration and removal of the lime rich cementing components of the concretes.

Table 1 Compressive and Splitting Tensile Strength results in N/mm^2

Age	Compressive Strength		Splitting Tensile Strength	
	CU_{SW} (N=23)	CU_{FW} (N=16)	CY_{SW} (N=23)	CY_{FW} (N=16)
15	16.30	18.60	1.40	1.40
30	19.40	25.80	1.80	1.90
60	25.70	30.20	2.00	2.10
75	29.60	32.60	2.40	2.20
90	32.90	34.40	2.70	2.40
120	21.70	44.80	1.90	2.50
135	15.90	53.50	1.30	2.60
150	31.80	54.50	1.70	2.90
180	41.80	56.90	3.00	3.20

Comparatively, the rate of increase in Fc for the concrete CU_{SW} specimens were observed to be low relative to CU_{FW}, as strength increases from 18.6N/mm^2 at 15 days to 56.9N/mm^2 at 90 days curing periods (Table 1). This may be due to the less concentration of chloride (242.3mg/l) and sulphate (41.56mg/l) in the freshwater used as curing fluid, hence, the absence of the negative impacts of the curing fluid on concrete strength.

Furthermore, the result of Ft, (Table 1), revealed a similar trend in strengths of CY_{SW} relative to the Fc. The Ft for the CY_{SW} specimens varies from 1.3 – 3.0N/mm^2 while F_t for the CY_{FW} specimens varies from 1.4 – 3.2 N/mm^2. Also the highest Ft of 3.0N/mm^2 and 3.2 N/mm^2 for the CY_{SW} and CY_{FW} respectively were observed at 180 days. However, the highest Ft of 3.2 N/mm^2 for CY_{FW} is most expected as concrete mix ratio of 1:1:2 are known to perform better under freshwater curing fluid without impacts of chloride or sulphate attacks that usually characterized seawater curing medium [3].

Hydrochemical Profiles of the Curing Fluids

Table 2 shows the initial chemical composition of the freshwater and seawater prior to curing relative to the composition of the Atlantic Ocean (Gopal, 2010). Table 3 presents the results of the physico-chemical characteristics of the curing waters at different curing durations.

The initial physico-chemical characters of the curing seawater aligned reasonably well with the Atlantic seawater thresholds with respect to EC, Na^+, Mg^{2+}, Cl^- and SO_4^{2-} concentrations. However, the freshwater exhibited low TDS of 680mg/l and low concentrations of 41.03 mg/l Na^+, 39.0mg/l Mg^{2+}, 134.2 mg/l Cl^- and 41.6 mg/l SO_4^{2-} compared to initially measured concentrations of 12,475 mg/l Na^+, 1,650.2 mg/l Mg^{2+}, 26,000 mg/l Cl^- and 180.0 mg/l SO_4^{2-} for the curing seawater (Table 2).

Table 2 Composition of initial seawater and freshwater (in mg/l) to relative Atlantic Ocean

Parameters	Freshwater	Seawater	Atlantic
Temp.	29	30	-
EC	1,000	32,500	35,370*
TDS	680.0	21,000	-
pH	6.9	8.0	-
Na^+	41.0	12,475	11,100*
K^+	28.1	451.06	-
Ca^{2+}	85.0	382.02	-
Mg^{2+}	39.0	1,650	1,210*
Cl^-	134.2	26,000	20,000*
HCO_3^-	242.3	185.2	-
SO_4^{2-}	41. 6	180.05	2,180*
PO_4^{3-}	20.1	2.59	-

*[7].

As presented in Table 3, the measured pH revealed steady increase for the curing seawater with curing duration from 8.0 to about 12.6 and from 6.9 to 11.9 for the control curing freshwater; suggesting increasing alkaline condition due to the dissolution / leaching of carbonates constituents of the cement concretes especially for those cured in seawater. Such dissolution will obviously lead to loss of cementing properties thereby affecting the strength of the concrete [8].

In addition, EC of the curing seawater also increases steadily from 32,500 to 53,500µS/cm during curing period 180 days. Likewise, for the control freshwater curing medium, the EC also increases slightly from 1,000 to 9,200µS/cm during the curing period. In general, the increase in EC is

clearly an indication of increasing dissolved solids apparently due to the dissolution / leaching of carbonates constituents of the cement concretes and possible reduction in strengths as highlighted earlier. As presented in Table 4, the results of the analysed chemical parameters of the curing fluids revealed varied enrichment and depletion of the dissolved solutes at the end of the different curing duration vis-à-vis the initial freshwater / seawater composition. There are clear decreases in Na^+ from 12,475mg/l to 3,412 mg/l and K from 451mg/l to 305mg/l alongside with decreases in Cl^- from 26,000mg/l to 17,160.2mg/l. This is a clear indication of uptake/ depletion due to reactions with the components of cement concretes.

Table 3 Profiles of the Physico-chemical Characteristics of the Curing Fluids with respect to the Curing Durations

Concrete Mix	Parameter	Curing Periods / Ages							
		0	15	30	60	90	120	150	180
BCU_{SW}	Temp. (°C)	30	31	30	30	28	28	27	28
	EC (µS/cm)	32,500	33,000	35,000	36,000	38,000	44,500	48,500	52,500
	TDS (mg/l)	21,000	16,000	17,500	19,000	18,000	22,500	24,100	26,900
	pH	8.0	8.3	8.8	11.1	11.5	11.5	12.5	12.6
BCY_{SW}	Temp. (°C)	30	29	30	30	29	28	26	26
	EC (µS/cm)	32,500	39,000	41,500	42,500	43,500	49,500	51,000	53,500
	TDS (mg/l)	21,000	19,500	20,800	21,850	21,450	24,000	25,400	26,070
	pH	8.0	8.4	9.0	11.1	11.4	11.6	12.9	12.5
BCU_{FW} and BCY_{FW}	Temp. (°C)	29	30	30	27	28	28	27	27
	EC (µS/cm)	1,000	3,500	5,500	6,500	7,500	8,400	8,900	9,200
	TDS (mg/l)	680.0	1,750	2,750	3,250	3,850	4,200	4,500	4,500
	pH	6.9	7.4	7.9	9.1	10.2	10.1	11.1	11.9

Table 4 Chemical Concentration of Curing Fluids at varying Curing Durations/ages

Concrete Mix	Para-meter	Curing Periods (in days)						
		15	30	60	90	120	150	180
BCU_{SW}	Ca^{2+}	590.1	777.6	790.1	805.2	695.4	337.7	227.40
	Mg^{2+}	1,750.0	2,400.6	3,280.6	4,140.0	4,090.8	2,856.5	1,940.20
	Na^+	11,325	11,000	9,400.1	8,050.1	7,250.4	5,500.3	3,411.60
	K^+	405.1	332.5	330.2	305.2	415.3	687.5	835.90
BCY_{SW}	Ca^{2+}	462.5	752.6	780.0	787.6	600.1	403.1	306.90
	Mg^{2+}	300.2	1,910.5	2,138.8	2,360.8	2,348.0	1,000.2	738.30
	Na^+	8,625.3	8,550.1	8,125.2	7,500.1	7,350.3	5,600.1	3,400.50
	K^+	425.3	417.5	405.3	367.6	399.6	422.6	682.40
BCU_{FW} and BCY_{FW}	Ca^{2+}	106.5	156.5	219.6	230.3	300.3	554.1	754.10
	Mg^{2+}	45.5	67.5	70.2	84.4	121.3	160.1	200.10
	Na^+	30.2	28.1	17.6	17.5	15.5	5.5	3.50
	K^+	286.5	266.2	157.1	137.5	201.4	300.5	476.70
BCU_{SW}	HCO_3^-	bdl	bdl	1,176.1	1,680.2	1,788.1	1,836.6	2,036.3
	CO_3^-	305.3	322.1	392.8	422.0	788.1	912.3	1,400.6
	Cl^-	24,660	22,860	20,360	18,800	17,160	14,556.6	13,483
	SO_4^{2-}	138.8	174.5	267.2	269.2	318.0	324.1	401.3
BCY_{SW}	HCO_3^-	1,980.0	2,500.1	2,756.1	2,968.0	3,256.4	3,976.2	4,135.4
	CO_3^-	244. 2	244.6	264.1	280.5	356.4	392.5	420.6
	Cl^-	18,540	16.672	16,640	15,800	15,640	11,700	9,705.7
	SO_4^{2-}	165.1	183.6	242.20	248.1	272.4	341.4	410.8
BCU_{FW} and BCY_{FW}	HCO_3^-	1,440.1	1900.1	2,040.2	2,064.1	2,252.2	2,688	3,274.7
	CO_3^-	bdl	bdl	bdl	bdl	45.1	46.4	60.0
	Cl^-	128.1	194.30	280.0	340.0	164.8	102.6	82.0
	SO_4^{2-}	42.4	52.40	54.3	74.6	76.3	78.9	80.6

However, Ca^{2+} and Mg^{2+} increased steadily till 90 days curing duration alongside with an increase in CO_3^{2-} from 122mg/l to 788.1mg/l. In addition, SO_4^{2-} ions steadily increase in the curing seawater from 139mg/l at 15days to 412mg/l at the end of 180days curing duration.

Hence it can be inferred that the enrichment of Ca^{2+}, Mg^{2+} and CO_3^{2-} are clear indication of leaching or dissolution of the carbonate components of cement concretes and it is consistent with the observed increase pH from 8.0 to 12.9 of the curing seawater.

Influence of Curing Durations on Strengths of the Concrete Moulds

There is no doubt as to the fact that sulphate and chloride attacks result in expansion, cracking, spalling and loss of bond between the cement paste and aggregate with eventual attendant reduction in strength of concretes [9]. As presented in Figs. 5a and b, there are steady increases in both compressive and tensile strengths until 90days curing duration. This can be attributed to progressive hydration as the concretes slowly set with resultant decrease in porosity and thus increase in strength.

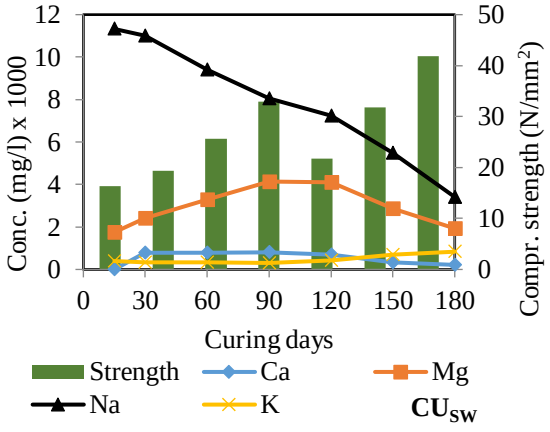

Fig 5a Chemical characters of the curing fluid and compressive strengths against curing durations

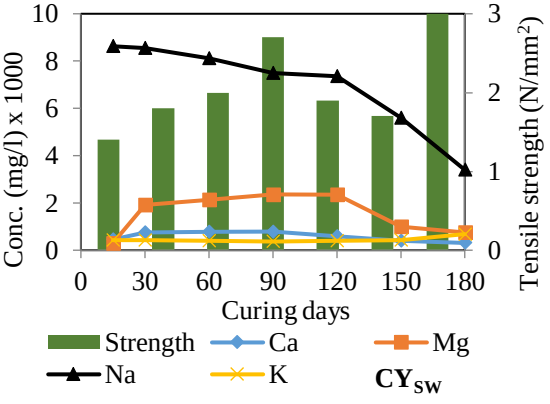

Fig 5b Chemical characters of the curing fluid and tensile strength profiles against curing durations

However, the observed reduction in compressive strength of cubes (CU_{SW}) from 32.9 – 21.7 N/mm^2) and the tensile strength of cylinders (CY_{SW}) from 2.7 – 1.9 N/mm^2 cured in seawater by 90days to 150days of curing (Fig.5a and b) can be attributed to the chemical activity between the components of the concretes and the curing fluids controlled principally by the pH of the medium. This is consistent with the study as in [10] that revealed increase in strengths of concrete when mixed & cured in sea water at early ages and a decrease after a curing period of 28 days and up to 90 days.

In addition, the decreases in strengths by 90days of curing are consistent with the decrease in Mg and Ca, Na, Cl and SO_4 in the curing fluid, which is an indication of alteration of the binding properties of the concretes through sulphate attack. The sulphate attack is related to the formation of expansive *ettringite* with the hydrated calcium aluminates of the set-cement leading to internal cracks and spalling as in Eq. 3:

$$MgSO_4 + CaH_2SiO_4 \cdot 2H_2O \rightarrow CaSO_4 \cdot 2H_2O + MgH_2SiO_4 \quad (3)$$

In summary, it can be inferred that ion exchange processes with attendant leaching of Ca^{2+} and CO_3^{2-} components of the cement concretes and corresponding exchange of Na and Cl ions are responsible for the observed variation in hydro-chemical characteristics of the curing fluid.

Implications of Changes in the Chemistry of the Curing Fluids

The implication of uptake of Na and K ions into the concretes is that after 90 days curing duration and at high basic pH, the presence of Na and K as (NaOH or KOH) will attack siliceous aggregates. This will lead to formation of soluble viscous alkali silicate gel (N-S-H or K-S-H); thus weakening the concrete as stated in Eq. 4.

$$2Na(OH) + H_4SiO_4 \rightarrow Na_2H_2SiO_4 \cdot 2H_2O \quad (4)$$

In absorbing water, soluble alkali silicate gels can swell and induce enough expansive pressure within the core of the aggregates to damage concrete:

Alkalies + Reactive Silica → Gel Product

Gel Product + Moisture → Expansion

However, sulphate (Na_2SO_4 or K_2SO_4 or $MgSO_4$) attacks on concretes are particularly damaging, forming soluble hydroxide ($Ca(OH)_2$; portandite) in the set-cement as in [11] and the resulting reaction to form gypsum which will cause weakening action on the cement paste as in [12] stated in Eq. 5.

$$\boldsymbol{Na_2SO_4} + Ca(OH)_2 + 2H_2O \rightarrow CaSO_4 \cdot 2H_2O + 2NaOH \quad (5)$$

Nonetheless, the implication of chloride attack at higher concentration in curing seawater is the volume expansion and cracking that accompanied

the formation of $CaO{\bullet}CaCl_2{\bullet}2H_2O$ (dicalcium dichloro-hydroxide hydrate) through thermal transformation of the calcium oxychloride salts as in [13] shown in Eq. 6:

$$\boldsymbol{3CaO \cdot CaCl_2} \cdot 15H_2O \rightarrow CaO \cdot CaCl_2 \cdot 2H_2O \quad (6)$$

Hence it can be inferred that under high basic pH of the curing water after 90days of curing, the observed reduction in strengths of test concrete moulds can be attributed to a combination of chloride and sulphate attacks with the resultant formation of crystallize salts within the pore system of the concrete / mortar leading to expansive pressure, internal cracks and spalling [14].

CONCLUSION

This work presents the chemical interactions of the curing fluid i.e. seawater on the compressive and splitting tensile strengths of ordinary portland (OPC) cement-based concretes. The study involved monitoring of the physico-chemical parameters and variations in chemical composition of the curing fluids at specified curing duration vis-à-vis the strengths of the test concrete moulds.

The study revealed that the observed changes in the curing seawater can be attributed to chemical interactions between the components of the cement concretes and the curing seawater. The reduction Na^+ (from 11,325 − 3,400mg/l) K^+ (from 425 − 305mg/l) and Cl^- (from 24,660 − 9,705mg/l) in the curing seawater as curing days progresses can be attributed to the cation exchange processes leading to enrichment of Ca^{2+} (from 462 − 805mg/l), Mg^{2+} (from 300 − 4,140mg/l) and HCO_3^- (from 980 − 4,135mg/l) in the curing seawater due to associated leaching.

In addition, detail evaluation of the controlling chemical processes revealed that the formation of crystallize chloride salts through ingress of chloride ions into pore system and the formation of gypsum salts through sulphate attack usually induce internal cracks and spalling [14]; hence contributed to the observed reduction in strengths of test concrete moulds. The implication is reflected in the observed reduction in compressive strength of cubes (CU_{SW}) from 32.9 – 21.7 N/mm^2) and the tensile strength of cylinders (CY_{SW}) from 2.7 – 1.9 N/mm^2 cured in seawater by 90days to 150days of curing duration.

In addition, this study highlighted that the strength of the concrete tends to increase initially during the early stage of saline attack, but later followed by loss of strength that accompanied the expansion of the set concrete with resultant spalling and cracking [10]. Therefore, there is the need for prior preventive measures such as coating of reinforcement steel /concretes to prevent the risk of seawater attacks on concrete structures in coastal environments.

REFERENCES

[1] Matthias, D. Properties of concrete, Retrieved November 11, 2010, from http://en.wikipedia.org/ wiki/concrete.

[2] Dimri, A., Varshney, J.Kr., Verma, V. K., Gupta, S. A Review on Strength of Concrete in Seawater. International Journal of Engineering Research & Technology (IJERT). Vol. 4, Issue 3, 2015, pp. 844–847.

[3] Islam, Md. M., Islam, Md. S., Al-Amin Md, and Islam Md. M. Suitability of sea water on curing and compressive strength of structural concrete. Journal of Civil Engineering (IEB), Vol. 40, Issue 1, 2012, pp. 37–45.

[4] Adeyemi, O.F. and Modupeola, A.G. The Effect of Seawater on Compressive Strength of Concrete. International Journal of Engineering Science Invention, ISSN: 2319-6734, www.ijesi.org, Vol. 3, Issue 7, 2014, pp. 23–31.

[5] Bansal, S.K., Bhutani, S., Kishanrao, W.M. and Pandey, K.K. Effects of Sulphate and Chloride contaminated Water on Concrete. International Journal of Advances in Mechanical and Civil Engineering, Vol. 3, Issue 3, 2016, pp.145–147.

[6] Prascal, G.H. and Regourd, M.L. Physico-chemical Studies on Concrete Paste, New Brunswick, Vol.2, 2006, pp. 112–128.

[7] Gopal, M. Concrete in Seawater, Retrieved November 8, 2010, http://www.theconstructor.org/concrete/concrete-in seawater/843/.

[8] Bing, T. and Menashi D.C. Expansion of alite paste caused by gypsum formation during sulphate attack. *Materials in civil engineering;* Vol. 12, Issue 1, 2011, pp. 24–25.

[9] Mehta, P.K. Durability of concrete in marine environment– A review, performance of concrete in marine environment, ACI Pub., SP 68, 2011, pp. 1–15.

[10] Wegian, F.M. Effects of sea water for mixing and curing on structural concrete Studies. The IES Journal Part A: Civil & Structural Engineering, Vol. 3, Issue 4, 2010, pp. 235–243.

[11] Swamy, R.N. The alkali-silica reaction in concrete. London: Spon Press, 1991.

[12] Uddin, T., Hidenori, H., and Yamaji, T. Performance of seawater-mixed concrete in the tidal environment. Cement and Concrete Research, Vol. 34, Issue 4, 2004, pp. 593–601.

[13] Birnin-Yauri, U.A. and Garba, S. The effect and mechanism of chloride ion attack on Portland cement concrete and the structural steel reinforcement. IFE Journal of Science, Vol. 8, Issue 2, 2006, pp. 131–134.

[14] Yang, C.C. and Cho, S.W. An electrochemical method for accelerated chloride migration test of diffusion coefficient in cement based materials, Mater. Chem. Phy., Vol. 81, 2003, pp. 116–119.

9thInt. Conf. onGeotechnique, Construction Materials andEnvironment, Tokyo, Japan,20-22 November 2019, ISBN: 978-4-909106025C3051

MULTIPLE PLANTS MULTIPLE SITES READY MIXED CONCRETE SCHEDULE DISPATCHING USING IMPROVED ANT COLONY OPTIMIZATION

Sakchai Srichandum

ABSTRACT

The purposes of this paper were to optimize the schedule of dispatching Ready Mixed Concrete (RMC) trucks with multiple plants multiple construction sites (MPMS) in order to minimize the transportation cost under various construction constraints i.e. limited traveling, casting time, number of truck, allowable weight for transfer and distance from multiple RMC Batch plants to different construction sites using Improved Ant Colony Optimization (IACO). The IACO introduces some additional techniques for improvement of search process such as neighborhood search and re-initializations. The procedures are: firstly, develop the mathematical model of MPMS for RMC truck schedule dispatching in term of optimization problem. After that, use the IACO to solve the optimal schedule dispatching of RMC with MPMS and truck operation. To show its efficiency, IACO is applied to test with two different problems, and its results are compared with those obtained from the conventional approaches such as genetic algorithm (GA) and conventional Ant Colony Optimization (ACO). The experimental results show that the IACO approach is comparatively capable of obtaining higher quality solution, faster computational time and efficiency schedule dispatch

Keywords:Ant colony optimization, Heuristic algorithm, Optimization problem, Ready mixed concrete, Truck dispatching

INTRODUCTION

Recently, the construction industry is continuously growing and developing in term of construction process, methods and materials. In modern construction, Ready Mixed Concrete(RMC) is one of the most popular building materials inconstruction industry due to RMC has several benefits. The advantages of RMC are convenient for management, reducing the labor cost, providing many concrete types for many construction site and high standards. Unfortunately, the RMC delivery has many constraints due to quick solidifying nature of the mixed concrete. RMC trucks dispatching must be scheduled to many requested construction sites continuously under limited traveling and casting time, number of truck, allowable weight for transfer and distance from RMC Batch Plants to many construction sites [1].

Effective and efficient of RMC delivering to construction sites is an important issue to the batch plant manager. The manager has to consider both timeliness and flexibility to develop an efficient schedule of dispatching RMC trucks, which balances the operations at the construction sites and the batch plant. The existing dispatching schedule mainly depends on the experiences and preferences of the dispatcher. A systematic approach to tackle stated problem has seldom been taken due to the complexity and uncertainty involved within the dispatching process. Consequently, there is a need to develop a systematic model that optimizes the schedule of dispatching RMC trucks as a combination optimization problem.

In the past, many studies under the literature reviews dedicated to the RMC production or truck dispatching scheduling based on optimization problems and solved the problem by heuristic algorithms such as Genetic Algorithm (GA) [2], and Bee Algorithm (BA) [3].

Practically, the RMC companies provide the multiple plants for supplying RMC with various types of concrete in different zone to satisfy more customers' demand. It effects to RMC dispatching due to add more complexity to the model.

This paper proposes a new mathematic model of the RMC dispatching problem in case of the multiple plants to multiple sites (MPMS) with 3 types of concrete (floor, column and beam) to minimize total fuel cost of RMC trucks which is considered from shortest route and minimum waiting time of RMC trucks at construction sites. Furthermore, the development of Ant Colony Optimization (ACO) called "Improved Ant Colony Optimization (IACO)" is purposed to solve this problem.The IACO can provide better solution in comparison to the conventional approaches such as GA, PSO and ACO.

PROBLEM FORMULATION

RMC Delivery Process

The RMC delivery process consists of five main components, which are material production, production loading, truck transport, placement and truck return as shown in Fig.1. This process needs to be carefully planned to avoid early concrete setting.Consequently, the RMC production scheduling and the truck dispatching are not only affect delivery efficiency, but also the operating cost. For the truck dispatching, there are many factors need to be considered as follows.

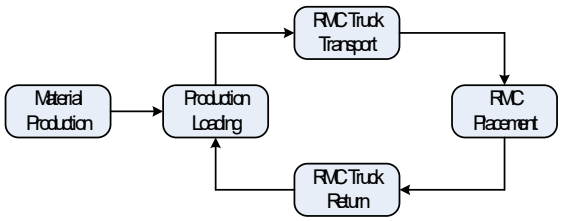

Fig.1. RMC delivery process

RMC dispatching Formulation

In this section, the RMC dispatching formulation in case of multiple plants and multiple sitescan be explained in three parts are dispatching model, feasible solution and fitness function.

Dispatching Model

The dispatching model consists of four components, which are input parameters, decision variables, constraints and system output as shown in Fig.2.

Input parameters: these parameters include the types of required concrete, the number of RMC deliveries, traveling time, pouring duration, mixing duration and allowable buffer duration. The allowable buffer duration presents the maximum duration that the construction site can wait for the arrival of RMC truck.

Decision variable: the sequence of assigning each RMC truck from the different plants to the different construction sites is defined as "dispatching sequence". Therefore, the dispatching sequence of RMC trucks is considered as the decision variable.

Constraints: The continuously pouring requirement restricts the duration that the construction site waits for the arrivals of the RMC truck is smaller than the allowable buffer duration. This constraint is applied to eliminating the infeasible dispatching schedules.

System output: The goal of developing an efficient schedule of dispatching RMC trucks is to minimize the total fuel cost of RMC trucks without breaking off the operation of pouring concrete.

Feasible Solution

The purpose of this study is to find the most efficient and effective sequence of RMC dispatching delivery in case of multiple plants and construction sites. Therefore, the feasible solutions are the sequence of RMC dispatching delivery.

Fitness Function

In order to evaluate fitness function of RMC MPMS problem, we first define indices, parameters and decision variables as follows.

Indices

i : Index of RMC plant, $i \in \{1, p\}$

j : Index of the construction site, $j \in \{1, m\}$

t : Index of RMC truck dispatching sequence from plant i to construction site j, $t \in \{1, n\}$.

Variables

p : Number of RMC plants.

m : Number of construction sites that request RMC deliveries.

n : Total number of the RMC delivery round for all construction sites, $n = \sum_{j=1}^{m} k_j$

NT : Total number of the RMC trucks that all batch plant owns.

D_{ij} : Distance RMC from plant i to construction site j (km).

SCT_j : Start casting time of construction site j.

R_j : Required quantity of the RMC by construction sites j (m^3).

PT_j : Placement type at construction site j. RMC recipe for each type requires pouring time. The pouring time for floor, beam and column is 4, 7, and 9 min/m^3 respectively.

ABD_j : Allowable buffer duration of construction site j (min).

ABT_j : Allowable buffer time of RMC truck (min).

MD_t : Mixed duration of RMC for each placement type for RMC dispatching sequence t which is 2 min/m^3.

CD_t : Casting Duration at construction for each placement type by RMC dispatching sequence t (min), where $CD_t = R_t \times PT_t$.

k_j : Required RMC truck deliveries for the construction site j.

TDG_{ij} : Traveling time from the plant to construction site j (min).

TDB_{ji} : Returning time from construction site j to the plant (min).

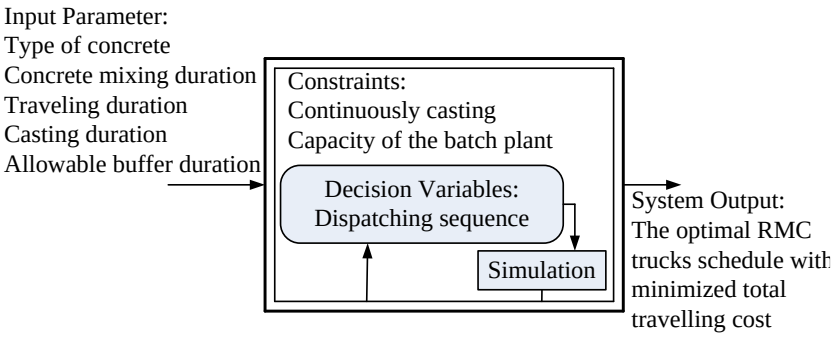

Fig.2. RMC dispatching model

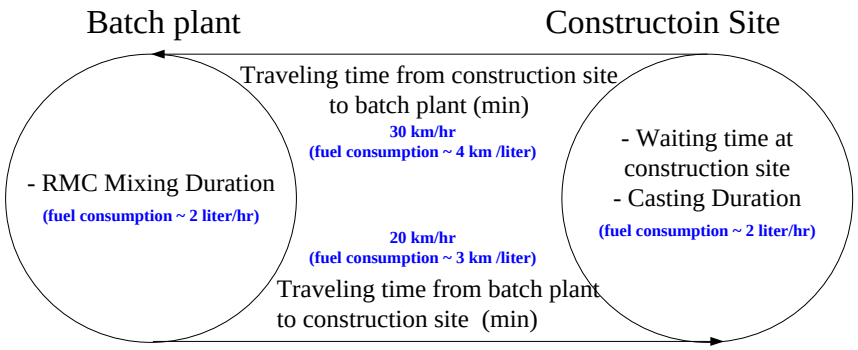

Fig. 3. RMC delivery process and vital variables.

FDT_i : First departing time of RMC truck from plant i .

DT_{it}: Departing time of RMC truck round t from plant i .

SDT_{it} : Simulated departing time of t dispatched truck from plant i .

TAC_{jt} : Arrival time of dispatched truck t at construction site j .

PTF_{jt}: Start pouring time of the construction j if t dispatched truck arrived at construction site j .

$WC_{jt} > 0$: Waiting Duration that dispatched RMC truck t waits at the construction site j .

$WC_{jt} < 0$: Waiting Duration that construction site j waits for the arrival of the dispatched RMC truck t .

LT_{jt} : Leaving time of t dispatched truck from construction site j .

ATB_{it} : Arrived Time of the t dispatched travels back to the batch plant i .

TFC_{ij} : Total fuel cost of RMC truck t for dispatching to construction site j .

The objective of RMC MPMS problem is to minimize fuel cost from multiple plants to multiple construction sites. This duration covers from loading and mixing concrete into RMC truck agitator, travelling from batch plant to construction, waiting time at construction site, casting duration and travelling back to batch plant. RMC truck process flow is shown in Fig. 3. The vital variables in fitness function are travelling speed and fuel consumption in each activity.

Total fuel cost of RMC trucks per minute for each operation is composed of two portions. In this paper, we use the fixed fuel cost of 1.33 $/liter. It is obtained from fuel cost in Thailand.

Firstly, during the transportation of RMC truck: According to the historical data, an average fuel consumption of RMC truck traveling from batch plant to construction site is around 3 km/liter while average traveling speed at 20 km/hr. Thus, fuel cost per minute of TDG_{ij} which is 0.1481 $/min. Meanwhile, average fuel consumption of RMC truck returning from construction site to batch plant is 4 km/liter at 30 km/hr. Hence, the fuel cost per minute of TDB_{ji} is 0.1667 $/min. In this portion, total fuel cost of RMC truck can be minimized by selecting shortest routing from plant i to construction site j .

In addition, the distance (km) from the batch plant to the construction site can be found by using Google map. In this study, the average velocity of RMC truck from batch plant to construction site is

20 km/hr. Therefore, traveling duration from t batch plant to construction site j (in minute), TDG_{ij} can be determined in Equation (1). Meanwhile, the average velocity of RMC truck from construction site back to batch plant is 30 km/hr. Thus, traveling duration from construction site j to batch plant (in minute), TDBj can be calculated in Equation (2).

$$TDG_{ij} = \frac{D_{ij} \times 60}{20} \quad (1)$$

$$TDB_{ji} = \frac{D_{ji} \times 60}{30} \quad (2)$$

Secondary, when RMC truck parks while mixing at the plant: casting at the construction time and waiting for pouring, it is assumed that the average fuel consumption is at 2 km/liter or 0.0444 $/min. This fuel cost could be reduced by minimizing the waiting duration at all construction sites because the mixing and casting times are fixed.

Three truck operations have an impact on the total fuel cost. They are 1) loading/mixing concrete at plant (MD_t), 2) waiting time of RMC truck (WC_{jt}), and 3) Casting time of RMC at construction site (CD_t). These operations occur when the truck parks with agitator rolling at the same time. When the truck is not move, the average fuel consumption is around 2 liter/hr and the fuel cost is 1.33 $/liter. Hence, the fuel cost per minute of MD_t , WC_{jt} , CD_t is 0.0444 $/min. As previously mentioned, an ideal of RMC truck dispatching is just in time delivery. Since mixing and casting times are required, total fuel cost of RMC trucks can be minimized by selecting the RMC truck sequence that have minimum waiting time at all construction sites or the summation of all WC_{jt} .

In summary, the fitness function is equal to the summation of fuel cost per minute multiplied by total duration for each operation of RMC trucks by Equation (3).

$$TC = 0.15 \times \sum_{t=1}^{n} TDG_{ij}^{t} + 0.17 \times \sum_{t=1}^{n} TDB_{ji}^{t} + 0.04 \times \left(\sum_{t=1}^{n} WC_{jt} + \sum_{t=1}^{n} MD_t + \sum_{t=1}^{n} CD_t \right) \quad (3)$$

IMPROVED ANT COLONY OPTIMIZATION

Inspired by the collective behavior of a real ant colony, Marco Dorigo first introduced the ant system (AS) in his Ph.D. thesis in 1992, and the study was further continued by Dorigo et al. [4]. The characteristics of an artificial ant colony include positive feedback, distributed computation, and the use of a constructive greedy heuristic. Positive feedback accounts for rapid discovery of good solutions, distributed computation avoids premature convergence, and the greedy heuristic helps to find acceptable solutions in the early stages of the search process.

A major weakness of conventional ACO algorithm is stagnation that is all ants take the same position. If this problem situation occurs, the algorithm may be trapped in a local optimal point [5]. To alleviate the stagnation problem of conventional ACO algorithms, two improvement procedures are applied in order to improve the ant colony optimization method to guarantee the diversity of ants. This approach is called improved ant colony optimization (IACO). The additional procedures are a specific improvement algorithm (called neighborhood search) and re-initializations.

During searching, the search process gets the repeated solution for a long time. That means the process could not be found the better solutions or escaped from this solution. So this solution could be either a local or global solution. In case the global solution is known, the search process will be stopped as it has been gotten the best solution. On the other hand the global solution is unknown. The algorithm will assume that this solution is a local solution. If the process is stroke on local solution for a long time, the re-initialization process will be applied. This mechanism helps the process to continue searching and find the better solutions. The flowchart of IACO as shown in Fig.4.

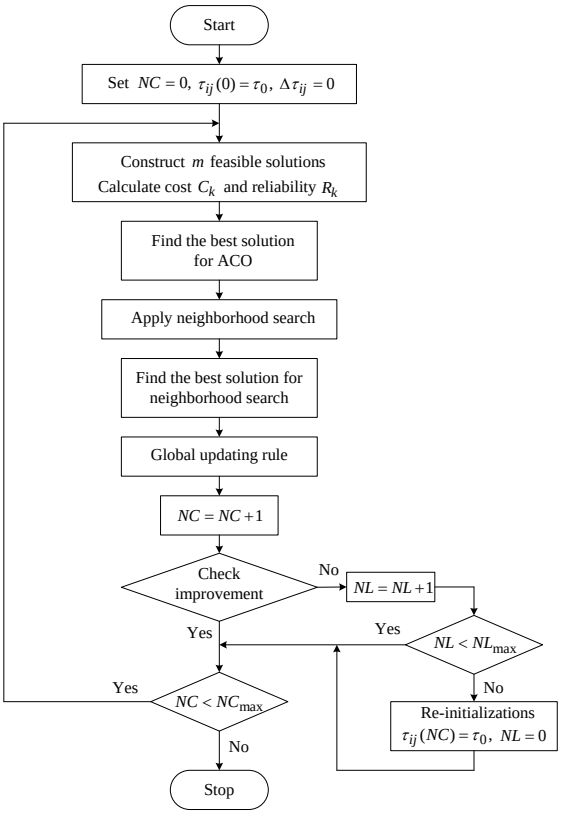

Fig. 4. Flow chart of IACO algorithm

NUMERICAL SIMULATION AND RESULTS

To assess the feasibility of the proposed IACO and the comparison methods i.e. ACO and GA, The different two cases studies are proposed. All methods are performed 30 trials, under the same fitness function and individual definition, in order to compare their solution quality, convergence characteristic and computation efficiency. The software was implemented using MatLab® languages on Intel® Core i5-5200u, 2.20 GHz Laptop with 4 GB RAM under Windows 8.

For case studies, the RMC Company has two batch plants, the first and the second batch plants have three and two RMC trucks, respectively. The Information of dispatching operation is listed in Table 1.

As mention in feasible solutions, There are 1.03×10^{7} and 1.96×10^{12} different dispatching schedules for case study 1 and 2. After solved the case studies with 30 trials, the best solutions for all case studies are shown in Table 2. The *Plant ID* and *Site ID* are determined RMC trucks dispatching sequence. For example in case study 1, the RMC truck starts dispatching from plant 2 in the first sequence of *Plant ID* to construction site 2 in the first sequence of *Site ID* for the first round. Next, RMC truck need to dispatch from plant 2 to construction site 3 and follow this sequence until finished total 8 dispatching orders.

All case studies could be obtained the minimum fuel cost without interruption time by IACO. In addition, the results in case studies 1 and 2 are also verified by exhaustively enumerating all possible solutions.

The interruption of pouring concrete occurs when the duration that the construction site waits for the arrival of the RMC truck is longer than the allowable buffer duration. As shown in Table 2, the best interruptions time is zero that mean without the interruption of pouring concrete.

Comparison of Three Methods

Solution Quality

The results of the IACO method are compared with those obtained by ACO and GA in terms of maximum, average, minimum cost, the standard deviation, and average computational time, as provided in Table 3. Obviously, all methods have succeeded in finding the satisfied solution in all case studies.

In order to demonstrate the efficiency of the IACO method, the distribution outlines of the best solutions of each trial are considered. Fig. 5 and 6 shows the distribution outlines of the best solution of each trial. Almost all optimum costs obtained by the IACO method are lower cost and variation in both case studies. This verifies that the IACO method has better quality of solution.

Computation Efficiency

Table 3 shows average computation time of 30 trials for all methods. The computation time was set running time within 500 seconds per trial. Clearly, the computational time of the IACO method is lowest in comparison to other methods.

Moreover, the convergence characteristics of the IACO, ACO and GA are shown in Fig. 7. The convergences of the IACO to the optimum solution are faster than other methods.

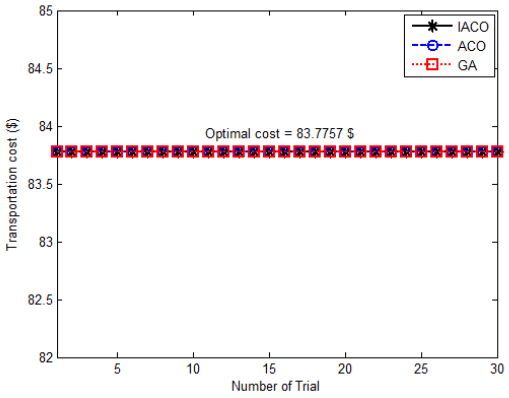

Fig. 5. Distribution of fitness values of all methods of case study 1.

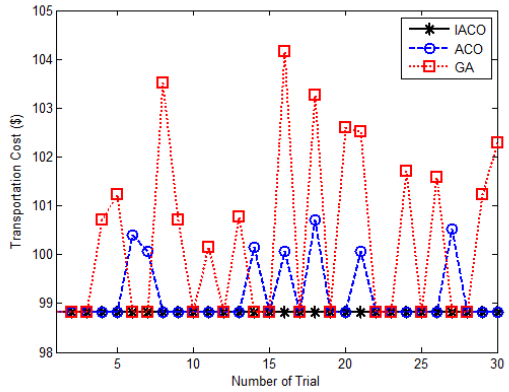

Fig. 6. Distribution of fitness values of all methods of case study 2.

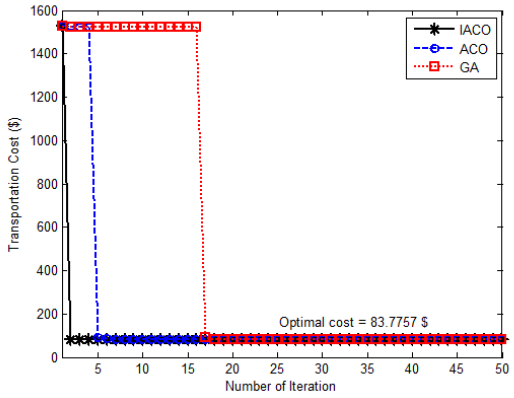

Fig. 7. Convergent graph of fitness values of case study 1.

Table 1 Information for RMC trucks scheduling for all problems.

Case Study	*Site*	SCT_j	$R_j\ (m^3)$	PT_j	D_{ij}		ABD_j	ABT_j
					$i=1$	$i=2$		
1	1	8:00	10	*Floor*	10	15	45	45
	2	8:00	14	*Beam*	8	10	45	45
	3	8:00	15	*Post*	15	12	45	45
2	1	8:00	8	*Floor*	10	15	45	45
	2	8:00	9	*Beam*	8	10	45	45
	3	8:00	10	*Post*	15	12	45	45
	4	8:30	12	*Beam*	8	12	45	45
	5	8:30	15	*Post*	11	14	45	45
Maximum load of trucks 5 (m^3) and the duration of mixing concrete (MD) is 2								

Table 2. Optimal solution by all methods of case studies.

Case Study	Optimal Dispatching Sequence		Min Fuel Cost ($)	Best Interruption Time (minutes)
	Plant ID	*Site ID*		
1	[2 2 1 1 1 1 1 2]	[2 3 1 1 3 2 2 3]	83.77	0
2	[1 1 2 1 2 2 1 1 1 1]	[1 1 3 5 2 3 2 4 4 5]	98.81	0

Table 3 Performance comparison for both case studies.

Case Study	*Algorithm*	*Min cost ($)*	*Avg cost ($)*	*Max cost ($)*	*S.D.*	*Avg CPU time(sec)*	*%Get Optimum*
1	GA	83.77	83.77	83.77	0	6.8	100
	ACO	83.77	83.77	83.77	0	30.06	100
	IACO	83.77	83.77	83.77	0	3.94	100
2	GA	98.81	99.98	102.70	1.39	445.91	53.33
	ACO	98.81	99.10	100.41	0.54	293.15	76.67
	IACO	98.81	98.81	98.81	0	78.08	100

CONCLUSION

This study presents a systematic approach to modeling the process of dispatching RMC trucks. Results show that by applying the proposed RMC dispatching model to the IACO and the simulation technique, the batch plant manager can quickly generate the efficient and flexible dispatching schedule of the RMC trucks, which not only improves the operations at the batch plant but also promotes the service of the RMC batch plant

REFERENCES

[1] S. Sakchai, T. Rujirayanyong "Production Scheduling for Dispatching Ready Mixed Concrete Trucks Using Bee Colony Optimization", American J. of Engineering and Applied Sciences, vol. 3, pp.7-14, January 2010

[2] C. W. Feng, T. M. Cheng, T. H. Wu, "Optimizing The Schedule Of Dispatching RMC Trucks Through Genetic Algorithms" Automation in Construction, vol. 13, pp. 327-340, October 2003

[3] N. Mayteekrieangkrai, W. Wongthatsanekorn, "Optimized ready mixed concrete truck scheduling for uncertain factors using bee algorithm", Songklanakarin Journal of Science and Technology, vol. 37, pp. 221-230, March-April 2015

[4] M. Dorigo, V. Maniezzo, and A. Colorni, "Ant system: Optimization by a colony of cooperative agents," IEEE Trans. Syst., Man, Cybern. B, Cybern., Vol. 26, no. 1, pp. 29-41, Feb. 1996.

[5] S.L. Ho, Shiyou Yang, H.C. Wong, K.W.E. Cheng, and Guangzheng Ni, "An Improved Ant Colony Optimization Algorithm and Its Application to Electromagnetic Devices Designs," IEEE Transactions on Magnetics, vol. 41, no. 5, pp.1764-1767, 2005.

9th Int. Conf. on Geotechnique, Construction Materials and Environment, Tokyo, Japan, 20-22 November 2019, ISBN: 978-4-909106025 C3051

EFFECT OF SUGARCANE BAGASSE ASH ON ALKALI SILICA REACTION OF CONCRETE WITH SODA LIME GLASS AS AGGREGATES

Richard De Jesus[1], Giancarlo A. R. Cruz[2], Kendrick B. M. Galang[2], and John D. M. Layson[2]
[1]Faculty, De La Salle University, Philippines; [2] De La Salle University, Philippines

ABSTRACT

Utilization of waste materials for construction use has received much attention lately in the hope of contributing to saving the environment by lessening the impact of construction. This study utilized soda lime glass in concrete as substitute for fine aggregates. However, since soda lime glass promotes alkali-silica reaction, its addition to concrete will not come without risk. Sugarcane bagasse, the unused stalk of sugarcane, when burnt into ash, is a good pozzolanic material. It also has the capability to arrest the expansion brought about by alkali-silica reaction. Therefore, when added to concrete with soda-lime glass, it can lessen the alkali-silica reaction. This study employed sugarcane bagasse ash, as partial replacement of cement, in concrete with soda-lime glass. The amount of soda-lime glass in concrete used in the study ranged from 10-40% replacement of sand, while that of sugarcane baggase ash are 5% and 10% replacement of cement. Compressive strength was determined in 7 and 28 days. Scanning electron microscopy (SEM) was conducted to examine the microstructural change in concrete. To investigate the alkali-silica reaction, measurement of mortar expansion using mortar bar test in accordance with ASTM C1260, was conducted. Some of the significant findings of the study are: (1) addition of soda lime glass, up to 30% replacement of sand, contributes to an increase in compressive strength, and (2) length expansion, due to alkali silica reaction, in concrete with soda lime glass was reduced with sugarcane bagasse ash.

Keywords: Sugarcane bagasse ash, Soda lime glass, Alkali silica reaction, Mortar bar test

INTRODUCTION

The use of glass aggregates in concrete as partial replacement for fine aggregates have been shown to be suitable for use in concrete [1]. Using glass aggregates in concrete is one way of utilizing waste materials and seen as contributing to lessening the impact of waste materials to the environment. Study of [2] have shown that using glass aggregates to replace sand can have beneficial effects on mechanical properties for as long as the replacement is kept below 20-30% of sand since it helps reduce the porosity of concrete. However, the use of soda lime glass (SLG), in particular, does not come without complication as it promotes occurrence of alkali silica reaction (ASR) in concrete due to siliceous content of soda lime glass. They [3] have stated that soda lime glass contains approximately 7-10% Calcium Oxide (CaO) which provides Calcium (Ca) needed for ASR gel formation. In this study, to counter the impact of SLG in causing alkali silica reaction, sugarcane bagasse ash (SBA) is employed.

Alkali-Silica reaction (ASR) is a reaction in concrete when alkali in cement paste reacts with silica present in most aggregates which causes volume expansion that can lead to cracking. This problem in concrete is considered common, and referred to as “cancer of concrete” [4]. One of the most common ways to mitigate ASR in concrete is by adding very fine siliceous material, like pozzolan, silica fume, or fly ash, which results to a controlled pozzolanic reaction during the early stages of cement setting [5]. These siliceous materials safely react with alkali in cement without any formation of expansive pressure because siliceous in fine particles transform into alkali silicate and into calcium silicate without semipermeable reaction rims [6]. They [4] investigated the effect to ASR of employing sugarcane bagasse ash in concrete. They have shown that 10% and 40% SBA replacement of cement resulted to expansion reduction in mortar bar specimens.

Waste glass, in general, contains alkali and silicon dioxide which may lead to ASR [7]. They showed that soda lime glass is composed of 68.4% SiO2, 14.1% Na2O, 9.5% CaO, while the remaining components are small amounts of several compounds. This high amount of silica in soda lime glass, when used as partial replacement of sand in concrete, promotes ASR. Moreover, they showed that ASR risk with an ASR expansion rate of above 0.2% is present in concrete having 30% glass aggregates as sand. Other researches ([2], [8], & [9]) have proven that glass aggregates promote the occurrence of ASR.

Sugarcane bagasse ash (SBA) is a by-product

Table 1. Concrete Design Mix in accordance with ACI 211.1 (for 1-m^3 concrete mix)

Mix ID	Portland Cement (kg)	Course Aggregates (kg)	Fine Aggregates (kg)	Water (kg)	Soda Lime Glass (kg)	Sugarcane Bagasse Ash (kg)
B0G00 (control)	8.40	25.21	16.83	4.25	0	0
B0G10	8.40	25.21	15.15	4.25	1.68	0
B0G20	8.40	25.21	13.46	4.25	3.37	0
B0G30	8.40	25.21	11.78	4.25	5.05	0
B0G40	8.40	25.21	10.10	4.25	6.73	0
B5G00	8.40	25.21	16.83	4.25	0	0
B5G20	8.11	25.21	13.46	4.25	3.37	0.29
B5G30	8.11	25.21	11.78	4.25	5.05	0.29

Note: B – sugarcane Baggase ash; G – soda lime Glass. B5G20 means sugarcane bagasse ash replaces 5% of cement, and soda lime glass replaces 20% of fine aggregates. All replacements were made by weight.

from combustion boilers in sugar industries. SBA is found to be rich in reactive silica giving it a cementitious property, hence, making it a suitable supplementary cementitious material. The use of supplementary cementitious materials (SCM), like sugarcane bagasse ash, is a common method to address ASR [10]. Study of [11] showed that the use of SCM reduces alkali concentrations in concrete hence, reducing the element responsible for producing hydroxyl ions that reacts with siliceous aggregates resulting to ASR. This potential of sugarcane bagasse ash, a waste material, in addressing ASR in concrete is seen as a good compliment for the use of another waste material – soda lime glass in concrete. SBA, through this study, is able to show that ASR caused by employing soda lime glasses in concrete can be mitigated by employing SBA in the same concrete.

MATERIALS AND METHODS

Sugarcane bagasse ash were obtained from local juice vendor. Literatures [12] & [13] have established that the optimal percentage of replacement of SBA to cement ranges from 5 to 10%, hence, this study opted to adopt 5%.

The soda lime glass used in this study was derived from beer bottles, soda bottles, and juice bottles bought commercially. These were crushed manually into bits using a hammer. After crushing, it was sieved to ensure that it is comparable to particle size of fine aggregates. Partial replacement of sand with SLG was done at 10% to 40% replacement by weight, at 10% interval.

Portland cement (Type I) was obtained from local hardware store, along with coarse aggregates, and fine aggregates. Physical characterization of materials (i.e. determination of moisture content, unit weight, and specific gravity) used in producing concrete were made prior to designing the concrete mix proportions and were all conducted in accordance with appropriate ASTM standards. Concrete mix proportion were made in accordance with ACI 211.1 (Table 1).

To figure out the effect of adding soda lime glass to concrete in terms of workability, slump test was conducted on fresh concrete. Justifying the use of alternative materials in concrete requires that the mechanical properties are not compromised. Hence, this study investigated compression and split tensile strength of concrete with 5% sugarcane bagasse ash and soda lime glass which ranged from 10 to 40% at 10% interval. Compressive strength, in accordance with ASTM C39, was tested in 7^{th} and 28^{th} day. Split tensile strength, in accordance with ASTM C496, was tested at 28^{th} day. Three (3) samples were prepared for each mix proportion. All samples were cured in water.

ASTM C1260 is a standard test for determining the potential alkali reactivity of aggregates using mortar bars. Similar to concrete, three (3) specimens were prepared for each mortar mix. The samples were initially immersed in a water bath for 24 hours before it was cured in NaOH solution in an oven for fourteen (14) days. During NaOH solution curing, temperature was maintained at 80 degrees celsius. Length readings were taken three times (3x) daily.

In addition to mortar bar test of potential alkali reactivity, scanning electron microscopy (SEM) was employed to acquire high resolution images of mortar's microstructure to detect the development of ASR gel from the reaction of silica in soda lime glass and alkali in cement.

DATA AND ANALYSIS

Concrete Test Results

Table 2 shows the slump test result for concrete with 0% and 5% SBA, and varying amount of soda lime glass. It shows that the addition of sugarcane bagasse ash reduces slump supporting the claims of [9], and [14] that sugarcane bagasse ash consumes water that is supposed to be for mixing, hence, reducing workability. Another observation

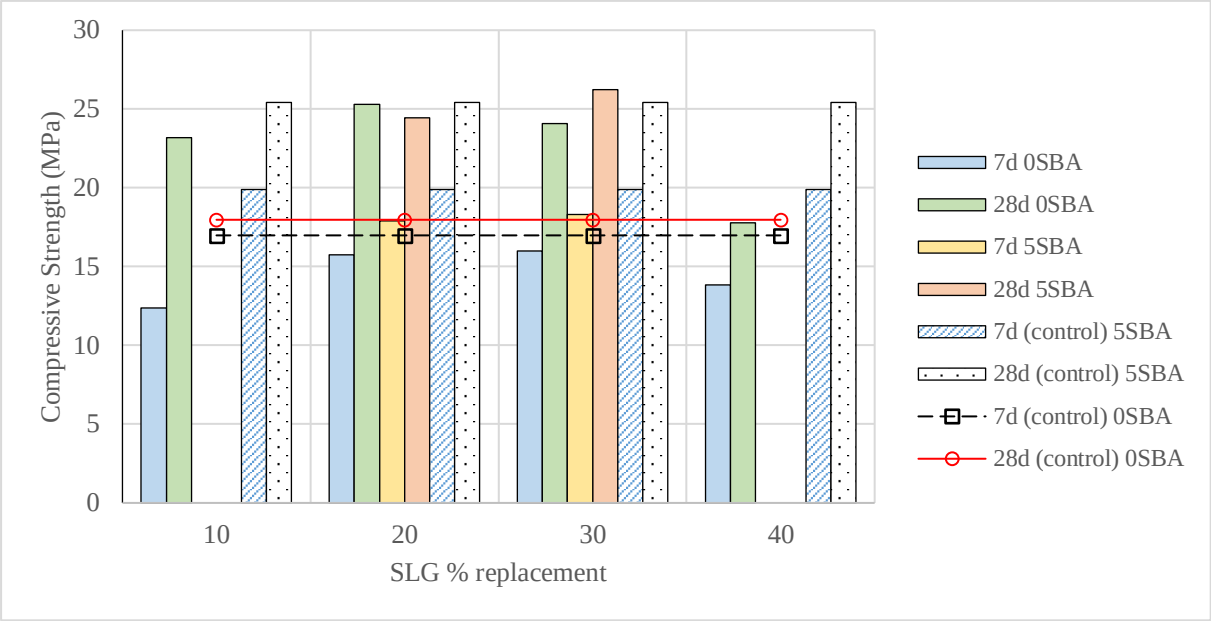

Figure 1. 7th & 28th day compressive strength of concrete with sugarcane bagasse ash and soda lime glass

made was increasing the amount waste glass resulted to increase in slump. This implies that glass aggregates promote workability.

Table 2. Slump test of concrete with SBA & SLG

Mix ID	Slump (mm)
B0G00	86
B5G00	52
B0G20	75
B5G20	56
B0G30	97
B5G30	70
B0G40	112
B0G10	65

Compressive strength test of concrete with SLG and SBA can be seen in Figure 1. Comparison between compressive strength of concrete with and without sugarcane bagasse ash revealed that there is no significant difference between the two. This implies that 5% replacement of cement with sugarcane bagasse ash will not compromise the compressive strength. For both 7th and 28th day strength, the highest strength can be observed at 20% SLG replacement, followed closely by strength values at 30% replacement. SLG replacement appeared to be viable for 20 to 30% replacement as its strength is higher compared to that of control concrete. At 40% replacement, strength fell below that of controlled concrete. All 28-day strength exceeded that of typical normal strength of 21 MPa and that of 28-day control concrete. In this study, it was not established that increasing SLG compromises strength though it was clear that at 40% SLG replacement of sand, strength decreases significantly. Table 3 summarizes the strength results for 7 and 28-day compressive strength and 28-day split tensile strength.

Table 3. Summary of strength results

Mix ID	Compressive strength (MPa)		Tensile strength (MPa)
	7 day	28 day	
B0G00	16.98	17.97	2.92
B0G10	12.39	23.19	1.86
B0G20	15.75	25.30	2.34
B0G30	15.97	24.07	1.87
B0G40	13.84	17.77	1.55
B5G00	19.89	25.42	2.28
B5G20	17.88	24.43	1.29
B5G30	18.29	26.21	1.79

Split tensile strength results showed all samples with SLG have strength lower than that of control sample. Comparison between sample with and without sugarcane bagasse ash show that concrete mix without sugarcane bagasse ash have higher tensile strength. Since this was not observed in compressive strength, it can be stated that for concrete that will utilize tensile strength for a particular purpose, the replacement of cement with sugarcane bagasse ash needs to be investigated thoroughly before application.

Mortar Test Results

The mortar test based on [15] was done to test if the substitute aggregates (i.e. soda lime glass) are potentially reactive to alkali in cement. Length measurement of mortar specimen, using a

Table 4. Length expansion of mortar bar specimens with sugarcane bagasse ash and soda lime glass

Mix ID	Ave. Length Change	Ave. Expansion	Interpretation of Expansion
B0G00	0.663 mm	0.231%	Potentially harmful
B5G00	0.433 mm	0.150%	Safe with slight chance of being harmful
B5G20	0.500 mm	0.173%	Safe with slight chance of being harmful
B5G30	0.537 mm	0.187%	Safe with slight chance of being harmful

length comparator, were done for fourteen (14) days while cured in NaOH solution and kept in an oven to maintain a temperature of 80 degree Celsius. Table 4 summarizes the result of length measurement. Specimen with no sugarcane bagasse ash experienced the highest average length expansion and was found to be potentially harmful with respect to alkali silica reaction. The test also showed that with increasing soda lime glass in concrete, the average length expansion has also increased. This supports the earlier claim that soda lime glass, with its high siliceous content, will contribute more to the occurrence of alkali silica reaction.

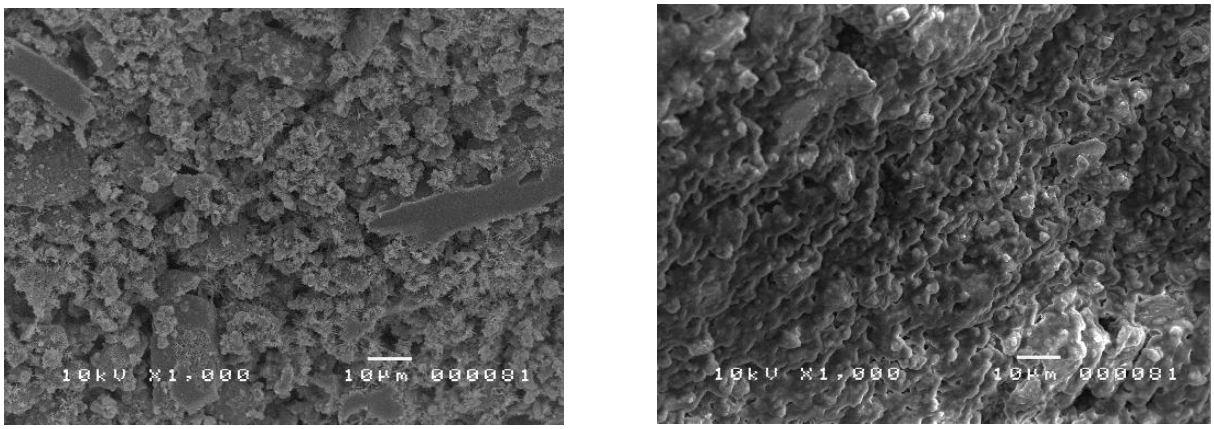

Figure 1a & 1b. B0G00 mortar microstructure before (a) and after 14-day immersion to NaOH (b)

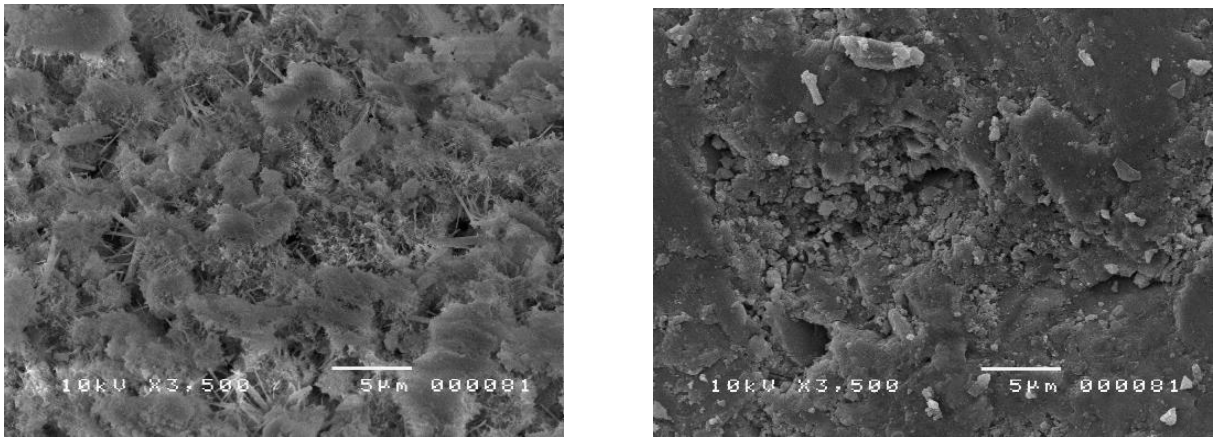

Figure 2a & 2b. B5G00 mortar microstructure before (a) and after 14-day immersion to NaOH (b)

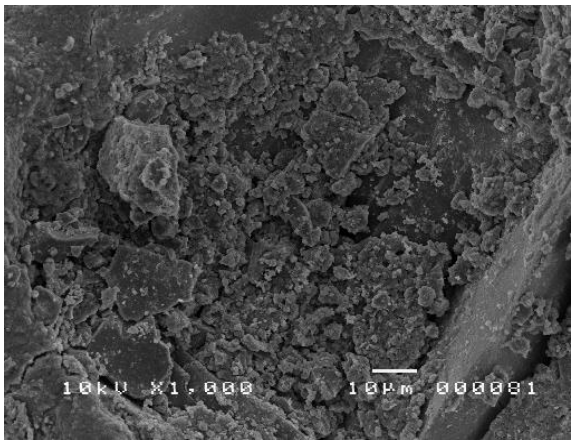

Figure 3a & 3b. B5G20 mortar microstructure before (a) and after 14-day immersion to NaOH (b)

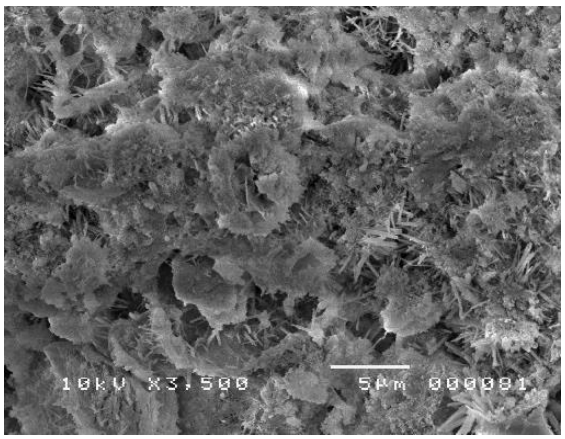

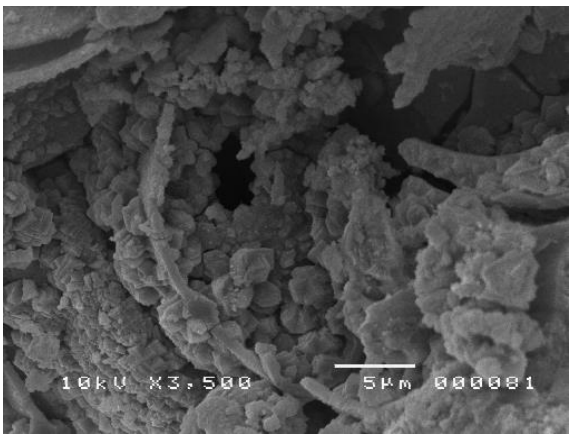

Figure 4a & 4b. B5G30 mortar microstructure before (a) and after 14-day immersion to NaOH (b)

The microstructure of mortar bars was investigated thru SEM before NaOH curing and after 14-day curing in NaOH, as shown from Figure 1 to 4. Common observation from SEM micrographs is the degrading effect of subjecting mortar samples to NaOH after 14 days.

CONCLUSIONS

The call for utilization of waste in construction is getting more loud with times due to continued depletion of resources and the negative impact to the environment. Hence, this study attempted to answer that call by utilizing soda lime glass in concrete by making it a partial substitute for fine aggregates. However, due to high siliceous content of SLG, the potential reaction of silica with alkali in cement pastes must be addressed as it may lead to alkali silica reaction which leads to concrete cracking. So, in order to address ASR, this study employed sugarcane bagasse ash as partial replacement of cement. Sugarcane bagasse ash (a by-product of sugarcane) is another waste where possible utilization in concrete is also being sought in this study.

Mechanical properties of concrete with 5% SBA and varying SLG showed no compromise in compressive strength. Comparison of compressive strength of concrete with increasing SLG amount showed higher values for SLG content not exceeding 30% of sand. 5% replacement of cement with sugarcane bagasse ash will not compromise compressive strength. However, split tensile strength demonstrated lower values for concrete with SLG and SBA. Hence, it is recommended by this study that for concrete applications where tensile strength might be of critical importance, a thorough investigation of tensile strength must be conducted.

Mortar bar test, in accordance with ASTM C1260, was also conducted to determine the potential alkali reactivity of mortar with SLG and to assess whether sugarcane bagasse ash contributes in mitigating the alkali silica reaction. Length expansion measurement showed that increasing SLG resulted to increasing length expansion. Sugarcane bagasse ash reduced the length expansion as compared to specimen without SBA.

Finally, SEM of mortar samples revealed deterioration after exposure to NaOH for 14 days in 80 degree celcius maintained temperature.

REFERENCES

[1] De Castro, S. and De Brito, J., Evaluation of the

durability of concrete made with crushed glass aggregates, Journal of Cleaner Production, Vol. 41, 2013, pp. 7-14.

[2] Mukesh, C., Bulk engineering and durability properties of washed glass sand concrete, Construction and Building Materials, Vol. 2, 2009, pp.1078–1083.

[3] Maraghechi, H., Rajabipour, F., Pantano, C. and Burgos, W., Effect of calcium on dissolution and precipitation reactions of amorphous silic at high alkalinity, Cement and Concrete Research, Vol. 87, 2016, pp. 1-13.

[4] Kazmi, S.M., Munir, M.J., Patnaikuni, I., and Wu, Y., Pozzolanic reactions of sugarcane bagasse ash and its role in controlling alkali silica reaction, Construction and Building Materials, Vol. 148, 2017, pp. 231-240.

[5] Ballard, Z., Caires, W., and Peters, S., Final Report: Alternate Mitigation Materials for Alkali-Silica Reaction in Concrete, Colorado Department of Transportation, 2008. Date Retrieved: October 8, 2017.

[6] Ramlochan, T., Thomas, M., and Gruber, K., The effect of metakaolin on alkali-silica reaction in concrete, Cement and Concrete Research, Vol. 30, Issue 3, 2000, pp. 339–344.

[7] Liu S., Wang, S., Tang, W., Hu, N., and Wei, J., Inhibitory effect of waste glass powder on ASR expansion induced by waste glass aggregate, Materials (Basel), Vol. 8., Issue 10, 2015, pp. 6849-6862.

[8] Schwarz N., and Neithalath N., Influence of a fine glass powder on cement hydration, comparison to fly ash and modeling the degree of hydration, Cement and Concrete Research, Vol. 38, 2008, pp. 429–436.

[9] Topcu, I.B., Boga, A.R., and Bilir, T., Alkali-silica reactions of mortars produced by using waste glass as fine aggregate and admixture such as fly ash and Li2CO3, Waste Management, Vol. 28, Issue 5, 2007, pp. 878-884.

[10] Thomas. M., The effect of supplementary cementing materials on alkali-silica reaction: a review, Cement and Concrete Research, Vol. 41, Issue 12, 2011, pp. 1224–1231.

[11] Thomas, M.D.A., and Bleszynski, R.F., The use of silica fume to control expansion due to alkali-aggregate reactivity in concrete – a review, in: A.J. Boyd, S. Mindess, J.P. Skalny (Eds.), Materials Science of Concrete VI, American Ceramics Society, Westerville, Ohio, 2001, pp. 377–434.

[12] Modani, P., and Vyawahare, M.R., Utilization of bagasse ash as a partial replacement of fine aggregate in concrete, Procedia Engineering, Vol. 51, 2013, pp. 25-29.

[13] Bahurudeen, A., and Santhanam, S., Performance evaluation of sugarcane bagasse ash-based cement for durable concrete. Conference Proceeding. 4th International Conference on the Durability of Concrete Structures, Purdue University, USA, 2014

[14] Afshinnia, K., and Rangaraju, P., Impact of combined use of ground glass powder and crushed glass aggregate on selected properties of Portland cement concrete, Construction and Building Materials, Vol. 117, 2016, pp. 263-272.

[15] ASTM C1260, Standard Test Method for Potential Alkali Reactivity of Aggregates (Mortar Bar Method), ASTM International, Conshohocken, PA, 2016, www.astm.org.

9th Int. Conf. on Geotechnique, Construction Materials and Environment, Tokyo, Japan, 20-22 November 2019, ISBN: 978-4-909106025 C3051

LESSON LEARNED IN MAINTAINING THE PRECAST CONCRETE BUILDINGS

Zul-Atfi Ismail
Civil Engineering Program, School of Environmental Engineering, Universiti Malaysia Perlis, Malaysia

ABSTRACT

The contemporary practice of conventional methods in the Precast Concrete (PC) building maintenance entails many issues due to poor service delivery and defect repetition. A key problem impeding the widespread adoption of emerging technologies is the lack of competent contractor supporting the effectiveness of implemented Information and Communication Technology (ICT) than conventional methods and the returns on investment. The shortcomings of conventional methods are assessed from the perspective of PC buildings. Data were collected through a case study of eight PC buildings from two type of design which were high-rise and complex building. The conventional methods had significantly little emphasis on defect diagnosis tools. It had also increased the inadequate strategic decision making to analyse information in improving the maintenance project outcomes for PC building. Building Information Modelling (BIM) tools is suggested from findings and lessons learned as a good practice to reduce the repetition of defect on the design specification used and construction practiced.

Keywords: Maintenance Management, Conventional Method, Maintenance Management System, Building Information Modelling, Malaysian PC Building

INTRODUCTION

Maintenance management is paramount in ensuring the effective and efficient monitoring process of maintenance activities, and Information and Communication Technology (ICT) could play fundamental role in delivering that maintenance management. Precast Concrete (PC) building maintenance depends on the design type (e.g. complex and high-rise building), size and building usability that require quality maintenance in order to achieve life-span prolongation. Structural repairing practice in managing PC building maintenance activities has been a hot issue in recent years due to lack of progress in the area of computer-aided maintenance management and difficulties with accessing information and data in maintenance support systems such as Computerised Maintenance Management System (CMMS) and Computerised Aided Facility Management (CAFM) [1]. Clients and contractors should use the high-quality building information from an emerging application of computerbased technology during the maintenance activities of the PC building's lifecycle. In response to the challenges of dynamic maintenance operations and the need for improving the quality of maintenance process in complex and high-rise structural building components, clients and contractors could change their method from conventional practices to more enabling technology to increase productivity and a new level of interoperability and collaboration. The conventional modus operandi (paper-based reports/unsystematic database), which is commonly being conducted in a sequential manner using CAFM and CMMS tools replaced to new business model which integrates various sources of data and knowledge such as CMMS with the Building Information Modelling (BIM) of the PC building in the maintenance activities [2, 3, 4].

Maintenance staff generally introduces ICT into PC building maintenance management for providing maintenance inspection records and results, including checklists, specification, and maintenance procedure by using software such as CMMS and CAFM. The CMMS and CAFM application provides various paper-based reports (such as inventory confirmation) related to maintenance and repair issues [3]. Furthermore, the traditional 2D Computer-Aided Design (CAD) technology is widely used for maintenance information illustration and even integrating related data for PC building construction design history purposes [5]. Despite the fact that the use of ICT solutions in assessing, planning or process execution takes place at a different scale and function, the emerging trend such as using sophisticated or innovative tools and techniques could improve productivity in PC building maintenance activities and have a great potential to redefine and re-engineer the conventional setting. The conventional method (paper-based reports/unsystematic database) is lack of knowledge support in coordination, maintenance monitoring, maintainability, automation and robot control systems. The PC building maintenance has different training or maintenance information to

address the issue of defects for particular component compared to the conventional building maintenance. The connection of PC component such as by using corbel and PCB need the expert knowledge to improve the quality and reliability of PC scheme in order to avoid any defect repetition in the long-term of life cycle building services. Failure to capture the data acquisition and monitor the defects effectively will influence the assessment process including maintenance planning and execution. This can contribute poor quality, productivity and performance in PC building construction projects [6, 7]. There is also give problematic and inefficient in the handling of information and integration of data of maintenance components within a post-construction site activity [8].

BIM FOR PC BUILDING MAINTENANCE

Recently on PC construction sites, there are many efforts to improve the efficiency of maintenance management activities through the use of more ICT-based systems (i.e. BIM). With the development of emerging technology such as BIM, maintenance management improvements in PC building construction has become possible [9]. Several other industry projects worldwide, for example real estate, waste management, transportation, supply chain and facility management, have been successfully completed by implementing BIM technology [10, 11, 12]. BIM can assist clients to determine the appropriate technology strategy and scope of each deliverable, with the intention of reducing redundancy and rework while improving performance and productivity of an operation and maintenance processes effectively in the future [13, 14]. Whereas BIM related studies mainly focus on utilising sophisticated tool and efficient technique, associating decision making support in diagnosis principles can help in achieving new levels of efficiency in PC building maintenance performance.

CASE STUDY

The case studies on the eight PC buildings were undertaken in order to identify the maintenance management problems, the current approaches to addressing the problems, the ICT implementation, use of emerging technologies and the maintenance management system (MMS) to obtain information relating to the maintenance identification, assessment, planning and execution processes. Eight maintenance clients/contractors are selected based on major problems of using conventional method (paper-based reports/unsystematic database) in the comparison to investigate the maintenance management practices in each PC building. There are around 51 contractors of Industrialised Building System (IBS) building maintenance from a classification of PC system have the highest of IBS building maintenance projects in Malaysia according to CIDB and almost are using conventional method and inadequately use of modern ICT tools. The number is considered very big indicating that the use of modern ICT is still very limited for PC system classification in IBS building maintenance management in Malaysia. The adopted synthesis of good practices of maintenance operations is based on the findings of the interviews and case studies conducted with professional engineers working in PC building maintenance departments [15]. This paper is part of a larger research and will only introduce and discuss the entire finding of the case study. This finding is illustrated in the following sections.

The interviews consisted of two types of PC building, namely, “Residential” and “Non-Residential”. The case study was based on eight cases (Case A-Case H) of PC buildings in Malaysia. There were two case studies (Cases A and E) on “Residential” due to housing maintenance operation such as the Putrajaya Quarters. In addition, six more case studies (Cases B, C, D, F, G and H) were classified as “Non-Residential” which manages the maintenance operation with fully equipped office buildings. The interviews reached a saturated point after the eighth interview session. The justifications for the selected case studies were according to the following main criteria: exposed to the conventional method used and major problems, attempted to implement computerised technology and the willingness of staff to share their experiences in improving the maintenance management processes at the PC building. The differences between the types of the PC building project provided an opportunity to explore variations in maintenance management issues for complex and high-rise PC building projects. The type of PC building under study for maintenance project were all varied from Quarters to Integration News Centre. The summary on the eight case studies is presented in Table 1.

Table 1 List of Case Studies

Interviewee	**A**
Type of IBS Building Project	Quarters
Type of Building	Residential
Design of IBS Building	High-rise
Interviewee	**B**
Type of IBS Building Project	Malaysian Institute of Pharmaceuticals and Nutraceuticals (IPHARM)
Type of Building	Non-Residential

Design of IBS Building	High-rise
Interviewee	**C**
Type of IBS Building Project	National Youth Skills Institute (IKBN)
Type of Building	Non-Residential
Design of IBS Building	Complex
Interviewee	**D**
Type of IBS Building Project	Anti-Corruption Agency Office Complex and Housing
Type of Building	Non-Residential
Design of IBS Building	Complex
Interviewee	**E**
Type of IBS Building Project	Double Storey Super link House
Type of Building	Residential
Design of IBS Building	Complex
Interviewee	**F**
Type of IBS Building Project	Inland Revenue Board Of Malaysia Complex
Type of Building	Non-Residential
Design of IBS Building	High-rise
Interviewee	**G**
Type of IBS Building Project	National Audit Department Office
Type of Building	Non-Residential
Design of IBS Building	Complex
Interviewee	**H**
Type of IBS Building Project	Integration News Centre
Type of Building	Non-Residential
Design of IBS Building	High-rise

The semi-structured interviews were conducted with the engineers who were responsible for the maintenance management of the entire PC's building structure under the Facility Management and Development Unit (UPPF) and Maintenance and Development Unit (UPS) including maintenance contractor. The interview sessions took around five hours to accumulate the data on the maintenance processes including the demonstration of the current maintenance management system with the implementation of the ICT tools by the engineer. All the data from the interviews were recorded using video camera and transcribed verbatim.

KEY FINDINGS

The eight case studies involved in this research were to identify the maintenance management problems, the approaches to address problems, ICT implementation, use of emerging technologies including the maintenance management system at the selected PC building. The problems identified from the eight case studies revealed that each case study experienced similar problems with defect repetition at the specific component part of PC building and are summarised and presented as below. The discussion involves a cross-case analysis and has been grouped into five main 'embedded units of analysis' identified which are (1) Maintenance Management Problems, (2) Approaches to Address Problems, (3) ICT Implementation, (4) Use of Emerging Technologies and (5) Maintenance Management System.

Table 2 Cross-Case Analysis

Case	Element of Analysis: Maintenance Management Problems
Case A	*Lack of commitment for handling defect* -Report delay and undelivered -Unsystematic database *Less competent contractor staff* -Less engineer competency -Technician's report is in general description -Technician's failure to identify defect problem *Defects repetition (surface cracking, leaking, scaling and jointing)* -Fault design *Poor quality work by contractor* -Less material quality *Poor buildability (M&E coordination)* -Lack coordination between design and maintenance team *Poor maintainability* -Unspecific accessibility to the defect location *Poor waterproofing* -Poor maintenance method
Case B	*Poor quality work by contractor* -Low repair requirements of the structure component *Lack of staff* -Lack of supervision *Limited Budgets* -Budget constraint *Defects repetition (surface cracking and aircond belting)* -Lack of technician -Less defect detection technologies *Less competent contractor staff* -Less engineer/technician competency
Case C	*Defects repetition (surface cracking, leaking and jointing)* -Low quality design control

	Surface cracks due to improper jointing -Less quality of joint material *Deep cracks due to settlement* -Less suitable soil *Less competent contractor staff* -Less engineer/technician competency
Case D	*Defects repetition (leaking and jointing)* -Design performance for concrete durability requirements -Structural installation method *Poor waterproofing* -Poor installation of the waterproof membrane *Poor quality work by contractor* -Lack of uniform standard -Poor material quality *Less competent contractor staff* -Less engineer/technician competency
Case E	*Defects repetition (surface cracking, leaking and jointing)* -Fault design -Poor material quality -Time gap of building repairs *Poor plumbing fitting* -Plumbing installation method
Case F	*Defects repetition (leaking and jointing)* -Design performance for concrete durability requirements *Less competent contractor staff* -Less engineer/technician competency
Case G	*Defects repetition (leaking, jointing and overload current trip)* -Fault design -Contractor ethics issues-Interested in making profits
Case H	*Defects repetition (heavy leaking)* -Poor quality of design -Less technician competency *Deep cracking on structure* -Limited experience by engineer -Poor maintenance method by contractor *Less competent contractor staff* -Less engineer/technician competency
Case	**Element of Analysis: Approaches to Address Problem**
Case A	-Improve the maintenance assessment for the building works did by contractor
Case B	-Provide more quality staff in managing the maintenance of critical defect -To replace the conventional defect detection method (e.g. visual inspection) with the sophisticated ICT application (e.g. CMMS)
Case C	-Improve the maintenance effectiveness for the building works did by contractor
Case D	-Proper supervision of work for the building works did by contractor
Case E	-Improve the building control for the building works did by main contractor
Case F	-Critical plan on maintenance repairs
Case G	-Conduct the maintenance assessment for evaluating the building works performance did by contractor
Case H	-Conduct the maintenance assessment for evaluating the building works performance did by contractor
Case	**Element of Analysis: ICT Implementation**
Case A	*mySPATA*-Data inventory for immobile facilities (e.g. building) *mySPA*-Data inventory for mobile facilities (e.g. furniture) *mySMS System*-for managing complaints
Case B	-Conventional (e.g. MS Word, MS Excel)
Case C	*mySPATA*-Data inventory for immobile facilities (e.g. building) *mySPA*-Data inventory for mobile facilities (e.g. furniture)
Case D	-Conventional (e.g. MS Word, MS Excel)
Case E	-Conventional (e.g. MS Word, MS Excel)
Case F	-Conventional (e.g. MS Word, MS Excel)
Case G	-Conventional (e.g. MS Word, MS Excel)
Case H	*Building Automation System (BAS)*-for detected building's heating, ventilation and air conditioning systems *Supervisory Control and Data Acquisition System (SCADA)*-to ensure that the building systems (e.g. fire alarm) were in good condition *E-Aduan*-for managing complaints
Case	**Element of Analysis: Use of Emerging Technologies**
Case A	-No
Case B	-No
Case C	-No
Case D	-No
Case E	-No
Case F	-No
Case G	-No
Case H	-No
Case	**Element of Analysis: Maintenance Management System**
Case A	-Conventional (e.g. paper-based reports/unsystematic database)

Case B	-Conventional (e.g. paper-based reports/unsystematic database)
Case C	-Conventional (e.g. paper-based reports/unsystematic database)
Case D	-Conventional (e.g. paper-based reports/unsystematic database)
Case E	-Conventional (e.g. paper-based reports/unsystematic database)
Case F	-Conventional (e.g. paper-based reports/unsystematic database)
Case G	-Conventional (e.g. paper-based reports/unsystematic database)
Case H	-Conventional (e.g. paper-based reports/unsystematic database)

SYNTHESIS OF GOOD PRACTICES

Table 3 below represents the suggested solutions from the case studies to improve the current practices on the maintenance management by implementing three approaches at the PC building. Case A, B, C, D, F, G and H suggested improving the transfer of knowledge in the defect diagnosis by combining with the related software technology such as CMMS and CAD. In fact, the problem of knowledge transfer in the defect diagnosis delivery also does affect the other PC buildings to some extent and the significance of this factor is quite obvious. The maintenance contractors will use the inadequate knowledge to handle the defect problem and less detail of the defect source explanation to gather accuracy information record for inspection and planning works. The other suggestion from the client/contractor was to provide the transfer of knowledge to improve the maintenance quality of structure and facility at the PC building (Case A, B, D, F, G and H). All the related cases are facing the impact of problems for the quality knowledge management, which are associated to the defect repetition for handling the defect of structures and facilities with IBS score usage about 70% on its structure development of PC building.

Case C, D, E, F and G suggested on efficient controlling of building performance based design and monitoring the defect diagnostic operation in maintenance through implementation of emerging technology (BIM) on the PC building maintenance. These are also recommended by Case A, B and H to integrate the design/construction and maintenance's database in order to facilitate better decision support and coordination within and across multiple field (e.g. civil, mechanical and electrical) for effective management of the PC building maintenance. This suggested solution is ranked as the most important solution due to suggest from almost case studies in order to manage the large and critical maintenance services for the PC building structure and facility. The using of emerging technology is also the lowest in terms of existing practice for better managing PC building components including mechanical and electrical control systems. As the overall results indicated in Table 3, it was deemed necessary to analyse the use of emerging technology further. Therefore, the systematic system with the emerging technology, defect diagnosis and decision making process should be developed to improve the building structure and facility performance by conducting effective knowledge transfer on the structure component maintenance defects.

Table 3 Suggested Solutions from Case Studies

Case	Suggested Solutions
A,B,C,D,F,G,H	Provide more transfer of knowledge in defect diagnosis
A,B,D,F,G,H	Provide more transfer of knowledge to improve the maintenance quality in maintenance execution
A,B,C,D,E,F,G,H	Implementation of emerging technology (BIM) (efficient control of building performance based design/ monitor the defect diagnostic operation in maintenance)

LESSON AND ENLIGHTMENTS

1) The PC building maintenance and the application of diagnosis techniques should be paid highly attention. Because of the defect repetition of structure components and limitation of understanding about the PC knowledge, the maintenance approach is very important. The application of modern ICT tools such as BIM integration can avoid or alleviate the defect of critical structure.
2) The appropriate modern ICT tools should be selected in assessment areas (diagnosis and decision making process on the design specification used and construction practiced) for PC buildings. The high-rise or complex structure should be given the priority for these types of PC buildings.
3) The maintenance quality of PC buildings should be strictly guaranteed.
4) The deficiency of PC buildings knowledge affected the quality of competent maintenance staff in Malaysia. The future work should be strengthened to guarantee the quality and knowledge in case of defect repetition.

The repetition of defect was frequent at PC building. The maintenance inspection and assessment was not able to address the building structure defect problems at the particular location due to the less knowledge

transfer between all members in maintenance management. Furthermore, the less competent contractor caused the maintenance faults to be increased to encourage the deterioration of the IBS building structure and facility.

In this research, the frontline approaches (new system development with BIM) is intended to counter the maintenance management problems on PC building which are:

a) Defect repetition information and knowledge due to failure to identify the actual reason of structure defect;
b) Defect repetition (leaking, jointing and cracking) information and knowledge due to design defect; and
c) Less competent contractor due to lack of knowledge regarding with materials, method and design of structure repair.

CONCLUSIONS

The data obtained in the case studies revealed that the PC buildings are using the conventional method such as paper-based reports in managing the maintenance processes for building structure and facility. This arise a problematic situation such as defects repetition (leaking, jointing and cracking) and poor quality work by contractor that need sophisticated tools towards a solution. Presently, the implementation of ICT tools in the new system is the better improvement to lead the tremendous saving in budget, time planning and to receive the precise data in handling the defect diagnosis and control. The suggestion for good practices was through the implementation of BIM to reduce the repetition of defect on the design specification used and construction practiced for the building structure and facility.

REFERENCES

[1] Duran, O. (2011). Computer-aided Maintenance Management Systems Selection based on a Fuzzy AHP Approach. Advances in Engineering Software, 42(2011), 821-829.

[2] Espindola, D. B., Fumagalli, L., Garetti, M., Pereira, C. E., Botelho, S. S. C., & Henriques, R. V. (2013). A Model-based Approach for Data Integration to Improve Maintenance Management by Mixed Reality. Computers in Industry, 64(2013), 376-391.

[3] Motamedi, A., Hammad, A., & Asen, Y. (2014). Knowledge-assisted BIM-based Visual Analytics for Failure Root Cause Detection in Facilities Management. Automation in Construction, 43(2014), 73-83.

[4] Nawi, M. N. M., Salleh, N. A., & Anuar, H. S. (2014). A Review Study of Maintenance and Management Issues in IBS Commercial Building. International Journal of Computer Informatics & Technological Engineering, 1(1), 42-46.

[5] Su, Y., Lee, Y. C., & Lin, Y. C. (2011). Enhancing Maintenance Management using Building Information Modeling in Facilities Management. 2011 Proceedings of the 28th International Symposium on Automation and Robotics in Construction (ISARC), IAARC, Seoul, Korea, 752757.

[6] Vaha, P., Heikkila, T., Kilpelainen, P., Jarviluoma, M., & Gambao, E. (2013). Extending Automation of Building Construction-Survey on Potential Sensor Technologies and Robotic Applications. Automation in Construction, 36(2013), 168-178.

[7] Kamaruddin, S. S., Mohammad, M. F., Mahbub, R., & Ahmad, K. (2013). Mechanisation and Automation of the IBS Construction Approach: A Malaysian Experience. Procedia Social and Behavioral Sciences, 105(2013), 106-114.

[8] Babic, N. C., Podbreznik, P., & Rebolj, D. (2010). Integrating Resource Production and Construction using BIM. Automation in Construction, 19(2010), 539-543.

[9] Nawari, N. O. (2012). BIM Standard in Off-Site Construction. Journal of Architectural Engineering, 18(2), 107-113.

[10] Cheng, J. C. P. & Ma, L. Y. H. (2013). A BIM-based System for Demolition and Renovation Waste Estimation and Planning. Waste Management, 33(2013), 1539-1551.

[11] Irizarry, J., Karan, E. P. & Jalaei, F. (2013). Integrating BIM and GIS to Improve the Visual Monitoring of Construction Supply Chain Management. Automation in Construction, 31(2013), 241-254.

[12] Love, P. E. D., Matthews, J., Simpson, I., Hill, A. & Olatunji, O. A. (2014). A Benefits Realization Management Building Information Modeling Framework for Asset Owners. Automation in Construction, 37(2014), 1-10.

[13] Love, P. E. D., Simpson, I., Hill, A. & Standing, C. (2013). From Justification to Evaluation: Building Information Modeling for Asset Owners. Automation in Construction, 35(2013), 208-216.

[14] Volk, R., Stengel, J. & Schultmann, F. (2014). Building Information Modeling for Existing Buildings-Literature Review and Future Needs. Automation in Construction, 38(2014), 109-127.

[15] Ismail, Z., Mutalib, A. A., & Hamzah, N. (2016). Case Study to Analyse Problems and Issues in IBS Building Maintenance. International Journal of Applied Engineering Research, 11(1), 226-232.

9th Int. Conf. on Geotechnique, Construction Materials and Environment, Tokyo, Japan, 20-22 November 2019, ISBN: 978-4-909106025 C3051

THE FIRE DYNAMIC SIMULATION IN A FACTORY WITH MULTIPLE STORAGE RACKS

Karin Kandananond
Faculty of Industrial Technology, Valaya Alongkorn Rajabhat University, Thailand

ABSTRACT

The fire protection in a factory is important to the manufacturing of any products since fire can cause a disruption in the manufacturing process and lost in the investment. As a result, the behavior of fire is well understood, the protection will be efficiently enabled. The factory with storage racks was modelled and the fire was simulated with a computational fluid dynamics (CFD) program, PyroSim. The source of a fire was set a corner of the warehouse and other fuel was the pallets and wooden containers. The spread of flame as well as the smoke were simulated and analyzed in a real-time manner. Other factors, e.g., heat flow and temperature, were also considered. Moreover, the capability of fire exhaustion equipment was also assessed. The research results also leads to the recommended design of the factory and the damage protection due to the fire.

Keywords: Computational fluid dynamics, Heat, Temperature, Warehouse

INTRODUCTION

The industrial safety is a critical concern for the industrial personnel and fire is one of the harmful sources which have a significant impact on the safety. Therefore, if the behavior of the fire in the workplace is fully assessed, the proper safety measures for the fire protection will be prepared. In a factory, warehouse is a potential source of fire eruption since there are a lot of materials which is the fire fuel. However, it is difficult to conduct a study by conducting the actual experiment in the real situation. As a result, the fire simulation is a powerful tool used to understand the behavior of the fire in a warehouse.

LITERATURE REVIEW

Pole, Chiu, and Wu [1] studied the airflow in the factory which has a clean room environment. The simulation was conducted to evaluate the effective installation of fans and the airflow when there is a fire and explosion in the factory. The assessment of an open fire in the pesticides storage facility was conducted by Kefalas, Chritolis, Nivolianitou, and Markatos [2] by the computational fluid dynamic (CFD) program. Two factors, fire strength and magnitude of the hear, were studied in order to evaluate the consequence of the fire in the facility. Another study regarding the fire experiment in the factory was carried out by Zhang, Zhu, Wang and Wu [3]. This study focused on the temperature of the fire source and the plant facility where fire broke out. Yang, Tan, and Xin [4] utilized the CFD program to simulate the fire in the storage house where there were shelves. The studied factors were temperatures, fire growth and heat release rate. Another study on fire factory was conducted by Lin, Wu, and Tsai [4]. The scenario is a textile factory in Taiwan. The analysis was based on three factors, temperature, smoke conditions, and smoke layer height.

METHODOLOGY

To understand the fire characteristics, the method of computational fluid dynamics (CFD) is utilized and the Fire Dynamics Simulator (FDS), a CFD model, is used to simulate the fire behavior in the factory. The computation is based on the solution of a large eddy simulation form of the Navier–Stokes equations. In this study, a FDS program, Pyrosim, was utilized to conduct a study.

OBJECTIVES

The objectives are the characteristics study of the fire spread and smoke in the warehouse. These also include how fast the fire can spread in 2 minutes and the studied parameters are temperature, heat release rate, and smoke. Moreover, another objective is the effectiveness study of the fire extinguishers, i.e., sprinkles installed in the warehouse.

SCENARIO

The study was set in a warehouse which consists of multiple storage racks. The size of palette is 1m x 1.2 m x 2 m while the size of the warehouse is 10 m x 10 m x 3 m. The total number of pallets and wooden containers are 21 and its size is 1 m x 1.2 m x 2 m. The pallets and containers were made of pine wood and the thickness of the containers is 2 cm. In this warehouse, there is a single door with the size of 1.5 m x 2 m. Different measuring devices were installed

as follows:

-Thermometer located at x-plane = 8 and y-plane = 2.5.

-Flowmeter located at y-plane = 8, x = [2,3], z =[0,2]

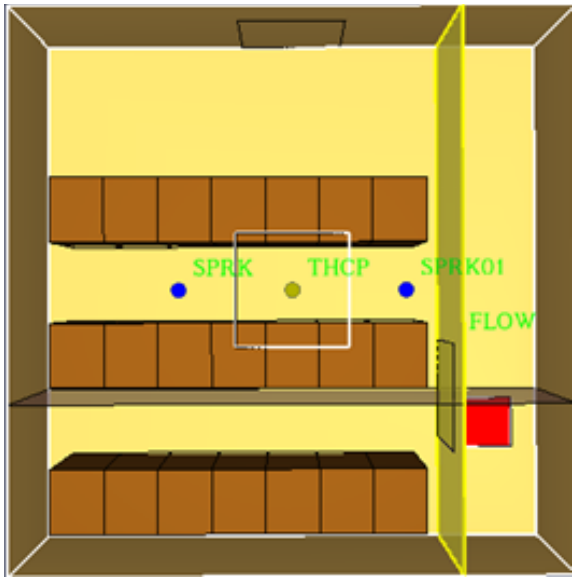

Fig. 1 Layout of the warehouse.

The free space near the first aisle is the place where spare pallets were placed. In this case, it was the potential spot that the fire might be lighted so the simulation was conducted by placing the surface burner with the heat release rate of 1000 kW. The heat release rate (HRR) graph from 0-120 seconds is shown in Fig. 2. The heat release is approximately 1000 kW.

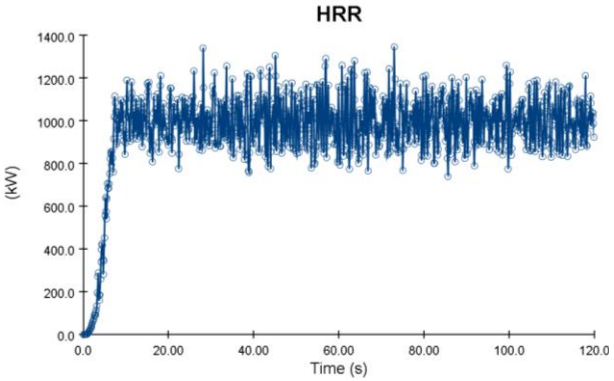

Fig. 2 Heat release from the burner.

RESULTS

The simulation was carried out in Pyrosim, a FDS package, in order to study the characteristics of the fire spread and the effective option to extinguish the fire. The time frame of the simulation is 120 seconds. The results are categorized into two cases, before and after installing the sprinkles in the warehouse.

Before installing sprinkles

The simulation was conducted and the thermometer installed at y-plane = 2.5 was measured at t = 10, 20, and 30 seconds consecutively. The isometric view of the temperature from the thermometer (y-plane = 2.5) was illustrated in Fig. 3. Color codes represent a different bands of temperatures

-red ≈ 155-170 Celsius degree

-orange ≈ 140-155 Celsius degree

-yellow ≈ 125-140 Celsius degree

-green ≈ 80-125 Celsius degree

-light blue ≈ 50-80 Celsius degree

-dark blue ≈ 20-50 Celsius degree)

The thermal images from the thermometer installed at y-plane = 2.5 were simulated at different time t = 10, 20, and 30 seconds as shown in Fig. 4, 5, and 6). Alternatively, Fig. 7, 8, and 9 illustrate the thermal images measured from the thermometer installed at x-plane = 8 for time: t = 10, 20, and 30 seconds.

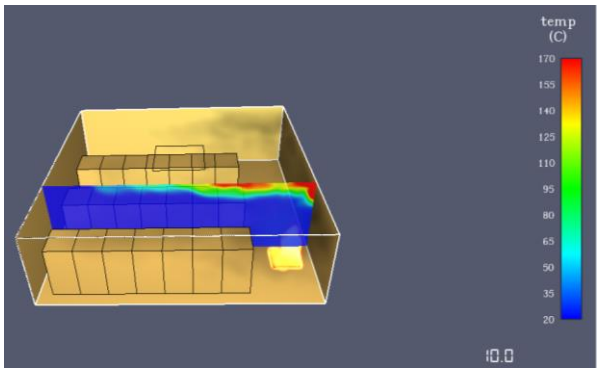

Fig. 3 Thermometer (y-plane = 2.5) at t = 10 sec (isometric view).

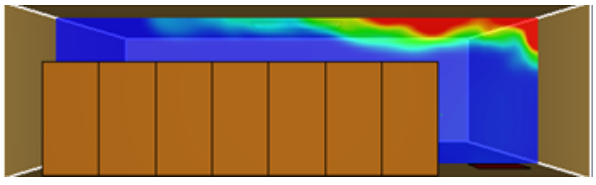

Fig. 4 Thermometer (y-plane = 2.5) at t = 10 sec (front view).

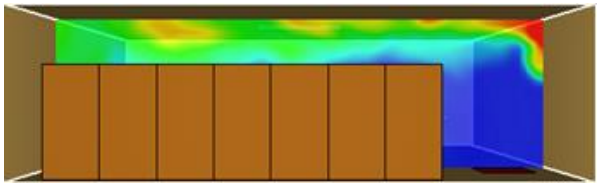

Fig. 5 Thermometer (y-plane = 2.5) at t = 20 sec (front view).

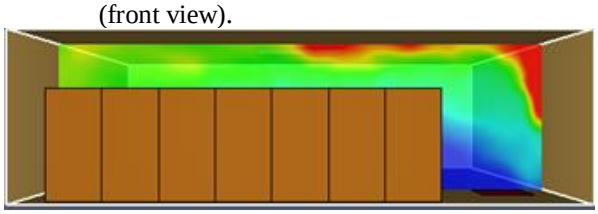

Fig. 6 Thermometer (y-plane = 2.5) at t = 30 sec (front view).

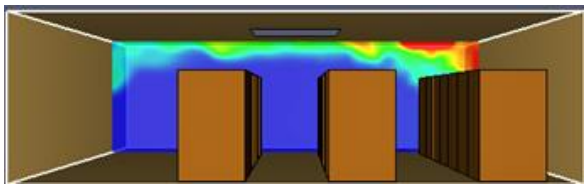

Fig. 7 Thermometer (x-plane = 8) at t = 10 sec (side view).

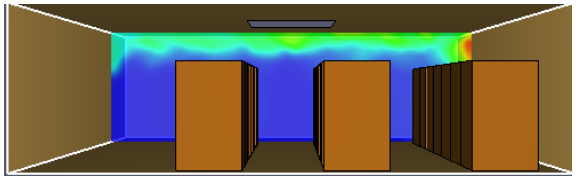

Fig. 8 Thermometer (x-plane = 8) at t = 20 sec (side view).

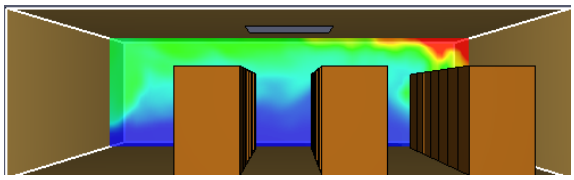

Fig. 9 Thermometer (x-plane = 8) at t = 30 sec (side view).

Fig. 10 Smoke view (front view) at t = 10 sec.

Fig. 11 Smoke view (front view) at t = 20 sec.

Fig. 12 Smoke view (front view) at t = 30 sec.

After installing sprinkles

To study the effect of fire extinguisher, two sprinkles were included in the simulation. They are located at (3, 5) and (7, 5). The orientation of the sprinkle is set at z = -0.01 and it will work at the temperature of 75 Celsius degree. After the simulation was run, the results show that he first sprinkle is activated at the time t = 6.7 second while the second is at time t = 65.2 second.

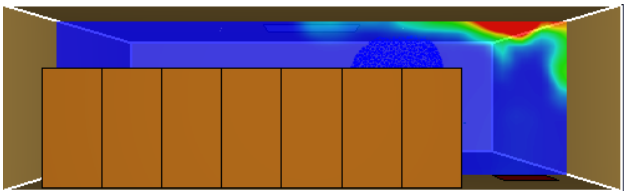

Fig. 13 Thermometer (y-plane = 2.5) at t = 6.7 sec.

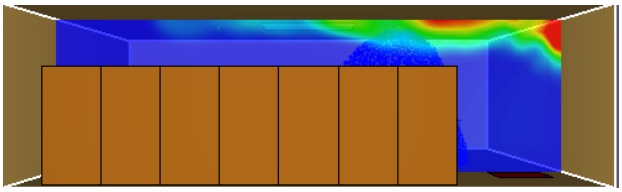

Fig. 14 Thermometer (y-plane = 2.5) at t = 10 sec.

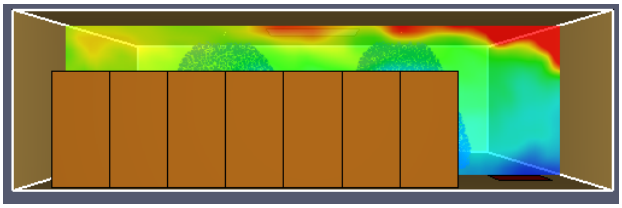

Fig. 15 Thermometer (y-plane = 2.5) at t = 65.2 sec.

The front view pictures of the smoke occurred in the warehouse was shown in Fig. 10, 11, and 12 for different time (t = 10, 20, and 30 seconds). According to Fig. 10-12, the smoke fully covers the warehouse in only 30 seconds.

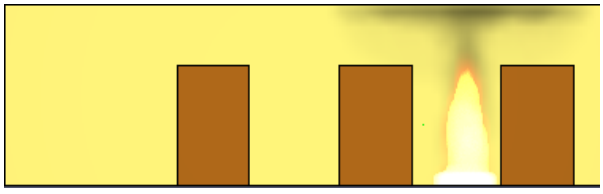

Fig. 16 Thermometer (x-plane = 8) at t = 5 sec.

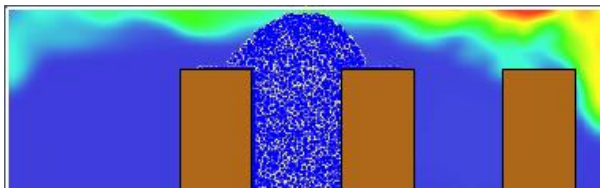

Fig. 17 Thermometer (x-plane = 8) at t = 10 sec.

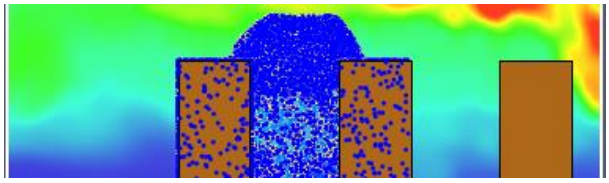

Fig. 18 Thermometer (x-plane = 8) at t = 65.2 sec.

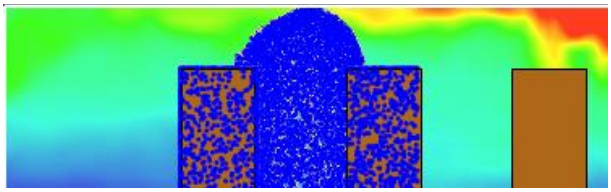

Fig. 18 Thermometer (x-plane = 8) at t = 120 sec.

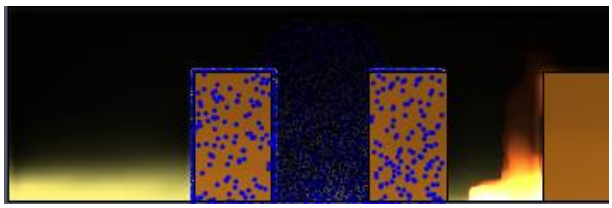

Fig. 19 Smoke view at t = 60 sec

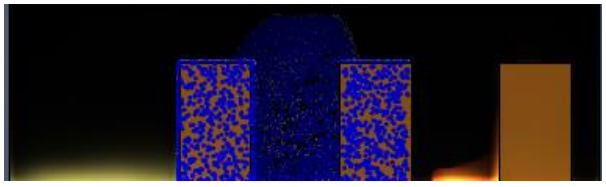

Fig. 19 Smoke view at t = 90 sec

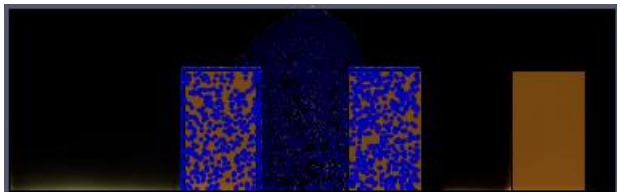

Fig. 20 Smoke view at t = 120 sec

The smoke view in the room at t = 60, 90, and 120 seconds is shown in Fig. 19, 20, and 21. From the smoke view, the fire is almost gone but the room is fully covered by the smoke.

The heat flow measured from the flow meter installed shows that the quantity of heat reaches the highest point (700 kW) at the approximate time of t = 5 second but gradually decreases after time t = 10 when the first sprinkle was activated. The quantity of heat decreases in the form of linearity and was reduced to almost zero at time t = 70 seconds which was after the second sprinkle was activated.

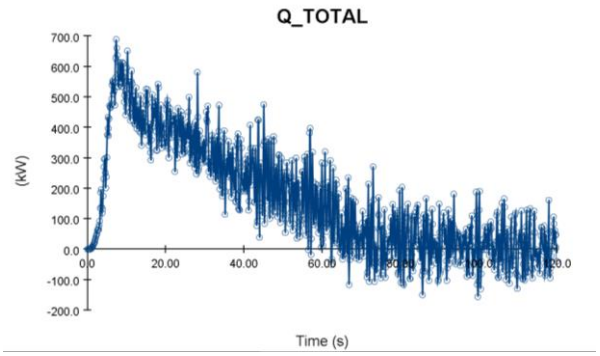

Fig. 20 Heat flow

CONCLUSIONS

The fire simulation was carried out to study the fire scenario in a warehouse. The burner surface with the heat release rate of 1000 kW was set as the fire source. There are 21 wooden pallets and containers in the warehouse. Different measuring devices, thermometer and flowmeter, were included in the simulation program. The period of simulation was 120 seconds. The results show that the fire quickly spreaded since the temperature of the another side of the room swiftly reach 120 Celsius degree in 30 seconds. On the other hands, the smoke also covers the warehouse in 30 seconds. The study also includes the sprinkles as the fire extiguisher. The simulation study show that the sprinkles were activated at time t = 10 and 65.2 seconds consecutively. The results also show that the sprinkle can help to sustainly contain the fire as shown in heat quantity graph. However, although the sprinkle can effectively work but the problem is the smoke which is still in the warehouse.

As a result, the future study should include the effective approach to ventilate the smoke from the warehouse.

REFERENCES

[1] Pole Y., Chiu Y.-L., and Wu S.-J., The Simulation of Air Recirculation and Fire/Explosion Phenomena Within A Semiconductor Factory. Journal of Hazardous Materials, Vol. 163, Issue 2-3, 2009, pp.1040-1051.

[2] Kefalas D.A, Christolis M.N., Nivolianitou Z., and Markastos N.C., Consequence Analysis of An Open Fire Incident in A Pesticide Storage Plant, Journal of Loss Prevention in the Process Industries, Vol. 19, Issue 1, 2006, pp. 78-88.

[3] Zhang G.-W., Zhu G.-Q., Wang X.-I., and Wu W.-H., Simulations based on the Large Space Factory Fire Experiment, Procedia Engineering, Vol. 111, 2011, pp. 649-657.

[4] Yang P., Tan X., and Xin W., Experimental Study and Numerical Simulation for A Storehouse Fire Accident, Building and Environment, Vol. 46, Issue 7, 2011, pp. 1445–1459.

[5] Lin C.S., Wu, M.G., and Tsai S.M., A Case Study on a Fire Disaster in a Textile Factory, Applied Mechanics and Materials, Vol. 763, 2015, pp. 134-139.

9th Int. Conf. on Geotechnique, Construction Materials and Environment, Tokyo, Japan, 20-22 November 2019, ISBN: 978-4-909106025 C3051

FTIR AND UV IN STEEL PIPELINE COATING APPLICATION

Omar Abdelkarim[1], Mohamed Hazem Abdellatif[1], Diaa Khalil[1] and Ghada Bassioni[1]
[1] Faculty of Engineering, Ain Shams University, Cairo, Egypt

ABSTRACT

Different spectrum can be used in characterization and upsetting the performance of our daily application. Fourier transform infrared (FTIR) spectroscopy is used to make structural analysis for materials. The need to have low cost, portable, and suitable size FTIR to be used onsite application is in need. A novel microelectromechanical system (MEMS)-based FTIR spectrometer device is made to solve this problem. Epoxy coating is used frequently to protect steel pipeline from environmental condition against corrosion. Its drawback is that is perform with low resistance for crack initiation and propagation. In addition, the absorption of ultraviolet radiation (UV) deteriorate its properties. Which reduce the lifetime of the coating. Having direct and indirect economical losses. The usage of alumina nanoparticles with small amount of weight percentage 0.25 wt. % can enhance the mechanical properties. The key factor is having good distribution of nanoparticles inside epoxy-resin matrix. The investigation of the mechanical properties, bulk properties as in flexural strength, and surface properties as in erosion resistance and hardness are studied. Furthermore, the effect of 48 h UVA absorption on the performance of these properties with different alumina nanoparticles wt. % is investigated. For the bulk properties, the addition of alumina nanoparticles having insignificant effect, while in surface properties, the effect of UV reduces with the increase in particle wt. %. The MEMS-FTIR has good agreement with mechanical properties. Indicating the distribution of particles inside the system. Supported by environmental scanning electron microscope (ESEM) images. Which shows that MEMS-FTIR is useful instrument used in non-destructive, low cost, onsite material analysis.

Keywords: MEMS-FTIR · Epoxy resin · Alumina nanoparticles · Mechanical properties

INTRODUCTION

Spectroscopy is an important characterization technique that analyze the interaction between matter and electromagnetic spectrum [1]. There are different type of spectroscopy, with wide range of electromagnetic wavelength, ranging from Gamma rays to radio waves [2]-[8]. Fourier transform infrared (FTIR) spectroscopic analysis is one way to analyze the structure of different materials [9]-[12]. The use of portable, low cost, average size near-infrared spectroscopy (NIRS) as a non-destructive testing technique is a major challenge. One way to solve this problem is by using microelectromechanical system (MEMS)-based FTIR spectrometer [13]. This device can be used for practical applications, onsite material analysis, which can save cost and time.

Steel pipeline manufacturing has been developed in the last decades [14]. Continuously increasing strength of pipeline, reducing its thickness that decreases the overall cost has been of major concern. A challenge remains corrosion of steel that depends on environmental and operational factors [15]. Many ways are used for protection including surface coating, which act as a barrier between steel and the environment [16]-[19]. Liquid epoxy coating is one type that is widely used, because of good electrical insulator, adhesion, chemical, and mechanical properties [20]-[26]. A drawback for epoxy coating is that it has a poor resistance for crack initiation and propagation, and surface damage through abrasion ware [27]. Furthermore, epoxy degrades when it is exposed to sunlight for a long time, due to absorption of ultraviolet radiation (UV) [28]. This degradation deteriorates the mechanical and physical properties [29]-[31], eventually causing direct and indirect economical losses [32].

Incorporation of nanoparticles in epoxy systems can enhance the properties at nanoscale. The factors that affect the properties are matrix-to-particle interaction and particle-to-particle interaction [33]. Nanoparticles with high surface to volume ratio tend to reduce its surface energy by interacting with each other to form agglomerates, which deteriorate the properties [34]. This interaction can be controlled through particle disruption, loading, and shape. The interface between matrix and particles, its quality enhances load transfer to nanoparticles, which enhance the mechanical properties [35].

In this study, two different spectra are used to investigate a system composed of epoxy resin with alumina nanoparticles with different weight percentage (wt. %). The effect of ultraviolet radiation A (UVA), which is the main cause for epoxy degradation, on the mechanical and physical properties, and MEMS-based FTIR spectroscopy used for material characterization.

EXPERIMENTAL

Alumina nanoparticles are used due to high

phase and dimensional stability, commercial availability, and hardness. The particles wt. % used are (0 – 0.25 – 0.5 – 0.75 – 1). The UVA exposure is for 48 hours for each sample. The detection of alumina nanoparticles distributed in epoxy-resin matrix in the near-infrared (NIR) range using an on-chip silicon micro-electro-mechanical for the application of coating steel pipelines is also studied.

Materials

KEMAPOXY epoxy-resin, mixing ratio 2:1 (resin: hardener), bought from CMB. α alumina nanoparticles, coated with aluminic ester, with 60 nm particle size, super hydrophobic, bought from US research nanomaterial, Inc.

Mold preparation

Silicon rubber mold is prepared according to ASTM D790. Using steel samples, with the same dimensions as the standard sample, as a positive pattern, then pouring silicon rubber mixture to cure on theses samples, providing the mold used for epoxy-resin/alumina nanoparticles composite samples. The ratio between resin and hardener for silicon rubber is 950:32. A vacuum pump is used to remove any air bubbles inside for 10 min. then poured over the steel samples.

Sample preparation

The epoxy resin is weighed, heated to 50ºC for 10 min to decrease the viscosity, and evacuated from any air bubbles through a vacuum pump for 30 min. Then alumina nanoaparticles with different wt. % are weighed, using sensitive scale, and added to the epoxy resin. The mixture is then stirred, using a magnetic stirrer, for 1 h. Subsequently evacuated for 30 min using vacuum pump. Then the hardener is added to the mixture, stirred for 15 min, evacuated for 5 min, and finally poured into the silicon rubber mold. The nanocomposite is left to cure at room temperature for 24 h, then post curing at 80ºC for 16 h. The samples are then exposed to ultraviolet lamp, in a sealed chamber, for 48 h at room temperature.

Characterization

MEMS-FTIR

The spectrum reflected by the samples is measured using MEMS FTIR spectrometer. Spectralon (diffuse reflectance standard) is used as a background and samples reflectance are measured with respect to it. All measurements are taken with 10 sec averaging time and a resolution of 16 nm. Samples with different concentrations are measured. For each concentration, different positions are tested to identify variation in nanoparticles distribution in the sample. The sample was placed on the source with free-space above to ensure no reflection from objects. The sample was coupled in the spectrometer's fiber.

ESEM

ESEM (Quanta FEG250) is used to take images for the cross-section of alumina/epoxy nanocomposite. Sample size 1 $cm* 1\ cm* 0.4\ cm$ is used. Samples are gold plated first to enhance the conductivity.

Mechanical properties

Bending test: 3-point bending test is used to test epoxy-resin and alumina/epoxy nanocomposites. The load is applied on the middle of specimens, supported by 2 spans. ASTM D790 (2004) specimens' specification. The machine used is 10 Ton LLYOD testing machine.
Erosion test: Sand erosion testing is performed on the samples. After projecting the samples to a stream of abrasive sand particles for 9 minutes, the weight of each sample is measured 9 times, each after 1 min, by sensitive scale, then the slope of the line is calculated as the erosion rate, which is converted to erosion resistance.
Hardness test: The same samples used for the bending test is used to measure the hardness of the composite. Each sample is tested 3 times, at 3 different locations. The test is performed using ZWICK/ROELL testing instrument, to determine the hardness behavior at room temperature.

The prepared samples are subjected to Ultraviolet radiation, before being tested, investigating the effect of UV radiation on the composites. Using a self-assembled sealed chamber, consisting of 3 partitions, UVA, UVB, and UVC is used to expose the specimens to ultraviolet radiation UVA. The exposure duration to UVA is 48 h at room temperature.

RESULTS AND DISCUSSION

Nanoparticles distribution are analyzed using MEMS-FTIR spectroscopy. The spectrum of different concentrations and positions is shown in Fig. 1. The spectrum shows that for the 0.25 wt. % sample, the alumina nanoparticle distribution is well dispersed inside the matrix, no difference with different positions. As we increase the particle wt. %, the spectrum varies from one position to the

other. The variation gradually increases as we increase the particle wt. % with the highest variation in 1 wt. %. These results indicate that agglomeration starts to occur as we increase the amount of alumina nanoparticles inside epoxy-resin matrix as well as the uneven distribution of the nanoparticles inside the system.

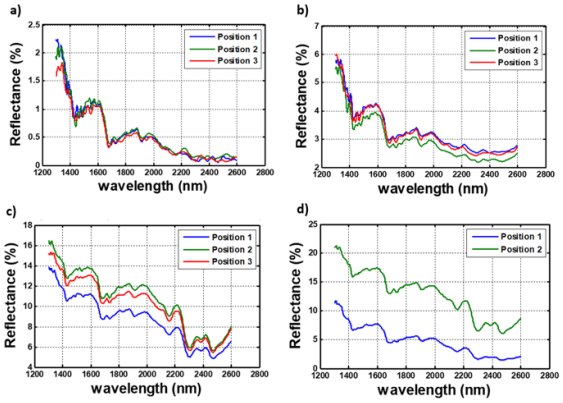

Fig. 1 MEMS-FTIR reflectance spectrum for a) 0.25 wt. % b) 0.5 wt. % c) 0.75 wt. % and d) 1 wt, % of alumina nanoparticles inside epoxy-resin matrix at different positions

The effect of increasing the amount of alumina nanoparticles wt. % on the spectrum is shown in Fig. 2. As we increase the amount of nanoparticles, the reflectance increases, from wavelength of 1300 nm to 1700 nm, then at higher wavelength, there are insignificant changes. These results indicate that the more nanoparticles we add to the system, the more interaction bonds occur between the chains and these nanoparticles. These bonds hinder the movement of the polymer chains during light exposure, and hence increase the reflectance peak for the same wavelength.

The effect of UV on the reflectance spectrum varies from one concentration to another. For pure sample without alumina nanoparticles the spectrum shifts upwards, which indicate that the UV exposure increases the amount of crosslinking inside the system, and hinders the movement of chains. While for the samples with different alumina nanoparticles a different behaviour is observed due to the inhomogeneous distribution of particles inside the matrix, as proven in Fig. 1.

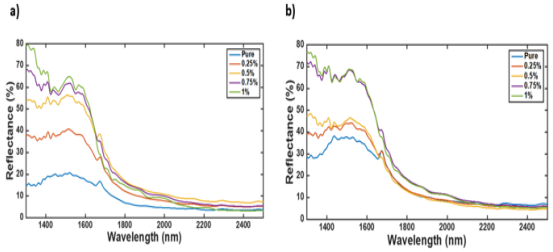

Fig. 2 : Effect of particle wt. % on the MEMS-FTIR reflectance spectrum a) before UV exposure b) after UV exposure

ESEM micrographs of the cross section of the samples are shown in Fig. 3. Those images support the results from MEMS-FTIR, showing the agglomerations that occur in different particle wt. %, in the indicated white circles. The more the particles wt. %, the more agglomeration occurs. From Fig. 1 and Fig. 3, we can conclude that as the amount of nanoparticles increases in the system, more particle-to-particle interaction increases, and more agglomeration occurs.

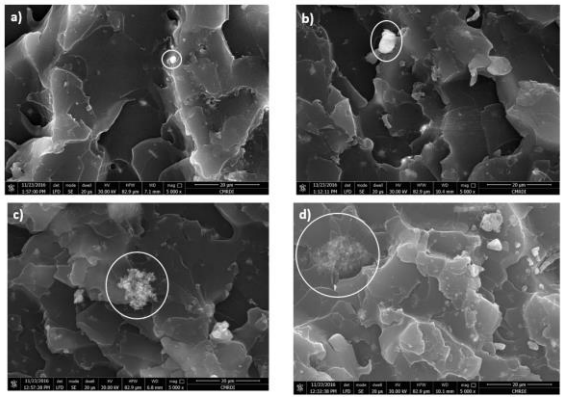

Fig. 3 ESEM microscopy of cross section surface at 20 µm of epoxy alumina nanoparticles composite with a) 0.25 wt. % b) 0.5 wt. % c) 0.75 wt. % and d) 1 wt. %

In order to investigate the effect of UVA exposure on the samples, different tests are performed: Three point bending test, Hardness test, and sand erosion test. All samples are subjected to these tests before and after UVA exposure. The effect of UVA for tests results, comparing before and after UVA exposure, are summarized in table 1.

Table 1 Mechanical properties of epoxy resin reinforced with alumina nanoparticles, difference between before and after exposure to UVA

Alumina Nanoparticles wt.%	Effect of UV on Flexural Strength (%)	Effect of UV on Erosion Resistance (%)	Effect of UV on Hardness (%)

0.00%	-1.11%	-23.0%	-20.4%
0.25%	1.11%	-19.8%	-16.9%
0.50%	-0.61%	-2.5%	-13.0%
0.75%	2.04%	-6.5%	-12.3%
1.00%	-5.06%	10.4%	0.8%

Flexural strength of epoxy-resin samples with different alumina nanoparticles, before and after exposure to UVA, is shown in Fig 4. The flexural strength increases in case of 0.25 wt. % with respect to pure sample with 7% from 77.1 MPa to 83.06 MPa. Then the strength gradually decrease with increasing wt. % till it reaches 62.45 MPa at 1 wt. %, which is 19% decrease compared to pure sample. The reason for increasing the strength is due to the good dispersion of alumina nanoparticles inside the matrix. More particle to matrix interface occurs, which transfers more load from matrix to the nanoparticles, carrying more load, and enhancing the strength of the system. However, further increase in alumina wt. %, increases particle agglomeration, so more particle-to-particle interaction occurs. These agglomeration works as stress concentration parts, which initiate cracks inside the system, lowering its performance. MEMS-FTIR and ESEM in Fig 1 and 3 can be used as a support for this statement.

The difference between the flexural strength, before and after exposure to UVA, is shown in Fig. 4. From these data, there is insignificant difference between the flexural strength before and after 48 h. UV exposure, as shown in table 1.

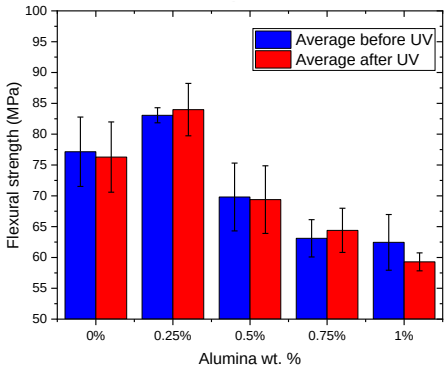

Fig. 4 Flexural strength of epoxy resin reinforced with alumina nanoparticles, before and after exposure to UVA

Erosion resistance of epoxy-resin samples with different alumina nanoparticles, before and after exposure to UVA, is shown in Fig. 5. Similar to flexural strength. The erosion resistance increases in case of 0.25 wt. % with respect to pure sample with 67% from 0.824 min/mg to 2.477 min/mg. Then the resistance gradually decrease with increasing wt. % till it reaches 1.23 min/mg at 1 wt. %, which is 49% increase compared to pure sample. The crosslinking density increases with the increase in particle wt. %, with good dispersion then gradually decreases in case of agglomeration.

From table 1, the increase in alumina nanoparticles reduces the UV effect gradually as we increase the wt. %. Starting from 23% reduction in pure sample to 10.4% improvement in 1 wt. %. These results show that the addition of alumina nanoparticles improves the surface properties of the coating against UV exposure.

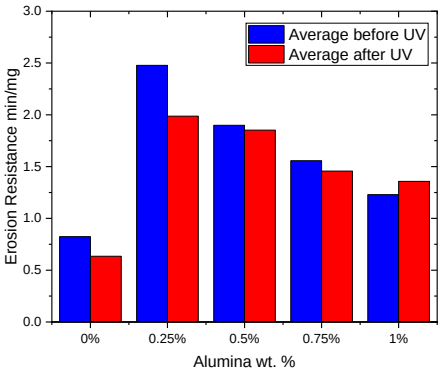

Fig. 5 Erosion resistance of epoxy resin reinforced with alumina nanoparticles, before and after exposure to UVA

Hardness of epoxy-resin samples with different alumina nanoparticles, before and after exposure to UVA, is shown in Fig. 6. In this case, The hardness slightly increases with the increase in particle addition. Starting with 75.6 Shore D for pure sample. Until it reaches 79.3 Shore D for 0.75 wt. %, with 4.9% increase. For 1 wt. %, a reduction in Hardness occur, due to inhomogeneous distribution of the nanoparticles, and Hardness test is a localized test.

The effect of UV on Hardness test is the same as in erosion resistance. As both are surface properties. The increase in alumina nanoparticles wt. % reduces the effect of UV gradually with the increase in wt. %. Staring from 20.4% reduction in pure sample to 0.8% improvement in 1 wt. %.

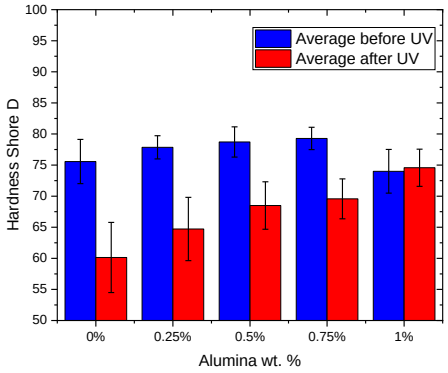

Fig. 6 Hardness Shore D of epoxy resin reinforced with alumina nanoparticles, before and after exposure to UVA

CONCLUSION

As a conclusion for this work a novel MEMS-FTIR method is used to identify the alumina nanoparticles distribution, using different positions, for the same material, in an epoxy-resin matrix. These results are supported by ESEM micrographs. The mechanical properties of different alumina nanoparticles wt. % is investigated before and after UV exposure. For flexural strength, the properties improved with the addition of 0.25 wt.% and reduced with increasing more of wt. %. The improvement is due to good particle dispersion, as indicated by MEMS-FTIR and ESEM. The reduction is due to formation of agglomeration, which reduces crosslinking density and acts as stress concentration points. The erosion resistance properties follow the same trend as flexural strength, while hardness improves slightly with increasing particle wt. %. The effect of 48 h UV exposure is insignificant in flexural strength, indicating that the UV does not affect the bulk properties. On the other hand, in case of erosion resistance and hardness, as surface properties, the addition of alumina nanoparticles reduces the effect of UV with increasing the wt. %.

REFERENCES

[1] Harvey, D. Analytical Chemistry 2.0. 2016.
[2] Colthup, N. Introduction to infrared and Raman spectroscopy. Elsevier, 2012.
[3] Jensen, Traci R., George C. Schatz, and Richard P. Van Duyne. Nanosphere lithography: Surface plasmon resonance spectrum of a periodic array of silver nanoparticles by ultraviolet− visible extinction spectroscopy and electrodynamic modeling. The Journal of Physical Chemistry B, Vol 103. Issue 13, 1999, pp. 2394-2401.
[4] Harris, R. K. Nuclear magnetic resonance spectroscopy. 1986.
[5] Gilmore, G. Practical gamma-ray spectroscopy. John Wiley & Sons, 2011.
[6] Briggs, D. ed. Handbook of X-ray and ultraviolet photoelectron spectroscopy. London: Heyden, 1977.
[7] Townes, Charles H., and Arthur L. Schawlow. Microwave spectroscopy. Courier Corporation, 2013.
[8] Gupta, S., Z. Hadzibabic, M. W. Zwierlein, C. A. Stan, K. Dieckmann, C. H. Schunck, E. G. M. Van Kempen, B. J. Verhaar, and W. Ketterle. Radio-frequency spectroscopy of ultracold fermions. Science, Vol 300, Issue 5626, 2003, pp. 1723-1726.
[9] Schmitt, J., & Flemming, H. C. FTIR-spectroscopy in microbial and material analysis. International Biodeterioration & Biodegradation, Vol 41, Issue 1, 1998, pp. 1-11.
[10] Colom, X., F. Carrillo, F. Nogués, and P. Garriga. Structural analysis of photodegraded wood by means of FTIR spectroscopy. Polymer degradation and stability, Vol 80, Issue 3, 2003, pp. 543-549.
[11] Baker, M.J., Trevisan, J., Bassan, P., Bhargava, R., Butler, H.J., Dorling, K.M., Fielden, P.R., Fogarty, S.W., Fullwood, N.J., Heys, K.A. and Hughes, C. Using Fourier transform IR spectroscopy to analyze biological materials. Nature protocols, Vol. 9, Issue 8, 2014, pp.1771.
[12] Rehman, Ihtesham, and W. Bonfield. Characterization of hydroxyapatite and carbonated apatite by photo acoustic FTIR spectroscopy. Journal of Materials Science: Materials in Medicine, Vol 8, Issue 1, 1997, pp. 1-4.
[13] Khalil, D. A., Mortada, B., Nabil, M., Medhat, M., & Saadany, B. A. 2013. U.S. Patent No. 8,531,675. Washington, DC: U.S. Patent and Trademark Office.
[14] Kagechika, H. Recent progress and future trends in the research and development of steel. NKK Technical Review (Japan), Vol, 88, 2003, pp. 6-9.
[15] Banach, J. Liquid epoxy coatings for today's pipeline coating challenges. In Proceedings of Northern Area Western Conference, Victoria. 2004.
[16] Caporali, S., Fossati, A., Lavacchi, A., Perissi, I., Tolstogouzov, A., & Bardi, U. Aluminium electroplated from ionic liquids as protective coating against steel corrosion. Corrosion Science, Vol 50, Issue 2, 2008, pp. 534-539.
[17] Shen, G. X., Y. C. Chen, and C. J. Lin. Corrosion protection of 316 L stainless steel by a TiO2 nanoparticle coating prepared by sol–gel method. Thin Solid Films, Vol. 489, Issue 1-2, 2005, pp. 130-136.

[18] Sathiyanarayanan, S., S. Syed Azim, and G. Venkatachari. A new corrosion protection coating with polyaniline–TiO2 composite for steel. Electrochimica Acta, Vol. 52, Issue 5, 2007, pp. 2068-2074.

[19] Sathiyanarayanan, S., S. Muthukrishnan, G. Venkatachari, and D. C. Trivedi. Corrosion protection of steel by polyaniline (PANI) pigmented paint coating. Progress in Organic Coatings, Vol. 53, Issue 4, 2005, pp. 297-301.

[20] Behzadnasab, M., S. M. Mirabedini, K. Kabiri, and S. Jamali. Corrosion performance of epoxy coatings containing silane treated ZrO2 nanoparticles on mild steel in 3.5% NaCl solution. Corrosion Science, Vol. 53, Issue 1, 2011, ppt. 89-98.

[21] Talo, A., P. Passiniemi, O. Forsen, and S. Yläsaari. Polyaniline/epoxy coatings with good anti-corrosion properties. Synthetic Metals, Vol. 85, No. 1-3, 1997, pp. 1333-1334.

[22] Shi, X., Nguyen, T. A., Suo, Z., Liu, Y., & Avci, R. Effect of nanoparticles on the anticorrosion and mechanical properties of epoxy coating. Surface and Coatings Technology, Vol. 204, Issue 3, 2009, pp. 237-245.

[23] Manning, David G. Corrosion performance of epoxy-coated reinforcing steel: North American experience. Construction and Building Materials, Vol. 10, Issue 5, 1996, ppt. 349-365.

[24] Hang, T. T. X., Truc, T. A., Nam, T. H., Oanh, V. K., Jorcin, J. B., & Pébère, N. Corrosion protection of carbon steel by an epoxy resin containing organically modified clay. Surface and Coatings Technology, Vol. 201, No. 16-17, 2007, pp. 7408-7415.

[25] Shao, Y., Jia, C., Meng, G., Zhang, T., & Wang, F. The role of a zinc phosphate pigment in the corrosion of scratched epoxy-coated steel. Corrosion Science, Vol. 51, Issue 2, 2009, pp. 371-379.

[26] Galliano, F., and D. Landolt. Evaluation of corrosion protection properties of additives for waterborne epoxy coatings on steel. Progress in Organic Coatings, Vol. 44, Issue 3, 2002, pp. 217-225.

[27] Spanoudakis, J., and R. J. Young. Crack propagation in a glass particle-filled epoxy resin. Journal of Materials Science, Vol. 19, Issue 2, 1984, pp. 473-486.

[28] Singh, B., & Sharma, N. Mechanistic implications of plastic degradation. Polymer degradation and stability, Vol. 93, Issue 3, 2008, pp. 561-584.

[29] Joseph, P. V., Marcelo S. Rabello, L. H. C. Mattoso, Kuruvilla Joseph, and Sabu Thomas. Environmental effects on the degradation behaviour of sisal fibre reinforced polypropylene composites. Composites Science and Technology, Vol. 62, No. 10-11, 2002, pp. 1357-1372.

[30] Woo, R. S., Chen, Y., Zhu, H., Li, J., Kim, J. K., & Leung, C. K. Environmental degradation of epoxy–organoclay nanocomposites due to UV exposure. Part I: Photo-degradation. Composites Science and Technology, Vol. 67, No. 15-16, 2007, pp. 3448-3456.

[31] Woo, R. S., Zhu, H., Leung, C. K., & Kim, J. K. Environmental degradation of epoxy-organoclay nanocomposites due to UV exposure: Part II residual mechanical properties. Composites science and technology, Vol. 68, Issue 9, 2008, pp. 2149-2155.

[32] Javaherdashti, R. How corrosion affects industry and life. Anti-corrosion methods and materials, Vol. 47, Issue 1, 2000, pp. 30-34.

[33] Schmidt, G, and Matthew M. Malwitz. Properties of polymer–nanoparticle composites. Current opinion in colloid & interface science, Vol. 8, Issue 1, 2003, pp. 103-108.

[34] Zare, Y. Study of nanoparticles aggregation/agglomeration in polymer particulate nanocomposites by mechanical properties. Composites Part A: Applied Science and Manufacturing, Vol. 84, 2016, pp. 158-164.

[35] Fu, S. Y., Feng, X. Q., Lauke, B., & Mai, Y. W. Effects of particle size, particle/matrix interface adhesion and particle loading on mechanical properties of particulate–polymer composites. Composites Part B: Engineering, Vol. 39, Issue 6, 2008, pp. 933-961.

9th Int. Conf. on Geotechnique, Construction Materials and Environment, Tokyo, Japan, 20-22 November 2019, ISBN: 978-4-909106025 C3051

INFLUENCE OF EMBEDDING POSITION ON THE PERFORMANCE OF BASALT GEOSYNTHETICS

Mohamed Eltaher[1], Zakaria Hossain[1], Jim Shiau[2,] and Hajime Takami[3]
[1]Graduate School of Bioresources, Mie University, Japan; [2]School of Civil Engineering and Surveying, University of Southern Queensland, Australia; [3]Tsuchiya TSCO Co., Ltd., Japan

ABSTRACT

This paper presents the experimental study of a new two types of eco-friendly basalt geosynthetics. Results are evaluated for its bearing capacity with one backfill soil using the California bearing ratio (CBR) test. The test results are compared based on interface mechanical properties of the reinforcements. One backfill sandy soil in combination with two different geosynthetics are tested at various loading conditions in the CBR test. Based on the analyses of the experimental data, the penetration strength and the penetration displacement of specimens due to the variation of the type of geosynthetic and location of embedment are examined. Load-penetration behavior of the backfill soil with the two types of geosynthetic shows a significant increment in the bearing capacity. It is found that the embedment position of the reinforcement affects the ground bearing capacity. Also, for each one of those reinforcements, there is an effective embedment position to reach the maximum bearing capacity. In particular, bearing capacity reached its maximum in the case of using two layers of geogrid on the surfaces of the upper and lower layers of the subgrade soil specimen.

Keywords: Geosynthetics, Sandy Soil, California Bearing Ratio Test, Bearing Capacity.

INTRODUCTION

Earth fill structures offer various advantages and can be used in airfields, highways, and other public facilities, depending on the purpose of the construction. Those structures must be stable under all static and dynamic loadings during construction and in-service [1]. The subgrade soils are generally defined by their resistance to deformation under load and the strong subgrade soil can reduce the cost of the airfield or highway construction. By using reinforced subgrade, which can be very complex depending on the nature and properties of the reinforcement [2] the required thickness of a flexible pavement can be reduced as compared to weaker subgrades. It will, therefore, result in a significant cost saving advantage due to resource-saving and durability [3]. This is the reason that the reinforcing the soft soil using various types of geosynthetics is a well-known technique to improve subgrade soils performance and enhance its bearing capacity.

The performance of the subgrade soils is widely evaluated by using the California bearing ratio (CBR) test which evaluates the strength of subgrade soils, sub-base, and base course material for the design of the pavement thickness. The CBR test often forms the basis of pavement design. For this reason, it finds favor with some design and control methods. Design testing is usually undertaken in the laboratory where the CBR can be measured for a variety of dry densities and soaked or unsoaked, corresponding to the groundwater or drainage conditions foreseen and where surcharges can be added to simulate the effect of construction thicknesses. Once a design CBR has been established, it can be controlled in the field by sampling the placed fill and testing at the site laboratory, or by adopting in situ CBR procedures.

The bearing capacity of reinforced soil with geosynthetics has been investigated using the CBR tests by several researchers. They used various types of geosynthetic materials i.e. polypropylene (PP), High-density polyethylene (HDPE), Polyester (PET) yarns, etc. [4] The present study dealt with a new type of geosynthetics which are made from basalt fiber. A series of CBR tests on the geosynthetic embedded inside one type of backfill soil have been conducted. Based on the test results, the load-penetration behavior of the reinforced subgrade soil along with different mechanical characteristics has been evaluated and discussed shortly.

PURPOSE OF THE STUDY

1. To investigate the relationship between the reinforced subgrade soil moisture content and the CBR value.
2. To investigate the influence of new types of basalt geosynthetics, (its embedding position, and the number of geosynthetic layers) with one backfill soil on CBR value, through a series of CBR tests.

MATERIALS AND METHODS

Backfill Material

One type of soil was used as backfill material in

this study. The soil sample had been collected from Handa area (半田地区), Tsu City, Mie Prefecture, Japan is shown in Fig. 1 and used in combination with geosynthetic materials to evaluate its bearing behavior.

Fig. 1 Soil from Hanada area, Tsu City, Mie Prefecture, Japan.

Fig. 2 represents the gradation curve of the experimental soil. According to the Japanese Geotechnical Society engineering classification system (JGS), this sandy soil is classified as SF.

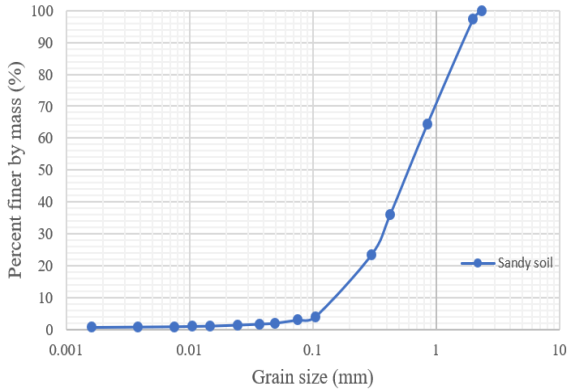

Fig. 2 Backfill soil particle size distribution curve.

The major physical properties of the soil are listed in table 1. While basically, the optimum water content of this sandy soil was 16.7%.

Table1. Backfill sandy soil physical properties.

Properties	Sandy backfill
Soil particles density, ρ_s	2.779 g/cm^3
Optimum water content, $W_{opt.}$	16.7%
Maximum dry density ($\gamma_{\text{dry max}}$)	1.713 g/cm^3
Liquid Limit, LL	36.664%
Plastic Limit, PL	30.587%
Plasticity Index, PI	6.08%
Gravel > 2 mm	2%
Sand (75 µm - 2 mm)	94%
Silt (5 µm - 75 µm	2%
Clay < 5 µm	2%

Geosynthetic Materials

The woven geosynthetics used in this study are made of basalt fiber and provided by Tsuchiya TSCO Co., Ltd. These materials possess the good property of elasticity and stretch tension with good resistance to acid, alkali, heat, and vibration. It has also nonconductive and non-magnetic resistance. The chemical composition and basic characteristics of basalt fiber used for manufacturing these geosynthetics are listed in Tables 2 and 3 respectively. Two types of geosynthetics have been used, one woven geotextile (with soft texture) and one woven geogrid (with stiff texture). For the purpose of discussion, the geotextile is noted as GTX and the geogrid is noted as GGR as shown in Fig. 3.

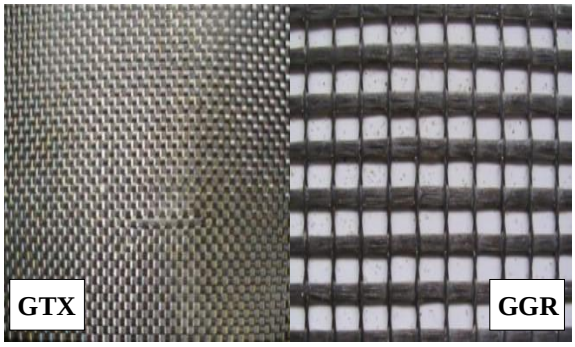

Fig. 3 Types of the used geosynthetics

Table 2. Chemical composition of basalt fiber [5]

Ingredient	Content by weight %
SiO_2	51.6 ～ 59.3
Al_2O_3	14.6 ～ 18.3
CaO	5.9 ～ 9.4
MgO	3.0 ～ 5.3
Na_2O+K_2O	3.6 ～ 5.2
TiO_2	0.8 ～ 2.25
Fe_2O_3+FeO	9.0 ～ 14.0
Others	0.09 ～ 0.13

Table 3. Basic characteristics of basalt fiber [5]

Characteristic		Basalt fiber
Thermal	Operating temperature (heat-resistant temp.) (℃)	-260～650
	Maximum continuous use temperature (℃)	700
	Heat transfer coefficient (W/mk)	0.031～0.038
	Melting temperature (℃)	1450
	Softening temperature (℃)	1050
	Thermal expansion coefficient (×10^{-6}/℃)	10

	Table 3 Continued	
Physical	Density (g/cm^3)	2.67
	Fiber diameter (μm)	10～17
	Tensile strength (Mpa)	1900
	Elastic modulus (GPa)	90
	Breaking elongation (%)	2.2
	Tensile strength thermal change (Tensile strain):	
	20℃ (%)	100
	200℃ (%)	95
	400℃ (%)	82
Electro-chemical	Electric resistance (Ω)	1×10^{12}
	Chemical stability (3h boiling mass loss):	
	2N-HCI (%)	2.20
	2N-NaOH (%)	2.75
	H_2O (%)	0.20

For convenience in drawing CBR specimens and diagrams, the used geosynthetic products were represented by abbreviations and graphical symbols as recommended by the International Geosynthetic Society (IGS) described in table 4.

Table 4. Abbreviations and graphical symbols of the used geotextile and geogrid products

Abbrev.	Geosynthetic Product	Graphical Symbol
GTX	Geotextile	
GGR	Geogrid	

Note: as recommended by the International Geosynthetics Society (IGS) [6].

CBR Test Apparatus and Equipment

In this research many tools have been used e.g. CBR stainless steel Mold (inner diameter 15 cm, height 17.5 cm), perforated base plate, collar (extension ring), spacer disc (diameter 15 cm, height 5 cm), manual compaction hammer (diameter 5.0 cm – mass 4.5 kg – height 45 cm), steel straight edge, balance (Max. capacity of 20 kg, minimum reading 10 g), filter papers, measuring cylinder, plastic squeeze bottle with water, moisture beakers, drying oven, loading plate**s** (split surcharge weight**s**), samples jack (Universal extruder), and CBR penetration testing machine.

For the convenience of the readers, the important components of the CBR penetration testing machine shown in Fig. 10 are numbered numerically starting from top left to down right in the increasing way such as, the number from (1) to (8), where the number (1) are a stainless steel screw columns, adjustable upper crosshead, and nuts, (2) is the proving ring with dial gauge for measuring the vertical load applied, (3) is the standard penetration piston (plunger), (4) is the CBR mold with a perforated bottom plate containing the specimen, (5) are the split surcharge weights outside the mold, (6) is the penetration measuring dial gauge, (7) is a stainless steel top board of a mechanical type jack (8) mechanical type jack manual operating wheel.

CBR Specimen's Preparation

At first, the CBR control specimen (soil only specimen) shown in Fig. 4 was prepared in the CBR mold. To prepare the control specimen layers, soil and water (12% - 13% of the soil weight) were mixed homogeneously. Then the soil was added into the mold after it had been assembled with the perforated bottom plate, spacer disc, and mold extension. While adding soil into the mold the soil was divided into three layers and tamped uniformly 67 times per layer using a manual hammer.

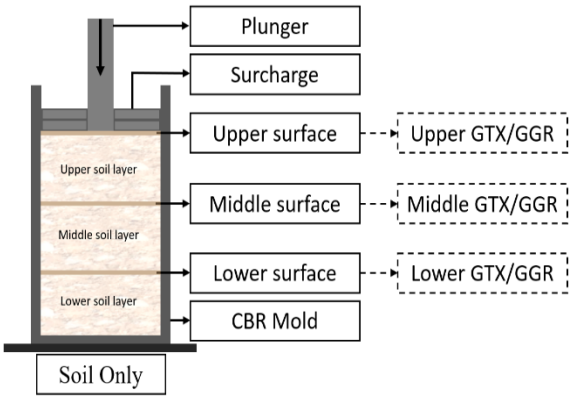

Fig. 4 Typical schematic diagram of CBR control specimen using a divided three layers of soil only with an indication of the surface of each layer where geosynthetics can be laid on.

For the preparation of CBR test specimens, in the same way, the mold had been assembled with the perforated bottom plate, spacer disc and mold extension, the wet soil sample was poured into it. The wet soil sample was divided into three layers then tamped uniformly 67 times per layer with the 4.5 kg hammer.

Fig. 5 GGR sample laid or flattened on a surface of a compacted soil layer inside the CBR mold.

Considering that in these CBR test specimens, the surface of each soil layer was leveled precisely and geosynthetic(s) of the same diameter of the mold were laid or flattened on the surface of a chosen soil layer(s) which had been tamped before to achieve the separation between specific soil layer(s) as shown in Fig. 5 resulting in six patterns of CBR test specimens with a total number of twelve specimens.

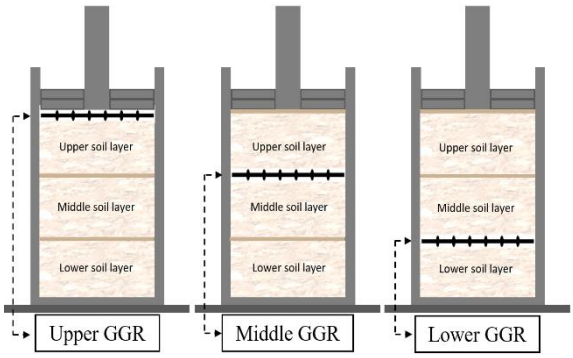

Fig. 6 Three specimens of one-layer GGR embedded in between three layers of compacted soil in three different positions (upper, middle and lower)

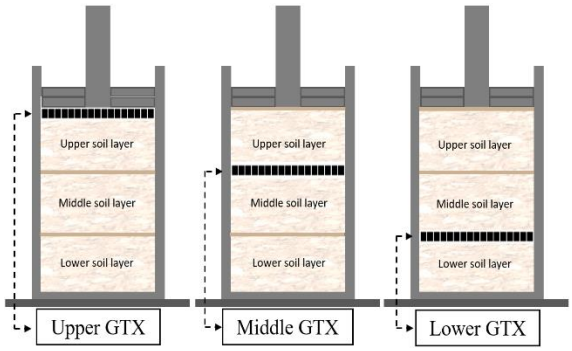

Fig. 7 Three specimens of one-layer GTX embedded in between three layers of compacted soil in three different positions (upper, middle and lower)

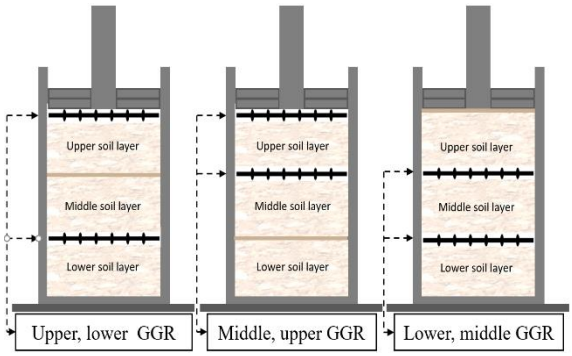

Fig. 8 Three specimens of two layers GGR embedded in between three layers of compacted soil in three different positions (upper and lower, middle and upper, lower and middle)

The six patterns of CBR test specimens were classified into two groups, three of one layer (upper GGR/GTX (pattern I), middle GGR/GTX (pattern II), and lower GGR/GTX (pattern III)) shown in Fig. 6, 7 and three of two layers (upper and lower GGR/GTX (pattern IV), middle and upper GGR/GTX (pattern V), lower and middle GGR/GTX (pattern VI)) shown in Fig. 8, 9.

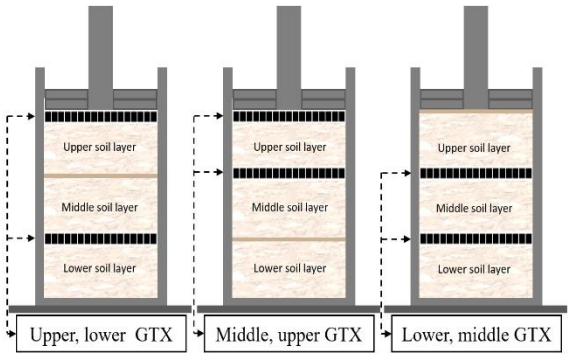

Fig. 9 Three specimens of two layers GTX embedded in between three layers of compacted soil in three different positions (upper and lower, middle and upper, lower and middle)

CBR Test Setup and Procedures

The California Bearing Ratio (CBR) test was developed by the Californian Division of Highways for the design of flexible pavements. The basic procedure of this test was adopted by the Corps of Engineers of the US Army. Certain modifications were made in the test procedure, and now the modified method is adopted by the Corps of Engineers and Regarded as the standard method of determining the CBR. The corps Engineers have developed design curves using CBR values for determining the required thickness of flexible pavements for airport runways and taxiways.

It has been widely used all over the world to evaluate the bearing capacity of soils and subgrades since its invention in 1930 by the California Division of highways, USA [7].

In the laboratory, the CBR test is typically performed on compacted soil samples. In this research, the CBR was calculated as follows:

After the specimen had been set up in the mold then the specimen is placed precisely on the top board of the CBR apparatus jack (No.7, Fig. 10). The required clearance between the split surcharge weights inside the mold (No.5, Fig. 10) and plunger (No.3, Fig. 10) was set by adjustable upper crosshead (No.1, Fig. 10) letting the plunger to touch the upper surface of the specimen freely without applying loads. The tests were conducted in the way of penetrating the specimens using the standard plunger with a constant velocity of 1.27 mm/min (0.05 in/min) by means of screw jack (No.7,8, Fig. 10) under mechanically

manual operated constant pressure.

While operating the CBR testing machine the load (pounds) measured using proving ring dial gauge (No.2, Fig. 10) versus depth of penetration (inches) of the piston (No.3, Fig. 10) as it is being pushed into the soil was recorded using penetration measuring dial gauge (No.6, Fig. 10) considering the penetration depths of 0.5 mm, 1.0 mm, 1.5 mm, 2.0 mm, 2.5 mm, 3.0 mm, 4.0 mm, 5.0 mm, 7.5 mm, 10.0 mm, and 12.5 mm.

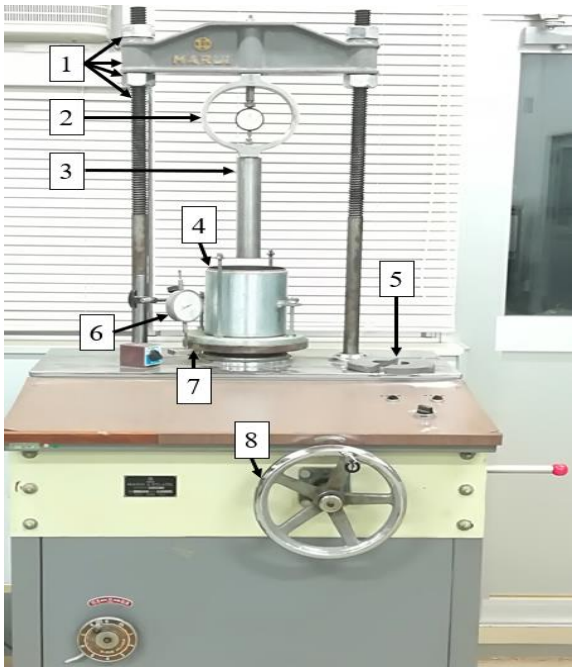

Fig. 10 CBR testing machine and its components

Then the stress (psi) on the piston by dividing the load by the area of the piston was calculated. A graph for the stress (psi) versus the depth of penetration (inches) relationship was plotted. The bearing value is normally the stress (psi) corresponding to a depth of penetration of the piston of 0.10 in. (2.54 mm). if the curve indicates surface irregularities or if the curve is initially concave upward, a correction is applied, in order to obtain the corrected stress for 0.10 in (2.54 mm) penetration of the piston. This bearing value is converted to a ratio by dividing it by 1000 psi, which represents the penetration resistance of compacted standard crushed rock.

This bearing ratio, which is a fraction, is multiplied by 100 and reported as the California Bearing Ratio. Typical CBR values range from less than 5 for soft clays up to 80 for dense sandy gravel.

In the above analysis, the stress corresponding to 0.20 in. (5.08 mm) of penetration should also be determined, and then the bearing value is converted to a ratio dividing by 1500 psi. if this bearing ratio is greater than the bearing ratio calculated for 0.10 in. (2.54 mm) penetration, then the test must be repeated. If, upon rerunning the test, there is a similar result, then the ratio at 0.20 in. (5.08mm) is used as the California Bearing Ratio value. In this study, the CBR tests were carried out for one control specimen and twelve test specimens with their repetitions.

It is vital to take care while interpreting the CBR data, because there is a possibility that the soil might be disturbed and loosened during the construction operations, resulting in a lower CBR than originally measured.

The CBR is defined as the ratio of the resistance to the sinking of a penetration piston having a velocity of 1.27 mm/min (0.05 in/min) into the soil to the resistance shown by a standard crushed rock sample for the same penetration depth [8].

Using this apparatus, the loads were recorded up to a penetration depth of 12.5 mm according to the Japanese Industrial Standards (JIS-A-1211) [9]. The CBR value was calculated according to the following equation:

$$CBR\,\% = \frac{Load\ Strenght}{Standard\ Load\ Strength} \times 100 \quad (1)$$

RESULTS AND DISCUSSION

In the present investigation, two types of basalt geosynthetics (geotextile (GTX) and geogrid (GGR)) were embedded inside soil layers with the purpose of reinforcing the subgrade soil. The reinforcing of subgrade soil by using basalt geosynthetics is expected to be used in infrastructure projects including those in the rural sector (highways, airports, and embankments) that require huge initial investments and low rate of returns on investment [10]. The performance of the non-reinforced and reinforced subgrade specimens was evaluated by using the CBR test. A high CBR value indicates the excellent quality of the material, although other relevant parameters may be necessary to re-confirm the material's performance [11].

In this study, six position patterns forming twelve different CBR test specimens of subgrade soil reinforced with geosynthetic were tested in order to understand their performance response based on CBR values.

The types of test specimens were classified into two groups, in the first group which contains three patterns of six specimens, only one layer of geogrid (GGR) was embedded inside the subgrade soil layers forming three different specimens according to its position which were GGR on upper layer, GGR on middle layer, and GGR on lower layer of the subgrade soil. In the same way, another three specimens using geotextile (GTX) instead of geogrid (GGR) were prepared.

On the other hand, also the second group contained six test specimens of three patterns but in which a combined layer of geogrid (GGR) was

embedded inside the subgrade soil layers forming three different specimens according to its position which were GGR on upper and on lower layers, GGR on middle and on upper layers, and GGR on lower and on middle layers of the subgrade soil. In the same way, another three specimens using geotextile (GTX) instead of geogrid (GGR) were prepared. In addition to the twelve test specimens, there was one control specimen which was a nonreinforced soil sample.

The results for the effects of different geosynthetic type and embedding position(s) at variable depths of soil as a subgrade layer are depicted and a pertinent discussion comparing the results with this control specimen is presented.

Moisture Content and CBR Value Relationship

Analysis in this part included the relationship between the subgrade soil moisture content and the CBR value. A graph had been created where the water content was plotted on the horizontal axis and the CBR value was plotted on the vertical axis as shown in Fig. 11. In Fig.11, a range of around 12 to 13.5% of water content, which is the water content ratio used for the preparation of all the CBR control and test specimens and slightly lower than the optimum moisture content of the used subgrade soil, was shown with a green frame.

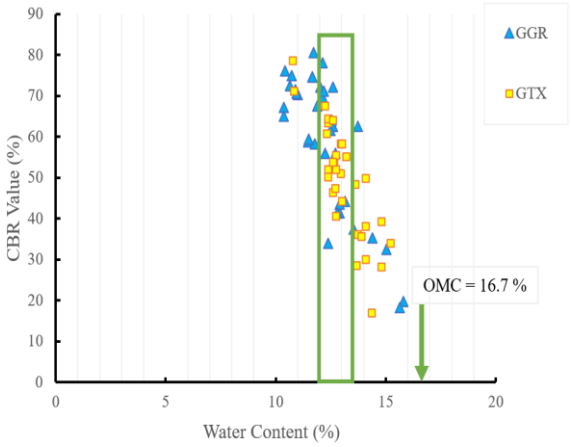

Fig. 11 Subgrade soil moisture content - CBR value relationship chart

Basically, the green frame in Fig. 11 had been picked to show the effect of the water content on the CBR value in the case of the water content is slightly lower than the optimum water content.

The experiments showed that the CBR values were significantly different near the optimum moisture content than in the place where the water content was low. It was found that the CBR value tends to decrease near the optimum moisture content where the water content is slightly high. In contrast, it was found that the CBR value tends to increase as the water content decreased.

While the main purpose of this research is to investigate the effect of embedding different types of basalt geosynthetics inside the subgrade soil layers in different positions at a water content slightly lower than the optimum moisture content on the CBR value, it was found that when the water content ratio becomes low, the CBR value is getting increased drastically. Thus, the CBR value was affected not only by the subgrade soil type, basalt geosynthetic type and/or location but also by the moisture content. And therefore, in this research, the percentage near 12-13.5%, which is slightly lower than the optimum moisture content, was carefully considered.

And that is why, when one is interpreting the CBR data, there is a possibility that the field moisture content of the soil could increase, which could soften fine-grained soils leading to a lower CBR than originally measured.

Influence of Embedding Geosynthetic Inside Subgrade Soil on CBR Value

A series of CBR tests were conducted to obtain the load-penetration relationship of CBR control and test specimens to understand the Influence of geosynthetic type, the number of layers, and position of embedment inside subgrade soil on the CBR value.

Influence of reinforcing the subgrade soil with one layer of basalt geogrid (GGR)

In addition to the CBR control specimen curve, three load-penetration curves obtained from the CBR tests of the three subgrade test specimens containing only one layer of GGR are shown in Fig. 12 in which three different embedding positions were implemented upper, middle and lower. From this figure, it can be seen that all curves follow a typical trend of a CBR test. And also, as the embedding position goes up, the piston load at a given penetration also increases considerably.

The calculated CBR values for the penetration depth of 2.5 mm in the subgrade soil reinforced with one layer of GGR are given in table 5. The results show that the CBR values can be improved by raising the embedding position of the GGR inside the subgrade soil as in the upper layer case, the CBR value was maximized. The CBR values for one-layer GGR reinforced soil in positions of upper, middle and lower layers are 70.89, 60.08, and 42.25% respectively. From these results, also it could be seen that the upper layer is closer to the surface of sinking, indicating more resistance in comparison to the lower layer.

The CBR value of the control specimen (soil only) in this research is 47.93%. This means that CBR values can approximately by 48% higher be achieved by embedding the GGR on the upper subgrade soil layer compared to the CBR value of the control.

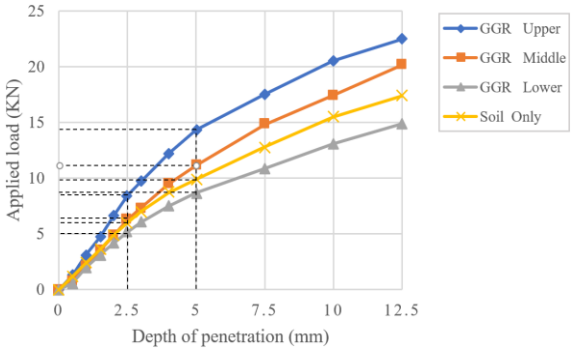

Fig. 12 Load penetration curves of control specimen and three subgrade soil test specimens containing one layer of basalt GGR on the upper, middle and lower soil layer respectively

Influence of reinforcing the subgrade soil with one layer of basalt geotextile (GTX)

The CBR test results for the subgrade soil test specimens containing one layer of basalt GTX on the upper, middle or lower soil layer all together are shown in Fig. 13 It can be seen that, the results of the control specimen (soil only) and the two specimens of soil containing one layer of GTX on the upper- and middle-layer display similar trend before and after penetration depth of 2.5 mm. while the specimen of soil containing one layer of GTX on lower layer showed a different increasing trend.

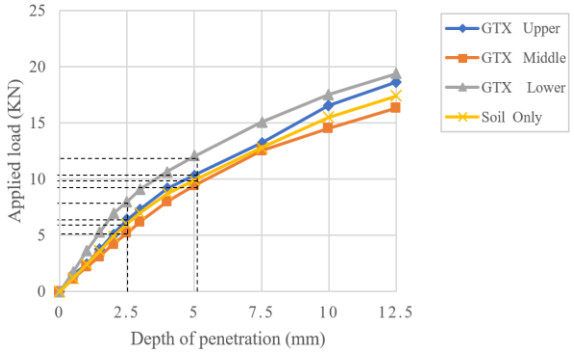

Fig. 13 Load penetration curves of control specimen and three subgrade soil test specimens containing one layer of basalt GTX on the upper, middle and lower soil layer respectively

The CBR test values for penetration depths of 2.5 mm in the subgrade soil reinforced with one layer of GTX are also given in table 5. From this table, it can be observed that in contrast to the GGR one layer the CBR values increase when the embedding position of GTX goes down inside the subgrade soil as in the GTX lower layer case, the supporting force was maximized. The CBR values for subgrade soil reinforced with one layer of GTX on upper, middle and lower layer are 49.72, 45.66, and 59.28% respectively.

This means that CBR values can at most by 24% higher be achieved by embedding the GTX on the lower subgrade soil layer compared to the CBR value of the control.

From Fig. 12 and Fig. 13 where the subgrade soil is reinforced with one-layer geosynthetics only, it is found that in the case of the stiff geosynthetics (as the used GGR), the closer to the upper layer, the sooner the bearing capacity is affected and the CBR value increases drastically. In contrast, softer geosynthetics (as the used GTX) are not immediately affected by the upper layer and are considered to affect significantly the bearing capacity when embedded in the lower layer.

Influence of reinforcing the subgrade soil with two layers of basalt geogrid (GGR)

Fig. 14 describes the relationship of applied load versus the penetration depth in subgrade double layers of basalt GGR upper-lower, middle-upper, and lower-middle. The CBR curves for the GGR double layer in subgrade soil are more pronounced before 2.5 mm penetration in comparison to the previous group of GGR and GTX one layer. It is evident that the penetration load increased for this case.

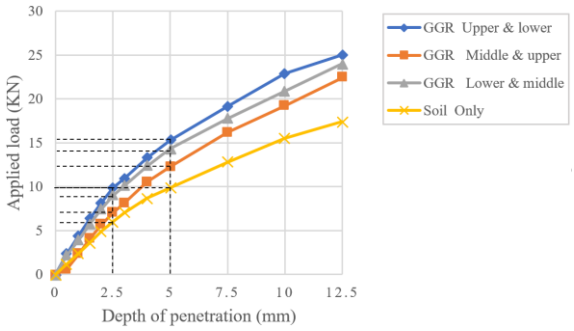

Fig. 14 Load penetration curves of control specimen and three subgrade soil test specimens containing two layers of basalt GGR on the upper-lower, middle-upper, and lower-middle soil layers respectively

The CBR values for the penetration depth of 2.5mm penetration are given in table 5. In comparison to the previous group of one layer of geosynthetic (GTX or GGR), the current CBR results show higher increments especially when the embedding position in the subgrade soil comes in upper-lower, and lower-middle layers. The CBR values for a penetration depth of 2.5 mm for subgrade double layers of GGR upper-lower, middle-upper, and lower-middle are 74.61, 64.48 and, 67.29% respectively.

Influence of reinforcing the subgrade soil with two layers of basalt geotextile (GTX)

The CBR test results for the subgrade soil test specimens containing two layers of GTX on the

upper-lower, middle-upper, and lower-middle soil layers all together are shown in Fig. 15 The CBR curves for the double layer GTX reinforced subgrade soil show close trends before and after penetration depth of 2.5 mm.

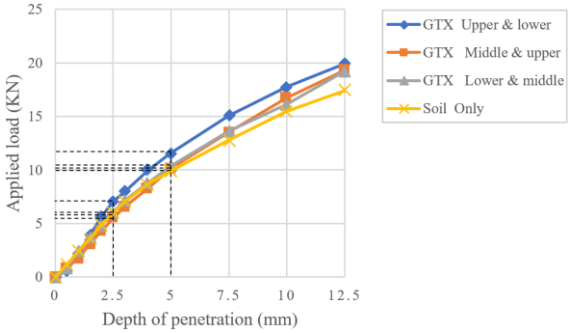

Fig. 15 Load penetration curves of control specimen and three subgrade soil test specimens containing two layers of basalt GTX on the upper-lower, middle-upper, and lower-middle soil layers respectively

The calculated CBR values for the penetration depth of 2.5 mm in the subgrade soil reinforced with two layers of GTX are given in table 5. The results illustrate that the CBR values, in general, had been slightly improved by using two layers of GTX, but this improvement was still less than the increment due to using only one-layer GTX on the lower subgrade soil layer. The CBR values for double layers GTX reinforced subgrade soil in positions of upper-lower, middle-upper, and lower-middle are 55.87 %, 56.07 % and, 52.87 % respectively.

Table 5 CBR values of subgrade soil specimen types

Specimen type or layering pattern		CBR Value	
		GGR	GTX
One layer test specimen	Upper	70.89	49.27
	Middle	60.08	45.66
	Lower	42.45	59.28
Two layers test specimen	Upper & middle	64.48	56.07
	Middle & lower	67.29	52.87
	Lower & upper	74.61	55.87
Control specimen (soil only)		47.93	

Table 5 summarizes the CBR values of the types of control and test specimens with various positions of geosynthetics embedment. It shows that embedding the eco-friendly basalt geosynthetic (geogrid and/or geotextile) inside the subgrade soil has a significant effect on improving the CBR value except in the case of using one GTX layer on the middle layer of subgrade soil and also using one GGR layer on the lower layer of subgrade soil.

Fig. 16 shows a bar graph to compare the difference in the CBR values depending on the geosynthetic layering pattern inside the subgrade soil where the CBR value is plotted on the vertical axis and the specimen type is plotted on the horizontal axis.

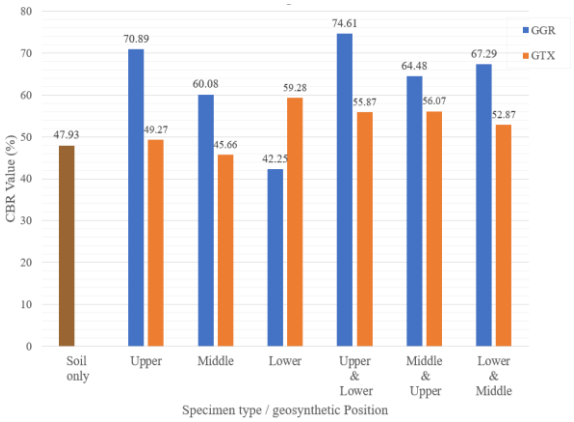

Fig.16 Comparison between CBR values of control and test specimens

The CBR value of one layer of GGR embedded on the lower subgrade soil layer specimen has the lowest value, whilst the specimen of GGR flattened on the upper subgrade soil layer has the highest CBR value among the one-layer GGR pattern. On the other hand, with changing the one-layer GGR pattern into one layer of GTX pattern, the case of embedding the GTX on the middle subgrade soil layer shows the lowest CBR value and on the lower subgrade soil layer the highest CBR value. At one-layer geosynthetic embedment in the subgrade soil, the maximum increment in the CBR value was 48% in the geogrid upper layer case and 24% in geotextile lower layer case.

Further addition of geosynthetic layers inside the subgrade soil layers to turn it into two layers instead of one layer alters the behavior of the ground conspicuously. It is observed that the GGR upper-lower double layers in the subgrade soil gave the highest CBR value compared to the other five double layer cases, whilst the GTX lower-middle double layers showed the lowest CBR value. In the two layers geosynthetic embedment case, the maximum increment in CBR value was 55.7% in the geogrid upper-lower layers specimen and 16.6% in the geotextile middle-upper layers specimen.

It was interesting to note that the GTX double layers embedded inside the subgrade soil layers are not as beneficial as originally expected when compared to a single GTX lower layer. And the effect of embedment was not that large when the number of geosynthetic layers was increased. indicating that there is no benefit in using a double GTX layer for the purpose of reinforcement in constructions. In general, even though the double layer gives the high CBR values, the single layer is more effective and

recommended for field application due to materials scarcity and economic reasons where it has the benefit on the budgeting aspect for design and construction.

This conclusion has certain economic implications for optimizing design and construction using these new geogrid and geotextile. And therefore, it is also recommended that more research be done to outline the correlation between CBR values and shear strength parameters.

CONCLUSIONS

Based on the study results of this paper, it can be concluded that embedding of these new types of eco-friendly basalt geotextile and geogrid inside the subgrade soil layers has a significant effect on improving the CBR value. Since it was found that the CBR value increases by a range from 2 to 55 % from the CBR value of the control specimen according to the layering pattern and the used geosynthetic type.

It could also be concluded that there are effective embedment positions for these geosynthetics according to its type to increase the bearing capacity where the highest CBR value (74.61%) was reached by using double layers of GGR on the upper-lower layers and the lowest CBR value (42.25%) was obtained by using the subgrade soil reinforced with one-layer of GGR on the lower soil layer. It was also interesting to note that the double geosynthetic layers patterns are not as beneficial as originally expected when compared to a single upper layer in the case of using GGR and to a single lower layer in the case of using GTX. This conclusion has certain economic implications for optimizing design and construction using these new basalt geosynthetics.

The increment of water content reduced the CBR value of all types of subgrade soil reinforced with geosynthetics which have been examined. The highest CBR value was achieved by the water content of 10.4%.

For practical and economic reasons, it is recommended to use the pattern of GGR upper layer for the field application. Even though the GGR two layers upper-lower pattern gives the highest CBR value, the upper GGR layer is more effective for field applications due to materials supplied and economic reasons. It has a benefit on the budgeting aspect for design and construction when using this type of geosynthetics.

ACKNOWLEDGMENTS

Thanks to Japan International Cooperation Agency (JICA), African Business Education Initiative for collaboration with International Environment Conservation Lab, Graduate School of Bioresources, Mie University, School of Civil Engineering and Surveying, University of Southern Queensland, Australia, Egyptian Airports Company (EAC) and Tsuchiya TSCO Co., Ltd. for the opportunity which they gave me to proceed in this

REFERENCES

[1] Hossain M.B., Sakai T., and Hossain M.Z., Evaluation of Sand/Geosynthetic Interface Behavior for Earth Reinforcement. International Journal of Geosciences Engineering, Vol. 7, No.3, 2013, pp.452-465.

[2] Shukla, S.K., Discussion of Applications of geosynthetics for soil reinforcement by M.I.M. Pinto, Ground Improvement, 7, 2004, pp. 61-72.

[3] Choudhary A.K., Jha J.N., and Gill K.S., A Study on CBR Behavior of Waste Plastic Strip Reinforced Soil. Emirates Journal for Engineering Research, 15 (1), 2010, pp.51-57.

[4] Eltaher M., Hossain M.Z., Shiau J., and Takami H., Ground Improvement Using Geosynthetics A Literature Review. Proceedings of the 5th International Conference on Science, Engineering & Environment (SEE), Bangkok, 11-13 November 2019, an accepted paper.

[5] Basalt Fiber Products Report, Tsuchiya TESCO Co., Ltd., 2nd Ed., 2018, pp. 1-15.

[6] Recommended Descriptions of Geosynthetics Functions, Geosynthetics Terminology, and Graphical Symbols, International Geosynthetics Society, 5th Ed. 2009, pp. 1-31.

[7] Hossain M.Z., and Sakai T., The Effectiveness of Nominal Dosage of Ordinary Cement on Strength and permeability of Clay Soil, Journal of Japanese Society of Soil Physics, No.110, 2008, pp.25-35.

[8] Yildirim B. and Gunaydin O., Estimation of California Bearing Ratio by Using Soft Computing Systems, Journal of Expert Systems with Applications, Vol.38, 2011, pp: 6381-6391.

[9] Test Method for the California Bearing Ratio CBR of Soils in Laboratory, Japan Industrial Standards Committee (JIS-A-1211), 2009.

[10] Satish P., Rural Infrastructure and Growth: An Overview, Indian Journal of Agriculture Economics, 62, 2007, pp. 32-51.

[11] Ekeocha N.E., and Egesi N., Evaluation of Subgrade Soils using California Bearing Ratio (CBR) in Parts of Rivers State, Journal of Applied Sciences Environmental Management, Vol.18, 2, 2014, pp.185-187.

9th Int. Conf. on Geotechnique, Construction Materials and Environment, Tokyo, Japan, 20-22 November 2019, ISBN: 978-4-909106025 C3051

GREEN CONCRETE HOLLOW BLOCKS UTILIZING BASIC OXYGEN FURNACE STEEL SLAG

Santiago, Karen Joyce B.[1]; and Juan, Jose Arnel P. [2]
[1]Faculty, Mariano Marcos State University, Philippines; [2]Faculty, Mapua University, Philippines

ABSTRACT

This study presented the effects of replacement of fine aggregates with high percentages of steel slag (BOF) on the properties of Concrete Hollow Blocks (CHB). The mix proportions of 1:3:4, 1:4:3, and 1:3.5:3.5 (cement: fine aggregates: coarse aggregates) incorporating various percentages of steel slag were designed. Fine aggregate was replaced 25, 50, 75, and 100 percentages of BOF steel slag by volume of fine aggregate. Elemental and chemical tests were conducted to determine the toxicity of BOF slag to the environment and its use as a partial replacement of fine aggregates thru optical microscopy and xrf spectrometer. Compressive test and statistical inference reveal that inclusion of steel slag as partial replacement with fine aggregates in CHB has a greater compressive strength than the conventional CHB. Moreover, the results of the xrf indicates the presence of calcium and iron oxides. Iron oxides, which are non-toxic, have inert, opaque, and water resistant properties. In raw cement manufacturing, calcium oxide and silica oxides are components and considered to be non-toxic.

Keywords: BOF Steel Slag, Compressive Strength, Green Concrete Hollow Blocks, Toxicity

INTRODUCTION

In the Philippines, Concrete Hollow Blocks (CHB) are commonly used for exterior and interior walls of buildings especially residential projects [1]. It is also used for perimeter fence, tank, septic vault, drainage canal, and many more. Fajardo [2] adds that CHBs are classified as bearing and non-bearing blocks. Load bearing blocks are those which thickness ranges from 15 cm to 20 cm and are used to carry load aside from their own weight. Non-bearing blocks, on the other hand, have thickness ranging from 7.5 cm to 10cm blocks and are intended for walls and partition fences carrying their own weight.

Hua-dong and Liu's [3] study as cited in Yi, Xu, Cheng, Wang, Wan and Chen [4] stated that basic oxygen furnace (BOF) steel slag is a solid waste from steel production. This slag is formed when scrap metals, molten iron, and various fluxes like lime are oxidized by injecting large amounts of pure oxygen into the molten mix to create molten steel and molten slag [5].

In the construction industry, concrete is one of the most commonly used material in variety of environment such as dry, water, underground and even in hot or cold climate zones. One of the advantages of concrete is the material's possibility to change its properties depending on the requirements of the construction project and the price. Concrete consists of three components: binder, filler, and water. Natural aggregates with different proportions are the most common filler. However, the status of depleting natural resources especially on natural aggregates is under question. This led to the conduct of studies using alternatives and replacements of natural aggregates using solid waste.

A global sand importer, Omnico Natural Resources (ONRI), has been exporting construction sand from Ilocos Norte, Philippines to Japan and Singapore since 2009. It has also been importing furnace slag aggregates from Taiwan since 2015 to develop a 112 hectare seaport reclamation project in Currimao, Ilocos Norte [6]. However, the use of this slag for embankment and backfilling materials has been stopped by the Ilocos Norte Provincial Quarry Council due to the alleged toxic slag elements. The council needed the slag to be re-examined in its toxicity and threat to the marine ecosystem of Currimao [7]. Due to the discontinue of the use of the BOF steel slag, which appears like mixed gravel and sand and furnace slag steel, wastes are stockpiled in the northern portion of ONRI seaport complex, measuring as high as 20 meters [8].

Yildirim and Prezzi [9] stated that it is essential to have knowledge of the chemical, mineralogical, and morphological properties of steel slag to utilize BOF steel slag as a replacement material in concrete development to produce green concrete. The use of the Currimao BOF steel slag will take care of the environmental issue as well as the scarcity of the use of natural aggregates for concrete. The use of the slag as a partial replacement for fine aggregates will lessen and eventually eliminate the stockpiled BOF steel slag in Currimao. It will address the problem in industrial waste and apply the recycle, reuse, and recover implementing rules and regulation of the Philippine's Ecological Solid Waste Management Act of 2000 (RA 9003)[10].

The study focused on the utilization of the BOF steel slag as a partial replacement of fine aggregates to produce green concrete hollow blocks. Establishment of proportions for the BOF as a partial replacement of fine aggregates was observed and its possibility as a substitute for natural aggregates.

METHODOLOGY

Concrete Mix Design

Sample design mixes of proportions 1:3:4; 1:3.5:3.5; and 1:4:3 (cement: fine aggregates: coarse aggregates) were used as presented in Table 1. The fine aggregates were replaced by BOF steel slag with various percentage replacement of 25%, 50%, 75%, and 100%, respectively.

Elemental Test by Optical Microscopy

Natural aggregates and BOF slag were collected, sorted, and dried before undergoing elemental analysis using OEM optical microscope.

Table 1. Concrete Mix Design

Mixture (Cement : Fine : Course)	Natural Fine Aggregates %	BOF Slag Aggregate %
1:3:4	0	100
	25	75
	50	50
	75	25
	100	0
1:3.5:3.5	0	100
	25	75
	50	50
	75	25
	100	0
1:4:3	0	100
	25	75
	50	50
	75	25
	100	0

Material Characterization

Natural aggregates and BOF steel slag were pulverized and characterized by the handheld X-Ray Fluorescence Spectrometer.

Slump Test

All procedures and test methods conducted were in accordance with ASTM C143, "Standard Test Method for Slump of Hydraulic-Cement Concrete" specification. Slump was maintained at 5 inches for all mix designs.

Compressive Strength of Cylindrical Concrete Specimens

One hundred fifty (150) 4 x 8 inches concrete cylinders have been tested in the uni-axial compressive test in order to obtain compressive strength. Every five (5) concrete cylinders was tested, respectively, on the same age set to 14^{th} and 28^{th} day period. The development of compressive strength of BOF steel slag aggregate at the age of 14 and 28 days was investigated.

Green Concrete Hollow Blocks Development

BOF steel slag was incorporated in the production of CHB to produce green concrete hollow blocks. Based on the results of the compressive test of the cylindrical samples, the mixture with the highest compressive strength value served as the proportion to be used in the fabrication of the green concrete hollow blocks.

RESULTS AND DISCUSSIONS

Optical Microscopy

The results obtained from the optical microscopy shows that the sample course aggregate had a 12.21mm diameter. This value conforms to the standard size used in concrete mix wherein the usual range employed is between 9.5mm and 37.5mm in diameter. Likewise, the sample fine aggregate had 1.432mm and 1.064mm diameter, respectively. Lastly, the result obtained for BOF steel slag aggregate had 1.218mm and 1.163mm diameter, as shown in Fig. 1. These values of fine aggregates and BOF steel slag conforms to the standard size of fine aggregate used in concrete mix with a range less than 9.5mm.

Figure 1. BOF steel slag

Table 2. Traced Chemical Composition of BOF Steel Slag

Element	PPM	+/-
Ca	37.61%	0.3706%
Fe	23.99%	0.2423%
LE	16.32%	0.2215%
Si	7.72%	0.1664%
Mg	7.10%	0.8808%
Al	3.38%	0.1362%
Mn	1.90%	0.0305%
P	1.34%	0.0266%
Ti	3072	286.68
Cr	1010	81.84
S	936	61.47
V	509	123.64
Sr	259	6.57
Zn	178	14.08
Cu	142	17.84
Nb	93	5.11
Zr	82	4.54
Ni	69	21.12
Pb	25	7.30
Mg	21	3.64
Se	9	2.89

Material Characterization

Table 2 shows the weight percentage of the element present on BOF steel slag. Its main chemical constituents are CaO, FeO/ Fe_2O_3, and SiO_2. The iron oxide (FeO/ Fe_2O_3) content of BOF slag was 23.99% which could be as high as 31%. This is the amount of oxidized iron that cannot be recovered during the conversion of molten iron into steel. The silica (SiO_2) content of BOF slag was 7.72% ranging from 6.9449% to 8.4951%. The Al_2O_3 and MgO contents were 3.38% and 7.10% ranging from 2.92-3.84% and 0.84-13.35%, respectively. Large quantities of lime were used during the process of conversion from iron to steel; hence, the CaO content of BOF steel slag was 37.61%, which was typically very high (CaO>35%).

In Table 3, Calcium oxides (ranges from 52.25 % to 72.15% parts per million) and iron oxide (ranges from 25.99 % to 42.61% parts per million) are the two major chemical constituent of BOF steel slag. According to Egirani, Latif, Poyi, Wessey and Acharjee [11] as discussed by Ohimain [12], oxides of iron ore are highly values and possess non-toxic, inert, opaque and water resistant properties. Calcium oxide and silica oxides are likewise non- toxic substances since these oxides are raw materials in producing raw cement [13].

Table 3. Oxides present in BOF Steel Slag

	Range Percentage (%)	
Oxides	Low	High
CaO	33.12	72.13
Fe_2O_3	25.99	42.61
SiO_2	13.77	19.26
MgO	1.40	22.15
Al_2O_3	5.52	7.26
MnO	2.38	2.53
P_2O_5	2.99	3.15

Compressive Strength Test

One hundred fifty cylindrical samples were subjected to compressive test. On the 14th and 28th days of curing, the cylindrical samples were tested at the Universal Testing Machine (UTM) to determine their compressive strength. The 150 samples comprised of 3 mixture proportions, namely 1:3:4, 1:4:3, and 1:3.5:3.5 (cement: fine sand: coarse aggregate) with different percentages of fine aggregates replaced by BOF steel slag of percentages 0%, 25%, 50%, 75%, and 100%, respectively.

Five samples on different percentages of slag (0%,25%,50%,75% and 100%) on the different proportions of cement, fine sand, and coarse aggregate (1:3:4, 1:4:3, and 1:3.5:3.5) were subjected to compressive test as presented in Table 4. From Fig. 2, it was presented that the proportion 1:3:4 (cement: fine sand: coarse aggregate) with 25% partial replacement of BOF slag had the highest compressive strength of 4.34 MPa. Furthermore, five samples on different percentages of slag (0%, 25%, 50%, 75%, and 100%) on the different proportions of cement, fine sand, and coarse aggregate (1:3:4,1:4:3, and 1:3.5:3.5) were subjected to compressive test as presented in Table 4 for 28 days curing. It presented that the proportion 1:3:4 (cement: fine sand: coarse aggregate) with 75% partial replacement of BOF slag had the highest compressive strength of 5.38 MPa.

The proportion of 1:3:4 (cement: fine sand: coarse aggregate) significantly presents a higher compressive strength compared to the conventional mix. In the mixture, the 25% BOF steel slag replacement attained the highest value of compressive strength for a 14-day-old concrete while a 75% BOF steel slag replacement attained the highest compressive strength for a 28-day-old concrete. Results indicate that the use of BOF steel slag in the 1:3.5:3.5 proportion yields a lower compressive strength than

those of the conventional mix made from the similar mix proportions.

In addition, there was a difference among the compressive strength of concrete which depended upon the percentage of BOF steel slag it contained. There was also a significant increase of the mean compressive strength between the 14 day age and 28 day age. The highest compressive strength of concrete was considered for the 28 day age since their mean values were significantly higher than the mean compressive strength of the 14 day age. For the mixture 1:3:4, 75% replacement of BOF steel slag showed the highest compressive among the different replacement with the value 5.38 MPa. In the mixture 1:4:3, 50% replacement of BOF steel slag presented the highest compressive strength of 4.39 MPa. While in the 1:3.5:3.5 mixture, 100% replacement of BOF steel slag had the highest mean compressive strength of 5.33MPa. Although the value of the mean compressive strength of the 100% BOF steel slag replacement was high, the values presented in the 1:3.5:3.5 proportions were not recommended since the values were all lower than the compressive strength of the control sample (0% BOF steel slag replacement) which was 5.53MPa.

Table 4. Comparison of Compressive Strength

Mixture	Percentage Replaced by BOF (%)	Compressive Strength, MPa 14 day Age	28 day Age
	0% BOF	2.76	4.84
	25% BOF	4.34	5.28
	50% BOF	3.06	5.31
	75% BOF	2.86	5.38
1:3:4	100%BOF	2.84	4.44
	0% BOF	3.11	3.65
	25% BOF	2.47	4.25
	50% BOF	3.01	4.39
	75% BOF	2.71	4.34
1:4:3	100%BOF	2.47	4.29
	0% BOF	3.21	5.53
	25% BOF	2.32	3.31
	50% BOF	2.42	3.85
	75% BOF	2.57	4.74
1:3.5:3.5	100%BOF	3.31	5.33

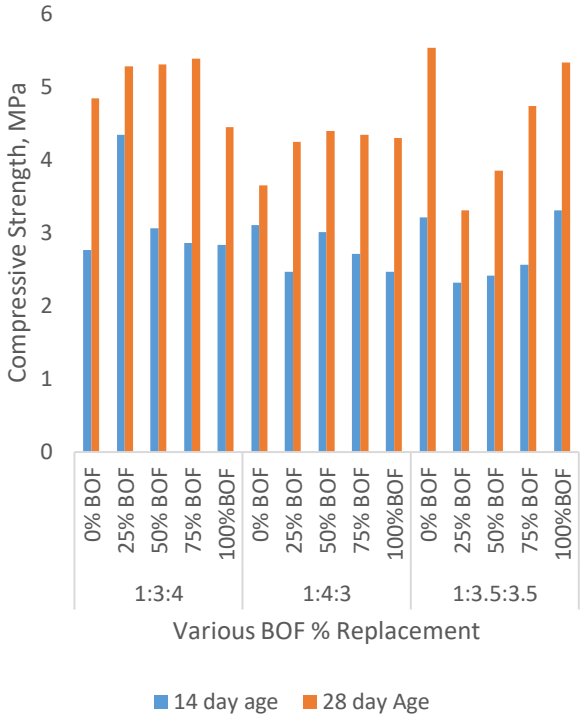

Figure 2. Comparison of compressive strength of various BOF percentages

Statistical Analysis T Test

The t-test analysis with 95% confidence is presented in Table 5. In the design mix 1:3:4, the t critical 2.54 was higher than the t actual 1.20 and the p value of 0.28 was higher than the level of significance. There was no significance between the control mix and the highest compressive strength generated of the design mix 1:3:4. However, this design mix actually generated the highest compressive strength among the mixes. Likewise, the two design mixes of 1:4:3 and 1:3.5:3.5, showed that most of the t actual was greater than the t critical ($t_{actual} > t_{critical}$). Moreover, the p values of these two design mixes were less than 0.05, the level of significance. Hence, the results show that there is a significance difference between the control mix and the fine aggregates replaced by BOF steel slag in the design mix 1:4:3 and 1:3.5:3.5. Likewise, the presence of BOF slag in the mixture of concrete increases the compressive strength of the concrete.

Table 5 Statistical Analysis T test for the compressive strength of concrete of all design mixes

Parameters	Mix Design		
	1:3:4	1:4:3	1:3.5:3.5
Compressive Strength, Control Design Mix, MPa	4.84	3.65	5.53
Highest Compressive Strength, MPa	5.38	4.39	5.33
Fine aggregates replaced by BOF steel slag, %	75	50	100
T actual	1.20	20.91	2.71
T critical	2.45	2.45	2.45
P value	0.28	0	0.04

Figure 3. Green CHB

Development of Green Concrete Hollow Blocks

The proportion 1:3:4 served as the basis for the fabrication of the green concrete hollow blocks since it generated the highest compressive strength of 5.38 MPa. Conventional procedure in the fabrication of hollow blocks was implemented. Fine aggregates were replaced by 75% BOF steel slag. After the molding of green CHB, a maximum of 10 days curing was observed to attain its maximum strength.

CONCLUSION

Green concrete, also known as a sustainable or 'high performance' concrete, uses sustainable materials which are made from recyclable materials or green materials. They are more efficient than the traditional products because they require fewer resources to produce. Green concrete is a material that exhibits better functional performance and capabilities than ordinary concrete. It is considered a maintainable construction material as it consumes less natural resources and less energy and emits a smaller amount of carbon dioxide. The concrete wastes are slag, power plant wastes, recycled concrete, mining and quarrying wastes, waste glass, incinerator residue, red mud, burnt clay, sawdust, combustor ash and foundry sand.

The results obtained from the optical microscopy shows that the BOF steel slag conforms to the standard size of fine aggregate used in concrete mix with a range less than 9.5mm. In determining the elements and oxides present in pure BOF steel slag specimen, it was found out that it contained oxides that had similar elements to the results of the previous studies. Calcium oxides (ranges from 52.25 % to 72.15% parts per million) and iron oxide (ranges from 25.99 % to 42.61% parts per million) are the two major chemical constituent of BOF steel slag. Iron oxides, which are non-toxic, have inert, opaque, and water resistant properties. In raw cement manufacturing, calcium oxide and silica oxides are components and considered non-toxic. Thus it can be concluded that the BOF steel slag treated specimen does not contain any toxic and harmful elements that can harm the environment. The slag can then be used as a suitable material for replacement of natural aggregates and can be categorized as a sustainable material to produce green concrete products.

This study attempts to optimize and develop proportions that can include steel slags as an ingredient for concrete hollow block. BOF slag replaced a certain percentage of fine natural aggregates and the specimens were tested according on the specimens curing days. Concrete hollow block proportion 1:4:3 has the highest value for compressive strength of a fourteen-day old CHB having a value of 4.34 MPa with 50% fine aggregate replacement by BOF steel slag. Likewise, concrete hollow block proportion of 75% replacement from the 1:3:4 proportion governed the value for compressive strength of a twenty-eight-day old concrete hollow block with a compressive strength of 5.38 MPa.

Based on statistical analysis, there was a great significance of the replacement of BOF steel slag in the concrete mixture. There was a significant increase of the compressive strength of concrete as the percentage

of BOF replacement also increases until it reaches its maximum strength. Also, the three mixture proportions were treated independently and presented increase of compressive strength as its age from 14 to 28 days, as well as the addition of BOF steel slag as a replacement of fine sand. As the percentage of fine aggregates replaced by steel slag increased, compressive strength of concrete samples slowly increased.

It can be concluded that BOF steel slag can be used as an aggregate in the manufacture of concrete hollow blocks. It can reduce the solid wastes present in Currimao, Ilocos Norte as well as environmental impacts. Moreover, the use of BOF steel slag makes it possible to reduce the consumption of natural sand which causes potential environmental damage in riverbeds.

REFERENCES

[1] Rabena, A. R. & Aman, N. V.. (2010). Analysis on the Strength of 5" CHB with Oyster Shell as Component of the Aggregates. *UNP Research Journal, 19(1)*. Retrieved from http://ejournals.ph/form/cite.php?id=6891

[2] Fajardo, M. B. (1980). *Simplified Construction Estimate*. National Bookstore.

[3] Hua-dong, M. E. N. G., & Liu, L. I. U. (2009). Stability processing technology and application prospect of steel slag [J]. *Steelmaking*, *25*(6), 74.

[4] Yi, H., Xu, G., Cheng, H., Wang, J., Wan, Y., & Chen, H. (2012). An overview of utilization of steel slag. Procedia Environ Sci 16: 791–801.

[5] Shi, C. (2004). Steel slag—its production, processing, characteristics, and cementitious properties. *Journal of Materials in Civil Engineering*, *16*(3), 230-236.

[6] Ilocos Norte's Global Sand Exporter Pushes Private Seaport Reclamation Project. (2015). *Northbound Philippines News Online*. Retrieved from http://northboundasia.com/2015/12/07/ilocos-nortes-global-sand-exporter-pushes-private-seaport-reclamation-project/

[7] Ilocos Norte Gov't Halts Importation of Alleged Toxic Materials for Port Expansion Project. (2015). *Balita*. Retrieved from http://balita.ph/2015/04/17/ilocos-norte-govt-halts-importation-of-alleged-toxic-materials-for-port-expansion-project/

[8] Adriano, Leilanie. (2015, April 17). Entry of 'toxic' materials for port project stopped. *Inquirer*. Retrieved from http://newsinfo.inquirer.net/685993/entry-of-toxic-materials-for-port-project-stopped#ixzz58NUrPQsT

[9] Yildirim, I., & Prezzi,M. (2011). Chemical, Mineralogical, and Morphological Properties of Steel Slag. *Advances in Civil Engineering*, 1-13.

[10] Sapuay, G. P. (2005, July). Ecological Solid Waste Management Act of 2000 (RA 9003): a major step to better solid waste management in the Philippines. In *International Conference on Integrated Solid Waste Management in Southeast Asian Cities, Siem Reap* (pp. 51-59).

[11] Egirani, D. E., Latif, M. T., Poyi, N. R., Wessey, N., & Acharjee, S. (2018). Genesis, Uses and Environment Implications of Iron Oxides and Ores. In *Iron Ores and Iron Oxide Materials*. IntechOpen.

[12] Ohimain, E. I. (2013). Scrap iron and steel recycling in Nigeria. *Greener Journal of environmental Management and public safety*, *2*(1), 1-9.

[13] Li, X., Yu, H., & Yuan, M. (2012). Modeling and optimization of cement raw materials blending process. *Mathematical Problems in Engineering*, *2012*.

9th Int. Conf. on Geotechnique, Construction Materials and Environment, Tokyo, Japan, 20-22 November 2019, ISBN: 978-4-909106025 C3051

CONCRETE STRUCTURES INTERACTING WITH SUBSOIL DEPENDING ON THE USE OF SLIDING JOINT

Michal Kropacek[1], Petr Mynarcik[2] and Radim Cajka[3]
[1, 2, 3]Faculty of Civil Engineering, VSB – Technical University of Ostrava, Czech Republic

ABSTRACT

Article describes the interaction of concrete structure (usually foundation structure or industrial floor) with subsoil, where unwanted friction occurs. Friction can be reduced with sliding joint. This generally known assumption is followed by research described in the article, which determines the effectiveness of sliding joints with respect to concrete volume changes on large-dimensional specimens. Large-dimensional specimens with dimension of 150 x 500 x 6000 mm were placed in the laboratory and outdoor environment, defining different boundary conditions. The research included various concretes in the same strength class and various sliding joints that respect the requirements of construction practice. The paper also describes the comparison of measured results with calculation models from technical standards and regulations, which allow calculation of volume changes on concrete structures. Regarding the subsoil and the sliding joint, this is one of the main long-term goals of the research, since the calculation models do not take these two parameters into account. Deformations from volume changes then deviate significantly from theoretical calculations, as friction in the sliding joint area affects the magnitude and course of volume changes.

Keywords: Concrete, Foundation, Subsoil, Sliding Joint, Volume changes

INTRODUCTION

When designing concrete structures, usually flat foundations and industrial floors, the subsoil has a major impact on the behavior of these structures. This is a well-known phenomenon and is also based on the regulations used to design these structures. In conjunction with the subsoil, a sliding joint is used on the footing bottom to reduce friction (for example, in connection with undermining, prestressing, etc.). The use of sliding joints is a long-term scientific topic of the Faculty of civil engineering, VSB – Technical University of Ostrava, where they are verified by experiments calculations for various types of concrete structures and sliding joints. Various boundary conditions and load methods enter to these calculations. [7], [8], [9], [10], [11], [13], [14], [15], [16], [17], [21], [30], [35], [36]

One of the branches of this research is the use of sliding joint in interaction with volume changes of concrete. From the perspective of concrete structures, volume changes cause unwanted friction on the base-subsoil. These volume changes caused by hydration of cement or also by the ambient temperature lead to stress that can lead to undesirable cracks [2], [3], [28], [29], [31], [32], [33].

For this reason, a sliding joint is used which allows friction to be reduced on this footing bottom. The sliding joint can also be understood as a simple treatment of the footing bottom, as evidenced by the friction coefficients in Tab. 1, where various subsoils and sliding joints are simulated. Mostly, however, the sliding joint is understood as an interlayer composed of one or more layers of different materials providing lower friction. The first option is a composition, where one or more layers are made of foil (PE, PVC) and between them can be, for example, sand or geotextile. The second option is to use asphalt membranes of different thickness and compositon, where viscoelastic properties of asphalt are used.[5], [6], [12], [17], [20], [24], [34]

Table 1 Friction coefficient for subsoil [34]

Base layer	Sliding joint	Friction coefficient
Gravel	No	1,4 – 2,1
Sand	No	0,9 – 1,1
Cohesive soil	No	0,5 – 0,8
Base concrete smooth	1 layer PE foil	0,8 – 1,4
Base concrete smooth	2 layers PE foil	0,6 – 1,0
Base concrete rough	2 layers PE foil	max. 2,0 (h=0,3m) max. 1,3 (h≥1,5m)
Base concrete rough	1 or 2 layers bitumen membr.	avg. 0,45 (h=0,3m) avg. 0,2 (h≥1,5m)

Note: h – thickness of foundation slab

The long-term intention of the author's research is to determine the volume changes of concrete in interaction with the use of sliding joint. Several practical experiments were conducted on this subject, and the results were further used as a basis for comparison by calculation models. From experiments performed on large-dimensional specimens, it was found that even one layer of PE foil can serve as an effective sliding joint (depending on the subsoil) and thus significantly different volume changes of concrete were measured in the laboratory and outdoor environment. The results also differ considerably from calculation models, which are currently the most widely used [22]. It is calculation model from the technical standard EN 1992-1-1 [18], a refined model of regulation Model Code 2010 [23], the American model ACI 209R-92 [1], and the most detailed model of a team Professor Bazant model B4 [4]. All these listed calculation models for determining final concrete shrinkage do not consider the effects of subsoil and possible sliding joint. [25], [26], [27]

EXPERIMENTAL PART

The main part of the experiment was the production of six large-dimensional specimens, which were made of two types of concrete. The first concrete was steel fiber reinforced concrete in strength class C 30/37-X0 and the second concrete was plain concrete in the same strength class C 30/37-XC4. Both concretes have been designed fully in accordance with technical standard EN 206 [19], with the intention that both concretes have the same composition. Minor variations in the composition of the concrete components are caused by the use of steel fibers. This made it possible to directly compare the effect of dispersed reinforcement.

Six large-dimensional specimens with dimensions of 150 x 500 x 6000 mm were made with the emphasis on building practices, where laboratory results on small specimens need to be verified. The dimensions of the specimens simulate the dilatation unit and correspond proportionally to the real structure. Of the total number of specimens, three specimens were placed in a test hall simulating laboratory conditions (hereafter referred to as laboratory) and three specimens were placed in outdoor environment. Two types of sliding joints were chosen for this experiment and the combination with the proposed concrete was as follows. Three combinations were chosen for laboratory and outdoor environments. The first pair of specimens was a combination of fibreconcrete and sliding joint from the asphalt membrane. The second pair of specimens was composed of fibreconcrete and two layers of PE foil with an intermediate layer of geotextile. The last pair of specimens consisted of plain concrete and the same type of asphalt membrane as in the first pair of specimens. The asphalt membrane was selected with a thickness of 4 mm based on modified asphalt (SBS) with sand on the strip surface and PE foil on the bottom. Volume changes, including temperature sensing, were measured inside of specimens using the EDS-20-E string strain gauges. Three string strain gauges were fitted in each specimen at a spacing of 1,5 m from the specimen edge along the length. The strain gauges were at a height of 50 ± 10 mm from the bottom of the specimen, see Fig. 1, where the location of the strain gauges can be seen together with the sliding joint from the asphalt membrane and the prepared formwork.

Fig. 1 Installation of string strain gauges

The concrete was cast into the prepared formworks directly from the truck mixer using a trough and compacted by submersible vibrators. After the concrete was casted, the curing was started immediately. Curing of concrete was performed for 5 days by spraying with water on specimens that were covered with geotextile, see Fig. 2.

Fig. 2 Large-dimensional specimens in laboratory during concrete curing

At the end of the curing, the specimens in laboratory were exposed to conditions with

temperature of 20 ± 2 °C and relative humidity of air 55 ± 5 %, the specimens stored outside the laboratory were fully exposed to ambient conditions.

EVALUATION OF RESULTS

The results were continuously evaluated at time 100 days, which is a sufficiently long period since concrete is usually evaluated in accordance with the regulations for a 28-day period. Since the article describes the interaction of concrete with subsoil, it is not an object to describe in depth concrete technology and processes occurring in concrete during hydration. That is why only graphs showing the comparison of volume changes (shrinkage) of concrete with calculation models are presented in the article and there are no detailed results of individual specimens with boundary conditions. A more detailed evaluation focused on concrete technology will be the subject of another article, but it is certain that specimens in the laboratory undergo different volume changes than specimens in the outdoor environment.

Specimens swell at the start of setting and hardening, and no shrinkage occurs during the curing period. However, since the calculation models do not consider initial swelling, the measured results from the experiment had to be customized. Specimens began to shrink after the end of the curing, which was the time defined as “zero” value, and from that time the volume changes read from the string strain gauges were further measured. The following calculation models were used for comparison with experimental results. Calculation model from EN 1992-1-1, Model Code 2010, ACI 209R-92 and Model B4.

Because of the stable conditions and thus the limitation of the external influences, it is advantageous to evaluate the results separately for the specimens placed in the laboratory and specimens placed in the outdoor environment. Figure 3 shows a graph of the comparison of the results on the specimens in the laboratory with the results of the calculation model. As mentioned above, drying shrinkage occurs in the laboratory after the curing is finished. All other volume changes can be neglected or cannot occur in a laboratory environment. For this reason, the shrinkage curves are continuous and have a regular course. This is important for comparing specimens to each other and for comparison to specimens placed in outdoor environment where more influences enter the experiment and it is not easy (or even possible) to accurately evaluate the volume changes or behavior of the specimens interacting with the subsoil. It can be seen from the graph in Fig. 3 that the combination of plain concrete and sliding joint from the asphalt membrane has the largest shrinkage. This result corresponds to the assumption, since the plain concrete without dispersed reinforcement is to generate the largest shrinkage and the asphalt membrane provides low friction. From the graph describing only shrinkage, the results of fibreconcrete is identical regardless of the sliding joint used. The results show that steel fibers in concrete regulate concrete shrinkage. Compared to calculation models, the measured results are comparable to the model assumptions of the technical standard EN 1992-1-1, which is in line with the requirements of a safe design. In contrast, the measured results differ significantly from the assumption of model B4. The other two models also differ. The results confirm considerably different behavior when using sliding joint.

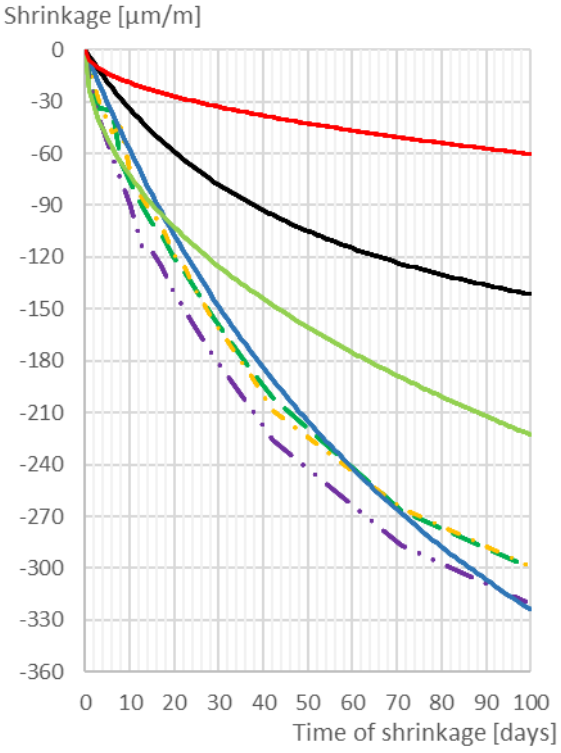

Fig. 3 Comparison of specimens from laboratory with calculation models. Legend: Dashed line – Fibreconcrete / Asphalt membrane; Dashed line one dot – Fibreconcrete / (PE foil + Geotextile + PE foil); Dashed line two dots – Concrete / Asphalt membrane; Blue line – EN 1992-1-1; Green line – MC 2010; Black line – ACI 209R-92; Red line – Model B4

When evaluating specimens from the outdoor environment, the situation is more complicated. Other boundary conditions, such as varying temperature, relative humidity of air and possibly precipitation, affect the measurement. In addition to drying shrinkage, thermal expansion also affects the volume changes. Since the specimens are in outdoor environment, they can be constantly doped with water and the average higher relative humidity of air also

ensures a slower shrinkage of the concrete specimens. Thus, it can be seen from the graph of Fig. 4 that the specimens alternately shrink and swell over time. The shrinkage of concrete is undoubtedly continuous, but shrinkage is outweighed by the expansion of the concrete due to changes in temperature and water supply. An important role is played by the use of a sliding joint that reduces friction and allows the specimen to move horizontally. For the reasons given above, it is very difficult to evaluate any trend, but the largest shrinkage again generates plain concrete in combination with the asphalt membrane sliding joint. The lowest shrinkage (but the largest volume changes) has a specimen of fibreconrete with a sliding joint from the PE foil + geotextile + PE foil. This finding again confirms the trend of laboratory results and the need to use dispersed reinforcement to control concrete shrinkage.

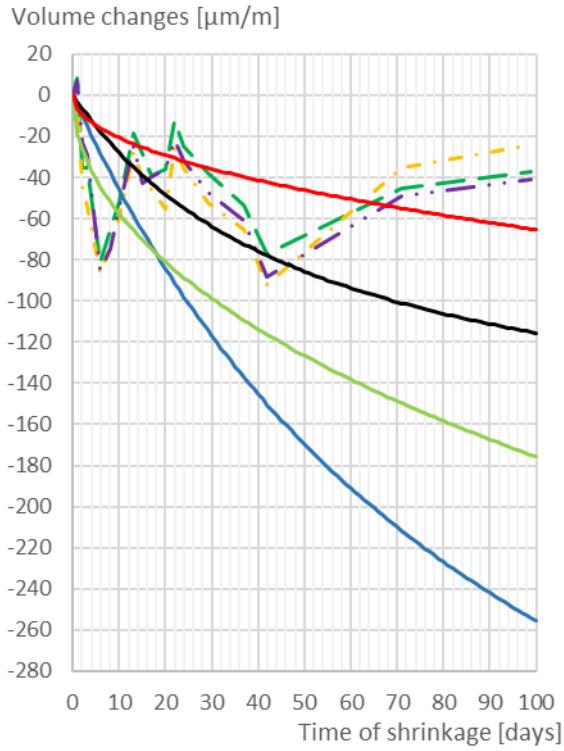

Fig. 4 Comparison of specimens from outdoor environment with calculation models. Legend: Dashed line – Fibreconcrete / Asphalt membrane; Dashed line one dot – Fibreconcrete / (PE foil + Geotextile + PE foil); Dashed line two dots – Concrete / Asphalt membrane; Blue line – EN 1992-1-1; Green line – MC 2010; Black line – ACI 209R-92; Red line – Model B4

Comparison of results with calculation models is significantly different from specimens in the laboratory. Regarding the different behavior of specimens in an outdoor environment, the B4 model is closest to the measured results. Calculation model from technical standard EN 1992-1-1 provides significantly oversized results, but the results are consistent with safe design of concrete structure. These results demonstrate that calculation models do not reflect the effect of sliding joint, which reduces friction and allows the concrete specimen to make volume changes easier.

CONCLUSIONS

An experiment dealing with the interaction of the sliding joint with the concrete specimen provides unique results in several areas. When designing concrete foundations as well as industrial floors, it is always necessary to consider and assess the influence of horizontal forces resulting from the load. However, horizontal forces also arise within the concrete structure through volume changes from hydration or climatic conditions. Large volume changes and high friction at the footing bottom result in high stress inside the structure, which can lead to cracks and weaken the durability of concrete. For this reason, sliding joints are designed in the footing bottom to reduce friction and allow concrete "free" volume changes. The results from experiment show that when using dispersed reinforcement in concrete, the volume changes of fibreconcrete compared to plain concrete are reduced. Steel fibres mixed into concrete have a positive effect on reducing volume changes (mainly shrinkage) in early stages of setting and hardening of concrete. This is particularly evident in laboratory specimens where only drying shrinkage occurs. As mentioned above, the use of sliding joints has its clear reason and importance. In direct comparison of selected sliding joint (and recalculation of results for use with calculation models), the actual use of sliding joint is particularly important. 4 mm thick asphalt membrane and formation of PE foil – geotextile – PE foil do not offer significant differences in friction coefficient.

Comparison of results with calculation models is another separate area to which the author has long focused. Calculation models allow to determine long-term final shrinkage of concrete. The lack of all current models is that they do not reflect initial swelling of concrete during the curing, do not reflect effect of dispersed reinforcement and, above all, do not reflect the influence of subsoil and sliding joint. There are only theoretical sub-calculations that work with a coefficient of friction, but these are not included in calculation models together with other effects such as concrete composition, temperature, relative humidity and time. The results point to the fact that large-dimensional concrete specimens behave very differently from the assumption of calculation models, especially in real conditions of concrete casting and construction conditions. The research of the volume changes of concrete in

interaction with the sliding joint is further focused on high performance and high strength concrete. The results will be further compared with calculation models with an emphasis on friction.

ACKNOWLEDGMENTS

This outcome has been achieved with the financial support of MEYS by the project of "The conceptual research and development 2019" in the Faculty of Civil Engineering, VSB TU – Ostrava.

REFERENCES

[1] American Concrete Institute – ACI, Guide for Modeling and Calculating Shrinkage and Creep in Hardened Concrete, American Concrete Institute, 2008.

[2] Baleviius R., Augonis M., Bistrickait R. and Dilinas S., Shrinkage effect on cracking resistance of flexural reinforced concrete members, Mechanika, Vol. 24 (1), 2017, pp. 11-18, DOI:10.5755/j01.mech.24.1.17901.

[3] Bandeli B., Saje D., Sustersic J., Lopatic J. and Saje F., Free shrinkage of high performance steel fiber reinforced concrete, Journal of Testing and Evaluation, Vol. 39 (2), 2011, DOI: 10.1520/JTE103028.

[4] Bazant Z, RILEM draft recommendation: TC-242-MDC multi-decade creep and shrinkage of concrete, Model B4 for creep, drying shrinkage and autogenous shrinkage of normal and high strength concretes with multi-decade applicability, Materials and Structures, Vol. 48, 2015, pp. 753-770.

[5] Bazant Z., Kristek V. and Vitek J., Drying and cracking effects in box – girder bridge segment, J Struct Eng. Vol. 118(1), 1992, pp. 305-321.

[6] Bilcik J., Sonnenschein R., Measures to Reduce the Formation of Early-Age Through Cracks in Foundation Slabs, Beton TKS, Vol. 18, 2018, pp. 46-50.

[7] Cajka R., Analytical derivation of friction parameters for FEM calculation of the state of stress in foundation structures on undermined territories, Acta Montanistica Slovaca, Vol. 18 (4), 2013, pp. 254-261, ISSN: 13351788

[8] Cajka R., Determination of Friction Parameters for Soil – Structure Interaction Tasks. 7th WSEAS International Conference on Continuum Mechanics, Energy, Environmental and Structural Engineering Series, Vol. 4, 2012, pp. 435-440, ISSN 2227-4359.

[9] Cajka R., Soil-structure interaction in case of expectional mining and flood actions, Improvement of Buildings' Structural Quality by New Technologies – Proceedings of the Final Conference of Cost Action C12, 2005, pp. 369-376.

[10] Cajka R., Burkovic K. and Buchta V., Foundation Slab in Interaction with Subsoil. Advanced Materials Research, Vol. 838-841, 2013, pp. 375-380, DOI: 10.4028/www.scientific.net/AMR.838 -841.375, ISSN 1662-8985.

[11] Cajka R., Manasek P., Numerical analysis of the foundation structures with sliding joint, Eleventh East Asia-Pacific Conference on Structural Engineering & Construction – Building a Sustainable Environment, Taipei, Taiwan, 2008, pp. 716-717, ISBN 978-986-80222-4-9.

[12] Cajka R., Manasek P., Effect of friction in the subsoil on the tension of fiber concrete floors, Conference Proceedings of the Conference with International Participation FC 2005 – Fiber concretes, Vol. 3, 2005, pp 237-242.

[13] Cajka R., Mateckova P., Modelling of foundation structure with slide joint depending up the temperature, 9th International Symposium on High Performance Concrete – Design, Verification & Utilization. Rotorua, New Zealand, 2011, ISBN 978-0-476-19028-6.

[14] Cajka R., Mateckova P., Temperature Distribution of Slide Joint in Reinforced Concrete Foundation Structures, 17th International Conference on Engineering Mechanics, Engineering Mechanics, 2011, pp. 95-98, ISBN 978-80-87012-33-8.

[15] Cajka R., Mynarcik P. and Labudkova J., Experimental measurement of soil-prestressed foundation interaction, International Journal of GEOMATE, Vol. 10 (4), 2016, pp. 2101-2108.

[16] Cajka R., Labudkova J., Comparison of Analysis of Linear Inhomogeneous and Nonlinear Half-Space in Foundation-Subsoil Interaction, International Journal of Mechanics, Vol. 10, 2016, 99. 90-98, ISSN 1998-4448.

[17] Cajka R., Sekanina D., Interaction between prestressed foundations and subsoil – influence of shear stress in contact area onto state of stress in foundation, Eleventh East Asia-Pacific Conference on Structural Engineering & Construction – Building a Sustainable Environment, Taipei, Taiwan, 2008, ISBN 978-986-80222-4-9.

[18] CSN EN 1992-1-1, Eurocode 2: Design of concrete structures – Part 1-1: General rules and rules for building, Czech standards institute, 2006.

[19] CSN EN 206, Concrete – Specification, performance, production and conformity, Czech Office for Standards, Metrology and Testing, 2014.

[20] Hornikova K., Foglar M., Kolisko J. and Kolar J., Experimental and Numerical Assessment of Slab-on-grade Friction Coefficient, Beton TKS, Vol. 16, 2016, pp. 42-49.

[21] Hrubesova E., Mohyla M., Lahuta H., Bui T.Q. and Nguyen P.D., Experimental analysis of

stresses in subsoil below a rectangular fiber concrete slab, Sustainability, Vol. 10 (7), 2018, DOI: 10.3390/su10072216.

[22] Chylik R., Fladr J., Bily P., Trtik T. and Vrablik L., An analysis of the applicability of existing shrinkage prediction models to concretes containing steel fibres or crumb rubber, Journal of Building Engineering, Vol. 24, 2019, DOI: 10.1016/j.jobe.2019.02.021.

[23] International Federation for Structural Concrete FIB, Model code 2010: first complete draft, Fédération internationale du béton, 2010.

[24] Janulikova M., Comparison of the Shear Resistance in the Sliding Joint between Asphalt Belts and Modern PVC Foils, Applied Mechanics and Materials, 2014, pp. 501-504, DOI: 10.4028/www.scientific.net/AMM.501-504.945.

[25] Kropacek M., Experimental measurement of volume changes of cement composites using Portland cements from different locations, WSEAS Transactions on Applied and Theoretical Mechanics, Vol. 13, 2018, pp. 193-198.

[26] Kropacek M., Cajka R., Experimental measurement and calculation of volume changes of concrete specimens, WSEAS Transactions on Applied and Theoretical Mechanics, Vol. 13, 2018, pp. 29-36.

[27] Kropacek M., Cajka R., Measurement of Volume changes of Cement Concrete in Large-Dimensional Samples, Solid State Phenomena, Vol. 272, 2018, pp. 102-106.

[28] Kucharczykova B., Danek P., Kocab D. and Misak P., Experimental Analysis on Shrinkage and Swelling in Ordinary Concrete, Advances in Materials Science and Engineering, 2017, DOI: 10.1155/2017/3027301.

[29] Marusic E., Stiimer N., Autogenous shrinkage and expansion related to compressive strength and concrete composition, Journal of Advanced Concrete Technology, Vol. 14 (9), 2016, pp. 489-501, DOI: 10.3151/jact.14.489.

[30] Mynarcik P., Cajka R., Experimental testing of post-tensioned concrete industrial floor model – Subsidence analysis, International Journal of Mechanics, Vol. 10, 2016, pp. 33-38, ISSN 1998-4448.

[31] Navratil J., Cajka R., Crack control in reinforced concrete liquid retaining structures, Materials Science Forum, Vol. 893, 2017, pp. 410-415, DOI: 10.4028/www.scientific.net/MSF.893.410

[32] Saje D., Bandeli B., Sustercic J, Lopatic J. and Saje F., Autogenous and drying shrinkage of fibre reinforced high-performance concrete, Journal of Advanced Concrete Technology, Vol. 10 (2), 2012, pp. 59-73, DOI: 10.3151/jact.10.59.

[33] Saje D., Bandeli B., Sustercic J, Lopatic J. and Saje F., Shrinkage of Polypropylene Fiber-Reinforced High-Performance Concrete, Journal of Materials in Civil Engineering, Vol. 23 (7), 2011, pp. 941-952, DOI: 10.1061/(ASCE)MT. 1943-5533.0000258.

[34] Schweighofer A. & Kollegger J., Reibungsfreie Gleitlagerung für vorgespannte Bodenplatten, Beton und Stahlbetonbau, Vol. 108, 2013, pp 335-345.

[35] Sucharda O., Bilek V., Smirakova M., Kubosek J. and Cajka R., Comparative Evaluation of Mechanical Properties of Fibre-Reinforced Concrete and Approach to Modelling of Bearing Capacity Ground Slab, Periodica Polytechnica – Civil Engineering, Vol. 61 (4), 2017, pp. 972-986, ISSN: 0553-6626, DOI: 10.3311/PPci.10688.

[36] Sucharda O., Smirakova M., Vaskova J., Mateckova P., Kubosek J. and Cajka R., Punching Shear Failure of Concrete Ground Supported Slab, International Journal of Concrete Structures and Materials, Vol. 12 (1), 2018, DOI: 10.1186/s40069-018-0263-6

9th Int. Conf. on Geotechnique, Construction Materials and Environment, Tokyo, Japan, 20-22 November 2019, ISBN: 978-4-909106025 C3051

INFLUENCE OF COARSE AGGREGATE PROPERTIES ON CONCRETE PERFORMANCE

Md Jahidul Islam[1*], Md Rabiul Alam[2], Mohammed Russedul Islam[3], Muhammad Hasanuzzaman [4]
[1]Department of Civil Engineering, Military Institute of Science and Technology, Dhaka-1206, Bangladesh,
[2]Department of Civil Engineering, Military Institute of Science and Technology, Dhaka-1206, Bangladesh, e
[3]Department of Civil Engineering, Military Institute of Science and Technology, Dhaka-1206, Bangladesh,
[4]Department of Glass and Ceramic Engineering, Bangladesh University of Engineering and Technology, Dhaka-1205, Bangladesh,

ABSTRACT

A good number of infrastructure projects are implemented in Bangladesh during the last decade and many more are still in pipeline. In the financial year 2017-18 approximately 12.7 million tons of aggregate are used by the construction industries. Local sources could supply only 11% of those aggregate and rest 89% are collected from foreign sources. Due to the wide variation of aggregate sources performance of concrete become unpredictable in some cases. Therefore, in the present study influence of coarse aggregate characteristics on concrete properties are investigated in the context of Bangladesh. To evaluate performance, six mostly used coarse aggregate sources are selected for this study. A series of laboratory test are conducted to evaluate the ACV, TFV, LAA, EI, FI, specific gravity, water absorption and unit weight for all six aggregates. Additionally, chemical composition and petrographic properties are also explored. Keeping the gradation of aggregate constant, two types of concrete mix (w/c ratio 0.3 and 0.4) were prepared to cast concrete cylinders and beams by using six sources of coarse aggregate. Concrete properties including compressive, tensile and flexural strength are determined. The study finds that physical properties of aggregate generally influence the properties of concrete. However the influence is significant in case of concrete requiring compressive strength higher than 50 MPa. The outcomes of the study will help the engineers to select appropriate sources of aggregate depending on concrete strength requirements.

Keywords: Coarse aggregate, Concrete, Compressive strength, Aggregate crushing value and Flakiness Index

INTRODUCTION

Bangladesh is a developing country where GDP growth rate has hit 7.86 % in the fiscal year 2017-18. It is often said that construction sector is one of the crucial drivers for accelerating economic growth in Bangladesh. Construction sector plays a great role in employment generation, expansion of markets for materials and other commercial activities. Aggregate is one of the mostly used construction materials in all most every construction work. Aggregates have a significant effect on the strength characteristics of concrete in case of high strength concrete. For normal concrete strength may be governed by the interfacial transition zone as it is the strength limiting factor for the case of normal concrete [1], [2]. Characteristics of cement matrix, the interfacial transition zone between the cement matrix and the coarse aggregate usually decide the strength of normal concrete. The usage of water reducing agents in the high strength concrete increases the strength of cement matrix as well as the mechanical properties of interfacial transition zone. Consequently, the properties of coarse aggregate have become dominant in making high strength concrete. In such high strength concrete, the cracks may get initiated either in matrix or aggregate and propagate across all the three phases making the fracture surface relatively less tortuous [3]. Chemical admixtures and some supplementary cementing materials can be used to improve the workability of concrete without negatively affecting hardened concrete [4]. Aggregate shape, texture, and grading have a significant effect on the performance of fresh concrete [4]. Extensive research works on aggregate properties are reported by many researchers including the effect of different types of coarse aggregates such as grey Granite, Anorthosite, Charnockite, Limestone, and Gneiss on the performance of concrete by Vishalakshi et al. [5], effect of maximum aggregate size on the concrete strength by Grabiec et al. [6], the influence of coarse aggregate minerology in mechanical properties of high strength concrete by Oraimi et al. [7], the influence of aggregate type on the elastic modulus of high strength concrete Beushausen et al. [8].

However, detail research work related to the development of high strength concrete using available aggregates in Bangladesh is yet to be completed. In Bangladesh, maximum 6,600 psi

concrete is made but it is not sufficient for making high-rise structures [9]. One of the challenges for making high strength concrete in Bangladesh is non-availability of good quality stone aggregates [10]. Bangladesh has limited sources of naturally occurring rock [11]. Due to shortage of aggregate researchers in Bangladesh are trying to establish recycled aggregate as an alternative. Study reports that by utilizing 100% recycled coarse aggregate and 100% recycled fine aggregate, it is possible to make concrete of strength over 27.5 MPa. Additionally, it is reported that induction furnace slag can be utilized as coarse aggregate for normal strength concrete [12].

Currently, this country depends largely on the various international sources and on few local sources for coarse aggregates. The geological and geo-morphological processes forming the rocks may vary in different locations leading to remarkable variations on the properties of aggregates from different sources. Therefore, it is essential to analyze the characteristics of local as well as known foreign aggregates to be used in various national important infrastructure projects.

In the present study, the influence of aggregate, collected from various sources, characteristics on concrete strength has been studied. A series of physical and mineralogical tests of aggregates have been performed. Concrete cylinders are then prepared and tested for strength evaluation. Finally, a correlation between the concrete strength and aggregate properties has been studied.

MATERIALS

Coarse Aggregate

The coarse aggregate were obtained from six different sources, three from sources within Bangladesh, such as Moddhapara (Mo), Bholaganj (Bh) and Jaflong (Ja) and three from sources outside Bangladesh, namely Pakur – India (PI), Seremban – Malaysia (SM) and Khuong – Vietnam (KV). Samples were crushed as shown in Fig. 1 before delivered by the local supplier.

Pakur Seremban Khuong

Moddhapara Bholagonj Jaflong

Fig. 1 Crushed samples of various coarse aggregates.

Physical Test

Gradation of coarse aggregate varies from source to source and has significant effect on concrete strength [5]. However, in order to study the influence of aggregate on concrete properties it is essential to keep the gradation of coarse aggregate same for all samples. Therefore, for the present study gradation of aggregate is kept constant for all six aggregate samples as shown in Fig. 2.

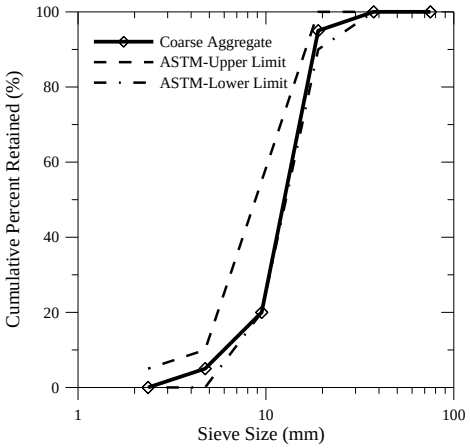

Fig. 2 Constant gradation of coarse aggregate used in this study along with ASTM limits (ASTM C 33).

It is reported that physical properties of aggregate, like strength, shape, size and texture has significant effect on both fresh and hardened properties of concrete [4]. Furthermore, mineralogical composition of aggregate also influences the compressive strength of concrete. Therefore, in the present study a series of physical test, such as aggregate crushing value (ACV), Los Angeles abrasion (LAA), ten percent fine value (TFV), flakiness index (FI), elongation index (EI), fractured face (FF), specific gravity (SG), absorption capacity (AC) and unit weight, has been performed. Properties of various aggregates are summarized in Table 1.

Table 1 Physical properties of coarse aggregate

Properti	PI	KV	SM	Mo	Bh	Ja

es						
ACV (%)	12	17	17	19	20	21
LAA (%)	12	21	16	26	28	32
TFV (kN)	290	220	240	190	210	170
EI (%)	23	23	16	21	19	20
FI (%)	17	15	12	22	19	20
FF† (%)	100	100	100	100	100	100
SG (SSD)	2.88	2.80	2.65	2.74	2.64	2.66
AC (%)	1.19	0.57	0.72	0.83	0.94	0.74
Unit wt. (kg/m^3)	1673	1677	1626	1682	1567	1669

† 100% of aggregates have 3 or more fractured faces

The aggregate crushing value (ACV) and ten percent fine value (TFV) indicate resistance of aggregate against crushing under a gradually applied compressive load. According the ACV result, Pakur-India (PI) has the highest resistance then SM, KV, Mo, Bh, and finally Ja. Based on TFV data, sequence of resistance is PI>SM>KV>Bh>Mo>Ja. Los Angeles abrasion (LAA) test measures toughness and abrasion characteristics of aggregate. Similarly, PI has highest toughness and lowest abrasion, and sequence for the other aggregates is SM>KV>Mo>Bh>Ja.

Elongation index (EI) and flakiness index (FI) represent shape and size of the aggregate. Fractured face signify rough surface of the aggregate and the test results show that 100% of all six aggregate samples have three or more fractured faces. Specific gravity and water absorption capacity of all six aggregates is similar except for PI and KV with slightly higher value. Unit weight of aggregate samples is almost similar apart from Bholaganj aggregate.

Chemical Test

Aggregate mineralogical composition has substantial effect on concrete strength as reported by [7]. Hence, in the current study chemical composition of all six aggregates are determined through a wavelength dispersive X-ray fluorescence (WDXRF) and the results are shown in Table 2. From the test results it is evident that only Khuong – Vietnam (KV) is calcium oxide based and all the other aggregates are silica based. Beside these other major components are ferric oxide, aluminum oxide, magnesium oxide and potassium oxide.

Table 2 Chemical composition of coarse aggregate

Properties	**PI**	**KV**	**SM**	**Mo**	**Bh**	**Ja**
SiO_2 (%)	56.2	4.59	67.2	57.3	83.3	82.0
Fe_2O_3 (%)	11.9	1.71	4.80	9.69	3.19	3.20
Al_2O_3 (%)	10.7	1.02	10.3	9.24	4.65	5.43
CaO (%)	10.4	78.7	5.10	11.6	2.77	2.68
MgO (%)	3.62	12.6	0.99	4.20	0.94	0.82
K_2O (%)	3.16	0.36	8.14	3.46	3.22	3.93
TiO_2 (%)	1.80	0.22	0.62	1.03	0.60	0.61
Na_2O (%)	1.54	0.17	1.94	2.26	0.83	0.91
P_2O_5 (%)	0.35	0.05	0.35	0.56	0.18	0.17
SO_3 (%)	0.22	0.24	0.17	0.09	0.10	0.12
SrO (%)	0.06	0.19	0.02	0.12	0.02	0.02
Cr_2O_3 (%)	-	0.03	0.06	0.07	0.05	-
MnO (%)	-	0.03	0.09	0.15	0.05	0.04
ZrO_2 (%)	0.02	-	0.03	-	0.14	0.07
ZnO (%)	0.02	0.02	0.06	-	-	-
Rb_2O (%)	0.02	-	0.08	0.01	0.02	0.02

Petrographic Analysis

Petrography analysis appraises the quality of course aggregate. In this analysis aggregate particles are initially subjected to geological classification. Analysis is done following ASTM C-295 and the results have been sketched out in Table 3. As shown in the table, parent rock for PI, SM and Mo is igneous type; whereas, parent rock for KV, Bh and Ja is sedimentary. On the other hand, PI is basalt, KV is lime stone and rest are granite type rock.

Table 3 Rock classification of aggregates

Aggregate Source	Origin	Rock Type
PI	Igneous	Basalt
KV	Sedimentary	Lime Stone
SM	Igneous	Granite
Mo	Igneous	Granodiorite
Bh	Sedimentary	Granite
Ja	Sedimentary	Granite

Fine Aggregate

Fine sand are river sand obtained from Sylhet district in Bangladesh. These particles almost entirely passing the 4.75 mm (No. 4) sieve and predominantly retained on the 75 µm (No. 200) sieve. The properties of fine aggregate are shown in Table 4.

Table 4 Properties of Sylhet sand

Name of properties	Ref. Standard	Test Results	Unit

Fineness Modulus (FM)	ASTM C 136	2.78	-
Specific gravity	ASTM C 128	2.61	-
Absorption capacity	ASTM C 128	1.7	%
Unit weight	ASTM C 29	1466	kg/m^3

Cement

For the present study an ordinary Portland cement (OPC) collected from local manufacturer has been used. The OPC cement, also classified as CEM I – 52.5 N, was produced following the Bangladesh Standard BDS EN 197-1: 2003. The physical and chemical tests were conducted in the laboratory and presented in Tables 5 and 6, respectively.

Table 5 Physical properties of cement

Name of properties	Ref. Standard	Test Results	Unit
Specific Gravity	ASTM C 188	3.15	-
Strength, 3 days	ASTM C 109	30.2	MPa
Strength, 7 days		36.3	MPa
Strength, 28 days		46.6	MPa

Table 6 Chemical composition of cement (ASTM C 114)

Name	Test Results (%)
Silicon di-Oxide (SiO_2)	19.74
Aluminum Oxide (Al_2O_3)	5.06
Ferric Oxide (Fe_2O_3)	3.21
Calcium Oxide (CaO)	64.67
Magnesium Oxide (MgO)	2.11
Insoluble Residue (IR)	0.7
Sulfur tri-Oxide (SO_3)	2.43
Trlcalcium Aluminate (C_3A)	9.7
Loss on Ignition (LOI)	1.63
Total Alkalis (Na_2O+0658K_2O)	46.6

Admixture

In order to maintain the workability at low water-cement ratio a modified polycarboxylate based admixture is used in this study. It is a high range water reducing super plasticizer with negligible sensitivity against aggregate variations. It has a relative density of 1.08 kg/l at 25°C. As per the manufacturer, recommended dosage is 0.5 to 2% by the weight of cement.

CONCRETE MIX PROPORTION AND PREPERATION

It is widely reported that influence of aggregate is insignificant for regular concrete with w/c ratios between 0.4 and 0.7. However, concrete with high compressive strength with low w/c ratio may depend on aggregate properties. Therefore, to study the effect of aggregate properties in concrete performance, two w/c ratios (0.3 and 0.4) has been considered in this study.

Mix design of concrete has been performed according to ACI 211-91. Mix proportions for 1 m^3 of concrete for each aggregate type are presented in Table 7. In total, twelve mix proportions have been considered with six different aggregate types and two different w/c ratios. Concretes were designated with coarse aggregate type and w/c ratio. For example, PI-03 represents Pakur-India coarse aggregate and 0.3 w/c ratio.

Table 7 Mix proportion for 1 cum of concrete

Designation	**Water (kg)**	**Cement (kg)**	**CA (kg)**	**FA (kg)**	**Admixture (ltr)**
PI-03	205	683	1037	501	6.83
PI-04	205	513	1037	650	3.85
KV-03	205	683	1040	470	6.83
KV-04	205	513	1040	618	3.85
SM-03	205	683	1008	449	6.83
SM-04	205	513	1008	597	3.85
Mo-03	205	683	1043	455	6.83
Mo-04	205	513	1043	603	3.85
Bh-03	205	683	972	480	6.83
Bh-04	205	513	972	629	3.85
Ja-03	205	683	1035	427	6.83
Ja-04	205	513	1035	575	3.85

Concrete cylinders, 100 mm by 200 mm, were prepared in two layers with the help of vibrator for compressive strength and split tensile strength. Beside these, concrete beams, 100 x 100 x 500 mm, were also casted for flexural strength test.

RESULTS AND DISCUSSION

At 28 days concrete cylinders were tested for compression and split tensile test in a 3000 kN capacity compression machine; beams were tested

for flexural strength in 1000 kN capacity universal testing machine. Just before the test samples were removed from the water tank and surface dried with rags.

Compressive Strength

Compression test were performed for twelve sets of cylinders for six aggregate types and two w/c ratios. Fig. 3 represents the test results. As shown in the figure, concrete with aggregate from the Seremban – Malaysia (SM) produced the highest compressive strength in case of both w/c ratios of 0.3 and 0.4. On the other hand, concrete with aggregate from Jaflong (Ja) showed lowest compressive strength. Beside these concrete with KV and Mo showed good compressive strength. Except for concrete with Pakur-India (PI) compressive strength concrete is related to strength properties of aggregate, such as ACV, LAA and TFV. Aggregate from PI has shown highest strength compare to other aggregates. However, because of its high elongation index (EI) and flakiness index (FI) the compressive strengths of concrete with PI fall short of the expected results. Furthermore, lime stone aggregate from KV showed good compressive strength despite having relatively high EI value.

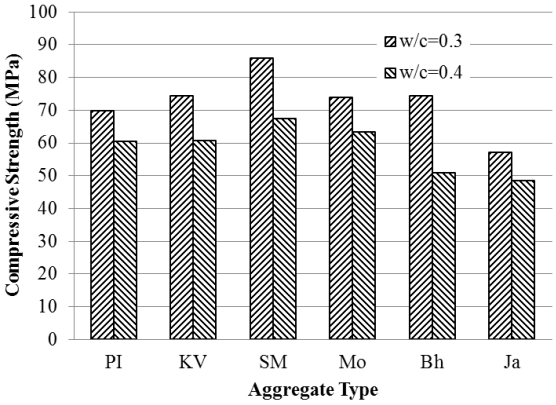

Fig. 3 Compressive strength of concrete with six coarse aggregate types at 28 days age for w/c ratios of 0.30 and 0.40.

Split Tensile Strength

Similar to compression test, split tensile tests were performed for concrete with six aggregate type and two w/c ratios. Fig. 4 displayed the tensile test results. Like compressive strength, concrete with SM aggregate showed the highest tensile strength; whereas, concrete with Ja aggregate gave the lowest strength. Concrete with KV and Mo also performed well.

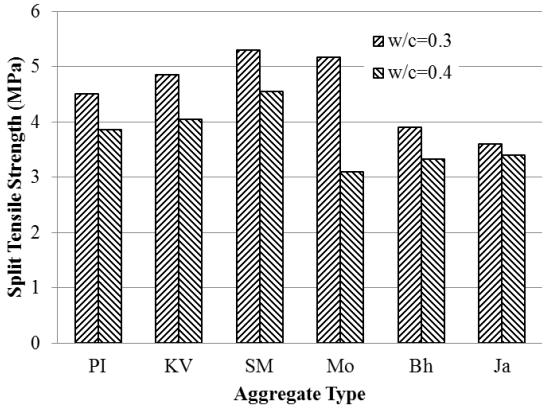

Fig. 4 Splitting tensile strength of concrete with six coarse aggregate types at 28 days age for w/c ratios of 0.30 and 0.40.

Flexural Strength

Concrete beams were tested for flexural strength. Loads were applied at one-third and two-third points and flexural loading capacity were calculated accordingly. Fig. 5 displayed the flexural strengths concrete with aggregate and w/c ratio variations. As shown in the figure, concrete with aggregate from KV and PI have shown the highest flexural strength despite having high EI and FI values. On the other hand, SM, with lowest EI and FI values, based concrete has not yield higher flexural strength. This implies that aggregate shape has very little effect on flexural strength of concrete.

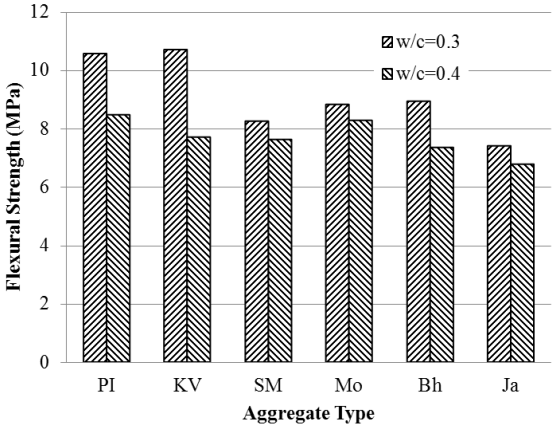

Fig. 5 Flexural strength of concrete with six coarse aggregate types at 28 days age for w/c ratios of 0.30 and 0.40.

Correlation between Aggregate Properties and Concrete Strength

One of the major objectives of this study is to

find a correlation between aggregate properties, such as shape and strength, with concrete strength. Shape of the aggregate is partly depends on the crushing procedure of the rock, and thus, will not be used for direct correlation for concrete strength. However, strength properties of aggregate, such as ACV, LAA and TFV, have significant effect on concrete compressive strength. Fig. 6 – 8 represent concrete compressive strength against ACV, LAA and TFV, respectively except for concrete with aggregate from PI. As mentioned earlier, concrete with PI showed scattered results because of its shape factor of aggregate. The figures also include linear trend lines with r-squared values. In all cases it showed good correlations.

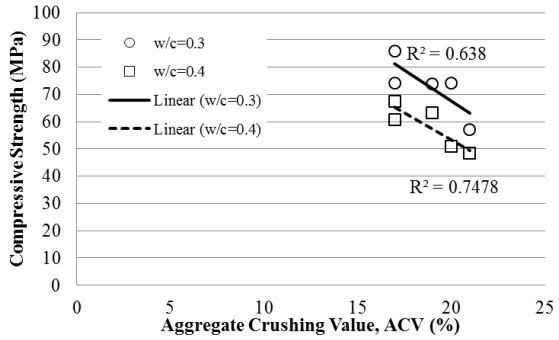

Fig. 6 Compressive strength of concrete at 28 days vs. aggregate crushing value (ACV).

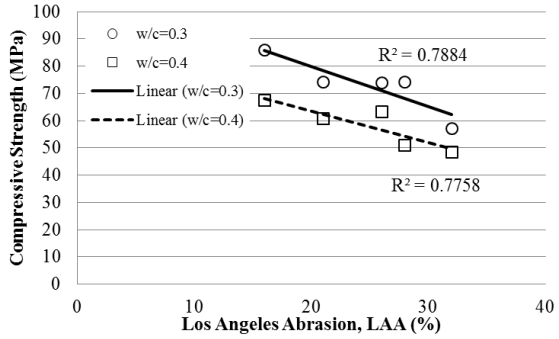

Fig. 7 Compressive strength of concrete at 28 days vs. Los Angeles abrasion (LAA) value.

As shown in Fig. 6, concrete compressive strength reduces with increasing ACV values. Similar is true for LAA values. As described in Fig. 7, higher the LAA values lower the compressive strength of concrete. For TFV opposite trend observed as presented in Fig. 8. With increasing values of TFV concrete compressive strength increases. It is also observed that in all cases influence of aggregate strength become insignificant for concrete with 50 MPa or less.

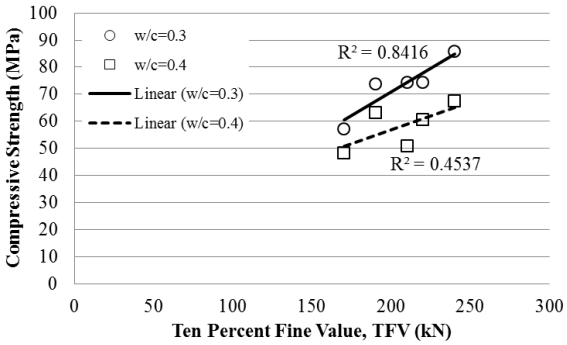

Fig. 8 Compressive strength of concrete at 28 days vs. ten percent fine value (TFV).

CONCLUSIONS

The conclusions that can be drawn from this study are as follows:

- Strength and shape properties of aggregate have significant effect on compressive and tensile strength of high strength concrete. However, for concrete with 50 MPa or less compressive strength this influence becomes trivial.
- Concrete compressive strength increases linearly with decreasing ACV and LAA values and with increasing TFVs. However, this is relation is only valid for 50 to 90 MPa strength and for relatively lower elongation and flakiness indexes.
- Shape of aggregates has insignificant influence on flexural strength of concrete.

ACKNOWLEDGMENTS

The authors express their profound thanks to Military Institute of Science and Technology for providing financial support to this project.

REFERENCES

[1] Davis DE, Alexander MG, Properties of aggregate in concrete (part 2). Hippo Quarries Technical Publication, Hippo Quarrie, Sandton, South Africa, 1992, pp 48.

[2] Ezeldin AS, Aitcin PC, Effect of Coarse Aggregate on the Behavior of Normal and High-Strength Concretes. Cem, Conc, and Aggr, 13(2), 1991, pp 121-124.

[3] Mohammed Seddik Meddah, Salim Zitouni, Said Belaabes, Effect of Content and Particle Size Distribution of Coarse Aggregate on the Compressive Strength of Concrete, Construction and Building Materials 24, 2010, pp 505–512.

[4] Pedro Nel Quiroga and David W. Fowler, The Effects of Aggregates Characteristics on the Performance of Portland Cement Concrete,

Report No. ICAR 104-1F, International Center for Aggregates Research, The University of Texas at Austin, 2004.

[5] K.P. Vishalakshi, V. Revathi, S. Sivamurthy Reddy , Effect of Type of Coarse Aggregate on the Strength Properties and Fracture Energy of Normal and High Strength Concrete, Engineering Fracture Mechanics Volume 194,1 May 2018, pp 52-60.

[6] Anna M. Grabiec , Daniel Zawal, Jakub Szulc, Influence of Type and Maximum Aggregate Size on Some Properties of High-Strength Concrete Made of Pozzolana Cement in respect of Binder and Carbon Dioxide Intensity Indexes, Construction and Building Materials , 98, 2015, pp 17–24.

[7] S.K. Al-Oraimi, R. Taha, H.F. Hassan, The effect of the Mineralogy of Coarse Aggregate on the Mechanical Properties of High-Strength Concrete, Construction and Building Materials 20, 2006, pp 499–503.

[8] Hans Beushausen, Thomas Dittmer, The influence of aggregate type on the strength and elastic modulus of high strength concrete, Construction and Building Materials 74, 2015, pp 132–139.

[9] Mohammad Abdur Rashid, Tanvir Hossain and M. Ariful Islam, Properties of Higher Strength Concrete Made with Crushed Brick as Coarse Aggregate, Journal of Civil Engineering (IEB), Vol.37(1) 2009, pp 43-52.

[10] Nafis Sarwar, Tarek Uddin Mohammed, Shamim Z. Bosunia and Jamal Khatib, Development of High Strength Concrete in Bangladesh, Third International Conference on Construction In Developing Countries (ICCIDC–III), Advancing Civil, Architectural and Construction Engineering & Management, Bangkok, Thailand, July 4-6, 2012.

[11] Road Master Plan, Volume I: Main Text, Roads and Highways Department, Bangladesh, March 2009.

[12] Tarek U. Mohammed, Aziz H. Mahmood, Ijaj M. Chowdhury, Akter M. Humayun, and Tanvir Ahmed, Sustainability of Construction Materials in Bangladesh, Fourth International Conference on Sustainable Construction Materials and Technologies , Las Vegas, USA, August 7-11, 2016.

9th Int. Conf. on Geotechnique, Construction Materials and Environment, Tokyo, Japan, 20-22 November 2019, ISBN: 978-4-909106025 C3051

A SIMPLE METHOD FOR STRENGTHENING THE BRICK MASONRY INFILLED IN THE REINFORCED CONCRETE FRAME STRUCTURE

Jafril Tanjung[1], Febrin Anas Ismail[1], Maidiawati[2] and Rudiansyah Putra[3]
[1]Engineering Faculty, Andalas University, INDONESIA; [2]Padang Institute of Technology, INDONESIA
[3]Syiah Kuala University, INDONESIA

ABSTRACT

The collapse of the brick masonry infill in the Reinforced Concrete (RC) structures has been known as one of the causes of the many casualties during the earthquake. This clay brick masonry has been commonly used as the partitions in the RC frame structures in earthquake-prone areas such as West Sumatera, Indonesia. Strengthening the brick masonry infill is expected to be able to increase the performance of the brick masonry against the earthquake motions, which also may improve the seismic performance of RC structures. In this study, four of 1/4 reduced-scale singe-bay and single-story RC frame specimens were prepared and tested under lateral static reversed cyclic loading. The specimens include one specimen of RC frame infilled with brick masonry and three specimens of RC frames infilled with strengthened brick masonry. Strengthening of the brick masonry infill has used three types of wire mesh, namely plastic wire mesh, steel wire mesh, and chicken wire mesh. The wire mesh was tacked on both sides of the diagonal area of the brick masonry infill. The wire mesh was then fastened to columns and beams of RC frame by using chemical epoxy adhesive. The purpose of this experimental study is to define an effective, inexpensive, and easy to apply the strengthening of the brick masonry infill such that may be applied by the local labors in West Sumatera, Indonesia. The structural test results have shown that all the strengthening methods increase the lateral strength of the RC frame and can delay the failure of the brick masonry infill. Even though the strengthening by using the steel wire mesh produced a higher increase in stiffness of the specimen compares to others, however strengthening by using chicken wire mesh performed the most effective strengthening method. The presence of the chicken wire mesh maintains the ductility of brick masonry infill and RC frame as well.

Keywords: RC building, strengthening brick masonry, seismic performance, reversed cyclic loading

INTRODUCTION

The presence of brick masonry as infill in the reinforced concrete (RC) structure has commonly in the earthquake-prone area such as West Sumatera, Indonesia. Based on the results of the post-earthquake investigation after the earthquake and the experimental results of RC frame subjected to static lateral loading showed that the presence of infilled brick masonry in RC frame structures influence the performance of its structures. The presence of brick masonry infill, on one side, increasing the lateral strength and the stiffness of the structure, however, decreases its ductility. On the other hand, the existence of this brick masonry infill may endanger the occupants.

In many cases, the brick masonry infill often collapses during the earthquake shaken and results in a loss of human life [1]-[2]. The studies for investigating the influence of brick masonry infill to seismic capacity and behavior of the RC frame structures have been conducted by many researchers covering various aspects. Tanjung [3]-[4] has examined the use of various types of brick masonry materials commonly used in West Sumatra, Indonesia for evaluating the seismic performance of the RC frame structures with infilled by the brick masonry. The RC specimens were subjected to the lateral static pushover loading only. More detail and complex studied have been carried out by Madiawati [5] Cavaleri [6] and Dautaj [7], where the brick masonry infilled of RC frame specimens were tested under the lateral static reversed cyclic loading. They concluded that the brick masonry infill plays an essential role in the damaged on the RC frame structure during cyclic loading.

One effort to reduce the vulnerability of this brick masonry infill is by strengthening its brick masonry infill with such ductile materials. Obviously, the research on the strengthening of the brick masonry has also been carried out by several researchers. Tanjung [8], for instance, has used the embedded plain steel on bed mortar joint to strengthen the brick masonry infill in the RC frame structure, while Ismail [9] uses wire mesh banded to strengthen the unconfined brick masonry housing in Pariaman, West Sumatera. Leeanansaksiri [10] also used the Ferro-cement for straightening the brick masonry infilled in RC frame structures. More advanced research is carried out by researchers have been well summarized

in the article [11]-[16]. The strengthening methods by using modern materials such as textile-reinforced mortar, welded wire mesh, and Carbon Fiber Reinforced Polymer (CFRP) have also been conducted and proposed by the researchers. Although their test results show that the strengthening materials and methods gave better RC frame construction, unfortunately, the strengthening methods require the relative expensive materials and specialized labor for applying the strengthening. Therefore, these methods are not suitable to apply in the West Sumatra area, since there is no available strengthening material and skilled labors as well.

In this study, the simple method based on the experimental works for strengthening the brick masonry infilled in the RC frame structure is proposed. For this purpose, four of 1/4 reduced-scale singe-bay and single-story RC frame specimens were prepared and tested under lateral static reversed cyclic loading. The purpose of this experimental study is to define an effective, inexpensive, and easy to apply the strengthening of the brick masonry infill such that may be applied by the local labors in West Sumatera, Indonesia.

EXPERIMENTAL PROGRAM

The experimental study explains in this paper was conducted by utilizing the structural testing facilities at Structure and Construction Material Laboratory of Syiah Kuala University, Banda Aceh, Indonesia. Four of 1/4 reduce-scaled one-bay and one-story RC frame specimens were prepared, i.e., one specimen of RC frame infilled with brick masonry and three specimens of RC frames infilled with strengthened brick masonry. The specimens represent the first story of the typical construction of low-rise RC frame structures in West Sumatra, Indonesia. Strengthening of the brick masonry has used three types of wire mesh, namely plastic wire mesh, steel wire mesh, and chicken wire mesh. The materials for constructing these specimens were collected from local markets in Banda Aceh, Indonesia. All the specimens were subjected to lateral static reversed cyclic loading.

The RC Frame Specimens

Figure 1. shows the details of the geometry and reinforcement applied for all RC frame specimens. The columns of the RC frame were detailed to yield in flexure before shear failure. The dimension of the cross-section of columns was 125 mm x 125 mm and reinforced with 4D10 longitudinal bars and ϕ4@50 transverse hoops. We designed the cross-section of the columns by considering the scale reduction. The clear height of the columns was 750 mm. The dimension of top-beam was 200 mm wide, 200 mm deep and 1550 mm long and reinforced with 4D13 longitudinal bars and ϕ6@50 transverse stirrups. The columns were then supported by the lower-beam, which was fastened to the strong-floor by using six post-tensioning rods. The dimension of the lower-beam was 700 mm wide, 150 mm deep and 1650 mm long and reinforced with 12D16 longitudinal bars and ϕ6@50 transverse stirrups.

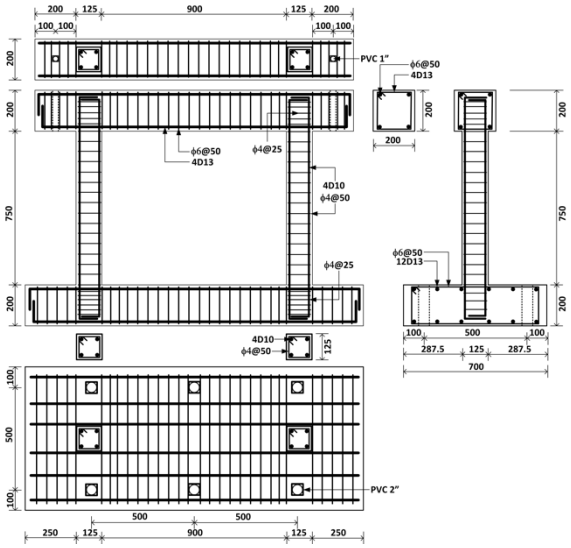

Fig. 1 Reinforcements Details of the RC Frame.

Four of 1/4 reduced-scale singe-bay and single-story RC frame specimens were constructed in this study. The specimens include one specimen of RC frame infilled with brick masonry (IF-SW) and three specimens of RC frames infilled with strengthened brick masonry. Strengthening of the brick masonry has used three types of wire mesh, namely plastic wire mesh (IF-SM-P), steel wire mesh (IF-SM-S) and chicken wire mesh (IF-SM-A). The wire mesh was tacked on both sides of the diagonal area of the brick masonry wall. The wire mesh was then fastened to columns and beams of RC frame by using chemical epoxy adhesive. The RC frame specimen with brick masonry infill is schematically shown in Fig. 2a while the RC frame with strengthened brick masonry infill is presented in Fig. 2.b

Experimental Setup and Instrumentation

As was mentioned above, during experimental works, the prepared RC frame specimens were subjected to static lateral reversed cyclic loading. A schematically image of the experimental setup for the current study is shown in Fig 3.a. For testing the specimen, at first, its specimen was placed on the rigid-floor. The lower-beam of the specimen was fastened to the rigid-floor by using six post-tensioning rods to keep the specimen remain in its position during the test. A double-action lateral actuator force equipment was attached and fastened to the strong wall by using four post-tensioning rods.

Two horizontal steel beams were used to restrain top-beam of the specimen from preventing the applied force on its top-beam causes out-of-plane deformation occurs during testing. These two horizontal steel beams were connected to the actuator force, which mounted on the strong wall. The displacement transducers (LVDTs) were installed at several points to measure the deformation of the RC frame specimen, as is shown in Fig. 3.b. A displacement transducer which was placed in the middle of top-beam was used as a displacement-control point.

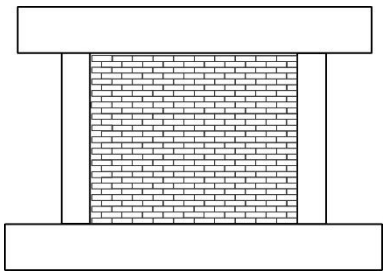

(a) RC Frame with Brick Masonry Infill Specimen

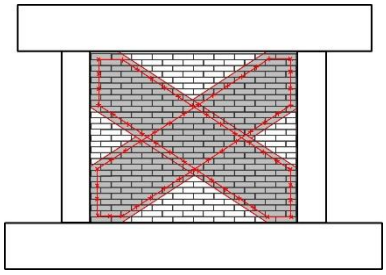

(b) RC Frame with Strengthened Brick Masonry Infill Specimen

Fig. 2 Design of the RC Frame Specimens.

The lateral static reversed cyclic loading applied in current experimental works was conducted by control the lateral displacement of the top-beam with the loading speed of approximately 0.05 mm/s. The procedure follows FEMA461 [17]. The amount of lateral movement of the top-beam was defined based on the drift ratio of the column R=δ/H, where δ is the lateral displacement at a tip of the top-beam measured by the displacement transducer and H is the distance between the transducer and the bottom of the column. The loading program was R=1/800, R=1/400, R=1/200, R=1/100, R=1/50, R=1/25, R=1/12.5 rad., and followed by a pushover to R=+1/10. Except for the first drift ratio R=+1/800, two cycles were applied for each drift ratio. Incremental of the applied lateral static load and the deformation of the specimen were monitored and recorded throughout the tests. An initial crack and its crack propagation were drawn on the RC frame and brick masonry infill in every loading cycle for identifying the failure mechanism of the specimen.

RESULTS AND DISCUSSION

Material Properties

The material properties used for constructing RC frame specimens, including their brick masonry infills, were obtained by standard material testing procedures. The compressive strength of concrete cylinder at 28 days after casting was 30.6 MPa, i.e., the sample of the concrete was cast to the RC frame specimens. The compressive strength of the brick masonry cube was 9.4 MPa. The nominal yield (tensile) strengths of the reinforcements, respectively for Ø4, Ø6, D10, and D13, were 390.2 (574.9) MPa, 346.8 (446.3) MPa, 324.6 (449.5) MPa, and 374.3 (535.4) MPa.

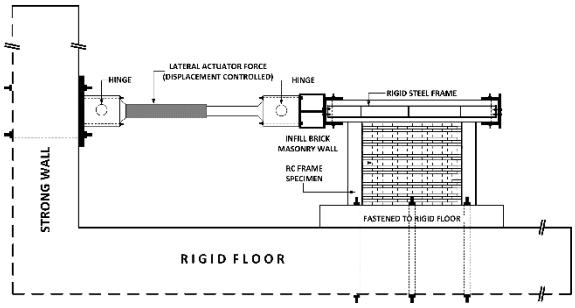

(a) The Experimental Setup

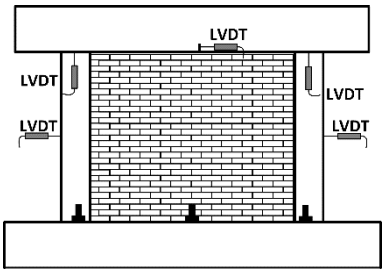

(b) The Position of the LVDTs

Fig. 3 Experimental Setup and Instrumentation.

Performance and Failure Mechanism

RC Frame with Brick Masonry Infill

Figure 4. shows the test results of the IF-SW specimen. The ultimate lateral strength was obtained about 93.5 kN at the first cycle of R =+1/100 and 94.5 kN at R=-1/100. An initial crack on the interface between columns and brick masonry infill firstly appeared at R = +1/400 at a load of 30 kN and the initial flexural crack in the column have also been seen at it R= +1/400 due to the lateral load of 47.6 kN. Meanwhile, the brick masonry infill started to crack on it diagonal at the first cycle of R =+1/200 caused

by the lateral loading of 78 kN.

Furthermore, the diagonal crack on the brick masonry infill spreads and widens when the specimen was loaded to 92 kN at cyclic R = +1/100. At the same time, the flexural cracks in the left column also increased. The shear crack on the upper of the left column occurred at the first cycle of R = +1/50, and the diagonal cracks on the brick masonry infill increased become wider than 5 mm. The surface plastering on the brick masonry infill started to peel off at R = +1/50 as it is shown in Fig. 4.b., then the diagonal crack on the brick masonry infill increased more than 10 mm wide when R = +1/25. Finally, the brick masonry infill collapsed at the second cycle of R = +1/12.5, and the transverse hoop in the left column ruptured when the specimen has been subjected a pushover loading to R = +1/10.

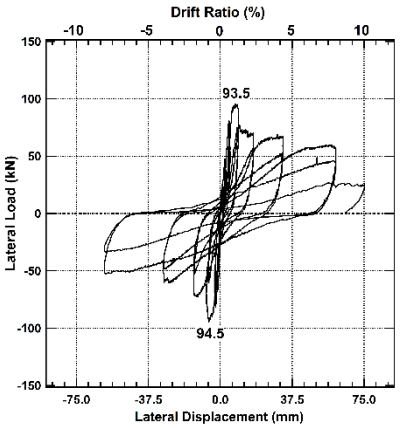

(a) Load-Displacement Hysteresis Curve

(b) Crack Pattern at R=1/12.5

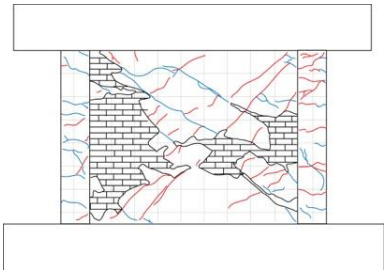

(c) Sketch of the Crack Pattern at R=1/12.5

Fig. 4 Experimental Setup and Instrumentation.

RC Frame with Strengthened Brick Masonry Infill

The comparison of the load-displacement hysteresis curves based on the experimental results for all three strengthed brick masonry infill specimens is shown in Fig. 5. Compare to the test results of the IF-SW specimen, increasing of the lateral strength due to the strengthening of brick masonry infill in IF-SM-P, IF-SM-S, and IF-SM-A specimens are 12.4%, 5.3%, and 22.6%, respectively. Although the increase in its lateral strength is not significant, however, the presence of the strengthed brick masonry infill in the RC frame significantly changed the deformation behavior, crack pattern and the progressive failure of the RC frame specimens.

In IF-SM-P specimen, the plastic wire mesh could not perfectly bond to brick masonry and surface plastering as well. Therefore, the strengthening of the brick masonry infill became imperfect. The initial crack on the wall has seen at the first cycle of R = + 1/400, and the surface plastering of the brick masonry infill has begun to release at the second cycle of R = + 1/200. The interface between the column and the brick masonry infill connected by wire plastic was also the weak area of this strengthening method. The cracks in this area have already appeared at the beginning of loading. The advantage this method is that the use of wire mesh plastic may delay the collapse of RC frame specimen and the brick masonry infill.

The material of the steel wire mesh has better tensile strength compared to plastic wire mesh and chicken wire mesh. Its material may bond to the brick masonry infill as well as to the surface plastering of the brick masonry infill. Strengthening using this steel wire mesh (IF-SM-S specimen) gave an excellent strengthening on brick masonry infill. The cracks that occur on the brick masonry wall were significantly reduced. The strengthening causes increase the stiffness of the brick masonry infill. Unfortunately, increasing of the brick masonry stiffness produced the high force on the diagonal brick masonry infill that compresses the column such that the column damaged relatively faster than other test specimens.

When compared these three types of strengthening materials shows that the strengthening by using chicken wire mesh (IF-SM-A specimen) provided the most optimal result. Although the cracks occurred on its brick masonry infill was more than those of the IF-SM-S specimen, the strengthening using chicken wire mesh can delay the collapse of the brick masonry infill. We noted that the cracks on the brick masonry infill generally occurred outside the area where the chicken wire mesh was installed. The cracks appeared in the columns were dominated by the flexure cracks. This result contrasts to the experimental results of the IF-SM-S specimen where

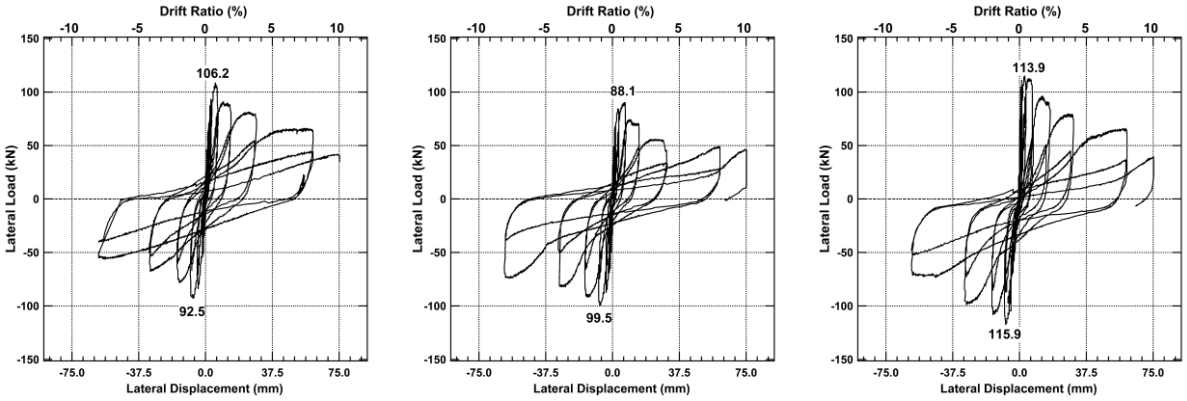

(a) IF-SM-P Specimen (b) IF-SM-S Specimen (c) IF-SM-A Specimen

Fig. 5 Comparison of the Load-Displacement Hysteresis Curves

(a) IF-SM-P Specimen (b) IF-SM-S Specimen (c) IF-SM-A Specimen

Fig. 6 Comparison of the Crack Pattern of the Specimens at R=1/12.5

the column damage was caused by shear failure. The experimental results were also indicated that the ductility of the IF-SM-A specimen better than other specimens. The images of the crack pattern of the RC frame specimen infilled by the brick masonry are shown in Fig. 6.

CONCLUSIONS

The simple method for strengthening the brick masonry infilled in the RC frame structures has been proposed. A proposed method is defined based on experimental works on several RC frame specimens. Comparing the experimental results of these specimens concluded that the strengthening by using the chicken wire mesh gave the optimal result. The strengthening increase in the lateral strength about 22,6% and delayed the failure of the RC frame and collapse of the brick masonry infill. This proposed strengthening method by using the chicken wire mesh also has good ductility compare to other material. The strengthening material is easy to find in the local markets and is easy to apply by unskill local labor. Therefore, this method will be useful and applicable in the seismic-prone area, such as West Sumatera, Indonesia.

ACKNOWLEDGMENTS

This research work is financially supported by the Institute of Research and Community Development of Andalas University through the Research Grand of Program Penelitian Skim Klaster Riset Percepatan Guru Besar (KRP2GB) with the contract number T/45/UN.16.17/PP.IS-KRP2GB/LPPM/2019. The authors also sincerely acknowledge to Professor Katsuki Takiguchi, Takiguchi Laboratory, Department of Mechanical and Environmental Informatics, Tokyo Institute of Technology, Japan; Dr. Abdullah, Civil Engineering Department, Syiah Kuala University; head and staffs of Structure and Construction Material Laboratory, Engineering Faculty, Syiah Kuala University, for supporting during prepared the specimens, provided the structural testing facilities and conducted the structural tests.

REFERENCES

[1] Maidiawati and Sanada Y., Investigation and Analysis of Buildings Damaged during the September 2007 Sumatra, Indonesia Earthquakes, Journal of Asian Architecture and Building Engineering (JAABE), Vol 7 No 2, 2008, pp. 371-378.

[2] Tanjung J., Post-earthquake Investigation Report of Damaged Reinforced Concrete Buildings after Pidie-Jaya Earthquake 2016, Civil Engineering Department, Andalas University, Unpublished Report, 2017.

[3] Tanjung J. and Maidiawati, Experimental Study on the Influence of the Brick Masonry Infill to the Lateral Strength of the Reinforced Concrete Structures (in Bahasa Indonesia), Jurnal Teknik Sipil ITB, Vol 23 No 2, 2016, pp. 99-106.

[4] Tanjung J. and Maidiawati, The Experimental Investigation on Beneficial Effects of the Local Brick Masonry Infills to Seismic Performance of R/C Frame Structures in West Sumatera, International Journal of Civil Engineering and Technology (IJCIET), Vol 8, Issue 10, 2017, pp. 687–697.

[5] Maidiawati and Sanada Y., R/C Frame–infill Interaction Model and Its Application to Indonesian Buildings, Earthquake Engineering & Structural Dynamic, Vol 46, 2017, pp. 221–241.

[6] Cavaleri L., Di Trapani F., Cyclic Response of Masonry Infilled RC Frames: Experimental Results and Simplified Modeling, Soil Dynamics and Earthquake Engineering, Vol. 65, 2014, pp. 224-242.

[7] Dautaj A.D., Kadiri Q.and Kabashi N., Experimental Study on the Contribution of Masonry Infill in the Behavior of RC Frame Under Seismic Loading, Engineering Structures, 165, 2018, pp. 27–37.

[8] Tanjung J., Maidiawati and Nugroho F., Experimental Investigation of the Seismic Performance of the R/C Frames with Reinforced Masonry Infills, Conference proceedings, AIP Conference Proceedings 1892, 020009, 2017; doi: 10.1063/1.5005640

[9] Ismail, F.A., Tanjung J., Hakam A., Fauzan and Boen T., Plastered Wire-mesh Bandaged: An Effective Alternative Technique for Seismic Strengthening of the Unconfined Brick Masonry Housing in Pariaman City, West Sumatera, Indonesia, Technology (IJCIET), Vol 6, Issue 7, 2015, pp. 44-52.

[10] Leeanansaksiri A., Panyakapo P. and Ruangrassamee A., Seismic Capacity of Masonry Infilled RC Frame Strengthening with Expanded Metal Ferrocement, Engineering Structures, 159, 2018, pp. 110–127.

[11] Benavent-Climent A., Ramírez-Márquez A. and Pujol S., Seismic Strengthening of Low-rise Reinforced Concrete Frame Structures with Masonry Infill Walls: Shaking-table Test, Engineering Structures, 165, 2018, pp. 142–151.

[12] Akhoundia F., Vasconcelos G., Lourenço P., Silva L.M., Cunha F., Fangueiro R., In-plane Behavior of Cavity Masonry Infills and Strengthening with Textile Reinforced Mortar, Engineering Structures, 156, 2018, 145–160.

[13] Guerreiro J., Proença J., Ferreira J.G., Gago A., Experimental Characterization of In-plane Behaviour of Old Masonry Walls Strengthened Through the Addition of CFRP Reinforced Render, Composites Part B, 148, 2018, pp. 14–26.

[14] Fagone M. and Ranocchiai G., Experimental Investigation on Out-of-plane Behavior of Masonry Panels Strengthened with CFRP Sheets, Composites Part B, 150, 2018, pp. 14–26.

[15] Can Ö., Investigation of Seismic Performance of In-plane Aligned Masonry Panels Strengthened with Carbon Fiber Reinforced Polymer, Construction and Building Materials, 186, 2018, pp. 854–862.

[16] Shermi C. and Dubey R.N., In-plane Behaviour of Unreinforced Masonry Panel Strengthened with Welded Wire Mesh and Mortar, Construction and Building Materials, 178, 2018, pp. 195–203.

[17] FEMA 461, Interim Testing Protocols for Determining the Seismic Performance Characteristics of Structural and Nonstructural Components, Federal Emergency Management Agency, 2007.

9th Int. Conf. on Geotechnique, Construction Materials, and Environment,
Tokyo, Japan, 20-22 November 2019, ISBN: 978-4-909106025 C3051

SEISMIC ANALYSIS OF DAMAGED BUILDINGS BASED ON POST-EARTHQUAKE INVESTIGATION OF THE 2018 PALU EARTHQUAKE

Maidiawati[1], Jafril Tanjung[2], Yasushi Sanada[3], and Syafri Wardi[1]
[1]Civil Engineering and Planning Faculty, Padang Institute of Technology, Indonesia;
[2]Engineering Faculty, Andalas University, Indonesia
[3]Architectural Engineering Department, Osaka University, Japan

ABSTRACT

On September 28, 2018, Palu city, the Central Sulawesi area suffered the M7.5 earthquake. An epicenter of its earthquake located 77 km from the capital of Central Sulawesi Province, Palu city. The main earthquake followed by a localized 4 to 7 meters high tsunami which swept shore-lying houses and buildings on its way. A large number of damages on reinforced concrete (RC) buildings, houses, and soil liquefaction spread in Palu city were observed after the earthquake. The post-earthquake observation reported in this paper was conducted in order to define the typical pattern of RC buildings' damages. The field investigation was focused on the damaged RC buildings. Several types of damage were detected on RC structures such as collapse due to the soft story, damage to beam-column joint, failure of short column, shear failure of the column, collapsed of brick masonry infills. Two damaged RC frame buildings, one in severe damage and the other in totally collapsed, were furthermore analyzed to define it seismic capacity based on Japanese standard. According to the analyses of the first story in the buildings, the distinct difference of seismic performance of both buildings was discovered.

Keywords: Post-earthquake investigation, Reinforced concrete, Seismic performance, The 2018 Palu earthquake

INTRODUCTION

Indonesia is a country located in the highest seismic region in the world. Indonesia has experienced many strong earthquakes [1]. During the last decades, the series of the intense earthquakes have struck several areas in Indonesia, for instance, Aceh in 2004 and 2016, West Sumatera in 2009 [3,4], Bengkulu in 2007 [5], Yogyakarta in 2006, [6], and Central Sulawesi in 2018. The Earthquake in Central Sulawesi was struck by the M7.5 earthquake on Friday, September 28, 2018, at about 6:03 pm local time in Indonesia and was followed by a tsunami with waves up to 7 m high. According to the U.S. Geological Survey (USGS) [7], the epicenter of the M7.5 earthquake was at 0.256ºS, 119.840ºE with a shallow depth of 10 km and it was 70 km away from the provincial capital, Palu. The earthquake rocked areas around the epicenter is shown in Fig.1.

The Palu earthquake **i**n September 2018, was preceded by series of small-to-moderate magnitude earthquakes over the hours leading up to the big one, the biggest of which was a magnitude M6.1 earthquake that occurred three hours earlier and just to the south of the M7.5 event as reported by the USGS. There was also followed by an active aftershock sequence, with about ten events of M4.7 and it got more significant in the three hours after the earthquake. The earthquake and tsunami destroyed large residential areas of more than 70,000 houses and nearly 3,000 schools. Moreover, the earthquake also triggered soil liquefaction and settlements in Palu, Donggala andSigiareas. Many multi-story buildings were reported being severely damaged as well as collapsed in Palu, for instanc**e**, the Anuntapura Hospital, Palu'sTatura Mall (the oldest shopping centers in Palu), the Roa-Roa Hotel, Fire Station, and Tadulako University.

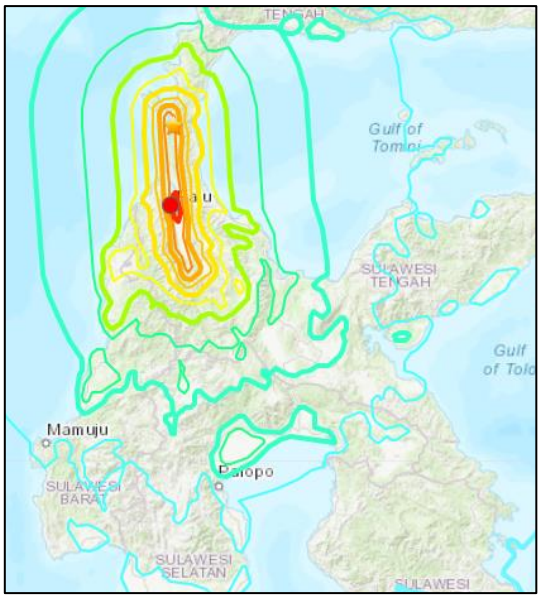

Fig. 1 Shock map of M7.5 Palu earthquake (Source: USGS)

According to the National Board for Disaster Management (BNPB), the earthquake and tsunami caused more than 3,000 death and more than 4,000 injuries in Palu, Donggala, Sigi, and nearby area [8].

This paper presents the report field investigation after Palu earthquake. The observation was conducted from October 4 to 6, 2018, in around Palu city. The investigation was focused on evaluating and discussed on the engineered damaged buildings.

OBSERVATION OF DAMAGED BUILDING

The observation of the damaged RC buildings took place in the areas of Palu, Donggala, and Biromaru cities of Central Sulawesi. Figure 2 shows the map of Sulawesi island dan surveyed areas.

a). Location of Palu city in Central Sulawesi (Source: Google map).

b). Surveyed areas (Source: Google map)

Fig. 2 Map of surveyed areas

The observation was initially done in Donggala, about 40 km west-north of Palu. The ground motion of the Palu earthquake destroyed most of the non-engineered houses, which were built in confined brick masonry wall type. The typical damages of these houses are shown in Photo 1.

Investigation on damaged buildings was carried out in Palu city on the second day. The collapsed RC buildings of Tadulako University (Faculty of Forestry, Faculty of Law, Faculty of political science buildings), building of Universitas Terbuka, The Sya Regency Hotel, Ramayana shopping center, Anuntapura Hospital, Mecure hotel, Fire Station and public apartment and the damaged RC buildings of shophouse and masonry infills were observed**.** Photo 2 shows an example of the damaged buildings observed during the post-earthquake investigation.

In the district Biromoru of Sigi area, the survey was conducted on the third day. In this region, massive liquefaction caused houses to be swept away and damaged public facilities, as shown in Photo 3.

Photo 1 Damage on confined masonry structures

Photo 2 Collapsed and damaged RC buildings: a) Mercure hotel, b) Faculty of Politic Science building of Tadulako University, c) Public apartment, d) Shophouse

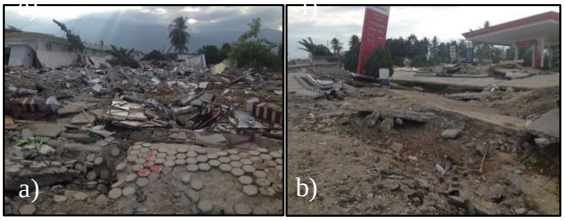

Photo 3 Damage due to liquefaction: a) Swept away homes, b) Damaged fuel station facility

TYPICAL DAMAGE OF RC STRUCTURES

Based on-site investigation, deficiencies were observed on damaged RC buildings according to Indonesian codes of SNI 03-2847-2002 [9] and SNI 03-2847-2013 [10], such as the use of plain round rebars for longitudinal and shear reinforcements of columns and beams, the absence of stirrups in beam-column joint regions, the use of stirrups with 90-degree anchorage on columns and beams, etc. These deficiencies might cause damage to building structures, as follows;

1. The total collapse of the first story that classified as soft-story collapse [11], as shown in Photo 4(a);
2. Failure of beam-column joint due to lack of transversal reinforcements in the joint region, as shown in Photo 4(b);
3. Shear failure of column caused by the use of shear reinforcements with 90-degree hooks, inadequate anchorage of hooks (Photo 4c) and the use of small rebars for stirrups;
4. Columns failed in flexure due to buckling the longitudinal reinforcements (Photo 4d);
5. Short columns failed in shear (Photo 4e);

Photo 4 Typical damage of RC structures: a) The first story collapsed due to the soft story, b) Failure of beam-column joint, c) Shear failure of short columns, d) Shear failure of columns e) Buckling of longitudinal reinforcements of a column

SEISMIC ANALYSIS OF DAMAGED BUILDINGS

Two damaged RC buildings, the Faculty of Forestry of Tadulako University and the Fire Station buildings, were thoroughly investigated. Structural specifics of both buildings were collected through on-site assessments. The Faculty of Forestry building was three-story RC frame structure building located at Jl. Soekarno-Hatta KM 9 Tondo, Mantikulore, Palu which collapsed on the first story as shown in Photo 5(a). The Fire Station building was two stories RC frame structure building located at Jl. Balai Kota Timur No. 1, Tanamodindi, Mantikulore, Palu. The Fire Station building was survived during the earthquake, but most of its columns were damaged, as shown in Photo 5(b). The calculation to identify the damaged grade of the Fire Station building is described as follow.

a). The Faculty of Forestry building of Tadulako University

b). The Fire Station building and damaged columns

Photo 5 The investigated damage buildings

Damage grade evaluation of building

The evaluation was conducted for the first story to identify the damage grade of The Fire Station building. Specifics of the building, correlated to cross-sectional dimensions of structural components, arrangements of reinforcing bars, and damages to columns, were collected on-site investigation. Based on the reference of Nagano [12], damage to the columns was grouped into five classes classified according to Table 1.

Table 1 Damage class definition of RC columns

Damage class	Descriptions of damage
I	– Visible narrow cracks on a concrete surface (crack width of less than 0.2 mm)
II	– Noticeable evident cracks on a concrete surface (crack width of about 0.2–1.0 mm)
III	– Local crushing of concrete cover – Remarkably wide cracks (crack width of about 1.0–2.0 mm)
IV	– Remarkable crushing of concrete with exposed reinforcing bars – Spalling off concrete cover (crack width of more than 2.0 mm)
V	– Buckling of reinforcing bars – Cracks in core concrete – Observable vertical and/or lateral deformation in columns and/or walls – Visible settlement and/or leaning of building

As a result, the damage classes of columns for the first story of the Fire Station building are indicated in Fig.3. The cross-sectional dimension of column C1 was 350x650 mm with 12ϕ19 longitudinal reinforcements and a hoop of ϕ8-100. The damage degree was decided according to the residual capacity index, R, calculated by Eq. (1) [12].

$$R = \frac{\sum_{j=0}^{5} \eta_j . A_j}{A_{org}} \quad (1)$$

where, A_j and A_{org} are the total numbers of columns possessing damage class 0 through V and the total number of the columns, respectively. η_j is seismic capacity reduction factor from Table 2.

Table 2. Damage class definition of RC columns

Damage class	Brittle column ($h_0/D \leq 3$)	Ductile column($h_0/D > 3$)
I	0.95	0.95
II	0.60	0.75
III	0.30	0.50
IV	0.00	0.10
V	0.00	0.00

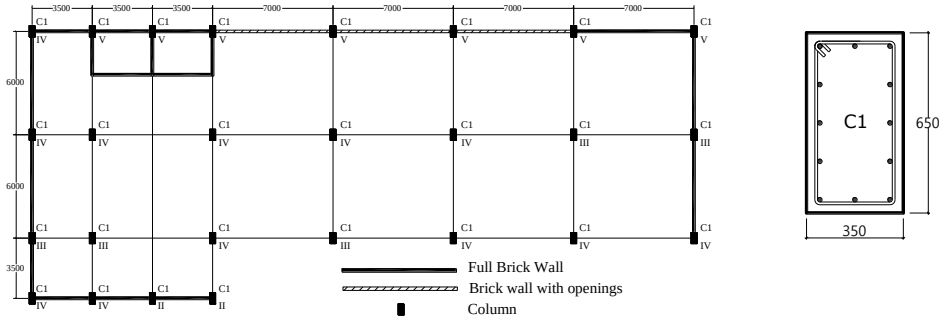

Fig. 3 Floor plan first story and damage class of columns of Fire Station building

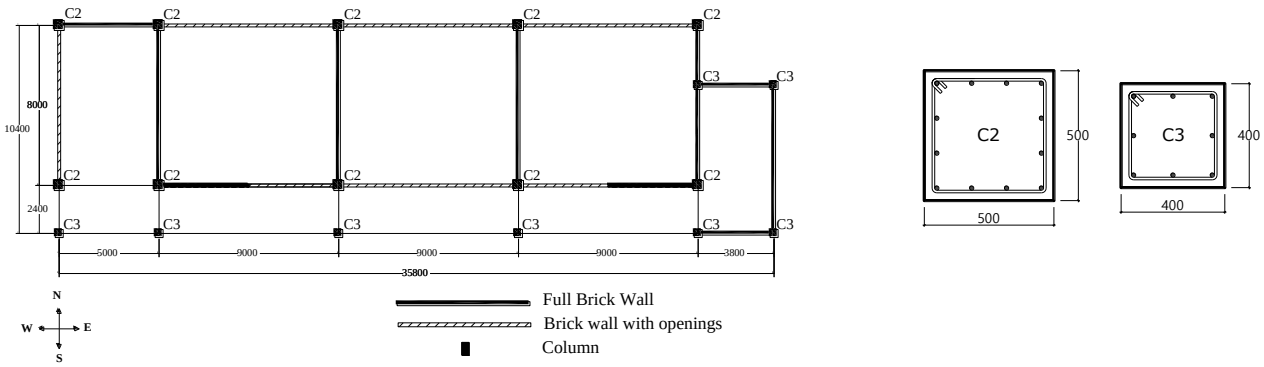

Fig. 4 Floor plan first story of Faculty of Forestry building of Tadulako University

where, h_0 is a clear height of the column, and D is column depth. Based on R-value, that are slight damage with 95 % ≤ R, light damage with 80 % ≤ R < 95 %, moderate damage with 60 % ≤ R < 80 %, heavy damage with R < 60 %, and collapse with R ≈ 0, the damage grade for the first story of the Fire Station building was classified as "a severe damage". On the other hand, the first story of the Faculty of Forestry building was totally collapsed.

Seismic performance of investigated buildings

Seismic performances of the Fire Station building and Faculty of Forestry building were evaluated based on the Japanese standard [13]. The seismic performances of both buildings were analyzed in each direction only for the first story, where the most severe damage was found out to both buildings. The rebars arrangement of the columns of each building is shown in Fig.3 and Fig.4. In the case of Forestry building, the cross-sectional dimension of column C2 was 500x500 mm with 12D22 longitudinal reinforcements and column C3 was 400x400 mm with 8D22 as shown in Fig.4. The stirrups of C2 and C3 were ϕ10-100. The infill walls were neglected in the seismic calculation assuming as non-structure, however, the partial walls were taken into account to calculate the clear heights of the columns.

Based on the reference of [13], the calculated seismic performance of the building was presented in the relationship between the cumulative strength index, C and ductility index, F. The C index was calculated by Eq. (2) [13,14, 15]

$$C = C_i + \sum_j \alpha_j \, C_j \tag{2}$$

$$C_i = \frac{Q_{ui}}{\Sigma W} \tag{3}$$

where, C_i: the strength index of the i-th group of columns having the same ductility index, calculated using Eq. (3), C_j: the strength index of the j-th group having the same ductility index larger than that of i-th group, α_j: the effective strength factor of the j-th group for considering differences between yield deformations of i-th and j-th groups as described in [13]. Q_{ui} is the ultimate lateral load-carrying capacity of the i-th group of columns which is evaluated as the smaller value between the shear force at flexural yielding, Q_{mu}, and the ultimate shear strength, Q_{su}, which are calculated by Eqs. (4) and (6), respectively [13, 14]. ΣW is the total weight of the building.

$$Q_{mu} = \frac{2M_u}{h_0} \tag{4}$$

$$M_u = 0.8\, a_t.D + 0.5N.D\left(1 - \frac{N}{b.D.f_c}\right) \tag{5}$$

$$Q_{su} = \left[\frac{0.053.p_t^{0.23}.(18+f_c)}{\frac{M}{(Q.d)}+0.12} + 0.85\sqrt{p_w.\sigma_{wy}} + 0.1\sigma_0\right] b.j \tag{6}$$

where, p_t is tensile reinforcement ratio calculated ($p_t = a_t/(b.D)$), M/Q is shear span length in which the default value is $h_0/2$, d is effective depth of column, p_w is shear reinforcement ratio calculated by ($p_w = a_w/(b.s)$), σ_{wy} is yield stress of shear reinforcement, σ_0 is axial stress in column (σ_o=N/(b.D)), j is the distance between tension and compression forces, default value is 0.8D. a_w is the cross-sectional area of shear reinforcing bars, s is spacing of hoops. If the value of M/(Q.d) is less than unity or greater than 3, the value of M/(Q.d) to be unity or 3, respectively, and the value of σ_0 is not more than 8 N/mm2.

The F index, which represents deformability of column, was calculated by Eq. (7) for the shear column. The F index for the flexural column was determined by Eq. (7) in the case $R_{mu} < R_y$ and by Eq. (8) in the case $R_{mu} \geq R_y$ [13]. This index, excepting extremely short ones, ranges between 1.0 and 3.2, which corresponds to a lateral drift ratio of 1/250 and 1/30, respectively.

$$F = 1.0 + 0.27\,\frac{R_{su}-R_{250}}{R_y-R_{250}} \tag{7}$$

$$F = \frac{\sqrt{2R_{mu}/R_y - 1}}{0.75\left(1+\frac{0.05R_{mu}}{R_y}\right)} \leq 3.2 \tag{8}$$

where, R_{mu} is the drift angle at the ultimate flexural strength of column = (h_0/H_0). ${}_cR_{mu} \geq R_{250}$, ${}_cR_{mu} = {}_cR_{my} + {}_cR_{mp} \leq {}_cR_{30}$, ${}_cR_{mp} = 10(Q_{su}/Q_{mu} - q).{}_cR_{my} \geq 0$, q = 1.0 for S≤ 100 mm, q = 1.1 for S >100 m. s: spacing of hoops, h_o= clear hight of the column, and H_o= height of column from bottom to top of the lower floor slab. ${}_cR_{150}$ = standard drift angle of column (measured in the clear height of column), 1/150. ${}_cR_{250}$ = standard drift angle of column (measured in the clear height of column), 1/250, R_{250} = standard inter-story drift angle, 1/250.

Consequently, a distinct difference in seismic performance was obtained in both investigated buildings, as shown in Fig.5. The maximum strengths are in South-North direction according to the C index of 0.39 and 0.32 for the Fire Station and Faculty of Forestry buildings, respectively. The strengths in the South-North direction of both buildings were dropped first at ductility index F of 0.1 due to failure of short columns. In the case of the Fire Station building, Its strength was maintained about 0.32 of C index after yielding point up to ductility index F of 3.05 as shown in Fig.5(a).

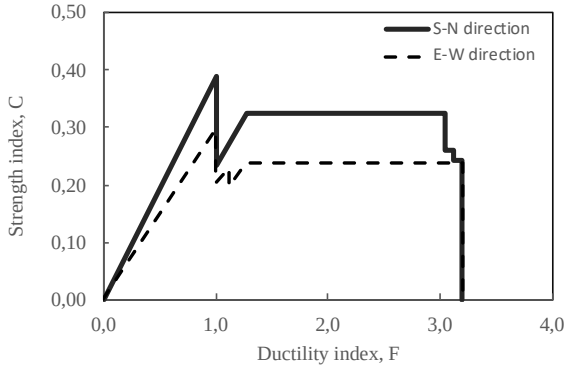

a). Fire Station building

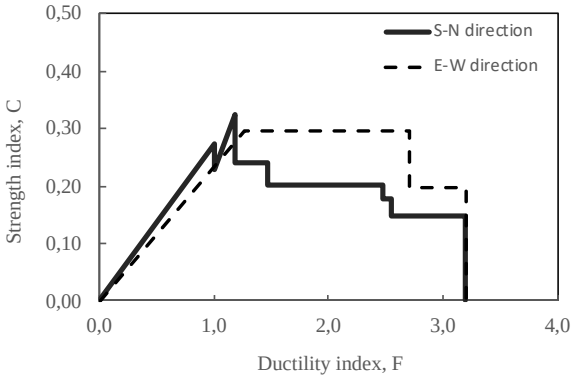

b). Faculty of Forestry of Tadulako University building

Fig. 5 Seismic performance of the investigated buildings

In the case of the building of Forestry Faculty, the strength capacity gradually dropped to 0.15 in the plastic region, as shown in Fig.5(b). Although its strength index of 0.29 was retained up to 2.7 ductility index in E-W direction, these values are low strength capacity and not ductile enough for a building which is located in a high seismic area. This result indicates that the building can be survived during the earthquake when it has strength index more than 0.3 with large plastic deformation.

CONCLUSIONS

According to a post-earthquake investigation conducted after the September 2018 Palu earthquake, several typical damages on building structures and house were observed such as the total collapse of RC buildings, the failure of beam-column joint, the flexural failure of columns, the shear failure of short columns, and the failure of masonry infills. A further analysis was conducted on two damaged buildings, one was survived building, and the other was collapsed on its first story. As a result, the survived building classified as severe damage. The survived building was able to maintain its lateral strength with large deformation. Therefore, it is concluded that the building can survive during the earthquake if such building has high strength capacity in large plastic deformation.

ACKNOWLEDGMENTS

This research was supported by JSPS KAKENHI Grant Number 16H05650 and Ministry of Research, Technology and Higher Education, Indonesia (326/27.O10.5/PN/II/2019). The author's acknowledgments to Dr. Nugroho F, and Dr. Medriosa H., Padang Institute of Technology, for their good collaboration in our observation. We are grateful to Rector and staffs of Tadulako University for their help and guidance during the investigation.

REFERENCES

[1] Biggest Earthquakes Near Indonesia. https://earthquaketrack.com/p/indonesia/biggest
[2] Muzli, Umar M., Nugraha A. D., Bradley K. E., Widiyantoro S., Erbas K., Jousset P., Rohadi S., Nurdin I., Wei S., The 2016 M_w 6.5 Pidie Jaya, Aceh, North Sumatra, Earthquake: Reactivation of an Unidentified Sinistral Fault in a Region of Distributed Deformation. Seismological Research Letters, Vol. XX, No XX, 2018, pp. 1-12.
[3] Choi H., Sanada Y., Kashiwa H., Watanabe Y., Tanjung J., and Jiang H., Seismic Response Estimation Method for Earthquake-Damaged RC Buildings, Earthquake Engineering and Structural Dynamics, Vol.45, Issue 6, 2016, pp. 999-1018.
[4] Earthquake Engineering Research Institute, Learning from Earthquakes, The M_w 7.6 Western Sumatra Earthquake of September 30, 2009. EERI Special Earthquake Report, 2009.
[5] Maidiawati, and Sanada Y., Investigation and Analysis of Buildings Damaged during the September 2007 Sumatra, Indonesia Earthquakes, Journal of Asian Architecture and Building Engineering, Vol.7, No.2, 2008, pp. 371-378.
[6] Pribadi K.S., Kusumastuti D., and Rildova, Learning from Recent Indonesia Earthquake: An Overview To Improve Structural Performance. Conference proceedings, in Proc. 14th Wold Conference on earthquake Engineering, 2008.
[7] https://earthquake.usgs.gov/earthquakes/eventpage/us1000h3p4/executive
[8] National Board for Disaster Management (BNPB), https://www.bnpb.go.id/warga-segera-bangkit-dan-beraktivitas-kembali-pascabencana-di-sulawesi-tengah
[9] Requirements for Structural Concrete for Buildings, National Standardization Agency of Indonesia, SNI 2847:2002, 2002
[10] Requirements for Structural Concrete for

Buildings, National Standardization Agency of Indonesia, SNI 2847:2013, 2013.

[11] McKenzie G., Samali B., and Zhang C., Review Collapse Mechanisms Causing Damage From Controlled and Uncontrolled Demolitions, International Journal of GEOMATE, Vol. 15, Issue 59, 2019, pp. 197-203

[12] Nakano Y., Maeda M., and Kuramoto H., Guideline for Post-Earthquake Damage Evaluation and Rehabilitation of RC Buildings in Japan, Conference proceedings, 13th World Conference on Earthquake Engineering, 2004.

[13] The Japan Building Disaster Prevention Association, English Version 1st, Standard for Seismic Evaluation of Existing Reinforced Concrete Buildings 2001, 2005

[14] Maidiawati and Sanada Y., R/C Frame-Infill Interaction Model and Its Application to Indonesian Buildings, Earthquake Engineering and Structural Dynamics, Vol.46, Issue 2, 2017, pp. 221-241.

[15] Maidiawati and Sanada Y., Modeling of Brick Masonry Infill and Application to Analyses of Indonesian R/C Frame Buildings, Conference proceedings, in Proc. 13th East Asia-Pacific Conference on Structural Engineering and Construction, EASEC, 2013.

9th Int. Conf. on Geotechnique, Construction Materials and Environment, Tokyo, Japan, 20-22 November 2019, ISBN: 978-4-909106025 C3051

SOLAR PANEL INSTALLATION ON SLOPES ~ A LITERATURE REVIEW

Jamie Ure Ovia[1], Zakaria Hossain[1] and Jim Shiau[2]
[1]Dept. of Environmental Science Graduate School of Bioresources, Mie University, Japan
[2]School of Civil Engineering and Surveying, University of Southern Queensland, Australia

ABSTRACT

Renewable energy is rapidly becoming the alternative to fossil fuel-based energy generation. With new innovative advances in renewable energy technology and the market improving, solar panel prices have become more affordable. Currently more and more countries are opting for solar power energy. Owing to urbanization and population increase on flat terrains, finding flat lands to accommodate this technology is becoming more difficult. Solar installation on slope terrains can provide an alternative solution to this problem. This concept is relatively new with only a handful of companies that have already designed and installed solar panels on slopes. This paper aims to provide a review of current practices used for installation on flat and sloping grounds. Furthermore, the potential effects of solar panel installation on slopes, such as slope instability and a number of foundation design considerations are identified.

Keywords: Slope, Solar panel installation, Foundation design, Slope instability

1. INTRODUCTION

Solar energy generation is a fast and effective way to produce clean energy without causing harm to the environment as seen when using fossil fuel energy generation. Solar energy has also increased in generation as compared to previous years. According to the International Renewable Energy Agency [1], solar energy generation increased 35% in 2017 compared to 2016.

One of the main forms on solar energy generation is using solar PV panels which require land to be utilized. Due to the different terrains solar PV farms can vary from the area of land used. A report done in the United States showed that on average a large fixed tilt PV plant that generates 1GWhr/year requires 2.8 acres or 11.33km^2 [2]. As seen in many solar projects around the world, flat lands are traditionally used because it is easily accessible and does not require landscaping. But now with increasing population and urbanization, most flat lands are being used for other development purposes. Therefore, unused sloping terrains is the answer to solving this problem.

Of course, these inclined terrains need to be thoroughly studied before any solar system is placed on them. The main siting factors include land topography, type of land use, proximity to load demand, accessibility and proximity to existing and planned transmission lines [3,4].

The installation technique and types of materials used for the solar panels also needs to be taken into consideration because sloping terrains pose different problems compared to flat terrains. For example, slope angle and height will play a pivotal difference and may take more time in installing panels.

Finally, a main topic of interest that has little research done is the effect the solar panels play on the slope stability. A failure in a slope occurs when a mass of soil beneath the slope slides or fails [5]. Internal factors such as material composition, physical and mechanical indexes, the topography, rock mineral composition, soil and rocks geological structure surface and slope shape can all influence a slopes stability [6]. The foundation type, position on slope and different parameters of the foundation (depth, load, etc.) for a solar panel may affect the integrity of a slope.

The use of sloping terrains with solar PV systems has only been used in very few countries and little research has been conducted in this area. This paper will review the present state of solar PV panel systems on sloped terrains.

2. CURRENT PRACTICES

There are very few companies who have managed to place solar PV systems on inclined terrains, and so this section will look at some examples from these projects in Japan. While also reviewing the various methods and factors that played a role in the completion of each project.

The first large-scale solar power plant known as the “Dream Solar Higuchi Nagasaki” is located in Togitsucho, Nishisonogi-gun, Nagasaki Prefecture, and construction was completed on September 2015 by the Daiwa Lease Co Ltd (Fig.1) [7]. This solar power plant has an output of about 15MW and is located on the southern slopes of a former hilly golf course.

The initial planning of the solar power plant was carefully taken into consideration, as well as the types of foundations for the solar panels. Since the mountain terrain was previously a golf course the Daiwa Group optimized on the situation and did not

do major landscaping of the slope, instead the company only cut down a few trees on site in order to array solar panels more evenly.

Fig.1: Aerial shot of the "Dream Solar Higuchi Nagasaki" (Source: Daiwa Lease/Daiwa House Industry)

Mortar was also used in some areas to prevent landslides. Water discharge capacity was a major concern for residents living close to the power plant, with landslides posing a risk. Therefore, with this risk in mind, the Daiwa Group maintained all previous water discharge facilities from the golf course and covered all areas under the solar panels with anti-weed sheets. The anti-weed sheets would help in the land's water retaining function because these sheets permeability are almost equivalent to that of previous grass on the ground surface. Next, the company used four different foundation methods in accordance with the slope and terrain of the area (Fig.2).

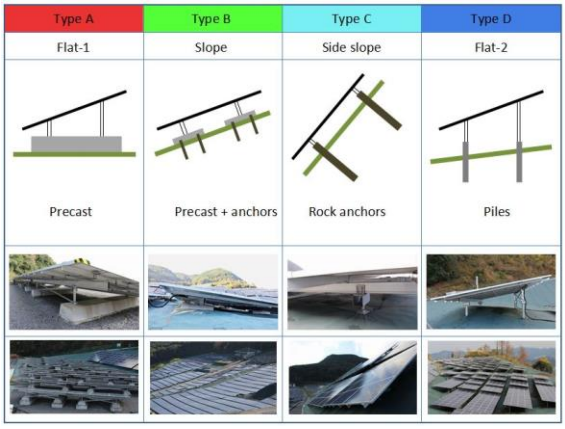

Fig.2: The four types of foundations used in accordance to area and shape of the terrain. (Source: top, Daiwa Lease/Daiwa House Industry; bottom, Nikkei BP; bottom, Photos of Type B Daiwa Lease/Daiwa House Industry)

The first type was a concrete secondary product foundation for flat areas (Type A). Next, on slight slopes a concrete precast foundation was used along with spiral anchors (Type B). For the slopes that were angled even higher a rock anchor foundation was used (Type C). The last type used was the steel tube-based pile foundation, in which a pile driving machine crushed the bedrock and boulders, while driving the pile foundation into the ground (Type D).

Afterwards, installation of the solar panels on the side slopes was done by lifting and supporting the panels with cranes, while the workers, secured by holding fixtures with ropes attached to them, helped to assemble the panels correctly (Fig.3). It should also be noted that the panels were fixed with the mounting system rails in advance before being lifted by the cranes.

Fig.3: Installation of solar panels on side slopes. (Source: Daiwa Lease/Daiwa House Industry).

Another mega solar power plant was constructed at the hills north of Nagasaki Fishing Port on a steep south-facing roadside slope by Sakuranosato Mega Power JV [8]. This solar power plant has 2.141MW output and is known as the "Sakuranosato Mega Power Plant" which was completed in October 2015 (Fig.4).

Fig.4: "Sakuranosato Mega Power Plant" located on a steep south-facing roadside slope. (Source: Nikkei BP)

The main challenge when constructing this solar power system was the angle of the slope which was 30º, a very steep slope. As a result of this steep slope almost no heavy machinery was used in construction. In the middle of the solar power plant there is road that runs east-west and this road was used when heavy trucks and crane vehicles needed to load or offload heavy materials. Transformers and PV inverters were

set up on this road afterwards. Furthermore, a monorail was set up to from bottom to top to transfer construction materials (Fig.5). Portable stairs (newly constructed) and pre-existing lanes running from east-west every 7 meters from the top of the slope were used as well. Next, steel pile foundations were first considered as is seen often on slopes, but due to the unavailability of heavy machinery a new type of foundation installation method was used.

Fig.5: A monorail was constructed to transfer heavy materials. (Source: Toda Corp)

The company decided on using a net as square mold measuring 45 x 45 x 25cm, steel beams were buried in the four corners and center of the square mold (Fig.6). Then mortar was sprayed inside and around forming the foundational structure of each panel (Fig.7). As for drainage capacity, no additional facilities were introduced, the facilities that had been used with the roadside slope was used without modifications.

Figure 6: Foundation method using a net square mold. (Source: Toda Corp)

3. RESEARCH GAP

The interaction between slopes and foundation of solar panels is a complicated topic and requires a great deal of study. Since there is no data on this matter found, deep stabilizing piles embedded in slopes to help reinforce slopes is a good reference to start with this research. Ashour [9], mentions that piles and soil interaction used in slope stabilization is difficult phenomenon due to its 3-dimensional nature and can be influenced by many factors such as the characteristics of deformation and the strength parameters of both pile and soil. As shown in Fig. 8, the driving force that acts along the pile segment above the slip surface is transmitted to the lower (stable) soil layers.

Fig.7: Foundation method of "spraying" mortar in a square mold with buried steel beams was used. (Source: Nikkei BP)

This is the typical reaction seen when piles are used in stabilization of slopes. But piles seen in the above cases do not have the typically long depth which is needed to penetrate the sliding surface.

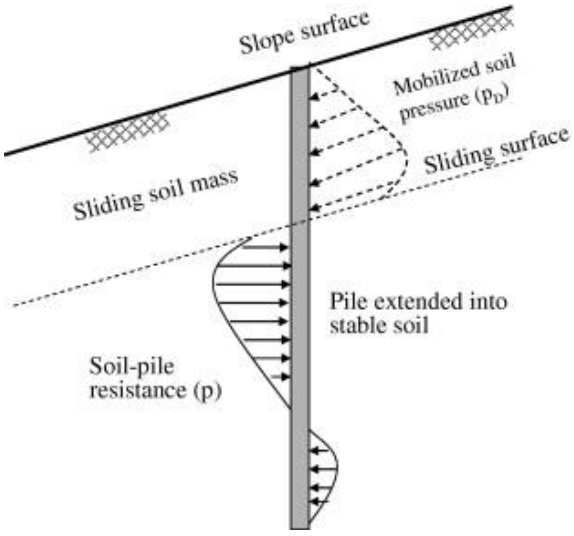

Fig.8: Pressure from the sliding soil mass is transferred to the more stable soil. (Source: Ashour, 2011)

Hence, further information on shallow foundation on slopes and its affects is needed. According to a study on embedded length of piles for slope reinforced with one row of piles [10], showed that the

factor of safety improves as the pile length increases and tends to remain constant after exceeding the critical length. Also, the paper concluded that the critical pile length for slopes with clayey soils is smaller than that for sandy soils for free head piles. There have been other studies as well on the embedded length of piles subjected to lateral soil movements or in unstable slopes. However, there has yet to be research on the short pile length that are in the upper unstable soil and with a load and its effects on the slope.

4. FUTURE RESEARCH

4.1 Proposed Methodology

Further research is needed in order to fully understand the effects of solar panels placed on slopes have on the overall stability of a slope. A proposed methodology for this research could be a numerical simulation with clearly defined parameters for both the slope and piles. The slope would have to have clear measurements such as slope angle, height, slope stability before and after installment of solar panels, shear strength, etc. And the piles would have a given load seen in regular solar panels and various spacing and embedded lengths to see the changes occurred from such variables.

4.2 Research Questions

Some of the research questions that may bring a clearer picture to further research ideas on this topic are presented below:

- What are the best foundation types for solar panels on slopes?
- What is the maximum or optimum slope angle for solar panels to be placed on slopes?
- What is the reduction of lateral capacity of the pile in slope?
- What is the reduction of pull-out capacity of the pile in slope?
- What is the factor of safety before and after installation of solar panels on slope?
- What is the optimum embedded length of pile that would not affect the factor of safety?
- What are the effects of seismic forces that act on the slope with and without the solar panels installed? Is there a difference?

5. CONCLUSION

This paper brings to light that solar panels on slopes is a great way to effectively use sloping land that would otherwise be left idle. After reviewing the current industry practices, a number of research questions were raised for answer in the future. The effect of pile installation on the overall stability of slope and the reduction of pile capacity with respect to the lateral loading and pullout force were identified as the key research items in the near future. This paper has also highlighted the need to bring industry partner and government body to join the research program.

6. ACKNOWLEDGEMENT

The first author would like to express his gratitude to the Japanese International Cooperation Agency (JICA) for providing scholarship to study and research at Mie University, Japan.

7. REFERENCES

[1]. International Renewable Energy Agency, Renewable Energy Highlights, IRENA, 2019.
[2]. Ong S, Campbell C, Denholm P, Margolis R, Heath G., Land-Use Requirements for Solar Power Plants in the United States, National Renewable Energy Laboratory (NREL), 2013.
[3]. Anasari M. F, Chatterji S., Iqbal A., A Fuzzy Logic Control Scheme for a Solar Photovoltaic System for a Maximum Power Point Tracker, International Journal of Sustainable Energy, Vol. 29, Issue 4, 2010, pp. 245-255.
[4]. Charabi Y., Gastli A., PV Site Suitability Analysis using GIS-Based Spatial Fuzzy Multi-Criteria Evaluation, Renewable Energy, Vol. 36, Issue 9, 2011, pp. 2554-2561.
[5]. Salunkhe D. P., Chvan G., Bartakke R. N., Kothavale P. R., An Overview on Methods for Slope Stability Analysis, International Journal of Engineering Research & Technology, Vol. 6, Issue 3, 2017, pp.528-535.
[6]. Wen S., La H., Wang C., Analysis of Influence Factors of Slope Stability, Applied Mechanics and Material, 256-259, 2012, 34-38.
[7]. Kato S., 4 Types of Foundations Adopted for 15MW Solar Plant, 2016, Retrieved from: https://tech.nikkeibp.co.jp/dm/atclen/news_en/15mk/021100369/.
[8]. Kato S., 2.1MW Solar Plant Built on Roadside Slope, 2015, Retrieved from Solar Power Plant Business: https://tech.nikkeibp.co.jp/dm/english/NEWS_EN/20150810/431534/?ST=msbe.
[9]. Ashour M., Ardalan H., Analysis of pile stabilized slopes based on soil-pile interaction, Computer and Geotechnics, Issue 29, 2012, pp. 85-97.
[10]. Yang S., Ren X., Zhang J., Study on embedded length of piles for slope reinforced with one row of piles, Journal of Rock Mechanics and Geotechnical Engineering, Volume 3, Issue 2, 2011, pp. 167-178.

Environment

9th Int. Conf. on Geotechnique, Construction Materials and Environment,
Tokyo, Japan, 20-22 November 2019, ISBN: 978-4-909106025 C3051

RAIN GAUGES NETWORK SIMULATION USING GEOSTATISTICS AND HYBRID PARTICLE SWARM-SIMULATED ANNEALING OPTIMIZATION

Mohd Khairul Bazli Mohd Aziz[1], Fadhilah Yusof[2], Zulkifli Yusop[3], Mohammad Afif Kasno[4]
[1]Centre for Mathematical Sciences, Universiti Malaysia Pahang, Malaysia,
[2]Faculty of Science, Universiti Teknologi Malaysia, Malaysia,
[3]Faculty of Civil Engineering, Universiti Teknologi Malaysia, Malaysia,
[4]Faculty of Electrical and Electronic Engineering Technology, Universiti Teknikal Malaysia, Malaysia.

ABSTRACT

In designing an effective and economical hydraulic structure for flood control, an optimal design of rain gauge network is important as it produces fast, accurate and important rainfall data. In this paper, the geostatistical method integrated with a hybrid of particle swarm optimization-simulated annealing is used to simulate the optimal locations and number of raingauges station. The simulation process used different generated rainfall data based on real rainfall data. The rainfall data randomly generated based on the exponential semivariogram model and it showed similar characteristics with the mean and standard deviation of real rainfall data. The proposed method successfully obtained the optimal number of rain gauges despite different sets of generated rainfall data. This situation shows that the proposed method is adequate to be applied in another case study, in other places or different data.

Keywords: Rain Gauges, Geostatistics, Particle Swarm Optimization, Simulated Annealing

INTRODUCTION

Numerous water resources management tasks such as water budget analysis and assessment, flood analysis and forecasting, streamflow estimation, and design of hydraulic structures, employed rainfall data provided by a reliable and optimal rain gauge network. Accurate and precise data will help the researchers to minimize the hydrological and economic risk and errors involved in different water resources projects. An optimal and well-designed rain gauge network thus should contain an appropriate number of rain gauges, which reflect the spatial and temporal variability of rainfall in a catchment [1].

Thus, identification and selection of the optimal rain gauge network configuration with optimal number and locations of rain gauge stations is the main objective of the network design. Hence, the optimal rain gauge network should contain the number and locations of rain gauge stations in such a way that it can produce optimum rainfall information and data with minimum uncertainty and cost [1]-[3]. One can approach the problem either by removing redundant stations from the network to minimize the cost or by expanding the network with the installation of additional stations to reduce the estimation uncertainty [4]. Some studies applied the kriging technique in combination with other techniques such as entropy [1] and multivariate factor analysis [5] for the network design. A few studies also combined optimization method based on simulation tools (e.g. simulated annealing) with the kriging technique [2], [6],[7] to obtain the optimal rain gauge network.

A network design methodology was developed in this paper to determine optimal number and locations of the existing stations in the current rain gauge network located in the Johor state, Malaysia using geostatistical and hybrid of particle swarm optimization-simulated annealing (PSO-SA) as an optimization method. A simulation is performed to verify the ability of the optimization method to determine the optimal number of raingauges using randomly generated rainfall data by the semivariogram model selected. The major contribution here is that unlike the work of [2], the developed methodology considered the hybrid of PSO-SA technique as an optimization method which capable of escaping from a local optimum with fast convergence.

METHODOLOGY

Geostatistical Method

The network design problem consists in obtaining the number *N* and the location of rain gauges stations that give the best estimate areal mean rainfall. An estimation variance σ^2 is a basic tool of variance reduction techniques for optimal selection of sampling locations. A semivariogram must be modelled for the application of the variance reduction method to the optimal location of sampling sites.

A semivariogram $\gamma(h)$ is one of the significant functions to indicate spatial correlation in observations measured at sample locations. Semivariogram is represented as a graph that shows the difference in measure with a distance between all pairs of sampled locations. The estimated variance depends on the semivariogram model, the number *N* of rain gauges and its spatial location. Therefore, choosing an appropriate semivariogram model is vital in determining the optimal estimation variance.

Let *h* be the lag or distance, and *Z* be an intrinsic random function and let $Z(x_i)$, for $i = 1,2,\ldots,N$ be a sampling of size *N*. Then the following expression is an unbiased estimator for the semivariogram of the random function:

$$\gamma(h) = \frac{1}{2n(h)} \sum_{i=1}^{n(h)} [Z(x_i + h) - Z(x_i)]^2 \quad (1)$$

Equation 1 is used to compute experimental semivariogram from the data under study. By changing *h*, both in distance and direction, a set of the sample (or experimental) semivariograms for the data is obtained [8].

The exponential semivariogram models are selected to fit the data. The exponential semivariogram model equation is as follow:

$$\gamma(h) = C\left(1 - e^{-\frac{3h}{a}}\right) \quad (2)$$

where *C* is the sill and *a* is the range.

Once the model of the semivariogram is fixed, the estimation variance only depends on the number *N* and the location of the rain gauges. To calculate the estimation variance using ordinary kriging,

$$\sigma^2(x_0) = 2\sum_{i=1}^{k} \lambda_i \gamma(x_i, x_0) - \sum_{i=1}^{k}\sum_{j=1}^{k} \lambda_i \lambda_j \gamma(x_i, x_j) \quad (3)$$

Where

$$\hat{Z}(x_0) = \sum_{i=1}^{k} \lambda_i Z(x_i) \quad (4)$$

Subject to $\sum_{i=1}^{k} \lambda_i = 1$.

This is an algorithm for the ordinary kriging estimation to calculate the estimation variance [9]:

1. Calculate each term in matrix *G*.

   Let x_i 's be the sampling sites of a sample subset of size k, $i = 1,2,\ldots,k$ and let $\gamma(x_i, x_j)$'s be the experimental variogram. Then the *G* is the matrix

$$G = \begin{bmatrix} \gamma(x_1,x_1) & \gamma(x_2,x_1) & \cdots & \gamma(x_k,x_1) & 1 \\ \gamma(x_1,x_2) & \gamma(x_2,x_2) & \cdots & \gamma(x_k,x_2) & 1 \\ \cdots & \cdots & \cdots & \cdots & \cdots \\ \gamma(x_1,x_k) & \gamma(x_2,x_k) & \cdots & \gamma(x_k,x_k) & 1 \\ 1 & 1 & \cdots & 1 & 0 \end{bmatrix} \quad (5)$$

2. Calculate each term in matrix g.

Let x_0 be the estimation location, then the *g* is the matrix

$$g = [\gamma(x_0,x_1) \quad \gamma(x_0,x_2) \quad \cdots \quad \gamma(x_0,x_k) \quad 1]' \quad (6)$$

3. Solve the system of equations

$$GW = g,$$

$$W = gG^{-1},$$

Where $W = [\lambda_1 \quad \lambda_2 \quad \cdots \quad \lambda_k \quad -\mu]$.

4. Calculate the ordinary kriging estimation variance

$$\sigma^2(x_0) = g'W = g'G^{-1}g. \quad (7)$$

Hybrid of Particle Swarm Optimization and Simulated Annealing

The basic idea of the hybrid optimization study in this research is based on running PSO algorithm first and then improving the result by employing simulated annealing. The most significant character of SA is the probabilistic jumping property, i.e. probability to accept a worse solution to be a new solution. Therefore, through the integration of SA to PSO, the proposed algorithm is capable of escaping from a local optimum with fast convergence. Based on the PSO and SA characteristics, the whole procedure of PSO-SA is described as follows:

1. Initialization:

1a. Randomly initialize the *x* particles representing different combinations of *N* rain gauge placements.

1b. Evaluate each particle in the population using the fitness function in Eq. (7) and minimum fitness function is set as *pbest*.

1c. Set all parameters, including c_1 and c_2, $v_{\max}$, initial temperature T_0, cooling rate α.

2. Repeat this step until the stopping criterion is satisfied:

2a. Evaluate the velocity and position of each particle by Eq. (8) and Eq. (9).

2b. Calculate the fitness of each particle, x'.

2c. Calculate $\delta = f(x') - f(x)$ and then randomly generate a number $\theta \in (0,1)$. If $\delta < 0$, as the objective is to minimum, meaning that the new position is improved, then the new position is accepted as the new position of particle *i*. Otherwise, a new position is accepted according to the following criterion: $\theta > e^{\frac{-\delta}{T_k}}$. Proceed to step 2d when the velocity of all particles are determined or return to step 2a for

those particles failing to be accepted and generate new velocities using the same evaluation process.

2d. Renew each particle to the new velocity and position and modify *gbest* and *pbest* by a simple comparison of their fitness values.

2e. When the evolution process has achieved a stopping criterion (or maximum iteration is reached), proceed to step 3, otherwise, modify the annealing temperature and return to step 2.

Output the best solution *gbest* and its fitness value. The output is the optimal number and location of stations with the minimum estimated variance.

Optimization Procedure

The optimization model to determine the optimal number and locations of rain gauge formulated mathematically as below.

Minimize

$$\sigma^2(x) = 2\sum_{i=1}^{k} \lambda_i \gamma(h_{i0}) - \sum_{i=1}^{k}\sum_{j=1}^{k} \lambda_i \lambda_j \gamma(h_{ij})$$

subject to

$$\sum_{i=1}^{k} \lambda_i = 1$$

where

$$\gamma(h) = C\left(1 - e^{-\frac{3h}{a}}\right)$$

RESULTS AND DISCUSSION

The optimization procedure to determine the optimal number of raingauges using the real rainfall data shows 59 raingauges stations, as in [10]. This procedure is performed by using monsoon rainfall data. It is because Johor recorded high rainfall amount during monsoon season. This procedure is needed to be verified by performed a simulation with randomly generated rainfall data.

For the simulation process, the rainfall data randomly generated based on the exponential semivariogram model obtained previously in Eq. (2) The semivariogram model used to estimate the rainfall data for each location as the geostatistics is a method of interpolation itself. The generated rainfall data is shown in Table 1. The true value for mean and standard deviation are 335.37mm and 490.63mm, respectively.

The box and whisker plot has been constructed to determine the variability of the mean and standard deviation of the simulated rainfall data as compared to the real rainfall data from monsoon season. It is due to the boxplot ability to interpret the asymmetric aspects of the data [11]. From Fig. 1 and Fig. 2, it shows that the boxplot manages to accurately capture the mean and the standard deviation of the real monsoon data. Indirectly, this proves that the exponential semivariogram model previously obtained is the best fitted and accurate model to represent the rainfall data. The estimates rainfall data showed similar characteristics to real data with the mean and standard deviation that is almost the same with real monsoon data.

Table 1 Mean and standard deviation for 30 generated rainfall data.

No.	Mean (mm)	Standard Deviation (mm)	No.	Mean (mm)	Standard Deviation (mm)
1	342.97	556.37	16	353.27	538.03
2	377.92	573.95	17	332.64	521.94
3	279.21	310.88	18	329.78	493.19
4	364.29	310.88	19	269.59	316.19
5	352.77	586.46	20	370.42	715.40
6	277.95	325.39	21	319.44	535.82
7	320.41	598.14	22	338.69	598.76
8	340.23	528.67	23	320.82	418.32
9	283.03	330.85	24	348.65	575.51
10	326.74	532.19	25	342.03	526.48
11	340.18	621.42	26	362.54	672.00
12	337.52	505.59	27	350.16	458.23
13	337.78	542.33	28	293.94	369.38
14	335.05	561.95	29	331.82	539.51
15	288.95	337.87	30	369.24	592.43

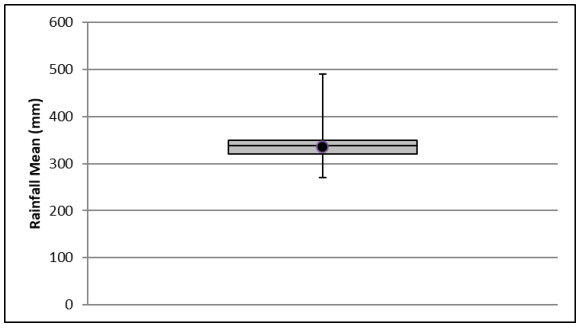

Fig. 1 Box and whisker plot for rainfall mean (mm).

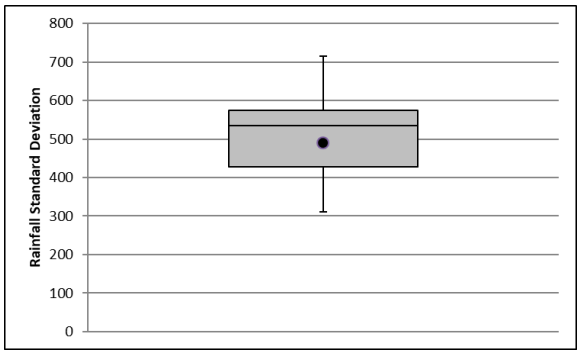

Fig. 2 Box and whisker plot for rainfall standard deviation.

The proposed method has been simulated 30

times, with 30 different generated rainfall data based on monsoon rainfall data. The computing procedure to obtain the optimal number and location for each data are repeated using the proposed method after the rainfall data has been successfully generated. The results are shown in Table 1 below.

The proposed method managed to determine the optimal number of rain gauges for each simulation. The optimal number of rain gauges for each simulation is not the same. This is because of the different generated rainfall data will give a different number of optimal rain gauges.

Table 2 The optimal number of rain gauges for 30 simulations.

Simulation	Optimal Number of Rain Gauge	Simulation	Optimal Number of Rain Gauge
1	59	16	63
2	62	17	59
3	60	18	63
4	60	19	61
5	60	20	58
6	58	21	58
7	57	22	58
8	59	23	61
9	62	24	59
10	61	25	61
11	58	26	55
12	55	27	61
13	63	28	58
14	56	29	59
15	56	30	55

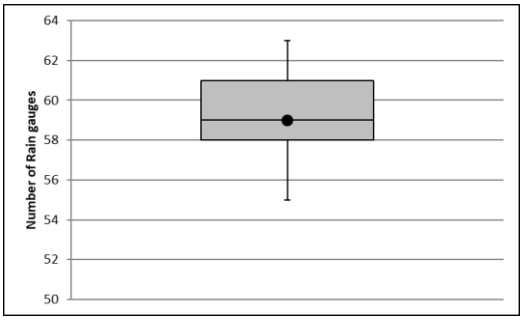

Fig. 3 Box and whisker plot of the number of rain gauges for 30 simulations.

Box and whisker plot (boxplot) used to investigate the symmetry of the results. The form of the box and whisker plot shown in Fig. 3 here is a graphical 5-number summary of a given dataset, which includes: the median, the interquartile range (shown by the box), the maximum and minimum value from Table 2. The distribution is shifted to the right; the mean should be greater than the median. From the plotted boxplot, the minimum number of rain gauges network is 55 rain gauges, and the maximum is 63. The median is 59, same as the results in [10]. In this case, the median is shifted toward the lower portion of the box with a wider range of observations in the upper quartile as compared to the lower quartile [11]. The box and whisker plot manages to capture the optimal value of the rain gauge network very well, and it proves the stability of the proposed method. Overall, the proposed method successfully obtained the optimal number of rain gauges despite different sets of generated rainfall data. The optimal locations of the generated shown in Fig. 4(a) and Fig. 4(b).

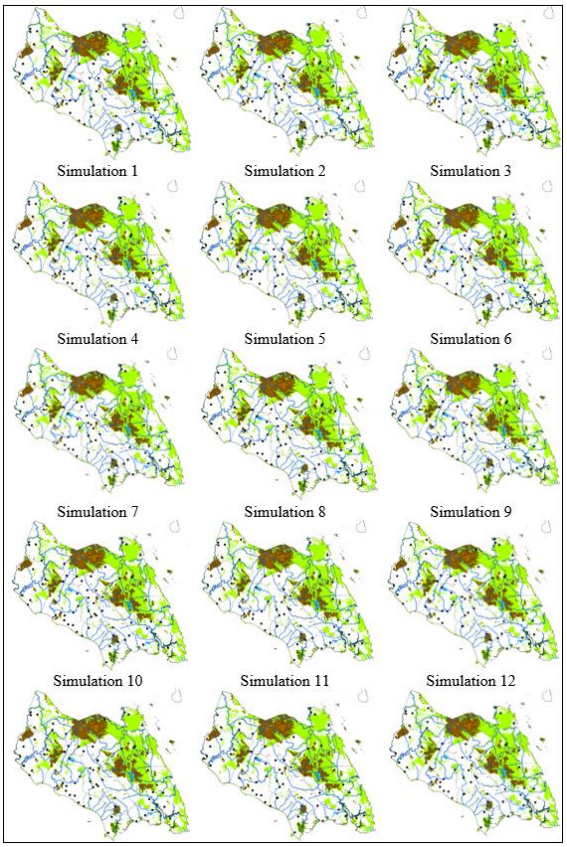

Fig. 4(a) The optimal locations for the raingauges stations.

CONCLUSION

The combination of PSO and SA successfully develop a new optimization method to determine the optimal number and location of the rain gauges in Johor. To this point, the unique characteristic of PSO and SA is utilized to form a PSO-SA hybrid optimization model. PSO ability to change the pace of the optimization procedure and SA ability to find new angles of solution at times when it is trapped in local optima has been a key factor in the optimization process. The simulation results verified the stability of the newly proposed method in determines the optimal number and locations for the rain gauge network. The optimal rain gauges network is essential

in helping understanding the rainfall patterns and acts as a guide in water resource management for extreme events like flood and drought. The optimal rain gauge network also helps us plan responses to droughts and floods, especially in flood prediction, flood warning and flood risk management. Since all of these events frequently occurred during the monsoon season, thus the results of monsoon data are the most appropriate result to be implemented in Johor.

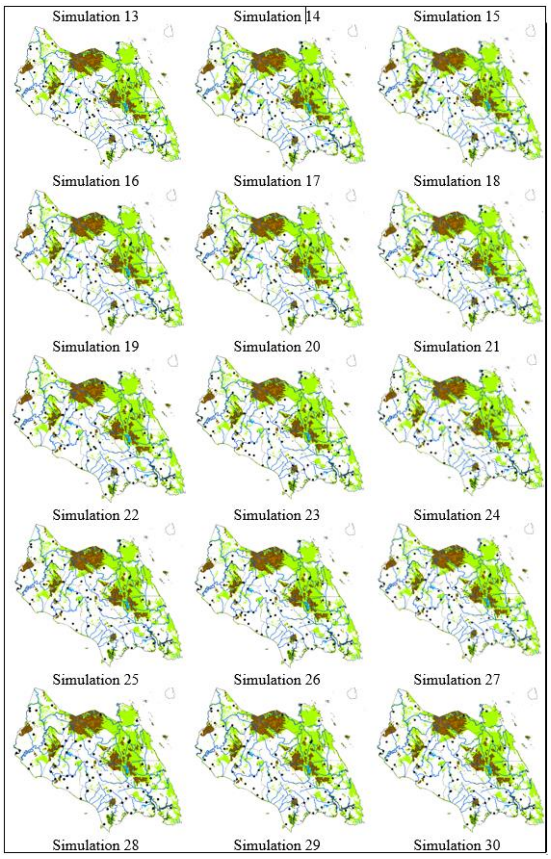

Fig. 4(b) The optimal locations for the raingauges stations.

ACKNOWLEDGEMENTS

The authors would like to thank Universiti Malaysia Pahang under UMP grant RDU1703196 for the technical and research support.

REFERENCES

[1] Yeh, H. C., Chen, Y.C., Wei, C., Chen, R. H., Entropy and kriging approach to rainfall network design. Paddy and Water Environment 9: 343–355. DOI: 10.1007/s10333-010-0247-x. 2011.

[2] Pardo-Igúzquiza, E. Optimal selection of number and location of rainfall gauges for areal rainfall estimation using geostatistics and simulated annealing. Journal of Hydrology 210: 206–220. DOI: 10.1016/S0022-1694(98)00188-7. 1998.

[3]Kassim, A. H. M., Kottegoda, N.T. Rainfall network design through comparative kriging methods. Hydrological Sciences Journal 36: 223–240. DOI: 10.1080/02626669109492505. 1991.

[4] Mishra, A. K., Coulibaly, P. Developments in hydrometric network design: a review. Reviews of Geophysics 47: RG2001. DOI: 10.1029/2007RG000243. 2009.

[5]Shaghaghian, M. R., Abedini, M. J. Rain gauge network design using coupled geostatistical and multivariate techniques. Scientia Iranica 20: 259–269. DOI: 10.1016/j.scient.2012.11.014. 2013.

[6] Barca, E., Passarella, G., Uricchio, V. Optimal extension of the rain gauge monitoring network of the Apulian regional consortium for crop protection. Environmental Monitoring and Assessment 145: 375–386. DOI: 10.1007/s10661-007-0046-z. 2008.

[7] Chebbi, A., Bargaoui, Z. K., Cunha, M. D. C., Optimal extension of rain gauge monitoring network for rainfall intensity and erosivity index interpolation. Journal of Hydrologic Engineering 16: 665–676. DOI: 10.1061/(ASCE)HE.1943-5584.0000353. 2011.

[8] Burrough, P. A. Principles of Geographical Information Systems for Land Resources Assessment. Clarendon Press, Oxford, pg. 147-165. 1987.

[9] Olea, R. A. Geostatistics for Engineers and Earth Scientists, Kluwer Academic Publishers, ISBN 0-7923-8523-3, Massachusetts, 2003.

[10]Aziz, M. K. B. M., Yusof, F., Yusop, Z., Kasno, M. A. Optimal Rain Gauges Network Using Geostatistics And Hybrid Particle Swarm-Simulated Annealing Optimization. 4th Int. Conf. on Science, Engineering & Environment (SEE), Nagoya, Japan, Nov.12-14, 2018, ISBN: 978-4-909106018 C3051

[11]Peter C. Banacos. (2011). Box and Whisker Plots for Local Climate Datasets: Interpretation and Creation using Excel 2007/2010. Eastern Region Technical Attachment. No. 2011-01 January.

9th Int. Conf. on Geotechnique, Construction Materials and Environment,
Tokyo, Japan, 20-22 November 2019, ISBN: 978-4-909106025 C3051

DIFFERENT RATIOS OF RICEBERRY RESIDUES AND WATER ON HEALTH DRINK PRODUCTION

Wattana Wirivutthikorn[1]

[1]Faculty of Agricultural Technology, Rajamangala University of Technology Thanyaburi (RMUTT)
2 Phaholyothin 87 Soi 2 Phaholyothin Road Thanyaburi Pathum Thani 12130 Thailand

ABSTRACT

The food industry has a lot of wastes from production processes, that are beneficial to the possible when used of by-product to reduce environmental pollution. There were research reports related to the production of various type of cereal drinks by using cereals as raw materials. The objective of this research was to study the optimum ratios of riceberry residues, agar and water on health drink production. There were four experiments: Experiment 1: (control formula) blended riceberry and water 30:70, Experiment 2: blended riceberry and water 15:85, Experiment 3: blended riceberry and water 20:80 and Experiment 4: blended riceberry and water 25:75 were obtained. The results from physical measurement (L*,a and b*) were significantly different ($P \leq 0.05$). The study chemical of measurements, i.e. pH, percentage of acidity and total soluble solid were performed. The results showed that Experiment 2 had the lowest pH and gave the highest percentage of acidity values of 5.96 and 0,28, respectively. The microbiological properties revealed that amount of microorganism in each treatment was not found. The sensory evaluation used a 9-point hedonic scale. The results indicated that Experiment 3 had the highest scores of overall liking. Based on the obtained data, the formulation of beverages produced from residues, there is a high possibility of using the residues from production process. It can be developed health drink to be accepted by consumer, which has increased steadily and reduced the amount of wastes that must be disposed of pollution that is toxic to the environment.

Keywords: Riceberry, Water, Health, Drink

INTRODUCTION

At the present, Thailand food industries generate large amount of wastes or by-products annually from a variety of raw material sources. In that food wastes or by-products are an excellent source of nutraceuticals, bioactives, inherently functional and possess many components that are good for human health. Food industrial wastes or by-products convert to the functional food ingredients, it is the healthy trends in the food industry. The waste management is one of the major parts of food industries. The large volume of the low cost by-product gives economical benefit of its potentially valuable components and environmental benefits. Therefore, the utilization of by-products to health beneficial product and economic benefit to labour and country. Now, as people become increasingly take care of the relation between foods and good health. Consumer attitude towards health foods is promising development and the scope of functional foods is growing very fast in Thailand. Consumers believe that foods are taken directly effects on their health as a good or as a bad. The market for the functional foods has seen a tremendous demand in the recent years. Today foods are not only used to demand our hunger but also to provide major and minor nutrients for human life and these nutrients having the health benefits, protecting and controlling from the diseases [1]. Rice is one of the commonly used stable foods around the world. The distribution of the rice anthocyanins depends on the rice cultivars. The consumption of colored rice varieties is increasing among the people, because of its health benefits. Riceberry is a good example as registered rice variety from Thailand, a cross-breed of Jao Hom Nin (JHN), a local non-glutinous purple rice and Khoa Dawk Mali 105 (hom mali_rice). The variety was created by the Rice Science Center, Kasetsart University, Thailand. The research for nutritional properties, anthocyanin stability, and physical and cooking properties is a deep purple whole grain rice with softness and a palatable aftertaste. Riceberry has been a popular brown rice due to its health promoting properties. Inducing people to consume more brown rice could help ameliorate food-related chronic diseases like diabetes, heart disease, high blood cholesterol, obesity, and cancers [2]. Agar is a mixture of two components: the linear polysaccharide agarose and a heterogeneous mixture of smaller molecules called agaropectin. It forms the supporting structure in the cell walls of certain species of algae, and is released on boiling. Agar has been used as an ingredient in dessert. Agar can be used as a laxative, an appetite suppressant, a vegetarian substitute for gelatin, a thickener for soups, in ice cream, and beverage, as a thickening agent. Agar is the phycocolloid of most ancient origin. Water contributes to the formation of gels in food. Originally, and even in the present times, it

was made and sold as an extract in solution (hot) or in gel form (cold), to be used promptly in areas near the factories; the product was then known as tokoroten [3]. Since this research focuses on the use of food waste residues for added values, therefore, the riceberry residues from the riceberry production process has been utilized since it still contains the necessary nutrients. There are some researches related to the processing of healthy beverages from Homnil rice by studying to optimize a suitable ratio between rice flour and water at 1:20, 1:30 and 1:40 ratios with rice flour extraction temperature at 50°C. The types and amount of sweeteners were 60°Brix sucrose syrup and 60°Brix. The banana syrup at concentration levels of 7 and 9°Brix. and amount of gelatin stabilizer were used at 0.0, 0.1, 0.2, 0.3 and 0.4 percent and suitable period for disinfection at 90°C was studied at 15, 20, 25 and 30 mins. It was found that the most suitable ratio between rice flour and water was 1:30. The batter viscosity was 14.73 centipoises, with pH, total soluble solids, protein content, fat content, and fiber content of 6.71, 1.1, 0.23, 0.05 and 0.83 percent, respectively. The amount of anthocyanin was 0.37 mg/ml. From adjustment of total soluble solids, it indicated that the use of 7°Brix sucrose syrup was most acceptable from testers in taste, texture, and overall liking ($p \leq 0.05$). The use of 0.3 percent gelatin (by weight) resulted in wholeness of the beverage, without layers. The beverage had viscosity of 18 centipoises, pH of 6.4, total soluble solids of 9.8 percent, and anthocyanin content of 0.7 mg/ml. It was also found that with disinfection at the temperature of 90°C for 25 minutes, the beverage could be kept for 15 days at the temperature of 4-6°C with standard amount of microbes [4]. The study on preparation of enhancing GABA in germinated brown rice and its products were conducted during 2008-2010 at Pathum Thani Rice Research Center, Thailand. The results revealed that an appropriate method was malting of selected healthy brown rice in a closed container at room temperature for 20 hours after the seeds being washed with clean water and steeped for 4 hours. This freshly malting rice can be used for making blended drinks of germinated brown rice by pre-boiling with intermittently stirring the mixture of ingredients as germinated Khao Dawk Mali 105 : germinated black glutinous rice: overnight steeped soy bean: roasted white sesame: water at a ratio of 1: 0.5 : 0.3 : 0.3 : 20 by weight for 20 mins. Filtering the mixtures twice and adding 5 g of sugar per 100 ml of the mixtures. The processing of instant germinated brown rice was also conducted by pre-preparation of soy milk from a mixture of overnight soaked soybean: roasted white sesame: water at a ratio of 1 : 0.8 : 14 by weight. Rice starch mixture was then prepared by mixing germinated Khao Dawk Mali 105 : germinated black glutinous rice: soy milk at a ratio of 7:3:9 by weight and wet milling. The mixture was dried with a double drum drier then ground to fine powder. Eight g of germinated rice powder were then mixed with 5 g of fine sugar, 4 g of maltodextrin and 2 g of non dairy cream packed in aluminium foil sachet. The another experiment was conducted at Ubon Ratchathani Rice Research Center using cooked germinated Khao Dawk Mali 105 and water at a ratio of 1 : 1 by weight. The mixture was slurred and drum dried prior to ground into powder. The powder was then packed with pre-cooked soy bean and job tear powder which were prepared by overnight soaked and steamed cooked before drum dried and ground to powder. The ingredient contained 7 g of dehydrated germinated brown rice, 2 g of dehydrated soy bean, 2 g of dehydrated Job's tear, 6 g of non dairy cream, 4 g of dairy powder and 10 g of sugar [5]. From above related researches, but there was no information about the formulation of riceberry residues juice mixed with agar and water. For this reason, of riceberry residues and agar advantages, the researchers are interested in producing water-based riceberry residues juice, agar and water with the healthy drink by studying and development an appropriate amount of riceberry residues, agar and water ratios on the physical, chemical, microbiological quality and sensory acceptability of the panelists, which help with the quenching of thirst and help relax or make the body. The data obtained from this research was an alternative to make riceberry residues juice as by-products and agar for beverage production to improve the quite appearance characteristic, nutritional quality, acceptability test and good health of consumers also solve the problems of bringing by- products from various food industries that are being commercially used in functional food ingredients for human consumption with higher values.

METHODOLOGY

The research was carried out at the Division of Food Science and Technology, Faculty of Agricultural Technology, Rajamangala University of Technology Thanyaburi. (RMUTT) Pathum Thani Province Thailand. The samples used in this study were purchased from Rangsit Market which located in Pathum Thani Province Thailand. This research was performed as four experiments)three replications(: 1) (control formula) blended riceberry and water 30:70; 2) blended riceberry and water 15:85; 3) blended riceberry and water 20:80 and Experiment 4: blended riceberry and water 25:75 details as the Table 1 [6].

Riceberry Juice Preparation

The riceberry was soaked in amount of water in a

stainless steel pot according as shown in Table 1. Then, allowed to mix homogeneously. The aliquot was filtered through a white cloth and again an aliquot was clarified. The aliquot was heated, then 50g of sugar was added and allowed to dissolve homogeneously after which pandan leaf juice was gradually added. An aliquot of this was heated at 65°C for 30 mins, then the temperature was reduced and the liquid poured into a sterilized plastic bottle [6],[7].

Preparation of Riceberry Residues Agar

Weigh 8.3 g of agar powder and 100 ml of water were placed in a stainless steel pot and heated to 90 °c for 6 mins until allowed to dissolve homogeneously. Then 100 g of sugar to simmer until it dissolved until a homogeneous aliquot. Then, put 30 ml of pandan juice was added and allow to dissolve homogeneously and then cooled at room temperature. (This step should add pandan juice before lifted down from the stove, because the aliquot of simmering for too long affecting on the pandan leaf color causing separation from each other). Put them in the prepared mold, then add the boiled rice berry residues from the riceberry juice (as 2.1), then let it cooled to be mixed well [6],[7].

Recording of Data

Collect and record numerical data from experiments (three replications) and calculate data and statistical analysis. The Experimental design for physical and chemical quality analysis were evaluated by using a completely randomized design (CRD). A randomized complete block design (RCBD) for sensory evaluation was used with analysis of variance. Analysis of the mean differences of experiments was performed using Duncan's new multiple range test [8].

Physical Measurement

The color brightness (L*), color as red (+a*) and yellow (+b*) were measured by using Minolta CR-10 [9] and recorded as values adapted from [9]. The sedimentation was detected by using eye detection adapted from [9].

Chemical Measurement

The pH, total soluble solid (TSS) and percentage of total acidity (calculated as citric acid) were measured by using pH meter OHAUS ST3100-F, using hand refractometer and titration with 0.1N sodium hydroxide (phenolphthalein as indicator) as values, respectively adapted from [10].

Microbiological Measurement

The total microbiology was measured as total plate count by using plate count agar adapted from [11].

Sensory Evaluation

The sensory evaluation was carried out by 30 untrained panelists in Rajamangala University of Technology Thanyaburi (RMUTT), Thailand. Panelists were asked to analyze their level of preference for each treatment by using a 9-point hedonic scale test based on the attributes of color, odor, taste, body, clarify and overall acceptability. A randomized complete block design was used with analysis of variance. Analysis of the mean differences of experiments was performed using Duncan's new multiple range test [12].

RESULTS AND DISCUSSION

Physical appearances of blended riceberry residues juice and agar

From the Fig 1, the study of the outside appearance of the riceberry products mixed with riceberry, agar and water. The images could be seen that the red color in all experiments were not significantly different. As a result of the ratio of riceberry juice, agar and water. When considering the appearance, it was found that all the experiments were suspended, which is the pulp of riceberry, which is derived from riceberry, agar and others. When considering the color, revealed that all the samples were dark brown as the color results of the anthocyanin [13]. The anthocyanin is water-soluble vacuolar pigments that, depending on their pH, may appear red, purple, blue or black. Food plants are abaundant in anthocyanins include the blueberry, raspberry, black rice, and black soybean, among many others that are red, blue, purple, or black. Some of the colors of riceberry are derived from anthocyanin. The color of anthocyanin is quite distinct and different chemical compositions and structures in riceberry. The color characteristics can be seen that when the amount of water is much, the color was pale. When considering the appearance, it indicated that the Experiment 1 gave a lot of suspended sediments of riceberry residues than the other experiments. The odor was varied with the amount of increased riceberry and the decreased amount of water which compared to control samples. The taste indicated that all experiments were little sweet and little salty taste. This is due the increasing proportion of riceberries, whereas reducing the amount of water that results in dilution effects caused the flavor to not be concentrated [14].

Physical Measurement

Table 2, The results showed that all of L*, +a* and +b* values and physical appearance depending on different ratios of riceberry residues, agar and water. The results showed that all values were different ($P \leq 0.05$). The physical characteristics of blended riceberry residues, agar and water, comparing the differences between the experiments of color values L*, +a* and +b*, they revealed the brightness value (L*) was of 33.3, 29.0, 31.2 and 32.1, respectively. The color values (+a*) was 4.1, 3.1, 3.6 and 2.5, respectively. The color values (+b*) was of 10.59, 12.13, 12.51 and 13.55, respectively [15]. Riceberry had a deep purple color. This may be caused by the ratios between riceberry residues, agar and water with different amounts due to each experiment to have different values. The experiment with a large amount of riceberry residues ratio had a darker color and more brightness than the experiment with ratio of the less amount of riceberry residues [16]. One possible reason ricebeery has a anthocyanin as a main pigment, a pigment that is red color and soluble in water well. The proportion of the amount of riceberry that increase redness will increase according to the amount of riceberry, but increasing the amount of riceberry residues results in an increasing trend of all values [17].

Chemical Measurement

Table 3, The results revealed that the pH, total soluble solid and percentage of total acidity in riceberry juice products with agar and water, depended on the different ratios. The result was found that the measured values (percent of acidity) were statistically significant differences ($P \leq 0.05$) while pH and total soluble solid were not statistically different. This value depends on the increasing riceberry residues, agar and water ratio, resulting in lower pH values (more acidity). The results indicated a tendency for the percent of total acidity decrease low values in comparison with the control samples. The analyzed values were consistent with the percentage of total acid content in the form of citric acid that is higher with organic acid (such as citric acid). The total soluble solid was not significantly different ($P > 0.05$). The anthocyanins are the most important water-soluble pigments that belong to the flavonoid group and are accountable for the different color in plant tissues [18]. The pH is one of the most influencing factors of stability, and color of the anthocyanins. The anthocyanins are more stable in acidic condition than in the alkaline condition. This reason be due to anthocyanin may be used as pH indicators because their color changes with pH; they are red or pink in acidic solutions ($pH < 7$), purple in neutral solutions ($pH \approx 7$), greenish-yellow in alkaline solutions ($pH > 7$) and colorless in very alkaline solutions, where the pigment is completely reduced. [19]. Apart from this, there was some main compounds of total phenolic content in riceberry. Therefore, if the riceberry was heated to a high temperature level and took too long time, it did not affect in pH change of riceberry. This can be seen that the pH value might not be very low. Because the heat was used to boil, it took short time, so the amount of pH was not very low [20],[21].

Microbiological Measurement

Based on the analysis of total microbial counts by using the total plate count method in blended riceberry residues, agar and water. the results showed that microorganisms were not found in all experiments. One reason possibility was due to the completed pasteurization process of blended riceberry residues juice agar and water before packaging. This processing is a thermal processing method with the main purpose to destroy pathogenic microorganisms, including microorganisms and enzymes that cause food degradation [22],[23].

Sensory Evaluation

Table 4, the results of the sensory analysis showed that there were differences in all experiments ($P \leq 0.05$) [24],[25],[26]. Based on the color, odor, taste, body, clarify and overall acceptability values. Experiment 1 had the greatest odor and taste from panelists due to the highest amount of riceberry residues being added [26],[27]. One possible reason might be due to the highest proportion of riceberry resiudes and the lowest of water. Color values showed that Experiment 4 was the most acceptable, but Experiment 2 gave the highest body score value. This may have been due to the riceberry residues and water ratios level resulted in preferred acceptance level or the panelists preferred the color of the drink containing reddish purple color of riceberry. The experiment with the highest clarify and overall acceptability were the Experiment 3. For one possible reason, the increased amount of water, if increased too much, caused the color and appearance to appear paled color. The amount of total soluble solids decreased as a result of dilution, causing the panelists did not accept it [28],[29].

Table 1 Different Ratios of blended riceberry residues juice agar and water

ingredient	Experiment			
	1	2	3	4
riceberry (g)	210	105	140	175
filtered water (ml)	490	595	560	525
sugar (g)	50	50	50	50
pandan leaf juice (ml)	52	52	52	52

Table 2 Physical measurement of blended riceberry residues juice agar and water

Experiment	physical values*		
	L*	a*	b*
1	33.3[c]	4.1[c]	10.59[c]
2	29.0[a]	3.1[b]	12.13[b]
3	31.2[b]	3.6[b]	12.51[ab]
4	32.1[b]	2.5[a]	13.55[a]

Note: a-d The different letters in the same column mean significant difference (P ≤ 0.05)

Table 3 Chemical measurement of blended riceberry residues juice agar and water

Experiment	chemical values		
	pH[ns]	TSS (°Brix)[ns]	percent of total acidity*
1	33.3[c]	4.1[c]	10.59[c]
2	29.0[a]	3.1[b]	12.13[b]
3	31.2[b]	3.6[b]	12.51[ab]
4	32.1[b]	2.5[a]	13.55[a]

Note: a-d The different letters in the same column mean significant difference (P ≤ 0.05) and ns non significant difference (P>0.05)

Table 4 Mean score of preference for sensory properties of blended riceberry residues juice agar and water

Exp	scores					
	color*	odor*	taste*	body*	clarify*	overall acceptability*
1	6.29[b]	6.42a	6.50[a]	6.30[b]	6.22[b]	6.64[b]
2	6.18[b]	6.38[b]	6.38[b]	6.67[a]	6.26[b]	6.60[b]
3	6.41[b]	6.03[b]	6.42[b]	6.44[b]	6.41[a]	6.91[a]
4	6.86[a]	6.02[b]	6.37[b]	6.39[b]	6.29[b]	6.82[b]

Note: a-d The different letters in the same column mean significant difference (P ≤ 0.05)

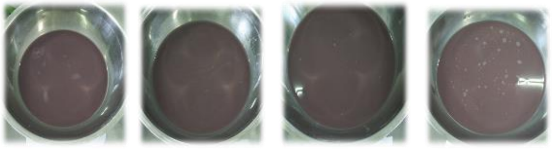

E1 E2 E3 E4

E1: blended riceberry and water 30:70
E2: blended riceberry and water 15:85
E3: blended riceberry and water 20:80
E4: blended riceberry and water 25:75

CONCLUSION

1. The uses of different ratios of by-products as raw material preparation had effects on the quality of mixed riceberry residues, agar and water.

2. The results of the physical properties analysis showed that all values were statistically significant differences (P≤0.05).

3. The results of the chemical analysis showed that the percent of total acidity (except pH and total soluble solid) were significantly different (P≤0.05).

4. Blended riceberry residues, agar and water 20:80 gave the most overall acceptability of 6.91 values from the panelists.

5. The results of total plate count indicated that the microorganism in each experiment was not found.

6.. Based on this research, researchers will be able to launch new health drink products in the future for functionalities and health benefits of food by-products and their functional ingredients.

ACKNOWLEDGMENTS

The researchers would like to thank the 4 the grade students and officials of the Division of Food Science and Technology, the Faculty of Agricultural Technology Rajamangala University of Technology Thanyaburi (RMUTT), Pathum Thani Thailand that contributed some parts in the research. The Faculty of Agricultural Technology provided support facilities and budgets for the research.

REFERENCES

[1] Helkar, P.B., Sahoo, A.K. and Patil, N.J., Review: Food Industry By-Products used as a Functional Food Ingredients, Int J Waste Resour, Vol 6, 2016, pp. 1-6.

[2] Luang-In, V., Yotchaisarn, M., Somboonwatthanakul, I. and Deeseenthum, S., Bioactivities of organic riceberry broken rice and crude riceberry rice oil, Thai Journal of Pharmaceutical Sciences, Vol 42, 2018, pp. 161-168.

[3] Abraham, A. Afewerki, B., Tsegay, B., Ghebremedhin, H., Teklehaimanot, B. and Reddy, K.S., Extraction of Agar and Alginate from Marine Seaweeds in Red Sea Region, [Internet] 2018 [cited 2019 July 1]. Available from: www.symbiosisonline.org.

[4] Tirasarot, J. and Thanomwong, C., Production of Healthy Beverage from "Homnil" Rice, Khon Kaen University Sci. J. Vol 43, 2015, pp. 395-402.

[5] Wongpiyachon, S., Sudtasarn, K. and Sukviwat, W., Germinated brown rice and beverage products from germinated brown rice, [Internet] 2014 [cited 2018 January 25]. Available from:

http://anchan.lib.ku.ac.th/agnet/bitstream/001/2985/3/brrd54001a.pdf.

[6] Bua Yam, P., Milk cereal and herbal tea formula to relieve the disease, Bangkok: Phongsarn Publishing., 1994.

[7] Kinchampa, A. and Anothaiwattana, A., Study of physical and sensory properties on the consumer of carrot juice products with passion fruit juice, Bachelor of Science degree Science and Food Technology, Faculty of Agricultural Technology, Rajamangala University of Technology Thanyaburi, Pathum Thani, 2009.

[8] Damnum, A., Statistical analysis and data analysis, Kasetsat University Press. Bangkok, 2006.

[9] Lozano, J.E., Fruit manufacturing: Scientific: basis, engineering properties, and deteriorative reactions of technological importance, Springer Science & Business Media, LLC.. USA, 2006.

[10] AOAC, Official Method of analysis, Verginia: The Association of official Analytical Chemists, 2000.

[11] American Public Health Association, Compendium of Methods for the Microbiological Examination of Foods, 2nd ed. APHA, Washington, DC, 1984.

[12] Anprung, P., Principle of food analysis by sensory evaluation, Bangkok.: Chulalongkorn University Press.

[13] Wirivutthikorn, W. and Jenkunawatt, S., Preference colors of gac fruit blended with pineapple juice, Tien-Rein LEE (Editor –in-Chief), The 2nd Conference of Asia Color Association URBAN COLOR FOR LIFE 4-7 September 2014, Taipei, Taiwan, 2014, pp.304-307.

[14] Wirivutthikorn, W., Effect of lemongrass and pandan leaf ratios on production of mixed juice with lycopene supplementation, In: Proc. International Conference of Agriculture and Natural Resources 26-28 April 2018, ANRES 2018, Bangkok, pp. 378-381.

[15] Wirivutthikorn, W. and Jenkunawatt, S., Factors affecting on drying of okra and gac fruit in okra blended with gac fruit powdered beverage production, Research Report. Faculty of Agricultural Technology, Rajamangala University of Technology Thanyaburi, 2017, pp. 1-44.

[16] Wirivutthikorn, W., Effect of ratio of okra gac fruit and passion fruit on color and preferences of mixed juice, International Journal of Food Engineering, Vol 4, 2018, pp. 212-215.

[17] Anonymous., Special characteristics of Khao Hom Hom Nil, [Internet] 2013 [cited 2013 December 10]. Available from: http://www.sininrice.com/insight sub1.html.

[18] Glover, B. J. and Martin, C., Anthocyanins, Current Biology, Vol 22(5), 2012, pp. R147-R150.

[19] Fleschhut, J., Kratzer, F., Rechkemmer, G. and Kulling, S.E., Stability and biotransformation of various dietary anthocyanins in vitro, European Journal of Nutrition, Vol 45(1), 2006, pp.7-18.

[20] Wirivutthikorn, W., Effect of passion fruit juice and sugarcane juice ratios on blended passion fruit juice and sugarcane juice production, Agricultural Sci. J. Vol 49(3) (Suppl), 2018, pp. 229-235.

[21] Wirivutthikorn, W., Effects of types and quantities of sweeteners on development of blended lotus root juice and goji berry product, In: Proc. the 6th Academic Science and Technology Conference 2018, 6 June 2018, pp. AS176-AS180.

[22] Ciuffreda, E., Bevilacqua, A., Sinigaglia, M. and Corbo, M.R., *Alicyclobacillus* spp.: New insights on ecology and preserving food quality through new approaches, Microrganisms, Vol 3, 2015, pp. 625–640.

[23] Gilchrist, J.E. Donnelly, C.B., Peeler, J.T. and Campbell, J.E., Collaborative study comparing the spiral plate and aerobic plate count methods, J. Assoc. Off. Anal. Chem. Vol 60, 1977, pp. 807-812.

[24] Obasi, B.C., Whong, C.M.Z. and Ameh, J.B., Nutritional and sensory qualities of commercially and laboratory prepared orange juice, African Journal of Food Science, Vol. 11, 2017, pp. 189-199.

[25] Figueiredo, L.P., Dias, M.V., Valenti, W.A., Borges, S.V., Pereira, A.G.T., Pereira, P.A.P. and Queiroz, F., Influence of process parameters on the color and texture of passion fruit albedo preserved in syrup, J Food Sci Technol Campinas, Vol 33(1), 2013, pp. 116-121.

[26] Wirivutthikorn W., Appropriate ratios of producing riceberry blended with gac fruit and roselle beverage, In: Proc 3rd National and International Research Conference 2019 : NIRC III 2019 "Challenges of Higher Education in Production of Graduate Students in the 21st Century" 1st February 2019, Buriram Rajabhat University, Buriram, Thailand: 2019, pp. 2117-2126.

[27] Wirivutthikorn, W., Effect of okra and tangerine ratios on production of mixed juice with lycopene supplementation, In: proceedings of the 4th Int. Conf. on Science, Engineering & Environment (SEE), November 12-14, 2018, Nagoya, Japan, 2018, pp. 15-19.

[28] Rinphon, A., Luang Saen, N. and Donmun, P., Development of cereal beverage products, In: Proc. the 49th Kasetsart University academic conference, Bangkok: Kasetsart University, 2011, pp. 141 – 147.

[29] Prikbunchan, P. and Rattanapan, B., Development of germinated brown rice with vegetable juice ready-to-drink beverage, In: Proc. the 5th Rajamangala University of Technology National Conference, RMUTP Research Journal Special Issue, 2013, pp. 87-92.

9th Int. Conf. on Geotechnique, Construction Materials and Environment, Tokyo, Japan, 20-22 November 2019, ISBN: 978-4-909106025 C3051

MICROPLASTICS INGESTION BY FRESHWATER FISH IN THE CHI RIVER, THAILAND

Pattira Kasamesiri[1] and Wipavee Thaimuangphol[2]
[1,2]Faculty of Technology, Mahasarakham University, Thailand; [1,2]Research Unit of Excellence for Tropical Fisheries and Technology, Mahasarakham University, Thailand

ABSTRACT

Microplastic pollution mainly emanates from terrestrial sources but studies of plastic contamination in freshwater ecosystems remain limited. Consumption of freshwater fish is widespread throughout all regions of Southeast Asia. Contamination of microplastics in fish is an important issue which leads to human health risk. Common freshwater fish in the Chi River, Thailand were caught by local fishermen and investigated for abundance, size, color and shape of microplastics. Eight fish species were investigated. Results showed that 72.9% of the collected fish were polluted with microplastics at mean abundance of 1.76±0.97 particles per fish and was no significant difference of abundance between species. Percentage occurrence of microplastics was highest in omnivorous fish *Puntioplites proctozysron* (86.7%) with the most common size of microplastics ingested by fish at over 0.5 mm (47.5%), of which 56.9% were blue color and 86.9% were fiber shaped. Results revealed that fishing nets and fish cages were major sources of microplastic contaminants in the Chi River.

Keywords: Microplastics Pollution, Freshwater fish, Ingestion, Aquatic Environment

1. INTRODUCTION

Plastic production has continually increased since 1950, reaching 332 million tons in 2015 [1]. Increasing plastic debris has become a serious pollution problem in the aquatic environment. The amount of plastic debris is now 10 times greater than a decade ago on the shores of South Atlantic islands [2]. Plastic debris is widely distributed over ocean shorelines and has also become a major component of riverine pollution [3]-[5], which impacts to aquatic animals such as zooplankton, aquatic invertebrates, fish, marine reptiles and mammals by ingestion [6]-[10].

Microplastics are small plastic items with particle size <5 mm which can be classified into primary microplastics (pellets, plastics used in cleansing, cosmetic products and manufactured plastic products) and secondary microplastics [11]. Secondary microplastics originate from degradation and fragmentation of large plastic items and enter the aquatic environment through different pathways [1], [12]. Microplastics are easily spread with wide distribution because of their small size, light weight and durability [13]. Oceans and many urban rivers are contaminated with microplastics [14].

Direct effects of pollution by microplastics on aquatic organisms hamper their ability to ingest natural prey by obstruction of the digestive tract [6] and reduction of swimming velocity which affects resistance time of fish when swimming against the water flow [15]. Microplastic ingestion also leads to neurotoxicity and oxidative damage in marine fish [16] and reduction in photosynthetic activity and chlorophyll *a* of algae [17]. Moreover, various chemical substances are contained in all plastic products such as styrene, toxic metals, polychlorinated biphenyls (PCB), bisphenol A (BPA), polycyclic aromatic hydrocarbons (PAHs) and phthalates for improving polymer properties [18]-[19]. Microplastics deliver these chemical substances to aquatic organisms and act as mediators for other chemical contaminants in aquatic environments [20].

Microplastics transfer from primary consumers to higher trophic levels via a trophic food web and, finally, may contaminate humans [12], [19], [21]. Thus microplastic contamination is a crucial issue for food safety and human health [19]. Reports concerning microplastic contamination in fish have mainly concentrated on oceans and shorelines with the minority assessing the effects in freshwater environments [22]-[27]. Thus, this study assessed the abundance, size, color and shape of microplastics ingested by freshwater fish in the Chi River. Results will provide useful data for fishery and aquaculture food security.

2. MATERIAL AND METHODS

2.1 Samples Collection

Fish samples were collected from four sampling stations along the Chi River in the northeast of Thailand (Fig. 1). The Chi River is the longest river flowing within Thailand at 765 kilometers and runs

Table 1 Species and number of fish samples caught in the Chi River

Species	Habitats	Feeding features	Total Length (cm)	Weight (g)	Total Number
Labiobarbus siamensis	benthic	Detritivore	9.6±0.7	8.0±2.3	15
Puntioplites proctozyson	midwater – benthic	Omnivore	11.1±3.2	20.4±17.7	6
Cyclochelichthy repasson	midwater – benthic	Omnivore	11.8±2.6	18.7±11.4	15
Henicorhynchus siamensis	midwater	Omnivore	12.4±1.2	20.1±6.1	27
Labeo chrysophekadion	benthic	Detritivore	17.0±2.8	57.5±23.7	14
Mystus bocourti	benthic	Carnivore	14.9±2.7	21.1±9.2	20
Hemibagrus spilopterus	benthic	Carnivore	20.4±3.9	56.7±27.2	6
Laides longibarbis	pelagic-benthic	Detritivore	15.8±1.3	22.5±2.4	4

through seven provinces. The four study sites were located along the middle region where the river flows through urban areas of Maha Sarakham Province. Sources of plastic pollution were composed of fishing activity, aquaculture, agriculture, and sewage from industrial factories and residential areas. Fish were caught by local fisherman using gill nets during the late rainy season (October 2018) and stored at -20°C prior to examination for microplastics.

2.2 Microplastic Extraction and Analysis

Fish samples were weighed and measured for total length to an accuracy of 0.1 g and 0.1 cm, respectively. After dissection, fish stomachs and intestines were placed in 50 ml Erlenmeyer flasks and 30% H_2O_2 was used to digest the organic matter (Jabeen 2017). Volume of H_2O_2 was based on weight of stomach and intestine samples (approximately 30 ml/sample). Extracted samples were placed in an incubator at 65°C for 24 h. A saturated NaCl solution (approximately 300 g/L) was filtered and added into the flasks to separate microplastics by flotation. The saline solution was kept for 12 h at room temperature and then the supernatant was pipetted and filtered through a glass microfiber filter (Whatman GF/C 1.2 μm pore size). The filter paper was placed on Petri-dishes to record the numbers of microplastic particles, and colors and physical characteristics were divided into fibers, rods, fragments, and pellets under a stereomicroscope (Nikon SMZ745/745T). Microplastics were measured for their longest dimension

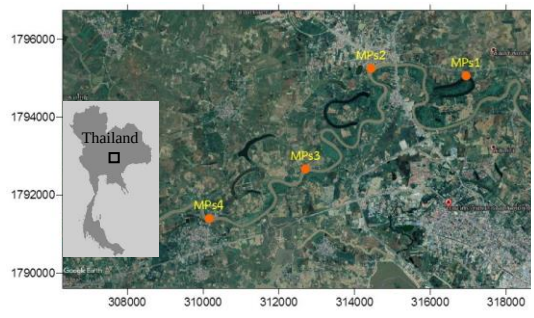

Fig. 1 Location (UTM; 48Q) of the sampling stations at Chi River, Maha Sarakham Province, Thailand

2.3 Statistical Analysis

Significant differences of microplastic abundance in fish gut among sampling stations and fish species were analyzed by Independent-Samples Kruskal-Wallis Test. Significant difference was set as p-value less than 0.05.

3. RESULT AND DISCUSSION

3.1 Abundance of Microplastics Ingested by Fish

A total of 107 individual fish were identified into 8 species (Table 1). We observed microplastics inside the gastrointestinal tract of 78 individuals (72.9% of total fish samples). Percentage occurrence of microplastics in each species ranged between 50.0-86.7% with the highest in *Puntioplites proctozysron* (Smith's barb) (Fig. 2). All feeding types (omnivore, carnivore, detrivore) showed high occurrence of microplastics (>50%) but less than planktivorous fish (77%) from Tokyo Bay, Japan [30]. Proportion of ingested microplastics was higher than fish in the English Channel (36.5% from 10 fish species) [22], islands in French Polynesia (37.2% from 4 fish species) [23] and estuaries of Brazil (9% of 69 fish species) [25]. Microplastics ingested by the fish samples varied from 1 to 2 particles per fish with an

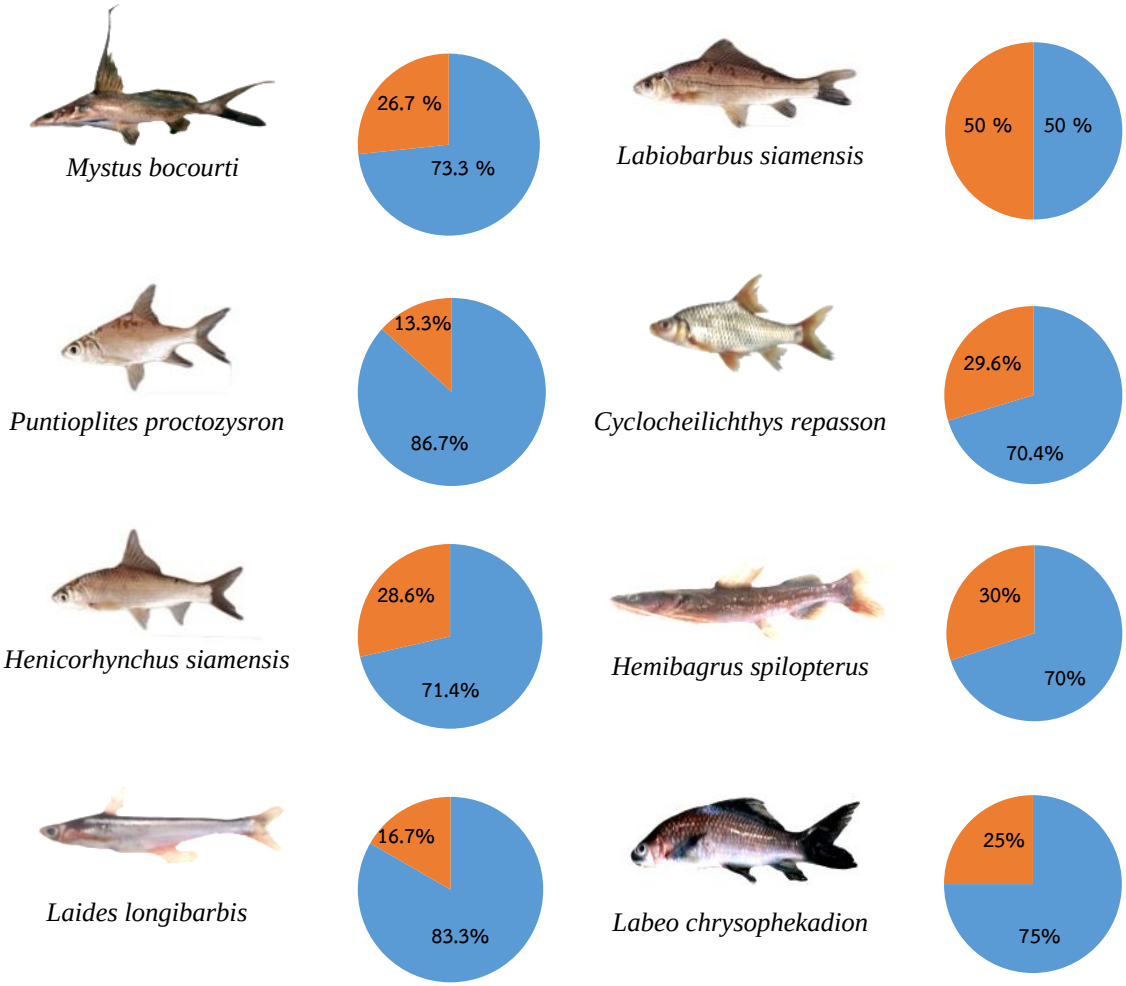

Fig. 2 The percent occurrence of microplastics ingested by fish in each species

average of 1.76±0.58 (Fig. 3). There was no significant difference in abundance of microplastics ingested between species (Kruskal-Willis Test, p-value=0.849). Omnivorous fish in intertidal zones of Chile recorded significantly higher numbers of microplastics than herbivorous and carnivorous fish [26], showing that occasions to ingest microplastics of feeding types were similar in present study. Abundance of microplastics was relatively high compared with fish from tropical estuaries of Brazil that affected from the anthropogenic pressures (0.12±0.37 particle per fish) [25]. Conversely, abundance of microplastics was lower than fish in the Pajeu River of Brazil (3.6 particles per fish) [7], possibly due to different flushing efficiency from river catchments and diverse microplastic sources [5], [12].

3.2 Colors, Shapes and Size of Microplastics Ingested by Fish

Six colors of microplastics were found in fish gut as blue, red, black, white, transparent and brown. The most common color was blue 56.9% (Fig. 4A). Most abundant color results concurred with former studies [8], [13], [28]. Variety of colored microplastics was higher in *Mystus bocourti* and *Cyclocheilichthys repasson* (Fig. 5) as carnivorous and omnivorous species, respectively. Fish may ingest microplastics as a result of visual confusion between prey [28] but our results gave similar color patterns between different feeding types.

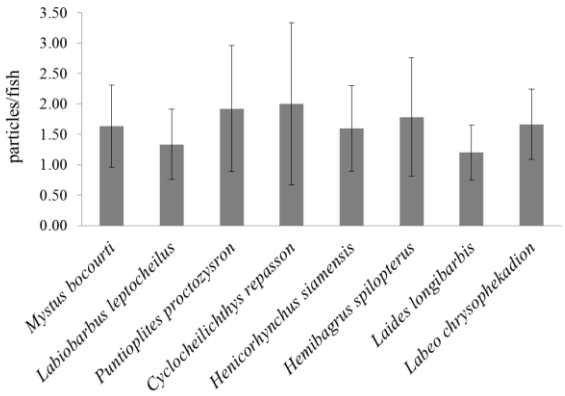

Fig. 3 The average number of microplastic ingested by fish (particles per fish) in each species. (Mean±SD)

Four shapes of microplastics were presented in fish gut (Fig. 6). The most abundance shape was fiber followed by rod-shaped, pellet and fragment, respectively (Fig. 4B). Fiber shape was a major type ingested by fish [7], [13], [28] and related to human activities [12]. An important source of fiber microplastics is from degradation of fishing gear, fish cages or nylon ropes [8] and sewage from washing clothes [29].

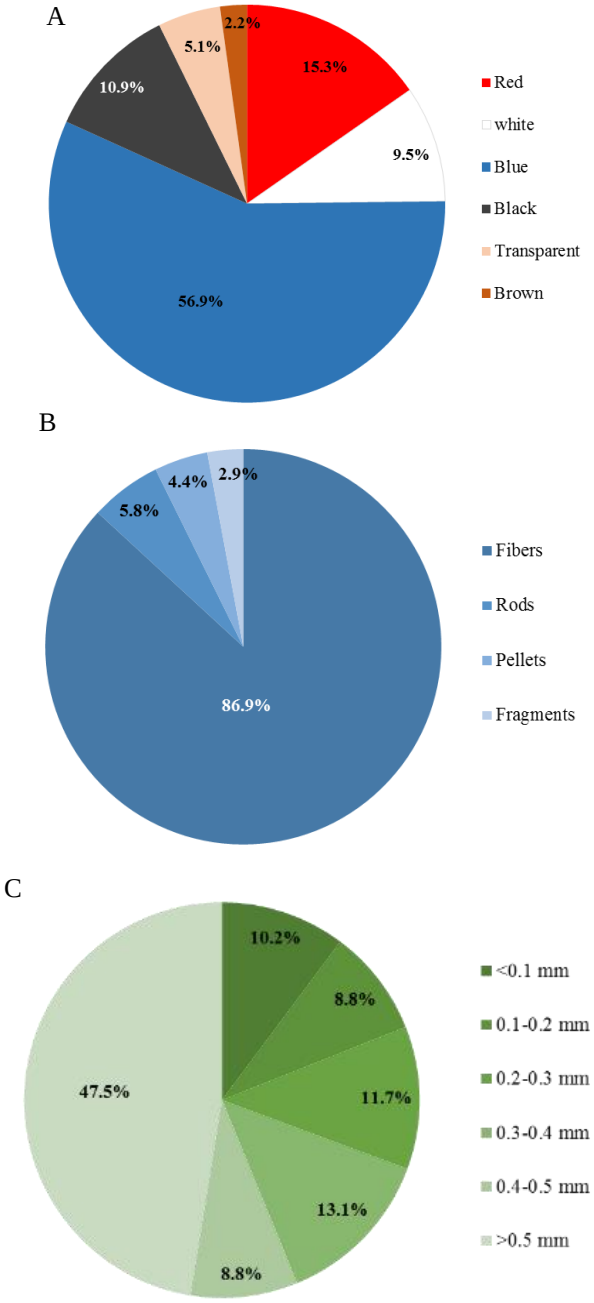

Fig. 4 The percentage of the total number of microplastics ingested by freshwater fish of color (A), shape (B) and size (C).

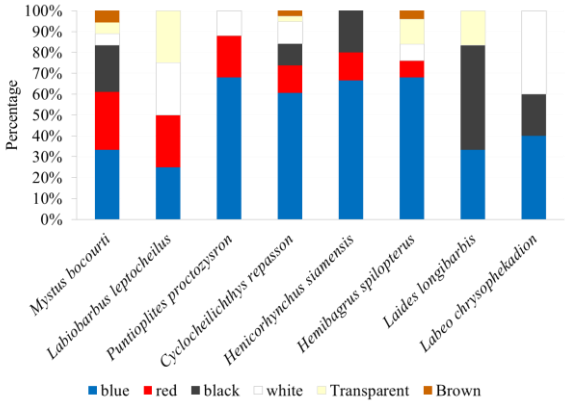

Fig. 5 The percentage of microplastics colors in each fish species.

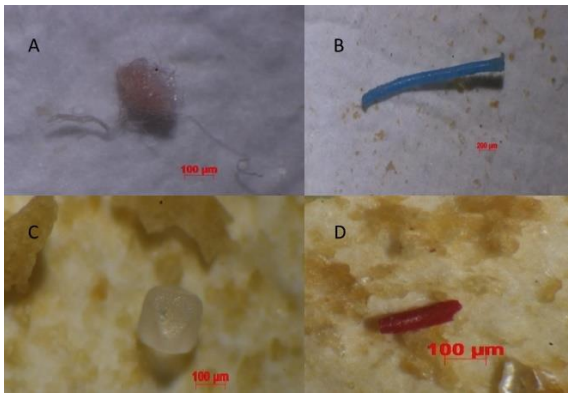

Fig. 6 Shape of microplastics found in gastrointestinal tract of fish: fiber (A), rod (B), pellet (C) and fragment (D).

Size distribution of microplastics ranged between 0.03-3.84 mm. The most abundant size was over 0.5 mm (47.5% of the total number of plastics) (Fig. 4C). Large particles were common in fiber type. Our results were similar to a previous report on surface water in reservoirs of China which found microplastic sizes ranging from 1 to 5 mm as more abundant [31]. Fish from coastal and freshwater areas of China contained microplastics ranging from 0.04-5 mm (76.3%) [13], while in our study, particles smaller than 5 mm were 100% of total number of plastics ingested by fish.

Size of plastics larger than 0.5 mm are used in fishing ropes or lines [30], indicating that the source of microplastics in the Chi River emanated from fishing gear and equipment used in aquaculture. The Chi River is an important fishery resource in the northeast of Thailand with abundant fishing activities [32]. Local fisherman usually use transparent or black gillnets to catch fish [32]. Blue fiber fish cages in Nile tilapia aquaculture may also be an important source

of microplastics ingested by freshwater fish in the Chi River. Plastic materials are used in fishing gear such as nets, traps, hooks and lines. These are commonly made from polyamide (PA) and polyethylene (PE) [1]. Polyamide is a low-density polymer that is found in both pelagic and demersal fish [22]. Results confirmed that the percentage occurrence of microplastics ingested by each fish species was not related to vertical habitat zonation but concerned feeding activities.

CONCLUSIONS

The abundance of microplastics ingested by fish in the Chi River indicated middle-level contamination in aquatic animals compared to results of previous studies in both freshwater and ocean fishes. Opportunities to convey microplastics through the food chain into the human body remain limited. Shapes of microplastics indicate their origin as mainly from fishing gear such as nets and synthetic fibers from clothing.

ACKNOWLEDGMENTS

The joint conference was supported by Mahasarakham University Development Fund. Laboratory operations were supported by the Research Unit of Excellence for Tropical Fisheries and Technology. We would like to convey our special thanks to Padchara Bupphahao and Pattarawut Kothaisong for assisting with field operations and ensuring project success.

REFERENCES

[1] Lusher A., Hollman P. and Mendoza-Hill J., Microplastics in Fisheries and Aquaculture. FAO Fisheries and Aquaculture Technical Paper, Vol. 615, 2017, pp. 1-126.

[2] Barnes D.K.A., Morley J., Bell J., Brewin K., Collins M., Glass T., Goodall-Copestake W.P., Henry L., Laptikhovsky V., Piechaud N., Richardson A., Rose P., Sands C.J., Schofield A., Shreeve R., Small A., Stamford T. and Taylor B., Marine Plastic Threaten Giant Atlantic Marine Protected Area. Current Biology, Vol. 28, Issue 19, 2018, pp. 1137-1138.

[3] Imhof H.K., Sigl R., Brauer E., Feyl S., Giesemann P., Klink S., Leupolz K., Loder M.G.J., Loschel L.A., Missun J., Muszynski S., Ramsperger A.F.R.M., Schrank I., Speck S., Steibl S., Trotter B., Winter I. and Loforsch C., Spatial and Temporal Variation of Macro-, Meso- and Microplastic Abundance on a remote coral island of Maldives, Indian Ocean. Marine Pollution Bulletin, Vol. 116, 2017, pp. 340-347.

[4] Lee J., Lee J., Hong S., Hong S.H. and Shim W.J., Characterics of Meso-sized Plastic Marine Debris on 20 Beaches in Korea. Marine Pollution Bulletin, Vol. 123, 2017, pp. 92-96.

[5] Hurley R. Woodward J and Rothwell J.J., Microplastic Contamination of River Beds Significantly Reduced by Catchment-wide Flooding. Nature Geoscience, Vol. 11, 2018, pp. 251-257.

[6] Cole M., Lindeque P., Fileman E., Halsband C., Goodhead R., Moger J. and Galloway S., Microplastic Ingestion by Zooplankton. Environmental Science & Technology, Vol. 47, Issue 12, 2013, pp. 6646-6655.

[7] Silva-Cavalcanti J.S., Silva J.D.B., de Franca E.J., de Araujo M.C.B., Gusmao F., Microplastics Ingestion by Common Tropical Freshwater Fishing Resource. Environmental Pollution, Vol. 221, 2017, 218-226.

[8] Thushari G.G.N., Senevirathna J.D.M., Yakupitiyage A. and Chavanich S., Effects of Microplastics on Sessile Invertebrates in the Eastern Coast of Thailand: An approach to Coastal Zone Conversation. Marine Pollution Bulletin, Vol. 124, 2017, pp. 349-355.

[9] Pinheiro C., Oliveira U. and Vieira M., Occurrence and Impacts of Microplastics in Freahwater Fish. Journal of Aquaculture & Marine Biology, Vol. 5, Issue 6, 2017, p. 00138.

[10] Campani T., Baini M., Giannetti M., Cancelli F., Mancusi C., Serena F., Marsili L., Casini S. and Fossi M.C., Presence of Plastic Debris in Loggerhead Turtle Standed along the Tuscany Coasts of the Pelagos Sanctuary for Mediterranean Marine Mammals (Italy). Marine Pollution Bulletin, Vol. 74, 2013, pp. 225-230.

[11] Wagner M. and Lambert S., Freshwater Microplastics: Emerging Environmental Contaminats?, 2017, pp. 1-301.

[12] Eerkes-Medrano D., Thompson R.C. and Aldridge D.C., Microplastics in Freshwater Systems: A Review of the Emerging Threats, Identification of Knowledge Gaps and Prioritisation of Research Needs. Water Research, Vol. 75, 2015, pp. 63-82.

[13] Jabeen K., Su L., Li J., Yang D., Tong C. and Mu J., Microplastics and Mesoplastics in Fish from Coastal and Fresh Waters of China. Environmental pollution, Vol. 221, 2017, pp. 141-149.

[14] Yan M., Nie H., Xu K., He Y., Hu Y., Huang Y. and Wang J., Microplastic Abundance, Distribution and Composition in the Pearl River along Guangzhou City and Pearl River Estuary, China. Chemosphere, Vol. 217, 2019, pp. 879-886.

[15] Barboza L.G.A., Vieira L.R. and Guilhermino L., Single and Combined Effects of Microplastics and Mercury on Juveniles of the European Seabass (*Dicentrarchus labrax*): Changes in Behavioural Responses and Reduction of

Swimming Velocity and Resistance Time. Environmental Pollution, Vol. 236, 2018, 1014-1019.

[16] Barboza L.G.A., Vieira L.R., Branco V.,Figueiredo N., Garvalho F., Carvalho C. and Guilhermino L., Microplastics Cause Neurotoxicity, Oxidative damage and Energy-related Changes and Interact with the Bioaccumulation of mercury in the European Seabass, *Dicentrarchus labrax* (Linnaeus, 1758). Aquatic Toxicology, Vol. 195, 2018, 49-57.

[17] Wu Y., Guo P., Zhang X., Zhang Y., Xie S., Deng J., Effect of Microplastics Exposure on the Photosynthesis System of Freshwater Algae. Journal of Hazardous Materials, Vol. 374, 2019, pp. 219-227.

[18] Hahladakis J.N., Velis C.A. Weber R., Lacovidou E. and Purnell P., An Overview of Chemical additives Present in Plastics: Migration, Release, Fate and Environmental Impact During Their Use, Disposal and Recycling. Journal of Hazardous Materials, Vol. 344, 2018, pp. 179-199.

[19] Barboza L.G.A., Vethaak A.D., Lavorante B.R.B.O., Lundebye A.K. and Guilhermino L., Marine Microplastic Debris: An Emerging Issue for Food Security, Food Safety and Human Health. Marine Pollution Bulletin, Vol. 133, 2018, pp. 336-348.

[20] Ha J. and Yeo M.K., The Environmental Effects of Microplastics on Aquatic Ecosystems. Molecular & Cellular Toxicology, Vol. 14, 2018, pp. 353-359.

[21] Batel A., Linti F., Scherer M., Erdinger l. and Braunbeck T., Tranfer of Benzo[a]pyrene from Microplastics to Artemia nauplii and Further to Zebrafish via a Trophic Food Web Experiment: CYP1A Induction and Visual Tracking of Persistent Organic Pollutions. Environmental Toxicology Chemistry, Vol. 35, Issue 7, 2016, pp. 1656-1666.

[22] Lusher A.L., McHugh M. and Thompson R.C., Occurrence of Microplastics in the gastrointestinal tract of Pelagic and Demersal Fish from the English Channel. Marine Pollution Bulletin, Vol. 67, 2013, pp. 94-99.

[23] Garnier Y., Jacob H., Guerra A.S., Bertucci F. and Lecchini D., Evaluation of Microplastic Ingestion by Tropical Fish from Moorea Island, French Polynesia. Marine Pollution Bulletin, Vol. 140, 2019, pp. 165-170.

[24] Pozo K., Gomez V., Torres M., Vera L., Nunez D, Oyarzun P., Mendoza G., Clarke B., Fossi M.C., Baini M., Pribylova P. and Klanova J., presence and Characterization of Microplastics in Fish of commercial Importance from the Biobio Region in Central Chile. Marine Pollution Bulletin, Vol. 140, 2019, pp. 315-319.

[25] Vendel A.L., Bessa F., Alves V.E.N. Amorim A.L.A., Patricio J. and Palma A.R.T., Widespread Microplatic Ingestion by Fish assemblages in Tropical Estuaries Subjected to anthropogenic Pressures. Marine Pollution Bulletin, Vol. 117, 2017, pp. 448-455.

[26] Mizraji R., Ahrendt C., Perez-Venegas D., Vargas J., Pulgar J., Aldana M., Ojeda F.P., Duarte C. and Galban-Malagon C., Is the Feeding Type Relation with the Content of Microplastics in intertidal Fish Gut?, Marine Pollution Bulletin, Vol. 116, 2017, pp. 498-500.

[27] Phillips M.B. and Bonner T.H., Occurrence and Amount of Microplastic Ingested by Fishes in Watersheds of the Gulf of Mexico. Marine Pollution Bulletin, Vol. 100, 2015, pp. 264-269.

[28] Alomar C., Sureda A., Capo X., Guijarro B., Tejada S. and Deudero S., Microplastic Ingestion by *Mullus surmuletus* Linnaeus, 1758 Fish and Its Potential for causing Oxidative Stress, Environmental Research, Vol. 159, 2017, pp. 135-142.

[29] Browne M.A., Crump P., Niven S.J., Teuten E., Tonkin A., Galloway T. and Thompson R., Accumulation of Microplastic on Shorelines Worldwide: Sources and Sinks. Environmental Science & Technology, Vol. 45, 2011, pp. 9175-9179.

[30] Tanaka K. and Takada H., Microplastic Fragments and Microbeads in Digestive Tracts of Planktivorous Fish from Urban Coastal Waters. Scientific Reports, Vol. 6, 2016, p. 34351.

[31] Zhang K., Xiong X., Hu H., Wu C., Bi Y., Wu Y., Zhou B., Lam P.K.S. and Liu J., Occurrence and Characteristics of Microplastic Pollution in Xiangxi Bay of Three Gorges Reservoir, China. Environmental Science & Technology, Vol. 51, 2017, pp. 3794-3801.

[32] Panchan R., Jutagate T. and Wigraiboon S., Fish Species Composition Caught by Gillnets: Case Study from Chi River, Mahasarakham Province, Thailand. Maejo International Journal of Science and Technology, Vol. 7, 2013, pp. 43-51.

9th Int. Conf. on Geotechnique, Construction Materials and Environment, Tokyo, Japan, 20-22 November 2019, ISBN: 978-4-909106025 C3051

CURRENT SITUATION EVALUATION OF TAKASAKI CITY BY FORMULATING MODEL OF URBAN POWER

Toshikazu Nishio[1], Tetsuo Morita[2] and Shinya Tsukada[3]
[1] Takasaki Technical High School, [2] Maebashi Institute of Technology, Maebashi City Office [3]

ABSTRACT

The aim of the present study is to indicate objective position of a local city other than the prefectural capital location by formulating model of urban power and current condition evaluation. Specific methods are as follows: 1) formulate a model of urban power; 2) evaluate the current situation of Takasaki City; and 3) clarify direction to tackle in order to improve Takasaki City in the future by formulating model of urban power and current condition evaluation. The results obtained in the present study can be summarized as follows: 1) In order to maintain urban power of local cities, it is necessary to industrial activities that create bustling communities such as commerce; 2) It is indispensable to enhance transportation system such as Shinkansen, railway and expressway, and to enhance the bases of home center and department store; and 3) The annual sales of goods value of Takasaki City is larger than that of Maebashi City, the prefectural office location in Gunma, and is considered to be contributed by department store, Shinkansen, and expressway.

Keywords: Provincial city, urban power, Takasaki City

INTRODUCTION

City data pack 2018 version is conveying movement of town of the whole country. [1] Toyo Keizai is published a livability ranking in July 2018. The purpose is to clarify urban power of each city area based on public statistics in various fields. The 16 indicators are based from 5 in terms of peace of mind degree, convenience degree, comfort, high-net-worth level. Deviation value for the 50 average values is calculated for 16 indicators. The overall rating is the calculation each average and the deviation value of the 5 point of view. The rankings of all 814 city blocks in 791 cities and 23 wards of the country are introduced on 2 pages each. For example, Inzai City is a livability ranking overall rating 1 of 2017. It is located in the northwestern Chiba, in a population of 92,000 people, accounting for more than half of the area of Chiba New Town. It is comfort third place, in the convenience of 10-position. Mori Memorial Foundation urban strategy Institute is published a "Japanese cities characterization" in October 2018. Six areas as elements that make up the city are economy, business, research and development, culture and exchange, living and living, environment, transportation and access. In each field, 26 indicator groups and 83 indicators are selected. Each index data is indexed as maximum value 100 and minimum value 0. The average value of each index group is summed up by field, and it is considered as the score of each field. The total score is calculated by adding up the six fields. For example, Kyoto City is a ranking first in culture and interaction, and second in research and development, and first in the total score of urban characteristics in Japan.

The present study is to formulate a model of the city force, intended to evaluate and organize the current state of Takasaki City (summary will be described later).

PREVIOUS STUDIES

As research on urban power, Ishikawa considers urban power to be a comprehensive value of seven indicators: production rate, population growth rate, land price rate, yield rate, lighting rate, tax rate, and savings rate. [2] Sakurai focuses on milk marketed in Tokyo. There is explained urban power from the milk producing area in the metropolitan area, the amount of milk transported from the milk producing area to Tokyo, the transportation distance, transportation means, and transportation route. There is clarified that the city's milk area connecting Tokyo from milk producing area was formed in Showa era. [3] Takano defines urban power as the total number of employees of the establishment targeting 23 urban areas in Aichi. Urban area index is the ratio to the total residential population. There is high in large cities like Nagoya and in developed areas of the industry. It is low in other areas. [4] Yoshisaka et al. define a numerical value corresponding to urban power in order to quantitatively grasp the size of the city the force index. A comprehensive index is obtained by multiplying the population concentration area population (DID population) by the population concentration area

(DID area). [5] Sawada uses the total value of the six indicators of the number of shops, the number of shop workers, the number of goods sold, the number of factories, the number of plant workers, and the amount of industrial shipments as urban power. [6] Yoshisaka et al. define urban power index corresponding to urban power from the road distance in the population concentration area. [7] Yoshisaka et al. consider the composition of a block from the city power index and the area corresponding to urban power. [8] Sakurai et al. define urban power as the force produced as a result of accumulation of urban functions. It is target within a radius 5km area of central area in Yokohama City. There is defined urban power as a comprehensive value of the active force produced in 4 function of residential, commercial, business, industry. In order to simulate the situation of city change and transformation in advance, there is formulated by multiple regression analysis. Objective variable is urban power. [9] Noda defines the urban power as a state that the transform the world, the quality of life, and the economic power are achieving balanced growth. The three areas are measured by intellectual capital / innovation, technology maturity, gateway function, transportation/ infrastructure, health/ safety/ security, sustainability and natural environment, population composition/ livability, economic influence, ease of business, the cost of industrial and life. [10]

In the field of urban planning, urban power is seen to have been professionally defined as a comprehensive indicator of quantitatively competitiveness between cities.

THE PURPOSE OF THE PRESENT STUDY

Urban power is professionally defined as a comprehensive indicator that quantitatively indicates the competitiveness between cities from the past research in the field of urban planning. Each item of indicators makes up urban power as a comprehensive evaluation, and there are variety previous studies. Therefore, a problem from the point of view of regional policy is to formulate a model of urban power by an objective analysis technique. It is necessary to be formulated on the model of urban power, evaluate and organize the current state of the specific city by case studies.

The aim of the present study is to reveal the state objectively the position of regional cities other than prefectural office location by modeling formulation of urban power and evaluating current. It is formulated a model of urban power by the objective analysis technique. Moreover, it is evaluated and organized the current state in Takasaki City as a case study (set reason will be described later). Based on the above-mentioned results, it reveals the direction that should be addressed in order to improve the future Takasaki City. That is, there is created a model that can be represented metrically on the scale of urban power. Based on the above-mentioned results, there is addressed the direction in order to improve the urban through case studies.

The specific method is as follows.

(1) There is described the concept of urban power model. There is selected a multiple regression analysis from the statistical analysis technique. From this, the evaluation index X is to formulate a model of urban power to predict the impact directly to the comprehensive evaluation Y.
(2) As a study area to expand the case studies, there is set Takasaki City, and described an overview of Takasaki City.
(3) There is organized and evaluated the current status of Takasaki City from the model of urban power formulated by predicting that the evaluation index and the general evaluation are related.
(4) There is revealed the direction that should be addressed in order to improve the future Takasaki City from the current state evaluation of the results.

URBAN POWER MODEL FORMULATION

Urban Power Model Concept

Model concept of urban power in this study are as follows. Urban power is able to capture and quantify the status of the city. Outlines of the analysis procedure are modeling of urban power, and prediction of urban power by simulation using model formula.

Prerequisites for Modeling

A prerequisite is to the following two assumptions to model construction for expressing to meter urban power.

[Assumption 1] To make city unit city.
[Assumption 2] To quantify the situation of the city at a certain point.

Model Formulation

Among various urban activities developed in a city, the base function and the transportation system are taken up as two representative functions. The total value of activity generated by these two functions is the annual product sales value. This is urban power. Annual sales of goods is based on 2016 economic general survey-activity investigation Table 1, the number of the establishments according to city and

Table 1 Index and Item of Urban Power
(Created by the author)

Index	Item
base function	1. number of household appliances, furniture, and home center 2. department store association merchant number
transportation system	3. Shinkansen stop station 4. number of railway station 5. number of interchange

Table 2 Statistics of multiple regression analysis
(Created by the author)

Index item	Partial regression coefficient	Standard partial regression coefficient	T value	Judgment
X1	18,918.076	0.303	3.548	**
X2	206,940.793	0.248	3.463	**
X3	190,712.134	0.142	2.085	*
X4	5,455.218	0.120	1.549	
X5	32,650.959	0.166	2.366	*
Constant term	128,625.126		1.656	
F value			22.577	**
Multiple correlation				0.679

**: the t value does satisfy the significance level for 1 %.
*: the t value does satisfy the significance level for 5 %.

district, the industrial classification subdivision, the number of the employees, the annual sales of goods. There is selected the number of household appliances, furniture, and home center, and department store association merchant number for the base function. Similarly, there is selected the presence or absence of Shinkansen stop station, the number of railway station, the number of interchange for the transportation system (Table 1). Therefore, objective variable is "annual sales of goods(Y)". Explanatory variable is "the number of household appliances, furniture, and home center(X1)", "department store association merchant number(X2)", "the presence or absence of Shinkansen stop station(X3), "the number of railway station(X4)", "the number of interchange(X5)". When formulated by multiple regression analysis, regression equation of formula (1) is obtained a precision shown in Table 2. In addition, the cities used for model creation are population of 150,000 or more excluding all ordinance-designated along with 790 cities in Japan based on the 2015 census.

$$Y=18918.076X1+206940.793X2+190712.134X3 +5455.218X4+32650.959X5+128625.126\cdots(1)$$

The results of the test for significance of regression equation is shown in Table 2. The results of the analysis of variance, the degree of freedom of the F value molecule is 5, and the denominator of freedom of the F value molecule is 132. F distribution of the upper side 1% is 22.577>F (5, 132, 0.01) =3.17. It is 1 % level of significance. The null hypothesis that the obtained regression equation is not useful for the estimation of Y is rejected. The F value is also large enough. Therefore, the resulting regression equation can be determined to be valid. Further, the multiple

Table 3 Annual sales of goods [13]
(Created by the author)

Population rank	Prefecture	Municipalitie	Annual sales of goods (one million yen)		
			Actual value	Estimated value	Difference
51	Nagano	Nagano City	1,685,006	1,290,507	−394,499
52	Aichi	Toyohashi City	1,089,863	1,162,887	73,024
53	Osaka	Suita City	1,919,875	497,317	−1,422,558
54	Gunma	Takasaki City	3,057,010	1,405,140	−1,651,870
55	Wakayama	Wakayama City	1,133,258	1,080,768	−52,490
56	Nara	Nara City	602,695	898,894	296,199
57	Osaka	Takatsuki City	555,036	796,800	241,764
58	Saitama	Kawagoe City	766,096	593,032	−173,064
59	Fukushima	Iwaki City	869,814	841,205	−28,609
60	Shiga	Otsu City	469,139	1,280,467	811,328
61	Saitama	Tokorozawa City	520,941	692,807	171,866
62	Hokkaido	Asahikawa City	1,063,246	708,319	−354,927
63	Saitama	Koshigaya City	822,471	456,038	−366,433
64	Kochi	Kochi City	972,508	1,193,206	220,698
65	Gunma	Maebashi City	1,147,867	1,015,305	−132,562
66	Fukushima	Koriyama City	1,402,963	1,114,169	−288,794
67	Okinawa	Naha City	849,364	639,226	−210,138
68	Akita	Akita City	1,147,819	1,076,333	−71,486
69	Mie	Yokkaichi City	993,011	894,490	−98,521
70	Aichi	Kasugai City	696,654	602,737	−93,917

correlation coefficient between the actual observed values with the theoretical value calculated by applying the regression equation of the object variables is 0.679. Therefore, as shown in Table 3, there is a difference between actual values and estimated values in the annual sales of goods, but resulting regression equation is valid.

Table 2 is clear that the number of household appliances, furniture, and home center, department store association merchant number, the number of interchange, and the number of railway station affected annual sales of goods, the t value does satisfy the significance level. Among them, the number of railway station and the number of interchange are a significant impact on annual sales of goods can be seen. On the other hand, although the t value does not satisfy the significance level for 5 %, “the number of railway station (5,455.218)” is also an important index item judging from the magnitude of the parameter (partial regression coefficient).

Based on the above-mentioned results, it is considered that the number of household appliances, furniture, and home center, department store association merchant number, the presence or absence of Shinkansen stop station, the number of railway station, and the number of interchange are important to capture urban power from the viewpoint of base function and traffic system.

STUDY AREA AND TAKASAKI CITY

Setting of study area

A city that represents the prefecture is generally prefectural office location. Even if Maebashi City is appeared in the national statistics in case of Gunma, Takasaki City is hardly found. However Takasaki City is merged with Haruna town, becomes a population of 340,000 in October 2006, exceeded

Fig. 1 Takasaki Station West Exit
(Photo taken by the author)

Fig. 2 Takasaki Station East Exit
(Photo taken by the author)

Maebashi City which has been merged with the previously Seta County area, etc. Takasaki City is the city with the largest population in Gunma. April 2011 or later, Takasaki City is a core city. In recent years, Takasaki City's position has been objectively shown throughout Japan. According to Takasaki Chamber of Commerce and Industry, Takasaki City has been posted on the city ranked by economic magazine in recent years. Happiness ranking with 42 core city nationwide of the Toyo Keizai newspaper is third across Japan, Nikkei city rankings with a vitality of the business is the 29 across Japan in 2016. According to statistical data, the urban population is 55th in the whole country (2015), the industrial scale is 31th in the national scale, commercial sales is 15th in the national scale, and the industrial shipments are 88th in the national scale. [11]

From above, the present study is set area the Takasaki City as local cities other than prefectural office location.

Summary of Takasaki City

According to Takasaki City Directory, Takasaki City is a commercial city that flourished as a strategic point of traffic. There is expanded exchange area by development of high-speed transportation network. Prefecture population in sphere that can travel in two hours from Takasaki City is said to be 46 million people. The annual 200 million 6,000 million people visit in Gunma. Visitors to Takasaki City are the most frequent in Gunma. Near Takasaki Station is accumulation of accommodation, is a base for businessmen and tourists. Headquarters of the consumer electronics retailer's largest and a broad-based sales offices nationwide company are integrated. The department stores and attractive commercial premises in the nucleus, town building has been carried out and full of bustle and vitality in the center city. Advanced use of Takasaki City center is progressed by urban redevelopment projects. Takasaki Station connects with large commercial facilities, office buildings and hotels via an air corridor called pedestrian deck. Castle district which is continuous from Takasaki Station West Exit (Fig. 1) commercial area is an integrated areas of public facilities such as the city hall and Medical Center, Gunma Music Center. Takasaki City is established a "Takasaki Cultural Arts Center (tentative name)" new music hall as the base of art and culture in Takasaki Station East Exit (Fig. 2) area, is planning a large-scale complex facility with commercial premises and industrial development function. [12]

CURRENT EVALUATION

Assuming the annual product sales amount as urban power, evaluation Takasaki City is formulated urban power model of formula (1). More specifically, the current state of Takasaki City is organized from the point of view of annual sales of goods, the number of installed university, department store association merchant number, the presence or absence of Shinkansen stop station, the number of railway station, and the number of interchange. It is evaluated by comparing with Maebashi City, the prefectural office location in Gunma.

Current Situation of Takasaki City

(1) Annual sales of goods

Wholesale trade is 2 trillion 569.2 billion yen, the retail industry is 487.7 billion yen in Takasaki City, 2016. Annual sales of goods which is their total amount are 3 trillion 57 billion yen. Takasaki City ranks 15th in the national ranking and 1st in the core city. The cities in within the 20th place are all designated cities except for Takasaki City. In the city in Gunma, Maebashi City is 1 trillion 147.8 billion yen (46th) (See Table 4, the same is true for the following.).

(2) Number of home center and so on

The number of household appliances, furniture, and home center are 24 shops, in the case of Takasaki City, as of March 2019; Yamada Denki, Cainz home,

Table 4 Current Situation of Takasaki City
(Created by the author)

Item	Current Situation
Annual sales of goods	1 trillion 147.8 billion yen
number of household appliances, furniture, and home center	24 shops
Department store association merchant number	2 shops
Shinkansen stop station	Takasaki Station
number of railway station	16 stations
number of interchange	4 places

Sekichu, Nitri, Super Viva Home, Tokyo interior furniture, Bic camera, and so on.

(3) Department store association merchant number

Department store association merchant number are 2 shops, in the case of Takasaki City, as of March 2019; Takasaki Takashimaya, Suzuran Takasaki store.

(4) Shinkansen stop station

The presence or absence of Shinkansen stop station is Takasaki Station, in the case of Takasaki City, as of March 2019. Takasaki Station gets into Joetsu Shinkansen and Hokuriku Shinkansen of JR East that have served.

(5) Number of railway station

The number of railway station are 16 stations, the case of Takasaki City, as of March 2019, JR Takasaki Line Takasaki Station, Kuragano Station, Shinmachi Station, JR Joetsu Line of Takasaki-tonyamachi Station, Ino Station.

(6) Number of interchange

The number of interchange are 4 places, in the case of Takasaki City, as of March 2019; Takasaki Tamamura SIC, Takasaki IC, Maebashi IC of Kanetsu expressway, Yoshii IC of Joshinetsu expressway.

Comparative Study of Maebashi City

In order to show the position of regional cities other than the prefectural capital objectively, as compared with Maebashi City, there is evaluated the estimated value of annual sales of goods of Takasaki City.

Substituting a numerical value into urban power model of formula (1); the number of household appliances, furniture, home center of X1=24, department store association merchant number of X2=2, the presence or absence of Shinkansen stop station of X3=1 (Yes), the number of railway station of X4=16, and the number of interchange of X5=4, the estimated value of annual sales of goods of Takasaki City is 1 trillion 405.1 billion yen.

Substituting the estimated value into urban power model of formula (1); the number of installed university of X1=12, department store association merchant number of X2=1, the presence or absence of Shinkansen stop station of X3=0 (no), the number of railway station of X4=19, and the number of interchange of X5=2, the estimated value of annual sales of goods of Maebashi City is 1 trillion 15.3 billion yen.

Compared to Maebashi City, there are 3 shops less than the number of household appliances, furniture, and home center, there are 3 stations less than the number of railway station, and there are acting on the negative. However, there is a Shinkansen stop station, there is 1 shop more department store association merchant, there are 2 places more than the number of interchange, and there are acting on the plus.

Based on the above-mentioned results, it is considered that the number of interchange, Shinkansen stop station, and department store association merchant number of Takasaki City contribute to the results above the estimated value of annual sales of goods of Maebashi City, the prefectural office location in Gunma.

CONCLUSIONS

The aim of the present study is to reveal the direction to be addressed in order to improve the future Takasaki City by urban power model formulation and present situation evaluation. The results obtained in the present study can be summarized as follows:

(1) It is considered that the number of household appliances, furniture, home center, department store association merchant number, the presence or absence of Shinkansen stop station, the number of railway station, and the number of interchange are important to capture urban power from the viewpoint of base function and traffic system.

(2) It is considered that the number of interchange, Shinkansen stop station, and department store association merchant number of Takasaki City contribute to the results above the estimated value of annual sales of goods of Maebashi City, the prefectural office location in Gunma.

(3) From (1) and (2), it is possible to show objectively indicate the position of a local city other than the prefectural capital location by formulating model of urban power and current condition evaluation. In order to maintain urban power of local cities, it is necessary to industrial activities that create bustling communities such as commerce. For that reason, it is considered that it is indispensable to enhance transportation

system such as Shinkansen, railway and expressway, and to enhance the bases of home center and department store. The annual sales of goods value of Takasaki City is larger than that of Maebashi City, the prefectural office location in Gunma, and is considered to be contributed by department store, Shinkansen, and expressway.

SUBJECT FOR NEXT STUDY

(1) Our future goal is creation of time consumption type sightseeing to create bustle of town. Tourism resources such as landmarks, sightseeing spots, and hot springs are indispensable to increase the residence time of tourists. It is difficult to make tourists stay for more than half a day with tourist resources such as historic sites and city parks, and invite them to local consumption. Therefore, it is considered that experience-type tourism such as farming experience, and making of daruma at a tourist farm, and leisure tourism by eating and drinking utilizing special products such as Takasaki pasta.

(2) Maebashi City is the 12th largest agricultural city in the country according to the 2016 agricultural production estimate. Therefore, in the future, it is necessary in Maebashi City to put emphasis on the sixth industrialization of agriculture which is processing and sales of agricultural products.

REFERENCES

[1] Toyo Keizai Shinpo Co., Ltd., City Data Pack 2018 Edition.

[2] Ishikawa lordliness, Japan land planning theory, Hachigensha, 1941, p. 5.

[3] Katsui Sakurai, The City of Tokyo (1) -Research on Urban Power-, Geography, Vol. 5, No. 4, 1942, pp. 413-437.

[4] Fumio Takano, Metropolitan area patterns on the regional structure theory research - as an example the Tokai region-[Summary], Geography critic, Vol. 36, No. 1, 1963, pp. 57-67.

[5] Takamasa Yoshizaka, Koichi Tonuma, Hiroshi Kobayashi, and Ryozo Nakamura, About the calculation of the city force, Japanese Architecture Society report Gallery and extras, extra edition Scientific Abstracts, Vol. 40 No. 0, 1965, p. 569.

[6] Sawada Kiyoshi, Urban Areas of Japan, Kokoku Shoin, 1978, p. 9.

[7] Takamasa Yoshizaka, Koichi Tonuma, Hiroyasu Higuchi, Arai KatsuSachi, and Ishida Yukihira, About the stage of the city force and road construction, Japanese Architecture Society report Gallery and extras, extra edition Scientific Abstracts, Vol. 40 No. 0, 1965, p. 570.

[8] Takamasa Yoshizaka, Koichi Tonuma, About the stage of the city force and city blocks configuration", "Japanese Architecture Society report Gallery and extras, extra edition Scientific Abstracts" Vol. 40 No. 0, 1965, p. 571.

[9] Shin-ichi Sakurai, Norihisa Yokouchi, Shozo Kazemi, Study on the transformation of urban power of the hinterland associated with the location of oceanic cities, The Proceedings of the Architectural Institute of Japan, Volume 373, 1987, p.87-97.

[10] Noda Yumiko, PwC's Urban Power Evaluation Index" "Urban Planning, Vol. 64, No. 1, 2015, pp. 44-47.

[11] Takasaki Chamber of Commerce and Industry, Special feature: City power of Takasaki seen by numbers, The Takasaki Chamber of Commerce Conference report Takasaki 5, 2018, pp. 6-11.

[12] Takasaki City, Takasaki City Directory, 2015, pp. 4-9.

[13] Ministry of Internal Affairs and Communications Bureau of Statistics, 2016 economic general survey-activity investigation Table 1, the number of the establishments according to city and district, the industrial classification subdivision, the number of the employees, the amount of annual product sales.

9th Int. Conf. on Geotechnique, Construction Materials and Environment,
Tokyo, Japan, 20-22 November 2019, ISBN: 978-4-909106025 C3051

CHARACTERISTICS OF CULTURAL LANDSCAPE IN THE GATEWAYTOWN OF KUDOYAMA

Tomoko Miyagawa[1], Sakura Yamaguchi[1], Sayuri Yoshino (Aoyama)[2], Shinpei Yamamoto [3] and Masahiro Takasago[1]
[1] Faculty of Systems Engineering, Wakayama University, Japan; [2] Wakayama Prefectural Office, Japan; [3] Kudoyama Town Office, Japan

ABSTRACT

Managing historic environment and cultural heritage are important not only from the conservation of cultural assets and local environment but it is also necessary to consider the perspectives from the community. This paper aims to examine a case study focusing on houses and local resources in the center of Kudoyama, known as the gateway town to the World Heritage Site, Koyasan in Wakayama, Japan. Study methods used are field observations and literature reviews. From the results, characteristics of the town center of Kudoyama became clear as follows; around a half of all houses have been built with single or semi-second story houses to form relatively reduced height of skylines. Thus, it creates viewpoints to surrounding mountains within the town center on undulating landform. In terms of local resources, a variety of natural and historic elements have been found to create a historic environment in town center of Kudoyama. In addition, some traditional design of houses is representing the similarities with surrounding areas of the World Heritage Sites of Yoshino and Koyasan. In future, managing cultural landscape may be necessary to balance the needs of the community and tourism.

Keywords: Historic environment, Cultural heritage, Cultural landscape, The World Heritage

INTRODUCTION

The Definitions of Cultural Landscapes

Managing historic environment and cultural landscape are important not only from the conservation of cultural assets and local environment but it is also necessary to consider the perspectives from the community. There are number of studies regarding on valuing cultural heritage and landscapes can be seen [1]–[2]. Melnick suggests the importance of 'viewing the landscape from a variety of perspectives' [1]. For instance, 'documented cultural imprints such as battles and literary connections' are well known by the 'outsiders', however, 'customs and experiences that may only be appreciated by the 'insiders'' [3]. Therefore, meaning to the people living in the area becomes important when it comes to consider thorough comparison which may deny what has been important to those people [1]. In terms of determining priorities, 'the level of significance', whether world, national, regional, and local 'does not reflect the absolute significance of the landscape' [1]. Moreover, cultural landscapes can be described from a wider scale to clarify the characteristics from the human and other species behavior patterns and understanding of mixture of variety of 'species, places and environmental conditions' in complexity [4]. Thus, it is necessary to focus on the diversity and identity of cultural landscapes in rapidly changing landscapes and the society to find out the importance of 'coherence between small composing elements in a broader spatial context' and to be able 'to tell the story of the place' [5]. Furthermore, it is suggested the needs of balancing between three aspects as follows; 'distinctive landform and cover, the indivisible multiplicity of functions, and the embedded fabric of stories and memories' [3]. Therefore, this study defines the meaning of cultural landscapes to be a variety of cultural landscape including value and meaning for the community in a wider scale than current situations of different levels of registrations as cultural properties for conservation.

The Aim of the Study and Study Methods

This paper aims to clarify characteristics of cultural landscape focusing on houses and local resources in the center of Kudoyama, known as the gateway town to Koyasan in Wakayama, Japan. It is one of the sites registered as the World Heritage Site by the UNESCO, Sacred Sites and Pilgrimage Routes in the Kii Mountain Range in 2004, and additional minor boundary modifications in 2016. The town has a World Heritage Site, Jison-in temple and Nyukanshofu shrine, along with pilgrimage routes of Choishi-michi and Kuroko-michi (added in 2016) to Koyasan, as well as a variety of cultural landscape managed by community. Study methods used are field observations and literature reviews regarding on cultural landscapes.

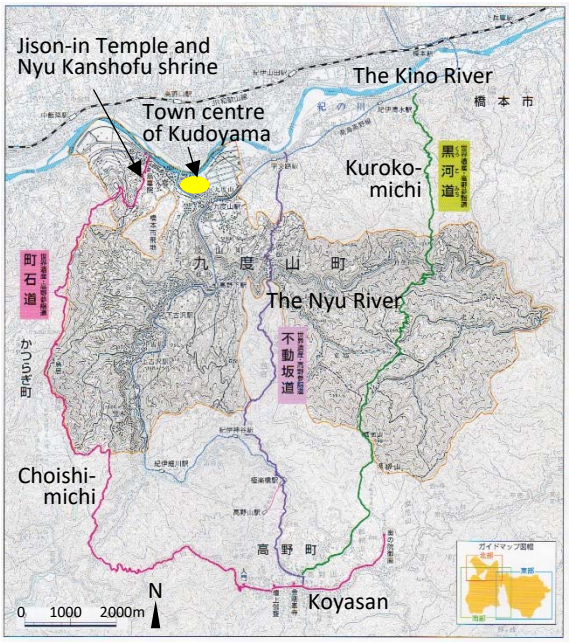

Fig. 1 A map of town of Kudoyama [6] with some amendments

Fig. 2 Undulating landforms and narrow streets

The Outline of the Case Study Location

The town is located at the northeastern part of Wakayama Prefecture. The town of Kudoyama is located along The Kino river which has been a major transportation route by ship between the town of Yoshino, Nara Prefecture and the Wakayama city to carry goods. Therefore, it became a center of a transportation and commerce as a place of unloading at Funato in the town of Kudoyama to Koyasan and surrounding areas since 1601 [7]- [9]. The town center of Kudoyama is located at the foot of mountains to Koyasan, therefore, it became a gateway town and the pilgrimage routes has been developed (Fig. 1). Choishi-michi has been completed in 1285 [10]. Kuroko-michi is documented as the route has been used by one of the famous warriors, Hideyoshi Toyotomi to run down with a horse from Koyasan in 1594 [11]. It is also known to be a place lived by famous warriors of Masayuki and Nobushige Sanada.

The town center has a characteristic of undulating landforms and traditional houses with narrow streets

Fig. 3 Traditional houses creating townscapes

placed on the independent plateau surrounded by two rivers [12], the Nyu river down the mountains of Koya which joins the Kino river (Fig. 1-3).

A CLASSIFICATION OF HOUSES IN THE TOWN CENTRE OF KUDOYAMA

The town is located at the regions of Koya, known as the World Heritage Site, as well as architectural characteristics of using steep sloped sites which can be seen in the neighboring Yoshino region [13]- [14]. It is also surrounded by towns and villages with architectural characters at local scale, i.e., village landscapes at Koya paper making villages [15], and townhouses at cities of Hashimoto [16] and Gojo [17].

A Classification by Numbers of Levels

Single story houses were found at 103 with 32 percent, semi second story houses at 50 with 15 percent, and second story houses at 175 with 53 percent out of 328 houses in total (Table 1, Fig.4). To sum up single and semi second story houses becomes about a half of all houses, which can be recognised to be built in traditional styles (Table 1, Fig.4). Single story houses can be found around the Sanada temple, while semi second story houses are located along the

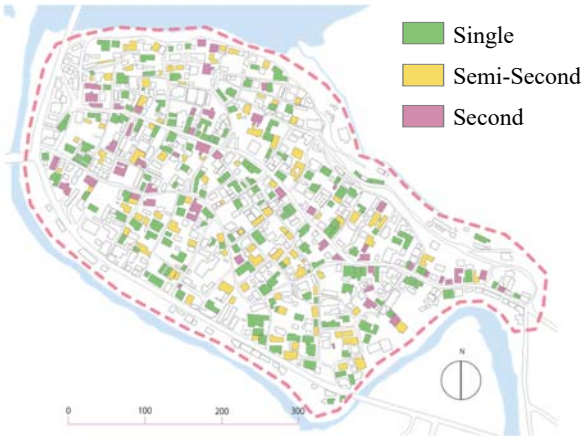

Fig.4 A map of Classification by Numbers of Levels [18]

second main street near the Sanada temple. Second story houses can be found throughout the town center (Fig.4) [12].

Table 1 A Classification by Numbers of Levels [18]

Items	numbers	percentages
Single story houses	103	32%
Semi second story houses	50	15%
Second story houses	175	53%
Total	328	100%

Characteristics of Traditional Houses

A significant number of single-story houses are plastered on the wall. To include partial plaster, it sums up to 50 houses. Semi second story houses can be divided into higher and lower height on the second floor which reflects architecture styles of different time. On the second floor, a window style called 'Mushiko' (refer to as an insect cage) was found at 14 houses, and 13 houses are plastered into a square timber like shaped. Second story houses are relatively newly built. However, some houses are built in the traditional style, i.e., lattice, plaster, etc [12].

A building style of 'Yoshinodate' was found at four houses. The building style can be seen around the region of Yoshino, Nara Prefecture. It utilizes steep slopes to create basements by adjusting to landforms, therefore, a bottom of basements became limited and a foundation are created by terraced stone walls [13]- [14]. Thus, it may be one of the reasons to utilize undulating landforms in town center of Kudoyama.

A Classification by Roof Styles

The results are as follows; gable roofs can be seen at around a half of all houses, at 173 with 53 percent, gambrel roofs are at 102 with 31 percent, and hipped roofs are at 35 with 11 percent (Table 2, Fig.5). Therefore, gable roofs are commonly seen, which

Table 2 A Classification by Roof Styles [18]

Items	numbers	percentages
Gable roofs	173	53%
Gambrel roofs	102	31%
Hipped roofs	35	11%
Semi-Gambrel roofs	8	2%
Flat roofs	4	1%
Thatched roofs	2	1%
Others	4	1%
Total	328	100%

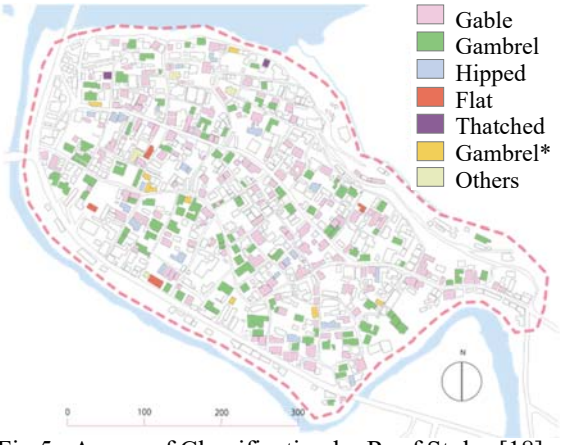

Fig.5 A map of Classification by Roof Styles [18]
Gambrel*: Semi-Gambrel

may be one of the reasons to build houses on the limited land with an independent plateau with higher density in comparison to surrounding areas, such as neighboring district of Nyugo. Gable roofs can be seen along the Sanada high street, and particularly concentrated around the Western area. On the other hand, gambrel roofs are located at the Southern area, along the Sanada temple (Fig. 5). Thatched roofs do exist although at a very limited numbers with two houses. It used to be thatched before, but now has been covered by the tin roofs [12]. This represents the traditional housing styles with the drawings in sites of interests of Kii area in the late Edo period [7].

A Classification by Ridge-end Tiles

The results are as follows; Ornamental borders are commonly seen at 190 with 65 percent, ogre shaped are seen at 63 with 21 percent, and jewel shaped are at 16 with 5 percent (Table 3, Fig. 6). Some ogre shaped are designed with other tiles and plasters. Some houses are decorating ogre shaped tiles in the entrances or gardens; therefore, it is possible to imagine that is used to be placed on the roof top in the past times. Ornamental borders can be seen throughout the town center, whereas ogre shaped are seen along the Sanada street (Fig.6) [12].

Table 3 A Classification by Ridge-end Tiles [18]

Items	numbers	percentages
Ornamental borders	190	65%
Ogre shaped	63	21%
Jewel shaped	16	5%
Family crest	2	1%
Others	22	8%
Total	293	100%

Notes: No ridge-end tiles at 28, and Unidentified at 17.

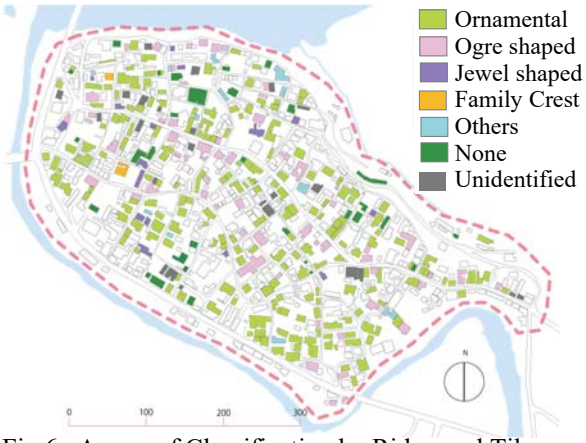

Fig.6 A map of Classification by Ridge-end Tiles [18]

Fig.10 A map of Classification by Uses of houses [18] Merchant*: Merchant houses

Fig. 7 A lattice under the eaves

Fig. 8 A traditionally designed window

Fig. 9 A chimney on a roof with tiles

Details of the design of houses

Traditional houses in town center of Kudoyama have details of the design, such as, lattices (Fig.7), traditionally designed windows called 'Mushiko' (Fig. 8), chimneys on a roof with tiles (Fig. 9), and wooden bars on the edge of the eaves. Houses with lattices were found at 35 houses. This may be due to keep privacy and surveillance from narrow streets with high density of houses in town center [12].

Traditionally designed windows were seen at 14 houses with semi-second story houses, and most of them were designed in square shapes to illustrate the characteristics of timbers. Chimneys on a roof with tiles were found at 5 houses, which can be seen in traditionally designed houses. Wooden bars on the edge of the eaves were seen at 15 houses, which is a common design feature in towns and villages around Koyasan [12].

A Classification by Uses of Houses

The most common uses of houses were residences, and merchant houses have been built along the Sanada street (Fig. 10). Some of residences at present have been built with a signboard architecture, so that it is possible to imagine the houses have been used to be merchant houses in the past. In addition, some merchant houses are single story or semi-second story houses, and it have been built with a traditional design. Moreover, a few factories have been confirmed. According to the interviews to the residents, a saw-tooth roof textile factory used to produce cotton fabrics and had been sold at the Sanada street in the past. From the above, these houses and buildings remaining at present can be said to be the important which represents the history and people's life of the town center [12].

LOCAL RESOURCES IN THE TOWN CENTRE OF KUDOYAMA

In this section, it aims to clarify the characteristics of local resources from a classification and a distribution in town center of Kudoyama. Local resources also reflect natural and historic environments of the area, and it may be necessary to examine the management and conservation as well as houses and buildings [19]. Miyayama and Kamihogi introduces the concept of local resources represented by 'natural elements' to inherit the local history and culture, i.e., landforms, rivers, and streets; and 'historic elements' of monuments and sights of interests, as well as the wider understandings of landscapes and spaces [20]. Therefore, this study aims to clarify natural elements and historic elements.

Characteristics of Local Resources

From the results, a variety of local resources have been become clear and managed by people in the area. In terms of classification, natural elements were found at 224, and historic elements were at 7. Natural elements can be divided into leveling at 115, pine trees at 94, and wells at 15. Historic elements were found with shrines for residences at 4 and monuments at 3 (Table 4-5) [19].

Levelling are largely formed with stone walls particularly along the Kino river and the Nyu river to

Table 4 A Classification of Natural Elements [19]

Items	numbers	percentages
Leveling	115	51%
Pine trees	94	42%
Wells	15	7%
Total	224	100%

Table 5 A Classification of Historic Elements [19]

Items	numbers	percentages
Shrines for residences	4	57%
Monuments	3	43%
Total	7	100%

Fig. 11 Stone walls forming townscapes

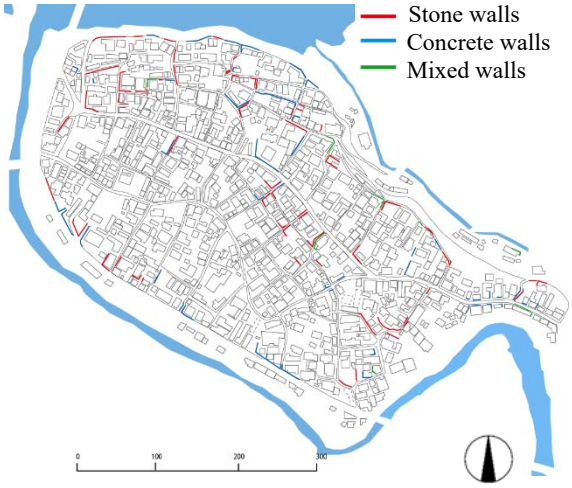

Fig. 12 A map of Levelling [21]

Fig.13 A map of Pine Trees [21]

Fig. 14 Pine trees creating townscapes

represent characteristics of undulating landforms. Chlorite schist, a locally produced stone, has a half of the numbers of all levelling with a count of 62 (Fig. 11, 12). Pine trees can be found in the gardens or entrances of houses (Fig. 13). There are a variety of sizes of pine trees from potted plants to large trees. Several trees planted nearby, and large trees are becoming as landmarks to create characteristics of historic environment and townscapes (Fig. 14) [19].

From the above, a variety of local resources can be seen in town center of Kudoyama which is managed

regularly by people in the area.

CONCLUSIONS

From the results, characteristics of the town center of Kudoyama became clear as follows; around a half of all houses have been built with single or semi-second story houses to form relatively reduced height of skylines. Thus, it creates viewpoints to surrounding mountains within the town center on undulating landform. In terms of local resources, a variety of natural and historic elements have been found to create historic environments in town center of Kudoyama. In addition, some traditional design of houses is representing the similarities with surrounding areas of the World Heritage Sites of Yoshino and Koyasan. In future, managing cultural landscape may be necessary to balance the needs of the community and tourism.

ACKNOWLEDGEMENTS

The authors would like to express our gratitude for the financial support provided by the cultural heritage utilization and community activation project from the Agency for Cultural Affairs.

REFERENCES

[1] Melnick R.Z., Protecting Rural Cultural Landscapes: Finding Value in the Countryside, Landscape Journal, Vol. 2, No. 2, 1983, pp. 85-96.
[2] Willemen L., Verburg P.H., Hein L., and Mensvoort M. E. F., Spatial characterization of landscape functions, Landscape and Urban Planning, Vol. 88, 2008, pp.34-43.
[3] Selman, P., Chapter 6, Landscape and sustainability at the national and regional scales, in Landscape and sustainability, 2nd ed., Benson and Roe, Ed. Taylor and Francis, 2007, pp. 104-117.
[4] Roe, M. and Taylor, K., Chapter 1, New cultural landscapes: emerging issues, context and themes, in New Cultural Landscapes, Roe and Taylor, Ed. Routledge, 2014, pp.1-23.
[5] Antrop M., Why landscapes of the past are important for the future, Landscape and Urban Planning, vol.70, Issue 1-2, 2005, pp.21-34.
[6] A committee of cultural heritage utilization and community activation project, the town of Kudoyama, Historic heritage visit guide map of Kudoyama town, 2018 (in Japanese).
[7] A committee of history of the town of Kudoyama, overview of history, 2009 (in Japanese).
[8] A committee of history of the town of Kudoyama, customs and cultural properties, 2003 (in Japanese).
[9] A committee of history of the town of Kudoyama, historical records, 2002 (in Japanese).
[10] A committee of cultural heritage utilization and community activation project, the town of Kudoyama, A guidebook of cultural properties of Kudoyama town, 2016.
[11] A committee of education, Wakayama Prefecture, The academic investigation report of Koyasan Kekkaido, Fudozaka, Kuroko-michi, Mitanizaka and related cultural properties, 2012 (in Japanese).
[12] Yamaguchi, S. and Miyagawa, T., Townscape of Kudoyama, in the investigation report of a committee of cultural heritage utilization and community activation project, the town of Kudoyama, 2017, pp.7-10.
[13] Motozuka, T., Kanki, K., and Miyagawa, T., A study on traditional houses and land uses in Koya Yoshino boundary areas, Summaries of technical papers of annual meeting, Architectural Institute of Japan, 2008, pp.471-474 (in Japanese).
[14] Katayama, S., Honda, T., and Hirata, T., A study on 'Yoshino-date' as an architectural vocabulary in Yoshino region', Summaries of technical papers of annual meeting, Architectural Institute of Japan, 2008, pp.619-620 (in Japanese).
[15] Kitano, Y., S., Honda, T., Yoshinaga, N. and Hirata, T., Village-landscape and spatial functions of Koya-paper making villages, Summaries of technical papers of annual meeting, Architectural Institute of Japan, 2011, pp.577-578 (in Japanese).
[16] Asano, K., Ougida, M., Hayashino, Z., Suzuki, Y., Kudo, K., and Aoyama, Y., Chronological Study on the Town Houses of Gojyo City Nara Prefecture, and on their Architectural Transition, Journal of technical papers, Architectural Institute of Japan, vol. 63-2, 1959, pp.601-604 (in Japanese).
[17] Umejima, O., Hirayama, I., and Nishizawa, K., Transition of town houses by the old Yamato Highway in Hashimoto city, Summaries of technical papers of annual meeting at Kinki Branch, Architectural Institute of Japan, pp.877-880 (in Japanese).
[18] Yamaguchi, S., A study of characteristics of houses in town center of Kudoyama, a dissertation submitted to the Dept. of Env. Systems, Wakayama Univ., 2011 (in Japanese).
[19] Aoyama, S. and Miyagawa, T., Local resources of Kudoyama, in the investigation report of a committee of cultural heritage utilization and community activation project, the town of Kudoyama, 2017, pp.37-39 (in Japanese).
[20] Miyayama, Y. and Kamihogi, A., Study about the succession of Kyokaido road, looked at from the continuation situation of the road, maintenance and the use situation, Landscape Research, Vol.74, (5), 2011, pp.773-778 (in Japanese).
[21] Aoyama, S., A study of local resources in town center of Kudoyama, a dissertation submitted to the Dept. of Env. Systems, Wakayama Univ., 2012 (in Japanese).

9th Int. Conf. on Geotechnique, Construction Materials and Environment, Tokyo, Japan, 20-22 November 2019, ISBN: 978-4-909106025 C3051

RESIDENTS' EVALUATION AND CONTINUITY IN THE CASE OF SHIKISHIMA OPEN GARDEN IN MAEBASHI CITY

Shinya Tsukada1, Kazuya Tsukada2, and Tetsuo Morita3
1Maebashi City Office, Japan, 2Seikei University, Japan,, 3Maebashi Institute of Technology, Japan

ABSTRACT

Living while feeling various green effects is considered an effective tool to adapt to the situation of declining population and the aging population or to live an environmentally friendly life. To realize this, it is necessary to have a green zone management policy through cooperation between the administration and residents. Particularly, open gardens (* OG) as one of the private greening areas are expected to have great effects on the viewpoint of town planning. In the task of OG, "trigger and form of activity", "increase participants" and "increase awareness" are soft issues in sustainability. We thought that these could greatly influence the citizen's future activities. Therefore, we focused on this research. Therefore, to solve the above three major problems, this research grasped "situation of efforts by administrators and OG organizers in the case of OG of Maebashi City" and "perception of neighborhood residents' OG activities". The purpose of this research was to obtain basic knowledge for improvement of "issues for the sustainability". As a conclusion, "Shikishima OG" was not a limited activity of merely a favorite group, but more than half of the residents were recognized in the area around Shikishima Park. In addition, 80% of those inhabitants regarded positively as "Shikishima OG contributes to local community development". Furthermore, we could grasp that "improvement of the landscape of the district" was the most expected by these inhabitants in terms of "community development".

Keywords: Open Garden, Actual Situation, Actual Evolution, Continuity

INTRODUCTION

In today's Japan, Japan's financial resources are constrained by the declining population, the aging of the population, and the increase in infrastructure stocks. Under these conditions, to promote environment-friendly living environment improvement and regional development, urban planning that fully demonstrates the various benefits of green and open space is required.

To carry out city planning that fully demonstrates the diverse benefits of greenery and open spaces, it is important that the government and residents work together to make greening activities in accordance with the characteristics of the area and the needs of the residents.

Japan's greening policy can be broadly divided into two. The first is greening of public facilities, which is led by the government. The second is greening of private land, which the residents take the lead.

As one of the private land reforestations, open garden is expected to have great effect based on the point of town development. The open garden (hereinafter referred to as OG) is an activity to open private garden into public. The purpose of this activity is to make citizens enjoy the garden of an individual. This is a greening activity developed in Japan at the late 1990s.

The pleasure of showing the owner's garden to the visitor and the pleasure of the visitor watching the owner's garden can be expected to have the effect of fostering exchanges and communities via flowers.

VIEWPOINTS

Previous research

Research on OG in Japan was accumulated as the activities of OG in Japan were developed.

For example, a study of features and problems in Obuse Town, Nagano Prefecture, conducted by Mr. Nonaka [1]. Another study conducted by Mr. Hirata focused on the impact of the open garden on the regional economy [2]. These are researches on the cause of OG introduction in Japan, and the effect and significance of activities.

After that, with the spread of the activities of OG in Japan, the research conducted by Nonaka "Focus on the behavior of the viewer at the time of the green event [3]", the research brought about by the open garden conducted by Sambuichi and Iwatomo et al. [4] [5] etc. These researches on the visitor's behavior and the actual activity concerning OG was conducted.

Viewpoints of this research

As a study of OG today, a study [6] was conducted focusing on the actual condition and continuity of the

open garden activities conducted by Park. In this study, 73 OGs in Japan were classified into three groups of 9 years or more, 5 years or more and less than 9 years, and 5 years or less. Because of the research, it is necessary to secure the parking lot on the hard side for the continuity of the activity of OG. In terms of software, it has been suggested that it is important to increase activity awareness, form of activity, increasing human resources to conduct activities, and to increase awareness of OG.

As mentioned above, although the research about OG has shown the subject in the activity actual condition and continuity of OG, there are few researches, which examined these subjects more deeply. In addition, “triggers and forms of activities,” “increase the number of participants,” and “increase awareness”, which are the software issues in OG's continuity of activities, are particularly important for promoting future activities. However, conventional research focusing on this has not been seen.

In this study, the above three major issues are summarized as "The issues of OG activity continuity". Then, for the open garden in Maebashi City, we conducted a questionnaire survey 1) on the status of efforts by administrative personnel, and 2) 0on the awareness of OG activities by nearby residents. In addition, it was considered as the originality of research to obtain basic knowledge for the improvement of "problem to OG continuity".

SHIKISHIMA OPEN GARDEN

In this study, OG (hereinafter referred to as Shikishima OG), which has been continuously addressed for 10 years at Shikishima area in Maebashi City, Gunma Prefecture, is used as an example. Firstly, in order to investigate the actual conditions and characteristics of "Shikishima OG", the actual situation was grasped by interviews with the administrative staff who were continuously involved in the work of open garden.

Figure 1 shows the location of the open garden being tackled in Maebashi City. The open garden that has been held continuously for 10 years in the central area of Maebashi City is "Shikishima OG." The "Shikishima OG" began when the National Urban Greening Gumma Fair was held in March 2008 in Gunma Prefecture. Shikishima Park is selected as the main site of the afforestation fair, and the open garden that residents of the adjacent Shikishima area have been working on is the "Shikishima OG Festival" (Fig. 2).

Before the National Urban Greening Gumma Fair

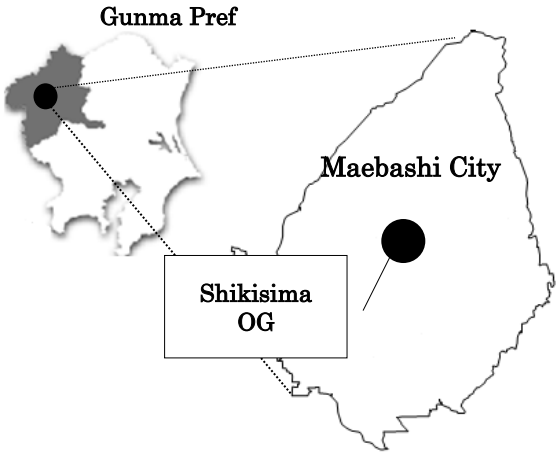

Fig. 1 Location map of Shikishima OG

Fig. 2 Shikishima OG Festival

In 2005, Maebashi City planned an open garden to promote the development of flowers and greenery with the participation of residents in conjunction with the holding of the urban greening fair.

First, in Maebashi City, a lecture was given by a lecturer by Katsue Suma (113 participants) to promote the project. Next, the gardening course and the flowerbed of the Shikishima Town Park were implemented as an approach for the practice of OG.

Shikishima Town Park is a familiar block park in Shikishima Town.

The administration (Maebashi government office) offered the block park of the district as a place of the flowerbed making practice, and there was a desire to want to plan the improvement of the facility environment.OG. Those who wish to participate had a desire to promote their activities to the district residents widely by utilizing the local block park. The interests of both the administration and OG participants agreed.

Gardening course was established in 1971 and was held in greening enlightenment business of

"committee to make town green" with citizen activity organization with history. By holding "seeding class" and "cutting tree class", the opportunity to discover flower lovers was established.

The first open gardening workshop was held in April 2007 at the “Fukaya Flower Festa” site (18 participants). In June of the same year, an open garden gardening class and a planting class for Jade Garden were held (19 participants).

By the time the greening fair was held in 2008 (about 1 year), OG practice classes were held 15 times and open garden gardening classes were held 3 times. Technology training and human resource development for the implementation of the open garden were carried out roughly once or twice a month. This training resulted in the participation of approximately 20 fixed flower lovers.

National Greening Gumma Fair Conducted-After

In the first "Shikishima OG Festival" in conjunction with the holding of " National Urban Greening Gumma Fair " on March 29-30, 2008, "Shikishima Park Flower Friends" with 18 participants are organized and the members' private garden is It was released.

The “Shikishima OG Festival” has been continued every year during the implementation period of the Rose Garden Festival at Shikishima Park after the greening fair (Fig. 3).

In 2019, the 10th "Shikishima Open Garden Festival" was held. Nineteen proud gardens were opened during the two days of the Rose Garden Festival.

As for the administrator, the lecture for citizens promoted citizen enlightenment for OG business is the reason that the activity of "Shikishima OG" continued for 10 years continued. Flower lovers gathered from interest to gardening course and maintenance of flower bed of Shikishimacho Park. In addition, flower lover activities such as open garden inspection training and the implementation of open garden practice classes led to OG. Furthermore, the findings obtained through regular inspection training were used for OG practice. It was evaluated that the continuous approach by such PDCA cycle was the starting point.

For the "Shikishima OG" approach, inspection training sessions and technical training increased the number of activities and participants. In addition, it was evaluated that the use of the block district park familiar to the district residents as a place of OG practice was effective in raising the awareness of the residents.

CITIZEN EVALUATION OF OPEN GARDEN ACTIVITY

Fig. 3 Implementation status of the Shikishima OG Festival

Table1 Neighborhood Resident Questionnaire Survey

Area	within 2.5 km Around Shikishima town
Target	Kawahara town Aramaki town Kamikoide town Shikishima town Midorigaoka town Iwagami town
Duration	2016.8.18～2016.8.31
Method	Posting
Distribution	1,800
Sample	472

The questionnaire survey shown in Table 1 was conducted in order to investigate the residents' evaluation of the activities of "Shikishima OG", which has been working on OG continuously for 10 years. The survey area was 6 towns around Shikishima Park where open gardens are being conducted (within 2.5 km around Shikishima town).

The land use of 6 cities is in the urbanized area in the Maebashi urban planning area, and the use area of the residential area from the first-class low-rise residential area occupies over 80% of the area.

In addition, around Shikishima Park is designated as scenic area. Table 2 summarizes the personal attributes of respondents. According to the table, although there is no significant difference in gender, by age 50 or more accounted for 77.3%. In terms of occupation, "no-employment (34.7%)" was the most frequent, followed by "company employee and public employee (28.0%)." In the family structure, the total of "one generation household" and "two generation household" accounted for 72.2% of the whole.

The residence type was "single-family house (85.2%)".

Table2 Respondent Attributes of the Neighborhood Resident Questionnaire

Sex	Men:56.1% Women:41.9% N.A.:1.9%
Age	19 under:0.2%、 20～29:2.8%、 30～39:6.6%、 40～49:12.1%、 50～59:17.2%、 60～69:25.8%、 70 more:34.3% N.A.:1.3%
Employment	Company employee and Public employee 28.0% Company-owner: 7.4% engage in agriculture: 0.0% housekeeper: 14.4% Student: .6% Part-time: 7.2% No-employment: 34.7% Other: 6.1% N.A. : 1.5%
composition of a family	Single-person household:16.5% One generation household:35.8% Two generation household:36.4% Three generation household:6.6% Other: 3.4% N.A.:1.3%
Habitation	Single-family house: 85.2% Cluster housing: 13.1% Other: 0.4% N.A.: 1.3%
Residence year	0～9: 20.8% 9～19: 17.8% 20～29: 12.9% 30～39: 15.9% 40～49: 14.8% 50～59: 8.1% 60～69: 3.4% 70～79: 3.0% 80～89: 1.1% N.A: 2.3%

Table 3 shows the outline of the questionnaire survey. 55.5% of respondents answered that they knew the activity of "Shikishima OG" and 44.5% answered that they did not know. The following questions were answered by 262 respondents who said, “I know”.

Table3 Results of Neighborhood Resident Questionnaire Survey

Q1: Do you know the Open Garden activities around Shikishima Park?	
They knew the activity	262(55.5%)
They did not know	210(44.5%) (No questions to follow)
Q2: Do you have visited Shikishima Open Garden activities, have you ever seen it?	
visited	87(33.2%)
Seen it	154(58.8%)
N.A.	21(8.0%)
Q3: What changes do you think the area around Shikishima Park will be due to Shikishima Open Garden activities?	
I think that the landscape of the district improves	137
I think that the greenery and flowers of the district will increase	124
I think that the greenery and attachment of the area will increase	84
I think that the community activity will be active	64
I think that nothing changes in particular	35
Do you think that Open Garden activities contribute to community development in the community?	
I think	206(78.6%)
I do not think	50(19.1%)
N.A.	6(2.3%)

Firstly, 33.2% of the respondents answered that they "visited" when I asked the question "Do you have visited Shikishima OG, have you ever seen it?". Next, I asked them to answer the question "What changes do you think the area around Shikishima Park will be due to Shikishima OG activities?"

As a result of the answer, "I think that the landscape of the district improves (137)" was the most frequent. The fact that the neighborhood residents most hoped for the improvement of the landscape of the district by the open garden activity was realized. Then "I think that the greenery and flowers of the district will increase (124)", "I think

that the greenery and attachment of the area will increase (84)", and "I think that the community activity will be active (64). In addition, when asked about "Do you think that open garden activities contribute to community development in the community", 78.6% of the respondents answered, "I think".

From the above, "Shikishima OG" was not just a limited activity of a lover's group, but activity was recognized by more than half of the residents in the area around Shikishima Park. And about 80% of the people who recognized it were positively regarded as "contributing activities to community development in the community".

In addition, in "the town development of area", expectation was most raised for "the scenery of district improves". From this result, the recognition of the activities of the nearby residents and the expectation for the community development were one of the factors that "Shikishima OG" could be continued.

CONCLUSIONS

In this research, we examined three aspects of open garden "motive for activity", "increase participants" and "increase awareness" as a problem of activity continuity, taking "Shikishima OG" as an example. Park's previous research [6] suggests that open garden activities tend to be continued toward activities starting with "a gathering of flower lovers" rather than "recommendation of administration."

"Shikishima OG" originated from the recommendation from the administration (Maebashi City Hall). I. I made an opportunity of activity centering on training of training courses and practical skills. After that, they voluntarily recruited participants of flower lovers' gatherings. II. The area block park familiar to the district residents was used as a place of practice. As a result of the above, the awareness of the residents was raised, and as a result, OG activities could be continued.

"Shikishima OG" was recognized by more than 50% of the respondents in the results of the questionnaire survey on the neighbors. In addition, more than 80% of the recognized residents were rated as "contributing to the area", and it was possible to know "the situation what they most expected these activities to create a local landscape"

The Shikishima OG, which has continued for 10 years, is considered to have received favorable evaluations from nearby residents as a result of working on activities characterized by the issue of activity and the issue of increasing the number of participants, which are the issues of activity continuity.

We will quantitatively verify the basic findings obtained in this research on the subject of activity continuity. In addition, I think that it is necessary to do a concrete study to solve the problem of activity inheritance.

REFERENCES

[1] Katsutoshi.N, The Characteristics and Problem of 'Open Gardens' in Obuse Town, Nagano Pref., journal of the Japanese Institute of Landscape Architecture, Vol.65, No.5, pp.805-810, 2002.3

[2] Fujio.H, Toshimitsu.T, Akira.M, The Study about the Estimation of Economic Effect to the Local Area by the Activity to Open the Private Gardens to the Public in Japan, journal of the Japanese Institute of Landscape Architecture , Vol.66, No.5, pp.779～782, 2003.3

[3] Katsutoshi.N, A Study on the Significance of 'Open Garden' in a Greenery Event, journal of the Japanese Institute of Landscape Architecture 69(5), pp.789-794, 2006.3

[4] Jun.S, Akira.Y, Minoru.K, An Examination about Structure of Consciousness of Open Gardener , journal of the Japanese Institute of Landscape Architecture 70(5), pp.391-396, 2007.3

[5] Hanae.I, Akiharu.K, The Study of the Activity of 'Open Gardens' and the Change in the Member's Consideration and Action in Sanda City, Hyogo Pref., journal of the Japanese Institute of Landscape Architecture 70(5), 657-662, 2007.3

[6] Hyeeun.P and Katsutoshi.N, A Study of the continuity on Actual Situation of ‘Open Garden’ Activity from opportunity and period: Transactions of AIJ. Journal of architecture, planning and environmental engineering , Vol.75 , No.648 , pp.427～435, 2010.2

9th Int. Conf. on Geotechnique, Construction Materials and Environment, Tokyo, Japan, 20-22 November 2019, ISBN: 978-4-909106025 C3051

WATER POLLUTION OF THE KAIZO-GAWA RIVER

Yukimasa Takemoto[1]・Masaaki Takahashi[1]・Maki Ooyagi[1]・Seiji Iwasaki[1], Masashi Sakakieda[2]・Jirou Ito[3]・Naoki Shimomura[3]・Takanori Terazawa[4] and Tadashi Kobayashi[4]

[1]. Yokkaichi University, Research Laboratory on Environmental Technology,
[2]. Azuma Sangyo Co. Ltd. [3]. Yokkaichi-Shi Kamiebi-Chou Suiri Kumiai
[4]. Mie Prefectural Environmental Conservation Agency,

ABSTRACT

The Kaizou-Gawa River is a middle size of the river which flows down to Ise Bay though the northern part of Yokkaichi city. Recently, in the catchment area of the river many pig farms and a semiconductor factory were constructed, In order to identify the influences on them, investigations were carried out over 5 years. High levels of pollution of nutrients and fluorine compounds were found. These pollutions are considered to be related with wastewater of the semiconductor factory and pig farms.

Keywords: Water, Pollution, IC industry, Pig farm, Waste-water

INTRODUCTION

The Kaizou-Gawa River is a middle size of the river which flows down from Komono-Cho town to Ise Bay though the northern part of Yokkaichi city[1)]. The river is situated in a rural area, and is well known by many citizens as the place of ECO-Activities because of its landscape and biological diversity. In the catchment area of the river, vast rice field is spread, and the river enacts an important roll as the source of the irrigation water. However, recently, some big pig farms were constructed upstream from them, and a semiconductor factory was constructed at the upper stream of the branch river. In order to identify the influences of both, an investigation was carried out[2)].

METHOD

Time and investigation site

The investigation was carried out in the years 2015 to 2018 at the stations St0 to St11 (12 stations, shown in Fig.1). In order to identify the source of the pollution, waste water discharged from the pig farms was also investigated.

Monitoring site

The feature of the monitoring sites are mentioned below.
St0: most upstream of the Heta-Kawa river, where has no influence of the semiconductor factory, St1: downstream of the discharge point of the semiconductor factory, St2: downstream of the Heta-Kawa river. St3: irrigation canal, which flows down to the mouth of the main stream. St4: situated at the most downstream of the river. St5: Eda-Gawa, one of the branch river, St6: Taketani-Gawa (branch river), St7: midstream of the main stream. St9: small irrigation canal which leads to the Taketani-gawa. St8: Ooguti-Gawa, branch river, near of Sato-pig farm, St10: upstream of St8, St11: situated at the most up-stream of the main stream, where no typical inflows of the pollutants.

Parameter and analytical methods

Parameter and analytical methods are shown in Table1.

RESULT AND DISCUSSION

At St 0 a high concentration of NO_3-N was found which was considered to be affected by the farm land around there. At St1, St2 and St4, high values of EC, Cl-ion, F-ion were found (Fig.4), these high pollutants level are considered to be due to the influence of the wastewater from the semiconductor factory. The pollution is considered to become significant because of the volume of the wastewater compared to the small original flow rate of the river. In order to solve the matter, much stricter waste water control will be needed. At the St3, some-time relatively high values of F-ion was found which is related to the introduction the irrigation water from the Heta-Gawa river.

At St8 and St9, high values of COD, NO_3-N, NH_4-ion and PO_4-P were found (Fig.2 and Fig.3). At St8, low values (2mg/L to 6mg/L) of DO were also found which is considered to be an influence of the pollutants. These pollutants are considered to be the influence of the wastewater from the pig farms around there. Many pig farms in the area have some waste water treatment facilities,

Table 1 Parameter and analytical methods

Parameter	Method	Parameter	Method
p H	Glass electrode method	NH_4-Ion	Indophenol method
EC	Plutonium electrode method	PO_4-P	Molybdenum color method
DO	Winkler method	F-Ion	Lanthanum-alizarin complexone method
COD	Acidic Manganese titration	CL-Ion	Silber nitrate titration
NO_3-N	UV absorbance		

Fig. 1 Investigation Site

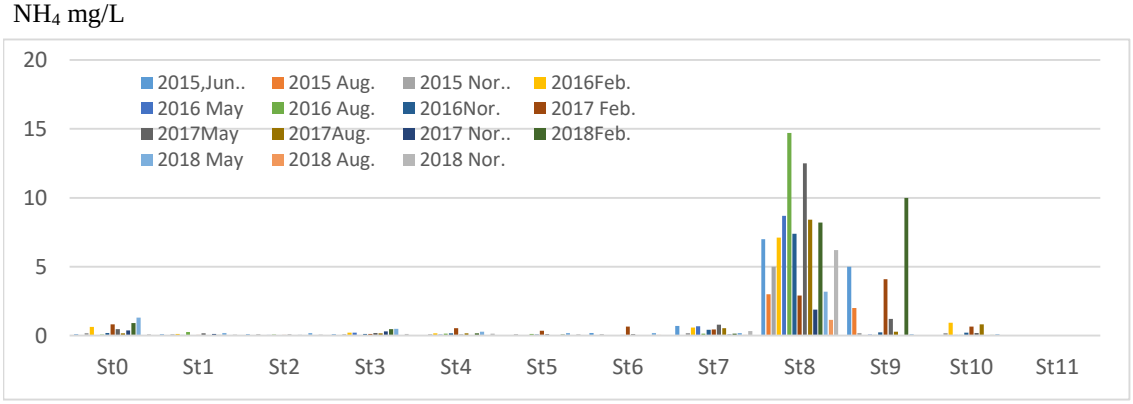

Fig. 2 Features of the NH_4-Ion

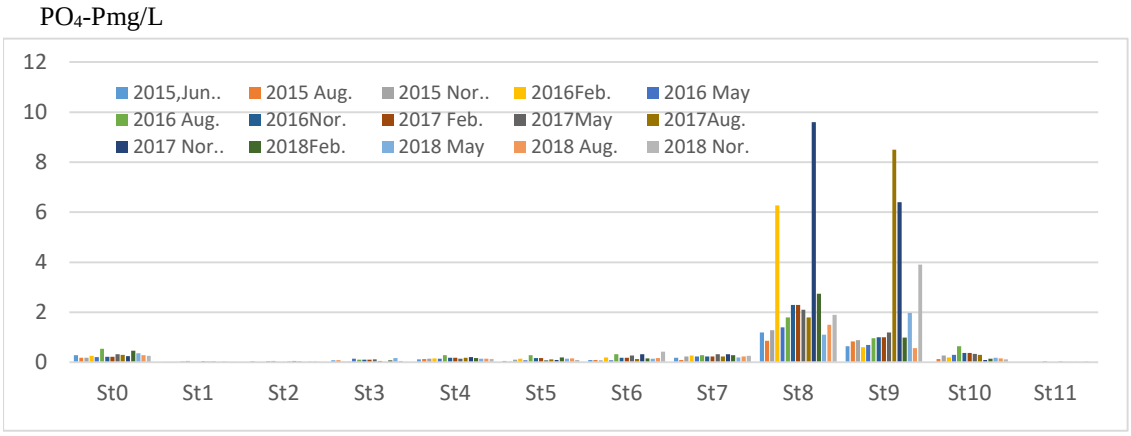

Fig.3 Features of the PO_4-P

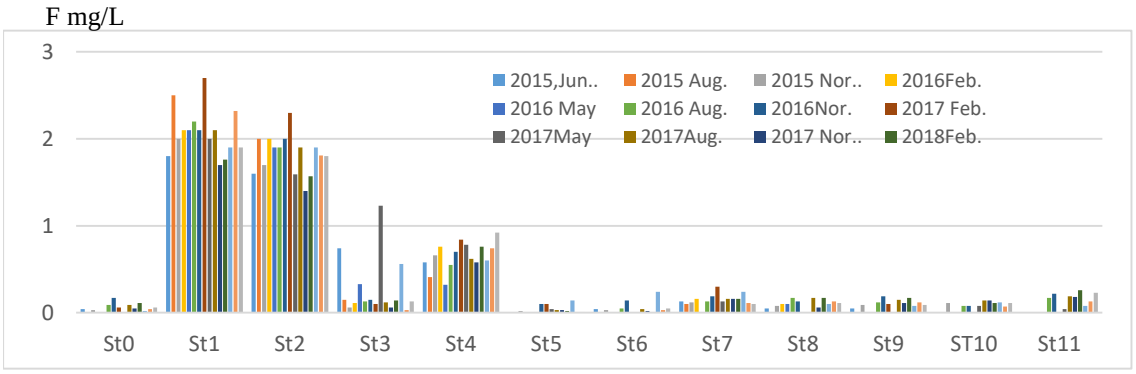

Fig.4 Features of the F -Ion

but these measures are not enough, and influences to the river cannot be ignored. The pollution tends to be lower toward the downstream of the river due to the dilution of the branch river.

At the other monitoring sites, no remarkable pollution was found, and water quality was maintained as pH value distributes around 7 to 8, and DO value 8mg/L to 11mg/L, and the river is judged to be a slightly polluted river like other rivers in this district[3].

CONCLUSION

In order to identify the degree of the pollution, investigations were carried out over 5 years on the Kaizo-gawa river. At the Heta-gawa (branch river), high concentrations of F-ion , Cl-ion was found, and also high values of EC was found. These pollution levels are considered to be due to the influence of the waste water from semiconductor factory near of the river. At the Ooguchi-gawa and Taketani river, (other branch river) high concentrations of COD, PO_4-P, NH_4-N were found which are considered to be caused by pig farms near of the river. At other monitoring sites, unusual levels of pollution was not found.

ACKNOWLEGEMENT

The authors wish to express their appreciation to Dr. Eric Bray (Professor of Yokkaichi University) for his advice on making the article.

REFERENCE

[1] Mie Prefectural Anural Report on the Environment. 3-6 Outline of the Monitoring Station (2016)

[2] Yukimasa Takemoto, Masaaki Takahashi, Maki Ooyagi, Masashi Sakakieda, Jirou Ito, Naoki Shimomura, Takanori Terazawa, Water pollution of Kaizo-Gawa River, Journal of, Yokkaichi University, Vol. 30, No.1,171-181 (2017)

[3] Yukimasa Takemoto, Peng Guo, Masaaki Takahashi: Water Quality Analysis and Environmental Education in the River (II)、Journal of Faculty Environmental and Information Science, Yokkaichi University, Vol. 16, No.2, 51-72 (2013)

9th Int. Conf. on Geotechnique, Construction Materials and Environment, Tokyo, Japan, 20-22 November 2019, ISBN: 978-4-909106025 C3051

THE CONTACT PATCH ANALYSIS OF THE SOLID TIRE TESTING BY FINITE ELEMENT METHOD

Chakrit Suvanjumrat[1,2] and Juthanee Phromjan[1,2]
[1]Department of Mechanical Engineering, Faculty of Engineering, Mahidol University, Salaya, Nakhon Pathom, 73170, Thailand
[2]Laboratory of Computer Mechanics for Design (LCMD), Department of Mechanical Engineering, Faculty of Engineering, Mahidol University, Salaya, Nakhon Pathom, 73170, Thailand

ABSTRACT

The solid tire performance can be characterized by the contact patch. The footprint is the particular method to achieve the contact patch between a tire and pavement. The flat surface is often equipped to support a pressure measurement film which is pressed by the tire tread. This derivative patch illustrates characteristic seems the probable result to predict tire performance. Practically, the contact patch happens by the rolling tire. To understand the patch characteristic, the contact patch between the rolling tire and pavement was studied. The 3D finite element model of solid tire which pressed on three different surfaces was developed. The experimental footprint on the flat surface was carried out to validate the finite element model. The contact patch of solid tire tread on the drum surface was investigated to discuss the effect of supporting floor of the testing method. The stress distribution in the solid tire model is the exceptional criteria to clarify the contact patch on the road. The developed models will be used to design the tire tread and pavement in the future work.

Keywords: Solid tire, Finite element method, Ride Contact patch, Pavement, Tread

INTRODUCTION

The solid tire has an excellent performance for supporting the heavy load. To develop solid tire performance, the tire testing is carried out to provide the physical behavior of tire. The tire stiffness testing is used to study the tire characteristic under the compression load which compose of the vertical stiffness and contact patch. Liang et al., [1] had been used the tire static loaded machine and tire pressure measurement system (Tekscan) to studied the footprint geometry. The footprint shape was described in order to build the relationship between the footprints and tread wear. Nowadays, the engineering design technology has been employed popularly to develop the tire performance. The computer aided design (CAD) and computer aided engineering (CAE) can be used to develop the solid tire. The performance testing by the stiffness tester is the compressing on flat surface which performed on solid tires to create benchmark for validation of the solid tire deformation models [2]. Alkan V. et al. [3, 4] had been investigated the static tire enveloping characteristic by experimental setting and 3D finite element model. The finite element method had been used to design tires popularly. The vertical stiffness of the rolling pneumatic tire was studied on a flat surface. To develop the tire safety and effective driving action, the carcass stiffness was studied [5]. The pneumatic tire was compressed on flat surface in laboratory. The carcass stiffness was carried out from experiment to validate the FE model. Subsequently, the FE model which can provide the gradient of contact stress was used to study the effect of carcass stiffness. Practically, the tire is used in the rolling state. The drum testing method is ideal for rolling tire testing in laboratory [6]. Then, the drum testing method which mimics the tire rolling on flat road was widely used to investigate the mechanical behavior of rolling tire. Phromjan J. and Suvanjumrat C. [7] had been carried out the drum testing method with a diameter of 1.7 m to study the vibration behavior of solid tire and pneumatic tire. The rolling velocity and compression load on tire was controlled. Wei C. and Olatunsun O. A. [8] were studied the effect of different height obstacle on pneumatic tire behavior traversing by finite element method. The drum testing method with a diameter of 2.44 m was performed in order to examine the transient dynamic responses of a pneumatic tire rolling over road obstacles and to validate the FE pneumatic tire model. Moreover, the drum testing method was modeled in 3D finite element model to develop the accurately simulation of pneumatic tire rolling over cleat by transient dynamic model [9]. The transient dynamic response was studied in time and frequency domain. The tire rolling speed gave the remarkable influence while the change of the tire inflation pressure only produced the remarkable variation in vertical dynamic force. Both flat and curvature surfaces were used to support tires under the performance testing without proofing its effect. Consequently, the effect of curvature of drum on tire/road contact is interesting.

In this research, the 3D finite element model of

solid tire was developed to study the contact patch characteristic by the compression on three tendentious difference pavements.

THE TIRE TESTING METHOD

The 6.00-9 inch solid tire was interesting to study in this research. The characteristics of solid tire are described in Table 1. According to the tire standards, the tire testing was set to characterize the tire performance. For example, the tire stiffness testing was performed in order to achieve the tire deformation, tire stiffness and tire-pavement contact patch by steel flat surface. On the other hand, the drum testing method which was performed by cylindrical steel surface provided the tire rolling characteristic. The curvature of steel drum surface might be effects to the rolling solid tire which was provided the deformable behavior as like as the tire testing on flat surface.

Table 1 The characteristic of solid tire.

Size (inch)	Rim Size (inch)	Tire Dimension (mm)		Weight (kg)
		Width	Outside Diameter	
6.00-9	4.00E-9	145	523	27

The tire stiffness testing

The tire stiffness testing has been performed by mounting a solid tire on axle of the tire stiffness tester EKTRON TEK model: PL-2003 of Research and Development Center for Thai Rubber Industry (RDCTRI) as shown in Fig. 1. The stiffness characteristic of solid tire was measured by loading the solid tire on measurement table which had a pressure measurement film. In order to investigate the contact patch, the solid tire was pressed by three different loads which were comprised of 400, 800 and 1200 kg. Fig. 2 shows the contact patch on pressure measurement film which illustrates contact area (CA) and footprint area (FA). The FA was calculated by a×b while the contact area was presented in red color. Moreover, the contact pressure distribution on pressure measurement film was presented by color intensity. The vertical force and deformation were measured by a load cell and position transducer while the measurement table was driven by hydraulic motor to lift and press the stationary solid tire.

The drum testing method

The mechanical behavior of rolling tire was investigated by mimicking rotation state of the tire. The drum testing method is an ideal testing in the laboratory. It is exclude the various factors such as road surface and vehicle system which are not the effect of the tire. The drum testing method has been performed by mounting a solid tire on a mounting arm which is driven by hydraulic motor to move and press the solid tire onto rolling steel drum as shown in Fig. 3. The solid tire was pulled to roll at the same velocity with the rolling steel drum by the friction between the contact areas.

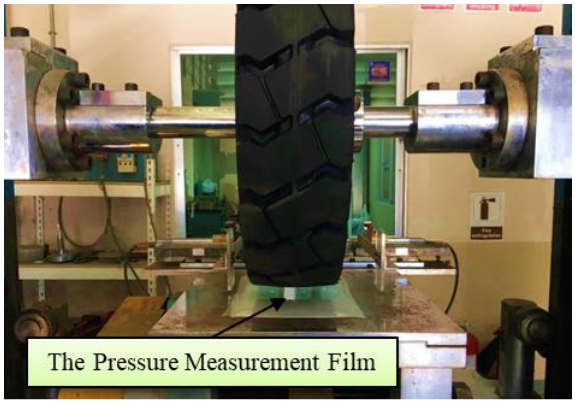

Fig. 1 The tire stiffness testing.

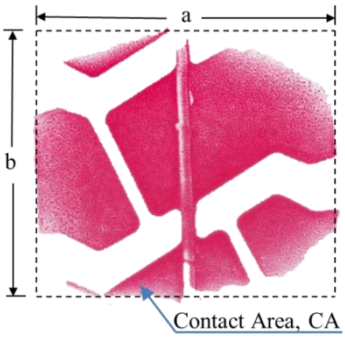

Fig. 2 The contact patch on pressure measurement film.

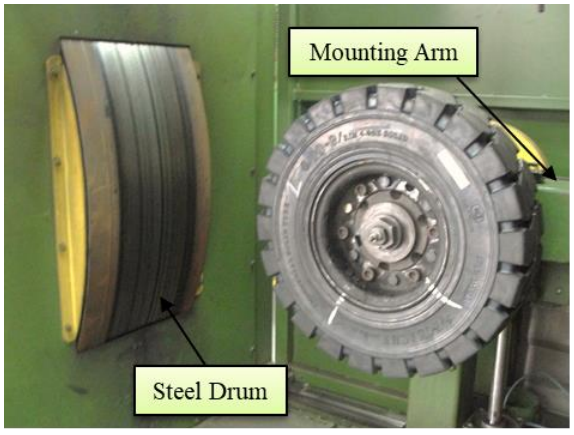

Fig. 3 The drum testing method.

FINITE ELEMENT METHOD

The finite element analysis (FEA) of the solid tire testing is governed by Eq. 1.

$$m\ddot{u}_i + c\dot{u}_i + ku_i = F_i \tag{1}$$

where u_i is the time-dependent displacement field, c is the damping coefficient, m is mass, F_i is the total force.

The Eq. 1 can be transformed into the form of system total work which balanced the work per unit element as shown in Eq. 2 [10]. Hence, V and s is the element's volume and element's surface, respectively.

$$\int \{\delta u\}^T \{f_i\} dV + \int \{\delta u\}^T \{\Phi\} ds + \sum_{i=1}^{n} \{\delta u\}_i^T \{p\}_i = \int \left(\{\delta u\}^T \rho \{\ddot{u}\} + \{\delta u\}^T c\{\dot{u}\} + \{\delta\varepsilon\}^T \{\sigma\} \right) dV \tag{2}$$

where f_i is body force, Φ is surface force, p is determined force, ρ is mass density, ε is strain, σ is stress and n is the number of nodes.

The solution of transient FEA can obtain by the Housbolt method. The general form of the single-step Housbolt is written in Eq. 3-4 [11].

$$\dot{u}_{n+1} = \dot{u}_n + \gamma \Delta t \ddot{u}_n + \gamma_1 \Delta t \ddot{u}_{n+1} \tag{3}$$

$$u_{n+1} = u_n + \Delta t \dot{u}_n + \beta \Delta t^2 \ddot{u}_n + \beta_1 \Delta t^2 \ddot{u}_{n+1} \tag{4}$$

where β_i is the constant and γ_i is the defined parameter.

In case of large strain, the hybrid formulation is effective for the analysis of rubberlike material [12]. The FEA of the solid tire testing was governed by the following equations which the strain energy density per unit volume, ${}_0^t\bar{U}$ is defined in Eq. 5.

$$d\,{}_0^t\bar{U} = {}_0^t\bar{S}\, d\,{}_0^t\varepsilon_{ij} \tag{5}$$

where $d\,{}_0^t\bar{U}$ and ${}_0^t\bar{S}$ are incremental potential energy and Piola-Kirchhoff stress which computed only from the displace field.

The integral form of total Lagrangian formulation is shown in Eq. 6.

$$\int_{V_0} {}_0^t S_{ij} \delta\, {}_0\varepsilon_{ij} dV_0 = R \tag{6}$$

The general form of principle of virtual work which written in the total Lagrangian formulation is given in Eq. 7.

$$\delta\left(\int_{V_0} {}_0^t U dV_0 \right) = R \tag{7}$$

where ${}_0^t U$ is the incremental potential which can be modified to include the effect of interpolated pressure by adding to the term of the displacement based total element pressure.

Material properties

The solid tire which is studied in this research is comprised of the three rubber layers and 4 steel wires (Fig. 4). The rubber layers were built by different formula of rubber compounds. The internal layer (M058) was hardest, the middle (M047) and the tread layer were softer, respectively. The material property of each rubber layer of solid tire was obtained by the tensile testing according to ASTM D412 standard. The stress-strain curve from the tensile testing was fitted by linear regression method. The Ogden hyperelastic constitutive model (Eq. 8) which is the strain-energy density function was the most suitable to represent the solid tire deformation behavior in all rubber layers [13]. The values in Table 2 are the constant of Ogden constitutive model of three rubber layers. The steel wire was specified with elastic modulus and Poisson's ratio of 200 GPa and 0.3, respectively.

$$\mathrm{U} = \sum_{\mathrm{i}=1}^{\mathrm{n}} \frac{\mu_i}{\alpha_i} (\bar{\lambda}_1^{\alpha_i} + \bar{\lambda}_2^{\alpha_i} + \bar{\lambda}_3^{\alpha_i} - 3) + 4.5K(J^{1/3} - 1)^2 \tag{8}$$

and $\bar{\lambda}_\mathrm{i} = \mathrm{J}^{-1/3}\lambda_\mathrm{i}$, $\mathrm{J} = \lambda_1\lambda_2\lambda_3$.

where λ_i is the deviatoric principle stretches, J is the Jacobean determinant, K is the initial bulk modulus, and μ_i, α_i is constant.

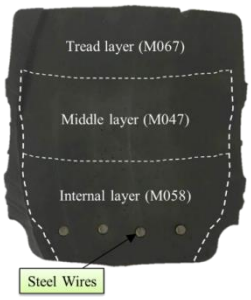

Fig. 4 The cross section of solid tire.

Table 2 The constant of Ogden constitutive model

Rubber layer	μ_1	μ_2	α_1	α_2	K
M067	1.075	154.616	2.927	1.14e-7	7,866
M047	0.362	510.855	3.233	0.0056	10,078
M058	3,615.31	2,915.36	0.0028	0.0024	42,449

Solid tire finite element model

The solid tire model was created in three dimensions using data from the 3D scanner (Artec 3D, Eva) and CAD software. The solid tire model was meshed by hexahedral elements. Consequently, the internal, middle, tread layer and steel wires are created using 16,623, 8,448, 14,366 and 7,040 elements, respectively (Fig. 5). The element of steel wire, internal, middle and inner tread layer are connected together with conjunct node while the outer tread layer is connected with the inner tread by glue contact condition as presented in different color as shown in Fig. 6.

The finite element model of tire stiffness testing

The finite element (FE) model of solid tire which was described in above section was compressed on a rigid flat plate according to the physical tire stiffness testing. Fig. 7 shows the boundary conditions of FE solid tire testing model which the RBE2 elements were defined to link the axis of solid tire model as the steel wheel. The fixed boundary condition was assigned on wheel fixed point as same as the solid tire mounting on the axis of the stiffness tester. The contact boundary condition between the solid tire model and rigid flat plate was specified with 0.8 of static friction coefficient. The vertical loads were assigned on a rigid flat plate to lift and press the solid tire model. Subsequently, the solid tire model was compressed by three different loads which were 400, 800 and 1,200 kg, respectively.

The finite element model of drum testing method

The cylindrical steel drum was created using the curvature rigid element with a diameter of 1.7 m according to the size of the drum testing machine, KAYTON; model: DTM-350PC of RDCTRI. It provided the diameter ratio of 3.25 between the diameter of drum and tire. First, the vertical load was assigned on a rigid drum to move and press the solid tire model by three different loads, 400, 800 and 1,200 kg. Next, the rigid drum was rotated with a constant velocity of 20 km/h. After that, the solid model was pulled by the rolling drum with the dynamic friction coefficient of 0.5 which referred to the principle of drum testing machine. The implicit dynamic transient with single-step Houbolt was used to operate the rolling solid tire finite element model. The constants for analysis were 1.5 and -0.5 for γ_1 and γ , respectively. Fig. 8 presents the boundary condition of rolling solid tire on steel drum to study the effect of curvature surface on contact patch by FEM. MSC. Marc software which was installed in a personal computer with a Core-i7 processor and 8 GB RAM memory had been used to process finite element method of solid tire testing.

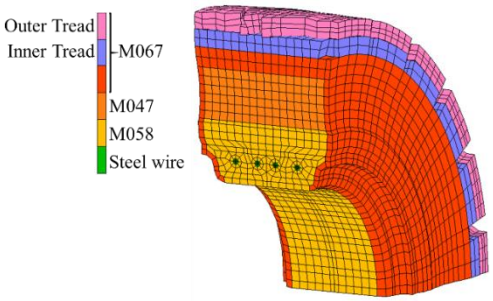

Fig. 5 The finite element model of solid tire.

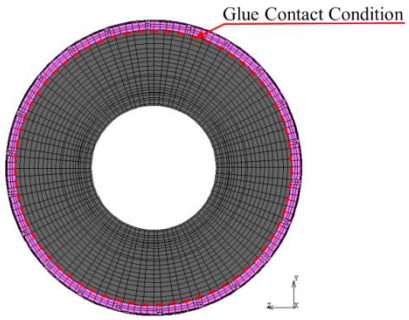

Fig. 6 The contact condition of solid tire model.

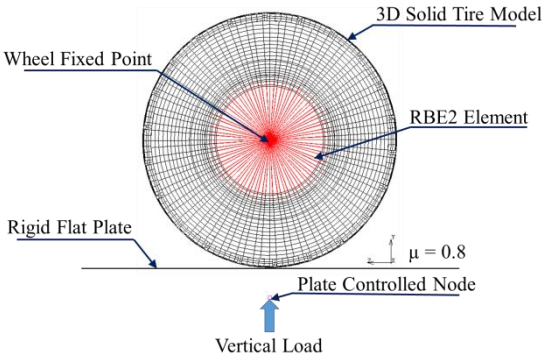

Fig. 7 The boundary condition of compressed solid tire finite element model.

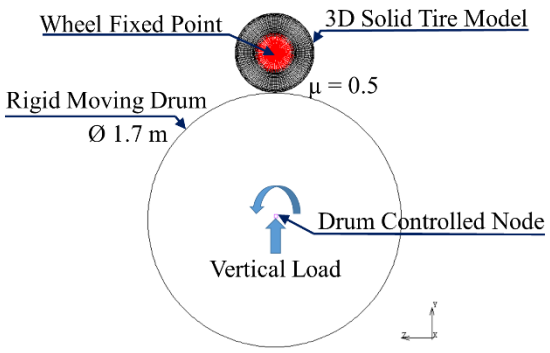

Fig. 8 The boundary condition of rolling solid tire finite element model.

RESULTS AND DISCUSSIONS

The results of compressed solid tire (size 6.00-9 inch) on rigid flat plate model were compared with the stiffness testing. The contact patch of compressed solid tire on rigid flat plate model found to be in agreement with the experimental result under compression loads of 400, 800 and 1,200 kg. Table 3 presents the contact patches of all studied conditions which observed at the same tread pattern position with experiment. The vertical deformations increase by the increase of compression loads as shown by graphs in Fig. 9. The comparison graphs in Fig. 10 also indicated that the footprint area of solid tire on measurement table under various compression loads by experiment is smaller than footprint area of compressed solid tire model on rigid flat plate. The maximum stress which happens on the tire tread can illustrate by FEM as shown in Fig. 11. The maximum normal stress happened at the contact area between solid tire model and pavements. At the same time, the concentrate stress also happened between glue contact area of inner and outer tread. This phenomenon affected to the poor distribution of contact patch. The better stress distribution of solid tire model compression on rigid flat plate provided the lower vertical deformation and maximum stress than stationary drum because of contact with the smooth curvature cylindrical drum surface. The maximum normal stress which happened on solid tire under rolling drum was higher than the rigid flat plate. The lateral force of rolling contact affected to the

Table 3 The contact patch characteristic of solid tire (size 6.00-9 inch)

Type of Testing		Vertical Load (kg)		
		400	800	1,200
Stiffness testing	Loaded (EXP)			
	Loaded (FEM)	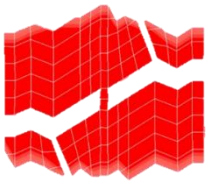	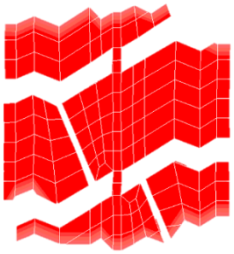	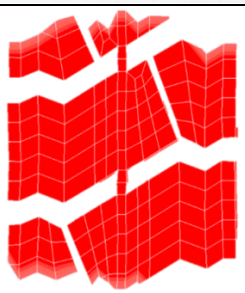
Drum testing method	Loaded (FEM)	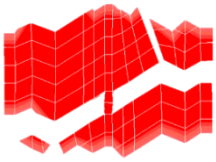	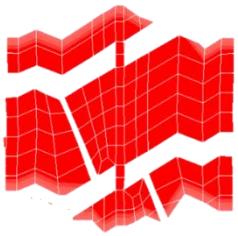	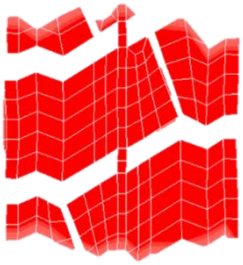
	Rotated (FEM)		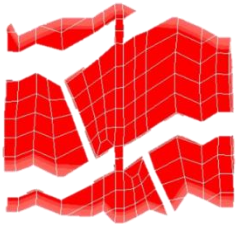	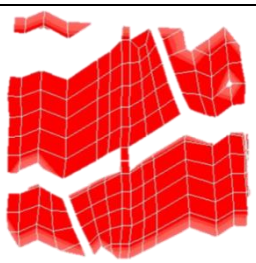

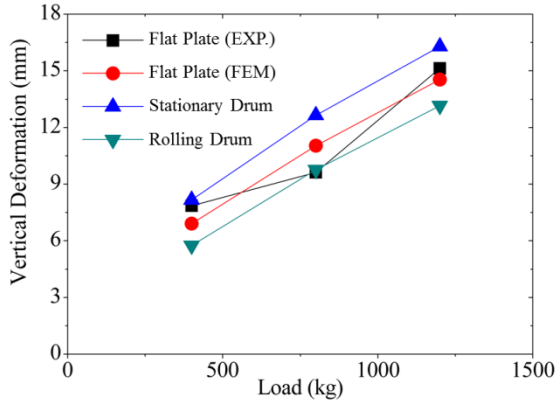

Fig. 9 The vertical deformation of solid tire by three different compression loads on three different pavements.

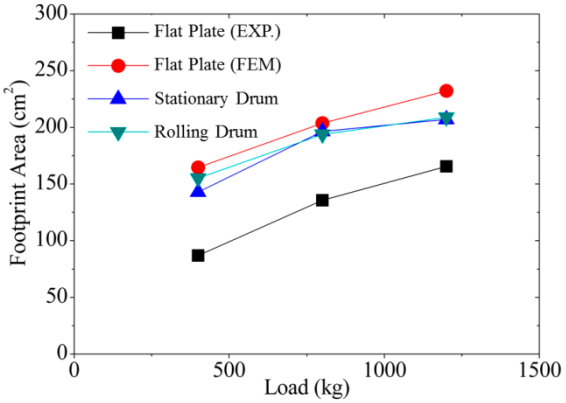

Fig. 10 The footprint area of solid tires by three different loads and pavements.

increase of maximum stress. Fig. 12 shows the comparison graphs of maximum stress between the flat plate and the curvature rolling drum. The contact patch was affected by drum pulling and then some of solid tire elements were deformed extremely. However, the contact coefficients (CA/FA) which represent the adhesion and wear behavior of solid tire were similar. Fig. 13 shows the comparison graphs of the contact coefficients. The average contact coefficient of experiment of solid tire stiffness testing, FE model of solid tire stiffness testing, FE model of loaded drum and FE model of rotated drum were 0.70, 0.70, 0.67 and 0.68, respectively. The error of contact coefficient of solid tire models on the rolling drum surface from the flat plate was less than 2.71%.

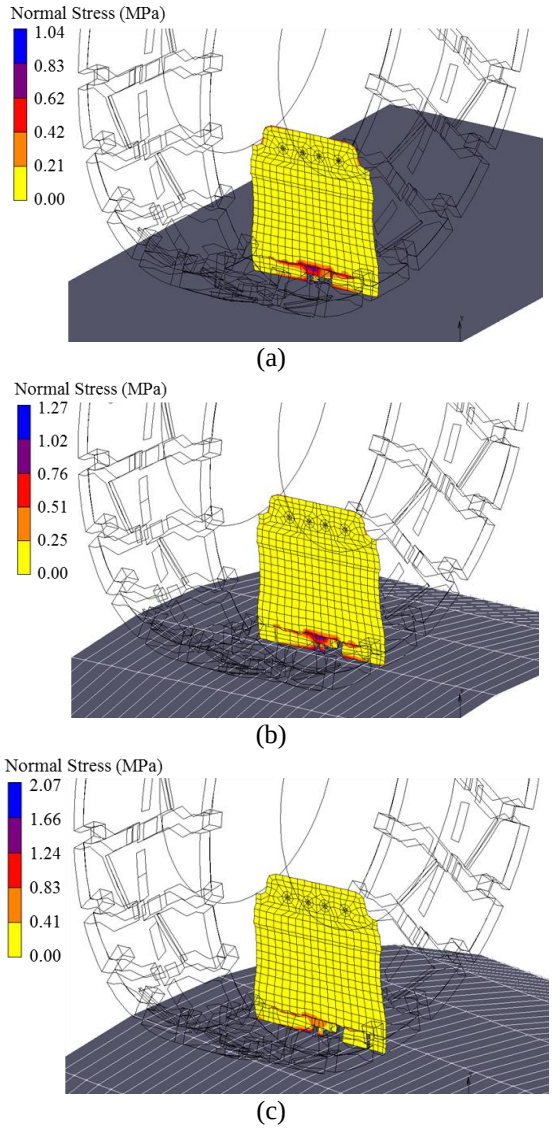

Fig. 11 The normal stress on the cross section of solid tire under the compression load of 3,924 N on (a) flat plate, (b) stationary drum and (c) rolling drum.

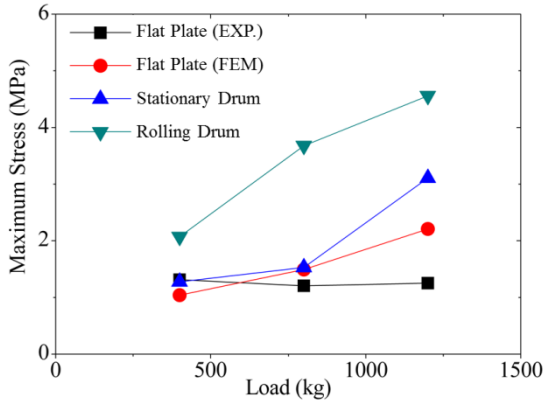

Fig. 12 The maximum stress of solid tires by three different loads and pavements.

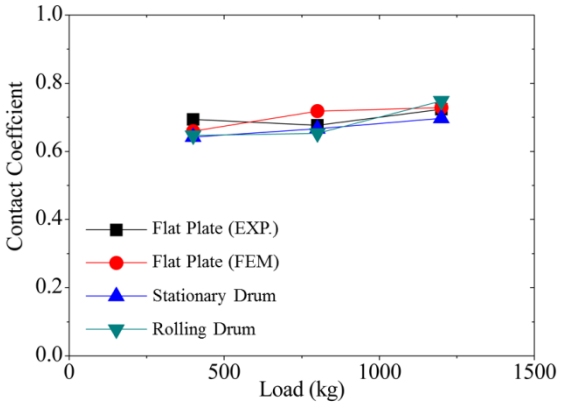

Fig. 13 The contact coefficient of solid tires by three different loads and pavements.

CONCLUSIONS

The contact patch which was used to characterize the solid tire perfomnce was studied by finite elememt method. The solid tire model was compressed on three different pavement with various loads which composed of 400, 800 and 1,200 kg. The contact patch characteristics, vertical deformations and maximum normal stresses were obtained by finite element anslysis (FEA). The results of FEA on rigid flat plate had a good agreement with the experiment under the error of 0.52%. The footprint area of solid tire model on drum was less than on rigid flat plate bacause of the curvature of cylindrical drum. Consequently, the stress distribution of solid tire on flat plate was better than drum. On the other hand, the contact coefficient of solid tire which was compressed on flat surface and drum were similar. It indicated that the contact patch characteristic on flat surface by stiffness testing can repesent the adhesion and wear behavior of rolling solid tire. The developed models will be used to design the tire tread and pavement in the future work.

REFERENCES

[1] Liang C., Wang G., An D., and Ma Y., Tread Wear and Footprint Geometrical of Truck Bus Radial Tires. Chinese Journal of Mechanical Engineering, Vol. 26, Issue 3, 2013, pp. 506-511.

[2] Phromjan J., and Suvanjumrat C., A Suitable Constitutive Model for Solid Tire Analysis under Quasi-Static Loads using Finite Element Method. Engineering Journal, Vol. 22, Issue 2, 2018, pp. 141-155.

[3] Alkan V., Karamihas S., and Anlas G., Experimental Analysis of Tyre Enveloping Characteristics at Low Speed. Vehicle System Dynamics, Vol. 47, Issue 5, 2009, pp. 575-587.

[4] Alkan V., Karamihas S., and Anlas G., Finite Element Modeling of Static Tire Enveloping Characteristics. International Journal of Automotive Technology, Vol. 12, Issue 4, 2011, pp. 529-535.

[5] Namjoo M., and Golbakhshi H., An Efficient Design Tool Based on FEM for Evaluating Effects of Components Properties and Operating Conditions on Interaction of Tire with Rigid Road. J. Cent. South Univ, Vol. 22, 2015, pp. 189-195.

[6] Andersen L. G., Larsen J. K., Fraser E. S., Schmidt B., and Dyre J. C., Rolling Resistance Measurement and Model Development. Journal of Transportation Engineering, Vol. 141, Issue 2, 2015, pp. 1-10.

[7] Phromjan J., and Suvanjumrat C., Vibration Effect of Two Different Tires on Baggage Towing Tractirs. Journal of Mechanical Science and Technology, Vol. 32, Issue 4, 2018, pp. 1539-1548.

[8] Wei C., and Olatunbosun A. O., Transient Dynamic Behavior of Finite Element Tire Traversing Obstacles with Different Heights. Journal of Terramechanics, Vol. 56, 2014, pp. 1-16.

[9] Cho J. R., Kim K. W., Leon D. H., Yoo W. S., Transient Dynamics Response Analysis of 3-D Patterned Tire Rolling Over Cleat. European Journal of Mechanics A/Solids, Vol. 24, 2005, pp. 519-531.

[10] Cook R. D., Malkus, D. S., Plesha M. E., and Witt R. J., Concepts and Applications of Finite Element Analysis, 4th ed. John Wiley & Sons, 2002.

[11] Chung J., Hulbert G. M., A family of single-step Houbolt time intergration algorithms for structural dynamics. Computer methods in applied mechanics and engineering, Vol. 118, 1994, pp. 1-11.

[12] K. J. Bathe, “Finite Element Nonlinear Analysis in Solid and Structural Mechanics,” in Finite Element Procedure, London, England: Pearson Education Limited, 1996, ch. 6, pp. 485–641.

[13] Phromjan J., and Suvanjumrat C., Material Characteristic for Capability Analysis of Solid Tire by Finite Element Mothod. Key Engineering Materials, Vol. 777, 2018, pp. 416-420.

9th Int. Conf. on Geotechnique, Construction Materials and Environment, Tokyo, Japan, 20-22 November 2019, ISBN: 978-4-909106025 C3051

DEVELOPMENT OF DYNAMIC FINITE ELEMENT MODEL FOR RIDE COMFORT EVALUATION OF NON-PNEUMATIC TIRE

Chakrit Suvanjumrat[1,2] and Ravivat Rugsaj[1,2]
[1]Department of Mechanical Engineering, Faculty of Engineering, Mahidol University, Salaya, Nakhon Pathom, 73170, Thailand; [2]Laboratory of Computer Mechanics for Design (LCMD), Department of Mechanical Engineering, Faculty of Engineering, Mahidol University, Salaya, Nakhon Pathom, 73170, Thailand

ABSTRACT

The non-pneumatic tire (NPT) has design potential to have desired mechanical characteristic upon usage requirements. The NPT also has no restriction on inflation pressure, maintenance, and less damage possibilities due to flat while driving. The optimum design of NPT to have required load carrying capacity and vertical stiffness can be easily achieved by mean of static finite element method (FEM) with appropriated material models. However the models to predict dynamic response such as tire structure to road pavement interaction, shock absorption and ride comfort are still needed. This paper aims to develop FEM to study dynamic characteristics and evaluate the ride comfort property of the NPT. The FEM of NPT, which composed of Tread band and Spokes, was model using 3D hexagonal and 2D Quadrilateral elements respectively. The rebar elements and tying equation were used to model steel belt layers of the NPT. The visco-hyperelastic constitutive model was used to model the mechanical behavior which depends on time of the NPT's components. The FEM of NPT was then assigned to traverse across cleats with different heights to study the effect of obstacle on tire-road interaction and dynamic response of NPT. The impact force history and deformation behavior of NPT at any given time was analyzed. The results were compared to discuss the validity of the model to capture important dynamic characteristic that considered useful in designing of NPT to have ride quality challenging the commonly used pneumatic tire.

Keywords: Non-pneumatic tire, Finite element method, Tire-road interaction, Ride Comfort, Impact force

INTRODUCTION

The basis function of pneumatic tire, which is an important vehicle component, is to provide the vehicle to road interface, to support vehicle load, to provide road surface friction, and to absorb road irregularities. In that regards, the design of pneumatic tire requires some performance parameters such as the riding comfort, handling and traction criteria to be engineered to meet desired characteristic. However, the pneumatic tires have several disadvantages since the tire possess the risk to undergo severed damage or flatted if the tire traversing across various types of critical obstacles [1]. The non-pneumatic tire (NPT) or airless tire was developed to overcome these disadvantage. The NPT was designed to exhibit desired characteristics of the pneumatic tires without requirement of the inflation pressure. The first available commercial NPT is TWEEL developed by Michelin. The Tweel, consists of two main components which are 1) circular shear beam and tread 2) elastic spokes which connected to a hub. The NPT can be designed to have required vertical stiffness and contact pressure upon spoke geometry and material without limit to size and pressure, unlike traditional pneumatic tire. The non-pneumatic tire's lateral stiffness which affects handling and cornering can also be independently optimized with vertical stiffness which affects the riding comfort [2].

The vehicle stability and ride comfort is important tire performance especially on off road vehicle which traversing over various type of irregular terrain and obstacles. The transient dynamic characteristic of a tire has significant effect on vehicle handling stability. However the transient dynamic effect is difficult to study due to its highly non-linear behaviors. The effects of obstacle geometric factors during tire-obstacle collision was study using soil-bin facility equipped with a single-wheel tester. The various obstacle shapes along with different depth were varied in the experiments which operation condition of wheel traversing such as speed and load were controlled. The maximum and minimum induced impact force were observed from highest triangular shape and trapezoidal shape obstacle respectively [3]. Normally transient dynamic characteristic of the rolling tire can be determined by using drum testing method. However the drum testing method has limitation if the effects of pavement surface, roughness, or obstacles such as cleat or ditch are interested. The finite element method (FEM) can be used to simulate the tire behavior during rolling under critical conditions. A FEM of tire was developed to perform tire enveloping tests in transverse obstacles

of different sizes using explicit dynamic solution in finite element software ABAQUS. The tire transient dynamic behavior was investigated by analyzing the effects of tire rolling velocity and obstacle height on spindle force, dynamic stiffness, and tire deformation. [4]. The 3D FEM based on dynamic transient approach of mechanical elastic wheel (MEW) traversing over a ditch was developed to study transient dynamic characteristic of MEW. The radial stiffness and footprint of MEW were analyzed and compared with the experiment to validate the model accuracy. A dynamic analysis of MEW over a ditch was conducted using ABAQUS. The equivalent stress and contact stress was analyzed to study effects of rolling speed over the ditch [5].

The tire, which is considered as viscoelastic material, undergoes cyclic deformation during rolling on the road surface. The stress and strain field under cyclic loading exhibit phase delay between strain and stress time histories, which is the cause of hysteresis energy loss [6]. Thus, the development of thermomechanical model with viscoelastic material is required to predict the dynamic characteristic of the rolling tire. NPT, which components are made from low viscoelastic energy loss materials, can be a good option for developing tires with low rolling resistance. The thermo-viscoelastic model of NPT with a lattice spoke was developed to predict rolling energy loss and the corresponding heat generation of NPT components. The Yeoh hyperelastic model was obtained from the tension and compression tests, while viscoelastic material properties were obtained from dynamic mechanical analysis (DMA) test. A 3-D stress analysis was performed using steady state rolling analysis, then the cyclic strain energy was converted into heat to obtain temperature and compared with temperature distribution from the experiments [7]. The effects of static and dynamic loading of NPT with honeycomb spoke was investigated using FEM. the three types of NPT with constant cell wall thickness but different cell geometries were numerically simulated to study the effects on deformation modes, stress distribution, load carrying capacity, and rolling resistance. While on dynamic loading, the effects of friction coefficient and angular velocity on rolling resistance were also studied. The maximum stress in spoke under dynamic loading was observed to be higher when compared to static loading [8].

Design of NPT is needed to consider the tire performances which dynamic characteristic such as tire–road interaction, rolling resistance, and riding comfort, play an important factor. This paper aimed to develop the 3D FEM of NPT based on viscohyperelastic material model that can be used to predict NPT performances regarding dynamic characteristic.

FINITE ELEMENT MODEL OF NON-PNEUMATIC TIRE

The commercial NPT Tweel 12N16.5 SSL ALL TERRAIN airless radial tire developed by Michelin (Fig. 1), which is the first available NPT, was selected to study the mechanical behavior and characteristic of NPT. The FEM of NPT was modeled using the FE software MSC.Patran. The NPT model composed of 4 main components which can be concluded as follows: 1) tread, 2) shear band, 3) belt layers, and 4) polyurethane spoke. The FEM of NPT along with its overall dimension and components is shown in Fig. 2, 3, and 4 respectively. The hybrid formulation or Hermann formulation was used to model the tread and shear band elements of NPT. The formulation utilized the separated integration of pressure and displacement field, which can be used to prevent volumetric locking that may occur during loading of rubber material elements. The thick shell approximation is used to model the spoke. The details of elements which are used in modeling of NPT which shown in Table 1. The thickness of each shell elements was assigned differently based on the actual thickness distribution measured from the real spoke. The thicknesses at outer and inner ring of the spoke were 6 and 7 mm, respectively, while the averaged thickness of the spokes could be calculated relating to the spoke weight that was 5.8 mm.

The belt layer consisted of four main layers which were 1) the outer layer, 2) the 1st middle layer, 3) the 2nd middle layer, and 4) the inner layer. The outer layer was composed of three sublayers while the inner layer was composed of two sublayers. The belt layer model was developed using reinforce bar or rebar element [9]. The rebar elements of the belt layer were embed into the rubber element using tying equations. The value of the degrees of freedom of the nodes in host body element was tied based on their isoparametric location in the elements. The cross section of shear band of the FEM and real TWEEL along with the embed belt layer position is shown in Fig. 5. The details of the elements using in each layer are described in Table 2.

Fig. 1 NPT Tweel 12N16.5 SSL ALL TERRAIN.

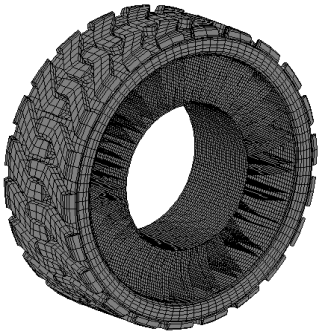

Fig. 2 Finite element model of non-pneumatic tire.

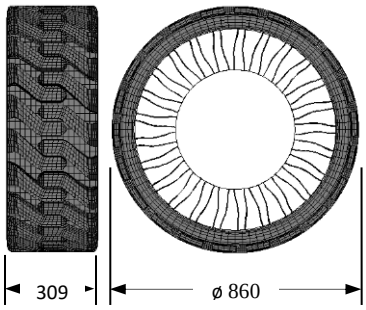

Fig. 3 Overall dimension of NPT's FEM.

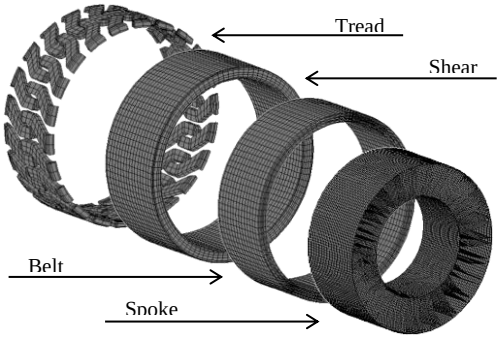

Fig. 4 Components of FEM of NPT.

Table 1 Details of elements used in FEM of NPT

	Element type	Number of element	Averaged element length (mm)
Tread	Hexagonal	2,228	19.89
Shear band	Hexagonal	11,904	16.15
Belt layers	Quadrilateral	6,144	20.38
Spoke	Quadrilateral	35,500	8.74

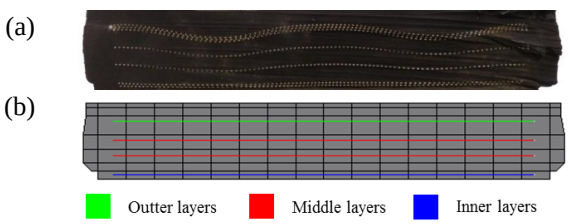

Fig. 5 Cross section of shear band with embed belt layers of (a) FEM (b) TWEEL

Table 2 Details of rebar element properties in each layers.

Layers	Number of sublayers	Bead wire diameter (mm)	Number of wires per unit length (mm^{-1})	Bead wire angle (degree)
Outer layers	3	1	0.3582	0°
1st middle layers	1	1	0.3582	0°
2nd middle layers	1	1	0.3582	0°
Inner layers	2	1	0.3582	0°

HYPERVISCOELASTIC MATERIAL MODEL

The Ogden hyperelastic constitutive model was used to model nonlinear elastic behaviors of rubber tread, shear band, and polyurethane spoke.

The general form of Ogden hyperelastic model [10] can be expressed as Eq. (1):

$$ {}^{t}_{0}\tilde{W} = \sum_{n=1}^{3} \frac{\mu_n}{\alpha_n}\left(\lambda_1^{\alpha_n} + \lambda_2^{\alpha_n} + \lambda_3^{\alpha_n} - 3\right) \quad (1) $$

Where λ_i are the principal value of the stretch tensor ${}^{t}_{0}U$, μ_i and α_i are material constants. The inelastic behaviors of NPT components were modeled using the generalized Maxwell viscoelastic material model. The generalized Maxwell viscoelastic model can be express as Eq. (2), (3).

$$ G(t) = G_0 - \sum_{i=1}^{n} G_i\left(1 - e^{-t/\tau_i}\right) \quad (2) $$

$$ \tau_i = \eta_i / E_i \quad (3) $$

Where $G(t)$ is Shear Relaxation Modulus, G_0 is Shear Modulus at time, *t=0*, G_i is i[th] term of Shear Modulus, τ_i is i[th] term of Relaxation Time (sec), E_i is Modulus of Elasticity, and η_i is viscoelasticity.

The parameters of Ogden hyperelastic and generalized Maxwell material model of tread and PU spoke, which are obtained and validated from mechanical testing in the previous research, are shown in Table 3 and 4, respectively [7, 11]. The compressive testing and tensile testing was performed on the cylindrical shape and dumbbell shape specimens, which were prepared from NPT's tread and spoke respectively. In addition, steel the belt layers were modeled using linear elastic material with modulus of elasticity (E) of 200 GPa and Poisson's ratio of 0.3.

Table 3 Hyperelastic constants of NPT components.

Constant	Component	
	Spoke	Shear Band
λ_1	0.112983	1.15673
λ_2	-11.0664	1.06228
α_1	3.1488	5.37146
α_2	-1.75206	-2.31827

Table 4 Viscoelastic constants of NPT components.

ith	τ_i	G_i	
		Spoke	Shear Band
1	0.2	0.125	0.2
2	0.02	0.125	0.2
3	0.002	0.125	0.2

FINITE ELEMENT ANALYSIS OF OBSTACLE TRAVERSING

The FEM of NPT was combined with road surface model for obstacle traversing analysis of NPT. The tread and shear band was assigned to be in contact with the road surface with friction coefficient of 0.8. The Coulomb's friction model was used to evaluate the friction force which occurred between the tire and road surfaces. The cleat surface was attached to road surface for the purpose of obstacle traversing simulation. Three size of rectangular shape cleat surface was selected in this research to study the effects of obstacle geometry to dynamic behaviors of NPT. The schematic diagram of installation and placement of NPT FEM onto the road and cleat surface along with its boundary conditions is shown in Fig. 6. The cleat surfaces are varied in height, which the schematic diagram of each cleat dimension is shown in Fig. 7 and are summarized in Table 5. The hub of NPT was modeled as rigid surface, which was assigned to be perfectly glued contact with the inner ring of spoke. The vertical load of 5 kN was assigned to the center of rigid hub, which was also applied to move forward at the speed (v) of 10 km/hr with corresponding angular velocity (ω) of 3055.6 rad/sec.

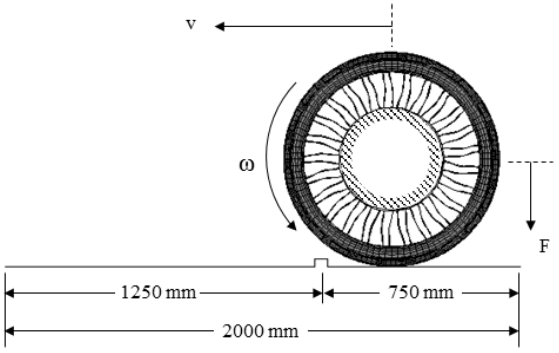

Fig. 6 Boundary conditions of NPT combined with road and cleat surfaces.

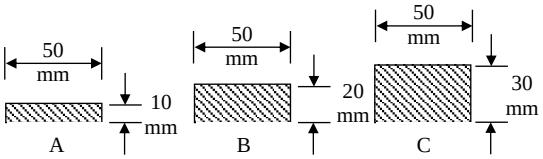

Fig. 7 Detail of cleats dimension with different height (A) 10 mm (B) 20 mm (C) 30 mm

Table 5 Details of cleat dimensions.

Cleat	Length	Width	Height
A	500	50	10
B	500	50	20
C	500	50	30

The dynamic transient analysis was performed using finite element software MSC.Marc, The analysis was divided into 2 main stage, which was 1) loading stage, and 2) rolling stage. At 0 < t < 1 sec., the NPT was assigned to be loaded with force gradually increase from zero to maximum force of 5 kN while the tire was assigned to be stationary. At 1 < t < 1.4 sec., after the NPT was fully loaded, the tire was assigned to be rotated and moved forward while the maximum force was still applied. The force and displacement history were collected after the analysis was complete at t = 1.4 sec to study the tire-road interaction and dynamic behaviors of NPT. The stress and deformation of NPT FEM at t = 1 sec., which is when the vertical force is fully applied, is shown in Fig. 8. It should be note that the analysis at this stage was corresponding to vertical stiffness testing of tire at maximum force 5 kN, which the vertical stiffness was founded to be 648.7078 N/mm. In addition, the spokes at the upper portion of NPT was observed to be in tension, while the spokes at lower portion was observed to be in bending mode. The tire-road interaction and deformation at various time t are shown in Fig. 9.

The impact force and vertical displacement history at hub center were collected, which the vertical displacement was normalized to exclude

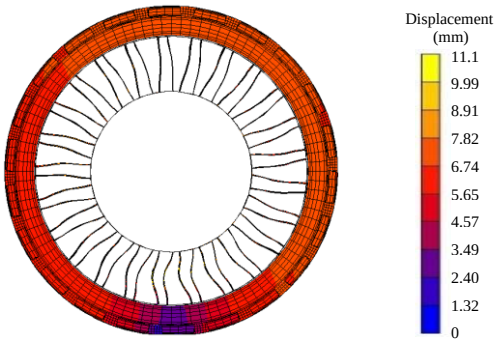

Fig. 8 Displacement and deformation result at t = 1 sec and F = 5 kN.

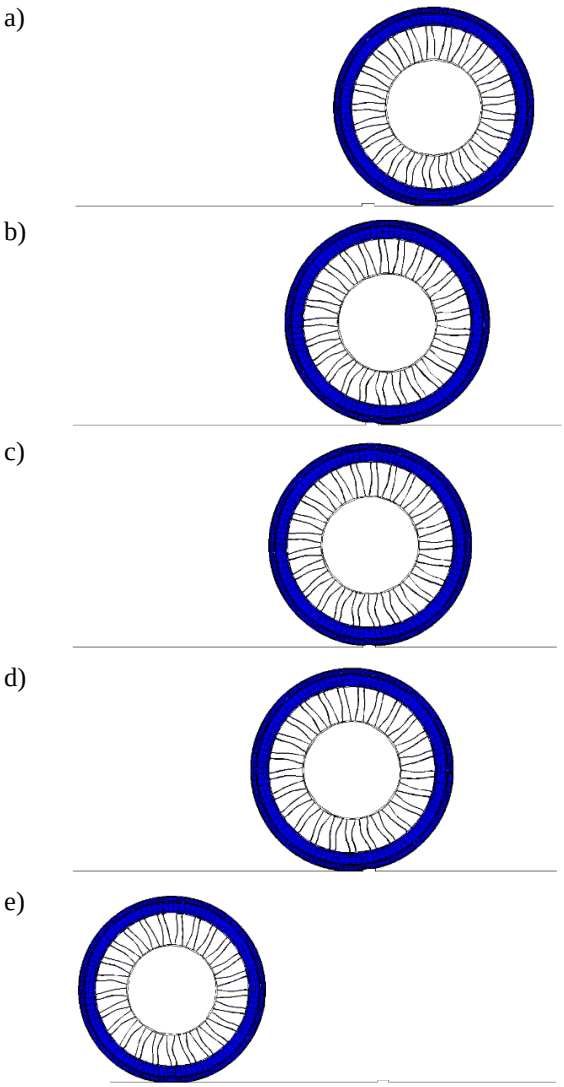

Fig. 9 Deformation and tire-road interaction of NPT at a) t = 1 sec, b) t = 1.72 sec, c) t = 1.88 sec, d) t = 1.14 sec, and e) t = 1.40 sec.

initial displacement due to deformation at t = 1 sec where the load was fully applied. The normalized vertical displacement of tire center and impact force at various time are shown in Fig. 10, 11 respectively. The average vertical displacement of tire center and average impact force along with their maximum values can be concluded as shown in Fig. 12 and Fig. 13, respectively. The summarization of average normalized displacement at tire center and average impact force can be concluded as shown in Table 6. The NPT model with highest cleat (height = 30 mm) was shown to yield greatest value of both average vertical displacement of tire center and average impact force. However the oscillatory response after the NPT rolled down a cleat was scant when compared with pneumatic tire [12-15]. Considering the observed underdamp characteristic of the oscillatory, the NPT has potential to be optimized the ride comfort properties for the vehicles.

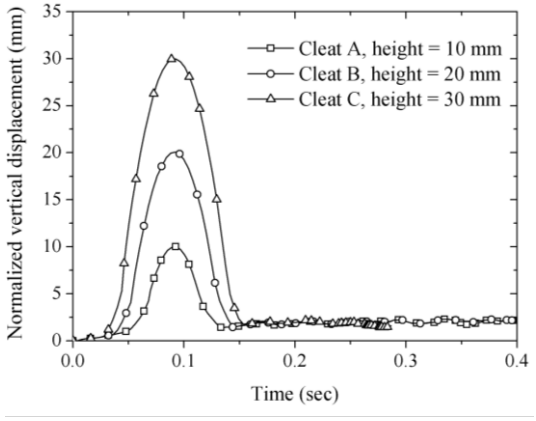

Fig. 10 Vertical displacement at various time.

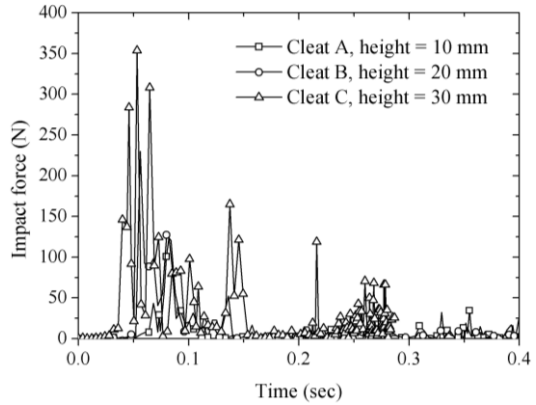

Fig. 11 Impact force at various time.

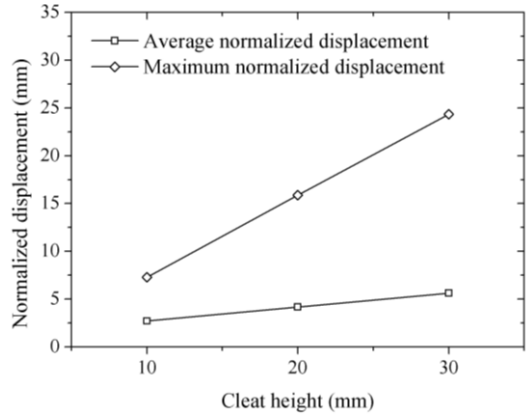

Fig. 12 Vertical displacement at various cleat heights.

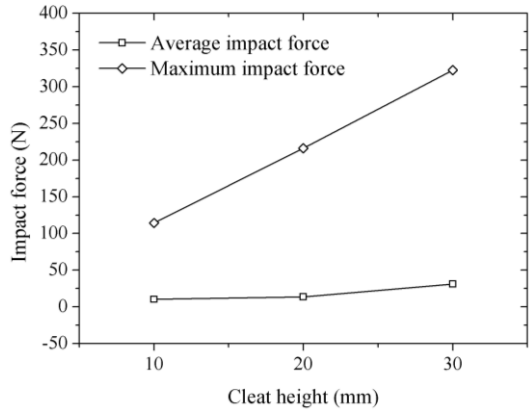

Fig. 13 Impact force at various cleat heights.

Table 5 Summarization of average normalized displacement and average impact force.

Cleat	Height	Average normalized displacement (mm)	Average impact force (N)
A	10	2.706719	10.26311
B	20	4.184955	13.68296
C	30	5.617848	30.87236

CONCLUSIONS

The FEM of NPT was developed to study dynamic characteristics and evaluate the ride comfort property of the NPT. The FEM of NPT, which composed of Tread, shear band and Spokes, was modeled using 3D hexagonal and 2D Quadrilateral elements respectively. The rebar elements and tying equation were used to model steel belt layers of the NPT. The validated Ogden hyperelastic material model and generalized Maxwell viscoelastic material model were used to model nonlinear elastic and inelastic behaviors of NPT components. The FEM of NPT was then assigned to traverse across cleats with different heights to study the effect of obstacle on tire-road interaction and dynamic response of NPT. The impact force history and deformation behavior of NPT at any given time was analyzed. The results were compared to discuss the validity of the model to capture important dynamic characteristic. The FEM of NPT with highest cleat (height = 30 mm) was shown to yield greatest value of both average vertical displacement of tire center and average impact force at 5.617848 mm and 30.87236 N respectively. The underdamped oscillatory behavior was observed from vertical displacement and impact force, which shown that NPT has potential to be optimized regarding ride comfort properties. The analysis results shown that the devloped hyperviscoelastic dynamic FEM of NPT can be used in designing of NPT to have dynamic characteristic such as ride quality for challenging the commonly used pneumatic tire.

ACKNOWLEDGMENTS

This work was financial supported by Rubber Technology Research Center (RTEC), Mahidol University and the Thailand Research Fund (TRF) under the TRF Research Grant No. RDG60T0140.

REFERENCES

[1] Gent A. N., and Watler J. D., The pneumatic tire. National Highway Traffic Safety Administration, 2006.

[2] Rhyne T. B., and Cron S. M., Development of a Non-Pneumatic Wheel. Tire Sci. Technol., Vol. 34, 2006, pp. 150-169.

[3] Taghavifar H., Motlagh A. M., Mardani A., Hassanpour A., Hosseinloo A. H., and Wei C., The Induced Shock and Impact Force as Affected by the Obstacle Geometric Factors during Tire-Obstacle Collision Dynamics. Journal of Measurement, Vol. 84, 2016, pp. 47-55.

[4] Wei C., and Olatunbosun A.O., Transient Dynamic Behavior of Finite Element Tire Traversing Obstacles with Different Heights. Journal of Terramechanics, Vol. 56, 2014, pp.1-16.

[5] Zhao Y. Q., Deng Y. J., Lin F., Zhu M. M., and Xiao Z., Transient Dynamic Characteristics of a Non-Pneumatic Mechanical Elastic Wheel Rolling Over a Ditch. International Journal of Automotive Technology, Vol. 19, Issue. 3, 2018, pp. 499-508.

[6] Montgomery T.S., MacKnight W.J., Introduction to Polymer Viscoelasticity, 3rd ed. John Wiley & Sons, Inc., 2005.

[7] Yoo S., Uddin M., Heo H., Ju J., and Choi S.J., Thermoviscoelastic Modeling of a Non-pneumatic Tire with a Lattice Spoke. Journal of Automobile Engineering, Vol. 231, Issue. 2, 2017, pp. 241-252.

[8] Jin X., Hou C., Fan X., Sun Y., Lv J., and Lu C., Investigation on the Static and Dynamic Behavior of Non-Pneumatic Tires with Honeycomb Spokes. Journal of Composite Structures, Vol. 187, 2018, pp. 27-35.

[9] Helnwein P., Liu C.H., Meschke G., and Mang H.A., A New 3-D Finite Element Model for Cord-Reinforced Rubber Composites-Applications to Analysis of Automobile Tires. Finite Elem. Anal. Des., Vol. 14, 1993, pp. 1-16.

[10] Bathe K. J., Finite Element Procedures, 1997, Prentice Hall, London.

[11] Rugsaj R., and Suvanjumrat C., Finite Element Analysis of Hyperelastic Material Model for Non-Pneumatic Tire, Key Engineering Materials, Vol. 775, 2018, pp. 554-559.

[12] Hans-Rudolf B.B., Herman A., Hamersma P., and Schalk E., Parameterisation, Validation and Implementation of an All-Terrain SUV FTire tyre model. Journal of Terramechanics, Vol. 67, 2016, pp. 11-23.

[13] Kazemi O., Ribaric A.P., Nikravesh P.E., and Kim S., Non-Rolling Mesh for a Rolling Finite-Element Tire Model. J Mech Sci Technol, Vol. 29, 2015, pp. 2615-2522.

[14] Palanivelu S., Rao K.V.N., and Ramarathnam K.K., Determination of Rolling Tyre Modal Parameters using Finite Element Techniques and Operational Modal Analysis. Mechanical Systems and Signal Processing, Vol. 64–65, 2015, pp. 385-402.

[15] Cho J., Kim K.-W., Jeon D.H., Yoo W.S., Transient Dynamic Response Analysis of 3-D Patterned Tire Rolling Over Cleat. European Journal of Mechanics A/Solids, Vol. 24, 2005, pp. 519-531.

9th Int. Conf. on Geotechnique, Construction Materials and Environment, Tokyo, Japan, 20-22 November 2019, ISBN: 978-4-909106025 C3051

IMPROVEMENT OF STRUCTURAL ANALYSIS BY MODIFICATION OF SITE RESPONSE ANALYSIS AND EARTHQUAKE FORCE DIRECTION

W. Partono[1], M. Irsyam[2], Asrurifak[3], U. C. Sari[1] and Hariyadi[1]
[1]Engineering Faculty, Diponegoro University, Indonesia; [2]Faculty of Civil and Environmental Engineering, Bandung Institute of Technology, Indonesia; [3]Research Center for Disaster Mitigation, Bandung Institute of Technology, Indonesia

ABSTRACT

The seismic resistance design of buildings in Indonesia is usually performed based on the most recent Indonesian Seismic Code (ISC). Improvement of the ISC will sometimes produce different (increasing or decreasing) earthquake forces for building design. This paper describes the study of building evaluation by conducting a modified site response analysis (SRA) with a modified incoming earthquake force direction. The modified SRA was performed by means of an in-complete soil boring investigation through the bedrock elevation, using 30 m (soil boring investigation) and 50 m (microtremor investigation) soil profile models. The earthquake force towards the building is analysed using a pair (North-South/NS and East-West/EW) of ground motion models. Due to the unpredictability of incoming earthquake forces, these models are improved by adjusting the ground motion direction to the building by rotating a pair of ground motion from 0^o to 180^o at 10^o intervals. The ground motion is developed based on the Probabilistic and Deterministic Seismic Hazard Analysis (PSHA and DSHA). The analysis was performed by evaluating the moment capacity ratio of the building's existing column reinforcement in resisting the earthquake force. The ground motion and spectral accelerations developed using the 50 m model is slightly greater (10%) than the ground motion and spectral accelerations developed using the 30 m model. In terms of the moment capacity ratio, the existing column reinforcement of the building is strong enough to resist seismic earthquake scenarios, and the minimum value is observed when the ground motion is rotated by 40^o.

Keywords: Site response analysis; Microtremor; Ground motion; PSHA; DSHA

INTRODUCTION

The seismic resistance design of buildings is usually performed by applying a seismic or earthquake force model in terms of spectral acceleration. For design purposes, the Indonesian Seismic Code describes an easier method for preparing the spectral acceleration. The spectral acceleration can also be developed using online software prepared by the Ministry of Public Works and Human Settlements of Indonesia, and is developed based on the updated earthquake data collected from all earthquake events in the whole of the country.

Seismic resistance design and evaluation can also be performed using surface ground motion in terms of acceleration time histories developed from the accelerograph data of a specific earthquake. To develop surface ground motion that can be used for structural analysis requires information of the bedrock elevation and all the soil deposit data from the bedrock up to the surface elevation. The bedrock elevation measurements can be performed using single or array microtremor tests. The soil deposit data can be obtained by conducting soil boring investigations and laboratory measurements.

A soil boring investigation is usually performed when preparing foundation design requirements. The depth of the soil boring investigation data has a direct correlation with the type of foundation used and the bearing capacity requirements of the foundations. Usually the soil boring investigation has no correlation with the bedrock elevation. For a building located on a soft soil layer having a bedrock elevation more than 100 meter, time and money will be needed to prepare soil deposit data, compared to the normal soil boring investigations used for foundation design purposes.

The spectral acceleration data applied to building structure design is usually obtained for two directions perpendicular to the building's position (X and Y, or 0^o and 90^o directions). As the building's position relative to the seismic source is unknown, it is difficult to ensure the seismic force direction for building structure design. This paper describes an example of structural analysis performed using modified ground motion or seismic force directions. The analysis is conducted by first improving the depth of the soil deposit model for SRA by taking a 30 m soil deposit model adapted

from a soil boring investigation. The spectral acceleration and the ground motion are then compared to the same analysis using a 50 m soil deposit model developed from microtremor investigation data. The purpose of this analysis is to obtain the differences between the surface ground motion and surface spectral accelerations developed based on the two models in order to improve them.

The second improvement is conducted by gradually modifying the two perpendicular directions of earthquake forces in terms of ground motion (NS and EW) from 0° to 180° at 10° intervals relative to the building position. The purpose of this second improvement is to obtain the minimum moment capacity ratio of the existing column reinforcement and the correlation between the moment capacity ratio and ground motion direction.

METHODOLOGY

The modified structural analysis in this research was conducted at the Diponegoro University Semarang (Indonesia) building (40.75 x 16.2 m^2 and 43.2 m height). The building was first open on March 10 2017 and was designed and constructed based on the Indonesian Seismic Code 2012 [1].

Soil Investigations

Two types of soil investigations were performed in the building area. The soil boring investigation was first performed to design the foundation system to support the upper structure and was conducted down to a 30 m depth. According to the N-SPT data obtained on site, the building was found to be located on medium site class soil/SD ([1] - [3]).

The second soil investigation was related with the measurement of the predicted bedrock elevation and was performed using single station three-component microtremor at 22 positions surrounding the building position. Fig. 1 shows the site plan of the study area, the building position, soil boring position and microtremor test positions. Fig. 2 and Fig. 3 show the microtremor results analysis in terms of the shear wave velocity profile. As can be seen in these figures the bedrock elevation is predicted at 40 to 50 m below the surface level. This prediction is based on [1], with a shear wave velocity ranging from 750m/s to 1500 m/s.

Site Response Analysis (SRA)

The SRA is conducted based on two different soil profiles. The first profile is applied using the actual bedrock elevation (50 m) and the second profile using the 30 m soil deposit model [4]. The second model is adjusted in this research due to incomplete data or soil boring investigation data from the bedrock elevation. The soil boring investigation data was performed until a maximum 30 m depth due to the requirement for the foundation design of the structure and the minimum requirement for site class calculation [1]. Fig. 4 shows the first soil profile model (Model-1) using the actual bedrock elevation. Fig. 5 shows the second soil profile model (Model-2). The Vs (shear wave velocity) values embedded in these two profiles (0-30 m) are developed using three empirical correlation proposed by ([5] - [7]) and the microtremor data. The actual bedrock elevation is predicted at 50 m below the surface level.

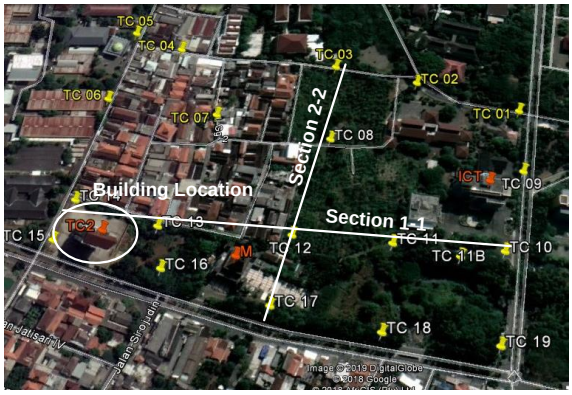

Fig. 1 Study area and building position.

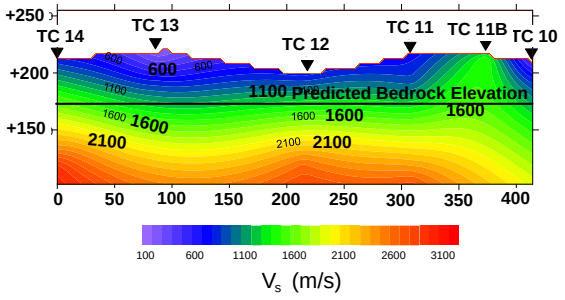

Fig. 2 Vs profile of Section 1-1.

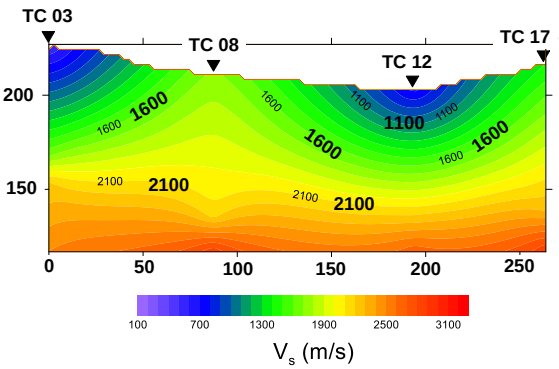

Fig. 3 Vs profile of Section 2-2.

The SRA is developed using two directions of ground motion (NS and EW) collected from a 6.52 Mw earthquake event with an epicenter distance of 5.07 km. To perform the SRA, two different response spectral targets are developed in this study

based on two different types of seismic hazard analysis: Probabilistic Seismic Hazard Analysis (PSHA) with a 2% probability of exceedance in 50 years (2500 years return period) and Deterministic Seismic Hazard Analysis (DSHA). The modified ground motions are then calculated using response spectral matching analysis. Fig. 6 shows the two spectral targets used for spectral matching analysis in order to obtain the modified ground motion at the bedrock elevation. The modified ground motions are used for SRA for obtaining the surface ground motion and spectral acceleration. The PSHA spectral acceleration target was developed based on the 2017 Indonesian Seismic Hazard Map [8]. However the DSHA spectral acceleration target was calculated using three different attenuation functions ([9]–[11]).

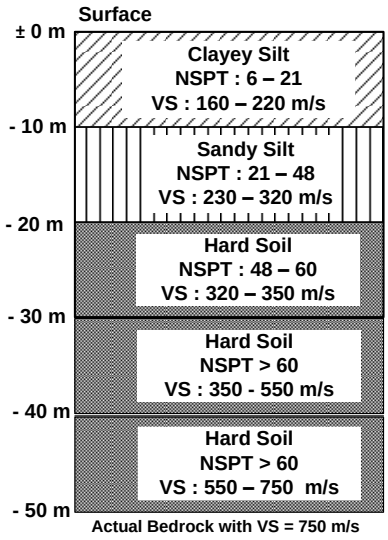

Fig. 4 Soil profile using 50 m soil deposit (Model-1).

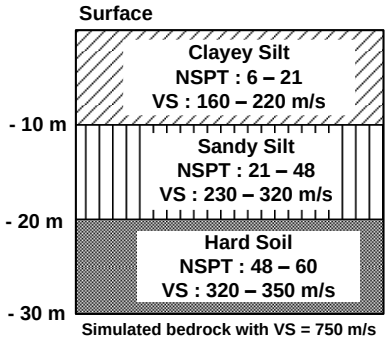

Fig. 5 Soil profile using 30 m soil deposit (Model-2).

The two directions of modified ground motion (NS and EW) developed using the PSHA and DSHA spectral acceleration targets are then used for the SRA using two different soil profile models as shown in Fig. 4 and Fig. 5. Fig. 7 and Fig. 8 shows the two different modified ground motions (NS and EW) developed based on the PSHA and DSHA spectral acceleration targets. As can be seen in those two figures the ground motion developed using PSHA has a peak acceleration almost equal (slightly greater) to the ground motion developed using DSHA. Based on the response spectral matching analysis, the ground motion developed using PSHA is used for SRA.

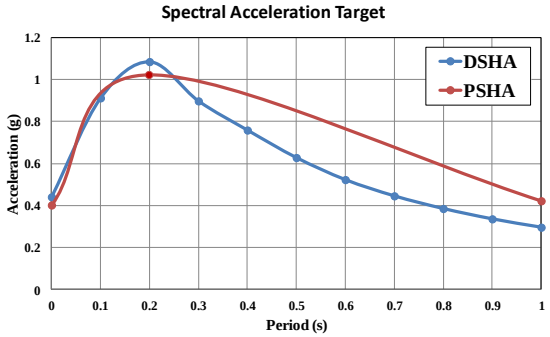

Fig. 6 PSHA and DSHA spectral acceleration target.

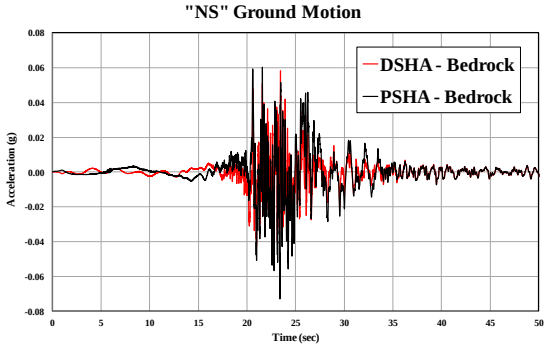

Fig. 7 Modified NS direction ground motion developed from response spectral matching analysis.

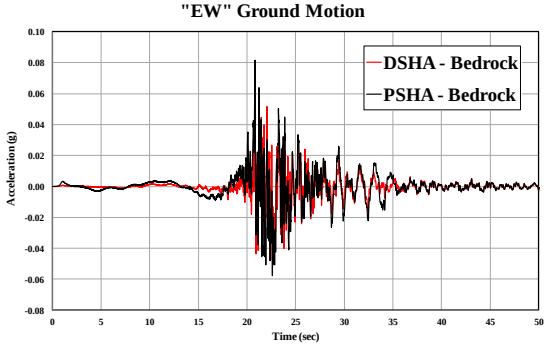

Fig. 8 Modified EW direction ground motion developed from response spectral matching analysis.

Structural Analysis

The earthquake forces model used and applied to the structures is based on surface ground motions in two directions, NS and EW obtained from SRA analysis. The NS direction is perpendicular to the

EW direction. Both ground motions directions are then gradually rotated from 0º to 180º at 10º intervals. The existing columns are evaluated to obtain the moment capacity ratio of longitudinal concrete column reinforcement. The moment capacity ratios for all earthquake force directions are then evaluated and compared to obtain the correlation chart between the earthquake force direction and moment capacity ratio. The minimum moment capacity ratio in terms of the force direction can be obtained using this chart. Fig. 9 shows the model of the earthquake directions used for the structural analysis.

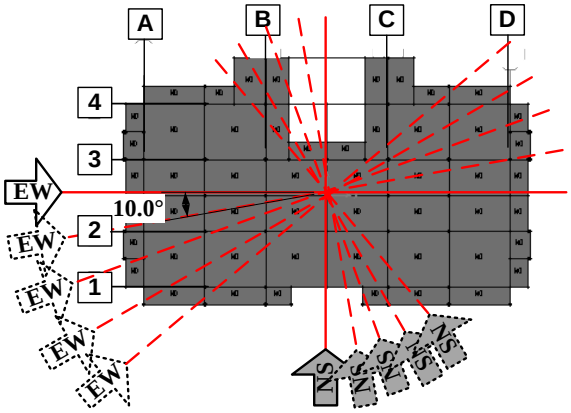

Fig. 9 Improvement of ground motion directions used for structural analysis.

RESULT AND DISCUSSIONS

Surface ground motions are developed using two different soil profile models, Model-1 and Model-2. According to the analysis performed for both models by employing the two different ground motions directions (NS and EW), the surface ground motions developed for the two models are almost equal. Fig. 10 shows the difference of the NS surface ground motions developed using the two models. As can be seen in Fig. 10 the absolute maximum acceleration developed using Model-1 is 0.22 g while the absolute maximum acceleration developed using Model-2 is 0.21g.

Fig. 11 shows the difference of the EW surface ground motions calculated using the two different models. The absolute maximum acceleration developed using Model-1 is 0.18 g and the absolute acceleration developed using Model-2 is 0.16 g. Based on the two different soil profile models developed for the SRA, the maximum surface acceleration for the NS and EW directions is almost equal. Fig. 12 shows the four different surface spectral accelerations developed using the two different SRA models and that the EW and NS spectral accelerations developed using the two models are almost equal.

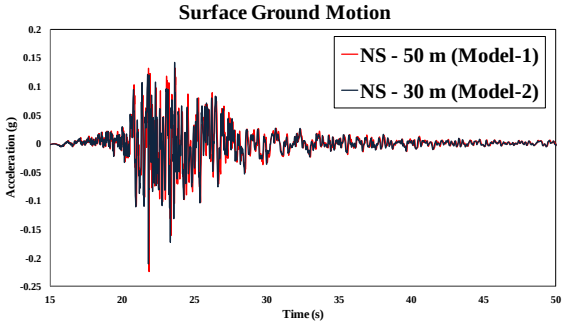

Fig. 10 Surface NS direction ground motion developed using two SRA models.

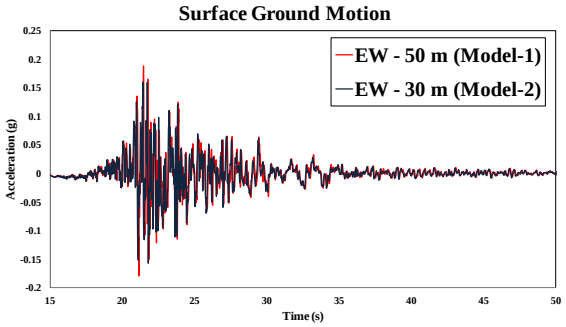

Fig. 11 Surface EW direction ground motion developed using two SRA models.

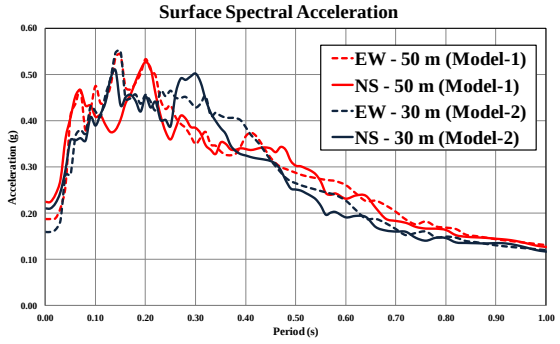

Fig. 12 Surface spectral acceleration developed using two SRA models.

Fig 13 shows the difference of the peak ground acceleration (PGA) profiles developed using the two different SRA models. The PGA values developed using Model-1 is greater than those calculated using Model-2. All the PGA profiles developed using the two models are almost equal (coincident) with maximum differences of surface PGA of 0.03 g (16%) for the NS direction and 0.01 g (5%) for the EW direction. The average surface PGA difference of Model-1 is 10.5% greater than Model-2. Table 1 shows the difference of the surface PGA developed based on the two models. Based on the analysis for developing surface ground motions using the two models, the 30 m soil profile model (Model-2) can

be used as an alternative for developing the surface ground motion. The second soil deposit model (Model-2) used for the SRA is based on the maximum soil boring investigation.

Table 1 Peak ground acceleration of two models

Model	Elevation (m)	PGA-NS (g)	PGA-EW (g)
Model-1	0	0.19	0.22
	50	0.07	0.07
Model-2	0	0.16	0.21
	30	0.07	0.07

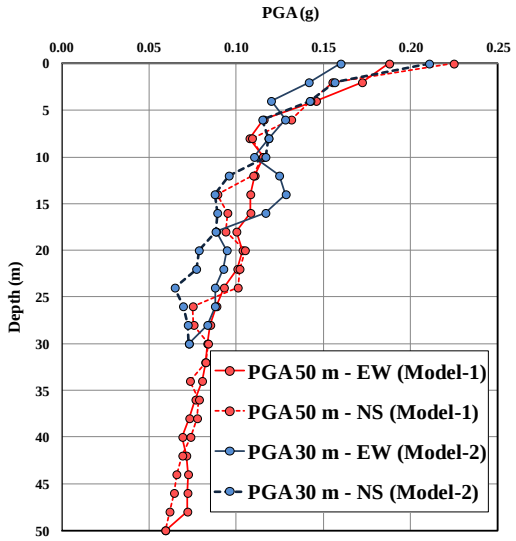

Fig. 13 PGA profiles developed using two different models.

The surface ground motions, EW and NS, used for structural analysis are two perpendicular ground motion developed based on SRA Model-2. Both ground motions are gradually increased and rotated from 0° through 180° at 10° intervals. The example column elements used for structural analysis have dimensions of 700x700 mm^2 and 700x900 mm^2 and longitudinal reinforcement 32D25 and 48D25 respectively. Fig. 14 shows the 700x700 column's longitudinal and transversal reinforcement. Fig. 15 shows the 700x900 column's longitudinal and transversal reinforcement.

The moment capacity ratio (ϕMn/Mu) is calculated for all element structures. Fig. 16 shows the moment capacity ratio of the 700x700 and 700x900 columns. The moment capacity ratios are calculated in terms of the earthquake force directions towards the structure. As can be seen in Fig. 16, the minimum moment capacity ratios for the 700x700 and 700x900 column are observed at earthquake force directions of 40°. The minimum moment capacity ratio for the 700x700 and 700x900 columns are 2.361 and 1.998 respectively. The minimum moment capacity ratios for the 700x700 column are 12.5% to 17.7% smaller than the moment capacity ratios calculated for 0° and 90°, while the minimum moment capacity ratios for the 700x900 are 14.5% to 20.7% smaller than the moment capacity ratios calculated for 0° and 90°.

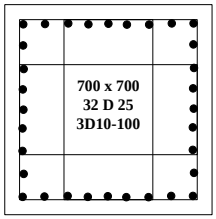

Fig. 14 Reinforcement of 700x700 mm^2 column.

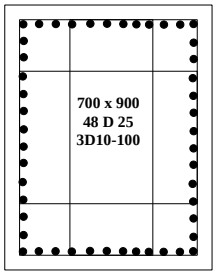

Fig. 15 Reinforcement of 700x900 mm^2 column.

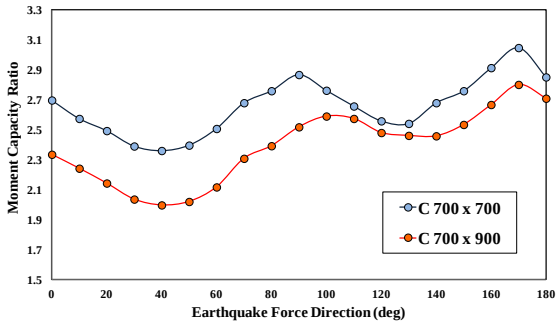

Fig. 16 Moment capacity ratio curves in terms of earthquake force directions for 700x700 and 700x900 columns.

Based on the analysis of moment capacity ratio for the 700x700 and 700x900 columns, the existing column size and reinforcements have a minimum moment capacity ratio of 1.998, greater than 1. All the exiting column reinforcements are predicted to be save enough to resist earthquake forces having a magnitude of 6.5 and a minimum distance 5 km. Table 2 shows the moment capacity ratio calculated for 0 and 90° (the X and Y directions usually used for building structural design) compared to the minimum moment capacity ratio obtained at the 40° direction of ground motion as can be seen in Fig. 16.

Table 2 Moment capacity ratio of 700x700 and 700x900 columns

Column Size	Force direction (°)	ϕMn/Mu	ϕMn/Mu minimum
700x700	0	2.698	2.361
	90	2.868	
700x900	0	2.336	1.998
	90	2.519	

CONCLUSIONS

An improved of SRA is conducted in this study for developing surface ground motion. Two different models of soil profiles, 50 m and 30 m soil deposit above the bedrock elevation are performed in this study. The surface peak ground acceleration developed using the 30 m soil deposit model is approximatelay 10% less than the real 50 m soil deposit model.

The modified SRA can be adjusted by using a 30 m soil deposit model instead of the real soil deposit model developed using the real bedrock elevation. The modified SRA can be applied whre there is in complete data from the soil boring investigation or when the bedrock elevation is greater than 30 m.

An improved analysis of the incoming earthquake force toward the building position was performed in this research by adjusting the earthquake directions from 0° to 180°. In terms of the moment capacity ratio of the column reinforcement, the minimum moment capacity ratio is at the 40° earthquake direction, and is reduced to approcximately 15% less than the normal X and Y (0° and 90°) directions.

ACKNOWLEDGMENTS

This research was financially supported by Direktorat Jenderal Penguatan Riset dan Pengembangan Kementerian Riset, Teknologi dan Pendidikan Tinggi, Republik Indonesia (Directorate General of Empowerment Research and Development, Ministry of Research Technology and Higher Education, The Republic of Indonesia). The Author also would like to thank to the Ministry of Public Works and Human Settlements of Indonesia and National Center for Earthquake Studies (PUSGEN) for providing data and technical supports during the development of this research.

REFERENCES

[1] SNI 1726:2012, Tata Cara Perencanaan Ketahanan Gempa untuk Struktur Bangunan Gedung dan Non Gedung (Seismic Resistance Design Code for Buildings and Other Structures), Jakarta, 2012, pp. 1-138.

[2] ASCE/SEI 7-10, Minimum Design Loads for Buildings and Other Structures, American Society of Civil Engineers, Virginia, 2010, pp. 1 – 608.

[3] ASCE/SEI 7-16. Minimum Design Loads and Associated Criteria for Buildings and Other Structures. American Society of Civil Engineers, 2017.

[4] Partono W., Prabandiyani S. P. R., Irsyam M. and Maarif S. Seismic Microzonation of Semarang Indonesia based on Site Response Analysis using 30 m Soil Deposit Model. Jurnal Teknologi, Vol. 78:8-5, 2016, pp. 31-38.

[5] Ohsaki Y. and Iwasaki R., On dynamic shear moduli and Poisson's ratio of soil deposits, Soils and Foundations, Vol. 13 (4), 1973, pp. 59-73.

[6] Ohta Y. and Goto N., Empirical Shear Wave Velocity Equations in terms of characteristic soil indexes, Earthquake Engineering and Structural Dynamics, Vol. 6, 1978, pp. 167-187.

[7] Imai T. and Tonouchi K., Correlation of N-Value with S-Wave velocity and Shear Modulus, Proceedings of Second European Symposium on Penetration Testing, Amsterdam, The Netherlands, 1982, pp. 67-72.

[8] Pusat Studi Gempa Nasional, Peta Sumber Dan Bahaya Gempa Indonesia Tahun 2017, Pusat Litbang Perumahan dan Pemukiman, Kementerian Pekerjaan Umum dan Perumahan Rakyat (National Center for Earthquake Studies, Indonesian Seismic Sources and Seismic Hazard Maps 2017, Centre for Research and Development of Housing and Resettlement, Ministry of Public Works and Human Settlements), ISBN 978-602-5489-01-3, 2017, pp. 1-377.

[9] Boore D.M. and Atkinson G.M., Ground-Motion Prediction Equations for the Average Horizontal Component of PGA, PGV, and 5%-Damped PSA at Spectral Periods between 0.01 s and 10.0 s, Earthquake Spectra, Earthquake Engineering Research Institute, Vol. 24, No. 1, 2008, pp. 99-138.

[10] Campbell K.W. and Bozorgnia Y., NGA Ground Motion Model for the Geometric Mean Horizontal Component of PGA, PGV, PGD and 5% Damped Linear Elastic Response Spectra for Periods Ranging from 0.01 to 10 s, Earthquake Spectra, Earthquake Engineering Research Institute, Vol. 24, No. 1, 2008, pp. 139-171.

[11] Chiou B. S. J. and Youngs R. R., NGA Model for Average Horizontal Component of Peak Ground Motion and Response Spectra, PEER 2008/09, Pacific Engineering Research Center, College of Engineering, University of California, Berkeley, 2008, pp. 1-94.

9th Int. Conf. on Geotechnique, Construction Materials and Environment, Tokyo, Japan, 20-22 November 2019, ISBN: 978-4-909106025 C3051

ESTABLISHMENT OF RESIDENTIAL FLOOD DAMAGE FUNCTION MODEL FOR KUANTAN, MALAYSIA

Noor Suraya Romali[1] and Zulkifli Yusop[2]
[1]Faculty of Civil Engineering Technology, Universiti Malaysia Pahang, Gambang, Malaysia; [2]Centre for Environmental Sustainability and Water Security, Universiti Teknologi Malaysia, Skudai, Malaysia.

ABSTRACT

Flood damage estimation is an essential element in the assessment of flood risk. However, the study on flood damage in developing countries is limited due to the scarcity of historical data. An attempt has been made to derive residential flood damage function models and flood depth-damage curve for the year 2013 flood in Kuantan, in the state of Pahang in Malaysia. A field survey was conducted to gather information regarding the flood event based on face to face interview technique. The education background, household income, and construction materials had significant influence on the variation of structural flood damages, whereas the content damage was found to be depended mostly on the types of occupation, household income, and house type. The flood depth-damage curves obtained in this study are satisfactory as content and structural damage show R^2 above 0.80 for both, and can be used for future studies on flood damage assessment of the study area.

Keywords: Flood damage estimation, Flood damage function, Flood depth-damage curve, Residential, Malaysia

INTRODUCTION

Flood risk assessment consists of two main parts i.e. a hazard and vulnerability assessment. Flood hazard is normally illustrated in flood inundation or flood extend maps, while flood vulnerability emphasizes the impact of flooding in flood damage map. Flood vulnerability is associated with the assessment of flood damages. Estimation of economic loss is essential to help the development of new housing away from the flood disaster area and reduce the damage loss.

The assessment of flood damages can be done using two methods; either evaluated directly from existing database or by using modeling approach. The modeling of damage estimates is either using unit loss model or a model that relates the flood damages with other factors that have linkage effect on the damages such as economic factor, the nature of damage, and possible relations between damage and flood parameters [1]. Unit loss method is defined as a property-by-property assessment of potential damage [1] and it uses the relationship between flood characteristics and damages to a unit [2]. In the latter method, three well known flood damage estimation models are FDAP (Flood Damage Analysis Package), ANUFLOOD and ESTDAM. Although various different approaches had been used to estimate flood damages, the estimation concept is basically the same, which considers the combination of flood hazard (hydrological characteristics), exposure, value of elements at risk, and the susceptibility of the elements at risk to particular hydrologic conditions which can be represented by a flood damage function curve [3]-[5].

Flood damage function curve is the plot of flood damages to flood parameters [6]. It shows the relationship between the flood parameters with the level of flood damage [7]. Examples of commonly used flood damage influencing factors for flood damage functions are flood depth, flood duration and velocity [1]. However, according to Thieken et al. [8], damage influencing factors consist of two types i.e. the impact parameters and the resistance parameters. The impact parameters reflect the specific characteristics of a flood event such as water depth and flow velocity, while resistance parameters represent the properties of the affected assets such as building type or materials and the emergency measures used.

Flood damage curve can be derived using two methods depending on the availability of the data. The first is based on damage data of past floods or also known as empirical method, and the second is termed as synthetic method, which is based on hypothetical analysis [1]. The curve based on empirical method, or also known as historical curve [10] is derived from historical loss data of actual flood events. While in the latter method, the development of synthetic flood damage function curve does not rely on the actual flood damage information, but derived from hypothetical analysis based on land cover and land use patterns, type of objects, information from questionnaire survey, interviews and expert judgements [1], [11], [12]. This synthetic method had been adopted by researchers who experienced data scarcity problem [10], [11].

Although the first research on flood damage

assessment field can be traced back almost forty years ago, there is still a lot of works to do related to few issues. In developing countries, especially Malaysia, the study on flood vulnerability assessment is still limited especially on flood damage estimation. There are many methodologies for estimating the flood damage worldwide. However, there is no common methodology applied to estimate flood damage in Malaysia. The effect of resistance parameters to the degree of flood damages are usually neglected in damage modelling, as most studies select more influencing parameters such as flood depth. In fact, flood risk assessment should cover all damage dimensions to obtain an extensive description of flood damages [13]. Therefore, with the aim to assist in the assessment of flood vulnerability, the purpose of this study is to investigate the relationship between flood damages and the local condition of the study area and to establish a residential flood depth-damage curve for future flood risk assessment works in Kuantan.

METHODS

Case Study Area

The Kuantan River Basin (KRB) was selected as the location for this case study because it is known for its frequent flooding. KRB has a catchment area of 1638 km^2 and the length of the river is approximately 93.44 km. Kuantan River is the main river in KRB where it flows from Mukim Ulu Kuantan through the Kuantan city and ends at the Perkampungan Tanjung Lumpur before flowing out to South China Sea. In the last few decades, the Kuantan River has experienced severe flood in 2001/02, 2011/12, and recently in 2013. There were major damages to properties, infrastructures and traffic, while around 14,044 people were evacuated during the 2013 flood [14]. The map of KRB displays the area, main river, tributaries and the streamflow station which is Kenau Flow Station is shown in Fig. 1 [15].

A few flood risk studies had been done [16]-[18] for flood mitigation at Kuantan River. However, to date, none flood vulnerability assessment has been studied within the river basin. Hence, a study on the assessment of flood damage is compelling to assess the impacts of flood to properties and the society of Kuantan.

Questionnaire and Field Survey

A field survey using face to face interview technique was conducted to gain a clearer picture of the 2013 Kuantan flood. A questionnaire was developed and distributed among the flood affected residence twice, with the initial survey was conducted in March 2018 and the second survey being conducted in February 2019.

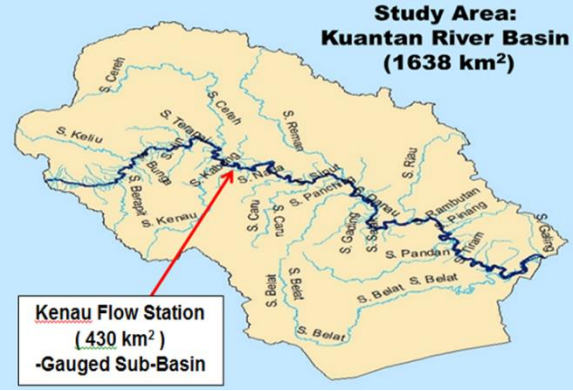

Fig. 1 Residential flood depth-damage curve for structural damage

The questionnaire was designed according to three scopes; demographic data, information on residential property and damage data. There are two sections; Section 1 and Section 2. Demographic and residential property were considered in Section 1, while Section 2 gathered information on the damage experienced by residents during the 2013 flood. Under demographic, various factors, such as gender, age, race, education level, occupation, and household income data were collected, whereas the price of the house, year bought, ownership status, house's type, numbers of storeys, house's material, house's insurance, and the estimated price of the house contents (furniture, gate etc) were investigated under the residential property scope. To gain information on damage, the flood depth and duration were considered, as well as the cost of damage to fabric/structural, cleaning, content damage, vehicle damage and loss of wages.

This survey used randomly selected sampling in the flood prone area of Kuantan to collect a representative sample, as suggested by Win et al. [19]. Information about the flood prone areas was collected from Drainage and Irrigation Department (DID) Kuantan, Kuantan Municipal Council and available flood maps. By using this information, a few 2013 flood affected village in Kuantan area were selected for the survey i.e. Permatang Badak, Sungai Isap, Bukit Rangin, Bukit Setongkol, Kampung Sungai Soi and Kampung Galing Besar. In each village, interviews were conducted randomly at different location and end up with a total of 201 samples.

Multiple Regression Analysis

A multiple regression model was used in this study to model the relationship between flood and various flood damage influencing variables. This method had been adopted by several previous researchers to analyze flood damage and its determinants [19]-[21].

In this study, every value of the independent

variable (flood influenced factor, *x*) is associated with the value of the dependent variable (flood damages, $Flood_D$). The dependent variable covers the level of property damages in terms of structural and content damage. While the independent variables are divided into two categories i.e. demographic and property characteristics. The demographic variables are gender, age, race, education background, occupation and house income, whereas the properties variables are ownership, price of properties, properties type, number of storeys, building material, and flood insurance status. The general regression equation is as Eq. (1) below:

$$Flood_D = f(x_{i1}, x_{i2}, x_{i3.} \ldots\ldots\ldots + x_{ip}) \quad (1)$$

The transformation of the functions for model in Eq. (1) resulted a regression model as shown in Eq. (2):

$$lnFlood_{Di} = \beta_0 + \beta_1 lnx_{i1} + \beta_2 lnx_{i2} + \cdots + \beta_p x_{ip} + \varepsilon_i \quad (2)$$

Where i = 1, 2, 3, …….n while p and ε refer to the numbers of independent variables and error term respectively. *lnFlood* is the logarithm of flood damages from surveys.

The analysis observed the value of coefficient of determination (R^2) and p-value (significance level), where a 5% significance level ($p < 0.05$) is used.

Flood Depth-Damage Curve

Flood damage function curve is the relationship between flood damages (in percentages) against flood parameters. The level of damage was measured according to flood depth and was taken as the ratio of overall replacement cost to the estimated total replacement value of the building. The damage percentage (D_p) was calculated according to the definition by Pistrika et al. (2014) as in Eq. (3):

$$\mathrm{D_p} = \frac{\text{Overall Replacement Cost}}{\text{Market Value of Properties}} \times 100 \quad (3)$$

The overall replacement is the expenses spent by the flood victim to mend their properties after flood, either at their own cost or compensation from the government or insurance company. The damage replacement was estimated for the structural, content, stock and equipment damage. The flood parameter chosen in the establishment of the damage curve is flood depth. Based on previous published work, inundation depth is considered as the principal factor and found to be the major variable for assessing direct tangible damages [1], [7], [22]. Furthermore, Chang et al. [23] suggested that the flood depth alone is sufficient for flood damage estimation without considering other factors.

The curve is plotted using Microsoft Excel and the curve fitting process was performed using trial and error. Curve fitting is the process of constructing a mathematical function that best fits to a series of data points [12]. The logarithmic trend line was selected as the type of trend line best fitted the data and the curve shape is similar with other damage curves from previous studies [1], [12], [14]. The average value of flood depth and percentages of damage was used in the construction of the damage curve.

RESULTS AND DISCUSSION

Survey Results

The field survey data collection yielded a wide range of useful parameters that may help in the assessment of flood damage [19]. Based on the primary collected data, more than 54% of the respondent were male while the rest were female. The average age of the respondents was 45 years old.

The house type that is mostly observed in Kuantan area is brick since 62% of the house interviewed during the survey are brick wall house. Further, 29% of the houses are built as the combination of brick and timber materials, whereas wooden houses are observed to be only 9% of the survey samples.

Most of the house sample was terrace (69%), while only 6% was semi-detached house, 9% was bungalow and 16% was other than these house types. Almost 97% of the house was one storey house.

Flood Damage Function Models

Structural Damage Functions

The relationship between structural damage and demographic and property variables is explained by Equation (4) with the regression results shown in Table 1. The R^2 obtained is low i.e. 0.19. However, the value is acceptable for cross sectional data and it is in agreement with the result observed in Poussin et al. [25] which relate the flood damage mitigation behavior amongst households in France where the R^2 was between 0.19 to 0.31.

$$Flood_{struc} = -10974 - 1422EDU + 1799\ln INC + 1066MAT + \varepsilon \quad (4)$$

where ε is error term and $Flood_{struc}$ is the structural flood damage in RM (Ringgit Malaysia) with the following influenced factors;

EDU	=	Education level of the respondent
INC	=	Household income of the respondents

MAT = Construction material of the houses

Table 1 Regression analysis results on the impact of demographic and property variables on structural flood damages

Variable	Coeffi-cient	Std. Error	t	p-value
EDU	-1421	467.24	-3.04	0.003
lnINC	1799	368.92	4.88	0.000
MAT	1066	458.44	2.33	0.021
Constant	-10974	2803	-3.92	0.000

The results in Table 1 show that the value of residential structural damage is positively correlated with the house material and household income but is negatively correlated with the respondents' education background. Assuming that all other variables are unchanged, a unit increment in household income will result in RM1799 increment in the structural damage when a linear relationship is assumed. These define the affordability of the high income respondent in buying more expensive house or wall furnishing, gate, etc., thus cause greater damage.

Meanwhile, the structural damage decrease by RM1421 if the respondent's educational background is at higher level. This result is consistent with Panic et al. [26] and Morrisey [27] who found that education also plays a crucial role in influencing the flood damage. The people with better educational background is more knowledgeable, hence tend to be more aware and prepared for any natural disaster event [20]. Based on the observation from survey, most of residents with high education level works at private sector or owns a business. Similarly, people with better occupation tend to be more exposed with advance mitigation options and well prepared. On the other hand, the damage increased by RM1066 if the house is built from concrete. This is in agreement with the finding by Win et al. [19] who stated that the rate of flood damage is commonly related to the total of household, household income, and building materials variables.

Content Damage Functions

The R^2 value is 0.19 which is similar with the structural damage model in Eqn. (4). The results for content damage are summarized in Table 2. The occupation and household income was found to have significant positive relationships to the total amount of content damage. However, the content damage is negatively related to house type. Assuming that all other variables are unchanged, a unit increment in household income will result in RM1586 increment in the structural damage when a linear relationship is assumed. The content damage increase by RM3157 if the respondent is businessperson. Respondent with better occupation may owned a high quality and expensive furniture thus experienced high damage if their house content is affected by flood. The content damage decrease by RM3396 for terrace house. This can be justified by the content of terrace house may be cheaper than the content damage of semi-detached house or bungalow.

$$Flood_{content} = -4040 + 3157OCCU + 1586\ln INC - 3396\ln TYPE + \varepsilon \quad (5)$$

where ε is error term and $Flood_{content}$ is the content flood damage in RM with the following influenced factors;

OCCU = Occupation of the respondents
lnINC = Household income of the respondents
TYPE = Types of the houses

Table 2 Regression analysis results on the impact of demographic and property variables on structural content flood damages

Variable	Coeffi-cient	Std. Error	t	p-value
OCCU	3157	1251	2.52	0.012
lnINC	1586	651	2.44	0.016
TYPE	-3396	858	-3.96	0.000
Constant	-4040	5143	-0.79	0.433

Flood Depth-Damage Curves

The flood depth-damage curve for structural and content damage is shown in Fig. 2 and Fig. 3 respectively. Both graphs show a significant correlation, where the percentages of damage increase with the flood depth, with R^2 values of more than 0.8 for all categories. This is in agreement with Pistrika et al. [12] for residential area, R^2 of 0.78.

The result shows that the 2013 flood victims experienced content damage higher than structural damage. Content damage estimates as high as 50% are expected at 6 meters' flood level, compared to 12% for structural damage. The finding is consistent with the observation by Pistrika et al. [12] in Greece where all the flood-affected buildings required only minor repair.

The percentages of content damage are quite low which is between 2% to 12% for a flood depth up to 6 meters. The study by Pistrika et al. [12] obtained a similar low percentages damage, range from 9% to 18% also for up to 6 meters inundation depth.

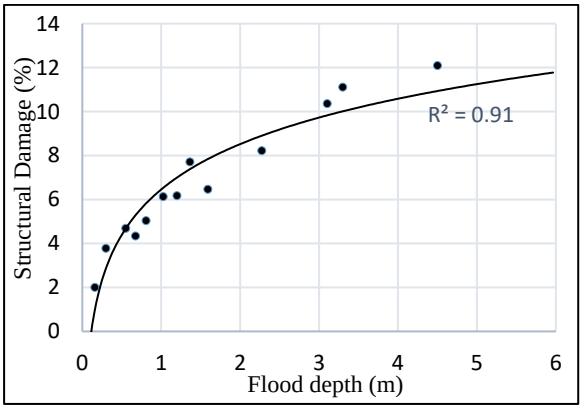

Fig. 2 Residential flood depth-damage curve for structural damage

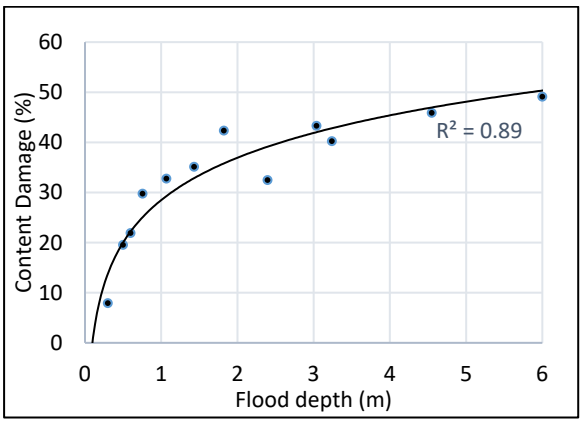

Fig. 3 Residential flood depth-damage curve for content damage

CONCLUSIONS AND RECOMMENDATIONS

Flood damage function model was developed based on interview survey data. The model considered the effects of demographic and property characteristics variables to the level of flood damages.

From this study, the structural damage was found to be depended mostly on the education background, household income, and construction materials, whereas the content damage was found to be depended mostly on the types of occupation, household income, and house type.

Flood depth-damage curves shows that the residents of Kuantan River Basin experienced content damage more than the structural damage during the 2013 flood. For the flood depth up to 6 meters, the percentages of content damage are in between 9% to 50% while the structural damage is in the range 2% to 12%. The damage curves obtained in this study is good enough with R^2 0.91 and 0.89 for structural and content damage respectively and can be applied in future flood damage assessment works at the study area.

A number of recommendations for the future flood damage assessment works are derived. An additional data collection is suggested to improve the flood damage function model, in terms of the coefficient of determination (R^2). Besides damage assessment for residential category, future works should also include commercial and industrial categories. These categories are rarely investigated as getting reliable damage data for the commercial and industrial category is expected to be more challenging. However, the damage assessment of these categories is compelling as it may show the effect of urbanization to the study area.

ACKNOWLEDGMENTS

The authors would like to acknowledge Universiti Malaysia Pahang and Universiti Teknologi Malaysia for the financial and technical supports. The study has been supported through research grant RDU1703115.

REFERENCES

[1] Dutta, D., Herath, S., and Musiake, K., A Mathematical Model for Flood Loss Estimation, Journal of Hydrology, 277, 2003, pp.24-49.

[2] Wagenaar, D. J., de Bruijn, K. M., Bouwer, L. M., and De Moel, H., Uncertainty in flood Damage Estimates and Its Potential Effect On Investment Decisions, Natural Hazards and Earth System Sciences Discussions, 3, 2015, pp.607–640.

[3] Hossain Meyer, V. and Messner, F., National Flood Damage Evaluation Methods - A Review of Applied Methods in England, the Netherlands, the Czech Republic and Germany. UFZ Discussion Papers, UFZ-Discussion Papers, Leipzig, 2005.

[4] Romali, N. S., Yusop, Z., Sulaiman, M. and Ismail, Z., Flood risk assessment: A Review of Flood Damage Estimation Model for Malaysia, Jurnal Teknologi, Volume 80:3, 2018, pp. 145-153.

[5] De Moel, H. and Aerts, J. C. J. H., Effect of Uncertainty in Land Use, Damage Models and Inundation Depth on Flood Damage Estimates, Natural Hazards, Volume 58(1), 2011, pp. 407–425.

[6] Yu, J. J., Qin, X. S., and Larsen, O., Joint Monte Carlo and Possibilistic Simulation for Food Damage Assessment, Stochastic Environmental Research and Risk Assessment, 27, 2013, pp. 725-735.

[7] Notaro, V., De Marchis, M., Fontanazza, C. M., La Loggia, G., Puleo, V., and Freni, G., The Effect of Damage Functions on Urban Flood Damage Appraisal, Procedia Engineering, 70, 2014, pp.1251–1260.

[8] Thieken, A. H., Müller, M., Kreibich, H., and Merz, B., Flood Damage and Influencing Factors: New Insights from the August 2002 Flood in

Germany. Water Resources Research, 41(12), 2005, pp.1–16.

[9] Velasco, M., Cabello, À., and Russo, B., Flood Damage Assessment in Urban Areas. Application to the Raval District of Barcelona using synthetic depth damage curves, Urban Water Journal, 2015, pp. 1-14.

[10] Vozinaki, A. E. K., Karatzas, G. P., Sibetheros, I. A., and Varouchakis, E. A., An Agricultural Flash Flood Loss Estimation Methodology: The Case Study of the Koiliaris Basin (Greece), February 2003 Flood, Natural Hazards, 2015, doi:10.1007/s11069-015-1882-8.

[11] Smith, D. I., Flood Damage Estimation – A Review of Urban Stage-Damage Curves and Loss Functions. Water SA, Volume 20, 1994, pp. 145-180.

[12] Pistrika, A., Tsakiris, G. and Nalbantis, I., Flood Depth-Damage Functions for Built Environment. Environmental Processes, Volume 1, 2014, pp. 553-572.

[13] Okazawa, Y., Yeh, P. J., Kanae, S., and Oki, T., Development of a Global Flood Risk Index Based on Natural and Socio-Economic Factors Socio-Economic Factors, Hydrological Sciences Journal, 56:5, 2011, pp.789-804.

[14] Zaidi, S. M., Akbari, A. and Ishak, W. M. F., A Critical Review of Floods History in Kuantan River Basin: Challenges and Potential Solutions, International Journal of Civil Engineering and Geo-Environment, Volume 5, 2014.

[15] Romali, N. S., Yusop, Z., Mohd Zaki, N. I. H., Sulaiman, M., Abdul Ghani, N. A. A., and Sulaiman, S., Flood Damage Function Model for Residential Area in Kuantan: A Preliminary Study, International Journal of Intergrated Engineering, Vol 11, No 1, 2019, pp. 203-213.

[16] Akbari, A., Slope Adjustment of Runoff Curve Number (CN) using Advanced Spaceborne Thermal Emission and Reflection Radiometer (ASTER) Global Digital Elevation Model (GDEM) for Kuantan River Basin, Proceedings of SPIE – The International Society for Optical Engineering, Volume 9644, 2015, Article number 96441W.

[17] Saudi, A. S. M., Juahir, H., Kamarudin, M. K. A., Toriman, M. E., aziz, N. A. A., Hasnam, C. N. C., and Samsudin, M. S., Flood Risk Pattern Recognition using Chemometric Technique: A Case Study in Kuantan River Basin, Jurnal Teknologi, Volume 72, Issue 1, 2015, Pages 137 -141.

[18] Ng, Z. F., Gisen, J. I. and Akbari, A., Flood Inundation Modelling in the Kuantan River Basin using 1D-2D Flood Modeler Coupled with ASTER-GDEM, IOP Conference Series: Materials Science and Engineering, Volume 318, 2018, 012024.

[19] Win, S., Zin, W. W., Kawasaki, A. and San, Z. M. L. T., Establishment of Flood Damage Function Models: A Case Study in the Bago River Basin, Myanmar, International Journal of Disaster Risk Reduction, Volume 28, 2018, pp. 688-700.

[20] Jaharudin, P., Anang, Z., Mat Alipiah, R., Kamaludin, M., Abd. Aziz, A. and Saat, S. A., Flooding Losses and Socio-economic Damage in Kelantan. Proceedings of the 3rd International Conference on Water Resources (ICWR 2015), 24-25th November 2015, Bayview Hotel, Langkawi, Kedah, Malaysia.

[21] Appelbaum, S. J., Determination of Urban Flood Damages, Water Resources Planning Management, 111, 1985, pp.269–283.

[22] Shaw, D. G., Huang, H., and Ho, M., Modeling Flood Loss and Risk Perception: The Case of Typhoon Nari in Taipei. Proceeding of 5th Annual IIASA-DPRI Forum on Integrated Disaster Risk Management: Innovations in Science and Policy, 14-18 September 2005, Ministry of Civil Affairs of China, China.

[23] Chang, L., Lin, C., and Su, M., Application of Geographic Weighted Regression to Establish Flood-Damage Functions Reflecting Spatial Variation. Water SA, 34(2), 2008, pp.209–216.

[24] Oliveri, E. and Santoro, M., Estimation of Urban Structural Flood Damages: The case study of Palermo. Urban Water 2, Volume 2(2000), 2000, pp. 223–234.

[25] Poussin, J. K., Botzen, W. J. W., and Aerts, J. C. J. H., Factors of Influence on Flood Damage Mitigation Behaviour by Households, Environmental Science and Policy, 40, 2014, pp.69–77.

[26] Panic, M., KovacevicMajkic, J., Miljanovic, D. and Miletic, R., Importance of Natural Disaster Education – Case Study of The Earthquake Near The City Of Kraljevo: First Results, Journal of the Geographical Institute Jovan Cvijic, Volume 63 (1), 2013, pp. 75-78

[27] Morrissey, M. Curriculum Innovation for Natural Disaster Reduction: Lessons from The Commonwealth Caribbean. International Perfectives on Natural Disasters: Occurrence, Mitigation, and Consequences Advances in Natural and Technological Hazards Research 21, 2007, pp. 385-396.

9th Int. Conf. on Geotechnique, Construction Materials and Environment, Tokyo, Japan, 20-22 November 2019, ISBN: 978-4-909106025 C3051

COMPOSITIONAL CHANGES IN SEA SLUDGE SAMPLES FROM HIDAKA PORT IN WAKAYAMA, SOUTHWEST JAPAN, COLLECTED MONTHLY FOR A PERIOD OF 16 MONTHS

Hirosuke Hirano[1, 2] and Davin H. E. Setiamarga[2, 3, 4]
1 Department of Civil Engineering, National Institute of Technology, Wakayama College, Japan
2 Department of Ecosystem Engineering, Faculty of Advance Engineering, National Institute of Technology, Wakayama College, Japan
3 Department of Applied Chemistry and Biochemistry, National Institute of Technology, Wakayama College, Japan
4 The University Museum, The University of Tokyo, Japan

ABSTRACT

The composition of sea sludge varies from location to location and from time to time, since it is affected by various external environmental factors. In this study, we analyzed the organic and inorganic contents of sludge samples collected for 16 months from the Hidaka Port in Wakayama. Weight-loss analyses for 16 months indicates that the highest inorganic content was in July 2016 (99.11%), and the lowest in June 2017 (94.42%). We then conducted EDX Spectrometry analyses on the samples, focused on Si, Al, Fe, and S. Our result indicated that while the dynamics of total inorganic content is naturally synchronized inversely with that of the organic content, it is not completely reflected in the dynamics of individual inorganic elements. For example, S is relatively stable throughout the year, and Fe changes are not congruent with the changes of the total organic and inorganic contents. However, Al and Si show a possible agreement with the changes of total inorganic and organic contents. From these results, we deduced that the dynamics were probably caused by environmental factors such as weather and water temperature, and the activities of living organisms such as diatoms, alga, and microbes.

Keywords: Sea sludge, Inorganic matter, Time series dynamics, Water temperature, Geochemistry

INTRODUCTION

Sedimental sea sludge is formed through the deposition of organic and inorganic matter brought in to the sea by river, rain, and sea currents, resulting in viscous mud-like sediment piling on the seafloor. Because of the organic material and sulfide compounds, sea sludge has a dark color and bad smell [1]. Information on the chemical compositions of sea sludge is important, since such information will help us to understand the interaction between different environments related to the formation of the sedimental sea sludge, but also about the interactions between the organisms living in the sea sludge as the matrix of their habitats. Such information might also bring insights about the effects of human activities on seafloor environment. However, the inter-relationships and interactions among climate and weather dynamics and other external environmental changes, and the dynamics of chemical compositions of the sea sludge, are rarely studied.

Several studies reported the compositional aspect of sea sludge samples collected from single sampling localities. For example, we have reported the chemical compositions of samples from the Funabashi Port in Chiba as 23.61% [2], and the Hidaka Port in Wakayama as 7.27% [3]. Although lacking detailed information, insights from such studies have allowed for the formulation of a generalized definition of the sea sludge [1]. However, since sea sludge composition itself is influenced greatly by small differences in the environs of the location, to do an objective and standardized comparison of sludge collected from different locations is difficult [1] [4].

To our knowledge, there was no report about sea sludge content changes collected in a time series from one particular sampling point, until our previous study reporting changes of the organic content in time-series samples collected from Hidaka Port in the Gobo coastal area [1]. The result of that study indicates that environmental data such as weather condition and water temperature might explain such dynamics, while possible influence of anthropogenic and microbial activities to such dynamics were also discussed.

In this study, we focused on the changes of inorganic content over time on samples collected from Hidaka Port for 16 months (samples collected

for 12 months analyzed in our previous paper plus additional samples collected in the following 4 months), from July 2016 to October 2017, besides also revisited and reanalyzed the organic content dynamics data from our previous study [1].

MATERIALS AND METHODS

1. Sea sludge sampling

Wet sea sludge from Hidaka Port in Gobo City (33°52'55.3"N, 135°09'10.7"E) in Wakayama Prefecture was collected manually. Details about sampling method and post-sampling oven treatments followed our previous study [1]. Sea sludge samples were collected once a month for 16 months from July 2016 to October 2017 from one sampling location at three different loci. The sludge from the three loci were mixed together for further analyses, in order to avoid compositional bias.

2. Analysis of total organic and inorganic contents

Thermo-Gravimetric (TG) analyses were conducted on oven-dried samples in order to obtain the information of organic content. TG analyses were conducted in three conditions: (1) the original dried sludge sample, (2) dried-up sample further burnt at 100ºC in order to obtain information about both inorganic and organic contents, and (3) dried sample burnt twice, first at 100ºC and later at 600ºC, to get rid of the organic matter completely. The mass lost after burning can be considered as the total mass of organic content. Inorganic content of a sample was inferred by calculating the mass left after burning at 100ºC and 600ºC, considering sample (1) (the solid/dried soil sample) as the standard.

The total organic and total inorganic contents analyses were conducted on all samples collected for 16 months.

3. Main elements analyses using EDX

We measured silicon (Si), aluminum (Al), iron (Fe), and Sulfur (S) in surface of sludge using the energy dispersive X-ray spectrometry (EDX) (SEM-EDX; Miniscope TM-3000; Hitachi Ltd.). Sample preparations were as follow: First, wet sludge samples were dried in an oven at 100ºC for 10–15 minutes. Dried sample clumps were then crushed to turn them into coarse powder. The powder were mounted on carbon stage using carbon tapes, were analyzed using the SEM-EDX. From the analysis, values in percentage showing proportions of the four elements analyzed relative to one another were obtained. For each sludge sample, three mounted powder samples were prepared and analyzed in order to avoid sampling bias.

We were unable to do EDX analyses for August and October, 2016, because of insufficient amount of samples for those two months. Therefore, we obtained only the information of total organic and inorganic contents for those two months.

4. Environmental data

Weather condition and rainfall precipitation data of the three consecutive days before and on the day of sludge collections were collected from the homepage of the Japan Weather Association (http://tenki.jp/) and from the homepage of the Japan Meteorological Agency (http://www.dta.jma.go.jp/obd/stats/etrn/index.php), respectively. Information of seawater mean temperature for the week of the sampling date was obtained from the homepage of the 5th Regional Coast Guard Headquarters (http://www1.kaiho.mlit.g o.jp/KAN5/).

RESULTS

1. Additional analysis of total organic content

a) The dynamics of total organic content

We have reported the dynamics of organic content in a set of time-series sludge samples collected for a year previously, from July 2016 to July 2017 [1]. In this study, we added the results obtained from more samples collected from the same sites in Gobo/Hidaka coast, for another three months (August–October, 2017), totaling in a series of samples showing monthly organic contents for 16 months. When we reconsidered our results to include the values for the whole 16 months, we saw a possible cyclical pattern of the organic content changes. The highest organic content was 8.82% in August 2017 (different from our previous study [1] = in June 2017, 3.93%), while the lowest value was 0.89% in July (similar to our previous study [1]).

b) Weather condition and weather temperature

The highest water temperature was observed during the sampling week of August in 2016 and 2017, after gradually increasing, and then gradually decreasing in other months. Interestingly, when the trends of organic content dynamics vs. water temperature changes during the months of July to October in 2016 vs. 2017 were compared, we observed that organic content decrease happened simultaneously with the gradual decrease of water temperature. Our data indicated that the organic content in 2016 started to decrease about a month

after water temperature decrease, while in 2017 the decrease started in the same month.

We also observed a possible relationship between weather condition and the changes in organic content, in agreement with our discussion given in our previous report [1]. Weather patterns in the months of August and September 2016, and June and August of 2017, heavy rains fell 1–3 days before the sampling date of each month. In these summer months, weather conditions around the sampling dates were similar. Interestingly, organic contents of the sea sludge samples from these months were observed to be relatively high. This observation is also in agreement with water temperature changes mentioned previously.

2. Analysis of inorganic content

a) The dynamics of total inorganic content

The dynamics of the total inorganic content of the time series samples correlate inversely with those of the total organic content. We found that the sea sludge collected from Hidaka Port is composed mainly of inorganic materials (mean percentage for 16 months = 97.96%). The maximum value of the total organic content was 99.11% in July 2016, while the minimum value was 91.18% in August 2017.

b) SEM-EDX Results of the four major elements (Si, Al, Fe, S)

We conducted SEM-EDX analyses to identify the compositional changes of the four main inorganic elements of a sea sludge: Si, Al, Fe, and S. The average value of Si for all samples collected for 16 months is 67.47% (maximum value: 69.18%, October 2017; minimum value: 62.82%, August 2017). The values for all months besides the maximum and minimum values are all more than 60%. When the low organic content mentioned previously (average value: 2.24%) is also considered along with the high Si content, it can be said that the sludge from Hidaka Port is very close to sand. Meanwhile, the average value of Al is 20.82%

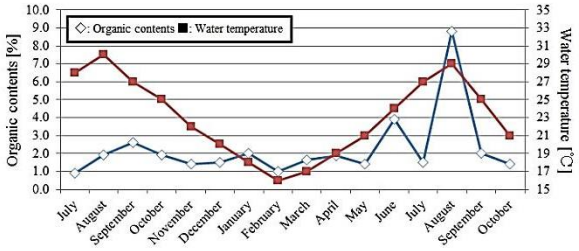

Fig. 1: Analysis of total organic content and water temperature

(maximum value: 22.33%, November 2016; minimum value: 19.59%, June 2017). This makes the composition of Si to be three times of Al (Si : Al ≒ 3 : 1). This compositional ratio is very close to the materials of cement such as blast-furnace slag [5] and fly ash [6].

Fe and S are the elements thought to affect the colorations and smell of sea floor sedimental sludge and mud. EDX analyses of our samples showed the average value of Fe to be 8.52% (maximum value: 11.19%, February 2017; minimum value: 6.73%, June 2017). Meanwhile, the average value of S is 0.90% (maximum value: 1.45%, July 2017; minimum value: 0.49%, November 2016). This composition could explain the gray color and slight rotten-egg smell of the sludge from Hidaka Port.

While random dynamic changes of compositional ration of Fe in the samples were seen, only slight changes of S were observed. Because the changes of S are very small, in order to confirm the stability of S, we conducted log approximation. We obtained the formula below to express our results:

$$Y = 0.286 + 0.298 \ln(x) \quad (1)$$

The result (Fig 1) showed that the changes of S across the whole observation period are very low, which means that for the whole 16 months, the composition of S is relatively stable.

4. DISCUSSIONS

1. Possible external factors affecting the organic matter composition dynamics of the seafloor sludge from Hidaka Port

In a previous study, we suggested that the change in the organic matter content in the sea sludge from Hidaka Port was probably caused by environmental factors such as water temperature and weather conditions, and biological factors such as living organism activities and life cycles [1].

In our present study, we conducted additional analyses on samples taken in the months of July to October 2017, making the total samples to be 16 months. The addition of the measurement results of the organic content has made comparisons among the corresponding months of 2016 and 2017, possible. The comparisons indicated a congruency of fluctuations between the corresponding months of 2016 and 2017 (July, August, September and October) for which data are available. The data showed that in both years, a decrease in the organic content rate was observed a month after the water temperature peaked in 2016, whereas in 2017 the organic matter decrease happened with the samples collected at the end of the month when the water

temperature peaked (Fig. 1). This probably suggests that during the hot months of summer, the warm water temperature might have caused microbe proliferations [7], which might then cause an increase in organic matter deposition. Meanwhile, a decrease in organic matter composition of the sludge samples collected when water temperature dropped at the end of summer might probably be explained in two ways. While warm temperature of water might cause an increase in microbial activities, temperature decrease might have caused microbial activities to also decrease. The decrease in organic content could be caused by it. Besides that, warm water is known to leach organic matter [8]. During summer months, increased microbial activities might replenish the leached out organic matter in the sedimental sludge. However, when microbe activities decrease, the replenishing pace might not be able to catch up with the leaching pace, hence the roughly one month time lag of the decrease of organic content. In our previous report [1], we also discussed possible contributions of the presence and absence of seaweed (a and b in Fig. 2, as change by season, in Hidaka port) caused by its life cycle [9] [10].

In this study, we found that our hypothesis about a possible correlation among microbial activities, water temperature, and seaweed life cycle, is not rejected. We observed that rain fell several days prior to the sampling dates. This might have contributed to the increase of organic content, which was probably caused by leached inland organic matter brought in to the sea by the river. However, while we found no contradiction with what we proposed in our previous paper [1], we are unable to decisively pinpoint any strong correlation between rainfall and the dynamics of organic content. Accordingly, further studies to specifically see if rain affects compositional changes of sea sludge must be conducted in the future.

2. Possible external factors affecting the inorganic matter composition dynamics of the seafloor sludge from Hidaka Port

In order to investigate the factors of change in the main components of inorganic matter, we conducted EDX analyses using the Scanning Electron Microscope (SEM) on the time-series sludge samples on the four main elements known as the main components of sea sludge: we compared fluctuation in organic matter and Si (Fig. 3), Al (Fig. 4), Fe (Fig. 5), and S (Fig. 6). We surprisingly found out that S is stable throughout the year, and Fe fluctuations are uncorrelated with any content changes. Therefore, at least in this study, we are unable to connect the stability of S and the irregular fluctuations of Fe during the whole sampling period with changes in organic components, or environmental factors. Further studies must be conducted to pinpoint the possible causes such as anthropogenic, biological, or environmental factors, and the mechanism.

We also noted that the average percentage of S of the Hidaka Port samples is very low (0.90%), when compared to samples collected from the

a) Feb. 2017 b) Jul. 2017

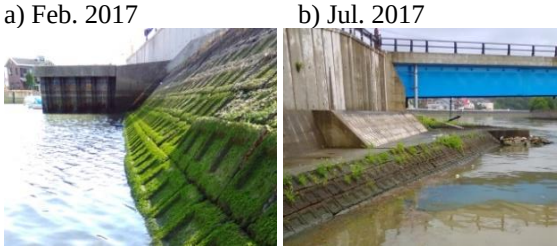

Fig. 2: Dynamics of seaweed in Hidaka port

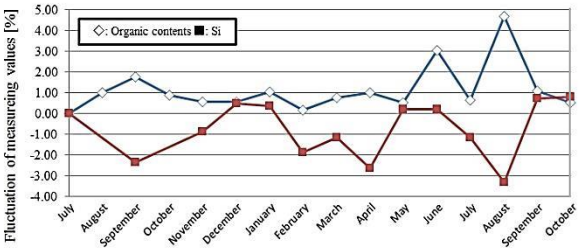

Fig. 3: Comparison with organic content and Si

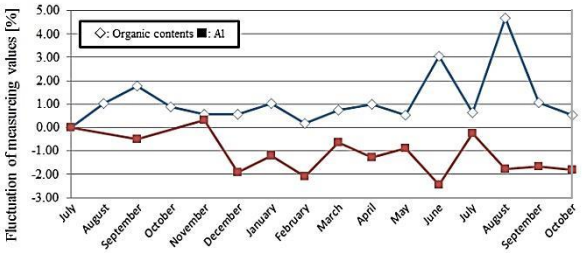

Fig. 4: Comparison with organic content and Al

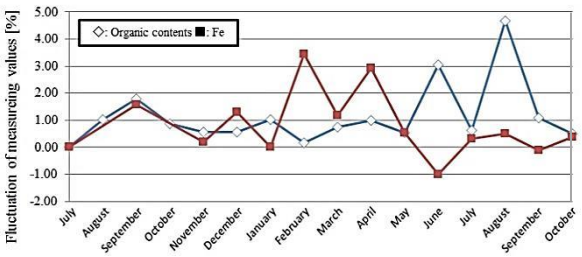

Fig. 5: Comparison with organic content and Fe

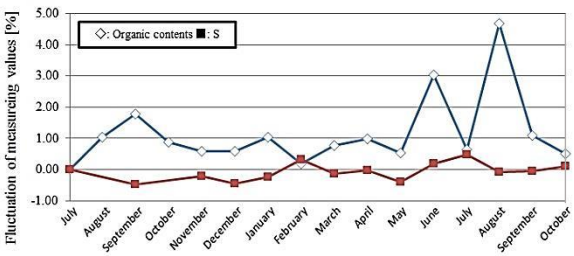

Fig. 6: Comparison with organic content and S

Funabashi Port in Chiba (10.29% [3]). A study of sludge collected from the Funabashi Port in Chiba [11] showed that the amount of dissolved oxygen (DO) is higher in sludge with lower content of sulfide. Therefore, the low S in Hidaka Port sludge might indicate high DO. Further studies, however, will be needed to confirm this suggestion.

In our present study, the changes of Si across time were found to be highly dynamics. When we looked at our non-EDX SEM data, we found traces of the phytoplankton diatoms (Fig. 7 a, b) from the sludge sample of the month October 2017, which is the time when we observed an increase in Si percentage (Fig. 5). Diatoms are classified as a type of algae, members of the superphylum Heterokonta. One of their main characteristics, besides their ability to photosynthesize, is their dense and heavy cell wall made of silica (SiO_2), which is also the cause of their non-motility. Because they are non-motile, they depend on water flow and turbulence to stay suspended in water with enough sunlight, and sink to the bottom of the sea when no external force keep them afloat [12]. As phytoplankton,their life cycle depends on water temperature and the availability of sunlight [12] [13].

A previous study focused on the abundance of diatoms collected from various depths in the Nada-Kumano coastal area, which is adjacent to our sludge-sampling location [14]. The study reported that diatoms from the area at the depth of 200 m are abundant during the months of April, August, and at the depth of 1000 m in October. This observation result sits very well with our results, which showed that Si percentage is high during the months of September 2016, May 2017, and August 2017 (Fig. 5), which means that high Si contents were observed on the month, or a month after diatoms high abundance was reported at the depth of 200 m. Takeuchi had reported the presence of an upwelling current from the bottom to the surface in the sea of the area [15]. Ishikawa et al also suggested that this upwelling could explain the abundance at different depths on different times, similar to previous studies in other areas [14] [16] [17]. Our samples were collected from shallow/surface waters (ca. 30 cm depth) at the Hidaka Port. Taking everything into account, a possible explanation of the relationship between the abundance of diatoms and high Si contents can thus be conceived. Probably, the upwelling brought many of the diatoms to the surface water level. Later, since the diatoms are non-motile, they settled down on the seafloor sludge close to the surface, contributing to the high Si content of the sludge. The one-month time lag between the abundance of diatoms at 200 m depth reported by Ishikawa et al [14] and peaks of Si content in the samples could be explained as the time the diatoms needed to move up from the depth of 200 m to the surface, and then to settle down on the shallow seafloor sludge.

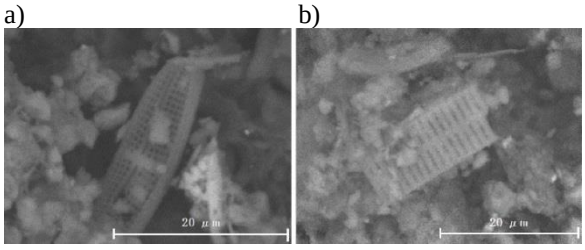

Fig. 7: phytoplankton diatoms in sludge samples

We also found that in our data, Si changes and fluctuations were in agreement with those of the total organic content (Fig. 3), indicating a possible connection. However, further studies to pinpoint the underlying connection are needed. When based on our present result only, however, we might hypothesize that changes in total organic content might be affected by the changes of Si content in the sludge, which most likely is caused by the abundance of diatoms in shallow water. This relationship might also explain the inverse relationship between Si and the amount of organic content (Fig. 3).

Al content fluctuations were found to be congruent to Si. Although we are unable to pinpoint a possible cause, this "synchronized" dynamics of Al to Si have caused the proportion of Si : Al to be relatively stable at 3 : 1. This also makes that both Si and Al changes are in agreement with the dynamics of total inorganic content of the sludge samples across the whole 16 months (Fig. 3, Fig. 4). Future studies will be needed to elucidate the reasons and mechanisms behind the changes and maintenance of the Si : Al proportion.

CONCLUSION

By adding data for three additional months, we were able to confirm our hypothesis conceived from our observation in the previous study [1]. That is, (1) the dynamics of the organic contents over time are probably directly and indirectly affected by external environmental factors such as water temperature, and weather condition. (2) The direct influence of water temperature and weather condition could involve warm-water leaching of organic content, (3) and organic materials from inland areas brought in by rain and river flow. (4) Indirect influence might be related to the presence of microbes and other biological agents such as seaweed and diatoms, which life cycles and biological activities probably depends on water temperature and weather. We also cannot rule out causes of anthropogenic origin, such as farming, contributing to the dynamic changes of sea sludge compositions.

We also concentrated on changes of percentage of some elements composing the inorganic content of sea sludge. Our result indicates that S content did not fluctuate over time, and Fe changes were

probably random and thus inexplicable with our present result. Meanwhile, Si changes are probably be connected to the presence/abundance of diatoms. Al changes were seemingly synchronized with those of Si across time, causing the ratio of Si to Al to be stable at 3 to 1. However, we were unable to pinpoint what exactly the cause of the dynamics of Al in the sludge samples.

We plan to continue our study in order to obtain more information across longer time span, in order to confirm the presence or absence of a cyclical pattern. More studies are needed to pinpoint the exact actual cause of organic content changes, most likely by using other methods including those of microbiology and molecular genetics, such as flow cytometry and eDNA. Similar biological methods can also be used to pinpoint the changes in Si content. Other studies to closely monitor the effects of rain and water temperature must also be conducted in the future.

ACKNOWLEDGEMENTS

HH would like to thank Gobo City municipal government for their cooperation during sampling collection. HH and DHES were partially supported by the National Institute of Technology, Wakayama College Competitive Internal Research Grant for Education and Research 2016.

REFERENCES

[1] Hirano H., Semura D., Sakamoto K., Toyama T., and Setiamarga D.H.E, A Dynamic changes of organic content over time in the sea sludge collected from the Gobo/Hidaka coastal area in Wakayama, southwest Japan. IOP Conference Series: Earth and Environmental Science, Vol. 176, 2018, Paper No. 012007.

[2] Hirano H., Toyama T., Nishimiya N., and Okamoto K., Removal of Cesium from Sea Sludge through Decomposition of Organic Matter with Aqueous Hydrogen Peroxide. International Journal of GEOMATE 8(1), 2015, pp. 1203-1206.

[3] Hirano H., Toyama T., Nishimiya N., Setiamarga D.H.E., Morita S., Uragaki Y., and Okamoto K., Artificial Sludge Based on Compositional Information of a Natural Sea Sludge. International Journal of GEOMATE 12(31), 2017, pp. 95-99.

[4] Yoshida T., About Generation and the Removal of the Sludge – In Bottom Sampler Examination of the Gulf of Minamata. Hedoro 1, 1974, pp. 11-27. [In Japanese]

[5] Inamoto I., and Saeki M., Preparation and Certification of Blast Furnace Slag for Japanese Iron and Steel. Tetsu to Hagane 75(10), 1989, pp. 1824–1828. [In Japanese]

[6] Nagataki S., Ohga H., and Inoue T., Effect of Fly Ash in Controlling Expansion Due to Alkali–Aggregate Reaction and ITS Mechanism, Doboku Gakkai Ronbunshu 1990(414), 1990, pp. 175-184. [In Japanese]

[7] Rasconi S., Gall A., Winter K., and Kainz MJ., Increasing Water Temperature Triggers Dominance of Small Freshwater Plankton. PLoS ONE 10(10), 2015, e0140449.

[8] Guigue J., Mathieu O., Lévêque J., Mounier S., Laffont R., Maron P.A., Navarro N., Chateau C., Amiotte–Suchet P., and Lucas Y., A Comparison of Extraction Procedures for Water–Extractable Organic Matter in Soils. European Journal of Soil Science 65(4), 2014, pp. 520-530.

[9] Uede T., Chemical Characteristics of Bottom Sediment at Sea Bed, Mud Flat and Zostera japonica Meadow in Uchinoura, Tanabe Bay, Wakayama Prefecture, Japan. Aquaculture Science 56(3), 2008, pp. 295-302. [In Japanese]

[10] Uede T., Yoshida G., Yamauchi M., Takahashi Y., and Iseki K., Influence of Environmental Factors on Biomass and Morphological Variability of Zostera japonica on the Coast of Uchinoura, Tanabe Bay, Wakayama, Japan. Aquaculture Science 59(1), 2011, pp. 29-40. [In Japanese]

[11] Okamoto K., Toyama T., and Komoriya T., Ocean Decontamination: High Ability Removal Method to Radioactive Cesium from Ocean Sludge by Using Micro Bubbles and Activating Microorganisms. International Journal of GEOMATE 12(32), 2017, pp. 57–62.

[12] Sournia A., Form and function in marine phytoplankton. Biological Reviews 57(3), 1982, pp. 347-394.

[13] Fogg G.E., The phytoplanktonic ways of life. New Phytologist 118(2), 1991, pp. 191-232

[14] Ishikawa A., Kitami S., Ishii K., Nakamura T., and Imai I.. Resting Stage Cells of Diatoms in Deep Waters in Kumano–Nada, Central Part of Japan. Plankton and Benthos Research 6(4), 2011, pp. 206-209.

[15] Takeuchi J., Warm water tongue and coastal upwelling in southern region of Kumano-Nada. Mar Sci Monthly 19, 1987, pp. 447-455. [In Japanese]

[16] Pitcher G.C., Phytoplankton Seed Populations of the Cape Peninsula Role Upwelling Plume, with Particular Reference to Resting Spores of Chaetoceros (Bacillariophyceae) and Their Role in Seeding Upwelling Waters. Estuarine, Coastal and Shelf Science 31, 1990, pp. 283-301.

[17] Takahashi M., Seibert D.L., and Thomas W.H., Occasional Blooms of Phytoplankton During Summer in Saanich Inlet, B. C. Canada. Deep Sea Research 24, 1977, pp. 775-780

9th Int. Conf. on Geotechnique, Construction Materials and Environment,
Tokyo, Japan, 20-22 November 2019, ISBN: 978-4-909106025 C3051

PUBLIC ACCEPTANCE OF MINING COMPANIES IN INDONESIA

Einde Evana[1], Lindrianasari[2], Hamartoni Ahadis[3], Yuztitya Asmaranti[4]
[1,2,4]Faculty of Economics and Business, University of Lampung, Indonesia;
[3]Ph.D. Student of Environmental Science, University of Lampung, Indonesia.

ABSTRACT

This study aims to provide empirical evidence on community acceptance of mining sector. The survey involved in particular the Department of Environment in all Regencies / Cities in Lampung Province. This survey model is very effective in obtaining data that is suitable for target participants, relatively faster because access to mining locations is easier, and cheaper. The questionnaire was compiled using simple sentences to avoid the possible maturation in a prolonged survey. There are seven variables measured in this study. First is governance, measured by the existence of rules and legislation. The assumption is that these rules and regulations can ensure companies carry out mining activities according to the rules and the government can guarantee the accountability of mining companies. The second is mining acceptance, measured by tolerance, accept, approve, and embrace. Third is living cost, measured by how much the community sacrifices to fulfill basic needs. Fourth is environmental costs, measured by environmental quality (low pollution). Fifth, improving infrastructure, measured by improvements and facilities in supporting economic activities. Sixth is the impact of other industries, measured by the growth of other industry sectors, and the seventh is increasing welfare and greater employment opportunities for the community. The study found empirical evidence that public acceptance of mining companies is influenced by several factors, including the cost of living, quality of the environment, community involvement, improved infrastructure, the impact of other industries, and public welfare.

Keywords: Regulation, Governance, Mining, Public Acceptance, Environmental Cost, Living Cost.

INTRODUCTION

Lampung Province's spatial planning rules have been prepared through Regional Regulation No. 1 of 2010 concerning Lampung Province Regional Spatial Planning for 2009-2029, and Regional Regulation Number 1 of 2018, concerning the Zoning Plan for Coastal Areas and Small Islands of Lampung Province for the period 2017- 2037. The location of the mining area has also been established as shown in Figure 1.

The right to a healthy environment and is well contained in Article 28H of the 1945 Constitution, Article 9 Paragraph (3) of Law No. 39/1999 concerning Human Rights and Article 65 Paragraph (1) of Law No. 32 / 2009 concerning Environmental Protection and Management. Thus, the state (government) and business actors are obliged to respect, protect and fulfill these rights. Article 66 of Law No. 32/2009 states that anyone who fights for the right to a good and healthy environment cannot be prosecuted in criminal or civil suit (https://www.mongabay.co.id/2017/05/17/ damage - environment-effect of coal-mining-continuous-what is the solution /).

Therefore, the community and / or environmental institutions have the right to fight for these rights. Not only to obtain a decent living environment for now, but also to ensure the sustainability of the ecosystem for future generations.

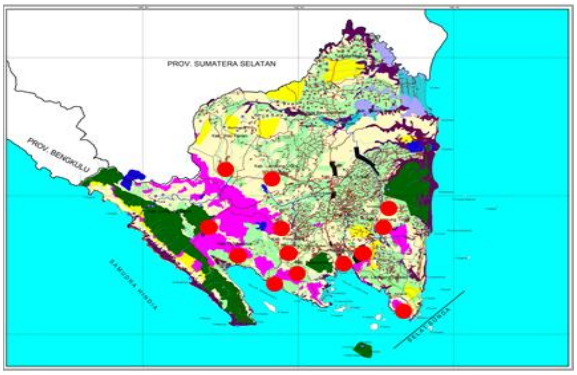

Fig. 1 The spatial layout of the Lampung Province.

Based on Law Number 23 of 2014, since 2015 the authority to administer government affairs in mineral and coal mining has been transferred to the Province. The purpose of transferring this authority to the Provincial Government is to control many conflicts that occur when the ownership rights of mining permits are in the hands of the Regional Head. Conflicts in various dimensions often occur, even though the reason of triggering the conflict is to prosper the community. But in fact, people always become victims of the conflict in the mining area (https://setkab.go.id/konflik-tambang-dan-manfaat-dana-desa/).

This research involves community participation in assessing environmental management in mining areas.

This assessment will provide relevant information for policy making related to the existence of mining. Data on reclamation guarantees, and post-mining guarantees recorded in the Provincial Government of all mining companies active in Lampung Province show that the compliance of mining companies in fulfilling the company's responsibility for the environment is very low.

The low awareness of mining companies to provide guarantees of reclamation and post-mining, is shown in Figure 2. From figure 2, it can be seen that there were only 36% of mining companies out of a total of 168 companies that paid collateral for reclamation. Meanwhile, companies that pay post-mining guarantees are only 18%, and all of them come from companies that also pay collateral for reclamation.

This study successfully confirmed both theories, legitimacy theory and stakeholder theory, that in its operational activities, companies must pay attention to the interests of their stakeholders. Community acceptance of mining companies is one of the keys for companies to perform and continue operations in a sustainable manner.

LITERATURE REVIEW

Social research in the area of the environment, using these two theories, namely the legitimacy theory and stakeholder theory. Both theories can explain that companies must carry out responsibility activities to society and the environment. In this study also uses these two theories and enriched with regulatory theory.

The Legitimacy Theory

Legitimacy was states that legitimacy is important for organizations because it explains the limits of emphasis on social norms and values [1]. Legitimacy is also a response to the importance of analyzing organizational behavior that takes into account the environment. The company's legitimacy will be obtained if there are similar results expected by the community from the company, so that there are no demands from the community. Companies can make social sacrifices as a reflection of the company's attention to society [2]. In order to gain legitimacy, companies must improve their image [3] by communicating their environmental activities with the disclosure of the social environment [4].

Legitimacy theory explains that companies must carry out operational activities in line with the expectations of the surrounding community [5: 8]. If the company's activities are contrary to the expectations of the community, then the company will not get the legitimacy of the community. This is what further tends to cause conflict between the company and the community [6].

The Stakeholder Theory

In general, stakeholder theory explains that a company is an entity that not only operates for its own interests, but also must provide benefits to stakeholders. The stakeholder theory also explains that each stakeholder group has an unequal impact on the environment. This explanation also indicates that all stakeholders have the right to obtain information about company activities so that their diverse decision-making can be used [7]. Consequently, the company has an obligation to fulfill all its obligations to stakeholders. Stakeholders have different expectations from the company [8]. To pursue this expectation, stakeholders can put pressure on the company directly or indirectly in making environmental disclosures. To deal with this, the company is required to always work with stakeholders so that the company's vision is in line with them. However, stakeholders can also choose not to use information and cannot play a role directly in the company [9].

This study attempts to confirm whether the legitimacy theory and stakeholder theory are in line with the real conditions of mining companies in Lampung Province. Where the two theories predict that in its operational activities, the company must pay attention to the interests of its stakeholders. If the company's activities are in line with the interests of stakeholders, the company will be legitimized in the community.

The Public Interest Theory

Public Interest Theory was introduced by Arthur C. Pigou in his book entitled The Economics of Welfare in 1932. Regulation refers to the availability and enforcement of legal instruments, such as laws and other government rules. In general, the Public Interest Theory explains that regulation provides protection and benefits to the wider community [10]. In the case of mining, the theory of public interest leads to the assumption that the legal instruments issued are to provide a balance of allocation of these scarce resources, for all parties. Communities that are powerless stakeholders and who cannot be sacrificed from mining activities. To provide protection to the public, regulation is needed.

Previous Research and Hypothesis Development

Mining companies are types of companies whose operations are very sensitive to the environment. This type of industry is very easy to generate profits, but on the other hand also has a negative impact on humans and the environment. Zhang and Moffat [11] conducted a study that aims to examine how people around mining companies evaluate the benefits and

negative impacts of mining, and from this evaluation data is obtained about the extent to which mining activities in Australia affect community acceptance of mining activities.

Conflicts between companies and communities (including indigenous peoples) are an integral part of the mining area. The frequency of this conflict occurs, resulting in mistrust of indigenous peoples in the government [12]. The Center for Social Responsibility in Mining (CSRM) also recognizes that conflict is an inherent part of the mining community throughout the world. Conflicts that occur in mining areas occur in various elements of society, on several scales, concerning a number of problems; politics, economy, socio-culture, and environment [13], [14].

The study conducted by Zhang and Moffat [10] found that the role of government can play a role (moderating) in public acceptance of the impact of mining activities. Literatures that discuss impact assessments especially on social impact assessments also find positive and negative impacts on mining activities on, especially on a small scale [15]. Islam [5] explains that one form of corporate social responsibility is assessed from the welfare of the community.

Meanwhile, Boyd and Banzhaf [16] explain that the explanation in ecosystem services must involve environmental costs. This explanation is quite a reason for the importance of research to assess the acceptance of people around the mining area for the impact caused by the company's activities. The hypothesis formulated is the role of government can play a role (moderating) in public acceptance of the impact of mining activities. Prolonged conflicts that occurred in the mining area, one of which was the conflict between diamond and mining areas (titanium oxide) in the Sierra Leone region. This conflict between the company and the people of Sierra Leone eventually contributed to the formation of the Revolutionary United Front (RUF) and civil war in Sierra Leone [17]. Conflict in the mining area is one of the centers of economic, social and environmental problems that are key to the country's development, therefore, the impact of the mining sector needs to be seriously assessed [18].

The rules issued by the Indonesian government through Law No. 23 of 2014, effectively valid for 2016, are essentially in favor of the public interest (see Public Interest Theory). So that the policy of business practices should properly create regional economic growth. In relation to mining companies, the law has the potential to reduce poverty and improve the quality of human development [19]. This explanation is quite a reason for the importance of research to assess the acceptance of people around the mining area for the impact caused by the company's activities. For theoretical explanations and previous research, the research hypothesis formulated: Government governance can play a role (moderating) in public acceptance of the impact of mining activities.

RESEARCH METHOD

This study will use a questionnaire survey to measure community acceptance (including indigenous peoples) of mining companies, by involving Regency / City / Province of Lampung. Government involvement will greatly influence the achievement of this research, because the government has easy access to meet people in mining areas. The participative design is very effective in order to obtaining data from participants, and also relatively faster because access to mining locations is easier, and cheaper. In addition, the government should also show concern for the community for the possibility of corporate irregularities in existing rules and regulations. Thus, the government has an interest in achieving the objectives of this research.

The surveys conducted are manual (not on-line) related to the condition of the community surrounding mining companies that may not have WIFI access. Even if they have WIFI access, their expertise in taking orders and filling out online surveys is predicted not to be as expected in this study. Questionnaires were built using research designs that had been carried out in previous studies [10], with adjustments as needed. This adjustment is considered important because of the different natural and community conditions between Australia and Indonesia.

Through the local government, this research will spread questionnaires to the community including indigenous peoples in the area where the mining company is located. Furthermore, the role of local governments to determine respondents (residents around the mining area) will greatly simplify the survey method of this study. At the end of the 20th century indigenous peoples were excluded from any important role in the management of the resource development environment in traditional lands [11].

The instrument of this study adopted the previous research instrument [10]. All variables used in their study were also measured in this study, with some modifications, if needed. Governance is measured using two question items, laws and government guarantees [20], [21], [10]. Participants were given 22 questions (consists of 8 criteria of questions) with a 7-point scale (1 = strongly disagree / very bad / very unsatisfactory, 7 = very agree / very good / very satisfying). Acceptance of mining was measured using four items of questions that tolerate / Accept / Approve / Embrace [22].

The questionnaire was compiled using simple sentences to avoid the possible maturation in a prolonged survey. There are seven variables measured in this study. The respondent group was

divided into two groups. The first group is the Regency / City, where the mining company is located, and also and Lampung Province (the first variable). The second group is community groups who live around mining companies (second-seventh variables).

The **first** is mining acceptance, measured by tolerance, accept, approve, and embrace. **second** is living cost, measured by how much the community sacrifices to fulfill basic needs. The **third** is environmental quality, measured by environmental quality (low pollution). The **fourth** is community involvement, measured by involvement of local residents in mining activities. The **fifth is** improving infrastructure, measured by improvements and facilities in supporting economic activities. The **sixth** is the impact of other industries, measured by the growth of other industry sectors, and **the last** the is increasing welfare and greater employment opportunities for the community.

Before collect the data, surveyors team educated by researcher to guide how data could be collected and why survey conducted. Each Regencies / Cities respondence was not similar, it was depended on the number of mining corporation in its area. The final participant of this study consisted 78 participants.

RESULT

The mean of the respondent's answer to this research questionnaire shows a reasonable value. The mean value for each study variable, respectively, is: (1) the Mining Acceptance = 3.52; (2) Living cost= 4,26; (3) Environmental Quality = 3.15; (4) Community Involvement = 3.36; (5) Infrastructure Improving = 3.38; (6) Impact of Others Industry = 3.09; and (7) Public Welfare = 3.48. The whole has a relatively similar value. Except for Living Cost which has a mean value that tends to be highest. Table 1 explains each correlation test result between variables. In addition, the mean and standard deviations are explained in the table. Furthermore, a discussion about the acceptance of mining companies using consideration of living costs.

The community will reject the existence of mining when the necessities of life are getting higher. Statistics on the correlation between mining receipts and living costs show a negative relationship (R = -0,531**). This finding also demonstrates that mining companies need to pay attention to the elements of community needs around mining activities carried out, such as the presence of clean water and ease as well as relatively low prices to obtain basic needs, and so forth.

Low environmental quality (indicated by poor air quality, high noise, garbage, declining soil fertility, damage to post-mining ecosystems, etc.), will result in more public acceptance of mining companies. Statistics shows a positive correlation value (R = 0.858 **). Other analysis shows that environmental quality has a negative impact on people's living costs (R = -0.607 **). This means that the lower the quality of the environment, the higher the cost of living that will be paid by the community.

Table 1 Relationship between variables

	1	2	3	4	5	6	7
1	1						
2	-,531**	1					
3	,858**	-,607**	1				
4	,874**	-,569**	,688**	1			
5	,875**	-,521**	,714**	,946**	1		
6	,922**	-,604**	,900**	,857**	,894**	1	
7	,759**	-,455**	,445**	,910**	,921**	,712**	1
Mean	3,52	4,26	3,15	3,36	3,38	3,09	3,48
SDev	0,69	0,48	0,96	0,99	0,91	1,3	0,84

Note: 1. Mining acceptance; 2. Living cost; 3. Environmental quality; 4. Community involvement; 5. Infrastructure Improving; 6. Impact of others industry; 7. Public welfare.
** Significant level <0,01

The relationship between community involvement and mining company revenue is positive (R = 0.874 *). This figure indicates that the higher the community involvement in mining companies, the higher their acceptance of the company. Community involvement in mining company activities will increase community income. That way, the community will be able and easier to meet the cost of living. The cost of living feels lower when the ability to pay is higher. Finally, with the low cost of living, community income to mining companies is higher (R = -0.569 **). The involvement of the community in mining must be considered by the company. The involvement of the community in mining companies can be as mining workers, or as providers of supporting activities for mining companies (such as transportation, food or food providers, business partners, etc.).

Road improvements around the company will result in a smooth production process. In addition, the community benefits from the infrastructure built in the company environment. In accordance with the concept of CSR, the company's concern for infrastructure will gain the sympathy of the surrounding community, so that it will gain legitimacy. The results of this study are in line with what the legitimacy theory predicts, where the relationship of infrastructure development is positively related (R = 0, 875 **) to the acceptance of mining companies.

Communities around mining companies also need infrastructure improvements, such as the availability of electricity and good main roads. As with conditions in the village area, the availability of electricity is still relatively limited. If the availability of electricity is

mostly absorbed by mining activities, it can be ascertained that the community will often experience a long duration of blackouts. Infrastructure that is not well developed will have a high cost of living. The quality of the main road to community settlements must be maintained quality. Damaged roads will cause economic movements to require a relatively long time, and ultimately increase the cost of goods. The study found that the worse the infrastructure, the lower the acceptance of mining (R = -0,521 **).

The correlation test results between industrial growth and mining company revenues were found to be positive (R = 0.922 **). These results indicate that the more industries grow around mining companies (especially if the mining company triggers the growth of the new industry), the higher the community's acceptance of the mining company. This result is in line with the legitimacy theory and stakeholder theory. Both theories predict that in its operational activities, the company must pay attention to the interests of its stakeholders. If it is in line with stakeholder interests, the company concerned will obtain legitimacy in the community.

This study also found empirical evidence that industrial growth reduced living costs (R = -0.604 **). The growth of other industries around mining companies was also a concern in this study. The presence of mining activities followed by the growth of other business activities in the surrounding areas indicates that mining activities can drive economic growth in the region. Economic growth will encourage the ability of the community to fulfill their needs.

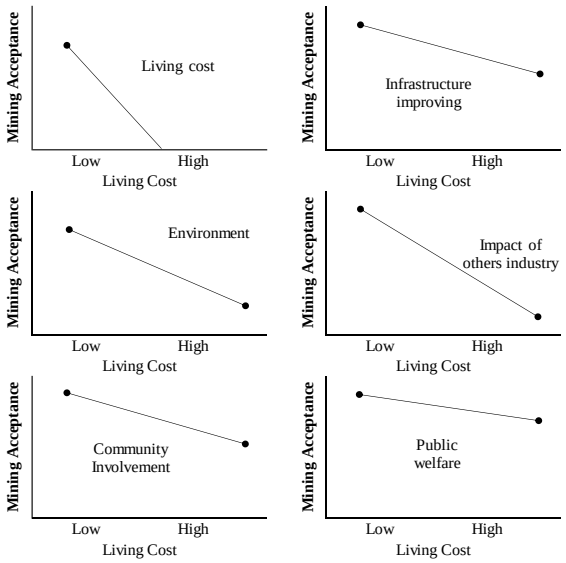

Fig. 2. Illustration of relationship between variables when living cost as situational factor.

Finally, this study found that community welfare was positively related to the acceptance of mining companies around them (R = 0.759 **). In general, the concept of community welfare is indeed the main measure of economic success. The results of this study also found a negative correlation between the welfare of the community and the acceptance of mining companies in their area (R = 0.455 **). Low people's welfare will encourage the difficulty of the community in fulfilling their needs. On the other hand, the cost of living will be increasingly heavy. The higher the cost of living, the lower the community's acceptance of mining. Figure 2 show the illustration of relation between variables and living cost as a situational factor. Living costs are a consideration in discussing the main variable relationship because this variable is very relevant and important in developing country society. Results generated discussion becomes more interesting.

CONCLUSIONS

The study found empirical evidence that public acceptance of mining companies is influenced by several factors, including the cost of living, quality of the environment, community involvement, improved infrastructure, the impact of other industries, and public welfare. These results are increasingly interesting when considering the cost of living in interacting between variables. These results are increasingly interesting when considering the cost of living in interacting between variables. Where it was found that the cost of living statistically was negatively related to the variable.

An important implication of this research is the need for attention from the company to maximize the interests of the community around the company. Because, community acceptance is absolutely needed by the company to ensure the sustainability of the company's operations.

Several limitations of the study were encountered, especially when the surveyor team went to the field to get respondents. The difficulty in reaching the location of the mining company and the research schedule that coincided with the days of Ramadan (when Muslims fasted for a full month) caused the low number of respondents to this study. However, the conduct of surveys is still carried out with a high level of caution, to obtain quality research results.

ACKNOWLEDGMENTS

This research was funded through the Professor Grant at the University of Lampung, 2019. Collaboration with the district/city/provincial government contributed greatly to maximizing secondary and primary data collection. Interesting discussion with a peer group of environmental science courses to strengthen practical argument, which resulted in this paper more attractive. For these reasons, we thank you for the involvement of all the parties we mentioned above. Hopefully this paper can contribute, especially to the Lampung Province.

REFERENCES

[1] Dowling, John and J. Pfeffer. Organizational Legitimacy: Social Values and Organizational Behavior. The Pacific Sociological Review Vol.18, Issue 1, 1975, pp.122-136.

[2] Deegan, C., M, R., and J. Tobin. An Examination of the Corporate Social and Environmental Disclosure BHP from 1983-1997 a Test of Legitimacy Theory. Accounting, Auditing and Accountability Vol. 15, Issue 3, 2002, pp. 312-343.

[3] Clarkson, P. M., Li, Y., Richardson, G.D., and Vasvari, F. P. Does it Really Pay to be Green? Determinants and Consequences of Proactive Environmental Strategies. Journal Account, Public Policy Vol. 30: 2011, pp.122-144.

[4] Berthelot and Robert. Climate change disclosure: An examination of Canadian oil and gas firms. Issues in Social and Environmental Accounting Vol. 5, Issue 1, 2011, pp.106-132.

[5] Islam, Muhammad Azizul. Social Compliance Accounting: Managing Legitimacy in Global Supply Chains. Springer International Publishing, Switzerland, 2015, pp.

[6] McKenzie, H. and F., Hoath, A. The socio-economic impact of mine industry commuting labour force on souce communities. Resources Policy Vol. 42: 2014, pp. 45–52.

[7] Lindrianasari, M. Kufepaksi, Y. Asmaranti, A. Komalasari. Social and Environmental Responsibility in Developing Countries: A Theoretical Approach to Regulation. International Journal of Geomate Vol. 15, Issue 49, 2018, pp. 47-52.

[8] Ghomi, ZB and P. Leung. An Empirical Analysis of The Determinants of. Accounting and Finance Research Vol. 2, Issue 1, 2013, pp. 110-127.

[9] Deegan, C. Environmental Disclosures and Share Prices−A Discussion about Efforts to Study this Relationship. Accounting Forum Vol. 28, 2004, pp. 87-97.

[10] Hantke-Domas, M. The Public Interest Theory of Regulation: Non-Existence or Misinterpre-tation? European Journal of Law and Economics Vol. 15, Issue 2, 2003, pp.165–194

[11] Zhang, A. and K. Moffat. 2015. A balancing act: The role of benefits, impacts and confidence in governance in predicting acceptance of mining in Australia. Resources Policy 44: 25–34.

[12] O'faircheallaigh, C. and T. Corbett. Indigenous Participation in Environmental Management of Mining Projects: The Role of Negotiated Agreements. Environmental Politics Vol. 14, Issue 5, 2005, pp. 629–647.

[13] Bridge, Gavin. CONTESTED TERRAIN: Mining and the environment. Annual Review of Environment and Resources Vol. 29, 2004, pp. 205–259

[14] Bury J. Transnational corporations and livelihood transformations in the Peruvian Andes: An actor-oriented political ecology. Human Organization Vol. 67, Issue 3, 2008, pp. 307–321

[15] Esteves, A.M., D. Franks, and F. Vanclay. Social impact assessment: the state of the art. Impact Assess. Project Apprais Vol. 30, 2012, pp. 34–42.

[16] Boyd, J. and S. Banzhaf. What are ecosystem services? The need for standardized environmental accounting units. Ecological Economics Vol. 63, 2007, pp. 616-626.

[17] Akiwumi, Fenda A. Global Incorporation and Local Conflict: Sierra Leonean Mining Regions. Antipode 2011, pp. 1-18.

[18] Marie Mazalto, Environmental Liability in the Mining Sector: Prospects for Sustainable Development in the Democratic Republic of the Congo. Mining, Society, and a Sustainable World. 2009, pp. 289-321

[19] Kemp, Deanna. Mining and community development: problems and possibilities of local-level practice. Community Development Journal Vol. 45, Issue 2, 2010, pp.198–218.

[20] Cadman, T. and Maraseni, T. The governance of REDD+: an institutional analysis in the Asia Pacific region and beyond. Journal Environmental Planning Management Vol. 55, 2012, pp.617-635.

[21] Jepson, P. Governance and accountability of environmental NGOs. Environmental Science Policy Vol. 8, 2005, pp. 515-526.

[22] Moffat, K., and A. Zhang. The Path of social license to operate: an integrative model explaining community acceptance of mining. Resource Policy Vol. 39, 2014, pp. 61-70.

9th Int. Conf. on Geotechnique, Construction Materials and Environment, Tokyo, Japan, 20-22 November 2019, ISBN: 978-4-909106025 C3051

VALIDATING CREATIVE THINKING PROCESS EFFECT IN THE 2011 TOHOKU DISASTER AREA: DESIGNING LANDSCAPE RESILIENCE

Misato Uehara[1], Rob Roggema[2] and Makoto Fuiji[3]
[1] Shinshu University, Japan; [2]Hanze University of Applied Sciences, Netherlands,[3] Tonich Engineering Consultant, Japan

ABSTRACT

In order to treat which is suitable for climate change and natural disasters beyond forecasting, drafting a flexible plan and consensus among the residents are important issues. However, empirical verification of successful creative discussion and planning processes are limited, because experimental verification of the effect of such planning theory and communication is extremely difficult. Our purpose was to prove benefits of the Swarm Planning's Centre for Development of Creative Thinking (COCD) tool which is one of creative planning processes. To make the member construction for each four design groups (General process, Swarm process), we questioned 41 universities' students about their opinions and interests in the 2011 Tohoku disaster area and its reconstruction conflict. These score allowed us to make the same allocation of people who were agree or disagree with current relocation housing and sea wall development plan, gender, interest of disaster area. We required all eight groups to plan relocation housing site for tsunami disaster victims, required to plan destroyed sea wall reconstruction of the Tohoku disaster area. Four groups used the general planning approach, while the other four groups use the COCD box tool. After this, every group presented their design proposals, and audiences scored them. After this, each student scored their proposal too. The research concluded that evaluation of proposals by Swarm Planning got higher evaluation than regular planning proposals on three criteria, habitability, appropriateness and originality in statistically.
Keywords: Participatory planning, Post-disaster, Design Charrette, Future Design

1. INTRODUCTION

At the 2011 Japan Earthquake Tsunami disaster, many Tohoku cities which had been built through proper processes were damaged: Dead or missing 18,430 people, destroyed 404,890 buildings. In addition, despite strong opposition by few residents and ecologists, a huge seawall was re- constructed, and relocation houses on the hill were developed in the disaster area. As a result, these developments used 4 billion yen, but about 100,000 victims did not choice to return to the reconstructed town, for residents on the hill were not convenient, and huge sea wall hid beautiful coastal line view. Alternative new planning process is required rather than past general planning process for adaptation to climate change and natural disaster recovering. This is our question.

Previous studies reported that digital technologies (GIS, 3Dmapping) in workshops can help to stimulate understanding and discussion of issues by the interview survey [1,2] and participatory observations [3-7]. Warden R et al [8] indicated the demerits of using digital tools. Zhang H et al and Valencia-Sandoval C et al [9,10] showed the importance of a simple discussion tool in disaster areas and rural areas where digital data resources are not available. Höppner C et al, Knox MW et al, Rohrbach B et al [11-13] verified the merits of the whole workshop program. Thus, there are very few quantitative empirical studies of the effects of workshops with citizen's participation. Therefore, the purpose of this paper is compare the final qualities the plans by two different workshop discussion process of reconstruction plans from 2011 Tsunami disaster by quantitative analysis.

2. STUDY MATERIALS AND METHODS

This article focused on setting up a process of comparative design, which should make it possible to identify the potential benefits of Swarm Planning over regular planning.

General planning process and design aims to provide limited solutions for relatively straight forward, 'tame' problems [14], while climate adaptation is seen as a 'wicked' problem [15]. General planning processes' main stakeholders are 'consulted', which means they are approached with some design proposals which have been already well thought through and proven. The role left for the stakeholders is in general to accept or reject such proposals. Real influence or a contribution in the form of suggestions is often not possible, nor welcomed. Though different opinions are introduced here, they are chosen in the final majority and the minority's opinion is ignored.

On the other hand, Swarm Planning approach's

key factor is to deal with complex issues [16]: it is the most important advantage of working in a design charrettes; the method that is possible to make complex issues, such as climate adaptation which is concrete and conceivable. Roggema developed workshop process using tool by the COCD-box methodology [17].

In this article, the benefits of the Swarm Planning's COCD-box thinking process are investigated. We required six students' groups to plan relocation housing site for Tsunami disaster victims, required them to consider destroyed sea wall reconstruction of the Tohuku Disaster area. Four groups used the general planning approach, while the other four groups used the COCD box tool. After group discussion and workshop, every group presented their design proposals, and the audience scored each proposals and own group's proposal too. To evaluate each proposal, a Semantic Differential Method questioner was used.

2.1 Defining the design teams

This study investigated the effect on quality of proposals by two different discussion process for reconstruction of the 2011 Tohoku earthquake and tsunami disaster. In order to make each group have students who had different opinion equally, we questioned the 41 university students about their opinions and interests in the 2011 Tohoku disaster area.

The score of answers to this questionnaire showed the difference of their premise knowledge and opinion of 2011 disaster area. This data was used to make member construction for each eight design groups. Additionally, in forming the group members, we considered the gender balance too. We allocated each eight groups had approximately five students under above process. As a result of this adjustment, each group had same allocation of people who had favor and against opinion for housing-relocation on the high land, and sea wall re-construction. In order to evaluate the usability of swarming planning statistically, Swarm Planning four groups used COCD-box tool, while the other general planning four groups did not used COCD-box tool. This design setting made it possible to compare proposal qualities by two different thinking process.

2.2 Planning theme and target issue

All eight groups were required to plan a new a sea wall development and relocation housing site planning for destroyed residential community by tsunami disaster. This subject is a very important issue. In the actual disaster area, 40 trillion yen of reconstruction budget was used, and the new sea wall and the new town were rebuilt [18]. However, planned population has not recovered because many of these new-residential sites and rebuilt apartments' rooms are left empty.

Our each workshop group had similar members, used same work time (One and a half hours), same design task, materials such as colored plasticine to proposed plan of sea wall (yellow cray), new housing site (red cray) and another land-use proposal (green cray) ,according to design charrettes setting [16]. All groups were given the same advance information; Disaster area's favor or against opinions for relocating houses to higher ground and reconstructing seawalls.

Fig.1 The COCD-box sheet with favor or against opinions for relocating houses to higher ground and reconstructing seawalls

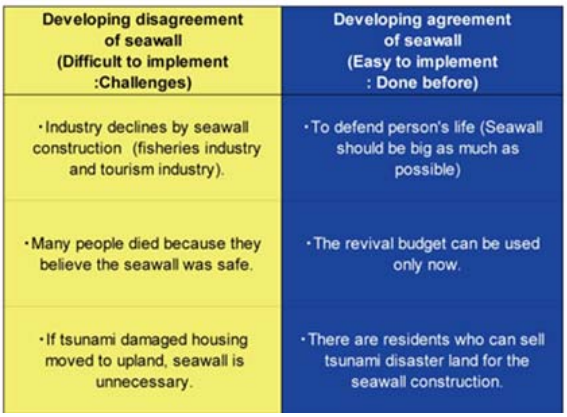

Fig.2 The simple tow column sheet with favor or against opinions for relocating houses to higher ground and reconstructing seawalls

The four groups of Swarm Planning were used the COCD-box tool, which was developed by COCD (Centre for development of Creative Thinking) (Fig.1). The COCD-box has 2 axes: 1. Difficulty or ease of implementation, 2. Agree or oppose to existing proposals, (Generality or uniqueness of planning idea). Therefore, compared to the column sheet, even if the discussion is based on the same positive and negative opinions, new discussion direction with the conflict of two opinions was assumed to be stimulated. Swarm Planning process groups (SG) discussed the matter with COCD box to focus on the new direction (red column of Fig.3); the ease of implementation normal idea and creative idea which is not (yet) feasible (SG1,2,3,4).

The control groups used simple tow column sheet (Fig.2). Every group was allocated the students by the result of questionnaire survey, so each group's favor and against opinion for current development (relocation and sea wall renovation) were same percentage. General planning process groups (GG) had discussion which is based on the original ideas. This is the ease of implementation and creative idea which is not (yet) feasible in parallel (Fig.2). Then, we assumed they tend to decide by majority rule, and tend to ignored minority's opinion (GG1,2,3,4).

2.3 Evaluation of proposal quality difference by two planning process using a Semantic Differential Method

After the workshop, all students scored each proposal using employing Semantic Differential Method including own team's plan, which took One and a half hours. In order to abandon potentially biases, the SG and the GG presented their proposals alternately. The respondents evaluated using Semantic Differential Method scale; A point value is assigned for each of the spaces on a seven-point scale so that a set of seven spaces or a continuous line between the opposing adjectives could be constructed. When the positive adjective is on the right side, assign the values 1 to7 from left to right; for example, 1 = uninhabitable, 4 = no opinion, 7 = habitable. After evaluation, the authors analyzed the evaluation score's difference between the four proposals by Swarm Planning and the four proposals by the General planning. This analysis used Welch's t test. This analysis showed the relationship between the type of planning process (Swarm planning way or General planning way) and these evaluation score's average of difference.

3.RESULTS

In this paper, we compared the quality of proposals by two different process, for we revealed the validity of the use of the Swarm Planning approach. First, we compared the design proposals' quality by the two different processes. Next, we compared the evaluation scores statistically.

3.1 Design proposals differences

Figure 3 showed the results of the proposals by general planning process. As a whole, all the groups made proposals to rebuild the sea wall for tsunami breakwaters (yellow clay) (Fig.3). This decision seemed to be same in actual disaster area.

The GG3 group also proposed to rebuild the residential area in the affected area of the tsunami again, and GG1 and GG2 proposed high land relocation. The remaining GG 4 group could not propose relocation sites. Especially GG3 plan did not seem to have considered on the cost aspect: the sea wall at twice the height as before (10 m), making a 100 m tower. In addition, the reason of the relocation housing site did not seem to be logical (Fig.3).

Although many seawalls could not save the coastal residents at 2011 disaster, from the GG's discussions and proposals, we can see that it is difficult to break away from the conventional and general decision. Furthermore, using the conventional discussion process, there were some cases when the proposal became childish, and cases when answers to the requested task could not be made.

Figure 4 showed the results of the proposals by Swarm Planning process. As a whole, all the groups' plan had no seawall construction, for all group also proposed to relocation site on the hill.

The SG1,2,3 plans seemed to be consideration on the both coastal site and hill site with road networking. They set the seawall cost to road networking construction cost.

Especially, we were interested in the SG1's housing resettlement site which was located in the highest altitude tsunami affected land ; they explained 'The reason for this choice was that it will achieved both minimum tsunami disaster risk and land cost was cheap than that of the area which was not affected inland.'

Unlike the regular planning process group, half of the group had additional proposal of seaside tide forest and network roads using green cray(Fig.4).

On the other hand, the regular planning groups were also given the same consultation option as green clay which proposes land use other than seawalls and relocation housing, their additional proposal such as seaside tide forest and roads were few(Fig.3).

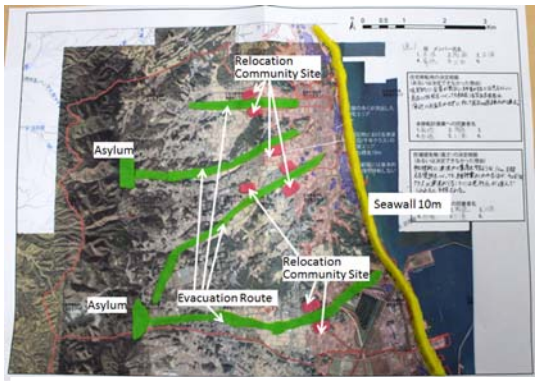

GG1

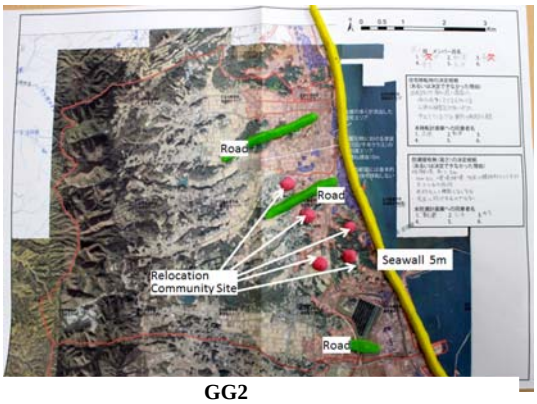

GG2

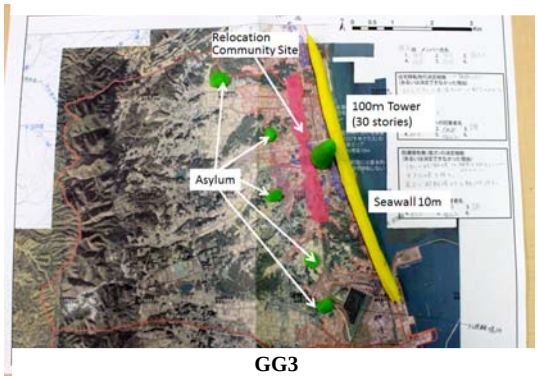

GG3

GG4

Fig.3 Results of land use plans using control general planning process

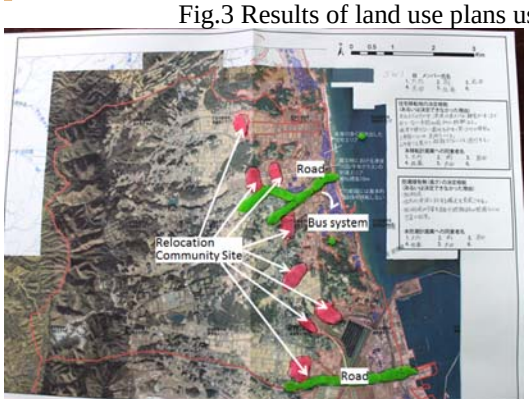

SG1

SG2

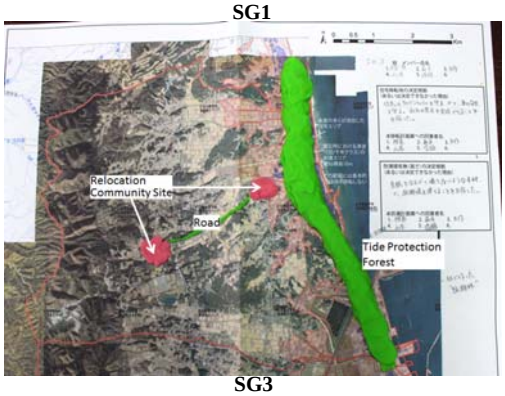

SG3

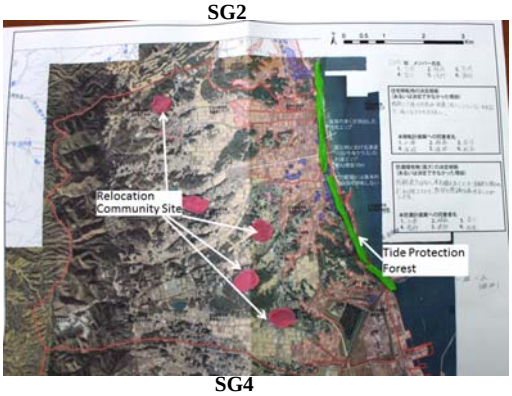

SG4

Fig.4 Results of land use plan using Swarm Planning COCD process

3.2 Evaluation scores and its comparison

In order to conduct a Semantic Differential Method test, a total of eight design proposals were introduced with a brief presentation.

The students evaluated each proposal using the method of semantic differential scale. The proposed plans in each of the methods of GG and SG had alternating announcements, to reduce the impact of order on evaluation; It was to avoid the possibility that the first half of the proposals are highly appreciated than the second half of the proposals.

In this test, preferences of each plans were scored along a seven-point scale. A score of seven points means that the subject has a strong positive

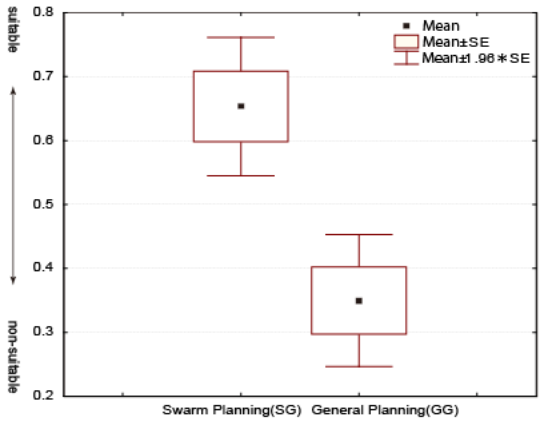

Fig.5 The comparison evaluation score of Swarm Groups and General Groups plan's suitability

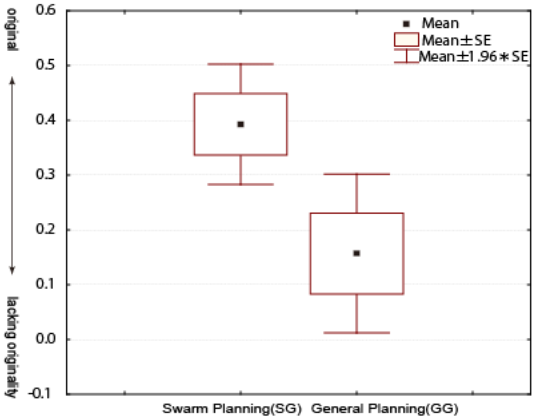

Fig.6 The comparison evaluation score of Swarm Groups and General Groups plan's originality

impression of the sample, while a score of one point denotes a strong negative impression: Each land use plan's appropriateness, habitability and originality. This result of the analysis showed the effect of Swarm Planning, as interpreted through the Welch's t test (Fig.5,6,7). Overall, the evaluated scores were significantly higher in Swarm Planning groups plans than general planning groups' ones. In other words, the majority of the 41students evaluated the Swarm Planning groups land use plans higher than the control general groups in statically (Fig.5,6,7).

The evaluation scores of suitable(2) to non-suitable(-2) was significantly higher in Swarm Groups (mean 0.65) than General Groups (mean 0.35) , with t=4.00 p<0.001 (two-tailed), df=489.2 (Fig.5). The evaluation scores of habitable (2) to non-habitable (-2) was significantly higher in Swarm Groups (mean 0.34) than General Groups (mean -0.04) , with t=4.59, p<0.001 (two-tailed), df=489.4(Fig.6). Similarly, the evaluation scores of Originality (2) to lacking-originality(-2) was significantly higher in Swarm Groups (mean 0.39) than General Groups (mean 0.16) , with t=2.56, p=0.011(two-tailed), df=454.1 (Fig.7).

The results suggested that Swarm Planning process using the COCD-box will lead to more favorable outcomes of planning than general planning process without the COCD-box. This analysis revealed that the relationship between the type of planning process and the quality of proposals in terms of resilience. And it proved that the Swarm Planning approach's result is as good as quantitative empirical studies.

CONCLUSIONS

In this paper, we investigated the relationship of planning processes and its proposal qualities, to reveal the validity of the use of the Swarm Planning process. First, we compared the design proposals' quality by planning process type. Second, we also compared each plan's evaluation scores by planning process type in statistically. Empirical verification of

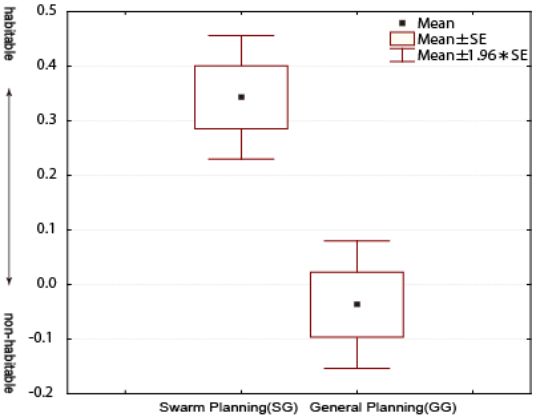

Fig.7 The comparison evaluation score of Swarm

successful and creative discussion and planning processes is limited, because experimental verification of the effect of such planning theory and communication is extremely difficult. Though this is based on qualitative interviews, Cheng P. et al. **[2]** points out the importance of using a matrix for thinking and forcing new ideas with different options. Kojima et al **[19]** also revealed that when members of an imaginary future generation are present during negotiations, groups tend to select more sustainable options. The results of this study support**ed** it quantitatively. In this article, we accomplished to analyze the suitability and usability of the Swarm Planning approach with COCD- box tool.

Additionally, this study reveal**ed** novel results in aspect of difference of planning effect's empirical verification. All groups had the same disagreement, because we assigned members with diverse opinions to each group. Despite above design setting, it can be concluded that the Swarm Planning approach performs better quality of proposal than regular planning approaches.

Each group also included students who opposed to the standard relocation housing and sea wall development idea of the 2011 disaster areas. After that, the same study time and the same materials

were given. Thus, although the group condition and design work task were unified, the proposal contents by two different processes appeared to be distinctly different. Also, in the individual evaluation of 41 students for the proposal, the proposals with COCD-box were statistically evaluated higher than the proposals by the conventional method of planning. This result seem**ed** to be one evidence that will overcome the general planning problem; Although different opinions were introduced on the table, they were chosen in the final majority and the minority opinion was ignored.

In fact, despite strong opposition, a huge seawall was constructed, and the relocation houses on the hill were developed in the affected area. As a result, the seawall and the relocation of houses were completed at a cost of 4 billion yen, but about 100,000 victims did not return to the reconstructed town. This fact indicates an inconsistency in the existing planning process. In that context, we could point out the possibility of flexible planning process using Swarming planning and COCD-Box. It is recommended to use the Swarm Planning approach in areas that suffer or potentially suffer after a climatic event. In these cases, the planning approach could help to minimize the damage after a disaster and/or to anticipate a disaster by designing a more resilient urban environment.

ACKNOWLEDGMENTS

This work was supported by JSPS KAKENHI Grant Number 15K21039 and 18K18570.

REFERENCES

[1] Luz F. Participatory landscape ecology–a basis for acceptance and implementation. Landscape and urban planning. 2000 Aug 15;50(1-3):157-66.

[2] Cheng P, Mugge R, Schoormans JP. A new strategy to reduce design fixation: Presenting partial photographs to designers. Design Studies. 2014 Jul 1;35(4):374-91.

[3] Stock C, Bishop ID, Green R. Exploring landscape changes using an envisioning system in rural community workshops. Landscape and Urban Planning. 2007 Mar 2;79(3-4):229-39.

[4] Al-Kodmany K. Using visualization techniques for enhancing public participation in planning and design: process, implementation, and evaluation. Landscape and urban planning. 1999 Sep 15;45(1):37-45.

[5] Arciniegas G, Janssen R. Spatial decision support for collaborative land use planning workshops. Landscape and Urban Planning. 2012 Sep 15;107(3):332-42.

[6] Janssen R, Dias E. A pictorial approach to geodesign: A case study for the Lower Zambezi valley. Landscape and Urban Planning. 2017 Aug 1;164:144-8.

[7] Vervoort JM, Kok K, Beers PJ, Van Lammeren R, Janssen R. Combining analytic and experiential communication in participatory scenario development. Landscape and Urban Planning. 2012 Sep 15;107(3):203-13.

[8] Warden R, Woodcock D. Historic documentation: a model of project based learning for architectural education. Landscape and Urban Planning. 2005 Oct 15;73(2-3):110-9.

[9] Zhang H, Mao Z, Zhang W. Design charrette as methodology for post-disaster participatory reconstruction: Observations from a case study in Fukushima, Japan. Sustainability. 2015 Jun;7(6):6593-609.

[10] Valencia-Sandoval C, Flanders DN, Kozak RA. Participatory landscape planning and sustainable community development: Methodological observations from a case study in rural Mexico. Landscape and Urban Planning. 2010 Jan 15;94(1):63-70.

[11] Höppner C, Frick J, Buchecker M. Assessing psycho-social effects of participatory landscape planning. Landscape and Urban Planning. 2007 Nov 19;83(2-3):196-207.

[12] Knox MW, Clevenger CM, Dunbar BH, Leigh KE. Impact of charrettes and their characteristics on achieved LEED certification. Journal of architectural engineering. 2013 Dec 31;20(3):04013012.

[13] Rohrbach B, Laube P, Weibel R. Comparing multi-criteria evaluation and participatory mapping to projecting land use. Landscape and Urban Planning. 2018 Aug 31;176:38-50.

[14] Conklin J. Wicked problems and social complexity. CogNexus Institute. 2001:11.

[15] Rittel HW, Webber MM. Dilemmas in a general theory of planning. Policy sciences. 1973 Jun 1;4(2):155-69.

[16] Roggema R, editor. Swarming landscapes: the art of designing for climate adaptation. Springer Science & Business Media; 2012 Dec 2.

[17] https://www.tuzzit.com/en/canvas/COCD_box

[18] https://www.kahoku.co.jp/tohokunews/201809/20180911_73006.html

[19] Kamijo Y, Komiya A, Mifune N, Saijo T. Negotiating with the future: incorporating imaginary future generations into negotiations. Sustainability science. 2017 May 1;12(3):409-20.

9thInt. Conf. on Geotechnique, Construction Materials andEnvironment, Tokyo, Japan,20-22 November 2019, ISBN: 978-4-909106025C3051

RESPONSES OF DIATOM COMMUNITIES TO CHEMICAL VARIABLES IN STREAM WATERS RUNNING IN SERPENTINE, LIMESTONE AND CLOSED-MINE AREAS IN KINKI AND CHUGOKU, JAPAN

Akio Nishida[1] and Hiroyuki Ii[2]

[1]CLERK Memorial International Highschool, Toyooka city, Hyogo, Japan

[2] Faculty of System Engineering, Wakayama University, Wakayama, Japan

ABSTRACT

The responses of diatom communities distributed on the surface of substrates in stream beds were investigated at 17 study sites in three areas with different geological characteristics: closed-mine, serpentine and limestone areas. Our aims were to describe how diatom communities in different geological areas respond to and are affected by water chemistry. High Mg^{2+} and Ni concentrations characterized stream water chemistry in the serpentine area. The limestone area was characterized by high pH , Ca^{2+} and $HCO3^-$ concentrations. Samples collected at 17 study sites were clustered into 5 groups, depending on diatom species similarities. Results from nonmetric multidimensional scaling(nMDS) and canonical correspondence analysis (CCA), showed chemical variables in running water were strongly related to diatom communities. Only four diatom communities belonging to cluster 3 (2 sites in closed-mine area and 2 sites in serpentine area) had positive correlations with three chemical variables (F^-, Zn and NH_4^+). Moreover, those communities at two sites in limestone area were affected by pH values. It is clear that species compositions of diatom communities were different for the three areas with different geological characteristics, and that those compositions were greatly affected by water chemistry.

Keywords: diatom, serpentine, limestone, water chemistry, geology

INTRODUCTION

Diatoms, green algae, and cyanobacteria typically comprise the majority of species in benthic algae communities. These occur within virtually all rivers, typically in intimate association with heterotrophic microbes and the extracellular matrix, known by the all-inclusive terms periphyton or biofilms [1]. Sheath and Cole [2] recorded 259 taxa of algae, of which 35% were green algae, 24% were cyanobacteria, 21% were diatoms and other chrysophytes, and 20% were red algae. Recently, water pollution has become a very important social problem, and benthic algae, including diatoms and other algae, have been used as tools to assess the degree of water pollution. Because of their ability to concentrate metals from aqueous solutions, marine and fresh water algae have great potential as biological monitors for anthropogenic waste [3]. As in Europe and the United States, many studies concerned with bio assessment have been conducted in Japan. Diatoms and other benthic algae play important roles as primary producers in aquatic food webs. Many benthic invertebrates, such as trichoptera, ephemeroptera and plecoptera, feed diatoms and other algae, and seetfish (*Plecoglossusaltivelis*) called Ayu in Japan is well known as one of the main diatom feeders [4]. However, studies concerning the response of diatom communities to bed rock geology, such as serpentine and limestone, have rarely been conducted in Japan. Therefore, the aim of this study was to make clear how diatom communities in streams respond to the bed rock geology.

STUDY SITES AND METHODS

STUDY SITES

Samples were collected at 17 study sites in streams running in areas with different characteristics. Seven sites from st.1 to st.7 were located around the Ikuno mine, in the central part of Hyogo Prefecture (Fig 1). That mine was closed in late March 1973, after operating for about 1200 years. The elevations of sites in this area ranged from 343m to 513m. Five sites (st.8–st.12) in the area of serpentine geology were located in Yabu City, in the northern part of Hyogo Prefecture, and were set in Oecho, Fukuchiyama City, Kyoto Prefecture (Fig.1). All of the streambeds of the five sites in those areas were composed of serpentine rocks, and the land aroundthe sites was largely covered by serpentine soils produced after weathering of the rocks. The serpentine rocks in Japan were described by Suzuki [5], and were found

along two south-northeast-trending belts in Kyushu, Shikoku, central and southern Honshu. The serpentine areas in Yabu City and Oecho are two wide spreading areas in Honshu. Two other sites (st.13 and st.14) in the limestone area were located inTaishaku valley, Tojocho, in the northern part of Hiroshima Prefecture (Fig.1). Those sites were selected in the Mito river and the Taishaku river respectively. The streambeds of the two rivers have substrates of limestone walls around the rivers. In addition to those sites, we have
three reference sites for comparison with results from serpentine, limestone and closed-mine areas, in the Yada River system in the northern part of Hyogo Prefecture. Three sites (st.15–st.17) were located in the Yamada river, Kumanami river, and Kyonyo river, respectively (Fig.1). These sites were chosen due to their geological characteristics (Yamada river: sedimentary rocks; Kumanami river: quartz porphyry, and Kyonyo river: basalt).

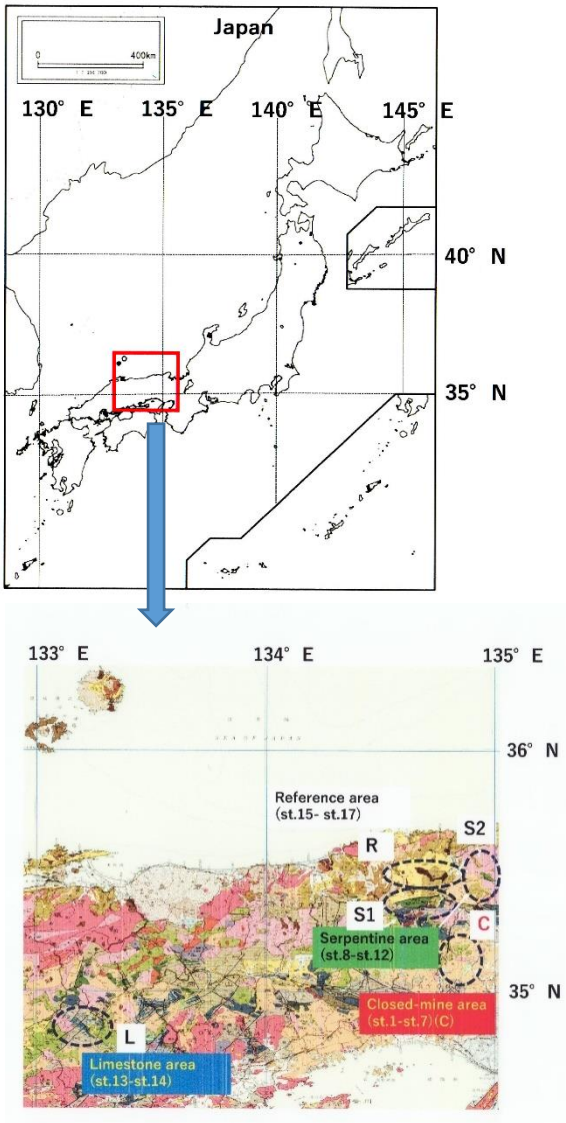

Fig. 1 Seventeen study sites: st.1–st.7 in closed-mine area; st.8–st.12 in serpentine area; st.13and st.14 in limestone area, and st.15–st.17 in reference area with sedimentary and igneous rocks.

SAMPLING AND ANALYTICAL METHODS

Benthic diatoms were collected from at least 5 stones from the lotic parts of the sampling sites. The upper surface of stones were scratched with a toothbrush in an area of 5cmX5cm and rinsed with river water on site. Collected materials were placed in 50ml plastic bottles, and then the samples were fixed in 5% formaldehyde. Diatom specimens for microscopy were mounted using Naphrax [3]. Diatom counts and identification were performed atx1000 magnification using a light microscope (Zeiss, Germany). Water samples were collected in spring and autumn from 2010 to 2012. Water temperatures, pH, and conductivity (EC), dissolved oxygen (DO) and total dissolved solids (TDS) were measured at each site by using a sensor probe (W-23XD, Horiba). Water samples were collected in two polyethylene bottles (100mL), with one bottle being acidified with nitric acid (HNO3) before transportation to the laboratory. The water samples were analyzed by ICP-AES (Inductivity Coupled Plasma Atomic Emission Spectroscopy) (SPS1700HVR) for measurements of heavy metal concentrations. The other samples were used for ion chromatographic analysis (DIONEX ICS-1500) for other nonmetallic ions, including Ca^{2+} and Mg^{2+}. Water samples were stored in a refrigerator running at about 10℃ until chemical analysis.

DATA ANALYSIS

Multivariate Analyses and Ordination

First, diatom communities were clustered into several groups by K-medoids [6,7]. The number of clusters was decided by maximizing the average silhouette width [6, 7]. Indicator species of each cluster were detected by using the indicator values (IndVal) [6,7]. For each site, we estimated exponential Shanon diversity {expH' = exp[-$\sum p_i \log_e(p_i)$], where pi is the proportion of abundance for species I }, and Shimpson's inverse diversity. Second, we performed nonmetric multidimensional scaling(nMDS) to investigate the similarities among 17 diatom communities. After that, canonical correspondence analysis (CCA)was performed to get more information with respect to the relationship between diatom communities and chemical variables. Species diversity, clustering, nMDS and CCA analyses were carried out using packages of cluster (pam) [8], labdsv (indval) [9] and vegan [10] in R 3.3.2 software.

RESULTS

Diatom Communities and Diversity

Seventeen diatom communities were clustered into 5 groups as follows (Fig.2); cluster 1 (st.1, st.7, st.3, st.8, st.15 and st.16), cluster 2 (st.2), cluster 3 (st.12, st.4, st.5 and st.9), cluster 4 (st.11, st.13, st.14. st.6 and st.10), and cluster 5 (st.17). Two clusters (cluster 3 and cluster 4) revealed higher values than the average

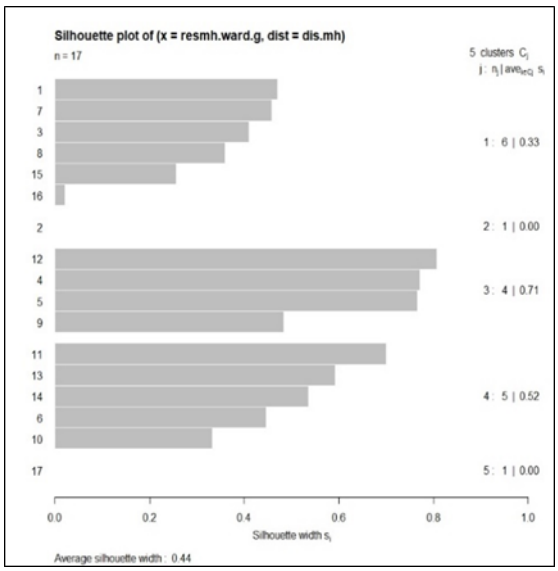

Fig.2 Silhouette plots of 17 study sites: average silhouette width = 0.44. The numerical number expresses study sites

value (0.44), and those values indicated that those communities closely

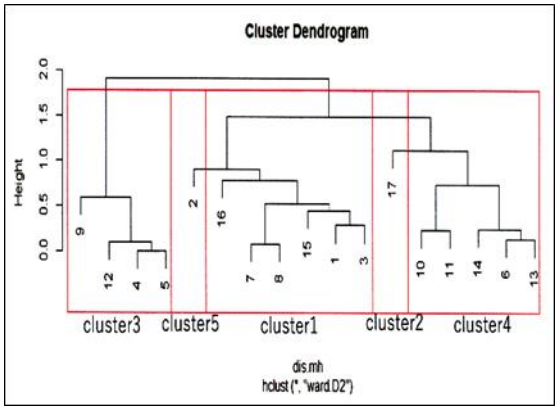

Fig.3 Cluster dendrogram with boxes around the five selected clusters of sites (Method= "ward.D2").

Table 1 Indicator species of each cluster. The number of (;) shows IndVal values and p-values of permutations.

Cluster	Number of sites	Average silhouette width	Indicator species (IndVal; permutation p<0.10)
Cluster1	6	0.33	
Cluster2	1	0.00	
Cluster3	4	0.71	*Cymbellade licatula*(0.842;. p<0.082)
Cluster4	5	0.52	*Naviculatri punctata*(1.000; p<0.058) *Navicularhynchocephala* (0.792; p<0.034) *Achnanthidiumsubhudsonis*(0.574; p<0.034)
Cluster5	1	0.00	*Gomphonemaangustatum*(0.739; p<0.078)
Total	17	0.44	

Table 2 Dominant species in each cluster.

Number of cluster	Dominant species
luster 1	*Achnanthidiumconvergens*(st.1, st.3, st.7,st.8,st.15,st.16) *Planothidiumlanceolatum*(st.1, st.16)
Cluster 2	*Gomphonema*spp.*(st.17)*
Cluster 3	*Achnanthidiumminutissimum*(st.4,st.5,st.9,st.12) *Achnanthidiumconvergens*(st.9) *Cymbelladelicatula* (st.9,st.12)
Cluster 4	*Achnanthidiumsubhudsonis*(st.6,st.10,st.11,st.13,st.14) *Sellaphorapupula*(st.10,st.11) *Vavicularadiosav.tenella*(st.10,st.11,st.14) *Gomphonema*spp.(st.14)
Cluster 5	*Cocconeislineata* (st.2) *Achnanthidiumconvergens*(st.2)

resembled each other within the same cluster. One cluster (cluster 1) showed a lower value than the average value (Fig.2), and revealed that that cluster had a great variety of species compositions. Indicator species of each cluster were designated by IndVal. However, species of two clusters (cluster 1 and cluster 2) were not detected by that method (Table.1). Dominant species observed at each site are listed above (Table 2). Exponential Shanon-Wiener diversity index (ESI) was estimated at each site (Fig.3 [A] [B] [C]). In the closed-mine area, the values of ESI at st.4 and st.5 revealed 1.357 and 1.124, representing quite low diversities with comparison to those of the reference area. The values of ESI at st.1 and st.3 were 12.415 and 13.486. In the serpentine area, ESI at st.9 showed a lower value of 2.542 rather than another site in the serpentine area. However, the value of ESI at st.10 was 11.295. In the limestone area, values of ESI at two sites (st.13–st.14) were 5.351 and 8.937. In the reference area, ESI value at st.15 was 16.829, which was the highest value among diatom communities collected at the 17 sites.

Water chemistry

The concentrations of zinc (Zn) at st.4 and st.5 were 1.273 (mgL^{-1}) and 1.457 (mgL^{-1}) respectively. These values were remarkably high compared with the values at sites in other areas (Table 1). In addition to that, iron (Fe) concentration at st.7 was 1.320 (mgL^{-1}), being the highest value in all sites. Nickel (Ni) concentrations showed higher values at five sites (st.8–st.12) in the serpentine area rather than other sites. Results of paired-tests, revealed that the concentrations of magnesium ion (Mg^{2+})were closely related to that of nickel (Ni)(paired test: p=0.731), and correlations among some chemical variables were observed. For instance, the concentrations of manganese (Mn) correlated with Pb (p=0.881), and the relationship between zinc (Zn) and fluoride ion(F^-) was strong (p=0.957). Moreover, we could see a high value (p=0.828) in the relationship between nickel (Ni) and phosphorus ion (PO_4^{3-}). We performed paired-tests among chemical variables, which are listed in Table 3.

[A] Closed-mine area

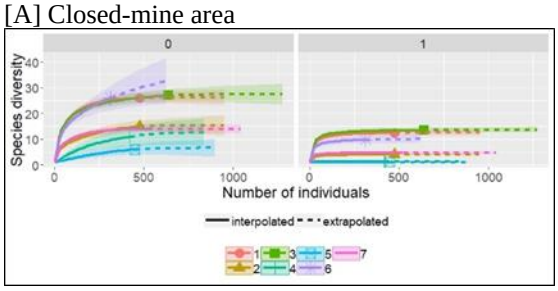

[B] Serpentine area

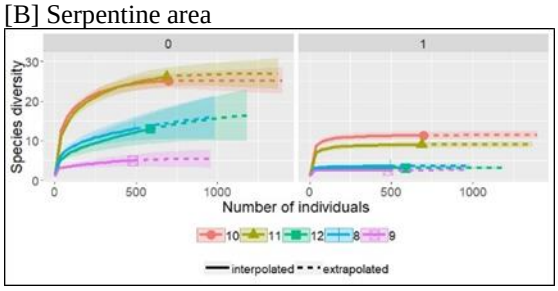

[C] Limestone (st.13-st.14) and reference area (st.15-st.17)

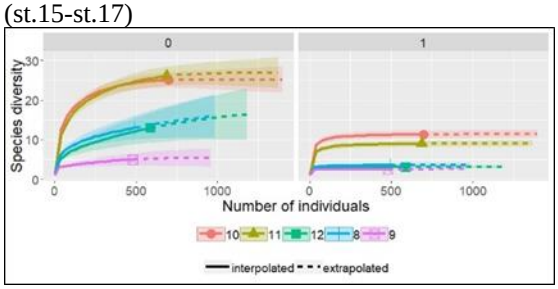

Fig.4 Exponential Shannon-Wiener diversity index {expH'=exp[-$\sum p_i \log_e(p_i)$], where pi is the proportion of abundance for species i. The number of "q=0" expresses taxa number collected at each site, and the number of "q=1" shows those indices. The dash lines express the expected values by attenuation, and the dot lines show 95% confidence intervals obtained using bootstrap methods.

Table 3 Chemical valuables (mean values) of 17 studying sites, especially for heavy metals, measured from spring 2010 to autumn 2012.

Site		Pb mg/L	Cu mg/L	Zn mg/L	Ni mg/L
St.1	M	0.007	0.001>	0.046	0.002
St.2	M	0.057	0.001>	0.004	0.003
St.3	M	0.013	0.001>	0.430	0.014
St.4	M	0.021	0.035	1.273	0.005
St.5	M	0.116	0.043	1.457	0.005
St.6	M	0.087	0.001>	0.014	0.002
St.7	M	0.098	0.138	0.039	0.002
St.8	S	0.008	0.001	0.001	0.022
St.9	S	0.007	0.002	0.003	0.062
St.10	S	0.014	0.001	0.111	0.011
St.11	S	0.008	0.001>	0.003	0.010
St.12	S	0.080	0.082	0.010	0.448
St.13	L	0.004	0.001>	0.001	0.002
St.14	L	0.002	0.001>	0.002	0.001
St.15	R	0.004	0.001>	0.001	0.001
St.16	R	0.004	0.001>	0.001	0.001
St.17	R	0.001>	1.300	0.001	0.001 >

Note: Geology: M-closed-mine area, S-serpentine area, L-limestone area and R-reference area with sedimentary rocks and basalt.

Table 4 Results of paired-test among chemical variables (p-value).

Chemical variables	
Ca^{2+}	F^-(0.662)
Cu	Fe(0.880)
Mn	F^-(0.633)
Ni	Zn(0.518), Mg^{2+}(0.731)
Pb	Fe(0.552), Mn(0.881)
$SO4^{2-}$	F^-(0.860), Zn(0.763)
NO_3^-	Mg^{2+}(0.665)
PO_4^{3-}	Ni(0.828)

Ordinations

Firstly, we analyzed the data of diatoms and chemical variables by using nonmetric multidimensional

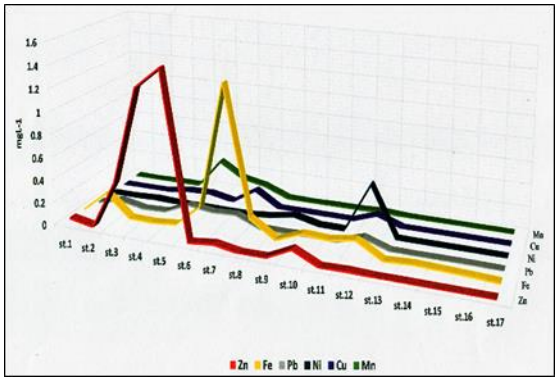

Fig.5 Concentrations of six chemical variables (Zn, Fe, Pb, Ni, Cu and Mn).

scaling (nMDS) (Fig. 6). The final stress value showed 10.421, representing a fair result. From the result of nMDS, five clusters located separately escape from two clusters (cluster 1 and cluster 4), which are very widespread. After that analysis, we carried out canonical correspondence analysis (CCA) with constructing some models. In this model from CCA with eight chemical variables, the constrained inertia (sum of squared distance) was 2.048 (51.5% of the total inertia). Eigenvalues ofthe first and second axes were 0.715 and 0.441, respectively. Permutation test of this model by ANOVA indicated significant results (F=1.364, Pr(>F)=0.033). Diatom communities belonging to cluster 3 (st.4, st.4, st.9 and st.12) had remarkably strong relations to Zn and F^- (Fig.6). In addition to this, the communities belonging to cluster 4 (st.6, st.10, st.11, st.13, and st.14) and cluster 2 (st.17) were affected by phosphorus ion (PO_4^{3-}). However, we could not see clear relations among the communities, belonging to cluster 1 (st.1, st.3, st.7, st.8, st.15 and st.17) and cluster 5 (st.2). Figure 7 indicates that st.13 and st.14 in limestone area are affected by pH values in comparison with Ca^{2+} concentration, and shows that six sites in cluster 1 and 5 tend to have negative relations to chemical variables.

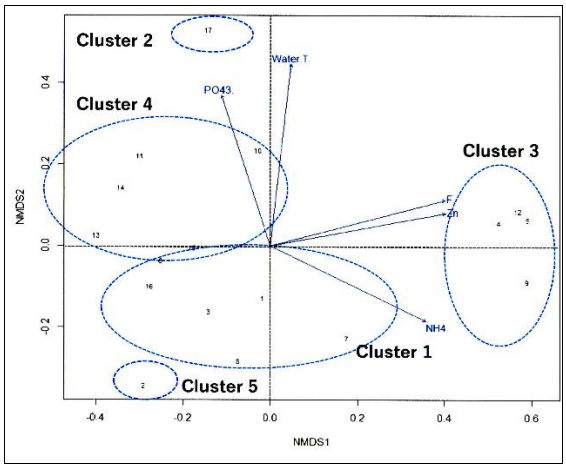

Fig.6 Ordination by nMDS of diatom communities sampled at 17 sites. Sites were classified into 5 clusters. Moreover, five significant chemical variables were plotted as vectors: water temperature (water T.)(r^2=0.384, Pr(>r)=0.032), F- (r^2=0.329, Pr(>r)=0.071), PO_4^{3-} (r^2=0.284, Pr(>r)=0.085), NH_4^+(r^2=0.307, Pr(>r)=0.078), and Zn (r^2 =0.320, Pr(>r)=0.071)

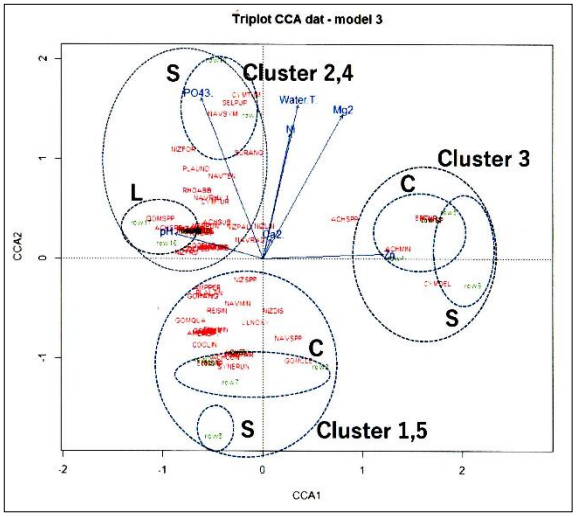

Fig. 7 Ordination by CCA based on triplot projections of the seven variables. Eigenvalues of CCA1 and CCA2 are 0.715 and 0.441, respectively. Study sites and area are expressed by numeric numbers (1–17) andfour capital letters: C = closed-mine area, S = serpentine area, L = limestone area, and R = reference area.Significant chemical variables were plotted as five vectors. Diatom species are expressed by CODE with four capital letters as followes;

CODE:ACHMIN=*Achnanthidium minutissimum*, ACHCON = *Achnanthidium convergens*, COCLIN= *Cocconeis lineata*, CYMDEL= *Cymbella delicatula*, SELPUP= *Sellaphora pupula.*

DISCUSSION

The values of exponential Shanon-Wiener diversity indices at four sites (st.4, st.5, st.9 and st.12) were significantly low, representing the effectiveness of three chemical variables (Zn, F^- and NH_4^+). The result of CCA also indicates the influence of those chemical variables on diatom communities (Fig.7). Those sites belonging to cluster 3 locate separately from other clusters (Figs.6, 7). In particular, diatom communities at st.4, st.5 and st.9 are mainly composed of *Achnanthidum minutissimum*, well known as a pollution-tolerant species [11]. In addition to that, from the result of CCA, we can see some influence of pH value on the communities at st.13 and st.14. It might be said that the influence of pH may be greater than the influence of the calcium ion (Ca^{2+}) . Diatom communities belonging to cluster 1 and 5 locate on the opposite side of chemical variables, and this location indicates that those communities are mainly composed of pollution-sensitive species such as *Cocconeis lineata*. It is possible to say that two chemical variables (Mg^{2+} and Ni) greatly affect the communities in the serpentine area, and that the pH value remarkably influences those in limestone areas. However, we need to consider many more factors, such as light, suspended solid invertebrates and so on, to control the diatom community composition.

CONCLUSION

It is clear that diatom communities are composed of very different species in areas with different geological characteristics of serpentine, limestone and closed-mine. In particular, zinc (Zn) partly affects the species composition in closed-mine and serpentine areas. However, it might be said that species composition in those communities is controlled by many factors such as substratum instability, light, suspended solid, invertebrates and fish. Geological characteristics of diatom habitats may be one of the important factors controlling their composition.

ACKNOWLEDGEMENTS

We gratefully thank Dr. Tomoko Shimodoi for the identification of diatom species and for providing us with much useful advice. We also thank Dr. Yoshinari (Idea Co.) and Dr. Taniguchi (Wakayama University) for help with analyzing the concentrations of chemical ions in stream waters and biostatistical analysis. Finally, we thank Dr. Noboru Nishimura (President of Hyogo Freshwater Biological society) for promoting our study in advance.

REFERENCES

[1] Allan J.D. and Castillo M.M., Stream Ecology – Structure and Function of Running Waters 2nd Edition, Springer, 2007, pp.106–107.

[2] Sheath R.G. and Cole K.M., Biogeography of stream macroalgae in North America, Journal of Phycology, Vol.28, 1992, pp.448–460.

[3] Stevenson R.J., An Introduction to Algal Ecology in Freshwater Benthic Habitats, Academic Press, 1996, pp.3–30.

[4] Nozaki K., Ecology of benthic invertebrate, Kawanabe H. and Mizuno N., Ed., Kodansha, 2013, pp.72–78.

[5] Brooks R.R., Serpentine And Vegetation - A Multidisciplinary Approach, Ecology, Phytogeography & Physiology series, vol.1, 1987, DIOSCORIDGE PRESS, Portland, Oregon, USA, pp.15–30.

[6] Borcard D., Gillet F., and Legendre P., Numerical ecology with R, Springer, New York, USA, 2011, pp.62; pp.107.

[7]Takada Y., Kajihara N., Sawada H., Mochizuki S., and Murakami T., Environmental factors affecting benthic invertebrate assemblages on sandy shores along the Japan Sea coast: implications for coastal biogeography, Ecological Research, Vol. 33 Number 1, 2018, pp.271–281.

[8]Maechler M., Rousseeuw P., Struyf A., Hubert K., Cluster: cluster analysis basics and extensions. R package version 2.0.6, 2017.

[9] Roberts DW., Labdsv: ordination and multivariate analysis for ecology. R package version 1.8-0., 2016.

[10]Oksanen J., Blanchert F.G., Friendly M., Kindt R., Legendre P., McGlinn D., Minchin PR., O'Hara RB., Simpson GL., Solymos P., Henry M., Stevens H., Sozoecs E., and Wagner H., Vegan: Community ecology package. R package version 2.0.6, 2017.

[11]Anazawa K., Kaida Y., Shinomura Y., Tomiyasu T., and Sakamoto H., Heavy-Metal Distribution in River Water and Sediments around a "Firefly Village", Shikoku, Japan: Application of Multivariate Analysis, ANALYTICAL SCIENCES, Vol.20, 2004, pp.79-84.

9th Int. Conf. on Geotechnique, Construction Materials and Environment, Tokyo, Japan, 20-22 November 2019, ISBN: 978-4-909106025 C3051

ANALYSIS OF WATER QUALITY OF RIVERS AND RESERVOIRS IN CHELYABINSK REGION, SOUTH URAL

Anastasiya M. Kostryukova, Irina V. Mashkova and Elena E. Shchelkanova
Chemistry Department, South Ural State University, Russia

ABSTRACT

Overland water resources of the Chelyabinsk region are presented by the basins of the Tobol, Ural, Volga (Kama) rivers. The total number or rivers exceeds 3.5 thousand, many of them are headwaters. This work assesses a ten-year change of water quality in 3 rivers and 3 reservoirs of the Tobol basin that are as well the source of drinking water for the residential area of the Chelyabinsk region. There are many ferrous, non-ferrous, power and machine building industry facilities in the region. As a result, most of the rivers in South Ural are affected by industrial and household wastewaters. Any significant improvement of the water quality in the studied rivers has not been monitored for 10 years. The water can be characterized as "polluted" - "very polluted". The Miass river has the most anthropogenic impact in the Chelyabinsk region. It used to be "extremely polluted". The given work aims to reveal interrelations between the water quality and the state of the studied water-bodies by means of principal component analysis. Principal component analysis allowed to distinguish 2 - 3 periods that are characterized by similar pollution. The environment of rivers under a human-made impact changes adversely and transforms into another ecological state for a couple of years.

Keywords: Rivers, Reservoirs, Pollution, Principal Component Analysis

INTRODUCTION

The pollution of natural waters, both sea and fresh, is a crucial issue all over the world [1]-[3]. Countries have various regulations that are aimed at assessing the environment of water-bodies and designing improvement strategies. The EU Water Framework Directive aims at improving the environment of all underground and overland waters in Europe [4], [5]. The Clean Water Act governs water pollution in the USA [6]. The Water Code of the Russian Federation addresses the issue in Russia [7]-[9].

Russia, as well as other countries, pays special attention to freshwater rivers and artificial reservoirs. The function of the national observation network in Russia is to control the pollution of overland waters, to monitor their environment and to analyze the overland water quality [10]. All the regions of the country including the Chelyabinsk region (South Ural) monitor chemical pollution of water-bodies [11]. According to the national report on environmental protection of 2017 [10] the Chelyabinsk region leads in the amount of wastewater discharge (691.3 million / $m^{3)}$ in the Ural Federal District.

More than 3.6 thousand rivers with a total length of about 18 thousand km run on the territory of the Chelyabinsk region. They belong to the basins of such large rivers of Russia as the Kama, the Tobol, the Ural. Most of the rivers are under an intensive man-made impact [11], [12].

Annual comprehensive reports on the environment in the Chelyabinsk region present information about chemical pollution of the large rivers of South Ural [11], [12]. It also refers to the rivers of the Tobol basin. Besides, separate studies of their environment and biota are being conducted [13], [14]. But these studies are scattered and do not usually consider one exact water-body and do not provide the long-term dynamics of water pollution.

The aim of the paper is to assess the change of water quality in the rivers of the Tobol basin as a source of drinking water in 2007-2016.

METHODOLOGY

Study Area

Three large rivers of more than 200 km, the Uy, the Uvelka, the Miass (Table 1), many smaller rivers such as the Syntashpy, the Ayat, the Kartaly-Ayat, the Kidysh, the Toguzak, the Sak-Alga, the Atkus, the Sinara, and three reservoirs Troitskoye, Argazinskoye, Shershnevskoye belong to the Tobol basin [15]. The head-rivers of the basin are mountain rivers (the Uy, the Miass) as they start in the Urals and then flow into the plain. The Tobol basin is 55 thousand km^2 [15].

The Uy river water in its chemical composition belongs to the hydrocarbonate class of the calcium group. Four towns, including Troitsk, are located in the Uy basin, as well as some villages where the river is the main water source. Troitskoye reservoir

with the volume of 45.1 million m^3 is built on the river [15], which flows mainly on farmland being polluted by effluents from cattle farms and fertilizers. The river is heavily affected by human activity within the limits of Troitsk where industrial and sewage facilities discharge effluents. Much of the pollution is then found in Troitskoye reservoir. The reservoir water in its chemical composition belongs to the hydrocarbonate class of the calcium group. Residential sewage comes into the river from all the catchment area.

Table 1 General characteristics of the Uy, Uvelka, Miass rivers

River	Total length, m	Maximum depth, m	Basin, km^2
Uy	462	15	34 400
Uvelka	234	4	5 820
Miass	658	7	21 800

The Uy river water in its chemical composition belongs to the hydrocarbonate class of the calcium group. Four towns, including Troitsk, are located in the Uy basin, as well as some villages where the river is the main water source. Troitskoye reservoir with the volume of 45.1 million m^3 is built on the river, which flows mainly on farmland being polluted by effluents from cattle farms and fertilizers. The river is heavily affected by human activity within the limits of Troitsk where industrial and sewage facilities discharge effluents [12]. Much of the pollution is then found in Troitskoye reservoir. The reservoir water in its chemical composition belongs to the hydrocarbonate class of the calcium group. Residential sewage comes into the river from all the catchment area [15].

The Uvelka is a left tributary, the largest one. Its water in its chemical composition belongs to the hydrocarbonate class of the calcium group. Like the Uy river, the Uvelka is polluted by farms, villages and industrial facilities of Yuzhnouralsk (a town in the Chelyabinsk region) [15].

The Miass river starts at the eastern slopes of the Ural [15]. It crosses all the forest-steppe zone of the Chelyabinsk region and then joins the Iset river. The Miass river water is widely used as a water supply for some cities including Chelyabinsk. Two reservoirs are built on the river: Argazinskoye and Shershnevskoye. Argazinskoye reservoir, the largest one, with the volume of 980 million m^3 [15], is the main source of water for the Chelyabinsk industrial hub. Shershnevskoye reservoir, with the volume of 176 million m^3 [15], is used as a water supply for Chelyabinsk [14]. The river water in its ion composition belongs to the hydrocarbonate class of the calcium group.

Effluents are discharged into the Miass river along its whole length. The river headwaters are the cleanest. Industrial and household effluents of Miass city come into the river water and then go into Argazinskoye reservoir. Along the way from Argazinskoye reservoir to Chelyabinsk sewage from farming and household activities of some villages are put into the Miass river. The river water then goes into Shershnevskoye reservoir where it is slightly cleaned. But the city industrial facilities and treatment plants of Chelyabinsk also discharge their effluents into the Miass river [12], [15].

Data of Monitoring of Chemical Pollution of the Studied Rivers and Reservoirs

To analyze the dynamics of how water quality in the Uy, Uvelka and Miass rivers, Troitskoye. Argazinskoye and Shershnevskoye reservoirs is changing, the data of monitoring chemical pollution of water-bodies in the Chelyabinsk region given in comprehensive reports on the environment of the Chelyabinsk region were taken. The reports are at an open access on the site of the Ministry of Ecology in the Chelyabinsk region [11], [12]. Monitoring sections are represented in Fig. 1.

Specific Combinatorial Water Pollution Index (SCWPI)

Specific combinatorial water pollution index (SCWPI) is used to assess water quality in Russia. RD 52.24.643-2002 [16] gives the methods of calculating the index.

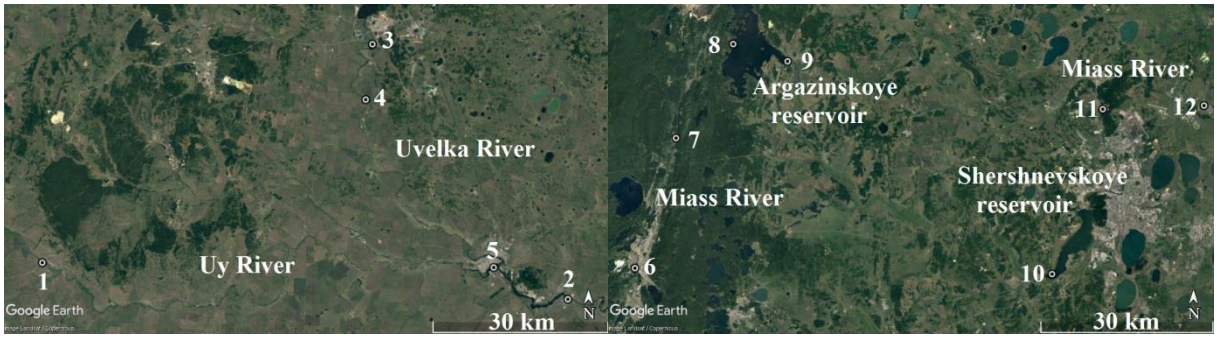

Fig. 1 Quick map of rivers and reservoirs of the Tobol basin (Chelyabinsk region).

It is calculated in 2 stages: first, each separate ingredient and pollution index is measured, and then all the pollutants are considered in complex, and the final assessment is given (Table 2). Maximum permissible concentration (MPC) of hazardous substance for fishery waters is taken for the standard.

Table 2 Effluent quality classification according to SCWPI [11]

Class	Category	Water pollution characteristics
1		conditionally clean
2		slightly polluted
3	a	polluted
	b	very polluted
4	a	dirty
	b	dirty
	c	very dirty
	d	very dirty
5		extremely dirty

RESULTS AND DISCUSSION

Monitoring of the Studied Water-bodies and Rivers Chemical Pollution

According to the Comprehensive reports on the environment in the Chelyabinsk region in 2007, 2008, 2012-2016 [11], average annual maximum permissible concentrations are exceeded for the following substances (Tables 3, 4).

Table 3 Intervals of pollutant concentration (C_i), C_i / MPC_i

Index	Uy river		Uvelka river		Troits-koye reservoir
	s. 1	s. 2	s. 3	s. 4	s. 5
Cu	2.0-4.0	1.6-3.5	1.8-4.2	2.2-4.2	1.9-4.1
Zn	2.9-12.0	2.7-9.6	2.7-3.6	3.0-3.7	2.8-13.7
Mn	11.9-45.6	5.7-9.5	4.0-7.5	12.0-26.2	6.2-13.9
Fe	2.3-4.0	-	-	1.1-1.8	-
PO_4^{3-}	-	1.1-1.5	-	1.1-3.5	-
SO_4^{2-}	1.4-2.4	1.5-2.0	1.2	1.1-6.8	1.3-2.8

Tables 3 and 4 show that such metals as Cu, Zn, Mn pollute the studied rivers and water-bodies constantly. Higher standard values for COD and petroleum products are registered in all the sampling sites. Phenols, Ni, sulfates and fluorides are rare, but that kind of pollution can't be called an isolated discharge, as the standard values for phenols, Ni, sulfates and fluorides are exceeded throughout the year.

Mn, Zn and Cu are registered as the main pollutants in all the sampling sites, except for 11 and 12.

Figure 2 shows the analysis of Mn content with the help of principal component analysis (PCA) for all monitoring period [17]. Most of the sampling sites are grouped in one locality and characterized by similar pollution. Sites 1, 4, 6 and 8 differ from the rest.

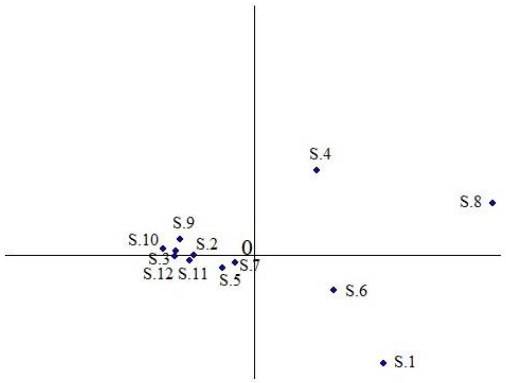

Fig. 2 Resulting diagram Mn content of PCA.

Exceeding of average annual Mn content over MPC in sampling sites 1 (the Uy river) and 8 (Argazinskoye reservoir) in some years was 45.6 - 47. Mining and ore-processing effluents come into the water of sampling site 1. Sampling site 2 is under an adverse impact of the Miass river tributary that is polluted by copper mining and processing facilities. Sewage, industrial and storm waters of Yuzhnouralsk are discharged into sampling site 4, site 6 is the head of the Miass river.

Figures 3 and 4 show the PCA of Cu and Zn content for all monitoring period. Unlike Mn, the situation with Cu and Zn is slightly different. Sampling site 8 is singled out of the rest with an average annual Zn content 2-5 and Cu 2.5-6 times higher than in the other sampling sites where these metals content in water is almost identical irrespective of the year.

Sampling sites 11 and 12 can also be marked. They are the furthest down the stream of the Miass river and take effluents from the city sewage systems, ferrous, non-ferrous, power and machine building facilities. The list of the main pollutants varies in sites 11 and 12. Mn is still leading with nitrites joining it in both sampling sites and petroleum products and phosphates being found in site 11.

Table 4 Intervals of pollutant concentration (C_i), C_i / MPC_i

Index	Miass river		Argazinskoye reservoir		Shershnevskoye reservoir	Miass river	
	s. 6	s. 7	s. 8	s. 9	s. 10	s. 11	s. 12
Cu	1.7-3.0	2.3-3.7	10.8-24.5	2.0-4.1	1.4-2.8	2.3-3.4	1.7-2.6
Zn	2.8-3.7	2.0-4.3	7.8-19.0	3.2-3.7	2.7-3.8	2.9-4.2	3.1-3.7
Mn	12.9-23.1	8.0-12.8	20.1-47.0	4.3-12.60	3.6-5.9	5.9-11.2	4.4-9.4
Fe	-	1.1-1.3	3.0-5.3	-	1.2	1.2	-
Ni	-	-	-	-	-	1.1-1.2	-
PO_4^{3-}	-	1.7-3.9	1.4-2.1	-	-	3.3-6.7	2.5-5.9
SO_4^{2-}	-	-	-	-	-	-	-
F^-	-	-	-	-	-	1.2	1.3
NO_2^-	-	3.2-6.7	1.2-2.5	-	-	3.8-12.3	2-12
NH_4^+	-	1.8-2.1	1.4	-	-	1.2-5.7	1.8-4.3
COD	2.0-2.4	2.1-2.6	1.5-2.3	1.5-1.9	1.9-2.2	2.1-3.1	2.2-2.9
BOD_5	1.2	1.1-1.7	-	-	1.2	1.8-3.0	1.6-2.5
Oil pipeline	1.2-1.5	1.4-1.9	1.3	1.2-1.3	-	3.9-10.2	2.8-6.8
Phenols	-	-	-	-	-	2	-

Fig. 3 Resulting diagram Cu content of PCA.

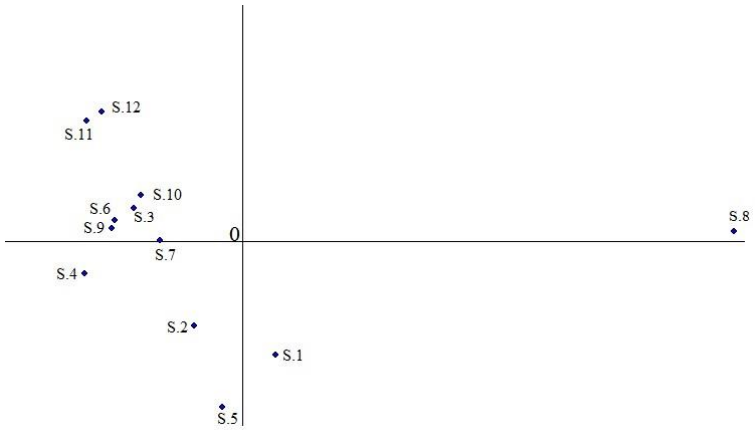

Fig. 4 Resulting diagram Zn content of PCA.

Water Quality Assessment of the Studied Rivers and Water-Bodies

Pollutant content ordination with the help of PCA for the sampling points in the Uy river, Troitskoye reservoir and its tributary (Fig. 5, a) and the Miass river and its reservoirs (Fig. 5, b) allows to distinguish 2-3 periods that are characterized by similar pollution.

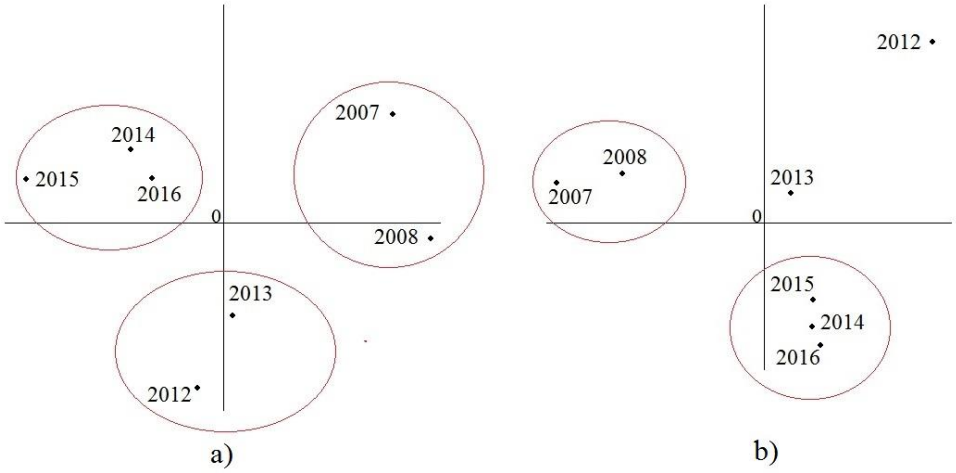

Fig. 5 Resulting diagram of PCA ordination of pollutants content in the Uy, Uvelka rivers, Troitskoye reservoir, the Miass river, Argazinskoye and Shershnevskoye reservoirs.

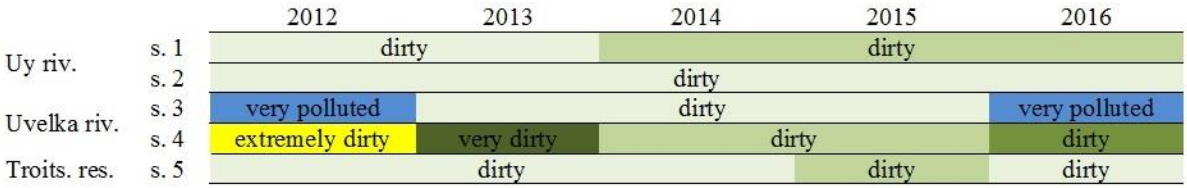

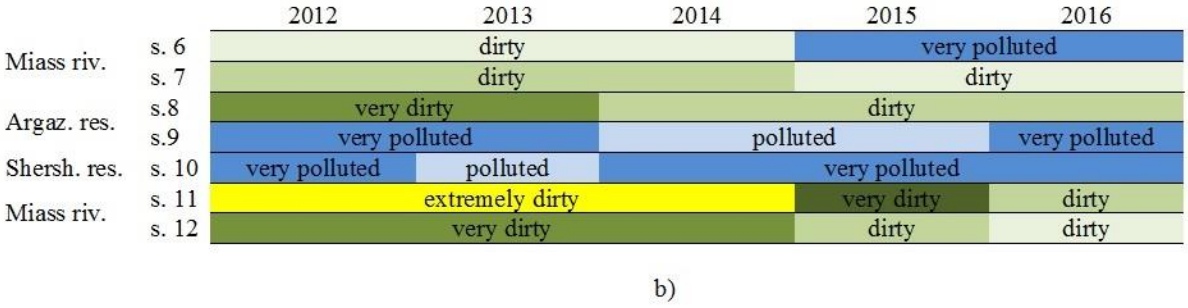

Fig. 6 Water pollution class of the studied rivers and reservoirs. Class 3 is blue, 4 - green, 5 - yellow. Colour density shows the category deterioration.

Thus, it can be noted that the environment of rivers under a human-made impact changes adversely and transforms into another category for a couple of years.

Figure 6 shows water pollution class of the studied rivers and reservoirs on the basis of specific combinatorial water pollution index (SCWPI) for 2012-2016. As the figure shows the water can't be called conditionally clean or slightly polluted. As these water-bodies are used as the main source of drinking water, there is a serious problem concerning the water quality and its influence on the population. Water quality is deteriorating downstream the rivers. The worst situation is in Chelyabinsk. Although, water quality in most of the sampling points is stated to become better since 2014-2015, the water is still not clean.

The situation is similar in many regions of Russia. Thus, the federal project "Clean Water" is designed within the limits of the national project [18]. The aim of the project is to improve drinking water quality by means of modern water supply and treatment systems with the help of innovative technologies. Its realization will provide 95.5 % of the city population with clean quality water.

CONCLUSIONS

Adverse environment of drinking water sources is one of the crucial issues of the Chelyabinsk region. Rivers and reservoirs of the Tobol basin have been

continuously polluted by the city sewage treatment facilities, industrial plants, agribusinesses, and spate flow. Higher concentrations of Cu, Zn, Mn, Fe, Ni, phosphates, sulfates, nitrites, ammonium ions, fluorides, COD, BOD_5, petroleum products and phenols were registered during the monitoring. Cu, Zn, Mn, COD and petroleum products are chronically exceeding the standard values. Unfortunately, water of the studied water-bodies in the Chelyabinsk region can't be qualified as satisfactory. In spite of some improvement the water is not clean enough. That is the matter of national concern, so the federal project "Clean Water" has been designed to tackle it.

REFERENCES

[1] Altenburger R., Brack W., Burgess R.M., Busch, W., Escher B.I., Focks A., Mark Hewitt L., Jacobsen B.N., de Alda M.L., Ait-Aissa S., Backhaus T., Ginebreda A., Hilscherová K., Hollender J., Hollert H., Neale P.A., Schulze T., Schymanski E.L., Teodorovic I., Tindall A.J., de Aragão Umbuzeiro G., Vrana B., Zonja B. and Krauss M., Future water quality monitoring: improving the balance between exposure and toxicity assessments of real-world pollutant mixtures, Environmental Sciences Europe, Vol. 31, Issue 1, 2019, pp. 12.

[2] Tian Y., Zheng B., Shen H., Zhang S. and Wang, Y., A novel index based on the cusp catastrophe theory for predicting harmful algae blooms, Ecological Indicators, Vol. 102, 2019, pp. 746-751.

[3] Lin C.-C., Lin J.-Y., Lee M. and Chiueh P.-T., Sector-wise mid site characterization factors for impact assessment of regional consumptive and degradative water use, Science of the Total Environment, Vol. 607-608, 2017, pp. 786-794.

[4] The EU Water Framework Directive - integrated river basin management for Europe, http://ec.europa.eu/environment/water/water-framework/index_en.html.

[5] Giakoumis T. and Voulvoulis N., The Transition of EU water policy towards the Water Framework Directive's integrated river basin management paradigm, Environmental Management, Vol. 62, Issue 5, 2018, pp. 819-831.

[6] United States Environmental Protection Agency. Summary of the Clean Water Act, https://www.epa.gov/laws-regulations/summary-clean-water-act.

[7] The Water Code of the Russian Federation (in Russian).

[8] Yasinskii S.V., Vishnevskaya I.A., Shaporenko S.I. and Bibikova T.S., Current problems in organizing water protection zones at water bodies: case study of the Uglich Reservoir, Water Resources, Vol. 45, Issue 4, 2018, pp. 490-502.

[9] Lopatin S.A., Redko A.A. and Terentyev V.I., The features of the establishment of zones of sanitary protection of the water source, Gigiena i sanitaria, Vol. 3, 2014, pp. 16-20.

[10] National report, On environment and environmental protection in the Russian Federation in 2017, Ministry of Natural Resources and Environment of the Russian Federation, Kadastr, 2018, pp. 81-151 (in Russian).

[11] Ministry of Ecology of the Chelyabinsk region, http://www.mineco174.ru.

[12] Ministry of Ecology of the Chelyabinsk Region 2016, Comprehensive report on the state of the environment of the Chelyabinsk region in 2016 (in Russian).

[13] Rogozin A.G., Zooplankton of the Argazi reservoir (Southern Urals, Russia) and its long-term changes, Inland Water Biology, 2013, Vol. 6, Issue 2, pp. 106-113.

[14] Mashkova I.V., Krupnova T.G., Kostryukova A.M. and Artyukov E.V., Determination of quality of water of a Shershnevskoe reservoir, International Multidisciplinary Scientific GeoConference Surveying Geology and Mining Ecology Management, SGEM, 2017, Vol. 17, Issue 31, pp. 191-198.

[15] Levit A.I., South Ural: Geography, Ecology, Nature Management, South Ural book publishing house, 2005, pp. 43-52 (in Russian).

[16] RD 52.24.643-2002, Comprehensive assessment methods of overland water pollution according to hydrochemical indices, (in Russian).

[17] Nowakowski A.B., Possibilities and principles of operation of the software module "Graphs". Automation of scientific research 7, 2004, (in Russian).

[18] Certificate of the federal project "Clean Water", http://www.minstroyrf.ru/docs/17692/ (in Russian).

9th Int. Conf. on Geotechnique, Construction Materials and Environment,

Tokyo, Japan, 20-22 November 2019, ISBN: 978-4-909106025 C3051

EFFECT OF SALINE SOIL ON GROWTH AND YIELD OF BLACK SESAME

Darika Bunphan[1*]

[1]Faculty of Technology, Mahasarakham University, Thailand

*Corresponding Author

ABSTRACT

Saline-soil is a major problem in northeast of Thailand. Several crops are sensitive with saline-soil, however some are moderate sensitive i.e. peanut, soybean and sesame. Sesame is moderate sensitive with saline-soil and drought tolerant, it is oil crop with short life cycle and attractive for being second crop, however, previous reports did not study on effect of saline-soil on growth and yield in black sesame clearly. Therefore, the objective was to study on effect of saline-soil on growth and yield in black sesame. The research was carried out in factorial in RCBD with three replications. The level of salinity was used as factor A, non-saline and saline soil (3 dS/m^{-2}) and six sesame cultivars were used as factor B. All black sesame was planted in pot with 9 kg soil contain. The results showed that all trait was not significant in 15 DAT except plant height. At 30 and 45 DAT, plant height, number of branches $plant^{-1}$, total chlorophyll content, number of capsules $plant^{-1}$ had significantly different whereas SCMR and chlorophyll fluorescence had response on level of saline-soil, however, these two traits of 6 cultivars were not significance. Total dry matter, capsule dry weight and harvest index at harvest day were significantly different. An interaction between salinity level and cultivar was found in all trait except plant height at 3 and 45 DAT, SCMR, total chlorophyll content and chlorophyll fluorescence.

Keywords: Salt tolerant, Saline soil, Black sesame, Agronomic traits

INTRODUCTION

Sesame (*Sesanum indicum* L.) is one of the oldest known oilseeds, with its origin being Central Africa is oilseed [1], it ranged the nine position among the most cultivated oilseed crops in the world and world production estimated at 3.5 M tons of grains [2]. It is widely used in food and in the nutraceutical, and pharmaceutical industry in many countries due to its high oil content, antioxidant and protein contents [3] and [4].

Sesame is cultivated in dry and semi-dry regions of the world where soil and/ or water salinization is common [5]. Sesame is an important oilseed crop rated moderately salt tolerance and capable of producing profitable crops in saline condition [6]. At seedling stage found that salinity reduced sesame growth [7]. Mahmood et al. [12] reported that salinity reduced growth, yield, yield components and oil content, but increased protein content of sesame cultivars. However, Ramirez et al. [8] evaluated sesame genotypes for their salt tolerance at germination, vegetative and maturity stages. Germination parameters, growth and yield of the genotypes increased under low salinity level, but decreased under high salinity level, they also detected high variability in tolerance to salinity among the genotypes. Gaballah et al. [9] also reported that low salinity level increased while high salinity level reduced growth parameters of sesame cultivars. The previous reports reviewed that sesame cultivars were subject to salinity stress using sandy soil [9] and [4].

In Thailand, sesame is second crop and it was planted after harvesting main crops because it is drought tolerance, short life cycle, it can be grown in marginal land and moderate sensitive with salt tolerance. In some area of northeast Thailand occupies with saline soil with low fertility and some crop cannot be grown. Therefore, sesame is one of the alternative crops for production in these area, however the study on sesame in saline soil is lacking especially in black sesame. The objective was to study on effect of saline-soil on growth and yield in black sesame.

MATERIALS AND METHODS

Plant Material

Six black sesame cultivars namely KU18, CM07, Kanchanaburi, Buriram, UBonratchathani3 and KKU2 were used. KU18 and CM07 were kindly donated from Kasetsart University, Kanchanaburi and UBonratchathani3 were donated from Ubon Ratchathani Farm Crops Research Center, KKU2 was kindly donated from Khon Kaen University.

Experimental Design

The experiment was conducted in Buriram province in plastic pots. It was randomized complete blocks in 2 × 6 factorial scheme (12 treatments), with three replications, a total of 72 experimental units. Factor A was two levels of soil salinity (A0 = no salt solution was added to soil in the pots and A1 = 27.45 g NaCl was added to soil and salinity was found 3 dS m^{-2}), Factor B was 6 cultivars of black sesame namely KU18 and CM07 were donated from Kasetsart University, KKU2 from Khon Kaen University, UB3 and Kanchanaburi from Ubonrachathani Field Crops Research Center and Buriram was donated from farmer. The pot was 20 cm diameter and 28 cm height, each pot contained 9 kg of soil. The soil properties with pH 7.25, EC 0.0067 dS m^{-2}, organic matter is 0.615%, exchangeable N is 21.09 mg kg^{-1} and soil texture is sand.

Agricultural Practice

After 15 days after planting (DAP), all of sesame was transplanted to 72 pots and 2 plants were transplanted in each pot, 27.45 g NaCl was mixed with soil and contained in 36 pots and other 36 pots had 0 g NaCl. Chemical fertilizer (NPK) at rate 156.25 kg ha^{-1} was applied as basal fertilizer and applied the same rate at 30 days after transplanting.

Data Collection

The following data were recorded at 15 30 and 45 days after transplanting and harvesting day. Plant height measurement: it was considered from the soil surface to the tip of sesame, no. of branches/plant; was recorded primary branch of sesame. The SCMR was measured using by SPAD-502 meter (Minolta SPAD-502 meter, Tokyo, Japan). The chlorophyll content in leaves was measured by the method described by Moran [10] Briefly, the leaf was cut one small leaf disc with the area 1 cm^2 using cork border, the leaf disc was placed in a vial containing 5 ml DMF (N, N-dimethyl formamide) and incubated in 4 °C for 24 h in dark. The chlorophyll extract was measured at 647 and 664 nm by a spectrophotometer. The equations to calculate for total chlorophyll, chlorophyll a (Chl a) and b (Chl b) were as follows: Chl a = 12.64 A664-2.99 A647, Chl b= -5.6 A664+23.24 A647, expressed in µg cm^{-2}. The CF was measured two positions in the middle of leaf and midrib was avoided, Fv/Fm was used and averaged as a single value, the CF was measured using chlorophyll fluorescence meter (PAM-2000, Heinz Walz GmbH, Germany). The measured leaf was dark-adapted for 30 min using leaf clips (FL-DC, Opti-Science) before fluorescence measurements. The chlorophyll fluorescence was determined following the procedures of Maxwell and Johnson [11]. Number of capsules $plant^{-1}$, total dry matter $plant^{-1}$, pod dry weight $plant^{-1}$, harvest index (HI) was recorded at physiological maturity.

Statistical Data Analysis

Analysis of variance (ANOVA) was conducted on the collected data using STATISTICS 9 and treatment means were separated using LSD at 5 % probability level.

RESULTS

Analysis of variance

At 15 DAT, SCMR, Total chlorophyll content and chlorophyll fluorescence were not significantly different and we did not found interaction between salinity level and sesame cultivars, plant height at 15 DAT was not significant when compared between non-saline and saline soil, however we found significantly plant height among six sesame cultivars and interaction between salinity level and sesame cultivar.

At 30 DAT, number of branches per plant, number of pods per plant were significantly different and we found interaction between salinity level and sesame cultivar. However, plant height showed significantly different both in salinity level and sesame cultivar but we did not found interaction in salinity and cultivar. SCMR and chlorophyll fluorescent were significantly in salinity level but they had no significant among cultivar and we did not found interaction between salinity level and cultivar. Total chlorophyll content was significant among sesame cultivar but it was not significant in salinity level and it had no interaction between salinity level and sesame cultivar.

At 45 DAT, number of pods per plant was significantly different and we found interaction in salinity level and sesame cultivar. We did not found

interaction in plant height but we found in number of branches per plant.

We found interaction between salinity level and sesame cultivar in total dry weight, pods dry weight and harvest index. Moreover, salinity level and sesame cultivar had significantly different of these traits but HI was not different when compared in salinity level.

Effect of salinity level on six sesame cultivars

Plant height at 15 DAT, CM07, UB3, Kanchanaburi and Buriram had higher than KKU2 and KU18. We found interaction in plant height at 15 DAT but did not find in 30 and 45 DAT. At 15 DAT when considered salinity level and sesame cultivar we found that Kanchanaburi in non-saline soil showed the highest plant height (31. cm) following Buriram, UB3 and CM07 (29.8, 28.2 and 28.0 cm respectively) when planting in saline soil.

KKU2 with non-saline soil had the highest number of branches plant^{-1} following UB3 and Kanchanaburi. At 45 DAT, CM07 with non-saline soil had the highest number of branches but it was not different to UB3 in saline soil (3.5 and 3.0 branches respectively). At 30 and 45 DAT, KKU2, UB3 and Kanchanaburi had the higher plant height.

We found interaction in number of branches per plant at 30 and 45 DAT. At 45 DAT, CM07 with non-saline soil had the highest number of branches but it was not different to UB3 in saline soil (3.5 and 3.0 branches respectively).

We did not find interaction between salinity level and cultivar in SCMR, total chlorophyll content and chlorophyll fluorescence at 15 and 30 DAT. However, at 30 DAT we found the difference of SCMR between salinity level. Total chlorophyll content at 30 DAT among six cultivars were significantly different and KKU2 had the highest chlorophyll content when compared to other five cultivars.

Number of capsules per plant at 30 and 45 DAT were significantly different and it had interaction between salinity level and cultivar. Number of capsules per plant in non-saline soil had higher than planting in saline soil both at 30 (10.7 and 5.4 capsules respectively) and 45 (9.6 and 5.1 capsules respectively) DAT. KKU2 had the highest capsules per plant both in 30 and 45 DAT (16.1 and 11.9 capsules). KKU2 in non-saline soil showed the highest number of capsules both at 30 and 45 DAT (21.3 and 17.3 capsules respectively) and higher than cultivars planting in saline soil, however at 30 DAT KKU2 planting in saline soil had higher capsules than other five cultivars that planting in saline soil. In the other hand, at 45 DAT Kanchanaburi planting in saline soil showed higher capsules than other five cultivars.

Total dry weight per plant in non-saline soil was higher than planting in saline soil (2.59 and 1.07 g respectively), KKU2, UB3, Kanchanaburi and Buriram had higher total dry weight that CM07 and KU18. Moreover, KKU2 planting in non-saline soil showed higher total dry weight that other cultivars. In saline soil, Kanchanaburi had higher total dry weight than other cultivars.

Capsules dry weight per plant in non-saline soil was higher than in saline soil (1.10 and 0.44 g respectively) and Buriram had higher capsules dry weight than other five cultivars. Moreover, Buriram in non-saline soil had higher capsules weight than other cultivars, however Kanchanaburi planting in saline soil had higher capsules dry weight than other cultivars.

HI was not different between salinity level, Buriram had highest HI that other cultivars. When planting in non-saline soil Buriram had highest HI, following KU18 planting in saline soil, UB3 planting in non-saline soil, UB3 and Kanchanaburi planting in saline soil

DISCUSSION

Many previous researches studied on effect of salinity to sesame, however they did not study on black sesame, some study used $CaCl_2$ and they found that salinity level had effect to dry matter and leaf area on sesame [12], it similar to our study that salinity affected to total dry matter. Suassuna et al. (2017) [13] and Bahrami et al. [14] reported that saline stress affected to reducing of plant height and number of capsules and theirs result were accordance to present study, in contrast to Gaballah et al. [9] reported that low salinity level increased while high salinity level reduced sesame height and there were significant differences between the cultivars for this trait. Their results were different with ours perhaps due to differences between salinity level, plant genotypes and environmental conditions. Reduction in the plant height could be due to drought stress caused by salt on water adjustment in plant tissues and cell enlargement as well as increase in leaf senescence and abscission [15].

Many previous studies varied salinity level but present study has set only 2 level of salinity (non-saline soil and slightly saline soil) because sesame is moderated sensitive salt tolerance. Moreover, our study used black sesame as a treatment and previous study did not clearly reported. Bahrami et al. [14] reported that plant height was negatively affected by salinity level, as salinity level increased number of

capsules per plant decreased, root dry weight, seed yield, 1000 seeds weight and oil content, some result was similar to our study however, our study did not focus on root dry weight. Present study also focused on SCMR, total chlorophyll content and chlorophyll fluorescence but previous study did not report. Reduction in the number of capsule per plant was perhaps due to reduction in the plant height and roots and shoots growth [14]. Not only capsules in sesame decreased as increased salinity level, but also canola [16].

In present study only study effect of saline soil in black sesame and root traits were not focused, in further study we would focus on white and red sesame and more traits would be studied.

CONCLUSIONS

Sesame is moderate sensitive with saline soil. Saline soil has effect to growth and yield of black sesame. All trait of black sesame when planting in saline soil decreased except at 15 DAT. At 30 and 45 DAT, plant height, number of branches plant^{-1}, total chlorophyll content, number of capsules plant^{-1} had significantly different whereas SCMR and chlorophyll fluorescence had response on level of saline-soil, however, these two traits of 6 cultivars were not significance. Total dry matter, capsule dry weight and harvest index at harvest day were significantly different. An interaction between salinity level and cultivar was found in all trait except plant height at 3 and 45 DAT, SCMR, total chlorophyll content and chlorophyll fluorescence.

ACKNOWLEDGMENTS

This research was supported by a grant from the National Research Council of Thailand. I am thankful the Department of Agricultural Technology, Faculty of Technology Mahasarakham University. The author would like to thank Kasetsart University, Kalasin University, Ubonrachathani University for kindly donated sesame seeds for our research.

Table 1 Effect of salinity level on plant height, number of braches per plant, SCMR, total chlorophyll content and chlorophyll fluorescence of black sesame

	Plant height (cm)			Number of branches per plant		SCMR (SPAD unit)		Total chlorophyll content (µg cm^{-2})		Chlorophyll fluorescence	
	15 DAT	30 DAT	45 DAT	30 DAT	45 DAT	15 DAT	30 DAT	15 DAT	30 DAT	15 DAT	30 DAT
Salinity level (A)											
Non-saline soil (A1)	24.7	50.3a	52.2a	2.1a	2.3	34.2	44.0a	5.86	10.72	0.810	0.825a
Saline soil (A2)	25.6	36.2b	42.3b	1.7b	2.1	35.0	38.6b	5.55	10.41	0.812	0.809b
Sesame cultivar (B)											
KU18 (B1)	18.8c	30.2c	35.1b	1.3b	1.3b	32.0	36.5	5.38	10.05b	0.809	0.809
CM07 (B2)	26.6a	40.2b	41.8b	2.3a	2.7a	35.6	42.4	6.38	10.68b	0.812	0.817
KKU2 (B3)	23.1b	53.8a	58.7a	2.3a	2.6a	36.5	46.8	5.49	12.56a	0.812	0.83
UB3 (B4)	27.7a	45.4ab	52.2a	1.9a	2.7a	34.7	38.4	5.60	10.52b	0.811	0.813
Kanchanaburi (B5)	26.6a	50.8a	56.1a	2.2a	2.5a	34.0	41.8	5.68	10.13b	0.809	0.818
Buriram (B6)	28.0a	38.9bc	39.7b	1.4b	1.6b	34.8	41.9	5.70	9.43b	0.813	0.817
A*B											
A1 x B1	16.1e	37.9	40.9	1.3e	1.3d	31.6	40.2	5.64	9.76	0.812	0.82
A1 x B2	25.2cd	41.4	41.4	3.0a	3.5a	36.5	45	6.62	11.5	0.807	0.82
A1 x B3	21.4d	63.3	65.9	2.7ab	2.7b	34.8	49.3	5.55	12.38	0.811	0.842
A1 x B4	27.3bc	56.1	57.2	2.3abc	2.3bc	34.1	44.4	5.75	11.17	0.808	0.83
A1 x B5	31.8a	60.7	61.8	2.3abc	2.5bc	33.4	43.6	6.33	10.5	0.812	0.824
A1 x B6	26.3bc	42.3	46.2	1.3e	1.8cd	34.6	41.5	5.28	9.02	0.808	0.816
A2 x B1	21.4d	22.4	29.3	1.3e	1.3d	32.4	32.7	5.13	10.35	0.807	0.799
A2 x B2	28.0abc	39.1	42.1	1.7cde	1.8cd	34.7	39.8	6.14	9.89	0.816	0.814
A2 x B3	24.8cd	44.3	51.5	2.0bcd	2.5bc	38.3	44.3	5.42	12.74	0.814	0.819
A2 x B4	28.2abc	34.8	47.2	1.5de	3.0ab	35.3	32.4	5.45	9.87	0.814	0.796
A2 x B5	21.4d	41	50.5	2.0bcd	2.4bc	34.6	40	5.03	9.77	0.806	0.812
A2 x B6	29.8ab	35.5	33.3	1.5de	1.5d	35	42.3	6.12	9.83	0.817	0.817
F-test											
A	ns	**	**	**	ns	ns	**	ns	ns	ns	*
B	**	**	**	**	**	ns	ns	ns	**	ns	ns
A*B	**	ns	ns	*	**	ns	ns	ns	ns	ns	ns
CV (%)	10.43	17.88	17.12	22.03	20.05	9.86	13.83	14.95	11.07	0.98	2.41

Ns,* and **; not significant, significantly different at 95 and 99% respectively.

Table 2 Effect of salinity level on number pf capsules per plant, total dry weight, capsule dry weight per plant and HI of black sesame

	Number of capsules/plant		TDW (g/pl)	CDW (g/pl)	HI (%)
	30DAT	45DAT			
Salinity level (A)					
Non-saline soil (A1)	10.7a	9.6a	2.59a	1.1.10a	42.4
Saline soil (A2)	5.4b	5.1b	1.07b	0.44b	40.4
cultivar (B)					
KU18 (B1)	3.2d	3.0e	0.64c	0.25d	43.8ab
CM07 (B2)	5.5c	4.6d	1.36b	0.52c	37.7bc
KKU2 (B3)	16.1a	11.9a	2.47a	0.81b	34.4c
UB3 (B4)	7.4b	8.0b	2.06a	0.95b	45.5a
Kanchanaburi (B5)	8.8b	10.5a	2.21a	0.95b	40.0abc
Buriram (B6)	7.2b	6.3c	2.25a	1.15a	47.0a
A*B					
A1 x B1	3.8f	3.9gh	0.88ef	0.31ef	34.8d
A1 x B2	7.5cd	6.8def	1.66c	0.65c	39.6cd
A1 x B3	21.3a	17.3a	4.08a	1.31b	33.0d
A1 x B4	11.0b	10.5bc	2.70b	1.33b	49.4bc
A1 x B5	10.8b	11.9b	3.22b	1.19b	37.3d
A1 x B6	9.8bc	7.2de	3.00b	1.78a	60.4a
A2 x B1	2.5f	2.0i	0.40f	0.20f	52.8ab
A2 x B2	3.5f	2.3hi	1.05de	0.38def	35.9d
A2 x B3	11.0b	6.5def	0.85ef	0.31ef	35.9d
A2 x B4	3.8f	5.5efg	1.42cde	0.57cd	41.5cd
A2 x B5	6.8de	9.1cd	1.20cde	0.70c	42.8bcd
A2 x B6	4.7ef	5.3fg	1.54cd	0.51cde	33.6d
F-test					
A	**	**	**	**	ns
B	**	**	**	**	*
A*B	**	**	**	**	**
CV (%)	16.90	14.92	19.58	16.76	15.48

Ns,* and **; not significant, significantly different at 95 and 99% respectively.

TDW; Total dry weight, CDW; Capsule dry weight

REFERENCES

[1] Cattan P. and Schiling, R. Sesame cultivation in tropical Africa. Oleagineux, 46, 1991, pp.129-13.

[2] Silva E.R., Martino H.S.D., Moreira A.V.B., Arriel A.C. and Ribeiro S.M.R. Capacidade antioxidante e composição química de grãos integrais de gergelim creme e preto. Pesquisa Agropecuária Brasileira, Brasília Vol.46 Issue7, 2011, pp.736-742.

[3] Morris J.B. Food, industrial, nutraceutical and pharmaceutical uses of sesame genetic resources. Janick J, Whipkey VA. 2002, pp. 153-156.

[4] Koca H., Bor M., Ozdemir F. and Turkan, I. The effect of salt stress on lipid peroxidation, antioxidative enzymes and proline content of sesame cultivars. Environmental and Experimental Botany, Vol.60, 2007, pp. 344-351.

[5] Yousef Y. H., Bingham F. T. and Yemanos D. M. Growth, mineral composition and seed oil of sesame *(Sesamum indicum* L.) as affected by NaCl. Soil Science Society of America Journal, Vol.36,1972, pp. 450-453.

[6] Bahrami H, Effect of salinity stress (NaCl) on germination and early seedling growth of ten sesame cultivars (*Sesamum indicum* L.). International Journal of AgriScience, Vol. 2, Issue 6, 2012, pp.529-537.

[7] Yahya, A. Salinity effects on growth and on uptake and distribution of sodium and some essential mineral nutrients in sesame. Journal of Plant Nutrition, Vol.21, 1998, pp.1439-1451.

[8] Ramírez R., Gutiérrez D., Villafañe R. and Lizaso J.I., Salt tolerance of sesame genotypes and germination, vegetative and maturity stages. Communication in Soil Science and Plant Analysis Vol.36 Issue17-18, 2007, pp.2405-2419.

[9] Gaballah, M. S., Abu Leila, B., El-Zeiny, H. A., & Khalil, S., Estimating the performance of salt- stressed sesame plant treated with antitranspirant. Journal of Applied Sciences Research, Vol. 9, 2007, pp.811-817.

[10] Moran R., Formulae for determination of chlorophyllous pigments extracted with N, N dimethylformamide, Plant Physiology Vol.69, 1982, pp.1376-1381.

[11] Maxwell K. and Johnson G.N., Chlorophyll fluorescence-A practical guide, Journal of Experimental Botany Vol.51, No.345, 2000, pp. 659-668.

[12] Mahmood, S., Iram, S., Ather, H. R. (2003). Intra-specific variability in sesame (Sesamum indicum L.) for various quantitative and qualitative attributes under differential salt regimes. Pakistan Journal of Science and Industrial Research, 14, 177-186.

[13] Suassuna J.F., Fernandes P.D., Brito M.E.B., Arriel N.H.C., de Melo A.S., Fernandes J.D., Tolerance to salinity of sesame genotypes in different phenological stages. American Journal of Plant Sciences Vol.8, 2017, pp. 1904-1920.

[14] Bahrami H., Jafari A.O. and Razmjoo J., Effect of salinity levels (NaCl) on yield, yield components and quality content of sesame (*Sesamum Indicum* L.) cultivars. Environmental Management and Sustainable Development Vol.5 No.2, 2016, pp. 104-117.

[15] Jaleel C. A., Gopi R., Manivannan P. and Panneveerselvam R., Soil salinity alters the morphology in carthamus roseus and its effects on endogenous mineral constituents. EurAsia. Journal of Biosciences, Vol.2, 2008, pp. 18-25.

[16] Bybordy A. Effect of salinity on yield and components characters in canola (*Brassica napus* L.) cultivars. Notulae Scientia Biologicae, Vol.2, 2010, pp.81-83.

9th Int. Conf. on Geotechnique, Construction Materials and Environment, Tokyo, Japan, 20-22 November 2019, ISBN: 978-4-909106025 C3051

QUANTITATIVE EVALUATION OF BUCKLING STRENGTH OF DAMAGED COLUMNS

Yazid Alkhatib, Hani Doummar and Yoshitaka Suetake
Graduated School of Engineering, Ashikaga University, Japan

ABSTRACT

The objective of the present investigation is to find an approach for evaluating buckling strength of damaged columns. Because of wars, natural disasters, explosion, or overloading, a lot of structures has been damaged in different levels. Some of these damaged structures can be repaired and reused by specifying their damaged levels. In order to do that, we focus on damaged levels of structural members through the buckling strength of column members. In the present investigation, the damage columns is represented by partial loss of their sections, which is modeled by step-formed changing cross sections. In addition, a damage index, which indicates damage levels, is defined by using the critical loads of damaged and non-damaged columns. Several numerical calculations are performed in order to study the efficiency of the present damage index. Especially, influences of the boundary conditions and the section parameters to the damage index are discussed through the numerical results.

Keywords: Buckling, Columns, Damaged index, Variable cross section

INTRODUCTION

Damaged members or damaged structures are found in natural disaster areas or war damaged areas. If the damage is not serious, however, we can repair the members or the structures and reuse them sometimes. In order to do that, we have to evaluate the level of the damage appropriately. Especially, we have to know the remaining strength of the members or the structures.

For columns, members are subjected to axial force, the buckling strength is one of the most important points of view. Therefore, in damaged members, it is also important to understand buckling behavior of damaged columns and to estimate critical loads. Investigation of the critical loads of columns has become the center of attention and got more and more systematic during the second half of the 20th century.

The problem is how to represent the damage columns. In the present investigation, it is represented by partial loss of their sections, which is modeled by step-formed changing cross sections. Therefore, we have to calculate the critical loads of columns with non-uniform sections. The determination of critical loads of columns with non-uniform cross-section can be a complex task that depends on several parameters and boundary conditions.

In the present investigation, the classical energy method is employed for determining the critical loads of the damaged columns. Since the energy method is approximate approach, we have to make sure the accuracy of the solutions. In this paper, a part of the numerical results is compared with the result obtained by the exact approach.

On the other hand, damage level of the columns also have to be evaluate appropriately. Damage levels of the structure and their corresponding displacements could be presented both qualitatively and quantitatively (based on the performance-based design method). For quantitative evaluation of damage level in structures, a damage index is used. Researchers have proposed several functions based on the nonlinear dynamic and cyclic behavior of the structural members for quantitative evaluation of damage. On the other hand, for evaluation of the damage index, various uncertain parameters such as load and resistance exist [1]. In this paper, we will focus on the definition based on the reduced stiffness [2] formulated with the following expression:

$$DI = 1 - \left[\frac{K_{final}}{K_{initial}} \right] \tag{1}$$

Where DI is the damage index, $K_{initial}$ is the initial stiffness or the initial tangent before the damaged impact and K_{final} is the tangent of the curve after the damaged impact. The amount of DI ranges from zero to one; zero represents no damages and one represents incipient collapse of the structure. Calibration of damage indices performed as [3] are presented in Table 1, as well as the degree of observed damage in the structures.

Table 1 Interpretation of the Damage Indices [4]

Degree of Damage	Damage Index, DI	State
Collapse	> 1.0	Loss of building
Severe	0.4 - 1.0	Beyond repair
Moderate	< 0.4	Repairable
Minor/Slight	< 0.2	

In this paper, we adopt Eq. (1) as the definition of the damage index. Then, we use the critical loads for columns with a uniform section as $K_{initial}$ and the one for columns with non-uniform sections as K_{final}.

Several numerical examples are performed in this paper. Especially, influences of the boundary conditions and the section parameters are discussed through the numerical results. It follows from the numerical results that the present damage index is effective to evaluate the buckling strength of the damaged columns.

METHODOLOGY OF ANALYTICAL MODEL

In this paper, damaged columns are modeled by using columns with step-formed changing cross sections. In order to calculate critical loads of the step-formed columns, two classical approaches are employed here; one is the eigenvalue analysis of the governing equations and the other is the energy method.

As an example, a two-steps column is used here. In the analyses, we assume that the line that goes through the centroids of all cross-sections is straight. In addition, the following assumptions are made: the column is assumed to be made of homogeneous material that obeys Hooke's law, the load P is concentrated and the deformations of the column are small.

Eigenvalue Analysis

In this section, we explain the eigenvalue analysis of the column buckling [5]. As an example, we treat with a two-steps cantilever type column as shown in Fig. 1. The compression load P acts at the top of the column, the point B.

As well-known, the governing equations of this column buckling are given by

$$\frac{d^2 y_1}{dx^2} + k_1^2 = k_1^2 \delta \quad ; \quad k_1^2 \equiv \frac{P}{EI_1} \ (i = 1, 2) \qquad (2)$$

where y is the deflection of the column, δ the deflection of the free end, E Young's modulus, and I the moment inertia of area. The subscript i represents a region of the column. The general solutions are

$$y_1(x) = D_{2i-1} \sin k_i x + D_{2i} \cos k_i x + \delta \qquad (3)$$

where D_i $(i = 1 \sim 4)$ are arbitrary constants.

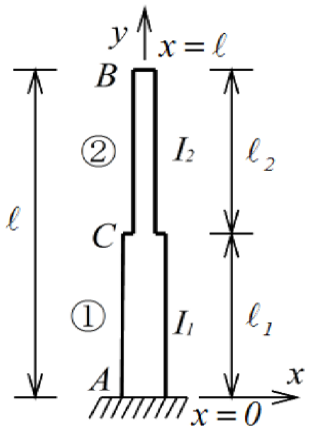

Fig. 1 Cantilever type two-steps column

The boundary conditions and the continuity conditions at the intermediate point C are as follows:

$$y_1(0) = 0 \quad , y_1'(0) = 0 \ , \ y_2(\ell) = \delta \qquad (4)$$

$$y_1(\ell_1) = y_2(\ell_1) \quad , \ y_1'(\ell_1) = y_2'(\ell_1) \qquad (5)$$

Applying these conditions to the general solu tions, we have the following matrix notation f or determining the arbitrary constants: (6)

$$\begin{bmatrix} \sin k_2\ell & \cos k_2\ell & 0 \\ \sin k_2\ell_1 & \cos k_2\ell_1 & \cos k_1\ell_1 \\ -k_2\cos k_2\ell_1 & k_2\sin k_2\ell_1 & k_1\sin k_1\ell_1 \end{bmatrix} \begin{Bmatrix} D_3 \\ D_4 \\ \delta \end{Bmatrix} = \begin{Bmatrix} 0 \\ 0 \\ 0 \end{Bmatrix}$$

A necessary and sufficient condition such that this equation has a non-trivial solution is that the determinant of the coefficient matrix of Eq. (6) becomes zero. Thus we have

$$(k_1 / k_2) \tan k_1\ell_1 \tan k_2\ell_2 = 1 \qquad (7)$$

The solutions of Eq. (7) are the eigenvalues of the coefficient matrix of Eq. (6) and the minimum eigenvalue corresponds to the critical load of the column.

For given values of I_2/I_1 and ℓ_1/ℓ, the critical load parameter $k_1\ell$ can be calculated by using the Newton Method as shown in Table 2.

The values in Table 2 are regarded as standard values in this paper.

Table 2 Critical load parameter (standard)

I_2/I_1 \ ℓ_1/ℓ	0.2	0.4	0.6	0.8
0.1	0.606	0.775	1.060	1.465
0.2	0.836	1.027	1.294	1.527
0.4	1.128	1.292	1.459	1.555
0.6	1.321	1.430	1.520	1.564
0.8	1.462	1.515	1.552	1.568

The same approach can be also used when number of steps in cross sections is greater than the above example. Naturally, with an increase in the number of steps, it is difficult to apply the eigenvalue analysis to calculations of critical load of columns. Therefore, it is desirable to use alternative approximate methods.

Energy Method

As an alternative approximate method, the energy method [5] is adopted in this investigation.

The internal energy of columns ΔU is given by

$$\Delta U = \int_0^\ell \frac{M^2}{2EI} dx = \frac{1}{2E} \int_0^\ell \frac{M^2}{I} dx \tag{8}$$

On the other hand, the external energy ΔT is given by the multiplication of the compression load P and the axial displacement, $\Delta\ell$, that is,

$$\Delta T = P\Delta\ell = \frac{P}{2} \int_0^\ell (\frac{dy}{dx})^2 dx \tag{9}$$

Since $\Delta U = \Delta T$ when the compression load P is equal to the critical one, we can obtain the following formula for determining the critical load:

$$\frac{1}{EP} = \int_0^\ell \frac{M^2}{I} dx = \int_0^\ell (\frac{dy}{dx})^2 dx \tag{10}$$

One end free and the other end fixed

We deal with the cantilever type column as shown in Fig. 1 in this subsection. First, we assume a buckling shape as

$$y(x) = \delta(1 - \cos\frac{\pi}{2\ell} x) \tag{11}$$

Substituting Eq. (11) into Eq. (10), in view of $M = P(y - \delta)$ for the cantilever type column, we can obtain the critical load parameter $k_1\ell$ as

$$K_1\ell = \sqrt{\frac{p_{cr}}{EI}}\ell = \frac{\pi}{2\sqrt{\alpha}} \tag{12}$$

$$;\alpha \equiv \frac{\hat{\ell}_1}{\hat{I}_1} + \frac{\hat{\ell}_2}{\hat{I}_2} + \frac{1}{\pi}(\frac{1}{\hat{I}_1} - \frac{1}{\hat{I}_2}) \sin \pi \hat{\ell}_1$$

where $\hat{I}_i \equiv I_i / I$ is a non-dimensional moment inertia, $\hat{\ell}_i \equiv \ell_i / \ell$ a non-dimensional length, and I a standard moment of inertia. The results calculated by Eq. (12) is shown in Table 3.

Table 3 Critical load parameter (cantilever)

I_2/I_1 \ ℓ_1/ℓ	0.2	0.4	0.6	0.8
0.1	0.615	0.819	1.147	1.489
0.2	0.845	1.061	1.333	1.532
0.4	1.133	1.306	1.467	1.556
0.6	1.323	1.434	1.522	1.564
0.8	1.462	1.515	1.551	1.568

Comparison of the results of Table 3 with those of Table 2 shows that the maximum error is 8.67%. Therefore, the approximation by using the energy method gives us satisfactory results. In this paper, we employ the energy method for the analyses of columns under the other boundary conditions.

Both ends fixed

We deal with columns with both ends fixed as shown in Fig. 2 in this subsection. We assume a buckling shape as

$$y = -\frac{M_0}{P}(1 - \cos\frac{2\pi x}{\ell}) \tag{13}$$

Substituting Eq. (13) into Eq. (10), in view of

$$M = -M_0 \cos\frac{2\pi x}{\ell} \tag{14}$$

we can obtain the critical load parameter $k_1\ell$ as

$$K_1\ell = \sqrt{\frac{p_{cr}}{EI}}\ell = \frac{2\pi}{\sqrt{\beta}} \tag{15}$$

$$;\beta \equiv (\frac{1}{\hat{I}_1} - \frac{1}{\hat{I}_2})(\hat{\ell}_1 + \frac{1}{4\pi} \sin 4\pi \hat{\ell}_1) + \frac{1}{\hat{I}_2}$$

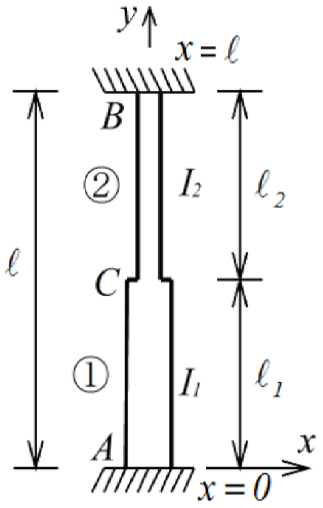

Fig. 2 Two-steps column with both ends fixed

The results calculated by Eq. (15) is shown in Table 4.

Table 4 Critical load parameter (fixed ends)

I_2/I_1 \ ℓ_1/ℓ	0.2	0.4	0.6	0.8
0.1	2.253	2.361	3.174	3.501
0.2	3.137	3.265	4.145	4.457
0.4	4.305	4.428	5.153	5.368
0.6	5.127	5.217	5.697	5.822
0.8	5.764	5.811	6.043	6.098

One end hinged and the other end fixed

We deal with columns with one end hinged and the other end fixed as shown in Fig. 3 in this subsection. We assume a buckling shape as

$$y(x) = -\frac{M_A}{P}\{\frac{\sin k_0(\ell - x)}{\sin k_0 \ell} - \frac{(\ell - x)}{\ell}\} \tag{16}$$

Substituting Eq. (16) into Eq. (10), in view of

$$M = \frac{M_A}{\sin k_0 \ell}\sin k_0(x - \ell) \tag{17}$$

we can obtain the critical load parameter $k_1\ell$ as

$$k_1 l^2 = \sin k_0 \ell \sqrt{\frac{2k_0{}^3\ell^3}{\gamma}}$$

$$;\gamma \equiv (\frac{1}{\hat{I}_1} - \frac{1}{\hat{I}_2})(\hat{\ell}_1 + \frac{1}{4\pi}\sin 4\pi\hat{\ell}_1) + \frac{1}{\hat{I}_2} \tag{18}$$

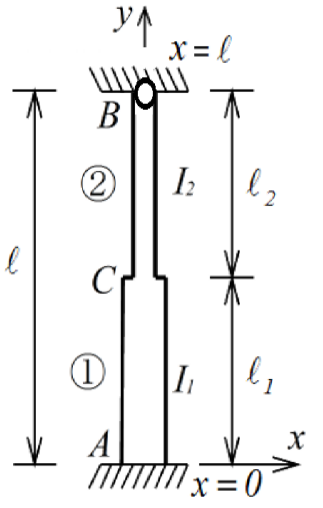

Fig. 3 Two-steps column with hinged-fixed ends

The results calculated by Eq. (18) is shown in Table 5.

Table 5 Critical load parameter (hinged-fixed ends)

I_2/I_1 \ ℓ_1/ℓ	0.2	0.4	0.6	0.8
0.1	1.616	1.642	1.963	3.290
0.2	2.249	2.280	2.646	3.819
0.4	3.084	3.115	3.439	4.200
0.6	3.670	3.693	3.920	4.356
0.8	4.124	4.136	4.250	4.440

DAMAGE INDEX

After war or Earthquake excitations often cause damage to structures, the extent of which can be quantitatively described by an advanced tool called damage index (DI). Many proposals are currently available to calibrate DI based on a number of parameters such as deformation, stiffness, energy absorption etc. To date, there is no universally accepted range for the magnitude of DI, although a scale varying between 0 (no damage) to 1 (total collapse) would be rational for this indicator [6]. Damage analysis has increasingly attracted many researchers to come up with both empirical and theoretical approaches in order to propose appropriate DIs. Last 30 years we have seen many concepts for DI proposed in order to calibrate the observed levels of damage. In recent years the damaged index has been introduced by some researchers which takes the stiffness before and after the damaged into account in order to determine damage index. Reference [2] defined a new relation between performance level and damage level for structures, based on the reduced stiffness.

They concluded [7] that the maximum drift

depends on the primary characteristics of the structure and independent of the stiffness of the structure at the beginning. Therefore, drifts cannot be merely considered for the assessment of damages index.

In this paper we will defined DI based on the reduced stiffness as Eq. (1). Damage index represents the degree of damage that may occur at each performance level. Damage extent to the structure also has a direct relationship with the structural stiffness variations. In the study of damaged columns, buckling loads of them plays a key role to evaluate the stiffness variations. In this paper, we regard the variation of the buckling loads as the stiffness variations. Therefore, we use the critical loads for columns with a uniform section as $K_{initial}$ and the ones for columns with non-uniform sections as K_{final} in Eq. (1).

NUMERICAL RESULTS

Numerical results are shown in Fig.4 to Fig.6 the damaged index in each case that depend on different boundary conditions.

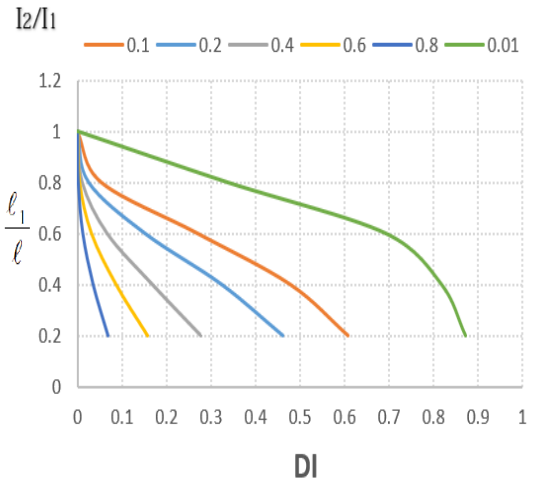

Fig.4 DI for column with one end fixed and the other end free

Figure 4 shows 6 curves for different moments of inertia (I2/I1) for columns with the fixed end and the free end boundary conditions.

The DI values increase in accordance with the decrease of the length ratio L1/L without regard to the moment inertia ratio I2/I1. The increase of I2/I1 leads to the decrease of DI.

When the range of L1/L is between 0.8 and 0.1, the 5 corves except I2/I1=0.01 are approaching from each other. In other words, the change of DI in this range is quite small depending on the moment inertia ratio I2/I1.

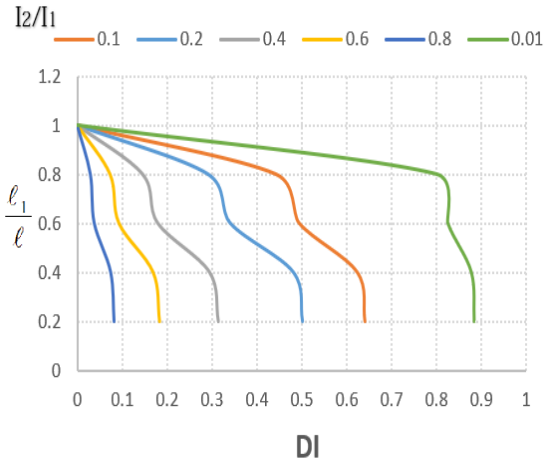

Fig.5 DI for column with both fixed ends supported

Figure 5 shows 6 curves for different moments of inertia (I2/I1) for columns with the fixed ends.

The DI's increase in accordance with the decrease of L1/L without regard to I2/I1, again. The increase of I2/I1 also leads to the decrease of DI. However, all curves are diverging from each other near to L1/L=1 unlike Fig. 4.

When we notice the range between L1/L =0.4 to L1/L=0.8, we can observe the sudden changes in curves, especially in the case of I2/I1=0.01. It is possible that the constraint of both ends deeply affect the buckling behavior.

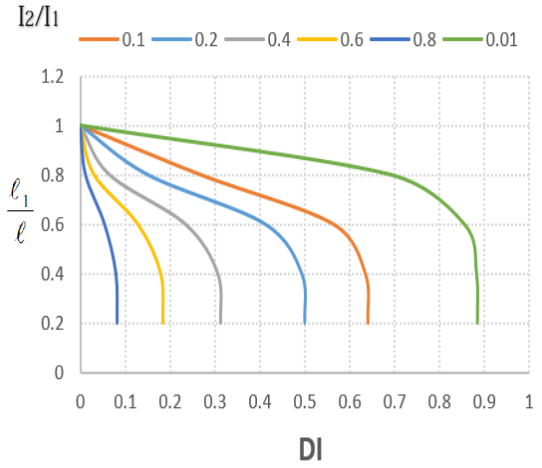

Fig.6 DI for column with fixed-pinned ends supported

Figure 6 shows DI-length parameter curves for columns with fixed-pinned ends.

In Fig. 6, we can observe intermediate tendency between Fig. 4 and Fig. 5. From I2/I1=0.1 to 0.4, the three curves are approaching from each other near to L1/L=1. On the other hand, in the case of I2/I1>0.4, the curves are diverging from each other near to L1/L=1.

When the length parameter L1/L decreases, DI

approaches a constant in all curves. The sudden changes are not observed in all curves.

It can be seen from these three figures that when the constraint at both ends intensifies, there exist stagnation parts of DI changes.

INTERPRETATION OF THE DAMAGE INDEX

The damage index DI has been recognized as an effective tool of quantitatively expressing the extent of damage. The Structure damage is described quantitatively according to the range of DI. To estimate the degree of the damage, we use Table 1 and adopt a column with one end fixed and the other end free as an example. The result is shown in Fig.7.

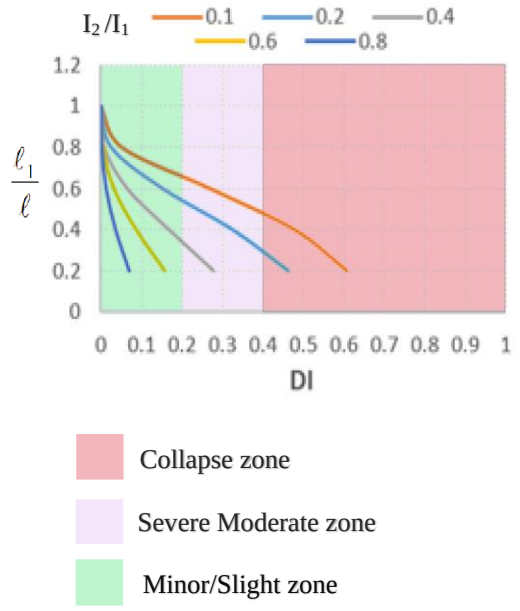

Fig.7 Degree of Damage for column with one end fixed and the other end free

Figure 7 shows the state of column depending on DI. When the parameter I2/I1 is over 0.2, the damage of the column does not reach the collapse zone even in the range of small L1/L. We can obtain the same results for the other boundary conditions.

CONCLUSIONS

In this paper we determine the buckling loads for columns with changing in the cross section with different end conditions. From the present investigation, the following conclusions may be drawn.

1- A damage index, DI, is redefined by using buckling loads of damaged and non-damaged columns.
2- The damage index, DI, increases in accordance with the decrease of the length and the moment inertia parameters. Namely, large loss of the sections leads to the increase of DI.
3- When the constraint at both ends of the columns intensifies, stagnation parts of DI occur.

REFERENCES

[1] Fardin Azhdary, Naser Shabakhty, performance-based design and damages estimation of steel frames with consideration of uncertainties, ISSN 1330-3651(Print), ISSN 1848-6339 (Online) UDC/UDK 624.014.2.042.7:620.191.3

[2] Ghobarah, A.; Abou-Elfath, H.; Biddah, A. Response-based damage assessment of structures. // Earthquake engineering & structural dynamics. 28, 1(1999), pp. 79-104.

[3] Park YJ, Ang AH, Wen YK. Damage-limiting aseismic design of buildings. Earthquake Spectra 1987; 3(1):1–26.

[4] Andre R. Barbosa1 Filipe L.A. Ribeiro2 and Luis A.C. Neves3, Influence of Earthquake Ground-Motion Duration on Damage Estimation: Application to Steel Moment Resisting Frames DOI: 10.1002/eqe

[5] Stephen P.Timoshenko , DH.Young , Theory of Elastice Stability .

[6] Kappos, A.J., (1997), "Seismic damage indices for RC buildings: evaluation of concepts and procedures".

[7] Arjomandi, K.; Estekanchi, H.; Vafai, A. Correlation between structural performance levels and damage indexes in steel frames subjected to earthquakes. // Sci Iranica Trans Civil Eng. 16, 2(2009), pp. 147-155.

9th Int. Conf. on Geotechnique, Construction Materials and Environment,
Tokyo, Japan, 20-22 November 2019, ISBN: 978-4-909106025 C3051

FRAMEWORK OF SUSTAINABLE ENERGY DEVELOPMENT IN A BEREFT POWER SUPPLY ECONOMY OF NIGERIA

Ibrahim Udale **Hussaini**[1], Sarile Kawuwa **Abubakar**[1], Muhammad Aliyu **Danmaraya**[2], Suleiman Khalid **Ibrahim**[1]
1. Department of Architecture, Abubakar Tafawa Balewa University Bauchi, Nigeria
2. Department of Architecture, Ahmadu Bello University Zaria, Nigeria

ABSTRACT

Issues of improving energy performance of any nation borders on increasing energy supply to meet up energy demand; and also reducing energy consumption through efficiency practices to attain sustainable energy utilization. Nigeria as a nation is bedeviled with the problems of inadequate energy supply as well as inefficient utilization of the low-supplied energy. In spite of the enormous and abundant energy resources across the country (renewable and non-renewable alike), the question of sustainable energy development in Nigeria remains a farce. All spheres of energy development (generation, transmission and distribution) together with consumption is occasioned by irregularities that have plunged the nation into a protracted energy crisis for decades due to its inability to harness adequately the abundant energy resources, and sustainably utilize the low-supplied energy. This study therefore attempts to review the state of energy development in Nigeria with its attendant limitations in terms of energy supply and its utilization in a bid to attaining a sustainable national energy development. Thus, a framework of strategies towards attaining sustainable energy development through the deployment of renewable energy resources and energy efficiency practices is therefore proffered.

Keywords: Sustainable energy development, Energy efficiency, Renewable energy resources, Nigeria

INTRODUCTION

Energy development involves all activities of policies and operations that bring about obtaining energy primarily from natural resources through conventional or non-conventional applications to power the national economy. A sustainable energy development has today become a global concern that requires the development and implementation of technologies as well as policies that can improve the energy situation of a country without exhausting resources for all generations; in a manner that the society is not adversely affected socially, economically and environmentally. However, this development mainly focuses on effective and efficient electrical energy supply essential for modern life and economy. It is generated from either renewable sources or non-renewable sources which are mainly fossil fuels, hydroelectricity, nuclear power and other sources like solar, wind, biomass, etc. Sources other than renewables are prone to depletion, and cause environmental degradation and pollution, climate change, etc. Thus, the need for a sustainable energy development which produces energy sources that meet today's demand and thereby eliminating the feared danger of depletion, environmental degradation and climate change; and can be used over and over again. Exploration of sustainable energy is harmless to the environment and equally cost-effective.

Electric energy is on the top grade in energy hierarchy and it is fundamental and inevitable to our daily lives. It is used in homes, industry, agriculture, education, defence and transportation. In fact, the economic growth of any nation depends heavily on the electrical power supply. The per capita consumption of electricity is an index of the standard of living of the people of the country; and to maintain a steady growth and development, the electricity

industry is always engaged in a continuous planning process which now calls for a sustainable dimension. Thus, sustainable generation, transmission and distribution planning becomes very crucial in the expansion planning of the utility alongside population growth [1].

Nigerian society has for many years being experiencing a critical problem of energy poverty occasioned by extreme electricity shortage. The power sector is characterized by low generating capacity in spite of the nation's abundant reserves of hydro-energy, petroleum, coal and gas. This has resulted in unsatisfactory electricity power supply that has left many of the citizens without access to steady power supply for decades unabated. Socio-political, financial and structural factors which are mutually exclusive are known to be responsible for this deficiency [2, 3]. Nigeria as a nation is endowed with enormous energy resources more than many countries combined that are exclusively out of energy poverty; yet, Nigeria presents a persistent and complex scenario of unresolved energy issues in the face of massive reserve of energy resources. In addition to the mentioned adverse factors, the menace of corruption in the Nigerian public service which has ravaged every sector of the economy, including energy, has drawn the country backward among community of nations [4].

Nigeria is the most populous black nation of the world with a population of about 180 million people with an annual growth rate of about 6%. It is heavily endowed with an abundance of natural resources which are grossly unharnessed. Nigeria is among the major oil producing and exporting countries in Africa with average of 2.5 million barrels per day. As an entity, it is among the countries with the largest natural gas reserves in the world, with an estimated 182 trillion cubic feet of established reserves. It is also endowed with extensive coal reserve of between 1.5 billion to 2.5 billion metric tonnes. In addition, there is the much availability of renewable resources like water, wind and sun energy, from which appreciable power can be generated as shown in table 1 [2, 4, 6].

The national grid is essentially hydro and thermal powered, in which less than 40% of the population is connected to the grid; and this meagre proportion is short of power for over 60% of the time [3]. In the face of the acute deficit in power supply, the energy sector operates at very high cost (over 8 billion Naira/53 million US dollars) and with more than 80% of this cost going into staff salaries and welfare. It is characterized with high energy losses in generation, transmission and distribution in both technical and non-technical dimensions; and with inadequate expertise [5]. With a lot of funds expended on the sector (over 40 billion US dollars) over the past decade, the country remains barely over 7,500 MW of installed generating capacity in a country of approximately 180 million people [6]. Regimes upon regimes; and energy programmes upon programmes, the story of energy poverty remains persistent. The scenario remains bleak for decades which require a strategic approach to address the constraints in all spheres of energy development in order to support national growth and economic development. Thus, the framework of sustainable energy development in a bereft power supply economy of Nigeria becomes essential.

THE CHALLENGES OF THE POWER SECTOR

As a nation, the power supply is expected to grow in line with power demand. But, according to David-

West [21], the Nigeria peak load demand in 2010 is 12, 800 MW compared to its maximum generation of 3, 400 MW; creating a supply/demand gap of 73%. However, the reported peak load is a misnomer of the actual demand for electricity. In fact, access to electricity at the national level is 51% in favour of the urban areas, while rural access to electricity is under 20%. This has actually put Nigeria among other nations in a very bleak economic situation in terms of power generation per capita as indicated in figures 1 and 2.

Nigeria has gone through successive power reforms from the earlier time as a British Protectorate to now as a Democratic Nation. But, the electricity supply crisis ensued with a decline in generating capacity of the power sector coupled with the population explosion without a corresponding improvement/maintenance of power supply/transmission/distribution facilities. This is occasioned by such challenges as slow growth in generation capacity, market deregulation process delay, power lines and power distribution vandalism, poor maintenance of existing power system, lack of adequate funding and corruption among others [20]. The generating capacity as at 1993 was just about 1,669 MW, which up to this moment (2019) has sparingly reached 7,000 MW [2] in spite of earlier intervening reforms. Consequent upon slow growth and inadequate supply of the needed power on demand, the Federal Government began a gradual process of power revitalization by setting up the Electric Power Sector Implementation Committee. This committee facilitated the passage of the Electric Power Sector Reform Act of 2005. The sole aim of this act was to ensure and promote efficiency of the power sector through privatization. The privatization exercise later took effect to unbundle the prime utility company (Power Holding Company of Nigeria) into several successor companies likely to be more efficient in services provision to undo the ugly power situation of the country.

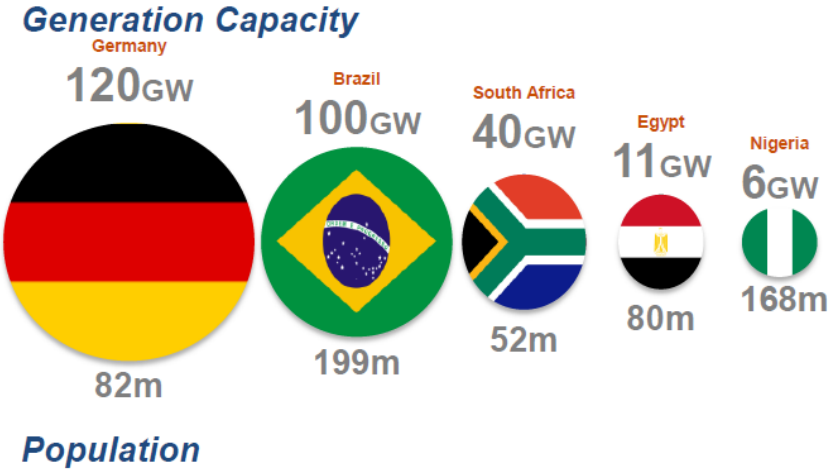

Figure 1: Putting Nigeria in Perspective of Population to Generation Capacity Ratio
Source: KPMG [8]

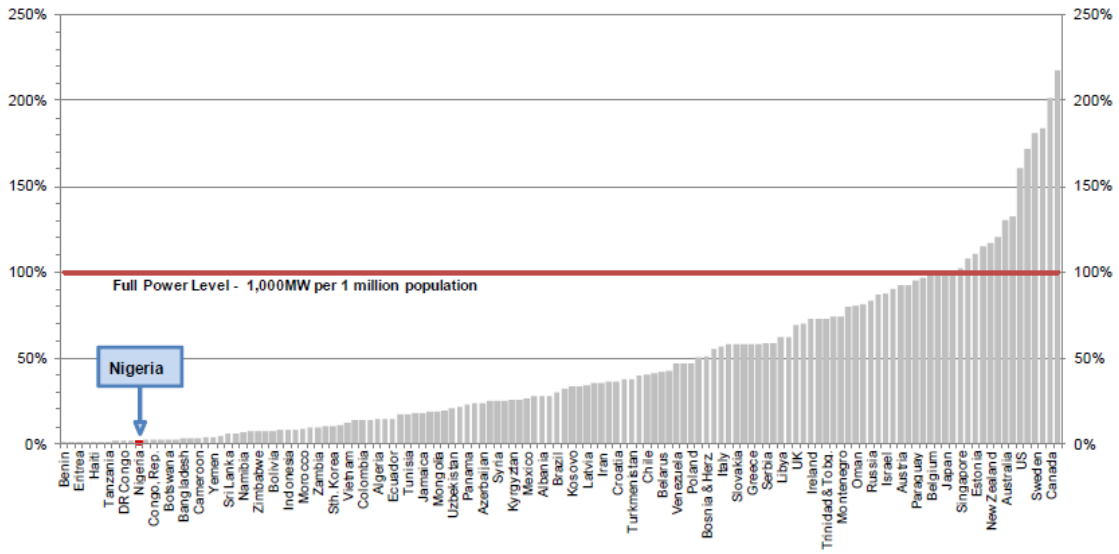

Figure 2: Generation Capacity per Capita (2010)
Source: US Energy Information Administration, CSL Research in David-West [20]

In fact, the challenges of the power sector are multifaceted and are witnessed at all levels of operation; - generation, transmission, distribution and consumption. The major root cause of these challenges is the preponderance of corruption resulting in lack of transparency and uncertified credibility of the government officials. In summary, the power sector of Nigeria is highly engrossed in inadequate power generation; inefficient technologies/equipment deployed for generation, transmission and distribution; and inefficient consumption in the industries and housing units due to inefficient behaviours.

To confront the surmounting challenges of the power sector, there is the need for further reforms focusing on sustainably increasing generation capacity to adequately meet the demand, in line with the expansion of both the transmission and distribution lines collectively with the deployment of sustainable and efficient technologies. Establishing public awareness and information programmes on energy efficiency and conservation equally becomes crucial. Sambo [7] has however, argued that the persistent energy poverty in Nigerian society is due largely to the lack of infrastructural development of the energy sector for decades

Adequate energy supply is the power drive of all nations as it promotes economic growth and global competitiveness. Therefore, the current gloomy state of the Nigerian power sector deserves to undergo further reform for a successful development outcome among nations. According to KPMG [8], "The Nigerian power sector remains adequately positioned as the next destination for massive power investments." To attain this, the identified challenges/obstacles must be adequately addressed. However, the current global trend in energy reforms include the unbundling of the sector into manageable sub-sectors, the privatization of ownership and the introduction of competition into the power generation sector. As part of the reform, the government has successfully embarked on the approach of unbundling. This, according to Washington Consensus, is being promoted by the World Bank and

IMF [2]. This reform pattern is necessary because of the need to rationalize the power sector development through liberalization that requires optimal resource allocation.

All the drive issues of reform are to be regulated by adequate and appropriate guidelines of operation for a successful and sustainable power industry. The guidelines include market issues, electricity transmission license, power purchase agreements, multi-year tariff order, grid code, metering code, market procedure and interim market rules [5]. To accomplish a successful mission of reform, the evolved frameworks must be in consideration of a sustainable outlook; and with the deployment of renewables in the energy-mix for grid production.

A SUSTAINABLE OUTLOOK APPROACH

The study focuses on attaining sustainable energy development for the Nigerian economy through formidable framework of energy resources utilization. To accomplish this goal, a textual analysis of the current state of energy development in conjunction with energy resources potentials of the country is undertaken. However, the current global energy development trend has a great and enhanced consideration for a sustainable outlook. This is consequent upon the fact of persistent depletion of the non-renewable sources; the environmental degradation and pollution due to resources exploitation; the associated climate change and loss of biodiversity etc.; and the fear of energy scarcity. The dimension of a sustainable outlook is mainly focused on the deployment of the renewables in the energy-mix in power generation. The Nigerian government has recognized this potential and has established renewable energy research and development centres across the country (at Usman Danfodio University Sokoto, University of Nigeria Nsukka, etc.) as subsidiaries of the Energy Commission of Nigeria (ECN). Unfortunately, the activities of these centres have been limited to solar photovoltaic development, and solar energy products and devices like solar cookers, water heaters, dryers, etc. on a very minimal level. Solar power generation has not actually been introduced into the power grid; and other renewables like wind, biomass, etc. have outrightly been ignored.

On a global scene, many countries are turning towards renewable energy sources in their power mix on a very significant level. Examples are; Germany already generates about 13% of its electricity from renewable sources; in the United Kingdom (UK), there is already a rule that any new building must reduce its carbon emission by 10% through use of renewables; member states of the European Union (EU) are required to generate one-fifth ($1/5^{th}$) of their power from renewable sources by the year 2020; and the United States of America (USA) has legislated that all publicly traded utility power companies should generate 15% of their power from clean sources like windmills, solar panels, etc. by the year 2020 [3], [4]. It is therefore necessary for the government of Nigeria to imbibe a sustainable outlook in recognition of global trends through a framework of sustainable energy development as presented in this study. The changing energy mix trend should include non-hydro renewables and natural gas. The hydropower generation as it is presently could be doubled to increase its contribution in the mix since much of the hydropower potential is grossly unexplored.

There is also the need to introduce a decentralized renewable energy capacity in the form

of off-grid solutions in all the six (6) regions of the country based on the local renewable sources potential to serve the regions including the remote and rural communities that have being deprived of access to electricity for decades [9] .

THE OPPORTUNITIES IN THE POWER SECTOR

Based on the geographical and socio-economic landscape of Nigeria, several opportunities abound in the bid to overturn the current scenario into a plausible and more sustainably efficient venture. Some of these opportunities as observed, and in line with Deloitte Global [9] presentations are as follows;

i. Renewable energy opportunities

There are ample opportunities to explore in renewable energy sources in all regions of the country. Principal among these are, solar, wind, tidal wave and biomass. These opportunities will become evident for firms in this sector in the form of research and development, project management, consulting, as well as capacity building and skills training.

ii. Restructuring utilities

This opportunity would tend to encourage greater private participation in the electricity market in which private sector players will emerge, with a particular focus on sources for project funding.

iii. New technologies and systems

There is the need to consider new innovations and adopting new technologies in order to modernize the national utilities. This can be achieved by the introduction of smart metering and process automation systems so as to ensure the sustainability of the power industry. Application of DSM (demand-side-management) in most utilities is essential.

iv. New-build and project supply opportunities

Within the traditional thermal and hydropower sectors, there are opportunities within the new build and civil construction and supply of inputs environment for power generation projects. There are also the noted renewable energy opportunities, spanning solar, wind, geothermal and biofuel related technologies.

v. Skills development

Presently, there is a substantial level of skills deficit in the power sector and sectors that support it that creates an opportunity for foreign investors to partner with the national government in order to develop technical training schools and fund more students enrolling in science and engineering programmes on long-term plans. But for immediate requirements of professionals in the sector, it is necessary for the government to import skills and facilitate skills transfer through tailor-made programmes.

vi. Technologies and systems for rural electrification

There is need for a rigorous focus on rural electrification and use of renewable energy technologies (RETs) in stand-alone off-grid or mini-grid systems to reach out to large sections of the rural communities. This will unlock opportunities for investors, financiers, technology owners, builders, project managers and entrepreneurs in rural electrification projects.

vii. Scenario planning

For the onward success or sustainability of the power industry, the government and the utility agencies will need to engage in scenario planning in order to get a

view of what is really required for successful operations.

viii. Improved stakeholder engagement

It is required and very important to develop clear stakeholder engagement strategies for new entrants, vis-à-vis policymakers, regulators, utilities and operators.

ix. Others are diversified investment attraction and portfolio optimization.

FRAMEWORK OF SUSTAINABLE ENERGY DEVELOPMENT

The proposed framework is intended to provide working plan/strategies for the operation of the power sector in terms of generation, transmission and distribution; and energy consumption efficiency in consideration of the overall energy resources potential of the country based on sustainability principles, and in recognition of the observed opportunities.

Nigeria as a country is divided into six (6) geopolitical regions, and each of the regions is endowed with enormous renewable (see tables 1) and non-renewable energy resources. They are; the North central, North west, North east, South west, South east and South south regions. The abound resources in these regions include; large and small water bodies for hydropower, sunshine for solar power, strong winds for wind power, ocean tides and biomass from the enormous waste disposal across the country.

Table 1: Renewable energy potential in Nigeria

Energy Resources	**Estimated Reserve**
Large Hydropower	11,250 MW
Small Hydropower (<30 MW)	3500 MW
Fuel Wood	11 million hectares of forest and woodland
Municipal Waste	30 million tonnes/year
Animal Wastes	245 million assorted animals in 2001
Energy Crops and Agricultural Residue	72 million hectares of agricultural land
Solar Radiation	3.5-7.0 kW h/m2/day
Wind	2-4 m/s at 10 m height Wind speeds in Nigeria range from a low 1.4 to 3.0m/s in the Southern areas, except for coastal line and 4.0 to 5.1m/s in the North. The Plateau area particularly interesting.

Source: Energy Commission of Nigeria (ECN), "Draft National Energy Master Plan [2014]"
Adapted from Energypedia at https://energypedia.info/wiki/Nigeria_Energy_Situation [22]

A. Framework of Sustainable Power Generation

This is undertaken in consideration of mostly, the renewable energy resources in the various regions of the country;

i. Hydropower source

The nation has a very high hydropower potential of large and small rivers; and some few water falls. According to Idris, Kura, Ahmed & Abba [2] the total technically exploitable large scale hydropower potential is estimated at over 10,000 MW capable of producing 36,000 GWh of electricity annually. Only about one-fifth of this potential has been developed as at 2001, and since then, there has not been any significant improvement. The small hydropower potential is estimated at over 734 MW. The current hydropower infrastructures are in dire need of rehabilitation; and their actual energy output is far below their operation capacity. The hydropower source cuts across all the regions of the country; as such, the maximal exploitation should be the prerogative of all regions.

ii. Solar Power Source

There is a great solar power generation potential in Nigeria which has been undermined and utilized on a very meagre scale (less than 5% of total generation). In fact, the entire geography of Nigeria has fairly well distributed solar radiation across all regions. This is because; Nigeria is located in a high sunshine belt of the equatorial region of the globe. The annual average of total solar radiation varies from about 12.6 MJ/m^2/day in the south-coastal areas to about 25.2 MJ/m^2/day in the far north. The solar radiation intensities range from 3.5 – 7.0 kWh/m^2/day; and sunshine duration ranges from 4.0 – 9.0 hours/day [2].

Solar power generation is also suitable for all regions of the country but most suitable for the northern regions. It is a very promising renewable energy sources because of its limitless potential and capacity to be installed at the very point of load or load centre making it suitable for remote and local communities not connected to national grid [10].

iii. Wind Power Source

The wind power source distribution in Nigeria varies greatly based on the regional climate variation. There is a very good wind power potential in the north which constitutes a great resource for power generation for the northern regions, particularly to communities not connected to the grid.

It is estimated that Nigeria has annual average wind speed of 10m heights, varying from 3m/s in the coastal areas and above 5- 7m/s in the far north where vegetation is less [2].

iv. Biomass

There is much biodegradable waste disposal in both the rural communities and the urban centres across the country. This situation presents biomass which is a plant derived matter a great renewable resource for power generation. This requires the deployment of biomass technologies such as “digesters” to generate biogas as a sustainable by-product for power generation. Biomass resources of Nigeria are in the form of wood, forage grasses and shrubs, animal waste, agricultural and forestry residue, municipal and industrial activities as well as aquatic biomass. Plant biomass can be utilized as fuel for small-scale industries [11, 12].

v. Tidal waves

Nigeria is a coastal country along the Atlantic Ocean making it a good potential for tidal energy from the

waves of the Atlantic. Tidal wave can be a very efficient and sustainable source of power if the difference between the high and low tide is great [13]. Therefore, the appropriate technology can be deployed to take advantage of the tidal waves for power generation for the coastal regions of the country.

B. Framework of Sustainable Power Transmission

Transporting electricity over long distances is technologically and economically challenging that the proponents of electricity market have tended to support regional markets as a more sustainable option. As such, there are fundamental changes away from traditional ways in the manner that grids are designed, built and managed today. The traditional grid transmission originates from the era of industrialization which never took cognizance of the challenges of the 21st century sustainable development. Therefore, an intelligent/smart grid system of transmission of renewable resources that would optimize a balance between demand and supply of electricity would be essential. This system should ensure transmission without loss of power even over long distances as exemplified today in China and some European countries using high-voltage direct current (HVDC) option of electric power transmission. However, the first sustainable approach is the 'unbundling' system in which production and transportation of electricity is separated to create room for competition and an open and transparent market. This should be supported by adequate grid planning to ensure technological developments and advancements in the aspect of energy transportation across long distances. This shall be based on specifications and objectives related to regional planning policy, environmental and nature protection targets and economic criteria in terms of efficient, considerate and timely infrastructure investments [14].

C. Framework of Sustainable Power Distribution

It is a fact that the power distribution system is the lifeline infrastructure that determines the level of development of any nation and it plays a significant role in its industrialization and the general economic development. As such, it becomes necessary that both the transmission and distribution systems should be reliable, efficient and sustainable. A reliable power distribution system ensures safety of energy end-users, and promises reliable and quality electricity at affordable prices. The advancement of the power distribution system is known to have direct impact on the development potential of economic growth particularly in the urban centres. Promoting efficient power distribution infrastructure according to the 'International Copper Association Asia' [15] has enormous benefits among which are;

i. The environment-link economic sizing of cables campaign in Japan, Korea and China creates annual energy saving potential of 51 Billion kWh which is enough to power 27% of total residential lighting in United States.

ii. Energy efficient distribution transformer programmes in India and China helps to reduce 192 Billion kWh or a net savings of USD 138 Billion.

Therefore, all nations of the world aspiring to attain a sustainable power supply to its citizenry must drive towards achieving reliability in power distribution infrastructure. This can be accomplished by the following;

i. Power loss reduction with the use of energy efficient transformers and power cables (high conductivity cables).

ii. Power reliability enhancement by use of underground cabling systems to prevent power theft and mitigate challenges caused by visual pollution.

iii. Mitigating power quality issues by creating awareness and deploying solutions to ensure reliability and quality in the energy supply.

D. Framework of Sustainable Power Consumption

The power consumption unit is the terminal (end) point of energy supply chain. It deals with the energy end-users and their pattern and manner of consumption. It is therefore necessary to establish a framework of sustainable consumption so that many of the benefits of greater technological efficiency attained may not be lost to irrational behaviour [16].

Sustainable power consumption typically targets energy efficiency which is the application of efficient appliances/equipment/installations; and energy conservation which concerns human behaviour in energy use. It is about shaping the behaviour of power consumers in the direction of energy efficiency and conservation. The framework focuses on the human dimension of energy use which according to Abdul Majid and Hussaini [17] can foster significant boost in the efficient use of all energy resources if well understood and implemented. The human dimension according to Lutzenhiser [18] can amplify or reduce the effects of technology-based efficiency improvements in energy consumption. Therefore, the prime agenda of the framework of sustainable power consumption is to attain energy efficiency and conservation which has countless benefits in environmental and socio-economic sense. This could be in the form of reduced running costs, reduced environmental impact, improved ambient conditions and increased productivity/equipment life [17]. Sustainable power consumption can be achieved through government policies and regulations on energy utilization; and by providing public awareness/information programmes on energy efficiency and conservation. On this note, Grady [19] has presented the proposal of the Garrison Institute which stipulates the 'TIME model' on attaining energy efficiency on the public or consumer domain as follows;

T – Targeting: to recognize consumption pattern so as to regulate it towards efficiency through targeting and auditing programmes, etc.

I – Informing/engaging: helping people to develop capacity to be mindful of their energy use through 'people-centered-initiative.'

M – Motivating: use financial and non-financial mechanisms to turn intentions into behaviour in efficient use of energy.

E – Empowering/enabling: use concerted effort to remove financial and structural barriers to power consumption; and to provide better choice sets through policies and legislation, etc.

CONCLUSION

The Nigerian Power Sector has been in operation for decades and has witnessed several transformative/initiative reforms in policy and pattern of operation; yet the energy poverty of the nation remains unabated. This is because a 'sustainable outlook' has not been deployed in the successive

reforms; and the policies evolved have not been sustainably strategic. As such, available opportunities could not be adequately tapped or harnessed for growth and posterity of the sector and the general society. The sustainable outlook calls for adequate maintenance of all infrastructures of electricity production and transportation, with an increase in generation capacity of existing facilities which are grossly under-utilized far below their installed capacities; and to be accompanied with broad introduction of renewable resources into the energy-mix. The enormous potentials of the renewable resources across all regions of the country have been subsequently ignored in past reforms. Therefore, efficient and sustainable utilization of the abundant renewable and non-renewable energy resources of Nigeria on the platform of effective and good governance is the panacea to the relentless energy/power problem of the nation.

In addition, the power sector has being subjected to several daunting challenges in power generation, transmission and distribution responsible for losses and failures over the years. In short, the power infrastructure in place is in a state of apathy, very unreliable, inefficient and unsustainable. As such, it needs to be strategically revitalized through a sustainable approach. The prelude to the approach is the 'unbundling' system in which production and transportation of electricity is separated to create room for competition and an open and transparent market. This is has been carried out by the government, and this study further recommends adequate grid planning to ensure technological developments and advancements in all the facets of operation so as to liberate the power industry out of the present state of impasse.

REFERENCES

[1] Akinbulire, T. O., Oluseyi, P. O., Awosope, C. O. A. & Okoro, O. I. (2008). *Data-based Analysis of Power System Crisis in Nigeria*. esptaee 2008, University of Nigeria,Nsukka

[2] Idris, A., Kura, S. M., Ahmed, M. A. & Abba, Y. (2013). An Assessment of the Power Sector Reform in Nigeria. *International Journal of Advancement in Research and Technology*. Vol. 2, Issue 2, February 2013. ISSN 2278-7763.

[3] Kennedy-Darling, J., Hoyt, N., Murao, K. & Ross, A. (2008). *The Energy Crisis of Nigeria: An overview and implications for the future*. BP – Energy, Nigeria. The University of Chicago, 6/3/2008.

[4] Olugbenga, T. K., Abdul-Ganiy, A. J. & Phillips, D. A. (2013). The Current and Future Challenges of Electricity Market in Nigeria in the Face of Deregulation Process. *African Journal of Engineering Research*. Vol. 1(2), pp. 33-39, March 2013.

[5] Nnaji, B. (2011). Power Sector Outlook in Nigeria: Governments Reviewed Priorities. Chairman, presidential Task Force on Power Securities and Exchange Commission, June 2011.

[6] World Economic Forum: Global Energy Architecture Performance Index, 2015. Available at www.weforum.org/global-energy-architecture-performance-index-report-2015report

[7] Sambo, A. S. (2008). Matching Electricity Supply with Demand in Nigeria. International Association for Energy Economics, Fourth Quarter 2008.

[8] KPMG – "Cutting through complexity." Overview of the Nigerian Power Sector and Post Privatization Expectations. A Korean trade delegation, July 2014.

[9] Deloitte Global (2015): Sub-Saharan African (SSA) Power Trends: Power Disruption in Africa Report, 2015. Deloitte Touche Tohmatsu Limited (DTTL) UK. Designed and Produced by Creative Services at Deloitte, Johannesburg. Available at www.deloitte.com/

[10] Hussaini, I. U., Onunze, C. N., Chiroma, A.H.,

Muhammad, S. I. & Ibrahim, S. K. (2014). Energy Resources Development in Nigeria: Prospects and Challenges. *Proceedings of the 7th International Conference on Sustainable Energy & Environmental Protection (SEEP 2014)* held in Dubai – UAE from Nov. 23rd – 25th, 2014, paper # S0 1137.

[11] Uduma, K. & Arcciszewski, T. (2010). Sustainable Energy Development: The way to a Stable Nigeria, *Open Access Journal of Sustainability*, 2, pp. 1558-1570, Published 3 June 2010. Available at www.mdp.com/journal/sustainability

[12] Uzoma, C. C., Nnaji, C. E. & Nnaji, M. (2012). The Role of Energy Mix in Sustainable Development of Nigeria, *Continental Journal of Social Sciences,* 5(1): 21-29, 2012. Available at http://www.wiloludjournal.com

[13] Uyigue, E. (2006). Renewable Energy and Sustainable Development in Nigeria, Being a paper presented at the *CREDC (Community Research and Development Centre) seminar proceedings on Renewable Energy*: The key to sustainable development in Nigeria held at the University of Benin, Benin City, Nigeria on July 18, 2006.

[14] Riese & Wilms: Overall idea for the planning of transmission grids and grid connections, pg. 108 in Klaus Rave (2010). Sustainable Energy Transmission – Challenges and Visions. Global Economic Symposium, 2010. Available at https://www.global-economicsymposium.org/knowledgebase/the-global-environment/towards-a-global-electricity-market/proposals/sustainable-energy-transmission-2013-challenges-and-visions

[15] 'International Copper Association Asia' (Cu). Copper Alliance

[16] Hussaini, I. U. & Abdul Majid, N. H. (2014). Energy development in Nigeria and the need for strategic energy efficiency practice scheme for the residential building sector. *Management of Environmental Quality: An International Journal,* Vol. 26 Iss 1 pp. 21 – 36

[17] Abdul Majid, N. H. & Hussaini, I.U. (2011). The challenges of energy efficiency in the Nigerian households. *Conference Proceedings of the 3rd International Conference on Applied Energy*, Perugia, Italy, 16-18 May, pp. 1471-1482.

[18] Lutzenhiser, L. (1993). Social and behavioral aspects of energy use. *Annual Review of Energy and Environment*, Vol. 18, pp. 247-289.

[19] Grady, E. (2011). Unlocking the behavioural wedge: tools for realizing sustainable energy use practices. P*aper presented at Behaviour, Energy and Climate Change (BECC) Conference*, Washington, DC, 30 November.

[20] Olugbenga, T. K., Jumah, A. A. & Phillips, D. A. (2013). The current and future challenges of electricity market in Nigeria in the face of deregulation process. *African Journal of Engineering Research.* Vol. 1 (2), pp. 33-39.

[21] David-West, Alowiba (2014). Nigerian Power Sector: Value Investment Opportunity or Value Trap? CSL Stockbrokers – a division of FCMB (UK) Limited.

[22] Energy Commission of Nigeria (ECN), "Draft National Energy Master Plan [2014]" Adapted from Energypedia at https://energypedia.info/wiki/Nigeria_Energy_Situation [22]

9th Int. Conf. on Geotechnique, Construction Materials and Environment, Tokyo, Japan, 20-22 November 2019, ISBN: 978-4-909106025 C3051

EXAMINATION OF CRUSHED LATERITE BRICK FOR REMOVAL OF CHROMIUM AND ARSENIC FROM WASTEWATER

A.B.P. Bandara[1], Yuki Yoshida[1], G.M.P. Kumara[1], Akihiro Matsuno[1] and Ken Kawamoto[1]
[1]Graduate School of Science and Engineering, Saitama University, Japan

ABSTRACT

Adsorption is one of cost-effective method to treat heavy metals in wastewater and the use of locally-available materials as adsorbents is receiving much attention especially in developing countries. This research was done to examine the potential use of laterite brick (from Vietnam) as a locally-available adsorbent to remove Chromium (Cr) and Arsenic (As) from wastewater. For comparison, commercially available zeolite and autoclaved aerated concrete (AAC) from Japan were used. Effect of initial metal concentration, pH and solid to liquid ratio (S:L) was examined for the fraction of 0.105-2 mm grains. The change in pH and electrical conductivity (EC) before and after the adsorption was measured. For laterite, both Langmuir and Freundlich models were fitted well for Cr and As adsorption isotherms and the maximum adsorption capacities (Q_m) became 1.3 mg/g for Cr and 8.2 mg/g for As. The measured Q_m for laterite became lower than zeolite but higher or equal to tested AAC. The change in pH became opposite between Cr and As adsorption, i.e., ΔpH (equilibrium pH–initial pH) increased with increase in Cr adsorption but ΔpH decreased with increase in As adsorption. Results revealed, for both As and Cr adsorption were dependent of initial pH and S:L ratio and desorption isotherms shown irreversibility of adsorbed metal ions onto laterite. Laterite has a possibility in treating Cr and As contaminated wastewater as commercially available zeolite. Further studies on the effects of competitive metal ions and ionic strength on adsorption process are highly recommended.

Keywords: Adsorption, Heavy metals, Laterite, Wastewater

INTRODUCTION

Adverse effects on the environment and human health is highly influence by heavy metal contamination in water is a global significance problem. Human population and environment are under severe dangers as treat to human by cancers, organ mutilation and death in serious cases through bioaccumulation of heavy metals [1]. Among them chromium (Cr) and arsenic (As) have become more hazardous pollutants. About 200 million people in worldwide are suffered due to arsenic contaminated drinking water [2]. The carcinogenic influence of Cr is also strong by making harm to the human [3]. Hence effective and efficient treatment technologies are essential to evade this issue.

Chemical precipitation, coagulation, membrane filtration, reverse osmosis, electrocoagulation and ion exchange can be identified as improved efforts among wastewater treatment methods [4]. High initial, maintenance and operation costs, expensive in large scale, severe pollution occurs due to regeneration of chemical reagents, chemical consumption and high sludge volume generation are drawbacks of them [5]. Positive image has received for adsorption process as an effective and economic technique for heavy metal removal because of low cost, high efficiency with easy operation conditions [6] and sometimes adsorbents can be regenerated [5].

There are various adsorbent materials as industrial products, natural and industrial geomaterials and biosorbents. Promoting the low cost adsorbents in adsorption process is needed to improve the economic feasibility and user-friendliness.

Therefore, laterite was used in this study as a locally-available and low cost adsorbent to examine the suitability for the removal of chromium and arsenic from wastewater.

MATERIALS AND METODS

Adsorbents Preparation and Physicochemical Characterization

In this study, laterite bricks from Vietnam was chosen to analyze adsorption characteristics expecting to be a better locally available material for Cr and As removal. Commercially available zeolite and autoclaved aerated concrete (AAC) in Japan were used as reference materials. All the materials were crushed by hand and sieved, and 0.105-2 mm particles were prepared and stored under natural moisture conditions. Determination of basic physical and chemical properties such as pH, electrical conductivity (EC), gravimetric water content of air-dried particles, specific gravity and loss of ignition (LOI) were done for all the tested materials, and are exemplified in Table 1.

The Batch Experiments for Adsorption Studies

Adsorption experiments under full contact conditions were followed according to the standard batch method proposed by the Organization of Economic Cooperation and Development (OECD) [7]. H_3AsO_4 and K_2CrO_4 reagents (Wako Pure Chemical Industries, Ltd., Japan) were used to preparation of adsorbates. Triplicate samples of adsorbents and adsorbates as 1:10 solid:liquid ratio (S:L) in 50 mL Violamo Centrifuge tubes (AO1350002, Sigma-Aldrich, USA) were shaken for 24 hours at 100 rpm at 20 ˚C in a reciprocating shaker. Subsequently 15 min centrifuge at 8000 rpm, membrane filtration (Millipore 0.22 µm) of supernatants and dilution with pure water to predetermined dilutions were conducted towards measurements of heavy metal concentrations by atomic adsorption spectrophotometry (AAS-AA-6200, Shimadzu, Japan). Both pH and EC values before and after the adsorption process were monitored.

The Effect of Initial Metal Concentration on Adsorption

Batch experiments for Cr and As adsorption at natural pH onto tested adsorbents by varying initial metal concentrations of 0-2,000 mg/L was accomplished to estimate the maximum metal adsorption capacity. Observed experimental data were fitted into Langmuir model [Eq. (1)] [8] and Freundlich model [Eq. (2)] [9] to examine the adsorption behaviors. Removal efficiency of metal contaminant was calculated using Eq. (3).

$$\frac{C_e}{Q_e} = \frac{1}{bQ_m} + \frac{C_e}{Q_m} \quad (1)$$

Where C_e=equilibrium aqueous metal ion concentration (mg/L), Q_e=amount adsorbed per adsorbent at equilibrium (mg/g), b=Langmuir constant related to binding strength (L/g), and Q_m= maximum adsorption capacity (mg/g).

$$\mathrm{Log}Q_e = \mathrm{Log}K_f + \frac{1}{n}\mathrm{Log}C_e \quad (2)$$

Where K_f =Freundlich adsorption capacity (L/g), and 1/n = adsorption intensity.

$$R = \frac{C_i - C_e}{C_i} x100 \quad (3)$$

Where R=Removal efficiency (%), and C_i=initial metal ion concentration (mg/L).

The Effect of Initial pH on Adsorption

Initial pH can be identified as one of a controlling factor for adsorption process [10]. Batch adsorption experiments were done in the pH ranges from 1 to 10, adjusted by adding either 1N HCl or 1N NaOH. S:L ratio was 1:10 and C_i was 500 mg/L for each solution.

The Effect of Solid:Liquid Ratio on Adsorption

Effect of S:L ratio on the adsorption was performed by using three different ratios as 1:5, 1:10 and 1:30, for 500 mg/L initial metal ion concentration at natural pH condition.

Desorption Experiments

Leaching of adsorbed metals from the adsorbent materials was examined by desorption experiments according to the sequential decant-refill technique [11]. Initially, the batch adsorption experiment under natural pH was performed. After centrifugation, 10 mL of the supernatant was removed, and the suspension was filled up with 10 mL of Millipore water (pure water). Then, samples were equilibrated under the same conditions as adsorption test. Consecutive desorption process was repeated at least three more times to achieve a well-fitting desorption isotherm. The hysteresis index (ω) [Eq. (4)] was valued according to the different between adsorption and desorption isotherms modeled by the Freundlich model [Eq. (2)]. Difficulty in detachment of the adsorbed metals to the adsorbent shows by higher ω value [12].

$$\omega = \left[\left(\frac{n_a}{n_d}\right) - 1\right] x100 \quad (4)$$

Where n_a=adsorption intensity and n_d=desorption intensity according to the Freundlich model [Eq. (2)]. Reversible metal adsorption indicated by $n_a=n_d$ or $n_a<n_d$, while $n_a>n_d$ shows irreversibility [11].

RESULTS AND DISCUSSION

Physical and Chemical Properties

Metal adsorption of liquid to solid phase is governed by adsorbent's characteristics [12]. Japanese AAC showed the high pH indicating capability of release OH^- in aqueous solution (Table 1). Narayanan [13] shows crystalline, semi-crystalline and near amorphous tobermorite group of calcium silicate hydrates (C-S-H) may cause to release OH^- . Hematite and Goethite are ion rich compounds in laterite which improve the positive charge governs to low pH in aqueous solution.

Table 1: Basic physical and chemical properties of tested materials.

Properties	Laterite	Zeolite	AAC
Water content (%)	0.7	0.04	10.2
Natural pH	4.2	8.4	10
EC (mS/cm)	0.02	5.6	1.8
LOI (%)	24	1.1	10.8
Specific gravity	3	2.7	2.5

The Effect of Initial Metal Concentration on Adsorption

Measured Cr and As adsorption isotherms fitted well in Langmuir model for entire range of C_i with high regression co-efficient (r^2>0.9) for laterite. Fitted with Langmuir model shows homogeneous and monolayer type adsorption [14]. Measured isotherms and fitted Langmuir models [Eq. (1)] data are shown in Fig. 1a and Fig. 1c for Cr and As respectively. The measured Q_m values became 1.3 mg/g for Cr and 8.2 mg/g for As, for laterite, lower than zeolite but higher or equal to tested AAC. Comparison of Q_m values with previous studies are summarized in the Table 2 and fitted Freundlich model [Eq. (2)] parameters are shown in Table 3.

Table 2: Comparison of Q_m (mg/g) values for Cr and As adsorption with previous studies.

Adsorbent	Cr	As	Reference
Laterite	1.3	8.2	This Study
Zeolite	5.4	14.6	This Study
AAC	-	4	This Study
Coir pith	11.6	-	[15]
Sepiolites	14.1	-	[16]
Chitosan	55.8	-	[17]
Cement	-	1.9	[18]
Brick	-	0.04	[18]

The ΔpH (difference between equilibrium pH and initial solution pH) relationship with equilibrium adsorption (Q_e) of Cr and As for laterite is shown in Fig. 1b and Fig. 1d. It indicated opposite behavior in Cr and As adsorption as decreasing ΔpH with increase in Q_e for As while positive ΔpH with increasing Q_e for Cr. This outcomes may due to the presence of Ca^{+2}, Mg^{+2}, Fe^{+2} and Cl^- like ions, which adsorption onto materials got affected.

Further studies are needed to interpret the results of metal adsorption process with relating to pH change and Ca^{+2} elusion before and after the adsorption process.

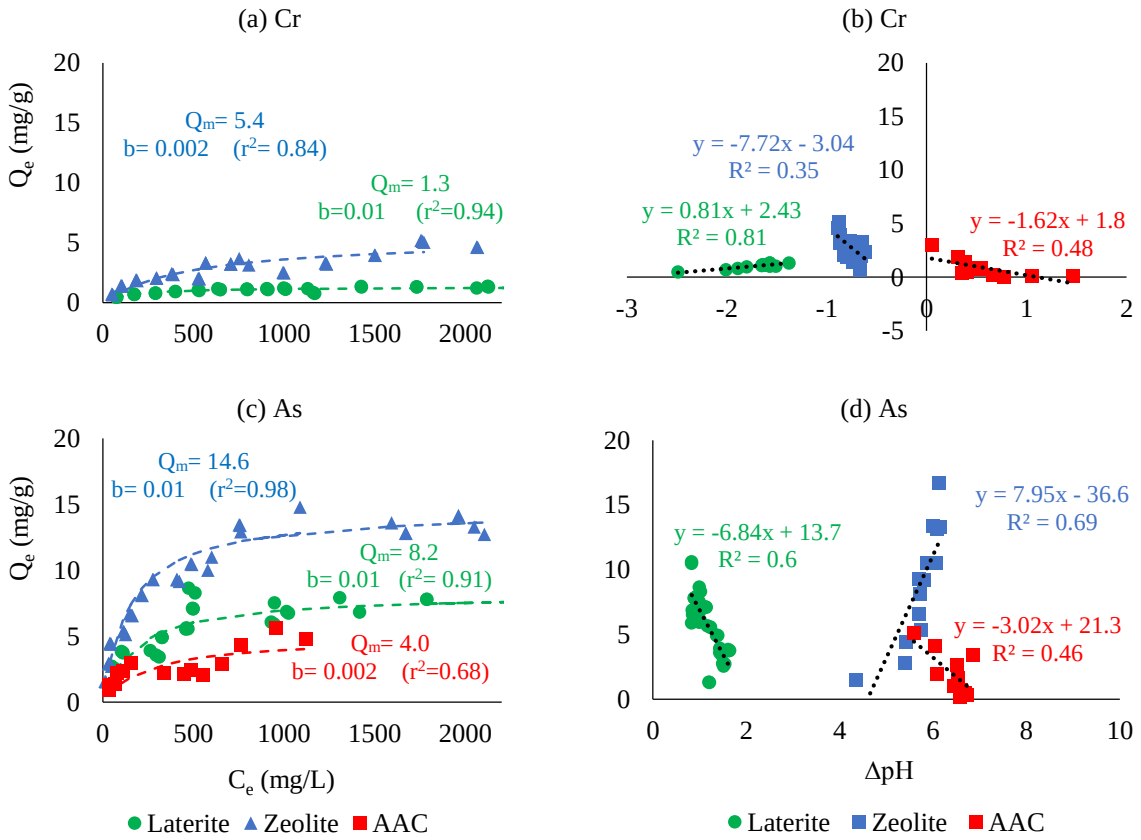

Fig. 1: Measured adsorption isotherms and fitted Langmuir models of (a) Cr and (c) As and the ΔpH relationship with equilibrium adsorption (Q_e) of Cr (b) and As (d) for all the tested materials.

The Effect of Initial pH on Adsorption

As the pH rises from 2 to 10 it was found to slight decrease in removal rate of Cr for all the materials as illustrated by Fig. 2a. In contrast, As removal shown in Fig. 2b increased from pH 1 to 2 in all the tested adsorbents and then decreased with pH increase in the solution. This results revealed that there is an effect on As and Cr adsorption with related to initial pH in the solution. Arsenic exists as neutral species in the pH range of 4-8.5 cause to slight reduction in adsorption [19]. Surface property of the adsorbent and adsorbate ionization degree may be changed with solution pH and it shows a significant impact on the heavy metal uptake [20].

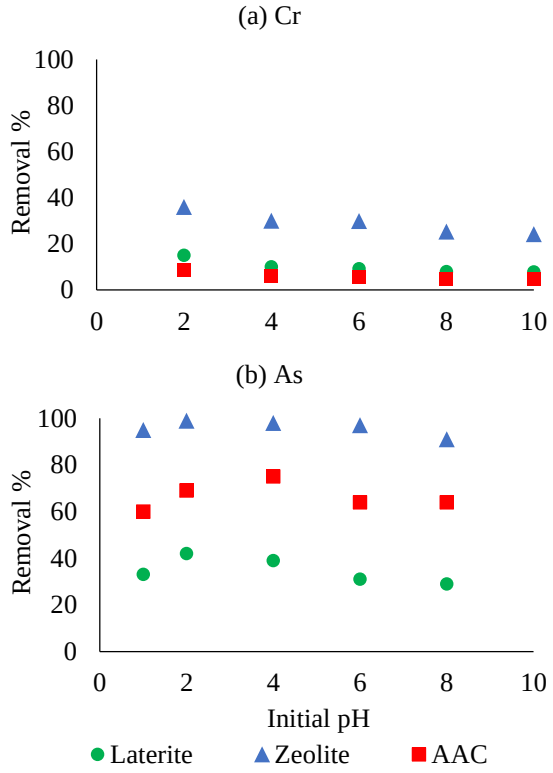

Fig. 2: Effect of initial pH of the solution for removal of (a) Cr and (b) As for tested materials.

The Effect of Adsorbent: Adsorbate (S:L) Ratio on Adsorption

As in the Fig. 3, higher solid content showed higher removal efficiency since increased in active adsorption sites. Removal efficiencies for laterite became lower than zeolite but higher or equal to tested AAC. S:L ratio of 1:10 can be suggested as a good ratio for laterite to remove both metals since it showed 7.8% and 42% of removal efficiency for Cr and As respectively at the natural pH conditions.

Reducing the pH condition of solution, removal efficiency of laterite was improved up to 15% for Cr as showed in the Fig. 2a. Therefore, there may be a possibility of improving the adsorption efficiency by doing some modifications to the materials, so; future studies are greatly recommended to improve the adsorption characteristics.

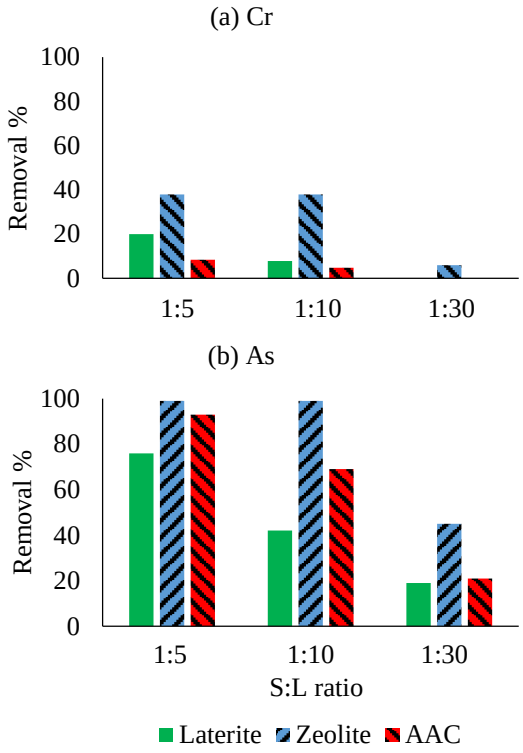

Fig. 3: Effect of S:L ratio for removal of (a) Cr and (b) As.

Desorption Experiments

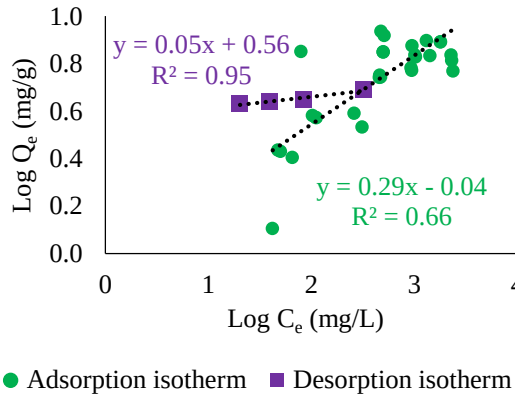

Fig. 4: Measured adsorption and desorption isotherms and fitted Freundlich models for As onto laterite.

Table 3: Fitted parameters for adsorption and desorption isotherm models (K_f, n, r^2) and hysteresis index (ω) for tested adsorbents.

Metals	Adsorbents	Adsorption			Desorption			ω
		K_{fa}	n_a	r^2	K_{fd}	n_d	r^2	
Cr	Laterite	0.24	0.24	0.69	2.16	0.07	0.28	242
	AAC	$1.5*10^{-4}$	1.38	0.78	2.8	0.03	0.06	4500
	Zeolite	0.22	0.4	0.74	0.84	0.17	0.67	135
As	Laterite	0.92	0.29	0.65	3.65	0.05	0.95	480
	AAC	0.37	0.69	0.69	0.87	0.25	0.81	176
	Zeolite	0.8	0.41	0.87	2.86	0.18	0.98	128

Reversibility and irreversibility behavior of the metal adsorption can be identified by consecutive desorption tests. For both adsorption and desorption data fitted with Freundlich model [Eq. (2)] are shown in the Table 3 with the estimated hysteresis index (ω) [Eq. (4)] (only adsorption and desorption isotherms were shown for the laterite fines in Fig. 4). All the tested materials showed higher regression coefficients (r^2) for As desorption higher than 0.8, while it is quite questionable for Cr desorption for both laterite and AAC compared to zeolite. Hence repeated experiments are essential to be followed for further studies.

Laterite has higher hysteresis index (ω) indicating irreversibility of adsorption process for As than other two adsorbents (Fig. 4). For all the materials, n_d values were lower than the n_a values, revealing strong bonds of adsorbed metal ions to adsorbents in water extraction conditions. Further studies are needed to examine the effect of pH onto the immobilization of sorbed ions.

CONCLUSIONS

Applicability of laterite bricks for As and Cr removal from wastewater was examined by a series of batch adsorption and desorption experiments. For laterite, both Langmuir and Freundlich models were fitted to the measured data. Arsenic adsorption showed higher Q_m value than chromium adsorption onto tested laterite, became 8.2 mg/g for As and 1.3 mg/g for Cr. It revealed higher adsorption capacity than AAC for both metal ions. For all the tested adsorbents, higher solid fraction affected in increasing the removal efficiency due to increase in active adsorption sites. Removal of Cr and As were high at pH 1 and 2 respectively, revealing pH dependency on adsorption. Lower leaching of adsorbed As was observed onto laterite with comparatively higher hysteresis index than other tested adsorbents. Based on the overall tested results, it suggested that laterite used in this study had a reasonable potential as an adsorbent to treat Cr and As contaminated wastewater.

Further studies on the effects of competitive metal ions in binary and multi-metals systems and ionic strength together with pH effect on adsorption process are essential to understand the adsorption mechanism in the typical wastewater conditions.

ACKNOWLEDGMENTS

This research was supported by JST - JICA Science and Technology Research Partnership for Sustainable Development (SATREPS) project (No. JPMJSA170).

REFERENCES

[1] Gunathilake S. K., Methods of Removing Heavy Metals From Indutrial Wastewater, Journal of Multidisciplinary Engineering Science Studies (Jmess), Vol. 1, Issue 1, 2015, pp. 12-18.

[2] Christine M. G., Laura S., Arias M. H. J., Mihali J., Cabrera L. Z., Danz D., Checkley W., and Gilman R. H., Arsenic Exposure in Drinking Water: An Unrecognized Health Threat in Peru, Bulletin of the World Health Organization, Vol. 92, Issue 8, 2014, pp. 565-572.

[3] Mohan D., Singh K. P., and Singh V. K., Removal of Hexavalent Chromium from Aqueous Solution using Low-Cost Activated Carbons Derived from Agricultural Waste Materials and Activated Carbon Fabric Cloth, Industrial and Engineering Chemistry Research, Vol. 44, Issue 4, 2005, pp. 1027-1042.

[4] Bissen M. and Frimmel F. H., Oxidation of Arsenic and its Removal in Wastewater, Clean Soil Air Water, Vol. 31, Issue 2, 2003, pp. 97-107.

[5] Fu F. and Wang Q., Removal of Heavy Metal Ions from Wastewaters: A Review, Journal of Environmental Management, Vol. 92, Issue 3, 2011, pp. 407-418.

[6] Aklil A., Mouflih M., and Sebti S., Removal of Heavy Metal Ions from Water by Using Calcined

Phosphate as a New Adsorbent, Journal Of Hazardous Materials, Vol. 112, Issue 3, 2004, pp. 183-190.
[7] Organization for Economic Co-Operation and Development Publications (OECD), Guidelines for the Testing of Chemicals, 2000.
[8] Langmuir I., The Adsorption of Gases on Plane Surfaces of Glass, Mica And Platinum, Journal of the American Chemical Society, Vol. 40, Issue 9, 1918, pp. 1361-1403.
[9] Freundlich H. M. F., Over the Adsorption in Solution, Journal of Physical Chemistry, Vol. 57, 1906, pp. 385-471.
[10] Kumarasinghe U., Kawamoto K., Saito T., Sakamoto Y., and Mowjood M. I. M., Evaluation of Applicability of Filling Materials in Permeable Reactive Barrier (PRB) System to Remediate Groundwater Contaminated with Cd and Pb at Open Solid Waste Dump Sites, Process Safety And Environmental Protection, Vol. 112, 2018, pp. 118-127.
[11] Mon E. E., Hirata T., Kawamoto K., Hiradate S., Komatsu T., and Moldrup P., Adsorption of 2,4-Dichlorophenoxyacetic Acid onto Volcanic Ash Soils; Effects of pH and Soil Organic Matter, Environ. Asia, Vol. 1, 2009, pp. 1-9.
[12] Kumara, G. M. P., and Kawamoto Ken., Applicability of Crushed Clay Brick and Municipal Solid Waste Slag as Low-Cost Adsobents to Refine High Concentrate Cd(II) And Pb(II)-Contaminated Wastewater, International Journal of Geomate, Vol. 17, Issue 63, 2019, pp. 133-142.
[13] Narayanan N., and Ramamurthy K., Structure and Properties of Aerated Concrete: A Review, Cement and Concrete Composites, Vol. 22, Issue 5, 2000, pp. 321-329.
[14] Cheng T. W., Lee M. L., Ko M. S., Ueng T. H., and Yang S.F., The Heavy Metal Adsorption Characteristics on Metakaolin-Based Geopolymer, Applied Clay Science, Vol. 56, 2012, pp. 90-96.
[15] Parab H., Joshi S., Shenoy N., Lali A., Sarma U. S., and Sudersanan M., Determination of Kinetic and Equilibrium Parameters of The Batch Adsorption of Co(II), Cr(III) and Ni(II) onto Coir Pith, Process Biochemistry, Vol. 41, 2006, pp. 609-615.
[16] Padilla O. E., Leyua R. R., Guerrero C. R. M., Jacobo A. A., and Aragon P. A., Adsorption of Heavy Metal Ions from Aqueous Solution onto Sepiolite, Adsorption Science and Technology, Vol. 29, 2011, pp. 569-584.
[17] Thinh N. N., Hanh P. T. B., Ha L. T. T., Anh L. N., Hoang T. V., Hoang V. D., Dang L. H., Khoi N. V., and Lam T. D., Magnetic Chitosan Nanoparticles for Removal of Cr(VI) From Aqueous Solution, Materials Science and Engineering: C, Vol. 33, Issue 3, 2013, pp. 1214-1218.
[18] Bibi S., Farooqi K. H., and Haider N., Evaluation of Industrial Based Adsorbents for Simultaneous Removal of Arsenic and Fluoride from Drinking Water, Journal of Cleaner Production, Vol. 87, 2015, pp. 882-896.
[19] Maiti A., Basu J. K., and De S., Removal of Arsenic from Synthetic and Natural Groundwater using Acid-Activated Laterite, Environmental Progress & Sustainable Energy, Vol. 29, Issue 4, 2010, pp. 457-470.
[20] Cho H., Oh D., and Kim K., A Study on Removal Characteristics of Heavy Metals from Aqueous Solution by Fly Ash, Journal of Hazardous Materials, Vol. 127, Issue 1-3, 2005, pp. 187-195.

9th Int. Conf. on Geotechnique, Construction Materials and Environment, Tokyo, Japan, 20-22 November 2019, ISBN: 978-4-909106025 C3051

CHARACTERIZATION OF TEMPERATURE ENVIRONMENT ON MIKURA-JIMA ISLAND, JAPAN WITH CONSIDEARATION OF VEGETATION RECOVERY

Teruo Arase[1], Tetsuo Okano[1], Masayuki Hino[2] and Taizo Uchida[3]
[1]Faculty of Agriculture, Shinshu University, Japan; [2] Botanist in Mikura-jima Island, Japan;
[3] Faculty of Engineering, Kyushu Sangyo University, Japan

ABSTRACT

Vegetation recovery following landslides caused by typhoons has been monitored on Mikura-jima Island. Despite having a temperature profile of a warm temperate zone, Mikura-jima has many plant species representative of a cool temperature zone. Temperature environment is an essential parameter for determining the development of vegetation and flora, but little data are available for the island. In the present study, we measured atmospheric temperature by thermographs at seven different elevations (130, 300, 400, 500, 600, 700 and 800 m) over a period of 5 years (from 2013 to 2017), and we determined the warm index, cool index and rate of decline with elevation. The lapse rate along elevation gradient was 0.98 ˚C per 100 m for elevations 500 m and below, and 0.66 ˚C per 100 m for elevations 500 m and above. Warm index (W.I.) was estimated to fall below 85 at elevations over about 800 m, which allows the existence of a cool temperature zone. The re-examination of temperature environment in the present study will facilitate planning of goals and evaluation or estimation of vegetational succession on Mikura-jima Island.

Keywords: Atmospheric Temperature, Warm index, Lapse rate, Vegetation, Mikura-jima Island

INTRODUCTION

Vegetation recovery projects require planning of remediation activities based on monitoring data and evaluation of success at the species level. The course of remediation efforts may differ greatly from project to project and will reflect the purpose of the project. In the case of urgently needing to stabilize the base of a slope to prevent landslides near populated areas, rapid establishment of ground cover may be achieved by using exotic pasture grasses owing to their superior germination and growth compared to native plant species. However, when restoration in a natural ecosystem is not so urgently required, it is desirable to focus on establishing native plant species. The importance of native species becomes greater in isolated natural ecosystems such as solitary islands due to its vulnerability to disturbance by non-native species [1].

What determines the distribution of native species? Humidity and temperature environment, which can be measured by precipitation and atmospheric temperature, have been demonstrated to influence the distribution of vegetation in various studies [2], [3]. In the 'Sino-Japanese Region' including China, the Korean peninsula and Japan, differences in atmospheric temperature are generally more critical than precipitation in determining the distribution of vegetation and flora because precipitation is abundant across this region [4]. Temperature environment is essential for determining the development of vegetation and flora [2]-[5] and, accordingly, it is an essential parameter for setting goals and evaluating or estimating the succession of vegetation.

The range of each plant species is determined by biomass production (i.e., photosynthesis, respiration, growth and storage), ability of survival in unfavorable seasons, as well as reproduction and competition [5]. From these points of view, several temperature indices such as the warm index (W.I.) and cool index (C.I.) [3] have often been used to characterize the habitat environment. For example, Kira [3] showed that the boundary between the cool temperature zone (deciduous broad-leaved tree forest) and a warm temperature zone (evergreen broad-leaved tree forest) is around 85 for the W.I. and -10 for the C.I. in Japan.

On Mikura-jima Island (Fig. 1), one of the solitary islands of the Izu Islands of Japan in the Pacific Ocean, vegetation recovery following landslides caused by typhoons has been monitored [6], [7]. Mikura-jima Island naturally has an 'irregular' vegetation distribution, having many plant species that are representative of a cool temperature zone but that are inconsistent with the previous placement of the entire island into a warm temperature zone. This inconsistency in classification poses challenges for setting goals for vegetation recovery and evaluating the succession of vegetation.

However, little data is available on the temperature environment of Mikura-jima Island. The only temperature dataset on Mikura-jima Island was recorded for 5 years from 1960 to 1964 at the village school located at an elevation of 130 m reported by Kawamoto [8]. Mikura-jima Island is encircled by a shoreline of uninhabitable sheer sea cliffs and has a highest peak (Mt. Oyama) with an elevation of 850.9 m [9]. Since clouds and fog usually cover the high elevation area of the island (Fig. 2), it is reasonable to consider that the atmospheric temperature shows a lapse rate along the elevation gradient in humid conditions: taking a lapse rate of 0.6 ˚C per 100 m produces an estimated difference of about 4.3 ˚C in temperature and 51.6 (= 4.3 × 12) in W.I. between at the village school and the mountaintop. This empirical estimation provides an W.I. of more than 100 at the top of Mt. Oyama, which exceeds the criteria of a cool temperature zone, which is W.I. of less than 85 [10].

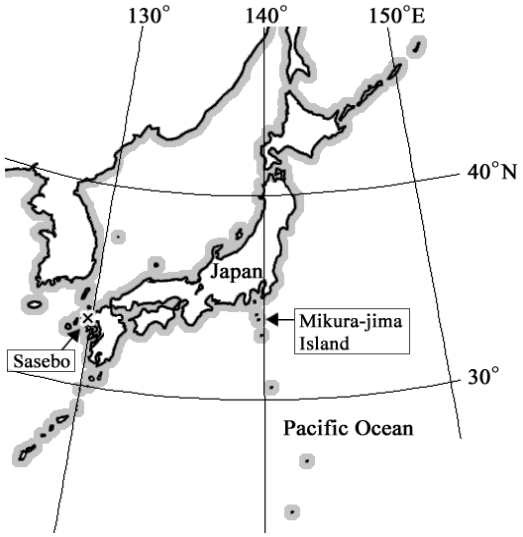

Fig. 1 Location of Mikura-jima Island, Japan with Sasebo, a city with nearly the same latitude, shown for reference.

Fig. 1 Photo of Mikura-jima Island. The shoreline is made up of sea cliffs, and the high-elevation area of the island is usually covered by clouds and fog.

In the present study, atmospheric temperature is measured continuously at several points with various elevations on Mikura-jima Island. We characterize the temperature environment of Mikura-jima Island and furthermore, re-examine the relationship between the distribution of vegetation and the temperature environment.

METHODS

Measurement of Atmospheric Temperature

Seven points at different elevations (130, 300, 400, 500, 600, 700 and 800 m) were established for the measurement of atmospheric temperature. Among them, six points were at an elevation of 300 m or higher and are located along a path leading to the top of Mt. Oyama. The observation point at 130 m is at a village school (elementary school along with a junior high school) in a residential area.

Atmospheric temperature at each observation point was measured using a waterproof self-registering thermograph (TR-51, T AND D Corporation). The thermographs were placed at the six points along a path leading to the top of Mt. Oyama in August 2012. Each was placed at a height of 1.5 to 2.0 m shaded from direct sunlight by placement under tree crowns along the path and in an instrument shelter at the village school.

Measurements were taken every hour on the hour, and the thermographs were exchanged every summer in order to collect registered data.

Measurements were continuously taken starting in August 2012 and are continually being taken as of publication of this report. In the present study, we analyzed the results of 5 years with entire-year data from 2013 to 2017.

Data Analysis

Based on the atmospheric temperature dataset, average monthly temperature and average annual temperature were calculated in each of the 5 years. From the viewpoint of the ‘irregular’ distribution of plant species in cool temperature zone, we also counted the number of days with freezing temperatures (i.e., the minimum temperature was below 0 ˚C) occurring each year.

The warm index (W.I.) at each point was calculated as follows,

$$W.I. = \Sigma (T - 5) \quad \text{(if T is higher than 5 ˚C)} \qquad (1)$$

where T is the average monthly temperature and the value of W.I. works out a positive number.

The cool index (C.I) at each point was calculated

by the similar formula to W.I.,

C.I. = Σ (T - 5) (if T is lower than 5 ˚C) (2)

and the value of C.I. gives a negative number. Equations (1) and (2) were proposed based on a general rule that plants can grow at temperatures above 5 ˚C [3].

The lapse rate along the elevation gradient was estimated by the relationship between elevation and each temperature index (average annual temperature, W.I, C.I and the number of days with freezing temperature). A simple regression model was employed to estimate the relationship, and the significance of fitness of the model was determined by an F-test based on the value of R^2.

RESULTS

Atmospheric Temperature

Table 1 Average monthly temperature and temperature indices by elevation on Mikura-jima Island over the period from 2013 to 2017.

Month	Elevation (m)						
	130	300	400	500	600	700	800
Jan.	9.4	7.2	6.5	5.4	4.8	3.6	3.1
Feb.	9.5	7.5	6.7	5.8	5.0	4.0	3.4
Mar.	12.4	10.6	9.6	9.1	8.1	7.0	6.5
Apr.	15.7	14.2	13.1	12.3	11.6	10.7	10.2
May	19.3	18.0	16.8	16.0	15.6	14.7	14.3
Jun.	21.4	20.1	19.1	18.6	18.2	17.4	16.9
Jul.	25.5	24.3	23.1	22.4	22.3	21.4	21.0
Aug.	26.8	25.2	24.1	23.5	23.1	22.4	21.9
Sep.	24.2	22.2	21.4	20.3	20.3	19.5	19.0
Oct.	20.7	18.6	18.0	17.0	16.7	15.9	15.3
Nov.	16.5	14.3	13.7	12.7	12.2	11.2	10.7
Dec.	11.8	9.6	9.0	7.6	7.3	6.1	5.6
An.ave.	17.8	16.0	15.1	14.2	13.8	12.8	12.3
W.I.	153	132	121	111	155	96.4	91.3
C.I.	-	-	-	-	-0.2	-2.4	-3.4
DF	-	0.4	1.0	2.0	10.0	18.8	24.7

An.ave.: the average annual temperature, W.I: warm index, C.I.: cool index, and DF: days with freezing temperature (below 0 °C).

Table 1 shows the average monthly temperature, average annual temperature and temperature indices (W.I, C.I, and days with freezing temperature) by elevation over the 5-year period from 2013 to 2017. The seasonal changes in atmospheric temperature on Mikura-jima Island presented as profiles of average monthly temperature at elevations of 130, 600 and 800 m (Fig. 3) show that the coldest month was January and the warmest month was August at all elevations. All temperature parameters showed that temperatures decrease with higher elevation throughout the year. C.I. was determined to be '0' at the points at elevation lower than 600 m because the average temperature did not fall below 5 ˚C in any month.

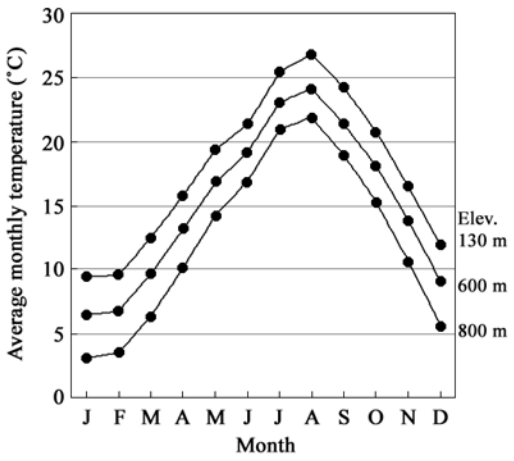

Fig. 3 Average monthly temperature in Mikura-jima Island, from 2013 to 2017.

Lapse Rate along Elevation Gradient

The lapse rate along the elevation gradient is shown for average annual temperature (Fig. 4), W.I. (Fig. 5) and days with freezing temperature (Fig. 6). We excluded C.I. from this analysis because only three observation points at high elevation had observations that could be used to calculate C.I.

For average annual temperature (Fig. 4), fluctuation among years seemed small (standard error (se) = 0.42 ˚C) at each elevation point. A statistically significant regression line using all data points (R^2 =0.951, p <0.0001, F-test) was obtained:

$y = 18.5 - 0.0080\ x$

where x is elevation and y is the average annual temperature. The slope (-0.0080) indicates a lapse rate in atmospheric temperature over the elevation gradient of approximately 0.80 ˚C per 100 m.

Regression lines fitted to data for lower and upper elevations separately (dashed lines in Fig. 4) showed a significant difference in slope (p<0.005, F-test by analysis of covariance). Lapse rate for elevations 500 m and below was 0.98 ˚C per 100 m, while the lapse rate for elevations 500 m and above was 0.66 ˚C per 100 m (R^2 = 0.954 and 0.742, respectively; p <0.0001, F-test).

For W.I. (Fig. 5), variation among years was also small (se = 5.1) at each elevation. A statistically significant regression line (R^2 =0.944, p <0.0001, F-test) was obtained as follows:

$y = 160.6 - 0.091\ x$,

where x is elevation and y is W.I. The slope (-0.091) indicates a lapse rate in W.I. over the elevation

gradient of approximately 9.1 per 100 m.

Breaking down the observation points by lower and upper elevation (dashed lines in Fig. 5) shows a significant difference in the slope of the regression line (p<0.0002, F-test by analysis of covariance) between lower elevations and upper elevations with a lapse rate of 11.7 per 100 m for elevations at 500 m and below and 6.5 per 100 m for elevations at 500 m and above (R^2 = 0.953 and 0.718, respectively; p <0.0001, F-test).

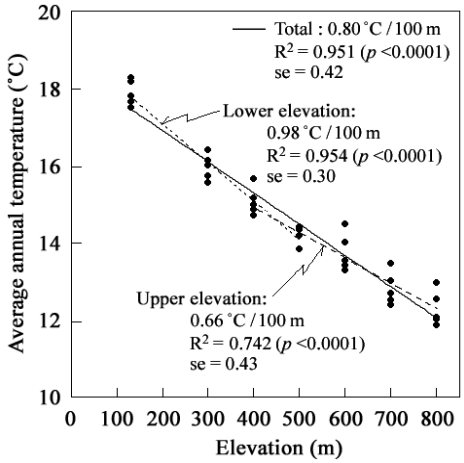

Fig. 4 Lapse rate for average annual temperature.

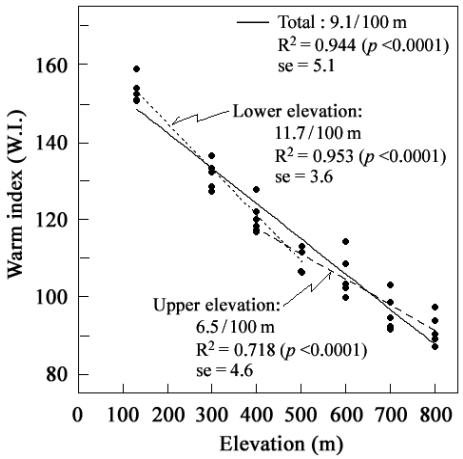

Fig. 5 Lapse rate for warm index (W.I.).

On the other hand, days with freezing temperature, or DF, showed large variation among years, especially at the points at higher elevations (Fig. 6). DF was zero or small up to elevations of 400 or 500 m and tended to increase with increasing elevation above 400 m. A statistically significant regression line was obtained for data over the elevations from 400 to 800 m (R^2 =0.717, p <0.0001, F-test):

$y = 25.9 + 0.062\ x$,

where x is elevation and y is days with freezing temperature. The slope (0.062) indicates that for elevations above 400 m, there is a rate of increase of approximately 6.2 days of freezing temperature per 100 m.

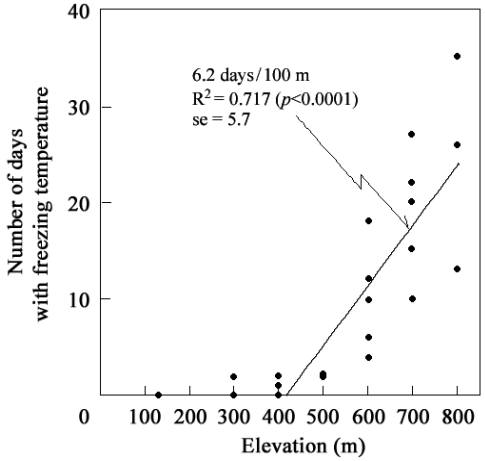

Fig. 6 Lapse rate for days with freezing temperature.

DISCUSSION

Temperature environment in Mikura-jima Island

Over the 5 years from 2013 to 2017, the average annual temperature was 17.8 ˚C and W.I. was 153 at an observation point in the residential area of Mikura-jima Island at an elevation of 130 m.

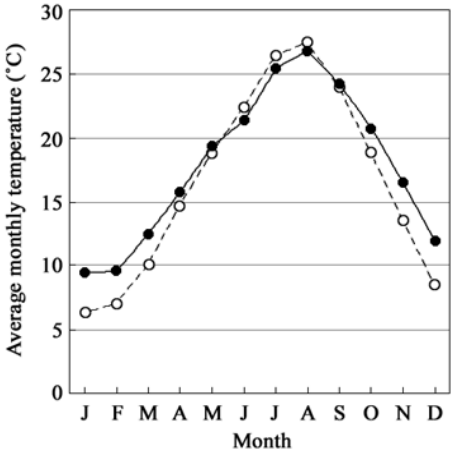

Fig. 7 Comparison of average monthly temperature between Mikura-jima Island at elevation 130 m (closed circles and solid line) measured in this study and Sasebo City (open circles and broken line) [11]. Data are averages over 5 years (2013 to 2017).

Kawamoto (2006) reported that the annual temperature range on Mikura-jima Island was smaller (i.e., cooler in summer and warmer in winter) than in Sasebo [3], a city at nearly the same

latitude (Fig. 1). From a plot of average monthly temperature on Mikura-jima Island using data collected in this study and in Sasebo city using data obtained by the Japan Meteorological Agency [11] over the same 5-year period from 2013 to 2017 (Fig. 7), we see a range in annual temperature on Mikura-jima Island of 17.4 ˚C, which is smaller than that in Sasebo City (21.0 ˚C). Further, the average monthly temperature was higher from October to April and lower from June to August on Mikura-jima Island than in Sasebo City. These data show that the temperature environment conditions on the island reported by Kawamoto [3] are as applicable in recent years as previously.

The lapse rate against elevation gradients differed between lower and higher elevations (Fig. 4 and Fig. 5). The patterns are classified as different patterns as for average annual temperature with the rate for elevations of 500 m and below of 0.98 ˚C per 100 m considered as a dry adiabatic lapse process, while the rate at elevations of 500 m and above of 0.66 ˚C per 100 m considered as a moist adiabatic lapse process [12]. These classifications are fitting with the clouds and fog that usually cover the high-elevation area of the island (Fig. 2). Other studies have also reported changes in lapse rate along the elevation gradient for other islands in Japan [13], [14], but the change in the lapse rate was relatively mild on Mikura-jima Island: the moist adiabatic lapse rate at higher elevations was larger than that on Mimami-Iwo-To Island (-0.47 ˚C [13] and 0.56 ˚C [14] per 100 m). We consider that this less distinct difference in lapse rate is due to the landform of Mikura-jima Island, or the strong winds that almost steadily blow up from the sea.

The regression equation on lapse rate enables us to estimate W.I. at any elevation and, conversely, to determine elevation from any W.I.. Using the regression equations in Fig. 5, we estimated the elevation corresponding to W.I. over the entire Mikura-jima Island. As W.I. is related to vegetation, the elevations with W.I. = 120 and W.I. = 85 were estimated to be at 409 ± 36 m and 895 ± 92 m, respectively (estimated elevation ± se). The lower confidence interval of W.I. = 85 involves the upper part of Mt. Oyama with elevations over 803 m, which implies that the temperature environment in Mikura-jima Island would support a cool temperature zone: W.I. can fall below 85 at elevations over about 800 m, where the days with freezing temperatures total up to about a month (Fig. 6).

Re-examination of Distribution of Vegetation

Fig. 8 shows the distribution of classes of vegetation on Mikura-jima Island by elevation with notation of W.I. The vegetation classes are as defined following Sanada [15] with the following examples:

(a) Forest vegetation:
A: Daphniphyllo - Trochodendretum aralioidis,
B: Carci - Castanopsietum sieboldii,
C: *Castanopsis* coppice forest,
D: Hydrangeo - Alnetum sieboldianae,
E: *Alnus sieboldiana* secondary forest,
F: Euonymo - Pittosporetum tobira,
(b) Harbaceous vegetation:
G: Patrinio - Calamagrostietum insularis,
H: Sasa community,
I: Chrysanthemo - Miscanthetum condensatus,
(c) Artificial vegetation:
J: *Buxus microphylla* plantation,
K: *Cryptomeria japonica*, *Chamaecyparis obtusa* plantation.

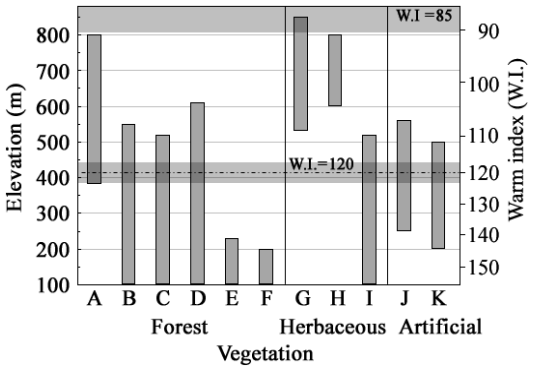

Fig. 8 Distribution of vegetation in Mikura-jima Island by elevation and estimated W.I.. A to K are the patterns of vegetation described in the text. Horizontal shading indicates confidence intervals (elevation ± se estimated by W.I.).

Compared to empirical estimations obtained by setting the lapse rate at 0.6 ˚C per 100 m, the temperature environment on Mikura-jima Island proved to be overall cooler. In particular, the distributions of Daphniphyllo - Trochodendretum aralioidis (A), Patrinio - Calamagrostietum insularis (G) and Sasa community (H) on the coastal wind-blown slopes are reasonably explained by the estimated W.I. in the present study (Fig. 8). These distributions of vegetation corresponding to W.I. were not inconsistent with those of previous reports [16], [17]. In addition to the lapse rate phenomenon, shading by clouds and fog and the occurrence of freezing temperature days likely contribute to cooling the environment in the high elevation area, which appears to enable plant species representative of a cool temperature zone to grow naturally on Mikura-jima Island.

CONCLUSIONS

We measured the atmospheric temperature on Mikura-jima Island over a period of 5 years using

thermographs placed at seven different elevations (from 130 to 800 m). Analyses of the temperature environment produced the following conclusions:
(1) Along elevation gradients, the average annual temperature ranged from 17.8 to 12.3 ˚C, and the warm index (W.I.) ranged from153 to 91.3 on the island.
(2) The lapse rate differed between lower and upper elevations with rates of 0.98 ˚C per 100 m for elevations of 500 m and below and 0.66 ˚C per 100 m for elevations of 500 m and above.
(3) W.I. was estimated to fall below 85 at elevations over about 800 m, which would produce a cool temperature zone, which reasonably explains the distribution of vegetation patterns.

These solved the inconsistency in the distribution of plant species and vegetation. Temperature environment re-examined in the present study will facilitate the planning of the goal and the evaluation or estimation of vegetational succession on Mikura-jima Island.

It should be noted that temperature observations were not taken at elevations over 800 m (e.g., the top of Mt. Oyama), and the lapse rate above 800 m can not be confirmed to maintain the 0.66 ˚C per 100 m at elevations over 800 m. It is desirable to achieve a more precise characterization of the temperature environment in Mikura-jima Island.

REFERENCES

[1] Ono M., Wildlife in solitary island. Tokyo: Iwanami Shoten, 1994, 239 pp.

[2] Tagawa H., Plant Ecology. Tokyo: Kyoritsu Shuppan Co., Ltd., 1982, 270 pp.

[3] Kira T., Forest zones in Japan. Tokyo: Japan Forest Technology Association, 1949, 42 pp.

[4] Kitamura S., Murata G. and Hori M, Colored illustrations of herbaceous plants of Japan Vol. I. Osaka: Hoikusha Publishing Co., Ltd., 2008, pp.246-264.

[5] Boysen-Jensen P, Casual plant-geography. Det Kongelige Danske Videnskabernes Selskab BIologiske Meddelelser, Bind 21, Nr. 3, 1949, pp.1-19.

[6] Arase T. and Okano T., Influence of fertilization on native plants and exotic pasture grasses on the fascined landslide slopes in Mikura-Jima Island, Japan. International Journal of GEOMATE, Vol. 8, Issue 16, 2015, pp.1316-1322.

[7] Okano T. and Arase T., Vegetation recovery process on landslide steep slope after *Alnus sieboldiana* and *Miscanthus condensatus* planting with simple terracing work in Mikura-jima Island, Japan. International Journal of GEOMATE, Vol. 10, Issue 21, 2016, pp.1884-1890.

[8] Kawamoto H., Chapter 3 (2) Weather conditions. History of Mikura-jima Village, the editorial committee of 'History of Mikura-jima Village' ed. Tokyo: Mikura-jima Village, 2006, pp.30-34.

[9] Issiki N., Geology of the Mikura-jima, Inamba-jima and Zenisu districts. Yatabe: Geological Survey of Japan, 1980, 35 pp.

[10] Kamijo T, Isogai T, Hoshino Y and Hakamada H, Altitudinal zonation and structure of warm-temperate forests on Mikura-jima Island, Izu Islands, Japan. Vegetation Science, Vol. 18, 2001, pp.13-22.

[11] Japan Meteorological Agency, Ministry of Land, Infrastructure, Transport and Turism, the web site of online search for past weather data < https://www.data.jma.go.jp/obd/stats/etrn/index.php>. (referred in 1st Apr., 2019)

[12] Ahrens C.D., Meteorology today –an introduction to weather, climate and the environment (7th edition). Pacific Grove: Books/Cole, a division of Thomson Learning, Inc. pp. 164-187.

[13] Shumiya T., Takayama K., Fujita T. and Kato H., Development of cloud zone and forest pattern along altitudinal gradients in Minami-Iwo-To Island, the Bonin Islands, southern Japan. Ogasawara Research, Vol. 33, 2008, pp.63-87.

[14] Shumiya T., Kato H. and Takayama K., Weather and soil moisture conditions along an altidunal gradient on Minami-Iwo-To Island. Ogasawara Research, Vol. 44, 2018, pp.153-166.

[15] Sanada M., Chapter 4 (2) Vegetation of Mikura-jima Island. History of Mikura-jima Village, the editorial committee of 'History of Mikura-jima Village' ed. Tokyo: Mikura-jima Village, 2006, pp.39-46.

[16] Ohba H., Die Vegetation von Mikura-Insel, Bulletin of the Kanagawa Prefectural Museum Natural Science, Vol. 1, No. 4, 1971, pp.26-53.

[17] Miyawaki A., Vegetation of Japan, Vol. 7 Kanto. Tokyo: Shibundo Co., Ltd. Publishers, 1986, 641 pp.

9th Int. Conf. on Geotechnique, Construction Materials and Environment, Tokyo, Japan, 20-22 November 2019, ISBN: 978-4-909106025 C3051

EXPERIMENTAL STUDY OF TWO-STAGE FORCED CONVECTION FURNACE FOR RIBBED RUBBER SMOKED SHEET (RSS) PRODUCTION

Machimontorn Promtong*
* Department of Mechanical Engineering, Faculty of Engineering, Mahidol University, Bangkok, 73170, Thailand

ABSTRACT

Due to improper design of the original rubber smoking-room, the Ribbed Smoked Sheets (RSS) productions at Thai Rubber Smoking Cooperatives (RSCs) are undergoing. In this research, a prototype of the two-stage forced convection system has been proposed to renovate the traditional smoking process. Generally speaking, to enhance the efficiency of fuel consumption and to increase the number of qualitative RSS, the new hot-gas supplying system was carefully designed and constructed. Eight small ventilating lids were specifically used at the smoking-room ceiling to improve the velocity and temperature distributions. To obtain the optimal temperature (60°C) for natural rubber smoking, the feeding rates of firewood and the supplying rates of hot gas while operating this new forced convection system were optimized. According to the RSS production (1458 sheets), the drying time and the fuel consumption were found at 90 hrs, and 1.04 ton per a ton of the dried sheets, respectively. Surprisingly, 92% (822 kg) of the dried RSS were found to be above the selling grades; nevertheless, the remaining was in the cutting-grade due to having the unacceptable thickness (> 3mm). Overall, the new two-stage forced convection system could save 25% of production time and 35% of fuel consumption compared with the original natural convection system. Because the harmful aerosol particles could be trapped, so this new forced convection system may be friendly to the environment as well. In future work, a Computational Fluid Dynamics (CFD) technique will be used to enhance the efficiency of this new smoking room system for RSS production.

Keywords: Forced convection flow, Ribbed Smoked Sheets (RSS), Natural rubber smoking, Temperature distribution, Energy efficiency

INTRODUCTION

Thailand has become one of the largest natural rubber (NR) producing and exporting country in the world. In 2018, 3.84 million tons ($1,000 million) of natural rubbers were produced and exported into four forms including Concentrated Latex (36%), Ribbed Smoked Sheet (RSS) (16%), Block Rubber (~1%), and miscellaneous other forms (47%). Due to the price decline of natural rubber, the production of RSS at the community's level has gained more attractive ($2.87 per kg in 2012 to $1.33 US in 2018). Nevertheless, the RSS producing time has taken up to 6 days and the consumed firewood has found as high as 1.5 tons per ton of dried RSS. Over 40 percent of the produced RSS has been also represented at low quality. According to this situation, more than half (over 300 groups) of the Rubber Smoking Cooperatives (RSCs) in Thailand cannot be operating. According to the literature reviews, the non-uniformity of the hot gas during the smoking-process has been mentioned and this is because of the improper design of the original smoking-room [1], [2] and [3].

Over a few decades, many researchers have studied the curing parameters for natural rubber drying. For instance, the effects of temperature, velocity, and moisture of inlet air were particularly demonstrated [4], [5], [6] and [7]. In order to lower the RSS production cost, the free and friendly environment energy like a solar house was designed. Basically, the solar heat could be used to preliminarily remove the moisture from the wetted rubber sheets prior to the smoking process [8], [9], [10], and [11]. Furthermore, a recently developed technology like the multiple hot-air jets was particularly suggested for curing the RSS and reducing the production time [12]. As well as, a Computational Fluid Dynamics (CFD) technique was introduced by Promtong and Tekasakul for improving the uniformity of hot gas flow inside the smoking-room. Regarding the recommendations, the original rubber smoking-room was suggested to modify further, then the smoking-time and RSS quality could be significantly improved [1] and [13].

As known, during the burning of the firewood for each RSS production, the harmful wood particles are usually released out to the environment. To protect the worker's health, many researchers have investigated the environmental pollutions at the RSCs. For example, the concentration of the aerosol particles inside the factory area was observed [14], [15], [16], and [17]. Electro Static Precipitator (ESP) was designed to trap a number of particles before

entering the smoking-room [18]. As explained, this way could improve not only the RSS quality but also reduce the number of detrimental chemicals released into the atmosphere [19], [20], and [21]. Similarly, the wastewater issue was found to be another critical problem as well [22] and [23]. Therefore, to renovate the current smoking process at the RSCs, the environmental effects should be seriously brought into consideration.

The main objectives of this research are i) to experimentally study the capability of the new forced convection smoking room system under various operating conditions, ii) to investigate temperature distribution inside the modified smoking-room while operates using two proposed functions and iii) to evaluate the performance of the new smoking-room system under real RSS production, especially in term of fuel consumption, production time, and the percent of the RSS satisfied the marketing grades.

THE RUBBER SMOKING-ROOM AND ITS MODIFICATIONS

The Original Smoking Room

The dimensions of the original rubber smoking room are 2.6-wide×6.2-depth×3.7 height-m (Fig. 1). On the room floor, twelve 10-cm diameter inlet gas supply ducts are used for hot-air introduction during the smoking period. At the ceiling, two 0.6×0.6-m ventilating lids are installed for the air outlets. Also, there is an 8-m chimney with a 200-mm-diameter used for hot air exhaust and temperature control inside the smoking-room.

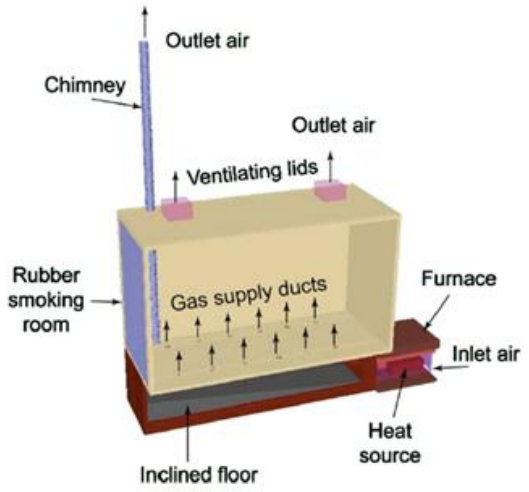

Fig. 1 The model of original rubber smoking-room used at Thai Rubber Smoked Cooperative [13]

Details of the New Smoking-Room System

Due to having a high-temperature variation inside the traditional rubber smoking room (~15°C), about 40% of the produced RSS were represented at low quality [6]. As a consequence, the parts of the rubber smoking-room were suggested to be modified. For instance, since it was found that a chimney is the cause of the loss of energy, thus the draft tube was disconnected from the heat supply system [5]. However, in this work, the size of the rubber smoking room was not modified because its capacity is suitable for daily RSS production at the community's level.

Modifications of the room inlet and outlet

The adjustment of sizes and positions of the inlets and the outlets of the rubber smoking-room could improve the uniformity of the flow [4]. At the room inlets, 12 round ducts remained the same diameter and positions for the hot gas introduction. However, they are directly connected to the new furnace via the main supply duct (Fig. 3). At the outlets, two original ventilating lids (0.6×0.6 m) at the ceiling were replaced by the eight lids of 0.25×0.25 m and their locations are identical with the simulation. Further details can be found in our previous simulation study [1].

Details of the new two-stage forced convection smoking room system

As shown in Fig. 3, the new forced convection system consisting of the heat exchanger unit, a 1-HP-motor with a fan set, and a piping loop, is mainly used for hot gas supplement and circulation. A Variable-Frequency Drive (VFD) is installed to control the fan speed and torque by varying motor input frequency and voltage. Adjustments of the firewood fed and the motor speed via the VFD, hence the velocity and temperature inside the smoking-room can be controlled within the desired range for RSS production [8].

In practical, this new forced convection system can supply the hot gas to either one or two rubber smoking-rooms. By using two rooms, about 3,150 wetted rubber sheets can be smoked at the same time. For a safety reason, a pressure relief valve is installed at the top of the furnace. Likewise, three dust-trap boxes are installed along the main pipes between the furnace and the smoking-room for blocking and collecting the fly ash (however they are not detailed).

Functions of the new forced convection system

The one-way flowing and the waste gas recirculation are two functions of the new forced convection system that are designed for RSS production. Basically, this first function is proposed to efficiently remove the moisture of the wetted rubber sheets. As shown in Fig. 3 the flow path of this one-way supplying mode is started from 1→2→3→4 respectively. Ideally, the desired length of the flow path of hot gas in the smoking-room should be a strength line (as short as possible) from the floor to the ceiling during this function operation. In this first stage, the ventilating lids should be fully opened to allow the moisture flowing out without any blockages.

The waste gas recirculation function is designed to enhance energy efficiency by utilizing the wasted gas. Briefly, the direction of the flow path is started from 5→6→2→3→5, respectively (Fig. 3). It should be noted that during this second stage the ventilating lids should be closed so that the wasted gas can be circulated and reused. Therefore, the circulation of the waste gas during this lateral function may reduce the number of soot particles released into the environments.

EXPERIMENTAL DETAILS

The experiments were carried out using two modified rubber smoking-rooms at Ban-Nong-Deang Samaggi Rubber Cooperative, Nakhon Si Thammarat province, Thailand. Details of tools, measuring positions, research methodology, and performance indicators are described as follows:

Measurement Tools

Type-K thermocouples were used for the temperature measurement, and a data logger (Data-Taker, DT 500) was used to record the temperatures at 5-min intervals to ensure a continuous reading. A hot-wire anemometer (Airflow, TA400T, 3% full display scale) was used for the velocity measurement. The firewood of known mass was fed to the burner to supply heat to the rubber smoking-room and its moisture content was determined on a dry basis. Drying the wood samples in a laboratory oven at 105°C until its mass did not change, then the moisture content and its heating value can then be examined [24].

Positions of Measurements

Three positions at the burner inlet were used to measure air velocities. The outlet gas velocities at eight ventilating lids of the rubber smoking-room were also measured for comparison purposes. These measurements were recorded every hour during the experimental period and their locations are presented in Fig. 4.

Moreover, the temperatures of fifteen positions in the modified rubber smoking-room were also investigated (Fig. 4). As well, the temperatures of two positions (T_{rear} and Tf_{ront}) at the ceiling were

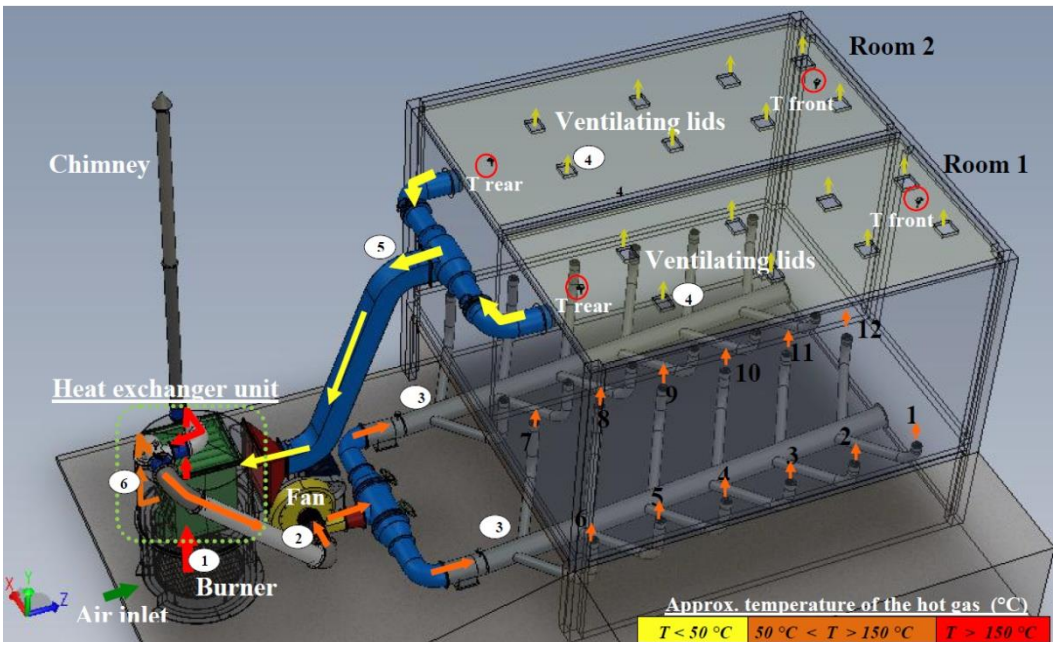

Fig. 3 Details of the new smoking room system and approximate hot gas temperature entering and leaving the smoking room

particularly monitored during the suitable rates of the firewood and the motor speeds were examined (Fig. 3). Their probe ends are situated at 0.40 m below the ceiling inside the rubber smoking-room. Ambient temperature was also measured, and this measurement was close to the air inlet of the burner.

optimize together with monitors of the temperature occurred inside the rubber smoking-room. To prevent the deterioration of the natural rubber sheet, the smoking temperature is specifically controlled to be around 60°C.

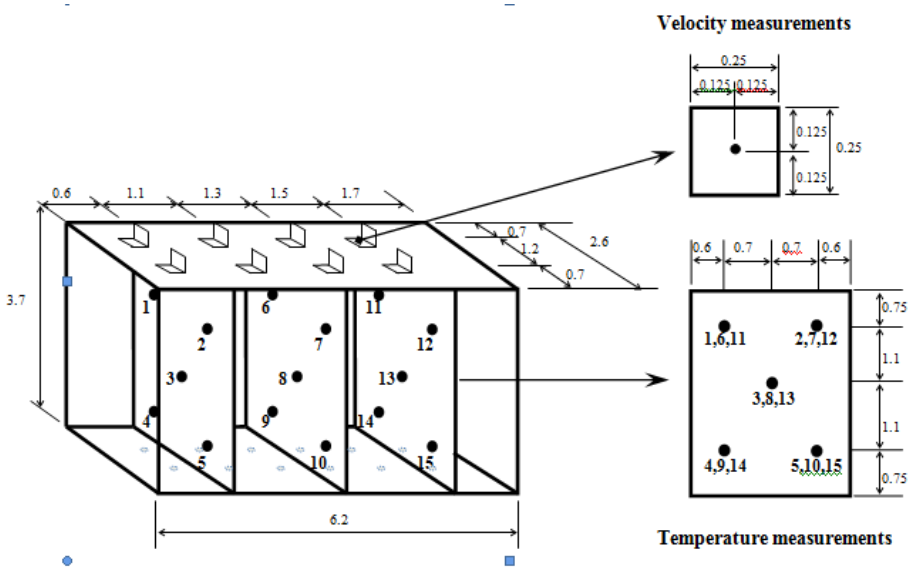

Fig. 4 Positions of temperature (side view), and velocity measurements (top view) at the smoking room (units in meters)

Research Methodology

In order to conduct the experiments for evaluating the capability of the new forced convection smoking room system, this research work is thus divided into four main steps as illustrated in Fig. 5. In brief, the fan speeds and the feeding rates of firewood are firstly focused to

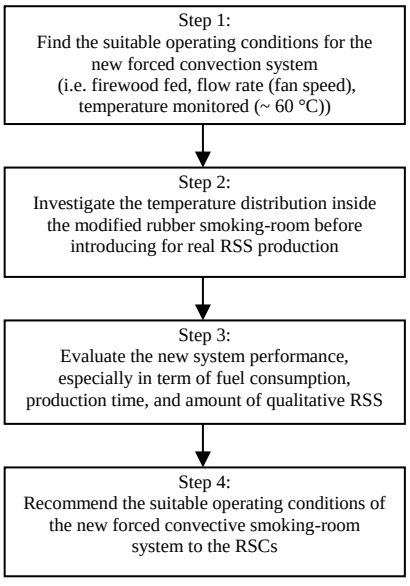

Fig. 5 A flow chart representing the main research methodology

A lower temperature is also acceptable; however, a longer time for RSS production may be required. Temperatures of fifteen positions in the modified rubber smoking-room are secondly investigated under the use of suitable operating conditions. During the experiment, the temperatures were monitored every 5 minutes for continuous reading. The interesting results from this investigation are presented and discussed in the following section.

Thirdly, the new forced convection smoking-room system is used for real RSS production. During the experimental investigations, the fuel consumption, the production time and the percent of qualitative RSS for the one-room operation are discussed. The performance of this new smoking room system is then evaluated and reported in this paper. Lastly but most importantly, the instructions regarding how to operate this new forced convection smoking-room system for RSS production are recommended to the RSCs.

Performance Indicators

Thermal efficiency and specific firewood consumption are normally used for estimating the performance of the new forced convection rubber-smoking system. However, in the section of results, only the specific firewood consumption is discussed.

Thermal efficiency ($\eta_{thermal}$) is calculated as shown as follows [25]:

$$\eta_{thermal} = \frac{m_L \times L}{(HV)_{firewood} \times m_{firewood}} \quad (1)$$

where $m_L, m_{firewood}$ are the evaporation mass of water (kg) and the firewood mass (kg), L is the latent heat of vaporization (kJ/kg), $(HV)_{firewood}$ is the heating value of the firewood (kJ/kg).

The specific firewood consumption per ton of dried rubber sheet while using the new smoking room system can be calculated by using the following equation:

$$Firewood-consumption = \frac{m_{firewood}}{m_{dried-RSS}} \quad (2)$$

As mentioned in [26], $m_{dried-RSS}$ is the total mass of dried RSS.

RESULTS AND DISCUSSION

The important results including the ambient temperature, inlet and outlet velocities (volumetric flow rate), firewood feeding rate as well as temperature variation are firstly presented in this section. To investigate the temperature variation, the experiments were conducted using the empty modified smoking-room, thus the moisture effects can then be ignored. Other interesting results including the ambient temperature, the firewood moisture are additionally given.

After the temperature investigation, this new forced convection smoking-room system was reintroduced for RSS production. So, in the second part of this section, the results regarding the performance indicators of the new smoking-room system, i.e. temperature variation, firewood consumption and percent of satisfied RSS are presented and discussed.

Case 1: Investigating temperature variations in the empty modified smoking room

Because the configurations of the two modified smoking-room are identical, thus only one room was used to conduct the experiment. The appropriate operating conditions from preliminary observations were adopted for this temperature distribution investigation. Generally speaking, the maximum difference of the temperature among fifteen locations for both available functions (one-way flowing and waste gas recirculation) was specifically observed and also compared with the original rubber smoking room.

Feeding rates of firewood and inlet/outlet velocities (volumetric flow rates)

To accelerate the temperature inside the modified smoking-room for the first 2 hrs, 60 kg of the firewood was fed at the furnace and the fan speed was specified by setting VFD at 60 Hz (Table 1). From the measurements, the average air velocity at the burner inlet was found about 2.68 m/s and the average hot gas velocity at the ventilating lid outlets was about 1.02 m/s. After calculations, the volumetric flow rates of inlet air and outlet gas were found to be 0.282 m^3/s and 0.421 m^3/s, respectively.

After the heating-up period, 40 kg of the firewood was fed at the burner in every 3 hrs during 2-14 hrs and the VFD frequency was reduced to 50 Hz. Average velocities of air entering the burner and the gas flowing out the ventilating lids were found at 2.17 m/s and 0.88 m/s, respectively. According to the values, the volumetric flow rates were 0.227 m^3/s and 0.365 m^3/s, respectively.

Table 1 The velocities measuring at furnace inlet and ventilating lids and their volumetric flow rate.

Operating function (Time/VFD frequency/Feeding rate)	INLET	OUTLET
	Average velocity (m/s)	Average velocity (m/s)
	The flow rate of inlet air (m^3/s)	The flow rate of outlet waste gas (m^3/s)
One-way flowing (0-2 hrs /60Hz /60 kg every 2 hrs)	2.68	1.02
	0.282	0.421
One-way flowing (2-14 hrs/ 50Hz/ 40 kg every 3 hrs)	2.16	0.88
	0.227	0.365
One-way flowing (14-32 hrs/ 50Hz / 35 kg every 3 hrs)	2.11	0.85
	0.222	0.349
Waste gas recirculation (32-64 hrs/ 40Hz/ 30 kg every 3 hrs)	-	-

The reductions of the firewood fed and the fan speed were due to a requirement of the temperature control around 60 °C. Lower feeding rate of the firewood (35 kg every 3 hrs) at the burner was attempted for the third period (14-32 hrs). As a result, the volumetric flow rates of inlet air and outlet exhaust gas were found slightly lower than the second period (0.222 m^3/s and 0.349 m^3/s).

For the last period (32-64 hrs), the waste gas recirculation function was introduced instead of the one-way flowing. During the operation, the ventilating lids were shut down and the waste gas temperature was circulated and reheated using the heat exchanger. Also, to maintain temperature around 60 °C, the feeding rate of the firewood required was found at only 30 kg every 3 hrs.

Temperature distribution and other interesting parameters

Fig. 6 shows the temperature results measured in the modified smoking-room. Clearly, the temperatures are quickly climbed up and reached 70°C within the first hour. With the selected firewood fed and the fan speed, the room temperature can be raised efficiently. During these two hours, the maximum variation of the temperature was found as high as 6.3°C.

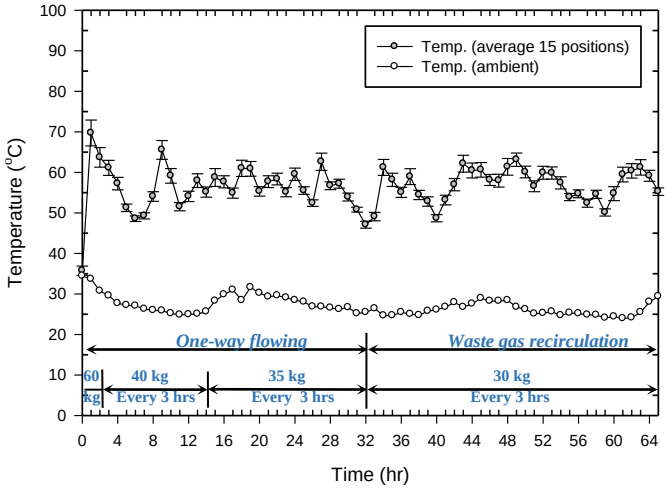

Fig. 6 The average temperature of fifteen positions measuring in the smoking-room and the ambient temperature

During the employment of one-way flowing function, all the ventilation lids were fully opened. For the second and third periods (2-32 hrs), the average temperature from the fifteen positions was 56.3°C and the maximum variation remained at 4.6 °C, occurred at a ninth of the experiment.

While the waste gas recirculation (32-64 hrs), the average temperature among the measuring positions was 57.3°C and the maximum variation was reduced to 3.8 °C. According to these results, with a lower feeding rate of the firewood (5 kg every 3 hrs), in general, the average temperature was higher than using the one-way flowing mode.

Using the waste gas recirculation for the last period, the average temperature from fifteen positions was found at 57.3°C, and the maximum variation remained only 3.8°C (Fig. 6). The firewood consumption fed in this period was less than that used in the one-way flowing mode about 5 kg every 3 hrs. Nevertheless, it still gave a higher average temperature in the rubber smoking-room.

Because the ambient temperature is usually high and the air humidity is also low during daytimes, hence heating up the room temperature and removing the rubber sheet moisture on this time may be easier and more efficient. According to this reason, the one-way flowing function is suggested to be first introduced during daytimes for RSS production.

Case 2: Evaluating the performance of the modified smoking-room system for RSS production

As aforementioned, the performance of the new smoking-room system used for RSS production is another focus to be observed in this work. Prior to the smoking process, the preparations of the wetted ribbed rubber sheets at the RSCs can be reviewed from the work of Dejchanchaiwong [26]. The number of wetted rubber sheets filled up the smoking room for the case of one-room smoking was 1458 sheets. The experiments were begun at 11.00 a.m.; hence the ambient temperature at the beginning was found near the highest on that date.

Feeding rates of firewood and inlet/outlet velocities (volumetric flow rates)

In this experiment, the operating conditions used during the RSS production (0-78 hrs) are similar to the previous study that the temperature variation was investigated. For instance, 60 kg of the firewood feeding rate was fed at the burner for raising the smoking temperature for the first 2hrs (Table 2). Due to an attempt to reduce fuel consumption in the low-moisture period (78-92 hrs), the feeding rate was reduced to 25 kg every 3 hrs.

Table 2 The inlet air velocities, outlet hot gas velocities and their volumetric flow rates

Operating function (Time/VFD frequency/Feeding rate)	INLET	OUTLET
	Average velocity (m/s)	Average Velocity (m/s)
	The flow rate of inlet air (m^3/s)	The flow rate of outlet waste gas (m^3/s)
One-way flowing (0-2 hrs /60Hz /60 kg every 2 hrs)	2.42	0.644
	0.254	0.266
One-way flowing (2-14 hrs/ 50Hz/ 40 kg every 3 hrs)	2.29	0.590
	0.240	0.244
One-way flowing (14-32 hrs/ 50Hz / 35 kg every 3 hrs)	2.28	0.619
	0.239	0.255
Waste gas recirculation (32-92 hrs/ 40Hz/ 30 kg every 3 hrs)	-	-

As shown in Table 2, the velocities of inlet air are between 2.28-2.42 m/s and the average velocities of outlet gas at the ventilating lids are between 0.590-0.644 m/s. The volumetric flow rates of inlet air and outlet gases were at 0.239-0.254 m^3/s and 0.255-0.266 m^3/s, respectively.

Also, the velocities and the flow rates measured at the outlets in this RSS production were lower than the previous study about 35%. This may be because the gas had a lower temperature and the rubber sheets also caused the pressure drop.

Temperature distribution and other interesting parameters

The temperatures of fifteen locations measured during the smoking process are presented in Fig. 7. As can be seen, for the first 2 hours the temperatures climbed up slowly and reached a maximum of about 55.2°C. During using the one-way flowing function (0–32 hrs), the average temperature was about 52.5 °C and the maximum variation of the temperature was 10 °C.

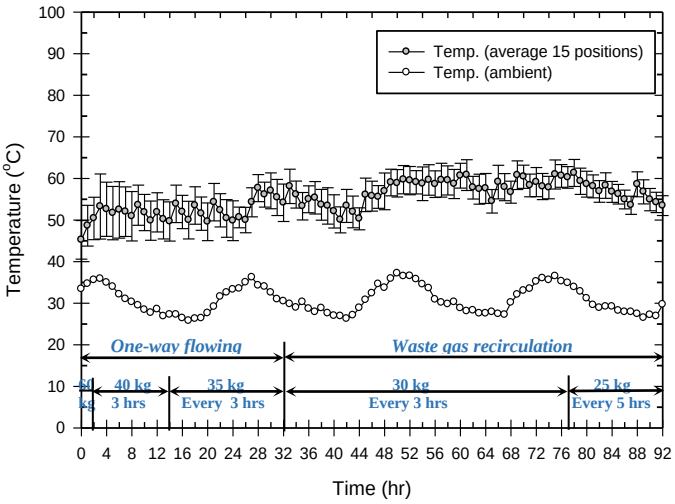

Fig. 7 The average temperature of fifteen positions measuring during the smoking process and ambient temperature

The reduction of the average smoking temperature (~8 °C) may be caused by the moisture removal process. During the drying process, the flowing heats were absorbed by the wetted rubber sheets and caused the moisture (mass) transferring to the surface. Afterward, the moisture was swept away by the carrier gas, as a consequence, the temperature of the hot gas was reduced. Anyways, with a higher rate of firewood fed, the smoking temperature could be increased.

During the waste gas circulation period (32-92 hrs), with the mentioned firewood fed (25-30 kg for every 3 hrs) the average temperature was about 57.1 °C. The maximum variation was found around 8.0 °C, which occurred at the 40th of the experiment. This high variation may be because having a low ambient temperature and high moisture in the smoking room.

CONCLUSIONS

The new two-stage forced convection smoking room system has been proposed to renovate the traditional natural convection smoking-process. To maintain the temperature around the optimal for natural rubber smoking (60 °C), the highest consumption rate was found at 30 kg every 3 hrs. Surprisingly, this consumption rate was less than the average feeding rate used at the RSCs around 35%.

According to the temperature investigation, the maximum difference (4.6 °C) inside the modified smoking-room was found less than approximately three times compared with the original smoking-room. Comparing between the one-way flowing and the waste gas recirculation functions, the maximum temperature variation of the recirculation was found at a lower value (3.8 °C). Also, this temperature result can confirm the previous simulation study.

From the RSS production (1458 sheets), the drying time and the consumption were required at 90 hrs and 1.04 ton per a ton of dried sheets, respectively. After the cutting process, around 822 kg (92%) of the produced RSS represented above the marketing grades. Therefore, it can be anticipated that this new forced convection system could save about 25% of the production time and 35% of the fuel consumption.

ACKNOWLEDGEMENTS

This research was financially supported by iTAP-Walailak University and the NSTDA, Thailand. Many thanks go to Wood Science and Engineering Research Unit, Walailak University and Mechanical Engineering Department, Prince of Songkla University, for the facilities. Special thanks go to Ban-Nong-Deang Samaggi Rubber Smoking Cooperative and Mr. Boonchod Romyen for the superb assistance. Many thanks go to Dr. Prachid Saramolee, Dr. Korakot Suwannarat, Mr. Puchong Dangrah, and Mrs. Leelanuch Leelapitak for the great supports during experimental works.

REFERENCES

[1] Tekasakul, P. and M. Promtong, Energy efficiency enhancement of natural rubber smoking process by flow improvement using a CFD technique. Applied Energy, 2008. 85(9): p. 878-895.

[2] Office of Industrial Economics. Rubber Intelligence Unit 2019; Available from: http://rubber.oie.go.th/ImExThaiByProduct.aspx?pt=ex.

[3] Office of the Rubber Replanting Aid Fund 2019; Available from: http://www.raot.co.th/ewtadmin/ewt/raot_en/rubber2012/rubberprice_yr_eng.php.

[4] Promtong, M. and P. Tekasakul, CFD study of flow in natural rubber smoking-room: I. Validation with the present smoking-room. Applied Thermal Engineering, 2007. 27(11-12): p. 2113-2121.
[5] Kalasee, W., Pongpariyawatee, Y., Tantaprapa W., Suwanjaras S., Kirirat P. and P. Tekasakul, Fuel efficiency enhancement in rubber smoking for rubber cooperative in Southern Thailand. The 17th conference on mechanical engineering network of Thailand,Prachinburi, Thailand, 2003: p. 560-564.
[6] Promtong, M., CFD study of flow in rubber smoking room and modification to improve uniformity of velocity and temperature distributions. 2006, Prince of Songkla University.
[7] Pomvisaid, J., Affecting of air velocity and temperature for rubber sheet drying. Project No. ME 6/2537, 1984(Department of Mechanical Engineering, Faculty of Engineering, Prince of Songkla University, Thailand).
[8] Prasertsan, S. and P. Kirirat, Factors affecting rubber sheet curing. RERIC Int Energy J, 1993. 15: p. 77–87.
[9] Prasertsan, S., Kirirat P., Sen-Ngam S., Prateepchaikul G. and N. Coovattanachai, Monitoring of the rubber smoking process. RERIC Int Energy J 1992. 15(1): p. 49-63.
[10] Tanwanichkul, B., S. Thepa, and W. Rordprapat, Thermal modeling of the forced convection Sandwich Greenhouse drying system for rubber sheets. Energy Conversion and Management, 2013. 74: p. 511-523.
[11] Pratoto, A., M. Daguenet, and B. Zeghmati, Sizing solar-assisted natural rubber dryers. Solar Energy, 1997. 61(4): p. 287-291.
[12] Pratoto, A., M. Daguenet, and B. Zeghmati, A simplified technique for sizing solar-assisted fixed-bed batch dryers: Application to granulated natural rubber. Energy Conversion and Management, 1998. 39(9): p. 963-971.
[13] Promtong, M., CFD Study of Flow in Rubber Smoking Room and Modification to Improve Uniformity of Velocity and Temperature Distributions in Department of Mechanical Engineering. 2006, Prince of Songkla University.
[14] Nuntadusit, C. and M. Waehahyee, Drying of Rubber Sheet Using Impingement of Multiple Hot Air Jets. Advanced Materials Research, 2013. 844: p. 502-506.
[15] Tekasakul, P., Furuuchi, M., Tekasakul, S.,Chomanee, J. and Y. Otani, Characteristics of PAHs in Particulates in the Atmospheric Environment of Hat Yai City, Thailand, and Relationship with Rubberwood Burning in Rubber Sheet Production. Aerosol and Air Quality Research, 2008. 8(3): p. 265-278.
[16] Chomanee, J., Effects of Moisture Content and Burning Period on Concentration of Smoke Particles and Particle-Bound Polycyclic Aromatic Hydrocarbons from Rubber-Wood Combustion. Aerosol and Air Quality Research, 2009.
[17] Purba, L. and P. Tekasakul, Computational Fluid Dynamics Study of Flow and Aerosol Concentration Patterns in a Ribbed Smoked Sheet Rubber Factory. Particulate Science And Technology, 2012. 30(3).
[18] Kalasee, W., Improvement Soot Particles Separation Equipments for Rubber Smoking Chamber. Aerosol and Air Quality Research, 2009.
[19] Tekasakul, P. and S. Tekasakul, Environmental Prolems Related to Natural Rubber Production in Thailand. Aerosol Research, Japan, 2006. 21(2): p. 122-129.
[20] Furuuchi, M., Furuuchi, M., Tekasakul, P., Murase, T., Otani, Y., Tekasakul, S., and Y. Bai, Characteristics of Particulates Emitted from Rubber-wood Burning. Journal of Ecotechnology Research, 2006. 12(1-2): p. 135-139.
[21] Choosong, T., Workplace Environment and Personal Exposure of PM and PAHs to Workers in Natural Rubber Sheet Factories Contaminated by Wood Burning Smoke. Aerosol and Air Quality Research, 2010.
[22] Ruttanachot, C., Application of Electrostatic Precipitator in Collection of Smoke Aerosol Particles from Wood Combustion. Aerosol and Air Quality Research, 2011.
[23] Chaiprapat, S. and S. Sdoodee, Effects of wastewater recycling from natural rubber smoked sheet production on economic crops in southern Thailand. Resources, Conservation and Recycling, 2007. 51(3): p. 577-590.
[24] Khullar, C., Effects of chemical additives on the reduction of particulate emissions and combustion deposits in solid fuel fired systems. 1995: p. 362–386.
[25] Dejchanchaiwong, R., Arkasuwan A., Kumar A., and P.Tekasakul, Mathematical modeling and performance investigation of mixed-mode and indirect solar dryers for natural rubber sheet drying. Energy for Sustainable Development, 2016. 34: p. 44-53.
[26] Dejchanchaiwong, R., Kumar, A., and P. Tekasakul, Performance and economic analysis of natural convection based rubber smoking room for rubber cooperatives in Thailand. Renewable Energy, 2019. 132: p. 233-242.

9th Int. Conf. on Geotechnique, Construction Materials and Environment, Tokyo, Japan, 20-22 November 2019, ISBN: 978-4-909106025 C3051

BEHAVIOR OF INDUSTRIAL BUILDING UNDER SEISMIC LOADING

Nontawit Muangnoi[1], Piyawat Foytong[1], Apichat Janpila[1] Maetee Boonpichetvong[1], Natthapong Areemit[1], Tanyada Pannachet[1] and Anat Ruangrassamee[2]
[1] Sustainable Infrastructure Research and Development Center, Department of Civil Engineering, Faculty of Engineering, Khon Kaen University, Khon Kaen, 40002, Thailand.
[2] Department of Civil Engineering, Faculty of Engineering, Chulalongkorn University, Bangkok, 10330, Thailand.

ABSTRACT

Every year, earthquakes cause injuries, deaths, severe structural damage to buildings and destruction of property in many countries. In developing countries, economic growth depends on industrial development. Therefore, if an earthquake occurs, it may cause severe damage to large industrial factories. This present study aims to examine the structural behavior of industrial buildings under the earthquake force which is a reinforced concrete building. The structure of an industrial building is different from a general building. In this study, the factory is a four-story building with the dimensions of 34.4 meter in width, 59.2 meters in length and 15.6 meters in height. In the analysis, the nonlinear dynamic procedure is applied to analyze the building behaviors. The 20 seismic waves are selected and adjusted with the ASCE41-13. LMSR wave are considered in x-direction and y-direction. From the results, the responses and damage of the industrial structure are analyzed. The building has performed the soft story irregularity. The performance level for the acceptance criteria, according to ASCE41-13 and FEMA365 is life safety performance level. Therefore, the industrial factory building is needed to enhance the seismic capacity for damage prevention.

Keywords: Seismic behavior, Reinforced concrete, Industrial factory building, Nonlinear time history procedure

INTRODUCTION

The industrial sector has had an important role in the economic growth in developing countries. Pricing instruments with technological innovation are installed in factories. Therefore, if an earthquake occurs, it may cause severe damage to industrial instruments and building structures. To prevent and reduce this potential damage, an industrial factory is analyzed under seismic loading in this present study. A four-story reinforced concrete building located in the Northeastern region of Thailand is analyzed. The building model comprises a linear elastic element, a fiber element and a rigid joint. The fiber element is located at both ends of structural members to represent the nonlinear behavior of them. This analysis applies a nonlinear time history procedure subjected to 20 seismic waves using PERFORM3D program [1]. A three-dimensional fiber model is used to model plastic hinges for columns and beams. The seismic waves are appropriately scaled with a design response spectrum of the Northeastern region according to the Earthquake Resistant Design code 1303 [2] of Thailand. The analysis results are reported in terms of maximum inter-story drift and rotation of fiber elements, which are used to specify the damage level related to the acceptance criteria of ASCE41-13 [3] and FEMA356 [4].

ANALYZED BUILDING

The analyzed industrial factory is a 4-story reinforced concrete building which is used as a cooling tower. The structural type is a moment-resisting frame with beams and columns. The first-floor plan with beam section is shown in Fig. 1. The dimensions of this factory building are 22.4 meters in width, 59.2 meters in length and 16.2 meters in height. There are eight spans of columns in length and four spans of columns in width with a span of 7.4 meters and 5.6 meters, respectively. As illustrated in Fig. 2, the height of each story from the first floor to the fourth floor is 1.80 meters, 7.45 meters, 3.82 meters and 3.11 meters, respectively. This building has a symmetrical appearance in the plan, but the structural configuration is an irregularity in the vertical. There are two rectangular column sections in the building as shown in Table 1. The 650x650 mm column section consists of 20-DB32mm longitudinal reinforcement bars and 5-DB12@200mm crossties stirrup. The 700x700 cm column section includes of 24-DB32mm longitudinal reinforcement bars and 7-DB12@200mm crossties stirrup. There are seventeen rectangular beam sections in the building. The section and reinforcement of beams are demonstrated in Table 2. Rotors and gearboxes are placed at the roof level, with the weights of 1,843

kilograms and 1,937 kilograms, respectively. In the construction drawing, the compressive strength of concrete is 23.54 MPa and the specified yield strength of reinforcement is 490.33 MPa.

Table. 1 Rectangular column sections and reinforcement details.

No.	Section (cm.)	Reinforcement	Stirrup
C1	650x650	20DB32	5DB12@200
C2	700x700	24DB32	7DB12@200

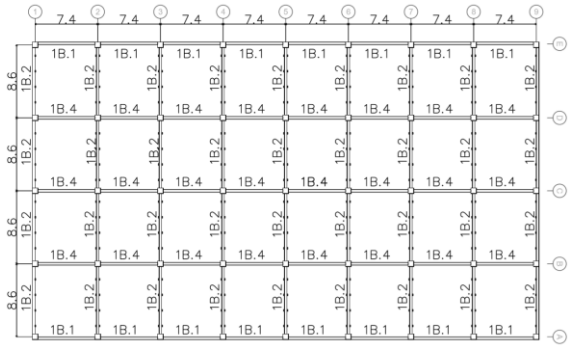

Fig. 1 First floor plan at an elevation of 1.80 meters.

Table. 2 Beam sections and reinforcement details.

No.	Section (mm.)	Upper Reinf.	Lower Reinf.	Stirrup
1B.1	300x750	4DB25	4DB25	DB12@125
1B.2	300x750	5DB25	5DB25	DB12@125
1B.4	300x750	6DB25	6DB25	DB12@200
2B.1	300x750	2DB25	2DB25	DB12@150
2B.2	300x750	4DB32 2DB16	6DB25	DB12@150
2B.4	300x750	4DB20	4DB20	DB12@150
2B.5	350x750	4DB16	4DB16	DB12@200
3B.1	300x750	4DB20	4DB20	DB12@200
3B.2	300x750	4DB32 2DB16	4DB25	DB12@125
RB1	300x700	2DB20	2DB20	DB12@200
RB2	250x600	4DB25	4DB25	DB12@200
RB3	300x800	5DB25	5DB25	DB12@150
RB4	300x700	2DB16	2DB16	DB12@200
RB5	300x700	2DB20	2DB20	DB12@150
RB6	300x700	2DB20	2DB20	DB12@150
RB7	250x600	2DB25	2DB25	DB12@150
RB8	500x800	8DB25	8DB25	DB12@150

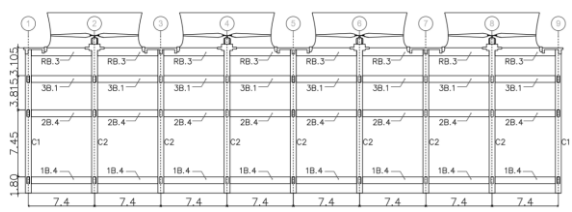

Fig. 2 Side view at gridline B.

SEISMIC HAZARD

Seismic behaviors under the seismic hazard of the factory building in the Northeast region of Thailand is analyzed by using the nonlinear time history procedure. The seismic waves are appropriately scaled with the design response spectrum constructed from the seismic hazard. The new seismic hazard for this area was proposed by Janpila [5]. which is approximately twice as high as the Earthquake Resistant Design code 1303 of Thailand [2]. The highest seismic hazard location is selected, which is in Nongkai province. According to the Earthquake Resistant Design code 1303 [2], the seismic hazard with the probability of exceedance of 10% in 50 years is used to evaluate the seismic behavior of an existing building structure. The seismic hazard map in the term of spectral acceleration (SA) at the structural periods of 0.2 and 1.0 second at base rock level with 5% critical damping ratio for reference return periods of 10% POE in 50 years are shown in Fig. 3 and 4, respectively. The spectral acceleration at the structural periods of 0.2 and 1.0 second at Nongkai province are 0.567 m/s^2 and 0.204 m/s^2, respectively. The target design response spectrum used to analyze the factory building is shown in Fig. 5.

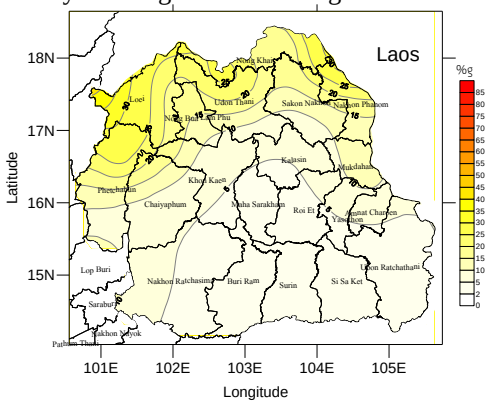

Fig. 3 Seismic hazard maps in the Northeast region of Thailand corresponding to a probability of exceedance of 10% in 50 years, SA0.2sec.

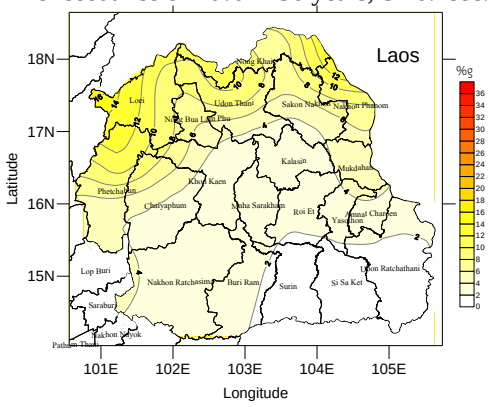

Fig. 4 Seismic hazard maps in the Northeastern Thailand corresponding to a probability of exceedance of 10% in 50 years, SA1.0sec.

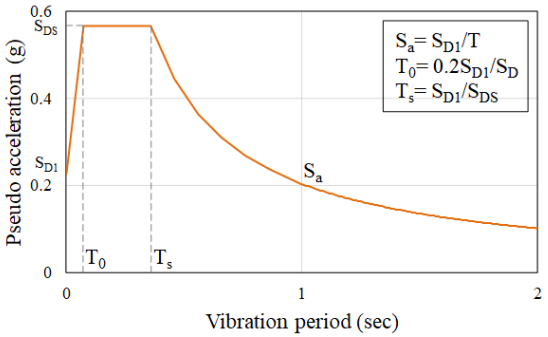

Fig. 5 Target design response spectrum at Nongkai province, Thailand at base rock level with 5% critical damping ratio for 10% POE in 50 years

BUILDING MODEL

Model calibration

The building model is analyzed with the nonlinear time-history procedure under 20 seismic waves by using PERFORM3D [1] program. The nonlinear behaviors of the structure are represented by fiber elements located at both ends of structural members. The fiber element is separately modelled by considering the behavior of each material, which primarily consists of unconfined concrete models, confined concrete models and longitudinal reinforcement models. The stress-strain relationships of unconfined concrete are modeled using the equation proposed by Kent and park [6]. The confined concrete behavior is modeled using the equation proposed by Hoshikuma et al. [7]. The longitudinal reinforcement is modeled using the equation proposed by Menegotto and Pinto [8]. When conducting a structural model validation, the results of RC columns experiment obtained from the study by Wehbe et al. [9] and RC frames experiment results received from Anil and Altin [10] are compared to analytical results. The plastic hinge lengths of beams and columns are evaluated by using the equation proposed by Paulay and Priestley [11] as shown in Eq. 1.

$$L_p = 0.08L + 0.022d_b f_y \quad (1)$$

where L is the distance from a critical section to the point of contraflexure (meters), d_b is the diameter of longitudinal reinforcement (meters) and f_y is the yield stress of longitudinal reinforcement (MPa).

RC columns experiment conducted by Wehbe et al. [9] yielded results of a rectangular column section with the dimensions of 610mm x 380mm and 2.050 m in height. The longitudinal reinforcements were 18-DB19mm. The transverse reinforcements were 2-RB6mm crossties and 2-RB10mm crossties with an equal space of 110mm interval along with the column height. The RC column was tested under cyclic loading with an axial force of 615 kN. The compressive strength of concrete was 27.2 MPa. The yield strengths of reinforcements were 445 MPa, 428 MPa and 448 MPa for DB19, RB10 and RB6, respectively. The column model consists of the fiber element and elastic element is shown in Fig 6. The plastic hinge is 0.352 m in length. The comparison of force and deformation obtained from the analytical results versus the experimental results is shown in Fig 7. The analytical results can also capture experimental behaviors. The analytical results give a slightly lesser amount of the maximum load and slightly greater estimates of the initial stiffness than the experimental results.

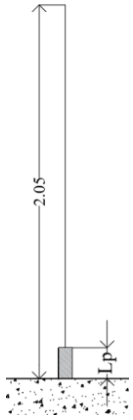

Fig. 6 Model of RC columns experiment results conducted by Wehbe et al. (1999).

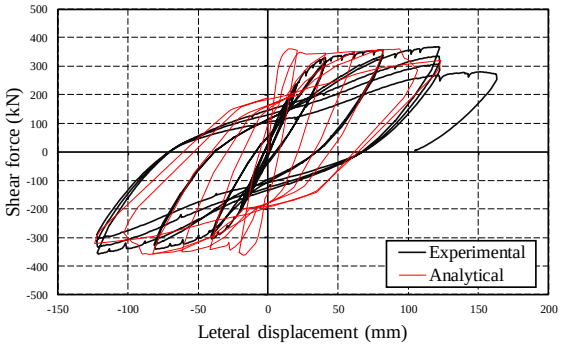

Fig. 7 The Comparison of analytical results versus experimental results by Wehbe et al. (1999).

For RC bare frame experiment results of the study by Anil and Altin [10], the rectangular columns were the 100x150mm section with 4-DB10mm for the longitudinal reinforcement and RB6 crossties with an equal space of 40mm interval along with the column height. The rectangular beam was 150x300mm section with 4-DB8mm for both top and bottom reinforcement and RB4 crossties with an equal space of 40mm interval along the beam length. The compressive strength of concrete was 21.8 MPa. The yield strengths of reinforcements

for DB10, DB8, RB6 and RB4 were 475 MPa, 592 MPa, 427 MPa and 326 MPa, respectively. The bare frame model which comprises the fiber element, elastic element and rigid joint connection is shown in Fig. 8. The plastic hinge lengths of beam and column are 0.174 m and 0.150 m, respectively. The comparison of the analytical results versus the experimental results is presented in Fig. 9. Experimental behaviors can be captured by analytical results.

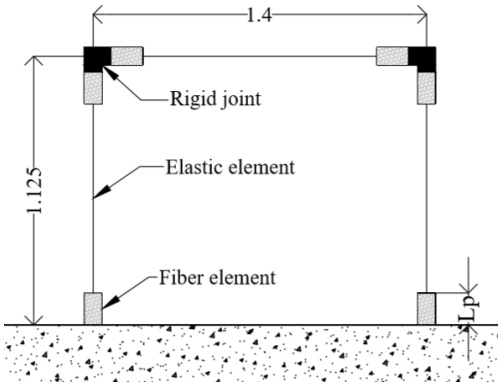

Fig. 8 Model of RC frame experiment results of the study by Anil and Altin (2007).

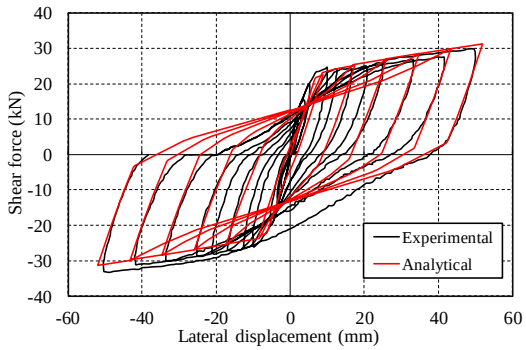

Fig. 9 The Comparison of analytical results vs. experimental results of the study by Anil and Altin (2007).

Analyzed model

An analysis of seismic behavior under seismic hazard of the factory building located in Northeastern Thailand applies the nonlinear time history procedure. The building model consists of the elastic elements in the middle of members, the fiber elements at both ends of members and the beam-column connection which is assumed to be rigid. The foundations are modelled as fixed support. RC slab in each floor is considered as a rigid floor. The fiber element is modelled by dividing the cross-section into the properties of each material, which are confined concrete, unconfined concrete and longitudinal reinforcement. Fig. 10 describes the fiber section of columns C1 and C2. For column C1, the fiber section is divided into 18 sub-elements for unconfined concrete, 8 sub-elements for confined concrete and 20 sub-elements for longitudinal reinforcement. For column C2, the fiber section is divided into 18 sub-elements for unconfined concrete, 8 sub-elements for confined concrete and 20 sub-elements for longitudinal reinforcement. The 3D building model is shown in Fig. 11. The Preliminary analysis of the building model is performed by determining the natural period in X and Y directions, which are used to scale the seismic waves. The natural periods of building model are 0.758 sec for X direction and 0.733 sec for Y direction.

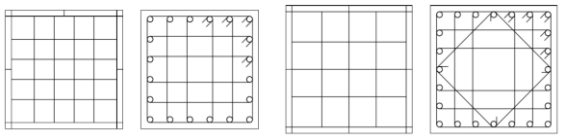

a) Column C1 b) Column C2

Fig. 10 Fiber section of column C1 and column C2.

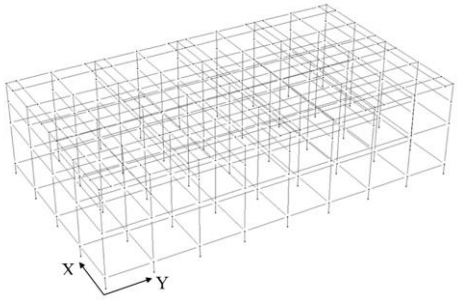

Fig. 11 Analyzed building

SEISMIC WAVE

The seismic waves, collected by the Pacific Earthquake Engineering Research Center (PEER) [12] database, are selected to analyze the building model. As mentioned before, although the Northeast region of Thailand is classified as a low seismic hazard region, there are two active faults. Therefore, the large-magnitude small distance (LMSR) seismic wave type is considered in this analysis. The wave selection criteria are as follows:

1 Distance from the earthquake epicenter to the considering site is in the range of 30 km to 50 km.
2 Earthquake magnitudes are in the range of 6.5 Mw to 6.9 Mw, which is the possibility maximum magnitude of the faults in this area.
3 The fault of earthquake events is a crustal fault and the epicenter is shallow.
4 The soil type in Northeastern Thailand is soil type D with the shear wave velocity (V_s30) of about 180-360 m/s.

Twenty seismic waves that are considered to be appropriate for the Northeast region are shown in Table 3. According to the Earthquake Resistance Design Code.1302 of Thailand, the response

spectrums of seismic waves are analyzed and compare with the target design response spectrum (Fig. 5). All seismic wave response spectrums have to be higher than the target design spectrum for the natural period in the range of 0.2T to 1.5T, where T is the natural period of the analyzed building model. The response spectrums of seismic wave are scaled at least 1.17 times. The scale factors of each seismic wave in X-direction and Y-direction are demonstrated in Table 3. The scaled response spectrum of twenty seismic waves as compared with the target design spectrum for X-direction and Y-direction are shown in Fig. 12 and Fig. 13, respectively.

Table 3 The appropriate selection of seismic waves for the Northeast region and scale factor.

No.	Earthquake Name	Year	Station Name	Magnitude	Scale factor x dir.	Scale factor y dir.
W1	San Fernando	1971	LA - Hollywood Stor FF	6.6	1.381	1.381
W2	Superstition Hills-02	1987	Brawley Airport	6.5	2.029	2.029
W3	Superstition Hills-02	1987	El Centro Imp. Co. Cent	6.5	1.17	1.17
W4	Superstition Hills-02	1987	Plaster City	6.5	1.506	1.506
W5	Superstition Hills-02	1987	Westmorland Fire Sta	6.5	1.174	1.174
W6	Loma Prieta	1989	Agnews State Hospital	6.9	1.439	1.439
W7	Loma Prieta	1989	Capitola	6.9	1.17	1.17
W8	Loma Prieta	1989	Gilroy Array #3	6.9	1.17	1.17
W9	Loma Prieta	1989	Gilroy Array #4	6.9	1.17	1.17
W10	Loma Prieta	1989	Gilroy Array #7	6.9	1.811	2.282
W11	Loma Prieta	1989	Hollister City Hall	6.9	1.557	1.475
W12	Loma Prieta	1989	Hollister Differential Array	6.9	1.29	1.17
W13	Loma Prieta	1989	Sunnyvale - Colton Ave.	6.9	1.153	1.153
W14	Northridge-01	1994	Canoga Park - Topanga Can	6.7	1.17	1.17
W15	Northridge-01	1994	LA - Fletcher Dr	6.7	1.233	1.268
W16	Northridge-01	1994	LA - Hollywood Stor FF	6.7	1.17	1.17
W17	Northridge-01	1994	LA - N Faring Rd	6.7	1.17	1.17
W18	Northridge-01	1994	LA - N Westmoreland	6.7	1.17	1.17
W19	Northridge-01	1994	Northridge - 17645 Saticoy St	6.7	1.17	1.17
W20	Northridge-01	1994	Pardee - SCE	6.7	1.17	1.17

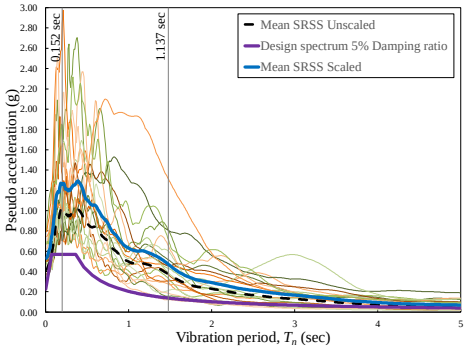

Fig. 12 Response spectrum and scaled SRSS spectrum LMSR for X- direction

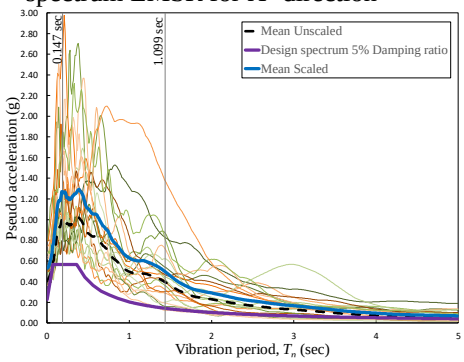

Fig. 13 Response spectrum and scaled SRSS spectrum LMSR for Y- direction

ANALYSIS AND RESULTS

The building model is analyzed under twenty seismic waves in both X-direction and Y-direction. According to the Earthquake Resistance Design Code 1303 of Thailand [2], the analyzed load combinations for the 3-dimensional model are defined into two case.

1) $$E = 1.00X + 0.30Y \quad (2)$$

2) $$E = 0.30X + 1.00Y \quad (3)$$

where E is the earthquake load, X is the load in X-direction and Y is the load in Y-direction. For conservative, the seismic waves in X-direction and Y-direction are switched to evaluate the maximum building responses. Therefore, four cases are considered in the analysis. From [3] and [4] , the acceptance criteria performance level for the plastic hinge rotation angle and the maximum inter-story drift are shown in Table 4 and Table 5, respectively. The acceptance criteria performance level is classified into 3 levels, which are immediate occupancy (IO), life safety (LS) and collapse prevention (CP).

Table 4 Acceptance criteria for the plastic rotation (ASCE41-13).

Performance Level	IO	LS	CP
Rotation Angle (radians)	0.005	0.045	0.060

Table 5 Acceptance criteria for the maximum inter-story drift (FEMA356).

Performance Level	IO	LS	CP
Maximum Inter Story Drift	<1%	<2%	<4%

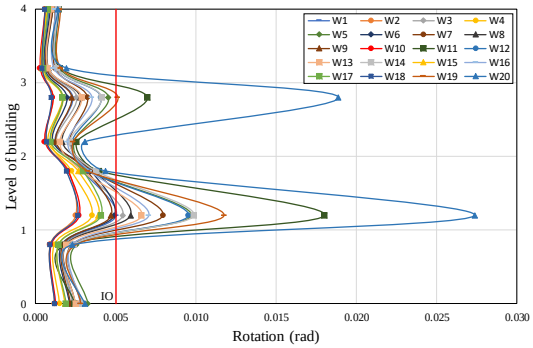

Fig. 14 Plastic rotation angle of the column

From the analysis result, the maximum plastic rotation of columns at all levels under each seismic wave are shown in Fig. 14. The top of columns under the second floor at an elevation of 9.25m has the highest rotation angle due to the long column. The maximum rotation angle is 0.0274 rad due to the W20 Northridge-01 seismic waveform which

occurs the immediate occupancy performance level and is reached about 61% of life safety performance level. The building model has performed the immediate occupancy performance level under eleven seismic waveforms.

The maximum inter-story drift has occurred int the weak direction of the structure as shown in Fig. 15. The maximum inter-story drift of column is on the second floor that has the highest column. The column height of this level is 7.45 meters. The performance level of the structure is life safety, which has the maximum inter-story drift more than two percentage, under the seismic wave number W12, W14, W5, W19, W11, and W20. The maximum inter-story drift under the seismic waveform W20 is closely reached the collapse prevention performance level.

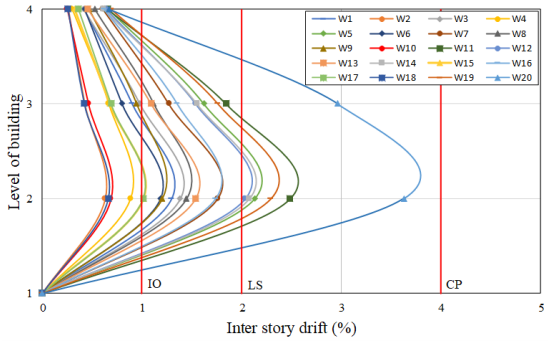

Fig. 15 Maximum inter-story drift

CONCLUSIONS

The industrial factory building is analyzed the seismic behavior under seismic hazard in Northeastern Thailand according to the Earthquake Resistant Design code 1303 [2]. Twenty seismic waveforms are selected and scaled for this area. The nonlinear time history procedure is applied to capture the building responses. The building model consists of the elastic elements in the middle of members, the fiber elements at both ends of members and the beam-column connection, which is assumed to be rigid. From the results, the maximum damage has occurred in the second-floor column with a height of 7.45 m. The columns in this floor perform the soft story irregularity. The building is severe damage due to the W20 Northridge-01 seismic waveform. The performance level for the acceptance criteria for the plastic rotation is immediate occupancy with the rotation angle of 0.0274 rad, and for the maximum inter-story drift is life safety with the inter-story drift of 3.63 percentage. Therefore, the industrial factory building is needed to enhance the seismic capacity for damage prevention.

ACKNOWLEDGMENTS

The authors gratefully acknowledge the funding support from the Electricity Generating Authority of Thailand (EGAT).

REFERENCES

[1] PERFORM3D, Computer and Structure Inc., PERFORM 3D Version 6.0.0, User ‘reference Manual, California Blvd, CA, 2016.

[2] Department of Public Works and Town & Country Planning (DPT)., Earthquake Resistant Design code 1302, Earthquake Resistant Design code, Bangkok, Thailand, 2009, pp. 1-113.

[3] American Society of Civil Engineers (ASCE), Seismic Evaluation and Retrofit of Existing Buildings. Standard ASCE41-13, 2014, pp.179-195.

[4] FEMA356, Prestandard and Commentary for the Seismic Rehabilitation of Buildings. Rehabilita tion Requirements, 2000, pp. 1–518.

[5] Janpila A., Seismic Hazard Assessment in the North-Eastern Area of Thailand, Master of Engineering Thesis in Civil Engineering, Graduate School, 2017, Khon Kaen University, Thailand.

[6] Kent D.C. and Park R., Flexural members with confined concrete. Journal of the Structural Division, ASCE, 97 (ST7), 1971, pp. 1969–1990.

[7] Hoshikuma J., et al., Stress-strain model for confined reinforced concrete in bridge piers. Journal of Structural Engineering, ASCE, Vol. 123, Issue 5, 1997, pp. 624–633.

[8] Menegotto M. and Pinto P. E., Method of analysis for cyclically loaded RC plane frames including changes in geometry and non-elastic behavior of elements under combined normal force and bending. In: Proceedings of the IABSE Symposium on Resistance and Ultimate Deformability of Structures Acted on by Well Defined Repeated Loads. Lisbon, Portugal. Vol. 13, 1973.

[9] Wehbe, N.I., Saiidi, M.S., and Sanders, D.H., Seismic performance of rectangular bridge columns with moderate confinement. ACI Structural Journal, Vol. 96, Issue 2, 1999, pp. 248–259.

[10] Anil Ö., and Altin S., An experimental study on reinforced concrete partially infilled frames, Engineering Structures, Vol. 29, Issue 3, 2007, pp. 449–460.

[11] Paulay T. and Priestley M. J. N., Seismic design of reinforced concrete and masonry buildings. New York, John Wiley, 1992.

[12] PEER, Pacific earthquake engineering research center, Strong Motion Database, https:// ngawest2.berkeley.edu, last access july 30th, 2019

9th Int. Conf. on Geotechnique, Construction Materials and Environment, Tokyo, Japan, 20-22 November 2019, ISBN: 978-4-909106025 C3051

DEVELOPMENT OF THE DISASTER PREVENTION AND MINIMIZATION EDUCATIONAL PROGRAM: CASE STUDY RECONSTRUCTION OF ASO AREA AFTER THE KUMAMOTO EARTHQUAKE

Reiko Machida[1], Hijiri Shimojima[1] and Junya MACHIDA[2] Naomasa Honda[1]
[1] Department of Regional Regeneration Science, Tokyo University of Agriculture, Japan
[2] Environment Design Institute, Japan

ABSTRACT

This study developed a disaster prevention education program for children who continued to live in the Aso area after the Kumamoto earthquake with the aim to enhance their disaster prevention capabilities and to help them take active roles in the reconstruction of the region. This study clarified the objectives, teaching materials, learning methods of the disaster risk prevention education program after the disaster, and clarified the educational effects of the program. The study set the evaluation criteria based on the ministry's curriculum guideline called "Zest for Living". It has become evident that, the knowledge based on the local historical experiences can be a good starting point for the reconstruction immediately after the Kumamoto Earthquake. One of the educational effects of the program was, as it became clear that the local children are deeply interested in the wisdom and customs of reading and understanding nature. The program successfully raised children's level of awareness from the classroom education of disaster prevention to regional disaster prevention in the three years it has been implemented. Furthermore, with the passage of time after the disaster, it has become apparent that the programs called 'Prediction of Danger and Taking Independent Action', which aims at recognizing dangers associated with various disasters and 'Contributing to Society and Basics for Disaster Service Workers' can also be implemented.

Keywords: Kumamoto Earthquake, Disaster Prevention Educational Program, Aso

1. INTRODUCTION

Disaster Risk Education plays an important role in overcoming the memory of the disaster and in providing preparation for future disasters. The objectives and programs of disaster risk prevention education differ according to the periods prior to the disaster, at the time of the disaster and in the periods of recovery and reconstruction.

Most of the disaster prevention programs deal with the pre-disaster phase. Many of these programs use simulation models [1] and hazard maps [2] [3]. The contents of learning include evacuation training to ensure safety and the understanding and prediction of the hazards associated with disasters [4].

On the other hand, there are not many disaster prevention education programs for recovery and reconstruction. In particular, there is a lack of disaster prevention training programs that would foster attitudes which promote participation, cooperation and contribution to the safety of the area during times of recovery and reconstruction [5].

It is important to provide such education to those children who will continue to live in disaster-stricken areas that fosters their attachment to the community and promotes attitudes which contribute to the recovery and reconstruction [6]. Two months after the Great East Japan Earthquake, Iwate Prefecture designed an education program called: "Iwate's Reconstruction Education" with the goal of "nurturing people who love their hometown and are involved in the reconstruction and development" [7].

As a response to the 2011 Great East Japan Earthquake, the Ministry of Education, Culture, Sports, Science and Technology (MEXT) set up an expert committee for reviewing disaster prevention education and management. MEXT published a revised material in 2013 titled Zest for Living. It includes not only evacuation procedures during disasters, but also educational programs from the viewpoint of local life and customs[8].

The Aso area suffered from recent natural disasters such as the Kumamoto earthquake (April 2016). From the viewpoint of reconstruction following the Kumamoto earthquake, promotion of disaster prevention education is required based on traditional lifestyle and knowledge that have helped local people to coexist with the volcano and overcome natural disasters, such as eruptions and landslides. Especially during times of disasters, the traditional lifestyle, knowledge and feelings of local patriotism are considered to have helped the children psychologically [9].On the other hand, education psychology studies reported that children who had experienced disasters have to deal with the effects of serious psychological stress in daily life [10].

Therefore, it is important to clarify the objectives of the educational program, the teaching material and learning methods that are to be considered during the post-disaster recovery and reconstruction period.

This study aimed to develop a disaster risk educational program, which promotes place attachment for reconstruction from disasters and fosters awareness for disaster prevention. This study carried out the disaster prevention education program in the three years immediately after the 2016 Kumamoto earthquake. It also clarified the objectives of the teaching materials, the learning methods of the disaster risk prevention education in the time after the disaster, and clarified the educational effects of the program.

2. DEVELOPMENT OF THE DISASTER PREVENTION EDUCATIONAL PROGRAM FOR RECONSTRUCTION AFTER KUMAMOTO EARTHQUAKE

The study set the evaluation criteria based on "Zest for Living", the Ministry's curriculum guideline. In "Developing disaster prevention education that fosters "Zest for Living"set the following three aims for disaster prevention education [11].

The following articles from the Education Ministry guidelines are incorporated into the elementary school curriculum: "to help pupils become aware of the close relationship between the national land, people's lives and livelihoods" - from the objectives of Social Studies; "to help pupils develop interest in the relationships between themselves, the people around them, the various local places, public facilities; to enable them to appreciate their locality and to develop a feeling of attachment to it; at the same time, to enable them to think about their roles and actions as members of their groups or society and to act safely and appropriately" - from the objectives of Life Environment Studies.

The education programs, based on the disaster situation, were planned in cooperation with the locals and the elementary teachers. The education programs were carried out in two Minami-Aso Elementary Schools, and Aso Elementary School a Minami-Aso Junior High School,Aso Elementary School,by scientist, locals and NPO, teachers.

The study looked at the effects of the program based on the selected keywords from children's oral comments and the interview survey results by children.

Table 1 Disaster prevention education of "Zest for Living"

The evaluation criteria of "Zest for Living"	The objective
Knowledge, Consideration, Judgment	To understand disasters that are likely to occur in the area, to learn from the past disasters of the area, and to use them in making decisions for taking safe actions
Danger Prediction, Independent Action	To recognize danger at the time of disaster and to be able to secure one's own safety using daily training etc.
The Foundation of Social Contribution	To respects one's own life and those of others, to be able to help the safety of other individuals, To be able to take useful action to help groups and areas during and after disasters that occur in the area.

3.1 The Disaster Prevention Educational Program 6 months after the Kumamoto Earthquake

The education programs were planned in cooperation with local elementary school teachers and NPOs from May 2016, two months after the Kumamoto earthquake. The conclusion of the advance meeting with local teachers was that the educational program aimed at helping children deal with the damage and trauma of the earthquake was too early. Therefore, this study established three disaster education programs. The first was a program to leverage the local historical experiences, such as the grassland management techniques（controlled burning, fire belt, seven plants in season）. The aim of the second program was to learn about the attractiveness of living together with volcanoes and grasslands through national parks and geoparks. The third program introduced the interaction between the inside and the outside of the area through the case of Kumamoto's reconstruction efforts in Tokyo. The teaching materials used numerous photos of grassland landscapes and local agricultural activities such as controlled burning, mowing and pasturage in the Aso area. In addition, this program featured a 3D terrain model to enhance the sensory perception of the volcanic terrain of the Aso area.

The program was carried out on September 24, 2016 with the participation of 30 children in total from 3rd grade and 4th grade of two elementary schools in Minami-Aso.The instruction method included the presentation of a 3D topography model of Aso with the purpose to enhance the understanding of the volcanic topography and caldera topography of

Aso. The 3D terrain model is 29 cm long, 25 cm wide, has a maximum of 3 cm in height, and was created at the scale of 1 to 100,000. In order to help children grasp the size of the secondary grassland areas of Aso we compared it to the Yahoo! Dome of Fukuoka which the local children are familiar with. In addition, when explaining the total distance of the secondary cut in the grassland, the idea was to make it easy for children to imagine the total area of the open area and the cut, so it was compared to the distance between Aso and Nagoya.

The second program explained about the purposes of National Parks, Globally Important Agricultural Heritage Systems, and Global Geoparks. In addition, the program explained that the reasons for recognitions as Global Agricultural Heritage Systems and Global Geopark are the livelihood of the people in the grasslands and the volcano of Aso.

The third program introduced a sales promotion event held in Tokyo in order to support the reconstruction after the Kumamoto earthquake.

The educational effect includes the appearance frequency of controlled burning, and the deepened understanding of the maintenance and management of the grassland and its relationship with people's activities. The educational effect was frequent in case of national parks (11 times). Therefore, it became clear that incorporating national parks and world geoparks into the educational materials would enhance understanding and interest in the area.

3.2 The Disaster Prevention Educational Program 1 year after the Kumamoto Earthquake

A year has passed since the Kumamoto earthquake, and following meetings with teachers, we planned an educational program that placed stronger emphasis on the perspective of disaster prevention education than the one in 2016.

The objective of the program continued to highlight the attractiveness of Aso through the activities of grassland management such as the fire controlled burning, and through the recognition as national park and geopark, in order to enhance the appeal of the hometown and to promote place attachment. In addition, learning points from a disaster prevention point of view about the wisdom of Aso that overcame natural disasters and the bond between the community were further included along with traditional land use techniques based on the caldera's topography [12]

The program was carried out for 60 5th grade students of Aso City's Aso Elementary School on December 11, 2017.

The educational methods of the continued program was the same as the previous one.

The program featured wisdom gained from overcoming natural disasters, reflected on the bond within the community, incorporated methods for passing on past disasters within the community and introduced traditions related to the natural disasters and the natural phenomena of the Aso region. For example, "Han"(the wooden plate is called) used to alert the neighborhood of impending disasters. It is not used anymore, of course, but it is kept there to remained people of the importance to help each other at times of disasters.

Concerning the local customs, the contents of the program did not investigate the question of scientific validity, but merely aimed at understanding the fact that local ancestors have faced nature by closely observing it.The program explained about the traditional land use from the walls of the caldera to the floor of the caldera, with the aim to learn about traditional land use.

As for the educational effect, from the high frequency of the appearance of words that refer to the management of the area (e.g. controlled burning), it was possible to confirm the educational effect that children possess an understanding of the management of the grassland and have a raised level of interest toward it.Furthermore, the frequency of appearance of the phrases 'National Park' (25 times) and 'Knowing' (26 times) was high. There were many children who did not know that Aso was designated as a National Park, Globally Important Agricultural Heritage System, or Global Geopark. The largest number of comments were about the natural disasters of Aso and its natural phenomena. It became apparent that children are interested in the area's traditional customs and wisdom. Furthermore, it was also confirmed that the wisdom gained from overcoming natural disasters and the bond within the community helps form a place attachment to the Aso area.

Photo. 1 Hann

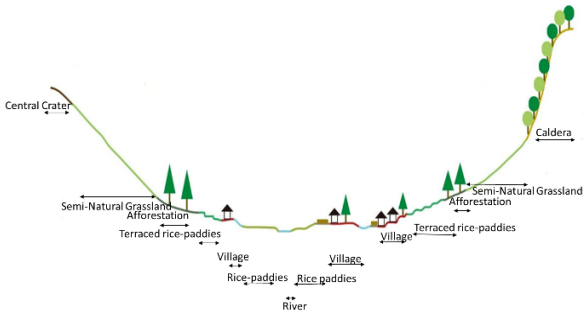

Fig. 1 The land use of Aso area

3.3 The Disaster Prevention Educational Program of Program 2 years after the Kumamoto Earthquake

As one of the educational effects of the program implemented so far, it turned out that the children have a strong interest in the wisdom and customs of reading and understanding nature. Therefore, in the educational program two years after the Kumamoto earthquake, sixty 6th grade students who participated in the educational program of the previous year were interviewed about the wisdom and customs they acquired from their families and neighbors related to understanding natural disasters in the Aso area. The range of the survey period is from July to December 2018.

The result is that 'tradition and wisdom about rain' was the most frequent with 43 mentions (36.4%).

There were as many as 18 stories (15.2%) of 'lore and wisdom related to earthquakes'.It was observed from comments that many of the surveyed have heard from family and neighbors about the experiences of the Kumamoto earthquake, such as: "I was helping (being helped by) neighbors or other local people at the time of the Kumamoto earthquake.". Furthermore, there were comments such as "My great grandmother had fled to the rice fields when there was an earthquake in the old days, because there were not many open places." which show that experiences related to past earthquakes are still kept alive.

There were 11 cases (9.3%) of 'lore and wisdom about snow'. "When there was a lot of snow, we shoveled the snow together with the people of the area to clear the road." These comments clearly indicate that children heard tales about living through the severe winters of the Aso area and providing mutual assistance.

There were 4 cases (3.4%) of 'lore and wisdom about frost'. Aso area is an area where early frost and late frost are likely to occur in May and in early autumn around October. As a result, we were able to confirm practices related to frost and agriculture.

There were two cases (1.7%) of 'lore and wisdom on grassland management', which were about the timing of the controlled burning and the necessity of grassland management.

There were two cases (1.7%) of `traditions and wisdom concerning firefighting`, and those referred to the prevention of fire spreads and related prediction techniques.

The learning points summarized by the children were compiled into a booklet which contain the wisdom of coexisting with nature and Aso, and were shared with families, multigenerational groups, and local communities. Therefore, the program was able to raise awareness of disaster prevention education from school education to regional disaster prevention.

In addition, a public workshop was conducted on September 8, 2018. The topics included the risk characteristics of Aso's natural disasters, forecasting, preparedness and fostering social contribution after disasters. Eleven students ranging from the 5th grade of elementary school to the 1st grade of junior high schools have participated from the local schools of the Aso area.

As part of the learning method, in order to learn about the risk characteristics of Aso, children were explained about the types of landslides (slump, topple, debris flow, rockfall), the differences between landslides that occurred as a result of the Kumamoto earthquake and the landslides that were the results of rain. Subsequently, children enhanced their learning by using confectioneries to simulate the differences of rock topples and slumps.

During the emergency food preparation session, participants used familiar natural resources, eco ovens and bamboo in order to learn the skills to survive natural disasters.

Finally, using elevation maps and 3D topographic models, the children deepened their understanding of the relationship between the topographical characteristics of the Aso area and the disasters. Then, imagining that a disaster occurred while the participants were at home, disaster prevention maps and evacuation action plans were created for each child simulating scenarios of volcanic eruption, landslide disasters and earthquake disasters.

There were several comments made by the participating students regarding the educational program's learning points: "I want to tell about the landslide disaster and the evacuation sites of Aso that I learned about today to my friends and family ", "I want to take advantage in my daily life of the many things I learned about, such as the nature of Aso, or making emergency food and disaster prevention plans.As a result of the educational program various learning points have been confirmed from understanding the blessings of nature, the understanding of the characteristics of disasters that are likely to occur in the area, to the 'knowledge' and 'social contribution' needed to take safe action.

3.4 Readjustment and future proposals for the educational materials of the Disaster Prevention Education Program for the recovery and reconstruction periods

This study developed a disaster prevention education program for children who continued to live in the Aso area after the Kumamoto earthquake with the aim to enhance their disaster prevention capabilities and to help them take active roles in the reconstruction of the region.

Immediately after the Kumamoto earthquake, the program incorporated 'knowledge' about natural environments, national parks, geoparks, and other local attractions into the educational programs. It became apparent that it is useful to raise children's interest and attachment to the Aso area. Furthermore, it has also become evident that, the knowledge based on the local historical experiences can be a good starting point for the reconstruction after the Kumamoto earthquake.

One year after the Kumamoto earthquake, and local traditions and disasters have been incorporated into the educational programs from the perspective of disaster prevention education. Consequently, 'knowledge' and 'decision' that are necessary for understanding disasters which are likely to occur and past disasters of the area were obtained as a result. Furthermore, valuable educational effects became evident as the result of deepening interest and awareness by linking past traditional wisdom and modern disaster management approaches.

In the second year after the Kumamoto earthquake, children have become proactive in learning about past regional disasters and their community and love of our homelands. Further, this study clarified that, immediately after the disasters, such educational curriculum, involving the learning of local historical experience, helps nurturing the sense of place attachment to local community. This study suggests that, with the passage of time after the disaster, the disaster prevent programs aspect of place attachments help 'Prediction of Danger and Taking Independent Action', which aims at recognizing dangers associated with various disasters and 'Contributing to Society and Basics for Disaster Service Workers' can also be implemented.

Table 2 Disaster Prevention Educational Program for Reconstruction after Kumamoto Earthquake

Time	After Kumamoto Earthfuake	Age (Number of students)	School curriculum	The evaluation criteria on "Zest for Living	Teaching material of Disaster Prevention Education	The objective of educational program	The word in frequency of oral comments and The word of Impression	Educational effects and issues
2016.Septem	5 months	9-10 years old 10-11 years old 11-12 years old (36) *Double class	Social stuc	Knowledge and unferstanding Local identity	・The landsape of Aso (Grassland,Volcano, controlled burning, fire belt, seven plants in season) ・3D topography model of Aso	・Instead of focusing the reality of the recovery from the disaster of Kumamoto Earthquake, it aims to turn children's attention to the values of the local historical experiences, such as the grassland management techniques (controlled burning, fire belt, seven plants in season). ・ The attractiveness of living together with volcanoes and grasslands through national parks and geoparks. ・The interaction between the inside and the outside of the area through the case of Kumamoto's reconstruction efforts in Tokyo.	【The word of Impression (Total words=75) Multiple answers allowed】】 Controlled burning (12) 16.0% Volunteers (17) 22.7% Natinadl Park (27) 36.0% Designation of Natinal Park (16) 21.3% Caldera(4) 5.3% Geo-Parkd (2) 2.7% Kind (3) 4.0% Tokyo (1) 1.3% thoughtfulness (1) 1.3% Kumamoto Earthquake (1) 1.3%	It became clear that incorporating national parks and world geoparks into the educational materials would enhance understanding and interest in the area
2017.Decem	1 year and 8 months	10-11 years old (41)	Life envetome nt studies	Knowledge and unferstanding Local identity	・The landsape of Aso (3D topography model of Aso) ・3D topography model of Aso ・ Local historical descriptions	・The objective of the program continued to highlight the attractiveness of Aso through the activities of grassland management. ・The wisdom of Aso that overcame natural disasters and the bond between the community along with traditional land use techniques based on the caldera's topography.	【The word of Impression (Total words=239) Multiple answers allowed】 Controlled burning (60) 25.1% Fire belt mowing (27) 11.3% Natinadl Park (41) 17.2% Geo-Parkd (19) 7.9% World Agricultural Heritage (19) 7.9% Local customs(72) 30.1% Hann :Past of disaster alarm (19) 7.9% Tinber forest (1) 0.4%	It was also confirmed that the wisdom gained from overcoming natural disasters and the bond within the community helps form a place attachment to the Aso area.
2018 Septem	2 yeasr and 5 months	9-10 years old 10-11 years old 11-12 years old 12-13 years old	Social studies Science	Knowledge and unferstanding Local identity Considertation of judgement Social contribution	・The landsape of Aso (Grassland,Volcano) ・3D topography model of Aso ・ local historical descriptions ・Simulation model experiment ・Hazard map	・The types of landslides (slump, topple, debris flow, rockfall) by using confectioneries to simulate the differences of rock topples and slumps. ・The emergency food preparation. ・It used the Simulation model experiment and hazard map for confirmation of evacuation sites and plan for volcanic eruptions, floods, earthquakes, and landslide disasters that are assumed in the Aso area.	【The oral comments 】 "I want to tell about the landslide disaster and the evacuation sites of Aso that I learned about today to my friends and family " "I want to take advantage in my daily life of the many things I learned about, such as the nature of Aso, or making emergency food and disaster prevention plans.	the understanding of the characteristics of disasters that are likely to occur in the area, to the 'knowledge' and 'social contribution' needed to take safe action.
2018 Decem	2 yeasr and 8months	11-12 years old	Social stuc	Knowledge and unferstanding Local identity Considertation of judgement Social contribution	・Local historical descriptions ・Interview of local their families and neighbors	・The interview about the wisdom and customs they acquired from their families and neighbors related to understanding natural disasters in the Aso area. ・The learning points summarized by the children were compiled into a booklet which contain the wisdom of coexisting with nature and Aso,	【The total number traditions and wisdom =60】 Rain : 43 (36.4%). Earthquakes : 18 (15.2%) Snow : 11 (9.3%) Frost : 4 (3.4%) Grassland management : 2 (1.7%) Firefighting : 2 (1.7%)	It was able to raise awareness of disaster prevention education from school education to regional disaster prevention

prevention. Then, the educational program provided an opportunity to share knowledge and awareness on disaster prevention among children, local residents and their families. The program successfully shifted from school education to regional disaster prevention.

Generally, such educational curriculum aimed at the development of the sense or belonging to the

4. CONCLUTIONS

The study set the evaluation criteria based on the ministry's curriculum guideline called "Zest for Living". It has become evident that, the knowledge based on the local historical experiences can be a good starting point for the reconstruction

immediately after the Kumamoto earthquake. One of the educational effects of the program was, as it became clear that the local children are deeply interested in the wisdom and customs of reading and understanding nature. The program successfully raised children's level of awareness from the classroom education of disaster prevention to regional disaster prevention in the three years it has been implemented. Furthermore, with the passage of time after the disaster, it has become apparent that the programs called 'Prediction of Danger and Taking Independent Action', which aims at recognizing dangers associated with various disasters and 'Contributing to Society and Basics for Disaster Service Workers' can also be implemented.

ACKNOWLEDGMENTS

This work was supported by JSPS KAKENHI Grant Number JP17K02130 and the strategic research project of Tokyo University of Agriculture. We received the support from Mr.Sumio Sei and The Takamori Higashi Junior High School, The Takamori Higashi elementary school and The Ryohei elementary school and Mr .Katsuya Mochzuki.

REFERENCES

[1] Takashi Yamada, Education method for sediment-related disaster prevention based on the combination of field seminar and teaching hydraulic apparatus use for school children, Japan Society of Erosion Control Engineering, Vol.59 No.3,2006, pp. 13-22(in Japanese with English abstract).

[2] Cheng-Chien LIU, Hsiao-Yuan YIN, Hsiao-Wei CHUNG, Wei LUO and Ke-Wei YAN, Towards an Auto-nowcasting System for Landslide Hazard, INTERPRAEVENT 2018 Symposium proceedings, 2018, pp. 336-340

[3] Kana NAKATANI, Kazuki YAMANOI, Yuji HASEGAWA, Seiya HAYASHI, Shusuke MIYATA and Masaharu FUJITA, Advanced Hazard Information and Methods for Appropriate Evacuation During Sediment Disasters, Modulus of Elasticity and Shrinkage Behaviour of Concrete Containing Waste Carpet Fiber, INTERPRAEVENT 2018 Symposium proceedings, 2018, pp. 327-335

[4] Dedi Hermon, Ganefri, Erianjoni, Indang Dewata, Paus Iskarni and Alexander Syam, A policy model of adaptation mitigation and social risks the volcano eruption disaster of sinabung in Karo Regency – Indonesia, International Journal of GEOMATE 17(60), 2019, pp. 190-196

[5] Ryoga Ishihara, Nobuhiko Matsumura, The Development and Evaluation of Teaching Material for Disaster Reduction in Daily Life, The Journal of Japan Society of Civil Engineers (H) (Education) Vol.70, No.1,2014, pp. 1-12 (in Japanese with English abstract)

[6] Misato Uehara, Holistic Landscape Planning`s Value For Natural Disaster Reconstruction Willingness to Pay For New Residence in Different Reconstruction Planning Approaches, International Journal of GEOMATE 17(60), 2019, pp. 92-97.

[7] Jyunichi Murakami, Interim report of the Educational programs of Iwate Prefecture-Viewpoint to the difference of the damage situation by area and "Iwate recovery education" (in Japanese, the title is tentatively translated by the author), Research on the present conditions and problems of the education field in the Great East Japan Earthquake by Hyogo Earthquake Memorial 21st,2018, pp. 7-16(in Japanese).

[8] The Ministry of Education, Culture, Sports, Science and Technology (MEXT), Development of disaster prevention education to bring up reference materials "Zest for Living" (in Japanese, the title is tentatively translated by the author), 2013,pp130 (in Japanese).

[9] Ryoga Isihara and Nobuhiko Matsumura, A Study on the Actual Condition and The Effects of Disaster Oral Trad ititon in the Coastal Regions, The Journal of Japan Society of Civil Engineers(D3) (Civil Engineering Planning)Vol.69, No.5, 2013, pp.I_101-I_114 (in Japanese with English abstract).

[10] Tateo Fijimori, The Care for the children who experience with a disaster (in Japanese, the title is tentatively translated by the author), Fukumra, 2011.

[11] The Ministry of Education, Culture, Sports, Science and Technology (MEXT), Development of disaster prevention education to bring up reference materials "Zest for Living" (in Japanese, the title is tentatively translated by the author), 2013,pp8-9 (in Japanese).

[12] The Aso City, The history of Aso, Vol 2 Material (in Japanese, the title is tentatively translated by the author),2016,pp195-196.

9th Int. Conf. on Geotechnique, Construction Materials and Environment, Tokyo, Japan, 20-22 November 2019, ISBN: 978-4-909106025 C3051

THE OPTIMAL METHOD FOR BUILDING DAMAGE FRAGILITY CURVE DEVELOPMENT

Apichat Janpila[1], Piyawat Foytong[2], Supakorn Tirapat[3], Nuttawut Thanasisathit[4] and Anat Ruangrassamee[5]
[1,2,3]Sustainable Infrastructure Research and Development Center, Department of Civil Engineering, Faculty of Engineering, Khon Kaen University, Khon Kaen, Thailand.
[4]Department of Civil Engineering, King Mongkut's University of Technology North Bangkok, Bangkok, Thailand.
[5]Department of Civil Engineering, Chulalongkorn University, Bangkok, Thailand.

ABSTRACT

A fragility curve is a primary component in the risk assessment, which is useful for evacuation planning, estimation of potential losses, and estimation of the damage to residential buildings caused by natural hazards. In general, a fragility curve represents the relationship between the probability of exceeding a specific damage state of a structure and natural hazard intensity. For determining such a curve, two parameters: the median and standard deviation are estimated. A fragility curve can be constructed using empirical data and analytical data. Numerical fitting data is used to develop the fragility curve. Various methods have been proposed using numerical fitting data to approximate the fragility curves. However, the most widely used methods for developing fragility curves are the least-squares method and the maximum likelihood method. In this present study, these two different numerical fitting data methods for fragility curve development are analyzed and compared. Basic assumptions and limitations of each method are also discussed. The building damage data used in all methods to derive the fragility curve is generated from hypothetical damage data assuming a lognormal distribution. Finally, the maximum likelihood method is proven to be optimal for developing fragility curve based on structural damage data.

Keywords: Optimal method, Fragility curve, Building damage, Risk assessment

INTRODUCTION

Each year, several countries are affected by a variety of natural hazards, including hurricanes, tropical storms, strong winds, floods, earthquakes, and tsunamis. Therefore, risk assessment is the key to provide a way to prevent and mitigate damages or losses resulting from natural disasters in the future. The risk assessment process includes natural hazard identification, building inventory, and fragility curve. The Natural hazard is identified at any given site to determine the likely impacts in the form of a hazard map. The building inventory is a classification procedure in which buildings are grouped based on similar damageability/loss characteristics into a set of predefined building classes. Model building types are further constructed by developing the damage and loss prediction models to represent the average building population characteristics within each class. A fragility curve is utilized to estimate a vulnerability, which expresses a relationship between the probability of being in or exceeding building damage state and the intensity of natural hazard. Therefore, a fragility curve is the key parameters in risk assessment for evaluating the damage probability at a specific damage level under the hazard. Statistical methodology is applied to establish a fragility curve. The building damage data, which is assumed to follow the lognormal distribution [1], is used in exploring the relationship of damage probability and hazard intensity. In general, methods most commonly used to develop the fragility curve are the least squares estimation (LSE) [2]-[3] and maximum likelihood estimation (MLE) [4]-[10]. Thus, in this study, the two most commonly used methods of estimation are compared, and the optimal method of fragility curve development is demonstrated based on statistical principles.

FRAGILITY CURVE

In this section, the concept and the key parameters of a fragility curve are described here to provide a basic understanding of analysis in fragility curve development for obtaining the appropriate method. A fragility curve describes a relationship between the level of damage probability and hazard. The probabilities defined in fragility curve are conditional probabilities as shown in Eq. (1):

$$F_d = \boldsymbol{P}\left[D \geq d \mid X = x\right] \quad d \in \{1, 2, \ldots N_D\} \tag{1}$$

where F_d represents the fragility function for damaged state d evaluated at the hazard level of x $P[A|B]$ is the probability that event A occurs given that event B has taken place. D is a damaged state of a particular component, which takes on a value of $\{0,1,\ldots,n_D\}$, and d is a damaged state. X is an uncertain excitation which is called demand parameter (DP) and x is a particular value of X.

The structural failure data follows a lognormal distribution as shown in Fig.1. The probability density function (PDF) as defined in Eq. (2) represents the probability of structural damage. The dispersion or width of distribution indicates the uncertainty of each damage state. Then the probability of the structural failure can be obtained by cumulative distribution function of the lognormal distribution with intensity measure on the horizontal axis The probability of structural failure is obtained through the cumulative standard log-normal distribution function in which the horizontal axis represents the intensity measure. The log-normal cumulative distribution function expresses the fragility curve as defined in Eq. (3).

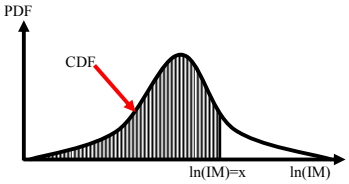

Fig. 1 Cumulative distribution function with intensity measure equal to x

$$f_d = \frac{1}{x\beta\sqrt{2\pi}} e^{(-1/2)\left[(\ln x-\alpha)/\beta\right]^2} \tag{2}$$

$$F_d = \int_{-\infty}^{\ln x} \frac{1}{x\beta\sqrt{2\pi}} e^{(-1/2)\left[(\ln x-\alpha)/\beta\right]^2} dx = \Phi\left(\frac{\ln(x/\alpha)}{\beta}\right) \tag{3}$$

where Φ[.] represents the standard normal cumulative distribution function, α and β are parameters which controls the shape of the fragility curve. Thus, α is the median which controls the location of the fragility curve and β is the log-normal standard deviation which represents the dispersion of the fragility curve.

ESTIMATION METHOD FOR FRAGILITY CURVE

In this paper, we compare the results of two different estimation methods, LSE and MLE, for establishing the fragility curve. The optimal method is statistically proven based on the assumptions and properties inherent to each method.

Least Squares Estimation

Least squares estimation is the method which gives the minimum sum of squared errors in finding the optimal parameter values. The error term expresses the difference between the sample values, Y_i, and the estimated values, $\hat{Y}_i$. The estimated values $\hat{Y}_i$ can be written as $E[Y_i|X_i]$. The least squares estimation is used for a simple linear regression. Given X is an independent variable, Y is a dependent variable, and β is a constant. Then, a linear relationship between Y and X can be set up as shown in Eq. (4):

$$Y = \beta_0 + \beta_1 X_1 + \beta_2 X_2 \tag{4}$$

Considering the population regression model with p parameters and n observations written as follows:

$$\begin{aligned}
\hat{Y}_1 &= E(Y_1|X_1) = \beta_0 + \beta_1 x_{1,1} + \beta_2 x_{2,1} + \ldots + \beta_{p-1} x_{p-1,1} \\
\hat{Y}_2 &= E(Y_2|X_2) = \beta_0 + \beta_1 x_{1,2} + \beta_2 x_{2,2} + \ldots + \beta_{p-1} x_{p-1,2} \\
&\vdots \quad \vdots \quad \vdots \quad \vdots \\
\hat{Y}_n &= E(Y_n|X_n) = \beta_0 + \beta_1 x_{1,n} + \beta_2 x_{2,n} + \ldots + \beta_{p-1} x_{p-1,n}
\end{aligned} \tag{5}$$

Then, the matrix form is cast in the following form:

$$\hat{\boldsymbol{Y}} = E(\boldsymbol{Y}|\boldsymbol{X}) = \boldsymbol{X}\boldsymbol{\beta} \tag{6}$$

$$\hat{\boldsymbol{Y}} = \begin{bmatrix} \hat{Y}_1 \\ \hat{Y}_2 \\ \vdots \\ \hat{Y}_n \end{bmatrix}; \boldsymbol{X} = \begin{bmatrix} 1 & x_{1,1} & x_{2,1} & \cdots & x_{p-1,1} \\ 1 & x_{1,2} & x_{2,2} & \cdots & x_{p-1,2} \\ \vdots & \vdots & \vdots & & \vdots \\ 1 & x_{1,n} & x_{2,n} & \cdots & x_{p-1,n} \end{bmatrix}; \boldsymbol{\beta} = \begin{bmatrix} \beta_1 \\ \beta_2 \\ \vdots \\ \beta_{p-1} \end{bmatrix}$$

Estimates of the error terms refers to the differences between the observed value of the dependent variable and its predicted value in the model:

$$Y_i - \hat{Y}_i = \varepsilon_i \tag{7}$$

$$\varepsilon_i = Y_i - \hat{Y}_i = Y_i - E\left[Y_i|X_i\right] \tag{8}$$

$$S = \sum_{i=1}^{n} \varepsilon_i^2 = \sum_{i=1}^{n} \left(Y_i - E\left[Y_i|X_i\right]\right)^2 = \sum_{i=1}^{n} \left(Y_i - \beta_0 - \beta_1 X_i\right)^2 \tag{9}$$

Eq. (9) can be expressed in matrix form as follows:

$$\begin{aligned}
\boldsymbol{S} &= \boldsymbol{\varepsilon}'\boldsymbol{\varepsilon} = (\boldsymbol{Y} - \boldsymbol{X}\boldsymbol{\beta})'(\boldsymbol{Y} - \boldsymbol{X}\boldsymbol{\beta}) \\
&= \boldsymbol{Y}'\boldsymbol{Y} - \boldsymbol{\beta}'\boldsymbol{X}'\boldsymbol{Y} - \boldsymbol{Y}'\boldsymbol{X}\boldsymbol{\beta} + \boldsymbol{\beta}'\boldsymbol{X}'\boldsymbol{X}\boldsymbol{\beta} = \boldsymbol{Y}'\boldsymbol{Y} - 2\boldsymbol{\beta}'\boldsymbol{X}'\boldsymbol{Y} + \boldsymbol{\beta}'\boldsymbol{X}'\boldsymbol{X}\boldsymbol{\beta}
\end{aligned} \tag{10}$$

It should be noted that $\boldsymbol{\beta}'\boldsymbol{X}'\boldsymbol{Y}$ and $\boldsymbol{Y}'\boldsymbol{X}\boldsymbol{\beta}$ are the same scalar. Then, the least squares estimation of β is shown in Eq. (11) and Eq. (12)

$$\frac{\partial \boldsymbol{S}}{\partial \hat{\boldsymbol{\beta}}} = \frac{\partial \boldsymbol{\varepsilon}'\boldsymbol{\varepsilon}}{\partial \hat{\boldsymbol{\beta}}} = -2\boldsymbol{X}'\boldsymbol{Y} + 2\boldsymbol{X}'\boldsymbol{X}\hat{\boldsymbol{\beta}} = 0 \tag{11}$$

$$\hat{\boldsymbol{\beta}}_{OLS} = \left(\boldsymbol{X}'\boldsymbol{X}\right)^{-1}\boldsymbol{X}'\boldsymbol{Y} \tag{12}$$

where $\hat{\boldsymbol{\beta}}_{OLS}$ is the least squares estimator of β.

Assumptions of LSE

1. The dependent variable, $\boldsymbol{Y}$, is continuous.
2. The relationship between the dependent variable, $\boldsymbol{Y}$, and the independent variable, $\boldsymbol{X}$, is linear.
3. Observations are independently and randomly drawn.
4. The error term has the expected value equal to zero and the variation equal to σ^2.
   $E\left[\varepsilon_i\right] = 0$; $Var\left[\varepsilon_i\right] = \sigma^2\mathbf{I}$
5. The error term is not auto correlated.
   $COV\left[\varepsilon_i, \varepsilon_j\right] = 0$; if $i \neq j$
6. The error term, ε, is independent of $\boldsymbol{X}$.
   $COV\left[X_i, \varepsilon_j\right] = 0$; for all i and j

7. The error term is approximately normally distributed.

$\varepsilon_i \approx N(0,\sigma^2)$; for i = 1, 2, …, n

We can write this in matrix form as $\boldsymbol{\varepsilon} \approx N(0,\sigma^2\mathbf{I})$ where $\mathbf{I}$ is identity matrix. From this assumption, the distribution of the dependent variable, $\boldsymbol{Y}$, is written as: $\boldsymbol{Y} \approx N(\boldsymbol{X\beta},\sigma^2\mathbf{I})$

The properties of LSE

1. The estimator of least squares method is unbiased estimator. The estimator is unbiased if and only if the expected value of an estimator, $E[\hat{\beta}]$ equals parameter β, that is,

$$E[\hat{\beta}] = \beta \tag{13}$$

From Eq. (12), we derive the following equation:

$$\begin{aligned}\hat{\boldsymbol{\beta}}_{OLS} &= (\boldsymbol{X'X})^{-1}\boldsymbol{X'Y} = (\boldsymbol{X'X})^{-1}\boldsymbol{X'}(\boldsymbol{X\beta}+\boldsymbol{\varepsilon}) \\ &= (\boldsymbol{X'X})^{-1}(\boldsymbol{X'X})\boldsymbol{\beta} + (\boldsymbol{X'X})^{-1}\boldsymbol{X'\varepsilon} \\ &= \boldsymbol{\beta} + (\boldsymbol{X'X})^{-1}\boldsymbol{X'\varepsilon} \end{aligned} \tag{14}$$

$$E[\hat{\boldsymbol{\beta}}_{OLS}] = E[\boldsymbol{\beta}] + E[\boldsymbol{X}^{-1}\boldsymbol{\varepsilon}] = \boldsymbol{\beta} + \boldsymbol{X}^{-1}E[\boldsymbol{\varepsilon}]$$

According to Assumption 4, if $E[\varepsilon_i]=0$ then $E[\hat{\boldsymbol{\beta}}_{OLS}] = \boldsymbol{\beta}$

Therefore, $\hat{\boldsymbol{\beta}}_{OLS}$ is an unbiased estimator of β.

2. The least squares estimator is an efficient estimator. The estimator is efficient if and only if the variance of estimator, $V[\hat{\beta}]$ is minimum

$$Var[\hat{\boldsymbol{\beta}}_{OLS}] = E\left[(\hat{\boldsymbol{\beta}}_{OLS}-\boldsymbol{\beta})(\hat{\boldsymbol{\beta}}_{OLS}-\boldsymbol{\beta})'\right] \tag{15}$$

From Eq. (14), we now obtain:

$$\hat{\boldsymbol{\beta}}_{OLS} - \boldsymbol{\beta} = (\boldsymbol{X'X})^{-1}\boldsymbol{X'\varepsilon}$$

$$\begin{aligned} Var[\hat{\boldsymbol{\beta}}_{OLS}] &= E\left[((\boldsymbol{X'X})^{-1}\boldsymbol{X'\varepsilon})((\boldsymbol{X'X})^{-1}\boldsymbol{X'\varepsilon})'\right] \\ &= (\boldsymbol{X'X})^{-1}\boldsymbol{X'}E[\boldsymbol{\varepsilon\varepsilon'}]\boldsymbol{X}(\boldsymbol{X'X})^{-1} \end{aligned}$$

According to Assumption 4, given

$Var[\varepsilon_i] = \sigma^2\mathbf{I} = E[(\varepsilon - E[\varepsilon])^2] = E[\varepsilon^2]$ then

$$\begin{aligned} Var[\hat{\boldsymbol{\beta}}_{OLS}] &= (\boldsymbol{X'X})^{-1}\boldsymbol{X'}\sigma^2\mathbf{I}\boldsymbol{X}(\boldsymbol{X'X})^{-1} \\ &= \sigma^2(\boldsymbol{X'X})^{-1} \end{aligned} \tag{16}$$

3. The estimator of least square method is the best unbiased estimator.

Given $\hat{\boldsymbol{\beta}}^* = [(\boldsymbol{X'X})^{-1}\boldsymbol{X'} + \boldsymbol{A}]\boldsymbol{Y}$, where $\boldsymbol{A}$ is a matrix which treats $\hat{\boldsymbol{\beta}}^*$ as the unbiased parameter.

$$E[\hat{\boldsymbol{\beta}}^*] = \boldsymbol{\beta}$$

$$\begin{aligned}\boldsymbol{\beta} &= [(\boldsymbol{X'X})^{-1}\boldsymbol{X'} + \boldsymbol{A}]E[\boldsymbol{Y}] \\ &= \boldsymbol{\beta} + \boldsymbol{AX\beta}\end{aligned}$$

Thus, if $\boldsymbol{AX} = 0$ then $\hat{\boldsymbol{\beta}}^* = (\boldsymbol{X'X})^{-1}\boldsymbol{X'Y} = \hat{\boldsymbol{\beta}}_{OLS}$

$$Var[\hat{\boldsymbol{\beta}}^*] = E\left[(\hat{\boldsymbol{\beta}}^*-\boldsymbol{\beta})(\hat{\boldsymbol{\beta}}^*-\boldsymbol{\beta})'\right]$$

$$= E\left[((\boldsymbol{X'X})^{-1}\boldsymbol{X'Y} + \boldsymbol{AY} - \boldsymbol{\beta})((\boldsymbol{X'X})^{-1}\boldsymbol{X'Y} + \boldsymbol{AY} - \boldsymbol{\beta})'\right]; \boldsymbol{Y} = \boldsymbol{X\beta} + \boldsymbol{\varepsilon}$$

$$= E\left[((\boldsymbol{X'X})^{-1}\boldsymbol{X'\varepsilon} + \boldsymbol{AX\beta} + \boldsymbol{A\varepsilon})((\boldsymbol{X'X})^{-1}\boldsymbol{X'\varepsilon} + \boldsymbol{AX\beta} + \boldsymbol{A\varepsilon})'\right]; \boldsymbol{AX} = 0$$

$$= E\left[((\boldsymbol{X'X})^{-1}\boldsymbol{X'\varepsilon} + \boldsymbol{A\varepsilon})((\boldsymbol{X'X})^{-1}\boldsymbol{X'\varepsilon} + \boldsymbol{A\varepsilon})'\right]$$

$$= \left[((\boldsymbol{X'X})^{-1}\boldsymbol{X'X}(\boldsymbol{X'X})^{-1}) + \boldsymbol{AA'} + (\boldsymbol{X'X})^{-1}(\boldsymbol{AX})' + (\boldsymbol{AX})(\boldsymbol{X'X})^{-1}\right]\sigma^2; \boldsymbol{AX} = 0$$

$$= \left[(\boldsymbol{X'X})^{-1} + \boldsymbol{AA'}\right]\sigma^2$$

Given $\boldsymbol{AA'} = \boldsymbol{B} = (b_{ij})$, where is $b_{ij} > 0$. Then, $Var[\hat{\boldsymbol{\beta}}^*]$ is minimum if and only if $b_{ij} = 0$ for all i=1, 2,…,p.

Given $\boldsymbol{A} = (a_{ij})$, $b_{ii} = \sum_{j=1}^{n} a_{ij}^2 = 0$ Therefore,

$a_{ij} = 0$ for i =1, 2, …, p and j = 1, 2, …, p

That is, when $\boldsymbol{A} = 0$, $\hat{\boldsymbol{\beta}}^* = (\boldsymbol{X'X})^{-1}\boldsymbol{X'Y} = \hat{\boldsymbol{\beta}}_{OLS}$ is the minimum variance parameter of β.

The least squares estimation has many assumptions. This estimation method is considered to be improper to develop the fragility curve using structural damage data due to some invalid assumptions. For instance, Assumption 4, $Var[\varepsilon_i]=\sigma^2\mathbf{I}$, which assumes the error term has a constant variance and Assumption 6, $COV[X_i,\varepsilon_j]=0$, which implies that the error is uncorrelated with all independent variables. The variance of the errors of structure damage is small when the IM (intensity measure) is small (most structures are not damaged). That is, the variance increases when the structure starts to damage and then the variance decreases again when IM is large because most structures are damaged. As a result, the variance of the errors is not constant and depends on IM. Thus, Assumption 7, $\varepsilon_i = N(0,\sigma^2)$ becomes invalid. In addition, review of the literature indicates that the data of structural component failure appear to fit the log-normal distribution well. Although the log-normal distribution can be transformed to linear logarithm, properties of the error term are changed.

The Method of Maximum Likelihood

Maximum likelihood estimation is a method for parameter estimation by maximizing the likelihood function. Given X is a random variable with probability distribution function $f(X\ \theta)$, where θ is a single unknown parameter. Let $x_1, x_2, ..., x_n$ be the observed values in a random sample of size n. Then, the likelihood function of a sample is defined as:

$$\begin{aligned} L(\theta|X) &= L(\theta|x_1,x_2,...,x_n) = \prod_i^n f(x_i|\theta) \\ &= f(x_1,\theta)\cdot f(x_2,\theta)\cdots f(x_n,\theta) \end{aligned} \tag{17}$$

The likelihood function depends on the unknown parameter θ only. Essentially, the maximum likelihood estimator is the value of θ that

maximizes the probability of occurrence of the sample by differentiating $L(\theta|X)$ with respect to θ and setting that derivative equal to zero:

$$\frac{\partial L(\theta|X)}{\partial \theta}=0 \tag{18}$$

Then, with the second derivative value being less than zero we have a maximum:

$$\frac{\partial^2 L(\theta|X)}{\partial \theta^2}<0 \tag{19}$$

The assumptions of MLE

1) The observations are independently and randomly drawn.
2) The parameter $\hat{\theta}$ maximizes the likelihood of the sample, i.e., it represents the maximum likelihood estimator of θ in which $L(\hat{\theta}|X)\geq L(\theta|X)$.

Properties of MLE

1. The maximum likelihood estimator does not need to be unbiased since it can be corrected. The estimator is unbiased if and only if the expected value of an estimator, $E[\hat{\theta}]$ equals parameter θ.

We consider the random sample $x_1, x_2, ..., x_n$, where n is the random sample size. The random sampling distribution is assumed to be normal which comprises two unknown parameters, μ and σ^2. The probability density function of normal distribution can be expressed as:

$$f(x)=\frac{1}{\sqrt{2\pi\sigma^2}}e^{-(1/2)[(x-\mu)/\sigma]^2} \tag{20}$$

$$L(\mu,\sigma^2|X)=L(\mu,\sigma^2|x_1,x_2,...,x_n)=\prod_{i=1}^{n}\left(\frac{1}{\sqrt{2\pi\sigma^2}}e^{-(1/2)[(x_i-\mu)/\sigma]^2}\right)$$

$$=\frac{1}{\left(2\pi\sigma^2\right)^{n/2}}e^{-(1/2\sigma^2)\sum_{i=1}^{n}(x_i-\mu)^2} \tag{21}$$

Simplifying Eq. (21) by taking the log of both sides yields:

$$\ln L(\mu,\sigma^2|X)=-\frac{n}{2}\ln\left(2\pi\sigma^2\right)-\frac{1}{2\sigma^2}\sum_{i=1}^{n}(x_i-\mu)^2 \tag{22}$$

Then, the estimator of μ and σ^2 is

$$\frac{\partial \ln L(\mu,\sigma^2|X)}{\partial \hat{\mu}}=\frac{\partial\left(-\frac{n}{2}\ln\left(2\pi\sigma^2\right)-\frac{1}{2\sigma^2}\sum_{i=1}^{n}(x_i-\hat{\mu})^2\right)}{\partial\hat{\mu}}=-\frac{1}{\sigma^2}\sum_{i=1}^{n}(x_i-\hat{\mu})=0$$

$$\hat{\mu}=\frac{1}{n}\sum_{i=1}^{n}x_i=\bar{x} \tag{23}$$

Next, we check that the estimator $\hat{\mu}$ gives maximum L:

$$\frac{\partial^2 \ln L(\mu,\sigma^2|X)}{\partial\hat{\mu}^2}=\frac{\partial\left(-\frac{1}{\sigma^2}\sum_{i=1}^{n}(x_i-\hat{\mu})\right)}{\partial\hat{\mu}}=-\frac{1}{\sigma^2}\frac{\partial\left(\sum_{i=1}^{n}x_i-\sum_{i=1}^{n}\hat{\mu}\right)}{\partial\hat{\mu}}=-\frac{n}{\sigma^2}<0$$

$$\frac{\partial \ln L(\mu,\sigma^2|X)}{\partial\hat{\sigma}^2}=\frac{\partial\left(-\frac{n}{2}\ln\left(2\pi\hat{\sigma}^2\right)-\frac{1}{2\hat{\sigma}^2}\sum_{i=1}^{n}(x_i-\mu)^2\right)}{\partial\hat{\sigma}^2}=\frac{-n}{2\hat{\sigma}^2}+\frac{1}{2\hat{\sigma}^4}\sum_{i=1}^{n}(x_i-\mu)^2=0$$

$$\hat{\sigma}^2=\frac{1}{n}\sum_{i=1}^{n}(x_i-\bar{x})^2 \tag{24}$$

And if the estimator $\hat{\sigma}^2$ treats maximum L then

$$\frac{\partial^2 \ln L(\mu,\sigma^2|X)}{\partial\left(\hat{\sigma}^2\right)^2}=\frac{\partial\left(\frac{-n}{2\hat{\sigma}^2}+\frac{1}{2\hat{\sigma}^4}\sum_{i=1}^{n}(x_i-\mu)^2\right)}{\partial\hat{\sigma}^2}=\frac{n}{2\hat{\sigma}^4}-\frac{1}{\hat{\sigma}^6}\sum_{i=1}^{n}(x_i-\mu)^2$$

$$=\frac{n}{2\hat{\sigma}^4}-\frac{1}{\hat{\sigma}^6}\left(n\hat{\sigma}^2\right)=\frac{n}{2\hat{\sigma}^4}-\frac{n}{\hat{\sigma}^4}=-\frac{n}{2\hat{\sigma}^4}<0 \quad \text{OK.}$$

According to Eq. (19), we obtain:

$$E[\hat{\mu}]=E[\bar{x}]=\frac{1}{n}E[x_1+x_2+x_3+\ldots+x_n]=\frac{1}{n}\sum_{i=1}^{n}E[x_i]=\frac{1}{n}(n\mu)=\mu \tag{25}$$

Thus, $\hat{\mu}$ denotes an unbiased estimator of μ. From Eq. (24), we now derive the following form:

$$\hat{\sigma}^2=\frac{1}{n}\sum_{i=1}^{n}(x_i-\bar{x})^2=\frac{1}{n}\sum_{i=1}^{n}(x_i-\mu+\mu-\bar{x})^2=\frac{1}{n}\sum_{i=1}^{n}\left((x_i-\mu)-(\bar{x}-\mu)\right)^2$$

$$=\frac{1}{n}\left(\sum_{i=1}^{n}(x_i-\mu)^2-2n(\bar{x}-\mu)^2+\sum_{i=1}^{n}(\bar{x}-\mu)^2\right)$$

$$E\left[\hat{\sigma}^2\right]=\frac{1}{n}E\left[\sum_{i=1}^{n}(x_i-\mu)^2-2n(\bar{x}-\mu)^2+\sum_{i=1}^{n}(\bar{x}-\mu)^2\right]$$

$$=\frac{1}{n}\left(\sum_{i=1}^{n}V[x_i]-nV[\bar{x}]\right)$$

Based on the properties of normal distribution in which $V[x_i]=\sigma^2$ and $V[\bar{x}]=\frac{\sigma^2}{n}$, we obtain

$$E\left[\hat{\sigma}^2\right]=\frac{1}{n}\left(\sum_{i=1}^{n}\sigma^2-n\frac{\sigma^2}{n}\right)$$

$$=\frac{1}{n}\left(n\sigma^2-n\frac{\sigma^2}{n}\right)$$

$$=\frac{(n-1)\sigma^2}{n}\neq\sigma^2 \tag{26}$$

$\hat{\sigma}^2$ is the biased parameter of σ^2. Then, $\hat{\sigma}^2$ is corrected to be unbiased as follows

$$\hat{\sigma}^2=\frac{1}{n}\left(\frac{n}{n-1}\right)\sum_{i=1}^{n}(x_i-\bar{x})^2=\frac{1}{n-1}\sum_{i=1}^{n}(x_i-\bar{x})^2 \tag{27}$$

2. The maximum likelihood estimator is efficient. The estimator is efficient if and only if the variance of an estimator, $V[\hat{\theta}]$ is minimal and unbiased:

$$V[\hat{\mu}]=Var\left[\frac{x_1+x_2+x_3\ldots x_n}{n}\right]$$

$$=\frac{1}{n^2}\left(E[x_1]+E[x_2]+E[x_3]+\ldots+E[x_n]\right)$$

$$=\frac{n\sigma^2}{n^2}=\frac{\sigma^2}{n} \tag{28}$$

To determine the variance of $\hat{\sigma}^2$, Chi-square distribution is utilized. Chi-square distribution is the distribution of the sum of squared standard normal deviates. Given the random variable for a Chi-square distribution with *k* degrees of freedom; that is,

$$Q=Z_1^2+Z_2^2+Z_3^2+\ldots+Z_k^2\sim\chi^2_{(k)} \tag{29}$$

where Z_i is a standard normal distribution which is independently and identically distributed, that is, $Z_i \sim N(0,1)$. The expected value and variance of Q are written as:

$$E(Q) = k$$
$$Var(Q) = 2k \quad (30)$$

According to Eq. (20), given $z = \frac{x-\mu}{\sigma}$ which can be written as $\frac{x-\mu}{\sigma} \sim N(0,1)$, it can be shown that

$$\sum_{i=1}^{n}\left(\frac{x_i-\mu}{\sigma}\right)^2 \sim \chi^2_{(n)}$$

$$\sum_{i=1}^{n}\left(\frac{x_i-\mu}{\sigma}\right)^2 = \sum_{i=1}^{n}\left(\frac{x_i-\mu-\bar{x}+\bar{x}}{\sigma}\right)^2 = \sum_{i=1}^{n}\left(\frac{x_i-\bar{x}}{\sigma}+\frac{\bar{x}-\mu}{\sigma}\right)^2$$

$$= \sum_{i=1}^{n}\left(\frac{x_i-\bar{x}}{\sigma}\right)^2 + \left(\frac{\bar{x}-\mu}{\sigma/\sqrt{n}}\right)^2$$

$$= \chi^2_{(n-1)} + \chi^2_{(1)} \quad (31)$$

Considering Eq. (28), the second term on the right-hand side of the equation is the normal distribution of $\bar{X}$ which gives a Chi-square distribution with 1 degree of freedom. Then, the formula becomes

$$\sum_{i=1}^{n}\left(\frac{x_i-\bar{x}}{\sigma}\right)^2 = \chi^2_{(n-1)} \quad (32)$$

From Eq. (27), the unbiased estimator of parameter σ^2, denoted as $\hat{\sigma}^2 = \frac{1}{n-1}\sum_{i=1}^{n}(x_i-\bar{x})^2$ or alternatively written as $\sum_{i=1}^{n}(x_i-\bar{x})^2 = (n-1)\hat{\sigma}^2$, is substituted into Eq. (32):

$$\frac{(n-1)\hat{\sigma}^2}{\sigma^2} = \chi^2_{(n-1)}$$

Now, from Eq. (30) we have

$$V\left[\frac{(n-1)\hat{\sigma}^2}{\sigma^2}\right] = 2(n-1)$$

$$V\left[\hat{\sigma}^2\right] = \frac{2\sigma^4}{(n-1)} \quad (33)$$

3. The maximum likelihood estimation method appears to be the best possible or optimal estimator because its variance of estimator equals the Cramér -Rao Lower Bound which yields a minimum variance estimator. Let $f(x|\ \theta)$ be the probability density function of the population and $\hat{\theta}$ denotes an unbiased estimator of parameter θ. The Cramér -Rao Lower Bound can be expressed as:

$$V(\hat{\theta}) \geq \frac{1}{n\mathrm{E}\left[\left(\frac{\partial \ln f(x|\theta)}{\partial\theta}\right)^2\right]} \quad (34)$$

Assuming normal distribution, it follows that

$$f\left(x|\mu,\sigma^2\right) = \frac{1}{\sqrt{2\pi\sigma^2}}e^{-(1/2)\left[(x-\mu)/\sigma\right]^2}, -\infty < x < \infty$$

$$\ln f\left(x|\mu,\sigma^2\right) = -\frac{1}{2}\ln\left(2\pi\sigma^2\right) - \frac{1}{2\sigma^2}(x-\mu)^2$$

$$\frac{\partial \ln f\left(x|\mu,\sigma^2\right)}{\partial\mu} = \frac{1}{\sigma^2}(x-\mu)$$

$$E\left[\left(\frac{\partial \ln f\left(x|\mu,\sigma^2\right)}{\partial\mu}\right)^2\right] = \frac{1}{\sigma^4}\mathrm{E}(x-\mu)^2 = \frac{V[x]}{\sigma^4} = \frac{\sigma^2}{\sigma^4} = \frac{1}{\sigma^2}$$

Taking into account Eq. (28), substituting the above equation into Eq. (34) yields

$$\frac{1}{n\mathrm{E}\left[\left(\frac{\partial \ln f\left(x|\mu,\sigma^2\right)}{\partial\mu}\right)^2\right]} = \frac{1}{n\left(\frac{1}{\sigma^2}\right)} = \frac{\sigma^2}{n} = V[\hat{\mu}] \quad (35)$$

$$\frac{\partial \ln f\left(x|\mu,\sigma^2\right)}{\partial\sigma^2} = -\frac{1}{2\sigma^2} + \frac{1}{2\sigma^4}(x-\mu)^2$$

$$E\left[\left(\frac{\partial \ln f\left(x|\mu,\sigma^2\right)}{\partial\sigma^2}\right)^2\right] = \frac{1}{4\sigma^4} + \frac{1}{4\sigma^4}\left[V\left[\left(\frac{x-\mu}{\sigma}\right)^2\right] + \left(E\left[\left(\frac{x-\mu}{\sigma}\right)^2\right]\right)^2\right] - \frac{1}{2\sigma^6}V[x]$$

From Eq. (30), since $V\left[\left(\frac{x-\mu}{\sigma}\right)^2\right] = 2$, $E\left[\left(\frac{x-\mu}{\sigma}\right)^2\right] = 1$

then,

$$E\left[\left(\frac{\partial \ln f\left(x|\mu,\sigma^2\right)}{\partial\sigma^2}\right)^2\right] = \frac{1}{4\sigma^4} + \frac{1}{4\sigma^4}(2+1) - \frac{1}{2\sigma^4} = \frac{1}{2\sigma^4}$$

Now, the above equation is substituted into Eq. (34) and Eq. (33) is taken into consideration:

$$\frac{1}{n\mathrm{E}\left[\left(\frac{\partial \ln f\left(x|\mu,\sigma^2\right)}{\partial\sigma^2}\right)^2\right]} = \frac{1}{n\left(\frac{1}{2\sigma^4}\right)} = \frac{2\sigma^4}{n} < V\left[\hat{\sigma}^2\right] = \frac{2\sigma^4}{(n-1)} \quad (36)$$

4. The maximum likelihood estimator is consistent because it converges to the true value of parameter being estimated.

From Eq. (26), despite having $E\left[\hat{\sigma}^2\right] = \frac{(n-1)\sigma^2}{n} \neq \sigma^2$, but $E\left[\hat{\sigma}^2\right]$ converges to σ^2 for a large sample size (n-1 $\approx$ n). In the same way, $2\sigma^4/n$ converges to $V\left[\hat{\sigma}^2\right] = \frac{2\sigma^4}{(n-1)}$ as shown in Eq. (36).

The development of fragility curve using the maximum likelihood method have been adopted in many previous studies [1], [4]-[10]. The review of literature shows that the structural component failure data fits with the lognormal distribution well. A log-normal distribution appears to set robust precedent in risk analysis and assessment. Furthermore, theoretically, applying a lognormal distribution yields zero probability density at and below zero intensity measure (IM).

TESTING ESTIMATION METHOD FOR FRAGILITY CURVE

As a first step of the method for the fragility curve development, the parameter values of μ and σ^2 assuming a lognormal distribution is chosen. Next, 100 groups of 50 data is randomly generated from these parameters. Finally, estimated values of the parameter mean and variance ($\hat{\mu}$ and $\hat{\sigma}^2$) are

obtained from using the MLE and LSE methods for each group of data. Precisely, $\hat{\mu}$ is not equal to μ for all groups of data, as well as the estimated value of $\hat{\sigma}^2$. A summary of findings is presented in Table 1. The distribution of estimated parameter value is shown in Fig.2. The estimated probability density function, which is inherent in Eq. (2), appears to have a bell-shaped curve. The maximum likelihood estimation gives μ = -0.80 and σ^2 = 0.40 which has a smaller variance than the variance of the least square estimation. The results show that the MLE method based on the lognormal approach yields better estimates than the LSE method.

Table 1 The estimated parameters by LSE and MLE

Methods in numerical fitting	Estimated parameter		Error (%)	
	μ	σ^2	μ	σ^2
Least Squares	-0.8116	0.3994	0.0065	0.0016
Maximum Likelihood	-0.7985	0.4003	0.0063	0.0016

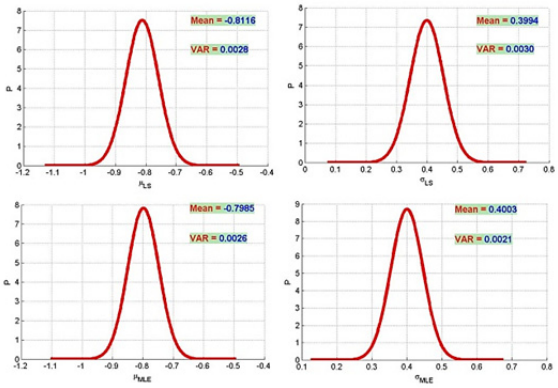

Fig. 2 The distribution of estimated value.

CONCLUSIONS

In this paper, the estimated parameter of mean (μ) and variance (σ^2) of a lognormal distribution are determined either by the maximum likelihood estimation (MLE) or by the least squares estimation (LSE). Then, the estimated results obtained from these two methods are compared with each other. To develop a fragility curve, the method starts by choosing the parameter values of μ and σ^2, assuming a lognormal distribution. The results indicate that the size of variance obtained with MLE is smaller than the variance obtained with LSE. In summary, the MLE method based on the lognormal approach gives better outcomes of the estimated parameter of mean (μ) and variance (σ^2) of lognormal distribution. In other words, fragility curves developed by the MLE method appears to be more consistent and efficient than those developed by the LSE method.

REFERENCES

[1] Porter K., Kennedy R. and Bachman R., Creating fragility functions for performance-based earthquake engineering. Earthquake Spectra, 2007, Issue 23, pp. 471-489.

[2] Mackie K. and Stojadinovic B., Fragility curves for reinforced concrete highway overpass bridges. 13th World Conference on Earthquake Engineering, Vancouver, B.C., Canada August 1-6, 2004, Paper No. 1553.

[3] Tien Y.M. and Pai C.H., Development of fragility curves for the 1999 Chi-Chi, Taiwan, earthquake. Proceedings of the 8th U.S. National Conference on Earthquake Engineering, San Francisco, California, USA April 18-22, 2006, Paper No. 401.

[4] Foytong P. and Ruangrassamee A., Fragility curves of reinforced-concrete buildings damaged by the 2004 tsunami. Engineering and Applied Science Research, Vol. 43, Issue S3, 2016, pp. 419-423.

[5] Karim K.R. and Yamazaki F., A simplified method of constructing fragility curves for highway bridges. Earthquake Engineering and Structural Dynamics, 2003, Vol. 32, pp. 1603-1626.

[6] Mander B., Fragility curve development for assessing the seismic vulnerability of highway bridges. University at Buffalo, 1999, State University of New York.

[7] Saxena V., Deodatis G., Shinozuka M. and Feng M.Q., Development of fragility curves for multi-span reinforced concrete bridges. International conference on Monte Carlo simulation Technical Program, Balkema Publishers, 2000.

[8] Shinozuka M., Feng M.Q., Kim H.K. and Kim S.H., Nonlinear static procedure for fragility curve development. Journal of Engineering Mechanics, 2000, Vol. 126, pp. 1287-1295.

[9] Singhal A. and Kiremidjian A.S., Bayesian updating of fragilities with application to RC frames. Journal of Structural Engineering, 1998, pp. 922-929.

[10] Yamazaki, F. and Murao, O., Fragility curves for buildings in Japan based on experience from the 1995 Kobe Earthquake. Institute of Industrial Science, 2000, University of Tokyo, Tokyo, Japan.

9th Int. Conf. on Geotechnique, Construction Materials and Environment, Tokyo, Japan, 20-22 November 2019, ISBN: 978-4-909106025 C3051

HEAVY METAL CONCENTRATION CHANGE IN OYSTER AFTER CHANGING LIVING PLACES WITH VARIOUS HEAVY METAL CONDITION IN OSAKA BAY, JAPAN

Tetsuya Fukano[1] and Hiroyuki Ii[2]
[1]Graduate School of Systems Engineering, Wakayama University, Japan
[2]Faculty of Systems Engineering, Wakayama University, Japan

ABSTRACT

Heavy metal concentration of oysters in the Osaka Bay were measured. As the result, high Zn and Cu concentration oyster was found in Takaishi fishing port in the Osaka Bay. In 2018, Cu concentration of oyster sampled at Takaishi fishing port was extremely high, 7.8 ‰ dry weight. On the other hand, Zn and Cu concentrations of these oysters gradually increased after these oysters living place changed from natural beach area of Takashinohama to the boat maintenance sloops of Takaishi fishing port. Similarly after changing living place from Takaishi fishing port to Izumiotsu port, heavy metal concentration of oyster at Takaishi fishing port gradually changed to heavy metal concentration of oyster at Izumiotsu port with 7 weeks. Cu, Mn, Fe, Ni, Pb and Zn concentrations of oyster sampled at Takaishi fishing port are high, but As concentration was low. Cu, Mn, Fe, Ni, Pb and Zn concentrations of oyster sampled at Izumiotsu port were low, but As concentration was high, 0.023~ 0.029 ‰ dry weight. The goal of the changing living place was concentration of naturally lived oyster at Izumiotu port. It means oyster do not keep accumulating the heavy metals. As the result heavy metal concentration of oyster was clarified to change with time. Each heavy metal concentration for various internal organs was measured. Cu, Fe, Pb and Zn concentrations in all internal organs decreased in direct ratio. Mn concentrations in mantle, gill showed various change. Ni concentration in gill showed various change. Concentrations of As in all internal organs increased in direct ratio. The speed of decrease, Pb was fastest in all heavy metal. Every metal concentrations of oyster changed gradually in Hepatic gland even the oyster was small one. And the speed of change was almost same to other tissues. Hepatic gland has blown or green color, so easy to find and separate. From this study, Hepatic gland has most high potential as an environmental index in oyster.

Keywords: Oyster, changing living place, heavy metal accumulation, internal organs, hepatic gland

INTRODUCTION

The absorption and accumulation of heavy metals in sea water by aquatic organisms was reported by Ikuta [1]. Concentration and distribution of toxic and essential metals in biological samples collected in Okayama prefecture were reported by Morita and Ogata [2]. Metal contamination of sea water was evaluated by seaweed [3] and in particular, metal concentration of seaweed along the Kii Peninsula was measured and high Cu, Fe and Zn concentrations were found around metal mines [4]. Use of seaweed is useful for sea contamination. The use of bivalves as possible sentinel marine organisms to monitor metal pollution in coastal water was reported by Takayanagi and Sakami [5].

"*Ostrea gigas*," a very popular coastal oyster, lives in the same location for several years, thus has high potential as a heavy metals index. The relation of Pb, Cd and Cr between sea water, sea sediment and oyster (*Crassostrea virginica*) was clarified and influence of metal contamination caused by the runoff of household and industrial discharge on oyster was evaluated in Mexico [6]. Then, this study is to clarify how to change heavy metal concentration of oyster with time and location condition, and determine the potential of oysters as an environmental index for heavy metal. Heavy metal concentration of oysters is measured with time after changing living place of oyster. Moved oyster was sampled every week for 7 weeks, and each heavy metal concentrations for various internal organ, mantle, gill, muscle, hepatic grand, others, and whole oyster were measured. The heavy metals measured were Cu, Mn, Fe, Ni, Pb, Zn and As. Cu concentrations of each oyster parts were analyzed at Oman Sea [7] and those of tissue were higher than those of shell although Pb concentrations of tissue were lower than those of shell.

METHOD

Shells of sampled oysters were opened carefully with a stainless-steel knife. The soft tissues of the oysters were cut into small pieces and put into pre-weighted laboratory dishes. The soft tissues were

dried at 60 degrees for a week. Each dried sample was ground manually into fine powder form by mortar and a pestle. Each dried ground sample was stored separately in airtight polypropylene bags.

0.020g of dried ground sample was mixed with 5.0 mL of concentric nitric acid in a glass vessel and then kept for a week at room temperature. After ground samples were dissolved by nitric acid completely, added 10mL water. And the solution was filtered with a 0.45μm filter and then dry weight concentrations of heavy metal were measured by Inductively Coupled Plasma (ICP).

RESULT

Oysters were changed living place from Takaishi fishing port to izumiotu port. At Takaishi, Oysters were lived on boat maintenance slope. On the slope, many small red paint flakes were peeled off from bottom of boats. The paint was anti-fouling paint, ingredient of the paint were Cu_2O and ZnO [8]. After changing place, oysters in polyethylene mesh net bags were hanged about 2m depth from surface at Izumiotsu port. At Izumiotsu port, anti-fouling paint flakes were not seen.

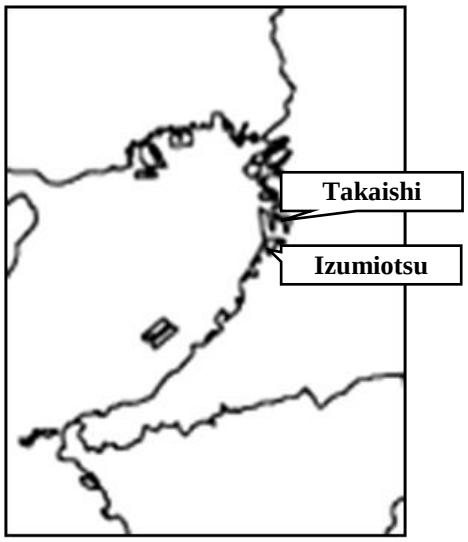

Fig.1 Sampling points
(Located at east side of Osaka Bay)

Oysters were sampled from Takaishi fishing port and moved to Izumiotu port at 5-Mar. 2019. Moved oyster was sampled every week for 7 weeks. And concentration of Cu, Mn, Fe, Ni, Pb, Zn and As for Mantle, Gill, Adductor muscle, hepatic gland, and whole oyster were measured. Samples were choose big oyster over 10g wet weight without shells. Concentrations of heavy metals in small oyster contained many irregular data. Last results of May in each figures showed heavy metal concentration in oyster naturally lived at Izumiotu port.

Cu concentration in oyster

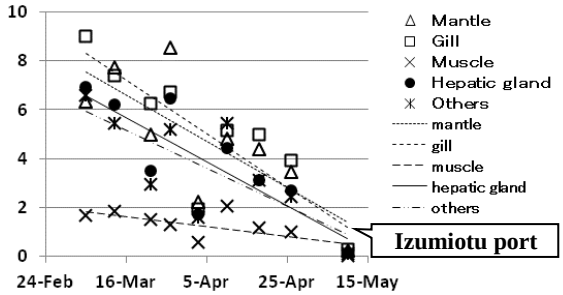

Fig. 1 Cu ‰ [dry wt.] in each internal organ

Fig.1 showed concentration of Cu in each internal organ decreased in direct ratio. Especially gill and hepatic gland were showed smooth decrease, R^2 were 0.72 and 0.68.

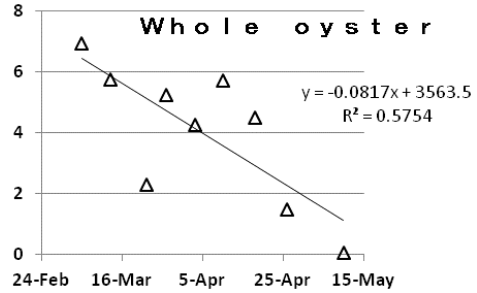

Fig. 2 Cu ‰ [dry wt.] in whole oyster

Fig.2 showed concentration of Cu in whole oyster decreased in almost direct ratio.

Mn concentration in oyster

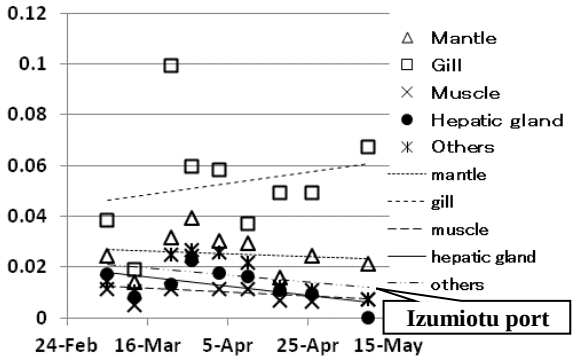

Fig. 3 Mn ‰ [dry wt.] in each internal organ

From Fig.3, Mn concentrations in mantle and gill showed various change.

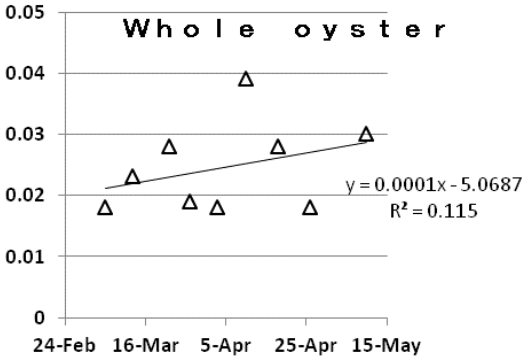

Fig. 4 Mn ‰ [dry wt.] in whole oyster

Fig.4 showed concentration of Mn in whole oyster gleatly changed. But concentration of Mn in hepatic gland decreased in almost direct ratio.

Fe concentration in oyster

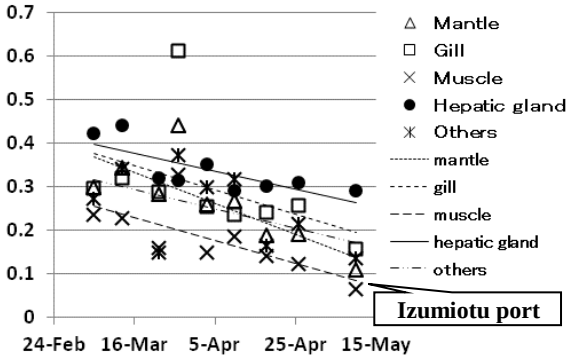

Fig. 5 Fe ‰ [dry wt.] in each internal organ

Fig. 5 showed concentration of Fe in each internal organ decreased in direct ratio roughly. Especially mantle and hepatic gland were showed smooth decrease, R^2 were 0.61 and 0.61.

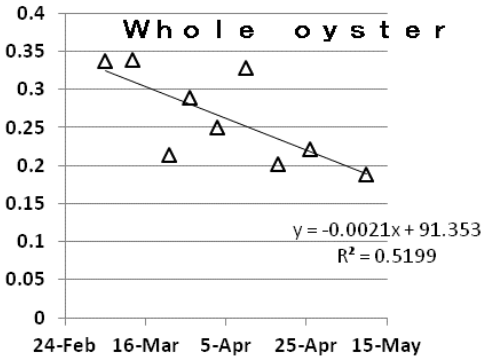

Fig. 6 Fe ‰ [dry wt.] in whole oyster

Fig. 6 showed concentration of Fe in whole oyster, decreased in almost direct ratio.

Ni concentration in oyster

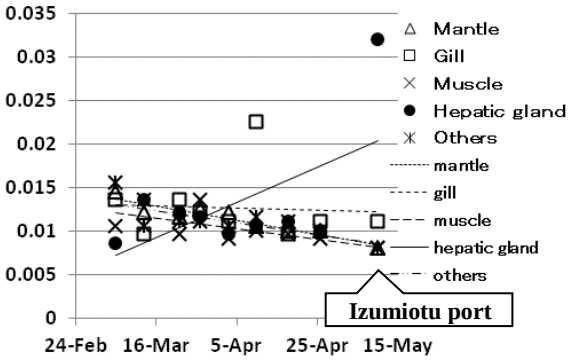

Fig. 7 Ni ‰ [dry wt.] in each internal organ

Fig. 7 showed concentration of Ni in each internal organ decreased in almost direct ratio except some errors. Especially mantle showed smooth decrease, R^2 was 0.86.

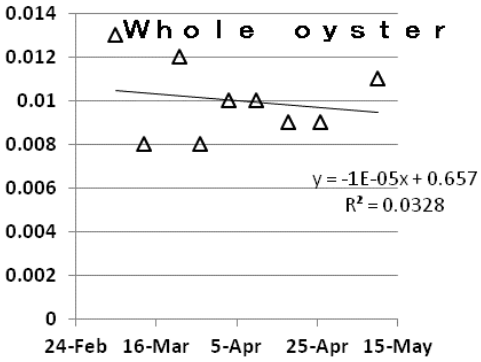

Fig. 8 Ni ‰ [dry wt.] in whole oyster

Fig. 8 showed concentration of Ni in whole oyster decreased in direct ratio roughly, R^2 were low 0.032.

Pb concentration in oyster

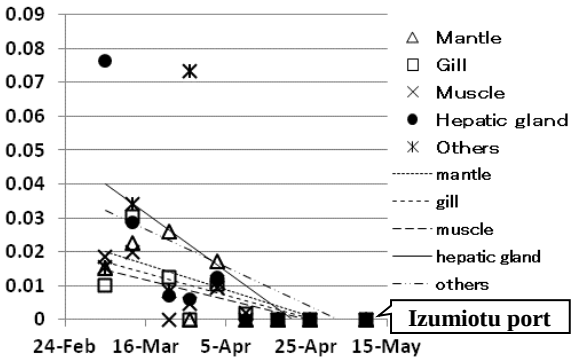

Fig. 9 Pb ‰ [dry wt.] in each internal organ

Fig. 9 showed concentration of Pb decreased in direct ratio. And the speed of decrease was fast.

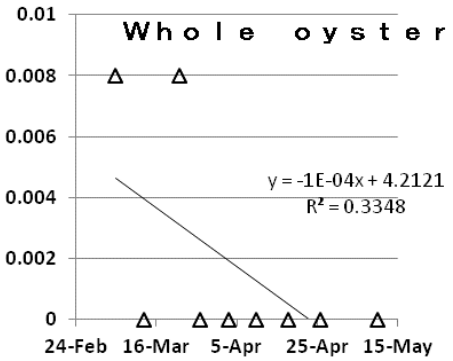

Fig. 10 Pb ‰ [dry wt.] in whole oyster

Fig. 9 and Fig. 10 showed concentration of Pb decreased in direct ratio. The speed of decrease, Pb was faster than other heavy metal.

Zn concentration in oyster

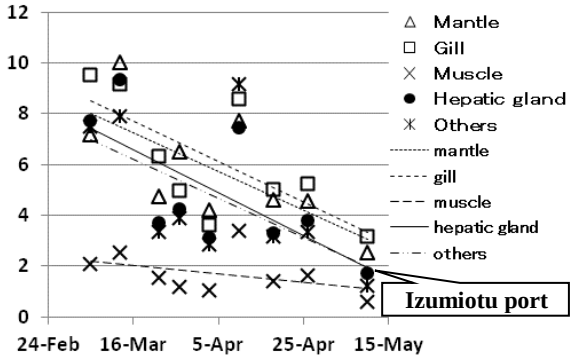

Fig. 11 Zn ‰ [dry wt.] in each internal organ

Fig. 11 showed concentration of Zn in each internal organ decreased in almost direct ratio.

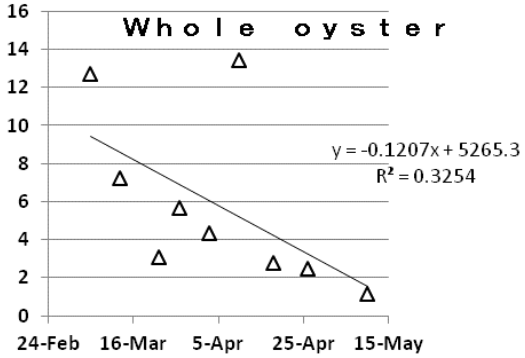

Fig. 12 Zn ‰ [dry wt.] in whole oyster

Fig. 12 showed concentration of Zn in whole oyster decreased in almost direct ratio except some errors.

As concentration in oyster

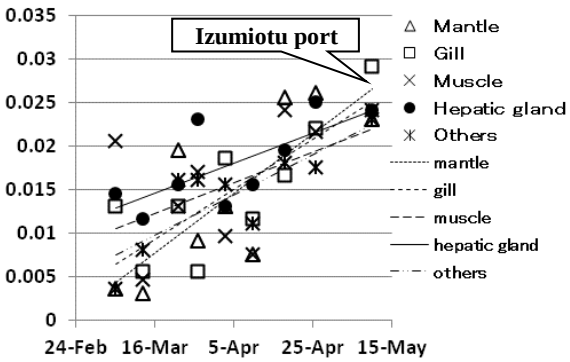

Fig. 13 As ‰ [dry wt.] in each internal organ

Fig. 13 showed concentration of AS in each internal organ increased in almost direct ratio.

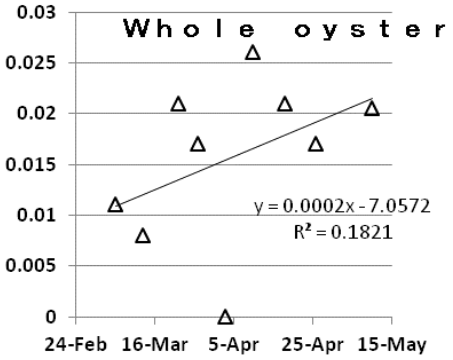

Fig. 14 As ‰ [dry wt.] in whole oyster

Fig. 14 showed concentration of As in whole oyster increased in direct ratio roughly.

From fig.1to14, results sometimes contained irregular data. But heavy metal concentrations of oyster changed gradually with relocation, and goal of the change was concentration of naturally lived oyster at Izumiotu port. Concentration of Cu, Fe, Ni in Mantle approach to goal in about 6 weeks, and bigger oyster showed smooth change. The change of Pb was fast, reached to goal in about 5 weeks. Concentration of As in oyster at izumiotu was higher than Takaishi, then concentration of As in moved oyster increased quickly.

Concentrations of Cu and Zn in changed living places oysters at Takashinohama port

Oysters were sampled from 10th January 2016 to 28th February 2016 at sampling point E1 and E3 to check for changes of Cu and Zn concentrations after changed living places.

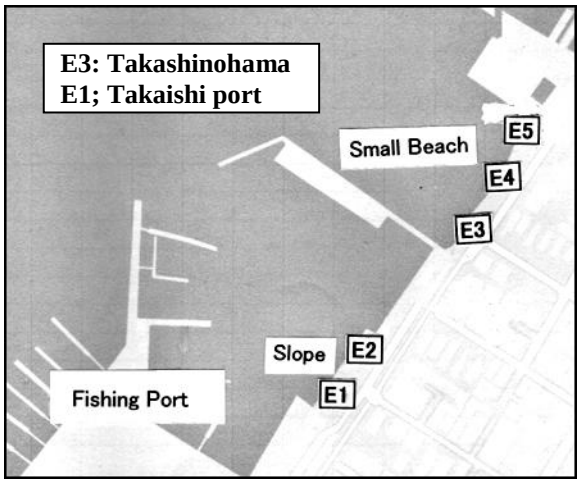

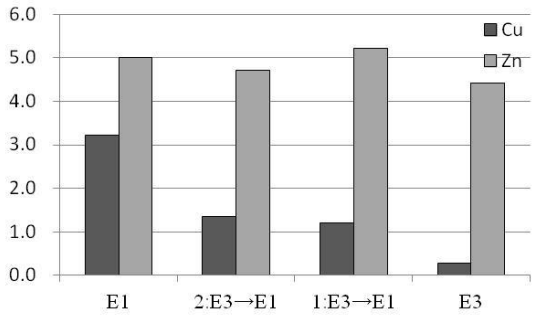

Fig.15 Concentrations of Cu and Zn in changed living places oysters. (‰ [dry wt.])

Oyster changing living places was done in the following way; "1:E3→E1" indicates that oysters were sampled 10th January 2016 at sampling point E3 and released at sampling point E1. Sampling point E3 was a beach area of Takashinohama, and sampling point E1 was an area of the boat maintenance sloops of Takaishi fishing port. Oysters changed living places were sampled again at sampling point E1, 23rd January 2016. Therefore, the "living time" at sampling point E1 was 13 days.

"2:E3→E1" indicates that oysters were sampled 11th February 2016 at sampling point E3 and released to sampling point E1. Oysters changed living places were sampled again at sampling point E1, 28th February 2016. Therefore, the "living time" at sampling point E1 was 17 days.

Fig.15 showed the relation between Cu and Zn concentrations of the oysters and living time at sampling point E1. Cu concentration increased with living time 0.3, 1.2, 1.7 and over 3.0 ‰ for living time from 0, 13, 17 days to long term. But Zn concentrations in oysters did not increased with location and living time at sampling point E1 and values were uniform. Therefore, sampling point E1 increased Cu concentration in the oysters but did not increase Zn concentration.

CONCLUSIONS

Cu, Fe, Ni, Pb, Zn, As concentrations of oyster changed gradually with relocation and goal of the change was concentration of naturally lived oyster at Izumiotu port. It means oyster do not keep accumulating the heavy metals. When changed living place 6~7 weeks, heavy metals concentrations of oyster approached to goal. And big oyster showed smooth change.

But concentration of Mn showed various change in Mantle and Gill. Mantle and Gill are outside tissues of oyster, so easy to be contaminated with fine particle size of mad or sand.

Every metal concentrations of oyster changed gradually in Hepatic gland even the oyster was small one. And the speed of change was almost same to other tissues. Hepatic gland has blown or green color, so easy to find and separate.

From this study, Hepatic gland has most high potential as an environmental index in oyster.

REFERENCES

[1] Ikuta K, Studies on Accumulation of Heavy Metals in Aquatic Organism-1.On the Copper Contents in Oysters, Bulletin of Japanese Society Fisheries, Vol.33, No.5, 1967, pp405_409.

[2] Morita K, and Ogata M, "Levels and distribution of toxic and essential metals in biological samples collected in Okayama Prefecture", Department of Public Health, Okayama University Medical School, 1983, pp359_376

[3] Ii, H., Cu, Zn and As contamination of Seaweed beside Shizuki and Kanayama Metal Mines in Japan, International Journal of GEOMATE, Vol. 9 (1), 2015, pp.1411-1417.

[4] Ii H., As, Sr, Zn, Fe, Mn, Pb, and Cu Concentrations of Seaweed at the Kii Peninsula, Japan, International Journal of GEOMATE, Vol.10 (1), 2016, pp. 2036-2042.

[5] Takayanagi K., and Sakami T., Bivalves as a possible sentinel marine organism to monitor metal pollution in coastal waters –A review-, Bull. Fish. Res. Agen.,No2.35-46,2002

[6] Guzmán-García1X., Botello A.V., Martinez-Tabche L. and González-Márquez H., Effects of heavy metals on the oyster (Crassostrea virginica) at Mandinga Lagoon, Veracruz, Mexico, Rev. Biol. Trop. Int. J. Trop. Biol. 2009, Vol. 57 (4), pp.955-962.

[7] F. Einollahi Peer, A. Safahieh, A. Dadollahi Sohrab, S. Pakzad Tochaii, Heavy metal concentrations in rock oyster Socostre Cucullata from Iranian Coasts of the Oman Sea, Trakia Journal of Sciences, Vol. 8, No. 1, 2010, pp. 79-86.

[8] Yamaguchi Y, Copper Speciation and oCncentration in Seawater of Japan-Toward the Risk Assessment of Copper Compounds for Anti-Fouling Paint, National Maritime Research Institute ISSN;2186-6598 http://www.nmri.go.jp/main/publications/paper/pdf/21/15/02/PNM21150205-00.pdf

9th Int. Conf. on Geotechnique, Construction Materials and Environment,
Tokyo, Japan, 20-22 November 2019, ISBN: 978-4-909106025 C3051

REPAIR SEQUENCE AND RECOVERY TIME IN WATER DISTRIBUTION NETWORK RESILIENCY

Janice Kaye L. Aquino[1], Richard M. De Jesus[2], Lessandro E. O. Garciano[2], Renan M. T. Tanhueco[2], and Agnes D. Garciano[3]
[1]Faculty, St. Louis University (Baguio), Philippines; [2]De La Salle University (Manila),
[3]Ateneo De Manila University

ABSTRACT

Recent disasters highlighted that water distribution systems (WDS) suffered greatly during seismic events. But people cannot afford to have extended water service interruption as it is essential for drinking, sanitation, and medical services. Thus, it is imperative that WDS provides adequate resistance to extreme events. And in the event of failure, it must recover functionality within short period. Resilience-based engineering ensures that infrastructures be robust to adequately resist seismic events and recover from failure fast. It also requires to have resources and redundant systems. This implies that WDS must satisfy resiliency requirements for it to function satisfactorily during and after seismic events. This study quantifies the resiliency of La Trinidad Water District (LTWD) through measuring the impacts of restoration sequences to recovery duration and knowing which sequence satisfies resiliency. LTWD, in Benguet, Philippines, is at risk to earthquake due to geologic and geographic setting, thus, it must be "resilient". In this study, restoration strategies were conducted using constrained spanning trees to determine the most efficient network connectivity. Horn's algorithm was applied for repair sequence. Results showed that restoration sequence is directly related to rapidity of resiliency. The shortest restoration resulted to a faster recovery to return back to its pre-event system functionality.

Keywords: Resilience, Horn's algorithm, Restoration curve, Earthquake, Water distribution network

INTRODUCTION

The Philippine Institute of Volcanology and Seismology (PHIVOLCS) [1] considered the province of Benguet to be, among the provinces in the Philippines, the third at risks to earthquakes considering its geologic and geographic setting. According to Mines and Geosciences Bureau (MGB) [2], La Trinidad - a municipality in Benguet is highly vulnerable to geologic hazards because of several active fault lines in the area. This makes the water infrastructure vulnerable to earthquake hazards.

The case study area is La Trinidad Water District (LTWD), located in La Trinidad in the province of Benguet (Fig. 1). La Trinidad is where Baguio City is located. Baguio city is considered to be the summer capital of the Philippines due to its cold weather and has become one of the country's top tourist destinations. LTWD is a local water district that serves 16 barangays with drinking water. It has been in operation for more than 30 years but has not received any technology-based upgrade yet. Its only upgrade is the continuous expansion of water pipe networks to serve a rapidly increasing demand. It has also increased its water source, from four to seventeen comprised of mixed spring and deep well sources. La Trinidad was devastated by a magnitude 7.8 earthquake in 1990 where casualties and damage to structure is considered to be among the deadliest earthquake that hits the country [3].

The area is surrounded by five (5) active major faults: (1) Philippine fault, (2) Digdig fault, (3) San Manuel fault, (4) Tebbo fault, and (5) Tubao fault. LTWD was lucky to have not suffered any major damage during the 1990 earthquake though there were reports of few pipe breakages due to joint pullout from the main transmission line, but was repaired immediately.

Because of great risks that earthquake hazard poses to the area of La Trinidad, it is important to for LTWD to satisfy water distribution network resiliency as it is of utmost importance that water supply remains functional during earthquake events for life safety, rescue, and healthcare operations. Hence, this study conducted the following: (1) assessment of the possible impact of earthquake hazard to LTWD, (2) evaluation of post-earthquake restoration strategy to ensure that functionality of LTWD can return back to its pre-event functionality at the soonest possible time.

THEORETICAL BACKGROUND

Graph theory [4] was employed to simplify the water distribution network, where pipelines are treated as "branches" or links of each "tree" joined by demand nodes. Here, $G = (V, E)$ represents the network configuration of a water pipeline system,

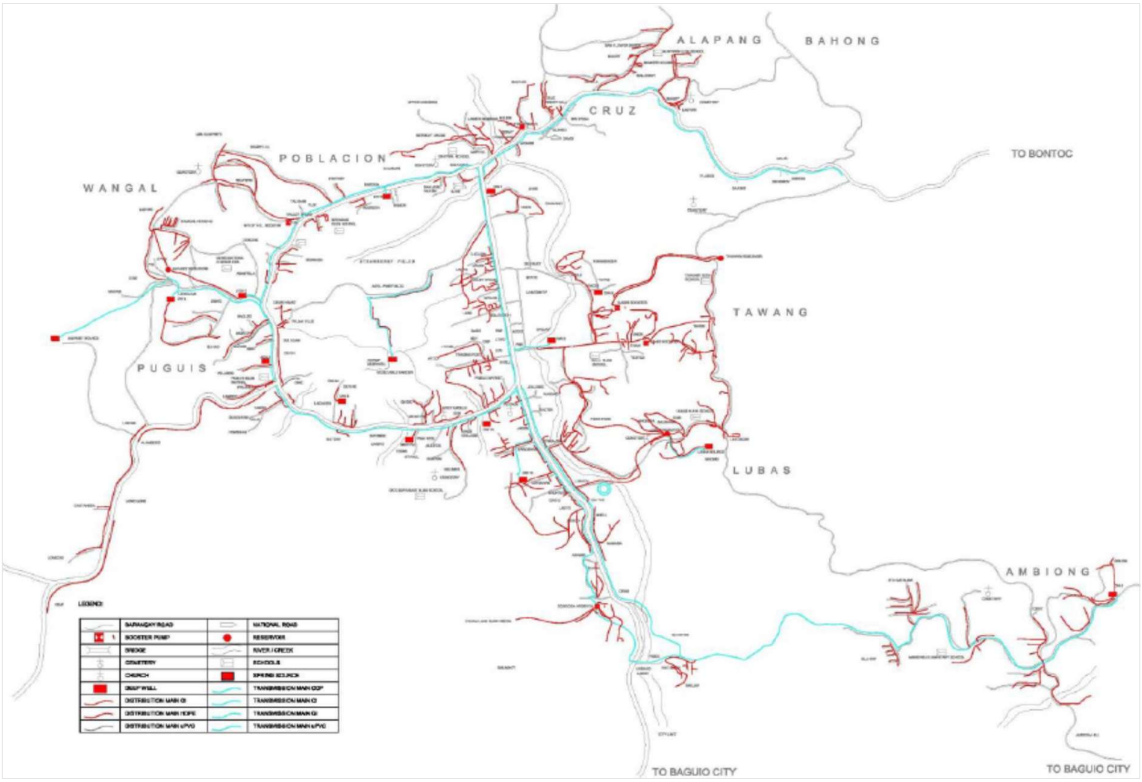

Figure 1. Digitized schematic diagram of LTWD (green lines – transmission; red lines – distribution)

where V and E are nodes and links, respectively. A series of single rooted tree, which is a finite directed network with a distinguished node root (i.e. supply node of the network) directed towards demand nodes along a single line with no closed loops, represents the system.

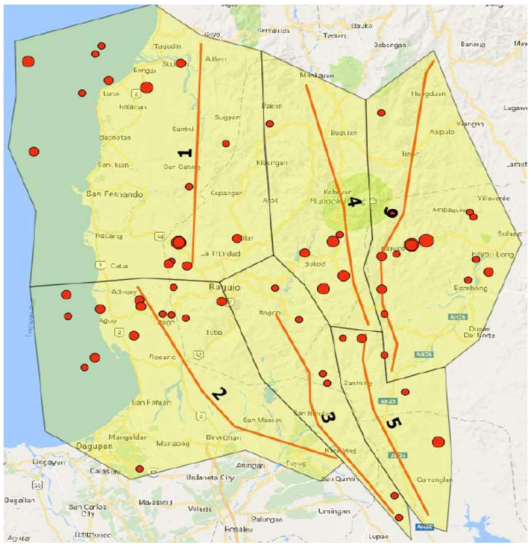

Figure 2. Faults considered in conducting PSHA

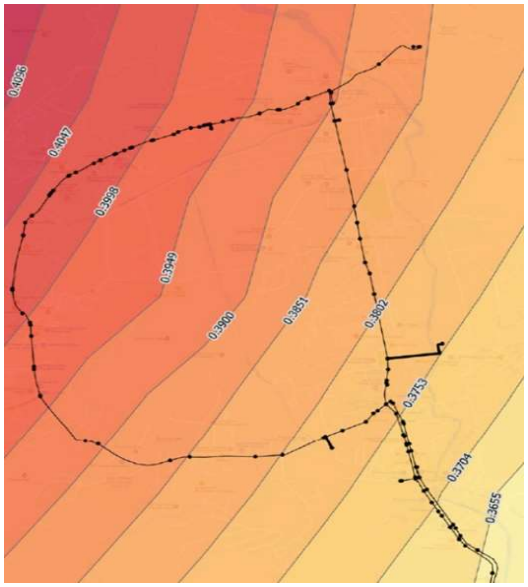

Figure 3. PGA contour map (as fractions of g)

In optimizing the restoration process, the study utilized restoration curve which is time-dependent function that represents the degree of restoration with respect to time. The restoration curve $R(Tj)$ is a stepwise function defined by the following equation:

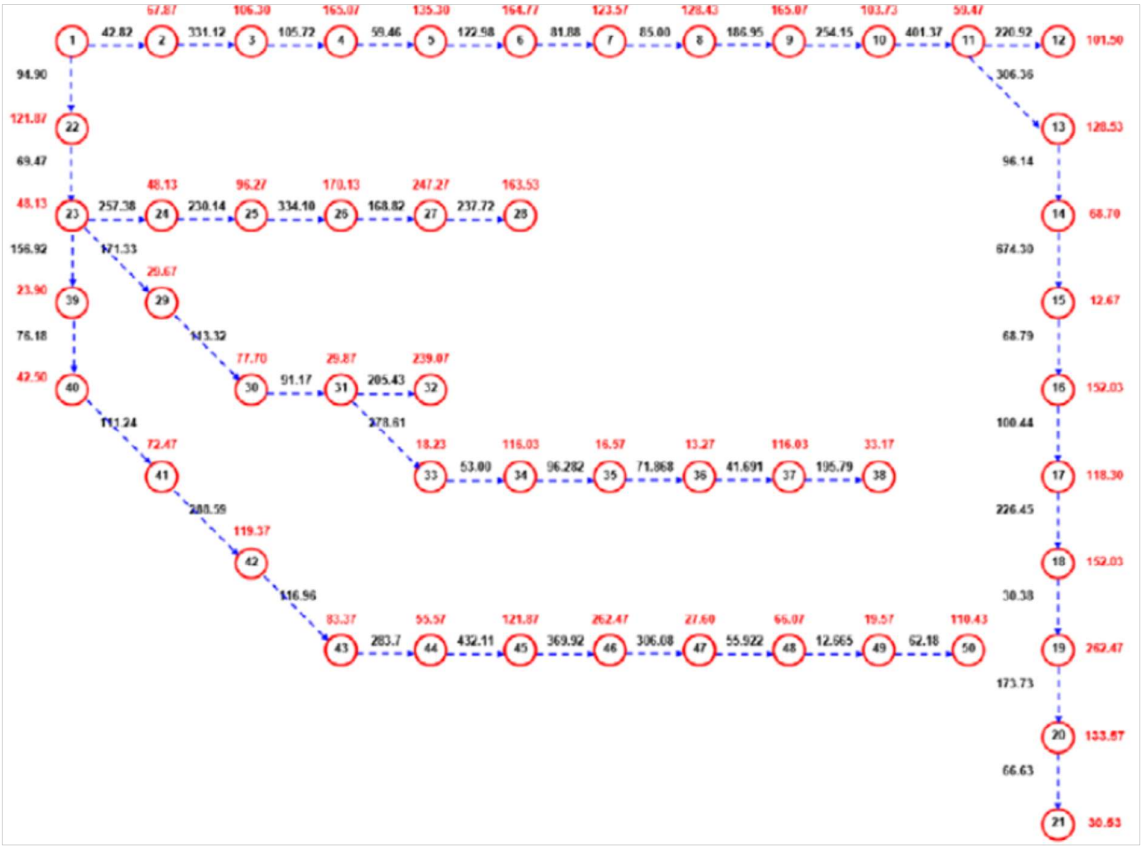

Figure 4. LTWD schematic scheme model (red – repair time, blue – node capacity)

$$R(Tj) = \sum_{\sigma(k)\leq\sigma(j)} h_k / \sum_{i=1}^{n} h_i \quad (1)$$

where $\sigma(j)$ = position number assigned to each node v_j in the recovery sequencing; t_j = net time required to repair each damaged component j. Also, h_i represents users that are linked to demand node (v_j) restored at time T_j after an earthquake event.

$$T_j = \sum_{\sigma(k)\leq\sigma(j)} t_k \quad (2)$$

Using Horn's algorithm [5], an optimized restoration sequence for damaged LTWD during a seismic event is achieved. In sequencing the repair of nodes, priority is given to demand nodes with higher efficiency. This is to restore service first to nodes that will supply water to more consumers in the shortest time possible.

Global optimization, through Horn's algorithm, is done by minimizing the area above the restoration curve. This is achieved using the improved efficiency parameter, γ_j*, and is computed by:

$$\gamma_j^* = \sum_{i\in U(j)} h_i / \sum_{i\in U(j)} t_i \quad (3)$$

where $U(j)$ is a subset of a set of nodes reachable from node v_j. It is determined so that γ_j* takes on the greatest value. The improved efficiency is taken along a directed path from supply nodes on a single line. Obviously, there are no directed cycles. The area above the restoration curve, called the linear delay penalty, is computed as follows:

$$t_A = \sum_{i=1}^{n} h_i T_i / \sum_{i=1}^{n} h_i \quad (4)$$

t_A represents the average time for restoration and can be regarded as the measure of the overall impact of lifeline malfunction.

Table 1. Horn's algorithm sequencing and efficiency parameter

Sequence	Node	γ*	Sequence	Node	γ*	Sequence	Node	γ*
1	22	0.73	18	8	0.57	35	42	0.45
2	2	0.70	19	9	0.54	36	43	0.46
3	3	0.68	20	10	0.51	37	44	0.44
4	4	0.76	21	11	0.52	38	45	0.49
5	5	0.69	22	13	0.61	39	46	0.60
6	23	0.65	23	14	0.65	40	47	0.51
7	29	0.65	24	15	0.64	41	48	1.50
8	30	0.85	25	16	1.27	42	49	1.74
9	31	0.91	26	17	1.17	43	50	1.78
10	32	1.16	27	18	1.16	44	33	0.42
11	6	0.63	28	19	1.58	45	34	0.64
12	7	0.60	29	20	0.68	46	35	0.44
13	24	0.59	30	12	0.46	47	36	0.53
14	25	0.70	31	21	0.46	48	37	0.63
15	26	0.78	32	39	0.44	49	38	0.17
16	27	1.01	33	40	0.46			
17	28	0.69	34	41	0.46			

METHODS, ANALYSIS, AND RESULTS

In conducting the probabilistic seismic hazard analysis (PSHA), seismic sources that will significantly influence the study area are the ones considered. Hence, foreshocks and aftershocks are not considered, earthquakes with magnitude less than 5.0 were removed, and only earthquake events within 100-kilometer radius are evaluated. Moreover, only six (6) seismic sources are considered (Fig. 2). These faults were divided into 100-meter segments and distances are measured from a point on the fault to a point on the grid. This is necessary to determine the probability of radius for each seismic zone.

Gutenberg-Richter equation [6] was used to generate the magnitude and frequency of the earthquakes from the six seismic sources mentioned. To translate PSHA output into a peak ground acceleration (PGA) map, the LTWD seismic map was subdivided into grids and points. For ground motion prediction, Youngs, Chiou, Humphrey, and Silva [7] ground motion prediction equation was used. The resulting PGA contour map was shown in Figure 3. It can be observed that PGA only ranged from a maximum of 0.409g to a minimum of 0.365g. Hence, this range is very narrow which validates the assumption that all pipes can fail during a seismic event.

The study's delimitation considered only the main transmissions that were laid out along the highway. This also caused many of the other water sources of LTWD to be excluded because they do not contribute to the transmission main. Hence, in the development of the schematic network model, for the optimization of repair sequencing, only a single supply source is applicable. The schematic diagram of the simplified network model is shown in Figure 4.

The rate of repair for the damaged pipes was taken as 1 kilometer of pipe-length per day. The schematic diagram (Fig. 4) shows six (6) trees, all rooted at node 1. Among these trees, the node in the tree with higher total efficiency is repaired first, followed by the next higher efficiency. This repair sequence goes on until all nodes are restored.

The result of repair sequence is shown in Table 1. It is derived after imposing Horn's algorithm. In this table, nodes were arranged based on repair sequence. The improved efficiency parameter is also shown. The total time of restoration is 8.62 days (Fig. 5). So, an all-pipe failure scenario will only take approximately 9 days to repair and bring back the water distribution network to its original pre-event functionality.

CONCLUSION

The six (6) identified seismic sources can each potentially damage and disrupt water supply service provided by La Trinidad Water District (LTWD). Based on PSHA, the north-western part of the municipality will experience the highest PGA implying that pipes located in that area will be highly

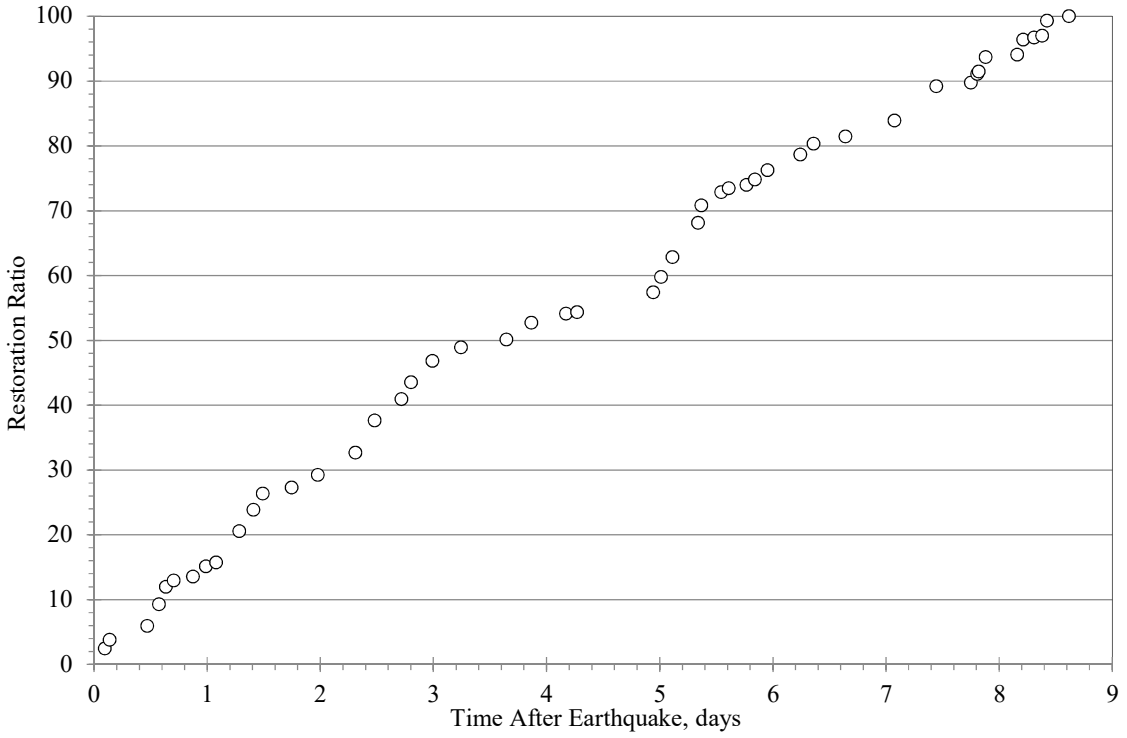

Figure 5. Restoration curve for LTWD during a seismic event using Horn's algorithm

vulnerable to damage due to earthquake. Moreover, about 3 kilometers (37.5%), serving about 39% of total demand, of the pipe network is projected to be damaged based on PGA derived from PSHA. Utilizing the average time for restoration (t_A) based from Horn's algorithm resulted to a t_A value of 3.95 days with a total restoration time of 8.62 days. In an event where earthquake causes an all-pipe-failure, following the repair sequence as derived from Horn's algorithm, it can be guaranteed that water demand can be met sooner at areas where demand is highest. This implies that more consumers get to have their water supply back faster.

REFERENCES

[1] Castillo E., Castillo C., Vicente C., and Villarin J., Mapping Philippine Risk: A GIS-Based Analysis of Climate-and Weather-related Disasters, Quezon City, Manila Observatory, 2005.

[2] Olsim V., Municipal Tourism Plan La Trinidad Benguet 2015-2019, 2014.

[3] Peralta-Malonzo T. A., Top 5 Most Destructive Earthquakes in the Philippines, www.sunstar.com.ph, August 1, 2015.

[4] Ruohonen K., Graph Theory, 2013.

[5] Horn W. A., Single-machine Job Sequencing with Treelike Precedence Ordering and Linear Delay Penalties, SIAM, Journal of Applied Mathematics, Vol. 23, No. 2, 1972, pp. 189-202.

[6] Gutenberg B., and Richter C.F., Earthquake Magnitude, Intensity, Energy, and Acceleration, Bulletin of the Seismological Society of America, vol. 32, 1942, pp. 163-191.

[7] Youngs R.R., Chiou S.J., Silva W.J., and Humprey J.R., Strong Ground Motion Attenuation Relationships for Subduction Zone Earthquakes, Seismological Research Letters, Vol. 68, Issue 1, 1997, pp. 58-73.

9th Int. Conf. on Geotechnique, Construction Materials and Environment,
Tokyo, Japan, 20-22 November 2019, ISBN: 978-4-909106025 C3051

CLUSTERING OF RAINFALL DATA USING K-MEANS ALGORITHM

Mohd Sham Mohamad[1], Yuhani Yusof[2], Ku Muhammad Na'im Ku Khalif[3] and Mohd Khairul Bazli Mohd Aziz[4]
[1,2,3,4]Faculty of Industrial Sciences & Technology, Universiti Malaysia Pahang
Lebuhraya Tun Razak, 26300 Gambang, Kuantan, Pahang, Malaysia

ABSTRACT

Clustering algorithms in data mining is the method for extracting useful information for a given data. It can precisely analyze the volume of data produced by modern applications. The main goal of clustering is to categorize data into clusters according to similarities, traits and behavior. This study aims to describe regional cluster pattern of rainfall based on maximum daily rainfall in Johor, Malaysia. K-Means algorithm is used to obtain optimal rainfall clusters. This clustering is expected to serve as an analysis tool for a decision making to assist hydrologist in the water research problem.

Keywords: Clustering, Data mining, K-Means, Rainfall

INTRODUCTION

Malaysia is located in Southeast Asia and near the equator where it receives higher concentration of solar energy since the sun rays strikes almost on all year round. It is also surrounded by the sea and the air is moist and is usually covered with clouds.

Every year, Malaysian experiences two types of monsoon, the Northeast Monsoon (wet) and Southwest Monsoon (dry). The Northeast Monsoon started from early November to March, originating from China and the north Pacific, brings heavy rainfall to the east coast states of the Peninsular Malaysia. The Southwest Monsoon from late of May and ends in September, and is dried period for the whole country. However, there is also a period that happens in between of both monsoon (April – October) and is known as the inter-monsoon.

Above are statements that usually heard by reader. Thus in this paper we evaluated all real rainfall data and classified all of them to differentiate the rainfall according to the period of time stated before. K-Means cluster analysis is used to obtain optimal month of rainfall clusters. This clustering is expected to give better rainfall forecasting result and rain caught.

Literature review is given in second part of this paper, continued by methodology as the third part. Next results and discussions are given followed by conclusion and references.

LITERATURE REVIEW

K-means clustering is a clustering algorithm that aims to partition n observations into k clusters. There are 3 steps which are initialisation (K initial centroids are generated at random), assignment (K clusters are created by associating each observation with the nearest centroid) and update (the centroid of the clusters becomes the new mean).

Many contries have done on rainfall data reserch via K-means clustering. Baeriswyl et. al in [1] has conducted clustering analysis of Australia using Principal Component Analysis and K-means cluster analysis. Results have shown that the regions identified by both analyses are largely same. While in [2], the entire region of Bangladesh is grouped into certain homogeneous regions based on temperature and rainfall by using K mean clustering method.

Munoz in [3] used Principal Component Analysis to divide Spain in to a number of climatically homogeneous zones. Ward's method is used for clustering. Then, optimum number of clusters is determined by plotting distance between merged clusters as a function of the stage analysis.

K-means all used in [4] to get a good regionalization in determining how many clusters are required according to the type of data or objective and how good is the clustering itself. To answer these questions, hierarchical and non-hierarchical algorithms were applied to six experiments based on the data sets for precipitation and temperature available from traditional weather stations.

A paper by Shirin & Thomas in [5] grouped the entire region of Kerala into an optimum number of clusters using Ward's method of clustering. The purpose of Clustering Analysis is to place objects into groups suggested by the data, so that objects which are similar to each other in some sense are grouped into one cluster, and dissimilar objects in different clusters.

In 67], an effective framework for landslide susceptibility mapping (LSM) is presented by integrating information theory, K-means cluster analysis and statistical models.

The RMSE value can be minimized by including seasonal elements in the model, both in BPS and K-Means clustering. In addition, the K-Means clustering done in [7] may also reduce the RMSE value of model, both on non-seasonal and seasonal models.

The best model for this case is GSTARK-Seasional ie Seasonal GSTAR model on K-Means clustering.

K-means are very useful as stated before. In this study, rainfall data from 8 stations in Johor are used and clustered by using K-means clustering.

METHODOLOGY

In this section, study area and method used are given.

Study Area and Data Description

Johor Bahru, capital of the Malaysian state of Johor, sits at the southern tip of the Malay Peninsula. With a causeway across the Straits of Johor connecting it to Singapore. For this study, the entire state of Johor Bahru which occupies the southernmost part of peninsular Malaysia, is selected that located at 1.4927° N, 103.7414° E. The total area of the state accounts to around 220 sq.km.

The main parameter required is the monthly rainfall of all the gauging stations in Johor Bahru. The monthly rainfall data are collected for a period of 31 years (1981-2012). Rainfall data each year for 9 stations are obtained from Department of Hydrology Malaysia.

Determination of Optimum Number of Clusters

In order to use the k-Means method we have to find the optimal number k of clusters for the given dataset. In some cases, the called elbow method can be used to determine a nearly-optimal number k of clusters. The elbow method consists in plotting in a graph the WCSS(x) value on y-axis according to the number x of clusters considered on the x-axis, the WCSS(x) value being the sum for all data points of the squared distance between one data point x_i of a cluster j and the centroid of this cluster j (as written in the formula below), after having partionned the dataset in x clusters with the k-means method.

$$\mathrm{WCSS}(k) = \sum_{i=1}^{k} \sum_{x_i \in \text{cluster } j} \left\| x_i - \bar{x}_j \right\|^2 .$$

RESULTS & DISCUSSION

In this section we state the optimal number for cluster and proceed with clustering the dataset. Results are discussed after that.

Number of Clusters

The optimal number of clusters is given by the points located on the curved WCSS curve that look like "elbows". We can visually search or we can use formal tricks consisting of finding the optimum point of the WCSS curve. In the following, we arbitrarily set the maximum number of clusters to the square root of the dataset size. This means that if the data is uniformly distributed and the partition is built with this maximum number of clusters, then the number of data points in each cluster will be equal to the number of clusters, which is considered to be quite large here.

Given the dataset, the function generates the WCSS curve data as given in Fig. 1.

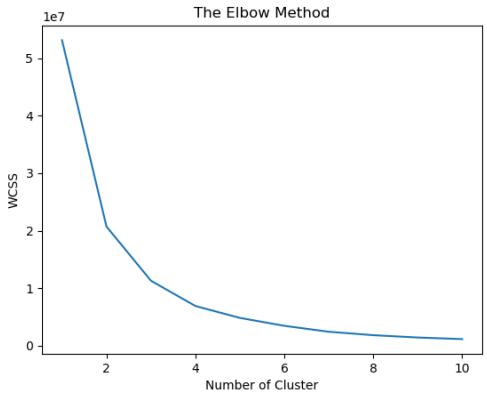

Fig. 1 The Elbow Method.

Here the x= 4, which leads to an optimal number of clusters. Once we found the optimal number of clusters we can launch k-means with this number and get the resulting y_kmeans classification of the given X data points.

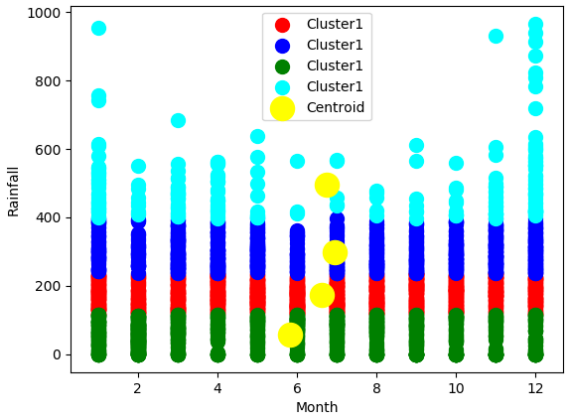

Fig. 2 Cluster of Rainfall

The number of groups in the K-means clustering in this study were four, which are region 1 (Cluster 1) in green, region 2 (Cluster 2) in red, region 3 (Cluster

3) in blue, and region 4 (Cluster 4) in cyan. This refers to the 4 clusters by Elbow Method.

We can see from that figure; each month has 4 groups. Only the fourth group distinguishes the monthly rainfall distribution. This proves that Malaysia has a humid climate throughout the year. More rainfall in December and January where plots abound in the fourth group. In June, on average, there is less rainfall compare to other months.

CONCLUSIONS

Johor Bahru is the selected area to study and monthly rainfall from 9 stations in Johor Bahru are used. The monthly rainfall data are collected for a period of 31 years (1981-2012). The optimal number of clusters is given by the points located on the curved WCSS is 4 which leads to an optimal number of clusters. There are four clusters in all and three clusters exist in all months except for the fourth cluster that is mostly large of data (most are December and January) and some less of data (June).

ACKNOWLEDGMENTS

The authors would like to thank the Department of Irrigation and Drainage Malaysia for providing the data of this research work. The authors also would like to acknowledge the Universiti Malaysia Pahang (UMP) for providing the internal research grant RDU1703265.

REFERENCES

[1] Baeriswyl P. A., Rebetez M. Regionalization of Precipitation in Switzerland by Means of Principal Component Analysis. Theoretical and Applied Climatology; 1996, pp. 31-41.

[2] Md. Mizanur Rahman, Sarkar S., Reza Najafi M., Rai R. K. Regional Extreme Rainfall Mapping for Bangladesh Using L-Moment Technique. Journal of Hydrologic Engineering © ASCE; 2013, pp. 603-615.

[3] Munoz-D´ıaz. D., Rodrigo F. S. Spatio-temporal patterns of seasonal rainfall in Spain (1912–2000) using cluster and Principal Component Analysis: comparison. Annales Geophysicae; 2004, pp. 1435-1448.

[4] Ildiko Pelczer, Judith Ramos, Ramón Domínguez, Fernando González. Clustering of Regional Homogeneous Zones in a Watershed Using Clustering Algorithms. National Autonomous University of Mexico, 2007.

[5] Shirin S. A. H., Thomas R. Regionalization of Rainfall in Kerala State Procedia Technology 24, 2016, pp.15 – 22

[6] Wang Q., Wang Y. Peng L. Integration of Information Theory, K-Means Cluster Analysis and the Logistic Regression Model for Landslide Susceptibility Mapping in the Three Gorges Area, China. Remote Sens. 2017, 9, pp. 938-966

[7] Hadi A. F., Yudistira I., Anggraeni D. and Hasan, M. The Geographical Clustering of the Rainfall Stations on Seasonal GSTAR Modeling for Rainfall Forecasting. J. Phys.: Conf. Ser. 1028 012238. 2018.

9th Int. Conf. on Geotechnique, Construction Materials and Environment, Tokyo, Japan, 20-22 November 2019, ISBN: 978-4-909106025 C3051

CLIMATE CHANGE IMPACTS ON HYDROLOGY REGIME AND WATER RESOURCES SUISTAINABILITY IN CIMANUK WATERSHED, WEST JAVA, INDONESIA

*Merri Jayanti[1], Arwin[2], Iwan K. Hadihardadja[3], Herto Dwi Ariesyady[4] and Jakobis J. Messakh[5]

[1]Environmental Engineering Program, Institut Teknologi Bandung, Indonesia; [2,4]Departement of Environmental Engineering, Institut Teknologi Bandung, Indonesia; [3] Departement of Water Resources Engineering, Institut Teknologi Bandung, Indonesia; [5] Departement of Environmental Science, Nusa Cendana University, Indonesia

ABSTRACT

The goal of this study is to analyze the impact of climate change on the hydrological regime changes in Cimanuk Watershed, West Java, Indonesia, analyzes the existing problems and contributes to the management of water resources in monsoon climate region in Indonesia. The results have shown that climate change is shown by the increasing temperature, meanwhile the air humidity, wind speed, sunshine duration, and evaporation are decrease. Changes of the hydrological regime have been known by the analysis of the main components of the hydrological cycle specifically discharge (Q) and precipitation (P). Precipitation and discharge had shown an increasing trend from 1987 to 2012, but with high variability in annual and monthly period. The critical condition of water availability for four months (June to September), while the excess water condition occurs during eight months (October to May). The Model of input-output correlation between precipitation and discharge have shown a positive correlation 0.9564 for the monthly average, and 0.5417 for the annual. The coefficient of annual water availability is high, shows that the region is monsoon with great potential for flooding. Therefore, need for optimal management of surplus water in the rainy season so not wasted.

Keywords: Climate Change, Hydrology Regime, Monsoon Area, Water Availability, Water Resources

INTRODUCTION

Water Resources states that water as a source of community life is dynamic existence naturally flow to a lower place without knowing the administrative boundaries. According to Arwin [1], Source of water is a natural resource that can be updated through the hydrologic cycle depending on the climate and weather be affected by cosmic factors, regional and local (watershed) form the hydrological regime. Where is the main component of the hydrological cycle of rainfall is input in the watershed system and the output is the discharge and the quality of surface water (river water) and groundwater reserves. The second component is characterized by random variables and stochastic as well as water drainage to the sea is a deterministic phenomenon. Uncertainties of climate and weather triggered by global warming from greenhouse gas emissions in the atmosphere result in temperature increases the earth [1,2]. The presence of water follows the hydrological cycle is closely related to the weather conditions in an area that causes uneven water availability in every time and every region. Changes in surface water availability extreme would be a serious problem in terms of the sustainability of water management [3,4,5]

In the monsoon area, water resource availability is a serious problem in terms of the sustainability of water management. Monsoon patterns are characterized by monthly V-shaped rainfall distribution with low seasonal rainfall in June, July or August. In normal conditions, when the west monsoon will get abundant rainfall (rainy season) while in the eastern monsoon the amount of rainfall is very little (dry season). In monsoonal rain patterns the region has a clear distinction between the period of the rainy season and the dry season. Numerous studies have been conducted, some of them are about the availability of water during the rainy season and the dry has a very high degree of variability about scenario development for watershed management [1,6,7,2,8].

Therefore, this research specifically examines: a) climate change and hydrological regime changes in Cimanuk Watershed and b) the impact on the water resources sustainability in monsoon regions. Conditions impact of climate change and land conversion may have occurred in the Cimanuk Watershed, as the main water source rivers Jatigede Reservoir.

MATERIAL AND METHOD

The quantitative approach has been done to analyze the impacts of climate change on the hydrological regime change. Series precipitation data are used daily and monthly throughout the 26 years (1987 to 2012) from 9 (nine) precipitation stations around the Cimanuk watershed. Data climate elements derived from Cimanuk Climatology and Wado Discharge Station, while the series of monthly discharge data for 32 years (1980 to 2013). Figure 1 shows the study area of Cimanuk Watershed, the discharge station namely Q Wado, and for the rainy station from P1 Pamegatan, P2 Pangauban, P3 Kepakan, P4 Tarogong, P5 Leuwigoong, P6 Darmaraja, P7 Pamulihan, P8 Cilimun, P9 Majalengka.

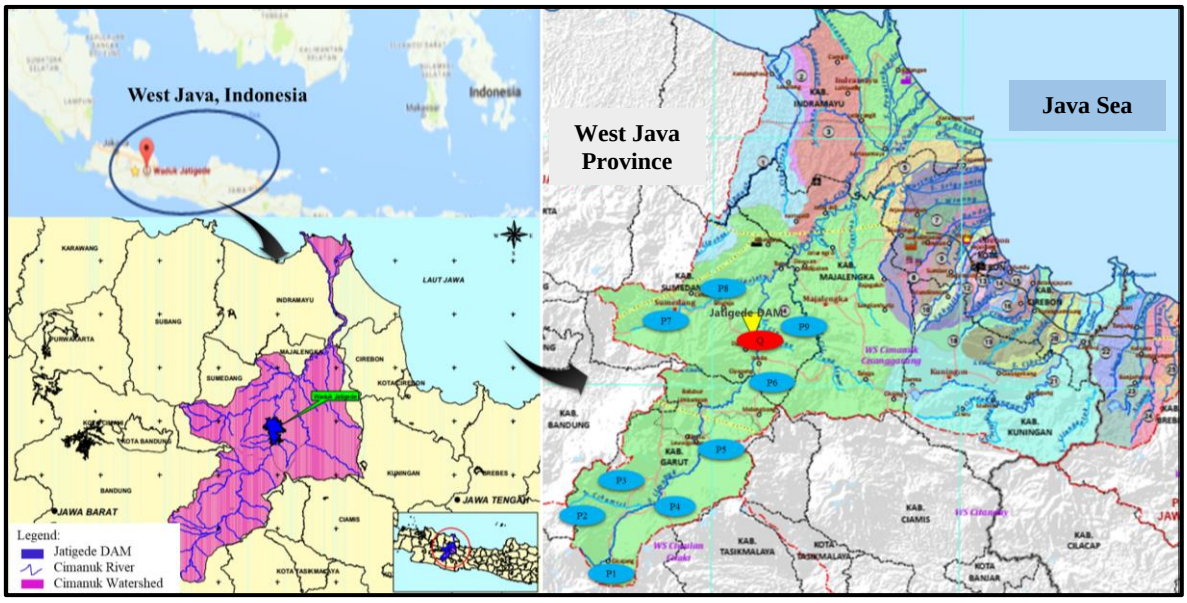

Fig.1 Study Area

The analysis of climate parameters, precipitation and discharge trends revealed by the data using the moving average method, the range of values and the average values were compared at different periods. In addition to the analysis of changes in precipitation are also using the IDF Curve method. The significance level between precipitation and discharge, using the Spearman Correlation Test model of a two-way with a significance level of 5%.

RESULTS AND DISCUSSION

Climate Change

Climate parameters which have been analyzed were: air temperature, wind speed, air humidity, sunshine duration, and evaporation. Results of the analysis showed that the average air temperature of 28,44°C, the lowest in March at 22,27 C and highs in October amounted to 31,35°C. Relative humidity average is 68,29% with the highest data in January by 98,01% and the lowest in September at 8,9%. For evaporation, the average is 60 mm/day, the highest evaporation occurs in August 88,70 mm and the lowest in October amounted to 43,01 mm. Average wind speed of 1325,66 km/day, the biggest in September amounted to 7861,87 km/day and the lowest in March at 33,8 km/day.

Figure 2 shows the trend of climate change parameters on average time series from 2000 to 2013 (14 years) as follows: temperature has shown an upward trend with changes in average temperature was 0.1037°C per-year, while the trend of global temperature changes 0.7°C every 100 years. IPCC [9] reported that the distribution of increase in the global temperature anomaly is uneven and varies between land and sea, between the northern hemisphere and southern hemisphere, and between regions and between types of land cover are different.

Other climate parameters results have shown a downward trend for the 14 year observation period, namely: humidity -1,3968 % per-year; wind speed 266,58 km/day per-year; and evaporation -0.6908 mm per-year. Result analysis shows the changes in temperature and evaporation are the same climate change theory that rising temperatures will lead to increased evaporation.

The temperature's rise is not evenly distributed around the earth cause low pressure and new high pressure. The pattern of wind is shifting and the precipitation patterns are changing either. Indonesia's geographic position greatly affects the extreme climate events, in this case is flooding and drought. The phenomenon that affects the climate in Indonesia is called ENSO because Indonesia is located between two oceans, the Pacific and Indian oceans. El Niño events will cause drought in

Indonesia, especially in areas that have a pattern of monsoonal precipitation. While La Niña phenomenon will lead to increased precipitation in Indonesia during the dry season and the rainy season led the advance [2]. The research of Jayanti et al [10] showed that in 2005 the last year, there was a wet-dry phenomenon happening throughout the year so that the rainy season. This is one example of the extreme climate that occurs as a result of climate change.

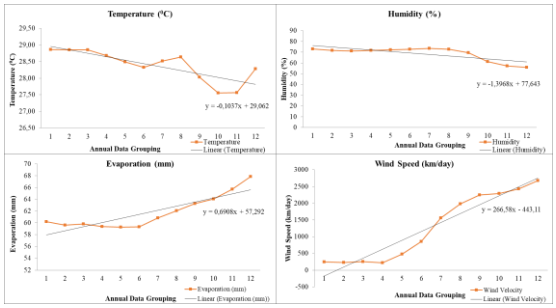

Fig.2 Trend of Climate Parameters Changes

The changes in climate parameters that occurred can result in a change of the magnitude and distribution of water, and the long-term sustainability of water resources being threatened and requires serious attention.

Hydrological Regime Changes

Changes in climate parameters will impact directly or indirectly on the hydrological response of the region further define the availability of water for various needs. Changes in the hydrological regime in this study were observed through changes in the main components of the hydrological cycle that is precipitation and discharge.

Changes of Precipitation Intensity

Changes of the hydrological regime (precipitation), observed among others by changes in precipitation intensity with curve IDF method (Intensity Duration Frequency). Precipitation intensity data over different time periods (1987 to 1999 and 2000 to 2012). Analysis of the results for the period of 2 years and 10 years as shown in Figures 3 and 4.

On the return period (RP) 2nd annual, overall precipitation stations have a higher intensity of precipitation for the current period (1987 to 1999) compared to the previous period (2000 to 2012). Pamegatan station has a value greater margin between the two periods of rain showers in the appeal of other stations and also has the highest intensity for a short period of rain (5 minutes).

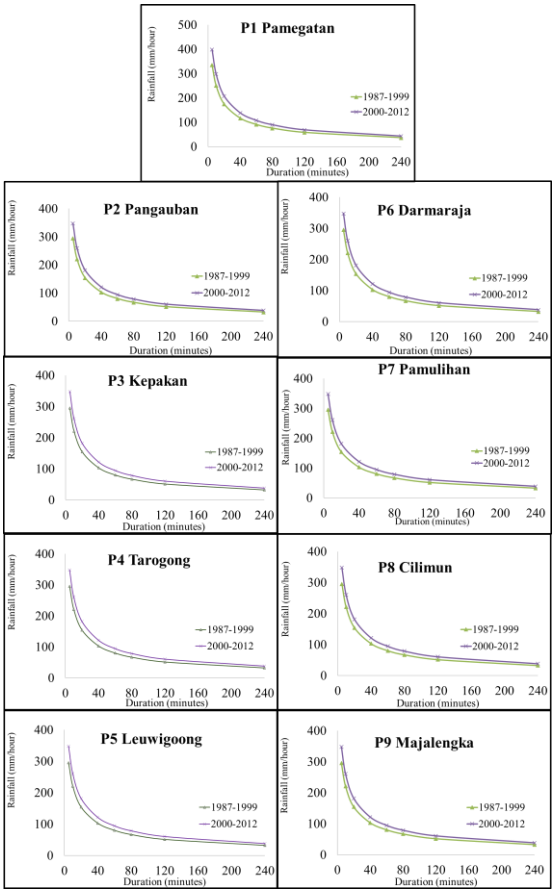

Fig.3 IDF Curve for 2nd Annual Return Period (1987-1999 and 2000-2012)

For the 10th annual return period (figure 4) the highest precipitation intensity occurred in urban areas (Darmaraja and Tarogong). The results of this analysis showed that differences in land use affect the value of the hydrological regime. Condition is consistent with that presented in the IPCC report (2007), that differences in the distribution of land use will result in the increase of global temperature anomalies uneven and different.At 10th annual return period, a trend increasingly little difference in intensity between the 2 periods of the calculation (the curves coincide).

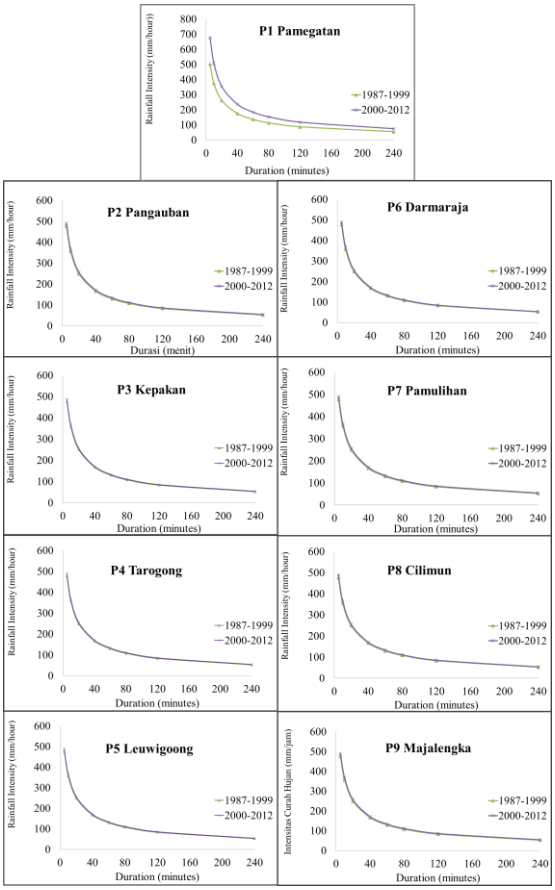

Fig.4 IDF Curve for 10th Annual Return Period (1987-1999 and 2000-2012)

The intensity of rain between the 2nd calculation period (1987 to 1999 and 2000 to 2012) is also getting random between stations because there are stations with the intensity of the period 1987-1999 is higher than the period 2000 to 2012 and on the contrary. From the analysis of the return period 25th, 50th and 100th annual also shows that the greater the return period, the smaller the value of the different intensity precipitation or curve formed by the overlaps.

Precipitation changes

The analysis results of precipitation changes show increases trend (Figure 5a) [10]. Distribution of precipitation monthly averages in Figure 5b shows the wet season occurs during the eight months (October to May), while the other four months (Juni to September) is a dry month, which means that the dominant dry season occurs in the study area. Monthly precipitation pattern that occurs is monsoon type [10].

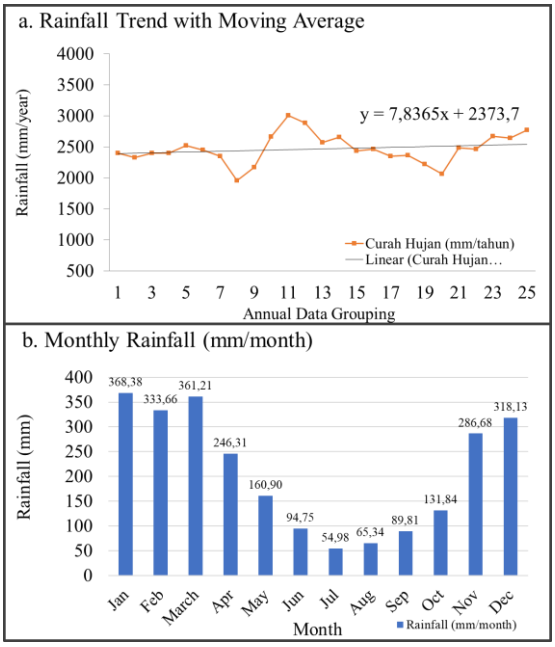

Fig.5 Trend and Distribution of Precipitation at Cimanuk Watershed, Indonesia (1987-2013)

Precipitation variability is also different in the wettest month (rainy season) and dry months (dry season). In the wet months, the more extreme precipitation in the dry season wet while getting extreme precipitation dried (figure 6).

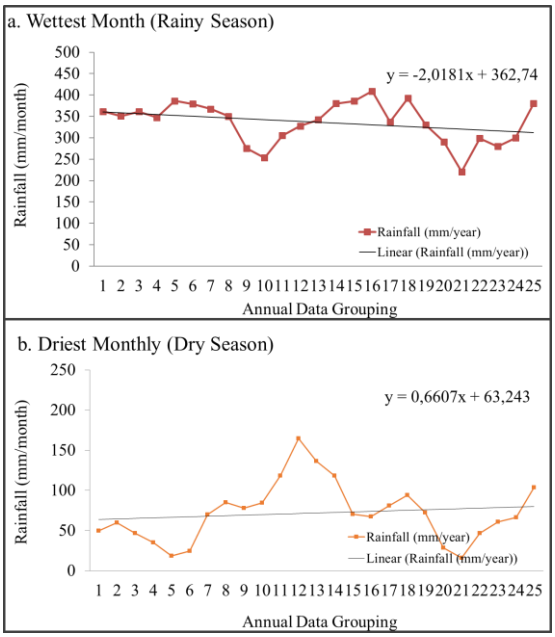

Fig.6 Trend of Average Precipitation in Rainy Season and Dry Season with 3rd Annual Moving Average Method

This means that climate change may lead to a shift of the season, which will last a long dry season, causing drought. The rainy season will take place with the trend of precipitation intensity is higher than normal precipitation, the impact of floods.

Precipitation data were grouped in two different periods shows the more extreme precipitation in the period 2000-2013 where the average precipitation of 2502,82 mm/year, while in the previous period (1987 to 1999) only amounted to 2386,28 mm/year. Which means that the change increased by 8.10%. If the precipitation data grouped by wet months (October to May) and dry months (June to September). The data also shows that the more extreme the current period in the previous period in the wet in the rain (2209,72 mm versus 2044,06 mm) and in dried drier (293,1 mm versus 342,22 mm).

Discharge Changes

Trend analysis shows an increase in annual discharge changes (Figure 7a). Changes occurring discharge is 96,48 m^3 per-32 years or 0,9648 m3/year. Monthly average discharge showed different distributions of per-month (Figure 7b).

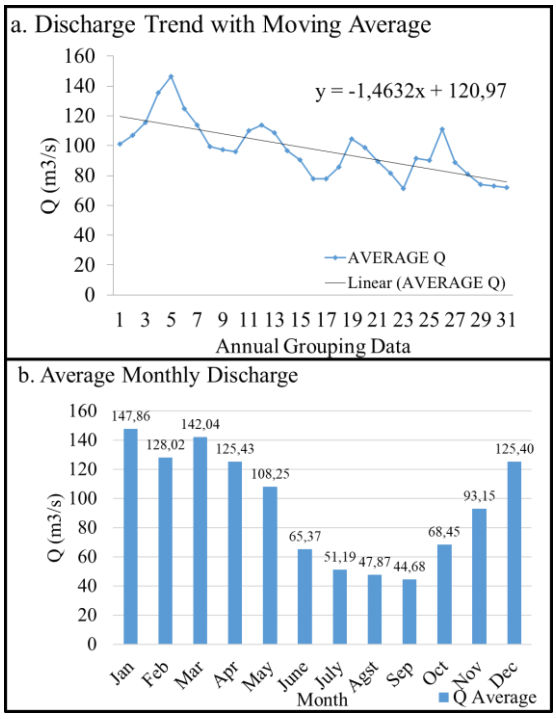

Fig.7 Trend and Pattern of Annual Discharge (1980-2013)

The amount of discharge change between wet months (October to May) is 117,34 m^3/s and dry (June to September) is 52,28 m^3/s. The monthly maximum discharge occurred in January amounted to 147,86 m3/second, and the smallest was 44,68 m3/second occurred in September with an average discharge of 95,64 m3/second /months. The Month from October to May is a condition in which the discharge that occurs above the average discharge, and the month from June to September is a condition in which the discharge occurred under average discharge. This differs from the pattern seen in the precipitation which occurred a shift in the months from October to May (for precipitation) to the month of June to September (for discharge). This happens because of the precipitation that occurred the previous month (October) used to fill the pores of the soil that had vacancies during the dry season. If the soil pores are fully charged (saturated) then becomes surface water (river flow).

Discharge changes also differ in the wettest and driest months. In the wettest month (January) shows the trend of increasing discharge (147,86 m^3/second per-year), as well as the driest month (October), increased 44,68 m^3/second per-year (Figure 8).

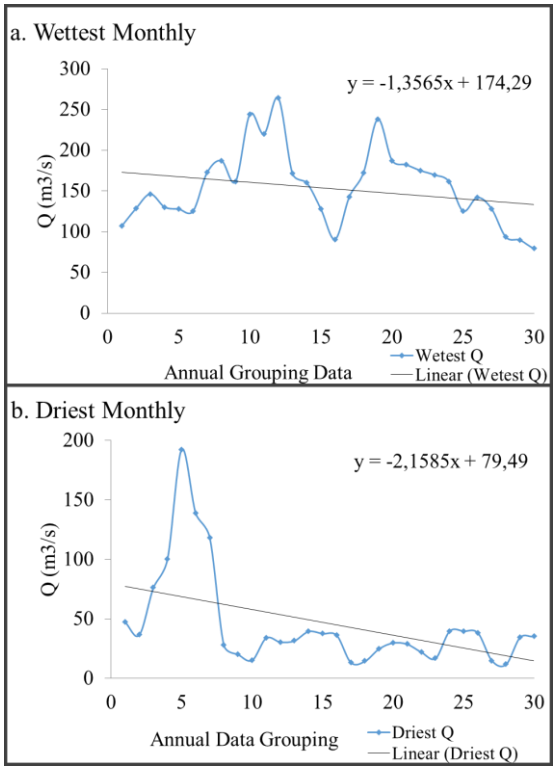

Fig.8 Trend of Discharge in The Wettest Month and Driest Month

Conditions of discharge increase during the driest season, although the value is not significant, in monsoon area that indicates improvements in the condition of the watershed water use planning.

Correlation between Precipitation and Discharge

Correlation between precipitation and discharge in this study is that the greater the precipitation intensity, the greater the discharge occurs. Spearman correlation test at a significance level of 0.05% two-way test, for a monthly average data shows a correlation value 0,9564 which means that the increase in discharge can be explained 95,64 % due to an increase in precipitation, while the

remaining 4.36% is explained by the variables others, such as in wet or dry conditions during the rains, the amount of base flow (baseflow), and other factors. On annual average data, the relationship between precipitation and discharge correlated at 0.5417. The results of this analysis showed that precipitation is the biggest input on discharge of Cimanuk watershed, West Java, Indonesia.

Hydrology in Monsoon Region

The study area is monsoon regions indicated by the following indicators: (a) the average precipitation 2422,09 mm/year, (b) the number of rainy days with an average of 240 days/year, (c) evaporation 747,14 mm/years, (d) potential evapotranspiration (ETo) 2600 mm/year, and (e) the annual water availability coefficient of 1,468, the water deficit as much as 1338,6 mm/year which results in a high risk of drought.

The critical condition of water availability for four months (June to September), while the excess water condition occurs during eight months (October to May) For the foreseeable future water needs of irrigation and drinking water will increase, especially in the dry season, because it's raw water supply challenges will be even greater.

CONCLUSION

Global climate change that also has occurred in the study area that will affect the hydrological response ie, the observed changes in the hydrological regime through the major components of the hydrological cycle that is precipitation and discharge. This change will determine the availability of water for various needs. Increased precipitation and discharge, though with little value, the observation period 1987 to 2012 is a favorable condition for the availability of water in the study area. But with the higher variability between dry season and rainy season that resulted in the need for optimal management of surplus water in the rainy season can be accommodated to be used in the dry season.

REFERENCES

[1] Arwin. (2009): Perubahan Iklim, Konversi Lahan, dan Ancaman Banjir dan Kekeringan di Kawasan Terbangun. Pidato Ilmiah Guru Besar ITB-Majelis Guru Besar ITB. CV Senatama Wikarya-Bandung. (Paper)

[2] Messakh, Jakobis Johanis; Arwin; Hadihardadja, Iwan K; Duppe, Zadrak (2013): Analysing Variability of the Precipitation and Discharge, for Sustainable Management of Water Resources in the Semi-arid Area (Case Tilong Watershed, Indonesia). (International Proceeding)

[3] Masih, Ilyas., Ahmad, Mobin-ud-Din., Uhlenbrook, Stefan,. Turral, Hugh., dan Karimi, Poolad (2009): Analysing Streamflow Variability and Water Allocation for Sustainable Management of Water Resources in the Semi-arid Karkheh River Basin, Iran, Physics and Chemistry of the Earth 34, 329–340. (Journal)

[4] Mugabe, F.T., Chitata, T., Kashaigili, J., dan Chagonda, I. (2011): Modelling the Effect of Precipitation Variability, Land Use Change and Increased Reservoir Abstraction on Surface Water Resources in Semi-arid Southern Zimbabwe. Physics and Chemistry of the Earth 36, 1025–1032. (Journal)

[5] Messakh, Jakobis Johanis; Arwin; Hadihardadja, Iwan K; Duppe, Zadrak (2013): Impact of Climate Change On The Hydrology Regime in Semi-Arid Region, West Timor. (International Proceeding)

[6] Indarto (2010): Hidrologi Operasional, Penerbit Andi, Yogjakarta. (Book)

[7] Kodoatie, Rober J., dan Sjarief, Roestam (2010): Tata Ruang Air, Penerbit Andi, Yogyakarta. (Book)

[8] Mahmoud, Mohammed I; Gupta, Hoshin C.; Rajagopal, Seshadri (2011): Scenario development for water resources planning and watershed management: Methodology and semi-arid region case study, Environmental Modelling & Software, Journal homepage: www.elsevier.com/locate/envsoft. (p873-885). (Journal)

[9] IPCC (2007): Climate Change 2007 - The Physical Science Basis. Contribution of Working Group I to the Fourth Assessment Report of the Intergovernmental Panel on Climate Change. Edited by Alley, R. et al. IPCC Secretariat. Switzerland. (Book)

[10] Jayanti, Merri (2019): Laporan Kemajuan Disertasi I. (Progress Dissertation)

[11] Asdak, Chay (2002): Hidrologi dan Pengelolaan Daerah Aliran Sungai, Gadjah Mada University Press, Jogjakarta. (Book)

[12] Georgakakos, A.P., Yao, H., Kistenmacher, M., Georgakakos, K.P., Graham, N.E., Cheng, F.Y., Spencer, C., dan Shamir, E. (2011): Value of Adaptive Water Resources Management in Northern California Under Climatic Variability and Change, Journal of HydrologyVolumes 412–413, 4 January 2012, 34–46. (Journal)

[13] Hyung-Il Eum., Simonovic, Slobodan P. (2010): Integrated Reservoir Management System for Adaptation to Climate Change: The Nakdong River Basin in Korea. Water Resources Management 24:3397–3417. (Journal)

[14] Kementrian Negara Lingkungan Hidup (1997): Agenda 21 Indonesia, Kementrian Negara Lingkungan Hidup Republik Indonesia, Jakarta. (Book)

9th Int. Conf. on Geotechnique, Construction Materials and Environment,
Tokyo, Japan, 20-22 November 2019, ISBN: 978-4-909106025 C3051

EFFECT OF CLIMATE VARIABILITY ON RICE PRODUCTION OF NORTHEASTERN THAILAND

Piyapong Wongkhunkaew[1], Supasit Konyai [2] and Vichai Sriboonlue [3]
[1] Graduate Student of Agricultural Engineering, Faculty of Engineering, Khon Kaen University, Thailand;
[2] Assistant Professor of Agricultural Engineering, Faculty of Engineering, Khon Kaen University, Thailand;
[3] Associate Professor of Agricultural Engineering, Faculty of Engineering, Khon Kaen University, Thailand

ABSTRACT

Rainfed rice cultivation is the key agricultural practice in the Northeast of Thailand. Climate variability is the main cause affecting the rice production. Climatic water balance index namely standardized precipitation evapotranspiration index (SPEI) indicates variation of climate conditions, whether the area is wet (positive) or dry (negative). Our study concerned the effect of climate variability on the production and yield of rice cultivations in five provincial stations in the northwestern of the Northeast which has one of the most extreme climatic conditions in Thailand. El Nino Southern Oscillation (ENSO) is also related to SPEI and related to rice production and yield.

For the study rainfall and meteorological data between 2005 to 2016 were used for analyses. Changes of monthly SPEI over all stations were abrupt compared to ENSO changes which were gradual. During the rice cultivation period, May to September, 1-month SPEI fluctuated from month to month. The summation SPEI values within that 5 months were compared to rice production and yield from each station. All of rice productions increased with SPEI values but only three stations had yields agreeing with SPEI. This shows that amount of production always relates to wetness but not the yield which depends on other factors such as soil fertility and good management. In marginal paddy fields, cultivation is limited to positive wet conditions. Production may increase depend on the area cultivate, but yields will reduce.

Keywords: climate variability, standardized precipitation evapotranspiration index, rice production and yield

INTRODUCTION

Rice is the main staple food of Southeast Asia and some other parts of the world. It has been believed that rice was originated from Southeast Asia region then spreading throughout the world [1]. Rice is a special crop that needs much more water than any other cereal crops it can survive even in standing water as long as the whole plant does not inundated [2]. The benefit of the standing water is that it controls weed growth. The climate of Southeast Asian countries is one of the best regions for cultivating rice crop since it has large amount of rain during wet season. The Northeast of Thailand is such a place that has plenty of rain during May to October each year [3]. It receives rain from two sources the southwest monsoon from Indian Ocean and the tropical cyclone from the Pacific Ocean [4]. The northwestern part of the Northeast is quite a special place because it has an orographic effect from the Phetchabun, Dong Phaya Yen, and Sankambeng mountain ranges to retard the flow of Southwest monsoon into the region. In case of the tropical cyclone from the Pacific, before reaching the region, the cyclone has to travel passing Vietnam, Laos, Cambodia, the eastern part of the Northeast before reaching the northwestern region. The region normally receives less rainfall than the other parts of Thailand even worse when the southwest monsoon is weak, and no tropical cyclone occurred. However, the area can be flooded during a year of strong summer monsoon and coupling with a large number of tropical cyclones. These dry and wet years are the result of atmospheric and Pacific Ocean interaction indicated by El Nino Southern Oscillation (ENSO) [5]. The majority type of rice growing in the region is glutinous (*Oriza Sativa var. Glutinosa*) [6]. Rice culture in the northwestern part of the Northeast, Thailand, mainly is planted in a paddy lot of irregular size, rectangular shape, and surrounding with small earth bunds to confine water in the paddy. These lowland rainfed paddy fields receive water from rainfall and runoff and loss water through evapotranspiration, the combination of evaporation and crop transpiration. The indicator of water availability for rice crop is the difference between rainfall and evapotranspiration, namely standardized precipitation evapotranspiration index (SPEI) [7], [8]. The SPEI index is superior to other indices that it can detect both extremes, flood and drought. Our objectives are to compare and correlate the rice productions and yields of the five northwestern provincials of the Northeast, Thailand, to their SPEI's then to ENSO.

STUDY AREA AND DATA COLLECTION

Our study area is in the northwestern part of Northeast, Thailand, between 15 31 -18 21 N and 100 83 -103 66 W. It covers 5 provincial areas namely Chaiyaphum, Nongbualamphu, Khonkaen, Udonthani, and Loei. The whole Northeast is one of the large sub-basin on the right bank of the Mekong River called the Khorat Plateau. The plateau is separated into two basins by Phu Phan mountain range lying in west to east direction. The upper (northern) basin is Sakol Nakhon Basin and the lower (southern) one is Khorat Basin. Interestingly, our study area involves both basins, the Khorat Basin comprises Chaiyaphum, and Khonkaen; whereas Udonthani and Loei are in the Sakol Nakhon Basin, however Nongbualamphu covers both basins.

Rainfall of the study area is in the range 1146 mm for Chaiyaphum to 1457 mm for Udonthani. Since the western part of our study area is a rather rain shadow therefore the amount of rain is increasing in the northeastern direction toward the Mekong River. Due to the Phu Phan Range, the topography of Loei and Udonthani is sloping down northward to the Mekong while that of the other two provinces, Chaiyaphum and Khonkaen is descending southward to the Chi River. Nongbualamphu is a special one because its northern part drains northward to the Mekong River while the southern drains southward to the Chi River. Drainage channels of the northern area are the Loei and the Huai Luang Rivers and those of the southern areas are the Nam Pong River and its tributaries. Undulating terrain is the typical landscape with majority of sandy soil which derived from the sandstone of the Khorat Group. Saline soil and groundwater are the environmental problems of the area.

The main land-uses are upland crops and forest covering the upper terrains and paddy fields on the lower and swampy areas. The main type of rice is glutinous rice of more than 80 % and other is white rice [6], [9], [10]. The major variety is RD6 which is a short plant and photosensitivity therefore it must be transplanted as early as possible to obtain higher production. Since being rain-fed agriculture, it is sensitive to both drought and flooding, especially drought at the vegetative period (first half) and flooding at the maturing period (later half) [9].

Three types of data to be used namely rice production and yield, hydrometeorological, and ENSO index data. The data of rice cultivation during 2005 to 2015 were obtained from the Office of Agricultural Economics (http://www.oae.go.th) for each province and nationwide. The data are planted areas, harvested areas, production, and yield. The hydrometeorological data for 2005 to 2016 were collected from the Department of Alternative Energy Development and Efficiency (DEDE) of Thailand and the Thai Meteorological Department (TMD). These data are essential for SPEI evaluation which are daily precipitation and referent crop evapotranspiration (ETo). The precipitation data were collected from provincial rain gauges. The ETo has to be determined from FAO-Penman-Monteith formula refer to Eq. (11) which is required a range of meteorological data, e.g. maximum and minimum temperatures, solar radiation, relative humidity, and wind speed, etc. The last set of data is ENSO indices which comprise several indices. We decided to use Oceanic Nino Index (ONI), which is the atmospheric pressure anomaly at Nino 3.4, for its simplicity and effectiveness. The ONI data set for 2005 to 2016 were retrieved from NOAA's National Weather Service's Climate Prediction Center [11].

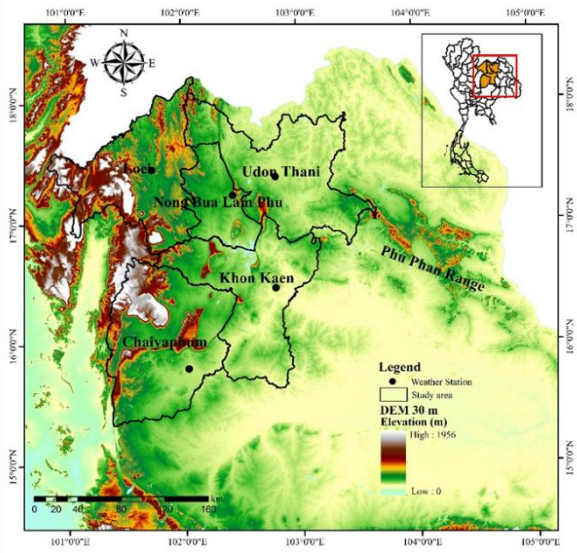

Fig. 1 Topography area of the five-province study region in Thailand.

METHODOLOGY

We hypothesized that the rice production and yield of the northwestern region of Northeast, Thailand, should be related to the appropriated amount of water availability for rice growing. The crop water supply for rain-fed agriculture depends on the timing amount of rainfall and evapotranspiration. Too much rain creates flooding whereas too much ET creates drought. Both flooding and drought deteriorate rice production and yield. We tied rainfall and ET together using an index of SPEI which is the function of the difference of rainfall and ET [12]. We also presumed that SPEI is related to ONI index, if so ONI can be used a proxy to forecast the rice production and yield of the interested area.

Standardized precipitation evapotranspiration index (SPEI) is an index to classify climate variable condition from the discrepancy of rainfall and ET. It was derived from standardized precipitation index (SPI) by adding the effect of ET. Its determination procedure is the same as that of SPI just by replacing rainfall by rainfall minus ET (D_i, mm) as:

$$D_i = P_i - ETo_i \quad (1)$$

We used log-logistic probability distribution to fit the monthly D data. It was found that 1-month time scale is the most appropriate for the Northeast [13]. The cumulative probability distribution function (cdf) for 3-parameter log-logistic distribution can be written as [12].

$$F(Di) = \left[1 + \left(\frac{\alpha}{D-\gamma}\right)^{\beta}\right]^{-1} \quad (2)$$

where α, β, and γ represent the scale, shape, and location parameters, respectively. These parameters can be estimated by several methods e.g. method of moment, probability weighted moment (PWM), maximum likelihood, and principle of maximum entropy [14]. For PWM, we compute frequency estimator F_i from [15],

$$Fi = \frac{(i-0.5)}{N} \quad (3)$$

where i is rank of observation in increasing order and N is number of data points. Then w can be determined from,

$$w_s = \frac{1}{N}\sum_{i=1}^{N}(1-F_i)^s D_i \quad (4)$$

where s is the order of PWMs ranking from 0 to 3, N is total number of data, and D_i is the data of rank i. The three parameters are now ready to be calculated from [14],

$$\beta = \frac{(2w_1 - w_2)}{(6w_1 - w_0 - 6w_2)} \quad (5)$$

$$\alpha = \frac{(w_0 - 2w_1)\beta}{\left[\Gamma\left(1+\frac{1}{\beta}\right)\Gamma\left(1-\frac{1}{\beta}\right)\right]} \quad (6)$$

$$\gamma = w_o - \alpha\Gamma\left(1+\frac{1}{\beta}\right)\Gamma\left(1-\frac{1}{\beta}\right) \quad (7)$$

where w_0, w_1, and w_2 can be obtained from Eq. 4, Γ is the gamma function.

Knowing α, β, and γ, we can calculate non-exceedance probability of D_i, $F(D_i)$, from Eq. 2. To transform $F(D_i)$ from log-logistic probability distribution to normal distribution we should compute exceedance probability first as:

$$P = 1 - F(Di) \quad (8)$$

For P is less than or equal to 0.5, then

$$W = (-2\,ln(P))^{0.5} \quad (9)$$

otherwise, for P is larger than 0.5, then P is replaced by 1-P. The value of W gives SPEI as [16]:

$$SPEI = W - \frac{(C_0 + C_1 W + C_2 W^2)}{(1 + d_1 W + d_2 W^2 + d_3 W^3)} \quad (10)$$

in which the values of the constants are C_0 = 2.515517, C_1 = 0.802853, C_2 = 0.010328, d_1 = 1.432788, d_2 = 0.189269, and d_3 = 0.001308.

Type of ET to be used in SPEI determination is critical. We decided to use crop reference ETo as in [17]. The ETo is the hypothetical ET of a large area of growing uniform grass at 12 cm high without lacking of water. It can be calculated from [18]:

$$ET_o = \frac{0.408\Delta(R_n - G) + \gamma\frac{900}{T+273}U_2(e_s - e_a)}{\Delta + \gamma(1 + 0.34U_2)} \quad (11)$$

Where
ETo: reference evapotranspiration [mm day^{-1}],
R_n: net radiation at the crop surface [MJ m^{-2} day^{-1}],
G: soil heat flux density [MJ m^{-2} day^{-1}],
T: mean daily air temperature at 2 m height [°C],
u_2: wind speed at 2 m height [m s^{-1}],
e_s: saturation vapour pressure [kPa],
e_a: actual vapour pressure [kPa],
e_s-e_a: saturation vapour pressure deficit [kPa],
Δ: slope vapour pressure curve [kPa °C^{-1}],
γ: psychrometric constant [kPa °C^{-1}]

RESULT AND DISCUSSION

Climate variability is the fluctuation of wet and dry condition along the time period which can be shown as the time series of SPEI. The main cause of climate variability is thought to be the interaction of the Pacific Ocean and the atmosphere which reflects through ENSO index e.g. Oceanic Nino Index (ONI). We therefore compared time series of ONI to SPEIs of the 5 provincial areas. We only illustrate the results of Udonthani province in Fig. 2a. The rice production and yield time series of the same province are also shown in Fig. 2b and 2c, respectively.

We only show the Udonthani's results however the other four provinces' results are very similar. ONI changes gradually with time while SPEI changes rapidly (Fig. 2a). The La Nina condition is represented by negative ONI whereas EL Nino by positive. For climatic condition, the wet one is shown by positive SPEI but the dry condition is by negative SPEI. Fig. 2a shows strong La Nina years at 2 periods 2007-2008 and 2010-2011, it shows El Nino at 2 periods at 2009-2010 and 2014-2015. Fig. 2a shows opposite signs for most of the time, by showing wet condition for La Nina and dry one for El Nino periods. When considering the time series of production and yield in Fig. 2b and 2c, both curves show their increases at the periods of La Nina at 2007 and 2011. The rising trends in both production and yield indicate the progress of rice breeding and

modern technology e.g. RD6 variety and combine harvesting have been popularly increasing [9], [10].

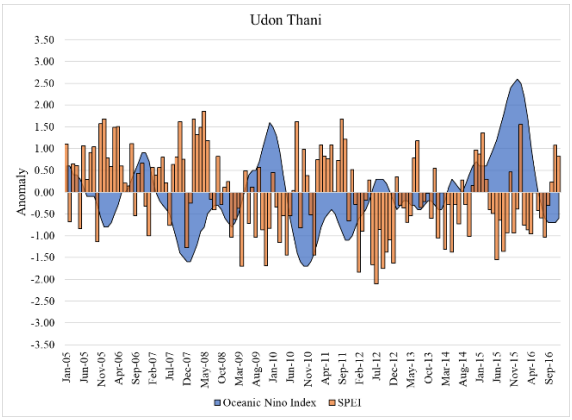

a)

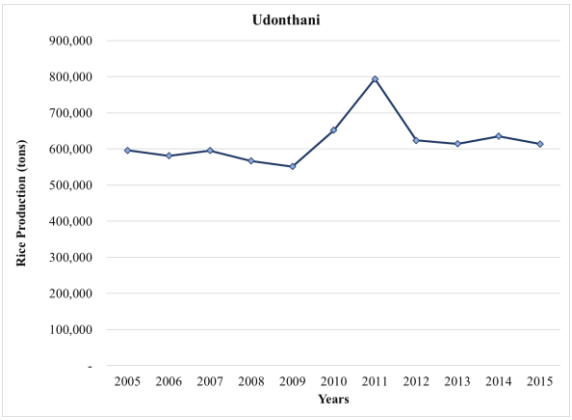

b)

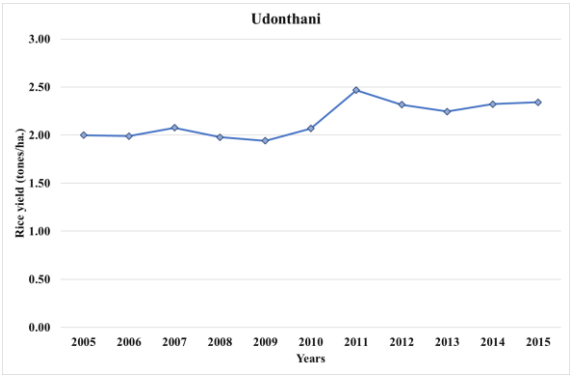

c)

Fig. 2 The time series of a) ONI and SPEI, b) rice production, and c) rice yield of Udonthani Province.

The spectral analyses were performed to the time series of ONI and SPEIs to see the dominated spectrums as shown in Fig. 3. The highest peaks together with second and third of these curves are shown as wave lengths in Table 1. The dominant return periods of ONI and SPEIs of the five provinces are shown in Table 1.

Table 1. The wave lengths of the highest, second, and third highest peaks of the spectrums of ONI and SPEIs.

		Return Period (year)		
		λmax	**λ2nd**	**λ3rd**
ENSO index		**3.00**	1.50	12.00
	Udonthani	**3.00**	12.00	1.71
	Loei	0.21	**3.00**	0.86
SPEI	**Khonkaen**	0.17	**4.00**	0.23
	Chaiyaphum	**12.00**	0.48	0.60
	Nongbualamphu	**6.00**	12.00	1.50

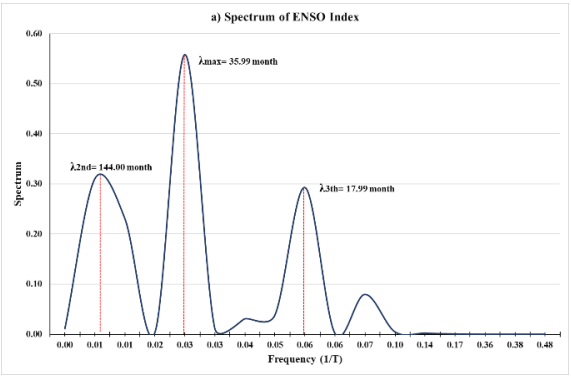

a)

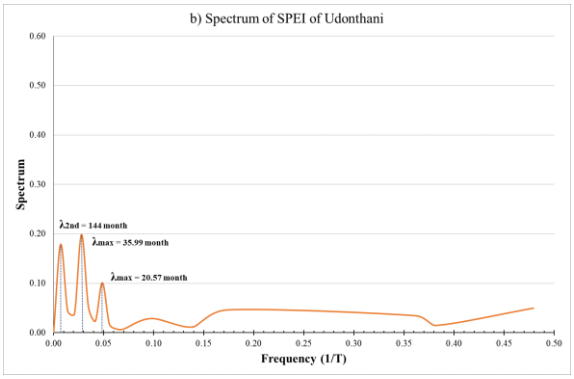

b)

Fig. 3 Spectrums of ONI and SPEI time series of Udonthani.

Table 1 shows that the recurrent time of ONI should be approximately 3 years which is the same as the SPEIs for Udonthani and Loei, while that of Khonkaen and Nongbualamphu are 4 and 6 years, respectively. The longest return period of SPEI is that of Chaiyaphum region which is 12 years. Drought in Chaiyaphum is common because it locates in the strong rain shadow and the longest distance from the landfall of tropical cyclone (Fig. 1).

An essential characteristic of SPEI is its time scale. We did check correlation of 5-time scales SPEIs with the rice production and yield of each

provincial regions using Pearson's correlation coefficient. Udonthani and Loei are both the provinces in Sakol Nakhon Basin, where Loei is mountainous but Udonthani is rather flat. For Udonthani, 2-month time scale of May-June is the best correlation at 0.66 and 0.71 for production and yield, respectively (Table 2). However, for Loei, the best ones are 5- month and 3-month time scales for production and yield. Khonkaen and Chaiyaphum are in Khorat Basin. Khonkaen is flatter whereas Chaiyaphum is rather hilly or more undulating. Khonkaen's production and yield are related to SPEI at 3- month and 2-month time scales, respectively (see Table 2). The best time scale for Chaiyaphum for both production and yield are at 2-month. The last province is Nongbualamphu which its area covers both basins (Fig. 1). Only its rice production correlates with SPEI at 0.42 of 2-month time scale, but not for the rice yield.

Table 2 The Pearson's correlation coefficients of SPEIs with rice production and yield at several time scales.

		Ud	L	KK	Ch	NB
Rice Production	May	-0.12	-0.28	-0.05	-0.25	-0.13
	May-June	0.66	0.15	0.25	0.50	0.42
	May-July	0.16	0.23	0.75	0.19	0.27
	May-August	-0.13	-0.06	0.20	-0.45	-0.20
	May-September	0.11	0.45	0.12	0.07	0.29
Rice Yield	May	0.03	-0.24	-0.13	-0.25	-0.13
	May-June	0.71	0.31	0.54	0.38	-0.16
	May-July	0.50	0.43	0.45	0.11	0.05
	May-August	-0.12	0.24	-0.24	-0.33	-0.09
	May-September	0.09	0.16	0.48	0.17	-0.14

CONCLUSIONS

The glutinous rice is the major staple food of the northwestern region of Northeast, Thailand. Orographic effect and the lengthy distance from tropical storm landfall render the region being drought prone. The rice productions and yields from 5 provincial regions of this northwestern part was correlated to the climatic conditions of the region using SPEIs and ENSO index using ONIs. The time series of 1-month SPEIs of all 5 provinces go against with that of ONI index. This means that positive SPEI (wet condition) is agreeable with La Nina (negative ONI) and vice versa dry condition go along with El Nino. From spectral analyses of ONI and 1-month SPEI time series, we found return period of ONI at 3 years and SPEIs at 3-12 years. Pearson correlation coefficient was used to determine the best time scale of SPEIs and found that two-month time scale is the most reasonable. The effect of climate variation on rice cultivation of the northwestern region of the Northeast of Thailand is needed to deeper study to get more information and understanding.

ACKNOWLEDGMENTS

The authors would like to thank the Graduate School and Applied Engineering for Important Crops of North East Research Group, Khon Kaen University for providing facilities, the Water Engineering Group, Faculty of Engineering, Khon Kaen University for funding and data supporting.

REFERENCES

[1] Van der Eng P., Productivity and Comparative Advantage in Rice Agriculture in South-East Asia since 1870, Asian Economic Journal, Vol. 18, Issue 4, 2004, pp. 345-370.

[2] Moormann F. R., and Breemen V.N., Rice: Soil, water, land., 2nd ed. International Rice Research Institute, Los Baños, Philippines, 1978.

[3] Thavorntam W., and Tantemsapya N., Vegetation Greenness Modeling in Response to Climate Change for Northeast Thailand, Journal of Geographical Sciences, Vol. 23, Issue 6, 2013, pp. 1052-1068.

[4] Delgado J. M., Merz B. and Apel H., A Climate-Flood Link for The Lower Mekong River, Hydrology and Earth System Sciences, Vol. 16, Issue 5, 2012, pp. 1533-1541.

[5] Rasanen A. T., and Kummu M., Spatiotemporal Influences of ENSO on Precipitation and Flood Pulse in the Mekong River Basin, Journal of Hydrology, Vol. 476, 2013, pp. 154-168.

[6] Varinruk, B., Thailand Rice Production and Rice R&D on Climate Change, Asia-Pacific Economic Cooperation, 2017.

[7] Vicente-Serrano S.M., Azorin-Molina C., Sanchez-Lorenzo A., Morán-Tejeda E., Lorenzo-Lacruz J., Revuelto J., López-Moreno I.J., Espejo F., Temporal Evolution of Surface Humidity in Spain: Recent Trends and Possible Physical Mechanisms, 2013, Climate Dynamics, Vol. 42, Issue 9-10, 2014, pp. 2655-2674.

[8] Weng, S-P., Constructing a 1-km Aridded Multi-Scalar Drought Index Dataset (1960-2012) in Taiwan base on the Standardized Precipitation Evapotranspiration Index-SPEI. Terrestrial, Atmospheric at Oceanic Sciences Journal, Vol. 27, Issue 5, 2016, pp. 625-648.

[9] Miyagawa S., Expansion of An Improved Variety into Rain-Fed Rice Cultivation in Northeast Thailand. Southeast Asian Studies, Vol. 33, Issue 2, 1995, pp. 187-203.

[10] Rerkasem B., The Agroecosystem of Thai Rice: A Review, Chiang Mai University Journal of

Natural Sciences, Vol. 14, Issue 1, 2015, pp. 1-21.

[11] CPC. El Niño-Southern Oscillation (ENSO). National Oceanic and Atmospheric Administration, Climate Prediction Center, 2019. <https://origin.cpc.ncep.noaa.gov/products/analysis_monitoring/ensostuff/ONI_v5.php> (accessed March 2019).

[12] Vicente-Serrano M. S., Begueria S., and Lopez-Moreno J. I., A Multiscalar Drought Index Sensitive to Global Warming: The Standardized Precipitation Evapotranspiration Index. Journal of Climate, Vol. 23, Issue 7, 2009, pp. 1696-1718.

[13] Prabnakorn S., Maskey S., Suryadi X. F., and Fraiture de C., Climate and Drought Trends and Their Relationships with Rice Production in The Mun River Basin, Thailand. 2nd World Irrigation Forum (WIF2), 2016, pp.1-10.

[14] Singh P.V., Guo H., and Yu X. F., Parameter Estimation for 3-Parameter Log-Logistic Distribution (LLD3) by Pome. Stochastic Hydrology and Hydraulics. Vol. 7, Issue 3, 1993, pp. 163-177.

[15] Hosking J.R.M., L-Moments: Analysis and Estimation of Distributions Using Linear Combinations of Order Statistics. Journal of the Royal Statistical Society: Series B (Methodological) Vol. 52, Issue 1, 1990, pp. 105–124.

[16] Abramowitz M., and Stegun A. I., Handbook of Mathematical Functions, with Formulas, Graphs, and Mathematical Tables, Dover Publications, 1965, 1046 pp.

[17] Begueria S., Vicente-Serrano M. S., Reig F., and Latorre B., Standardized Precipitation Evapotranspiration Index (SPEI) Revisited: Parameter Fitting, Evapotranspiration Models, Tools, Datasets and Drought Monitoring. International Journal of Climatology, Vol. 34, Issue 10, 2014, pp. 3001-3023.

[18] Allen G. R., Pereira S.L., Raes D., and Smith M., Crop Evapotranspiration: Guidelines for Computing Crop Water Requirements, FAO Irrigation and Drainage Paper 56, 1998, 300 pp.

9th Int. Conf. on Geotechnique, Construction Materials and Environment, Tokyo, Japan, 20-22 November 2019, ISBN: 978-4-909106025 C3051

STUDY ON EXTRACTION FROM CESIUM IN CONTAMINATED SOIL PACKED IN FLEXIBLE CONTAINER BAG AND ADSORPTION USING RICE HUSK

Keiichiro Shibata[1], Hidenori Yoshida[2], Shota Nishioka[3], Matsumoto Naomichi[4] and Ayane Yanaka[5]
[1, 3, 5] Graduate school of engineering, Kagawa university, [2] Faculty of engineering and design, Kagawa university, Japan; [4] Technical staff, Kagawa university, Japan

ABSTRACT

A large amount of radioactive cesium was diffused by the accident at Fukushima Daiichi nuclear power station. Most of the diffused radioactive cesium deposited on Fukushima soil, and most of the contaminated soil was recovered by the stripping work. The contaminated soil including the radioactive cesium is currently placed in a flexible container bag and stored in a temporary storage facility. In the future, the contaminated soil is going to be burned at the intermediate storage facility. However, the storage facilities are insufficient and a disposal method has an agenda. In order to solve these problems, it is demanded to reduce the contaminated soil by decreasing the dose of radioactive cesium in the contaminated soil. Therefore, in this study, the test equipment simulating the actual flexible container bag is primarily made. Secondly, the two methods are combined; one is the extraction method using the electrophoresis, and another is the adsorption method using an adsorbent in order to decrease the concentration of cesium included in the simulated contaminated soil. As the adsorbent, the rice husk is focused on. Its material cost is reasonable and it can be acquired in bulk. Two types of the electrophoresis test are carried out, one with the use of the rice husk and another with the use of zeolite. The test with the zeolite is positioned as a control test for the test with the rice husk. It is clarified that the adsorption effect of rice husk for cesium is similar to that of zeolite.

Keywords: Radioactive cesium, Electrophoresis, Rice husk, Zeolite

INTRODUCTION

The huge tsunami caused by the Great East Japan Earthquake brought devastating damage to the Pacific coast of the Tohoku and Kanto regions. Even now, about eight years have passed since the tsunami disaster, and the reconstruction of Fukushima Prefecture has not been completed due to the serious nuclear accident of the diffusion of a large amount of radioactive materials at the Fukushima Daiichi Nuclear Power Plant of Tokyo Electric Power Company. Among the released radioactive materials, the radioactive cesium is still detected in a wide range in Fukushima Prefecture since it is released in large quantities and has a long half-life as in [1]. In addition, it is known that it is difficult to extract cesium due to the elective fixation of cesium by the clay mineral in soil as in [2]. The soil distribution map in Fukushima prefecture is shown in Fig.1 as in [3], [4]. From Fig. 1, the soil in Fukushima prefecture has a relatively large amount of clayey soil, and cesium is likely to be incorporated into the soil under these circumstances. Fig. 2 shows the abundance of radioactive cesium in multiple soils when one year has passed since the nuclear accident as in [5]. It can be seen that almost all of the radioactive cesium is fixed in the soil as a fixed state. It has been confirmed that a large amount of fixed radioactive cesium is fixed between the layers, called as Frayed Edge, in which mineral particles such as vermiculite are involved. The vermiculite is broadly distributed in the soil of Fukushima prefecture. Therefore, the development of effective removal technology of cesium from vermiculite is an urgent issue. The biggest issue in the decontamination project in Fukushima prefecture is how to treat the contaminated soil generated by decontamination. Since much of the deposited radioactive cesium exists in the surface layer of about 10 cm of the contaminated soil, the radiation dose has been reduced by the surface decontamination such as the peeling of the topsoil. Large amounts of collected contaminated soil are temporarily stored in flexible container bags in temporary storage areas in Fukushima prefecture. The contaminated soil enclosed in the flexible container bags is scheduled to be sequentially delivered to intermediate storage facilities in Fukushima prefecture in the future. However, it is not easy to carry out a large amount of contaminated soil from the temporary storage place to the intermediate storage facility, in fact, only about 2.18 million m3, which is about 15.6% of about 14 million m3 of the transported objects which should be transported to the intermediate storage facility, has been carried out of the temporary storage place. Furthermore, the contaminated soil transported to intermediate storage facility will be sorted by a sieve,

and incinerated at a high temperature of 800 ° C or higher as in [6]. However, not only the transportation cost of a large amount of contaminated soil but also the incineration cost has not been clarified. Therefore, it is necessary to establish a technology for reducing the volume of contaminated soil by removing cesium from the contaminated soil in the flexible container bags at a temporary storage place. The technology can reduce the radiation dose of the contaminated soil without transporting it to an intermediate storage facility. Thus, in this, study, the simulated flexible container bad is produced on the assumption of the removal of cesium in the flexible bag at the temporary storage place, and the test is conducted with the sand in which vermiculite and Toyoura standard sand are mixed as a simulated contaminated soil. As a cesium removal method from the contaminated soil, and it is verified whether cesium in the soil can be moved and adsorbed to adsorbents by means of the electrophoresis method. The purpose of this study is to examine the effective cesium extraction conditions and the possibility of volume reduction of contaminated soil through the obtained results of various tests.

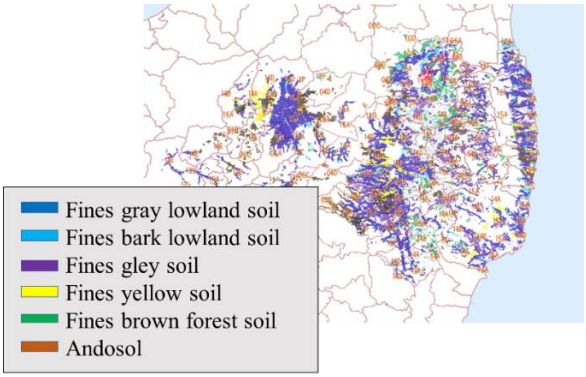

Fig. 1 Soil distribution map in Fukushima prefecture

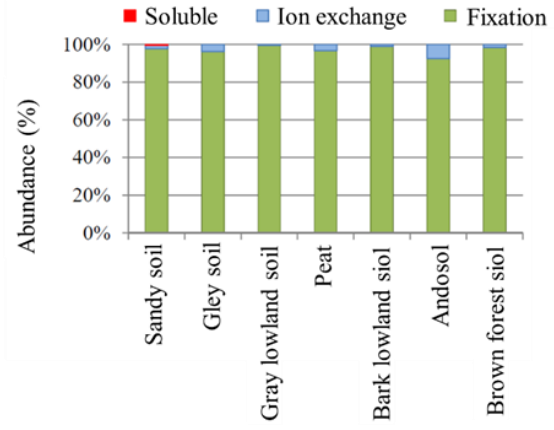

Fig. 2 Abundance of cesium in the soils

CESIUM IN SOIL

Cesium exists as a monovalent cation in soil and is adsorbed to the soil particles which is charged with a negative in soil. Additionally, cesium is easily adsorbed in and on the clay particles whose size is small. It is the 2: 1 layered silicate constituting a clay mineral that cesium adheres to the soil. The 2: 1 layered silicate is a generic term of the minerals in which the relation between the thickness of silicon tetrahedral sheet and those of aluminum octahedral sheet is 2: 1. In a silicon tetrahedron sheet and an aluminum octahedron sheet, either sheet or both of the sheets become insufficient in positive charge when a part of silicon or aluminum is replaced with another element having a small amount of positive charge. After that, the negative charge is appeared by the lack of positive charges in the sheet, and the cations are adsorbed to neutralize the interlayers of the sheet. The layer charge shows high selectivity to cesium ions as in [7]. This is because the size of cavity called a six-membered ring formed by oxygen atoms on the basic plane of a silicon tetrahedral sheet is approximately equal to the ionic radius of cesium ion. In addition, the bonding strength to the six-membered ring increases as the hydration energy decreases, which means that cesium ion has the highest bonding strength. However, the potassium ion occupies the six-membered ring because the abundance of potassium ion is decisively large in the soil (see the top of Fig. 3). The end of the clay mineral layer is frayed by weathering of soil, and the potassium ion is released. As a result, the region into which other cations can penetrate is formed and called as frayed

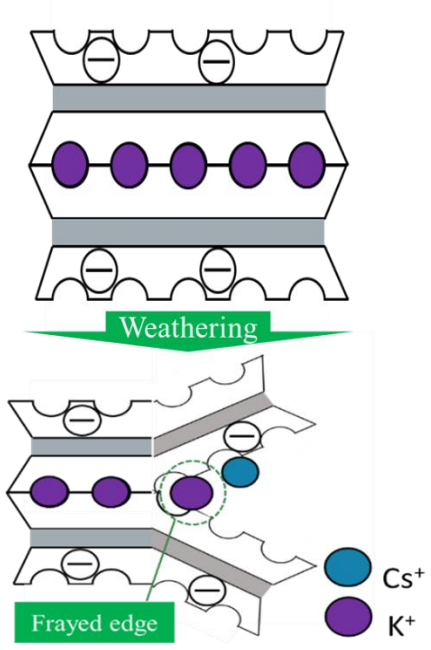

Fig. 3 Top part of 2:1 type of lamellar silicate and bottom part of the Frayed edge

edge site (see the bottom of Figure 3). It is difficult to replace cesium ions fixed to the frayed edge site with other cations as in [8].

ADSORBENTS

Rice husk and Rice husk powder

A large amount of rice husk is generated in the process of threshing and hulling after harvesting, and 2 million tons are discarded every year. In this study, the cesium adsorption ability of rice husks is focused on in order to effectively utilize it as a resource. Various researches on the adsorption ability for cesium of rice husk have been studied as in [9], [10]. For example, the research by Shozugawa et al. states that radioactive cesium is trapped by viscous fungi on the rice husks as in [11]. The possibility as a new adsorbent to replace zeolite is examined by using rice husk as an adsorbent in an electrophoretic test. Raw rice husk and commercially available rice husk powder as shown in Photo 1 are used in the test.

Photo 1 Rice husk (left) and Rice husk powder (right)

Zeolite

Zeolite is a clay mineral with regular tubular pores and cavities. Zeolite crystals have adsorption properties and ion exchange properties because they have many pores. In particular, it is known that the zeolite has high ion exchange properties against cesium. Thus, the zeolite is selected so as to exam the adsorption ability of the rice husk through the results of adsorption tests as a comparative material for rice husk. In the test, powdered rice husk is used (see Photo 2).

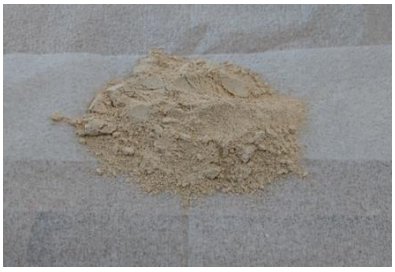

Photo 2 Powdered zeolite

TEST METHOD

Electrophoresis

In this study, the electrophoretic method is employed in order to transfer cesium ions extracted from clay minerals in soil. The cesium ions transferred to the cathode are adsorbed by an adsorbent placed in front of the cathode. An electrophoretic phenomenon is the movement of charged particles in a liquid medium under an electric field. Cesium ions are transferred to the cathode side by using the electrophoretic phenomenon, and are adsorbed in or on the zeolite or rice husk which are placed in front of the cathode side.

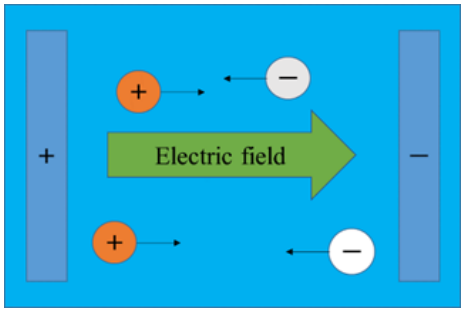

Fig. 4 Mechanism of electrophoresis

Electrophoresis test

The experiment device which simulates the flexible bag packing the soil contaminated by radioactive cesium is produced in the course of conducting the electrophoresis test. First, a simulated contaminated soil is prepared by adding 1 mL of the cesium standard solution so as to assume a real contaminated soil. The simulated soil consists of vermiculite and standard sand. Next, the simulated contaminated soil is placed in an acrylic container bag, and a carbon rod (diameter of 15 mm and length of 40 mm) serving as an anode is placed vertically in the center of the soil. Additionally, the simulated contaminated soil is placed in a simple container that combines filter paper and bolding cloth (mesh size 37 μm) to prevent mixing with the adsorbents. Moreover, the simulated contaminated soil is immersed in ammonium acetate aqueous solution (3.0% of concentration, 60 - 70 mL) and the adsorbent is placed in front of an aluminum plate so as to enclose the simulated contaminated soil (see Fig. 5). After an energization for a specified time, the soil is collected and washed out by stirring. The extracted amount of cesium contained in the solution and soil after the test is quantified by an atomic absorption spectrophotometer for the solution separated through filtration. The extraction rate is determined by the following equation (1).

Extraction ratio (%)
= extracted amount (mg)
/added amount (mg)
× 100 (1)

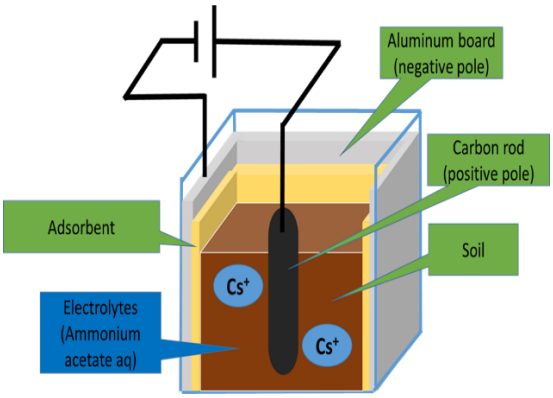

Fig. 5 Test device

TEST RESULTS

The volume ratio of standard sand to vermiculite contained in simulated contaminated soil is 1: 1, and the mass of simulated contaminated soil is 120 g. The current values during the electrophoresis test are 25, 50, and 100 mA, and the energizing time is 48 hours. The results of tests using three types of adsorbents are shown in graphs, respectively. Each test is conducted three times to ensure a reproducibility, and the average value for three batches is listed in the graphs. The test conditions are shown in Table 1.

Table 1 Test conditions

Soil		Standard sand: 114 g, Vermiculite: 6 g
Electrolyte		Ammonium acetate aqueous solution (3.0 %): 60-70 mL
Sample		Cesium standard solution: 1mL
Adsorbents	Zeolite	10 g
	Rice husk	3 g
	Rice husk powder	10 g
Curing time		168 hours
Energizing time		48 hours
Current value		25, 50, 100 mA (under 40 V)

Test results of zeolite

Fig. 6 shows the test results when zeolite is used as the adsorbent. The vertical and horizontal axes of the graph represent the extraction ratio of cesium and the current value, respectively. The results of the test with and without zeolite are compared. As a result of the test, the extraction rate of cesium decreases with increasing of the current value regardless of the presence or absence of the adsorbent. It is found that about 20% of the added cesium is extracted, which can help the volume reduction of the contaminated soil. On the other hand, about 80% of the added cesium remains in the soil. These facts indicate the difficulty of extracting cesium from the soil. Before the electrophoretic test is carried out, the curing period of 168 hours is set to fix the cesium sufficiently to the soil. Most of the cesium is adsorbed to the vermiculite during the curing period, which makes it difficult to extract the cesium from the vermiculite. Alternatively, the most effective extraction of the cesium form the soil appears when the current value is 25 mA in the electrophoresis test. It is found that the extraction of cesium is inhibited if the current value becomes too high. This is caused by the re-adsorption of cesium, temperature rise, the promotion of evaporation of electrolyte, etc. The investigation of the cause should be examined in the future. Considering the practical operation, it can be said that the low current value is advantageous from the viewpoint of running cost. Suppose the difference between the extraction ratios of specimens with and without zeolite is the adsorption ability of zeolite for cesium, the adsorption ability hardly changes with increasing or decreasing current value. In other words, it is found that the current value has little significant influence on the adsorption ability.

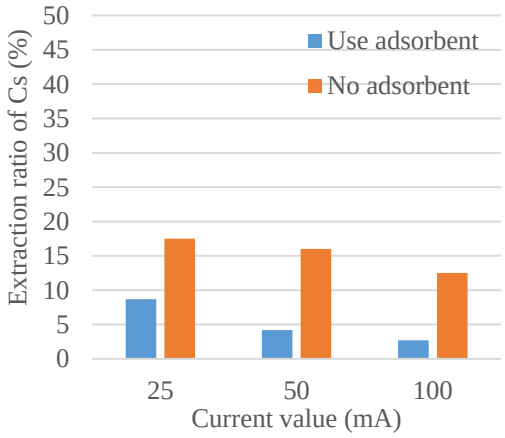

Fig. 6 Extraction ratio of Cs using zeolite

Test results of rice husk

Fig. 7 shows the test results when the rice husk is used as the adsorbent. The test results are very similar to those of zeolite. The smaller the current value, the larger the extraction ratio r, and the current value has little significant influence on the adsorption ability of rice husk. It is clarified that the rice husk has almost

the same adsorption capacity for cesium as the zeolite. It is noted that the used amount of adsorbent is 10g of zeolite and 3g of the zeolite. There is a difference in mass since the apparent volumes of both adsorbents are tried to be equalized. Thus, from the viewpoint of mass, the rice husk has higher adsorption capacity per unit volume than the zeolite. As these results, it may be most useful to use raw rice husk as adsorbent from the viewpoint of both volume reduction and processing cost of rice husks when the amount of adsorbent and adsorption performance is focused on.

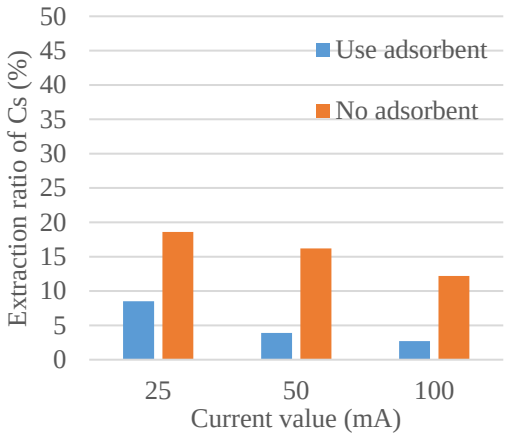

Fig. 7 Extraction ratio of Cs using rice husk

Test results of rice husk powder

Fig. 8 shows the test results when the rice husk powder is used as the adsorbent. The test results are similar to those of zeolite and rice husk. The mass of the adsorbent is 10g of rice husk powder as well as zeolite, and the rice husk powder has the more or less same adsorption ability as zeolite. The adsorption to cesium is largely due to the micorpore distribution of the adsorbent and the constituent elements. In the future, it is necessary to investigate the cause by comparing the micropore distributions with using a facility such as a BET specific surface area measurement device.

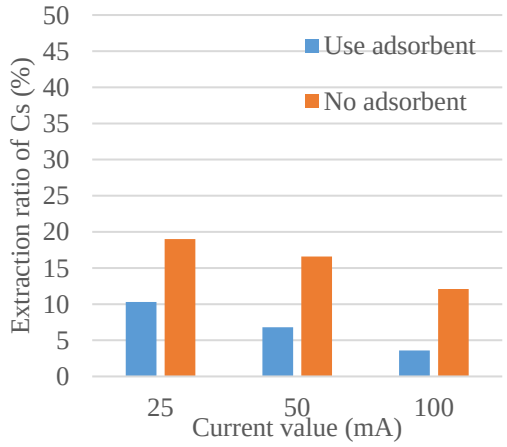

Fig. 8 Extraction ratio of Cs using rice husk powder

CONCLUSIONS

・In this study, the experiment device which simulates the flexible bag packing the soil contaminated by radioactive cesium is produced, and the electrophoresis tests are conducted under various conditions in order to investigate appropriate transfer conditions of cesium to the adsorbents (zeolite, rice husk and rice husk powder).

・ The extraction rate of cesium is the highest at the minimum current value (25 mA) when the cesium is extracted by electrophoresis without an adsorbents.

・ The adsorption rate of cesium at 50 mA of current value shows the maximum value to compare with the other current value (25, 100 mA) when the zeolite is used as the adsorbent. However, the difference due to the current is not so large.

・ The adsorption rate of cesium at 50 mA of current value also shows the maximum value to compare with the other current value (25, 100 mA) when the rice husk or the rice husk powder are used as the adsorbent, the difference due to the current is not so large.

・ The test results with zeolite, rice husk and rice husk powder as an absorber for cesium are similar, which shows that their adsorption properties for cesium are more or less same.

・ It is not clear whether there is a clear correlation between the mass and the amount adsorbed, but it is venture to discuss them here. It can be seen that the rice husk adsorbs the cesium in a smaller amount. It is considered that the adsorption principle of rice husk is one of the factors that enables rice husk to adsorb cesium in a smaller amount than rice husk powder.

・Some of the cesium can be trapped by viscous fungi that attach to the rice husk surface. The reason why the absorbent performance of rice husk powder is inferior to that of rice husk can be that the adsorption property mentioned above is lost during the powder processing from rice husk to powder form.

・ It is identified that a rice husk is an excellent adsorbent for cesium because the powder processing is not necessary and the required amount is small.

ACKNOWLEDGMENTS

This work was supported by Japan Society for the Promotion of Science, the Grants-in-Aid for Scientific Research (C) (Grant number: 18J12343).

REFERENCES

[1] Ministry of the Environment, Unified basic data

on health effects from radiation, 2014, p. 32.
[2] Okumura M., Numerical simulation studies on cesium adsorption to clay minerals, Abstracts of Annual Meeting of the Geochemical Society of Japan, Vol. 64, 2017, pp. 156-157.
[3] Agricultural Environmental Technology Research Institute, Soil information browsing system, 2001.
[4] Adachi T., Maeda T. and Takenaka H., Special soil in Japan (No. 2), Journal of the Agricultural Engineering Society, Japan, Vol. 51, Issue 9, 1983, pp. 841-849.
[5] The Japanese Geotechnical Society, Review of the behavior of radioactive cesium in soil, 2015, pp. 1-7.
[6] National Institute for Environmental Studies, Proper disposal of waste containing radioactive materials, 2012, pp. 1-20.
[7] Suzuki N., Ochi K. and Chikuma T., Cesium Adsorption Behavior of Vermiculite and It's Application to the Column Method, Journal of Ion Exchange, Vol. 25, Issue 4, 2014, pp. 122-125.
[8] Motokawa R., Endo H., Yokoyama S., Nishitsuji S., Kobayashi T., Suzuki S. and Yaita T., Collective Structural Changes in Vermiculite Clay Suspensions Induced by Cesium Ions, Scientific Reports (online), Vol. 4, 2014, article number 6585 (online).
[9] Miura T., Kabir M., Suzuki M., Nakajima S and Mori S., Effect of Organic Acids on Cesium Removal from Contaminated Soil by the Electrokinetic Remediation, Vol. 40, Issue 1, 2016, pp. 14-19.
[10] Hatakeyama Y., Kabir M., Suzuki M. and Nakajima S., Development of Flexible Ion Adsorption Electrode by Using the Burnt Rice Husk (Kuntan) and Zeolite, J. Inst. Electrostat., Vol. 41, Issue 2, 2017, pp. 111-116.
[11] Shozugawa K., Nogawa N. and Matsuo M., Decontamination of Radioactive Cesium from Environmental Water Using Rice Chaff and Straw, BUNSEKI KAGAKU, Vol. 62, Issue 6, 2013, pp. 547-554.

9th Int. Conf. on Geotechnique, Construction Materials and Environment, Tokyo, Japan, 20-22 November 2019, ISBN: 978-4-909106025 C3051

HISTORICAL HYDROLOGICAL DATA GENERATION FOR UNGAUGED WATERSHED BY WATER BALANCE TOOL

Wachirawit Plinruttanadet[1], Supasit Konyai[2]*, Vichai Sriboonlue[3]
[1]Graduate Student, Faculty of Engineering, Khon Kaen University, Thailand
[2]Assistant Professor, Faculty of Engineering, Khon Kaen University, Thailand
[3]Associate Professor, Faculty of Engineering, Khon Kaen University, Thailand

ABSTRACT

Effective water resources planning and management need accurate historical hydrological data for simulation and prediction. Many watersheds in Thailand are ungauged and many have unreliable or incomplete data. This study focuses on using available meteorological data to generate accurate monthly hydrological data, including direct runoff, evapotranspiration, and groundwater recharge for Lam Takhong watershed in Buriram Province, Thailand, as a case study. The Lam Takhong River is a tributary of the Mun River in northeastern Thailand covers an area of 1,560 square kilometers. This study examined nine years of daily meteorological data, including rainfall, temperature, relative humidity, and solar radiation obtained from a meteorological station, Buriram 436401, Royal Meteorological Department, from January 1, 2006 to December 31, 2014. Direct runoff values were evaluated from rainfall data using SCS-CN method. The CN and λ parameters were evaluated from accurate GIS maps of soil and land-use. Evapotranspiration values were determined from recorded climatic data using Morton's CRAE method. Results from the study period indicated that the wettest and driest years were 2008 and 2007, respectively. Groundwater recharge occurred every year except in 2007 with the greatest recharge occurring in 2011. Water balance was demonstrated to be a valuable tool for generating accurate historical hydrological data.
Keywords: Lam Takhong, water balance tool, SCS-CN, Morton's CRAE,

INTRODUCTION

Burirum is a fast growing township located in southern part of Northeast, Thailand. Lam Takhong (Burirum) is a small river that supports livelihood of its population. It is one of the main tributaries of the Mun River that flowing to the great Mekong River. The Lam Takhong, apart from the only water supply source for the Burirum township and its satellites, is responsible for surrounding agriculture, ecology, and socio-economic of the area. The river is subjected to flood and drought almost every year and recently increasing in frequency and intensity. There are three medium reservoirs and several small scale ones along the river. Water resource and watershed planning and management are therefore extremely important so that river flood and droughts are to be mitigated and so water pollution.

The hydrological data of the area in the past are crucial for the river and its watershed planning and management studies. Surprisingly, the past hydrological data of the Lam Takhong (Burirum) watershed are very scarce and not reliable even though serious problems are always at hand. The river is so called ungauged river [1]. Fortunately, meteorological data from the township's weather station are fairly reasonable, therefore, historical, hydrological, data can be generated.

The foremost driving force of river flow is the rainfall on the watershed. Total rainfall can be divided into vegetation interception, surface detention and retention, direct runoff, interflow, and groundwater flow. The interception, detention, and retention are evaporated back to the atmosphere. The interflow and groundwater flow become base flow. The direct runoff together with base flow constitutes the river flow [2]. The Burirum weather station recorded precipitation and other meteorological data since 2006. The objective of this study was to construct monthly hydrological data namely river flows and groundwater recharges of the Lam Takhong (Burirum) watershed from 2006 to 2014 by utilizing the daily meteorological data. The SCS-CN method was used for rainfall-runoff modelling. Monthly actual evapotranspiration was evaluated by Morton's CRAE method. The water balance tool was used to generate the time series of direct runoffs and groundwater recharges of the watershed. The river flow was finally the results of direct runoff and base flow.

STUDY AREAS AND DATA SETTING

Our study area is the Lam Takhong (Burirum) watershed which is located in the southern part of Northeast Thailand (Fig. 1). It is a sub-basin of the Mun River, one of the main tributaries of the Mekong River. It covers the area of 1560 km2 in between 14º41’ 54” to 15º 17’ 51” latitude and 102º 56’ 15” to 103º 17’ 15” longitude Takhong flows northward with a length of about 95 km. From the two southern most tributaries Huai Jorkhemak and Huai Raj, they form the Lam Takhong

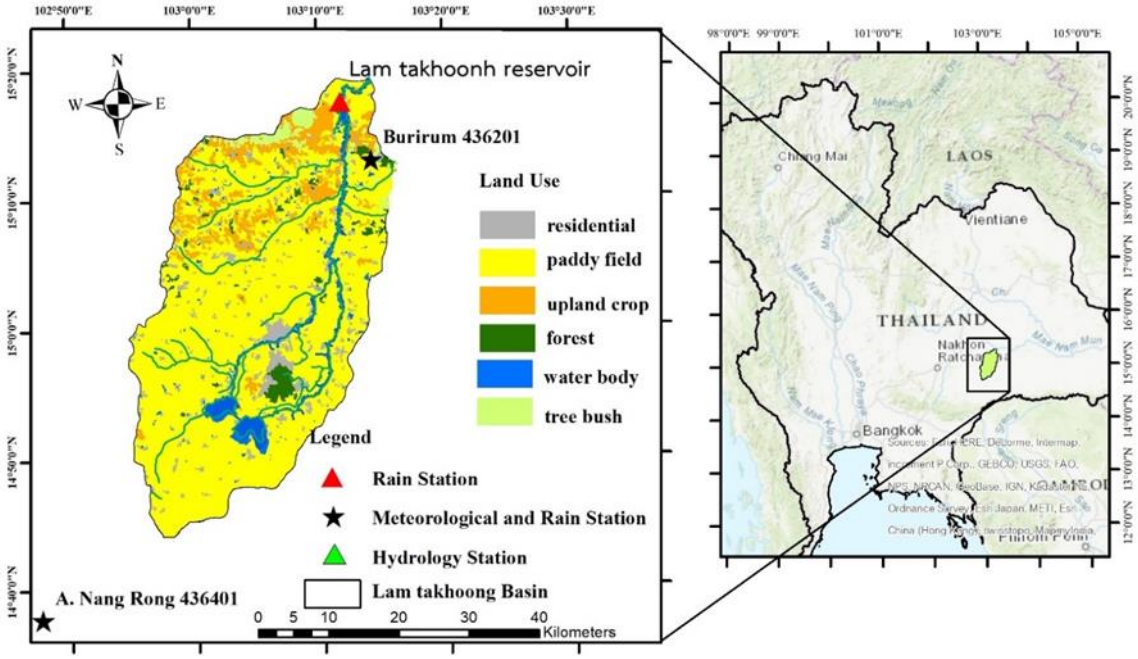

Fig. 1 Study area with drainage networks and other information.

River which drains in to the Mun River. The climate of Lam Takhong is the typical Northeast, Thailand, climate demonstrating wet and dry cycle each for half a year. Humidity causes of rainfall come from two sources namely, the southwest monsoon and the tropical cyclone. The mean annual rainfall of the region is 1,420 mm (2006 to 2014) and normally peaks in August. The mean annual of actual evapotranspiration of the same periods as rainfall is about 910 mm and also peaks in August due to large amount of soil water availability (Fig. 2).

The landform of the study area is a mild undulating terrain with highest elevation of 180 m (from the annual mean sea level) at the southernmost of the watershed and the lowest at the confluence with the Mun River of about 140 m (amsl.). Its geology is the Khorat Group with the majority of Mahasarkham formation. The formation consists of sandstone, mudstone, and rock salt producing sandy, clayey, and saline soils. The soils of the whole watershed were studied for hydrological properties and classified into 4 hydrological soil groups as shown in Table 1 and Fig. 3. The main soil groups are C and D which can produce large amount of runoff. This is one of the reasons for frequent flooding of the downstream area.

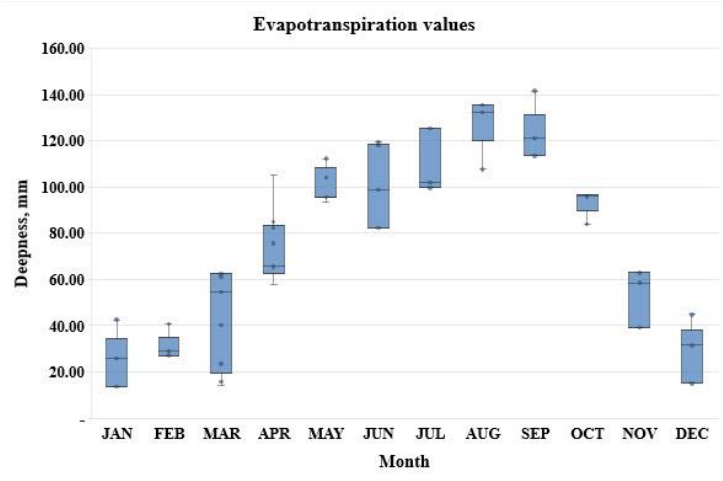

Fig. 2 Actual evapotranspiration of the region.

Table 1 Hydrological soil groups and their hydrological properties.

	Land use	Area km^2	% Area	CN II				CN*%Area	CN II
				Soil A	Soil B	Soil C	Soil D		
2014	residential	109.60	7.02	77	85	90	92	6.18	77.64
	paddy field	1,167.06	74.76	59	70	78	81	57.51	
	upland crop	178.73	11.45	62	71	78	81	8.99	
	forest	31.94	2.05	30	55	70	77	1.12	
	tree bush	35.15	2.25	30	55	70	77	1.37	
	water body	38.56	2.47	100	100	100	100	2.47	
2010	residential	108.39	6.94	77	85	90	92	6.10	77.58
	paddy field	1,206.16	77.27	59	70	78	81	59.43	
	upland crop	160.60	10.29	62	71	78	81	7.95	
	forest	36.78	2.36	30	55	70	77	1.24	
	tree bush	10.42	0.67	30	55	70	77	0.38	
	water body	38.67	2.48	100	100	100	100	2.48	

Table 2 Land-use classification and curve numbers class 2 (CN2).

HSG	Description	Area km^2	Final Infiltration Rate (mm/h)	Field capacity (%)	Wilting point (%)
A	Lowest Runoff Potential. Includes deep sands with very little silt and clay, also deep	128.21	8-12	5.5	2
B	Moderately Low Runoff Potential. Mostly sandy soils less deep than A	201.23	4-8	28.4	12.15
C	Moderately High Runoff Potential. Comprises shallow soils and soils containing considerable clay and colloids,	604.75	1-4	33.95	13.4
D	Highest Runoff Potential. Includes mostly clays.	626.84	0-1	33.5	20.2

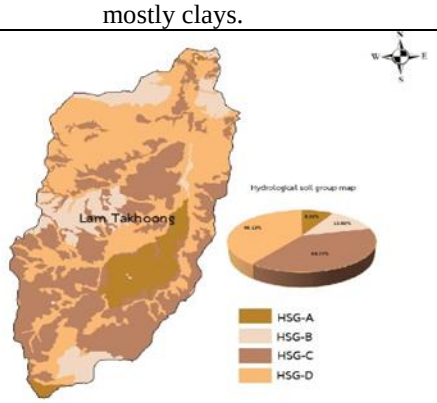

Fig. 3 Hydrological soil groups of the Lam Takhong Watershed.

The land-use of the study area was derived from the two land-use maps (2010 and 2014) of the Department of Land Development of Thailand. The land-use types were classified into 6 types with the majority of paddy fields and upland crops (Fig. 1 and Table 2). The change of 2010 land-use to 2014 one is negligibly small therefore we used the 2014 one in our curve number (CN) calculations. The CN value is the function of soil, land-use, and antecedent soil moisture. We normally estimate CN2 first from look-up tables then it is changed to CN1 or CN3 for dry or wet conditions, respectively, using antecedent rainfall see Eqs. (6) and (7).

METHOLOGY

Water balance of Lam Takhong watershed

Water balance can be defined as inflow rate subtracted by outflow rate equals to time rate of change of the soil water. We are only interested in the critical zone which range from the base of effective root zone up to the crown of the plant [3]. Considering the whole watershed, the only input is assume to be precipitation even though there are some other inflows but they are so negligibly small [4]. There are three outputs namely runoff, evapotranspiration, and groundwater recharge. Water balance equation for the effective root zone can be written as [3]:

$$\frac{Zd\theta}{dt} = P - E - R - D \quad (1)$$

where Z is thickness of effective root zone, θ is moisture content of the soil, P is precipitation, E is evapotranspiration, R is runoff, and D is deep drainage below the root zone. In the form of finite difference Eq. 1 is:

$$Z(\theta_t - \theta_{t-1}) = P_t - E_t - R_t - D_t \quad (2)$$

where subscript t and t-1 are the present time and the past time for one period, respectively. In case of daily time series t and t-1 are today and yesterday. The definition of effective root zone, Z, is loosely defined as the depth of soil with rather constant moisture content plant root can however penetrate much deeper than that [3]. Several studies of variability of soil moisture content in the Northeast of Thailand found that northeastern soil profiles normally keep moisture constant at about 1 m depth [5]-[6]. So we presume Z value at 1 m deep that $Z\theta_t$ and $Z\theta_{t-1}$ are the soil water depths of today and yesterday, respectively. The equation to predict soil water depth for today can be written as:

$$Z\theta_t = Z\theta_{t-1} + P_t - E_t - R_t - D_t \quad (3)$$

The upper and lower limits of soil moisture content are the field capacity and permanent wilting point conditions, respectively. By deducing from the study of, for example, [5]. we obtained soil water depths of 10 and 150 mm for lower and upper limits.

Direct runoff

A direct runoff (R) is a part of the whole precipitation that flow along the soil surface and shallow interflow to constitute the river flow. One of the most popular methods to evaluate direct runoff is the soil conservation service curve number (SCS-CN) method [7]. It is the function of total precipitation (P) and potential retention of soil (S) at the time of runoff occurring which can be written as [8],

$$R = \frac{(P - Ia)^2}{(P - Ia + S)} \quad \text{for } P > Ia \quad (4a)$$

$$R = 0 \quad \text{otherwise} \quad (4b)$$

where I_a is initial abstraction (mm) meaning the volume of precipitation loss before runoff to begin and is a function of potential retention, S, as

$$Ia = \lambda S \quad (5)$$

where λ is the ratio of initial loss to potential retention which was assigned to 0.2 at the beginning [9]. Several studies found the values of λ in the range of 0 to 0.3 [10]-[11]. Most of the studies in semiarid regions obtained the λ values less than 0.2 at the average of 0.05 [12] however for the area of humid climate the λ values are higher than 0.2 or up to 0.3 [13]. Lam Takhong (Burirum) watershed is in sub humid climate which its initial abstraction may be in the middle between humid and semiarid climates. We decided λ to be 0.1 in this watershed.

For simplicity, the value of S is related to a dimensionless parameter called curve number (CN) which depends on land use, soil type, and antecedent soil moisture [7]. The CN values are classified with antecedent soil moisture into three groups. The values of CN1, CN2 and CN3 are for antecedent wet soil, normal, and dry soil respectively. The CN2 value can be determined from the prepared tables e.g. [2] then CN1 and CN3 can be evaluated from CN2 as:

$$CN1 = \frac{4.2CN2}{(10 - 0.058CN2)} \quad (6)$$

$$CN3 = \frac{23CN2}{(10 + 0.13CN2)} \quad (7)$$

The antecedent soil moisture in this study was classed using the depth of rainfall of two previous days plus half of today. The potential retention of watershed, S, can be calculated from CN value as

$$S = \frac{25400}{CN} - 254 \quad (8)$$

Evapotranspiration

In majority of water balance models the value of actual evapotranspiration (E_a) is always the unknown or output of the model, but in this study we estimated E_a directly from climatic data with the model of Morton's complementary relationship areal evapotranspiration (CRAE). [14]. extended the assumption of [15] which stating that the sum of regional actual evapotranspiration (E) and potential evapotranspiration (E_p) rates equals to twice the wet environment evapotranspiration rate (E_w), namely

$$E + E_p = 2E_w \quad (9)$$

Morton (1983) solved this equation using two equations, the energy balance and vapour transfer equations, respectively,

$$E_p = R_T - [\gamma f_T + 4\varepsilon\sigma(T_P + 273)^3](T_P - T) \quad (10)$$

$$E_p = f_T(e_P - e_d) \quad (11)$$

in which T_P and T are the equilibrium and air temperatures, respectively, in degree C; R_T is the net radiation at critical zone at air temperature; γ is psychrometric constant; σ is the Stefan-Bolzmann constant; ε is the surface emissivity; f_T is the vapour transfer coefficient; e_P and e_d are the saturated vapour pressure at T_P and at dew point temperatures, respectively. Eq. (10) and (11) can be solved for Ep and Tp by iterative technique. The value of E_w can be estimated from [16]:

$$E_w = b_1 + b_2[\frac{\Delta_p}{(\Delta_p+\gamma)}][R_n - 4\varepsilon\sigma T_P{}^3(T_P - T_a)] \quad (12)$$

where b_1 accounts for large scale advection during season of low net radiation is equal to 14 W/m^2, and b_2 equals to 1.20, Δ_p is the slope of the saturated vapour pressure curve at T_p. Eqs (9) to (11) can be solved for actual evapotranspiration, E, [14].

Since solving simultaneously Eqs (9) to (11) is very complicated however [17] presented a computer programming in R language to solve them. The daily climatic data from 1/1/2006 to 31/1/2014 were used in this calculation. The accurate output results from MortonCRAE model must be in monthly forms.

Groundwater recharge

Groundwater is one of the important hydrologic components. It resides in aquifers far below the bottom of effective root zone. Top of the upper most aquifer is a water table. The drainage water from the root zone feeds the groundwater system through the unsaturated zone down to the water table called groundwater recharge. The drainage from root zone begins when the root zone reaching field capacity which is about 150 mm of soil water of the root zone [18]. Groundwater can be lost from an aquifer by two ways discharging to rivers as baseflow and flowing upward to a root zone as capillary action.

River flow

River flow is composed of direct runoff and baseflow. The former comes from precipitation whereas the later from groundwater discharge. The baseflow of the interest region is one of the lowest in the Mekong Basin which is about 53 mm/year [18]. We estimated baseflow from the concept of baseflow index, i_b, which is

$$ib = \frac{R}{Q} \quad (13)$$

where R and Q are runoff and river flow, respectively. We obtained the value of baseflow index from [19]. Which is about 0.17.

RESULTS AND DISCUSSION

The time series of rainfall, runoff, and actual evapotranspiration of the study area from 2006 to 2014 are shown in Fig. 4**.** It shows the distributions of rainfall, runoff, and ETa for each year. The runoff and ETa are always followed the pattern of rainfall. The daily distribution of rainfall for each month of the years dictates the amounts of runoff and ETa.

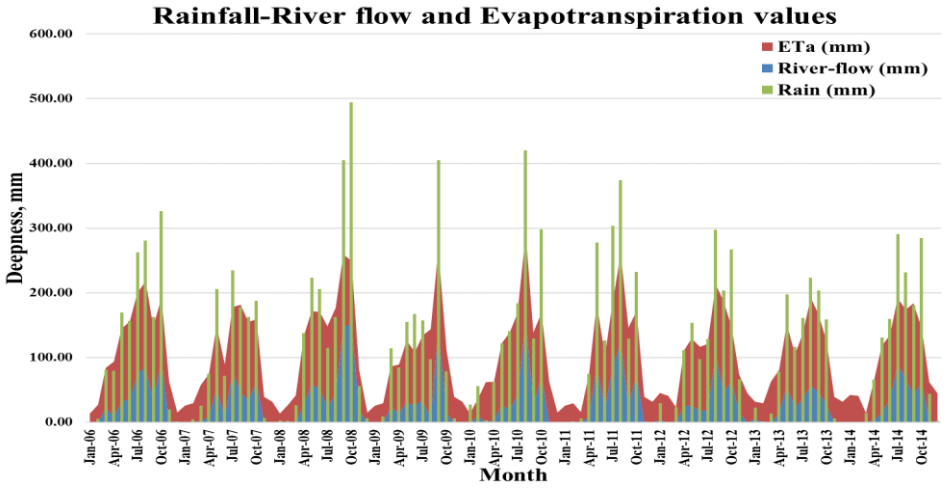

Fig. 4 The time series of rainfall, runoff, and actual evapotranspiration of the study area.

Table 3 Summarized results of water balance.

Year	Rain	Runoff	Eta	GW	Base flow	River flow	ETa/ Rain	Runoff/ Rain	River-flow/ rain
	(mm)	(mm)	(mm)	(mm)	(mm)	(mm)	(mm)	(mm)	
2006	1,545.03	391.52	964.04	160.90	80.67	472.19	0.62	0.25	0.31
2007	1,152.68	291.90	878.96	0.00	60.06	351.97	0.76	0.25	0.31
2008	1,838.57	524.08	963.29	294.96	89.19	613.27	0.52	0.29	0.33
2009	1,302.67	295.65	882.40	148.58	50.26	345.91	0.68	0.23	0.27
2010	1,445.71	362.14	920.77	125.66	62.99	425.13	0.64	0.25	0.29
2011	1,527.00	425.30	838.90	255.59	72.49	497.79	0.55	0.28	0.33
2012	1,378.98	318.42	934.55	93.69	54.91	373.33	0.68	0.23	0.27
2013	1,183.48	265.18	885.48	44.69	45.43	310.61	0.75	0.22	0.26
2014	1,404.69	316.67	901.27	190.57	54.29	370.96	0.64	0.23	0.26
Mean	1,419.87	354.54	907.74	146.07	63.36	417.91	0.65	0.25	0.29

Table 3 summarizes the results of the water balance during 2006 to 2014 period. The highest annual rainfall were in the years 2008, 2006, and 2011 at 1839, 1545, and 1527 mm, respectively which produced runoff at 524, 392, and 425 mm while ETa at 963, 964, and 838 mm, and river flow at 613, 472, and 498 mm. The second largest precipitation (2006) produced the least river flow among these three years due to its lower runoff and higher ETa. This shows that the higher precipitation does not mean to produce higher river flow.

The lowest annual rainfall were in the years 2007, 2013, and 2009 at 1,153, 1,183, and 1,303 mm respectively which produced surface runoff at 292, 265, and 296 mm, ETa at 879, 885, and 882 mm, and groundwater recharge at 0, 45, and 149 mm. The precipitation of the year 2007, even though, was much less than that of the year 2013 but it produced runoff as high as that of the year 2013, that is why it could not produce groundwater recharge, it was the only year without groundwater recharge.

From Table 3, we can evaluate runoff coefficient of the study area as 0.25 for surface runoff and even higher for that of river runoff at 0.3 which is quite high for the mean value of Northeast region e.g. for the Chi-Mun Basin the runoff coefficient is 0.1-0.15 [20]. This discrepancy indicates that the runoff from the study watershed is exceptionally very large due to soil and land-use types. The soils of the watershed are mostly clayey and compact sandy soils of Roi-et series which is the paddy soil (Fig. 2). The main land-use of the study area is paddy field which is saturated most of the time during rice growing season (Fig. 1). The saturated and heavy soil creates high rate of runoff [2].

CONCLUSIONS

We presented an effective water balance tool for generating hydrological data from the available and accurate meteorological data for an ungauged or poorly gauged watershed. Rainfall data as well as other essential meteorological data were needed for our procedure. The soil water conservation service-curve number (SCS-CN) method was used to transform rainfall data to surface runoff values with the helped of land-use and soil information. The actual evapotranspiration (ETa) was evaluated from meteorological data using Morton's CRAE method. Knowing 3 hydrological components namely rainfall, runoff, and ETa, the water balance of the root zone was proceeded. The groundwater recharge and the river flow were evaluated with the help of baseflow index. The generation of hydrological data for a watershed is very useful for watershed and reservoir management. It is interesting to compare this method to any accurate gauged data in the future.

ACKNOWLEDGMENTS

The authors would like to thanks the Graduate School and Applied Engineering for Important Crops of North East Research Group, Khon Kaen University for funding support. We would also like to thanks the Water Engineering Group, Faculty of Engineering, Khon Kaen University for data supporting

REFERENCES

[1] Bloschl, G., Sivapalan, M., Wagener, T., Viglione, A., and Savenije, H., Runoff Prediction in Ungauged Basins,1st ed. Vol.1, Cambridge University Press, 2013, pp189-225

[2] Chow, V.T., Maidment, D.R., and Mays, L.W., Applied Hydrology., 1988, McGraw-Hill.

[3] Scott, R.L. and Biederman, J.A., Critical Zone Water Balance Over 13 Years in a Semiarid Savanna, Water Resources Research, Vol.55, Issue 1, 2019, pp. 574-588.

[4] Cook, P.G., Hutton, T.J., Pidsley, D., Herezeg, A.L., Held, A., O'Grady, A.O., and Eamus, D., Water Balance of a Tropical Woodland Ecosystem, North Australia: A Combination of Micro-Meteorological, Soil Physical and Groundwater Chemical Approaches, Journal of Hydrology, Vol.210, Issue 1-4, 1998, pp. 161-177.

[5] Hamada, H. and Sukchan, S., Relationship Between Soil Water Content of a Surface Sandy Soil and Groundwater Level in a Study Site in Northeast Thailand, Journal of Japanese Society of Soil Physics, Vol. 110, 2008, pp. 79-87

[6] Moroizumi, T., Hamada, H., Sukchan, S. and Masahiro, I., Soil Water Content and Water Balance in Rainfed Fields in Northeast Thailand, Agricultural Water Management, Vol.96, Issue 1, 2009, pp. 160-166

[7] Hawkins, R.H., Ward, T.J., Woodward, D.E., and Van Mullem, J.A., Curve Number Hydrology: State of the Practice, American Society of Civil Engineers, 2009, pp6-20,

[8] Tailor and Shrimali, Rainfall-runoff Estimation of Bojiang Lake Watershed Using SCS-CN Model Coupled with GIS for Watershed Management, Journal of Applied and Advanced Research Vol.4, Issue 1, 2016, pp. 16-24

[9] Rallison, R.E., Origin and Evolution of the SCS Runoff Equation, Proceeding of the Symposium on Watershed Management 80, 1980, ASCE

[10] Bosznay, M., Generalization of SCS Curve Number Method, Journal of Irrigation and Drainage Engineering, Vol.115, Issue 1, 1989, pp. 139-144.

[11] Ponce, V.M. and Hawkins, R.H., Runoff Curve Number: Has it Reached Maturity? , Journal of Hydrologic Engineering, Vol.1, Issue 1, 1996, pp. 11-19.

[12] Shi, Z-H., Chen, L-D., Fang, N-F., Qin, D-F. and Cai, C-F., Research on the SCS-CN Initial Abstraction Ratio using Rainfall-runoff Event Analysis in the Three Gorges Area China, Catena Vol.77, Issue 1, 2009, pp. 1-7.

[13] Satheeshkumar, S., Venkateswaran, S., and Kannan, R., Rainfall-runoff Estimation Using SCS-CN and GIS Approach in the Pappiredipatti Watershed of the Vaniyar Sub basin South India, Modeling Earth Systems and Environment, Vol.3, Issue 24, 2017, pp. 1-8.

[14] Morton, F.I., Operational Estimates of Areal Evapotranspiration and Their Significance to the Science and Practice of Hydrology, Journal of Hydrology, Vol.66, Issue 1-4, 1983, pp. 1-76.

[15] Bouchet, R.J., Evapotranspiration Reelle et Potentielle, Signification Climatique, International Association of Hydrological Sciences, Symposium Publication Number 62,1963, pp. 134-142

[16] Xu, C.-Y. and Singh, V.P., Evaluation of Three Complementary Relationship Evapotranspiration Models by Water Balance Approach to Estimate Actual Regional Evapotranspiration in Different Climatic Regions, Journal of Hydrology, Vol.308, Issue 1-4, 2005, pp. 105-121.

[17] Guo, D., Westra, S. and Peterson, T., Evapotranspiration: Modelling Actual, Potential, and Reference Crop Evapotranspiration, CRAN-Package Evapotranspiration,2019

[18] Lacombe, G., Douangsavanh, S., Vongphachanh, S. and Pavelic, P., Regional Assessment of Groundwater Recharge in the Lower Mekong Basin, Hydrology, Vol.4, Issue 4, 2017, pp. 1-18

[19] Swatpru, K. and Konyai, S. Base flow index evaluation for Yom River, Thailand. The 2nd International Conference on Engineering and Applied Science (ICEAS), 2013, pp.523-532.

[20] Floch, P. and Molle, F., Water Traps:The Elusive Quest for Water Storage in the Chi-Mun Basin, Thailand, University of Natural Resources and Applied Life Sciences,2009.

9th Int. Conf. on Geotechnique, Construction Materials and Environment, Tokyo, Japan, 20-22 November 2019, ISBN: 978-4-909106025 C3051

REGIONALIZATION OF RAINFALL IN NORTHEASTERN THAILAND

Pongpinid Pinidluek [1], Supasit Konyai [2] and Vichai Sriboonlue [3]
[1] Graduate Student of Agricultural Engineering, Faculty of Engineering, Khon Kaen University, Thailand;
[2] Assisttant Profressor of Agricultural Engineering, Faculty of Engineering, Khon Kaen University, Thailand;
[3] Associate Profressor of Agricultural Engineering, Faculty of Engineering, Khon Kaen University, Thailand

ABSTRACT

Rainfall is one of the most valuable natural resources for northeastern Thailand, a region whose livelihood of more than 80% of the population depend predominantly on rainfed agriculture. Rainfall events can also cause severe natural hazard, therefore proper water resources and flood management is crucial to this region. Regionalization of rainfall can facilitate the management of water resources and floods by delineating a region with rainfall patterns that vary in both time and space into areas with more homogeneous rainfall characteristics. This study applied both hierarchical and K-means clustering methods to separate the entire Northeast into three precipitation zones using monthly rainfall data from 38 stations over 30 years from 1987 to 2016. The temporal variation of zoning was also investigated by dividing the data into three 10-year periods, 1987-1996, 1997-2006, and 2007-2016. The regionalization by both methods gave similar results that are comparable to the mean annual rainfall of the entire region. Mean annual rainfall values were highest in the northeastern part of the region with a gradual decreasing trend to the southwest. The clustering methods, on the other hand resulted in the highest rainfall zone in the northern part, the moderate rainfall on the southeastern, and the lowest on the southwestern part. As it relates to temporal variation, the results from 1987-1996 for both methods are mostly the same but those from 1997-2006 and 2007-2016 are not quite the same especially results from the last decade. Homogeneous rainfall regionalization by clustering methods is preferable to merely geographical and mean annual rainfall values because they take into account several factors such as monthly rainfall distribution.

Keywords: hierarchical clustering, K-means clustering, homogeneous rainfall, temporal variation, northeastern Thailand.

INTRODUCTION

Rainfall is the primary cause of flood, drought, and other hydrological consequences. Many hydrological and water resources analyses, designs, and operations are needed to know the rainfall homogeneous regions [1]. Traditionally, homogeneous rainfall region has been determined from the mean annual precipitation and geography of the region [2]. Since the northeastern Thailand climatic condition is monsoonal the area is wet during the southwest monsoon from mid-May to mid-October and dry from mid-October to mid-May by the northeast monsoon [3], [4]. This is actually the result of the dynamics of Intertropical Convergence Zone (ITCZ) [5], [6] that moves across the northeast region during the wetting period by touching the southern boundary of the region at about mid-May and keep on moving up passing the northern boundary at about early July and moving further north then returning to touch the northern boundary again at about mid-July then slowly moving southward across the Northeast region again until mid-October then passing the southern boundary of the region. Mobility of the ITCZ causes rainfall pattern of the Northeast region to be ever changing [7].

The Northeast topography is a plateau-like with mountain ranges on the west and the south boundaries. The rainy season starts when the ITCZ band first approaching the southern boundary about mid-May and ends when the ITCZ about to leave the same boundary at mid-October. During the ITCZ band moving further north, the rainfall of the Northeast decreases allowing dry spell to interfere with its rainfall pattern. Two types of wind bring moist air from the oceans to the Northeast region namely the southwest monsoon from the Indian Ocean and the tropical cyclone from the Pacific Ocean. These phenomena make the rainfall pattern very complicate. Regionalization of rainfall in this part of Thailand cannot be performed just by subjectively observing the mean annual rainfall and its geography but must be applying cluster analyses. Two well known clustering algorithms being generally used for this type of work are hierarchical and k-means methods [1], [8].

Our study objective is to partition the whole Northeast region into three uniform precipitation sub-regions using the two cluster analyses with monthly rainfall data on scatter rainfall stations all over the region during three 10-year periods.

STUDY AREA AND DATA ACQUISITION

Our study area is the whole northeast region of Thailand. It covers the area of 168,854 km^2 of a relatively mild rolling plain with the elevation of about 150 to 500 m above mean sea level. Due to its plateau-like topography it is called the Khorat Plateau [9]. There are mountain ranges on the west and south borders, the Phetchbun and Dong Paya Yen on the west boundary which border with the Central and the Sankambeng and Phanom Dangreg Ranges on the south which border with the Central and Cambodia (Fig. 1). These mountain ranges create orographic effects as rain shadows retarding the flow of southwest monsoon to the region. The Phu Phan Range divides the Khorat Plateau into two basins the upper is smaller called the Sakol Nakhon Basin and the lower part is called the Khorat Basin. Both basins drain to the Mekong River in the north and east boundaries by the Songkhram River for the upper basin and the Chi-Mun System for the Khorat Basin. Geology of the northeast composts of sandstone of the Mesozoic Khorat Group [10]. Following the parent materials of sandstone, typical soils of the northeast are sandy soils which are very infertile and sometime saline [9]. Hydrologically, there are only wet and dry seasons in the northeast, Thailand, each sharing half of the year. Two sources of humidity to produce rainfall in the northeast region namely the southwest monsoon and the tropical cyclone. The topographic and climatic conditions complicate the rainfall pattern of the northeast region, therefore it is essential to partition the whole northeast region into more compact, homogeneous areas. We used monthly rainfall data from 38 rainfall stations for 30 years during 1987 to 2016 from the Thai Meteorology Department for our study. The names, locations, and elevations of the rainfall stations are shown in Table 1 and Fig. 1.

METHODOLOGY

Traditional method of rainfall regionalization is by using mean annual depth of precipitation e.g. low, modulate, and high rainfall [11]. Objectively, rainfall regionalization can be performed by mean of a cluster analysis [12], which is a set of algorithms to group the similar objects from a diverse observations. In this study we tried to partition 38 rainfall stations of the whole Northeast region (Fig. 1 and Table 1) into 3 groups of homogenous rainfall characteristics as in [13]. From 30-year data we investigated each of three 10-year periods, i.e. 1987-1996, 1997-2006, and 2007-2016, to evaluate temporal variation.

Two types of clustering algorithms, i.e. hierarchical and k-means, were used with monthly rainfall depths which were arranged in the forms of 3 tables. Each table contains monthly rainfall data with 120 columns of months of the years, say from January 1987 to December 1996 for the first table, and 38 rows of the stations in Table 1. The hierarchical algorithm and the k-means one are totally different [8]. The former produces a dendrogram of the stations with similar rainfall characteristics [14].

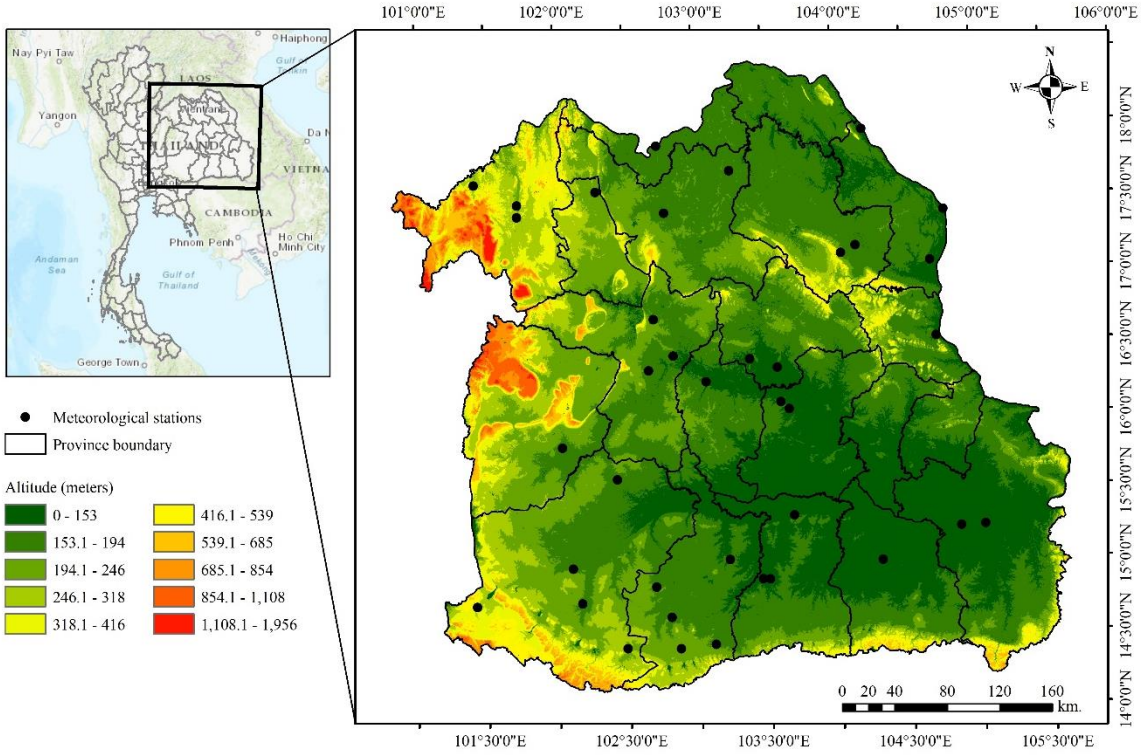

Fig. 1 Topography of the northeast and locations of rain gauges.

Table 1 Details of rainfall stations

Code	Name	Elevation (m)	Latitude	Longitude
352201	Nong Khai	168	17°52'44.63"	102°44'14.11"
353004	Tha Li	266	17°38'25.64"	101°25'50.36"
353201	Loei	244	17°28'54.86"	101°42'55.42"
353301	Loei Agrometeorological Station	286	17°23'44.08"	101°44'16.82"
354005	Ban Dung	176	17°41'1.34"	103°16'0.62"
354201	Udon Thani	178	102°47'22.12"	102°47'22.12"
356201	Sakon Nakhon	164	17°10'53.67"	104°9'58.38"
356301	Sakon Nakhon Agrometeorological Station	193	17°6'58.07"	104°2'22.05"
357003	Renu Nakhon	156	17°2'31.12"	104°40'46.36"
357005	Ban Phaeng	153	17°58'52.35"	104°12'46.61"
357301	Nakhon Phanom Agrometeorological Station	150	17°24'13.61"	104°47'12.42"
360004	Suwan Khuha	206	17°34'34.27"	102°18'9.30"
381017	Ubonrat Dam Self-Supporting Settlement	187	16°41'54.34"	102°41'7.94"
381201	Khon Kaen	164	16°25'56.53"	102°49'22.69"
381301	Tha Phra Agrometeorological Station	179	16°19'57.09"	102°38'13.41"
383201	Mukdahan	152	16°31'56.92"	104°42'21.08"
387401	Maha Sarakham	160	16°15'21.23"	103°4'7.05"
388008	Kalasin Seed-Multiplication Station	152	16°24'16.31"	103°22'6.17"
388401	Kalasin	146	16°19'53.19"	103°34'27.44"
403201	Chaiyaphum	185	15°48'31.42"	102°2'28.95"
405201	Roi Et	151	16°2'57.83"	103°38'41.08"
405301	Roi Et Agrometeorological Station	163	16°5'45.84"	103°36'15.77"
407301	Ubon Ratchathani Agrometeorogical Station	132	15°13'55.05"	105°2'3.04"
407501	Ubon Ratchathani	123	15°13'8.59"	104°52'29.69"
409301	Si Sa Ket	132	15°0'36.30"	104°18'37.16"
431002	Bua Yai	173	15°34'25.59"	102°25'20.42"
431013	Soeng Sang	228	14°24'33.08"	102°29'10.29"
431201	Nakhon Ratchasima	191	14°58'56.35"	102°5'39.37"
431301	Pak Chong Agrometeorological Station	313	14°42'13.17"	101°25'6.81"
431401	Chok Chai	196	14°43'24.48"	102°9'19.40"
432201	Surin	149	14°52'23.58"	103°29'20.55"
432301	Surin Agrometeorological Station	142	14°52'26.48"	103°26'52.24"
432401	Tha Tum	134	15°18'36.57"	103°40'51.98"
436002	Lahan Sai	215	14°25'14.20"	102°51'24.6"
436009	Ban Kruat	190	14°26'42.64"	103°5'53.88"
436012	Nong Hong	185	14°50'10.10"	102°40'32.14"
436201	Burirum	157	15°1'17.07"	103°12'52.11"
436401	Nang Rong	190	14°37'40.43"	102°47'44.51"

At the beginning procedure the two most similar rainfall characteristics being merged together and then the third station (or another cluster of stations) to be merged with the Ward's criteria that is the sum of euclidean distances among the stations in the new cluster must be minimum [8]. Each dendrogram (not shown herein) illustrates 38 clusters at its base and 1 cluster at its top.

The k-means algorithm needs to be provided with k seeds randomly [12] among each of the three data sets. In our case, we set up 3 seeds since we need to group into three clusters as probably of low, medium, and high rainfall. From the 3 predetermined seeds, the rainfall data that are more similar to a seed are grouped together with the seed, therefore we have three groups for the whole data. Consequently, new seed is to be determined for each group e.g. at the centroid of the group, then the process to be

performed all over again until the stations in each group do not change [8].

The similarity are always measured by euclidean distance which is not really a distance but it is a square root of sum square of the coordinates difference between two points. The points are the rainfall stations and their coordinates are monthly rainfall data from each ten year period. Since rainfall depths in the wet seasons are much larger than those in the dry seasons, therefore the data in each station must be normalized so that the wet season data do not dominate the dry season ones.

Tables of monthly rainfall data from 38 stations were prepared using Excel software then transformed into text files to be used with the R programming. The text file tables of rainfall data were input as data frames. The data frames were normalized using *scale* function. The normalized table can be clustered by hierarchical method using *hclust* function together with the Ward's criteria, e.g.

```
ne.rainh1  <-  hclust(table1, method = 'ward')
```

This is an R code to cluster by hierarchical algorithm the data fame of 10-year monthly rainfall data of 38 rainfall stations called table1 with Ward's method for merging criteria. The result of hierarchical clustering on the data frame is kept in *ne.rainh1*.

For k-means algorithm we use *kmeans* function to group the similar rainfall stations from the same data frame *table1* into 3 clusters in R code as:

```
ne.raink1  <-  kmeans(table1, 3)
```

RESULTS AND DISCUSSIONS

The three 10-year rainfall data (1987-1996, 1997-2006, and 2007-2016) were grouped into three clusters using the hierarchical and K-means algorithms. The results are shown in Fig. 2 as triangles, squares, and hexagons for each group, the results from hierarchical on the left and those from K-means on the right, the three pairs represent each period from the first to last. The isohyets are also shown on Fig. 2 illustrating that the highest rainfall is in the northeastern part of the region and the lowest is in the southwestern part for all three periods. The annual means rainfall of the region were 1306, 1391, and 1438 mm, for the first to the last periods, respectively. The increases of annual means from the first to the second period is 6.6 % and from the second to the third is 3.4 %. These are likely to be the effect of climate change [15].

The top pair of Fig. 2, the first period of 1987-1996, demonstrate hexagons to occupy the northern part of the region, the squares the southeastern, and the triangles the southwestern part. The positions of the three symbols from both algorithms, left and right in Fig. 2, are exactly the same. We presumed that the hexagons represent the high rainfall region, the squares the moderate, and the triangles are the low rainfall.

The positions of the three symbols from both methods for the second period are not exactly the same as in the first period. For this 2nd period, the hexagons still occupy the northern region, but the squares cover most of the middle zone including the southeast portion. The K-means method give preferable pattern for this period.

For the last period, the hierarchical algorithm gives preferable pattern of the 3 symbols to the K-means one. The hexagons cover the north and northwest zones, the squares on the eastern, while the triangles occupy the southwestern region. We cannot conclude that the hexagons are indicated the high rainfall zone and the triangle the low rainfall one. For the K-means method of the 3rd period showing 4 hexagons in the zone of low rainfall (Fig. 2).

Fig. 3 illustrates rainfall distributions throughout the year. The triangles are of the top pair, the squares of the middle, and the hexagons of the bottom one. The hierarchical clustering is on the left and the K-means on the right. Fig. 3 and Table 2 show that peaks of hexagon group of rainfall always being in the month of August but for those of square and triangle groups being in both August and September. The dry spell during rainy season were in the month of July for all groups of the 1st period. For the 2nd and 3rd periods, there was no dry spell during the rainy season except for the triangles were in June. These phenomena were the consequence of the movement of ITCZ rain band. The ITCZ band moved much farther north creating dry spell in July for all groups (triangle, square, and hexagon). Only the triangle group did show the dry spell in June, there was no dry spell for other groups.

The above phenomena demonstrate that the hexagons always peak before the others since the ITCZ band, on the way back, reaching the hexagons before the others. The absent of dry spell with a few in June, for the 2nd and 3rd periods, show the ITCZ band did not move too far off from the north border of the Northeast.

CONCLUSIONS

The regionalization of homogeneous rainfall pattern of the Northeast, Thailand, was done by hierarchical and K-means methods with data from 38 rain gauges for three periods, 1987-1996, 1997-2006, and 2007-2016. The rainfall characteristics were partitioned into three groups illustrating by triangle, square, and hexagon. These groups did not exactly match with the amounts of the mean annual rainfall. However, the triangle group got along with the low

rainfall zone, the square with the moderate, while the hexagon agreed with the high rainfall region. The hexagon group occupied the northern part of the Northeast, the square the southeastern, whereas the triangle covered the southwestern part. The movement of the ITCZ band went farther from the northern boundary of the region creating dry spell during rainy season in July for the 1st period (1987 to 1996). For the 2nd and 3rd periods, rainy season came early and the ITCZ band did not move further away from the northern border, by majority no dry spell existed. The mean annual rainfall of the region increased from the 1st period to the 2nd then to the 3rd at 1306, 1391, and 1438 mm, respectively. This is a sign of climate change.

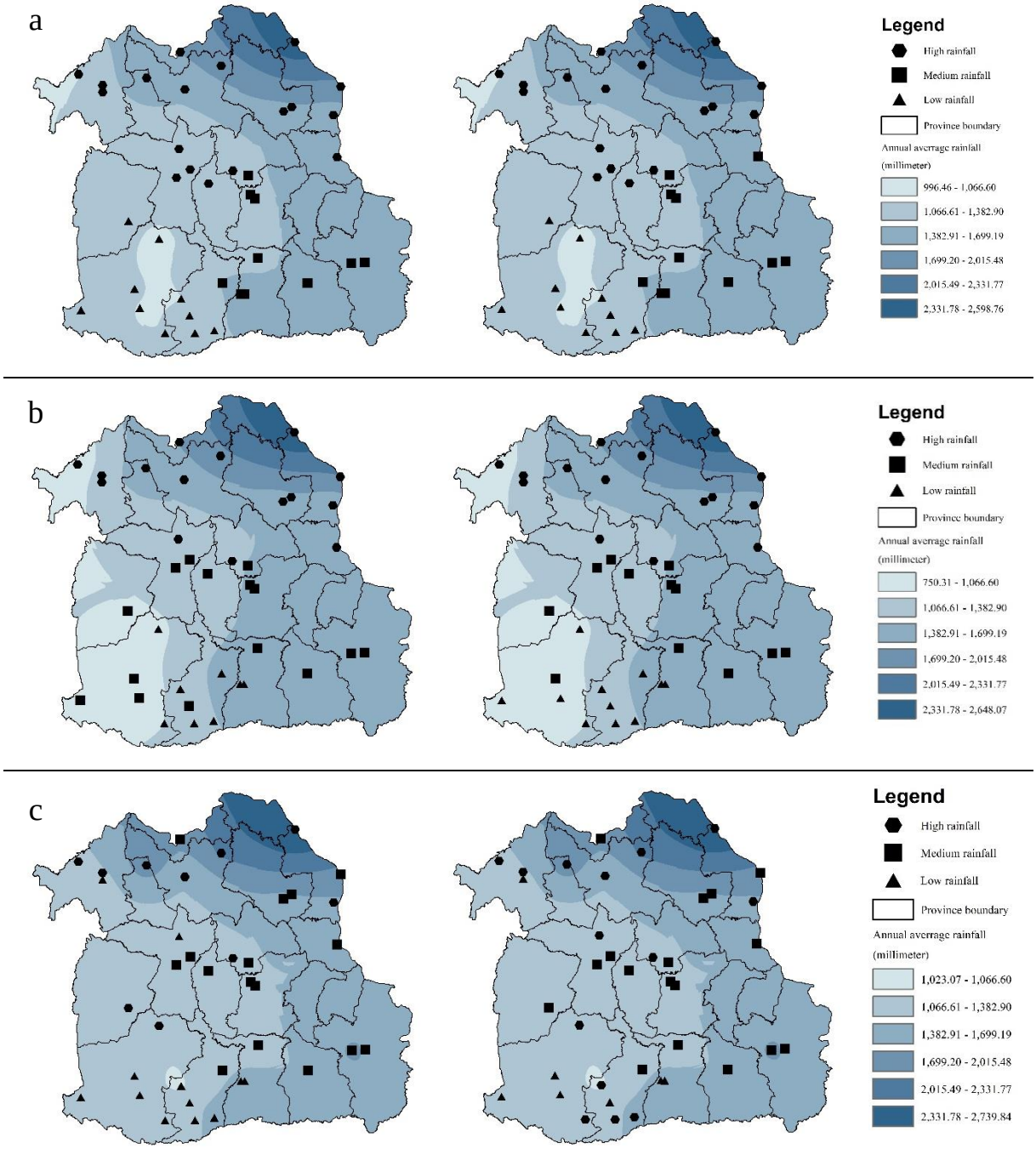

Hierarchical clustering method K-mean clustering method

Fig. 2 Identification of clusters for hierarchical and K-mean clustering method: (a) period 1987-1996; (b) period 1997-2006 and (c) period 2007-2016.

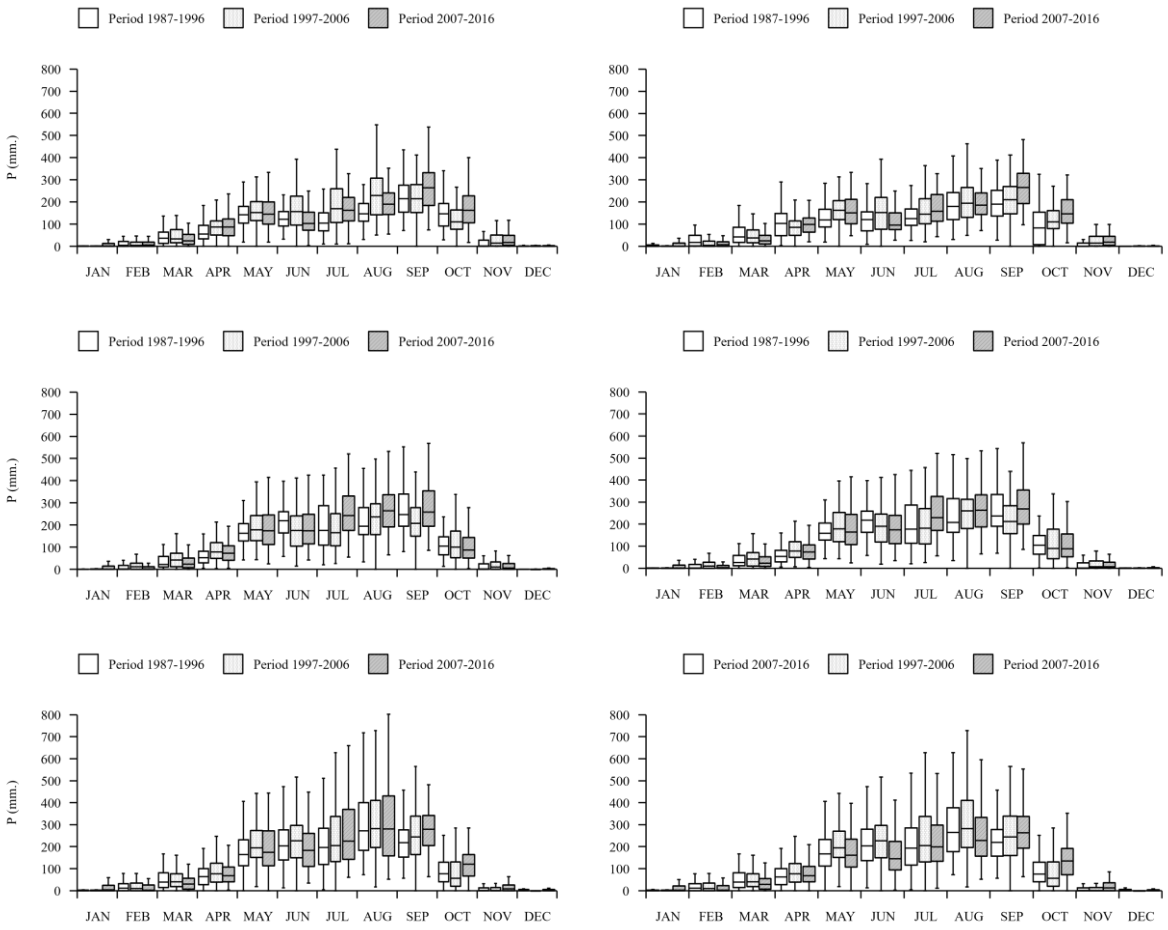

Fig. 3 Monthly rainfall distributions in three 10-year periods.

Table 2 Monthly rainfall cluster by using Hierarchical and K-means methods. (H= Hierarchical, K= K-means)

Periods	Zones	Method	Peak	Dry spell	Mean annual rainfall
1987-1996	low	H	Sep.	Jul.	1,078
		K	Sep.	Jul.	1,078
	medium	H	Sep.	Jul.	1,331
		K	Sep.	Jul.	1,346
	high	H	Aug.	Jul.	1,417
		K	Aug.	Jul.	1,413
1997-2006	low	H	Aug.	N	1,294
		K	Aug.	Jun.	1,245
	medium	H	Aug.	N	1,309
		K	Aug.	N	1,357
	high	H	Aug.	N	1,555
		K	Aug.	N	1,555
2007-2016	low	H	Sep.	Jun.	1,258
		K	Sep.	Jun.	1,274
	medium	H	Aug.	N	1,475
		K	Sep.	N	1,463
	high	H	Aug.	N	1,594
		K	Aug.	N	1,488

ACKNOWLEDGMENTS

The authors would like to thank the Graduate School and Applied Engineering for Important Crops of North East Research Group, Khon Kaen University and the Water Engineering Group, Faculty of Engineering, Khon Kaen University for funding and data supporting.

REFERENCES

[1] Zhang Y., Moges S., and Block P., Optimal cluster analysis for objective regionalization of seasonal precipitation in regions of high spatial-temporal variability: Application to western Ethiopia. Journal of Climate, Vol. 29, 2016, pp. 3697-3717.

[2] Ahuja S., and Dhanya C.T., Regionalization of rainfall using RCDA cluster ensemble algorithm in India. Journal of Software Engineering and Applications, Vol. 5, 2012, pp. 568-573.

[3] Sangwaldach P., Wongwises P., Exell R.H.B., and Sukawat D., The surface features of southwest monsoon onset over Thailand. The 2nd Joint International Conference on "Sustainable Energy and Environment (SEE 2006)" D-015 (O).

[4] Naeimi V., Leinenkugel P., Sabel D., Wagner,W., Apel H., and Kuenzer C., Evaluation of soil moisture retrieval from the ERS and Metop scatterometers in the Lower Mekong Basin. Remote Sensing, Vol. 5, 2013, pp. 1603-1623.

[5] Byrne M.P., Pendergrass A.G., Rapp A.D., and Wodzicky K.R., Response of the intertropical convergence zone to climate change: Location, width, and strength. Current Climate Change Reports, Vol. 4, 2018, pp. 355-370.

[6] Chokngamwong R. and Chiu L.S., Thailand daily rainfall and comparison with TRMM products. Journal of Hydrometeorology, Vol. 9, 2008, pp. 256-266.

[7] Weesakul U., and Lowanichchai S., Rainfall forecast for agricultural water allocation planning in Thailand. Thammasart International Journal of Science and Technology, Vol. 10, Issue 3, 2005, pp. 18-27.

[8] Rogerson P.A. (2010) Statistical Methods for Geography: A Student's Guide. Third edition, Sage.

[9] Loffler E., Thompson W.P., and Liengsakul M., Geomorphological development of the Thung Kula Ronghai, Proceedings of the 1st Symposium on Geomorphology and Quaternary Geology of Thailand, 1983, pp.123-130.

[10] Wongsomsak S., Salinization in Northeast Thailand, Southeast Asian Studies, Vol. 24, Issue 2, 1986, pp. 133-153.

[11] Limsakul A., and Singhruck P., Long-term trends and variability of total and extreme precipitation in Thailand. Atmospheric Research, Vol. 169, 2016, pp. 301-317.

[12] Carvalho M.J., Melo-Goncalves P., Teixeira J.C., and Rocha A., Regionalization of Europe based on a k-means cluster analysis of the climate change of temperatures and precipitation. Physics and Chemistry of the Earth, Vol. 94, 2016, pp. 22-28.

[13] Venkatesh B., and Jose M.K., Identification of homogeneous rainfall regimes in parts of Western Ghats region of Karnakata. Journal of Earth System Science, Vol. 16, Issue 4, 2007, pp. 321-329.

[14] de Bodas Terassi P.M., and Galvani E., Identification of homogeneous rainfall regions in the eastern watersheds of the State of Parana, Brazil. Climate, Vol. 5, Issue 3, 2017, pp. 53.

[15] Babel M.S., Agawal A., Swale D.K., and Herath S., Evaluation of climate change impacts and adaptation measures for rice cultivation in Northeast Thailand. Climate Research, Vol. 46, Issue 2, 2011, pp. 137-146.

9th Int. Conf. on Geotechnique, Construction Materials and Environment, Tokyo, Japan, 20-22 November 2019, ISBN: 978-4-909106025 C3051

THE HABITAT CONDITION ANALYSIS OF LUEHDORIFIA JAPONICA, THE SIMBOL OF CONSERVATION AREA

Michiko Masuda[1], Yoriko Gido[2], Yukimaru Tashiro[3], Atsushi Tanaka[4], and Fumitake Nishimura[5]
[1,2,3,4] Department of Civil Engineering, Nagoya Institute of Technology, Japan; [5] Department of Environment Engineering, Kyoto University, Japan

ABSTRACT

It has been pointed out that the vegetation succession brings out the reduction of the *Luehdorifia japonica*. But some researcher insisted that thinning cannot increase the population of the butterfly. Then we cut down half of the forest and reverse succession, in order to study the influence of the population of *Asarum rigescens* var. *brachypodion*, larval food plant, and the mass of reward of the butterfly by cut off the forest. It was being thought that thinning in a forest obstructed growth of forest floor plant, but the growth of *A. rigescens* that was famous of forest floor plants, was promoted. On the other hands, *A. rigescens* did not grow up in the climax forest despite of survive. In the green house experiment we can get the proof of the growth condition. The growth of open light condition was superior to that of the 40% light penetration condition. And more the number of flowering of plants was more increased than ever. It was indicated that the thinning in a forest is important for the habitat of the symbolic butterfly, *L. japonica*, and it increased other plants bloom, and to secure source of nutrition of much insect kinds

Keywords: thinning, light condition, larval food plant, the mass of flowering, biodiversity

INTRODUCTION

The 2005 World Exposition, Aichi, Japan, Nature's Wisdom, was held at Aichi Prefecture. Some *Accipiter gentilis* built nests and many *Luehdorfia japonica* grew up in the main site, so that area would be conserved in order not to develop [1] [2]. The main site of the 2005 World Exposition moved to the next place. The area was divided 6 sections along the objection for the natural conservation [3]. Almost sections were adopted as untouched nature conservation.

Almost 10 years passed from the 2005 World Exposition, Aichi, Japan, we cannot find out the feature of *L. japonica* anymore. The untouched conservation management is not good for the butterfly. In 2012 only one *L. japonica* observed and in 2013 and 2014 there was no *L. japonica* in the area [4].

Ishii (2005) pointed out the half of the endangered species in Japan was distributed in Satoyama [5]. Satoyama has been affected by human disturbance in order to get energy, construction and food materials for some centuries. The moderate disturbance maintained high biodiversity. It suggested the moderate disturbance is important for the *L. janonica*.

But some researchers insisted that the disturbance is not good for the forest floor plants, *Asaram* species, that is larval food plants of *L. japonica* [6]. And some conservationists argue that the conservation should be un-disturbed. The cause of the butterfly decrease should be explained for the conservation management. The insects cannot live when the decrease of larval food plant and the decrease of adult food resource occurred. Then we investigate the influence of the thinning to both the larval food plant growth and the mass of flower resources.

We have three hypothesis, 1) the thinning doesn't increase the death rate of *Asarum rigescens* var. *brachypodion*, 2) The lighter condition promote the growth of *A. regescens* var. *brachypodion*, 3) the thinning increase the mass of flower reward. It was paid attention to the three points and analyzed.

MATERIALS AND METHODS

The Study Site

The study was carried out on the Kaisho-no-mori Conservation area (600 ha) at the center of Aichi Prefecture, the middle of Japan (Fig. 1).

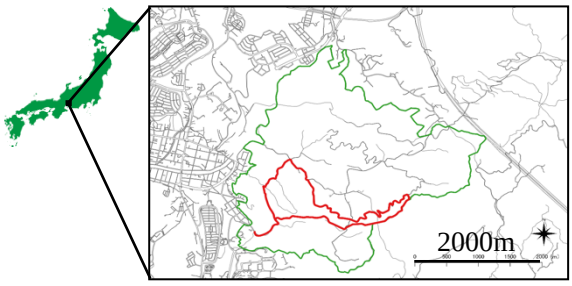

Fig. 1 The area of the study site (green line) and route of the phenology census (red line).

The area has been conserved from 2005 in order to prevent the disorder construction and over use. Especially no one step into northeastern conservation area. The geological feature of the area assumes rich groundwater and the soil of the oligotrophy base. 16 Tokai hilly land elements [7] that are endangered species grown up in the area.

The Study Plant

Asarum rigescens var. *brachypodion* (ARISTOLOCHIACEAE) is a perennial herb in the temperate forest distributed in Chubu Japan (Fig. 2). The habitat of the species is deciduous or evergreen forest floor. From January to March the species is flowering close to the ground 1 to 10 flowers. From April to May the seed dispersal is occurred by some kinds of ants. The each of seeds has elaiosome that is nutritional source for many ants. The seedling emergence is occurred in April. Despite of the leaves of the species have aristolochic acid, the leaves of the species is larbal food of *L. japonica* (Fig. 3), then the butterfly species have tolerance to the toxin.

Fig. 2 Photos of *A. rigescens* var. *brachypodion*, under right photo shows the flowers of the species.

Fig. 2 Photos of *L. japonica* and under right photo shows the eggs of the species.

The Field Census

To know the distribution of *A. rigescens* var. *brachypodion*, we walked everywhere of Kaisho-no-mori along the ridges and the valleys using GPS from January to March in 2016 and made a distribution map.

In order to investigate the effect of shinning, we set up the quadrat (10 m x 10 m) and cut off every woods and weeds except *Asarum* in June 2016. And we set up the same size quadrat at 100 m away. At each quadrat we made a map of distribution of every *A. rigescens* var. *brachypodion*, and measured the size of the species. The individual size was estimated by five index, number of leaves (n), largest leaf length (l_{max}), largest leaf width (w_{max}), smallest leaf length (l_{min}), and smallest leaf width (w_{min}). Then size index (S_{index}) showed equation (1).

$$S_{index} = \frac{n}{2} (l_{max} \text{ x } w_{max} + l_{min} \text{ x } w_{min}) \quad (1)$$

From June 2016 to Nov. 2018, we measured every individual size index in early summer and autumn in each year to detect the difference of growth rate in each quadrat.

And we took the photographs to investigate light condition at each individual location using omnidirectional camera (RICOH THETA S) and calculated the open sky degree using software (CanopOn2).

To measure the mass of flowering reward, we took every flower photographs a week interval from March to April in 2016 and 2018 along the field census route 4m wide 20m long (Fig. 1 red line). Using the phots we grasped the number of flowers. In 2016 to measure the honey amount of each flower of Rhododendron and Viola (the flowers attract the butterfly). To compare the reward of the flowers, we counted another place (where we can observe a lot of *L. japonica*).

Comparison of Growth Rate

Two condition were prepared to measure the growth rate of the species. One condition was open light condition (where 50% open sky) and the second condition was closed by cheesecloth (where 20% open sky). We collected from the field 84 individuals of *A. rigescens* var. *brachypodion* on October 2017. After collecting, each individual was washed to remove the soils in order to measure fresh weight. After wiping water by paper towel, we measured fresh weight, we planted 10cm diameter pot with cultivation soils. We divided two groups that has same size distribution, one group lay in open area, and the other lay in closed area. One years later, we measured fresh weight and calculated the growth rate.

RESULTS

The Field Census

Fig. 4 showed the distribution of now and two decade ago [4]. The distribution of the present time is very different from 20 years ago. Half of the populations disappeared, and we can find out new populations in the different area.

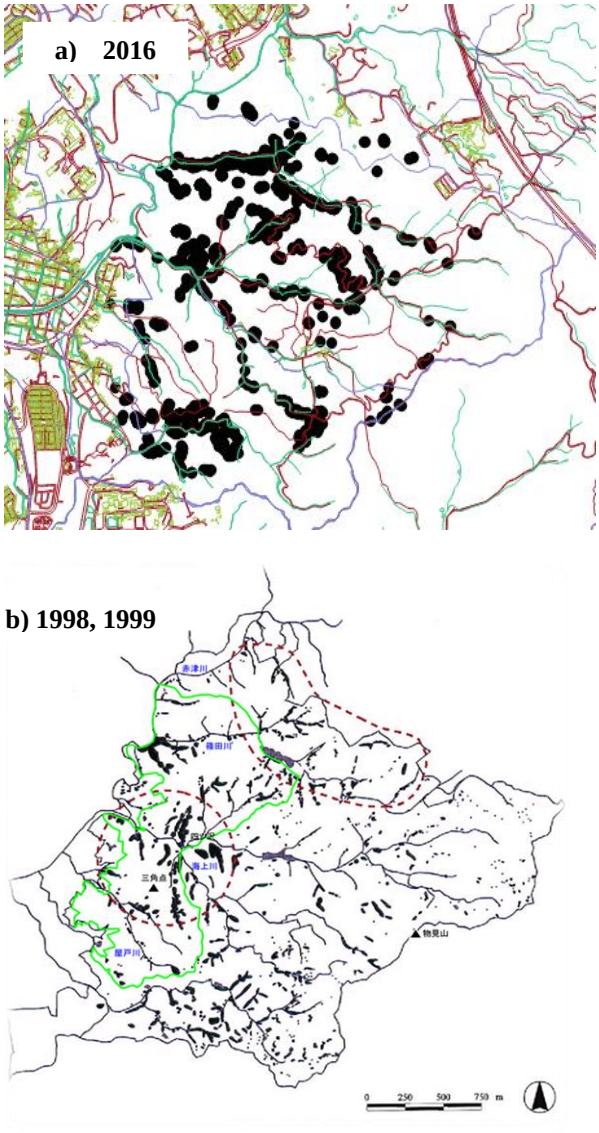

Fig. 4 The distribution of *A. rigescens* var. *brachypodion*, a) in 2016 and b) from 1998 to 1999.

Fig. 5 showed the size distribution between shinning area and controlled area from 2016 to 2018. In the shinning area, we can find out the increase of $S_{index,}$ especially from autumn to summer. There was a difference between the growth of shining area and that of the control area. From the Steel Dwass test of each season distribution 15 pairwise within each area, there were 8 significant differences ($p<0.05$) observed in shining area, but in control area there were 3 significant difference observed. The growth rate of shining area was superior to that of control area. We also found out the difference between the variance. The variance of the sinning area was largerer than that of the control area.

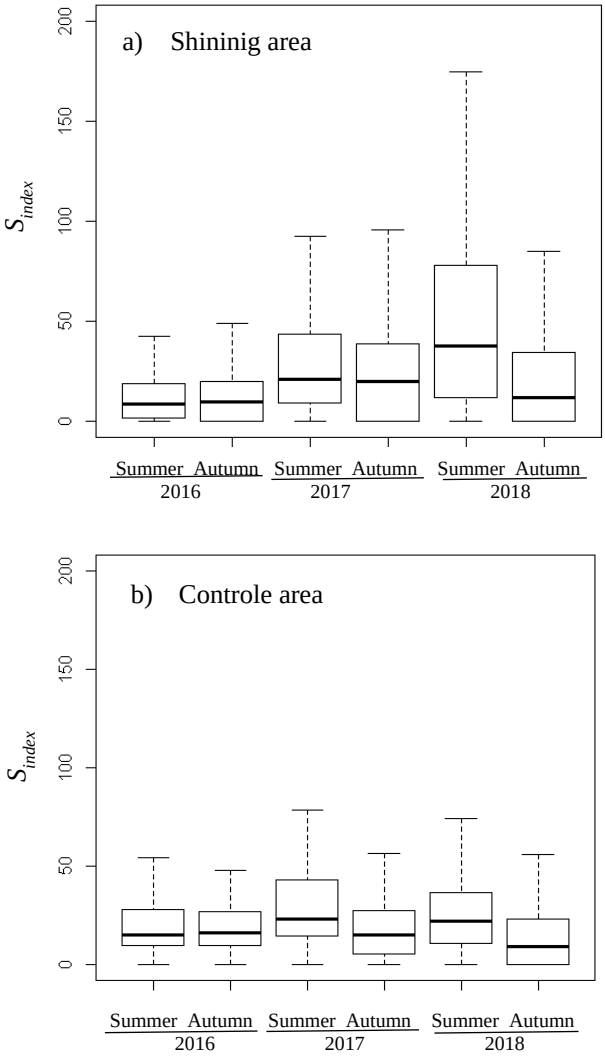

Fig. 5 The S_{index} distribution of *A. rigescens* var. *brachypodion*, from summer in 2016 to autumn in 2018. a) shinning area, b) controle area.

Fig. 6 showed the relationship between light condition (open sky percentage) and the growth rate (increase percentage of S_{index}) from summer in 2016 to summer in 2018. Remarkably growth rate was observed in 40% to 50% open sky percentage condition.

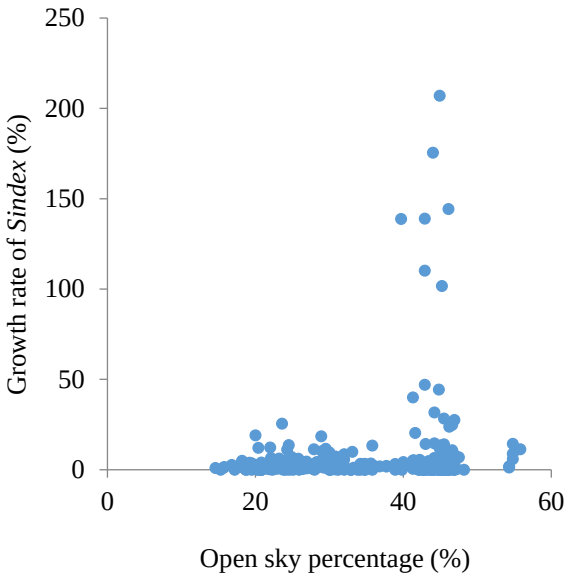

Fig. 6 The relationship between light condition and growth rate of S_{index} of each individual.

The amount of flower from 2016 and 2018 in spring showed in Fig.7. Amount of the nectar was increasing after shining. The histogram skewed to right. The number of the increased nectar quadrats was larger than that of decreased quadrats.

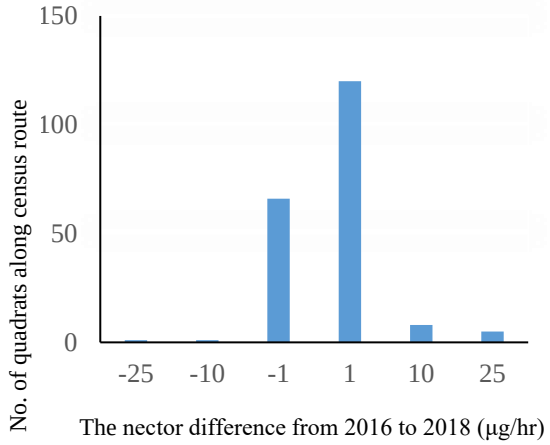

Fig. 7 The difference of nectar at each quadrat along the route of phenology census from 2016 to 2018.

The growth amount at open environmental condition and closed condition showed in Fig. 8. From the Wilcoxon test, the growth rate of open condition was superior to that of closed condition ($p<0.05$). And we could observe the variance difference between the two condition.

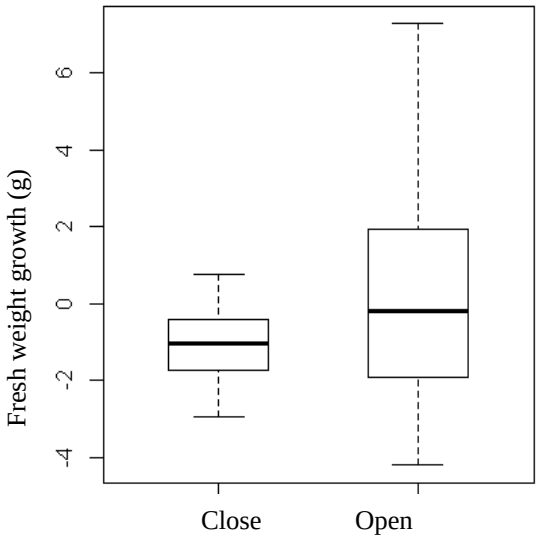

Fig. 8 The growth amount in closed by cheese cloth and open for one year.

DISCUSSIONS

IUCN (International Union for Conservation of Nature) has developed a system of classifying protected areas that ranges from minimal (nature reserves, national parks, etc.) to intensive use of the habitat by humans, with six categories [8]. There strict nature reserves and wildness areas have the high quality of biodiversity. So almost people believe that the untouchable nature is very precious. Nature should be leave as they are. That is a true because the development destroys the biodiversity. But recently the role of moderate disturbance regard as important.

Jacobson et al. (1991) reported the human moderate disturbance reverse the vegetation succession and formed the valuable biodiversity [9]. The mechanism of disturbances were reported many other researchers [10][11]. These researches were about wetlands and grasslands where affected vegetation succession seriously. Stop the succession is very important for the special vegetation. In the forest, people think that biodiversity of forest will be increasing along succession. Because there were many kinds of species that likes closed, humidity and nourishment condition can live under the condition, so the disturbances destroy such a condition and shade species.

The data of the biodiversity was investigated because of the 2005 World Exposition, Aichi, Japan, Nature's Wisdom. After 18 years passed some nature conservation association reported the decrease of biodiversity, especially *L. japonica*. The cause of butterfly decrease was undetected. Every conservationist insisted the conservation area closed and no one affect the biodiversity.

In order to realize the cause of butterfly decrease,

the resource condition of both larva and adult were investigated. The distribution of larva food plant, *A. rigescens* var. *brachypodion* was changed from 18 years ago. The center of distribution moved to the area of Japanese oak die. It was suggested that the light condition is darker and darker, the growth condition is worse and worse. *A. rigescens* var. *bracypodion* is a famous of forest floor plant, but almost individuals have a few leaves only. It is not sufficient to serve larva, because it is needed at least 3 leaves to nurse the butterfly. The difference about the condition of the forest is disturbance. 20 years ago, the forest supply as fuel, building materials and food to near agriculture village people. Utilization by people can make the oligotrophic and intolerant tree forest.

In fact, the growth rate of the species accelerates by shining, and growth experiment showed the light condition is very important for the species. Each light condition in the field, the 40-50% open sky conditions are very good condition for the growth. By the experiment the light condition is very important of the forest floor plant. But there is large variance observed in shining, it is showed the open light condition is very strict condition, some individuals can grow up, but the other cannot grow up. The severe natural selection occurred in open condition, especially more than 50% open sky. Perhaps drying and strong light inhibition prevent the growth.

The shining brought another effect of the mount of reward to the adult butterfly. The increase amount of reward is not so much, but the light condition brought a good condition for photosynthesis and rhododendron (short tree) and viola (herb) can produce many flowers than before. The condition will be good for the butterfly and other insects.

From the experiment, the cause of the butterfly decrease is succession of the forest. Shinning is very important of the management for biodiversity. But there is problems in the management. How much may we cut down in order to maintain biodiversity? The best condition for *A. rigescens* var. *bracypodion* is 40 to 50% open sky. But it is very difficult to cut down such a condition, and it is very difficult to maintain the condition because of vegetation succession.

The management plans are needed to maintain the biodiversity. Succession is always progress, the zoning is needed to shining. Every 10 years interval each zone should be cut off. The first year 1/10 forest part cut, and the second year the next section of forest cut of, the third year and so on. The moderate disturbance management is very difficult, but the succession will repair the over shining condition.

CONCLUSIONS

We get four main conclutions.

1) The forest thinning is important for the iconic butterfly habitat, increasing the flowering of other plants and securing nutrients for many insect species.
2) The distribution of *A. rigescens* var. *brachypodion* greatly changed for 18 years.
3) The growth rate of *A. rigescens* var. *brachypodion* that is forest floor plant, is larger in shining area than that in closed area.
4) In light control experiment, growth of *A. rigescens* var. *brachypodion* in open area was accelerate than in closed area.
5) The shinning increased the flower nectar amount in spring.

From these conclusions, it is suggested that t the cause of the decline of *L. japonica* is the decline of larval food plant and adult food plant.

Based on the conclusions, two proposals about the conservation activities

1) Human disturbance is very important to maintain the biodiversity at the mountain named ‘Satoyama’ near the agriculture field because of the light condition maintenance.
2) The conservation activities should be done by shining or felling instead of untouchable nature conservation.

We should remake the zoning of Kaisho no mori for maintain the biodiversity return to the 20 years ago.

ACKNOWLEDGMENTS

We wish to thank the members of Kaisho no mori Conservation Association for research support and section of environment at Aichi Prefecture Government for permission to work in the conserved area. We also thank Mr. Kamio and the members of our laboratory for their assistance in the field works.

REFERENCES

[1] Tsuboi T., The 2005 World Exposition, Aichi, Japan. The Journal of the Institute of Electrical Installation Engineers of Japan, Vol. 25, Issue 3, 2005, pp. 173-174.
[2] Hatta K., and Hiroki S., The conservation of Luehdorfia japonica which becomes an index of the Satoyama ecosystem. Lepidoptera Secience, Vol 58, Issue 2, 2007, pp. 145-156.
[3] Aichi Prefecture, Conservation management plan of Kaisho-no-mori 2025, Aichi Prefecture, 2016, pp. 17-29.
[4] Aichi Prefecture, Conservation Plan of Leuhdorfia japonica in Kaisho-no-mori, Aichi Prefecture, 2016, pp. 1-36.
[5] Ishii M., Conservation of Satoyama in Ecological Aspect. Kodansha Publisher, Tokyo, 2005, pp. 1-20.
[6] Koizumi T., Phytogeographical study on the

distribution of 3 species of Asarum in Tama region of Tokyo district from the development of landform. Gakugei Geography, Vol. 73, Issue 1, 2017, pp. 3-15.

[7] Ueda K., Phytogeography of Tokai Hilly Land Element: I. Definition. Acta Phytotaxonomica et Geobotanica, Vol. 40, Issue 5-6, 1989, pp. 190-202.

[8] Primack R.B., Essentials of Conservation Biology 4th ed. Sinauer Associate, Inc. Sunderland, 2010, pp. 341-366.

[9] Jacobson G.L.Jr., Almquist-Jacobson H. and Winne J.C., Conservation of rate plant habitat: Insights from the recent history of vegetation and fire at Crystal Fen, northern Marine USA. Biology Conservation, Vol. 57, Issue 3, 1991, pp. 287-314.

[10] Yuan S.Y., Jiao F., Li Y.H. and Kallenbach R.L., Anthropogenic disturbance are key to maintaining the biodiversity of grassland. Scientific Reports, Vol. 6, Article number: 22132, 2016.

[11] Hughes A.R., Byrnes J.E., Kimbro D.L. and Stachowicz J.J., Rreciprocal relationships and potential feedback between biodiversity and disturbance. Ecology Letters, Vol. 10, Issue 9, 2007, pp. 849-862.

9th Int. Conf. on Geotechnique, Construction Materials and Environment, Tokyo, Japan, 20-22 November 2019, ISBN: 978-4-909106025 C3051

GROUNDWATER VULNERABILITY OF THAILAND'S LOWER CHAO PHRAYA BASIN

Pinit Tanachaichoksirikun[1], Uma Seeboonruang[2] and Graham E. Fogg[3]
[1] Ph.D. Student, Department of Civil Engineering, Faculty of Engineering, King Mongkut's Institute of Technology Ladkrabang, Thailand;
[2] Associate Professor, Department of Civil Engineering, Faculty of Engineering, King Mongkut's Institute of Technology Ladkrabang, Thailand;
[3] Professor, Department of Land, Air and Water Resources, Faculty of Hydrology, University of California, United State of America

ABSTRACT

Since global warming effects water resources, especially, surface water sources, groundwater is an essential water source, when facing the critical drought, because groundwater in less sensitive than surface water. However, groundwater response is delayed in some area. Thus, groundwater vulnerability is a tool to identify critical areas for maintaining water quantity and quality. The Fuzzy-Catastrophe-based DRASTIC model, drought persistence and several climate scenarios were combined to estimate the vulnerability on the confined aquifers of Thailand's Lower Chao Phraya basin. Thus, critical areas that may face groundwater shortage were identified. Our analysis predicted that most of basin would have few effects on climate change. However, vulnerability maps showed that 5% of the basin may be critical areas that may show groundwater shortage, especially, drought persistent areas with low rainfall. Generated maps identify 'hotspots' and can help decisions on groundwater development and economic growth and aid planning policy.

Keywords: DRASTIC, Climate change, Groundwater vulnerability, Groundwater resource, Groundwater resources planning

INTRODUCTION

Groundwater is a very important natural resource and can be a second source of water supply, when facing critical droughts or limited accessible surface water, since surface water is more sensitive than groundwater to climate fluctuation. So, groundwater is an important water source because groundwater response is delayed relative to climate changes on the surface water (Seeboonruang, 2014) [1]. Decrease in surface water level contributes significantly to the groundwater decline. Although groundwater is a renewable resource, much groundwater cannot be renewed in the human life spans (Foster and Chilton, 2004) [2]. Then, groundwater will become a limited resource and must be conserved.

Hydrological systems and water resources affect the global climate change, such as flood, drought and seawater intrusion. They are very significant in the tropical climate, especially, groundwater vulnerability and sustainability (Chris et al., 2012 [3]; Green et al., 2011 [4]; Taylor and Callist, 2012 [5]; White and Tony, 2012 [6]). Thailand is in the tropical zone. Then, groundwater resource in Thailand will face these problems. The linkage between groundwater and climate change is inherently complicated. Therefore, these are the need to study the impact of climate on groundwater quickly, before it becomes exhausted.

The effect of drought on water resources has been studied by Wongsa (2015) [7]; Rangsiwanichpong et al. (2016) [8] and several others. Tanachaichoksirikun et al. (2018) reported that groundwater affected the climate change: especially, in Thailand's Lower Chao Phraya (LCP) basin, groundwater is still sustainable but shortage may be faced in some aquifers [9].

The DRASTIC framework consists of seven indices i.e. depth to water table (D), net recharge (R), aquifer media (A), soil media (S), topography or slope (T), impact of the vadose zone (I) and hydraulic conductivity (C). These factors were assigned by ratings and weighting by Aller (1987) [10]. The model succeeded in predicting groundwater quality in unconfined aquifers (Huan et al., 2012 [11]; Ouedraogo et al., 2016 [12]; Shrestha et al., 2016 [13]). Seeboonruang (2016) modified DRASTIC to show that the groundwater vulnerability affected climate change in the unconfined aquifers [14]. However, the DRASTIC model has disadvantages,

because the regional characteristics vary the appropriate weightings and ratings (Sadat-Noori and Ebrahimi, 2016) [15]. So, the DRASTIC framework was modified to the Fuzzy-Catastrophe DRASTIC Framework (FCF) for confined aquifers by Nadiri (2017) [16] and Nadiri (2018) [17]. However, the modified DRASTIC has not been used to determine climate change impact on groundwater vulnerability.

Therefore, we investigated the impact of climate change on the groundwater vulnerability, by combining climate change, history of drought persistent and FCF, to investigate critical areas that affect the climate change. This is the first time, FCF has been used to evaluate the challenge of confined aquifers: it was applied to the LCP basin, because it is a confined aquifer, that was affected by climate change (Tanachaichoksirikun et al., 2018) [9].

STUDY AREA

Thailand's LCP basin locates in the central plain; it covers ~41,300 km^2, which covers Bangkok, the capital city, and 21 provinces. Groundwater flows from the north to south. The Tenasserim Hills are located in the north and west and there are small hills in the east, while the south connects to the Gulf of Thailand. The northeast connects to the Upper Chao Phraya basin - see Fig. 1. The hydrogeology is Tertiary-Quaternary formation that the depositions are coastal and fluvial deposits (Piancharoen, 1977 [18]; Piancharoen and Chuamthaisong, 1978 [19]). The aquifers consists mainly of sands, gravels and clay lenses, that can be divided into eight confined aquifers - the Bangkok (BK), Phra Pradaeng (PD), Nakorn Luang (NL), Nonthaburi (NB), Sam Khok (SK), Phayathai (PT), Thonburi (TB), and Pak Nam (PN) aquifers (Seeboonruang, 2014 [1] and Tanachaichoksirikun et al., 2018 [9]).

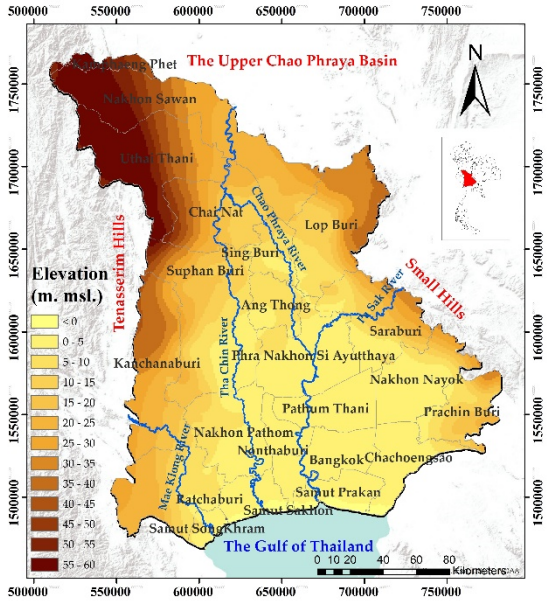

Fig. 1 Lower Chao Phraya basin, Thailand

DATA AND METHOD

Climate and rainfall

Climate records from LCP monitoring stations indicated that the average annual temperature has increased from 27.1°C (1983-1998) to 27.4°C (1999-2014) and the maximum temperature is nearly 40.6°C in April, while the minimum temperature is ~12.7°C in December. In addition, the average annual rainfall had increased from 1,191 mm (1983-1998) to 1,208 mm (1999-2014) and the maximum monthly rainfall is ~348 mm in September, the minimum rainfall is ~11 mm in December and the average monthly rainfall is 83-139 mm.

Wattanasetpong (2015) predicted the future climate in the LCP basin based on 30 years weather records and several other criteria [20]. Future climates were separated into the 'near' future predictions for 2020-2049 and 'far' predictions for 2050-2099. We preferred the IPSL-CM5A-MR climate model, from the Coupled Model International research group (CMIP5) from the Institute Pierre Simon Laplace, which offers the minimum bias and root mean square error on past data for the annual precipitation in the Chao Phraya watershed which closely covers the LCP basin (Ruangrassamee, 2015) [21].

Representative Concentration Pathway (RCP) is a map of greenhouse gas concentration (not emissions) trajectory in the fifth Assessment Report (AR5) 2014 (IPPC, 2014) [22]. We selected three pathways for climate modeling, which could be considered, depending on the quantity of greenhouse gases emitted in 2100. Three RCPs - RCP2.6, RCP4.5 and RCP8.5, which cover the range of likely future radiative forcing values, were selected.

Climate exposure

Climate exposure is an index level for the fluctuation of rainfall between past and future (Fig. 2a and 2b). The south boundary produces the local increase in rainfall. The maximum increase in rainfall occurs near the Gulf of Thailand ~10% (RCP8.5) and the minimum increase in rainfall occurs near the Tenasserim Hills ~6% (RCP2.6). We classified the climate exposure into four classes (ΔR^0, ΔR^{1+}, ΔR^{2+} and ΔR^{3+}) as shown in Table 1. The worrisome factor is rainfall increase because it contributed to flood. Therefore, the basin may show groundwater vulnerability from future rainfall which will affect climate change.

Drought persistence

Drought persistence is the historical report and frequency of droughts. It was monitored and calculated by several factors of Thailand Land Development Department (LDD). Drought persistence was divided into four classes, 0, <3, 4-5

and >6 times/10 years as shown in Table 1 and Fig. 2c. Drought persistence highlighted the adaptation of groundwater management. In this basin, droughts occurred near the boundary, but the central area remains fertile.

Impact of climate change

Droughts contributed to change in climate change index (Fig. 2d), that divided into six classes, as shown in Table 1. When an area did not have enough rainfall and a high frequency of droughts, it had a high impact of the climate change on that area, but if the area had high rainfall and no drought, the area had no impact on climate change.

Table 1 Impact of climate change index

Climate exposure	Drought persistence (times/10years)			
	0	≤ 3	4-5	> 6
$\Delta R^{3+} > 3.36\%$	I^{2+}	I^{+}	I^{0}	I^{-}
$1.68\% < \Delta R^{2+} \leq 3.36\%$	I^{+}	I^{0}	I^{-}	I^{2-}
$0.36\% < \Delta R^{1+} \leq 1.68\%$	I^{0}	I^{-}	I^{2-}	I^{3-}
$-1.68\% < \Delta R^{0} \leq 0.36\%$	I^{-}	I^{2-}	I^{3-}	I^{4-}

Note: I^{2+} = best, I^{+} = good, I^{0} = no impact, I^{-} = low impact, I^{2-} = moderate impact, I^{3-} = high impact, I^{4-} = very high impact

Fuzzy Catastrophe DRASTIC Framework

DRASTIC was designed by the US Environmental Protection Agency (Aller et al., 1987) [10]: it is a method that describes the allowable pollution potential hydrogeologic setting. The system has two major steps: (a) is the hydrogeologic settings map design, and (b) overlaying the relative rating system. DRASTIC uses seven parameters to classify the pollution potential of an aquifer. The sensitivity index of our study modified weightings and ratings for FCF by Nadiri et al. (2017) [16] and Nadiri et al. (2018) [17] shown in Table 3.

The DRASTIC index (D_i) was analyzed:

$$D_i = D_r D_w + R_r R_w + A_r A_w + T_r T_w + I_r I_w + C_r C_w \quad (1)$$

where D_i = DRASTIC index for a mapping unit, r = rating, w = weighting factor for D, R, A, S, T, I, C.

Depth to water (D) = depth from ground surface to the top of the confining layer. If the groundwater aquifer is deep, water is harder to infiltrate.

Net recharge (R) = average monthly infiltration from the ground surface and becomes groundwater.

Aquifer media (A) = the porous media between bedrock and the confining layer. An aquifer, that has larger grain size or more openings, leads to higher permeability and lower attenuation capacity.

Soil media (S) = media between ground surface and unsaturated zone. Soil has a significant impact on the recharge that infiltrates the aquifer.

Topography (T) = slope of land surface. It makes recharge take longer to infiltrate.

Impact of vadose zone (I) = material above the water table below topsoil, which is clay in the confined aquifer. Hence, the impact of vadose zone was set to 1 due to the clay lenses.

Hydraulic conductivity (C) = ability of an aquifer to transmit water, controlling the rate at which groundwater will flow under a given hydraulic gradient.

Groundwater vulnerability

Groundwater vulnerability is a major problem because it is a key to groundwater management. The groundwater vulnerability was derived from the combination of FCF and the impact of climate change. The indicators used are shown in Table 2. The groundwater impact is critical, when the impact of climate change and the FCF is high, it implies the risk of change is very high. The degree of groundwater-climate change vulnerability can affect the groundwater management. In addition, in the red areas, identified as highly sensitive areas – high drought persistence, a slight increase in rainfall and high values of DRASTIC – are causes for concern (Fig. 4).

Table 2 Groundwater vulnerability indices

Drought exposure	DRASTIC index				
	33-41	42-49	50-57	58-65	66-73
I^{2+}	Ex	Vg	B	G	N
I^{+}	Vg	B	G	N	N
I^{0}	B	G	N	N	L
I^{-}	G	N	N	L	M
I^{2-}	N	N	L	M	H
I^{3-}	N	L	M	H	Eh

Note: Ex = excellent, Vg = very good, B = better, G = good, N = none, L = low, M = moderate, H = high, Eh = extremely high vulnerability

RESULTS AND DISCUSSTION

Future groundwater vulnerability

The future groundwater vulnerability map is represented in Fig. 4. The extreme risk values are shown in warms tone and change to better qualities are shown with cold tones. When the RCP 2.6 was used for 2020-2049 and 2050-2099, it shows highest vulnerability indices (5%) of the total area that the area may face future drought. Most of these areas are located near the boundary of basin, where lower rainfall rate recharged the groundwater and there was the history of drought. However, the RCP 8.5 model, for the same periods, shows the highest groundwater resilience, i.e. the groundwater would cause only small climate change: the high rainfall would recharge and there would be few droughts. However, in RCP 4.5, groundwater vulnerability was predicted for 2050-2099, because this period would have relatively high rainfall near the Gulf of Thailand but low rainfall near the Tenasserim hills.

The main reason of the greater vulnerability to impact of climate change in the central area is the area

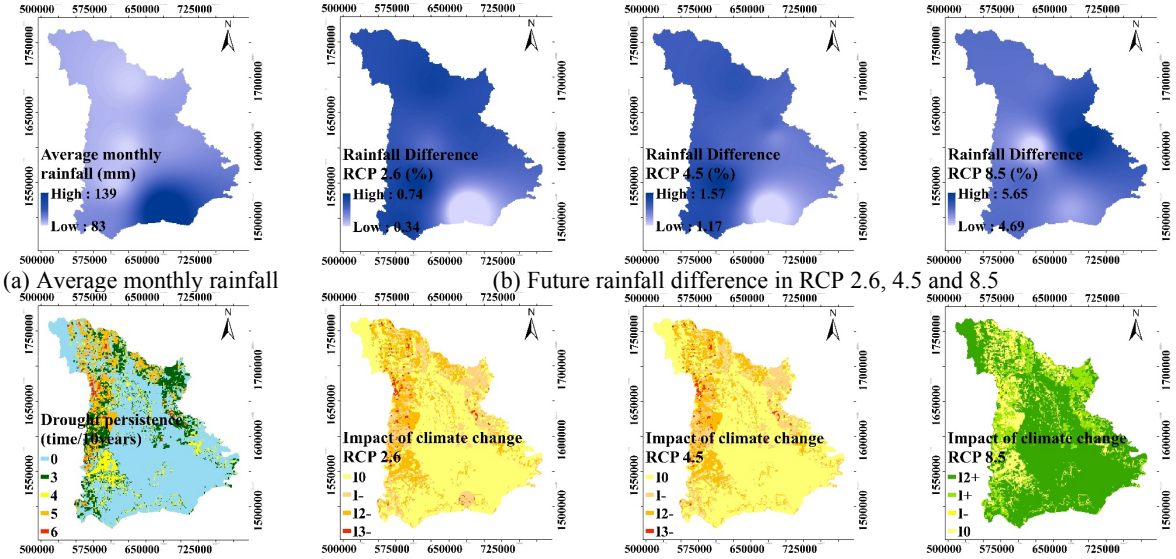

(a) Average monthly rainfall (b) Future rainfall difference in RCP 2.6, 4.5 and 8.5

(c) Drought persistence (d) Impact of climate change in RCP 2.6, 4.5 and 8.5

Fig. 2 Impact of climate change index

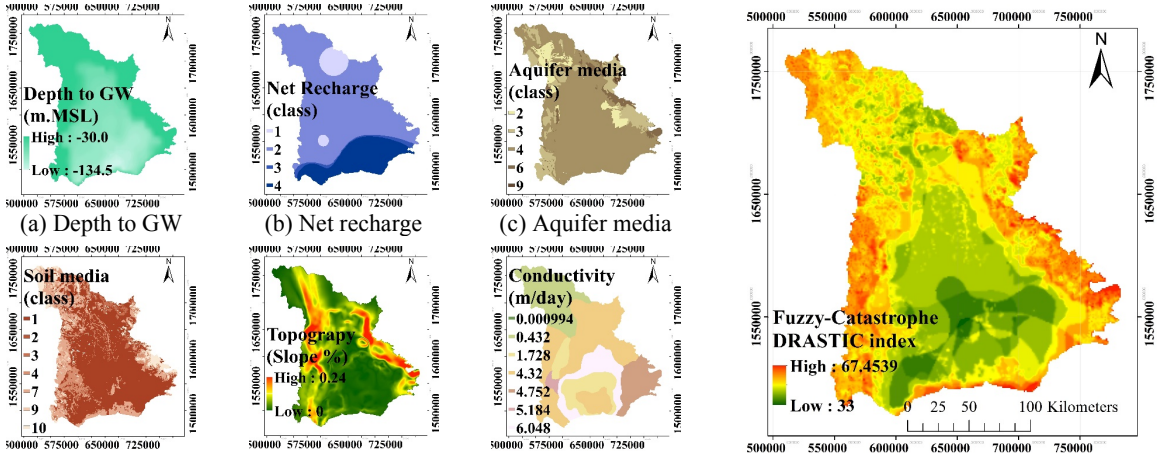

(a) Depth to GW (b) Net recharge (c) Aquifer media

(d) Soil media (e) Topography (f) Conductivity (g) Fuzzy-Catastrophe DRASTIC index

Fig. 3 Combining Fuzzy-Catastrophe DRASTIC index

Table 3 Fuzzy Catastrophe DRASTIC index

DRASTIC parameter	Classification range			Mean	Normalized Value of mean	Catastrophe fuzzy membership function	Priority	Catastrophe Drastic Weight
Depth to groundwater (m)	-77.18	class 1	-49.82	-58.49	1.00	1.00	0.67	5
	-49.82	class 2	-37.42	-42.86	0.67	0.87		
	-37.42	class 3	-25.02	-30.95	0.42	0.80		
	-25.02	class 4	-12.62	-18.81	0.16	0.69		
	-12.62	class 5	-10.00	-11.03	0.00	0.00		
Recharge (mm/year)	7.12	class 1	8.24	8.11	0.00	0.00	0.63	4
	8.24	class 2	10.46	9.07	0.22	0.61		
	10.46	class 3	11.57	10.95	0.66	0.90		
	11.57	class 4	13.33	12.38	1.00	1.00		
Aquifer media (rate)	2	class 1	3	2.74	0.00	0.00	0.62	3
	3	class 2	4	3.81	0.31	0.67		
	4	class 3	6	4.12	0.40	0.79		
	6	class 4	9	6.23	1.00	1.00		
Soil media (rate)	1	class 1	2	1.10	0.00	0.00	0.69	6
	2	class 2	3	2.53	0.17	0.55		
	3	class 3	4	3.06	0.30	0.74		
	4	class 4	7	5.95	0.57	0.89		
	7	class 5	9	7.37	0.74	0.95		
	9	class 6	10	9.60	1.00	1.00		
Topography (percent)	0	class 1	2	0.04	-	-	1.00	7
Impact of vadose zone	0	class 1	1	1	-	-	0.00	1
Conductivity (m/day)	0.00	class 1	1.10	0.43	0.00	0.00	0.56	2
	1.10	class 2	4.00	1.73	0.30	0.67		
	4.00	class 3	12.00	4.73	1.00	1.00		

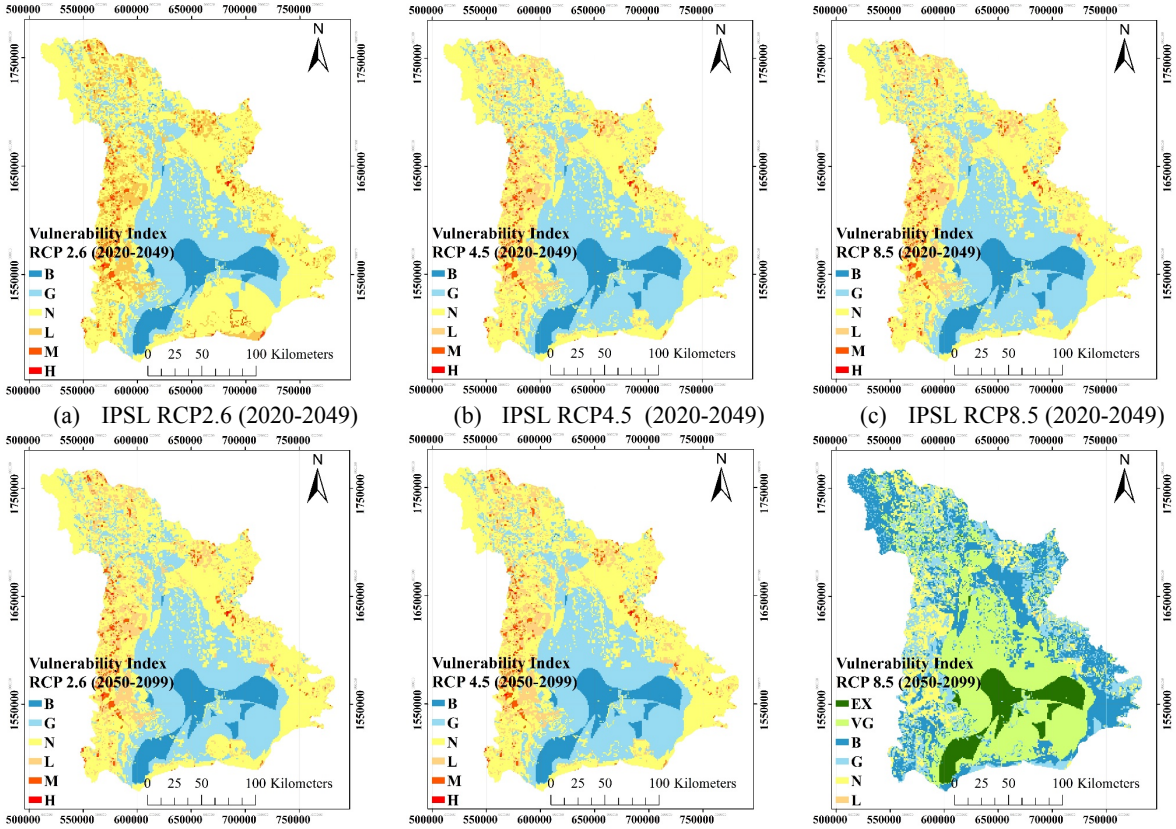

(a) IPSL RCP2.6 (2020-2049) (b) IPSL RCP4.5 (2020-2049) (c) IPSL RCP8.5 (2020-2049)

(d) IPSL RCP2.6 (2050-2099) (e) IPSL RCP4.5 (2050-2099) (f) IPSL RCP8.5 (2050-2099)

Fig. 4 Groundwater vulnerability maps of LCP basin, Thailand

is relatively flat and the soil media is clay lenses. Whereas, near the area with persistent drought, it has slight vulnerability because the rainfall is low.

CONCLUSION

We investigated the groundwater vulnerability under climate change in Thailand's Lower Chao Phraya (LCP) basin to aid decisions in groundwater management. We combined the Fuzzy Catastrophe DRASTIC Framework (FCF), climate scenarios, and drought persistence to consider groundwater characteristic, climate exposure and history of drought occurrence. The climate scenarios used in Representative Concentration Pathway (RCP) were 2.6, 4.5 and 8.5. The Geographic Information System technique was used to analyze the periods 2020-2049 and 2050-2099.

The critical areas in the LCP basin had 5% because that area has low rainfall, history of high drought frequency and high values of FCF. However, the groundwater vulnerability continuously decreased in all scenarios, because the rainfall increased, especially under the RCP 8.5 scenario. Although with RCP 2.6 was lower rainfall (but higher than the base case (1983-2014)), the groundwater vulnerability still resilient.

The climate change has lower impact on groundwater vulnerability in a confined aquifer when compared with the unconfined aquifers, because the FCF index shows that the low impact of the vadose zone value. However, the topography, soil media, and depth to groundwater are the most important factors in the LCP basin because they show the high FCF weight.

The impact of climate change was significantly affected on the drought persistence. However, we did not include future land use, which should probably be considered in an extension of this work.

We concluded the groundwater vulnerability in the Lower Chao Phraya basin has a little impact in RCP 2.6 scenario and no impact on the RCP 8.5 scenario, because it included increased rainfall.

At this stage, we did not consider human activities, e.g. land use and pumping, which can have more impact on the groundwater system. However, these will be considered in the future work.

ACKNOWLEDGMENTS

We thank the Thailand Research Fund through the Royal Golden Jubilee PhD Program, Grant No. PHD/0189/2556. Special thanks to the Thailand Land Development Department, Thailand Meteorological Department, and Thailand Department of Groundwater Resources for the data.

REFERENCES

[1] Seeboonruang U., An Empirical Decomposition of Deep Groundwater Time Series and Possible

Link to Climate Variability, Global NEST Journal, Vol. 16, Issue 1, 2014 pp. 87–103.
[2] Foster S. S. D., and Chilton P. J., Downstream of Downtown: Urban Wastewater as Groundwater Recharge, Hydrogeology Journal, Vol. 12, Issue 1, 2004, pp. 115–120.
[3] Chris M. H., Harm D., Diana M. A., and Dirk K., Groundwater Recharge and Storage Variability in Southern Mali, Climate Change Effects on Groundwater Resources: A Global Synthesis of Findings and Recommendations, Taylor and Francis Group, London, United Kingdom, 2012.
[4] Green T. R., Taniguchi M., Kooi H., Gurdak J. J., Allen D. M., Hiscock K. M., and Aureli A., Beneath the Surface of Global Change: Impacts of Climate Change on Groundwater, Journal of Hydrology, Vol. 405, Issue 3–4, 2011, pp. 532–560.
[5] Taylor R., and Callist T., The Impacts of Climate Change and Rapid Development on Weathered Crystalline Rock Aquifer Systems in the Humid Tropics of Sub-Saharan Africa: Evidence from South-western Uganda, Climate Change Effects on Groundwater Resources: A Global Synthesis of Findings and Recommendations, 2012, pp. 17–32.
[6] White I., and Tony F., Reducing Groundwater Vulnerability in Carbonate Island Countries in the Pacific, Climate Change Effects on Groundwater Resources: A Global Synthesis of Findings and Recommendations, 2012, pp. 75–110.
[7] Wongsa S., Impact of Climate Change on Water Resources Management in the Lower Chao Phraya Basin, Thailand, Journal of Geoscience and Environment Protection, Vol. 3, Issue 3, 2015, pp. 53–58.
[8] Rangsiwanichpong P., Kazama S., and Ekkawatpanit C., Assessment of Flood and Drought Using Ocean Indices in the Chao Phraya River Basin, Thailand, The 7th International Conference on Water Resources Engineering, in Proc. the 7th International Conference on Water Resources Engineering, 2016.
[9] Tanachaichoksirikun P., Seeboonruang U., and Saraphirom P., Impact of Climate Change on the Groundwater Sustainability in the Lower Chao Phraya Basin, Thailand," The 4th International Conference on Engineering, Applied Science and Technology, in Proc. the 4th International Conference on Engineering, Applied Science and Technology, 2018, pp. 119–122.
[10] Aller L., Bennett T., Lehr J. H., Petty R. J., and Hackett G., DRASTIC: A Standardized System for Evaluating Ground Water Pollution Potential Using Hydrogeologic Setting, 1987.
[11] Huan H., Wang J., Zhai Y., Xi B., Li J., and Li M., Quantitative Evaluation of Specific Vulnerability to Nitrate for Groundwater Resource Protection Based on Process-based Simulation Model, Science of the Total Environment, Vol. 550, 2016, pp. 768–784.
[12] Ouedraogo I., Defourny P., and Vanclooster M., Mapping the Groundwater Vulnerability for Pollution at the Pan African Scale, Science of the Total Environment, Vol. 544, 2016, pp. 939–953.
[13] Shrestha S., Semkuyu D. J., and Pandey V. P., Assessment of Groundwater Vulnerability and Risk to Pollution in Kathmandu Valley, Nepal, Science of the Total Environment, Vol. 556, 2016, pp. 23–35.
[14] Seeboonruang U., Impact Assessment of Climate Change on Groundwater and Vulnerability to Drought of Areas in Eastern Thailand, Environmental Earth Sciences, Vol. 75, Issue 1, 2016, pp. 1–13.
[15] Sadat-Noori M., and Ebrahimi K., Groundwater Vulnerability Assessment in Agricultural Areas Using a Modified DRASTIC Model, Environmental Monitoring and Assessment, Vol. 188, Issue 1, 2016, pp. 1–18.
[16] Nadiri A. A., Sedghi Z., Khatibi R., and Gharekhani M., Mapping Vulnerability of Multiple Aquifers Using Multiple Models and Fuzzy Logic to Objectively Derive Model Structures, Science of the Total Environment, Vol. 593–594, 2017, pp. 75–90.
[17] Nadiri A. A., Sedghi Z., Khatibi R., and Sadeghfam S., Mapping Specific Vulnerability of Multiple Confined and Unconfined Aquifers by Using Artificial Intelligence to Learn from Multiple DRASTIC Frameworks, Journal of Environmental Management, Vol. 227, 2018, pp. 415–428.
[18] Piancharoen C., Groundwater and Land Subsidence in Bangkok, Thailand, IAHS Publication, Issue 121, 1977, pp. 355–364.
[19] Piancharoen C. and Chuamthaisong C., Groundwater of Bangkok Metropolis, Thailand, IAH Memoire, Vol. 11, 1978, pp. 510–528.
[20] Wattanasetpong J., Charoenvaravut P., and Laosinwattana W., Downscaling Climate Models in Thailand by Artificial Neural Network Method, Thesis of Civil Engineering, King Mongkut's Institute of Technology Ladkrabang, Bangkok, Thailand, 2015.
[21] Ruangrassamee P., Khamkong A., and Chuenchum P., Assessment of Precipitation Simulations from CMIP5 Climate Models in Thailand, The 3rd EIT International Conference on Water Resources Engineering, in Proc. the 3rd EIT International Conference on Water Resources Engineering (ICWRE3), 2015.
[22] IPCC, Climate Change 2014: Synthesis Report. Contribution of Working Groups I, II and III to the fifth Assessment Report of the Intergovernmental Panel on Climate Change, 2014.

9thInt. Conf. onGeotechnique, Construction Materials andEnvironment, Tokyo, Japan,20-22 November 2019, ISBN: 978-4-909106025C3051

RESILIENCY OF A TWO-STOREY DEPEd STANDARD SCHOOL BUILDING USING THE REDi FRAMEWORK

Ray Anthony V. Ausan[1], Kyle Didacus V. Cabatit[2], Megan Angela S. Quiaem[3], and Richard M. De Jesus[4]
[1,2,3]Undergraduate Students, De La Salle University (Manila), Philippines;[4]Faculty, De La Salle University (Manila), Philippines

ABSTRACT

Public school buildings in the Philippines are built with a code-based design philosophy, wherein the life safety of the occupants is the sole performance objective. While the loss of life is the primary consideration for design, other losses such as cost of repair or replacement and service losses are to be expected after an earthquake. The 2017 Surigao Earthquake damaged 47 schools and caused a 10-day suspension of classes. Three years after the 2013 Bohol Earthquake, 279 classrooms from 696 schools are still under construction. A resilience-based design philosophy takes into consideration safety and other losses including recovery. To assess the resilience of a structure, a resilience-based seismic assessment methodology was adopted after the REDi Framework. Other tools utilized for the seismic assessment were the FEMA P-58, their accompanying software PACT, as well as SeismoStruct. It consists of the identification of losses in terms of cost and time, as well as the evaluation of proper building management and design practices. As a pilot study, a two-story four-classroom template designed by the Department of Education was assessed for seismic resilience. Numerical simulations and analysis showed that upgrade/retrofit must be done for both non-structural and structural components to comply with minimum resiliency requirement.

Keywords: Resilient buildings, School buildings, loss assessment, REDI rating

INTRODUCTION

The Philippines is a seismically active country due to its location along the Ring of Fire, or the Circum-Pacific belt. This Circum-Pacific belt is defined as a 40,000 kilometer-long zone of earthquakes, volcanic eruptions, and plate boundaries where the majority of the world's earthquakes occur [1]. Due to the frequency of earthquake occurrence within the Ring of Fire, structures in these countries must be built to withstand seismic activity. In Metro Manila, the looming threat of a high-magnitude earthquake named "The Big One" prompts the revisiting of seismic resistance of essential structures, most especially public school buildings, in the country. These public schools serve a dual purpose: the first and primary cause of operation is as centers of education for Filipino children and the second is as evacuation facilities during times of disaster [2].

In the event of an earthquake, the damaging or collapse of the school building will put the lives of youth at risk of injury or loss of life. Similarly, a collapsed school building will not be able to serve its second purpose as temporary shelters for victims of the disasters. Past instances wherein school buildings were affected by seismic activity include the 2013 earthquake located in Bohol wherein 696 schools were either damaged or destroyed and a student population of 270,000 individuals was affected [3].

Public school buildings in the Philippines follow the design philosophy of code-based design, wherein they designed based on the National Structural Code of the Philippines (NSCP). Adapting this design philosophy ensures that structure are life-safe when a certain magnitude earthquake occurs, though it does not ensure that the building suffers no damage nor will it remain operational after the seismic event, as per Section 208.1.1 of the NSCP [4]. The performance of a school after an earthquake is an essential aspect in its operation, and total collapse will render it unusable for an extended period of time. The Bohol Earthquake rendered 279 classrooms inoperational three years after the event [5].

Seismic resilience is defined as the ability for an organization or a community to recover from an earthquake [6]. The existing and prevalent design philosophy is the code-based design, which addresses the loss of life after an earthquake but fails to consider structural damage. Resilience-based design (RBD) takes additional factors into consideration to improve the seismic performance of a building. A key component in RBD assessment is the minimization of structural and non-structural damage during an earthquake. Such damage minimization increases occupant confidence in the structure as there is a level of unpredictability on the performance of the building as it reaches its limits.

Additionally, the goal of a prompt recovery after the occurrence of a disaster is greatly emphasized in the RBD philosophy. This parameter can be measured using the investigation of both the building performance and the building environment after the earthquake.

The REDi Rating System was developed by Arup to measure the level of resiliency of a structure by assigning a certain resilience rating, namely gold, silver, and platinum. Each resilience rating has certain criteria that a building needs to achieve under three resilient design and planning categories: organizational resilience, building resilience, and ambient resilience. Organizational resilience includes the assessment of factors beyond the structure itself, such as emergency evacuation systems and procedures and plans for utility disruption. Building resilience quantifies the performance of the building components during an earthquake event. Ambient resilience considers the environmental factors and other facilities that may impact the building in consideration. The final method of quantification is the criteria under evaluation, in the form of a loss assessment. This is done to determine the financial losses and the downtime of the structure in the event of an earthquake.

The resilience objectives for loss assessment can be seen in Table 1. Once all the criteria are met, the building qualifies for a resilience rating [7].

Table 1 REDi Baseline Resilience Objectives for Different Resilience Rating

Rating	Re-occupancy	Functional recovery	Direct financial loss	Occupant safety
Platinum	**Immediate**	**< 72 h**	**< 2.5%**	**Injuries Unlikely**
Gold	**Immediate**	**< 1 month**	**< 5%**	**Injuries Unlikely**
Silver	**< 6 months**	**< 6 months**	**< 10%**	**Injuries Possible**

This study aimed to perform an RBD assessment on a two-storey standard school building by the Department of Public Works and Highways (DPWH) and Department of Education (DEPEd).

Fig. 1 Two-Storey Standard School Perspective

METHODOLOGY

In order to determine the resiliency of the two-storey public school building, the following analyses procedure were used to determine the resilience rating.

Checklist

The REDi Rating System was used as the basis for the creation of the assessment tool used to determine the seismic resilience of the structure. The criteria taken under consideration to be adapted in the checklist were the silver-required, gold-required, and the platinum-required criteria from the REDi Framework.Within the checklist are the four resilience categories explained beforehand, namely: building resilience, ambient resilience, organizational resilience, and loss assessment. Each category is assessed differently and further elaborated below.

Direct Financial Loss Assessment

First, a loss assessment was conducted to assess whether the building will minimize injuries, repair costs, and repair times at the scenario expected earthquake. This was done by following the FEMA P-58 [8] procedure for the seismic assessment of buildings. The procedure comes with the accompanying software PACT, which can be used to estimate the earthquake losses.

First, basic building information were inputted into PACT. These include the number of stories, the total replacement cost, the core and shell replacement cost, the replacement time, floor areas per floor, and the max number of workers per square foot. The replacement cost was estimated to be around Php 11,250,000 as the typical project cost for the construction of a two-storey four classroom building is around Php 9,000,000. Additionally, according to the REDi, rating system, demolition costs could increase replacement costs by around 20-30%. Thus, an additional 25% of the project cost was added to the replacement cost, totaling at Php 11,250,000.

Then, the population of the building was modelled. The type of occupancy and population distribution per floor was inputted. As the classroom holds an estimated 40 people and each floor is around 2500 square feet, the number of occupants per 1000 square feet was set to 33.

Next, the component fragilities were determined. Since the building is a reinforced concrete building and a special moment resisting frame, the fragilities for concrete column and beam joints were selected. The closest possible size to the actual column dimensions (24” by 24”) was selected. For the non-structural components, a distribution panel was

selected. The panel was specified to have a capacity from 100 to 350 Amperes and not vibration isolated. For piping, the fragility for SDC D, E and F piping were selected.

Next, the performance groups were specified. Performance groups are the components of the building per floor that are subject to the same earthquake demands such as story drift, floor acceleration, and floor velocity. They can be directional or non-directional. The quantity of components per performance group was specified.

Next, structural analysis was conducted using the procedure for Intensity-Based Assessment as per FEMA P-58. The Simplified Analysis procedure (FEMA P-58 3.2.2) was used as the building is regular in plan and only two stories high. Through the procedure, the collapse fragility of the structure was determined. Also, the distribution of demands such as story drift, peak floor acceleration, peak floor velocity, and residual story drift were determined.

Next, PACT calculated the expected fatalities, repair costs, and repair time at the scenario expected level. The median number of fatalities and repair cost was compared to the baseline REDi objectives. The repair time needs further modification using the REDi Modified Downtime Methodology.

Static Pushover Analysis

First, the structure was modelled in the Building Modeler facility of SeismoStruct. The Building Modeler is a tool provided for easier visual modelling of the structure. A static pushover analysis with a uniform distribution of lateral loadswas used. The columns were laid out according to the plan. The beams were connected between columns. Slabs were added to the corresponding bound boxes. Longitudinal and transverse reinforcements of the elements were inputted. A project was made after exiting and saving the model.

Then, the project was setup for analysis. Project properties can be changed in the Pre-Processing Tab. Acceptance criteria based on Tables 10-7 and 10-8 of ASCE 41-17 were used for the performance criteria of the structure. SeismoStruct computes the yield chord rotation capacity automatically. A residual strength of 20% was used when chord rotation capacity was reached based on ASCE 41-17.

Next, the analysis was run in the Processing Tab. The results were seen in the Post-Processing Tab. The pushover curve graph and values were obtained from the Hysteric Curves under the Global Response Parameters.

For the pushover curve in the y-direction, project properties under loading phases and applied loads were changed to the y-direction. The same procedure for the y-direction will follow. For convergence and loading problems, the model was checked for errors.

User Defined Stair Fragility Curve

First, the staircase was modelled in the building Modeler facility of SeismoStruct. An Incremental Dynamic Analysis (IDA) was used. Ten earthquake records were matched to the response spectrum of the school using SeismoMatch. The records were incremented by 0.1 Peak Ground Acceleration(PGA). The results yielded IDA curves with a damage measure of maximum inter-storey drift ratio and an intensity measure of PGA. The drift ratio at the threshold of structural damage is based on FEMA Hazus MR4. The mean of the lognormal cumulative distribution was obtained from the average of the natural logarithm of the PGA at the drift ratio threshold for the ten records. The standard deviation was obtained from natural logarithm of the PGA at the drift ratio threshold for the ten records.

Downtime Assessment

First, repair times and damage states were extracted from the analysis from PACT. The median repair time for each component accordingfloor from the maximum direction on all realizations was calculated. The average damage state for each component according to floor from the sum of both directions on all realizations was calculated.

Then, repair classes for each component were assigned based on the average damage state. Repair classes for structural and non-structural components for each corresponding damage state were provided by the Framework. A desired probability of non-exceedance was selected. The median probability of non-exceedance was advised.

Next, downtime due to repairs was considered. The number of workers was computed based on building area and damage units corresponding to the repair sequence. Repair time at each floor was then computed based on the worker days required for each repair sequence at each floor and the number of workers. A repair schedule that considered the series of work according to floor and number of workers was made.

Then, downtime due to delays was considered. Impeding curves, median and dispersion values of delay based on building characteristics were provided by the Framework. The probability of non-exceedance was used in determining the delay times. Delays caused by post-earthquake inspection were based on building importance. Delays caused by engineering mobilization were based on the maximum structural repair class and the engineer on contract. Delays caused by financing were based on the type of financing availed. Delays caused by contractor mobilization were based on the maximum repair class, number of stories, and building

importance. Delays caused by permitting were based on maximum repair class. The highest delay of post-earthquake inspection & financing, post-earthquake inspection, engineering review & permitting, and post-earthquake inspection & contractor mobilization was selected.

Then, downtime due to utility disruption was considered. Utility disruption curves for electrical, water, and natural gas systems were provided by the Framework. The probability of non-exceedance was used in determining the delay times. Delays due to natural gas and water system disruption were based on repair rate. Repair rate was calculated based on the peak ground velocity.

Full recovery is required for repairs with repair class 1. Functional recovery is required for repairs with repair class 2. Reoccupancy is required for repairs with repair class 3. Reoccupancy downtime is the sum of downtime due to repairs and delays. Full and Functional downtime is the sum of downtime due to repairs, delays, and utility disruption.

Seismic Resilience

The checklist was evaluated for whether the building is resilient or not. The final output was the rating of the structure as either platinum, gold, silver or not resilient. In order for the building to be considered as seismically resilient, it should be able to fulfill all of the silver-required criteria. If all silver-required criteria were met, then the next resilience tier is taken into consideration. If it did not fulfill even one of the silver-required criteria, it was not considered to be resilient and retrofitting was done in the form of adding CFRP wrapping. Only the detailed analysis will be repeated for the modeled retrofitted structure. In the case that the building was not seismically resilient, the researchers outlined the suggested plans and retrofitting methods in order to make the structure resilient.

DATA AND ANALYSIS

Fig.2 shows the derived fragility curve of the reinforced stairs. The demand parameter chosen was peak ground acceleration. The damage states based on drift were matched to the qualitative description from the fragility library. The median of the three curves are 0.072, 0.228, and 0.457. The dispersion of the three curves are 0.250, 0.250, and 0.249.

Fig. 3 shows the derived collapse fragility curve of the structure. The demand parameter required by PACT was spectral acceleration. The median collapse is 0.6. The dispersion is 1.7.

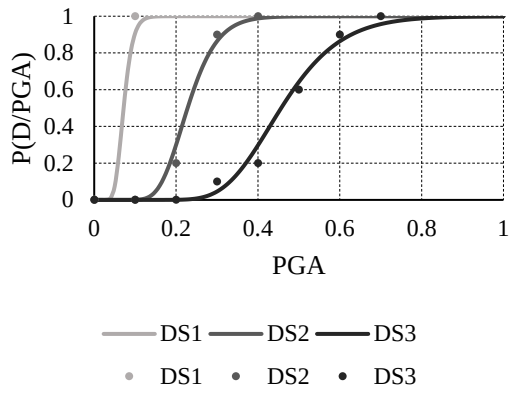

Fig. 2 User Defined Stair Fragility

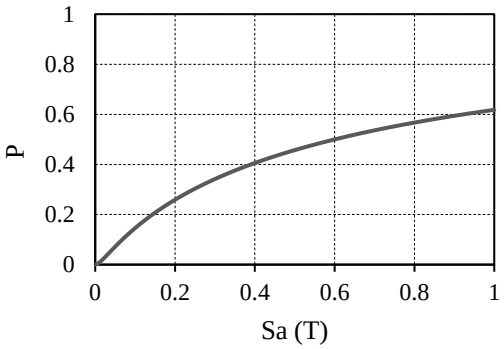

Fig. 3 Simplified Procedure Collapse Fragility

The probability of non-exceedance of the repair cost against the repair cost is presented in Fig.4. The abscissa presents the probability at which the total repair cost is less than or equal to the total replacement cost of the structure at total collapse. The median value of repair cost is taken to be equal to USD 218,360.00. The repair cost is almost equal to the replacement cost of USD 218,998.00. This puts direct financial loss at 99.7%. REDi suggests replacement for a structure with a direct financial loss greater than 40%.

The median values for repair cost indicate that the structure is not resilient in terms of direct financial loss.

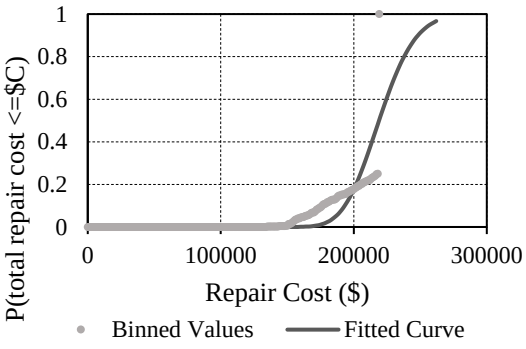

Fig. 4 Repair Cost

Fig. 5 determines the probability of non-exceedance of total fatalities against the number of deaths that occurred after the earthquake was simulated. The median value of deaths is taken to be equal to 0.

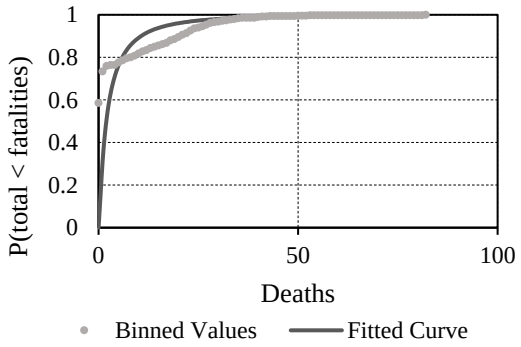

Fig. 5 Deaths

In Fig. 6, the probability of non-exceedance of total number of injured individuals versus the number of injuries is also presented. The plot provides a median value of 0.

The median values for deaths and injuries indicate that the structure is resilient in terms of occupant safety.

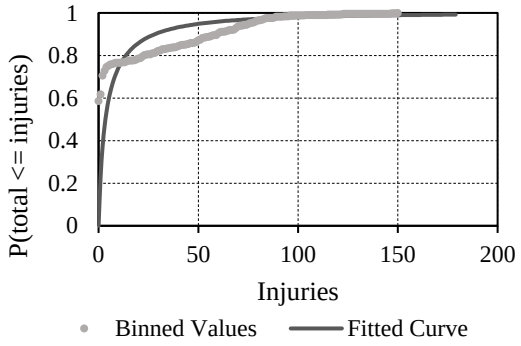

Fig. 6 Injuries

Fig. 7 illustrates the repair sequence of the structure. The structural repairsequence is first considered before other sequences. The interior and stair sequence occur simultaneously. The per floor sequences occur consecutively.Using modified repair time, the total delay due to repairs is 31.13 days.

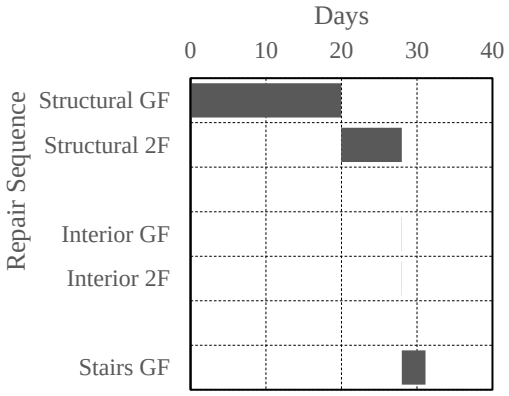

Fig. 7 Modified Repair Time

Fig. 8 shows the Reoccupancy, and Functional Recovery. All components to be repaired was of repair class 3. No component to be repaired was of repair classes 2 or 1. The Reoccupancy and Functional Recovery are the same. It would take 442.13 days for the Reoccupancy and Functional Recovery of the structure.

The median values for Reoccupancy and Functional Recovery for a year and two months indicate that the structure is not resilient in terms of recovery

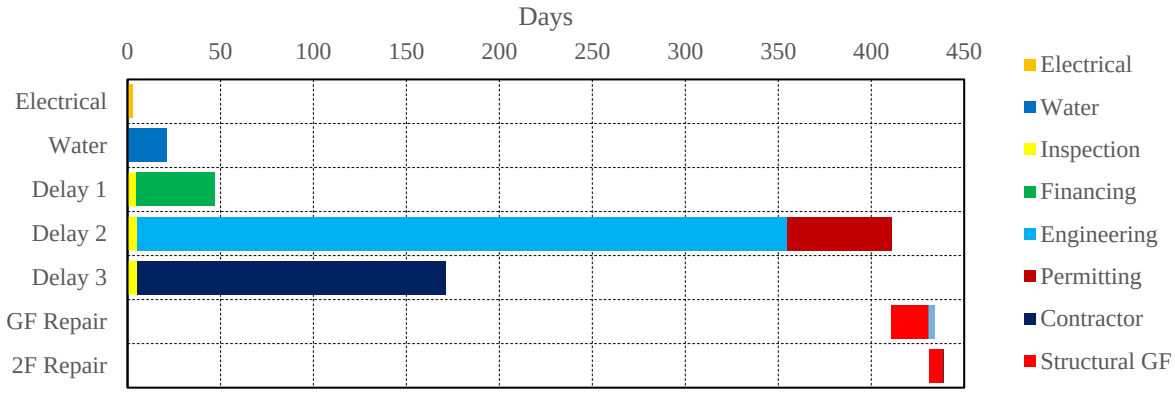

Fig 8. Total Downtime Timeline

CONCLUSIONS

In conclusion, the two-storey four classroom DPWH standard school building is not resilient based on the REDi Framework as it failed to comply with all of the silver-required criteria.

ACKNOWLEDGMENTS

The researchers wish to acknowledge their institution, De La Salle University, for their continuous support in providing the necessary tools for the preparation and execution of this research. They are also grateful to Seismosoft for sharing a student license of their software, SeismoStruct.

REFERENCES

[1] Rafferty, J. P. (2011). Ring of Fire. Retrieved from https://www.britannica.com/place/Ring-of-Fire

[2] Ilumin, R. C., & Oreta, A. W. (2018). A Post-Disaster Functional Asset Value Index for School Buildings. Procedia Engineering, 212, 230-237. doi:10.1016/j.proeng.2018.01.030

[3] UNICEF (2014, January 20). Philippines Humanitarian Situation Report (Rep.). Retrieved https://www.unicef.org/appeals/files/UNICEF_Philippines_Bohol_Earthquake_SitRep_22_January_2014.pdf

[4] ASEP. (2015). National Structural Code of the Philippines (7th ed., Vol. 1). Quezon City: ASEP.

[5] Vestil, J. K. (2016, October 17). 279 classrooms still being built in Bohol, 3 years after quake. Retrieved from https://www.sunstar.com.ph/article/104495

[6] Almufti, I., & Willford, M. (2013). REDi Rating System. Retrieved from http://usrc.org/files/technicalresource/REDi_Final Version 1.0_October 2013.pdf

[7] Almufti, I., & Willford, M. (2014). THE REDi™ RATING SYSTEM: A FRAMEWORK TO IMPLEMENT RESILIENCE-BASED EARTHQUAKE DESIGN FOR NEW BUILDINGS. Retrieved from https://datacenterhub.org/resources/12400/download/10NCEE-001055.pdf

[8] Applied Technology Council. (2012). Seismic Performance Assessment of Buildings. FEMA, P58(1). Retrieved August 20, 2018 from https://www.fema.gov/media-library-data/1396495019848-0c9252aac91dd1854dc378feb9e69216/FEMAP-58_Volume1_508.pdf

9th Int. Conf. on Geotechnique, Construction Materials and Environment, Tokyo, Japan, 20-22 November 2019, ISBN: 978-4-909106025 C3051

BLACK CARBON IN PM2.5 AT ROADSIDE SITE IN BANGKOK, THAILAND

Pornsuda Phanukarn[1], Hatairattana Gariyavech[2] and Sopa Chinwetkitvanich[3,*]
[1,3] Faculty of Public Health, Mahidol University, Thailand;
[2]Department of Environmental Quality Promotion, Ministry of Natural Resources and Environment, Thailand

ABSTRACT

Traffic is typically a major source of air pollution in urban areas of developing countries. The exhaust emissions include gaseous substances and particulate matter, which PM2.5 (particulate matter less than 2.5 micrometers in aerodynamic diameter) is the majority. In urban areas, the composition of PM2.5 at roadside site dominated by the carbonaceous combustion component, the major constituent wherein was represented as black carbon (BC). This study aimed to investigate the diurnal concentrations of BC related to PM2.5 by using a seven-wavelength aethalometer. Study site was located near one of congested roads in Bangkok, Thailand. The correlation between traffic volumes and BC concentrations at roadside were also discussed. Results showed that the 24-h average BC concentrations of this site were in the range of 1.5 – 15 μg/m^3. The diurnal pattern of BC levels exhibited two peaks of BC concentrations occurring during 0500 to 0700 LST and 2100 to 2300 LST. The morning peak of BC evidently governed by traffic condition while the evening peak resulted from traffic associated with meteorological effect. In addition, the density of heavy-duty diesel vehicles (HDDVs) played an important role to the diurnal pattern of BC concentrations. Interestingly, the highest BC level from this study site was observed on Sunday, where the lowest was found on Monday and Friday. This involved with traffic volumes caused by particular activity around this study site.

Keywords: Black carbon, PM2.5, Heavy-duty diesel vehicle, Bangkok urban area, Air pollution.

INTRODUCTION

Black carbon (BC) is a major constituent of particulate matter (PM) in urban environments resulted from incomplete combustion processes of fossil fuels or burning of biomass and biofuels. BC plays an important role in climate change [1]. It has been estimated that the direct radiative forcing of BC aerosol is around 0.2 – 1 W/m^2, suggesting that BC is the second contributor to climate warming next to carbon dioxide [1], [2]. In addition, BC also causes harmful health effects, including several respiratory diseases and cardiovascular system [3], [4].

The rapid growth of industrialization and urbanization has created high levels of air pollution in Thailand, especially in urban areas. Vehicles and factories were stated to be major contribution to air pollution, particularly in Bangkok [5]. The Asian Development Bank [6] reported that the main source of inhalable particulate matter at roadside of Bangkok came from in-use diesel vehicles. Health risk assessments for Bangkok indicated that as much as a third of all heart disease deaths might be caused by air pollution, primarily from motor vehicles exhausts [7]. Likewise, several studies reported high levels of air pollutants, including PM and BC, at roadsides in Bangkok Metropolitan Region. The increasing severity of road transportation has the potential to greatly increase pollutant emissions, which also have the effect on health, economy and society. Nowadays, the routine automatic ambient air quality monitoring of roadside stations in Bangkok mainly focuses on parameters of NO_x, CO, O_3 and PM10, while PM2.5 was only an addition available in some monitoring stations. The measurements of BC, which are more health damaging, are not included in routine monitoring programs.

At present, BC concentrations in Thailand are only reported by researchers, and mostly related to biomass burning and its haze problem in Northern provinces of Thailand. Though BC observed in Bangkok area was noticeably traffic-related, the correlation between measured BC and traffic characteristics was not clearly stated. Thus, the purpose of this study was to investigate the diurnal concentrations of BC related to PM2.5 and traffic characteristics nearby roadside site in Bangkok area.

MATERIALS AND METHODOLOGY

Study area

Bangkok is the capital of Thailand, covering an area of 1569 km^2, and has a population of 6 million inhabitants [8]. In 2016–2017, there were about 9.4–9.8 million registered vehicles in Bangkok, including 65% gasoline vehicles and 25% diesel vehicles [9]. Samples of BC were collected at an automatic

continuous air quality monitoring station operated by Bangkok Metropolitan Administration (BMA), namely Ratchathewi station, situated at Ratchathewi District Office. This was a roadside station located at the west-northwest side of Phayathai Road (Fig.1), which was 5 meters away from the curbside of the road and approximately 150 meters from Phayathai Intersection. Phayathai Road is one of the main roads in the center of Bangkok with high traffic density and congestion in rush hours. This road is surrounded by several commercial buildings, hospitals and academic institutes. Moreover, there is the BTS Skytrain structure covering some part of this road, especially near this monitoring station. Black carbon sampling was conducted on the rooftop of the monitoring station, which was approximately 5 meters above the ground.

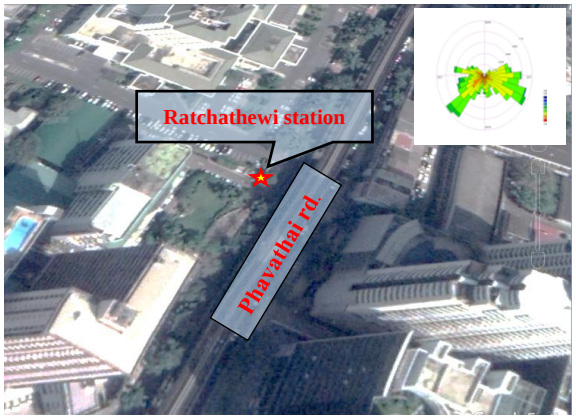

Fig. 1 Location of Ratchathewi monitoring station

Samples collection and data analysis

Real-time measurement of BC concentrations was conducted at the Ratchathewi station during the dry season (January 4 – 30th, 2017). Measured data was separated into two groups of weekday (Monday to Friday) and weekend (Saturday and Sunday). Total days of measured BC data were 27 days, consisting of 19 days of weekday data and 8 days of weekend data (four Saturdays and four Sundays). However, there were some missing data during January 10 – 11th due to heavy rain.

Black carbon measurements were carried out using the equipment called aethalometer, Model AE-42 (Magee Scientific, USA) with seven different wavelengths (370, 470, 520, 590, 660, 880, and 950 nanometer). The aethalometer was equipped with a cyclone to allow only particles smaller than 2.5 µm in aerodynamic diameter. Sampled particles were collected on a quartz fiber tape. The flow rate was controlled at 2 liters/minute, and the measured cycle was set at every two minutes. Hourly averaged values from the measurement at 880 nanometer wavelength were regarded as BC mass. If measured BC data in any hour or any day were missing more than 40%, their hourly or daily averages were not calculated and presented.

Traffic volumes passing by the monitoring site were evaluated from CCTV camera obtained from Traffic and Transportation Department, Bangkok Metropolitan Administration. The number of vehicles passing in the image were manually counted for twenty minutes' duration for every hour, then, they were interpolated to be hourly data. Eight different vehicles; passenger car, pick-up, van, taxi, motorcycle, three–wheeler (or "Tuk–Tuk"), bus and truck were categorized. Particulate matter (PM2.5) data simultaneously monitored at the same sampling station were provided by Bangkok Metropolitan Administration (BMA).

RESULTS AND DISCUSSION

BC concentrations and BC/PM2.5 ratios

The daily concentrations of BC observed at Ratchathewi station were in the range of 1.5 to 15.0 µg/m^3, which their average and median were 4.5±1.9 and 4.1 µg/m^3, respectively. Secondary data of PM2.5 concentrations from BMA were in the range of 1.0 – 58.0 µg/m^3, with the average of 27.2 µg/m^3. In comparison to several studies monitoring BC nearby roadways (Table 1), BC concentrations measured in this study were somehow lower than those previously reported, e.g., the average BC concentration of 17.9±6.6 µg/m^3 observed in Bangkok area during dry season [10], the ones of 8.9±3.6 µg/m^3 monitored in Istanbul, Turkey [11], and 9.7 ± 0.8 µg/m^3 reported in London, UK [12].

Table 1 Reported BC concentrations at different locations during dry season

Location	BC (µg/m^3)	BC/PM2.5 (%)	Ref.
Bangkok, Thailand	18±6.6	30	[10]
Istunbul, Turky	8.9±3.6	38	[11]
London, England	9.7 ± 0.8	–	[12]
Shanghai, China	3.3±2.1	5.0 – 12	[13]
Gwanju, Korea	2.4±2.2	–	[14]
Ostrava, Czech republic	3.5±4.1	–	[15]
Jiaxing, China	5.1	7.1	[16]
Guadalajara, Mexico	1.3 – 14	1.4 – 9.6	[17]
Bangkok, Thailand	4.5±1.9	18	This study

However, this average BC concentration was slightly higher than those observed in Shanghai, China (3.3±2.1 μg/m^3) [13], or in Gwangju, Korea (2.4±2.2 μg/m^3) [14] and Ostrava, Czech Republic (3.5±4.1 μg/m^3) [15]. During the period of BC monitoring (January 4 – 30th, 2017), total of 557 hourly data of BC concentration were gathered, excluding missing data. The majority of BC data (76.5% of total data) were in the range of 2 – 5 μg/m^3 and the second (20.5% of total data) were found in the range of 6 – 10 μg/m^3. Those of BC data, which were smaller than 2 μg/m^3 and higher than 10 μg/m^3, were observed only 2.2 and 0.9%, respectively.

The mass fraction of BC in PM2.5 (or BC/PM2.5 ratios) in this study were ranging from 6.2 to 69.8%, the average of which was 18.0% while the median was 16.1%. These BC/PM2.5 ratios on weekdays and weekends obviously peaked during morning hours (6:00 – 8:00) and night hours (20:00 – 21:00), while they remarkably decreased in the afternoon (15:00 – 16:00). Those peaks of BC/PM2.5 ratios in the morning and the night were related to traffic flow.

Moreover, the mass fraction of BC in PM2.5 (BC/PM2.5) of weekdays data were significantly different ($p<0.05$) from weekends data. Throughout the sampling period, the results between daytime and nighttime either on weekdays or weekends did not show significant difference. The average BC/PM2.5 ratio (18.0%) from this study was clearly lower than the previous studies at roadside site in urban Bangkok (30.0 – 37.0%) [10] and in Instunbul, Turkey (38.0%) [11]. However, it was relatively higher than those found in Shanghai (5.0 – 12.0%) and Jiaxing (7.1%) of China, and in Guadalajara of Mexico (1.4 – 9 .6%) (Table 1). The fraction of BC in PM2.5 depended on pollution sources and meteorological conditions. Reddy et al. [18] mentioned that their high BC/PM2.5 ratios of Anantapur in India during winter affected by biomass burninng, while increase of non-carboneceous PM2.5 during monsoon period might decrease the ratios.

Effects of day of the week on BC concentrations

Due to the sampling site represented a roadside type, traffic emission was expected to be a major contribution of BC and PM2.5 mass. Therefore, the sampling period was assigned to obtain enough data of weekdays and weekends BC concentrations. In addition, daytime and nighttime data were separately considered in order to understand the diurnal variation of BC. Daily BC concentrations categorized as weekly pattern were averaged and illustrated in Fig.2. The average daily BC concentrations on weekdays (Monday to Friday) ranged from 4.1 to 4.9 μg/m^3, with their average of 4.4 μg/m^3. For Saturdays and Sundays, these averages were 4.4 and 5.3 μg/m^3, respectively. Surprisingly, higher BC concentrations were observed on Sundays and they were significantly higher than those on Saturdays or weekdays ($p<0.05$).

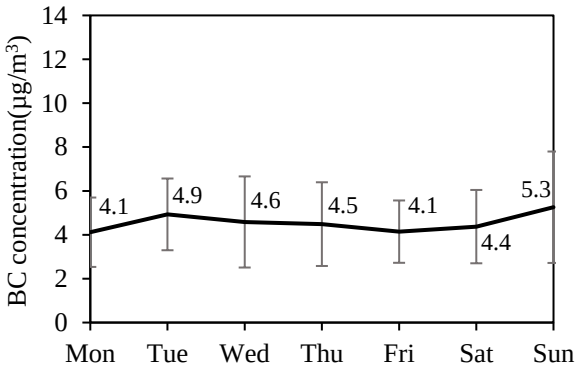

Fig. 2 The average daily BC concentrations in weekly pattern.

The hourly BC concentrations during weekdays were in the range of 1.5 – 12.1 μg/m^3, and their average was 4.4±0.2 μg/m^3. During weekends, the hourly BC were in the range of 1.7 – 15.0 μg/m^3 with the average of 4.8±2.2 μg/m^3. Though the average daily BC concentration on Sundays was significantly different from others as mentioned above, there was no significant difference between hourly BC concentrations of weekdays and weekends data ($p=0.075$).

Diurnal BC concentrations

During weekdays, hourly BC concentrations recorded between daytime (06:00-18:00) and nighttime (18.00-06.00) were in the ranges of 1.8 – 12.1 and 1.5 – 9.2 μg/m^3, respectively. Their averages were 4.1 and 4.8 μg/m^3, respectively. On weekends, hourly of BC concentrations during daytime ranged from 1.8 to 15.0 μg/m^3, while those of nighttime ranged from 2.6 to 11.6 μg/m^3. The averages of weekends were 4.6 and 5.1 μg/m^3, respectively. Interestingly, these results showed that the average BC concentrations during daytime were significantly lower than nighttime ($p<0.05$).

All hourly BC concentrations of weekdays and weekends were averaged, and their diurnal patterns were plotted as shown in Fig.3. Two curves of average daily BC concentrations representing weekdays and weekends data in diurnal pattern exhibited similar two peaks in the morning (5:00 – 7:00) and the night (21:00 – 23:00). During weekdays, the average hourly BC concentrations started to increase from 5:00 and reach its peak (6.2 μg/m^3) on 6:00, while the peak of weekends (6.4 μg/m^3) occurred at 7:00. In addition, some data higher than 10 μg/m^3 were mostly observed during these hours. The second peak happened in the night (21:00 to 23:00), which the evening peak of weekdays and weekends were 5.2 and 6.0 μg/m^3, respectively.

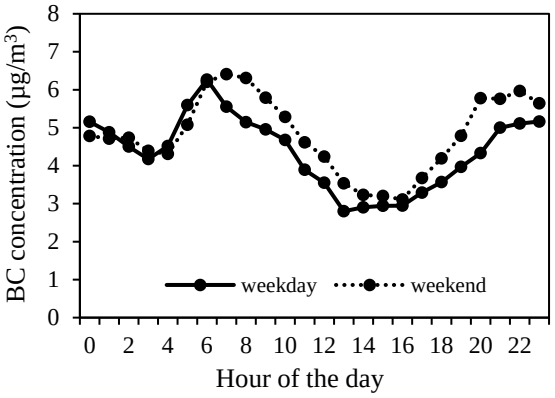

Fig. 3 Diurnal variation of BC concentrations

These two peaks of BC concentrations presented in the morning and the night, which should be related to traffic emission and the formation of boundary layer height, [10], [15]. Due to Thailand is the tropics, sunrise usually occurs during 5:00 – 6:00. The solar heat may disturb the nighttime stable layer and agitate nocturnal aerosols with some residuals near the surface. The lowest BC concentrations were found during 13:00 – 16:00 both weekdays and weekends data. The decrease after rush hours was mentioned to be associated with the atmospheric turbulent mixing and meteorological conditions [19]. Nonetheless, the diurnal pattern of BC observed at Ratchathewi station was unlike those observed in other urban cities such as London [12] and New Delhi [20] due to traffic rush hours on Phayathai road was uncommon.

Traffic characteristics on Phayathai road

Traffic volumes on Phayathai road were also counted during the same period, the traffic density ranged from 510 to 5342 vehicles/hour, resulting in the average of 2671 vehicles/hour. When weekdays and weekends data were categorized, their average densities were 2759 and 2451 vehicles/hour, respectively. The diurnal patterns of traffic flow pass through Phayathai road near the sampling station on weekdays and weekend are presented in Fig.4. The most congested traffic flows were observed during 7:00 – 8:00 and 16:00 – 17:00, which the traffic densities increased up to 3796 and 3871 vehicles/ hour, respectively.

However, Figure 4 illustrated that traffic densities during 8:00 – 16:00 were not drastically decreased in comparison with those peaks. This should be due to Phayathai road leads to Victory monument (a center of public transportation), and several public hospitals located nearby, resulting in substantial traffic congestion almost all daytime. Besides, there were several public organization or academic institutes nearby Victory monument. Their office hours mostly ended at 16:00, resulting in traffic congestion happened since 16:00 and started to decrease after 17:00. For weekends, traffic congestion still exhibited substantially, but not the same early hours as those on weekdays. The morning traffic density during the weekends observed at 9:00 and reach the highest densities of 2844 vehicles/hour at approximately 10:00. For nighttime, their peak of 3722 vehicles/hour was found during the hour of 20:00 – 21:00.

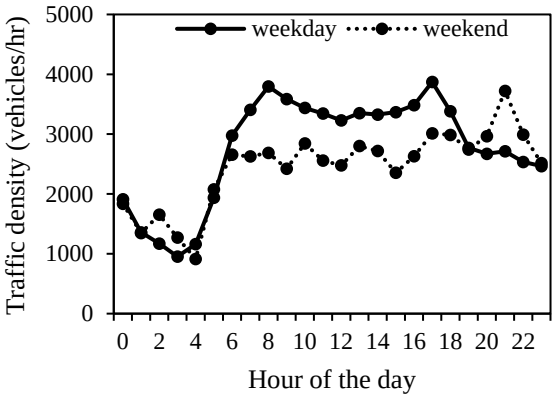

Fig. 4 Diurnal patterns of traffic density

The average traffic densities during daytime on weekdays was about 3382 vehicles/hour, which was clearly higher than the daytime average density on weekends (2675 vehicles/hour). In contrast, the average traffic densities during nighttime on weekdays (1969 vehicles/hour) was lower than that of 2185 vehicles/hour on weekends. This could be noticed that fluctuation of traffic densities on weekends were smaller than that of weekdays.

Table 2 categorized traffic composition passing through this station during the same sampling period. Traffic composition affected the emission of pollutants. The vehicle fleets were dominated by private car (29-30%), taxi (25-33%) and motorcycle (21-25%), while pickup, van, bus, and Tuk–Tuk (three-wheel vehicle) proportions were 8, 4, 4 and 2%, respectively. Truck showed the smallest proportion of less than 1%.

Table 2 Percentage of traffic fleets composition

Vehicle type	Weekdays	Weekends
Private car	30.0±4.0	29.0±3.9
Pickup	8.4±0.8	6.8±3.5
Van	4.1±0.8	3.3±0.8
Taxi	25.0±5.6	33.0±3.8
Motorcycle	25.0±13.0	21.0±6.5
Tuk–Tuk	2.0±0.2	2.2±1.0
Bus	4.7±1.7	4.0±1.1
Truck	0.4±0.1	0.6±0.0
Average (vehicles/hour)	2759±660	2451±679

The high proportions of private car, taxi, motorcycle and pickup were observed both on

weekdays and weekends while the proportion of Tuk–Tuk and truck were still smaller than other fleets. In comparison with weekdays, the major fleets (private car, pickup, motorcycle, etc.) showed smaller proportion on weekends. But, there were some fleet increased their proportions on weekends, e.g., taxi, Tuk–Tuk and truck.

Correlation between BC concentration and traffic

Figure 4 illustrated that traffic densities started to increase from pre-dawn at 4:00, similar to the increase of BC concentration in Fig. 3. However, BC concentration reached its peak at 6:00 and decreased afterward, while traffic densities still kept rising until 8:00. After the morning peak, the decrease of BC concentrations was more drastically than traffic densities. The BC concentrations lowered to the smallest during the hours of 13:00 – 16:00 (Fig. 3), but traffic densities were still substantial amount at the same hours. Therefore, the correlation between BC concentrations and traffic densities in this study could not be affirmative. Subsequently, traffic fleets were further considered, which truck vehicles (Fig. 5) showed interesting correlation with BC concentrations. (Remarks: Some other fleets also showed a weak correlation, but data were not discussed here.)

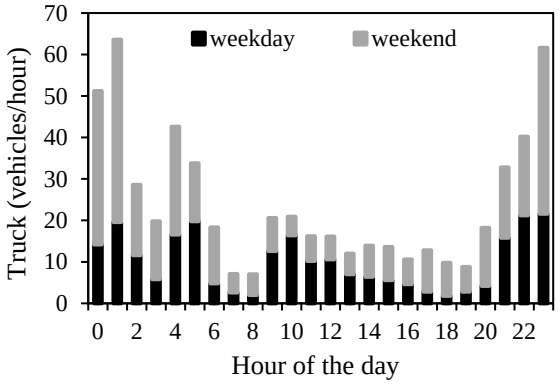

Fig. 5 The diurnal pattern of truck density

Trucks transportation within Bangkok area were regulated and allowed only between 10:00 – 15:00 and after 21:00, resulting in similarity of diurnal pattern of truck and BC concentrations. Figure 5 showed high densities of truck during 4:00 – 5:00 and drastically decreased afterward, as well as, another high truck densities during the night similar to diurnal pattern of BC concentrations (Fig. 3). In addition, more truck densities on weekends than weekdays were consistent with the higher averages BC concentrations on weekends. The possible explanation for this correlation between BC concentrations and truck densities might be due to diesel was their majority fuel. Particularly during nighttime, heavy-duty diesel vehicles should be an important source of black carbon emission.

Effects of meteorological parameters on BC concentrations

Wind speeds during the sampling period were monitored and found in the range of 0.5 – 2.5 m/s with their average of 1.3 m/s. Wind speed is an important factor related to accumulating BC concentration. Higher wind speed could contribute more emission dispersion, lowering pollutant concentrations in the ambient. Wind speed higher than 0.5 m/s illustrated a significant inverse relation with BC concentrations ($R_{pearson}$ = –0.377, P<0.01).

Predominant wind directions were observed from east–southeast (ESE), east (E), southwest (SW) and south–southwest (SSW), the frequency percentages of which were 16.4, 10.1, 13.7, and 10.6%, respectively. The contribution of hourly BC concentrations from different wind directions was shown in Fig. 6. During sampling period, BC concentrations larger than 5 µg/m^3 occurred when the wind blowing from the directions of ENE/E/ESE (28%) and SE/SSE/S/SSW directions (27%). As the monitoring station is located on the west–northwest curbside of the road, traffic emission from nearby roads and Phayathai road itself were clearly sources of these winds. The results indicated that BC mass should be influenced by traffic emissions, which was consistent to the relation between BC concentrations and heavy-duty diesel vehicles on weekends.

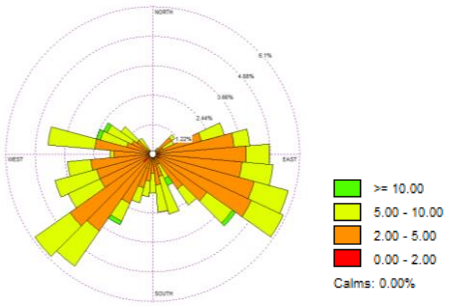

Fig. 6 Pollution rose of hourly BC concentrations

CONCLUSIONS

Hourly BC concentrations in this study were measured at roadside station in the center of Bangkok during dry season in year 2017. The averages of hourly BC concentration and BC/PM2.5 ratio were observed as 4.5±1.9 µg/m^3 and 18%, respectively. The results were lower than a previous study in Bangkok [10]. Diurnal pattern showed two peaks of BC concentrations during the periods of 5:00 – 7:00 and 21:00 – 23:00. Two peaks of BC concentrations in this study were more likely due to rush hour traffic concurrently with meteorological condidition. When the prevail wind direction blowed from traffic congestion on the road to the monitoring station, high BC concentrations were sometimes observed. Heavy-duty diesel vehicles should be an important

fleet affecting on BC concentrations, especially during nighttime and weekends.

ACKNOWLEDGMENTS

The authors gratefully acknowledge assistance for BC analyzer from the Environmental Quality Promotion Department. Special thanks for ambient air quality data and sampling station accessibility from Bangkok Metropolitan Administration.

REFERENCES

[1] Ramanathan V, Carmichael G. Global and regional climate changes due to black carbon. Nature Geoscience, 2008, pp.221-227.

[2] IPCC. Climate change 2007: synthesis report. Intergovernmental Panel on Climate Change, Geneva, Switzerland, 2007.

[3] Jansen KL, Larson TV, Koening JQ, Mar TF, Fields C, Stewart J, Lippmann M. Associations between health effects and particulate matter and black carbon in subjects with respiratory disease. Environ Health Perspect, 2005, 1741-1746.

[4] Mordukhovich I, Wilker E, Suh H, Wright R, Sparrow D, Vokonas PS, Schwartz J. Black carbon exposure, oxidative stress genes, and blood pressure in a repeated- measure study. Environ Health Perspect, 2009, 1767-1772.

[5] BMA (Bangkok Metropolitan Administration). Bangkok state of the environment 2003. BMA Report, 2004.

[6] Asian Development Bank. Country synthesis report on urban air quality management: Thailand. Journal of the Air&Waste Management Association, 2006, 652-697.

[7] Buadong D., Jinsart W., Funatagawa I., Karita K., Yano E., 2009. Association between PM10 and O3 levels and hospital visits for cardiovascular diseases in Bangkok, Thailand. J. Epidemiol, 2009, 182–188.

[8] Bangkok Metropolitan Administration. Stratistics of traffic in Bangkok. Department of Traffic and Transportation, BMA Report, 2017.

[9] Department of Land Transport. Number of vehicle classified by fuel used registered in Bangkok as of 31 December. DLT Report, 2015.

[10] Hung NTQ, Lee SB, Hang NT, Kongpran J., Kim Oanh NT. , Shim SG. , Bae GN. Characterization of black carbon at roadside sites and along vehicle roadways in the Bangkok Metropolitan Region. Atmospheric Environment, 2014, 231-239.

[11] Ozdemir H., Pozzoli L., Kindap T., Demir G., Mertoglu B., Mihalopoulos N., Theodosi C., Kanakidou M., Ime U. Unal A. Spatial and temporal analysis of black carbon aerosols in Istanbul megacity. Science of the Total Environment, 2014, 451–458.

[12] Singh V., Ravindra K., Sahu L., Sokhi R. Trends of atmospheric black carbon concentration over the United Kingdom. Atmosphric Environment, 2018, 148-157.

[13] Feng J., Zhong M., Xu B., Du Y. Wua, M. Wang H. , Chen C. Concentrations, seasonal and diurnal variations of black carbon in PM2. 5 in Shanghai, China. Atmospheric Research, 2014, 1–9.

[14] Park SS., Lee KH. Characterization and sources of black carbon in PM2. 5 at a site close to roadway in Gwangju, Korea, during winter. Environ Sci. 2015.

[15] Kucbel M., Corsaro A., Svedova B., Raclavska H., Raclavsky K., Juchelkova D. Temporal and seasonal variations of black carbon in a highly polluted European city: Apportionment of potential sources and the effect of meteorological conditions. Journal of Environmental Management, 2017, 1178-1189.

[16] Shen L., Li L., Lu S., Zhang X., Liu J., An J., et al. Characteristics of black carbon aerosol in Jiaxing, China during autumn 2013. Paricuology, 2015, 10-15.

[17] Limon- Sanchez MT. , Carbajal- Romero P. , Hernandez- Mena L. , Saldarriaga- Norena H. , Lopez-Lopez A., Cosio-Ramirez R., et al. Black carbon in PM2.5 data from two urban sites in Guadalajara, Mexico during 2008. Atmospheric Pollution Research, 2011, 358-365.

[18] Reddy BSK., Kumar KR., Balakrishnaiah G., Gopal KR., Reddy RR., Reddy LSS., et al. Potential source regions contributing to seasonal variations of black carbon aerosols over Anantapur in Southeast India. Aerosol and Air Quality Research, 2012, 344- 358.

[19] Tiwari S., Srivastava AK., Bisht DS., Parmita p., Srivastava MK., Attri SD. Diurnal and seasonal variations of black carbon and PM2. 5 over New Dalhi, India: Influence of meteorology. Atmospheric Research, 2013, 50-62.

[20] Sharma MC., Pandey VK., Kumar R., Latief SU., Chakrawarthy E. , Acharya P. Seasonal characteristics of black carbon aerosol mass concentrations and influence of meteorology, New Delhi (India). Urban Climate, 2018, 968-981.

9th Int. Conf. on Geotechnique, Construction Materials and Environment,
Tokyo, Japan, 20-22 November 2019, ISBN: 978-4-909106025 C3051

WEB APPLICATION SUPPORT FOR CARBON FOOTPRINT MANAGEMENT OF PETROL STATIONS IN THAILAND

Amika Srikritsanarat[1] and *Suphaphat Kwonpongsagoon[2]
[1,2]Department of Sanitary Engineering, Faculty of Public Health, Mahidol University, Thailand;
Center of Excellence on Environmental Health and Toxicology (EHT), Thailand

ABSTRACT

The release of greenhouse gases from anthropogenic activities in many organizations of the country has induced the effect labeled global warming. In Thailand, a "petrol station" is considered an "organization" that not only sells fuels and engine lubricants for motor vehicles but also includes many other facilities provided to satisfy the modern lifestyle of customers. In other words, a petrol station in Thailand comprises a large complex service center offering a wide range of services that contribute greenhouse gas emissions to the atmosphere. This paper aimed to present a specific web application tool developed to estimate the carbon footprint for petrol stations in Thailand. The application system comprises three core components: 1) a web-based user interface; 2) a processing system, incorporating the carbon footprint of the organization (CFO) framework and the calculated model and 3) a database. The site-specific input data or activity data provided by the user was primarily required for the data entry in the system. The processing system will then quantify the amount of greenhouse gas emissions by multiplying the activity data by the emission factor (EF). A database was also created containing default EFs readily used for the calculation, but users can change these values at any time when a more appropriate one is indicated. Finally, the CF calculation results can be evaluated in various functional units: monthly or yearly, per fuel sold, or per area of the petrol station, and visualized in graphs. In addition, the results can be reported by categorizing the emission sources according to the scope of the CFO and the GHGs reporting guidelines (scopes 1, 2 and 3).

Keywords: Carbon footprint, Organization, Petrol station, Web application

INTRODUCTION

Petrol stations in Thailand have increased continuously. From 2007 to 2016 the number of petrol stations in Thailand has increased by 29%, corresponding to the increasing trend of fuel sales at 22% [1]. Currently, more than 26,000 petrol stations are located across the country [1]. In Thailand, petrol stations not only sell fuel and engine lubricants for motor vehicles, but also include many other facilities provided to satisfy the modern lifestyle of customers such as convenience stores, restaurants, souvenir shops, coffee shops, food stalls, toilet facilities, including automatic teller machines (ATMs) and auto mechanic services. In other words, the petrol station is a large complex service center with a wide range of activities that could contribute greenhouse gas emissions to the atmosphere, resulting in the effect labeled global warming.

Carbon Footprint for Organization (CFO) is a quantitative method to measure greenhouse gas emissions from all activities in the organization, including energy used in the building, industrial processes and company vehicles [2]. According to our previous research, studies have developed special carbon footprint calculation programs for food and beverage packaging using Visual Basic for Applications (VBA) in Microsoft Excel [3], [4]. One advantage of this type of program is that it works on Microsoft Excel in a desktop or laptop. However, the VBA's disadvantage is its unattractive appearance and limited functions compared with other types of available programs, like a web-based application (web app).

In fact, a web app is a subset of information technology (IT) that has become an integral part of modern lifestyle. People use it to facilitate the functioning of nearly all life domains. With the help of information technology, users now can acquire information, connect with people and achieve much more with speed and precision [5]. The web application has the advantage of being easily accessible to show users. Just by having a computer or smartphone device, a web browser and connecting to the internet, users can access the program from anywhere at any time. At the moment, although numerous web applications for carbon footprint calculation are available online, they are all simple carbon footprint calculators for individuals, events or businesses [6], [7], [8]. Researchers have paid little attention to the GHGs of an organization that are needed to estimate accurately the complex service activities that are common to petrol stations in Thailand.

As a result, the aim of this paper was to create a web application to analyze carbon footprint for petrol station in Thailand in the form of web application software. Thus, the owner or petroleum company in Thailand can use our developed web-based application to calculate greenhouse gas emissions released from their activities. The web app will be served as a supporting tool for carbon management of their organizations.

METHODOLOGY

Data Requirements and Calculation Method

To develop the web application in this study, petrol stations in Thailand were first surveyed to receive an overview of their various service activities. Activity data were collected relating to GHG emissions from different sources situated in the petrol stations including offices, convenience stores, fast food shops, restaurants, coffee shops, retailers and toilet facilities. The examples of data related to those activities were mainly electricity, water and chemical use and waste generated. In addition, the secondary data required in this study were emission factors (EFs). Main sources of the EFs include Thailand Greenhouse Gas Management Organization (TGO) and the international database, e.g., Ecoinvent. Other sources involve published and unpublished articles.

For carbon footprint calculation in this study, the method was based on guidelines for carbon footprints of organizations by the Thailand Greenhouse Gas Management Organization (TGO) [9] and World Business Council for Sustainable Development (WBCSD) [10]. The GHG emission is simply calculated by multiplying activity data with the related emission factor as expressed in Eq. (1) as shown below.

$$CF = \text{Activity Data} \times \text{Emission Factor} \quad (1)$$

where CF is the carbon footprint estimated in unit of kilograms carbon dioxide equivalent (kg CO_2eq); the activity data represents a factor that quantifies an activity used to calculate the emissions generated, and emission factor represents a factor that allows GHG emissions to be estimated from a unit of available activity data.

Programing Languages for Web App Development

To develop the web-based application, five programming languages were used to write the code to support two system components of the software – client and server side. The data processing is handled by the server while results are returned to the client. These five languages include Hypertext Markup Language (HTML), Cascading Style Sheets (CSS), JavaScript, Active Server Pages (ASP.NET) and Structured Query Language (SQL). At the client side, HTML is used to create a web application structure, in conjunction with CSS and JavaScript that are used to control the appearance and to make user interactions. At the server side, ASP.NET is used for server processing and to connect to databases, while the database management is achieved with Structured Query Language (SQL). A program called, "Microsoft Visual Studio Community 2017" was used as a platform tool to support writing the code of these five languages.

RESULTS AND DISCUSSION

Description of the Web Application

The developed web application is available online at http://www.carbonfootprintthailand.com /petrolstation. It can run on all electronic devices such as desktop computers, laptops, tablets and smartphones through a web browser. It can calculate the carbon footprint of a petrol station by referring to the resources used and activity information of the petrol station. Using the software, developers have designed three different functions of user access level: 1) general user for petrol station level; 2) group user for corporate level, e.g., Shell, ESSO, Bangchak, PTT, Chevron and 3) administrative user for general system management level. Using these levels, allows users to access various parts of the application. At the petrol station level, a general/owner user involves a group of users that can use the main part of the CF calculation system. The general user will be able to create, browse, edit and delete historical results, including being able to edit the EF values. At a corporate level, a group user is in the business level that provides a network of fuel distribution services across the country. This group of users can only browse the calculation results of petrol stations under their business group. The group users will not be able to edit any input data or results of any petrol stations. At the system management level, an administrative user can generally manipulate the overall software system such as deleting user and updating EF default values etc.

To calculate the carbon footprint, the developer has gathered all related EFs needed for the calculation by setting them as the software's default values, so they can be retrieved for the estimations instantly. The software also provides a special function that allows users to change these values at any time when a more appropriate one is indicated.

The CF calculation results can be evaluated in various functional units: monthly, yearly, per fuel sold or per area of the petrol station. These functional units can help entrepreneurs to calculate their GHGs (or CF), and to compare the CF results among petrol stations under the same corporate group.

The application system comprises three core components as shown in Fig. 1: 1) a web application user interface; 2) a processing system, incorporating the carbon footprint of the organization (CFO) framework and the calculation model and 3) a database. The user interface involves the display section of the web application, where the user can connect and send a request to the web server via a web browser. The processing system will then process the requests, connect to the database to manipulate data and send results to show to the user interface. The database of this developed web application is a data storage system called the Relational Database Management System (RDBMS). More details are described in a later section of this paper.

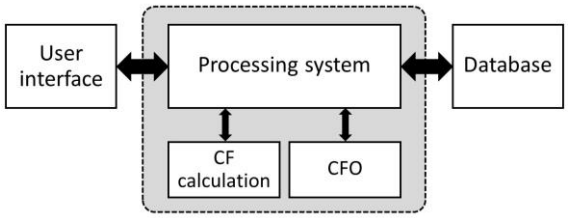

Fig. 1 Main components of the web application

Database Model with RDBMS

The database in this study involved a set of data stored in the application system, designed by using the SQL language of the Relational Database Management System (RDBMS). This database is a type of relational database model to organize and store data as a set of eight database tables (see Fig. 2). These database tables store account information, related companies or associations, petrol station information, EFs, shops and facility types and details, historical data of calculation options and input data related to carbon footprint results. To organize all databases, interaction needs to be created among tables, so a "primary key" which is a column in a database table that uniquely identifies rows in that table, and a "foreign key" which is a column of a table that is the primary key on another table, are assigned to define relationships between the two tables. The relationship was defined in this software as an one-to-many relationship. For example, one User ID of the 'User Table' may create many emission factor values in the 'Emission Factor Table'. Moreover, each user in the 'User Table' can create many petrol stations in the 'Company Table', and each petrol station can estimate CF many times in the 'Save Table'.

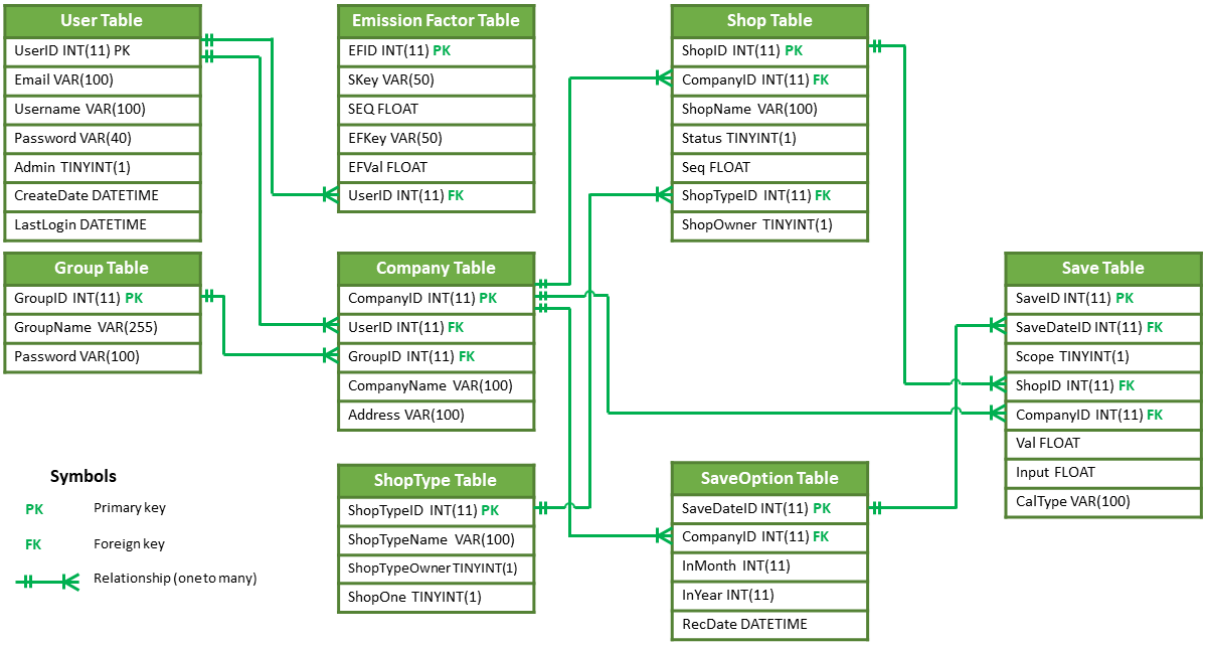

Fig. 2 Relational database model of the web application

Three Scopes of Emission Sources

According to the guidelines for CFO and the GHG reporting standard [9], [10], the application was designed to categorize and report the activity or emission sources of a petrol station separately in three scopes (scopes 1, 2, and 3), as presented in Fig. 3. Direct GHG emissions of scope 1 are released from sources that are owned or controlled by the petrol station while indirect GHG emissions of scope 2 are emissions from the generation of purchased electricity. Finally, indirect GHG emissions of scope 3 are emitted from sources not owned or controlled by the petrol station. Considering the definition of

these scopes and petrol station activities, scope 1 emissions involve onsite electricity generation, vehicle fuel consumption, onsite wastewater treatment system and use of chemicals, refrigerants and fire extinguishers while scope 2 emissions come from the consumption of purchased electricity. Lastly, scope 3 emissions come from several sources such as fuel consumption of outsourced vehicles, electricity consumption of the rental businesses, use of fuel sold and waste management by the local authority. Moreover, scope 3 also involves raw material acquisition such as use of paper, packaging and water.

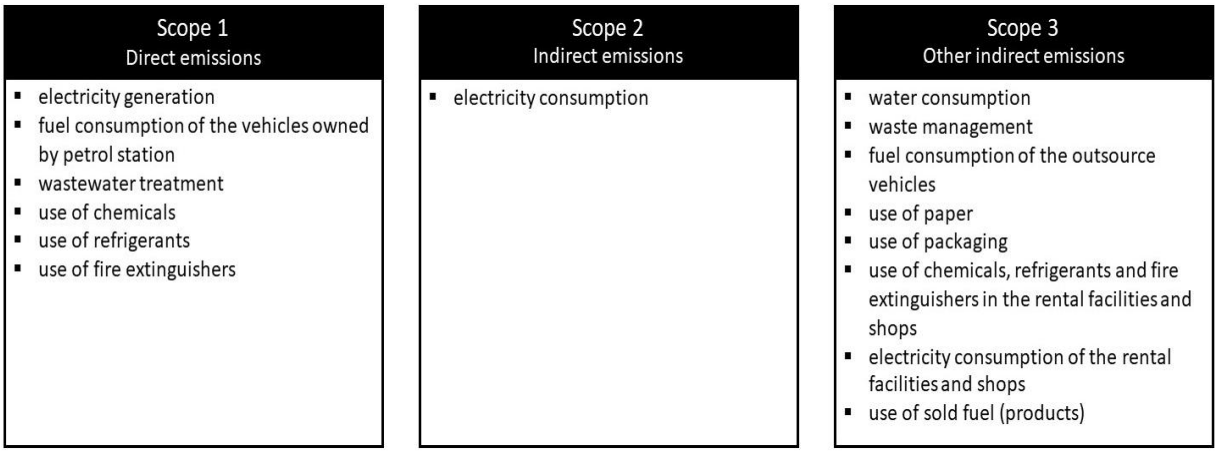

Fig. 3 GHG emissions from a petrol station relating to the scopes of GHG reporting guidelines

Calculation Sequence

Figure 4 shows the sequence of carbon footprint calculation, 12 processes connected to 3 user groups and 8 database tables (described above in database model section). First is process 1.0, where the general user has to create an account or log in to access the software. User information such as username, password and the level of user will be stored in the database named 'User table' and 'Group table'. After login, the general users can browse or modify EF values in process 2.0. In process 3.0, the general user has to create information about the petrol station. In the case the petrol station information is already created, the user can select the existing petrol station which he/she wants to calculate the CF. Process 4.0 allows a user to identify the time period of entering data, e.g., monthly or yearly meaning that all data have to be entered in relation to the selected time period. In process 5.0, the general user has to create and edit the details of shops and service facilities. Another important information needed is whether each shop/service facility is owned by the petrol station or rented. Such information will allow the software to categorize activities and emission sources according to the scope of the CFO and GHG reporting guidelines at a later step. Next, process 6.0 allows a general user to input activity data such as the volume of water, electricity, and fuel consumption for each shop/service facility previously selected. After completing process 6.0, the web app will use those data to calculate CF in process 7.0. Process 8.0 will use the CF results to create pie and bar graphs, comparing the CF among various shops, activities, the three scopes of the CFO guidelines and showing them all in process 9.0. Here the user can change the displayed functional unit to monthly, yearly, per volume of selling fuel or per petrol station areas. When the functional unit is selected, the software will automatically recalculate CF, recreate graphs and illustrate the results on the web page. The software can export all input data and results in PDF format at process 10.0. For process 11.0, the general user can browse the calculation history and edit the input data. Finally, process 12.0 is the system management tool, which only administrative users can access.

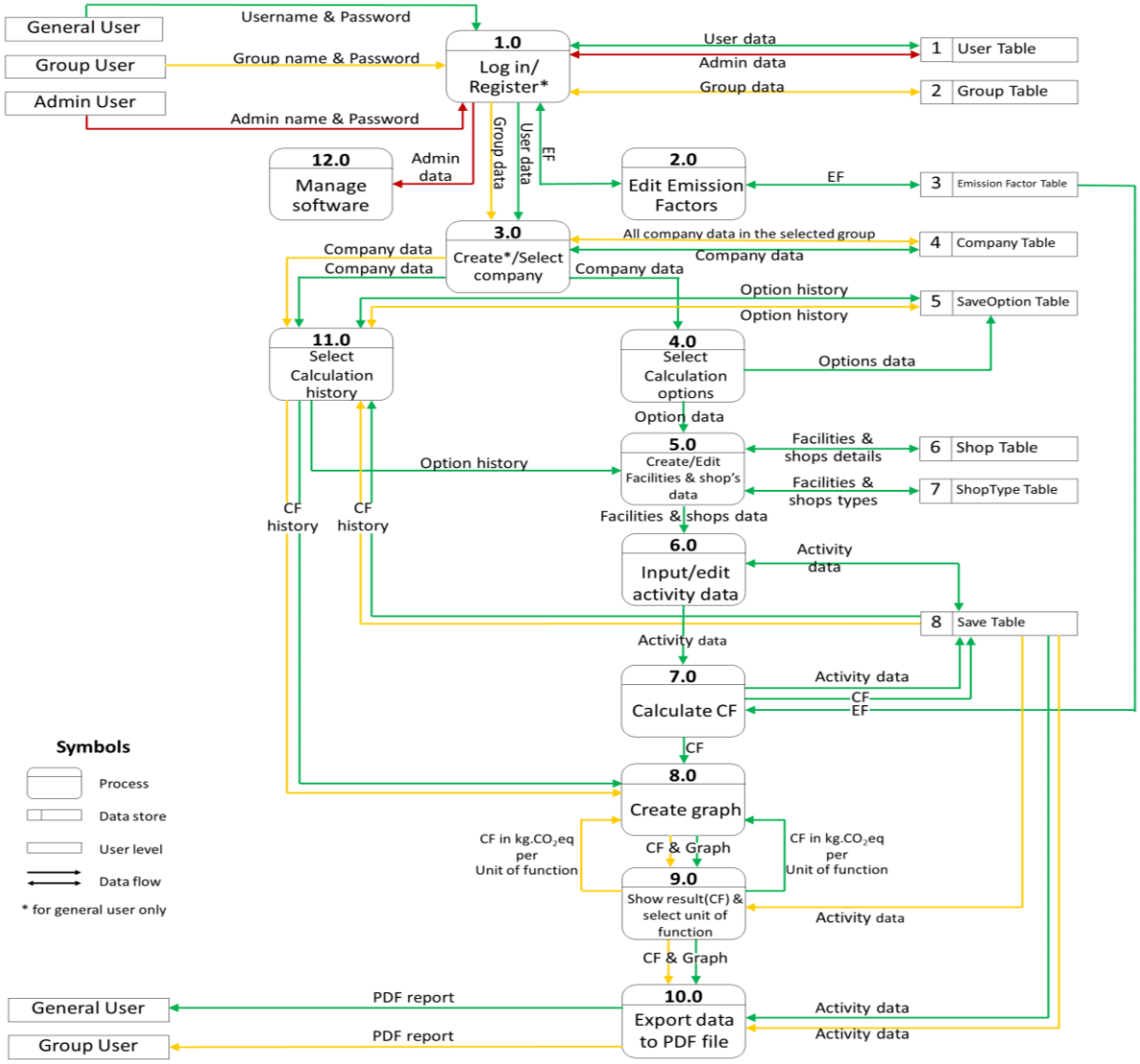

Fig. 4 The sequence of the carbon footprint calculation

Web Application User Interface

Figure 5 shows the main graphical user interface (GUI) of the developed web application, namely, main page, input data page and result page. Main page is well designed as a snapshot of a petrol station, consisting of all twelve categories of shops and service facilities currently provided in petrol stations of Thailand. This page allows users to work easily on relevant service facilities (see Fig. 5a). Fig. 5b depicts an example of an input data page where users have to fill in activity data and resource use. Several web pages of input data were enhanced by adding checklist options, drop down list options, and illustrations to make it more attractive and easier for users to enter their input data. The result page displays the calculated results in units of kilogram CO_2-eq relating to the functional units chosen: monthly, yearly, per fuel sold or per area of the petrol station and illustrated in graphs (Fig. 5c). In addition, the results can be reported following scopes 1, 2 and 3 of the CFO and the GHGs reporting guidelines as mentioned above.

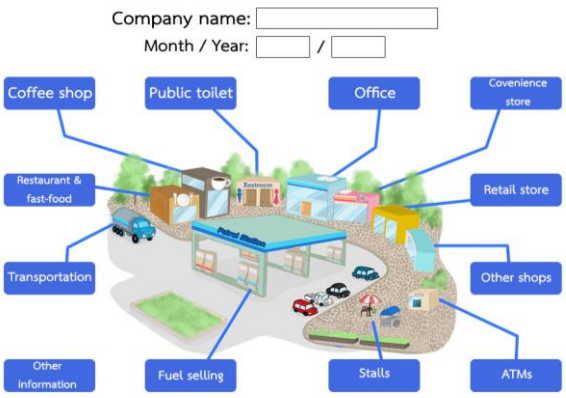

(a) Main page

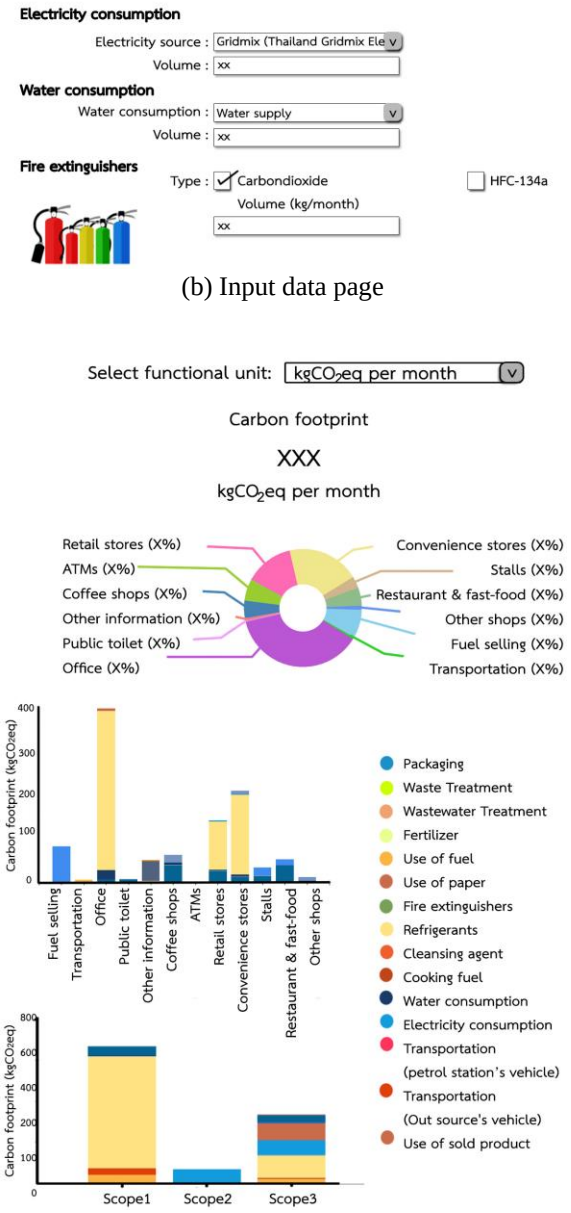

(b) Input data page

(c) Result page

Fig. 5 Main graphical user interface

CONCLUSION

Clearly, the advantage of web application software is being easily accessible to any user. With a computer or smartphone device, a web browser and connection to the internet, users can access the web app from anywhere at any time. The CF calculation results of the web app can be estimated in various functional units: monthly, yearly, per fuel sold or per area of the petrol station. Therefore, the developed web application in this study can help petrol station owners, petroleum companies and associations in Thailand to account GHG emissions released from their boundaries and operations and to compare the CF results among petrol stations under the same corporate group. Ultimately, it will lead to guidelines for future planning to reduce their emissions.

ACKNOWLEDGMENTS

This research work was financially supported by the Center of Excellence on Environmental Health and Toxicology (EHT), Science & Technology Postgraduate Education and Research Development Office (PERDO), Ministry of Education, Thailand. Moreover, the study was partially supported for publication by the Faculty of Public Health, Mahidol University, Bangkok, Thailand.

REFERENCES

[1] Department of energy business. Number of petrol stations in Thailand [Internet]. 2017 [cited 2019 Apr 21]. Available from http://www.doeb.go.th/2017/#/article/statistic

[2] Tao G., Qing L., and Jianping W., A comparative study of carbon footprint and assessment standards. International Journal of Low-Carbon Technologies, Vol.9, Issue 3, 2014, pp. 237–243.

[3] Chansod K. The development of a compact, easy-to-use carbon footprint analysis software for the standard design of corrugated boxes and plastic containers for food packaging [Master Thesis]. Bangkok: Mahidol University; 2011.

[4] Thongiem A. The development of a compact easy-to-use carbon footprint analysis software for the standard design of glass and aluminum beverage containers [Master Thesis]. Bangkok: Mahidol University; 2011.

[5] Sigerson L., Angel Y., Cheung M., and Cheng C., Examining common information technology addictions and their relationships with non-technology-related addictions. Computers in Human Behavior, Vol.75, 2017, pp. 520-526.

[6] TGO. Web-based Thai carbon footprint calculator [Internet]. 2013 [cited 2019 May 12]. Available from http://carbonmarket.tgo.or.th/carbonfootprint/thai/index.php

[7] Myclimate. Myclimate carbon footprint calculators [Internet]. 2019 [cited 2019 May 12]. Available from https://co2.myclimate.org/en/offset_further_emissions

[8] Carbon Footprint Ltd. Carbon footprint calculator [Internet]. 2019 [cited 2019 May 12]. Available from https://www.carbonfootprint.com/measure.html

[9] Thailand Greenhouse Gas Management Organization (Thailand). Guidelines for Carbon Footprint of Organization. Bangkok: 2016.

[10] World Business Council for Sustainable Development (Switzerland). The greenhouse gas protocol: a corporate accounting and reporting standard. Geneva: 2011

9th Int. Conf. on Geotechnique, Construction Materials and Environment,
Tokyo, Japan, 20-22 November 2019, ISBN: 978-4-909106025 C3051

DEVELOPMENT OF A WEB APPLICATION FOR ESTIMATING CO_2-EQUIVALENT EMISSIONS OF POULTRY AND SWINE SLAUGHTERING PROCESSES

Salinee Ratchadaariyachat[1] and *Suphaphat Kwonpongsagoon[2]
[1,2]Department of Sanitary Engineering, Faculty of Public Health, Mahidol University, Thailand;
Center of Excellence on Environmental Health and Toxicology (EHT), Thailand

ABSTRACT

Thailand is one of the top productions and trade of poultry and pig meat to the world, making the slaughterhouse an important contributor to the release of greenhouse gases (GHGs) in the environment. This study aimed to create a web application to evaluate GHG emissions of poultry and swine slaughtering processes. The development was based on the carbon footprint of the product and life cycle assessment approach. The designed scope involved a cradle-to-gate assessment. The CO_2-eq estimation results are based on the following functional units: per kilogram of animal live weight, or per number of live animals, or a product-based perspective as per kilogram of animal meat or carcass. The developed application can be conceptualized in three main components. First is a web-based user interface, separated in input and output parts. Slaughterhouse information and activity data were required to be entered as site-specific input data while CO_2-equivalent emission was shown as carbon footprint output. Next, the processing system was designed to function regarding various conditions of input data, ranging from minimum to detailed data sets providing a simple, coarse, and detailed estimation. Finally, the system database used to access and store emission factors, historical data, and carbon footprint results was created using a relational database model to organize data in a set of 6 tables. Moreover, many functionalities were considered and incorporated in the application to facilitate the user's estimation such as navigation tool, functional unit selection, data validation and null check, emission factor management, report/export documentation, and data confidentiality and security. The potential of this developed application is expected to aid the Thai slaughterhouse industry calculating their GHG emissions released in the environment, and subsequently leading to CO_2 mitigation.

Keywords: Carbon footprint, Slaughtering process, Poultry and swine, Web application

INTRODUCTION

The prediction of the world's population increase is expected to result in significantly increasing meat production possibly affecting the greatest environmental impacts as a result of global consumption [1], [2]. With the FAO report, it has become evident that the quantity of global meat consumption per capita is likely to continue increasing, which corresponds to the trend of meat production and slaughtered animals [3]. Slaughtering is a core sector of meat production for domestic consumption and export, especially in Thailand. During the last 20 years, overall meat production in Thailand has increased by almost 30%, especially poultry and swine, about 56% and 23%, respectively [3], [4]. It was reported that the Thai animal slaughtering industry is one of the most important and rapidly growing markets for poultry meat exports, placing Thailand in the Top 5 ranking of the world and the first among Southeast Asian countries [5]. Currently, international market opportunities are joining the environmental agenda, and more consumers emphasize green products. Especially consumers in developed countries are becoming concerned about climate change effects, so greenhouse gas (GHG) emissions during the slaughtering process in Thailand contributing to environmental degradation should be taken into account for industrial management and sustainability.

One method used to measure climate change impact in terms of the amount of GHGs generated from human/industrial activities is called, "Carbon Footprint (CF)" and is based on the life cycle assessment (LCA) approach. CF analysis of a product/process can provide an idea of resource consumption efficiency, affecting the amount of GHGs or CO_2 equivalent (eq) released in the atmosphere. The method can also identify hot spots where the most significant impacts occur for improving performance. In general, numerous studies have been conducted using CF and LCA to evaluate climate change and other environmental impacts for a variety of specific food products such as meat products, organic foods, wine, and milk [6]–[9]. In our previous studies, "CFPack" was first developed for carbon footprint analysis of food and beverage packaging [10], [11], using the Microsoft Excel Visual Basic for Application (Excel/VBA). In the current digital era with the popularity of the World Wide Web (www), most activities are conducted over the internet. According to researchers, the recent growth of web applications has been helpful in

developing environmental management and sustainability [12]–[14]. However, until now, few specific software packages have been developed and published to help entrepreneurs identifying their GHG emissions online. Therefore, this study aimed to create a web application to estimate CO_2-eq emissions of poultry and swine slaughtering processes in Thailand. The application is expected to aid the Thai slaughterhouse industry measure their greenhouse gas emissions, subsequently leading to reduced emissions.

METHODOLOGY

Scope and System Boundary

The web application was developed to estimate CO_2-eq emissions (or Carbon Footprint of Product – CFP) of the slaughterhouse industry according to the Life Cycle Assessment (LCA) concept. As can be seen in Fig. 1, the scope and system boundary of the estimation defines what is covered in the web application design and development starts by raw material acquisition, raw material transportation to the factory, the slaughtering process and product transportation to customers. In other words, the designed scope is a cradle-to-gate assessment. The CO_2-eq estimation results are based on the following functional units: per kilogram of animal live weight, or per a number of live animals, or a product-based perspective as per kilogram of animal meat or carcass. As all these functional units are the most commonly used in meat production [15], the estimation results will help the industry to monitor the emissions released and to compare the GHG inventory in terms of live animal-based units and carcass-based units.

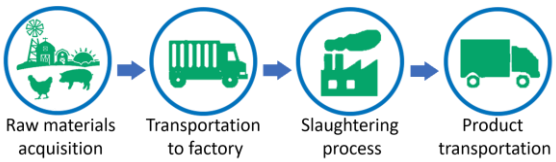

Fig. 1 Scope of this study

Data Requirements and Calculation Method

In this study, data involves all relevant activities of raw material acquisition, the slaughtering process, and transportation, for example, total amount of raw materials, energy, water, packaging, and chemical use, waste disposal, vehicle type, fuel type, and transportation distance. These activities are required to be entered in the software by users. In addition, the emission factors which are basically collected from Thailand Greenhouse Gas Management Organization (TGO), the international database, e.g. Ecoinvent and published articles, are also required to develop the web application.

The GHG emissions associated with the activities mentioned above can be generally estimated by multiplying the activity data with emission factors as expressed in Eq. (1) [16]

$$CF = \Sigma \text{ (Activity Data} \times \text{Emission Factor)} \quad (1)$$

where CF is the carbon footprint (or GHG emissions) estimated in kilograms of carbon dioxide equivalent (kg CO_2-eq), activity data represents a factor that quantifies an activity used to calculate the emissions generated, and emission factor represents a factor that emits the amount of greenhouse gases per unit of the activity data.

RESULTS AND DISCUSSION

Software Description

The web application was developed using a cradle-to-gate assessment scope to quantify the CO_2-eq emissions of poultry and swine slaughtering processes were conceptualized as comprising three main components: a web-based user interface, processing system and a database as shown in Fig. 2. The web-based user interface (UI) is separated in input and output parts. At the input UI, the user needs to provide site-specific data, namely, slaughterhouse general information, activity data, and the user's defined emission factor (EF) if any user wants to calculate with his/her own EF values. Next, the data/program processing system was designed to function using three different data entry conditions, ranging from minimum to detailed data sets providing a simple, coarse, and detailed estimation of the CO_2-eq emissions. Finally, the database was created to access and store EF, historical data, and calculated results. This database enables users to access, query, visualize, analyze, and download data. As a result, this increases the performance of the web application and user interactivity as a whole.

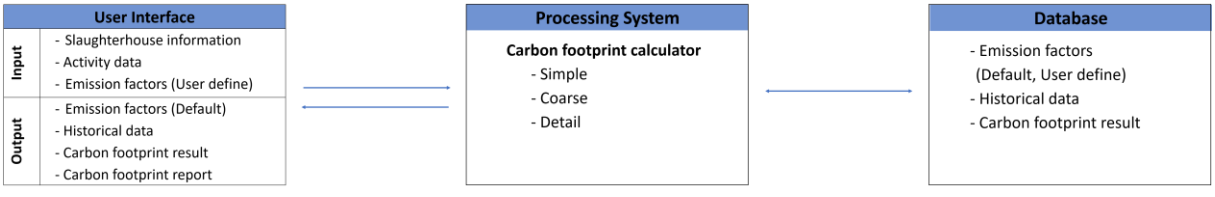

Fig. 2 Major components of the application

Data Processing Sequence

Figure 3 shows data flow of the developed web application. The tool is broken down in 11 sequential steps, six gather user input (process 1.0-6.0), two are background processing (process 7.0-8.0), two provide feedback to the user (process 9.0-10.0), and the last one manages software by an administrator (process 11.0). At the home page, a general/company user (non-admin and non-group user) can select either a new registration or log-in as current user to access the web application. The system will then connect to the database of the 'user table' and 'group table' to classify the user account in 3 levels as an administrator, the general user or group user, to receive the data accessibility level. After log-in, the general/company user could add a new company or select a company to estimate GHG emissions of the slaughterhouse. At process 2.0, the application will access the database of the 'company table' to show the historical information for the selected company. However, when 'add new company' is selected at this process, the pop up will appear for the data entry of its location and general information of the slaughterhouse. After finishing the process 2.0, the user could add new calculations (process 4.0) or go to process 5.0 to 'select historical calculation'. In the case of 'add new calculation' mode, the user has three options to select: simple, coarse or detailed for the data entry in the next process (process 6.0). The selected option will be stored at the database of 'save option table'. At process 7.0, while the calculation process is working, the EF value from the EF table (process 3.0) will be used to multiply with the inventory of activity data input to estimate the GHG emissions. However, when 'select historical calculation' mode is chosen, the user selects to open a previous estimation (process 5.0); he/she can see or edit the existing input data through the web application directly (process 6.0), and recalculate on process 7.0 or see the CF results (process 8.0-9.0). When each mode is running ('add new calculation' mode or 'select historical calculation' mode), the system will connect to the database of the 'save option table' and 'save input table' to record and retrieve all data to show on a web page. The CF result will be used to create graphs (process 8.0) to present in the next process. At process 9.0, the user is able to change the displayed functional units based on live animals, carcasses or product weight. Once the user changes, the web app will then recalculate and send back the new CO_2-eq results per the functional unit selected by the user. The results will be stored after finishing work at the back end and can be retrieved conveniently for reviewing and updating at the next visit. In addition, all inputs and results can be exported as a PDF file (process 10.0).

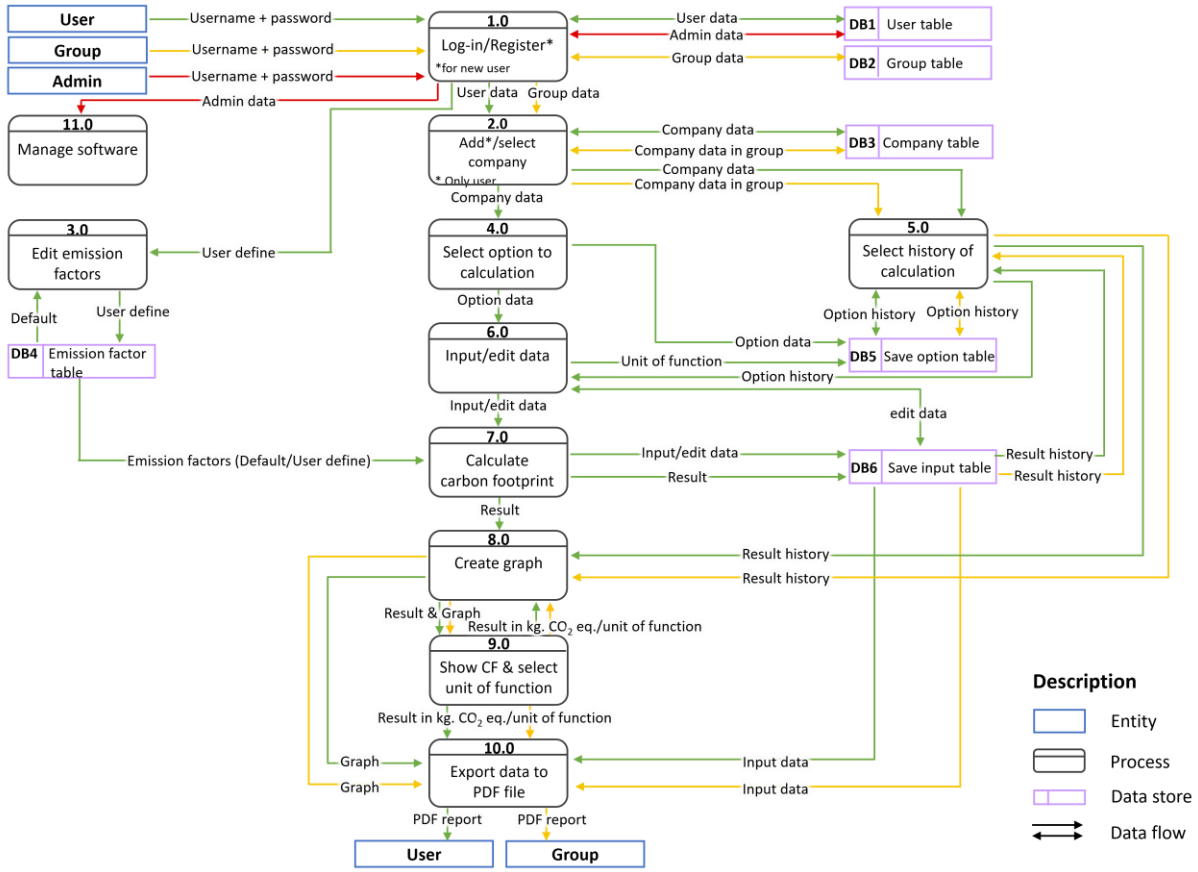

Fig. 3 Data flow diagram with entity, process, and data store

Relational Database Model

The database of this application was developed using a relational database model to organize and store data as a set of six database tables that has the primary key-foreign key rapport to create interaction among all tables (see Fig. 4). The database is the table storing account information, related companies or associations, slaughterhouse information, EFs, historical data of calculation options, and input data related to carbon footprint result. Databases (or tables) are linked in an one-to-many relationship, meaning the data which is a primary key of the first table is associated with the foreign key of the second table as multiple matching rows. For example, the user can create many companies under each user account and each company can estimate its carbon footprint many times. These relations can help to represent accurate data when the user accesses and queries the historical data of each slaughterhouse because the primary key of the 'User ID', 'Company ID', and 'Save Input ID' is uniquely identified in each row of this web application.

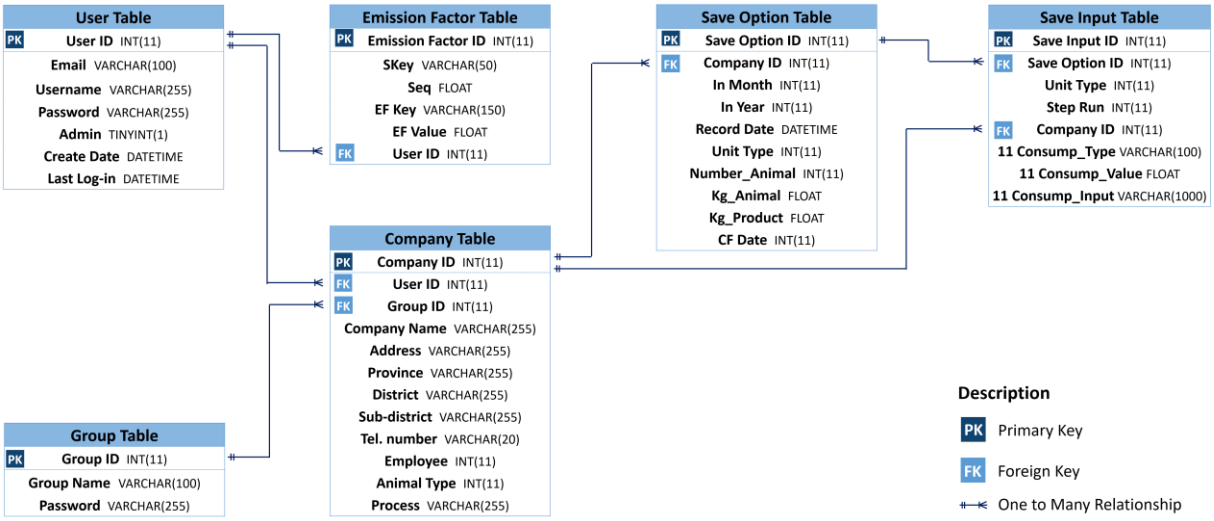

Fig. 4 Relational database model of the web application

Web User Interface

Figure 5 shows examples of the graphical user interface (GUI) of the developed web application: main page, input data page, and result page. The main page depicts the general information of the slaughterhouse involving address, contact number, and types of animal to be slaughtered. Regarding input data, several web pages of different activity data have been created for user's data entry, depending on the analysis option chosen as mentioned above (simple, coarse, or detailed). These pages contain several data items that were reviewed accordingly to the current slaughtering process of the country. In addition, the relevant graphic icons, visual indicators, and drop-down lists were added to the created web pages instead of texts. These features will give an easy-to-understand overview of the data input and make the application more attractive to the user. The result page can present the total CO_2-eq emitted based on live animal-based units or carcass-based units and illustrated as a pie chart or bar graph for different consumption categories or detailed slaughtering activities, respectively.

Web Application Functionalities

Three functions of various estimation levels

Unlike many other simple web apps, this tool offers three methods for entering consumables used at the slaughterhouse, covering the easiest to detailed ways to provide input data, called "simple", "coarse", and "detailed", so a small to large scale slaughterhouse will be able to use this tool. When using the easiest method by entering minimal input data, the user will receive a roughly calculated result of total CO_2-eq emissions. On the other hand, the coarse and detailed methods are more complicated but the informative results will be analyzed and visualized for further discussion on different resource type consumption and how the company uses resources for each slaughtering activity. In addition, because of a large number of such inputs is required for coarse and detailed estimation, a navigation tool is provided on the left menu to help the user easily navigate slaughtering steps to indicate where the data entering is up to. At the transition between steps, designed necessary data validation and null check are automatically implemented by

setting data requirements for user input to avoid errors. These involve functional units (number of live animals, carcasses, and product meat weight), and mass balance between live animals and meat product (product weight ≯ live animals).

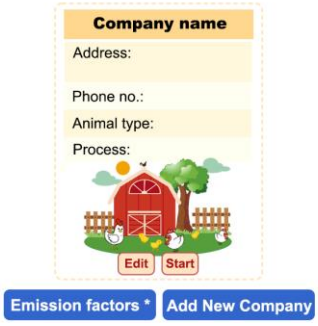

(a) Main page

(b) Input data page

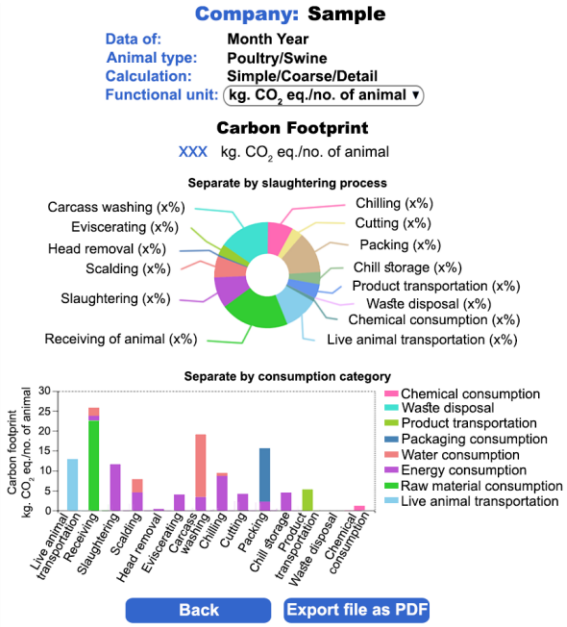

(c) Result page

Fig. 5 Examples of web user interface of the developed application

EF management

As mentioned in the methodology section, the default EFs basically collected from various databases can be categorized in eight groups, namely raw material, energy, water, packaging, chemicals, waste disposal, transportation, and product. They were stored and manipulated as in the database table named 'Emission Factor Table'. Most users do not know the EF related to the activity data, so these default values will allow users to immediately estimate the CO_2-eq emitted from their processes by using our web app. These EF values were well chosen from many reliable sources both national and international databases (when not available in Thailand). In addition, when any user knows his/her own EFs and desires to use them for the estimation, the tool is also designed to change, save, and reset these values easily.

Report/export documentation

In addition to displaying the CO_2-eq results over the web page, the application is also able to generate a report and export it in PDF file format. The report contains all general information of the slaughterhouse, the inventory of input data, and calculated CO_2-eq emission results (carbon footprint), including graphs. This will allow the user to easily print and view all information together. It will be useful to assist further discussion on reducing CO_2 emissions.

Confidentiality to Access the Database

The system offers confidentiality and security for the general/company user to access his/her data. All information including input data inventory and GHG emissions can be saved privately. This means it is available only to the specific company owner to open and edit the historical data and estimation results.

Software Availability

The developed web application to estimate CO_2-eq emissions (carbon footprint) of the Thai poultry and swine slaughtering industry can be accessed through any device such as desktop computers, laptops, tablets, and mobile phone over an internet connection using Hypertext Transfer Protocol (HTTP) via modern web browser. The web application can be found online at http://www.carbonfootprintthailand.com/Slaughter

CONCLUSION

The web application developed in this study is an analytical tool to estimate CO_2-eq emissions for poultry and swine slaughtering processes. The usefulness of this application is to aid Thailand

slaughterhouse industries to calculate and understand how much and how they contribute GHG emissions to the environment. It implies the current resource use (inputs) and change, subsequently leading to reduced GHG emissions. The output generated by the web application is reliable because of our careful emission facter selection. Moreover, many functionalities are considered and incorporated in the application to facilitate the user's estimation such as data input conditions (simple, coase, and detailed data entry), navigation tool, functional unit selection, data validation and null check, EF management, report/ export documentation, and data confidentiality and security. All these features are necessary, but the tool should not require too much effort from the user.

ACKNOWLEDGMENTS

This research work was financially supported by the Center of Excellence on Environmental Health and Toxicology (EHT), Science & Technology Postgraduate Education and Research Development Office (PERDO), Ministry of Education, Thailand. Moreover, the study was partially supported for publication by the Faculty of Public Health, Mahidol University, Bangkok, Thailand.

REFERENCES

[1] FAO. How to Feed the World in 2050 [Internet]. 2009 [cited 2019 Apr 9]. Available from http:// www.fao.org/fileadmin/templates/wsfs/docs/expe rt_paper/How_to_Feed_the_World_in2050.pdf

[2] Henchion M., McCarthy M., Resconi V. C., and Troy D., Meat consumption: Trends and quality matters. Meat Science, Vol. 98, 2014, pp. 561–568

[3] FAO. Livestock Primary [Internet]. 2019 [cited 2019 Apr 9]. Available from http://www.fao.org/ faostat/en/#home

[4] BLSC. Bureau of Livestock Standards and Certification Annual Report 2014 [Internet]. 2014 [cited 2017 Aug 27]. Available from http://certify. dld.go.th/certify/index.php/th/2016-05-01-14-50-24/ 50-2016-05-03-02-34-53/108-2016-05-27-01-52-19

[5] USDA-FAS. Livestock and Poultry: World Markets and Trade [Internet]. 2017 [cited 2017 Dec 10]. Available from http://usda.mannlib.cornell.edu/Mann Usda/viewDocumentInfo.do?documentID=1488

[6] Reyes Y. A., Barrera E. L., Valle A. S., Gil M. P., García O. H., and Dewulf J., Life Cycle Assessment for the Cuban pig production: Case study in Sancti Spiritus. Journal of Cleaner Production, Vol. 219, 2019, pp. 99-109.

[7] Treu H., Nordborg M., Cederberg C., Heuer T., Claupein E., Hoffmann H., and Berndes G., Carbon footprints and land use of conventional and organic diets in Germany. Journal of Cleaner Production, Vol. 161, 2017, pp. 127-142.

[8] Meneses M., Torres C.M., and Castells F., Sensitivity analysis in a life cycle assessment of an aged red wine production from Catalonia, Spain. Science of The Total Environment, Vol. 562, 2016, pp. 571-579.

[9] O'Brien D., Capper J. L., Garnsworthy P. C., Grainger C., and Shalloo L., A case study of the carbon footprint of milk from high-performing confinement and grass-based dairy farms. The Journal of Dairy Science, Vol. 97, Issue 3, 2014, pp. 1835-1851.

[10] Chansod K. The development of a compact, easy-to-use carbon footprint analysis software for the standard design of corrugated boxes and plastic containers for food packaging [Master Thesis]. Bangkok: Mahidol University; 2011.

[11] Thongiem A. The development of a compact easy-to-use carbon footprint analysis software for the standard design of glass and aluminium beverage containers [Master Thesis]. Bangkok: Mahidol University; 2011.

[12] Machwitz M., Hass E., Junk J., Udelhoven T., and Schlerf M., CropGIS – A web application for the spatial and temporal visualization of past, present and future crop biomass development. Computers and Electronics in Agriculture (2018), https://doi.org/10.1016/j.compag.2018.04.026

[13] Delipetrev B., Jonoski A., and Solomatine D. P., Development of a web application for water resources based on open source software. Computers & Geosciences, Vol. 62, 2014, pp. 35–42.

[14] Carlson B.R., Carpenter-Boggs L.A., Higgins S.S., Nelson R., Stöckle C.O., and Weddell J., Development of a web application for estimating carbon footprints of organic farms. Journal of Computers and Electronics in Agriculture, Vol. 142, 2017, pp. 211-223.

[15] Djekic I. and Tomasevic I., Environmental impacts of the meat chain - Current status and future perspectives. Trends in Food Science & Technology, Vol. 54, 2016, pp. 94-102

[16] BSI. Guide to PAS 2050 How to assess the carbon footprint of goods and services [Internet]. 2008 [cited 2017 Sep 12]. Available from https:// www.bsigroup. com/PAS2050

9th Int. Conf. on Geotechnique, Construction Materials and Environment,
Tokyo, Japan, 20-22 November 2019, ISBN: 978-4-909106025 C3051

SAFETY AND OPERATIONAL ANALYSIS FOR MEDIAN U-TURN INTERSECTIONS IN THAILAND

Nopadon Kronprasert, Ph.D.[1], Pavee Kuwiboon [2] and Wachira Wichitphongsa[3]
[1,2,3]Department of Civil Engineering, Chiang Mai University, THAILAND

ABSTRACT

At major conventional intersections along high-speed divided highways, road users experience serious accident risks and long travel delay. Specifically, vehicles from minor roads at unsignalized intersections have to make a direct crossing at the main intersection. To solve safety and mobility problems at conventional intersections. a median U-turn intersection design has recently proposed among highway authorities in Thailand. This design removes the median opening at the main intersection, restricts vehicles from making a direct crossing, guides them to make a U-turn at the downstream median U-turn opening, and returns to the main intersection. For such design, the distance between the median U-turn opening downstream and the main intersection (called a median U-turn offset) is the most important design parameter that influences the safety and operating efficiency. Too short median U-turn offset will result in harsh lane-change conflict for minor-road traffic, while too long median U-turn offset will increase vehicle travel time. This paper proposes the framework to rationally recommend the median U-turn offsets of such design. The microscopic traffic simulation models are developed to estimate vehicle travel time, and the crash surrogates are used to estimate the number of vehicles involved in conflicts. The median U-turn offsets that balance the operating and safety efficiencies are recommended. It is found that the recommended median U-turn offsets are sensitive to volumes on major and minor roads, vehicle speed, and vehicle composition. The proposed framework is then applied to the real-world highway improvement projects.

Keywords: Safety, Surrogate safety assessment, Traffic simulation, Intersection, Median u-turn

INTRODUCTION

Managing traffic mobility and safety at intersections is one of the most challenging tasks for highway engineers. At major intersections, road users often experience travel delay during peak periods and suffer serious accident risks. To solve such problems, various alternative intersection designs have recently been proposed among highway authorities, such as roundabouts, restricted-crossing U-turn intersections. [1] The basic premise of such designs is to separate different traffic movements, provide more uninterrupted flow, and minimize severe traffic conflicts.

In Thailand, road users experience severe far-side angle accident risks and long travel delay at a conventional unsignalized intersection where a minor road intersects a high-speed multilane road. To improve safety and mobility at an intersection, a median U-turn intersection design is gaining acceptance. This design prohibits vehicles from a minor road to directly cross the main intersection, but guides them to make a U-turn at the downstream median U-turn opening and return to the intersection. [1]-[2] The design features of conventional unsignalized and median U-turn intersection designs considered in this study are shown in Fig. 1.

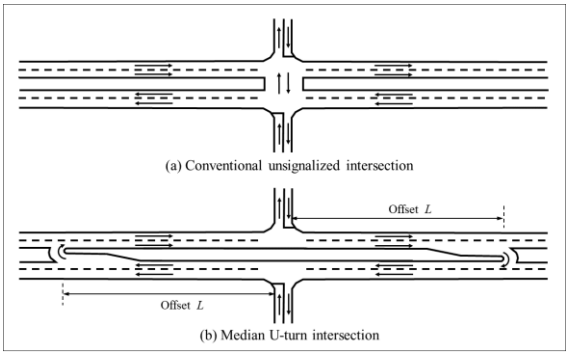

Fig. 1 Intersection configuration

For this type of intersection design, the distance between the median U-turn opening and the main intersection, called median U-turn offset (L) shown in Fig.1(b) is the most important design parameter that influences the operating and safety efficiency. Too far median U-turn offset will increase vehicle travel time, while too short offset will result in harsh lane-change conflicts for minor-road traffic. The objectives of this study are (i) to propose the model framework that can rationally recommend the median U-turn offsets for median U-turn intersection designs; and (ii) to apply it to determine the U-turn openings for a real-world highway intersection improvement projects.

LITERATURE REVIEW

Median U-Turn Intersection Design

A median U-turn treatment is an alternative low-cost at-grade intersection design that offers the potential to improve safety and mobility of conventional intersections along multi-lane divided highways. The design restricts some or all of the direct turn movements at the main intersection and provides the median U-turn downstream to make a turn. [3] Past studies on this subject mainly focused on determining the operational or safety benefits of intersection designs. For the operational benefits, the alternative design performs better than the conventional design in terms of average delay, average queue length, and total throughputs. [4-5] For the safety benefits, the alternative design theoretically reduces the number of conflicts by half.. The before-and-after studies also showed the reduction in numbers of crashes. [5]-[7]

By its design, there are a number of factors affecting the safety and efficiency of median U-turn intersections, such as the number of traveled lanes, the presence of acceleration lane, the U-turn opening configuration, and the median U-turn offsets.

In practice, the median U-turn offset are varied. For unsignalized types, the median U-turn offsets range from 100 to 900 m. [2], [9] For signalized types, the median U-turn openings are relatively short. The openings are located closer to the main intersection, typically 100 to 180 m based on signal timing [8]

Microscopic Traffic Simulation Model

A microscopic traffic simulation is a powerful tool that can analyze the complex traffic flow and represent traffic movement under various scenarios. It is used to simulate and replicate several driving behaviors. In highway and traffic engineering applications, a microscopic traffic simulation is widely accepted and used as a reliable decision tool. In general, the development of microscopic traffic simulation model involves network coding, model calibration, and model validation. [9]

Surrogate Safety Assessment Model

The surrogate safety assessment model is an analytical tool to identify conflict events by assessing surrogate safety measures, such as time to collision, post encroachment time, deceleration rate, maximum speed, and speed difference. The model analyzes the frequency of conflict events (or traffic crash avoidance) in a traffic network using vehicle trajectories recorded in a microscopic traffic simulation. Typically, three categories of conflict events can be identified: rear-end conflict events, lane-change conflict events, and path-crossing conflict events. [10]

METHODOLOGY

Model Framework

The study proposes the model framework to analyze the safety and operational performance of intersection designs as shown in Fig. 2. The details are as follows.

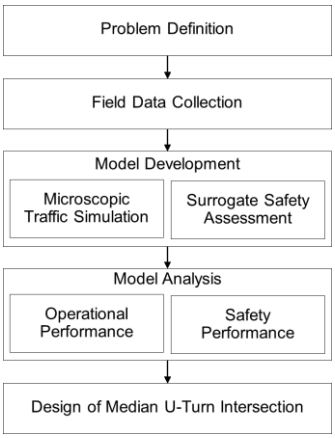

Fig. 2 Model framework

Problem Definition and Data Collection

This study focuses on recommending the median U-turn offsets of median U-turn intersections located on a 4-lane divided major road intersecting with a 2-lane minor road. Although the scope of the study is limited to this intersection configuration, the proposed model framework can be applied to other intersection configurations.

Next, the parameters required to develop traffic simulation models were identified. These parameters include road network geometry, input traffic on major and minor road, turning movements on all intersection approaches, traffic compositions, desired vehicle speed, and gap acceptance for all types of vehicle and movement.

All necessary data were collected from the intersections on a high-speed corridor. The relevant data are road geometry (i.e. the configuration of intersections and U-turn openings), traffic data (i.e. traffic volume, speed, traffic composition, gap acceptance), and socio-economic data (i.e. value of time, unit cost of accident)

Model Development

The simulation models were developed using the microscopic traffic simulation package (PTV Vissim) and surrogate safety assessment model (SSAM) for evaluating operational and safety performances. [11]-[12] The models were built for various sets of input variables including traffic volume ranges from 200 to 600 vehicles per hour per lane; the median U-turn offset ranges from 100 to 800 m.

Model Analysis

The recommended median U-Turn offsets were determined by minimizing the marginal user costs at an intersection**.** The marginal user costs represent the operational and safety effects of traffic flows at an intersection**.**

Operational Performance

The operational performance is measured by the excess travel time cost. Using a microscopic traffic simulation, travel times that all vehicles used to maneuver through the intersection for both conventional and proposed intersection designs were recorded. The excess travel time cost is then calculated by the difference of travel times between two designs, and conerting it to the annual costs by taking into consideration the annual traffic and value of time.

Safety Performance

The safety performance is measured by the accident cost saving. Using a surrogate safety assessment model, the reduction in number of conflicts that vehicles encountered when making a U-turn compared with the direct turn at the intersection. The accident cost saving is then calculated by converting the number of conflicts by taking into consideration the accident to onflict ratio and the unit cost of accident.

Determination of Median U-Turn Offset

The median U-turn offsets are then determined based on minimum total (marginal) user cost concept as shown in Fig. 3.

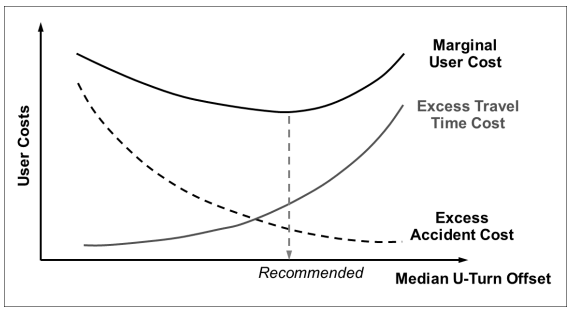

Fig. 3 Minimum user cost concept

APPLICATION TO INTERSECTION DESIGN

The proposed framework was applied to a real-world highway improvement project in Chiang Mai, Thailand. The existing corridor is a 12-kilometer 4-lane divided high-speed highway in a suburban area. There are many intersections and U-turn openings along this corridor as shown in Fig.4; and as a result, there are many road crashes at these locations. The goal of the improvement project is to relocate the median U-turn openings by introducing median U-turn intersection design concept along this corridor. Figure 5 illustrates the snapshot of traffic simulation model developed for evaluating the operational performance of this case study.

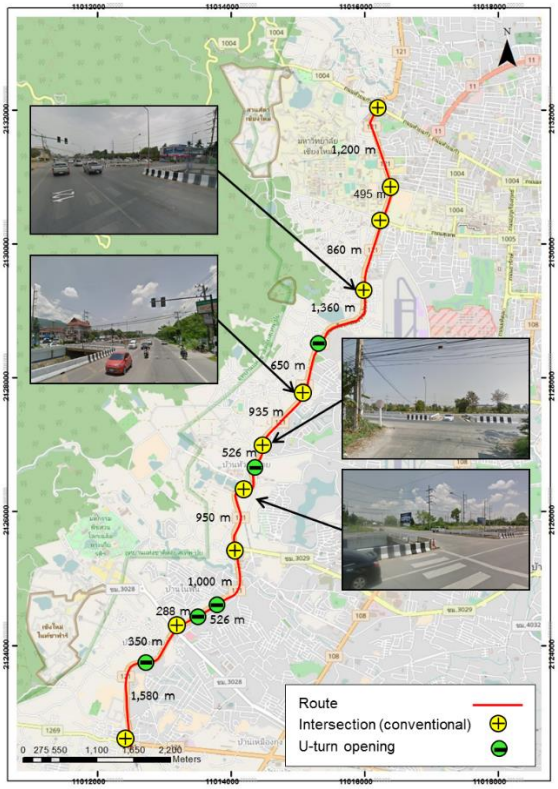

Fig. 4 Existing corridor

Fig. 5 Snapshot of simulation model

Using a microscopic traffic simulation model, travel time associated with conventional and proposed design were measured, and then travel time costs were calculated. The result shows that travel time cost increases with the increase in median U-turn offset for any given major- and minor-road traffic volumes as shown in Fig. 6. The figure also shows that the travel time costs increase significantly when the median U-turn offset increase greater than 500 m.

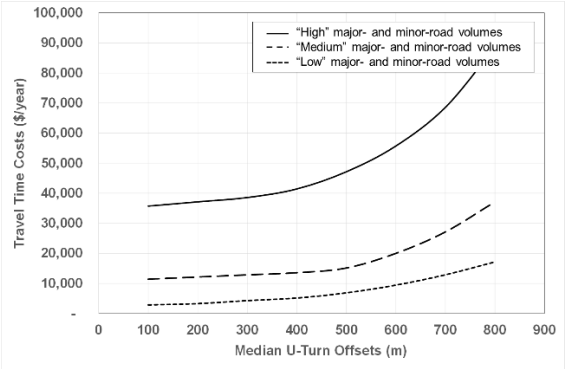

Fig. 6 Travel time costs with respect to different median U-turn offsets

Using a surrogate safety assessment model, the conflict points associated with a given intersection design can be measured. Figure 7 shows the conflict points obtained from a surrogate safety assessment model. Three conflict types were marked by different colors: red is for crossing conflict, green is for lane-change conflict, and yellow is for rear-end conflict.

The result intuitively shows that accident costs decrease with the increase in median U-turn offsets for any given major- and minor-road traffic volumes as shown in Fig. 8. The figure shows that the long median U-turn offsets can reduce the loss of accident.

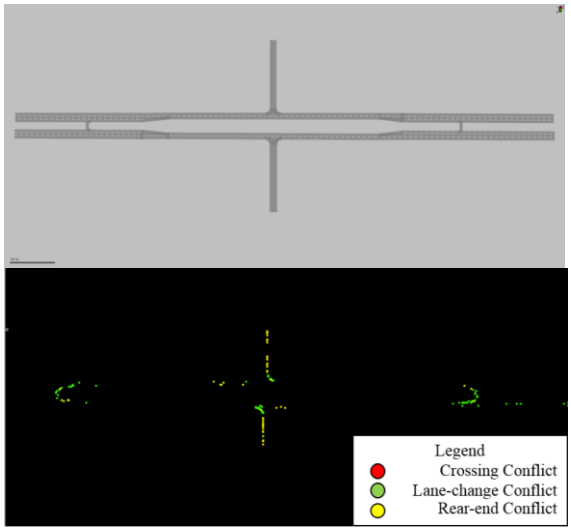

Fig. 6 Conflict points by surrogate safety assessment

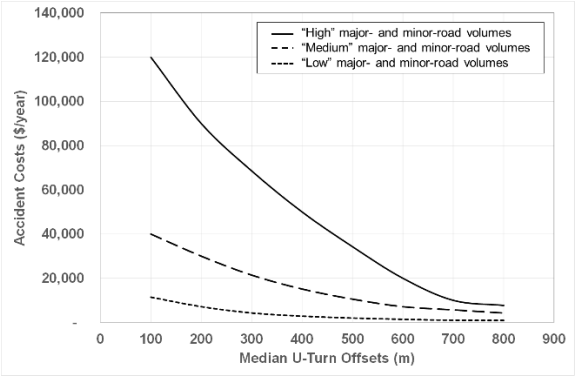

Fig. 8 Accident costs with respect to different median U-turn offsets

For a given traffic condition and design setup, the median U-turn offset can be determined by minimizing the total user cost (which combines travel time costs and accident costs.) Figure 9 illustrates the relationship of total user costs and median U-turn offsets. The results show that for a given traffic volume, there is an optimal value of median U-turn offset. Too short offset may cause low travel time cost with very high accident cost, while too long offset may cause very high travel time cost with low accident cost.

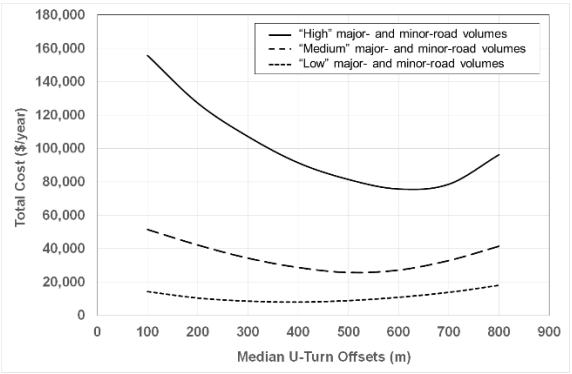

Fig. 9 Recommended median U-turn offsets based on minimum costs

Table 1 presents the set of recommended median U-turn offsets in meters for different traffic volumes on major and minor roads (100 to 600 vehicles per hour per lane).

Figure 10 plots the recommended offsets for different combination of major-road and minor-road traffic volumes. The higher traffic volumes, the longer median U-turn offsets are. Table I and Fig. 10 are complementary; the former shows in specific values, while the latter is a look-up chart for practitioners. The recommended offsets can be determined if traffic volume on a major- and a minor road are given.

Table 1 Recommended median U-turn offsets for different traffic volumes

Major road (veh/hr/ln)	Minor road (veh/hr)					
	100	200	300	400	500	600
100	270	295	310	330	340	345
200	310	330	347	360	370	380
300	345	370	390	410	430	445
400	390	420	435	470	495	520
500	445	475	495	520	550	570
600	535	550	565	580	595	630

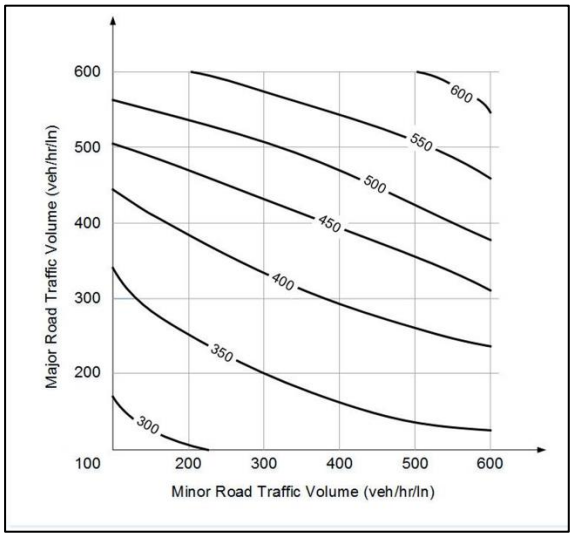

Fig. 10 Look-up chart on recommended median U-turn offsets for different sets of major-road and minor-road traffic volumes

Sensitivity Analysis

The study performs the sensitivity analyses to determine which parameters are significant and should be taken into account to the proposed model. The effects of some parameters on the median U-turn offsets are discussed below.

- Effect of heavy vehicles. The heavy vehicles require longer gap to merge the traffic and change lanes than other vehicles. The proposed model suggests the need to consider the percentage of heavy vehicles. The median U-turn offset should be longer than what is proposed in Fig. 10 by 15-20% for every 5% increase of heavy vehicles.
- Effect of vehicle operating speed. The operating speed on a major road significantly affect the median U-turn offset. The higher operating speed on a major road creates difficulties for vehicles to enter the major road, and at the same time force them to the risky situation.
- Effect of socio-economic factors. The economic factors that used to convert operational and safety performance to single comparable performance have insignificant effect on the optimal median U-turn offsets. For example, the value of time and unit of accident cost will proportionally shift the total costs, but not the recommended median U-turn offsets.

Recommended Median U-turn Offsets

To apply the simulation analysis to search for the optimal median U-turn offsets in the real-world situations, the recommended offsets from Table I and Fig. 10 can be used. It is however noted that the recommended offsets are proposed based on typical simulation models. When multiple intersections are considered or the intersections are varied from the typical one, the model framework must be applied together with the simulation model of the entire corridor. Figure 11 presents the locations of the median U-turns proposed for the highway improvement project in the application.

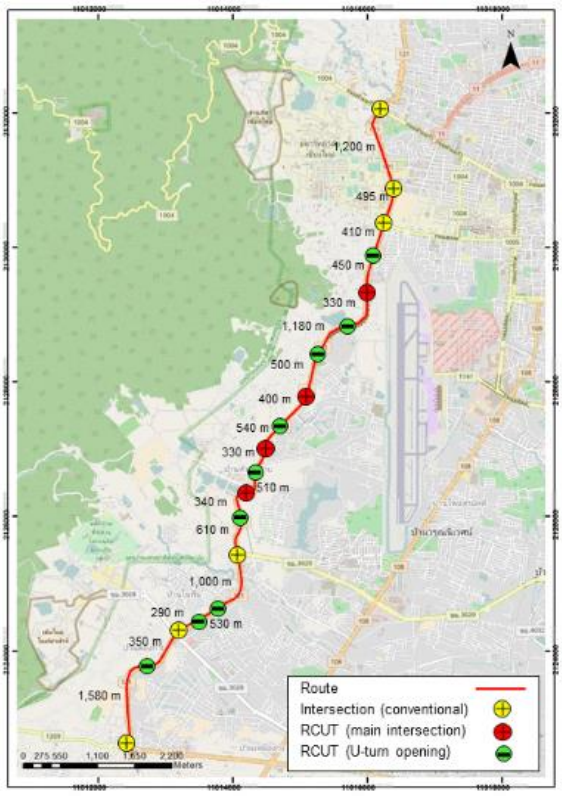

Fig. 13 Proposed RCUT intersections and their median U-turn offsets

CONCLUSIONS

A median U-turn intersection is an alternative

design that helps improve safety and mobility at major at-grade intersections by eliminating the median opening at the main intersection and converting severe crossing conflicts into merging and weaving conflicts. For its design, the distance between the main intersection and the downstream U-turn opening (or median U-turn offset) is the critical design parameter influencing efficiency and safety of the intersection.

This paper develops a model framework for determining the median U-turn offsets of median U-turn intersection design using simulation analysis. The analysis considers the trade-off between the increase of travel time required to make a U-turn downstream and the reduction of potential accident risks due to fewer number of conflicts. The study recommends the median U-turn offsets for a given traffic condition which minimizes the cost of road users including the travel time cost and accident cost. The results also note that the median U-turn offsets are sensitive to the major-road and minor-road traffic volumes, vehicle composition, and vehicle operating speed.

The proposed model framework and the exhibits allow the engineers to examine the proper locations of median U-turns for median U-turn intersection design. Therefore, the model framework is useful for both practitioners and researchers in real-world highway improvement projects.

ACKNOWLEDGMENTS

The authors would like to gratefully acknowledge financial support of the research project from Thailand Research Fund MRG5980074, and the Excellence Center in Infrastructure Technology and Transportation Engineering (ExCITE) of Chiang Mai University for technical support.

REFERENCES

[1] R.P. Kramer, “New combination of old techniques to rejuvenate jammed suburban arterials” Proc. of ITE Nat. Conf., pp.139-148, 1987

[2] T.H. Maze, J.L Hochstein, R.R. Souleyrette, H. Preston, and R. Storm, Median Intersection Design for Rural High-Speed Divided Highways, NCHRP Report 650. Washington, D.C., Transportation Research Board, 2010.

[3] J. Hummer, B. Ray, A. Daleides, P. Jenior, and J. Knudsen, Restricted crossing U-turn inersection: information guide, Washington, D.C., FHWA, 2014.

[4] R.L. Haley, S.E. Ott, J.E. Hummer, J.E. Foyle, C.M. Cunningham, and B.J. Schroeder. “Operational Effects of Signalized Superstreets in North Carolina” Trans. Res. Rec., vol. 2223, pp.72-79, 2011.

[5] W. Zhang, N. Kronprasert, and J.G. Bared, “Restricted Crossing U-Turn Intersection Design for Improving Safety and Mobility at High Speed Stop Controlled Intersections” Road Safety & Sim, Italy, 2013.

[6] S.E. Ott, R.L. Haley, J.E. Hummer, R.S. Foyle, and C.M. Cunningham, “Safety effects of unsignalized superstreet in North Carolina” Acc. Anal. & Prev., vol. 45, pp.572-579, 2012.

[7] W. Zhang, and N. Kronprasert, “The ABCs of designing RCUTs” Public Roads, vol.78, no.2, 2014.

[8] F. Koupke, and H. Levinson, Access management guidelines for activity centers. NCHRP Report 348, Washington, D.C., Transportation Research Board, 1992.

[9] R. Dowling, A. Skabardonis, and V. Alexiadis, Traffic analysis toolbox volume III: Guidelines for applying traffic microsimulation software. FHWA-HRT-04-040, Washington, D.C.. 1994.

[10] F. Huang, P. Liu, H. Yu, and W. Wang, Identifying if VISSIM simulation model and SSAM provide reasonable estimates for field measured traffic conflicts at signalized intersections. Acc. Anal. & Prev. vol.50, pp.1014-1024, 2013.

[11] Planung Transport Verkehr AG, Vissim 8.0 User Manual. (PTV), Karlsruhe, 2015.

[12] D. Gettman, and L. Head, Surrogate Safety Measures from Traffic Simulation Models. FHWA-RD-03050, Washington, D.C., 2003.

9th Int. Conf. on Geotechnique, Construction Materials and Environment, Tokyo, Japan, 20-22 November 2019, ISBN: 978-4-909106025 C3051

EFFECTIVENESS OF RIVER INSECTS AND WATER PLANTS AS AN INDEX OF ZN AND FE CONTAMINATION FOR RIVER IN THE KINOKAWA RIVER CATCHMENT

Takuma Kubohara[1] and Hiroyuki Ii[2]
[1]Kinokawa City Office, Japan; [2]Faculty of Systems Engineering, Wakayama University, Japan

ABSTRACT

It has not been studied whether river insects and water plants are useful for an index of Zn and Fe contamination in the Kinokawa River catchment. Useful species as an index of Zn and Fe contamination needs a high metal concentration in a contaminated area, a low metal concentration in a non-contaminated area, and a high and a wide range of metal concentration. Zn and Fe concentrations of crane fly larva were high around the closed Cu mine area (88 to 420 and 1,300 to 9,300 mg/kg-dry for Zn and Fe) and were low in the other areas (81 to 180 and 110 to 5,700 mg/kg-dry for Zn and Fe). Crane fly larva had high and a wide range of Zn and Fe concentration among river insects. Zn and Fe concentrations of bryophyte were high around the closed Cu mine area (34 to 8,900 and 110 to 58,000 mg/kg-dry for Zn and Fe) and were low in the other areas (24 to 1,100 and 110 to 34,000 mg/kg-dry for Zn and Fe). Bryophyte had the highest and a wide range of Zn and Fe concentration among water plants. Therefore, it was thought that crane fly larva in river insects and bryophyte in water plants were useful species for an index of Zn and Fe contamination. Bryophyte was useful species for an index of Zn and Fe contamination among river insects and water plants because bryophyte had the highest and a wide range of their concentrations among them.

Keywords: Zn, Fe, Bryophyte, Crane fly larva, River

INTRODUCTION

Metal concentration of river water and river sediment (soil and mud) are measured in order to investigate the influence of heavy metals for aquatic life in river. However, metal concentration of river water is always very low and is changeable depending on the change of flow rate. Heavy metals of river sediment are soluble or insoluble. Many kinds of heavy metals of river sediment elute in river water. Then, total concentration of heavy metal of river sediment does not represent the heavy metal mass transfering in river. Therefore, the metal concentrations of river water and river sediment were not always useful for an index of the influence of heavy metals for aquatic life in river. On the other hand, it is thought that the metal concentrations of river insect and water plant to be useful for investigating the influence of heavy metals for aquatic life in river because river insect and water plant intake and accumulate heavy metal from river water and sediment in the long term.

At past, metal concentrations of caddice-worm [1]-[2], dobsonfly larva [3]-[4], stonefly larva [5], mayfly larva [5]-[6], reed [7]-[8], fern [9]-[10], bryophyte [11]-[12] have been studied. However, few reports were available on useful species as metal contamination index using river insects [13]-[14]. Then, we have studied Cu, Co and Ni concentrations of river insects and water plants in the Kinokawa River catchment and have determined useful species for an index of Cu, Co and Ni contamination for river [15]. However, it has not been studied whether river insects and water plants are useful for an index of other metal contamination, in particular Zn and Fe, in the Kinokawa River catchment. Therefore, Zn and Fe concentrations of river insects and water plants were measured in the Kinokawa River catchment and then the relation between Zn and Fe concentration of river insects and water plants and Zn and Fe contamination for river was analyzed. Useful species as an index of metal contamination needs a high metal concentration in a contaminated area and low metal concentration in a non-contaminated area. Moreover, it needs a high and a wide range of metal concentration and also very popular.

STUDY AREA

Figs.1 and 2 show location of study area and the Kinokawa River catchment. The Kinokawa River is located in the center of Kinki district and flows into the Kii Channel through the Kii plain. The Kinokawa River is classified into A river based on the Ministry of Land, Infrastructure, Transport and Tourism of Japan. The length and total area of the Kinokawa River are 136 km and 1,750 km^2 [16]. The Sanbagawa Belt composed of metamorphic rocks, serpentinite and crystalline schist is distributed in the southwest

part and the northeast part of the catchment. The Hidakagawa Group composed of sedimentary rocks, sandstone and shale is distributed from the southern part to the northeast part of the catchment. The Chichibu Belt composed of sedimentary rocks, sandstone, mudstone, limestone and chert is distributed in the eastern part of the catchment. The Izumi Group composed of sedimentary rocks, sandstone, mudstone and conglomerate is distributed in the northwest part of the catchment [17]. The Ryoke Complex composed of plutonic rocks, granite and gneiss is distributed in the northeast part of the catchment. In the Kinokawa River catchment, there are the closed Cu mines and serpentinite. The closed Cu mine produced a lot of Cu and Fe sulfide ore and the waste water was low pH and high concentration of sulfate with metal. The chemistry of serpentinite is quite different from the other rocks and in particular Mg and Ni concentrations of serpentinite are high.

STUDY METHOD

River insects and water plants in the river bed were sampled in the Kinokawa River catchment. Sampling points were shown in fig.2. Investigation period is July 2013 to April 2016. The number of sampling points was 109 points. Those sampling points were classified into three groups, the serpentinite area, the Cu mine area and the normal area. The kinds of sampled river insects were Japanese freshwater crab, caddice-worm, dobsonfly larva, dragonfly larva, stonefly larva, crane fly larva, mayfly larva and corixidae. However, crane fly larva was not sampled in the serpentinite area. The kinds of sampled water plants were reed, fern, moss, Japanese knotweed and coix. However, reed was not sampled in the serpentinite area. Moreover, Japanese knotweed was not sampled in the normal area. Zn and Fe concentrations of river insects and water plants were measured. The sampled river insects and water plants were desiccated by dryer at first. After drying, they were dissolved with concentrated nitric acid and it was filtered with the membrane filter with 0.45 micrometer of pore size before analysis. Zn and Fe concentrations of river insects and water plants were measured by ICP-AES (Seiko Instruments Inc., SPS1700HVR) in the laboratory of Wakayama University. The actual detection limit of ICP-AES is 0.01ppm for Zn and Fe. Water plants excluding bryophyte were divided into leaf, upper part stem, middle part stem, lower part stem and root and each part was separately analyzed.

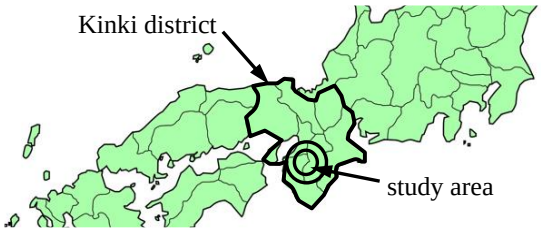

Fig.1 Location of study area.

RESULTS AND DISCUSSION

Effectiveness for Zn

Fig.3 shows Zn concentrations of river insects and water plants. Solid mark indicates Zn concentration of water plant under the detection limit, 0.01 ppm of concentration for sample solution.

Zn concentrations of caddice-worm, dobsonfly larva, dragonfly larva, crane fly larva and corixidae in the Cu mine area were 76 to 250, 310, 88 to 260, 88 to 420 and 370 mg/kg-dry, respectively. Zn concentrations of caddice-worm, dobsonfly larva,

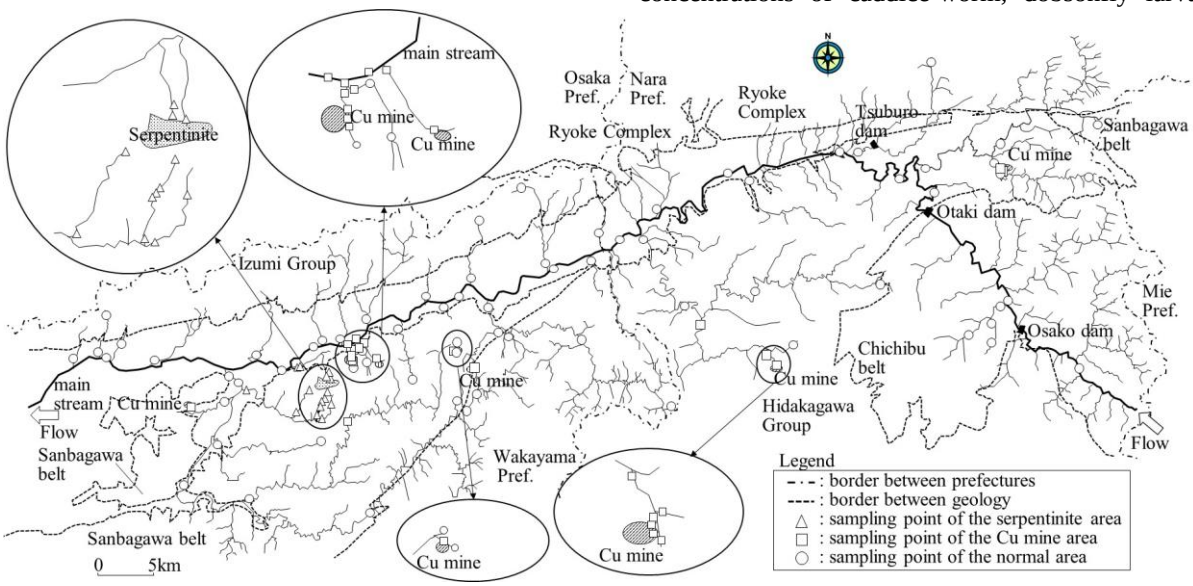

Fig.2 Study area.

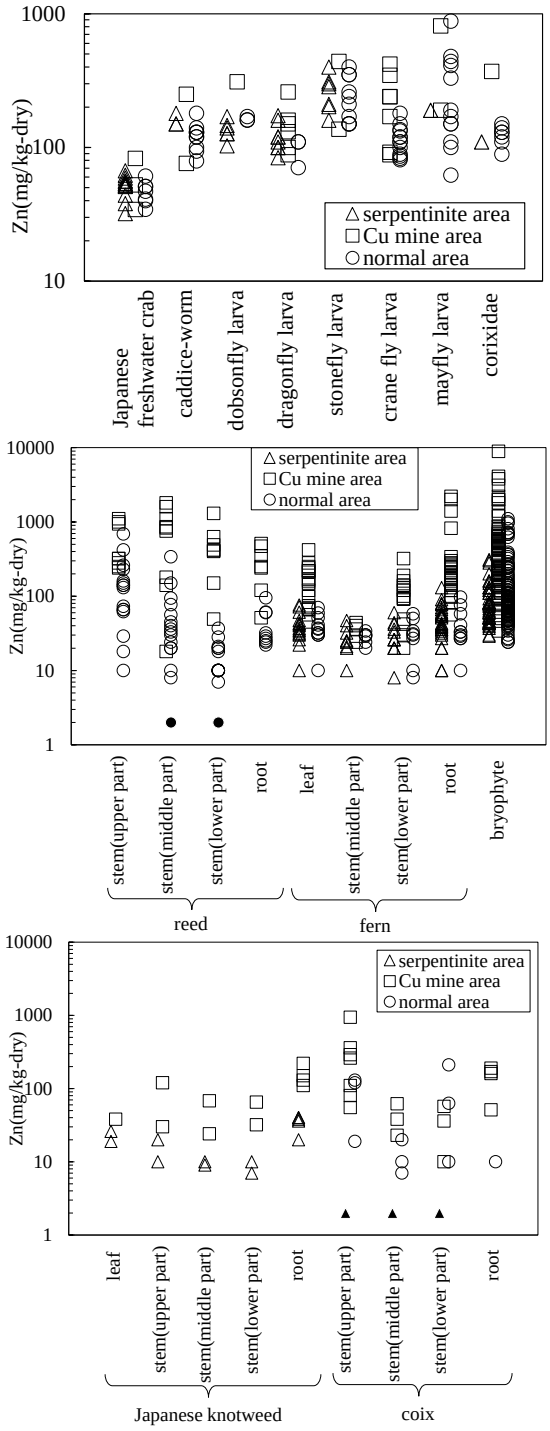

Fig.3 Zn concentrations of river insects and water plants.

dragonfly larva, crane fly larva and corixidae in the other areas were 79 to 180, 103 to 170, 70 to 173, 81 to 180 and 89 to 150 mg/kg-dry, respectively. Zn concentrations of reed, leaf and lower part stem and root of fern, bryophyte, stem and root of Japanese knotweed and upper and middle part stem and root of coix in the Cu mine area were 18 to 1,800, 20 to 2,200, 34 to 8,900, 24 to 220 and 23 to 940 mg/kg-dry, respectively. Zn concentrations of reed, leaf and lower part stem and root of fern, bryophyte, stem and root of Japanese knotweed and upper and middle part stem and root of coix in the other areas were 2 to 690, 8 to 130, 24 to 1,100, 7 to 40 and 2 to 130 mg/kg-dry, respectively. Therefore, their Zn concentrations in the Cu mine area were higher than those in the other areas. The closed Cu mine produced a lot of Cu and Fe sulfide ore and then the waste water was low pH and contained high concentration of sulfate with metal. It is reported that Zn concentrations of the cupriferous pyrite in the closed Cu mine in the Kinokawa River catchment were 100 to 25,000 ppm [18]. Therefore, it was thought that high Zn concentrations of caddice-worm, dobsonfly larva, dragonfly larva, crane fly larva, corixidae, reed, leaf and lower part stem and root of fern, bryophyte, stem and root of Japanese knotweed and upper and middle part stem and root of coix in the Cu mine area were caused by waste water and Cu and Fe sulfide ore from the closed Cu mines. On the other hand, Zn concentrations of Japanese freshwater crab, stonefly larva, middle part stem of fern and Japanese knotweed leaf in the Cu mine area were 34 to 82, 137 to 440, 24 to 44 and 38 mg/kg-dry, respectively. Zn concentrations of Japanese freshwater crab, stonefly larva, middle part stem of fern and Japanese knotweed leaf in the other areas were 32 to 67, 150 to 400, 10 to 47 and 19 to 26 mg/kg-dry, respectively. Therefore, their Zn concentrations in the Cu mine area were about the same as those in the other areas. Zn concentrations of mayfly larva and lower part stem of coix in the Cu mine area were 190 to 810 and 10 to 57 mg/kg-dry, respectively. Zn concentrations of mayfly larva and lower part stem of coix in the other areas were 62 to 880 and 2 to 210 mg/kg-dry, respectively. Therefore, their Zn concentrations in the Cu mine area were not higher than those in the other areas.

Zn concentrations of Japanese freshwater crab, caddice-worm, dobsonfly larva, dragonfly larva, stonefly larva, crane fly larva, mayfly larva and corixidae were 32 to 82, 76 to 250, 103 to 310, 70 to 260, 137 to 440, 81 to 420, 62 to 880 and 89 to 370 mg/kg-dry, respectively. Therefore, mayfly larva had the highest and a wide range of Zn concentration among river insects. Zn concentrations of reed, fern, bryophyte, Japanese knotweed and coix were 2 to 1,800, 8 to 2,200, 24 to 8,900, 7 to 220 and 2 to 940 mg/kg-dry, respectively. Therefore, bryophyte had the highest and a wide range of Zn concentration among water plants.

From the above results, mayfly larva had the highest and a wide range of Zn concentration among river insects. However, Zn concentrations of mayfly larva in the Cu mine area were not higher than those in the other areas. Useful species as an index of metal contamination needs a high metal concentration in a contaminated area and low metal concentration in a non-contaminated area. Therefore, mayfly larva was not useful species for an index of Zn contamination. On the other hand, crane fly larva also had high and a

wide range of Zn concentration among river insects. Moreover, Zn concentrations of crane fly larva in the Cu mine area were higher than those in the other areas. Bryophyte had the highest and a wide range of Zn concentration among water plants. Moreover, Zn concentrations of bryophyte were high in the Cu mine area and were low in the other areas. Therefore, crane fly larva and bryophyte were useful species for an index of Zn contamination.

Effectiveness for Fe

Fig.4 shows Fe concentrations of river insects and water plants. Solid mark indicates Fe concentration of water plant under the detection limit, 0.01 ppm of concentration for sample solution.

Fe concentrations of dobsonfly larva, dragonfly larva, crane fly larva and corixidae in the Cu mine area were 9,100, 280 to 9,100, 1,300 to 9,300 and 3,200 mg/kg-dry, respectively. Fe concentrations of dobsonfly larva, dragonfly larva, crane fly larva and corixidae in the other areas were 326 to 3,500, 250 to 2,500, 110 to 5,700 and 460 to 2,000 mg/kg-dry, respectively. Fe concentrations of middle and lower part stem and root of reed, leaf and root of fern, bryophyte, Japanese knotweed root and coix root in the Cu mine area were 10 to 13,000, 46 to 12,000, 110 to 58,000, 2,600 to 43,000 and 140 to 440 mg/kg-dry, respectively. Fe concentrations of middle and lower part stem and root of reed, leaf and root of fern, bryophyte, Japanese knotweed root and coix root in the other areas were 2 to 1,100, 79 to 3,500, 110 to 34,000, 1,600 to 6,000 and 130 mg/kg-dry, respectively. Therefore, their Fe concentrations in the Cu mine area were higher than those in the other areas. The closed Cu mine produced a lot of Cu and Fe sulfide ore and then the waste water was low pH and contained high concentration of sulfate with metal. It is reported that Fe concentrations of the cupriferous pyrite were 41.72% (417,200 mg/kg) [19]. Therefore, it was thought that high Fe concentrations of dobsonfly larva, dragonfly larva, crane fly larva, corixidae, middle and lower part stem and root of reed, leaf and root of fern, bryophyte, Japanese knotweed root and coix root in the Cu mine area were caused by waste water and Cu and Fe sulfide ore from the closed Cu mines. On the other hand, Fe concentrations of Japanese freshwater crab, caddice-worm, stonefly larva, mayfly larva, upper part stem of reed, fern stem and upper and middle part stem of coix in the Cu mine area were 46 to 465, 790 to 1,800, 183 to 240, 630 to 1,100, 20 to 370, 10 to 590 and 10 to 230 mg/kg-dry, respectively. Fe concentrations of Japanese freshwater crab, caddice-worm, stonefly larva, mayfly larva, upper part stem of reed, fern stem and upper and middle part stem of coix in the other areas were 32 to 3,500, 83 to 5,100, 11 to 1,300, 29 to 2,800, 20 to 1,500, 20 to 1,600 and 10 to 320 mg/kg-dry, respectively. Therefore, their Fe concentrations in the

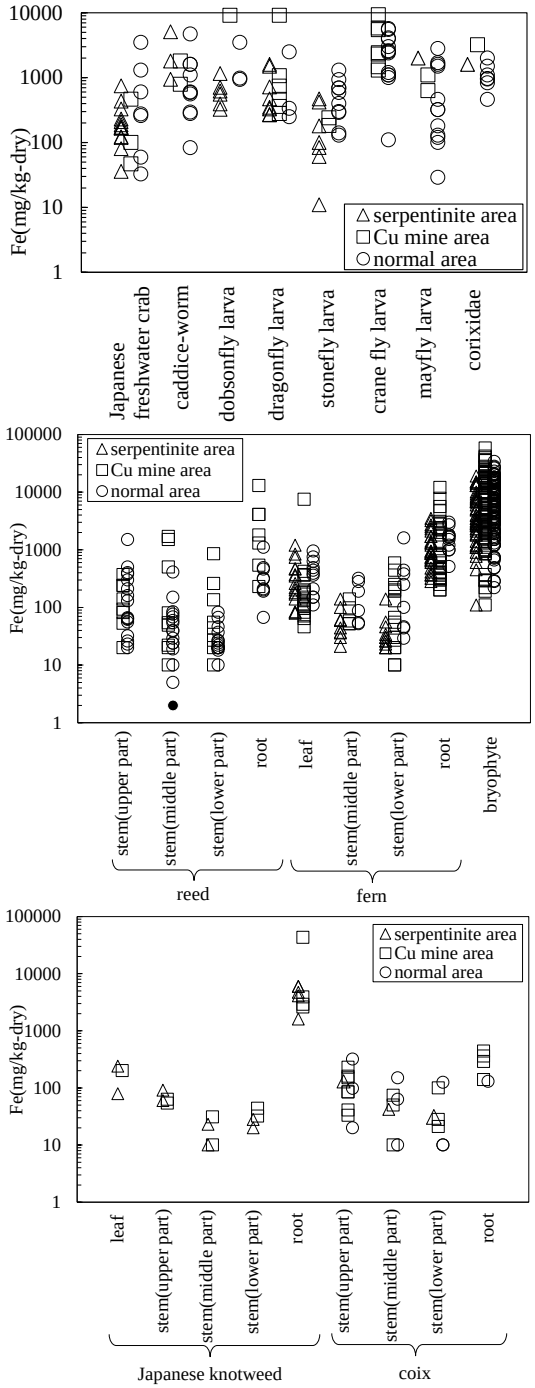

Fig.4 Fe concentrations of river insects and water plants.

Cu mine area were not higher than those in the other areas. Fe concentrations of leaf and stem of Japanese knotweed and lower part stem of coix in the Cu mine area were 10 to 200 and 21 to 100 mg/kg-dry, respectively. Fe concentrations of leaf and stem of Japanese knotweed and lower part stem of coix in the other areas were 10 to 240 and 10 to 125 mg/kg-dry, respectively. Therefore, their Fe concentrations in the Cu mine area were about the same as those in the other areas.

Fe concentrations of Japanese freshwater crab,

caddice-worm, dobsonfly larva, dragonfly larva, stonefly larva, crane fly larva, mayfly larva and corixidae were 32 to 3,500, 83 to 5,100, 326 to 9,100, 250 to 9,100, 11 to 1,300, 110 to 9,300, 29 to 2,800 and 460 to 3,200 mg/kg-dry, respectively. Therefore, crane fly larva had the highest and a wide range of Fe concentration among river insects. Fe concentrations of reed, fern, bryophyte, Japanese knotweed and coix were 2 to 13,000, 10 to 12,000, 110 to 58,000, 10 to 43,000 and 10 to 440 mg/kg-dry, respectively. Therefore, bryophyte had the highest and a wide range of Fe concentration among water plants.

From the above results, crane fly larva had the highest and a wide range of Fe concentration among river insects. Bryophyte had the highest and a wide range of Fe concentration among water plants. Moreover, Fe concentrations of crane fly larva and bryophyte were high in the Cu mine area and were low in the other areas. Therefore, crane fly larva and bryophyte were useful species for an index of Fe contamination.

Estimation of Most Useful Species among River Insects and Water Plants

From figs.3 and 4, Zn concentrations of bryophyte and river insects and other water plants were 24 to 8,900 and 2 to 2,200 mg/kg-dry, respectively. Fe concentrations of bryophyte and river insects and other water plants were 110 to 58,000 and 2 to 43,000 mg/kg-dry, respectively. Therefore, bryophyte had the highest and a wide range of Zn and Fe concentrations among river insects and water plants. Moreover, Zn and Fe concentrations of bryophyte in the Cu mine area were higher than those in the other areas. River insects absorb heavy metals included in the water and food from the intestine. Reed, fern, Japanese knotweed and coix are vascular plant and absorb heavy metals included in the water and soil from the roots. Therefore, the absorption path of heavy metals of river insects and their plants are limited. However, bryophyte absorbs heavy metals from the whole surface of the body [20]. Therefore, bryophyte is easy to absorb heavy metals compared with river insects and vascular plants. Furthermore, bryophyte in the river bed absorbs heavy metals from not only river water but also high concentration of sulfate with metal from the closed Cu mines. It is thought that bryophyte is little metal consumption because growth rate of bryophyte is generally slow [21]. From the above reasons, it was thought that bryophyte had the highest and a wide range of Zn and Fe concentrations among river insects and water plants. Therefore, bryophyte was useful species for an index of Zn and Fe contamination among river insects and water plants.

CONCLUSION

In this study, Zn and Fe concentration of river insects and water plants in the Kinokawa River catchment were investigated in order to find useful species for an index of Zn and Fe contamination for river. Useful species as an index of metal contamination needs a high metal concentration in a contaminated area and low metal concentration in a non-contaminated area. Moreover, it needs a high and a wide range of metal concentration and also very popular.

Zn concentrations of crane fly larva, mayfly larva and bryophyte in the Cu mine area were 88 to 420, 190 to 810 and 34 to 8,900, respectively. Zn concentrations of crane fly larva, mayfly larva and bryophyte in the other area were 81 to 180, 62 to 880 and 24 to 1,100, respectively. Zn concentrations of crane fly larva, mayfly larva and other river insects were 81 to 420, 62 to 880 and 32 to 440, respectively. Zn concentrations of bryophyte and other water plants were 24 to 8,900 and 2 to 2,200, respectively. Fe concentrations of crane fly larva and bryophyte in the Cu mine area were 1,300 to 9,300 and 110 to 58,000, respectively. Fe concentrations of crane fly larva and bryophyte in the other area were 110 to 5,700 and 110 to 34,000, respectively. Fe concentrations of crane fly larva and other river insects were 110 to 9,300 and 11 to 9,100, respectively. Fe concentrations of bryophyte and other water plants were 110 to 58,000 and 2 to 43,000, respectively.

Then, Zn and Fe concentrations of crane fly larva and bryophyte in the Cu mine area were higher than those in the other areas. Moreover, crane fly larva had the highest and a wide range of Fe concentration among river insects. Bryophyte had the highest and a wide range of Zn and Fe concentration among water plants. Mayfly larva had the highest and a wide range of Zn concentration among river insects. However, Zn concentrations of mayfly larva in the Cu mine area were not higher than those in the other areas. Useful species as an index of metal contamination needs a high metal concentration in a contaminated area and low metal concentration in a non-contaminated area. Therefore, mayfly larva was not useful species for an index of Zn contamination. On the other hand, crane fly larva also had high and a wide range of Zn concentration among river insects. Therefore, crane fly larva and bryophyte were useful species for an index of Zn and Fe contamination.

Bryophyte had the highest and a wide range of Zn and Fe concentrations among river insects and water plants. Therefore, bryophyte was useful species for an index of Zn and Fe contamination among river insects and water plants.

In future work, it is necessary to study whether this study results can be confirmed in other catchments.

REFERENCES

[1] Tochimoto H., Study of Aquatic Insect, Caddisfly, *Stenopsyche marmorata* as a Bio-monitor of Trace Element Contamination in Rivers and Streams: Cadmium and Copper, Journal of Japan Society on Water Environment, Vol. 17, No.11, 1994, pp.737-743.

[2] Aizawa S., Tsunoda A., Yasuda M., Tsunoda K. and Itabashi H., Concentrations of Heavy Metals in Caddisfly Larvae of the Tone River System and Their Seasonal Variations, BUNSEKI KAGAKU, Vol.58, No.4, 2009, pp.273-285.

[3] N. H. Tarras-Wahlberg, A. Flachier, S. N. Lane and O. Sangfors, Environmental Impacts and Metal Exposure of Aquatic Ecosystems in Rivers Contaminated by Small Scale Gold Mining: the Puyango River Basin, Southern Ecuador, The Science of the Total Environment, vol.278, 2001, pp.239-261.

[4] Fujino A. and Ii H., Importance of Corydalidae as an Index of Metal Contamination of River, International Journal of Geomate, Vol.9, No.2, 2015, pp.1483-1490.

[5] Nehring R. B., Aquatic Insects as Biological Monitors of Heavy Metal Pollution, Bulletin of Environmental Contamination and Toxicology, Vol.15, Issue 2, 1976, pp.147-154.

[6] Ishizaki S. and Yamanouchi K., Benthic Communities and Heavy Metal Concentrations of Mayflies (*Baetis* spp. and *Epeorus latifolium*) in Sasu and Se Rivers, Annual Report of Nagasaki Prefectural Institute of Public Health and Environmental Sciences, Vol.30, 1987, pp.46-52.

[7] Ogino T., Endou Y. and Kurosawa K., Heavy Metal Concentration of Water, Soil and Plant in Wetland, Report of the Geological Survey of Hokkaido, Vol.72, 2001, pp.115-120.

[8] Sasaki S., Environmental Characteristics around River Area Based on Analysis of Chemical Contaminants in Reed, Soil Mechanics and Foundation Engineering, Vol.55, No.8, 2007, pp.28-30.

[9] Ogino T. and Endou Y., Basic data on the accumulation of metal component plant, Report of the Geological Survey of Hokkaido, Vol.80, 2009, pp.133-139.

[10] Okada H., Sakakibara M., Sueoka Y and Sera K., Heavy Metals Accumulation of *Athirium yokoscense* in Polluted River Basin, Southeast Japan, NMCC Annual Report, Vol.22, 2015, pp.168-184.

[11] Aikawa Y., Nagano I., Sakamoto S., Nishiyama M. and Matsumoto S., Contents of Heavy Metal Elements in Copper Mosses: *Scopelophila ligulata*, *Scopelophila cataractae*, and *Mielichhoferia japonica* and Their Substrates, Soil Science and Plant Nutrition, Vol.45, Issue 4, 1999, pp.835-842.

[12] Laura R. E. B., Tanner B. H. and William B., Bryophytes of Adjacent Serpentine and Granite Outcrops on the Deer Isles, Maine, U.S.A., RHODORA, Vol.111, No.945, 2009, pp.1-20.

[13] Hatakeyama S., Satake K. and Fukushima S., Flora and Fauna in Heavy Metal Polluted Rivers I Density of *Epeorus latifolium* (Ephemeroptera) and Heavy Metal Concentrations of *Baetis* spp. (Ephemeroptera) Relating to Cd, Cu and Zn Concentrations, Research Report from the National Institute for Environmental Studies, No.99, 1986, pp.15-33.

[14] Ii H. and Nishida A., Effectiveness of Using River Insect Larvae as an Index of Cu, Zn and As Contaminations in Rivers, Japan, International Journal of Geomate, Vol.12, No.33, 2017, pp.153-159.

[15] Kubohara T. and Ii H., Cu, Co and Ni Contamination Index for River Using River Insects and River Plants, International Journal of GEOMATE, Vol.11, Issue 26, 2016, pp.2651-2658.

[16] Ministry of Land, Infrastructure, Transport and Tourism Kinki Regional Development Bureau, http://www.kkr.mlit.go.jp/river/kasen/kinokawa.html

[17] Wakayama City Children's Science Museum, Wakayama no ishi, 2002, pp.7-10.

[18] Itoh S., Geochemical Study of Bedded Cupriferous Pyrite Deposits in Japan, Bulletin of the Geological Survey of Japan, Vol.27, No.5, 1976, pp.245-377.

[19] Sakai N., Ishizaki C., Chida T. and Shimoiizaka J., A Kinetic Study of Pyrite Oxidation by Ferric Sulfate, Journal of the Mining and Metallurgical Institute of Japan, Vol.103, Issue 1192, 1987, pp.395-400.

[20] Yoshio Hada, Okayama University of Science, http://had0.big.ous.ac.jp/thema/moss/moss.htm

[21] Graduate School of Agricultural and Life Sciences, The University of Tokyo, https://www.a.u-tokyo.ac.jp/topics/2018/20180327-3.html

9th Int. Conf. on Geotechnique, Construction Materials and Environment,
Tokyo, Japan, 20-22 November 2019, ISBN: 978-4-909106025 C3051

EFFECT OF AUTOMATED SPEED ENFORCEMENT SYSTEMS ON DRIVING BEHAVIOR AND ATTITUDES ON MOUNTAINOUS ROADS IN THAILAND

Nopadon Kronprasert, Ph.D.[1], Chomphunut Sutheerakul[2]
[1,2] Department of Civil Engineering, Chiang Mai University, THAILAND

ABSTRACT

Speeding is one of the leading causes of road traffic accidents in mountainous areas in Thailand. Recently, the government has been gaining attention to employ automated speed enforcement systems for monitoring speeding behavior on major highways. This study aims to evaluate the effectiveness of an automated speed enforcement system implemented along mountainous road sections in Thailand. Specifically, the study examines whether such system changes driving behavior and attitudes. The study has two thrusts. First, the study conducted the observational before-and-after speed study and performed the statistical analyses to evaluate driving behavior. Second, the study conducted the questionnaire surveys and applied the sequential equation modelling analyses together with the Theory of Planned Behavior concept to evaluate driving attitudes toward speeding and speed enforcement system. The study used the Highway No.118, one of the most hazardous mountainous corridors in Thailand as a case study. The results showed the changes in both driving behavior and attitudes. After implementing automated speed enforcement system. there were significant reductions in speed and the number of violators. Moreover, psychologically, drivers believe that they would increase the opportunity to perform overspeed if there is no speed control. Therefore, this study provides decision-makers better understand the characteristics of driving attitudes and behavior in Thailand and ensures the effectiveness of automated speed enforcement system.

Keywords: Safety, Speeding, Automated speed enforcement, Risk, Theory of planned behavior

INTRODUCTION

Like many other countries, speeding is one of the most leading causes of road traffic accidents on highway networks in Thailand. According to the 2006-2016 national accident statistics [1], speeding contributes 75% in road traffic accidents as shown in Fig. 1. Reducing speeding is now becoming a high-priority target for many road safety authorities. To this aim, proper and effective safety countermeasures have been proposed to reduce speeding lowering crash risk.

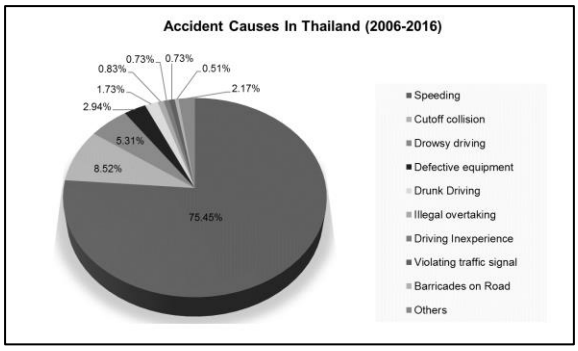

Fig. 1 Causes of accident on highway network in Thailand between 2006 and 2016.

An automated speed enforcement system is one of emerging speed control technologies, which has been proved to be a success safety measures in many developed countries. Recently, Thai government has been gaining attention to employ automated speed enforcement systems for monitoring speeding behavior on major highways. The main objective of this study is to evaluate the effectiveness of the proposed automated speed enforcement systems being implemented on mountainous roads in Thailand. The major contribution of this study is the examination of the changes in driving behavior and driving attitudes affected by the speed enforcement system on a high-risk mountainous corridor.

LITERATURE REVIEW

Various studies worldwide focused on evaluating the effectiveness of speed enforcement applied in different road functions and areas, such as freeways [2], arterial roads [3, 4], local streets [6], and residential streets and school zones [7, 8]. These studies measured the effectiveness of speed control in terms of speed reduction and the number of violators reduced. Table 1 lists some examples of research studies regarding the effectiveness of speed enforcement.

Table 1 Examples of Speed Enforcement Literature

Studies	Area	Measures of effectiveness
IIHS [3]	Freeways in Scottsdale, Arizona	Number of violators
Cunningham et al. [4]	14 corridors across Charlotte, North Carolina	Speed reductions and Crash reduction
Retting et al. [7]	Residential streets and school zones in Montgomery County, Maryland	Speed and Public attitude
D'Elia et al. [6]	Local streets in Melbourne and Victoria, Australia	Crashes, Casualty crashes,
Freedman et al. [8]	School zones in Portland, Oregon	Public awareness, Speed, Proportion of traffic exceeding the speed limit by 10 mph

The study by Lu [9] compared the effectiveness of different speed control measures. The study showed that the speed cameras have high efficiency and enhance the speed continuity of speed control. Moreover, the study by Marciano et al. (2015) [10] discussed the pros and cons of overt and covert speed cameras and suggested that the covert speed cameras (the drivers cannot notice) with the immediate feedback to the violators is the most efficient approach to motivate drivers to maintain their speeds.

While speed camera programs seem to be success in many countries today, the use of enforcement cameras is certainly contentious. It is found that several international programs were initially met with public resistance. There were a number of public concerns, which road safety professionals should consider when implementing a speed camera program. They include ticket procedures, how ticket revenues will be distributed, and whether or not automated enforcement results in reduced accident rates. [11]

RESEARCH APPROACH

This section is divided into three parts: the study area, the method to analyze driving behavior, and the method to analyze driving attitudes.

Study Area

Chiang Mai is the major city in the northern region of Thailand. About 89-percent of the area is mountainous terrain. Most of the roads connected to other neighboring cities are mountainous roads. One of the most dangerous roads is Highway No.118 (Chiang Rai - Chiang Mai) connected between Doi Nangkaew and Doi Saked districts. This road corridor has more than 7% grades and continuous curvy roads 3 kilometers or more. As a result, it has numerous road accidents. Most of the accidents on this road are caused by speeding and unfamiliarity of drivers. Drivers fail to control the vehicles and the accidents result in massive loss of life and property. The annual average daily traffic (AADT) of this corridor is 11,982 veh/day (both directions) in 2015 and the percent share of vehicle type is 11% of motorcycles, 39% of passenger cars, 36% of light trucks or pick-ups, 9% of heavy trucks, and 5% of buses. Figure 2 shows the example of road section on Highway No.118.

Fig. 2 Example of road section in a study area

Highway No.118 in Chiang Mai was built in 1984. It is about 52-kilometer long. It consists of 37-km two-lane mountainous road section and 15-km four-lane divided road section. At the end of 2016, five automated speed cameras were installed along this corridor at the following stations: km 50+400, km 43+050, km 35+800, km 21+700, and km 15+600. The first four stations are on a two-lane mountainous road section with the speed limit of 80 km/h, while the last station is on a four-lane divided road section with the speed limit of 90 km/h as shown in Fig. 3.

Fig. 3 Locations of automated speed camera

Analysis of Speeding Behavior

The study examines the speeding behavior by using the statistical *t*-test analysis of speed data. The observational before-and-after speed analysis is performed. The hypothesis of the speed study is that there is no difference between the vehicle speed data before and after implementing automated speed cameras along the corridor (H0). The *t*-test method calculates the *p*-value to find whether the difference between the means of two speed data groups is statistically significant within a specified confidence interval. The *t*-value is calculated using Eq. (1).

$$t = \frac{\overline{X_B} - \overline{X_A}}{\sqrt{\frac{S_B^2}{N_B} + \frac{S_A^2}{N_A}}} \quad (1)$$

where t = the value of statistical test, and $\overline{X_B}$ and $\overline{X_A}$ are the average speed of sample vehicles before and after installing automated speed camera, respectively. S_B and S_A are the standard deviation of sample vehicles before and after installing automated speed camera, respectively. N_B and N_A are the sample sizes of vehicles before and after installing automated speed camera, respectively.

Analysis of Speeding Attitudes

The study examines the speeding attitudes by using the statistical analysis of drivers' opinions. Questionnaire surveys are conducted by asking the opinions of drivers within the study area regarding speeding behavior, speed control measures, and factors affecting speeding behavior.

This study applies the Theory of Planned Behavior (TPB) to examine the psychological factors influencing the speeding behavior of road users. TPB firstly proposed by Icek Ajzen [12] in 1985 is one of the psychological theories explaining that the personal behavior is determined by three direct factors: attitude towards behavior (ATT), subjective norm (SN), and Perceived Behavioral Control (PBC), and one indirect factor: behavioral intention (I) as shown in Fig. 4.

Attitude towards behavior **(**ATT**)** is a personal belief accrued from individual attitude or feeling that he/she favors or does not favor the behavior**.**

Subjective Norm **(**SN**)** is a personal belief accrued from the people who are important to him/her think he/she should or should not perform the behavior**.**

Perceived Behavioral Control **(**PBC**)** is a personal perception of the ease or difficulty of performing the behavior**.**

Intention **(**I**)** is a willingness to perform the defined action or the behavior**.**

The more positive a person's belief, the stronger is his/her intention to perform the behavior.

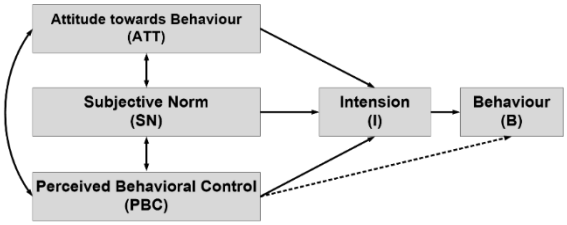

Fig. 4 Theory of planned behavior

RESULTS AND DISCUSSION

The analysis results are divided into two-fold: the analysis of driving behavior and driving attitudes. The details of each test are described as follows.

Results on Driving Behavior

The observational speed data were collected 2-month before and 2-month after introducing the speed cameras along mountainous roads in the study area. The speed of more than 3,000 vehicles at five station locations along the corridor were observed and three vehicle types were classified including passenger cars, trucks, and buses.

Figure 5 shows the frequency and cumulative frequency distributions of all speed data collected before and after the speed camera installation. The cumulative distribution of the observed "after" speed data is shifted to the left of the observed "before" speed data. The mean speed of all vehicles was reduced from 76.0 km/h to 70.4 km/h (or reduced by 8.0%). The 85th percentile speed of all vehicles was reduced from 93.0. km/h to 82.0 km/h (or reduced by 13.4%). It implies that most drivers lower their speed through the road sections in the study area.

Table 2 also summarizes the before-and-after speed data. The mean, 85th percentile, and the deviation of vehicle speed before and after the implementation of automated speed enforcement system are compared. The statistical *t*-test showed the significant reduction on the average vehicle speeds at 95% confident interval.

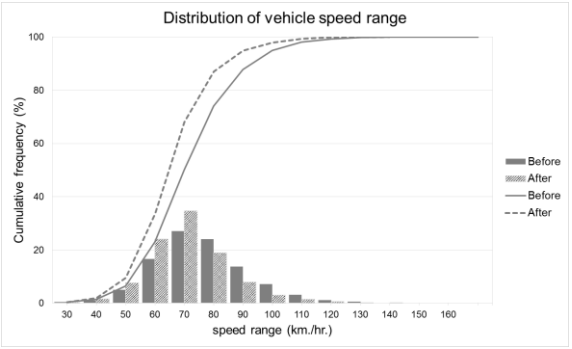

Fig. **5** Comparison of speed distribution

Table 2**:** Comparison of Driving Speed Before-and-After Implementation of Speed Enforcement System

Locations	Period	Speed Limit (km/h)	Sample Size	Speed (km/hr.)			*t*-value	Sig*
				Mean	85th percentile	Standard deviation		
Station 1: km 50+400	Before	80	244	72.9	84.0	12.1	4.90	0.00
	After		272	67.8	78.0	11.1		
Station 2: km 43+050	Before	80	258	68.7	82.0	11.8	4.24	0.00
	After		245	64.6	74.0	10.0		
Station 3: km 35+800	Before	80	267	80.8	94.0	13.0	8.39	0.00
	After		240	71.9	82.0	10.8		
Station 4: km 21+700	Before	80	321	68.3	77.0	9.0	5.89	0.00
	After		282	64.3	72.8	8.0		
Station 5: km 15+600	Before	90	516	83.5	103.0	19.7	4.60	0.00
	After		456	78.2	93.7	16.2		
All data	Before	-	1606	76.0	93.0	16.0	10.54	0.00
	After		1495	70.4	82.0	13.5		

Note: * Confident interval at 0.95

In this study, the numbers of violators before and after the implementation were also compared. The number of violators was considerably reduced at all station locations along the corridor. The percentage of violators was reduced from 31% to 11%, from 19% to 7%, from 53% to 19%, from 12% to 3%, and from 39% to 21% at Stations 1 to 5, respectively.

Results on Driving Attitudes

The questionnaire contains three parts**.** For the first part, the basic characteristics of 400 respondents are presented in Table 3**.**

Table 3**:** Basic Characteristics of Respondents

Characteristics		Number (Person)	Percent %
Gender	Male	275	68.6
	Female	125	31.4
Age	Less than 23 years	21	5.2
	23-40 years	217	54.1
	More than 40 years	162	40.6
Occu-pation	Government officers	82	20.4
	Private employees	80	20
	Students	27	6.7
	Private business	93	23.2
	Contractor	100	24.9
	Other	18	4.7
Educa-tion	High school or lower	185	46.4
	Undergraduate	194	48.4
	Graduate or higher	21	5.2
Type of vehicle	Motorcycle	18	4.7
	Passenger car	272	67.8
	Van	37	9.2
	Bus	23	5.7
	Truck	50	12.5

The classification of the respondents' characteristics represents the characteristics of driving population within the study area.

For the second part, the frequency analysis was performed. Some interesting statistics of drivers' opinions are summarized as follows.

- Sixty-four percent of respondents were aware that speeding is the major cause of road traffic accidents on mountainous roads, followed by illegal overtaking, drivers' unfamiliarity with the roads, and slippery pavement condition.
- Sixty-nine percent of drivers were unaware of the speed limit of mountainous roads.
- Seventy-one percent of drivers agreed with the speed enforcement measure on mountainous roads, and seventy percent agreed with automated speed camera enforcement.

It implies that the majority of drivers accept the speed control measure on mountainous roads because they realize the consequences of speeding behavior.

Psychological Factors Affecting Driving Behavior

For the last part of the questionnaire, the study uses Analysis of Moment Structure (AMOS) to perform the structural equation modelling (SEM) analysis. In the questionnaire, psychological factors are measured based on a seven-point Likert scale ranging from "Strongly Agree" to "Strongly Disagree". Each factor is measured by asking the respondents to rate different numbers of latent statements as follows: Attitude towards Behavior (ATT) factor group has four statements (ATT1 to ATT4). Subjective Norm (SN) factor group has four statements (SN1 to SN4). Perceived Behavioral Control (PBC) factor group has three statements (PBC1 to PBC3), and Intention (IN) factor group has three statements (IN1 to IN3). All the latent factors are listed in Table 4.

Table 4**:** Latent factors in each factor group based on Theory of Planned Behavior

Factor Group	Question	Variable
Attitude towards behavior (ATT)	For me, in the next time I drive faster than the speed limit, I think it is …….	
	Bad – Good	ATT1
	Not useful - Useful	ATT2
	Unacceptable - Acceptable	ATT3
	Wrong – Not wrong	ATT4
Subjective Norm (SN)	I believe that my important people (e.g. family members/friends) think next time I should not/should drive over the speed limit.	SN1
	I believe that my important people (e.g. family members/friends) will disagree/agree when I drive over the speed limit.	SN2
	I believe that my important people (e.g. family members/friends) will not support/support me to drive over the speed limit.	SN3
	I believe that speeding behavior of my important people (e.g. family members/friends) is impossible/possible.	SN4
Perceived Behavioral Control (PBC)	In my next driving, I am unconfident/confident that I can drive over the speed limit.	PBC1
	It is difficult/easy for me to drive over the speed limit in my next driving.	PBC2
	I feel dependent/independent to drive over the speed limit in my next driving.	PBC3
Intention (IN)	"I intend to drive over the speed limit in my next driving" is very impossible/possible.	IN1
	"I have a tendency to drive over the speed limit in my next driving" is very impossible/possible.	IN2
	"I am willing to drive over the speed limit in my next driving" is very impossible/possible.	IN3

The questionnaire was first tested for its reliability using the Cronbach's alpha in the SEM analysis. The result shows that the Cronbach's alpha ranges from 0.81 to 0.92, which represent the very high reliability of the questionnaire. Then the AMOS analysis was carried out and the TPB structure was constructed. The relationship among psychological factors and their latent factors were evaluated. The results of AMOS analysis are shown in Fig. 6.

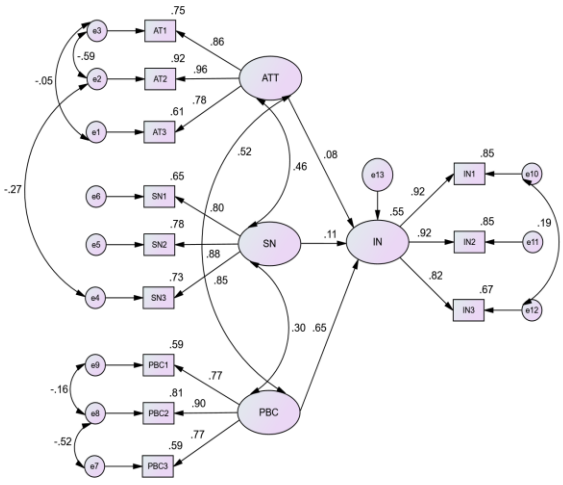

Fig**.** 6 The result of AMOS analysis

This diagram shows that three basic psychological factors: attitude towards behavior (ATT), subjective norm (SN), and perceived behavioral control (PBC) are highly influenced on intention (IN). All statistical indicators are accepted compared to their threshold values: Chi-square/df = 2.46 (recommended between 2 and 3), Goodness-of-fit indices (GFI) = 0.959 (recommended close to 1), Comparative Fit Index (CFI) = 0.981 (recommended close to 1), Standardized Root Mean Squared Residual (SRMR) = 0.045 (recommended close to 0.05), and Root-mean square error of approximation (RMSEA) = 0.061 (recommended close to 0.08) [13].

The diagram shows that among the three factors, PBC is the highest influential factor to the intention and to the speeding behavior. It implies that the speeding drivers are willing to drive fast whenever he or she has an opportunity to perform speeding. Therefore, breaking the opportunity to overspeed by introducing speed camera enforcement would affect the speeding behavior of drivers within the study area.

CONCLUSIONS

The paper presents the effect of automated speed enforcement system installed along the hazardous sections of mountainous roads in Thailand. Although the automated speed enforcement system has been successfully implemented in many developed countries, such system has not yet been widely introduced and comprehensively analyzed their effectiveness in Thailand. This study evaluated the effects in terms of the speeding behavior and drivers' perception and attitudes.

An automated speed camera enforcement system in this study becomes an effective speed control technology on mountainous roads because of three respects. First, the speed camera enforcement helps reduce the speed of vehicles significantly. The 85th percentile of vehicle speed is reduced by 13,4%, while the number of violators is reduced by 16%. Second, it helps increase public awareness of the risk of speeding behavior as the drivers perceive the speed limit more while driving on mountainous roads. In this study, the public resistance is minor because the drivers realize that the speed camera is a tool to enhance the speed regulation. Finally, the speed enforcement program helps minimize the opportunity of the drivers to perform overspeed. In other words, it enhances the safe driving speed and sustains the safe behavior.

This study has two further recommendations. One, this paper presents the 2-month before-and-after speed data. Data collection including speed data, speed tickets, and accident records should be carried out in a longer time period to ensure the sustainable speeding behavior and their positive consequences. Two, it should be noted that automated speed enforcement is one of the possible and practical safety countermeasures to improve the perceived behavioral control of drivers' speed on mountainous roads. More comprehensive studies on safety measures in other regards, such as engineering and education measures, should be emphasized in order to more effectively sustain the safe speeding culture.

ACKNOWLEDGMENTS

The authors would like to gratefully acknowledge financial support of the research project from Thailand Research Fund MRG5980074, and the Excellence Center in Infrastructure Technology and Transportation Engineering (ExCITE) of Chiang Mai University for technical support.

REFERENCES

[1] World Health Organization. Global status report on road safety 2015: supporting a decade of action. Switzerland, 2015.

[2] Bureau of Highway Safety. Department of Highways, Thailand. Accident statistic. http: / / bhs. doh. go. th/ statistics, accessed on February 1st, 2017.

[3] Insurance Institute for Highway Safety Highway Loss Data Institute, *Cameras help lower speeds on Arizona freeway.* Status Report, 2008, 43(1).

[4] Cunningham, C., J. Hummer, and J. P. Moon, *Analysis of automated speed enforcement cameras in Charlotte, North Carolina*. Transportation Research Record: Journal of the Transportation Research Board, 2008, 2078: p. 127-134.

[5] Tay, R. *Do speed cameras improve road safety*. In Traffic and transportation studies: international conference on traffic and transportation studies. Beijing, China, 2000, 44: p. 44-51.

[6] D' Elia, A. , S. Newstead, and M. Cameron, *Overall impact during 2001-2004 of Victorian speed-related package*. Prevention, 2007, 17(1): p.47-56.

[7] Retting, R. A., C. M. Farmer, and A.T. McCartt, *Evaluation of automated speed enforcement in Montgomery County, Maryland*. Traffic injury prevention, 2008, 9(5): p.440-445.

[8] Freedman, M., D. De Leonardis, Raisman, et al. *Demonstration of Automated Speed Enforcement in School Zones in Portland, Oregon*, 2007.

[9] Lu, F. and Z. Cheng, *Study on the Effects of Speed Camera*. In ICCTP 2010: Integrated Transportation Systems: Green, Intelligent, Reliable, 2010, p. 824-831.

[10] Marciano, H., Setter, P., Norman, J. *Overt vs. covert speed cameras in combination with delayed vs. immediate feedback to the offender*. Accident Analysis and Prevention, 79, 2015, pp.231-240.

[11] Boos, M. A., *Speed cameras as a tool to reduce road fatalities.* Research Synthesis Bibliography No. 23. 2009: Virginia Department of Transportation.

[12] Ajzen, I. *The theory of planned behavior*. Organizational behavior and human decision processes, 1991, 50(2): p. 179-211.

[13] Hair J.F., Black W.C., Babin B.J, Anderson R.E., Tatham RL. *Multivariate data analysis*. 6th ed. Upper Saddle River, New Jersey: Pearson Prentice Hall, 2006.

9th Int. Conf. on Geotechnique, Construction Materials and Environment, Tokyo, Japan, 20-22 November 2019, ISBN: 978-4-909106025 C3051

CHLORIDE ION MEASUREMENT SYSTEM FOR RC STRUCTURE BY NEAR-INFRARED SPECTROSCOPY

Yoko Sakakihara[1], Yoshihiro Kabeyama[2], Hiroshi Kanasaki[3], Kazushi Hamada[4], Shinichiro Okazaki[5], Kenji Wada[6], Ichiro Ishimaru[7]
[1,2]Graduate School of Engineering, Kagawa University, Japan;
[3,4]NISSIN KIKAI Co., Ltd., Japan
[5,7]Faculty of Engineering and Design, Kagawa University, Japan;
[6]Faculty of Medicine, Kagawa University, Japan

ABSTRACT

Aging deterioration of reinforced concrete structures is mainly due to chemical reactions of rebar corrosion, carbonation, alkali-aggregate reaction, and the like, whereas collection of chemical information is effective to accurately grasp these signs. The recently introduced nondestructive measurement method of chloride ion concentration using a near-infrared (NIR) spectroscopy system detects an NIR peak of Friedel's salt that is immobilized on a concrete surface, followed by application of a multispectral method. Herein, a prototype of a small-scale, NIR spectroscopy system that does not require seismic isolation was developed, using imaging-type two-dimensional Fourier spectroscopy technology, and the applicability of two-dimensional imaging of chloride ion concentration on concrete surfaces by this system was evaluated. Apparently, measurement by the system could be performed in a short time and with measurable accuracy. Moreover, the two-dimensional imaging of chloride ion concentration was possible in an outdoor environment with almost no associated difficulty. In addition to measuring Friedel's salt, it was possible to observe cracks on the concrete surface by measuring water.

Keywords: Two-dimensional imaging, Chloride ion concentration, Near-infrared spectroscopy, Nondestructive measurement

INTRODUCTION

Since its period of economic boost, Japan has been engaged in the fast-paced reconstruction of social infrastructures that are reportedly estimated at present to cost around 800 trillion yen. Measures to slow down the aging of buildings and structural units is of dire need. Implementation of deterioration measures presupposes the collection of information on signs of degradation before deterioration and preventive maintenance measures. Present-day nondestructive inspections, however, which carry out every five years, such as visual inspection and concrete hammering test, are geared to obtaining information after deterioration. Time-related deterioration is mainly due to chemical wear-and-tear, i.e., corrosion, where chemical information is of vivid necessity for understanding the signs and pinpoint the source.

Nondestructive measurement of chloride ion on a concrete surface via near-infrared (NIR) spectroscopy is a recently developed method of collecting chemical information relative to deterioration of structures, which emerged subsequently after the discovery of the NIR peak of Friedel's salt immobilized on concrete surface by Dr. Kanada, followed by practical application of the multispectral method [1],[2]. A new NIR spectroscopy system is introduced in this paper, mainly to perform the objectives of measuring chloride ion concentration and moisture content on a concrete surface, and then the applicability of two-dimensional imaging obtained from the spectrum data is reported [3], [4].

NIR SPECTROSCOPY SYSTEM

Overview of the Conventional System

So far, with the spectroscopic measurement in the outer region of the NIR, the 1300–2350 nm band could not be covered with high sensitivity and two dimensions due to the characteristics of the detector. It was confirmed that the imaging-type two-dimensional Fourier spectroscopy technology developed by one of the authors, Prof. Ishimaru, could cover the required wavelength band cited [5].

In the conventional mechanism, if this instrument receives vibration during measurement, the mirror is shifted, and interference does not occur. The proposed method overcomes the disadvantage in that spectral data cannot be acquired and thus, is suitable for on-site measurements.

Additionally, an angle of view correction function to correct the error caused by the difference in optical path length caused by the difference in the pixel position of the camera, as illustrated in Fig. 1, was implemented.

Consequentially, the conventionally used

demonstration machine was reduced to 203.5 × 398 × 140.5 mm; its original mass of 9.0 kg with camera was lessened to 7.1 kg, and from 6.5 to 2.5 kg in the spectroscopy section alone, thus, showcasing improved portability.

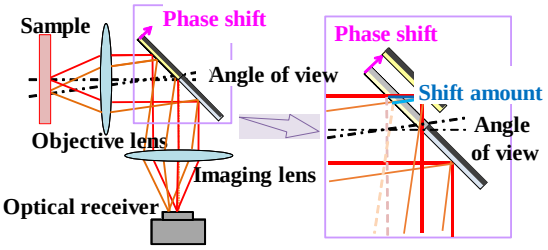

Fig. 1 Field angle correction technology of imaging-type two-dimensional Fourier spectroscopic technique

INDOOR MEASUREMENT

Outline of Indoor Measurement

Indoor measurements for mortar specimens was carried out to validate the accuracy of the system. Ordinary Portland cement (OPC) and blast furnace cement B (BB) were the cement samples considered. The water–cement ratio applied was 50 %, whereas the fine aggregate in the mortar specimens had a volume ratio of 48 %. Sodium chloride was added in specimens. The chloride ion concentrations are 0, 1, 2, 3, 4, 5, 10, 15, 20, 30 kg/m^3. Thirty plastic molds (10× 30 cm in size) were used for 10 kinds of specimens (3 molds each). Sealed curing was performed in a 20 °C environment for 7 days, before the molded specimens were exposed indoors. Specifically, the specimens were named according to the combination of cement type and chloride ion concentration. For example, an OPC paste sample with chloride concentration of 1 kg/m^3 was labeled as NP01, whereas a BB 30 kg/m^3 of chloride ion concentration is labeled as BBM30.

Indoor Measurement

The indoor measurements followed a schematic procedure depicted in Fig. 2. A standard reflector with 99 % reflectance was the reference, and a spot heater unit was used for illumination. A high-resolution SWIR lens was attached to the objective lens of the instrument, and measurement was performed at a sample angle of 0 degree and an illumination angle of 45 degrees to the sample.

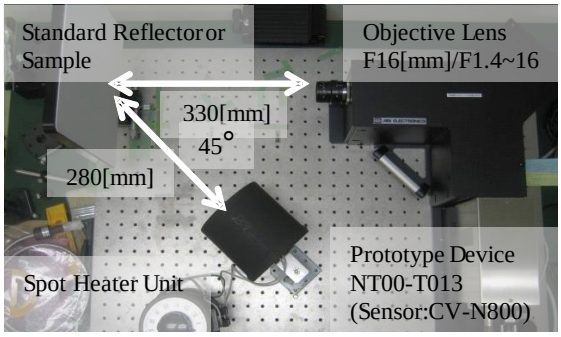

Fig. 2 Setup for indoor measurement

Measurement Results

Spectrum data of the specimens with each chloride ion concentration were examined. The relationship between the chloride concentration of the specimen and the absorbance value in the absorption wavelength range derived from Friedel's salt is shown in Fig. 3. Note that the absorbance value for 20 and 30 kg/m^3 of chloride concentration for the same specimen was almost identical, probably because the chloride fixed to the cement was saturated. Except for the 30 kg/m^3, the one for which the calibration curve was prepared is represented as a dotted line in the figure. The coefficient of determination was 0.9272.

It is considered that this calibration curve can estimate the chloride amount with high accuracy from the peak value of the absorbance of Friedel's salt.

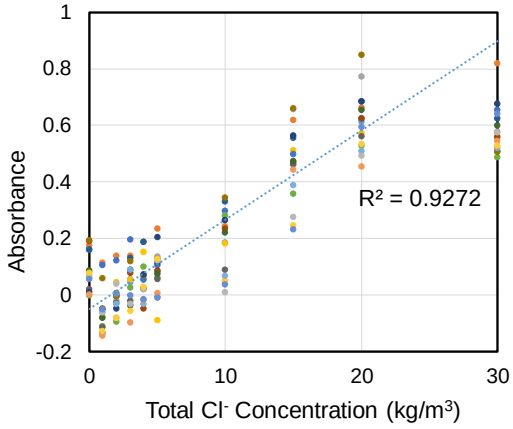

Fig. 3 Chloride concentration vs. absorbance of specimens

Use of Two-Dimensional Imaging Software

Along with the development of this NIR camera system was the creation of a two-dimensional imaging software. Accordingly, specimens BBP0, BBP30, and BBM30 were placed in a metal mortar and manually (hand) made into a powder, prior to

measurement. Sample output by the software is shown in Fig. 4.

The image on the left of the output plot was the result of the two-dimensional imaging, and that on the right side was the spectrum at five target points of the center in the left image. At the two-dimensional imaging, where the salinity is higher the color is closer to red and where the lower salinity is closer to blue.

(a)

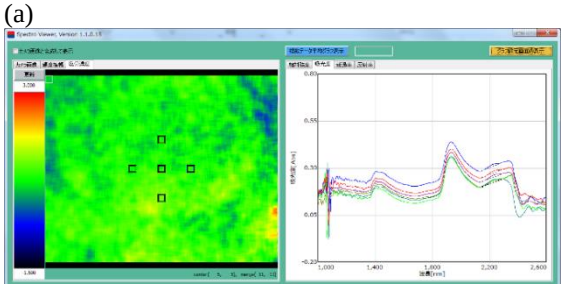

(b)

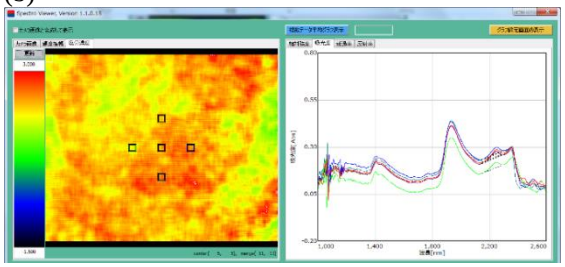

(c)

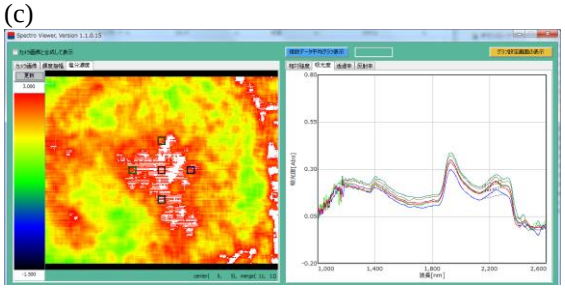

Fig. 4 Left: Output of two-dimensional imaging
Right: Output of absorbance spectrum
(a) Powdered BBP0
(b) Powdered BBP30
(c) Powdered BBM30

For example, in BBP0, the chloride concentration was almost 0, and the heat map was blue almost entirely. In contrast, almost the whole area in BBP30 was uniformly yellow-to-red, given the high chloride concentration. In the case of BBM30, in which the specimen was hand-pulverized (and thus powderization was insufficient), the presence of uneven colors was observed. Very high concentration appeared near the center, and low-density parts locally occurred in the heat map. Since pulverization of the aggregate was not enough. Accordingly, the difference in the properties of the specimens is apparent in the two- dimensional imaging. It was confirmed that such a difference could be measured indoors with no associated difficulty.

APPLICABILITY VERIFICATION BY OUTDOOR MEASUREMENT

Objects and Measurement Outline

The target structure was once used near the coastal area of Shikoku Chuo City, removed for salt damage, and transferred to the Shikoku Technical Office, Shikoku Regional Development Bureau, Ministry of Land, Infrastructure, Transport, and Tourism. Of the hollow girder bridges, one girder that was not relatively salt-damaged (Fig. 5, near side, girder 1) and another from which concrete cover was peeled off due to salt damage (Fig. 5, back-side, girder 2) were used in the measurement. Prior to removal, the girders were 15.6 m long and had served for 51 years since they were built in 1967.

Fig. 5 PC digit removed due to salt damage

Measurement Results

Measurement values for girders 1 and 2 are provided in Fig. 6, respectively. Here, the heat map for girder 1 confirmed the appearance of yellow-to-red areas that were larger than those for girder 2, whereas the degree of salt damage and the tendency of the amount of surface chloride tended to almost coincide. Moreover, the average values of the absorbance at the target points were respectively 0.32 and 0.41 for girders 1 and 2; it is considered that the difference in the degree of salt damage can be interpreted from the degree of the evaluation value.

Results of the Fourier transform infrared spectrophotometer (FTIR) analysis for the concrete powder that was scraped off the surface of the girder, to confirm the validity of the outdoor test, are displayed in Fig. 7. Moreover, the powder was collected from two places in girder 2, namely, girder 2-1 and girder 2-2. Although a clear peak could be confirmed in the portion indicated by the arrow in girder 1, this was not derived from Friedel's salt.

On the contrary, in girders 2-1 and 2-2, the peak derived from Friedel's salt could be confirmed in the

part shown by the arrow (Fig. 7), thus, indicating that the result of outdoor measurement with the system is generally appropriate. However, regardless of the presence of the absorbance peak of Friedel's salt, other peaks could be confirmed on the shorter wavelength side than that of the peak wavelength, which interferes with the result of absorbance of Friedel's salt. Thus, a study on peak separation was conducted, with the aim of improving the system's evaluation accuracy.

(a)

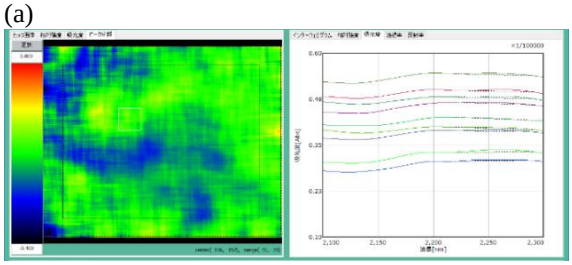

(b)

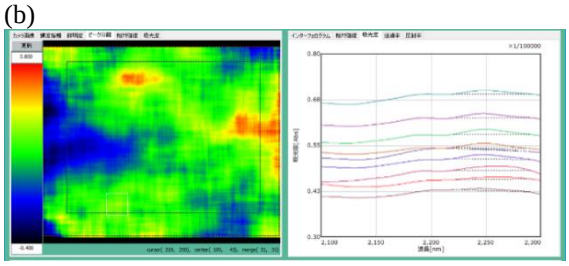

Fig. 6 Measurement result
(a) In girder 1
(b) In girder 2

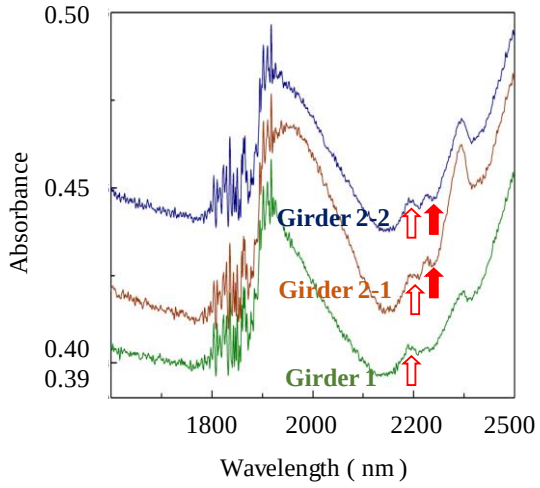

Fig. 7 Measurement result by FTIR
Bold arrows show peak of Friedel's salt
Hollow arrows show peak of others

Improvement of Evaluation Accuracy by Peak Separation

The Friedel's-salt-derived absorbance spectrum of the indoor test shows the difference from the baseline created from absorbance values of 2180 and 2290 nm. Apparently, the wavelength at which the peak was taken differed depending on the measurement cases. Although this is under investigation, this waveform is not the peak derived from Friedel's salt. Therefore, assuming a Gaussian function, the waveforms not derived and that derived from Friedel's salt were decidedly separated.

For example, at a specimen with a total chloride ion concentration of 10 kg/m^3, both peaks could be separated by two Gaussian distributions (Fig. 8). The absorbance after peak separation is shown in Fig. 9, and what prepared the standard curve using the absorbance value after peak separation is shown in Fig. 10.

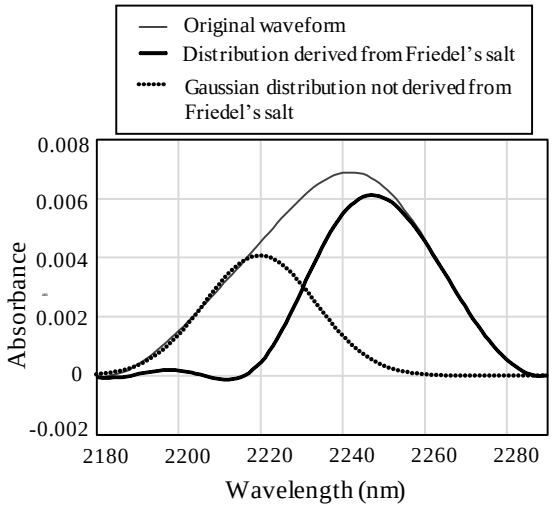

Fig. 8 Peak waveform separation

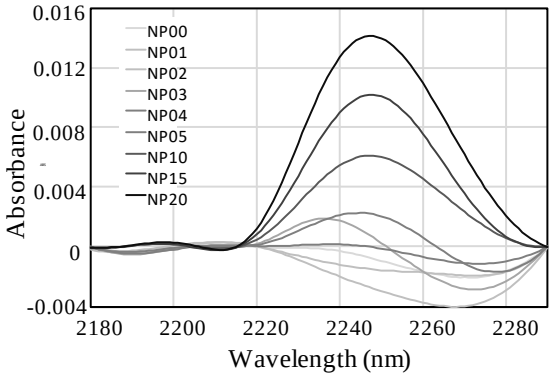

Fig. 9 Peak derived from Friedel's salt after separation and extraction of waveform

Here, the coefficient of determination was 0.9658, and accuracy was greatly improved. The same peak separation scheme was imposed on the BB type

specimens, and the result of preparing a calibration curve is shown in Fig. 11. Although not listed for the convenience of the paper, the coefficient of determination was 0.5494 before peak separation but rose to 0.7474 by peak separation. Such value of determination coefficient was small compared with that using OPC. The reason is under investigation.

A notable point in this measurement was the short measurement time. More specifically, the time required to obtain a single case of two-dimensional imaging results was approximately 60 s, including the time required for measurement on the imaging, which is much shorter than in conventional methods.

However, points that should pay attention are shown. Suspects of the progress of carbonation on the girder are typical, especially being constructed in a considerably long time, and such girders were also set outdoors for a long time in this study. With the system, the chloride content could be estimated from the amount of friedel's salt on the surface of the concrete; nonetheless, if friedel's salt gets liberated via carbonation, then the total amount of chloride actually attached to the surface of concrete may be larger than those confirmed by ftir or the proposed system. Interestingly, the preparation of a calibration curve that takes into account the effect of friedel's salt release due to carbonation is a future direction for the present study.

Accordingly, approximately 1 cm of the test piece of the NP group was cut dry with a concrete cutter, and the cut surface was subjected to the proposed measurement system. Results are shown in Fig. 12. Here, the heat generated at the time of the cutting may have caused alteration of the Friedel's salt; nonetheless, there were visible color shifts in the heat map from blue and green to yellow as the set chloride concentration increased. Based on the cross-sectional view of this specimen, two-dimensional imaging was possible.

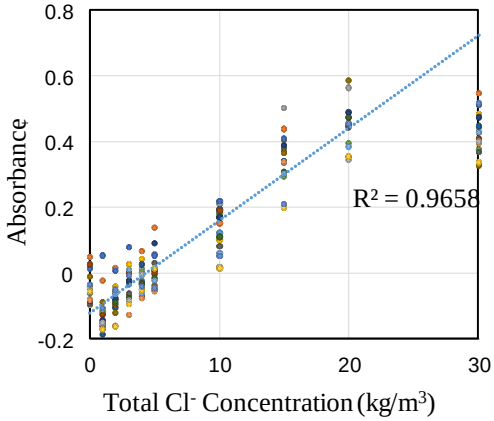

Fig. 10 Calibration curve in ordinary cemen

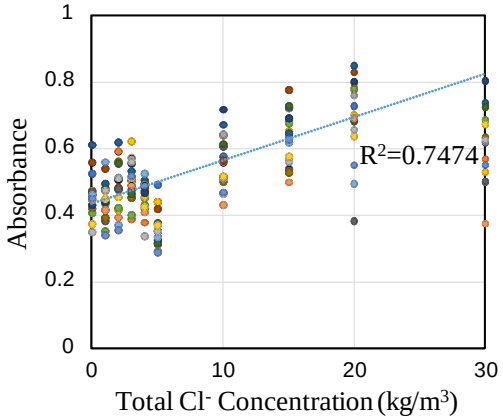

Fig. 11 Calibration curve in blast furnace cement

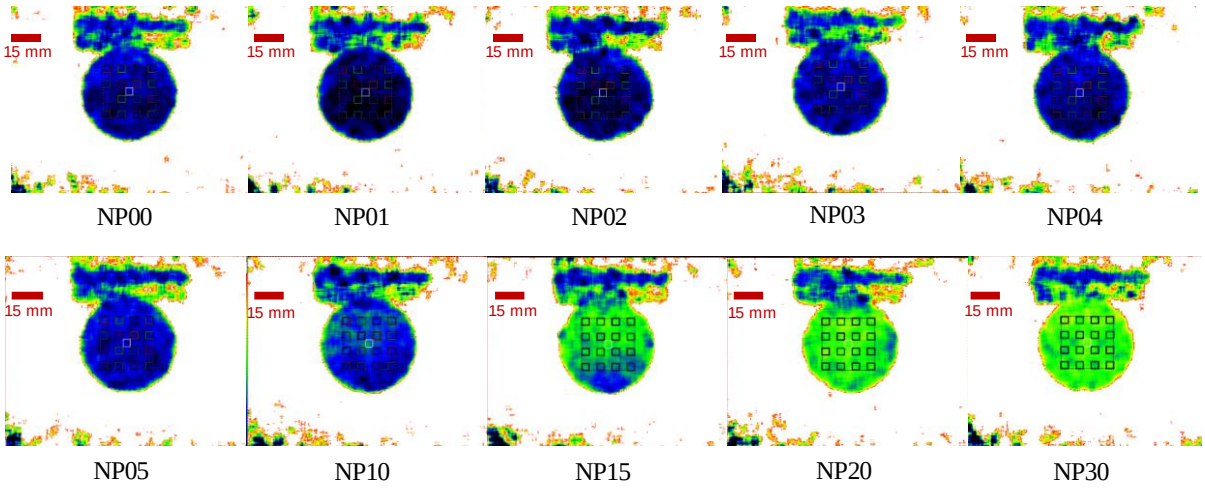

Fig. 12 Two-dimensional imaging of chloride in NP specimen cross section

Measurement regarding Water Distribution

In the NIR spectroscopy, a spectrum analysis on the OH group is frequently performed, especially on the spectrum of water. In this study, given that the concrete has water content, moisture measurement and imaging of water intrusion at the crack site were examined.

Using the proposed system, specimens that had been artificially cracked in advance were measured. A stone material with thermal expansion coefficients different from concrete was placed at the center of the specimen, and the specimen was heated to a maximum of 80 °C and then cooled. Cracks were generated due to the difference in the thermal expansion coefficients between the materials. The observed crack width was 0.15 mm at the top half and 0.10 mm at the bottom. Moisture content on the specimen was 3.3 %, as indicated by a concrete moisture meter.

Imaging results of the dried specimen are given at the left side in Fig. 13. Here, water was not confirmed in the original image of the NIR camera. After that, a specimen supplied with water from the outside by atomizing and re-imaged after visual confirmation that it had been substantially dried, is shown at the right side in Fig. 13. Moisture in the specimen could not be confirmed visually, but by imaging, this became possible with the moisture remaining in the crack. Here, moisture content was 4.3 %.

More accurately, through the proposed system, the presence of even the slightest amount of water adhering to concrete surface may be sufficient to make a proper evaluation, and fine cracks that cannot be grasped by visual inspection were shown. This issue is another direction for future study.

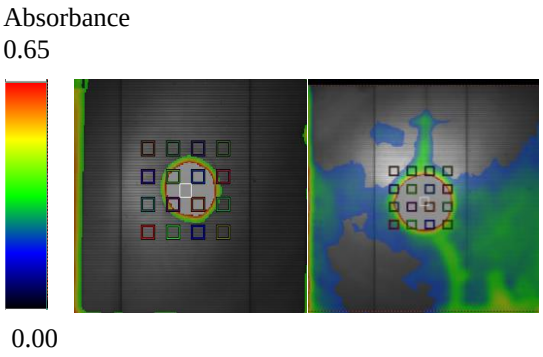

Fig. 13 Mortar specimen before wetting and after wetting
Left: Dry specimen
Right: Slightly wet specimen

CONCLUSIONS

The NIS system presented in this paper was fundamentally geared to the measurement of chloride concentration on concrete surfaces and the evaluation of applicability of two-dimensional imaging of the chloride concentration. These points can be generalized from the findings: (1) A compact, non-seismic-free two-dimensional imaging spectrometer was developed using Fourier spectroscopy technology; (2) Because the peak waveform considered to be Friedel's salt is adhered to a waveform other than it, waveform peak separation was essential to extract that of Friedel's salt. Doing so, the determination coefficient of the calibration curve increased greatly; (3) The two-dimensional imaging for the chloride concentration in the cross section of the specimen could be performed in a short time and with high accuracy; (4) Moreover, the two-dimensional imaging of chloride concentration is possible for measurement in open air with no associated difficulty.

ACKNOWLEDGMENTS

We would like to appreciate the immense support of the 99th New Technology Development Grant by Ichimura Kiyoshi Technology Foundation, for the success of this research.

REFERENCES

[1] Kanada T., Development of a method for detecting degraded material in concrete by multispectral method, The University of Tokyo thesis, 2004

[2] Kanada T., Ishikawa Y., and Uomoto K., Application of Near Infrared Method to Concrete Survey, Concrete Engineering, Vol. 43, No. 3, 2005, pp. 37-44

[3] Toda K., Nakamura Y., and Kurata T., Development of a diagnostic system for degradation of concrete using spectroscopic methods, IHI Technical Report, Vol. 52, No. 1, 2012, pp. 53-58

[4] Nakajima Y., Shirane Y., Suenaga R., Hantani K., and Sakamura R., Development of survey system of chloride ion content on concrete surface using near infrared spectroscopy and application to maintenance of RC structure, Maeda Journal of technical research institute, Vol. 57, 2016, pp. 6

[5] Inoue Y., Ishimaru I., et al., Variable phase-contrast fluorescence spectrometry for fluorescently stained cells, Applied Physics Letters, Vol. 89, 2006, pp. 121103

9th Int. Conf. on Geotechnique, Construction Materials and Environment, Tokyo, Japan, 20-22 November 2019, ISBN: 978-4-909106025 C3051

RECYCLED POROUS CONCRETE EFFECTIVENESS FOR FILTRATION MATERIAL ON WASTEWATER TREATMENT

Evi Nur Cahya[1], Eva Arifi[2] and Riyanto Haribowo[3]
[1]Faculty of Engineering, Universitas Brawijaya, Indonesia; [2,3] Universitas Brawijaya, Indonesia

ABSTRACT

The use of concrete waste from demolition of buildings is one of the conservation efforts to reduce its environment impact. In this study, concrete waste was destroyed by the size of coarse aggregates, then made into porous concrete. Porous concrete from recycled coarse aggregate was used as filtration media to reduce the pollutants in wastewater to satisfy the water quality standards. For this purpose, wastewater from communal wastewater treatment plant was filtrated through two layers of porous concrete made of recycled coarse aggregate with several different sizes, and the water quality output of the system was measured according to water quality parameter standard. The objective of this study is to examine the effectiveness of the aggregate sizes of normal coarse aggregate compared to recycled coarse aggregate as filtration media. From the result of water treatment filtration model, it was found that size of coarse aggregate in porous concrete mix has a significant effect for reducing the water pollutants, as biological oxygen demand (BOD), chemical oxygen demand (COD) and total suspended solid (TSS). As a result of this study, porous concrete made from recycled coarse aggregate shows better performance on filtrating the water pollutants.

Keywords: wastewater treatment, porous concrete, recycled coarse aggregate, water quality

INTRODUCTION

Domestic wastewater comes from residential businesses and activities, restaurants, offices, commerce, apartments and dormitories. It is generally called grey water and black water, which is very influential in decreasing water quality. Some parameters such as the total coliform content, BOD (Biological Oxygen Demand), COD (Chemical Oxygen Demand), Ammonia, pH, temperature, and TSS (Total Suspended Solid) are very dominant and each is affected in different ways [1, 2, 3].

Porous concrete is concrete which is permeable or can absorb water. By relying on the absorption and pore power of the porous concrete, it is expected to be a filtration medium to reduce some contaminants in the wastewater. Porous concrete is composed of water, cement and coarse aggregate. The coarse aggregate used in this study, is recycled aggregate which is derived from concrete that has been unused and reused. The use of concrete waste from demolition of buildings is one of the conservation efforts to reduce its environment impact.

Porous concrete is also called previous concrete which generally only use coarse aggregates with a uniform gradation size so that it has a larger size pore, which allows drainage to drain water through the pore. Porous concrete has several advantages, including a high void content of about 30%, so it is potential to reduce run off to the drainage system with a flow rate of 0.34 cm/second, making it effective for pavement, footpaths, and sidewalks [4], beside that it can be a constructive alternative with low environmental impact and protect water quality. Porous concrete also has a higher void ratio and permeability compared to conventional concrete, so that it can be used for construction of wastewater treatment plants and as a construction material for sea walls [5]. In addition, porous concrete can also be used for groundwater refilling [6]. Also, as a detention system, porous concrete can remove stormwater pollutants from the runoff, which significantly decreases the concentrations of total suspended solids, nitrite, chemical oxygen demand, and increases the values of pH and sulfate [7].

Recycle aggregate is an aggregate derived from conventional concrete that is no longer used, and then destroyed to become an aggregate for a new concrete mix. Coarse aggregates used in this study were natural concrete aggregates (NCA) and recycle concrete aggregates (RCA). The aggregate variations used are aggregates with a diameter of 0.5-1 cm, 1-2 cm, and well graded 0.5-2 cm for RCA and NCA. NCA comes from natural aggregate material, while RCA was taken from conventional concrete crushing with f'c compression strength of 22.5 MPa.

Water absorption in concrete is obtained from the ratio of the weight of pore absorbable water to dry concrete, which is expressed in percent, which serves to determine the amount of water content in the concrete. Void can be interpreted by the total percent of the pore number on the total volume. For the average, porous concrete has a pore percent value of 15-25% and the permeability is generally between 2 -

30 mm/sec [8]. The pore number is determined according to ASTM CI688.

Permeability is generally influenced by aggregate size and proportion [8]. Permeability measurements are calculated based on ACI-522R. The falling head method is used for measuring permeability in concrete. This permeability measurement usually uses a cylindrical test object with a size of 150 mm x 150 mm. the cylinder is placed in a PVC pipe. For testing is done after 28 days of curing [8]. Urban water needs include 25-35% for industry, 5-10% for public use, 10-20% for commercial, firefighting, and 30-50% for housing [9].

Wastewater released by disposal can be analyzed through the discharge of the needs of each resident. According to Tchobanoglous [9], the amount of wastewater produced ranges from 50-80% of the use of clean water. For the calculation of the amount of wastewater produced by the service area, 80% of the consumption of clean water is determined. The value of 80% versus 20% is the comparison between direct connections to urban public hydrants for medium economic communities, while the value of 30 L/person/day is the standard of clean water needs for urban public hydrants. The wastewater factor for drinking water is 0.5-0.8 [9].

Quality standards for domestic wastewater according to the Minister of Environment and Forestry of the Republic of Indonesia as a reference for this study can be seen in Table 1.

Table 1 Quality standards for domestic wastewater

Parameter	Units	Maximum level
pH	-	6 – 9
BOD	mg/L	30
COD	mg/L	100
Oil and Grease	mg/L	5
Amonia	mg/L	30
Total Coliform	Amount/100 ml	3000
Discharge	L/person/day	100

The parameters of domestic wastewater are a measure of the waste water content that can calibrate the wastewater. This parameter is used as a reference for domestic wastewater to achieve quality standards. Parameters for each type of waste vary. In domestic wastewater, the parameters used as reference quality standards are pH, BOD, COD, TSS, oil and grease, ammonia, total coliform and discharge.

The purpose of this study is to examine the effectiveness of the aggregate sizes of normal coarse aggregate compared to recycled coarse aggregate, on filtrating the water pollutants to satisfy the water quality parameter standard.

METHODS

The research sets at a local integrated domestic wastewater treatment plant in Malang, Indonesia, which covered domestic wastewater (gray water and black water) from 112 family with a total of 14 tanks. In this study the concrete material uses natural concrete aggregates (NCA) and recycle concrete aggregates (RCA) with three variations, namely, 0.5-1 cm, 1-2 cm and 0.5-2 cm.

The tested domestic wastewater treatment plant single model is 60x60x100 cm in size with two slab concrete dividers as filtration mediums, which is 60x60x5 cm. The water used as a sample is domestic wastewater (gray water and black water) from a local wastewater treatment plant in the first tank (after the crushing tank). Inlet discharge is 2 L/min, with calculation of deposits every 18 hours, calculation of water level every 1 hour and samples were taken at the end of the three hours running experiment.

Water quality of wastewater treatment plant in the original tanks and at the experiment tank model after filtered is tested at the time of each layer (BOD, COD, TSS, Ammonia, Oil and grease, Total Coliform) in addition to measuring pH and temperature, water level and height of sediments. Void ratio of porous concrete and concrete permeability are tested separately.

The output of water quality testing is the effectiveness of porous concrete as a filter for wastewater treatment where normal porous concrete aggregates become a comparative material for porous recycle aggregate concrete.

Comparison of the ratio of the proportion of weight in the manufacture of porous concrete, namely Cement: Gravel: Water is 1: 4: 0.3. The composition of NCA (Normal coarse aggregate) and RCA (Recycled coarse aggregate) aggregate sizes can be seen in Table 2.

Table 2 Aggregate size compotition in porous concrete

Aggregate		A (0.5 cm - 1 cm)	B (1 cm - 2 cm)	C (0.5 cm – 2 cm)
I	NCA	100% NCA 0.5-1	100% NCA 1-2	100% NCA 0.5-2
II	RCA	100% RCA 0.5-1	100% RCA 1-2	100% RCA 0.5-2
III	NCA: RCA	50%RCA 50% NCA 0,5-1	50% RCA 50% NCA 1-2	50% NCA 50% RCA 0.5-2

From each variation, two slab test specimens were made for each trial session in the form of concrete plates measuring 60 cm wide, 60 cm long and 5 cm thick. Concrete samples will also be made specifically for the calculation of void ratio and permeability of the nine existing variants.

RESULT AND DISCUSSION

This study is aimed for the efficiency value of the aggregate sizes of normal coarse aggregate compared to recycled coarse aggregate, on filtrating the water pollutants to satisfy the water quality parameter standard.

Void Ratio and Permeability

The pore number shows the number of pores in the concrete. The concrete pore number is in line with the amount of porosity in the concrete. This permeability analysis is used to see how much absorption by the porous concrete is displayed with the symbol k. Permeability measurements are calculated based on ACI-522R. The results of pore and permeability calculation are explained in Table 3. The relationship between pore number and permeability does not appear to be significant because the pore number testing method uses fresh concrete while permeability using dry concrete is 28 days old.

Table 3 Calculation Results of Void Ratio and Permeability

Coarse Aggregate Mix	Void Ratio %	Permeability (mm/s)
100%NCA 0.5-1	9.772	4.878
100%NCA 1-2	10.615	4.824
100%NCA 0.5 -2	8.720	9.248
50%NCA50%RCA 0.5 -1	8.587	7.317
50%NCA50%RCA 1-2	11.672	11.367
50%NCA50%RCA 0.5-2	5.940	7.332
100%RCA 0.5-1	4.865	6.264
100%RCA 1-2	5.186	8.865
100%RCA0.5-2	8.263	8.052

Analysis of Water Quality and Efficiency Results

The water quality tested in this study is in accordance with the quality standards of domestic wastewater namely temperature, pH, BOD, COD, TSS, Oil and grease, Ammonia and Total Coliform. To see the relationship between the efficiency of the reduction of the parameter and the void ratio and permeability, several graphs are made. In this graph the value of oil and grease and total coliform is not included because there is no reduction value of these parameters in this study. Oil and grease and total coliform can only be decomposed and reduced using biological and chemical methods [10, 11, 12].

For comparation of the effect of aggregate sizes to the filtration ability, one of the results from the 50%NCA 50%RCA is shown for COD, BOD and TSS, as shown in Figure 1. It can be seen, that aggregate size of 0,5-1 cm and 0,5-2 cm show good numbers of efficiency compare to concrete with bigger aggregate size of 1-2 cm, due to it bigger pores.

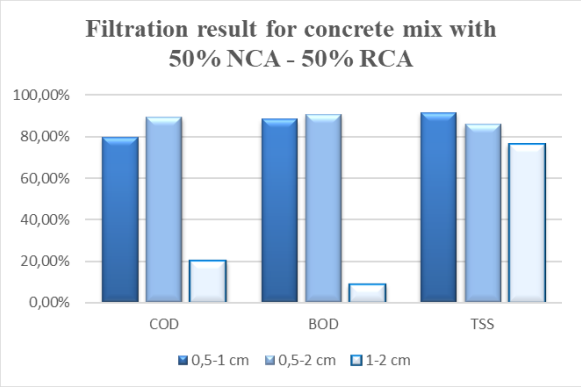

Fig. 1 Filtration result for different aggregate sizes for COD, BOD and TSS parameters

Comparison of aggregate types with various sizes can be seen in Figure 2, 3 and 4. In these figures, the effectiveness is compared for different type of coarse aggregate in concrete mixture with the same sizes.

In Figure 2, for an aggregate size of 0.5-1 cm, the best percentage of efficiency is seen in the 50%RCA 50%NCA mixture type. But it has the lowest ammonia efficiency. This is because ammonia is not reduced only by physical methods, but by the addition of biological methods or by adding aeration to processing.

While for 1-2 cm aggregate size, the highest value of TSS efficiency in 50%NCA 50%RCA mixture while BOD, COD is at 100% NCA. However, the highest ammonia reduction efficiency value is 100% RCA.

The largest pore number is at 100% NCA. The biggest permeability is at 50% RCA 50% NCA. For 0.5-2 cm aggregate size, it can be seen, that the efficiency value of TSS, COD, BOD has the highest value at 50%NCA 50%NCA. With a pore value lower than 100% NCA and higher than 100% RCA as well as its permeability value.

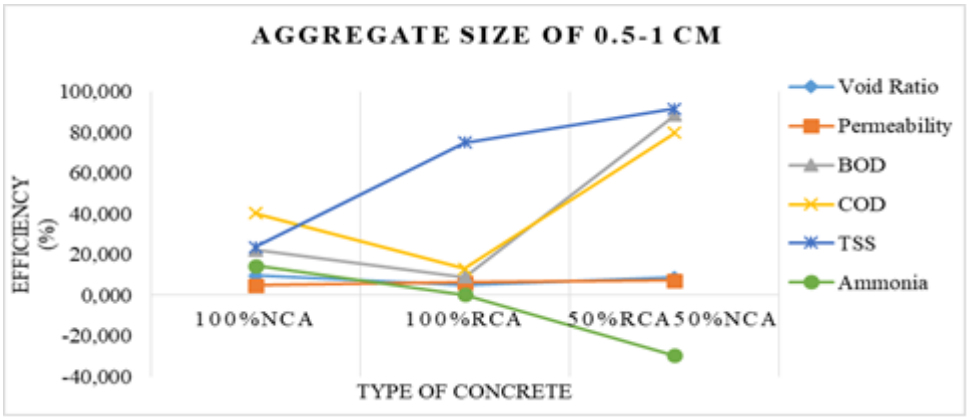

Fig. 2 Void ratio, permeability and efficiency for every mixture with aggregate size of 0.5-1 cm

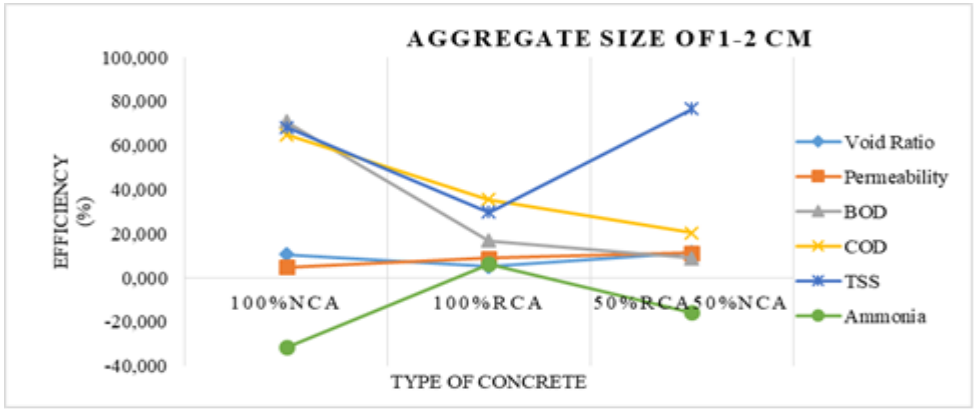

Fig. 3 Void ratio, permeability and efficiency for every mixture with aggregate size of 1-2 cm

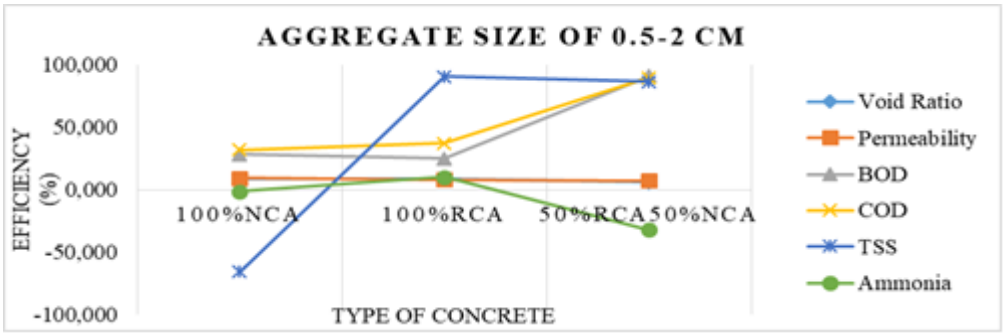

Fig. 4 Void ratio, permeability and efficiency for every mixture with aggregate size of 0.5-2 cm

Comparison of the types of aggregates in each type of concrete mixture is presented with a graph in Figure 5,6, and 7. In these figures, the effectiveness is compared for different size of coarse aggregate in concrete mixture with the same coarse aggregate type. For the 100% RCA aggregate type, it can be seen that the highest efficiency values of TSS, BOD, COD and Ammonia are in the mixture of 100% RCA size 0.5-2 cm. But the highest value of the pore is 1-2 cm. Whereas permeability is at 0.5-2 cm. In 100% NCA mixture 1-2 cm aggregate size has the highest efficiency for TSS, COD, BOD parameters. However, the lowest ammonia reduction efficiency is 1-2 cm. In 1-2 aggregate sizes with 100% NCA mixture types, the pore value is the largest compared to 0.5-1 and 0.5-2. 100% NCA 1-2 has the smallest permeability compared to 0.5-1 and 0.5-2 cm. For the 50% RCA50% NCA aggregate type, the greatest efficiency of TSS, BOD and COD is 0.5-2 cm. But the biggest ammonia reduction efficiency value is 1-2 cm. Efficiency results of 0.5-1 and 0.5-2 in the 50% RCA50% NCA mixture are not much different.

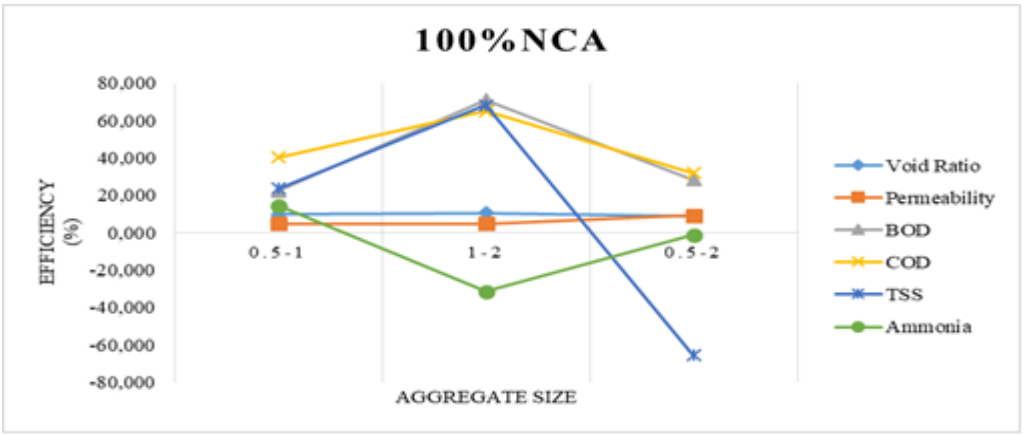

Fig. 5 Efficiency for water quality parameter at porous concrete with 100% of natural coarse aggregate

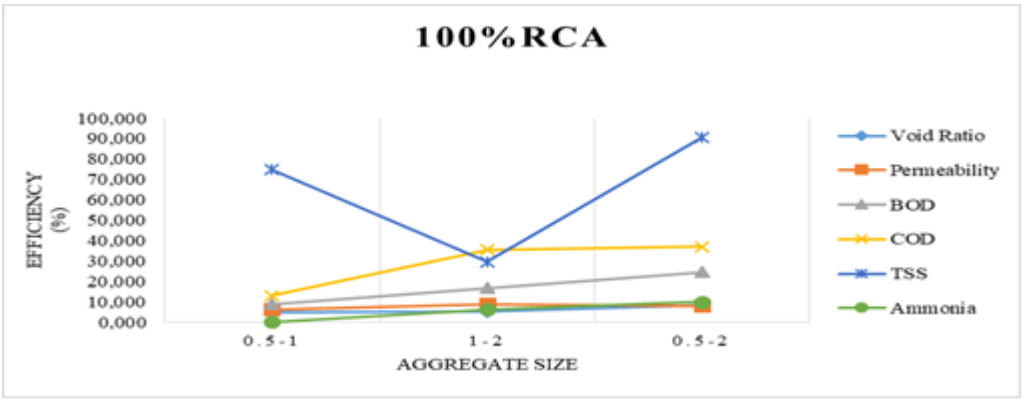

Fig. 6 Efficiency for water quality parameter at porous concrete with 100% of recycle coarse aggregate

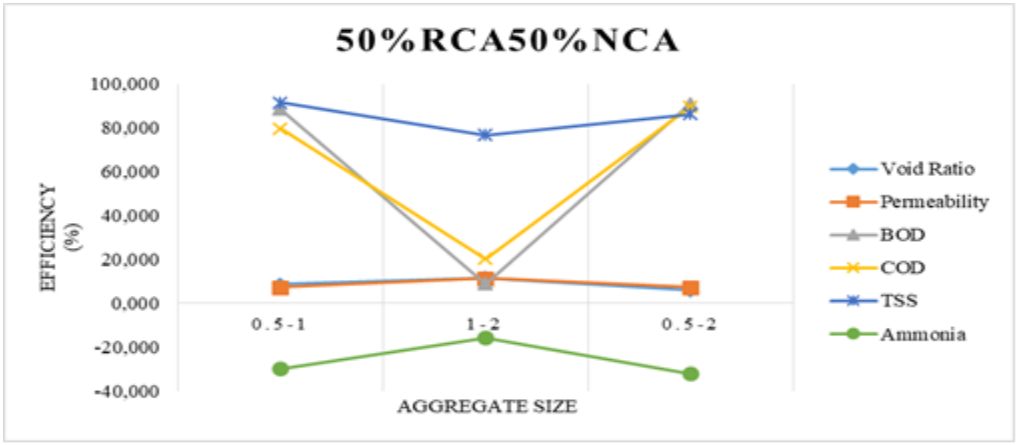

Fig. 7 Efficiency for water quality parameter at porous concrete with 50% RCA and 50% NCA

From the results of the analysis, the size of coarse aggregate in porous concrete mix significantly affected to its filtration ability for reducing water pollutants. Generally, concrete mix with 0.5-2 cm agreggate sizes gives the best result, for the decrease of biological oxygen demand (BOD), chemical oxygen demand (COD) and total suspended solid (TSS), due to its well graded sizes. The porous concrete made from recycled coarse aggregate (RCA) shows better performance on filtrating the water pollutants compared to one made from natural coarse aggregate (NCA).

CONCLUSIONS

In conclusion, the size of coarse aggregate in porous concrete mix has a significant effect and highly efficient for reducing the water pollutants, as biological oxygen demand (BOD), chemical oxygen demand (COD) and total suspended solid (TSS), with 0.5-2 cm agreggate sizes for best result, due to its well graded sizes. The porous concrete made from recycled coarse aggregate (RCA) shows better performance on filtrating the water pollutants compared to one made from natural coarse aggregate (NCA). Void ratio and permeability values cannot determine the efficiency of reducing pollutants by porous concrete. The outcome of this study can be used to develop an improved filtration system model of wastewater for residents with limited land in urban areas. In order to appropriately meet the water quality standart criteria, it is recommended in the future work to improve the filtration model by considering adding more layers, adding wetland system, or combining with adding some additives. The cumulative sediments in the model should be well predicted as well.

REFERENCES

[1] Tiwari, S., Water Quality Parameters –A Review, International Journal of Engineering Science Invention Research & Development, Vol. I, Issue t

[2] Mishra, R., Prajapati, R.K., Dwivedi, V.K., Mishra, A., Water Quality Assessment of Rani Lake of Rewa (M.P.), GERF Bulletin of Biosciences, 2011, 2 (2), pp. 11-17.

[3] Yimrattanabavorn, J., Rungrueang, O., Karuchit, S., Wirikitkhul, P., Assessing Urban Water Supply System in Northeastern Thailand: Water Quality and Authority Organization, International Journal of GEOMATE, Aug. 2018 Vol.15, Issue 48, pp.187-194.

[4] HarshavarthanaBalaji M., Amarnaath M.R., R.A.Kavin, S. Jayapradeep, "Design of Eco Friendly Pervious Concrete", International Journal of Civil Engineering and Technology (IJCIET), Vol. 6, Issue 2, February (2015), pp. 22-29.

[5] Pratap Singh H., Sharma K., Sakale R., Kumar K.S., "Enhancement the Strength of Pervious Concrete with Different Water Cement Ratio and Admixture", International Journal of Engineering Research & Technology (IJERT), Vol. 5, Issue 01, Januari 2016, pp. 582-588.

[6] Vikram, Mahla R.P., "Experimental Study of Pervious Concrete Pavement", International Journal for Research in Applied Science & Engineering Technology (IJRASET), Vol. 3, Issue 7, July 2015, pp. 40-48.

[7] Pilon, B.S., Tyner, J.S., Yoder, D.C., Buchanan, J.R., The Effect of Pervious Concrete on Water Quality Parameters: A Case Study, Water 2019, Vol. 11, no. 2, 263.

[8] Joshi T., Dave U., Evaluation of Strength, Permeability and Void Ratio of Pervious Concrete With Changing W/C Ratio and Aggregate Size, International Journal of Civil Engineering and Technology (IJCIET), Vol. 7, Issue 4, July-August (2016), pp. 276-284.

[9] Tchobanoglous G., Burton F.L, Stensel H.D., Wastewater Engineering, Treatment and Reuse, 4rd edition, McGraw- Hill, New York (2003).

[10] El-Gawad, H.S.A., Oil and Grease Removal from Industrial Wastewater Using New Utility Approach, Hindawi Publishing Corporation Advances in Environmental Chemistry, Volume 2014, Article ID 916878.

[11] Mueller, A.SS, et.al, Removal of Oil and Grease and Chemical Oxygen Demand from Oily Automotive Wastewater by Adsorption after Chemical De-emulsification, Practice Periodical of Hazardous, Toxic, and Radioactive Waste Management, Vol 7, no. 3, 2003, pp. 156–162.

[12] Scholz, M., Mineral and Biological Contamination of Soil and Crops Irrigated With Recycled Domestic Wastewater, Sustainable Water treatment, Elsevier, 2019, Pages 55-83.

9th Int. Conf. on Geotechnique, Construction Materials and Environment, Tokyo, Japan, 20-22 November 2019, ISBN: 978-4-909106025 C3051

WATER MOVEMENT AND DEFORMATION IN UNSATURATED MULTI-LAYERED SLOPE UNDER HEAVY RAINFALL

Tang Junfeng[1], Uchimura Taro[1], Tao Shangning[1,] Huang Dong[3], Xie Jiren[2]
[1]Department of Civil & Environmental Engineering, Saitama University, Saitama, 338-0825, Japan;
[2]Department of Civil & Environmental Engineering, University of Tokyo, Tokyo, 113-8654, Japan;
[3]Institute of Mountain Hazards and Environment, Chinese Academy of Science, Cheng Du, 610041, China

ABSTRACT

In 2013, a number of shallow landslides triggered by heavy rainfall affected a mountainous area which located on Izu-Oshima island (Eastern Japan). These slopes are consist of fine soil layers and coarse soil layers which have a different permeability coefficient and soil water characteristic curves. To clarify the characteristics of water infiltration in such unsaturated multi-layered slope and to assess the influence of the water content distribution on slope failure, 4 column tests and 2 groups of inclined slope model experiments were conducted. Silica No 1(D_{50}=3.10 *mm*) and silica No 7(D_{50}=0.16 *mm*) were used as the slope materials. The results indicated that advancing wet front apparently stopped at the interface between the silica No 7 layer and silica No 1 since the capillary barrier works and then lateral water flow occurred along with the interface and infiltrate into next layer when soil approaches saturation. It was found that when lower water content θ in fine and coarse layer, unsaturated permeability coefficient *K* in coarse layer (*K*=5.54E-06 *cm/s*) is smaller than fine layer (*K*=1.08E-04 *cm/s*) since matric suction is 2.5 kPa, which result that capillary barrier works. In addition, higher water zone still exists at the bottom of the fine layer after drainage for a long period which results in the failure in this zone firstly when second rainfall was applied. Piping occurred at the bottom of the model when amount of water exists inside the slope. Although toe of slope reach to saturated condition is later in multi-layer slope, failure time is earlier.

Keywords: Unsaturated soil; Water infiltration; Capillary barrier; Permeability coefficient; Multi-layer slope; soil Piping;

INTRODUCTION

This study deal with a slope consist of fine layer and coarse layer. It has a deep influence on the process of rainfall water infiltration and volume water content distribution in slope, thus governing the failure of slope. These kinds of multilayer slopes are present in many landscapes. For example, the catastrophic landslides that occurred in May 1998, involved pyroclastic covers laying upon the slopes of Pizzo D'Alvano, in Campania Southern Italy [1]. Another example is the multi-layer slope consists of volcanic sand and loess in Japan, which have the failure on the surface in Izu-Oshima in 2013. Rainfall infiltrating water owing to the build-up of capillary barriers [2] that occur at the interface between unsaturated fine and coarser soil layers. Capillary barriers can maintain a high degree of saturation in the soil above them which result into a different failure part in multi-layer slope [3]. These phenomena are related to capillary tension that limits the downward movement of water from a finer soil into underlying coarser soil. In some situations, capillary forces in the upper fine layer can no longer hold water, any additional infiltration is transmitted to the lower coarse layer. This situation happens at a critical distance from the top of the slope that can be estimated using a model proposed by Ross [4].

In this paper, building up and breakthrough point of the capillary barrier has been taken into consideration and its influences on slope failure time and failure modes are discussed based on column tests, inclined model slope experiments and mathmatic calculation.

The main objectives of this study are to evaluate the influence of capillary barrier and its diversion capacity on slope failure and the different failure modes between single layer and multi layer slope. SWCC tests of fine sand and coarse layer were also conducted to estimating the different hydraulic conductivities to explain how the capillary barrier works.

TESTING MATERIALS AND METHODS

Two soils from Japan, Silica No 1 and Silica No 7 were used in the lab experiments, which were excavated from Tono-Area Gigu Province. The sieve tests were conducted using the JGS Geotechnical Society standard test methods (JGS0131-2009). The details of the experiment properties are shown in Fig 1. The dry density of the coarse layer is 1.43 g/cm^3 while that of the fine layer is 1.33 *g*/*cm*^{3}. In addition, Table 2 and Fig 5 show soil water characteristic

curves of silica No 1 & 7 in both drying and wetting process and the fitting parameters by the VG model. It was found that saturated water content and residual water content in silica No 1 is lower than silica No 7, and volume water content is also lower under the same matric suction condition.

The other basic physical properties of test materials, including specific gravity G_s, maximum dry density, soil grain size distribution was measured in accordance with JGS standard test methods and the result are shown in Table 1. According to the soil classification system (USCS), Silica No 1 is classified as the coarse sand while No7 is fine sand.

Table 1 Basic properties of Silica No 1 and No 7

Description	Silica No 7	Silica No 1
Specific gravity G_s	2.63	2.62
Gravel content (>4.75*mm*; %)	0	97.13
Sand content (%)	87.31	2.86
Fines content (<0.075*mm*; %)	11.64	0
D_{10} (*mm*)	0.043	2.26
D_{50} (*mm*)	0.152	3.52
D_{60} (*mm*)	0.165	4.21
Maximum dry density (g/cm^3)	1.556	1.52
Minimum dry density (g/cm^3)	1.271	1.38

SWCC Tests and Unsaturated Hydraulic Conductivity of Testing Materials

SWCC and unsaturated hydraulic conductivity of sands was obtained in lab. Fig. 1 shows the relationship between matric suction and volume water content. Both drying process and wetting process experiments were conducted showing a difference in both sands. In this case, hydraulic conductivity increased with water content increase in coarse and fine sand.

The soil-water characteristic curves of the soil have been modeled with the van Genuchten-Mualem model [5], namely:

$$S_e = \left\{1+(-\alpha h)^n\right\}^{-m}$$
$$S_e = \frac{\theta-\theta_r}{\theta_s-\theta_r} \quad (1)$$
$$m = 1-\frac{1}{n}$$

In the above equation, the water retention curve has been expressed in terms of effective degree saturation. Where θ is the volumetric water content; θ_r and θ_s indicate residual and saturated values of the water content; a, m and n are the fitting parameters. h is the matric suction. a is a scaling parameter (units of m^{-1}) and the exponents n and m are parameters that determine the shape of the retention curve The hydraulic parameters are given in Table 2.

Table 2 Hydraulic properties of the silica No 1 and silica No 7

Description	Symbol (unit)	Soil	
		No 7	No 1
Drying curve			
Saturated volume water content	θ_s	0.44	0.42
Air-entry value	ψ_a (kPa)	2.44	0.62
Residual volume water content	θ_r	0.12	0.05
van Genuchten model	a	0.41	1.59
Fitting parameter	n	4.07	3.11
	m	1.42	0.67
Wetting curve			
van Genuchten model	a	0.42	0.03
Fitting parameter	n	4.51	1.42
	m	0.78	0.29

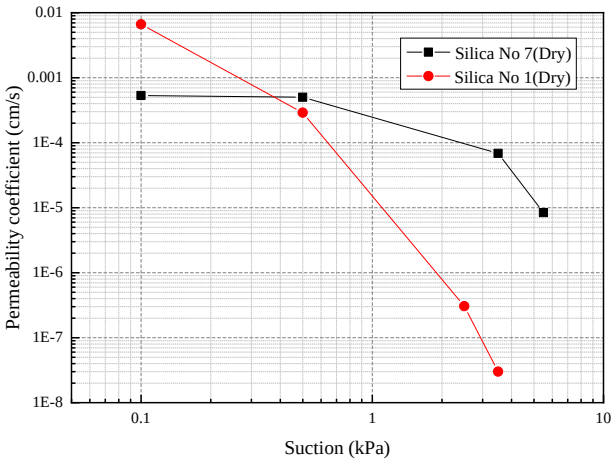

Fig. 1 Hydraulic conductivity of Silica No1 & No 7 in drying process and wetting process

Fig. 1 shows that the volume water content in silica No 7 is higher than No 1 when under the same suction, which could explain how the capillary barrier works. Suction in fine layer decrease as the water content increase, capillary will breakthrough and rainwater start to infiltrate into the next layer.

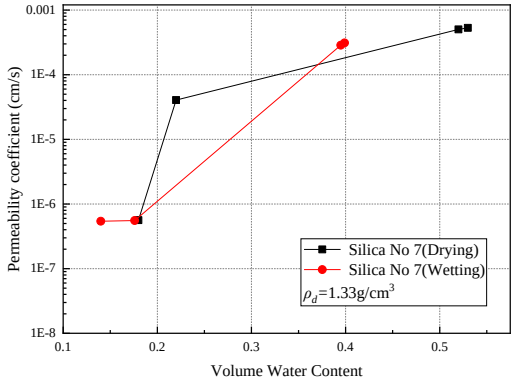

Fig. 2 Permeability coefficient functions of fine-grained sand and coarse-grained

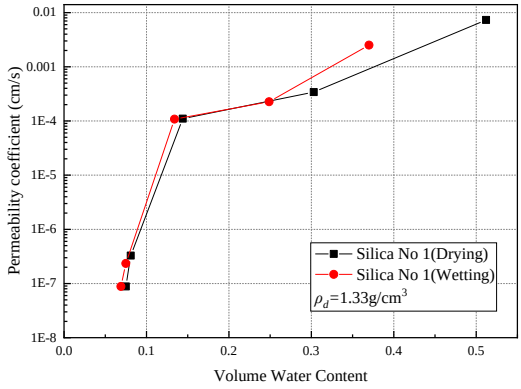

Fig. 3 Relationship between permeability coefficient and volume water content of Silica No1 in both Drying and Wetting process

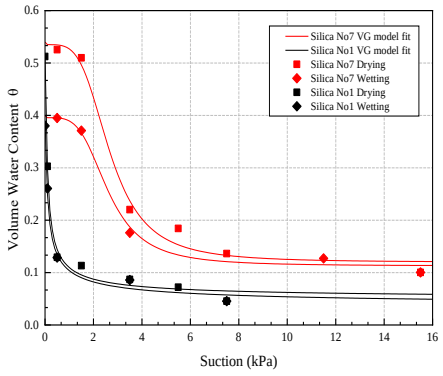

Fig. 4 Relationship between permeability coefficient and volume water content of Silica No7 in both Drying and Wetting process

MODEL EXPERIMENTS

Column Infiltration Tests Through Layered Soil

A series of laboratory column infiltration tests have been performed in the laboratory to observe and to analyze the capillarity barrier behavior at the laboratory scale. The apparatus consisted of the transparent column, whose diameter is 155mm and height is 450mm. In the experiments, moisture sensors (METRE, EC-5) were placed, at various locations, at four different depths within the three soil layers (at 10 *cm*, 15 *cm*, 22.5 *cm* and 30 *cm* below the top surface, respectively) in test I and II while 5 different depths in test III and IV(at 10 *cm*, 15 *cm*, 22.5 *cm* and 30 *cm* below the top surface, respectively). HOBO-loggers were used to get the data of water content every 10 seconds. The density of coarse layer and the fine layer are 1.43 g/cm^3 and 1.33 g/cm^3 while the initial water content is 5%. Results from four sets of tests are reported on Fig. 6. In the column Test I ,II, III and IV.

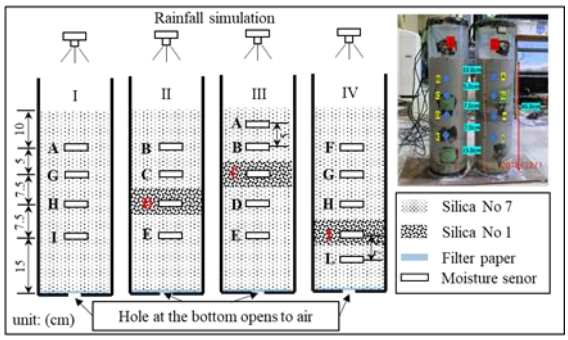

Fig. 5 Schematic view and photo of the experimental apparatus for column Test I, II, III and IV

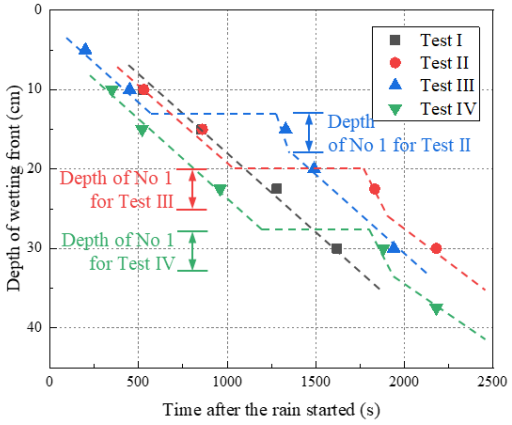

Fig. 6 Measured wetting front advancement for test I, II, III, and IV

Test procedures

The sand was packed into the cylinder and hammered to get the designed density in 5cm increments. During the wetting experiments, all of the column tests I, II, III and IV (Fig.5) has been subjected to a rainfall intensity of 75*mm*/*h* for about 2 hours (rainfall stage) until the attainment of a nearly steady state condition. And to a water drainage process of about 72 hours (dry stage). The bottom of the column has a hole (diameter = 35*mm*) covered with filter paper, which is open to the atmosphere.

Test results and analysis

Fig. 6 shows the progress of the infiltrate wetting front to a different depth. The advancement in the beginning of rain for 4 tests of the wetting front was similar for all cases because they had the same soil types in the upper soil layer. The difference occurred at the interface of the fine layer and coarse. For example, in tests I and II, the arrived time of water at the depth of 100 *mm* and 150*mm* are 510 seconds and 890 seconds respectively. However, the arrived time at central coarse layer (depth of 225 *mm*) were 1380 seconds and 1890 seconds respectively, which showed a time delay around 13minutes at this area. These results show that the progress of the wet front apparently stopped at the interface between the silica No 1 & No 7 when fine layer overlying the coarse layer since capillary barrier worked. In tests III and IV, the same phenomenon could also be observed at the interface when the depth of upper fine layers were different.

In addition, time histories of the volume water content of Test I ,II, III and IV (in Wetting Process) at different depths are illustrated in Fig. 7. Taking the original dada of Test I as an example (Fig. 7 I), Point B, C, D and E showed a sharp increase of soil water content when the wetting front arrived, which soon reached a stable and nearly saturated value. The probe D and E were higher than that at Probes B and C. This indicated that ponded infiltration had caused sealed air and result in an unsaturated condition in the top soil layer while it was not so obvious in the bottom layer. For Probes E in column, the obvious increase of soil water content not only occurred when the wetting front arrived but also after the wetting front had reached the bottom of the soil column (at about 56 min).

The reason is that the wetting front stopped for a while above the interface between the silica No 7 (which was fine layer) and silica No 1(which was coarse layer) while rainfall on the surface did not stop and rainfall water accumulated. Therefore, water started accumulating from the bottom and upwardly rewetting the sand.

As a result, the bottom of the upper fine layer had a higher water content in the multi-layered model (Tests II, III, IV) while it is lower in single layer test (Tests I). It means that water accumulation at the interface results a higher water content zone above the coarse layer in the multi-layer test. Compared Test III with IV, the area of higher water content zone became lager while the thickness of the fine layer overlying the coarse layer is lager.

Model Tests of the Multi-layered Slope Under Rainfall

To evaluate the effect of capillary barrier acting on a slope resembling, the experiments of multi-layered slope have been set up. The apparatus for the physical model experiments consisted of an inclined steel box, a rainfall simulator, water content sensors and in soil (Fig. 8 b). Details pertaining to each subsystem are as follows: (i) the inclined steel box was 1.0 m long, 0.3*m* wide, and 0.5*m* high; (ii) the sidewalls of the box were made of acrylic plate to visually observe the advance of the wetting front and failure process during rainfall infiltration; (iii) pictures were taken every 30 seconds by cameras (Fig. 8).

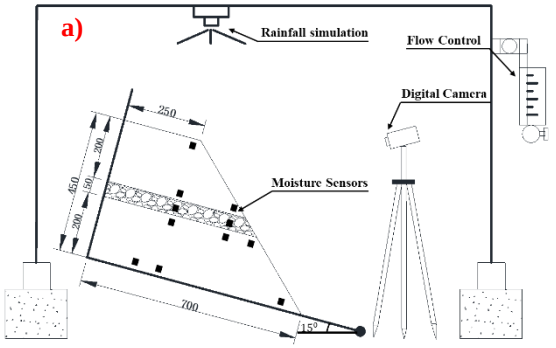

Fig. 8 a) Schematic diagram of the experimental apparatus for multi-layered slope under rainfall: side-view of the multi-layered slope

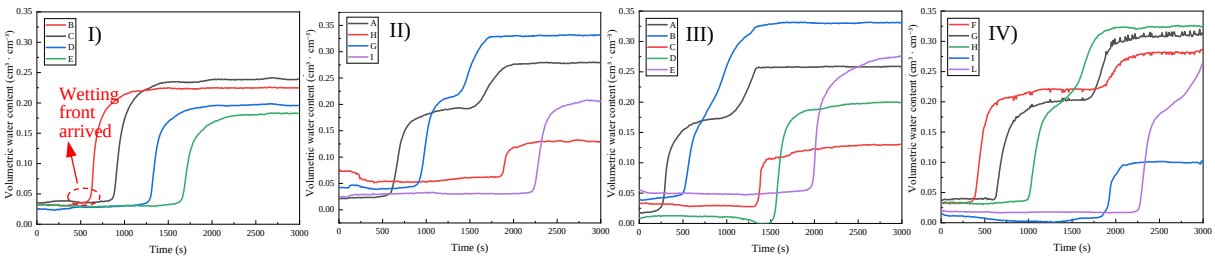

Fig.7 Variation in water content versus time in different observation points in the column tests. I) single layer column; II) multi-layer column; III) upper multi-layer column; IV) lower multi-layer column.

Fig. 8 b) Schematic diagram of the experimental apparatus for multi-layered slope under rainfall: apparatus for the physical model experiment

Testing procedure

Soil preparation. The silica No 1 and silica No 7 used to make the slope was dried in an oven for 48 hours. Then, the amount of water was added to the soil to achieve the initial water content.

Compaction of soils. Slope model was constructed in the model box when the soil has been prepared. The prepared soil was compacted and placed in a series of horizontal layers. Silica No 7 and No 1 were placed into the model box in layers and compacted to achieve the dry density of 1.33 g/cm^3 and 1.43 g/cm^3, respectively. Each layer was tamped equally rod to a thickness of 5cm and repeat the procedures until the height of slope was achieved. Fig. 8 a) shows the information about slope completed. Layers of Silica No 1 was placed as the coarse layer in multi-layer slope.

Positions of sensors and cameras. During the soil placement, moisture sensors were placed at the specific locations within the slope and time of recording the quantity of water content was 10 seconds. Cameras were put in 6 different locations to record the failure condition of the slope every 30 seconds. And 6 blacks dots were inserted laterally into the surface of the slope to as the marks.

Rainfall Simulation. When the initial readings of all sensors and camera were stable, the rainfall simulation commenced. A rainfall sprinkler (Fig. 8) was used to simulate artificial rainfall at different intensities from 45 *mm/h* to 85 *mm/h*. During the first rainfall, 4 hours was applied with 45 *mm/h*. Then the slope model was subjected to a drying process without rainfall; The second rainfall was applied for 4 hours with intensity was 45 *mm/h*. The experiment was stopped with the assumption that seepage had reached a steady-state condition.

Table 3 General information for the slope model experiment

		Group 1	Group 2
Inclined degree		0	15
Initial water content		5%	5%
Unit weight of dry soil (g/cm^3)		No 1 14.4 No 7 13.3	No 1 14.4 No 7 13.3
Rain 1	Intensity	45 *mm/h*	45 *mm/h*
	Duration	4 *h*	4 *h*
Drying Period 1		72 *h*	72 *h*
Rain 2	Intensity	45 *mm/h*	45 *mm/h*
	Duration	4 *h*	4 *h*
Drying Period 2		72 *h*	72 *h*

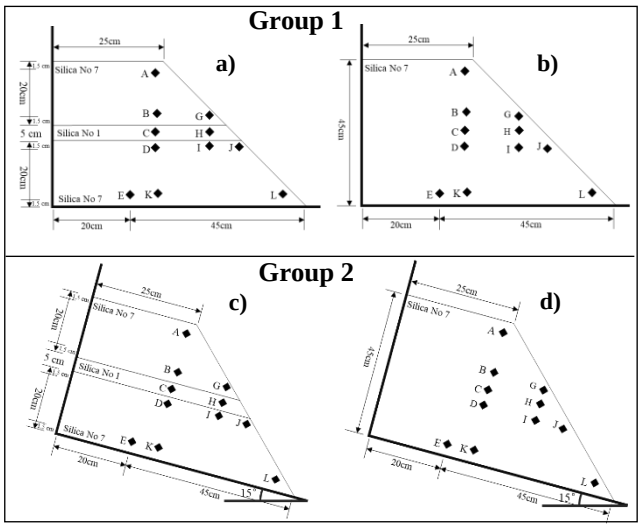

Fig. 9 Schematic diagram of the experimental apparatus for different groups of slopes under rainfall

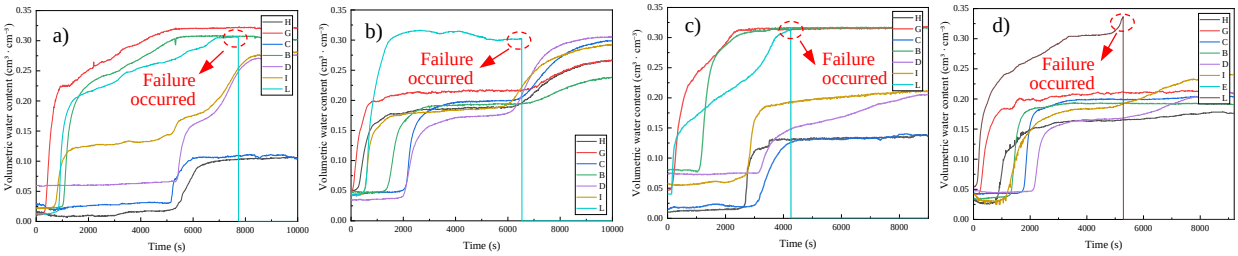

Fig. 10 Water content variation with time at different locations in the flat and inclined groups slopes. a) flat multi-layer slope; b) flat single layer slope; c) inclined multi-layer slope; d) inclined single layer slope.

Experiment result and discussion

In Fig. 10, water content decreases sharply which means the failure occurred at this point since the separation of sensors and soil. Comparing the water content at point L in the flat group (Fig. 10 a and b), point L reached to the saturated condition later in multi-layer since capillary barrier prevents the water infiltrate into the bottom which makes the slope more stable and caused a time delay in failure time. Comparing the water content at point L in the inclined group (Fig. 10 c and d), point L reached to saturated condition still later but the failure time is earlier (about 20 minutes) than single layer slope which means the multi-layer slope is more dangerous under rainfall situation.

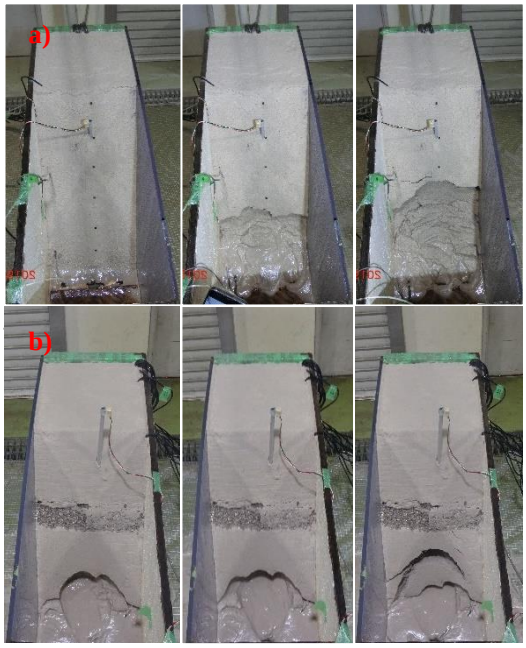

Fig. 11 Different failure modes occurred in the toe of slope under rainfall condition. a) sliding from toe in inclined single layer slope; b) piping occurred at the bottom in inclined multi-layer layer slope.

From Fig.11, different failure modes were observed during the slope experiments. Sliding occurred from the toe of slope (Fig. 11 a) gradually in single layer slope when the rainfall was applied. In the inclined multi-layer slope, piping occurred at the bottom of the slope. Piping (Fig. 11 b) occurred at the bottom when amount of water exists in inside the slope. Although point L reach to saturated condition is later in multi-layer slope, a failure time is earlier.

In order to clear the water movement across the interface, more sensors were put in the coarse layer (Point H, M, C, N and O) in inclined multi−layer slope experiment, 1st and 2nd rainfall were also applied which durations were 20 minutes and 50 minutes respectively.

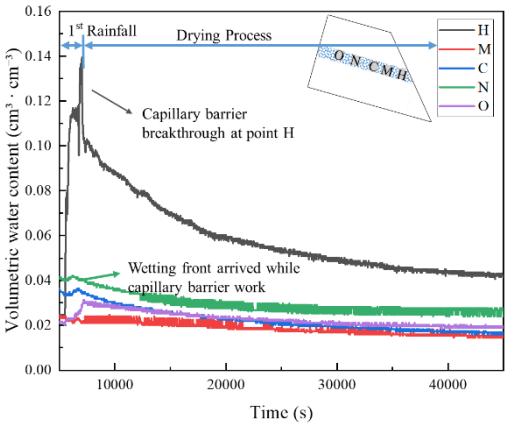

Fig. 12 Volume water content variation with time at different locations along the coarse layer during the first rainfall (20 minutes)

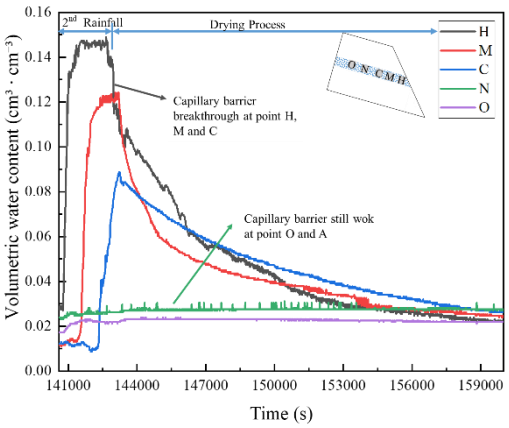

Fig. 13 Volume water content variation with time at different locations along the coarse layer during the second rainfall (70 minutes)

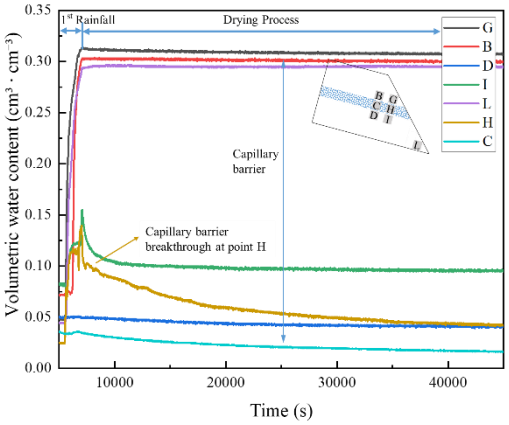

Fig. 14 Comparison between water content in different layers during the first rainfall (20 minutes)

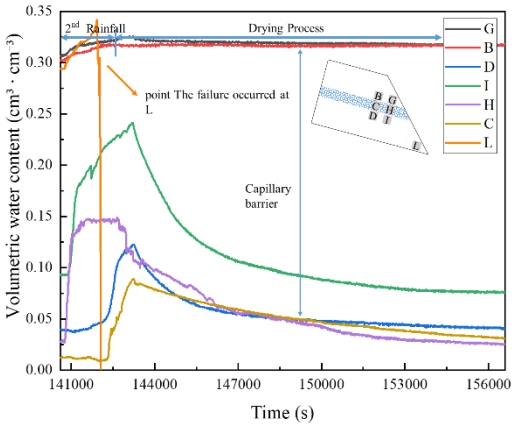

Fig. 15 Comparison between water content sensors in different layers during the second rainfall (70 minutes)

Fig. 12 (case c) shows the water content at point H, M, C, N, and O which at different locations in the coarse layer. The graph shows that when 1st rainfall was applied, the water content at point O and M increased firstly since the location was closest to surface, then N, C and M increased when wetting front arrived the interface and have a small flux before capillary barrier breakthrough. Meanwhile, water content at point H increased quickly and showed a higher water content in Silica No 1 since the capillary barrier didn`t work. When rainfall was stopped and the dry process started, water drained down easily with a rapid reduction in water content in the coarse layer. Similar behavior was also observed when the second rainfall was applied. It was found that the water content in point H, M and C increased gradually with the rainfall continued while water content at point O and N were stable (Fig. 13).

Fig. 14 shows the water content history of point B and G (above the coarse-grained layer), C and H (in the coarse layer) D and I (below the coarse layer) which were put in three different soil layers. This graph shows that water content above the coarse layer (point B and G) remain wetter than the soil below the coarse layer (point D and I). The sand above coarse layer showed 30% of volume water content all the time, suggesting that water didn`t drain down through the coarse layer when first rainfall was stopped while the below showed a sharp reduction in the dry process. A similar phenomenon was also observed when the second rainfall was stopped. When the second rainfall started, the sand above coarse layer at point B and G approached to saturated condition, and capillary barrier breakthrough at point H with water content increased quickly from H and I. Meanwhile, water content at point C and D were still in a lower condition and capillary barrier still work at the same time. Then water content increased at point C infiltrate into the next layer (point D). since the capillary barrier breakthrough gradually from point H to point C in the coarse layer.

DISCUSSION

The diversion capacity is the maximum flow that a capillary barrier can divert water flux and the diversion length is the horizontal length from the top of the slope to the breakthrough. In order to evaluate the diversion length of a capillary barrier, following assumptions are made: (1) suction profile in the fine layer could be estimated using the linear method [6]; (2) upper fine layers are thick enough; (3) the interface is inclined and longer than the diversion length; (4) continuous rainfall is applied on the top of the slope.

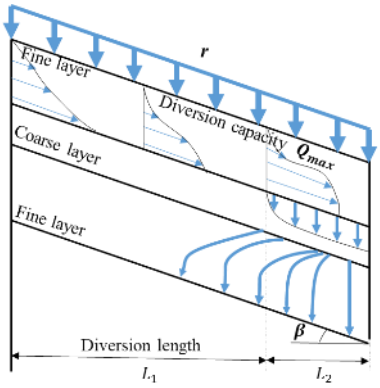

Fig. 16 Calculation of diversion length and capacity in an inclined slope

Based on these situations [4], diversion capacity and diversion length of capillary could be calculated, as the equation:

$$Q_{max} = \int_{z_{0_c}}^{z_{con_c}} v_h(z)dz \tag{2}$$

Where, Q_{max} is the maximum unsaturated lateral diversion capacity (cm^2/s); $v_h(z)$- velocity profile as the function of elevation (cm^2/s); z_{0c} - elevation of base of the upper fine layer (cm); z_{conc} - elevation where the maximum suction in the upper coarse layer (cm);

According to the linear method, elevation can be transformed into suction, and matric suction ψ at the contact interface between two layers must be continuous across the boundary:

$$\begin{aligned} z_{0_f} &= z_{con_c} \\ \psi_{0_f} &= \psi_{max_c} \end{aligned} \tag{3}$$

According to the equation (2) and (3), equation (4) can be obtained and can be deducted via Darcy`s law.

$$Q_{max} = \int_{\psi_{con_c}}^{\psi_{con_f}} v_h(\psi)d\psi = \int_{\psi_{con_c}}^{\psi_{con_f}} i_h k(\psi)d\psi \tag{4}$$

Where, i_h - the lateral hydraulic gradient, which equals to the tangent of slope tan β; $k(\psi)$– k function; β -inclined angle of slope(°).

The maximum lateral diversion flux is

$$\begin{cases} Q_{max} = k_{sat} tan\beta \int_{\psi_{con_c}}^{\psi_{con_f}} k_{rw}(\psi) d\psi \\ k_{rw}(\psi) = \dfrac{\left\{1-(\alpha\psi)^{mn}\left[1+(\alpha\psi)^{n}\right]^{-m}\right\}^{2}}{\left[1+(\alpha\psi)^{n}\right]^{m/2}} \end{cases} \quad (5)$$

According to the formulas (5), the lateral diversion capacity of the inclined capillary barrier can be diverted downdip per unit time per unit length along with the interface. Assuming the water lateral diversion length is L_1, the water lateral flux $Q(x)$ can be calculated by

$$Q(x) \approx r * L_1 < Q_{max} \quad (6)$$

Substituting the equation (6) into equation (5), Equation (7) can be

$$r * L_1 < k_{sat} tan\beta \int_{\psi_{con_c}}^{\psi_{con_f}} k_{rw}(\psi) d\psi \quad (7)$$

Diversion length is bounded by

$$L_1 < \frac{k_{sat} tan\beta \int_{\psi_{con_c}}^{\psi_{con_f}} k_{rw}(\psi) d\psi}{r} \approx 0.56m \quad (8)$$

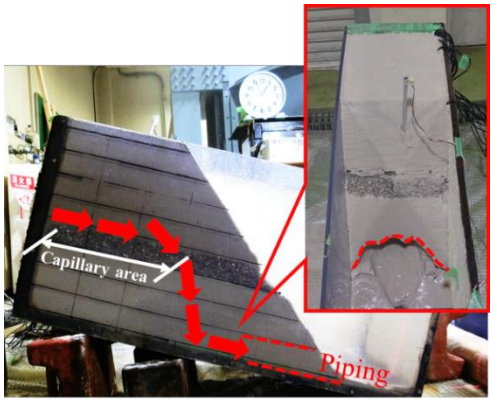

Fig. 17 Accumulated rainfall water infiltrate into the middle part of the slope which cause soil piping

According to the calculation of diversion length by simplified model, length of capillary area (Fig. 17) of this case is smaller than the length of interface. As a result, infiltrating water accumulated above the coarse layer and lateral water flow occurred along with the interface and capillary barrier breakthrough in the middle part of interface which results that water starts to infiltrate into the lower coarse layer at this location. A large amount of rainfall water will pass across the coarse layer and exist in the middle part of the lower fine layer, with rainfall event continued, soil pipes contribute to the quick discharge of rainfall water which results in slope stability.

CONCLUSIONS

The following conclusions are drawn from the present study. Different failure modes occurred in under rainfall condition in inclined multi-layer slope and single layer slope.

In the flat group, multi-layer slope was safer since capillary barrier works which prevent the rainwater infiltrate into coarse layer. Failure occurred at the bottom of slope, the toe of slope reach to saturated condition is later while failure time is also late. In inclined group, failure occurred at the same location, Although toe of slope reach to saturated condition is still later, the failure time is earlier.

According to calculate the length of capillary area and compared with experiment pictures, the diversion length is smaller in this case which allows the accumulated rainfall water infiltrate at the middle part of slope, which causes the soil piping and has an influence on the slope stability.

REFERENCES

[1] D. Mancarella, A. Doglioni, and V. Simeone, “On Capillary Barrier Effects and Debris Slide Triggering in Unsaturated Layered Covers,” Eng. Geol., vol. 147–148, pp. 14–27, 2012.

[2] S. D. Shackelford, M. K, and J. W. Savell, “Evaluation of Longissimus Dorsi Muscle pH at Three Hours Post Mortem as a Predictor of Beef Tenderness,” vol. 37, pp. 195–204, 1994.

[3] E. F. Garcia, C. P. K. Gallage, and T. Uchimura, “Function of Permeable Geosynthetics in Unsaturated Embankments Subjected to Rainfall Infiltration,” Geosynth. Int., vol. 14, no. 2, pp. 89–99, 2007.

[4] B. Ross, “The Diversion Capacity of Capillary Barriers,” Water Resour. Res., vol. 26, no. 10, pp. 2625–2629, 1990.

[5] M. T. van Genuchten, “A Closed-form Equation for Predicting the Hydraulic Conductivity of Unsaturated Soils1,” Soil Sci. Soc. Am. J., vol. 44, no. 5, p. 892, 1980.

[6] M. Kisch. “The theory of Seepage From Clay-Blanketed Reservoirs,” Géotechnique, vol. 9, no. 1, pp. 9–21, 2009.

[7] H. J. Morel-Seytoux and J. R. Nimmo, “Soil Water Retention and Maximum Capillary Drive from Saturation to Oven Dryness,” Water Resour. Res., vol. 35, no. 7, pp. 2031–2041, 1999.

[8] H. Yang, H. Rahardjo, E. C. Leong, and D. G. Fredlund, “A study of Infiltration on Three Sand Capillary Barriers,” Can. Geotech. J., vol. 41, no. 4, pp. 629–643, 2004.

9th Int. Conf. on Geotechnique, Construction Materials and Environment,
Tokyo, Japan, 20-22 November 2019, ISBN: 978-4-909106025 C3051

EVALUATING PASSENGER EVACUATION STRATEGIES IN A MASS RAPID TRANSIT STATION IN THAILAND

Nopadon Kronprasert, Ph.D.[1], Wisarute Kussalanuparb[2] and Thodsapon Hunsanon[3]
[1,2,3]Department of Civil Engineering, Chiang Mai University, THAILAND

ABSTRACT

Rail transit plays a significant role to serve major commuters in many metropolitan areas. In Bangkok metropolitan region in Thailand, several mass rapid transit (MRT) lines and stations are currently being constructed and operated. To perform efficient safety and operational performances, the analysis of pedestrian traffic flow within transit stations under normal and emergency circumstances is a crucial step for planning, design, and operations of station facilities. This study focuses on applying the pedestrian traffic simulation to model the characteristics of passengers and then evaluate passenger evacuation strategies in mass rapid transit stations. The pedestrian's walking behavior and characteristics were observed. Three evacuation strategies were examined including (i) Evacuation to Ground Level; (ii) Evacuation to Train; and (iii) Evacuation to Track Level. The evacuation times under a given number of evacuate occupants were evaluated, and the bottleneck of evacuation strategies was identified. A case study of Tao Poon mass rapid transit station was carried out. The results showed that the pedestrian traffic simulation technique provides great flexibility in modeling different scenarios in emergency situations and evaluating the dynamic nature of pedestrian flow characteristics. It is also useful to planners, designers, and operators of rail transit systems in practice.

Keywords: Rail transport, Evacuation, Safety, Pedestrian simulation, Station design

INTRODUCTION

Rail transit plays a significant role to serve commuters in many large and congested cities. In Bangkok metropolitan area, Thailand, two mass rapid transit (MRT) lines are now being operated: Blue Line and Purple Line; and ten more lines are being planned and constructed. According to the ridership data, the growth of passenger ridership is about 6% each year. With the increasing number of MRT lines and stations along with the estimated growth of passengers, evaluating the performance of station facilities and emergency evacuation strategies in MRT stations are needed.

Many international standard codes defined minimum evacuation requirements and calculation procedures, such as China CDM, Japanese Safety Evacuation and National Fire Protection Association (NFPA 130) [1]-[3]. For instance, NFPA 130, which is also being implemented by Mass Rapid Transit Authority of Thailand, specified two criteria for station evacuation efficacy. The first is referred to the time required to evacuate the platform within 4 minutes or less; and the second gives the time frame to evacuate the whole station and reach a point of safety within 6 minutes or less.

However, such standard codes provide macro-scale equations, which rely on static hand calculation. To overcome the limitation, a microscale study on evacuation using microscopic traffic simulation models is proposed. It is capable to simulate the dynamic environment of evacuation situations and to provide visible results through 3-D animations. More importantly, the use of simulation models in emergency situations provides great flexibility in modeling and evaluating various evacuation strategies.

This research aims to evaluate the effectiveness of evacuation strategies for passengers within mass rapid transit stations in Thailand. The focus of this research is on applying a microscopic pedestrian traffic simulation model to the evaluation of evacuation plans.

LITERATURE REVIEW

Research studies on emergency evacuation of passengers in a metro station have mainly focused on the development of sound and applicable evaluation methods for emergency evacuation. Two leading approaches were found in the literature.

First, the traditional approach, is a macroscopic equation of traffic flow theory [1]-[2]. The macro approach has failed to deal with interactions among pedestrians and between pedestrians and facilities [3]. However, they are still widely used due to its simplicity.

Second, the groundbreaking approach, is a microscopic pedestrian traffic simulation. The number of research studies on pedestrian evacuation using microscopic pedestrian traffic simulation have been increasing greatly since last decade. This is

because the micro approach accounts for the detailed representation of space, individual person and personal abilities and characteristics [4]. As a result, it is more reasonable and more realistic.

Using a micro approach, research studies have focused on determining the effects of a proposed policy on pedestrian facilities, evacuation behavior, and evacuation process. For example, Credit [5] developed various microscopic simulation scenarios to gain more understanding about pedestrian characteristics. The study compared one-way and two-way pedestrian traffic; examined the effect of an elderly pedestrian on system behavior; and evaluated the performance of lane-like segregation policy.

Moreover, Asano [6] proposed a microscopic simulation model for pedestrian flow evaluation. The study combined an operational model with a tactical model. The former considered anticipation behavior between two pedestrians based on collision avoidance concept and using the two-player game, and the latter considered the route choice behavior of individuals. The study suggested the usefulness of a micro simulation for precisely evaluating the Level of Service of the building design layout.

However, limited studies were a consideration of different evacuation strategies on pedestrian facilities, such as escalators and staircases. This subject is in fact needed for the safety design. Shi [7] investigated safety strategy of evacuation in a metro station in China by proposing a calculation method for evacuation time, and taking into consideration the metro station structure and layout features. The study used an agent-based simulation model to compare the evacuation time with the China CDM requirement.

Kallianiotis [8] compared two evaluation methods of evacuation performance in an underground metro station: the calculation method based on NFPA 130 design guidelines and Pathfinder software evacuation simulation package. The study showed both static hand calculation and dynamic environment simulation produce consistent results, but the static hand calculation requires a number of assumptions.

RESEARCH APPROACH

Study Area

The research selected Tao Poon MRT station, an aboveground interchange station connecting between 2 train lines (Blue and Purple Lines) as a case study. The station consists of 4 levels and details on station facilities of each level are shown in Fig. 1 to Fig. 4.

- Ground level (with four entrances/exits);
- Concourse level (with six emergency exits and two staircases);
- Blue-line platform (with six emergency exits and two staircases); and
- Purple-line platform (with two emergency exits and two staircases).

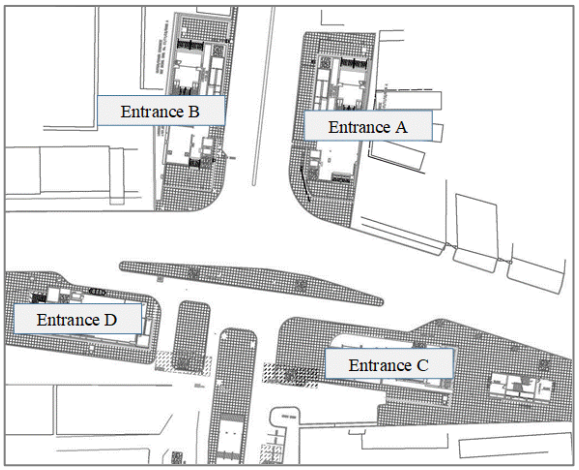

Fig. 1 Locations of main entrances/exits on Ground Level of Tao Poon MRT station

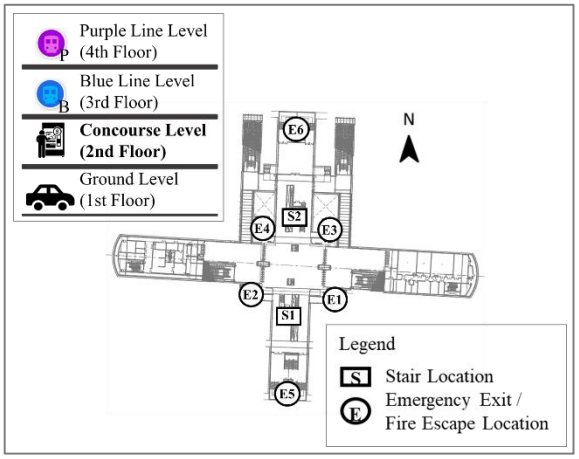

Fig. 2 Locations of emergency exits and staircases on Concourse Level

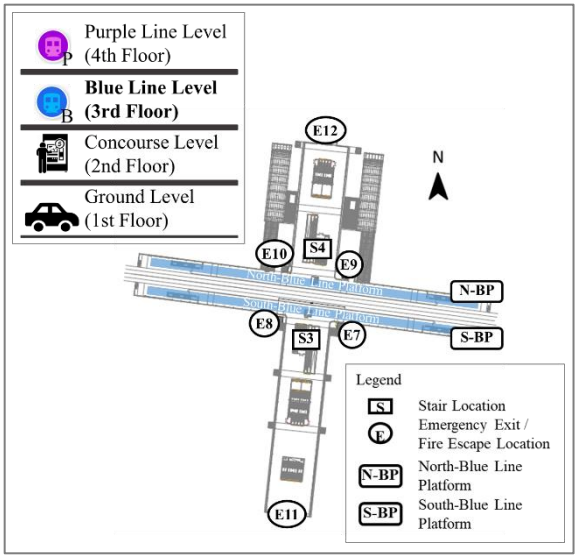

Fig. 3 Locations of emergency exits and staircases on Blue-line platform Level

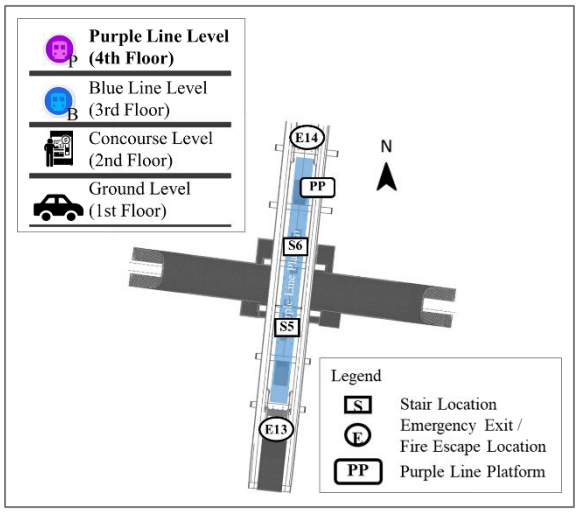

Fig. 4 Locations of emergency exits and staircases on Purple-line platform Level

Data Collection

To build up the model, the data collection is necessary to improve the model accuracy and realistic. Data needed for building the models include

Occupant Load

One of the key inputs in developing the evacuation model is the occupant load, which directly affects evacuation time. For Tao Poon MRT station, passenger volume was first collected during October to December in 2016 as shown in Fig. 5. The peak-hour period passenger volume was converted to occupant load.

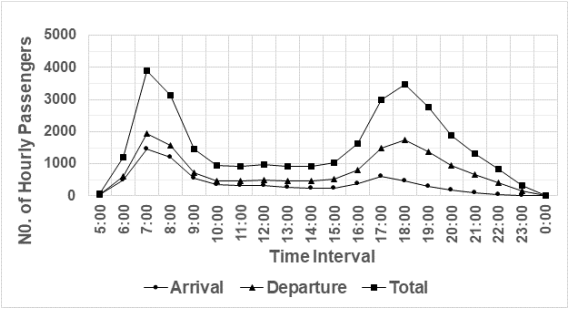

Fig. 5 Hourly passenger volume

The total number of occupants to be evacuated in the model is 1,010 passengers during the peak hour. They include 50 occupants on the Concourse level, 483 on Blue-Line platform, 322 on Purple-line platform, 105 occupants boarding on Blue-Line trains, and 50 occupants boarding on Purple-Line trains.

Walking Speed

Walking speed is another important parameter affecting the performance of evacuation strategies. Walking speed on different facilities: concourse and staircase were measured from CCTV installed in the station. Table 1 presents the calculated average walking speed by age group. A cumulative distribution function of Walking Speed is also shown in Fig. 6.

Table 1 Average walking speed by age group

Age	Average walking speed (m/s)		
	Concourse	Staircase (upward)	Staircase (downward)
Children	1.36	0.61	0.75
Adult	1.45	0.82	1.15
Elderly	1.06	0.55	0.81

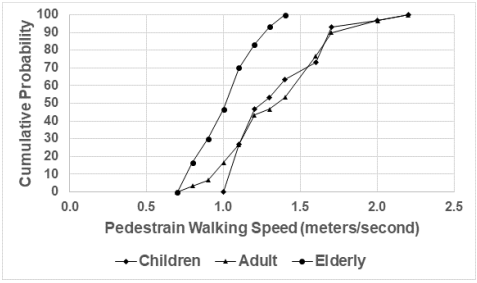

Fig. 6 Walking speed distribution by age group

EVACUATION MODEL

Evacuation situations of the case study were developed using a microscopic pedestrian traffic simulation program, PTV Viswalk. Figure 7 shows the snapshot of the simulation model of the Tao Poon MRT station.

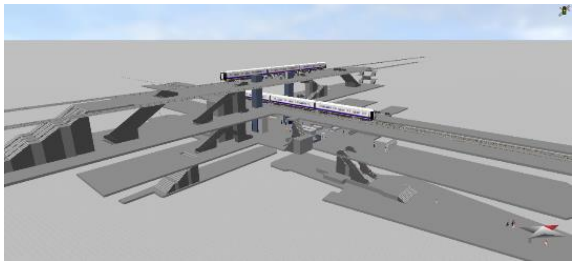

Fig. 7 Snapshot of Tao Poon MRT Station model

Three emergency evacuation strategies are proposed according to MRTA evacuation action plans. The effectiveness of each evacuation strategies were evaluated in the model.

- Strategy I: Evacuation to ground level: applied when fire is present.
- Strategy II: Evacuation to trains: applied when entrances and exits are not accessible or not considered as a safe area.
- Strategy III: Evacuation to track level: applied to the same situations as Strategy II, but trains are unable to operate by any means.

Strategy I: Evacuation to Ground Level

In this evacuation strategy, evacuation occupants in Tao Poon MRT station from all floors need to evacuate to the Ground Level through 4 entrances including Entrance A, B, C, and D. There are in total 6 designated evacuation routes as shown in Fig. 8.

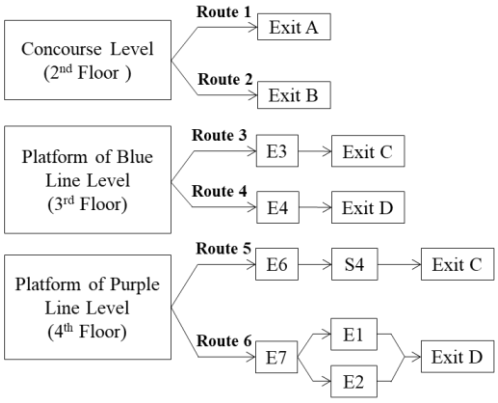

Fig. 8 Evacuation routes to Ground Level

Strategy II: Evacuation to Train

This evacuation strategy is to evacuate all occupants in the station to the nearest platforms and evacuated them by trains. This strategy consists of 9 designated evacuation routes, of which 6 routes evacuating from Concourse Level, 2 routes from Blue-line platform and 1 route from Purple-line platform as shown in Fig. 9.

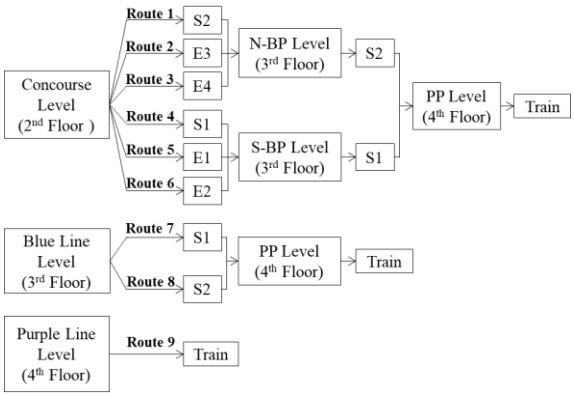

Fig. 9 Evacuation to Train Platform Strategy

Strategy III: Evacuation to Track Level

This evacuation strategy is similar to the Evacuation to Train strategy (Strategy II). Instead of evacuating occupants by trains, this strategy evacuates them to railway tracks, which are out of operation. It should be noted that to deploy this strategy, the electrical system needs to be cut off for the safety reason. This strategy consists of 9 designated evacuation routes as shown in Fig. 10.

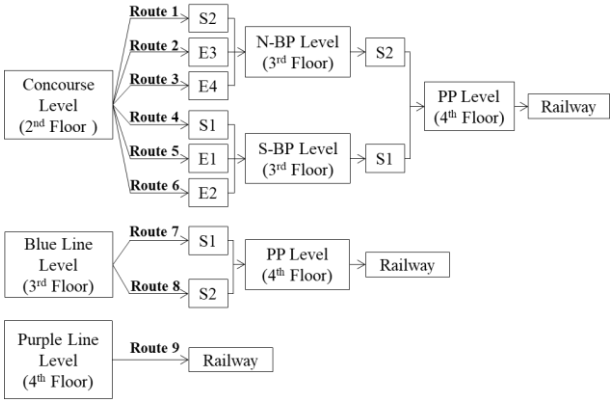

Fig. 10 Evacuation to the Track Level Strategy

RESULTS AND DISCUSSION

Evacuation time and pedestrian density of three strategies were measured, and their level-of-service (LOS) were evaluated based on Highway Capacity Manual [10] criteria shown in Table 2.

Table 2 Level-of-Service Criteria

LOS	Pedestrian Density (peds/sq.meter)	Color defined in the model
LOS A	≤ 0.179	Blue
LOS B	0.180 – 0.269	Cyan
LOS C	0.270 – 0.454	Green
LOS D	0.455 – 0.713	Yellow
LOS E	0.714 – 1.333	Orange
LOS F	≥ 1.334	Red

Strategy I: Evacuation to Ground Level

This strategy evacuates occupants to Ground Level or where entrances are located. Table 3 suggests that the evacuation time of 6 different evacuation routes meets the NFPA 130 thresholds. Route 2 evacuated occupants from Purple-Line platform has the longest evacuation time, yet it meets NFPA standard.

It should be noted the evacuation preparation time is excluded in the model. If 1-minute preparation time are included, the total evacuation time will be no more than 4 minutes.

Routes 3 and 4 are evacuating routes from Blue-line platform. They result in the evacuation time less than 2 minutes. Routes 5 and 6 are evacuating routes on Concourse Level, which are not as crowded as the platform levels. Thus, the evacuation times are also

less than 2 minutes including preparation time. Evacuation time and evacuation rate are shown in Table 3. The heat maps presenting pedestrian density are shown in Fig. 11.

Table 3 Evacuation time and Evacuation rate of Evacuation to Ground Level Strategy

Route	Evacuation time (mins)	Evacuation rate (peds/min)
Route 1	0.87	11
Route 2	0.72	11
Route 3	1.83	82
Route 4	1.62	94
Route 5	2.85	57
Route 6	2.95	58

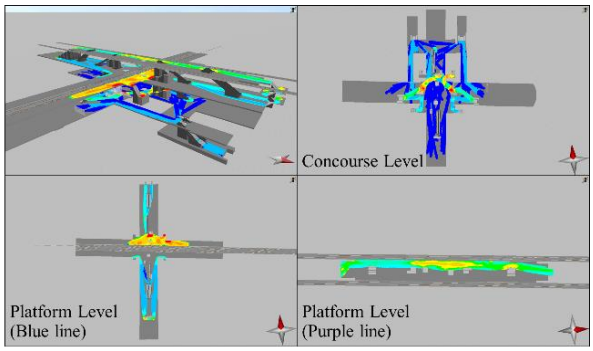

Fig. 11 Pedestrian Density in Evacuation to Ground Level Strategy

Strategy II: Evacuation to Train

In this evacuation strategy, all occupants are evacuated through trains. Table 4 shows that the longest evacuation time including 1-minute preparation time is below 6-minute threshold. However, if the preparation stage takes longer than 1 minute, this strategy may fail. Hence, more trains should be allocated in this evacuation situation. The pedestrian density heat maps are in Fig. 12.

Table 4 Evacuation time and Evacuation rate of Evacuation to Train Strategy

Route	Evacuation time (mins)	Evacuation rate (peds/min)
Route 1	3.6	1
Route 2	3.7	2
Route 3	4.5	1
Route 4	4.3	1
Route 5	4.3	1
Route 6	4.4	2
Route 8	3.9	87
Route 9	2.1	154

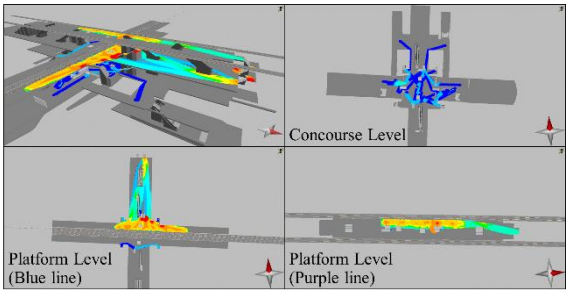

Fig. 12 Pedestrian density of evacuation to train strategy

Strategy III: Evacuation to Track Level

Evacuation to Track Level strategy can be deployed when the ground level or the road outside the station is not safe anymore, or in the case that trains are not available to help evacuate. In this strategy, occupants will be evaluated through train tracks. The results showed that evacuation time of this strategy are less than 3 minutes including preparation time. This is because occupants can evacuate immediately when an emergency occurs.

When deploying this strategy, safety concern is needed. There should be trained staff helping navigate occupants to the safe areas, and no train must be operated. The evacuation time in each route and density heat map are shown in Table 5 and Fig. 13.

Table 5 Evacuation time and Evacuation rate of Evacuation to Track Level Strategy

Route	Evacuation Time (mins)	Evacuation Rate (peds/min)
Route 1	1.8	4
Route 2	1.8	5
Route 3	1.7	2
Route 4	1.8	2
Route 5	1.9	2
Route 6	1.8	4
Route 8	1.6	211
Route 9	1.0	337

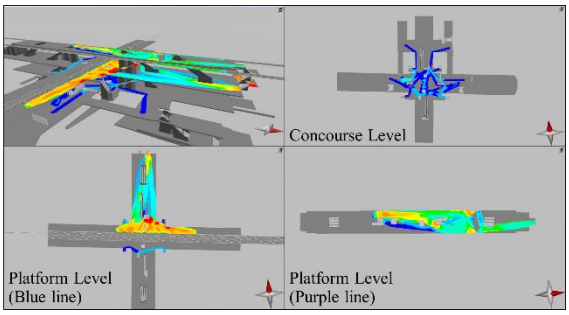

Fig. 13 Pedestrian density of evacuation to track level strategy

CONCLUSIONS

This research applies the microscopic pedestrian traffic simulation models to evaluate the effectiveness of passenger evacuation strategies within mass rapid transit stations in Thailand. Three strategies: Evacuation to Ground Level, Evacuation to Train, and Evacuation to Track Level. Input parameters in the models are the number of occupants, the distribution of walking speed and the locations of station facilities.

Evacuation strategies were evaluated in terms of the evacuation time, evacuation rate and pedestrian density. The results showed that all three evacuation strategies meet the requirement of NFPA evacuation time.

This research emphasizes the capability of a microscopic traffic simulation in modeling dynamic environment of evacuation events and its flexibility in testing different evacuation routes and strategies. It allows planners, designers, and operators of rail transit systems to determine whether certain building designs meet the requirement of a standard.

In future research, more operational strategies should be taken into consideration in order to obtain the most effective evacuation strategy, such as the use of escalators, and types of exit gates. Moreover, the severity of emergency incidents should be included in the model to evaluate more comprehensive and realistic passenger evacuation strategies for a mass rapid transit station.

ACKNOWLEDGMENTS

The authors would like to gratefully acknowledge the Excellence Center in Infrastructure Technology and Transportation Engineering (ExCITE) of Chiang Mai University for technical support and also appreciate the Mass Rapid Transit Authority of Thailand and Bangkok Expressway and Metro Public Company Limited for providing data and financial supports of this project.

REFERENCES

[1] Zhang B., Xu Z. S., Zhao Q. W., and Liu, Y. Y., A Study on Theoretical Calculation Method of Subway Safety Evacuation. Procedia Engineering, Vol. 14, 2014, pp.597-604.

[2] Chen S., Di Y., Liu S., and Wang B., Modelling and Analysis on Emergency Evacuation from Metro Stations. Mathematical Problems in Engineering, Vol. 17, 2017, pp.1-11.

[3] NFPA 130, Standard for Fixed Guideway Transit and Passenger Rail Systems. National Fire Protection Association, 2014.

[4] Teknomo K., Application of microscopic Pedestrian Simulation Model. Transportation Research Part F Traffic Psychology and Behavior, Vol. 9, Issue 1, 2006, pp.15-27.

[5] Credit K., Transit-oriented Economic Development: The Impact of Light Rail on New Business Starts in The Phoenix, AZ Region, USA. Urban Studies, Vol. 55, Issue 13, 2018, pp.2838-2862.

[6] Alonso V., Abreu O. V., Cuesta, A., and Silió D., A New Approach for Modelling Passenger Trains Evacuation Procedures. Procedia Social and Behavioral Sciences, Vol. 160, 2014, pp.284-293.

[7] Shi C., Zhong M., Nong X., He L., Shi J., and Feng G., Modeling and Safety Strategy of Passenger Evacuation in a Metro Station in China. Safety Science, Vol. 50, Issue 5, 2012, pp.1319-1332.

[8] Kallianiotis A., Papakonstantinou D., Arvelaki V., and Benardos A., Evaluation of Evacuation Methods in Underground Metro Stations. International Journal of Disaster Risk Reduction, Vol. 31, 2018, pp.526-534.

[9] Transportation Research Board, Highway Capacity Manual, National Research Council, Washington, D.C., 2010.

9th Int. Conf. on Geotechnique, Construction Materials and Environment, Tokyo, Japan, 20-22 November 2019, ISBN: 978-4-909106025 C3051

SPACE RHYTHMS AND TECHNOLOGIES OF ASTRONOMIC NAVIGATION AS FACTORS OF CULTURAL GENESIS AND SAPIENTATION

Alina Paranina
Faculty of Geography, Herzen State Pedagogical University, Russia

ABSTRACT

The article proposes a new approach to these problems, developed on the basis of the navigation concept of the information modeling of the world. From the position of the navigation concept, the development of the geographical space-time played a leading role in the processes of human biological and supra-biological adaptation. Such an approach takes into account the fundamental role of the planetary-cosmic factors in shaping the structure of the geocultural space of the Earth and is consistent with the main provisions of the modern scientific picture of the world. On the basis of field and laboratory research, the instrumental possibilities of stone labyrinths and other prehistoric cultural heritage sites are determined. According to the results of the analysis of the structure of uneven-age objects, the reconstruction stages of the development of prehistoric astronomical orientation technologies are proposed. Comparison of classical signs and symbols with sun shadow charts allowed to substantiate the astronomical nature of the sign. The analysis of ethnographic materials has provided the preservation of archaic navigation technologies in everyday life practice, ornaments, mythological scenes, and sacral traditions. On the basis of generalization of materials, new models of cultural genesis and anthropogenesis, based on solar navigation, have been developed.

The results of the study show that the invariant structures of genetic and social memory are associated with the order of geographical space-time, which is determined by the shape, daily and annual movements of the planet Earth.

Keywords: Adaptation, Evolution, Intellect, Culture, Astronomical navigation technologies

INTRODUCTION

The primary process in the system of biological and supra-biological adaptation is navigation – movement and orientation in the geographical space-time. The main source of energy and information for processes occurring on the surface of the Earth is the sun. For most living organisms, sunlight is, at the same time, a “signal” and a “food” (productivity of nursing populations).

The exploration of space and its resources, the survival and development of living organisms provide various types of astronomical navigation: phototaxis, geo- and heliotropism, photoperiodism, biological clock, near and far migrations, orientation reflex. The ancestors of modern human were nomadic and accumulated skills of instrumental astronomical navigation, representatives of *Homo erectus* settled most widely.

By examples of historical time, it is possible to trace how transport communications and product flows shaped the structure and maintained the stability of socio-natural and socio-economic systems. Today, the direction of flows of matter, energy and information determines the network of water, land, air routes. However, even with a well-developed communications infrastructure, the need for navigation tools is preserved, and space remains the most reliable basis for navigation (while both GPS navigation and popular methods of orientation by the Sun and the stars are widely used).

The purpose of the article is to show the role of instrumental astronomical navigation in the processes of anthropogenesis and cultural genesis.

OBJECTS AND METHODS

The navigational models of cultural genesis and anthropogenesis were developed by the authors based on studies of the instrumental functions of cultural heritage sites (Stone and Bronze Ages). Reconstructions of algorithms for creating and navigating the use of northern labyrinths and petroglyphs of Karelia, objects of the Central Russian Upland, the Urals, the Caucasus and Gorny Altai and other objects were proposed.

We used standard field and cameral methods of geography and astroarcheology. The measurements of object sizes and distances, the definition of azimuths in the structure of objects, paleoastronomic calculations and anthropometric analysis were carried out. Lineament analysis of surrounding landscapes was carried out on the basis of maps and satellite images: lineaments were distinguished in

the landscape design – linear structures (straightened relief elements, chains of lakes, borders of wetlands, forests), rose diagrams of measured directions were constructed.

Studies have shown that at all sites, regardless of age (from 12,000 to 4,000 years old), the main tool was the shadow of the gnomon (reverse sighting). However, in the surrounding landscape stands out coarse and heavily destroyed boulder material, convenient for conducting near-horizon observations (direct sighting). In addition, linear relief elements and the shape of the horizon at the location of objects are convenient for astronomical observations, since they correspond to astronomically significant azimuths (*azimuth* is the angle between the direction to the north and the object or point of the horizon). The technological multi-layeredness of such complexes testifies to the continuous tradition and rational basis of the sacral status associated with the information function of the object and its place.

A comparative analysis of the graphs of the shadow of a sundial for the year (Fig. 1) and the structure of signs and images of different ages – from the Stone Age to our days (petroglyphs, solar signs, mythological images, modern sign systems) was carried out. Proof of the astronomical nature of the sign was received.

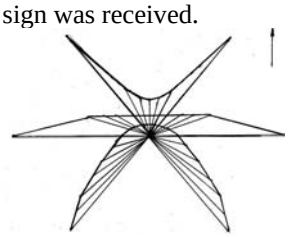

Fig. 1 The scheme of drawing the shadows of the gnomon in the days of the equinoxes and solstices is the basis of the solar signs and images: "horns", "wings", "fish tail", "lotus".

The results of the research have been summarized by the authors in the navigation concept of information modeling of the world [1, 2, 3]. The concept served as the basis for further research and theoretical constructions.

RESULTS AND DISCUSSION

Solar navigation as the basis of abstract thinking

Astronomical signs are abstract in shape (directions to horizon points, shadow graphics), but are specific in terms of content aimed at life support. The lack of road infrastructure, ready-made calendars and timers forced the ancient human to constantly reproduce information about space and time. This suggests that it was not the person who created the sign, but *the sign created the person.*

Let us list some arguments confirming our thesis that navigation in space-time by the Sun could become the basis for the formation of abstract thinking.

1. Astronomical landmarks are more reliable than objects in a dynamic landscape (because the super-system is more inert).

The dynamism of objects is determined by their mass (mass is a measure of the inertia of bodies). The mass of the Sun and the Universe is greater, and the rate of change is smaller compared to landscapes covering the surface of the Earth. The relative stability of astronomical landmarks was emphasized by ancient philosophers, who called the space surrounding the planet, the cosmos – "order". The dynamism of the elements of the landscape is reflected in ancient sayings "one cannot enter the same river twice", "everything flows, everything changes", "nothing lasts forever under the Moon". The inertial properties of objects of nature were taken into account in everyday practice. Thus, for astronomical observations of fixing important dates of the calendar, the most stable elements of the landscape were selected: weathering-resistant bedrock, tectonic cracks, large erosion and tectonic forms (outcrops, mountain peaks and ravines). High resistance to movement and destruction allowed to use the tool for a long time, to transmit information from generation to generation, thanks to the monumentality, many objects have survived to this day.

2. Light is the most powerful signal in geographic space.

This provision probably does not require special explanation. It is obvious that all living organisms obey daily and annual rhythms of illumination, because the whole range of environmental conditions (temperature, moisture, food supply) depends on the mode of lighting. The main correlations of the mode of illumination, physiological processes and behavioral reactions are "recorded" in the genetic program of biological species. Human evolution is associated with instrumental activity in general and instrumental astronomical navigation – in particular. In general, the development of technology is a factor in increasing human emancipation from environmental conditions. Reducing the power of direct environmental influences mitigates the effect of natural selection and the "editing" of genetic programs for space-time orientation. Hence the role of instrumental navigation technologies (positive feedback) is increasing.

3. Regular repetition of the light signal, with food reinforcement, shapes a conditioned reflex.

This provision is formulated in the studies on the physiology of higher nervous activity. It is based on the well-known experiments of academician I.P. Pavlov, who explained the mechanisms of formation of the conditioned reflex. Experiments with the dog, in the stomach of which the fistula was sewn to divert part of the gastric juice. Repeated combination of feeding with switching on the lamp leads to the formation of a stable connection between the two stimuli (1st irritant – light, 2nd – food). Subsequently, it was enough to switching on the lamp so that the dog started secreting gastric juice, which confirmed the excitation of the two nerve centers between which the connection was formed. Other conditioned reflexes are formed in the same way. Regular reinforcement of connections underlies the development of automatism (a dynamic stereotype is formed), and the lack of reinforcement leads to a complete weakening of communication. Navigation in space-time is carried out in order to efficiently use resources and predict adverse conditions that should be avoided. The combination of the sun's light signals and actions supported by food or other obvious success can form a stable link between the visual and other nerve centers.

4. The orientation reflex is paramount for adaptation.

This position is formulated in ethology – the science of animal behavior. It has been experimentally proved that the main unconditioned reflex that solves the problem of self-preservation of the body is the orientation reflex. For example, an animal placed in an unfamiliar room (or other new conditions) will not start eating until it has examined the room. All life requirements, including manifestations of the breeding instinct, are inferior in strength and meaning to the orientation reflex. When traveling in unfamiliar territory, the primacy of orientation can be felt on personal experience. According to the rules of navigation at each stop for rest, you should navigate around the map and compass, mark a point and record the track in the GPS navigator.

5. Language, as a model of the surrounding world and means of communication, begins with the designation of a place and time.

In the presence of road infrastructure it is much easier to navigate. However, the questions most frequently asked by strangers in a locality relate to the location of objects and directions. Since the information on space-time is of paramount importance, it can be assumed that the first words created by human meant space, time, distance and direction. The global invariant of the main geographical areas and universal solar navigation technologies easily explain the phenomenon of the Nostratic kinship of languages.

6. Position in space-time is unique for each object and can be the basis of its designation.

More than one object cannot be located at one point in space-time. The coordinates of an object in the geographical space-time reflect its functional connections in the structure of the system, and hence its quality. The positioning system is based on measurement and is associated with a number. Many languages have personal names and pronouns derived from numerals: Ivan is the first, Ben is the second, Thor is the third; I am the first, you are the second.

7. In anthropogenic, the average temperatures on Earth were negative, which increased the value of astronomical navigation.

A decrease in temperature is accompanied by a decrease in biomass, a restructuring of landscapes, a change in the ranges of biological species, and massive migration of biological species outside a well-developed and intuitively recognizable territory. By the example of the polar regions of the planet it can be seen that the increase in continental climate is accompanied by an increase in its contrast in space and in time, and a decrease in biomass is accompanied by a decrease in the stability of the landscape to any effects. Therefore, in a cold climate, it is advisable to nomadic (extensive) management of natural resources, the distribution of anthropogenic loads over large areas.

8. About 2.62 million years ago human led nomadic lifestyle and accumulated navigation skills.

The Paleolithic occupies 99% of anthropogenesis, this is the time of the Pleistocene cold spells and the appropriating economy (hunting, gathering). In the Holocene (about 10-14 thousand years ago), in the conditions of global climate warming, the human moved to a productive type of economy and settlement. In navigation, as in other activities, the complexity of practical tasks determines the level of mass knowledge and skills. Ethnographic studies on the comparison of the culture of hunters and farmers showed a significant simplification of the calendar, inventory and vocabulary in conditions of exhausting work in a limited space. This is consistent with the general rule of evolution – slow-moving and attached forms, as a rule, are simpler in

their organization than moving related biological species. Similar differences associated with the level of mobility can also be observed in individuals who are representatives of the same species.

9. Astronomical navigation is most in demand at sea, where there are no other landmarks.

There are no landscape landmarks in the open sea, and it is impossible to avoid access to the open sea (as a last resort, this may be the result of a storm). Sailing along the coast is dangerous: you can be aground or hit the ship on the rocks. Coastal waters are particularly variable in tidal seas with a shallow shore. The rugged coastline (with strongly inlet bays) makes one move from cape to cape. The development of the islands also makes you move away from the mainland and sail without landmarks on the way.

10. Solar navigation has no competition in polar days and white nights.

In the polar regions and in circumpolar regions, such phenomena of illumination as polar days and white nights are observed. Under the conditions of the polar day, the Sun is the only astronomical reference point that can be observed. During the white nights, the stars lightly stand out in the bright sky. The season of marine navigation in the seas of the Arctic Ocean is in the summer. In the polar regions, the summer season is a period of vigorous economic activity; the connection between solar heat and life is most noticeable here, which may not be so obvious in subtropical and tropical regions (especially in the arid part). For this reason, the ancient solar cult is most closely associated with the North. In ancient sources, the North is called the House of the Sun and by the fact that it spends the night there (goes beyond the horizon).

11. The regions of the Arctic are the most dynamic in the lighting regime (56° N – the Arctic boundary according to Eudoxus Cnidus).

In ancient times, classifications were created, with the release of the Tropic, the Arctic Circle, and other important boundaries. In the model of Eudoxus Cnidus, the boundary of the Arctic was drawn at a latitude of 56 °; in the history of science, this boundary was associated with the conditions of orientation according to the constellation Ursa Major. The azimuth calculations for each degree of latitude in the northern hemisphere show an additional navigational meaning of this boundary. At latitude 55.5 ° (latitude of Moscow), the points of sunrise / sunset at the solstice deviate from the meridian by 45 ° (azimuths drawn from the center of observation form a regular oblique cross, which, together with the main geographic directions, forms a wind rose or a solar sign with radial symmetry). Moreover, the navigation conditions to the north and south of this latitude differ dramatically: from the equator to this latitude (0 ° - 55.5 °), the azimuth of the sunrise changes gradually by 21.1 ° (66.6 ° - 45 °), and when moving north to the polar circle (55.5 ° - 66.5 °) – very dynamic: at 45 ° (45 ° - 0 °).

Solar navigation as the basis of cultural genesis

In the studies on historical geography V.I. Paranin showed that navigation by the Sun became the basis of the spatial structure and toponymic labeling of territorial systems [4]. These results are consistent with our results and conclusions obtained earlier – in studies of near-horizon observatories and the history of astronomical and mathematical knowledge [5, 6].

Today it is known that the images of the maps are preceded by the written language, and the earliest known maps are the maps of the starry sky. The oldest read entries are the tables by Ancient Babylon (6000 years ago) with calculations of the angular height of the midday Sun and the shadow of the figure of average height measured by the feet. The tables are compiled for seven latitudes (90° / 7) • n (where n = 1, 2, 3, ... 7), which are marked by the most grandiose ancient structures and graves of chiefs. For example, at a latitude of about 51.5 ° Stonehenge, Arkaim, Arjan, and many large cities in Europe are located. At latitudes 52 ° and 38°, the length of the shadow at the winter and summer solstice is 7:1 and can be recorded on a standard staff 7 feet long (the wish “7 feet under the keel” is associated with depth measurements of a pole of this size).

The development of navigation and the lack of state borders ensured freedom of movement and extensive intercultural communications, an intensive exchange of products and technologies. Still in the studies of V.I. Paranin it was proved that the Great Mussel of ancient authors was not a country in the modern view, but was a steppe region, symmetrical about 45 ° N. – the golden mean between the pole and the equator. The characteristics of the nomadic way of life, when in the summer the herds were distilled to the north and in the winter to the south of the Caucasus, is in good agreement with the conditions of the steppes of the temperate and subtropical belt and the position of the Caucasus as a regional climate-section. This model well explains the significant concentration of hydronyms with Iranian roots in the steppes of the European territory of Russia. The meridional connections are well traced along the major rivers of Eurasia, along the distribution areas of labyrinths in northern Europe, in the Mediterranean and in the Caucasus.

As was shown in our study on the ecology of

civilizations, the development of navigation technologies played the role of a locomotive of public consciousness and became the basis of the socio-cultural paradigm. Based on the technology of near-horizon observations, a model of consciousness is inevitably formed, reflecting the systemic "unity of significant parts". Examples of such thinking can be: the pantheon of the gods – the planets, the Moon and the Sun, the personification of the 12 months of the year and the forces of nature. In the structure of society, such ideas correspond to the institutions of chiefdom, social equality and democracy.

The gnomon sundial calendars allowed us to determine the geographical latitude and increase the reliability of the navigation system, link existing observatories to a regional and global network, measure the planet – i.e. create a world of chaos. But, the altered space was broken by a system of borders, and the mono-instrument itself became a model of the organizing center. Reflection in consciousness of the processes of polarization of reality (center – periphery, one's own – alien, living – inert, good – bad) is first noted in the culture of the Iron Age, and in the artificial urban environment reaches its apogee (war, all forms of dependence and the systemic crisis of civilization a consequence of limited thinking).

In the epoch of new technologies of navigation and communications, the humankind has the opportunity to return to holistic thinking, restore ties and, therefore, stability in the "human-nature" system.

We list some of the main directions of the influence of navigation technologies on culture.

1. Measurement forms a system of notation.

This item can also be considered primary for sapientation, since its processes are inseparable from the development of social culture and modern civilization. It is the *measurement with the help of tools* – the new field of activity on which a new system of concepts could have formed (all other spheres of life activity exist in animals, especially in social forms: construction, raising offspring, moving long distances). The very first measuring tool, a landscape transformed for orientation in space-time, is a powerful factor in the development of abstract thinking, since makes read artificially introduced markers, reflecting its vital quantitative characteristics (positive feedback).

2. On the petroglyphs of the Stone and Bronze Ages, simple geometric signs precede more complex artistic images.

The researcher of the Karelian petroglyphs F. Ravdonikas was the first to measure the azimuths of simple geometric signs (solar and lunar) and showed their high correlation with the astronomically significant azimuths of the Sun and the Moon (at the time of imaging, 6000 years ago). Our studies on synchronous objects of Karelia and Gorny Altai show that rocks with petroglyphs everywhere function as a scale / dial of a sundial calendar, and their creation and use is based on shadow fixation [7].

The sequential drawing of the shadow of the vertical gnomon gives an idea of the origin of the solar signs and typical attributes of mythological images (horns, fishtail, lotus and others). The shadow of a bent or T-shaped staff continuously draws the sign of the swastika. On the Tiunovsky stone (Vologda region, Russia), you can trace the stages of creating images from the Stone Age to the Middle Ages: first, graphical signs (lines, grids, radial labyrinths) oriented astronomically significant directions appeared, and a graphic image of a deer, a marquee , wood), then runic writing, and finally Christian crosses added.

3. The shadow graphics of the gnomon of sundial calendars correspond to a matrix of modern signs and sign systems;

It is known that the Phoenician script consisted of solar signs, and in linguistics and philology the first successful steps were taken in solving the task of "throwing a bridge" from solar signs to modern sign systems. Hermann Wirth created the phonetic systems of vowels and consonants associated with the annual solar cycle. In the studies of Olzhas Suleimenov, continuity in the morphology of existing sign systems is analyzed. The discussed communication is so obvious that it became a subject for discussion at classes in preschool educational institutions of St. Petersburg (children perform the task: on the matrix of 6 intersecting lines to find all the letters of the alphabet). It remains to add that the graph of the shadow of the gnomon in the days of the solstices and equinoxes represents the same six directions, but fills them with a concrete meaning.

4. On the height of a person, two basic measurement systems of the ancient world are intersected - anthropometric (fathom, foot) and astronomical (the length of the shadow of the figure measured by the feet).

Anthropometric measures of length were used almost everywhere until the twentieth century [8]. However, there is still no correlation of this measurement system with the astronomical system. Since they are related, it is obvious that all anthropometric measurements have an astronomical standard, i.e. linked to space.

5. Archaic measures of weight, money supply and nominal retain connection with the solar calendar system.

Studies in the history of the use of the gnomon have shown that many standards of measures and weights, a measure of money supply, music theory and the practice of creating musical instruments are associated with this astronomical instrument and calendar.

6. The consolidation of territorial boundaries, the development of all forms of social dependence, the struggle of urban religions with popular culture led to the loss of navigation skills and traditions.

Oases of traditional culture are preserved in different regions of the world. The territories that preserve the continuity of cultures from the Stone Age include the North and East of Russia. For example, the Mari people maintain the ecological traditions of respectful care for the landscape as a living organism, non-antagonistic world perception (there is no “evil”, there is only good and un-manifest good) cosmogonic thinking (Mari is the day of the heavenly girl, daughter Yume, who descended to Earth the sunbeam through the top of the birch; the holidays of the year – the creation of the universe, the solar system, the earth, life). In the culture of the Mari preserved traditions that are described by ancient authors during the practice of the Hyperborean peoples (voluntary death, burial in a basket on a tree, recollections of how a person knew how to joke and gave joy – laughter at the wake of the funeral immediately after the funeral). Many images of the gnomon have been preserved (a stick in the courtyard, an image of a golden needle and an embroidered shawl along which one can find a way, the word "bull" means "time"). However, the tradition of orientation is forgotten, because the territories are well known.

7. Improvement of technologies and the transition to new navigation tools is accompanied by the loss of the primary rational content of ancient objects of tangible and intangible culture.

Oblivion of ancient technologies is associated with the development of new technologies and road infrastructure. However, as revered objects and objects of tourism, they continue to provide a link between generations and cultures. Moreover, the ancient navigation tools continue to perform information functions – these are sources of information about the nature and culture of the prehistoric past.

Solar navigation in traditional culture

Based on an analysis of Paleolithic art, B.A. Frolov concluded that combined astronomical and mathematical knowledge manifests itself invariantly from the Atlantic to the Pacific Ocean, and the calendar can even be very different in the embodiment with peoples who live next to each other.

Traditional cultures retain the system of festivals tied to the astronomical calendar and the concept of the divine-cosmic nature of human (the goddess-mother, gods who preserve life on Earth: the Sun, planets, constellations). According to the literature and oral reports of the respondents, until the end of the twentieth century, in all regions of Russia and in adjacent regions, the gnomon was used for navigation (a human figure, a staff or a shepherd’s whip, wood and stone, as well as the shadow of an object sandwiched between the fingers, move on the palm).

In ethnography, only formal similarity of objects and contexts is considered, but functional analysis is also possible. In practice, you can make sure that there is no difficulty in uncovering objectively the reflection of astronomical navigation technologies in the structure and decoration of clothing and household items, sacred objects and mythopoetic subjects. As an example, we compare the gnomon of sundials, calendars, and a number of the most typical images presented in all archaic cultures and with surprising similarities.

World tree

In terms of shape and characteristics, the World Tree is one of the most obvious options for reflecting the real gnomon and the abstract concept of the earth axis: the Tree of Life, as it is called, connects cosmic and terrestrial space, cyclical and linear time. The crown of a tree can be represented as a set of rays passing through the top of the gnomon, into the roots – as lines of shadows radially diverging from its base. But another option is also possible – an inverted tree (in the hands of Varuna): its roots go back to Space, and the branches are directed to Man. In all cases, it seems that the real instrument-gnomon is primary in relation to the abstract concepts "earth axis" and "axis of the world", since they could be formed only on its basis.

The Maypole is still set on the eve of May 1 in the center of many European settlements – it is a birch, spruce or a tall trunk cleared of bark, decorated with ribbons and a wreath. In calendar (astronomical) holidays, the world tree is placed in the center of the labyrinth, on the main square, in the house. Round dances lead, gifts and ribbons are hung on the top.

In the labyrinth, the place of the world tree can be occupied by a girl, with ribbons in hand, the other ends of the ribbons can be held by the participants of the round dance. Archaeologists note that even in the art of Paleolithic, the theme of the world tree is closely intertwined with the theme of the Great Goddess.

Mother Goddess image

Research conducted by P.I. Kutenkov, devoted to the female calendar of the Eastern Slavs, allow us to distinguish the features of the Mother Goddess in dress and status of the woman, preserved in traditional culture from the Stone Age.

Comparing the image of the Mother Goddess in different cultures allowed Yu. Ratnikova to show the continuity of the main functions (fertility and ancestor worship) and the relationship with the equinoxes (Beltyne and Samhayn of the Celtic calendar), which for several millennia have shifted due to the precession of the equinoxes. The image of the goddess with snakes (figurines from Crete) is convincing as a symbol of the equinox axis, which divides the annual circle into winter and summer, the time of withdrawal, immersion in deep sleep (anabiosis), and the time of returning to life.

The researcher of the traditional cultures of the Volga region I. Kulyazheva gives evidence that the image of the Mother Goddess is the embodiment of the earth's axis. The horses held by the Mother Goddess in the canonical plot (in some cases, birds or deer) symbolize the unity of the diametrical positions of the starry sky, describing a 360° circle in 24 hours (the constellation Ursa Major and Ursa Minor, the cosmogonic legends of the Mari people can be replaced by elk or bird).

It should also be remembered that the formation of ideas about the axial rotation, shape and size of the planet is associated with the practical use of the vertical gnomon, one of the variants of which was a human figure. The traditional account of the months of the year among the peoples of Siberia is connected with parts of the human body. In parts of the palm of your hand were the solar-lunar calendar and the countdown of the hours of the day, many peoples of Europe and Asia. Calendar functions in traditional culture were performed by jewelry and clothing items (hats, embroidery and ornament).

Mount Meru

The use of the first protractor, the solar gnomon, in contrast to previous technologies at near-horizon observatories, allows us to determine the spherical shape of the Earth, the geographic latitude of the observation point, to build a regional and global geodetic network. The oblique gnomon can be viewed as a projection of the earth's axis.

From the epoch of mastering gnomon technology and the information function of a spear, whip, belt and staff, *the World* exists as *measured* chaos, and the centers of territorial systems are the starting points and the place where standards are preserved. In local territorial systems, the role of the gnomon and the markup can be performed by the combination “Sacred tree-stone” (traditionally symbolically preserved in the Baltic States), “The sacred grove with elements oriented along the horizon is stone” (in Mari El), a pole in the yard of a rural house (Mari El, Poland), stone stela (in villages of Armenia, Dagestan). The centers of large territorial systems at different times were Kailas – In Tibet, omphaly – Delphic (Greece), Tours (Ireland), Jerusalem and many others.

According to the authors of the article, in the considered navigation context, the center of the planetary scale could only be a pole – a point on the earth's surface, lying on the axis of rotation of the planet and the celestial sphere. Today, the poles are the fixed base of the network of coordinates, the intersection of the *meri*dians "meridianus" is "midday" (from "meridians" to "noon", the addition of the *medius* "middle" and dies "day"). In ancient culture, the pole and the earth's axis could receive the status of sacred objects, thanks to its stability and reliability (the direction to the north is easily determined and therefore serves as the main reference point and reference point). In this context, the location of the mythical Mount *Meru* in the North is the result of the fusion of mathematical, conceptual and mythological modeling of reality, characteristic of science as a form of knowledge.

Bowl

The axial rotation of the Earth and the time of day can be determined using a bowl filled with water. This tool replaces the gnomon at night and in cloudy weather. Water, like Foucault's pendulum, retains its initial position in space, and the bowl rotates along with the earth and the meridian (like a dial). The role of an arrow in such a watch can be performed by a light object placed on the surface of the water mass, and the time stamps are the shape of an edge or an ornament. Observation of a circular motion of such an “arrow” (15° per hour) inevitably gives rise to the idea of the axis of rotation, and the absence of a tangible physical body leads to the search for means of expression of this important knowledge. So the bowl is combined with the image of the world tree. Another option for combining the bowl and the gnomon is scafis (Fig. 2).

In ethnography, steady (canonical) compositions

depicting a bowl and a world tree are considered as a display of three levels of the world: the lower one – the roots (the older generations, the past, the underworld, a different light), the middle world – the earth (the human world, the family, the present), the upper – the sky (world of gods, future). Two birds facing the trunk are a pair ready to make a nest.

Comparison with astronomical navigation technology allows us to associate the three-part composition as a whole (the presence of the 3rd axial element) with the definition of the middle of the day, and the triplicity of symmetric elements with three nodal points in the trajectory of the midday shadow, which allow to distinguish astronomical seasons: solstice, medium – at equinox, short – in summer solstice.

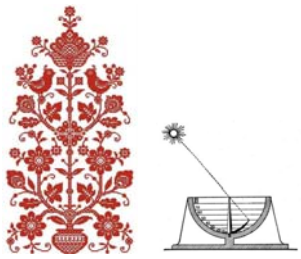

Fig. 2 The World Tree in the Bowl and the Tool – Bowl with a needle of Eratosthenes.

In ancient art this story has a wide distribution and independent significance (sometimes birds are replaced by two half-opened flowers submerged in water). It can symbolize the relationship of astronomical navigation, the cycles of the planet and biological rhythms (birds singing and blooming at the dawn – the biological clock). The consistency of astronomical and phenological cycles is also recorded in folk calendars.

INFORMATION POTENTIAL OF ASTRONOMIC NAVIGATION TECHNOLOGIES

Planetary invariant, regional specificity and unique local conditions

From the definition of culture as a form of suprabiological adaptation, it follows that its diversity is associated primarily with the dynamics of the geographic environment. Then the cultural invariant reflects the general that is necessary and accessible anywhere in the geographic space.

The universality of solar navigation technologies is based on the Earth-Sun global invariant: at every point of geographic space at noon the N-S direction can be determined, at sunrise / sunset at the equinoxes – the W-E direction.

The greatest regional differences can be observed in different zones of illumination (separated by the tropics and the polar circles).

The ratio of the general and the particular in the objects of navigation purpose transfers the rule “technologies are universal – the objects are unique”. Objects are unique because they differ: in latitude, position of the earth's axis at the time of creation, height above sea level, the shape of the horizon.

Unified language of the Universe

Since there are planetary systems like ours, extrapolation of this experience beyond the limits of the geographical envelope allows us to simulate a single language of the Universe.

CONCLUSIONS

The navigation concept of information modeling provides a holistic view of the development of the "nature-man" system as a breed and an inseparable part of the Universe.

REFERENCES

[1] Paranina A.N., Gnomon as sours of information on planet rhythms. International Journal of GEOMATE, Vol. 10, No. 2, 2016, pp. 1815-1821.

[2] Paranina A., Archaeological objects as elements informational life support system and as sources of information about evolution of environment. International Journal of GEOMATE, Vol. 13, Issue 35, 2017, pp. 100-107.

[3] Paranina A., Paranin R., Information in geographical space as the basis of crossdisciplinary researches in culture geography. European Journal of Geography, Vol. 8, No. 3, 2017, pp. 67-77.

[4] Paranin V.I., Historical geography of chronicles of Russia, Petrozavodsk, Karelia, 1990, pp. 1-152.

[5] Stafeev S.K., Tomilin M.E., Five millennia of optics: prehistory, St. Petersburg, Polytechnic Publisher, 2006, pp. 1-304.

[6] Van der Waerden B., The Awakening Science II. The birth of astronomy, Moscow, Science Publisher, 1991, pp. 1-384.

[7] Paranina A., Paranin R., Primary navigation purpose of petroglyphs: reconstruction on the basis of the gnomon. OALib Journal is an all-in-one open access journal, No. 4, 2017, pp. 1-13.

[8] Marsadolov L.S., Paranina G.N., Grigoryev A.A., An integrated approach to the study of megalithic legacy. Bulletin of Tomsk State University. History, Vol. 22 No. 2, 2013, pp. 72-75.

9th Int. Conf. on Geotechnique, Construction Materials and Environment, Tokyo, Japan, 20-22 November 2019, ISBN: 978-4-909106025 C3051

DRAINAGE DENSITY AND RAINFALL INTENSITY AS SLOPE FAILURE SUSCEPTIBILITY INDEX IN SMALL CATCHMENT AREA

Hirohisa Kinoshita[1], Shuichi Hasegawa[2], Shinji Nakai[1], Atsuko Nonomura[2], Minoru Yamanaka[2]
[1]Fukken Co., Ltd, [2] Faculty of Engineering and design, Kagawa University

ABSTRACT

Drainage density exhibits spatial characteristics that provide important information about the nature of the drainage basin. For example, permeability of the bedrock, ground-water movement, infiltration capacity of the soil mantle, surface-water discharge, erodibility of the surface materials. These characters represent the dominant factors that affect to frequency of slope failure, landslide and debris flow. And mainly incentive of slope failure is rainfall. The rainfall intensity is proportional to the susceptibility of slope failure occurrence. The authors investigated the relationship between drainage density and rainfall index, through the past disasters in southwest Japan. The drainage density of occurred debris flows are higher than the basin of occurred landslide. And the rainfall intensity leading to slope failures are higher than debris flows. Drainage density would be good index for evaluation of susceptibility that rainfall-induced landslide, slope failure and debris flow in small catchment area.

Keywords: Drainage density, Slope failure, Small catchment area, Rainfall index R', Risk management

1. INTRODUCTION

Recently, extreme weather related to global warming frequently occurs with many record-setting rainfall event all over the Japan, which have induced slope failure. Examples of recent rain-induced slope failure and debris flow are Hiroshima disasters in 1999 and 2014, West of Japan disasters in 2018. Slope failure and debris flow are shown to be parts of denudational processes that developing drainage net. The geomorphic character of drainage basin has suggested by Horton [1], thus defined drainage density as total stream length per unit area of a river basin. Drainage density varies according to several environmental factors. For example, highly erodible and impermeable rocks tend to have higher drainage density than areas dominated by resistant or permeable rocks, slope, mean relief and vegetation cover can also affect drainage density. Carlston [2] described the relation between hydrology and geomorphology, which presented evidence that drainage density, surface-water runoff, and the movement of ground water are parts of a single hydrologic system controlled by the transmissibility of the bedrock and its overlying soil mantle. Transmissibility or permeability is the most important characteristic that provide drainage density in terrain. Onda [3] stated that terrain with higher drainage density and thin soil layer was comparatively damaged more by shallow seated landslides, because of perched ground water at the soil-bedrock interface. On the other side, in the lower drainage density area occurred deep seated landslides due to the rise of ground water level in the fractured bedrock. Hasegawa [4] noticed that during heavy rainfall, area having higher drainage density is usually prone to shallow seated landslide , in the other hand, Large scale landslide tend to occur in area with lower drainage density, And large scale landslide is frequent in area having lesser than drainage density (Fig.1).

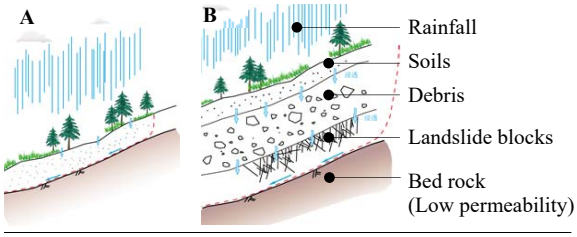

Model	Thickness of soil and debris	erodibility of slope	infiltration capacity	runoff character
A	thin	less resistant	small	surface water
B	thick	more resistant	large	ground water

Fig. 1 Relation between drainage density and hydrological structure of slope [4].

Consequently, drainage density may indicate the slope failure type of mass movement and proportional to susceptibility or frequency of slope failure. In this study, relation between drainage density and the rainfall index for landslides and debris flows occurrence are analyzed in southwest Japan. The area of study comprises 45 debris flows, slope failures and landslides whose occurrence times are confirmed were selected from Hiroshima disasters in 1999 and 2014, 2004 Typhoon 21 and 23 disasters in Shikoku, 2009 Hofu rainstorm disasters, 2010 Shobara rainstorm disasters and 2011 Kii Peninsula rainstorm disasters (Fig.2).

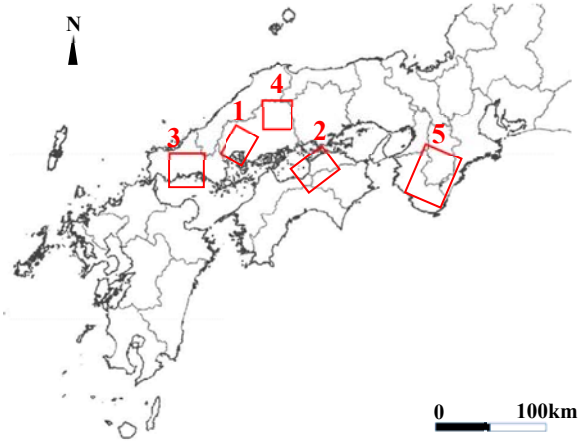

Fig. 2 Study area. 1: 1999 and 2014 Hiroshima disaster of debris flows by rainstorm, 2: 2004 Typhoon 21 and 23 disaster of slope failures in Sikoku, 3: 2009 Hofu disaster of debris flows by rainstorm, 4: Shobara disaster of debris flows by rainstorm, 5: 2011 Kii Peninsula and Mountains disaster of landslide and rock avalanches by Typhoon 12.

2. METHODS

We examined relationship between drainage density and frequency of debris flows and slope failures occurred by intensity of precipitation.

2.1 Drainage density measurement

The extent of channelization can be represented by measuring drainage density (Dd), where Dd=L/Ad, the total length of all channels (L) divided by the area of the drainage basin (Ad). In this study, measurement of drainage density conformed to methods that proposed by Kinoshita [5]. In the paper, dissected correlation coefficients between drainage density (Dd) that were calculated from several scale base map, basin area, channel line and density of slope failures (Df) of a small catchment area. It was derived the approximately equation, Df=2.50×Dd+0.28. In the measuring of drainage density several criterions and rules were used following, (1) Base map; Using base map is 10-m resolution DEM, (2) Definition of valley; Valley is defined by pixel whose average curvature is equal or larger than 1.0. (3) Draw thin line on valley; If width of valley is over one pixel, the maximum pixel is selected. (4) Calculation of drainage density; Drainage density [km^{-1}] is total pixel of channel lines per unit area, where numbers of pixels defined as valley by 10m per numbers of pixels defined as catchment area. (5) Size of catchment area; Catchment areas were selected by topographic map. Area of a catchment area is around 1km2 that located in divides. Fig.3 shows an example of measuring drainage density of small catchment area.

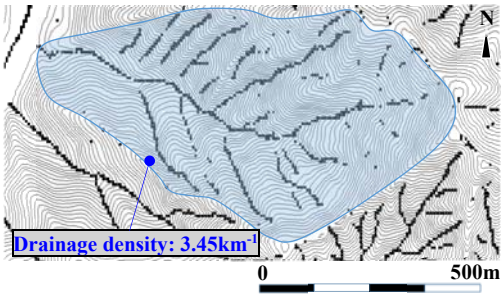

Fig. 3 An Example of measuring drainage density, using 10-m resolution DEM. The extracted channel lines are comprised of pixels. Drainage density equal number of channel line pixel per all number of drainage basin.

2.2 Rainfall index R'

Generally, the probability of slope failure occurrence varies with the precipitation. Rainfall indexes relating to rainfall-induced landslides and debris flows have two parameters which long-term rainfall such as duration and rainfall intensity for a short term. But it is difficult that using two parameters for comparison with drainage density. So, in this study, we apply a new rainfall index R' proposed by Nakai [6]. It became possible to express influence of both preceding-long term rainfall and present-short term rainfall by a single value of R' showed Figure 4 and Equation (1).

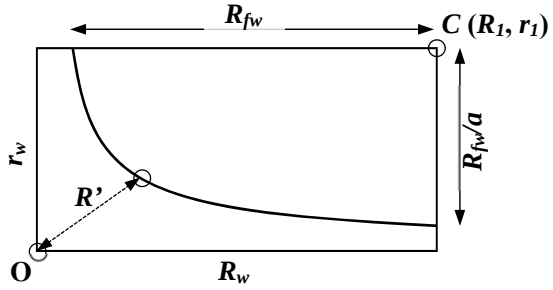

Fig. 4 Definition of the rainfall index R_{fw} and R' [6]. This parabola model depicting the variation of R' value from long-term effective rainfall to Short-term effective rainfall.

$$R' = R_{fw0} - R_{fw} \quad (1)$$

$$R_{fw} = \sqrt{(R_1 - R_W)^2 + a^2(r_1 - r_w)^2}$$

Where
R_w: Long-term effective rainfall (mm)
r_w: Short-term effective rainfall (mm)
R_1: Point of reference on horizontal axis
r_1: Point of reference on vertical axis
a: Weight of coefficient
R_{fw0}: Value of R_{fw} when Long-term and short-term effective rainfall are zero

3. RESULT

3.1 Drainage density in the basin of include slope failures

At the measurement of drainage density, we have adopted slope failure and debris flow disasters which can be referred to occurrence place and time record. The extent of calculation is set a limit to small catchment area where ranged from 1 to 1.5 km^2, abide by Kinoshita [5]. Figure 5 showed an example of drainage density in the basin of include landslide which induced by 2011 Typhoon 12 in the Kii Peninsula and Mountains. Upper of Fig.5, showed the aerial photograph around the landslide that occurred in Nosegawa village, Nara prefecture. The topographical map (lower figure) express the aspect of drainage net which represented by pixel lines. Red area and line are approximately moving body and point of main scarp of landslide. Table.1 shows the values of drainage density in the basin where occurred disasters of landslide, rock avalanche, slope failure, debris flow. As previous studies stated, the frequency of debris flow where Granite region are higher than the other bedrock region. And the drainage densities are larger than other lithologic basins.

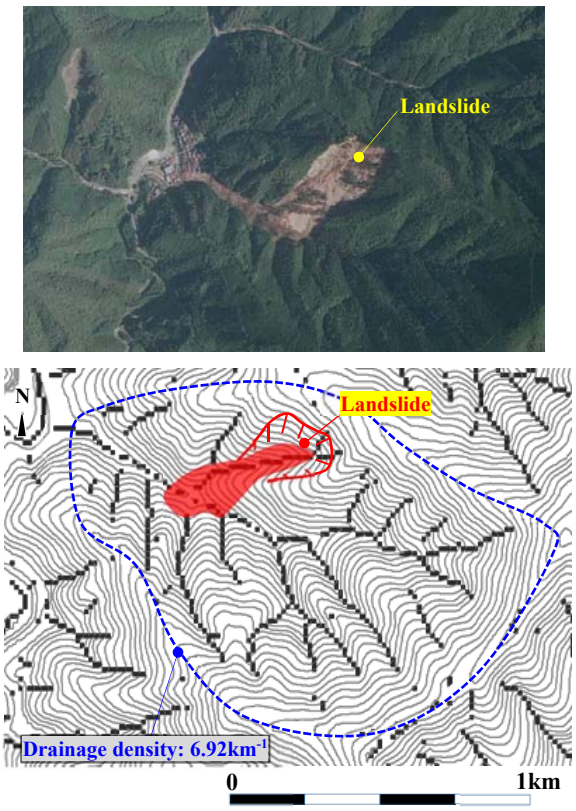

Fig. 5 A result of measuring drainage density where occurred landslide in Kitamata, Kii Mountains. The measuring area (blue dashed line) is monolithologic basin.

Table 1 Drainage density of past disaster region

No. (fig.1)	Facter of failure	Main type of failure	Bedrock lothology	Average of D_d (km^{-1})
1	1999 rainstorm	debris flow slope failure	Granit Rhyolite	8.34
1	2014 rainstorm	debris flow slope failure	Granit Andesit	7.86
2	2004 Typhoon21	slope failure debis flow	Sandstone Mudstone	6.64
2	2004 Typhoon23	slope failure landslide	Metamorphic -rock	4.81
3	2009 rainstorm	debris flow slope failure	Granit Rhyolite	7.51
4	2010 rainstorm	debris flow slope failure	Granit Rhyolite	10.53
5	2011 Typhoon12	rock avalanch landslide	Sandstone Mudstone	5.87

Figure 6 shows example that drainage density in the basin formed large landslide block. This site located in metamorphic rocks area, in Tosa town, central Shikoku Mountains.

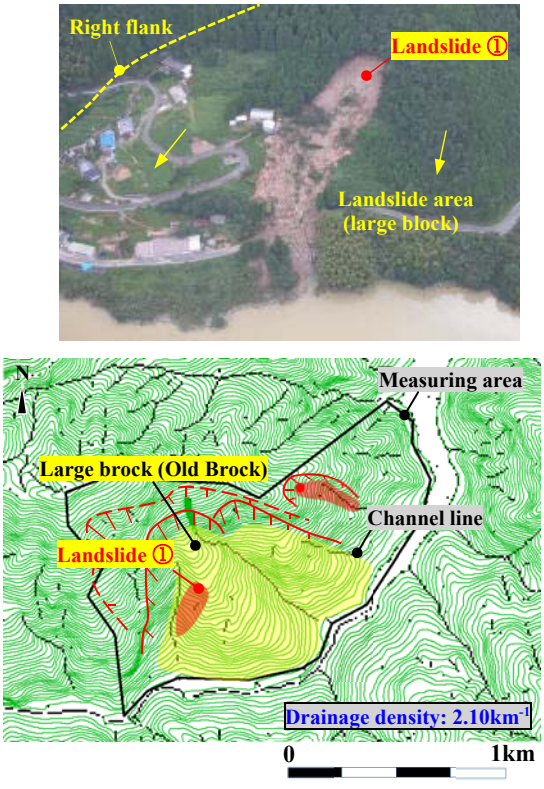

Fig. 6 Example of landslide that included larger landslide brock (old brock).

Lower part of fig.6, result of measuring drainage density around large landslide basin. The channel lines are fewer than the other basin (in this case, D_d=2.10 km^{-1}).

3.2 Application of the rainfall index R' to past rainstorm disasters

We establish rainfall index R' that adjusted to regional rainfall properties. Equation (1) indicate the state that the risk of landslide increases into increment of R'. The calculation of R' value may be affected by distance from drainage basin to gaging station. Therefore, in this study, the rainfall data adopted gaging station data, less than 2.5 km. Table 2 shows R' values on several place where occurred debris flow or landslide disasters.

Table 2 The results of estimating R' in the basin of disaster occurred (examples of 1 and 5, fig1).

Locality name	Gaging station	distance (km)	Time of disaster	R' (mm)
1999 rainstorm (debris flow)				
Ichihara	Ushirobata	1.0	06.29 15:20	413.1
Ichihara	Ushirobata	0.3	06.29 15:30	417.3
Yashiro	Ushirobata	1.9	06.29 14:40	370.3
Itsukaich	Uogiri-dam	1.9	06.29 15:20	414.0
Itsukaich	Ushirobata	1.6	06.29 14:30	353.1
Itsukaich	Ushirobata	1.3	06.29 14:30	353.1
Ban	Numata	2.2	06.29 15:20	327.9
Asa	Kuji-PA	2.5	06.29 15:30	394.6
Asa	Asa	1.0	06.29 15:15	301.1
Asa	Myojin	2.1	06.29 15:30	282.8
Kabe	Myojin-dam	1.9	06.29 15:30	323.9
			Av.	359.2
2011 Typhoon12 (rock avalanch)				
Kitamata	Kitamata	1.6	09.04 10:10	561.9
Ui	Ui	0.7	09.04 07:07	488.6
Sako	Sako	0.8	09.04 17:20	417.5
Nojiri	Kazeya	2.0	09.03 18:38	746.6
Tsujido	Sarutani	2.2	09.04 06:45	535.1
Kumano	Kumano	1.6	09.04 06:35	811.8
Tsubouchi	Tsuzurao	0.6	09.04 12:00	549.5
Tsubouchi	Tsuzurao	1.3	09.03 20:00	612.1
Tsubouchi	Tsuzurao	1.0	09.04 08:00	598.4
Fudono	Kushizaki	2.0	09.04 00:40	685.1
			Av.	600.7

The average of R' in landslide site, are larger than debris flow site.

Figure 7 showed one measuring result of R' values spatial distribution that involved by rainstorm of2011 typhoon12, in Kii Mountains. The R' value increase into warm color. Middle and Lower map of Fig.6 are expanded A (Ui) site and B (Tsubouchi) site with round number contour.

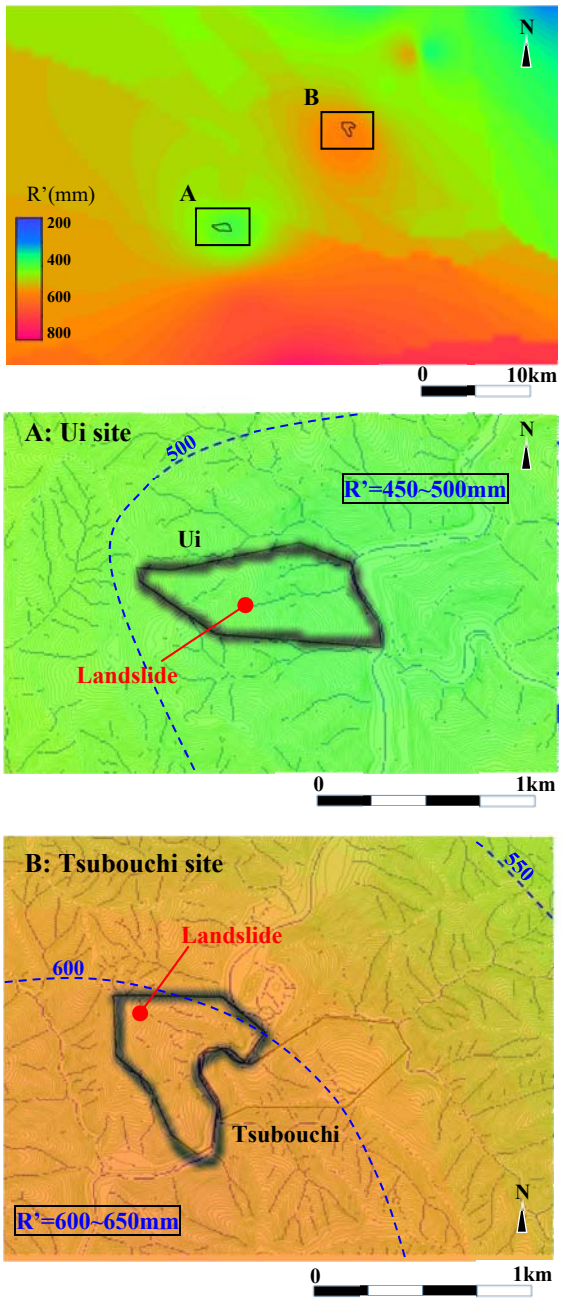

Fig. 7 Example of mapping R' distribution. Upper map: R' distribution around Yoshino country in Kii Mountains. A: Ui (R'= 488.6mm), B: Tsubouchi (R'= 598.4mm).

Both sites are occurred landslide at R' range about 450 to 650mm. In Tsubouchi site, places where occurred landslides located along R'= 600mm contour line curve.

3.3 Relation between drainage density and slope failure density

Figure 8 shows relation between drainage density and rainfall index R'. Generally, the value of R' decrease, as drainage density increase. In this study, lower limit of R' is about 250mm, regardless of drainage density accretion. The frequency of slope failures converges in the extent which drainage density range from 5 to 10km^{-1}, R' value range from 250 to 550mm. This relationship indicates that drainage density will be a good susceptibility index for rainfall-induced landslides and debris flows in small catchment area.

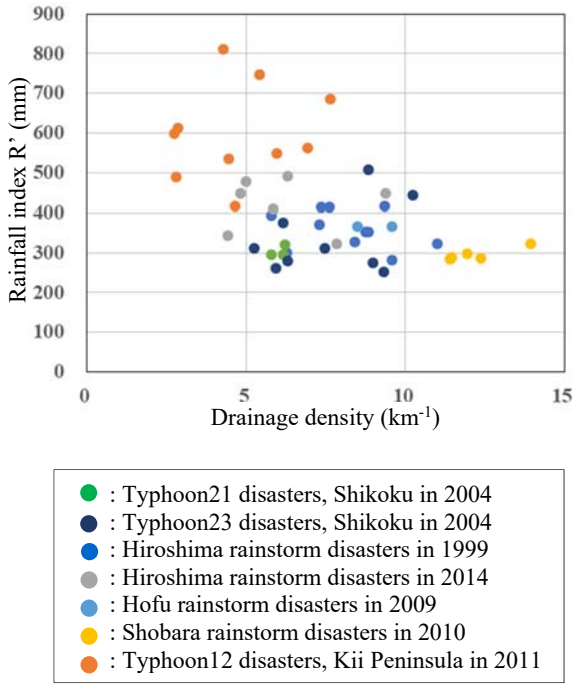

Fig. 8 Relation between drainage density and rainfall index R'.

4. DISCUSSION

4.1 Applicability to rainfall index for occurrence of slope failure

This paper presented the relationship between drainage density of small catchment area and rainfall index R'. Both values are roughly indicated inverse proportion. In the case of the rainfall index R' is nearly or equal, the frequency of slope failure increase, according to the drainage density increasing. Therefore, these two values are important parameter, for evaluation to susceptibility of slope failure and deduced occurrence time that estimated by rainfall index R' variation. However, there are points of remember. One is the area scale of measuring drainage density. In this study, calculation area of drainage basin established in small catchment area that range from 1 to 1.5km^2. If the area changed wider or smaller, affected to results of drainage density value, so may be appeared disagreement with the rainfall index R'. Another one, measuring of lowest drainage density basin. As previous statements, the drainage density of landslide block tend to smaller. Because, generally landslide block is comprised with debris, cracked rocks. These blocks become highly permeable. Therefore, the drainage density of landslide basin is extremely decrease. This low drainage density area that less than about 5km^{-1} needed to verification of measuring method, for example using 2 or 5-m high resolution DEM. Other attention, 2011 typhoon12 disasters in Kii Peninsula, occurred in the above R' = 400mm. And the distribution spread in the range which the drainage density is about 2 to 5km^{-1}. This showed apparently in case of Typhoon12 disasters, Kii Peninsula. It may be noticed that the difference of correlation is affected by base rock lithology. This area is mainly comprised by the bedrocks of accretionary complexes. Thus, plot on the data of divided by rock type (Fig.9). Generally, the area of distribute mainly Igneous rocks (Granite and Rhyolite group) located range of the drainage density over 5km^{-1} and the R' value less than 500 mm. While Other lithological area, for example Metamorphic rocks group, Lowest drainage density is about 2.5km^{-1}. In the other hand, Lowest R' value is about 250 mm through both base rocks. And the area of Lower drainage density, Higher R' value, tend to form Landslide (mass movement). For example, Kumano landslide induced by 201 Typhoon21, drainage density is 2.8km^{-1} and R' value is 612mm.

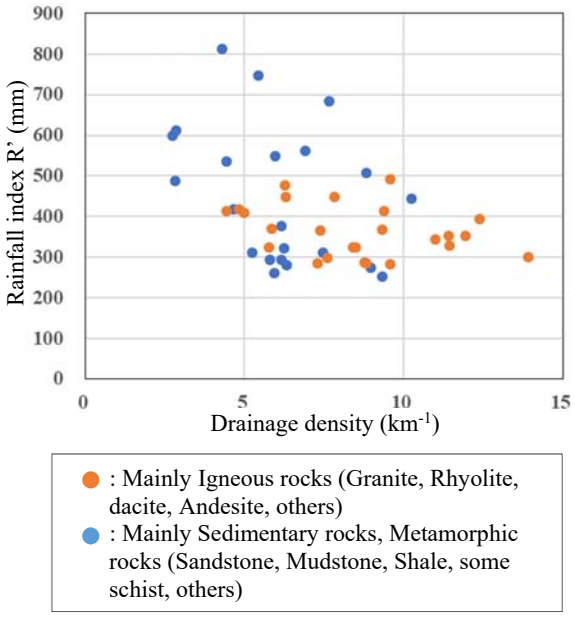

Fig. 9 Relation between drainage density and rainfall index R' divide two rock group.

4.2 Deploy to index of risk for rainfall-induced slope failure disasters.

The prediction of occurrence place, scale and type of slope failures, time of occurrence are important for risk management of rainfall-induced slope failure disasters. Relationship between drainage and rainfall index R' is avail to approximately indication for warning and evacuation. For example, indicate the slope failure risk according to frequency and limit of rainfall intensity (Fig.10).

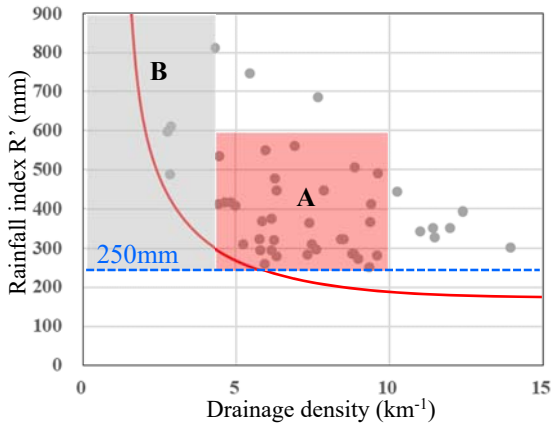

Fig. 10 Example of evaluate of disaster risk based on drainage density and rainfall index R'.

The red line in Fig.10, show change of R' values during a prospective hourly rainfall, this is generally equal to lower limit line of occurrence of slope failure. And the lower limit of R' value is about 250mm (blue line). Region A is a range that the drainage density is from 4 to 10km^{-1} and the R' value is from 250 to 600mm. In this region, frequency of slope failure occurrence is comparatively higher. And the range that the drainage density is larger than 10km^{-1}, the slope failure is mainly debris flow. On the other hand, the drainage density is less than about 4km^{-1}, the occurrence of landslide become dominant and increase the value of R' (region B). It suggested that the resistance for rainfall intensity is higher with the decrease of drainage density. However, the low drainage density area is needed more review, as above discussion that measuring drainage density of landslide character of channel distribution.

5. CONCLUSION

In this study, examined relationship between drainage density and rainfall index R' in small catchment area (1 to 1.5 km^2), through the past disasters data. Drainage density of the basin which occurrence of disaster, the value of including debris flow is higher than including landslide. The former is in range of about 6 to 12km^{-1} and the latter is in range of about 3 to 6km^{-1}. The relationship to rainfall index R', both values are roughly indicated inverse proportion. The value of R' decrease, as drainage density increase. Therefore, drainage density would be an effective index for evaluation the susceptibility of slope failures. In this study case, the lowest limit of rainfall index R' was about 250mm. It suggested that the possibility of rainfall-induced every slope failure are very unlikely during the value of R' is in less than 200 to 250mm. Particular, the frequency of slope failure is very rare at the condition that drainage density is less than about 5km^{-1}. Drainage density is easy to measure without field survey, and drainage basin scale is moderately small, therefore, drainage density is beneficial to warning and estimating of evacuation for regional disasters risk management.

ACKNOWLEDGMENTS

The authors thank to the undergraduate and master of Kagawa University for their help in measuring drainage density and rainfall index R'. And express sincere gratitude to all Agencies who have provided rainfall data during disasters, which was useful to estimating rainfall intensity along with change over time.

REFERENCES

[1] Robert E. Horton., Erosional development of streams and their drainage basin; Hydrophysical approach to quantitative morphology, Bulletin of the geological society of America, Vol.56, Issue 40, 1945, pp.275-370.

[2] Charles W. Carlston., Drainage density and streamflow, Geological survey professional paper, 422-C, 1963, pp. c1-c8.

[3] Onda Y., Underlying rock type controls of hydrological processes and shallow landslide occurrence, IAHS Publ, No. 217,1993, pp. 47–55.

[4] Hasegawa S., Yamanaka M., Miura T., Dahal R.K., and Nonomura A., Drainage density as rainfall-induced landslides susceptibility index, International Seminar on Hazard Management for Sustainable Development in Kathmandu, Nepal, 2009, pp.72-75.

[5] Kinoshita H., Hasegawa S., Nonomura A., and Yamanaka M., Drainage density as slope failure susceptibility index in small catchment area., Jour. Japan Soc. Eng. Geol., Vol.59, Issue6, 2019, pp472-484.

[6] Nakai S., Kaibori M., Sasaki Y., Moriwaki T., Applicability of a new rainfall index R' for recent cases and proposal of the method for warning against sediment-related disaster, Article of the Jour. Japan Soc, Erosion Control Eng, Vol.60, Issue1, 2007, pp37-42.

9th Int. Conf. on Geotechnique, Construction Materials and Environment, Tokyo, Japan, 20-22 November 2019, ISBN: 978-4-909106025 C3051

ANALYSIS OF ENERGY SECURITY CHANGES ON ENERGY REDUCER DUE TO BASIC REDUCTION OF ENERGY REDUCERS USING THE HYDRAULIC PHYSICAL MODEL TEST

Syaiful Anam[1], Very Dermawan[2] and A. B. Sambah[3]
[1]Doctoral Student of Civil Engineering, University of Brawijaya, Indonesia.
[2]Faculty of Engineering, University of Brawijaya, Indonesia
[2]Faculty of Fisheries and Marine Science, University of Brawijaya, Indonesia

ABSTRACT

The main building (Headworks) in an irrigation network building can be defined as a building complex along the river where buildings can divert water to an irrigation channel so that the water can be used for irrigation purposes. If a weir is built, a water jump will occur downstream of the weir. The speed in the area is still high so that a construction of energy absorbers is made. Energy reducer is a hydraulic building which built to reduce energy of water that caused from the runoff of the top of the dam lighthouse. The construction of energy absorbers has several types including the type of Vlughter, Schoklitsch, Bucket, USBR, and The SAF Stilling Basin. In this study, the type of USBR II energy reducer is used, which is an energy reducer which has sharp channel blocks (dispersing teeth) at the upstream end and near the end of the downstream (end sill) and this type is suitable for flow with hydrostatic pressure greater than 60 m. The purpose of this study is to efficiently the model of energy absorbers by modifying the reduction the elevation in the energy absorbing floor type USBR II. This research was conducted at the Laboratory of River and Swamp, Water Resources Engineering, Faculty of Engineering, University of Brawijaya Indonesia by testing the physical model in accordance with the design work of South Borneo Kambat Dam, with a physical model of open channels with a width of 40 cm, fixed base, scalatic and using clean water.

Keywords: Irrigation, energy reducer, USBR II, ground floor reduction

INTRODUCTION

Main building (headworks) in an irrigation network can be defined as a building complex on or along a river where the building as a whole can divert water to an irrigation channel so that the water can be used for irrigation purposes. The main building consists of a complex of buildings, among others: (i) Building a dodger that is part of the main building that functions to divert the direction of the flow of the river into the channel (for example: weir) with energy absorbers; (ii) Energy dampening, which is part of the evacuation building which functions to reduce the flow of water when passing dam (for example: olak pond); (iii) Mud bag, which is part of the main building that functions to deposit or contain sediment from the river so that it does not enter into the irrigation canal until during rinsing; (iv) Rinsing building, which is part of the main building that functions to rinse the sediment.

If a weir construction is built on the river flow both on the trough and on the line, then on the downstream of the weir there will be a water jump. The speed in the area is still high, this will cause local scouring. To reduce the high speed, an energy damper construction is made. The hydraulic form is a form of meeting between a sloping cross section, a curved cross section, and a straight cross section. In general, the construction of energy absorbers is divided into five types, namely: (1) Vlughter type ponds; (2) Schoklitsch type ponds; (3) Bucket type pool; (4) USBR type pool; (5) Natural swimming type The SAF Stilling Basin (SAF = Saint Anthony Falls).

The Vlughter type olak pool was specifically developed for the plunge building in the irrigation channel. The limits given for z / hc 0.5; 2.0 and 15.0 are associated with the Froude 1.0 number; 2.8 and 12.8. The Froude numbers are taken at z depth below the upstream energy level, not on the pool floor as for the water jumping pool. The Vlughter pool can be used up to z height difference of not more than 4.50 m and or in the olak to mercury room floor (D) no more than 8 meters and consideration of soil porosity conditions at the weir location in the context of drying.

The use of the type of USBR energy absorbers in Indonesia began in 1970 [1]. This type is usually used for head drop that is higher than 10 meters. This processed space has various variations and most importantly there are four types that are distinguished by the hydraulic regime of flow and construction. These types, namely the processing space type USBR I, USBR II, USBR III, and USBR

IV.

The use of energy absorbers for weirs based on graphs and published formulas will be over design, this is due to; (1) Sometimes there is no back jump on the floor and sometimes the flow that occurs is higher than the tail water; (2) There is a difference in the determination of the Froude number in full jump (Fr1) and reverse jump (Fr2) conditions where Fr2 <Fr1; (3) Types of energy absorbers can be used for weirs provided that the size needs to be adjusted to the results of the Physical Model Test.

Experiments to determine the hydraulic spring length are not easy due to the occurrence of strong turbulence and the presence of one-phase and two-phase currents which add to the difficulty in measuring flow depth, pressure distribution and hydraulic jump length. According to the Elevatorski (1959), the initial formulation for the hydraulic jump length was carried out by [2]. Then in 1927-1929, Safranez carried out a systematic study of the length of the roll (roller) on hydraulic leaps. Furthermore [3]-[4] define that the end of the hydraulic jump is a position where the free surface reaches the maximum height. Peterka (1984) [5] examines that the hydraulic spring end is assumed to be the position where the highest beam velocity starts to detach from the base and then glides downstream. The results of Peterka's research are one that is often used to calculate the length of the hydraulic jump in the olak pool.

This research tried to find out the flow behavior in a flat pool and to find out the energy attenuation in the basic olak pool.

METHOD

Research Variable

The research was conducted at the Laboratory of River and Swamp, Water Resources Engineering, Faculty of Engineering, University of Brawijaya Malang, Indonesia. The implementation of this hydraulic physical model test research uses laboratory facilities, including; (a) physical overflow model with open channel, spillway uses upright Ogee type as fixed parameter with slope of launcher channel is 1:4, fixed channel width is 40 cm; (b) three pieces of water pump to supply clean water flow to the model; (c) water reservoir to supply water to the model and equipped with a discharge measuring device; (d) rechbox discharge measurement tool; (e) point gauge, pitot tube, water pass, measuring rod, measuring cup, bucket, telemetry, and stopwatch.

In this study several variables were used to support the results of this study. The dependent variable consist of; (a) critical depth (Yc); (b) y_1, y_2, y_3; (c) Froude number (Fr); (d) Jump Length (Lj); (e) Jump height (YJ). Moreover, the independent variable consist of ; (a) discharge (Q); (b) ogee spill upright; (c) slope of the launch channel; (d) high damping; and (e) USBR olak pool type II.

Energy Dissipation

Specific energy is energy relative to the channel base. The amount of this energy as illustrated in Fig. 1 and Eq. (1).

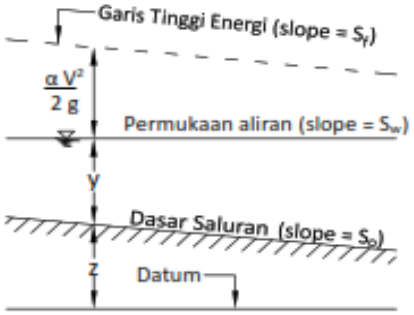

Fig. 1 Energy flow in open channel [6]-[7]

$$E = \frac{av^2}{2g} + y \qquad (1)$$

The velocity distribution coefficient (a) can be seen in Table 1.

Table 1. Velocity Distribution Coefficient (a) [8]

Channel	Minimum	Average	Maximum
Ordinary canals, overflow gutters	1.10	1.15	1.20
Natural rivers and heavy rivers	1.15	1.30	1.50
The river is covered by ice	1.20	1.50	2.00
River valleys are flooded	1.50	1.75	2.00

Froude Number (Fr) is defined as the average velocity *v* divided by the root of gravity *g* and the depth of water written as Eq. (2) [9].

$$Fr = \frac{v}{\sqrt{\frac{gy}{\alpha}}} \qquad (2)$$

Flow in open channels based on Froude numbers can be classified into three parts, namely sub-critical, critical and super critical flow, with the the criteria of; (a) sub-critical flow: when Fr<1; (b) critical flow: when Fr=1; (c) super critical flow: when Fr>1.

Hydraulic jumps are the fast transition from supercritical to subcritical flow. This is an extreme turbulence process, which is characterized by large-scale turbulence, surface waves and pounding, energy reduction and air entrainment. The nature of

the flow in the downstream and the energy lost in the hydraulic jump can be inferred from the momentum principle as a function of the Froude number upstream and the depth of the upstream flow.

For rectangular channels with horizontal flat shapes, the downstream flow depth is described as Eq (3).

$$\frac{y_2}{y_1} = \frac{1}{2}\left(\sqrt{1 + 8F_r{}^2} - 1\right) \quad (3)$$

The depth before hydraulic jump (y_1) and the depth after hydraulic jump (y_2) are also called the conjugation depth. Hydraulic jumps can be distinguished based on Froude numbers like the following Table 2.

Table 2. Classification of Hydraulic Jumps on Horizontal Square Channels [10]

Fr	Definition	Information
1	Critical flow	No jumps are formed
1.0 - 1.70	Choppy jumps	There are waves on the surface of the water
1.70 - 2.50	Weak jumps	Small energy loss
2.50 - 4.50	Oscillating leaps	Irregular oscillating bursts produce large waves towards the downstream, damaging and eroding the dikes.
4.50 - 9.00	Steady jumps	Energy reduction is 45–70%. Hydraulic jumps are very balanced. Not too affected by downstream conditions. The best economic planning
> 9.00	Strong jump	Strong jump. Energy reduction up to 85%. The risk of erosion at the bottom of the channel to watch out for.

Energy Loss

The loss of energy in jumping is the same as the specific energy difference before and after the jump. The amount of energy loss as defined in Eq (4).

$$\Delta E = E_{1-}E_1 = \frac{(y_2 - y_1)^2}{4y_1y_2} \quad (4)$$

An equation for energy loss in uniform flow and non-uniform flow in smooth launch channels as shown in Eq (5) [9].

$$\Delta E = y_w \cos\theta + \alpha \frac{{q_w}^2}{2g{y_w}^2} \quad (5)$$

Previous research was developed kinetic energy coefficients for sinking flows on launchers with values a is 1.1 - 1.6 [10]-[11]-[12]. The research step is described in the flow chart of the research on Fig. 2.

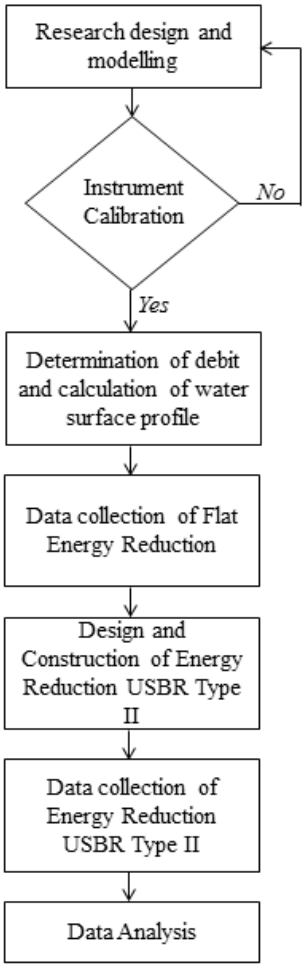

Fig. 2 Research flow chart

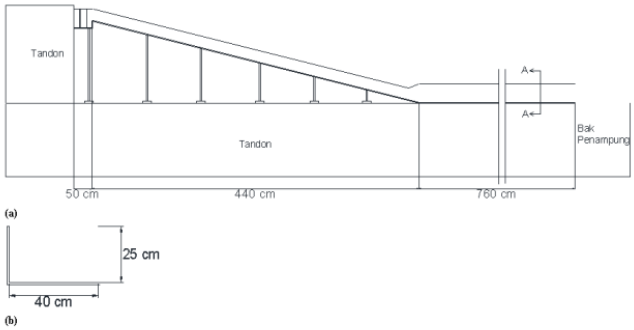

Fig. 3 (a) Research Channel Model in the Laboratory; (b) A-A Pieces of the Research Channel Model

RESULT AND DISCUSSION

New Discharge Calculation between Thompson Discharge and Measure Discharge

The calculation of the new discharge is done by finding a relative error and correction discharge between the Thompson discharge and the measuring discharge. Then look for a new discharge value through the equation from the graph obtained from the correction discharge.

The steps to find a new discharge value are as follows:

Example of calculation (*h* thompson = 5.1cm);

1. Finding Relative Mistakes (Kr)

$$Kr = \frac{Qmeasure - Qthompson}{Qmeasure}$$
$$= \frac{0.850 - 0.842}{0.850} = \mathbf{0.010}$$

2. Finding the Correction Discharge Coefficient (K)

$$K = \frac{Qmeasure}{Qthompson}$$
$$= \frac{\mathbf{0.850}}{\mathbf{0.842}} = \mathbf{1.010}$$

From the calculation of the correction discharge coefficient it shown the smallest correction discharge coefficient value is 0.978 at h thompson 6.75 cm.

3. Finding Corrected Discharge

$Q_{correction} = Q_{measure} \; x \; K$

= 0.850 x 0.978 = 0.831 l/s

4. Finding the relative error of Correction Discharge

$$Kr = \frac{Qmeasure - Qcorrection}{Qmeasure}$$
$$= \frac{0.850 - 0.831}{0.850} = \mathbf{0.022\ l/s}$$

5. Finding New Discharge

The calculation is obtained from the graph of the relationship between h thompson and correction discharge. The graphs as shown on Fig. 4.

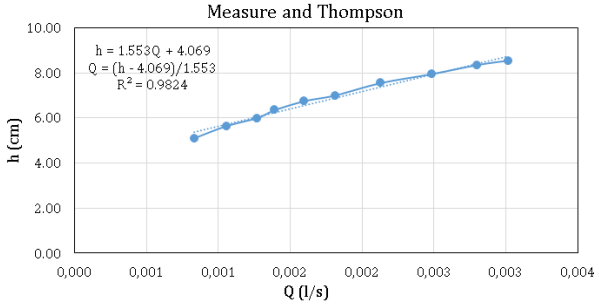

Fig. 4 Graph of the relationship between Q and h

From the graph above, statistics are used to calculate Thompson's new discharge. Calculation as follows;

Example of calculation (h thompson = 5.1 cm)

$$\boldsymbol{h = 1.553Q + 4.069}$$

from above algoritm, $\boldsymbol{a = 1.553}$ and $\boldsymbol{b = 4.069}$, so:

$$h = aQ + b$$
$$Q = \frac{h - b}{a}$$
$$= \frac{5.1 - 4.069}{1.553} = \mathbf{0.664\ l/s}$$

Discharge value at h thompson 5.1cm is 0.664 l/s.

Calculation of Flat Energy Reduction

The measured data is critical depth (*yc*), y_1, y_2, *Lj*. Measurement data as shown in Table 2.

Table 2. Calculation and Measurement Results of Flat Energy Reduction

h Rechbox (cm)	Q (l/s)	Theoretical		
		Yc (cm)	y_1 *(cm)*	y_2 *(cm)*
7.00	11.004	4.257	1.392	9.855
8.00	13.019	4.762	1.544	11.080
9.00	15.102	5.257	1.692	12.287
10.00	17.246	5.744	1.836	13.478
11.00	19.446	6.222	1.981	14.636

Measurement of Flat Energy Reduction				
Yc (cm)	y_1 *(cm)*	y_2 *(cm)*	*Kr* y_2 *(%)*	*Lj (cm)*
4.300	1.400	10.650	8.071	154
4.750	2.550	11.500	3.787	159
5.250	1.700	12.300	0.103	162
5.750	1.850	13.150	2.431	181
6.300	2.000	14.700	0.435	87

From the data above, it can be seen that the critical depth (*yc*) and y_1 between the theoretical results and the measurement results have relatively the same value, whereas for the value of y_2 it has a relative error of less than 10%.

Calculation of Energy Reduction Buildings (USBR Type II)

The energy absorbers used in this study are USBR Type II energy absorbers. The calculation of the USBR Type II energy absorbing building uses data from a 9 cm rechbox h discharge. The calculation steps are as follows:

Known data;

Discharge (Q) = 15.102 l/s

Y_1 = 1.692cm

Y_2 = 12.287cm

1. Calculation of Olak Pool Length (*L*)

   L = 4.16 x y_2 = 4.16 x 12.287 = 51,115cm

2. Chute Block Design

   a. Chute Block high (h_1)

   $h_1 = y_1$ = 1.692cm

   b. Chute Block width (W_1)

   $W_1 = y_1$ = 1.692cm

   c. Distance between Chute Block (S_1)

$S_1 - y_1$ = 1692cm

d. Chute Block distance with the wall
0.5 x y_1 = *0.846cm*

3. Block Edge Design
   a. Block Edge high (h_2)
   h_2 = 0.2 x y_2 = 0.2 x 12.287 = 2.457cm
   b. Block Edge width (W_2)
   W_2 = 0.15 x y_2 = 0.15 x 12.287 = 1.843cm
   c. Distance between Block Edge (S_2)
   S_2 = 0.15 x y_2 = 0.15 x 12.287 = 1.843cm
   d. Upper End Block Thickness
   0.02 x y_2 = 0.02 x 12.287 = 0.246cm

Result of Launcher Slope 1:4 Measurement without Decreasing Energy Reduction Using Type USBR II

The measurements are made by measuring water level and the velocity. The following are the results of measurements carried out on 5 variations of discharge.

Table 3 Data on Water Level, Jump Length and Velocity on h Rechbox 7 cm

Water Level and Length					
Q = 11.004 l/s		Calculation (cm)	Measurement (cm)	Froude	Kr (%)
Yc	=	4.257	4.300	1	1.01
Yb	=	3.044	3.050		0.21
Lc min	=	12.771	11.000		13.87
Lc max	=	17.028			35.40
Y_1	=	1.392	2.2		58.04
Yj	=		10.9		
Y_3	=		13.4		
Y_2	=	9.855	11.9	0.2	20.76
Ysill	=		11.6	0.2	
Lyj	=		25.5		
Lj	=		54		

Velocity		
Cp	=	0.98
		Measurement (cm/s)
Vtransition	=	9.706
Vc	=	63.154
V_{10}	=	148.797
V_{12}	=	174.086
V_{14}	=	181.072
Vy_1	=	225.975
Vj_1	=	9.706
Vj_2	=	9.706
Vy_2	=	16.812
Vsill	=	19.413

CONCLUSIONS

It can be concluded that the value of the discharge has a value that is relatively the same as the discharge value using the rechbox and thompson discharge equations, but with the rechbox discharge equation the relative error value is 0.013 compared to the relative error with the Thompson discharge equation which is 0.022, so that the calculation of new discharges is based on the value of the discharge rate and the value with the rechbox discharge equation. In the measurement of flat energy absorbers, the value of *Lj* (jump length) has a greater value at each increase in discharge, namely 154cm, 159cm, 162cm, 181cm. However, at the largest discharge, the value of *Lj* is smaller than 4 other discharges, due to the limited channel length of 87cm. In the measurement of energy absorbers USBR type II, the value of *LJ* (Leap Length) has a greater value at each increase in discharge, namely 54cm, 70cm, 114cm, 124cm, 152cm. The *Lj* value of the USBR type II energy reducer measurement has a smaller value than the measurement of flat energy absorbers because there is a type II USBR energy reducer. For the value of the water level and velocity in each section it has a greater value at each increase in discharge, and the Froude value at critical depth is 1, the flow is critical, whereas in *y2* the Froude value is less than 1 (Froude <1), ie the flow is subcritical.

ACKNOWLEDGMENTS

Authors are thankful to Laboratory of River and Swamp, Water Resources Engineering, Faculty of Engineering, University of Brawijaya Malang, Indonesia. We also thank to postgraduate program of Faculty of Engineering, University of Brawijaya Malang, Indonesia.

REFERENCES

[1] Mawardi Erman, Memed Moch, Desain Bendung Tetap Untuk Irigasi, Bandung: Alfabeta, 2002
[2] Woodward S. M., Beebe J. C., Riegel R. M., Theory of The Hydraulic Jump and Backwater Curves, Dayton, Ohio : State of Ohio, Miami Conservancy District, 1917, Technical reports (Miami Conservancy District (Ohio)), pt. 3.
[3] Bakhmeteff B. A., Hydraulics of Open Channel, 1936, p. 70.
[4] Bakhmeteff B. A., and Matzke, Trans, ASCE 101, 1936, pp. 630-680.
[5] Peterka A. J., Hydroulic Design of Stilling Basins and Energy Dissipators, a Water Resources Technical Publication, Engineering Monograph No. 25, 1984, United State Department of Interior, Beureau of Reclamation.
[6] Chaudhry H., Schleip R., Ji Z., Bukiet B., Maney M., Findley T., Three-Dimensional Mathematical Model for Deformation of Human Fasciae In Manual Therapy, J Am Osteopath Assoc, 108 (8), 2008, pp. 379-90.
[7] Chaudhry H., Open Channel Flow, Springer US, Edition Number 2, 2008, p. 523
[8] Chow, Velocity Distribution in Open Channel

Flow, Journal of Hydraulic Engineering 115 (5), 1989.

[9] Chow, V. T., Open Channel Hydroulic, New York: McGraw-Hill, 1959.

[10] Chanson, H., The Hydraulics of Open Channel Flow: An Introduction, Butterworth-Heinemann, Oxford, UK, 2nd edition, 2004, 630 pages.

[11] Boes R. M., and Willi H., Hager Closure to Hydraulic Design of Stepped Spillways, Journal of Hydraulic Engineering, 131 (6), 2005.

[12] Matos J., Sanchez M., Quintela A., and Dolz J., Characteristic Depth and Pressure Profiles In Skimming Flow Over Stepped Spillways, in: *Abstrs. of the XXXVIII IAHR Congr.*, Graz, 1999.

9th Int. Conf. on Geotechnique, Construction Materials and Environment, Tokyo, Japan, 20-22 November 2019, ISBN: 978-4-909106025 C3051

ASSESSMENT OF POLLUTION CARRYING CAPACITY IN THE LOWER PART OF MAE KLONG RIVER, THAILAND

Boontarika Thongdonphum[1] and Shettapong Meksumpun[2]
[1]Faculty of Agricultural technology, Rajamangala University of Technology Thanyaburi, Thailand
[2]Faculty of Fisheries, Kasetsart University, Thailand

ABSTRACT

Assessment of aquatic environmental impacts, nutrient transfer and the clarification of contaminated sites were conducted based on water quality analysis of the Mae Klong River. Twelve sampling stations were surveyed between April 2015 and April 2016 covering Kanchanaburi, Ratchaburi and Samut Songkhram Provinces. Results showed that aquatic environmental factors varied seasonally. A mathematical model developed using the box modeling method showed that middle (Ratchaburi Province) and lower (Samut Songkhram Province) riverine zones were point source areas. Highest DIN and PO_4^{3-}-P loads were found in Samut Songkhram Province. Results implied that PO_4^{3-}-P levels were higher than the standard criterion for aquaculture (< 1.45 μmol L^{-1}). Levels of PO_4^{3-}-P continued to increase, downriver, particularly in the estuary. Recent PO_4^{3-}-P levels suggest that the number of agroindustry plants discharging waste effluent into the river should be reduced. Monitoring to assess the aquatic status of the Mae Klong River and estuary using the PO_4^{3-}-P database is urgently required to control water quality and reduce contamination levels.

Keywords: Pollution, Carrying Capacity, Environmental impact, Mae Klong River

INTRODUCTION

The Mae Klong at approximately 140 km long with a catchment area of 22,075 km^2, is the most important river in Western Thailand. The Mae Klong diversion dam is located in the upper zone, about 10 km from the river basin and forms the headworks of the Greater Mae Klong Irrigation Project which divert and distribute water to about 3.0 million rai (1 ha = 6.25 rai) of the cultivated area in 10 irrigation subprojects [1]. The river flows across the lower plain and passes through Ratchaburi Province, before discharging into the Gulf of Thailand in Samut Songkhram Province, where the important estuarine ecosystem supports a residential population as well as various industries [2]. More than 100 industrial factories are located along the banks of the Mae Klong River. Apart from industry and fisheries, other activities supported by the river include intensive agriculture [3].

[4] reported that freshwater inputs to the river depend on rainfall, irrigation control systems, and natural tributaries that flow through agricultural areas. Paddy rice is cultivated in about two-thirds of the area with the other third under sugar cane cultivation [5]. The aquatic environmental parameters, particularly dissolved oxygen and ammonia nitrogen, have deteriorated to critical levels over the past decade [6]. Rapid urbanization and industrial and agricultural development, coupled with inadequate sewerage systems, contribute to elevated material inputs in the water resources, e.g. nitrogen (N) and phosphorus (P) [7].

The abundance of nitrogen and phosphorus compounds causes eutrophication problems [8]. Thus, this study aimed to describe the impacts of aquatic environmental parameter variations. Assessment of non-point source nutrient loads was a major focus, together with clarification of nutrient transfer patterns and a pollution carrying capacity assessment at the impacted sites using a mathematical model. Results will contribute to water quality conservation to maintain acceptable and sustainable utilization management of river ecosystems.

MATHEMATICAL MODEL

Sampling sites

Twelve localities along the Mae Klong River were selected as sampling stations (Fig. 1). They were clustered in an 'upper' zone in Kanchanaburi Province (stn. 1-2), a 'middle' zone in Ratchaburi Province (stn. 3-7), and an 'estuarine' zone in Samut Songkhram Province (stn. 8-12). Water sampling was conducted during two separate time periods to take account of the effects of seasonal variability on nutrient loadings as April 2015 (dry season) and September 2015 (rainy season). Under the influence of monsoon winds, Thailand has three seasons: rainy season (May-September), winter season (October-February) and dry season (March-April) [9].

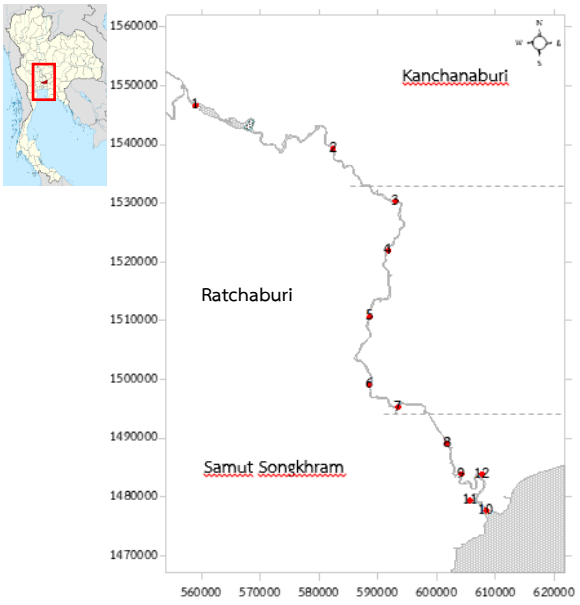

Fig. 1 Sampling stations (stn.1-12) of the Mae Klong River with the 'upper' zone in Kanchanaburi province (stn. 1-2), a 'middle' zone in Ratchaburi province (stn. 3-7), and an 'estuarine' zone in Samut Songkhram province (stn. 8–12).

Sample collection and analysis

Temperature, dissolved oxygen (DO), salinity and pH of the water samples were measured using a multi-parameter probe (YSI-6600 Sonde Instrument) at the sampling sites (stn.1-12). For nutrient analysis, water samples were pre-filtered through GF/F (Whatman) and then immediately stored at 4 °C before transportation to the laboratory where they were kept at -20 °C until required for analysis. Ammonium (NH_4^+), nitrite and nitrate (NO_2^- and NO_3^-), and orthophosphate (PO_4^{3-}) concentrations were determined using a Skalar segmented flow analyzer with corresponding detection limits of 0.70-57.14, 0.70-14.28 and 0.03-3.87 µmol L^{-1}. Specifically, the DIN and P loads were assessed at stn. 1-10 cross-sectional sites using a two-dimensional Surfer model. Nutrient loads were approximated by equation (1)

$$M_i = [Conc]A_iUh_i\Delta t_i \quad (1)$$

where M_i is the amount of nutrient load (ton/day), Conc is the nutrient concentration (µg L^{-1}), A_i is the cross-sectional area of section *i* (m^2), Uh_i is the flow velocity of section *i* (cm/s) and Δt_i is the length of time (i.e. 1 day) [2].

DIN and P loads were used for making decisions regarding the focus areas for pollution carrying capacity assessment using the mathematical model (Fig. 2). Pollution carrying capacity was conducted at two separate time periods: September 2015 and April 2016.

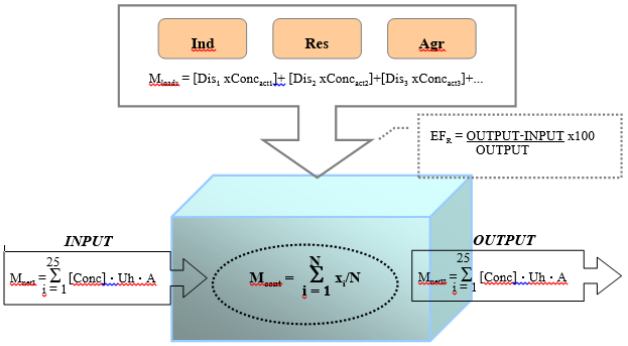

Fig. 2 Mathematical model for pollution carrying capacity assessment of the Mae Klong River.

In Fig. 2, M_{loads} is the amount of nutrient discharge (ton day^{-1}) from industrial (Ind.) residential (Res.) and agricultural (Agr.) activity, Dis_1 is the amount of discharge in each activity (l day^{-1}), $Conc_{act1}$ is the average concentration of DIN or PO_4^{3-}-P (µg L^{-1}) M_{cont} is the amount of nutrients within the box (ton/day), x_i is the concentration of DIN or PO_4^{3-}-P (µg L^{-1}) at the present time within the box, M_{net} is the amount of each nutrient load (ton/day), [Conc] is the concentration of DIN or PO_4^{3-}-P (µg L^{-1}) in the time focus (1-25 hrs). Uh is the flow velocity (cm s^{-1}) passing through the section in the time focus, and A is the cross-sectional area (m^2) of the section in focus.

Data analysis

Physicochemical properties of the water samples associated with both sampling periods (April 2015 and September 2015) were determined using descriptive statistics and presented as means ± standard deviations (SD). T-test was used to verify statistical differences between the two study periods, with $p \leq 0.05$.

RESULTS

Table 1 shows the physicochemical characteristics of the water samples for both study periods (rainy and dry seasons). Results revealed that water temperature and salinity varied minimally from season to season ($p \leq 0.05$) and were lower during the rainy season. Sampling locations (stn.1-12) and seasonal variability had no significant impact on pH levels which remained relatively constant throughout. The DO varied in response to seasonal variability ($p > 0.05$) at alarmingly higher than Thailand's minimum threshold of 4 mg L^{-1}. Average levels of NH_4^+ and NO_2^-+NO_3^- also varied significantly ($p \leq 0.05$) with the season. Minimum and maximum

concentrations of NH_4^+ and PO_4^{3-} associated with dry and rainy seasons were respectively 1.73 and 28.92 μmol L^{-1}, and 0.10 and 5.23 μmol L^{-1}. Observations also revealed that NH_4^+ and NO_2^-+NO_3^- were high during the dry season.

Table 1 Physicochemical properties of water samples (mean±SD)

Parameters	Study period	
	April 2015 (dry)	September 2015 (rainy)
Temp (°C)	31.85±0.71[a]	29.19±0.72[b]
DO (mg L^{-1})	5.62±2.26[a]	5.47±1.11[a]
Salinity (psu)	2.79±5.19[a]	0.39±0.62[a]
pH	7.63±0.22[a]	7.18±0.19[a]
NH_4^+ (μmol L^{-1})	8.57±8.41[a]	5.13±2.08[a]
NO_2^-+NO_3^- (μmol L^{-1})	26.83±13.34[a]	11.55±3.76[b]
PO_4^{3-} (μmol L^{-1})	1.31±1.90[a]	1.77±1.18[a]

Table 2 shows the cross-sectional area, water volume and current velocity associated with the 10 cross-sectional sites (stn. 1-10). During the dry season (April), stn. 10 exhibited the highest volume and velocity of 78.49 x 10^6 ton day^{-1} and 39.7 cm s^{-1}, respectively. Meanwhile, stn. 2 recorded the lowest volume (3.09 x 10^6 ton day^{-1}) and stn. 7 had the lowest velocity (12.5 cm s^{-1}).

Table 2 Water volume and velocity of the 10 cross-sectional sites during the dry (April 2015) season

Zone	Stn.	Section area (m^2)	Volume (10^6 ton day^{-1})	Velocity (cm s^{-1})
Upper	1	1,217.05	31.34	29.8
	2	196.58	3.09	18.2
Middle	3	253.98	4.37	19.9
	4	536.14	10.84	23.4
	5	531.77	10.93	23.8
	6	564.10	9.07	18.6
	7	732.09	7.91	12.5
Lower	8	747.91	10.15	15.7
	9	1,213.72	26.95	25.7
	10	2,288.23	78.49	39.7

Nutrient loads (DIN and P) associated with stn. 1-10 were estimated using (1). Results indicated that the DIN and P loads were respectively in the range of 2.09-31.00, and 0.03-5.25 ton day^{-1}. The highest DIN and P loads were registered at stn. 10, 31.00 ton day^{-1} and 5.25 in the dry season (Table 3). Results of nutrients loads indicated that the lower zone (Samut Songkhram Province) should focus on a point source area in the Mae Klong River.

Table 3 DIN and P transport (ton day^{-1}) at three cross-sectional sites during the dry season (April 2015)

Zone	Sectioned codes	DIN (ton day^{-1})	PO_4^{3-}-P (ton day^{-1})
Upper	St1	9.80	0.13
	St2	2.09	0.03
Middle	St3	3.22	0.04
	St4	3.36	0.10
	St5	3.35	0.11
	St6	4.71	0.12
	St7	4.54	0.11
Lower	St8	5.97	0.13
	St9	12.64	0.44
	St10	31.00	5.25

DIN and P transport for pollution carrying capacity were calculated using the equation shown in Fig. 2, with primary and secondary data collected from government officials (Table 4).

Table 4 Parameters for calculating the mathematical model in the lower area (Samut Songkhram Province) of the Mae Klong River

Type of waste water	Waste water volume	No.	Levels of concentration (μg/l)	
			DIN	PO_4^{3-}-P
Industry*	5 $x10^5$ $Lday^{-1}$	80 factory	23.6 $x10^3$	4.45 $x10^3$
Domestic	342 $Lcap.^{-1}day^{-1}$	194,069 cap.	10.9 $x10^3$	1.4 $x10^3$
Shrimp pond	1.9 $x10^4$ $LRai^{-1}day^{-1}$	1,613 Rai	2.7 $x10^3$	43.1
Rice field	2.3 $x10^3$ $LRai^{-1}day^{-1}$	-	3.6 $x10^3$	49.6

Results revealed that DIN and P transport during the rainy season were higher than levels in the dry season. However, output levels of DIN and P loads in both seasons were lower than input levels (Fig.3). To improve self-remediation of the river, especially during the dry season, high DIN and P levels in the box require larger recharge from the Mae Klong River in the dry season and imposition of restrictions on the discharge of wastewater into the river.

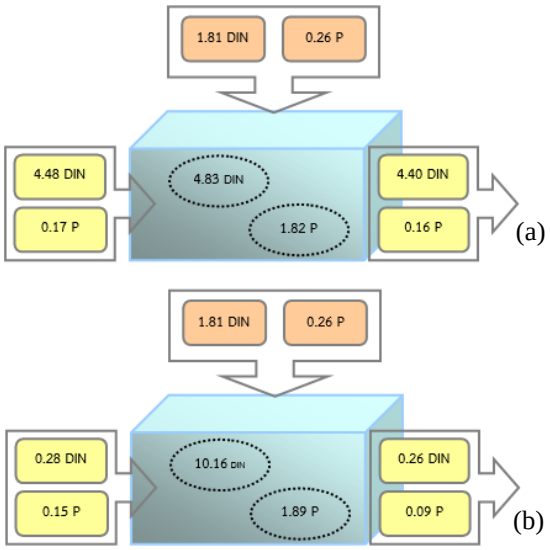

Fig. 3 DIN and P transport (ton day^{-1}) for pollution carrying capacity assessment using the mathematical model in the rainy (September 2015) and dry (April 2016) seasons in the lower part of the Mae Klong River.

DISCUSSION

Research results indicated that temperature and salinity of the river water varied minimally with seasons, while pH levels also remained relatively constant throughout. According to [2], freshwater inflow and precipitation-induced drainage influence the salinity level. Findings also revealed that dissolved oxygen (DO) was higher than Thailand's minimum threshold of 4 mg L^{-1}, rendering the water unfit for aquatic animals [10].

Furthermore, high DIN and P nutrient concentrations suggested anthropogenic contamination from the high population density along and near both sides of the river. Nutrient loads from the major areas revealed the impact of anthropogenic activity, while water flow characteristics influenced water quality in those areas [2]. Generally, nutrient loadings in a river are linked to natural and anthropogenic sources, e.g. runoff from urban areas and plantations, and inflow through organic-rich ground [11]. In addition, non-point sources e.g. storm water runoff and runoff from agricultural and urban areas contribute significantly to riverine biogeochemistry [12].

In water quality assessment, NH_4^+ is an important determinant [13]. The NH_4^+ levels in water bodies should be below 1 mg L^{-1} (or 71.4 µmol L^{-1}) [14], and the PO_4^{3-} levels below 1 µmol L^{-1} to avert eutrophication [2]. The PO_4^{3-} levels in the Mae Klong River were in excess of the limit.

Anthropogenic activity and water mass transfer direction of the Mae Klong River, especially in the lower zone (Samut Songkhram Province), contributed to high DIN and P loads. Nutrient input-outputs were high in the dry season when nutrient loads were excessive. [11] reported that nutrients in water could be diluted or enhanced in response to areas that the water flows through, and that nutrient concentrations influence the self-remediation of the waterways. In addition, land use contributes to nitrogen enrichment in the river [15], while phosphorus emission from wastewater is prevalent in highly populated areas [16].

The mathematical model for pollution carrying capacity of the area (lower zone) was positive, indicating adequate self-remediation and nutrient input-output balance. However, nutrient loads should be monitored, especially during the dry season.

CONCLUSIONS

Effects of seasonal variability (rainy and dry seasons) and nutrient transfer patterns on the anthropogenic nutrient loads (DIN and P) and the self-remediation of the Mae Klong River in Thailand were investigated. Findings revealed maximum DIN and P loads of 31.0 ton day^{-1} and 5.25 ton day^{-1}, respectively during the dry season in the lower part of the river. The predominantly positive nutrient transport for DIN and P indicated adequate self-remediation with subsequent nutrient input-output still in balance. To address self-remediation in the area requires enhanced recharge from the Mae Klong River during the dry season. Observations also indicated that water mass transfer direction influenced drainage, nutrient dilution and nutrient accumulation in the area.

ACKNOWLEDGMENTS

The authors would like to extend their deep gratitude to the Research Institute and Faculty of Agricultural Technology, Rajamangala University of Technology Thanyaburi (RMUTT) for financial support.

REFERENCES

[1] EGAT, Srinakarind Dam, Electricity Generating Authority of Thailand. accessed http://snr.egat.com/topography.htm. (28 April 2007).

[2] Thongdonphum B., Meksumpun S. and Meksumpun C., Nutrient Loads and their Impacts on Chlorophyll *a* in the Mae Klong River and Estuarine Ecosystem: An Approach for Nutrient Criteria Development, Water Science and Technology, Vol. 64(1), 2011, pp. 178-188.

[3] Chulalongkorn University. Environmental Conservation Plan for the Don Hoi Lord in the Mud Beach Area, Changwat Samut Songkram.,The Office of Environmental Policy and Planning, Ministry of Science, Technology and Environment, Thailand, 1996.

[4] Poolpak,T., Pokethitiyook,P., Kruatrachue, M.,Arjarasirikoon, U. and Thanwaniwat, N., Residue analysis of organochlorine pesticides in the Mae Klong river ofCentralThailand, Journal of Hazardous Materials 156, 2008, pp. 230–239.

[5] Vudhivanich, V., Pajongkitkran, S., Bunpian, A. and Cherdchanpipat, N., Irrigation efficiency of the greater Chao Phraya and the greater Mae Klong irrigation projects, Kasetsart Journal 36, 2002, pp. 110–118.

[6] PCD, Inland Water Quality Information System. Pollution Control Department, Thailand. accessed http://iwis.pcd.go.th/IWIS/intranet/inland/rep_stat_overview2.php (15 July 2010).

[7] Glibert P.M., Mayorga E. and Seitzinger S., *Prorocentrum minimum* Tracks Anthropogenic Nitrogen and Phosphorus Inputs on Global Basis: Application of Spatially Explicit Nutrient Export Models, Harmful Algae, Vol. 8, 2008, pp. 33-38.

[8] Flemer, D. A. and Champ, M. A., What is the future fate of estuaries given nutrient over-enrichment, freshwater diversion and low flows?, Marine Pollution Bulletin 52, 2006, pp. 247–258.

[9] TMD, Climate of Thailand, Thai Meteorological Department, Thailand, accessed https://www.tmd.go.th/info/info.php?FileID=53 (April 4, 2017)

[10] PCD, Water Quality Standard, Pollution Control Department, Thailand, accessed http://www.pcd.go.th/info_serv/reg_std_water06.html (March 20, 201**8**)

[11] Xia Y., Ti C., She D. and Yan X., Linking River Nutrient Concentrations to Land Use and Rainfall in a Paddy Agriculture-urban Area Gradient Watershed in Southeast China, Science of the Total Environment, Vol. 566-567, 2016, pp. 1094-1105.

[12] David S.E., Chattopadhyay M., Chattopadhyay S. and Jennerjahn T.C., Impact of Human Interventions on Nutrient Biogeochemistry in the Pamba River, Kerala, India, Science of the Total Environment, Vol. 541, pp. 1420-1430.

[13] Wang S., Lu A., Dang S. and Chen F., Ammonium nitrogen Concentration in the Weihe River, central China during 2005-2015, Environmental Earth Science, Vol. 75, 2016, 512.

[14] PHILMINAQ, Water Quality Criteria and Standards for Freshwater and Marine Aquaculture, Mitigating Impact from Aquaculture in Philippines, accessed https://www.researchgate.net/file.PostFileLoader.html?id=571b93653d7f4b012861d0a1&assetKey=AS%3A354056255098880%401461424997739. (Mar 2, 2016)

[15] Li R., Liu S., Zhang G., Ren J. and Zhang J., Biogeochemistry of Nutrients in an Estuary Affected by Human Activities: the Wanquan River Estuary, eastern Hainan Island, China, Continental Shelf Research, Vol. 57, 18-31.

[16] Mockler E.M., Deakin J., Archbold M., Gill L., Daly D. and Bruen M., Sources of Nitrogen and Phosphorus Emission to Irish Rivers and Coastal Waters: Estimates from a Nutrient Load Apportionment Framework, Science of the Environment, Vol. 601-602, 2017, pp. 326-229.

9th Int. Conf. on Geotechnique, Construction Materials and Environment, Tokyo, Japan, 20-22 November 2019, ISBN: 978-4-909106025 C3051

A RELIABILITY BASED CONSISTENT FUZZY PREFERENCE RELATIONS FOR RISK ASSESSMENT IN OIL AND GAS INDUSTRY

Ku Muhammad Naim Ku Khalif[1], Ahmad Syafadhli Abu Bakar[2, 3], Alexander Gegov[4] , Adam Shariff Adli Aminuddin[1], Noor Zuraidin Mohd Safar[5]

[1]Centre for Mathematical Sciences, Universiti Malaysia Pahang, Malaysia; [2]Centre for Foundation Studies in Science, University of Malaya, Malaysia; [3]Centre of Research for Computational Sciences and Informatics in Biology, Bioindustry, Environment, Agriculture and Healthcare (CRYSTAL), University of Malaya, Malaysia; [4]School of Computing, University of Portsmouth, United Kingdom; [5]Faculty of Computer Science and Information Technology, Universiti Tun Hussien Onn Malaysia, Malaysia

ABSTRACT

In decision making, linguistic variables tend to be complex to handle but they make more sense than classical fuzzy numbers. Fuzziness is not sufficient enough to deal with information and degree of reliability of information is critical. Z-numbers is proposed to model the uncertainty produced by human judgment when eliciting information. Therefore, the implementation of z-numbers is taken into consideration, where it has more authority to describe the knowledge of human being and extensively used in the uncertain information development. This issue has motivated the authors to propose fuzzy multi criteria decision making methodology using z-numbers. The proposed methodology is demonstrated the capability to handle knowledge of human being and uncertain information for risk assessment in oil and gas industry. This assessment is due to periodic basis, which will give insights from the operational until the strategic level of decision making process that is capable of dealing with uncertainty in human judgment. The consistent fuzzy preference relations is developed to calculate the preference-weights of the criteria related based on the derived network structure and to resolve conflicts arising from differences in information and opinions provided by the decision makers. The proposed methodology is constructed without losing the generality of the consistent fuzzy preference relations under fuzzy environment.

Keywords: Multi criteria decision making, Consistent fuzzy preference relations, Z-numbers, Reliability, Risk assessment, Oil and gas industry

INTRODUCTION

Risk assessment is an evaluation process for identified hazards or undesirable events. It is a process of categorizing and measuring the risk related outcomes from a specific incident in a particular scenario [1]. It can cause individual wounds of workers, environmental damages, degradation and damage of the assets which have high effects on the reputation of the industry. In the human decision making process, the risk is present because of uncertainty and imprecision [2]. Commonly, uncertainty and imprecision exist due to the lack of information, incompatible evidence, vague information and individual information. In oil and gas industries, risk assessment and decision making have been considered as crucial aspects. The investigation on risk assessment factors assists the decision makers to minimize the risk related and take the appropriate decisions about risk level [3].

Multiple criteria decision making (MCDM) approach has become a discipline of operations research which has been widely explored by experts or practitioners [4]. It is the process of making decision in the appearance of multiple criteria or objectives. Nowadays, uncertainty affected strongly in the world where much of the information on which decisions are based is uncertain [5] [6]. Thus, consistency is crucial for achieving correct solutions in decision process.

Consistent fuzzy preference relations was proposed by [7] for constructing the decision matrices of pairwise comparisons based on additive transitivity property. Due to each positive reciprocal matrix is described by fuzzy numbers in fuzzy linguistic terms, so to satisfy the consistency is very difficult [8]. Besides, establishing a fuzzy positive reciprocal matrix requires $\frac{n\times(n-1)}{2}$ judgments to be made for a level with n criteria. Hence, the number of comparison increase with the number of criteria, so inconsistent conditions are likely to occur. To solve the consistency problem, the consistent fuzzy preference relations technique is adopted in order to construct fuzzy decision matrix instead of fuzzy positive reciprocal matrix. The utilisation of consistent fuzzy preference relations in this phase yields decision matrices for making pairwise comparison matrices using additive transitivity. There are only *n-1* comparisons judgments are

required to ensure the consistency on a level that contains *n* criteria.

In the literature of fuzzy set, Zadeh [9] introduced fuzzy set theory in representing vagueness or imprecision in a mathematical approach. In order to do so, the main motivation of using fuzzy sets shows its ability in appropriately dealing with imprecise numerical quantities and subjective preferences of decision makers [10]. Zadeh [11] proposed a notion of z-number, which is an order pair of fuzzy numbers $(\tilde{A},\tilde{B})$. The $\tilde{A}$ component plays the role of a fuzzy restriction and represent the information about an uncertain variable, while the $\tilde{B}$ component is a reliability of $\tilde{A}$ component and enable to represent an idea of certainty or probability [12] [13]. The idea of z-numbers is to provide a basis for computation with numbers which are not completely reliable and more intelligent to describe the knowledge of human being and capable to cater uncertain information.

In real world decision making problems, linguistic variables tend to be very complex to handle but makes more sense than classical fuzzy numbers. Rather than use classical fuzzy numbers, the linguistic scales are expressed in a more details and flexible way by z-numbers. The membership functions of type-1 and type-2 fuzzy sets have no information regarding knowledge of human being. This issue motivates us to propose consistent fuzzy preference relation that has capability to handle knowledge of human being and uncertain information properly using z-numbers. Then, apply for risk assessment in oil and gas industry problem.

The rest of this paper is organized as follows: Section II introduces the concept of z-numbers. Section III presents the proposed methodology of consistent fuzzy preference relation using z-numbers. In Section VI, a case study for risk assessment in oil and gas industry. Section V summarises the conclusion.

PRELIMINARIES

In this section, the authors briefly review basic concept and definition of z-number that are illustrated as follows.

Z-numbers

A z-number is an ordered pair of fuzzy numbers

$$\mu_{\tilde{A}}(x)=(a_1,a_2,a_3,a_4)=\begin{cases}\dfrac{(x-a_1)}{(a_2-a_1)} & if \quad a_1\le x\le a_2\\ 1, & a_2\le x\le a_3\\ \dfrac{(a_4-x)}{(a_4-a_3)} & if \quad a_3\le x\le a_4\\ 0 & otherwise\end{cases}$$

$$\mu_{\tilde{B}}(x)=(b_1,b_2,b_3,b_4)=\begin{cases}\dfrac{(x-b_1)}{(b_2-b_1)} & if \quad b_1\le x\le b_2\\ 1, & b_2\le x\le b_3\\ \dfrac{(b_4-x)}{(b_4-b_3)} & if \quad b_3\le x\le b_4\\ 0 & otherwise\end{cases} \quad (1)$$

denoted as $Z=(\tilde{A},\tilde{B})$. First component, $\tilde{A}$ is known as restriction component whereby it is a real-valued uncertain on X while second component, $\tilde{B}$ is a measure of reliability for $\tilde{A}$ [11]. The illustration for z-number is depicted in Fig. 1 [12].

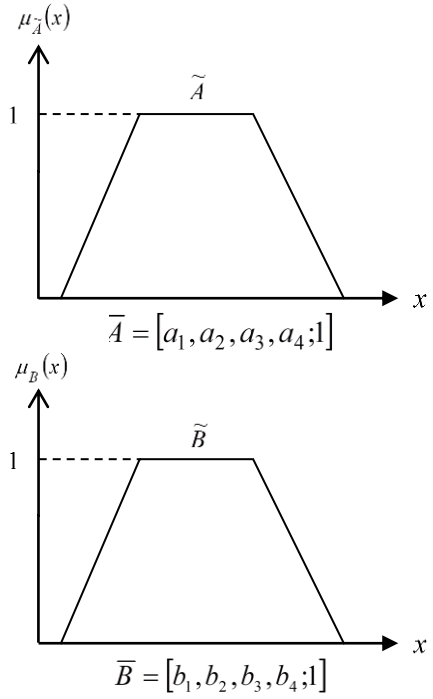

Fig. 1: Z-number, $Z=(\tilde{A},\tilde{B})$

PROPOSED METHODOLOGY

This section focuses on the development of integrated fuzzy risk assessment using z-numbers. It is worth mentioning that the structure of the proposed methodology is depicted as Figure 2.

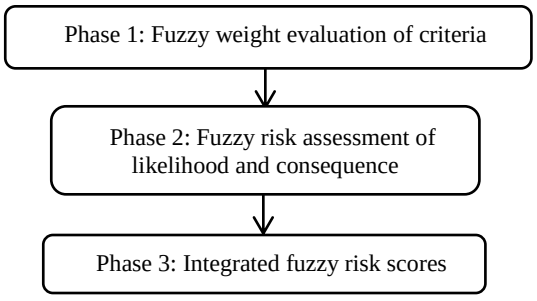

Fig. 2: Structure of fuzzy risk assessment in the presence of z-numbers.

Phase 1: Fuzzy Weights Evaluation of Criteria

Stage 1: Construct a pair-wise comparison matrices
The pairwise comparison matrices are constructed among all preferences elicited that comprise all criteria in z-numbers form as following matrix *A*:

$$A=\begin{bmatrix} 1 & \tilde{a}_{12} & \cdots & \tilde{a}_{1n} \\ \tilde{a}_{21} & 1 & \cdots & \tilde{a}_{2n} \\ \vdots & \vdots & \ddots & \vdots \\ \tilde{a}_{n1} & \tilde{a}_{n2} & \cdots & 1 \end{bmatrix}=\begin{bmatrix} 1 & \tilde{a}_{12} & \cdots & \tilde{a}_{1n} \\ 1/\tilde{a}_{12} & 1 & \cdots & \tilde{a}_{2n} \\ \vdots & \vdots & \ddots & \vdots \\ 1/\tilde{a}_{1n} & 1/\tilde{a}_{2n} & \cdots & 1 \end{bmatrix} \quad (2)$$

The risk analystss use the linguistic terms as depicted in Table 1 to present the weights and Table to present relibilility.

Stage 2: Convert the z-numbers into type-1 fuzzy numbers and aggregate them.
All z-numbers in fuzzy decision matrices are converted into type-1 fuzzy numbers by reduction process using intuitive vectorial centroid. The intuitive vectorial centroid is an extension of the classical vectorial centroid methods for fuzzy numbers that proposed by [14]. Compare to other centroid methods in the literature, the way to get the centroid value is more intelligent manner, easy to compute, more balance, and consider all feasible cases of fuzzy numbers. Intuitive vectorial centroid can be computed as

$$IVC(\tilde{x}_{\tilde{A}},\tilde{y}_{\tilde{A}})=\left(\frac{2(a_1+a_4)+7(a_2+a_3)}{18},\frac{7h_{\tilde{A}}}{18}\right) \quad (3)$$

where

$\tilde{x}$: the centroid point on the horizontal *x*-axis

$\tilde{y}$: the centroid point on the vertical *y*-axis

$(\tilde{x},\tilde{y})$: the centroid coordinate of fuzzy number $\tilde{A}$

The reduction process of z-numbers into type-1 fuzzy sets using intuitive vectorial centroid can be computed using [15].

Then, aggregate fuzzy decision matrix from risk analysts' evaluation.

$$\tilde{x}_{ij}=(\tilde{x}_{ij}^1\times\tilde{x}_{ij}^2\times\ldots\times\tilde{x}_{ij}^n)^{1/k} \quad (4)$$

where $\tilde{x}_{ij}$ is the performance rating of criteria, A_i with respect to criterion C_j evaluated by *kth* experts and $\tilde{x}_{ij}=(a_1^k,a_2^k,a_3^k,a_4^k;h^k)$.

Stage 3: Compute the criteria evaluations using consistent fuzzy preference relations.

Step 1: Construct a hierarchy structure.
The construction of hierarchy model needs judgment matrix filled by risk analysts about the evaluation of all criteria.

Step 2: Construct a pair-wise comparison matrices.
Consistent fuzzy preference relations is adopted to evaluate the weights of difference criteria for the performance of alternatives. The pairwise comparison matrices are constructed among all criteria in the dimension of the hierarchy systems based on the risk analysts preferences in stage 1 as following matrix *A*:

$$A=\begin{bmatrix} 1 & \tilde{a}_{12} & \cdots & \tilde{a}_{1n} \\ \tilde{a}_{21} & 1 & \cdots & \tilde{a}_{2n} \\ \vdots & \vdots & \ddots & \vdots \\ \tilde{a}_{n1} & \tilde{a}_{n2} & \cdots & 1 \end{bmatrix}=\begin{bmatrix} 1 & \tilde{a}_{12} & \cdots & \tilde{a}_{1n} \\ 1/\tilde{a}_{12} & 1 & \cdots & \tilde{a}_{2n} \\ \vdots & \vdots & \ddots & \vdots \\ 1/\tilde{a}_{1n} & 1/\tilde{a}_{2n} & \cdots & 1 \end{bmatrix} \quad (5)$$

Step 3: Convert risk analysts' preferences from z-numbers into regular fuzzy numbers.
Conversion process is computed by using [15] .

Step 4: Aggregate the risk analysts' preferences.
The pairwise comparison matrices of risk analysts' preferences are aggregated using equation below:

$$\tilde{a}_{ij}=(\tilde{a}_{ij}^1\times\tilde{a}_{ij}^2\times\ldots\times\tilde{a}_{ij}^n)^{1/k} \quad (6)$$

where *k* is the number of risk analysts and *i=1,2,…m; j=1,2,…n*.

Table 1 Trapezoidal fuzzy numbers preference scale [16]

Linguistic variables	Scale of relative important crisp numbers	Trapezoidal fuzzy numbers	Reciprocal trapezoidal fuzzy number
Equally important (EI)	1	(1, 1, 1, 1; 1)	(1, 1, 1, 1; 1)
Intermediate value (IV)	2	(1, 3/2, 5/2, 3; 1)	(1/3, 2/5, 2/3, 1; 1)
Moderately more important (MMI)	3	(2, 5/2, 7/2, 4; 1)	(1/4, 2/9, 2/5, 1/2; 1)
Intermediate value (IV)	4	(3, 7/2, 9/2, 5; 1)	(1/5, 2/9, 2/7, 1/3; 1)
Strongly more important (SMI)	5	(4, 9/2, 11/2, 6; 1)	(1/6, 2/11, 2/9, 1/4; 1)
Intermediate value (IV)	6	(5, 11/2, 13/2, 7; 1)	(1/7, 2/13, 2/11, 1/5; 1)
Very strong more important (VSMI)	7	(6, 13/2, 15/2, 8; 1)	(1/8, 2/15, 2/13, 1/6; 1)
Intermediate value (IV)	8	(7, 15/2, 17/2, 9; 1)	(1/9, 2/17, 2/15, 1/7; 1)
Extremely more important (EMI)	9	(8, 17/2, 9, 9; 1)	(1/9, 1/9, 2/17, 1/8; 1)

Table 2 Reliability linguistic terms and their corresponding z-numbers [17]

Linguistic Terms	Generalised fuzzy numbers
Very-low (VL)	(0,0,0,0.25;1)
Low (L)	(0,25,0.25,0.5;1)
Medium (M)	(0.25,0.5,0.5,0.75;1)
High (H)	(0.5,0.75,0.75,1;1)
Very-high (VH)	(0.75,1,1,1;1)

Step 5: Defuzzify the fuzzy numbers of aggregation's result of risk analysts' preferences.
Intuitive vectorial centroid for z-numbers is used for conversion process using [15].

Step 6: Compute the criteria values as weightage/ fuzzy weight, *FW* for alternatives' evaluation using consistent fuzzy preference relations.
Consistent fuzzy preference relations was proposed by [7] for constructing the decision matrices of pairwise comparisons based on additive transitivity property. Referring to [18], a fuzzy preference relation R on the set of the criteria or alternatives A is a fuzzy set stated on the Cartesian product set $A \times A$ with the membership function $\mu_R : A \times A \to [0,1]$. The preference relation is denoted by $n \times n$ matrix $R = (r_{ij})$ where $r_{ij} = \mu_R(a_i, a_j) \quad \forall i, \ j \in \{1,...,n\}$. The preference ratio, r_{ij} of the alternative a_i to a_j is determined by:

$$r_{ij} = \begin{cases} 0.5 & a_i \text{ is different to } a_j \\ (0.5,1) & a_i \text{ is preferred than } a_j \\ 1 & a_i \text{ is absolutely preferred than } a_j \end{cases}$$

The preference matrix R is presumed to be additive reciprocal, $p_{ij} + p_{ji} = 1, \ \forall i, \ j \in \{1,...,n\}$. Several propositions are associated to the consistent additive preference relations as follows:

Proposition 1 [19]**:** *Consider a set of criteria or alternatives,* $X = \{x_1,..., x_n\}$*, and associated with a reciprocal multiplicative preference relation* $A = (a_{ij})$ *for* $a_{ij} \in \left[\frac{1}{9}, 9\right]$*. Then, the corresponding reciprocal fuzzy preference relation,* $P = (p_{ij})$ *with* $p_{ij} \in [0,1]$ *associated with A is given by the following formulation:*

$$p_{ij} = g(a_{ij}) = \frac{1}{2}(1 + \log_9 a_{ij}) \tag{7}$$

Generally, if $a_{ij} \in \left[\frac{1}{n}, n\right]$*, then* $\log_n a_{ij}$ *is used, in particular, when* $a_{ij} \in \left[\frac{1}{9}, 9\right]$*;* $\log_9 a_{ij}$ *is considered as in the above proposition because* a_{ij} is between $\frac{1}{9}$ *and 9. If* a_{ij} is between $\frac{1}{7}$ *and 7, then* $\log_7 a_{ij}$ *is used.*
.

Proposition 2 [19]**:** *For a reciprocal fuzzy preference relation* $P = (p_{ij})$ *, the following statements are* equivalent

(1) $p_{ij} + p_{jk} + p_{ki} = \frac{3}{2}, \ \forall i, j, k$ (8)

(2) $p_{ij} + p_{jk} + p_{ki} = \frac{3}{2}, \ \forall i < j < k$ (9)

Proposition 3 [19]**:** *For a reciprocal fuzzy preference relation* $P = (p_{ij})$ *, the following statements are equivalent:*

(1) $p_{ij} + p_{jk} + p_{ki} = \frac{3}{2}, \ \forall i < j < k$

(2) $p_{i(i+1)} + p_{(i+1)(i+2)} + ... + p_{(j-1)j} + p_{ji} = \frac{j - i + 1}{2}$, $\forall i < j$ (10)

Proposition 3 is crucial because it can be used to construct a consistent fuzzy preference relations form the set of $n-1$ values $\{p_{12}, p_{23},..., p_{n-1}\}$. A decision matrix with entries that are not in the interval $[0,1]$, but in an interval $[-c, 1+c]$, $c > 0$, can be obtained by transforming the obtained values using a transformation function that preserves reciprocity and additive consistency with the function:

$$f : [-c, 1+c] \to [0,1], \ f(x) = \frac{(x + c)}{(1 + 2c)} \tag{11}$$

Phase 2: Fuzzy Risk Assessment of Likelihood and Consequence

Stage 1: Assess the real risk matrix into z-numbers for likelihood, consequence and risk level.
Z-numbers are utilised in capturing knowledge of human being in term of consideration of reliability aspect.

Stage 2: Establish a risk matrix using z-numbers as depicted in Table 3 and Table 4, then convert into type-1 fuzzy sets.
Z-numbers are converted into type-1 fuzzy sets using Eq. (3).

Stage 3: Aggregate the results for likelihood and consequence process.
Aggregate the likelihood and consequence process using Eq. (6).
Stage 4: Compute the fuzzy risk assessment for likelihood and consequence process.
The fuzzy risk assessment, *FRA* process can be computed by equation as follows:

$$FRA = \frac{\sum_{k=1}^{n}\left(Likelihood_i \times Consequenc_i\right)}{\sum_{k=1}^{n}\left(Likelihood\right)} \quad (12)$$

The risk matrix shows in Figure 3 has been used to generate the likelihood, consequence and risk in the model. The risk matrix has been applied by oil and gas industry to evaluate the overall risk of hazard by qualitatively.

Table 3 Linguistic fuzzy scale of likelihood

Likelihood	Trapezoidal fuzzy numbers
Rare	(1,1,2,3;1)
Unlikely	(2,3,4,5;1)
Possible	(4,5,6,7;1)
Likely	(6,7,8,9;1)
Almost Certain	(8,9,10,10;1)

Table 4 Linguistic fuzzy scale of consequence

Consequence	Trapezoidal fuzzy numbers
Insignificant	(1,1,2,3;1)
Minor	(2,3,4,5;1)
Moderate	(4,5,6,7;1)
Major	(6,7,8,9;1)
Severe	(8,9,10,10;1)

Table 5 Linguistic fuzzy scale of risk level

Risk level	Trapezoidal fuzzy numbers
Low	(0,2,3,4;1)
Medium	(3,4,5,6;1)
High	(5,6,7,8;1)
Very high	(6,7,8,10;1)

	Consequence				
Likelihood	**Insignificant**	**Minor**	**Moderate**	**Major**	**Severe**
Almost Certain	Medium	High	High	Extreme	Extreme
Likely	Medium	Medium	High	Extreme	Extreme
Possible	Medium	Medium	High	High	Extreme
Unlikely	Low	Medium	Medium	High	High
Rare	Low	Low	Medium	High	High

Fig. 3: Risk assessment matrix

Stage 4: Rank the criteria evaluated according to risk vales.
Risk value can be referred to Table 5 and Figure 3.

Phase 3: Integrated Fuzzy Risk Scores

Integrated fuzzy risk scores, *IFRS* for risk assessment are computed in this phase using equation below:

$$IFRS = FW^{0.1} \times FRA \quad (13)$$

The final score is compulsorily in the range of $0 \le IFRS \le 10$. The value of IFRS capable to determine the scaling and assignment of risk levels (Table 5) that best suits its priorities and available resources. In addition, it capable to rank the criteria/ inputs related to knowledge of human being properly without losing the nature of fuzzy/ uncertain environment.

FUZZY RISK ASSESSMENT IN OIL AND GAS INDUSTRY

Mercury exposure hazard has been used as a case study. Mercury is a natural component of oil and gas, and may be present at high concentrations in some formations. When these gas reservoirs are produced and the processed fluids are cooled, liquid mercury can condense within heat exchangers, separators, coolers, valves, and piping. When this equipment (particularly components made from magnesium or aluminum alloys) is taken apart for maintenance or repair, workers can be exposed to mercury vapour. The risk analyst must conduct a hazardous materials survey and a risk assessment for mercury exposure during decontamination of turnaround in refinery plant. Risk analysts assessed individually the effects of mercury exposure as likelihood and consequence of four categories; personnel safety, environment, property damage, and reputation.

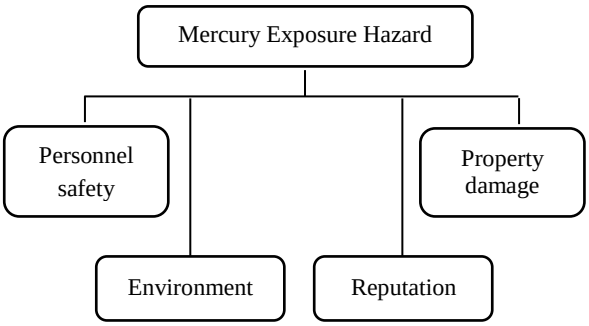

Fig. 4: Structure of risk assessment on mercury exposure hazard.

Phase 1: Fuzzy Weights Evaluation of Criteria
Table 6 depicts the fuzzy weight results for each criterion using the proposed reliability model. Personnel safety criterion depicts the highest weight value with 0.3299, followed by property damage with 0.2693, environment with 0.2279 and reputation with 0.1729. Based on risk analysts' evaluations, personnel safety , property damage and environment play important role in risk assessment in chemical hazardous.

Table 6 Fuzzy weight dimension results

Criteria	Reputation	Property Damage	Environment	Personnel Safety	Average	Weight	Rank
Reputation	0.5	0.3071	0.39	0.1858	0.3457	0.1729	4
Property Damage	0.6929	0.5	0.5829	0.3788	0.5387	0.2693	2
Environment	0.61	0.4171	0.5	0.2958	0.4557	0.2279	3
Personnel Safety	0.8142	0.6212	0.7042	0.5	0.6599	0.3299	1

Phase 2: Fuzzy Risk Assessment of Likelihood and Consequence
Table 7 depicts the evaluation of each criterion based consequence and likelihood assessment from three risk analysts with reliability assessment as well. Table 8 shows the risk assessment results and risk ranking of four criteria. It indicating the risk level of criterion personnel safety has the highest ranking with its value 8.341. However, the other criteria; property damage, environment, asset and reputation have the least priority as compared to personnel safety.

Table 8 Risk assessment results of each criterion based on likelihood and consequence

Criteria	Risk level	Rank
Personnel Safety	8.341	1
Environment	7.131	3
Property Damage	8.175	2
Reputation	6.022	4

Table 7 Risk assessment of likelihood and consequence process

Criteria	Risk Analyst 1		Risk Analyst 2		Risk Analyst 3	
	Consequence	Likelihood	Consequence	Likelihood	Consequence	Likelihood
Personnel Safety	5 (VH)	5 (VH)	5 (H)	5 (H)	4 (VH)	4 (VH)
Environment	4 (VH)	4 (VH)	4 (H)	4 (H)	4 (VH)	4 (VH)
Property Damage	4 (VH)	4 (VH)	5 (VH)	3 (VH)	5 (H)	4 (H)
Reputation	4 (VH)	3 (VH)	3 (VH)	3 (VH)	3 (VH)	4 (VH)

Phase 3: Integrated Fuzzy Risk Scores

Table 8 Integrated fuzzy risk scores between fuzzy weight and fuzzy risk level.

Criteria	Integrated fuzzy risk score (IFRS)	Rank
Personnel Safety	7.4658	1
Environment	6.1506	3
Property Damage	7.1702	2
Reputation	5.0529	4

Aforementioned in Section 3, the final score/ IFRS of risk assessment is the integration of two different methodologies which are from phase 1 and phase 2. The value of IFRS has capability to double check the ranking evaluated in earlier phase. The final ranking depicts personnel safety as the highest rank, followed by property damage, environment and reputation.

CONCLUSION

This study introduces the integrated fuzy risk assessment using consistent fuzzy preference relations and fuzzy risk assessment using z-numbers. In dealing with the uncertainty and complexity in the information, the reliability of information is taken into consideration efficiently. Z-numbers have better capability in describing uncertain and complex knowledge. For this reason, z-numbers are used in this work. The proposed methodology is developed by improvising several steps in computing the consistent fuzzy preference relations and fuzzy risk assessment using z-numbers to make sure both methodologies are well integrated. The proposed

model is capable of interacting or cooperating with unlimited criteria in dealing with real world decision making problems.

The proposed fuzzy risk assessment in human based decision making by capturing uncertainty in human judgement. Due to access information and availability of the incomplete and uncertain data, it is hard to make a right decision. In this sense, it is important to modify some classical techniques and models by adding intuitive reasoning and human subjectivity. As compared with the existing risk ranking method, the proposed fuzzy risk assessment is able to provide the risk level score more precisely and accurately and will also assist to reduce the risk ranking ties wherever possible and it can integrate the opinions of experts in a more accurate way and can rank the risk levels quantitatively. As a consequence, the proposed fuzzy risk assessment offers a robust and reliable methodology that provides best assessment with regard to available resources. Therefore, this methodology can be further extended in order by considering complicated case studies drawn from a wide range of human based decision making problems.

ACKNOWLEDGMENTS

This research work is funded by Universiti Malaysia Pahang Research Grant RDU190306, Malaysia Ministry of Education Research Grant FRGS/1/2019/STG06/UMP/02/9. University of Malaya Research Grants RF001H-2018, Malaysia Ministry of Education Research Grant FRGS/1/2018/STG06/UM/02/14.

REFERENCES

[1] K. Shuaib, H. Hussin, M. Amin, and A. Majid, "Fuzzy Multi-Criteria Decision Making Model for Risk Assessment," *ARPN J. Eng. Appl. Sci.*, vol. 11, no. 22, pp. 13072–13077, 2016.

[2] H. Hussin, S. Kaka, M. Amin, and A. Majid, "A Case Study on Fuzzy Logic-Based on Risk Assessment in Oil and Gas Industry," vol. 11, no. 5, pp. 3049–3054, 2016.

[3] C. Yeh, H. Deng, S. Wibowo, and Y. Xu, "Multicriteria Group Decision Support for Information," in *International Conference on Industrial, Engineering and Other Applications of Applied Intelligent Systems*, 2009, pp. 152–161.

[4] A. Mardani, A. Jusoh, and E. K. Zavadskas, "Fuzzy multiple criteria decision-making techniques and applications – Two decades review from 1994 to 2014," *Expert Syst. Appl.*, vol. 42, no. 8, pp. 4126–4148, Jan. 2015.

[5] X. Zhi-quan, "Application of Z-numbers in Multi-criteria Decision Making," in *International Conference on Informantive and Cybernatics for Computational Social Systems (ICCSS)*, 2014, pp. 91–95.

[6] A. Gegov, F. Arabikhan, D. Sanders, B. Vatchova, and T. Vasileva, "Fuzzy networks with feedback rule bases for complex systems modelling," *Int. J. Knowledge-Based Intell. Eng. Syst.*, 2017.

[7] E. Herrera-Viedma, F. Herrera, F. Chiclana, and M. Luque, "Some issues on consistency of fuzzy preference relations," *Eur. J. Oper. Res.*, vol. 154, no. 1, pp. 98–109, 2004.

[8] T.-C. Wang and Y.-H. Chen, "Consistent Fuzzy Linguistic Preference Relations for Computer Integrated Manufactory Systems Selection," *Proc. 9th Jt. Conf. Inf. Sci.*, pp. 2–5, 2006.

[9] L. A. Zadeh, "Fuzzy Sets-Information and Control-1965.pdf." Information and Controls, pp. 338–353, 1965.

[10] H. Deng, "Comparing and ranking fuzzy numbers using ideal solutions," *Appl. Math. Model.*, vol. 38, no. 5–6, pp. 1638–1646, Mar. 2014.

[11] L. A. Zadeh, "A Note on Z-numbers," *Inf. Sci. (Ny).*, vol. 181, no. 14, pp. 2923–2932, Jul. 2011.

[12] B. Kang, D. Wei, Y. Li, and Y. Deng, "A Method of Converting Z-number to Classical Fuzzy Number," *J. Inf. Comput. Sci.*, vol. 9, no. 3, pp. 703–709, 2012.

[13] A. Azadeh, M. Saberi, N. Z. Atashbar, E. Chang, and P. Pazhoheshfar, "Z-AHP: A Z-number extension of fuzzy analytical hierarchy process," *2013 7th IEEE Int. Conf. Digit. Ecosyst. Technol.*, pp. 141–147, 2013.

[14] K. M. N. Ku Khalif and A. Gegov, "Generalised Fuzzy Bayesian Network with Adaptive Vectorial Centroid," in *16th world congress of the international fuzzy systems association (IFSA) and the 9th conference of the European society for fuzzy logic and technology (EUSFLAT)*, 2015, pp. 757–764.

[15] K. M. N. Ku Khalif, A. Gegov, and A. S. Abu Bakar, "Hybrid fuzzy MCDM model for Z-numbers using intuitive vectorial centroid," *J. Intell. Fuzzy Syst.*, vol. 33, no. 2, 2017.

[16] G. Zheng, N. Zhu, Z. Tian, Y. Chen, and B. Sun, "Application of a trapezoidal fuzzy AHP method for work safety evaluation and early warning rating of hot and humid environments," *Saf. Sci.*, vol. 50, no. 2, pp. 228–239, Feb. 2012.

[17] B. Kang, D. Wei, Y. Li, and Y. Deng, "Decision Making Using Z-numbers under

Uncertain Environment," *J. Comput. Inf. Syst.*, vol. 8, no. 7, pp. 2807–2814, 2012.

[18] N. H. Kamis, K. Abdullah, H. Mohamed, S. Sudin, and W. Z. A. W. Ishak, "Decision making models based on consistent fuzzy preference relations with different defuzzification methods," *2011 IEEE Colloq. Humanit. Sci. Eng. CHUSER 2011*, no. Chuser, pp. 845–850, 2011.

[19] T. C. Wang and Y. H. Chen, "Applying consistent fuzzy preference relations to partnership selection," *Omega*, vol. 35, no. 4, pp. 384–388, 2007.

9th Int. Conf. on Geotechnique, Construction Materials and Environment, Tokyo, Japan, 20-22 November 2019, ISBN: 978-4-909106025 C3051

LEAD IMMOBILIZATION IN ARTIFICIAL CONTAMINATED SOIL USING SULFUR-IMPREGNATED CARBONACEOUS BAMBOO

Takaaki Wajima[1]
[1]Department of Urban Environment Systems, Chiba University, Japan

ABSTRACT

A novel carbonaceous immobilizing agent for heavy metal contaminated soil was prepared from bamboo using sulfur immersion and pyrolysis, and the lead immobilization in artificial contaminated soils using sulfur-impregnated carbonaceous material was estimated. The bamboo was powdered, dried, and then immersed in 0.1 - 1 M K_2S solution for 0 - 24 h to prepare sulfur-immersed materials. The immersed-materials were heated at 400 ^oC for 1 h in nitrogen gas to produce the sulfur-impregnated carbonaceous material by pyrolysis. The abilities of the product to immobilize lead from aqueous solution were examined to obtain the product with high lead immobilization ability. With increasing K_2S concentration, the immobilization ability of the product for lead gradually increases and then above 0.75 M K_2S those are almost constant, while 15 min is sufficient for the immersed time to obtain the product with high lead immobilization ability. The product prepared from material immersed in more than 0.75 M K_2S solution for more than 15 min has a maximum immobilization ability for lead ion of 2.78 mg/g. The lead immobilization using the sulfur-impregnated product is sustainable due to the formation of leadhillite [$Pb_4SO_4(CO_3)_2(OH)_2$] and lead carbonate [$Pb(CO_3)_2O$]. The product can immobilize lead ion in various artificial lead contaminated soils. By mixing artificial lead contaminated soil with the sulfur-impregnated product, the eluted solution became neutral, and the eluted concentrations of lead ion dropped below the Japanese elution standard for soil.

Keywords: Sulfur-impregnation, Lead immobilization, Bamboo, Artificial contaminated soil, Pyrolysis

INTRODUCTION

Soil contamination with heavy metals is a worldwide problem. Accumulation of heavy metals in soils affect soil ecology, agricultural productivity, quality of agricultural products, water resources, and serious health problems for human and animal [1]. In the United States, for example, approximately 63 % of the sites on the National Priority List (NPL) for the treatment of contaminated soils are contaminated by metals, and lead is the most common metal, found at 15 % of the sites. In Japan, according to a report by the Ministry of Environment, 43 % of the contaminated sites that exceed the environmental quality standards are contaminated by lead compounds. Soil contamination by lead compounds is also prevalent in other developed and developing countries where lead compounds are used extensively in industrial activities without careful contamination management.

Lead is a ubiquitous heavy metal pollutant in soils due to their use widely. The primary sources of Pb contamination include industrial activities such as mining, smelting of metals, and the use of Pb-containing products such as paints, lead-acid batteries, bullets, gasoline and pesticides [2]. It can damage human nervous (especially children) and reproductive systems [3]. The high concentration of Pb in the soil poses risks to human and animal health by the leaching of metals from the soil into water and the consumption of edible plants growth in the contaminated soil. Therefore, proper remediation is necessary to reduce metal availability in soil for protecting human health.

Among available remediation technologies, in situ immobilization of heavy metals using a chemical amendment can be a cost-effective and environmentally sustainable remediation approach for the immobilization of heavy metals by reducing the mobility and availability. This immobilization technique may provide a long-term remediation solution if low solubility minerals and/or stable precipitates are produced in situ [4]. Therefore, the choice of the soil amendments need that the amendments must reduce heavy metals transfers from contaminated soils to the surface water or groundwater and uptake by plants and organism. The most common agents for lead immobilization are phosphate-based compounds [5-7]. Although these studies have successfully demonstrated that phosphates effectively immobilize lead in various contaminated soils, there are several concerns about the use of phosphate as agents for lead immobilization. First, from an environmental protection point of view, excessive supplied phosphate can lead to eutrophication in the natural environment. Second, from a resource conservation point of view, phosphate is becoming a precious element, especially in countries such as Japan that import a major portion of their phosphate

requirements. For these reasons, research on other types of lead immobilization agents is needed. Soil amendments, lime [8], calcium carbonate [9], red-mud [10], fly ash [11] and so on, may decrease leachable concentrations of contaminants and thus reduce the detrimental effects of heavy metals on environmental receptors, such as microorganisms, plants, animals, water and humans [12].

In previous studies, sulfur-impregnated adsorbents with high removal abilities for heavy metals were prepared from paper sludge, cedar bark and rice husk using K_2S solution [13-15]. According to the Pearson theory, the sulfur, as a soft base, should interact with heavy metals such as Zn^{2+}, Pb^{2+}, Cd^{2+} and Ni^{2+} (soft acids) rather than with oxygen (a hard base) in the activated carbon. From these results, it would be possible to produce a low cost agent to immobilize the metal ions in contaminated soils from agricultural waste.

Bamboo is a renewable bioresource and abundantly found in different geographic areas of the world. Bamboos, fast growing plants, are natural composite materials useful in construction, textile industry and so on. Large quantities of bamboo waste are generated every year, which could be a biomass feed stock for char production due to its high fraction of lignocelluloses [16]. Bamboo charcoal is one of the promising adsorbents enriched with microporous structure and higher surface area. The surface area of bamboo charcoal is generally 3-10 times higher than compared to the world charcoal. The surface porous structure and heterogeneity of charcoal materials can be improved by modification process which has significant effects on adsorption performance. The physical and chemical modification of bamboo charcoal can enhance its affinity to adsorbate ions which is evidenced by earlier studies [17]. In recent years, very few studies have been conducted for adsorption of heavy metals using bamboo charcoal [18, 19].

From these background, in this study, we attempted to prepare the lead immobilization agent from bamboo using sulfur-impregnation, and lead immobilization ability of the sulfur-impregnated product was estimated using artificial lead contaminated soils.

MATERIALS AND METHODS

Raw Sample

Bamboo, which was collected from a forest area in Chiba prefecture, Japan, first pulverize under 3 mm length, then washed with distilled water, and dried and stored for use. Properties of bamboo sample are shown in Table 1, and mineralogical composition of bamboo is shown in Fig. 1, which indicates that bamboo mainly composed of cellulose. All reagents were purchased from Wako Chemical Co., Japan at analytical grade.

Table 1 Properties of bamboo sample

Moisture	Ash	Fixed carbon and Volatile matter		
		C	H	N
11 %	2 %	44.9 %	5.4 %	0.2 %

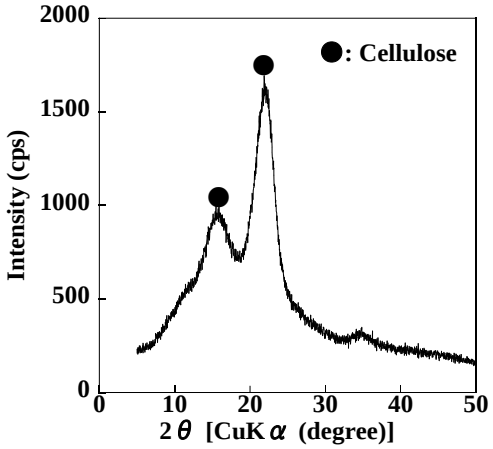

Fig. 1 XRD patterns of bamboo.

Sulfur Impregnation

20 g of sample was immersed in 200 mL of 0.1 - 1 M K_2S solution for 0 - 24 h, then filtered, and dried in a drying oven overnight to obtain sulfur-immersed samples. These samples were pyrolyzed using a horizontal reactor. Sulfur-immersed samples were put in a ceramic board, and installed in a transparent quartz tube of 0.45 mm inside diameter and 1 m in length. Before pyrolysis, N_2 gas was injected into the tube for 30 min at a rate of 1.0 L/min to replace the air in the tube. The board was heated in an electric furnace at 400 ^oC for 1 h, with a continuous flow of N_2 gas at a rate of 1.0 L/min. After heating, the solid was cooled to room temperature with a steady N_2 gas flow (1.0 L/min) in the tube, then washed with distilled water and dried in drying oven overnight to obtain the sulfur-impregnated material.

The abilities of the material for immobilization of lead ion from aqueous solution were examined as follows. 0.1 g of the sample was added to 10 mL of $Pb(NO_3)_2$ solution with 10 mM in 50 mL centrifuged tube, and was shaken in a reciprocal shaker for 24 h. After shaking, the slurry was centrifuged, and the pH of the supernatant and the concentration of Pb^{2+} in the supernatant were measured by pH meter (D-53, Horiba) and atomic absorption spectrophotometer (AAS) (AAnalyst200, PerkinElmer), respectively. The immobilization ratios of Pb^{2+} were calculated using the following equation:

$$R = \frac{(C_0 - C_e)}{C_0} \times 100 \quad (1)$$

Here, R = Immobilization ratio of Pb^{2+} (%), C_0 = Initial concentration of Pb^{2+} in the solution (mg/L), and C_e = Measure concentration of Pb^{2+} in the solution (mg/L).

After lead immobilization, each sample (1.0 g) was added into 10 mL of distilled water in 50 mL of centrifuged tube, and tube was shaken for 6 h. After shaking, the slurry was centrifuged, and the concentration of Pb^{2+} in the supernatant was measured by AAS to calculate the elution of lead

The samples were analyzed by powder X-ray diffraction (XRD) with monochromate CuKα radiation (Ultima IV, Rigaku).

Lead Immobilization

Four soil samples, Akadama soil, Kanuma soil, black soil and river sand, were used to prepare artificially lead-contaminated soils. Lead-contaminated soil was artificially prepared by mixing 30 g of soil sample and 300 mL of 1000 mg-Pb/L aqueous solution (provided by $Pb(NO_3)_2$) using a rotary stirrer for 6 h. After mixing, the mixture stands at room temperature for 7 days, and then filtrate. The concentration of Pb^{2+} in the filtrate was measured by AAS to calculate the content of lead in artificially contaminated soils. The solid was dried in air for 7 days to obtain artificially contaminated soil.

1 g of artificially contaminated soil without or with 0.01 – 0.1 g of sulfur-impregnated product was added into 50 mL of a conical flask, and 10 mL of distilled water was then poured. The flask was shaken with shaking incubator at 50 °C for 6 h, and then filtrate. The pH of the filtrate was measured by pH meter, and the eluted concentration of Pb^{2+} in the filtrate is measured by AAS.

RESULTS AND DISCUSSION

Lead Immobilization of Sulfur-Impregnated Product

Figure 2 shows the lead immobilization of the product from bamboo via pyrolysis of the bamboo immersed in 0.5 mol/L K_2S solution for various times, and pH of the solution after lead immobilization. With increasing immersion time, lead immobilization of the product rapidly increases, and then be almost constant (about 55 %) after 15 min. It is noted that pH of the solution is almost 5.2 after addition of the product.

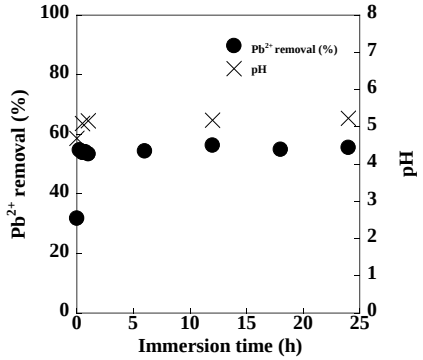

Fig. 2 Lead immobilization of the product from bamboo via pyrolysis of the bamboo immersed in 0.5 mol/L K_2S solution for various times, and pH of the solution after lead immobilization.

Figure 3 shows the lead immobilization of the product from bamboo via pyrolysis of the bamboo immersed in K_2S solution with various concentrations, and pH of the solution after lead immobilization. With increasing K_2S concertation to 0.75 mol/L, lead immobilization of the product increases, and be almost constant (approximately 80 %) above 0.75 mol/L K_2S solution, which is more than 2 times higher than the product without sulfur-impregnation. It is noted that pH of the solution after lead immobilization of the product with sulfur-impregnation is 5.0 - 5.5, which is higher than that without sulfur-impregnation (4.8).

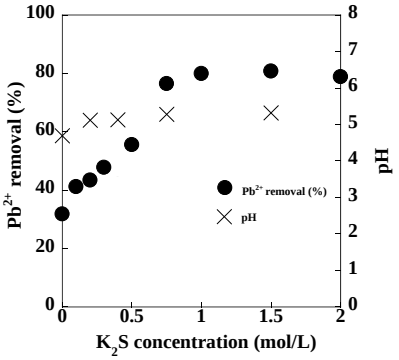

Fig. 3 Lead immobilization of the product from bamboo via pyrolysis of the bamboo immersed in K_2S solution with various concentrations, and pH of the solution after lead immobilization.

Figure 4 shows the XRD patterns of (a) immersed bamboo and (b) the products from bamboo via pyrolysis of the bamboo immersed in 0.5 mol/L K_2S solution for various times, and Figure 5 shows the XRD patterns of (a) immersed bamboo and (b) the products from bamboo via pyrolysis of the bamboo immersed in K_2S solution with various concentrations. Regardless of the immersed conditions, the bamboo after K_2S immersion have cellulose peaks, which is almost same as raw bamboo (Fig. 4 (a), Fig. 5 (a)). After pyrolysis, the pyrolyzed bamboo products have amorphous structure (Fig. 4 (b), Fig. 5 (b)).

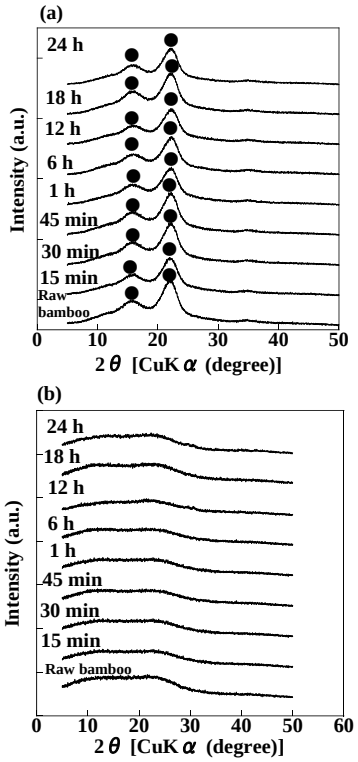

Fig. 4 XRD patterns of (a) immersed bamboo and (b) the products from bamboo via pyrolysis of the bamboo immersed in 0.5 mol/L K_2S solution for various times.

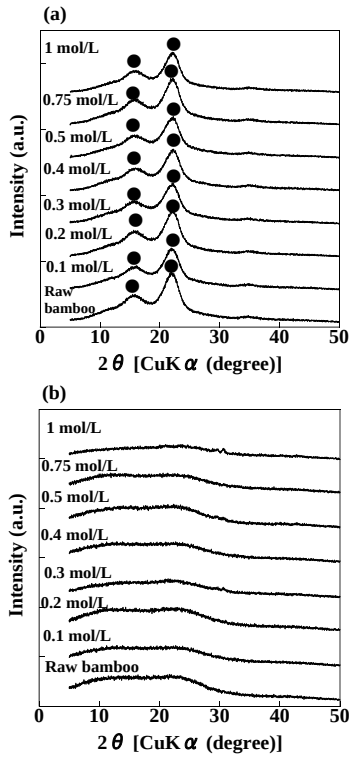

Fig. 5 XRD patterns of (a) immersed bamboo and (b) the products from bamboo via pyrolysis of the bamboo immersed in K_2S solution with various concentrations.

Figure 6 shows the XRD patterns of the products after lead immobilization test using (a) the products from bamboo via pyrolysis of the bamboo immersed in 0.5 mol/L K_2S solution for various times and (b) the products from bamboo via pyrolysis of the bamboo immersed in K_2S solution with various concentrations. After lead immobilization test, while lead carbonate [$Pb(CO_3)_2O$] appears in the product without sulfur-impregnation, lead carbonate and leadhilite [$Pb_4SO_4(CO_3)_2(OH)_2$] appear in the product with sulfur-impregnation, which means that sulfur-impregnated product has higher lead removal ability than the product without sulfur-impregnation, due to the formation of leadhilite by sulfur content in the product.

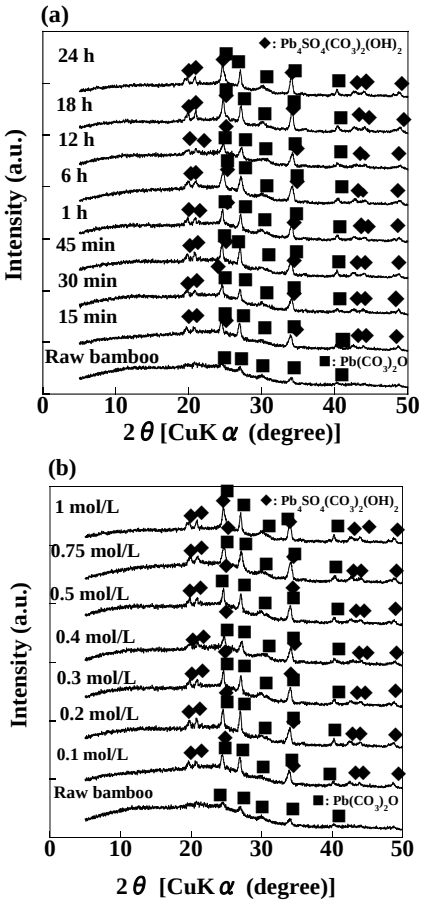

Fig. 6 XRD patterns of the products after lead immobilization test using (a) the products from bamboo via pyrolysis of the bamboo immersed in 0.5 mol/L K_2S solution for various times and (b) the products from bamboo via pyrolysis of the bamboo immersed in K_2S solution with various concentrations.

From these results, lead immobilization agent can be prepared from bamboo via pyrolysis of the bamboo immersed in higher than 0.75 mol/L K_2S solution for more than 15 min, indicating a maximum immobilization ability for lead ion of 2.78 mg/g.

Figure 7 shows the lead elution from the products from bamboo via pyrolysis of the bamboo immersed in K_2S solution with various concentrations. Lead elution from the product without sulfur impregnation is 35 %, while that of the product with sulfur-impregnation is zero, which means that the sulfur-impregnated product can strongly immobilize lead in the product.

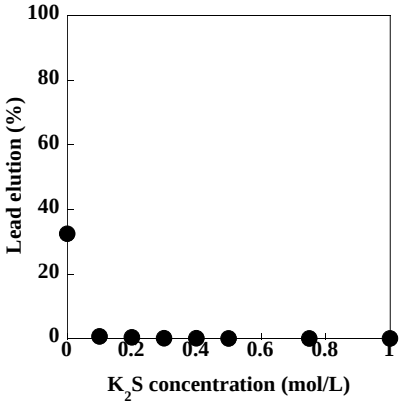

Fig. 7 Lead elution from the products from bamboo via pyrolysis of the bamboo immersed in K_2S solution with various concentrations.

Lead Immobilization

The lead immobilization of the obtained product was examined using artificial contaminated soils. It is noted that the lead content of artificial contaminated soils used in this experiment is black soil (9799 mg/kg) > akadama soil (8347 mg/kg) > kanuma soil (6969 mg/kg) > river sand (4185 mg/kg).

Figure 8 shows the pH of the solution and the eluted lead concentrations after elution test using artificial contaminated soils with addition of sulfur-impregnated product. Without addition of the product, pH of the solution is weak acidic (pH 4-6), and with increasing addition of the product, pH of the solution increased. With addition of 0.1 g product, pHs of the solution using akadama soil, kanuma soil and black soil are neutral, while that using river sand is weak alkaline. It is considered that the product is alkaline material and three soils have pH buffering ability.

Without addition of the product, high concentrations of lead were eluted from kanuma soil (85.5 mg/L) and akadama soil (63.5 mg/L), while elution from black soil (1.0 mg/L) and river sand (1.1 mg/L) are low. With increasing addition of the product, the lead elution decreases, and with addition of 0.1 g product, the lead elution from all samples are not detected using AAS. It is noted that Japanese standard of soil elution is less than 0.01 mg/L. It would be considered that the product can immobilized lead ion in various soils.

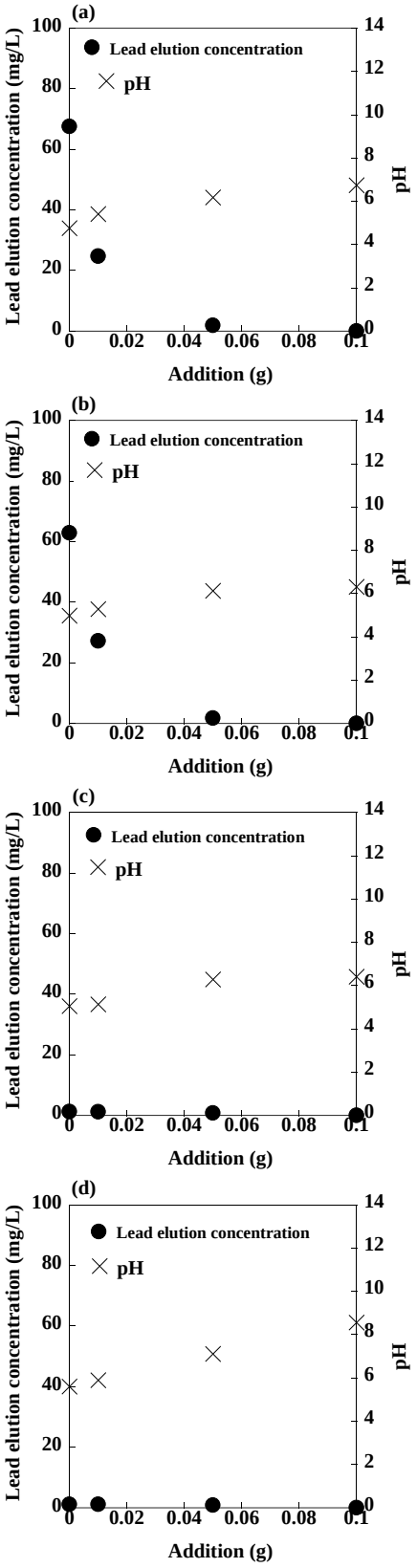

Fig. 8 The pH of the solution and the eluted lead concentrations after elution test using artificial contaminated soils with addition of sulfur-impregnated product: (a) Akadama soil, (b) Kanuma soil, (c) Black soil, and (d) River sand.

From these results, it would be possible that, by mixing lead contaminated soil with sulfur-impregnated product, the eluted solution becomes neutral and the concentration of lead drops below the Japanese eluted standard for soil.

CONCLUSIONS

A novel carbonaceous immobilizing agent for heavy metal contaminated soil can be prepared from rice straw using sulfur immersion and pyrolysis, and can immobilize lead ion in various artificial lead contaminated soils.

ACKNOWLEDGMENTS

This work was supported by JSPS KAKENHI Grant Number 16K00609.

REFERENCES

[1] Raicevic, S., Kaludjerovic-Radoicic, T. and Zouboulis, A. I., In situ Stabilization of Toxic Metals in Polluted Soils using Phosphates: Theoretical Prediction and Experiment Verification, J. Hazard. Mater., Vol. B117, 2005, pp. 41-53.

[2] Cao, X. D., Wahbi, A., Ma, L. N., Li, B. and Yang, Y. L., Immobilization of Zn, Cu, and Pb in Contaminated Soils using Phosphate Rock and Phosphoric Acid, J. Hazard. Mater., Vol. 164, 2009, pp. 555-564.

[3] Agency for Toxic Substances and Disease Registry (ATSDR), Toxicological Profile for Lead, Atlanta, 2007.

[4] Vangronsveld, J. and Cunningham, S. D., Introduction to the concepts. In Metal Contaminated Soils: in situ Inactivation and Phytorestoration, New York: Springer, 1998. pp. 1–15.

[5] Cui, Y. S., Du, X., Weng, L. P., Riemsdijk, W. H., Assessment of in situ Immobilization of Lead (Pb) and Arsenic (As) in Contaminated Soils with Phosphate and Iron: Solubility and Bioaccessibility, Water Air Soil Pollut., Vol. 213, 2010, pp. 1-4.

[6] Munksgaard, N., Lottermoser, B. G. and Blake, K., Prolonged Testing of Metal Mobility in Mining-Impacted Soils Amended with Phosphate Fertilisers, Water Air Soil Pollut., Vol. 223, 2011, pp. 2237-2255.

[7] Mignardi, S., Corami, A. and Ferrini, V., Evaluation of the Effectiveness of Phosphate Treatment for the Remediation of Mine Waste Soils Contaminated with Cd, Cu, Pb, and Zn, Chemosphere, Vol. 86, 2012, pp. 354-360.

[8] Gray, C. W., Dunham, S. J., Dennis, P. G., Zhao, F. J. and McGrath, S. P., Field Evaluation of in situ Remediation of a Heavy Metal Contaminated Soil using Lime and Red-mud, J. Environ. Pollut., Vol. 142, 2006, pp. 530–539.

[9] Wang, Y. M., Chen, T. C., Yeh, K. J. and Shue, M. F., Stabilization of an Elevated Heavy Metal Contaminated Site, J. Hazard. Mater., Vol. 88, 2001, pp. 63-74.

[10] Lee, S. H., Lee, J. S., Choi, Y. J. and Kim, J. G., In situ Stabilization of Cadmium-, Lead-, and Zinc-Contaminated Soil using Various Amendments, Chemosphere, Vol. 77, 2009, pp. 1069-1075.

[11] David, H., Jonathan, P. and Philippe, S., Heavy Metal Immobilization by Cost-Effective Amendments in a Contaminated Soil: Effects on Metal Leaching and Phytoavailability, J. Geochem. Explor., Vol. 123, 2012, pp. 87–94.

[12] Lombi, E., Zhao, F. J., Zhang, G., Sun, B., Fitz, W., Zhang, H. and McGrath, S. P., In situ Fixation of Metals in Soils using Bauxite Residue: Chemical Assessment, J. Environ. Pollut., Vol. 118, 2002, pp. 435-443.

[13] Wajima, T., Preparation of Carbonaceous Heavy Metal Adsorbent from Cedar Bark using Sulfur-Impregnation, Int. J. Chem. Eng. Appl., Vol. 18, 2017, pp. 272-276.

[14] Wajima, T., A New Carbonaceous Adsorbent for Heavy Metal Removal from Aqueous Solution prepared from Paper Sludge by Sulfur-Impregnation and Pyrolysis, Process Saf. Environ. Prot., Vol. 112, 2017, pp. 342-352.

[15] Wajima, T., Preparation of Sulfur-Impregnated Carbonaceous Adsorbent from Rice Husk for Heavy Metal Removal from Aqueous Solution, Int. J. Environ. Sci. Dev., Vol. 9, 2018, pp. 38-42.

[16] Shen, S., Nges, I. A., Yun, J. and Liu, J., Pre-treatments for Enhanced Biochemical Methane Potential of Bamboo Waste, Chem. Eng. J., Vol. 240, 2014, pp. 253-259.

[17] Fan, Y., Wang, B., Yuan, S., Wu, X., Chen, J. and Wang, L, Adsorptive Removal of Chloramphenicol from Wastewater by NaOH Modified Bamboo Charcoal, Bioresour. Technol., Vol. 101, 2010, pp. 7661-7664.

[18] Wang, F. Y., Wang, H. and Ma, J. W., Adsorption of Cadmium (II) Ions from Aqueous Solution by a New Low-Cost Adsorbent Bamboo Charcoal, J. Hazard. Mater., Vol. 177, 2010, pp. 300-306.

[19] Tan, Z., Niu, G. and Chen, X., Removal of Elemental Mercury by Modified Bamboo Carbon, Chin. J. Chem. Eng., Vol. 23, 2015, pp. 1875-1880.

9th Int. Conf. on Geotechnique, Construction Materials and Environment, Tokyo, Japan, 20-22 November 2019, ISBN: 978-4-909106025 C3051

ESTIMATION OF TRANSPORT DEMAND USING SATELLITE IMAGE: CASE STUDY OF CHIANG MAI, THAILAND

Masanobu Kii[1], Nopadon Kronprasert[2] and Boonsong Satayopas[2]
[1]Faculty of Engineering and Design, Kagawa University, Japan;
[2] Faculty of Engineering, Chiang Mai University, Thailand

ABSTRACT

Transport demand is one of the essential datasets for urban / transport planning and policy development. However, the full size of travel demand survey requires large amount of cost, therefore the survey is merely conducted in developing countries. Their policy decision might be based on the old and limited datasets. In this study we propose a new approach to estimate transport demand using the night-time light satellite image based on the correlation of these two factors. Taking the case of Chiang Mai Metropolitan area, we found a soft relationship between the night-time light intensity and trip generation/trip attraction. Transport survey data is provided by Chiang Mai University for the year 2016. NOAA provides cloud free monthly composite of night-time light satellite image (VIIRS-DNB) by Suomi-NPP satellite of which resolution is 15 arc-second (about 500m by 500m at equator). It is spatially more precise than zones of travel demand survey and monthly frequency. Applying the relationship between transport demand and night-time light intensity, we propose a method to update the transport demand with higher spatial resolution.

Keywords: Transport demand update, Night-time light satellite image

INTRODUCTION

Current and future transportation demand are essential information for urban / transport planning and policy development. As input for transport demand analysis like traditional four step models [1] massive number of samples are required in travel survey to achieve enough accurate demand modeling to apply in policy and planning practice. They were often as big as 1-3% of the population [2]. This big sample size requires huge budget for the survey, therefore the frequency of the full-size survey is quite low even in the developed countries. Recently tracking devices like GPS and smart phone are found to have enough performance for accurate and low-cost travel survey [3], however the data privacy issue limits the use of those data in public policy.

In developing countries, the urbanization is rapidly progressing, that induces increase and expansion of urban activities including travel and land development [4]. That requires frequent monitoring of urban activities however the full-size survey is merely conducted due to its high cost.

Meanwhile several studies indicate night-time light satellite images can represent economic activities of a region [5-7]. Especially, the Visible Infrared Imaging Radiometer Suite (VIIRS) sensor on the Suomi National Polar-orbiting Partnership (NPP) Satellite [8-12] provides a Day-Night Band (DNB) in which nighttime light is observed and it has higher performance in detecting the radiation range comparing the Defense Meteorological Satellite Program's Operational Line-scan System (DMSP-OLS) that enables to detect the light intensity within cities.

Travels are also induced by economic activities, so the night-time light image could be a cue to estimate the transport demand. For the VIIRS-DNB, National Oceanic and Atmospheric Administration (NOAA) provides monthly composite of cloud free images since April, 2012. This update frequency is enough high to capture the urban dynamics in developing countries. If this night-time light information can be applicable in updating the travel demand, it will be a very powerful tool in urban and transportation planning in developing countries.

In this study, we examine the applicability of VIIRS-DNB in travel demand update taking the case of Chiang Mai, Thailand. We focus on the zonal trip generation and attraction and try to explain the travel demand by night-time light intensity statistically. Based on this statistical relationship, we attempt to update the trip generation and attraction using the updated night-time light image.

DATA

In this study, we examine the relationship between trip generation / attraction and night-time light. Chiang Mai household travel survey data in 2016 is used as data for travel demand, and monthly composite of Suomi-NPP VIIRS DNB in January 2016 is used as night-time light data.

Chiang Mai household travel survey was

conducted by Department of Civil Engineering, Chiang Mai University in February 2016 in which 6,236 households were visited and travel information of household members from 6 years old and above were collected. This is equivalent to an overall sample size of 3.4%. The survey area comprises of Chiang Mai Metropolitan and surrounding sub-district municipalities. Its total area is 1,606.35 sq.km. This area is divided into 142 zones. The population of target region is 761,986 in 2016. The population trip generation and attraction were estimated by expanding that of zonal sample statistic by zonal sample size expansion factor. The estimated trip generation per zone area for each zone is shown in Fig.1. The number is standardized by area because the area is different by zones. The estimated total number of trip generation / attraction is 3.6 million per day. The correlation between zonal trip generation and attraction per day is 0.95 and they have quite similar figure of spatial distribution.

The monthly composite of Suomi-NPP VIIRS DNB in January 2016 is obtained from NOAA website. We choose the image for January because it is dry season and effect of cloud on the observation is smaller than that in the months of rainy season. The projection is WGS84 latitude-longitude coordinate system, resolution of the image is 15 arc-second and the unit of the light intensity is given in nanoWatts/cm2/sr. The data overlaid with travel survey zone system is shown in Fig. 2.

Comparing the figures of spatial distribution of trip generation and night-time light, the volume and the intensity looks to have similar pattern. Fig. 3 shows the relationship between trip generation per area (horizontal axis) and average night-time light intensity (vertical axis) of each zone. A positive relationship between the night-time light and trip generation can be found in this figure. Based on this fact, we investigate the relationship between these two factors using simple non-linear model in the next section.

MODEL AND PARAMETER ESTIMATION

We assume that trips are generated/attracted only at meshes where the night-time light is more than zero and it is also assumed that the trip volume is larger as higher the level of night-time light radiation. With this assumption, we presume the following model for trip generation/attraction.

$$\frac{q_j}{a_j} = \alpha_0 l_j^{\alpha_1} \qquad (1)$$

Where q_j is trip generation or attraction at mesh j, a_j is area of mesh j, l_j is night-time intensity at mesh j, and α_0, α_1 are parameters. Here trip generation data for each mesh is not obtained, but that for the zonal data is obtained. So above equation is aggregated by zonal level.

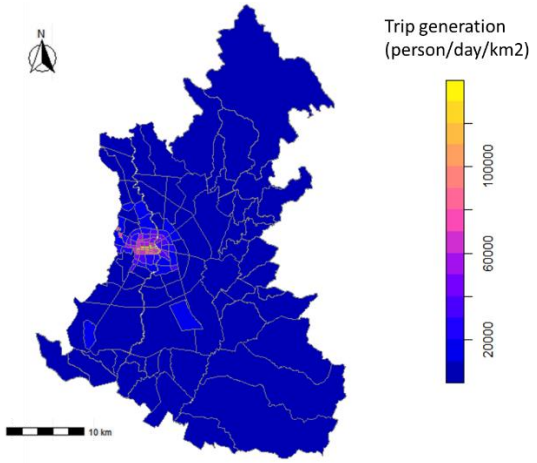

Fig.1 Spatial distribution of trip generation

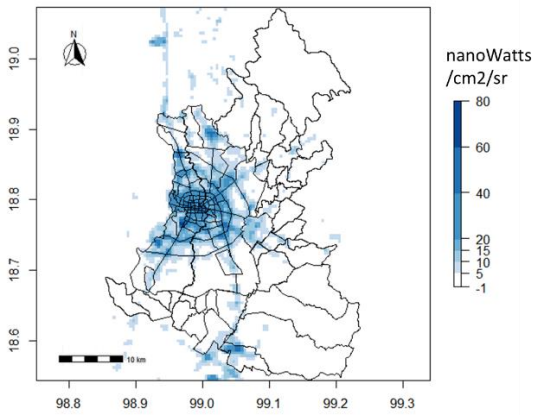

Fig.2 Night-time light intensity

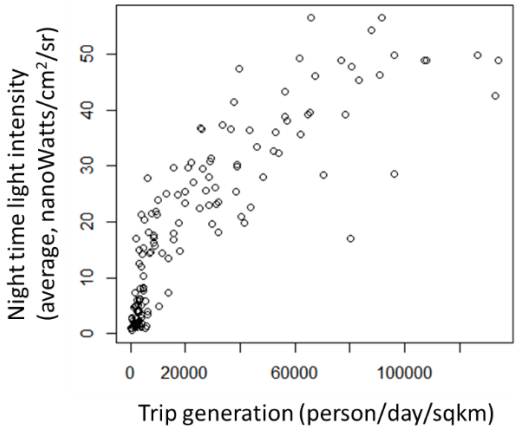

Fig.3 Relationship between trip generation and night-time light intensity

$$\frac{Q_i}{A_i} = \alpha_0 \frac{\sum_{j\in\Omega_i} l_j^{\alpha_1} a_j}{\sum_{j\in\Omega_i} a_j} = \frac{\alpha_0}{|\Omega_i|} \sum_{j\in\Omega_i} l_j^{\alpha_1} \qquad (2)$$

Where Ω_i is set of mesh whose night-time light intensity is more than zero in zone i, Q_i and A_i are trip

generation/attraction and mesh area where night-time light intensity is more than zero in zone *i* respectively. The last term assumes area of all mesh is identical and $|\Omega_i|$ represents the number of mesh. Here Q_i is obtained from travel survey, A_i and l_j can be derived from VIIRS-DNB datasets.

The parameters are estimated by solving the following problem.

$$\min_{\alpha_0,\alpha_1}\left(Q_i/A_i - \frac{\alpha_0}{|\Omega_i|}\sum_{j\in\Omega_i} l_j^{\alpha_1} \right)^2 \quad (3)$$

If we assume that the error term follows normal distribution, the above equation is variable part of log-likelihood function by α_0, α_1. This means the estimated parameters are maximum likelihood estimators. The statistics of estimated model is shown in Table 1. R^2 denotes the R squared of observed and estimated trip per area. Fig. 4 shows the relationship between observed and estimated trip generation. The trip attraction has quite similar figure with trip generation.

Table 1 Estimated parameters

	Trip generation		Trip attraction	
	parameter	t-value	parameter	t-value
α_0	12.73	3.45	183.5	2.94
α_1	2.28	30.29	1.58	17.42
R^2	0.70		0.74	

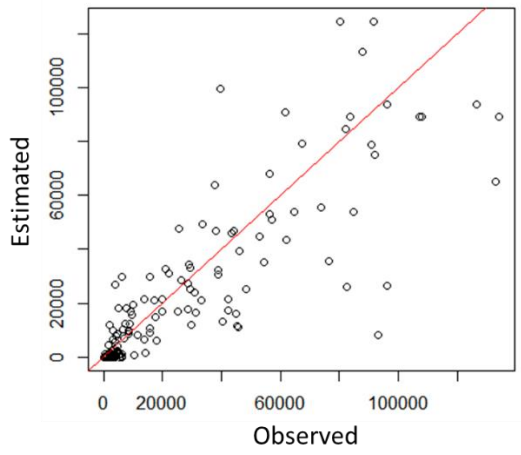

Fig.4 Plot of observed and estimated trip generation (trips/sq.km/day)

The parameter α1 is positive and more than unity. This means as stronger the intensity of night-time light larger trips is generated/attracted. It reflects the relationship between the night-time light and trip generation as shown in Fig.3. Its t-value is enough high so this parameter is statistically significant. The representability of the model is not satisfactory. Obviously, trip generation is affected by various factors, including population, floor area of buildings, land use, and the other urban activities, and it is not necessarily determined by night-time light solely. However, this result indicate that the night-time light can represent a certain part of urban activities and also have the correlation with trip generation and attraction.

Purpose of this study is to investigate a method to update the travel demand without huge survey. The statistical significance of estimated parameter indicates the night-time light image can be a clue for the travel demand update in dynamically growing cities in developing countries.

ESTIMATION OF FINER RESOLUTION OF TRAVEL DEMAND

The relationship between the night-time light and travel demand would suggest the possibility of travel demand estimation in finer spatial resolution especially in suburban zones. The zone system in this transport survey, the average size of a zone is 8.4km^2 and the largest size is 158km^2. For transport policy practice, it is desirable to capture the travel demand in finer spatial scale when the demand drastically change because it affect first local traffic situation and not zone wide situation.

It would be possible to estimate the travel demand using equation (1), however Fig.4 suggests there are substantial errors in the estimation. Here we introduce following adjustment factor β_i for zone *i* to make the estimation fit to the zonal observation of traffic demand.

$$\beta_i = \frac{Q_i}{A_i} \Big/ \frac{\alpha_0}{|\Omega_i|}\sum_{j\in\Omega_i} l_j^{\alpha_1} \quad (2)$$

The numerator is observed travel demand and the denominator is zonal sum of estimated demand by mesh level night-time light. Fig.5 shows the adjustment factor level of each zone on the map. This figure shows that the adjustment factor looks higher value at outer zones in the region. That would suggest the error might have relationship with the development level which may have correlation with the night-time light intensity. Fig.6 shows the relationship between zonal average of night-time light intensity (horizontal axis) and the adjustment factor (vertical axis) in logarithm scale for both axes.

From this figure, there is a tendency that the average night-time light is weaker the adjustment factor is larger. In addition, the adjustment factor tends to distribute around one when the night-time light intensity is enough high. So it would be suggested that the adjustment factor should not be fixed in lower night-time light zones. In this study we

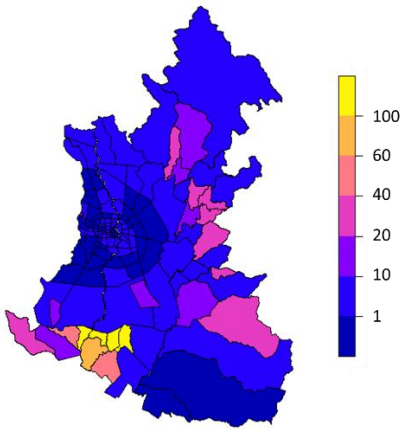

Fig.5 Adjustment factor of travel demand

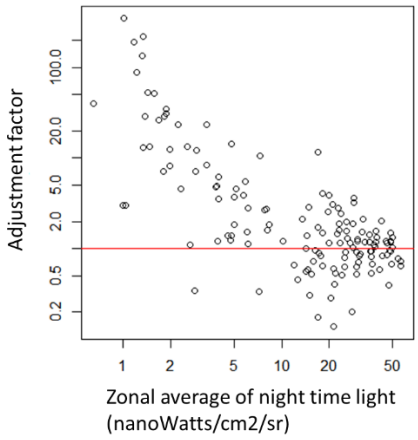

Fig.6 Night-time light and adjustment factor

do now examine the relationship further, but for future study, at the weaker night-time light like less than 10 nanoWatts/cm^2/sr it should be modified as night-time light getting to be stronger.

The estimated mesh level trip generation maps with and without adjustment are shown in Fig.7 and 8 respectively. The estimated trip generation with adjustment (Fig.7) indicates that trips are generated at Chiang Mai city center as well as along the corridors of major radius and circular roads. That is consistent with the experience in the target city where the major economic activities are located on those places.

Without adjustment (Fig.8), trip generation in suburban area is clearly underestimated and some nodes looks over estimated compare with the adjusted estimation. This result indicates that night-time light solely does not have enough performance to estimate the travel demand and the combination with the other appropriate information is required.

TRAVEL DEMAND UPDATE

Taking the case of Chiang Mai Metropolitan area, we found loose relationship between trip generation

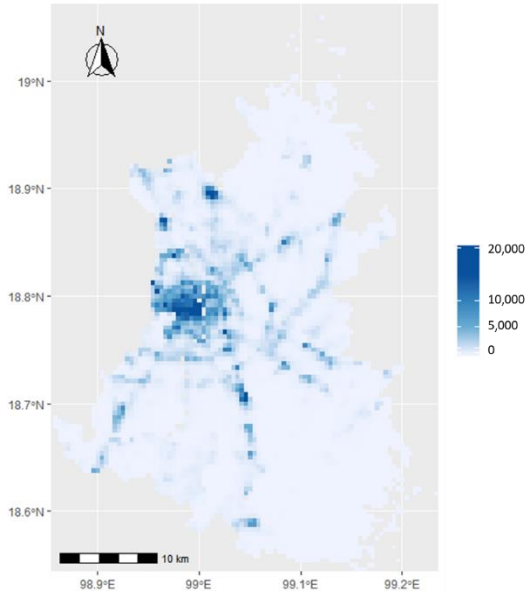

Fig.7 Estimated trip generation (adjusted)

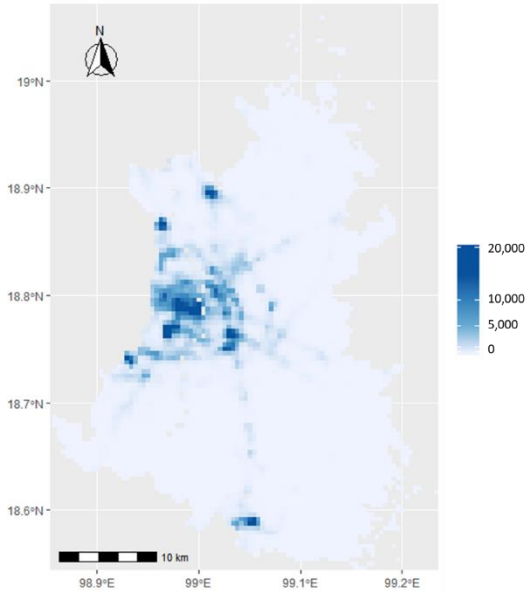

Fig.8 Estimated trip generation (non-adjusted)

/attraction and night-time light observed by VIIRS-DNB. This result indicates possibility of the travel demand update using the updated night-time light observation. In this section, we attempt to update the travel demand using the newly observed night-time light image.

Fig. 9 shows the histogram of the difference of night-time light intensity in target region between January 2016 and February 2019. The difference ranges -28 ~ +29 nanoWatts/cm^2/sr. This figure indicates that the most of the grids has almost the same intensity between the periods, but the distribution shifts towards brighter direction. The average of the change of nigh time light in the target

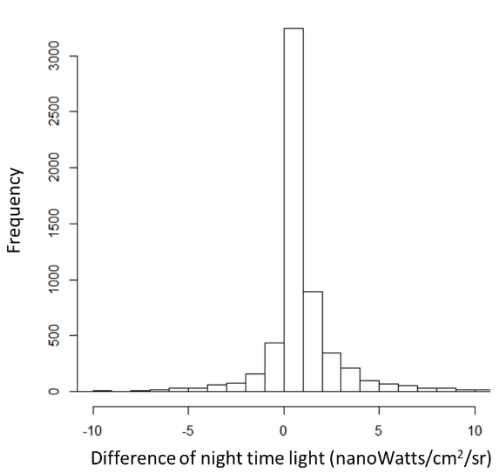

Fig.9 Difference of night-time light between January 2016 and February 2019

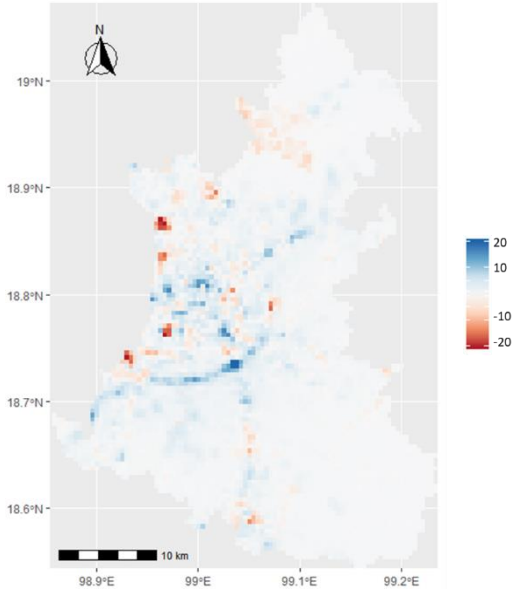

Fig.10 Spatial distribution of night-time light change between January 2016 and February 2019

region is 0.82 nanoWatts/cm^2/sr and the standard deviation is 2.49 nanoWatts/cm^2/sr.

The spatial distribution of night-time light change between 2016 and 2019 is shown in Fig. 10. It is noted that night-time light has gotten darker particularly at the east of target area. One site is at the north near the crossing point of Chiang Mai Outer Ring Road and Chotana Road, and the other place is Chiang Mai International Airport. Military facilities are located near these sites therefore the night-time light would occasionally change without reflecting the civil urban activities.

On the other hand, night-time light intensity has increased at two specific sites. One is at the center north of Chiang Mai city. This could reflect to the service expansion of a major provincial hospital at center north. The other is at the south part of the Outer Ring Road especially its crossing point with Chiang Mai-Lampang Highway. Alongside the south part of the Outer Ring Road, residential estates and commercial development resulting from the road being widen to 4 and 6 lanes has also been observed. This would be a factor on the night-time light change.

Applying the updated night-time light to equation (1), the updated traffic volume is estimated. The trip generation and attraction are estimated to increase 14% and 16%, respectively during this period. Compare with the total night-time light which is increased 18%, the travel demand increase is estimated to be moderate due to the non-linear relationship between the night-time light and travel demand. It is difficult to examine quantitatively due to lack of data, empirically the road traffic situation is getting severe with higher concentration of vehicle traffic recently. The method proposed in this paper can be provide a clue to investigate the updated spatial distribution of traffic demand.

DISCUSSION AND RECOMMENDATION

In this study, we attempt to examine the relationship between night-time light observed by satellite and trip generation in Chiang Mai Metropolitan Region 2016. We found that these two factors have non-linear positive relationship and estimated a model to calculate the travel demand from night-time light intensity. Based on the estimated model, we demonstrated the estimation of travel demand in finer spatial resolution compare to the ordinaly zone system. Additionally we applied this model to update the travel demand 2019. As a result, the total travel demand is estimated to increase about 15% from 2016. Looking at the spatial distribution of night-time light change, north city center and south part of outer ring road are the place where the travel demand is expected to increase significantly.

The proposed appraoch would be useful especially in developing cities where the temporal transport and economic statistics and surveys are limited at the same time the urban activities are growing and spatially shifting rapidly. The satellite image employed here is published periodically which can be a clue to capture the progress of urban and transprot situation and updating the urban and transport policy and planning.

CONCLUSION

In this study we proposed a new method to estimate the travel demand from night time light satellite image which is periodically published and distributed through the internet. The method was examined taking the case of transport demand estimation in Chiang Mai Thailand. We found a

cetrain level of representability of the transport demand observation and demonstrated the applicatiblity to a developing city.

The results in this study can be supported empirically however still need further examination to check its accuracy and reliability, and we also need further upgrading the method incorporating with the other data sources.

First, the estimation error shown in Fig. 4 is not neglegible as a projection model of travel demand. In this study we just employed adjustment factor to fit with the observed travel demand, but of course upgrade the model incorporating the other explanatory variable is desired. Sometimes population or floor area of buildings are employed as explanatory variables, however those input statistics are not surveyed frequently. It would be needed to explore the other information including open location data like Open street map and google place.

Second, further examination of the satellite image is needed. In this study we only utilize the image taken in January 2016 and February 2019. The VIIRS-DNB lose its accuracy by cloud cover because it observes visible light. Therefore the accuarcy of rainy season, for example July in Chiang Mai, is extremely low. However the images taken in the other dry month will also support the analysis. Of course another periodical satellite image products would support the analysis, but at this moment, the VIIRS-DNB is the most convenient periodical product for the urban activity analysis.

Finally, we need to investigate methods for travel survey. The data utilized in this study is relatively small sample survey and is expected to have substantial error especially in the peripheral zones in the target area. It would have induced analytical errors in this study. Travel survey methods using positioning device like smart phone and traffic counts survey are expected to improve the travel data quality.

ACKNOWLEDGMENTS

This study was supported by JSPS grants-in-aid for scientific research (KAKENHI) grant number 16kk0013, JST E-ASIA JRP and SATREPS by JST and JICA entitled “Smart Transport for Thailand 4.0”.

REFERENCES

[1] Mitchell, R.B., Rapkin, C., Urban Traffic: A Function of Land Use, Columbia, University Press, New York, NY. 1954.

[2] Stopher, P.R., Greaves, S.P., Household travel surveys: Where are we going?, Transportation Research Part A: Policy and Practice, Volume 41, Issue 5, 2007, pp. 367-381

[3] Safi, H., Assemi, B., Mesbah, M., Ferreira, L., An empirical comparison of four technology-mediated travel survey methods, Journal of Traffic and Transportation Engineering, 4 (1), 2017, pp. 80-87.

[4] Gao, Z., Kii, M., Nonomura, A., Nakamura, K., Urban expansion using remote-sensing data and a monocentric urban model, Computers, Environment and Urban Systems, In Press.

[5] Li, X., Xu, H., Chen, X., Li, C., Potential of NPP-VIIRS nighttime light imagery for modeling the regional economy of China, Remote Sensing, 5 (6), 2013, pp. 3057-3081.

[6] Qi, K., Hu, Y., Cheng, C., Chen, B., Transferability of economy estimation based on DMSP/OLS night-time light, Remote Sensing, 9 (8), 2017 art. no. 786.

[7] Wang, L., Fan, H., Wang, Y., Estimation of consumption potentiality using VIIRS night-time light data, PLoS ONE, 13 (10), 2018, art. no. e0206230.

[8] Lee, T. E., Miller, S. D., Turk, F. J., Schueler, C., Julian, R., Deyo, S., Dills, P. and Wang, S.: The NPOESS VIIRS day/night visible sensor, Bull. Am. Meteorol. Soc., Vol. 87, pp. 191-199, 2006.

[9] Miller, S. D., Mills, S. P., Elvidge, C. D., Lindsey, D. T., Lee, T. F. and Hawkins, J. D.: Suomi satellite brings to light a unique frontier of nighttime environmental sensing capabilities, Proc. Natl. Acad. Sci. USA, Vol. 109, pp. 15706-15711, 2012.

[10] Cao, C., Shao, X. and Uprety, S.: Detecting light outages after severe storms using the S-NPP/VIIRS day/night band radiances, IEEE Geosci. Remote Sens. Lett., Vol. 10, pp. 1582-1586, 2013.

[11] Cao, C., de Luccia, F. J., Xiong, X., Wolfe, R. and Weng, F.: Early on-orbit performance of the visible infrared imaging radiometer suite onboard the suomi national polar-orbiting partnership (S-NPP) satellite, IEEE Trans. Geosci. Remote Sens., Vol. 52, pp. 1142-1156, 2014.

[12] Liao, L. B., Stephanie, W., Steve, M. and Bruce, H.: Suomi NPP VIIRS day-night band on-orbit performance, J. Geophys. Res. Atmos., Vol. 118, pp. 12705-12718, 2013.

9th Int. Conf. on Geotechnique, Construction Materials and Environment, Tokyo, Japan, 20-22 November 2019, ISBN: 978-4-909106025 C3051

NITROGEN SULFIDE AND BOD REDUCTION OF DOMESTIC WASTEWATER USING AQUATIC PLANTS

Thitinun Pongnam[1] and Chaichan Yuwanasiri[2]
[1] Department of Civil Technology Education, Rajamangala University of Technology of Technology Khon Kaen Campus, Thailand; [2] Department of Civil Engineering, Faculty of Engineering, Northeastern University, Thailand

ABSTRACT

The reduction of Nitrogen Sulfide and BOD in the wastewater from buildings using aquatic plants was a study to find the ability to reduce nitrite and nitrate in the form of Total Kjeldahl Nitrogen (TKN) Sulfide and Biochemical Oxygen Demand (BOD) in the wastewater from office buildings and dormitories using 3 types of aquatic plants that were beautiful in terms of bringing it to arrange landscape in public areas, and it could be easily grown in the test pond, including 20 reeds per square meter, 10 cattails per square meter, and 10 cannas per square meter. Tested by filtering the wastewater through the sand filter layer before entering into the test pond, and retaining the water in the test pond for 1, 7 and 15 days. The results showed that the canna had the highest efficiency in BOD treatment during the 1 day storage period of 89.04% and the cattail had the highest efficiency in BOD treatment at 7 and 15 days of 92.53 % and 95.71 %, respectively. The efficiency in the treatment of TKN values during storage period at 1 day was 67 %, 7 days at 75 %, and 15 days at 82.33 %. But the cattail and canna after entering the treatment system, they had TKN values increased, it caused by not controlling the quality of the planting soil. The efficacy of sulfite treatment showed that the reed was the most effective in the treatment of sulfite during the storage period of 1, 7 and 15 days, that was 100 %. The Canna was during the storage period of 1, 7 and 15 days, it had efficiency in the treatment of sulfite at 100 % , 39.99 % and 65.21 % respectively, as well as the Cattail had efficiency in the treatment of sulfite at 100 % , 55.75 % and 91.30 % respectively.

Keywords: Total Kjeldahl Nitrogen (TKN,) Sulfide, Biochemical Oxygen Demand (BOD), Domestic Wastewater and Aquatic Plants.

INTRODUCTION

The water is an important resource in the lives of humans, plants and animals, it is the resource that indicates the abundance of living things on the world endlessly. For this reason, when the water is used for consumption, it causes the wastewater which is mixed into natural water sources. At present, it can see that the economic and social development, the expansion of agriculture and industry when they were compared to the beginning of the century. The water consumption has increased 5 times in the agricultural sector, and 26 times in the industrial sector [1]. In terms of population, it is estimated that in 2047 [2], the world population will increase to 9.2 billion people resulting the higher use of water for consumption, therefore the effluent is more. Especially, the effluent is from community buildings, houses with increasing population. If it was not treated before releasing to natural water sources, it will cause a balance loss. Until it will lead to problems that require enormous budgets to fix, such as the water in the water source causes the foul rot because on the water surface, it can grow well, and it covered over the surface of the water causing oxygen content in the water to be low. It makes various living things In the water cannot live, and the people can no longer use the water from that source for consumption any more.

The effluent is released from the building, which is the center of the population that uses the water throughout the day. The standards for controlling the drainage of effluent from some size and types of the buildings according to the announcement of the Ministry of Science, Technology and the Environment are used to measure the control indicators such as pH, BOD, Suspended Solids, Settleable Solids, Total Dissolved Solid, Sulfide, Total Kjeldahl Nitrogen (TKN), Fat, Oil and Grease. From the test of [3], they studied the quality of effluent from school buildings of the Faculty of Health Sciences which has many building users, it was found that it had higher BOD and TKN values than other faculty buildings. These indicators are water qualities that indicate the amount of organic and inorganic substances that are mixed with human daily life when there is more water consumption, there will be more waste affecting water quality as well. The disadvantage that comes from the quality of the effluent from the building when there is more, it can affect the environment such as the growth of abnormal water plants,

unpleasant smell, the water sources lack of oxygen, including the changing scenery. The treatment of wastewater from communities or buildings is therefore very necessary in order to maintain the quality of water sources to be balanced in accordance with the standards. At present, the wastewater treatment system used in single buildings or homes is the Onsite Treatment. The most commonly used wastewater treatment systems include septic tank, cesspool, and anaerobic pond systems, which are effective in the removal of organic matter but it cannot eliminate nitrogen and phosphorus. [4]

Wastewater treatment systems from other types of houses that are currently studied and widely used throughout the world are Wetland system using water plants to effectively eliminate contaminants in the waste, and provide beautiful scenery. It can be designed to be a recreation place in the form of small park and low cost. There is also a relatively low cost in the construction of the system, the system operation and maintenance. Therefore, the investment in the construction of the wetland system is therefore economical, suitable for economic conditions. The use of artificial ponds is therefore a suitable way to treat the wastewater from homes or communities, which reduces the discharge of wastewater into natural water sources, it also brings the wastewater back to use again, and to promote environmental conservation and biodiversity as well. [5]

Therefore, in this research, three types of aquatic plants that can be easily found in Thailand, which have already been studied, are effective in treating the wastewater, including 20 reed trees per square meter, 10 cattail trees per square meter, and 10 canna trees per square meter. The reed can treat the wastewater from the slaughterhouse until it receives the standard of industrial wastewater, both in the form of COD, TNN and it can reduce the COD, BOD and SS of the wastewater by 40-50 % [7] The cattail trees has potential to reduce the pH of the water, and it can also change the color of wastewater to fade, and reduces the toxicity in the wastewater such as it can be absorbed 56.36 % Cr and 68.47 % Cu. In addition, it was found that it can eliminate nitrogen from wastewater. [8], [9] and 20 canna trees per square meter can eliminate BOD, SS and TKN values up to 90.7 %, 98.5 %, 99.00 %, respectively. The test was conducted by filtering the wastewater through sand filter layer before entering the test pond, and the water was retained in the test pond for 1, 7 and 15 days to determine the ability to reduce nitrite, and nitrate content in the form of Total Kjeldahl Nitrogen (TKN) Sulfide and Biochemical Oxygen Demand (BOD) in the effluent from office buildings and dormitories.

MATERIALS AND METHODS

This study used 3 types of aquatic plants, Reed, Cattail, and Canna (Fig1). For use in reducing nitrite and nitrate content in the form of Total Kjeldahl Nitrogen (TKN) Sulfide and Biochemical Oxygen Demand (BOD) in the wastewater from office buildings and dormitories together with the permeability of effluent through sand filter layer using a pond of 1 .0 m diameter. Then, the effluent was released to store in the pond that planted 3 types of plants for 1, 7 and 15 days, as shown in Figure 2. In the test pond, it contained 20 reed trees per square meter, 1 0 cattail trees per square meter, and 1 0 canna trees per square meter. The test was conducted by releasing the effluent by allowing the effluent to permeate through sand filter layer before being released into the pond growing plants when the time is specified, it collected the samples at the point of discharge as shown in Figure 3.

Fig. 1 The picture of 3 types of aquatic plants., Reed, Cattail, and Canna.

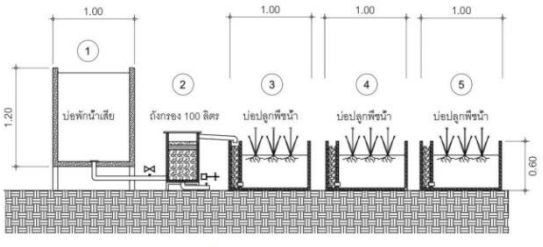

Fig. 2 The picture of wastewater treatment system from buildings using 3 types of aquatic plants.

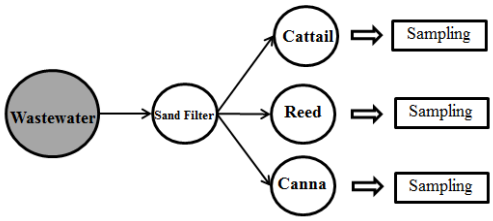

Fig. 3 The picture of the point for collecting the samples of wastewater treatment system from buildings using 3 types of aquatic plants.

From Figure 3, the nitrite and nitrate reduction test in the form of Total Kjeldahl Nitrogen (TKN) Sulfide and Biochemical Oxygen Demand (BOD) in the effluent from office buildings and dormitories using 3 types of plants. When placing the piping system and the pond according to the diagram, then growing the experimental plants in the experimental pond prepared. The plants were left to be strong for a period of 1 month, then released the effluent to store in the pond growing each type of plant for 1, 7 and 15 days, respectively. The water was collected before entering the system and after quarantine according to the specified period to test the quality of effluent according to standard testing methods from the laboratory.

RESULTS AND DISCUSSION

The analysis of the sample quality of the effluent from the building was tested with 3 types of aquatic plants to compare the efficiency of wastewater treatment by using 3 types of plants. All 3 ponds used the same effluent quality, and the effluent samples in and out of the treatment pond system was collected for quality analysis every 1 day, 7 days and 15 days from the sampling point. The effluent samples were analyzed the parameters such as nitrile and nitrate in the form of Total Kjeldahl Nitrogen (TKN) Sulfide and Biochemical Oxygen Demand (BOD). The results of the experiment were as follows:

The efficiency in BOD treatment when stored at 1, 7 and 15 days

The effluent that was fed into the treatment system growing 3 types of plants at 1, 7 and 15 days, it was found that there were BOD 73, 67 and 70 mg liters, and when passed into the treatment system, it was found that BOD removal efficiency as shown in Figure 4.

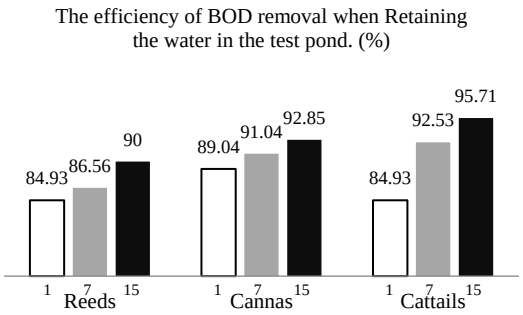

Fig. 4 The relationship between BOD value and treatment efficiency of each type of plant at 1, 7 and 15 days

From Figure 4, it was found that Canna trees had the highest efficiency in BOD treatment at 1 day of 89.04%, and the Cattail trees at 7 and 15 days it was found that it had the highest efficiency in BOD treatment for 92.53 % and 95.71 % respectively. Therefore, when considering the graphs, it showed that the BOD value tended to decrease according to the duration of storage, and when using the treatment system using 3 types of aquatic plants, BOD values were in the standard criteria of effluent from buildings. (Not more than 20 mg / l)

The efficiency in the treatment of TKN values in effluent treatment from buildings when stored at 1, 7 and 15 days

The effluent that was fed into the treatment system growing 3 types of plants when stored at 1, 7 and 15 days, it was found that there were TKN Value at 59.7, 61.2 and 60 mg liters, respectively. When it passed into the treatment pond system, it can be effective in the treatment of TKN as shown in Figure5.

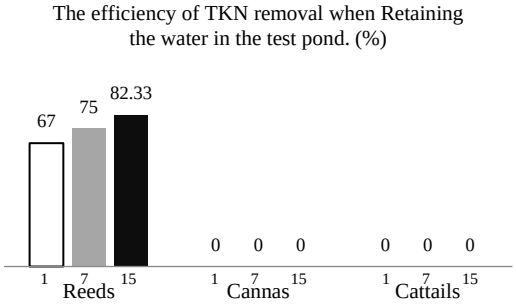

Fig. 5 The relationship between TKN values and treatment efficacy of all 3 types of plants at 1, 7 and 15 days.

From Figure 5, it was found that the reed was

effective in the treatment of TKN during the 1 day storage period was 67 % , 7 days was 75 %, 15 days was 82.33 %. But canna trees and cattail trees after entering to the treatment system, TKN values were increased due to the lack of quality control of the cultivated soil. Therefore, when considered the graph, it showed that the reed tended to decrease TKN values according to the increased retention time, and the TKN value was in the standard criteria of effluent from the building (not more than 35 mg / l)

Efficiency in the treatment of TKN values in the effluent treatment of sulfide values in the treatment of wastewater from buildings when stored at 1, 7 and 15 days

The effluent that was fed into the treatment system growing 3 types of plants at 1, 7 and 15 days, it was found that there were Sulfide Value at 1.44, 1.65 and 2.30 mg liters, respectively. When it passed into the treatment pond system of 3 types of plants, it can be effective in the treatment of sulfide as shown in Figure 6.

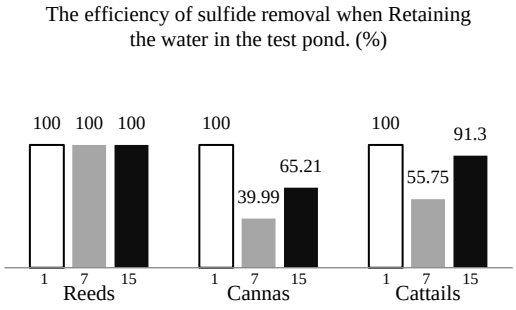

Fig. 6 Relationship between sulfide value and treatment efficiency of all 3 types of plants in storage period at 1, 7 and 15 days

From Figure 6, it was found that the reed tree had the highest efficiency in the treatment of sulfite at 1, 7 and 15 days, that was 100 %. The canna tree at 1, 7 and 15 days, it had efficiency in the treatment of sulfite of 100 %, 39.99 % and 65.21%, respectively, and the cattail tree had efficiency in the treatment of sulfite of 100 %, 55.75 % and 91.30 %, respectively. Therefore, when considered the graph, it showed that the reed is the most effective in the treatment of sulfite, and it was found that there was a tendency to decrease the sulfide value according to the storage time and the sulfide value was in the standard criteria of the effluent from the building (Not more than 1.0 mg / l)

CONCLUSIONS

The experiment results found that the cattail tree could reduce the BOD value most effectively at 15 days. It could reduce the BOD value 95.71 %, which the BOD concentration from 70 to 3 and it was found that the reed could reduce TKN value to be the most effective at 15 days, and it could reduce TKN value of 82.33 %, which the TKN concentration from 60 to 10.6 . In addition, it was found that the reed could reduce the sulfite value most effectively at 1, 7 and 15 days, it could reduce the sulfite value of 100 %. It showed that all types of plants could increase the effluent quality to be in the standard criteria of effluent quality from the building.

ACKNOWLEDGMENTS

The authors wish to thank Department of Civil Technology Education, Rajamangala University of Technology of Technology Khon Kaen Campus and Department of Civil Engineering Northeastren University for facilitating the study. Finally, special thanks of Faculty of Technical Education , Rajamangala University of Technology of Technology Khon Kaen Campus for funding support , and all the help.

REFERENCES

[1] Suteera Tulyasathien, Kosol Wongsawan and Satid Wongsawan.(2001). Pollution environment (Thai social problems). 1(1997).

[2] Asna-urai Techasawat. (2011). The individual's responsibility for sustainable consumption. University of the Thai Chamber of Commerce Journal . 31(3), 150-161.

[3] Noppharit Thongda and Ratchaneewan Viengwa-lai.(2558). The study of effluent quality from Naresuan University building. Senior. Department of Natural Resources and Environment, Naresuan University.

[4] Punpaphatporn Bunprom, Jindawan Wibulouti, and Chavayut Phornpimolthape. (2009). Efciency of Canna warscewiezii Dietr for Domestic Wastewater Treatment Using Subsurface System Constructed Wetlands. Journal of Enviromental Management. 5(2), 89-99.

[5] Punpaphatpron Bunprom. (2011). Constructed Wetland for Wastewater Treatment. Engineering Journal of Siam University. 22,2014

[6] Suwasa Kantawanichkul. (2014). Slaughter-house Wastewater Treatment by Constructed Wetland System. Chiang Mai: Department of Environment Engineering, Chiang Mai University.

[7] Sakundee Tungsakul, Kanyavee Thanaphomi-chai, Jatuphorn Promma and Pavena Chaiya-mo. (2011). Comparison of Silk Dyeing Treatment Efficiency of Sedge, Elephant Grass and Screw Pine in Pilot-Scale Constructed Wetland. Khon-kaen. Department of Environment Engineering, Khon-Kaen University.

[8] Sumol Nilratnisakorn. (2010). Effect of Silicon, Sulfur and Glutathione on The Mechanism of Textile Wastewater Treatment by Narrow-Leaved Cattails. Phayao: Phayao University.

[9] Supat Buddee, Parintip Rattanaburi, Prakit Chaithada, Phakarat Rotduang and Tarnhatai Malawet. (2016).Adsorption of Metal Ions by Using Vetiver Grass and Cattail. 4th Rajabhat University National and International Research and Academic Conference (RUNIRAC IV) November 22-2, 2016. (Page 1111-1117). Buriram: Buriram Rajabhat University.

[10]Punpaphatporn Bunprom, Jindawan Wibulouti, and Chavayut Phornpimolthape. (2009). Efficiency of Canna warscewiezii Dietr for Domestic Wastewater Treatment Using Subsurface System Constructed Wetlands. Journal of Environmental Management, 5(2),.89-99.

9th Int. Conf. on Geotechnique, Construction Materials and Environment,
Tokyo, Japan, 20-22 November 2019, ISBN: 978-4-909106025 C3051

THE EFFICIENCY OF SOLAR POWERED WATER PUMPING SYSTEMS FOR DRIP IRRIGATION

Pattaraphon Na Nongkhai[a], Suphattaradids Rachatha[b], Thitinun Pongnam[c*], Banjob Chumchong[d]

[a] Director, Medium Scale Irrigation Project, The Regional Irrigation Office 6, KhonKaen Thailand 40000
[b] Researcher, Medium Scale Irrigation Project, The Regional Irrigation Office 6, KhonKaen Thailand 40000
[c] Department of Civil Technology Education, Rajamangala University of Technology of Technology Khon Kaen Campus, Thailand 4000
[d]Department of civil engineering, Faculty of engineering, North Eastern University, KhonKaen Thailand 40000

ABSTRACT

In this research, the efficiency of solar powered water pumping systems for drip irrigation is studied through solar powered water pumping systems and drip irrigation by doing the actual tests on the agricultural land by dividing into 3 tests, 1. the relationship between the discharge and water level, 2. the relationship between the light intensity measured from the solar meter and the discharge of the water and 3. the efficiency of solar powered water pumping machine in the form of efficiency of emission uniformly drip irrigation (EU). The tests were conducted on an agricultural field with the area of 1600 m^2. From the tests, it was observed that the solar powered water pumping machine reached the maximum efficiency in the period of 11:00h to 13:00h. The maximum value of light intensity was 1038.9 W/m^2. The discharge of the water varies as functions of water level in the tank and efficiency of emission uniformly drip irrigation. There were 28 lines of drip irrigations spread on the hold area of the testing field. When all of the drippers were opened, it was observed that the efficiency of emission uniformly drip irrigation from the lowest until the highest water level was 71% to 84% which was in the condition of an acceptable design, and when switching by opening only 14 lines (one line was closed, its neighbor was opened) of drip irrigation, it was found that the efficiency of emission uniformly from the lowest to the highest water level was 81% to 86% which was in the condition of a good design.

Keywords: Water Resources Management, Irrigation, Solar Powered, Pumping System and Drip Irrigation

INTRODUCTION

Water plays a very important role in plant productions since it is an important factor for plant growth and improving the productivity in both quantity and quality which is the farmers' main goal. In some areas, water resources for agricultures are insufficient for cultivation; especially, in the year of drought or irregular rainfall, typically in the north-east part of Thailand which is a hot and dry weather region, resulting the plants demand high amount of water. Therefore, the requirement of drip irrigation in this region is high. However, the type of soil in most areas here is sandy soil with low water holding capacity. When the amount of drip water irrigation is greater than the water holding capacity of soil, the state of water repellency in soil occurs, and the plant nutrients stay beyond the area or length of the plant roots. In this case, the water drip irrigation should be provided in low amount, but frequently. This method could cost some budgets on labors and water losing from leaks while transporting water along the pipes in the water drip irrigation systems [1]. To avoid these problems, farmers should consider carefully about the water sources, methods of water transportation, water storages, and appropriate procedures of making drip irrigation systems to make plants grow well in all seasons by trying to use water at the maximum level of effectiveness because in the north-east part of the Kingdom is the irregular rainfall area and may lead to have water crisis in some seasons. Water resource management for the north-east part of Thailand is now a very important issue for farmers in order to be able to use the existing limited amount of water reach the maximum results.

By receiving the helps from Drought Relief Volunteer Center, The Regional Irrigation Office 6, Khon Kaen Province, a solar powered water pumping system has been implemented. This pumping machine generates by using the power from the sunlight instead of diesel fuel, gas, and coal. This solar powered water pumping system is not only cheaper than diesel, gas, and coal, but it can also reduce noise and pollutions in the environment

as well. In short, using the solar powered water pumping system provides lower cost than using diesel fuel from 2 to 4 times. Moreover, it can keep the atmosphere clean, low cost in maintenance, no need to spend money on any type of fuel [2]. By applying this method together with water resource managements using drip irrigation systems, water can be transported from the sources and stored in a certain place to be used in cultivation or other agricultural purposes in the drought season. This solution can be counted as an efficient method in using water and suitable for the north-east area of Thailand since the drip irrigation system is a system that provides water at the base of the plants little by little which is more economical than other types of irrigations. However, in the real process, it has not had any research on the efficiency of this system yet.

Therefore, it is necessary to do the research and collect the data to find the efficiency of solar powered water pumping systems for drip irrigation. The tests were done on a farmer's agricultural land located in Khum Kao Sub district, Khao Wong District, Kalasin Province to get information and data to be used and applied so that it can produce good benefits for farmers in the future.

MATERIALS AND METHODS

To reach the goals of the study, the data and analyses of the efficiency of solar powered water pumping systems for drip irrigation must be collected. The methodologies are as below:

1.1 Install the solar powered water pumping system which consisted of a 1-inch pump controller, 2 panels of solar cell with the capacity of 150 W, 1 set of motor brushless of 350 W, a motor controller box, an airware, water tanks, pipes, pipe fittings, an agricultural water filter, and a valve as shown in Fig 1.

1.2 Collect the data of the light intensity every 1 hour from 6.00h until 18.00h by using solar power meter measuring 5 times per day. Then calculate the average value of 7 days to find the efficiency of solar cells at the different light intensities.

1.3 The test of the relationship between the discharge and water level in the tank can be done by measuring the discharge of water in the tank and divide the water level into 200 liters per portion to calculate the discharge as a function of height (water level).

Fig 1. The solar powered water pumping systems

1.4 The calculation of the efficiency of the emission uniformly full and half drip irrigation systems can be done by collecting the average discharge of all drippers on the field, and the value of emission uniformly (EU) can be calculated from equation 1.

$$Eu = qn/qa \times 100\% \quad (1)$$

where

Eu = Emission uniformly of water measured on the testing field

qn = average discharge of the minimum values (1/4) of the data measured from the testing field

qa = average discharge of all drippers on the testing field

The value of Eu for drip irrigation system is sometimes considered as an efficiency of drip irrigation on the testing field (Ea). For the drippers which are used with plants planted very close to each other, Eu is considered as follow [3]:

Eu>80% considered as a good drip irrigation system

70<EU<80% considered as an acceptable drip irrigation system

70>Eu considered as a weak drip irrigation system, and the system should be redesigned

RESULTS AND DISCUSSION

1. Results of the test on the relationship between light intensity and discharge

After the analysis, a result is obtained in the function of solar power and time period as shown in Fig 2.

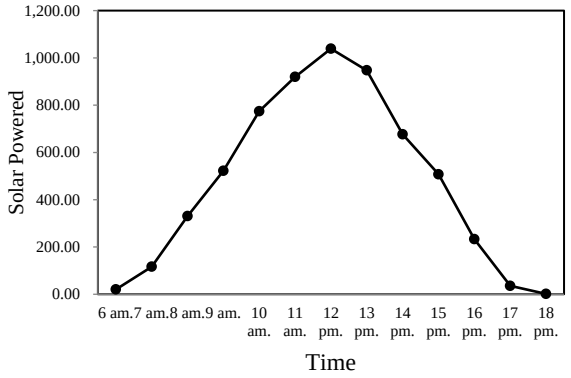

Fig 2 The relationship between solar powered and time

Fig 2 shows that the relationship between the average light intensity and time period happens in the form of parabolic curve. The light intensity increases while the time period also increases until it reaches the maximum value at 12:00h (vertex of the curve) . Then the light intensity decreases slowly until zero at 18:00h.

Therefore, choosing the average intensity of solar power which is suitable to the needs of different plants can be done from the amount of water requirement subjected to the relationship between time period and light intensity which lead to make the comparison between the discharge and the solar power as shown in Fig 3.

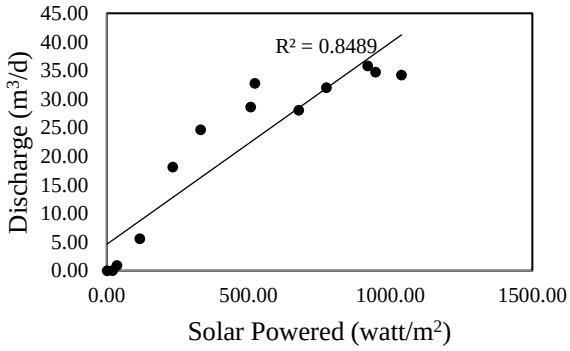

Fig 3 The efficiency of solar powered water pumping systems

Fig 3 proves that the test results of the data collection of light intensity is compared to the discharge of the pumping machine. Based on the analysis, the results of the test of the light intensity data collection compared to the discharge of the pumping machine varies as functions of time and light intensity. The maximum discharge of the pumping machine is 2.55 L/s at 11:00h. The study [4] of developed solar powered pumping machine showed that it can pump at the maximum discharge of 3.15 liters per second, where, the discharge varies as a function of time, and the period for pumping is limited only 4 hours per day. However, if the solar cells are charged while pumping, the pumping machine can work longer in the constant amount of discharge of 1.5 liters per second.

2. Results of the test on the relationship between the discharge and water level in the tank

The test of the relationship between the discharge Q and the water level in the tank can be done by measuring the discharge of water in the tank and divide the water level into 200 liters per portion to calculate the discharge Q compared to the water level h as shown in Fig 4.

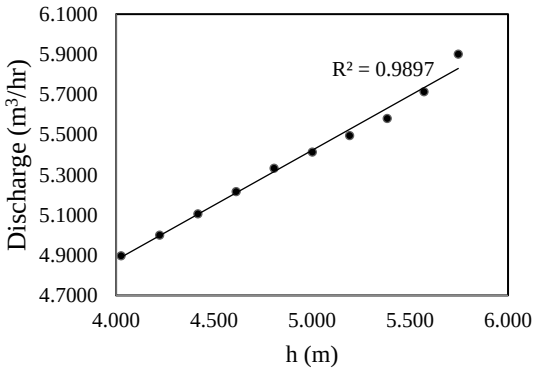

Fig 4 Relationship between the discharge and water level in the tank

Fig 4 shows about the relationship between the discharge and water level in the tank. After releasing water from the state of full tank at the level of 5.746 until the tank runs out of water at the level of 4.025, it has been observed that the discharge varies as a function of water level in the tank. The maximum discharge at full water tank and the minimum discharge when the tank runs out of water are 5.9016 m^3/hr and 4.898m^3/hr , respectively.

3. The efficiency of emission uniformly (EU) drip irrigation

The calculation of the efficiency of emission uniformly can be done by collecting the average discharge data of all drippers on the testing field. In this step, the test is divided into 2 types. Type 1: Find the value of EU by opening all of the drippers in the field (28 lines of drippers). Type 2: Find the value of EU by opening only 14 lines of drippers in the field (switching). Then note the results from 3 points per line. The results from the test are as the following:

3.1 Value of EU when all drippers are opened

From the test, when all the drippers (28 lines) are opened and note the results from 3 points per line, it provides a result as shown in Fig 5.

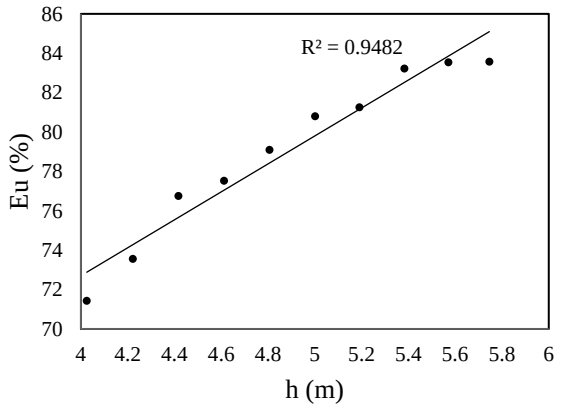

Fig 5 Efficiency of emission uniformly drip irrigation when all drippers are opened

By measuring the results from all 28 lines of the hanging drippers, it is shown that the value of emission uniformly (EU) at the lowest to highest water level lies from 71%s to 84%, which is considered to be an acceptable design.

3.2 Value of EU when 14 lines of drippers are opened

The drippers on the hold testing field are opened only 14 lines by switching one by one (one line is opened, its neighbor is closed). The results are measured from 3 points per line. After finishing the test, it provides the value of EU as shown in Fig 6.

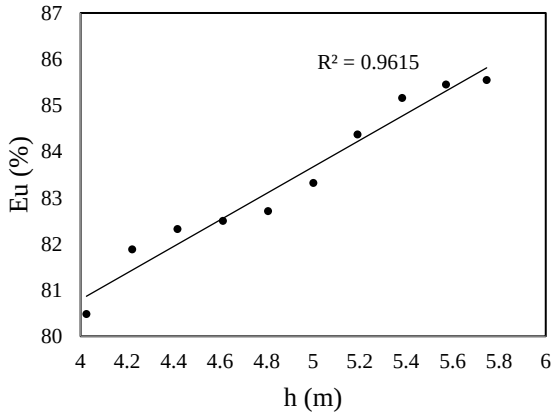

Fig 6 Efficiency of emission uniformly drip irrigation opened only 14 lines of drip irrigation

By measuring the results from 14 lines of the hanging drippers, it is shown that the value of emission uniformly (EU) at the lowest to highest water level lies from 81% to 86%, which is considered to be a good design of drip irrigation.

CONCLUSIONS

The study of the efficiency of solar powered water pumping systems for drip irrigation is done by pumping the water using solar powered water pumping machine from the canal to store in the tank with the volume of 2000 liters. The tank is installed at 2 meters above ground surface, and the water is transported to the drip irrigation. Based on this study, it has been concluded that the solar powered pumping machine under the petty patent of Drought Relief Volunteer Center, The Regional Irrigation Office 6, Knon Kaen, Thailand provides a good efficiency and can be pumped in the discharge of 0.43 L/s during 7:00h. This period is a low solar power absorbing period. The solar power increases all the way up to 11:00h which is the period that provides high intensity of light and can be pump up to 2.5 L/s. When this solar powered water pumping machine is brought to work with the drip irrigation system by installing the tank at high level above ground surface, it has been found that in the area of the testing field, 1600m^2, filled with the drip irrigation systems for 28 line provided the efficiency of emission uniformly (EU) from 70% to 80% which lies in the condition of acceptable design. In case of opening the drippers only 14 lines (switching) which conform to the farmers' real work, it provides the efficiency of emission uniformly greater than 80%, and this is considered as a good design.

REFERENCES

[1] Wonprasaid, S (2014). Development of Techniques in Micro Irrigation andFertigation for Chili and Tomato Production in the Northeast,. Institute of Research and Development , Suranaree University of Technology ,. Thailand.

[2] Saenrak, D. Application of solar electricity for water pumping in a village water supply system. Naresuan Phayao Journal,. Vol.8 No.3 (2015): September - December

[3] Kulapatsangtong, A., Choekaew, S., and Poodduang, T. (1994). Field Evaluation of Drip Irrigation System. Irrigation research project. Department of Irrigation Engineering, Kasetsart University,. Thailand.

[4] Tongsangiem, S. Puangpiw, A. (2012) The development of solar pumps. Irrigation research project. Department of Irrigation Engineering. Kasetsart University,. Thailand.

9th Int. Conf. on Geotechnique, Construction Materials and Environment, Tokyo, Japan, 20-22 November 2019, ISBN: 978-4-909106025 C3051

PREPARATION OF DESALINATION AGENT FROM CA-TYPE CLAY MINERALS

Fumika Sekihata[1], Takaaki Wajima[2]
[1,2]Graduate School to Science and Engineering, Chiba, Japan

ABSTRACT

The desalination technology of seawater is considered to secure water and food in recent years, and a new simple desalting material to decrease the high concentration of sodium chloride in seawater is desired. In this study, preparation of the desalting agent from two Ca-type clay minerals, natural zeolite and Ca-Fe type layered double hydroxide (LDH), attempted to desalinate seawater for agricultural water.

Natural zeolites used in this study were mordenite-type zeolite from Fukushima prefecture, Japan and clinoptilolite-type zeolite from Kagoshima prefecture, Japan, and raw and Ca-substituted zeolites were used for seawater desalination. Regardless of zeolite type, desalination behaviors of Ca-substituted zeolite were almost same as those of raw zeolite. The salinity and pH of seawater were 3.46% and 8.0, respectively, while clinoptilolite decreased the salinity to 3.20%, mordenite decreased to 2.09%, above 5.0 g/L zeolite addition. As increasing the Calcined Ca-Fe LDH addition to seawater, the salinity decreased to 3.3%, and pH of the solution increased to pH 11.5, and then became almost constant above 2.0 g/L addition of Calcined Ca-Fe LDH. As increasing the mixing ratio of Calcined Ca-Fe LDH to raw mordenite, the salinity decreased to 0.8% (79.2% reduction) while pH of the solution was neutral (about 7.6~8.0). Radish sprouts could be harvested using the seawater treated with a mixture of raw mordenite-type natural zeolite and Calcined Ca-Fe LDH, although those could not be harvested using seawater, the seawater treated with natural zeolite or Calcined Ca-Fe LDH.

Keywords: Natural Zeolite, Calcined Ca-Fe LDH, Desalination, Agricultural Water

INTRODUCTION

The total amount of water resources on the earth is about 1.3 billion km^3, but seawater is about 97.5% and freshwater is only about 2.5%, and the freshwater available to mankind is only about 0.01% of total water resources. About 70% of freshwater is used for the agricultural uses. In recent years, water demand has increased due to the increase in the world population, and the development of technology to obtain agricultural water from high salinity water, such as seawater, is considered in order to secure food. Multi-stage flash evaporation and reverse osmosis membrane are typical seawater desalination techniques and are often used for the securing of drinking and industrial water, which required high purity. Therefore, it is a high cost for the production of agricultural water and a simple new desalination method is desired.

In this study, we try to develop a new desalting material that reduces the high concentrations of sodium chloride in seawater causing salt damage to the level at which crops can grow [1]. In previous studies, we can prepare the cultivation solution, which can be used for radish sprout growth, from seawater by two-stage treatment of seawater with calcined hydrotalcite and mordenite natural zeolite [1]. Additionally, radish sprouts can be grown in the solution prepared from seawater treated by Ca-A synthetic zeolite [2], and in calcined-layered double hydoroxide (LDH), Ca-Fe LDH calcined at 500°C has high desalting ability [3].

In this study, a simple desalting material with high desalting ability was prepared using two Ca-type clay minerals, Ca type natural zeolite and calcined Ca-Fe LDH. We evaluated the desalting capacity of the new desalting material for two Ca-type clay minerals.

EXPERIMENTAL

Two types natural zeolites, clinoptilolite type natural zeolite obtained from Koriyama, Kagoshima prefecture, Japan, and mordenite type natural zeolite obtained from Iizaka, Fukushima prefecture, Japan, were used as natural zeolite sample in this study.

The following operations were performed to prepare Ca type natural zeolite. 5 g of natural zeolite was added to 100 mL of 5 mol/L $CaCl_2$ solution. Stirring (1000 rpm) was carried out at 80 ° C for 1 hour and then filtered. The filtered solid was added into the fresh $CaCl_2$ solution and stirring was carried out again. This process was repeated 2 times. After that, the soiled was washed with 1 L of distilled water, dried in a drying oven to obtain Ca-type natural zeolite sample.

Calcined Ca-Fe LDH was prepared as follows. A

mixed solution of Ca^{2+} and Fe^{3+} (Ca/Fe = 2) was prepared from 0.2 M $CaCl_2$ solution and 0.1 M $FeCl_3$ solution, and dropped into a 0.3 M NaCl solution at 4 mL/min. Stirring was performed for 6 hours with bubbling nitrogen gas, and the pH of the NaCl solution was maintained at 12.5 by dropwise addition of NaOH during stirring. After stirring, the product was filtered and dried, and the resulting product was calcined at 500°C for 1 hour in electric furnace to obtain calcined Ca-Fe LDH.

Desalination Ability

Seawater was collected from the surface layer of Imari bay, Saga prefecture, Japan and filtered. Chemical composition, salinity and pH of seawater are shown in Table 1.

Table 1 Chemical composition, salinity and pH of seawater (mg/L)

	Sea Water
SO_4^{2-}	3137
Cl^-	26137
Na^+	9686
K^+	478
Mg^{2+}	1527
Ca^{2+}	471
Fe^{3+}	0.02
Salinity(%)	3.46
pH	8.0

The desalting ability was evaluated as follows. Raw and Ca-type natural zeolite, calcined Ca-Fe LDH, and the mixtures of natural zeolite and calcined Ca-Fe LDH with various mixing rations was added to 20 mL of seawater, and shaken for a predetermined time. After shaking, the solution is filtered, and the pH of the filtrate is measured by pH meter (Horiba, F-72), salinity is measured by salinity meter (Mothertool, YK-31SA), the concentrations of Na^+ K^+, Mg^{2+}, Ca^{2+}, Cl^-, and SO_4^{2-} in the filtrate, were measured with an ion chromatograph (Tosho, IC-2010) and Fe^{3+} content in the filtrate was determined using an atomic absorption spectrophotometer (Perkin Elmer, AAnalyst 200). The reduction rate of each ion after treatment was calculated using equation (1).

$$R=(C_0-C)/C_0\times 100 \quad (1)$$

where R is reduction rate (%), C_0 is each ion concentration (mg/L) in initial solution, and C is each ion concentration (mg/L) in the solution after desalination of the seawater.

Furthermore, the residue was dried, and the structure was confirmed by a powder X-ray diffraction apparatus (Rigaku, MiniFlex 600).

Growth Test

Radish sprouts (30 seeds) were used for 10 days growth Test. Seawater solution, seawater treated with mordenite type natural zeolite (10 g/ 20 mL), the seawater treated with Calcined Ca-Fe LDH (0.6 g/ 20mL) and the seawater treated with a mixture of mordenite type natural zeolite (10 g/ 20mL) and Calcined Ca-Fe LDH (8 g/ 20mL) was given by a spray every day, and germinations of radish sprouts were observed.

RESULT AND DISCUSSION

Seawater Desalination of Zeolites

Fig. 1 shows the salinity and pH of seawater after treatment with natural zeolite. The white plots indicate clinoptilolite use and the black plots indicate mordenite use. For the raw and Ca-type clinoptilolite natural zeolite, when the addition amount increased to 1.0 g/ 20 mL, the salinity decreased to about 3.20% (about 5% reduction), and became constant above 1.0 g/ 20 mL. For the raw and Ca type mordenite natural zeolite, the salinity decreased to about 2.09% (about 38% reduction) when the addition amount increased to 10 g/ 20 mL. It was noted that the pH of the solution after desalination was 7.4 to 8.0 for all samples.

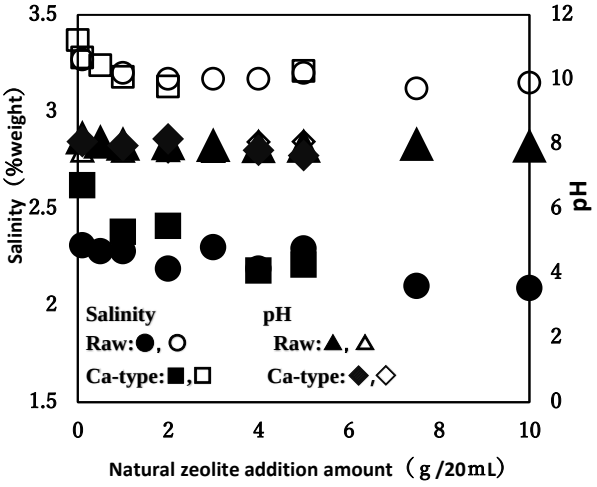

Fig. 1 Salinity and pH of seawater after treatment of natural zeolite

Fig. 2 shows the reduction of each ion in seawater after treatment with clinoptilolite zeolite. Fig. 3 shows the reduction of each ion in seawater after treatment with clinoptilolite zeolite and mordenite zeolite, respectively.

In clinoptilolite zeolite, the contents of Na^+, Mg^{2+}, Cl^- and SO_4^{2-} in the solution treated with raw and Ca

type natural zeolite are reduced (about 15~30%) when the addition amount is more than 1.0 g/ 20 mL. K^+ reduction is about 60~75% at more than 0.5 g/ 20 mL. In mordenite zeolite, the reduction of Na^+ and K^+ in the solution after zeolite treatment is about 65% when the addition amount is 10 g/ 20 mL, Mg^{2+} reduction was about 17~26% at more than 0.5 g/ 20 mL addition, and Cl^- and SO_4^{2-} reduction are about 31~51% at more than 0.1 g/ 20 mL.

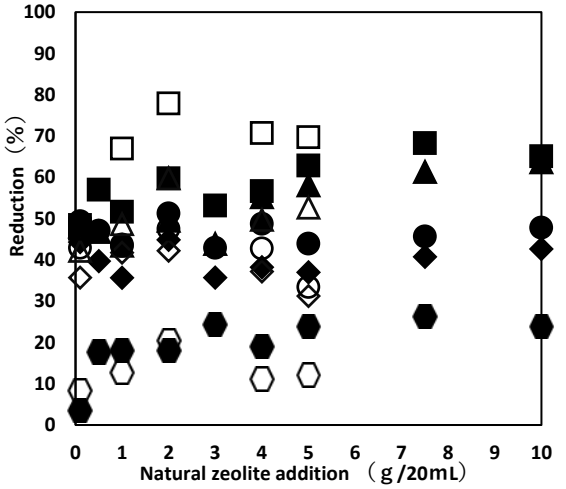

Fig. 2 Reduction of each ion in seawater after treatment of clinoptilolite natural zeolite
Raw: ◆:SO_4^{2-} ●:Cl^- ▲:Na^+ ■:K^+ ⬣:Mg^{2+}
Ca-type: ◇:SO_4^{2-} ○:Cl^- △:Na^+ □:K^+ ⬡:Mg^{2+}

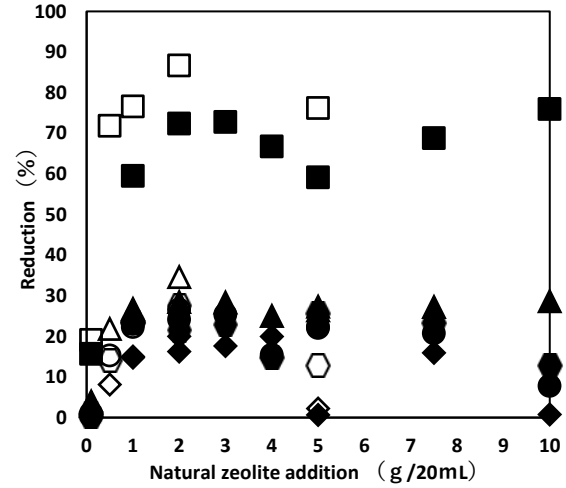

Fig. 3 Reduction of each ion in seawater after treatment of mordenite natural zeolite
Raw: ◆:SO_4^{2-} ●:Cl^- ▲:Na^+ ■:K^+ ⬣:Mg^{2+}
Ca-type: ◇:SO_4^{2-} ○:Cl^- △:Na^+ □:K^+ ⬡:Mg^{2+}

From these results, it was found that the desalting ability of Ca-type substituted natural zeolites is the same as that of raw zeolites, and mordenite type natural zeolite has higher desalting ability than clinoptilolite type natural zeolite. The decrease of Na^+, Mg^{2+}, Cl^- and SO_4^{2-} in seawater after treatment of mordenite-type natural zeolite is more than that of clinoptilolite type natural zeolite.

Fig. 4 shows the XRD patterns of clinoptilolite before and after desalination treatment. Fig. 5 shows the XRD patterns of mordenite before and after desalination treatment. It was confirmed that the peak intensity and pattern after treatment were the same for both raw and Ca-type natural zeolites.

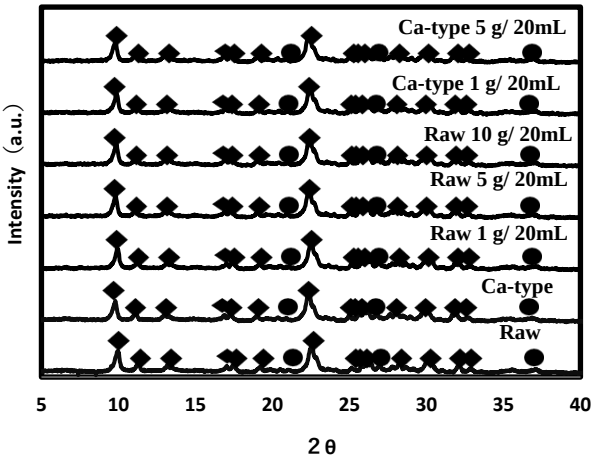

Fig. 4 XRD patterns of clinoptilolite type natural zeolite before and after desalination

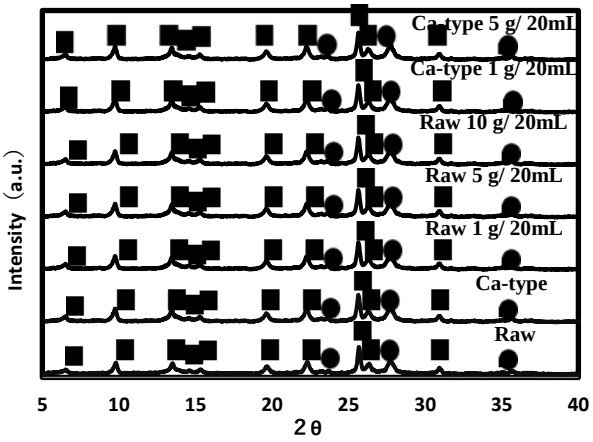

Fig. 5 XRD patterns of mordenite natural zeolite before and after desalination
◆: Clinoptilolite ■: Mordenite ●: Quartz

Seawater of Desalination Calcined Ca-Fe LDH

Fig. 6 shows the salinity and pH of seawater after treatment with calcined Ca-Fe LDH. The salinity was reduced until 0.6 g/ 20 mL of calcined Ca-Fe LDH addition, and the salinity of seawater was reduced from about 3.55% to about 3.30% (about 6.5% reduction). The pH after desalination increased to about 11.0 ~ 11.5 when more than 0.4 g/ 20 mL of calcined Ca-Fe LDH was added because OH^- is released when calcined Ca-Fe LDH intercalates anions into layers by reconstruction of LDH structure [3].

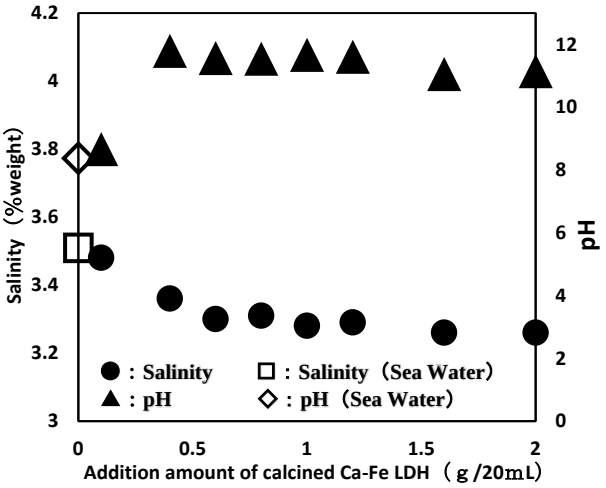

Fig. 6 Salinity and pH of seawater after desalination of calcined Ca-Fe LDH

Fig. 7 shows reduction of each ion concentration in seawater after treatment. The reduction of SO_4^{2-}, Cl^-, Na^+ and K^+ increased to 20 ~ 30% up to 0.6 g/ 20 mL of calcined Ca-Fe LDH. The reduction of Mg^{2+} was about 70 ~ 80% regardless of additional amount of calcined Ca-Fe LDH. It is considered that these decrease causes the decrease of salinity. It is noted that after the desalination of seawater, the concentration of Ca^{2+} and Fe^{3+} increased. Because the Ca^{2+} and Fe^{3+} would be released from calcined Ca-Fe LDH into the seawater.

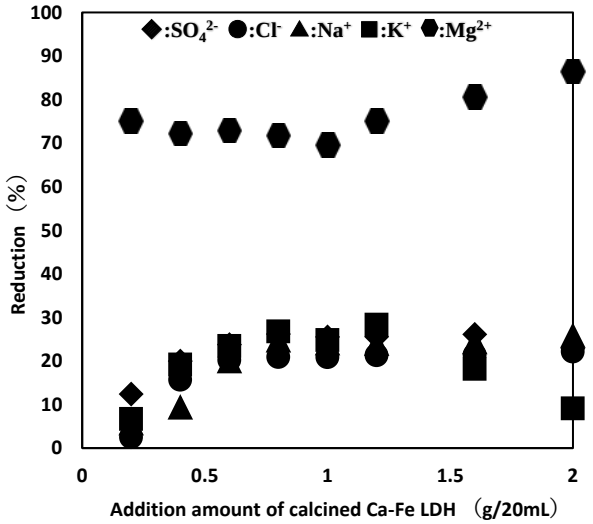

Fig. 7 Reduction of each ion concentration after seawater desalination using calcined Ca-Fe LDH

The XRD of Ca-Fe LDH, calcined Ca-Fe LDH after seawater desalination are shown in Fig. 8. The peaks of Ca-Fe LDH were confirmed before calcination. After calcination, it was confirmed that no Ca-Fe LDH peak appeared. The peaks of LDH were confirmed in all the calcined Ca-Fe LDH after desalination of seawater. It is considered that desalination was occurred by the reconstruction of calcined LDH. It is noted that the formation of calcium carbonate ($CaCO_3$) were confirmed in calcined Ca-Fe LDH after desalination.

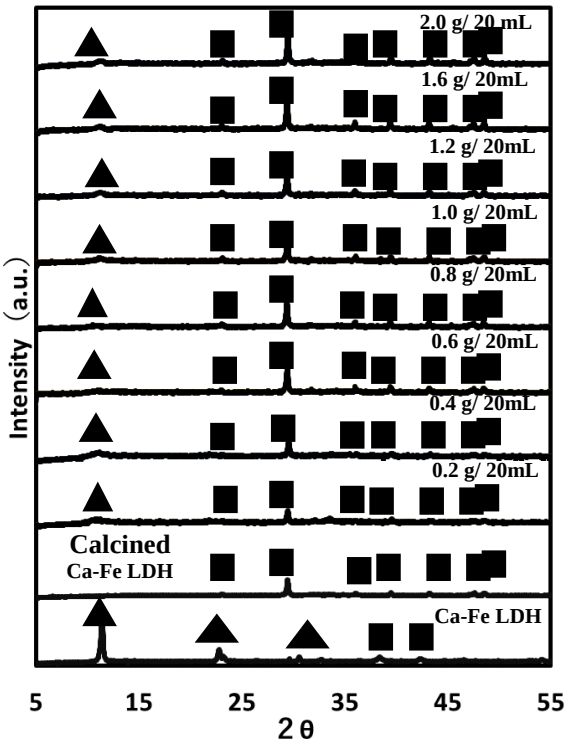

Fig. 8 XRD pattern of Ca-Fe LDH, calcined Ca-Fe LDH and the product after treatment with various Ca-Fe LDH
▲:Ca-Fe LDH ■:$CaCO_3$

Desalination of Seawater with a Mixture of Natural Zeolite and Calcined Ca-Fe LDH

In order to determine the optimum ratio for maximizing desalting ability of the mixture of natural zeolite and calcined Ca-Fe LDH, 0 to 8.0 g of calcined Ca-Fe LDH is mixed with 10 g of raw mordenite zeolite, and the desalting ability was examined. Fig. 9 shows the salinity and pH of seawater obtained by treatment of the mixture of various amount of calcined Ca-Fe LDH and 10 g of raw mordenite type natural zeolite.

The salinity decreased to 0.70% when 8.0 g of calcined Ca-Fe LDH was added to 10 g of raw mordenite zeolite (about 79.2% reduction) and the pH after treatment was about 7.6 to 8.0.

Fig. 10 shows the reduction of each ion and Fig. 11 shows each ion concentration in seawater after treatment with a mixture of calcined Ca-Fe LDH and mordenite zeolite. It was confirmed that the concentration of Na^+, K^+, Mg^{2+}, Cl^- and SO_4^{2-} decreased. When 8.0 g of calcined Ca-Fe LDH is added to 10 g of raw mordenite zeolite, NaCl which

causes salt damage is reduced, and 59% of Na^+ and 71% of Cl^- were removal by natural zeolite with cation exchange ability and calcined Ca-Fe LDH with anion removal ability, respectively. The decrease rate of each ion in seawater was SO_4^{2-}: about 87.7%, Mg^{2+}: 96.8%, and K^+: about 64.0%. Ca^{2+} and Fe^{3+} increased with increase of the amount of calcined Ca-Fe LDH. It is considered that the increase in contents of Ca^{2+} and Fe^{3+} is released into seawater from mordenite zeolite and calcined Ca-Fe LDH.

From these result, it is considered that when the mixture of two clay minerals is used, the salinity decreases to the level that can be used for agriculture because more than 80% of SO_4^{2-}, Cl^-, Na^+ and Mg^{2+} decrease.

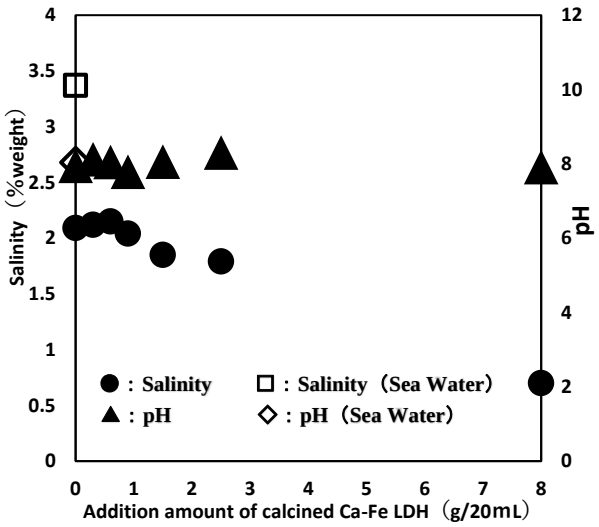

Fig. 9 Salinity and pH of seawater after treatment with mixtures of mordenite natural zeolite and calcined Ca-Fe LDH

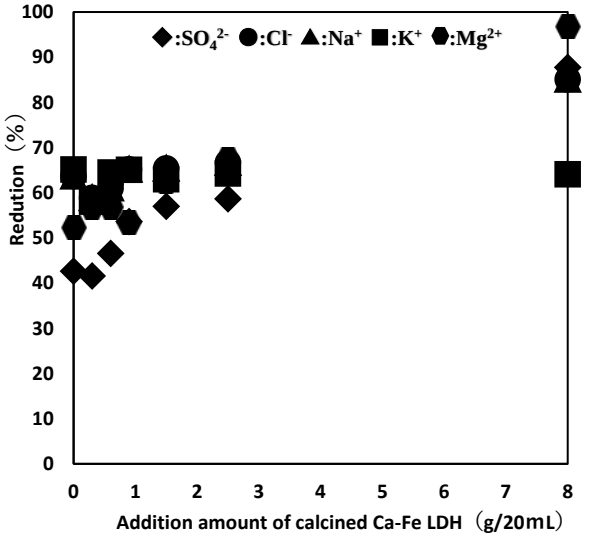

Fig. 10 Each ion reduction of seawater after treatment with a mixture of mordenite type natural zeolite and calcined Ca-Fe LDH.

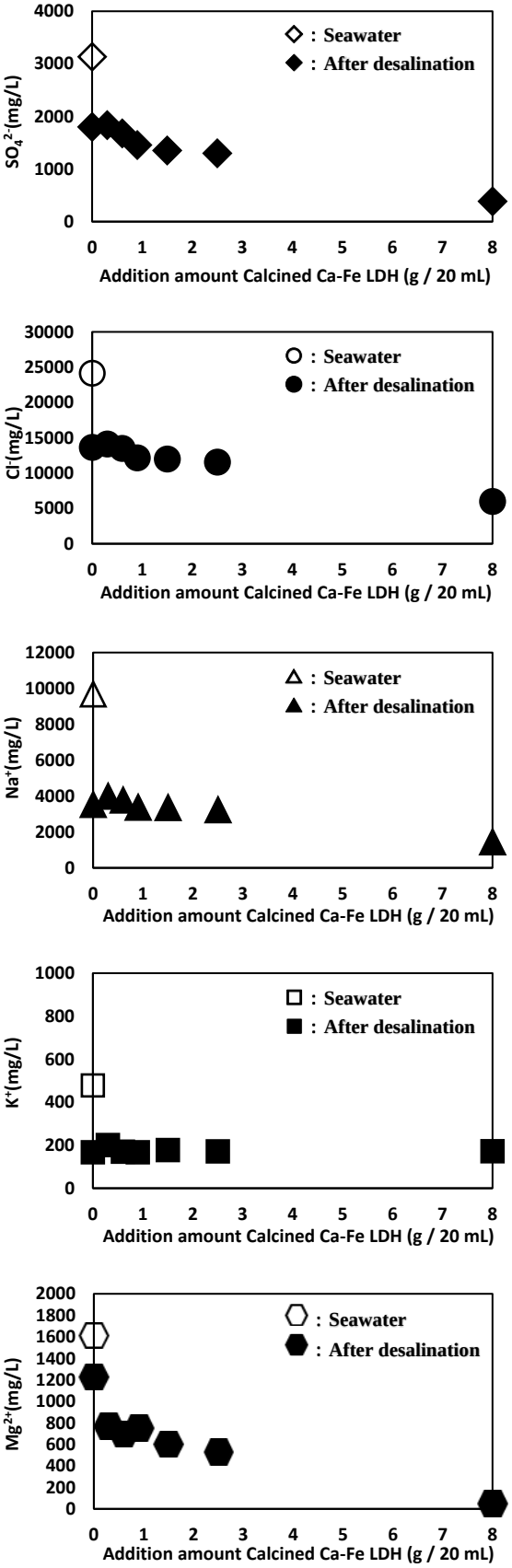

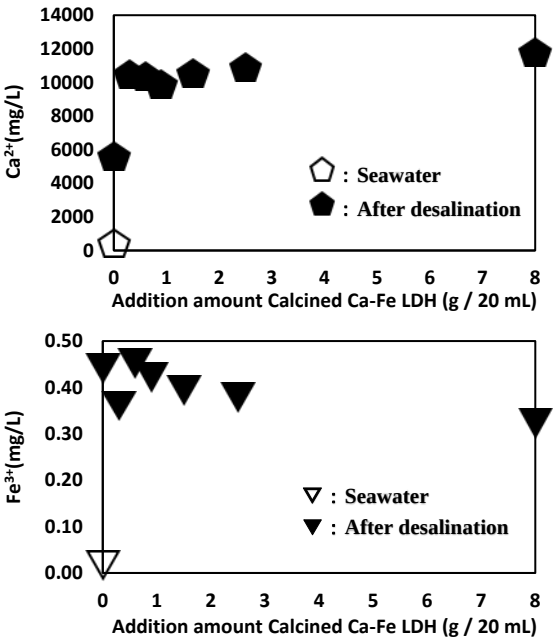

Fig. 11 Each ion concentration of seawater after treatment with the mixture 10 g of mordenite type nature zeolite and various amounts of calcined Ca-Fe LDH

Cultivation of Radish Sprouts

Table 2 shows the concentration of each ion of (a)seawater, and the seawater treated with (b) raw mordenite zeolite (10 g/20 mL), (c) calcined Ca-Fe LDH (0.6 g), and (d) the mixture of raw mordenite zeolite (10 g) and calcined Ca-Fe LDH (8.0 g). When desalting seawater with natural zeolite, calcined Ca-Fe LDH, and a mixture of natural zeolite and calcined Ca-Fe LDH, the concentrations of Na^+, K^+, Mg^{2+}, Cl^- and SO_4^{2-} decreased, and Ca^{2+} and Fe^{3+} increased.

The germination of radish sprouts was confirmed using seawater treated with a mixture of mordenite type natural zeolite and Calcined Ca-Fe LDH, while they can't germinate using seawater, the seawater treated with natural zeolite and that with Calcined Ca-Fe LDH (Fig. 12).

Table. 2 Each ion concentration of seawater and seawater after addition of desalination material (mg/L)

Sample	(a)	(b)	(c)	(d)
SO_4^{2-}	3137	1800	2391	386
Cl^-	26137	13646	20859	5997
Na^+	9686	3524	7758	1446
K^+	478	167	366	172
Mg^{2+}	1527	1225	431	51
Ca^{2+}	471	5644	2202	11860
Fe^{3+}	0.02	0.44	0.17	0.39
Salinity(%)	3.46	2.09	3.29	0.70
pH	8.0	7.83	11.6	7.80

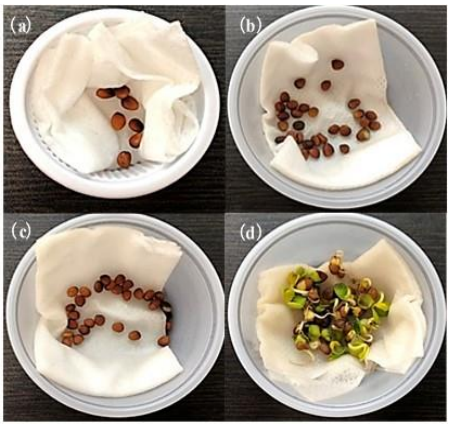

Fig. 12 Observation of radish sprouts after 10 day growth using (a) seawater, and the seawater treated with (b) raw mordenite zeolite (10 g/20 mL), (c) calcined Ca-Fe LDH (0.6 g), and (d) the mixture of raw mordenite zeolite (10 g) and Calcined Ca-Fe LDH (8.0 g)

CONCLUSION

For the development of desalination material to obtain agriculturally usable freshwater from seawater for stable supply of water resources, two Ca types clay minerals, Ca type natural zeolite and calcined Ca-Fe LDH, were used for desalting from seawater.

When adding 10 g of mordenite zeolite, the salinity decreased to about 2.09% (about 38% reduction), and mordenite indicates higher desalting ability than the clinoptilolite zeolite. Reduction of the salinity using Calcined Ca-Fe LDH was about 6.5%, and pH rises to about 11-11.5 from about 8.0.

Seawater were treated with the mixture of raw mordenite zeolite (10 g) and Calcined Ca-Fe LDH. With increasing the Calcined Ca-Fe LDH addition, the salinity decreased to 0.70% below the available salinity for agriculture (about 1.0%) and pH is neutral. When using desalting of seawater treated with a mixture of mordenite zeolite and Calcined Ca-Fe LDH, the germination of radish sprouts was confirmed.

REFERENCES

[1] Wajima. T., Ikegami.Y., Desalination Properties of a Natural Zeolite and Calcined Hydrotalcite Mixture in Seawater. Clay Science, Vol.14, 2008, pp.7-12.

[2] Wajima.T., Desalination of Seawater using Ca-A Zeolite for Agricultural Utilization. Bulletin of the Society of Sea Water Science, Japan, Vol. 72, Issue 6, 2018, pp.325-328.

[3] Tsutsui.D., Wajima.T., Desalination property of various calcined layered double hydroxides from seawater. International Journal of Environmental and Agriculture Research, Vol. 4, Issue 11, 2018, pp.15-21.

9th Int. Conf. on Geotechnique, Construction Materials and Environment, Tokyo, Japan, 20-22 November 2019, ISBN: 978-4-909106025C3051

STABLE TRAJECTORIES CONTROL OF UNMANNED GROUND VEHICLES

Thanapat Wanichanon[1], Jiraphat Noppajattupons[2], Nattaphat Thanaussawanun[3], and Natithorn Traisrisuvan[4]
[1,2,3,4]Faculty of Engineering, Mahidol University, Thailand

ABSTRACT

Route tracking's stabilization control in autonomous vehicles is the system invented to response to the need of use of vehicles' transportation in various industrial factories. This system helps in controlling the autonomous vehicles to move in programmed routes and time efficiently and provides safety from work of other vehicles in the factories. The study of this work uses transportation routes regarding to one of the automobile factories to calculate the transportation paths by using Microsoft Excel program. The paths are scaled in comparison with the factory patterns and the data is used to create equations with a linear relation between the speed and time of vehicles. The acquired equations are further applied with the Fundamental Equations of Constrained Motion to find a force that controls the system so that the vehicles move in their designated routes. The analyzing processes consist of three parts: unconstrained system, constraint equations, and constrained system respectively. According to the study and simulation of vehicles' movement, it is found that the approach using the Fundamental Equations of Constrained Motion is easy especially in calculation when there are a complex system with many constraints. Furthermore, there are some flexibility in choosing parameters to control errors to be small or approaching to zero with less time. The results guarantee that satisfaction because not only vehicles move along the routes and time specified but also they can move according to all conditions that are set perfectly. That is the main reason for more efficient future production of industrial plants.

Keywords: Stability, Tracking Control, The Fundamental Equation, Constrained Motion

INTRODUCTION

In various industrial plants, loading or unloading objects may result in errors such as wrong loading places or relocation time. According to the need to control inventions, the incompetent person can make moving objects more valuable and more accurate.

Unmanned Ground Vehicles (UGVs) can be used to transport items from one point to another as needed. It is driven by a computer-controlled automation system [1] – [3]. A creation of control is a significant part that has an effect on controlling errors of UGV's maneuvers. From literatures, it is found that the adaptive control is a controller that requires multiple adapting parameters used in calculation, causing complexity. The sliding mode control [3] is a controller that takes into account an uncertainty in the environment and requires fewer calculation parameters. However, it causes chattering of a control signal that may encourage high frequency dynamics, which are usually ignored in the model. Therefore, we have chosen to use the Fundamental Equations of Constrained Motion [8] to create a controller and learn how to reduce error values in a short time. This is a reason that motivates us to develop the stability control of the UGV system to follow paths and to be more stable with least time as possible. However, in order to make movements of vehicles to be more effective, both conditions in terms of position and time are considered. Therefore, it is expected to result in more efficient driving of unmanned vehicles

In general, studying movements of any objects uses Newton's law of motion, which is the main rule in calculating movements of various objects. It is an equation that relates to an acceleration of masses which is a vector quantity, making it necessary to consider directions in studying movements of objects [4]-[5]. However, in this work, Lagrange's equation related to kinetic energy and potential energy, which are scalar quantities, is chosen, thus eliminating the need to consider the direction in studying movements of unmanned ground vehicles. When applying this movements, which are relying on moving conditional equations, a stable trajectory control of unmanned ground vehicles is achieved by analyzing the movements using the Fundamental Equations of Constrained Motion (FECM) [6]-[8]. A development of a numerical simulation is also done in order to verify stability of the movements of the unmanned ground vehicles (UGVs).

In real life, work does not consist of the sole purpose of working. But we still have to think about the correctness and safety in that work especially by working in conjunction with various vehicles. There are errors that can cause accidents, resulting in the development of unmanned vehicle control systems in order to meet the need to reduce the risk of work hazards caused by human work and the above limitations.

THE FUNDAMENTAL EQUATIONS

The uncontrolled system is described in which the coordinates are all assumed independent of each other. The equation of motion of this system is given using Lagrange's equation, by

$$M\ddot{q} = Q \tag{1}$$

with the initial conditions $q = 0$ and $\dot{q} = 0$. q is the generalized coordinate n-vector, $M > 0$ in the n by n mass matrix which is a function of q and t. Q is an n-vector, called the 'given' force. From Eq. (1) the acceleration of the uncontrolled system is given by

$$a := \ddot{q} = M^{-1}Q. \tag{2}$$

On this uncontrolled system, a set of control requirements is imposed as constraints. The uncontrolled system is now subjected to the m sufficiently smooth control requirements given by

$$\phi(q, \dot{q}, t) = 0 \tag{3}$$

where $r \leq m$ equations in the equation set Eq. (3) are functionally independent. The control constraints described by Eq. (3) include all the usual varieties of holonomic or non-holomonic constraints. The presence of the control requirements does not permit all the components of the n-vector $q = 0$ and $\dot{q} = 0$ to be independently assigned. The initial conditions are assumed to satisfy the m control requirements.

Differentiating the control requirements Eq. (3) with respect to time t, the constraint relation is obtained as

$$A(q, \dot{q}, t)\ddot{q} = b(q, \dot{q}, t) \tag{4}$$

where A is an m by n matrix whose rank is r and b is an m-vector. It is noted that each row of A arises by appropriately differentiating one of the m control requirements in the set given in Eq. (3). The equation of constrained motion of the system is given by

$$M\ddot{q} = Q(q, \dot{q}, t) + Q^C(q, \dot{q}, t) \tag{5}$$

where Q^C is the control force n-vector that arises to ensure that the control requirements Eq. (4) are satisfied. Thus the explicit equation of motion of the system is given by [8]

$$M\ddot{q} = Q + A^T(AM^{-1}A^T)^{+}(b - Aa) \tag{6}$$

where + is a Moore-Penrose inverse of the matrix [8]. The control force that the uncontrolled system is subjects to, because of the presence of the control requirements Eq. (4), can be explicitly expressed

$$Q^C = A^T(AM^{-1}A^T)^{+}(b - Aa). \tag{7}$$

The control force given in Eq. (7) is optimized in the sense that it minimizes the control cost $Q^{C^T}M^{-1}Q^C$ at each instant of time. The weighting matrix in the control cost has been chosen to be M^{-1}, although other positive definite matrices can be easily chosen. Pre-multiplying both side of Eq. (6) with M^{-1}, the acceleration of the system that satisfies the constraint Eq. (3) can be expressed as

$$\ddot{q} = a + M^{-1}A^T(AM^{-1}A^T)^{+}(b - Aa). \tag{8}$$

DYNAMICS OF THE UNMANNED GROUND VEHICLE

The design process for 2 Unmanned Ground Vehicles (UGVs) using the Fundamental Equations of Constrained Motion (FECM), which consists of 3 steps (Unconstrained system, Constraint equation, and Constrained system) is hereto discussed.

Unconstrained system

For the dynamics of the UGV system, let two vehicles that are considered as point masses which each has 1000 kilograms move freely in the Cartesian coordinate as seen on Fig. 1.

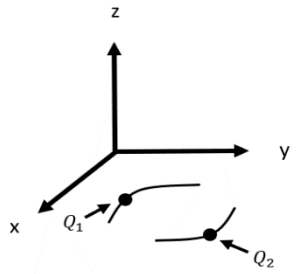

Fig. 1 Planar motion of two vehicles

Using Lagrange's equation, it is described by

$$\frac{d}{dt}\left(\frac{\partial T}{\partial \dot{q}}\right) - \frac{\partial T}{\partial q} + \frac{\partial V}{\partial q} = Q \tag{9}$$

where q is the generalized coordinate, T is the kinetic energy, V is the potential energy, and Q is the generalized force of the system. Whereas we consider

that the vehicles move on a planar motion, so the potential energy of the system is zero. The unconstrained system is considered as

$$M := \begin{bmatrix} m_1 & 0 & 0 & 0 \\ 0 & m_1 & 0 & 0 \\ 0 & 0 & m_2 & 0 \\ 0 & 0 & 0 & m_2 \end{bmatrix} \begin{bmatrix} \ddot{x}_1 \\ \ddot{y}_1 \\ \ddot{x}_2 \\ \ddot{y}_2 \end{bmatrix} = \begin{bmatrix} Q_{x1} \\ Q_{y1} \\ Q_{x2} \\ Q_{y2} \end{bmatrix} := Q \quad (10)$$

where $m_1 = m_2 = 1000$ kg and we assume that there is no applied force to the system, so that $Q_{x1} = Q_{y1} = Q_{x2} = Q_{y2} = 0$.

Constraint Equation

We bring a factory's map to set designated routes by specifying the distance of each square block to be 5 meters wide and 3 meters long and also using time to relate the movements of vehicles in each period as seen on Fig. 2. The red line shows movement of the first vehicle, while the blue one represents that of the second vehicle. The starting point (0,0) of both vehicles is at the top of the warehouse.

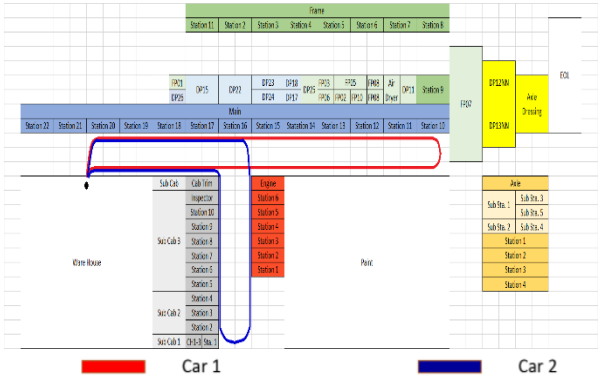

Fig. 2 Factory map and movement path model

For generating constraints of vehicle's movements, we divided motions of the system into 16 periods. And since lengthy limitation is considered, we only illustrate an example of some periods of motions of the two vehicles in this paper. From Fig. 2, we use the vehicle's paths to create the positioning coordinates on x, y graph by Microsoft Excel program and create the path equations of motion for each period as seen on Figs. 3 and 4 for the first and second vehicles respectively.

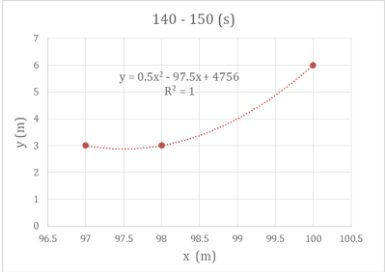

Fig. 3 Motion of the first vehicle at 140 - 150 sec

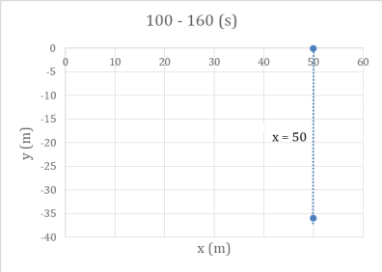

Fig. 4 Motion of the second vehicle at 100 - 160 sec

By appropriately differentiating equations of constraint in Fig. 3 and Fig. 4, they are then used to create path constraint equations in the linear function of acceleration form as

$$\phi_1 := A_1(q, \dot{q}, t)\ddot{q} - b_1(q, \dot{q}, t) = 0 \quad (11)$$

where A_1 is the path constraint matrix and b_1 is the path constraint vector.

Beside the path condition equations, the speed condition equation that is related to time is an aid for the vehicles to run within the specified time limit and allows both vehicles to be related. Such equation is generated from the relationship of time and motion with a linear function

$$x_2 - x_1 = p(t_2 - t_1) \quad (12)$$

where x_i is the displacement in X-axis of vehicle *i*, t_i is the time used of vehicle *i*, and p is the slope of linear relation between x_i and t_i.

Differentiating Eq. (12) twice and put it in the form of the linear function of acceleration as

$$\phi_2 := A_2(q, \dot{q}, t)\ddot{q} - b_2(q, \dot{q}, t) = 0 \quad (13)$$

where A_2 is the time constraint matrix and b_2 is the time constraint vector.

In order to guarantee that both vehicles will move on the designed paths at the right time, the constraint

equations Eq. (11) and Eq. (13) are modified using the Trajectory Stabilization [9].

$$\alpha\ddot{\phi} + \beta\dot{\phi} + \gamma\phi = 0 \quad (14)$$

where $\phi = \begin{bmatrix} \phi_1 & \phi_2 \end{bmatrix}^T$ is the modified constraint function equation and α, β, γ are any positive constants.

Trajectory stabilization can also help finding initial conditions which can be difficult for a complex system that has a large number of conditional equations. The equation will force the function ϕ to approach zero when the time enters to infinity, which results in the system being able to follow the specified conditions.

Here is a concluded procedure of calculations of the constraint equations for the linear functions of acceleration. First, the equations for the movements of various periods are arranged in the form of the Trajectory Stabilization as well as the velocity condition equations associated with time. Second, based on the calculations of the above motion conditions, rearranging the equations to the linear form of acceleration (see Eq. (4)), we then obtain the parameters *A* and *b*, which are the constraint matrix and constraint vector of the constraint equation respectively.

Constrained System

Taking the parameters *M* and *Q* from the unconstrained system and parameters *A* and *b* from the constraint equation to create a controller by the Fundamental Equations of Constrained Motion, we obtain the constrained system.

$$M(q,t)\ddot{q} = Q(q,\dot{q},t) + A^T(AM^{-1}A^T)^+(b - Aa). \quad (15)$$

The obtained controller is then used to calculate on the MATLAB program to verify the accuracy of the movements of both vehicles by using the ODE45 function.

RESULT

ODE45 is the integration procedure using Runge-Kutta method for velocity and displacement of any movements. In calculation, ODE45 function requires 3 parameters which are the acceleration of the constrained motion, time, and initial conditions. When calculated by the ODE45 function, we can check the validity of the designed controller generated from the Fundamental Equations of Constrained Motion.

Experiment and results are analyzed in this section. The results are divided into periods. As written on MATLAB, they consist of 16 ranges, which are divided by relative time of the two vehicles. The first vehicle has a period from 0 - 280 seconds, which is divided into ranges 1 - 14. The second vehicle is set to have a period from 20 - 310 seconds, which is also divided into periods 3 – 16.

The results of the experiments presented include the movements of both vehicles during that control periods, the errors of the movements of the vehicles, the speed conditions associated with the time, and the control forces (constraint forces: Q^C).

As mentioned that there is a page limitation in this paper, we choose to show some examples of the experimental results**.**

Movement of the First Vehicle at 0 - 10 sec

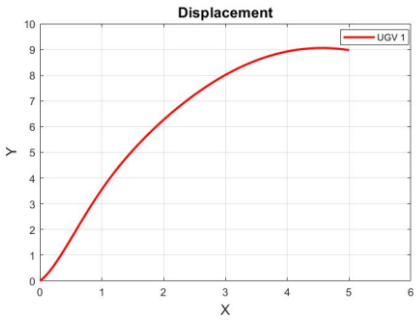

Fig. 5 Moving route of vehicle 1

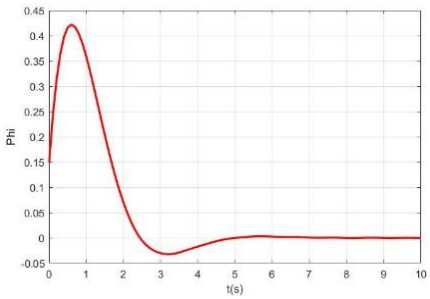

Fig. 6 Error of movement of vehicles 1

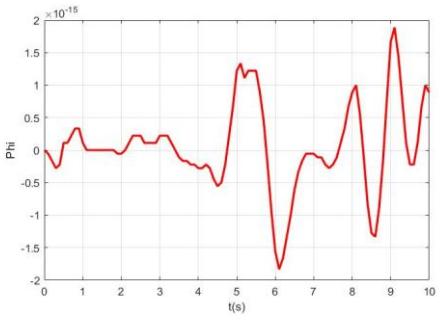

Fig. 7 Error of speed condition of vehicle 1

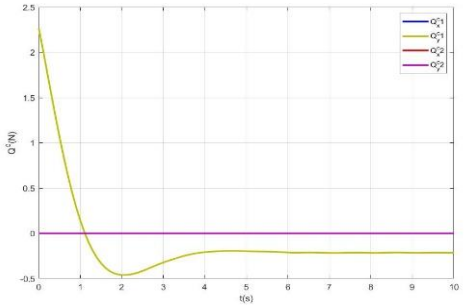

Fig. 8 Effect of Control forces (Q^C)

Movement of the Second Vehicle at 230 - 240 sec

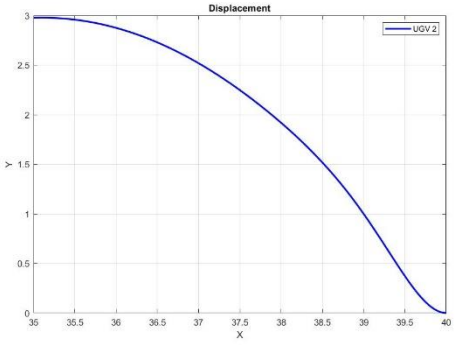

Fig. 9 Moving route of vehicle 2

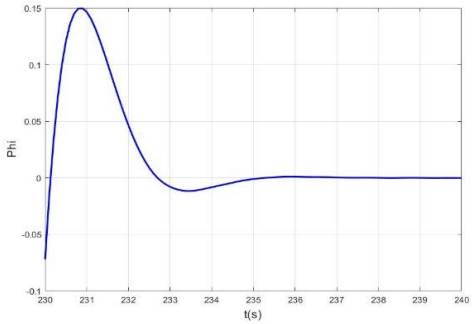

Fig. 10 Error of movement of vehicles 2

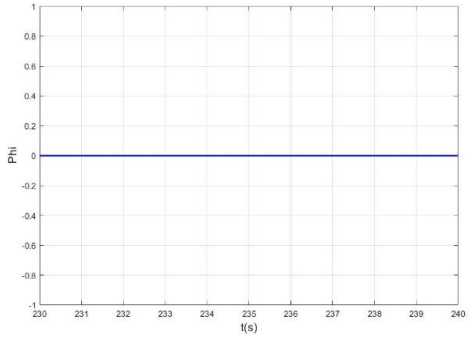

Fig. 11 Error of speed condition of vehicle 2

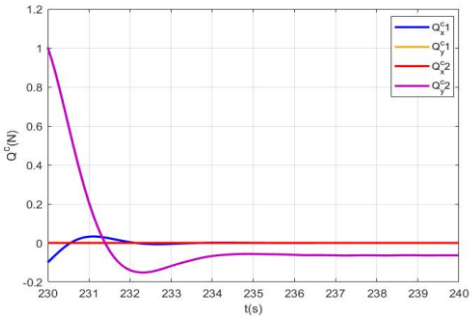

Fig. 12 Effect of control forces (Q^C)

Figures 5 and 9 show path movements of the vehicles 1 and 2 respectively on the X-Y plane. Figures 6 and 10 correspondingly illustrate the errors in tracking the designated routes of vehicles 1 and 2 in their own period. The results of the errors of the speed conditions associated with time of the vehicle 1 and vehicle 2 are presented in Figs. 7 and 11 respectively. All the errors are values that approach zero or into balance. This verifies that even each vehicle of that period has different convergence speeds, but all errors are acceptable values and still make unmanned vehicles able to work efficiently.

The control forces (Q^C) which are shown in Figs. 8 and 12 are the force that help in driving the unmanned ground vehicles to follow the conditions of path tracking and the speed of both vehicles

After creating the graphs in each phase, the entire 16 stages are combined as a result of the movement routes of the two vehicles together as seen on Figs. 13 and 14.

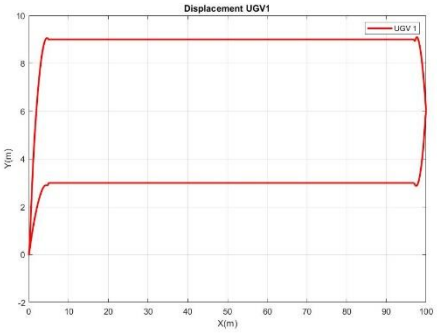

Fig. 13 Moving result on all routes of vehicle 1

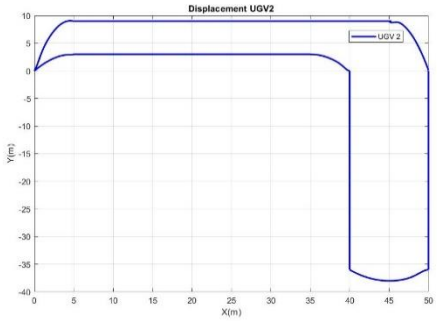

Fig. 14 Moving result on all routes of vehicle 2

Figure 15 displays the total movements of both vehicles which are similar to the one that of shown in the designed factory map in Fig. 2.

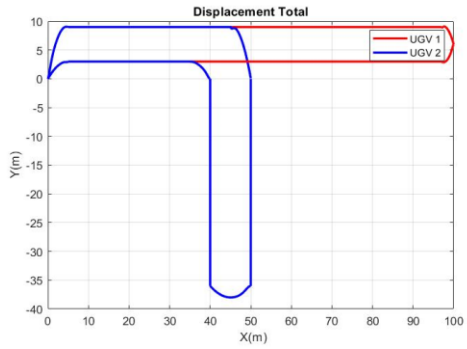

Fig. 15 Moving results of both vehicles

CONCLUSION

It is concluded that the research and experimentation in this work make it possible to see the results that are satisfactory and fulfilled at the intended purpose. Vehicles' movement inspection is done by using ODE45, which is the function in MATLAB program, to inspect the movement positioning' s data. The processes show that the control forces, which this research found from the Fundamental Equations of Constrained Motion, guarantee the movements of the vehicles. The errors of movements of both vehicles are very low and are satisfying. Moreover, the size of the errors and the speed in approaching stability can be controlled with the flexibility in choosing the proposed control parameters. We thus see that in the future, if the proposed controller is to be developed more or less, such as considering uncertainty in the system, we believe and hope that the proposed control system can actually be used in controlling movements of any vehicles in the real industrial factories.

ACKNOWLEDGEMENT

We would like to thank Dr. Thanapat Wanichanon for providing advice and assistance in this work. We also thank to the administrative staffs of the Department of Mechanical Engineering for providing all useful facilities. We also thank friends for both physical and mental support. Finally, we would like to thank to the faculty members of the Faculty of Engineering at Mahidol University, who convey various knowledge, as a result, there is a driving force for this work. The authors hope that this work will help to understand the stability control of unmanned vehicles in tracking system. For those who are interested, this work is a guideline for further system development and applying technology.

REFERENCE

[1] Kanayama Y., Kimura Y., Miyazaki F., and Noguchi T., A Stable Tracking Control Method for an Autonomous Mobile Robot. Conference proceedings, IEEE International Conference on Robotics and Automation, Vol. 1, 1990, pp. 384-389.

[2] Xu H. and Yang S.X., A Novel Tracking Control Method for a Wheeled Mobile Robots. Electronic Journal of Computational Kinematics, Vol. 1, Issue 1, 2002, pp. 1-11.

[3] Pears N.P., Mobile Robot Tracking of Pre-Planned Paths. Advanced Robotics, Vol. 15, Issue 1, 2001, pp. 97-107.

[4] Banjerdpongchai D., Dynamical Control Systems Analysis, Design and Applications, Chulalongkorn University Press, 2008.

[5] Boonchuy S., Mechanics Classic 1, Kasetsart University Press, 2013.

[6] Udwadia F.E. and Kalaba R., Nonideal Constrained and Lagrangian Dynamics, Journal of Aerospace Engineering, Vol. 13, Issue 1, 2000, pp. 17-22.

[7] Udwadia, F.E and Koganti, P.B., Optimal stable Control for Nonlinear Dynamical Systems: An Analytical Dynamics Based Approach. International Journal of Nonlinear Dynamics, Vol. 82, Issue 1-2, 2015, pp. 547-562.

[8] Udwadia F.E. and Wanichanon T., Control of Uncertain Nonlinear Multibody Mechanical Systems. International Journal of Applied Mechanics, Vol. 81, Issue 4, 2013, pp. 041020-1-041020-11.

[9] Udwadia F.E., A New Perspective on the Tracking Control of Nonlinear Structural and Mechanical Systems. Proceedings of the Royal Society A, Vol. 459, Issue 2035, 2003, pp. 1783-1800.

9th Int. Conf. on Geotechnique, Construction Materials and Environment, Tokyo, Japan, 20-22 November 2019, ISBN: 978-4-909106025 C3051

SPATIAL ESTIMATION OF CADMIUM CONTAMINATED SEDIMENT FROM THE UPSTREAM OF THE REMOTE CONTAMINATED AREA OF THE MAE TAO BASIN, THAILAND

Sinsantithet M.[1], Somprasong K.[2]
[1,2]Department of Mining and Engineering, Faculty of Engineering,
Chiang Mai University, Thailand

ABSTRACT

Overland sediment, occurred during rainfall incident, has been verified as one of the transcendent media transporters of cadmium contaminant in the Mae Tao Basin, Thailand since 2011. The integrated spatial approach based on the Revised Universal Soil Loss Equation (RUSLE) was applied for illustrating the area where a high volume of cadmium can be leached out with acceptable precision. However, this estimation technique, is subjected to the inclusiveness of the secondary data, applied as inputs in the calculation. In order to overwhelm this limitation, the alternate integrated spatial procedure should be applied for the better estimation's results, compared to the previous one. In this study, the Revised Morgan-Morgan and Finney erosion model (RMMF) was applied with the purpose of overwhelming the limitation in utilizing secondary data. The RMMF model can reflect both of erosion potential of the monitoring area and the sediment transportation capacity after the occurrences of the erosion. As stated by RMMF, which is based on the interaction of kinetic energy from the contact between rainfall intensity and the specific soil surface. Consistent with the estimation's results, the potential erosion of the downstream area of the basin were ranged from 6.22 to 99.346 t/ha/year. In order to compare the efficiency of this method to the previous RUSLE, the potential cadmium fluxes from erosion of the same area, from 2006 to 2009, were analyzed, using the relative standard error. The results indicate that RMMF can perform better %RSD to the previous RUSLE ranged from 4.204 to 16.550.
Keywords: Erosion, GIS, RMMF, Spatial technologies, Contamination

INTRODUCTION

The Mae Tao basin is a large important basin of Mae Sot district, Tak, Thailand. The development of the area for the expansion of agricultural lands is necessary in order to support the population growth of the area nearby. This situation can cause a major change in land use resulting as the alternation of factors that contribute to soil erosion, such as rainfall runoff, soil erodibility and plant canopy. Soil erosion can cause a migration of heavy metal contaminants through sediment transport and sediment accumulation over the watershed area especially cadmium, born in association with zinc - deposition [1].

The Revised Universal Soil Loss Equation (RUSLE) erosion model has developed to replace the USLE and incorporates new material. It has been widely applied as an accommodating equation for estimating surface erosion by requiring less data and necessitating a short period of time to run compared to other erosion estimation [1]. The model propagates estimated soil loss through increasing the parameter of rainfall erosivity, soil erodibility, slope gradient and length, cover management and confirmation practice. This makes RUSLE a consequence of topography model which is a consideration for the slope length multiplier. According to the study of [2] which applied the RUSLE equation with remote sensing technique and geographic information system (GIS) technology the amount of potential cadmium flux from erosion was 279.86 to 703.73 t/ha/year in 2002-2016. Although, RUSLE can be an effective tool for the estimation of potential flux that can be occurred during rainfall's erosion, thus the model itself cannot exemplify the plausible quantity of sediment's migration. It is subjected to the inclusiveness of the secondary data, applied as inputs in the calculation especially the correctness of the elevation map applied during model construction. In order to overwhelm this limitation, alternate integrated spatial procedure should be applied for the better estimation's results, compared to the previous one.

While RUSLE is the empirical estimation for potential soil loss of the area, the application of Revised Morgan-Morgan and Finney (RMMF) erosion model was developed to suits annual soil loss in hill slope [3]. This model is divided into two phases, the water phase, and the sediment phase. The water phase determines the energy of the rainfall available to detach soil particle from soil mass and the volume of runoff. In the sediment phase, rate of soil particle detachment by rainfall runoff is determined along with transporting capacity of [4].

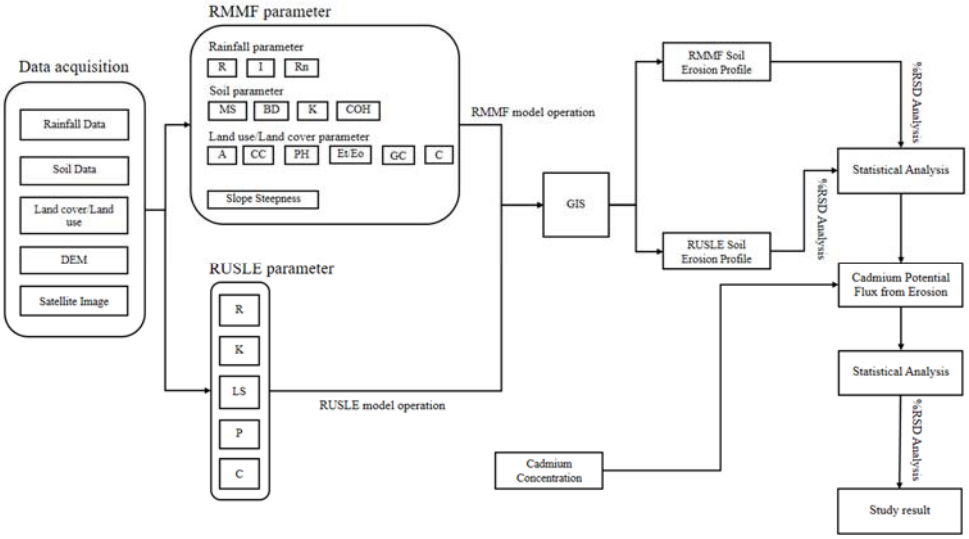

Figure 1. Overall framework of the study

In this study, the RMMF model is applied in association with remote sensing technique and geographic information system (GIS) to estimate soil loss in the Mae Tao basin. Data inputs of the RMMF model were provided in a geographic information system (GIS) which is consisted of spatial data linked to the attribute data. The process is creating data as a parameter map by using interpolation and the data were collected in raster files. The result of annual soil loss rate in the form of raster data, retrieved from RMMF model were used to conduct the contamination assessment by integrating it with cadmium concentration layer. The estimation's results from RMMF model were compared with the results of the RUSLE model, according to the study of [2]. In order to elucidate the efficiency of each estimation's method, relative standard error analysis of the same monitoring area was accomplished.

METHODOLOGY

The overall framework of this study is demonstrated in Fig.1 The study instigated with data acquisition. The secondary data from various sources were gathered to be assigned as the RMMF 's inputs. The model computes the proportion of rainfall amount that reaches the ground surface after allowing for the interception to derive effect rainfall. It is further distributed into two parts. First, rainfall that reached the ground surface after being intercept by plant canopy as leaf drainage and another part is the rainfall without an interception. Then the kinetic energy is calculated by the difference of direct through fall and leaf drainage. The annual runoff is calculated by using three parameters including soil moisture storage capacity, annual rainfall and mean rainy days. The soil moisture storage capacity is a function of bulk density, effective hydrological depth, a ratio of actual to potential evaporation and soil moisture content at field capacity. The estimation of soil particle detachment by raindrop and runoff are divided into two part. The soil particle detachment by a raindrop is a combination of the total kinetic energy of rainfall and soil erodibility. The calculation of detachment by runoff is a function of runoff, soil resistance, ground cover, and slope steepness. Total detachment is as a sum of both soil particle detachment by raindrop and runoff. The transport capacity is estimated by using runoff, surface cover factor, and slope. To obtain annual soil loss prediction, the RMMF model compares the total detachment and transport capacity for each grid and the minimum erosion rate is selected as the estimation of annual soil loss. The result of annual soil loss from the RUSLE model is obtained from the study of [2]. The cadmium potential flux from erosion is computed by using cadmium profile and annual soil loss. Finally, the annual soil loss and potential cadmium flux from the RMMF method is compared with the result of the RUSLE model by using a statistical analysis technique as relative standard deviation (%RSD).

Site Description

The Mae Tao Basin described as the largest zinc deposition area of Thailand. The basin covers 59.61 km^2, as can be followed in Fig.2. The basin contains 4 main significant land use type which are rice paddy field, mining production area, cornfield and deciduous forest [4]. The contamination over the Mae Tao Basin has been widely spread and was mostly detected to exceed the acceptable standards [5].

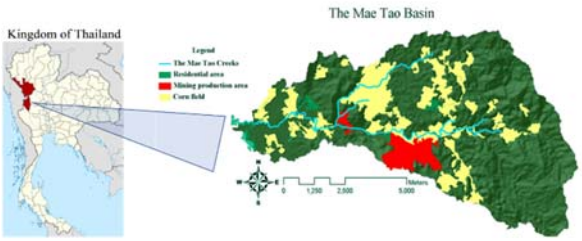

Fig. 2 Location of the Mae Tao Basin [1]

Data acquisition

All input data were prepared at a 30 m resolution. The Rainfall data were obtained from The Thai Meteorological Department, with a 5 km spatial resolution. Rainfall data is interpolated on the model grid using IDW interpolation. Soil textural fractions (sand, clay, and silt) and soil organic matter content are obtained from The Land Development Department (LDD). The land use data are obtained from The Land Development Department (LDD) at 30 m resolution. A digital elevation model was obtained from the Royal Thai Survey Department (RTSD). The satellite image of the basin, covering the study period from 2002-2016 were afforded by GISTDA.

Integrated RUSLE Estimation

The revised universal soil loss equation (RUSLE) is an empirical model, modified from the USLE [6]. It estimates sheet and rill erosion using Eq.1. Since cadmium, contaminated in the basin adsorb with the overland sediment as residue from surface runoff (Somprasong et.al, 2015), so the RUSLE can effectively estimate the fluxes of the contamination migrated over the study area [1].In this study, the results from integrated RUSLE estimation were referenced from [2].

$$A = R \times K \times LS \times C \times P \quad (1)$$

Revised Morgan – Morgan and Finney Model

RMMF model is developed from the MMF physical model that divides the erosion process into 2 phases which are the water phase and the sediment phase. The water phase is calculated by using the evaluation of kinetic energy from rainfall and runoff. The sediment phase consists of the estimation of soil particle detachment by raindrop and runoff along with the runoff's transporting capacity [4].

Different from the MMF, the simulation of soil particle detachment by raindrop takes a parameter of plant canopy height and leaf drainage and a component has been added for soil particle detachment by the flow, while estimation of soil erosion is computed by comparing total soil particle detachment and transport capacity of runoff.

Estimation of Rainfall Energy

Rainfall energy, determined by RMMF, is a function of the difference between kinetic energy of direct through fall and kinetic energy of leaf drainage. First, the model computes the proportion of rainfall amount that reaches the ground surface after deducting for rainfall interception as effective rainfall. as presented in (6).

$$ER = R \times A \quad (6)$$

R indicates annual rainfall (mm), while A refers to rainfall interception value range from 0 to 1 based on the study of [6] According to RMMF, effective rainfall is divided into direct through fall (DT, mm) and leaf drainage (LD, mm). Leaf drainage is a function of effective rainfall and canopy cover. The leaf drainage can be retrieved from (7), while direct through fall is calculated by (8) respectively.

$$LD = ER \times CC \quad (7)$$

$$DT = ER - LD \quad (8)$$

The kinetic energy of direct through fall can be calculated by distribution of the effective rainfall intensity on leaf drainage and direct through fall, whereas kinetic energy of leaf drainage is a function of plant height, the kinetic energy of direct through fall is presented in (9) and the kinetic energy of leaf drainage is according to (10).

$$KE(DT) = DT(11.9 + 8.7\, log\, I) \quad (9)$$

$$KE(LD) = LD(1.58 \times PH^{0.5}) - 5.87 \quad (10)$$

Where KE (DT) is kinetic energy of direct through fall (j/m^2), I represents the rainfall intensity, KE (LD) stands for the kinetic energy of leaf drainage (j/m^2) and PH is plant height (m). The total kinetic energy (KE_{total} (j/m^2)), is obtained from (11)

$$KE_{total} = KE(DT) - KE(LD) \quad (11)$$

Estimation of Rainfall Runoff

Runoff can be calculated, using three factors consist of soil moisture storage capacity, annual rainfall and mean rainy days. Equation (12) expresses the calculation of soil moisture storage capacity.

$$R_C = 1000 \times MS \times BD \times EHD \times (E_t/E_0) \quad (12)$$

As stated by the equation, MS stands for soil moisture content at the field, BD is expressed as the density of the topsoil layer (Mg/m^3) and EHD is an effective hydrological depth of rainfall. E_t/E_o refers to the ratio of actual evapotranspiration to potential transpiration of the cover plant over the monitoring area

For mean rainy days, the calculation can be retrieved from (13), where R and R_n indicates annual rainfall (mm) and numbers of rainy days in a year respectively.

$$R_0 = R/R_n \quad (13)$$

Estimation soil particle detachment by raindrop and runoff

The estimation of soil particle detachment is divided in two part. First, the soil particle detachment by a raindrop is derived from the combination between total kinetic energy and soil erodibility parameter are applied following Eq. (14).

$$F = K \times KE_{total} \times 10^{-3} \quad (14)$$

Where K indicate soil erodibility (g/j) which is a unique characteristic of each soil types. The soil detachment by runoff can be derived from surface cohesion slope steepness (degree) and ground as can be followed in Eq.15 and Eq.16.

$$Z = 1/(0.5COH) \quad (15)$$

$$H = Z \times Q^{1.5} \times sin\, S \times (1 - GC) \times 10^{-3} \quad (16)$$

Where Z refers to the soil resistance. COH is the surface cohesion (kpa) that can be follow in Table 1. Total particle detachment (D, kg/m^2) is finally calculated as a sum of both soil particle detachment by raindrop and runoff. The calculation is presented in (17).

$$D = F + H \quad (17)$$

Table 1 demonstrates the input parameters, applied as soil properties in the estimation of this study

Table 1 Input parameters of soil properties

Soil Texture	K (gJ^{-1})	MS ($\%ww^{-1}$)	BD (mg^{-3})	COH (KPa)
Clay	0.05	0.45	1.10	12
Clay loam	0.70	0.40	1.30	10
Silty clay	0.50	0.30	-	10
Sandy loam	0.70	0.28	1.20	2
Silt loam	0.70	0.25	1.30	3
Loam	0.80	0.20	1.30	3
Fine sand	1.00	0.15	1.40	3
Sand	1.20	0.08	1.50	2

Estimation of transport capacity of runoff

The transport capacity of runoff can be retrieved from (18)

$$\mathrm{TC} = \mathrm{C} \times \mathrm{Q}^2 \times \sin \mathrm{S} \times 10^{-3} \quad (18)$$

C is the crop or plant cover factor. Q refers to annual runoff (mm). TC stands for the transport capacity of the runoff (g/m^2) S is slope angle of the monitoring area (degree). This is then compared with the annual transport capacity and the lesser of the two values is the annual erosion rate [7].

Table 2 Input parameter of land use/land cover data

Land cover	A (gJ^{-1})	E_t/E_o ($\%ww^{-1}$)	C (mg^{3})	EHD (KPa)
Paddy field	0.25	0.60	0.525	0.12
crop	0.25	0.60	0.525	0.12
Grassland	0.20	0.88	0.1	0.14
Perennial	0.20	0.90	0.3	0.15
Orchard	0.20	0.70	0.3	0.15
Forest	0.30	0.90	0.048	0.2
Mine	0	0.05	0	0.05
Village	0	0	0	0

Table 3 Input parameter of land use/land cover data (Cont.)

Land cover	CC (gJ^{-1})	GC ($\%ww^{-1}$)	PH (mg^{-3})
Paddy field	0.49	0.37	1.8
crop	0.49	0.37	1.8
Grassland	0.93	0.95	1.5
Perennial	0.49	0.37	1.8
Orchard	0.31	0.5	7.3
Forest	0.81	0.91	19.4
Mine	0	0	0
Village	0	0	0

Estimation of erosion in turn of soil loss rate

Soil loss rate is generated by comparing between total soil particle detachment and transport capacity of runoff. The minimum value is applied following the last step in the script. For the calculation of soil loss (SL) rate is computed by using equation (19).

$$\mathrm{SL} = \min\{\mathrm{D}, \mathrm{TC}\} \quad (19)$$

Potential cadmium flux from erosion estimation and comparison

The estimation of potential cadmium contamination fluxes over the basin can be achieved according to Eq. (20).

$$\mathrm{PE} = [\mathrm{Cd}] \times \mathrm{SL} \quad (20)$$

Where, PE is the potential availability of cadmium. [Cd] stands for the cadmium concentration of the monitoring area in form of calculation layer in GIS application. The potential cadmium flux from erosion, obtained from both methods were analyzed using relative standard deviation formula following [1],[9].

RESULTS & DISCUSSION

The potential erosion of the Mae Tao basin, estimated using RMMF, are established in Table 3. The highest potential erosion was determined to be 99.346 ± 3.502 t/ha/y at the downstream of the basin in 2009. The soil loss map then was classified into erosion prone area, determined according to the threshold values from [8] The tolerance of soil loss rate that agriculturist should be concern was more than 10 ton/ha/year [4] The potential erosion map of the Mae Tao Basin is shown in Table 5 and Fig.3 According to the estimation results, the erosion occurred upon the study area were mostly determined to be very slight class.

Table 4. Estimation results from the RMMF's estimations

Year	Potential Erosion (t/ha/y)			
	Minimum	Mean	Maximum	SD
2006	0	41.11	82.22	3.118
2009	0	49.67	99.35	3.520
2012	0	3.11	6.22	0.771
2016	0	42.46	92.85	2.687

Table 5 demonstrates the potential cadmium flux from erosion of the Mae Tao Basin, based on the calculation of both methods. For RUSLE, the highest value of potential cadmium flux from erosion was found to be 687 t/ha/y, while 3.42 t/ha/y were determined to be the highest value of the contamination's fluxes from the estimation using RMMF model.

Table 5. Potential cadmium flux from erosion, obtained from RUSLE and RMMF

Year	Potential cadmium Fluxes from erosion (t/ha/y)		Relative standard deviation (RSD) (%)	
	RUSLE	RMMF	RUSLE	RMMF
2006	687.5	3.42	381.11	15.98
2009	142	0.73	355.21	16.55
2012	62.02	0.29	274.12	4.2
2016	32.5	0.94	385.02	15.73

Even supposing that the results from RMMF demonstrate the lower value than the those, obtained from RUSLE, but only the pixels value cannot represent the quality of the estimation so that relative standard deviation analysis was then conducted.

According to the analytical outcomes, the %RSD of RMMF ranges from 4.20 to 16.55 % while 274.12 to 385.02. As smaller % RSD represents the better value of precision and consistency of the estimation, RMMF, based on the combination between real field observation and detailed recorded data, can perform better precision in the determination of the distribution of cadmium contamination from erosion.

As stated by the estimation results, the estimation, using RMMF, contains better results. Since its calculation method is mostly subjected to the rainfall intensity data, which is classified as primary data, so there are less interferences from the initial errors of the data input, compared to the previous integrated model. Furthermore, since the calculation method of RMMF model is based on the actual interaction between rainfall and soil surface, therefore hydrological properties, soil surface and plant cover properties are integrated, resulting in better precision of the estimations.

To achieve better estimation's results for migration availability, the enhancement of the assigned parameter such as cadmium concentration profile should be conduct. Although the estimation's results of RMMF can perform better precision thus the gathering all data required in the erosion model is limited. Therefore, most of the parameters' values used in the erosion model were acquired from literature which may cause uncertainty on the results. To overwhelm this limitation, the direct field measurement must be conducted in the reachable area of the basin to elucidate the performance of the RMMF model 'estimation.

Conclusion

In conclusion, it appears that RMMF model can be efficiently used as tools to assess the severities for soil degradation evaluation. By accounting real interaction between rainfall and soil surface during rainfall incident, the model can give better precision than the previously proposed integrated RUSLE estimation. Even though the result of estimation of soil erosion may not be according to the exact value, but this result can illustrate the potential migration availability of the contaminant over the study area, therefore, more field measurement is recommended for the other parameter in order to achieve the realistic model results.

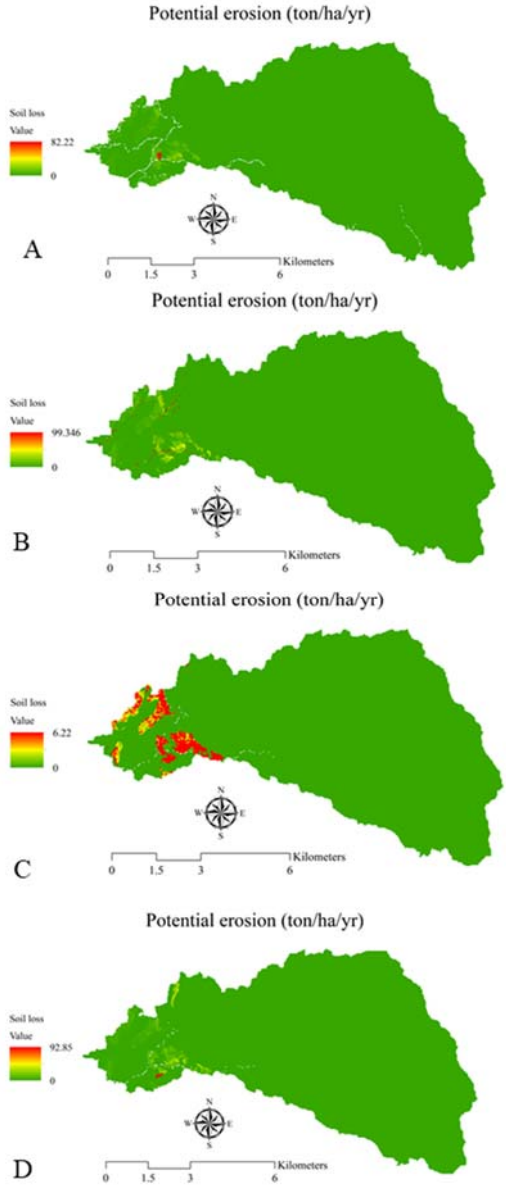

Fig.3 Potential erosion of the study area (A) 2006, (B) 2009, (C) 2012, (D) 2016

REFERENCES

[1] Somprasong, K. and Chaiwiwatworakul, P., Estimation of potential cadmium contamination using an integrated RUSLE, GIS and remote sensing technique in a remote watershed area: a case study of the Mae Tao Basin, Thailand. Environmental earth sciences, Vol.73, Issue 8, 2015, pp.4805-4818.

[2] Somprasong, K., Spatial Monitoring of Potential Overland Sediment from Significant Land Use Types, for the Remote Contaminated Area of the Mae Tao Basin, Thailand: 15 Years Monitoring Period. International Journal of Environmental Science and Development, Vol 8, Issue 9, (2017).

[3] Gebrekirstos, T., Use of simplified field tests and revised MMF model for assessing soil erosion: case study Lom Kao area, Thailand, ITC, Enschede, 2003, 94 pp.

[4] Morgan, R.P.C., A simple approach to soil loss prediction: a revised Morgan-Morgan-Finney model. CATENA, Vol. 44, Issue 4, 2001, pp 305-322.

[5] Karoonmakphol, P., Evaluation of cadmium contamination due to stream sediment transport in Mae Tao Creek, Mae Sot District, Tak province (Doctoral dissertation, Chulalongkorn University).9, Issue 17, 2015, pp. 1441-1446.

[6] Department of Primary Industries and Mines (DPIM). Report of the study on the solution of cadmium contamination in the Mae Tao Basin Mae Sot district, Tak province. Bangkok. Thailand, 2016.

[7] Renard, K.G., Foster, G.R., Weesies, G.A., McCool, D.K. and Yoder, D.C., Predicting soil erosion by water: a guide to conservation planning with the Revised Universal Soil Loss Equation (RUSLE) (Vol. 703), 1997. Washington, DC: United States

[8] Morgan, R.P.C., Morgan, D.D.V. and Finney, H.J., A predictive model for the assessment of soil erosion risk, 1984, Argicult. Engineering Res: 245-253

[9] Pryseley, A., Mintiens, K., Knapen, K., Van der Stede, Y. and Molenberghs, G., Estimating precision, repeatability, and reproducibility from Gaussian and non-Gaussian data: a mixed model's approach. Journal of Applied Statistics, 37(10), 2010. pp.1729-1747.

9th Int. Conf. onGeotechnique, Construction Materials andEnvironment,
Tokyo, Japan, 20-22 November 2019, ISBN: 978-4-909106025C3051

STABILITY ANALYSIS OF AN ACTIVE VEHICLE SUSPENSION SYSTEM

ThanapatWanichanon[1], ChayadaThidrasamee[2] , Thana Pornrattanaprasert[3], and Palita Mahachotikul[4]
[1.2.3.4]Faculty of Engineering, Mahidol University, Thailand

ABSTRACT

A car suspension is widely applied due to its use in smoothening a car when driving or absorbance of impacts made to the car. With its usefulness, developments and creations of new suspensions are being continuously conducted. This results in having better experience with less impact when driving from rough road for drivers and passengers.

This work conducts a research in developing an active suspension by analyzing a working process of a car suspension using the fundamental equations of constrained motion and Lyapunov theory. MATLAB software is used in the analyzing process and to examine the correctness of the results.

With the research conducted, the analysis found that the results from the analyzing process set to the satisfaction. The work is also completed according to the objectives and limitations which are successful in finding a mathematical model for the design and controller of the active suspension in a car. This also includes the ability to analyze functions of the controller and it is found that spring constant of choke, spring constant of tire and damping constant affect smoothness of a car suspension.

Keywords:Stability, Suspension system, The fundamental equation, Constrained motion

INTRODUCTION

Nowadays, smooth driving is the main objective in developing modern cars and is one of the significant key satisfactions of customers. If cars have a suspension with better response to the roads, passengers will have better satisfaction towards those particular cars. The suspension that is currently favored for further development is an Active Suspension [3]-[5]. This dues to its ability to constantly adjust the force applied to the suspension system by calculating suitable forces for each kind of roads at any period of time. In the model of study it is assumed that the suspension could apply forces to both sprung mass and unsprung mass, which are comparable to a car cabin and a car suspension respectively. As in many references of researches related to the active suspension [1]-[2], it is easier to consider a dynamic model of a quarter car and control the system with feedback controller [6]-[7]. With that, if errors were to be found, the controller will try to correct the system back to the equilibrium point. In this paper, the fundamental equations of constrained motion is used to solve the dynamic equations of the mathematical model for a quarter car in order to verify that the controller could perform according to the stability's criterions [8]. In addition, Lyapunov theory is applied in the process of determining the stability constraint of the system. The linear constraint function in the form of acceleration is then received. Its condition helps diminishing the energies in the system to be zero or close to the equilibrium point, which meets the designed expectation. The verification of the effectiveness of the proposed controller is done by a numerical computation in MATLAB to find the displacement and velocity in each period of time of the sprung and unsprung masses of the quarter car. This is to prove that the system meets the stability's expectations and designed objectives.

DYNAMICS

On the dynamics we analyze our interested system by using the fundamental equations of constrained motion. The approach is divided into three steps.

Unconstrained System

First, Newton second law of motion is used to create unconstrained motion's equation to find a non-constrained system's equation.

$$\sum F = ma. \tag{1}$$

Equation (1) can be written as

$$M\ddot{q} = Q \tag{2}$$

where

M is a mass matrix (kg)
$\ddot{q}$ is a generalized acceleration ($\mathrm{m/s^2}$)
Q is a generalized force (N).

Pre multiplying Eq. (2) with M^{-1}, we can find the unconstrained system's acceleration as

$$a := \ddot{q} = M^{-1}Q\,. \tag{3}$$

Constraint Equation

For this part, a constraint (or a part which forces the system back to a desired stage) is defined for the system to be back to the equilibrium

$$\phi(q,\dot{q},t) = 0\,. \tag{4}$$

Differentiating Eq. (4) and rewriting it in an acceleration form, we have

$$A(q,\dot{q},t)\ddot{q} = b(q,\dot{q},t) \tag{5}$$

where

A is a constraint matrix
b is a constant vector.

Constrained System

In order the system to satisfy the constraint (5), from the Newton second law of motion (Eq. (2)), we add forces from feedback controller as a control force.

$$M\ddot{q} = Q(q,\dot{q},t) + Q^C(q,\dot{q},t) \tag{6}$$

where

Q^C is a control force (N), which is computed from Ref. [11] as

$$Q^C = A^T(AM^{-1}A^T)^+(b - A\ddot{q}) \tag{7}$$

where

+ is the Moore-Penrose inverse of the matrix [8].

Then substituting Eq. (7) into Eq. (6) and pre-multiplying the equation with M^{-1}, we finally get the dynamic equations in the form of acceleration

$$\ddot{q} = a + M^{-1}A^T(AM^{-1}A^T)^+(b - Aa). \tag{8}$$

In order to verify motions of the constrained system, we integrated Eq. (8) twice to compute velocity and displacement of the system respectively in any period of time.

METHOLOGY

Analyzing the Unconstrained System

In this work a quarter car is modeled with an active suspension as seen in Fig. 1. In its free body diagram a vertical movement of a two-degree of freedom system of sprung and unsprung masses is considered. By the virtue of the unconstrained motion, the Newton second law of motion [1] yields mathematical models of the system without any control force from hydraulic (Q^c) (see Eq. (2)):

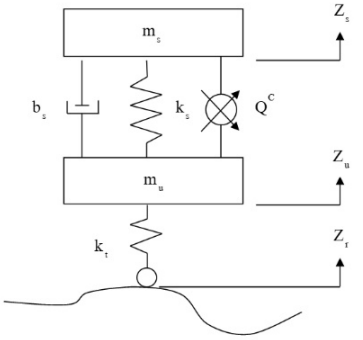

Fig. 1 Quarter car

For sprung mass

$$m_s\ddot{z}_s = -k_s(z_s - z_u) - b_s(\dot{z}_s - \dot{z}_u) \tag{9}$$

and for unsprung mass

$$m_u\ddot{z}_u = k_s(z_s - z_u) + b_s(\dot{z}_s - \dot{z}_u) + k_t(z_r - z_u) \tag{10}$$

where

m_s is sprung mass (kg)
m_u is unsprung mass (kg)
z_s is displacement of sprung mass (m)
z_u is displacement of unsprung mass (m)
$\dot{z}_s$ is velocity of sprung mass (m/s)
$\dot{z}_u$ is velocity of unsprung mass (m/s)
k_s is spring constant of sprung mass (N/m)
b_s is damping constant of sprung mass(Ns/m)
k_t is spring constant of tire (N/m)
z_r is displacement from road (m).

Rearranging Eqs. (9) and (10) into a matrix form, we obtain

$$\begin{bmatrix} m_s & 0 \\ 0 & m_u \end{bmatrix}\begin{bmatrix} \ddot{z}_s \\ \ddot{z}_u \end{bmatrix}=\begin{bmatrix} k_s(z_u-z_s)+b_s(\dot{z}_u-\dot{z}_s) \\ k_s(z_s-z_u)+b_s(\dot{z}_s-\dot{z}_u)+k_t(z_r-z_u) \end{bmatrix}. \tag{11}$$

The matrix in front of the acceleration is considered as the mass matrix (*M*) and another one on the right handed side of the equation is the generalized force vector (*Q*). So we get these two parameters of the unconstrained system

$$M(q,t):=\begin{bmatrix} m_s & 0 \\ 0 & m_u \end{bmatrix}$$

$$Q(q,\dot{q},t):=\begin{bmatrix} k_s(z_u-z_s)+b_s(\dot{z}_u-\dot{z}_s) \\ k_s(z_s-z_u)+b_s(\dot{z}_s-\dot{z}_u)+k_t(z_r-z_u) \end{bmatrix}. \tag{12}$$

Assigning a Constraint Equation

This step is to define a function that controls the system. Let us begin with the constraint equation from Eq. (4). Since stability of the movements of the sprung and unsprung masses are considered, Lyapunov stability criterion is used in this work [7].

Now let us talk about Lyapunov stability criterion. It composes of a function of V, which is also known as Lyapunov candidate function. In our work, we assume that it is a function of displacement, velocity and time. Stability in Lyapunov sense is satisfied with two conditions

1. *A positive definite function of the Lyapunov candidate*

$$V(q,\dot{q},t)>0. \tag{13}$$

2. *Differentiation of the Lyapunov candidate is negative definite function*

$$\frac{d}{dt}(V(q,\dot{q},t))<0. \tag{14}$$

To satisfy the first condition is not a challenge. However, in order to find a positive definite function that also has negative definite differential function is not an ease. We thus consider any positive definite function V that satisfies

$$\dot{V}(q,\dot{q},\ddot{q},t)=-\alpha V(q,\dot{q},t) \tag{15}$$

as a constraint.

In Eq. (15), V is a Lyapunov candidate which is a function of generalized coordinate, generalized velocity and time. α is a positive constant parameter which is to show the speed in which the system can be back to equilibrium.

Our goal is to reduce and bring back displacement and velocity of the sprung and unsprung masses into equilibrium. To prove that this constraint equation suits with the goal, we solve the Eq. (15) so we can get the solution of this equation as

$$V=e^{-\alpha t}V_0. \tag{16}$$

This equation is in the form of an exponential decay. When the time goes to ∞. The function will bring V back to zero. So the parameters that are defined as the function of V is also brought back to zero, which is our equilibrium.

In our case, we use the Lyapunov candidate function [7] as

$$V=\frac{1}{2}a_1q^Tq+\frac{1}{2}a_2v^Tv+a_{12}q^Tv \tag{17}$$

where a_1, a_2, a_{12} are positive constants that satisfy

$$a_1>0,\ a_2>0,\ 0<a_{12}<\sqrt{a_1a_2}, \text{ and}$$

$$\alpha=\frac{2a_{12}}{a_2} \text{ (see Eq. (15))}$$

$$q:=\begin{bmatrix} z_s \\ z_u \end{bmatrix},\ v:=\dot{q}:=\begin{bmatrix} \dot{z}_s \\ \dot{z}_u \end{bmatrix},\ a:=\ddot{q}:=\begin{bmatrix} \ddot{z}_s \\ \ddot{z}_u \end{bmatrix},$$

q is the generalized displacement, v is the generalized velocity, and a is the generalized acceleration.

The derivatives of Eq. (17) is

$$\begin{aligned}\dot{V}=&a_1\begin{bmatrix} z_s & z_u \end{bmatrix}\begin{bmatrix} \dot{z}_s \\ \dot{z}_u \end{bmatrix}+a_2\begin{bmatrix} \dot{z}_s & \dot{z}_u \end{bmatrix}\begin{bmatrix} \ddot{z}_s \\ \ddot{z}_u \end{bmatrix}\\ &+a_{12}\begin{bmatrix} \dot{z}_s & \dot{z}_u \end{bmatrix}\begin{bmatrix} \dot{z}_s \\ \dot{z}_u \end{bmatrix}+a_{12}\begin{bmatrix} z_s & z_u \end{bmatrix}\begin{bmatrix} \ddot{z}_s \\ \ddot{z}_u \end{bmatrix}.\end{aligned} \tag{18}$$

From this part we substitute Eq. (17) and Eq. (18) into Eq. (15)

$$a_1\begin{bmatrix} z_s & z_u \end{bmatrix}\begin{bmatrix} \dot{z}_s \\ \dot{z}_u \end{bmatrix} + a_2\begin{bmatrix} \dot{z}_s & \dot{z}_u \end{bmatrix}\begin{bmatrix} \ddot{z}_s \\ \ddot{z}_u \end{bmatrix}$$
$$+a_{12}\begin{bmatrix} \dot{z}_s & \dot{z}_u \end{bmatrix}\begin{bmatrix} \dot{z}_s \\ \dot{z}_u \end{bmatrix} + a_{12}\begin{bmatrix} z_s & z_u \end{bmatrix}\begin{bmatrix} \ddot{z}_s \\ \ddot{z}_u \end{bmatrix} = -\alpha V. \quad (19)$$

Rearranging Eq. (19) into the acceleration form (see Eq. (5)), we have

$$\begin{bmatrix} a_2\dot{z}_s + a_{12}z_s & 0 \\ 0 & a_2\dot{z}_u + a_{12}z_u \end{bmatrix}\begin{bmatrix} \ddot{z}_s \\ \ddot{z}_u \end{bmatrix}$$
$$= -\left(a_1 z_s \dot{z}_s + a_1 z_u \dot{z}_u + a_{12}\dot{z}_s{}^2 + a_{12}\dot{z}_u{}^2\right) - \alpha V. \quad (20)$$

From Eq. (20) we can find parameter *A* and *b* which are the constraint matrix and the constraint vector respectively as

$$A := \begin{bmatrix} a_2\dot{z}_s + a_{12}z_s & 0 \\ 0 & a_2\dot{z}_u + a_{12}z_u \end{bmatrix}$$
$$b := -\left(a_1 z_s \dot{z}_s + a_1 z_u \dot{z}_u + a_{12}\dot{z}_s{}^2 + a_{12}\dot{z}_u{}^2\right) - \alpha V. \quad (21)$$

Computing Control Forces of the Constrained System

Substituting *M*, *Q* from the unconstrained system and *A*, *b* from the constraint equation in Eqs. (6) and (7). The dynamic equation of our constrained suspension system with control forces is

$$M\ddot{q} = Q(q,\dot{q},t) + A^T(AM^{-1}A^T)^+(b - Aa). \quad (22)$$

After we get the dynamic equation of the constrained system. We could verify its displacement and velocity in any period of time by using MATLAB to compute and validate the result.

RESULT

Consider parameters of the system and the controller as m_s = 208 kg, m_u = 28 kg, k_s = 18709 N/m, k_t = 127200 N/m, b_s = 1300 Ns/m, a_1 = 1, a_2 = 8, a_{12} = 1, and $\alpha = 1/4$.

Given the system mathematical model, consider that both masses have separate equilibrium points related to CG of their particular masses. In the experiment, the values of a_1, a_2, a_{12}, and α are varied until the suitable values are found. In the simulation, the values of the initial conditions of the system are defined as z_s = 0, z_u =0, $\dot{z}_s$ = 0.01, and $\dot{z}_u$ = 0.05. These values are assumed and might not be the correct initial values that are related to the constraint equation of the system. Therefore, the nonlinear solver *fsolve* command in MATLAB is used to solve for the right initial conditions of the non-linear system. We found that the initial conditions that are met with the constraint equation are z_s = -0.0028, z_u = -0.0140, $\dot{z}_s$ = 0.0014, and $\dot{z}_u$ = 0.0070.

In this work we have tested the proposed active suspension controller with three types of road:

1. A sinusoidal wave road with the height of slope equals to 0.075 meters and frequency equals to 0.242 Hz (see Fig. 2). This model represents for a normal road condition.
2. A sinusoidal wave road with natural frequency with the height of slope equals to 0.015 meters and frequency equals to 0.625 Hz, which is the value of natural frequency of the system (see Fig. 5). This case shows the model that has the least suitable frequency for the car of our system.
3. A random road with all random height of the slope and frequency by MATLAB function *rand* (see Fig. 8). This is the example model of an unexpected road type.

The results in the paper only show for displacements of the sprung mass from each road types (see Figs. 3, 6, and 9) which are comparable to the trembling in the car cabin and the additional control forces (see Figs 4, 7, and 10) which negate with the given forces of the system.

Figure 3, 6, and 9 show that the sprung mass which is considered as a car cabin goes back to the equilibrium set point within a short period of time. While Figs. 4, 7, and 10 verify the possibility in generating our control forces.

If the force which controls the system is close to the force generated by the system, it could be a possibility in which we could control the system using the calculated control force.

Response from Sinusoidal Wave

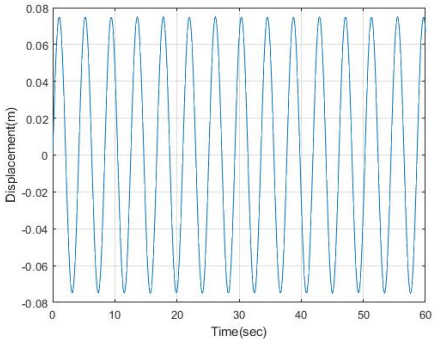

Fig. 2 Road distribution

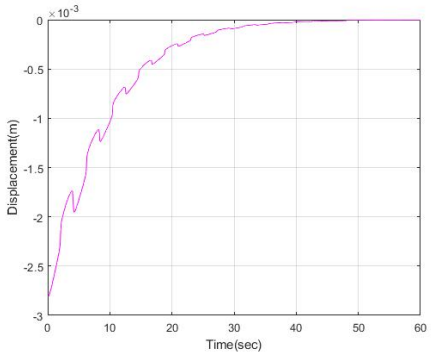

Fig. 3 Displacement of sprung mass

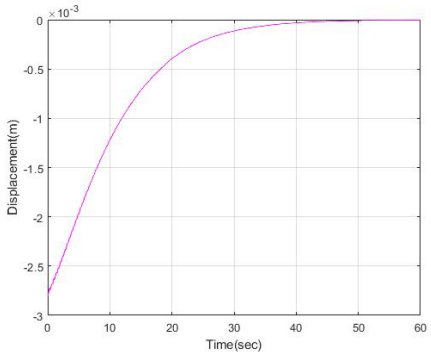

Fig. 6 Displacement of sprung mass

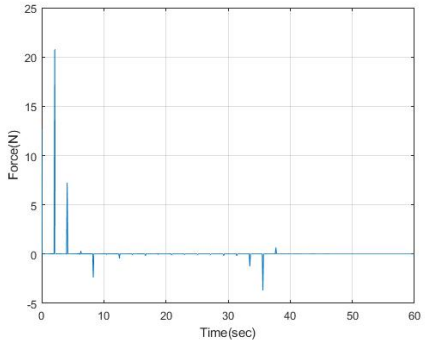

Fig. 4 $Q^C - Q$

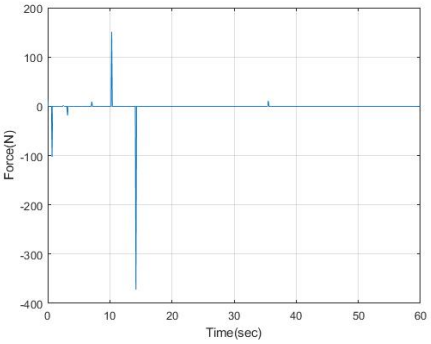

Fig. 7 $Q^C - Q$

Response from Sinusoidal Wave with Natural Frequency

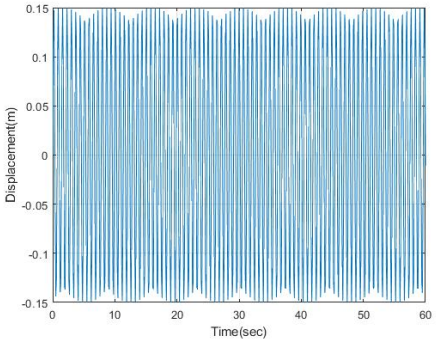

Fig. 5 Road distribution

Response from Random Road Distribution

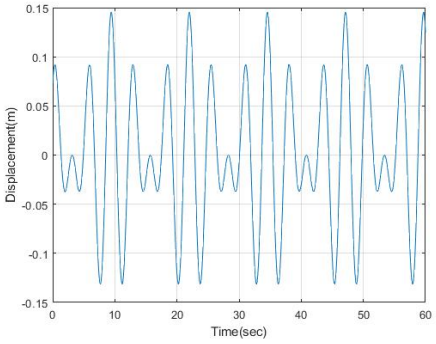

Fig. 8 Road distribution

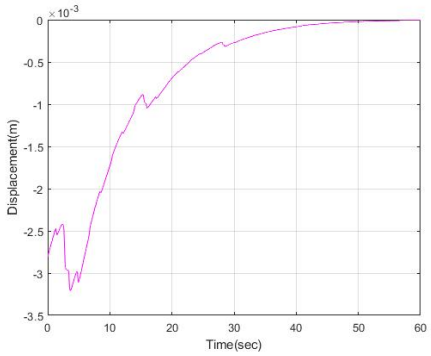

Fig. 9 Displacement of sprung mass

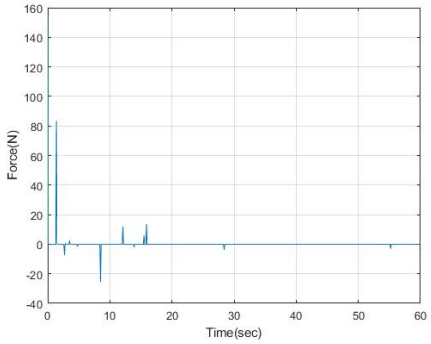

Fig. 10 $Q^C - Q$

CONCLUSIONS

In this work the fundamental equations of constrained motion is applied with a quarter active suspension car. We use Lyapunov theory in part of the constraint equation because this theory is based on reducing energy of the system to the equilibrium or zero. We thus finally get the dynamic equation of the constrained system. Then the results are verified by computing the dynamic constrained equation on MATLAB. As the expectation that displacements of the sprung mass and unsprung mass could be brought back to the equilibrium, the results shown verify that the system could do our expectation. Moreover with the experimentation we found that we could adjust the speed that the system goes to the equilibrium by varying the constant parameter α . The greater of α makes the system back to equilibrium faster but the control forces (Q^C) might increase respectively to α. The bigger control force from the generalized force, the less opportunity to succeed in applying the physical part to the suspension system.

Reducing and bringing back the displacement of the system to equilibrium point using the fundamental equations of constrained motion is the way to improve the stability of the suspension. According to the results, we can bring back the car cabin to the equilibrium as we expect. So it is possible that this system could be applied in a real car but it needs further research on the study of physical equipment.

ACKNOWLEDGMENTS

Firstly, I would like to express my sincere gratitude to my advisor Dr. Thanapat Wanichanon for the continuous support of my work and related research, I could not have imagined having a better advisor and mentor for my study.

Besides my advisor, I would like to thank the rest of my thesis committee: Dr. Ittichote Chuckpaiwong, and Dr.Chokchai Chutakositkanon, for the hard questions which incented me to widen my research from various perspectives.

Finally, I must express my very profound gratitude to my parents and to my wonderful faculty members for providing me with support.

REFERENCES

[1] Li H., Yu J., Hilton C., and Liu H., Adaptive SlidingMode Control for Nonlinear Active Suspension VehicleSystemsUsing T–S FuzzyApproach. IEEE Transactions on Industrial Electronics,Vol. 60, Issue 8, 2013, pp. 3328-3338.

[2] Shiuh-Jer H. and Wei-Cheng L., Adaptive Fuzzy Controller with Sliding Surface for Vehicle Suspension Control. IEEE Transactions on Fuzzy Systems, Vol. 11, Issue 4, 2003, pp. 550-559.

[3] Alexandru C. and Alexandru P., A Comparative Analysis between the Vehicles' Passive and Active Suspension. International Journal of Mechanic, Vol. 5, Issue 4, 2011, pp. 371-378.

[4] Bhise A.R., Desai R.G., Yerrawar R.N., Mitra A.C., and Arakerimath R.R., Comparison between Passive and Semi-Active Suspension System Using Matlab/Simulink. IOSR Journal of Mechanical and Civil Engineering,Vol. 13, Issue 4, 2016, pp. 01-06.

[5] Rijumon K., Murtaza M.A., and Ajith K., A Comparisonbetween Passive & Semi Active Suspension Systems.International Journal of Innovative Research in Science, Engineering and Technology,Vol. 2, Issue 6, 2013, pp. 01-05.

[6] Li H., Jing X., and Karimi H.R., Output-Feedback-Based H_∞ Control for Vehicle Suspension Systems with Control Delay. IEEE Transactions on Industrial Electronics,Vol. 61, Issue 1, 2014, pp. 436-446.

[7] Udwadia, F.E and Koganti, P.B., Optimal stable Control for Nonlinear Dynamical Systems: An Analytical Dynamics Based Approach. International Journal of Nonlinear Dynamics,Vol. 82, Issue 1-2, 2015, pp. 547-562.

[8] Udwadia F.E. andWanichanon T.,Control of Uncertain Nonlinear Multibody MechanicalSystems. International Journal of Applied Mechanics, Vol. 81, Issue 4, 2013, pp. 041020-1-041020-11.

9th Int. Conf. on Geotechnique, Construction Materials and Environment, Tokyo, Japan, 20-22 November 2019, ISBN: 978-4-909106025 C3051

STUDY ON LAND SURFACE EMISSIVITY ESTIMATION OVER EAST ASIA

Nozomu Hirose[1], Kenji Taniguchi[2] and Ichiro Kaihotsu[3]
[1] National Institute of Technology, Matsue College, Japan; [2] Faculty of Environmental design, Kanazawa University, Japan; [3] Hiroshima University, Japan

ABSTRACT

Estimation of the land surface emissivity is crucial to evaluate the boundary conditions of atmospheric modeling data assimilation. Brightness temperatures observed by satellite passive microwave radiometer give information on emission forma raindrops and scattering by frozen particles. By applying radiative transfer model of the atmosphere, we can estimate the atmospheric hydrological process (i. e., rainfall, snowfall, water vapor, cloud water, etc.). However it is difficult to estimate microwave land surface emissivity at higher frequencies over land. Because land use, land cover and surface wetness over land are various and heterogeneous by comparing with over ocean. Therefore, we aim to estimate the microwave land surface emissivity over East Asia by using observed data and numerical models.

Firstly, we investigate the characteristics of land surface emissivity derived from SSM/I, AMSR-E and AMSR2 over Asia and the relationship between land surface emissivity and land hydrological variables based on satellite data sets and numerical models. Secondary, we estimate the land surface emissivity by applying the Community Microwave Emission Model (CMEM) and Community Radiative Transfer Model (CRTM).

Keywords: Microwave land surface emissivity, CRTM, CMEM, Japan, Mongolia

INTRODUCTION

Microwave land surface emissivity at higher frequencies is crucial for cloud data assimilation for heavy rainfall. Cloud data assimilation has great potential to improve the prediction of heavy rainfall area because it can directly obtain information on locations of rain systems. Clouds can be observed globally by satellite-based microwave remote sensing. Therefore, satellite-based microwave remote sensing has Retrievals of land surface emissivity (LES) are challenging due to the high variability of emissivity and its sensitivity to land surface hydrological parameters [1], [2], [3]. Passive microwave remote sensing such as AMSR-E and AMSR2 has the advantages of considerably high revisit time and having multiple channels that are sensitive to different atmospheric variables and surface properties [4], [5], [6].

The objectives of our study are to investigate the temporal and spatial variability of LSE over East Asia, to reveal the relationship between LES at low frequency (6.9GHz and 10.7GHz) and high frequency (36.5GHz and 89.0GHz) by exploring the AMSR-E Monthly Global Microwave LSE dataset obtained from National Snow and Ice Data Center (NSIDC) and to estimate the LES at Mongolia observation sites from 2002 to 2008 by applying the Community Microwave Emission Model (CMEM) and Community Radiative Transfer Model (CRTM).

CMEM is developed by ECMWF for low frequency passive microwave brightness temperatures from 1 GHz to 20 GHz of the surface.

To estimate LES at higher frequencies by applying CMEM, we should clarify the relationship of LES between low and high frequency using NSIDC LES data set. On the other hand, CRTM with the land microwave emissivity component is used in a wide frequency range from 1 GHz to 100 GHz. Microwave LES at higher frequency is directly estimated by applying CRTM.

CARACTERISCS OF LAND USE AND LAND SURFACE EMISSIVITY OVER EAST ASIA

Microwave land surface emissivity strongly depends on the land surface condition (i. e., land use, land cover, vegetation type, surface wetness, surface roughness, etc.). Therefore, we investigate the relationship between land surface emissivity and land use by using satellite observation date.

All of the seven channels with vertical and horizontal polarizations of AMSR-E/Aqua Global Monthly LSE at 0.25° latitude/longitude for the study period from July 2002 to June 2008 were obtained from data providing service at NSIDC.

Our target areas are Mongolian Plateau and Japan.

Mongolian Plateau

Firstly, Mongolian Plateau area is shown in Fig. 1a. These figures also show the classification of land cover by using the dataset of USGS (Unite States Geological Survey) Global Land Cover Characterization Version 2.0. Figure 1b shows the relative frequency of land cover in the histogram. Glassland, shurabland and Barren or Sparesly vegetated are mainly covered with our target area. The characteristics of land cover in our area is less vegetated condition.

Fig. 2a presents the comparison between land surface emissivity at low frequencies (6.9GHz and 10.7GHz) and other high frequencies in July 2002 at grassland area. It represents the relationship between land surface emissivity and land hydrological variables (land type, land use, vegetation and soil moisture) in summer. The LSE at 6.9GHz with horizontal polarization is related with at higher frequencies. However, variation is large in the relationship between LSE at 6.9GHz and at 89.0GHz with horizontal polarization.

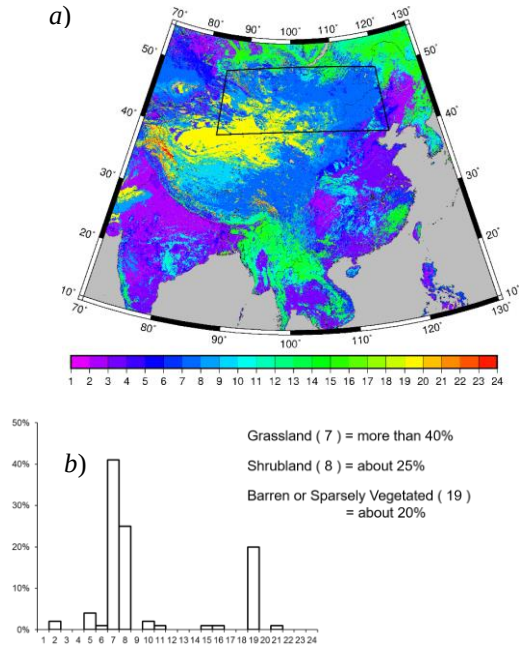

Fig. 1 *a*) Land cover classes and *b*) the relative frequency of land cover over Mongolian Plateau area.

Relationship between LES at low frequency and high frequency

Fig. 2b shows the comparison between LSE at low and high frequencies at bare soil area. By comparing Fig. 2a, we found that liner relationship between low-frequency LES and high frequency LES is clear. These figures implies that microwave LSE at high frequency is estimated by using microwave low-frequency LES in summer.

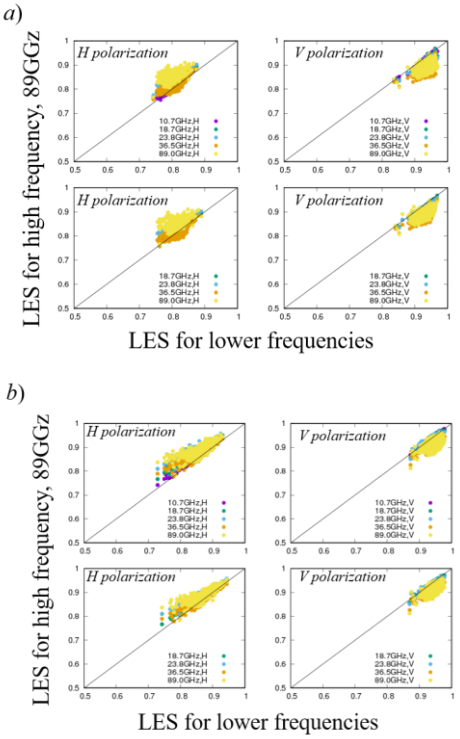

Fig. 2 Relationship between low-frequencies and high frequency LES over *a*) glass-land area and *b*) bare soil area shown in Fig. 1a.

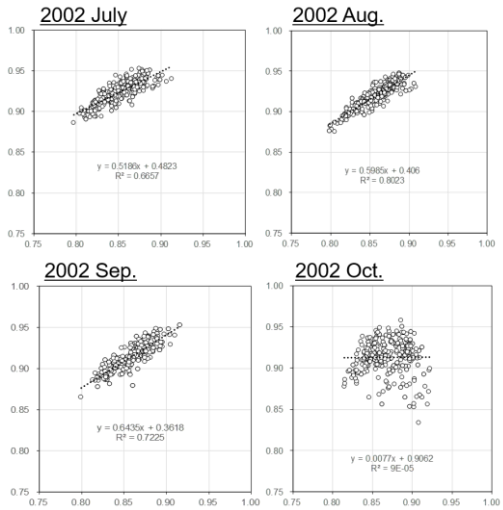

Fig. 3a Seasonal change of relationship between low-frequencies and high frequency LES from July 2002 to October 2002 at bare soil area shown in Fig. 1a.

Relationship in barren or sparsely vegetated area

Fig.3 shows the seasonal change of its relationship over barren or sparsely vegetated area. It is found that correlation coefficient in summer (from July to September) is higher compared with one in winter.

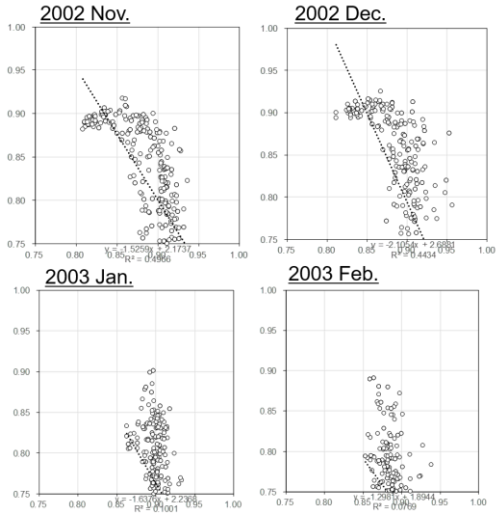

Fig. 3b Seasonal change of relationship between low-frequencies and high frequency LES from November 2002 to February 2003 at bare soil area shown in Fig. 1a.

Japan

Secondary, Fig. 4 shows the relative frequency of land cover over Japan in the histogram by using the dataset of USGS Global Land Cover Characterization Version 2.0. As compared with Mongolian Plateau, Japan area is covered with forest more than 90% as show in Fig. 4.

We investigate the relationship between low frequency LES and high frequency LES. However, we could not found its relationship. It is because that our target area is cover with dens vegetated and various land cover.

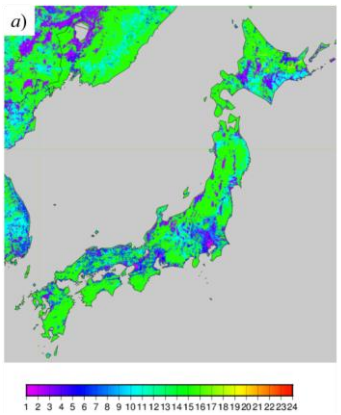

Fig. 4a Land cover classes over Japan.

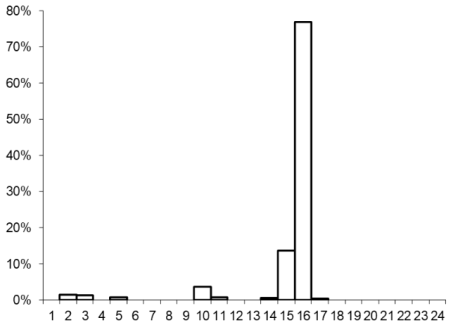

Fig. 4b Relative frequency of land cover classes over Japan.

ESTIMATION OF LAND SURFACE EMISSIVITY

The Community Microwave Emission Model, CMEM comprises the physics and parameterizations used in the Land Surface Microwave Emission Model (LSMEM) [7] and the L-Band Microwave Emission of the Biosphere (L-MEB) [8], [9].

Community Microwave Emission Model (CMEM)

CMEM was developed by the ECMWF for numerical weather prediction applications and is used to simulate passive microwave brightness temperatures of the surface at low frequencies (from 1 GHz to 20 GHz) [10], [11], [12]. For polarization (p), the brightness temperatures over snow-free areas at the top of the atmosphere (TOA) $T_{Btoa,p}$, which result from the contributions of three dielectric layers (soil, vegetation, and atmosphere), can be expressed as follows:

$$T_{Btoa,p} = T_{Bau,p} + e^{-\tau_{atm,p}} \cdot T_{Btov,p} \quad (1)$$

$$T_{Btov,p} = T_{Bsoil,p} \cdot e^{-\tau_{veg,p}} + T_{Bveg,p}(1 + r_{r,p} \cdot e^{-\tau_{veg,p}}) + T_{Bad,p} \cdot r_{r,p} \cdot e^{-2\tau_{veg,p}} \quad (2)$$

where $T_{Btov,p}$ is the top-of-vegetation brightness temperature when the vegetation is represented as a single-scattering layer above a rough surface; $\tau_{atm,p}$ is the atmospheric optical depth; $T_{Bau,p}$ and $T_{Bad,p}$ are the upward and downward atmospheric emissions, respectively; and $T_{Bsoil,p}$ and $T_{Bveg,p}$ are the soil and vegetation layer contributions, respectively. Here, $r_{r,p}$ is the soil reflectivity of a rough surface (one minus the emissivity $e_{r,p}$), and $\tau_{veg,p}$ is the vegetation optical depth along the viewing path.

Simulation Results

We address long-term land hydrological dataset measured at Mongolia observation sites. By applying to CMEM, land surface emissivity at 6.9GHz with horizontal and vertical polarization are estimated at Mongolia site.

Fig. 5a and 5b present the comparison between simulation results at Mongolia site by using CMEM and AMSR-E Monthly Global LSE. Fig. 4a shows the simulated microwave LSE at 6.9GHz with horizontal polarization is overestimated and its temporal variability is very large.

On the other hand, Fig. 5b shows the simulation result with vertical polarization is good agreement with AMSR-E Monthly LSE at Mongolia observation site.

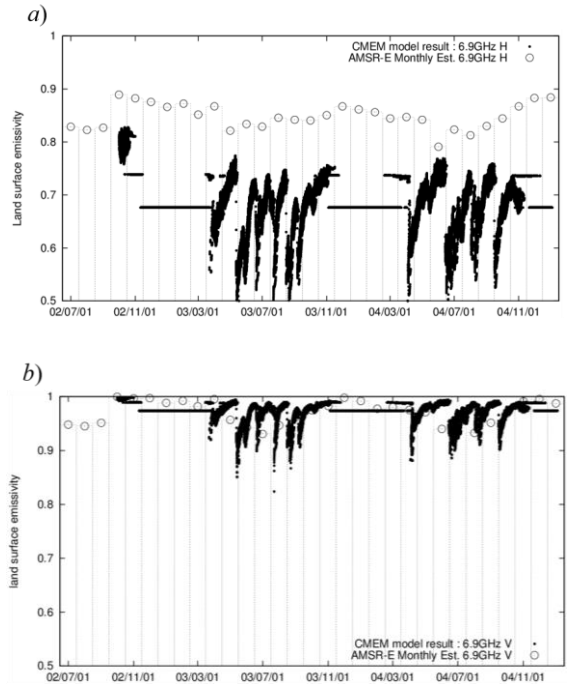

Fig 5. Comparison between the observed microwave LES and simulation results with *a*) Horizontal polarization and *b*) Vertical polarization.

CONCLUTION

In this study, we investigate the temporal and spatial variability of LSE over Asia and the relationship between LES at low frequency (6.9GHz and 10.7GHz) and high frequency (36.5GHz and 89.0GHz) and try to estimate microwave land surface emissivity from July 2002 to January 2005 at Mongolia observation sites.

Firstly, Microwave LES at high frequencies is related to LES at low frequencies in summer. It implies effect of land surface hydrological variables to LES. Therefore, we try to identify the effect of snow, vegetation type and soil moisture by using Land use and MODIS dataset. Secondly, Microwave LES at 6.9GHz with horizontal and vertical polarization is simulated at Mongolia observation sites. Simulation results shows the estimated LSE is overestimated and its variability is large by comparing the observed data.

We should reveal the effect of snow and vegetation type to the relationship between LES at low and high frequencies and calibrate CMEM model parameters to represent the temporal and spatial variability of LSE obtained from AMSR-E and AMSR2.

ACKNOWLEDGMENTS

The data sources used in the study are graciously acknowledged. This work was supported by JAXA PMM RA8 and JSPS KAKENHI Grant Number JP26289162.

REFERENCES

[1] Hirose, N., 2016. Estimation of land surface emissivity for atmospheric modelling data assimilation. Abstracts of the 61th autumn conference of the remote sensing society of japan, B15, pp.10.

[2] Hirose, N., 2017. Relationship between land surface emissivity and land hydrological variables. Proceeding of International Symposium on Remote Sensing 2017, D-37, pp.507-508.

[3] N. Hirose, K. Taniguchi, and I. Kaihotsu, Estimation of microwave land surface emissivity over East Asia, 39th Asian Conference on Remote Sensing 2018 Proceeding, 2018, pp.1567-1569.

[4] Tian, Y., C. D. Peters-Lidard, K. W. Harrison, Y. You, S. Ringerud, S. Kumar, and F. J. Turk, An examination of methods for estimating land surface microwave emissivity, J. Geophys. Res. Atmos., 120, 11,114–11,128, doi:10.1002/2015JD023582, 2015.

[5] Prakash, S., H. Norouzi, M. Azarderakhsh, R. Blake, and K. Tesfagiorgis, 2016. Global land surface emissivity estimation from AMSR2 observations, IEEE Geoscience and Remote Sensing Letters, 13(9), pp.1270-1274.

[6] de Rosnay, P., M. Drusch and J. Muñoz Sabater, 2009a. Milestone 1 Tech Note - Part 1: SMOS Global Surface Emission Model.

[7] de Rosnay P., M. Drusch, A. Boone, G. Balsamo, B. Decharme, P. Harris, Y. Kerr, T. Pellarin, J. Polcher and J.-P. Wigneron, 2009b. The AMMA

Land Surface Model Intercomparison Experiment coupled to the Community Microwave Emission Model: ALMIP-MEM. J. Geophys. Res., Vol 114, doi:10.1029/2008JD010724.

[8] Drusch, M. and Jacson, T., 2001. Vegetative and atmospheric corrections for soil moisture retrieval from passive microwave remote sensing data: Results from the Southern Great Plains Hydrology Experiment 1997. J. Hydrometeor., 2, pp.181-192.

[9] Wigneron, J. et al, 2007. L-band Microwave Emission of the Biosphere (L-MEB) model: Description and calibration against experimental data sets over crop fields. Remote Sens. Environ., 107, pp.639-655.

[10] Holmes, T., M. Drusch, J.-P. Wigneron, et al., 2008. A global simulation of microwave emission: Error structures based on output from ECMWF's operational Integrated Forecast System, IEEE Trans. Geosci. Remote Sens., 46, 846–856.

[11] Drusch, M., T. Holmes, P. de Rosnay, et al., 2009. Comparing ERA-40 based L-band brightness temperatures with Skylab observations: A calibration/validation study using the Community Microwave Emission Model, J. Hydrometeor., 10, 213–226.

[12] Jia, B., and Z. Xie, 2011:Evaluation of the community microwave emission model coupled with the community land model over East Asia. Atmospheric and Oceanic Science Letters, 4, 209–215.

9th Int. Conf. on Geotechnique, Construction Materials and Environment, Tokyo, Japan, 20-22 November 2019, ISBN: 978-4-909106025 C3051

WATER QUALITY INDEX ANALYSIS OF LAKE RAWA BESAR, DEPOK, WEST JAVA, AND ITS RELATIONSHIP WITH LAND USE

Mangapul Parlindungan Tambunan[1], Elgi Lukiyansah[1] and *Kuswantoro Marko[1]
Department Geography Faculty of Mathematics and Science, Universitas Indonesia, Indonesia

*Corresponding Author

ABSTRACT

The lake's catchment area is one of the objects of land use conversion as a space for community needs. The boundary of the Lake Rawa Besar has been widely used by the surrounding community to carry out activities. Human activity and land use around lake borders can affect water quality. This study aims to look at the pattern of spatial distribution of Lake Rawa Besar water quality and its relationship with land use in the border. Water quality was tested based on the instant surface water sampling method in 30 samples evenly distributed in the water body and laboratory testing based on 6 water quality parameters such as turbidity, BOD, total phosphate, total solid, pH, and nitrate. Water quality is measured based on the water quality index level of WQI (Water Quality Index) and interpolated using the IDW method. Large-scale land use is used from digitizing large resolution images and potential sources of pollutants obtained from field observations. The results showed that the water quality in water bodies was almost evenly distributed with mild polluted criteria. Land use in the form of domestic activities affecting the quality of water in the Lake Rawa Besar is characterized by high turbidity and BOD values, while the total phosphate, total solid, nitrate, and pH value is low. The high correlation between turbidity and BOD which is impacted from land use concluded that the poor quality of the lake's water was caused more by organic waste.

Keywords: Water Quality Index, Inverse Distance Weighted, interpolation, land use, pollutant source

1. INTRODUCTION

The lake's catchment area is also one of the objects of land use conversion as a space for community needs. Various activities that make people live around the lake's catchment area to make use of land [1] Water bodies located in urban areas serve as reservoirs for surface runoff and are sensitive to activities around them, especially settlement activities [2].

Dense population settlements are a sign of the many human activities in the area around Lake Rawa Besar. Lake Rawa Besar also has varied land uses, namely settlements, trade, gardens, neighborhood roads, and public facilities. The effect of land use resulted in an increase in the amount of pollutants and domestic wastewater which were disposed of in Lake Rawa Besar [3].

Domestic wastes are at risk of disrupting the quality of water in a body of water and affecting several types of parameters, namely BOD, nitrate, and total phosphate [4] – [5]. Water runoff containing waste such as industrial products and waste trees and chemicals will affect the parameters of water quality such as turbidity, total solid, and pH [6] – [8].

For this reason, this study is important. The reason for the importance of the study is that the quality of water in a water body requires serious attention and management, especially from surrounding communities and governments that have authority [9]. In addition, water sources and water buildings, including those there, must be protected, secured, maintained and preserved [10].

2. DATA AND METHODS

2.1. Study Area

This research was conducted in Lake Rawa Besar and its surrounding area. Lake Rawa Besar is located in Pancoran Mas District, Depok City, West Java Province. The Lake is located between two villages, namely Depok and Depok Jaya Villages. The absolute location of the Lake Rawa Besar is 6º23'27" - 6º23'53"S and 106º48'54" - 106º49'2"W. Lake Rawa Besar has an area of about 12.92 hectares.

2.2. Water Quality

Water samples tested based on water quality parameters have 30 locations spread in Lake Rawa Besar. The location of the water sample has its own characteristics. The distribution map of the location of the water sample and the imagery of the area is shown in Fig. 1.

Water quality data used are turbidity, BOD, total phosphate, total solid, pH, and nitrate parameters. Water quality data with the 6 parameters are produced from the results of testing 30 water samples in the

AAS Cilodong laboratory. The data will then be compared with the quality standards that have been previously set as a comparison between the water quality standard value.

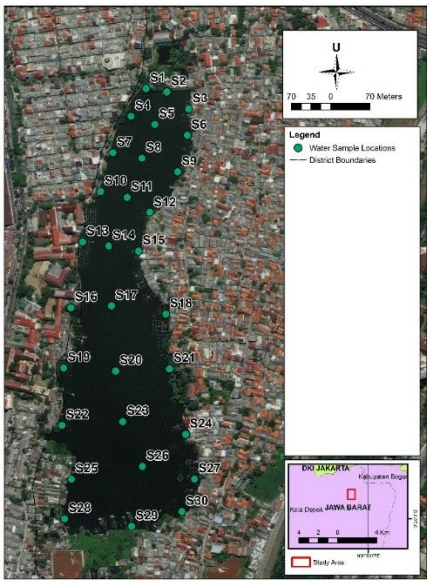

Fig. 1 Water Samples in study area

Water quality data processing is the first step that needs to be done in this study, because spatial pattern data is obtained from the processing of water sample data that has been tested. The water quality index is first calculated using WQI. Each sample point location was calculated to determine the water quality index amount at each point. The formula used to calculate WQI is in Eq. (1) [11]. The standard value used in the WQI calculation are shown in Table 1.

$$WQI = \frac{\Sigma\left[\frac{C_i}{Pl_i}\right]}{n} \quad (1)$$

WQI = Water Quality Index
C_i = Concentration of i variable
Pl_i = Standard value allowed for i variable
n = number of variable

Table 1 Standard value of water quality

Parameters	Standard Values
Turbidity	25 NTU
BOD	2 mg/L
Total Phosphate	0.2 mg/L
Total Solid	1050 mg/L
pH	6,5 – 8,5
Nitrate	10 mg/L

Water quality data is prepared to be interpolated. The interpolation that will be used is Inverse Distance Weighted (IDW) interpolation. Interpolation methods can be used to estimate objectively the spatial distribution of data [12]. Interpolation was carried out to determine the spatial distribution of WQI calculation results in the waters of Lake Rawa Besar. Data to be generated from interpolation is the distribution of WQI for each parameter and total distribution of WQI.

After that, categorization of the water quality level was carried out to see the spatial distribution of the water quality index of each parameter and the total water quality index in the Lake Rawa Besar area. The level of water quality used is the water quality classification criteria [13]. The criteria classification for WQI can be seen in Table 2.

Table 2 Water Quality Index Criteria

WQI value	Criteria
WQI ≤ 0,30	Excellent
0,31 ≤ WQI ≤ 0,89	Clean
0,90 ≤ WQI ≤ 2,49	Mild Polluted
2,50 ≤ WQI ≤ 3,99	Moderately Polluted
4,00 ≤ WQI ≤ 5,99	Heavily Polluted
WQI ≥ 6,00	Dirty

2.3. Land use

Secondary data used in this study is Digital Globe imagery data. The imagery is then digitized to obtain several land use variables. The variables used in digitizing land use are buildings, gardens, and environmental roads. Land use is digitized at a scale of 1:5000. Pollutant sources within land use also identified by field observing the land study area.

3. RESULTS AND DISCUSSION

3.1. Turbidity

The results of WQI calculation of water turbidity parameters indicate an index based on a review of water quality turbidity standards. The WQI level based on turbidity parameters produces 5 criterias for water quality level, which are clean, mildly polluted, moderately polluted, and heavily polluted. Two samples counted as water with clean water quality, 3 samples were mildly polluted water, 9 samples were moderately polluted water, 12 samples were heavily polluted water, and there were 3 samples which were dirty water based on turbidity parameters.

Spatially, the turbidity in Lake Rawa Besar has a high value in areas close to the land. Turbidity with high numbers also exists in the northern part of the

lake. The more center part of the lake showing the smaller turbidity value. This is shown in samples 17 and 20 in the middle of the lake. In the north, water samples show small values in samples 4, 8, and 9. The more toward the edge of the lake, the turbidity value increases. Turbidity WQI spatial pattern in Lake Rawa Besar is shown in Fig. 2.

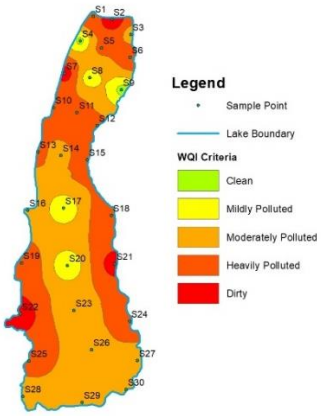

Fig. 2 Turbidity WQI Spatial Pattern within Lake Rawa Besar

3.2. BOD

The BOD in Lake Rawa Besar shows a number that is quite varied. Samples 1 to 30 have a variety of values. Spatially, the BOD in Lake Rawa Besar has higher value at several sample points, such as in the north of the lake and in the middle of the lake near the edge of the lake. The BOD in Lake Rawa Besar is quite uniform with mildly polluted criteria scattered throughout the lake. BOD with a high value is on the edge of the lake with a presence that is not too dominant towards the overall value of BOD. BOD WQI spatial pattern in Lake Rawa Besar is shown in Fig. 3.

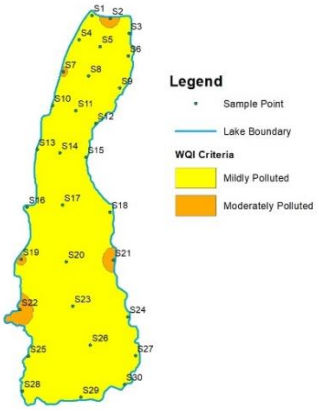

Fig. 3 BOD WQI spatial pattern within Lake Rawa Besar

3.3. Total Phosphate

The total phosphate present in Lake Rawa Besar shows almost uniform values. Spatially, the total phosphate present in Lake Rawa Besar has a higher value at several sample points, such as in the western part of the lake, precisely in the middle and at the southern edge of the lake. Total phosphate in Lake Rawa Besar is quite uniform with excellent criteria spread throughout the lake. Total phosphate with clean criteria is at the edge of the lake with a less dominant presence in the total value of total phosphate. Total phosphate WQI spatial pattern in Lake Rawa Besar is shown in Fig. 4.

Fig. 4 Total Phosphate WQI spatial pattern within Lake Rawa Besar

3.4. Total Solid

The total solids value shows that 30 water samples have total solids that do not exceed the quality standard which is valued 1050 mg / L. Spatially, the total solids present in Lake Rawa Besar have uniform WQI values. There is only one water quality criteria based on the total solids parameter, which is water that is considered excellent.

Fig. 5 Total Solid WQI spatial pattern within Lake Rawa Besar

3.5. pH

WQI level based on pH parameters produces 1 type of water quality criteria, which is lightly polluted. All water samples have a pH value that is included in the criteria for mild contamination. Spatially, the existing pH in Lake Rawa Besar has a uniform WQI value. There is only one water quality criterion based on pH parameters, namely water which is critically polluted.

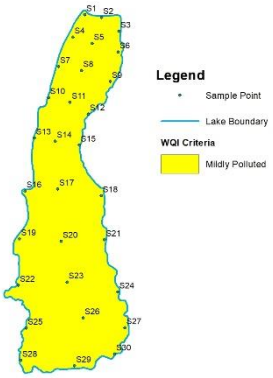

Fig. 6 pH WQI spatial pattern within Lake Rawa Besar

3.6. Nitrate

The nitrate value also shows that 30 water samples have nitrates that do not exceed the water quality standard which is worth 10 mg / L. Spatially, nitrates in Lake Rawa Besar have uniform WQI values. There is only one water quality criterion based on the nitrate parameter, that is, water that is critically clean.

Fig. 7 Nitrate WQI spatial pattern within Lake Rawa Besar

3.7. Landuse

The lake's catchment area has different uses around it, such as settlement, market, public buildings, and vegetation cover. The details of the building classification such as permanent and semi-permanent house, permanent and semi-permanent commercial building, house with garden cover, and also public building differentiate by the difference of the uses. The figure can be seen on Fig. 8

The west side of Lake Rawa Besar also has a permanent house built in Depok City Housing. In addition, there is also a school complex consisting of several elementary, middle, high school, vocational schools, and foundations that have several levels of schools. On the same highway there are also many buildings that are used as trade.

Utilization in the form of a garden house is in the eastern part of Lake Rawa Besar. In the garden house, this house is in a garden that grows wild trees and there is no path to the house. Around the garden house there is a garbage dump and a chicken coop.

In addition to land use in the form of area, there are also places for surrounding community activities such as poultry cages, fish cages, iron workshops, wood sawmills, tofu factories, garbage dumps, and food stalls that have the potential to become pollutant sources for Lake Rawa Besar. Some chicken coops are in slums in the west of Lake Rawa Besar, but there are also several locations in the north and east of Lake Rawa Besar.

The type of land use in the north tends to be dominated by permanent houses. The northern part of Lake Rawa Besar on the edge of Lake Rawa Besar also has a lot of semi-permanent commercial building. Public buildings in the form of schools are mostly located in the west of Lake Rawa Besar. In the southwest there are semi-permanent houses because of the existence of slum settlement located on the banks of Lake Rawa Besar. There are uses of many garden lands in the edge around the lake. Permanent commercial buildings on the edge of highways are found in the western part of public buildings. There are several garden houses around slums and gardens.

There are some pollutant sources such as chicken coops in slums behind the school area and in the north and east of Lake Rawa Besar. Fish cages located on the edge of the Lake Rawa Besar are spread almost evenly in water bodies near permanent settlements in the eastern part of the lake and slums.

The boundary of the Lake Rawa Besar also has an inlet flow in the form of sewers and culverts flowing into the lake body. The use of land and sources of pollutants that exist in the boundary of the Lake Rawa Besar has the potential to affect the lake and flow through the inlet to the water body.

3.8. The Effect of Landuse to The Water Quality

This study found that turbidity and BOD parameters is more variative scattered in the water body than total phosphate, total solid, pH, and nitrate. These may indicate that the water turbidity and BOD level in the waters of Lake Rawa Besar can be affected by the land use surrounding the lake. The lake's catchment area mostly in the form of built-up land, such as settlements, commercial areas, and school zones are heavily filled with pollution source caused by human activities. The existence of settlements producing household waste can be a major cause of high BOD values so that water becomes turbid [14].

The dominance of permanent home land use and environmental roads does not affect water quality, but the use of trade land in the north with the type of trade land use and source of pollutant landfills affects several water quality parameters, such as turbidity entering the dirty criteria and BOD entering the moderately polluted criteria. Uneven turbidity in Lake Rawa Besar has varying characteristics of land use, such as extensive garden areas in the south, as well as several landfills in parts of the slum area around semi-permanent houses area. Turbidity with dirty levels is also found in the north of Lake Rawa Besar with the type of land use dominated by gardens and the use of semi-permanent commercials, but there are several landfill locations on the edge of Lake

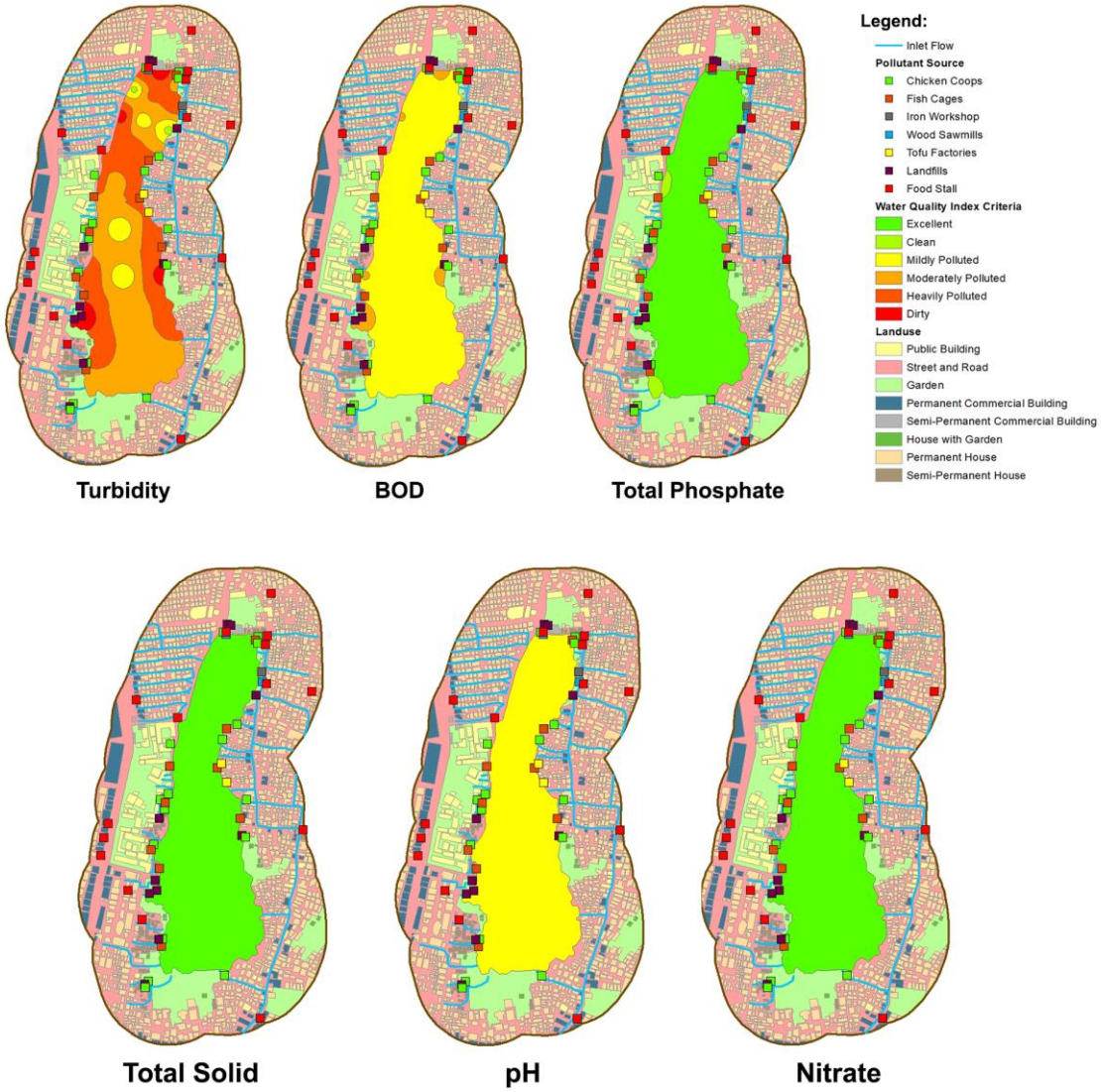

Fig. 8 WQI parameter values with landuse around Lake Rawa Besar

Rawa Besar. Some locations for food stalls and chicken coops do not affect the total phosphate value, but some locations of chicken coops and landfills are related to the location of BOD values that are included in the medium polluted criteria.

The total phosphate parameters are related to agricultural and plantation activities that produce chemical waste and runoff of large and small materials. The total phosphate value is only slightly higher in the western part of the back of the school area and gardens near the southern part of the housing complex. It is possible that more disposal of chemicals and wastes is found in the vicinity of slums, especially there are also poultry cages in that location.

4. CONCLUSIONS

The pattern of spatial distribution of Lake Rawa Besar water quality based on the total value of the WQI produces a relatively clean and increasingly dirty central part of the lake towards the edge of the lake. The spatial distribution of water quality turbidity and BOD parameters has a similar pattern, which is high on the edge and lower in the middle. The water quality of the total phosphate parameters has an almost uniform pattern, namely the excellent criteria that is evenly distributed in the Lake Rawa Besar water body. The pattern of spatial distribution of water quality is closely related to land use and the existence of potential sources of pollutants. The high BOD and turbidity values are caused by domestic waste.

REFERENCES

[1] Marisa, Basri, H., and Anhar, A., Kajian Perubahan Penggunaan Lahan di Daerah Tangkapan Air Danau Laut Tawar Tahun 2007-2015. Jurnal Ilmiah Mahasiswa Pertanian, Vol. 1, Issue 1, 2016, pp. 110-118.

[2] Anand, A., Linking Urban Lakes: Assessment of Water Quality and Its Environmental Impacts. University of Twente Faculty of Geo-Information and Earth Observation (ITC), 2014.

[3] Susilowati, W., Dampak perubahan penggunaan tanah pada kualitas air Lake Rawa Besar, Doctoral dissertation Universitas Indonesia, 2004.

[4] Bhateria, R. and Jain, D., Water quality assessment of lake water: a review. Sustainable Water Resources Management, 2(2), 2016, pp. 161-173.

[5] Wang, L., Ye, M., Rios, J. F., Fernandes, R., Lee, P. Z., and Hicks, R. W., Estimation of nitrate load from septic systems to surface water bodies using an ArcGIS-based software. Environmental Earth Sciences, Vol. 70, Issue 4, 2013, pp. 1911–1926.

[6] Faiilagi, S. A., Assessing the impacts of land use patterns on river water quality at catchment level: a case study of Fuluasou River Catchment in Samoa: a thesis presented in partial fulfillment of the requirements for the degree of Master of Environmental Management at the Institute of Agriculture and Environment, Massey University, Palmerston North, New Zealand. Doctoral dissertation Massey University, 2015.

[7] Ohrel, R. L. and Register K. M., Volunteer Estuary Monitoring: A Methods Manual Second Edition. Washington DC: US Environmental Protection Agency, 2006.

[8] Rinawati, Hidayat, D., Suprianto, R., and Dewi, P. S., Penentuan Kandungan Zat Padat (Total Dissolved Solid dan Total Suspended Solid) di Perairan Teluk Lampung. Analit: Analytical and Environmental Chemistry, Vol. 1 Issue 1, 2016, pp. 36-45.

[9] Sutjiningsih, D., Water Quality Index for Determining the Development Threshold of Urbanized Catchment Area in Indonesia. International Journal of Technology, Vol. 8 Issue 1, 2017.

[10] Undang-Undang Nomor 11 Tahun 1974 Tentang Pengairan. Indonesia Constitution, 1974.

[11] Lathamani, R., Janardhana, M. R., and Suresha, S., Application of Water Quality Index Method to Assess Groundwater Quality in Mysore City. International Journal of Innovation Research in Science, 2014, pp. 501-508.

[12] Ke, W., Cheng, H. P., Yan, D., and Lin, C., The application of cluster analysis and inverse distance-weighted interpolation to appraising the water quality of three Forks Lake. Procedia Environmental Sciences, Vol. 10, 2011, pp. 2511-2517.

[13] Ramadhani, F. T. W., Harisuseno, D., and Yuliani, E., Penerapan Metode Water Quality Index (WQI) dan Metode STORET untuk Menentukan Status Mutu Air pada Ruas Sungai Brantas Hilir. Jurnal Pengairan Universitas Brawijaya, 2016.

[14] Khatri, Nitasha, and Tyagi S., Influences of Natural and Anthropogenic Factors on Surface and Groundwater Quality in Rural and Urban Areas. Frontiers in Life Science, Vol. 8, Issue 1, 2015, pp. 23–39.

9th Int. Conf. on Geotechnique, Construction Materials and Environment,
Tokyo, Japan, 20-22 November 2019, ISBN: 978-4-909106025 C3051

GIS FOR COASTAL HAZARD ANALYSIS

A. B. Sambah[12*], F. Miura[3], D. O. Sutjipto[1], T. D. Lelono[1]
[1]Faculty of Fisheries and Marine Science, University of Brawijaya, Indonesia
[2]Marine Resources Exploration and Management Research Group, University of Brawijaya
[3]Faculty of Engineering, Yamaguchi University, Japan

ABSTRACT

Coastal areas have been used as a settling ground for human population as they provided abundant fisheries and marine resources and possibilities for business sectors. Coastal hazards cause loss of life and the degradation of coastal environment. It defined as physical phenomena that expose a coastal area to risk of property damage. Coastal areas are frequently changing, in which natural hazards such as tsunamis is one of the sources. The management of coastal hazard currently has become an important aspect for coastal planning in order to improve the resilience of society to coastal hazards. Coastal disaster management can be done based on the risk analysis using several vulnerability and risk parameters. The current research tried to analyze the potential risk area due to tsunami hazard using the parameter of vulnerability in the coastal area of East Java Indonesia. Risk map produced from the geospatial database analysis in the concept of the geographical information system (GIS). Risk assessment combines the outputs of vulnerability assessments and the hazard, in which the topography elevation, type of building, land cover, coastal vegetation density, and the type of coastline build the vulnerability map. Historical data of some tsunami events indicates that some of the damage caused by the coastal elevation as one of the physical parameters of tsunami vulnerability, as well as social parameters. The study describes an important result related to multi-criteria processing in predicting the tsunami risk area. GIS plays as important approaches in combining the geospatial database of each parameter and displays it in geographical perspective.

Keywords: Geographical information system, hazard, tsunami, risk, vulnerability

INTRODUCTION

The development of coastal areas today is more focused on the consideration of environmental degradation. Various kinds of hazard threats to the coastal environment, such as natural disasters and other natural phenomena, are also considered in the management of coastal areas. Coastal areas are one of the areas that are susceptible to environmental damage, both caused by the pressure of human activities and the consequences of natural disasters.

Coastal hazards can be defined as physical phenomenon that exposes a coastal area to risk of property damage, loss of life and environmental degradation. In the term of coastal zone management, coastal hazard management has become an increasingly important aspect. This is important to improve the resilience of society to coastal hazards. Possible management options include the design of coastal structures, application of natural coastal green for coastal protection, various accommodation approaches as well as a managed infrastructure in the area close to the coastline. For overcoming coastal hazards, it is also important to have early warning systems and emergency management plans in order to be able to address sudden and potential disastrous hazards i.e. major flooding events, tsunami, or hurricane. Events as the 2004 Indian Ocean earthquake and tsunami, the Hurricane Katrina affecting the southern USA in 2005, the cyclone Nargis affecting Myanmar in 2008, the 2011 Tohoku, Japan earthquake and tsunami, and also the 2018 Sulawesi, Indonesia earthquake and tsunami provides clear examples of the importance of timely coastal hazard management.

The purpose of mitigation is not only to minimize the loss of property damage but also minimize the damages of environmental due to development. Disaster mitigation program also important approaches in order to avoid impacts by not taking actions, to reduce impacts by rehabilitation the affected environments or constructing long-term maintenance operations, and compensating for impacts by providing substitute environments for resources.

Through human history, developing technology has increased the range of adaptation options in the face of coastal hazards, and there has been a move from retreat and accommodation to hard protection and active seaward advance via land claim as exemplified by the Netherlands [1].

in general coastal hazards can be grouped into five main impacts, usually with several contributing

processes causing cumulative harm; (1) coastal erosion and coastline stability (including the area of river mouths, tidal inlets and cliffs) from waves, storm tide, changes in sediment budgets, river floods, coastal structures, storm water, and sea-level rise; (2) coastal flooding cause from storm tide, river floods, tsunami, and sea-level rise; (3) the level of groundwater in the coastal area due to storm tide, intense rainfall, sea-level rise, and salinization; (4) recreational activities together with hazards arising from surf zone conditions (e.g. rips, wave conditions, long-wave surges); (5) oceanic activities together with marine navigation hazards arising from wave conditions, storm tide, strong winds, long-wave surges and also tsunami.[2].

The application of Geographical Information System (GIS) for disaster research provides an important integrated contribution in order to assess the risk of the coastal area due to the natural disaster [3]. The development of satellite remote sensing technology and its applications enable the use of satellite imagery for mapping the distribution of an area damaged by a disaster. Satellite images have the advantage of being able to deliver simultaneous images of wide areas [4]-[5]-[6]. In addition, with the aid of the GIS, spatial multi criteria analysis helps prioritize the decision-making process using spatial database. Spatial multi criteria analysis is vastly different from conventional Multi Criteria Decision Making (MCDM) techniques, due to the inclusion of an explicit geographic element.

GIS mapping of tsunami vulnerability has also applied using the Shuttle Radar Topography Mission (SRTM) to obtain the topographic data of the study area [7]-[8]. Another geospatial analysis approach has applied soil type, urban form and social type system for the potential natural hazard mapping [9] and has assessed the tsunami vulnerable area by comparing building damage map with the physical topography data includes elevation, land use, and the distance from the coast [10]. Mapping of the 2011 Tohoku earthquake tsunami inundation and run-up by in-situ survey also has been published in order to develop create appropriate disaster mitigation concepts [11].

This study tried to apply several physical topography data for analyzing coastal hazard and its affected areas, especially caused by the tsunami disaster using GIS approach.

METHOD

Study Area

The analysis was applied in three different case study areas around the coastal area of Indonesia in order to know the different result of applying physical topographic dataset. The area includes the coastal area of Java Island and divided into the western part of Java which is represented by Banten Regency areas, the eastern part of Java Island which represent by Banyuwangi Regency, and also Malang regency area which represents the area that directly faces to the Indian Ocean. The study area as describe on Fig. 1.

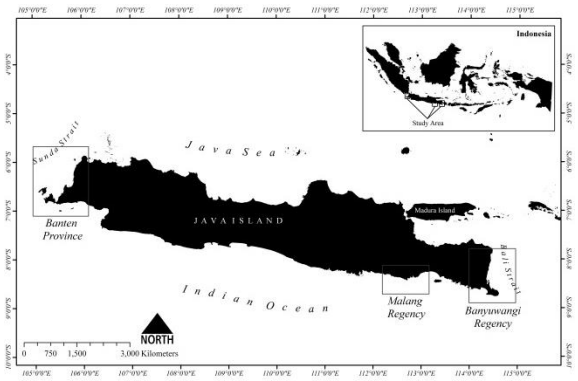

Fig. 1 Study area

Dataset

Physical data set for assessing the affected area of tsunami disaster in all coastal areas of case study was collected. This dataset includes topography elevation, slope, building area, coastal proximity and coastal type, and also population density as well. For providing the physical topographic parameters, the dataset of The ASTER Global Digital Elevation Model (ASTER GDEM) version 2 was collected from *https://gdex.cr.usgs.gov/gdex/*. This data are available from the Land Processes Distributed Active Archive Center (LP DAAC). Moreover, The NASA Shuttle Radar Topographic Mission (SRTM) also collected for preparing topographic elevation dataset. SRTM has provided digital elevation data (DEMs) for over 80% of the globe and distributed by USGS and is available for download from the National Map Seamless Data Distribution System, or the USGS ftp site. The SRTM data is available as 3 arc second and downloaded from *http://srtm.csi.cgiar.org/srtmdata/*.

In addition to provide land use map that describe also the building areas, Sentinel 2 satellite image was applied. Sentinel-2 is a European wide-swath, high-resolution, and multi-spectral imaging mission. The full mission specification of the twin satellites flying in the same orbit but phased at 180°, is designed to give a high revisit frequency of 5 days at the Equator. Sentinel-2 carries an optical instrument payload that samples 13 spectral bands: four bands at 10 m, six bands at 20 m and three bands at 60 m spatial resolution. The orbital swath width is 290 km [12]. This data was collected from *https://scihub.copernicus.eu/dhus/#/home.*

The type of coastal, distance from coastline to hinterland (coastal proximity), and other land use

feature were created from vector data of base map. This data was collected from Indonesia Geospatial Information Agency. Dataset that used in the analysis as described in Table 1, Table 2, and Table 3.

Table 1 Specification of DEM data

	Aster GDEM	SRTM
Data source	ASTER	Space shuttle radar
Generation and distribution	METI/NASA	NASA/USGS
Release year	2009 ~	2003 ~
Data acquisition period	2000~ongoing	11 days (in 2000)
Posting interval	30m	90m
DEM accuracy (stdev)	7-14m	10m
DEM coverage	83°N~83°S	60°N~60°S

Table 2 Specification of satellite image data

Satellite specification			
Data source	The Copernicus Sentinel-2 mission		
swath width	290 km		
revisit time	10 days at the equator with one satellite, and 5 days with 2 satellites under cloud-free conditions which results in 2-3 days at mid-latitudes		
coverage limits	56°S~84°N		
Sensor specification			
No	Band	Wave length (µm)	Spatial resolution
1	Band 2 – Blue	0.490	10m
2	Band 3 – Green	0.560	10m
3	Band 4 – Red	0.665	10m
4	Band 5 – Vegetation Red Edge	0.704	20m
5	Band 6 – Vegetation Red Edge	0.740	20m
6	Band 8 – NIR	0.835	10m
7	Band 8a – Vegetation Red Edge	0.865	20m

Table 3 Specification of vector base map data

Location	Type	Scale	Coordinate system
Banten, Malang, and Banyuwangi, Indonesia	**Point type:** boundaries of administrative areas, road edge, elevation, buildings **Line type:** Shoreline, water, road edge, boundaries of administrative areas **Polygon type;** Boundary of the district	1:25000	UTM WGS 88, Zona 48 S

Data Analysis

As one of the potential natural disasters that affect to the dynamic of coastal area, the affected area due to tsunami could be assess through the analysis of risk and vulnerability. In order to analyse this assessment, all parameters will be analyzed using GIS. GIS helps in the integration of all dataset geographically.

DEM dataset collected will be calculated for producing topographic elevation data and slope. This elevation and slope data will then be analyzed spatially based on the risk standard and vulnerability of these two parameters to produce a map of coastal area vulnerability to tsunami hazards. DEM data will be visualized using surface analysis in GIS as well as the slope was created from the DEM data. DEM data will be visualized using surface analysis in GIS as well as the slope was created from this DEM data.

The distance from coastline to the hinterland (coastal proximity) and the radius zone from river was calculated and created using vector base map of the study area and analyzed through multi-ring buffer of proximity analysis in GIS. In order to set the radius number of coastal proximity for assessing the risk area due to tsunami, Eq. (1) was applied.

$$log X_{max} = log 1400 + {}^{4}/_{3}\, log\left({}^{Y_0}/_{10}\right) \quad (1)$$

In which, X_{max} is represent the maximum reach of the tsunami over land, and Y_0 is the height of the tsunami at the coast. For applying this algorithm, a set of tsunami historical data which describe the information of maximum run-up in the area of study was collected. The class number of this coastal proximity was different for three research areas. Type of coastline was created also using vector base map of the study area by digitizing polyline data of the coastline and categorized it based on the coastal morphology type.

For preparing the land use data and build area of the study area, Sentinel-2 satellite image was analyzed using image classification process. The satellite image processing starts with the computation of TOA (Top of Atmosphere) Reflectance. The numeric digital counts (CN) of each pixel image (*i*,*j*) and each spectral band (*k*) are converted in TOA reflectance (ρ). This conversion takes into account the equivalent extra-terrestrial solar spectrum (*Es*), the incoming solar direction defined by its zenith angle (θs) for each pixel of the image and the absolute calibration (*Ak*) of the

Multispectral Instrument (MSI). As explained in Sentinel-2 technical guides [13], The TOA conversion equation as described in Eq. (2).

$$\boldsymbol{\rho_k(i,j) = \frac{\pi \times CN_{k.NTDI}(i,j)}{A_{k.NTDI} \times E_S \times d(t) \times \cos(\theta_s(i,j))}} \quad (2)$$

where:
$CN_{k.NTDI}$ is the equalized numeric digital count of the pixel (*i,j*) with NTDI, the number of Sentinel-2 TDI lines. E_s is the equivalent extra-terrestrial solar spectrum and depends on the spectral response of the Sentinel-2 bands. The component *d(t)* is the correction for the sun-Earth distance variation (as described in Eq. (3)). It utilises the inverse square law of irradiance, under which, the intensity (or irradiance) of light radiating from a point source is inversely proportional to the square of the distance from the source [13].

$$\boldsymbol{d(t) = \frac{1}{(1 - 0.01673 \times \cos(0.0172 \times (t-2)))^2}} \quad (3)$$

Where :
t is the Julian Day corresponding to the acquisition date. 0.01673 is the Earth orbit eccentricity. 0.0172 is the Earth angular velocity (radians/day). The parameters *Ak* and *Es* are provided by the GIPP and are also included in the ancillary data of the Level-1 products. The sun zenith angles are determined at this level too. A sun angle grid is computed by regularly down-sampling the target geometry (Level-1C tile). The cosine of the zenith angle *θs* is defined at each point of the grid using the ground coordinates and the datation of the corresponding pixel acquisition.

Reflectance value, often between 0 and 1, is converted into integer values, in order to preserve the dynamic range of the data by applying a fixed coefficient (1000 by default). This reflectance value was used as standard value in image classification process in which the supervised classification method was applied using several training area.

All geospatial databases will be analyzed through a spatial overlay process, where all parameters were in the form of a raster data base and processed based on the standard value of each parameter, as illustrated in Table 4 and Table 5. Analysis carried out through GIS with a pixel-based weighted overlay process. The weights of the parameter were constructing using pair-wise comparison matrix of Analytical Hierarchy Process (AHP) method.

Table 1 The physical vulnerability value range for elevation, slope, and landuse

Vulnerability class	Elevation (m)[1]	Slope (%)[2]	Landuse[3]
High	<5	0-2	Urban
Slightly high	5-10	2-6	Agriculture
Moderate	10-15	6-13	Bare soil
Slightly low	15-20	13-20	Water
Low	>20	>20	Forest

[1] [4]
[2] [5]
[3] [6]

Table 2 The physical vulnerability value range for coastline distance, river distance, and coastal type

Vulnerability class	Coastline distance (m)[4]	River distance (m)[5]	Coastal type[5]
High	<293	0-100	V bay
Slightly high	293-514	100-200	U bay
Moderate	514-762	200-300	Cape
Slightly low	762-1032	300-500	Straight
Low	>1032	>500	Neutral

[4] Based on Eq. 1 calculations and it will be different result for different study area
[5] [7]

RESULT AND DISCUSSION

This study was one of the approaches in the integrated coastal hazard assessment, in which the analysis for describing the affected area caused by tsunami wave was studied. Analysis of all disaster risk parameters in this study obtained thematic maps of each parameter. This map illustrates the potential areas affected by the tsunami disaster. To get a conclusion of the risk area based on a combination of all parameters, a spatial overlay process for all parameters was carried out, with the multiplication concept of each pixel of parameter with its weight. The weight of each parameter was obtained from expert judgment and calculated based on the AHP approach. The conclusion of this calculation is the form of pair-wise comparison matrix with the required consistency ratio of less than 10% (2.9%), as explained in Fig. 2. The result of AHP calculation through pair-wise comparison matrix described that the elevation was parameters with the highest weight that affect the creating of risk maps. In contrast, the parameter of river distance was the lowest. In the future analysis, the different type of landcover would be important to be separated. The area with a high density of vegetation would be included in the low class of tsunami risk compare with the bare land.

In the application of parameter's weight for creating risk area map, a research on tsunami vulnerability in Alexandria was applied all parameter in equal weight due to the limitation of knowledge regarding to the study area [14]. The use of pair-wise comparison matrix in weight calculation also applied in the tsunami vulnerability mapping along coastal area of Miyagi Prefecture, Japan and. illustrated a similar pattern of tsunami vulnerability

area to the real tsunami inundation area during the 2011 Tōhoku's tsunami [15].

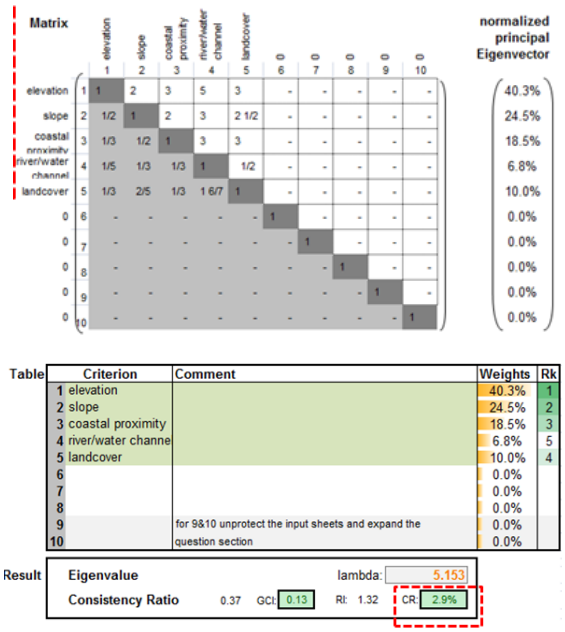

Fig. 2 Pair-wise comparison matrix and normalized principal eigenvector

The result of the analysis as describe on Fig. 3, Fig. 4, and Fig. 5. The map shows that in general the high risk areas were mostly found in the coastal area with the sloping coast type. Elevation and slope play an important role in determining the stability of the terrain in the coastal [16]. The research of tsunami vulnerability along coastal area of Bali, Indonesia described that the distribution of vulnerability is not uniform and physically it is highly influenced by the distance from coastline to the hinterland, topography elevation, and also slope [17]. The most risk area due to tsunami disaster in depends on the direction of tsunami source or the epicentre of the earthquake.

The results of this study illustrate that areas with low vegetation density, high distribution of build area, flat areas, and areas close to large rivers will have greater disaster risk. The existence of rivers in the coastal area will enable it to act as the successor to the tsunami wave that comes and takes it far towards the land until it reaches a certain elevation.

The outputs of the tsunami hazard analysis are very much dependent on data availability and the application of methods. The approaches range from simple empirical methods to sophisticated numerical simulations. Empirical methods use simplified formulas to derive tsunami hazard maps. In general, information on the elevation and the distances from coastline are applied in combination with empirical formulas to estimate the inundated areas on coastal areas [18].

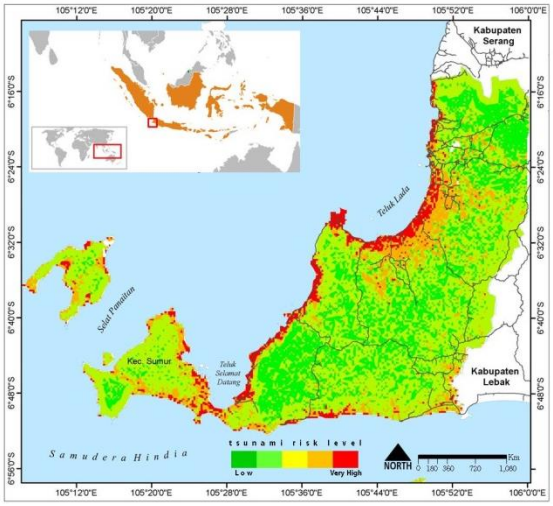

Fig. 3 Tsunami risk area in the coastal area of Banten, Indonesia

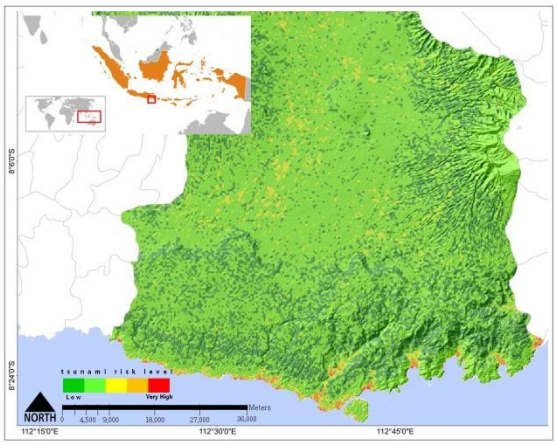

Fig. 4 Tsunami risk area in the coastal area of Malang, Indonesia

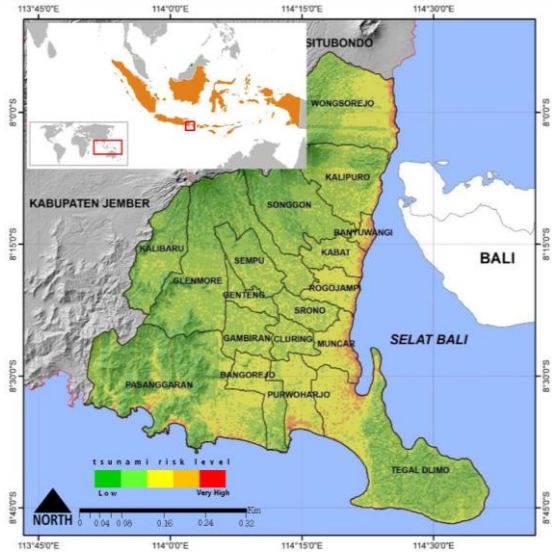

Fig. 5 Tsunami risk area in the coastal area of Banyuwangi, Indonesia

CONCLUSIONS

Risk and vulnerability assessment is one of the important steps in contributing the information regarding to the coastal hazard analysis. The concept and methods have been applied to compare the importance of using risk parameters by testing them in three different coastal regions. From the analyses key parameters are derived and integrated for assessing the risk and vulnerability map. The result will be act an important role for effective early warning system. In the future work, the social and ecological parameter will be an important parameter for analysis.

ACKNOWLEDGMENTS

Authors are thankful to Laboratory of Marine Resources Exploration, University of Brawijaya Indonesia and Laboratory of Disaster Prevention System, Yamaguchi University, Japan. We also thank to Indonesia Geospatial Information Agency for providing the basic map of the study area, METI/NASA for Aster GDEM data, NASA/USGS for SRTM data, and ESA for Sentine-2 data.

REFERENCES

[1] Van Koningsveld, M.; Mulder, J.P.M.; Stive, M.J.F.; van der Valk, L., and van der Weck, A.W., Living with sea-level rise and climate change: a case study of the Netherlands. Journal of Coastal Research, Vol. 24, 2008, pp. 367–379.

[2] https://www.niwa.co.nz/natural-hazards/hazards/coastal-hazards

[3] Sambah A.B., Miura F., Guntur, and Fuad., Integrated Satellite Remote Sensing And Geospatial Analysis For Tsunami Risk Assessment, International Journal of GEOMATE, Vol.14, Issue 44, 2018, pp.96-101.

[4] Karen, E., Joyce K. C., Wright S., Samsonov V., and Ambrosia V. G., Remote Sensing and the Disaster Management Cycle, In Advances in Geoscience and Remote Sensing, edited by G. Jedlovec. Croatia: InTech, 2009.

[5] Yamazaki, F., Kouchi K., and Matsuoka M., Tsunami Damage Detection Using Moderate-Resolution Satellite Imagery, Proceeding of the 8th U.S. National Conference on Earthquake Engineering, San Francisco, CA, April 18–22, 2006.

[6] Yamazaki, F., and Matsuoka, M., Remote sensing technology in post-disaster damage assessment, Journal of Earthquakes and Tsunamis, World Scientific Publishing Company, vol. 1, no. 3, 2007, pp. 193-210.

[7] Sinaga, T.P., Adhi, N., Yang-Won, L. and Yongcheol, S., GIS Mapping of Tsunami Vulnerability: Case Study of the Jembrana Regency in Bali, Indonesia, KSCE Journal of Civil Engineering, Vol. 15, No. 3, 2011, pp. 537-543.

[8] Abu Bakar Sambah Fusanori Miura, Remote Sensing and Spatial Multi-Criteria Analysis for Tsunami Vulnerability Assessment, Disaster Prevention and Management, Vol. 23 Issue 3, 2014, pp. 271 – 295.

[9] Hsien, L.C. and Sheng, C.H., The Use of Spatial Analysis Techniques In Mapping Potential Natural Hazard Areas: A Case Study of Taiwan", Procedia Environmental Sciences, Vol. 10, No. Part B, 2011, pp. 1092-1097.

[10] Gokon, H. and Koshimura, S., Mapping of Building Damage of The 2011 Tohoku Earthquake Tsunami in Miyagi Prefecture, Coastal Engineering Journal, Vol. 54, No. 1, 2012, pp. 126-138.

[11] Mori, N., Takahashi, T., Yasuda, T. and Yanagisawa, H., Survey of 2011 Tohoku earthquake tsunami inundation and run-up, Geophys. Res. Lett, Vol. 38, 2011, L00G14.

[12] Sentinel-2 User Handbook. Issue 1 Rev 2. ESA Standart Document. European Space Agency, 2015.

[13] https://sentinel.esa.int/web/sentinel/technical-guides/sentinel-2-msi/level-1c/algorithm

[14] Eckert, S., Jelinek, R., Zeug, G. and Krausmann, E., Remote sensing-based assessment of tsunami vulnerability and risk in Alexandria, Egypt", Applied Geography, Vol. 32 No. 2, 2012, pp. 714-723

[15] Sambah A.B. and Miura F., "Remote Sensing and Spatial Multi-Criteria Analysis for Tsunami Vulnerability Assessment", Disaster Prevention and Management, Vol. 23 (3), 2014, pp. 271–295.

[16] Yashon O. Ouma, and Tateishi R., Urban Flood Vulnerability and Risk Mapping Using Integrated Multi-Parametric AHP and GIS: Methodological Overview and Case Study Assessment, Water, Vol. 6, 2014, pp. 1515-1545.

[17] Eddy, GIS in Disaster Management: a Case Study of Tsunami Risk Mapping in Bali, Indonesia, Masters (Research) Thesis, 2006, Jamas Cook University, Australia.

[18] Strunz, G., Post, J., Zosseder, K., Wegscheider, S., Muck, M., Riedlinger, T., Mehl, H., Dech, S., Birkmann, J., Gebert, N., Harjono, H., Anwar, H. Z., Sumaryono, Khomarudin, R. M. and Muhari, A., Tsunami risk assessment in Indonesia, Natural Hazards and Earth System Science, Vol. 11, 2011, pp. 67-82.

9th Int. Conf. on Geotechnique, Construction Materials and Environment, Tokyo, Japan, 20-22 November 2019, ISBN: 978-4-909106025 C3051

WHEEL LOAD DISTRIBUTION IN STRAIGHT AND SKEWED CONCRETE SLAB BRIDGES STIFFENED WITH RAILINGS

Ghassan Fawaz[1], Mounir Mabsout[2], and Kassim Tarhini [3]
[1]Dept. of Civil, Architectural and Environmental Engineering, Univ. of Texas at Austin, USA; formerly Dept. of Civil and Environmental Engineering, Amer. Univ. of Beirut, Lebanon
[2]Dept. of Civil and Environmental Engineering, Amer. Univ. of Beirut, Lebanon
[3]Dept. of Civil Engineering, U.S. Coast Guard Academy, USA

ABSTRACT

This paper presents the parametric investigation of the influence of railings on the wheel load distribution in simply-supported, one-span, three- and four-lane straight and skewed reinforced concrete slab bridges using the finite element method. A total of 96 bridge cases were modeled using finite-element analysis (FEA) and bridge parameters such as span length, slab width, and skew angle are varied within practical ranges. Typical railings built integrally with the bridge were placed on both edges of the deck slabs. AASHTO HS20 truck loadings were positioned transversely and longitudinally to produce maximum longitudinal live load bending moments in the slabs. The FEA wheel load distribution and bending moments were compared with reference straight bridges without railings as well as to the AASHTO Standard Specifications for Highway Bridges and the AASHTO LRFD Bridge Design Specifications. AASHTO overestimates FEA moments for almost all bridge cases and this overestimation increases with the increase in the skew angle, and it is more significant in the presence of two railings. Also, it was found that the reduction in slab moment due to skewness and railings is cumulative. The presence of railings can be considered to be a possible method for strengthening and rehabilitating straight and skewed concrete slab bridges.

Keywords: Concrete slab bridges, Multi-lane, Skew angle, Railings or parapets, Finite-element analysis, AASHTO procedures, Load-carrying capacity.

INTRODUCTION

A significant number of highway bridges are short-span reinforced concrete slabs that are owned and maintained by local and state governments. The main advantage of concrete slab bridges is the ease of construction and the ability to field adjustment of the roadway profile during construction.

Skewed bridges are often encountered in highway design when the geometry cannot accommodate straight bridges. The skew angle can be defined as the angle between the normal to the centerline of the bridge and the centerline of the abutment or pier cap as described in Fig. 1.

The design of highway bridges in the United States conforms to the American Association of State Highway and Transportation Officials (AASHTO) procedures, either to the Standard Specifications for Highway Bridges (2002) prior to 2007 – thereafter referred to as AASHTO Standard [1], or to the current Load and Resistance Factor Design (LRFD) Specifications (2014) – thereafter referred to as AASHTO LRFD [2]. The current AASHTO procedures do not consider the effect of railings that are built integrally with the bridge deck, and only AASHTO LRFD accounts for skewness in the evaluation of the load-carrying capacity of bridges. Therefore, this study investigates the combined effect of railings and skew angle in resisting highway loading and increasing the load-carrying capacity of reinforced concrete slab bridges.

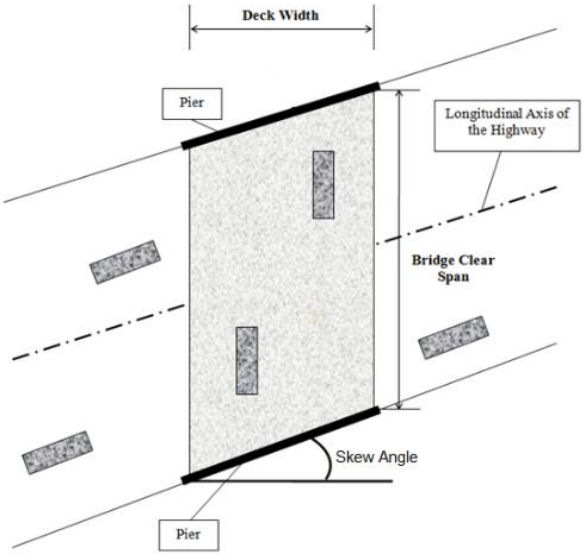

Fig. 1 Description of skewed bridge.

Several studies were conducted on the influence of sidewalks and railings on wheel load distribution in steel and prestressed girder bridges which was shown to increase the stiffness of the superstructure and improve the load-carrying capacity of these bridges [3]-[4]-[5]-[6]-[7].

A parametric study of straight, single-span, multi-lane (1 to 4 lanes) simply-supported reinforced concrete slab bridges, using finite-element analysis (FEA) was also reported [8]. Results indicated that AASHTO Standard moments overestimate the FEA moments for short spans, one-lane bridges and agreed with FEA moments for short spans in combination of two or more lanes. Also, AASHTO Standard underestimates the FEA moments for longer spans. As for AASHTO LRFD procedure, it overestimates FEA moments for all bridge cases. This study was extended to study the influence of skew angle on the same concrete slab bridges [9]. The ratio between the FEA longitudinal moments for skewed and straight bridges was almost one for bridges with skew angle less than 20 degrees. This ratio decreased to about 0.75 for bridges with skew angles between 30 degrees and 40 degrees, and further decreased to about 0.50 skew angle of the bridge increased to 50 degrees. Further, a study investigated the influence of one standard railing built integrally on either one or both edges of the slab deck, for the same straight bridges [10]. The results indicated that placing two railings on the bridge slab, AASHTO Standard overestimated the FEA moments by 100% for one-lane bridges, and by 20% for bridges with two or more lanes, while AASHTO LRFD overestimated the FEA moments in all bridge cases by 150% for one-lane, 70% for two-lanes, and a 30% for three- and four-lanes. Finally, a preliminary study considered the combination of railings and skewness on the concrete slab bridges previously analyzed for the cases of one and two lanes [11]. With no railing, AASHTO Standard generally tends to give similar results to the FEA slab moments for skew angle up to 20 degrees. As skew angle increases, AASHTO overestimation increases till it reaches 100% for bridges with skew angle of 50 degrees. Also, generally AASHTO overestimation is higher for one-lane bridges as compared to two-lane bridges and it decreases with the increase in span length. Adding two railings, AASHTO overestimates FEA moments for all bridge cases and this overestimation increases with the increase in skew angle reaching 140% for a skew angle of 50 degrees. Further, AASHTO LRFD overestimates the FEA slab moments in almost all bridge cases with or without railings. This overestimation increases with the increase in the skew angle and it is most significant for bridges with two railings and a skew angle of 50 degrees. For straight bridges with no railings, AASHTO LRFD overestimates the FEA slab moments by about 50% for one-lane bridges and about 30% for two-lane bridges. When the skew angle increases to 50 degrees, AASHTO LRFD overestimates the FEA slab moments by about 125% for one-lane bridges and about 100% for two-lane bridges. When two railings are present, and for straight bridges, the AASHTO LRFD overestimation of the FEA slab moments becomes more significant reaching an average high of 150% in one-lane bridges or 70% in two-lane bridges. As for bridges of skew angle of 50 degrees this overestimation reaches its maximum values and is 190% for one-lane bridges and 140% for two-lane bridges.

This paper builds on the previously published research, namely in [8]-[9]-[10]-[11], by performing a parametric study investigating the influence of railings and skweness on wheel load distribution in simply-supported, one-span, three- and four-lane concrete slab bridges. The FEA slab moments will be assessed with AASHTO Standard and LRFD, as well as with the reference straight bridge cases without railing.

AASHTO STANDARD AND LRFD PROCEDURES

For simply-supported concrete slab bridges, AASHTO Standard [1] suggest three approaches in determining the live-load bending moment but only one procedure is used in this study that was compared with the finite-element analysis results.

$$M = 13{,}500S \quad for\ S \le 15m \tag{1a}$$

or

$$M = 1{,}000(19.5S - 90) \quad forS > 15m \tag{1b}$$

where:
S = span length (m)
M = longitudinal bending moment per unit width (N-m/m)

AASHTO Standard Section 3.2.6 suggests that slab bridges with a skew angle less than 30 degrees be designed as a typical slab at right angles, or as straight bridges, with no modifications. However, if the skew angle exceeds 30 degrees, AASHTO suggests the use of an alternate superstructure configuration.

AASHTO LRFD [2] Section 4.6.2.3 provides an equivalent strip width procedure to design reinforced concrete slab bridges that is comparable to procedures specified in the AAHSTO Standard. However, the AASHTO LRFD Section 3.6.1.2 requires the use of HL93 (addition of HS20 Truck plus lane loading) live loading. This approach is to divide the total bending moment by an equivalent width to obtain a statically design moment per unit width. The equivalent width

"*E*" of longitudinal strips per lane for both shear and moment is determined using the following formulas:

The width for one lane loaded is:

$$E = 250 + 0.42\sqrt{L1 \times W1} \quad (2)$$

while the width for multi-lanes loaded is:

$$E = 2{,}100 + 0.12\sqrt{L1 \times W1} \quad (3)$$

where:

M = longitudinal bending moment per unit width (N-m/m)

E = equivalent width of longitudinal strips per lane (mm)

L1 = span length (mm), the lesser of the actual span or 18,000 mm

W1 = edge-to-edge width of the bridge (mm) taken to be the lesser of the actual width or 18,000 mm for multi-lane loading, or 9,000 mm for single-lane loading.

For skewed bridges, AASHTO LRFD 4.6.2.3-3 reduces longitudinal force effects by a factor "*r*" which is a function of the skew angle:

$$r = 1.05 - 0.25\tan\theta \le 1.\ldots \quad (4)$$

where θ is the skew angles in degrees.

The current AASHTO procedures (Standard or LRFD) do not consider the influence of railings that are built integrally with the bridge deck on the increase of the bridge stiffness and its load-carrying capacity.

BRIDGE CASES AND LOADING

Typical simply-supported one-span, three-lane and four-lane, straight and skewed reinforced concrete slab bridge cases were analyzed in this study, without and in the presence of integral railings. Four span lengths were considered, 7.2, 10.8, 13.8, and 16.2 m (24, 36, 46, and 54 ft) with corresponding slab thicknesses of 450, 525, 600, and 675 mm (18, 21, 24, and 27 inches), respectively. The lane width was assumed to be 3.6 m (12 ft) and therefore the overall slab widths were taken as 10.8 m (36 ft) for three lanes and 14.4 m (48 ft) for four lanes. Six skew angles varying between 0° and 50° by increments of 10° were considered. A straight bridge is defined as having a 0° skew angle. Standard railings, 200 mm (8 inches) wide and 760 mn (30 inches) high above roadway, were placed integrally on both sides of the slab edges (labeled as R2). Straight bridges without railings were first analyzed and considered as the reference cases (labeled as R0). Figure 2 shows a typical cross-section and plan layout of a 13.8 m (46 ft) span, three-lane bridge case, with 30° skew angle and railings placed on both edges of the slab deck.

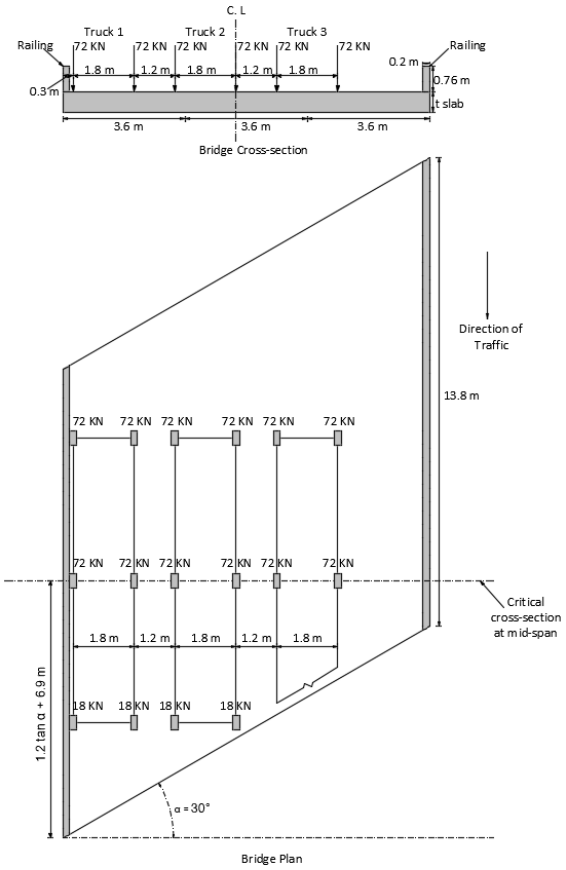

Fig. 1 Typical cross-section and layout for a 13.8 m (46 ft) span, three-lane, 30 degrees skewed bridge with railings, subject to HS20 Edge loading condition.

The bridge cases considered were subjected to AASHTO HS20 design trucks assumed to be traveling in the same direction placed longitudinally and transversally to produce maximum moments. For HS20 loading, the line wheel loads are 18 KN (4 Kips), 72 KN (16 Kips), and 72 KN (16 Kips) with axle spacing of 4.2 m (14 ft).

The longitudinal location of HS20 axle loads that produce maximum positive moment in one-span loading condition bridges was placed such that the centerline of bridge aligned with the location of centerline halfway between the resultant load of the truck and the middle axle. However, a previous study reported that the difference between placing the middle axle aligned with the mid-span versus the actual location mentioned above was negligible in determining the maximum bending moment in concrete slab bridges, which will therefore be adopted in this study [8]. Transversely, an Edge loading condition was applied, where the first design truck was placed close to one edge of the slab, such that the center of the left wheel of the left most truck is

positioned at 0.3 m (1 ft) from the left edge of the slab, and the other trucks were placed side-by-side with a distance 1.2 m (4 ft) between the adjacent trucks in order to produce the worst live loading condition on the bridge [8]. It is also worth noting that only the left-most truck was centered longitudinally, while adjacent trucks were aligned with the edge truck as shown. This condition resulted in slightly higher moments than for the case where each adjacent truck was centered longitudinally in its own lane [9]. Figure 2 shows the Edge loading condition for the bridge case described earlier.

The material properties used in modeling the highway bridges were normal-strength reinforced concrete. The compressive strength of the concrete was 27,500 kPa (4,000 psi), the modulus of elasticity was 25×10^6 kPa (3.6×10^6 psi), and Poisson's ratio was 0.2. Grade 60 reinforcing steel could be assumed in the design of slab reinforcement, but the FEA models did not include such property in the analysis.

FINITE ELEMENT MODELING AND RESULTS

A total of 96 slab bridge cases were investigated using the FEA using the general computer program SAP2000 [12]. The bridge discretization was tested in previous studies where shell elements with six degrees of freedom at each node were used to model the slab [8]-[9]. A typical four-node square element size of 0.3x0.3 m (1x1 ft) was adopted and for the slab discretization four-node quadrilateral and three-node triangular elements were additionally used at the supports to accommodate for skewness. Railings placed both edges of the slab were modeled as space frame elements placed "eccentrically" along the slab edges with the second moment of area calculated about its base. This was based on previous studies which investigated the appropriate railing modeling on straight concrete slab bridges [10]-[11]. This study considered all elements to be linearly elastic and the analysis assumed small deformations and deflections. Figure 3 shows a typical FEA model for the bridge case described earlier subjected to AASHTO HS20 Edge loading condition.

The FEA results are reported in terms of the maximum longitudinal bending moments at critical cross-section locations in the concrete slab bridges, shown in Fig. 3. The FEA results for skewed bridges with railings were compared with straight reference bridge cases without railings (R0- 0 degrees) as well as with AASHTO Standard [1] and LRFD [2] procedures. Figure 4 shows sample plots of the FEA longitudinal bending moment at the critical sections for 13.8 m (46 ft) span, three-lane bridge cases with the various railing configurations (R0 for no railing; and R2 for two railings), and select skew angles (only 0, 30, and 50 degrees for clarity) subject to Edge HS20 loading conditions. The corresponding AASHTO moments are also plotted in the figure. It is worth mentioning that the maximum FEA longitudinal moments in Fig. 4 for the concrete slabs was defined as the first peak value occurring after the maximum value at the leftmost edge which is assumed to be resisted by the edge beam and/or railing when present.

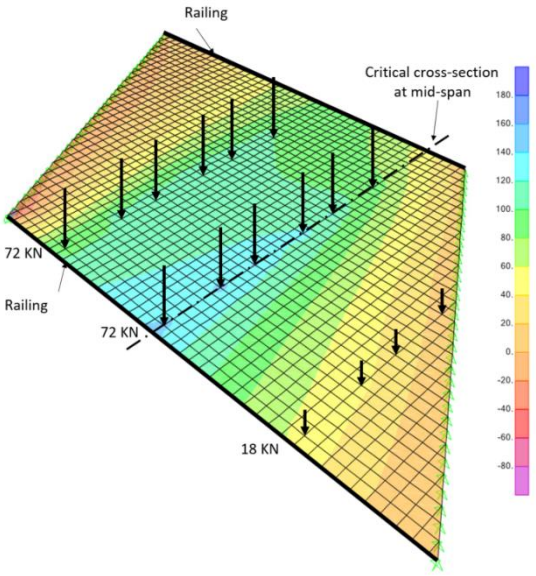

Fig. 2 FEA discretization and moments (KN-m/m) in a 13.8 m (46 ft) span, three-lane, 30° skewed bridge with railings, subject to HS20 Edge loading condition.

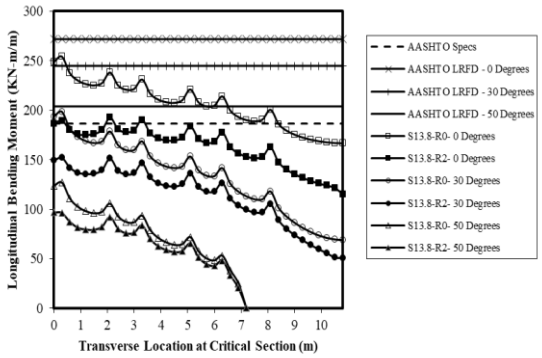

Fig. 3 FEA and AASHTO Standard (Specs) and LRFD moments for 13.8 m (46 ft) span, three-lane skewed bridges with railings and reference straight bridges without railing.

FEA RESULTS VS. AASHTO PROCEDURES

Table 1 summarizes the increase or decrease in predicting the bending moments in the concrete slabs when comparing the maximum FEA with the AASHTO moments for all bridge cases analyzed.

Using Table 1, it can be observed that, for short-span bridge cases with no railing, AASHTO Standard generally tends to give similar results to the FEA slab moments for skew angle up to 20 degrees, and overestimates the FEA moments by about 20 to 50%

for skew angle up between 30 and 50 degrees. For longer span bridge cases with no railing, AASHTO Standard generally tends to underestimate to the FEA slab moments by about 10 to 35% for skew angle up to 20 degrees, and gives similar results or overestimates the FEA moments by about 10 to 45% for skew angle up between 30 and 50 degrees. Adding two railings, AASHTO Standard overestimates FEA moments for almost all bridge cases and this overestimation increases with the increase in skew angle reaching about 60% for short-span bridges with skew angle of 50 degrees; only in few long-span bridge cases with two railings and for skew angles up to 20 degrees, then AASHTO gives similar results or underestimates the FEA moments by about 10 to 20%.

Table 1 Comparison of FEA Maximum Moments and AASHTO Moments

Number of Lanes	Span Length (m)	FEA Maximum Longitudinal Moments and LRFD Moments (KN-m/m)						AASHTO Standard (KN-m/m)
		0 Degrees			10 Degrees			
		R0	R2	LRFD	R0	R2	LRFD	
3	7.2	98	78	102	96	77	102	97
	10.8	169	129	190	167	128	190	146
	13.8	238	192	272	234	190	272	186
	16.2	293	249	347	286	244	347	226
4	7.2	100	86	97	99	84	97	97
	10.8	176	142	180	174	141	180	146
	13.8	249	208	269	244	205	269	186
	16.2	305	267	347	298	261	347	226
Number of Lanes	Span Length (m)	FEA Maximum Longitudinal Moments and LRFD Moments (KN-m/m)						AASHTO Standard (KN-m/m)
		20 Degrees			30 Degrees			
		R0	R2	LRFD	R0	R2	LRFD	
3	7.2	90	71	98	76	60	91	97
	10.8	152	119	183	130	103	171	146
	13.8	213	175	261	181	151	245	186
	16.2	261	225	333	223	194	312	226
4	7.2	91	73	93	76	60	87	97
	10.8	158	127	173	132	106	162	146
	13.8	221	186	258	186	157	242	186
	16.2	271	239	333	229	203	312	226
Number of Lanes	Span Length (m)	FEA Maximum Longitudinal Moments and LRFD Moments (KN-m/m)						AASHTO Standard (KN-m/m)
		40 Degrees			50 Degrees			
		R0	R2	LRFD	R0	R2	LRFD	
3	7.2	63	51	86	48	39	77	97
	10.8	103	84	160	80	63	143	146
	13.8	144	123	228	111	92	204	186
	16.2	180	158	292	138	119	260	226
4	7.2	63	51	81	48	39	72	97
	10.8	104	85	151	80	63	135	146
	13.8	146	125	226	110	91	202	186
	16.2	183	162	292	138	120	260	226

Also with reference to Table 1, it can be deduced that AASHTO LRFD generally overestimates the FEA slab moments in almost all bridge cases with or without railings, and gives similar results in a few cases without railing. For short-span bridge cases with no railing, AASHTO LRFD generally tends to give similar results to the FEA slab moments for skew angle up to 20 degrees, and overestimates the FEA moments by about 15 to 40% for skew angle up between 30 and 50 degrees. For longer span bridge cases with no railing, AASHTO LRFD overestimates the FEA slab moments by about 10 to 20% for skew angle up to 20 degrees, and by about 25 to 50% for skew angle between 30 and 50 degrees. Adding two railings, AASHTO LRFD overestimation of the FEA moments increases with the increase in skew angle from about 20% for straight bridges with no skewness to about 50% for bridges with skew angle of 50 degrees.

It is worth noting that generally AASHTO overestimation is higher for three-lane bridges as compared to four-lane bridges except for high skew angles of 40 to 50 degrees when the results of three- and four-lane bridges become similar.

FEA RESULTS OF SKEWED BRIDGES WITH RAILINGS VS. REFERENCE BRIDGES

The maximum slab bending moments are summarized in Table 2 for all bridge cases in terms of ratios of FEA results for skewed bridges with railings to the corresponding reference straight bridges without railings. Table 2 shows that the maximum longitudinal slab moment reduces with the increase in skew angle and it is more pronounced for bridges with two railings. For angle of skewness less than 20º, the reduction in the moment reaches 30% for bridges with two railings, and about none for bridges with no railing. For angle of skewness equal to 20º, the reduction in the moment reaches 30% for bridges with two railings, and about 10% for bridges with no railing. For angle of skewness equal to 30º, the reduction in the moment reaches 40% for bridges with two railings, and about 25% for bridges with no railing. For angle of skewness equal to 40º, the reduction in the moment reaches 50% for bridges with two railings, and about 40% for bridges with no railings. For angle of skewness equal to 50º, the reduction in the moment reaches 65% for bridges with two railings, and about 55% for bridges with no railing.

It is worth noting that generally the reduction in FEA moments due to skewness and railings is slightly affected by the number of lanes or span lengths considered.

SUMMARY AND CONCLUSIONS

AASHTO Standard [1] and AASHTO LRFD [2] empirical equations do not account for the presence of railings as integral parts of a bridge slab, and these elements are neglected during the design stage, and only AASHTO LRFD considers skewness to reduce the designs slab moments.

A parametric study using finite-element analysis was performed to investigate the influence of railings and skewness on the longitudinal slab moments in simply-supported, one-span, three- and four-lane concrete slabs bridges. The bridge parameters considered were the span length, number of lanes, railings on both edges, and skew angle. The FEA

moments were assessed with AASHTO procedures and with reference bridge cases without railing.

The study concluded that the presence of railings increases the load carrying capacity of the bridges if they are modeled as integral parts of the slab, and that the slab moments reduce with the increase in the increase of skew angle. Further the influence of railings and skew angle is cumulative and becomes significant with high skewness and two railings. It can also be noted that integral railings can be used as one alternative strengthening technique to upgrade already existing bridges that require rehabilitation or upgrading, or if heavier loads are foreseen.

Table 2 Ratio of FEA Maximum Moments to Reference Bridge Cases

Number of Lanes	Span Length (m)	Ratio of FEA Maximum Longitudinal Moments to Reference Straight Bridge Cases without Railing					
		0 Degrees		10 Degrees		20 Degrees	
		R0	R2	R0	R2	R0	R2
3	7.2	1.00	0.80	0.98	0.79	0.92	0.73
	10.8	1.00	0.77	0.99	0.76	0.90	0.71
	13.8	1.00	0.81	0.98	0.80	0.89	0.73
	16.2	1.00	0.85	0.98	0.83	0.89	0.77
4	7.2	1.00	0.86	0.98	0.84	0.91	0.73
	10.8	1.00	0.81	0.99	0.80	0.90	0.72
	13.8	1.00	0.84	0.98	0.82	0.89	0.75
	16.2	1.00	0.88	0.98	0.86	0.89	0.78
Number of Lanes	Span Length (m)	Ratio of FEA Maximum Longitudinal Moments to Reference Straight Bridge Cases without Railing					
		30 Degrees		40 Degrees		50 Degrees	
		R0	R2	R0	R2	R0	R2
3	7.2	0.77	0.61	0.64	0.52	0.49	0.40
	10.8	0.77	0.61	0.61	0.50	0.47	0.38
	13.8	0.76	0.63	0.61	0.52	0.47	0.39
	16.2	0.76	0.66	0.62	0.54	0.47	0.41
4	7.2	0.76	0.60	0.62	0.51	0.48	0.39
	10.8	0.75	0.60	0.59	0.48	0.45	0.36
	13.8	0.75	0.63	0.59	0.50	0.44	0.37
	16.2	0.75	0.67	0.60	0.53	0.45	0.39

ACKNOWLEDGMENT

This research was supported by a grant from the University Research Board (URB) at the American University of Beirut to whom the authors are indebted and thankful.

REFERENCES

[1] American Association of State Highway and Transportation Officials (AASHTO), Standard Specifications for Highway Bridges, 17th ed, Washington D.C., 2002.

[2] American Association of State Highway and Transportation Officials (AASHTO), LRFD Bridge Design Specifications, 7th ed, Washington D.C., 2014.

[3] Mabsout M., Tarhini K., Frederick G., and Tayar C., Finite Element Analysis of Steel Girder Highway Bridges, Journal of Bridge Engineering, ASCE, Vol. 2, No. 3, 1997, pp. 83-87.

[4] Eamon C. and Nowak A., Effects of Edge-stiffening Elements and Diaphragms on Bridge Resistance and Load Distribution, Journal of Bridge Engineering, ASCE, Vol. 7, No. 5, 2002, pp. 258-266.

[5] Chung W., Liu J., and Sotelino E.D., Influence of Secondary Elements and Deck Cracking on the Lateral Load Distribution of Steel Girder Bridges, Journal of Bridge Engineering, ASCE, Vol. 11, No. 2, 2006, pp. 178-187.

[6] Conner S. and Huo X.S., Influence of Parapets and Aspect Ratio on Live-load Distribution, Journal of Bridge Engineering, ASCE, Vol. 11, No. 2, 2006, pp. 188-196.

[7] Akinci N.O., Liu J., and Bowman M.D., Parapet Strength and Contribution to Live Load Response for Superload Passages, Journal of Bridge Engineering, ASCE, Vol. 13, No. 1, 2008, pp. 55-63.

[8] Mabsout M., Tarhini K., Jabakhanji R., and Awwad E. Wheel Load Distribution in Simply Supported Concrete Slab Bridges, Journal of Bridge Engineering, ASCE, Vol. 9, No. 2, 2004, pp. 147-155.

[9] Menassa C., Mabsout M., Tarhini K., and Frederick G., Influence of Skew Angle on Reinforced Concrete Slab Bridges, Journal of. Bridge Engineering, ASCE, Vol. 12, No. 2, 2007, pp. 205-214.

[10] Fawaz G., Waked M., Mabsout M., and Tarhini K., Influence of Railings on Load Carrying Capacity of Concrete Slab Bridges, Bridge Structures, IOS Press, Vol. 12, No. 3-4, 2017, pp. 85-96.

[11] Fawaz G., Mabsout M., and Tarhini K., Wheel Load Distribution in Straight and Skewed Concrete Slab Bridges Stiffened with Railings, Proceedings of the Istanbul Bridge Conference, Istanbul, Turkey, 8-10 August, 2016.

[12] SAP2000, User's Manual, Computers and Structures Inc., Berkeley, California, 2017.

9th Int. Conf. on Geotechnique, Construction Materials and Environment, Tokyo, Japan, 20-22 November 2019, ISBN: 978-4-909106025 C3051

INFLUENCE OF RAILING STIFFNESS ON SINGLE-SPAN TWO-LANE STEEL GIRDER BRIDGES

Wassim Nasr Eddine[1], Kassim Tarhini[2], and Mounir Mabsout[3]
[1]Dept. of Civil and Environmental Engineering, Rutgers Univ., New Jersey, USA; formerly Dept. of Civil and Environmental Engineering, Amer. Univ. of Beirut, Lebanon
[2]Dept. of Civil Engineering, U.S. Coast Guard Academy, New London, CT, USA
[3]Dept. of Civil and Environmental Engineering, Amer. Univ. of Beirut, Lebanon

ABSTRACT

The presence of railings or parapets acting integrally with the concrete deck placed on steel girders has the effect of stiffening and therefore altering the lateral wheel load distribution on highway bridges. The American Association of State Highway and Transportation Officials (AASHTO) Standard Specifications for Highway Bridges and AASHTO LRFD Bridge Design Specifications procedures do not account for the presence of railings when evaluating the load-carrying capacity of highway bridges. This paper presents a parametric study using 3D finite element analysis to investigate the influence of railing stiffness on one-span, two-lane steel girder bridges. Railings of different sizes were placed on one or both sides of the bridge deck, in combination with various span lengths and girders spacing. AASHTO HS20 design trucks were placed longitudinally and transversally in order to produce maximum longitudinal bending moments in the steel girders. The wheel load distribution obtained from finite element analysis at the critical section of each bridge were compared with the AASHTO procedures and with reference cases for bridges without railing. This study confirmed that the presence of concrete railings modeled and built integrally with the deck tends to stiffen the bridge superstructure. Further, the study quantified the effect of railing in increasing the load-carrying capacity of steel bridges. The results of this research will therefore assist structural engineers in better designing new steel girder bridges and/or evaluating more precisely the load-carrying capacity of existing bridges with railings of different sizes. Bridge engineers can consider adding or stiffening railings/parapets as a practical method for strengthening existing steel girder bridges.

Keywords: Steel girder bridges, Railings or parapets stiffness, AASHTO procedures, Finite-element analysis, Wheel load distribution factor, Load-carrying capacity

INTRODUCTION

A common type of highway bridge deck is a reinforced concrete slab placed on steel I-beams that is referred to as a steel girder bridge. The analysis and design of highway bridges in the United States must conform to the American Association of State Highway and Transportation Officials (AASHTO) procedures, either to the Standard Specifications for Highway Bridges (2002) prior to 2007 – thereafter referred to as AASHTO Standard [1], or to the current Load and Resistance Factor Design (LRFD) Specifications (2014) – thereafter referred to as AASHTO LRFD [2]. Typically, the analysis of a three-dimensional (3D) bridge superstructure is reduced to the analysis of a two-dimensional (2D) single girder by using a wheel load distribution factor (DF). The current AASHTO wheel load distribution factors (Standard or LRFD) do not consider the influence of raised sidewalks and/or railings that are built integrally with the bridge deck, nor their effect on the increase of the bridge's stiffness and its load-carrying capacity.

A previous study reported the results of a parametric study that investigated, using finite element analysis (FEA), of various modeling techniques on one-span, two-lane, simply supported, composite steel girder bridges without the presence of sidewalks or railings [3]. In this study, the span length and girder spacing were varied within practical ranges, and the FEA results were used to calculate the longitudinal bending moments and wheel load distribution factors in the steel girders for the composite slabs, which were compared with AASHTO procedures. A follow-up study extended the latter analysis to investigate the influence of sidewalks and railings of standard sizes on wheel load distribution for the same bridges [4]. The presence of sidewalks and railings was shown to increase the stiffness of the superstructure and improve the load-carrying capacity of steel bridges by as much as 30%.

Another study investigated the influence of secondary elements and deck cracking on the lateral load distribution of steel girder bridges [5]. The presence of secondary elements such as lateral bracing and parapets produces load distribution factors up to 40% lower than the AASHTO LRFD values. Other work investigated the effect of parapets

and bridge aspect ratio on live-load moment distribution in bridge girders [6]. The finite element analysis was used to investigate 34 two-span continuous bridges with different skew angles and overhang lengths. The presence of parapets was shown to reduce the wheel load distribution factors by as much as 36% and 13% for exterior and interior girders, respectively. Another research reported the parapet strength and contribution to live-load response for permit super-load passages were tested [7]. The results of this study showed that girder distribution factors (GDFs) can be decreased by as much as 30%, depending on the stiffness of the girders and the transverse truck position if the parapets are included in the analysis. The effect of secondary elements on load distribution in prestressed bridge girders was examined showing the effect of including barriers (railings) in calculating the wheel load distribution and bending moments in girders [8].

This paper builds on the previously published research, namely in [3]-[4], by performing a parametric study investigating the influence of railing stiffness on wheel load distribution in simply-supported, one-span, two-lane steel girder bridges. The results of 240 bridge cases that are modeled using FEA are presented in this paper. The various bridge parameters investigated in this study are the span length, girder spacing, and various railings stiffness and configurations, subject to HS20 truck loadings positioned transversally and longitudinally in order to produce the maximum longitudinal live load bending moments. Parapets or railings are assumed to be placed on either edge or both edges of the bridge deck, built integrally with the concrete slabs that is placed over steel girders under composite action. The effect of railing stiffness on the maximum live load wheel load distribution factors are assessed by calculating and comparing the FEA bending moments with both AASHTO Standard and LRFD, as well as with the reference bridge cases without railing.

AASHTO STANDARD AND LRFD PROCEDURES

The AASHTO Standard [1] specifications specify the load distribution factor for a steel girder to be a function of the girder spacing only. The use of distribution factors reduces the three-dimensional (3D) bridge deck analysis to a two-dimensional (2D) beam analysis and design process subject to AASHTO HS20 loadings. Typically, AASHTO design wheel loads are positioned on a 2D girder using influence lines to produce the maximum design live load moment, which is then multiplied by an empirical wheel load distribution factor (DF) such as S/5.5, where S is the girder spacing in feet (S/1676, where S is in millimeters) – thereafter referred to as "S/5.5" formula. If the girder spacing is greater than 14 ft (4.27 m), AASHTO recommends the use of simple beam distribution for estimating the wheel load distribution factor. This AASHTO Standard procedure has been criticized for being conservative due to its simplistic load distribution factors.

The AASHTO LRFD [2] specifications introduced relatively new wheel load distribution factors based on published research in the last few decades. AASHTO LRFD wheel load distribution formulae presented in Table 4.6.2.2.2b-1 account for parameters such as span length, girder spacing, and cross-sectional properties of the bridge deck. The wheel load distribution factor for bending moment in two-lane steel girder bridges is, in Imperial units:

$$g = 0.075 + \left(\frac{S}{9.5}\right)^{0.6}\left(\frac{S}{L}\right)^{0.2}\left[\frac{K_g}{12.0Lt_s^3}\right]^{0.1} \quad (1a)$$

The equivalent equation in SI units is:

$$g = 0.075 + \left(\frac{S}{2{,}900}\right)^{0.6}\left(\frac{S}{L}\right)^{0.2}\left[\frac{K_g}{Lt_s^3}\right]^{0.1} \quad (1b)$$

where:

S = girder spacing (ft, $3.5 \le S \le 16.0$) or (mm, $1{,}100 \le S \le 4{,}900$)

L = span length of beam (ft, $20 \le L \le 240$) or (mm, $6{,}000 \le L \le 73{,}000$)

K_g = longitudinal stiffness parameter (in^4, $10{,}000 \le K_g \le 7{,}000{,}000$) or ($mm^4$, $4x10^9 \le K_g \le 3x10^{12}$) $= n\,(I + A\,e_g^2)$

n = modular ratio between beam and deck material

I = moment of inertia of beam (in^4 or mm^4)

A = girder gross area (in^2 or mm^2)

e_g = distance between the centers of gravity of the basic beam and deck (in or mm)

t_s = depth of concrete slab (in, $4.5 \le t_s \le 12.0$) or (mm, $110 \le t_s \le 300$)

Equation (1) is recommended for highway bridges with at least two lanes, composite or non-composite, single- and multi-span steel girder bridges. Even though this equation was recommended for bridge decks with at least four girders, the presence of three girders in a bridge deck was also investigated in this paper and the FEA results were evaluated and compared with Eq. (1).

BRIDGE CASES AND LOADING

Typical one-span, simply supported, two-lane straight steel girder bridges were selected for this parametric FEA investigation. The bridge deck consisted of a 7.5 inches (190 mm) reinforced concrete slab thick supported by structural steel girders (W36x160). The various span lengths "*L*" considered in this study were 40, 60, 80, 100, and 120 ft (12, 18, 24, 30, and 36 m). The girder spacing "*S*" was set at 6, 8, and 12 ft (1.8, 2.4, and 3.6 m). A standard lane width of 12 ft (3.6 m) was used with a shoulder width of 4 ft (1.2 m), and the overall bridge

slab width was 32 ft (9.6 m) for two lanes with a shoulder on each side. These dimensions accommodate the possible presence of sidewalks and/or railings on the bridge deck. A typical bridge cross-section with 6 ft (1.8 m) girder spacing is shown in Fig. 1.

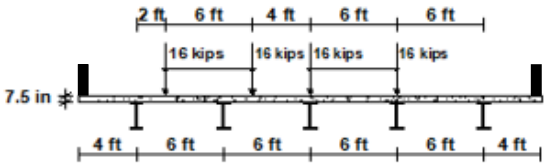

Fig. 1 Typical two-lane bridge cross-section with standard railings on both edges (x1, 2R) and HS20 trucks loading.

A reinforced concrete railing or parapet, 8 inches (200 mm) thick by 30 inches (760 mm) high, was selected as the standard railing (labeled as x1) and placed on the left, right, and on both sides of the deck (labeled respectively as RL, RR, and 2R) for all bridge combination parameters considered, as shown in Fig. 1 for the case (2R). Four additional railing sizes were considered in this study by varying the stiffness to half, double, triple and quadruple the standard railing stiffness (labeled respectively as x0.5, x2, x3, and x4), and all railings cross-sections are shown in Fig. 2. It was assumed that the railings were properly reinforced and connected integrally to the bridge deck in order to transmit the shear forces, bending moments, and to act integrally with the superstructure. Reference bridge decks with no railing were also analyzed using for comparative analysis (labeled as NoR).

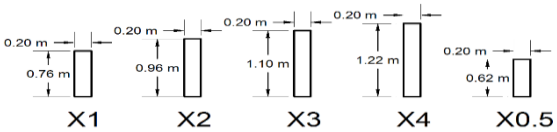

Fig. 2 Various railing sizes (x1, x2, x3, x4, x0.5).

The bridge live loadings considered in this investigation were limited to the AASHTO Standard [1] of either applying AASHTO HS20 design truck or a train of HS20 trucks depending on the span length. The single HS20 truck has a total weight of 72 Kips (324 kN), distributed over two rear axles of 32 Kips (144 kN) each and one front axle of 8 Kips (36 kN), with a distance of 14 ft (4.2 m). For the train of trucks, HS20 trucks were placed longitudinally in each lane of a given bridge, with a spacing of 30 ft (9 m) separating each of the trucks. Only one truck per lane can fit on a given bridge, and the design truck or train of trucks using influence lines in order to achieve the most severe live loading conditions. In all cases, the trucks in multiple lanes assumed to be traveling in the same direction. Transversally, the AASHTO HS20 design trucks were positioned side-by-side on the bridge superstructures with a distance of 4 ft (1.2 m) between the loading points. Note that the transverse position of the trucks was selected in order to produce the most severe loading conditions on the bridge to result in the maximum bending moment in the critical girder, as shown for the 6 ft (1.8 m) girder spacing in Fig. 1.

Typical material properties used in modeling the bridge superstructure were normal-strength reinforced concrete with compressive strength of 4,000 psi (27.5 MPa), modulus of elasticity of 3.6×10^6 psi (24.8 GPa), and Poisson's ratio of 0.20. The modulus of elasticity of steel beams were selected to be 29×10^6 psi (200 GPa).

FINITE ELEMENT MODELING

The 3D-FEA model and mesh discretization adopted to analyze the 240 bridge cases considered is based on previous studies reported earlier [3]-[4] using the general FEA program SAP2000 [9]. This study considered all elements to be linearly elastic and the analysis assumed small deformations and deflections.

The concrete slab was modeled using quadrilateral 2x2 ft (0.60x0.60 m) shell elements (SHELL, with 6 degrees of freedom at each node) and the steel girders were idealized as space-frame elements (FRAME, with six degrees of freedom at each node). The railings were also modeled as concentric space-frame elements with a moment of inertia and stiffness equivalent to an eccentric element applied on top of the slab [4]. Hinges were assigned at one bearing location and rollers at the other to simulate the simple support conditions. AASHTO HS20 wheel loads were applied at isolated nodes, located longitudinally and transversally in order to produce maximum longitudinal bending moments. Figure 3 shows a typical 3D-FEA model for a two-lane bridge with span length of 80 ft (24 m) and girder spacing of 6 ft (1.8 m) subjected to AASHTO HS20 truck loading.

The 3D-FEA results reported are stresses or moments for the slab shell elements and moments for the girders and railings frame elements. The moments in the girders were calculated using two parts: (a) the bending moment contribution of the tributary or effective concrete slab, and (b) the bending moment in the steel girder element. Figure 4 shows the longitudinal bending moment distribution in all girders (no slab contribution) and railings for the same bridge case shown in Fig. 3.

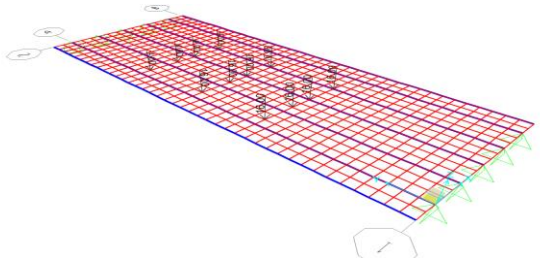

Fig. 3 Typical 3D-FEA model of a two-lane bridge with standard railings on both edges (x1, 2R) and HS20 trucks loading.

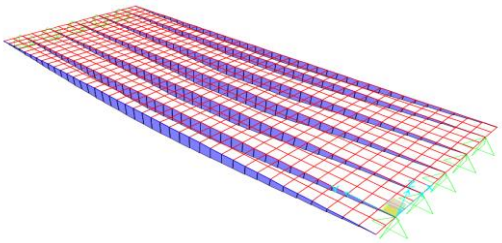

Fig. 4 Typical girders moment diagrams in a two-lane bridge with standard railings on both edges (x1, 2R) and HS20 trucks loading.

SUMMARY OF RESULTS

The maximum FEA moments from each and all girders, with the corresponding moments contributed from the slabs and railings, are obtained for all the 240 bridge cases analyzed. The presence of railings were considered as a part of the concrete section that contributed to the exterior girders in resisting wheel loads which tends to overestimate those moments as compared to interior girders. However, when considering girder and slab without railings, the moments in the critical interior girder will be larger than in exterior girders, and will therefore be considered as the effective moments used for design.

Table 1 shows a typical summary of those moments for the 80 ft (24 m) span, 6 ft (1.8 m) girder spacing with standard railings (x1) at either or both sides of the bridge deck; the case with no railing is also shown for reference. The maximum FEA moments in the critical interior girder (M_{max}) for the latter bridge cases can be obtained for each railing configuration (NoR, RL, RR, and 2R) by combining girder and slab moments; this is shown in the "Max-Total" value in the last column of the table. It is also worth noting that the total moment summed from all girders, slabs, and railings, or "Total-Total", is the same for all railings configurations, and is equal to four times the maximum statical girder moment (M_o) obtained from 2D-beam analysis with one line of wheel loads applied, for all the two-lane bridges.

Table 1 FEA moments in girders, slabs, and railings for two-lane bridges with 80 ft span, 6 ft girder spacing, and standard railings (x1).

Bending Moments (kip-ft), Two Lanes, L=80 ft, S=6 ft, Standard Railings (x1)								
Case	Zone	Girder 1	Girder 2	Girder 3	Girder 4	Girder 5	Total	Max
NoR	Girder	514.8	503.3	472.9	405.4	311.5	2208.0	514.8
	Slab	28.1	30.4	28.2	20.9	14.0	121.6	
	Railling	0.0	0.0	0.0	0.0	0.0	0.0	
	Total	542.9	533.7	501.1	426.4	325.5	2329.6	533.7
RL	Girder	348.3	407.9	429.0	398.8	336.2	1920.1	429.0
	Slab	22.4	29.4	28.7	21.9	15.5	118.0	
	Railling	291.5	0.0	0.0	0.0	0.0	291.5	
	Total	662.1	437.4	457.7	420.7	351.7	2329.6	457.7
RR	Girder	526.6	498.2	447.6	353.9	227.9	2054.1	526.6
	Slab	28.9	30.8	28.3	20.2	10.6	118.7	
	Railling	0.0	0.0	0.0	0.0	156.7	156.7	
	Total	555.4	529.0	475.9	374.1	395.2	2329.6	529.0
2R	Girder	353.6	398.1	398.6	339.0	238.0	1727.3	398.6
	Slab	23.1	30.0	29.0	21.2	11.8	115.2	
	Railling	305.5	0.0	0.0	0.0	181.6	487.1	
	Total	682.2	428.2	427.6	360.3	431.4	2329.6	428.2

The wheel load distribution factor (DF) from FEA was calculated by dividing the maximum FEA moment in the critical interior girder (M_{max}), considering the combination of moments from steel girder and concrete slab, by the maximum girder moment (M_o), or DF = M_{max}/M_o. This FEA DF for interior girders for the bridge cases with various configurations and sizes of railings will be compared with the DF from AASHTO Standard formula ("S/5.5") and LRFD Eq. (1), as well as with the reference bridges without railings, in order to determine the effect of these elements on the bridge superstructure. The maximum statistical girder moment (M_o) and FEA wheel load DF for interior girders are summarized in Table 2 for the two-lane bridge cases considered, for all span lengths and girder spacing analyzed with standard railings (x1) at either or both sides of the bridge deck, including the case with no railing as a reference. The FEA wheel load DF are also plotted with the span lengths in Fig. 5, along with AASHTO Standard formula ("S/5.5") and AASHTO LRFD Eq. (1) for the two-lane bridges with 6 ft (1.8 m) girder spacing and standard railing stiffness (x1). Finally, Table 3 shows the maximum interior AASHTO and FEA DF for all 240 bridge cases, with the various railings stiffness considered in this study.

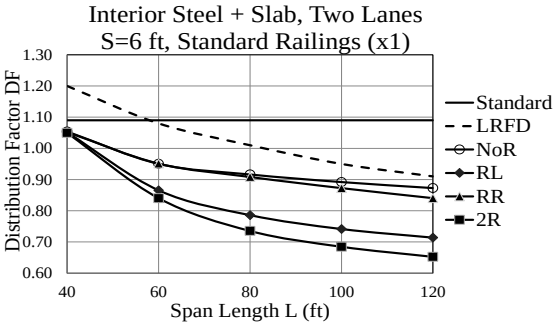

Fig. 5 AASHTO and FEA distribution factors in interior girders for two-lane bridges with 6 ft girder spacing and standard railings (x1).

Table 2 FEA distribution factors in interior girders for two-lane bridges with standard railings (x1)

Mo (kip-ft) and FEA DF, Interior Steel + Slab, Two Lanes, Standard Railings (x1)						
L (ft)	S (ft)	Mo (kip-ft)	DF-NoR	DF-RL	DF-RR	DF-2R
40	6	224.8	1.05	1.05	1.05	1.05
	8	224.8	1.36	1.31	1.36	1.31
	12	224.8	1.91	1.88	1.90	1.86
60	6	403.2	0.95	0.87	0.95	0.84
	8	403.2	1.20	1.07	1.19	1.05
	12	403.2	1.58	1.46	1.50	1.37
80	6	582.4	0.92	0.79	0.91	0.74
	8	582.4	1.14	0.95	1.10	0.91
	12	582.4	1.48	1.29	1.35	1.15
100	6	825.4	0.89	0.74	0.87	0.68
	8	825.4	1.10	0.90	1.04	0.83
	12	825.4	1.43	1.20	1.26	1.02
120	6	1163.5	0.87	0.71	0.84	0.65
	8	1163.5	1.07	0.87	1.00	0.77
	12	1163.5	1.39	1.14	1.20	0.94

ANALYSIS OF RESULTS

For the particular bridge cases shown in Table 1 of the two-lane bridges with 80 ft (24 m) span and 6 ft (1.8 m) girder spacing, the FEA results shows that the contribution of bending moment from the concrete slab is about 5% to the overall total girder bending moment when there is no railing on the bridge. It was also observed that this percentage contribution ranges from about 5% to 15% for other two-lane bridge cases considered with no railing. However, when introducing railing or parapet on one or both sides of the bridge deck, the concrete slab and railing contribute largely to the total bending moment of the exterior girder in bridges, which can reaches about 50% with the standard railing stiffness (x1) for the bridge cases shown in Table 1. The FEA moments results in exterior girders showed that the percentage of the deck contribution (slab and railing) to the overall moments increased due to changes in railing stiffness and span lengths, but not with girder spacing, ranging from about 25% to 35% for (x0.5), 35% to 50% for (x1), 40% to 65% for (x2), 40% to 75% (x3), and 45% to 80% for (x4).

In this study, since the AASHTO HS20 trucks were placed 2 ft (0.60 m) from the left outside girder, the maximum bending moment predicted to occur in either one of the two left side girders, except for the shortest span, where in the case of 6 ft (1.8 m) girder spacing, the maximum was always at the center girder. Therefore, when the railings were placed on the left side or on both sides of the bridge, the maximum bending moment occurred in the left exterior girder when adding the contribution of the railing but, as discussed earlier, the effective critical girder will be an interior one. As a result, the wheel load DF to be used in the girders will be identified based on the maximum moment occurring in the interior critical girder.

This FEA maximum design moment or FEA-DF will therefore be compared with AASHTO procedures/equations, with and without railings. Also, the maximum FEA-DF for cases with railings on either edge or both edges will be compared with the reference FEA-DF cases without railing for all railings stiffness considered. Note that for exterior girders, the railings when present should be designed to take the large moments attracted to those stiffening elements.

FEA results vs. AASHTO procedures

As shown in Table 3, AASHTO Standard [1] formula is highly conservative when compared with the FEA DF without railing which was also previously reported [3] for all the two-lane bridge cases considered. This will be even more the case with any railing size. This study will therefore focus on comparing the FEA DF with AASHTO LRFD [2] Eq. (1), where a good correlation in the pattern of results was observed as shown in Fig. 5. Using Table 3, the following general observations can be made:

- No railing (NoR): FEA DF were smaller than Eq. (1) by about 10% for spans up to 80 ft (24 m), and by about 5% for spans between 80 and 120 ft (24 to 36 m).
- Railing on one side (Largest of RL or RR): FEA DF were smaller than Eq. (1) by about: 10% for railing stiffness (x0.5), 15% for railing stiffness (x1) and (x2), and 20% for railing stiffness (x3) and (x4).
- Railings on both sides (2R): FEA DF were smaller than Eq. (1) by about: 20% for railings stiffness (x0.5), 30% for railings stiffness (x1), 45% for railings stiffness (x2), 50% for railings stiffness (x3), and 60% for railings stiffness (x4).

Influence of railings stiffness vs. reference base cases without railing

Using Table 3, the following general observations can be made:

- Railing on one side (Largest of RL or RR): FEA DF with one railing is reduced when compared to reference case without railing by an average of about: 5% and 10% for railing stiffness (x0.5) through (x4) for spans between 40 and 80 ft (12 to 24 m), and 10% and 20% for railing stiffness (x0.5) through (x4) for spans for spans between 80 and 120 ft (24 to 36 m).
- Railings on both side (2R): FEA DF with two railings is reduced when compared to reference case without railing by an average of about: 10% and 30% for railings stiffness (x0.5) through (x4) for spans between 40 and 80 ft (12 to 24 m), and 15% and 50% for railings stiffness (x0.5) through (x4) for spans for spans between 80 and 120 ft (24 to 36 m).

Table 3 AASHTO and FEA distribution factors in interior girders for all bridges with various railings stiffness

AASHTO and FEA DF, Interior Girders (Steel + Slab), Two Lanes, All Railings Stiffness																			
L (ft)	S (ft)	Stand.	LRFD	NoR	RL					RR					2R				
					x0.5	x1	x2	x3	x4	x0.5	x1	x2	x3	x4	x0.5	x1	x2	x3	x4
40	6	1.09	1.20	1.05	1.05	1.05	1.05	1.05	1.05	1.05	1.05	1.05	1.05	1.05	1.05	1.05	1.05	1.05	1.05
	8	1.46	1.48	1.36	1.32	1.31	1.30	1.30	1.29	1.36	1.36	1.36	1.36	1.36	1.32	1.31	1.30	1.30	1.30
	12	2.18	1.98	1.91	1.89	1.88	1.87	1.87	1.87	1.90	1.90	1.89	1.89	1.89	1.87	1.86	1.85	1.85	1.85
60	6	1.09	1.08	0.95	0.88	0.87	0.85	0.85	0.84	0.95	0.95	0.95	0.95	0.95	0.86	0.84	0.82	0.81	0.80
	8	1.46	1.32	1.20	1.11	1.07	1.02	1.00	0.99	1.19	1.19	1.18	1.18	1.18	1.10	1.05	1.00	0.97	0.96
	12	2.18	1.77	1.58	1.49	1.46	1.42	1.40	1.39	1.53	1.50	1.48	1.47	1.47	1.44	1.37	1.31	1.28	1.26
80	6	1.09	1.01	0.92	0.81	0.79	0.76	0.74	0.73	0.91	0.91	0.91	0.90	0.90	0.80	0.74	0.68	0.65	0.63
	8	1.46	1.23	1.14	1.02	0.95	0.92	0.91	0.90	1.11	1.10	1.09	1.08	1.08	0.99	0.91	0.82	0.77	0.74
	12	2.18	1.64	1.48	1.35	1.29	1.22	1.19	1.17	1.39	1.35	1.31	1.28	1.27	1.26	1.15	1.03	0.97	0.93
100	6	1.09	0.95	0.89	0.78	0.74	0.70	0.69	0.69	0.88	0.87	0.86	0.86	0.86	0.76	0.68	0.59	0.54	0.51
	8	1.46	1.16	1.10	0.97	0.90	0.86	0.85	0.83	1.06	1.04	1.02	1.01	1.00	0.93	0.83	0.70	0.63	0.59
	12	2.18	1.54	1.43	1.28	1.20	1.11	1.06	1.03	1.32	1.26	1.19	1.16	1.14	1.17	1.02	0.86	0.77	0.72
120	6	1.09	0.91	0.87	0.76	0.71	0.68	0.67	0.66	0.85	0.84	0.83	0.82	0.81	0.74	0.65	0.54	0.47	0.43
	8	1.46	1.10	1.07	0.94	0.87	0.82	0.80	0.78	1.02	1.00	0.96	0.94	0.93	0.89	0.77	0.63	0.55	0.50
	12	2.18	1.47	1.39	1.23	1.14	1.03	0.97	0.93	1.27	1.20	1.11	1.07	1.04	1.11	0.94	0.76	0.65	0.59

SUMMARY AND CONCLUSIONS

A parametric study using finite-element analysis was performed to investigate the influence of railing stiffness on wheel load distribution in simply-supported, one-span, two-lane steel girder bridges. The bridge parameters considered were the span length, girder spacing, and railings stiffness and configurations, subject to HS20 truck loadings positioned transversally and longitudinally in order to produce maximum girder bending moments.

The effect of railing stiffness on the maximum live load wheel load distribution factors were assessed by calculating and comparing the FEA moments or wheel load distribution factors with both AASHTO Standard and LRFD, as well as with the reference bridge cases without railing. The study confirmed that AASHTO Standard [1] formula is highly conservative when compared with the FEA DF without railing or with railings, and that FEA DF were smaller than AASHTO LRFD [2] Eq. (1) by about 5-10% with no railing, to about 20-50% for two railings with stiffness (x0.5) to (x4), depending on span lengths. The study also showed that the presence of one or two railings reduces the FEA-DF about 5-20% or 10-50%, respectively, depending on railings stiffness and span length. Such reduction in DF due to railings implies an increase in the bridge. Therefore, bridge engineers can consider adding, replacing, or stiffening railings/parapets as a practical method for strengthening existing steel girder bridges.

ACKNOWLEDGMENTS

This research was supported by a grant from the University Research Board (URB) at the American University of Beirut to whom the authors are indebted and thankful.

REFERENCES

[1] American Association of State Highway and Transportation Officials (AASHTO), Standard Specifications for Highway Bridges, 17th ed, Washington D.C., 2002.

[2] American Association of State Highway and Transportation Officials (AASHTO), LRFD Bridge Design Specifications, 7th ed, Washington D.C., 2014.

[3] Mabsout M., Tarhini K., Frederick G., and Tayar C., Finite Element Analysis of Steel Girder Highway Bridges, Journal of Bridge Engineering, ASCE, Vol. 2, No. 3, 1997, pp. 83-87.

[4] Mabsout M., Tarhini K., Frederick G., and Kobrosly M., Influence of Sidewalks and Railings on Wheel Load Distribution in Steel Girder Bridges, Journal of Bridge Engineering, ASCE, Vol. 2, No. 3, 1997, pp. 88-96.

[5] Chung W., Liu J., and Sotelino E.D., Influence of Secondary Elements and Deck Cracking on the Lateral Load Distribution of Steel Girder Bridges, Journal of Bridge Engineering, ASCE, Vol. 11, No. 2, 2006, pp. 178-187.

[6] Conner S. and Huo X.S., Influence of Parapets and Aspect Ratio on Live-load Distribution, Journal of Bridge Engineering, ASCE, Vol. 11, No. 2, 2006, pp. 188-196.

[7] Akinci N.O., Liu J., and Bowman M.D., Parapet Strength and Contribution to Live Load Response for Superload Passages, Journal of Bridge Engineering, ASCE, Vol. 13, No. 1, 2008, pp. 55-63.

[8] Roddenberry M.R., Chipperfield J., and Tawfiq, K.S., Effect of Secondary Elements on Load Distribution in Prestressed Bridge Girders, Structures Congress, ASCE, pp. 215-226.

[9] SAP2000, User's Manual, Computers and Structures Inc., Berkeley, California, 2017.

9th Int. Conf. on Geotechnique, Construction Materials and Environment, Tokyo, Japan, 20-22 November 2019, ISBN: 978-4-909106025 C3051

THE EFFECT OF SPAN LENGTH AND BEAM TYPE VARIATIONS TO THE BRIDGE DECK ANALYSIS

Asyadzili Bukhari[1], Anizahyati Alisibramulisi[2], Ekarizan Shaffie[3], Mohd Raizamzamani Md Zain[4] and Haryati Awang[5]
[1,2,3,4]Faculty of Civil Engineering, Universiti Teknologi MARA (UiTM), Selangor, Malaysia;
[2,3]Institute for Infrastructure Engineering and Sustainable Management (IIESM), UiTM, Selangor, Malaysia;
[1]KL Prima Consult Sdn Bhd, Selangor, Malaysia
[5]Faculty of Civil Engineering and Earth Resources, Universiti Malaysia Pahang (UMP), Pahang, Malaysia

ABSTRACT

The aim of this study was to determine the suitability of three different configurations of beam type and analyze these beam type with variation of span lengths as well as its effects to bridge deck by considering maximum bending moment, shear force and deflection. This study focuses on single span bridge of TM-beam, I20-beam and U12-beam with varying span lengths of 30m, 28m and 24m. These pre-cast concrete beams were spaced equally. The bridge deck analysis was carried out by using STAAD.Pro software. Maximum bending moment, shear force and deflection were found from U12-beam, followed with TM-beam and I20-beam respectively. Thus, it can be concluded that I20-beam is the best option as compared to TM-beam and U12-beam. Apart from the beam shape, the span length also affects the bridge deck analysis, as the longer the span length, the values of bending moment, shear force and deflection will also increase. Note that, other factors should also be considered, namely; ease of construction, the amount of reinforcements, formworks, concrete and tendon. Nevertheless, the design choices are in the hand of the engineer and the final decision will still be in the hand of the client.

Keywords: Span length, Beam type, Bridge Deck, Analysis, STAAD.Pro

INTRODUCTION

Standard bridge beams have been developed to cover a wide variety of applications. Although there is a recognized range of spans for which each standard section is generally used, the fields for various types overlap and the final selection is normally based on experience relating to a specific situation. Currently, the common bridge beams in Malaysia are; TM-Beam, I-Beam and U-Beam. But the main selection of the type of beams for a bridge should be based on structural condition, functional, available of materials, effectiveness of cost, geometric requirements, geological condition, construction sequence as well as its aesthetic factor.

This paper discusses about the effect of three different configuration of beam types to the bridge deck analysis and analyze it further with span length variations. Comparisons were made in terms of maximum bending moment, shear forces and deflection. This study focused on single span bridge of TM-beam, I20-beam and U12-beam with varying span lengths of 30m, 28m and 24m. The bridges were modeled using STAAD.Pro [1] software. Bending moment and shear force results obtained during the analysis stage, leads to the reinforcement details during the design stage. The results were checked under the Ultimate Limit State (ULS) condition, whereas, the deflection was checked under the Serviceability Limit State (SLS) condition. The limits are vital in ensuring that the structure remains in elastic phase under loading [2].

METHODOLOGY

Overall, nine (9) simply supported bridge were modeled with varying span length of 30m, 28m and 24m. Three (3) types of beams shape were selected; TM-10 (T-beam), I-20 (I-beam) and U-12 (U-beam). Six (6) equally spaced concrete girders with 1.90m spacing (1.9m c/c). The girders support 180mm thick concrete deck and 100mm thick asphalt concrete premix. The abutments are supported by six (6) numbers of 1200mm diameter concrete piles of 16m length. Figure 1 and 2 illustrate the plan and longitudinal section of the bridge.

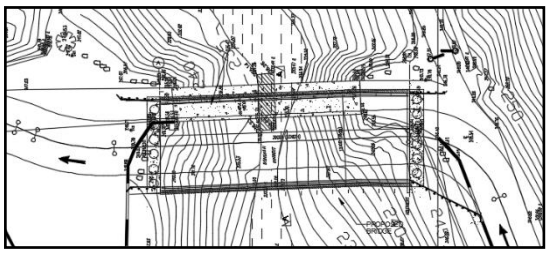

Fig.1: Plan view of the simply supported bridge

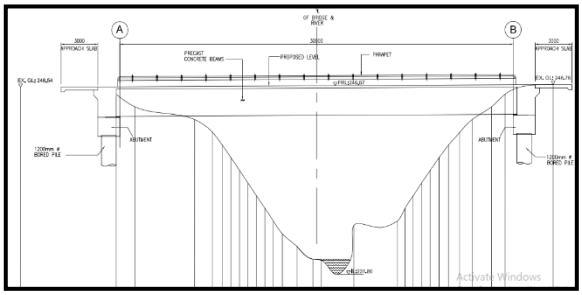

Fig.2: Longitudinal section of the simply supported bridge, crossing river channel

Section properties of the TM-10, I20 and U12 pre-cast concrete girders were taken from supplier catalogue and calculated further by using Integrated Bridge Design Software (SAM Leap 5). In this study, SAM was used to obtain the accurate section properties of TM-10, I20 and U12 pre-cast concrete girders. Figure 3 show the beam arrangements, whereas Fig. 4-6 show its typical sections.

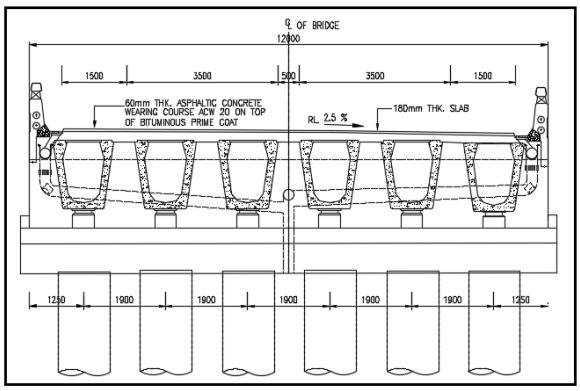

Fig.3: Beam arrangements

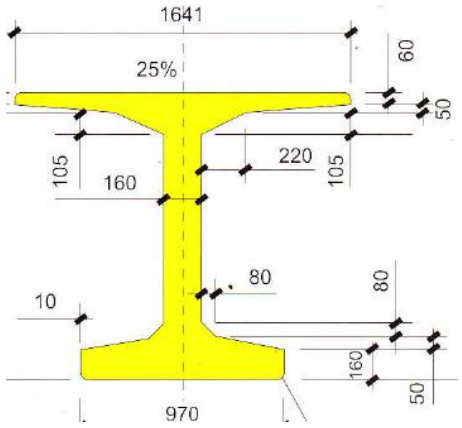

Fig.4: Typical section of TM-Beam

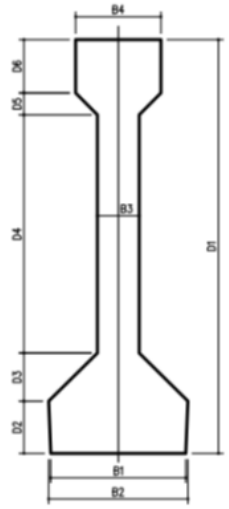

Fig.5: Typical section of I-Beam

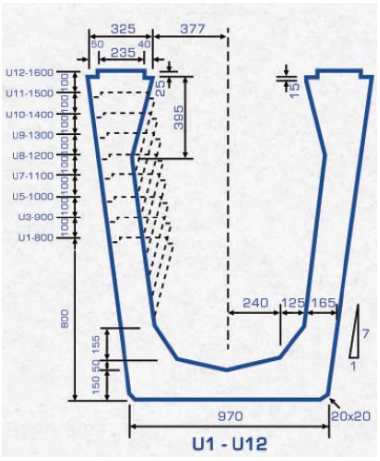

Fig.6: Typical section of U-Beam

The bridge superstructures comprise of precast concrete TM-10, I20 and U12 beams placed at 1.9m centre to centre and 180 mm thick cast in-situ reinforced concrete deck slab for the varying span lengths of 30m, 28m and 24m. The substructure consists of reinforced concrete abutments and piers/pile that are located outside the natural river profiles to improve water-flow and reduce scouring. Pier/pile type abutments that are located outside RS-wall are adopted for high approach road embankment to retain the horizontal earth pressure. As such, earth pressure is not considered in designing abutment column and abutment piles. Bank seat type abutment is adopted at the locations where the height of embankment is less than 3m. 1200mm diameter bored pile is used at the abutment with appropriate design loads. The whole structure is supported on 1200mm diameter bored pile for foundation system.

The modelling of the single span bridge was done by using STAAD.Pro V8i software. Three-dimensional (3D) model of single span bridge was adopted. The concrete slab (considered as plate) was supported by six (6) concrete longitudinal girders and abutment was modelled as shell element. Six (6) bored piles concrete were connected to each abutment with connectivity node. Figure 7 shows the 3D model of the single span bridge.

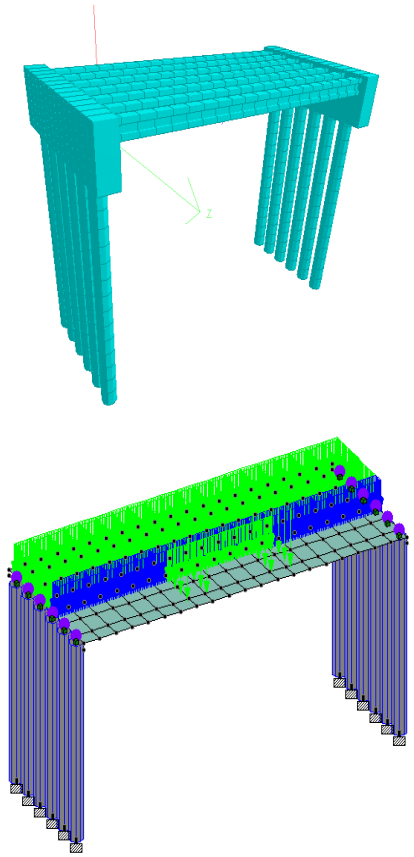

Fig.7: Three-dimensional model of the bridge

Grades of concrete used:

Location	Grade
Prestressed precast beams	C50
Parapets in-situ concrete	C40
Piers	C40
Pilecaps, deck slab, diaphragm beams	C40
Bored cast in-situ piles	C40

Grades of steel reinforcement used:

Steel type	Fy(N/mm^2)	E(kN/mm^2)
Mild Steel	250	200
High Yield Deform Type 2	500	200

The design was carried out in accordance with the design standards and specifications. The structure has been analyzed for self-weight, traffic load, and superimposed dead load. Local analysis due to concentrated wheel loads on deck slab has been done by using STAAD.Pro and STAAD BEAVA software. All loads considered in the analysis are applied in conjunction with the Design Statement and in accordance with BS 5400 [3] or BD 37/01 [4] whichever is relevant.

RESULTS AND DISCUSSIONS

Manual calculation was carried out to compare it with the Finite Element Analysis (FEA) of varying beam types and span lengths for validating the bridge models. To obtain the reliable data, only self-weight loading was considered for bending moment and shear force. Table 1, 2 and 3 show comparison results of manual calculation vs FEA.

Table 1: Manual calculation vs FEA: 30m span

Beam	Item*	Manual calc.	FEA	Diff. (%)
TM	BM	2694.86	2826.90	4.67
	SF	359.31	377.92	4.92
I20	BM	2690.99	2813.87	4.37
	SF	358.80	373.28	3.88
U12	BM	3000.54	3123.51	3.94
	SF	400.07	418.02	4.29

*Units for BM (kNM) and SF (kN)

Table 2: Manual calculation vs FEA: 28m span

Beam	Item*	Manual calc.	FEA	Diff. (%)
TM	BM	2347.52	2473.83	5.11
	SF	335.36	354.30	5.34
I20	BM	2344.15	2404.90	2.53
	SF	334.88	352.07	4.88
U12	BM	2613.81	2731.94	4.32
	SF	373.40	391.73	4.68

*Units for BM (kNM) and SF (kN)

Table 3: Manual calculation vs FEA: 24m span

Beam	Item*	Manual calc.	FEA	Diff. (%)
TM	BM	1724.71	1835.66	6.04
	SF	287.45	306.52	6.22
I20	BM	1722.23	1780.62	3.28
	SF	287.45	303.71	5.49
U12	BM	1920.35	2025.09	5.17
	SF	320.06	338.63	5.48

*Units for BM (kNM) and SF (kN)

Based on the comparison above, the differences are between 2.5-6.2%, thus, it has proven that the models carried out can be considered as acceptable. The FEA results were also validated further with F.Sahaya et al [5] and were found in good agreement.

Normally, different type of beam is chosen based on the span lengths of the bridge and its application. I-beam section is one of the most popular types implemented, as it has both flange at the bottom and top in order to cater more compressive and tensile forces. T-beam has no flange member at the bottom which then lack in terms of tensile forces. The web of these beams is used to cater shear stress as well as provide greater separation for the coupled forces of bending moment. On the other hand, U-Beam has void that helps to improve torsional stiffness of the beam. Note that, these beams having different shapes also means that they have different depth, width, area, centroid, second moment of area, section modulus and self-weight. And these will affect the beam behaviour.

According to Fig.8 to Fig.10, types of beam and span lengths have significant impact on the bending moment, shear force and deflection of the bridge deck analysis. Logically, the longer the span length of a bridge, the more load it must carry and of course the more tendency for it to be bended, sheared and deflected as illustrated in Fig. 8, Fig. 9 and Fig.10 respectively. Thus, bending moment, shear force and deflection increases as the span length increases.

Based on Fig.8, U12-beam has the highest maximum bending moment among the three type of beams, with values of 10586.006kNm, 9480.087kNm and 7258.018kNm for span length 30m, 28m and 24m respectively. Whereas, TM-beam has maximum bending moment value of 10291.522kNm, 9220.179kNm and 7066.969kNm for span length 30m, 28m and 24m respectively. Among the three beams, I20-beam has the lowest maximum bending moment value of 10105.610kNm, 8349.121kNm and 6561.723kNm for span length 30m, 28m and 24m respectively.

Similarly, for the shear force, based on Fig.9, U12-beam has the highest maximum shear force among the three type of beams, with values of 1276.682kN, 1255.682kN and 1174.735kN for span length 30m, 28m and 24m respectively. Whereas, TM-beam has maximum shear force value of 1230.95kN, 1212.709kN and 1140.113kN for span length 30m, 28m and 24m respectively. Among the three beams, I20-beam has the lowest maximum shear force value of 1217.216kN, 1209.759kN and 1134.851kN for span length 30m, 28m and 24m respectively.

Finally, Fig. 10, illustrated the maximum deflection for each beam with 3 different span length. Again, U12-beam has the highest value, but now for the deflection with values of 155.642mm, 124.317mm and 74.769mm for span length of 30m, 28m and 24m respectively. While for TM-beam, its maximum deflection values are 134.265mm, 107.388mm and 64.746mm for span length 30m, 28m and 24m respectively. The lowest maximum deflection is obtained from I20-beam with values of 111.137mm, 78.927mm and 47.433mm for span length 30m, 28m and 24m respectively.

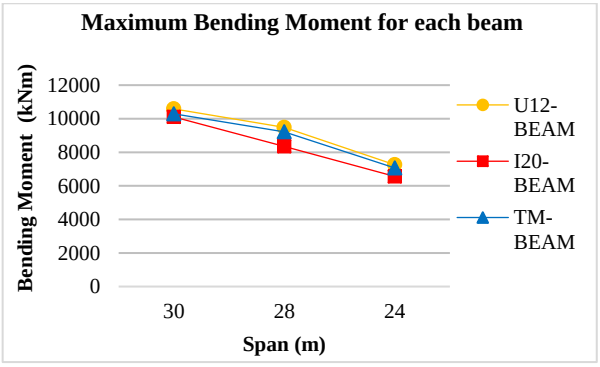

Fig.8: Maximum bending moment for each beam

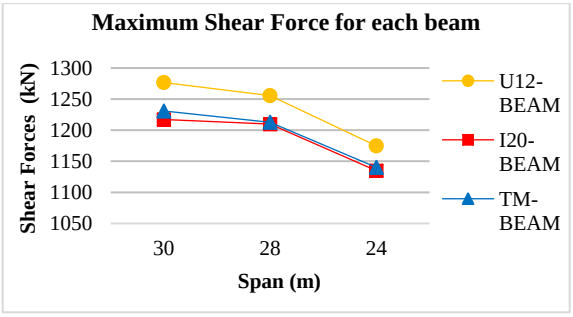

Fig.9: Maximum shear force for each beam

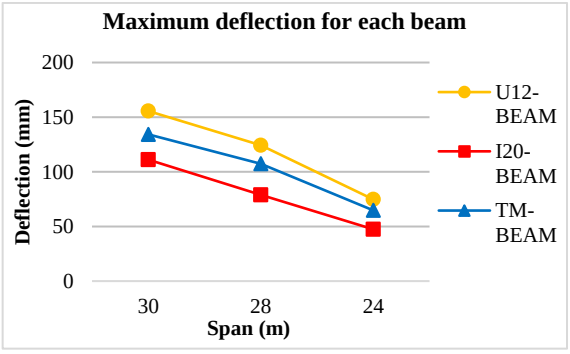

Fig.10: Maximum deflection for each beam

For the same span lengths and loads of the three beams types, I20-beam has the least value of maximum bending moment, shear force and deflection. And as expected, these values decrease as the span length decreases. Thus, I20-beam is strongly recommended. Note that, other factors should also be considered for the final decision, namely; ease of construction, the amount of reinforcements, formworks, concrete and tendon. Nevertheless, the design choices are in the hand of the engineer and the final decision will still be in the hand of the client.

CONCLUSIONS

Maximum bending moment, shear force and deflection were found from U12-beam, followed with TM-beam and I20-beam respectively Thus, it can be concluded that I20-beam is the best option as compared to TM-beam and U12-beam. Apart from the beam shape, the span length also affects the bridge deck analysis, as the longer the span length, the values of bending moment, shear force and deflection will also increase. Note that, other factors should also be considered for the final decision, namely; ease of construction, the amount of reinforcements, formworks, concrete and tendon. Nevertheless, the design choices are in the hand of the engineer and the final decision will still be in the hand of the client.

ACKNOWLEDGMENTS

The authors would like to acknowledge the financial support for this work from Universiti Teknologi MARA (UiTM), Selangor, Malaysia, in particular; Faculty of Civil Engineering and Institute for Infrastructure Engineering and Sustainable Management (IIESM). The industrial support from KL Prima Consult and collaboration support from Universiti Malaysia Pahang (UMP) are also gratefully acknowledged.

REFERENCES

[1] STAAD.Pro V8i, Technical Reference Manual, 2012, Bentley System Incorporated

[2] Anizahyati Alisibramulisi, Mohammad Noor Abu Hassan, Ahmad Ramlan Abu Talib, Hamidah Ramaley, Aqilah Ahmad Zaini and Renga Rao Krishnamoorthy, Transverse Analysis and Design of Box Girder Bridge, IOP Conf. Series: Materials Science and Engineering 431, 2018, 112005, doi:10.1088/1757-899X/431/11/112005

[3] BS 5400-4:1990 Steel, concrete and composite bridges. Part 4: Code of practice for design of concrete bridges

[4] BD37/01: Design Manual for Roads and Bridges, 2001, Vol.1, Highway Structures: General Design, Loads for Highway Bridges

[5] F. Sahaya Sachin and Sandesh Upadhyaya K, A Comparative Study of T-beam bridges for Varying Span Lengths, International Journal of Research in Engineering & Technology, Vol 5, 2016, pISSN 2321-7308

9th Int. Conf. on Geotechnique, Construction Materials and Environment, Tokyo, Japan, 20-22 November 2019, ISBN: 978-4-909106025 C3051

OPTIMIZATION OF BIOGAS PRODUCTION FROM CO-DIGESTION OF WASTE ACTIVATED SLUDGE AND MODIFIED TAPIOCA STARCH SLUDGE

Piyavadee Srivichai[1] and Orathai Chavalparit[2,3]
[1]Interdisciplinary Program in Environmental Science, Graduate School, Chulalongkorn University, Thailand.
[2] Department of Environmental Engineering, Chulalongkorn University, Thailand
[3] Research Program: Sustainable management of industrial and agricultural wastes for transitioning to a circular economy, Center of Excellence on Hazardous Substance Management (HSM), Bangkok 10330, Thailand

ABSTRACT

Waste activated sludge (WAS) obtained from a modified tapioca starch wastewater treatment plant has potential for use as feedstock for biogas production. However, it has a very low C/N ratio of 4.3, leading to a low methane yield. Co-digestion of WAS with starch sludge (SS) can potentially provide balanced nutrients and can enhance biogas production. The results from a biochemical methane potential (BMP) test showed that using WAS as a single feed stock provided a low biogas production at 80 L/kg TVS_{added}. In co-digestion, the addition of 30% and 50% SS increase the biogas yields by as much as 150 and 209 L/kg TVS_{added}, respectively. However, the addition of 70% SS reduces the biogas yield to as low as 117 L/kg TVS_{added}. The result also showed that the optimum condition for biogas production is achieved at 2% TVS_{added} of mixed WAS and SS (1:1) with a desired C/N ratio of 23.56. The increase in % TVS_{added} of the mixed feedstock resulted in a reduction of the biogas yield. The co-digestion of WAS and SS (1:1) also improved the rate of digestion and enhanced the system stability. TVS removal efficiency of the mixed WAS and SS was 41.44% higher than the efficiency when using WAS alone. Moreover, the result of continuous stirred tank reactor (CSTR) confirmed that the co-digestion ratio of WAS:SS (1:1) can enhance biogas yield and methane yield at 301 and 142 L/kg TVS_{added}, respectively at retention time of 11 days.

Keywords: Waste activated sludge, Starch sludge, Co-digestion, Biogas yield

INTRODUCTION

Modified tapioca starch is a value-added product. Thailand is the world's largest exporter of modified tapioca starch, it exported approximately 1.01 million tons with a value of 649 million dollars in 2017 [1]. The modified starch is produced from native tapioca starch that has been changed in its properties to provide the characteristics needed for specific uses. Two major sources of solid waste generation from the production process commonly consist of starch sludge (SS) from a primary sedimentation tank and excess waste activated sludge (WAS) from a secondary sedimentation tank. The reaction and drying starch processes are expressed as mostly a loss of SS. Generally, the tapioca starch loss rate discharges as large quantities, with wastewater comprising approximately 1 percent of raw starch [2]. SS was dewatered and sold at a low price of approximately 73-97 dollars per ton [3] to produce animal feeds that were not economically valuable.

Due to the large quantities and nutrients of WAS, many researchers have studied the biogas production potential from various sources of WAS. For example, Wang et al.[4] reported that the methane production from WAS of an oil refinery plant was 228 L/kg COD_{added}. Karlsson et al.[5] found that the WAS of six Swedish pulp and paper plants could produce methane in the range of 100-200 L/kg TVS_{added}, and Bolzonella et al. [6] found that WAS from four Italian wastewater treatment plants could produce methane between 500-900 L/kg TVS_{added}. WAS is a substrate with high potential for biogas generation. However, WAS has a very low C/N ratio that typically ranges from 6 to 9, thereby possibly limiting the efficiency of biogas production [7]. An excessive amount of nitrogen in the WAS can lead to an overabundance in ammonia accumulation and result in a subsequent inhibition to methanogenesis. [8].

The co-digestion with a rich carbon substrate may be an effective option for improving nutrient balances and biogas production. According to the co-digestion of 95% sewage sludge with 5% glycerol that is rich in carbon content, the biogas yield may be increased by almost 67.4% compared to the digestion of sewage sludge alone [9]. Moreover, co-digestions may offer several advantages such as an improved buffer capacity, an increased biodegradation of feedstock as well as dilutions of toxic substances, which will lead to increases in biogas yields [10].

Thus, it is more appropriate to use SS as a co-substrate with WAS. Meanwhile, this approach helps to tackle the limitation of the pH drop at the beginning of single SS digestion. Because WAS, consisting of 95 percent of bacterial cells [11], has a slower digestion rate than SS consisting of mostly carbohydrates.

This research aims to study the biogas production potential, system performance and TVS removal efficiency of different co-digestion ratios between WAS and SS using the biochemical methane potential method (BMP) for experimentation and the response surface methodology (RSM) for analysis.

MATERIALS AND METHODS

Feedstock and inoculum preparation

The WAS and SS were sampled from a primary sedimentation tank and a secondary sedimentation tank of an activated sludge wastewater treatment process of the modified tapioca starch factory in Rayong province, Thailand. The feedstocks were analysed for moisture, pH, total solids (TS), total volatile solids (TVS) and the carbon to nitrogen (C/N) ratio. Then, the WAS and SS were stored at 4°C before the experiment.

The feedstock was prepared at different ratios of WAS and SS. The %TVS of each substrate in the feedstock were calculated using the following Eq. (1):

$$TVS_1W_1 = TVS_2W_2 \quad (1)$$

Where:

TVS_1 = TVS of the feed substrate (% by wet weight);

W_1 = Weight of substrate (g);

TVS_2 = TVS of feedstock (% by wet weight); and

W_2 = Weight of feedstock (g).

The seed sludge from the up flow anaerobic sludge blanket (UASB) tank of the beverage factory in Pathum Thani province, Thailand was used as an inoculum in this experiment. The TVS of inoculum was prepared at 2.5%.

Experimental design

The co-digestion ratios of WAS with SS were established using Design Expert Software version 10 based on a central composite design (CCD) with an alpha value of 1.414. The TVS of each substrate was specified within the range of 0-2% in which the codes and scales of the variables are shown in Table 1. This experiment consisted of 13 runs, and each run was conducted in triplicate.

The experimental design of the variables was 13 runs with the biogas yield as the response value (Table 3). The proportions of each substrate were varied at 0, 30, 50, 70 and 100 percent while the C/N ratios were in the range from 6.06 to 56.44, which covered the optimum C/N ratio ranging between 20 and 30.

Table 1 The codes and scales of variables

Independent variable	Unit	Coded level				
		-1.414	-1	0	+1	+1.414
WAS concentrations	% TVS	0	0	1	2	2.414
SS concentrations		0	0	1	2	2.414

Biochemical methane potential (BMP) test

A biochemical methane potential (BMP) test was applied to assess the biogas production efficiency of the AD system based on the earlier suggestion of Owen et al. [12]. The ratio of feedstock to active inoculum of 60:40 (by volume) was added to 125 ml serum bottles with working volumes of 80 ml. The pH was initially adjusted using a digital pH meter in the range of 6.8-7.2 by adding sodium bicarbonate ($NaHCO_3$). The headspace of the prepared serum bottles was purged with nitrogen gas before being sealed with airtight rubber stoppers and covered by an aluminium cap. Then, they were incubated on a rotary shaker at a room temperature of 25-30°C with a speed of 140 rpm for 45 days. The volume of biogas was monitored daily using a syringe. The produced biogas was measured by reading the scale on the syringe (Fig. 1).

(A) (B)

Fig. 1 BMP test (A) BMP bottle incubated on the shaker and (B) biogas measurement

Continuous stirred tank reactor (CSTR) test

The optimum co-digestion ratio of WAS:SS obtained from the BMP test was used for further batch CSTR test. The ratio of inoculum to feedstock was 40:60 by volume. The CSTR working volume was 5 L and mixed with a speed of 70 rpm. The entire pH of the mixture between 6.8 and 7.2 by adding sodium bicarbonate ($NaHCO_3$). The biogas volume was measured by a gas counter based on a water-gas displacement system connected to a sensor counter (Fig. 2). The CH_4 content in biogas was analysed by GC (Model Shimadzu GC-2014, Shimadzu Corp., Japan).

Fig.2 CSTR reactor and gas counter

Calculations and statistical analysis

The biogas yield (L/kg TVS_{added}) after 45 days of incubation was calculated using the following Eq. (2):

$$\text{Biogas yield} = BV/TVS_{added} \quad (2)$$

Where:

BV = Cumulative biogas volume (L); and

TVS_{added} = Weight of TVS of feedstock added to the bottle (kg).

An R squared (R^2) analysis was applied to evaluate the RSM model's appropriateness. The optimum co-digestion ratios can be obtained by considering a three-dimensional RSM plot of biogas yields, the system performance and the TVS removal efficiency.

The pH, volatile fatty acids (VFA), alkalinity (ALK) and TVS of the effluent were analysed. All analytical methods were performed by following the American Public Health Association (2017) standard method for the examination of water and wastewater.

RESULTS AND DISCUSSION

The characteristics of the feedstock

The characteristics of the feedstock and inoculum are presented in Table 2. The WAS collected from the secondary sedimentation tank contained a low total solids content at 7.56% by wet weight. Since the major composition is an aerobic bacterial cell, it has a high TVS/TS ratio at 0.78 that was suitable for an anaerobic digestion (AD) system. The pH of WAS was 6.5, and the C/N ratio was 4.3, which can lead to a low biogas yield. Therefore, the digestion of WAS alone may not suitable for biogas production. Thus, such waste may have a substantial advantage on the nutrient balance when co-digested with SS.

The SS from the primary sedimentation tank consisted of the residual starch in the acidic slurry, at a low pH of 4.48. Generally, tapioca starch contains a large amount of amylopectin at up to 83%, which is easy to digest [13]. Additionally, the high C/N ratio of 242 may lead to VFA accumulation and an important drop in pH. Both its pH property and VFA accumulation have a similar adverse effect on the system pH drop, which consequently inhibits methanogenic activity. Concern about this limitation was an important reason for why the AD of SS alone was not appropriate. The useful application of SS was co-substrate with WAS that may help to solve the prior problem by balancing the nutrients and enhancing the biogas yield higher than using WAS alone.

Table 2 Characteristics of co-digestion feedstock and inoculum

Parameter	WAS	SS	Inoculum
Moisture (%)	92.44±1.01	39.09±0.62	93.05±0.14
pH	6.50±0.03	4.48±0.01	-
TS (% by wet weight)	7.56±1.01	61.00±0.45	6.95±0.14
TVS (% by wet weight)	5.92±0.04	31.26±0.03	6.73±0.03
C/N ratio	4.3	242	8.51
TVS/TS	0.78	0.51	0.97

Note: n = 3

Effect of the initial feedstock concentration on the digestion time

Fig. 3 showed the cumulative biogas yield from the WAS and SS feedstocks at various concentrations of TVS_{added}. The digestion time was affected by source of feedstock for both WAS and SS (as a single digestion or co-digestion system). When using WAS as a single substrate, the biogas yield was highest at a reaction time of 38 days, while when using SS as a single substrate the reaction time was 45 days at 1% TVS. Various co-digestions of WAS and SS may reduce the digestion time to less than 30 days. The co-digestion of WAS:SS at a ratio of 1:1 and 2% TVS_{added} achieved the shortest digestion time of 25 days. At this condition, the biogas yield was 209 L/kg TVS_{added}. We emphasize that SS has high potential for co-digestion with WAS.

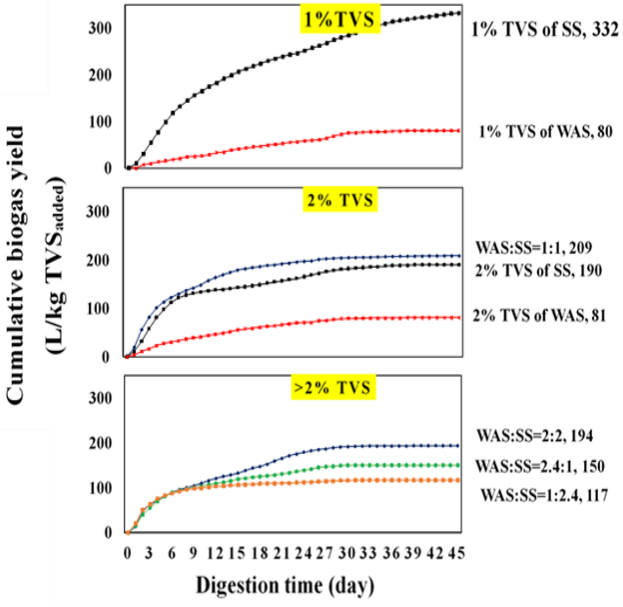

Fig. 3 The cumulative biogas yields from different feedstock and TVS concentrations

Effect of the co-digestion ratio on biogas yields

A three-dimensional plot (Fig. 4) was developed by relating the WAS and SS concentrations to the biogas yields by using RSM analysis. The determination coefficient (R^2) was 0.9561, which indicated that the model is highly capable of explaining up to 95.61% of the experimental condition. The result showed that the major factors impacting biogas yield were the ratios of WAS and SS and the initial concentrations of TVS_{added}. The biogas yield increase with the SS ratio is shown in Fig. 4. At 1% TVS_{added}, the highest predicted biogas yield may be achieved at 301 L/kg TVS_{added} by using SS alone, while the lowest predicted biogas yield occurred at 80 L/kg TVS_{added} by using WAS alone (Table 3). Many studies reviewed that the methane yield from WAS varied in the range of 100-900 L/kg TVS_{added} depending on the source of feedstock, such as: 100-200 L/kg TVS_{added} from pulp and paper plants [5], 500-900 L/kg TVS_{added} from a municipal wastewater treatment plant in Italy [6], 183-200 L/kg TVS_{added} from a municipal wastewater treatment plant in China [14] and 190 L/kg TVS_{added} a municipal wastewater treatment plant in France [15].

The co-digestion of WAS: SS at ratio 1:1 is able to achieve the highest predicted biogas yield at 210 L/kg TVS_{added}. The co-digestion of WAS and SS (1:1) enhanced the biogas yield by 159% compared to the WAS alone (2:0). Meanwhile, the biogas yield from using SS as a single feedstock at 2%TVS_{added} (0:2) was 10% lower than using a mixed feedstock (1:1). Thus, the co-digestion of the WAS:SS at a ratio of 1:1 is suitable for usage at 2% TVS_{added}.

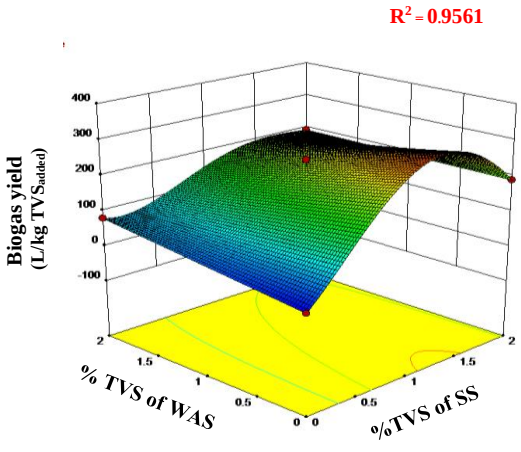

Fig. 4 The RSM pot of the influences of WAS and SS concentrations on the predicted biogas yields

Effect of the C/N ratio on biogas yields

Table 3 showed the C/N ratios of biogas feedstock and biogas yields in each CCD experimental run. The result showed that the C/N ratio of the initial feedstock influenced the biogas yield. The optimum C/N ratio was in the range of 20-30 [16]. The results showed that the optimum biogas yield depended on the ratio of WAS and SS that resulted in a suitable C/N ratio for methanogens. The addition of the SS to WAS feedstock resulted in the increase of the C/N ratio, which may thus increase the biogas yield. For example, the mixed feedstock of WAS and SS at a ratio of 1:1 and the C/N ratio of 23.56 and 29.30 (2% and 4% TVS, respectively) may achieve a biogas yield as high as 209 and 194 L/kg TVS_{added}, respectively. However, the addition of SS to WAS at a higher ratio than 1:2.4 would reduce the biogas yield since the C/N ratio was 43.57, which exceeds the optimum range.

In the case of using SS alone at 1% TVS_{added}, the highest biogas yield was achieved 332 L/kg TVS_{added}. This is because during the preparation of feedstock, seed was added to the SS feedstock (40:60) before the BMP test. Thus, the C/N ratio of using SS alone was 35.2. Meanwhile, the C/N ratio of 2% TVS of SS alone was 56.44.

Table 3 C/N ratio of the biogas feedstock and biogas yield in each CCD experimental run.

Run	TVS concentration (% by wet weight)		Proportion (%)		C/N ratio	Biogas yield (L/kg TVS_{added})	
	WAS	SS	WAS	SS		Actual value	Predicted value
1	0	0	0	0	8.51	0	0
2	1	0	100	0	6.79	80±0.42	80
3	2	0	100	0	6.06	81±16.62	81
4	2.41	1	70	30	16.86	150±5.56	119.43
5-9	1	1	50	50	23.56	209±25.55	210.42
10	2	2	50	50	29.30	194±8.42	193.92
11	1	2.41	30	70	43.57	117±3.23	116.8
12	0	1	0	100	35.21	332±3.57	301.41
13	0	2	0	100	56.44	190±13.08	189.88

Performance of AD

Fig. 5C showed the pH and the ratios of VFA and ALK of each experimental run after 45 days of operation. At the beginning of the experiment, all reactors were adjusted so that the pH of the reactor was in range in 6.8-7.2 with $NaHCO_3$. The reactors using WAS alone and the co-digestion of the WAS:SS ratio were 2.4:1 and 1:1 (run 2-9), while the final pH values were in the range of 7.01-7.27 (Fig. 5B). VFA/ALK ratios of these reactors were in the range of 0.09-0.23. These values may be an indicator that the reactors were working within the optimum interval for methane formation, which should be lower than 0.4 [17]. This may be because WAS had the low concentrations of readily available organic carbon [14]. Typically, it is not quickly degraded to VFA by the hydrolysis, acidogenesis and acetogenesis stages. Therefore, the VFA produced in the co-digestion ratios of 2.4:1 and 1:1 can be converted into biogas through the methanogenesis stage with a suitable conversion rate that resulted in

no excess VFA accumulation occurring. This result was confirmed by the neutral pH value and the lower VFA/ALK ratio in this digestion system.

For reactors using SS alone and the co-digestion of the WAS:SS ratio of 1:2.41 (run 11-13), the pH values were in the range of 4.16-6.86, while VFA/ALK ratios were in the range of 2.55-15.8. The co-digestion that added the high ratio of SS had the low biogas yields. The SS is too much starch content, causing the speed of the VFA production in the early stage to be faster than the speed of VFA consumption by methanogenic bacteria, which resulted in a high VFA accumulation. This dynamic may inhibit the methanogenesis process [18]. These results are in line with those obtained by Cuzin et al. [19], who reported that the AD of cassava peels consists of a major biodegradable starch that usually results in excess acid production, which affects the pH drop and is highly toxic to methanogens. Anunputtikul and Rodtong [20] showed that there was the decrease in pH in the initial fermentation of rich starch cassava tubers.

Meanwhile, the co-digestion of WAS:SS at the ratio of 1:1 may give the highest biogas yield compared with other co-digestion ratios. Additionally, it can enhance the performance and system stability with a lower VFA/ALK ratio of 0.23 and a neutral pH of 7.01 compared to the digestion of SS alone. Thus, selecting the optimum co-digestion ratio should also consider the biogas yield, the system stability and the TVS removal efficiency.

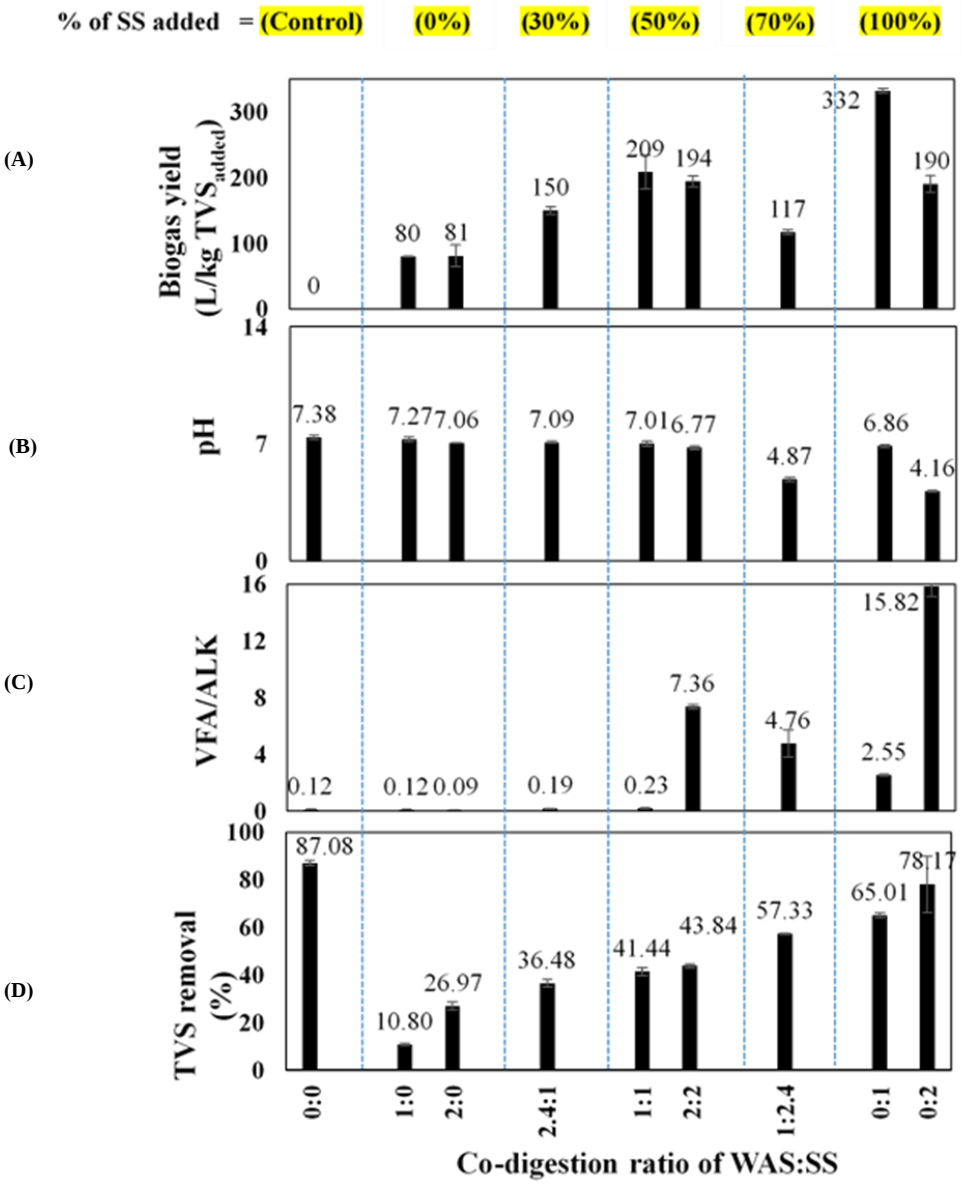

Fig. 5 The performance and system stability in the co-digestion of WAS:SS (A) Biogas yield, (B) pH, (C) VFA/ALK ratio and (D) TVS removal

TVS removal efficiency

Increasing the ratios of the added SS (at the co-digestion of WAS:SS ratios of 1:0, 1:1 and 1:2.4) resulted in significant increases in the TVS removal efficiency of 10.80%, 41.44% and 57.33%, respectively (Fig. 5D). Since WAS consists of a combination of microorganisms, approximately 95% of bacteria and 5 percent of higher organisms [11], it is more difficult to digest than SS [14]. Thus, increasing the TVS removal efficiencies depends mostly on the SS, which is easy to digest. Specifically, at the co-digestion ratio of 1:1 (WAS:SS), the TVS removal efficiency was 41.44% higher than it was when using WAS alone, which achieved an efficiency of 10.80%. Thus, this result verified that the co-digestion ratio of 1:1 may be a promising and practical option for the use of WAS and SS as feedstock in the anaerobic digestion process due to improved TVS removal efficiency, high biogas yield and proper system stability.

CSTR test

Fig.6 showed that the biogas yield at the co-digestion of WAS and SS (1:1) in the CSTR was 301 L/kg TVS_{added} at retention time of 11 days. Since the CSTR digestion was carried out with complete mixing, so the biogas yield was higher than those obtained from BMP test. Moreover the reaction time was also faster than BMP test. Considering the methane (CH_4) yield and content equal to 142 L/kg TVS_{added} and 47%, respectively. The final pH and VFA/Alk ratio was equal to 7.04 and 0.36, respectively. It was emphasis that the system has good performance.

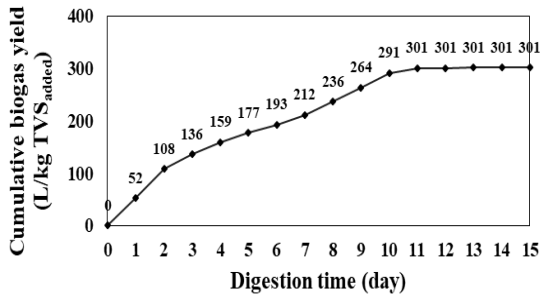

Fig. 6 The biogas yield in the CSTR

CONCLUSIONS

WAS and SS may be used as feedstocks for biogas generation. The optimum condition for biogas production was the co-digestion of WAS:SS at the ratio 1:1 at 2% TVS_{added}. At this condition, biogas yields may be achieved at 209 L/kg $TVS_{added.}$ Result from CSTR batch experiment of such condition showed that biogas yield and methane yield were high as 301 and 142 L/kg TVS_{added}, respectively. After operation for 11 days, the pH and VFA/ALK ratio was7.04 and 0.36, respectively. The biogas obtained in this anaerobic digestion can be used as an alternative fuel in a hot air generator for the starch drying process. Moreover, there are cost-saving for WAS sent to landfills and environmental advantages in reducing the greenhouse gas emissions from landfills.

REFERENCES

[1] Thai Tapioca Starch Association (TTSA), Export Tapioca Products. 2018, http://www.thaitapiocastarch.org/en/information/statistics/export_tapioca_products

[2] Kumoro A.C.B., Primaloka D.A., Ardhannari L., Matin H.A. and Sumardiono S., Study of Biogas Production from Cassava Industrial Waste by Anaerobic Process. MATEC Web of Conferences, Vol. 156, 2018, pp. 1-6.

[3] The Thai Tapioca Products Factory Association, The Price of Tapioca By-Product in Thailand, 2017, http://thaitapioca.org/

[4] Wang Q., Liang Y., Zhao P., Li Q. X., Guo S. and Chen C., Potential and Optimization of Two-Phase Anaerobic Digestion of Oil Refinery Waste Activated Sludge and Microbial Community Study, Scientific Reports, Vol. 6, 2016, pp. 1-10.

[5] Karlsson A., Truong X.B., Gustavsson J., Svensson B.H., Nilsson F. and Ejlertsson J., Anaerobic Treatment of Activated Sludge from Swedish Pulp and Paper Mills--Biogas Production Potential and Limitation, Environmental Technology, Vol. 32, Issue 13, 2011, pp. 1559-1571.

[6] Bolzonella D., Pavan P., Battistoni P. and Cecchi F., Mesophilic Anaerobic Digestion of Waste Activated Sludge: Influence of The Solid Retention Time in The Wastewater Treatment Process, Process Biochemistry, Vol. 40, Issue 3, 2005, pp. 1453-1460.

[7] Liu C., Li H. and Zhang Y., Improve Biogas Production from Low-Organic-Content Sludge through High-Solids Anaerobic Co-Digestion with Food Waste, Bioresource Technology, Vol. 219, 2016, pp. 252-260.

[8] Mawioo P. M., Garcia H. A., Hooijmans C.M., Velkushanova K., Simonic M., Mijatovic I. and Brdjanovic D., A Pilot-Scale Microwave Technology for Sludge Sanitization and Drying, Science of The Total Environment, Vol. 601, 2017, pp. 1437-1448.

[9] Maragkaki A.E., Fountoulakis M., Kyriakou A., Lasaridi K. and Manios T., Boosting Biogas Production from Sewage Sludge by Adding Small Amount of Agro-Industrial By-Products and Food Waste Residues. Waste Management, Vol. 71, 2018, pp. 605-611.

[10] Rabii A., Aldin S., Dahman Y. and Elbeshbishy E., A Review on Anaerobic Co-Digestion with a Focus on the Microbial Populations and the Effect of Multi-Stage Digester Configuration, Energies, Vol. 12, Issue 6, 2019, pp. 1-25.

[11] Tomasik, B., Microorganisms Created by Wastewater-Treatment Systems. 2017, https://reducing-suffering.org/microorganisms-wastewater-treatment/#Microorganism_composition

[12] Owen W.F., Stuckey D.C., Healy L.B., Jr., Young L.Y. and McCarty P.L., Bioassay for Monitoring Biochemical Methane Potential and Anaerobic Toxicity, Water Research, Vol. 13, 1979, pp. 485-492.

[13] Promthong S., Kanto U., Tirawattanawanich C., Tongyai S., Isariyodom S. and Markvichitr K., Comparison of Nutrient Compositions and Carbohydrate Fractions of Corn, Cassava Chip and Cassava Pellet Ingredients: Animals, in Proc 44th Kasetsart University Annual Conference, 2006, pp. 211-220.

[14] Liu X., Xu Q., Wang D., Zhao J.,Wu Y., Liu Y., Ni B.J., Wang Q., Zeng G., Li X. and Yang Q., Improved Methane Production from Waste Activated Sludge by Combining Free Ammonia with Heat Pretreatment: Performance, Mechanisms and Applications, Bioresource Technology, Vol. 268, 2018, pp. 230-236.

[15] Carrrea H., Rafrafia Y., Battimellia A., Torrijosa M., Delgenes J.P. and Ruysschaert G., Methane Potential of Waste Activated Sludge and Fatty Residues: Impact of Co-digestion and Alkaline Pretreatments, The Open Environmental Engineering Journal, Vol. 3, 2010, pp. 71-76.

[16] Dioha I.J., Ikeme C.H., Nafi'u T., Soba N. I. and Yusuf, M.B.S., Effect of Carbon to Nitrogen Ratio on Biogas Production. International Research Journal of Natural Sciences, Vol. 1, Issue 3, 2013, pp. 1 - 10.

[17] Janejadkarn A. and Chavalparit O., Biogas Production from Napier Grass (Pak Chong 1) (Pennisetum purpureum × Pennisetum americanum). Advanced Materials Research, Vol. 856, 2014, pp. 327-332.

[18] Dobre P., Farcas N. and Matei F., Main Factors Affecting Biogas Production - An Overview Romanian Biotechnological Letters, Vol. 19, Issue 3, 2014, pp. 9283 - 9296.

[19] Cuzin N., Farinet J.L., Segretain C. and Labat M., Methanogenic Fermentation of Cassava Peel Using A Pilot Plug Flow Digester, Bioresource Technology, Vol. 41, 1992, pp. 259-264.

[20] Anunputtikul W. and Rodtong S., Laboratory Scale Experiments for Biogas Production from Cassava Tubers, in Proc. Int. Conf. on Sustainable Energy and Environment (SEE), 2004, pp. 238-243.

9th Int. Conf. on Geotechnique, Construction Materials and Environment,
Tokyo, Japan, 20-22 November 2019, ISBN: 978-4-909106025 C3051

HEAVY METAL SEDIMENT AVAILABILITY ASSESSMENT OF THE REMOTE CONTAMINATED UPSTREAM OF THE MAE TAO BASIN

Khunin. T. [1], Wongyai s.[2] Somprasong K.[3]
[1,2,3] Department of Mining and Engineering, Faculty of Engineering,
Chiang Mai University, Thailand

ABSTRACT

The Mae Tao Basin in Mae Sot district, Thailand, was a large remote cadmium contaminated area. This area has been reclaimed after the closing of two zinc mine in 2016. Even supposing that the contamination of cadmium in this area is related to the mine operation, but the investigation of other heavy metal in the upstream area has not been completely established. In this study, the Portable X-ray Fluorescence Spectroscopy (P-XRF) were assigned as the analysis tool for retrieving the primary concentration levels of heavy metals. Since the upstream area of the Mae Tao Basin is a remote area, covered with deciduous forest, therefore must collect samples for analysis. The recorded concentrations of heavy metals were analyzed and transformed into data input in form of raster calculation layers. These layers were combined with Revised Universal Soil Loss Equation (RUSLE) incorporated with geographic information system (GIS) with the intention of estimating the heavy metal sediment availability. The study's result the discovered heavy metals, other than cadmium, are arsenic (As), manganese (Mn), lead (Pb), zinc (Zn) and mercury (Hg). Additionally, the concentration of arsenic revealed by the investigation is ranged from 6.104 – 297.122 mg/kg while its highest sediment availability is equal to 38.36 g/m 2 /y. This contamination level is exceeding the acceptable level for arsenic in soil of Thai at 3.9. According to study's result, the further investigation on arsenic in the upstream area of the basin is strongly recommended to be conducted.
Keywords: Erosion, GIS, Contamination, Sediment, RUSLE

INTRODUCTION

The Mae Tao Basin covers 6090.75 ha (59.61 km^2). The basin contains four significant land utilizations which are mining production areas, corn field, rice paddy fields, and deciduous forest areas. This area has been considered to be Thailand's largest zinc deposit, is in Mae Sot district, Tak province as can be followed in Fig1. It is a remote area where the contamination of cadmium has been continuously reported. [1] According to the existence of cadmium which naturally born in association with the occurrence of zinc- composite mineral, so the contamination was widely detected over the area, especially in the main water resource, named as the Mae Tao Creeks.

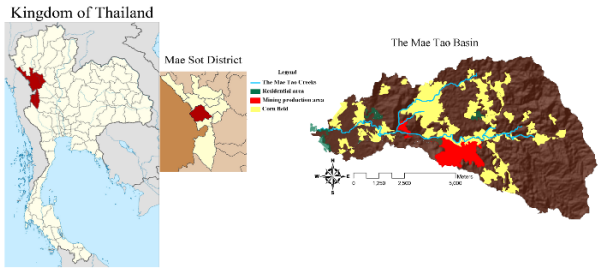

Fig1. Location of the Mae Tao Basin

While cadmium has been considered to be the main contaminants, degrading the qualities of the environmental phases of this area, thus the study of the availability of other heavy metals has not been archived especially in the upstream area of the basin.

Rainfall erosion was found to be one of the major mechanics that make cadmium available for spreading throughout the basin [2]. In order to illustrate this circumstance as a spatial model, the Revised Universal Soil Loss Equation (RUSLE) has been applied to evaluated possible amount of the surface erosion. Application of RUSLE is accustomed to the remote sensing for land surveying and development.

The integration between geographic information system (GIS) technology and this erosion models has been proven to be effective at estimating the magnitude and distribution of erosion. It has been effectively applied in the monitoring of contaminated area. [3] successfully applied RUSLE as a main tool in the identification of heavy metals distribution patterns and the likely sources of pollution in the Songkhla Lake Basin, southern Thailand.

Recently, X-ray fluorescence analysis has been developed into portable analytical device and emerged as a very powerful technique for in-situ elemental analysis of environmental samples [3]. The Portable X-ray fluorescence spectroscopy (PXRF) , demonstrated in Fig.2, offers non-destructive analysis of both quality and quantity of the mineral composition in multi-element samples. This instrument provides a competence in conducting a reliable on filed-chemical analysis with a short period of time.

Figure 2. Portable X-ray fluorescence spectroscopy (PXRF)

The application of PXRF in the environmental and mining sector to determine elemental distributions and quantifying element contents were found to be reasonable. It can generate reliable, high quality elemental concentration data for metal-contaminated soils [4].

By combining the concentration profiles of the area, analyzed directly PXRF with the results from RUSLE, the potential migration fluxes of the heavy metals, including Arsenic (As), Lead (Pb), and Mercury (Hg), the sediment availability of these contaminants in the upstream of these study area can be illustrated.

METHODOLOGY

The overall framework of the study is established in Fig.3

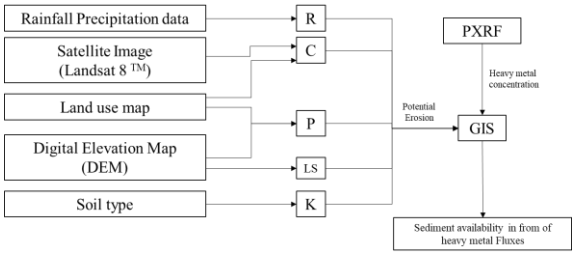

Fig.3 Framework of the study

Rainfall precipitation data were attained by Thai Meteorological Department (TMD). The soil classification and land use maps were acquired from the Land Development Department of Thailand (LDD). The Digital Elevation Map (DEM) of the study area was afforded by the Royal Thai Survey Department (RTSD). The satellite image of the basin, covering the study period were supported by GISTDA.

The data sets were separately analyzed in the purpose of preparing the required data input of RUSLE using GIS application. The potential erosion results were estimated in association with the concentration profile, gathered from the on-site analysis, using PXRF for establishing the potential heavy metal flux from erosion that occurred over the upstream of the Mae Tao Basin Area.

Heavy metal concentration analysis.

The upstream area of the Mae Tao Basin, is classified as a remote area, where the hauling of sampling out of the area for chemical analysis is merely possible. Accordingly,PXRF, capable for on-site analysis, then applied as analytical instrument. Since the standard method for PXRF has not been release, the analysis on heavy metal content in the soil surface of the area were conducted following ASTM E 1626 – 13 [5] at the sample preparation state. Soil samples with a depth of 30 cm were analyzed to determine contents of heavy metal including Arsenic (As), Lead (Pb), and Mercury (Hg). Fifty two samples, cover the reachable area in the upstream of the basin,were colected and analyzed into the concetration profile,using GIS application.

Revised universal Soil Loss Equation.

Soil loss or soil erosion refers to the amount of soil moved from one particular area to another. This phenomenon were based on the relationship between raindrops, runoff and the erodibility of a certain area. RUSLE can give a quantifiable results of the erosion amout by extending the terms of cover management and support practices into the equation.

Cadmium contaminats in the basin adsorb with the overland sediment as residue from surface runoff, so the applying of RUSLE to illustrate the potential erosion of the area can reflect the possibility of the cadmium that can be release into the environmental phases. The Revised Universal Soil Loss Equation is presented in (1)

$$A = R \times K \times LS \times C \times P \qquad (1)$$

The R factor is the erosivity by rainfall runoff at a location. The K factor refers to the specific value of the inherent erodibility of the soil surface material at a specific area. The LS reflects the effects of topography, specifically a hill's slope, length, and steepness, on the rates of soil loss at a site.

The C factor expresses the effects of surface cover and roughness from the biomass to the rate of soil loss, while the P factor represents effects of soil conservation practices such as buffer strips for cover vegetation [3].

Parameter Determination

R factor

R factor calculations were conducted base on the study of [6] as can be seen in (2).

$$R = 0.4669X - 12.1415 \qquad (2)$$

K factor

The land use and soil classification map of the Mae Tao Basin are afforded from LDD in association with the study 's result of [2].

C factor

The familiar spatial estimation method for C factor is to assign values into land cover classes using classified remotely sensed images. Basically, the classification using NDVI analysis presents a high correlation with ecological variables as leaf-area-index, total vegetation cover or above ground biomass [7]

The C factor assigned in this study were based on the study of which were derived from the NDVI analysis result of the satellite images. According to [2], the method performs high accuracy when applied the calculation to the South-East Asia's NDVI analysis. The calculations were performed following (3) to (4)

$$NDVI = (NIR - R)/(NIR + R) \qquad \textbf{(3)}$$

$$C = 0.6 - 0.77NDVI \qquad \textbf{(4)}$$

Where NIR and R indicate channel or band of Landsat which are near infrared and visible red respectively.

P factor

The support practice factors (P) were assigned, according to [8] as a combination between slope data from the spatial analysis of DEM and land use map based on the criteria, prescribed in Table 1.

Table1 P factor assigned in this study

Land cover	P factor
Agricultural Area with Slope ≤ 8 %	**0.5**
Agricultural Area with Slope between ≥ 8 % and 20 %	**0.75**
Agricultural Area with Slope ≥ 20 %	**0.9**
Shrub, Secondary Forest and Forested Area	**0.1**

LS factor

LS-factor calculation was operated under the remote estimation technique using GIS application, following the equation of which is presented in (5). The calculation of LS factor for the surface area of The Mae Tao Basin is presented in Fig 4.

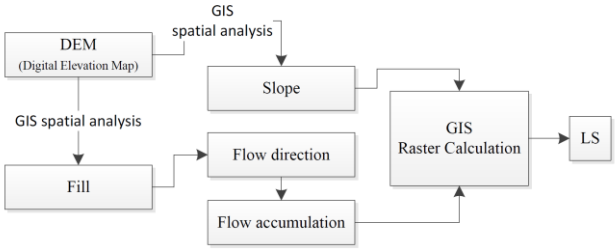

Fig.4 LS factor determination process

$$LS = \left(\frac{Flowacc \times resolution}{22.13}\right)^{m} (65.41\sin^2\theta + 4.56\sin\theta + 0.0654) \qquad (5)$$

The LS-factor refers to the surface terrain of the basin, affect by the slope gradient of in the form of percent gradient [9,10]. The slope gradient of the study area was calculated and analyzed based on spatial analysis technique [10]. The value of m, referred to a coefficient related to the ratio of rill to inter-rill erosion, was varied from 0.2 to 0.5, depending on the slope gradient and m, defined previously, was equivalent to 0.5 for slope > 5 %, 0.4 for slope between 3 %s to5 %, 0.3 for slope range pf 1 % to 3 %, and 0.2 for under 1 % slope.

In a purpose of calculating the flow accumulation, a DEM (30 m resolution) of the basin from the Royal Thai Survey Department (RTSD) was obtained and analyzed under the fill spatial analysis technique to avoid any discontinuity in the flow simulation which can be existed when water is trapped by cells of higher elevation. After that, the flow direction was generated from these filled grids. Flow accumulation was calculated based on the direction acquired from the flow direction analysis. As a final process, the raster calculation was applied to determine the LS-factor.

Potential heavy metal flux from erosion estimation

Potential erosion estimation. The calculation for potential erosion of the Mae Tao Basin was operated under the spatial analysis for raster calculation in GIS application, based on (1).

The potential erosion, obtained from RUSLE's estimation were combined with the heavy metal profile, using (6), to illustrate the sediment contaminated by heavy metal in the study area. In this equation, P_E is the potential availability of cadmium, while [H] stands for the heavy metal's concentration of the monitoring area.

$$P_E = [H]A \qquad (6)$$

RESULTS AND DISCUSSIONS

Potential erosion of the Mae Tao Basin

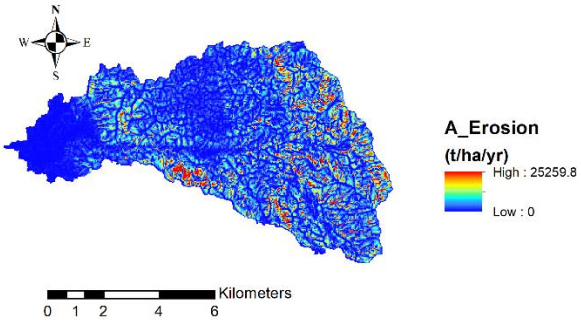

Fig.5 Potential cadmium flux from erosion of the basin

Figure 5 illustrates the potential erosion of the Mae Tao Basin in 2018. The potential erosion can be defined in form of raster map. High potential erosion was significantly detected in the mining production area and the upstream of the basin. The results also designate some other areas with high potential due to high soil erosion capabilities. The highest value of potential was found to be 25259.8 t/ha/y.

Heavy metal concentration's profile

As previously stated, the concentration of each contaminants was analyzed by PXRF and then transformed into raster-calculation layers. The analytical results indicated that high level of heavy metals can be notified in some parts of the basin as can be seen in Fig.6 to Fig.8.

Pb, As and Hg, considered to be lethal hazardous substances that can cause both long term and short-term diseases, were diffusely sensed all over the area of the basin as can be followed in Fig.6 to Fig.8.

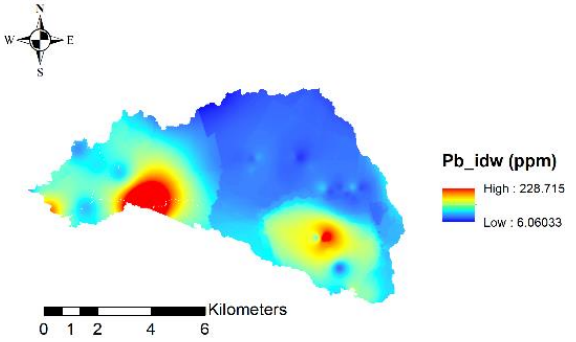

(a)

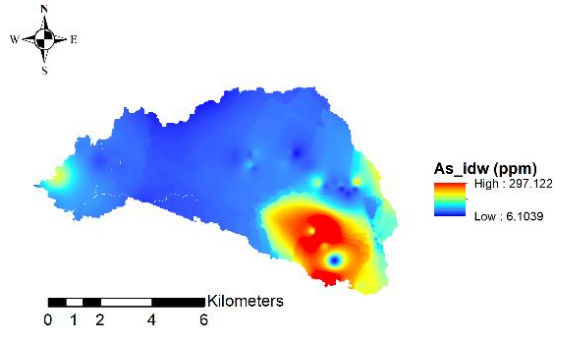

(b)

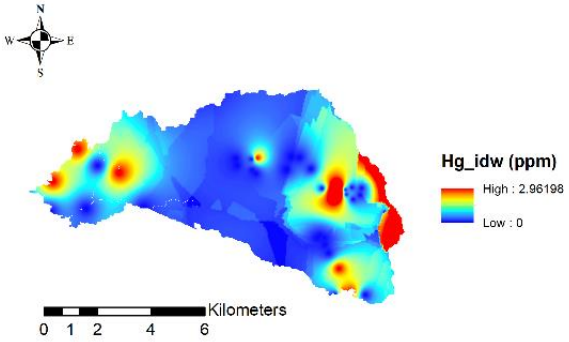

Fig.6 Heavy metal concentration profile (a) Pb, (b) As (c) Hg

Table 2 Comparison between heavy metal contents from the analysis and existed standards.

Heavy Metals	Concentration (ppm)				
	Max	Avg.	Min	SD	Standard in soil
Pb	228.175	36.98	9.27	1.62	400.00
As	297.122	44.88	6.00	0.59	3.90
Hg	2.961	0.53	< 0.02	0.13	23.0

In accordance with Table 2, Arsenic, mostly found in the agricultural area of the basin's upstream range from 6.00 to 297.122 ± 4.78 ppm were exceed the acceptable standards of Thailand [PCD] at 3.9 ppm. The concentration level of Pb and Hg is under the acceptable standard at 400 ppm and 23 ppm respectively. Pb's content, detected during the monitoring period were ranged from 9.27 to 228.175 ± 1.62 ppm, while Hg's concentration was ranged from 0.02 to 2.961± 0.13 ppm respectively.

Estimation result of potential cadmium flux from erosion

Consistent with Eq.6, the potential heavy metal fluxes from can be defined in form of raster map as established in Fig.7 and Table3.

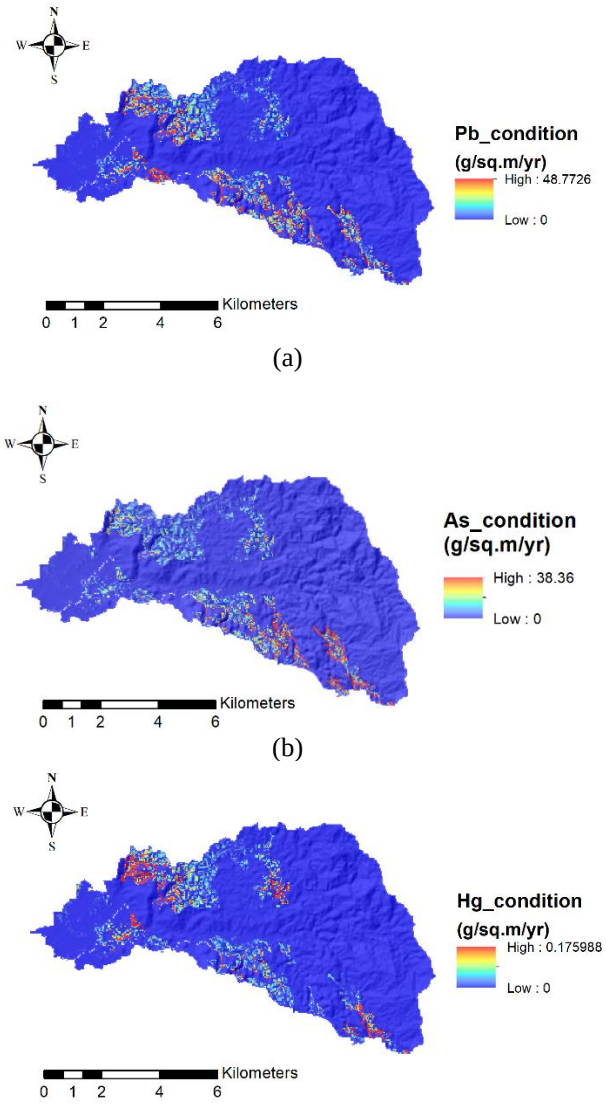

Fig.7 Potential heavy metal fluxes from erosion ($g/m^2/y$) (a) Pb (b) As (c) Hg

Table 3. Estimation results of potential cadmium flux from erosion

Heavy metals	Potential heavy metal fluxes from erosion ($g/m^2/y$)			
	Max	Min	Avg	SD
Pb	48.770	0.000	0.210	1.010
As	38.360	0.000	0.730	1.040
Hg	0.176	0.000	0.001	0.005

Along with the spatial analysis' results, the high potential flux value was perceived in the upper stream of the and some other areas, containing high soil erosion capabilities.

High level of the potential lead flux from erosion was compactly located in the downstream of the basin, as well as mercury. Lead discovered in the study area, contained potential migration availability at 0 to 48.77 ±1.01 $g/m^2/y$, while mercury contained 0.176±1.01 $g/m^2/y$ is mercury availability. The highest value of potential arsenic fluxes from erosion was found in the agricultural region in the upstream area at 38.36 ± 1.04 t/ha/y. The location where high availability of arsenic was densely sense was in the south-eastern upstream area of the basin.

Discussion & suggestion

Despite the fact that the Mae Tao basin has been contaminated by cadmium, but the degradation of environmental phases, caused by other heavy metals must be concerned. Arsenic, possesses abilities in causing both acute and chronic effect to the residents in the contaminated area such as hyperkeratosis, leading to skin cancer, were the most deleterious substance that need further remediation. There are two possible sources of arsenic in this study area. Firstly, the geological characteristic of the basin which is considered to be secondary deposition area of zinc and other metal compositions so that the high content of arsenic and other heavy metal contaminants can be sensed.

Likewise, the dense contaminated area with high potential erosion is the also classified as the agricultural area in which corn field are planted and vegetated. According to this circumstance, the contamination of heavy metal especially arsenic can be the results from fertilizers' utilization and irrigation.

Since the distribution process of arsenic can be different from cadmium, the monitoring on fate and transport of the contaminant must be conduct in a purpose of establishing a recommendation on the remediation procedure. Parts of the corn plant, including tassel, leaf, stalk, root and corn fruit sample should be separately analyzed to determine the accumulated arsenic content.

Mercury and lead, compactly sense in the downstream area of the basin, contains low level of potential flux during the rainfall incident. According to the heavy metal content and the detected location, the migration availability of these two contaminants is insignificant, compared to the exposing of arsenic, however long-time monitoring on the accumulation of them into forage plants must be considered.

As a suggestion to improve the quality of the estimation, the statistical analysis of the study's results should be accomplished in order to examine the accuracy and the precision of the results. Extended field observation for other input data should be concerned so that the estimation will be more fitted to the real incident occur in the study area.

CONCLUSIONS

The contaminant flux from erosion in the upstream area of the Mae tao basincan be estimated, based on RUSLE. It can illustrate the significant potential area which have a capability in releasing heavy metal attaching in form of the residue in the rainfall runoff. This integrated spatial techniques can effectually map out the potential sources of contamination especially in the remote area. This study has shown the capability of customizing this integrated method to characterize a remote heavy metal contaminated area.

The combination between the effects of low erosion resistance and being situated in a mountainous area results in high potential in releasing cadmium during the erosion incident.

For arsenic contamination, discovered in this case, further study of potential sources of the contaminant and its fate and transport must be accomplished in order to establish the suitable remediation and protection scheme

The further study and development in utilizing more precise parameter for soil erosion estimation will enhance the estimation efficiency of this integrate method and can be applied to another similar contaminated site.

REFERENCES

[1] Department of Primary Industries and Mines (DPIM)., Report of the study on the solution of cadmium contamination in the Mae Tao Basin Mae Sot district, Tak province. Bangkok. Thailand, 2016.

[2] Ladachart, R., Sutthirat, C., Hisada, K. and Charusiri, P., Soil Erosion and Heavy Metal Contamination in the Middle Part of the Songkhla Lake Coastal Area, Southern Thailand. In Coastal Environments: Focus on Asian Regions. Springer Netherlands, 2012, pp. 106-129.

[3] Somprasong, K., Spatial Monitoring of Potential Overland Sediment from Significant Land Use Types, for the Remote Contaminated Area of the Mae Tao Basin, Thailand: 15 Years Monitoring Period. International Journal of Environmental Science and Development, Vol 8., Issue 9. 2017.

[4] Ussath M., Grimmer M., Hoth N. and Alcalde J., Hand-held X-ray fluorescence (hXRF) measurements as a useful tool in the environmental and mining sector–Comparative measurements and effects of water content.13th International Mine Water Association Congress. Mine Water & Circular Economy, Finland Vol. 2,2017, pp. 979 – 987.

[5] ASTM E1621-13, Standard Guide for Elemental Analysis by Wavelength Dispersive X-Ray Fluorescence Spectrometry, ASTM International, West Conshohocken, PA, 2013, www.astm.org

[6] Vityakon, P., Trelo-ges, V. and Sriboonlue, V., Soil erosion in some land use systems in an agroforestry landscape of Northeast Thailand. Ministry of Agriculture and Cooperatives. Bangkok, Thailand,1993, pp.149 (in Thai with English abstract).

[7] Lawrence, R.L. and Ripple, W.J., Comparisons among vegetation indices and band wise regression in a highly disturbed, heterogeneous landscape: Mount St. Helens, Washington. Remote sensing of Environment, Vol. 64, Issue 1., 1998 pp.91-102.

[8] Van der Knijff, J.M., Jones, R.J.A. and Montanarella, L., Soil erosion risk assessment in Europe, 2000.

[9] Nontananandh, S. and Changnoi, B., Internet GIS, based on USLE modeling, for assessment of soil erosion in Songkhram Watershed, Northeastern of Thailand. Kasetsart J, Vol.46, 2012, pp.272-282.

[10] Mitasova, H., Hofierka, J., Zlocha, M. and Iverson, L.R., Modelling topographic potential for erosion and deposition using GIS. International Journal of Geographical Information Systems, Vol.10, Issue 5., 1996, pp.629-641.

9th Int. Conf. on Geotechnique, Construction Materials and Environment, Tokyo, Japan, 20-22 November 2019, ISBN: 978-4-909106025 C3051

DIFFERENCE OF FLOODING PHENOMENON WITH BANK BREACH BY DIFFERENCE OF BACK WATER EFFECT IN 2016 FLOOD AT TOKORO RIVER

Sho Adam Fukazawa[1], Yasuharu Watanabe[2] Tomonori Shimada[3]
[1,2]Kitami Institute of Technology, Japan, [3] Civil Engineering Reserch Institute for Cold Region

ABSTRACT

In recent years, bank breaching has occurred with high frequency. In August 2016, the eastern part of Hokkaido, Japan was hit by a heavy rainfall and the tributaries of Tokoro River (Sibayamsawa River and Toua River) had a bank breach caused by the back water of Tokoro River. Although both tributaries were almost identical in size and both junctions were very close, the situation of inundation significantly differed. At the breaching point of the Sibayamasawa River, the inundation flowed toward the upstream side of the inland, while at the Toua River it was perpendicular to the channel.

In order to understand the cause of the difference in phenomena, the reproduction of the breaching situations of both rivers at tributaries were attempted using the numerical simulation model "iRIC Nays 2D Breach".

Keywords: Four or five keywords (First characters of each keyword are in uppercase letters), Italic

1. INTRODUCTION

In recent years, heavy rainfall has occurred highly frequently due to the effects of climate change, and many cases of damages cause through bank breaches in small and medium-sized rivers and tributaries of large rivers have been reported. In August 2018, the torrential rain experienced in the western part of Japan lead to a total of five separate bank breakages at three tributaries of Odagawa River in the area of Mabicho[1], Kurashiki City's. Also in August 2016, while the heavy rainfall caused various disasterous situations as a result of bank breaches and river flow fluctuations in many parts of Hokkaido, in Tokoro River many disastrous cases such as bank breach, bank erosion sand blast, etc. were reported. Under such circumstances as this, a bank breach with inundation occurred seemingly as a result of the back water phenomenon arisen in the tributaries Tokoro River (Sibayamasawa River and Toua River). The Figure 1 shows the location of the main stream of Tokoro River and the tributaries of Sibyamasawa River and Toua River. Although both tributaries were almost identical in size and both junctions were very closely located, the situation of inundated were largely differed. Toua River's bank breach phenomenon occurred 300m away from the bank position and the scour scars which was formed by the inundation flow streched perpendicularly to the river channel. In contrast, the Sibayamasawa River's bank breach phenomenon made the scour scars that the embankment ground been formed by inundated flow more toward the upstream side of the inland. The width of scour scars was wider than Toua River, but the length was shorter than Toua River. In fact, it was half length of Toua River, extending only for a length of 150m from the bank. Although there are examples illustrating the phenomenon of bank breach widening had the examples of bank breach including a scale model[2] made with a bank breach experiment[6] using a full size model of water channel and numerical calculation of bank breach widening performed by Shimada[5] and Tujimoto[4]. they were all for self-flowing sections and the process of bank breach widening in the case of bank breach occurring in the section of back water channel isn't clear yet. It will be an important piece of information for the reduction of natural disaster occurring at the time of bank breach, if how bank breach widening progresses is clarified not only at the self-flowing section but also at the section of back water. In this research an analysis was carried out to understand the cause of difference in phenomena between the two tributaries of Sibayamasawa River and Toua River. As the impression after the bank breach was grasped by field survey, but the phenomenon during bank breach was not confirmed, the numerical simulation software model called "iRIC Nyas 2D Breach"[6] was used to confirm the bank breach widening phenomenon.

2. OUTLINE OF THE CALAULATION MODEL

The fundamental model of the Nays 2D Breach is iRIC Nays 2D[7] which is a two dimensional computational model for shallow water riverbed fluctuations. The model of dike break expansion progress is modified with the non-dimensional bed flow force obtained from the dike break experimental results[3] discovered using the Chiyoda experimental channel and the following relational expression of the dike collapse amount (1).

$$q_* = \frac{dV}{dt}\frac{1}{\sqrt{sgd_{50}^3}B_m}(1-\lambda) = \alpha_*(\tau_* - \tau_{*_c})^{\beta_*} \quad \textbf{(1)}$$

Where, q_*: volume of non-dimensional dike collapse, V: volume of dike collapse, t: time, s: underwater relative density of sand granules, g : gravitational acceleration, d_{50}: 50% passage grain size of sand granules, B_m: bottom width of the dike, lambda: void percentage, τ_*: non-dimensional bed flow force, τ_{*c}: non-dimensional limiting bed flow force, α_*, β_*: model constants. τ_*: is calculated from the amount of the hydraulics of the flood flow of the upstream and downstream near the dike break opening, which is used as the external force acting on the dike. From the relational expression (1) above, the dike break expansion is developed according to the calculated dV/dt of dike collapse. For details, refer to the literature of Kakinuma et. al.[9]

3. BANK BREACH OF SIBAYAMASAWA RIVER

3.1 OVERVIEW OF DISASTER AT THE SIBAYAMASAWA RIVER

Hokkaido was devastated by three typhoons in one week between August 17 and August 23 had in a week with heavy rainfall causing flood and landslide in several areas mainly in the eastern part of Hokkaido. The typhoons affected Tokoro River, causing slope failure, base water leakage from the bank embankment, and the sand blast at two of its tributaries. The bank breakage, sand blast and discharge of low water channel revetment, etc. was evident in the middle basin of Sibayamasawa River in the range of KP 12.5 ~ KP 40.0. This area is a narrow strip in mountainous terrain where water level tends to rise easily and has a river course characteristics of high water level flow continuing for an extended length. These characteristic could be the highly possible cause of the damages such as bank breach.

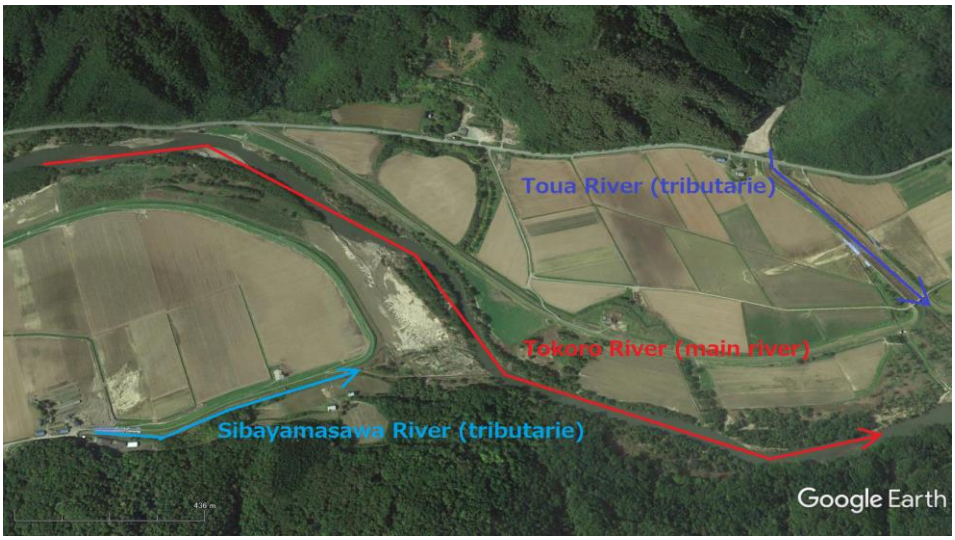

Figure 1 Location at Tokoro River and rtibutaries

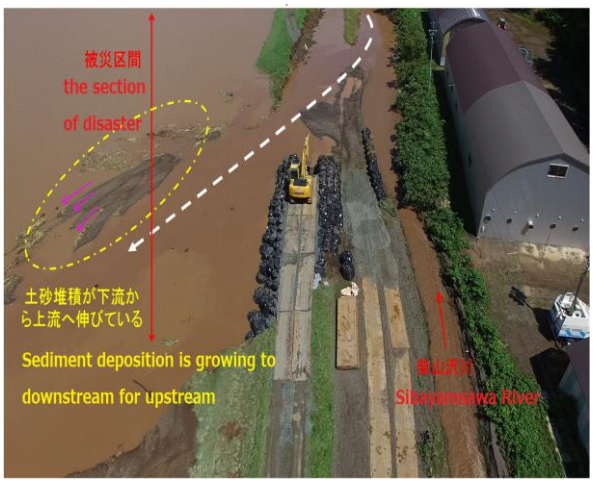

Figure2 Disaster summary at Sibayamasawa River

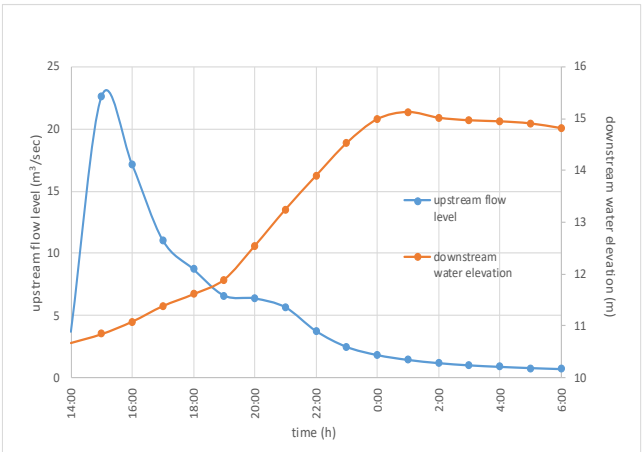

Figure 3 Sibayamasawa hydro and water elevation graph

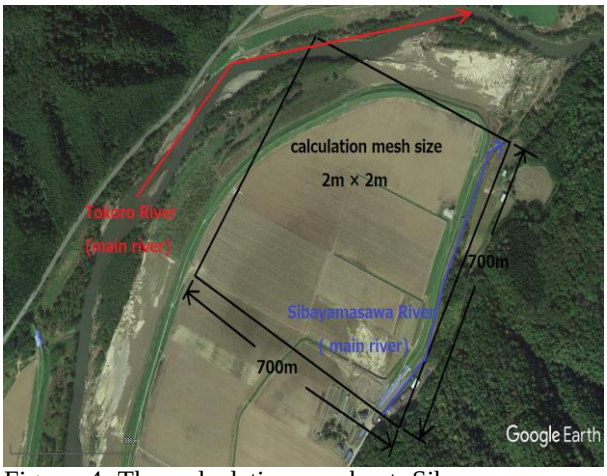

Figure 4 The calculation mesh at Sibayamasawa River

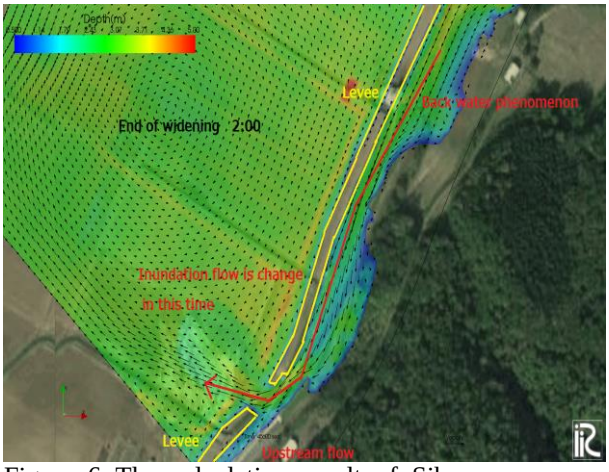

Figure 6 The calculation result of Sibayamasawa River (End of widening)

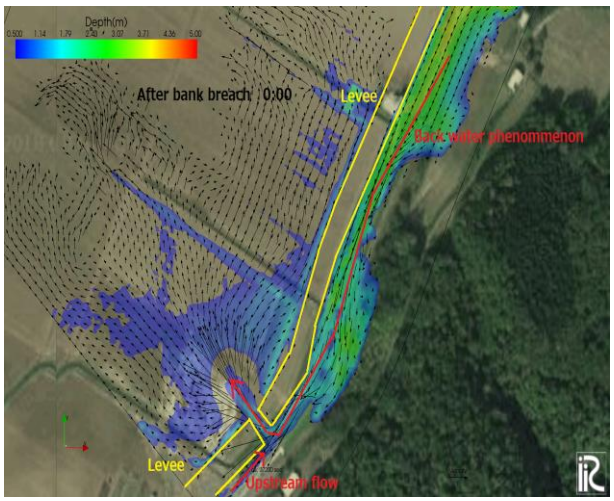

Figure 5 The calculation result of Sibayamasawa River (After bank breach)

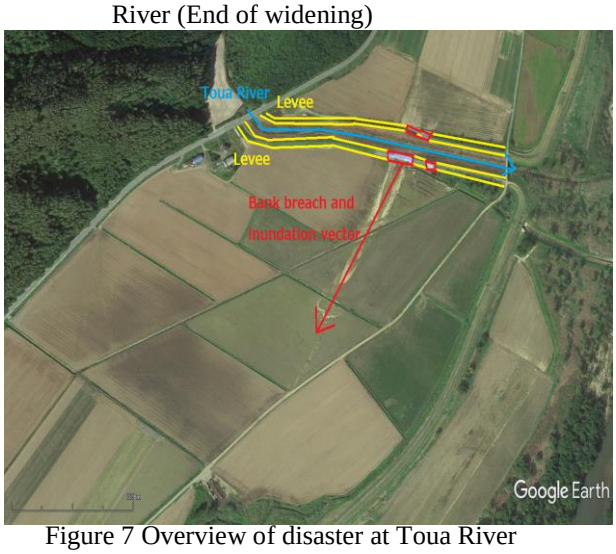

Figure 7 Overview of disaster at Toua River

The bank breach was estimated to have occurred at 0:00 on August 21[10], at which the inundation was confirmed by a manager patrolling the area and though hearing with nearby residents. Figure 2 also shows the disaster situation of Sibayamasawa River resulted in bank breach. The Figure 3 contains 2 hydro graphs of the water elevation at the junctions of Tokoro River and Sibayamasawa River and another graph to illustrate the flow of Sibayamasawa River. According to Figure 3, the estimated time of bank breach occurring at Shibusawa River isn't the time when the flow peaked in Sibayamasawa River but is much closer to the time when flow peaked in Tokoro River. It could mean that Sibayamasawa River's bank breach had a different phenomenon with which the inundation flow headed toward inland upstream. This is different from the conventional knowledge, therefore, we decided to analyse the reason behind it.

3.2 CALCULATIONAL CONDITIONS FOR SIBAYAMASAWA RIVER

The calculating area is as shown in Figure 4, set at SP400-SP1100m toward the junction of Tokoro River and Sibayamasawa River in the longitudinal direction and at 700m in transverse direction, considering the conditions about the inundation area and the stream flow at the time of the bank breach. Moreover, for Figure 4 the calculating area of Sibayamasawa River and the grid spacing is set at 2m mesh in both longitudinal and lateral directions. Here the manning roughness coefficient is set to 0.035, and the time step for calculation is set to 0.04 second. As a boundary condition, the actual results of flow at Sibayamsawa River was given for upstream and the water elevation level at the junction of Tokoro River was given for downstream. The Figure 3 illustrates the hydro of Sibayamsawa River's flow and the water elevation at the junction in the time series. The time that is the object of calculation is between 14:00 on August 20, 2016 and 6:00 on August 21, 2016, including the time of flow peak in Sibayamsawa River and the time of the highest water elevation in Tokoro River. On the calculation, conditions are set so that the bank breach occurrs when water flows over the bank levee crown at a width of 8m in the of

longitudinal distance to initiate the breaching. In addition, the material gain diameter of levee body is set to 4.8mm; and the material gain diameter of river bed is set to 1.5mm using the data obtained from the field test result of soil.

3.3 CALCULATION RESULTS OF SIBAYAMASAWA RIVER

How the behavior of inundation changed the time between the beginning of bank breach and the end of widening is compared. Firstly, the inundation situation of bank breach is shown in Figure 5. At this time, it can be confirmed that the direction of inundation flow from waterside land to inland is vertical to the levee. Once the bank breached the flow at the Sibayamasawa river is instantly almost out of flow and the bank breach occurred this time can be confirmed to have been effected by the main stream. Secondly, Figure 6 shows the behavior of inundation flow at the time of bank breach widening and here it can be seen that the inundation flow direction was changed toward the end of widening, and that the direction is changing to upstream from vertical to levee due to the effects of the Tokoro river's back water phenomenon.The inundation flow going upstream makes the upstream side of the breached section to erode and the erosion extends in the direction of the upstream side the breach point. Also, the inundation situation at the time of breaching and widening was completed is shown in Figure 6. At this stage, there's hardly any difference between the water elevation of waterside land's and inland and inundation flow decreasing with time.

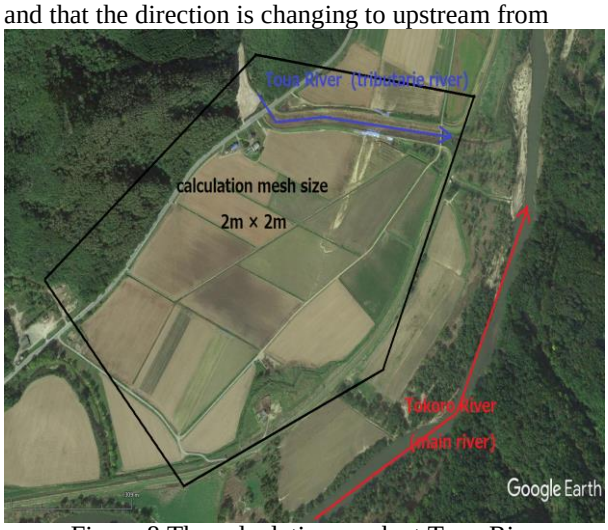

Figure 8 The calculation mesh at Toua River

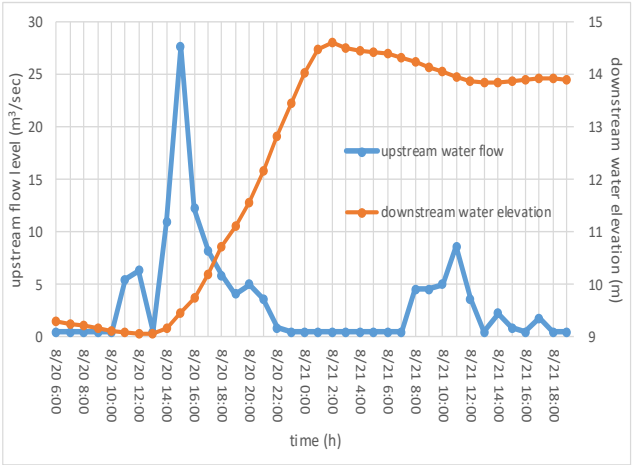

Figure 9 Toua hydro and downstream water elevation graph

4. BANK BREACHING CASE AT TOUA RIVER

4.1 OVERVIEW OF DISASTER AT THE TOUA RIVER

A total of 3 Over flow incidents occurred at Toua river. At the Toua river's right bank, the bank breached at around SP400-SP450 and the bank collapsed at the foot of slope in the region of SP350-SP365. Additionally, on the left bank, bank collapse occurred at the foot of slope between SP365 and SP374[10]. Figure 7 shows the bank conditions of the right side and the left side. Although the river characteristics are quite similar to those of Sibayamsawa, inundation flow ran in the direction vertical to the bank when the bank was breached, therefore, it can be estimated that the bank breach mechanism of Toua River is quite different to that of Sibayamsawa River. The difference is noticeable in the direction of inundation remained vertical to the bank at all times.

4.2 CALCULATION CONDITION AT TOUA RIVER

The calculation area of Toua river is, as Figure 8 indicates, includes the entire area containing the right bank and the right side of inland.

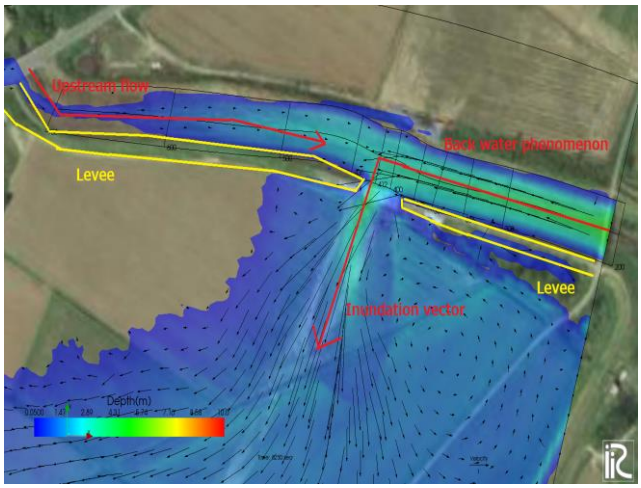

Figure 10 The calculation result at Toua River (Part of inland)

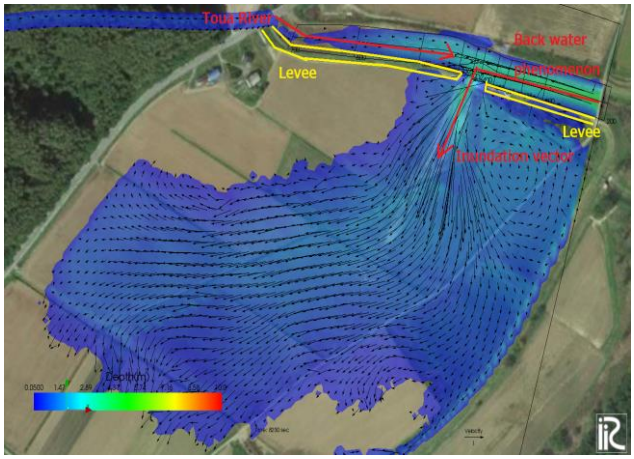

Figure 11 The calculation result at Toua River (All of the inland)

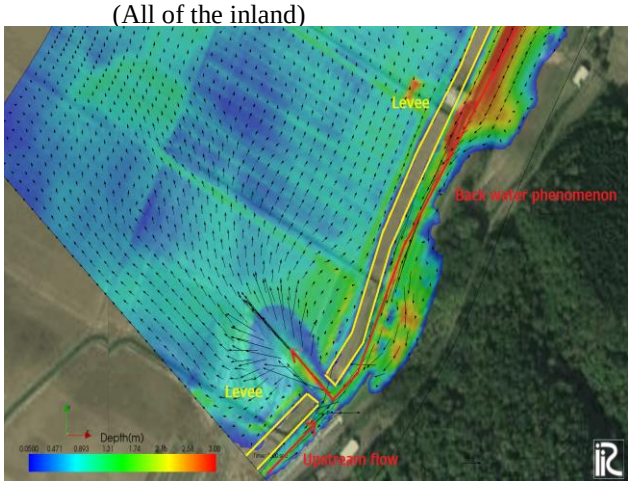

Figure 12 The calculation result of changing the upstream flow at Sibayamasawa River (After bank breach)

The calculation mesh is set at 2m grid spacing each for longitudinal and lateral directions. For this calculation the same values for manning roughness coefficient, calculation time step, riverbed material gain diameter and levee body material gain diameter was used as Sibayamasawa river. Figure 9 shows the boarding condition of the Toua river's upstream flow hydro graph and the downstream water elevation graph where the junction of Tokoro River and Toua River lies. Toua river's bank breach conditions are set similarly to those for Sibayamasawa River and the bank breach to occur at the moment of water flooding over the bank levee crown with the longitudinal distance of 8m in width to initiate the breach.

4.3 THE CALCULATION RESULT OF TOUA RIVER

For Toua River, like Sibayamasawa River, comparison of the Rivers of Toua and Sibayamsawa were made right after the bank breach and at the end of widening to see how the inundation flows. The inundation flow did not change direction and

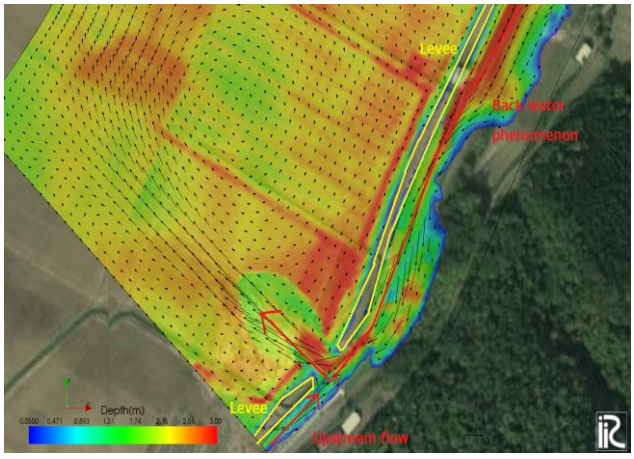

Figure 13 The calculation result of changing the upstream flow at Sibayamasawa River (End of widening)

continued to flow from waterside land to inland keeping the state of the inundation flow vertical to the bank. Figure 10 illustrates the flow state right after bank breach and Figure 11 shows the flow state of the entire inland location at that time. Studying the vector of river channel immediately after the bank breach, it can be confirmed that the water flowed in the forward direction. Moreover, it shows that the inundated flow rate is faster compared to that of Sibayamasawa river. It can be assumed that inundated water run fast in the vertical direction to bank resulted in leaving the scar far from the bank. Similar to the actual phenomena, calculation results reproduced the overflow occurring at two places on the right bank and one place on the left.

5. THE DIFFERENCE FACTOR OF BANK BREACH WITH BOTH TRIBATARIES

5.1 THE DIFFERENCE OF BANK BREACH PHENOMMENA WITH TWO TRIBUTARIES

From the result of calculation described above, with regard to inundation flow state, the flow direction in the case of Sibayamasawa River was from downstream to upstream, whereas in the case of Toua River it was at a right angle to the levee normal vector. Following the findings illustrated Figure 6 and Figure 10, it can be considered that it is the differing natural upstream flow rate that makes the difference of the mechanisms of bank breach and widening. On one side, with Sibayamsawa River's bank breach mechanism, it can be considered that the effects of back water from the main stream largely contributed to inundation flow as almost no natural flow of its own was present upstream immediately after the bank breach. On the other side, with Toua River, it is considered that the bank breach widening was affected by its own natural flow condition and back water phenomenon from the main stream as certain level of its own natural flow was present after the

bank breach. Responding to the findings stated above, the effects of the relation of upstream flow and back water phenomenon from main steam on bank breach widening mechanism were studied with the geographical features of Sibayamasawa river.

5.2 EFFECTS OF THE UPSTREAM FLOW ON THE BANK BREACH PHENOMENA

Of the reproduction calculation of Sibayamasawa river above, calculations were carried out, making changes in the condition of upstream flow level. More specifically, natural upstream flow hydro was continued to be passed with a fixed level of peak flow. The idea was to focus on the effects of the difference in the river's natural flow on the phenomena of bank breach widening, as at the natural upstream flow continued in Sibayamasawa River even after bank breach. Figure 12 shows the contour of depth and vector of velocity after bank breach. As the figure illustrates, inundation flow is running from water side land to inland at right angle against the vector of bank, this result is the same as the reproduction calculation of Sibayamasawa river. Additionally, the inundation flow velocity is faster than the reproduction calculation and this is considered that the upstream flow and the inundation flow from the main stream side to aperture is getting bigger and that makes the effects of inundation flood velocity make faster. Figure 13 shows the contour of depth and the vector of velocity when the bank breacwidening had almost ended. The time is the same as Figure 6 where reproduction calculation was carried out but the reproduction calculation of inundation flow vector travels from downstream to upstream whereas this case is different in that the inundation flow continues at right angle vector to the levee. It seems that the presence of upstream flow remains after bank breach and it collides with the back water phenomenon from main steam near the aperture of bank breach that makes it closely resembles the inundation vector to right angle from levee after the bank breach. From the above, it was clarified that difference in bank breach widening mechanism are evident even with the same point of tributaries levee that has affected section by the back water phenomenon as the tributaries own flow and flow peak appearance time differ. This indicates the need of considering multiple conditions for damage reduction measures at the time of bank breach.

6. CONCLUSION

The obtained knowledge through this research is briefly summarized below.

・The bank breach calculation model of "Nays 2D Breach

・the bank breach of Shibayamasawa River had low" enabled the reproduction of the back water phenomenon with the bank breach. level of upstream flow from tributaries and due to the effects of back water phenomenon made the inundation vector to change to right angle to bank to the upstream shown above in Sibayamasawa river reproduction calculation case.

・The condition of the upstream flow from tributaries affected the back water phenomenon making the inundation flow vector of right angle to bank immediately after bank breach widening ended.

・The fact that tributaries' own flows and back water levels affects the mechanism of inundation vector and widening vector have been confirmed from the results.

・Bank breaching and widening model of "Nays 2D Breach" enabled us to confirm the travelling direction of widening vector and inundation vector, and the details of river side flood vector after the bank breach.

REFERENCES

[1] Committee of researching bank at Odagawa. http://www.cgr.mlit.go.jp/emergency/odagawateibochosa.htm

[2] Yuuitirou Fujita, Takashi Tamura, Yosio Muramoto:Process of bank breach and widening in experiment and research, Researching disaster prevention Kyoto University, Number27, B-2, pp369-392,1984.

[3] The repot of bank breach and over flowing bank breach phenomenon within widening phenomenon experiment reports: Hokkaido Reginal Development Bureau, Ministry of Land, Infrastructure, Transport and Tourism, Civil Engineering Reserch Institute for Cold Region, 2012.

[4] Teturou Tujimoto, Tadanori Kitamura, Masahiko Kisimoto: Simulation and hydrology with breach in the condition of arenaceous bank and the phenomenon of widening: Japan Society of Cicil Engineers of River Development Reports Number8, pp31-36, 2002.

[5] Tomonori Shimada, Yasuharu Watanabe, Hirokazu Okabe, Riki Iwasaki, Yasuhiro Nakasima: How the effecting to the bank breach in condition of River width and bed slope Japan Society of Cicil Engineers Reports B1, Vol73, No4, I_1345-1350, 2017.

[6] Civil Engineering Reserch Institute for Cold Regionhttp://river.ceri.go.jp/contents/tool/nays2d-breach.html.

[7] iRIC, http://i-ric.org/ja/.

[8] [9]Kouji Kakinuma, Daisuke Hida, You Yokoyama, Takuya Inoue, Atusi Takeda: Developing the numerical calculation model and experiment of Tiyoda, Civil monthly reports, No, 732 p10-19

[10] Committee of researching bank at Tokoro https://www . hkd . mlit . go.jp/ab/tisui/v6dkjr00000006el.htm

9th Int. Conf. on Geotechnique, Construction Materials and Environment, Tokyo, Japan, 20-22 November 2019, ISBN: 978-4-909106025 C3051

REALITY IN PACKAGE ON-SITE GREASE TRAP PERFORMANCE: SUCCESS OR FAILURE IN FOG REMOVAL?

Sopa Chinwetkitvanich[1,*] and Piti Ektaku[1]
[1] Department of Sanitary Engineering, Faculty of Public Health, Mahidol University, Bangkok, Thailand

ABSTRACT

Package on-site grease traps are widely used in household and restaurant in Thailand for oil and grease removal although frequent failures in FOG removal have been reported. Theoretically, too small of operating hydraulic retention time (HRT) takes the blame, but some suppliers claim that their grease traps can be well operated even with HRT of 15 minutes. This study was to investigate the performance of grease trap with various HRTs (15 minutes to 20 hours) and FOG concentrations in the feed (50 to 600 mg/l). Results showed that the operating HRTs of 15, 30 and 60 minutes could represent a kind of shock hydraulic loading condition, which insufficient FOG removal efficiencies were observed. Also, the experiment to enhance the grease trap's performance was set up by withdrawing certain volume of grease trap waste. The operating HRT of 60 minutes with the feed contained FOG of 200 mg/l and dishwashing detergent of 0.5% (v/v) was investigated for seven-day period. The experiment without daily withdrawal was operated in parallel as a control. The results showed that the FOG removal efficiencies in the control began to fall down to 50% on the fifth day of operation. The experiment with daily withdrawal showed more stable FOG removal efficiencies, which its efficiencies was still higher than 50% after seven days of the experiment. However, this could be said that the 15-litre package on-site grease trap fed with operating HRT of 60 minutes (or lower) could not maintain sufficient removal efficiency for long period (months).

Keywords: Package on-site grease trap, Fat oil and grease (FOG), Dishwashing detergent, Oil and grease removal, Hydraulic retention time (HRT).

INTRODUCTION

Fats, oils and greases contaminated in water or wastewater are commonly referred to FOG, which can be categorized based on their origin. That is, FOG based on animal and vegetable is considered to be edible, and that based on mineral (petroleum and coal sources) is not edible. FOG in domestic wastewater is mostly generated from food processing either in household or commercial scale (e.g., restaurant, canteen, food plaza, etc.). FOG is a major problem for both onsite or public sewer systems due to it may continually accumulate and cause clogging problem within the drainage system [1]–[3]. Sometimes, clogging occurs in the crossover line between compartments of grease traps [3]. Although grease traps are supposed to remove FOG before entering a septic tank or sewer system, high FOG loads or emulsified oils as well as surge wastewater flows often cause FOG bypassing through the sewer system.

Oil contaminated in water or wastewater may exist in several forms such as free oil, physically or chemically emulsified oil, or dissolved oil. Usually, FOG in wastewater from households or restaurants is a free oil, which eventually rise to surface of the container or the receiving water. Most conventional grease traps are basically designed to allow free oil to float up to the surface. Physically emulsified oil means a free oil broken into small droplets by agitation or mixing with water. Also, high water temperatures concurred with liquid vegetable oils can promote physically emulsification. However, these physically emulsified oils will eventually separate from water again when enough hydraulic retention time is given. Chemically emulsified oil is a mixture of oil and water caused by chemical reagents, resulting in very small oil particles and not able to separate and float up to the surface of water regardless how much retention time is allowed. Kitchen wastewater may contain high chemically emulsified oil proportion due to the use of detergents and other alkalis.

The package on-site grease traps are widely used by household for oil and grease removal. Typically, a grease trap is used to intercept liquid grease waste or garbage and retain it for an adequate period of time. The configuration of the tank allows cooling down the incoming liquid, which helps solidify this grease and separation from water. However, sufficient detention time will be required to enhance an efficient floatation of this oil and grease.

In Thailand, there are several types and sizes of commercial package on-site grease traps sold in the market. However, failures of grease traps have been frequently mentioned among customers, whereas too small operating hydraulic retention time (HRT) should be the cause. Pollution Control Department

(PCD) of Thailand suggested that HRT for grease removal should not be less than 6 hours [5]. However, some suppliers declared their grease traps could be operated with design HRT of 15 minutes. Therefore, this study was to investigate a performance and optimum HRT for oil and grease removal by a package on-site grease trap. In addition, the effects of dishwashing detergent mingling in wastewater were compared.

MATERIALS AND METHOD

Synthetic oil contaminated wastewater

Cooking oil made from soybeans was used for preparation of synthetic wastewater by mixing cooking oil with tap water till the designated FOG concentrations were reached. The cooking oil was boiled for a few minutes in order to imitate used cooking oil. Then, boiled oil was diluted in tap water using mixer with speed of 110 rpm

Reactor Setup

A package on-site grease trap used in this study is a commercial type generally found in Thailand market. It was made of polypropylene (PP) with effective volume of 15 L, dimension of which was 290 mm (W) x 395 mm (L) x 330 mm (H) as shown in Fig. 1. Reactor setup consists of a 15-litre package on-site grease trap, storage influent container equipped with mixer and pump feeding, and effluent container (Fig. 2). The mixer in storage container is to prevent separation of oil from water before fed into the grease trap.

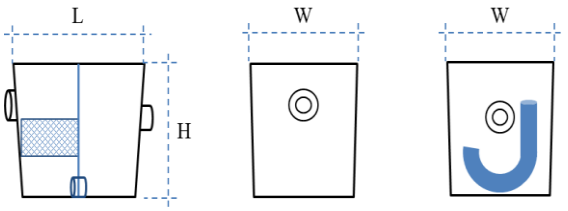

Fig. 1 A package on-site grease trap

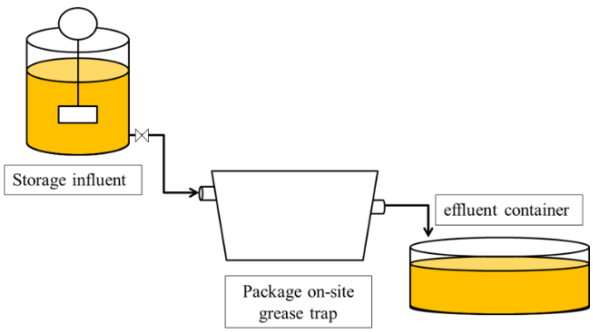

Fig. 2 A schematic diagram of reactor setup

Experimental procedures

This study was divided into two parts; the first part was to investigate effect of operating hydraulic retention time (HRT) and dishwashing detergent addition on FOG removal efficiencies. Factorial design of four FOG concentrations (50, 200, 400 and 600 mg/l) and five operating HRTs (15, 30, 60 minutes and 6 and 20 hrs.) were assigned, resulting in total of twenty experiments. Another twenty experiments were setup in parallel, with the addition of 0.5% (v/v) dishwashing detergent into the synthetic wastewater.

For experiments with HRTs of 15, 30 and 60 minutes, the synthetic wastewater was fed into the package on-site grease trap with designated HRTs for four hours continuously. Then, the feed was stopped for the rest hours of the day with the package on-site grease trap filled. Effluent samples were collected hourly and acidified for preservation till analysis. The same feeding was repeated on the next day for four days continuously. Therefore, for each operation, there were totally sixteen (4x4) samples for analysis. For experiments with HRTs of 6 and 20 hours, the synthetic wastewater was fed into the package on-site grease trap with designated HRTs. The operating hours of each day was according to HRTs, then, the feed was stopped for the rest hours of the day with the grease trap filled. The same feeding was repeated on the next day for four days continuously. Effluent samples were collected after each operating HRT was finished; therefore, there were four samples for analysis.

After four-day operation of each experiment were achieved, the reactors were cleaned to remove all residual oil attached within reactor before the operation was repeated. Each experiment was conducted in triplicates to obtained reasonably statistical results. Those samples were determined for oil and grease (as FOG) and COD according to Standard Methods for the Examination of Water and Wastewater [6].

The second part was set up to investigate the performance of the grease trap in case of daily withdrawing certain amount of floated grease trap waste was applied. The experiment was operated for seven days with selected HRT of 60 minutes for four hours each day. The synthetic wastewater composed of FOG concentration of 200 mg/l and dishwashing detergent of 0.5% by volume. Two reactors were operated in parallel, one of which was acted as a control with no daily withdrawing (named as Reactor G1), while another one was operated with daily withdrawing of certain amount of floated grease trap waste from the first compartment (Reactor G2). After seven-day operation, reactors were cleaned and the experiments were done in triplicates.

RESULTS AND DISCUSSION

Part I: Effects of operating HRT on FOG removal

Figure 3 showed the removal performance of fat, oil and grease (FOG) from the experiments with four influent FOG concentrations. The experiments with small operating HRTs, i.e., 15, 30 and 60 minutes, clearly showed less FOG removal efficiencies than the others (6 and 20 hours) either with or without addition of dishwashing detergent. That is, the daily FOG removal efficiencies with operating HRTs of 15 – 60 minutes were in the ranges of 60 – 76% and increased to the range of 88 – 94% with the operating HRTs of 6 – 20 hours in the case of without dishwashing detergent.

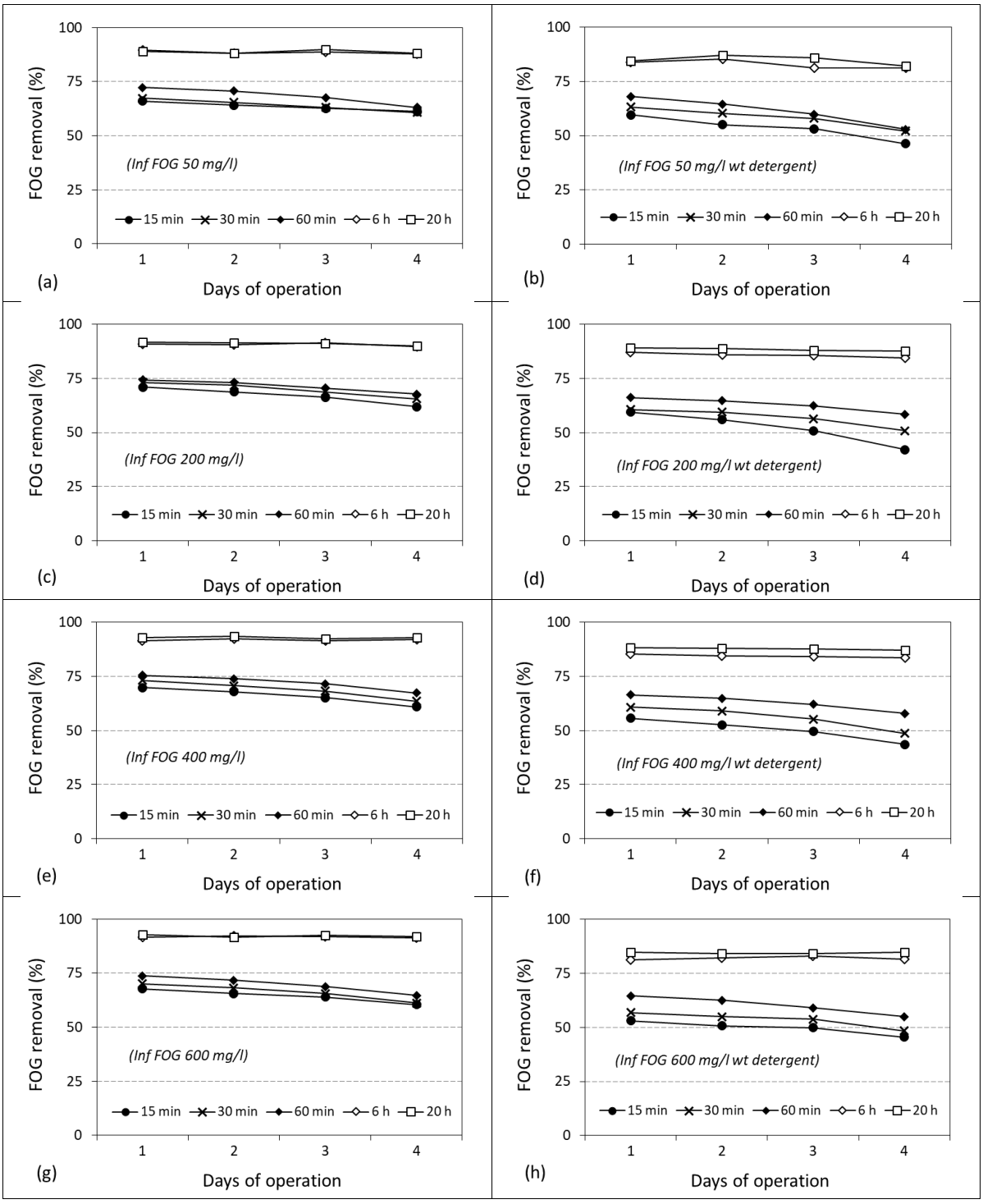

Fig. 3 Performance of FOG removals at various influent FOG concentrations and operating HRTs

Obviously, dishwashing deteriorated FOG removal performance of the trap, especially with the smaller HRTs (15 – 60 minutes). Their daily FOG removal efficiencies were in the ranges of 42 – 68% and 81 – 89%, respectively.

Table 1 concluded the averages of FOG removal efficiencies from this study. The results of both groups (without and with dishwashing detergent) illustrated that higher operating HRTs (6 and 20 hours) resulted in more FOG removal efficiencies. The variation of HRTs in the range of 15 to 60 minutes did not make substantial difference in FOG removal efficiency. The experiments with influent FOG concentration of 50 mg/l without addition of dishwashing detergent obtained a little less removal efficiencies than other concentrations. However, with addition of dishwashing detergent, their removal efficiencies of FOG 50 mg/l experiments were similar to the others.

Table 1 The average FOG removal efficiencies

Average FOG removal efficiencies (%)								
	Influent FOG concentrations (mg/l)							
	50		200		400		600	
HRTs	No D	wt D	No D	wt D	No D	wt D	No D	wt D
15 min.	63	54	67	52	66	50	64	50
30 min.	64	58	70	57	69	56	66	53
60 min.	68	61	71	63	72	63	70	63
6 h.	89	83	91	86	92	84	92	82
20 h.	89	85	91	88	93	88	92	84

Remark: D = dishwashing detergent

It could be said that the variation of influent FOG concentrations (50, 200, 400 and 600 mg/l) did not affect on the FOG removal efficiencies, especially in the same operating HRT. Consistently, Chu and Ng [7] similarly reported their COD and FOG removal efficiencies were not influenced by influent FOG concentrations ranging from 400 to 1600 mg/l. They also mentioned that a grease trap should be implemented with appropriate HRT that most of oil droplets would be separated and floated to water surface. Unfortunately, the grease trap often came across with these short HRTs in practice, especially during the peak hours of kitchen activities. Large quantities of wastewater both from meal processing or utensils washing were generated within a couple hours. This high volume of wastewater forced the grease trap to be overloaded with both high FOG concentration and hydraulic flow.

In addition, the adverse effect of dishwashing detergent was obviously found in every operating HRTs. The dishwashing detergent substantially reduced FOG removal efficiencies in comparison with the experiments without detergent, especially when the operating HRTs of 15, 30 and 60 minutes were employed. This could be explained that dishwashing detergent caused higher emulsification of oil and grease in wastewater, resulting in more difficulty to be separated from water. Thus, more retention time (or operating HRT) would be extensively required for this slower separation. Besides, hot oil and grease contaminated (from meal processing) in wastewater should be cooled within grease trap, then, they could be more solidified and easily separated from liquid bulk. Hence, short HRT in grease trap will hinder cooling step, which can double the adverse effect of short HRT on FOG removal efficiency. Therefore, the time for allowing oil and grease separated from wastewater was the key.

Part II: Effects of daily grease trap waste withdrawing

Due to oil and grease separated from the water by floating and accumulating on the surface of water, this accumulated grease trap waste required regular removal to maintain the capability of the grease trap. This experimental part was fed with the FOG of 200 mg/l and conducted with operating HRT of 60 minutes. Two reactors were set up, one of which was acted as a control with no daily grease trap waste withdrawing (Reactor G1), while another one with daily withdrawal (Reactor G2). Figure 4 illustrated profiles of the influents and effluents of FOG concentrations during seven–day operation.

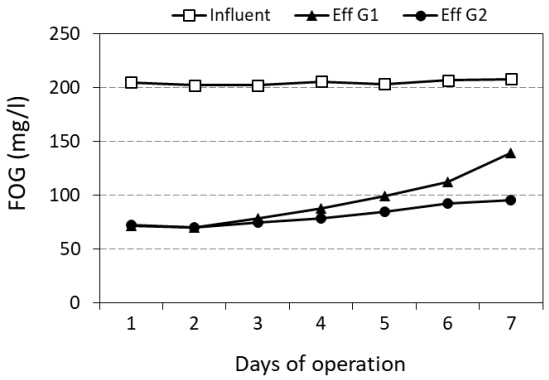

Fig. 4 Profiles of FOG concentrations

Effluent FOG concentrations of both reactors clearly increased after three days of operation. Then, effluent FOG concentrations in the control reactor (G1) gradually increased up to 139 mg/l on the last day of operation (day 7), resulting in FOG removal efficiency less than 40%. Figure 4 showed slower increase of effluent FOG in the reactor G2 (with daily withdrawing) than the reactor G1, resulting in its lower effluent FOG on the last day of 96 mg/l. It could be clearly seen that withdrawal of grease trap waste

helped reduce accumulated FOG in the trap and prolong its capability before failure. With this FOG loadings (FOG concentration of 200 mg/l, HRT of 60 minutes and 4 hours operating), the control reactor (G1) lost its 50% efficiency since the fifth day of operation while daily withdrawing could maintain FOG removal efficiency over 50% after seven days of operation.

Mass balance of FOG

Due to operating HRT of 60 minutes and four hours of operation, sixty liters of the feed were used. Therefore, total FOG mass of around 12.3 g/day were calculated and total FOG mass fed into the trap after seven days was about 86 g. For the reactor G1, which there was no daily withdrawing of grease trap waste, those retained FOG mass of 8 g on the first day was the highest, then, they declined throughout the seven days of operation (Fig 5a). Totally, accumulated FOG mass after seven-day operation was about 47 g. If density of soybean at 23.9°C was 0.9193 g/ml [8], this 47 g of retained FOG should require volume of around 51 ml (0.34% of the trap volume of 15 liter)

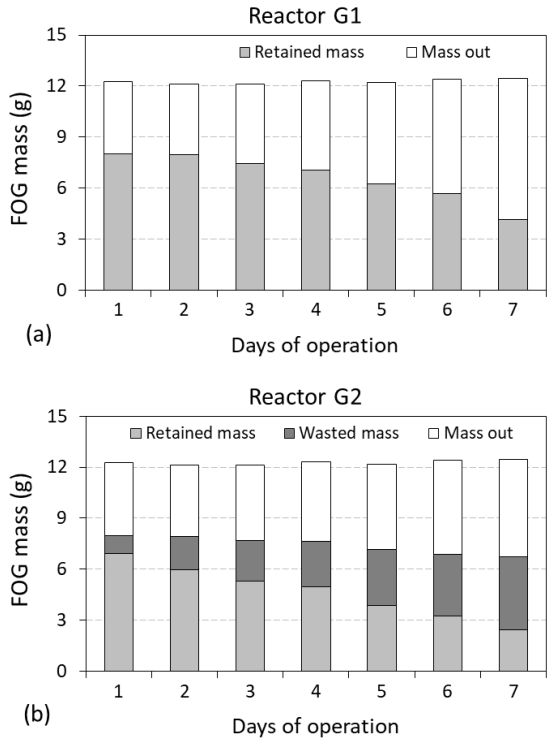

Fig. 5 Mass balance of FOG

In the reactor G2, the same seven days of operation was applied, but 0.5 liter of floated grease trap waste) was daily withdrawn. Grease trap waste mostly composed of water up to 86% [9]. The withdrawal was done in the first compartment of the grease trap (influent part). Total wasted FOG mass was about 20.3 g, considering as 23.6% of total influent FOG mass of 86 g. Apparently, daily withdrawing could help retard accumulation of retained FOG mass within the trap, resulting in less FOG mass discharged through the effluent ('mass out'). FOG removal efficiency was still higher than 50% on the last day of operation. The total accumulated FOG mass after seven-day operation was about 33 g, which was much less than those of the reactor G1 (47 g). Thus, no matter how effective grease trap was designed, lacking of proper maintenance could induce failure in FOG removal [2].

Observational opinions in configuration of commercial package on-site grease trap

From this study, there are some observational opinions about the design of the package on-site grease trap to be mentioned. That is, the difference of the traps between two sizes (15 and 30 liters) was the enlargement of the second compartment, while the first compartment of both sizes was the same dimension. Therefore, the first compartment of 15–liter grease trap acting as an inlet compartment is comparatively larger than the latter compartment (oil separation chamber). The 30–liter grease trap seems to have more suitable dimension (larger oil separation part). Unfortunately, the first compartment of 15–liter grease trap cannot be lessened because of those necessary inlet pipe and fittings. Moreover, they were also equipped with basket-shape screening for trapping food scrap or else as shown in Figure 6 [10]. Hence, the package on-site grease trap with a size as small as 15 liters would require more attention before implementation.

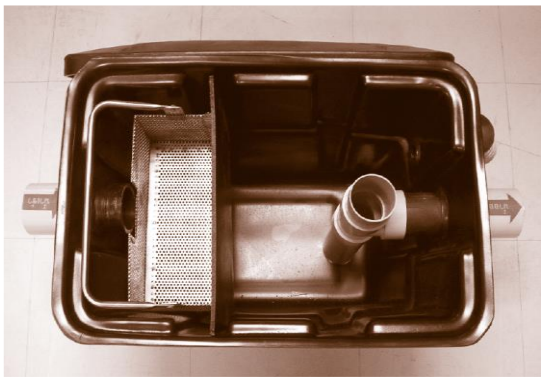

Fig. 6 Typical package on-site grease trap [10]

Besides, solid waste or food scrap contaminated in wastewater as in practice has not been included in this study. These solid wastes would be detained within the trap and deteriorate FOG removal efficiency by reducing effective volume of the trap. Also, the retained solid wastes could be further rotten and stinking within the trap faster than FOG. In practice, the small package on-site grease trap such as 15-liter type would not handle any solid wastes effectively. For this case, solid wastes or food scrap

in wastewater must be removed well enough before entering the grease trap.

In consideration of HRT equation (HRT = V/Q; where V = required tank volume and Q = hydraulic flow), hydraulic flow should be carefully selected before calculation and selection the size of grease trap. Therefore, it is important that hydraulic flow passed into the very small trap (such as 15- or 30-liter) must be carefully concerned and managed.

CONCLUSIONS

The influent FOG concentrations varied between 50 to 600 mg/l did not make substantially difference in removal efficiency of the package on-site grease trap. The operating HRTs plays an important role in FOG removal. Several operating HRTs for the grease trap were recommended and published, but some confusion occurred to users. Especially, for household level, too small operating HRT of 15 minutes used to be advertised. In practice, the package on-site grease trap commercially marketed in Thailand are mostly too small for proper FOG removal. In addition, dishwashing detergent made oil and grease more soluble, then, more difficult to separate off water. Therefore, the operating HRTs of more than 6 hours (or up to 20 hours) were recommended for reliable FOG removal. However, maintenance program for grease trap, such as regular removal of floated FOG waste, should be applied to extend their capability and prevent failure of FOG removal.

ACKNOWLEDGMENTS

The authors would like to thanks the Department of Sanitary Engineering, Faculty of Public Health, Mahidol University for laboratory assistance. This article was financially supported for presentation by Faculty of Public Health and Faculty of Graduate Studies, Mahidol University.

REFERENCES

[1] He X., de los Reyes F.L., Leming M.L., Dean L.O., Lappi S.E., Ducoste J.J., Mechanisms of Fat, Oil and Grease (FOG) deposit formation in sewer lines, Water Research, Vol. 47, 2013, pp. 4451–4459.

[2] Williams J.B., Clarkson C., Mant C., Drinkwater A. and May E., Fat, oil and grease deposits in sewers: Characterisation of deposits and formation mechanisms, Water Research, Vol. 46, 2012, pp. 6319–6328.

[3] Ashley R.M., Fraser A., Burrows R., Blanksby, J., The management of sediment in combined sewers, Urban Water, Vol. 2, Issue 4, 2000, pp. 263–275.

[4] Hussin M.S.F., Shamsuddin M.A., Jumaidin R., Zakaria A.A., Jenal N., Portable grease trap for wastewater management system: A conceptual design approach, Journal of Advanced Research in Fluid Mechanics and Thermal Sciences, Vol. 49, Issue 1, 2018, pp. 18–24.

[5] Pollution Control Department, On-site wastewater treatment manual for producers and designers [In Thai], Bangkok, Reunkaew Printing, 1994.

[6] APHA, AWWA, WEF. (2012). Standard methods for the examination of water and wastewater (22nd ed.). Washington, DC: American Water Works Association.

[7] Chu W. and Ng F.L., Upgrading the conventional grease trap using a tube settler, Environment International, Vol. 26, 2000, pp. 17–22.

[8] Noureddini H., Teoh B.C. and Clements L.D., Densities of Vegetable Oils and Fatty Acids, Papers in Biomaterials, 14, 1992, http://digitalcommons.unl.edu/chemeng_biomaterials/14.

[9] Tu Q. and McDonnell B.E., Monte Carlo analysis of life cycle energy consumption and greenhouse gas (GHG) emission for biodiesel production from trap grease. J. Clean. Prod. Vol.112 (Part 4), 2016, pp. 2674–2683.

[10] Pollution control department, Guidelines for Restaurant in Management of Oil and Grease from Grease Trap and Utilization [In Thai], Bangkok, TQP Co., Ltd., 2008.

9th Int. Conf. on Geotechnique, Construction Materials and Environment, Tokyo, Japan, 20-22 November 2019, ISBN: 978-4-909106025 C3051

NUMERICAL SIMULATION FOR SEASONAL AND INTER-ANNUAL CHANGE OF DISSOLVED OXYGEN IN LAKE BIWA, JAPAN

Jinichi Koue[1], Hikari Shimadera[1], Tomohito Matsuo[1] and Akira Kondo[1]
[1] Graduate School of Engineering, Osaka University, Japan;

ABSTRACT

The dynamics of dissolved oxygen in lake is a fundamental issue of comprehending the water environmental habitats of aquatic organisms. In recent years, the decrease in dissolved oxygen has been observed at the bottom of the northern part of Lake Biwa, Japan. In recent years, eutrophication and global warming caused the decrease in the dissolved oxygen in the deep layer. Under these circumstances, in order to preserve the ecosystem of Lake Biwa and to provide water resources, the environmental changes in Lake Biwa should be accurately grasped. In our present study, a water quality model considering the flow field from hydrodynamic model was developed in order to grasp the concentration of phytoplankton, zooplankton, nitrogen, phosphorus, dissolved oxygen and chemical oxygen demand in Lake Biwa. Numerical simulation was carried out for 3 years from 2007 to 2009. Comparisons of the simulations with the observations showed that the seasonal and inter-annual change of dissolved oxygen was well reproduced. The dissolved oxygen decreased during decomposing the organic matter by bacteria in the bottom layer with little oxygen supply from the atmosphere and the photosynthesis from the phytoplankton under the thermocline from spring to autumn. The simulation confirmed that in each year, the dissolved oxygen was supplied in all layers by the overturning in winter.

Keywords: Dissolved Oxygen, Water Quality Model, Thermocline, Overturning, Lake Biwa

1. INTRODUCTION

Water quality in lakes and reservoirs are of importance to daily life water but are vulnerable to external load. In various lakes, eutrophication due to increased nutrient loadings from the watershed and global warming caused deterioration of lake water quality [1] [2].

Lake Biwa which is the largest freshwater lake in Japan serves drinking water for approximately 15 million people in Shiga and other surrounding prefectures. Lake Biwa has undergone eutrophication since 1950s. After the improvement of water quality by promoting the use of non-phosphorus synthetic detergent from the late 1970s, the trends in the eutrophication in Lake Biwa had decreased. Until 1980, eutrophication was the main reason why the dissolved oxygen decreased in the deep layer. However, after the 1980s, low levels of dissolved oxygen under 2 mg/L in the bottom layer became evident. At this level, aquatic life cannot breathe naturally. The reason for the decrease in dissolved oxygen has been considered to be the strengthening of stratification due to global warming in recent years [3] [4].

The meteorological elements have direct and indirect impacts on the change of dissolved oxygen in the bottom layer. Direct impacts are due to changes in forcing factors such as air temperature, wind speed and precipitation. In particular, the rise in air temperature and the decrease in wind speed have been thought to weaken the vertical mixing of lake water, which maybe the cause of the hypoxia [5] [6].

Indirect impacts are changes in biogeochemical cycles and related biological activities. The biological metabolism to change in water temperature was observed in the deep layer after 1990, therefore the meteorological elements could cause the significant influences on the ecosystem of Lake Biwa.

In many lakes, eutrophication and climate change impacts causes the deterioration of water quality so that it is difficult to distinguish their effects [7]. It is necessary to figure out the biochemical processes together with considering the hydrological processes.

A box model was used to calculate the division of one box for the south lake and 2 boxes for the north lake in upper and lower part in Lake Biwa [8]. However, box models cannot consider spatial distribution because values in the box are uniform. The ecological simulation for the eutrophication in Lake Biwa were performed [9], [10]. It is better to use a one-dimensional model to predict long term changes in water quality ecosystem. However, three-dimensional physical processes such as the surficial flow, internal waves and turbulence caused by the wind should be included to capture the nutrient circulation.

In the present study, a water quality model considering the flow field from hydrodynamic model was developed in order to grasp the concentration of phytoplankton, zooplankton, nitrogen, phosphorus, dissolved oxygen and chemical oxygen demand in

Lake Biwa. Numerical simulation was carried out for 3 years from 2007 to 2009. The seasonal and inter-annual changes of vertical distribution of dissolved oxygen in Lake Biwa was simulated to compare with the observations from 2007 to 2009.

2. Water Quality Model in Lake Biwa

2.1 Calculation domain

This study focused on Lake Biwa in Japan. Fig. 1 shows the calculation domain and water depth in the water quality model of Lake Biwa. The horizontal domain is 36 km × 65.5 km with a horizontal resolution of 500 m. The vertical domain consists of 86 layers from the lake surface to the depth of 107.5 m. The vertical grid size is 0.5 m from the surface to the depth of 20 m and gradually increases up to 2.5 m.

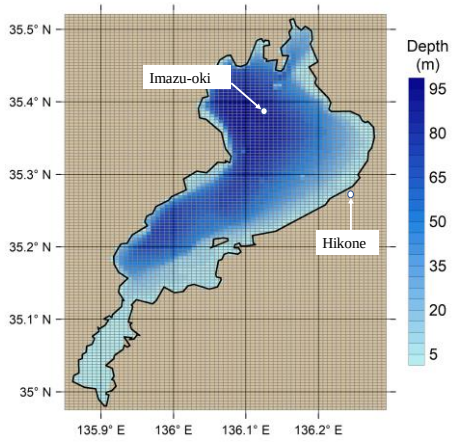

Fig. 1 Calculation domain with the topography of Lake Biwa

2.2 Each component in water quality model

Many factors are involved in water environment with large and complicated ecosystem like Lake Biwa. For simplifying this ecosystem, this model consists of nine state variables such as phytoplankton, zooplankton, particulate and dissolved organic chemical oxygen demand, inorganic and organic phosphorus and nitrogen, and dissolved oxygen. Phytoplankton have chlorophyll a, b and c. Based on the amount of each chlorophyll, the amount of phytoplankton is calculated. Phosphorus and nitrogen are two limiting nutrients that control the photosynthesis. Fig. 2 shows a conceptual diagram of a water quality model considering chemical and biological change terms.

The components are shown in Table 1. A summary of the chemical and biological processes of each component is shown in Table 2.

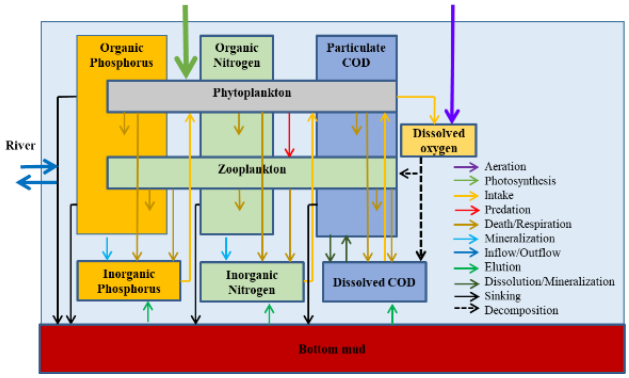

Fig.2 Conceptual diagram of water quality model

Table 1 Each component of water quality model

Component	Symbol	Unit
Phytoplankton	C_{PX}	mgC/l
Zooplankton	C_Z	mgC/l
Inorganic nitrogen	C_{IN}	μgN/l
Organic nitrogen	C_{ON}	μgN/l
Inorganic phosphorus	C_{IP}	μgP/l
Organic phosphorus	C_{OP}	μgP/l
Dissolved oxygen	C_{DO}	mgO/l
Particulate COD	C_{PC}	mg/l
Dissolved COD	C_{DC}	mg/l

Table 2 Balance of water quality elements

C_{PX}	Proliferation by photosynthesis－Respiration of phytoplankton－Predation by zooplankton－Sinking of phytoplankton
C_Z	Proliferation by predation of phytoplankton－Death of zooplankton
C_{IN}	－Intake by phytoplankton through photosynthesis－Intake by zooplankton + Death of zooplankton + Mineralization of organic nitrogen + Elution from the bottom mud
C_{ON}	Death of phytoplankton－ingestion of zooplankton + Death of zooplankton－Mineralization of organic nitrogen + Sinking of organic nitrogen
C_{IP}	－Intake by phytoplankton through photosynthesis－Intake by zooplankton + Death of zooplankton + Mineralization of organic phosphorous + Elution from the bottom mud
C_{OP}	Death of phytoplankton－Intake of zooplankton + Death of zooplankton－Mineralization of organic phosphorous + Sinking of organic phosphorous
C_{DO}	Supply by photosynthesis－Consumption by Respiration of phytoplankton－Consumption by Respiration of

	zooplankton－Consumption by suspended organic matter－Consumption by dissolved organic matter－Consumption at the bottom mud +Aeration
C_{PC}	Death of phytoplankton－Ingestion by zooplankton＋Death of zooplankton－Dissolution of Suspended COD＋Suspending of dissolved COD－Sinking of COD
C_{SC}	Respiration of phytoplankton－Ingestion by zooplankton＋Respiration of zooplankton－Mineralization of dissolved COD＋Dissolution of dissolved COD＋Elution from the bottom mud

The advection-diffusion equation of constituent elements is shown in Equation (1). The left-hand side represents the time-varying term and the advection term, and the right-hand side represents the diffusion term and the change by the biochemical process.

$$\frac{\partial C_i}{\partial t} + u\frac{\partial C_i}{\partial x} + v\frac{\partial C_i}{\partial y} + w\frac{\partial C_i}{\partial z} = \kappa_h\frac{\partial^2 C_i}{\partial x^2} + \kappa_h\frac{\partial^2 C_i}{\partial y^2} + \kappa_z\frac{\partial^2 C_i}{\partial z^2} + Q_{C_i} \quad (1)$$

C_i : Concentration of each component
i : Component
Q_{C_i} : Amount of change per unit time due to chemical and biological processes

The formulation of material circulation for each component and the details of each term are also shown in [8].

2.3 Initial conditions

As for the initial condition, the current velocity was set to be 0 m/s. The initial concentration of each component on April 1st, 2006 was derived from linear interpolation of observed data on March 20th and April 10th, 2006. The observations were conducted by the Lake Biwa Environmental Research Institute twice a month at the monitoring point Imazu-oki (35°23'41" N., 136°07'57" E.), the depth of which was 0.5 m, 5 m, 10 m, 15 m, 20 m, 30 m, 40 m, 60 m, 80 m, approximately 90 m.

2.4 Boundary conditions

The boundary conditions for hydrodynamic model were used as the same conditions described in [11]. Air temperature, atmospheric pressure, wind direction and speed, and relative humidity over Lake Biwa were derived from the Grid Point Value produced by the Meso-Scale Model (GPV MSM) of the Japan Meteorological Agency. GPV MSM data has a spatial resolution of 0.0625° longitude by 0.05° latitude (approximately 5 km) and a temporal resolution of one hour. The data was horizontally interpolated into each surface mesh of the hydrodynamic model. Solar radiation was derived from hourly observation data at the Hikone Local Meteorological Observatory (35°16'30" N, 136°14'36" E), (Fig. 1). Solar radiation was assumed to be horizontally uniform over the lake. The water temperature and flow rate simulated by the Yodo river basin model [12] were used as the boundary conditions for 56 rivers flowing into Lake Biwa.

2.5 Simulation conditions

The data of water temperature, flow direction, and flow velocity used in water quality model are input using the calculation results of the flow field model every three hours, and the calculation results of each component from the Yodo river basin model are used for the inflow from the river. The simulation was conducted for a period from 1st April 2007 to 31st March 2010 (Japanese fiscal year (JFY) 2007 to 2009) with a spin-up period from 1st April 2006 to 31st March 2007 using meteorological data derived from GPV MSM. Table 3 shows the simulation conditions for water quality model. The parameters of chemical and biological processes are based on [8].

Table 3 Simulation conditions for biological model

Parameter		Condition
Time step		45 s
Output interval		Every 3 hour
Horizontal grid size		500 m
Vertical grid size		0.5-2 m
Meteorological Data		GPV MSM data
Flow field data		Hydrodynamic Model
Inflow from river	Dissolved oxygen	Observed data from Ado river
	Inorganic nitrogen, Organic nitrogen, Inorganic phosphorus, Organic phosphorus, COD	Yodo river basin Model
Initial value	Phytoplankton (chl a,b,c)	Observed data from Imazu-oki
	Inorganic nitrogen	
	Organic nitrogen	
	Inorganic phosphorus	
	Organic phosphorus	
	Dissolved oxygen	
	Particulate COD	
	Dissolved COD	
	Zooplankton	Vertical uniform

3. RESULTS AND DISCUSSIONS

3.1. Seasonal change of nutrients and dissolved oxygen at Imazu-oki

Fig. 3, 4 and 5 show the seasonal changes in vertical distribution of observed and simulated total nitrogen (TN), phosphorous (TP), and dissolved oxygen (DO) at the monitoring point in Imazu-oki in 2007. The vertical distributions of TN, TP, and DO each year are not very different from each other, therefore we picked the values in 2007 as a representative year. The concentration of TN in the simulation didn't change seasonally above the thermocline. This may be because the amount of intake of inorganic nitrogen by phytoplankton was not enough in summer and autumn in this model. The concentration of TP in the simulation at the bottom layer was underestimated. The possible reason for it is that the amount of elusion in the bottom layer was not sufficient in this model. On the other hand, the trend of vertical distribution of DO in the simulation was well reproduced. In a stratified season, DO decreased under the thermocline while the organic matter was decomposed. In winter, DO increased because of the supply of the oxygen from the upper layer during overturning.

3.2. West-east vertical cross sections through Imazu-oki for DO in the simulation

The distributions of simulated DO along the line passing from west to east through the monitoring point in Imazu-oki are shown in Fig. 6. The snapshots were taken at 12:00 p.m. from April 2007 to February 2008 every two months. DO in the eastern coast tended to decrease from spring to autumn compared with the one in western side. One reason for it was the water temperature increased more in the eastern coast and less oxygen could be dissolved in water. The other reason for it was that since the slope in the eastern coast was more moderate than that in the western side, the organic carbon in the bottom layer was accumulated more in the eastern coast than in the western coast.

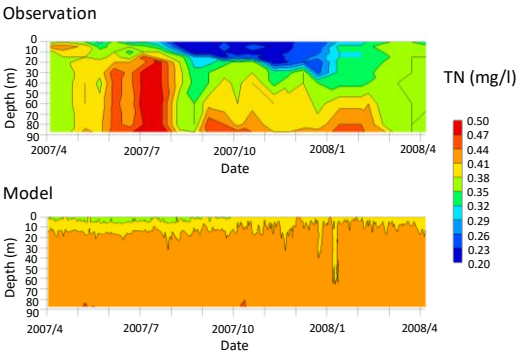

Fig. 3 Seasonal change of vertical distribution of observed and simulated total nitrogen at Imazu-oki in 2007.

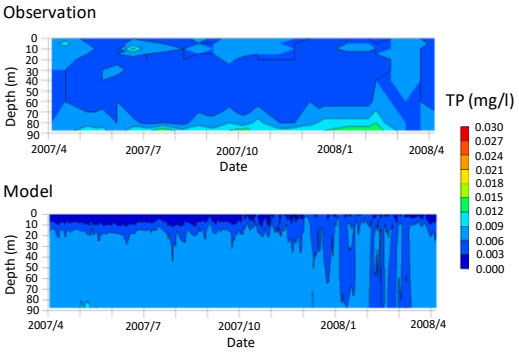

Fig. 4 Seasonal change of vertical distribution of observed and simulated total phosphorous at Imazu-oki in 2007.

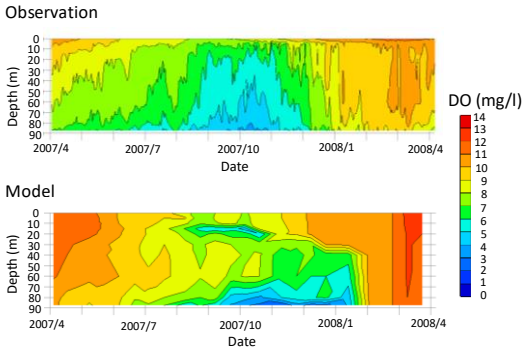

Fig. 5 Seasonal change of vertical distribution of observed and simulated dissolved oxygen at Imazu-oki in 2007.

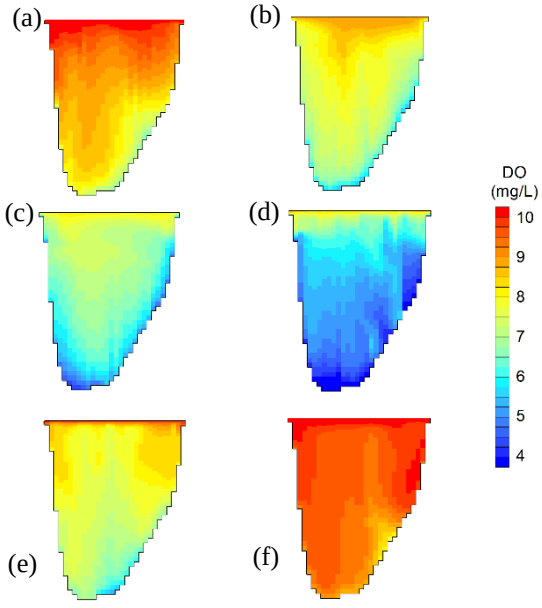

Fig. 6 Seasonal change in vertical distribution of simulated dissolved oxygen (Color contour: dissolved oxygen (mg/l)) (a) 3rd April; (b) 4th June; (c) 6th August; (d) 1st October; (e) 3rd December; and (f) 4th February.

3.3. Inter-annual change of DO at Imazu-oki

Fig. 7, 8 and 9 show the inter-annual changes in vertical distribution of observed and simulated TN, TP, and DO at depths of 0.5 m, 20 m, and 90 m at the monitoring point in Imazu-oki. The inter-annual change of TN was not well reproduced because the parameter of intake of inorganic nitrogen could be a small value during photosynthesis every year. The inter-annual change of TP in the simulation didn't agree well with the one in the observation in the bottom layer, because the amount of elution from the bottom of the lake could be insufficient. The inter-annual change of DO in the simulation approximately agreed with the one in the observation above the thermocline. In the surface layer, the seasonal change of DO was influenced by the dissolution rate.

The saturated concentration of DO is 11.8 mg/l in 8°C water in winter and 7.8 mg/l in 28°C water in summer every year. DO in the bottom layer decreased during decomposing the organic matter by bacteria with little oxygen supply from the atmosphere and the photosynthesis from the phytoplankton from spring to autumn every year. DO was supplied in all layers by the overturning in winter and the timing of recovery of DO depended on the start of overturning. The difference of DO between simulation and observation in the bottom layer possibly derived from not giving enough parameter values of consumption of DO during decomposing organic matters.

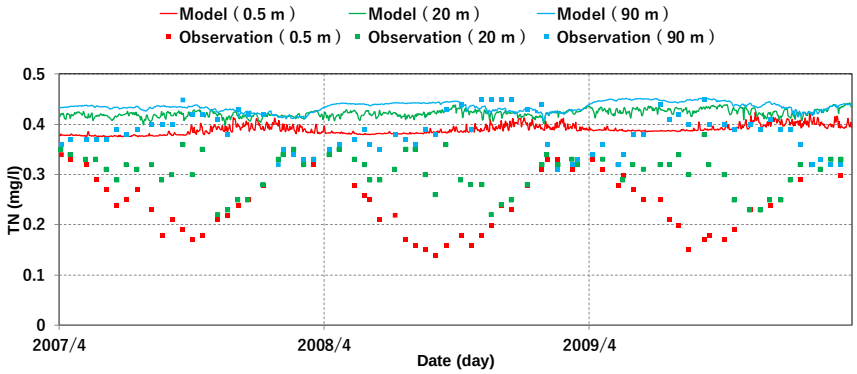

Fig. 7 Inter-annual change of vertical distribution of observed and simulated total nitrogen at Imazu-oki.

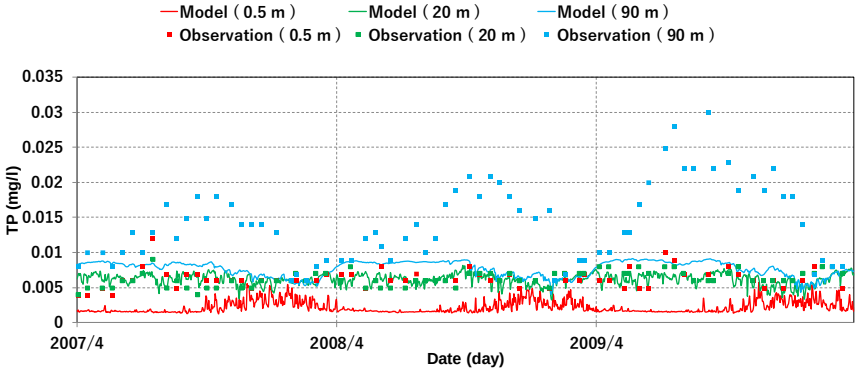

Fig. 8 Inter-annual change of vertical distribution of observed and simulated total phosphorous at Imazu-oki

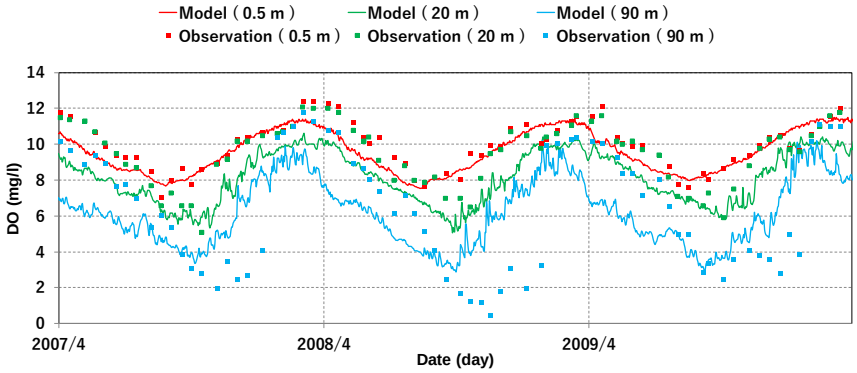

Fig. 9 Inter-annual change of vertical distribution of observed and simulated dissolved oxygen at Imazu-oki.

4. CONCLUSION

A three-dimensional water quality model considering the hydrodynamic processes is necessary for understanding the dynamic analysis of DO in Lake Biwa. Numerical simulations were carried out for 3 years from 2007 to 2009. This model was based on a low trophic level ecosystem. It consisted of phytoplankton, zooplankton, nitrogen, phosphorus, dissolved oxygen and chemical oxygen demand as state variables. In this model, the inflow load from the river was considered and the vertical mesh was in detail for reproducing the thermocline which suppressed the transportation of the substances.

The trend of the seasonal changes in the vertical distributions of DO were approximately reproduced by the water quality model considering the flow field. The simulated DO concentration above the thermocline approximately agreed with the observed one. DO solubility in water is influenced by the water temperature. In the surface water, DO was always saturated. As water depth increased, DO decreased due to the thermocline suppressing the transport from DO in the upper layer. The dynamics of DO above the bottom of the lake was controlled by consumption by bacteria and the supply from DO in the upper layer during overturning.

In order to better reproduce observed DO, minimal and maximal growth temperatures of phytoplankton and bacteria should be considered more in detail. Water temperature affects the biological processes such as algal growth, photosynthesis and decomposition of organic matters which cause the change in oxygen at the bottom of the lake.

As for TN and TP, there was a difference between simulation and observation, because the amount of intake by phytoplankton and mineralization of organic matter could be different from the observed ones. In order to reproduce the change in nutrients concentrations more precisely, the water quality model should consider the biochemical processes in detail to give the exact parameter and include the model of transportations of nutrients at the boundary conditions between bottom water and sediments. The decrease in DO at the bottom of the lake triggers the elution of nitrogen and phosphorus from the bottom sediment.

The model which can reproduce the seasonal and inter-annual change in concentrations of nutrients accurately leads to clarifying the reason why DO in the bottom of the lake decreased in a certain year. It is important to elucidate the effects of global warming and eutrophication. That leads to preserving the water quality and ecosystems of Lake Biwa.

5. REFERENCES

[1] Kumagai, M., Vincent, W.F., Ishikawa, K., and Aota, Y. Lessons from Lake Biwa and other Asian lakes: Global and local perspectives, in Freshwater Management (eds. M. Kumagai, W.F. Vincent), Springer, Tokyo, 2003, pp.1-23.

[2] O'Reilly, C.M., Alin, S.R., Plisner, P.D., et al. Climate change decreases aquatic ecosystem productivity of Lake Tanganyika, Africa. Nature, 24, 2003, pp.766-768.

[3] Matzinger A., Schmid M., Veljanoska-Sarafiloska E., and Wuest A., "Eutrophication of ancient Lake Ohrid: global warming amplifies detrimental effects of increased nutrient inputs." , Limnology and Oceanography, Vol. 52, 2007, pp.338-353

[4] Coats R., Perez-Losada J., Schladow G., Richards R., and Goldman C., "The warming of Lake Tahoe.", Climate Change, Vol.76, 2006, pp.121-148.

[5] Kumagai, M.; Ishikawa, K.; Jiao, C.; Aota, Y. Climate change and hypoxic phenomena in the norther part of Lake Biwa. Res. Rep. Lake Biwa Environ. Res. Inst. 2005, 22, pp.171-177.

[6] Koue J., Shimadera H., Matsuo T., Kondo A., Numerical Analysis of Sensitivity of Structure of the Stratification in Lake Biwa, Japan by changing Meteorological elements, Water, Vol. 10, 2018,1492.

[7] Moss, B., Kosten, S., Meerhoff, M., et al .Allied attack: climate change and eutrophication. Inland Waters, 1, 2011, pp.101-105.

[8] Iwasa Y., Engineering Limnology, Sankaido, Chapter 4, 1990, pp. 299-356.

[9] Ikeda, S. and Adachi, N., A dynamic water quality model of lake biwa, - A simulation study of the lake eutrophication -, Ecological Modelling, 4: 1978, pp.151-172.

[10] Hosoda, T. and Hosomi, T., A simplified model to predict seasonal variations of vertical water quality distributions in Lake Biwa and its applications, Advances in River Engineering, JSCE, 8, 2002:pp.495-500.

[11] Koue, J.; Shimadera, H.; Matsuo, T.; Kondo, A. Evaluation of Thermal Stratification and Flow Field Reproduced by a Three-Dimensional Hydrodynamic Model in Lake Biwa, Japan. Water, Vol.10, 2018, 47.

[12] Shrestha, K.L.; Kondo, A. Assessment of the Water Resource of the Yodo River Basin in Japan Using a Distributed Hydrological Model Coupled with WRF Model. In Environmental Management of River Basin Ecosystems; Part of the Series Springer Earth System Sciences; Springer: Berlin, Germany, 2015, pp. 137-160.

9th Int. Conf. on Geotechnique, Construction Materials and Environment,
Tokyo, Japan, 20-22 November 2019, ISBN: 978-4-909106025 C3051

NUMERICAL STUDY OF THE FACTORS THAT AFFECT THERMAL EFFICIENCY DURING INFRARED GAS STOVE HEATING

P. Keangin[1,*], A. Charoenlerdchanya[1] and P. Rattanadecho[2]
[1]Department of Mechanical Engineering, Faculty of Engineering, Mahidol University,
25/25 Phutthamonthon 4 Road, Salaya, Nakhon Pathom, 73170, Thailand.
[2]Department of Mechanical Engineering, Faculty of Engineering Thammasat University,
99 mu 18, Paholyothin Road, Klong Nueng, Klong Luang, Pathumthani, 12120, Thailand.
*Corresponding Author: E-mail: pornthip.kea@mahidol.ac.th.

ABSTRACT

The Energy Policy and Planning Office, Ministry of Energy, Royal Thai Government reported that from 2007 to 2015, the using of fuel increase in every year. In addition, the price of fuel increases continuously. The way of most efficiently of energy using is important. This paper aimed to study about the thermal efficiency of infrared gas stove by varies with the parameters which were diameters of pot (220, 240 and 260 mm), distances between burner (20, 25 and 30 mm) and pot and diameter of burner head (135, 145 and 155 mm) in 9 cases by simulation method. The numerical model was validated with the results from the experiment in 220, 240 and 260 mm of diameter of pot, average error are 10.85011, 6.754703 and 2.13054 percentages, respectively. The results of this study showed that with three sizes of pot, huger distances between burner and pot decrease thermal efficiency. The highest thermal efficiency was in 260 mm of diameter of pot. Within 9 cases by vary the parameters, the highest thermal efficiency was 260 mm of diameter of pot, 20 mm of distance between burner and pot and 145 mm of diameter of burner head condition and the less thermal efficiency was 220 mm of diameter of pot, 20 mm of distance between burner and pot and 145 mm of diameter of burner head condition. The obtained results provide useful for the development of heating process by infrared burner technologies and to guide the development of effective infrared burner too lead the way in energy-saving way and reduce environmental impacts.

Keywords: Infrared Gas Stove ; Temperature Distribution ; Thermal Efficiency ; Finite Element

INTRODUCTION

Data from the Energy Policy and Planning Office, Ministry of Energy, Royal Thai Government found that the usage of fuel gas in the year 2007 to 2015 is likely to increase every year [1]. In addition, the price of fuel gas in Thailand was found to have a tendency to rise every year as well [2]. However, because energy is limited, in order to reduce the energy consumption of the country should be find ways to use energy most efficiently as possible.

Infrared burner is a type of low gas pressure. The working principle of infrared burner is relying on heat transmission by radiation. Infrared (IR) is a part of the electromagnetic spectrum. IR is invisible radiant energy, electromagnetic radiation with longer wavelengths than those of visible light, extending from the nominal red edge of the visible spectrum at 700 nanometers (frequency 430 THz) to 1 mm (300 GHz). From survey the market, it is found that the infrared burner that supplied in Thailand all have the same type of radiation is the release of gas using ceramic plate [3]. The other characteristics are not as popular or widespread in the country because the producers lack knowledge and technology in production. Current infrared burner is gaining more popularity in households due to the infrared burner is a low gas pressure of no flames. The advantages of infrared burner are reducing the consumption of cooking gas stove over conventional, characterized by burning smokeless, clean applications and can be easily controlled as desired. Results in the annual sales volume of all operators in Thailand of infrared burners is 430,000 stoves per year.

Many previous researches studied on drying products using infrared radiation. The study found that drying using infrared reduces drying time less than the traditional drying (using hot air). There are some researches described the basic principles of infrared radiation and applications in the food industry such as baking, roasting and drying, the study found that the infrared can transfer heat to the food more efficiently and it can be reducing the time and cost of process [4-6]. It was also found that the products from infrared heating have better quality than conventional heating [7]. The rate of gas consumption was compared during the cooking of meat products using a gas stove with a traditional model and an infrared gas burner of ceramic plates [8]. It is observed that the infrared gas burner can help reducing gas consumption by about 55%. However, a few studies considered model of heat transport during heating by infrared burner,

especially a detailed study of the effect of heating time, temperature of the burners, the distance between the burners and the boiling pot of water and the size of the burners on temperature distribution and thermal efficiency of the infrared burner. This is because complexity of the mathematical model of pot and infrared burner

In this study, the influences of diameters of pot, the distances between the burner and the boiling pot of water and the size of the burners on temperature distribution and thermal efficiency during heating using infrared burner are investigated. In order to verify the accuracy of the present model, the computer simulation study is validated with an experimental study. The test method is reference from the low-pressure gas burner in households with LPG test (TIS No. 2312-2549) and the Development of energy efficiency standards infrared burner project. An axially symmetric model of pot and infrared burner are considered in this study, which minimized the computation time while maintaining good resolution and represents the full 2-D result. The governing equations as well as initial and boundary conditions are solved using the axisymmetric finite element method (FEM). The results of the study will be the basis for the study and analysis the effects of various parameters on temperature distribution and thermal efficiency during heating using infrared burner.

EXPERIMENT SETUP

For experiment, the test method is referenced from the low-pressure gas stove in households with LPG test (TIS No. 2312-2549) and the Development of energy efficiency standards infrared burner project [3].

The experimental testing apparatus

Infrared gas stove is used in the experiment. The infrared gas stove is composed of ceramic plate that it emits heat to the pot. The infrared gas stove that was used in the experiment was shown in Fig. 1. In this experiment, the three sizes of aluminum pots (220, 240 and 260 mm) as shown in Fig. 2 are used to compare the temperature and thermal efficiency.

Fig. 1 Infrared gas stove which is used in the experiment.

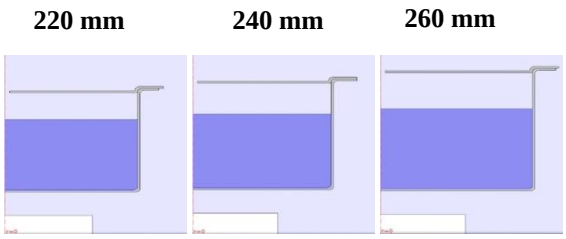

Fig. 2 Aluminum pots for experimental study.

Experimental methods to determine the thermal efficiency of the infrared gas stove in this study are in the Fig. 3 and follow by the steps. Starting with check and prepare experimental equipment, set up stove and connect the stove with gas gauge, pressure equipment, gas temperature gauge and valve gas as shown in Fig. 4. Then adjust the gas valve to the maximum gas inject position at gas pressure of 280 millimeters water (mm H_2O). Warm the burner for 5 minutes to remove stains dirt and oil. Turn off the stove and place the pot on the center of stove then put the thermometer to measure temperature. The initial water temperature should be set up at 25 ± 2 °C. In addition, the testing room is controlled room temperature at 25 ± 2 °C. Before the test, the temperature of gas and water temperature are recorded. The position for measuring the temperature of the center of the water at the height of 5 mm from the bottom of the pot is considered. Follow this procedure until the temperature of water increase from initial for 50 °C. Finally, turn off the stove; record the last temperature of water and quantity of gas. An experiment is repeated 5 times. The data of the test will be used to calculate the thermal efficiency of infrared gas stoves. Before do the test again, pot cleaner clearly to minimize heat loss. The temperature measured in experimental is recorded by using digital thermometer during heating. The dimension of pot and infrared gas stove and conditions in this experiment setup is used for the simulation.

Fig. 3 The water in the container is boiled in the experiment.

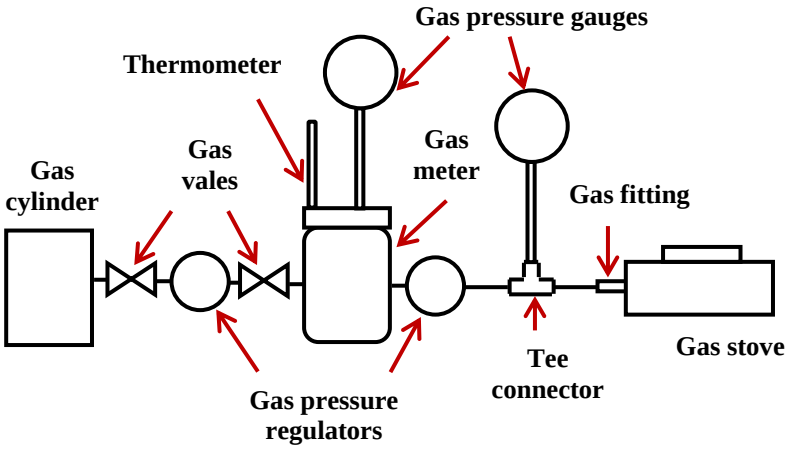

Fig. 4 Experimental apparatus.

Physical model

Analysis of heat transfer in water during heating by using infrared gas stove is presented. The system of governing equations as well as initial and boundary conditions are solved numerically using the FEM via COMSOL™ Multiphysics. In order to verify the accuracy of the present model, the simulation results are validated against the experimental results with the same conditions. The mathematic model used in computer simulation is divided into two parts, namely a container (pot) and infrared gas stove as sown in Fig. 5. The pot made of aluminum material. Because of the pot and burner are cylinder shape and the pot are located on the center of burner, an axially symmetric model is considered in this study for save the computation time. The axially symmetric model of pot and infrared gas stove for heat transfer analysis of water heating by using infrared gas stove is proposed. Heat absorbed by the water and converted into internal heat generation, which causes its temperature of water to rise. The convergence test is carried out to identify the suitable numbers of element required. The properties of materials are based on properties of equipment that use in experiment. There are properties of air, water and aluminum as shown in Table 1.

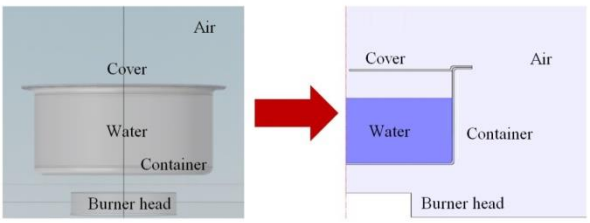

(a) (b)

Fig. 5 The numerical model that used in the simulation (a) 3D model and (b) 2D axial symmetry model.

Table 1 The properties of materials [9-11].

Properties	Air	Water	Aluminum
Density (kg/m^3)	1.186	1000	2700
Heat capacity (J/kg·K)	1005	4186	897
Thermal conductivity (W/m·K)	0.0259	0.6065	204

Equations for heat transfer analysis

The heat transfer model is developed to predict the temperature distribution in the water. The assumptions have been offered for computer analysis is as follows: lack of the combustion of gas fuel, unconsidered a container base and no phase change and no chemical reaction in the water. Also, thermal properties of water, aluminum pot and air are constant. Fig. 6 shows the internal and external boundary condition of pot. Temperature boundary condition is to specify the temperature from the burner head. The boundary condition of heat continuity is to temperature continuity in the different domain. The specification of the insulate boundary is in thermal insulation boundary condition. The inlet condition is to add the velocity to the model. The condition outflow is used in the flow problem with the unknowns of flow velocity and pressure. The boundary condition of wall is specific $\vec{u} = 0$. The open boundary is used to specify at the outlet. The initial condition of water is defined as $T_0 = 25$ °C at $t = 0$ s in order to comply with the experiment. The simulation measured point of water temperature to find thermal efficiency and water velocity measured point at 5 mm above inside bottom of pot.

The governing equation describing the heat transfer phenomenon is given in Eq. (1):

$$\rho c \frac{\partial T}{\partial t} + \rho c \vec{u} \cdot \nabla T = \nabla \cdot (k \nabla T) = 0 \qquad (1)$$

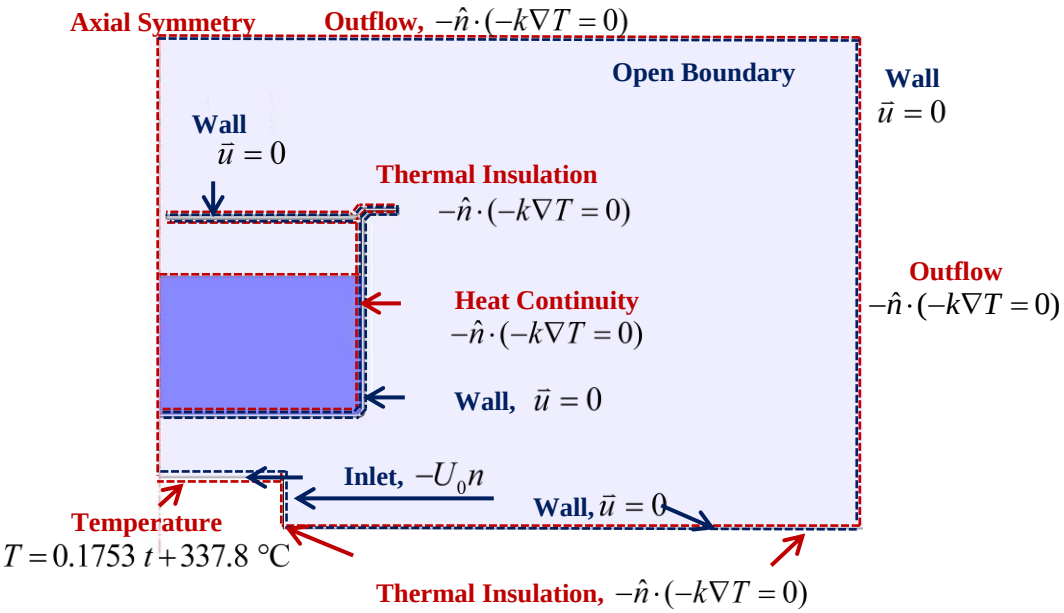

Fig. 7 Boundary condition for numerical analysis

Where ρ = 1000 kg/m^3 is the density, c = 0.004186 MJ/kg.K is the specific heat capacity, T is the temperature (°C), t is the time (s), $\vec{u}$ is the velocity (m/s) and k = 0.6065 W/m·K is the thermal conductivity.

Corresponding to heat transfer analysis, fluid flow analysis inside the water and air is assumed in axially symmetric model. Fluid flow analysis is formulated to describe the water and air velocity distributions. Using standard symbols, the governing equations describing the fluid flow are given as follows:

Continuity equation:

$$\frac{\partial \rho}{\partial t}+\nabla\cdot\left(\rho\vec{u}\right)=0 \tag{2}$$

Navier-Stokes equation:

$$\rho\frac{\partial u}{\partial t}+\rho(\vec{u}\cdot\nabla)\vec{u}= \nabla\cdot\left[-pl+\mu\left(\vec{u}+\nabla\vec{u}\right)^T-\frac{2}{3}\mu\left(\nabla\cdot\vec{u}\right)l\right] \tag{3}$$

Where ρ is the density (kg/m^3), t is the time (s), $\vec{u}$ is the velocity (m/s), p is the pressure (Pa), μ is the viscosity (Ns/m^2) and l is the identity matrix tensor.

The equation for calculate the thermal efficiency is given in Eq. (4) [1]:

$$\eta=\frac{m\times c\times(T_2-T_1)}{V\times Q}\times\frac{273+T_g}{298}\times\frac{101.3}{P_s+P_m-P_{sat}}\times 100\,\% \tag{4}$$

When η is the thermal efficiency (-), m is the mass (kg), c = 0.004186 MJ/kg.K is the specific heat capacity, T_1 = 25 ± 2 °C is the initial temperature of water, T_2 = 75 ± 2 °C is the final temperature of water, V is the amount of gas used test (m^3), Q = 107.86 MJ/m^3 is the lower heating value, T_g is the temperature of the gas during the test (°C), P_s is the atmospheric pressure during test (kPa), P_m is the pressure of the gas during the test (kPa), P_{sat} is the pressure of saturated stream at a temperature of gas during test (kPa).

RESULTS AND DISCUSSION

Verification of the Model

The number of elements where solution is independent of mesh density is found to be 26,754 elements. It is reasonable to confirm that, at this number of elements, the accuracy of the simulation results is independent from the number of elements through the calculation process. The water temperature during boiling the water with the infrared gas stove of the experimental study and

numerical study in condition pot size 220, 240 and 260 mm, distance between burner and pot 25 mm and diameter of burner head 145 mm are shown in Table 2, Table 3 and Table 4, respectively. The water temperature of the experiment and simulation (experiment:simulation) at 720 s of 220, 240 and 260 mm of pot size are 70.1:61.095, 65.2:60.55 and 57.7:61.19, respectively. The average error between the experimental results and simulation results of water temperature with the different 220, 240 and 260 mm of diameters of pot are 10.85011, 6.754703 and 2.13054 percentages, respectively. The average error of the experimental result and simulation results is part of the initial water temperature. The initial temperature of the simulation is specified at 25 °C but the experimental initial temperature is 25 ± 2 °C. It is found that the results of experiment and simulation are consistent. The results also indicate that an increase in the heating times results in an increase temperature. Even though there have a little different, the both of trends is similar. Therefore, this model can use to analyse and study thermal efficiency of infrared gas stove.

Table 2 The comparison between the experimental study and simulation study of 220 mm of diameters of pot, 25 mm of distance between burner and pot and 145 mm of diameter of burner head.

Time	Water temperature of the experiment (°C)	Water temperature of simulation (°C)	Error (%)
0	25.2	25.00001	0.714809
60	28.4	27.86652	1.87844
120	31.8	30.11759	5.350123
180	35.6	32.38299	8.934223
240	39.4	34.81065	11.60323
300	43.1	37.447	13.19656
360	47.1	40.27288	14.49494
420	50.9	43.29045	14.94999
480	54.4	46.53052	14.4974
540	58.5	49.92689	14.65489
600	62.4	53.52855	14.27202
660	66.3	57.24255	13.6092
720	70.1	61.09507	12.89554
		Average error (%)	10.85011

Table 3 The comparison between the experimental study and simulation study of 240 mm of diameters of pot, 25 mm of distance between burner and pot and 145 mm of diameter of burner head.

Time	Water temperature of the experiment (°C)	Water temperature of simulation (°C)	Error (%)
0	25.0	25.00001	0.0799
60	27.7	27.94727	0.892688
120	31.3	30.25616	3.334943
180	34.0	32.53411	4.311436
240	37.8	34.93435	7.532159
300	41.0	37.53286	8.45645
360	44.4	40.30004	9.23415
420	47.8	43.24168	9.574064
480	51.7	46.38212	10.25131
540	55.1	49.7054	9.856007
600	58.5	53.19229	9.073008
660	61.8	56.7887	8.138628
720	65.2	60.54902	7.076398
		Average error (%)	6.754703

Table 4 The comparison between the experimental study and simulation study of 260 mm of diameters of pot, 25 mm of distance between burner and pot and 145 mm of diameter of burner head.

Time	Water temperature of the experiment (°C)	Water temperature of simulation (°C)	Error (%)
0	24.6	25.00003	1.70883
60	27.0	28.04433	3.714232
120	29.5	30.46776	3.210564
180	32.4	32.83231	1.334285
240	35.1	35.31972	0.625977
300	37.9	37.96444	0.275861
360	40.7	40.76823	0.118438
420	43.6	43.73269	0.258345
480	46.4	46.95739	1.114098
540	49.4	50.25008	1.803234
600	52.2	53.79481	3.094697
660	55.0	57.38981	4.383071
720	57.7	61.19396	6.055386
		Average error (%)	2.13054

Effect of parameters varying

The different parameters are studied with the numerical method to compare the water temperature and thermal efficiency. The different pot sizes (220, 240 and 260 mm), distances of the burner and pot (20, 25 and 30 mm) and the diameters of burner head (135, 145 and 155 mm) are studied in 9 cases which are shown in Table 5. When the parameter changes, the other parameters are constant. For example, in the first three cases, the diameters of pot are 220, 240 and 260 mm with the constant parameters of 25 mm of distance between burner and pot and 145 mm of diameter of burner head. The cases number 2, 4 and 8 are in the same conditions because there is one vary parameter with two constant parameters.

The effect of parameters of diameters of pot (220, 240 and 260 mm), distance between burner and pot (20, 25 and 30 mm) and diameters of burner (135, 145 and 155 mm) to thermal efficiency of an infrared burner were studied in this research in 9 cases as shown in Table 5. In various parameters, the other parameters are fixed. The bigger pot size has thermal efficiency more than the small pot size. The thermal efficiency in the small gap between burner

and pot is higher than the widely size. In various diameters of burner head, the middle size which is 145 mm has the thermal efficiency more than the other sizes. Figure 8 shows the comparison of thermal efficiency by parameters varying.

Table 5 The thermal efficiency of infrared burner with varying parameters which are diameters of pot (220, 240 and 260 mm), distances between burner (20, 25 and 30) and pot and diameter of burner head (135, 145 and 155 mm).

Case	Diameters of pot size (mm)	Distances between burner and pot (mm)	Diameters of burner head (mm)	Thermal efficiency (%)
1	220	20	145	46.452
2	240	20	145	56.863
3	260	20	145	56.891
4	240	20	145	56.863
5	240	25	145	54.680
6	240	30	145	53.531
7	240	20	135	50.684
8	240	20	145	56.863
9	240	20	155	54.671

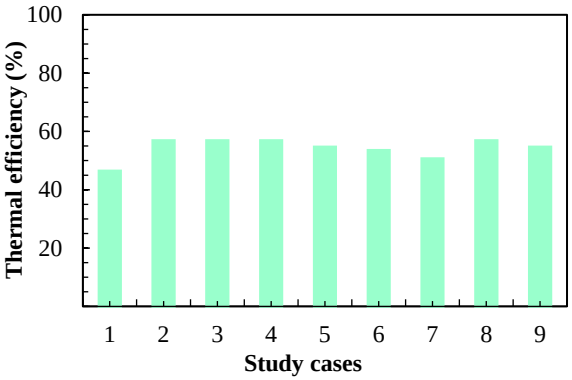

Fig. 8 Comparison of thermal efficiency by parameters varying.

The graph of thermal efficiency of parameters which are diameters of pot, distances between burner and pot and diameters of burner head is shown in Fig 8. When compared the thermal efficiency in various diameter of pot and distance between burner and pot conditions, the results of various size of pot have the difference more than the other parameters. The highest thermal efficiency of 9 cases is 260 mm of diameter of pot, 20 mm of distance between burner and pot and 145 mm of diameter of burner head at 56.891 percentages and the minimum thermal efficiency is 220 mm of diameter of pot, 20 mm of distance between burner and pot and 145 mm of diameter of burner head condition at 46.452 percentages.

Figure 9 shows the temperature distribution of 9 cases studied. The temperature distributions above the burner head of 155 mm of diameter of burner head are higher than the temperature distributions of 145 and 135 mm. The small head of burner and less area for heat transfer than the huge diameters of burner head and final temperature of water agree with the heat transfer. However, temperature distribution of 135 mm of diameter of burner head is different from the other burner head sizes. The area of head of burner and bottom of pot make the shape of temperature distribution different from the 145 and 155 mm of diameters of burner head. Water temperature of 135 mm of diameter of burner head is less than water temperature of 145 mm and 155 mm, respectively. In addition, the water temperature of small gap between burner and pot is more than water temperature of the huge distances between burner and pot. The huge distances between burner and pot have longer distance to transfer the heat than the small distance and have an opportunity for heat loss to surrounding more than little distance.

CONCLUSIONS

Thermal efficiency of infrared burner in varying of parameters which are diameters of pot (220, 240 and 260 mm), distances between burner (20, 25 and 30 mm) and pot and diameter of burner head (135, 145 and 155 mm) are studied in this research. The 26,754 elements are used in this simulation and are compared with the experimental results.

(1) This numerical model can solve the results of the heating of water by infrared gas stove. The average error of water temperature between simulation results and experimental results in 220, 240 and 260 mm of diameter of pot are 10.85011, 6.754703 and 2.13054 percentages, respectively.

(2) The parameters are effect to the water temperature and thermal efficiency. In 9 cases by varying of the parameters, the simulation results show that the less distances between burner and pot increase thermal efficiency of infrared burner and the highest thermal efficiency was in 260 mm of diameter of pot condition.

(3) The 260 mm of diameter of pot, 20 mm of distance between burner and pot and 145 mm of diameter of burner head has the maximum thermal efficiency and the 220 mm of diameter of pot, 20 mm of distance between burner and pot and 145 mm of diameter of burner head condition has the minimum thermal efficiency.

The complete mathematical model is useful for the development of heating process by infrared burner technologies and is a way to increase the thermal efficiency of various devices

ACKNOWLEDGMENTS

The authors gratefully acknowledge the Mahidol University for supporting this research.

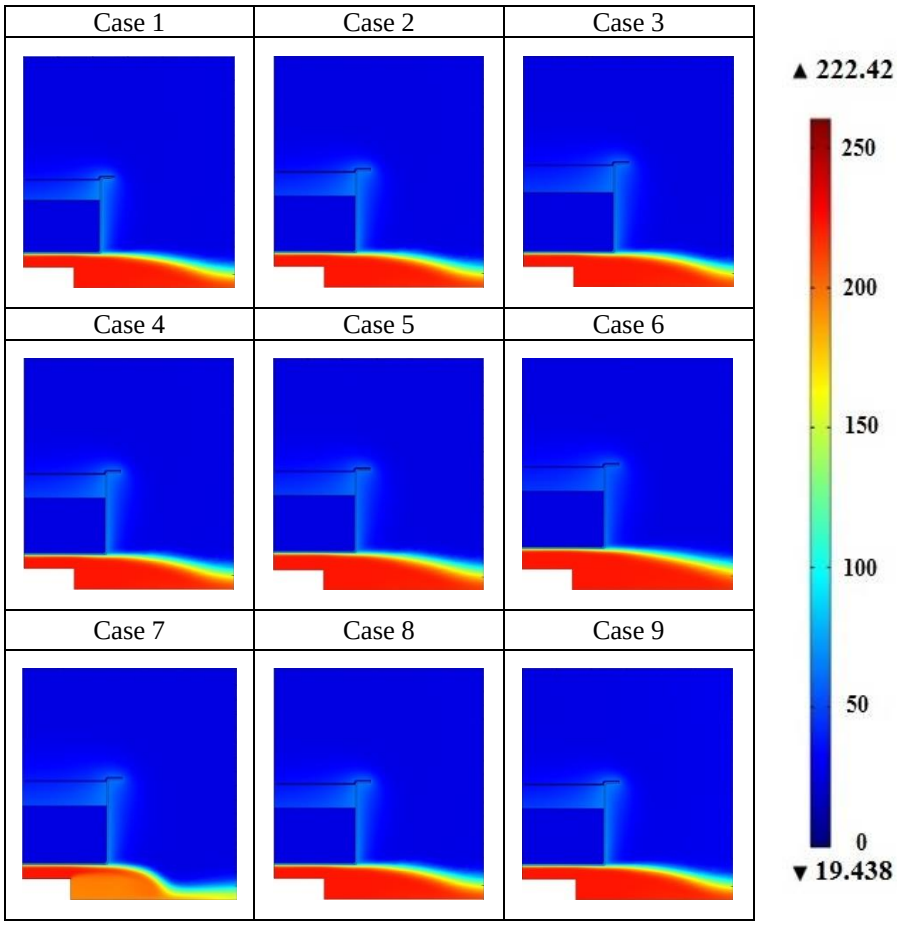

Fig. 9 Comparison of water temperature of experiment and simulation by parameters varying.

REFERENCES

[1] The Energy Policy and Planning Office, Energy Statistics of Thailand 2016, pp. 36.

[2] Chuenwong K., Chiarakorn S., and Sajjakulnukit B., Specific energy consumption and carbon intensity of ceramic tablewares: Small enterprises (SEs) in Thailand, Journal of Cleaner Production, Vol. 147, 2017, pp. 395-405.

[3] Department of Mechanical Engineering, Faculty of Engineering, Mahidol University, Final Report, Development of energy efficiency standards infrared burner project.

[4] Tamir A., Elperin I. and Yotzer, S., Performance Characteristics of A gas Burner with A Swirling Central Flame, Energy, Vol. 14, Issue 7, 1989, pp. 373-382.

[5] Carleton F.B., Tamir, A. and Weinburg F.J., Heat Recuperation Applied to a Gas Ring Burner, Combustion Science and Technology, Vol. 83, Issue 5, 1992, pp. 327-332.

[6] Trewetaskson W., Efficiency Improvement of LPG Domentics cooking stove, Master. Engineering (Chemical Engineering), King Mongkuts University of Technology Thonburi, 1998.

[7] Wade P. (1989). Biscuit Baking by Near Infrared Radiation, Journal of Food Engineering, vol. 6, pp. 165-175.

[8] Sheridan P. and Shilton N., Application of Far Infrared Radiation and Measurement of Equipment Performance, Japan Food Science, Vol. 27, 1999, pp.23-29.

[9] The Engineering ToolBox. Air properties. Inc.; ©2001. Accessed August 25, 2017. Available from https://www.engineeringtoolbox.com/air-properties-d_156.html

[10] The Engineering ToolBox. Water thermophysical properties. Inc.; ©2001. Accessed August 25, 2017. Available from https://www.engineeringtool box.com/water-thermal -properties-d_162.html.

[11] The Engineering ToolBox. Thermal Conductivity of Metals. Inc.; ©2001. Accessed August 25, 2017. Available from https://www.engineeringtool box.com/thermal-conductivity-metals-d_858.html.

9th Int. Conf. on Geotechnique, Construction Materials and Environment, Tokyo, Japan, 20-22 November 2019, ISBN: 978-4-909106025 C3051

EVALUATION OF BUS RAPID TRANSIT (BRT) TRANS KOTA TANGERANG SERVICE PERFORMANCE

Bella Fauziah[1], Lita Sari Barus[2] Jachrizal Sumabrata[3]
[1]Urban Studies, University of Indonesia, Jakarta.

ABSTRACT

The Tangerang City Government is one of the cities that has implemented BRT policy as public transportation since December 2016. However, its operation is considered to be lonely. This study aims to assess and analyze of BRT Trans Kota Tangerang Service Performance. The study used a quantitative method with servqual analysis to find out the comparison between expectations and reality from the service side with data analysis techniques using SEM analysis. From the results of the analysis it can be seen that the results of the study show that the perception of service performance provided by BRT Trans Kota Tangerang has been in line with expectations of 87.3%, while the remaining 12.70% is still not in accordance with the expectations of respondents. The results of the perception Gap analysis with the expectation of having a gap of -0.5 (Not Satisfied). The results of factor analysis show that the most influential and priority factor is the Tangible point 21 dimension with the highest loading factor of 0.885 (Information on bus services to be skipped in the form of visual / audio on the bus is functioning properly).

.

Keywords*: BRT Trans Kota Tangerang, Perception, Expectation of BRT Users, Service Performance, Servqual*

INTRODUCTION

The existence of transportation is intended to facilitate the movement of people or goods to a place, as a support for the running of activities of daily life. Transportation plays an important role in the development of the region related to accessibility which is the ease and ability of an area to be reached by outside parties. According to Andiriansyah (2015) the function of means of transportation "as a way to make it easier for humans or goods to move from one place to another they want to go".

In the sustainable development agenda of 2030 the Sustainable Development Goals (SDGs) consist of 17 Sustainable Development Goals (SDGs) with 169 targets aimed at ending all forms of poverty, combating inequality and overcoming climate change, while ensuring that "nothing is left behind. There are SDGs target where transportation directly contributes to five targets, namely road safety targets (Target 3.6), energy efficiency (target 7.3), sustainable infrastructure (Target 9.1), urban access (Target 11.2) and fossil fuel subsidies (Target 12.3) (Low Sustainable Carbon Transportation 2018).

Urban transportation is specified in Target no. 11.2 namely;

"Local governments are responsible for encouraging the use of public transportation in urban areas in order to improve traffic safety and reduce emissions. Providing a safe, affordable, accessible and sustainable transportation system for all, increasing traffic safety, increasing public transportation, and paying special attention to vulnerable communities, women, children, people with disabilities and the elderly "(United Cities and Local Governments Asia-Pacific 2019).

The government is responsible for making policies to make decisions in realizing public transportation. This is stated in Law No. 22 of 2009 concerning Road Traffic and Transportation (LLAJ), one of the policies in which regulates mass public transportation, and the government guarantees the availability of road-based mass transportation. In this law, it also regulates that public transport service providers must meet "Minimum Service Standards (SPM), which include" security, safety, comfort, affordability, equality and orderliness "".

In the 2013 Global Report on Human Settlements UN-Habitat concluded that public transport must be the highest priority form of motorized transportation. Joan Clos (Deputy Secretary General of UN-Habitat 2013) stated in the

global report that many cities in developing countries could easily reach public transportation, but most of them chose not to use it because they found that public transport safety and security was inadequate (because of sexual abuse or other forms of criminal behavior). This causes people to prefer to use private transportation (motorbike or car) to support their daily activities.

The high level of private vehicle use has resulted in traffic congestion and inadequate quality of public transport services. The government as a stakeholder and responsible for issuing policies must have the right planning in overcoming urban transportation problems. One of the policies implemented by the government in improving quality is by applying the Bus Rapid Transit (BRT) concept as public transportation. This BRT mass transport system has been well-known throughout the world as a cost-effective alternative to urban mass transit investments. According to Cervero (2014) there are successes for cities that adopt BRT as urban public transportation such as Curitiba and Ottawa

After the success of the operation of the concept of BRT public transportation in Jakarta, "Transjakarta" is a public transportation that has attracted many people. This also had a positive impact on the direct border areas with the capital city, such as Tangerang City, which was also one of the cities that implemented the BRT policy as mass transportation to reduce congestion.

In the Tangerang City Transportation Agency 2017 report (Figure 1.1) that there is an increase in the number of private vehicles each year. This shows that the increasing volume of vehicles that are on the road, and will have an impact on traffic congestion on the road. The Tangerang City Government made a BRT mass transportation policy in the hope that it could attract the public to use public transportation, diverting people who use private vehicles to ride public transportation so that it is expected to reduce traffic congestion.

the number of Trans City Tangerang BRT passengers is quiet, and even has a downward trend every month. This trend needs to be studied further so that in the future the Trans City Tangerang BRT program can still be a public transportation that still exists to serve the people of Tangerang City. The initial step taken was to assess the services provided by the Trans City Tangerang BRT to Trans City Tangerang BRT users. Supranto (2006) argues that;

"A 'company' must be able to give satisfaction to 'customers' to be able to compete. Customers must be satisfied because otherwise they will leave the company and become competitors' customers. This will cause a decrease in customers and cause losses.

"Companies" in the context of this case are the government as service providers and "customers" of the community in terms of service users. The government must measure the community satisfaction assessment of BRT users to immediately find out what factors make the BRT user community satisfied and dissatisfied as an evaluation to improve the quality / quality / services provided.

THEORY REVIEW

Parasuraman et.al in Mukarom and Wijaya (2016), factors that determine the quality of SERVQUAL (Service Quality) services, an approach based on a comparison of two main factors, namely consumer perceptions of the services they receive and services that are actually expected / desired. This model has five dimensions, namely:

1. Tangibles, appearance or physical facilities
2. Reliability, the ability to carry out the promised service accurately
3. Responsiveness, willingness to help consumers and provide fast service
4. Assurance, employee ethical knowledge and ability to convey trust and confidentiality
5. Emphathy, care and individual attention that is given to consumers

Furthermore, this study will classify variables and indicators as a measurement tool based on these five servqual dimensions which are related to the perception of the Trans City BRT service in Tangerang. Then it will be used as a questionnaire for Trans City Tangerang BRT service users.

METHODOLOGY

Servqual method

The purpose of servqual is intended to be able to measure the expectations and perceptions (reality) of customers here, namely the Trans City BRT users of Tangerang, as well as the gaps that exist in the service quality model. By referring to the 5 dimensions of service according to Parasuraman et al which are integrated with the Public Transport Service Standards (Director General Decree No. 687 of 2002, Minimum Minimum Service Standard for Mass Transportation of Transportation Minister Regulation No.10 of 2012 and changes in Permenhub No.27 of 2015 and BRT standards ITDP 2016) which consists of:

1. Tangible (Appearance or Physical Facilities)

Aspects that can be seen and touched on are related to bus facilities and supporting facilities such as at bus stops

2. Realibility (Ability to Accurately Promise Services)

In this aspect it aims to show and realize the service according to what has been promised

appropriately.

3. Responsiveness (Willingness to help consumers and provide fast and responsive services)

This aspect is related to the speed of response from service providers in providing services and can capture customer aspirations

4. Assurance (Knowledge of employee ethics and the ability to generate trust and confidence)

This aspect puts forward guarantees about services provided in terms of security, as well as competent resources in providing services that meet standards.

5. Emphaty (Concern and Attention to Customers)

This aspect emphasizes the attitude of service providers to service with friendliness, communication, and understanding the needs of consumers who want.

The sum of the average dimensions of each servqual item will be entered into the formula as follows.

Serqual Formula = Perception (reality) - Hope

- Servqual = 0 (means Value of Satisfied Service)
- Servqual> 0 (means Service Value is Very Satisfied)
- Servqual <0 (means Value of Service Not Satisfied)**Equations**

ANALYSIS OF SERVICE QUALITY FACTORS

In order to answer the 3rd problem formulation, the results of the Main Priority Quality of Service results from the Gap analysis need to be tested using factor analysis to obtain the most dominant (most dominant) factor so that decision making is more targeted, in this case the method used is Confirmatory Factor Analysis (CFA), while the tool used is AMOS software, where using this tool will be known to the recommendations of dominant factors which are the top priority for decision makers to take policy.

Evaluation of the validity of the measurement model can be done by looking at the results of estimating the load factors. A variable is said to have decent validity for its latent construct if the value of the t-factor is greater than the charge of the standard factor ≥ 0.5. While the evaluation of the reliability of the measurement model in CFA-SEM can use Composite Reliability (CR 7 0.7) and Average Variance Extracted (AVE ≥ 0.50). To see where the most dominant factors can be seen from the highest Loading Factor value, the Recapitulation of the results of priority factors can be seen in the following table:

Paper Submission Method and Copyright

Variabel Laten	Variabel Manifes	Validitas Parsial (LF > 0,5=Valid)		Rank	Validitas OverAll (AVE > 0,5=Valid)		Construct Reliability (CR > 0,7)	
		Loading Factors	Ket		AVE	Kesim-pulan	CR	Ket
Faktor Faktor Prioritas Utama Kualitas Layanan	**T3**	**0,694**	**Valid**	**4**	**0,814**	**Valid**	**0,897**	**Reliabel**
	T7	**0,638**	**Valid**	**8**				
	T14	**0,544**	**Valid**	**9**				
	T16	**0,652**	**Valid**	**7**				
	T18	**0,653**	**Valid**	**6**				
	T19	**0,689**	**Valid**	**5**				
	T20	**0,785**	**Valid**	**2**				
	T21	0,868	Valid	1				
	T22	**0,762**	**Valid**	**3**				

Based on the table above, it can be seen that all values of the loading factor partially every factor ≥ 0.50 (Valid / Eligible), as well as the results of OverAll each construct / concept has been declared feasible, ie with AVE value ≥ 0.50 (Valid / Eligible) Thus it can be concluded that the validity of all manifest variables on the latent variable is good. While the results of the reliability calculation show that all values of construct reliability (CR) ≥ 0.70 (reliable), thus it can be concluded that all these latent variables have reliable reliability. In detail, in order to find out the most dominant key factors in contributing to latent constructs are explained as follows.

1. Main Priority Factors The quality of service that is the most dominant rank 1 is T21 (Information on bus services to be passed in the form of visual / audio on the bus works properly) with a factor loading of 0.868.

2. Main Priority Factors The most dominant service quality ranked second is T20 (Supporting facilities and infrastructure for people with special needs available and functioning properly (priority seats, special seats for wheelchairs, slope of the floor and special texture at bus stops)) with loading factor of 0.785.

3. Main Priority Factors The most dominant service quality ranked 3rd is T22 (There is information on the delivery of the arrival time of the bus in the form of visual / audio / brochure that works well) with a loading factor of 0.762.

4. Main Priority Factors The most dominant service quality ranked 4th is T3 (Available security officers at the bus stop) with a factor loading of 0.694.

5. Main Priority Factors The most dominant service quality ranked 5th is T19 (There is information on disruption and disruption of car

travel in the bus stop via the bulletin board) with a factor loading of 0.689.

6. Main Priority Factors The most dominant service quality ranked 6th is T18 (Available bins at bus stops) with a factor loading of 0.653.

7. Main Priority Factors The service quality that is the most dominant ranked 7th is T16 (Room temperature control facilities at the bus stop function well (fan, ventilation)) with a factor loading of 0.652.

8. Main Priority Factor The most dominant service quality ranked 8th is T7 (Available bins on the bus) with a loading factor of 0.638.

9. Main Priority Factors The service quality that is the most dominant ranked 8th is T14 (Stop service information to be passed in the form of visual / audio on the bus works properly) with a factor loading of 0.544.

So that if the decision maker wants to increase the value of Service Quality (X), the statistic recommendation is to prioritize the increase in the value of the most dominant key factor in T21 (Stop service information to be passed in the form of visual / audio on the bus works properly) with the highest factor loading amounting to 0, 868. Broadly speaking, the Analysis of Confirmatory Factor can be seen through the following path diagram.

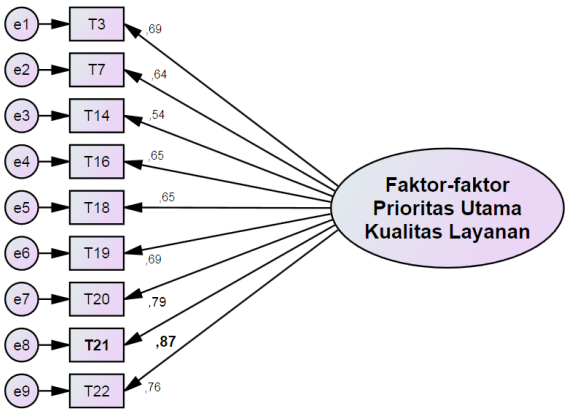

Figure 4.12 Confirmatory Factor Analysis Diagram (CFA)

CONCLUSIONS AND RECOMMENDATIONS

From the results of research on Perception (Perception) with the Expectations of Respondents, the authors can draw conclusions as follows:

1. Research Results show that the average description of respondents' expectations is 3.7, while the Perception average is 3.2, so it can be concluded that the perception of services provided by the Trans Kota Tangerang BRT has been as expected at 87.3%, while The remaining 12.70% is still felt to be less than the respondent's expectations.

2. The results of Gap Analysis show that between Service Perception and Desired Expectations Respondents have a gap that is quite far, with an average of -0.5 (Dissatisfied). The results were caused by all negative Trans City Tangerang BRT service factors, meaning that the Trans City Tangerang BRT Service Perception perceived by respondents was not satisfying the Trans City Tangerang BRT user.

3. The results of Factor Analysis show that if the decision maker wants to increase the value of Service Quality (X), the statistic recommendation is to prioritize the increase in the value of the most dominant key factor in T21 (Information on bus services to be passed in the form of visual / audio on the bus functions with good) with the highest loading factor of 0.885.

Future studies can use qualitative methods to get descriptive results directly in the field that cannot be explained in this study. In addition, in the future, the relevant agencies can work together with academics to survey and interview directly with BRT users. This can help agencies get evaluation reports on work programs in real time. And know what things must be improved in terms of service and that are maintained.

REFERENCES

[1] M Abdul, Suharto Majid. 2009. *Custommer Service Dalam Bisnis Jasa Transportasi.* Jakarta: Rajawali Press

[2] Andriansyah. 2015. *Manajemen Transportasi Dalam Kajian dan Teori*. Jakarta : Fakultas Ilmu Sosial dan Politik Universitas Prof. Dr. Moestopo Beragama

[3] Cervero, Robert. 2014. BRT TOD: *Leveraging transit oriented development with bus rapid transit investments*. Elsevier Journal Transport Policy page 127- 138. Departement of City and Regional Planning. University California Berkeley

[4] David A. Henser dan Thomas F. Golob. 2008. *Bus Rapyd Transit Systems: a Comparrative Assesment.* Journal Transportation 35:501–518. Institute of Transport and Logistics Studies, Faculty of Economics and Business, The University of Sydney

[5] Dinas Perhubungan Kota Tangerang

[6] Direktorat Bina Sistem Transportasi Perkotaan, *Studi Perencanaan Teknis Sistem Pengelolaan (Manajemen) Angkutan Umum Massal Berbasis Jalan di Wilayah Perkotaan*. Kementrian Perhubungan (II-23)

[7] Elisabet. 2006. *Analisis Indikator Kinserja Transportasi Angkutan Kota Di Surakarta*. Jurusan Teknik Industri. Fakultas Teknik Universitas Sebelas Maret

[8] Gukert, Wes PTP. 2015. *Bus Rapid Transit Systems : A Viable Tansit Solution.* ITE Journal;

Nov 2015 . Institute of Transportation Engineers.
[9] Global Report on Human Settlements. 2013. *Planning and Design For Sustainable Urban Mobility*. United Nations Human Settlements Programme. UN-Habitat
[10] Info HUBDAT. 2015. Berpikir Jernih Membangun Transportasi Darat. Edisi September 2015. Jakarta: Humas Direktorat Jenderal Perhubungan Darat
[11] Khisty, C. J and Lall, B.K.2003, Editor : Lemeda Simarmata 2005, Judul asli : *Transportation Engineering : An Introductiun/ Third Edition*, Judul Terjemahan: *"* Dasar-Dasar Rekayasa Transportasi / Edisi Ke-3 / Jilid 1**".** Jakarta : Erlangga.
[12] Kunchayani, Risti. 2012. *Analisis Persepsi Angkutan Umum Perdesaan Kabupaten Sidoarho (Studi Kasus Trayek Sidoarjo - Krian)*. Jurusan Teknik Sipil : Fakultas Teknik Universitas Jember
[13] Limar, Kinanti Shynde. 2018. Structural Equation Modeling. https://swanstatistics.com/structural-equation-modeling-sem. Diakses pada 13 Mei 2019 pukul 12.33 WIB
[14] Lohansen. 2004. *Tingkat Kepuasan Pelayanan Jasa Angkutan Umum Pada Koperasi Taksi Indonesia di Wilayah DKI Jakarta*. Tesis. Jakarta : Universitas Indonesia
[15] Lynch, K. (1981). *A Theory of Good City Form.* Massachussetts: The MIT Press
[16] Miro, Fidel. 2012. *Pengantar Sistem Transportasi. Jakarta:Penerbit Erlangga*
[17] Nasution, A. 1996. *Menajemen Transportasi*. Jakarta : Ghalia Indonesia
[18] Pembangunan dan Kota, Universitas Diponegoro
[19] Permenhub no. 10 Tahun 2012 tentang Standar Pelayanan Minimal Angkutan Massal.
[20] Permenhub no. 27 Tahun 2015 tentang Perubahan atas Peraturan Permenhub no.10 tahun 2012 tentang pelayanan minimal angkutan massal berbasis jalan
[21] Pradana Putra. Rully. 2012. *Evaluasi Kebijakan Trans Pakuan Kota Bogor*. Skripsi, Fakultas Ilmu Sosial Politik. Universitas Indonesia
[22] Sabari, Yunus Hadi, 2008. *Manajemen Kota Perspektif Spasial*. Yogyakarta: Pustaka Pelajar.
[23] SK Dirjen no. 687 Tahun 2002 tentang Standar Pelayanan Angkutan Umum Perkotaan.
[24] Sugiarto, Endar. 2002. *Psikologi Pelayanan dalam Industri Jasa*. Jakarta: Gramedia
[25] Sugiyono. 2012. *Metode Penelitian Pendidikan Pendekatan Kuantitatif, Kualitatif, dan R&D. Bandung* : Alfa Beta
[26] Supranto. 2006. *Pengukuran Tingkat Kepuasan Pelanggan Untuk Menaikkan Pangsa Pasar* . Jakarta : Rineka Cipta
[27] Tamin, Ofyar Z. 2000. *Perencanaan dan Pemodelan Transportasi. Edisi ke dua*. Bandung: Penerbit Institut Teknologi Bandung.
[28] Ulfa Dewi, Nabilah. 2017. *Efektivitas, Pelayanan Transportasi Publik (Studi Kasus : BRT Mamminasata)*. Skripsi. Fakultas Ilmu Sosial Politik. Universitas Hasanuddin
[29] Undang-Undang No. 22 Tahun 2009 tentang Lalu Lintas dan Angkutan Jalan (LLAJ)
[30] Zeithaml, V.A, Parasuraman, AA, Berry, L.L. 1990. "*Deliverning Service Quality Balancing Customer Perception and Expectation,* New York: The Free Press.
[31] Zuliansyah, Rangga Agung. 2017. BRT Kerap Sepi, Pemkot Tangerang Siapkan e-tiketing**,** http://tangerangnews.com/kota-tangerang/read/19787/BRT-Kerap-Sepi-Pemkot-Tangerang-Siapkan-e-tiketing , diakses 7 Maret 2018 pukul 11.25 WIB
[32] United Cities and Local Governments Asia-Pacific (UCLA). 2019. Tujuan Pembangunan Berkelanjutan yang Harus Diketahui Pemerintah Daerah. https://www.uclg.org/sites/default/files/tujuan-sdgs.pdf diakses 20 Juni 2019 pukul 11:29 WIB
[33] Stichting Partnership on Sustainable, Low Carbon Transport (SLoCaT). 2018. http://www.slocat.net/sdgs-transport

9thInt. Conf. onGeotechnique, Construction Materials andEnvironment,
Tokyo, Japan,20-22 November 2019, ISBN: 978-4-909106025C3051

A MULTI-SPATIAL ASSESSMENT FRAMEWORK TO GEOLOGICAL HAZARD FOR HIGH-RISE BUILDING PROJECT IN METRO MANILA, PHILIPPINES

Michael V. Almeid[1] and Andres Winston C. Oreta[2]
[1,2]De La Salle University, Philippines

ABSTRACT

On Metro Manila Earthquake Impact Reduction Study (MMEIRS) conducted from 2002 to 2004 by Japan International Cooperation Agency (JICA) together with the Philippine Institute for Volcanology and Seismology (PHIVOLCS) and the Metro Manila Development Authority (MMDA), a worst-case scenario with a 7.2 earthquake magnitude in Makati, would have structural impacts on 50% of infrastructures from partial to heavy damage, 18.3% would be heavily damaged, 32.8% would be partially damaged, and major lifelines and utilities that provide electricity, telephones, and water could be cut off. There will be 2,300 casualties, 7,700 injuries, and 156,000 displacements. In this study, we model the earthquake risk of high-rise building projects in Global City, located at the eastern portion of Makati City near Marikina Valley Fault System. To accomplish this, we identified important geological hazard-related factors and distributed survey question to experts to gather estimation of the importance of each factors, and Monte Carlo Analytic Hierarchy Process (MCAHP) was used to determine the consistency of the expert's judgment as well as the relative weights of each factor. These factor weights from the MCAHP are applied to the gathered data, and a Quantum GIS software tool was utilized for visualization, producing a geo-hazard map that is color-coded representing weighted-simulation levels of estimated earthquake hazard risks. Such a GIS weighted overlay analysis map will guide city government councils and other stakeholders to prepare or proactively promote appropriate land-use policy that will minimize threat to life and property each time an extreme natural event such as earthquake occurs.

Keywords: Monte Carlo analytic hierarchy process (MCAHP), Geographic information system (GIS), Geological hazard, High-rise building

INTRODUCTION

In a recent survey conducted by Skyscraper center, within the last decade an average of about seven (7) new high-rise buildings every year is completed making the Philippines top ten among countries around the world with the most number of high-rise buildings 150 meters and taller. Metro Manila provides a salient example almost all new buildings, office towers and particularly residential buildings have more than thirty floors as shown in Fig. 1 Progression of High-Rise Buildings in the Philippines.

Moreover, the rapid progression of high-rise building in high seismic areas in Metro Manila has led the greatest risk associated in its development. Geological hazard threaten safety and health of the City residents and its attractiveness of as the preferred residential and business location in the country. Disaster risks have to be carefully assessed so that measures may be introduced to avert potential danger to life and damage to property. In this study, we model the earthquake risk of high-rise building projects located at Makati City.

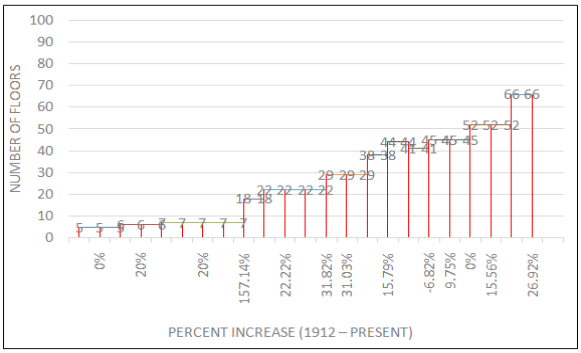

Fig. 1 Progression of High-Rise Buildings in the Philippines. Source: www.skyscraper.com

Makati City is occasionally beset by natural and man-made disasters brought about by geological, meteorological, and technological hazards. The proximity to West Valley Fault System contributes to geologic hazards, notwithstanding the density of high-rise building, infrastructure and technological development in the City.

Makati lies within a tectonically active region in the Philippines known as the Philippine Mobile Belt, and has experienced numerous destructive earthquakes in its recorded history. There are six (6)

known tectonic earthquake generators affecting the area, namely (MGB, 2003 and Daligdig and Besana, 1993): (1) the Valley Fault System, (2) the Philippine Fault Zone, (3) the Lubang Fault, (4) the Casiguran Fault, (5) the Philippine Trench, and the (6) Manila Trench. The nearest active fault within the City is the West Valley Fault.

Based on Metro Manila Earthquake Impact Reduction Study (MMEIRS), a worst-case scenario with a 7.2 earthquake magnitude would have the following impacts in Makati based on 2004 data:

- Structural Impacts: 50% of infrastructures would suffer partial to heavy damage
  - 18.3% (9,200)would be heavily damaged
  - 32.8%(16,500) would be partially damaged
  - Major lifelines and utilities that provide electricity, telephones, and water could be cut off due to seismic activity
- Human Impacts: There will be 0.5% (2,300) casualties, 1.6% (7,700) injuries, and 156,000 displacements.

As shown in Fig. 1, the official trace of the Marikina Valley Fault System can be seen on the eastern portion of Makati City. This fault system cuts across Barangays East Rembo, West Rembo, Comembo, Pembo and Rizal in District II. Earthquakes are part of a natural process and the damage it causes to urbanized areas affects decisions made on where and how to build. Whether these are houses, roads, skyscrapers, malls or any other structure needed for habitation or commerce, the structural system must fit the type of underlying material on which it rests.

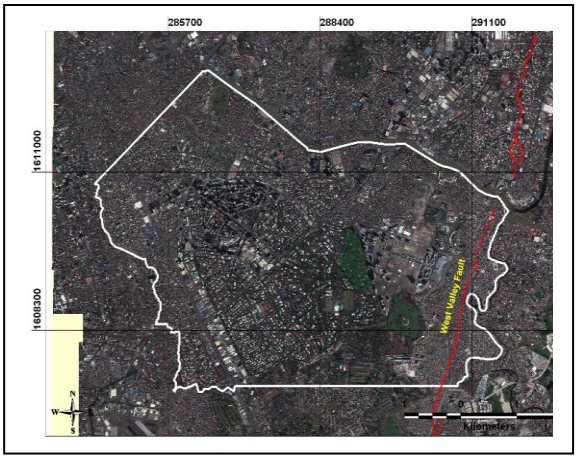

Fig. 1 Trace of the Valley Fault within Makati City. *Source: Philippine Institute of Volcanology and Seismology; Google Earth*

The objective of this study is to determine the importance of the identified earthquake risk factors on a highly urban Central Business District in Metro Manila. Furthermore, this study explores how the Analytic Hierarchy Process (AHP) can be combined with Monte Carlo method and spatial modeling using GIS for vulnerability assessment due to earthquake hazard. AHP is popular as a practical decision making tool applied in different fields. It converge traditional judgments of decision makers to a single numeric preference in order to estimate the pairwise comparisons of all pairs of objectives and decision alternatives while Monte Carlo method is known in testing statistical significance and variation due to uncertainty (Banuelas and Antony, 2004) . This paper proposes the use of both methods to test the statistical significance and variation due to uncertainty of the resultant rankings of earthquake risk factors.

The Analytical Hierarchy Process (AHP) is a decision-aiding method developed by Saaty (Saaty, 2008). It aims at quantifying relative priorities for a given set of alternatives on a ratio scale, based on the judgment of the decision-maker, and stresses the importance of the intuitive judgments of a decision-maker as well as the consistency of the comparison of alternatives in the decision-making process (Saaty, 1980). Since a decision-maker bases judgments on knowledge and experience, then makes decisions accordingly, the AHP approach agrees well with the behavior of a decision-maker. The strength of this approach is that it organizes tangible and intangible factors in a systematic way, and provides a structured yet relatively simple solution to the decision-making problems (Skibniewski and Chao, 1992). In addition, by breaking a problem down in a logical fashion from the large, descending in gradual steps, to the smaller and smaller, one is able to connect, through simple paired comparison judgments, the small to the large (Al-Subhi Al-Harbi, 2001). AHP is MCDM method where the process factors are hierarchically organized. Vertically, objective is on the highest level, with criteria, subcriteria and alternatives on lower levels, respectively, as it is showed on the hierarchical structure on Fig. 2 (Petronijevic et al., 2015).

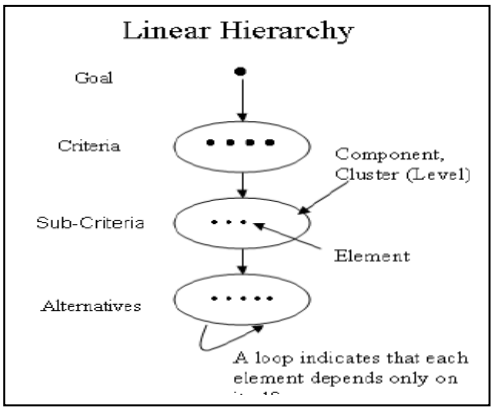

Fig. 2 Hierarchical structure for AHP model

For each level − the criteria, subcriteria and alternatives, elements are compared in pairs. It means that one unfamiliar with the methodology of AHP can compare two elements from the same level according

to verbal description scale. Fundamental scale used to compare the elements consists of verbal judgments ranging from equal to extreme (equal, moderately more, strongly more, very strongly more, extremely more) (Petronijevic et al., 2015). Corresponding to the verbal judgments are the numerical values (1, 3, 5, 7, 9) and intermediate values (2, 6, 8).

Comparison results of n elements belonging to Saaty's scale and AHP hierarchical structure levels are comparison matrices. These matrices ensue vectors priority or $\omega = (\omega 1, \omega 2, \ldots \omega n)^T$, ω is the eigenvector of corresponding matrix. Vector priority involves normalized values which determine importance of the elements – weights of the elements which are compared. This is the method for determination of the priority vector of criteria, the priority vector of alternatives, and as the final result the priority vector of the objective. The priority vector of objective ranks alternatives respect to the importance of the criteria. Judgment consistency ratio (CR) of $CI = (\lambda_{max} - n)/ (n - 1)$, n is the matrix size with the appropriate value in Table 1. If CR is more than 0.10, the judgment matrix is inconsistent (Saaty, 1990).

Table 1 Random consistency index (RI)

n	1	2	3	4	5	6	7	8	9	10
RI	0	0	.58	.90	1.12	1.24	1.32	1.41	1.45	1.49

GIS-multi-criteria evaluation have been used intensively in environmental planning and ecology management. Most analyses within this application area concern land suitability, resources allocation, plan/scenario evaluation, impact assessment and site search/selection problems (Chakhar & Mousseau, 2007). The application of MCDM in general and especially spatial MCDM in the context of geological risk management is still rare. However several methods have previously been employed and developed for vulnerability assessment. Among them, the analytic hierarchy process (AHP) is one of the most commonly used method of assessment (Ying, et al., 2007; Li, et al., 2007), which works on a premise that decision making of complex problems can be handled by structuring the complex problem into a simple and comprehensible hierarchical structure. Li, et al. (2007) utilized the GIS model approach to research the current condition of eco environment quality for typical area of red soil hilly region. Li et al. (2009) established an environmental information system database. Based on the database, an eco-environmental vulnerability assessment method using integrated fuzzy AHP (FAHP) and GIS was developed for the Danjiangkou Reservoir Area. According to eco environmental conditions and entropic effects, vulnerability was classified into five levels: potential, light, medium, heavy and very heavy.

METHODOLOGY

Weighted simulation analysis using MCAHP is applied and integrates with the spatial data in order to describe the causative factors of a phenomenon under concern. The selection of criteria was based on the expert's opinion and availability of data. This overlay was carried out as a Boolean overlay.

In the second phase, Ranking Method was used, where every criterion under consideration was ranked in the order of the decision maker's preference. Each factor was weighted according to the estimated significance. The inverse ranking was applied to these factors. Factor of rank 1 is the least important and 9 is the most important factor. In the third phase, the formula=P($X \leq x$) will be used to draw a random number equal to or greater than 1/9 and not greater than 9 in the Pair-wise Comparison Matrices to test the statistical significance, and variation due to uncertainty of the resultant rankings of each risk factors using Monte Carlo simulation. The simulation of iterations *n* will provide estimates of the probabilities associated with the vector of priorities of the following criteria below:

- Six contributing factors for Earthquake are:

(Q1) Distance from Valley Fault –Areas within 5-meter buffer zone are exposed to ground rupture

(Q2) Alluvial and Rock Material Deposits – Areas with this type of material underneath produces deterministic Possible Ground Acceleration or shaking.

(Q3) Loose sand and Shallow Ground Water Table – Areas with this type of subsurface soil are prone to liquefaction.

(Q4) Very Steep and Unprotected Slopes – Areas of rock slides from towering walls of adobe are susceptible to landslide.

(Q5) Infrastructure Density- Above and underground utilities particularly electrical line and gas pipes may cause fire outbreak.

(Q6) Distance from Sea Coast – Proximity to source of tsunami.

For the Mapping and Table inputs, the CBD barangay maps were then subdivided into equidistant square grids for distance reference using a customized Python Application Programming Interface (API) on Google Maps. Vertical elevation intersections and horizontal boundaries were identified and marked for analytical measurement. For the AHP Expert Judgment portion, a survey Questionnaire was distributed. The data for AHP was gathered, analyzed and tabulated to calculate the weight of each disaster criteria.

RESULTS AND DISCUSSION

Pair-wise comparison matrix is created by assigning weights by experts. The weights are further

evaluated in finding alternatives and estimating associated absolute numbers from 1 to 9 in fundamental scales of the AHP. These weights can be computed automatically in Microsoft Excel. Hence, the results of the relative weights of Q1 = Distance from Valley Fault , Q2 = Alluvial and Rock Material Deposits , Q3 = Loose sand and Shallow Ground Water Table, Q4 = Very Steep and Unprotected Slopes , Q5 = Infrastructure Density and Q6 = Distance from Sea Coast.

The MCAHP computation results reveal that the Very Steep and Unprotected Slopes (Q4) at 31.00% is assessed by experts to be the largest contributing factor for earthquake hazard, followed by (Q2) Alluvial and Rock Material Deposits at 19.00%, (Q3) Loose sand and Shallow Ground Water Table at 16.00%, (Q6) Distance from Sea Coast at 15.00%, (Q1) Distance from Valley Fault at 11.00% and (Q5) Infrastructure Density at 9.00%. The consistency as measured in the in pair-wise comparisons of *C.R.* = 0.014 (value < 0.10) indicates that the basis expert judgment is reasonably consistent.

For the simulated weights, (Q4) Very Steep and Unprotected Slopes at 31.00% to be the largest contributing factor for earthquake hazard as shown in Table 2.

Table 2. Simulated priority weights for earthquake related factors

	Q1	Q2	Q3	Q4	Q5	Q6	Wt	C.R
Q1	1	0.6	0.6	0.3	1.1	0.9	.11	1.4%
Q2	1.7	1	1.8	0.6	1.6	1.0	.19	
Q3	1.7	0.6	1	0.5	2.3	1.1	.16	
Q4	2.9	1.7	2.2	1	3.4	1.8	.31	
Q5	0.9	0.6	0.4	0.3	1	0.7	.09	
Q6	1.1	1.0	0.9	0.6	1.4	1	.15	

Finally, a Geo-hazard map was generated from the integration of criteria weights from MCAHP with the criteria maps into the GIS software. The map presents a rank of highest and lowest suitability areas. The geo-hazard classification is divided into three classes: Low Risk, Moderate Risk and High Risk (see Fig. 3, 4 and 5).

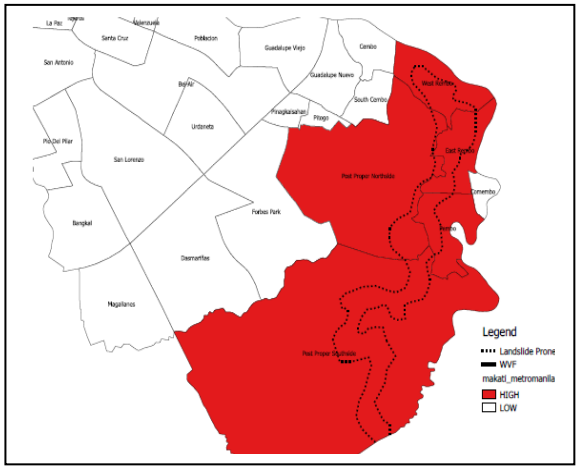

Fig. 3 Makati city urban CBD Earthquake-hazard map (Landslide prone areas) using AHP weighted overlay analysis on existing quantum GIS for earthquake

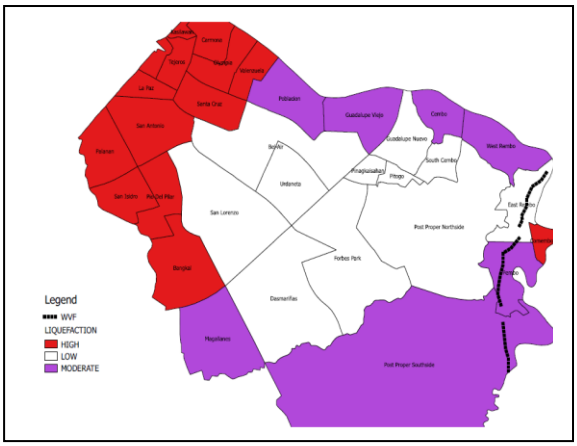

Fig. 4. Makati city urban CBD Earthquake-hazard map (Liquefaction prone areas) using AHP weighted overlay analysis on existing quantum GIS for earthquake.

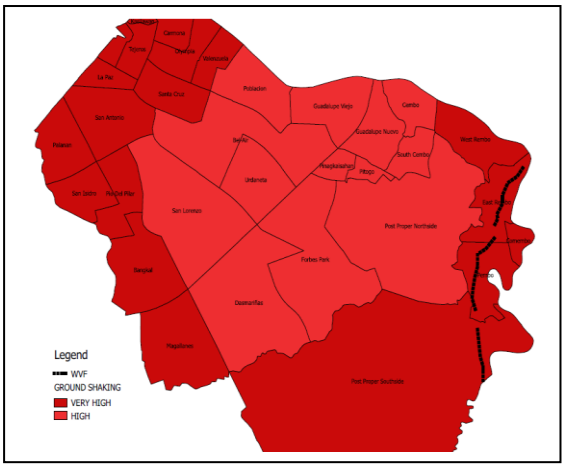

Fig. 5. Makati city urban CBD Earthquake-hazard map (Ground Shaking prone areas) using AHP weighted overlay analysis on existing quantum GIS for earthquake.

CONCLUSIONS

In this study, MCAHP is combined with GIS to come up with a tool for evaluating geological hazards in the CBD areas in Makati City. Such tool was developed after gathering topological information about the city and also reliable (C.R.< 0.10) expert criteria assessment for each earthquake related risk factors, and then applying multi-criteria analysis techniques based on AHP to an open source Quantum GIS software.

The developed tool will be a very valuable resource for consulting, planning agencies and local governments managing risk, land-use zoning, damage estimates, land tax valuation, life and property insurance claim validation, good governance, lifeline emergency services and remediation efforts to mitigate risks. Moreover, the technique applied in this study can easily be extended to other areas, where other factors may be considered, depending on the availability of data.

Provision of more community open spaces as staging areas during disasters and the control of development in identified risk areas are some of the needed land use interventions. Highly-congested, sub-standard housing near the West Valley Fault Zone need some re-blocking to clear the 5-meter easements on both sides of the fault line. Re-blocking will allow for more efficient development of medium rise housing facilities and the conversion of fault zone easements into linear parks. The West Valley Fault Zone traverses the congested barangays in the Eastside Cluster (i.e., Barangays Pembo, Comembo, Rizal, East Rembo) including West Rembo and Post Proper Southside. Barangay Rizal has been identified as the most vulnerable barangay, the presence of the West Valley Fault Zone and its impact such ground rapture, ground shaking, liquefaction and land-slide.

ACKNOWLEDGMENTS

The main author would like to thank Dr. Andres Winston Oreta for his support, guidance and motivation to complete this paper. Also

REFERENCES

[1] Al-Subhi Al-Harbi, K.M., Application of AHP in project Management. International Journal of Project Management 19 (2001) 19-27.

[2] Banuelas, R., & Anthony, J. (2004).Modified analytic hierarchy process to incorporate uncertainty and managerial aspects.International Journal of Production Research, 42(18), 3851-3872.

[3] Daligdig, J., & Besana, G. (1993). Seismological hazards in Metro Manila, in Disaster Prevention and Mitigation in Metropolitan Manila, Quezon City, Philippines. Department of Science and Technology and Philippine Institute of Volcanology and Seismology. (pp.9-42).

[4] Earthquake Impact Reduction Study for Metropolitan Manila, Republic of the Philippines, Final Report Volume 1, March 2004.

[5] Li, L., Shi, Z.-H., Yin, W., Zhu, D., Ng, S. L., Cai, C.-F., et al. (2009). A fuzzy analytic hierarchy process (FAHP) approach to eco-environmental vulnerability assessment for the danjiangkou reservoir area, China.

[6] Li, Z. W., Zeng, G. M., Zhang, H., Yang, B., & Jiao, S. (2007). The integrated eco-environment assessment of the red soil hilly region based on GIS--A case study in Changsha City, China.

[7] Petronijevic, M., Nikolic, A., Mikic, M., Ivanisevic, N. (2015 September). AHP Based Contractor Selection Procedure for Highway Infrastructure Projects in Serbia. Croatian Association for Construction Management. pp. 206-214.

[8] Saaty, T.L. (2008). Decision making with the analytic hierarchy process. Int. J. Services, Vol.1, No.1, pp.83-98.

[9] Skibniewski, M. and Chao, L. " Evaluation of Advanced Construction Technology with AHP Method." Journal of Construction Engineering and Management 118(3); (1992), 557-593.

[10] Satty, T.L., "The Analytic Hierarchy Process", McGrawHill, New York, 1980.

[11] Thomas L. Saaty. How to make a decision: The Analytic Hierarchy Process. European Journal of Operational Research 48;(1990) 9-26.

[12] Ying, X., Zeng, G. M., Chen, G. Q., Tang, L., Wang, K. L., & Huang, D. Y. (2007). Combining AHP with GIS in synthetic evaluation of eco-environment quality.

[13] www.makati.gov.ph;

[14] www.mgb.gov.ph

9th Int. Conf. on Geotechnique, Construction Materials and Environment, Tokyo, Japan, 20-22 November 2019, ISBN: 978-4-909106025 C3051

EXTREME HAZE DURING NON-DROUGHT (ENSO) YEARS: ASSESSMENT ON AEROSOLS CHARACTERIZATION OVER PENINSULAR MALAYSIA IN JUNE 2013

Nur Atiqah Aainaa Abd Latiff[1], and Takashi Machimura[2]
[1,2] Division of Sustainable Energy and Environmental Engineering,
Graduate school of Engineering, Osaka University, Japan

ABSTRACT

Population and economic growth over the Southeast Asia region had triggered to the increasing of pollutant that been released by automotive emission, industrial activity or biomass burning. The occurrence of intense haze episodes become severe in every year degrading the surrounding air quality and reduce visibility which may cause economic loses. However, detailed study on the aerosols concentration, source and its properties remain a challenge due to the limitation of in-situ data. Therefore, this study aimed to analyze the aerosols properties over Southern Peninsular Malaysia by utilizing the satellite and ground based remote sensing. Thus, by emphasizing on 2013 intense haze episode, PM10 concentration combine with aerosols from Aerosol Robotic Network (AERONET) data and some environmental parameters, i.e. rainfall, visibility, and hotspot numbers were investigated. Southern Peninsular Malaysia experience a dry and dense condition in June 2013 with highest temperature with less rainfall were recorded. The aerosols concentration and properties through aerosol optical depth (AOD), Angstrom Exponent (AE) parameter and particle size distribution indicate the presence of fine aerosols during the June 2013 haze episode, which is associates with biomass burning aerosols. Meanwhile, the MODIS fire activity data represents more than 3000 hotspots were recorded over Sumatera region. HYSPLIT modeling shows the pollutant substance from biomass burning activity were transported to the study area on 21st of June 2013 from southwest area which mainly from the Sumatera area.

Keywords: Aerosols, Biomass burning, Air quality, ENSO, Malaysia

INTRODUCTION

Anthropogenic pollution from aerosols and trace gases emission contributing a huge impact towards the air quality not only regional basis but also to the global scales [1], [2]. Moreover, a depth knowledge regarding the aerosols characteristic and properties are important to understand more on its impact on the surrounding environment. The aerosols particle concentration, size distribution and pollutant source may differ in temporal and spatial aspect. Generally, the South East Asia had experienced numerous intense polluted condition which due to several factor such as aerosols emission from industries, transportation and burning activities including land clearing for agriculture, open burning, and fossil fuel [3]. This factors inducing the transboundary pollution to occur and affecting the surrounding area. Nevertheless in Malaysia, intense haze episodes that occurs almost every year especially during southwest monsoon season (that prevail from May to September annually) which usually caused by: emission from automotive and industrial area and transboundary pollution (due to biomass burning) [3], [4]. Previous studies on air quality in Peninsular Malaysia shows that intense aerosols loading were taken place mostly in west Peninsular Malaysia which consist of high urbanized areas [3], [4], [5], [6]. In addition, the increasing number of vehicles which causing heavy traffic in the urban area and rapid development industrialization were led to severe pollution especially near the Klang Valley [3], [7]. However, these studies were largely focusing specifically on the urban area with data obtained during field campaigns over specific region. Furthermore, most of the studies previously analyzing on the spatio and temporal characteristic of the aerosols loading which neglecting on the aerosols properties and the pollutant sources. Therefore, a comprehensive study on the aerosol properties and its impacts need to be addressed in order to provide more understanding on atmospheric pollution.

In addition, the Malaysian haze episodes is also associated with the occurrence of inter-annual climatic changes that affecting the dry and wet season in Malaysia. These variations were associated with the El-Nino / Southern Oscillation (ENSO) and the Indian Ocean Dipole (IOD) event which prevail for a longer period [8], [9]. As been recorded in the previous study by [10], intense haze episode in 1997 and 2006 was not only caused by the forest fire and burning activities but also coincided with the El-Nino occurrence which prolonged the dry season in that year. The dry spell condition had induced the fire to start especially at the peatland area which worsened the air quality in Malaysia and neighboring region [9]. However, in June 2013, a non-ENSO year, an intense haze episodes occurred which affecting the

atmosphere in the southern part of Peninsular Malaysia. These intense haze event had caused negative impacts not only to the human's health but also to the tourism, transportation and economic activity to Malaysia and surrounding country [7], [11]. Based on news reported by the British Broadcasting Corporation (BBC), many schools and universities in Johor and Singapore were closed and flight delays due to low visibility during June 2013 [12]. Therefore, these intense haze on non-ENSO year encouraged us to identify the cause and source of the pollution in greater detail.

In addition, less documentation on the aerosols variation and its particle properties were done in Malaysia which may due to the limitation of data availability. In previous studies, the ground-based measurement or in-situ data were used which will provide point data with high accuracy in certain time period, but they have limited spatial coverage [13]. However, in recent years, both satellite and ground-based remote sensing have provided the ability to retrieve aerosol properties over large areas continuously. There are few satellite remote sensing available to provide useful data for aerosol studies such as, MODIS (TERRA and AQUA sensor), Sea-Viewing Wide Field-of-View Sensor (SeaWiFS), and Cloud-Aerosol Lidar and Infrared Pathfinder Satellite Observation (CALIPSO) which helps to provide long-term aerosol information with well-calibrated techniques and cloud screening, together with reliable accuracy (i.e. ±0.05 AOD under clear skies and ±0.15 AOD under moderately contaminated atmosphere) over land [13]. Besides that, the existence of Aerosol Robotic Network (AERONET) that introduced by NASA provides the ground based continuous cloud-screened observations of spectral aerosol optical depth (AOD), clouds, and others aerosol information.

Therefore, in this study we utilized the satellite and ground-based measurement for aerosol products, meteorological data and active fire/hotpots information to analyze the aerosols properties and characteristic by emphasizing on 2013 intense haze episode. Air quality data which been acquired from Malaysian Department of Environment (MDOE) and HYSPLIT trajectory model were used to identify the probable aerosols source and its impact towards the Southern Peninsular Malaysia atmosphere during the study period.

MATERIALS AND METHODS

Study Area and Dataset

Malaysia is located at the Southeast Asia which consist of 14 states which separated by the South China Sea into two regions; Peninsular Malaysia and East Malaysia (Sabah and Sarawak). Peninsular Malaysia also called as West Malaysia is a part of Malaysia which lies on the Asia continent and shares the land border with Thailand in the north and with Singapore at the southern part of Peninsular Malaysia. Fast growing economic development in industrial activities and increasing in population had expose this area with numerous atmospheric pollution in recent years. Numerous haze episodes had been recorded since 1980's and become severe in this last 10 years which caused by the transportation emission, land clearing for agriculture and trans boundary smokes from neighboring country [14]. In 2013, peninsular Malaysia had experienced intense haze episodes with the Southern Peninsular Malaysia (Johor, Melacca and Selangor) were adversely affected and the air quality deteriorated to unhealthy level. Hence, this hazardous situation in the Southern Peninsular Malaysia was lead to poor visibility, serious health problem towards the community and disrupt the economic growth.

In order to examine the aerosol variations in Southern Peninsular Malaysia during 2013, four air quality monitoring station located at Johore Baharu, Malacca, Sultan Abd Aziz International Airport (here after SAAIA) and Setiawan were used with the PM10 concentration as the indicator parameter for the aerosols (as shown in Figure 1). Meanwhile, the metrological parameters such as rainfall amount, temperature, wind speed, and visibility were gathered from NOAA's National Climatic Data Center (NCDC). Daily mean composites of wind vector were computed over the Southeast Asia region. In this region, it strategically depicts the tropospheric flow patterns where; it covers Malaysia and other neighboring countries. The maps were constructed from NCEP/NCAR Reanalysis Product developed by NOAA-ESRL9.

Characterization of aerosol properties has been done using the atmospheric radiation data taken from the AERONET station in Singapore as it the nearest AERONET station to the Southern Peninsular Malaysia. AERONET is a ground-based remote sensing instrument that provided by National Aeronautics and Space Administration (NASA). Furthermore, it provides long term, authentic and continuous data for aerosol research that can also be used to validate the satellite retrievals of aerosol properties and comparison with other databases for climate studies. The AERONET Singapore station (1.30° N, 103.77° E) that were used in this study is located at the southern part of the Peninsular Malaysia where it is the nearest AERONET station to our study area. Also, this site is an ideal for monitoring regional pollution events such as transboundary biomass burning emissions, clouds, local anthropogenic emissions and climate variability [15].

In order to understand more about the aerosols properties for this study, we use the daily average Aerosol Optical Depth (AOD) at 500 nm since this specific wavelength represents the visible spectrum,

which is the most relevant to the aerosol measurement during day time [16]. Besides AOD, Ångstrom exponent (AE) and aerosol particle size distribution are also assessed. In order to complement the quantitative assessment, HYSPLIT trajectory model has been applied for Southern Peninsular Malaysia during the entire haze period.

Further analysis on the source of pollution that occurred in 2013 were done with additional data of the active fire and hotspots which was obtained from the Moderate Resolution Imaging Spectroradiometer (MODIS) from the TERRA and AQUA satellite. This MODIS Active Fire Data acquired from the NASA/LANCE – FIRMS website to monitor the distribution of hotspots within the Sumatera area. Only hotspot counts with confidence level higher than 30% were included in this study.

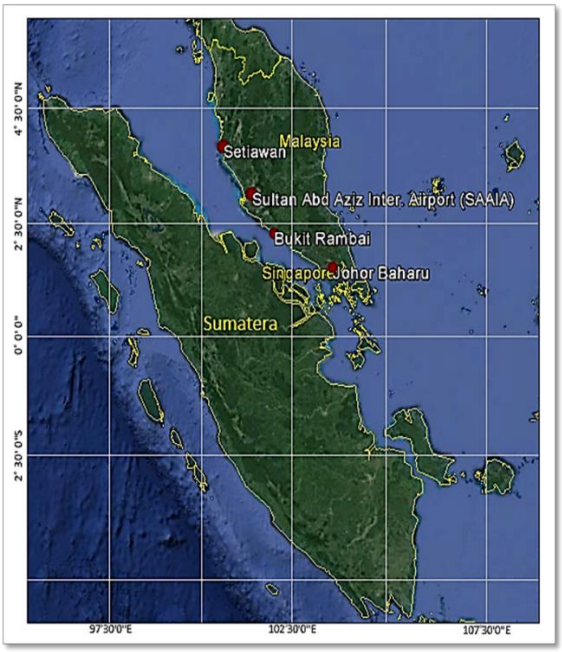

Fig.1 Monitoring stations at the Southern Peninsular Malaysia (Setiawan, Sultan Abdul Aziz International Airport, Bukit Rambai (Malacca) and Johore Baharu)

Methodology

In order to study on the air quality variation during the intense haze during 2013 in Southern Peninsular Malaysia, a quantitative analysis were done for the daily average PM10 concentration and meteorological data (rainfall amount, temperature and wind speed). Then, we identified the period that reached the peak of PM10 concentration and analyzed its relationship with the metrological parameter. Then, the AERONET data (which focusing on AOD, AE, and aerosol particle size distribution) were analyzed to justify the aerosols physical properties. Subsequently, the pollutant source and air masses transportation were tracked by using 5-days trajectories from NOAA HYSPLIT model. Additionally, MODIS Active Fire Data and hotspot count were used as the supporting information for the results acquired from those analysis. Analyzes on the social and economic impact of fire have been done by collecting data and information through secondary data gathered from literature reviews and legal documents.

RESULTS AND DISCUSSION

In general, during the normal conditions, these four stations experiencing the same fluctuation of PM10 concentration level on weekend and weekdays, as shown in Figure 2. These figures represent the weekly variation of PM10 concentration at Setiawan, SAAIA, Malacca and Johor Baharu stations based on daily data recorded from 2000 to 2013. The PM10 concentration were recorded high on weekdays (>40-60 μg m^{-3}), where the concentration level were increased from Monday on to the next day and remain high until Friday. Then, the concentration relatively decreased (<40 μg m^{-3}) during Saturday and Sunday. This was believed to be happened due to automobile emission that occur during weekdays compared to weekend. This situation also had been proved by [3] in previous study which stated that PM10 concentration level keep increasing due to the automobile and industry emissions which classified as anthropogenic causes during normal condition (without haze episodes). The increasing number of car on the road is a major contributor to high PM10 level at these four stations.

However, the PM10 concentration level may vary due to natural annual monsoon changes or inter-annual changes [17]. Trough out the year, Malaysia experiencing dry and wet monsoon season which associate with meteorological factors variation (such as rain rate, wind speed and direction and surface temperature) that causing the fluctuation of PM10 level.

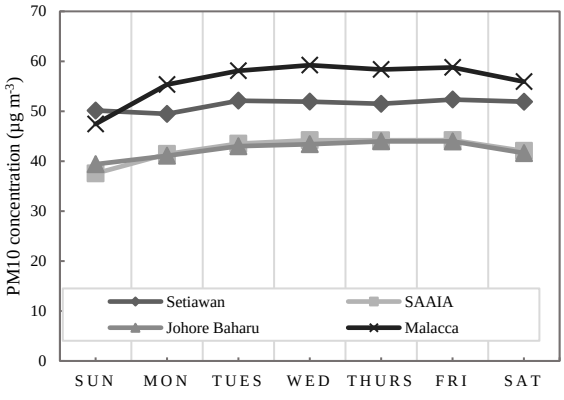

Fig.2 Weekly variation of PM10 concentration at Setiawan, SAAIA, Malacca and Johor Baharu

stations based on daily data recorded from 2000 to 2013

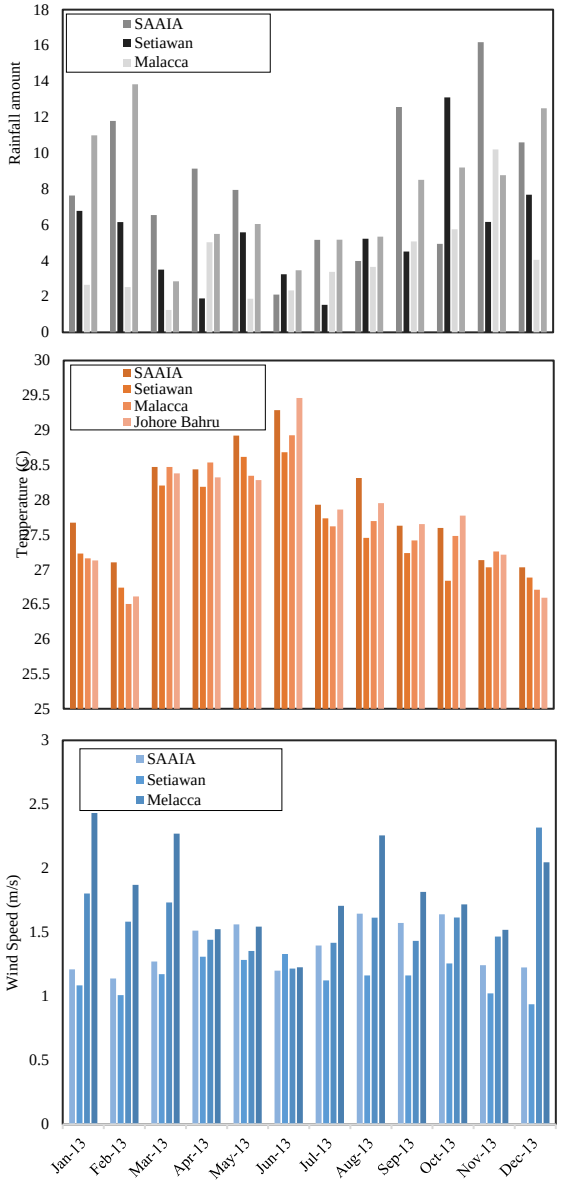

Fig.3 Monthly variation of meteorological parameter which includes (a) rainfall amount, (b) temperature, and (c) wind speed over four stations in Southern Peninsular Malaysia for 2013

Figure 3 presents the monthly meteorological variation which include rainfall amount, wind speed and temperature during 2013 over four stations at the southern part of Peninsular Malaysia. Based on the monthly rainfall amount in Figure 3(a), in the month of June, the rainfall amount for all four stations were recorded low, with the lowest rainfall was at SAAIA station and followed by Malacca, Setiawan and Johore Bahru. This dry condition is also associated high temperature which was observed to be increased in June 2013 as compared to the previous months. Based on Figure 3(b), the highest temperature was recorded at Johore Bahru station (29.46℃) and followed by SAAIA, Malacca, and Setiawan (29.30, 28.92, and 28.68℃). In Figure 3(c) the wind speed variation were started to decrease from April until June, with the lowest wind speed was recorded on June 2013. All four station in Southern Peninsular Malaysia were experienced low wind speed with the average value (less than 1.5 m/s) in June 2013.

These results can be relate with the southwest monsoon season where Malaysia normally experiencing high temperature and low southwesterly wind. These climatic changes are a huge impact toward the aerosols variation and its dispersion. In normal condition, the PM10 concentration tends to be minimal during the northeast monsoon (rainy season) where Malaysia experiences northeasterly winds. While, the PM10 concentration will increase during southwest monsoon, where the region experiences dry season with less rainfall and low level of wind speed (southwesterly winds).

Besides focusing on the seasonal variation of PM10 concentration, inter-annual changes such as ENSO modulations may also amplify the impact of aerosols concentration in Malaysia. In previous studies of intense haze in Southeast Asia, high polluted atmosphere from 1997 until 2007 had associated with dry and low rainfall condition which induced by the ENSO phenomena [18, [19], [20]. During the strongest 1997-1998 ENSO, an intense haze episode were recorded with the PM10 level concentration reached more than 200mg/m3 and been classified in hazardous air condition across the Southeast Asia [20]. In the other hand, 2013 was a year without ENSO yet the Southern Peninsular Malaysia experienced short-term intense haze during June, with increasing level of PM10 concentration and remaining high from 15th to 23rd of June 2013 (MDOE report 2013). By referring to Figure 4, the PM10 concentration level with normal reading (<100 µg/m^3) were recorded in May 2013 and fluctuated until mid-June 2013, where the PM10 concentration trends for all four stations were start to increase until 24th of June 2013. Then, the highest PM_{10} was recorded in the Malacca Station from 21st until 23rd of June (PM_{10} concentration more than 400 µg/m^3). PM_{10} concentration were also recorded high in the other three stations over Southern Peninsular Malaysia which are; Johore Bahru, SAAIA and Setiawan.

Optical and physical properties of aerosols during June 2013 haze episode

In order to explore on the aerosols microphysical and optical properties during haze episode in June 2013 AERONET data from Singapore station were used in this study. Figure 5 shows the daily variation of AOD at 500nm at the AERONET (Singapore Station) during 1st of June until 30th of June 2013. The highest

level of AOD were recorded on 21st of June 2013 with 3.61, and followed by 20th and 22nd June 2013 with the AOD values are 3.16 and 3.01, which indicating the intense level of air pollution happened in this region. The variability in box (b) (Figure 5) representing the normal condition (1st until 2nd of June 2013), which defined as clear condition with the AOD value (< 1.0). Meanwhile, the highest aerosols loading period starting 20th until 23rd of June 2013 recorded over 6 times higher than the AOD value observed on normal day. The increasing of AOD level during 21st of June 2013 significantly shows the presence of large source pollutants to this area.

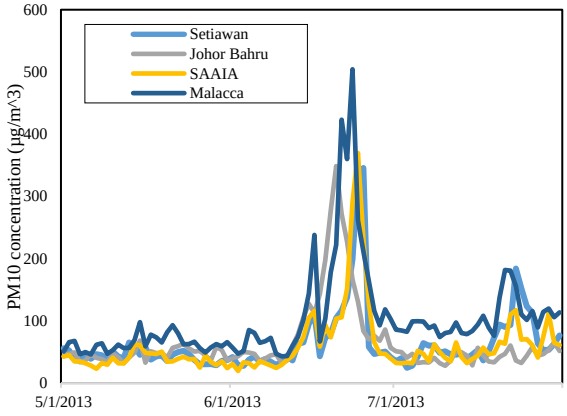

Fig.4 Comparison between daily PM10 concentrations from 1st of May until 31st of July 2013 at the four stations at Southern Peninsular Malaysia.

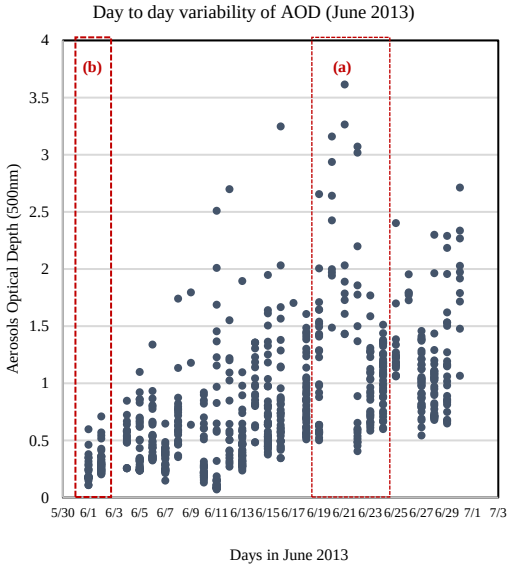

Fig. 5 Daily variability of AERONET derived AOD during haze June 2013.

Aerosol particle's size distribution is one of the parameter that normally being used to distinguish the aerosols particle type [21], [22]. Furthermore, the volume size distribution of aerosols at a certain location is affected by the mixture of different aerosol types. Thus, by referring to this parameter, it is not only provides information on particle size composition, but also describing the pollutant source, its dispersion mechanism, impact on climate system and visibility. In addition, the volume size distribution is characterized by the sum of two lognormal distributions. For each mode, it can be given as follows:

$$dV/d\ \ln\ r = \left(\frac{C_v}{\sigma\sqrt{2\pi}}\right)\exp\left[-\frac{1}{2}\left(\frac{\ln\left(\frac{r}{rv}\right)^2}{\sigma}\right)\right] \qquad (1)$$

Where; $C_v$the columnar concentration of aerosol particles is, σ is the standard deviation, while r refer to the particle radius and rv is the volume mean radius. These algorithm was formulated by [21], which widely being used to derive particle size distributions.

Figure 6 illustrates the available AERONET retrieved aerosols size distribution during June 2013. A bimodal lognormal distribution is observed with fine mode aerosols having radii < 0.7 µm and coarse mode aerosols with radii > 0.7 µm as shown in Figure 6. The occurrence of these two modes of volume size distribution was caused by few reasons. For instance, combination of different air masses with diverse aerosol types [23], homogenous nucleation of heteromolecules into fine mode aerosols or mixed nucleation [24]. It is clearly shown in the Figure 6 that volume concentration for fine mode was increased on 19th until 28th of June 2013 as compared to rest of the days. The fine mode peak value was found within the radius of ~0.26 to 0.33 µm and coarse mode peak value within ~3.86 to 6.64 µm.

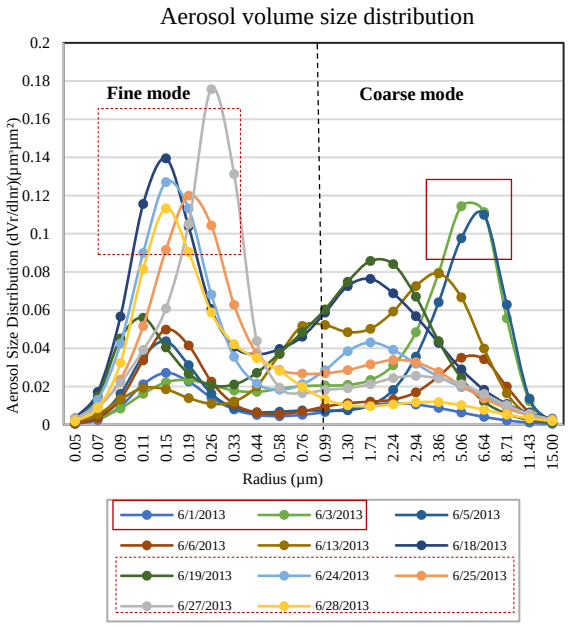

Fig.6 Aerosols size distribution during June 2013 at AERONET Singapore station which describing the size of the pollutant during the intense haze.

The microphysical properties of aerosol are highly relate on their sources. Various techniques have been used to classify aerosol types, and one of the way to do it is with correlation analysis based on Aerosol Optical Depth (AOD) and Angstrom Exponent (AE)(440-870 nm) [25], [26], [27]. These techniques use different threshold to differentiate the types of aerosols. Additionally, the AOD normally represents the level of pollutant during the hazy condition and AE parameter is known as the first derivative (negative slopes) of AOD at specific wavelength which also define the size of aerosol particles. Hence, these two combination of parameter would contribute to a better interpretation of aerosols source classification [15], [16], [28].

The Figure 7 represent the correlation between available AOD (500 nm) and AE (440-870 nm) which been used to classify the dominant aerosol types over study area. This scatterplot shows that there are three different classes presents in this area which been marked as biomass burning, dust or sea salt, and urban or industrial. The AE with value of less than 1 (< 1) indicates that the size of the aerosol is dominated by coarse particles (radius > 2.5 μm) from dust and sea salt, whereas the AE value of more than 1 (> 1) represent the presence of fine aerosol (radius < 2.5 μm) which associated with urban pollution and biomass burning emissions [15], [16], [28]. Aerosol from urban and industrial areas has a higher value of AE with AOD variation based on the level of pollution (concentration of aerosols) in the atmosphere as a result of urban activity. On the other hand, AOD from biomass burning can reach up to 6 in heavy smoke coming from peatland fire [29].

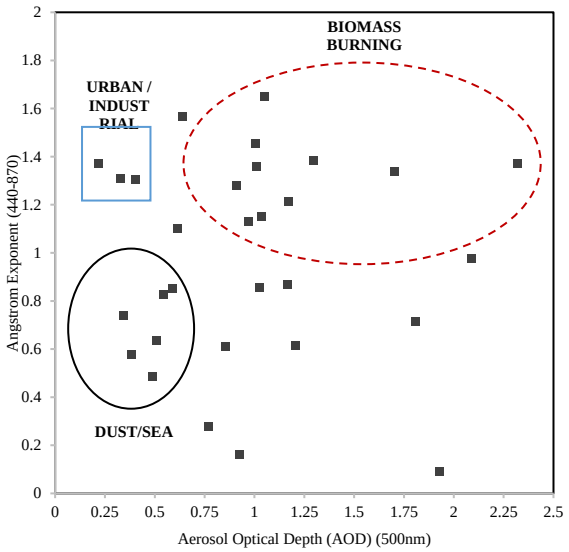

Fig. 7. Scatter plot between Angstrom Exponent (AE) and aerosol optical depth AOD at 500nm over AERONET Singapore station with the classes of different aerosols type.

Higher AOD in the range of 0.8 to 1.3 and AE varies from 1.3 to 1.7 (showed by the dashed line circle) indicates the domination of fine particles during a biomass burning event. Furthermore, this condition occurred when Singapore station experienced air quality degradation as a result of haze based on the AOD level recorded. While, the solid line circle on Figure 7 indicated the existence of coarse aerosol particles with lower AOD variations from 0.25–0.75 and AE values lower than 1.0. This type of aerosol may originate from dust and sea-salt considering this region near to Melacca Strait. Studies by [28] and [30] showed similar result which found dust contamination and sea-salt in Singapore and Kuching (Malaysia) under normal condition.

In order to investigate the possible source locations of pollutant and to examine the dispersion pathways of the air masses before reaching the AERONET station in Singapore, 5 days backward trajectories from NOAA HYSPLIT model was used. As shown in Figure 8, the 5days backward trajectories from HYSPLIT model shows that the polluted substance were transported to the study area from the southwest region and across Sumatera region at lower altitudes.

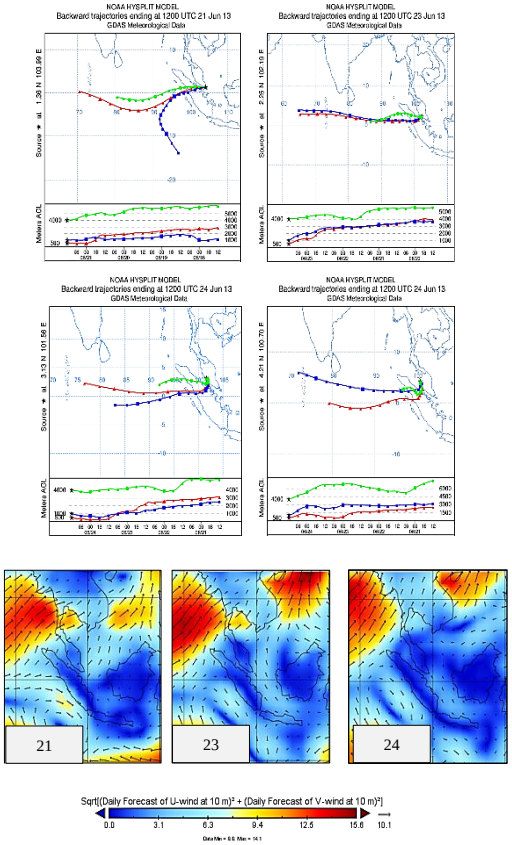

Fig.8. Backward trajectories from NOAA HYSPLIT model for the study area during the highest aerosols loading day (21st – 24th of June 2013) with additional information of the wind speed and direction.

This condition can best be relate with the influenced of Southwest Monsoon that normally occur from June to September which transporting the pollutant particles from biomass burning that originate from the neighboring country to the Peninsular Malaysia and Singapore. It clearly shown in Figure 8, the lower altitude trajectories (500m) were originated from the Sumatera region which may become the high contributors for the intense haze or smokes cover to the Southern Peninsular Malaysia and Singapore atmosphere within 24 hours.

Hence, the wind direction map shows low surface wind over study region on 21st, 22nd and 24th of June 2013. Generally, the southwest monsoon season flow was strengthened by a south to north pressure gradient, with northern hemisphere having a lower surface pressure than southern hemisphere. The pressure gradient is a consequence of the temperature contrast between the northern and southern hemisphere due to seasonal variations. Moreover, the aerosols concentration at Southern Peninsular Malaysia was largely dependent on these direction of the prevailing wind pattern. In which, the southern to southwesterly winds were transporting the pollutant substance towards Southern Peninsular Malaysia and Singapore.

Impact of the biomass burning during June 2013 haze episodes towards the Southern Peninsular Malaysia atmosphere

As been discussed in the previous section, Southern Peninsular Malaysia experiencing a short-period intense haze in June 2013 which dominated with fine particle distributed that were characterized due to biomass burning event that occurred during that period. Once again the PM10 concentration data sets from MDOE over Southern Peninsular Malaysia were plotted together with hotspot count over the Sumatera Island. Figure 9 illustrates the monthly mean fire active data from MODIS Terra and Aqua Satellite over Sumatera, the Fire radiative power (FRP) which defines the rate of electromagnetic energy released by fire was recorded high on June 2013 (with the highest peak of FRP = 484GW) [31]. Daily fire hotspots from MODIS Terra and Aqua satellite shows some high peak had been recorded in Sumatera area during 19th until 25th June 2013. In addition, this peaks correlated with the high PM10 level in Southern Peninsular Malaysia as illustrated in the Figure 9 (b). Respectively, a prominent peak on 19th of June 2013 with more than 3000 hotspot were found over Sumatera, Indonesia which may attributed to the existence of active fire activity that occurred in the Riau Province which had been reported previously. Therefore, biomass burning in surrounding area had indicate on the increasing of PM_{10} concentration in Peninsular Malaysia during June 2013.

These condition can be attributed from the meteorological results in Figure 3, which high temperature and low rainfall during June 2013 had creates a dry condition which may inducing soil moisture loss and led to wild and forest fire occurrences at surrounding region. Meanwhile, low wind speed which inducing less mixing depth promotes a 'stuffy condition' at the Southern Peninsular Malaysia atmosphere which trapped the smokes particle and slow dispersion may happen.

Even though the hotspot count shows some decreasing from 20th of June but it is still considered as higher than the normal days with more than 1500 fire hotspot were detected over Sumatera which related with high PM10 concentration level in all four monitoring station. This condition was caused due to the effect of peatland burning, which it occurs with smoldering combustion and underground fire [32]. Thus, although there is less fire activity or fire hotspots were detected, the emission is still continuously released to the surrounding atmosphere [33]. These results were supported with previous studies that proved the short period haze episodes of 2013 due to peatland burning activities for domestic agriculture and plantation purposes in several provinces in Sumatera [34]. Even tough 2013 was not listed as ENSO year, a similar dry condition as ENSO occurred due to deforestation and land clearing activities that rapidly happen in the Sumatera region [35]. Indirectly, these may increases local temperature, reduced precipitation process and more soil moisture loss; this heightens climatic variability will intensifies drought and influences regional climate [35], [36].

CONCLUSIONS

In this study an effort has been made to analyze the aerosol optical and physical properties during intense haze event in June 2013 over Southern Peninsular Malaysia. Based on the results in Figure 3, the highest AOD value (3.61) was observed on 21st of June 2013 which associated with the intense episode of air pollution that occurred due to large scale crop residue burning in Sumatera region. Plus, the highest peak of daily mean AOD value was six times higher than the AOD value (0.6) observed on clear and normal day. The fine mode volume concentration was found to be more than 1.5 times greater than the coarse mode volume concentration on the high aerosol burden day. While, the scatter-plot between AOD (500 nm) and Angstrom exponent (440-870 nm) showed that biomass burning aerosols were the

dominant aerosol type on the heavy aerosol loading day - 21st to 24th June 2013. NOAA HYSPLIT model of 5 day backward trajectories at different heights were drawn in order to track the pollutant source which been transported to the AERONET station. Figure 7 shows that the polluted substance were transported to the Southern Peninsular Malaysia on 21st of June 2013 were mainly from southwest area and across Sumatera within 24 hours.

In summary, the intense haze episodes in June 2013 was identically characterized by the dominance of fine-sized aerosol that represent as biomass burning pollutant. Besides, MODIS fire activity and hotspot counts over Sumatera region suggested that the existence of transboundary pollution in Southern Peninsular Malaysia and Singapore were caused by biomass burning activities over few province in Sumatera with over 3000 hotspots were detected on 19th of June 2013.

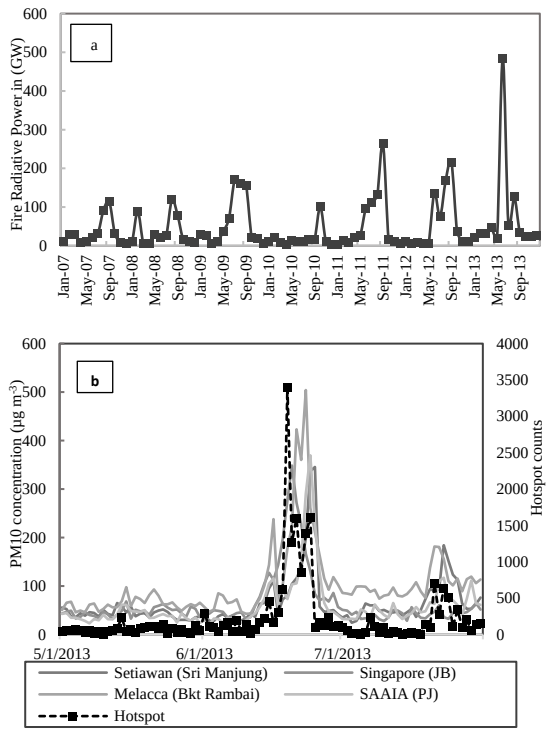

Fig. 9 a) The monthly mean fire active data from MODIS Terra and Aqua Satellite over Sumatera (Jan 2007 until December 2013); and b) Comparison between daily PM10 concentration at the four monitoring stations over Southern Peninsular Malaysia and daily hotspot count over Sumatera.

REFERENCES

[1] **(**MMS), Malaysian Meteorological Service. "Report on Air Quality in Malaysia as Monitored by the Malaysian Meteorological Service 1994." Technical Note Malaysian Meteorological Service 1995.

[2] Adelin Anwar, Liew Juneng, Mohamed Rozali Othman, Mohd. Talib Latif. "Correlation between Hotspots and Air Quality in Pekanbaru-Riau, Indonesia in 2006-2007." *Sains Malaysiana* 39 no. (2) (2010): 169-74.

[3] Anne M. Thompson, Jacquelyn C. Witte, Robert D. Hudson, Hua Guo, Jay R. Herman, Masatomo Fujiwara. "Tropical Tropospheric Ozone and Biomass Burning." *Science* Vol 291, no. Issue 5511, (2001): 2128-32.

[4] Annisa Puspa Kirana, Imas Sukaesih Sitanggang, Lailan Syaufina. "Hotspot Pattern Distribution in Peat Land Area in Sumatera Based on Spatio Temporal Clustering." *Procedia Environmental Sciences* Volume 33, (2016): Pages 635-45.

[5] Aswin Usup, Yoshihiro Hashimoto, Hidenori Takahashi, Hiroshi Hayasaka. "Combustion and Thermal Characteristics of Peat Fire in Tropical Peatland in Central Kalimantan, Indonesia." *Tropics* Vol. 14, no. 1 (2004).

[6] Awang M B, Jaafar A B, Abdullah A M, Ismail M B, Hassan M N, Abdullah R, Johan S, Noor H. "Air Quality in Malaysia : Impact, Management Issues and Future Challenges." *Journal of Respirology* 5, no. 2 (2000): 183-96.

[7] B. N. Holben, D. Tanré, A. Smirnov, T. F. Eck, I. Slutsker, N. Abuhassan, W. W. Newcomb, *et al.* "An Emerging Ground-Based Aerosol Climatology: Aerosol Optical Depth from AERONET." *Journal of Geophysical Research* Volume 106, no. Issue D11 (2001): 12067–97.

[8] Christopher D. Elvidge, Mikhail Zhizhin, Feng-Chi Hsu, Kimberly Baugh, M Rokhis Khomarudin, Yenni Vetrita, Parwati Sofan, Suwarsono, Dadang Hilman. "Long-Wave Infrared Identification of Smoldering Peat Fires in Indonesia with Nighttime Landsat Data." *Environmental Research Letters* Volume 10 (2015).

[9] Doreena Dominick, Hafizan Juahir, Mohd Talib Latif, Sharifuddin M. Zain, Ahmad Zaharin Aris "Spatial Assessment of Air Quality Patterns in Malaysia Using Multivariate Analysis." *Journal of Atmospheric Environment* 60 (2012): 172-81.

[10] G. R. van der Werf, J. T. Randerson, L. Giglio, G. J. Collatz, P. S. Kasibhatla, and A. F. Arellano Jr. "Interannual Variability in Global Biomass Burning Emissions from 1997 to 2004." *Atmospheric Chemistry and Physics* 6, (2006): 3423-41.

[11] Hendon, Harry H. "Indonesian Rainfall Variability: Impacts of Enso and Local Air–Sea Interaction." *Journal of Climate* Volume 16 (2003).

[12] Hiroshi Hayasaka, Izumi Noguchi, Erianto Indra Putra, Nina Yulianti, Krishna Vadrevu. "Peat-Fire-Related Air Pollution in Central Kalimantan, Indonesia." *Environmental Pollution* Volume 195, (2014): 257-66.

[13] Jeffrey S.Reid, Edward J.Hyer, Randall S. Johnson,Brent N. Holben,Robert J. Yokelson,Jianglong Zhang,James R. Campbell,Sundar A. Christopher,Larry Di Girolamo,Louis Giglio,Robert E. Holz,Courtney Kearney,Jukka Miettinen,Elizabeth A. Reid,F. Joseph Turk,Jun Wang,Peng Xian,Guangyu Zhao,Soo Chin Liew. "Observing and Understanding the Southeast Asian Aerosol System by Remote Sensing: An Initial Review and Analysis for the Seven Southeast Asian Studies (7seas) Program." *Journal of Atmospheric Research* Volume 122, (2013): 403-68.

[14] Jennifer A. Logan, Inna Megretskaia, Ray Nassar, Lee T. Murray, Lin Zhang, Kevin W. Bowman, Helen M. Worden, Ming Luo. "Effects of the 2006 El Niño on Tropospheric Composition as Revealed by Data from the Tropospheric Emission Spectrometer (TES)." *Geophysical Research Letters* Vol 35 (2008).

[15] Johannes J. Feddema, Keith W. Oleson, Gordon B. Bonan, Linda O. Mearns, Lawrence E. Buja, Gerald A. Meehl, Warren M. Washington. "The Importance of Land-Cover Change in Simulating Future Climates." *Science* Vol. 310,, no. Issue 5754, (2005): 1674-78.

[16] Jukka Miettinen, Aljosja Hooijer, Jianjun Wang, Chenghua Shi, Soo Chin Liew. "Peatland Degradation and Conversion Sequences and Interrelations in Sumatra." *Regional Environmental Change* Volume 12, no. Issue 4, (2012): 729–37.

[17] Jukka Miettinen, Chenghua Shi, Soo Chin Liew. "Two Decades of Destruction in Southeast Asia's Peat Swamp Forests." *Frontier in Ecology and the Environment* 10 (2011): 124-28.

[18] Kasturi Devi Kanniah, Norbaizura Yaso "Preliminary Analysis of the Spatial and Temporal Patterns of Aerosols and Their Impact on Climate in Malaysia Using Modis Satellite Data " Paper presented at the International Archives of the Photogrammetry, Remote Sensing and Spatial Information Science, Kyoto Japan 2010.

[19] Khan Alam, Salman Qureshi, Thomas Blaschke "Monitoring Spatio-Temporal Aerosol Patterns over Pakistan Based on Modis, Toms and Misr Satellite Data and a Hysplit Model." *Journal of Atmospheric Environment* 45 (2011): 4641-51.

[20] Kita K., Fujiwara M., Kawakami S. "Total Ozone Increase Associated with Forest Fires over the Indonesian Region and its Relation to the El Niño-Southern Oscillation." *Atmospheric Environment* Volume 34, no. Issue 17, (2000): 2681-90.

[21] Liew Juneng, Fredolin T. Tangang. "Evolution of Enso-Related Rainfall Anomalies in Southeast Asia Region and Its Relationship with Atmosphere–Ocean Variations in Indo-Pacific Sector." *Climate Dynamics* Volume 25, , no. Issue 4, (2005): 337–50.

[22] Liew Juneng, Mohd Talib Latif, Fredolin T. Tangang, Haslina Mansor. "Spatio-Temporal Characteristics of Pm10 Concentration across Malaysia." *Journal of Atmospheric Environment* 43 (2009): 4584–94.

[23] Liew Juneng, Mohd Talib Latif, Fredolin Tangang. "Factors Influencing the Variations of Pm10 Aerosol Dust in Klang Valley, Malaysia during the summer." *Journal of Atmospheric Environment* 45 (2011): 4370-78.

[24] Lorraine A. Remer, Richard G. Kleidman, Robert C. Levy, Yoram J. Kaufman, Didier Tanré, Shana Mattoo, J. Vanderlei Martins, *et al.* "Global Aerosol Climatology from the Modis Satellite Sensors." *Journal of Geophysical Research* Volume 113, no. Issue D14 (2008).

[25] M. Radzi Bin Abas, Bernd R.T. Simoneit. "Composition of Extractable Organic Matter of Air Particles from Malaysia: Initial Study." *Atmospheric Environment* Volume 30, no. Issue 15 (1996): Pages 2779-93.

[26] Marlier M. E. , De Fries R. S. , Voulgarakis A., Kinney P. L., Randerson J. T., Shindell D. T., Chen Y., Faluvegi G. "El Niño and Health Risks from Landscape Fire Emissions in Southeast Asia.". *Nature Climate Change* 3 (2013): 131-36.

[27] Nan Feng, Sundar A. Christopher. "Satellite and Surface-Based Remote Sensing of Southeast Asian Aerosols and Their Radiative Effects." *Journal of Atmospheric Research* Volume 122 (2013): 544-54.

[28] Nan Feng, Sundar A. Christopher. "Satellite and Surface-Based Remote Sensing of Southeast Asian Aerosols and Their Radiative Effects." *Atmospheric Research* Volume 122 (2013): Pages 544-54.

[29] Dubovik, A. Smirnov, B. N. Holben, M. D. King, Y. J. Kaufman, T. F. Eck, and I. Slutsker. "Accuracy Assessments of Aerosol Optical Properties Retrieved from Aerosol Robotic Network (AERONET) Sun and Sky Radiance Measurements." *Journal of Geophysical Research* Volume 105, no. Issue D8 (2000): 9791–806

[30] Oleg Dubovik, Brent Holben, Thomas F. Eck, Alexander Smirnov, Yoram J. Kaufman, Michael D. King, Didier Tanré, Ilya Slutsker. "Variability of Absorption and Optical Properties of Key Aerosol Types Observed in Worldwide Locations." *Journal of Atmospheric Science* Volume 59 (2002): 590-608.

[31] Rafia Afroz, Mohd Nasir Hassan, Noor Akma Ibrahim. "Review of Air Pollution and Health Impacts in Malaysia." *Environmental Research* Volume 92, no. Issue 2 (2003).

[32] Robert D. Field, Guido R. van der Werf, Samuel S. P. Shen. "Human Amplification of Drought-Induced Biomass Burning in Indonesia since

1960." *Nature Geoscience* Volume 2, (2009): pages 185–88

[33] Robert D. Field, Samuel S. P. Shen. "Predictability of Carbon Emissions from Biomass Burning in Indonesia from 1997 to 2006." *Journal of Research - Biogeosciences* Vol. 113, no. G4 (2008).

[34] Rona A. Dennis, Judith Mayer, Grahame Applegate, Unna Chokkalingam, Carol J. Pierce Colfer, Iwan Kurniawan, Henry *Geophysical* Lachowski, Paul Maus, Rizki Pandu Permana, Yayat Ruchiat, Fred Stolle, SuyantoThomas P. Tomich. "Fire, People and Pixels: Linking Social Science and Remote Sensing to Understand Underlying Causes and Impacts of Fires in Indonesia." *Human Ecology* Vol. 33, , no. Issue 4, (2005): 465–504.

[35] Sang-WooKim, Soon-Chang Yoon, Jiyoung Kim, Seung-Yeon Kim. "Seasonal and Monthly Variations of Columnar Aerosol Optical Properties over East Asia Determined from Multi-Year Modis, Lidar, and AERONET Sun/Sky Radiometer Measurements." *Journal of Atmospheric Environment* Volume 41, no. Issue 8 (2007): 1634-51.

[36] Santo V. Salinas, Boon Ning Chew, Jukka Miettinen, James R.Campbell, Ellsworth J. Welton, Jeffrey S. Reid, Liya E. Yu, Soo ChinLiew. "Physical and Optical Characteristics of the October 2010 Haze Event over Singapore: A Photometric and Lidar Analysis." *Journal of Atmospheric Research* Volume 122, no. Pages 555-570 (2013): 555-70.

[37] Santo V. Salinas, Chew B. Ning, Soo C. Liew. "Characterization of Aerosol Physical and Optical Properties from a Combination of Ground–Based and Hand–Held Sun–Photometer Data of Singapore." Paper presented at the International Geoscience and Remote Sensing Symposium (IGRSS), 2009.

[38] Sheil, Douglas. "How Plants Water Our Planet: Advances and Imperatives." *Trends in Plant Science* Volume 19, no. Issue 4, (2014): 209-11.

[39] Tacconi L., Moore P. F., Kaimowitz D. "Fires in Tropical Forests – What Is Really the Problem? Lessons from Indonesia." *Mitigation and Adaptation Strategies for Global Change* Volume 12, no. Issue 1 (2007): 55–66.

[40] Thomas Eck, Brent Holben, David Giles, Alexander Smirnov, Ilya Slutsker, Alexander Sinyuk, Joel Schafer, Mikhail Sorokin, Jeffrey Reid, Andrew Sayer, Christina Hsu, Robert Levy, Alexei Lyapustin, Yujie Wang, Muhammad Arif Rahman, Soo-Chin Liew, Santo V. Salinas Cortijo, Tan Li, Daniel Kalbermatter, Kwoh Leong Keong, Muhammad Elifant Y., Fanni Aditya, Maznorizan Mohamad, Tan Kok Chong, Lim Hwee San, Yeap Eng Choon, Gumilang Deranadyan, Sheila DA Kusumaningtyas, and Mastura Mahmud. "Remote Sensing Measurements of Biomass Burning Aerosol Optical Properties During the 2015 Indonesian Burning Season from Aeronet and Modis Satellite Data." *Geophysical Research Abstracts* Vol. 18, EGU2016-2391-3, no. EGU General Assembly 2016 (2016).

[41] Thomas Eck, Brent Holben, Jeffrey Reid, Alexander Smirnov, Ilya Slutsker, Oleg Dubovik, O'Neill N. T. "Wavelength Dependence of the Optical Depth of Biomass Burning, Urban, and Desert Dust Aerosols." *Journal of Geophysical Research* Volume 104, no. Issue D24 (1999): 31333–49

[42] Wolterbeek, Bert. "Biomonitoring of Trace Element Air Pollution: Principles, Possibilities and Perspectives." *Environmental Pollution* 120 (2002): 11–21.

[43] Wooster M., Roberts G., Perry G., Kaufman Y., "Retrieval of Biomass Combustion Rates and Totals from Fire Radiative Power Observations: FRP Derivation and Calibration Relationships between Biomass Consumption and Fire Radiative Energy Release." *Journal of Geophysical Research* Volume 110 (2005).

[44] Xueliang Deng, Chune Shi, Biwen Wu, Zhenghua Chen, Suping Nie, Dongyan He, Hao Zhang. "Analysis of Aerosol Characteristics and Their Relationships with Meteorological Parameters over Anhui Province in China." *Journal of Atmospheric Research* 109–110 (2012): 52-63.

[45] Yonghe Wang, Robert D. Field, Orbita Roswintiarti. "Trends in Atmospheric Haze Induced by Peat Fires in Sumatra Island, Indonesia and El Niño Phenomenon from 1973 to 2003." *Geophysical Research Letters* Vol 31 (2004).

9thInt. Conf. on Geotechnique, Construction Materials, and Environment, Tokyo, Japan,20-22 November 2019, ISBN: 978-4-909106025C3051

PEOPLE'S PERCEPTION AND ATTITUDE TO ENVIRONMENTAL POLLUTION AND ITS IMPACTS ON DHAKA CITY, BANGLADESH

Najmun Nahar[1, 2], Zakaria Hossain [1] and Sanjia Mahiuddin[2]
[1]Graduate School of Bioresources, Mie University, Japan,[2]Life and Earth Science, Jagannath University, Bangladesh

ABSTRACT

Dhaka, the capital city of Bangladesh is one of the most polluted cities in the world due to unplanned urbanization, rapid population growth, and resident's irresponsible behavior and attitudes to the environment. Therefore, the study tries to assess the level of people's perception and attitude and also to show the association between people's demographic characteristics with their perception and attitude towards 'Environmental Pollution and Its Impacts' of Dhaka City Corporation as the study area. The study was conducted mainly based on the primary data which were collected through a questionnaire survey, KII and direct observation. Secondary data was collected from various published and unpublished sources. Data were processed from surveyed questionnaire using SPSS software where mean score, percentage, and Standard Deviations were calculated for assessing the level of people's perception and attitude and the Pearson's Chi-square test were done for showing the association between demographic characteristics with the people's perception and attitude. The study results reveal that respondents have a higher level of environmental perception and an environment-friendly attitude in most cases. Age, Education, occupation, and income significantly affect the respondents' environmental perception and attitude exception sex types. It is urgent to change the dweller's environmental behavior for the sustainable environment of this city.

Keywords: Environmental pollution, Environmental Perception, Environmental attitude, Chi-square Test

1. INTRODUCTION

At present, environmental pollution is one of the major global concern in this century [1-2] because it adversely alters the quality of the environment and also affects the human health particularly for developing countries [3-4]. As a developing country, Dhaka, the primate and capital city of Bangladesh is not only the most polluted cities in this country but also the third most polluted city for having the worst level of air pollution [5-6], the second least livable city considering the critical environmental condition [7] and one of the most densely populated cities in the world and more than 15 million people are living in this city [8] with a density of 23,234 people per sq. km. living within a total area of 300 sq. km. [9]. Uncontrolled population growth, rapid urbanization, industrialization, inadequate and improper traffic management and inefficient solid waste management, etc. are the main causes of environmental pollution of this city [10-11].

It is undoubtedly true that our surrounding environment is facing acute problems and most of these problems are the consequences of irresponsible behavior and the attitudes of people on the environment [12] because people's perception and behavior influence their actions through a decision-making process to the environment [13]. Environmental perception and attitude of a person also depend on his demographic characteristics (i.e. age, sex, education, occupation, income, religion, marital status, etc.) and also differs from a community to a community or a country to country [14-15]. For making a better urban environmental management plan, it is important to know people's perception and attitude to environmental components and its quality [16-17] and the people have the right to know and use about environmental information held by public authority who can ensure the availability of environment-related information and can achieve sustainable development through the public response [18]. Therefore, the present study was designed to assess the level of perception and attitude of peoples towards environmental pollutions and its impacts and correspondingly to examine the status of the relationship among the people's perception and attitude with their demographic characteristics of Dhaka City Corporation (DCC) as the study area (Figure 1).

2. METHODS AND MATERIALS

The present study was conducted mainly based on primary data through secondary data were used. For primary data collection, the questionnaire survey, Key Informant Interview (KII) and direct observation were followed. For understanding the people's perception and attitude to environmental

pollution and its impacts on the study area, a semi-structured questionnaire was prepared, checked and then the pilot survey was conducted before questionnaire finalization. In the questionnaire, theme-wise 20 questions were arranged for both people's perception and attitude (positive and negative) related questions and questions pattern were designed according to five-point Likert-Scale where 1= strongly disagree; 2= disagree; 3= undecided/ neutral; 4= agree; 5= strongly agree (Tables 2 and 3). For conducting questionnaire survey conveniently, in total 400 households were selected randomly with 95% confidence level and ±5 precision level [19] from jointly 15,76,746 households from Dhaka City Corporation (DCC) area which is now divided into Dhaka North City Corporation (DNCC) and Dhaka South City Corporation (DSCC) [20-21] where each city corporation has 5 zones (Figure 1) and equally 40 respondents were taken from each zone. The demographic characteristics of the respondents are shown in Table 1. Moreover, 20 KII was done from two city corporations who were engaged in a different responsible position in society. The field survey was carried out from 2nd March to 16th March in 2018 by a research team consisting of 10 surveyors. The sources of secondary data were various published and unpublished documents. All collected data were compiled, processed, statistically analyzed and incorporated in text and tables including frequency, percentages, mean score, and standard deviations; and Chi-square (χ^2) test using SPSS (Statistical Package for the Social Sciences) software Version 23 and MS Excel. ArcGIS Version 10.3 software was used for the preparation of a map of the study area.

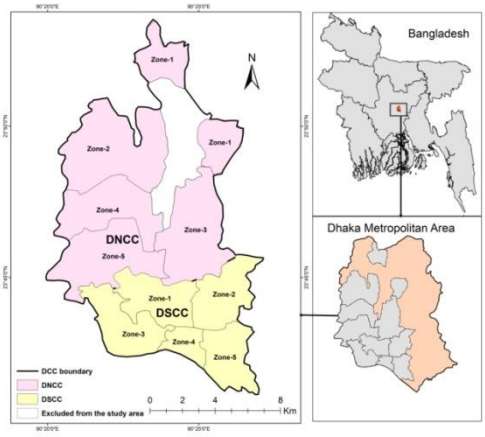

Fig. 1 Location of the Study Area. (Note: Modified from Kabir, 2015)

The level of people's perception and attitude is analyzed by using the mean score and standard deviation from the processed data from the questionnaire survey (Tables 2 and 3). In terms of evaluation of perception, mean score above 3.5 (X>3.5) means the higher level of perception of the respondents; mean scores between above 2.5 and below 3.5 (2.5 >X <3.5) indicates the neutral level and below 2.5 (X<2.5) means the lower level of perception. In terms of evaluation of the attitude level of the respondents in the study area, there is a difference between positive and negative statements for assessing the attitude level of the respondents. In the case of positive statement, score above 3.5 (X >3.5) means the environment friendly attitude of the respondents; mean scores between above 2.5 and below 3.5 (2.5 >X <3.5) indicates the neutral level and below 2.5 (X<2.5) means the not environment friendly attitude but it reverses for the negative statement.

For showing the association between people's perception and attitude with their demographic characteristics in the study area, data were processed from the same questionnaire (Tables 2 and 3) which was also used for assessment of the level of perceptions and attitudes. In this study, 5 independent variables (sex, age, education level, occupation and monthly income) were considered as the vital demographic characteristic of the respondents and used Pearson's Chi-square (χ^2) test to show the significant association among people's perception and attitude and their demographic characteristics about "environmental pollution and its impacts on the study area; where, p>0.05 indicates Non-Significant; p<0.05 is Significant and p<0.01 is Strong Significant [22]. For testing the association among the people's perception and attitude with their demographic characteristics, the formulated hypothesis was *"there will be a statistically significant association between people's perception and attitude with their demographic characteristics (sex, age, education, occupation and monthly income) about environmental pollution and its impacts on the study area".*

Table 1 Demographic Characteristics of the Study Area

Demographic Characteristics		Frequency (n=400)	Percentage
Sex	Male	265	66.3
	Female	135	33.8
Age Group	18-20	6	1.5
	21-30	111	27.8
	31-40	179	44.8
	>40	104	26.0
Education Level	Illiterate	16	4.0
	Primary	48	12.0
	Secondary	151	37.8
	Tertiary	185	46.3
Occupation	Unemployed	27	6.8
	Business	112	28.0
	Service	134	33.5
	Homemaker	74	18.5
	Student	53	13.3
Monthly Income (in BDT)	<10000	133	33.3
	11000-15000	26	6.5
	16000-20000	45	11.3
	21000-30000	110	27.5
	>30000	86	21.5

3. RESULTS AND DISCUSSION

3.1 Assessment of Level of People's Perception and Attitude in The Study Area

From the processed data in Table 2, it is found that people's perception level is high about environmental pollution and its impacts in the study area. If we observe all the data, there is a slight difference among the processed data from 20 questions with 2 themes. In terms of theme "Causes of environmental pollution", the mean scores are found above 3.65 to 4.35 (X>3.5) for the responses against 7 questions (1-7 no.), which means that the perceived level of the respondents is high and they are knowledgeable about the environment of the city. The mean scores are above 3.63 to 4.67 (X>3.5) for the theme "Effects of environmental pollution" which have 13 questions (8-20 no.) which also shows that the perceived level of residents of Dhaka City is also high and they are also informed about the effects of environmental pollution.

In terms of environmental attitude of residents in the study area, from the Table 3, considering the theme "*Negative Attitude to environmental pollution and its impacts*" consisting of 5 questions (1-5 no.), it is observed that the mean scores of the responses against the questions are above 1.86 to 3.34 (X<2.5) for the questions 2-4 no., which shows the environment friendly attitude of the respondents but the mean scores for question no. 1 and 5 are found between above 2.5 and below 3.5 (2.5 >X <3.5), which shows a neutral attitude. The theme "*positive attitude to environmental pollution*" consisting of 6 questions (6-11 no.) and the theme "*Attitude to Initiatives and Legislations for Environmental Management*" consisting of 9 questions (12-20 no.), the mean scores of those questions are 3.54 to 4.36 (X>3.5) which also shows the people's environment friendly attitude; except for question no. 20 which shows a neutral attitude.

Table 2 Level of People's Perception of Environmental Pollution and Its Impacts on the Study Area

Q.N.	Aspects of Evaluation	Strongly Disagree (%)	Disagree (%)	Undecided (%)	Agree (%)	Strongly Agree (%)	Mean Score	S.D.	Perception level
1	Rapid population growth is one of the main reasons for environmental pollution in Dhaka City.	0.0	1.3	9.8	48.8	40.3	4.28	0.68	High
2	Unplanned and ill planned urbanization also proliferate the pollution in this city.	0.0	1.0	10.5	41.3	47.3	4.35	0.70	High
3	Less vegetation has increased pollution in this city.	1.0	8.5	21.0	44.0	25.5	3.85	0.93	High
4	Improper waste disposal contaminates soil, water and air of this city.	1.0	0.0	14.0	52.5	32.5	4.16	0.73	High
5	Industries and Automobiles are the major sources of air and noise pollution.	0.0	1.0	24.3	38.0	36.8	4.11	0.80	High
6	Fossil fuels cause high level air pollution and also contribute to soil contamination and water pollution.	0.0	0.8	50.5	32.0	16.8	3.65	0.76	High
7	Water bodies are contaminated by a variety of chemicals and wastes.	0.0	0.0	11.8	62.5	25.8	4.14	0.59	High
8	Environmental Pollution is a serious problem of urban life.	0.3	0.0	9.5	35.0	55.3	4.45	0.68	High
9	Pollution deteriorates the environmental components adversely and affects the whole environment.	4.3	2.5	10.8	42.3	40.3	4.12	0.99	High
10	Environmental pollution can create a number of environmental hazards.	0.0	0.3	30.3	47.0	22.5	3.92	0.72	High
11	Pollution destroys biota and habitat and leads to the imbalance of ecosystems.	0.0	1.3	21.5	46.0	31.3	4.07	0.75	High
12	Environmental Pollution is harmful to human health and other living species.	0.0	1.0	3.3	23.3	72.5	4.67	0.58	High
13	Landfills by wastes deteriorate the beauty of the city and also create land pollution.	1.0	1.0	10.5	58.8	28.8	4.13	0.71	High
14	Air pollution alters the elements of weather and climate and seriously affects the human health.	0.0	0.8	24.5	49.0	25.8	4.00	0.73	High
15	Global temperature has increased due to air pollution.	0.0	1.0	17.5	48.8	32.8	4.13	0.72	High
16	Wetlands reduction increases level of water pollution and the frequency of flood, water logging in Dhaka city.	0.3	4.8	18.5	43.0	33.5	4.05	0.85	High
17	Noise pollution affects the personal and working life silently.	0.8	0.5	6.8	40.0	52.0	4.42	0.70	High
18	Noise pollution also seriously affects the health of the dwellers in this city.	0.0	3.3	7.8	41.8	47.3	4.33	0.75	High
19	Electromagnetic pollution directly effects on our health.	0.0	5.5	35.5	50.0	9.0	3.63	0.72	High
20	Water, food and air borne diseases are increasing day by day due to environmental pollution in this city.	0.0	0.3	8.8	53.3	37.8	4.29	0.62	High

Note: Q.N. = Question Number; Questions 1-7 belongs to Theme: *Causes of Environmental Pollution* and Questions 8-20 belongs to Theme: *Effects of Environmental Pollution*

Table 3 Level of People's Attitude to Environmental Pollution and Its Impacts on the Study Area

Q.N.	Aspects of Evaluation	Strongly Disagree (%)	Disagree (%)	Undecided (%)	Agree (%)	Strongly Agree (%)	Mean Score	S.D.	Attitude level
1	I am not sure what will be helpful or harmful for environment.	10.8	40.8	34.8	11.5	2.3	2.54	0.91	Neutral
2	Environmental problems are not affecting me personally	26.0	67.5	2.5	2.3	1.8	1.86	0.71	EF
3	I do not have enough time to concern about how my activities influence the environment.	12.0	39.3	40.8	6.0	2.0	2.47	0.85	EF
4	Environmental maintenance is only the responsibility of Government, so it is not essential to me to concern about it and not to do enough for it.	16.8	66.0	7.0	7.5	2.8	2.13	0.87	EF
5	I think that environmental pollution related issues have been overstated.	0.0	12.8	49.8	28.3	9.3	3.34	0.81	Neutral
6	Environmental protection is very significant to us and our future generation.	0.0	1.0	7.3	53.5	38.3	4.29	0.64	EF
7	Everyone should concern about environmental pollution.	0.8	0.3	7.3	45.8	46.0	4.36	0.69	EF
8	I feel better when my initiatives keep the environment sound.	0.3	0.8	20.5	54.3	24.3	4.01	0.70	EF
9	I feel worried when I see my surrounding environment has been contaminated.	0.5	1.5	31.0	42.3	24.8	3.89	0.80	EF
10	We should keep land, water and air pollution-free in order to get a beautiful and clean environment.	0.0	0.0	23.5	46.0	30.5	4.07	0.73	EF
11	I would be embarrassed if my acquaintance people caught me not recycling my daily waste.	0.0	6.5	28.0	43.3	22.3	3.81	0.85	EF
12	Personal and Economic interest should be removed for better environment.	5.3	11.5	23.3	41.5	18.5	3.57	1.07	EF
13	Everyone should know about the information how to control and mitigate environmental pollution.	0.0	0.5	23.8	42.3	33.5	4.09	0.76	EF
14	Use of science and technology should be environmentally viable.	0.0	1.3	23.3	45.0	30.5	4.05	0.76	EF
15	Local environmental groups may be a source of authentic information and may give realistic ideas to lessen the different environmental pollutions.	4.0	10.8	26.3	45.0	14.0	3.54	0.99	EF
16	The electronic and print media can create awareness about environmental pollution amongst the peoples.	0.0	1.3	11.8	52.5	34.5	4.20	0.68	EF
17	We need to control population migration to maintain the balance between population and ecosystem.	0.0	6.5	20.3	41.5	31.8	3.99	0.88	EF
18	Pollution free environment should be our prime policy before any development work.	0.8	2.0	10.8	54.5	32.0	4.15	0.74	EF
19	Environment friendly law should make and implement for managing our environment.	0.0	1.0	31.0	51.5	16.5	3.84	0.69	EF
20	The pollution control laws and rules should not be so strict as to discourage industrial development.	9.0	26.3	36.8	21.0	7.0	2.91	1.05	Neutral

Note: Q.N. = Question Number; Questions 1-5 belongs to Theme: *Negative Attitude to Environmental Pollution*, Questions 6-11 belongs to Theme: *Positive Attitude to Environmental Pollution* and Questions 12-20 belongs to Theme: *Attitude to Initiatives and Legislations for Environmental Management*; EF= Environment-Friendly &N. EF= Not-Environment Friendly.

3.2 Association Among People's Perception and Attitude with Their Demographic Characteristics

The statistical results (P-value) of the study reveals that people's perception and attitude to environmental pollution and its impacts on the study area are influenced more or less by their five demographic factors (sex, age, educational level, occupation and monthly income). In terms of the environmental perception of the residents in Dhaka City, from Table 4 it is noticed that exception question no. 18, there is no association between people's perception of environmental issues with people's gender types as a vital demographic factor. Considering the different age groups, questions no.1, 2, 4, 6, 11, 13, 15 and 18 show strong association (p<0.01) and question no. 12, 17 and 20 show significant association (p<0.05) with the environmental perception of the respondents in the study area. In terms of educational level, question no.1, 6, 10 and 19 show a strong association and the questions no. 3, 5, 12 and 15 show significant association. In terms of occupation, questions no. 7, 11, and 18 also show a strong association and question no. 15, 16 show significant associations. Moreover, question no. 1, 3, 4, 6, 10, 14, 16 indicates a strong association and question no. 2, 11 and 19 show a significant association between different income groups and the environmental perception of the dwellers in Dhaka City.

Considering the environmental attitude of peoples in the study area, the statistical results notices from Table 5, that only for questions no. 5 shows strong association (0.00<0.01) and question no. 14 and 15 show a significant association (p<0.05) between gender types and the environmental attitude of the respondents. In terms of different age groups, question no. 8, 14, 15 and 19 show strong association and question no.3, 5, 16, 17, 18, and 20 show significant association. In terms of education level, questions no. 1,3, 6-13, 15-16 and 19 show statistically strong association (p<0.01) and question no. 2, 5 and 20 show a significant association. In different occupations, question no. 1, 5, 10-13, 15 and 19 shows the strong association and question no. 2, 8, 9, 16 and 17 show significant associations. Besides, question no. 1, 3, 5, 9-13, 15 and 19 show the strong association and question no. 6, 8, and 18 show a significant association between people's environmental attitudes with their monthly income.

Table 4 Association between People's Perceptions with Their Demographic Characteristics showing P-Value

Q.N.	Aspects of Evaluation	Sex	Age	Education	Occupation	Income
1	Rapid population growth is one of the main reasons for environmental pollution in Dhaka City.	0.378	0.003**	0.000**	0.080	0.003**
2	Unplanned and ill planned urbanization also proliferate the pollution in this city.	0.288	0.000**	0.946	0.424	0.043*
3	Less vegetation has increased pollution in this city.	0.221	0.258	0.042*	0.219	0.008**
4	Improper waste disposal contaminates soil, water and air of this city.	0.148	0.002**	0.193	0.918	0.009**
5	Industries and Automobiles are the major sources of air and noise pollution.	0.793	0.529	0.026*	0.907	0.593
6	Fossil fuels cause high level air pollution and also contribute to soil contamination and water pollution.	0.213	0.000**	0.001**	0.507	0.000**
7	Water bodies are contaminated by a variety of chemicals and wastes.	0.379	0.096	0.668	0.003**	0.188
8	Environmental Pollution is a serious problem of urban life.	0.237	0.201	0.077	0.350	0.122
9	Pollution deteriorates the environmental components adversely and affects the whole environment.	0.393	0.537	0.192	0.228	0.052
10	Environmental pollution can create a number of environmental hazards.	0.722	0.107	0.025**	0.432	0.004**
11	Pollution destroys biota and habitat and leads to the imbalance of ecosystems.	0.595	0.002**	0.102	0.005**	0.033*
12	Environmental Pollution is harmful to human health and other living species.	0.426	0.010*	0.011*	0.186	0.056
13	Landfills by wastes deteriorate the beauty of the city and also create land pollution.	0.435	0.000**	0.881	0.060	0.516
14	Air pollution alters the elements of weather and climate and seriously affects the human health.	0.238	0.072	0.083	0.088	0.000**
15	Global temperature has increased due to air pollution.	0.080	0.000**	0.016*	0.030*	0.199
16	Wetlands reduction increases level of water pollution and the frequency of flood, water logging in Dhaka city.	0.262	0.073	0.155	0.023*	0.004**
17	Noise pollution affects the personal and working life silently.	0.427	0.038*	0.056	0.355	0.537
18	Noise pollution also seriously affects the health of the dwellers in this city.	0.031*	0.000**	0.222	0.000**	0.309
19	Electromagnetic pollution directly effects on our health.	0.478	0.276	0.006**	0.253	0.020*
20	Water, food and air borne diseases are increasing day by day due to environmental pollution in this city.	0.905	0.039*	0.461	0.079	0.909

Note: Q.N. = Question Number; Questions 1-7 belongs to Theme: *Causes of Environmental Pollution* and Questions 8-20 belongs to Theme: *Effects of Environmental Pollution;* N.S.: Non-Significant (p>0.05), *****Significant at p<0.05 and ****** Strong Significant at p<0.01

Table 5 Association between People's Attitudes with Their Demographic Characteristics showing P-Value

Q.N.	Aspects of Evaluation	Sex	Age	Education	Occupation	Income
1	I am not sure what will be helpful or harmful for environment.	0.074	0.115	0.000**	0.000**	0.000**
2	Environmental problems are not affecting me personally	0.207	0.480	0.018*	0.043*	0.095
3	I do not have enough time to concern about how my activities influence the environment.	0.619	0.047*	0.001**	0.126	0.000**
4	Environmental maintenance is only the responsibility of Government, so it is not essential to me to concern about it and not to do enough for it.	0.151	0.171	0.367	0.390	0.019
5	I think that environmental pollution related issues have been overstated.	0.004**	0.020*	0.022*	0.000**	0.008**
6	Environmental protection is very significant to us and our future generation.	0.628	0.099	0.001**	0.281	0.033*
7	Everyone should concern about environmental pollution.	0.725	0.341	0.000**	0.094	0.835
8	I feel better when my initiatives keep the environment sound.	0.526	0.009**	0.000**	0.028*	0.038*
9	I feel worried when I see my surrounding environment has been contaminated.	0.495	0.202	0.000**	0.022*	0.008**
10	We should keep land, water and air pollution-free in order to get a beautiful and clean environment.	0.290	0.251	0.000**	0.000**	0.001**
11	I would be embarrassed if my acquaintance people caught me not recycling my daily waste.	0.717	0.673	0.000**	0.001**	0.000**
12	Personal and Economic interest should be removed for better environment.	0.116	0.083	0.001**	0.001**	0.040**
13	Everyone should know about the information how to control and mitigate environmental pollution.	0.078	0.242	0.000**	0.001**	0.000**
14	Use of science and technology should be environmentally viable.	0.020*	0.001**	0.149	0.158	0.143
15	Local environmental groups may be a source of authentic information and may give realistic ideas to lessen the different environmental pollutions.	0.040*	0.000**	0.000**	0.000**	0.000**
16	The electronic and print media can create awareness about environmental pollution amongst the peoples.	0.074	0.019*	0.000**	0.030*	0.374
17	We need to control population migration to maintain the balance between population and ecosystem.	0.217	0.015*	0.263	0.046*	0.161
18	Pollution free environment should be our prime policy before any development work.	0.421	0.035*	0.025	0.187	0.032*
19	Environment friendly law should make and implement for managing our environment.	0.187	0.000**	0.000**	0.001**	0.000**
20	The pollution control laws and rules should not be so strict as to discourage industrial development.	0.324	0.025*	0.030*	0.059	0.108

Note: Q.N. = Question Number; Questions 1-5 belongs to Theme: *Negative Attitude to Environmental Pollution,* Questions 6-11 belongs to Theme: *Positive Attitude to Environmental Pollution* and Questions 12-20 belongs to Theme: *Attitude to Initiatives and Legislations for Environmental Management*; N. S.: Non-Significant (p>0.05), *****Significant at p<0.05 and ****** Strong Significant at p<0.01

4. CONCLUSIONS

This study attempts to demonstrate the current scenario of the people's environmental perceptions and attitudes toward environmental pollution and its impacts on Dhaka City. The result of the study represents that peoples of different sectors are knowledgeable about environmental pollution and its impacts of the study area but visually the environment of the city is terribly contaminated which means the dwellers of the city do not maintain their environmental behavior and attitude toward this issues and not tried to follow the rules and regulation strictly implemented for protecting environment from different pollution. The outputs of the study strongly support the need for creating awareness among people by providing more environmental education to reduce environmental pollutions and its impacts and also need to make people obliged in following environmental laws for protecting the environment from pollutions. More detailed research about this issue is needed to identify the gaps and associations between people's environmental perceptions and attitudes with their demographic characteristics in the future.

5. ACKNOWLEDGMENTS

The authors wish to gratefully acknowledge the financial assistance from the University Grants Commission and Jagannath University (UGC-JnU Project, 2017-18) of Bangladesh for the research presented in the paper.

6. REFERENCES

[1] Khan, M. A., and Ghouri, A. M., Environmental Pollution: Its Effects on Life and Its Remedies, International Refereed Research Journal, Vol. II, Issue 2, 2011, pp.276-285.

[2] Majumder, A. K., Assessments of Environmental Awareness Among the Some Selective University Students of Bangladesh, American Journal of Education and Information Technologies, Vol. 1, Issue 2, 2017, pp. 38-42. DOI: 10.11648/j.ajeit.20170102.12

[3] Landrigan, P.J. and Fuller, R., Global health and environmental pollution, International Journal Public Health, Springer, 2015; DOI 10.1007/s00038-015-0706-7

[4] The Lancet Planetary Health, Our polluted world: the need for a global pollution strategy, Elsevier, Vol. 1, Issue 6, 2017.

[5] Kabir, M. R., Municipal Solid Waste Management System: A Study on Dhaka North and South City Corporations, Journal of Bangladesh Institute of Planners, Vol. 8, 2015, pp. 35-48. [Online] 2017; Available at: http://www.bip.org.bd/SharingFiles/journal_book/20170119110116.pdf [Accessed: 22 May 2019]

[6] The Daily Star, (02 May 2018), Dhaka air ranked world's 3rd most polluted: WHO. [Online] 2018; Available at: https://www.thedailystar.net/city/air-pollution-in-bangladesh-dhaka-air-ranked-world-3rd-most-polluted-who-1570399 [Accessed: 17 November 2018]

[7] Haque, A.N.M.N., (14 March 2017), Environmental pollution in Bangladesh, The Daily Sun. [Online] 2017; Available at: https://www.daily-sun.com/printversion/details/211962/2017/03/14/Environmental-Pollutionin-Bangladesh- [Accessed: 17 November 2018]

[8] Amin, M.A., (14 October 2018), Dhaka remains the world's most densely populated city, Dhaka Tribune. [Online] 2018; Available at: https://www.dhakatribune.com/bangladesh/dhaka/2018/10/14/dhaka-remains-the-world-s-most-densely-populated-city [Accessed: 18 November 2018]

[9] Dhaka Population 2018, World Population Review. [Online] 2018; Available at: http://worldpopulationreview.com/world-cities/dhaka-population/ [Accessed: 18 November 2018]

[10] Khan, S.M.M.H., Environmental Education and Awareness, Bangladesh National Conservation Strategy. Government of the People's Republic of Bangladesh, 2016.

[11] Siddiqy, M. Ruhullah, Urban Environment and Major Challenges in Sustainable Development: Experience from Dhaka City in Bangladesh, South East Asia Journal of Public Health, Vol. 7, Issue 1, 2017, pp.12-16. DOI: http://dx.doi.org/10.3329/seajph.v7i1.34673

[12] Uddin, M. M. M., A Study of Knowledge on Consequences and Practices about Environmental Pollution of Secondary level Students' in Bangladesh, Universal Journal of Environmental Research and Technology, Vol. 3, Issue 5, 2013, pp. 571-584, Available at http://www.environmentaljournal.org/3-5/ujert-3-5-5.pdf [Accessed: 18 May 2019]

[13] Sarkar, M., Secondary Students' Environmental Attitudes: The Case of Environmental Education in Bangladesh, International Journal of Academic Research in Business and Social Sciences, Vol. 1, Issue 3, 2011, pp.106-116. Available at: https://core.ac.uk/download/pdf/25737860.pdf[Accessed: 14 July 2018]

[14] Patchen, M., Public attitudes and behavior about climate change: what shapes them and how to influence them, PCCRC Outreach Publications 0601, East Lafayette, Indiana, University of Purdue, 2006, pp. 1-53.

[15] Hasan, Z. and Akhter, S., Determinants of public awareness and attitudes on climate change in urban Bangladesh: Dhaka as a case, European Journal of Social Sciences, Vol. 21, 2011, pp.154-162.

[16] Aretano, R., Petrosillo, I., Zaccarelli, N., Semeraro, T., and Zulini, G., People perception of landscape change effects on ecosystem services in small Mediterranean islands: A combination of subjective and objective assessments, Landscape and Urban Planning, Vol. 112, 2013, pp. 63–73. [Online] 2012; Available at: https://doi.org/10.1016/j.landurbplan.2012.12.010 [Accessed: 23 May 2019].

[17] Islam, M. S., Rana, M. M. P., and Ahmed R., Environmental perception during rapid population growth and urbanization: A case study of Dhaka city, Environment Development and Sustainability, Vol. 16, 2014, pp. 443–453. DOI 10.1007/s10668-013-9486-5.

[18] Babalola, Yemisi T., Babalola, Akhinola D. and Okhale, Faith O., Awareness and Accessibility of Environmental Information in Nigeria: Evidence from Delta State, Library Philosophy and Practice, 2010.Available at: https://www.webpages.uidaho.edu/~mbolin/babalola-babalola-okhale.pdf, [Accessed: 23 April 2018].

[19] Yamane, T., Statistics; An Introductory Analysis, 2nd Ed., Tokyo: Harper and Row, New York, Evanston and Londonnd John Weatherhill, Inc., 1967.

[20] BBS, Population and Housing Census 2011, National Report, Volume-3: Urban Area Report, 2014, Bangladesh Bureau of Statistics, Statistics and Informatics Division (SID), Ministry of Planning, Government of the People's Republic of Bangladesh, 2011.Available at: http://203.112.218.65:8008/WebTestApplication/userfiles/Image/National%20Reports/Population%20%20Housing%20Census%202011.pdf[Accessed at: 26 November 2018].

[21] Swapan, M. S. H., Zaman, A. U., Ahsan, T., and Ahmed, F., Transforming Urban Dichotomies and Challenges of South Asian Megacities: Rethinking Sustainable Growth of Dhaka, Bangladesh, Urban Science, Vol. 1, Issue 4, Article No. 3, 2017. DOI:10.3390/urbansci1040031.

[22] Tesfai, M., Nagothu, U. S., Šimek, J. and Fučík, P., Perceptions of Secondary School Students' Towards Environmental Services: A Case Study from Czechia, International Journal of Environmental Science & Science Foundation, Vo.11, Issue 2, 2016, pp. 5533-5553.

9th Int. Conf. on Geotechnique, Construction Materials and Environment, Tokyo, Japan, 20-22 November 2019, ISBN: 978-4-909106025 C3051

THE CHALLENGE OF DEVELOPING HIGH-SPEED RAIL PROJECTS: RECENT EVIDENCE FROM DEVELOPING COUNTRIES

Aleksander Purba
Engineering Faculty, University of Lampung, Indonesia

ABSTRACT

The plan by Indonesian government to build a high-speed rail (HSR) has previously existed for years. Both the Japanese and Chinese government had both showed interest in the project, and both of them have the technological capacity to build a railway that would connect Jakarta and Bandung. This project was however awarded to China because they made a provision of soft loans for the project, while Japan on the other hand wanted the Indonesian government to completely provide the fund required to execute the project from the beginning to the end of the project. The proposed construction of the railway lines will cut travel time between Jakarta and Bandung from about three hours by car to just 45 minutes only. The project will include integration of the HSR with developments along its corridor through transit oriented developments. The line would attract around 10 million passengers per year in first year of operation, this is because of Jakarta's huge population size in addition to the number of pairs of destinations that the HSR would connect.

Keywords: High-speed rail, Indonesia, Travel time, Ridership, Transit oriented development

INTRODUCTION

A brief history into the railway system in Indonesia showed that the railway transport system was created in mid-19th century when Indonesia was still under the colonial rule of the Dutch. The railway system was created in 1939 so as to facilitate the movement of cargoes and passengers. As at that time, the length of the railway line was 6,324 km long on Java and 1,833 km long on the Sumatera Island. In 2009, the total railway length had fallen substantially from 6,324 km to 3,464 km on Java and 1,833km to 1,350 km on Sumatera Island [1]. The main reason for this decline was the competition of railway transport with road transport, thus more funds were utilized for building more roads at the expense of the railway lines. Hence, Law No. 23/2007 was approved to make railway transport an important means of transportation within Indonesia. This clearly maps out the development guide for the national railway system.

METHODOLOGY: CASE COMPARISONS

Author compare the proposed Jakarta-Bandung HSR corridor with the some of HSR corridors in Asia and Europe regions and to identify key factors that have contributed to its successful. International comparison is especially important in HSR because the research shows important differences across countries due to topography, demographics, nature of transit demand and government investment schemes [2, 3].

EARLY JAPANESE'S PROPOSAL

Japan had already indicated their interest to replicate their Shinkansen HSR technology in Indonesia since 2008. That same year, Japan had displayed their Shinkansen technology and also done a feasibility study. Considering that the Island of Java is identical to the pre-HSR Honshu in Japan, the Japanese government under the Japanese International Cooperation Agency (JICA) therefore proposed the construction of HSR for the Indonesian island of Java, backed by soft loans from the Japanese government, connecting the densely populated capital of Indonesia, Jakarta which suffers from freight and passenger congestion to Surabaya which is about 730 km apart.

A new proposal that focus on building 150 km of HSR from Jakarta to Bandung, which will result in the drastic reduction of the time spent to cover the 150 km from 3 hours to just 45 minutes as shown in Fig.1. Japan which is widely known for the manufacturing of world-class trains was the most favorable to win the contract for construction of HSR from Indonesian government. However, change in government after the 2014 Indonesian gubernatorial election which saw the swearing in of Joko Widodo in October 2014 put an end to this project. The Joko led administration basically the HSR project in January 2015, reason for this action was that the HSR project was quite too expensive for the government to execute and there were several other more important and significant infrastructural projects that were required in the underdeveloped islands outside of Java.

Fig. 1 Japanese proposed route [4]

CHINA'S APPROACH

In 2004, China's State Council adopted the Mid- and Long-Term Plan for railway development and the country decided to venture into the development of HSR. The government proceeded to invest huge sums of money into this plan and, in 2008, it affirmed and upgraded the Plan. Part of China's strategy was the purchase of rail technologies developed countries. This helped to accelerate China's HSR development and led to the development of China's indigenous HSR technology in 2007. This culminated in the manufacture of China's first high-speed train on 1st August, 2008, China vigorously promoted its HSR technology, transitioning and positioning their HSR technology.

Internally, China plans to establish four major train lines, connecting the north to the south and another four lines connecting the east to the west, across the entire length and breadth of the whole country. Externally, several major rail lines are also being planned, one linking Asia and Europe via Russia, another connecting China to Europe via Central Asia and the Middle East, and a third connecting southern China with Indo-China and Southeast Asia [5]. China's HSR strategy has become part an integral belt-and-road strategy and core of China's foreign policy, all these have occurred just within the past decade or thereabout [6]. The 'belt' component comprises of many land routes and the 'road' component on the other hand comprises of many sea routes. This also arise from the fact that both systems of land and sea routes link China to Europe. This initiative also led to the development of special funding and investments [7].

HISTORY AND RECENT DEVELOPMENT

The HSR project was forecasted to cover a distance of about 143 km, linking Jakarta and Bandung, thus becoming Indonesia's first ever HSR project. As highlighted earlier, the Japanese and Chinese government made known their intention. Although the Japanese and Chinese governments had carried out previous comprehensive studies, it was only Japan that went the extra length of issuing a study for a project extending to Surabaya, which was estimate to be about 730 km. This was followed by a counter bid which was submitted by the Chinese government in April 2015, must to the chagrin of the Japanese.

This was followed by a state visit by Joko Widodo, who had a successful meeting with the Chinese president, Xi Jinping on March 26, 2015. After the meeting Xi Jinping publicly announced the support of the Chinese government for the development of Indonesian high-speed project, this was followed by the signing of a memorandum of understanding between the two governments. In July 2015, Indonesia led by Jodo Widodo officially announced their plan to commence the construction of the HSR, this would connect Jakarta and Bandung, the bidding process was then made public, therefore the contest was between the potential bidders which included both the Japanese and Chinese train-makers had. The contest became interesting as the Chinese train-maker organized a Chinese HSR Technology exhibition in August 2015. This was a brilliant move which was not new to either contenders since both the Chinese and Japanese have been engaged in fierce business competition in the past, often using intense lobbying to outdo each other. It was widely acclaimed that the primary reason behind the high display of domineering campaign displayed goes further.

The Chinese government played another card in mid-September 2015, they submitted a new proposal that offered to fully meet the Indonesian government's demands while also eliminating funding required to commence. This was followed closely by several months of bidding, negotiations, between the two countries. It temporarily led to the cancellation of the project, however, the Indonesian government made a decision to select China as the preferred bidder for the US$5 billion project because of its financial structure which was so hard to ignore, considering the fact that this was completely different from what the Japanese plan had proposed.

China's triumph can be alluded to China's willingness fund the project. This would in fact lead to a waiver, which was different from what the Japanese had offered, and the Japanese had also refused to shift their grounds. China had even gone further ahead alleviate its deal by including its commitment to institute a program for the manufacture of light and electric rail system in partnership with local businesses. These products would be targeted at the Indonesian market, and exported neighboring markets, thus creating a seamless technology transfer system that would lead to growth of local technology for renovating and train stations.

Therefore, it looked like Indonesia had benefitted immensely from the Japan-China competition, as the

Indonesian HSR bid earmarked continuous competition between Japan and China in their bid for other infrastructure projects with Asia. The HSR system has 71.63 km of the track on the ground level, while 53.54 km of the track will be raised, and the remaining 15.63 km will be below the surface. This was followed by the groundbreaking ceremony, held on January 21, 2016 to commence the construction of the HSR. The HSR system would be open to the public after its official launch in 2021.

PROJECT'S DESCRIPTION

The HSR is part of the governments' grand ambition of upgrading Indonesia's lagging infrastructure. If successful executed, the project will drastically reduce travel time to just 45 minutes only. The HSR has four stations as seen in Fig. 2.

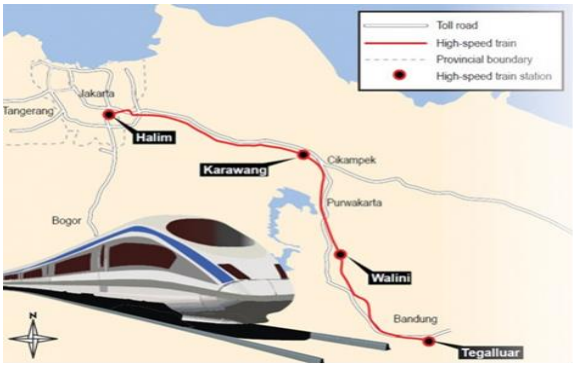

Fig. 2 Route of Jakarta to Bandung HSR

The HSR project will be financed exclusively by China. The project will include integration of the HSR stations with developments along its corridor through transit oriented developments (TOD) [8, 9].

The ambitious proposal for the national railway network comes amid recent news that the cost of the Jakarta-Bandung HSR has swelled to almost US$6 billion, from US$5.2 billion. On the other hand, rail ridership in Indonesia has risen substantially in recent years, making decades of underinvestment and growing urban congestion important considerations for transport stakeholders as they upgrade and construct new lines. Statistics Indonesia (BPS) reports that total rail passengers rose from 199 million in 2011 to 202 million in 2012, 216 million in 2013, 277 million in 2014 and 325 million in 2015. The average length of a passenger journey has simultaneously fallen from 95 km to 68 km, while the country's rail network remains limited to Java and Sumatra, with 22,296 km of total line operational in 2015. The Medium-Term Development Plan 2015-2019 includes an infrastructure development agenda that outlines projects such as having 3,258 km of newly built or rehabilitated rail lines, made up of 2,159 km of intercity railways and 1,099 km of urban railway, and boosting rail cargo volumes to 1.5 million twenty-foot equivalent units annually. Urban rail lines, including a planned light rail transit (LRT) system in Jakarta, are also expected to help reduce congestion and transport costs, which have become the highest in South-east Asia. It was forecast that the new line would attract around 10 million passengers per year in first year of operation, as shown in Fig. 3.

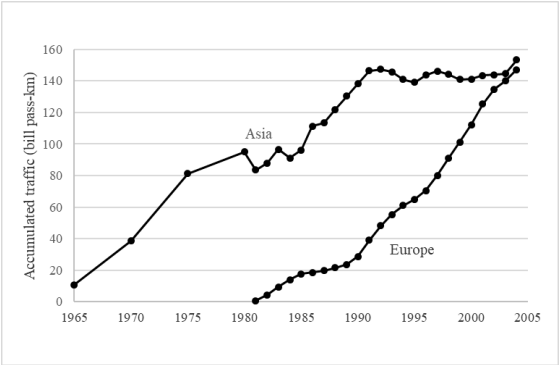

Fig. 3 Accumulated HSR traffic [10]

For 20 years, Shinkansen services in Japan enjoyed a sustained traffic, it gained 100 billion passengers-kilometer. From 1994 to 2004, within the next 20-years interval, the demand halved, because only 50 billion additional passengers-kilometer used HSR. When compared with most European HSR projects which are still in their first 20-year period, it is natural to expect high growth rates as expressed by Fig. 3. Figure 4 shows accumulated traffic used the HSR services in Asia and Europe based on traffic data from each operator during the 2010 to 2016 period. As confirmed by Fig. 4 the only China is still in it incredible constant growth and gained a huge accumulated traffic around 850 billion passenger-km. Two other Asian countries i.e. South Korea and Taiwan started HSR services in first decade of 21 centuries only gained accumulated traffic of 31.4 and 20.2 billion passenger-km respectively during the same period.

Based on long experienced of HSR services in Japan and Europe countries it is easy to predict that most China HSR projects still enjoyed a constant traffic growth for the next two decades most triggering by combined building new dedicated electrified lines and upgrading existing lines. Both South Korea and Taiwan HSR service expressed constant demand growth for the following first decade even the Korea Train Express (KTX) has transported approximately 150 million passengers since the four years after its opening. Taiwan HSR

itself has carried about 100,000 passengers per day for fifty first months of commercial service. However, Shinkansen services is still in its positive growth and gained accumulated traffic of 196 billion passenger-km from 2010 to 2016, two times higher than France figures of 99 billion passenger-km during the same period. France HSR had stagnant traffic growth from 2010 to 2016; in 2016 as an example, SNCF collected accumulated traffic of 49 billion passenger-km, otherwise in 2010 it figures stood at 51 billion passenger-km. Other Europe HSR operators include Dutch, England, and Sweden indicated sustained traffic growth and collected accumulated traffic around 42 billion passenger-km until the end of 2016.

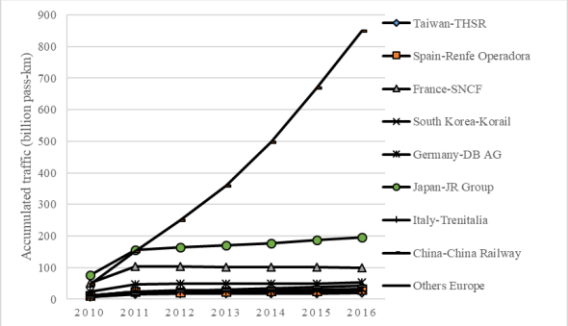

Fig. 4 Accumulated HSR traffic during the 2010 to 2016 period [11]

Based on passenger traffic data obtained from Europe and Asia, the first HSR line constructed in Indonesia is expected to gain considerable amounts of demand. However, it is important to state that in Europe and Asian countries, the construction of HSR lines was as a result of the inability of their conventional lines being unable to meet their demands, thus they needed to add a new capacity to increase rail service. It is also noteworthy to mention that many of these existing rail lines had already been doubled or tripled in a bid to increase the capacity. Therefore, the high demand for conventional rail can be said to have created a market for HSR in these countries. It is inevitable to mention that Indonesia include Jakarta and Bandung lacks of this factor that triggered HSR services successful in Europe and Asian countries.

PROPOSAL OF SG-KL HSR PROJECT

The Malaysian and Singaporean governments signed an agreement on February 2013 that would result in the construction of HSR line, connecting Malaysia [12]. It is of utmost important and key to the successful implementation of Malaysia's national development strategy, (one of the main objective is to increase the country's GDP per person by 150%) by the time this HSR line will be completed in 2020, the Malaysian government is also looking forward to a further boost in the country's economics by closely-tied cooperation with the Singaporean government.

Cost of this project is estimated at RM 40 billion (USD 12 billion). The source(s) of the funding, however, has not been officially disclosed; although some private sources say that Private-Public-Partnership (PPP) funding will be used, others claim that it will be jointly co-funded by both the Malaysian and Singaporean governments considering the fact 335 km of the line will be in Malaysia while the remaining 15 km will be in Singapore. The HSR will have a total of eight stops, seven of which will be within Malaysia and one will be within Jurong East. The high speed rail line which will consist of bullet trains moving at top speed, above an estimated 300 km/hour is projected to become operational in 2026. This would therefore reduce the land journey between Kuala Lumpur and Singapore from about five hours to a mere 90 minutes' journey as shown in Fig. 5.

This project has attracted keen interest from various large corporations within Asia and Europe. However, Mahathir Mohamad who is the current Malaysian Prime Minister had announced on Monday May 28, 2018 that the HSR project will be axed, but he had also explained that it will take some time to execute because the Malaysian government and Singaporean government had also signed a contract on the multi-billion-dollar project. Meanwhile, Dr Mahathir Mohamad, the Malaysian Prime Minister had also assured that the government will remain "business friendly" to all investors involve in the project [13].

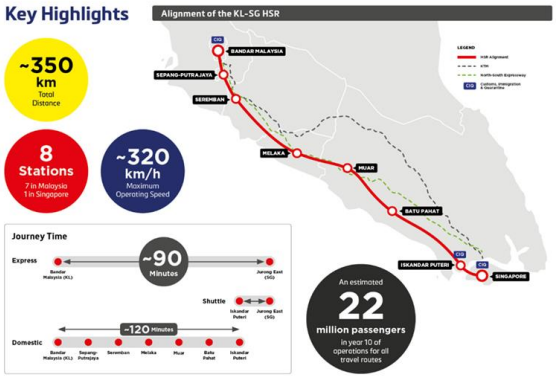

Fig. 5 Proposed Kuala Lumpur – Singapore HSR line [14]

The relationship existing between Malaysia and Singapore is considered unique because of certain factors, these include the geography of both countries, economy, politics, historical background, cultural

heritage, and ethnicity. It is also attributed to the fact that Singapore separated from Malaysia in 1965, hence the similarity. It is also intriguing to know that although both countries have been characterized by healthy competition in economic and social matters, they however enjoy a very high level of economic interdependence as major trading partners. The existing relationship between Singapore and Malaysia has been described as symbiotic. However, this mutually symbiotic as the relationship has been beneficial to both countries, although the relationship has faced some challenges in the past, it has existed since 1965. The Mahathir administration which was in control in Malaysia from 1997 to 2002, was believed by many to be the most stressful period between both Singapore and Malaysia. However, the situation changed after Abdullah Badawi got into power and became the prime minister of Malaysia in 2003, and since then there has been enhanced contact and cooperation between both governments. History is starting to repeat itself again in the part of the SG – KL HSR project [13].

CONCLUSIONS

In conclusion, the Jakarta-Bandung HSR project, linking Jakarta to Bandung was executed by PT Kereta Cepat Indonesia China (KCIC), through mutually agreed business-to-business plan basis, with the Indonesian government. China, which was not only the contender had been awarded the project because of the provision of soft loans for the project; on the other hand, Japan which had showed interest in the project had requested that the Indonesian government funded the project. Surprisingly, Japan was the first to have indicated interested in the project and had even gone ahead to commence working on a feasibility study for HSR track, connecting Jakarta to the country's second largest city, Surabaya, which is about 730 kilometers apart.

Indonesia went further in 2012 to commence another feasibility study focused on the Jakarta-to-Bandung leg, this study was finalized in 2014. The highest operating speed of the trains is estimated at about 350 km/hour, the Jakarta-Bandung high speed rail would result in shortened travel time between the two hubs, reducing the time spent to cover this distance from three hours to 45 minutes only, therefore pushing forward economic development along the line through transit oriented developments. It was projected that the line would also attract about 10 million passengers each year within the first year of operation. This high figure is however a reflection of the densely populated city of Jakarta, and the several number of origin destination pairs that the HSR line would simultaneously serve.

The Kuala Lumpur-Singapore HSR is a strategic project between the Malaysian government and Singaporean government, with its primary goal of facilitating seamless travel between the two capital cities of Kuala Lumpur and Singapore, enhancing business linkages, and connecting the citizens of both countries. The high-speed rail link is expected to reduce the travel time between the two cities from about four to five hours by road to 90 minutes only. However, it is also noteworthy to mention that the surprising decision arrived not long after the newly elected Malaysian prime minister raised the possibility of dropping the project because of its cost implications.

ACKNOWLEDGMENTS

Author would like to express my special thanks of gratitude to Ministry of Research and Higher Education thorough DRPM for funding the research.

REFERENCES

[1] Directorate General of Railway, Ministry of Transportation, Master Plan of National Railway, April 2011.
[2] Campos, J., and de Rus., G. Some stylized facts about high-speed rail: A review of HSR experiences around the world, Journal of Transport Policy, Vol. 16, 1, 2009, pp. 19-28.
[3] Albalate, D., and Bel, G. High-Speed Rail: Lessons for Policy Makers from Experiences Abroad, Research Institute of Applied Economics, Universitat de Barcelona, 2010.
[4] The Ministry of Economy, Trade and Industry, Study on the High Speed Railway Project (Jakarta-Bandung Section), Republic of Indonesia, Final Report, November 2012.
[5] Chan, G. From Laggard to Superpower: Explaining China's High-Speed Rail 'Miracle', The Japan Institute of International Affairs, 2017.
[6] Chan, G. China's high-speed rail diplomacy: global impacts and East Asian responses, EAI working paper, East Asian Institute, Seoul, 2016.
[7] Chan, G. China's New Silk Roads: a new global financial order in the making? in Bo Zhiyue (ed), China-US relations in global perspective. Wellington: Victoria University Press, 2016, pp. 91-107.
[8] Purba, A., Nakamura, F., Niken, C., Jafri, M., and Pratomo, P. A Current Review of High Speed Railways Experiences in Asia and Europe, AIP Conference Proceedings 1903, 060004, 2017, pp. 1-8.
[9] PT Kereta Cepat Indonesia China. High Speed Railway (HSR) Jakarta - Bandung, the Acceleration of Infrastructure in West Java. Rapat Kerja Kementerian Perhubungan (Ministry of Transportation), Jakarta, 2016.
[10] International Union of Railways (UIC). Estimation des resources et des activités

économiques liées a la grande vitesse. Prepared by CENIT (Center for Innovation in Transport, Universitat Politecnica de Catalunya). Paris, 2005.

[11] International Union of Railways (UIC). Railway Statistics, 2015.

[12] Retrieved from: www.railwaygazette.com/news/infrastructure/single-view/view/kuala-lumpur-singapore-high-speed-railway-agreement.html [Accessed: 2018-05-30].

[13] Retrieved from: https://www.straitstimes.com/asia/.../mahathir-spore-will-be-told-of-kls-wish-to-scrap- [Accessed: 2018-05-31]

[14] Retrieved from: http://www.myhsr.com.my/ [Accessed: 2018-05-30]

9th Int. Conf. on Geotechnique, Construction Materials and Environment, Tokyo, Japan, 20-22 November 2019, ISBN: 978-4-909106025 C3051

EXPLORATION OF THE POTENTIALS OF CARBONIC ANHYDRASE-PRODUCING BACTERIA UTILIZATION IN GEOPOLYMER-BASED BIOCONCRETE DEVELOPMENT

*Davin H. E. Setiamarga[1,†], Masahide Uomi[1,†], Diana Waturangi[2], Maggy T. Suhartono[2,3], Maya Shovitri[4], Masataka Kusube[1], Hiroshi Yonemitsu[1], Hirosuke Hirano[1], *Januarti Jaya Ekaputri[4]

[1] National Institute of Technology, Wakayama College, Gobo, Wakayama, Japan
[2] Atmajaya Catholic University, Jakarta, Jakarta, Indonesia
[3] Bogor Agricultural University (IPB University), Bogor, West Java, Indonesia
[4] Institut Teknologi Sepuluh Nopember, Surabaya, East Java, Indonesia

ABSTRACT

Using fly ash (FA; a by-product of coal-based powerplant) as an alternative material to produce concrete might contribute to the reduction of CO_2 emission in the field of general construction. Recent studies have shown that the application of biomineralizing bacteria during concrete production could improve concrete strength. In this research, we aimed to develop a bioconcrete using fly ash as the main binder, and bacteria with $CaCO_3$ precipitation capability to produce concrete micropore filler. In order to do so, we isolated a strain of the bacteria genus *Bacillus* from natto sold in Indonesia, because *Bacillus* are known to precipitate $CaCO_3$ through the production of the carbonic anhydrase enzyme (CA). Next, two types of three variations of FA-mixed concrete (with/without Natto bacteria, with three different ratios of FA/cement), NaOH, and Na_2SiO_3 were prepared, and their compressive strengths measured. We specifically used FA produced by the Suralaya power plant in Indonesia, because of its high percentage of calcium. The results indicated that the durability of concrete specimens made from 100% cement and 100% geopolymer were increased in samples with the natto bacteria added. The presence of bacteria in the specimens was confirmed by SEM, and the presence of $CaCO_3$ precipitates was confirmed by XRD. 16S-rRNA analysis of the bacteria indicated that it is *Bacillus safensis*. A PCR survey using CA specific primers showed that our *B. safensis* strain possesses the *carbonic anhydrase* gene. From these results, we deduced that the specimens containing natto bacteria were stronger probably because $CaCO_3$ produced by the CA-producing bacteria, precipitated and filled the micropores in the concrete specimens.

Keywords: fly ash, concrete, carbonic anhydrase, bioconcrete, CO_2

INTRODUCTION

In recent years, global warming caused by the emission of carbon dioxide (CO_2) from the field of general constructions has caused great concerns. This is because the production of cement, which is the main ingredient of concrete, generates CO_2 in an amount equivalent to that of the produced cement (CO_2/cement = 0.95) [1]. Therefore, reducing the amount of cement might contribute to the reduction of anthropogenic CO_2 emissions. However, rapid economic development in Indonesia has caused the demand for concrete in the country to increase [2].

About half of the power suppliers in Indonesia are thermal power plants. There are more than 100 coal-based thermal power plants in Indonesia, disposing millions of tons of fly ash annually. In Indonesia, fly ash is considered as a hazardous industrial waste. One of the legally accepted methods of treating fly ash is to solidify them into blocks. The blocks were then piled up in a specific "ash yard" inside the power plants.

In recent years, fly ash has been considered as a potential alternative building material. Unlike cement, fly ash is not water-soluble. Therefore, in order to use fly ash as a precursor to produce pozzolan binder, the fly ash is mixed with alkaline solution to form geopolymer paste, which is then used to produce concrete [3][4]. However, such concretes are still in the development stage because in most cases, their strength is weaker than cement-based concrete. Since concrete strength also depends on the presence of micropore fillers, finding methods to fill the micropores in geopolymer concrete might solve this particular problem. Moreover, geopolymer-based concrete was shown to be denser when compared to portland cement-based concrete, and thus has other advantages such as low permeability to chloride ions, which might increase the durability of constructed structures [5].

Table 1. Chemical properties of binders by XRF

Oxydes	fly ash	OPC
SiO	44.83	20.92
Al_2O_3	29.23	5.49
Fe_2O_3	4.66	3.78
TiO_2	0.84	-
CaO	4.47	65.21
MgO	1.62	0.97
Cr_2O_3	0.01	-
K_2O	0.68	-
Na_2O	1.32	-
SO_3	0.62	2.2
MnO_2	0.09	-
P_2O_5	0.25	-
LoI	11.13	-

Current research has focused on the potentials of biomineralizing microbes as agents to produce fillers in concrete [6]. This is carried out by including microorganism-induced calcite precipitate (MICP) agents [6][7], such as the urease-producing micro-organisms into concrete, in order to induce calcium carbonate ($CaCO_3$), precipitations. However, urease-based approach reduces the durability of concrete because urea must be added into the concrete. Urea is known to produce the highly acidic nitrates and nitrites, which could dramatically decrease concrete alkalinity, which in turn might corrode reinforce-ment metals [8].

Another MICP method is by using carbonic anhydrase (CA)-producing microbes [6][9]. Carbonic anhydrase works by catalyzing the inter-conversion between HCO_3^- and CO_2, which might lead to the precipitation of calcium carbonate. This enzyme is known to be present in *Bacillus* bacteria. *Bacillus* is also known to survive in extreme environment, including in alkaline condition [10].

In this study, we focused on carbonic anhydrase-producing *Bacillus* bacteria to induce precipitation of calcium carbonate ($CaCO_3$) as micropore fillers in concrete. We expect carbonate precipitates in the micropores would improve the durability and decrease chloride ion permeability [5]. *Bacillus* species used in this bioconcrete study were isolated from natto in Japan and Indonesia. Meanwhile, the fly ash used in this study was obtained from the Suralaya Power Plant in Indonesia. In order to simplify the experimental system, we used OPC paste and geopolymer paste (with and without bacterial addition) to make test specimens.

Figure 1.
A. Specimens made from geopolymer paste;
B. Specimens made from OPC paste;
C. Compressive strength test on specimens

MATERIALS AND METHODS

(1) Isolation of natto bacteria

Natto packs were purchased from a supermarket in Surabaya, Indonesia, and from a convenience store in Japan. A quick swab using the platinum loop was done, and then spread over a plate, and cultured overnight at 37ºC. Single colonies were picked and then cultured by shaking in an LB liquid medium overnight at 37ºC. The resulting bacterial solution was spread over an LB plate, and cultured at 37 ºC for 10 hours to obtain single colonies. The single colony was then picked, and again cultured overnight in LB liquid medium, streaked again on LB plate medium, and statically cultured at 37 ° C. for 10 hours to obtain single colony. This operation was repeated 5 times to obtain single natto bacteria. Glycerol stocks of the bacteria deriving from a single colony were made and stored in a -80°C freezer. The following experiments were all performed on cultured samples obtained from the glycerol stocks.

(2) Molecular identification of the natto bacteria

Picked single colony as inoculated in an LB liquid medium and cultured with shaking at 37ºC for 24 hours. Afterward, bacterial cells were precipitated through centrifugation (15,000 rpm, 1 minute). DNA extraction was conducted using the alkaline lysis method following the standard protocol. The 16S-rRNA gene was amplified using the standard PCR protocol for microorganisms using the bacterial universal primers 27F / 1492R [11]. Successfully amplified DNA were then sent to FASMAC Inc. in

Table 2. Compressive Strength at 7 and 28 days (MPa)

Paste	Non Bacteria		*B. safensis*		*B. subtills*	
Age (days)	7	28	7	28	7	28
OPC	100.8	109.5	66.2	88.9	55.4	73.8
Geo-polymer	45.0	71.8	32.9	77.34	41.2	41.0

Japan for sequencing. Obtained sequences were then used as queries for BLASTn searches on Genbank nr database for species identifications.

(3) Preparation of test specimens

In this study, we used fly ash collected from the Suralaya Power Plant, West Java, Indonesia, as the binder to make specimens. Fly ash from this power plant is classified as class F fly ash [12]. Specimens for comparisons were made from the Ordinary Portland Cement (OPC) as the binder, with the density of 3.14 g/cm^3. The chemical compositions of the fly ash and the OPC are listed in Table 1.

The geopolymer specimens were made by mixing fly ash and alkali activators. Two types of alkali activators, sodium silicate (Na_2SiO_3) and sodium hydroxide (NaOH) were used. The concentration of sodium hydroxide was 8M. Meanwhile, the mass ratio of sodium silicate to sodium hydroxide was kept constant at 2. The mass ratio of binder (the fly ash) and akali was kept at 7:3 to obtain water to solid ratio of 0.23. Specimens made with portland cement were prepared with mixing Ordinary Portland Cement and water with water to cement ratio of 0.23.

The specimens were created with two variations: with and without addition of natto bacteria. Two types of natto bacteria were used: those isolated from natto available in Indonesia, and those isolated from natto sold in Japan. In specimens with bacteria addition, after mixing with a mixer, the bacteria solution was added to the homogenous paste mixture and thoroughly mixed again using a mixer. Concentration of microbial agent in liquid form is 1000 mL/m^3. Afterward, the mix was cast in a cylindrical mold and allowed to set for 24 hours, and

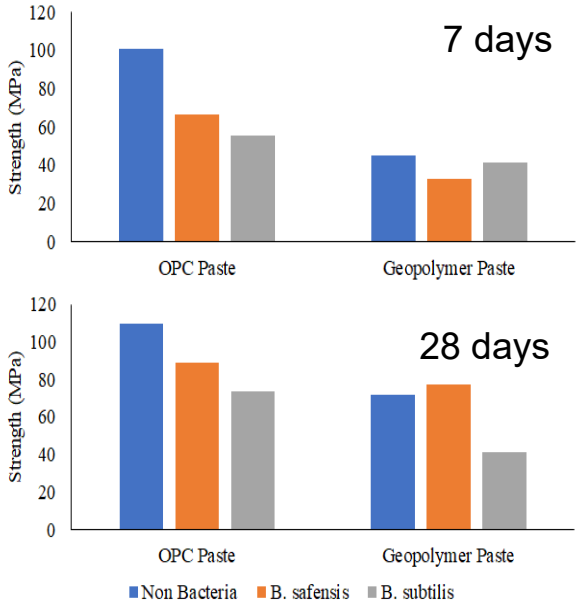

Figure 3. Compressive strength of the specimens at seven days and 28 days.

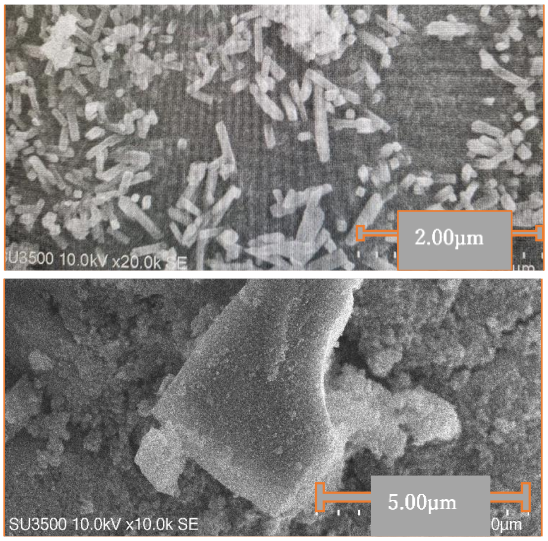

Figure 4. SEM analyses showed the presence of bacterial colony on geopolymer specimens with bacterial addition during production (UPPER). The lower picture showed the absence of any microbe in specimens produced without bacterial addition.

then de-molded and cured in moist condition until the age of seven and 28 days for compressive test. Cylindrical specimens (Figure 1) with a diameter and height of 2 am and 4 cm respectively were prepared for compressive strength test at seven and 28 days according to ASTM C39 (Figure 2) [13]. Microbe-free specimens from both geopolymer and OPC paste were also made as control specimens.

(4) SEM and XRD analysis

SEM analyses were conducted to confirm the presence of bacteria in the specimens. XRD analyses of specimens at the age of 28 days were conducted to confirm the presence of $CaCO_3$ crystals. The analyses were conducted at The Research Center for Nanosciences and Nanotechnology, Bandung Institute of Technology, Indonesia.

(5) PCR exploration to determine the presence of the *carbonic anhydrase* (CA) gene

Amino acid sequences of the CA enzyme from 7 strains of *B. safensis* and 1 strain of *B. subtilis* were downloaded from the UniProt web server [14], and the corresponding nucleotide sequences were downloaded from GenBank. The sequences were used as references to design two sets of CA specific primers we used to do the PCR survey of the *carbonic anhydrase* gene. PCR were conducted following the standard protocol, with the annealing temperatures of 54ºC. Successfully amplified sequences were sent to FASMAC Inc. for sequencings. Obtained sequences were used as queries for BLASTn searches.

RESULTS AND DISCUSSION

(1) Molecular identification of the bacterial species

A 820 base-long sequence was obtained from the 16S-rRNA gene sequencing. For the bacteria isolated from the Japanese natto, BLASTn search using the sequence as the query suggested that the Japanese natto bacteria was *Bacillus subtilis* (*B. subtilis*) with 99% sequence similarity and e-value, 0. Meanwhile, a BLASTn search using the sequence of the Indonesian natto as the query suggested that the bacteria species was *Bacillus safensis* (*B. safensis*) (sequence similarity = 99%, e-value = 0).

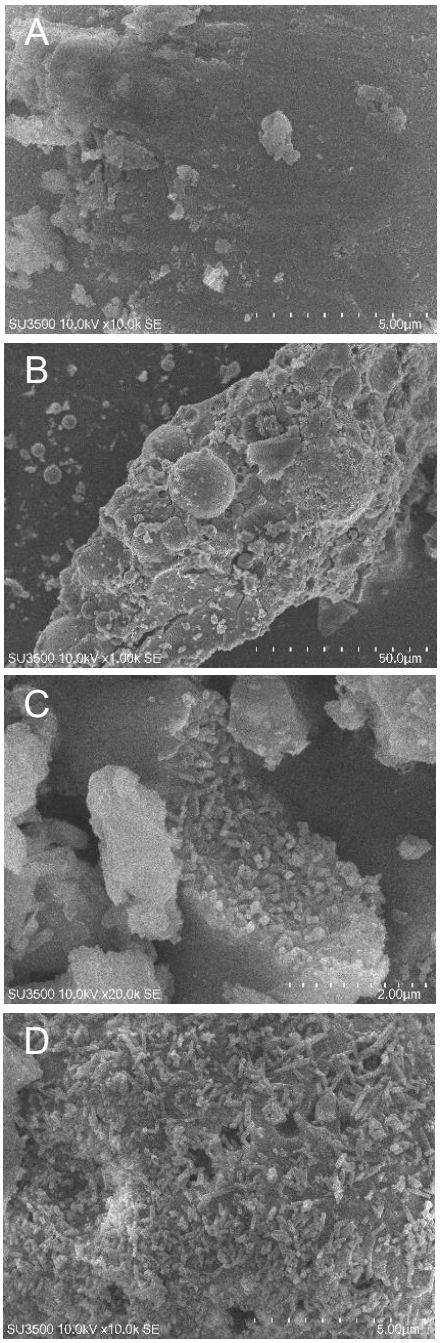

Figure 5. SEM analyses to track the presence of microbes on the specimens.
A. OPC specimen without microbial agent; B. Geopolymer specimen without microbial agent; C. Geopolymer specimen containing *B. subtilis*; D. Geopolymer specimen containing *B. safensis.*

(2) The compressive strength of specimens

Compressive-strength test (Figure 1C) was conducted for bacteria-free specimens, specimens containing *B. safensis*, and specimens containing *B. subtilis*. Average compressive strength was calculated from five identical specimens for each variation. The resulted strength values are shown in Table 2 and Figure 3.

As expected, OPC specimens showed higher strength than the geopolymer ones. This is most likely because, while all particles of cement are water-reactive, the reactivity of geopolymer particles (alumina-silica-based particles) depends on the quality of the fly ash.

The compressive-strength difference was large when specimens containing microbes were compared between those of the age of seven days and those at the age of 28 days (Table 2; Figure 3). This is probably because the specimens did not reach maturity, and thus the strength did not increase to a comparable level on day seven. Therefore, strength comparisons should be performed at the age of 28 days.

Some references suggested using 400–500 ml microbial agent per cubic meter concrete mixture [18][19]. This is roughly only half the amount we used in this study. A comparison between microbe-containing and microbe-free specimens suggested that microbe-free specimens were cured in seven days, while microbe-containing specimens might need more time to cure. This is probably because of the excessive amount of microbes in the mixture acted as CO_2 contributor that did not react with calcium hydroxide in the cement paste.

Our result also indicated that geopolymer specimens containing *B. safensis* showed higher strength compared to those containing *B. subtilis* (Table 2; Figure 3). Our result also indicated that the presence of *B. safensis* might affected the increase in compressive strength to reach the highest value on day 28 (Table 2; Figure 3).

(3) SEM analyses results confirmed the presence and absence of microbes in the specimens

From the Figure 5, we can confirm the presence of 1.00 µm –2.00 µm rod-shaped bacterial particles in the geopolymer specimen containing *B. safensis* (Figure 5C and 5D). This is not seen in specimens without microbes (Figure 5A and 5B). The results also suggested the prominent presence of *B. safensis*

population (Figure 5C), compared to *B. subtilis* (Figure 5D), in the geopolymer specimens. From this observation, we deduced that *B. safensis* probably could survive better than *B. subtilis* in geopolymers, as indicated by the presence of bacterial populations inside the specimen.

(4) XRD analyses to confirm the presence of calcium carbonate

Our compressive strength result indicated that the presence of bacteria increased the strength of geopolymer specimens (Figure 3). If we focused on the ability of *Bacillus* bacteria to produce $CaCO_3$, this could be explained by the possibility that the bacteria precipitated $CaCO_3$, and the precipitates filled the micropores inside the specimens. Figure 6 shows the results of XRD analysis of specimens with and without microbes. The intensity of the peaks indicating mineral presences in Figure 6B (*B. safensis*-containing specimen) is higher that in Figure 6A (microbe-free specimen). Also, the result indicated the presence of aragonite and calcite, crystal aggregates of $CaCO_3$, that could be formed in the presence of living organisms, including CA enzyme-producing bacteria [7][9][20]. This suggests that mineral formation in the geopolymer specimens was probably caused by the presence of *B. safensis*.

(5) The presence of the *carbonic anhydrase* (CA) gene in the bacterial genome

Our survey of the presence of the *carbonic anhydrase* gene in the genomes of the bacteria indicated that both *B. safensis* and *B. subtilis* possess the the gene in question. Sequencings using primers designed to amplify a conserved region of the CA gene of the *Bacillus* family produced 280 base-long sequences from both *Bacillus* (*B. safensis* = sequence similarity = 100%, e-value = 0; *B. subtilis* sequence similarity = 100%, e-value = 1e-138). Although further experiments are still needed for confirmation, we can deduce that both *Bacillus* species have the ability to precipitate $CaCO_3$ using the CA enzyme.

(6) Why the increase in compression strengths can be attributed to bacterial CA

Considering all results together, the increase of compression strengths on geopolymer specimens could be attributed to the presence of *B. safensis*, which, by producing the CA enzyme, precipitated $CaCO_3$ in the micropores of the specimens. We hypothesized the following process to explain this phenomenon. First, water and *B. safensis* were present in the micropores. *B. safensis* releases CO_2 through respiration, filling the micropores with the gas. The CO_2 dissolves in the surrounding water and is catalyzed by the CA enzyme produced by *B. safensis*, forming carbonate ions. The ions then combined with calcium ions abundantly present in the fly ash, forming calcium carbonate ($CaCO_3$) particles. The particles then filled the micropores, and causing the specimens strength to increase.

Our result, and the hypothesis conceived based on the result, presented here, must be further tested. Additional informations about the microbiology of *B. safensis*, the biochemistry and molecular biology of the CA enzyme, as well as informations obtained from further tests on various types of paste and concrete specimens, are still needed. However, we are confident that our progress report presented here contains valuable pieces of information on the development of geopolymer-based alternative construction materials.

ACKNOWLEDGEMENTS

The authors would like to thank Varia Usaha Beton, Co. Ltd. for providing Ordinary Portland Cement (OPC). DHES were partially supported by the National Institute of Technology, Wakayama College Competitive Internal Research Grant for Education and Research 2016 and 2017. JJE was funded by Penelitian Unggulan Strategis Nasional (PUSN) Grants-in-aid Batch 1 2018 from the Ministry of Research, Technology, and Higher

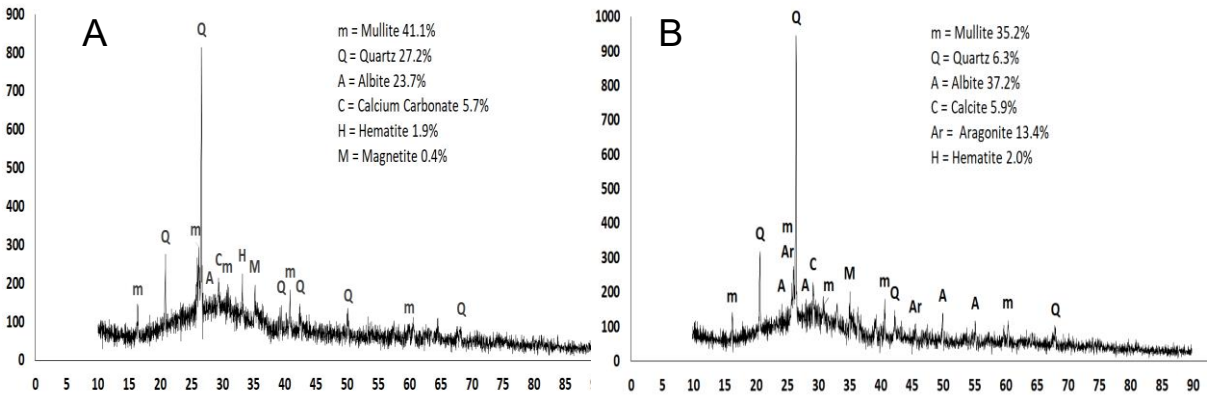

Figure 6. XRD analyses results on specimens, to determine the presence of organic $CaCO_3$. A: The result of microbe-free specimen; B: The result obtained from *B- safensis*-containing specimen.

Education of Indonesia. MU stay in Indonesia was supported by the JASSO Scholarship for Japanese students to study abroad 2018.

REFERENCES

[1] J Davidovits. Global warming impact on the cement and aggregates industries. World Resource Review, Vol. 6, No.2, pp. 263-278, 1994

[2] 建設経済レポート62号2014.4, pp. 263, http://www.rice.or.jp/regular_report/construction_economic_report.html

[3] AL Wijaya, JJ Ekaputri, Triwulan. Factors influencing strength and setting time of fly ash based-geopolymer paste. MATEC Web of Conferences Vol. 138, 01010, 2017

[4] P Risdanareni, P Puspitasari, JJ Ekaputri. Chemical and Physical Characterization of Fly Ash as Geopolymer Material. MATEC Web of Conferences Vol. 97, 01031, 2017, ETIC 2016

[5] JJ Ekaputri, IS Mutiara, S Numinarsih, DHE Setiamarga. The effect of steam curing on chloride penetration in geopolymer concrete. MATEC Web of Conferences Vol. 138, 01019, 2017, EACEF 2017

[6] AF Alshalif, JM Irwan, N Othman, A Al-Gheethi, A Hassan, IMA Nasser. Potential of carbonic anhydrase and urease bacteria for sequestration of CO_2 into aerated concrete. MATEC Web of Conferences Vol. 138, 01019, 2017.

[7] SP Chaparro-Acuña, ML Becerra-Jiménez, JJ Martínez-Zambrano, HA Rojas-Sarmiento. Soil bacteria that precipitate calcium carbonate: mechanism and applications of the process. Acta Agronomica, Vol. 67, No. 2, pp. 277-288, 2018

[8] M Sadegzadeh, CL Page, PRW Vassiet. Effects of urea on durability of reinforced concrete. Magazine of Concrete Research, Vol. 45, No. 164, pp. 179-186, 1998

[9] S Sundaram, IS Thakur. Induction of calcite precipitation through heightened production of extracellular carbonic anhydrase by CO2 sequestering bacteria. Bioresource technology, Vol. 253, pp. 368-371, 2018

[10] Z Zhang, B Lian, W Hou, M Chen, X Li, Y Li. *Bacillus mucilaginosus* can capture atmospheric CO_2 by carbonic anhydrase. African Journal of Microbiology Research Vol. 5(2) pp. 106-112, 18 January, 2011

[11] WG Weisburg, SM Barns, DA Pelletier, DJ Lane. 16S ribosomal DNA amplification for phylogenetic study. Journal of Bacteriology, Vol. 173, No.2, 697-703, 1991.

[12] ASTM C 618-05. 20015. Standard Specification for Coal Fly Ash and Raw or Calcined Natural Pozzolan for Use in Concrete. ASTM International.

[13] ASTM C 39-05. 20015. Standard Test Method for Compressive Strength of Cylindrical Concrete Specimens. ASTM International.

[14] Uniprot Consortium. UniProt: a hub for protein information. Nucleic Acids Research Vol. 43, D204-12, 2015

[15] F Hammes, N Boon, G Clement, J de Villiers, SD Siciliano, W Verstraete. Molecular, biochemical and ecological characterisation of a bio-catalytic calcification reactor. Applied microbiology and biotechnology, Vol. 62, No 2-3, pp. 191-201, 2003.

[16] GA Silva-Castro, I Uad, A Gonzalez-Martinez, A Rivadeneyra, J Gonzalez-Lopez, MA Rivadeneyra. Bioprecipitation of calcium carbonate crystals by bacteria isolated from saline environments grown in culture media amended with seawater and real brine. BioMed research international 816102, 2015.

[17] S Kumar, G Stecher, K Tamura. MEGA7: Molecular Evolutionary Genetics Analysis version 7.0. Molecular Biology and Evolution Vol. 33, 1870-1874, 2016.

[18] TH Bagio, M Basoeki, J Tistogondo, SA Pradana. Optimum concrete compression strength using bio-enzyme. MATEC Web of Conferences 138, EACEF 2017.

[19] KD Wulandari, JJ Ekaputri, Triwulan, C Fujiyama, DHE Setiamarga. Effects of microbial agents to the properties of fly ash-based paste. MATEC Web of Conferences 195, ICRMCE 2018

[20] AF Alshalif, JM Irwan, N Othman, MM Zamer, LH Anneza. Carbon Dioxide (CO2) Sequestration In Bio-Concrete, An Overview. MATEC Web of Conferences, Vol. 103, 05016, 2017.

9th Int. Conf. on Geotechnique, Construction Materials and Environment,
Tokyo, Japan, 20-22 November 2019, ISBN: 978-4-909106025 C3051

ABILITY AND WILLINGNESS TO PAY FOR WASTE WATER MANAGEMENT MAINTENNACE SERVICES (IPAL)

*Marselina Djayasinga and Tsra Subianto

Economic and Business Faculty, University of Lampung, Indonesia

ABSTRACT

Infrastructure sustainability must be maintained through public participation payment for the utilization of these public facilities. However, it is difficult to determine the appropriate tariff of public utilization. Ability and Willingness to Pay (ATP and WTP) are used to get it. This study aims to estimate ATP and WTP of beneficiary of waste water management maintenance services (IPAL). Using a purposive random sampling and cluster technique from 300 RT, there are 153 are selected as samples. There are 3 classification of household: household native inhabitans , household comers without experience with PDAMs, and household comers with experience PDAM. PDAM is another alternative of water supply produced by government. The results of this study are, the highest ATP is household inhabitants compared to the other 2 household categories. The WTP for IPAL is 30% higher than the rate set by the government initially. Increasing WTP is affected by the level of education, reference cognition, level of income and satisfaction. Continuous improvement in technology of water treatmenty, socialization to the community and use of tariffs based on volume of usage must be carried out for the continuity of infrastructure.

Keywords: Willingness to pay, Ability to pay, Waste water management services

INTRODUCTION

Lack of public awareness of waste water treatment has caused some areas to become a crisis of clean water and polluted the environment. Recently, waste water management maintenance services is becoming an important issue in the water protection in Indonesia. According to Hua (2010) the increasing population and reduced water resources have caused the need for clean water to be a very pressing problem in almost all parts of the world and lack of awareness of proper waste water.. This habit is driven by the low charge even free of charge of this services. As a public good, waste water management maintenance services IPAL) in Indonesia, is not on market mechanism. The tariff cannot be determine because no one can express their preference. So, it is needed the method to get the tariff which reflect the ability and willingness to pay of beneficiaries in order to maintenance this public facilities sustain for long time and arose awareness community to protect the water. Community is expected to respond for this public facilities by expected to be willing to participate through pay some cost to maintain the sustainability of this public infrastructure.

Langkapura Baru Sub district, in Bandar Lampung City is one of the worst sanitation areas, where domestic waste water, both black water and gray water, is thrown into the environment without any prior treatment, thus polluting surrounding groundwater and often experiencing drought. Now, the village is being built a Waste Water Treatment Plant, we called IPAL and immediately operating precisely at RT. 05 LK.II Langkapura Baru. The total population of households who will use the service is 350 families.

The IPAL program aims to overcome the problems of clean water and sanitation through the provision of assistance to Low-Income Communities by building communal IPAL. This public facility will treat household black water and gray water waste so that treated wastewater can be returned safely to household and environment in accordance with environmental quality standards. This processed wastewater will be the next source of clean water. The regional government cooperating with the Islamic Development Bank (IDB) only build the IPAL infrastructure, meanwhile for operational and maintenance costs are expected to come from community participation. So that the amount of the tariff is needed to cover this operational and maintenance costs of the IPAL, which will be charged to the community, especially the beneficiaries, which is in accordance with the ATP and WTP beneficiary households

Now, the city government has set a tariff for Communal IPAL in the Langkapura Baru Village for operation and maintenance of this public infrastructure by IDR 100,000 / month / household. This tariff is set by the city government with the consideration that the government will

provide a subsidy of IDR 50,000 / household, and honestly this subsidy can build the same infrastructure in other regions if burden to community. Allen Consulting Group (2003) states that one source of financing for public goods can come from fees in the form of tariffs, where the levy rates are influenced by the ability to pay (Ability to Pay) and Willingness to Pay. Based on this background, it is a technique for estimating tariffs that cover operational and maintenance costs and encourage environmental awareness. One of the methods to estimate is the Ability to Pay (ATP) and Willing to Pay (WTP).

ATP is the ability to pay for public services received based on income that is considered ideal. According to Rubiani (2004), ATP is the amount of money that can be paid by the community to replace the service costs it receives While Russel (1995) states that ATP is a consideration in spending his income / expenditure to buy goods or other services. ATP is related to the limitations of household income, where household need make priorities economically in choosing maximum satisfaction. ATP is the rest of income after deducted by essential expenditure, non-food expenditure, non-essential expenditure.

According [14] one form of participation of community can be seen from their willingness to pay.WTP according to Wedgwood. A (2003) is the maximum amount of an individual's status for willingness to pay for an item or service, Mankiw (2004) defines WTP as the highest price that each beneficiary is willing to pay using the consumer surplus approach of the demand curve . The consumer surplus is the willingness of a person to pay an economic value less the value actually paid by him. Economists, psychologists, and marketing researchers rely on measures of consumers' willingness to pay (WTP) in estimating demand for private and public goods and in designing optimal price schedules [22] and customers pay what they bid (s) so they must bid less than their true WTP if they want to obtain surplus from the transaction.. Using WTP to avoid the problem of free-riders in the determination of tariffs for public goods services [3].

OBJECTIVES

This study aims (1) to calculate the ability and willingness to pay off household to waste water management maintenance services (IPAL) in order to get the tariff in which is resulting which cover operational and maintenance cost and arouse the awareness of households to be more responsible in water protection, (2) to investigate the relationship between respondent’s characteristic with their WTP. This study is expected to provide policy to set tarrif in which keep infrastructure sustainable and community awareness.

LITERATURE REVIEW

Public participation is essential t and may lead to enormous benefits for sustainability development [5, 22] agree that public goods are build by the government should be managed by the community which requires active community involvement. Involvement, participation and some characteristic of household determine their choices in WTP. WTP is a technique to know the willingness of individuals to pay for public goods benefit in which the price of it cannot be determined by market mechanism because of the lack of information or preferences. Some experts also define WTP is the maximum price beneficiaries willing to pay for a given quantity of product or services [21]. WTP as a way of calculating the ability of each individual on an aggregate basis to pay in order to improve environmental conditions to conform to desired standards. Economic valuation is an attempt to provide a quantitative value to goods and services produced by natural resources and environment regardless of whether the market value is available or not [17] and. CVM is done by asking directly to benefit about the value of benefits of public goods includes resources and environment. [12] found that almost 85% of respondents are willing to pay a higher tariff and this WTP is effected by the level of education, family income This result also supported by [11] that the average WTP of consumers on waste treatment services is higher than the tariffs paid.

WTP is based on the user's perception of the public services. To get user perception, it can be used the Contingent Valuation Method (CVM). According to [7] CVM is one technique to analyze the valuation function that can provide qualitative information that is difficult to identify using other conventional valuation techniques. CVM is conducted because people is unable to express its preference for economic, such as for tourism hunting services, dumping tariffs, pollution, waste management, utilizing wildlife, environmental quality, etc. CVM is a method of measuring someone's preference [8]. CVM is measuring WTP by eliciting stated user preferences through direct surveys. The useris directly asked about their WTP by using open-ended questions [17]. In these surveys, household or beneficiaries are offered some alternative services or condition with varying attributes. WTP is inferred indirectly from their ranking or ratings of these alternative services.

Some characteristics of community such as education level, gender, age, lines of class, race,

ethnicity, house type, house distance, income and service quality, awareness, perception and household satisfaction level toward the benefits of public goods in correlating with WTP [4, 13]. Effects on WTP is high when they are interactions with each other.. Community awareness of the environment is influenced by the level of education and knowledge about the environment [7]. According to [17] household concerning will affect WTP and it increases along with improving the quality of services. Income inequalities can influence environmental degradation. Inequalities may affect the overall extent of environmental quality so that the higher income the higher WTP .High level of awareness and knowledge and positive attitude will increase environmental protection [2].

METHODOLOGY

The location of IPAL construction is in the RT. 05 .LK II Langkapura Baru, City of Bandar Lampung. There are 350 households will receive direct benefits from this infrastructure are 350 families. With a quota purposive sampling technique with the cluster method,158 respondents were selected. Through structured questionnaires and interview techniques, to determine the amount of tariff for operational and maintenance services based on their ATP and WTP. The Contingent Valuation Method (CVM) method with game bidding techniques are conducted by giving repeated questions about the desire to pay for wastewater management maintenance services with a number of services. The frequency of water flowed into the household is service scenario. At the starting point, tariffs are used and the service promised by the government is IDR 100,000 / month / RT and water is supplied to household twice a week. The 7 scenarios are designed as follows:

Table 1. 7 Scenarios of Services IPAL

Scenarios	Services	Tariff/ month
Scenario A	Water will be flowed to household once a week	90.000
Scenario B (starting point)	Water will be flowed to household 2 times a week	100.000
Scenario C	Water will be flowed to household 3 times a week	110.000
Scenario D	Water will be flowed to household 4 times h a week	120.000
Scenario E	Water treatment will be flowed 5 times a week	130.000
Scenario F	Water treatment will be flowed times a week	140.000
Scenario G	Water treatment will be flowed every day (7x a week)	150.000

The starting point of IPAL services scenario at B, in which wastewater treatment will be flowed to household 2 times a week with tariff IDR 100.000. IPAL services is decreased or increased by flowing water to household once a week, Increased scenario using IDR 10.000 every stage .If most respondents answer to one scenario selected, then his scenario is the actual WTP desired mostly

Hypothesis Development

To answer the second objective that the relationship between the characteristics of the respondent with their WTP, correlation technique and crosstab analysis techniques are used. The respondent's characteristic consists of 5 elements, namely the number of family members, the level of education, reference cognition. Level of income and satisfaction of the services. The hypothesis developed as follows:

Ha (1):Numbers of Family has a positive correlation with WTP.
Ha (2):Level of education has a positive correlation with their WTP
Ha(3):The reference cognition has a positive relationship with WTP.
Ha(4):Level of income level has a positive relationship with WTP.
Ha(5):The level of satisfaction of respondents has a positive relationship with WTP.

RESULT

Descriptive Respondent

Questioner distributed to 350 households. There are 158 households that returned and responded the questioner or 45%. The purpose of the household classified is to prove the correlation between reference cognition with their WTP. It may be correlated between perceptions of RTs who have no reference at all about clean water management, and households that have already felt

clean water management services such as IPAL, namely PDAM

Table 2. Family Categories of Respondent

Family Categories	KK	Percentage
Household stay formerly	78	49%
Household comers without experience with PDAM service.	43	27%
Household comers with experience with PDAM service.	37	24%

The original RT was obtained by 78 households, namely the RTs that settled in that location and had never moved. During this time they have experience in the difficulty of obtaining water, especially during the dry season. The second is 43 newcomer RT groups, namely RTs who moved to that location and have settled in that location and this household has never experienced water treatment services like the previous PDAM. PDAM is a water treatment service that is managed by the city government where the source of the spring is from a river or mountain or other source, then it is channeled to RT. Third, namely immigrant households that live in that location but already have experience in experiencing PDAM services. They already know a little about the quality of PDAM water, the tariff, the frequency of the water flowing to the previous household. The characteristics of respondents based on the number of family members and the level of education obtained the following results.

Table 3. Descriptive of Respondents

	A	B	C
Family member :			
< 5 person	40 %	65%	60%
≥ 5 person	60%	35%	40%
Level of Education			
< 9 years	40%	20%	15%
9 ≤ x < 12 years	25%	25%	20%
≥ 12 years	35%	55%	65%

Note: A is household stay formerly and never move to other location, B is household comers without PDAM service experience, C is household comers with PDAM experience

Households which stay formerly in that location have a greater number of family members than household comers with relatively lower levels of education than comers. On the other hand, household comers is dominated by small family . They have a family members less than 5 people, but they have with a relatively higher level of education than formerly household.

ATP dan WTP

The Ability to Pay for household stay formerly on average, is lower than to ATP in household comers, but their willingness to pay (WTP) is highest than to the other 2 categories of households. This is presumably because the former households have experience having difficulty obtaining water so they highly value water and realize how difficult it is to obtain clean water. While ATP for household comers with experience using PDAM services is the highest compared to the other two household categories, but they have the lowest WTP compared to the other two household categories. Household comers with PDAM experience have had references to the quality and quantity of clean water provided by the city government so far with cheaper rates because PDAM tariffs have been subsidized by the government.

Table 4. ATP and WTP IPAL (IDR ,000)

Family Category	ATP	WTP
Household stay formerly	295	125
Household comers without experience with PDAM	305	115
Household comers with experience with PDAM	315	95

Based on the questionnaire, the average tariff for PDAM water services, ranges from IDR 100,000 - 300,000 / month with water can be used not only for bathing and MCK but for drinking and cooking. Household comers consider that wastewater management from IPAL are still unsure about the quality of water produced This condition happen because of the source of wastewater from IPAL is come from black and gray water. Whether it is hygienic or not to be consumed, the use of waste water that has been processed by IPAL is still bog question. Based on the IPAL experience, water is usage only limited for non-eating, drinking purposes such as washing clothes, flush for toilet, washing vehicles, flushing plants. Household who stay formerly do not really care about wastewater quality. The important for them is, that water supply is always there regularly every day. For this condition and they want to pay higher because of the benefits of water and water difficulties so far.

WTP

Of the 158 respondents who were filled with the questionnaire, respondents were dominantly chosen scenario F, by 35,7%. They desired the wastewater management services working 6 times a week to flow the water. They agreed to pay IDR140.000 charged per month. If it compares with government tariff which is IDR 100.000, this WTP can increases 40%. A total of 31,4 % of respondents are willing to pay IDR 110.000 or scenario D, in which wastewater treatment is flowed to the household by four times a week, A, B, C, E, F. The respondent's choice is shown in

Table 5. Validity of WTP of IPAL (IDR)

Scenario	Tarif WTP	Valid (%)
A	90.000	10,5%
B	100.000	26,3%
C	110.000	30,8%
D	120.000	31,4%
E	130.000	24,2%
F	140.000	35,7 %
G	150.000	20,8%

The actual WTP is that it is willing to pay IDR 140,000 a month or increase 40% as long as the quality of water treatment is improved, by increasing the flow of water to household 6 times a day. This result is higher than what [7] found in WTP of water supply in Nigeria. It 's mean that the WTP can be pushed to increase if their satisfaction of public services is increased.

Correlation Between the Characteristics of Respondent with Their WTP of IPAL

The relationship of some characteristics of respondents with their WTP used Pearson Product Moment Test. Characteristics of respondents consist of 5 elements, namely family members, the level of education, reference recognition, the level of income and satisfaction. The result on

Correlation Between the Characteristics of Respondent with Their WTP of IPAL

Relationship of some characteristics of respondents with WTP used Pearson Product Moment Test. Characteristics of respondents consist of 5 elements, namely family members, the level of education, reference recognition, the level of income and satisfaction. The result on

Table 6. Correlation Between Characteristics of Respondents with Their WTP

Characteristic Respondent	coefficient	Sign
The family member	0,593	0,230
Level Education	0,786	0,036*
Reference Cognition	0,155	0,025*
Level of Income	0,733	0.090**
Level of Satisfaction	0,740	0.010*

*) significant on 95%
**) significant on 0,1%

From 5 characteristics of respondent, only the family members has no correlation with their WTP of IPAL, others such as level of education, level of income, reference cognition and satisfaction of IPAL services have correlation positively. The more the number of families is not relevant to the more their WTP. The family members has no correlation with WTP because IPAL tariff setting initially, is fixed cost, does not depend on the number of usage. Wastewater treatment by IPAL is not equipped with a meter or water volume meter distributed such PDAM's did. Increasing WTP is also supported by level of education and awareness of wastewater treatment with coefficient correlation equal to 78,6%. The higher level of education, the higher their WTP of IPAL. With higher levels of education and knowledge, household tend to wish and better understand about water protection. The more knowledge about environmental, the higher their WTP. Respondents who have good knowledge about the benefits and damage of the environment, they will tend to be more likely to be willing to pay [15]. Level of income is also correlated with WTP with 73.3%. It means that if the household has more income, the family has more WTP, with a coefficient correlation of 56.8%.

Reference cognition is used as a variable because of past experiences either satisfied or un satisfied of the services, has a big influence on their WTP. For formerly household who often difficult to get clean water especially in the dry season, they have highest appreciate with wastewater treatment, whatever its form. He [6] shows that experience is positively correlated

with environmental awareness. People who have environmental experiences are willing to pay higher. Respondents will have more knowledge that will not be environmentally damaging and are likely to be willing to make conservation efforts environment.

Level satisfaction of household from IPAL services, affects their WTP. Comers households who had experienced the benefits of other water sources, especially those provided by the government, such as the PDAM, The satisfaction of household increases if the quality of water treatment by implementing new technology will increase the quality of wastewater treatment. He [10] shows that more services are added, more WTP increases. Management service in Kampala City, Uganda can be improved by improving the quality of waste services [3].

Level of income does not have a significant effect with degree of freedom 5%, but significant on its 10%. For households, water is a vital goods, requirement and is determined by the government in a fixed rate. So whatever the tariff is charged to household, it will still to pays it unaffected by its income.

CONCLUSIONS

(1) The ATP of household which stay formerly on the location, , on average is lower than others the ATP from other household classification, but their WTP is relatively higher than the 2 other categories of households, because they highly value water and know how difficult it is to obtain clean water when dry season arrives;
(2) The average ATP of household comers who have never had the experience of using PDAM services is relatively highest compared to the other two categories of household, but on average, their WTPs are medium, because they feel the importance of water and feel the quality of wastewater quality treats IPAL is quality standard;
(3) Household comers that have had experience using PDAM services, their ATP is medium, but their WTP are lowest, compared to 2 sample categories of household. They have had experience enjoying water supplied by the government that has better quality and this household is still unsure, is the quality of wastewater of IPAL to be supplied is high such as PDAM did;
(4) Reference cognitive is positively correlated with their WTP because previous references are mainly on experiences with PDAMs with better quality and with tariffs so far;
(5) The city government needs to improve continually wastewater treatment by IPAL using high technology so that the quality of wastewater is quality standards, at least the same with other drinking water and government promote it;
(6) Tariff per household, should be determination as a variable costs or a number of uses.

REFERENCES

[1] Altaf MA, Haroon J, Whittington D. 1992. Willingnes to Pay for Water for Rural Punjab.Pakisatan. World Bank Water and Sanitation Programme.
[2]Afroz R, Using a Contingent Valuation Approach for Improved Solid Waste Management Facility. Journal Elsevier Waste Management, Vol.31,2011,pp.800-808.
[3] Meinrad Z, Sharifah ZB, Sayed ZASH, Mahyar Sakari., Relationship Between Awareness, Knowledge and Attitudes Towards Environmental Education Among Secondary School Students in Malaysia, World Applied Sciences Journal, 22 (9),2013, pp. 1326-1333.
[4] Banga,Margaret, Households Willingness to Pay for Improved Solid Waste Collection Services in Kampala City, Uganda.The Journal of Environment and Development, 2011.
[5] Brahim, Djemaci, Using a Contingent Valuation Approach for Improved Household Solid Waste Management in Algeria. Munich Personal. 2015.
[6] Chutarat Chompunth, Role of Public Participation in Environmental Impact Assessment in Thailand, International Journalof GEOMATE, Volume12, Issue 33, 2017.
[7] Finger, M, From Knowledge toAction? Exploring the Relationship Between Environmental Experiences,Learning, and Behavior, Journal of Social Issues 50(3), 1994, pp.141-160.
[8]Fonta.W.Metall. Using a Contingent Valuation Approach for Improved Solid Waste Management Facility: Evidence from Enugu State Nigeria. Journal of African Economics. 2008.
[9] Ghanem Samar Khairy, The Relationship Between Population and The Environment and Its Impact on Sustainable Development in Egypt Using a MultiEquation Model ,Environment, Development And Sustainability, Vol.20,2018, Issue1pp. 305-340.

Hagos,Households Willingness To Pay for Improved Urban Waste Management in Mekelle City, Ethiopia, Discussion Paper Series, 2012, EfDDP12-06

[10]Hua Wang. Water pricing with household surveys: A study of acceptability and willingness to pay in Chongqing, China. China Economic Review . 21(1):136-149 · March. 2010

[11]James K. Boyce., Inequality and Environmental Protection. Paper, Political Economy Research Institute MIT, 2003.Ladiyance,Sand Yuliana, L., Variable Effected Willingness To Pay Household at Bidaracina Jatinegara, East Jakarta, Widya Journal.Vol 2.No 2., 2014.

[12]Marselina, Djayasinga., Ria Virsa. Willingness to Pay (WTP) By Contingent Valuation Method (Case Study: Waste Management Services. Journal of GEOMATE, Vol 17, Issue 62, pp 59-64.2019.

[13]Steven Russel. Julian Fox Rusbhi. Dina Arhin.. Ability to Pay for Health Care: Concepts and Evidence. Health Policy and Planning, 1996; 11(3):219-37

[14]Takehisa Kumakawa, Altruism,and Willingness to Pay for Environmental Goods: A Contingent valuation study, Journal of Geoscience and Environment Protection, 5, 63-68, 2017.

[15]Tolulope J. Akeju. Gbenga J. Oladehinde and Kasali Abubakar, An Analysis of Willingness to Pay (WTP) for Improved Water Supply in Owo Local Government, Ondo State, Nigeria, Asian Research Journal of Arts & Social Sciences 5(3): 1-15, 2018.

[16]Whittington D, Briscoe J, Mu X, Barron W. 1990.Estimating the willingness to pay for water services in developing countries: A case study of the use of contingent valuation surveys in Southern Haiti. Economic Development and Cultural Change38 (2):293-312.

[17]WASH (Water and Sanitation for Health). 1988. Guidelines for Conducting Willingness-To-Pay Studies for Improved Water Services in Developing Countries. WASH Field Report No. 306, October 1988.Washington DC:USAID.

9th Int. Conf. on Geotechnique, Construction Materials and Environment, Tokyo, Japan, 20-22 November 2019, ISBN: 978-4-909106025 C3051

WHAT EFFECT OF DIFFERENT APPLICATIONS (AMENDMENT) OF SEWAGE SLUDGE ON RAPESEED OIL QUALITY

Najla Lassoued[1,2] and Essaid Bilal[3*]
[1] National Agronomic Institute of Tunisia, Tunisia; [2] National Institute for Rural Engineering' research, Water and Forestry, Tunisia; [3] Ecole Nationale Supérieure des Mines de Saint Etienne, CNRS UMR 5600, France

ABSTRACT

Application of sewage sludge rich in organic matter and nutrients such as nitrogen, phosphorus and potassium tends to improve crop yields. Nevertheless, this use is limited because of their heavy metal content. The objective of this work is to study the effect of sewage sludge on the accumulation of metallic trace elements in seeds and rapeseed oil. For this purpose, two different types of sludge by their metal composition were tested. Compared to the control, the supply of industrial sludge increases the metallic load of seeds and rapeseed oil. This increase is noted with the highest doses 50 and 100 t/ha. The same trend was observed during the two years of application. This effect is due to the richness of these slurries in chrome, cadmium and lead. This modification of the metal composition was accompanied by the decrease in the oil content. Analysis of the fatty acid composition of total lipids shows an increase in the percentage of oleic acid at the expense of linoleic and linolenic acids. On the other hand, the increase of 18: 1 at the expense of linoleic and linolenic acids may be the result of metal-induced alteration. For urban sludge, we noticed a variation in Cr, Co, Cu, Ni and Zn contents in the seeds depending on the doses. However, for Cd and Pb no variation was recorded. An increase in metal trace element levels was well reported at the seed level during the second amendment. We also detected a decrease in oil content with the contribution of industrial sludge. The composition of the total lipids in fatty acids shows an increase in the percentage of oleic acid (C18: 1) at the expense of linoleic (C18: 2) and linolenic (C18: 3) acids under the effect of heavy metals brought by the industrial sludge while no difference is recorded with urban sludge regardless of the dose. No significant differences in heavy metals were observed with the addition of the different doses of urban sludge even after two years of application. Urban sludge has no effect on oil content or fatty acid composition. However, we detected increases in most heavy metals, especially for high doses of industrial sewage sludge.

Keywords: Rapeseed Oil, Industrial Sludge, Urban Sludge, linoleic acids, Metallic Trace Elements.

INTRODUCTION

Rapeseed crop has in recent years a renewed interest in the world for the production of oil, for human consumption and as biofuels besides its use in the feed of cattle in the form of cake. The introduction of rapeseed farming in Tunisia is essentially aimed at increasing the production of oil for human consumption and that of oilseed meal (by-product of rapeseed) rich in proteins sought for animal feed [1]. Despite the adaptation of this crop and the place it occupies in cereal rotation, it is not well developed in Tunisia. The Pactol variety has been recommended for large-scale cultivation in the north of the country where the rainfall exceeds 400 millimeters per year. Rapeseed is also a model plant for phytoremediation. It is known for its ability to extract and accumulate toxic metals [2].

In addition to the nutrients, the residual sludge contains heavy metals, which is one of the repelling factors of their agricultural reuse [3], [4]. The presence of these elements in cultivated soils poses health safety problems because of their possible passage into plants consumed by humans and animals [5], [6].

Numerous studies have tested the accumulative potential of rapeseed [7]-[9] and its effectiveness on some heavily contaminated surfaces with many physiological and morphological advantages [10]. It is for this reason that we chose it to study the effect of sewage sludge especially on the chemical composition of the seeds and the quality of the oil. Few studies have been undertaken in this direction.

For this purpose, two types of sludge (industrial and urban) different in their composition of metals were tested to highlight the impact of heavy metals present in sewage sludge on certain physiological and biochemical parameters of rapeseeds.

MATERIALS AND METHODS

Culture conditions

The test device is installed in the open field at the Oued Souhil - Nabeul Agricultural Experiment Station, located about 60 km from Tunis. For each

type of sludge, 4 doses (5, 25, 50 and 100 t / ha) were put into play and compared to a control without any input. The trial comprising 9 treatments is conducted in four randomized blocks. The semi rapeseed (Brassica napus L.) Pactol variety was carried out in December with a density of 50 seeds/m² and a spacing of 40 cm from which 13 rows per colza plot were obtained.

The rape crop was conducted in two successive seasons, each time; sewage sludge was applied in the prescribed doses before sowing. However, during the second year, each plot was divided in two, the first part received sludge while the second part received nothing. This division was carried out to study the cumulative effect and the aftereffect of the sludge.

Characteristics of the spread sewage sludge

The chemical analysis of Korba's urban sludge (Table 1) showed that iron and zinc are the most represented elements. The average contents found are organized according to the following sequence: Fe >> Zn> Cu> Cr> Pb> Ni> Co> Cd. As for Bou Bouboub Industrial Sludge's (Table 1), they have very high levels of Cr, Pb and Cd. The sequence found is Cr >>> Pb >> Zn> Cd> Cu> Ni> Co.

Table 1: Sewage sludge chemical composition (ppm) during the first and second spreading. (The values represent the average of four individual repetitions ± (SD)). BU: Urban sewage sludge, BI: Industrial sewage sludge.

	Urban sludge (BU)		Industrial sludge (BI)	
	1st spreading	2nd spreading	1st spreading	2nd spreading
Co	3.6	5.1	20.6	18.3
Cd	n.d.	n.d.	163.0	200.8
Cr	73.1	102.6	11387.0	13965.0
Cu	188.8	210.4	142.4	164.0
Ni	19.8	17.3	61.8	63.2
Pb	54.9	63.3	2854.1	3175.9
Zn	463.2	506.9	821.8	698.5

Analysis method

Oil analysis

Seed oil extraction is carried out by the Soxhlet method [11]. A sample of milled rapeseeds is placed in a cellulose cartridge in the extractor which is connected on the one hand to a ball cooler and on the other hand to a flask containing 100 ml of hexane, pumice and a pinch of anhydrous sodium sulfate. The solvent is boiled using a regulated flask heater. The solvent vapors are condensed in the refrigerant and impregnate the sample placed in the cartridge thus extracting the oil. The appropriate time for the extraction used to obtain a better oil yield is 6 hours. The oil content (OC) expressed in% is given by the following formula:

$$\% \text{ oil} = (m/w) * 100$$

(m: mass of the oil; w: weight of the sample)

Oil yield (OYH) per hectare is determined by multiplying the seed yield (SY) by the oil content (OC)

$$OYH\ (qx/ha) = SY\ (qx/ha) * OC/100$$

The analysis of the fatty acids is carried out by gas chromatography after their conversion into more volatile compounds: the methyl esters. For this we use hot methylation using a methanolic solution of sodium methoxide followed by esterification in an acid medium [12]. The methyl esters thus prepared are analyzed by gas chromatography on a capillary column. Fatty acids are identified according to their retention times. Their rate is determined by the ratio between the area of the corresponding peaks and the sum of the peak areas of all the fatty acids [13] according to the formula:

$$\% \text{ Fatty acids} = (S / \Sigma S) * 100$$

The detection of metal trace elements in the oil is determined by the ICP-AES (Inductively coupled plasma atomic emission spectroscopy) technique. A mixture of rapeseed oil and 10% nitric acid is stirred and then centrifuged at 2800 rpm for 10 minutes. The assay is performed on the lower aqueous layer [14].

Chemical Analysis of Sewage Sludge

For sewage sludge and soil, the pH is measured by potentiation in 1 M KCl after 24 h in the water/soil ratio of 5. The organic carbon was determined by the method of [15]. Total nitrogen (N_t) was determined by the Kjeldahl method. For trace elements, soil and sludge samples were digested with a mixture of HCl/HNO_3 [16] and total concentrations were determined by plasma flash emission spectroscopy (ICP-OES). The apparatus used is of the HORIBA Jobin Yvon type.

Determination of metallic trace elements in seeds

The parched seeds were crushed into powder using a porcelain mortar and pestle to obtain a fine powder. Digestion is done hot with aqua regia. Then, the contents of heavy metals were determined by plasma emission spectroscopy (ICP-OES).

Statistical analysis

All data were subjected to an analysis of variance. The comparison of the means with the threshold of 5% of significance was carried out by the Newman-Keuls test using the Statistica 7 software.

Table 2: Variation of seed weight/m² and thousand seeds weight at the end of the Rapeseed (Brassica napus L) harvest. The values represent the average of four individual repetitions (SD). T: soil control, TSW: Thousand seeds weight, BU: Urban sewage sludge, BI: Industrial sewage sludge.

	First effect		Cumulative effect		After effect	
	Seeds weight/m²	WTS	Seeds weight/m²	WTS	Seeds weight/m²	WTS
T	48.03 ±5.9	2.60 ±0.2	45.81 ± 7.6	2.73 ± 0.10	52.43 ± 2.94	2.74 ±0.17
5BU	81.35 ±7.3	2.75 ±0.2	42.21 ± 4.95	2.86 ± 0.14	43.61 ± 2.44	2.66 ± 0.04
25BU	116.68 ±13.6	2.90 ±0.1	55.75 ± 3.25	2.73 ± 0.10	53.55 ±6.8	2.71 ± 0.06
50BU	121.90 ±17.6	2.82 ±0.3	62.38 ± 7.43	2.64 ± 0.10	81.96 ±4.75	2.70 ± 0.09
100BU	117.68 ±21.7	2.70 ±0.3	98.98 ± 3.66	2.73 ± 0.11	92.90 ±4.54	2.66 ± 0.19
5BI	64.40 ±4.3	2.74 ±0.3	43.50 ± 2.91	2.75 ±0.07	57.56 ±5.06	2.61 ± 0.06
25BI	80.30 ±5.3	2.74 ±0.2	54.95 ± 5.1	2.68 ± 0.02	62.79 ±8.72	2.61 ± 0.04
50BI	107.80 ±7.8	2.90 ±0.2	67.34 ± 10.7	2.43 ± 0.1	75.12 ±4.03	2.53 ± 0.05
100BI	108.95 ±7.7	2.67 ±0.1	59.98 ± 7.09	1.90 ± 0.15	80.97 ±7.22	2.36 ± 0.2

Table 3. Variation of total fatty acid composition (%) in rapeseed oil treated with different doses and types of sludge during the first and 2nd spreading. The values are averages of three repetitions.

		C16:0	C16:1	C17:0	C17:1	C18:0	C18:1	C18:2	C18:3	C20:0	C20:1
First spreading	T	4.74	0.27	0.040	0.07	1.91	60.57	22.15	8.40	0.69	1.12
	5BI	5.15	0.32	0.042	0.08	1.69	60.63	21.38	8.87	0.66	1.15
	25BI	5.06	0.32	0.042	0.07	1.73	60.10	21.85	8.96	0.69	1.14
	50BI	4.57	0.30	0.032	0.07	1.70	69.62[b]	15.81	5.99	0.67	1.22
	100BI	5.09	0.32	0.045	0.07	1.76	72.42[b]	12.57	5.82	0.72	1.16
	5BU	4.77	0.29	0.037	0.067	1.78	61.44	21.41	8.32	0.69	1.17
	25BU	5.25	0.33	0.040	0.072	1.67	59.44	22.71	8.72	0.64	1.11
	50BU	4.84	0.30	0.042	0.072	1.77	59.31	23.50	8.25	0.74	1.14
	100BU	4.90	0.31	0.042	0.077	1.79	60.10	21.97	8.84	0.70	1.24
2 and spreading	T	5.13	0.26	0.05	0.08	1.85	61.28	22	6.55	0.58	1.22
	5BI	5.55	0.30	0.03	0.09	1.62	64.34	19.23	7.02	0.56	1.26
	25BI	5.46	0.30	0.04	0.06	1.66	63.81	19.7	7.11	0.60	1.26
	50BI	4.96	0.28	0.03	0.09	1.63	73.33	13.66	4.14	0.54	1.33
	100BI	5.48	0.30	0.05	0.08	1.69	76.13	10.42	3.97	0.61	1.28
	5BU	5.16	0.27	0.04	0.08	1.72	65.15	19.26	6.47	0.57	1.28
	25BU	5.64	0.31	0.05	0.07	1.60	66.15	20.56	6.87	0.52	1.23
	50BU	5.23	0.28	0.04	0.07	1.71	67.02	21.35	6.4	0.64	1.26
	100BU	5.30	0.29	0.05	0.07	1.72	66.81	19.82	6.99	0.60	1.36

RESULTS

Effect of sewage sludge on rapeseed grain production

The results obtained during the two test campaigns showed that the sludge used as fertilizer improves the production of rapeseed whatever the type of sludge. The increases observed are all the greater as the sludge dose is higher and the lower production is recorded with the treatment without sludge. However, these increases are less important in the presence of industrial sludge compared to urban sludge or a difference of 39.41% for the same sludge input 100t/ha. In addition, the cumulative sludge inflow (2nd spreading) gave less pronounced improvements than those obtained during the 1st spreading. It is important to note that the increase in grain production is due to an increase in the number of seeds and not to an improvement in the weight of the seed. Indeed, the weight of one thousand grains (Table 2) did not undergo any sludge effect in the presence of the 1st application and decreased slightly with the cumulated application. As for the after effect, we note that regardless of the type of mud brought during the previous year, treatments that had previously received sludge gave better yields than those of the control treatment without any input. This is very clear for the 50 and 100t / ha doses. This result can be explain in large part by the mineral-rich soil richness favorable to growth from continuous mineralization of sludge even after stopping spreading. In addition, the sludge supply significantly improved the nitrogen content of the seed (Fig.1). This improvement is more pronounced with the addition of urban sludge and could be related to the essential nutrients provided by the sludge.

Effect of sewage sludge on oil content

The oil content of rapeseed is on average 30% (Table 4). As for the sludge effect, we notice that for all treatments of the first campaign no noticeable effect was recorded. While during the second season, we detected a decrease in oil content of 11.42% and 19.65% with the input of industrial sludge respectively at 50t/ha and 100t/ha.

This is essentially relate to the decrease in the weight of the seed. As for the oil yield / ha, it follows the evolution of the production with increases on the sludge plots compared to the soil control.

Effect of sludge on fatty acid composition in rapeseed oil

Rapeseed oil has a very good fatty acid profile, it consists of a minor fraction of 8% saturated fatty acids and about 92% unsaturated fatty acids (fig. 2) including 60% monounsaturated fatty acids mainly oleic acid (c18: 1), which is also found in peanut, olive and sunflower oils and 32% poly unsaturated fatty acids: linoleic acid (c18: 2) and linolenic (c18: 3) [17], [18].

The analysis of the fatty acid composition of total lipids shows an increase in the percentage of oleic acid (c18: 1) at the expense of linoleic (c18: 2) and linolenic (c18: 3) acids under sludge effect (Table 3). This increase in c18: 1 may be a consequence of metal-induced alteration of the process of sequential desaturation of 18-carbon fatty acids. For other acids, such as palmitic, palmitoleic, heptadecanoic, heptadecenoic, stearic, arachidic and gadoleic acids, no effects were recorded. Similarly no difference is recorded with the intake of urban sludge regardless of the dose.

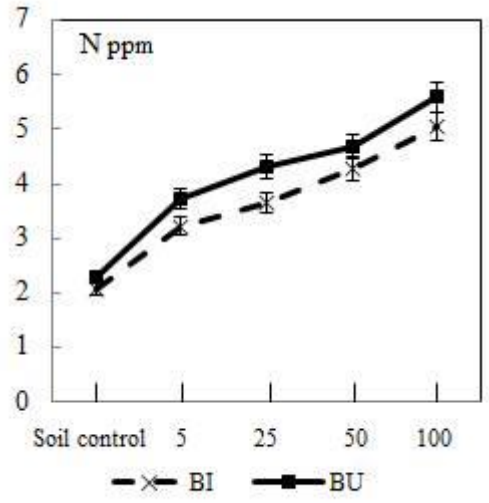

Fig.1: Nitrogen variation content of rapeseeds with increasing sewage sludge doses.

If we compare the composition of total fatty acids for the two companions (table 3), we note during the second application a considerable increase in oleic acid at 50t/ha dose. This acid went from 61.28% (soil control) to 73.33% (50t/ha bi treatment), an increase of 12%. The content of linoleic and linolenic acids in the oil undergoes a greater decrease under the cumulative effect. The highest dose of industrial sludge (100t/ha) resulted in a 52.64% decrease in linoleic acid and 39.39% in linolenic acid. These changes in fatty acid composition do not affect the nutritional quality of the oil. The fatty acid composition of total lipids, shows an increase (fig. 2) in the percentage of mono-unsaturated fatty acids (oleic acid) at the expense of poly-unsaturated fatty acids) in the presence of sludge industrial. The increase of the acid at the expense of linoleic and linolenic acids can be explained by an alteration induced by the metal.

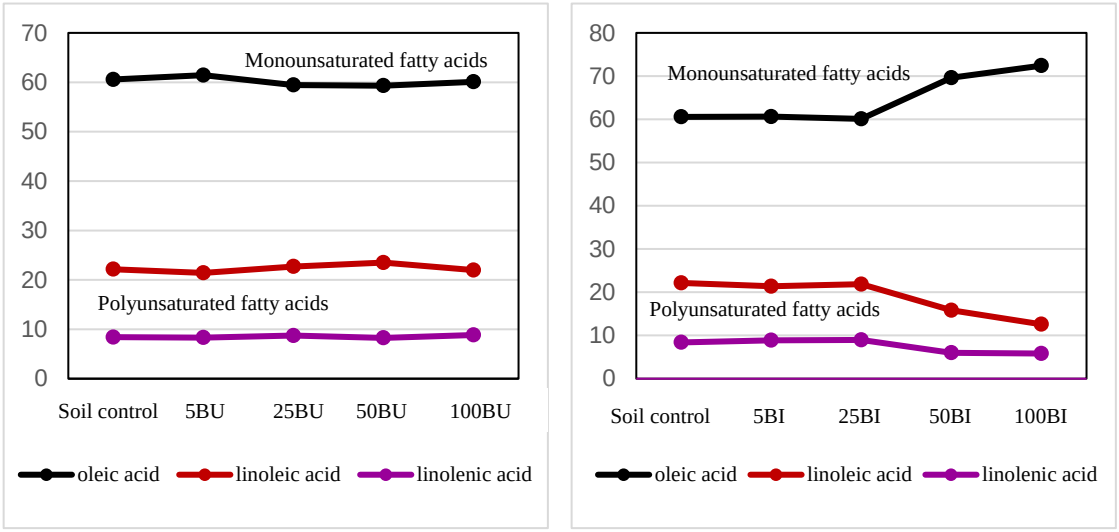

Fig.2 Composition of fatty acids % in Urban and Industrial sewage sludge.

Accumulation of heavy metals in rapeseed

Regarding the action of sludge on the trace metal content of rapeseed, we noticed that the response of the plant differs according to the type of sludge spread, the amount of sludge added and the year of cultivation. The application of industrial sludge essentially modified the Cd and Pb content in the seeds. Thus, we observed an accumulation of Cd with the addition of 100t/ha of sludge during the first year (Fig. 3). This effect was accentuated with the second intake, for which there is an accumulation of 25t/ha (50t/ha cumulative). At the 100t/ha rate (200t/ha cumulative), the contents become 4 times higher. The bioavailability of Cd after cessation of application was also manifested by an accumulation in seeds at 25, 50 and 100t/ha industrial sludge doses. Similarly, we report that, compared to the control, lead levels increase with the addition of 50t/ha of industrial sludge during the first application and the addition of 25t/ha of industrial sludge during the second application.

For the other elements, most grades increase with the addition of sludge. This increase becomes sharper following the second sludge supply for Cr, Ni and Zn contents.

The Cr content (Fig. 4) increase is clearly visible in the presence of industrial sludge where the levels reach with the highest dose of 10 ppm and 15 ppm for the first and second year of application. This accumulation is less pronounced with urban sludge, a maximum of 6 ppm is obtained only with the dose of 100t/ha following the second campaign. The after effect follows the same evolution as for the first spreading in the case of urban sludge. On the other hand for industrial sludge, the rear effect exceeds that of the 1st application but remains lower than the cumulative effect.

Table 4: Evolution of oil content and yield (The values represent the average of four individual repetitions ± (SD)). BU: Urban sewage sludge, BI: Industrial sewage sludge and T: soil control.

	Oil Content (%)		Oil Yield (qx/ha)	
Spreading	1st	2nd	1st	2nd
T	31.28± 0.5	31.62 ±0.5	1.502	1.449
5BI	30.91 ±1.2	31.41 ±0.5	2.013	1.339
25BI	29.88 ±1.6	30.56 ±0.9	2.399	1.684
50BI	31.10 ±0.4	28.07 ±1.6	3.145	2.093
100BI	31.8 ±0.7	25.40 ±0.8	3.335	1.873
5BU	31.26 ±0.9	30.79 ±1.1	2.514	1.326
25BU	29.88 ±1.8	30.65 ±0.8	3.486	1.704
50BU	29.18 ±1.7	31.08 ±1.3	3.791	1.751
100BU	30.61 ±0.5	31.23 ±1.7	3.739	2.514

The same Cr evolution is observed for Ni for the mud effect, cumulative effect and aftereffect. During the second crop, we also observed Ni increases from 5t/ha, regardless of the type of sludge (Fig. 4). This is quite normal given the quality of the two types of sludge spread including the very high load of industrial sludge in Cd, Cr, Ni and P.

For zinc (Fig. 5), the only difference with the elements previously reviewed is the rear effect which is slightly less important than the first spread for both types of sludge. This could be explained by the high

Zn mobility, which would probably have migrated laterally, or at depth which has blurred the after effect.

The Co contents increase significantly in the seeds (Fig. 6) with the contribution of 5t/ha of urban sludge and remain constant whatever the year of the application whereas for the industrial sludge the Co levels increase significantly from the 25t/ha dose. All effects (direct, cumulative and aftereffect) are very close. The Co contents are higher in the presence of 100t/ha of sludge (Fig. 6).

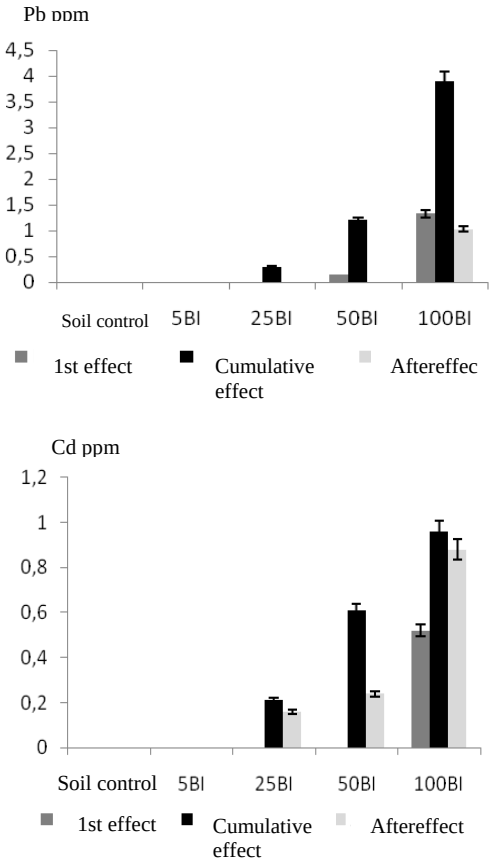

Fig.3: Cd and Pb content variation in rapeseeds grown in the presence of increasing doses of urban and industrial sludge in the first and second year of application.

Evolution of heavy metal contents in rapeseed oil

Analysis of heavy metal data in rapeseed oil (Table 5) shows that all trace metals are present in the oil. Nevertheless, some modifications have been noted.

For urban sludge, no significant difference in heavy metal concentrations was observed with the addition of different doses, even after two years of application. On the other hand, we detected differences with the contribution of industrial sludge loaded with metallic trace elements.

We have observed increases in most heavy metals especially for high doses. The Cd levels increase significantly with the addition of 100t/ha of industrial sludge, from 1.1 ppb (soil control) to 7.3 ppb during the first year and reach 25ppb following cumulative intake. During this 2nd year, the sludge effect was observed at 25t/ha. The Pb and Cr contents increase is mostly visible at 100t/ha. These increases become more important in the second year when the 100t/ha dose levels are 3 to 10 times higher than the soil control. For nickel, grades are higher compared to the control when 50t/ha of industrial sludge is applied to both applications. Regarding Cu, Zn and Cot no effect doses or sludge types were noted.

DISCUSSION

Intensification of human activities, especially industrial and agricultural activities, have contributed in recent decades to the contamination of agroecosystems by heavy metals [19]. The agricultural valorization of the waste sludge can be a source of pollution in the sense that they can contain toxic compounds [20], in particular the metallic trace elements (Pb, Cd, Ni, Cr) whose presence constitutes an obstacle to their use [21]-[23]. This sludge is rich in nutrients and is a significant source of nitrogen, phosphorus and micronutrients that must be used to save fertilizer and provide environmentally beneficial sludge removal [24]-[26].

In this perspective and to contribute to the valorization of sludge, several studies have been carried out. The present work on an open-field rape crop aims to study the effects of different types and doses of sewage sludge on seed yield, seed chemistry and rapeseed oil quality.

During the first and second spreading's, the grain yield increased significantly following the application of urban sewage sludge. The increase in biomass and grain yield has been reported by several authors [27]-[29]. This beneficial effect can be related to a continuous release of nitrogen and phosphorus sludge. We also found that industrial sludge improves production but in a less important way than urban sludge. This may be due to a depressive effect relating to the heavy load of industrial sludge including Cd, Cr, Ni and Pb.

At the same time, industrial sludge caused a decrease in the weight of thousand seeds following the second intake from the 50t / ha dose. This has been accompanied by a decrease in oil production. The metal load of this sludge can be the cause of this disturbance. Ben Youssef et al. [30] showed that the oil content shows a decrease proportional to the metal dose.

The application of industrial sludge also induces increases in metal contents in rapeseeds, while for urban sludge, the modifications are attenuated.

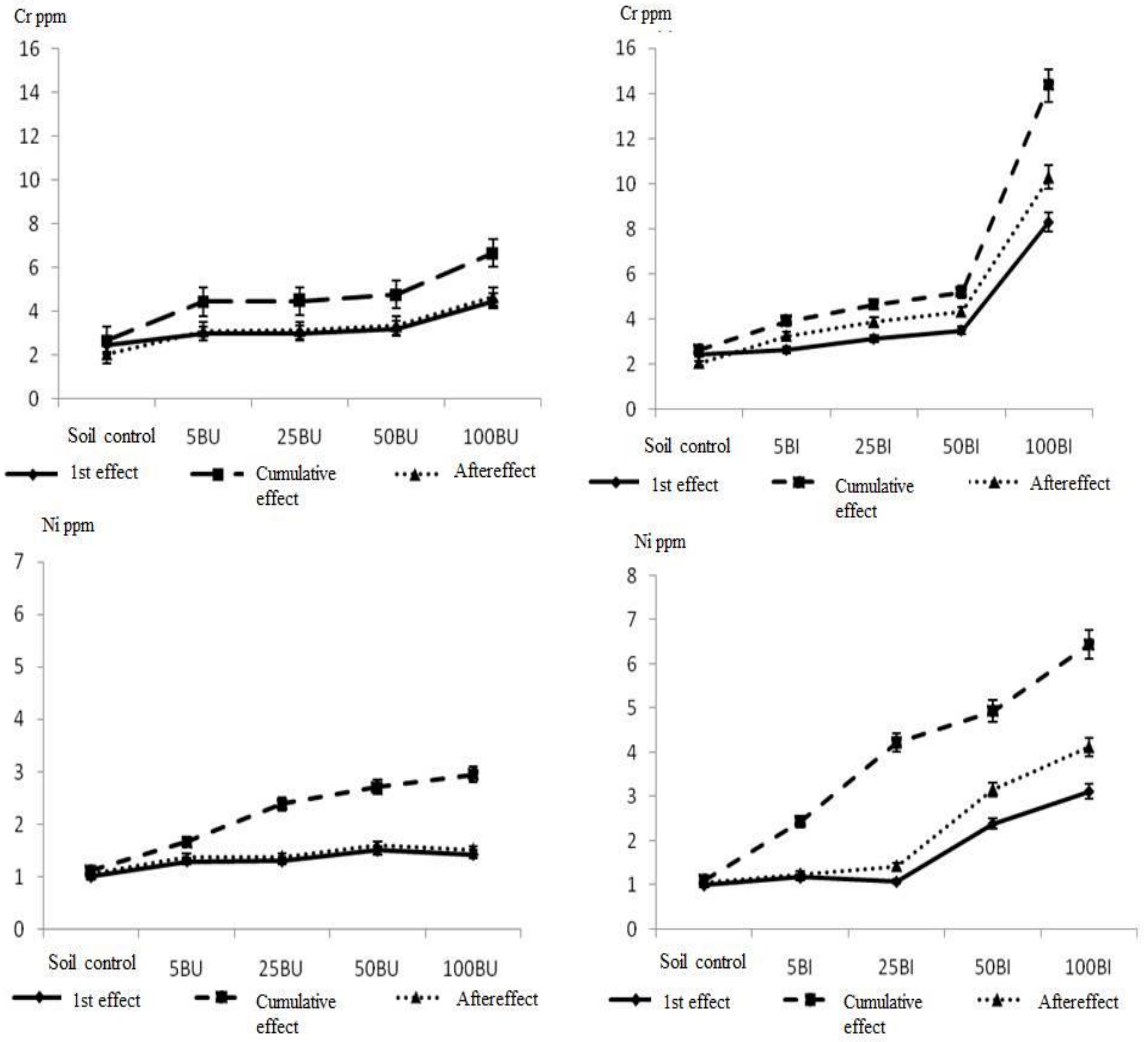

Fig. 4: Cr and Ni content variation in rapeseeds grown in the presence of increasing doses of urban and industrial sludge in the first and second year of application.

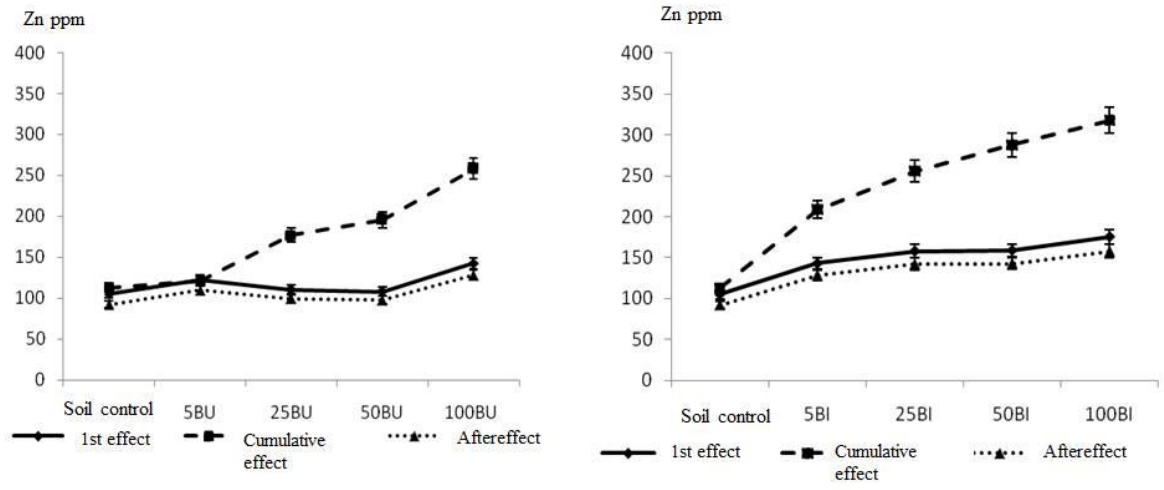

Fig. 5: Variation of zinc accumulation in rapeseeds grown in the presence of increasing doses of urban and industrial sludge in the first and second year of application.

Table 5: Evolution of metal trace element contents (ppb) in rapeseed oil during the first and second year of application. BU: Urban sewage sludge, BI: Industrial sewage sludge and T: soil control.

		Urban sludge t/ha					Industrial sludge t/ha			
Spreading		T	5	25	50	100	5	25	50	100
Cd	1st	0.8	0.7	0.9	0.7	0.9	1.0	0.7	1.1	7.3
	2nd	0.7	0.8	0.6	0.8	0.6	0.6	2.1	8.0	25.0
Cr	1st	0.6	0.5	0.6	0.5	0.5	0.7	0.4	1.6	1.0
	2nd	0.5	0.4	0.6	0.7	0.7	0.4	0.8	1.0	5.1
Pb	1st	1.6	1.7	1.6	1.5	1.5	1.5	1.6	2.1	3.2
	2nd	1.6	1.4	1.7	1.6	1.7	1.6	1.7	1.5	5.2
Ni	1st	4.3	4.7	4.2	5.2	4.7	4.2	3.7	5.1	4.2
	2nd	4.1	4.9	5.1	4.2	5.1	3.9	4.3	5.0	5.2
Zn	1st	33.4	32.1	33.5	34.1	37.4	33.2	31.0	32.0	36.0
	2nd	30.0	30.0	32.9	37.4	38.4	33.0	41.0	33.0	32.0
Co	1st	1.1	1.0	1.2	1.3	1.0	1.1	1.0	1.1	1.0
	2nd	1.0	1.0	1.0	1.0	1.0	1.0	1.5	1.0	1.2
Cu	1st	10.4	10.9	11.0	11.6	13.0	10.0	11.9	12.6	11.6
	2nd	9.5	9.0	10.6	10.0	11.0	10.6	10.4	10.6	12.1

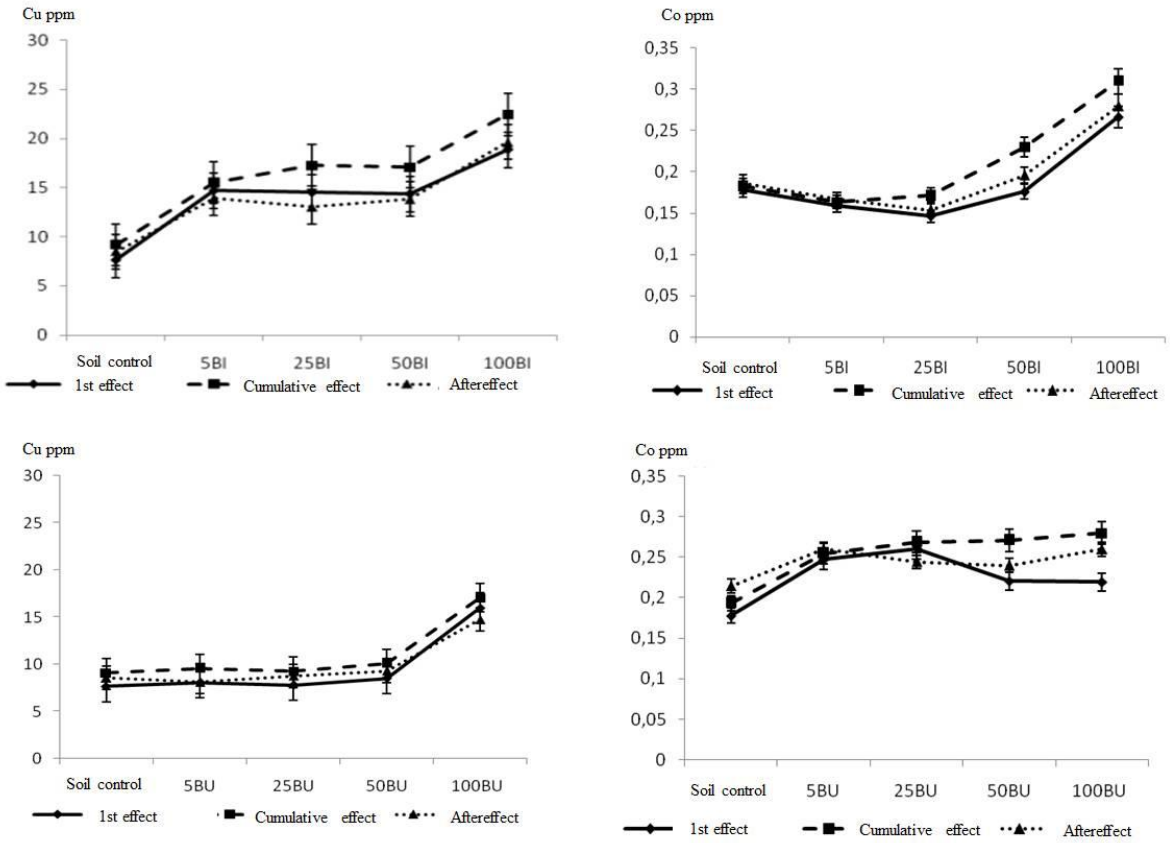

Fig.6: Co and Cu content variation in rapeseeds grown in the presence of increasing doses of urban and industrial sludge in the first and second year of application.

The typical effect of sludge is clear. For both types of sludge, the dose effect is visible. The highest levels are recorded with high doses including 100t/ha. For industrial sludge, the levels obtained at this dose exceed the authorized limits for cadmium, chromium, copper and zinc [31]. Amin and Sherif [32] found the same result where lead, cadmium, nickel and chromium concentrations of bean seed due to sludge application were generally higher than normal values.

The analysis of the fatty acid composition of total lipids shows an increase in the percentage of oleic acid (18: 1) at the expense of linoleic (18: 2) and linolenic (18: 3) acids in the presence of industrial sludge. From a nutritional standpoint, these modifications do not seem to call into question the quality of the oil despite the drop in its yield. According to Darrakech et al. [33] after the refining stage, no risk to human health could be identified with respect to rapeseed oil as it will have decreased levels of heavy metals. On the other hand, increasing the level of 18: 1 acid at the expense of linoleic and linolenic acids can be explained by a metal-induced alteration of the process of sequential desaturation of 18-carbon fatty acids.

ACKNOWLEDGMENTS

This work was supported by the National Institute for Rural Engineering research, Water and Forestry, Tunis and Ecole Nationale Supérieure des Mines de Saint Etienne, France.

REFERENCES

[1] Ben Salah, H., Jouhri, A. and Marzouk, B., Effet de la date de semis sur certaines composantes du rendement et sur la durée du cycle végétatif chez deux variétés de colza de printemps (Brassica napus L.) en Tunisie. Annales de l'INRAT, Vol. 73, 2000, pp. 211-221.

[2] Marichiol, L., Asooolari, S., Sacco, P., and Zerbi, G., Phytoextraction of Heavy Metals by Canola (Brassica napus) and Radish (Raphanus sativus) grown on multicontaminated soil. Environmental Pollution, Vol. 132, 2004, pp 21-27.

[3] Adriano, D.C., Bioavailability and Risks of Metals. Trace Metals in Terrestrial Environments: Biogeochemistry. Springer-Verlag, New york, Second ed., 2001, pp. 866.

[4] Alkorta, I., Hernandez-Allica, J., Becerril, J.M., Amezaga, I., Albizu, I., and Garbisu,C., Recent findings on the phytoremediation of soils contaminated with environmentally toxic heavy metals and metalloids such as zinc, cadmium, lead and arsenic. Environ. Sci. Biotechnol., vol. 3, 2004, pp. 71-90.

[5] Ashworth, D.J., and Alloway, B.J., Soil mobility of sewage sludge- derived dissolved organic matter, copper, nickel and zinc. Environmental pollution, vol. 127, 2000, pp. 137-144.

[6] Richards, B.K., Steenhuis, T.S., Pevverly, J.H. and Mc Bride, M.B., Metal mobility at an old, heavily loaded sludge application site. Env. Poll., vol 89, 1998, pp. 365-377.

[7] Kchaou R., Khelil M.N., Gharbi F., Rejeb S., Henchi B., Hernandez T. et Destain J.P., Isotopic evaluations of dynamic and plant uptake of N in soil amended with 15N-labelled sewage sludge. Polish J. of Environ. Stud. Vol. 19, Issue 2, 2010, pp. 363-370.

[8] Angelova, V., Ivanova, R., Todorov, G., and Ivanovi, K., Heavy metal uptake by rapeseed. Communications in Soil Science and Plant Analysis, vol. 39, 2008, pp. 344–357.

[9] Marichiol, L., Asooolari, S., Sacco, P., and Zerbi, G., Phytoextraction of Heavy Metals by Canola (Brassica napus) and Radish (Raphanus sativus) grown on multicontaminated soil. Environmental Pollution, vol. 132, 2004, pp. 21-27.

[10] Salt, D., Blaylock,M., Kumar,M., Dushenkov,N., Ensley,N., Chert, D., Raskin, I., Phytoremediation : A novel strategy for the removal of toxic metals from environment using plants. Biotechnology, vol. 13, 1995, pp 468-474.

[11] Harwood, H.J., Oleochemicals as a fuel: Mechanical and economic feasability,J.Am.Oil Chem.Soc., vol. 61, 1984, pp. 315-324.

[12] Cecchi G., S. Biasini and Castano, J., Méthanolyse rapide des huiles en solvant. Corps Gras, Vol. 4, 1985, pp. 163-164.

[13] James,A.T. and Martin, A.J.P., Gas liquid partition chromatography: the separation and microestimation of volatile fatty acids from formic acid to dodecanoic acid. J.Biol.Chem., vol. 50, 1952, pp. 679-690.

[14] Leonardis DA, Macciola V, and Felice DM., Copper and iron determination in edible vegetable oils by graphite furnace atomic absorption spectrometry after extraction with diluted nitric acid. Int. J. Food Sci. Technol., vol. 35, 2000, pp. 371-375.

[15] Kalra,Y.P. and Maynard, D.G., Methods for Forest Soil and Plant Analysis. Information Report NOR-X-319, Forestry Canada, Northwest Region, Northern Forestry Center, 1991, pp. 116 p.

[16] McGrath, S.P. and Cunliffe, C.H., A simplified method for the extraction of the metals Fe, Zn, Cu, Ni, Pb, Cr, Co and Mn from soils and sewage sludges. J. Sci. Food Agriculture, vol. 36, 1985,

pp. 794–798.

[17] Pehlivana, E., Arslanb G., Godec F., Altuna T., and Musa Özcand, M., Determination of some inorganic metals in edible vegetable oils by inductively coupled plasma atomic emission spectroscopy (ICP-AES). GRASAS Y ACEITES, Vol. 59, 2008, pp. 239-244.

[18] Szmigielski R., Surratt J. D., Vermeylen R., Szmigielska K., Kroll J. H. Ng, N. L., Murphy S. M., Sorooshian A., Seinfeld J. H. et Claeys, M., Characterization of 2-methylglyceric acid oligomers in secondary organic aerosol formed from the photooxidation of isoprene using trimethylsilylation and gas chromatography/ion trap mass spectrometry. J. Mass Spectrom., 42, 2008, pp 101–116.

[19] Rascio, N., Dallavecchia, F., Feretti, M., Merlo, L., and Ghisi, R., Some effects of cadmium on maize plants. Arch. Environ. Contam. Toxicol., vol. 25, 1993, pp. 244–249

[20] Chaney, R.L., Bruins, R.J.F., Baker, D.E., Korcak, R.F., Smith, J.E. and Cole, D., Transfer of sludge applied trace elements to the food chain. Land Application of Sludge-Food Chain Implications. Page A.L., Logan T.J., Ryan J.A. eds., Lewis Publishers, Chelsea, MI, 1987, pp. 67-99.

[21] Gupta, U.C., and Gupta, S.C., Trace element toxicity relationships to crop production and livestock and human health. Implications for management. Commun. Soil Sci. Plant Anal., vol. 29, 1998, pp. 1491-1522.

[22] Järup, L., Berglund, M., Elinder, C.G., Nordberg, G. and Vahter M., Health effects of cadmium. The literature and a risk estimate. Scand. J. Work Environ. Health, vol. 24, 1998, pp. 1-52.

[23] McLaughlin, M.J., Parker, D.R., and Clarke, J.M. 1999. Metals and micrantrients – food safety issues. Field crops Res., vol. 60, 1998, pp.143-163.

[24] Brofas, G., Michopoulas, P., Alifragis, D., Sewage sludge as an amendment for calcareous bauxite mine spoils reclamation. J. Environ. Qual., vol. 29, 2000, pp. 811-816.

[25] Kosobucki, P., Chmarzyeski,A. and Buszewski, B., Sewage Sludge Composting. Polish Journal of Environmental Studies, vol. 9, 2000, pp. 243-248.

[26] Rejeb S., Khelil M.N., Gharbi F. et Ghorbal M.H., Effet des boues urbaines sur la production de la pomme de terre. Cahiers Agricultures, vol. 12, 2003, pp. 39-42.

[27] Christodoulakis, N.S. and Margaris, N.S., Growth of corn (Zea mays) and sunflower (Helianthus annuus) plants is affected by water and sludge from a sewage treatment plant. Bull. Enviro. Contam. Toxical., vol. 57, 1996, pp. 300-306.

[28] Singh R.P. and Agrawal M., Potential benefits and risks of land application of sewage sludge Waste Management, vol. 28, Issue 2, 2008, pp. 347–358.

[29] Togay, N., Effects of municipal sewage sludge doses on the yield, some yield components and heavy metal concentration of dry bean (Phaseolus vulgaris L.). African Journal of Biotechnology, vol. 7, 2008, pp. 3026-3030.

[30] Ben youssef, N. Taammli,W. Ben Temime,S. Daoud, D. Zakrouk, M. and Ghorbel, M. H., Cadmium induced changes in growth and seed storage lipids of rape (Brassica napus L.), Rivista Italiana delle Sostanze Grasse, vol. 81, 2004, pp. 364-370.

[31] Darracq, S., Bernhard-Bitaud, C., Bourrie, B., Evrard, J., and Burghart, P., Heavy metals transfer from soil to rapeseed oil. Sustainable Organic Waste Management for Enviromental Protection and Food Safety, 2004, pp. 63.

[32] Amin, A.W.,and Sherif, F.K., Heavy metals in maize as affected by sewage sludge application: Morphological characters and yield. Pakistan Journal of Biological Sciences. Vol. 4, 2001, pp. 1451-1455.

[33] Darrakech S., Bernhard-Bitaud C., Bourrie B., Evrard J. and Burghart P., Heavy metals transfer from soil to rapeseed oil. Sustainable Organic Waste Management for Enviromental Protection and Food Safety, 2004, 63p.

9th Int. Conf. on Geotechnique, Construction Materials and Environment, Tokyo, Japan, 20-22 November 2019, ISBN: 978-4-909106025 C3051

MINING REGULATION AND IT'S IMPACT ON PUBLIC WELFARE

Hamartoni Ahadis[1], Wan Abbas Zakaria[2], Irwan Sukri Banuwa[3], Lindrianasari[4]
[1]Ph.D. Student of Environmental Science, University of Lampung, Indonesia;
[2,3,4]University of Lampung, Indonesia.

ABSTRACT

This study aims to provide empirical evidence on the impact of mining company policies in Lampung Province on improving community welfare. The issue used in this study was the enactment of Law No. 23 of 2014 which transferred the authority to manage mineral and coal mining to the Province (previously managed by the Regency/City). This study separates two periods of observation, namely before and after the authority to administer affairs in the mineral and coal mining sector has shifted to the provincial government. Using secondary data derived from records of receipts sourced from mining companies in each region for five years of observation (2010-2014 for the before period). While the 2015-2018 data will be collected from the government of Lampung Province, because since 2015 the authority to administer affairs in the mineral and coal mining sector has shifted to the Provincial government (2015-2018 for the after period). This welfare is measured using local original income. The greater the annual average local original income from mining received by the Province compared to the average accumulated annual local original income from mining received in all districts / cities in Lampung, the welfare index in Lampung Province also increases. The results of the 2010-2018 analysis show an increase in local original income from mining companies after the enactment of Law No. 23 of 2014. This finding indicates that mining regulations issued by the government improve community welfare and confirm regulatory theory, especially the theory of public interest.

Keywords: Regulation, Mining Companies, Public Welfare.

INTRODUCTION

Mining companies are companies that are very sensitive to the environment, because their operational activities are exploiting natural resources. Because the impact of environmental damage caused by the activities of this company is quite large, the policy on social responsibility and the environment of mining companies must be designed by the government. Without policy, ecosystems in the region will be threatened, and conflicts between communities and companies will increase. In this condition, government interference must be able to deal with problems that might arise from mining activities. From the company side, the social and environmental responsibility of mining companies should not be limited to Philanthropy but must be within the company's business strategy [1]. Thus, social and environmental accountability will indeed be managed by considering the relevance of the program to the activities of the company.

Through Law 23 of 2014 concerning Regional Government, mandates the authority of the Provincial Government in the field of energy and mineral resources. This law is strengthened by the Minister of Energy and Mineral Resources Circular Letter Number 04.E / 30.DJB / 2015 which confirms that the Regents / Mayors no longer have authority in the administration of minerals and coal.

This condition may be driven by the note that funds that must be deposited from mining companies to regional governments are still very low. Government revenues from mining activities are defined contributions, such as; exploration fees (work contracts/ feasibility studies, construction), exploitation contributions (Royalties) and other payments related to the granting of mining rights (Decree of the Minister of Finance of the Republic of Indonesia number 344 / kmk.06 / 2001).

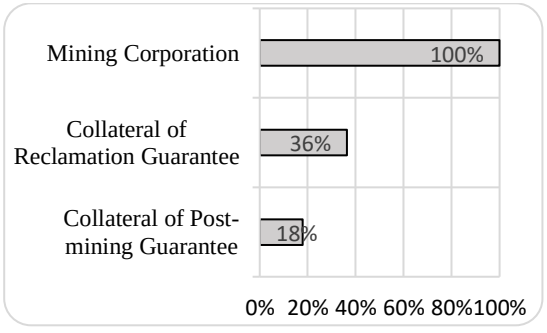

Fig. 1 Collateral for reclamation and post-mining guarantee in Lampung Province, 2018.

The low awareness of mining companies to provide guarantees of reclamation and post-mining, is shown in Figure 1. From figure 1, it can be seen that there were only 36% of mining companies out of a

total of 168 companies that paid collateral for reclamation. Meanwhile, companies that pay post-mining guarantees are only 18%, and all of them come from companies that also pay collateral for reclamation.

LITERATURE REVIEW

Regulatory theory, specifically public interest theory, introduced 1934 in the book The Economics of Welfare [2], explains that the policies issued by regulators are in the interests of the people, namely improving inefficiency and injustice in practices that occur in the field. Lindrianasari et al. [3] found that the theory of regulation (particularly for public interest theory) can explain clearly the reasons why the four variables research has increased after the environmental regulations issued. Their research found similar results in all companies listed on stock exchanges in three developing countries, namely Indonesia, Malaysia and Thailand, related to new policies on social and environmental responsibility.

Deegan and Unerman [4] explained that policies will not only bring benefits to the people but also to protect the environment and maintain sustainability. Regulatory theory predicts that policies issued by the government related to the authority of environmental management (in terms of activities of exploitation of natural resources), should be able to improve the quality and sustainability of the environment.

The stakeholder theory explains which parties the company must be responsible for [5]. At the very least, the company must be able to maintain its relationship with stakeholders, by fulfilling obligations that are the will and needs of stakeholders, including powerless-stakeholders. In this case, the company must ensure the availability of resources used for the operational activities of the company and the surrounding community.

In line with Law 23 of 2014 concerning Regional Government which mandates the authority of the Provincial Government in the field of energy and mineral resources, the assessment of social impacts on mining is an important matter. The purpose of this social impact assessment is to see whether regulatory theory can be confirmed in the application of the law. At present, there is no global regulatory system or an international legal system can force companies to be responsible for their operations in weak governance zones [6]. Because in weak governance zones, social and environmental problems are relatively higher, vice versa. Therefore, there must be an alternative accountability mechanism that applies at least within the scope of the state and the region that regulates corporate social responsibility. Enforcement of the Act 23 of 2014 has become the answer to the needs of regulation in mining issues in Indonesia.

As the company aims, mining activities are managed to generate profits. But if there is mismanagement, mining activities can have a negative impact on human society, the environment, even for the sustainability of the company. The study conducted a test of how people around mining companies evaluate the benefits and negative impacts of mining has been carried out in Australia. Evaluation is carried out on communities around mining about the influence of the order of life of communities around mining [7]. They found that strong governance will increase the respect of the community towards the company relatively higher compared to when governance is weak, even when environmental conditions get worse.

Mining companies, are one of the companies that can be the highest source of state income. Even in the Democratic Republic of Congo (DRC) mining companies are expected to contribute 50% of GDP in 2015 (Reuters, 25 October 2010) up from 23-25% in 2010 [8].

From theoretical, practical explanations, and supported by previous studies, the research hypothesis is formulated as follows:

Ha: Government policies on management authority in the field of energy and mineral resources improve public welfare.

RESEARCH METHOD

This research is a preliminary study conducted on the impact of the issuance of Law 23 of 2014 concerning Regional Government, regarding the transfer of management authority in the field of energy and mineral resources from the Regency / City Government to the Provincial Government. This law has also been strengthened by the issuance of the Minister of Energy and Mineral Resources Circular Letter Number 04.E / 30.DJB / 2015.

The research method used in this study is to involve the mining office in all cities and districts in Lampung Province. By using secondary data from two different recording sources. First, sourced from the mining offices of each district / city for data on revenues from mining companies in each region for the five-year period (2010-2014). Second, sourced from the environmental office for data acquisition from 2015-2018. The mechanism for obtaining data is by collecting it centrally at the Lampung Province government office. Moreover, since 2015 the authority to carry out affairs in mineral and coal mining has shifted to the provincial government.

This study will investigate the benefits of central government policies through Law 23 of 2014 concerning Regional Government. Whether after the authority in administering government affairs in the field of mineral and coal mining is transferred to the Province, public welfare will be better. This welfare will be measured by using Regional Original Income (PAD). The greater the annual average PAD from

mining received by the Province compared to the average accumulated annual PAD from mining received in all districts / cities in Lampung, the welfare index in Lampung Province also increases.

RESULT

This research will determine the different test of regional original income from mining obtained in Lampung Province. Before and after the enactment of Law Number 23 Year 2014, which transferred the authority to manage mineral and coal mining to the Province (previously managed by Regency /City). This regulation of substance is not only transferring management, but furthermore, this movement aims to provide greater authority to the Province to apply the pattern of uniformity that is applied to the mining sector to be responsible for the exploration and exploitation activities they carry out. With this pattern of uniformity, it is expected that the transparency and accountability of fund management from the mining sector will be better, and the misuse of funds can be minimized.

Regional Original Income when authority for the management of mineral and coal mining in Regency/City

Regional original income obtained from the mining sector four years before the transfer of authority for the management of mineral and coal mining to the Province, in accumulated from 15 Regency/City in Lampung Province, is shown in figure 2 and figure 3. Figure 2 shows local revenue originating from contributions fixed and royalty, while Figure 3 shows the total regional income from the mining sector.

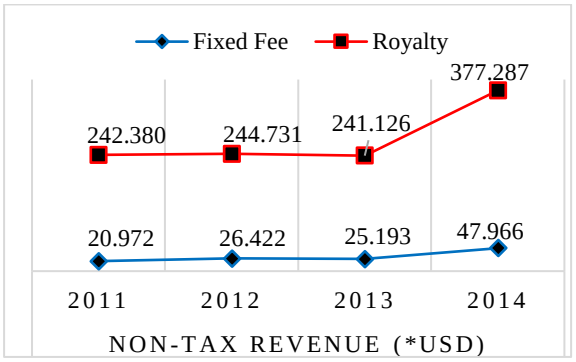

Fig. 2 Non-tax Revenue from fixed fee and royalties (Before).

Figure 2 shows that income from fixed royalty fees before 2014 tends to be low (stable). But this was not the case in 2014, when the government issued its new policy. Even though Law number 23 of 2014 was effectively implemented in 2015, the fixed fees and royalties obtained from the mining sector showed an increase. So that we can visually see how the new regulation affects regional revenues. In Figure 3, it shows how the total revenue from the mining sector increased in 2014, in line with the income from each fixed contribution and royalty increase in 2014. These findings indicate that regulations will form a legal certainty of how a person or entity behaves, in line with the rules made.

Fig. 3 Total Non-tax Revenue from fixed fee and royalties (Before).

Regional Original Income when authority for the management of mineral and coal mining in Province

Data from the Lampung Provincial Government shows an increase in the total non-tax revenue from the mining sector over the past 4 years (2015-2018). These results indicate an increase in the welfare of the community, assuming the rate of return to the community is directly proportional to the total non-tax income.

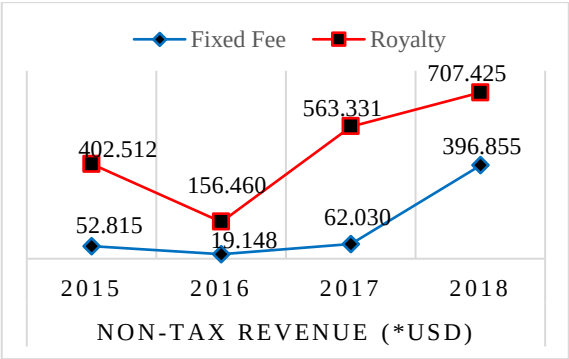

Fig. 4 Non-tax Revenue from fixed fee and royalties (After).

Since the enactment of Law 23 of 2014 which transferred the authority to manage mineral and coal mining to the Province (previously managed by the Regency/City), there has been an increase from sources of income from mining to the government. Figure 4 shows the growth of non-tax revenues originating from fixed fee and royalties of mining companies. Meanwhile, figure 3 shows the total non-tax revenue obtained by the province. Both images

show non-tax revenues from mining over the past 4 years after the management of mineral and coal mining management was transferred to the province, which was previously managed in the district /city.

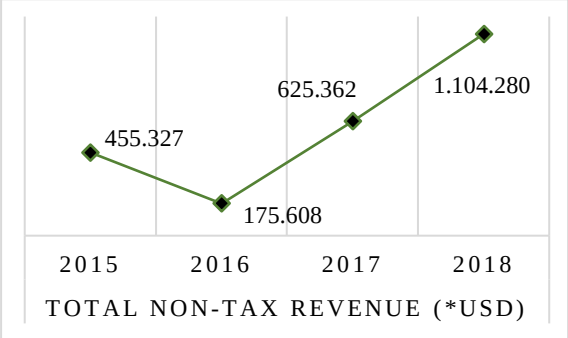

Fig. 5 Total Non-tax Revenue from fixed fee and royalties (After).

Figure 4 and Figure 5 show the growth of non-tax revenues obtained from mining companies. The income of the provincial government from the mining sector has been able to increase the amount of local revenue. Therefore, it is assumed that the higher the local revenue, the better welfare of the people in Lampung province.

The main operation of a mining company is to explore and exploit natural resources. Meanwhile, around the area where the company is exploring and exploiting, there are other interests that require a balanced ecosystem for a good life. For this reason, the function of the government is required to cover all the interests of the parties in this area, so that no party can obtain maximum benefits, while other parties only get negative impacts from mining activities.

The government must show its role as regional leader. The role of the government must be to minimize gaps between community groups and groups of companies, and / or in one region with other regions. Therefore, the existence of regulations that take over the authority at the lower level to a higher level is highly expected to create better welfare equality. Law 23 of 2014 concerning Regional Government which mandates the authority of the Provincial Government in the field of energy and mineral resources is one of the regulations that is expected to create welfare equality. This law is also strengthened by the Minister of Energy and Mineral Resources Circular Letter Number 04.E / 30.DJB / 2015 which confirms that the Regent / Mayor no longer has the authority to administer government affairs in mineral and coal mining.

Test the Comparison of Original Regional Income Before and After the Enactment of Law 23, 2014

We conducted an independent sample t-test to assess differences in government revenues from the mining sector before and after the enactment of Law 23 of 2014. The reason for using this test is because we use the average income for 4 years before and 4 years after, so the total sample used is < 30.

Table 1 Comparison test

Levene's Test for Equality of Variances	
F	10.100
Sig	.034
Equal variances not assumed	
t	-4.177
Sig. (2-tailed)	.047*

Note: *significant at the 0.05 level.

The results of the homogeneity test using the Levene's test method show the value based on Mean, which is 0.001 with p value (sig) of 0.034 where > 0.05. These results indicate that there are inequalities in variance between groups or heterogeneous. Therefore, we use the value of equal variances not assumed to determine whether there are any differences between the groups tested. Table 1 shows the results of the independent sample t-test.

The result of equal variances not assumed shows the t -4,177 with sig. (2-tailed) 0.047 <0.05 which indicates that the regional original income from the mining sector after the application of Law 23 of 2014 was significantly higher. These results mean that what is predicted by regulatory theory (public interest theory) that policy should be publicly confirmed is confirmed through this research. Because with the increase in the amount of local revenue, the greater funding can also be made in the area to improve the welfare of the community.

This finding is in line with previous research which found that the intervention of developing country governments greatly determines the company's compliance in considering social and environmental aspects [8]. This finding also indicates that the government issued a new policy to regulate the management of funding revenues from mining activities to improve community welfare. This finding concludes that the hypothesis of this study which states that government policies on management authority in the field of energy and minerals improve public welfare, is supported.

CONCLUSIONS AND SUGGESTIONS

This study found a significant increase in regional original income in Lampung Province after the enactment of Law No. 23 of 2014. This finding also shows that the aim of the government in issuing a new policy is to manage the amount of funds in the regions from mining activities which has succeeded in increasing the revenue of the Province.

Although this study was only conducted in Lampung Province, this study can be used as a reference that the regulations issued turned out to be in favor of the interests of the community. Because with the increase in local revenue, capital expenditure for the community is also expected to increase. That way, people's welfare will increase with this new policy.

This study can be applied to other regions in Indonesia. Future research can use the same approach and / or use other approaches, to test the superiority of the issuance of laws relating to the management of mining (related to the environment and social community). Further studies are also expected to expand research content, by combining secondary and primary data (surveys into the community) so that subsequent studies can provide more comprehensive and useful results.

The limitation of this study is that it is difficult to collect data from each district / city mining office because, since 2015, this section has been abolished and merged with the environmental office. This transition might cause the existence of documents to be incomplete.

ACKNOWLEDGMENTS

This paper can be completed thanks to the support of many parties. A valuable discussion with my colleague is the Doctor of Environmental Sciences program, University of Lampung, fellow practitioners from a mining company in Indonesia, head of the mining service, head of the environmental office, in Lampung province. All discussions and data help have made this paper more qualified. For all support, we are happy to thank you.

REFERENCES

[1] Hamann, Ralph and P. Kapelus. Corporate Social Responsibility in Mining in Southern Africa: Fair accountability or just greenwash? Development, Vol. 47, Issue 3, 2004, pp. 85–92.

[2] Pigou, A. C. *The Economics of Welfare*. London: Macmillan and Co. 1932, pp. 1-948.

[3] Lindrianasari, M. Kufepaksi, Y. Asmaranti, A. Komalasari. Social and Environmental Responsibility in Developing Countries: A Theoretical Approach to Regulation. *International Journal of GEOMATE*, Vol. 15 Issue 49, 2018, pp. 47 -52.

[4] Deegan, C., and Unerman, J. 2011. *Financial Accounting Theory*. Maidenhead: McGrawHill Education.

[5] Freeman, R.E., J.S., Harrison, A.C. Wicks, B. Parmar, S. de Colle. Stakeholder Theory. The State of the Art. Cambridge University Press. New York. 2010. pp. 1-364.

[6] Coumans, Catherine. Alternative Accountability Mechanisms and Mining: The Problems of Effective Impunity, Human Rights, and Agency. Canadian Journal of Development Studies Revue canadienne d'etudes du developpement. Special Issue: Rethinking Extractive Industry Issue 1-2, 2010, pp. 27-48.

[7] Zhang, Airong and K. Moffat. A balancing act: The role of benefits, impacts and confidence in governance in predicting acceptance of mining in Australia. Resources Policy, Vol. 44, 2015, pp. 25–34

[8] Hanlin, Rebecca and Hanlin, Christopher. The view from below: ‘lock in’ and local procurement in the African gold mining sector. Resources Policy, Vol. 37, Issue 4, 2012, pp. 468–474.

9th Int. Conf. on Geotechnique, Construction Materials and Environment, Tokyo, Japan, 20-22 November 2019, ISBN: 978-4-909106025 C3051

FOUNDATION, SUPPORT AND DEVELOPMENT OF THE REPUTATION IN COMPANY

Svetlana D. Gurieva[1]

[1]Professor, Department of Social Psychology,
Saint Petersburg State University, Saint Petersburg, Russia

ABSTRACT

This research work covers issues related with the main principals of foundation, support and development the reputation. We have collected a variety of definitions of the concept of “reputation" that are presented in different spheres: economics, marketing, sociology, organization theory, and received the modern understanding the reputation phenomena. Considering the structure of reputation, the main role in the formation and maintenance of reputation plays the owners, managing staff, employees, clients. The study involved 350 people from the Company, of which 14.2% were men and 85.8%, were women from 18 to 67 years old. The objective of our research is to study the socio-psychological representations of reputation in the context of the organizational culture. The study used the following tools: Questionnaire, Sacks sentence completion test by Sacks and Levy. A meaningful and statistical analysis of the results based on the method "Unfinished sentences" allows us to formulate several statements. We found practical confirmation that the foundation of reputation is perceived as honesty, credibility, openness, reliability, quality of products and services that is the core of company′ reputation. Theoretical analysis of strategies for the formation, maintenance and development of reputation shown that its can be a platform for the development of intra-organizational strategies aimed at maintaining the high reputation of the company. The development of the reputation is based on visibility, transparency, coordination and emotional appeal. All the above is a confirmation of the existence of a strong internal corporate reputation management that studies the specifics of building reputation.

Keywords: reputation, social representation of reputation.

INTRODUCTION

Fombrun C., Shanley M.S. (1990) suggests that reputation itself should be understood as a social assessment of someone's specific characteristics, “the reputation is an active assessment of respect for a man by himself and showing the respect for people’s opinion about him" [8]. According to S. Gorin (2006), who considers a business reputation as the economic-legal category that is the “general prevailing opinion about the qualities, merits and demerits of the organization in the field of business turnover, which determines the attitude of the environment and can generate above-standard profits" [11, P. 25-26]. R.J. Varey [19] focuses on the use of the term “reputation" in the business environment and provides these definitions and statements about the concept of corporate reputation: the combined experience of all people who interact with the organization (Friedman, 2009) [9, P. 229-244]. The assessment of respect for the organization that reflects the image created by people (Dowling, 2001) [5]; the reputation of a company is partly the function of its own activity (including PR-actions) and partly of the behavior of those groups of people who show interest in it or are directly related to (Griffin, 2009) [12]. V. Safón gives the following definition of the reputation as “perceptual presentation of the past actions of the company and its future plans which describe the overall attractiveness of the company according to its key components compared to the competitors” [18, P. 205]. Thus, as it is seen from the definitions of reputation, most authors agree that the reputation is certain information concerning the qualitative aspect of human activity or company [1], [3], [12], [10]. We have collected a variety of definitions of the concept of “reputation" presented in Fig.1.

In the specialized literature, the most commonly used concept of reputation is used in conjunction with the concept of corporate image. The set of beliefs and feelings associated with a particular image that enriches it with meaning or psychological content. This is the interaction of a company’s presentations of itself, the way it would like view and the real public opinion about it, whose changes are difficult to understand [19]. From our point of view, the essence of the reputation and image have a number of common points, but they are not the same [2]. Thus, an image is a specific symbol, a position being deliberately created and promoted by a person or an organization in public. A reputation is the way the image of a company is perceived and how it is viewed in the public eye. The authors argue that reputation is a broader concept and includes the image [13], [16], [13], [15].

Having considered the model of confidence and the structure of relationships in the organization let us pay attention to the specifics of the confidence in the organization (Fig. 2).

Discipline	Definition
Economics	Reputations are traits or signals that describe a company's probable behavior in a particular situation.
Strategy	Reputations are intangible assets that are difficult for rivals to imitate, acquire or substitute.
Marketing	Reputation describes the corporate associations that individuals establish with the company name.
Communications	Reputations are corporate trails that develop from relationships companies establish with their multiple constituents.
Organization theory	Reputations are cognitive representations of companies that develop as stakeholders make sense of corporate activities.
Sociology	Reputational ranking are social constructions emanating from the relationships firms establish with stakeholders in their shared institutional environment.

Fig. 1. The definition of corporate reputation.

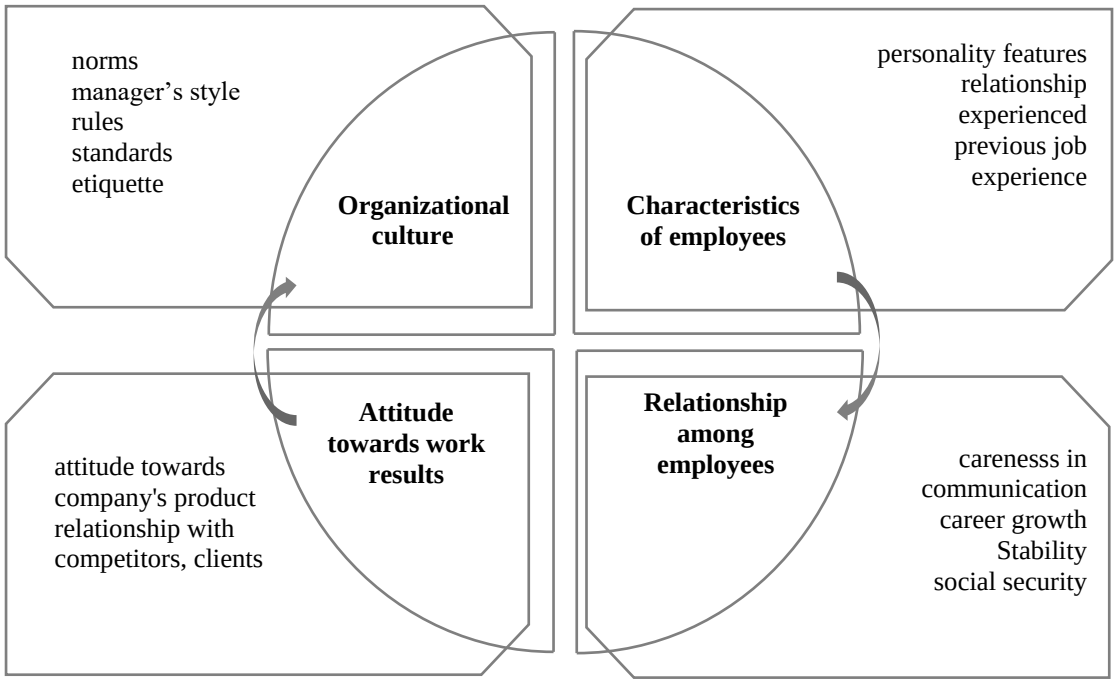

Figure 2. The model of confidence forming in the organization (Gurieva S., and others, 2016).

According to M. Armstrong (2006), the basis for forming the reputation, organizational confidence and image is the organizational culture being shaped under the control of company's management representing, a set of beliefs, attitudes, norms of behavior and values that are common to all the employees of the organization. Not always they can be clearly expressed, but in the absence of direct instructions they determine the ways people act and interact and they greatly affect the progress of the work. By forming the organizational culture, managers have the ability to control and modulate the optimal level of the staff. Also, the employees themselves may affect the common standards by their attitude towards them, duty and aim to meet them. Each of them does not only possess his own personal features that determine the ability to confidentially interact, but also the experience of previous professional relationships. This should be taken into consideration at the stage of adaptation of an employee, thus attitudes formed towards the image of the leaders, colleagues and subordinates have a direct impact on building relationships within the new team.

There are two factors affecting both level of trust in the organization and company's reputation. First of all, what does mean is the level of common well-being, satisfaction of such needs as the need for stability, security, career opportunities. Second, it is made up of confidence in the product, in the result of the organization, in the value of the staff themselves. These are the consumers and customers for goods and

services who affect the attitude towards the product, as well as competitors forming a picture of the position of the organization in the market.

The company's reputation is built on the values, which are the features of a particular company (authenticity, integrity, responsibility to customers, etc.). However, at some point, the author begins to use the concepts of image and reputation, separated by commas, without making distinctions between them [5]. Reputation is a better-considered, reasonable perception of the object, based on the achieved experience, containing the assessment. The image is the upper stage of knowledge and is a correlation of the communication process with the personal human experience, through which stereotypes and certain models of behavior are created [2]. Thus, it can be concluded that the reputation is more complicated concept compared to the other two. It includes brand (emotional) and substantive (based on personal experience) parts, the latter of which is based on the image [8].

Reputational nature of organizational culture in its turn, has an impact on the marketing symbol (brand assets), strengthening the positive association with the company, the perception of quality, increasing commitment and loyalty (Dowling, 2001; Martin, G., Hetrick S., 2006). It is necessary to demonstrate ethical values, the importance of employees and customers [15]. However, in different social groups, the strategies for building reputation differ and corporate identity and corporate image in people's minds are not always identical [5]. One may say that for building business reputation it is necessary to communicate with different target audiences, focus on their opinions and preferences, as the decision about quality of the reputation is being made on the auditor's assessment. It is subject to be assessed by the state, the competitors, the partners, the investors, the customers, the staff and the local community (Dowling, G. R., 2001; Martin G., Hetrick S., 2006; Griffin A., 2009; Fombrun C., Shanley M., 1990; Fombrun C., Van Riel C., 2004; Friedman B. A., 2009). G. Dowling (2001) divided all these types of social groups into 4 ones:

1. Regulations (establishing general laws and rules of doing business: authorities, government and non-government organizations, international credit rating agencies);
2. Functional (influencing the daily life of the organization: staff, suppliers, distributors, consulting and juridical firms);
3. Diffuse (indirectly related to the organization, but influencing its reputation, there can be potential customers i.e. journalists, environmental organizations, etc.);
4. Consumers [5].

Making the reputational strategy involves the goal setting, development of certain activities in order to form it and understanding the features of target social group. Mailath G., Samuelson L., (2001) view a reputation as an asset, and building a reputation requires three following principles:

- *Reputation is built gradually*. The consumer trust that lies at the basis of a reputation is accumulated in response to sustained, high-quality work.
- *Reputation disappears gradually*. A firm that stops investing in its capital stock and lowers the quality of service does not experience an immediate decline in reputation till a consumer adjust to the new level of working standard.
- *Reputation can be managed*. The quantity of investment can be regulated. Thus, the initial periods of development demand higher investment level than later periods when the company is mature and its reputation is sustained without essential investment.

This and much more will make the company be more attractive for both employees and customers, and increase its value. In order to create reputational strategy due to modern conditions it is necessary to take into consideration the following features of the world affecting the quality of companies' reputation:

1. *Widening boundaries of the world* (widening the boundaries of movement and increasing information streams make a man's life more public and available for society);
2. *Increasing dangerous cases* (the will to feel safe and secure under the current circumstances of increasing life intensity causes the keen attention to the risks);
3. *Informational saturation of the world* (the increased speed of reaction to new event, information acquisition and production);
4. *Society obtained true power* (attention to the needs of its target audience i.e. the consumers, the employees, the state etc.);
5. *Increasing influence of non-governmental organizations on the society and economics;*

«State remains strong but business weakens» (the demands and critical to the companies and their reputations increase) [12].

Reputation is one of the factors in building trust in a company. Many researchers have studied relationship between trust and reputation, as well as the mechanism of their formation in the conditions of market economy. The relational approach is commonly used, according to which the company's reputation and credibility of the system are considered as complementary components (Fig. 3).

That is the example of creating trust according to G. Dowling (2001). In this regard, to build the reputation companies should be able to differ from others, to carry out the obvious and consistent strategic actions, express their beliefs and values openly. It is necessary to show sincerity, interest in their target groups, thereby causing confidence.

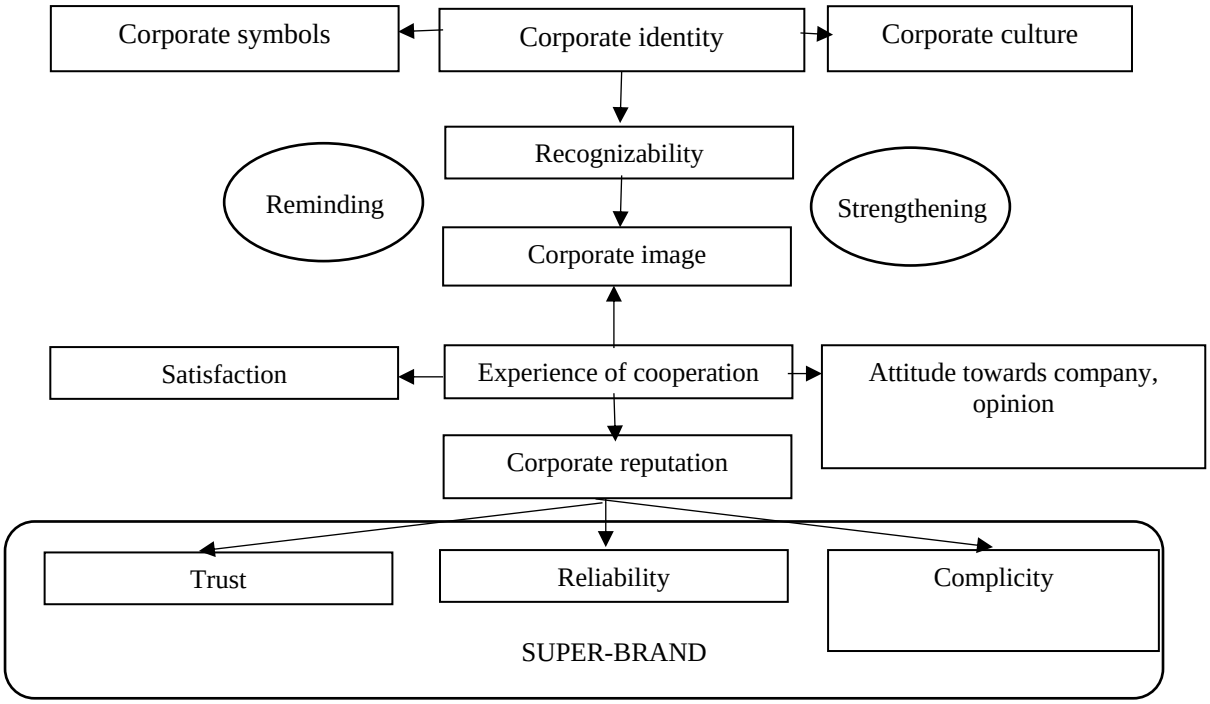

Fig.3. Reputation components (based on: Fombrun, Van Riel, 2004; Gurieva, Manichev, 2016).

THE IMPORTANCE OF ORGANIZATIONAL CULTURE FOR BUILDING A STABLE POSITIVE REPUTATION.

The transformation of a favorable image of an organization to the intangible asset ***starts from inside***, it must be transparent and integrated not only in the strategic management of the company (affecting goals, vision and mission of the company), but also embedded in the ***organizational values.*** Features of the organizational culture, reflected in both the actions of employees and the organization as the whole, play a major role in determining the nature of the company's business reputation in public, media and the state, as well as the specifics of corporate reputation, which is important for shareholders, creditors and investors. In other words, the concern for creating a stable reputation should be reflected in the organizational culture of the company, and corporate reputation should be perceived as a part of it. Many theorists and practitioners studying the reputation of companies agree with that thesis including A. Griffin (2009), S. Greyser (2009), B. Friedman (2009), O. Harpur (2001), V. Safon (2009) and others.

Proper human resource management as an element of organizational culture obtains particular importance to create a strong reputation. "Styles of behavior affecting the reputation and brands depend on the level of education, skills and abilities of the total human capital bank" (Martin G., Hetrick S., 2006, p. 36). In order to increase the loyalty of employees, according to Fraser P. Seitel (2014), one must keep the following principles: respect, frank feedback, moral encouragement, right to vote. However, this might not be sufficient. According to Griffin A. (2009), the company's reputation is appreciated by employees only when caring about it is embedded in the system of bonuses. In this situation, the special role in building the organizational reputational culture is given to the Department of HR, which increases the motivation of employees and their identification as a part of the organization through the following roles (Friedman, 2009).

No less significant is the *figure of the manager* who seems to reflect the company's values and transmits them first of all to the internal organizational environment, defining the character of the organizational culture. The manager carries the weight establishing delicate balance among organizational identity, corporate image and brand necessary for building the reputation. If the direction chosen by the selected leaders is not approved by employees, then there is a gap between the leader and his vision of culture. If values stated by the brand are not implemented that shows the divergence of image and corporate culture, which leads to confusion of customers and employees. In the case in practice when image and vision diverge, managers' aspirations do not coincide with the external image of the company (Martin G., Hetrick S., 2006).

The manager is the first person of the company both for employees and for all external audiences, to a greater or lesser extent related to the activities of the company. The image and reputation of the head definitely affect the nature of the company's reputation, but to use the head as a symbol of the company's

reputation would be the risk [5]. In this regard, the leader must not be only famous, but also authoritative, which is not synonymous. Accordingly, a successful manager who wants to create a favorable image of his company, should have the following features:

- a clear definition of objectives;
- the ability to inspire confidence;
- the ability to exercise effective crisis management;
- mergers and acquisitions management;
- formation of the company's reputation in the media;
- the influence on stock prices changes [5].

REPUTATIONAL NATURE OF ORGANIZATIONAL CULTURE.

Reputational nature of organizational culture in its turn, has an impact on the marketing symbol (brand assets), strengthening the positive association with the company, the perception of quality, increasing commitment and loyalty (Dowling, 2001; Martin, G., Hetrick S., 2006). It is necessary to demonstrate ethical values, the importance of employees and customers. However, in different social groups, the strategies for building reputation differ and corporate identity and corporate image in people's minds are not always identical (Dowling, 2001). One may say that for building business reputation it is necessary to communicate with different target audiences, focus on their opinions and preferences, as the decision about quality of the reputation is being made on the auditor's assessment. It is subject to be assessed by the state, the competitors, the partners, the investors, the customers, the staff and the local community (Dowling, G. R., 2001; Martin G., Hetrick S., 2006; Griffin A., 2009; Fombrun C., Shanley M., 1990; Fombrun C., Van Riel C., 2004; Friedman B. A., 2009). G. Dowling (2001) divided all these types of social groups into 4 ones:

1. *Regulations* (establishing general laws and rules of doing business: authorities, government and non-government organizations, international credit rating agencies);
2. *Functional* (influencing the daily life of the organization: staff, suppliers, distributors, consulting and juridical firms);
3. *Diffuse* (indirectly related to the organization, but influencing its reputation, there can be potential customers i.e. journalists, environmental organizations, etc.);
4. *Consumers*.

Thus, it is important to emphasize that the broadcasting reputation in a wide range of social

groups that are interested in cooperation with the organization, starts with the values of the atmosphere and culture, rooted in the company. Therefore, the type of organizational focus is crucial in determining the company's reputation.

APPROACH

The main goal of our project is studying the phenomenon of reputation. The study involved 350 people, 14.2% were men and 85.8%, were women from 18 to 67 years old. The participants of the study were asked to complete the 7 sentences which were grouped into 5 major scales and processed using content analysis. 1.Reputation is …? 2. Our company is …3. Reputation is based on the principles of …? 4.I trust the company because … and etc. While studying the phenomenon of reputation, priority is, first, the understanding and further investigation of implicit representations about the notion of "reputation". How to understand the reputation, what they put into the content, what related concepts are mentioned, why they are important. For the frequency analysis of words in tasks with an open response, the stamping procedure was used hat is bringing the words to a unique form. To stemmize the answers, the MyStem program (Yandex LLC) was used. The program MyStem makes a morphological analysis of the text in Russian. A special feature of this program is the possibility of constructing the presupposing parsing for words that are not in the main dictionary, and full support for the Russian language. The text was processed by means of a package for the study of the natural language tm (Feinerer I., Hornik K., Meyer D., 2008) for the statistical medium R (R Core Team, 2017). To provide the results, words that occur at least 5 times were selected.

RESULTS

To test the hypotheses put forward in the study the following mathematical-statistical methods of statistical data processing were used: Content analysis; Comparison of the mean values and standard deviations (Mann-Whitney U-test). For the frequency analysis of words in tasks with an open response, the stamping procedure was used hat is bringing the words to a unique form. Semantic analysis the results of meaning the reputation. Employees of the company consider that the reputation is: the company itself, society, opinion and people; The most frequently repeated terms in the description are the following statements: it is opinion about a stable company, a reliable partner (Fig. 4).

Staff.Reputation.word	Staff.Reputation.freq	percent
Opinon	56	10.7
Company	46	8.8
Society	25	4.8

Fig. 4. Representation of reputation among the interviewed employees.

During its existence on the market, company has proved that it can be perceived as a reliable, partner company, as a reliable and good company, as a stable

and reliable partner company. The main reasons why the interviewed respondents consider company to be reliable and stable is following the basic principles and values of the company. Among them, for example, the consultants note the honesty, quality of products; the leaders and the staff mention the spirit, togetherness and passion (Fig. 5).

Staff. principle. word	Staff. principle. freq	percent
spirit	108	16.2
togetherness	107	16.0
passion	104	15.6
people	17	2.5

Fig. 5. Basic principles of the company among the interviewed staff.

In our opinion, an important achievement and a high level of loyalty and commitment to the company are the responses to the statement "I feel myself the part of the company ...". The overwhelming majority of respondents perceive the company as their own, as part of themselves, as the greatest value in their lives (Fig. 6).

Staff. part. word	Staff. part. freq	Percent
company	27	8.9
my	14	4.6
be a part	11	3.6

Fig. 6. Staff about their attitude to the company.

A meaningful and statistical analysis of the results based on the method "Unfinished sentences" allows us to formulate several statements. Our company has stable, positive implicit ideas about the company itself, as well as the company's reputation, from the point of view of the employees. We found practical confirmation that the reputation of the company is perceived as honesty, credibility, openness, reliability, quality of products and services.

Conclusion

The results of our research were reflected with the main principles of forming the reputation and raising the emotional predisposition towards the company described by Charles Fombrun and Cees Van Riel (Fombrun C., Van Riel, S., 2004). Theoretical analysis of strategies for the formation, maintenance and development of reputation can be a platform for the development of intra-organizational strategies aimed at maintaining the high reputation of the company and its further development. The foundation of reputation is perceived as honesty, credibility, openness, reliability. Theoretical analysis of strategies for the formation, maintenance and development of reputation shown that its can be a platform for the development of intra-organizational strategies aimed at maintaining the high reputation of the company. The development of the reputation is based on visibility, transparency, coordination and emotional appeal. The company management should pay attention to the revealed differences in the assessment of the main components of the reputation between the staff, on the one hand, the leaders and consultants, on the other. It is possible to propose for the HR staff the development of special mixed training programs, which will involve representatives of three groups: leaders, consultants and company staff. In the program, include a meaningful analysis of cases, the reflection of experience, and the exchange of experience.

REFERENCES

[1] K.S. Cameron,. R.E. Quinn, Diagnosing and changing organizational culture: Based on the competing values framework (Rev. ed.). San Francisco, CA: Jossey-Bass. (2006).

[2] S. Gurieva, M. Borisova, Kawabata Takeyasu. Trust as a Mechanism of Social Regulation the Modern Youth's Behavior. American Journal of Applied Sciences, Volume 13, Issue 1, 2016, Article number 100.110, (2016). Pp. 100-110. http://thescipub.com/PDF/ajassp.2016.100.110.pdf

[3] S. Gurieva, S. Manichev, and set., Values and Hardiness: Entrepreneurs of Former Soviet Countries // Indian Journal of Science and Technology, Vol 9 (46), 2016. pp.333-342. DOI: 10.17485/ijst/2016/v9i46/107510, http://www.indjst.org/index.php/indjst/article/view/107510

[4] V.J. Doby, R.D Caplan, Organizational Stress as Threat to Reputation: Effects on Anxiety at Work and at Home // The Academy of Management Journal, Vol. 38, No. 4 (Aug., 1995), pp. 1105-1123.

[5] G.R. Dowling, Creating corporate reputations: identity, image and performance. New York: Oxford University Press. 2001.

I. Feinerer, K. Hornik, D.Meyer, Text mining infrastructure in R. Journal of

Statistical Software, 25 (5):1-54, March. 2008.

[6] C.J. Fombrun, C.B.M Van Riel, Fame & Fortune: How Successful Companies Build Winning Reputations. Upper Saddle River, N.J.: Financial Times/Prentice Hall. 2004. 272 p.

[7] C.J. Fombrun, M. Shanley, What's in a Name? Reputation Building and Corporate Strategy // The Academy of Management Journal, Vol. 33, No. 2 (Jun., 1990), pp. 233-258.

[8] B.A. Friedman, Human Resource Management Role Implications for Corporate Reputation // Corporate Reputation Review, Vol. 12, No. 3, 2009, pp. 229–244.

[9] St. Greyser, Corporate brand reputation and brand crisis management. Management Decision Vol. 47. No. 42009, pp. 590-602. DOI 10.1108/00251740910959431

[10] S.V. Gorin, Business reputation of organisation. Rostov-na-Donu, 2006. Горин С. В. (2006).

A. Griffin, New Strategies for Reputation Management: Gaining Control of Issues, Crises and Corporate Social Responsibility. 2009.

[11] S.C.Jones, J.S. Shrauger, Reputation and Self-Evaluation as Determinants of Attractiveness // Vol. 33, No. 3 (Sep., 1970), pp. 276-286.

[12] D. Knocha, F. Schneiderb, D. Schunkb, M. Hohmanna, E. Fehrb, Disrupting the prefrontal cortex diminishes the human ability to build a good reputation // PNAS vol. 106 (no. 49). . p.p. 20895–20899.

[13] G. Martin, S. Hetrick, Corporate Reputations, Branding and People Management: A Strategic Approach to HR. First edition, Elsevier Ltd, – 2006. 384 p.

[14] R.K. Merton, Social Theory and Social Structure (1968 enlarged ed.). New York, NY, US: Free Press. 1968.

[15] J.M. Sacks, S. Levy, The sentence completion test // Bellak L. (ed.) Projective psychology. - N.Y.: Knopf, 1950pp. 357-397.

[16] V. Safón, Measuring the Reputation of Top US Business Schools: A MIMIC Modeling Approach //Corporate Reputation Review, Palgrave Macmillan.Vol. 12, No. 3, 2009. pp. 204–228.

[17] R.J. Varey, Marketing communication: Principles and Practice. – Routledge, 2001.

9th Int. Conf. on Geotechnique, Construction Materials and Environment, Tokyo, Japan, 20-22 November 2019, ISBN: 978-4-909106025 C3051

ECOTOURISM DEMAND FORECASTING AT NATIONAL PARK, KUALA TAHAN, PAHANG

Noratikah Abu[1], Megat Muhammad Afif[2], Wan Nur Syahidah[3]and Zuhaimy Ismail[4]
[1,2,,3]Faculty of Industrial Science & Technology, Universiti Malaysia Pahang, Malaysia; [4] Faculty of Science, Universiti Teknologi Malaysia, Malaysia

ABSTRACT

Tourism forecasting can lead to an important element in tourism industry to ensure that each investment by individuals, companies and government was worth it. From economy perspective, ecotourism is a growing business nowadays and can be an important indicator to the tourism industry. Hence, this study attempt to forecast the ecotourism product demand in Pahang based on number of tourist arrivals in National Park Kuala Tahan, Pahang. Box-Jenkins (Seasonal ARIMA) model is used to make analysis and forecast of the number of international and domestic tourist since 2013 until present. The accuracy and validation of the results is measured using mean absolute percentage error (MAPE). Results obtained by applying the proposed model and numerical calculation shows that Seasonal ARIMA models is effective for forecasting the number of tourist arrivals in National Park Kuala Tahan. The best model in forecasting ecotourism product demand in Pahang is $\mathrm{SARIMA}(0,0,1)(2,0,1)_{12}$ with MAPE value 13.92%.

Keywords: Ecotourism, Forecasting, Box-Jenkins, Tourism

INTRODUCTION

Tourism industry is one of the main economy indicators in the world and is growing very fast from day to day. According to The World Tourism Organization (UNWTO), tourism can be classified to 14 types such as cultural tourism, ecotourism, rural tourism, adventure tourism, health tourism, wellness tourism, medical tourism, business tourism, gastronomy tourism, urban and city tourism, mountain tourism, education tourism, sports tourism, and coastal, maritime and inland water tourism. In this study, we will focus on ecotourism industry as ecotourism industry received less attention among researcher. Ecotourism involved of natural, communities and sustainable travel. The International Ecotourism Society (TIES) defined ecotourism as responsible tourist to natural areas that maintain the environment, sustain the well-being of the local people and includes education. Pahang, which is located at East Coast Malaysia and the population around 5.1% from total Malaysian population always, be the tourist attraction because of its natural beauty of flora and fauna, covered by thousands of hectares of rainforest. Estimated exist more than 130 million year's old, national park located at Jerantut, gazetted as National Park since 1938, it is the largest national park more than 4000 square kilometers. The beautiful and unique natural scenery undeniable natural lovers around world. Based on this information, it can be seen that nature is the main source of tourism product in Pahang which lead to ecotourism product. Hence this study proposes to forecast the ecotourism product in Pahang. Thus, the discussion of this paper is organised as follows. The second section of this paper will discuss the selected literature review. The third section focuses on methodology used. The fourth section touches on empirical results and the final section concludes.

LITERATURE REVIEW

Tourism forecasting can lead to an important element in the tourism industry to ensure that each investment by individuals, companies and government was worth it. According to Song and Li [9], the number of tourist arrivals is a most popular measure for demand tourism. Past research has shown that modelling and forecasting tourism demand is numerous with various type of empirical analysis. ARIMA method is a famous modelling approach to forecast tourism industry. Many studies have applied this method such as Lim and McAller [7]. They suggested shorter forecast horizon is more accurate than a longer forecasting horizon for tourist arrivals in Australia when using ARIMA method. While Kim and Moosa [6] has modified direct and indirect method to forecast international tourist flows in Australia which result indirect method provides more accurate forecasts for than the direct method. On the other hand, Chu [2] forecast tourism demand by using ARMA models that is perform well when MAPE is lower than 2%. Besides that, Loganathan and Ibrahim [8] forecast international tourism demand in Malaysia by using Box-Jenkins SARIMA application and concluded smoothing techniques should be included

to forecast tourism demand. Song et al. [10] compared between Box-Jenkins, naïve and exponential smoothing via a web-based tourism demand forecasting the finding shows that accuracy of the judgmental forecast increased for the second round compared to first round. Scheyvens [11] proposed in her study of ecotourism and the empowerment of local communities, ecotourism should promote conservation and development at the local area. Besides that, local peoples can maximise their benefit by control over ecotourism places for their region and tradition. Dimitrov [3] assert model to estimate the size of rural tourism and ecotourism located near Bulgarian's border. Data was provided by local authority. The result indicated increment between 1416 and 1631 number of foreign visitor arrivals with lower MAPE value. Iasha et al. [4] estimated economic value for ecotourism product in west Sumatera, Indonesia. Data collected were primary data which is the questionnaire was developed using a dichotomous choice-questioning format. Result showed ecotourism visitor monopolized by the group of middle and highly educated people and average income for domestic visitor was Rp 2.5 million while international visitors were Rp 132.1 million. Since ecotourism give a lot of benefits to the tourism industry, researchers should focus on this area. There are few studies regarding ecotourism forecasting. Hence, this paper proposes to forecast ecotourism demand in Pahang using Box-Jenkins method.

METHODOLOGY

Time Series Model

According to Hanke and Wichern [4], Box-Jenkins methodology refers to a set of procedures to identify, fit, and check the ARIMA models with time series data and forecast that follows directly from the form of the fitted model. The extension to the autoregressive AR(p) and moving average MA(q) models is the mixed ARMA(p,q) model which has the form (Bowerman et. al [1]),

$$z_t = \delta + \varphi_1 z_{t-1} + \varphi_2 z_{t-2} + ... + \varphi_p z_{t-p} + a_t - \theta_1 a_{t-1} - \theta_2 a_{t-2} - ... - \theta_q a_{t-q}$$

Many observe that non-stationary time series exhibit certain homogeneity, which can be counted by making simple modification on the ARMA model called integrated processes. By adding and integrating process, the ARMA(p,q) model will become an ARIMA(p,d,q) namely autoregressive integrated moving average model, thus it writes as;

$$\varphi(B) z_i = \theta(B) a_i$$

where $\phi(B)$, the generalized autoregressive operator, is a polynomial of degree with exactly d zeroes equal to unity. Therefore;

$$\phi(B) = \varphi_p(B)(1-B)^d = \varphi_p(B)\nabla^d$$

where $\varphi_p(B)$ is a stationary autoregressive operator of order p.

Seasonal ARIMA (SARIMA) models are generalization of an ARMA model. Forecasting SARIMA can be expressed as ARIMA $(p,d,q)(P,D,Q)_n$. For P and p are the orders of autoregressive, D and d are the differences and Q and q are the orders of moving average value of non-seasonal and seasonal which is consist of values greater or equal to zero respectively. While, n^{th} refers to seasonal pattern of data. If the seasonal pattern monthly the n value will be 12, quarterly equal to 4.

Box-Jenkins methodology consists of five-step iterative procedures as follows:

Step 1: Removal of Non-stationary Components: The first step in model identification is to determine whether the series is stationary or non-stationary. The stationary of data can be determined by looking at autocorrelation function (ACF) and partial autocorrelation function (PACF). If the model is non-stationary, differencing will be used to convert it to stationary model.

Step 2: Model Identification: The selection of an appropriate model is generally a complicated task. Analysis of the historical data is used to identify an appropriate Box-Jenkins model by looking at their ACF, PACF, stationary, and seasonality behavior if any.

Step 3: Estimation: After selecting the tentative model, the parameter will be estimated. The estimation method used is ordinary least square method with available historical data.

Step 4: Diagnostic Checking: Various diagnostic checking especially analysis of residual are used to check the adequacy of the tentatively identified model and, if need be, to suggest and improve as a tentatively new identified model. In diagnostic checking, we look at the residual plot of the autocorrelations.

Step 5: Forecasting: Once the final model is obtained, the forecasting process for future will be conducted.

Data

This study used a 5-year monthly data of tourist arrival at National Park Kuala Tahan, Pahang. Therefore, the data is obtained from Department of Wildlife and National Parks Peninsular Malaysia. This study focuses on total number of tourist entered the National Park Kuala Tahan from January 2013 until December 2017.

EMPIRICAL RESULTS AND DISCUSSIONS

Seasonality means a pattern data related to the calendar and repeated over a particular time. Seasonal can be defined as a pattern of change that repeats itself year after year (Hanke et al [4]). The data from January 2013 until December 2017 with seasonal effect of monthly basis is shown clearly in Figure 1.

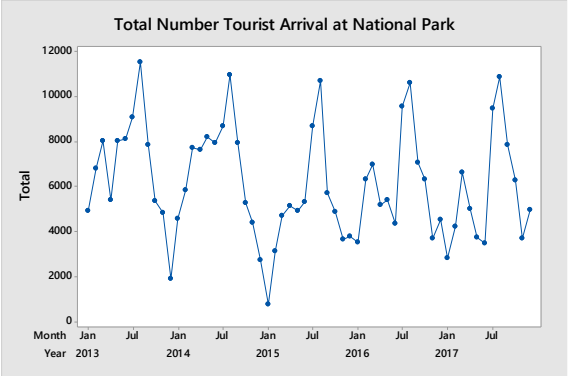

Fig. 1 Number of Tourist Arrivals at National Park from 2013 to 2017

Number of tourists came to National Park clearly depends on seasonal pattern. There are peak number of tourists on July every year and decreasing at the end of year because of monsoon season during that time. Thus, we begin first step in SARIMA that is model identification by looking at ACF and PACF as shown in Figure 2a and 2b.

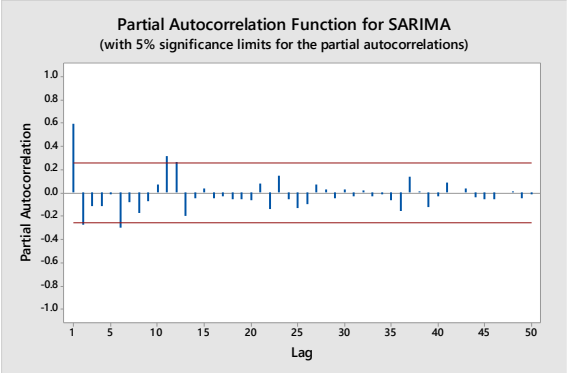

Fig. 2a PACF for non-stationary data

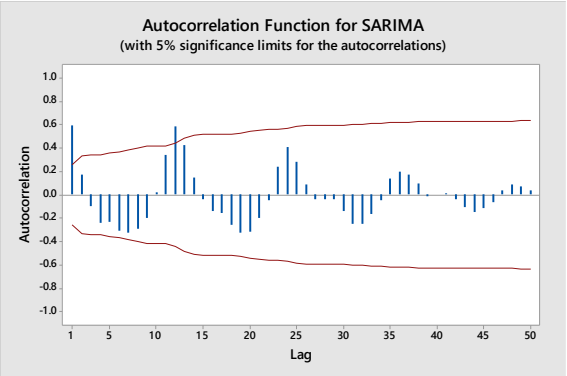

Fig. 2b ACF for non-stationary data

Figure 2a and 2b shows PACF and ACF for non-stationary data respectively. For non-seasonal (p,d,q) PACF pattern, there are spike at first 2 lags and tend to dies out pattern which indicate AR (2). As for ACF, only lag 1 spike and trail off to zero gradually after lag 2 which is indicate MA (1) behavior. PACF for seasonal (P,D,Q) which indicate autoregressive shown there are spike in lag 1, 2, 12, and 13, in addition there were small blip for lag 24 and 36. This suggested the series was monthly seasonal. This behavior also suggests AR (2) term at the seasonal lag 12. While ACF indicates there were significant spike at lag 1 and 12 then dies out. This is consistent with MA (1) pattern. Since the data are influenced by seasonal pattern, a trend pattern exists and trend is not a stationary. Therefore, the data can will be transform into stationary series by differencing. The seasonal differenced are computed as Figure 3.

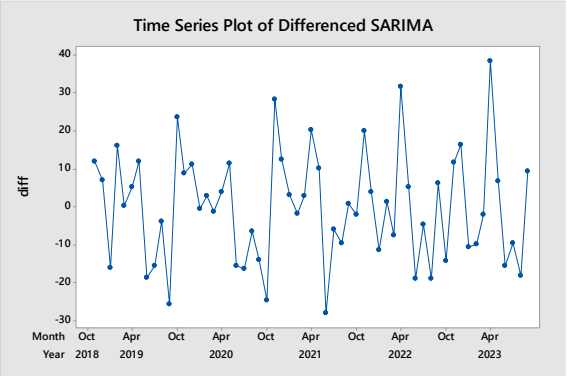

Fig. 3 Time Series plot first differencing

Figure 3 shows time series plot after differencing for SARIMA. The time series plots satisfy the stationary condition since means and variance are constant over time. The ACF and PACF for the differenced series are presented in Figure 4a and 4b.

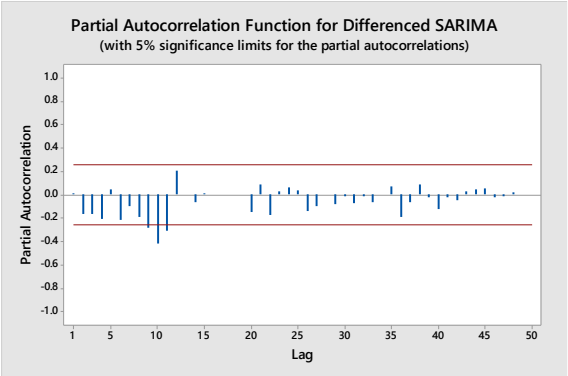

Fig. 4a PACF first differencing

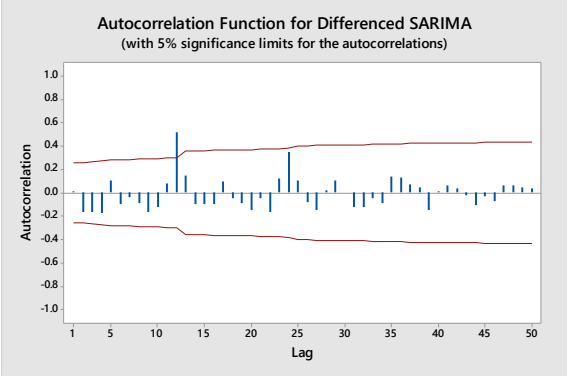

Fig. 4b ACF first differencing

The PACF have one significant spike at lag 10 then dies out, and the ACF have significant spike at lag 12 and 24 tend to follow die down pattern, it is indicating seasonal pattern of AR (0), AR (1) and MA (2). At non-seasonal level, the PACF and the ACF dies out indicate AR and MA behavior of (1). Hence, we tend to estimate model by using information of PACF and ACF earlier. The tentative models stated as Table 1.

Table 1 SARIMA tentative model

SARIMA	
$(2,0,1)(2,0,1)_{12}$	$(1,1,0)(1,1,2)_{12}$
$(1,0,1)(2,0,1)_{12}$	$(0,1,1)(0,1,2)_{12}$
$(1,0,0)(2,0,1)_{12}$	$(1,1,1)(0,1,2)_{12}$
$(0,0,1)(2,0,1)_{12}$	$(1,1,0)(0,1,2)_{12}$
$(1,1,1)(1,1,2)_{12}$	$(0,1,1)(1,1,2)_{12}$

The standard procedure for model estimation involved parameter estimation by using least square method for tentative models. The parameters are not significant if the *p-value* greater than 0.05. Based on the estimation results, from 10 models only 6 models are significant and can proceed to next step. After the estimation process, diagnostic tests have been applied to the six models to check the adequacy. The result is shown in Table 2.

Table 2 Ljung-Box Result for Model of SARIMA

Model	Ljung-Box Value	Result
SARIMA $(1,0,0)(2,0,1)_{12}$	0.051	Significant
SARIMA $(0,0,1)(2,0,1)_{12}$	0.079	Significant
SARIMA $(1,1,0)(1,1,2)_{12}$	0.319	Not Significant
SARIMA $(0,1,1)(1,1,2)_{12}$	0.179	Not Significant
SARIMA $(1,1,1)(0,1,2)_{12}$	0.256	Not Significant
SARIMA $(1,1,0)(0,1,2)_{12}$	0.368	Not Significant

LBQ for each model stated whether models are significant or not significant. If the result of LBQ values greater than 0.05, it indicates the model is not significant. Thus, we eliminated 4 models which are not significant because their large LBQ values. Only SARIMA $(0,0,1)(2,0,1)_{12}$ and SARIMA $(1,0,0)(2,0,1)_{12}$ are adequate. Then, we generate forecasts for sixty periods to compare values of forecast error. Mean absolute percentage error (MAPE) is used as forecast accuracy; SARIMA $(1,0,0)(2,0,1)_{12}$ generated 8.77% and SARIMA $(0,0,1)(2,0,1)_{12}$ 8.61%. Table 3 shows result for MAPE for both models.

Table 4 MAPE Result for Model of SARIMA

Model	MAPE Result
SARIMA $(1,0,0)(2,0,1)_{12}$	8.77%
SARIMA $(0,0,1)(2,0,1)_{12}$	8.61%

Figure 5 shows time series plot for both models SARIMA. Both models have slightly different forecast values middle of 2015. Thus, for seasonal ARIMA $(0,0,1)(2,0,1)_{12}$ was selected as best model since values of MAPE are lowest compared to

SARIMA $(1,0,0)(2,0,1)_{12}$.

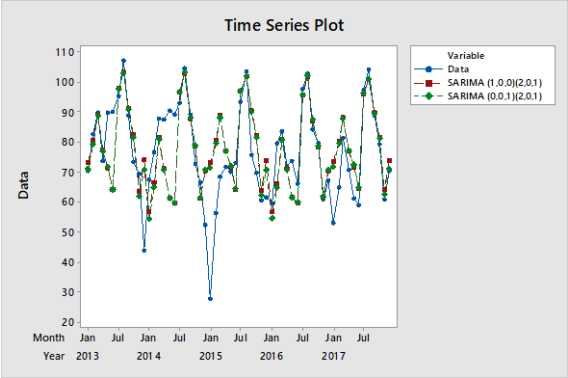

Fig. 5 Time Series Plot for SARIMA $(0,1,1)(1,1,2)_{12}$

CONCLUSIONS

This study found that SARIMA $(0,1,1)(1,1,2)_{12}$ is the best model to capture seasonality effect in forecasting number of tourist arrivals at National Park Kuala Tahan, Pahang. Forecasting number of tourist in National Park can help Malaysian government as well as stakeholder in tourism industry to perform better strategic planning and to help them in maximizing profits. This study shows that Box-Jenkins method has the ability to forecast number of tourists accurately. Since this study only focuses on SARIMA models, further researches can be conducted using other forecasting methods. Given the difficulty of finding a largest data, further researches could focus on largest set of data which may help to identify the best models. The analysis on the comparison between local and foreign tourist could be an interesting research analysis.

ACKNOWLEDGMENTS

This research is supported by Faculty of Industrial Sciences & Technology, Universiti Malaysia Pahang and funded under UMP internal grant RDU1703183. The supports are gratefully acknowledged.

REFERENCES

[1] Bowerman, O' Connell, and Koehler. (2005). Forecasting, Time Series, and Regression. (1st ed). USA: Thomson Brooks/Cole.

[2] Chu, F. L. (2009). Forecasting tourism demand with ARMA-based methods. Journal of Tourism Management, 30, 740-751.

[3] Dimitrov, P. (2013). Long-run forecasting of the number of the ecotourism arrivals in the municipality of Stambolovo, Bulgaria. Journal of Tourism & Management Studies, 9(1), 41-47.

[4] Hanke, J. E. and Wichern, D.W. (2005). Business Forecasting. (8th ed). USA: Pearson Prentice Hall.

[5] Iasha, A., Yacob, M. R., Kabir, I. and Radam, A (2015). Estimating economic value for potential ecotourism resources in Puncak Lawan Park, Agam District, West Sumatera, Indonesia. International Conference on Environmental Forensics 2015, 30, 326-331.

[6] Kim, J. H. and Moosa, I. A. (2005). Forecasting international tourist flows to Australia: A comparison between the direct and indirect method. Journal of Tourism Management, 26, 69-78.

[7] Lim, C. and McAleer, M. (2002). Time series forecasts of international travel demand for Australia. Journal of Tourism Management, 23, 389-396.

[8] Loganathan, K. and Ibrahim, Y. (2010). Forecasting International Tourism Demand In Malaysia Using Box-Jenkins Sarima Application. South Asian Journal of Tourism and Heritage, 3(2), 50-60.

[9] Song, H., and Li, G. (2008). Tourism demand modelling and forecasting-a review of recent research. Journal of Tourism Management, 29, 203-220.

[10] Song, H., Gao, B. Z. and Lin, V. S. (2013). Combining statistical and judgmental forecasts via a web-based tourism demand forecasting system. International Journal of Forecasting, 29, 295-310.

[11] Scheyvens, R. (1999). Case study of ecotourism and the empowerment of local communities. Tourism Management, 20, 245-249.

9th Int. Conf. on Geotechnique, Construction Materials and Environment, Tokyo, Japan, 20-22 November 2019, ISBN: 978-4-909106025 C3051

EMBODIED CARBON EMISSIONS OF CONSTRUCTION MATERIALS: A CASE STUDY OF BUILDING IN THAILAND

Nantamol Limphitakphong[1], Pipat Thaipradit[2], Premrudee Kanchanapiya[3], Thanapol Tantisattayakul[4] and Orathai Chavalparit[2,5,6]

[1]Interdisciplinary Program of Environment Development and Sustainability, Graduate School, Chulalongkorn University, Thailand; [2]Research Unit of Environmental Management and Sustainable Industry, Chulalongkorn University, Thailand; [3]National Metal and Materials Technology Center, National Science and Technology Development Agency, Thailand; [4]Faculty of Science and Technology, Thammasat University, Thailand [5]Faculty of Engineering, Chulalongkorn University, Thailand; [6]Research Program : Toxic Substance Management in the Mining Industry, Center of Excellence on Hazardous Substance Management (HSM), Thailand

ABSTRACT

Regarding a moving towards development with no threat to our future generations, an overwhelming consumption of natural resources is the dominant sustainability and environmental concerns argued either in international or national conferences. In particular, to heavily seek for high potential solutions in minimizing environmental impacts, building sector should firstly be considered practically since it is responsible for almost forty percent of both global energy and materials used and contributed around one-third to global greenhouse gases emission. This research, therefore, is aimed at evaluating a level of embodied carbon emissions derived from building construction materials, using educational institutes as case studies to represent an environmental performance of construction materials based on reinforce concrete structure in tropical climate. The results reveal that on weighted average, mass intensity and embodied carbon intensity of construction materials are 1,627 kg/m^2 and 322 kgCO_2/m^2. In addition, the taller the building height the more it is likely to help improve such intensities. Almost 90% of mass intensity contributed to structural component materials whereas the embodied carbon emissions attributed 69% to structural component materials and 24% to decorating component materials. The results also indicate that the building with reinforce concrete structure might focus only on six materials namely concrete, steel, aluminium, cement, paint, and ceramic tile since the contribution of such materials to embodied carbon emission do account for 94%. The findings will be useful for planning proactive strategies in mitigating embodied carbon of building to cope with the challenges of global warming in the future.

Keywords: Embodied carbon emission, Educational building, Building materials, Construction phase, Reinforce concrete structure

INTRODUCTION

Globally, building sector has played an important role in a moving towards sustainable development goals as it accounted for 40% of energy consumption, 40% of raw materials use, 12% of potable water consumption, one-third of carbon emission and 40% of waste to landfill [1,2]. Formally, numerous studies of buildings mostly focused on the operation phase in order to reduce energy consumption which will be consequently decreased an amount of carbon emission [3]. However, the construction phase performances should take into consideration since the amount of material used for building construction will proportionally affect the level of total building's embodied carbon and different types of building material will additionally result in different amount of energy demand in operation phase [4,5].

In Thailand, even a quarter of construction permission of commercial buildings was found to be school and institutions, merely less than one percent of such number is regulated under the energy conservation act [6,7]. A million of resources is prioritized for educational system with aiming to enhance capacity building and support the needs of the country whilst an efficiency of resources consumption is not considered significantly.

This study, therefore, aimed at evaluating a level of embodied carbon emissions derived from building construction materials of buildings located in educational institute in Thailand and identifying the key materials effecting a proportion of embodied carbon intensity in order to propose the alternative solutions for minimizing environmental impacts throughout building service life. The findings will be useful for building owner or decision maker in designing a sustainable building based on low carbon approach and in planning proactive strategies in mitigating embodied carbon of building to cope with the challenges of global warming in the future.

METHODOLOGY

Cases Description

Four buildings with different purpose of Chulalongkorn University located in Bangkok were assessed to evaluate the environmental performances through mass intensity and embodied carbon emission. All building cases were built based on reinforce concrete structure. Three of them were classified as a mix-used building with total floor area of 16,143 m^2, 21,627 m^2 and 3,225 m^2 for Building A (12-storey building served with conference rooms, classrooms, laboratory rooms, research units, gym), Building B (13-storey building occupied with classrooms, conference rooms, offices and a cafeteria) and Building C (2-storey building with a cafeteria on the ground floor and an information center on the first floor) respectively, whilst the last was a 17-storey dormitory building (Building D) with total floor area of 31,500 m^2. Due to a difference in building size, in order to be comparable, a square meter of floor area was used as a functional unit to quantify each building's performances.

Building Materials Analysis

Regarding building construction components, the construction materials in this study were classified into four categories named structural materials (SM), decoration materials (DM), materials supplied for ventilation and air condition (VA) system, and for sanitary and fire protection (SF) work. To analyze building construction performance, either data of material types or number were obtained from bill of quantities. In particular, twenty different types of building material that commonly used in building construction were addressed, then a record of each material number was calculated in term of kg/m^2 as demonstrated in equation 1.

$$MI = \sum_{j=1}^{4} \sum_{i} (Q_i \div A) \quad (1)$$

Where MI – the mass intensity (kg/m^2) represents the consumption rate of construction materials, Q – Quantity (kg) represents an amount of material used, A – area (m^2) represents a total floor area of building, i refers to the type of materials, and j refers to the four class of construction component.

Carbon Emission Assessment

Embodied carbon emission of building is an emission arose from a consumption of all materials used for building construction. A boundary of such emission calculation involves raw material extraction, transportation from raw material site to material production plant, and production process of material. Due to a lack of available data in Thailand, however, the BEES (Building for Environmental and Economic Sustainability) database was used as an emission factor (EF) to determine the embodied carbon emissions as demonstrated in equation 2.

$$ECI = \sum_{j=1}^{4} \sum_{i} (MI_i \times EF_i) \quad (2)$$

Where ECI - the embodied carbon intensity ($kgCO_2/m^2$) represents the carbon emissions rate of construction materials and EF – the emission factor ($kgCO_2/kg$) refers to the corresponding embodied carbon coefficient of materials.

RESULTS AND DISCUSSION

Mass Intensity

Table 1 illustrated values of MI of reinforce concrete building in a range of 1,595 – 2,252 kg/m^2 which meant in every square meter of building floor area, more than fifteen thousand of building materials were consumed in this study. In addition, because of a complexity of scientific laboratory room design, a greater amount of construction material required rather than the other conventional rooms, resulting in the highest MI revealed in Building A. The proportion of mass intensity on weighted average classified by building construction components and materials type revealed that the largest share of material used contributed to SM component with the major source of various concrete types used for sole plate, foundation, structure and precast as illustrated in Fig. 1. The finding was in agreement with the data discoursed in previous study [5,8].

With an exclusion of Building A, high-rise building (Building B and D) seem to exhibit more environmental-friendly performance in term of resources depletion since such buildings required slightly less resources per functional unit than low-rise building (Building C) even the total resources consumption would be higher. Moreover, a consumption of materials in DM component also emphasized that MI value of such component in Building C was almost twice more than the value presented in the other buildings which was mainly influenced by the consumption of cement group for wall finishing. Although a consumption of materials in DM component is uncontrollable since it is heavily determined by individual satisfaction, however, to reduce such environmental performance, a loft design building, a building polished with neither ceramic tile nor paint, was recommended as it could reduce nearly 4% of total mass intensity (Fig.1).

Embodied Carbon Intensity

Based on weighted average with an exclusion of Building A, an intensity of embodied carbon in building construction materials in this study was 347 $kgCO_2/m^2$. As similar to the result of MI, apart from Building A, Building C showed the higher point of

ECI than Building B and D. It could be concluded that, a smaller floor area is, a larger amount of embodied carbon intensity presents. The finding was in disagreement with the research on embodied carbon emission of office building in China, which concluded that the higher buildings area, the larger number of carbon emissions per unit area emitted [9]. However, that study was focused on the comparison between multi-story building, high-rise building and super-high-rise building, which this research was an investigation of small building and high-rise building. Therefore, it might be implied that difference in height of building has significant contribution in global warming in different range.

In addition, whilst a category of SM component was employed for more than 70% of total embodied carbon emission, about one-fourth of such intensity was associated with DM component. As presented in Fig 2, the two major materials generated a great amount of carbon emission were a group of concrete (44%) and aggregate (34%). To reduce carbon emission embodied from structural materials, a suggestion for new building construction, fly-ash or blast furnace slag are encouraged to substitute instead of using virgin cement, mortar, or concrete [10].

A Relation of Mass and Embodied Carbon Intensity

Excluding construction materials in a group of concrete which shared the highest contribution either in building material profile or in the embodied carbon content as mentioned above, Fig. 2 presented a contribution of ten building construction materials to the total mass or embodied carbon intensities in the bar chart.

Table 1 Mass and carbon intensities of major construction materials in educational buildings

Unit: Mass intensity (kg/m^2), Embodied Carbon Intensity ($kgCO_2/m^2$)

Materials	Building A		Building B		Building C		Building D	
	MI	ECI	MI	ECI	MI	ECI	MI	ECI
Structural Materials (SM)								
Group of Concrete	1,875.74	197.23	1,281.54	134.63	1,287.43	136.13	1,363.19	144.51
Sawnwood	124.86	1.90	72.79	1.11	80.57	1.23	79.87	1.22
Aggregate	11.13	0.02	44.49	0.08	4.39	0.01	3.81	0.01
Group of Steel	63.56	140.87	35.48	79.10	31.39	73.01	36.57	82.61
Sub-total	**2,075**	**340**	**1,434**	**215**	**1,404**	**210**	**1,483**	**228**
Decoration Materials (DM)								
Group of Cement	66.54	15.55	58.15	15.18	146.69	33.98	67.44	16.61
Brick	36.75	8.62	23.34	5.47	29.38	6.89	9.65	2.26
Aggregate	32.06	1.27	37.41	0.07	15.23	0.81	36.65	0.12
Ceramic Tile	4.15	1.55	10.70	4.00	63.47	23.71	21.12	7.89
Gypsum Fibreboard	13.20	9.90	8.17	6.13	3.79	2.85	4.24	3.18
Group of Steel	8.57	22.68	6.10	14.51	3.49	14.14	3.49	9.16
Sawnwood	1.99	0.03	-	-	-	-	0.92	0.13
Tap Water	4.63	0.00	4.77	0.00	3.07	0.00	5.52	0.00
Group of Paint	3.03	13.30	2.11	9.11	2.46	10.40	2.61	10.81
Aluminium	-	-	1.63	63.42	15.21	47.78	0.39	1.21
Insulation	0.60	2.58	-	-	8.60	20.92	-	-
PVC	1.09	2.07	0.62	1.89	2.74	5.21	0.99	1.88
Sub-total	**173**	**78**	**155**	**120**	**294**	**167**	**153**	**53**
Materials supplied for Ventilation and Air Condition (VA) system								
Copper	0.31	0.55	0.23	0.40	0.03	0.06	0.12	0.21
Steel	0.15	0.41	0.47	1.26	-	-	0.09	0.25
PVC	0.07	0.22	0.04	0.14	0.01	0.02	0.05	0.17
Polyurethane	0.02	0.10	0.02	0.10	-	0.01	0.01	0.06
Supply Air Inlet	n.d.	0.04	n.d.	0.04	n.d.	0.03	n.d.	0.01
Exhaust Air Outlet	n.d.	0.03	n.d.	0.17	n.d.	0.05	n.d.	0.02
Glass Fibre	-	-	0.04	0.10	-	-	-	-
Sub-total	**1**	**1**	**1**	**2**	**0**	**0**	**0**	**1**
Materials supplied for Sanitary and Fire Protection (SF) work								
Group of Steel	3.12	13.45	3.94	13.40	0.01	0.05	2.63	7.19
Glass fibre	-	-	0.58	1.41	0.45	1.10	0.21	0.52
Piping	0.21	0.67	0.13	0.38	0.48	1.54	1.48	4.70
Thermoforming	-	-	-	-	0.03	0.09	0.18	0.67
Sub-total	**3**	**14**	**5**	**15**	**1**	**3**	**5**	**13**
Total	**2,252**	**433**	**1,595**	**352**	**1,699**	**380**	**1,641**	**295**

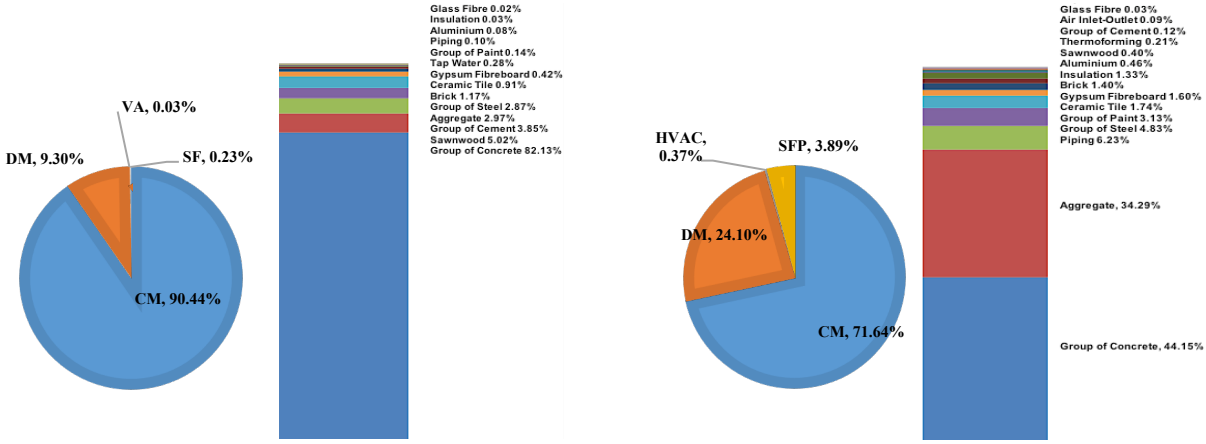

Fig. 1 Proportion of mass (left) and embodied carbon (right) in construction materials

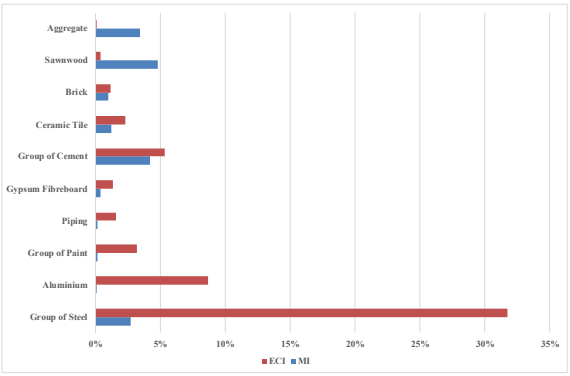

Fig. 2 Contribution of building materials to mass and embodied carbon intensities

The result revealed that there were three kinds of relation among the contribution of materials to both variables. Firstly - high consumption material with high emission, similar to a group of concrete, the high contribution was found in a group of cement and ceramic tile to both material mass and embodied carbon. Secondly – high consumption material with less emission, sawnwood and aggregate highly contributed to the total mass (3-4%) with insignificant in contribution to the embodied carbon (less than 0.4%). Lastly – less consumption material with high emission, due to its high embodied carbon efficient of steel, brick, gypsum fiberboard, aluminium, paint, and piping, even such materials were less consumed in construction process, its contributed greatly amount of carbon emission. Therefore, considering possible alternatives for alleviating global warming through building sector should involve either high carbon emitting materials or mass materials. Based on the results of this study, the building with reinforce concrete structure should focus on six materials namely concrete, steel, aluminium, cement, paint, and ceramic tile since the contribution of such materials to carbon emission accounted for 94% of the total embodied carbon. To roughly estimate building coefficient, a specific carbon emission of building based on reinforce concrete structure in Thailand was 0.198 $kgCO_2/kg$ of material mass.

A Comparison of Embodied Carbon Intensity with Other Studies

A comparison of embodied carbon intensity between the results of this study and the previous findings was presented in Table 2. Based on the same building typology, it was found that the ECI of this study was lower than the other cases. It might be because of the newly innovation and advance technology that has been developed occasionally from the past and the impact of the more total floor area that resulting in the decreasing of embodied carbon emission. However, by considering the concept of zero emission building (ZEB), it could be implied that to moving towards low carbon society, all new building construction should be designed based on such theme since the building will emit zero emission during the operation phase whilst the contribution to carbon profile during the construction phase will be compromised with the benefits gained of the utilization of building waste after its end-of-life stage.

Alternative Insulation Materials for Improving Environmental Performance of Existing Building

For improving existing building, energy efficiency performance was mainly focused on and energy simulation was introduced to anticipate the changing of energy consumption in building after implementation. Since more than half of total energy used in building in tropical countries is supplied for cooling system, various kinds of external wall insulation, therefore, were selected to examine an amount of energy-related emissions that will be reduced and to identify the best solution for optimizing energy-related emissions throughout a

Table 2 Embodied carbon emissions of various educational buildings

No.	Year	Location	Structure Type	No. of floor	Total Floor area (m^2)	ECI ($kgCO_2e/m^2$)	Ref.
1	2003	Michigan	Reinforced concrete	6	7,300	554.79	[11]
2	2011	Catalonia	Reinforced concrete	1	3,168	616.67	[12]
3	2015	Korea	Reinforced concrete	-	-	419.74[a]	[13]
4	2018	Sri Lanka	Reinforced concrete	7	5,967	490.93	[14]
5	2018	Norway[b]	Reinforced concrete	2 5	1,140 26,356	384.60 418.20	[15]
6	2018	Bangkok	Reinforced concrete Reinforced concrete Reinforced concrete	2 13 17	3,225 21,627 31,500	379.90 352.11 295.39	This study

[a] The average data of 7 educational buildings in Suwon city, Korea.
[b] Demonstration of zero emission building (ZEB) case studies

Table 3 Properties of base case and alternative external wall insulation materials

Indicator \ Insulation Material[a]	Unit	Base Case	Cellulose	Aerogel	Poly-urethane	Glass Wool
Embodied carbon co-efficient[16]	$kgCO_2/kg$	-	4.60	47.3	22.9	5.60
Embodied carbon of insulation used[b]	$kgCO_2$	-	32,324	332,377	160,918	39,351
Embodied carbon of all building materials[c]	tCO_2/BSL	7,000	7,162	8,663	7,805	7,198
Energy consumed in use phase	MWh/year	2,926	2,885	2,884	2,886	2,885
Reduction due to energy saving	$kgCO_2/year$	-	23,284	23,763	23,136	23,588
Energy-related emission[d]	tCO_2/BSL	82,874	81,710	81,686	81,717	81,695
Emissions reduction compared to Base case	tCO_2/BSL	-	1,002	-475	352	981

[a]Assumed all insulation life time of 10 years.
[b]Wall area for insulation installation in entire building is 7,027 m^2 and wall insulation thickness is 100 mm for all cases, except aerogel (50 mm)
[c]Building service life (BSL) is 50 years, thus 5 sets of insulation were installed throughout BSL.
[d]CO_2 emission due to electricity use in Thailand is 0.5664 $kgCO_2/kWh$ [17]

building service life of 50 years. In this study, Building A was selected to simulate energy use through EnergyPlus 8.8.0 model.

The results revealed that implementing all external wall insulation types certainly reduce energy required during building use phase since it helps lesser heat gain through building from the outside, and different types of external wall insulation showed no difference in the amount of energy saving. The best option of external wall insulation in reducing carbon emission for entire building service life was cellulose followed by glass wool and Polyurethane. Whilst aerogel insulation showed no gain in reduction potential because of its high embodied carbon coefficient, as demonstrated in Table 3.

For entire building service life, installation of cellulose insulation could reduce about 1,164 tCO_2e due to the energy saving during use phase. Such number can be used to compensate for the amount of embodied carbon increased in building due to the increase of material (insulation) consumed, the payback period of carbon offset was 1.4 years for every 10 years of insulation replacement.

CONCLUSION

As the global trend is moving towards nearly zero carbon building, this study is aimed at quantifying the amount of embodied carbon in construction materials and identifying the key materials effecting a proportion of embodied carbon intensity in order to propose the alternative solutions for minimizing environmental impacts throughout building service life. Buildings located in Thai academic institute were used to demonstrate the intensities of materials mass and embodied carbon. The results illustrated that on weighted average, the intensities of mass and embodied carbon in building construction materials were 1,627 kg/m^2 and 322 $kgCO_2/m^2$. In addition, in term of building size, high-rise building was found to contribute to both intensities less than low-rise building. To roughly estimate building coefficient, a specific carbon emission of educational building in Thailand was 0.198 $kgCO_2/kg$ of material mass.

The findings also indicated that either mass or embodied carbon intensities had contributed the highest share to structural material component, followed by decoration materials component, materials supplied for sanitary and fire protection work and for ventilation and air condition system respectively. Moreover, in order to mitigating embodied carbon of building, two group of materials that should be focused on were a group of high

embodied carbon efficient materials and a group of materials used in huge number.

For improving existing building, a solution for reducing energy consumption in cooling system was investigated as it requires the highest loads of energy. The result of energy simulation from applying four different external wall insulations revealed that even all insulations provide a better benefit in term of less energy consumption required during operation phase compared to Base case, however, when considering the entire building service life of 50 years, installation aerogel insulation has failed to improve building performance because of its high embodied carbon coefficient.

The characteristic of all buildings in this study is very similar to most of typical buildings in Thailand since the material used for foundation and structure was based on reinforce concrete and the envelope pattern was an opaque wall constructed from brick. The findings of this study therefore could be widely applied to the other buildings. The initiative of reducing carbon emissions of building sector either on loft style building or on zero emission building could lead to sustainable consumption and production in Thailand, enabling the country in moving towards low carbon society successfully as planned.

ACKNOWLEDGMENT

The authors thank the Thailand Research Fund through the Royal Golden Jubilee Ph.D. Program (Grant No. PHD/0071/2559) for student financial support as well as the Office of Higher Education Commission (OHEC) and the S&T Postgraduate Education and Research Development Office (PERDO) for the financial support of the Research Program. We also would like to express our sincere thanks to the Faculty of Engineering, Chulalongkorn University, and the Center of Excellence on Hazardous Substance Management (HSM) for their invaluable supports in terms of facilities and scientific equipment.

REFERENCES

[1] UNESCAP. Low Carbon Green Growth Roadmap for Asia and the Pacific. Buildings: Policy recommendations for the development of eco-efficient infrastructure (2012).

[2] Intergovernmental Panel on Climate Change (IPCC), Climate Change 2014: Synthesis Report, Contribution of Working Groups I, II and III to the Fifth Assessment Report of the Intergovernmental Panel on Climate Change, Geneva, Switzerland, 2014, 151 pp.

[3] Ramesh T., Prakash R. and Shukla K.K., Life cycle energy analysis of buildings: An overview, Energy and Buildings, Vol. 42, Issue 10, 2010, pp. 1592-1600.

[4] Jeong Y.S., Lee S.E. and Huh J.H., Estimation of CO_2 emission of apartment buildings due to major construction materials in the Republic of Korea, Energy and Buildings, Vol. 49, 2012, pp.437-442.

[5] Kumanayake R., Lao H. and Paulusz N., Assessment of material related embodied carbon of an office building in Sri Lanka, Energy and Buildings, Vol. 116, 2018, pp.250-257.

[6] Department of Alternative Energy Development and Efficiency (DEDE), Thailand, Lists of designated buildings, 2018

[7] Thaipradit P., Limphitakphong N., Kanchanapiya P., Tantisattayakul T. and Chavalparit O., The influence of building envelop materials on its life cycle performance: a case study of educational building in Thailand, Key Engineering Materials, Vol. 780, 2018, pp.74-79.

[8] Oyeshola F.K. and Shabbir H.G, Life cycle energy assessment of a typical office building in Thailand, Energy and Buildings, Vol. 41, Issue 10, 2009, pp. 1076-1083.

[9] Luo Z., Yang L. and Liu J., Embodied carbon emissions of office building: A case study of China's 78 office buildings, Building and Environment, Vol. 95, 2016, pp. 365-371.

[10] Shams S., Mahmud K. and Al-Amin M., A comparative analysis of building materials for sustainable construction with emphasis on CO_2 reduction, International Journal of Environment and Sustainable Development, Vol. 10, Issue 4, 2011, pp. 364 – 374.

[11] Scheuer C., Keoleian G. and Reppe P., Life cycle energy and environmental performance of a new university building: modeling challenges and design implications, Energy and Buildings, Vol.35, 2003, pp.1049-1064.

[12] Pons O. and Wadel G., Environmental impacts of prefabricated school buildings in Catalonia, Habitat International, Vol.35, 2011, pp.553-563.

[13] Kanga G., Kim T., Kim Y.W., Cho H. and Kang K.I., Statistical analysis of embodied carbon emission for building construction, Energy and Buildings, Vol.105, 2015, pp.326-333.

[14] Kumanayake R. and Lao H., A tool for assessing life cycle CO2 emissions of buildings in Sri Lanka, Building and Environment, Vol.128, 2018, pp.272-286.

[15] Wiik M.K., Fufa S.M., Kristjansdottir T. and Andresen I., Lessons learnt from embodied GHG emission calculations in zero emission buildings (ZEBs) from the Norwegian ZEB research centre, Energy and Buildings, Vol.165, 2018, pp.25-34.

[16] Kunic R., Carbon footprint of thermal insulation materials in building envelopes, Energy Efficiency, Vol. 10, Issue 6, 2017, pp.1511–1528.

[17] Thailand greenhouse gas management organization (public organization), Thailand Grid Emission Factor for GHG Reduction Project/Activity, 2017.

9th Int. Conf. on Geotechnique, Construction Materials and Environment, Tokyo, Japan, 20-22 November 2019, ISBN: 978-4-909106025 C3051

THE EFFECTIVENESS OF FLOOD OCCURRENCE COUNTER MEASURE PLAN DUE TO LOCAL CONDITION

Agus Suharyanto
Faculty of Engineering, Universitas Brawijaya, Indonesia

ABSTRACT

Kali Bogel river is a river flowing in Blitar regency, East Java province, Indonesia. The outlet of the river is located in Brantas river with river long of Kali Bogel is 25 km. The river mouth is located between two dams i.e. Wlingi dam and Lodoyo dam. The distance between two dams is 10 km. Consequently, in the rainy season most of the water level of Kali Bogel river mouth is lower than water level of Brantas river. The submerge flow almost occurred in river mouth during rainy season. Therefore, in rainy season almost every year the floods were occurred in the area beside of Kali Bogel river. The main reason is the water from Kali Bogel river cannot flowing smoothly to the Brantas river and consequently the overflow were occurred at many river bank. There are some plans were done to minimize the flood occurrences. Among them are normalized the river channel dimension, constructing small dams in upper stream area, and finally constructing floodway to minimize the submerge flow occurred in the river mouth. In this paper the effectiveness of three plans due to the civil work and social impact were discussed. The advantages and disadvantages of each plan was analyzed base on hydraulic – hydrologic conditions and will be described in this paper. Finally, it can be found that floodway is the best recommended to minimize the flood occurrences in Kali Bogel river but costly and have little bit high social impact.

Keywords: Flood, Small dam, Floodway, Return period, submerge flow.

INTRODUCTION

Flood is one of natural phenomenon which can be occurred in many places. There are many reasons of flood occurrences. Among them are high intensity of rainfall, not enough channel dimension, and watershed condition [1]. To minimize the flood occurrence, the several method can be applied due to the local condition. Evaluating of channel dimension, development of small dam, and applied of floodway can be used as counter measure method to minimize the flood occurrence. Evaluating of the channel dimension normally have result to enhance the channel dimension. If the land beside of channel still available, this method is easy and cheaper one. Due to the land availability, in area have high density population, this method is difficult to apply.

The second method is developed the small dam in upper stream area to hold the runoff discharge. If the runoff discharge can be hold until peak discharge at the reservoir, the flood occurrence can be minimized. The amount of reducing peak discharge is depend on the reservoir volume [2]. The reservoir volume design is depend on the topographic condition. Therefore, this method is fully depend on the local condition. If this method is effective to minimize the flood occurrence, the budget to construct the small dam is expensive.

The third method for minimizing flood occurrence usually is floodway. This method is easy to evaluate and easy to apply, but need land and budget consuming for constructing. This method is very common as the last alternative to reduce the flood occurrence especially in urban area or in area with special condition.

Kali Bogel river is one of a river located in Blitar regency, East Java province, Indonesia. This river as tributary of the biggest river in East Java province namely Kali Brantas river. The outlet of Kali Bogel river is located between two dams namely Wlingi and Lodoyo dams. These dams are located in Kali Brantas river and separated about 10 km distance. Wlingi dam is upper side of Lodoyo dam. Because of two dams only separated by 10 km distance, the high water level is occurred along the year in channel between these two dams. Due to this condition, the submerge flow is almost occurred at Kali Bogel outlet during rainy season. Consequently, the flow from Kali Bogel have big obstacle and back water occurred along the river. Due to this condition, flood almost occurred along Kali Bogel river especially during raining season. In this paper, the most effective plan based on the local condition as counter measure of the flood occurrence of Kali Bogel will be discussed. The hydrologic and hydraulic formulas were applied in channeling, dam construction plan, and floodway design analyses.

The counter measure of the flood occurrence of Kali Bogel river still in the plan stage. The implementation of the plan will be done in the near future. This research result is take account as consideration to decide which method will be implemented to minimize the flood.

RESEARCH AREA

The research area is Kali Bogel river. This river located in Blitar regency, East Java province, Indonesia. The location of research area can be shown in Fig.1. The Kali Bogel river have long 25 km and the watershed occupied 55,000 ha or 55.5 km^2. The outlet of Kali Bogel is located between two dams namely Wlingi dam in upstream and Lodoyo dam in downstream. The distance between two dams is about 10 km. The outlet of Kali Bogel river is separated about 2.3 km from Lodoyo dam to Wlingi dam direction. The layout of Kali Bogel watershed and river network is shown in Fig. 2.

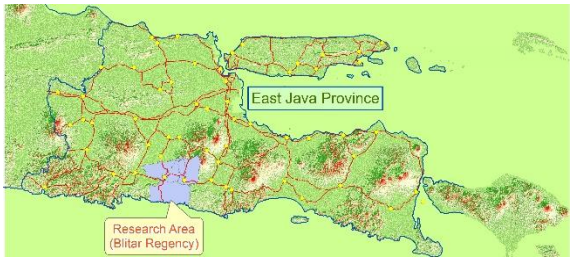

Fig.1 Location of research area.

Fig. 2 Layout of Kali Bogel watershed.

MATERIALS AND METHODS

The materials used in this research are topographic map in scale 1:25,000, remotely sensed satellite imageries, rainfall intensity data, soil map, and channel cross sectional data. From the topographic map, the watershed boundary, river network, river long, and watershed slope were analyzed. The remotely sensed satellite imageries is used to generate the land use map. The maximum daily rainfall intensity was selected for each rainfall station gauge along 10 years. The suitable statistical method is used to analyze the rainfall intensity with certain return period. The soil map in scale 1:25,000 was collected from Agriculture agency, East Java province government. The cross section data with interval 50 m was surveyed directly to the field. Base on the collected data, the channeling analyses, small dam plan, and floodway plan were done to minimize the flood occurrences. The analyses methods of each will discussed in the next paragraph.

Channeling Analysis

Flood can be occurred caused by the channel dimension is not enough to receive the runoff discharge. Therefore, the channel dimension should be increased until the water level is not over topped through the channel bank. In this research, the runoff discharge was analyzed using Nakayasu Synthetic Unit Hydrograph (SUH) [3]. The channel dimension was analyzed using Manning's continuity equation [4].

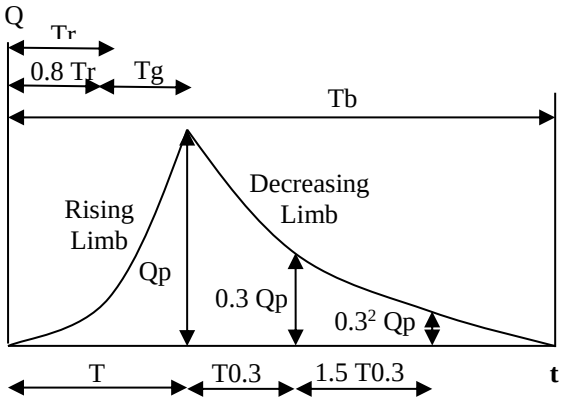

Fig. 3 Typical Hydrograph of Nakayasu SUH.

$$Qp = \frac{C.A.Ro}{3.6(0.3Tp.T0.3)} \quad (1)$$

$$Qa = Qp\left(\frac{t}{Tp}\right)^{2.4} \quad (2)$$

Where:

Qa	= rising limb discharge (m^3/se.)
t	= time (sec. or hour)
Qp	= peak discharge (m^3/sec.)
C	= surface runoff coefficient
A	= watershed area (km^2)
R_o	= rainfall unit (mm)
T_p	= time to peak (hour)
$T_{0,3}$	= time need in decreasing from peak discharge to 30% of peak discharge.

The part of decreasing limb can be calculated using eq. 3 - 5.

$$Qd > 0.3Qp \qquad Qd = Qp.0.3^{\frac{t-Tp}{T0.3}} \quad (3)$$

$$0.3Qp \geq Qd > 0.3^2 Qp \qquad Qd = Qp.0.3^{\frac{t-Tp+0.5T0.3}{1.5T0.3}} \quad (4)$$

$$Qd \leq 0.3^2 Qp \qquad Qd = Qp.0.3\frac{t-Tp+1.5.T0.3}{2.T0.3} \quad (5)$$

$$Tp = tg + 0{,}8\ tr \quad (6)$$

If L < 15 km, $tg = 0{,}21\ L^{0,7}$ (7)
If L > 15 km $tg = 0{,}4 + 0{,}058\ L$ (8)
where:
L = length of channel (km)
tg = time concentration
tr = 0,5 tg to tg (hour)
$T_{0,3}$ = α tg (hour)
tr = flood unit time (hour)
α = hydrograph parameter

$$\alpha = \frac{0.47(A.L)^{0.25}}{tg} \quad (9)$$

The rainfall intensity usually recorded in daily data. Due to the data requirement to analyze the runoff discharge, it is necessary to convert the daily to hourly rainfall data. The Mononobe formula is used in this analysis. The formula can be shown in eq. 10 [5].

$$I = \frac{I_{24}}{24}\left[\frac{24}{t_c}\right]^{2/3} \quad (10)$$

Where:
I = rainfall intensity (mm/hour)
R_{24} = daily rainfall intensity (mm/day)
tc = rainfall duration

By using peak runoff discharge and channel geometry as input data, the water level in channel is analyzed using hydraulic formula such as Manning's continuity equation. The HEC-RAS software was applied in channel water profile analysis.

$$V = \frac{1}{n} S^{1/2} R^{2/3} \quad \text{and} \quad R = A/P \quad (11)$$
$$Q = V \cdot A \quad (12)$$

Where:
Q = Discharge (m^3/sec.)
V = Velocity of flow in channel (m/sec.)
S = channel slope
R = wetted radius (m)
A = channel cross sectional area (m^2)
P = wetted perimeter (m)

Small Dam Plan

The location of dam was selected based on topographic condition. The deep reservoirs with narrow inundated area is better than the shallow reservoir with broad inundated area. Consequently, deep reservoirs with small inundated area usually can be found in the upstream area. The dam capacity was evaluated using water balance equation. The equation can be shown in eq. 13.
$St = St\ (t-1) + lt - Ot - Et - Lt$ (13)
and $0 < St < C$

where:
C = effective dam capacity (m^3)
St = intercept water volume in t period (m^3)
St (t-1)= intercept water volume in t-1 period (m^3)
lt = river discharge inflow in t period (m^3/sec.)
Ot = outflow discharge in t period (m^3/sec.)
Et = reservoir evaporation in t period (m/sec)
Lt = discharge loses in t period

Floodway

Floodway is designed to reduce the discharge flowing through the existing channel. If the existing channel dimension is not enough to receive the runoff discharge in spite of the others effort to reduce the runoff discharge was applied, finally the floodway will be applied. The design of floodway is depend on the local condition. Channel alignment are depend on the topographic condition and land availability. Channel dimension is depend on the amount of runoff discharge want to reduce from the discharge flowing through the existing channel. HEC RAS software will be used to analyze the hydraulic properties. The principle model of floodway is shown in Fig. 4. Basically, the continuity equation as shown is eq. 11 and 12 and energy equation in steady flow condition at open channel were used to analyze the channel dimension. The standard step is applied to analyze the water level profile. The energy equation in steady flow condition is shown in eq. 14 [6].

$$h_1 + \alpha_1 \frac{U_1^2}{2g} + z_1 = h_2 + \alpha_2 \frac{U_2^2}{2g} + z_2 + h_f + h_e \quad (14)$$

Where:
h = water depth (m) α = velocity coefficient
U = average velocity (m/sec.) z = elevation (m)
g = gravitation (m^2/sec.)
hf = friction energy looses
he = energy loses (cross section change)

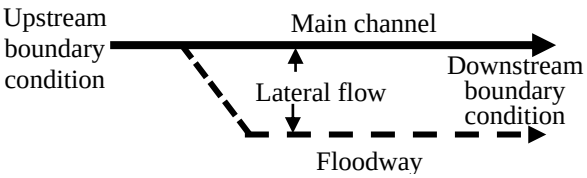

Fig. 4 Floodway model by HEC-RAS

RESULTS AND DISCUSSION

Six sheets of topographic maps in scale 1:25,000 were used in this research. From these maps the watershed boundary, length of main river, river network, others physical watershed data were found. The area of watershed is 55,000 ha and the length of main river is 25 km. There are four rainfall stations affected to the Kali Bogel watershed, namely Lodoyo, Judeg, Kanigoro, and Bacem stations. The 10 years daily rainfall data from 2004 to 2013 were collected. From the four location of rainfall stations, the

Thiessen polygon was drew to analyze the average rainfall in Kali Bogel watershed. The maximum daily rainfall from the each rainfall station can be shown in Table 1. By using the Thiessen polygon, the average rainfall for each year was analyzed. Table 2 is shown the average rainfall of Kali Bogel watershed.

Table 1 Maximum daily rainfall data

Year	Maximum daily rainfall (mm)			
	Lodoyo sta.	Judeg sta.	Kanogoro sta.	Bacem sta.
2004	289.67	288.68	264.33	276.63
2005	113.87	115.67	114.35	114.65
2006	87.50	87.25	86.75	85.95
2007	103.86	104.67	66.00	80.32
2008	23.25	58.95	59.75	40.25
2009	16.25	36.00	37.25	44.25
2010	26.50	25.50	30.00	47.50
2011	16.00	57.00	39.00	33.25
2012	20.25	39.75	55.75	57.50
2013	66.00	68.15	69.00	66.15

Table 2 Average maximum daily rainfall

No.	Year	Av. Maximum rainfall (mm)
1	2004	289.67
2	2005	115.67
3	2006	87.50
4	2007	104.67
5	2008	59.75
6	2009	44.25
7	2010	47.50
8	2011	57.00
9	2012	57.00
10	2013	69.00

Based on the average maximum daily rainfall data, the statistical distribution data was tested. The Log Pearson type III distribution is the best fit for this sequence data. By using this distribution formula, the daily rainfall data with several return periods were analyzed. Finally, the rainfall data in Kali Bogel watershed with several return periods can be shown in Table 3. To calculate the runoff discharge using Nakayasu SUH, the hourly rainfall data is needed. Therefore, the daily rainfall data as shown in Table 3 was convert to hourly rainfall using Mononobe formula. Base on the rainfall data from each rainfall station, the rainfall duration can be decided is equal to six hours. Consequently, the daily rainfall data was converted to hourly data for six hours rainfall duration. The hourly rainfall data after converted from daily rainfall data using Mononobe formula can be shown in Table 4.

Table 3 Daily rainfall data with many return periods

No.	Return period (year)	Rainfall intensity (mm/day)
1	2	68.37
2	5	115.06
3	10	165.16
4	20	224.12
5	50	365.66
6	100	509.33

Table 4 Hourly rainfall data

Time	Return periods rainfall (mm)			
(hour)	2 years	5 years	10 years	20 year
1	26.32	44.30	63.59	86.29
2	6.84	11.52	16.53	22.43
3	4.79	8.05	11.56	15.69
4	3.83	6.44	9.25	12.55
5	3.21	5.40	7.75	10.51
6	2.87	4.83	6.94	9.41

After finishing the rainfall data, the next step is analyzed runoff occurrence. Runoff data was analyzed using Nakayasu SUH as shown in eq. 1 to 9. With 55,000 ha area of watershed, 25 km river length, 0.7 runoff coefficient, and rainfall data as shown in Table 4, the runoff occurrence was analyzed. From the analyzed results the time to peak and peak discharge of rainfall data with return periods 2 and 5 years are 1.5 hours, 2 hours, 200.31 m^3/sec., and 331.44 m^3/sec., respectively. This data as main input data to simulate the water level profile in the channel using HEC-RAS software. The location of cross section area using in this research is shown in Fig. 5. In this figure, the red points are indicated the location of cross sections to check the water level from the simulation results. In this paper only cross section in point 18 is discussed. The simulation result of water profile using HEC-RAS in point 18 can be shown in Fig. 6. From this figure it can be concluded that the flood in Kali Bogel river will be occurred if the rainfall is bigger or equal than rainfall intensity with return period 5 years. The water level in point 18 is 2 m higher than river bank. For point 16, the water level is 1.2 m higher than river bank.

To reduce the water level, the river channeling was proposed. From the existing cross sectional dimension, to reduce the water level until under river bank level it is necessary to dike 0.75 m deeper and 1.5 m wider of channel width. To increase the channel cross sectional dimension a long river length, about 750 thousand US$ is needed. Base on the topographic situation, the location of points 11 to 15 is located in lower area. Therefore, after channeling, the flood still occurred in this area.

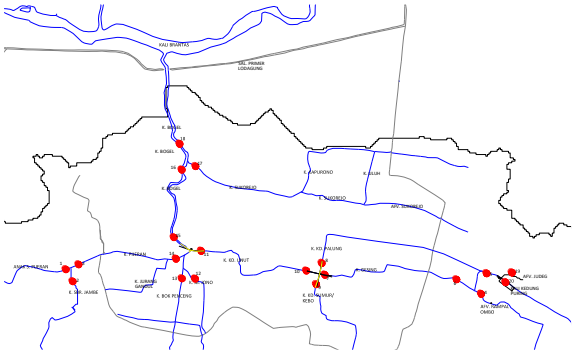

Fig. 5 Points of cross section area.

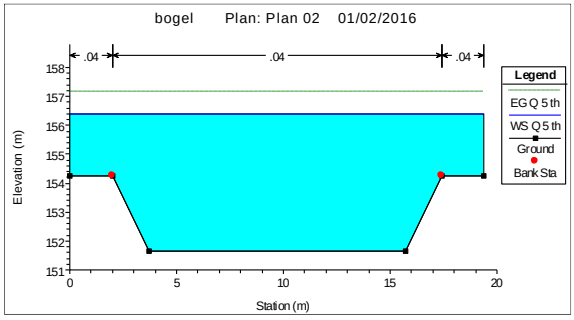

Fig. 6 Water level at cross section point 18.

The second plan is by constructing of small dam to reduce the water level. The function of small dam is to catch the surface runoff before flowing to the channel. In this research, two small dams were applied to reduce the runoff discharge. To find the biggest reservoir volume, the locations were decided on the upstream area. From three alternative location, the location dam 2 and dam 3 were selected to develop the small dams. The three proposed location of dams is shown in Fig. 7. Two selected location of dams are location dam 2 namely Bacem dam and location dam 3 namely Kedung Puring dam. From the analysis results base on the topographic map, for Bacem dam the dam height is 12 m and the reservoir can be intercepted of runoff is 147,064 m^3. For Kedung Puring dam, the dam height is 12 m and the reservoir can be intercepted of runoff is 170,708 m^3. The total volume of runoff can be intercepted by two dams is 317,772 m^3. Comparing with the runoff discharge occurred at outlet of Kali Bogel river (200.31 m^3/sec. and 331.44 m^3/sec. for rainfall with 2 and 5 years return period), the water volume can be intercepted in two dams is very small. The effect of two dams can only decrease the water level 0,5 m. To construct two dams, the budget need is equal to 2.0 million US$. From this analysis it can be concluded that the development of small dam to reduce the water level in Kali Bogel river outlet is ineffective and inefficient.

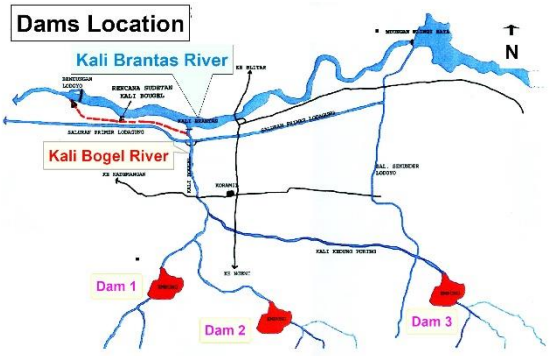

Figure 7. Proposed of dams location.

The third plan was proposed to reduce the flood discharge of Kali Bogel river. The proposed plan is by constructing of floodway. The floodway will differ the Kali Bogel flow direction about 500 m before outlet. The flow direction of floodway is to the new outlet which is located in downstream of Lodoyo dam. The distance from floodway gate to outlet is about 3 km. Because of the floodway outlet is located in downstream of Lodoyo dam, the submerge flow will not occur along the year. The layout of the floodway can be shown in Fig. 8. The trapezoidal cross section type was choose for floodway channel. If the cross section dimension are channel width 10 m, side slope 1:2, channel depth 3 m, channel slope 0.005, and Manning's coefficient 0,025 the floodway way can be carried the discharge equal to 175.91 m^3/sec. The typical of the floodway cross section is shown in Fig. 9. The material of the floodway channel is rubble stone. The discharge flowing through the Kali Bogel river with rainfall intensity equal to the 5 years return period rainfall is equal to 331.44 m^3/sec. If the floodway fully operated, the remained discharge flowing through in Kali Bogel river is equal to 155.53 m^3/sec. With this discharge, the water level in Kali Bogel river will be lower than river bank. Consequently, the flood will not occurred along the river. The discharge which is should be flew to the flood way can be control by the sluice gate on the floodway point. The cost to construct the floodway with 3 km long approximately equal to 1 million US$. This price is chipper than dam construction budged and little bit higher than channeling budged. By considering the construction budged need and decreasing of discharge amount the most effective and efficient of flood counter measure for Kali Bogel river is floodway. Some advantages of the floodway are the submerged flow will not occur at the floodway outlet, the construction budged is reasonable, and the land acquisition can done smoothly. The most difficulties may occurred on floodway construction is land acquisition. This work can done smoothly

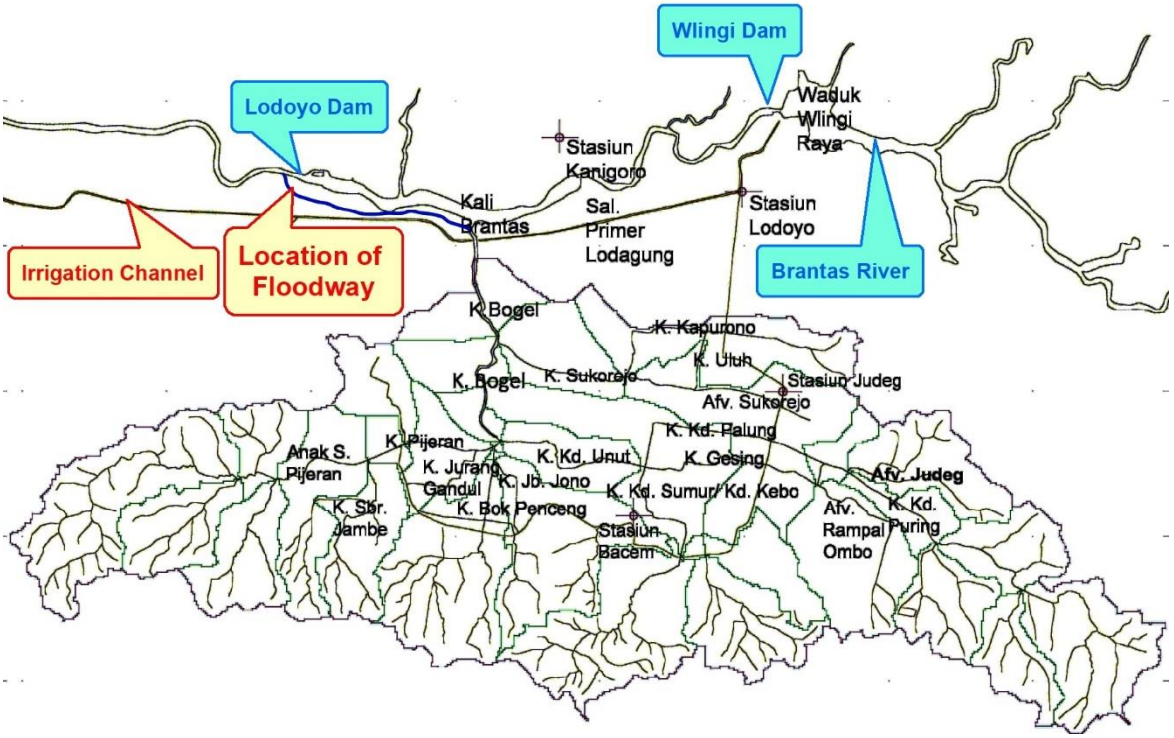

Fig. 8 Layout of floodway

if government can be explained well the purposed of the floodway and the advantaged of floodway. From Fig. 8 it can be seen that the floodway is located between Kali Brantras river and irrigation channel in narrow distance. Normally, land acquisition process for the land located between big river and irrigation channel with narrow distance is easy for government development purpose.

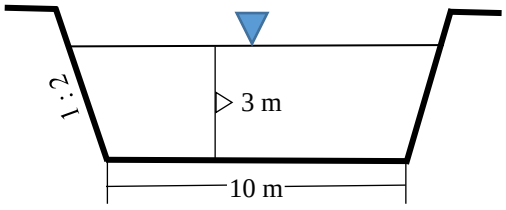

Fig. 9 Typical of floodway cross section

CONCLUSIONS

From this research it can be concluded that the most effective and efficient to reduce the flood occurrences of Kali Bogel watershed is by constructing the floodway. The main reason is the water level at the floodway outlet is higher than Kali Brantas river water level. Therefore, the submerged flow will not occurred. The second reason are the floodway can be reduced the discharge of Kali Bogel river significantly, the construction budged is reasonable, and the project implementation especially for land acquisition look easier than the other method (channelization and dam construction).

REFERENCES

[1] Papagiannaki K., Lagouvardos K., Kotroni V., and Bezes A., Flash flood occurrence and relation to the rainfall hazard in a highly urbanized area, Natural Hazards Earth System. Sci. Discuss., 3, 2015, pp. 3119–3149.

[2] Eui Hoon Lee, Yong Sik Lee, Jin Gul Joo, Donghwi Jung, and Joong Hoon Kim, Flood Reduction in Urban Drainage Systems: Cooperative Operation of Centralized and Decentralized Reservoirs, MDPI Water, 8, 469, 2016, doi:10.3390/w8100469.

[3] I Gede Tunas, Nadjadji Anwar, and Umboro Lasminto, The Improvement of Synthetic Unit Hydrograph Performance by Adjusting Model Parameters for Flood Prediction, International Journal of Engineering and Technology, Vol. 9 No 2, 2017, pp. 847-858.

[4] Song S., Schmalz B., Zhang J. X., Li G., and Fohrer N., Application of modified Manning formula in the determination of vertical profile velocity in natural rivers, Hydrology Research, · 2016.

[5] Chow V.T., Maidment D.R., Mays L.W., Applied hydrology, McGraw-Hill Book Co., Singapore, 1988.

[6] Marangu PK, Mwenda E., and Theuri DM., Modeling Open Channel Fluid Flow with Trapezoidal Cross Section and a Segment Base, Journal of Applied & Computational Mathematics, 5: 292, 2016.

9th Int. Conf. on Geotechnique, Construction Materials and Environment,
Tokyo, Japan, 20-22 November 2019, ISBN: 978-4-909106025 C3051

LANDING PREFERENCE OF MOSQUITOES ON HUMAN SKIN AMONG ABO BLOOD SYSTEM IN KELURAHAN KEMELAK BINDUNG LANGIT, KABUPATEN OGAN KOMERING ULU SUMATERA SELATAN

Farah Nuriessa Aputri[1], Yuanita Windusari[2*], Dwi Septiawati[3], Laila Hanum[4]
[1]Student in Departement of Biology, Faculty Mathematic and Natural Sciences, Sriwijaya of University Indonesia
[2,3]Departement Public Health and Mathematic and Natural Sciences Faculty Sriwijaya of University Indonesia
[4]Departement of Biology, Mathematic and Natural Sciences Faculty Sriwijaya of University Indonesia

ABSTRACT

Mosquitoes have their own preferences in determining hosts to be targeted in finding food. Some of the factors that can attract mosquitoes in finding their host are blood type. This study aims to determine the blood type preference by mosquitoes to landing and characteristics of mosquitoes that like landing and species of mosquitoes that landing on volunteers in Kemelak Bindung Langit Ogan Komering Ulu Regency, South Sumatra. This study uses 12 people who have different blood types. The time of observation of preference landing was carried out for 12 hours from (18.00-06.00) with a time ratio of 40 minutes / hour. with 3 repetitions. Data analysis using quantitative analysis used to determine the blood type needed is by discussing the Method Neu et, al 1974 (Preference Index). The results show that blood type O (1.12), AB (1.08), and B (1.08) are the blood groups that are the preference of mosquitoes to landing compared to blood group A (0.18). The characteristics of mosquitoes in each genus are different, the groups of Anopheles sp mosquitoes have proborcis and palpi characteristics are almost the same length, the Armigeres sp group has a characteristic scutellum consisting of 3 lobes and has a clear wing color. And in the genus Aedes sp has characteristics with the tip of the abdomen that has cerci, and has symmetrical wings and clear colored. The Culex vishnui mosquito species is the dominant mosquito species landing on all blood type systems.

Keywords: Landing preference, Mosquito, ABO blood group, Kemelak bindung langit

INTRODUCTION

Mosquitoes are animals that are ectoparasite which can disrupt the activities and health of humans and animals. This is because mosquitoes generally can be a vector in the spread of disease. In Indonesia there are 457 mosquito species consisting of 18 genera, including 80 Anopheles, 125 Aedes, 82 Culex and 8 Mansonia [26]

Kemelak Bindung Langit is one of the villages located in East Baturaja District, Ogan Komering Ulu Regency, South Sumatra. Kemelak Village is a low-lying area that has several types of habitats such as rice fields, swamps, rivers and plantations. Such environmental conditions are conducive habitats and suitable for breeding mosquitoes. Based on reports from the Ogan Komering Ulu Timur District Health Office it was found there were several diseases caused by Anopheles, Aedes and Culex mosquitoes [12].

Mosquito's preference for sucking blood of different hosts, one of which is a mosquito that likes to suck human blood (anthropophilic). Anthropophilic mosquitoes like to be close to human activities, because it is a very comfortable habitat for breeding these mosquitoes [24].

Female mosquitoes use odor and heat as a reference for locating blood feed so that mosquitoes can detect the blood content of the host over long distances. Mosquito's flight speed will be faster if there is a smell and heat stimulus from the host [39]. Every human being has a different blood group so that the blood and protein constituents of each individual also have different levels. Humans have blood which is included in the ABO blood group system which consists of four main blood groups namely A, B, AB, and O. This causes many people's opinions regarding blood feed preferences based on ABO blood pressure.

Research on mosquito characteristics both morphology, physiology, spread of mosquitoes and mosquito bite patterns on their hosts has been

widely carried out, but research on host characteristics that mosquitoes like has not been done much. Therefore, it is necessary to do further research regarding the host characteristics that mosquitoes like, entitled "Landing Preference for Mosquito Based on Blood Types of ABO System in Humans in the Kemelak Bindung Langit Regency Ogan Komering Ulu Districts".

MATERIALS AND METHODS

Location and Time of Research

The study was conducted from January to March 2019. Located in the Kelurahan Kemelak Bindung Langit of Komering Ulu Regency, and Mosquito Identification in the Entomology Laboratory of the Baturaja Health Research and Development Center.

Materials

There are also tools that are used include, stationery, aspirator, autoclick, blood lancet, petri dish, rubber, alcohol cotton, camphor, digital camera, blood group paper, kuteks, chloroform, hygrometer, insect box, insect pin, sergeant needle , paper labels, microscopes, papper cups, pinning blocks, point pouches, and thermometers. While the material of this study was mosquitoes as the object of research, 12 volunteers with different blood groups and Anti A, Anti B, Anti AB, and Anti D Reagents were used to see the presence of agglutination in the blood group.

Methods

Determination of Blood Type

Clean your fingers with alcohol cotton. Capillary blood taken using autoclik. The first blood is cleaned and the blood is then used for examination. Then place it in the column available on blood type paper. Dropped by each reagent according to the available column. Homogeneous. Judging by agglutination and the results recorded.

Observation of Landing Preferences Mosquito Based on Differences in Blood Types

Preference observations of landing mosquitoes were carried out in the neighborhoods of the Kemelak Village of Komering Ulu District. This study used 12 volunteers consisting of 3 blood groups (A, B, AB, and O). When observing the preferences of landing mosquitoes carried out for 12 hours from (18.00-06.00) with a time ratio of 40 minutes / hour. Mosquitoes that land on their hands and feet are captured using an aspirator and count the amount based on each blood group. This research was conducted with 3 repetitions with the same method and location.

Mosquito identification

Identification of mosquitoes to species level is carried out at the Baturaja Health Center Laboratory. The mosquito samples obtained were identified by observing the characteristics of the mosquitoes using a microscope while to find out the mosquito species name using the O'connor mosquito identification book, C.T. and T. Sopa, 1981 and Rattanarithkul, R., 2010.

Data analysis

Quantitative analysis used to determine the most preferred blood group is the Neu Method approach (Preference Index). According to Neu *et al*. (1974), If $w \geq 1$, the blood group concerned is preferred. The *w* value obtained from the calculation results is a preference index, then the Preferemsi Index value of the type of blood group is divided into two criteria. that is :

a. If $w \geq 1$ = preferred
b. If $w \leq 1$ = not liked

Determination of the Neu Method (Preference Index) according to Neu *et al*. (1974) can be seen in Table 1.

Table 1 The criteria measured in determining the Neu index

Blood Type	availability		Use		Preference Index		
	b	p	n	u	E	w	b
x1	a1	p1	n1	u1	e1	w1	b1
x2	a2	p2	n2	u2	e2	w2	b2
x3	a3	p3	n3	u3	e3	w3	b3
x4	a4	p4	n4	u4	e4	w4	b4
Total	an	pn	nn	un	E n	wn	bn
		1,00		1,00			

Description:
a = number of volunteers in blood group
p = proportion of the number of blood groups
n = number of each type of blood group infested by mosquitoes
u = proportion of each type of blood group that is infested by mosquitoes (ni / ∑n)
e = expectation value
w = preference index (ui / pi)
b = standardized selection index (wi / ∑w)

RESULTS AND DISCUSSION

Based on the research that has been done on the preference of mosquito perch based on ABO system blood type in humans in Kemelak Bindung Langit Village, South Sumatra Komering Ulu Regency, the results showed that the total number of mosquito samples obtained in this study were 361 individuals. The preference of mosquito perch based on ABO system blood type in humans in Kemelak Bindung Langit Village, South Sumatra Komering Ulu Regency can be seen in Table 4.1.

Table 4.1. Index and preference level of mosquito landing prefer based on blood type on volunteers in Kemelak Bindung Langit Village, Komering Ulu Regency, South Sumatra

Blood Type	Volunteer availability	Mosquito Landing Total	Preference Index (w)	Level Preference
A	3	64	0,72	4
B	3	97	1,08	3
AB	3	99	1,08	2
O	3	101	1,12	1

In Table 4.1. shows that blood groups O, AB, and B tend to be preferred by mosquitoes to perch. This is indicated by the index value of the mosquito perch obtained, in blood group O the preference index is 1.12 which tends to be higher than the other blood groups. While blood group AB and B get a preference index value of 1.08 and for blood group A get a preference index value of 0.72. Blood type A is included in the category of dislikes for mosquitoes to perch because of the preference index of blood type A> of 1.

Based on the results, it was found that the tendency of mosquitoes to perch on blood type O was in line with the research conducted by Shirai et al., (2004) (83.3%) compared to other blood groups.

The blood provides high iron levels as hemoglobin in erythrocytes and as transferrin iron. Iron plays an important role in living cells as a cofactor of proteins involved in various metabolic pathways such as DNA synthesis and repair, energy metabolism and immunity, and in mosquitoes, iron and proteins found in blood play an important role in the production and development of mosquito eggs. The tendency of mosquitoes to perch on blood type O is thought to be due to differences in levels of protein and iron contained in human blood. According to the results of Geiseret al., (2006), one of the proteins associated with iron in mosquito metabolism is ferritin. Besides ferritin protein according to transferrin also plays a role in mosquito metabolism[17].

Transferin iron and heme iron (ferrritin) found in human blood play a role in metabolism and the development of mosquito life cycles. That ingested iron from the blood which has been eaten by the Aedes aegypty mosquito in the form of 3.6 ng Transferin-Fe by (77%) is used for the development process maturation of mosquito eggs, (15%) is used for the body's metabolic processes and (8%) is excreted as waste from waste metabolism. Whereas from 1881.1 ng Heme-Fe absorbed by mosquitoes by (6%) was used for body metabolism, (7%) was used for egg maturation and (87%) was excreted as waste from waste products from metabolism [44]. However iron derived from heme and transferrin is distributed differently at the end of the gonotropic cycle. The majority of iron stored by the Aedes aegypty mosquito at the end of the first gonotropic cycle comes from heme because of the much greater heme level in the blood.

Regarding the level of ferritin and serum iron in the ABO blood group system in Enugu Southeast Nigeria the results showed that blood group O had a ferritin value of (116.75 ± 46.34) (ng / mL) and serum iron of (24.00 ± 6.75) (ng / mL) while blood group B has lower ferritin and iron iron values which are equal to (83.58 ± 57.7)

(ng / mL) and (20.20 ± 8.07) (ng / mL) compared to other blood groups [27]. However, for transferrin levels there was no significant difference in all blood groups. It is suspected that there are differences in levels of iron and proteins that distinguish the preference of mosquito perch on the ABO system blood group.

Characteristics of mosquitoes landing the results of identification of mosquitoes that landed on volunteers were found as many as 5 genera of mosquitoes consisting of 17 species. The mosquito species obtained can be seen based on the table as follows :

4.2. Table of Species of Mosquitoes that Perch on Volunteers Based on the Four Blood Types of the ABO System

No	Genus	Spesies	Golongan Darah			
			A	B	AB	O
1.	*Aedes*	*Aedes albopictus*	-	1	-	-
		Aedes albolineatus	-	-	1	-
		Aedes lineatopenne	-	1	1	1
		Aedes vexans	1	1	-	-
2.	*Anopheles*	*Anopheles barbumbrosus*	-	1	-	-
		Anopheles barbirostris	-	2	-	-
		Anopheles flavirostris	1	-	-	-
		Anopheles sinensis	1	-	-	-
		Anopheles vagus	25	32	31	23
3.	*Armigeres*	*Armigeres subalbatus*	-	2	6	4
4.	*Culex*	*Culex bitaeniorhyncus*	1	-	-	-
		Culex gellidus	-	2	-	1
		Culex tritaeniorhyncus	4	2	2	5
		Culex quinquefasciatus	4	7	8	10
		Culex vishnui	25	44	45	49
5.	*Mansonia*	*Mansonia annulifera*	2	4	4	2
		Mansonia uniformis	-	-	1	-

The mosquito species obtained in this study are variously seen because the mosquito samples obtained represent the five genera of mosquitoes in Indonesia, namely from the genus Anopheles, Aedes, Mansonia, Armigeres, and Culex. This is also influenced by ecological factors

The study area in Kemelak Village, Bindung Langit, is a low-lying area that has several types of habitats such as rice fields and plantation land. In addition, at the research location there are also cattle sheds. So that with a diverse habitat for living habitat, this is what supports it as a habitat for various species of mosquitoes [12].

In table 4.2. It can be seen that the mosquito species that dominates more on the blood group are the Culex vishnui mosquito species 49 perched on the blood group O while the mosquito species which are the least perched are Aedes albopictus, Aedes albolineatus, Aedes lineatopenne, Aedes vexans, Anopheles barbumbrosus, Anopheles flavirostris, Anopheles sinensis, Culex bitaeniorhyncus and Mansonia uniformis.

Culex vishnui has a habit of biting humans and animals at night. The time usually used by Culex

mosquitoes to suck blood is a few hours before the sun rises and after the sun sets [40] This caused the Culex vishnui to dominate the study because the study was conducted at 6:00 a.m. to 6:00 a.m. which was the time when the Culex mosquitoes were active in their activities.

The place that is usually used by Culex sp mosquitoes to breed is dark, protected from sunlight, the surface is wide open, contains clear water, and calm [37]. In the study site, there were several open sewers, puddles of water and swamps and trees. Which stated that Culex mosquitoes usually chose puddles of groundwater as their breeding places, such as in hollow trees. bamboo stems and stumps, and other water reservoirs [33]

Table 4.3. Characteristics of mosquitoes that land on volunteers

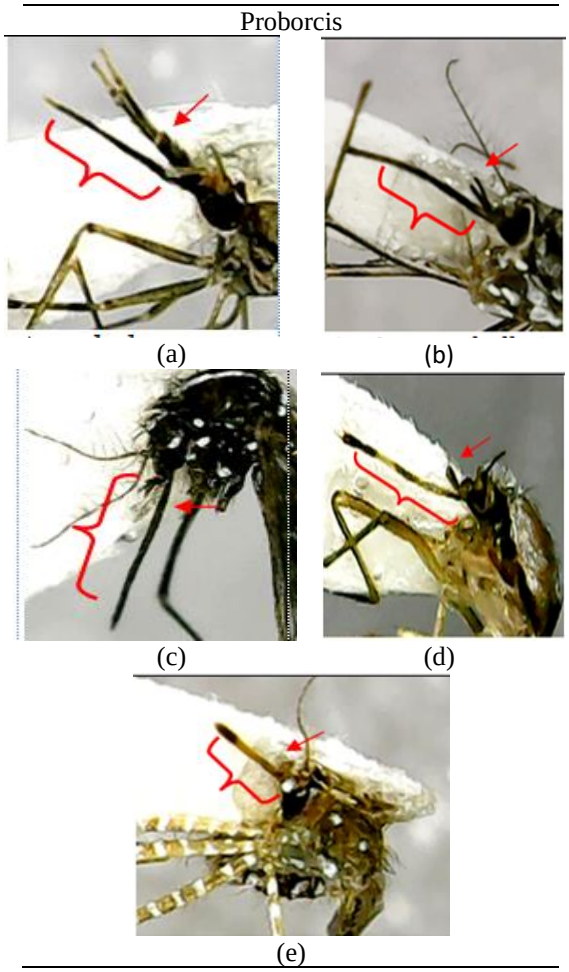

Figure. (a) *Anopheles vagus*
(b) *Armigeres subalbatus*
(c) *Aedes albopictus*
(d) *Culex gellidus*
(e) *Mansonia annulifera*
Source : Aputri (2019)

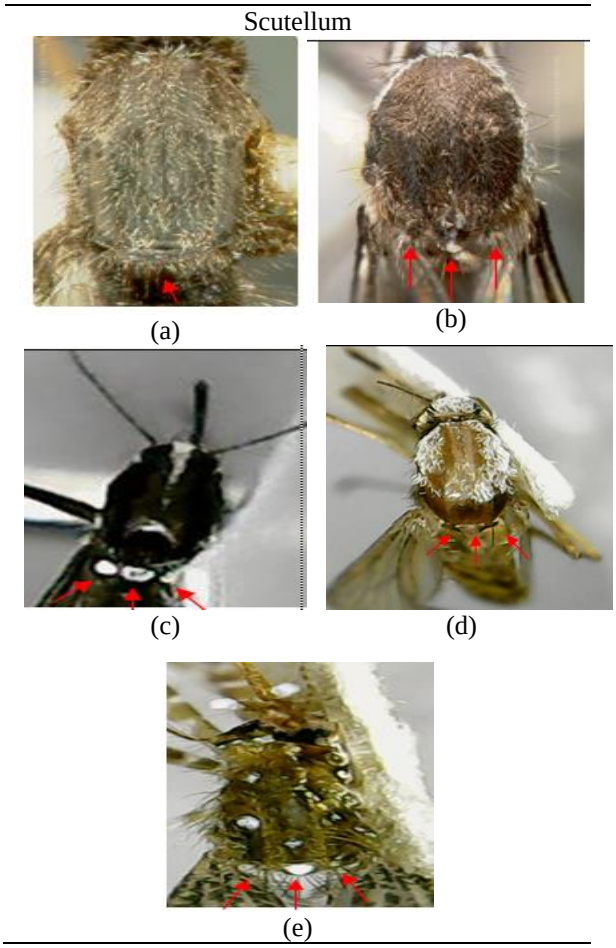

Figure. (a) *Anopheles barbirostris*
(b) *Armigeres subalbatus*
(c) *Aedes albopictus*
(d) *Culex gellidus*
(e) *Mansonia annulifera*
Source : Aputri (2019)

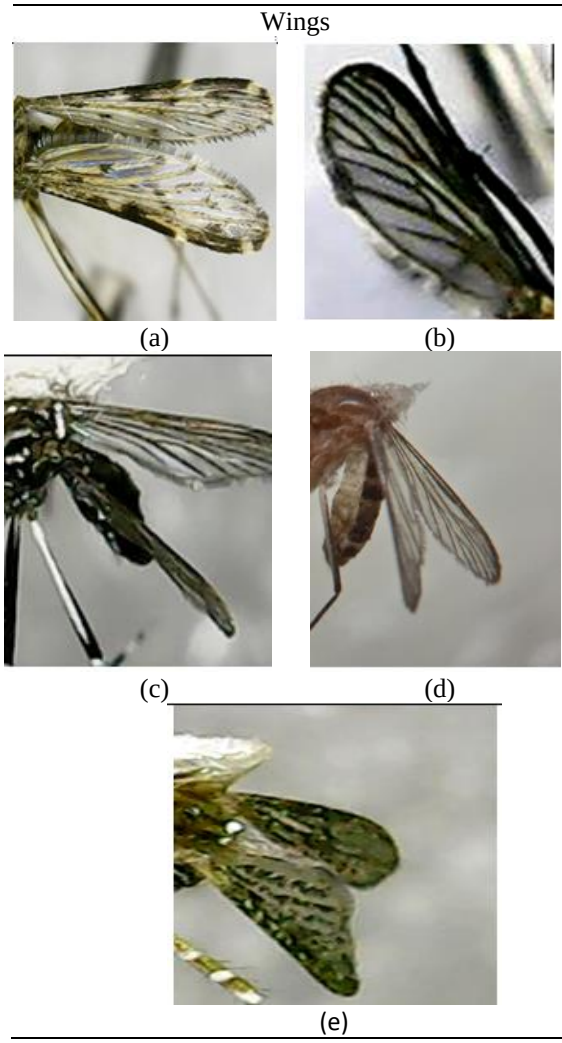

Figure. (a) *Anopheles vagus*
(b) *Armigeres subalbatus*
(c) *Aedes albopictus*
(d) *Culex vishnui*
(e) *Mansonia annulifera*
Source : Aputri (2019)

Based on table 4.3 mosquitoes have different characteristics. Anopheles sp mosquitoes have the main characteristics that distinguish anopheles sp mosquitoes from other mosquito groups which have proborcis not bent down with proborcis and palpi sizes almost in the long term whereas for the other genera it has probiotic size and palpi not equal length [26]. While the Armigeres mosquito has characteristics with a larger body size compared to Aopheles sp, Culex sp, Aedes sp, and Mansonia sp mosquitoes and has a rather curved probosis [30]. for groups of genus Culex sp and Mansonia sp have scutellum which consists of 3 lobes and has a clear wing color. As well as in the genus Aedes sp has characteristics with the end of the abdomen that has cerci, and has wings that have symmetrical wings and are generally clear in color [26].

4. CONCLUSION

Based on the research that has been done, it can be concluded as follows:

1. Blood type O (1.12), AB (1.08), and B (1.08) are blood groups that are the preference of mosquitoes to perch compared to blood group A (0.18)
2. Characteristics of mosquitoes in each genus are different, groups of Anopheles sp mosquitoes have proborcis and palpi characteristics are almost the same length, the Armigeres sp mosquito group has characteristics with a larger body size compared to other mosquito groups whereas with other mosquito groups while for the genus Cules sp and Mansonia sp it has the characteristics of scutellum consisting of 3 lobes and has a clear wing color. As well as in the genus Aedes sp has characteristics with the end of the abdomen that has cerci and has symmetrical and clear wings
3. The Culex vishnui mosquito species is the dominant mosquito species prevailing in all blood type systems.

5. REFERENCES

[1] Andiyatu, 2005. Fauna Nyamuk di Wilayah Kampus IPB Darmaga dan Sekitarnya. *Tesis*. Bogor. Institut Pertanian Bogor.

[2] Annisugiyarti, 2012. *Penentuan Golongan Darah*. Jakarta : Erlangga.

[3] Anwar, C., R. A. Lavita, D., Handayani. 2014. Identifikasi dan Distribusi Nyamuk *Aedes* sp Sebagai Vektor Penyakit Demam Berdarah *Dengue* di Beberapa Daerah Sumatera Selatan. *MKS*. 2(1) : 111-117.

[4] Arsin A,A, 2012. *Malaria di Indonesia Tinjauan Aspek Epidemiologi*. Makassar: Masagena Press.

[5] Arunchalam, N., Samuel P. P., Hiriyan J., RajendranR., Dash A. P. 2005. *Short Report: Observationon The Multiple Feeding Behavior of Culextritaeniorrhyncus*(Diptera: Culicidae), *The Vector of Japanes Encephalitis in kerala, in Southern India*. *Am J Trop Med Hyg*. 72(2): 198-200.

[6] Beerntsen BT, James AA, Christensen BM. 2000. *Genetics of Mosquito Vector Competence*. *Microbiol Mol Biol Rev*. 64(91) :37- 115.

[7] Cahyati, Widya H., 2006, Dinamika Aedes Aegypti Sebagai Vektor Penyakit Kemas. *Jurnal Kesehatan*. 2(1): 40-50.

[8] Chaves, L. F., Harrington L. C., Keogh C. L., NguyenA. M., Kitron U. D. 2010. *Blood Feeding Patterns of Mosquitoes: Random or Structured*.*Front Zool*.7(3): 1-11.

[9] Constantini C, Sagnon N, Torre AD, Diallo M, Brady J, Gibson G. 1998. *Odor Mediated Host Preferences of West African Mosquitoes With Particular Reference to Malaria Vector*. *AM J Trop Med Hyg*. 38(1): 56-63.

[10] Das S, Dimopoulus G. 2008. Moleculer *Analysis of Photic Inhibition of Blood Feeding in Anopheles gambiae*. *BMC Physiol*. 8(23).

[11] Dharmawan R.1993. *Metode Identifikasi Spesies Kembar Nyamuk Anopheles.* Sebelas Maret University Press. Surakarta.

[12] Dinas Kesehatan OKU Timur. 2017. *Profil Dinkes OKU Timur*. Dinas Kesehatan Kabupaten OKU Timur

[13] Foley, D. H., Wilkerson R. C., Birney I., Harrison S.,Christensen J., Rueda L. M. 2010. *Mosquito Map and The Malaria Calculator: New Web Tools to Relate Mosquito Species Distribution With Vector Borne Disease*. *Journa; health geographics*.9 (11): 1-8.

[14] Foster, W. A., E. D Walker. 2002. *Medical and Veterinary Entomology*. Terjemahan oleh Gary M. Dan Lanced. London: Academic Press.

[15] Geiser DL, Mayo JJ, Winzerling J,. 2006. *Secreted ferritin: mosquito defense against iron overload*. *Insect Biochemistry and Molecular Biology.* 36(1) :177–187.

[16] Harbach, R. E. dan T, M. Howard. 2007.*Index of Curently Recognized Mosquito Species* (Diptera: Culicidae*). Journal of the European Mosquito Control Association*. 23(1): 1-66.

[17] Harizanova N, Georgieva T, Dunkov BC, Yoshiga T, Law JH.2005. *Aedes aegypti*transferrin: gene structure, expression pattern, and regulation. *Insect Molecular Biology*. 14(1) :79–88.

[18] Kilpatrick AM, Kramer LD, Jones MJ, Marra PP, Dazak P, Foseca DM. 2007. *Genetic Influences on Mosquito Feeding Behavior and the Emergence of Zoonotic Pathogens*. *Am Journal Trop Medical Hyg*. 77(4): 71-667.

[19] Lefevre T, Gougna LC, Dabire KR, Elguro E, Fontenille D, Renaud F. 2009. *Beyond Nature and Nurture: Phenotypic Plasticity in Blood Feeding Behavior of Anopheles gambiae s.s. when humans are not readily accessible*. *Am Journal Trop Medical Hyg*. 81(1).

[20] Lestari, B.D, Gama Z.P, Rahadian B. 2010. *Identifikasi Nyamuk di Kelurahan Sawojajar Kota Malang*. Fakultas Matematika dan Ilmu Pengetahuan Alam Universitas Brawijaya. Malang.

[21] Macdonald, W,W. 1967. *Host Feeding Preference. Bull. Wld Hlth Org*. 36(1):597-599.

[22] McMeniman JC, Hughes GL, Oneill S. A. 2011. *Wolbachia Symbiont in Aedes aegypti disrupts mosquito egg development to a greater extent when mosquitoes feed on nonhuman versus human blood.Journal medical entomology*. 48(1) :76-84.

[23] Montgomery, D. D. 1974. *A Guide to The Common Mosquitoes of Jackson Country Vector Control District*. Oregon: Southern Oregon State Collage

[24] Noshirma, M., R. W. Willa, dan N. W. D. Adnyana. 2012. Beberapa Aspek Perilaku Nyamuk *Anopheles barbirostris*di Kabupaten Sumba Tengah. *Media Litbang Kesehatan* 22(4): 161-166.

[25] Novelani, B. 2007. Studi Habitat dan Perilaku Mengigit Nyamuk *Aedes* serta Kaitannya dengan Kasus Demam Berdarah di Kelurahan Utan Kayu Utara. *Tesis*. Program Pascasarjana, IPB.

[26] O'connor, C.T. & T. Sopa. 1981. *A Checklist of The Mosquitoes of Indonesia*. U.S. Naval Medical Research Unit No. Jakarta: 1-26.

[27] Ositadinma IM, Ifeoma AG, Martina NA, Okorie OG, Ejike OA.2014. Ferritin and Serum Iron Levels among the ABO Blood Groups in Enugu, South Eastern Nigeria. *J Blood Disord Transfus*. 5(1) 204-209.

[28] Pagaya, J., M Nihdatu, dan F. Ririhena. 2005. Analisa Kepadatan Larva dan Survei Tempat Perindukkan Nyamuk *Aedes* (Diptera: Culicidae) di Dusun Waimahu Kecamatan Nusaniwe Kota Ambon. *Tropical Medicine Journal*. 6(1):12-20.

[29] Pratama, G.Y. 2015. Nyamuk *Anopheles* sp dan Faktor yang Mempengaruhi di Kecamatan Rajabasa, Lampung Selatan. *Jurnal Majority*. 4(1): 20-27.

[30] Rattanarithkul, R., R. E. Harbach, B. A. Harrisson, P. Panthusiri, R. E. Coleman, dan J. H. Richardson. 2010. *Illustrated Keys to The Mosquitoes of Thailand VI. Tribe Aedini*. Bangkok.: SEAMO Regional Tropical Medicine and Public Health Network.

[31] Rueda, L, M. 2004. *Pictorial Keys for The Identification of Mosquitoes* (Diptera: Culicidae) *Associated with Dengue Virus Transmission*. *Zootaxa 589*. 1-11.

[32] Sembel, D. 2009. *Entomologi kedokteran*. Yogyakarta: Penerbit Andi: 49-105.

[33] Setiawan, B., 2008. Faktor Risiko Yang Berhubungan Dengan Kejadian Filariasis Malayi Di Wilayah Kerja Puskesmas Cempaka Mulia Kabupaten Kotawaringin Timur Propinsi Kalimantan Tengah. *Jurnal Jurusan Epidemiologi dan Penyakit Tropik*. FKM Universitas Ahmad Dahlan, Yogyakarta. 1(1):2-4.

[34] Shirau, Y., Hisashi F.,Hisao T., Taisuke, S., Masaaki M., and Kiyoshikamimura. 2004.*Landing Preference of Aedes albopictus* (Diptera: Culicidae) *on Human Skin Among ABO Blood Groups, Secretors or Nonsecretors,and ABH Antigens. Journal Medical Entomologi*. 41(4): 796-799.

[35] Siagian, F. E., Janno B. B. B., Robiatul A., dan Esy M. 2011. Nyamuk: Peran Pola Gigit dan Pilihan Inang Dalam Kompetensisebagai Vektor. *Jurnal Ilmu Kedokteran*. 5(2): 63-124.

[36] Soegijanto, S., 2006. *Demam Berdarah Dengue*. Edisi 2. Malang: Airlangga University Press.

[37] Subowo. 1992. *Histologi Umum*. Jakarta: PT Bumi Aksara

[38] Syahribulan, F., M, Biu dan M, S. Hassan.2012. Waktu Aktivitas Menghisap Darah Nyamuk *Aedes aegypty* dan *Aedes albopictus* di Desa Palanassang Kelurahan Barombong Makassar Sulawesi Selatan. *Jurnal Ekologi Kesehatan*. 11(4): 306-314.

[39] Thomson R.C.M., 2009. *The Reactions of Mosquitoes to Temperature and Humidity*. *Bulletin of Entomological Research*. 29(2): 125-140.

[40] Tiawsirisup, S. & Nithiuthai, S., 2006, Vector Competence of *Aedes aegypti (L.) And Culex quinquefasciatus* for Dirofilaria imitis (Leidy), http://www.tm.mahidol.ac.th/ diakses pada 25 Maret 2019.

[41] Vosshall LB. 2018. *Modulation of Complex Behaviors by Internal Physiological State and Ekternal Chemosensory Cues*.

[42] Wibowo, Sutyo Agus, 2010. Pengaruh Pencucian Kain Payung yang Dicelup Insektisida Permetherine Terhadap Daya Bunuh Nyamuk *Culex* sp. *Skripsi*. Fakultas Kesehatan Masyarakat Universitas Muhamadiyyah Semarang, Semarang

[43] Widayati, opik. 2010.*Sediaan Apus Darah*. Fakultas Matematika dan Ilmu Pengetahuan Alam Universitas Muhammadiyah Prof. DR. Hamka; Jakarta.

[44] Zhou G.,Pete Kohlhepp., Dawn Geiser., Maria del Carmen F., Luz VM dan Joy K. Winzerling. 2007. Fate of Blood Meal Iron In Mosquitoes. *Journal Insect Physiol*. 53(11) : 1169-1178.

[45] Zwibel LJ, Takken W. 2004. *Olfactory Regulation of Mosquito Host Interactions*

9thInt. Conf. onGeotechnique, Construction Materials andEnvironment, Tokyo, Japan,20-22 November 2019, ISBN: 978-4-909106025C3051

ORGANIC CYCLE SYSTEM IN BIOGAS SYSTEM: THE RECYCLING OF BIOGAS SLUDGE FROM COW MANURE AS BIOCHAR FOR BIOGAS PURIFICATION

Ambar Pertiwiningrum[1,3,5], Andang Widi Harto[2], Margaretha Arnita Wuri[3,4], Adam Gemilang[2], Rachmawan Budiarto[2,3,4] and Misri Gozan[3,4]

[1]Faculty of Animal Science, Universitas Gadjah Mada, Indonesia; [2]Faculty of Engineering, Universitas Gadjah Mada, Indonesia; [3]Center for Development of Sustainable Region (CDSR); [4]Center of Energy Studies, Universitas Gadjah Mada; [5]Agrotechnology Innovation Center; [6]Faculty of Engineering, Universitas Indonesia, artiwi@mail.ugm.ac.id

ABSTRACT

The increase in intensive using of production elements has been reflected on the increasing amount of organic waste. Without appropriate treatment, waste leads to the contamination of environment. The conversion of organic waste into material with economic value will contribute to increasing productivity, for example in biogas system. Today, the utilization of waste from biogas processing (biogas sludge) as bio-fertilizer has been developed. However, the utilization of biogas sludge from cow manure as biochar is still rare. The aims of this study were to investigate the recycling of biogas sludge from cow manure as biochar in biogas purification. Biochar made of biogas sludge from cow manure as adsorbent in biogas purification leads to the cycle loop of biogas system. We also investigated the effect of mass variation of biochar made of biogas sludge from cow manure on biogas purification performance. The variation of zeolite and biochar made of biogas sludge with mass ratio of 0:80; 20:60; 40:40; 60:20; and 80:0 per each column had been put inthe adsorption column of biogas purification. The results showed that the increase in biochar mass affected on methane enrichment of biogas. The highest methane enrichment (22.57%) was performed by biogas purification using biochar with ratio 40:40. The utilization of biochar mass above 50% of the total mass per each column decreased methane enrichment. From this study, we concluded that biogas sludge has potential to be used as adsorbent in biogas purification. The recycling of biogas sludge into biochar leads to organic cycle system in biogas system that provides option in sustainable energy and additional benefits for farmers.

Keywords:Organic cycle system, Biogas sludge, Biogas purification, Biochar

INTRODUCTION

Livestock contribution to environmental problems is on a massive scale. Along with economic growth, food demand including meat and milk will increase day by day. The global production of meat is projected to be more than 460 million tonnes in 20150 [1]. The impact on environment may be direct, through grazing and organic waste, or indirect, such as the expansion of land for feeding. The organic waste from livestock comes from their manure. Livestock manure is primarily composed of organic material and water, and it is accumulated annually without treatment. If the waste get into the water or accumulate, it can contaminate freshwater and soil. Moreover, in aerobic condition, the organic material is decomposed, producing methane and carbon dioxide gases.

The population of livestock in Indonesia increases annually and unfortunately is not accompanied by a good waste management. Most of the livestock farmer groups in Indonesia still maintain conventional management without waste treatment. The organic cycle system is expected to be an alternative solution in livestock waste management. The cycle of organic material is managed through 9R (reuse, reduce, recycle, refill, replace, repair, replant, rebuild, and reward) [2]. It means livestock manure can be recycled into renewable resources to high value product like biogas. Biogas technology allows us to use methane generated in anaerobic condition for cooking or lighting. The organic cycle system can provide sustainable economic, social, and environmental aspects out of organic waste. Moreover, if organic cycle system is developed with circular economy system model, it will give a good local economic. The development of circular economy does not only utilize organic waste but also practice a profitable business from organic waste [3]. The circular economy in livestock sector means maximizing natural resource yields by circulating the production

[4] for example by turning livestock waste into energy. Today, the development of circular economy model in livestock sector does not only change waste into energy but also waste into material.

In biogas production, the waste will produce solid by-product like biogas sludge. Many reported the use of biogas sludge for fertilizing [5]-[6]. The studies about the use of biogas sludge as biochar are still rarealthough biochar has the economic added value. Biochar is a solid material obtained from thermochemical conversion of biomass in limitless oxygen condition [7]. Biochar is commonly used as soil enrichment. In this study, we tried to investigate biogas sludge utilization as biochar for biogas purification.

METHODOLOGY

Materials

Biogas sludge from cow manure is used for raw material in biochar production. Before the biochar production process beginned, biogas sludge was dried under the sunlight for 24 hours. Then dried biogas sludge was pyrolyzed at 225^{o}C for four hours in pyrolysis reactor. The pyrolysis of biogas sludge generated biochar that can be used for biogas purification.

Biogas Purification

Biogas purification is a method to clean biogas content from impurities such as carbon dioxide, hydrogen sulfide, volatile organic compound, et cetera [8]. In this study, we investigated the utilization of biogas sludge-basedbiochar to capture carbon dioxide in biogas. Carbon dioxide capturing on the surface of biochar was expected to increase methane composition and calorific value.

The increasing number of biogas plants will also increase adsorbent demand. To fulfill the demand, biochar production from biogas sludge will be an alternative solution.

Biogas purification was carried out by the adsorption method with two integrated adsorption columns. The length and diameter of the column was 200 mm and 40 mm respectively (Fig. 1). The design of the column was adopted from Lalhmingsanga [9] with modification.

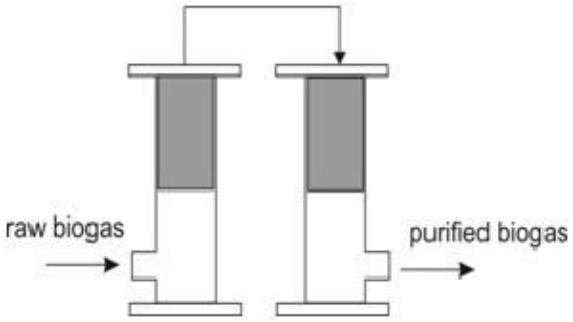

Fig. 1. Design of adsorption column [10]

Each column contained 80 grams of adsorption. The composition formulation of adsorbents is shown in Table 1.

Table 1. Formulation of adsorbents in biogas purification

Samples	zeolite (grams)	biochar (grams)
AS 1	80	0
AS 2	60	20
AS 3	40	40
AS 4	20	60
AS 5	0	80

The adsorption process was carried out at gas pressure ranged between 5-7 bar for 10 minutes. The methane compositions in biogas were analyzed by gas chromatography (GC).

RESULTS AND DISCUSSION

Biogas Purification

Biogas purification aims to minimize impurities in biogas such as carbon dioxide and increase its methane composition. Before and after the adsorption, the composition of biogas was analyzed using gas chromatography (GC). In this study, the capability of biochar to capture carbon dioxide (CO_2) was shown by the increase in methane (CH_4) composition. The biogas compositions before and after the adsorption are presented in Table 2.

Table 2. Methane compositions in biogas before and after adsorption

Samples	CH_4 before adsorption (ppm)	CH_4 after adsorption (ppm)	The increase in CH_4 (%)
AS 1	139448.78	140112.10	0.48
AS 2	138768.05	148754.20	7.20

AS 3	103153.36	126439.67	22.57
AS 4	113874.55	120584.95	5.89
AS 5	148599.30	143036.02	-3.74

Table 2 shows that after the adsorption using biogas sludge-based biochar, the methane in biogas increased. It means the biochar was capable to capture carbon dioxide. The performance of livestock waste-based biochar in capturing carbon dioxide is also reported by Minh-Viet and Byeong [11]. The combination of zeolite and biochar that could increase methane were AS 1, AS 2, AS 3, and AS 4. Carbon dioxide adsorption capacity at different mass of biochar resulted in different methane enrichment. The increase in methane performed by AS 1 was the lowest increase (0.48%). The higher increase in methane was performed by AS 2 (7.20%). By adding biochar composition in the combination of adsorbent, methane content increased. The highest methane enrichment was performed by AS 3 with the composition of 40 grams of zeolite and 40 grams of biochar.

Biochar is a solid material formed by thermochemical decomposition of biomass.The main element of biochar is carbon (C). Because of the carbonization process, biochar has a porous structure that can be used to capture carbon dioxide [12]. The surface pores of biochar havea key role in capturing carbon dioxide so the increase of biochar mass will increase the surface pores of biochar [13]. However, the increase in methane was lower compared to AS 3 when biochar was added to be 60 grams. Even the use of 80 grams of biochar actually decreased the methane composition of biogas from 148599.30 ppm to 143036.02 ppm. In other words, there was a decrease of -3.74% in methane concentration.

Previous study reported that biochar captures carbon dioxide more than methane [14]. It means biochar can adsorb methane, but not as much as adsorbing carbon dioxide. In fact, the use of 80 grams of biochar under these conditions caused the reduction of methane. It was possible that carbon dioxide had been maximally adsorbed and in these conditions, methane was also adsorbed.

The optimum combination of adsorbent in this study was performed by AS 3 with the formulation of 40 grams zeolite and 40 grams of biochar (see Fig. 2).

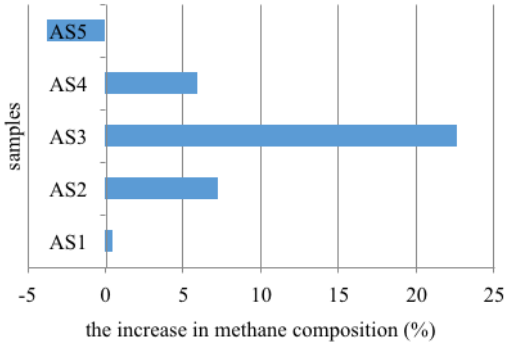

Fig. 2 The increase in methane composition after adsorption using AS 1, As 2, AS 3, AS 4, and AS 5

Recommendation of Organic Cycle System in Biogas Technology

Based on this study, biochar from biogas sludge has the potential to be developed to advance carbon dioxide capturing in biogas purification. Although this investigation is an initial study but the use of biogas sludge as biochar for biogas purification will lead to organic cycle system and circular economy.

Therefore, in this study we recommended a new concept in biogas system that is integrated with biogas purification using biogas sludge. Biogas sludge was recycled to be adsorbent in biogas purification. This concept aims to develop a model that has no effect on environment and ensure that there is no reduction in waste production [15]. It also becomes a solution in managing livestock waste, upgrading the quality of biogas, and increasing self-sufficiency energy. Moreover, biochar that have been used for purification can be used as soil enrichment. In this concept, no waste is wasted.

Biochar utilization that is integrated with biogas system is appealing because it is a safer method of organic waste management. The concept of organic cycle system in biogas system is shown in Fig. 3.

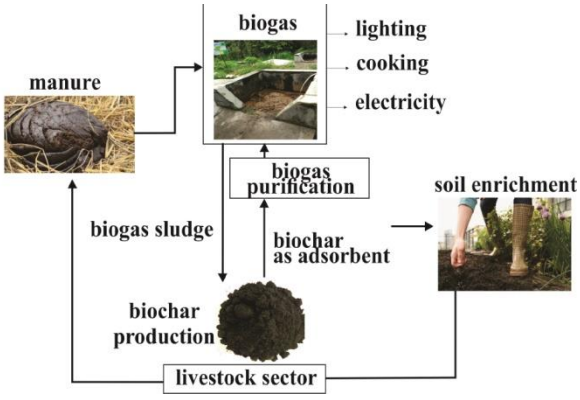

Fig. 3. Concept of organic cycle system in biogas

system

CONCLUSIONS

From this study we concluded that the optimum mass of biochar in the combination of adsorbent for biogas purification was 40 grams. The combination of zeolite and biochar with the composition of 40:40 can increase 22.57% of methane composition in biogas compared to biogas before purification. In this study, the utilization of biochar from biogas sludge is more appealing in biogas system. Besides being able to increase methane composition in biogas purification, the concept of organic cycle system in biogas system leads to zero waste management.

ACKNOWLEDGMENTS

The research was supported by Grant Program from Gadjah Mada University, Indonesia through PTUPT program. We gratefully acknowledge the support from USAID through the SHERA program – Centre for Development of Sustainable Region (CDSR). In year 2017-2021, CDSR is led by Center for Energy Studies - UGM. The authors also would like to thank the students of Faculty of Animal Science for the contribution in collecting the data.

REFERENCES

[1] Food and Agriculture Organization (FAO), *Livestock's Long Shadow: Environmental Issues and Options*, 2006, pp. 1-377.

[2] Ambar P., Cahyono A.D.K., and Margaretha A.W., "Renewable Energy of Biogas Through Integrated Organic Cycle System in Tropical System", *Energy Management for Sustainable Development*, 1st ed., 2018, pp.99-117.

[3] Trisha A.T., Shane W., Thomas O., Maria H., and Michael K.T., Agro-Cycle – "Developing A Circular Economy in Agriculture". *Energy Procedia*, 2017, pp.1-6.

[4] EIP-AGRI Agriculture & Innovation (Europe Commission), *Opportunities for Agriculture in Circular Economy*, 2015, pp.1-23.

[5] Nurzainah G. and Novilda E.M., "The Application of Biogas Sludge as Organic Fertilizer on The Growth of Spinach Plant", in *The Proceeding of The 2nd Annual International Conf*., 2012, pp. 154-156.

[6] Yoyo S. and Maswar, "Integration of Crop-Livestock-Biogas and The Effect of Dried Sludge Manure on The Growth and Yield of Maize on Ultisol Soil". *Agrivita*, 2014, Vol.2, No.2, pp.160-168.

[7] Simon S., Greet R., Kor Z., and Bruno G., Routledge, *Biochar in Europe Soils and Agriculture Science and Practice*. Taylor & Francis Group, 2016, pp.1-301.

[8] Irini A., Laura T., Panagiotis T., Gang L., Stefano C., Henrik W., Panagiotis G.K., "Biogas Upgrading and Utilization: Current Status and Perspectives". *Biotechnology Adv*., Vol.36, pp.452-466.

[9] Lalhmingsanga H. and Pinakeswar M., "Carbon Dioxide Adsorption on Zeolite and Activated Carbon by Pressure Swing Adsorption in Fixed Bed". *Int.J. Energy Environ. Eng*.,2014, Vol.5, pp.349-356.

[10] Ambar P., Margaretha A.W., Andang W.H., Rachmawan B., and Misri G., "Heating Value Enhancement by Biogas Purification Using Natural Zeolite and Rice-Straw-Based Biochar". *Int. J. of GEOMATE*, 2019, Vol.16, Issue 55, pp.80-85.

[11] Minh-Viet N. and Byeoung-Kyu L., "A Novel Removal of CO_2Using Nitrogen Doped Biochar Beads as A Green Adsorbent". *Process Safety and Environ. Protect*., 2016, Vol. 104, pp.490-498.

[12] Jin S.C., Sung H.P., Sang-Chul J., Changkook R., Jong-Ki J., Min-Chul S., and Young-Kwon P., "Production and Utilization of Biochar: A Review". *Journal of Industrial and Eng. Chem*., 2016, Vol. 40, pp.1-15.

[13] Yu-Fong H., Pei-Te C., Chun-Hao S., Shang-Lien L., Liping S., Yuan Z., and Chungsheng Q., *Microwave Pyrolysis of Rice Straw to Produce Biochar as An Adsorbents for CO_2 Capture*. Energy, 2015, Vol.84, pp.75-80.

[14] Anne E., Bin G., and Ming Z., "Carbon Dioxide Capture Using Biochar Produced from Sugarcane Bagasse and Hickory Wood". *Chem. Eng. Journal*, 2014, Vol. 249, pp.174-179.

[15] T.A. Toop, S. Ward, T. Hull O., M.E. Kirby, and M.K. Theodorou, Agrocycle – "Developing A Circular Economy in Agriculture". *Energy Procedia*, 2017, pp.1-6.

9th Int. Conf. on Geotechnique, Construction Materials and Environment, Tokyo, Japan, 20-22 November 2019, ISBN: 978-4-909106025 C3051

SEMANTIC OUTLINES OF MODERN GEOGRAPHY

Viacheslav D. Sukhorukov, Yuriy N. Gladkiy
Herzen University, 48, Moika Emb., St. Petersburg, Russia, 191186
E-mail: suhor@herzen.spb.ru; gladky43@rambler.ru

ABSTRACT

The authors consider the process of geographical knowledge of spatial reality, perceived as a multi-level structure. The image of geographical science is presented in new contour lines and research opportunities. There is hardly sufficient reason for geographers to "privatize" space – one of the three categories of the world (space, time and matter), since all Sciences have spatial quality. Geography is not a "super science" of spatial relations, since this assumption automatically narrows the field of study of many other Sciences, as well as can not be considered a generalizing or law-making science of spatial relations. It is argued that by its very nature topology does not and cannot answer the basic question of geography about the identification of the subject of science. The authors' position is reduced to rethinking the structural content of modern geography and actualization of its subject image. This does not change the main object of geography - connections, interactions, circuits, correlation relations, etc., confined to a specific spatial arena and beyond the microcosm. The role of praxiology - the doctrine of human activity, the realization of human values in real life-is increasing.

Key words: geographic factology, geographical phenomenology, geographic modeling, geographical conceptology, geographical praxeology, popularization of geographical knowledge.

INTRODUCTION

The public and disciplinary status of any area of knowledge depends on condition of a subject, semantic depths, presence (or absence) paradigm effect, a method, a point of view (and, certainly, degrees of error of the scientist). A number of knowledge, including geographical, is distinguished by its multifunctionality, being simultaneously a *science* and *not a science*. Some geographers operate with measures of scientists, others with measures of travelers or specialists in art. It is remarkable the lot of philosophy in which frameworks (natural philosophy) the first geographical views have been arisen. Today it doesn't serve neither to the science s nor theology though we can duffer in it the scientific and religious philosophy together with existentialism, postmodernism etc. Therefore the statement about existence of different kinds of philosophical knowledge is fair. Acting as a reflection over the world outlook universalism, basic values of culture, the philosophy has as though passed in the development two stages: the first associates with transformation universalism of cultures in philosophical categories (here vainly to search for visible scientific achievements); the second - it is connected with judgment primary category samples turning to strict definitions with which philosophers operate as theoretical ideal constructions. In this being the philosophy appears as enough strict theoretical science in spite of the fact that it contains obviously unscientific components in other quality.

It is known the part of knowledge exists at a joint of social, natural and existential, in "a backlash" (in "a condensation kernel") between objective and subjective, natural-scientific and humanitarian. (Hence, the "vicious" division of sciences into natural and humanitarian, their vision in a "black-and-white" range). This knowledge in many respects associates with *geography in general and in particular with human geography*.

Geography deals with the study of the earth's space. It is believed that the earthly reality for the past time thoroughly studied geography, so now it remains only information and didactic functions. However, the world is conceived by an extended eternity, rejected from direct vision. Therefore, the power of geography is now moving into the semantic area, which is proportional to the experiences and feelings of life. This orientation of comprehension of space clearly distinguishes modern geography among other areas of knowledge.

PURPOSE AND METHOD OF STUDY

Now modern geographical science understands the subject of all that is required in the act of judgment, representation and sense of spatial reality through the stages of self-consciousness, culture, morality, art, religion, philosophy. The embodiment of the world now takes place in a plentiful and polysemous association of images, closely related to the semantic experience of understanding space. That is, the scope of the current geography includes not only the universality of natural nature, built on the principle of determinism, but summarizes the

total existence, located outside the predicates of physical phenomena.

The aim of this study is to highlight the main cognitive projections of the new geography. In this case, the leading method the authors recognize *the idiographic analysis* of structural and cognitive levels of geographical science in the context of a holistic perception of theory and practice. At the same time, *the homothetic approach* advocated by many theorists of geography (the essence of which is to establish laws, to quantify geography, to mathematize it, to develop isomorphic models of spatial structures, etc.), is considered by the authors to be at best auxiliary in relation to the homothetic.

RESEARCH RESULT

Geographical Factology

Geographical knowledge contains a huge amount of empirical and factual information and materials. The study of facts and methods of their knowledge as a result provides scientific comprehension of geographical reality. Thus, geographical factology is the area of scientific knowledge about the methods of description and analysis of geographical objects, phenomena and processes in order to systematize them.

Geographical fact is a phenomenon, event or process realized by the researcher, the reliability of which corresponds to objective reality and is established empirically. Many questions arise here. For example, should geography study the whole complex system of supra-biological programs of human activity or only its separate fragments? Is it not more logical to put the external, materialized, objectified part of history related to the real geospheres into the subject field of cultural geography research, and to leave the culture that is fixed in the mentality, morals, customs, in the living experience of people's life together, mainly to the representatives of related sciences? Where are the boundaries separating cultural geography from economic and social geography, sociology, philosophy of culture, cultural anthropology, cultural studies, cognitive psychology?

Phenomenological approach in geography (rooted in the works of *Carl Sauer*), can be perceived as a valuable scientific reflection only when it comes to the study of perception and subconscious structuring of the natural environment and geospatial, the assessment of the quality of the natural environment (with access to the project and district planning), and even when subjected to the analysis of works of art, to illuminate the pages of paleography (how the landscape of a country). In those cases, when instead of facts it is proposed to study the perception of phenomena and to distinguish the relationship between them by means of visual, auditory or taste sensations, we can not talk about valuable scientific rationality. Recall: in phenomenology, a special place is given to imagination, fantasy (for *Edmund Husserl* - German philosopher, founder of phenomenology fantasy is more important than perception!), giving the possibility of free, unlimited variation of examples necessary for the comprehension of the essence.

Thus, the concept of fact in geographical knowledge remains one of the most difficult, since spatial givens are based on the multiple nature of what is happening. Therefore, the boundaries of geographical fact are usually fixed by its meaning and logical position of the researcher.

It should be emphasized that in spatial reality the fact can not only appear, exist, but also disappear. This suggests that the fact of science must be present in a holistic system of geographical knowledge, in the operational, semantic and conceptual sections of the entire subject area of geography. In these meanings, geographical fact embodies the semantic structure and information potential of space.

The formation of geographical fact is carried out by means of factual search in the logic of understanding and explanation of the object under study. This means that the actual data in geography are of particular value for science and practice. In this case, the description of the facts without their analysis and generalization (*factography*) is usually used to characterize the experience or for other purposes. Systematized facts that reflect the essence of the studied object, the connection between phenomena and events (*factology*), reveal features of the organization of individual components into the whole process. Thus, factography and factology to create the *texture* of the geographical space. On its basis the General statements having explanatory power are formulated [4].

Geographical facts have multiple parameters and characteristics by which the regularities of spatial reality are fixed. Interpretation of geographical facts can be carried out in various ways and techniques. The intensive development of geographical factology in recent decades has led to the formation of a special science - *geoinformatics*, which is engaged in the collection, processing and presentation of information about the properties of objects, processes and phenomena occurring on Earth. Geographic information systems (GIS) databases are used to gain new knowledge and to solve practical problems. Figuratively speaking, GIS technologies in geography are simultaneously “a telescope, a microscope and a computer” [3].

Geographical Phenomenology

Phenomenology is a field of research that contains the roots of various sciences and concentrates the researcher’s attention on the

problem of perception of space and space. The leading approach of phenomenology is the description of "animate natural reality." At the same time, phenomenology reveals the "sources" from which the basic concepts and ideal laws of pure logic "flow". In turn, the latter should provide the required understanding of the subject, “clarity and distinctness” of concepts and laws, which give objective knowledge and theoretical unity to all knowledge. Consequently, phenomenology means the seizure of objects, “that everything subject to analysis should be worked through in direct demonstration and direct proof” [6], [7].

If a phenomenon is considered only what constitutes being, then phenomenology in turn implies a descriptive philosophical method capable of providing science with reliable cognitive tools. At the same time, phenomenology is not limited to the “real” orientation. Above the reality is the opportunity. Therefore, phenomenology embraces realities and opportunities, the present and the future. Thus, geographical phenomenology is a conscious experience of the embodiment of spatial reality and possibility, represented by unique essential attributes. In the study of phenomenal images of space, the phenomenological methodology of knowledge should be decisive as a dialectical translational movement from sensual immediacy through the stages of science to “absolute knowledge” [5]. The thinking of such a plan is capable of producing a kind of phenomenological reduction, meaning the reduction of being to phenomena and putting the world beyond the brackets. The most important feature of this consciousness is its intensity, that is, the focus on any object. The “entities” generated in this way have the meaning of “individual data” belonging to the corresponding “essence”. In other words, the universality of entities and constituent of the ultimate task of geographical phenomenology. Consequently, the phenomenological consciousness is the reliance of the world, that is, a direct focus on this, on the subject of "intensionality". As a result of the “Intentional Experience”, the world becomes a “world phenomenon”. In this sense, phenomenological attitudes make it possible to construct such structures of being that are of ideal subjectness for a particular person. These actions are carried out in the experiences of consciousness that give rise to the value meaning of geographic space in its “intensionality” images [7].

With the help of phenomenological consciousness, all kinds of theoretical dualisms are overcome. At the same time, the human world, in essence, turns into “for-itself-being”. Hence, a person strives to become being itself, and any human desire is only a lack of being [5].

This imperative sets a perfectly defined ontology, in which the external world is viewed as permeable to a person and possessing the necessary semantic density. This world has its own tension, able to bring outrage in the field of human consciousness and action. Such a world becomes transparent to the thinking individual. This semantic substantiality means that in every decision a person chooses the whole world.

Geographic Modeling

Modeling as a method of knowledge acts as an intermediate link connecting the object of study with the subject. At the same time, modeling is an integral part of a scientific concept, a kind of skeleton of theory. Much has already been said about the role of modeling and the significance of models in geography. In general, it can be argued that geographical modeling is the process of constructing and researching a standard image of a spatial object, on which scientific theory and practice are oriented.

The whole process of geographical modeling is based on the structural limitation of the qualitative content of the object to be cognized. The result is a strictly defined structure that covers only the elements and relationships of a certain composition and character. It follows that for large geographic complexes the stock of models is practically unlimited.

The final stage of the simulation is a mental or material realizable construction reflecting the object of study. The model allows you to formalize the analyzed problem and integrate a way of understanding and explaining the essence of a geographical phenomenon or process. At the same time, the model performs the function of scientific foresight, has a heuristic value, and provides for obtaining new object data hidden from empirical measurements.

The main tool of geographic modeling and search criteria for the optimization of spatial structures are now GIS technologies. With their help, it is possible to ensure the proportionality of the main ingredients of the geographical space. Efforts in this direction are focused on creating a universal model of the world.

Summarizing the accumulated experience, we can distinguish functional and dynamic models of geographic space. The first fixes the relationship of components within the space. The latter are designed to identify and analyze various state variables of the analyzed geographical objects.

Information models of natural complexes and world systems, which have received many interpretations, are particularly well known in geography. In the meantime, the causal matrix underlying the actual picture of geographic space is extremely complex. The tangle of systemic interdependence in the real world, in the words of

the American geographer W. Isard, is "truly monstrous." However, taking into account the concept of geographic space, its universal dominant is the space of human society. It localizes the socio-economic practice of people, which is a sphere of interaction between society and the natural environment.

Geographical Conceptology

A concept is a semantic unit of representation of one or another form of scientific judgment. This may be related to a concept, idea, theory, or training. They, in turn, determine the boundaries and scope of scientific knowledge development and the possibility of its transformation into reality [1].

Thus, the geographical conceptology is a system of views and considerations that reflect the scientific point of view in the form of ideas and constructive principles in explaining and changing the subject of the study.

The main attributes of geographical conceptology are social conditionality and the scientific and practical need for new ideas, but also the depth of the subject coverage and targeting of recommendations. The degree and level of conceptuality may vary. Therefore, there are many variants of geographical concepts - from scientific justifications and declarations to applied design and experimental actions.

The theoretical constructs of the classics of geographical science and authoritative modern scientists (including representatives of the regional economy) - *W. Christaller, N. Kolossovskii, T. Hagerstrand, F. Perroux, Yi-Fu Tuan, D. Harvey, E. Soja, D. Massey, B. Rodoman, M. Porter, P. Krugman,* etc, are outstanding examples of geographical conceptology. Despite the high level of abstraction of many geographical concepts, they tend to be problem-oriented. This is confirmed by the theories of geographical determinism, numerous concepts of regional development, etc. In the content of geographical conceptology, the most important fact is the process of transition from the essence of the interpreted object to the normative part. It provides a general idea of what should be considered an ideal and how this can be approached. Finally, the agreed standards are transformed into projects that acquire the language of practical action.

The set of geographical ideas, reflecting the measure of knowledge and scientific understanding of the studied spatial reality, creates a kind of conceptual field of geography. His condition is directly related to the structure and directions of development of geographical science. The current stage of the formation of the conceptual field of geography can be named by paradigmatic. Therefore, modern geographical studies use systems of developing concepts and explanatory procedures that correspond to the genesis and logic of science in understanding and constructing an ideal plan of action.

Geographical Praxeology

Praxiology is the doctrine of human activity, the realization of human values in real life. As a research area, it covers the sphere of socio-economic practice of society. the most developed section of praxiology now is sociological and economic theory. Geographical praxiology identifies special structural range of scientific disciplines, making effective substantive reflection of the achieved level of knowledge. thus, the essence of geographical praxiology is the research specifics and practical recommendations for the arrangement of geographical space. One of the clearest examples of geographical praxiology is *currently geopolitics*. now this term has a very wide circulation. Its frequent use directly or indirectly indicates the demand for geopolitical thought, the conceptual topic of which has a synthetic character. In this sense, geopolitics is a holistic methodology that explains the "attitude of the state and society to space" [2].

At least "praxeological" is also *geoeconomics*. It is a complex transregional economic space that includes economic, ethno-cultural and social structures aimed at long-term planning for large-scale redistribution of resources, financial flows and world income as the main source of systemic profit. There is an opinion, geoeconomics is a "global economic federation, a kind of way of intensive economic development of the material world" [10].

Special praxeological role of *geoecology*. It is based on the idea of reasonable interaction of geographical space and human society. This is a kind of reaction of public consciousness, which came to understand the place of man in nature. The core of modern geo-ecology is the phenomenon of the value of the world and the self-value of life in general. To date, this idea of geoecology has become widespread and of global importance [8], [11]. Of course, the mentioned areas of "modernistic" scientific knowledge do not reduce the enormous role of traditional scientific disciplines: physical geography, economic, social, etc.

Popularization of geographical knowledge

The main organizational form uniting geographers of the whole world is the international geographical union (IGU), established in 1922. The international geographical union has the following main goals:

1. To promote the study of geographic problems;
2. Initiate and coordinate geographic research requiring international cooperation, ensure their

broad scientific discussion and publication of results;

3. To ensure the participation of geographers in the work of international organizations;

4. Assist in improving the collection and dissemination of geographic data and documentation;

5. To facilitate the holding of International Geographical Congresses, regional conferences and specialized symposia, the themes of which correspond to the goals of the Union.

6. Participate in any other forms of international cooperation to promote geographical research and the application of their results in practice;

7. To promote international standardization and unification of methods, nomenclature and symbols used in geography.

Geographical societies also play a huge role in the popularization of geographical knowledge. One of the oldest and most honored is the Russian Geographical Society (RGS), founded in 1845. Its founders, among whom were well-known naturalists, travelers and seafarers, identified the cultivation of Russia's geography as the main task of the Russian Geographical Society.

Today, the Russian Geographical Society is an all-Russian public organization that unites almost 30 thousand members in all constituent entities of the Russian Federation and abroad and has regional and local branches, as well as branches and representative offices throughout Russia. One of the priority tasks of the RGS now is the dissemination of geographical knowledge, propaganda of the achievements of domestic and world geography, education of geographical culture, assistance in improving the quality of geographical education among various age and professional groups of the population, teaching geography in secondary and higher education.

Currently, in Russia, in order to popularize geography and increase the prestige of the geographer's profession, a professional holiday is being set - Geographer's Day, which will be celebrated on August 18, the day the Russian Geographical Society was founded.

In Russia, the question is being considered of entering the All-Russian Classifier of the Geographers Study Group, the types of economic activities "Conducting Geographic Research" and the professional standard "Geographer". The establishment of centers for studying geography for schoolchildren at educational institutions of higher education, including within the framework of the national project "Education", is envisaged. The agenda also includes proposals for the implementation of measures aimed at improving the quality of teaching the subject "Geography" in general education organizations, taking into account the priorities and objectives of the scientific, technological and spatial development of the Russian Federation, as well as taking into account the results of monitoring and other forms of objective knowledge assessment students in the field of geography [12].

CONCLUSION

The above considerations lead to the following main generalizations:

- geographical science is constantly being improved, introduces new layers of knowledge into the sphere of its cognitive interest, which requires clarification of its semantic contours;
- modern geography is experiencing a pronounced humanitarian stage of its development, demonstrating a fundamental appeal to the human consciousness;
- in the development of geographical science significantly increases the role of praxiology - the doctrine of human activity, the implementation of human values in real life;
- geographical knowledge is currently embodying the integral representations of the "life world" [9], [13]. These areas of geographical thought also should be reflected in educational geography.

REFERENCES

[1] Bordovskaya N.V. The dialectics of pedagogical research: the Logical and methodological problems. - Sankt-Petersburg, 2001, p. 227.

[2] Dugin A.G. Geopolitics: the textbook for high schools. Moscow, 2011, pp. 4-5.

[3] Gladkiy Yu.N. Humanitarian geography: scientific explication. - Sankt-Petersburg, 2010, p. 625.

[4] Goldstein M., Goldstein I. How we know: an exploration of the scientific process. Moscow, 1984, pp. 42-43.

[5] Hegel G. Phenomenology of the Spirit. Philosophy of history. Moscow, 2007, pp. 458-471.

[6] Heidegger M. Being and time. Moscow, 2011, pp. 31, 35.

[7] Husserl E. Logical Studies. Vol. II. Part 1: Research on phenomenology and theory of knowledge. Moscow, 2011, pp. 8-9, 347-349.

[8] Kochurov B.I., Antipova A.V. Geography as a science for the future // Problems of regional ecology, №5, 2013, pp. 76-91.

[9] Mitin I.I. From cognitive geography to mythogeography: interpretations of space and place. Kazan, 2004, pp. 163-165.

[10] Neklessa A. Geo-Economics. Introduction to the problem. URL: http://tower-libertas.ru/research/ (Date of request 18.05.2019)

[11] Petrov K.M. The Ecology: Proc. benefit. Sankt-Petersburg, 2004, 274 p.

[12] President of Russia. The list of instructions on the popularization of geography. May 15, 2019. URL: http://kremlin.ru/acts/assignments/orders/60537 (Date of request 25.05.2019)

[13] Sukhorukov V.D. Cognitive levels of geography // Geography at school, №1, 2015, pp. 36-44.

9th Int. Conf. on Geotechnique, Construction Materials and Environment, Tokyo, Japan, 20-22 November 2019, ISBN: 978-4-909106025 C3051

ALTERNATIVE OPTIONS FOR ROAD MAINTENANCE MANAGEMENT IN BANGLADESH UNDER CLIMATE CHANGE CONDITION

M. R. Islam, S. M. Muniruzzaman, Md. K. A. Masud, S. S. Morshed
Department of Civil Engineering, Military Institute of Science and Technology, Bangladesh

ABSTRACT

Bangladesh is one of the worst climate vulnerable countries in the world. It is predicted that temperature and precipitation of the country will increase 1-3% and 20% respectively by 2050. Bangladesh being a flood prone country, roads in the low lying areas will likely to be flooded more frequently than before due to increased rainfall. The study has developed a methodology by Mechanistic-Empirical (M-E) method to find out the effect of moisture on the pavement. It has also provided solutions to minimize the additional damage due to traffic movement on the affected pavement. It is found that damage by a standard axle load during saturation period of 30 days is almost 3 times than that in dry condition. However, during 30 days of saturation if the axle is overloaded by 6 ton, damage is 20 times than that of a standard axle at dry condition. By M-E method it is found that imposing 30 % restriction on standard axle load during pavement saturation condition will minimize the additional damage. The outcome of the study will help road engineers of Bangladesh to combat with the climate change effect by adopting axle load restriction.

Keywords: Climate change, Mechanistic-Empirical method, Pavement saturation, Axle load restriction

INTRODUCTION

The climate change adaptation becomes more critical development issues for Bangladesh. According to scientists, it is predicted that temperature will increase 1-3% and precipitation 20% by 2050 in Bangladesh [1]. Moreover Bangladesh is a flood prone country. Flood water causes enormous damage to the road infrastructure of the country.

Although the road agency of Bangladesh requires 4-days soaked CBR value for design of pavement [2] but usual flooding duration is more than 4 days in Bangladesh and may increase in future. Due to increase in precipitation and flooding duration pavement will remain in saturated condition for longer time. Saturated layers of the pavement cannot bear the wheel load of the vehicle. So, pavement life will reduce and road maintenance cost will be increased. Moreover, increase in pavement temperature will affect the functioning of the asphalt layer and will reduce the pavement life.

However, it is important to quantify the pavement damage done by moisture. If quantification of the damage can be done it will be possible to show the significance of the problem. Since road infrastructure is the main mode of transport of goods and passengers in Bangladesh, it should be safe against adverse climate change effect. Moreover, a developing country like Bangladesh has a limited budget allocation for road construction and maintenance. So, road design, materials selection, and traffic loading should be such that road construction and maintenance become economic and durable.

The study has attempted to quantify the effect of moisture for a typical national highway with consideration of vehicle overloading. In Bangladesh, vehicle overloading is common as mentioned in the road master plan [3].To predict the life of the flexible pavement due to changes in saturation period, the study has adopted mechanistic-empirical (M-E) approach. However, dynamic effect of entrapped water due to vehicular movement is not considered in the study. In this study mechanistic analysis was done with a software GAMES (General Analysis on Multi-layered Elastic system). GAMES provide strain values at critical location of the pavement. Pavement life is then predicted by using empirical model of Asphalt Institute with the critical strain values. Finally it has suggested probable solutions to fight against the moisture effect.

METHODOLOGY

Moisture Effect on Pavement

Finding moisture effect on pavement is based on measuring the damage occurred during flood by a standard axle. Due to flooding, stiffness values of layers reduce. With the reduced stiffness values of layers, pavements will exhibit less fatigue and rutting strength. It is reported that reduction of strength of pavement can be 1.5% to 50% within a short time [4] .This means damage induced by a

single axle during flood will be more.

It is found that Marshall stability value decreases and flow value increases with the increase of inundation period [5].Marshall stability-flow ratio decreases to approximately 38% of the initial after 30 days of inundation as shown in figure 1. Stability-flow ratio is proportional with resilient modulus (M_r) of asphalt concrete [6]. Table 2 shows M_r value of HMA for different saturation period. In this study, assumed M_r for dry condition is reduced according to stability-flow ratio for different saturation period

. Figure 2 shows, if saturation period is 30 days, subgrade CBR value reduces to 89% - 69% of the 4-days soaked CBR value depending on the condition of compaction [6]. CBR value for subgrade is linearly correlated with the resilient modulus [7]. So, resilient modulus of the subgrade modulus also decreases with inundation period. Additionally, resilient modulus for base and sub-base layer is assumed to be decreased with same rate as that of subgrade value. In this study, M_r values for dry granular layers are determined from standard CBR values by using correlation charts developed by Van Til. et al.[7].Table 1 shows the resilient modulus (M_r) values for different saturation period. Table 2 shows the typical layer thickness values for a national highway of Bangladesh.

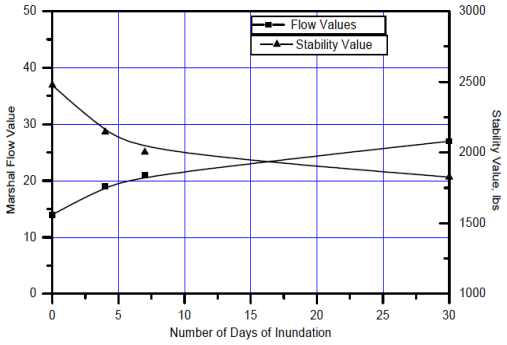

Fig. 1: Effect of inundation on CBR of subgrade. [5]

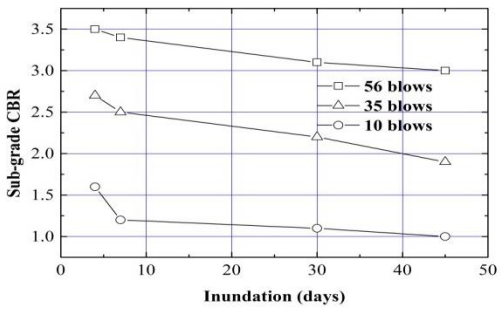

Figure 2: Effect of inundation on flow and stability of bituminous surface layer. [5]

Table 1 Values of Resilient Modulus (M_r) at saturated conditions

Layer	M_r (Mpa) for saturation period of			
	0 day	4 days	7 days	30 days
HMA	2760	1762	1488	1055
Base	210	210	158	144
Sub-base	140	140	105	96
ISG	83	83	62	57
Sub grade	62	62	47	43

Table 2 Layer properties of the highway.

Layer	Layer thickness(cm)	Poisson's ratio
HMA	12.5	0.30
Base	15	0.35
Sub-base	18	0.35
ISG	20	0.40
Sub grade	200	0.40

Axle Load

Standard single axle load for Bangladesh is 80 kN. However, to simulate overloading effect axle load of 100 kN, 120 kN, and 140 kN consecutively are also considered. Since overloading is a common practice in Bangladesh, it is taken into consideration while simulating saturation effect. Tire pressure for the study is considered to be 0.5 Mpa

Damage by a Standard Axle

Two failure mechanisms are considered to determine the damage done by a standard axle load. One is fatigue and another is rutting failure. To measure the pavement life, critical strain values are determined by general analysis of multi-layered elastic system (GAMES) software. Following steps have detailed the approach:

1. Resilient modulus (MR), Poisson's ratios, layer thicknesses and layer interface slip values, wheel load and tire pressure are needed as inputs to run GAMES.
2. To determine the fatigue and rutting life of the pavement, tensile strain value at the bottom of the asphalt layer and compressive strain value at the top of the subgrade layer as shown in Figure 3 is calculated first by GAMES. After getting the strain values for critical location of the pavement layers, life was predicted by Asphalt Institute model [8], [9].

$$N_{f_1} = 0.0796 {\varepsilon_t}^{-3.291} {E_1}^{-0.854} \quad (1)$$

$$N_{f_2} = 1.365E-07\varepsilon_v^{-4.477} \quad (2)$$

Where N_{f_1} = allowable number of load repetition to prevent fatigue cracking, N_{f_2} = allowable number of load repetition to prevent rutting cracking, ε_t = tensile strain at the bottom of Asphalt layer, ε_v = compressive strain at the top of sub-grade layer, E_1 = elastic modulus of asphalt layer.

Moreover, the damage (D_i) caused by each application of axle load is given by:

$$D_i = 1/N_i \quad (3)$$

Where N_i is the minimum number of load repetitions required to cause either fatigue or rutting failure.

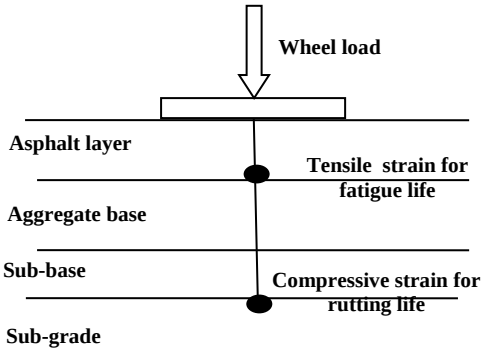

Fig. 3: Critical location of strain values for analysis.

RSULTS AND DISCUSSIONS

Moisture Effect on Pavement

From the Mechanistic-Empirical (M-E) analysis it is found that fatigue failure governs for the typical pavement of the national highway of Bangladesh as shown in the figure 4. Fatigue damage by a single axle is considered for making critical decision in this study as it is higher than that of rutting.

Figure 5 shows damage by a single standard and overloaded axle for different saturation periods. Here, damage are normalized by the damage value of a standard axle load during dry period. It is found that damage by a standard axle during 30 days of saturation period is approximately 3 times than that of dry period. Other study reveals that, the relative damage due to a single axle load for wet sections varies from 5 to 70,000 times in comparison to drained sections [10]. In this study it is found that if axle is overloaded by 6 ton the damage is approximately 20 times higher than that of dry period.

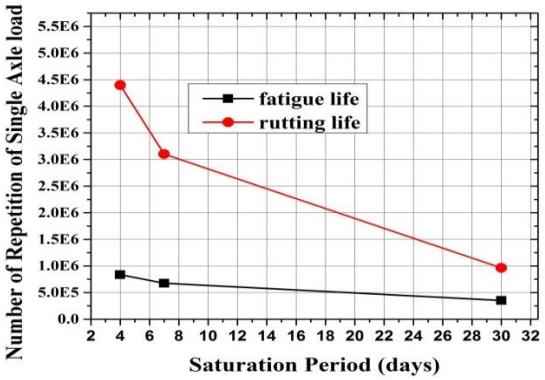

Fig. 4 Comparison between fatigue and rutting life of the pavement.

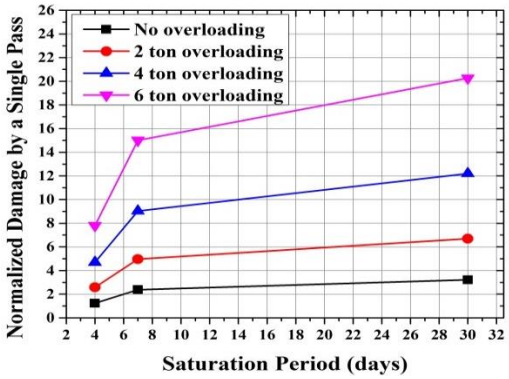

Fig. 5 Effect of saturation and overloading on pavement.

Figure 6 shows a standard axle in saturation period causing additional damage to the pavement. Actually, layer's stiffness reduces during saturation condition and hence the standard load causes additional damage. As a result, even if a standard axle load is allowed to pass during saturation condition pavement life will reduce drastically. However, we can prevent the pavement from losing its life by allowing a load less than the standard axle load so that it does not cause additional damage to the pavement.

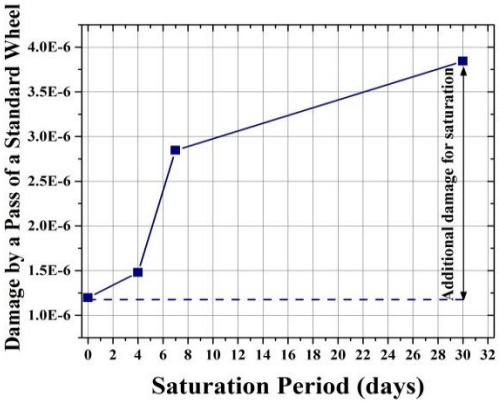

Fig. 6 Damage done by a single pass of a standard wheel load.

Figure 7 shows relationship between wheel load and damage for different saturation period of the pavement. By using the fitted equation shown in the figure 7, it is found that for a saturation period of 30 days a wheel load of approximately 28 kN causes the same damage as that of a 40kN wheel load in dry condition. If 70% of the standard axle load is allowed for the pavement with 30 days saturation period, it will not create additional damage. Figure 8 shows the allowable axle load for different saturation period. If axle load is restricted to the allowable limit until the dry back period of the pavement, its life will not reduce at all.

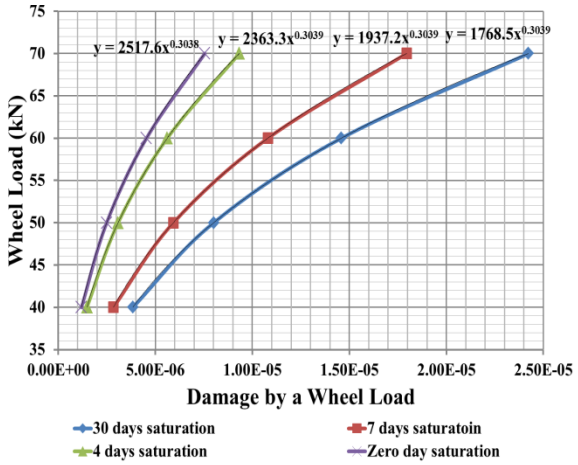

Fig. 7 Load damage correlation for different saturation periods.

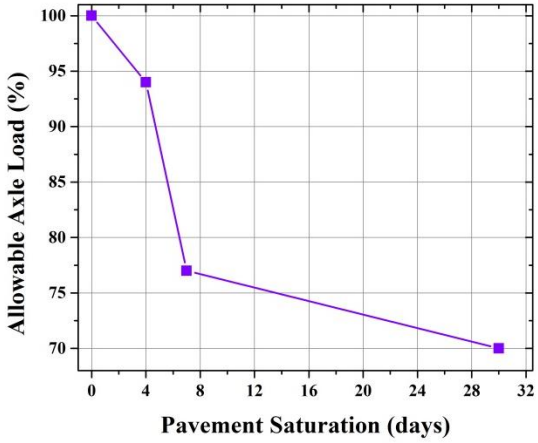

Fig. 8 Allowable axle load during saturation period.

CONCLUSION

The study has made an attempt to simulate the effect of climate change on roads of Bangladesh. It has developed a methodology for finding the effect of moisture by M-E method. It has also proposed a methodology to impose axle load restriction on pavement to minimize the moisture effect. The study concludes with the following findings :

1. Damage by a standard axle load to the 30-days saturated pavement is approximately 3 times of damage to the dry pavement.
2. However, damage by a 6 ton overloaded axle to the 30-days saturated pavement is 20 times of that by a standard axle to the dry pavement.
3. Reduction of the standard axle load will be necessary during saturation period to keep the pavement design life unaffected. For a sturation period of 30 days, 70% of the standard axle load should be allowed to minimize the effect of pavement saturation.
4. Moreover, overloading should be totally restricted during pavement saturation period.

REFERENCES

[1] The World Bank, "The cost of adapting to extreme weather events in a changing climate", Bangladesh Development Series, Paper No. 2, executive summary, pp. xiii, 2011.

[2] Ministry of Communication, "Technical specifications," Bangladesh Roads and Highways Department, Vol. 7, 2011.

[3] Ministry of Communication, Bangladesh, "Road master plan", Roads and Highways Department, Vol. 1, 2007

[4] Sultana, M. et al. "A review of the structural performance of flooded pavements", in the proc. 26th ARRB, 2014, pp.1-11, Sydney, New South Wales, Australia

[5] Alam, M. J. B. and Zakaria M., "Design and construction of roads in flood affected areas", Engineering Concerns of Floods a1998 Perspective. Directorate of Advisory, Extension and Research Services, BUET, Dhaka, Bangladesh, pp91-99, 2002.

[6] Ahmad H. Al-Zassar et. al., "Using Marshall test to assess asphalt-concrete modulus for mixes used in Kuwait", Kuwait J. Sci. Eng. 30(2), pp169-182, 2003.

[7] Mamlouk, M.S. "Design of flexible pavements", The Handbook of Highway Engineering edited by Fwa, T.F, Boca Raton, T& F groups, , 2006, ch.8, pp. 8.1-34.

[8] Huang, Y.H., Pavement Analysis and Design, Pearson Education, Inc., 2nd edition, 2004, ch. 11.

[9] Salem, H.M.A., "Effect of excess axle weights on pavement life", Emirates Journal for Engineering Research, 13 (1), 21-28, 2008.

[10] Gartin, R.S., Raad, L., "Mechanistic behavior of saturated cohesionless layers in pavements", Report no. INE/TRC 92.06, Transportation Research Center, Institute of Northern Engineering, School of Engineering, University of Alaska Fairbanks, AK 99775:1- 2, 1992

9th Int. Conf. on Geotechnique, Construction Materials and Environment, Tokyo, Japan, 20-22 November 2019, ISBN: 978-4-909106025 C3051

QUANTITATIVE EVALUATION OF WATER POLLUTANT LOAD FROM KINOKAWA RIVER BASIN BY HIGH-FREQUENCY WATER QUALITY OBSERVATION

Hiroto Tanouchi[1], **Akihisa Imoto**[1], **Kouichi Ishiura**[1] and **Nobuyuki Egusa**[1]
[1]Faculty of Systems Engineering, Wakayama University, Japan

ABSTRACT

In the Kinokawa river basin, as same as other watersheds around the world, excess runoff of nutrients to the ocean mainly due to human activities has become an environmental issue. This study conducted high-frequency total nitrogen (TN) and total phosphorus (TP) monitoring at several monitoring posts along the Kinokawa river in the Kii peninsula, Japan in order to evaluate water pollutant load from the basin quantitatively. The water sampling has been conducted about 90 times for over a year from May in 2018 at several monitoring posts set along the downstream of the Kinokawa river. In the calm or the drought periods, TN concentration at Kinokawa river mouth were basically about 0.8 ~ 1.1 mg/L, TP were under 0.05 mg/L. On the other hand, TN concentrations could exceed 5.0 mg/L after one of the most intense storms, it was shown the TN concentration had a tendency extremely to rise especially in flooding condition. This tendency was similar in TP. In addition, the results of analysis including flow rate indicated that about 65% of the nitrogen load and 80 % of the phosphorus load from the basin was generated during a few and heavy flooding which were included in 5 % flow exceedance probability. These results suggested that almost all pollutant loads from basin was occurred in flooding conditions. It was also implied an improvement of the prediction accuracy of nutrient runoff simulation during flooding condition was vitally important.

Keywords: Pollutant loads, River water quality, Total nitrogen, Flooding, Kinokawa river basin

INTRODUCTION

Water quality conservation of rivers, lakes and ocean has still been a global issue. Therefore, a number of water quality observations and numerical analyses aiming at elucidating nutrients runoff mechanism has been conducted around the world. Donald and William (2001) showed that nitrogen flux from the basin to Gulf of Mexico was significantly increased in 1970s by using nitrogen concentration data of Mississippi river water during 100 years [1]. As studies targeting smaller spatial scale, [2] compared pollutant loads of pre-European settlement with ones of current into Great Barrier Reef by using numerical model. They utilized ten kind of pollutant substances as indicators, almost all substances increased over 5 times from pre-European settlement. We also evaluated water quality and pollutant loads targeting in Kinokawa river basin, which is also the target basin in this study, by using numerical water-nutrient runoff model [3]. This study showed the indicator "2-MIB" tended to increase when total phosphorus (TP) concentration exceeded 0.02 mg/L. It was concluded that the measures to combine TP mass load reduction with an increase in river flow rate could reduce TP concentration to less than 0.015 mg/L and prevent increases in 2-MIB in tap water.

As well as long-term fluctuation characteristic, extreme events like storm and resulting floodings are also important in river and ocean water quality. Several studies indicated almost all nutrients flux were generated by floodings. [4] conducted stormwater nutrients monitoring at the monitoring posts distributed whole Singapore. In [4], it was ascertained parklands could become main nutrient sources, including TN, TP and TSS in urbanized area. Although [5] also targeted in urbanized watershed in Korea to indicate mainly source of nutrients based on water quality monitoring, they concluded it was difficult to determine the non-point source by specific characteristics such as land cover.

These studies suggested nutrient runoff mechanism driven by storm has not explained well still now. In order to reveal the mechanism of nutrient runoff, there remains a need for an accumulation of nutrient monitoring data in a various of basins. In addition, former studies to evaluate flooding influence mainly targeted on small/urban scale runoff phenomena, water quality monitoring data including flooding condition on the watersheds with middle or large spatial scale (>1000km^2) is insufficient.

In this study, firstly we conducted high-frequency water quality observation in downstream of Kinokawa river in order to accumulate vital data to understand the system of nutrient runoff. River water was sampled manually once every three or four days at four observation points on bridges. Then we estimated relationships between water volume and

TN/TP concentrations. Finally, the estimated river flow rates were multiplied by estimated concentrations of TN and TP, we calculated the all nutrient loads from the Kinokawa river basin.

STUDY AREA

Figure 1 shows the land use in 2014 and observation points to sample river water. The length of Kinokawa river is about 136km, total watershed area is about 1750km^2. The basin extends from east to west, and after passing through the mountainous area in the eastern area (central massif of Kii peninsula), the river flows to the east and flows into the Seto Inland Sea. Majority of land use is forest (about 75%), followed by agricultural fields (farmland and rice paddy fields were 10% and 6%, respectively). Urbanized areas are concentrated downstream area, and the ratio of cities to the total is 9%. We conducted 80~90 times of water sampling from Musota bridge, Iwade bridge, Isaka bridge (across Kinokawa main river) and Kitajima bridge (across Kishi river, a large branch of Kinokawa river). In addition, we sampled water at the mouth of small canal and tributaries located between Musota and Iwade (1) ~ 4)) on 2018/6/15 in order to evaluate the influence of small water flows.

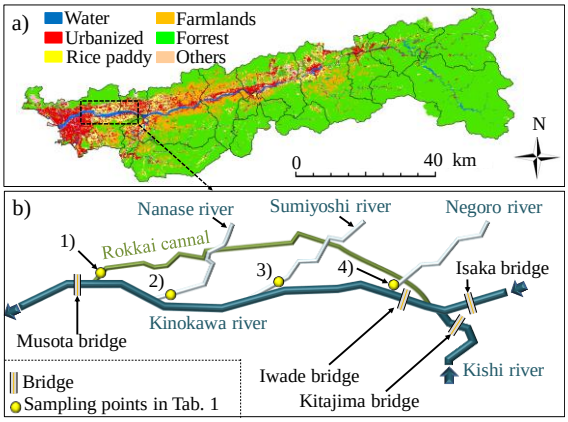

Fig. 1 a) Land use map in Kinokawa river basin based on Land Use Fragmented Mesh Data [6] and b) a thematic map indicated flow paths of Kinokawa main river and branches, canal, bridges and points we conducted water sampling. The numbers of sampling points were corresponding to ones of Tab. 1.

METHODOLOGY

River Water Sampling

Samplings were performed by lowering tinplate bucket from center of Musota bridge, Iwade bridge, Isaka bridge and Kitajima bridge. Drowned water by the bucket was put in polyethylene bottle, immediately installed in a cooler and kept to cold. Here, temperature in the cooler was kept about 2 ~ 8 degrees Celsius. Sampled waters were chemically analyzed basically within 4 hours after sampling. In this article, we mainly analysed and discussed about nutrients concentrations observed at Musota and Iwade.

Measurement of TN and TP concentrations

Figure 2 shows equipment for chemical analysis to measure TN concentration and TP concentration. TN and TP concentrations were estimated by TNP-10 produced by TOA DKK [7]. TN concentration was measured based on peroxodisulfate 120°C decomposition method [8]. In this method, firstly all nitrogen compounds are replaced into nitrate ion. Secondly nitrate ion is reduced to nitrite ion. Then, sulfanilamide added into chemical sample is diazotized by nitrite ion. Finally, the absorbance of the red azo compound formed by adding N-1-naphthylethylenediamine to the sample is measured to estimate the concentration.

Fig. 2 Equipment for chemical analysis to measure Total Nitrogen (TN) concentration and Total Phosphorus (TP).

TP concentration was measured based on peroxodisulfate 120°C decomposition method [8]. Here, all phosphorus compounds are firstly oxidized to phosphate ion by added acidic reagent to the sample. Then a mixed solution of ammonium molybdate and ascorbic acid is added to the sample. Finally, the absorbance is measured to determine the concentration of TP.

The detection limits for TN concentration and TP concentration in this device are 0.2 mg / L or more and 0.05 mg / L or more, respectively. Detected values below these limitations are untrustworthy.

Flow Rate Estimation

In this study, hourly river flow rate was estimated by using hourly time series data of water level and rating curve. hourly water level data observed at Funado (almost at the same place as Iwade) water level observation station has been provided by

Japanese ministry of land, infrastructure, transport and tourism [8]. The rating curve at Funado station was also developed by the ministry, we used this curve directly. Although the rating curve is state of the art we can obtain, it was optimized to calculate 2016's flow rate. In addition, the scope to apply this curve was obviously stated, heavy flooding that water levels exceed 2.93m and strong drought with water levels below -1.25m out of applicable. However, the rating curve was also applied in this study to calculate the flow rate under the un-applicable range because of no other way to estimate flow rate. Note that errors of flow rate under extreme storm/drought events could be large.

Estimation of Flow Rate - Concentration Relationship

We created regression lines of flow rate and TN/TP concentrations based on the assumption that there is a linear relationship between the flow rate at Funado and the TN and TP concentration at Iwade and Musota, respectively. Although this assumption might not appropriate for expression of nutrient runoff, we adopted it because of model simplification. This obvious weak point to express relationship between flow rate and nutrient concentrations should be discussed in future study. The reason why we used Musota's TP concentration data instead of Iwade's data here was because Musota had more data, and data on extreme phenomena such as floodings and droughts were also abundant.

Annual Pollutant Loads Estimation

Hourly TN and TP pollutant loads from Kinokawa river basin for target period were calculated by multiplying the flow rate at Hunado by the nutrient concentrations estimated by the regression lines. Secondly, we created flow duration curves of water quantity, hourly loads of TN and TP. Then, we, we estimated TN load and TP load that runoff in the top 5% of the flow rate in the target period, and calculated the ratio of them in the all pollutant loads. By this comparison, we evaluated flooding impact in total nutrient loads quantitatively.

RESULTS AND DISCUSSION

Temporal Variation of TN/TP Concentrations

Figure 3 shows flow rate at Funado station and TN, TP concentrations of river water at Musota bridge and Iwade bridge from 2018/5/15 to 2019/6/10. Average TN concentration for whole observation period at Musota and Iwade were 1.00 mg/L and 0.87 mg/L, respectively. Although TP was monitored simultaneously, TP concentrations were basically under detection limit. Therefore, we discussed about TN concentrations here.

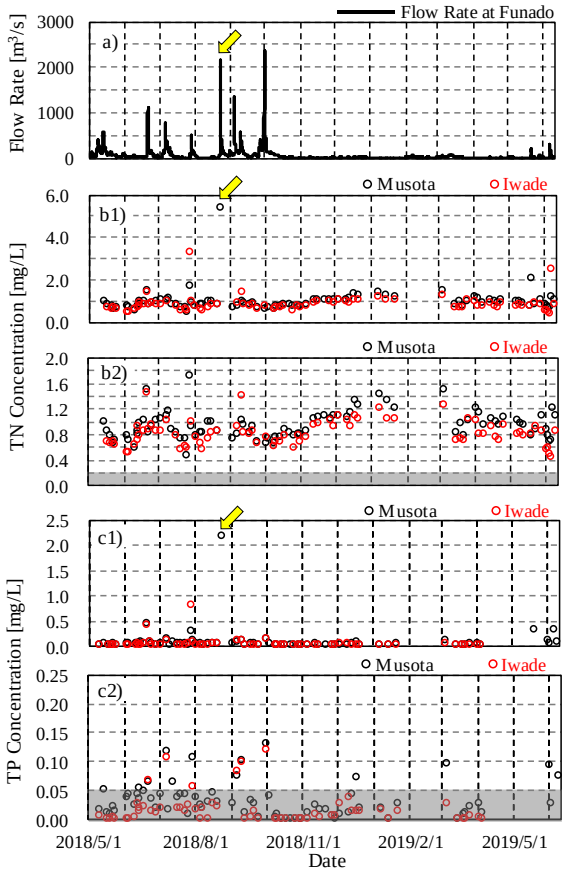

Fig. 3 a) Flow rate estimated at Funado water level station, b1) & b2) TN concentrations observed at Musota bridge and Iwade bridge, c1) & c2) TP concentrations observed at Musota bridge and Iwade bridge. b2) & c2) are engaged figures of b1) and c1). Yellow arrow shows the observation on 2018/8/24. Grey masks in b2) and c2) indicate under detectable limitations.

Fig.3 b2) indicates Musota's TN concentrations were chronically about 0.1~0.2 higher than Iwade's ones on the same date. This tendency implied the possibility that inflows with high TN from small tributaries or agricultural canal influenced total environment on Kinokawa river. Therefore, we conducted additional TN concentration observations at the mouths of these tributaries and canal. Fig. 1 also shows a map of tributaries/canal between Musota and Iwade. Table 1 shows TN concentrations observed at the mouth of each tributary or canal on 2018/6/15, all of them seems to be sampled under calm condition. The concentrations of TN at Musota and Iwade on June 15, 2018 were 0.98 mg / L and 0.79 mg/L, respectively. Although all TN concentrations of them were higher than ones of main Kinokawa river, Rokkai canal located at about 500 m

upper Musota bridge was especially higher than the others. Therefore, inflow from Rokkai canal mainly could influence for Kinokawa river environment.

Table 1 TN concentrations observed at 1)Rokkai canal, 2)Nanase tributary, 3)Sumiyoshi tributary and 4)Negoro tributary. 1)~ 4) were sampled at the mouth of them on 2018/6/15.

	1)	2)	3)	4)
Sampling time	8:28	8:45	9:00	9:17
TN[mg/L]	2.00	1.27	1.48	1.76

Rokkai canal supplies water for rice paddies located in right bank of the Kinokawa Plain. The canal was opened only when irrigation period (2018/6/1~2018/9/30), no water flowed except this perido. The upstream end of the irrigation canal is located about 500 m upstream of the Iwade Bridge, and it is designed that water of 4.96 m^3/s is always withdrawn from the Kinokawa river. Although the exact flow rate has not been confirmed, a portion of the water irrigated by the rice paddy fields will return to the canal and finally re-enter the Kino River at 1). Such hypothesis could be reasonable, however, it was difficult to prove them quantitatively due to the lack of TN observation data so far. In addition, since the discharge data of channel and tributaries are also insufficient either, data accumulation of TN concentration and flow rate to assess of agricultural activities in the Kinokawa plains will be necessary.

Fig. 3 also shows that there were the data observed extremely high concentrations of TN and TP, such as 2018/8/24 (Yellow arraied points). High TN and TP concentrations were tended to be generated when flow rate at Funado were getting over 200m^3/s, which was equivalent to 3 times of average flow rate in target period (62.9m^3/s). Figure 4 shows relationships between flow rate at Funado and the concentrations. Because the number of TN concentration data was totally 90, we considered TN data could be analyzed statistically here. On the other hand, TP concentrate data at Iwade whose values exceeded 0.05 mg/L (detection limit) were only two. Therefore, we utilized TP concentration data at Musota insteadly, the number of Musota's TP was 13.

Although there was no obvious relationship between TN concentrations and the flow rate in calm condition (Flow rate < 100 m^3/s), we could confirm that the concentrations rises with increasing the flow rate when it got over 100 m^3/s. A coefficient of determination between TN and flow rate was calculated as 0.46, it was met the significance level of 5%. The increasing tendency of concentration with the increase of flow rate was much stronger in TP than TN. A coefficient of determination between TP and flow rate was as high as 0.97. However, this unnaturally high coefficient could be influenced by the extremely high concentration observed in August 24, 2018 (red circle in Fig. 4 b1)). In addition, the evaluation by calculating regression line, the value of segment became -0.081. minus value in the segment can be inappropriate because negative concentration values could occur. Therefore, the coefficient excluding data observed on 2018/8/24 was also calculated, we obtained the value as 0.66. This value was also significant met the significance level of 5%.

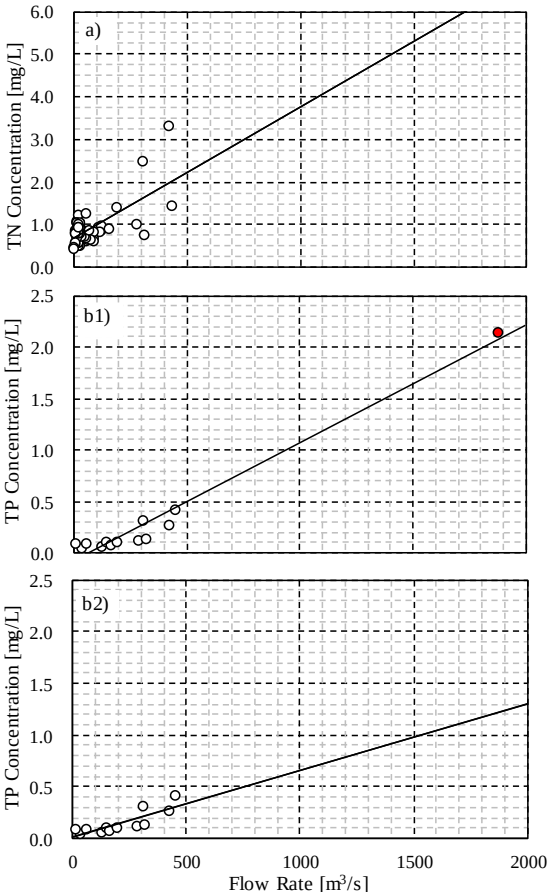

Fig. 4 a): Relationship between TN concentration at Iwade and flow rate at Funado. b1): Relationship between TP concentration at Musota and the flow rate. Although b2) also shows relationship between TP concentration and flow rate, extremely large value observed 2018/8/24 is excluded. Each figure has regression lines.

The tendency of this concentration rise could be considered caused by the increase in suspended solid in river water accompanying the increase in flow rate. Figure 5 shows pictures of sampled waters at Musota bridge and river flow at Iwade headwork which are located at 500m upstream of the Iwade bridge. They were taken on 2018/8/24 under flooding condition, indicated that river water contained a large amount of suspended solid such as soil particles, and the flow velocity looked large therefore these suspended solid was difficult to sink. Suspended solid have function as a nutrient carry, and it has been reported that this property in river water to be remarkable with

phosphorus than nitrogen [10]. In order to evaluate an influence of suspended solid, suspended phosphorus and suspended nitrogen contained in river water during floods should be measured separately from TN and TP. This is a future issue.

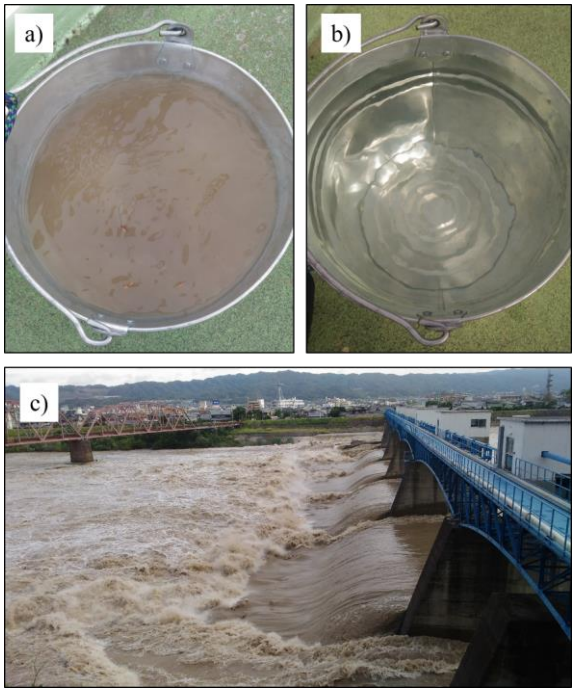

Fig. 5 a) River water under flooding condition sampled at Musota taken at 7:02 am, 2018/8/24. b) River water under calm condition sampled at Musota taken at 9:19 am, 2018/8/16. c) river flow at Iwade headwork on the same date as a).

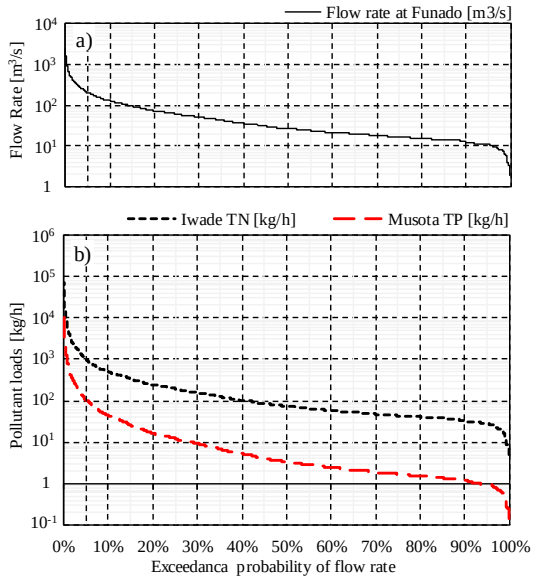

Fig. 6 Flow exceedance probabilities of a) flow rate, b) TN load and TP load.

Finally, we created regression lines between flow rate and concentrations. Relationship between TN at Iwade and flow rate at Funado was expressed as follows;

$$C_{TN} = 0.0031Q + 0.687 \quad (1)$$

where C_{TN} and Q are TN concentration at Iwade and hourly flow rate at Funado, respectively. Then, the relationship between the TP at Musota and flow rate at Funado became as follows;

$$C_{TP} = 0.0006Q + 0.019 \quad (2)$$

where C_{TP} is TP concentration at Musota. Both segments in (1) and (2) were larger than 0, it is guaranteed that the concentration is 0 or more in these equations even if little flow rate.

Annual Pollutant Loads Estimation

Figure 6 shows flow duration curves of the flow rate and pollutant loads of TN and TP, whose vertical axis are logarithmic. Both TN load and TP load were calculated by multiplying flow rates with TN and TP concentrations which were obtained by equation (1) and (2), respectively. In other words, these load calculations used estimated concentrations obtained assuming a linear relationship with the flow rate, the load amounts in this study are, as a result, proportional to the square of the flow rate. By analysis of fig.6, TN load and TP load were only about 150 kg/h and 15 kg/h when the flow rate was 100m^3/s whose excess probability was 10%. It was also shown, however, as excess probability of the flow rate decreases further, not only the flow rate itself but also the TN load and TP load more rapidly increased. This tendency could be caused that the loads proportional to the square of flow rate value because the loads were calculated by multiplying the concentration which were estimated by flow rate with the flow rate again. Whether such estimation is appropriate will be necessary to be discussed in the future. By a comparison TN with TP, the rapid increase in loads associated with floodings were more pronounced in TP than in TN, which is consistent with the characteristic that phosphorus was more likely to flow out as suspended solid.

Tab.2 shows the annual equivalent of TN and TP loads calculated by using fig.6. The annual equivalent of TN load was about 3300[t], and the sum of TN load on the flooding (included top 5% excess probability of flow rate) was 2100[t]. This result indicated that 65% of TN load runoff in the flooding condition. Sum of TP loads on the flooding was 326[t], which was equivalent to 80% of total annual TP runoff. These results suggest that accurate prediction of huge nutrient discharge during floods will be essential for quantitative assessment of nutrient discharge from the

basin.

Table 2 Total amount of annual TN, TP loads, the summed loads generated top 5% excess probability of flow rate, and ratios of Sum of top 5% / annual total loads.

	TN load	TP load
Annual total [t]	3263.6	408.4
Sum of top 5% [t]	2019.9	326.7
Ratio [%]	64.6	80.0

CONCLUSION

In this study, we conducted high-frequency water quality observation especially TN and TP aiming at quantitative evaluation of water pollutant loads from Kinokawa river basin. Results of the analysis based on TN and TP concentrations, flow rate of Kinokawa river and pollutant loads provided following considerations;

1) TN concentrations at Musota was chronically higher than ones of Iwade. The scales of agricultural canal and three tributaries flowing into Kinokawa river located between the bridges seems to be too small to impact on the environment of Kinokawa main stream. In order to understand the impacts of them, it will be necessary to accumulate quantitative data of flow rate and TN concentration.
2) In flooding condition, TN and TP concentrations in river water rapidly increased. It might be caused by increase of nitrogen and phosphorus attached suspended solid under flooding condition.
3) Almost all TN and TP loads were runoff in flooding whose flow rate were over 5 % flow exceedance provability. It was strongly suggested an accurate understanding of the nutrient discharge mechanism during floodings are essential for understanding the nutrient discharge phenomenon to the sea area.

Finally, we stress the limitations of this research and discuss some remaining future issues. It should be emphasized that river water quantity in heavy flooding and strong drought condition might include large errors because of out of scope of H-Q equations. Especially there was a possibility the results of this study might be affected, if the estimated flood flow rate contained large errors. In addition, in calculation of the annual runoff loads of TN and TP, we made the strong assumption that these concentrations are linearly related to the flow rate for simplifying the models. Further work is necessary to investigate how the approach can be improved in this respect.

ACKNOWLEDGMENTS

In this study, H-Q curve equations were provided from Wakayama office of Rivers and National Highways, Kinki Regional Development Bureau, Japanese ministry of land, infrastructure, transport and tourism. We express our gratitude, here.

REFERENCES

[1] Goolsby A.D., and Battaglin A.W., Long-term changes in concentrations and flux of nitrogen in the Mississippi River Basin, USA. HYDROLOGICAL PROCESSES, Vol. 15, 2001, pp.1209-1226.
[2] Frederieke J.K., Petra M.K., Brent L.H., Scott N.W., Anne K.-H., Brett A., Jon E.B. and Ryan D.R.T., River loads of suspended solids, nitrogen, phosphorus and herbicides delivered to the Great Barrier Reef lagoon, Vol. 65, Issues 4–9, 2012, pp. 167-181.
[3] Ryota H., Nobuyuki E., Yasuhiro W., Masahide I. and Tatemasa H., Restraint effects of 2-MIB concentration increases due to total phosphorus management in the upper Kinokawa watershed, *Int. J. of GEOMATE,* Vol. 13, Issue 37, 2017, pp. 141-148.
[4] Haihong S., Tingchao Q., Jianbin W. and Tony H.F.W., Characteristics of stormwater quality in Singapore catchments in 9 different types of land use, *Water,* Vol. 11, No.5, 2019, 1089.
[5] Minji P., Young S. C., Hyung J.S., Inhong S., Chun G.Y., Joong D.C. and Soon J.Y., A comparison study of runnof characteristics of non-point source pollution from three watersheds in South Korea., *Water,* Vol. 11, No.5, 2019, 966.
[6] Japanese Ministry of Land, Infrastructure, Transport and Tourism, Land Use Fragmented Mesh Data 2014., http://nlftp.mlit.go.jp/ksj-e/index.
html, accessed 2019/6/15.
[7] TOA-DKK, Portable simple total nitrogen and total phosphorus measuring instrument, https://www.toadkk.co.jp/product/sci/por/tnp.html, accessed 2018/4/2.
[8] Japanese ministry of the environment, water pollution load measuring method manual (in Japanese), http://www.env.go.jp/water/heisa/tplc/manu_npami/index.html, accessed 2019/6/15.
[9] Wakayama river national highway office, Japan, https://www.kkr.mlit.go.jp/wakayama/, accessed 2019/6/15.
[10] Ayako S., Yasuo N., Keisuke E., Miho U., Kyosuke S. and Satoshi O., Nutrient and cod loads in the edo, ara, tama and naka rivers under flood flow conditions, *Proc. of Hydraulic Engineering,* Vol. 52, 2008, pp.1117-1122 (in Japanese).

9th Int. Conf. on Geotechnique, Construction Materials and Environment, Tokyo, Japan, 20-22 November 2019, ISBN: 978-4-909106025 C3051

VARIATION OF STRAIN DURING THE CONSTRUCTION OF AN INCREMENTALLY LAUNCHED CONCRETE BRIDGE

Norisham Ibrahim[1], and Norhayati Abdul Hamid[2]
[1,2]Faculty of Civil Engineering, Universiti Teknologi MARA, Malaysia

ABSTRACT

Incremental launching is an alternative method of construction for medium span prestressed concrete bridges. However, the design and analysis of the concrete box girders are complicated due to the construction process and many other factors including the creep and shrinkage behaviour of the structure during and after the construction is completed. To gain better understanding of the strain variation, an incrementally launched prestressed concrete box girder bridge was instrumented with several vibrating wire strain gauges. The installation of vibrating wire strain gauges were done as not to miss the earliest possible data. The locations of vibrating wire strain gauges were selected to evaluate strains at critical sections. Strain variation at ten minute intervals captured during the launching operation is illustrated. Variation of strain due to other major construction activities such as concrete pouring and stressing of tendons are also shown. As expected, the abrupt change in strain can be seen immediately after launching

Keywords: Incremental launching, Vibrating wire strain gauge, Prestressed, Strain

INTRODUCTION

Incremental launching [1] construction method has become competitive since many years ago due to the advantages offered over the conventional construction method such as reduction of environmental constraints and use of road access. It also eliminates the distance between the casting yard (where a cast of segments take place) and the construction site. By using an incremental launching technique, it is essential for a bridge designer to understand the construction technique and how the construction technique affects the design parameters.

For an incrementally launched bridge, the location of a particular concrete segment changes from the beginning till the end of the construction. As a result, at any point on the concrete segment the value of stress vary throughout the construction process. Change of stress is also accompanied with shift in of concrete age and environmental condition. Since there are design parameters which are dependent on stress value, concrete age and environmental condition, the determination of these parameters has become very complicated. Among the design parameters which are highly influenced by concrete age and environmental condition are creep strain and shrinkage strain. Furthermore, the creep strain is also dependent on stress.

.

CREEP AND SHRINKAGE STRAIN

Both creep strain and shrinkage strain are critical parameters in the design of a prestressed concrete bridge, and these values must be predicted in order to be utilized in the design. The wrong prediction may cause the failure of the structure since these two parameters cause loss of stress force in the prestressing tendons as shown in [2] and [3]. Loss of stress force affects the capacity of the prestressing tendons installed in the concrete segments which finally affect the whole bridge structure.

Development of creep strain sand shrinkage strain is complicated as explained in [4] and there are many uncertainties in the prediction as shown in [5] due to the influence factors which occur concurrently. The investigation of creep and shrinkage have been shown in many literatures as given in [6], [7], [8] and [9]. Recent papers about shrinkage include [10], [11] and [12] and [13]. Many prediction models have been developed and investigated as given in [14], 15 and [16] in order to better predict the creep strain and shrinkage strain values. The development of creep prediction model is in the separation of the shrinkage prediction model and vice versa. However, in the real structure, the creep strain and shrinkage strain occur simultaneously and can only be measured in the form of total strain.

Monitoring the strain variation during and after construction is an excellent opportunity to better understand how the strain varies when exposed to the change of stress, concrete age as well as the environmental condition. The result may help the designers to better predict the values of creep strain and shrinkage strain which are very important in the design of a prestressed concrete bridge. Therefore it is a great opportunity to have Tauranga Harbour Link

(THL) installed with strain gauges in the concrete segments in order to monitor the concrete strain during and after construction. The monitoring system of THL has been produced in [17]. Several figures are reproduced here for clarity.

DESCRIPTION OF THL

THL is a bridge in New Zealand constructed by incremental launching. The bridge alignment is a circle situated on an inclined plane with a radius of 682.4 m. The Reduce Level (RL) of the circle centre is -86.061 m. The RL for Abutment A (AA) and Abutment B (AB) are 5.377 m and 3.917 m respectively. The total horizontal length is 467 m with 12 spans altogether built up by 23 box girder segments as shown in Figure 1(a). Length of Segment 1 (S1) and Segment 23 (S23) is 23,753 mm while the length of Segment 2 (S2) to Segment 22 (S22) is 19985 mm. Height (H) of the segment is 2700 mm. Length of span 1 (L1) and span 12 (L12) is 33.75 m while the length of span 2 to span 11 (L2 to L11) is 39.97 m. The typical cross section is shown in Figure 1(b). The view is from AA towards AB. The top 450 mm of the box girder is called deck slab while underneath of the deck slab is called soffit slab.

CONSTRUCTION OF THL

The construction activities may be divided into 6 major part namely installation of reinforcement for soffit slab, pouring of concrete for soffit slab, installation of reinforcement for deck slab, pouring of concrete for deck slab, stressing of tendons and launching of segments. Using incremental launching, all the box girder segments were cast in situ on one side of the waterway, in this case at AA. The cast area is called a Casting Shed (CS). Once a new segment was completed, the whole segment(s) was pushed from AA heading to AB leaving the Casting Shed empty. The emptied Casting Shed was then used to cast a new segment.

This process was repeated until all the box girder segments were completed. All the segments are connected to each other by reinforcement steel and prestressing tendons. As shown in Figure 1(a), the identification numbers of piers and segments are according to the cast sequence. The first box girder and pier cast were numbered as Segment 1 (S1) and Pier 1 (P1) respectively. However, when the bridge was completed, Segment 1 is located on AB while Pier 1 is situated close to AA. The launching activities may be illustrated as given in Figure 2.

.

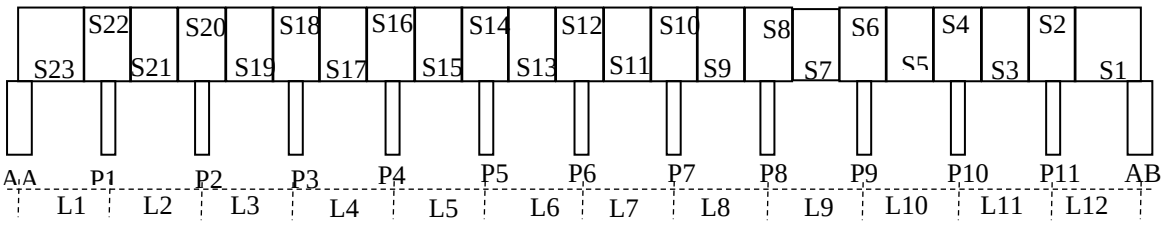

Fig. 1(a) Elevation of the box girder bridge

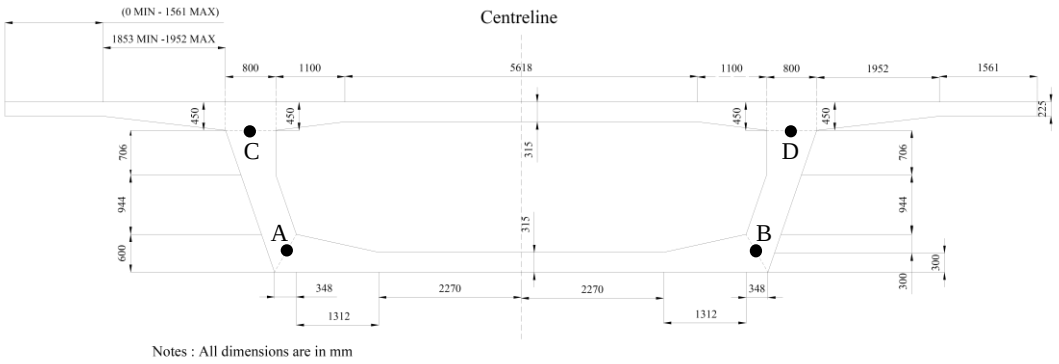

Fig. 1(b) Typical cross section of the box girder segment

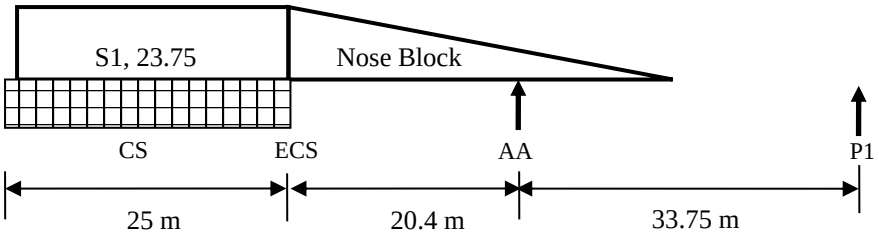

Fig 2(a). Location of segment 1 before launching

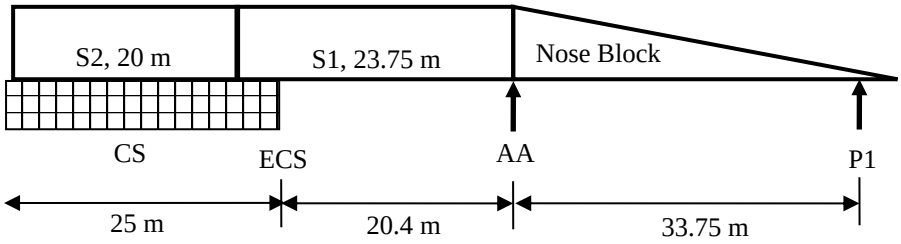

Fig 2(b). Location of segment 1 and 2 after first launching

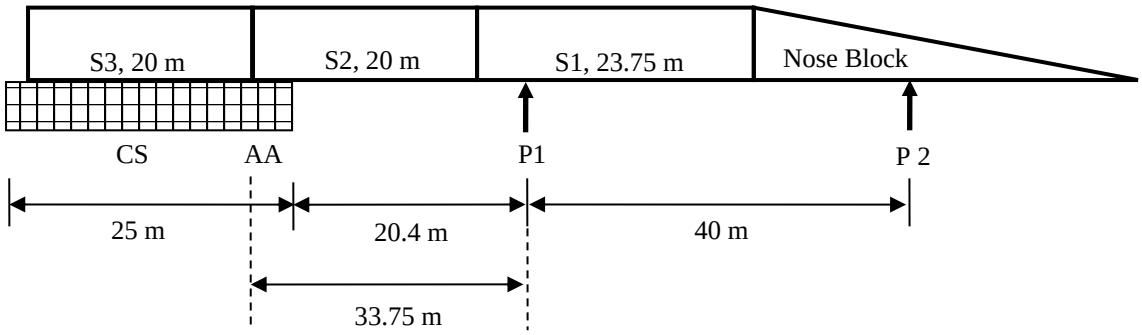

Fig. 2(c) Location of segment 1, 2 and 3 after second launching

MONITORING SYSTEM OF THL

The instrumentation system was based on [18]. Other researchers include [19] and [20]. One of the objectives to instrument THL was to measure concrete strains during and after, construction of the high strength concrete post-tensioned box girder bridge. The instruments used to measure the strain are vibrating wire strain gauges (VWSG). The segments instrumented are segment 15, 16, 17 and 18. According to the construction sequence, the first installation was done in segment 15, followed by segments 16, 17 and 18. There are four gauges in a segment. Location of the gauges are shown in Figure 1 as Point A, B, C and D. In segment 15 the gauges are known as BL15, BR15, TL15 and TR15 respectively. The bottom VWSGs were located at the depth of 300 mm from the bottom of the concrete face while the top VWSGs were positioned at 420 mm from the top of the concrete face. The installation of the instruments was done as not to miss the earliest possible data because most of the creep and shrinkage occur early after casting [4]. However, due to several problems, data from the instrumented gauges could only be logged after certain days of age.

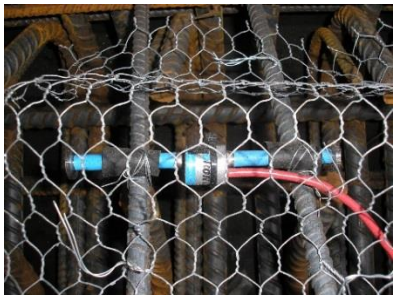

Fig. 3 A vibrating wire strain gauge

RESULTS

Results from BR15 is selected to be presented in this paper. The graph is plotted in the form that negative shows bigger compression than positive value. For clarity, the results are divided into several parts according to month. BR15 was connected to the datalogger on 24 Feb 09. At that time, the age of soffit was already 13 days and the segment already went through stressing and launching twice. As a result of launching, gauges BR15 was at about 9.6 m after Abutment A and 24.15 m before Pier 1 when the first data logged.

After the third launching, BR15 was at about 29.6 m after Abutment A and 4.15 m before P1. This strain variation after during and launching is shown in Figure 4(a). After launching 3, the strain is indicated as AL3. The next few launches are launching 4, 5 and 6. The variation of strain after each launching is indicated as AL4, AL5 and AL6 respectively.

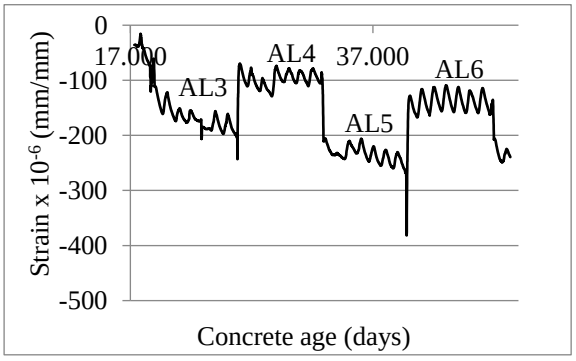

Fig. 4(a) Strain versus concrete age from BR15 recorded in March

Variation of strain during and after launching 7 and 8 are given in Figure (b). No more major launching was done after that because the segment already reached its final position. Any minor launch was only to correct if there was any misalignment of the bridge.

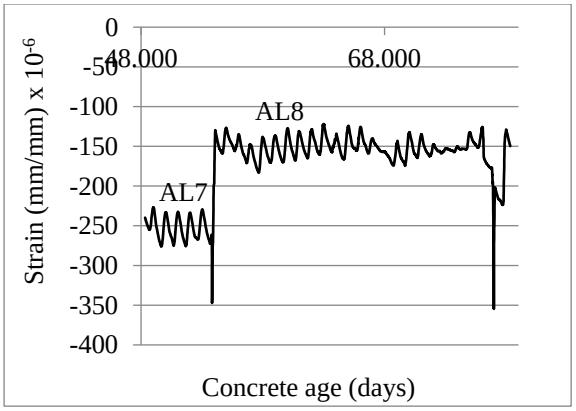

Fig. 4(b) Strain versus concrete age from BR15 recorded in April

CONCLUSIONS

In general, the location of BR15 may be divided into two major positions; close to pier or close to mid span. In comparison between these two locations, it is found that the soffit of the box girder is more compressed when it is located very close to the pier, as expected. The results would then be analyzed to study the creep and shrinkage behaviour of the bridge.

ACKNOWLEDGMENT

The author would like to acknowledge the help she received while conducting this research from Rudolph Kotze and Kelvin Reid of Transit New Zealand, Tim Grammer, Bryce Irving and Tony Pike of Fletcher Construction and Piotr Omenzetter, Jason Ingham, Noel Perinpanayagam, Sujith Padiyara and Mark Byrami of Auckland University.

REFERENCES

[1] Rosignoli, M. (1999). "Prestressing Schemes for Incrementally Launched Bridges." Journal of Bridge Engineering 4(2), pp. 107-115.
[2] Krishna Raju. N., Prestressed Concrete, Mcgraw Hill India, 2007, pp. 116-139.
[3] Rajagopalan. N., Prestressed Concrete, Alpha Science International U.K., 2005, pp. 120-153.
[4] Gardner, N.J. and Zhao, J.W., Creep and Shrinkage Revisited. ACI Materials Journal 90(3), 1993, pp. 236-246.
[5] Wendner, R., Hubler, M. H. and Bazant, Z. P., Creep and Shrinkage Models for Concrete: Uncertainty Quantification, Workshop Proceedings In Proc. 11th Int. Probablistic Workshop, 2013.
[6] Rosst, A. D., Creep of Concrete under Variable Stress, Journal of The Concrete Institute 29(9) 1958, pp. 739-758.
[7] Arshad A. K., William D. C. and Mitchel, D.,, Creep, Shrinkage and Thermal Strains in Normal, Medium and High Strength Concretes during Hydration, ACI Materials Journal 94(2) 1997, pp. 156-163.
[8] Altoubat, S. A. and Lange, D. A., Creep, Shrinkage and Cracking of Restrained Concrete at Early Age. ACI Material Journal 98(4), 2001, pp. 323-331.
[9] Adam Neville, In My Judgment. Creep Of Concrete and Behavior of Structures, Part 1: Problems, Concrete International, 2002, pp. 59-66
[10] Badrinarayan R, Shirish D, and Gangadhar, R, A., A Study on Early Age Shrinkage Behaviourof Cement Paste With Binary and Ternary Combination of Fly Ash And Pond Ash, Indian J. Of Science And Technology 9(44), 2016, pp. 1-9.

[11] Zemanova A, Tej P., Pokorny P. and Kolisko, J., Comparison of Currently Used Prediction Models for Creep and Shrinkage of Concrete, Conference Proceedings In Proc. Int. Conf. on Advanced Material and Env. Eng., 2016.

[12] Kucharezykova, B., Karel, O., Danek, P., Kocab, D. and Possl, P., Comparison of Measurement Methods Intended to Determination of The Shrinkage Development In Polymer Cement Mortars, Procedia Eng. 195, 2017, pp. 17-23.

[13] Misak, P., Experimental Analysis on Shrinkage and Swelling in Ordinary Concrete, Journal of Advances in Materials Science and Engineering, 2017.

[14] Zemanova, A., Tej, P., Pokorny, P. and Kolisko, J., Comparison of Currently Used Prediction Models for Creep and Shrinkage of Concrete, Conference Proceedings In Proc. International Conference on Advanced Material Science and Environmental Engineering, 2016.

[15] Fanourakis, G. C. and Bailim, Y., An Assesment of The Accuracy of Nine Design Models for Predicting Creep in Concrete, Journal of The South African, Institution of Civil Engineering 48(4), 2006, pp. 2-8.

[16] Goel, R., Kumar, R., and Paul D.K., Comparative Study of Various Creep and Shrinkage Prediction Models for Concrete, Journal of Materials In Civil Engineering, 19(3), 2007, pp. 249-260.

[17] Ibrahim, N., Instrumentation System and Total Strain of An Incrementally Launched Bridge, Conference Proceedings, In Proc. Int. Conf. On MISG, 2014, pp. 79-90.

[18] Lee, A. and Robertson, I. N., Instrumentation and Long-Term Monitoring of The North Halawa Valley Viaduct Report UHM/CE/95-08, University Of Hawaii, Honolulu, Hawaii, 1995.

[19] Barr, P. and Eberhard, M., High Performance Concrete InWashington State SR 18/SR 516 Overcrossing: Final Report on Girder Monitoring**.** Washington, Washington State Transportation Center (TRAC), University Of Washington, 2000.

[20] Dolinajová, K. And Moravčík, M., Monitoring and Numerical Analysis of Construction Stages on The Bridge Realized By The Free Cantilever Method Procedia Eng. 65, 2013, pp. 321-326.

9th Int. Conf. on Geotechnique, Construction Materials and Environment, Tokyo, Japan, 20-22 November 2019, ISBN: 978-4-909106025 C3051

MAPPING OF SEAWATER INTRUSION INTO COASTAL AQUIFER (CASE STUDY: PEKALONGAN COASTAL AREA, CENTRAL JAVA)

Muh. Irham Sahana[1], Roh Santoso Budi Waspodo[2], and Heriansyah Putra[3]
[123]Department of Civil and Environmental Engineering, Faculty of Agricultural Technology and Engineering, IPB University (Bogor Agricultural University), Indonesia

ABSTRACT

The intrusion of seawater has reported able to promote the degradation of groundwater quality. Seawater intrusion can be due to excessive exploitation of the groundwater or through natural phenomenon such as the tide floods. The inclusion of seawater in the land is not only being treated by the continued use of shallow wells but rather due to the phenomenon of seawater tide flood which is brought by the Bremi river and Tirto river causing a decline in quality of Groundwater. One of the areas that are affected by this disaster is Pekalongan City. Analysis of seawater intrusion in Pekalongan is conducted by referring to the decision of PAHIAA 1986 and the decree of Minister of Energy and Mineral Resources (ESDM). This study was conducted at 64 points spread across 4 sub-districts entire Pekalongan coastal area, which is 46.972 km^2. The result of this study shows that seawater intrusion in this location already affects the quality of groundwater is not depressed until it reaches a distance of 6.52 km from the seashore for the parameters of total dissolved solids (TDS) and electrical conductivity (EC), and 7.22 km from the seashore has been exposed to seawater intrusion based on the parameters of chloride ion. The magnitude of the safety zone decreased groundwater quality amounted to 23.324 km^2 or approximately 50% of Pekalongan area. Meanwhile, due to seawater intrusion, as much as 9.094 km^2 or 19% of the territory of the city of Pekalongan has been categorized into the damaged zone.

Keywords: Chloride, electrical conductivity, groundwater, seawater intrusion, total dissolved solids

INTRODUCTION

Seawater can influence groundwater quality and quantity through the intrusion and sea-level rise phenomenon. Seawater intrusion is the migration of seawater into freshwater aquifers under the influence of groundwater development [1]. Seawater intrusion is triggered by several factors, such as excessive pumping, land-use change, reduction in recharge because of global warming, and overtopping that caused by sea-level rise, storm surges, and tsunamis [1]. The increase in water withdrawals from the wells have caused unacceptable drawdowns and deterioration of the quality of water pumped by some of the wells. Fresh groundwater in the coastal aquifer is drained seas or lakes under natural conditions, and the interface line between fresh and salt water occurs. Massive exploitation of coastal aquifers also has an impact on the evolution of hydraulic gradient. This phenomenon is called seawater intrusion [2].

Seawater intrusion has a significant effect on human living, such as health disruption, decreasing of soil fertility, and buildings damaged, especially for people who live in coastal areas [3]. One of the coastal areas that have a big issue on the seawater intrusion is Pekalongan City. This city is located on the northern coast of Central Java Province, Indonesia. Tidal floods which have been inundating Pekalongan since 2013 became preliminary investigation that Pekalongan City experienced seawater intrusion, especially in North and West Pekalongan Districts. Fulfilling daily clean water needs by shallow groundwater wells also caused seawater intrusion in Pekalongan coastal area. The increasing exploitation of groundwater over time is thought to have resulted in seawater intrusion in aquifers in the coastal area. It also initiated the replacing groundwater in aquifers by sea water. This is indicated by the increasing number of population wells which has been turning into brackish. The objectives of this study are to investigate, analyze, and map the dispersion of seawater intrusion based on the relation between the electrical conductivity (EC), total dissolved solids (TDS), and chloride ion (Cl^-) to the distance of the well from the coast.

METHODOLOGY

This study was conducted in Pekalongan City, which has 4 sub-districts with the highest number of sampling points in the North and West Pekalongan Districts. These locations were the coastal areas and affected by the tidal flood. The primary and secondary data were used in this study. Firstly, the secondary data composed of the administrative map, Digital Elevation Map (DEM) data, and shapefile data of Pekalongan City were collected and used to obtain the sampling point.

The primary data of the unconfined groundwater samples were collected from 64 shallow wells, spread in 4 sub-districts. The measurements of the concentration of groundwater were conducted in the North and West Pekalongan Districts of 20 and 22 points, respectively. The distribution of the sampling point is depicted in Figure 1. The measurement was carried out using the instrument of AMTAST AMT03R to obtain electrical conductivity (EC), total dissolved solids (TDS), and chloride ion (Cl^-).

Furthermore, these results were analysed consider the coordinates of the location and distance from the coast. Then, a regression curve was made to improve the accuracy of the measurement results.

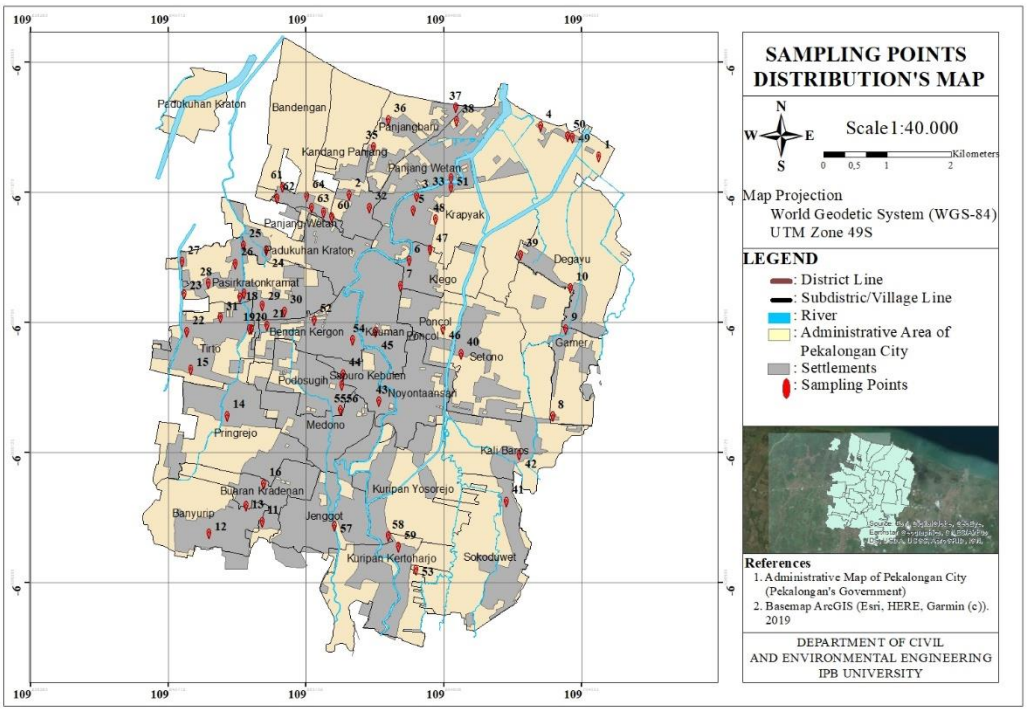

Fig. 1 Distribution of sampling points.

The dispersion map of seawater intrusion was based on the groundwater quality parameters which developed by refers to the Decree of the 1986 Ad Hoc Sea Water Intrusion (PAHIAA) Committee [3]. It contained 5 qualities of groundwater, namely, fresh, rather brackish, brackish, salty, and brine. Analysis of the data used was based on the values of electrical conductivity (EC), total dissolved solids (TDS), and chloride (Cl^-). The details of the classification of groundwater salinity level based on PAHIAA, 1986 were shown in Table 1.

Table 1 Classification of groundwater salinity level based on PAHIAA, 1986 [3].

Water Quality	TDS (mg/L)	EC (µmhos/cm)	Cl^- (mg/L)
Freshwater	<1,000	<1,500	<500
Rather brackish	1,000-3,000	1,500-5,000	500-2,000
Brackish	3,000-10,000	5,000-15,000	2,000-5,000
Salty	10,000-35,000	15,000-50,000	5,000-19,000
Brine	>35,000	>50,000	>19,000

Then, the alignment of the results from the plotting of coordinate data and the parameters of DHL, TDS, and Cl using Surfer 13 software. Furthermore, a general description of the zone of spreading seawater intrusion is seen through maps created using ArcGIS software.

The analysis was conducted using ArcGIS 10.4.1 software with the integrated distance weighted (IDW) method. The IDW method is a conventional interpolation method which considers distances as weights [4]. The interpolation refers to the flat distance from the data point (sample) to the block. The closer distance between the sample point and the block is estimated, the higher the weight is created [4]. The general weighting function is the inverse of the square of the distance, and the equation is used in the inverse distance weighted method. The advantage of this IDW method lies in the interpolation characteristics that can be controlled by limiting the input points used in the interpolation process. In addition, the selection of the IDW method compared to other interpolation methods such as spline and natural neighbor is that the use of IDW is able to interpolate values with considerable height differences [5].

RESULTS AND DISCUSSION

Groundwater quality parameters

The measurements of groundwater quality parameters show the highest concentrations of TDS, EC, and Cl^- are were 14330 mg/L, 21724 µmhos/cm, and 11360 mg/L, respectively. This value was obtained from Panjang Baru Village, North Pekalongan District with a distance of 440.220 m from the coast. Based on the classification of PAHIAA 1986, the quality of groundwater at this point was categorized to brackish water for TDS and EC parameters. Whereas, for the Cl^- parameter, it was categorized into salty water with concentration ranges from 5,000 to 19,000 mg/L. The difference of these parameters classification was due to salt ions (Cl^-) that affected the groundwater quality higher than the concentration of total dissolved solids (TDS) and electrical conductivity (EC) which were more influenced by metal elements in the groundwater. The amount of concentration obtained at that location was also influenced by the surrounding environment conditions which were flooded by tidal floods or sea tides so that salt and metals were more easily infiltrated and concentrated in the region.

Moreover, the smallest concentration was found in the Kuripan Yosorejo Village, South Pekalongan District, with a distance of 6,954.12 m from the coast. The magnitude of the concentration values of TDS, EC, and Cl^- were measured respectively at 142 mg/L, 213 µmhos/cm, and 104 mg/L. Based on this value, the quality of groundwater in the area was also classified as fresh water due to the TDS concentration was less than 1000 mg/L, the EC concentration was below 1500 µmhos/cm, and the salinity level was less than 500 mg/L. The result of measurements in West Pekalongan District, TDS concentrations ranged from 332 to 12356.8 mg/L, EC concentrations were 499 to 18740.02 µmhos/cm, and Cl^- concentrations were in the range 249 to 9798 mg/L. The highest concentration was obtained around the Tirto River, which was 3.65 km from the coast. It affected the pattern of the dispersion of seawater intrusion which tended to extend to the south. Then, the range of TDS values in North Pekalongan District ranged from 374 to 14330 mg/L, EC was in the range of 561 to 21724 µmhos/cm, and the chloride concentration was 281 to 11360 mg/L. In addition, the maximum concentration was found at a distance of 440.2 m from the coast. The result of this study indicated that the pattern of intrusion in North Pekalongan District was influenced by the phenomenon of sea tides due to its geographical location, which intersected the coast.

The results of measurements in West Pekalongan District had a range of TDS, EC, and Cl^- values of 314 to 844 mg/L, 471 to 1,266 µmhos/cm, and 235 to 633 mg/L, respectively. The distribution of the results of measurements of the concentrations of TDS, EC, and Cl^- in South Pekalongan District ranged between 142-460 mg/L, 213 to 690 µmhos/cm, and 104 to 345 mg/L. In general, the quality of groundwater in the South and East Pekalongan Districts were still feasible and classified into freshwater.

Correlation of TDS, EC, and Cl^- to distance from the coastline and Bremi river

The accuracy of the value of total dissolved solids, electrical conductivity, and chloride ion were evaluated based on measurement distance both from the shore and Bremi River to obtain the dispersion model entire groundwater quality parameters.

Correlation of TDS, EC, and Cl^- to distance from the coastline

The model distribution curves of TDS, EC, and Cl^- were presented using the logarithmic regression method because this regression method had the highest determinant coefficient or R^2 which approached the value of 1 (one) compared to the other regression methods. An intrusion of seawater was able to be predicted by connecting the values of TDS, EC, and Cl^- to the distance from the coastline. The results of the dispersion model are shown in Figure 2-4.

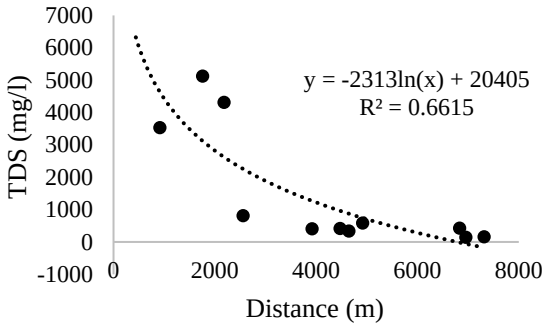

Fig. 2 Model dispersion curve of TDS in shallow wells to the distance from the coastline.

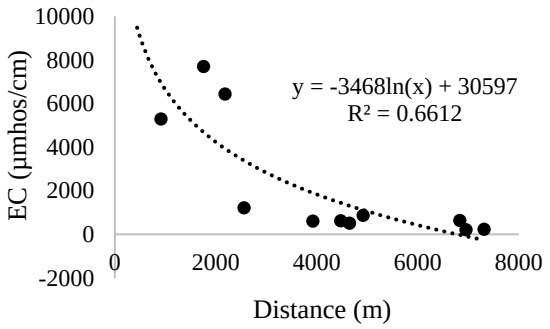

Fig. 3 Model dispersion curve of EC in shallow wells to the distance from the coastline.

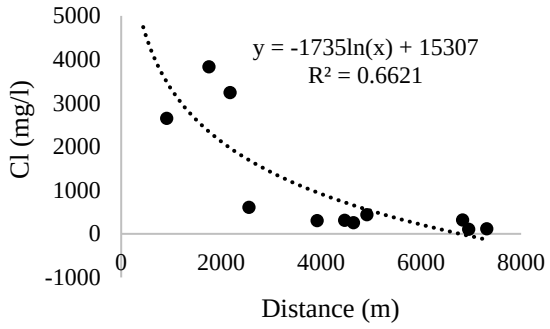

Fig. 4 Model dispersion curve of Cl^- in shallow wells to the distance from the coastline.

Based on observation from the curves above, the value of the three parameters decreased as the area farther away from the coast. The value of the equation obtained for the TDS relationship with distance was y = -2313ln(x) + 20405 with R^2 value of 0.6615. Then the equation value between the relationship of EC and Cl^- to the distance from the coastline respectively were y = -3468ln(x) + 30597 and y = -1735ln(x) + 15307, and the regression value respectively amounting to 0.6612 and 0.6621. Based on the value of the equation trend (R^2), the equations were not able to be used for regression analysis because R^2 value was less than 0,6750 or 67.50% [6].

Correlation of TDS, EC, and Cl^- to distance from the Bremi river

Although all parameters had been analysed from the coastline and had a strong relationship because R^2 had accuracy between 0.6-0.799 [7], but it couldn't be used for regression analysis. So, it was necessary to be re-analysis to the distance from Bremi river because of tidal floods. The model distribution curves of TDS, EC, and Cl^- were also presented using the logarithmic regression method to predict seawater intrusion model by connecting the values of TDS, EC, and Cl^- to the distance from the Bremi river. The dispersion curve and model are shown in Figure 5-7.

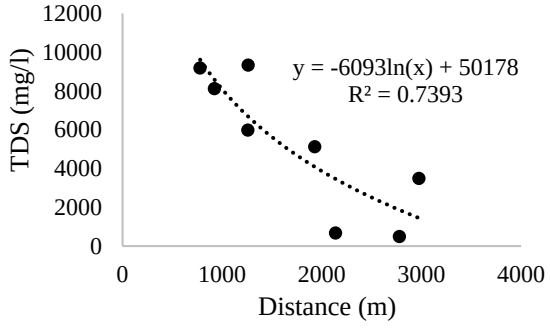

Fig. 5 Model dispersion curve of TDS in shallow wells to the distance from Bremi river.

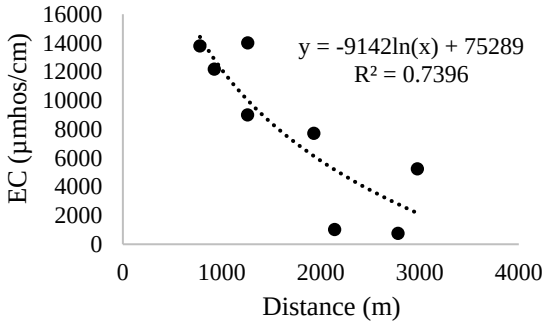

Fig. 6 Model dispersion curve of EC in shallow wells to the distance from Bremi river.

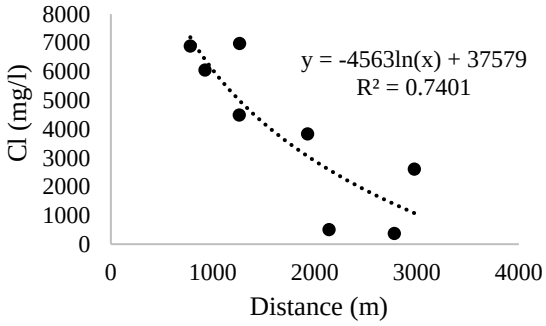

Fig. 7 Model dispersion curve of Cl^- in shallow wells to the distance from Bremi river.

Based on logarithmic regression analysis above, seawater intrusion dispersion in Pekalongan Coastal Area was mostly influenced by tidal floods phenomenon which was carried out by Bremi River. This analysis was proven by the accuracy of logarithmic regression analysis was 73.93% to 74.01%. So, it met the requirements that R^2 was suitable for regression analysis if it must be above 67.50% [6]. The value of the equation obtained for the TDS relationship with distance was y =-6093ln(x) + 50178 with R^2 value of 0.7393 or 73.93% for its accuracy. Then the equation value between the relationship of EC to the distance from the coastline were y = -9142ln(x) + 75289 and had an accuracy of 73.96%. While, the value of the equation obtained for the Cl^- relationship with distance was y = -4563ln(x) + 37579 with R^2 value of 0.7401 or 74.01% for its accuracy. Analysis was also conducted using linear regression, but it had smaller ratio of 0.7132 to 0.7139. Thus, the ratio in saline water was best described by logarithmic equation [11].

Correlation of TDS, EC, and Cl^- parameters

In addition, the three parameters also had a high correlation, so the measurement data which was used had high strength are shown in Fig. 8 to 10.

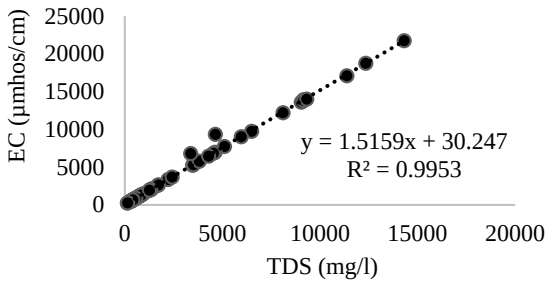

Fig. 8 Correlation curve between EC and TDS.

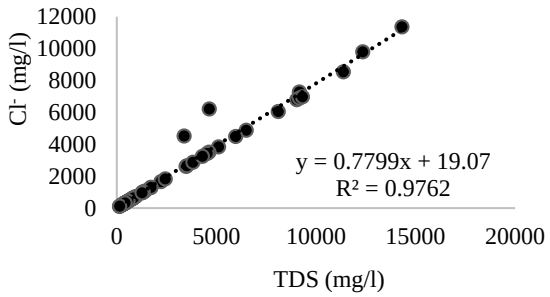

Fig. 9 Correlation curve between Cl^- and TDS.

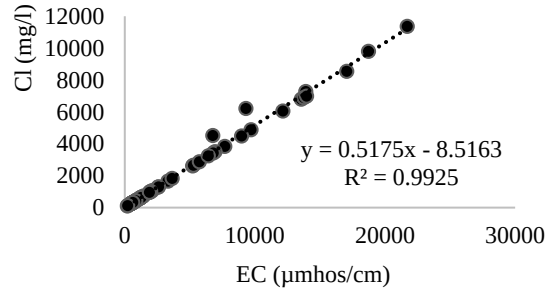

Fig. 10 Correlation curve between Cl^- and EC.

The correlation curve between TDS, EC, and Cl^- had a linear trend with R^2 values ranged from 0.9762-0.9953 or had an accuracy rate of 97.62% to 99.53%. This showed that the three parameters had a strong relationship and the data used was so accurate because it met the requirements that R^2 was suitable for regression analysis if it must be above 67.50% [6]. The linear regression equation for the correlation between TDS and EC was y = 1,5159x + 30,247 with accuracy reaching 99.53%. Then, the linear regression equation between TDS and Cl^- was y = 0.7799x + 19.07 with an accuracy of 97.62%. Furthermore, the equation between the value of EC and Cl^- was y = 0.5175x - 8.5163 with the accuracy of the data reaching 99.25%.

This difference indicates that the correlation of both parameters is strongly influenced by the EC values [10]. Whereas a high ratio between TDS and EC also has almost the same correlation (R^2 = 0.96) [10]. Even so, all the findings are in agreement with the conclusion drawn by McNeil and Cox (2000) [11] in which the obtained variation of TDS/EC ratio for freshwater can be vary 0.5 till ≥ 1.00 [11]. The type of freshwater is generally sodium, calcium, magnesium, bicarbonate type or calcium, sodium, bicarbonate, chloride type [11]. In line with this, it has been found that the most correlated major ions, especially to TDS, are chloride, sodium, and magnesium [12].

Dispersion Analysis of Seawater Intrusion

Dispersion pattern and flow direction of seawater intrusion

The pattern and flow direction of the dispersion of seawater intrusion were analyzed by the values of TDS, EC, and Cl^- carried out with Surfer 13 software. The analysis was performed using contour tools, the values of these three parameters combined with grid vector map tools to get the distribution and flow direction or flow net.

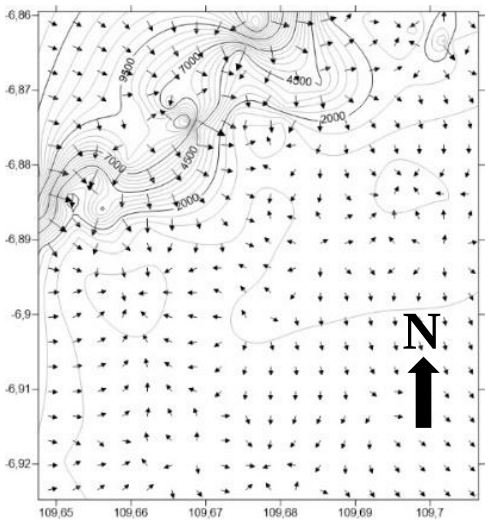

Fig. 11 Pattern and flow direction of TDS.

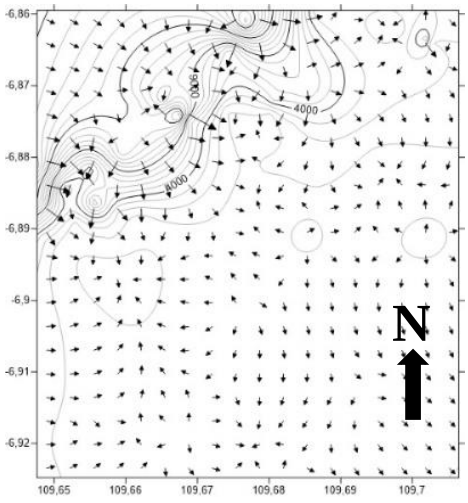

Fig. 12 Pattern and flow direction of EC.

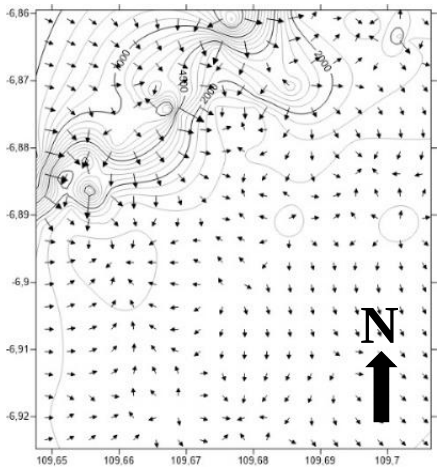

Fig. 13 Pattern and flow direction of Cl^-.

The dispersion pattern and flow direction were influenced by the distance and the magnitude of the measured parameter value. Based on Fig. 8 to 10, the direction of the dominant dispersion of seawater intrusion lead to the south or away from the coast and extended eastward. This meant that the concentration values of TDS, EC, and Cl^- decreased with the location of groundwater samples away from the coast and away from the Bremi and Tirto rivers in the western region. The pattern of the dispersion of seawater intrusion in Pekalongan City was influenced by tide flood or sea level rise, which was carried by Bremi and Tirto rivers. The inability of the river to accommodate sea tide loads due to river inflow discharge was smaller than the sea tide discharge, so seawater was intruded and polluted shallow groundwater. "Melo [5] states that seawater intrusion is not only influenced by excessive pumping (groundwater exploitation), but seawater intrusion is also able to be caused by changes in land-use, changes in recharge area conditions and rising sea levels to land due to global warming".

Mapping of seawater intrusion dispersion

Mapping of seawater intrusion dispersion based on the groundwater quality parameters, which refers to the Decree of the 1986 Ad Hoc Sea Water Intrusion (PAHIAA) Committee [3]. There are 5 qualities of groundwater, namely fresh, rather brackish, brackish, salty, and brine. Analysis of the data used was based on the values of electrical conductivity (EC), total dissolved solids (TDS), and chloride (Cl^-).

Table 2 Intruding distance from the coastline

Parameter	Intruding Distance (km)
TDS	6.52
EC	6.52
Cl^-	7.22

Seawater intrusion in Pekalongan coastal area had intruded to land as far as 6.52 km for TDS and EC parameters. Meanwhile, the farthest distance of 7.22 km was obtained for seawater intrusion, which was reviewed based on the level of salinity (Cl^-). The direction of the dispersion of seawater intrusion from the three parameters was to the south away from the coast. The seawater content which was found at that distance was caused by the phenomenon of sea level rise as tidal floods that inundated that region. Maps of seawater intrusion dispersion were shown in Fig. 14 to 16 based on total dissolved solid, electrical conductivity, and chloride parameters.

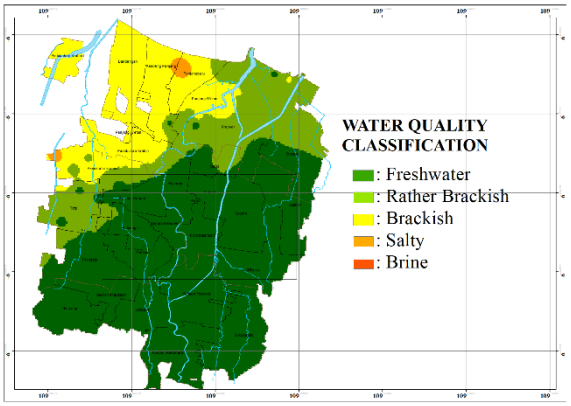

Fig. 14 Dispersion map of seawater intrusion based on TDS parameter.

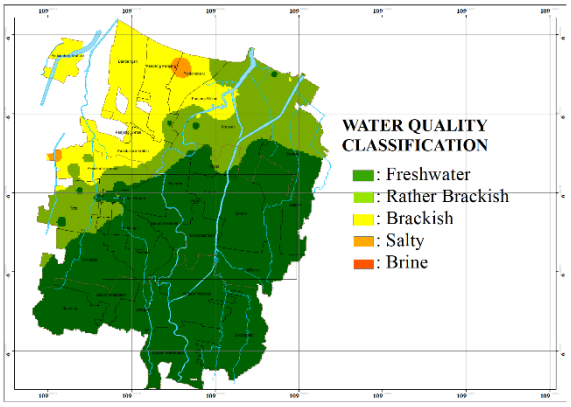

Fig. 15 Dispersion map of seawater intrusion based on EC parameter.

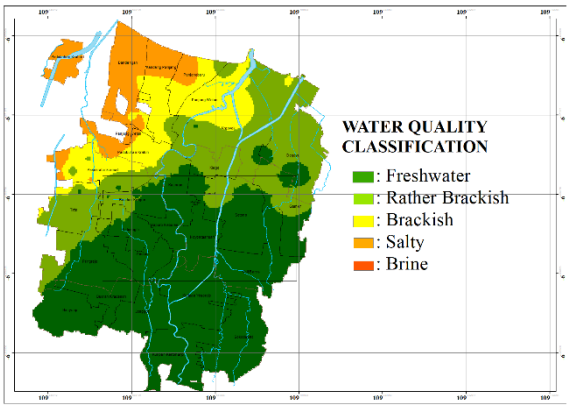

Fig. 16 Dispersion map of seawater intrusion based on Cl^- parameter.

The furthest location affected by seawater intrusion is in Pringrejo Village, West Pekalongan District. The tide was carried by the Bremi River and the Tirto River which directly emptied into the sea. The area passed by the flow of the two rivers mostly had rather brackish to salty water quality.

Based on the analysis of seawater intrusion dispersion in Pekalongan coastal area, the freshwater zone in Pekalongan was still 28.588 km^2 for TDS parameters and 28.357 km^2 for EC parameters. In addition, the area belonging to the freshwater zone was based on Cl^-parameters of 23.945 km^2. So based on the average of the three parameters, South Pekalongan District had the highest average with a region of 100% of its freshwater zone, East Pekalongan District at 86.97%, and West and North Pekalongan District at 57.23% and 8.59%

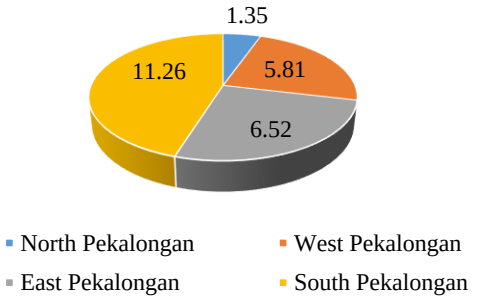

Fig. 17 Diagram of average availability of freshwater zone (km^2) in Pekalongan coastal area.

Based on the results of analysis and mapping, the villages in North Pekalongan District which still had a freshwater zone was a small portion of the southern part of Degayu Village and the southern part of Krapyak with a total area of 1.35 km^2. Whereas all other villages in North Pekalongan District which included Padukuhan Kraton, Bandengan, Kandang Panjang, Panjangbaru, Panjang Wetan, Krapyak, and Degayu villages had been exposed to seawater intrusion with a rather brackish water quality to salty. The study in 2019 was still in accordance with the research conducted in 2013 that in the coastal area of North Pekalongan District, fresh groundwater with EC <650 µmhos / cm was found in the south with the northern boundary through Dukuh, Krapyak Kidul to Degayu section South. For rather brackish groundwater with EC between 600 µmhos/cm - 1,500 µmhos cm found in the middle, including Kandang Panjang Village, Panjang Wetan, Krapyak Lor, and partially Degayu village. Whereas for brackish groundwater with EC > 1,500 µmhos / cm found in the north, covering Bandengan, Panjang Wetan, Kandang Panjang, Panjangbaru, and Degayu village [8]. So that in this case, in a period of 4 years, the availability of freshwater in Padukuhan Kraton Village is not available which indicated a decrease in groundwater quality in the Padukuhan Kraton Village due to infiltration of seawater through tidal floods or sea tides.

Analysis of Shallow Groundwater Quality Decreasing (Unconfined Aquifer)

Specific water quality requirements are theoretically determined by a number of parameters that are specific to a certain range of levels. Above these levels generally, tend to be indicative of contamination or to the level of water pollution or even environmental damage. The level of damage to groundwater conditions and environment can be determined by analysis of groundwater quality based on the parameters of electrical conductivity (EC) and total dissolved solids (TDS). Electrical conductivity (EC) or conductivity is a numerical representation of the ability of water to conduct electric current. The value depends on the content of the dissolved salt, which can be ionized in the water at the temperature when the measurement is made.

Table 3 Decreasing rate classification of confined and unconfined groundwater [9]

Classification Zone	EC (µmhos/cm)	TDS (mg/L)
Safety	< 1,000	< 1,000
Vulnerable	1,000-1,500	1,000-10,000
Critical	1,500-5,000	10,000-100,000
Damaged	> 5,000	>100,000

Based on the value of EC concentration obtained also categorized the level of decline in groundwater quality into 4 zones (safe, vulnerable, critical, and damaged) based on Minister of Energy and Mineral Resources ESDM Number 1451.K / 10 / MEM / 2000. From the results of the analysis with the IDW method in ArcGIS, the quality of groundwater in Pekalongan City which was still in a safe zone is

23.324 km^2, the vulnerable zone was 4.675 km^2, the critical zone was 9.879 km^2, and the damaged zone was 9.094 km^2.

Then, the dispersion map of declining groundwater quality due to seawater intrusion was presented in Fig. 18.

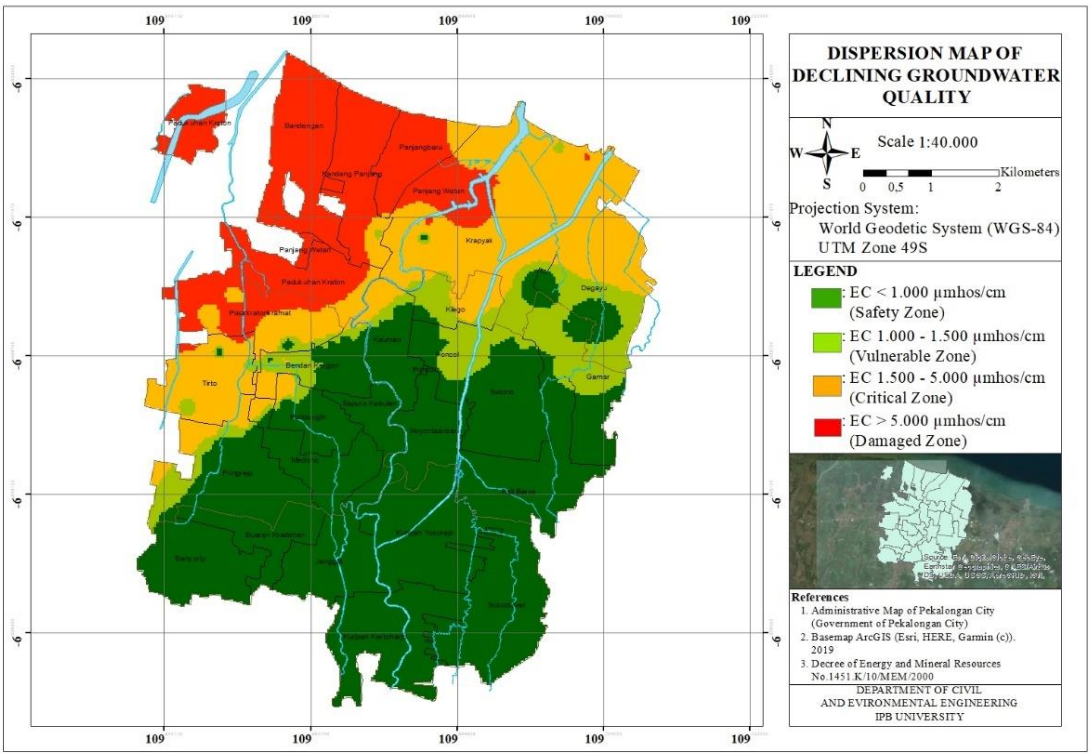

Fig. 18 Dispersion map of declining groundwater quality

The results of the analysis of the decrease in shallow groundwater quality were presented in Table 4 to 7.

Table 4 Dispersion of groundwater quality in West Pekalongan District

Village	Classification Zone
Sapuro Kebulen	Safety
Bendan Kergon	Safety-critical
Pasirkratonkramat	Critical-damaged
Medono	Safety-critical
Podosugih	Safety-critical
Pringrejo	Safety-critical
Tirto	Critical-Damaged

Table 5 Dispersion of groundwater quality in South Pekalongan District

Village	Classification Zone
Kuripan Yosorejo	Safety
Banyurip	Safety
Buaran Kradenan	Safety
Sokoduwet	Safety
Jenggot	Safety
Kuripan Kertoharjo	Safety
Kuripan Yosorejo	Safety

Table 6 Dispersion of groundwater quality in North Pekalongan District

Village	Classification Zone
Krapyak	Safety-damaged
Panjangbaru	Safety-critical
Bandengan	Damaged
Degayu	Safety-critical
Padukuhan Kraton	Critical-damaged
Kandang Panjang	Vulnerable-damaged
Panjang Wetan	Critical-damaged
Setono	Safety-vulnerable
Gamer	Safety-vulnerable

Table 7 Dispersion of groundwater quality in the East Pekalongan District

Village	Classification Zone
Kauman	Safety-critical
Klego	Safety-critical
Noyontaansari	Safety
Poncol	Safety-critical
Kali Baros	Safety

Based on classification zone of declining groundwater quality in Pekalongan coastal area,

South Pekalongan District still had a good groundwater quality because this district didn't have tidal flood area. East Pekalongan District was also dominated by village/subdistrict which had safety classification zone. But, West and North Pekalongan Districts were dominated between critical to damaged zone classification of declining groundwater quality. The type of saline water was usually dominated by sodium and chloride [10]. Other than cations and anions, organics are also associated with TDS but only in small quantities [10].

CONCLUSIONS

Area of Pekalongan coastal area was 46.972 km^2. Seawater intrusion in this region had affected the quality of groundwater which had intruded into 6.52 km from the coast for TDS and EC parameters, and 7.22 km from the coast had been affected by seawater intrusion based on Cl^- parameters. The intruding of seawater was not only affected by the use of continuous shallow wells but more due to the phenomenon of sea tides through tidal flooding carried by the Bremi and Tirto rivers, causing a decrease in the quality of groundwater. The safety zone for decreasing the quality of the groundwater or that was still suitable for use was 23.324 km^2 or about 50% including Banyurip Village, Buaran Kradenan, Jenggot, Kuripan Kertoharjo, Sokoduwet, Kuripan Yosorejo, Baros River, Noyontaansari, Sapuro Kebulen, part of Pringrejo Subdistrict, Medono, Podosugih, Bendan Kergon, Kauman, Poncol, Setono, and Gamer. Whereas, due to seawater intrusion, 9.094 km^2 or 19% of Pekalongan City's territory had been categorized into a damaged zone of shallow or unconfined groundwater.

The relationship between TDS, EC, and Cl^- was not always linear. This situation highly depended on water salinity and material contents. The higher the salinity level or material contents, the more complex mathematical equations were needed in describing those parameters.

REFERENCES

[1] Melo M. T. C., Coastal Aquifers Understanding Saltwater Intrusion, Tecnico Lisboa, 2015, pp.5.

[2] Naderi M. N., Kermani M. R., Barani G. A., Seawater Intrusion and Groundwater Resources Management in Coastal Aquifers, European Journal of Experimental Biology, Vol. 3, Issue 3, 2013, pp.80-94.

[3] Widada S., Phenomenon of Seawater Intrusion in Pekalongan Coastal Area, Journal of Marine Science, Vol. 12, Issue 1, pp.45-52.

[4] Hadi B. S., Spatial Interpolation Methods in Geography Studies (Brief Reviews and Sample Applications), Journal of Geomedia, Vol. 11, Issue 2, 2013, pp.235-252.

[5] Pasaribu J. M., Haryani N. S., Comparison of Interpolation Technical DEM SRTM Using Inverse Distance Weighed (IDW), Natural Neighbor, and Spline Method, Journal of Remote Sensing, Vol. 9, Issue 2, 2012, pp.126-139.

[6] Drapper N. R., Smith H., Applied Regression Analysis, John Wiley and Sons Inc. Canada, 1981, pp.

[7] Kusumarini S., Seawater Intrusion Prediction Based on Value of Electrical Conductivity and Total Dissolved Solid in Tangerang Regency [Thesis], IPB University, 2013, pp.6

[8] Hidayat M. R., Mapping of Seawater Intrusion of North Pekalongan District, State University of Semarang, 2015, pp.60.

[9] Ministerial Decree of Energy and Mineral Resources Decree Number 1451.K/10/MEM/2000 concerning on Government Technical Guidelines in The Field of Groundwater Treatment, Ministry of Energy and Mineral Resources, 2000

[10] Rusydi A. F., Correlation Between Conductivity and Total Dissolved Solid in Various Type of Water: A Review, IOP Conf. Series: Earth and Environmental Science 118 012019, 2018, pp.1-6.

[11] McNeil V., Cox M. E., Relationship Between Conductivity and Analyzed Composition in A Large Set of Natural Surface-water Samples, Queensland, Australia, Journal of Environ. Geol., Vol. 39, 2000, pp. 1325-1333

[12] Thirumalini S., Joseph K., Correlation Between Electrical Conductivity and Total Dissolved Solids in Natural Waters, Malaysian Journal of Science, Vol. 28, 2009, pp.56-61.

9th Int. Conf. on Geotechnique, Construction Materials and Environment, Tokyo, Japan, 20-22 November 2019, ISBN: 978-4-909106025 C3051

BIMODAL NUCLEAR THERMAL PROPULSION FOR INTERPLANETARY EXPLORATION

Elia D'Ambrosi[1] and Sam M Dakka[2]
[1,2] Department of Mechanical, Materials and Manufacturing Engineering, University of Nottingham, UK.

ABSTRACT

Interplanetary exploration is not only a proven recipe for advancement in science and technology; it is also a realistic and profitable goal for long-term human survival. However, current state-of-the-art Chemical Propulsion (CP) systems are inadequate for our future interplanetary objectives. In fact, a combination of low specific impulse and low efficiency lead to narrower launch windows, longer flights, and higher exposure to radiation.

The aim of this study is to make the case for Bimodal Nuclear Thermal Propulsion (BNTP) as the best alternative to today's rocket technologies for a manned mission to Mars. BNTP is a combination of Nuclear-Thermal-Propulsion (NTP) rockets and Nuclear-Electric-Propulsion (NEP) thrusters. The former generates high thrust, the latter high specific impulse; combined, they ensure both high payloads and short transit-times.

The split/sprint mission architecture is outlined as follows: the spacecraft with six astronauts departs in the June 2033 launch window with a fast-conjunction trajectory. The Pewee-class NTP engines provide the initial thrust for escaping Earth and for the propulsive capture at Mars, while the auxiliary NEP ion thrusters deliver constant acceleration during the transfer. The nuclear reactor is used as a power source for the entire spacecraft. This study shows that, using BNTP, the transit time could be reduced from the 260 days of a conventional Hohmann transfer to approximately 80 days, with a total outbound ΔV budget of 11.57 km/s and a spacecraft Initial Mass in Low Earth Orbit (IMLEO) of 250.27t.

Keywords: Mars exploration, Nuclear propulsion, Manned space mission, Orbital mechanics

INTRODUCTION

Problem Identification

It is likely that the next decades will see the development of ambitious space projects, not least in the context of interplanetary exploration. For this reason, it is important to investigate and analyze the different technologies that can enable deep space exploration.

Among these technologies comes propulsion: because of a combination of low specific impulse and low efficiency, current CP systems are insufficient for our future interplanetary objectives. Long transit times pose substantial risks to crews traveling to destinations such as Mars, due to the presence of Solar Radiation (SR) and Galactic-Cosmic Radiation (GCR). Physiological issues, such as bone and vision degradation, muscular atrophy and destruction of the circadian rhythm, combine with psychological problems such as claustrophobia and depression due to confinement. The only alternative to mitigate those effects, without sacrificing the scientific return of a manned mission, is by traveling faster.

Aims and Objectives

The aim of this project is to make the case for Bimodal Nuclear Thermal Propulsion (BNTP) as the best alternative to today's rocket technologies.
The first objective is to examine BNTP technology, presents its characteristics, and outline its benefits by defining key performance parameters.
The second objective is to include BNTP in the design of a preliminary mission architecture for the manned exploration of Mars.

NOMENCLATURE

Table 1 Nomenclature

BNTP	Bimodal Nuclear Thermal Propulsion
CP	Chemical Propulsion
ERV	Earth Re-entry Vehicle
GCR	Galactic Cosmic Radiation
IMLEO	Initial Mass in Low Earth Orbit
ISRU	In-Situ Resource Utilization
LEO	Low Earth Orbit
LH_2	Liquid Hydrogen
MOC	Mars Orbital Capture
NERVA	Nuclear Engine for Rocket Vehicle Applications
NTP	Nuclear Thermal Propulsion
SR	Solar Radiation
TMI	Trans-Mars Injection
Xe	Xenon

METHODOLOGY

Following an analytical methodology, this study examines how to exploit BNTP to decrease transit time and maximize the spaceship operational capability for a crewed mission to Mars.

The first section is descriptive: after defining key parameters for rocket propulsion, it presents the working principles for NTP rockets, NEP thrusters, and for BNTP using a combination of both.

The second section is based on estimation and analytical modelling. First, the transit time and minimum ΔV budget of the mission are calculated based on a Hohmann transfer. After that, a different trajectory is proposed, where NTP generates the high thrust of the planet-centric maneuvers, and NEP provides the high specific impulse necessary during heliocentric transfer. The ΔV budget for the new trajectory is estimated, and the NTP and NEP system are in turn sized to meet the requirements using Tsiolkovsky rocket equation. The total mass budget and the new transit time are thus linearly calculated.

TECHNOLOGY OUTLINE

Figures of Merit

Three figures of merit for space propulsion are established to evaluate the suitability of different propulsion systems, namely the specific impulse I_{sp}, the specific mass α, and the thrust-to-weight ratio.

The specific impulse I_{sp} [s] is a measure of the total impulse delivered by the engine per unit weight of propellant consumed. It measures how effectively the propellant is being used: a rocket with higher I_{sp} needs less propellant for a given mission.

The specific mass α [kg/kW] is the constant of proportionality between the engine system mass and the power delivered to the engine [1]; it measures the mass of the engine system for every kW produced.

Thrust-to-weight ratio is the ratio between the thrust F [N] delivered by the engine and the weight of the engine system [N]; it controls travel time.

When compared between each other, NTP has higher thrust-to-weight ratio and lower α but is limited by a lower I_{sp}. On the contrary, NEP has a very high I_{sp} but suffers from a low thrust-to-weight ratio and a higher α. In addition, burn time t_b for NTP is measured in minutes; for NEP in months or years. Hence the need for BNTP: a propulsion system that combines the best parameters of the two.

Nuclear Thermal Propulsion (NTP)

NTP working principles and components

NTP working principle is the following: hydrogen propellant is directly heated by a nuclear fission power source and then expanded out a nozzle, creating a thrusting force on the rocket. During operation, hydrogen (H_2) propellant is pumped through coolant channels where it is superheated to high temperatures and then expanded out a supersonic nozzle to generate high thrust at more than twice the specific impulse of today's best chemical rockets.

Advantages and disadvantages of NTP

NTP has always been an attractive space propulsion option for several reasons:

- The high I_{sp} reduces the in-orbit total mass for high ΔV missions.
- High F translates into more reasonable interplanetary trip times.
- Since NTP can utilize any gaseous propellant, it has the best potential for using in situ planetary propellant resources [1].
- It requires no large technology scale-up: the smallest tested *Pewee Engine* is adequate if used in a clustered arrangement [2].

However, NTP technology faces some technical issues with increased weight due to the thermal and radiation-shielding requirements [1]. Moreover, the high temperature desirable to maximize the thermodynamic efficiency is limited in a solid core reactor by the materials' thermal limits. Finally, radiation contamination in the case of uncontrolled explosion of the rocket shall be considered, and the reactor shall not become operational until it has been boosted into an orbit well away from Earth surface [6].

Nuclear Electric Propulsion (NEP)

NEP working principles and components

NEP working principle is outlined: heat coming from the reactor core is transferred by a working fluid to a power conversion unit. The electricity is then conditioned to the voltage and current needed and applied to the electric thrusters. Thrust is generated by flowing propellant along with electrical power through the thrusters.

Electrostatic propulsion is currently the only variant of electric propulsion that can enable long-term deep space missions [1].

The most popular and advanced means of electrostatic propulsion are ion thrusters. Molecules of the propellant are first ionized, and then accelerated by Coulomb body force driven by the electrostatic field. A neutralizer emits electrons to counterbalance the accelerated ions' charge.

Advantages and disadvantages of NEP

The reason for NEP popularity is based on some robust advantages:

- It has large mass carrying capabilities, coming from its high I_{sp}.
- Because of the high exhaust velocity of ion engines, less propellant is needed [3].
- The long burn time t_b is essential to provide constant acceleration for deep space exploration missions lasting months or years.
- The EU and the USA have extensive know-how in ion thrusters' technology.

However, the low thrust means that significant spacecraft acceleration requires either engine-on time comparable to the entire mission duration, or that tens or hundreds of individual modules must be used in a clustered arrangement, with a corresponding demand of electric power [4]. Another drawback of NEP is the dumping via a high-area space radiator, which can grow massive and increase the overall mass budget.

Bimodal Nuclear Thermal Propulsion (BNTP)

Overall, NEP is feasible for heavy-payloads propellant-efficient missions with a constant but slow acceleration, but a long mission duration is inevitable. On the other hand, NTP can ensure shorter trip times and more agility at the price of increased weight.

The best rocket propulsion system for deep space is a hybrid, dual-mode NTP-NEP system, the components of which are shown if Fig. 1. NTP would deliver the initial impulsive high thrust to reach escape speed quickly, and the balance between NTP and NEP during the mission trajectory would be optimized based on transit time and propellant.

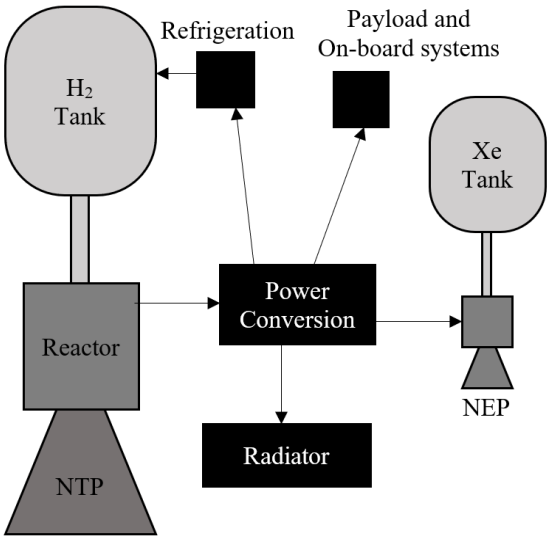

Fig. 1 BNTP components schematic

By reconfiguring the nuclear reactor for bimodal operation, abundant electrical power can be generated to support spacecraft environmental systems, high data rate communications, and an active refrigeration system for long term LH_2 storage [5]. The reactor could also be employed for in-situ operations, avoiding the need to deploy large photovoltaic arrays. Furthermore, using a nuclear reactor as power source for other propulsive methods appears to be the only possibility for powers at the hundreds of kW level.

Standard conversion is based on closed thermal cycles (e.g., Brayton) producing mechanical power driving alternators or dynamos. This technology is now mature in the MW power range, with a feasible conversion efficiency of ~25% [4].

MISSION ARCHITECTURE

The proposed architecture is a split/sprint mission with three spaceships. Two cargo ships pre-deploy the in-situ resource utilization (ISRU) equipment, the habitable module and the Earth Re-entry Vehicle (ERV). The manned spacecraft with six astronauts departs in the June 2033 launch window, uses a fast-conjunction trajectory, and performs a propulsive capture at Mars. It comprises BNTP with three 110kN Pewee-class NTP rockets and a cluster of nine NEP Radio-Frequency Ion Thrusters (RFIT-45).

Ground Rules and Assumptions

The reference NTP system is found in NASA DRA 5.0: a Pewee-class engine with expander cycle capable of $F = 110kN$, $I_{sp} = 900s$ and thrust-to-weight ratio of $F/W = 3.5$ [7]. For the NEP system, the parameters correspond to the RFIT-45 ion thruster, under development since 2010 at the Keldysh Research centre in Moscow [8]. A single RFIT-45 requires a power input of $P_e = 50kW$ and produces an $I_{sp} = 6880s$ at $F = 1.083N$.

Trajectory

To calculate the ΔV budget of the mission, it is first necessary to decide the spacecraft's trajectory. Figure 2 shows the difference between a fast-conjunction class trajectory and its alternative, an opposition class trajectory. Fast-conjunction is preferable because it provides adequate time at Mars for the crew to explore and sample the planet's rich geological diversity while reducing the transit time to and from Mars. In addition, an opposition class trajectory would require a higher ΔV, affecting the propellant mass and increasing the IMLEO.

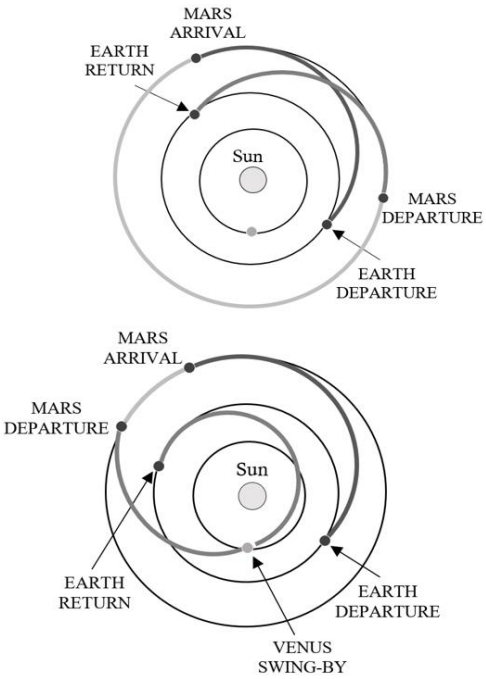

Fig. 2 Fast-conjunction class (top) vs Opposition class (bottom) trajectories

The smallest possible ΔV budget corresponds to a Hohmann transfer manoeuvre, where the spacecraft moves from one circular orbit to another coplanar circular orbit via an elliptical transfer orbit. This manoeuvre is energetically optimized and is therefore the most fuel-efficient. It consists in two impulsive burns: Trans-Mars Injection (TMI) and Mars Orbital Capture (MOC). ΔV_{TMI} indicates the velocity increment required to go from the spacecraft's parking orbit around Earth onto the hyperbolic departure trajectory to Mars. ΔV_{MOC} indicates the velocity change necessary to approach Mars parking orbit velocity from the hyperbolic arrival trajectory.

Assuming the two planets have circular orbits and are coplanar, and that arrival at Mars corresponds to an angle of 180° between the two planets, the ΔV budget for a Hohmann transfer can be calculated.

First, the initial impulsive burn is computed:

$$\Delta V_{TMI} = v_E \cdot \left(\sqrt{(1+e)} - 1\right) \qquad (1.1)$$

Where: $v_E = \sqrt{\mu_s / r_E}$ is the velocity of the Earth in a circular orbit around the Sun.
$e = (r_M - r_E)/(r_M + r_E)$ is the eccentricity of the elliptical transfer.
$\mu_s = 1.327 \cdot 10^{20}\ m^3/s^2$ is the Sun's gravitational parameter.
$r_E = 150 \cdot 10^9 m$ is Earth's orbital radius.
$r_M = 228 \cdot 10^9 m$ is Mars' orbital radius.

Substituting the values yields:

$$\Delta V_{TMI} = 2.94\ km/s \qquad (1.2)$$

Secondly, the final impulsive burn is determined:

$$\Delta V_{MOC} = v_M \cdot \left(1 - \sqrt{(1-e)}\right) \qquad (2.1)$$

Where: $v_M = \sqrt{\mu_s / r_M}$ is the velocity of Mars in a circular orbit around the Sun.

Substituting the values yields:

$$\Delta V_{MOC} = 2.63\ km/s \qquad (2.2)$$

The total ΔV budget for a Hohmann transfer is:

$$\Delta V_{Hohmann} = \Delta V_{TMI} + \Delta V_{MOC} = 5.57\ km/s \qquad (3)$$

Figure 3 displays the Hohmann transfer just described, where "1" is Earth orbit, "3" is Mars orbit, and "2" indicates the transfer trajectory.

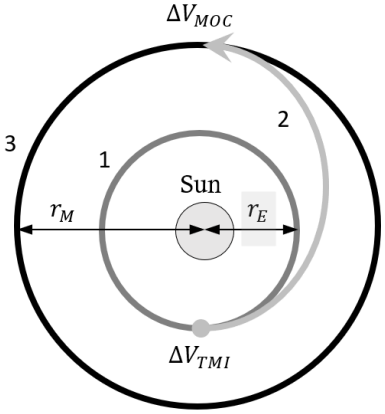

Fig. 3 Earth-Mars Hohmann Transfer

This corresponds to a 1-way transit time of:

$$T = \pi\sqrt{(r_E + r_M)/8\mu_s} = 260\ days \qquad (4)$$

Such transit time is deemed unacceptable for the prolonged risks posed to the crew and the spacecraft, and for the number of contingencies and resources needed during the transfer. This study attempts at finding a compromise between transit time, spacecraft mass and scientific return of the mission, and show how BNTP is a viable propulsion technology for these objectives.

Mars interplanetary transfer by means of BNTP consists of a combination of high- and low-thrust manoeuvres: the high-thrust NTP provides for TMI and MOC, whereas the low-thrust NEP defines the heliocentric transfer. This way, a continuous acceleration is provided, instead of boosting the spacecraft at the start and then coasting all the way to

Mars with the engines off. This concept is illustrated in Fig. 4, where "1" is Earth orbit, "3" is Mars orbit, and "2" indicates the transfer trajectory.

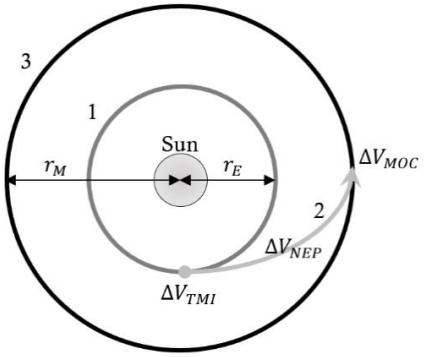

Fig. 4 Earth-Mars Proposed Trajectory

Propulsion Unit

If the spacecraft is constantly accelerating, the ΔV budget of the mission would evidently increase. ΔV_{TMI} and ΔV_{MOC} are kept the same, since TMI and MOC are still performed by NTP, with their sum being $\Delta V_{NTP} = \Delta V_{Hohmann} = 5.57\ km/s$. To account for the constant acceleration imparted by the NEP system, a new $\Delta V_{NEP} = 6km/s$ is added, which is an educated guess and duplicates the total mission ΔV budget. This allows to perform a separate analysis of the engine requirements for NTP and NEP.

Using Tsiolkovsky rocket equation, it is possible to infer the two ratios (R_{NTP} and R_{NEP}) between the spacecraft's wet and dry mass (m_w and m_d).

$$R_{NTP} = NTPm_w/NTPm_d = e^{(\Delta V_{NTP}/(I_{sp}(NTP)\cdot g_E))} = e^{(5770/(900\cdot 9.81))} = 1.922 \quad (5)$$

$$R_{NEP} = NEPm_w/NEPm_d = e^{(\Delta V_{NEP}/(I_{sp}(NEP)\cdot g_E))} = e^{(6000/(6880\cdot 9.81))} = 1.093 \quad (6)$$

The NTP propellant is liquid hydrogen (LH_2) and the corresponding mass is m_{LH2}. For the NEP unit, the propellant is Xenon (Xe) and the corresponding mass is m_{Xe}. The wet mass m_w is the sum of dry mass m_d and propellant mass, hence:

$$R_{NTP} = (NTPm_d + m_{LH2})/NTPm_d \quad (7.1)$$

$$\therefore m_{LH2} = 0.922 \cdot NTPm_d \quad (7.2)$$

$$R_{NEP} = (NEPm_d + m_{Xe})/NEPm_d \quad (8.1)$$

$$\therefore m_{Xe} = 0.093 \cdot NEPm_d \quad (8.2)$$

Mass Budget

Figure 5 illustrates the mass distribution of the spacecraft. The payload is estimated at 50t and includes a crew of six and suits (1.5t), consumables (5.5t), descent stage (4t), aerodescent shell and parachutes (7t), propellant for descent stage (7t) and surface payload (25t). Data for such subsystems is taken and approximated from [5] and reflects a six-astronauts spaceship of similar dimensions.

The LH_2 and Xe propellant masses (m_{LH2} and m_{Xe}) are still to be determined.

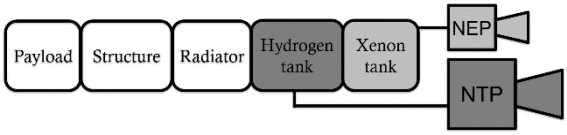

Fig. 5 Structural breakdown

As Borowsky and Dudzinsky explain in [5], other mass must be added, which accounts for the spacecraft's structure: the empty mass of the fuel tanks (14.5t), the Brayton conversion unit (1.5t), the nuclear reactors (18t), the radiation shields (9t), the LH_2 refrigeration system (0.5t), and the avionics (1.5t). Consequently, the total mass of the structure is 45t, and the dry mass $NTPm_d$ becomes:

$$NTPm_d = m_{payload} + m_{structure} + m_{Xe} = 50 + 45 + m_{Xe} = 95 + m_{Xe} \quad (9)$$

It can be noticed that the NEP unit starts operating only once the NTP has performed the TMI. At this point, a good portion of the LH_2 has been consumed, and it would be incorrect to perform the same calculations as in Eq. (9) without taking this into account. Since the ΔV is similar for the two main manoeuvres, it can be assumed that, when the NEP unit comes into operation, the LH_2 tank is half empty.

Therefore, the dry mass $NEPm_d$ becomes:

$$NEPm_d = m_{payload} + m_{structure} + 0.5m_{LH2} = 95 + 0.5m_{LH2} \quad (10)$$

With these figures at hand, the total IMLEO can be computed. Equations (7.2) and (8.2) can be substituted into Eq. (9) and (10) to yield:

$$\frac{m_{LH2}}{0.922} = 95 + m_{Xe} \quad (11)$$

$$\frac{m_{LH2}}{0.093} = 95 + 0.5m_{LH2} \quad (12)$$

This is a two-variables system, and the values of m_{LH2} and m_{Xe} are easily calculated:

$$m_{LH2} = 100.03t \quad (13)$$

$$m_{Xe} = 13.53t \quad (14)$$

These can now be added to the payload and structural masses to give the total IMLEO.

$$IMLEO = m_{payload} + m_{structure} + m_{LH2} + m_{Xe} = 50 + 45 + 100.03 + 13.53 = 208.56t \quad (15)$$

The waste power of the energy converter in the NEP system will have to be radiated to space. To account for the mass of the radiator, the result of equation (18) is multiplied by a factor of 120%.

$$IMLEO = 208.56 \cdot 1.2 = 250.27t \quad (16)$$

Transit Time

Borowsky, McCurdy and Packard [9] indicate that, with a total outbound ΔV of 11.41km/s, a launch in June 2033 could result in a fast conjunction of 80 days. The research in [9] is based on NTP only, and the values for ΔV_{TMI} and ΔV_{MOC} are therefore imprecise. However, since the ΔV budget of the mission proposed here is 11.57km/s, it can be inferred that a similar transit time could be achieved.

This result is a 325% improvement over the Hohmann transit time of 260 days calculated in Eq. (4) and would sensibly reduce the total dosage of hazardous radiation experienced by the crew as well as the total mass of necessary food and water resources.

CONCLUSION

Literature preceding this study has consistently ruled out CP technology for deep-space exploration for its low specific impulse and low efficiency. A tested near-term alternative could come from new propulsive methods powered by nuclear fission.

A descriptive overview has been presented about the technology principles underlying nuclear space propulsion. Relevant parameters have been defined: specific impulse I_{sp}, specific mass α, and thrust-to-weight ratio. In NTP, liquid hydrogen propellant is directly heated by a nuclear reactor and expanded through a nozzle, creating a thrusting force on the rocket. In NEP, electricity generated from the nuclear fission reactor ionizes the molecules of the Xenon propellant and accelerates them out of the thruster by an electrostatic field. When compared between each other, NTP has higher thrust-to-weight ratio and lower specific mass α but is limited by a lower specific impulse I_{sp}, and vice versa. BNTP is a propulsion technology that combines the high thrust of NTP with the high I_{sp} of NEP. In such hybrid mode, NTP could help a Mars spaceship reach escape speed quickly and NEP could operate at high efficiencies for a long duration.

A split/sprint Mars mission with three spaceships has been designed. Two cargo ships pre-deploy the ISRU equipment, the habitable module and the ERV. The manned spacecraft departs in June 2033 launch window with a fast-conjunction trajectory and uses BNTP. It was found that a Hohmann transfer trajectory would result in a ΔV budget of 5.57 km/s and a transfer time of 260 days for the crew. With the bimodal configuration, an auxiliary NEP system could deliver constant acceleration during the transfer, after the impulsive NTP burn. The nuclear reactor could be used as a power source for the spacecraft systems and ISRU, eliminating the need for a large photovoltaic array. The additional NEP ΔV is estimated at 6 km/s, causing the total ΔV budget to become 11.57 km/s and the transit time to be reduced to approximately 80 days. The IMLEO of the manned spacecraft is determined to be 250.27t.

REFERENCES

[1] Sforza P.M., Theory of Aerospace Propulsion, Butterworth-Heinemann, 2012, pp. 517-565.

[2] Borowski S.K., Nuclear Thermal Propulsion: Past Accomplishments, Present Efforts, and a Look Ahead, Journal of Aerospace Engineering, Vol. 26(2), 2013, pp. 334-342.

[3] Keaton P.W. and Tubb D.J., Nuclear Electric Propulsion, Manned Mars Missions, Working Group Papers, NASA TM-89320, Vol. 1, Sect. 1-4, 1986, pp. 129-141.

[4] Bruno C. and Dujarric C., In-space Nuclear Propulsion, Acta Astronautica, Vol. 82, 2012, pp. 159-165.

[5] Borowsky S.K., Dudzinsky L.A., Vehicle and Mission Design Options for the Human Exploration of Mars/Phobos Using Bimodal NTR and LANTR Propulsion, 34th AIAA / ASME / SAE / ASEE Joint Propulsion Conference and Exhibit, 1998.

[6] D.G. Shepherd, Aerospace Propulsion, Elsevier, 1972, pp. 240-242.

[7] Borowsky S.K., McCurdy D.R. and Packard T.W., Nuclear Thermal Rocket/Vehicle Characteristics and Sensitivity Trades for Nasa's Mars Design Reference Architecture (DRA) 5.0 Study, NASA, Proceedings of Nuclear and Emerging Technologies for Space 2009, Atlanta, GA, 2009.

[8] Loeb H.W., Petukhov V.G., Popov G.A., Mogulkin A.I., A realistic concept of a manned Mars mission with nuclear-electric propulsion, Acta Astronautica, Vol. 116, 2015, pp. 299-306.

[9] Borowsky S.K., McCurdy D.R., Packard T.W., Nuclear Thermal Propulsion (NTP): A Proven Growth Technology for Fast Transit Human Missions to Mars, NASA, AIAA Space 2013 Conference and Exposition, San Diego, CA, 2013.

9th Int. Conf. on Geotechnique, Construction Materials and Environment, Tokyo, Japan, 20-22 November 2019, ISBN: 978-4-909106025 C3051

TRIHALOMETHANE AND HALOACETIC ACID FORMATION POTENTIAL OF TROPICAL PEAT WATER: EFFECT OF TIDAL AND SEASONAL VARIATIONS

Muammar Qadafi[1], Suprihanto Notodarmojo[2], Yuniati Zevi[3], and Yusuf Eka Maulana[4]

[1]*Environmental Engineering Program, ITB Bandung, Indonesia*; [2,3]*Departement of Environmental Engineering, ITB Bandung, Indonesia,* [4]*Integrated Laboratory, Poltekkes Kemenkes Bandung, Indonesia*

ABSTRACT

The existence of humic substances in peat water impacts on the presence of the dissolved organic matter (DOM) which is the precursor of trihalomethanes (THMs) and haloacetic acids (HAAs). However, information on DOM characteristics, THMs and HAAs Formation Potential (THMFP and HAAFP) in tropical peat water are still limited. This study aimed to determine the correlations between DOM, THMFP, and HAAFP during dry and rainy seasons in tropical peat water in Indonesia. Samples of peat water are taken from the water canal and tidally affected river on Sumatera's peatland during the rainy season and dry season to determine the effects of the seasons and tides. DOM measured by dissolved organic carbon (DOC), specific ultraviolet absorbance and the ratio of UV_{465}/UV_{665} while THMFP determined from a total of THMFP4 measurements and HAAFP determined from measurement of total HAAFP5. Compared to dry season, values of all organic parameters on rainy season were higher but fewer in river. Canal water has a higher DOC while river water has a higher chloride and bromide content. Increasing of DOC in the rainy season correlates with increasing of THMFP4 and HAAFP5. THMFP4 is dominated by chloroform on canal while brominated THMs predominate in river water which correlates with the presence of bromide. Chlorinated HAAs dominate HAAFP5 in canal water while brominated HAAs increases in the river. Seasons and tides affect the appearance of bromide contaminants in water that affects the form of THMFP and HAAFP.

Keywords: Trihalomethanes, Haloacetic acids, Dissolved organic matter, Tropical peat water, Tides and seasons effect

INTRODUCTION

Peat water is colored and acidic and has a nutrient content [1]. Peat water is acidic with a pH <5.2 due to dissolved organic matter (DOM) in the form of humic acid [2]. Humic acid contained in soil and peat water comes from the decomposition of animals and plants from microbial activity. Humic acid is a weak acid that gives brownish color to peat water. The content of organic compounds in peat water depends on the condition of peat soils and the climatic conditions of peat swamps [3]. Peat water is raw water that is not suitable for drinking water. Compared to other better surface water, peat water requires special processing to be used as a source of drinking water.

The composition of DOM in raw water can be different due to land use pattern [4]. The source of organic compounds present in peat water comes from peat soil itself because peatlands are wetlands where the land will be flooded throughout the year so that there are considerable water reserves [5]. Peat soil itself is soil derived from the accumulation of decomposition of plants that are rich in organic matter. Distribution of land or peatland in Indonesia covers all regions in Indonesia. Some of them are in Sumatra, Papua, and Borneo. The peatland which located in each of these regions has different thicknesses [6].

Humic acid is not a hazardous material and has many beneficial environmental effects [7]. However, humic acid is a precursor for the formation of potentially hazardous carcinogen disinfection by-products (DBPs) during the chlorination of water. Besides containing DOM, peat water also contains pathogenic bacteria and halogenated ions (Cl^-, Br^-, F^-, I^-) [8]. The process of chlorine disinfection produces DBPs in the form of THMs and HAAs [9].

The use of chlorine as disinfection has the advantage because the remaining chlorine in water can disinfect introduced pollutants into the water during the storage and distribution process [10]. However, carcinogen disinfection by-products (DBPs) simultaneously generated during the chlorination process including trihalomethanes and haloacetic acids, formed from reactions between chlorine and natural organic matter in water [11,12]. In general, trihalomethane and haloacetic acid concentrations are substantially greater than other By-products [12].

Trihalomethane is a halogenated organic

compound in which three of the four hydrogen methane (CH_4) atoms are replaced by halogen atoms. THM is also a large pollutant that is considered carcinogenic [13]. THM4 (chloroform/TCM, bromodichloromethane/ BDCM, dibromochloro methane/DBCM, and bromoform/TBM) are carcinogens of Cancer Group B (proven to cause cancer in laboratory animals). The United States Environmental Agency (USEPA) established a maximum pollution level of 80 µg/L for total THM4.

The second most important DBPs, haloacetic acids is a carboxylic acid in which halogen atoms replace hydrogen atoms in acetic acid. The United States Environmental Agency (USEPA) sets a maximum pollution level of 60 µg/L of total HAA5 including dichloroacetic acid (DCAA), trichloro-acetic acid (TCAA) monochloroacetic acid (MCAA), monobromoacetic acid (MBAA) and dibromoacetic acid (DBAA), while four other HAAs including tribromoacetic acid (TBAA), bromochloro-acetic acid (BCAA), bromodichloroacetic acid (BDCAA) and chlorodibromoacetic acid (CDBAA) were not included in the regulation [13].

The effect of chloride and bromide ions on THM and HAA formation in the chlorination process was investigated, and it was found that brominated DBP concentrations (Br^-DBP) increased with increasing bromide concentration [14,15]. Experiments show that with increasing bromide concentration, the total THM and HAA results in an increase [16]; The formation of brominated THM and HAA species are increased during chlorination with an increase in bromide concentration [16].

The purpose of this study was to determine the THM and HAA formation potential of peat water based on tidal and seasonal influences that have an impact on the presence of bromide and chloride ions in peat water. As the result of this work, we hope to identify the information on the relationship between tides and seasons in THM and HAA generation characteristics in treatment processes, and finally, to provide suggestions for the control of THM and HAA in water treatment processes.

MATERIAL AND METHOD

Chemicals

A standard mixture of trihalomethanes contain of THM4 (chloroform/TCM, bromodichloromethane /BDCM, dibromochloromethane/DBCM, and bromoform/TBM) in methanol and haloacetic acids containing HAA9 (dichloroacetic acid/DCAA, trichloroacetic acid/TCAA, monochloroacetic acid/MCAA, mono-bromoacetic acid/MBAA, dibromoacetic acid/DBAA, tribromoacetic acid /TBAA), bromochloroacetic acid/BCAA, bromo-dichloroacetic acid/BDCAA and chlorodibromo-acetic acid/CDBAA) in methyl tert-butyl eter (MTBE) were purchased from Sigma Aldrich (USA). GC solvent grade of methyl tert-butyl eter (MTBE), sodium sulfate, sodium bicarbonate, copper II sulfate pentahydrate, sodium sulfite, phosphate buffer, methanol, and sulfuric acid were purchased from Merck (Germany). Chlorine solution (sodium hypochlorite 25%) were purchased from Pudak Scientific (local). All solutions were diluted with mili-Q grade water.

Instrumentations

UV absorbance (UV_{254}, UV_{465}, and UV_{665}) was measured using a UV-Vis Spectrophotometer (Shimadzu UV-1700). TOC Analyzer (Shimadzu TOC VCSH) are used to measure DOC (dissolved organic carbon) using EPA 415.3 method. Bromide was determined with APHA 4500 Br^- B using phenol red colorimetric method. Chloride was determined by APHA 4500 Cl^- B using argentometric method.

Gas Chromatography (GC) Agilent 7890A and Agilent 5975C Mass Selective Detector (MSD) were used to analyze HAA and THM. Agilent 7693 Series Automatic Liquid Sampler is used for sample injection and Agilent MSD ChemStation software is used to process data.

Trihalomethane Analysis

In the THM analysis, 1.0 µl of the sample was entered into GC by splitless injection and completed in the HP-5MS capillary column 30 m × 0.25 mm, 0.25 mm thick. The gas carrier (helium) rises at a constant inlet pressure of 15 kPa with a flow rate of 1.5 ml/minute. The injector temperature is 93 °C. The oven temperature is set to 90 °C, and the setting temperature is set to 300 °C.

Haloacetic acids Analysis

In the HAA analysis, setting GC conditions was carried out based on EPA 552 modified with Xie et al [17] for GC-MS analysis. 40 mL water sample was extracted using 4 mL MTBE after acidified to pH 2 using concentrated sulfuric acid and the addition of 16 g sodium sulfate and 3 g of copper II sulfate pentahydrate. Approximately 3 mL of the organic phase was methylated with acidic methanol in 50 ˚C ±2 for 2 hours. 1.0 µL of the sample was entered into GC by splitless injection and filled in the HP-5MS capillary column thickness 30m × 0.25mm, 0.25mm. The flow rate of the carrier gas (helium) is 1.0 mL/minute (constant flow). The oven temperature is set at 35 ˚C for 10 minutes and then raised to 75 ˚C at a level of 5 ˚C/minute and increased for 15 minutes, then raised to 100 ˚C with 5 ˚C/minute for 5 minutes, 135˚C with rose 5 ˚C/minute for 2 minutes, and 185

˚C by increasing 25˚C/minute for 2 minutes. The injector temperature is 200 ˚C and the line transfer is received at 280 ˚C. MSD is operated in Electron Impact (EI) mode. The ion source temperature is regulated 230 ˚C with electron energy being 70 eV.

Trihalomethane and Haloacetic Acids Formation Potential

The trihalomethane and haloacetic acid formation potential (THMFP and HAAFP) is the quantity of THMs and HAAs formed where the water sample is dosed with excess chlorine for 7 days at 25 °C and pH 7. The chlorine dosage was determined so that the remaining chlorine was 3-5 mg/L after 7 days of incubation. The method was adapted from standard method 5710B procedure [18]. In this method, 97.5 mL samples were dosed with 2 ml 0.5 M phosphate buffer solution to buffer the sample at pH 7 and 0.5 mL NaOCl. The sample was incubated for 7 days in a dark at 25 °C. After 7 days, 0.5 mL of cooling solution (sodium sulfite 10%) was added to prevent further reaction and the sample was cooled until analysis.

Sample Extraction

Trihalomethane extraction

The sample extraction procedure for THM analysis was carried out based on the EPA 551.1 Method [19] with minor modification. 50 mL of sample water was extracted with 3 mL MTBE by adding 20 gr of sodium sulfate anhydrous to increase the strength of the aqueous phase ion. After an organic phase (MTBE) and the water phase were separated, micro pipette used to remove approximately 1µL MTBE to autosampler vial for GC/MS analysis.

Haloacetic acid extraction

The sample extraction procedure for HAA analysis was carried out based on the EPA 552.2 Method. [20]. After adding 1mL of concentrated sulphuric acid, 16gr of sodium sulfate anhydrous, 2gr of copper II sulfate pentahydrate and surrogate (2,3-dibromopropionic acid), 40 mL of water sample was extracted with 4 mL MTBE and added internal standard, 1,2,3-trichloropropane, manual for 2 minutes. 2.5mL of extract was methylated by adding 1.0 mL of 10% sulphuric acid solution in methanol and heated at 50˚C for 2 hours. After neutralization with 4mL of saturated sodium bicarbonate solution, the extract was analyzed using GC/MS.

Samples

Sampling was carried out in Peria River and water canal found in Indragiri Hilir Regency's peatland, Riau Province, Indoneisa to see the effects of tides. Samples were taken in two different places, in the rainy and dry season. River water that affected by tides and canal water that was not affected by tides. the water samples are canal water at dry season (CWD), river water at dry season (RWD), Canal water at rainy season (CWR) and river water at rainy season (RWR). The sampling location shows in Figure 1.

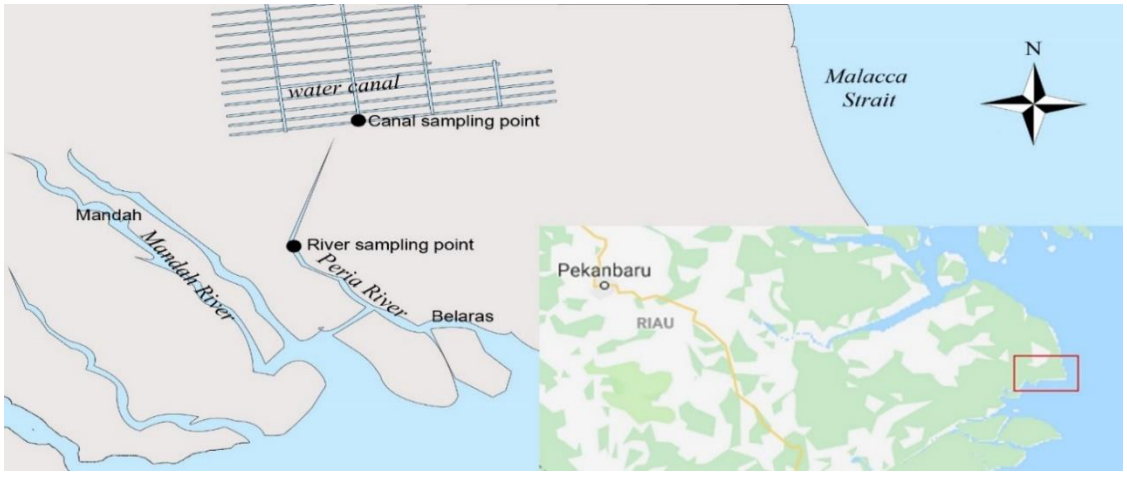

Fig.1 Sampling locations

RESULT AND DISCUSSION

Properties of Peat Water

Table 1 shows that the DOC values are ranging from 22.2 mg.C/L-56.2 mg.C/L where the highest concentration is found in peat water originating from CWR and the lowest comes from RWD. The DOC value corresponds to the UV_{254} absorbance. The highest UV_{254} absorbance was found in canal water during the rainy season which was 3.175/cm and the lowest was in river water during the dry season which

was 1.246/cm. The SUVA values range from 5.5 L/mg.m-5.9 L/mg.m which indicates that the compounds of NOM in peat water consist mostly of humic compounds that have high aromaticity and are strongly hydrophobic. Increasing of DOC in the rainy season can occur due to the leaching process that dissolves NOM from peat soil [21].

The E4/E6 ratio illustrates the presence of high molecular weight NOM in water [22]. The smaller E4/E6 ratio is found in peat water originating CWR, which is 4,914, whereas a large E4/E6 ratio is found in peat water originating from rivers in the dry season (= 8,286). The presence of chloride ions in river greater than canal due to the tidal influence. Bromide ions are only found in river peat water.

Table 1 Properties of peat waters

	CWD	RWD	CWR	RWR
DOC (mg.C/L)	44.46	22.2	56.2	47.4
UV_{254} (1/cm)	2.61	1.24	3.17	2.60
SUVA (L/mg.m)	5.9	5.6	5.6	5.5
E_4/E_6	7.8	8.28	4.91	5.57
Cl^- (mg/L)	94	192	88	200
Br^- (mg/L)	-	175.47	-	100

Trihalomethane Formation Potential

THMFP was determined from the total formation of THM4 after chlorination for seven days due to variations in the dominant compounds formed shows in Fig. 2. THMFP on peat water increase in the rainy season because increasing of DOC [23] during the rainy season due to NOM leaching from peat soil [22]. THMFP in peat water originating from canals dominated by TCM formation. According to Stuart et al. [23], Garrido and Ponseca [24], Panyapinyopol et al. [25], Sururi et al [4] TCM was the largest THM formed during chlorination. TCM concentration in the dry season from 658.27 µg/L in dry season becomes 1024.82 µg/L during the rainy season.

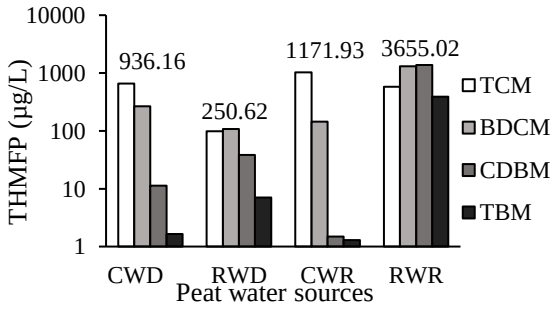

Fig. 2 Trihalomethane formation potential of peat water based on THM4 formation

The total THM4 which was THMFP was also increased in the rainy season from 936.16 µg/L to 1171.93 µg/L. In the river, THMFP is dominated by BDCM and CBDM in accordance with the Rajamohan [26] study. The presence of TBM is a significant difference between canal water and river water where the presence of TBM has a higher concentration in river water. This is in accordance with Marhaba et al [27] and Padhi et al [28] that bromide-containing water produce higher brominated THM. The pattern of THM formation in river water has the same pattern in peat canal water where the concentration of each THM increases during the rainy season. The THMFP increased from 250.65 µg/L to 1171.93 µg/L.

Haloacetic acid Formation Potential

HAAFP was determined from the total formation of HAA5 after chlorination for seven days due to variations in the dominant compounds formed (Fig.3). HAAFP in the canal water is dominated by DCAA and TCAA that corresponds to the results of He et al. [29] which indicate chlorine reactivity with low molecular weight compounds during the disinfection process. The DCAA and TCAA concentrations increased from 3387.50 µg/L and 3329.19 µg/L to 6898.31 µg/L and 5894.21 µg/L during the rainy season.

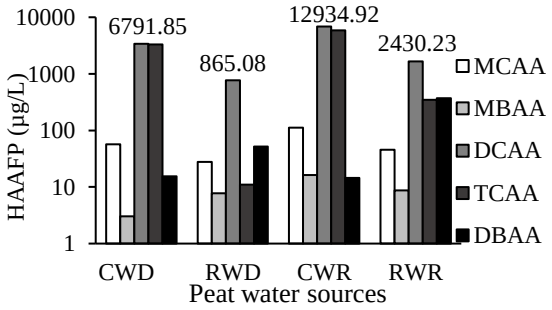

Fig. 3 Haloacetic acid formation potential of peat water based on HAA5 formation

Increased concentrations of DCAA and TCAA resulted in an increase in total HAA5 which was HAAFP from 6791.85 µg/L to 12934.92 µg/L. The same pattern occurs in peat water originating from rivers but HAAFP is only dominated by DCAA. This result corresponds to Yu et al. [30] and Yue et al. [31] where the low concentration of TCAA is influenced by the high concentration of bromide ions originating from the sea, so the presence of TCAA is replaced by bromine-based HAA (DBAA). Total HAAFP in river water increases in the rainy season from 856.08 µg/L to 2430.23 µg/L.

Specifc Formation Potential

Figure 4 shows the Specific Trihalomethane Formation Potential (STHMFP) and Specific

Haloacetic Acid Formation Potential (SHAAFP). Compared with DOC values, STHMFP of peat water ranged from 11.28-77.0 µg/mg.C. There was no big difference in HAAFP on canal water between dry and rainy seasons. On the other hand, STHMFP of river water in the dry season rise significantly compared to the rainy season that related to E4/E6 ratio. The ratio of E4/E6 of river water in the dry season was higher than a rainy season but the DOC value was smaller that relate to the appearance of low molecular weight NOM-THMs precursor.

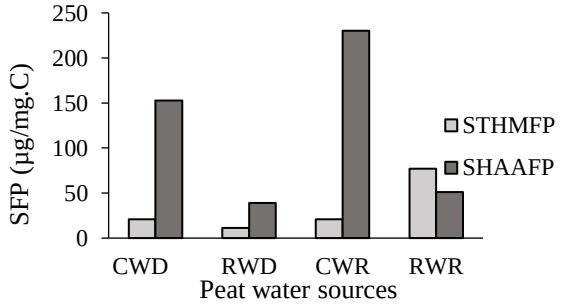

Fig. 4 Specific Trihalomethane and Haloacetic acid formation potential of pat water

SHAAFP of peat water range from 38.96-230.15 µg/mg.C where the highest value is found in canal water during the rainy season and related to higher E4/E6 ratio. This value is not much different from raw water originating from Bangkhan Water Treatment at 288 µg / mg.C [32]. Canal water has a higher E4/E6 ratio indicated that canal water has more humic content that major precursor to HAAs. SHAAFP of river water was raised but has a smaller ratio than canal water indicated that low molecular weight was not a major precursor of HAA compared to humic substances.

CONCLUSIONS

This work is conducted to identify the information on the relationship between tides and seasons in THM and HAA generation characteristics in tropical peat water during the chlorination process. The peat water has high DOC values ranged from 22.2-56.2 mg/L that the highest value found in canal water in the rainy season. THMFP and HAAFP are higher in the canal water and the rainy season. Bromide ion contains in river water influence the formation of brominated THM and HAA during chlorination. THMFP is dominated by TCM in canal water and dominated by BDCM and CBDM in river water. HAAFP in the canal water is dominated by DCAA and TCAA then in river water only dominated by DCAA.

ACKNOWLEDGMENTS

This research work was funded by The Indonesia Endowment Fund for Education (Lembaga Pengelola Dana Pendidikan/LPDP), Ministry of Finance Indonesia.

REFERENCES

[1] Kuokkanen, V., Kuokkanen, T., Rämö, J., and Lassi, U., Electrocoagulation treatment of peat bog drainage water containing humic substances. Water Research, Vol. 79, 2015, pp.79–87.

[2] Notodarmojo, S., Mahmud, and Larasati, A., Adsorption of natural organic matter (NOM) in peat water by local Indonesia tropical clay soil. International Journal of Geomate, Vol 13, 2017, pp.111–119.

[3] Ritson, J.P., Bell, M., Graham, N.J.D., Templeton, M.R., Brazier, R.E., Verhoef, A., Freeman, C., and Clark, J.M., Simulated climate change impact on summer dissolved organic carbon release from peat and surface vegetation: Implications for drinking water treatment, Water Research, Vol 67, 2014, pp.66-76.

[4] Sururi, M.R., Notodarmojo, S., and Rosmini, D, Aquatic organic matter characteristics and thmfp occurrence in a tropical river, International Journal of GEOMATE, Vol 17, 2019, pp.20–211.

[5] Raghunandan, M.E., dan Sriraam, A.S., An overview of the basic engineering properties of Malaysian peats, Geoderma Regional, Vol 11, 2017, pp.1-7.

[6] Ramadhan, M.L., Palamba, P., Imran, F.A., Kosasih, E.A., and Nugroho, Y.S., Experimental study of the effect of water spray on the spread of smoldering in Indonesian peat fires, Fire Safety Journal, Vol 91, 2017, pp.671–679.

[7] Abouleish, M.Y.Z., and Wells, M.J.M., Trihalomethane formation potential of aquatic and terrestrial fulvic and humic acids: sorption on activation carbon, Science of Total Environment, Vol 521-522, 2015, pp.293-304.

[8] Chan, C.M., Kamis, N.S., dan Mohamed, R.M.S.R., Using a Peat Media for Laundry Greywater Filtration: Geochemical and Water Quality Check, Middle-East Journal of Scientific Research, Vol 21, 2014, pp.1365-1370.

[9] Sillanpää, M., Ncibi, M.C., and Matilainen, A., Advanced oxidation processes for the removal of natural organic matter from drinking water sources: A comprehensive review, Journal of Environmental Management, Vol 208, 2018, pp.56-76.

[10] Lantagne, D.S., Cardinasli, F., and Blount, B.C., Disinfection by-product formation and mitigation strategies in point-of-use chlorination with sodium dichloroisocyanurate in Tanzania, The American Society of Tropical Medicine and Hygiene, Vol 8, 2010, pp.135–143.

[11] Tawabini, B, Al-Mutair, M., and Bukhari, A., Formation potential of trihalomethanes (THMs) in blended water treated with chlorine, Journal

of Water Reuse and Desalination, Vol 01, Issue 3, 2011, pp.172-178.

[12] Nitter, T.B., Kampel, W., Spendsen, K.V.H., and Aas, B., Comparison of trihalomethanes in the air of two indoor swimming pool facilities using different type of chlorination and different types of water, Water Science & Technology: Water Supply, 2017, pp.1–8.

[13] Wu, S., Anumol, T., Gandhi, J., and Snyder, S.A., Analysis of Haloacetic acids, Bromate, and Dalapon in Natural Waters by Ion Chromatography – Tandem Mass Spectrometry, Journal of Chromatography A. 2017.

[14] Zhang, Y., Collins, C., Graham, N., Templeton, M.R., Huang, J., and Nieuwenhuijsen., Speciation and variation in the occurrence of haloacetic acids in three water supply systems in England, Water and Environment Journal, Vol 24, 2009, pp.237-245.

[15] Hua, G. dan Reckhow, D.A., Effect of Pre-Ozonation on the Formation and Speciation of DBPs, Water Research, Vol 47, 2013, pp.4322-4330.

[16] Bond, T., Oslan, E.H., Parsons, S.A., and Jefferson, B., A critical review of trihalomethane and haloacetic acid formation from natural organic matter surrogates, Environmental Technology Reviews, Vol 1, 2012, pp.93-113.

[17] Xie, Y, Technical note analyzing haloacetic acids using gas chromatography/mass spectrometry, *Wat. Res*., Vol 35, 2001, pp.1599–1602.

[18] American Public Health Association, American Water Works Association, Water Environment Federation, 20th ed., Standard Methods for the Examination of Water and Wastewater, Washington, DC, 1998.

[19] U.S.EPA, Method 551.1. Determination of chlorination disinfection byproducts, chlorinated solvents, and halogenated pesticides/herbicides in drinking water by liquid-liquid extraction and gas chromatography with electron-capture detection. Environmental monitoring systems laboratory office of research and development., Cincinnati, 45268. 1990.

[20] U.S. EPA, Method 552.2. Determination of haloacetic acids in drinking water by liquidliquid extraction, derivatization, and gas chromatography with electron capture detection. Environmental monitoring systems laboratory office of research and development, Cincinnati, 45268, 1995

[21] Konskinen, M., Sallantaus, T., and Vasander, H., Post-restoration development of organic carbon and nutrient leaching from two ecohydrologically different peatland sites, Ecological Engineering, Vol 37, 2011, pp.1008–1016.

[22] Yu, J., Sun, D.D., and J.H. Tay., Characteristics of coagulation-flocculation of humic acid with effective performance of polymeric flocculant and inorganic coagulant. Water Science and Technology, Vol 47, Issue 1, 2002, pp.89-95.

[23] Stuart, M.E., Goody, D.C., Kinniburgh, D.G., dan Klinck, B.A., Trihalomethane formation potential: a tool for detecting non-specific organic groundwater contamination, Urban Water, Vol 3, 2001, pp.173-184.

[24] Garrido, S.E and Fonseca, M.G., Speciation and kinetics of trihalomethane formation in drinking water in Mexico, Ground Water Monitoring & Remediation, Vol 30, 2010, pp.77-84.

[25] Panyapinyopol, B., Kanokkantapong, V., Marhaba, T.F., Wattanachira, S., dan Pavasant, P., Kinetics of trihalomethane formation from organic contaminants in raw water from the bangkhen water treatment plant, Journal of Environmental Science and Health, 40, pp.2005, 1543–1555.

[26] Rajamohan, R., Ebenezer, V., Rajesh, P., Venugopalan, V.P., Natesan, U., Murugesan, V., and Narasimhan, S.V., Trihalomethane formation potential of drinking water sources in a rural location, Advances in Environmental Research, Vol 1, 2012, pp.181-189.

[27] Marhaba, T.F. Mangmeecha, A., Chaiwatpongsakorn, C., and Pavasant, P., Trihalomethanes formation potential of shrimp farm effluents, Journal of Hazardous Materials, Vol 136, 2006, pp.151–163

[28] Padhi, R.K., Subramanian, S., Mohanty, A.K., and Satpathy, K.K., Comparative assessment of chlorine reactivity and trihalomethanes formation potential of three different water sources, Journal of Water Process Engineering, Vol 29. 2019.

[29] He, K., Okuta, E., Cordero, J.A., Echigo, S., Asada, Y., and Itoh, S., Formation of chlorinated haloacetic acids by chlorination of low molecular weight compounds listed on Pollutant Release and Transfer Registers (PRTRs), Journal of Hazardous Materials, Vol 351, 2018, pp.98-107.

[30] Yu, J., D.D. Sun and J.H. Tay., Characteristics of coagulation-flocculation of humic acid with effective performance of polymeric flocculant and inorganic coagulant. Water Science and Technology, Vol 47, Issue 1, 2002, pp.89-95.

[31] Yue, Z., Vakili, A., and Wang, J., Activated carbon fibers from meltblown isotropic pitch fiber webs for vapor phase adsorption of volatile organic compounds, Chemical Engineering Journal, Vol, 330, 2017, pp.183-190.

[32] Kanokkantapong, V., Marhaba, T.F., Panyaponyopol, B., and Pavasant, P., FTIR evaluation of functional groups in the formation of haloacetic acids during the chlorination of raw water, Journal of Hazardous Material, Vol B136, 2006, pp.188-196.

9th Int. Conf. on Geotechnique, Construction Materials and Environment, Tokyo, Japan, 20-22 November 2019, ISBN: 978-4-909106025 C3051

ENHANCED SAFE CONDUCT AND PREPARATION FOR EFFECTIVE EVACUATION (ESCAPEE) USING GAMA

Shaun Manalili[1], Hannah Rafols [2], Joaquin Ramos[3], Syyida Shah[4]
[1] Lessandro Estelito Garciano, De La Salle University, Philippines

ABSTRACT

Hospitals are essential structures with the purpose of providing healthcare and assistance especially during disasters. These facilities are also prone to fire due to the presence of electrical equipment, oxygen tanks, chemicals, and other flammable materials. In an event of a fire, the layout of the hospital must be able to provide an effective evacuation. In this paper, the evacuation of ten emergency rooms (ER) was simulated. The simulation for the rooms utilized an agent-based model (ABM) by using GAMA Platform. Varying densities were simulated per ER and a fire simulation was done. The simulations resulted to total evacuation time for the different ERs and the mortality rate considering a fire inside the room. The results show that the number of occupants affected the evacuation time by 10 to 20 seconds. Considering a minimum evacuation time of 30 seconds, the simulations showed that three hospitals will never evacuate longer than 30 seconds, 3 needed a required density, while 4 would always take longer than 40 seconds. In addition, there is also a weak correlation between the area of the ER and the evacuation time. Based on observation of the simulations, the location of the exits plays a significant role in safe evacuation.

Keywords: Evacuation, Fire, Agent based model, Hospitals, GAMA Platform

INTRODUCTION

A disaster, according to the International Federation of Red Cross and Red Crescent Societies [1], is a sudden phenomenon that disrupts a unit's functionality. Shaluf [2] stated that disasters can be classified into three types: natural, man-made, and hybrid. Among the various disasters, fire alone accounts for 39.2% of the major disasters worldwide [3]. The Philippines are among those countries that have a tragic and significant record of fire incidents that resulted to numerous casualties. Some incidents are the Ozone Disco Fire in 1996 that resulted to a casualty count of 162, the Valenzuela Factory fire in 2015 that resulted to 74 deaths and the fire in NCCC mall in 2017 that resulted to 39 deaths [4].

Almost any building or structure is vulnerable to fire. This study focuses on hospitals, which are essential structures. Its purpose is to provide healthcare, assistance and accommodation during times of disasters. However, hospitals can be very vulnerable to disasters as well, especially to fire. The presence of volatile substances, extremely flammable materials and equipment with high tendency of overheating make hospitals more susceptible to fire. In the event wherein a fire may occur, hospitals must readily have a proper evacuation plan and layout. This may reduce the likelihood of casualties as a result of the fire.

Evacuation is needed when a hazard poses harm to the health and safety of people inside a facility or structure. This must be observed, practiced and executed especially in unforeseen and urgent instances when fire occurs. To preserve life and safety, the occupants of the building need to evacuate by following the building's evacuation plan. Accurate and effective evacuation plans are created and improved based on real-time evacuation drills. In the case of hospitals, it may be difficult to commence. Conducting drills may cause commotion, inconvenience and disruption in operations. In this study, evacuation simulation is used instead. It is an alternative quantitative method to determine evacuation times based on the concepts of crowd dynamics and pedestrian motion. This study uses an agent-based model through the use of GAMA Platform, a simulation software that is capable of modelling explicit multi-agent simulations.

Ten hospital emergency room layouts were obtained in this study. The research includes two phases of evacuation simulations. The first set of simulations involve the evacuation of ten hospital emergency layouts, where graphs of evacuation time versus occupancy density are plotted. The second set of simulations involve the evacuation of three representative layouts for small, medium and large areas. The division of the areas are determined by the researchers based on the obtained layouts. The second

phase of simulations, fire was introduced at random location with a rate ranging from 0.5 m/s to 2.0 m/s.

RELATED LITERATURE

Allowable Unit Area per Occupant

A facility or structure can only occupy a certain density at a time. According to the National Building Code of the Philippines [5], the allowable unit area per occupant of a hospital or sanitaria is 8.4 m^2/person.

Evacuation Models

There are many ways to simulate an evacuation model. Such methods include flow-based models, agent-based model (ABM) and cellular automata (CA). A flow-based model is one that considers a continuous flow movement between evacuees, without the consideration of varying human characteristics and direction [6]. The second type of model is the agent-based model, an improvement of the flow model that already considers a number of factors like the building configuration and the evacuees' proximity between each other. The last type of model is the CA model which utilizes cell grids and some rules of movement to come across this area of grids.

This research utilizes agent-based modeling or ABM. Agent interactions in multiplex systems can be simulated through this type of model. Therefore, several factors among agents and the floor layout can be investigated. Ha and Lykotrafitis [7] investigated the effect of the architectural complexity of a building on the crowd motion while commencing an evacuation. In their study, they explored the effects of the evacuees' panic level by varying desired agent speeds. They also explored the effect of the complexity of the floor plan by varying the door sizes. It was found that as the room door size and the desired speed increase, the evacuation time immediately decreased. The study employed a relationship between the size of the egresses having to match the configuration of the room and the speed of the occupants leaving the room.

Kasereka, Kasoro, Kyamakya, Doungmo Goufo, Chokki, & Yengo [8] used ABM to simulate evacuation of people in the case of fire. They were able to explore different factors and establish relationships between these factors. As the number of evacuees are higher, the fatality increases. As the speed of the agents increased, the number of survivors increased. The ABM model allows integration of different factors that influence the model, opening new doors of possibilities in mimicking real life scenarios. The study utilized GAMA to simulate an evacuation of supermarkets in case of fire and they have concluded that the faster the velocity of the occupants in the buildings, the higher the number of people who have evacuated. In addition, the number of deaths had decreased. Addition of exit doors had significantly influenced the model in such a way where the evacuation time of the occupants had significantly decreased and that the number of survivors had increased.

GAMA Platform

Claridades, Villanueva and Macatulad [9] conducted a simulation of an evacuation using GAMA Platform and they have discovered that several factors regarding human behavior such as original states, panic, eating and studying will hasten the evacuation process while sleeping and going to the bathroom are considered as impedances in the evacuation. Aside from that, the results of the evacuation time suggest that altering the width of the corridor and pathways towards the exit can affect the response time. When the width of the pathways increased, the response time decreased.

Macatulad and Blanco [10] conducted an evacuation simulation of the Melchor Hall building at the Univeristy of the Philippines, Diliman. The researchers have incorporated ABM and GIS to model the evacuation of the people and to look at different scenarios for evacuation planning. Simulating the ABM in GAMA allowed the researchers to construct a 3DGIS-BASED model of the structure. The test simulation in GAMA was satisfactory assuming only 6% room capacity. Considering only the first floor, the researchers discovered that the people at the first floor managed to evacuate at 9 seconds on average while the total evacuation time for the five-storey building is 96 seconds.

MODEL DESCRIPTION

The model works by first dividing the layout of the ER into square grids size 0. 4 m x 0.4 m. An example of the layout being divided into the grids are shown in Fig. 1. The obstructions are determined when they overlap cells. These cells are then obstructions and the agents will not be able to pass through those cells. Agents are also considered to obstacles to other agents, this prevents overlapping of cells.

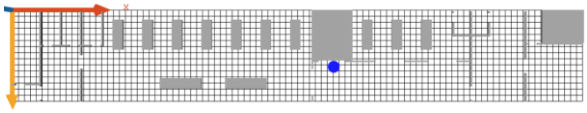

Fig. 1 Sample ER layout divided into square grids

The agents in the model move by utilizing a Moore Neighborhood. This means that an agent can have the option of moving to eight different directions as explained by Brugiere [11]. Figure 2 shows the

illustration of the neighborhood. Given an agent in the center shown as a blue circle, the agent will be able to move into any of the eight directions. The agent will choose the shortest path going towards a selected exit. The only time that there will be less than 8 options is when an obstacle is present in the cell.

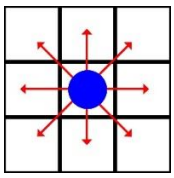

Fig. 2 Agent movement using Moore neighborhood

In choosing the exits, the agents select the closest direct exit. The agents then move towards the exit using the shortest path possible. Once the agent reaches a distance less than or equal to 0.4 m from the location of the exit, they are considered to be safe and have exited the layout. The program records the number of people that have exited at a given time and which exit they used. The independent variables used in the study are occupancy density, velocity of fire, number of people. The dependent variables are evacuation time and casualties. Controlled variables include the ER layout, exit location and fire source.

The research determined the amount of time steps and total time to complete the evacuation for 10 different hospital emergency rooms to acquire the evacuation time. In addition to the 10 hospitals, 3 hospitals were selected to be simulated considering a fire within the room. The controlled variables for each setup were the emergency room layout, with the nonstructural components or obstacles, the locations of the exits, and the source of fire. The independent variables in each experimental setup included the density of the occupants and the rate of spread of fire. Five trials of the simulation were done for each density for 11 varying densities of the ten hospitals. Three trials were simulated considering a fire source for three densities for three different hospitals. In total, 658 simulations were done. In the ABM model the layout of each hospital was considered including the obstructions present such as walls, chairs, beds, tables, and other immovable equipment. In order to simulate the most realistic evacuation simulation possible, factors that contribute to the decision-making of the agents such as distance effects and location of exits were also taken into account. The results of the simulation were the evacuation times with corresponding densities and the number of casualties due to fire. These results were analyzed to assess the efficiency and effectiveness of the evacuation, as well as to evaluate and recommend a solution to improve the plan layout.

DATA AND RESULTS

Prior to simulations, the researchers investigated ten hospital emergency room layouts as shown in Table 2. The smallest of the surveyed hospitals is about 200 m^2 and the largest about 2000 m^2.

Table 2 Areas of the ten surveyed hospitals

Hospital	ER Area (m^2)	Total Floor Area (m^2)
A	212	1,804
B	241	9,206
C	321	10,644
D	382	8,670
E	393	4,806
F	665	18,964
G	959	6,712
H	1,038	6,404
I	1,071	13,851
J	1,820	96,358

Based on the values shown in Table 2, there is a weak correlation between the total floor area and the area of the hospital ER. However, it is evident that the area of the ER ranges from 2% to 16% of the total hospital area.

The evacuation time for the varying densities for all the ten hospitals are shown in Fig. 3 and Fig. 4. The hospitals named alphabetically are in increasing order. Hospital A has the least ER area while hospital J has the largest area. It was found that the minimum and maximum evacuation time considering the different densities are shown in Table 3. The change in density effected the evacuation time by about 7 – 20 seconds.

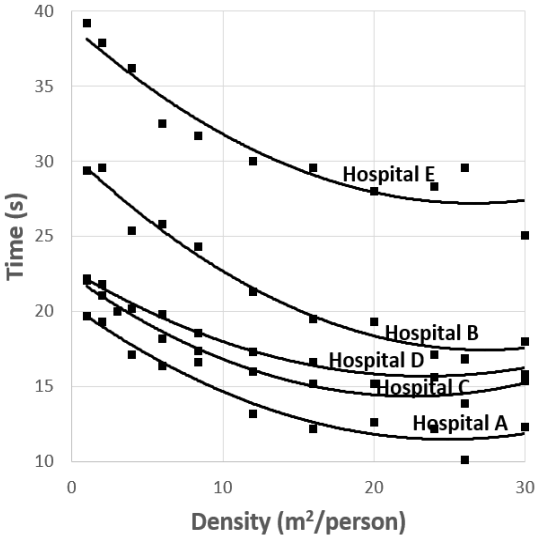

Fig. 3 Density versus time graph for Hospitals A-E

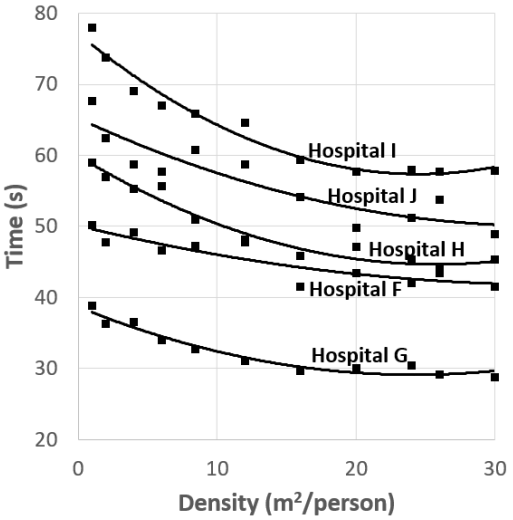

Fig. 4 Density versus time graph for Hospitals F-J

Table 3 Minimum and maximum evacuation times

Hospital	No. of Exits	Minimum Evac Time (s)	Maximum Evac Time (s)
A	2	10.1	19.7
B	1	18	29.6
C	2	15.4	22.2
D	2	15.2	22.1
E	1	25.1	39.2
F	2	50.2	41.5
G	3	28.8	38.9
H	2	45.3	59
I	2	57.8	78
J	3	48.9	67.7

The graph of the area of the ten hospitals versus the evacuation time for three different densities are shown in Fig. 5. the best fit polynomial curve for a high, medium, and low densities using the estimated area from all ten emergency room layouts. It can be observed that the area of the hospital has an effect on the evacuation time, however, there are some points where the evacuation of one room can be faster than that of a smaller room due to other factors such as the locations of the exits and the layout itself which includes the walls and obstacles. The number of exits ranged from one exit to three exits and it was found that there was no correlation with the number of exits.

Fire hazards were simulated by assuming it to start as a circle in the agent-based model with a diameter of 0.4 m. The hazard then continued to expand given varying velocities and the casualties and mortality rates were acquired for Hospital B, G, and J which were determined as the representative areas for small, medium and large areas for the ten hospitals gathered.

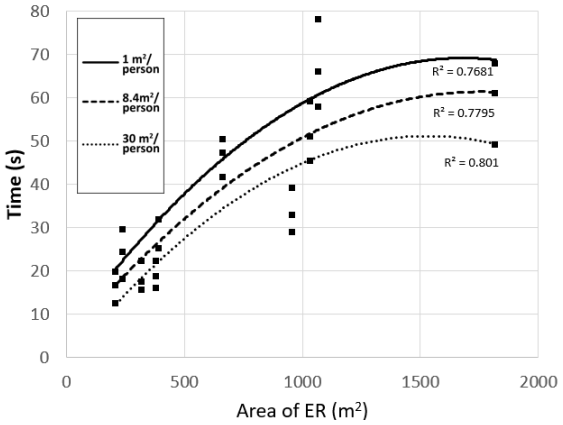

Fig. 5 Effect of ER area on evacuation time

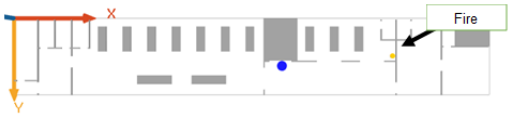

Fig. 6 ER Layout of Hospital B and the fire source

Figure 6 shows the layout of Hospital B and where the fire was assumed to start. The resulting graph of the mortality rate for varying velocities of the hazard is plotted in Fig. 7. The starting location of fire is placed near the oxygen tanks. Upon simulating, the curves produced by introducing fire to the layout of hospital B were steep. This may be due to the single exit located at the center of the layout. As the fire increases in diameter, it slowly spreads towards the exit. Therefore, agents who are travelling from the right side of the layout when engulfed by the growing radius of the fire, were already considered to be casualties. The maximum mortality rate of hospital B ranges from 80% to 90%.

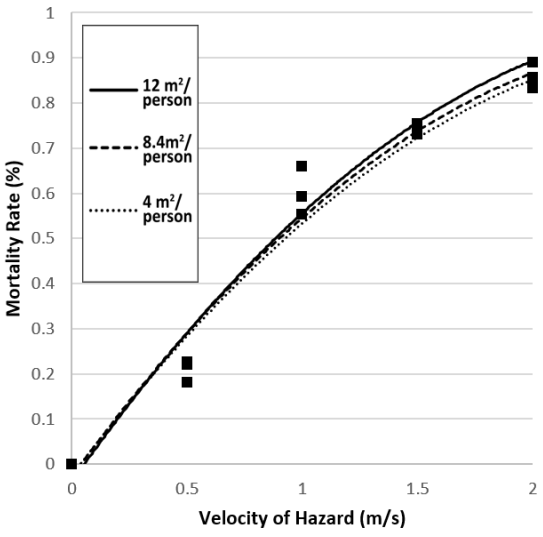

Fig. 7 Velocity of Hazard vs. Mortality Rate of Hospital

Figure 8 shows the layout of hospital G. It is evident that hospital G has a larger area and has more exits as compared to hospital B. The starting location of the fire is assigned at the equipment room of the layout where fire will most likely to occur.

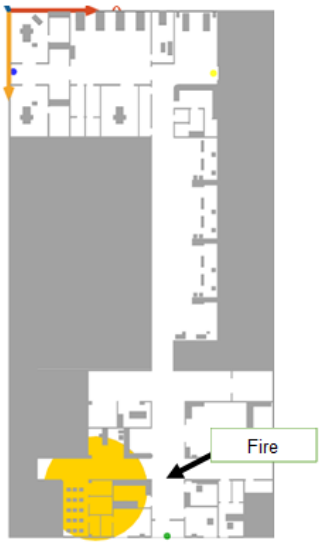

Fig. 8 ER Layout of Hospital G and the source of fire

The graph of the velocity of fire versus the mortality rate of hospital G shown in Fig. 9. The graph produced flatter slopes compared to the curves produced for hospital B. This implies that hospital G's layout is effective since it produced a flatter slope for the curves showing the relationship of the rate of fire with respect to the mortality rate. The highest speed of fire which is 2 m/s produced a smaller mortality rate for Hospital G as compared to Hospital B. Some of the factors that have contributed to the results are the location and number of exits as well as the presence of obstructions near the exits.

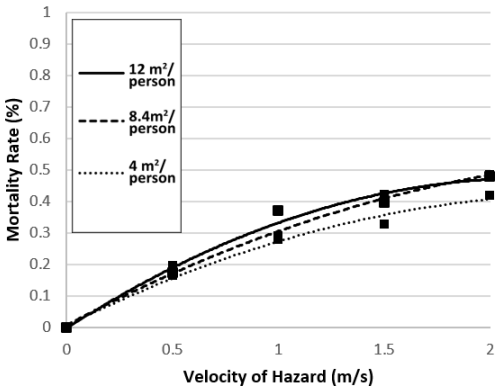

Fig. 9 Velocity of Hazard vs. Mortality Rate (Hospital G)

Figure 10 shows the layout of Hospital J and where the fire was assumed to start. The resulting graph of the mortality rate for varying velocities of the hazard is plotted in Fig. 11. Hospital J has the largest area among the ten hospitals. Fire was introduced in the simulation and was placed near the third exit. Over time, the fire spreads towards the exit, engulfing the area and the agents that chose that specific exit.

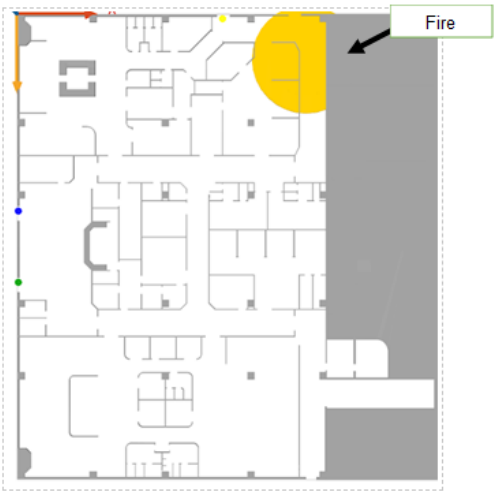

Fig. 10 ER Layout of Hospital J and the source of fire

The graph of Hospital J, as shown in Fig. 11, shows curves that are slightly steeper than hospital G but flatter than hospital B. The implication of this is although fire was initially near the exit, the highest velocity of fire produced a smaller mortality rate as compared to hospital B. The maximum mortality rate of hospital J ranges from values of approximately 58% to 72% took the exit at the rear side of the layout. Its distinct features include three exits: one at the top and two on the side as shown in Fig. 10.

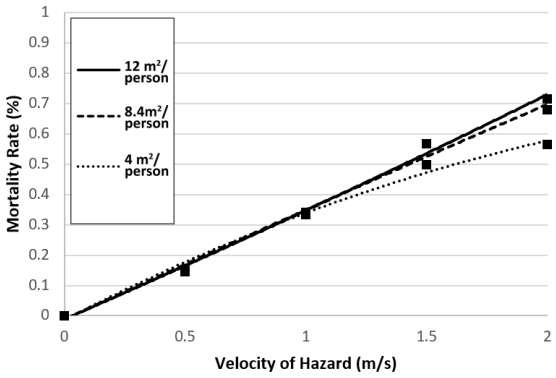

Fig. 11 Velocity of Hazard vs. Mortality Rate (Hospital J)

CONCLUSION

Ten emergency rooms were simulated for the evacuation time and fire. The researchers were able to

develop an ABM program to simulate the evacuation. Varying the densities of the room effected the time by 10 to 20 seconds, which were graphed. Moreover, it was found that although the area of the hospital has a weak correlation with time, it still has an effect on the evacuation time. Evacuation time becomes faster when the exits are more spread out from one another, and serve equal number of occupants. The mortality rate is also based on how fast the fire is, where the fire source is, and locations of the exits. Having more alternative routes lessens the mortality rate.

ACKNOWLEDGEMENTS

The researchers would like to extend their sincerest gratitude to their thesis adviser for helping them in analyzing and interpreting the data. In addition to their thesis adviser, their heartfelt gratitude extends to the Structural Engineering Division and to the Civil Engineering Department for providing them insightful ideas to improve their study. Lastly, the researchers wish to acknowledge their institution, De La Salle University, for the opportunity to conduct their study.

REFERENCES

[1] International Federation of Red Cross and Red Crescent Societies. (n.d.). *What is a disaster?* From International Federation of Red Cross and Red Crescent Societies: https://www.ifrc.org/en/what-we-do/disaster-management/about-disasters/what-is-a-disaster/

[2] Shaluf, I. M. (2007). Disaster Types. *Disaster Prevention and Management: An International Journal*, *16*(5), 704-717.

[3] Sigma (2018). Natural catastrophes and man-made disasters in 2017: a year of record-breaking losses. Retrieved from https://www.swissre.com/dam/jcr:1b3e94c3-ac4e-4585-aa6f-4d482d8f46cc/sigma1_2018_en.pdf

[4] De Guzman, N. (2019). The Ozone Disco Tragedy: 23 Years and Still Burning Our Minds. Retrieved from https://www.esquiremag.ph/culture/lifestyle/ozone-disco-tragedy-1996-a1729-20190318-lfrm

[5] Department of Public Works and Highways. (2005). *Implementing Rules and Regulations of the National Building Code of the Philippines*. Manila, Philippines: Manila Standard Today. Retrieved fromhttp://www.stii.dost.gov.ph/442-prepare-for-the-big-one-dost-makes-valley-fault-atlas-available-online

[6] Yuan, W., & Tan, K. H. (2007). An evacuation model using cellular automata. *Physica A: Statistical Mechanics and its Applications*, *384*(2), 549-566. doi:10.1016/j.physa.2007.05.055

[7] Ha, V., & Lykotrafitis, G. (2012). Agent-based modeling of a multi-room multi-floor building emergency evacuation. Physica A-Statistical Mechanics and Its Applications, 391(8).doi:doi:10.1016/j.physa.2011.12.034

[8] Kasereka, S., Kasoro, N., Kyamakya, K., Doungmo Goufo, E., Chokki, A. P., & Yengo, M. V. (2018). Agent-Based Modelling and Simulation for evacuation of people from a building in case of fire. *Procedia Computer Science*, *130*, 10-17. doi:10.1016/j.procs.2018.04.006

[9] Claridades, A. R., Villanueva, J. K., & Macatulad, E. G. (2016). EVACUATION SIMULATION IN KALAYAAN RESIDENCE HALL, UP DILIMAN USING GAMA SIMULATION SOFTWARE. *ISPRS - International Archives of the Photogrammetry, Remote Sensing and Spatial Information Sciences, XLII-4/W1*, 83-87. doi:10.5194/isprs-archives-xlii-4-w1-83-2016

[10] Macatulad, E. G., & Blanco, A. C. (2018). A 3DGIS multi-agent geo-simulation model for assessment of building evacuation scenarios considering urgency and knowledge of exits. *International Journal of Urban Sciences*, 1-17. doi:10.1080/12265934.2018.1549505

[11] Brugiere, A. (2019). Grid Species. Retrieved from https://github.com/gama-platform/gama/wiki/GridSpecies.

9th Int. Conf. on Geotechnique, Construction Materials and Environment, Tokyo, Japan, 20-22 November 2019, ISBN: 978-4-909106025 C3051

GREEN BUSINESS MODEL OF BIOMASS VERY SMALL POWER PRODUCERS IN THAILAND

Paron Vongchan[1], Chutarat Chompunth[2] and Wisakha Phoochinda[3]
[1] Graduate School of Environmental Development Administration, National Institute of Development Administration, Thailand

ABSTRACT

Thailand has traditionally been an agricultural economy which is appropriate for biomass energy because electricity can be produced from agricultural waste in large quantity. However, without proper management, electricity production from biomass, specifically biomass very small power plants located in communities across the country, may cause pollution and health threats impacting the environment, public health, and conflict from the pollution-affected communities around the biomass power plants. This research aimed to construct Green Business Model for electricity production using biomass for Biomass Very Small Power Producers in Thailand by applying the Sustainability Balanced Scorecard and to evaluate the model by interviewing experts and stakeholders of biomass electricity production. The study showed that the concept of green business model of Biomass Very Small Power Producers consisted of four key aspects namely 1) Stakeholders perspective including business entrepreneurs, feedstock producers/suppliers, feedstock transport operators, community, government, and non-governmental organizations 2) Sustainability management perspective including economic management, social management, and environmental management 3) Effectiveness perspective including Social Return on Investment and 4) Learning & growth perspective including training/learning and innovation/technology. Biomass Very Small Power Producers could deploy the concept of this model to generate profit coupled with responsibility for the environment and society. As a consequence, the green business model of Biomass Very Small Power Producers could benefit the agricultural and community sectors such as energy security, reduction of energy import, support of agricultural waste management, local occupation in community, and revenue generation within communities from agricultural waste. It would lead to sustainable development and benefit all stakeholders in the biomass energy supply chain.

Keywords: Green business model, Biomass, Sustainability Balanced Scorecard, Social Return on Investment

1. INTRODUCTION

The growth of the economy focuses on highly consumption-oriented production which in turn relies on limited natural resources and cannot generate a new replacement or may require a longer period of time to build up a replacement such as petroleum, coal, and natural gas which are unclean raw materials for energy production**.** The rising raw material costs and the use of natural resources in the international market cause higher production costs for the industry, as well as climate change, and increase waste, wastewater, and air pollution**.**

The concept of green economy has been presented by the United Nations Environment Programme to adjust the current capitalist economic system towards more sustainable economic system**.** An economic system enhances quality of life and social justice. At the same time, it can reduce the environmental risk and the problem of resource scarcity in accordance with business outcomes in the economic, social, and environmental dimensions based on the Triple Bottom Line concept [1]. The concept of "Green Business" emerged at the end of the 20th century in the wake of the ever-increasing public concern about the sustainability of economic development as an ideology and practice for business unit in the economic system**.** However, green business practices are still not universally embraced and applied by different business entities around the world [2].

Electricity from non-renewable energy comes from natural resources such as fossil fuels**.** However, burning fossil fuels is harmful to the environment**.** When fossil fuels are combusted **(**heated**),** they release carbon dioxide **(**CO_2**)** into the atmosphere**.** Carbon dioxide is a gas that keeps heat in the earth's atmosphere, a process called the "greenhouse effect**.**" This causes temperatures to rise faster than organisms can acclimate [3] .

Renewable energy such as solar, hydropower, wind power, biogas, waste, and biomass are related to people's well-being and the country's development**.** In the past, the Thai government was the only producer and manager of electricity production from non-renewable energy. But the undertaking was not

sufficient to cover the needs of communities in such a developing country like Thailand that was growing rapidly and affected the investment of power supply as it required large budget each year. Therefore, to reduce the burden on government investment in the construction of the power plant to meet the demand and to stabilize the country's electrical system, in 1994 Electricity Generating Authority of Thailand encouraged private sector participation in power generation business through purchasing of electricity from cogeneration power plants of the Independent Power Producers that used waste or residues in the agricultural sector (Biomass) as feedstock to produce electricity and heat. Heat left over from the manufacturing process could be used to produce electricity for sale to a transmission line to promote generation efficiency and public investment in the production and distribution of electricity. Private power producers therefore had a role as business unit in Thailand's electricity production. Subsequently in 1998, the National Energy Policy Council approved Very Small Power Producers (VSPP) (capacity not larger than 10 MW). More VSPPs were set up in remote areas to participate in the production of electricity from renewable energy in accordance with Thailand Power Development Plan 2015-2036 with the focus on (1) Energy security, to supply energy in response to the energy demand which was consistent with the rate of economic growth, the rate of population growth, and the growth of urban areas, as well as the diversification of energy to appropriate resources. (2) Economy, taking into account the reasonable energy costs without posing obstacle to the country's long-term economic and social development. The structure of fuel prices was reformed in line with costs and tax burden reasonable to level up national energy utilization performance with the promotion of energy efficiency. (3) Ecology, with increased domestic renewable energy production and energy production with high performance technologies to reduce the impact on environment and community [4] .

In 2017, biomass could produce electricity to Thailand about 651.1 MW, highest of all renewable energy sources [5]. Although Thailand is an agricultural country and is appropriate for biomass energy, electricity production from biomass may cause pollution impacting the environment, public health, and resistance from the affected citizens, if there is no proper management. Another factor is the provision of law that stipulates VSPP to conduct an Initial Environmental Examination (IEE) instead of Environmental Impact Assessment (EIA) that is a full assessment of the effects of the project on the environment which is a more detailed and comprehensive study of environmental impact than IEE [6]. In Thailand the biomass power plant with the generating capacity of 9.9 MW (<10MW) is not required to conduct the EIA, only conduct the IEE. Therefore, entrepreneurs can avoid conducting the environmental impact assessment by constructing the VSPP with lower investment in pollution management and technology than small power producers (SPP) (>10MW capacity). Subsequently, VSPP tend to pollute more than SPP. Therefore, VSPP must ensure that they carry out their business responsibly.

Under the green business topics, there are several education issues about green business practices in consumer products and services such as the ecolabeling (also known as green or environmental labeling, or green branding) [7], green behavior "4Rs" – reduction, reuse, recycling, and recovery [8], increased revenue from green business [9], etc. Therefore, the researchers anticipated that the concept of green business constructed from Sustainability Balanced Scorecard (SBSC) concept [10] and Biomass Supply Chain for Energy Production concept [11] could be deployed with public utility business such as biomass very small power producers electricity production. Consequently, biomass very small power (BVSPP) could generate profit coupled with responsibility for the environment and society.

2. OBJECTIVE

The objective of this study was to construct the Green Business Model of Biomass Very Small Power Producers which could bring sustainable benefit to BVSPP by-product from cost reduction along with reducing environmental impact and establishing good relation to society and communities surrounding the power plant.

This model was suitable for adoption by BVSPP which would assist in develop the green business potential of the biomass power plants as it was an economic approach that promoted sustainable development in all sectors of the country, including economy, society, and environment.

3. METHODOLOGY

This study was qualitative research. Secondary data was collected through books, documents, information media, and research works relevant to green business, biomass energy, stakeholders, and SBSC to formulate the (draft) of the Green Business Model of Biomass Very Small Power Producers conceptual framework.

Then, the Green Business Model of Biomass Very Small Power Producers was constructed by semi-structured interviews relevant to indicator criteria of SBSC concept to investigate the appropriateness of the issues in the (draft) of the Green Business Model of Biomass Very Small Power Producers conceptual framework, as well as the appropriateness of the content and language. Total of semi-structured interviews were conducted with 18 stakeholders each

from biomass supply chain including 3 business entrepreneurs of BVSPP, 3 feedstock producers/suppliers, 3 feedstock transport companies, 3 community leaders, 3 government officers and 3 non-governmental organizations (NGOs) as shown in Table 1.

Table 1 Key Informants of the Study

Types of stakeholders	Participants
Business entrepreneurs	1-3 BVSPP entrepreneurs
Feedstock producers/ suppliers	1-3 Farmers as biomass feedstock suppliers
Feedstock transport	1-3 Private companies providing transport services
Community	1-3 Community leaders living within the radius of 3 kms from the power plant
Government	1 Ministry of Industry officer 1 Local administration organization officer 1 Electricity Generating Authority of Thailand (EGAT) officer
NGOs	1 NGO 2 Academics

The (draft) of Green Business Model of Biomass Very Small Power Producers conceptual framework investigated and suggested by 18 interviewed persons usage of main structure to create the Green Business model of Biomass Very Small Power Producers in accordance with the context of SBSC concept.

4. GREEN BUSINESS MODEL OF BIOMASS VERY SMALL POWER PRODUCERS

This research was the study of the green business model of BVSPP by using the green business concept taking into account the economic, social, and environmental contexts as foundation, and the conceptual framework of SBSC [10,12,12–15] developed from the balanced scorecard concept [16]. The objective was to apply it to the business context of biomass power generation covering the stakeholders in the overall process in line with the concept of biomass supply chain Management [11,17–20] consisting of the following contexts in line with the green economy concept. The researchers formulated the green business model of Biomass Very Small Power Producers conceptual framework as shown in Figure 1.

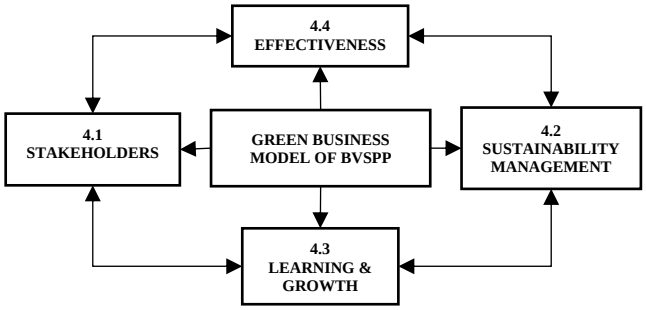

Fig. 1 Green Business Model of Biomass Very Small Power Producers

The green business model of Biomass Very Small Power Producers presented the four key aspects similar to four key perspectives of the SBSC consisting of: Learning and growth aspect, Sustainability management aspect, Stakeholder aspect, and Effectiveness aspect. Each aspect is detailed as follows:

4.1 STAKEHOLDERS

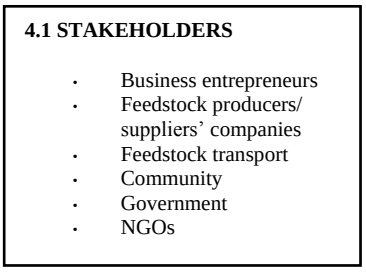

Fig. 2 STAKEHOLDERS aspect in Green Business Model of Biomass Very Small Power Producers

The conceptual framework of stakeholders aspect was investigated by 18 key informants from stakeholders of biomass supply chain. It focused on specifying type of stakeholders and reflected on how the business was creating stakeholders' value through its strategy and actions. In other words, it was the perspective on how to specify the stakeholders in the concept of Biomass Supply Chain [11,17,18,18–20]. The conceptual framework of stakeholders aspect was developed from the customer perspective in line with the SBSC concept.

To specify the target groups of stakeholders in green business model of biomass energy power plant, business should use the stakeholder's guideline framework developed from the evaluation of key informants to define type of stakeholders relevant to own operation of biomass power plant as shown in Table 2.

Table 2 Guideline Framework of Stakeholders

Types of stakeholders	Stakeholders
Business entrepreneurs	- BVSPP entrepreneurs - Shareholders - Officials relevant to process of biomass power generation
Feedstock producers/ suppliers	- Farmers as biomass feedstock suppliers - Communities as biomass feedstock suppliers
Feedstock transport	Feedstock logistics includes all of the unit operations necessary to move biomass feedstock from the land to the bio refinery and to ensure that the delivered feedstock meets the specifications of the bio refinery conversion process [21]. - Private companies providing transport services
Community	- Community leaders - Locals living within the radius of 3 kms from the power plant
Government	Responsible officials from: - Provincial Industry Office - Department of Industrial Works - Ministry of Industry - Office of Energy Regulatory Commission - Local administration organization - Metropolitan Electricity Authority, Provincial Electricity Authority, Electricity Generating Authority of Thailand
NGOs	- NGOs - Academics

4.2 SUSTAINABILITY MANAGEMENT

4.2 SUSTAINABILITY MANAGEMENT

Variable Costs

Economic management
- Feedstock provision
- Feedstock transport management
- Biomass feedstock storage
- Shareholder management
- Personnel management
- Quality control of power generation

Social management
- Participation of personnel and community
- Employment of local labor force
- CSR
- Agreement between BVSPP and community
- Community development fund in area surrounding power plant

Environmental management
- Environmental impact management in Biomass Supply Chain (air, energy, water, eco system, noise, waste)
- Raise environmental awareness to personnel
- Comply with law on power plant operation

Fig. 3 SUSTAINABILITY MANAGEMENT aspect in Green Business Model of Biomass Very Small Power Producers

Sustainability management aspect based on the evaluation of business entrepreneurs' interviews was the internal business process perspective that indicated business processes in key internal dimensions. It was the perspective of the management process of BVSPP in the economic, social, and environmental contexts. Most of the business entrepreneurs and officers commented that each activity in Sustainability management aspect including Economic management, Social management, and Environmental management was the variable cost of the investment in power generation. Sustainability management aspect was developed from the internal process perspective in line with the SBSC concept consisting of:

1. Economic management

- Feedstock provision: Rigorously inspect the quality of biomass bought in each lot in accordance with the standards of quality control of feedstock (Certification of testing of biomass composition).

- Feedstock transport management: Process to manage removal and storage of biomass feedstock during transport from feedstock suppliers to power plant.

- Biomass feedstock storage: Systematic feedstock storage management worth the investment, quality control of storage, prevention, reduced loss of operation for minimum operating costs and maximum use of storage space for biomass feedstock (depending on distance and seasons).

- Shareholder management: Safeguard and distribute return to shareholders to prevent conflict of themselves, partners, and business.

- Quality control of power generation: Control the process of power generation with stability (Output of electrical units was consistent depending on quality of feedstock such as humidity causing brownout).

2. Social management

- Community participation: Provide opportunity for the public to determine their own needs for resouce management, decision-making, and control of various activities related to community.

- Employment of local labor force: Employment of local people as part of business operation of BVSPP.

- Social responsibility: Organize Corporate Social Responsibility (CSR) and environmental activities both in and outside the organization towards sustainable development such as donation for social assistance.

- Agreement between BVSPP and community (Commitment): Contribute to the fund according to installation capacity of power plant, grant scholarship to community, improve basic infrastructure to community such as roads, temples, clinics, restrooms.

3. Environmental management

- Management of environmental impact from power generation processes (air, water, eco system, noise, waste): Determine measures to reduce environmental impacts from power generation processes such as dust filter system from combustion chamber, management of impact on water system, management of eco system around biomass power plant, management of noise pollution, "Eco efficiency" strategies or 4Rs such as disposal or use of waste from combustion.

- Raise environmental awareness: Campaign to raise awareness to personnel in power plant to learn about environment, as well as raising awareness of the environmental problems at national and global levels.

- Compliance with law relevant to operation of power plant: Implementation of policy, targets, rules and regulations, including law, stipulations, standards of environment and safety.

4.3 LEARNING & GROWTH

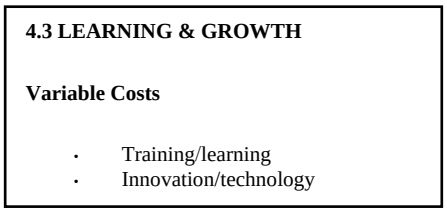

Fig. 4 LEARNING & GROWTH aspect in Green Business Model of Biomass Very Small Power Producers

Based on information from business entrepreneurs' interview, learning and growth aspect was measures of how well the business prepared to meet the challenges of the future obstacles through leveraging its organizational and human assets. It was BVSPP's learning and growth strategy by which each activity was the variable cost of the investment in power generation covering the impact on the stakeholders of the overall biomass supply chain management consisting of:

- Training / learning: Process of systematic learning management to create or enhance knowledge, skills, ability, and attitude that would improve the efficiency of operation, including raising awareness and campaigning for environment.

- Innovation / technology: Technology usage to increase efficiency in working system, reduce Input (feedstock) and increase Output (electric current) and pollution disposal system.

4.4 EFFECTIVENESS

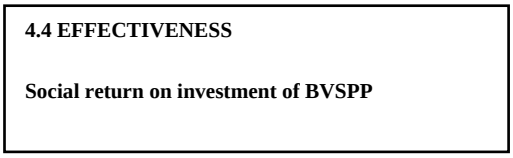

Fig. 5 EFFECTIVENESS aspect in Green Business Model of Biomass Very Small Power Producers

Based on information from stakeholders' interview, effectiveness aspect of Biomass Very Small Power Producers production should show the stakeholders' interests and the link between strategic objectives and financial, social, and environmental impacts. It was the perspective that BVSPP executives could inspect the success of BVSPP in economic, social, and environmental fields. Measure the results by using the processing tools from the social return on investment (SROI) analysis [22] existing in cost–benefit analysis. Which was a methodology for calculating SROI to explain that, for every investment of every single baht, the amount of money the society would receive in return (effectiveness) from the use of biomass to generate power. The analysis and the division of SROI covered economic, social, and environmental dimensions, both in monetary and non-monetary terms, in line with the sustainable development guideline [23]. The SROI could be calculated as follows:

SROI of BVSPP =

$$\frac{\text{Benefits received by BVSPP from investment in power generation}}{\text{Cost of investments in biomass power generation}}$$

The information from key informants revealed that the investment costs in biomass power generation consisted of the following: Fixed costs were the total costs that did not change according to the amount of power generation during the time of operation (machinery useful life) including equipment, machinery, construction, land, feedstock, etc. as shown in Table 3.

Table 3 Guideline Framework of Fixed Costs

Fixed costs	Value
Project development	Baht/Useful Life
Land value	Baht/Useful Life
Equipment, machinery	(Cost Price of Asset – Scrap Value) / Useful Life
Construction (basic infrastructure)	Baht/Useful Life
Commissioning	Baht/Useful Life
Lending interest all through the project	Baht /Useful Life

Variable Costs were the total costs that changed in proportion to the change in the level of activity or amount of power generation which included the following: sustainability management costs and learning & growth costs as shown in Table 4.

Table 4 Guideline Framework of Variable Costs

Variable costs	Value
Fuel	Baht/year
Labor	Baht/year
Feedstock storage	Baht/year
Utilities	Baht/year
Machinery repair and maintenance	Baht/year
Feedstock transportation	Baht/year
Personnel training	Baht/year
Contribution to community development fund in the area around power plant	Baht/year

The information of the value added received by BVSPP from investment in power generation consisted of the following: economic, social, and environmental benefits as shown in Table 5.

Table 5 Guideline Framework of Benefits

Economic benefits	Value
Income from sale of electricity	Baht/year
Reduce import value of petroleum	Baht/year
Social benefits	**Value**
Employment of local labor force	Baht/year
Community income from feedstock of biomass fuel	Baht/year
Feedstock transport in community	Baht/year
CSR activities	Baht/year
Community income from community development fund in the area around the power plant	Baht/year
Environmental benefits	**Value**
Reduced amount of greenhouse gas emission from biomass fuel usage instead of fossil fuel	Baht/year (value of carbon credit from the reduced CO_2)

The effectiveness aspect of Biomass Very Small Power Producers production analysis was then conducted on the SROI Ratio assigning a monetary value to investment costs and benefits (inputs and outcomes), using that assignation to calculate a ratio. For example, if the SROI Ratio is 5:1, which means that every baht allocated on investment costs will generate benefit worth five baht.

CONCLUSION

Without establishment of effective mechanism for sustainable management of the business combine with Economic, environmental and social impacts from biomass power production may pose a risk and conflicts to stakeholders of biomass business sectors in Thailand. Green Business Model of Biomass Very Small Power Producers concept is an effective scheme for Biomass Very Small Power Producers as business strategy and its performance focusing on four specific aspects: Learning and growth aspect, Sustainability management aspect, Stakeholders aspect, and Effectiveness aspect. Each aspect has shown a strong and positive link between successful implementation of a business strategy of Biomass Very Small Power Producers with social and environmental strategies.

Green Business Model of Biomass Very Small Power Producers is innovative and required at a specified time for sustainable operations of biomass power plants in Thailand. It directly leads to sustainable management and benefit in term of social return on investment for all of the stakeholders in biomass energy supply chain (Economic benefits), all of which respond to the environment and reduce greenhouse gas emissions, particle pollution and carbon-monoxide emissions (Environmental benefits). That also makes immense and positive contribution to rural economy of Thailand **(**Social benefits) in terms of income and employment to farmers, entrepreneurs at village level, and rural youth. Which also leads to development of other value-added products such as biofuels and establishment of small-scale industries such as biomass briquetting plants.

REFERENCES

[1] Elkington J. Enter the triple bottom line. The triple bottom line: Does it all add up. 2004;11(12):1–16.

[2] Cekanavicius L, Bazyté R, Dicmonaité A. Green business: Challenges and practices. Ekonomika. 2014;93(1):74.

[3] Böhmer W. Understanding the Thai renewable energy market [Internet]. Sun & Wind Energy. 2016 [cited 2017 Jan 29]. Available from: http://www.sunwindenergy.com/review/understanding-thai-renewable-energy-market

[4] Thailand Ministry of Energy. Alternative Energy Development Plan (AEDP 2015-2036) [Internet]. 2015 [cited 2017 Oct 26]. Available from: www.dede.go.th/download/files/AEDP2015_Final_version.pdf

[5] Electricity Generating Authority of Thailand. Private power plant capacity [Internet]. 2017 [cited 2017 Oct 12]. Available from: https://www.egat.co.th/index.php?option=com_content&view=article&id=355&Itemid=116

[6] Environmental Impact Evaluation Bureau. Environmental Impact Assessment in Thailand [Internet]. 2012 [cited 2018 Jan 25]. Available from: http://www.onep.go.th/eia/images/7handbook/Environmental_Impact_Assessment_in_Thailand.pdf

[7] Lavallée S, Plouffe S. The ecolabel and sustainable development. Int J LCA. 2004 Nov 1;9(6):349–54.

[8] Kassaye WW. Green dilemma. Mrkting Intelligence & Plan. 2001 Nov 1;19(6):444–55.

[9] Swallow L. Green Business Practices For Dummies. John Wiley & Sons; 2009. 388 p.

[10] Figge F, Hahn T, Schaltegger S, Wagner M. The Sustainability Balanced Scorecard – linking sustainability management to business strategy. Bus Strat Env. 2002 Sep 1;11(5):269–84.

[11] Toka A, Iakovou E, Vlachos D. Biomass Supply Chain Management for Energy Polygeneration Systems. 2010 Oct 1;

[12] Dias-Sardinha I, Reijnders L, Antunes P. Developing sustainability balanced scorecards for environmental services: A study of three large Portuguese companies. Environ Qual Manage. 2007 Jun 1;16(4):13–34.

[13] Epstein MJ, Wisner PS. Using a Balanced Scorecard to Implement Sustainability. Environ Qual Manage. 2001 Dec 1;11(2):1–10.

[14] Hansen EG, Schaltegger S. The Sustainability Balanced Scorecard: A Systematic Review of Architectures. J Bus Ethics. 2016 Jan 1;133(2):193–221.

[15] Kalender ZT, Vayvay Ö. The Fifth Pillar of the Balanced Scorecard: Sustainability. Procedia - Social and Behavioral Sciences. 2016 Nov 24;235:76–83.

[16] Kaplan RS, Norton DP. The Balanced Scorecard: Measures That Drive Performance [Internet]. Harvard Business Review. 2005 [cited 2017 Feb 4]. Available from: https://hbr.org/2005/07/the-balanced-scorecard-measures-that-drive-performance

[17] Iakovou E, Karagiannidis A, Vlachos D, Toka A, Malamakis A. Waste biomass-to-energy supply chain management: A critical synthesis. Waste Management. 2010 Oct;30(10):1860–70.

[18] Ji J, Raoupatham V, Sittibud N, Nananukul N. Biomass power generation supply chain planning. In: Smart Grid and Smart Cities (ICSGSC), 2017 IEEE International Conference on. IEEE; 2017. p. 115–119.

[19] Rentizelas AA, Tolis AJ, Tatsiopoulos IP. Logistics issues of biomass: The storage problem and the multi-biomass supply chain. Renewable and Sustainable Energy Reviews. 2009 May;13(4):887–94.

[20] WANG L, WATANABE T, XU Z, University K. STAKEHOLDERS' RISK PERCEPTION OF SUSTAINABLE BIOMASS POWER PLANT DEVELOPMENT ---A CASE STUDY OF WANGKUI COUNTY, CHINA. :13.

[21] Energy Alternatives India. Business Opportunities in Biomass Energy Sector [Internet]. 2017 [cited 2018 Oct 23]. Available from: http://www.eai.in/ref/ae/bio/biz/biomass_biz_opp.html

[22] Phoochinda W. Social Return on Investment of electricity generation using renewable energy after the opening of AEC. National Institute of Development Administration; 2017.

[23] Baker S. Sustainable development. Reprinted. London: Routledge; 2007. 245 p. (Routledge introduction to environment series).

9th Int. Conf. on Geotechnique, Construction Materials and Environment, Tokyo, Japan, 20-22 November 2019, ISBN: 978-4-909106025 C3051

DIRECT SHEAR STRENGTH OF HEATING AND HYDRATION BENTONITE-SAND MIXTURE SAND

Tomoyoshi Nishimura[1]
[1]Ashikaga University, Japan

ABSTRACT

It is important one of environmental geotechnical problems that relevant researches of thermal-hydration-mechanical-chemical have been progressed for radioactive waste disposal in further deep geological repositories combined highly compacted bentonite. The compacted bentonite engineered barrier is constructed under unsaturated condition which is as liner. Many couple models and investigation at in-site were reported that these results really have contributed to establish certain interpretation of engineered barriers system with detail. The model gradually solve, and reproduce comparison with measurement data on account of complex experimental test associated to thermal-hydration-mechanical. This study focused on shear strength of bentonite-sand mixture, which treated by thermal-hydration efforts as one of great significance like a predicted environmental problems to engineered barrier. Shear strength was measured using direct shear apparatus that constant vertical stress was applied at remaining of constant horizontal displacement speed. Prepared all samples were mixture Na-type bentonite and silica sand having uniformity grain size distribution. Compacted sample had a dry density of 1.600 g/cm^3. Also, heating control was supplied under 80 degrees as thermal effort in the heating oven. Heating flow was isotropic condition and soil moisture decrease, became to a like dry condition. The paper summarized on direct shear strength, influences of thermal-hydration was described certainly.

Keywords: Bentonite, Thermal effort, Suction, Direct shear strength, SWCC

INTRODUCTION

During long-term periods operation radioactive disposal waste repository at large deep underground, bentonite as natural swelling material apply one composed of barrier system [1][2]. Many investigation reports were published, mentioned in widely world and could commonly take data base from various research facilities. These results were based on laboratory, large scale testing at underground site and developed mathematical simulation model analysis [3]. The constitutive models was quiet difference with classical soil mechanical theory on saturated clay soil and consist of hydration, thermal effort and chemical effort. THMC analysis models [4][5] have been significant developed according to compare between experimental results in laboratory and underground site investigation works and to determine high quality parameters associate to predict barrier system composed by bentonite remain processing development of models.

PURPOSE OF THIS STUDY

This study conducted out direct shear test at constant vertical stress which used compacted bentonite-sand mixture sample subjected to heating process. Also other samples were applied hydration effort due to controlling relative humidity using vapor pressure technique. It was found out the influence of thermal effort on direct shear strength including reduction of mount of soil moisture and in addition various horizontal displacement speeds were focused other factors to strength of compacted bentonite-sand mixture.

SOIL MATERIALS AND APPARATUS

Sodium bentonite （Kunigel V1）taken in Japan was used for direct shear test and chemical component SiO_2 of the material occupied 62 %. The bentonite has been widely used for investigation of mechanical properties of high level radioactive disposal barrier system in Japan. Often, the material specimen was employed as one of reference materials and had comparison to other swelling clay materials in the outside. A sand was mixture into the bentonite which uniformity grain size distribution was indicated from grain size test and evaluated to classify as siliceous sand. Water supply was performed to material and was regulated to water content of 5.9 %.

Previously, soil-water characteristic curve [6] was described at high suction ranges which was defined relationship between suction and water content in Fig.1. The SWCC consisted various temperature until suction was 296 MPa. Range of temperature was from 20 degrees and 80 degrees that influence of temperature was further slight. Bentonite with sand mixture was statically compacted in the shear box.

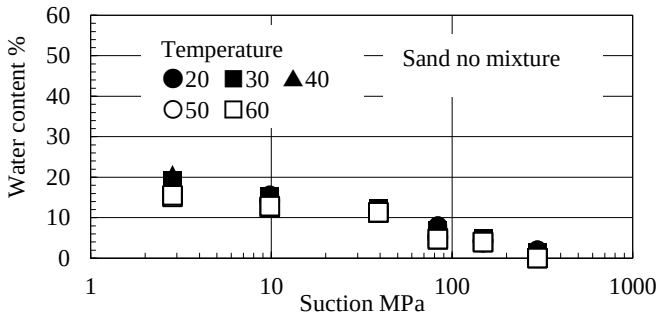

Fig. 1 SWCC with various temperatures.

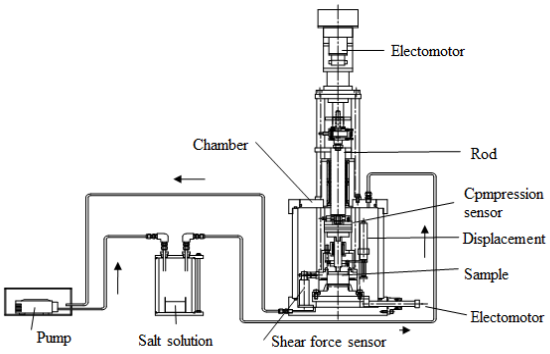

Fig. 2(a) Illustration of direct shear apparatus.

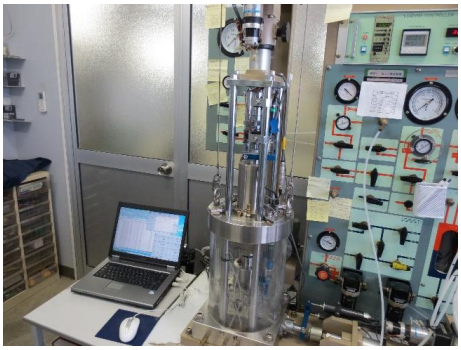

Fig. 2(b) Direct shear test apparatus

The specimen corresponding suction of 105 MPa had a dry density of 1.600 g/cm^3 which a diameter of 6.00 cm and a height of 2.50 cm.

This testing program used a modified direct shear apparatus as shown in Fig.2(a) (b). The modified direct shear apparatus was possible to maintain constant vertical stress and suction which was developed to evaluate unsaturated soil behavior with suction stress. Shear box was placed in the cell chamber and shear forces induced by horizontal moving of lower box was measured during test. Vertical stress was produced due to control pressure cylinder installed at outside cell chamber.

This study considered how magnitude of pore pressure in specimen under increasing of temperature

Fig. 3 Steel mould for measurement of pore pressure under 80 degrees.

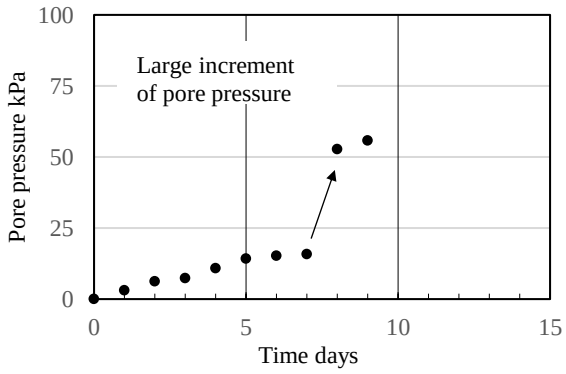

Fig. 4 Increment of pore pressure due to isotropic heating under 80 degrees.

and conducted out measurement of pore pressure specimen installed into stiffness steal mould. The steal mould was covered by two steal plate as shown in Fig.3 and specimen was closed completely.

TESTING CONDITIONS

This testing program consist of various horizontal displacement speed, difference vertical stress, thermal effort on direct shear test. Controlled horizontal displacement speed had a range from 0.0005 mm per min to 0.5 mm per min that it was further difference testing times. Measured vertical stresses were both 100 kPa and 200 kPa. Influence of thermal effort was consider under both temperatures between 20 degrees and 80 degrees. When 80 degrees was controlled, all specimen with shear box were placed in large oven chamber.

PRESSURE IN SAMPLE DUE TO HEATING

It is knowledge that heating loading developed pore pressure in void structure and this study investigated changing of pore pressure as shown in Fig.3. Obtained pressures were averaged using results both upper portion and lower portion that were described as shown in Fig.4 At beginning of heating for approaching to 80 degrees,

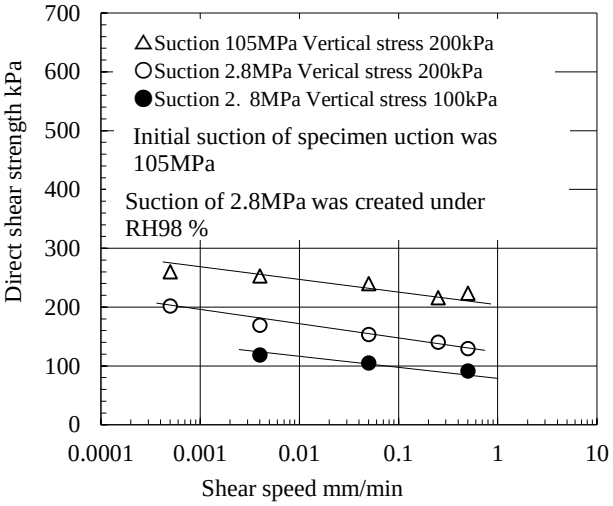

Fig. 5 Influence of some factor on direct shear strength.

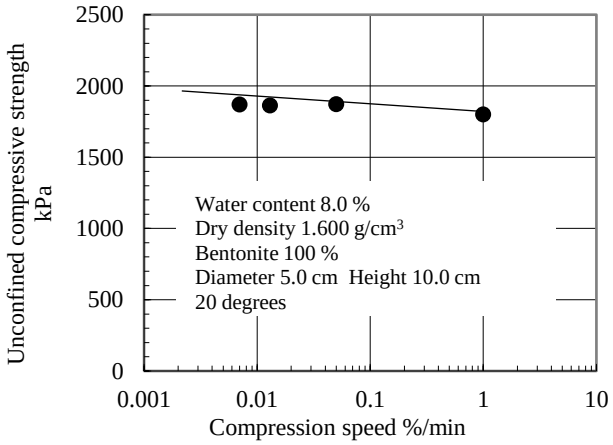

Fig. 6 Influence of compression speed on unconfined compressive strength.

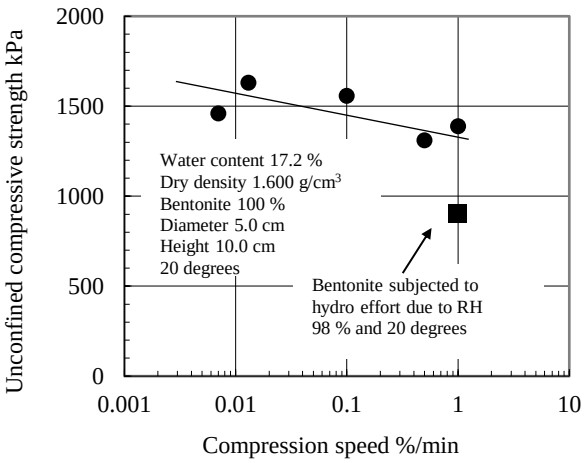

Fig. 7 Influence of compression speed on unconfined compressive strength.

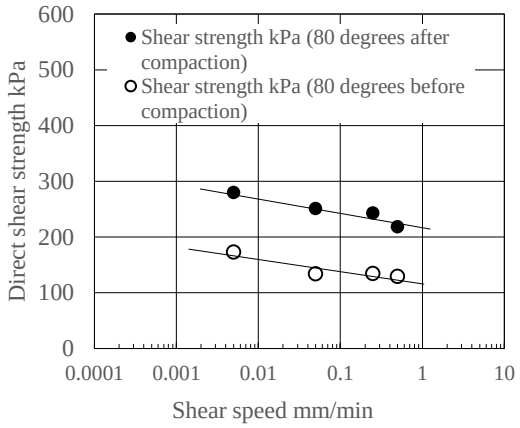

Fig. 8 Direct shear strength subjected to thermal effort.

pore pressure was smoothly produced, increased linearly with days. Large increment was observed beyond 7 days from 15.7 kPa and the pressure improved to over 50 kPa due to jumping growing. Interpretation and accumulation of experimental data sets regard to changing of pore pressure have been required to confirm mathematical models correctly.

SHEAR STRENGTH AT 20 DEGREES

Measurement of direct shear strength of compacted bentonite was conducted with two difference vertical stress such as 100 kPa and 200 kPa. Relationship between horizontal displacement speed and strength was mentioned as shown in Fig.5. Shear strength increased with high vertical stress that following to failure envelope line. In addition, it was of interesting phenomena that direct shear strength decreased according to increase horizontal displacement. Thus results were indicated regardless of both vertical stress. Unconfined compressive strength that reduction of strength closely related increasing of compression speed as shown in Figs.6 and 7.

Also, suction effort was observed that two difference suction (i.e. 105 MPa and 2.8 MPa) were applied to specimen and conducted out direct shear test. Reduction of strength due to decreasing of suction was further clear.

DISCUSSION ON THEARMAL EFFORT

Compacted specimens were placed into oven chamber, which was remained at temperature of 80 degrees. The specimen was with shear box and seven days were prepared for applying heating at least.

Beyond heating, the specimen within shear box was established into direct shear apparatus and specimen was equilibrium with laboratory room temperature (i.e. 20 degrees). Subsequently, applying of vertical stress of 200 kPa was processed and direct shear strength was measured at various horizontal displacement speeds. Also, powder material was prepared for compaction specimen which applied heating effort under 80 degrees and water content at equilibrium was 0.21 %. The powder material was statically compaction in the shear box according to dry density of 1.600 g/cm^3. Direct shear strength was measured similar to previous process. Two difference specimen described the difference strength as shown in Fig.8 and it was found that strength was lower than that of compacted specimen under 5.9 % water content subjected to heating. Even both water content and dry density were same, reduction of shear strength was observed. In addition, it was evidenced that shear speed affected to change of shear strength.

CONCLUSIONS

This study consider the influence of thermal effort through constant vertical stress direct shear test and applied temperature was up to 80 degrees. Also, results of direct shear strength with various horizontal displacement speed described significant properties associated to the influence of strain speed on strength regardless of thermal effort or no thermal effort.

Direct shear strength of compacted bentonite-sand mixture increased with vertical stress and indicated the increasing of strength with growing of horizontal displacement speed. Thus like an experimental tendency, it was found similar to unconfined compressive strength of compacted bentonite with various compression speed.

Also, tow difference specimens were prepared in thermal effort and lower strengths were demonstrated comparison with compacted specimen subjected to heating action which compacted using powder sample subjected to heating action.

REFERENCES

[1] Gen, A., Vallejian, B., Zandrain, M. T. and Sanchez, M, Homogenization in clay barrier and seals: two case studies. Journal of Rock Mechanics and Geotechnical Engineering, 2013, 5, pp.191-199.

[2] Nagra, Annual report 2015, National Cooperative for the Disposal of Radioactive Waste, 2015.

[3] Hossain M.Z., For Chapter in a Book, Soil Mechanics, 4th ed. Vol. 2, Sakai, Ed. SanAlonso, E.E., Gens, A. Josa, A, A constitutive model for partially saturated soil, Géotechnique, 1990, 40(3), 405–430.

[4] Cui, Y.J., Tang, A.M., Qian, L.X., Ye, W.M., Chen, B, Thermo-mechanical behavior of compacted GMZ bentonite. Soils and Foundations. 2011, 51(6), pp.1065-1074.

[5] Wiebe, B., Graham, J. Tang, G.X.M., Dixon, D, Influence of pressure, saturation, and temperature on the behavior of unsaturated sand-bentonite, Canadian Geotechnical Journal, 35, 1998, pp.194-205.

[6] Villar, M.V, Water retention of two natural compacted bentonites, Clays Clay Miner, 55(3), 2007, pp.311–322.

GEOMATE 2020

The Tenth International Conference on

Geotechnique, Construction Materials & Environment

10-12 November 2020

Melbourne, Australia

- The "International Journal of GEOMATE" is a Scientific Journal of the GEOMATE International Society that encompasses a broad area in Geotechnique, Construction Materials and Environment.
- The key objective of this journal is to promote interdisciplinary research from various regions of the globe.
- The editorial board of the journal is comprised of extensively qualified researchers, academicians, scientists from Japan and other countries of the world.
- It is peer-reviewed Journal that is published quarterly till 2015 and now monthly. All articles published in this journal are available on line.
- Contributors may download the manuscript preparation template for submitting paper or contact to the Editors-in-Chief

[editor@geomatejournal.com].